



28TH EUROPEAN SYMPOSIUM ON COMPUTER AIDED PROCESS ENGINEERING

PART A

Edited by
ANTON FRIEDL, JIŘÍ J. KLEMEŠ, STEFAN RADL,
PETAR S. VARBANOV AND THOMAS WALLEK



COMPUTER-AIDED CHEMICAL ENGINEERING, 43

28TH EUROPEAN SYMPOSIUM ON
COMPUTER AIDED PROCESS
ENGINEERING

PART A

28TH EUROPEAN SYMPOSIUM ON COMPUTER AIDED PROCESS ENGINEERING

PART A

Edited by

Anton Friedl

*Institute of Chemical, Environmental and Bioscience Engineering, TU Wien
Getreidemarkt 9/166, A-1060 Vienna*

Jiří J. Klemeš

*NETME Centre, Faculty of Mechanical Engineering, Brno University of Technology
Technická 2896/2, 616 69 Brno*

Stefan Radl

*Institute of Process and Particle Engineering, Graz University of Technology
Inffeldgasse 13/III, A-8010 Graz*

Petar S. Varbanov

*NETME Centre, Faculty of Mechanical Engineering, Brno University of Technology
Technická 2896/2, 616 69 Brno*

Thomas Wallek

*Institute of Chemical Engineering and Environmental Technology
Graz University of Technology
8010 Graz, Inffeldgasse 25/C/II*



ELSEVIER

Amsterdam – Boston – Heidelberg – London – New York – Oxford
Paris – San Diego – San Francisco – Singapore – Sydney – Tokyo

Elsevier
Radarweg 29, PO Box 211, 1000 AE Amsterdam, Netherlands
The Boulevard, Langford Lane, Kidlington, Oxford OX5 1GB, UK
50 Hampshire Street, 5th Floor, Cambridge, MA 02139, USA

Copyright © 2018 Elsevier B.V. All rights reserved.

No part of this publication may be reproduced or transmitted in any form or by any means, electronic or mechanical, including photocopying, recording, or any information storage and retrieval system, without permission in writing from the publisher. Details on how to seek permission, further information about the Publisher's permissions policies and our arrangements with organizations such as the Copyright Clearance Center and the Copyright Licensing Agency, can be found at our website: www.elsevier.com/permissions.

This book and the individual contributions contained in it are protected under copyright by the Publisher (other than as may be noted herein).

Notices

Knowledge and best practice in this field are constantly changing. As new research and experience broaden our understanding, changes in research methods, professional practices, or medical treatment may become necessary.

Practitioners and researchers must always rely on their own experience and knowledge in evaluating and using any information, methods, compounds, or experiments described herein. In using such information or methods they should be mindful of their own safety and the safety of others, including parties for whom they have a professional responsibility.

To the fullest extent of the law, neither the Publisher nor the authors, contributors, or editors, assume any liability for any injury and/or damage to persons or property as a matter of products liability, negligence or otherwise, or from any use or operation of any methods, products, instructions, or ideas contained in the material herein.

British Library Cataloguing in Publication Data

A catalogue record for this book is available from the British Library

Library of Congress Cataloging-in-Publication Data

A catalog record for this book is available from the Library of Congress

ISBN (Part A): 978-0-444-64237-0
ISBN (Set): 978-0-444-64235-6
ISSN: 1570-7946

For information on all Elsevier publications visit our website at <https://www.elsevier.com/>



Working together
to grow libraries in
developing countries

www.elsevier.com • www.bookaid.org

Publisher: Joe Hayton
Acquisition Editor: Kostas Marinakis
Editorial Project Manager: Emily Thomson
Production Project Manager: Paul Prasad Chandramohan
Designer: Greg Harris

Typeset by SPi Global, India

Contents

Preface	xxi
Scientific Committee	xxiii
Plenary Lectures	
1. Resilient Design and Operations of Chemical Process Systems <i>Jian Gong, Fengqi You</i>	1
2. Developing key PSE skills for the workforce of the future <i>Concepción (Conchita) Jiménez-González</i>	7
3. COSMO-RS: From Quantum Chemistry to Fluid Phase Thermodynamics <i>Andreas Klamt</i>	9
4. Multi-Parametric Optimization in Smart Manufacturing & Process Intensification <i>Efstathios Pistikopoulos</i>	11
Model Development and Simulation	
5. LCSOft as a Tool for LCA: New LCIA Methodologies and Interpretation <i>Tanathip Rattanatum, Rebecca Frauzem, Pomthong Malakul, Rafiqul Gani</i>	13
6. Modeling the Performance of Low Pressure Reverse Osmosis Membrane System for N-nitrosamine Rejection <i>Mudhar A. Al-Obaidi, Chakib Kara-Zaitri and Iqbal M. Mujtaba</i>	19
7. Model of a Formaldehyde Absorption System Based on Industrial Data <i>Catarina G. Braz, Henrique A. Matos, A. Mendes, J. Rocha, R. Alvim</i>	25
8. A multi-fluid approach to simulate separation of liquid-liquid systems in a gravity settler <i>Anurag Misra, Cyrille Bonamy, Luís M. de Souza, Lena Hohl, Markus Illner, Matthias Kraume, Jens-Uwe Repke and Dominique Thévenin</i>	31
9. Comparative Life Cycle Assessment of Ethylene from Wet Shale Gas and Biomass <i>Minbo Yang, Xueyu Tian, Fengqi You</i>	37

10. Model-based Design of Experiments Using a Flowsheet-Simulator
Norbert Asprion, Juliane Ritter, Roger Böttcher, Michael Bortz 43
11. Modeling of Non-Isothermal Adsorption Process in a Silica Gel Desiccant Packed Bed
Siripan Murathathunyaluk, Koranut Srichanvichit, Amata Anantpinijwatna, Prakob Kitchaiya 49
12. Modeling the Effect of Temperature on Microalgal Growth under Outdoor Conditions
Pooya Darvehei, Parisa A. Bahri, Navid R. Moheimani 55
13. Prediction of stability and thermal conductivity of nanofluids for thermal energy storage applications
B.H. Mahmoud, M. Fairweather, L.F. Mortimer, J. Peakall, H.P. Rice, D. Harbottle 61
14. Multiobjective optimization of eco-industrial parks: evaluation of environmental impacts at the watershed scale
Laura Garcia de Dios, Marianne Boix, Sabine Sauvage, Iréa Touche, Roxelane Cakir, Ludovic Montastruc, Jose Miguel Sanchez Perez 67
15. Coke Formation Model in Crude Oil Furnace for Maintenance Scheduling
Amata Anantpinijwatna 73
16. Microbubble coalescence during transport in vertical channel flows
K.S. Asiagbe, M. Fairweather, D.O. Njobuenwu, M. Colombo 79
17. Kinetic Modeling of Methanol Synthesis - Impact of Catalyst Deactivation
Carsten Seidel, Andreas Jörke, Bert Vollbrecht, Andreas Seidel-Morgenstern, Achim Kienle 85
18. Assessing the GHG emissions footprints of newly ultra-sour gas developments in the Middle East region for electricity production
Alberto Betancourt-Torcat, Mohammed Alkatheri, Ali Almansoori 91
19. Influence of cylinder-to-particle diameter ratio and filling speed on bed porosity of random packed beds of spheres
Johanna Fernengel, Jennie von Seckendorff and Olaf Hinrichsen 97

20.	Analyzing the link between G^E -model parameter regression and optimal process design <i>Mirko Skiborowski, Philipp Temmann, Chrstoph Brandenbusch</i>	103
21.	Kinetic Modeling of Precipitation Terpolymerization for Functional Microgels <i>Franca A. L. Janssen, Agnieszka Ksiazkiewicz, Michael Kather, Leif C. Kröger, Adel Mhamdi, Kai Leonhard, Andrij Pich, Alexander Mitsos</i>	109
22.	Towards predictive models for organic solvent nanofiltration <i>Rebecca Goebel, Tobias Glaser, Ilka Niederkleine and Mirko Skiborowski</i>	115
23.	COSMO-derived descriptors applied in ionic liquids physical property modelling using machine learning algorithms <i>Ismael Díaz, Manuel Rodríguez, María González-Miquel and Emilio J. González</i>	121
24.	A CFD investigation of the effect of particle sphericity on wellbore cleaning efficiency during oil and gas drilling <i>Emmanuel I. Epelle, Dimitrios I. Gerogiorgis</i>	127
25.	Process network modelling for the assessment of environmental impacts <i>Raul Calvo-Serrano, Gonzalo Guillén Gosálbez</i>	133
26.	Data-driven degradation model for batch processes: a case study on heat exchanger fouling <i>Ouyang Wu, Ala E.F. Bouaswaig, Stefan M. Schneider, Fernando Moreno Leira, Lars Imsland and Matthias Roth</i>	139
27.	Applying New Sustainability Metric in Different Natural Gas Liquid (NGL) Recovery Configurations to Extend Investment Decision and Incorporate Sustainability Analysis <i>Saad A. Al-Sobhi, Ahmed AlNouss</i>	145
28.	Identification of Mass Flow Dynamics in a Pretreatment Continuous Tubular Reactor <i>Ismael Jaramillo, Arturo Sanchez</i>	151
29.	Exploiting meta-modeling approach to investigate the effect of oil characteristics on the optimal operating conditions and biodiesel properties <i>P. Chhabra, L. Zhou, I. A. Karimi and M. Kraft</i>	157

30. Mixed-integer multiparametric Metamodeling: A machine learning tool applied to reactive scheduling
Gicela Lupera, Ahmed Shokry, Georgios M. Kopanos, Antonio Espuña 163
31. Resolved Numerical Analysis of Drying on a Vibrating Grate
Bernhard Peters, Mohammad Mohseni, Marc Demouling and Thorsten Kläs 169
32. Assessing the Performance of Industrial Ethanol Fermentation Unit Using Neural Networks
Rauber D. Pereira, Alberto C. Badino, Antonio J. G. Cruz 175
33. Thermal and hydraulic performance of pillow-plate heat exchangers
Olga Arsenyeva, Julian Tran, Eugeny Y. Kenig 181
34. Predicting Research and Motor Octane Numbers based on Near Infrared Spectroscopy: Models based on Partial Least Squares Regression and Artificial Neural Networks
Ana L. Leal, Jorge C. Ribeiro, Artur M. S. Silva, F. G. Martins 187
35. Modeling of an air quality monitoring network with high space-time resolution
Daniele Sofia, Aristide Giuliano, Filomena Gioiella, Diego Barletta, Massimo Poletto 193
36. Modelling of biomass residence time distribution and xylan depolymerization kinetics analysis in a Pilot-Scale Pretreatment Continuous Tubular Reactor
Felicia Rodríguez, Arturo Sánchez 199
37. Simulation and Analysis of Indian Residential Electricity Consumption Using Agent-Based Models
Sohini Dhar, Babji Srinivasan and Rajagopalan Srinivasan 205
38. Dull or bright you still get electric delight: A new approach to the design of all-weather panels
Sahar Hajizeinalibioki, Daniel Sebastia Saez, Oleksiy V. Klymenko, Harvey Arellano-Garcia 211
39. Direct Reduction of Iron-Ore in Fluidized Beds
M. Efe Kinaci, Thomas Lichtenegger and Simon Schneiderbauer 217

40. Experiments and Direct Computer Mapping Based Model for Photo-Fenton Process
Francesca Audino, Mónica Varga, Montserrat Pérez-Moya, Moisès Graells, Antonio Espuña and Béla Csukás 223
41. Surrogate-based modeling in flotation processes
Achref Rabhi, Abdellah Chkifa, Saad Benjelloun, Abderrazak Latifi 229
42. From Process Graph to Process Simulation with Proper Model Documentation
Arne Tobias Elve and Heinz A. Preisig 235
43. Graph-Based Modelling with Distributed Systems
Heinz A. Preisig and Arne Tobias Elve 241
44. Closure Development for Multi-Scale Fluidized Bed Reactor Models: A CLR Case Study
Stefan Radl, Federico Municchi, Schalk Cloete, Hendrik Cloete, Stefan Andersson, Joana Francisco Morgado, Thomas Gurker, Rosa Quinta-Ferreira, Christoph Kloss, Christoph Goniva, Shahriar Amini 247
45. Life Cycle Assessment of calcium carbonate loop CO₂ capture technology for brown coal power plant unit of the Czech Republic
Kristína Zakuciová, Vladimír Koči, Karel Ciahotný, Ana Carvalho, Jiří Štefanica, Jana Smutná 251
46. Computer-Aided Simulation of the Volumetric Efficiency of a 2 MW Gas Engine
Guillermo E. Valencia, Franklin E. Consuegra, Marisol Osorio 259
47. The Ordinary Kriging in Multivariate Dynamic Modelling and Multistep-Ahead Prediction
Ahmed Shokry, Antonio Espuña 265
48. Modelling and advanced dynamic optimization strategies for hydrological and water quality management in continental water bodies
A.G. Siniscalchi, L. Fritz, C. Garcia Prieto, V. Estrada, M. Hoffmeyer, R.J. Lara, M.S. Diaz 271
49. Recursive Model Estimation for the Plasma Parameters Quality Control
Junmo Koo, Damdae Park, Sangwon Ryu, Gon-Ho Kim, Youn-Woo Lee 279

50.	Model transformations and integration for process plant simulation, optimization and visualization <i>Manuel Rodriguez, Ismael Diaz</i>	285
51.	Property Prediction of Pharmaceuticals for Designing of Downstream Separation Processes <i>Getachew S. Molla, Lukasz Ruszczynski, Jens Abildskov, Gürkan Sin</i>	287
52.	Incorporating fouling model in plate heat exchanger modelling and design <i>Olexiy Demirskyy, Petro Kapustenko, Olga Arsenyeva, Olexandr Matsegora, Pavlo Arsenyev, Vladimir Tovazhnianskyi, Alisher Khusanov</i>	284
53.	Multi-scale modelling and simulation of Ca-looping cycle process for CO ₂ post-combustion capture <i>Carla I.C. Pinheiro, Rui Filipe, Miguel Abreu Torres, João M. Silva, Henrique A. Matos</i>	291
54.	Good modelling practice for process engineering: pitfalls and requirements to develop fit for purpose models <i>Ingmar Nopens</i>	293
Methods, Software and Tools		
55.	Efficient simulation of ion exchange chromatography with application to bioseparations <i>Marcus Fechtner, Malte Kaspereit and Achim Kienle</i>	295
56.	Virtual splitting of shared resource networks for price-based coordination with portfolio tariffs <i>Simon Wenzel, Lukas Samuel Maxeiner and Sebastian Engell</i>	301
57.	Ensuring $(n - 1)$ -reliability in the optimal design of distributed energy supply systems <i>Dinah Elena Hollermann, Dörthe Franzisca Hoffrogge, Maike Hennen and André Bardow</i>	307
58.	Integrating Real-time Operational Constraints in Planning of Water and Energy Supply <i>Negar Vakilifard, Parisa A. Bahri, Martin Anda, Goen Ho</i>	313
59.	Leveraging the Power of Big Data Analytics for Process Scheduling under Uncertainty using a Stochastic Robust Optimization Approach <i>Chao Ning, Fengqi You</i>	319

60. A hierarchical approach for solvent selection based on successive model refinement
Kai Fabian Kruber, Jan Scheffczyk, Kai Leonhard, André Bardow, Mirko Skiborowski 325
61. Optimal synthesis of mass exchange networks through a state-task-representation superstructure
Miguel Angel Velázquez-Guevara, Agustin Ramon Uribe-Ramirez, Fernando Israel Gómez-Castro, Juan Gabriel Segovia-Hernandez, Salvador Hernández, Jose Maria Ponce Ortega 331
62. Optimization of Cryogenic Carbon Capture and LNG process by Mathematical programming
Orakotch Padungwatanaroj, Kitipat Siemanond 337
63. A methodology of a hybrid hydrogen supply network (HHSN) under alternative energy resources (AERs) of hydrogen footprint constraint for sustainable energy production (SEP)
Soonho Hwangbo, ChangKyoo Yoo 343
64. Kinetic Modeling of Plastic Waste Pyrolysis in a Laboratory Scale Two stage Reactor
Zoltán Till, Tamás Varga, János Sója, Norbert Miskolczi, Tibor Chován 349
65. Experimentally Driven Guaranteed Parameter Estimation: a Way to Speed up Model-Based Design of Experiments Techniques
Arun Pankajakshan, Marco Quaglio, Federico Galvanin 355
66. Optimal Design of a Dividing Wall Column for The Separation of Aromatic Mixtures using the Response Surface Method
Pedro Barbosa de Oliveira Filho, Marcio Luis Ferreira Nascimento, Karen Valverde Pontes 361
67. Simulation/optimization of bio-hydrogenated diesel process with techno-economic analysis
Phooreerat Tawai, Kitipat Siemanond 367
68. A Bilevel Decomposition Method for the Simultaneous Synthesis of Utility Systems, Rankine Cycles and Heat Exchanger Networks
Cristina Elsidio, Emanuele Martelli, Ignacio E. Grossmann 373
69. Energy and exergy analysis for cryogenic process design/retrofit
Nattawat Threerachannarong, Kitipat Siemanond 379

70. Ammonia/Urea Production Process Simulation/Optimization with Techno-Economic Analysis
Jiranart Jeenchay, Kitipat Siemanond 385
71. Towards a Quantitative Food-Energy-Water Nexus Metric to Facilitate Decision Making in Process Systems: A Case Study on a Dairy Production Plant
Styliani Avraamidou, Aaron Milhorn, Owais Sarwar, Efstratios N. Pistikopoulos 391
72. Numerical Evaluation of Different Turbulence Models for Single-Phase Flow in the Outer Pillow-Plate Channel
Marco Vociante, Mark Piper, Alexander Zibart, Eugeny Y. Kenig 397
73. Improving Convergence Behavior of Nonlinear Equation Systems in Intensified Process Models by Decomposition Methods
Saskia Bublitz, Erik Esche, Jens-Uwe Repke 403
74. Optimizing Decolorization Efficiency of Methylene Blue by Photo-Fenton Process over Fe-Diatomite using Central Composite Design
Pongsert Sriprom, Varocha Champa, Prakob Kitchaiya, Pornsawan Assawasaengrat 409
75. An optimization method to estimate the SOFC market in waste water treatment
Sonja Sechi, Sara Giarola, Andrea Lanzini, Marta Gandiglio, Gbemi Oluleye, Massimo Santarelli, Adam Hawkes 415
76. Optimal Chemical Grouping and Sorbent Material Design by Data Analysis, Modeling and Dimensionality Reduction Techniques
Melis Onel, Burcu Beykal, Meichen Wang, Fabian A. Grimm, Lan Zhou, Fred A. Wright, Timothy D. Phillips, Ivan Rusyn, Efstratios N. Pistikopoulos 421
77. Solution of the Population Balance Equation by the Meshless Moving Particle Method (MMPM)
Menwer Attarakih, Hans-Jörg Bart 427
78. Multi-objective optimization of a CO₂-EOR process from the sustainability criteria
Juan Pablo Gutierrez, Eleonora Erdmann, Davide Manca 433

79. A software tool for optimizing intra-logistic activities
Dimitrios Poulimenos, Dimitrios Bechtsis, Dimitrios Vlachos, Eleftherios Iakovou 439
80. Electricity mix assessment of the EU member countries using DEA and EffMixF
Patricia Zurano-Cervelló, Carlos Pozo, Josep María Mateo-Sanz, Laureano Jiménez, Gonzalo Guillén-Gosálbez 445
81. CFD modelling of pulsed sieve plate liquid extraction columns using OOSPM as a reduced population balance model: hydrodynamics and mass transfer
Samer Alzyod, Menwer Attarakih, Hans-Jörg Bart 451
82. Systematic generation of insulation materials via DEA and Building modelling
A. Torres-Rivas, C. Pozo, A. Ewertowska, D. Boer and L. Jiménez-Esteller 457
83. Simulation-Based Optimization of Chemical Processes Using the Extended Cutting Plane Algorithm
Juan Javaloyes-Antón, Jan Kronqvist, José A. Caballero 463
84. Towards a Methodology for Reusable Ontology Engineering: Application to the Process Engineering Domain
Nikolaos Trokanas, Linsey Koo, Franjo Cecelja 471
85. Simultaneous Optimization for Integrated Cooling Water System with Chemical Processes
Fei Song, Nan Zhang, Robin Smith, Yujiao Zeng, Jie Li, Xin Xiao 477
86. Parameter Estimation of Biosurfactant Production from Agro-industrial Waste Using Genetic Algorithm
Ana Luiza Campos, Júlia Nogueira, Filipe A. Coelho, Brunno F. Santos 483
87. Comparison of reformulations of the Duran-Grossmann model for Work and Heat Exchange Network (WHEN) synthesis
Haoshui Yu, Matias Vikse, Truls Gundersen 489
88. Semantic Networking Facility for the Biorefining Community
Edlira Kalemi, Linsey Koo, Franjo Cecelja 495

89.	Economic and environmental benefits of waste-based energy closed-loop integration in process industries under uncertainty <i>Shabnam Morakabatchiankar, Kefah Hjaila, Fernando D. Mele, Moisés Graells, Antonio Espuña</i>	501
90.	Minimum Entropy Based PFR Analysis <i>David Rosa, Paulo Goes, João Manzi</i>	507
91.	Exergy Analysis of an Extractive Distillation Column for Reducing Energy Consumption in a Bioethanol Production Process <i>J. Cristóbal García-García, Danahe Marmolejo-Correa, J. Carlos Cárdenas-Guerra, Ricardo Morales-Rodríguez</i>	513
92.	A Relaxed Knapsack-Problem Based Decomposition Heuristic For Large-Scale Multistage Stochastic Programs <i>Zuo Zeng, Selen Cremaschi</i>	519
93.	A Time-series-based approach for robust design of multi-energy systems with energy storage <i>Paolo Gabrielli, Florian Fürer, Portia Murray, Kristina Orehounig, Jan Carmeliet, Matteo Gazzani, Marco Mazzotti</i>	525
94.	Ordinary Kriging: A Machine learning tool applied to mixed-integer multiparametric approach <i>Gicela Lupera, Ahmed Shokry, Sergio Medina-González, Eduardo Vyhmeister, Antonio Espuña</i>	537
95.	Assessment of technology portfolios with enhanced economic and environmental performance for the energy, water and food nexus <i>Rajesh Govindan, Tareq Al-Ansari, Anna Korre, Nilay Shah</i>	537
96.	Multi-objective Optimization for Plant Design via Tabu Search <i>Faiz Mandani, Kyle Camarda</i>	543
97.	Alternative mixed-integer reformulations of Generalized Disjunctive Programs <i>Miloš Bogataj, Zdravko Kravanja</i>	549
98.	LES of particle collision and agglomeration in vertical channel flows <i>T. Ogholaja, D.O. Njobuenwu, M. Fairweather</i>	555
99.	Improved modeling of membrane separation in integrated hybrid processes <i>Bettina Scharzec, Mirko Skiborowski</i>	561

100. Ontology engineering approach to support process of model integration <i>Linsey Koo, Edlira Kalemi, Nikolaos Trokanas, Franjo Cecelja</i>	563
101. Approximation Algorithms for Process Systems Engineering <i>Dimitrios Letsios, Georgia Kouyialis, Ruth Misener</i>	565
Process Synthesis, Process Design and Life Cycle Modelling	
102. Alternative processes for obtaining solar grade silicon <i>Cesar Ramírez-Márquez, Marta Vidal Otero, José Antonio Vázquez-Castillo, Mariano Martin, Juan Gabriel Segovia-Hernández</i>	567
103. An Engineering Tool to Screen and Integrate Biomass Valorization Paths in Multiple-Feedstock Biorefineries <i>Konstantinos A. Pyrgakis, Antonis C. Kokossis</i>	566
104. Processes Separation to Furfural, Design and Optimization Involving Economical, Environmental and Safety Criteria <i>G. Contreras-Zarazua, E. Sánchez-Ramírez, J.A. Vázquez-Castillo, C. Ramírez-Márquez, J.G. Segovia-Hernández</i>	579
105. Techno-economic assessment of a lignocellulosic biorefinery co-producing ethanol and xylitol or furfural <i>Aristide Giuliano, Diego Barletta, Isabella De Bari, Massimo Poletto</i>	585
106. Endpoint-oriented Life Cycle Optimization Models for Sustainable Design and Operations of shale Gas Supply Chains with Modular Manufacturing <i>Jiyao Gao, Fengqi You</i>	591
107. Surrogate-based Optimization Approach to Membrane Network Synthesis in Gas Separation <i>Jos E.A. Graciano, Rita M.B. Alves and Benoit Chachuat</i>	597
108. Balancing Costs, Safety and CO ₂ Emissions in the Design of Hydrogen Supply Chains <i>Anton Ochoa Bique, Leonardo K. K. Maia, Fabio La Mantia, Davide Manca, Edwin Zondervan</i>	603
109. Process Integration as an Effective Route Towards Sustainable Oil Refinery Development <i>Poland Jelihi, Timo Wassermann, Edwin Zondervan</i>	609

110. Experimental Study of a Biomass Downdraft Gasifier with Multi-tube Gas Outlets to Improve Synthesis Gases Quality
Ajaree Suwatthikul and Paisan Kittisupakorn 615
111. Design and Optimisation of Novel Cascade Refrigeration Cycles for LNG Production
Fernando Almeida-Trasvina, Robin Smith 621
112. Method of Removing water from Products of Dehydration Reaction of 3-hydroxypropionic acid in Acrylic acid Process
Jae-Hyeon Yang, Chul-Jin Lee 627
113. Multi-floor process plant layout using mixed-integer optimization
Jude O. Ejeh, Songsong Liu and Lazaros Papageorgiou 633
114. Feasibility study of using reactive distillation for the production of renewable aviation fuel
Maritza Lisette Soria-Ornelas, Claudia Gutiérrez-Antonio, Fernando Israel Gómez-Castro, Salvador Hernández 639
115. Extended Value Chain Synthesis towards the Design of Multi-Feedstock Algae Biorefineries
Melina Psycha, Maria Kapnisi, Antonis C. Kokossis 645
116. Selection of fractionation pathways and intermediates for mixed consumer products
Alberto Castiglioni, Jochem Jonkman, Renzo Akkerman, Albert van der Padt 651
117. Sustainable Optimal Strategic Planning for Shale Water Management
Alba Carrero-Parreño, Rubén Ruiz-Femenia, José A. Caballero, Juan A. Reyes-Labarta, Ignacio E. Grossmann 657
118. Compact and Multi-Stream Heat Exchanger Design
Somei Hayashi, Kitipat Siemanond 663
119. Optimal design of biogas supply chains
Grégoire Alain Chomette, Theodoros Damartzis, François Maréchal 669
120. Retrofit of mass exchange networks using a reduced superstructure synthesis approach
Adeniyi J. Isafiade 675

121. Optimization-Based Process Synthesis for Integrated Crystallizer-Wet Mill System for Improved Crystal Shape Control <i>Botond Szilagy, Zoltan K. Nagy</i>	681
122. Mathematical Modeling and Simulation in Natural Flavors and Fragrances Bioproduction Intensification <i>Ivan Červeňanský, Mário Mihal', Jozef Markoš</i>	687
123. Simulation and economic evaluation of NO _x removal in wet scrubbers of low-speed two-stroke vessels using H ₂ O ₂ as a replacement for conventional EGR <i>Yeongryeol Choi, Junghwan Kim</i>	693
124. Comparative Performance Analysis of Industrial Scale Catalytic Steam Reformer with Membrane Steam Reformer <i>Arun Senthil Sundaramoorthy, Arun Prem Anand Natarajan, Sundaramoorthy Sithanandam</i>	699
125. Towards the synthesis of modular process intensification systems with safety and operability considerations - application to heat exchanger network <i>Yuhe Tian, M. Sam Mannan, Zdravko Kravanja, Efstratios N. Pistikopoulos</i>	705
126. Design, Control and Economics of a Process for Isobutyl Acrylate Production <i>Mihai Daniel Moraru, Diana Adela Berinde, Costin Sorin Bildea</i>	711
127. Optimization based design of an industrial cluster for economic and environmental benefits <i>D. Varshney, P. Mandade, Yogendra Shastri</i>	717
128. Process Simulation and Optimization of 10-MW EFB Power Plant <i>Jaechan Han, Junghwan Kim</i>	723
129. Dimethyl Carbonate Production Process from Urea and Methanol <i>Daniel Vázquez, Juan Javaloyes-Antón, Juan D. Medrano-García, Rubén Ruiz-Femenia, José A. Caballero</i>	731
130. Design and Analysis of Edible Oil Processes Containing Lipids <i>Olivia A. Perederic, Sten Appel, Bent Sarup, John M. Woodley, Georgios M. Kontogeorgis, Rafiqul Gani</i>	737

131. Multi-objective optimization of sustainability criteria in the design of chemical plants <i>Federico Scotti, Nicola Fabricatore, Davide Manca</i>	743
132. Evaluating the effect of separation and reaction systems in industrial symbiosis <i>Ana Somoza-Tornos, Moisés Graells, Antonio Espuña</i>	749
133. A framework for optimised sustainable solvent mixture and separation process design <i>Eduardo Sánchez-Ramírez, Jaime D. Ponce-Rocha, Juan G. Segovia-Hernandez, Fernando I. Gómez-Castro, Ricardo Morales-Rodriguez</i>	755
134. Optimal Design and Operation of Hybrid Osmosis Processes for Simultaneous Production of Water and Power under Different Demand Conditions <i>Jyh-Cheng Jeng, Heng-Yi Chu</i>	761
135. Superstructure optimization (MINLP) within ProSimPlus Simulator <i>Qiao Zhao, Thibaut Neveux, Mounir Mecheri, Romain Privat, Philippe Guittard, Jean-Noël Jaubert</i>	767
136. Sustainable Supply Chain: Monetization of Environmental Impacts <i>Cátia da Silva, Ana Paula Barbosa-Póvoa, Ana Carvalho</i>	773
137. Design of Biotechnological Production of 2-Phenylethanol <i>Peter Vargai, Ivan Červeňanský, Mário Mihal', Jozef Markoš</i>	779
138. Process Innovation through bio-inspired design <i>Anne Marie Barthe-Delanoë, Stéphane Negny, Jean Marc Le Lann</i>	785
139. Heat pump assisted azeotropic DWC for enhanced biobutanol separation <i>Iulian Patraşcu, Costin Sorin Bildea, Anton A. Kiss</i>	791
140. Optimization based design of a resilient biomass to energy system <i>Ashish Soren, Yogendra Shastri</i>	797
141. Optimal on-grid hybrid power system for eco-industrial parks planning and influence of geographical position <i>Florent Mousqué, Marianne Boix, Stéphane Negny, Ludovic Montastruc, Louis Genty, Serge Domenech</i>	803

<i>Contents</i>	xix
142. Life cycle assessment of pulp and paper production – A Portuguese case study <i>Andreia Santos, Ana Barbosa-Póvoa, Ana Carvalho</i>	809
143. Modelling and Analysing Supply Chain Resilience Flow Complexity <i>João Pires Ribeiro and Ana Barbosa-Póvoa</i>	815
144. A model-based approach to design miniaturised structured packings for highly efficient mass transfer in gas/liquid multiphase flows <i>Daniel Sebastia-Saez and Harvey Arellano-Garcia</i>	821
145. Preliminary economic ranking of reactive distillation processes using a navigation method <i>Rahma Muthia, Aloijsius G.J. van der Ham, Anton A. Kiss</i>	827
146. Multi-scale system modelling under circular bioeconomy <i>Miao Guo</i>	833
147. An Integrated Reactive Separation Process for Co-Hydrotreating of Vegetable Oils and Gasoil to Produce Jet Diesel <i>Miriam García-Sánchez, Mauricio Sales-Cruz, Teresa López-Arenas, Tomás Viveros-García, Alberto Ochoa-Tapia, Ricardo Lobo-Oemichen and Eduardo S. Pérez-Cisneros</i>	839
148. Understanding the dynamic behavior of Semicontinuous distillation <i>Pranav Bhaswanth Madabhushi, Edgar Iván Sánchez Medina and Thomas Alan Adams II</i>	845
149. Integrated Solvent-Membrane and Process Design Method for Hybrid Reaction-Separation Schemes <i>Yuqiu Chen, Evangelia Koumaditi, John Woodley, Georgios Kontogeorgis, Rafiqul Gani</i>	851
150. Exergy efficiency based design and analysis of utilization pathways of biomasses <i>Hongliang Qian, Weiwei Zhu, Chang Liu, Xiaohua Lu, Georgios M. Kontogeorgis, Rafiqul Gani</i>	857
151. Systematic tool for sustainable synthesis and design of flexible processes and supply chains under uncertainty <i>Klavdija Zirngast, Žan Zore, Lidija Čuček, Zorka Novak Pintarič, Zdravko Kravanja</i>	863

152. Processing Systems Synthesis with Embedded Reliability Consideration <i>Akos Orosz, Zoltan Kovacs, Ferenc Friedler</i>	869
153. A Multi-stage and Multi-level Computer Aided Framework for Sustainable Process Intensification <i>Nipun Garg, Georgios M. Kontogeorgis, John M. Woodley, Rafiqul Gani</i>	875
154. Thermodynamic Network Flow Approach for Chemical Process Synthesis <i>Georg Liesche, Dominik Schack, Karsten Hans Georg Rätze and Kai Sundmacher</i>	881
155. A General Model-based Methodology for Chemical Substitution <i>Spardha Jhamb, Xiaodong Liang, Rafiqul Gani, Georgios M. Kontogeorgis</i>	887
156. Synthesis, design and analysis of energy efficient sustainable process alternatives <i>Rafiqul Gani, Ramsagar Vooradi, Sarath Babu Anne</i>	893
157. Process synthesis and optimization of membrane systems with superstructure approach for the mitigation of CO ₂ emissions from a coal-fired power plant <i>Sunghoon Lee, Jin-Kuk Kim</i>	901
158. Semantically-enabled CAPE platform: Towards a generic and dynamic formulation for the synthesis and optimisation of value chains <i>Eirini Sioumkrou, Foteini Barla, Antonis Kokossis</i>	903
159. A novel Graphical Gibbs Energy-Driving Force Method for the Optimal Design of Non-reactive and Reactive Distillation Columns <i>Mauricio Sales-Cruz, Rafiqul Gani, Eduardo Perez-Cisneros</i>	905

Preface

This volume of the Computer-Aided Chemical Engineering series puts together a selection of the contributions presented at the 28th European Symposium on Computer-Aided Process Engineering (ESCAPE28), held in Graz, Austria, from June 10th to 13th, 2018.

This 28th event of the ESCAPE series is a continuation of the conferences under the auspices of the CAPE Working Party of the European Federation of Chemical Engineering. The conference has been organised since 1992, starting with two meetings in 1992 in Denmark and France, then having one event annually since then. Hosts to the conference have been Ireland (1994), Slovenia (1995, 2016), Greece (1996, 2011), Norway (1997), Belgium (1998), Hungary (1999, 2014), Italy (2000, 2010), Denmark (1992, 2001, 2015), The Netherlands (2002), Finland (2003, 2013), Portugal (2004), Spain (2005, 2017), Germany (2006), Romania (2007), France (1992, 2008), Poland (2009), and the United Kingdom (2012). Having organised the event in 1993, Graz takes on the torch of research and knowledge exchange with organising ESCAPE28.

ESCAPE28 is jointly organized by TU Graz and TU Wien (Austria), and the Scientific Coordination Team also spans Brno University of Technology (Czech Republic). The vision was to collaborate in organizing the event, which - besides traditional themes - also offers a platform for topics that were not explicitly mentioned in the two previous editions of ESCAPE: food, (bio-)pharma, bioresources, and the open science movement.

The themes of ESCAPE28 have been selected after a comprehensive discussion with the CAPE Working Party members and the scientific community. These include: Model Development and Simulation; Methods, Software and Tools; Open Science Movement and Education; Process Synthesis, Process Design and Life Cycle Modelling; Process Operation and Control; Bioresources, Bioprocesses and Biomedical Systems; Environment and Energy; Food, (Bio-)Pharma, and Fine Chemicals. The individual topics within these overarching themes have been formulated for allowing researchers from CAPE-related sciences to present their results and exchange valuable knowledge and experience.

ESCAPE28 attracted 321 contributions from five continents (Europe, Americas, Africa, Asia and Australia), and the International Scientific Committee (ISC) selected 163 oral presentation out of these contributions. 4 plenaries given by renowned experts from academia and industry, as well as 16 keynotes, given by leaders in their field, rounds up the scientific program. Putting together all this would have been impossible without the help of nine topic coordinators, as well as the 96 members of the ISC. We are deeply thankful for timely and careful review by these committees, as well as their invaluable help in suggesting plenary and keynote speakers.

We hope that the contributions in this edition of Computer Aided Process Engineering shine bright as illustrations of the current state of the art in their respective field.

Anton Friedl

TU Wien

Jiří J. Klemeš, Petar S. Varbanov

Brno University of Technology

Stefan Radl, Thomas Wallek

TU Graz

Scientific Committee

Scientific Coordination Team

Anton Friedl (TU Wien, AUT)
Jiří J. Klemeš (Brno University of Technology, CZ)
Petar S. Varbanov (Brno University of Technology, CZ)
Thomas Wallek (Graz University of Technology, AUT)

Topic Coordinators

Ana Paula Barbosa-Póvoa (University of Lisbon, PT)
Antonio Espuña (Technical University of Catalonia, ES)
Ferenc Friedler (Pázmány Péter Catholic University, HU)
Rafiqul Gani (PSE for Speed Ltd., DK)
Christoph Herwig (TU Wien, AUT)
Zdravko Kravanja (University of Maribor, SLO)
Jean-Marc Le Lann (INP ENSIACET Toulouse, FR)
Péter Mizsey (Budapest University of Technology & Economy, HU)
Fengqi You (Cornell University, US)

Members of the Scientific Committee

Jens Abildskov (Technical University of Denmark, DK)
Thomas A. Adams II (McMaster University, CAN)
Raymond Adomaitis (University of Maryland, US)
Harvey Arellano-Garcia (University of Surrey, UK)
Parisa Arabzadeh Bahri (Murdoch University, AUS)
Nadav Bar (Norwegian University of Science & Technology, NOR)
André Bardow (RWTH Aachen University, DE)
Fernando Bernardo (University of Coimbra, PT)
Lorenz T. Biegler (Carnegie Mellon University, US)
Miloš Bogataj (University of Maribor, SLO)
Stanislav Boldyryev (University of Zagreb, CRO)
Jose Caballero (University of Alicante, ES)
Yi Cao (Cranfield University, UK)
Elisabet Capón-García (ABB Ltd., CH)
Ana Isabel Carvalho (University of Lisbon, PT)
Pedro Castro (University of Lisbon, PT)
Franjo Cecelja (University of Surrey, UK)
Benoit Chachuat (Imperial College London, UK)
Xi Chen (Zhejiang University, CN)
Selen Cremaschi (Auburn University, US)
Lidija Čuček (University of Maribor, SLO)
César de Prada (University of Valladolid, ES)
María Soledad Díaz (Universidad Nacional del Sur, AR)

Urmila Diwekar (Vishwamitra Research Institute, US)
Mario R. Eden (Auburn University, US)
Nimir Elbashir (Texas A&M University in Doha, QA)
Erik Esche (Technische Universität Berlin, DE)
Michael Fairweather (University of Leeds, UK)
Pascal Floquet (Université de Toulouse, CNRS, INPT, UPS, FR)
Dominic Foo (University of Nottingham Malaysia Campus, MY)
Eric S. Fraga (University College London, UK)
Daniel Garcia (Northwestern University, US)
Michail Georgiadis (Aristotle University of Thessaloniki, GR)
Krist V. Gernaey (Technical University of Denmark, DK)
Moisés Graells (Technical University of Catalonia, ES)
Gonzalo Guillen Gosálbez (Imperial College London, UK)
René Hofmann (TU Wien and Austrian Institute of Technology, AUT)
Christian Jallut (Université Claude Bernard Lyon, FR)
Iftekhhar A. Karimi (National University of Singapore, SG)
Achim Kienle (Otto von Guericke University, Magdeburg, DE)
Antonis Kokossis (National Technical University of Athens, GR)
Emilia Kondili (Technological Education Institute of Piraeus, GR)
Juraj Kosek (University of Chemistry and Technology Prague, CZ)
Andrzej Kraslawski (Lappeenranta University of Technology, FI)
Grégoire Léonard (University of Liège, BE)
Filip Logist (BASF NV, BE)
Teresa López-Arenas (Universidad Autónoma Metropolitana – Cuajimalpa, MX)
Sandro Macchietto (Imperial College London, UK)
Davide Manca (Politecnico di Milano, IT)
Flavio Manenti (Politecnico di Milano, IT)
Christos Maravelias (University of Wisconsin, US)
François Maréchal (École Polytechnique Fédérale de Lausanne, CH)
Emanuele Martelli (Politecnico di Milano, IT)
Mariano Martín (University of Salamanca, ES)
Miguel Mauricio-Iglesias (University Santiago de Compostela, ES)
Ruth Misener (Imperial College London, UK)
Alexander Mitsos (RWTH Aachen University, DE)
Ludovic Montastruc (Université de Toulouse CNRS/INPT/UPS, FR)
Ricardo Morales-Rodriguez (Universidad de Guanajuato, Mexico)
Iqbal Mujtaba (University of Bradford, UK)
Stéphane Negny (Université de Toulouse CNRS/INPT/UPS, FR)
Andreja Nemet (University of Maribor, SLO)
Nuno M. C. Oliveira (University of Coimbra, PT)
Leyla Ozkan (TU Eindhoven, NL)
Stavros Papadokostantakis (Chalmers University of Technology, SE)
Lazaros Papageorgiou (University College London, UK)

Radoslav Paulen (Technische Universität Dortmund, DE)
Eduardo Salvador Perez-Cisneros (Universidad Autónoma Metropolitana, MX)
Bernhard Peters (University of Luxemburg, LU)
Carla I. C. Pinheiro (University of Lisbon, PT)
Tânia Pinto-Varela (University of Lisbon, PT)
Vicenç Puig (Technical University of Catalonia, ES)
Luis Puigjaner (Technical University of Catalonia, ES)
Marco Reis (University of Coimbra, PT)
Mauricio Sales-Cruz (Universidad Autónoma Metropolitana – Cuajimalpa, MX)
Nilay Shah (Imperial College London, UK)
Kitipat Siemanond (Chulalongkorn University, TH)
Elena Simone (University of Leeds, UK)
Gürkan Sin (Technical University of Denmark, DK)
Sigurd Skogestad (Norwegian University of Science & Technology, NOR)
Oliver Spadiut (TU Wien, AUT)
Rajagopalan Srinivasan (Indian Institute of Technology Gandhinagar, IN)
Hirokazu Sugiyama (The University of Tokyo, JP)
Kai Sundmacher (Max Planck Institute Magdeburg, DE)
Constantinos Theodoropoulos (University of Manchester, UK)
Andrasz Jozsef Toth (Budapest University of Technology and Economics, HU)
Franz Winter (TU Wien, AUT)
Yoshiyuki Yamashita (Tokyo University of Agriculture and Technology, JP)
Yuan Yao (Tsinghua University, CN)
Zhihong Yuan (Tsinghua University, CN)
Victor M. Zavala (University of Wisconsin-Madison, US)
Lei Zhang (Dalian University of Technology, CN)
Nan Zhang (University of Manchester, UK)
Jinsong Zhao (Tsinghua University, CN)
Edwin Zondervan (Bremen University, DE)

Local Organising Committee

Core Team

Heidrun Gruber-Wölfler (Graz University of Technology, AUT)
Ulrich Hirn (Graz University of Technology, AUT)
Stefan Radl (Graz University of Technology, AUT)

Lead Assistant

Julia Weissinger (Graz University of Technology, AUT)

Resilient Design and Operations of Chemical Process Systems

Jian Gong, Fengqi You^{*}

Cornell University, Ithaca, New York, 14853, USA

Abstract

Resilience in response to disruption events is critical to the economic performance of process systems, but this concept has received limited attention in the literature. We propose a general framework for resilience optimization to incorporate an improved quantitative measure of resilience and a comprehensive set of resilience enhancement strategies for process design and operations. The proposed framework identifies a set of disruptive events for a given system, and then formulates a multiobjective two-stage adaptive robust mixed-integer fractional programming model to optimize the resilience and economic objectives simultaneously. The model accounts for network configuration, equipment capacities, and capital costs in the first stage, and the number of available processes and operating levels in each time period in the second stage. A tailored solution algorithm is developed to tackle the computational challenge of the resulting multi-level optimization problem. We demonstrate the applicability of the proposed framework through applications on a shale gas processing system.

Keywords: resilience, process design and operations, superstructure optimization.

1. Introduction

Resilience is the ability to mitigate hazards and minimize the reduction in the quality of life (Bruneau et al., 2003). A resilient system is always capable of absorbing a portion of the impacts from disruptive events and recovering to the original state rapidly. A resilient plant could move fast and smoothly from one operating condition to another and dealt effectively with disturbances (Morari, 1983). A relevant concept of resilience was flexibility (Grossmann et al., 2014) which can help predict the probability of feasible operation for a design (Straub and Grossmann, 1990). Another relevant concept was reliability, which described the failure rate due to equipment aging (Rajagopalan et al., Thomaidis and Pistikopoulos, 1995). As resilience deals with safety and operability, the worst-case realization of disruptive events is of paramount importance. However, resilience was not quantified explicitly as an intrinsic property of the system.

In this work, we propose a general framework for resilience optimization with three steps. First, a preliminary risk assessment is performed to identify the disruptive events and the numbers of failed processes for the identified disruptive events. Then a multiobjective two-stage adaptive robust mixed-integer fractional programming (ARMIFP) model is formulated to maximize the resilience under the worst-case realization of disruptive events, and to minimize the total capital cost. To tackle the computational challenges from the multilevel structure and the nonlinear objective function, a tailored global optimization method is proposed by integrating the inexact parametric algorithm and the column-and-constraint generation algorithm. The applicability of the proposed framework is illustrated through the superstructure optimization of shale gas processing and natural gas liquids (NGL) recovery processes.

2. General framework for resilience optimization

We propose a general framework for resilience optimization that incorporates the quantitative measure of resilience and the five resilience enhancement strategies. There are three steps in the proposed resilience optimization framework. In the first step, a preliminary risk assessment is performed for a given system. A set of disruptive events are identified, and the related information, such as the number of failed processes in the given system and the recovery time of each process, is used as input parameters in the second step to formulate a multiobjective two-stage ARMIFP model. In the third step, the multiobjective two-stage ARMIFP problem is solved by a tailored global optimization method that integrates the parametric algorithm and the column-and-constraint generation algorithm.

2.1. Novel quantitative measure of resilience

$$\text{Resilience} = \frac{\sum_{w=0}^{t_n-t_0-1} [F(t_0 + w \cdot ti) \cdot ti]}{[F(t_0) \cdot (t_n - t_0)]} \quad (1)$$

where $F(t) = \sum_k [\omega_k \cdot M(t)_k]$, $M(t)_k$ and ω_k are the flow rate and the weight of product k , respectively; ti is the length of each time period.

We propose a novel quantitative measure as in (1). The disruptive events occur at t_0 and the time horizon is $[t_0, t_n]$. The denominator calculates the accumulated system performance from t_0 to t_n and the numerator calculates the accumulated system performance in the same period but assumes that no disruptive event occurs. This quantitative measure accounts for recovery time and performance degradation simultaneously. Moreover, as the quantitative measure is normalized by the accumulated system performance without disruptions, the resilience analysis results can be compared among distinct process systems. The failed processes of a given system can be reused only if they are fully repaired and tested. Therefore, system performance remains the same in each time period, and the system performance functions are step-wise functions.

2.2. Uncertainty set

$$\sum_{i \in ID_d} SI_{i,d} \leq \Gamma_d \cdot (1 - \varepsilon_d), \quad \forall d \quad (2)$$

$$\sum_{i \notin ID_d} SI_{i,d} = 0, \quad \forall d \quad (3)$$

The availability of process i after the occurrence of disruptive event d is modeled as an uncertain 0-1 variable $SI_{i,d}$. $SI_{i,d}$ is equal to one if the operating units in process i fail after the occurrence of disruptive event d , and 0 otherwise. Given the same operating conditions, parallel operating units are assumed to show the same availability after the occurrence of disruptive event d . Additionally, constraints (2) and (3) are introduced to provide an upper bound of the number of failed processes in the given system. Γ_d denotes the number of failed processes of disruptive event d based on historical records or simulation results. As a decision-maker may consider it too conservative to hedge against the realization where Γ_d processes fail, a tolerance level ε_d is introduced to adjust the degree of conservatism of the optimal solution. Since a disruptive event may influence only a set of processes, the summation in constraint (2) are limited to a subset of sections ID_d . The processes not in subset ID_d are fixed to be 0 as enforced by constraint (3). Uncertainty set U is formed by constraints (2) and (3).

2.3. Model formulation and tailored solution algorithm

Given the definition of resilience and uncertainty constraints, a multiobjective two-stage ARMIFP model is developed for resilient design and operations (Ning and You, 2017b, Ning and You, 2017a, Shang et al., 2017). The decisions are determined sequentially in two stages (Shi and You, 2016, Yue and You, 2016). The first-stage decisions, including network configuration, equipment capacities, and capital costs, are determined before the occurrence of the disruptive events; the second-stage decisions, including the number of available processes and operating levels in each time period, are determined after the occurrence of the disruptive events. There are two objective functions in the general form of the proposed model (shown below). The first objective is to maximize the resilience under the worst-case realization of the availability of process units, and the second objective is to minimize the total capital cost of the given system.

$$\begin{aligned} & \max_{C1} \min_U \max_{C2} \text{ Resilience} \\ & \min_{C1} \text{ Total capital cost} \end{aligned}$$

where $C1 = \{\text{network design; equipment capacity constraints; capital cost evaluation}\}$;

$C2 = \{\text{recovery constraints; operating level constraints}\}$.

Since the proposed multiobjective two-stage ARMIFP model has a multilevel structure, it cannot be handled directly by any off-the-shelf optimization solvers. Additionally, due to the combinatorial nature and nonconvexity stemming from the mixed-integer terms and the fractional objective function, the optimization problem is challenging to solve (Gong and You, 2017). To tackle the computational challenge, we employ a tailored optimization algorithm to efficiently solve this ARMIFP problem (Gong et al., 2016). Specifically, the nonlinear, nonconvex fractional objective function in the ARMIFP is tackled by a parametric algorithm (Zhong and You, 2014) that solves a sequence of auxiliary mixed-integer linear programming (MILP) problems.

3. Case study

The application of the proposed resilience optimization framework is illustrated through the superstructure optimization of shale gas processing and NGLs recovery processes (He and You, 2014, He and You 2016). Figure 1 shows a superstructure that integrates 108 possible process designs for shale gas processing and natural gas liquids recovery processes (Gong et al., 2017). The superstructure consists of four sections, namely acid gas removal, dehydration, NGLs recovery, and sulfur recovery (Yang and You, 2017). The correlation parameter $ri_{i,d}$ is equal to 1 and the tolerance level ϵ_d is equal to 5% for all disruptive events. A total of 4 case studies are considered: Case studies 1–3 involve only one disruptive event with 2, 4, and 6 failed processes, respectively, while Case study 4 involves two disruptive events with 3 and 2 failed processes in the first and second disruptive events, respectively.

All computational experiments are performed on a DELL OPTIPLEX 7040 desktop with Intel(R) Core(TM) i7-6700 CPU @ 3.40GHz and 32 GB RAM. The solution procedure is coded in GAMS 24.8.5 (Rosenthal, 2016), with CPLEX 12.7 used as the MILP solver. The relative optimality tolerances for the inexact parametric algorithm and the column-and-constraint generation algorithm are 10^{-6} .

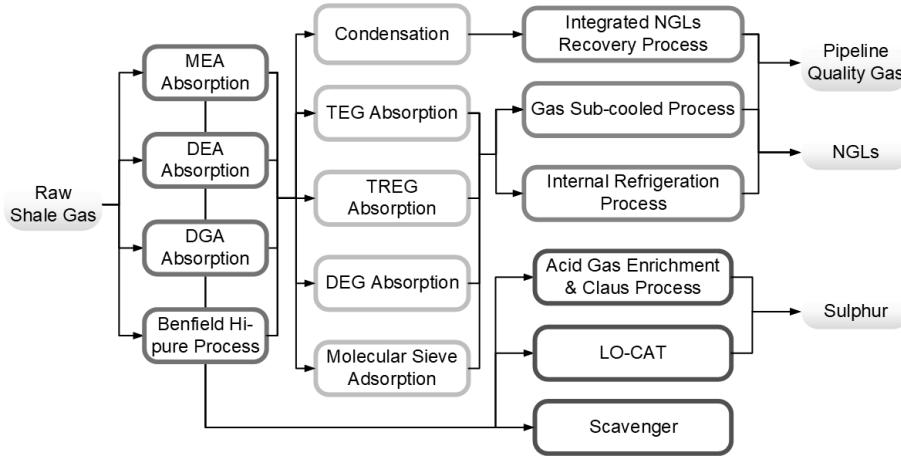


Figure 1. Superstructure of shale gas processing and NGLs recovery processes.

The optimal solutions and the selected optimal process design are plotted in the Pareto-optimal curve in Figure 2. Since the shale gas processing and NGLs recovery processes form a tandem system, the entire system will be disrupted even if only one process in the system fails. In order to operate after the occurrence of disruptive events, backup processes must be built for all the operating processes simultaneously regardless of the number of failed processes. Although four different cases have been considered in this application, the optimal solutions and the optimal objective function values are the same across all the case studies, and only one Pareto-optimal curve is exhibited in Figure 2.

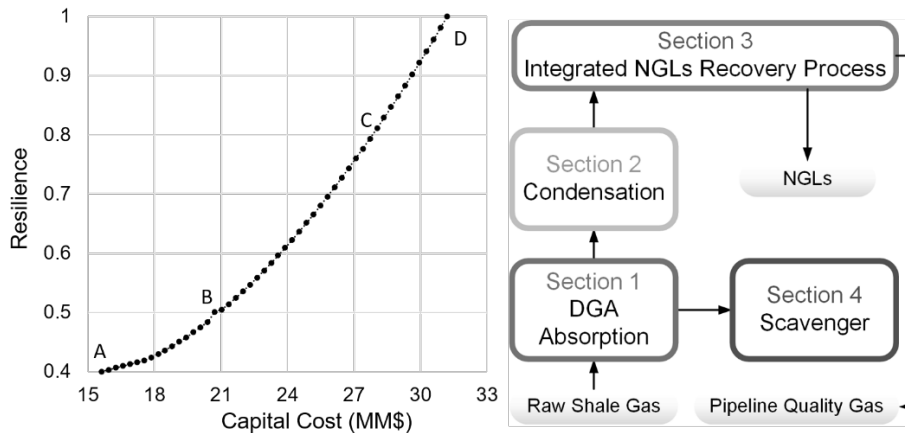


Figure 2. Pareto-optimal curve and optimal process design.

The most resilient solution demonstrates a resilience of 1 and a capital cost of \$31.22 MM, while the most cost-effective solution demonstrates a resilience of 0.4 and a capital cost of \$15.61 MM. There is a tradeoff between the two competing objective functions. A resilience of 1 for the most resilient solution means that the production rate is not affected by the disruptive events, but such an ideal performance corresponds to the highest capital cost, which is twice the cost of the most cost-effective solution. All the optimal solutions the same technologies/processes, namely diglycolamine (DGA) adsorption in the acid gas removal section, condensation in the dehydration section,

integrated NGLs recovery process in the NGLs recovery section, and scavenger in the sulfur recovery section. The resilience of a process system would be higher if additional products can be generated in the same process system. However, the technology alternatives that generate additional sulfur in the sulfur recovery section are not selected by the optimal process design, because of the relatively high capital costs of these technology alternatives. Although the selected scavenger process does not generate a sulfur product, the capital cost of this process is much lower. Therefore, the resilience will be higher if the saved capital cost is invested in alternative resilience enhancement strategies, such as employing multiple parallel processes. Overall, the optimal process design selects technologies that enhance resilience by either directly generating products or by saving capital investment for other resilience enhancement strategies.

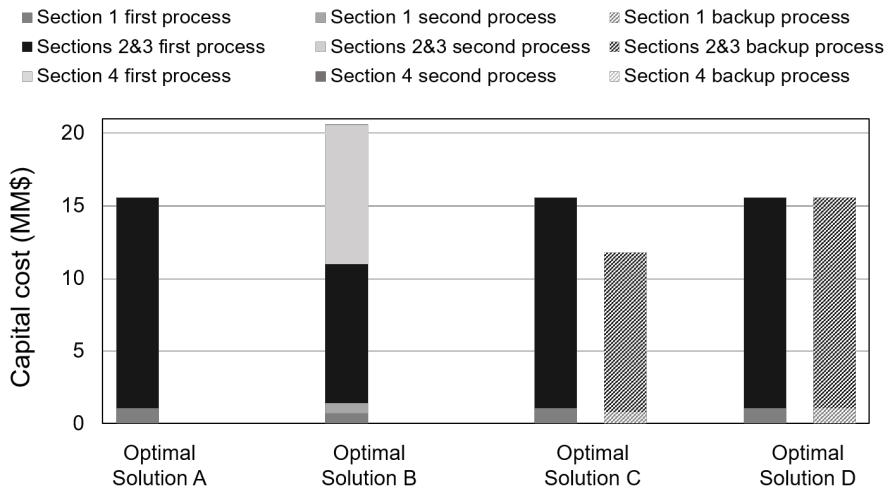


Figure 3. Capital cost breakdowns of the optimal solutions.

The breakdowns of capital costs of the optimal solutions A, B, C, and D are presented in Figure 3. The integrated dehydration and NGLs recovery process contribute to over 90% of the total capital cost. It is noted that the optimal solution B employs two parallel operating processes for the integrated dehydration and NGLs recovery process, while backup processes are built for all the sections in the optimal solutions C and D. The results also indicate that employing parallel processes can lead to a higher resilience with a low capital investment, but backup processes is desirable with higher capital investment.

4. Conclusions

We proposed a general framework for resilience optimization to incorporate the quantitative measure and the resilience enhancement strategies. The framework involves developing a multiobjective two-stage ARMIFP model, and solving the optimization problem with a tailored solution algorithm. The applicability of the proposed resilience optimization framework was illustrated through the superstructure optimization of shale gas processes. The optimal process design selected DGA adsorption, condensation, integrated NGLs recovery process, and scavenger. The maximum resilience ranged from 0.4 to 1, while the minimum capital cost ranged from \$15.61 MM to \$31.22 MM.

References

- M. Bruneau, S. E. Chang, R. T. Eguchi, G. C. Lee, T. D. O'Rourke, A. M. Reinhorn, M. Shinozuka, K. Tierney, W. A. Wallace, D. Von Winterfeldt, 2003, A framework to quantitatively assess and enhance the seismic resilience of communities, *Earthquake Spectra*, 19, 4, 733-752.
- J. Gong, D. J. Garcia, F. You, 2016, Unraveling Optimal Biomass Processing Routes from Bioconversion Product and Process Networks under Uncertainty: An Adaptive Robust Optimization Approach. *ACS Sustainable Chemistry & Engineering*, 4, 3160-3173.
- J. Gong, M. Yang, F. You, 2017, A systematic simulation-based process intensification method for shale gas processing and NGLs recovery process systems under uncertain feedstock compositions, *Computers & Chemical Engineering*, 105, 259-275.
- J. Gong, F. You, 2017, Optimal processing network design under uncertainty for producing fuels and value-added bioproducts from microalgae: Two-stage adaptive robust mixed integer fractional programming model and computationally efficient solution algorithm, *AIChE Journal*, 63, 2, 582-600.
- I. E. Grossmann, B. A. Calfa, P. Garcia-Herreros, 2014, Evolution of concepts and models for quantifying resiliency and flexibility of chemical processes, *Computers & Chemical Engineering*, 70, 22-34.
- C. He, F. You, 2014, Shale gas processing integrating with ethylene production: Novel process designs, exergy analysis, and techno-economic analysis. *Industrial & Engineering Chemistry Research*, 53, 11442-11459.
- C. He, F. You, 2016, Deciphering the true life cycle environmental impacts and costs of the mega-scale shale gas-to-olefins projects in the United States, *Energy & Environmental Science*, 9, 3, 820-840.
- M. Morari, 1983, Design of resilient processing plants—III: A general framework for the assessment of dynamic resilience, *Chemical Engineering Science*, 38, 11, 1881-1891.
- C. Ning, F. You, 2017a, Data-driven adaptive nested robust optimization: General modeling framework and efficient computational algorithm for decision making under uncertainty, *AIChE Journal*, 63, 9, 3790-3817.
- C. Ning, F. You, 2017b, A data-driven multistage adaptive robust optimization framework for planning and scheduling under uncertainty, *AIChE Journal*, 63, 10, 4343-4369.
- S. Rajagopalan, N. V. Sahinidis, S. Amaran, A. Agarwal, S. J. Bury, B. Sharda, J. M. Wassick, Risk analysis of turnaround reschedule planning in integrated chemical sites, *Computers & Chemical Engineering*.
- R. E. Rosenthal, 2016, *GAMS - a user's guide*, Washington, DC, USA.
- C. Shang, X. Huang, F. You, 2017, Data-driven robust optimization based on kernel learning, *Computers & Chemical Engineering*, 106, 464-479.
- H. Shi, F. You, 2016, A computational framework and solution algorithms for two-stage adaptive robust scheduling of batch manufacturing processes under uncertainty, *AIChE Journal*, 62, 3, 687-703.
- D. A. Straub, I. E. Grossmann, 1990, Integrated stochastic metric of flexibility for systems with discrete state and continuous parameter uncertainties, *Computers & Chemical Engineering*, 14, 9, 967-985.
- T. V. Thomaidis, E. N. Pistikopoulos, 1995, Optimal design of flexible and reliable process systems, *IEEE Transactions on Reliability*, 44, 2, 243-250.
- M. Yang, F. You, 2017, Comparative Techno-Economic and Environmental Analysis of Ethylene and Propylene Manufacturing from Wet Shale Gas and Naphtha, *Industrial & Engineering Chemistry Research*, 56, 14, 4038-4051.
- D. Yue, F. You, 2016, Optimal supply chain design and operations under multi-scale uncertainties: Nested stochastic robust optimization modeling framework and solution algorithm, *AIChE Journal*, 62, 9, 3041-3055.
- Z. Zhong, F. You, 2014, Globally convergent exact and inexact parametric algorithms for solving large-scale mixed-integer fractional programs and applications in process systems engineering, *Computers & Chemical Engineering*, 61, 90-101.

Developing key PSE skills for the workforce of the future

Concepción (Conchita) Jiménez-González^a

^a*GlaxoSmithKline, Global Program Lead – GMS, Research Triangle Park,
5 Moore Drive Research Triangle Park North Carolina 27709-3398, US*

conchita.j.gonzalez@gsk.com

Abstract

Process systems engineering (PSE) skills are imperative for the success of the chemical enterprise in a competitive and ever-changing world. Unfortunately, the importance of developing these skills is not always understood or accepted in industry or academia. Thus, engineers early in their careers sometimes have a steep learning curve applying PSE tools, and some may not be fully aware of the discipline and its possibilities.

This presentation will cover the author's perspective on key PSE skills to develop as part of the toolbox of successful engineers given ongoing trends. Developing and enhancing these key skills would enable the chemical enterprise to become more effective, sustainable, and innovative. Some of the skills to be discussed include sustainability evaluations, molecular design, process and supply chain modelling, process control and optimization, relevant data analytics, amongst others.

The talk will incorporate experience obtained through 20+ years of work from the following viewpoints: industrial PSE practice and research, development of technical engineering leaders in the chemical enterprise, and academic formation of new engineers at both graduate and undergraduate level.

The talk will provide perspective of some actions that can be taken by industry and academia to better prepare engineers in training for the demands of the chemical enterprise. When engineers are versed on the right tools, the challenges currently face by PSE become the opportunities of the innovators of tomorrow.

Keywords: education, training

COSMO-RS: From Quantum Chemistry to Fluid Phase Thermodynamics

Andreas Klamt^a

^a*COSMOlogic GmbH & Co. KG, and Inst. of Physical and Theoretical Chemistry,
University of Regensburg, Imbacher Weg 46, 51379 Leverkusen, DE*

klamt@cosmologic.de

Abstract

Thermodynamic data is the fundament of any process design. While accurately measured experimental data almost always is the most reliable source of information for the thermodynamic data required for process design, there are many situations in which this data is not available. In such situations predictive models are required. Correlative models as NRTL or SAFT, or group contribution methods as UNIFAC are the traditional approaches for property prediction in chemical engineering. Correlative methods require some experimental data for exactly the compounds and mixtures under consideration and only extrapolate to other state points. UNIFAC extrapolates to new compounds, but only if the compounds are well describable by the additive group concept and do not have major intramolecular interactions.

For structurally really new and demanding compounds, robust predictions require sound physical concepts for the description of the molecular interactions. The Conductor-like Screening Model for Realistic Solvation, COSMO-RS, is the most fundamental of such models, combining the sound quantum chemical polarity information with the efficient concept of surface segment interactions, also known as quasi-chemical approach. Thus, it provides reliable predictions for pure compound vapor pressures and mixture activity coefficients.

COSMO-RS has been initially published more than 20 years ago, and meanwhile it has become a popular method in academia and industry. The talk will cover the basic concepts of the method, its potential and limitations, and outline several extensions and new application areas which have opened up by the various methodological improvements developed during the past 20 years.

Keywords: Thermodynamics, Property prediction, Quantum chemistry

Multi-Parametric Optimization in Smart Manufacturing & Process Intensification

Efstratios Pistikopoulos^a

^a*Texas A&M University, Texas A&M Energy Institute, 1617 Research Pkwy, College Station, TX 77845, US*

stratos@tamu.edu

Abstract

Smart Manufacturing and Process Intensification are major initiatives in the US and worldwide in which process systems engineering core areas, such as modelling, optimization, control and data analytics, play key role. In Smart manufacturing real-time optimization and on-line control based on big data analytics and modelling efforts constitute important challenges. In Process Intensification the in-silico modelling, synthesis and optimization of operable and safe process intensification alternatives constitutes a key research direction.

Multi-parametric optimization provides a complete map of solutions of an optimization problem as a function of, unknown but bounded, parameters in the model, in a computationally efficient manner, without exhaustively enumerating the entire parameter space. In a Model-based Control framework, multi-parametric optimization can be used to obtain the governing ‘control laws’ – the optimal control/optimization variables as an explicit function of the state variables/parameters. This offers opportunities to (i) significantly accelerate and facilitate real-time/on-line optimization solution strategies - in the context of smart manufacturing applications, and (ii) effectively enable the systematic integration of operability criteria in the synthesis and optimization steps - in the context of process intensification.

In this presentation, we will first provide a historical progress report of the key developments in multi-parametric optimization and control. We will then describe PAROC, a systematic framework and prototype software system which allows for the representation, modelling and solution of integrated design, operation and advanced control problems – with focus on sustainable energy systems, smart manufacturing and process intensification.

Keywords: optimization, process intensification, sustainable energy systems

LCSoft as a Tool for LCA: New LCIA Methodologies and Interpretation

Tanathip Rattanatum,^a Rebecca Frauzem,^b Pomthong Malakul,^{a*} Rafiqul Gani,^{b*}

^a*The Petroleum and Petrochemical College, Chulalongkorn University, 254 Phyathai Road, Patumwan, Bangkok, 10330, Thailand*

^b*PSE for SPEED, Skyttemosen 6, DK-3450 Allerød, Denmark*

pomthong.m@chula.ac.th, rgani2018@gmail.com

Abstract

Life Cycle Assessment or LCA is a technique to evaluate and analyse environmental impacts through the entire life cycle of products and its associated processes. In order to evaluate environmental impacts and develop sustainable processes, LCSoft has been developed as a tool for LCA calculations that also integrates with other tools such as process simulation & design software, economic analysis and sustainability analysis. Apart from normalization, sensitivity analysis, uncertainty estimations, alternative comparison and eco-efficiency evaluation are also provided as results. In this paper, new Life Cycle Impact categories (LCIA) methodologies and new interpretations are added in order to improve performances, application range and flexibilities. ReCiPe, including midpoint and endpoint impacts, is added into LCIA method selection, water scarcity footprint and ecological footprint are added as a new feature of interpretation. Also, LCSoft can estimate water scarcity footprint and ecological footprint in different countries and periods of time. Finally, LCA calculations for bioethanol production from cassava rhizome and a carbon dioxide conversion process are validated by comparing with SimaPro, which is another LCA software. The results show that the new LCIA methodologies and LCA interpretation of LCSoft has the ability to evaluate environmental impacts of biochemical and petrochemical processes.

Keywords: Life Cycle Assessment, Life Cycle Inventory, Sustainable process design, Environmental footprint

1. Introduction

For decades, the increase of world population along with the growth of industries caused the increase of demand in natural resources. Policies are being implemented to prevent the reduction of natural resources and focus on environmental issues. Therefore, the assessment of environmental impacts has become an important issue to improve and develop new as well as existing processes. One of the most popular techniques that are widely used around the world is life cycle assessment, also known as LCA.

Currently, several commercial software are available to evaluate LCA, such as, SimaPro (Goedkoop et al., 2016), Gabi (PE, 2012), and Umberto (Ifu Hamburg GmbH, 2016). Although commercial tools for LCA are available, for sustainable process design a number of additional software are needed to obtain an overall perspective of the designed process. For this purpose, LCSoft (Chavewanmas et al., 2017) has been developed as a tool for LCA calculations for chemical and biochemical processes that also integrates with other design and analysis tools, such as, PROII (process

simulation), ECON (economic analysis, Saengwirun, 2011) and SustainPro (sustainability analysis) (Carvalho et al., 2013).

The new version of LCSOFT calculates the Life Cycle Inventory (LCI) as well as LCIA by using a systematic calculation strategy consisting of retrieval of appropriate system data, data of substances involved and process utility data (such as, consumptions of steam, electricity, and water) and the corresponding models. LCSOFT calculates and evaluates environmental impacts organized in different impact categories, which depend on the use of specific LCIA methodologies (General Impact Categories, ILCD 2011 midpoint, ILCD 2011 endpoint, ReCiPe midpoint and ReCiPe endpoint) that are currently available. LCSOFT provides the following impacts and factors: acidification, global warming potential, ozone depletion, particulate matter, photochemical oxidant formation, human toxicity, freshwater ecotoxicity, terrestrial ecotoxicity, marine ecotoxicity, ionising radiation, terrestrial eutrophication, freshwater eutrophication, marine eutrophication, water depletion, fossil depletion, water resource consumption, energy resource consumption for midpoint impact categories and ecological system, human health, resource depletion for endpoint impact categories as well as carbon footprint. The potential environmental impacts are calculated by using characterization factors of specific LCIA methodologies. The new characterization factors in LCSOFT are able to cover a wide range of chemical substances and the implemented model is also able to handle multiple products because of the use of predictive group contribution-based models. Several optional interpretations now available in LCSOFT consist of normalization, sensitivity analysis, uncertainty estimations, alternative comparison and eco-efficiency evaluation. In order to evaluate the impact of water and ecological resource consumption at different periods and locations, a water scarcity footprint and an ecological footprint are also now calculated.

2. Description of New Features in LCSOFT

Two of the features developed for LCSOFT are briefly described below.

2.1 New LCIA methodologies

Midpoint and endpoint impact categories are provided in the new version of LCSOFT, compared to the previous, which only calculated the midpoint impact. In order to broaden the application range of usage, ReCiPe and ILCD endpoints are included in the LCIA methodology. Normally, midpoint impact focuses only on single environmental problems. For other environmental problems, midpoint indicators are transformed by multiplication with characterization factors and aggregation of each environmental problem to higher levels, also known as endpoints. Also, each midpoint and endpoint of ReCiPe are classified in terms of individualist (short term), hierarchist (consensus model) and egalitarian (long term). The LCIA methodologies currently available in LCSOFT are listed in Table 1.

Table 1: LCIA methodologies in LCSoft

Impact level	LCIA methodologies in LCSoft	
	Previous version	Latest version
Midpoint	General Impact categories ILCD 2011	General Impact categories
		ILCD 2011
		ReCiPe (Egalitarian)
		ReCiPe (Individualist)
Endpoint		ReCiPe (Hierarchist)
		ILCD 2011
		ReCiPe (Egalitarian)
		ReCiPe (Individualist)
		ReCiPe (Hierarchist)

2.2 New interpretation and analysis options

To ease the communication with users, new interpretation and analysis options have been added. In addition to carbon footprint, which is defined as the total set of greenhouse gas emissions expressed in terms of carbon dioxide equivalent, LCSoft calculates other environmental footprints: water scarcity footprint (Boulay et al., 2017) and the ecological footprint. The water scarcity footprint shows the impact score of consumed water per kg product, which is compared with data from different countries and time periods. Ecological footprint is defined as the area used to support population and industrial consumption. Water scarcity footprint is calculated by Eq. (1).

$$Water\ Scarcity\ Footprint = Water\ consumption \times Characterization\ factor \tag{1}$$

The ecological footprint (Global Footprint Network, 2013) shows, in terms of global hectares, how much area is needed to produce all resources, instead of it being consumed, and absorb the waste generated from all activities.

LCSoft also provides options for analysis of sensitivity and uncertainty in the calculated impacts, as well as alternative comparison. Sensitivity analysis is calculated by perturbing each parameter to study the effect on the impacts. Uncertainties in the calculated impacts are obtained through the available variations in the system data.

3. Case Study

Here, LCA for two processes are calculated and compared with results from SimaPro.

Case-1: A process for production of bioethanol from cassava rhizome as the feed stock is assumed to be located in Thailand. The data (mass and energy flows) for this evaluation, are taken from simulation results (Mangnimit, 2013). The LCA for this process is evaluated in terms of environmental impacts calculated by LCSoft and SimaPro using the same simulation data and LCIA methodology, ReCiPe (H) methodology. LCA results from both programs for different environmental impacts calculated on the basis of 1 kg of pure ethanol produced are listed in Table 2.

Table 2: Comparison of bioethanol result with the ReCiPe (H) methodology

Impact Categories	Unit	LCSoft	SimaPro	Uncertainty (10%)
ReCiPe Midpoint				
Climate Change	kg CO2 eq.	2.31133	2.36460	2.38824
Ozone Depletion	kg CFC-11 eq.	1.61E-12	1.73E-12	1.61E-12
Terrestrial Acidification	kg SO2 eq.	0.00362	0.00959	0.00343
Freshwater Eutrophication	kg P eq.	5.18E-06	5.18E-06	5.39E-06
Marine Eutrophication	kg N eq.	0.00012	0.00014	0.00012
Human Toxicity	kg 1,4-DB eq.	0.00369	0.16753	0.00378
Photochemical Oxidant Formation	kg NMVOC	0.00213	0.00263	0.00210
Particulate Matter Formation	kg PM10 eq.	0.00077	0.00196	0.00072
Terrestrial Ecotoxicity	kg 1,4-DB eq.	3.96E-07	5.35E-07	3.98E-07
Freshwater Ecotoxicity	kg 1,4-DB eq.	0.00045	0.00211	0.00046
Marine Ecotoxicity	kg 1,4-DB eq.	0.00118	0.00195	0.00120
Ionising Radiation	kg U235 eq.	0.00E+00	0.00E+00	0.00E+00
Agricultural Land Occupation	m2a	0.00E+00	0.00E+00	0.00E+00
Urban Land Occupation	m2a	0.00E+00	0.00E+00	0.00E+00
Natural Land Occupation	m2a	0.00E+00	0.00E+00	0.00E+00
Water Depletion	m3	0.00007	0.00007	3.70E-05
Metal Depletion	kg Fe eq.	3.82E-08	3.83E-08	3.83E-08
Fossil Depletion	kg oil eq.	0.39005	0.31975	0.38954
ReCiPe Endpoint				
Ecosystem	species/y	1.94E-08	1.8787E-08	2.00E-08
Human Health	DALY	4.73E-06	3.9378E-06	4.82E-06
Resources	\$	0.06454	0.05284	0.06445

Case-2: Carbon dioxide capture and utilization (CCU) processes make an effort to reduce carbon dioxide emissions by converting them into useful chemicals. Dimethyl carbonate is one of those high value chemical selected in this work for production by a CCU process. The LCA calculated for this process is also compared with SimaPro (see Table 3). Also, for this case study, the water scarcity footprint and ecological footprint are calculated. For these footprint calculation, location of the process is an important factor because there are differences in climate, geography, resources and time-period. The plant location is assumed to be in Denmark and the results of the footprint calculations are given in Table 4.

Table 3: Dimethyl carbonate produced from carbon dioxide capture processes with ReCiPe (I) methodology

Impact Categories	Unit	LCSoft	SimaPro	Uncertainty (10%)
ReCiPe Midpoint				
Climate Change	kg CO2 eq.	81.30233	76.90087	82.0665
Ozone Depletion	kg CFC-11 eq.	5.20E-12	3.919E-11	5.10E-12
Terrestrial Acidification	kg SO2 eq.	0.01061	0.03924	0.01075
Freshwater Eutrophication	kg P eq.	0.00E+00	0.00E+00	0.00E+00
Marine Eutrophication	kg N eq.	0.00033	0.00024	0.00033
Human Toxicity	kg 1,4-DB eq.	1.11E-02	0.0655291	1.12E-02
Photochemical Oxidant Formation	kg NMVOC	1.86E-02	0.0321535	1.88E-02
Particulate Matter Formation	kg PM10 eq.	0.00372	0.00906	0.00379
Terrestrial Ecotoxicity	kg 1,4-DB eq.	4.04E-06	4.863E-06	4.11E-06
Freshwater Ecotoxicity	kg 1,4-DB eq.	0.00382	0.01132	0.00386
Marine Ecotoxicity	kg 1,4-DB eq.	9.41E-03	0.0103197	9.40E-03
Ionising Radiation	kg U235 eq.	0.00E+00	0.00E+00	0.00E+00
Agricultural Land Occupation	m2a	0.00E+00	0.00E+00	0.00E+00
Urban Land Occupation	m2a	0.00E+00	0.00E+00	0.00E+00
Natural Land Occupation	m2a	0.00E+00	0.00E+00	0.00E+00
Water Depletion	m3	0.00110	-0.00110	0.00116
Metal Depletion	kg Fe eq.	0.00E+00	0.00E+00	0.00E+00
Fossil Depletion	kg oil eq.	4.85606	2.55786	4.73952
ReCiPe Endpoint				
Ecosystem	species/y	9.68E-05	6.099E-07	9.59E-05
Human Health	DALY	1.96E-06	9.393E-05	1.94E-06
Resources	\$	0.25109	0.13246	0.25712

4. Conclusions

The latest version of LCSoft covers a broader application range for users, more LCIA methodologies are included and also impacts sub-level, including midpoint and endpoint are calculated. Environmental impacts from case study results confirm that LCSoft, integrated with design and analysis software tools, has the ability to efficiently evaluate biochemical, petrochemical, chemical and related processes. In addition, new interpretation results connected to, water scarcity footprint and ecological footprint are helpful additions to get a sound overall picture with respect to sustainability.

Table 4: Water scarcity footprint and ecological footprint of CCU process in Denmark

Water Scarcity Footprint		Ecological Footprint		
Month	m3/kg		Biocapacity (gha per person)	Ecological Footprint (gha per person)
January	3.50788	Built up Land	0.2297	0.2297
February	3.77053	Carbon	0.0000	3.113
March	3.51443	Cropland	2.189	1.1304
April	4.50688	Fishing Grounds	1.8083	0.2414
May	6.31094	Forest Products	0.3391	0.8932
June	9.98980	Grazing	0.0078	0.5007
July	13.35375			
August	15.56875			
September	15.22631			
October	11.66483			
November	8.11415			
December	4.63876			

References

- Boulay, A.-M., Bare, J., Benini, L., Berger, M., Lathuilière, M. J., Manzardo, A., Pfister, S., 2017, The WULCA consensus characterization model for water scarcity footprints: assessing impacts of water consumption based on available water remaining (AWARE). *The International Journal of Life Cycle Assessment*.
- Carvalho, A., Matos, H. A., Gani, R., 2013, SustainPro—A tool for systematic process analysis, generation and evaluation of sustainable design alternatives. *Computers & Chemical Engineering*, 50, 8-27.
- Chavewanmas, Y., Malakul, P., Gani, R., 2016, Improvement of Life Cycle Assessment Software and Its Applications, MSc-thesis, The Petroleum and Petrochemical College, Chulalongkorn University, Bangkok, Thailand.
- Global Footprint Network, “Ecological Footprint of Countries 2013”. 8 Dec 2017 <<http://data.footprintnetwork.org/#/compareCountries?cn=all&type=EFctot&yr=2013>>
- Goedkoop, M., Oele, M., Vieira, M., Leijting, J., Ponsioen, T., Meijer, E., 2016, SimaPro Tutorial, Pré Consultants.
- Ifu Hamburg GmbH, 2016, Umberto NXT LCA (v.7.1) User Manual.
- Mangnimit, A. S., 2013, Sustainable Process Design of Biofuels :Bioethanol Production from Cassava rhizome, MSc-thesis, The Petroleum and Petrochemical College, Chulalongkorn University, Bangkok, Thailand.
- PE International Sustainability Performance, 2012, GaBi Paper Clip Tutorial.
- Sangwiron, P., 2011, Cost Calculations and Economic Analysis, MSc-thesis, The Petroleum and Petrochemical College, Chulalongkorn University, Bangkok, Thailand.

Modeling the Performance of Low Pressure Reverse Osmosis Membrane System for N-nitrosamine Rejection

Mudhar A. Al-Obaidi ^{a,b}, Chakib Kara-Zaïtri ^a and Iqbal M. Mujtaba ^{a,*}

^a *School of Engineering, Faculty of Engineering and Informatics, University of Bradford, Bradford, West Yorkshire BD7 1DP, UK*

^b *Middle Technical University, Iraq – Baghdad*

I.M.Mujtaba@bradford.ac.uk

Abstract

In this work, a one-dimensional model of a low-pressure reverse osmosis (LPRO) membrane process has been developed using an augmented model previously developed by the same authors to analyse the rejection of N-nitrosamine from wastewater. The model, based on the principles of the solution-diffusion coupled with the concentration polarization theory, is validated using experimental data of N-nitrosamine rejection from the literature for three different types of membranes in an RO process. Finally, detailed simulation of the LPRO process is carried out for variety of operating conditions such as inlet feed flow rate, pressure, feed concentration, and temperature.

Keywords: Wastewater Treatment, Low Pressure Reverse Osmosis (LPRO), Distributed Modelling, Simulation, N-nitrosamine Rejection.

1. Introduction

The population growth is one of the important factors that drives the exploitation of other alternatives to ensure potable water supply around the world. In the last few decades, wastewater has become a supplementary source of high quality recycled water and a number of techniques including membrane and oxidation based processes have been explored to treat the wastewater (Farré et al., 2011). NDMA (N-nitrosodimethylamine) is one of the most highly toxic compounds in N-nitrosamine family, which has been classified as a carcinogenic compound to human (Fujioka, 2014). To minimize the risk of releasing NDMA into the recycled water, several treatment approaches has been implemented, such as adsorption on activated carbon, hydrolysis, metal complexation, ozonation (Lee et al., 2005). Particularly, ultraviolet radiation-hydrogen peroxide advanced oxidation process (UV/H₂O₂) is considered as the efficient standard treatment procedures used for N-nitrosamine removal from recycled water (Steinle-Darling et al., 2007).

The interest to use the RO process as a treatment method has increased in response to avoid the need for costly conventional methods in addition to satisfy the increasingly stringent limits of N-nitrosamine concentration. Flat sheet membranes are preferred for laboratory scale experiments to illustrate the intrinsic membrane properties with respect to permeate flux and separation efficiency. To the best of authors' knowledge, the distributed modelling of a flat sheet membrane under low pressure for the rejection of wastewater solutions has not been reported in the peer review literature. Fujioka (2014)

used the irreversible thermodynamics model (lumped version) to predict and simulate the rejection of N-nitrosamines in LPRO membranes. Al-Obaidi et al. (2016) developed a one-dimensional model based on the irreversible thermodynamics model to simulate the rejection of N-nitrosamine compounds but using a high-pressure spiral-wound RO process. In general, LPRO membranes are typically used for water reclamation applications (Fujioka., 2014). This is due to low concentration of impurities that can be found in wastewater compared to seawater. This in turn requires much lower values of operating pressure with the consideration of lower energy consumption in addition to lower cost of filtration. Most importantly, the outputs of Fujioka (2014) experiments show that N-nitrosamine rejection and recovery of low-pressure membrane (40 cm²) (small-scale RO system) and high-pressure membrane (7.9 m²) (pilot-scale of three RO modules in series) are 37-52% and 31-54% respectively. Note, in high pressure system pressure around 40-45 atm is used while in low pressure system pressure around 5-12 atm is used. In this work, the removal of a suite of three N-nitrosamines by three different LPRO membranes under different conditions is considered using a one-dimensional model based on the concepts of solution-diffusion model. The model is validated against experimental data gathered from the literature. Reliable design of membrane systems depends heavily on the understanding of the interaction of different parameters, which model based simulation can provide easily and cheaply compared to time-consuming experimental studies and therefore is the focus of this study.

2. Modelling of Spiral-wound Reverse Osmosis

A one-dimensional model includes the physical properties equations has been earlier developed for a spiral-wound RO system by Al-Obaidi et al. (2017) for the removal of chlorophenol and based on solution-diffusion model. Their work provides the basis for the development of a distributed model for a flat sheet LPRO in this work to estimate the rejection of N-nitrosamine. The new model equations are presented in Table 1.

The model equations of Al-Obaidi et al. (2017) are moderated to be compatible with the assumption of no pressure drop along the x-axis (assuming zero friction parameter). Therefore, several equations were included in the proposed new model. Eq. (9) used to calculate the mass transfer coefficient $k_{(x)}$. Eq. (10) is used to predict the viscosity parameter $\mu_{b(x)}$. The dependency of diffusivity parameter of N-nitrosamine solute on feed temperature (T_b) is approximated using Eq. (13). The diffusivity parameters at 20 °C for each N-nitrosamine are reported in Table 2. The calculation of solute concentration $C_{b(x)}$ along the feed channel is conducted using the proposed correlation of Eq. (14). Furthermore, the effect of temperature variation on both water permeability A_w and solute permeability B_s coefficients are described in Eqs. (19) and (20) respectively. Interestingly, the model developed can be used for other pollutants by providing the proper mass transfer coefficient and viscosity correlation for the given pollutant. A simulation model was developed for a flat-sheet LPRO membrane element that describe the variation of all variables with spatial dimensions using the gPROMS.

3. Experiments of Fujioka (2014)

Fujioka (2014) used a laboratory bench-scale filtration system of a flat sheet LPRO element to remove N-nitrosamines from its aqueous solutions, which consists of a rectangular stainless-steel membrane cell that holds a flat-sheet membrane of 4 cm x 10 cm of width and length respectively with a channel height of 2 mm. Three thin film composite LPRO membranes listed in Table 2 are separately packed into the membrane cell for different experiments. The experiment was carried out by introducing 250 ng/L

of each target N-nitrosamine. The feed was pumped at a constant volumetric flow rate of $3.36\text{E-}6 \text{ m}^3/\text{s}$. The temperature was kept at $20\pm 0.1 \text{ }^\circ\text{C}$. More details about the experiments can be found in Fujioka (2014). The characteristics of the membranes used are given in Table 2. The transport parameters for N-nitrosamines through these membranes and its feed concentrations and diffusivity parameters at $20 \text{ }^\circ\text{C}$ are given in Table 3.

Table 1. The model equations of LPRO membrane element

Model Equations	Eq. no.
$F_{b(x)} = \{F_{b(0)} - (W \theta x \Delta P_{b(0)})\}$, where x is the dimension of x-axis under considering	1
$\theta = \frac{A_{w(T_b)} B_s(T_b)}{B_s(T_b) + R (T_b + 273.15) A_{w(T_b)} C_{p(av)}}$, θ is a parameter in Eq. (1)	2
$U_{b(x)} = \frac{F_{b(x)}}{t_f W}$ $P_{b(x)} = P_{b(0)}$ $\Delta P_{b(x)} = \Delta P_{b(0)}$	3,4, 5
$J_{w(x)} = \theta (\Delta P_{b(0)})$, $J_{s(x)} = B_s(T_b) (C_{w(x)} - C_{p(av)})$	6, 7
$\frac{(C_{w(x)} - C_{p(av)})}{(C_{b(x)} - C_{p(av)})} = \exp\left(\frac{J_{w(x)}}{k(x)}\right)$	8
$k(x) = 0.664 \left(\frac{D_{b(x)}}{2 t_f}\right) \left(\frac{2 F_{b(x)} \rho_{b(x)}}{W \mu_{b(x)}}\right)^{0.5} \left(\frac{\mu_{b(x)}}{\rho_{b(x)} D_{b(x)}}\right)^{0.33} \left(\frac{2 t_f}{L}\right)^{0.33}$	9
$\mu_{b(x)} = 2.141x 10^{-5} x 10^{\left(\frac{247.8}{(T_b + 273.15) - 140}\right)}$	10
$\rho_{b(x)} = 498.4 m_{f(x)} + \sqrt{[248400 m_{f(x)}^2 + 752.4 m_{f(x)} C_{b(x)} (18.0153)]}$	11
$m_{f(x)} = 1.0069 - 2.757E - 4 (T_b)$	12
$D_{b(x)(T_b)} = D_{b(T_{bo})} \left(\frac{T_b + 273.15}{T_{bo} + 273.15}\right) \left(\frac{\mu_{b(x)(T_{bo})}}{\mu_{b(x)(T_b)}}\right)$	13
$\frac{C_{b(x)}}{t_f W} \frac{dF_{b(x)}}{dx} + \frac{F_{b(x)}}{t_f W} \frac{dC_{b(x)}}{dx} = \frac{d}{dx} \left[D_{b(x)} \frac{dC_{s(x)}}{dx} \right] - \frac{(J_{w(x)} C_{p(x)})}{t_f} + \frac{(J_{w(x)} C_{b(x)})}{t_f}$	14
$C_{p(av)} = \frac{C_{p(0)} + C_{p(L)}}{2}$, $C_{p(0)} = \frac{B_s(T_b) C_{b(0)} e^{\frac{J_{w(0)}}{K(0)}}}{J_{w(0)} + B_s(T_b) e^{\frac{J_{w(0)}}{K(0)}}}$, $C_{p(L)} = \frac{B_s(T_b) C_{b(L)} e^{\frac{J_{w(L)}}{K(L)}}}{J_{w(L)} + B_s(T_b) e^{\frac{J_{w(L)}}{K(L)}}}$	15, 16, 17
$F_{p(x)} = \{F_{p(0)} + (W x \theta \Delta P_{b(0)})\}$, where x is the dimension of x-axis under consideration	18
$A_{w(T_b)} = A_{w(T_{bo})} \left(\frac{\mu_{b(x)(T_{bo})}}{\mu_{b(x)(T_b)}}\right)$, $B_s(T_b) = B_s(T_{bo}) \left(\frac{T_b + 273.15}{T_{bo} + 273.15}\right) \left(\frac{\mu_{b(x)(T_{bo})}}{\mu_{b(x)(T_b)}}\right)$	19, 20
$Rec_{(Total)} = \frac{F_{p(L)}}{F_{b(0)}} x 100$ $Rej = \frac{C_{b(0)} - C_{p(av)}}{C_{b(0)}} x 100$	21, 22

Table 2. LPRO membrane characteristics (Fujioka, 2014)

Membrane	Manufacturer	NaCl rejection %	Pure water permeability A_w (m/s atm)
ESPA2	Hydranautics	99.6	1.4073E-6
TFC-HR	KMS	99.6	7.8808E-7
70LW(TML)	Toray	99.7	7.0364E-7

Table 3. Specification of N-nitrosamines (Fujioka, 2014)

N-nitrosamine	Feed concentration $C_{b(0)}$ (kmol/m ³)	Molecular weight (g/mol)	Diffusion coefficient $D_{b(20 \text{ }^\circ\text{C})}$ (m ² /s)	Transport parameter B_s (m/s) and operating feed pressure P_b (atm)		
				ESPA2	TFC-HR	70LW
NDMA	3.38E-09	74.05	9.7E-10	5.35E-6	4.15E-6	3.32E-6
				4.4510	6.0237	8.4776
NMEA	2.84E-09	88.06	8E-10	1.14E-6	1.07E-6	8.24E-7
				4.4510	6.0237	8.4776
NDEA	2.45E-09	102.08	8E-10	2.26E-7	2.49E-7	1.47E-7
				4.4510	6.0237	8.4776

4. Model Validation

Fig. 1 depicts the comparison of the model predictions of N-nitrosamine rejection of NDMA, NMEA and NDEA and experimental data of Fujioka (2014) for the specific LPRO membranes. The operating conditions of the experiments are as follows: inlet feed concentration of each N-nitrosamine and feed pressure of each membrane is listed in Table 3, inlet feed flow rate of $3.36E-5$ m³/s and feed temperature of 20 °C. Generally, Fig. 1 shows that the predicted values of the model are in a good agreement with experimental ones. Furthermore, LPRO membranes have poor rejection for NDMA in comparison to NMEA and NDEA. Also, it is expected that the low rejection of NDMA is largely due to its effective diffusion through these membranes.

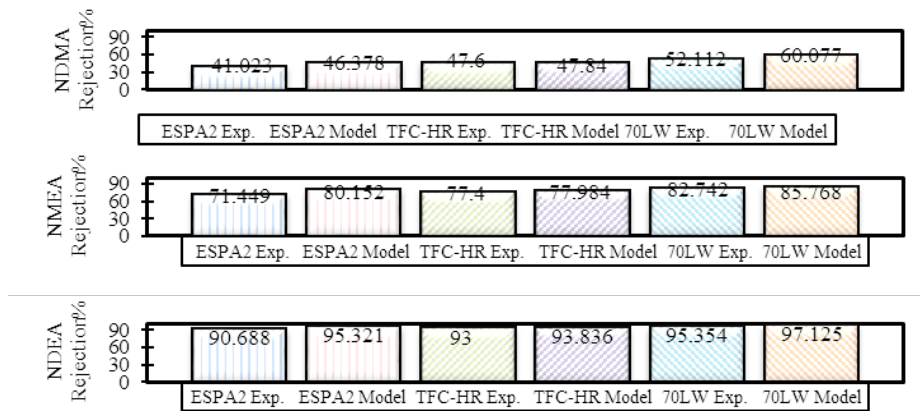


Fig. 1. The comparison of experimental results and model predictions of three types N-nitrosamine rejection by three LPRO membranes (ESPA2, TFC-HR and 70LW)

Fig. 2 shows the variation of feed concentration of NDMA and wall membrane concentration respectively at operating conditions of $3.38E-09$ kmol/m³, $3.36E-05$ m³/s 6.0237 atm and 20 °C for TFC-HR membrane. The concentrations are increased due to the permeated water passing through the membrane.

5. Effect of Operating Parameters on N-nitrosamine Rejection

5.1 Effect of Inlet Feed Concentration

The effect of inlet feed concentration variation from 250 to 1000 ng/L on steady-state rejection was tested by Fujioka (2014) at constant operating conditions of $3.36E-5$ m³/s, 6.0237 atm, 20 °C and for three representative nitrosamines, NDMA, NMEA and NDEA. Fig. 3 shows that the operating feed concentration has a negligible effect on N-nitrosamine rejection. Also, the model can give an accurate estimation of N-nitrosamine rejection at different feed concentration.

5.2 Effect of Feed Temperature

Fig. 4 shows that the operating temperature has a substantial impact on N-nitrosamine rejection, which is dropped due to an increase in feed temperature. The simulation results show that an increase in feed temperature increases N-nitrosamine permeability coefficient, which readily causes a reduction in N-nitrosamine rejection. It can be

mentioned that the model tends to only underestimate N-nitrosamine rejection at high feed temperature. Apparently, this might be attributed to an inaccurate estimation of the transport membrane parameters at such temperature.

5.3 Effect of Inlet Feed Pressure

The effect of inlet feed pressure on NDMA rejection while other variables remain constant can be distinguished through the simulation study shown in Fig. 5 where the pressure is increased from 6 to 10 atm at constant operating feed flow rate, concentration, and temperature of $3.36\text{E-}5 \text{ m}^3/\text{s}$, $3.38\text{E-}9 \text{ kmol/m}^3$ and $20 \text{ }^\circ\text{C}$ respectively for membrane type TFC-HR. It is clearly noted that the rejection parameter increases due to an increase in operating pressure since the water flux increased has diluted the permeate.

5.4 Effect of Inlet Feed Flow rate

The effect of the inlet feed flow rate on N-nitrosamine rejection is shown in the simulation results of Fig. 6 at 250 ng/L , 6.0237 atm , $20 \text{ }^\circ\text{C}$. The variation of feed flow rate from $3.36\text{E-}5$ to $9.8\text{E-}5 \text{ m}^3/\text{s}$ causes a little increase in rejection parameter, which might be attributed to decrease in wall concentration that causes an increase in water flux and decreases permeate concentration. Please note, the study of Fujioka (2014) does not include the impact of feed pressure and feed flow rate on N-nitrosamine rejection.

6. Conclusions

In this work, a one-dimensional model is developed for the low-pressure RO (LPRO) membranes considering the removal of three N-nitrosamine from wastewater. The findings of simulation results were compared to experimental one and shows a good match. The influence of operating parameters was investigated on the process performance. The study shows that inlet feed concentration and flow rate have no apparent impact on N-nitrosamine rejection in comparison to inlet feed pressure and temperature, which have clear influence. Also, the removal of N-nitrosamines is quite correlated to the type of membrane used. Thus, the membrane selection is one of the priorities to be considered in N-nitrosamine removal.

References

- Al-Obaidi M.A., Li Jian-Ping, Kara-Zaïtri C., Mujtaba I.M., 2017. Optimisation of reverse osmosis based wastewater treatment system for the removal of chlorophenol using genetic algorithms. *Chemical Engineering Journal*, 316, 91-100.
- Al-Obaidi M.A., Kara-Zaïtri C., Mujtaba I.M., 2016. Development and Validation of N-nitrosamine Rejection Mathematical Model Using a Spiral-wound Reverse Osmosis Process. *Chemical Engineering Transactions*, 52, 1129-1134.
- Farré M.J., Döderer K., Hearn L., Poussade Y., Keller J. and Gernjak W., 2011. Understanding the operational parameters affecting NDMA formation at Advanced Water Treatment Plants. *Journal of Hazardous Materials*, 185, 1575-1581.
- Fujioka, T., 2014. Assessment and optimisation of N-nitrosamine rejection by reverse osmosis for planned potable water recycling applications. PhD Thesis, University of Wollongong.
- Lee C., Choi W., Kim Y.G. and Yoon J., 2005. UV photolytic mechanism of N-nitrosodimethylamine in water: Dual pathways to methylamine versus dimethylamine. *Environmental Science and Technology*, 39, 2101-2106.

Steinle-Darling E., Zedda M., Plumlee M.H., Ridgway H.F. and Reinhard M., 2007. Evaluating the impacts of membrane type, coating, fouling, chemical properties and water chemistry on reverse osmosis rejection of seven nitrosoalkylamines, including NDMA. *Water Research*, 41, 3959-3967.

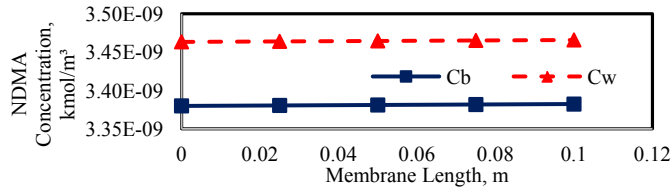


Fig. 2. Variation of feed and wall membrane concentrations along the membrane length

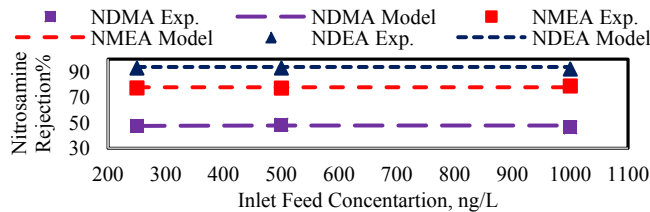


Fig. 3. Experimental results and model predictions of N-nitrosamine rejection verses inlet feed concentration (membrane: TFC-HR)

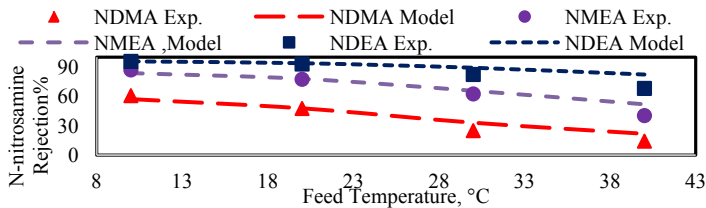


Fig. 4. Experimental results and model predictions of N-nitrosamine rejection verses feed temperature (membrane: TFC-HR)

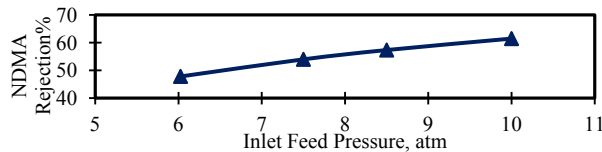


Fig. 5. Simulation results of NDMA rejection verses feed pressure (TFC-HR)

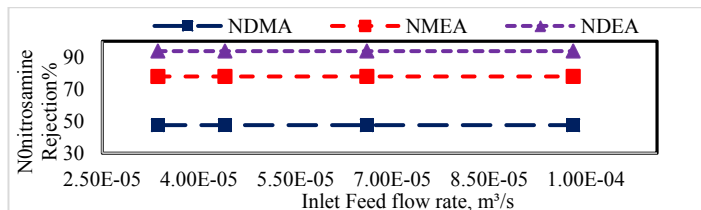


Fig. 6. Simulation results of N-nitrosamine rejection verses feed flow rate (membrane: TFC-HR)

Model of a Formaldehyde Absorption System Based on Industrial Data

Catarina G. Braz^a, Henrique A. Matos^{a*}, A. Mendes^b, J. Rocha^c, R. Alvim^c

^a*Centro de Recursos Naturais e Ambiente, Instituto Superior Técnico, Universidade de Lisboa, Av. Rovisco Pais 1, 1049-001 Lisboa, Portugal*

^b*Laboratory for Process Engineering, Environment, Biotechnology and Energy, Faculdade de Engenharia, Universidade do Porto, R. Dr. Roberto Frias, 4200-464 Porto, Portugal*

^c*EuroResinas – Indústrias Químicas S.A., Plataforma Industrial de Sines – Lote Industrial I, 7520-064 Sines, Portugal*

henrimatos@tecnico.ulisboa.pt

Abstract

This work focused on the simulation of an industrial system of formaldehyde absorption columns. For this purpose, a rate-based stage model of the system subjected to study was developed in *gPROMS[®] Modelbuilder 4.2.0* and the simulation results compared with the operational values. The results are mainly in accordance with the plant data. The columns temperature and composition profiles generated by the model will be validated in future work.

Keywords: Simulation, Model development, Absorption Columns, Formaldehyde.

1. Introduction

Formaldehyde is produced on a large scale due to its many applications as a raw material in industrial and end-use products. One of its main production processes consists of the methanol partial oxidation using an iron-molybdenum oxide catalyst. In this process, a mixture of air and lean methanol is vaporized and passes through a fixed bed multitubular reactor, the product gas stream is sent afterwards to a system of absorption columns with water, represented in Figure 1. The gaseous stream coming from the reactor enters the base of column T-1 and goes through two sections of random packing with two sieve trays in between, followed by a second column T-2 with bubble-cap trays that include internal coils in contact with the liquid. Process water is added at the top of T-2. In the first column, the formaldehyde aqueous solution (formalin) is collected with a concentration of around 55% and in the second column with a concentration of 35%.

The aim of this work was to develop a model that described the behaviour of the above-presented absorption system. The model will be used together with a previously developed model of an industrial reactor for formaldehyde production by Braz et al. (2017) to simulate the entire formaldehyde production unit. The final process model will allow a better understanding of the system as a whole and find the optimal operating conditions that reduce waste and increase the production profitability.

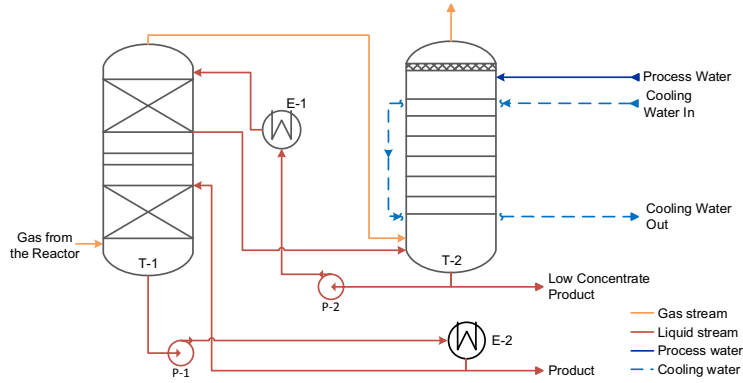


Figure 1 – Scheme of the industrial absorption system.

The design and optimization of formaldehyde absorbers is highly complex, mainly due to the reactions occurring in the liquid phase and the exothermicity of the process. According to Hasse & Maurer (1991), formaldehyde reacts with water to form methylene glycol by reaction (1).

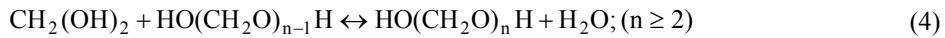


With kinetics:

$$r_1 = k_1 \left(C_F C_W - C_{WF_1} / K_1 \right) \quad (2)$$

$$K_1 = \left(\frac{C_{WF_1}}{C_F C_W} \right)_{eq} \quad (3)$$

Methylene glycol then polymerases to poly(oxymethylene) glycols by a series of reversible reactions, according to equation (4).



$$r_n = k_n \left(C_{FW_1} C_{FW_{n-1}} - C_{WF_n} C_W / K_n \right) \quad (5)$$

$$K_n = \left(\frac{C_{WF_n} C_W}{C_{WF_1} C_{WF_{n-1}}} \right)_{eq} \quad (6)$$

The good apparent solubility of formaldehyde in water is, in fact, the good solubility of methylene glycol, and the capacity of the solution to accommodate poly(oxymethylene) glycols. Like most gases, formaldehyde itself is only mildly soluble in water.

2. Model development

The rate-based stage model was chosen as the method to model the absorption columns. According to Kenig & Seferlis (2009), this approach is a more consistent modelling method when considering reaction and transport kinetics. The mass and energy balances for each phase were written separately for a stage, which represents either a tray or a

packed segment of a column unit. The differential equations were then numerically integrated for the total packed height. The mass transfer at the interface is described using the two-film model, Figure 2.

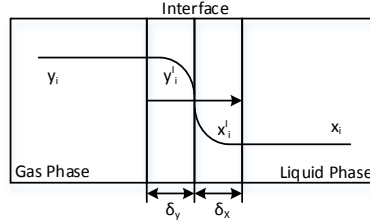


Figure 2 – Two_film model for the stage description.

The model major assumptions are: (1) The absorption system operates in steady-state; (2) A plug-flow regime is considered for both liquid and gas phase, i.e. there is no axial dispersion for mass and heat transfer; (3) The absorption column operates adiabatically; (4) The packing is fully wetted, i.e. the interfacial area is the same for mass and heat transfer; (5) There is only gas to liquid mass transfer of water and formaldehyde; (6) The liquid in the distributor above the bottom packing of column T-1 and at the bottom of both columns is ideally mixed and the heat and mass transfer between liquid and gas is negligible.

2.1. Differential balances in the gas and liquid phases

Considering the above assumptions, the mass balances for the components in the gas and liquid phases are defined by equations (7) and (8), respectively.

$$0 = -\frac{d}{dz}(y_i G) - N_{i,g} a^I A_c \quad \sum_i y_i = 1 \quad (7)$$

$$0 = \frac{d}{dz}(x_i L) + \left[N_{i,l} a^I + \phi_l \sum_{j=1}^{n_{\max}} \nu_{i,j} r_j \right] A_c \quad \sum_i x_i = 1 \quad (8)$$

Where, n_{\max} represents the largest polymer considered. The energy balances for the gas and liquid phases are:

$$0 = -\sum (y_i G C_{p,i,g}) \frac{dT_g}{dz} - q_g a^I A_c \quad (9)$$

$$0 = \sum (x_i L C_{p,i,l}) \frac{dT_l}{dz} + \left[q_{i,l} a^I + \phi_l \sum_{j=1}^{n_{\max}} r_j (-\Delta H_{R,j}) \right] A_c + Q_{\text{loss}} \quad (10)$$

In the case of column T-1 $Q_{\text{loss}} = 0$. For trays, the differential terms of equations (7) to (10) become finite differences and the balances are converted to ordinary differential equations. The correlations to calculate the holdup of the liquid, ϕ_l , were taken from Billet & Schultes (1993) for the packed sections and from Bennett et al. (1983) for the tray sections. Q_{loss} in column T-2 was taken from a previous master thesis by Branco (2014).

2.2. Equations for the film region

In the film region, the mass transport is normal to the interface and simultaneous with the reactions. The differential components balance is given by equation (11).

$$D_{i,l} \frac{d^2 C_i}{dx^2} = - \sum_j \nu_{i,j} r_j \quad (11)$$

$$x = 0 : C_i = C_{i,l}$$

$$x = \delta_l : N_{ix} = 0 \Rightarrow \frac{dC_i}{dz} = 0$$

2.3. Physical and chemical parameters

The mass transfer coefficients, $k_{i,g}$ and $k_{i,l}$, and the specific gas-liquid interfacial area, a^l , were calculated from the correlation taken from Onda et al. (1968) for packed columns and from AIChE (1958) for tray columns. The reaction rate and equilibrium constant for the hydration reaction (2) were taken from Winkelman (2003) and for the polymerization reaction (4), were taken from Hahnenstein et al. (1994) and Hahnenstein et al. (1995).

2.4. Vapour-liquid equilibria

The thermodynamic equilibrium at the gas-liquid interface was calculated by equation (12). Values for $\gamma_j P_i^s$ were taken from Winkelman (2003).

$$y_i P = \gamma_j P_i^s x_i, \quad i = F, W \quad (12)$$

2.5. Percentage of formaldehyde in the liquid

Since free formaldehyde is present in the liquid in traces quantities, the percentage of formaldehyde that is absorbed by the liquid is calculated by equation (13), considering an overall fraction of formaldehyde, \tilde{x}_F , that includes the formaldehyde converted in the formation of the methylene glycol and its polymerization, using equation (14).

$$W_F = \frac{\tilde{x}_F M_F}{\tilde{x}_F M_F + (1 - \tilde{x}_F) M_W} \quad (13)$$

$$\tilde{x}_F = \frac{x_F + \sum_{i=1}^{n_{\max}} i x_{WF_i}}{1 + \sum_{i=1}^{n_{\max}} i x_{WF_i}} \quad (14)$$

3. Results and discussion

The absorption system presented in Figure 1 was simulated using data supplied by the licensor of an industrial unit for formaldehyde production as input values of the model. The temperature and the formaldehyde mass percentage profiles are presented in Figure

3. Although these profiles were not yet compared with the real plant data, the simulation results are in agreement with what would be expected.

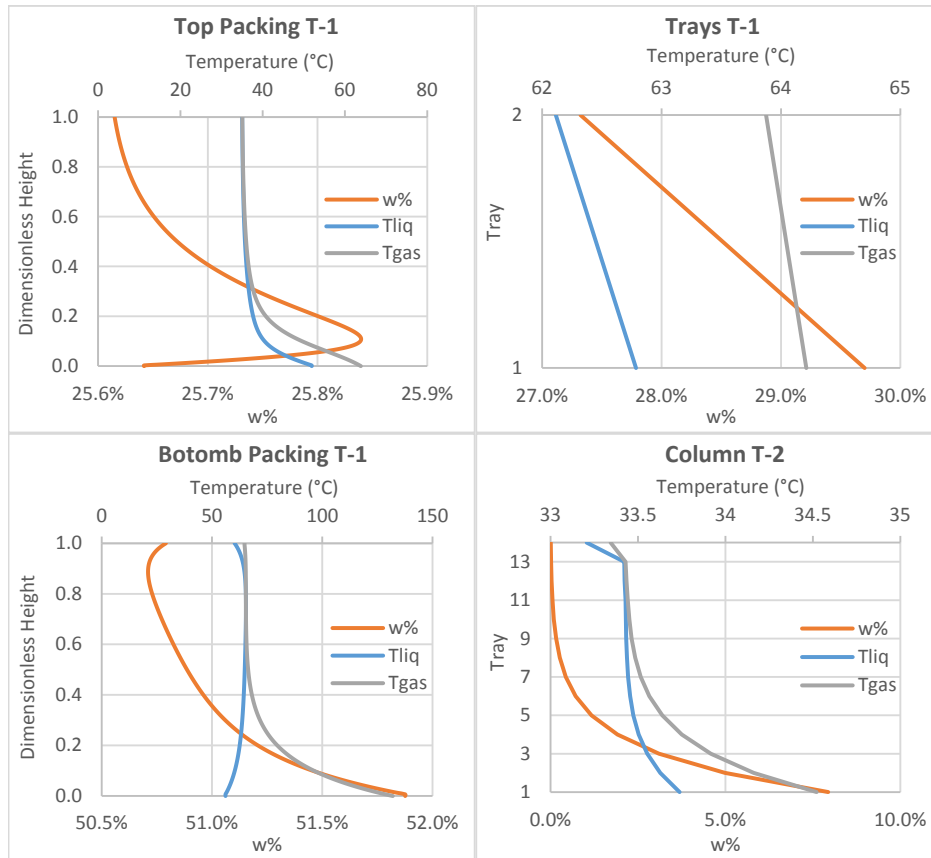


Figure 3 - Temperature and formaldehyde mass composition profiles of the absorption system.

Table 1 compares the simulation results with the typical values from the industrial unit and presents the absolute relative deviation between them, calculated by equation (15). Note that the T_{liq} from the bottom of column T-2 is not the temperature of the liquid after the first tray, but the temperature after mixing with the liquid coming from the top packing of column T-1. The simulation results are in general within the typical ranges of the plant operation values, presenting absolute relative deviations below 6.5%.

$$\varepsilon_{rel} = \frac{|x_{operational} - x_{simulation}|}{x_{operational}} \times 100 \quad (15)$$

Table 1 – Simulation results compared with the typical operational values.

	Typical operational values	Simulation	ε_{rel} (%)
W% bottom of T-1	50-58	51.9	5.8
T_{liq} bottom of T-2 (°C)	52-56	51.9	3.9
T_{gas} top of T-2 (°C)	22-38	33.2	6.4
% of Recovered HCHO	98-100	100	1

4. Conclusions

In this work, a first model of a formaldehyde absorption system was developed in *gPROMS*[®] and the simulation results were compared with typical operational data. The simulation results are in agreement with the operational data with absolute relative deviations below 6.5%. The compositions and temperature profiles of the absorption columns obtained by the model will be posteriorly validated using results from the industrial unit.

In future work, the authors intend to include the absorption and reaction of methanol in water and use the final model in the simulation and optimization of the complete formaldehyde production unit.

Acknowledgements

The authors greatly acknowledge EuroResinas and FCT support through the project UID/ECI/04028/2013 and the PhD grant number PD/BDE/113539/2015.

References

- AIChE, 1958, Bubble Tray Design Manual: Prediction of Fractionation Efficiency.
- D.L. Bennett, R. Agrawal, P.J. Cook, 1983, New pressure drop correlation for sieve tray distillation columns. *AIChE Journal*, 29, 3, 434–442.
- R. Billet, M. Schultes, 1993, Predicting mass transfer in packed columns. *Chemical Engineering & Technology*, 16, 1, 1–9.
- N. Branco, 2014, Aumento da Rentabilidade da Fábrica de Formaldeído. Instituto Superior Técnico.
- C.G. Braz et al., 2017, Model of an Industrial Multitubular Reactor for Methanol to Formaldehyde Oxidation in the Presence of Catalyst Deactivation.
- I. Hahnenstein et al., 1994, 1H- and 13C-NMR Spectroscopic Study of Chemical Equilibria in Solutions of Formaldehyde in Water, Deuterium Oxide, and Methanol. *Industrial & Engineering Chemistry Research*, 33, 1022–1029.
- I. Hahnenstein et al., 1995, NMR Spectroscopic and Densimetric Study of Reaction Kinetics of Formaldehyde Polymer Formation in Water, Deuterium Oxide, and Methanol. *Industrial & Engineering Chemistry Research*, 34, 440–450.
- H. Hasse, G. Maurer, 1991, Kinetics of the Poly(oxymethylene) Glycol Formation in Aqueous Formaldehyde Solutions. *Industrial & Engineering Chemistry Research*, 30, 2195–2200.
- E. Kenig, P. Seferlis, 2009, Modeling reactive absorption. *Chemical Engineering Progress*, 105, 1, 65–73.
- K. Onda, H. Takeuchi, Y. Okumoto, 1968, Mass transfer coefficients between gas and liquid phases in packed columns. *Journal of Chemical Engineering of Japan*, 1, 1, 56–62.
- J.G.M. Winkelman, 2003, Absorption of formaldehyde in water. University of Groningen.

A multi-fluid approach to simulate separation of liquid-liquid systems in a gravity settler

Anurag Misra^{a,*}, Cyrille Bonamy^b, Luís M. de Souza^a, Lena Hohl^b, Markus Illner^c, Matthias Kraume^b, Jens-Uwe Repke^c and Dominique Thévenin^a

^a*Lab. of Fluid Dynamics and Technical Flows, University of Magdeburg "Otto von Guericke", Universitätsplatz 2, Magdeburg, D-39106, Germany*

^b*Laboratoire des Écoulements Géophysiques et Industriels, Université Grenoble Alpes, 38058 Grenoble Cedex 9, France*

^c*Process Dynamics and Operations Group, Technische Universität Berlin, Straße des 17. Juni 135, Sek. KWT-9, D-10623 Berlin, Germany*

^b*Chair of Chemical and Process Engineering, Technische Universität Berlin, Ackerstraße 76, D-13355 Berlin, Germany*

anurag.misra@ovgu.de

Abstract

Industrial processes employing homogeneous catalysis face the difficulty of an economic recovery of the catalyst. In order to be able to design an optimal process route, a comprehensive understanding of the separation process is essential. In this work, the gravity-driven separation of a multi-phase system composed of water, 1-dodecene, and a non-ionic surfactant, is investigated. Within the employed ranges of temperature and phase composition, this system exists in a three-phase configuration, consisting of an aqueous, an organic, and a surfactant-rich middle phase. Following the reaction step, a complete separation of the aqueous phase, in which the expensive rhodium catalyst is dissolved, is essential. Extensive experiments have been carried out to determine the drop size distribution (DSD) of the disperse phases using an endoscopic measurement technique. Based on these experimental data, a Computational Fluid Dynamics (CFD) model employing the Euler-Euler multi-fluid framework coupled with the Extended Quadrature Method of Moments (EQMOM) for the solution of the population balance equations (PBEs) for each disperse phase is implemented using OpenFOAM. Within the framework of this CFD-PBE model, a buoyancy-induced coalescence model, which has been previously shown to accurately predict the degree of separation, has been employed. This multi-fluid CFD-PBE model has been used for simulating the separation of the three-phase system in a double-wall glass tank. The time-evolution of observed phase heights is used to fit the model parameters of the coalescence kernel. Subsequently, this numerical model has been used for simulating the gravity-driven separation in a horizontal settler equipped with a coalescer. The predictions of this numerical model are in good agreement with the experimentally observed values.

Keywords: gravity separation, population balance, method of moments, coalescer, multi-fluid

1. Introduction

Hydroformylation is an important industrial process for the conversion of long-chain alkenes to aldehydes. In this process, homogeneous catalysis is often employed due to its better performance and higher selectivity (Fang et al., 2011). However, this process path is also accompanied by

the problem of catalyst leaching which can make the process economically impracticable (Müller et al., 2015). The choice of recovery methods is also of essence since severe process conditions may be detrimental to the catalyst efficiency as well as to the environment (Peddie et al., 2017). A gravity-driven separation process is often employed in such cases owing to its simplicity and low cost of operation (Panda et al., 2017). In this light, an understanding of the separation process in general, and coalescence in particular, is critical to design an optimal process route. In recent years, there have been multiple investigations of drop coalescence in separating liquid-liquid systems (Frising et al., 2006; Liao and Lucas, 2010; Kamp and Kraume, 2016). Noik et al. (2013) reported the combined coalescence and sedimentation characteristics of a water-in-oil emulsion under the effect of gravity. In addition, a one-parameter model based on batch-settling data was also proposed for the process. However, the model assumes a mono-size droplet distribution as an initial condition. More recently, Mazumdar et al. (2017) investigated the effects of phase composition and surfactant concentration on the gravity-driven separation kinetics of oil-water emulsions. They reported the time-evolution of drop-size distributions in different layers of the emulsion and concluded that the concentration of surfactant in the system greatly influenced the coalescence mechanism. Panda et al. (2017) studied three-phase flow in a continuously-operated gravity settler with the help of Computational Fluid Dynamics. They reported a reduction in the thickness of the dispersion layer with increasing droplet diameter. However, their model only considered a constant droplet diameter for each dispersed phase.

The use of CFD coupled with the population balance equation (PBE) is an effective method in the solution of dispersed multiphase flows (Favero et al., 2015). Of the multiple available solution algorithms for PBE, the method of moments is perhaps the most frequently utilized one. Such moment-based methods convert the PBE to a set of transport equations of integral moments of the associated number density function. Thus, transport equations for just the moments are solved rather than for the full distribution. However, an additional closure condition is required in most practical cases for which a quadrature method of moments (QMOM) is often employed (McGraw, 1997; Marchisio et al., 2003). A number of quadrature-based moment methods (QBMMs) have been proposed in recent literature, for example Sectional Quadrature Method of Moments, SQ-MOM (Attarakih et al., 2009) and Extended Quadrature Method of Moments, EQMOM (Yuan et al., 2012). In particular, EQMOM is a notable method as it improves upon traditional QMOM by utilizing a continuous function instead of a Dirac delta function in the quadrature approximation which results in greater robustness as well as computational efficiency (Pigou et al., 2017).

In the present work, the separation process of a non-ionic surfactant containing water-oil emulsion is investigated through a coupled CFD-PBE Eulerian multi-fluid approach. Within the employed ranges of temperature and surfactant concentration, this mixture exists as a three-phase system consisting of an organic, an aqueous and a surfactant-rich (bicontinuous) middle layer (Hohl et al., 2016). This specific configuration is of particular interest as the presence of a distinct bicontinuous phase allows for better separation, as well as faster separation times. The open source CFD toolbox OpenFOAM 4.1 (Weller et al., 1998) has been used to simulate flow behavior in addition to an EQMOM-based PBE solution for each Eulerian dispersed phase (OpenQBMM, 2016). A buoyancy-driven coalescence model based on the one proposed by Prince and Blanch (1990) has been used to model droplet-droplet interactions. The results obtained using this approach seem promising and a good agreement with experimental data can be achieved, as discussed later. This multi-fluid framework makes it possible to simulate multiphase flows with independently-evolving drop-size distributions. The ultimate intention of the present work is to enhance our knowledge of gravity-driven separation processes in emulsion systems.

2. Multiphase model

The employed multiphase model is based on the solution of averaged mass and momentum transport equations for, both, continuous (organic) as well as dispersed (bicontinuous, aqueous) Eu-

lerian phases as shown in Eqs. (1) and (2), respectively. This means that each phase i , having a density ρ_i , viscosity μ_i and volume fraction α_i , has its own unique velocity \vec{u}_i . As opposed to the Euler-Lagrangian approach, the Euler-Euler multi-fluid method has the advantage of lower computational cost. The efficiency is especially noticeable for simulations with higher dispersed phase fraction. At the same time, however, a choice of appropriate closure terms is critical. In the present study, the effects of drag, surface tension and porous medium are included in the momentum equation as additional terms $\vec{F}_{D,i}$, $\vec{F}_{S,i}$ and $\vec{F}_{P,i}$, respectively. Surface tension is assumed to be constant and drag forces on the dispersed phase are calculated based on the model of Schiller and Naumann. A more detailed description of the model parameters can be found in our previous work (Misra et al., 2017).

$$\frac{\partial}{\partial t}(\alpha_i) + \vec{u}_i \cdot \nabla \alpha_i = 0, \quad i = 1 \dots N_{phase} \quad (1)$$

$$\frac{\partial}{\partial t}(\rho_i \alpha_i \vec{u}_i) + (\rho_i \alpha_i \vec{u}_i \cdot \nabla) \vec{u}_i = -\alpha_i \nabla p + \nabla \cdot (\mu_i \alpha_i \nabla \vec{u}_i) + \rho_i \alpha_i \vec{g} + \vec{F}_{D,i} + \vec{F}_{S,i} + \vec{F}_{P,i} \quad (2)$$

An additional set of moment transport equations given by Eq. (3) for each dispersed phase are also solved. EQMOM is used in order to close the source term \vec{S}_i^k on the right hand side of the equation. As Marchisio et al. (2003) have noted, the use of two quadrature nodes to describe the time evolution of the drop-size distribution is usually sufficient. Thus, transport equations for the first k integral moments of the distribution m^k have been solved in the present case. The initial values of the moments have been obtained from experimental data of Hohl et al. (2016). Moreover, a buoyancy-driven coalescence kernel $\beta(d, d')$ as given by Eq. (4) has been used to describe droplet-droplet interactions in each dispersed phase (Prince and Blanch, 1990; Misra et al., 2017). This approach models binary coalescence of droplets with diameters d and d' approaching each other with a relative velocity u_{rel} . The relative velocity of approach can be obtained based on the Sauter mean diameter and the velocity of the dispersed phase. The term u_{crit} is the only model parameter and can be determined from batch experiments (Noïk et al., 2013).

$$\frac{\partial}{\partial t}(m_i^k) + \nabla \cdot (m_i^k \vec{u}_i) = \vec{S}_i^k, \quad i = 2 \dots N_{phase}; k = 0 \dots 2N_{node} \quad (3)$$

$$\beta(d, d') = \left[\frac{\pi}{4} (d + d')^2 u_{rel} \right] \exp \left[\frac{-u_{rel}}{u_{crit}} \right] \quad (4)$$

2.1. Implementation in OpenFOAM

The OpenFOAM solver *multiphaseEulerFoam* (Wardle and Weller, 2013) already provides a multi-fluid Eulerian framework. Moreover, the OpenQBMM library (OpenQBMM, 2016; Passalacqua et al., 2018) implements solution of moment transport equations for OpenFOAM using QMOM as well as EQMOM closures. However, to the best knowledge of the authors, a coupled implementation of the two methods in a multiphase system has not yet been released. In order to implement the aforementioned model, the class *phaseModel* in *multiphaseEulerFoam* was modified to include a member function of the type *populationBalanceModel*. This ensures that the OpenQBMM library utilizes the phase velocity for transport of quadrature nodes using the buoyancy-driven coalescence kernel as defined by Eq. (4). Coupling between the two algorithms is achieved by adding a new member function to the *diameterModel* class which evaluates the Sauter mean diameter of the dispersed phase as a ratio of the third and second moments of the distribution. In order to ensure a physical solution, user-defined upper and lower limits have been set on the calculated diameter values. Finally, a source term is appended to the file *UEqns.H* through the *fvOptions* framework which enables a run-time selection of sources or constraints on the momentum transport equations. In this manner, the effect of porous media on flow based on the Darcy-Forchheimer relation has been included in the solver. The mesh non-orthogonality has a significant influence on the

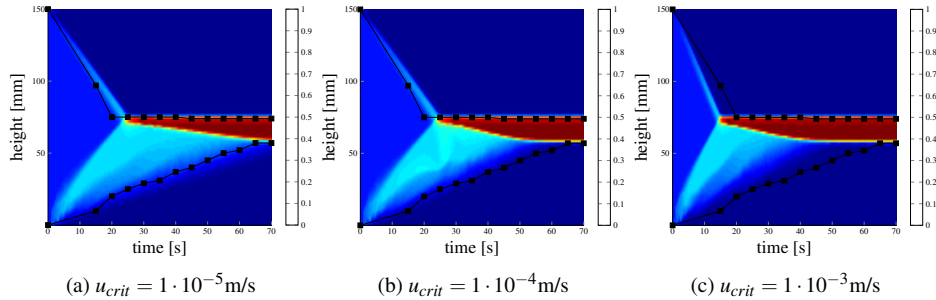


Figure 1: History of phase separation in time, starting from homogeneous conditions. Experimentally-measured phase boundaries (black lines) and computed volume fraction of the bicontinuous phase (color plot).

quality of the solution, regardless of the number of grid points in the mesh. Further, the choice of the time step size is also critical as the moment transport equations impose an additional stability restriction.

3. Results

3.1. Calibration of the buoyancy-driven coalescence kernel

Preliminary experiments to calibrate the model parameter u_{crit} were carried out in a double walled glass tank (DN 150, $H/D = 1$). Starting with a completely mixed system ($t = 0$), the initial drop-size distribution as well as the change in phase heights with time was recorded. A two-dimensional CFD-PBE simulation for the same configuration was performed, and a best-fit value of the parameter u_{crit} has been determined by repeating the simulations for different values of u_{crit} . The range of values considered for u_{crit} has been based on similar approaches reported in literature. In this manner, a good fit of the predicted separation profile with experimental data could be obtained with $u_{crit} = 10^{-5}$ m/s. While it is possible to fit u_{crit} for each phase independently, a single value for both dispersed phases has been set. Since the coalescence kernel only accounts for phase properties in an indirect manner (Misra et al., 2017) and the rheological properties of the bicontinuous and aqueous phases are similar, this is a reasonable assumption to make. Fig. 1 shows a comparison of the predicted phase separation profile of the bicontinuous phase (color) using 3 different u_{crit} values with experimentally observed phase boundaries (black lines). It is noteworthy that a ten-fold change in u_{crit} results only in a relatively small change in the predicted phase separation profile of the organic phase. At the same time, an influence on the separation characteristics of the dispersed phases is evident. However, a hundred-fold increase in u_{crit} leads to a noticeable change in the predicted separation time of the the organic phase as well.

3.2. Simulation of separation in a horizontal settler

Following the determination of u_{crit} , the solver is used to simulate separation in a continuously-operated settler. The real settler is modular and has one inlet for the reaction mixture, and three outlets for the separated products as depicted in Fig. 2. The initial condition is a completely mixed system with a fixed inlet flow rate and a Neumann boundary condition at the outlets. In a previous work, a simplification of the settler with only two outlets was investigated (Misra et al., 2017) and is, therefore, also presented here for a comparison. In the following discussion, the terms "top" and "bottom" outlets refer to the common outlets in both settler geometries. Figures 2a and 2b show the volume fractions of the bicontinuous phase in the settler at $t = 4$ s and $t = 7$ s, respectively. Unlike the top and bottom outlets, the third outlet begins in the center of the settler.

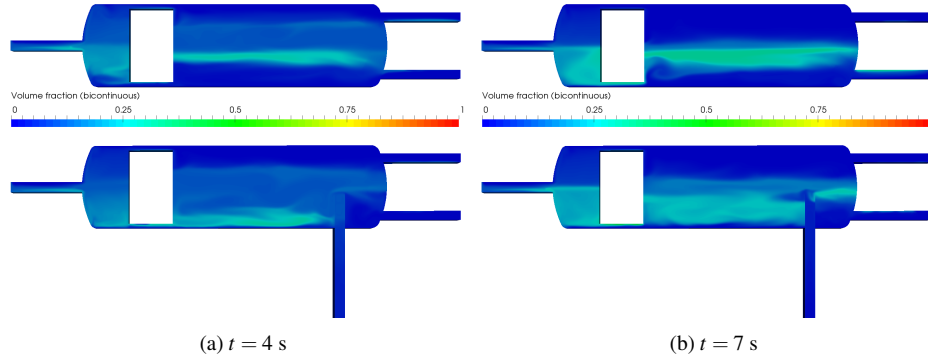


Figure 2: Volume fraction of the bicontinuous phase at different times in two different settler geometries as predicted by the buoyancy-driven coalescence kernel (color plot).

As is evident from the figure, the inclusion of a third outlet pipe in the settler geometry changes the separation profile inside the settler. This is expected as the pipe acts as an internal baffle. However, Figure 3 enunciates that this observed difference inside the settler does not affect the predicted volume fractions of the aqueous and bicontinuous phases at the bottom outlet. Moreover, the predictions of the model in both the cases are quite close to the experimentally observed values.

Although the employed coalescence kernel only approximates the several competing physical phenomena affecting droplet coalescence with the aid of a single lumped parameter, it is still able to predict the separation remarkably well. However, as can be observed in Figure 3, the model tends to slightly overestimate the degree of separation. But this is an acceptable drawback of using a single-parameter coalescence kernel. Since the presence present coalescence kernel does not account for the effects of surfactant concentration and temperature on separation, its direct application to a wide range of operating conditions is limited. An extension of the present model based on further experiments is planned for future work.

4. Conclusions

In this contribution, a multi-fluid CFD-PBE framework has been implemented in OpenFOAM to describe the gravity-driven separation process in a three-phase system. A buoyancy-driven coalescence kernel is used to describe droplet-droplet interactions in each dispersed phase. The effect of surfactant on coalescence has been incorporated in the lumped model parameter u_{crit} . This parameter is set to 10^{-5} m/s for both dispersed phases, based on the best-fit of preliminary investigations of batch separation experiments in a cell. Subsequently, this numerical model is used to simulate three-phase flow in a continuously operated horizontal settler. The predictions obtained from the model are in good agreement with the experimental observations. While the

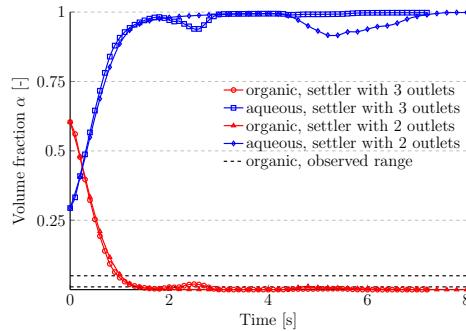


Figure 3: Time-evolution of volume fractions of organic and aqueous phases at the bottom outlet of the settler. The two horizontal dashed lines represent the upper and lower bounds of the organic phase volume fraction observed experimentally during the measurement campaign and are not associated with the time axis (color plot).

proposed framework is flexible, the choice of coalescence kernel still plays a critical role. In the present work, the employed one-parameter coalescence kernel has the advantage of reducing the model complexity. At the same time, it also prevents the model from being applicable to a wider range of operating conditions. A generally-valid coalescence model should take into account the effects of local surfactant concentration and temperature. Thus, further work on coalescence modeling is essential to explicitly incorporate the effects of phase properties as well as process conditions.

Acknowledgments: This work is part of the Collaborative Research Centre Integrated Chemical Processes in Liquid Multiphase Systems (TRR 63). The financial support by the German Research Foundation (DFG) is gratefully acknowledged.

References

- M. M. Attarakih, C. Drumm, H.-J. Bart, 2009. Solution of the population balance equation using the sectional quadrature method of moments (SQMOM). *Chem. Eng. Sci.* 64 (4), 742 – 752.
- J. Fang, R. Jana, J. A. Tunge, B. Subramaniam, 2011. Continuous homogeneous hydroformylation with bulky rhodium catalyst complexes retained by nano-filtration membranes. *Applied Catalysis A: General* 393 (1), 294 – 301.
- J. L. Favero, L. F. L. Silva, P. L. Lage, 2015. Modeling and simulation of mixing in water-in-oil emulsion flow through a valve-like element using a population balance model. *Comput. Chem. Eng.* 75, 155 – 170.
- T. Frising, C. Nořk, C. Dalmazzone, 2006. The liquid/liquid sedimentation process: From droplet coalescence to technologically enhanced water/oil emulsion gravity separators: A review. *J. Dispersion Sci. Technol.* 27 (7), 1035–1057.
- L. Hohl, J. Schulz, N. Paul, M. Kraume, 2016. Analysis of physical properties, dispersion conditions and drop size distributions in complex liquid/liquid systems. *Chem. Eng. Res. Des.* 108, 210–216.
- J. Kamp, M. Kraume, 2016. From single drop coalescence to droplet swarms scale-up considering the influence of collision velocity and drop size on coalescence probability. *Chem. Eng. Sci.* 156, 162 – 177.
- Y. Liao, D. Lucas, 2010. A literature review on mechanisms and models for the coalescence process of fluid particles. *Chem. Eng. Sci.* 65 (10), 2851–2864.
- D. L. Marchisio, R. Vigil, R. O. Fox, 2003. Quadrature method of moments for aggregation-breakage processes. *J. Colloid Interface Sci.* 258 (2), 322–334.
- M. Mazumdar, A. S. Jammoria, S. Roy, 2017. Effective rates of coalescence in oil-water dispersions under constant shear. *Chem. Eng. Sci.* 157, 255 – 263.
- R. McGraw, 1997. Description of aerosol dynamics by the quadrature method of moments. *Aerosol Sci. Technol.* 27 (2), 255–265.
- A. Misra, L. de Souza, M. Illner, L. Hohl, M. Kraume, J.-U. Repke, D. Thévenin, 2017. Simulating separation of a multiphase liquid-liquid system in a horizontal settler by cfd. *Chem. Eng. Sci.* 167, 242 – 250.
- D. Müller, E. Esche, T. Pogrzeba, M. Illner, F. Leube, R. Schomäcker, G. Wozny, 2015. Systematic phase separation analysis of surfactant-containing systems for multiphase settler design. *Ind. Eng. Chem. Res.* 54 (12), 3205–3217.
- C. Nořk, T. Palermo, C. Dalmazzone, 2013. Modeling of liquid/liquid phase separation: Application to petroleum emulsions. *J. Dispersion Sci. Technol.* 34 (8), 1029–1042.
- OpenQBMM, 2016. OpenQBMM 2.0.0 stable for OpenFOAM 4.x.
URL https://github.com/OpenQBMM/OpenQBMM/releases/tag/OpenQBMM_2.0.0_stable
- S. K. Panda, K. Singh, K. Shenoy, V. V. Buwa, 2017. Numerical simulations of liquid-liquid flow in a continuous gravity settler using OpenFOAM and experimental verification. *Chem. Eng. J.* 310, Part 1, 120–133.
- A. Passalacqua, F. Laurent, E. Madadi-Kandjani, J. Heylmun, R. Fox, 2018. An open-source quadrature-based population balance solver for openfoam. *Chem. Eng. Sci.* 176, 306 – 318.
- W. L. Peddie, J. N. van Rensburg, H. C. Vosloo, P. van der Gryp, 2017. Technological evaluation of organic solvent nanofiltration for the recovery of homogeneous hydroformylation catalysts. *Chem. Eng. Res. Des.* 121, 219 – 232.
- M. Pigou, J. Morchain, P. Fede, M.-I. Penet, G. Laronze, 2017. An assessment of methods of moments for the simulation of population dynamics in large-scale bioreactors. *Chem. Eng. Sci.* 171, 218 – 232.
- M. J. Prince, H. W. Blanch, 1990. Bubble coalescence and break-up in air-sparged bubble columns. *AIChE J.* 36 (10), 1485–1499.
- K. E. Wardle, H. G. Weller, 2013. Hybrid multiphase CFD solver for coupled dispersed/seggregated flows in liquid-liquid extraction. *Int. J. Chem. Eng.* 2013, 1–13.
- H. G. Weller, G. Tabor, H. Jasak, C. Fureby, 1998. A tensorial approach to computational continuum mechanics using object-oriented techniques. *Computers in Physics* 12 (6), 620–631.
- C. Yuan, F. Laurent, R. Fox, 2012. An extended quadrature method of moments for population balance equations. *J. Aerosol Sci.* 51, 1 – 23.

Comparative Life Cycle Assessment of Ethylene from Wet Shale Gas and Biomass

Minbo Yang, Xueyu Tian, Fengqi You

Cornell University, Ithaca, New York, 14853, USA

Abstract

This paper presents comparative techno-economic and environmental analyses of three ethylene manufacturing pathways based on wet shale gas, corn stover, and corn grain. A distributed-centralized processing network that consists of distributed ethane/bioethanol production and centralized ethylene manufacturing is employed for each of the three pathways. Based on the detailed mass and energy balances and life cycle inventory results, we conduct techno-economic and life cycle analyses to systematically compare the economic and environmental performances of the three pathways. The results indicate that the shale gas-based pathway is the most attractive due to the lowest breakeven ethylene prices; however, it leads to the highest greenhouse gas emissions. On the contrary, the corn stover-based pathway results in the lowest greenhouse gas emissions but the highest breakeven ethylene prices.

Keywords: shale gas, corn stover, corn grain, breakeven price, greenhouse gas emissions.

1. Introduction

Ethylene is the most important building block for the chemical industry (Zimmermann and Walzl, 2009). In recent decades, advancements of hydraulic fracturing and horizontal drilling have resulted in a boom of the U.S. shale gas production (Gao and You, 2017), which provides a tremendous increase in the yield of ethane for ethylene production (DeRosa and Allen, 2015). Taking into account the non-renewability of fossil fuel-based feedstocks for ethylene production, dehydration of bioethanol derived from renewable biomass demonstrates significant potential for ethylene production (Zhang and Yu, 2013). In the U.S., corn grain serves as the leading feedstock for bioethanol production. Besides, producing bioethanol from cellulosic biomass, such as corn stover, is of increasing interest, as corn stover not only is an abundant agricultural residue but also can avoid controversies over food versus energy (Ou et al., 2014). Based on the aforementioned feedstocks, manufacturing ethylene may result in different economic performances and environmental impacts (He and You, 2015). For judicious selection of feedstocks for ethylene production, it is necessary to systematically compare ethylene manufacturing from these feedstocks under the same conditions from economic and environmental perspectives.

In this work, we perform comparative techno-economic and environmental life cycle analyses for three ethylene production pathways. We consider a distributed-centralized processing network that combines distributed ethane/bioethanol production with centralized ethylene manufacturing for the three pathways. High-fidelity process simulation models are developed for processing steps including shale gas processing,

ethane steam cracking to ethylene, and bioethanol dehydration to ethylene. The three ethylene production pathways are modeled considering five different ethylene production scales. Next, we conduct techno-economic and environmental life cycle analyses for the three ethylene production pathways. The economic performances of the three ethylene production pathways are compared in terms of breakeven ethylene prices. The life cycle environmental impacts of ethylene manufactured via the three pathways are compared in terms of GHG emissions, which are of special interest in both academia and industry.

2. Distributed-centralized ethylene manufacturing

Figure 1 and Figure 2(a) and (b) illustrate the block flow diagram for ethylene production based on wet shale gas, corn stover and corn grain, respectively.

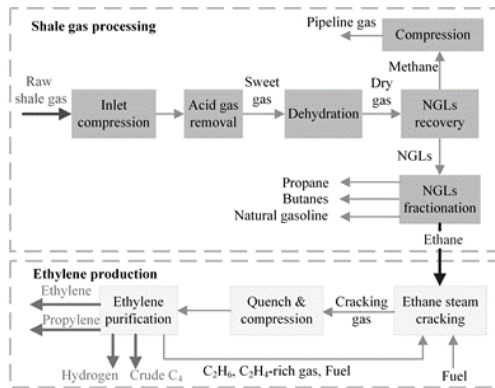


Figure 1. Block flow diagram for manufacturing ethylene from wet shale gas

2.1. Shale gas-based ethylene production

In the shale gas processing step, raw shale gas is first pressurized to satisfy the downstream operating conditions and maximize the recovery of natural gas liquids (NGLs) (Kidnay et al., 2011). The pressurized shale gas is then introduced into an acid gas removal unit to remove acid components. In the following dehydration unit, the water content in shale gas is reduced to prevent hydrate formation. Next, the obtained dry gas is sent to a cryogenic separation unit to recover NGLs (Gong et al. 2017). The resulting methane-rich gas is compressed and sent out as pipeline gas. The recovered mixture of NGLs is fractionated into ethane, propane, butanes, and natural gasoline in an NGLs fractionation unit (He and You, 2014). In the ethylene production step, ethane derived from shale gas is cracked in cracking furnaces first. The cracking gas from furnaces is then quenched and pressurized. Finally, in an ethylene purification unit, the cracking gas is separated into ethylene, ethane, and other byproducts (Yang and You, 2017).

2.2. Corn stover-based ethylene production

This process consists of two processing steps: bioethanol production from corn stover and ethylene production from bioethanol. In the bioethanol production step, corn stover is first delivered to a feed handling unit consisting of weighing and uploading stations, queuing storage, and conveyors. In the following pretreatment and conditioning unit, corn stover is pretreated with dilute sulfuric acid to liberate hemicellulose sugars and

break down biomass, and ammonia is then added to the pretreated slurry to adjust its acidity to be suitable for enzymatic hydrolysis. Next, the resulting hydrolysate is sent to an enzymatic hydrolysis and fermentation unit, where a cellulase enzyme is used for enzymatic hydrolysis. The hydrolyzed slurry is then fermented to convert cellulose and xylose into bioethanol. The required cellulase enzyme is produced on-site in an enzyme production unit using glucose as the primary carbon source. In a production recovery section, the resulting beer is separated into bioethanol, water, and residual solids via distillation and solid-liquid separation. Wastewater streams generated during bioethanol production are gathered and treated by anaerobic and aerobic digestion in a wastewater treatment unit. Solids and biogas from product recovery unit and wastewater treatment unit are combusted to produce HP steam, which is used to generate electricity and satisfy the process heat demand. Detailed process flowsheets for the production of bioethanol from corn stover are available in the literature (Humbird et al., 2011). In the ethylene production step, bioethanol derived from corn stover is first dehydrated into ethylene, water, and other byproducts. Next, the dehydration reactor effluent is quenched and pressurized. Finally, the effluent is sent to an ethylene purification unit, where it is separated into ethylene, water, and others.

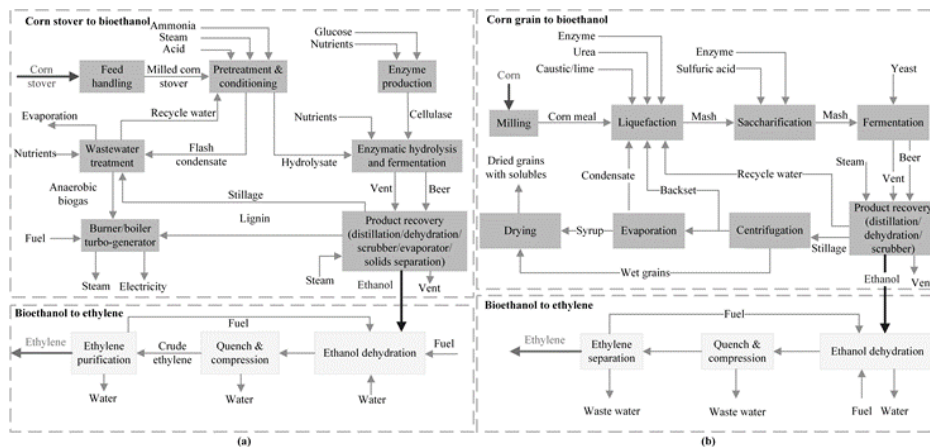


Figure 2. Block flow diagram for manufacturing ethylene from biomass

2.3. Corn grain-based ethylene production

In the bioethanol production step, corn is first conveyed to grain-cleaning equipment and then milled to fine meal by hammer mills. Next, the corn meal is sent to a liquefaction unit, where it is mixed with water and alpha-amylase. Also, caustic and lime are added to provide suitable acidity and calcium for the alpha-amylase, and urea is consumed to supply nitrogen for the downstream yeast fermentation. Maltose and higher oligomers are produced from corn starch using the alpha-amylase enzyme in the liquefaction unit. The resulting mash is introduced into a saccharification unit and mixed with gluco-amylase and sulfuric acid to create sugars. After saccharification, the mash is cooled and then fed to four continuous cascade fermenters with yeast added. Bioethanol and carbon dioxide are produced during the yeast fermentation. In a product recovery unit, bioethanol is obtained from the whole beer by distillation, scrub, and dehydration. The conserved stillage is partially evaporated and then fed to a centrifugation unit. A part of the thin stillage from the centrifugation unit is recycled as backset to the liquefaction unit, and the rest is concentrated to syrup in the following

evaporation unit. Finally, the wet grains from the centrifugation unit and the syrup from the evaporation unit are dried and sent out as distiller's dried grains with solubles (DDGS). Detailed information for the production of bioethanol from corn grain can be found in the literature (Wallace et al., 2005). The ethylene production step in the corn grain-based pathway is the same as that in the corn stover-based pathway described in the previous subsection.

2.4. Distributed-centralized processing network for ethylene production

We consider the distributed-centralized processing network as in He and You (2016) for shale gas and in You and Wang (2011) for biomass processing, we assume that ethane is first produced at several distributed shale gas processing plants and transported to a centralized ethane cracking plant by trucks. In the typical shale gas production process, multiple shale gas wells are drilled at a well pad. Raw shale gas extracted from shale gas wells is gathered at a well pad and transported to a nearby gas processing plant by pipelines. The distributed-centralized processing network is also employed for manufacturing ethylene from corn stover and corn grain. Bioethanol is first produced at several distributed ethanol plants, and then transported to a centralized ethylene plant by trucks. The average transportation distances for the upstream feedstocks are calculated based on the distributed-centralized processing network. The average transportation distances for the downstream feedstocks are assumed to be 100 km.

3. Techno-economic and life cycle analyses results

For systematic comparisons, we consider five different ethylene production scales for each pathway, namely, 1,000 kt/y, 800 kt/y, 600 kt/y, 400 kt/y, and 200 kt/y, according to commercial capacities of ethylene plants. In terms of the distributed ethane/bioethanol production, on each ethylene production scale, three cases are analyzed considering different numbers of distributed shale gas processing/bioethanol plants, i.e. 5, 10, and 15. Therefore, 45 ethylene production cases are investigated in this work.

3.1. Economic analysis

The breakeven prices of ethylene manufactured via the shale gas-based pathway, corn stover-based pathway, and corn grain-based pathway are evaluated and compared in Figure 3. For each of the three ethylene production pathways, the breakeven ethylene price increases as the ethylene production scale decreases and the number of distributed shale gas processing/bioethanol plants increases. On each ethylene production scale, the shale gas-based pathway results in the lowest breakeven ethylene prices. The breakeven prices of ethylene produced via the corn grain-based pathway are notably higher than that of ethylene produced via the shale gas-based pathway by 21%~284%. The corn stover-based pathway leads to the highest breakeven ethylene prices, which are 2.4~6.3 times of the breakeven prices of ethylene produced via the shale gas-based pathway. Also, we find that the breakeven ethylene prices of ethylene manufactured via both the corn stover-based pathway and the corn grain-based pathway are higher than the market ethylene price. This means that the corn stover-based pathway and the corn grain-based pathway have no economic advantage for ethylene production currently. On large ethylene production scales, the shale gas-based pathway could result in lower breakeven ethylene prices than the market ethylene price. Such results indicate that manufacturing ethylene from ethane-rich shale gas on large scales is cost-effective. In summary, the shale gas-based pathway is more competitive than from both the corn stover-based pathway and the corn grain-based pathway regarding the breakeven ethylene prices.

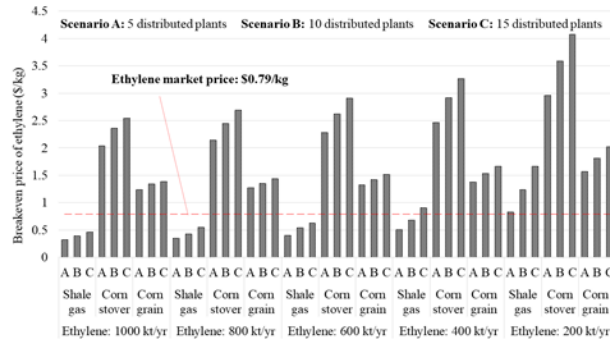


Figure 3. Breakeven prices of ethylene manufactured from ethane-rich shale gas, corn stover, and corn grain.

3.2. Environmental analysis

The environmental impacts of manufacturing ethylene from ethane-rich shale gas, corn stover, and corn grain are systematically analyzed following the LCA approach. The objective of this LCA study is to evaluate and compare the life cycle environmental impacts of ethylene manufactured via the shale gas-based pathway, corn stover-based pathway, and corn grain-based pathway. The functional unit of this LCA study is defined as 1 kg of ethylene manufactured at the plant gate. The impact category to assess the life cycle environmental performance of manufacturing ethylene via the three pathways is dedicated to GHG emissions. The environmental burdens are allocated using the economic value-based allocation method.

Regarding each of the three pathways, differences among the net GHG emissions of ethylene produced on different scales are insignificant, as illustrated in Figure 4. This is because the GHG emissions contributed by feedstock transportation are negligible compared with the total GHG emissions across the product life cycle. The net GHG emissions of ethylene produced via the shale gas-based pathway are positive. In comparison, the corn stover-based pathway and the corn grain-based pathway could result in negative net GHG emissions of ethylene, due to the sequestration of renewable carbon. Such results indicate that the corn stover-based pathway and the corn grain-based pathway are more advantageous over the shale gas-based pathway for ethylene production in terms of the net GHG emissions.

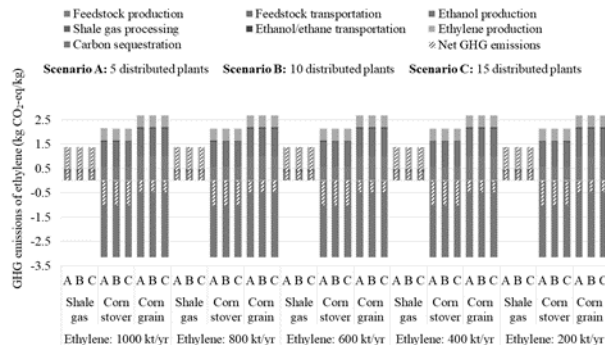


Figure 4. Life cycle greenhouse gas emissions of ethylene manufactured from shale gas, corn stover, and corn grain.

4. Conclusions

We conducted techno-economic and life cycle analyses for distributed-centralized ethylene production based on three feedstocks on five different scales. The shale gas-based pathway showed the best economic performance, but led to the highest net GHG emissions of ethylene. In comparison, the corn stover-based pathway was more competitive than the other two pathways in terms of the net GHG emissions of ethylene, although it resulted in the highest breakeven ethylene prices. The corn grain-based pathway was pinched between the other two pathways regarding both the breakeven ethylene prices and the net GHG emissions of ethylene.

References

- S. E. DeRosa, D. T. Allen, 2015, Impact of natural gas and natural gas liquids supplies on the United States chemical manufacturing industry: production cost effects and identification of bottleneck intermediates. *ACS Sustain. Chem. Eng.* 3, 451-459.
- J. Gao, F. You, 2015, Shale Gas Supply Chain Design and Operations towards Better Economic and Life Cycle Environmental Performance: MINLP Model and Global Optimization Algorithm. *ACS Sustainable Chemistry & Engineering*, 3, 1282-1291.
- J. Gao, F. You, 2017, Design and optimization of shale gas energy systems: Overview, research challenges, and future directions. *Computers & Chemical Engineering*, 106, 699-718.
- J. Gong, M. Yang, F. You, 2017, A systematic simulation-based process intensification method for shale gas processing and NGLs recovery process systems under uncertain feedstock compositions, *Computers & Chemical Engineering*, 105, 259-275.
- J. Gong, F. You, 2018, A new superstructure optimization paradigm for process synthesis with product distribution optimization: Application to an integrated shale gas processing and chemical manufacturing process, *AIChE Journal*, 64, 123-143.
- C. He, F. You, 2014, Shale Gas Processing Integrated with Ethylene Production: Novel Process Designs, Exergy Analysis, and Techno-Economic Analysis. *Industrial & Engineering Chemistry Research*, 53, 11442-11459.
- C. He, F. You, 2015, Toward more cost-effective and greener chemicals production from shale gas by integrating with bioethanol dehydration: Novel process design and simulation-based optimization. *AIChE Journal* 2015, 61, 1209-1232.
- C. He, F. You, 2016, Deciphering the true life cycle environmental impacts and costs of the mega-scale shale gas-to-olefins projects in the United States. *Energy & Environmental Science*, 9, 820-840.
- D. Humbird, R. Davis, L. Tao, et al., 2011, Process design and economics for biochemical conversion of lignocellulosic biomass to ethano, NREL: Golden, CO, USA.
- A. J. Kidnay, W. R. Parrish, D. G. McCartney, 2011, Fundamentals of natural gas processing. 2nd ed.; CRC Press: Boca Raton, FL.
- L. Ou, T. R. Brown, R. Thilakarathne, G. Hu, R. C. Brown, 2014, Techno-economic analysis of co-located corn grain and corn stover ethanol plants. *Biofuel. Bioprod. Bior.* 8, 412-422.
- R. Wallace, K. Ibsen, A. McAloon, W. Yee, 2005, Feasibility study for co-locating and integrating ethanol production plants from corn starch and lignocellulosic feedstocks; National Renewable Energy Laboratory: Golden, CO, USA.
- M. Yang, F. You, 2017, Comparative Techno-Economic and Environmental Analysis of Ethylene and Propylene Manufacturing from Wet Shale Gas and Naphtha. *Industrial & Engineering Chemistry Research*, 56, 4038-4051.
- F. You, B. Wang, 2011, Life Cycle Optimization of Biomass-to-Liquid Supply Chains with Distributed-Centralized Processing Networks. *Industrial & Engineering Chemistry Research*, 50, 10102-10127.
- M. Zhang, Y. Yu, 2013, Dehydration of ethanol to ethylene. *Ind. Eng. Chem. Res.* 52, 9505-9514.
- H. Zimmermann, R. Walzl, 2009, Ethylene. In *Ullmann's Encyclopedia of Industrial Chemistry*, Wiley-VCH Verlag GmbH & Co.: Weinheim, Germany.

Model-based Design of Experiments Using a Flowsheet-Simulator

Norbert Asprion,^{a,*} Juliane Ritter,^a Roger Böttcher,^a Michael Bortz^b

^a BASF SE, Chemical Process Modeling, Carl-Bosch-Str. 38, 67056 Ludwigshafen, Germany

^b Fraunhofer Institute for Industrial Mathematics ITWM, Fraunhofer Platz 1, 67663 Kaiserslautern, Germany

norbert.asprion@basf.com

Abstract

The quality of process optimization depends on model parameters. The use of operating data from mini-, pilot or production plants can help to improve model agreement with operation. To support the design of experiments (DoE) in plants with many operability limitations a model-based DoE was implemented into a flowsheet simulator. In this contribution, the implementation of the method is described and its use for the identification of kinetics is demonstrated for a cumene process.

Keywords: model-based design of experiments, process simulation, multi-criteria optimization.

1. Introduction

The validity of simulation and optimization results based on flowsheet simulation models depends significantly on the quality of these models and their model parameters. The estimation and validation of the parameters is based on experiments that, depending on the complexity of the process, can be cost- and time-intensive. Especially experiments in integrated mini-, pilot or production plants are very expensive. The goal of model-based design of experiments (DoE) is to determine a set of experiments that yields the highest information content, which here means the lowest uncertainty in the model parameters. Since integrated processes are usually modeled in flowsheet simulators, an integration of DoE methods in such simulators is obvious and beneficial. In this contribution, the experience gained by the integration of methods of model-based DoE into BASF's flowsheet simulator CHEMASIM for steady state processes are described. The methods are generic in the sense that in principle any other flowsheet simulator could have been used.

2. Theory: Design of experiments for parameter estimation using process simulation

Often parameter estimation is based on the minimization of a sum of weighted least-square residuals

$$\min_p \sum_{i=1}^{N_e} \sum_{j=1}^{N_m} r_j(p, x_i)^2 \quad \text{with } r_j(p, x_i) = \sqrt{w_{i,j}} \left(\frac{\tilde{y}_{i,j} - y_j(p, x_i)}{\sigma_{\tilde{y}_{i,j}}} \right) \quad (1)$$

Herein $r_j(\mathbf{p}, \mathbf{x}_i)$ denotes the residue of the j -th measured property $\tilde{y}_{i,j}$ and depends on the parameter vector \mathbf{p} (with N_p elements) and the design variable vector \mathbf{x}_i of the i -th experiment. $y_j(\mathbf{p}, \mathbf{x}_i)$ is the model prediction, $w_{i,j}$ a weighting factor and $\sigma_{\tilde{y}_{i,j}}$ the standard deviation of the measured property $\tilde{y}_{i,j}$. N_e and N_m are the number of experiments and measured properties. For unconstrained least squares problems, the Fisher information matrix (FIM) F (dimension $N_p \times N_p$) can be estimated based on an initial estimate of the parameter vector \mathbf{p} (cf. e.g. Schittkowski, 2007a)

$$F = \sum_{i=1}^{N_e} J(\mathbf{p}, \mathbf{x}_i)^T J(\mathbf{p}, \mathbf{x}_i) \quad (2)$$

with the Jacobians $J(\mathbf{p}, \mathbf{x}_i)$ (dimension $N_p \times N_m$)

$$J(\mathbf{p}, \mathbf{x}_i) = \left((\nabla_{\mathbf{p}} r_1(\mathbf{p}, \mathbf{x}_i))^T; \dots; (\nabla_{\mathbf{p}} r_{N_m}(\mathbf{p}, \mathbf{x}_i))^T \right) \quad (3)$$

Herein $\nabla_{\mathbf{p}} r$ denotes the gradient of the residual with respect to the parameters \mathbf{p} . The covariance matrix C , which is the inverse of the FIM F , shows how reliable the parameter estimates are and is also used to estimate confidence intervals of parameters. Therefore, the FIM (respectively the covariance matrix) is a good measure of the information content of designed experiments. A number of scalar functionals on the FIM F serve as quality indicators of experimental designs (cf. e.g. Franceschini and Macchietto, 2008), for example:

- A-criterion: $\text{trace}(F^{-1}) = \sum_{i=1}^{N_p} \frac{1}{\lambda_i}$
- D-criterion: $\det(F^{-1}) = \prod_{i=1}^{N_p} \frac{1}{\lambda_i}$

λ_i are the eigenvalues of the FIM. These criteria can be used as objectives to be minimized in a subsequent step to identify optimal designs.

The foundation of the implemented methods is the automated calculation of the Fisher information matrix (FIM). For this purpose, analytical first derivatives have to be available for example via algorithmic differentiation. When for optimization of the designs gradient-based optimization solvers are used, derivatives of the scalar measure of the FIM with respect to the experimental design variables \mathbf{x} are needed. Here the use of numerical derivatives is possible, but in general it is prohibitive to use numerical differentiation in both steps due to the accuracy. In this work, the DoE results are generated using integrated optimization solvers (NLPQLP, NLP-LSQ and MISQP from Schittkowski (2007b, 2009) and Exler et al. (2012)). A further requirement for the implementation of DoE and parameter estimation into a flowsheet simulator is the possibility to run one simulation model with different operating conditions for the experiments in a sequence and to collect data. This is necessary for the setup of the objective for the optimization either for the parameter estimation according to Eq. (1) or for the design of several experiments with the Fisher Matrix according to Eq. (2). This possibility was already realized in CHEMASIM in a previous work (Asprion et al., 2015).

This approach was developed and validated using simple analytical model functions and transferred to a cumene process as an example for a realistic industrial case study. For this process, a comparison between two strategies for the determination of kinetics are shown: The first strategy uses the negative trace of the FIM to be minimized besides the minimization of the operational expenditures (OPEX) in a multi-criteria optimization

(Bortz et al., 2014) to identify an interesting point. The negative trace of the FIM (also called A*-criterion, see Schittkowski 2007a) is used as measure of information content, since the FIM for only one design is (in most cases for $N_p > 1$) singular. Around this point a statistical design is used. The other strategy is to solely optimize a scalar measure of the Fisher information matrix (A-criterion) to estimate the designs. For both strategies, operational limitations like for example loading ranges are taken into account as constraints of the optimization.

3. Application: Design of Experiments for a Cumene process

For an application test an available simulation model for a cumene process (Asprion et al., 2017) has been used. As shown in Fig.1 the process model includes a tubular reactor which is modeled with ten segments with an initial kinetic model for the formation of cumene and the side product p-di-isopropyl-benzene (DIPB). This model was used for the design of the plant and is the basis of the design of experiments. Details of the design, costs and operability limits (used as constraints) are given in Asprion et al. (2017).

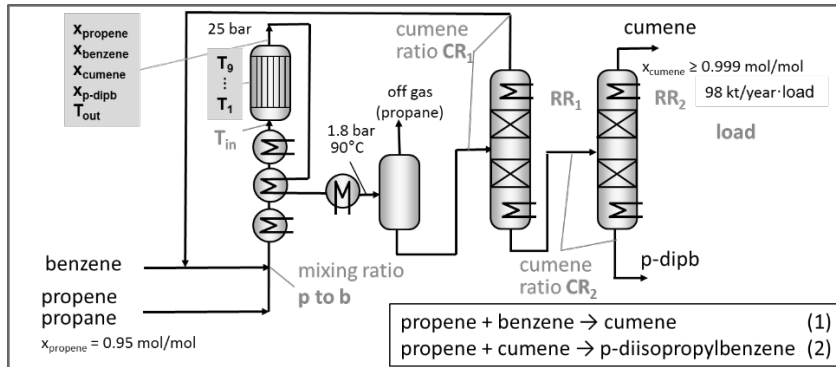


Figure 1: Design variables for the experiments are the operating variables (shown with gray font) of the cumene process. The measurements used in the sum of least squares for the determination of the kinetics are shown in the gray boxes.

The ranges of the operating variables which are used in the optimization of both strategies are given in Table 1.

Table 1: Range of the operating variables for the design of experiments. This range is used in the multi-criteria optimization step before applying the statistical DoE and for the optimization of the A-criterion in the model-based DoE.

	$T_{in}/^{\circ}\text{C}$	p to b	RR_1	$\ln(CR_1)$	RR_2	$\ln(CR_2)$	load
min	340	0.2	0.1	-12	0.1	-12	0.6
max	400	0.9	1	-1	1	-1	1.2

The results of the multi-criteria optimization (minimization of -trace F and OPEX) are shown in Fig. 2. Obviously, there is one dominated solution included, which emphasizes the need to start optimization from different initial values. Furthermore, the obtained Pareto-frontier is partly non-convex probably caused by active constraints and/or bounds on the variables. Starting from a typical operating point with low OPEX in the right corner, there is a huge trade-off in the information content (measured by -trace F) by increasing only a little the OPEX, before OPEX increases significantly,

while the additional gain in information content remains small. Therefore, a solution in the so-called Pareto “knee” was chosen. Starting from this point, a statistical design in a closed vicinity (operating variables at selected point and ranges see Table 2) has been setup using a fractional factorial design scheme, which leads to 8 experimental designs.

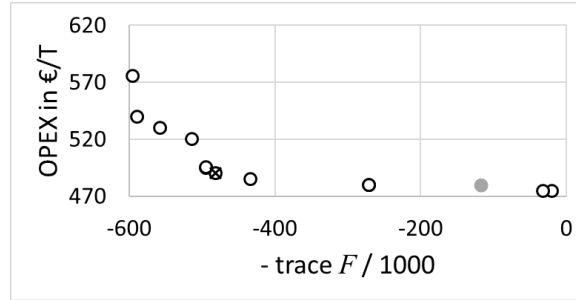


Figure 2: Results of the multi-criteria optimization: ○ Pareto points, ● dominated point, ✕ selected point as basis of a statistical DoE.

Table 2: Results of the operating variables of the cumene process for the selected point (cf. Fig. 2). Statistical design of experiments is based on a fractional factorial design using the min and max values. Italic values of the variables were already on lower or upper bounds and were not varied.

	$T_{in}/^{\circ}\text{C}$	p to b	RR_1	$\ln(\text{CR}_1)$	RR_2	$\ln(\text{CR}_2)$	load
selected	340	0.641	0.1	-1	0.428	-9.92	0.755
min	340	0.6	0.1	-1	0.4	-10.5	0.7
max	340	0.68	0.1	-1	0.45	-9.5	0.8

For the model-based DoE 8 parallel experiments with 7 operating variables (in total 56 variables) have been used to minimize the A-criterion (subject to in total 176 constraints). For both designed experimental plans “virtual” experiments with the model assuming a different kinetic (called “true” to distinguish from the kinetic used for the design). For the statistical design simulations for 7 and for the A-criterion simulations for 6 design points converged. The remaining ones failed. This behavior is conceivable for real experiments as well: Designs based on an initial guess of the parameters might fail as well because reality is different from the supposed model and limitations prevent to run an experiment. To the inlet stream conditions and the measured molar concentrations and temperatures of the reactor noise based on a normal distribution with standard deviations (1% for the total molar flow to the reactor, $\sigma_x=10^{-4}$ mol/mol and $\sigma_T=1$ K) has been added. For the parameter estimation, the inlet conditions are set and only the measured data (cf. gray boxes in Fig. 1) of the reactor are used in the least squares Eq. (1) with $w_x=w_T=10^{-4}$.

In Table 3 the parameters of the kinetic models based on the Arrhenius ansatz

$$k_i = k_{0,i} \cdot \exp\left(-\frac{E_{A,i}}{RT}\right) \quad (4)$$

used for the initial design and for the virtual experiments (“true”) as well as the estimated parameters based on the statistical and A-criterion design are given. Herein k denotes the kinetic, k_0 the pre-exponential factor, E_A the activation energy, R the universal gas constant. Instead of estimating the parameters k_0 and E_A of the i -th reaction directly, factors F_1 and F_2 initially set to 1 have been introduced

$$k_i = \exp(F_{1,i} \cdot \ln k_{0,i}) \cdot \exp\left(-\frac{F_{2,i} \cdot E_{A,i}}{RT}\right) \quad (5)$$

with the following ranges: $F_{1,1} \in [-3;15]$; $F_{1,2} \in [-3;30]$; $F_{2,1}$ and $F_{2,2} \in [0.1;20]$.

Table 3: Kinetic model parameters of the cumene (1) and p-dipb (2) reaction for different models: design - was used for plant design and design of experiments, “true” - is the kinetic model used for generating the virtual plant experiments, statistical and A-criterion – estimated parameters based on these experimental designs

model	$k_{0,1}$ / (l/mol)	$E_{A,1}$ / (J/mol)	$k_{0,2}$ / (l/mol)	$E_{A,2}$ / (J/mol)
design	2.8E+07	104251	2.32E+09	146873
“true”	1.054E+08	111546	6.101E+08	139577
statistical	2.208E+08	115773	1.275E-01	14687
A-criterion	2.513E+08	116160	6.207E+06	114756

These kinetic models are also shown in Figure 3 for temperatures between 340 and 440°C for the cumene and the p-dipb reaction (cf. Fig. 1). As can be seen, the estimated kinetics for the cumene reaction for both designs are in good agreement with the “true” kinetics, but for the p-dipb reaction the estimated kinetics based on the A-criterion design is much better than for the statistical design. The remaining deviations are caused by the noise as a comparison to the results without noise have shown (not presented here).

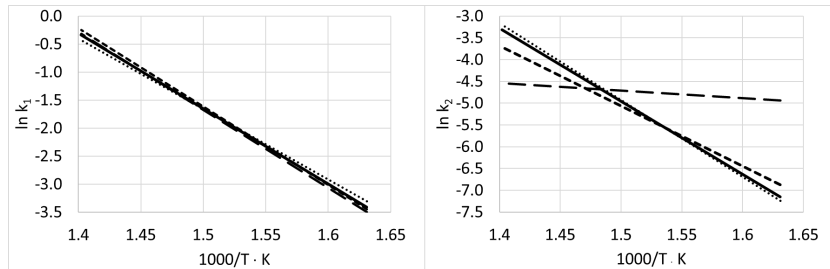


Figure 3: Comparison of the different kinetic models for the cumene (1, left) and the p-dipb (2, right) reaction: — “true” model, ... initial design model, -- estimated model based on statistical design around selected point from MCO and - - estimated model based on A-criterion design.

Comparisons of the outlet molar fractions of the virtual experiments and the predictions of the estimated kinetic models are shown for both designs in Figure 4. As can be seen there is more variance in the data for the A-criterion design.

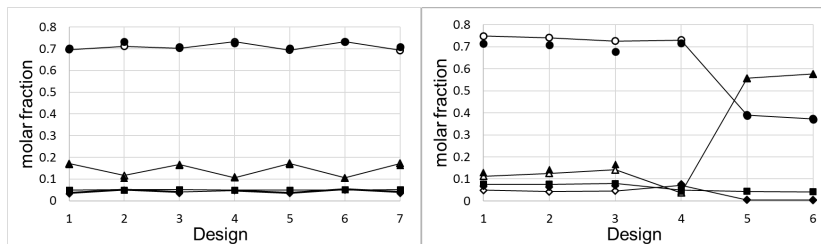


Figure 4: Reactor outlet concentration: full symbols are results of virtual experiments based on “true” kinetic model. Hollow markers with lines are results of estimation of kinetic parameters to this data. Left: based on statistical design, right: based on A-criterion design. O, ●: cumene, △, ▲: benzene, ◆, ◇: dipb, ■, □: propane

This is also true for the temperature profiles of the different designs as can be seen in Figure 5. This higher variance of the data reduces the impact of noise and improves parameter identifiability. There is a good agreement between the models with the estimated data and the virtual experiments.

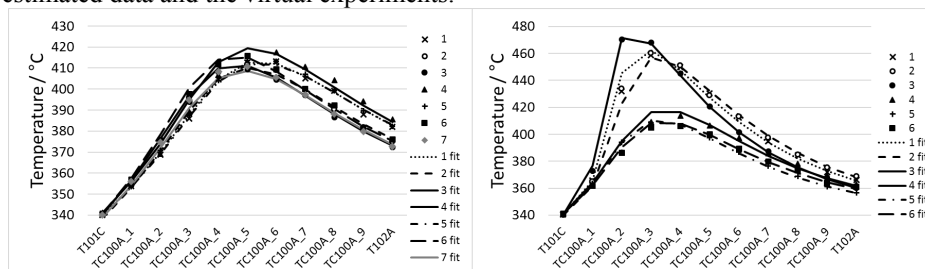


Figure 5: Reactor temperatures: symbols are results of virtual experiments based on “true” kinetic model. Lines are results of adjustment of kinetic parameters to this data. Left: based on statistical design, right: based on A-criterion design.

4. Conclusions and Outlook

The example of the cumene process has shown how a model-based design of experiments implemented into a flowsheet simulator helps to identify kinetics in an experimental setup with operability limitations. The method and the workflow of the two experimental plans as well as the results will be discussed in the presentation.

Following aspects will be considered for future improvements of the implementation:

- Automatic initialization strategies for the optimization
- Extension of existing experimental designs
- Use of singular value decomposition and estimation of parameter identifiability (Lopez et al., 2015, Schittkowski, 2007a)
- Robust design by considering uncertainties in initial parameter guesses
- User support in problem formulation

References

- N. Asprion, R. Benfer, S. Blagov, R. Böttcher, M. Bortz, M. Berezhnyi, J. Burger, E. von Harbou, K.-H. Küfer, H. Hasse, 2015, *Chem. Ing. Tech.*, 87 (12) 1810-1825,
- N. Asprion, S. Blagov, R. Böttcher, J. Schwientek, J. Burger, E. von Harbou, M. Bortz, 2017, *Chem. Ing. Tech.*, 89 (5) 665-674, DOI: 10.1002/cite.201600098.
- M. Bortz, J. Burger, N. Asprion, S. Blagov, R. Böttcher, U. Nowak, A. Scheithauer, R. Welke, K.-H. Küfer, and H. Hasse, 2014, *Comp. Chem. Eng.*, 60, 354–363.
- O. Exler, T. Lehmann, K. Schittkowski (2012), Report, Dept. of Comp. Sci., Univ. of Bayreuth
- G. Franceschini, S. Macchietto, 2008, *Chem. Eng. Sci.* 63, 4846 – 4872.
- D.C. López C. , T. Barz, S. Körkel, G. Wozny, 2015, *Comp. Chem. Eng.*, 77, 24–42.
- K. Schittkowski, 2007a, *Ind. Eng. Chem. Res.*, 46, 9137-9147.
- K. Schittkowski, 2007b, Report, Dept. of Comp. Sci., Univ. of Bayreuth
- K. Schittkowski, 2009, Report, Dept. of Comp. Sci., Univ. of Bayreuth

Modeling of Non-Isothermal Adsorption Process in a Silica Gel Desiccant Packed Bed

Siripan Murathatunyaluk^{a*}, Koranut Srichanvichit^a, Amata Anantpinijwatna^a,
Prakob Kitchaiya^a

^a *Department of Chemical Engineering, Faculty of Engineering, King Mongkut's
Institute of Technology Ladkrabang, 1 Chalongkrung Rd., Ladkrabang, Bangkok 10520,
Thailand*

* siripan.mu@kmitl.ac.th

Abstract

This study investigated a numerical simulation of a column packed bed using silica gel. This bed is either stationary or steadily rotating, leading to different operation-regeneration schemes. Although models of these systems have already been developed and fitted with available data, they require large number of costly and time-consuming experiment to be applicable. Therefore, the development of a fundamental predictive mathematical model is necessary. The present model is a one-dimensional numerical solution of the conservation equations for heat, water vapor, and adsorbed water inside the silica gel desiccant under the constraint of local equilibrium between the two phases, which is characterized by fundamental sorption isotherms. The system of a non-isothermal adiabatic under constant pressure containing heat and mass transfer phenomena between vapor and solid phases are considered. The numerical results show good agreement with a maximum root of mean square of errors of 6.6% and 9.6% for exit air temperature and humidity, respectively

Keywords: Adsorption, Packed bed, Desiccant, Dehumidification.

1. Introduction

Adsorption process has been used in various applications, for example, in purification processes, whereby a packed bed filled up with solid desiccant material is used to remove the impurity of the adsorbate. The most widely used materials in the adsorption processes are silica gel, activated alumina and zeolite. The choice of the material depends on the type of application to be used. Silica gel is considered as good alternatives and commonly used in air dehumidification systems due to its high performance in the removal of water vapor. It is non-toxic, non-flammable, non-reactive and stable with ordinary usage. One of the advantages of using silica gel desiccant packed bed is the low operating cost. It also does not pollute environment, and can be generated using low temperature. Silica gel desiccant is widely used in applications like food drying, air conditioning, storage of chemical and pharmaceutical products, etc.

Dehumidification is related to physical adsorption. It is an exothermic process. This involves the transfer of water vapor from the humid air onto the solid desiccant surface due to vapor pressure different between the air and the desiccant surface. It is a function of operating temperature with the degree of adsorption decreasing as

Nomenclature	
A_b	bed cross section area [m^2]
a	volumetric surface area [m^2/m^3]
c	specific heat [$J/kg\ K$]
d	diameter [m]
H_A	heat of adsorption [J/kg]
h	convective heat transfer coefficient [$W/m^2\ K$]
h_m	convective mass transfer coefficient [$kg/m^2\ s$]
k	thermal conductivity [$W/m\ K$]
L	bed length [m]
\dot{m}	mass flow rate [kg/s]
m	mass [kg]
P	pressure [kPa]
P_{sat}	saturated water vapor pressure [kPa]
q	average water content [$kg_w/kg_{dry\ silica\ gel}$]
R	particle radius [m]
Re	Renolds number, $Re = 2Rv / \nu$
RH_s	equilibrium relative humidity [%]
T	temperature [$^{\circ}C$]
t	time [s]
v	superficial velocity of air stream [m/s]
w_a	air humidity [kg_w/kg_a]
w_s	equilibrium humidity [kg_w/kg_a]
z	axial position [m]
Greek	
ρ	density [kg/m^3]
ε	bed porosity
ν	kinematic viscosity [m^2/s]
Subscripts	
0	initial condition
a	air side
b	bed
s	silica gel side
v	water vapor
w	water
z	axial direction

temperature increases. After the desiccant adsorbs moisture, it is usually desorbed or reactivated by heating. Isothermal dehumidification process is an ideal for applying to small systems. An adiabatic (non-isothermal) process is a common process that can occur with a heat insulating system.

In this study, the numerical model for heat and moisture transfer in the non-isothermal packed bed is described and analyzed. The objective of the present theoretical study is to investigate the desiccant bed dynamics during adsorption process and predict the influence of design parameters, such as air velocity and inlet air humidity for adsorption processes without the need of measured data. The model has been validated using the experimental data found in open literatures. The simple explicit finite difference method is applied to solve the model numerically.

2. Theoretical

2.1. Mathematical modeling

The physical system considered in this analysis is illustrated in Fig. 1. The moisture and energy conservation law are applied to the incremental volume of desiccant packed bed of spherical silica gel particles with a height of dz . To simulate the moisture and heat transfer processes in the desiccant packed bed, the following assumptions are used:

- (i) The bulk air stream contains only water vapor as adsorbate.
- (ii) The desiccant particles are porous spheres of uniform diameter d_p .
- (iii) Average bed porosity is assumed at all locations in the packed bed.
- (iv) The pressure drop along the bed is negligible, thus air velocity is constant.
- (v) The variation of humidity in radial direction is neglected.
- (vi) The heat transfer through the bed is along the z -direction only, and column wall is assumed to be adiabatic wall.
- (vii) The dispersion of moisture along axial direction of the bed, which is less than the convective mass transfer in the bed, can be neglected.
- (viii) Lumped capacitance method is adopted for moisture and energy balances.

Applying the moisture balance on the air stream through the bed, the equation of the gas phase moisture balance is:

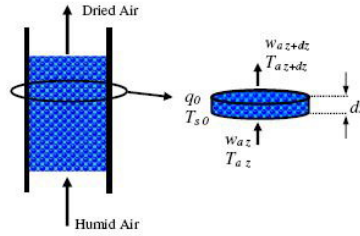


Fig. 1. Physical model for adsorptive packed bed.

$$-v \frac{\partial(\rho_a w_a)}{\partial z} = \rho_a \varepsilon \frac{\partial w_a}{\partial t} + \rho_s (1-\varepsilon) \frac{\partial q}{\partial t} \quad (1)$$

In the solid phase, the accumulation of moisture in the silica gel particles can be represented as the amount of water vapor transferred from the bulk air stream to particles as shown in eq. (2).

$$\frac{\partial q}{\partial t} = \frac{h_m a}{\rho_s (1-\varepsilon)} (w_a - w_s) \quad (2)$$

Substituting Eq. (2) into Eq. (1), and rearranging, the equation of gas phase moisture balance is as follows:

$$\frac{\partial w_a}{\partial t} = -\frac{\dot{m}_a}{\rho_a \varepsilon A_b} \frac{\partial w_a}{\partial z} - \frac{h_m a}{\rho_a \varepsilon} (w_a - w_s) \quad (3)$$

For simplification, the moisture balance is implemented on incremental volume of spherical desiccant particles. Thus, the moisture content in the solid phase is given by,

$$\frac{\partial q}{\partial t} = \frac{\dot{m}_a}{m_s} (w_{a,z} - w_{a,z+dz}) \quad (4)$$

Applying the energy balance to the following air stream, the gas phase energy equation can be expressed as,

$$\frac{\partial T_a}{\partial t} = -\frac{\dot{m}_a}{\rho_a \varepsilon A_b} \frac{\partial T_a}{\partial z} + \left(\frac{ha}{\rho_a c_a \varepsilon} + \frac{c_v h_m a}{\rho_a c_a \varepsilon} (w_a - w_s) \right) (T_s - T_a) \quad (5)$$

The solid phase energy balance equation is derived by applying the energy conservation law as follow:

$$k_b \frac{\partial^2 T_s}{\partial z^2} + H_A h_m a (w_a - w_s) + ha (T_a - T_s) = c_s \rho_s (1-\varepsilon) \frac{\partial T_s}{\partial t} \quad (6)$$

Where the first term in the left-hand side is the heat transferred by conduction, the second term accounts for the heat released during adsorption (or heat adsorbed during desorption) and the third term represents the convective heat transferred from/to the air stream.

Eqs. (3)-(6) have the following initial and boundary conditions during adsorption processes:

$$\begin{aligned} T_a(z, t=0) &= T_{a0}, & T_s(z, t=0) &= T_{s0}, & w_a(z, t=0) &= w_{a0}, & q(z, t=0) &= q_0, \\ T_a(z=0, t) &= T_{a,in}, & w_a(z=0, t) &= w_{a,in}, & \frac{\partial T_s}{\partial z} \Big|_{z=0} &= \frac{\partial T_s}{\partial z} \Big|_{z=L} &= 0 \end{aligned}$$

2.2. Auxiliary data

In this study, the average silica gel particle diameter and density are 3.88 mm and 1,200 kg/m³, respectively. The bed porosity has been taken as 0.31 for bed spherical particles. The cylindrical column diameter is 0.13 m. The physical properties used by Pesaran and Mills (1987) and Kafui (1994) are as followed:

$$\text{Thermal conductivity} \quad k_b = k_a^\varepsilon k_s^{1-\varepsilon} \quad (7)$$

$$k_s = 0.37 + 0.97q + 0.0014T_s \quad (8)$$

$$\text{Specific heat of silica gel} \quad c_s = 4,186q + 921 \quad (9)$$

$$\text{Specific heat of humid air} \quad c_a = 1,884w_a + 1,004(1-w_a) \quad (10)$$

$$\text{Specific heat of water vapor} \quad c_v = 1,859 + 0.382T_a \quad (11)$$

$$\text{Heat of adsorption} \quad H_A = \begin{cases} 1,000(3,500 - 12,400q) & q \leq 0.05 \\ 1,000(2,950 - 1,400q) & q > 0.05 \end{cases} \quad (12)$$

$$\text{Convective heat transfer coefficient} \quad h = 1.60\rho_a v c_a Re^{-0.42} \quad (13)$$

$$\text{Convective mass transfer coefficient} \quad h_m = 1.70\rho_a v Re^{-0.42} \quad (14)$$

The equilibrium isotherm of water-silica gel system for regular density silica gel is

$$RH_s = 100(0.0078 - 0.05759q + 24.16554q^2 - 124.478q^3 + 204.226q^4) \quad (15)$$

After calculating RH_s and the bed temperature (T_s), the equilibrium moisture content of air adjacent to the particle surface (w_s) is calculated using the following expression:

$$w_s = \frac{0.622RH_s \times P_{sat}(T_s)}{P_a - RH_s \times P_{sat}(T_s)} \quad (16)$$

The relation between water vapor pressure and temperature from Antoine equation is

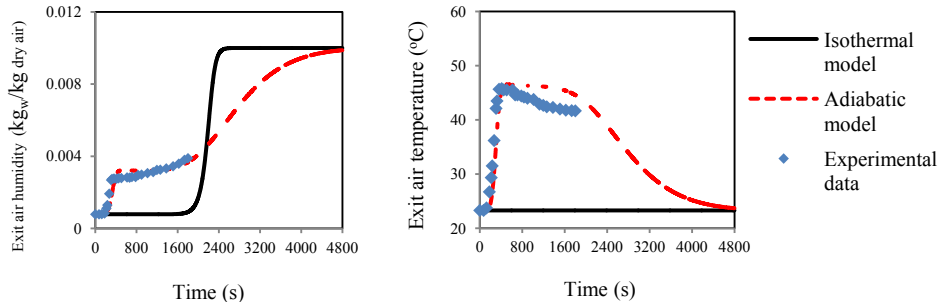
$$\ln P_{sat} = 16.3872 - \frac{3,885.70}{T_s - 42.980} \quad (17)$$

3. Numerical procedure

The nonlinear partial differential equation, moisture and energy balance of gas and solid phase as Eqs. (3)-(6), have been solved using explicit finite difference method. Computer codes are developed using programming MATLAB to obtain the result of the numerical model. Time step of 1.0 s and grid size of less than 1.0 mm with total 100 grid points have been used. The numerical procedure starts with the parameters definition and initialization for all variables. Finally, the variables w_a , q , T_a and T_s at the current grid point are calculated.

4. Numerical results

Fig. 2. illustrates the comparison between results of this numerical model and experimental data reported by Pesaran and Mill, 1987, which shows the variation of exit air temperature and humidity with time for adsorption processes. Regular density silica gel is packed in the desiccant bed. The height of the bed is less than 0.15 m to avoid pressure drop effects. The time of successful experiment is about 30 min. It can be seen that the present model results are consistent with the measured data. It is a maximum root of mean square of errors of 6.6% and 9.6% for exit air temperature and exit humidity, respectively. For the adiabatic model, there is an acceptable error that is



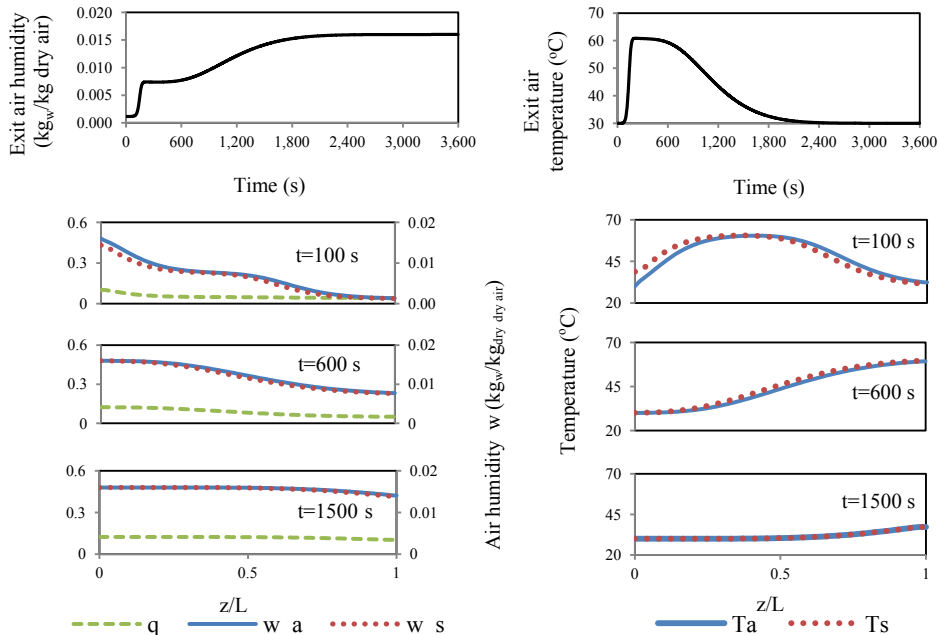
$L=0.0775$ m, $v=0.21$ m/s, $T_{a,in}=23.3$ °C, $w_{a,in}=0.01$ kg_w/kg_{dry air}, $q_0=0.0417$ kg_w/kg_s

Fig. 2. Variation of exit air temperature and exit air humidity with time.

due to heat transfer through packed bed’s wall during the experiment. The heat adsorption in packed bed has caused high deviation of isothermal model.

Fig. 3. shows the simulated results of axial variation of humidity, bed water content and temperature profile along the column. Top two graphs present exit air humidity and temperature. For 100 s, there is no change at the exit air humidity and temperature. However, air humidity, bed moisture and heat have been accumulated along the bed length. Later on, the developed humidity, moisture and temperature have moved toward the exit. Humidity and moisture have been increasing smoothly, while temperature wave has moved out by the air convection cooling. As the bed saturates, there is no humidity and temperature difference along the column.

Inlet air condition has been investigated and presented in Fig. 4. The results are



$L=0.1$ m, $v=0.5$ m/s, $T_{a,in}=30.0$ °C, $w_{a,in}=0.016$ kg_w/kg_{dry air}

Fig. 3. The axial distribution variation of desiccant bed during adsorption process.

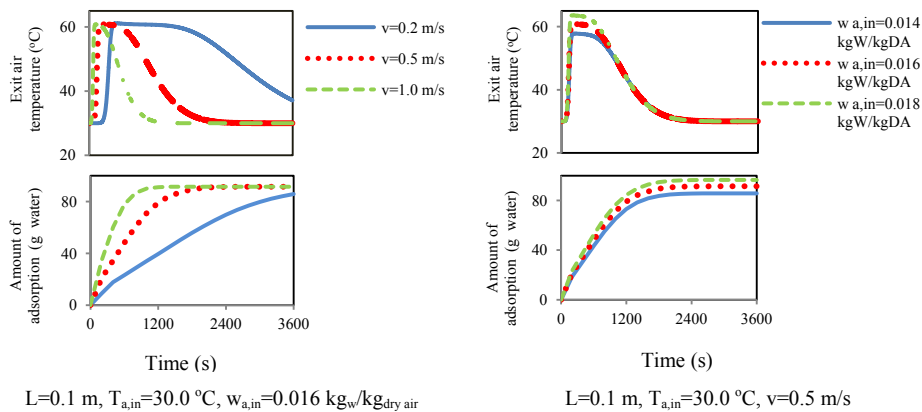


Fig.4. Effect of inlet air humidity and air velocity on exit air temperature and amount of adsorption.

consistent with the experimental data from A.E. Kabeel (2009). Initially, the rate of adsorption is high and gradually decreases when the adsorbent begins to saturate. The exit air temperature rises sharply due to the initial high heat of adsorption, which raises the temperature of bed particles and consequently heats up the air stream by convective heat transfer. When the bed temperature increases, the adsorption capacity decreases, resulting in the decline of heat released and a gradual decrease in the exit temperature. Different inlet humidity has a predictable amount of water adsorption and exit air temperature. In conclusion, the exit air temperature depends on the moisture content adsorbed. As the silica gel saturates, the exit air temperature will equal to the inlet air temperature. However, if the silica gel is still adsorbing moisture, the exit temperature will increase as a result of heat of adsorption.

5. Conclusions

A general numerical model for simulating transient heat and moisture transfer in silica gel packed bed has been presented and validated by comparing with experimental data from public literature reviews. The result of this numerical model is consistent with the experimental data and can accurately explain the physical properties existing in the bed. It can also forecast adsorption capacity by varying the independence variables, such as inlet air humidity and air velocity. The increasing of heat released from adsorption significantly reduces the adsorption capacity. If this numerical model, which is used as a basis for designing adsorption packed bed system, can be designed to reduce the temperature in packed bed, the efficiency of adsorption process will improve.

References

- A.A. Pesaran, A.F. Mills, 1987, Moisture Transport in Silica Gel Packed Beds-I Theoretical Study, *Int. J. Heat Mass Transfer*, 30, 1037-1049.
- A.A. Pesaran, A.F. Mills, 1987, Moisture Transport in Silica Gel Packed Beds-II Experimental Study, *Int. J. Heat Mass Transfer*, 30, 1051-1060.
- A.E. Kabeel, 2009, Adsorption-desorption operations of multilayer desiccant packed bed for dehumidification applications, *Renewable Energy*, 34, 255-265.
- K.D. Kafui, 1994, Transient Heat and Moisture Transfer in Thin Silica Gel Beds, *J. Heat Transfer*, 116, 946-953.

Modeling the Effect of Temperature on Microalgal Growth under Outdoor Conditions

Pooya Darvehei^{*a} Parisa A. Bahri,^a Navid R. Moheimani^b

^a*School of Engineering and Information Technology, Murdoch University, 90 South St Murdoch, WA 6150, Australia*

^b*Algae R&D Centre, School of Veterinary and Life Sciences, Murdoch University, 90 South St Murdoch, WA 6150, Australia*

p.darvehei@murdoch.edu.au

Abstract

Many factors affect the growth of microalgae among which temperature and light intensity are amongst the most important factors. While these two factors heavily influence the growth in outdoor microalgae cultures such as open ponds, they also have a significant correlation in this environment which makes studying their effects separately rather difficult. A method has been introduced in this paper which models the effect of temperature on long-term growth of microalgae based on the assumption that the effect of light and temperature are independent and can be separated. This method was obtained by binning the data and using the derivatives of the growth to eliminate the effect of light. For this study, long-term growth of *Tetraselmis* sp. grown in Murdoch University, Perth, Australia was used. The result showed that the calculated temperature function is similar to what has been reported in the literature for other types of microalgae. Although raw data did not show any decline in growth at high temperatures due to the increase in light exposure, the proposed model successfully demonstrated this effect and confirmed that elevated temperature can lower the growth of microalgae.

Keywords: microalgae, growth model, outdoor cultivation, temperature function

1. Introduction

Microalgae have attracted the attention of many researchers due to its high potential in production of various chemicals. From pharmaceuticals to nutrition and cosmetic industries as well as wastewater treatment, microalgae showed to be valuable source for wide range of applications (Acién et al. 2014). However, despite the beneficial characteristics, it is still pursuing the path to industrialization. One of the critical steps in this route is clear understanding of microalgal behavior from mathematical point of view. Design and control of a system is not feasible as long as there is not a clear formulation of the system's behavior. When it comes to microalgae production, one of the most important parameters to understand is growth which ultimately facilitates calculation of production rate and other economical values. Growth, in form of specific growth rate, has been subject to numerous studies and effect of various parameters including light, temperature, and nutrients have been investigated. However, there is still a noticeable lack of studies for outdoor cultures from modelling perspective (Béchet et al. 2013).

Mass production of microalgae is only possible in outdoor systems. Given the different nature of indoor and outdoor systems, data acquired indoor does not seem reliable to explain the behavior of an outdoor system. Hence, modelling based on outdoor data seems crucial. This paper specifically focuses on the effect of temperature on the growth of microalgae for which experimental data for growth of *Tetraselmis* sp. in an outdoor open pond is used. When it comes to outdoor data, there is little to control over factors that affect the growth. Temperature, likewise, is rarely controlled as it significantly increases the operating cost of a pond. Hence, the two influential parameters, light and temperature, vary continuously which makes studying the effect of solely one of them challenging. Moreover, these two factors have a strong correlation which makes separating their effect even more difficult. Figure 1 shows the correlation between daily light and pond temperature. However, this correlation is not strong enough to make an accurate prediction of one based on the other and hence it is critical to extract their individual effects from data for better analysis.

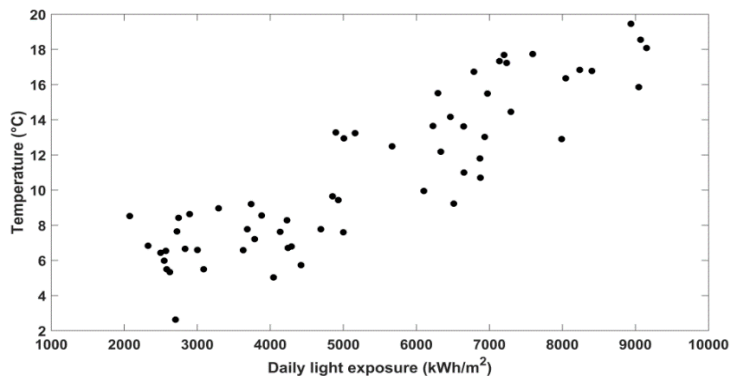


Figure 1 Temperature of the pond against total daily light exposure

Modeling and extracting the effect of temperature from outdoor data is essential since it helps in understanding the difference between the behavior of algal cells in indoor and outdoor cultures, and a pathway to more accurate prediction of growth based on weather conditions. Moreover, understanding the effect of temperature can be useful for cultures that have a temperature control system, which facilitates the optimization of temperature for better growth.

2. Methodology

2.1. Experiments

The data for this study was obtained by Isdepsky (2015) in Murdoch University Algae R&D Centre, Perth, Australia. As part of a long-term feasibility study, *Tetraselmis* sp. was grown in 1 m² open air raceway pond for a period of 20 months (from January 2009 to August 2010). The pond (2 m by 0.5 m) was divided into two channels and the culture was circulated continuously using a paddlewheel at 18 rpm which created a flow of approximately 0.2 m/s. The culture was maintained in a semi-continuous way using a dilution frequency of three times per week.

Light intensity data was collected from Murdoch University Weather Station (<http://www.met.murdoch.edu.au>). Using this data, total daily light exposure was calculated. Pond temperature measurements were collected during the experiments.

2.2. Numerical modeling

Light intensity and water temperature are very closely related in an outdoor culture. Therefore, to make the analysis of data possible, researchers often assume that their effects are independent of each other. Each factor is used to calculate an efficiency function which varies between zero and one. Multiplication of these functions is used frequently in the literature to describe the combined effect of light and temperature (Bordel et al. 2009, Bernard and Rémond 2012, Franz et al. 2012):

$$\mu = \mu_m f(I) g(T) \quad (1)$$

In Eq.(1), μ is specific growth rate, μ_m is theoretical maximum specific growth rate, and $f(I)$ and $g(T)$ are efficiency functions for light and temperature, respectively. The goal is to identify the temperature function, which is difficult since we do not have any information regarding light function either. However, assuming $f(I)$ is independent of temperature, the partial derivative of specific growth rate can be easily calculated:

$$\frac{\partial \mu}{\partial T} = \mu_m f(I) g'(T) \quad (2)$$

Now, by dividing Eq.(2) by Eq.(1), the terms μ_m and $f(I)$ will be cancelled out and hence removed from the calculations.

$$\frac{1}{\mu} \frac{\partial \mu}{\partial T} = \frac{g'(T)}{g(T)} = (\ln(g(T)))' \quad (3)$$

Although using the derivatives are theoretically simple, when it comes to using actual data other issues will appear. To properly calculate the derivatives, data at various temperatures are required for each light intensity value. Unfortunately, data from outdoor cultivation systems are not acquired under such controlled condition, and are far from the ideal form due to errors caused by sudden weather changes and being exposed to atmosphere and many more. One way to tackle this issue is by choosing small ranges of light intensity within which it is fair to assume the effect of light is negligible. Thus, any change in the growth would be due to temperature variations and fitting a line through data using regression can estimate the value of derivatives.

The integration of Eq.(3) results in the following equation:

$$\int_{T_{ref}}^T \frac{1}{\mu} \frac{\partial \mu}{\partial T} dT = \int_{T_{ref}}^T (\ln(g(T)))' dT \quad (4)$$

In Eq.(4) T_{ref} is the reference temperature which is arbitrary. Therefore, by selecting T_{opt} as the reference temperature and solving the integrals Eq.(5) will emerge:

$$\ln\left(\frac{g(T)}{g(T_{opt})}\right) = \int_{T_{opt}}^T \frac{1}{\mu} \frac{\partial \mu}{\partial T} dT \quad (5)$$

T_{opt} is the temperature at which $g(T)$ reaches its maximum value of one and can simplify the equation to the following form:

$$\ln(g(T)) = \int_{T_{opt}}^T \frac{1}{\mu} \frac{\partial \mu}{\partial T} dT \quad (6)$$

The values for $\frac{1}{\mu} \frac{\partial \mu}{\partial T}$ can be obtained from data; however, since the value of T_{opt} is not known, integration cannot be performed. Using an arbitrary temperature (T_0), which is set to be lowest temperature in the dataset, Eq.(6) is transformed to Eq.(7) :

$$\ln(g(T)) = \int_{T_0}^T \frac{1}{\mu} \frac{\partial \mu}{\partial T} dT - \int_{T_0}^{T_{opt}} \frac{1}{\mu} \frac{\partial \mu}{\partial T} dT \quad (7)$$

The first integral can be solved easily using the data. The value of the second integral is still unknown but it is constant and independent of temperature, since both upper and lower bounds are fixed temperatures. Let the value of the second integral be γ_0 . Using the maximum value of both sides of Eq.(7), the value can be determined:

$$\max(\ln(g(T))) = \max\left(\int_{T_0}^T \frac{1}{\mu} \frac{\partial \mu}{\partial T} dT - \gamma_0\right) \quad (8)$$

Knowing that γ_0 is constant and also the maximum value of $g(T)$ is one (or maximum value of $\ln(g(T))$ is zero):

$$\gamma_0 = \max\left(\int_{T_0}^T \frac{1}{\mu} \frac{\partial \mu}{\partial T} dT\right) \quad (9)$$

Eq.(9) shows that the value of the second integral in Eq.(7) is the maximum of the first integral. Therefore, first the integral should be solved using T_0 and all temperatures in the dataset, then the maximum value is γ_0 . Finally, the temperature function can be determined using Eq.(10):

$$g(T) = \exp\left(\int_{T_0}^T \frac{1}{\mu} \frac{\partial \mu}{\partial T} dT - \gamma_0\right) \quad (10)$$

3. Results and discussion

The data was classified into eight groups based on daily light exposure from 2,000 to 10,000 kWh/m² to make sure each group contains at least three data points while keeping the range of light exposure narrow and maintaining validity of assumptions. Within each group a linear regression was used for relationship between the specific growth rate and temperature to estimate the value of $\frac{1}{\mu} \frac{\partial \mu}{\partial T}$ in Eq.(3). The results are summarized in Figure 2. The calculated points follow a clear trend except for one instance associated with light range of 7,000 to 8,000 kWh/m² (Figure 2a). While the values are decreasing with temperature, at this data point (labelled in Figure 2a) there is a sharp increase. This issue occurs because all of the groups experienced a temperature range of

over 2.5 °C (Figure 2b), while for this specific group (7,000 to 8,000 kWh/m²) the range did not exceed 0.5 °C, and there were only three data points available. The combination of

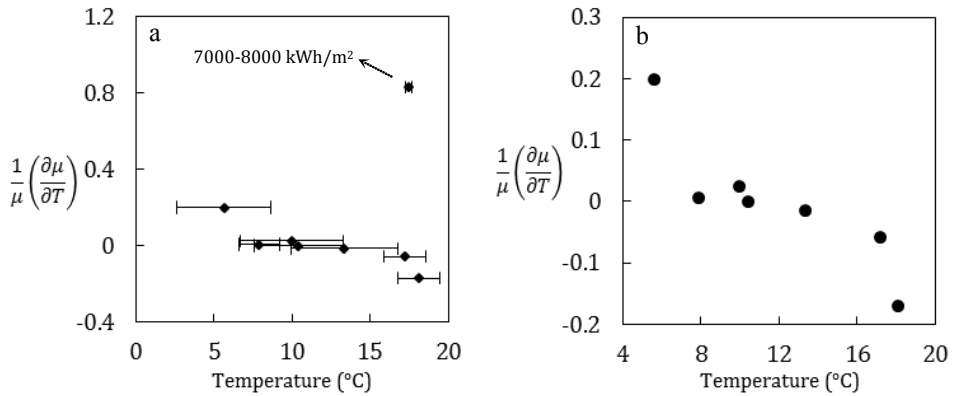


Figure 2 (a) Value of the derivative function for all group and their temperature range (b) Value of the derivative function for all groups, excluding the outlier.

these two factors aggravates the effect of any small error in the data and hence deteriorates the reliability of the result from this group. Therefore, it was decided to flag this point as an outlier and remove it from the rest of the calculations.

Figure 2b also shows that the temperature ranges overlap in certain areas, which produces multiple values at some temperatures and makes integration operation unfeasible. Therefore, where multiple values existed, an average of them was used in the calculation.

After calculating the value of $\frac{1}{\mu} \frac{\partial \mu}{\partial T}$ for all temperatures, numerical integral of the dataset was calculated from $T_0=2.6$ °C to temperature T. As shown in Eq.(9) the value of γ_0 is the maximum of integration which is calculated to be 0.9456 and was inserted into Eq. (10) to find the temperature function ($g(T)$).

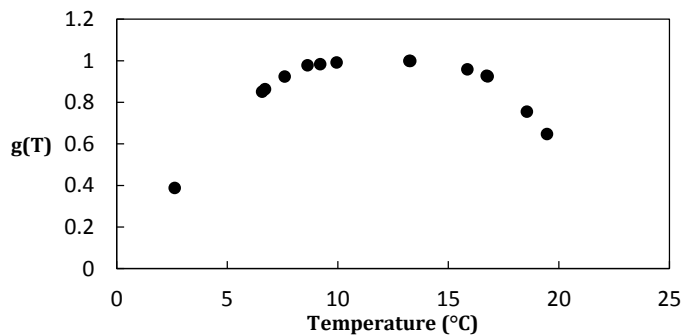


Figure 3 The calculated temperature functionality of growth

Figure 3 shows the final form of $g(T)$ which represents the effect of temperature factor on the growth. The shape of the function is similar to what is reported for other types of microalgae in the literature (Bernard and Rémond 2012). The growth is lower at low temperatures and it increases rapidly until it approaches T_{opt} where it reaches the maximum value and then drops thereafter. Here the growth is maximized at $T = 13.2$ °C which is T_{opt} . It is worthwhile to mention that this value is a daily average and does not mean that at this temperature the growth is maximized, but it shows that on the days

with average temperature of 13.2 °C the growth was at its highest value. The result shows the behavior of the culture under a wide range of temperature. Although, it does not cover the minimum and maximum temperature, at which no growth takes place, it describes the change in growth based on the sole factor of temperature in the range that is commonly experienced by the culture in the location of experiments.

4. Conclusion

A numerical modeling approach was presented to describe the effect of temperature on the growth of microalgae for long-term outdoor cultivation systems and decoupled it from light exposure. The effect of temperature was assumed to be independent of light intensity, which made separation of its effect from other factors possible. This effect was represented in form of a function for which the values were calculated within the temperature range of experiments. The result showed a fairly smooth function which to a good extent had a similar shape to the previous reported functions based on indoor data. In other words, the effect of average daily temperature in outdoor cultures seem to be very close to the effect of temperature in controlled indoor experiments. However, due to differences in the conditions of indoor and outdoor experiments there are a few distinctions between the result of this paper and temperature functions based on indoor experiments. For instance, in indoor experiments the temperature function usually is skewed. They tend to increase rather slowly with temperature and after reaching the maximum value decrease rapidly. But the result of this study shows the temperature function is rather symmetrical (Figure 3) and resembles a Gaussian distribution function, a function which has been used before by Franz et al. (2012) to describe the effect of temperature on the growth of microalgae.

Although a look at the raw data did not show any negative effect due to high temperature, this method managed to unravel this effect successfully. The results, however, heavily depend on availability of extensive data. As experienced in one instance, the lack of sufficient data in one of the groups can result in highly unreliable values.

Moreover, this model was based on half-monthly data for long-term cultivation in an open pond. More frequent data, enables us to do the analysis on a more accurate and more detailed scale, which can result in a more robust model. But despite these limitations, the presented framework resulted in a model that describes the temperature functionality of growth with a high quality. Additionally, instead of relying on controlled indoor experiments, it uses the data from long-term cultivation in real outdoor condition, which makes applying it to simulate an outdoor culture more reliable.

References

- F. Acién, J. Fernández and E. Molina-Grima, 2014, Economics of microalgae biomass production, *Biofuels from Algae*, Elsevier, 313-325.
- Q. Béchet, A. Shilton and B. Guieysse, 2013, Modeling the effects of light and temperature on algae growth: State of the art and critical assessment for productivity prediction during outdoor cultivation, *Biotechnology Advances*, 31, 8, 1648-1663
- O. Bernard and B. Rémond, 2012, Validation of a simple model accounting for light and temperature effect on microalgal growth, *Bioresource Technology*, 123, 520-527
- S. Bordel, B. Guieysse and R. Muñoz, 2009, Mechanistic model for the reclamation of industrial wastewaters using algal-bacterial photobioreactors, *Environmental Science and Technology*, 43, 9, 3200-3207
- A. Franz, F. Lehr, C. Posten and G. Schaub, 2012, Modeling microalgae cultivation productivities in different geographic locations - estimation method for idealized photobioreactors, *Biotechnology Journal*, 7, 4, 546-557
- A. Isdepsky, 2015, Saline microalgae for biofuels: outdoor culture from small-scale to pilot scale Murdoch University

Prediction of stability and thermal conductivity of nanofluids for thermal energy storage applications

B.H. Mahmoud^{a*}, M. Fairweather^a, L.F. Mortimer^a, J. Peakall^b, H.P. Rice^a, D. Harbottle^a

^a*School of Chemical and Process Engineering, and* ^b*School of Earth and Environment, University of Leeds, Leeds LS2 9JT, UK*

**bgy9bm@leeds.ac.uk*

Abstract

This study assesses the stability of nanofluids using a computational modelling technique based on Lagrangian particle tracking. A multiphase liquid-solid model is used where the motion of embedded nanoparticles in the suspended fluid is treated by an Eulerian-Lagrangian hybrid scheme with fixed time stepping. This technique enables various multiscale forces, whose characteristics (length and timescales) are quite different, to be established. The system under consideration consists of 50 nm Al₂O₃ ceramic nanoparticles at various volume fractions ranging between 1.0 and 5.0% suspended in fluids of different density ratios, including water with homogeneous temperature distributions from 5 to 95 °C. The simulation results demonstrate the effectiveness of the technique, with predictions elucidating the role of Brownian motion, particle collision and DLVO forces, and their influence on the level of nanoparticle agglomeration. The nano-aggregates formed are found to play a key role in the thermal behaviour of the nanofluid at various particle concentrations, with predictions in agreement with theoretical and experimental results obtained in similar studies. The results of the work are used to consider the heat transfer characteristics of nanofluids and their potential applications.

Keywords: Nanofluids, stability, thermal conductivity, thermal energy storage

1. Introduction

Both heat transfer fluids and thermal energy storage media are commonly used as thermofluids in large-scale power generation units, including solar thermal and nuclear plants. However, the poor thermal properties of many fluids (e.g. water, oil, ethylene glycol and molten salt) are a major limitation in developing more energy-efficient power generation processes. New methods have recently been introduced to improve their thermal heat transfer properties by doping them with small concentrations of selected nanoparticles (ranging in size from 10 to 100 nm) to form so-called nanofluids. Work in this area has therefore received increased attention in recent years, with extensive experimental and computational research having been carried out (Wang and Mujumdar, 2008a,b). The reported enhancement in heat transfer characteristics obtained using different types of nanoparticles such as metal oxides, non-metallic and carbon nano-tubes is described in the literature, with substantially higher thermal conductivities found. The most significant is for samples containing aluminium-trioxide (Al₂O₃) nanoparticles with volume fractions ranging between 1.0 and 2.5%, for which increases

in thermal conductivity of between 2 and 36% (Choi and Eastman, 1995; Wang and Mujumdar, 2008a,b) have been obtained.

For numerical simulations, most researchers have dealt with nanofluids as a single-phase fluid rather than a two-phase mixture (Wang and Mujumdar, 2008a). The single-phase approach assumes that continuum principles are still valid for fluids with suspended nano-sized particles following the flow, and as such is much simpler and computationally less expensive than explicitly accounting for both phases. The alternative two-phase modelling approach clearly better describes the separate phases, but this approach is not commonly found in the literature due to its computer run-time limitations. The latter technique is to be preferred when modelling nanosuspensions, as it is able to describe the key mechanisms and dynamic processes involved in such multi-phase fluids and their flows, such as nanoparticle clustering, aggregation and thermal property enhancement.

This paper describes the model used, and evaluates the key dynamic forces involved in nanofluids, demonstrating some results and findings. General conclusions are also drawn on the model's capabilities and its potential applications.

2. Computational Setup

The numerical multiscale model applies a Lagrangian particle tracking approach to investigate the dynamics of, and heat transfer mechanisms in, nanofluids. The three-dimensional computational region examined consists of a $1\mu\text{m}$ cube filled with stagnant water. This volume element is composed of a collection of 50 nm- Al_2O_3 spherical nanoparticles (40-2000 in number) that are injected uniformly across the domain. The motion of the embedded nanoparticles in the fluid is treated using an Eulerian-Lagrangian hybrid scheme with fixed time stepping. Two directions (x and z) use periodic boundary conditions while the third y direction limits are treated as walls. The particle equations of motion are integrated using the fourth order Runge-Kutta algorithm with a very small time step, $\Delta t = 10^{-11}$ s. The dynamic properties of both phases are coupled to the ambient temperature of the fluid suspension, that being water at 5 to 95 °C.

3. Model Description

The motion of each nanoparticle is described using the Langevin equation (Sloan et al, 2012), where the translational velocity of the i -th particle is obtained from the principle of conservation of linear momentum, using:

$$m_p \frac{\partial \mathbf{v}_i}{\partial t} = \mathbf{F}_i \quad (1)$$

where,

$$\mathbf{F}_i = \mathbf{F}_i^C + \mathbf{F}_i^e + \mathbf{F}_i^v + \mathbf{F}_i^f + \mathbf{F}_i^B \quad (2)$$

Here, m_p and \mathbf{v}_i are the mass and the transitional velocity vector of the i -th nanoparticle, respectively. \mathbf{F}_i^C is the particle contact force, \mathbf{F}_i^e is the electric double layer repulsive force, \mathbf{F}_i^v is the van der Waals attractive force, \mathbf{F}_i^f is the fluid force and \mathbf{F}_i^B is the random Brownian motion force. Other body forces such as gravity and buoyancy are found to be negligible for all length and time scales, since their magnitudes are much smaller than the aforementioned surface forces. The present model simulates the dynamics and

mechanisms responsible for nanoparticle aggregation, including particle collisions and DLVO (theory named after Derjaguin, Landau, Verwey, and Overbeek) inter-particles forces (Israelachvili, 2011), and the fluid force and Brownian motion as random forces. Particle collisions are resolved using a soft sphere approach as described by the Hertzian normal contact theory (Timoshenko and Goodier, 1970). The model describes the collision force between the i -th and j -th sphere in the normal unit direction, \mathbf{n}_{ij} , according to the approach of Fujita and Yamaguchi (2008). For the estimation of inter-surface forces, the DLVO theory is used, with surface separations down to 5 nm. This consists of a repulsive electric double layer exerted between the two spheres, together with an attractive van der Waals force that can be expressed mathematically as:

$$\mathbf{F}_i^e + \mathbf{F}_i^v = \sum_j (f_{ij}^e + f_{ij}^v) \mathbf{n}_{ij} \quad (3)$$

The magnitude of the electrostatic repulsive force exerted on two homogeneously charged spheres can be determined by Derjaguin's approximation (Israelachvili, 2011) using:

$$f_{ij}^e = -\frac{64\pi a n k_b T \theta^2 e^{-\kappa H_{ij}}}{\kappa} \quad (4)$$

and for the attractive van der Waals force:

$$f_{ij}^v = \frac{Aa}{12H_{ij}^2} \quad (5)$$

where a is the radius of a sphere, n is the number density of electrolyte ions, k_b is the Boltzmann constant, T is the temperature of the suspension, θ is the polarizability factor, κ is the inverse of the Debye length, H is the inter-surface distance between spheres and A is the Hamaker constant. The magnitude of the van der Waals force is limited below a maximum value to prevent divergence when the inter-surface distance becomes zero. For the Brownian force exerted on the spherical nanoparticles, the components are modelled using a Gaussian white noise process given by Kim and Zydney (2004):

$$f^B = \xi \sqrt{\frac{12\pi a \mu_f k_b T}{\Delta t}} \quad (6)$$

in which ξ is the coefficient of Stokes drag for a sphere and μ_f is the fluid dynamic viscosity. To determine the magnitude of the fluid force responsible for nanoparticle aggregation in a quiescent system, the following Stokesian equation is applied:

$$f^f = -6\pi a \mu_f V \quad (7)$$

The above nanofluid dynamic model is further coupled to a thermal energy model to predict the overall heat transfer properties of the system. The applied model works on the basis of inter-particle distances which are tracked at every time step in the simulation. The thermal model has also been coded to precisely determine the volume of aggregates formed at each time step, using a depth-first search method to iterate through aggregated particle chains and clusters. The applied technique considers both aggregation kinetics (responsible for the formation of particle percolation pathways) and Brownian motion (responsible for the induced micro-convection). These physical phenomena are found to be responsible for the effective thermal conductivity, k_{eff} , in nanofluids, as noted by Prasher et al. (2006), and can be expressed mathematically as:

$$k_{eff} = (1 + ARe^m Pr^{0.333} \phi) \left\{ \frac{[k_{ag} + 2k_{bf} + 2(k_{ag} - k_{bf})\phi_{ag}]}{[k_{ag} + 2k_{bf} - (k_{ag} - k_{bf})\phi_{ag}]} \right\} k_{bf} \quad (8)$$

where Re is the Brownian Reynolds number, Pr is the Prandtl number, and A and m are constants determined from experiment. Additionally, k_{ag} and k_{bf} represent the thermal conductivity of aggregates and the base-fluid, respectively. The particle volume fraction is given as ϕ for a primary particle and as ϕ_{ag} for aggregated particles that are characterized by their radius of gyration R_a , determined using the depth-first search method.

4. Results and Discussion

Different simulations were performed using the model described, with results analysed to elucidate the forces and mechanisms responsible for nanoparticle dynamics, aggregation and subsequent thermal property enhancement. First, the spontaneous ordering process of the particles in the suspension was examined, followed by clustering and agglomeration with time. Different time step snapshots of the simulations are presented in Fig. 1.

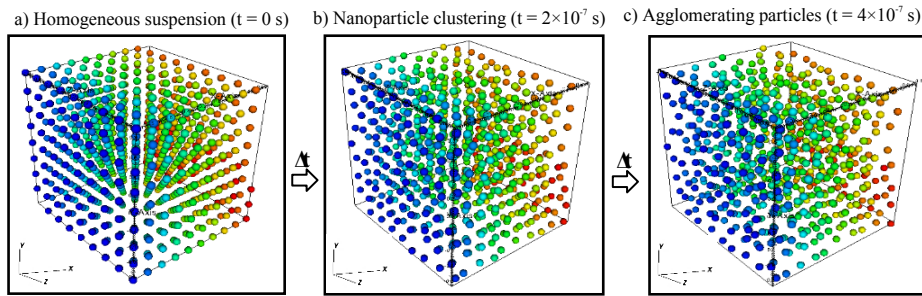


Figure 1. Representation of spherical 50nm Al_2O_3 particles in $1\mu m$ cubic-cell filled with water showing: a) homogenous distribution of particles; b) formation of clusters; and c) nano-aggregation.

The model allows the size of the different forces exerted on nanoparticles in a suspension to be predicted, with Fig. 2 giving the various multiscale forces plotted as a function of the normalized inter-surface distance, H , and the particle radius, a . These predictions indicate the magnitude of the various forces exerted on the particles in the test cell which drive particle aggregation. They also illustrate that when enough distance is maintained between nanoparticles, the effects of both the fluid (drag) and Brownian random motion forces dominate over other contributions as these forces are dependent on the velocity of the nanoparticles and interactions between the particles and the fluid. As the inter-surface distance between particles diminishes, the electric double layer (EDL) repulsive force starts to have a significant effect on the nanoparticles. When two particles are close to colliding, the attractive van der Waals force (VDW) starts to become dominant over all others. After a collision of two nanoparticles, the repulsive force increases rapidly and matches well with the attractive force. This change in the magnitude of the forces with inter-particle distance leads to the conclusion that every single force noted has to be considered in the dynamic modelling of nanofluids. The values noted in Fig. 2 are in excellent agreement with similar results in the literature

(Sloan et al, 2012; Fujita and Yamaguchi, 2008). The present model has been validated against experimental thermal conductivity data obtained in some of the studies described earlier, with good agreement found. This validation will be the subject of future publications. The model can also determine the number of nanoparticle collisions and the volume of each agglomerate formed in the system, with Fig. 3 giving predictions of the average number of inter-particle collisions occurring with time at different volume concentrations.

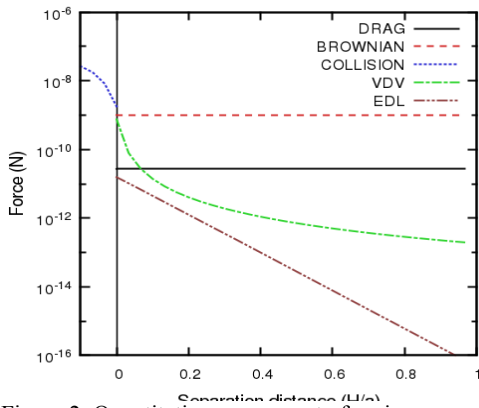


Figure 2. Quantitative assessment of various forces driving aggregation in nanofluids.

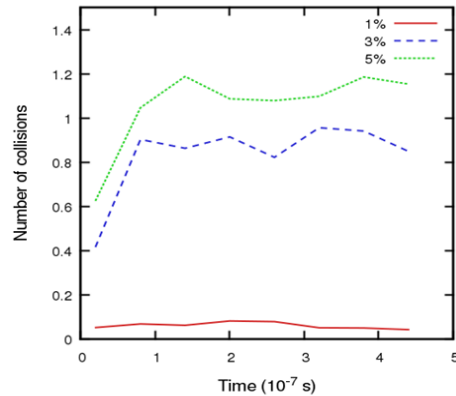


Figure 3. Collisions of particles in nanofluids as a function of particle volume concentration.

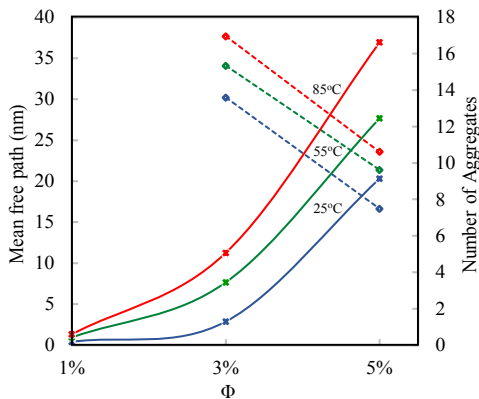


Figure 4. Mean free path (----) and number of aggregates (—) at different volume fractions.

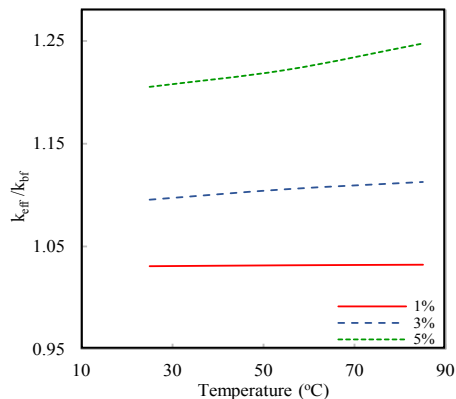


Figure 5. Enhancement in thermal conductivity of Al₂O₃-water nanofluid with temperature.

It is clear from Fig. 3 that the average number of collisions increases as a function of nanoparticle volume concentration. Very few collisions take place when the system concentration is 1 vol%. However, above 3 vol%, the system enters a regime where both collision and agglomeration begin to take place more frequently. Mean free path results corresponding to the results in Fig. 3 are given in Fig. 4, leading to the same conclusion. Hence, at 3% volume fraction, the mean free path clearly decreases with time due to collisions and agglomeration taking place in the system. Such dynamic forces also govern the thermal behaviour of nanofluids, with a direct relationship between the normalized thermal conductivity and temperature at different volume fraction of particles evident in the results of Fig. 5. The results for the thermal

conductivity demonstrate an almost 13% increase with time for a 5 vol% Al₂O₃ nanofluid, as is evident in Fig. 5. These predictions were performed for the given range of temperatures 25 to 85 °C, and shows that further enhancement is expected due to increases in kinetic energy and hence in the fluid and Brownian motion forces. The increasing number of collisions and aggregation with time and concentrating indicates the effect of direct particle contact and the agglomerates' percolation effects on the conductivity. The observed combined effects of convection and conduction of thermal enhancement in nanofluids has been reported by Prasher et al. (2006), and is of the same magnitude. It predicts a linear relationship between the thermal conductivity, temperature and volume fraction. All these results support the use of nanofluids in thermal energy storage applications.

5. Conclusions

Key variables related to the stability and thermal conductivity of nanofluids have been examined using multiscale simulation. The model enables the prediction of various dynamic forces, and gives quantitative predictions of the magnitude of those forces, including their role in particle aggregation. It has also been found to perform well in comparison with similar studies, and provides confirmation of the effect of particle size and concentration on the thermal conductivity of the system. Future work will extend the model's application to include other fluids such as molten salts (used for thermal energy transfer and storage applications), and to flow situations by coupling the tracking approach with direct numerical simulations.

Acknowledgements

BHM gratefully acknowledges the financial support of the Kuwait Institute for Scientific Research (KISR).

References

- S.U.S. Choi and J.A. Eastman, 1995, Enhancing thermal conductivity of fluids with nanoparticles, Developments and Applications of Non-Newtonian Flows, ASME, New York, FED-Vol 231/MD-Vol 66, 99-105.
- M. Fujita and Y. Yamaguchi, 2007, Multiscale simulation method for self-organization of nanoparticles in dense suspension, *J. Comput. Phys.*, 223, 108-119.
- J.N. Israelachvili, 2011, Intermolecular and surface forces, Elsevier, Amsterdam.
- M. Kim and A.L. Zydney, 2004, Effect of electrostatic, hydrodynamic, and Brownian forces on particle trajectories and sieving in normal flow filtration, *J. Colloid Interface Sci.*, 269, 425-431.
- R. Prasher, P.E. Phelan and P. Bhattacharya, 2006, Effect of aggregation kinetics on the thermal conductivity of nanoscale colloidal solutions, *Nano Lett.*, 6, 1529-1534.
- G. Sloan, Z.-G. Feng, K. Bhaganagar and D. Banerjee, 2012, Coupled direct numerical simulation and experimental approach to develop framework for nano fluids, ASME International Mechanical Engineering Congress and Exposition, 7, 2877-2882.
- J. Israelachvili, 2011, Intermolecular and surface forces, Academic Press, London.
- S.P. Timoshenko and J.N. Goodier, 1970, Theory of elasticity, McGraw-Hill, New York.
- X.Q. Wang and A.S. Mujumdar, 2008a, A review on nanofluids – Part I: Theoretical and numerical investigations, *Braz. J. Chem. Eng.*, 25, 613-630.
- X.Q. Wang and A.S. Mujumdar, 2008b, A review on nanofluids – Part II: Experiments and applications, *Braz. J. Chem. Eng.*, 25, 631-648.

Multiobjective optimization of eco-industrial parks: evaluation of environmental impacts at the watershed scale

Laura Garcia de Dios^a, Marianne Boix^a, Sabine Sauvage^b, Iréa Touche^a,
Roxelane Cakir^b, Ludovic Montastruc^a, Jose Miguel Sanchez Perez^b

^a*Laboratoire de Génie Chimique (LGC), UMR 5503 INPT-CNRS-UPS, 4, Allée Emile Monso, 31432 Toulouse, France*

^b*Laboratoire d'Ecologie Fonctionnelle (ECOLAB), UMR 5245 CNRS-UPS-INPT, Avenue de l'Agrobiopole, 31326 Castanet-Tolosan, France*

Abstract

Water, as everybody knows, is a limited and fragile resource. In fact, water faces several challenges in the future due to the increase of population, pollution, climate change, etc. To overcome these problems, some concepts linked to sustainable development such as “Industrial Ecology” have emerged. The concept of industrial ecology is defined as a group of companies, close in proximity to each other, who cooperate with the objective of sharing resources such as energy, water or services in order to act in a more efficient way and more respectfully to the environment. However, environmental impacts of such organizations are still difficult to identify and the impacts on the local environment could be very different from a larger surrounding ecosystem such as a watershed. The aim of this work consists in defining the optimal configuration of EIP in the watershed so that impacts of industrial activities are minimized considering a large-scale system. This study develops a multiobjective optimization based approach by combining two models. The first one consists of the optimisation of the water networks of clusters of companies to make them work as eco-industrial parks where a multi-objective optimisation approach is used. Secondly, the impact of this ecological strategy/policy is studied at a bigger scale: the Garonne watershed, in France modelled through a Material Flow Analysis (MFA). This model helps to track and measure the quality of the water, before and after the implementation of the eco industrial parks. In each scenario studied, there is a significant reduction of the pollutant concentration, proving the benefits of the implementation of an industrial ecology policy at a larger scale. Depending on which industrial area is transformed into an EIP, one can observe a diminution of the pollutant concentration up to 70% at the estuary.

Keywords: eco-industrial parks, multi-objective optimization, watershed scale, Material Flow Analysis

1. Introduction

Water is a fragile, precious and limited resource and is not only important for domestic or sanitary purposes, but every human economic activity relies on the existence of this element. In addition, leaving the human scope, every marine and terrestrial ecosystem depends on water somehow. This fact underlines the huge importance of this resource. Nevertheless, many recent reports have demonstrated that water is in danger. Indeed,

there is a clear evidence that in many rivers and aquifers there has been a reduction in its water quantity and quality. Water scarcity is a problem in many countries and many ecosystems have been modified until a point of no return. One of the most prominent problem is the pollution caused by agriculture and industry. This situation can cause significant damages, not only to ecosystems, but also to humans.

In conclusion, most of the problems evoked have a human origin and as a result, governments and society in general must act to reverse this situation. Efficiency in water use must be increased, technology must be developed and in this situation, research has an important role, because there are still many questions to answer and strategies to establish.

All this concern about resources in general, not only water, led to the birth of a great deal of new concepts such as sustainable development or industrial ecology. Industrial ecology consists of understanding human industrial activities as a natural ecosystem (Frosh and Gallopoulos, 1989). Indeed, a natural ecosystem represents equilibrium, sustainability and the use of every resource in the most efficient way as possible, reducing consumption and waste. One of the most important ideas in implementing Industrial Ecology is to establish eco-industrial parks. An eco-industrial park can be understood as a group of facilities in the same geographic region that try to optimise the use of energy, water and raw material flows, looking for economic benefits for all of them and for a better environmental performance (Lowe, 1997). Nevertheless, among all the eco-industrial parks that have been built, most of them are working in sub-optimal conditions because they have been built somehow, spontaneously. In other words, gradually some improvements were introduced, but a complete industrial park reconfiguration was never established.

The objective of this research is to introduce the conception of robust mathematical methods to design eco-industrial parks while taking into account the effects of such a policy at a bigger scale: the watershed scale. In order to convince the industries owners to be a part of these changes and to obtain real profits from them through a multiobjective optimization.

2. Objectives and methodology

During this research, several EIPs are going to be established within a region, from existing facilities or existing industrial areas. The reconfiguration of these facilities into eco-industrial parks is going to be limited to their water networks. The idea is to investigate deeply the impact of this politic at a bigger scale, the scale of the whole watershed. The objectives of this work are summarized below:

- To model a watershed. A Material Flow Analysis (MFA) to track and measure the quality of the river water is developed based on Lopez-Diaz et al. (2015).
- To develop a multi-objective optimization model for the water networks reconfiguration.
- To study the impacts of these changes on the watershed.
- To look for data to apply, specifically, this model to the Adour-Garonne watershed in France.

According to Figure 1, the two models interact with firstly the run of the MFA model to obtain the parameters of the watershed without the eco-industrial park's effects. Then, in the optimization model (MILP), the data related to water network of the industries are changed to make the industries work as eco-industrial parks. Finally, the results of the EIPs reconfiguration are loaded again into the MFA model to obtain the effects of these

modifications in the watershed, following the methodology developed by Lopez-Diaz et al. (2015).

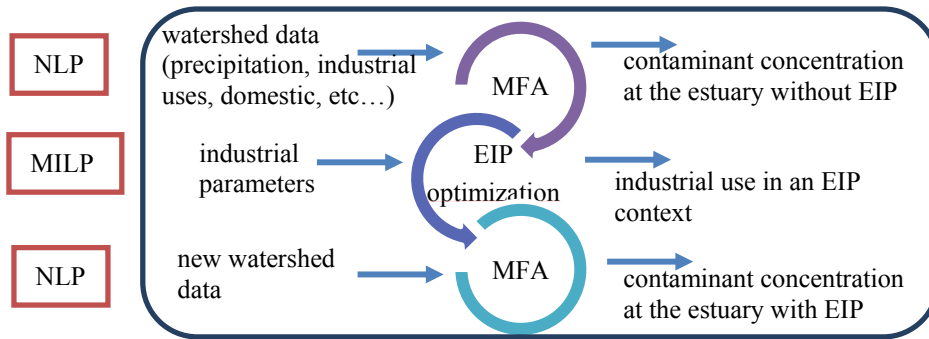


Figure 1. Methodology used in this study

3. Material Flow Analysis

The river flow along the watershed is modeled through a Material Flow Analysis (MFA), so its quality can be studied before and after the reconfigurations of the eco-industrial parks. To start with, the river is divided into several parts (Figure 2). The main parts are going to be called reaches and the secondary sections will be the tributaries. In general, this model is going to consist of some mass balances per reach and tributary, this allows to solve several consecutive small problems rather than a big non-linear one, more difficult to solve. This problem is formulated as a Non-Linear Problem (NLP) that has been solved within GAMS environment with DICOPT solver. Its most important variable is the pollutant concentration at the final disposal. With the changes on this variable before and after the establishment of the eco-industrial park their effects on the environment will be evaluated.



Figure 2: Decomposition of the river basin in reaches and tributaries (from Lopez-Diaz, 2015)

4. Multi-objective optimization of eco-industrial parks

As it has been showed in the previous figure, within a single watershed there can be several industrial parks or clusters of companies. Moreover, these industrial complexes are constituted by individual plants modelled as a group of process sources (i) and process sinks (j) to be reconfigured as EIP. Besides, a regeneration to clean the water

that has been used is added. This unit can be called an interception unit as well. The interception unit consists of several interceptors (int).

The superstructure defines the whole set of available solutions in a network so that all the possible links between units can be seen. For instance, the water used by a process unit leaves the sources to be used again in a process sink if some conditions, in relation to quality, are achieved. This water can also be sent to the regeneration unit. Furthermore, the flow leaving the sources can be sent directly to the environment without any previous treatment if the concentration constraints are respected. The process sinks can receive water from the sources, the interception unit or from fresh water sources directly. Finally, the interception unit is constituted by several interceptors, as it has been mentioned before. Each interceptor receives used water from process sources, it cleans the water and it can send it, either to the environment or to other process sinks so the water can be used again.

The companies that constitute the industrial parks are going to be working on their own at the beginning. With this methodology, all the plants characterized by their sources, sinks and interceptors are going to start working together, by sharing their water networks. For example, the water of one source of one specific plant can feed any sink of any plant; it can go to any interceptor of the industrial complex, etc. This way, the industrial plants will integrate an eco-industrial park. This optimization step will give a new optimal topological configuration of the water network as a solution by minimizing the total cost and environmental impact (fresh water consumption).

The problem is formulated as an MILP and solved within GAMS environment with CPLEX solver. The main equations are mass balances for each sink, source and interceptors, the total cost and environmental functions and more constraints that complete the model (Boix et al., 2012).

5. Case study: the Garonne watershed in France

5.1. Description of the case study

In this study, four possible eco-industrial parks are considered to be placed in the Garonne watershed. To model the Garonne watershed firstly, it is necessary to divide the watershed into different sub-watersheds, as the MFA model requires. Secondly, some information about the watershed was needed for each partition that had been done, for example the precipitations rate, industrial, residential and agricultural discharges, losses, usages, initial flows, etc.

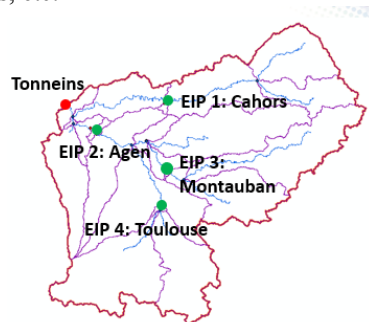


Figure 3: Garonne watershed

To reach this purpose, a model is developed in ArcSWAT (Arnold et al., 2012) for the watershed of Garonne. The watershed has been divided into 22 sub-basins and the final disposal has been placed in Tonneins. Also, it has been decided to place the possible eco-industrial parks in Toulouse, Montauban, Cahors and Agen (Figure 3). Firstly, with all this information, the MFA model for the Garonne watershed with normal industrial parks (without any collaboration) was developed and the concentration of pollutant at the final disposal is obtained: 2.03 ppm. Then, the multi-objective optimization of all the four industrial parks is carried out and the information obtained in relation to the pollutant concentration and the wastewater is introduced again into the MFA model to evaluate the changes in the pollutant concentration.

5.2. Reconfiguration of industrial parks into EIP by multi-objective optimization

In this study, four possible eco-industrial parks are considered to be placed in the Garonne watershed. For each of them a multi-objective optimisation process has been carried out. The optimisation variables were fresh water, regenerated water, number of connections, total cost and the pollutant concentration expelled to the environment. To solve this problem, for each eco-industrial park a Pareto front has been drawn and, from this set of optimal solutions, the optimal TOPSIS solution has been chosen. In order to illustrate this step, Figure 4 represents one of the four EIP Pareto fronts that have been built; the figure is related to EIP n°1 and represents the fresh water consumption (environmental objective) with the regenerated water (economic objective) for several number of connexions.

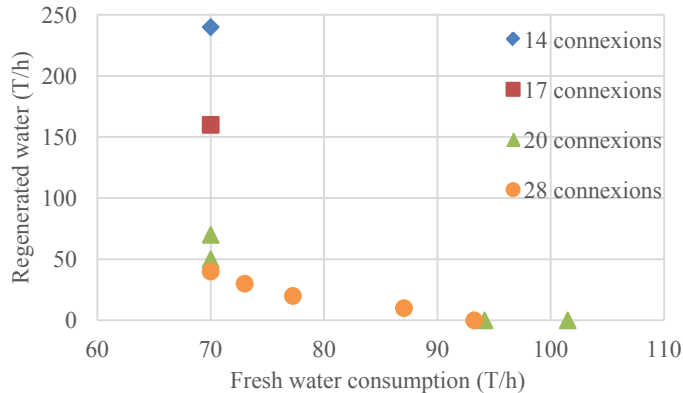


Figure 4: Pareto Front of the EIP 1

5.3. Environmental impacts of EIP policy at the watershed scale

Several strategies were studied: first, only one of the four EIP is working while the others stay as classical industrial parks, then some combinations of them and finally all of them are working at the same time. All these configurations were then compared to the pollutant concentration at the final disposal, without any eco-industrial park in the watershed. Figure 5 summarizes the results obtained during this study where the pollutant concentration at the final disposal is reported for the different strategies explored.

Some important results must be underlined:

- A global diminution of the pollutant concentration at the estuary is observed for every strategy of EIP development

- Each EIP does not have the same effect on the overall watershed, for example, EIP 3 leads to a greater reduction than EIP 4. This is mainly because EIPs have different sizes and are located at different places in the watershed what causes different environmental impacts.

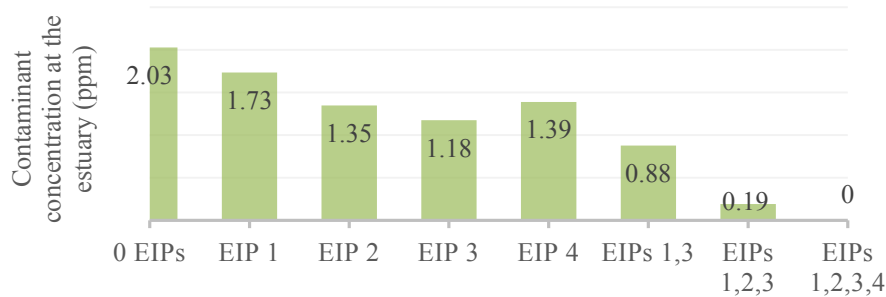


Figure 5: Pollutant concentration at the final disposal under several strategies of EIP development

6. Conclusions

As a general conclusion, it must be highlighted that the implementation of industrial ecology strategies is always interesting. The development of eco-industrial parks reduces pollution and studying the eco-industrial parks effects on a bigger perspective or scale, such as the scale of a whole watershed. This study helps us to understand their influence or beneficial impacts in a better way and the strategy developed aims at implementing this strategy with a higher performance. The optimal location for these eco-industrial parks in the watershed has a major influence in their final environmental impact. Nevertheless, this task is not completely finished. Some improvements can be added to both models, the EIP's model and the MFA model. Starting with the first one, this model can be enhanced by making the code multi-pollutant, the cost equations can be improved, other ways of introducing the ecological effects into the code or more ecological parameters could be studied. Moreover, the eco-industrial park concept can be extended by sharing not only water but also more resources such as energy or other materials.

References

- Arnold, J.G., Kiniry, J.R., Srinivasan, R., Williams, J.R., Haney, E.B., Neitsch, N.L., 2012. Soil and Water Assessment Tool (SWAT), Introductory Manual, Texas Water Resources Institute.
- Boix, M., Montastruc, L., Azzaro-Pantel, C., Pibouleau, L., Domenech, S., 2012. Industrial water management by multiobjective optimization: from individual to collective solution through eco-industrial parks. *Journal of Cleaner Production*, 22, 85-97.
- Frosch, R. A., & Gallopoulos, N. E. (1989). Strategies for manufacturing. *Scientific American*, 261(3), 144-152.
- López-Díaz, D. C., Lira-Barragán, L. F., Rubio-Castro, E., Ponce-Ortega, J. M., & El-Halwagi, M. M. (2015). Synthesis of eco-industrial parks interacting with a surrounding watershed. *ACS Sustainable Chemistry & Engineering*, 3(7), 1564-1578.
- Lowe, E. A. (1997). Creating by-product resource exchanges: strategies for eco-industrial parks. *Journal of cleaner production*, 5(1-2), 57-65.

Coke Formation Model in Crude Oil Furnace for Maintenance Scheduling

Amata Anantpinijwatna

Department of Chemical Engineering, Faculty of Engineering, King Mongkut's Institute of Technology Ladkrabang, 1 Chalongkrung Rd., Lat Krabang, Bangkok, TH-10520, Thailand

amata.an@kmitl.ac.th

Abstract

A crude oil distillation unit (CDU) is one of the most important unit in petroleum industry. Its main function is to separate the crude oil into many kinds of petroleum products. Generally, the CDU's design includes the crude oil preheater, which are either cabin or vertical cylindrical furnace, for adjusting the crude feed properties and increasing feed temperature. Carbon coking inside the furnace during the preheating process leads to accumulating of the coke, deteriorating of the product quality, increasing of the pressure drop across the furnace, and increasing of the energy consumption. The de-coking process is normally executed on demand based on the measured heat loss or performed every fixed period of time. However, due to the different rate of coke formation of various crude oil grades, as well as the difference in cost of product, process operation, and maintenance operation; both on-demand and fixed maintenance practices are not optimal method for de-coking. Model of the coking rate and accumulation inside of the furnace could be a useful tool for scheduling the de-coking. The model includes the balance equations for the heat generated, the heat transfer in forms of convection and radiation, the changes of the temperature and the amount of crude oil and coke, the constitutive equations for the coke formation and accumulation, and the conditional equations for optimization of the de-coking schedule. The model parameters are fitted to the data provided by the refinery in Thailand with absolute average deviation below 3%; the operation and maintenance costs are also estimated from the financial activity report of the similar sources. It is found that with different sources of crude oil, the optimal furnace maintenance schedules are different. The improvements, in term of cost per maintenance, are found to be 15 - 34% depending on the operation scenario. Although, the initial results look promising and the initial goal is accomplished, the application of the model toward multiple crude oil feed for better operation is under development.

Keywords: Modelling, Crude Oil Furnace, Coke Formation, Scheduling, Optimization

1. Introduction

A crude oil distillation unit (CDU) is one of the most critical and important unit in petroleum industry. Its main function is to separate the crude oil into many kinds of petroleum products (Motlaghi et al., 2008). General design of the CDU includes the crude oil preheater, which are either cabin or vertical cylindrical furnace, for adjusting the crude feed properties and increasing the feed temperature (Jegla et al., 2011; Pelini, 2008). The crucial issue found in the furnace is carbon coking, which occurred at the

inner-side of the crude oil tube in the furnace during the preheating process. The carbon coking and coating of the inner tube leads to the coke accumulating, the product quality deteriorating, the pressure drop increasing across the furnace, the energy consumption increasing, and the tube wall carbonization corroding (Jegla et al., 2011). Therefore, occasional de-coking of this furnace is required.

Generally, the de-coking is executed on demand based on the measured heat loss, or performed every fixed period of time (Towfighi et al., 2002). However, due to the different rate of coke formation of various crude oil grades, as well as the difference in cost of product, process operation, and maintenance operation; both on-demand and fixed maintenance practices are not optimal method for de-coking. Modelling of the coke's formation and accumulation rates at the inner tube of the furnace could be a useful tool for optimizing, predicting, and scheduling the de-coking period.

2. Model Development

The model has been developed with the modelling methodology proposed by Cameron and Gani (2011) based on the typical cabin furnace shown in Figure 1A.

2.1. Furnace Model

The furnace increases the temperature of the crude from 231 °C to 362 °C; consisting of 5 natural gas burners at the bottom. The crude is fed into the upper convection section, receiving the heat from the convection and radiation of the combusted gas, and raising the temperature to 288.5 °C. The heated oil is then passed through the bottom radiation section where the radiation directly from the burner flame is the main source of the heat; in this section, the crude temperature is increased to 362 °C.

The models for both convection and radiation sections have been developed similarly as presented in Figure 1B. The system consists of the heat transfer to the crude by convection as displayed in equations 1 - 3. It is worth mentioned that the coke inner

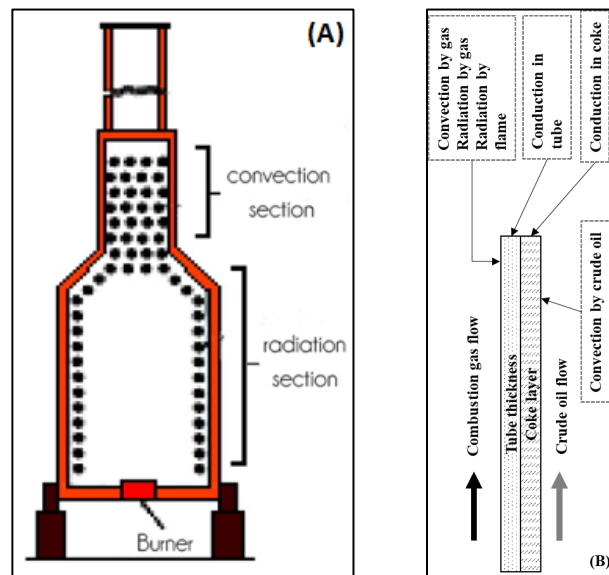


Figure 1. A: typical cabin furnace configuration (KLM Technology Group, 2013) and B: Representation of the radial cut of the system

tube radius ($r_{Co,i}$) is calculated from the amount of coke formed described in the next section.

$$Q_C = m_c c_C^p (T_{C,i} - T_{C,o}) \quad 1$$

$$A_{Co,i} = 2\pi r_{Co,i} L_{Co} \quad 2$$

$$T_{Co,i} = \frac{Q_C}{h_C A_{Co,i}} + T_{C,o} \quad 3$$

The heat transfers through the coke layer and the tube wall by conduction are displayed by equations 4 - 6.

$$T_{w,i,t} = T_{Co,o,t} = \frac{Q_C x_{Co,t}}{k_{Co} A_{w,i}} + T_{C,i} \quad 4$$

$$A_{w,o} = 2\pi r_{w,o} L_w \quad 5$$

$$T_{w,o,t} = \frac{Q_C \Delta x_w}{k_w A_{w,o}} + T_{w,i,t} \quad 6$$

And the outside tube wall heat transfers by the convection from the combusted gas and the radiations from the combusted gas and the flame are described with the equation 7, where the first term is only considered in the radiation section calculation.

$$Q_{r,t} = \frac{\sigma(T_f^4 - T_{w,o,t}^4)}{\frac{1 - \varepsilon_w}{\varepsilon_w A_{w,o}} + \frac{1}{A_f F_{ij}}} + h_g A_{w,o} (T_g - T_{w,o,t}) + \frac{\sigma(T_g^4 - T_{w,o,t}^4)}{\frac{1 - \varepsilon_w}{\varepsilon_w A_{w,o}} + \frac{1}{A_g F_{ij}}} \quad 7$$

As already discussed, the radius of the coke inner tube ($r_{Co,i}$) and the convective length of the coke ($x_{Co,t}$) are changing by time, depending on the amount of the coke formed throughout the operation, which is discussed in the next section.

2.2. Coking Mechanism

From the work of Towfighi et al. (2002), there are 3 mechanisms for coke formation in the furnace: catalytic coking, polyaromatic condensation, and radical coking.

2.2.1. Catalytic coking

Typical furnaces consist of iron, chromium, and nickel which behave catalysts-like; where the hydrocarbon is chemisorbed and react into crystalline filament on the metal surface as shown in Figure 2A.

2.2.2. Polyaromatic condensation

As displayed in Figure 2B, some polynuclear aromatics are produced by trimerization reaction; then these aromatics are dehydrogenated and condensed as tar droplets or soot particles onto the surface of the furnace.

2.2.3. Radical coking

At the interface between the coke and the crude, the unsaturated molecules can react with the remaining free-radical position of the coke, following with the decomposition and dehydrogenation reaction. Thus, resulting in the growing of the aromatic structure and regenerating of the free-radical molecules and sites, as shown in Figure 2C.

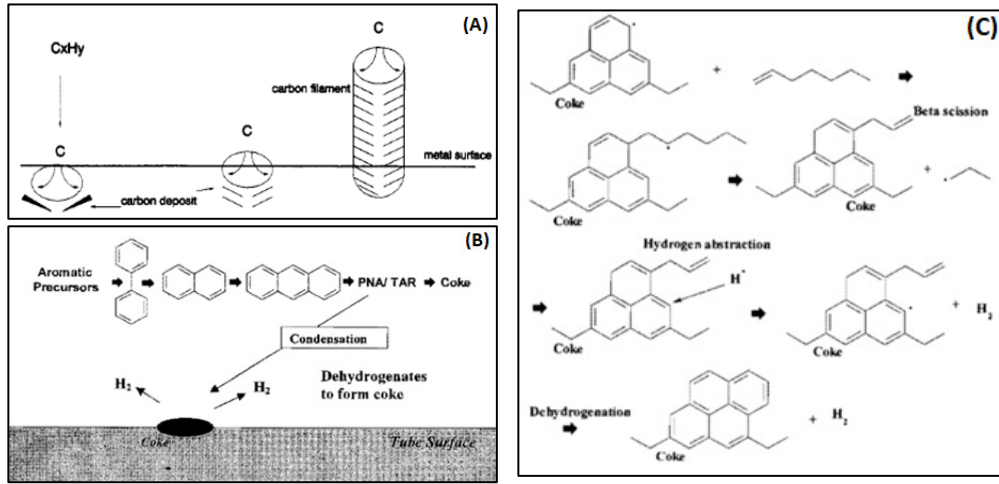


Figure 2. Coking mechanisms (Towfighi et al., 2002)

The rate of the coke formation is described by non-elementary reaction rate law, where the rate constant follows the Arrhenius equation, as displayed in equations 8 - 10.

$$k_{m,n} = Ae^{\frac{-E_{a,m,n}}{RT_{av}}} \quad 8$$

$$r_{m,n} = k_{m,n} C_m^{\alpha_{m,n}} \quad 9$$

$$x_{Co,t} = \frac{r_{m,n} MW_m t V}{\rho_{Co} \cdot A_{tu,i}} \quad 10$$

The composition of the crude is also considered to have an effect to the formation rate of the coke. In this study, the crude is divided by the cut-point temperature into 5 compositions as shown in Table 1.

The compositions of the crude are calculated from equation 11, where the volume average boiling points (VABP) are estimated from Figure 3.

$$VABP = \frac{T_0 + 4T_{50} + T_{100}}{6} \quad 11$$

Table 1. Crude category and their cut-point temperature (Uppaluri, 2010)

Crude Composition Category	Cut-point temperature (K)
Naphtha	Less Than 463.71
Kerosene	463.71 - 552.04
Light Gas Oil (LGO)	552.04 - 594.26
Heavy Gas Oil (HGO)	594.26 - 633.15
Residue	More Than 633.15

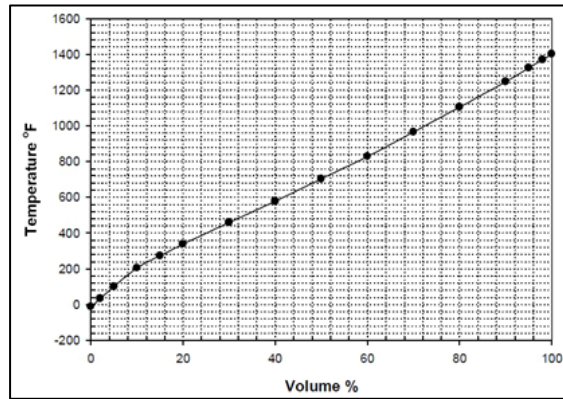


Figure 3. Total boiling points by volume of the crude generally used in Thailand (Thai Customs Department, 2016; Uppaluri, 2010)

3. Results

The data for the coke formation and accumulation inside the furnace and the furnace configuration are taken from various researcher (Bayat et al., 2012; Chaibakhsh et al., 2015; Coletti and Macchietto, 2011; Jafari Nasr and Majidi Givi, 2006; Jegla et al., 2011). Figure 4 shows the comparison between the measured data and the model predicted amount of the coke accumulation inside the furnace; the overall absolute average deviation is less than 3% with maximum deviation below 15%.

The regressed parameters are then utilized for the optimization of the crude oil furnace maintenance scheduling. As presented in Figure 5, the cost of natural gas consumed as fuel for the fixed maintenance schedule is undoubtedly highest, since the scheduling maintenance period tend to be longer than the optimum period; while the proposed optimum scheme costed the lowest since it could predict accurately the maintenance period. On the other hand, the expense of the routine maintenance scheduling is the lowest amongst all schemes because there will be no extra “urgent” scheduling involved; however, the optimum scheduling requires not much more maintenance cost

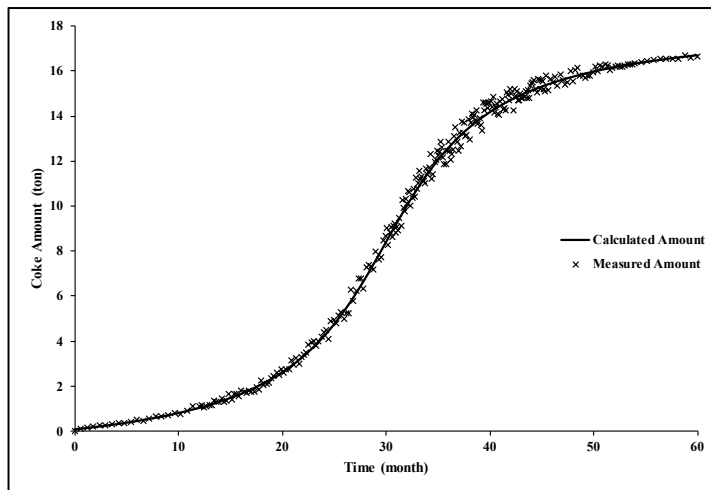


Figure 4. Comparison between the calculated coke amount (line) and the measured coke amount (dotted) inside the furnace tube

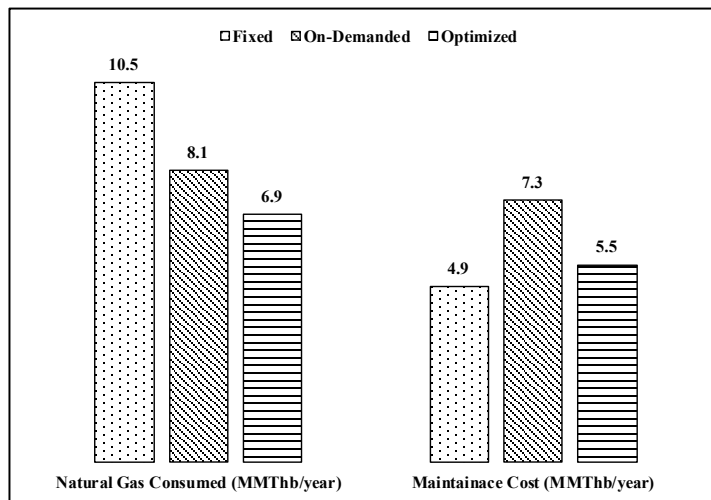


Figure 5. Comparison of the involved cost between the different operation scheme

compare to the on-demand scheduling. Moreover, the sum of the operation and maintenance cost of the optimum case is by far lower than the other cases.

4. Conclusion

In this work, the time-dependent lumped model of the coke formation in the furnace of the CDU has been developed. The model parameters have been regressed and validated with the measured data from various sources. The model has been then applied for the optimization of the furnace maintenance scheduling; around 20% of the operating and maintenance cost could be saved with the optimum operation scheme.

Although, the objective of this model development has been achieved; further study on the one or two dimension models and their applications are desired, since they could provide more detailed option for the maintenance and operation.

References

- Bayat, M., Aminian, J., Bazmi, M., Shahhosseini, S., Sharifi, K., 2012. *Energy Convers. Manag.* 64, 344–350.
- Cameron, I.T., Gani, R., 2011. *Product and Process Modelling : a Case Study Approach*. Elsevier Science.
- Chaibakhsh, A., Ensansfat, N., Jamali, A., Kouhikamali, R., Najafi, H., 2015. *Appl. Therm. Eng.* 83, 57–70.
- Coletti, F., Macchietto, S., 2011. *Ind. Eng. Chem. Res.* 50, 4515–4533.
- Jafari Nasr, M.R., Majidi Givi, M., 2006. *Appl. Therm. Eng.* 26, 1572–1577.
- Jegla, Z., Kohoutek, J., Stehlik, P., 2011. *Int. Conf. Heat Exch. Fouling Clean.* 7–14.
- KLM Technology Group, 2013. *Furnace (Engineering Design Guideline)*, 2nd ed. KLM Technology Group, Johor Bahru.
- Motlaghi, S., Jalali, F., Ahmadabadi, M.N., 2008. *Expert Syst. Appl.* 35, 1540–1545.
- Pelini, R.G., 2008. *Chem. Eng.* 115, 34–41.
- Thai Customs Department, 2016. *Statistic data of December 2016 - by country* [WWW Document]. http://www.customs.go.th/statistic_report.php?tab=by_country.
- Towfighi, J., Sadrameli, M., Niaei, A., 2002. *J. Chem. Eng. JAPAN* 35, 923–937.
- Uppaluri, R., 2010. *Refinery Process Design*. Department of Chemical Engineering Indian Institute of Technology Guwahati, Assam, India.

Microbubbles coalescence during transport in vertical channel flows

K.S. Asiagbe^{*}, M. Fairweather, D.O. Njobuenwu, M. Colombo

School of Chemical and Process Engineering, University of Leeds, Leeds LS2 9JT, UK

**pmksa@leeds.ac.uk*

Abstract

Large eddy simulation coupled to a Lagrangian bubble tracker, previously developed to study two-way coupled turbulent bubbly flows in channels, is extended to cover four-way coupling. The bubble tracker accounts for bubble collisions with a hard-sphere model and bubble coalescence using a film-drainage model. Upward and downward vertical channel flows of water at shear Reynolds numbers of 150 and 590 are examined, with air bubbles of diameter $d_b = 220 \mu\text{m}$ dispersed within the flows. Turbulence is found to significantly impact the level of bubble interaction, increasing the number of collisions and coalescences, but at the same time also increasing the number of collisions that do not result in a coalescence event (coalescence efficiency). The different behaviour of the bubbles, and the impact it has on the turbulence field in the two flow configurations examined, also plays a major role in the coalescence process. The paper demonstrates the capabilities of the overall model for predicting coalescence in bubbly flows, and its ability to model flows of industrial relevance such as enhanced oil recovery, fermentation processes etc, the results from which are also of value in increasing our understanding of such flows

Keywords: Eulerian-Lagrangian, microbubbles, coalescence, turbulent flow

1. Introduction

In many processes that rely on bubbly flows, such as those that use bubble column reactors and mixing equipment, mineral processing, fermentation, and oil and gas transportation and treatment, interfacial transfer is mainly governed by the interfacial area density. This drives exchanges of mass, momentum and energy between the phases and evolves continuously as a function of the bubble size distribution. In turbulent flows, most of the changes that occur within the flow result from bubble collision, coalescence and break-up that follow from interactions between the bubbles and the turbulence field. At present, knowledge of these processes is still limited and no general agreement on a commonly accepted modelling framework has been reached. This study has considerable industrial relevance such as enhanced oil recovery, fermentation processes, mineral processing etc.

In the present paper, a bubble collision and coalescence model is introduced into a Lagrangian bubble tracking routine previously developed to study bubbly flows in channels (Asiagbe et al., 2017). In this routine, individual bubble trajectories are deterministically predicted, differently from in Eulerian-Eulerian methods, where phases are treated as interpenetrating continua and, consequently, the behaviour of individual bubbles, including their position, velocity and the size of each bubble, is not

directly known. In this work the continuous phase flow field is predicted using large eddy simulation (LES), the use of which, when coupled to a Lagrangian bubble tracking routine, is less demanding computationally than studies based on direct numerical simulation. LES is, however, of sufficient accuracy when contrasted with the more commonly used Reynolds-averaged Navier-Stokes approach to allow confidence in using its predictions to understand and reliably predict bubbly flows that are of industrial importance. This is largely because in LES, accurate turbulence field predictions are obtained through full simulation of large scale anisotropic turbulent motions, with only the smaller scale isotropic motions having to be modelled.

In the tracking routine, the bubbles are assumed to be non-deformable and momentum coupled with the fluid, and are treated as pointwise spheres. The overall model is applied to vertical upward and downward channel flows of water at shear Reynolds numbers of 150 and 590. At the beginning of each simulation, air bubbles with $d_b = 220 \mu\text{m}$ are uniformly dispersed in the channel. With the aim of improving current understanding of, and the ability to predict, bubble coalescence, the impact of turbulence, and the different behaviour of bubbles in the two channel flow configurations noted, the rate of collision and coalescence is carefully analysed and discussed.

2. Computational Methods

LES was adopted to compute the continuous phase flow field. In LES, the fluid flow is divided into large scale turbulent motions, which are resolved by the computation, and small, sub-grid scale (SGS) fluctuations by use of a filtering operation. The flow field was calculated by integrating the mass and momentum balance equations, with results made dimensionless using the half-channel height, h , the fluid density, ρ , and the shear velocity, u_τ , defined as the square root of the ratio of shear at the wall, τ_w , to the fluid density. The SGS stress arising from the top-hat filtering operation on the Navier-Stokes equations was modelled using the Germano dynamic model (Germano et al., 1991).

The trajectory of each microbubble was tracked in a Lagrangian framework using the following equation of motion:

$$\frac{d\mathbf{v}}{dt} = \left(1 - \frac{\rho_l}{\rho_b}\right)g + \frac{\mathbf{u} - \mathbf{v}}{\tau_b} C_{SN} + C_L \frac{\rho_l}{\rho_b} [(\mathbf{u} - \mathbf{v}) \times \boldsymbol{\omega}] + \frac{\rho_l}{\rho_b} \frac{D\mathbf{u}}{Dt} + \frac{\rho_l}{2\rho_b} \left(\frac{D\mathbf{u}}{Dt} - \frac{d\mathbf{v}}{dt}\right) + \boldsymbol{\chi}_{sgs} \quad (1)$$

In Eq. (1), the terms on the right-hand side represent the different forces acting on the bubble motion, which are the gravity/buoyancy, drag, shear lift, pressure gradient and added mass forces, respectively. The final term, $\boldsymbol{\chi}_{sgs}$, represents the effect of SGS velocity fluctuations on the bubble motion which was determined using a stochastic Markov model (Bini and Jones, 2008). Subscripts l and b depict the liquid and bubble, respectively. τ_b is the bubble response time, expressed as $\tau_b = \rho_b d_b^2 / 18\mu$, with d_b the bubble diameter and μ the fluid viscosity. C_{SN} and C_L represent the drag and lift coefficients. C_{SN} modifies the Stokesian drag force for large bubble Reynolds numbers (Schiller and Naumann, 1935) and is equal to $(1 + 0.15 \text{Re}_b^{0.687})$. The lift coefficient C_L is a function of the flow Reynolds number and was calculated using the model of Legendre and Magnaudet (1997). The bubble position vector $\mathbf{x}_b = (x_b, y_b, z_b)$ was obtained by further integration of Eq. (1).

Deterministic, inter-bubble collisions were assumed to be binary (Breuer and Alletto, 2012) and modelled using a hard-sphere approach. For modelling the coalescence process, the film drainage theory proposed by Prince and Blanch (1990) was adopted. In the film drainage model, the coalescence process is divided into three steps: (i) two bubbles collide and trap a small amount of liquid between them; (ii) while both bubbles stay in contact, the liquid film drains out to a critical thickness and (iii) ruptures, leading the bubbles to coalesce. Otherwise, the bubbles bounce off one another without coalescing. The constraint for coalescence to occur is that the duration of the contact time of the bubbles must be sufficiently long for the liquid film to drain. For bubble coalescence, the contact time is expressed by $\tau_{ij} = (C_c R_{ij}) u_n^{-1}$, where R_{ij} is the equivalent bubble radius, given by $R_{ij} = 2.0(2/d_{b1} + 2/d_{b2})^{-1}$, u_n is the relative approaching velocity in the normal direction, and C_c is the deformation distance as a fraction of the effective bubble radius; a value of 0.25 gives the best agreement with experimental data (Sommerfeld et al., 2003). The film drainage time is given as $t_{ij} = (R_{ij}^3 \rho_l / 16\sigma)^{0.5} \ln(h_0/h_f)$, with the initial film thickness h_0 for air-water was set to 1.0×10^{-4} m, the final film thickness before rupture h_f was set to 1.0×10^{-8} m, (Prince and Blanch, 1990), and σ is the surface tension. The properties of the new bubble after coalescence were calculated from a mass and momentum balance. During coalescence, the total bubble volume was conserved and the bubble diameter after coalescence obtained from $d_{b,new} = (d_{d1}^3 + d_{d2}^3)^{1/3}$.

3. Computational Conditions

The computational domain employed was a vertical channel with the z , y and x axes in the streamwise, spanwise and wall normal directions, respectively. The dimensions of the computational domain was set to $4\pi h \times 2\pi h \times 2h$ for $Re_\tau = 150$ case, and $2\pi h \times \pi h \times 2h$ for the $Re_\tau = 590$ flow. The grid nodes were uniformly distributed along the y and z axes and non-uniformly in the wall-normal direction, giving a total of $128 \times 128 \times 129$ nodes. Periodic boundary conditions were imposed in the streamwise and spanwise directions, with no-slip boundary conditions enforced at the channel walls for the liquid phase, and elastic collisions assumed between the bubbles and the channel walls.

Air bubbles with diameter $d_b = 220 \mu\text{m}$ and density $\rho_b = 1.3 \text{ kgm}^{-3}$ were injected uniformly into fully-converged single-phase flow solutions at shear Reynolds numbers of $Re_\tau = 150$ and 590, with the liquid phase kinematic viscosity and density set to $\nu = 10^{-6} \text{ m}^2\text{s}^{-1}$ and $\rho = 1000 \text{ kgm}^{-3}$. The bubble volume fraction was $\Phi_v = 10^{-3}$ (corresponding to 226,662 bubbles for the $Re_\tau = 150$ case and 56,647 for the $Re_\tau = 590$ flow), high enough for the microbubbles to affect the continuous phase flow field as well as permitting significant bubble-bubble interactions. Simulations were performed for both upward and downward vertical flow configurations. The total flow time for the bubbles was 30 s for the $Re_\tau = 150$ and 3 s for the $Re_\tau = 590$ flows (corresponding to at least 12 passes through the channel in each case).

4. Results and Discussion

Bubble mean streamwise velocity and normalised concentration predictions from the simulations in the wall-normal direction at both Reynolds numbers, and for upflow and downflow conditions, are shown in Fig. 1. A clear distinction between the upflow and downflow velocity profiles is evident at $Re_\tau=150$. Having a much lower density, the

bubbles move faster than the fluid in upflow and, for the same reason, are slower in downflow. This difference is much smaller in the $Re_\tau=590$ flow as the fluid velocity is much higher. However, the relative velocity between the bubbles and the fluid remains almost constant, being mainly a function of the bubble diameter exerted through the drag force. The bubble concentration at $Re_\tau=150$ is mainly affected by the lift force that pushes the bubbles towards the wall in upflow and away from the wall, and towards the centre of the channel, in downflow. At $Re_\tau=590$ the lift force effect remains dominant but the bubble segregation is greatly reduced because of the enhanced mixing promoted by the higher levels of turbulence.

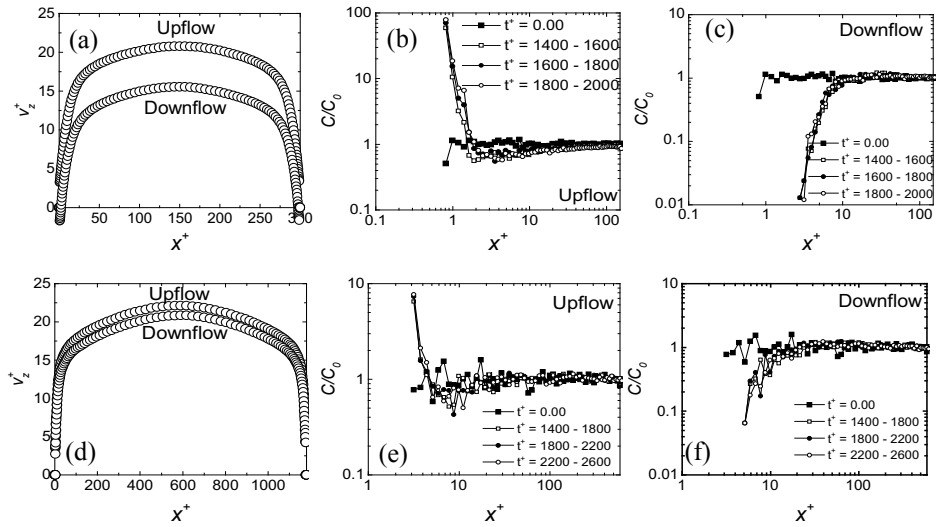


Figure 1. Bubble velocity statistics for four-way coupled vertical channel flows: (a) and (d) bubble mean streamwise velocity profiles; (b), (c), (e) and (f) bubble wall-normal concentration profiles; (a), (b) and (c) $Re_\tau=150$; (d), (e) and (f): $Re_\tau=590$.

Microbubble interactions are considered in Fig. 2, which shows normalised (by the initial number of bubbles) bubble collisions and coalescences, and the formation of larger bubbles, in upflow and downflow, for the two Reynolds number cases. Figure 2(a) and (d) show bubble collisions, whilst (b) and (e) gives coalescence events. Figure 2(c) and (f) shows the distribution of different bubble sizes with time (where (2) signifies a bubble formed from the coalescence of two bubbles of original size $220 \mu\text{m}$ (1), etc.). Note that some bubble sizes have been omitted from the latter plots for clarity, although the formation with time of increasingly larger bubbles is evident. It is immediately clear that, at $Re_\tau=590$, the higher levels of turbulence increase bubble interaction and, consequently, the number of coalescence events. Additionally, the number of multi-sized bubbles formed is higher than for the lower Reynolds number case, with the largest bubbles also forming at the higher Re_τ . However, turbulence also impacts on the bubble contact time, which decreases with the level of turbulence. Therefore, the coalescence efficiency decreases at $Re_\tau=590$, with a significant number of collisions not resulting in coalescence (cf. Fig. 2(a) and 2(b)).

It has been observed that bubbles tend to increase turbulence levels in upflow and decrease them in downflow (Molin et al., 2012), and this was confirmed in the present work. Therefore, the number of collisions is greater in upflow, as well as the number of coalescences. Because of the lower turbulence levels in downflow, the decrease in coalescence efficiency at $Re_\tau = 590$ noted above is limited to the upflow case and is not observed for the downflow.

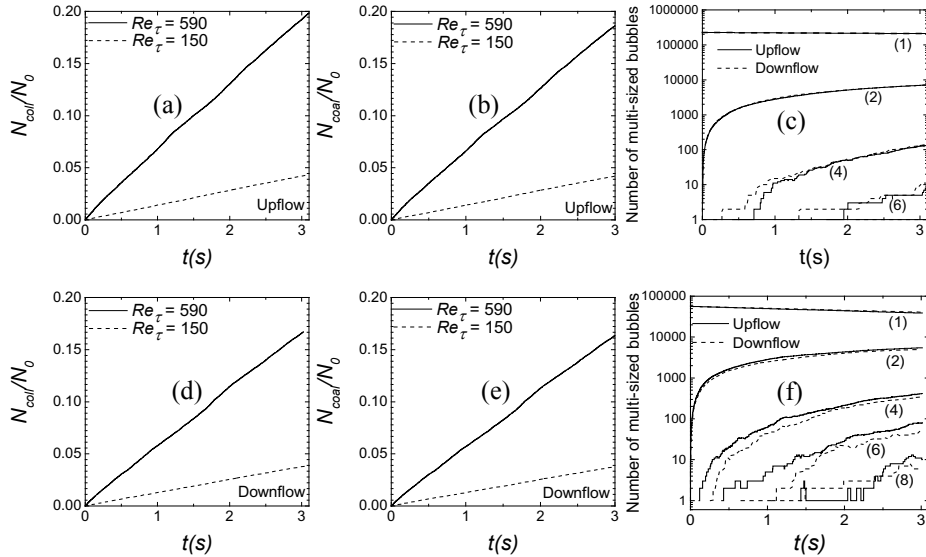


Figure 2. Normalized number of bubble collision, (a) and (d), and coalescence, (b) and (e) events, and bubble size distribution, (c) and (f) with time: (c) $Re_\tau = 150$; (f) $Re_\tau = 590$.

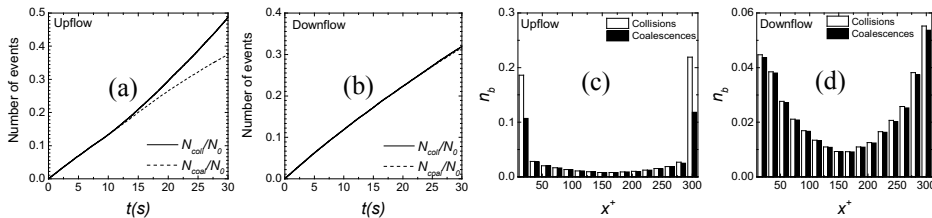


Figure 3. Normalized total number of collisions (a) and coalescences (b), and instantaneous distribution of collisions and coalescences across the channel at $t = 28$ s in upflow (c) and downflow (d), for the $Re_\tau = 150$ flow.

The $Re_\tau = 150$ flow simulation was extended to $t = 30$ s and the results are presented in Fig. 3. These confirm that the greatest number of collisions, and coalescences, is found in the upflow case. At the same time, the coalescence efficiency is reduced because of the higher turbulence level in upflow (Fig. 3(a)). For the latter case, the number of collisions is observed to deviate from a linear trend at around 10-15 s. The spatial distribution of collisions and coalescences in Fig. 3(c) and (d) help to explain this trend. Because of the lift force segregating bubbles near the wall in upflow, a larger number of them are located in regions of high turbulence, resulting in enhanced bubble interaction with respect to the downflow, where the majority of the bubbles are in the lower turbulence central region of the channel. However, although the coalescence rate remains higher, the bubbles experience lower contact times in those regions of high turbulence, and again not all collisions in the upflow case result in coalescence (Fig. 3(a)).

5. Conclusions

Four-way coupled simulations of bubbly flows in channels have been performed using a Lagrangian bubble tracking routine that includes bubble collision and coalescence, coupled to large eddy simulation of the liquid phase. Vertical upward and downward flows of water at shear Reynolds numbers of 150 and 590 were simulated, with air bubbles initially of 220 μm diameter. A greater number of collision and coalescence events occurs at $Re_\tau = 590$ due to enhanced bubble mixing and interaction promoted by high levels of turbulence. For the same reason, the associated lower bubble contact time resulted in a reduced coalescence efficiency than for the lower Reynolds number case. More collisions and coalescences, but at a reduced efficiency of coalescence, occur in upflow than in downflow, due partially to bubbles increasing the turbulence level in upflow but reducing it in downflow. The lift force affects the bubble distribution, pushing bubbles towards the highest turbulence regions near the wall in upflow, whereas in downflow the bubbles are concentrated in lower turbulence regions in the centre of the channel. Overall, the results demonstrate the potential of the overall model for predicting bubble behaviour in these types of flow. Future developments will enable full predictions of bubble size evolution with the introduction a model of bubble break-up.

Acknowledgements

KSA gratefully acknowledges the financial support of the Niger Delta Development Commission in Nigeria, and the opportunities that funding has given him.

References

- K.S. Asiagbe, M. Fairweather, D.O. Njobuenwu and M. Colombo, 2017, Large Eddy Simulation of Microbubble Transport in Vertical Channel Flows, 27th European Symposium on Computer Aided Process Engineering, A. Espuña, M. Graells, L. Puigjaner (Eds.), Elsevier, 73-78.
- M. Bini and W.P. Jones, 2008, Large-Eddy Simulation of Particle-Laden Turbulent Flows, *J. Fluid Mech.*, 614, 207-252.
- M. Breuer and M. Alletto, 2012, Efficient Simulation of Particle-Laden Turbulent Flows with High Mass Loadings using LES, *Int. J. Heat Fluid Fl.*, 35, 2-12.
- M. Germano, U. Piomelli, P. Moin and W.H. Cabot, 1991, A Dynamic Subgrid-Scale Eddy Viscosity Model, *Phys. Fluids*, 3, 1760-1765.
- D. Legendre and J. Magnaudet, 1997, A Note on the Lift Force on a Spherical Bubble or Drop in a Low-Reynolds-Number Shear Flow, *Phys. Fluids*, 9, 3572-3574.
- D. Molin, C. Marchioli and A. Soldati, 2012, Turbulence Modulation and Microbubble Dynamics in Vertical Channel Flow, *Int. J. Multiphas. Flow*, 42, 80-95.
- M.J. Prince and H.W. Blanch, 1990, Bubble Coalescence and Break-Up in Air-Sparged Bubble Columns, *AIChE J.*, 36, 1485-1499.
- L. Schiller and Z. Naumann, 1935, A Drag Coefficient Correlation, *Z. Ver. Dtsch. Ing.*, 77, 318-320.
- M. Sommerfeld, E. Bourloutski and D. Broder, 2003, Euler/Lagrange Calculations of Bubbly Flows with Consideration of Bubble Coalescence, *Can. J. Chem. Eng.*, 81, 508-518.

Kinetic Modeling of Methanol Synthesis - Impact of Catalyst Deactivation

Carsten Seidel^{a,*}, Andreas Jörke^a, Bert Vollbrecht^c, Andreas Seidel-Morgenstern^{a,b}
and Achim Kienle^{a,b}

^a*Otto-von-Guericke-Universität, Universitätsplatz 2, D-39106 Magdeburg, Germany*

^b*Max-Planck-Institut für Dynamik komplexer technischer Systeme, Sandtorstrasse 1, D-39106 Magdeburg, Germany*

^c*Siemens AG Engineering & Consulting, Industriepark Höchst B598, D-65926 Frankfurt am Main, Germany*

**carsten.seidel@ovgu.de*

Abstract

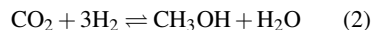
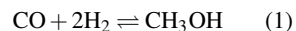
Recently, we developed a new kinetic model for the methanol synthesis from H₂, CO₂ and/or CO using a commercial Cu/ZnO/Al₂O₃ catalyst (Seidel et al., 2017), where different active surface species for CO and CO₂ hydrogenation and dynamic changes of the catalyst morphology were taken into account. This effect is crucial for the description of the dynamic transient behavior. The model is therefore suitable for evaluating new applications in chemical energy storage, where strongly varying feed ratios of CO and CO₂ are possible (Raeuchle et al., 2016). The model parameters were fitted to steady state and dynamic experimental data for varying CO/CO₂ feed ratios (Vollbrecht, 2007) using global optimization. Identifiability was studied using the profile-likelihood method. In the present contribution, the effect of catalyst deactivation observed during the experiments is explicitly taken into account. For that purpose different catalyst activity levels are considered and parameters are refitted to the experimental data to achieve better quantitative prediction. Further, the influence of possible additional side reactions is discussed.

Keywords: renewable resources, methanol synthesis, kinetics, catalyst deactivation

1. Introduction

Methanol is important for the chemical industry. It can be used as a starting material for paraffins, olefins or various organic chemicals like acetic anhydride and as fuel. It is produced continuously in large amounts from synthesis gas using Cu/ZnO/Al₂O₃ catalysts. The reaction network

comprises three main reactions, i.e. hydrogenation of CO and CO₂ as well as the water-gas shift reaction according to Eq. (1)-(3). With the upcoming focus on renewable resources as basis for energy supply, methanol becomes an important energy carrier in addition to its relevance as chemical industrial raw material. Excess wind or solar energy can supply an electrolysis for hydrogen, which reacts with CO/CO₂ to methanol for chemical energy storage. If an energy deficit occurs, methanol can be converted back into electrical energy. This results in a more flexible grid and more efficient usage of renewable resources. In this case the methanol reactor will face strongly varying ratios in the feed, where established kinetics are insufficient (Raeuchle et al.,



2016). These changing requirements were recently summarized by Kalz et al. (2017). In contrast to established kinetics (Bussche and Froment, 1996; Graaf et al., 1988), the proposed novel Langmuir-Hinshelwood kinetic for the methanol synthesis takes dynamic changes of catalyst morphology into account (Seidel et al., 2017). The model is able to reproduce steady state and dynamic data over a large range of CO/CO₂ feed ratios from previous experiments (Vollbrecht, 2007). For long term operation the catalyst deactivation has to be considered. In this paper, two approaches for deactivation are investigated. Furthermore, possible side reactions and their influence on catalyst activity are discussed.

2. Kinetic Model

The recently developed Langmuir-Hinshelwood kinetics describe the reactions Eqs.(1)-(3) with the following rate expressions:

$$r_1 = k_1 p_{\text{CO}} p_{\text{H}_2}^2 \left(1 - \frac{1}{K_{\text{P1}}} \frac{p_{\text{CH}_3\text{OH}}}{p_{\text{CO}} p_{\text{H}_2}^2} \right) \Theta^\ominus \Theta^{\otimes 4} \quad (4)$$

$$r_2 = k_2 p_{\text{CO}_2} p_{\text{H}_2}^2 \left(1 - \frac{1}{K_{\text{P2}}} \frac{p_{\text{CH}_3\text{OH}} p_{\text{H}_2\text{O}}}{p_{\text{CO}_2} p_{\text{H}_2}^3} \right) \Theta^{*2} \Theta^{\otimes 4} \quad (5)$$

$$r_3 = k_3 p_{\text{CO}_2} \left(1 - \frac{1}{K_{\text{P3}}} \frac{p_{\text{CO}} p_{\text{H}_2\text{O}}}{p_{\text{CO}_2} p_{\text{H}_2}} \right) \Theta^* \Theta^\ominus \quad (6)$$

The corresponding relative amounts of free surface centers will be denoted by Θ^\ominus for oxidized centers, Θ^* for reduced centers, and Θ^{\otimes} for hydrogen. Temperature dependence of the rate constants is described by the reformulated Arrhenius equation with six additional parameters ($\beta_1 - \beta_6$ for \tilde{k}_i & \tilde{E}_A) (Vollbrecht, 2007).

$$\Theta^\ominus = \left(1 + \underbrace{K_{\text{CO}} p_{\text{CO}}}_{\beta_{11}} + \underbrace{K_{\text{CH}_3\text{OH}}^\ominus p_{\text{CH}_3\text{OH}}}_{\beta_{12}} + \underbrace{K_{\text{CO}_2}^\ominus p_{\text{CO}_2}}_{\beta_{14}} \right)^{-1} \quad (7)$$

$$\Theta^{\otimes} = \left(1 + \underbrace{\sqrt{K_{\text{H}_2}} \sqrt{p_{\text{H}_2}}}_{\beta_7} \right)^{-1} \quad (8)$$

$$\Theta^* = \left(1 + \underbrace{\frac{K_{\text{H}_2\text{O}} K_{\text{O}}}{K_{\text{H}_2}} \frac{p_{\text{H}_2\text{O}}}{p_{\text{H}_2}}}_{\frac{\beta_{10} \beta_9}{\beta_7^2}} + \underbrace{K_{\text{CO}_2} p_{\text{CO}_2}}_{\beta_{13}} + \underbrace{K_{\text{CH}_3\text{OH}}^* p_{\text{CH}_3\text{OH}}}_{\beta_8} + \underbrace{K_{\text{H}_2\text{O}} p_{\text{H}_2\text{O}}}_{\beta_9} \right)^{-1} \quad (9)$$

The unknown parameters $\beta_1 - \beta_{14}$ were fitted to steady state experiments using global optimization (Seidel et al., 2017). Results are given in Tab. 1. Equilibrium constants $K_{\text{P1}} - K_{\text{P3}}$ are taken from Skrzypek et al. (1994); Vollbrecht (2007).

2.1. Extension to a variable fraction of reduced and oxidized surface centers

A fixed amount of reduced and oxidized surface centers was not able to explain transient effects, as seen in (Choi et al., 2001; Muhler et al., 1994; Nakamura et al., 2003; Peter et al., 2012) after feed changes. Therefore, a conversion of reduced to oxidized and vice versa was considered. Following

the work of Ovesen et al. (1997) the amount of reduced and oxidized centers was reformulated for a variable amount:

$$\tilde{\Theta}^{\ominus} = (1 - \phi) \cdot \Theta^{\ominus} \quad \tilde{\Theta}^* = \phi \cdot \Theta^* \quad (10)$$

where the fraction of reduced centers is denoted as ϕ and under transient conditions described by the following dynamic equation (Seidel et al., 2017):

$$\frac{d\phi}{dt} = k_1^+ \left(y_{\text{H}_2}(1 - \phi) - \frac{1}{K_1} y_{\text{H}_2\text{O}} \phi \right) + k_2^+ \left(y_{\text{CO}}(1 - \phi) - \frac{1}{K_2} y_{\text{CO}_2} \phi \right). \quad (11)$$

The additional rate constants were fitted to transient data (Vollbrecht, 2007). This dynamic equation allows the kinetic model to take the dynamic catalyst morphology changes by oxidation and reduction into account.

3. Catalyst deactivation

The developed Langmuir-Hinshelwood kinetics was fitted to experimental data without considering a deactivation especially due to sintering of the catalyst during the experiments. To account for the impact of possible deactivation, two deactivation models are considered and implemented in Eq.(4)-(6). The parameter estimation was done again for each deactivation model in the same way as in stated in (Seidel et al., 2017).

3.1. Model from experimental data

The first approach was formulated by Vollbrecht (2007) and assumes a deactivation of the catalyst only over time which gives the following equation:

$$a(t) = a_0 \exp(-k_s(t - t_0)) \quad (12)$$

The deactivation constant $k_s = -6.274 \times 10^{-4} \text{h}^{-1}$ is estimated from the decrease of methanol yield under identical experimental conditions at different time points. The steady state results and the corresponding parameters are given in Fig. 2 and Tab. 1.

3.2. Temperature dependent model

This model was formulated by Hanken (1995), it takes the impact of the temperature on the deactivation process into account.

$$\frac{da}{dt} = K_d \exp\left(-\frac{E_D}{R} \left(\frac{1}{T} - \frac{1}{T_{ref}}\right)\right) a^5 \quad (13)$$

The parameters are given with $T_{ref} = 513 \text{K}$, $E_d = 91 \times 10^3 \text{Jmol}^{-1}$ and $K_d = 4.39 \times 10^{-3} \text{h}^{-1}$. The steady state results and the corresponding parameters are given in Fig. 2 and Tab. 1. The difference over time and experiments between both deactivation models is pictured in Fig 1. The Vollbrecht model assumes a loss of 30% over all experiments and the Hanken model gives a loss of 20%. In both cases the parameter estimation could be done using global optimization strategies (GAMS, 2013; Sahinidis, 2014). As expected the parameter values shift, but stay in the same order of magnitude as without catalyst deactivation. Largest deviations are observed for β_4 , β_{10} and β_{12} . The profile likelihood method was used to investigate the structural identifiability for the parameters in both cases (Raue et al., 2014). It was shown that in both cases catalyst deactivation has no influence on structural identifiability, which is discussed in detail in Seidel et al. (2017).

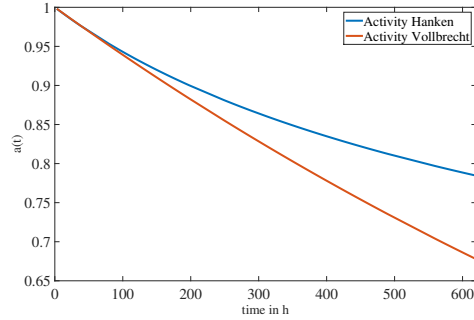


Figure 1: Activity over time as described by the models of Vollbrecht (2007) and Hanken (1995) at $T = 523 \text{K}$.

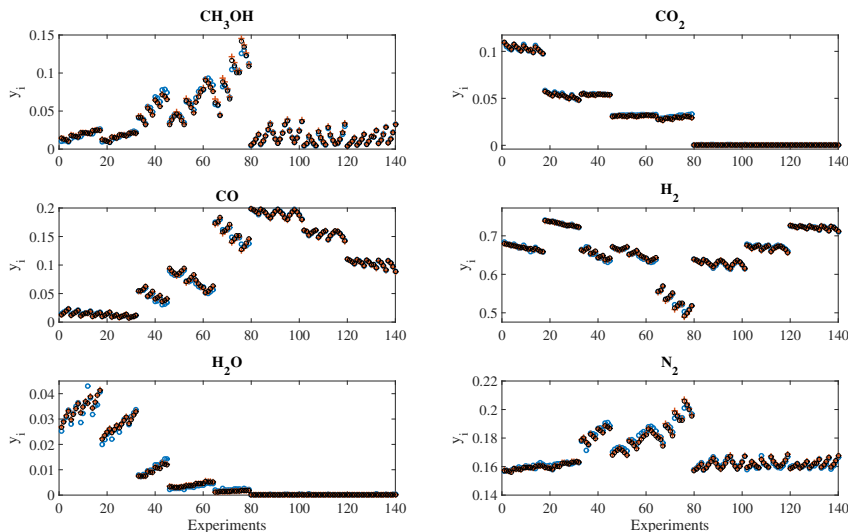


Figure 2: Steady state experiments (blue) with deactivation model by Vollbrecht (2007)(red) and deactivation model by Hanken (1995)(black).

4. Additional Side Reactions

During the dynamic experiments of Vollbrecht (2007), small amounts of CO_2 were measured at the output of the reactor for a pure CO/H_2 feed. This formation of CO_2 in the reactor has two possible reasons. The first possibility is the existence of side reactions and the second is a proceeding reduction of the catalyst. Vollbrecht (2007) mentioned various side reactions in his work for a commercial $\text{Cu}/\text{ZnO}/\text{Al}_2\text{O}_3$ catalyst which are listed in Tab. 2. It is obvious that all reactions contain at least one carbon compound which is not part of the methanol synthesis Eq. (1)-(3). However, these products were not detected in the experiments with the applied method (gas chromatography with ion-molecular-reaction mass spectroscopy). For some quantification we refer to Asinger (1986). The last side reaction to consider is the Boudouard reaction. In the experimental investigated temperature and pressure range, the reaction equilibrium lies on the side of carbon dioxide. In this case carbon would stay on the catalyst and would lead to a coking process that decreases the activity of the catalyst. A possible way to examine the influence of the Boudouard reaction is a stoichiometric consistency analysis (Felder and Rousseau, 1986). In a first step, the Boudouard reaction is neglected and the rank of the stoichiometric matrix in Tab. 3 is two. According to Tab. 4 CH_3OH and CO_2 are suitable key components and the reaction rates of all other components are calculated from the measured reaction rates of the key components. Results in Fig. 3 show good agreement between measured and calculated reaction rates of the nonkey components. If the Boudouard reaction is added, the rank of the stoichiometric matrix is 3. Therefore H_2 is added as a suitable third key component. This however, leads to a large differences

Table 2: Possible additional side reactions on a $\text{Cu}/\text{ZnO}/\text{Al}_2\text{O}_3$ catalyst (Asinger, 1986).

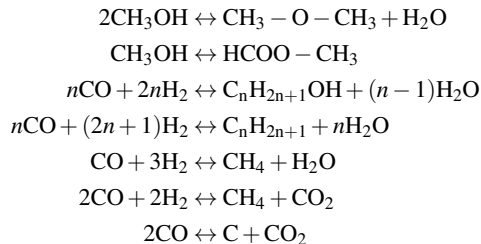


Table 1: List of estimated parameters with Vollbrecht model, Hanken model and no deactivation.

Unknown parameter	Estimated Vollbrecht	Estimated Hanken	Estimated no deactivation	Units
β_1	-4.5543	-4.5144	-4.7636	-
β_2	26.7823	26.2079	26.1883	-
β_3	-2.8991	-3.0118	-3.4112	-
β_4	6.0614	5.3356	3.4470	-
β_5	-5.3857	-5.5203	-5.7239	-
β_6	23.2372	22.5643	23.4744	-
β_7	1.2075	1.2446	1.1665	bar ^{-1/2}
β_8	0	0	0	bar ⁻¹
β_9	0.0043	0.0043	0.0297	bar ⁻¹
β_{10}	1.5018×10^4	1.4297×10^4	1.60×10^3	-
β_{11}	0.1284	0.1362	0.1362	bar ⁻¹
β_{12}	0.0514	0.000	0	bar ⁻¹
β_{13}	0	0	0	bar ⁻¹
β_{14}	0.0725	0.06	0.04712	bar ⁻¹

between measured and calculated reaction rates for the nonkey components, also illustrated in Fig. 3, indicating that the network with Boudouard reaction is not consistent with the experimental data. It is therefore conjectured that the measured CO₂ formation for a pure CO/H₂ feed is due to reduction of the catalyst which in the longer term can also result in a reduced catalyst activity.

Table 3: Stoichiometric matrix for standard model and with Boudouard reaction.

Species	r_1	r_2	r_3	$r_{Boudouard}$
CO	-1	0	1	-2
CO ₂	0	-1	-1	1
H ₂	-2	-3	-1	0
CH ₃ OH	1	1	0	0
H ₂ O	0	1	1	0
C	0	0	0	1

Table 4: Element-Species-Matrix for standard model and with Boudouard reaction.

Species	C	O	H
CO	1	1	0
CO ₂	1	2	0
H ₂	0	0	2
CH ₃ OH	1	1	4
H ₂ O	0	1	2
C	1	0	0

5. Conclusion

A kinetic model for methanol synthesis, which considers strongly varying CO/CO₂ feeds was extended with two different models describing catalyst deactivation. This results in a more precise kinetic model and improves the prediction for long term operation. Both accordingly extended models yield similar parameter values with some differences to our previous model without deactivation especially for β_4 , β_{10} and β_{12} . It is further suggested that for a pure CO feed, catalyst activity might also be lowered by catalyst reduction that is caused by CO₂ formation. Hence it is confirmed that a long term operation with pure CO feed is not reasonable. Further, CO₂ formation is caused by side reactions but seems to be small. The developed kinetic model explicitly accounts for dynamic changes of the catalyst morphology but has moderate complexity, therefore it provides a good basis for further studies on reactor dynamics and operation.

References

- F. Asinger, 1986. Methanol - Chemie und Energierohstoff. Springer.

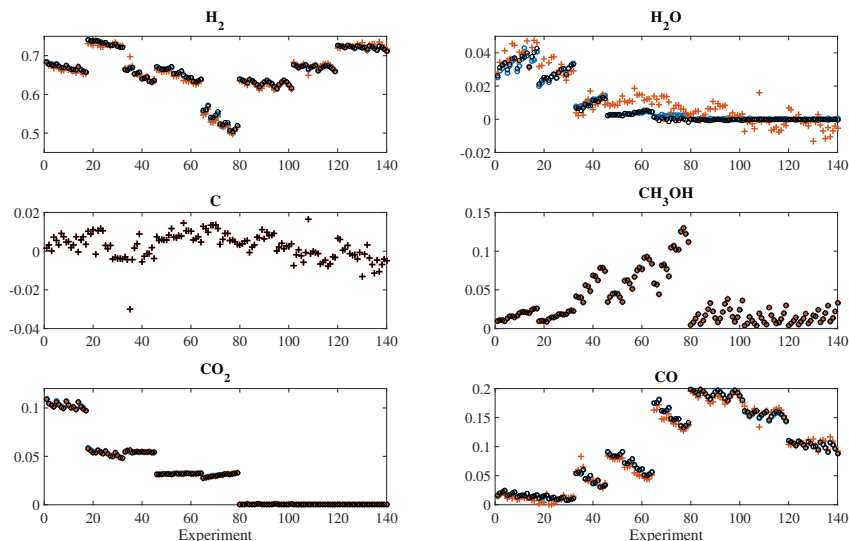


Figure 3: Predicted reaction rates considering the Boudouard reaction (red), without neglecting it (black) and experimental data (blue).

- K. M. V. Bussche, G. F. Froment, 1996. A steady-state kinetic model for methanol synthesis and the water gas shift reaction on a commercial Cu/ZnO/Al₂O₃ catalyst. *Journal of Catalysis* 161 (1), 1–10.
- Y. Choi, K. Futagami, T. Fujitani, J. Nakamura, 2001. The difference in the active sites for CO₂ and CO hydrogenations on Cu/ZnO-based methanol synthesis catalysts. *Catalysis Letters* 73 (1), 27–31.
- R. M. Felder, R. W. Rousseau, 1986. *Elementary principles of chemical processes*.
- GAMS, 2013. *GAMS - A User's Guide*, GAMS Release 24.2.1. GAMS Development Corporation, Washington, DC, USA.
- G. H. Graaf, E. J. Stamhuis, A. A. C. M. Beenackers, 1988. Kinetics of low-pressure methanol synthesis. *Chemical Engineering Science* 43 (12), 3185–3195.
- L. Hanken, 1995. *Optimization of methanol reactor*. Master's thesis.
- K. F. Kalz, R. Kraehnert, M. Dvoyashkin, R. Dittmeyer, R. Gläser, U. Krewer, K. Reuter, J.-D. Grunwaldt, 2017. Future Challenges in Heterogeneous Catalysis: Understanding Catalysts under Dynamic Reaction Conditions. *ChemCatChem* 9 (1), 17–29.
- M. Muhler, E. Törnqvist, L. P. Nielsen, B. S. Clausen, H. Topsøe, 1994. On the role of adsorbed atomic oxygen and CO₂ in copper based methanol synthesis catalysts. *Catalysis Letters* 25 (1-2), 1–10.
- J. Nakamura, Y. Choi, T. Fujitani, 2003. On the issue of the active site and the role of ZnO in Cu/ZnO methanol synthesis catalysts. *Topics in Catalysis* 22 (3-4), 277–285.
- C. V. Ovesen, B. S. Clausen, J. Schiøtz, P. Stoltze, H. Topsøe, J. K. Nørskov, 1997. Kinetic implications of dynamical changes in catalyst morphology during methanol synthesis over Cu/ZnO catalysts. *Journal of Catalysis* 168 (2), 133–142.
- M. Peter, M. B. Fichtl, H. Ruland, S. Kaluza, M. Muhler, O. Hinrichsen, 2012. Detailed kinetic modeling of methanol synthesis over a ternary copper catalyst. *Chemical engineering journal* 203, 480–491.
- K. Raeuchle, L. Plass, H.-J. Wernicke, M. Bertau, 2016. Methanol for Renewable Energy Storage and Utilization. *Energy Technology* 4 (1), 193–200.
- A. Raue, J. Karlsson, M. P. Saccomani, M. Jirstrand, J. Timmer, 2014. Comparison of approaches for parameter identifiability analysis of biological systems. *Bioinformatics*, btt006.
- N. V. Sahinidis, 2014. *BARON 14.3.1: Global Optimization of Mixed-Integer Nonlinear Programs, User's Manual*.
- C. Seidel, A. Jörke, B. Vollbrecht, A. Seidel-Morgenstern, A. Kienle, 2017. Kinetic modeling of methanol synthesis from renewable resources. *Chemical Engineering Science* 175, 130–138.
- J. Skrzypek, J. Słoczyński, J. Słoczyński, S. Ledakowicz, 1994. *Methanol synthesis: science and engineering*. Polish Scientific Publishers.
- B. Vollbrecht, 2007. *Zur Kinetik der Methanolsynthese an einem technischen Cu/ZnO/Al₂O₃-Katalysator*. Ph.D. thesis, Otto-von-Guericke-Universität Magdeburg.

Assessing the GHG emissions footprints of newly ultra-sour gas developments in the Middle East region for electricity production

Alberto Betancourt-Torcat^a, Mohammed Alkatheri^{a,b}, Ali Almansoori^{a,*}

^a*Department of Chemical Engineering, Khalifa University of Science and Technology, Sas Al Nakhl Campus, P.O. Box 2533, Abu Dhabi, United Arab Emirates.*

^b*Department of Chemical Engineering, University of Waterloo, 200 University Avenue West, Waterloo, Ontario, Canada N2L 3G1.*

aalmansoori@pi.ac.ae

Abstract

The Middle East is a hydrocarbon-rich region. Nonetheless, the majority of its natural gas reserves are ultra-sour in nature. Previously these resources were left untapped; but latest technology advances and growing energy security concerns have motivated the exploitation of such resources. Ultra-sour gas processing is particularly very energy intensive and generates noteworthy greenhouse gas (GHG) emissions during its whole lifecycle (e.g., from well-extraction to grid transmission). This study aims to quantify in detail the ultra-sour gas well-to-electricity transmission GHG emissions in terms of per kilowatt hour (kWh) delivered. This is, the GHG emissions involved in delivering one kWh of electricity produced from ultra-sour gas. A mathematical model of a power generation infrastructure was developed in GAMS®; whereas a simulation model for gas transportation and treatment was developed in ProMax®. The two aforementioned models together with engineering principles were employed in the present study. The United Arab Emirates is considered as case study. The results indicate that GHG emissions associated with ultra-sour gas-based power averages 564 g CO₂ eq./kWh delivered. This is over 11% larger than average US conventional gas-based power. Likewise, gas processing and electricity production account for more than 92 % of the lifecycle emissions.

Keywords: Greenhouse Gas, Life cycle assessment, Electricity generation, Optimization, Simulation.

1. Introduction

In most Middle Eastern countries the power generation capacity is dominated by fossil fuels; being gas one of the most important fuels (Betancourt-Torcat and Almansoori, 2015). Although most of these countries possess significant gas reserves, the majority of the untapped reserves are ultra-sour in nature (very high concentration of acid gases). The region features one of the highest electricity consumption rates in the world (Energy Information Administration, 2015). Accordingly, the countries in the region have been forced or plan to develop its unconventionally ultra-sour gas resources.

Although natural gas is commonly regarded as a relatively clean energy feedstock, it still represents a significant focus of greenhouse gas (GHG) emissions. For instance, the United Arab Emirates (UAE) is currently developing nuclear and renewable power capacities to increase the country's energy mix and reduce GHG emissions (Almansoori

and Betancourt-Torcat, 2015). In general, the literature on GHG emissions lifecycle for both ultra-sour gas resources and UAE's electricity sector is very scarce. For instance, the processing of ultra-sour gas featuring H_2S concentrations exceeding 20% is very unique; the first type of such development was recently inaugurated in the UAE in late 2016. Therefore, due to the high concentration of acid gases (particularly H_2S) in the country's gas reserves, and the highly energy-intensive processes employed to sweeten the ultra-sour gas, conducting a lifecycle assessment of the UAE's electricity sector is needed and is novel. To the authors' knowledge the level of detailed accounted in this analysis in terms of the power system, gas processing, and gas transmission simulations for the UAE cannot be found in any other study. Moreover, currently this is the only analysis covering these rarely ultra-sour gas resources.

ProMax® was used to simulate the upstream ultra-sour gas transportation and treatment processes, while an optimization mathematical model developed in the General Algebraic Modeling System (GAMS®) (Almansoori and Betancourt-Torcat, 2015) was used to illustrate the downstream gas combustion at UAE's power plants along with the electricity transmission and distribution. Unlike the inventory method, the proposed modeling-based approach allows conducting uncertainty analyses on key process parameters with major effects on the GHG emissions lifecycle. This is required to understand the environmental impacts of the cradle-to-grave UAE's electricity sector. This work is organized as follows: Section 2 presents the assessment methodology. Section 3 presents a case study of the UAE. Concluding remarks are presented at the end of this work.

2. Methodology

In the present work the lifecycle assessment method was employed to estimate the GHG emissions of ultra-sour gas electricity generation. The employed framework corresponds to those of the International Organization for Standardization (ISO) methodology reported in ISO 14040/44 (International Organization for Standardization, 2006). This study accounts for the GHG emissions associated with CO_2 , CH_4 , N_2O , and SF_6 . The analyzed well-to-transmission (WTT) lifecycle is given as follows: 1) extraction of ultra-sour gas, 2) raw gas collection and transfer to gas treatment facilities, 3) raw gas treatment, 4) sweet gas transfer to power plants, 5) gas combustion at power plants, and 6) electricity transmission and distribution.

The GHG emissions related to gas extraction and electricity transmission and distribution are estimated based on typical values reported in the literature (Skone et al., 2012). Likewise, fugitive and venting emissions for upstream processes are estimated according to guidelines for gas transmission and storage (Interstate Natural Gas Association of America, 2005). Moreover, all energy forms and GHG emissions from gas pipeline transmissions and treatment are calculated using a simulation model built in ProMax® v3.2. Most of the lifecycle GHG emissions are associated with energy consumption during operations. In gas extraction most of the energy is spent in drilling, generating GHG emissions. Also, some episodic natural gas emissions occurred in the well during gas extraction.

Then, the natural gas is sent to surface processing, where it is sweetened, dehydrated, and compressed for pipeline transmission. The ultra-sour gas is treated/sweetened using di-glycol amine (DGA) as solvent. The energy consuming units in this stage are: coolers (cooling water and electricity), reboilers (low and high pressure steam), pumps

(electricity), condensers (cooling water), and compressors (electricity). The wet sweet gas is dehydrated while the acid gases are sent to the sulfur recovery units.

In sulfur recovery, steam is generated contributing to meet part of the steam requirement in gas processing. The units consuming energy in sulfur recovery are condensers (cooling water) and re-heaters (high pressure steam). To estimate the amount of fuel gas required to produce process steam, it is assumed that the gas first combines with air and then combust in a burner. The heat generated is used to boil water and generate high and low pressure steam. The average emission per slandered of fuel gas was found to be approximately 66.7 g CO₂ eq./scf.

Part of the produced dry sweet gas can also be combusted onsite to generate electricity. The electricity requirements for the cooling water loop can be estimated using the cooling water flowrate (\dot{V}). This can be done calculating the power demands in pumps and cooling tower fans. The power for cooling water pumps ($Power_{pump}$) is given as:

$$Power_{pump} = \frac{\dot{V} \Delta P}{\eta} \quad (1)$$

where ΔP is the pressure drop and η is the pump's efficiency. Moreover, the power requirements in tower fans ($Power_{tower}$) can be estimated as:

$$Power_{tower} = \dot{V} (Area) Surface \quad (2)$$

where $Area$ is the tower fan's effective area, and $Surface$ is the fan's surface area.

To estimate the GHG emissions of dry sweet gas transfer from the currently only existing ultra-sour gas processing facility at Al Hosn Gas (Abu Dhabi Gas Development Ltd., 2016) to the different power plants' stations (main five stations) through the pipeline network, it was required to find: the pipeline lengths between the gas processing facilities and the power stations, the number of compression stations, and required compression power. The first compression station is considered to compress the sales gas from 330 psig to 1300 psig; whereas the remaining compression stations compress the gas from 500 to 1300 psig. This study considers the gas compression stations to be powered by the domestic electricity grid.

On the other hand, the GHG emissions of UAE's electricity generation system as well as power transmission and distribution were obtained from a proven GAMS® model (Almansoori and Betancourt-Torcat, 2015). The model is a Mixed Integer Linear Programming (MILP) formulation. The set of decision variables includes: types of power plants, number of power plants, plants' operating capacities, and plants' location. The model takes into account potential structural decisions through discrete (integer) variables to find the most suitable combination of power plants for a geographical area. The power production balance by type of power plant is given as follows:

$$EP_p = IE_p IC_p CF_p, \quad \forall p \quad (3)$$

where EP_p is the quantity of electricity produced by the p^{th} power plant, IE_p is an integer variable that denotes the number of plants p selected for the power structure, whereas IC_p and CF_p are model's parameters denoting the installed capacity and capacity factor

of the p^{th} power plant, respectively. The GHG emissions generated by the power plants can be estimated as:

$$EG_{e,p} = EP_p AEF_{e,p}, \quad \forall e, p \quad (4)$$

where $EG_{e,p}$ is the amount of emission e generated by plant p , and $AEF_{e,p}$ is a parameter representing the air emission e produced by the p^{th} power plant. The total balance of gas consumed (TNG) by the gas-based power plants (g) can be estimated as follows:

$$TNG = \sum_p IE_p NG_p, \quad p = g \quad (5)$$

where NG_p is the amount of natural gas consumed by the gas-based (g) power plants. The model's simulation results show an average gas volume of 7.78 scf of gas/kWh of power delivered, and an average GHG emission of 409.8 g CO₂ eq./kWh delivered. Finally, the average GHG emissions of electricity transmission and distribution were taken from the literature: 3.2 g CO₂ eq./kWh delivered (Skone et al., 2012).

3. Results and Discussion

The United Arab Emirates was taken as Case Study because is pioneering the development of ultra-sour gas facilities where the concentration of H₂S is much higher than that of CO₂. This is a rare characteristic which can only be found in the Middle East region. The natural gas considered in this study corresponds to that of a typical UAE ultra-sour gas reserve. This type of resource accounts for an annual production of 184 billion cubic feet (bcf) of natural gas; which currently represents roughly 20% of the gas consumed by the UAE power sector. The production of ultra-sour gas is expected to increase significantly in the near-to-medium term future. Table 1 shows a typical composition for ultra-sour natural gas produced in the UAE.

Table 1. Typical composition for ultra-sour natural gas in the United Arab Emirates (Abu Dhabi Gas Development Ltd., 2016).

Components	Mole %
H ₂ S	22
CO ₂	10
C1	54
C2	4
C3+	5
H ₂ O	5

ProMax® v3.2 was used to estimate the utilities (e.g., high/low pressure steam, cooling water, and electricity) required in the treatment of ultra-sour natural gas. The processing of ultra-sour gas requires a significant amount of energy (three to four times higher than conventional gas) per unit of sweet gas yield. This is explained by the fact that as the amount of H₂S in the feed gas increases so does the absorption facility utility requirements. This since more acid gases must be removed by the absorber leading to higher recirculating solvent flowrates. Therefore, the power consumed to cool and pump the regenerated solvent back into the absorber, as well as the steam used to regenerate the alkanolamines increases. Both energy forms (i.e., steam and electricity) account for

the majority of the utilities consumed in the absorption plant. Likewise, more sulfur must be processed by the sulfur recovery units. Moreover, the sweet gas product net recovery rate for ultra-sour gas is around 50 % (after internal fuel consumption); which is very low. For example, the net recovery rate for conventional gas resources is typically higher than 80 % in volume. The electricity requirements for the cooling water loop were estimated using Eq. (1)-(2). The GHG emissions values for ultra-sour gas processing are reported in Table 2. The values are given in terms of per standard cubic feet (scf) of net dry sweet gas yield.

Table 2. Greenhouse Gas emissions involved in ultra-sour natural gas processing.

Type of Utility	GHG emissions (g CO ₂ eq./scf)
High Pressure Steam	0.8
Low Pressure Steam	2.8
Electricity	10.8
Overall Energy Consumption	14.4

From the table it can be clearly noticed that around 75 % of the GHG emissions are due to electricity consumption. The WTT GHG emissions life cycle of UAE’s domestic ultra-sour gas electricity generation can be estimated as the summation of the GHG emissions from the six stages. Table 3 displays the single components of the GHG emissions life cycle for electricity produced from ultra-sour natural gas in the UAE. The GHG emissions were calculated using the 100 year global warming potential.

Table 3. Single GHG emissions for domestic ultra-sour electricity generation in the United Arab Emirates.

Type of Utility	GHG emissions (g CO ₂ eq./kWh)
Raw gas extraction	10 ± 7
Raw gas collection and transfer	0.2
Raw gas treatment/processing	112 ± 8
Sweet gas transfer	29 ± 9
Gas combustion – Power plants	409 ± 29
Electricity distribution and transmission	3 ± 1

As shown in Table 3, raw gas processing and electricity generation account for more than 92 % of the total GHG emissions in the life cycle. Figure 1 shows a comparison between the GHG emissions life cycles of ultra-sour gas electricity generation in the UAE and different power generation options in the United States (Skone et al., 2012). As shown in the Figure, the GHG emissions of ultra-sour gas electricity generation in the UAE are approximately 6% and 11% higher than the averages for the United States’ shale gas and conventional gas, respectively. Nevertheless, it is worth pointing out that the GHG emissions corresponding to UAE’s ultra-sour gas electricity generation place in the middle range of global values according to the literature (e.g., 416-730 g CO₂ eq./kWh). This since the majority of the UAE’s current power fleet is composed of gas-fired combined cycle plants; which are comparatively more efficient than other gas-based plants.

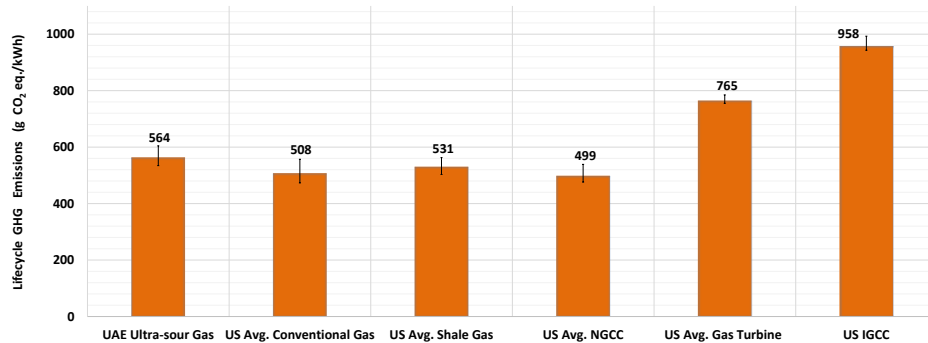


Figure 1: Comparison between the GHG emissions lifecycles of ultra-sour gas electricity generation in the UAE and different power options in the United States.

4. Conclusion

The results of the analysis show that UAE's ultra-sour gas electricity generation is more emission intensive than most gas-based power options employed in the United States. This because significant amounts of energy must be consumed during ultra-sour gas processing in addition to the very low sweet gas yield. Also, sour gas processing and electricity production account for over 90 % of the total GHG emissions.

References

- Abu Dhabi Gas Development Company Ltd. (Al Hosn Gas), 2016, Our Business, Al Hosn Gas.
- A. Almansoori, A. Betancourt-Torcat, 2015, Design optimization model for the integration of renewable and nuclear energy in the United Arab Emirates' power system, *Applied Energy*, 148, 234-251.
- A. Betancourt-Torcat, A. Almansoori, 2015, Design multiperiod optimization model for the electricity sector under uncertainty – A case study of the Emirate of Abu Dhabi, *Energy Conversion and Management*, 110, 177-190.
- Energy Information Administration (EIA), 2015, Country Profile: United Arab Emirates, U.S. Department of Energy.
- International Organization for Standardization (ISO), 2006, Environmental Management: Life Cycle Assessment: Requirements and Guidelines, ISO.
- Interstate Natural Gas Association of America (INGAA), 2005, Greenhouse gas emission estimation guidelines for natural gas transmission and storage, Natural Gas Association of America.
- T. Skone, J. Marriot, J. Littlefield, B.A. Hamilton, 2012, Life Cycle Assessment of Natural Gas Extraction, Delivery and Electricity Production, U.S. National Energy Technology Laboratory.

Influence of Cylinder-to-Particle Diameter Ratio and Filling Speed on Bed Porosity of Random Packed Beds of Spheres

Johanna Fernengel^{a,b,†}, Jennie von Seckendorff^{a,b,†} and Olaf Hinrichsen^{a,b,*}

^aTechnical University of Munich, Department of Chemistry, Lichtenbergstraße 4, 85748 Garching b. München, Germany

^bTechnical University of Munich, Catalysis Research Center, Ernst-Otto-Fischer-Straße 1, 85748 Garching b. München, Germany

† These authors contributed equally to this work.
olaf.hinrichsen@ch.tum.de

Abstract

Packed beds of monosized spherical particles in cylindrical confined walls are simulated using DigIDEMTM, LIGGGHTS[®] and blenderTM. Parameter studies to characterise the influence of the cylinder-to-particle diameter ratio and the filling speed on mean bed porosity are conducted for all three approaches. It is shown that the results obtained for bed configuration are in agreement with experimental results. A clear trend illustrating the influence of filling speed on mean bed porosity is presented. Moreover, new insights on local packing structure are revealed.

Keywords: random packed beds, bed porosity, filling speed, cylinder-to-particle diameter ratio.

1. Introduction

Packed beds are widely used within the chemical and pharmaceutical industry for numerous applications in all kinds of variations and come in a wide range of sizes. In principle, spherical particles were incorporated to form packed beds generally described as being random. However, the formation of an underlying order in the arrangement of the spheres in the bed, especially when using cylindrical containers, is widely accepted throughout the scientific community. This results in an inhomogeneous void space distribution across the packing. In fixed-bed reactors this leads to uneven velocity distributions, expressed by regions of fast channel flow on the one hand and dead zones on the other hand. As a consequence, problems evoke concerning heat and mass transfer. Further, the particle arrangement affects the mean bed porosity. It can easily be shown by error propagation of the respective correlations that small variations in mean bed porosity influence the pressure drop across the bed by a factor of about four. Since pressure drop is directly related to energy consumption, this is of major importance for industry. It is thus decisive to know the influence of parameters on the degree of order and on the mean bed porosity of packed beds.

The radial porosity profile as a function of the distance from the tube wall serves as a well established tool to describe order effects in packed beds. Experimental data, limited to a small selection of investigated cylinder-to-particle diameter ratios $\frac{D}{d}$ and incorporating different experimental techniques, were for example presented by Giese et al. (1998) and Mueller (2010). Altogether, it is shown that spheres order themselves in concentric rings starting from the tube wall. This is indicated by minima in the radial porosity profile at half sphere diameters and maxima at sphere

diameter multiples from the confining wall. However, this trend is not perfect: firstly, the amplitude of the porosity oscillation decreases with higher wall distance, indicating smaller degrees of order towards the tube centre. Secondly, the extrema are shifted closer to the tube wall than expected as the concentric rings of spheres intertwine and thus reduce the radial positions of the extrema away from integral multiples of half the particle diameter.

Experimental studies were performed concerning the dependency of mean bed porosity $\bar{\epsilon}$ and cylinder-to-particle diameter ratio $\frac{D}{d}$, for example by de Klerk (2003) as well as Benyahia and O'Neill (2005). A fast decrease of the mean bed porosity until reaching a constant value at $\frac{D}{d} > 10$ was generally observed and described by correlations. In this work, Benyahia and O'Neill's correlation for packed beds of spheres as given in Eq. (1) was representatively chosen.

$$\bar{\epsilon} = 0.390 + \frac{1.740}{\left(\frac{D}{d} + 1.140\right)^2} \quad \text{for } 1.5 \leq \frac{D}{d} \leq 50 \quad (1)$$

Further parameters possibly influencing bed porosity include filling procedure, material properties and deviations from the commonly assumed ideal geometrical properties. For example Afandizadeh and Foumeny (2001) investigated the difference between fast and slow filling of spheres into cylinders, resulting in a smaller bed porosity when particles were filled slower. Their findings were verified by Pottbäcker and Hinrichsen (2017).

Here, an attempt is made to characterise the influence of the cylinder-to-particle diameter ratio and the filling speed on the mean bed porosity using three different numerical simulation tools.

2. Methodology

The software packages DigiDEMTM (Caulkin et al. (2009)), LIGGGHTS[®] (Kloss et al. (2012)) and blenderTM (Blender Foundation (2015)) are used to generate packed beds of monosized spherical particles in cylindrical confined walls.

DigiDEMTM is a voxelated particle simulation software incorporating a digital packing algorithm based on the Monte Carlo Approach whilst explicitly considering physical interaction forces similar to the discrete element method (Caulkin et al. (2009)). In particular, DigiDEMTM uses the spring-dashpot contact force model between overlapping voxels. The particles are introduced at a random position along the cylinder cross sectional area at the upper end of the container where the number of particles added at each time step varies based on the available space within the cylinder. Thus a maximum filling speed, similar to experimental pouring, is obtained. The simulation finishes after reaching a set final time which is selected such that the cylinder is completely filled with spheres and the particles are at rest in the resulting bed.

LIGGGHTS[®] is a particle simulation software using the discrete element method. Details on the applied Hertz-Mindlin contact model can be found in Jahani et al. (2015) and Kloss (2016). To investigate the influence of the filling speed, particles are introduced above the cylinder at random positions across the cylinder diameter. The insertion rate is kept constant while the number of particles introduced at each insertion instance is varied. To examine the influence of $\frac{D}{d}$, particles are introduced at grid points in a plane above the cylinder with small random variation of the position about the grid points (cf. Boccardo et al. (2015) filling strategy 3). The number of particles is adjusted such that a square with a maximum number of particles per side fits into the considered cylinder. The total kinetic energy of the system is used as stopping criteria to determine whether the particles are at rest.

blenderTM is a computer graphics software used for animation movies and computer games. Boccardo et al. (2015) were the first to apply this software to the generation of packed beds. Particle deposition in blenderTM is achieved by integrating the Bullet physics library (Coumans (2015)). The simulation loop is based on collision detection and rigid body dynamics components (Coumans (2015); Bender et al. (2014)). After collision detection the contact points are handled and the collisions resolved. The particle velocity is updated and in the subsequent time integration the

Table 1: Parameters used for packing generation.

parameter	DigiDEM TM	LIGGGHTS [®]	blender TM
cylinder-to-particle diameter ratio, $\frac{D}{d}$ (-)	2 - 9	2 - 14	2 - 14
cylinder height-to-particle diameter ratio (-)	30	approx. 30	approx. 30
particle density (kg m^{-3})	3000	4000	4000
Young's modulus (GPa)	-	200	-
Poisson's ratio (-)	0.3	0.3	-
coefficient of restitution (-)	0.7	0.7	0.7
coefficient of friction (-)	0.3	0.3	0.3

resulting new particle position evaluated. Particles are positioned above the cylinder as single particles, a pair of particles, in triangle, rhombic and cross arrangement, as squares of 3x3 and 4x4 as well as in a honeycomb structure to investigate the influence of the filling speed. For simulations concerning $\frac{D}{d}$, particles are introduced at random positions across the cylinder diameter one at a time with minimal time between two insertions. The simulation times are chosen such that the particles are at rest in the resulting bed.

Geometry and material settings used for the packing generation simulations are provided in Tab. 1. Parameter studies to characterise the influence of the filling method and the cylinder-to-particle diameter ratio are conducted for the three approaches and compared to literature.

3. Results and Discussion

First, the obtained packed bed structures of all three simulation approaches are compared to experimental data. Two packed beds with $\frac{D}{d} = 8$ and $\frac{D}{d} = 5.6$ are selected as there is experimental data available by Mueller (2010) to characterise the packing structure.

In Fig. 1 (a) and (b) scatter plots of the sphere centre positions are depicted accordingly. Fig. 1 (a) compares the simulated results from all three applied software packages with experimental data, showing the results in the four quarters respectively. It can be seen that the outermost ring is almost perfect, whereas the order of the packing is decreasing towards the centre. Nonetheless, four complete rings with a stack of single spheres in the centre are visible. In case of $\frac{D}{d} = 5.6$, shown in subfigure (b), the positioning in rings is more pronounced as compared to the packing with $\frac{D}{d} = 8$. Small deviations between the software packages can be seen, where the second ring from the wall appears to be least ordered for the results obtained with LIGGGHTS[®].

These observations are reflected in the corresponding radial porosity profiles displayed in subfigures (c) and (d). Overall, for the packed bed with $\frac{D}{d} = 8$ (subfigure (c)) a perfect agreement of all three simulations and the experimental data from literature could be obtained. As expected, the first minimum in the radial porosity profiles appears at an exact position of half a sphere diameter from the containing cylindrical wall and the first maximum at a distance from the wall of one particle diameter. In addition, the amplitude of the porosity oscillations decreases towards the centre of the packing. In contrast to this, subfigure (d) depicting the bed with $\frac{D}{d} = 5.6$ shows generally less but still good agreement between simulated and experimental results. The radial porosity profiles of the simulated packings show less damping as compared to the experimental data. This deviation is especially distinct close to the cylinder centre. As opposed to the other two software packages, the results obtained with LIGGGHTS[®] are extraordinary close to the experimental data at the outermost one and a half particle diameters from the wall. Further into the bed, the LIGGGHTS[®] profile strongly approaches the other two simulated curves. The first minimum and maximum are once more at the expected positions whereas there is a perceptible shift in position of the following extrema between experimental and simulated data. Especially the last minimum is shifted away from the centre for the simulated results as compared to the experimental data. Consequently, a duct at the centre of the cylinder can be observed in the simulated data which is considerably more pronounced as compared to the experimental data.

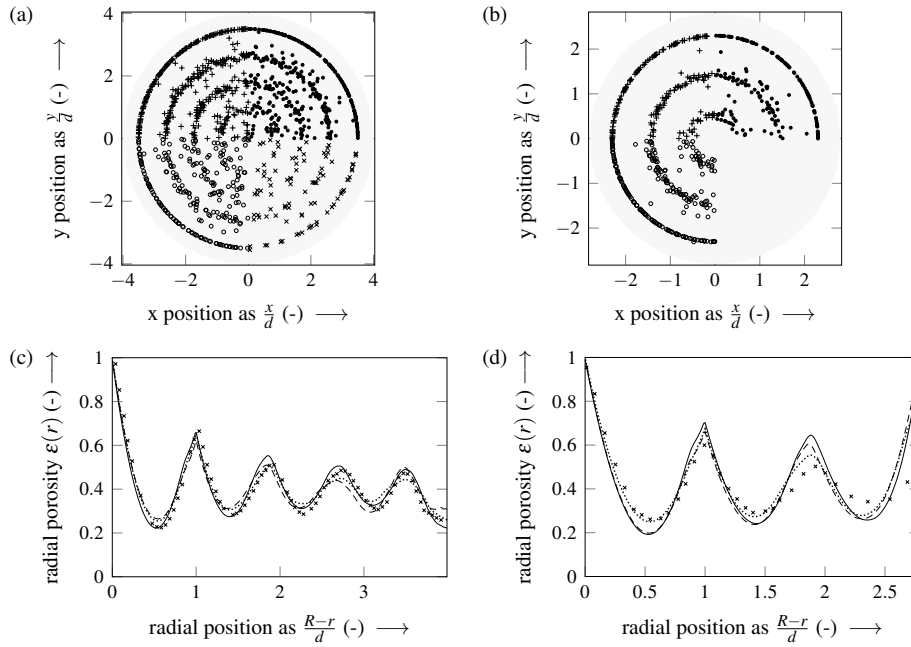


Figure 1: Scatter plots of sphere centre points and radial porosity profiles for beds with $\frac{D}{d} = 8$ (a,c) and $\frac{D}{d} = 5.6$ (b,d), simulated with DigiDEMTM (+ and —), LIGGGHTS[®] (• and), and blenderTM (◦ and ---); experimental data by Mueller (2010) for $\frac{D}{d} = 8$ (×).

Comparing the position of the minima corresponding to the third ring of spheres from the wall for both diameter ratios shown reveals different degrees of shifting. In case of $\frac{D}{d} = 8$ the minimum of the third ring is at a radial position of $2.25 \cdot d$ whereas for the packed bed with $\frac{D}{d} = 5.6$ the corresponding value is about $2.3 \cdot d$ for the simulated and $2.4 \cdot d$ for the experimental data. The positions of these extrema would be $2.5 \cdot d$ in an ideal packing, but due to intertwining rings of spheres the extrema positions are shifted towards the confining wall. This occurring deviation in the positions of the minima is worth being investigated further.

In Fig. 2 results showing the influence of $\frac{D}{d}$ on the mean bed porosity are provided for all three simulation approaches and compared to the correlation by Benyahia and O'Neill (2005). A good agreement between the simulated results and the correlation is presented. The data points obtained by simulation of beds with $\frac{D}{d} = 2$ are in perfect agreement with the correlation as well as an analytical solution presented by Govindarao et al. (1992). The following group of values from $\frac{D}{d} = 2.2$ to 2.8 are very similar for all numerically obtained data and close to the correlation. For $\frac{D}{d} = 3$ an apparent minimum can be identified for all three simulation approaches. This refers to a very dense packing based on one concentric ring at the wall with a stack of spheres in the centre of the cylinder. The experimental data by de Klerk (2003) shows a similar minimum. In the following, the data depicted in subfigures (a) and (b), representing DigiDEMTM and LIGGGHTS[®] respectively, show similar courses close to the correlation with values slightly above the predicted. The data obtained by simulation with blenderTM, presented in subfigure (c), shows a considerably steeper initial slope. As a result, the mean bed porosity is significantly below the other simulation results and the correlation from $\frac{D}{d} = 3$ and beyond, whereby an earlier but faster levelling off is observed. Altogether, the results obtained with blenderTM are slightly below the correlation.

Experimental studies by Afandizadeh and Fomeny (2001) and Pottbäcker and Hinrichsen (2017)

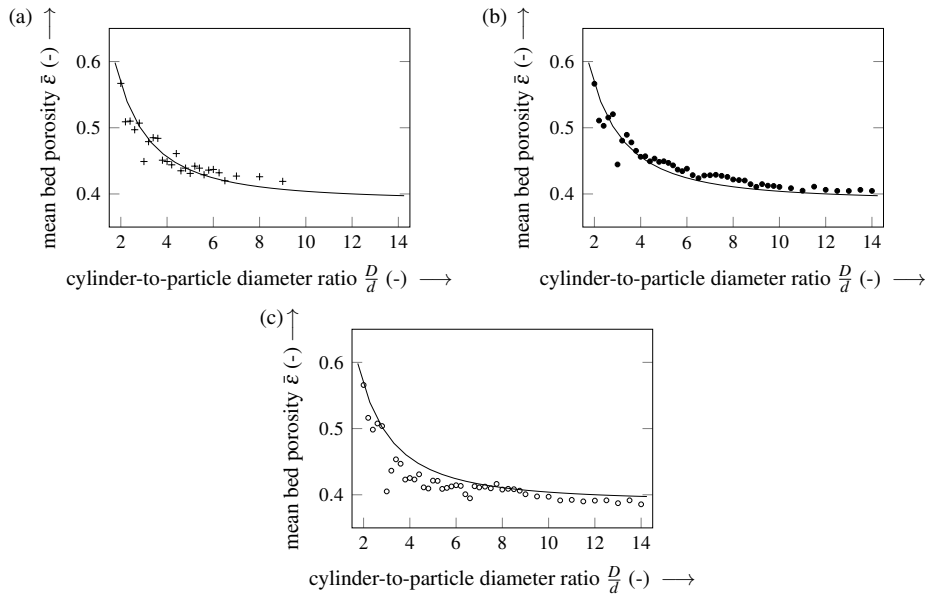


Figure 2: Mean bed porosity as a function of $\frac{D}{d}$, simulated with (a) DigiDEMTM (b) LIGGGHTS[®] and (c) blenderTM, compared to correlation of Benyahia and O'Neill (2005).

indicate an influence of the filling speed with a significantly lower mean bed porosity for slow filling as compared to poured beds, where the difference in both procedures is the amount of particles filled to a container within a given time. Here, the influence of filling speed, expressed as number of spheres per insertion layer, on the mean bed porosity of packed beds with $\frac{D}{d} = 6.25$ is simulated with LIGGGHTS[®] and blenderTM as presented in Fig. 3. It is apparent from both subfigures that the simulated bed porosities increase with filling speed, which is in line with the expected trend. For comparison, experimental bed porosity values are provided for poured beds, beds obtained by single particle dropping and subsequently densified beds (Pottbäcker and Hinrichsen (2017)). It would have been expected that at high filling speeds the porosity values should approach the experimental results for poured beds whereas at low filling speeds porosities close to single dropping should be obtained. Despite trying to establish comparable settings for the different simulation approaches, LIGGGHTS[®] overestimates whereas blenderTM underestimates the bed porosity at fast filling conditions.

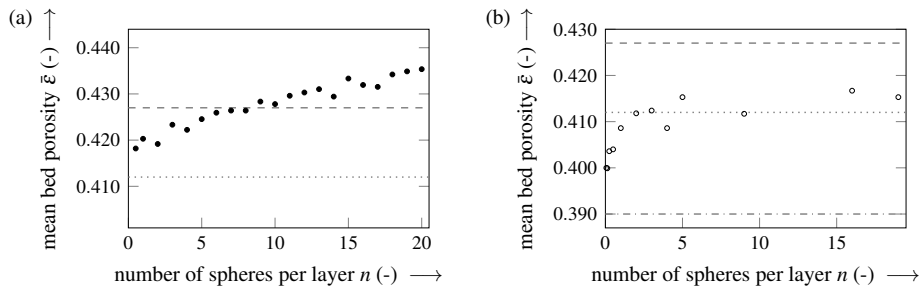


Figure 3: Mean bed porosity as a function of filling speed for beds with $\frac{D}{d} = 6.25$, simulated with (a) LIGGGHTS[®] and (b) blenderTM; experimental porosities for loose (---), dense (.....) and densified (-.-.-) beds shown for comparison (Pottbäcker and Hinrichsen (2017)).

4. Conclusions

All three applied software packages, although being based on different numerical methods, are well suitable to generate random packed beds of spheres. The results match the trends known from experimental studies. However, small differences in the obtained results are identified. Further, it could be shown that mean bed porosities simulated with DigiDEMTM and LIGGGHTS[®] are well in accordance with the experimental correlation of Benyahia and O'Neill (2005) for a wide range of $\frac{D}{d}$. Adequate consistency can be obtained using blenderTM, whereby slight deviations are balanced by considerably faster simulation times. Hence, blenderTM may be the tool of choice for initial assessments. A clear trend concerning the influence of filling speed on mean bed porosity was revealed. As a consequence, the filling speed could be utilised to adjust the bed porosity and thus for example the pressure drop of a packing. Moreover, the remarkable spread in the obtained mean bed porosities when varying the filling speed indicates that more care should be taken when designing numerical packed bed simulation set-ups as small changes may result in significant porosity deviations. This should be kept in mind when drawing conclusions from numerical simulations for technical applications.

Superimposing both influences of cylinder-to-particle diameter ratio and filling speed on the bed porosity as well as the influence of material properties are currently under investigation.

Acknowledgments

J. Fernengel and J. von Seckendorff gratefully acknowledge the support by the Departmental Graduate Center Chemistry of TUM Graduate School at Technische Universität München, Germany.

References

- S. Afandizadeh, E. A. Foumeny, 2001. Design of packed bed reactors: guides to catalyst shape, size and loading selection. *Applied Thermal Engineering* 21, 669–682.
- J. Bender, K. Erleben, J. Trinkle, 2014. Interactive Simulation of Rigid Body Dynamics in Computer Graphics. *Computer Graphics Forum* 33 (1), 246–270.
- F. Benyahia, K. E. O'Neill, 2005. Enhanced Voidage Correlations for Packed Beds of Various Particle Shapes and Sizes. *Particulate Science and Technology* 23, 169–177.
- Blender Foundation, 2015. Blender 2.76b. software package.
- G. Boccardo, F. Augier, Y. Haroun, D. Ferré, D. L. Marchisio, 2015. Validation of a novel open-source work-flow for the simulation of packed-bed reactors. *Chemical Engineering Journal* 279, 809–820.
- R. Caulkin, X. Jia, C. Xu, M. Fairweather, R. A. Williams, H. Stitt, M. N. A. Aferka, M. Crine, A. Léonard, D. Toye, P. Marchot, 2009. Simulations of Structures in Packed Columns and Validation by X-ray Tomography. *Industrial & Engineering Chemistry Research* 48, 202–213.
- E. Coumans, 2015. Bullet 2.83 Physics SDK Manual.
- A. de Klerk, 2003. Voidage Variation in Packed Beds at Small Column to Particle Diameter Ratio. *AIChE Journal* 49 (8), 2022–2029.
- M. Giese, K. Rottschäfer, D. Vortmeyer, 1998. Measured and Modeled Superficial Flow Profiles in Packed Beds with Liquid Flow. *AIChE Journal* 44 (2), 484–490.
- V. M. H. Govindarao, K. V. S. Ramrao, A. V. S. Rao, 1992. Structural characteristics of packed beds of low aspect ratio. *Chemical Engineering Science* 47 (8), 2105–2109.
- M. Jahani, A. Farzanegan, M. Noaparast, 2015. Investigation of screening performance of banana screens using LIGGGHTS DEM solver. *Powder Technology* 283, 23–47.
- C. Kloss, 2016. LIGGGHTS[®]-PUBLIC Documentation, Version 3.X. DCS Computing GmbH, Linz, Austria.
- C. Kloss, C. Goniva, A. Hager, S. Amberger, S. Pirker, 2012. Models, algorithms and validation for opensource DEM and CFD-DEM. *Progress in Computational Fluid Dynamics* 12, 140–152.
- G. E. Mueller, 2010. Radial porosity in packed beds of spheres. *Powder Technology* 203, 626–633.
- J. Pottbäcker, O. Hinrichsen, 2017. Experimental Study on the Influence of Filling Method and Particle Material on the Packed-Bed Porosity. *Chemie Ingenieur Technik* 89 (4), 454–458.

Analyzing the link between G^E -model parameter regression and optimal process design

Mirko Skiborowski^{a*}, Philipp Temmann^{ab}, Christoph Brandenbusch^b

^a*TU Dortmund University, Department of Chemical and Biochemical Engineering, Laboratory of Fluid Separations, Emil-Figge-Straße 70, 44227 Dortmund, Germany*

^b*TU Dortmund University, Department of Chemical and Biochemical Engineering, Laboratory of Thermodynamics, Emil-Figge-Straße 70, 44227 Dortmund, Germany*

mirko.skiborowski@tu-dortmund.de

Abstract

The importance of accurate thermodynamic models, capable of describing vapor-liquid and liquid-liquid equilibria, is generally acknowledged for the design of chemical processes. However, the parameterization of thermodynamic models and the development of chemical processes are usually treated as two different disciplines. More importantly, the objectives of each discipline do not necessarily align. While the quality of a thermodynamic model is often judged purely on the basis of its average mean deviation from experimental data, process design aims at minimizing the overall process costs, assuming that the underlying thermodynamic models (especially model parameters) are reliable/accurate. Assessing the uncertainty of the thermodynamic model parameters is the link between both disciplines. However, this link is rarely established, and even the effect of the consideration of uncertainties in parameter regression by means of a deterministic process design is rarely investigated. Within this work this effect was taken into account for vapor-liquid equilibrium modeling and optimal design of a distillation column. The results indicate the necessity of a consistent consideration of uncertainties both during parameter regression and process optimization. Furthermore, the results highlight that a special treatment of experimental data and uncertainty information is required for specific applications (e.g. distillation of tangent pinch systems) in order to obtain reliable results in process design.

Keywords: Thermodynamic equilibria, Parameter regression, Optimization, Distillation

1. Introduction

Thermodynamic data is required for a wide variety of applications in the chemical industry including the development, design, planning, and operation of processes. Especially phase equilibrium modeling is one of the most important fundamental sciences for process development in the chemical industry (Zeck & Wolf, 1993). It provides the basis for a model-based evaluation of a variety of separation processes, such as e.g. distillation and liquid-liquid extraction, and enables the evaluation of individual process concepts by means of flowsheet simulations. The availability of accurate thermodynamic models and corresponding parameters for a wide range of chemicals are the foundation of today's accelerated process development by means of process simulators. This circumvents a good number of previously required time consuming and expensive experiments. A famous quote of Roger Sargent states that

“design methods have been developed to such a point that any plant design can be carried through with confidence, provided the requisite basic data is available.” (Doherty et al., 2016). Today, this optimistic statement of Sargent is for sure more realistic than 60 years ago. However, the necessary confidence and even more a quantification of the level of confidence is still a challenge. One possibility to deal with uncertainty related to this basic data is to perform a robust process design. Thereby, the process specifications will be met for all probable variations of the property parameters considering a quantification of their uncertainty. Interestingly, Sargent was also one of the pioneers in the area of process design under uncertainty and specifically robust optimization approaches, more than 20 years after his previously quoted statement (Grossmann & Sargent, 1978). Today, in order to deal with uncertainty related to thermodynamic property models, methods like robust optimization or two-stage stochastic optimization become increasingly popular (Steimel & Engell, 2016). Nevertheless, these methods are not the state-of-the-art in application and uncertainty is almost always estimated, instead of properly propagated from the experimental data through parameter regression. One potential reason for this is the missing information on uncertainties (or their quantification) in published experimental data. This was recently documented by the results of the working party on thermodynamics and transport properties of the EFCE, which evaluated information from 28 chemical engineering companies (Hendriks et al., 2010). They specifically pointed out that quality is more important than quantity. An essential step in quantifying this quality by a regular reporting of uncertainties in thermochemical experimental data was established by the National Institute of Standards and Technology (NIST) through the concept of dynamic data evaluation more than 10 years ago (Frenkel et al., 2005).

In order to motivate the necessity of a consistent consideration of uncertainties, this work presents an investigation of the effect of different uncertainty considerations in parameter regression on a deterministic process design of distillation processes. Therefore, different objective functions for the parameter regression are taken into account, followed by an optimization-based process design for different product specifications. Various systems with different degrees of non-ideality are considered. It is shown that significant deviations in process design may occur from marginal deviations in equilibrium modeling: These can be caused by minor modifications of the parameter regression, especially the way uncertainties are considered. The results mandate a stronger integration between the disciplines of thermodynamics, fluid separations and process systems engineering in order to consider the effect of uncertain experimental data on process design already at the level of thermodynamic modelling.

2. Methodology

The methodology that is applied in the current study is illustrated in Figure 1. At first adequate experimental data, including reported uncertainty information is selected. Next, the parameters of a thermodynamic model for the free enthalpy (G^E -model), in this case the non-random two liquid (NRTL) model are regressed against the experimental data, using selected objective functions. Finally, an economic process optimization of a distillation column for different product specifications is performed.

2.1. Data acquisition

For the subsequent evaluation suitable vapor-liquid equilibrium (VLE) datasets with uncertainty information need to be selected from the NIST TDE as a first step.

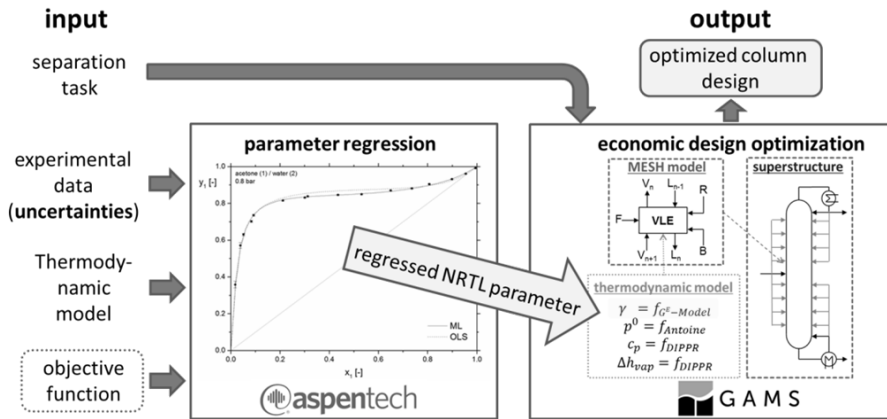


Figure 1: Illustration of the applied method for evaluating the effect of uncertainty consideration in parameter regression on the final process design.

Only datasets that contain a sufficient amount of data points, with full information on pressure, temperature, both compositions, as well as information on standard deviations for each measurement were considered. Although the NIST TDE provides a significant number of binary VLE datasets, yet, only a limited subset satisfies these constraints. Unfortunately, mostly default values for standard deviations are considered. These relative values are based on literature estimates and assume e.g. an error estimate of 1% for the vapor mole fraction (Sandler, op. 2015). The effect of these default values is briefly addressed in the subsequent subsection.

2.2. Parameter regression

While a proper choice of the thermodynamic model is important, even for the best available model the effect of uncertainties in the experimental data can result in significant uncertainties in the model parameters (upon regression based on these data) and a subsequent process design (Xin & Whiting, 2000). As one of the industrially most applied G^E models, the NRTL model is selected and the a_i and b_i parameters (Aspen nomenclature) are regressed to the selected VLE datasets. The NRTL c parameter is fixed according to the suggestions in ASPEN Plus® (Schefflan, 2017). Parameter regression is performed by means of the available regression methods in ASPEN Properties. In order to evaluate the effect of considering the uncertainty information, different objective functions are considered.

The statistically most reliable parameter estimates are obtained by means of a maximum likelihood estimation (MLE). Assuming that all measurements are independent of each other and that the measurement noise follows a Gaussian distribution with zero mean, the MLE can be obtained by a weighted least squares minimization, for which the weights are equivalent to the standard deviation of the measurement (Beck & Arnold, op. 1977). In ASPEN Plus® the MLE considers all compositions, the temperature and the pressure:

$$\min \sum_{i=1}^{N_{dp}} \left[\left(\frac{p_i^{est} - p_i^{exp}}{\sigma_{p,i}} \right)^2 + \left(\frac{T_i^{est} - T_i^{exp}}{\sigma_{T,i}} \right)^2 + \sum_{j=1}^{N_c-1} \left(\frac{x_{i,j}^{est} - x_{i,j}^{exp}}{\sigma_{x,i,j}} \right)^2 + \sum_{j=1}^{N_c-1} \left(\frac{y_{i,j}^{est} - y_{i,j}^{exp}}{\sigma_{y,i,j}} \right)^2 \right] \quad (1)$$

Since, the standard deviation of the liquid phase composition is usually zero, this term is often not considered. In case all standard deviations are equal, the method simplifies to the so called ordinary least squares (OLS) minimization (Beck & Arnold, op. 1977). Among others, *OLS* is also a possible objective function in ASPEN Plus® (Schefflan, 2017). However, this option presents a weighted least squares minimization that takes into account the reported standard deviation for the temperature and a relative error of 1% for the vapor composition:

$$\min \sum_{i=1}^{N_{dp}} \left[\left(\frac{T_i^{est} - T_i^{exp}}{\sigma_{T,i}} \right)^2 + \sum_{j=1}^{N_c-1} \left(\frac{y_{i,j}^{est} - y_{i,j}^{exp}}{0.01 \cdot y_{i,j}^{exp}} \right)^2 \right] \quad (2)$$

It therefore does not comply with the textbook definition of OLS and is rather equivalent to the MLE without the pressure and liquid composition, and default relative deviation for the vapor composition. Thus, a comparison between results obtained by both objective functions allows for an evaluation of the effect of considering reported uncertainty information for the vapor phase or a default estimate of a relative 1% error. The latter is not an accurate estimate of the variance of the measurement, but it introduces strong bias to measurements at small compositions, such that measurements close to pure components are fitted more accurately to the measurement value.

2.3. Rigorous economic optimization of a distillation column

The regressed parameters are further evaluated in a rigorous economic optimization of a separation by means of a distillation column for different separation tasks. Therefore, a superstructure optimization based on an equilibrium tray model, including sizing and costing correlations is performed in GAMS. Refer to the article of (Skiborowski *et al.*, 2015) for a detailed description of the models and the applied optimization approach. In the optimization the determined parameters are considered as deterministic values, while the process design is determined by minimizing the total annualized costs (TAC).

3. Results

Within this work three close-boiling, four azeotropic, and five tangent pinch systems were investigated. After parameter regression (Aspen properties) the NRTL was used as thermodynamic model within process optimization (GAMS), considering different product specifications (taking into account an equimolar saturated liquid feed mixture of 10 mol/s). Product specifications with high purities of 99 – 99.9 mol% were assumed for the close boiling and tangent pinch systems, while the product specifications for azeotropic systems were adapted to the azeotropic composition.

Table 1: Results of the parameter regression for both objective functions for selected systems.

System	BVLE [Nr]	p [bar]	T - AAD%		K ₁ - AAD%		K ₂ - AAD%	
			MLE	OLS	MLE	OLS	MLE	OLS
1: isopropanol/water	120	1.013	0.04	0.20	1.3	0.9	1.8	1.3
2: acetone/water	120	0.8	0.60	1.60	0.8	1.5	6.3	9.4
3: methanol/nitromethane	006	1.013	0.45	0.45	1.4	2.0	3.1	3.0
4: acetone/water	122	1.013	0.39	0.42	3.8	3.5	4.8	5.6
5: n-propanol/n-butyl acetate	003	1.013	0.05	0.65	2.0	1.3	7.5	2.1
6: acetonitrile/p-xylene	001	1.013	0.37	0.76	3.6	3.2	6.0	5.1

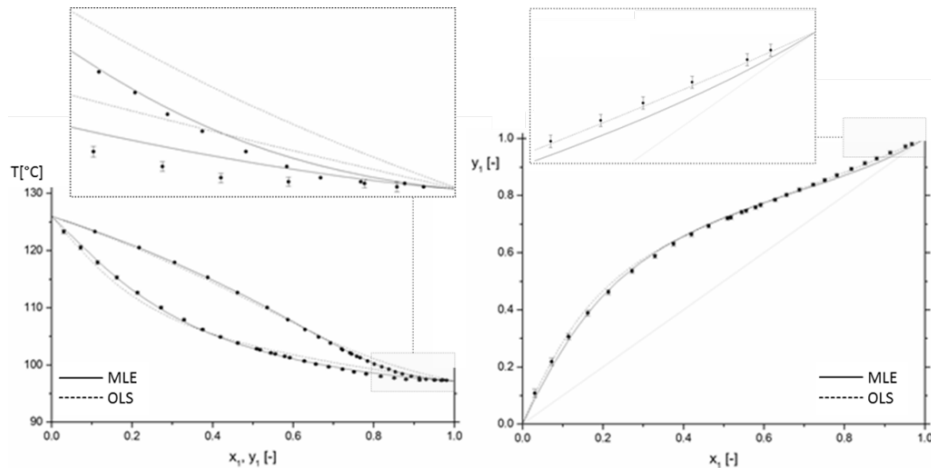


Figure 2: Illustration of the fit of the VLE model prediction according to the MLE and OLS objective function, for the binary the n-propanol/n-butyl acetate system.

In general, the results of the parameter regression in terms of the average absolute deviation (AAD%) are comparable for both objective functions. This is illustrated for a selection of the considered systems and the AAD% values for the temperature and the distribution coefficients (K) of both components in Table 1. Additionally, the specific dataset for the binary VLE data (BVLE) in the NIST TDE and the pressure are given. The subsystems selected are either azeotropic or tangent pinch systems, which show the comparably largest deviations in the subsequent process design results. The regression results for all narrow boiling systems show an excellent “goodness of fit” and are hardly distinguishable for both objective functions. This applies also for the selected subsystems with respect to the AAD% values, as well as corresponding T-xy and x-y diagrams. Deviations between the resulting VLE predictions and experimental data become apparent upon close up investigations. Especially in case of the tangent pinch systems the parameters fitted in accordance with the MLE objective function provide a better fit to the temperature and the T-xy diagram, while the OLS provides smaller deviations in terms of the K -values and accordingly the yx-diagram. This is illustrated for the n-propanol/n-butyl acetate system in Figure 2, which represents one of the largest visible deviations between the fits using the two objective functions.

While the deviations in VLE modeling are close to negligible, the differences in the resulting process designs can be substantial. Figure 3 illustrates the deviations between the resulting process designs in terms of relative deviations of the TAC. The small deviation in the VLE prediction for the n-propanol/n-butyl acetate systems results in a deviation in the subsequent process design that exceeds a factor of two in TAC for the highest product purity specifications of 99.9 mol%. Taking into account the deviation between the OLS and MLE fit for the yx-diagram in Figure 2 it can be suspected that the MLE results in a severe overdesign of the column, since the VLE equilibrium line of the model runs closer to the 45° degree line as indicated by the experimental data. However, there is no clear trend, as the differences in terms of TAC of an optimized design can go both ways. Nevertheless the trend towards higher deviations for higher purities is the same for all tangent pinch systems (4-6), whilst for the azeotropic systems one of the designs becomes infeasible (Inf) due to small differences in the azeotropic composition. Consequently, the differences in these cases are also significant.

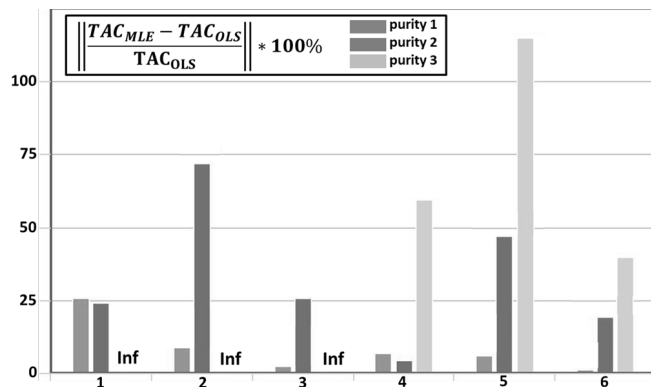


Figure 3: Resulting deviations in the TAC of the optimized process design for different product specifications for each of the listed binary systems (cf. Table 1).

4. Conclusion and Outlook

The results of this work highlight the importance of the choice of the objective function and the way uncertainties are considered in parameter regression. It is illustrated that severe differences in the subsequent process design can even result from minor deviations in the consideration of uncertainties (taking into account reported standard deviations or a default relative deviations). Especially small deviations in very narrow boiling regions of systems with non-constant relative volatility, such as azeotropic or tangent-pinch systems are of superior importance for the design of distillation processes. Thus, these regions have to be described with extreme accuracy in order to avoid process misdesign. Future work needs to evaluate if process design under uncertainty can avoid such misdesign without severely conservative overdesign.

References

- Beck, J., Arnold, K., 1977, Parameter estimation in engineering and science. New York, Wiley.
- Doherty, M. F., Grossmann, I. E., Pantelides, C. C., 2016, A Tribute to Professor Roger Sargent: Intellectual Leader of Process Systems Engineering, *AIChE J.*, 62, 2951–2958.
- Frenkel, M., Chirico, R. D., Diky, V., Yan, X., Dong, Q., Muzny, C., 2005, ThermoData Engine (TDE): Software implementation of the dynamic data evaluation concept, *J. Chem. Inf. Mod.* 45, 816–838.
- Grossmann, I. E., Sargent, R. W. H., 1978, Optimal design of chemical plants with uncertain parameters, *AIChE J.* 24, 1021–1028.
- Hendriks, E., Kontogeorgis, G. M., Dohrn, R., Hemptinne, J.-C. de, Economou, I. G., Žilnik, L. F., Vesovic, V., 2010, Industrial requirements for thermodynamics and transport properties, *Ind. Eng. Chem. Res.* 49, 11131–11141.
- Sandler, S. I., 2015, Using Aspen plus in thermodynamics instructions. Hoboken: Wiley.
- Schefflan, R., 2017, Teach yourself the basics of Aspen plus. Hoboken, Wiley.
- Skiborowski, M., Harwardt, A., Marquardt, W., 2015, Efficient optimization-based design for the separation of heterogeneous azeotropic mixtures, *Comp. Chem. Eng.* 72, 34–51.
- Steimel, J., Engell, S., 2016, Optimization-Based Support for Process Design under Uncertainty: A Case Study, *AIChE J.* 62, 3404–3419.
- Xin, Y., Whiting, W. B., 2000, Case Studies of Computer-Aided Design Sensitivity to Thermodynamic Data and Models, *Ind. Eng. Chem. Res.* 39, 2998–3006.
- Zeck, S. & Wolf, D., 1993, Requirements of thermodynamic data in the chemical industry, *Fluid Phase Equilibria.* 82, 27–38.

Kinetic Modeling of Precipitation Terpolymerization for Functional Microgels

Franca A. L. Janssen^a, Agnieszka Ksiazkiewicz^b, Michael Kather^b, Leif C. Kröger^c, Adel Mhamdi^a, Kai Leonhard^c, Andrij Pich^b and Alexander Mitsos^{a*}

^a*Aachener Verfahrenstechnik - Process Systems Engineering, RWTH Aachen University, Aachen, Germany*

^b*Institute for Technical and Macromolecular Chemistry, RWTH Aachen University, Aachen, Germany*

^c*Chair of Technical Thermodynamics, RWTH Aachen University, Aachen, Germany*

**amitsos@alum.mit.edu*

Abstract

Microgels based on poly(*N*-isopropylacrylamide)- and poly(*N*-vinylcaprolactam) can be synthesized by precipitation polymerization. To get a better insight into the kinetics of the microgel synthesis, a model-based approach is pursued. Herein, the approach proposed by Janssen et al. (2017) is extended to the terpolymerization system. The kinetic model for a two-phase terpolymerization is combined with parameter values from quantum mechanical calculations. The remaining unknown parameter values are estimated from experimental data using reaction calorimetry and Raman spectroscopy. Acceptable agreement of simulation and experimental measurements is obtained. The prediction of the gel phase growth is combined with the consumption of comonomers and the cross-linker *N,N'*-methylenebis(acrylamide) to predict the average distribution of comonomers, thus giving insight into the microgel structure. The resulting particle structures indicate uniform *N*-vinylcaprolactam and *N*-isopropylacrylamide compositions in the core and an outer layer with a high *N*-vinylcaprolactam fraction, while the cross-linker distribution decreases from core to shell.

Keywords: Method of moments, kinetic modeling, microgels, polymerization

1. Introduction

Precipitation polymerization is a commonly used method to synthesize poly(*N*-vinylcaprolactam) (pVCL)- and poly(*N*-isopropylacrylamide) (pNIPAM)-based microgels and copolymer microgels thereof (Pich and Richtering (2011)). Monomers and the cross-linker *N,N'*-methylenebis(acrylamide) (BIS) are initially dissolved in water. The thermal initiator 2,2'-azobis(2-methylpropionamide) dihydrochloride (AMPA) initiates the free radical polymerization. Due to low solubility of the growing polymer chains in water, the radicals precipitate to form small precursor particles. The particles continue to grow by both, aggregation as well as ongoing polymerization. Propagation of growing radicals with the pendant double bonds (PDB) of cross-linker lead to the formation of stable microgel particles.

In batch polymerization, the distribution of comonomers and cross-linker within the microgels is determined by the reaction kinetics. Balaceanu et al. (2013) reported for microgels from pVCL and pNIPAM uniform internal structures, although NIPAM is the more reactive monomer. Model-based approaches can help understanding the driving forces of the microgel synthesis and give

insight into their internal composition. Hoare and McLean (2006a) predict the local distribution of functional groups in pNIPAM-based microgels from reaction rate constants in a solution polymerization model. Further, they propose an approach for controlling the local polymer composition in multi-component systems (Hoare and McLean (2006b)). However, solution polymerization models simplify the system as they neglect any mass transfer mechanisms between the phases. The preferential accumulation of one monomer in the gel phase can equally cause an inhomogeneous copolymer composition. To elucidate the underlying phenomena causing the particle structures, models should address the distinction of the two-phase system and mass transfer mechanisms.

Precipitation polymerization models, such as proposed by Arosio et al. (2011) for a different polymer system, focus on the impact of mass transfer among the phases and predict the reaction locus. In Janssen et al. (2017) we propose a precipitation polymerization model for pVCL-based microgels. Thereby, the gel phase is determined to be the primary reaction locus due to a short critical chain length and an accumulation of monomer and cross-linker in the gel phase. Different cross-propagation reaction rates for VCL and BIS (Kröger et al. (2017)) cause an inhomogeneous cross-linker distribution in the particles.

In this contribution, we adapt our approach (Janssen et al. (2017)) to the terpolymerization precipitation of VCL, NIPAM and BIS. The model is fitted to previously published and new experimental data and applied for a rough prediction of the particles internal structure.

2. Modeling of Precipitation Terpolymerization

In Janssen et al. (2017) we describe the synthesis of pVCL-based microgel by precipitation copolymerization model with two phases. Mass balances for all reaction species are formulated, whereas the primary chains of polymers are balanced applying the terminal model and the method of moments. Mass transfer between the phases is described for small molecules by phase equilibrium with distribution coefficients D and for polymer by precipitation of the radicals at a finite critical chain length η . The key feature of this approach is that the high number of unknown parameter values is reduced by the use of reaction rate constants and distribution coefficients calculated from transition state theory and COSMO-RS. In this contribution, we apply this approach to a model for the terpolymerization of VCL (1) and NIPAM (2) with the cross-linker BIS (3).

Few alterations are applied to the model in order to reduce the number of parameter values to be estimated and decrease the model complexity without loss of information. These alterations are: 1.) Constant initiator efficiencies $f_i = 0.6$ in liquid and gel phase, which is a mean efficiency for azo-initiators. 2.) Cross-linking in the liquid phase is neglected ($f_{\text{pdb}}^l = 0$) while in the gel phase, cross-linking reactions are assumed to be equally limited by the formation of the polymer network, resulting in one cross-linking efficiency factor f_{pdb}^g . 3.) Termination rate constants k_t^g in the gel phase represent the apparent rate constants which account for diffusion limitation (k_{diff}^g). They are linked to the termination rate constants of the liquid phase by $k_t^g = (k_t^l k_{\text{diff}}^g) / (k_t^l + k_{\text{diff}}^g)$ (Buback et al. (1992)). 4.) The gel phase volume, V^g , is calculated from the pure polymer densities ρ and 50 w% water. The volume of the liquid phase, V^l follows from $V^{\text{tot}} = \text{const} = V^l + V^g$. 5.) The liquid phase serves as initiation phase, due to a small critical chain length and $D > 1$. To calculate the mass flow by precipitation, first the pseudo-homopolymerization approach (Storti et al. (1989)) and then the quasi-steady state assumption (QSSA) for radicals are applied. Thus, the $n_C(\eta - 1)$ differential equations for n_C comonomers are replaced by $n_C + 1$ algebraic equations.

Quantum mechanical calculations (QMC): The chain propagation rate constants k_p with the corresponding reaction enthalpies ΔH_R are calculated by transition state theory depending on the composition of both phases: For the liquid phase infinite dilution and for the gel phase a composition of 50 w% polymer and 50 w% water is assumed. The corresponding parameter values are used as listed in Kröger et al. (2017) and Janssen et al. (2017). VCL and NIPAM cross-propagation

rate constants are calculated accordingly for the liquid phase ($k_{p12}^l = 47.3 \text{ m}^3(\text{mol s})^{-1}$, $k_{p21}^l = 620.0 \text{ m}^3(\text{mol s})^{-1}$) and the gel phase ($k_{p12}^g = 19.6 \text{ m}^3(\text{mol s})^{-1}$, $k_{p21}^g = 315.7 \text{ m}^3(\text{mol s})^{-1}$). The unknown distribution coefficient for NIPAM is calculated with COSMO-RS ($D_{M_2} = 2.52$).

Experiments: All experiments are performed in a Mettler Toledo RTcal 0.5 L real-time calorimeter in isothermal control mode at 70 °C and ambient pressure. The reactor is filled with 0.3 L water and all reaction species, monomers (homo- and copolymerization: 0.106 molL⁻¹ VCL or NIPAM; terpolymerization: 0.053 molL⁻¹ VCL and NIPAM) with or without cross-linker BIS (2.5 mol% of monomer) are dissolved as well as the stabilizer Cetyltrimethylammoniumbromide (CTAB, 1 w% of monomer). Before the reaction, the reactor is purged with nitrogen. 0.1 g thermal initiator AMPA is added. The experiment runs for 1.5-2 h after initiation before it is terminated. Calorimetry and Raman spectroscopy are performed simultaneously. VCL and BIS experiments are used as published in Janssen et al. (2017). In-line Raman spectra are evaluated with Indirect Hard Modeling (IHM) according to the methods described in Meyer-Kirschner et al. (2016) and Meyer-Kirschner et al. (Submitted) to determine monomer mass fractions w_{M_i} of VCL and NIPAM. Despite purging, the experimental data reveal an inhibition phase right after initiation, which is removed for parameter estimation and comparison with simulation data.

The remaining unknown parameter values for initiator distribution coefficient D_1 , termination rate constants k_t^l , k_{diff}^g , and cross-linking efficiency f_{pdb} are determined by parameter estimation. The experimental data from Raman spectroscopy and the model are linked by the weight fraction balance for the monomers VCL and NIPAM:

$$\frac{dw_{M_i}}{dt} = \frac{MW_{M_i}}{m_{\text{tot}}} \left(-V^l \sum_{j=1}^3 (k_{pji}^l + k_{fmji}^l) c_{\lambda_0}^l c_{M_i}^l - V^g \sum_{j=1}^3 (k_{pji}^g + k_{fmji}^g) c_{\lambda_0}^g c_{M_i}^g \right). \quad (1)$$

Thereby, the termination rate constants influence w_{M_i} only indirectly by affecting the radical concentrations c_{λ_0} . In addition, reaction calorimetry provides information on the overall polymerization progress. The enthalpy transfer rate of the reaction, Σ_R , represents the heat released at constant temperature by the exothermic propagation reactions of monomer and cross-linker:

$$\Sigma_R = \sum_{p=1,g} \sum_{i=1}^3 \left(\sum_{j=1}^3 \left(-\Delta H_{Rij} V^p k_{pij}^p c_{\lambda_0}^p c_{M_j}^p \right) - \Delta H_{Ri3} V^p f_{\text{pdb}} k_{pi3}^p c_{\lambda_0}^p c_{\text{pdb}}^p \right). \quad (2)$$

It also accounts for the consumption of BIS and reactions of the PDBs, while the BIS concentration is below the detection limit of the utilized Raman spectrometer and therefore cannot be measured directly. Thus, both measurement techniques complement each other.

3. Results

Modeling and parameter estimation with the maximum likelihood method are both performed with gProms version 4.2.0 on a 64-bit Intel Core i3-3225 CPU with 3.3 GHz running Windows 7. The parameter values are estimated sequentially and transferred, beginning with homopolymerizations of VCL and NIPAM, followed by their copolymerizations with BIS, respectively, and last terpolymerization of VCL, NIPAM and BIS.

3.1. Homo- and Copolymerization of VCL and NIPAM

The model with parameter values from QMC is evaluated for polymerization reactions of pure VCL and NIPAM. Figure 1a shows the enthalpy transfer rate Σ_R calculated from measurements in comparison to the results with the fitted model. Σ_R is plotted over time, whereas $t = 0$ s corresponds to the moment of initiation in simulation and for experiments is located after the observed inhibition phase. Both curves, VCL and NIPAM, show a good agreement of the fitted model with

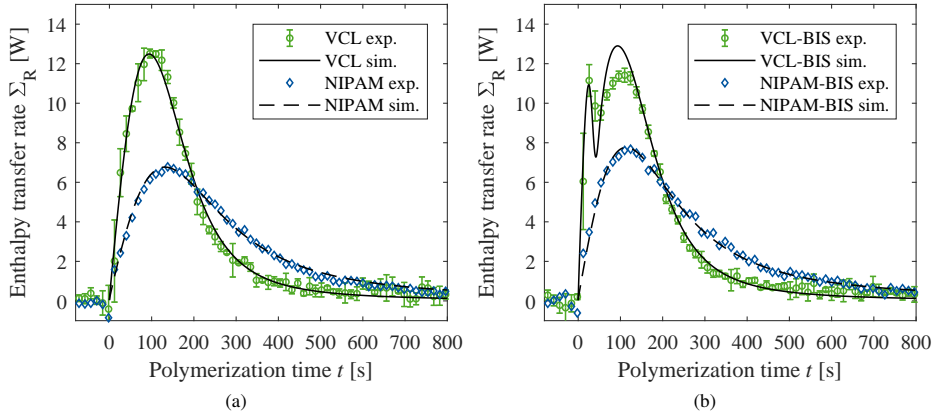


Figure 1: Comparison of experiments and fitted model for (a) homopolymerizations and (b) copolymerizations with BIS in terms of Σ_R .

experimental data.

The experimental data shows that the overall polymerization of VCL proceeds faster than of NIPAM, as Σ_R for VCL increases faster after initiation and obtains its maximum after 100 s while the curve for NIPAM obtains its significantly lower maximum after 150 s. This is counter-intuitive, as the calculated k_p (Kröger et al. (2017)) indicate a faster propagation rate for NIPAM. However, the estimated k_t to fit the experimental data differ significantly. A low estimated value $k_{diff}^g = 3.54 \cdot 10^{-2} \text{ m}^3(\text{mol s})^{-1}$ for VCL dominates k_t^g , expressing a significant diffusion limitation of the termination reaction. This accelerates the overall polymerization reaction. For NIPAM, the higher estimated $k_{diff}^g = 9.89 \cdot 10^3 \text{ m}^3(\text{mol s})^{-1}$ suggests that the termination reaction is less affected and the overall polymerization reaction proceeds slower.

Figure 1b depicts the results of the fitted model in comparison to experimental data for copolymerizations with the same amount of cross-linker. For both reaction systems, the parameter values from QMC can be employed to calculate the reaction progress, as the experimental data can be fitted with good agreement. For VCL-BIS, the first maximum in the Σ_R measurement results from the faster consumption of cross-linker, represented by higher cross-propagation reaction rate constants (Janssen et al. (2017)). Note that the improved fit for VCL-BIS results from a reevaluation of the experimental data regarding the inhibition phase. Σ_R for NIPAM-BIS on the other hand does not indicate such inhomogeneous consumption.

The estimated k_{diff}^g for both reactions differ significantly. A good fit for VCL-BIS is only obtained, when individual diffusion limitations for the termination reactions are introduced ($k_{diff11}^g < k_{diff13}^g < k_{diff33}^g$). For NIPAM-BIS, a constant k_{diff2}^{g*} for the different termination reactions is sufficient, but it needs to be determined for reactions with different cross-linker concentrations individually. Then, k_{diff2}^{g*} decreases with increasing cross-linker concentration, causing the overall polymerization to proceed faster. Thus, for the system of NIPAM-BIS, diffusion limitation depends on the cross-linker concentration, whereas for the VCL-BIS system, the monomer VCL itself, e.g., by steric limitation of the molecular structure, causes a limitation of the termination reaction.

3.2. Terpolymerization

The model is applied to the terpolymerization system. Thereby, the observations from copolymerization are incorporated in terms of the fitted parameter values: while k_{diff11}^g and k_{diff13}^g are

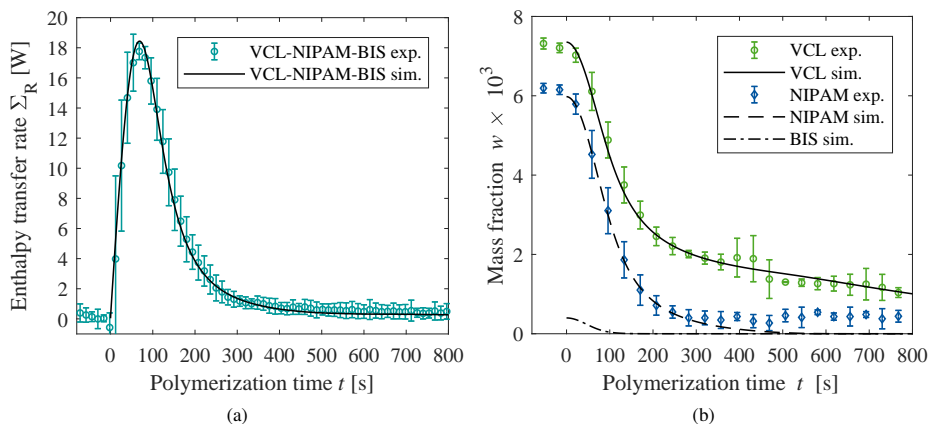


Figure 2: Comparison of experiments and simulation with fitted model for terpolymerization in terms of (a) enthalpy transfer rate from calorimetry and (b) monomer mass fractions from Raman spectroscopy. BIS concentration is below the detection limit and hence cannot be determined from in-line spectra. Time $t = 0$ s denotes the initiation.

transferred as previously estimated, the k_{diff2}^{g*} is estimated again due to the different composition. Figure 2a shows good agreement between Σ_R determined from experiments and the fitted model. The maximal enthalpy transfer rate is significantly higher (> 18 W) than for the copolymerizations and the overall reaction proceeds fast. For the fitted model, this results from high k_{p12} and k_{p21} in combination with low estimates for k_{diff12}^g and k_{diff2}^{g*} . Hence, the overall reaction is accelerated. The comparison of the measurements of the mass fractions w_M of VCL and NIPAM with the fitted model is illustrated in Figure 2b. NIPAM is consumed slightly faster than VCL. Still, high VCL cross-propagation rate constants and the preferential accumulation of VCL in the gel phase ($D_{M1} > D_{M2}$) promote the consumption of VCL in the presence of NIPAM and BIS. After 300 s, w_{M2} is below $1 \cdot 10^{-3}$ and thereby in the size range of the prediction error of the chemometric model (Meyer-Kirschner et al. (Submitted)). With the combination of both measurements, the cross-linker consumption can be predicted with the fitted model.

The comonomer consumptions in combination with the predicted gel phase growth provide a rough prediction of the internal microgel structure, as illustrated in Figure 3. The instantaneous copolymer fraction F_{CM} represents the reaction rate fractions of the comonomers in the gel phase and V^g is predicted from the mass transfer due to phase equilibrium and precipitation. The instantaneous BIS mole fraction declines over the radius. As the cross-linker is incorporated in the polymer network, the instantaneous radius represents the maximum range of its position in the microgel, indicating a higher cross-linked core. The instantaneous

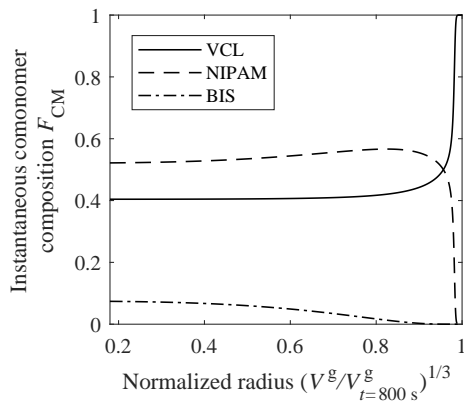


Figure 3: Instantaneous comonomer mole fraction compared to the instantaneous normalized radius.

mole fractions of VCL and NIPAM are mostly constant over the radius, though the faster NIPAM consumption results in a higher NIPAM fraction. For the normalized radius close to unity, VCL is the only monomer left. Hence, the final microgels have a core with radially uniform composition of VCL and NIPAM and a thin outer corona of pure pVCL. The prediction of the microgel structure agrees with the uniform distribution of VCL and NIPAM described by Balaceanu et al. (2013).

4. Conclusion

In this contribution, we extend our precipitation polymerization model for VCL-based microgels (Janssen et al. (2017)) to the synthesis of microgels based on pVCL and pNIPAM. Parameter values from QMC are employed to reduce the number of unknown parameter values. The unknown termination rate constants are estimated from experimental data for increasing system complexities. Thereby, substantial differences in the termination rate constants are observed for homo- and copolymerizations of VCL and NIPAM: A lower termination rate for VCL causes the overall reaction to proceed faster, despite its lower propagation rate constants. For terpolymerization, the overall polymerization proceeds faster due to high propagation reaction rates and low termination rate constants. Thereby, NIPAM is consumed slightly faster due to its higher propagation rate constants. In agreement with previous experimental observations, the prediction of the internal microgel structure shows a radially uniform distribution of the comonomers VCL and NIPAM.

Acknowledgements: The authors thank the Deutsche Forschungsgemeinschaft (DFG) within the Collaborative Research Center SFB 985 “Functional Microgels and Microgel Systems”, projects B4 and G2, and the Volkswagen Stiftung for financial support. Further, we thank Julian Meyer-Kirschner and Jörn Viell for valuable discussions and for sharing the Raman spectroscopy measurements.

References

- Arosio, P., Mosconi, M., Storti, G., Banaszak, B., Hungenberg, K.-D., Morbidelli, M., 2011. Precipitation copolymerization of vinyl-imidazole and vinyl-pyrrolidone, 2 - Kinetic model. *Macromol. React. Eng.* 5 (9-10), 501–517.
- Balaceanu, A., Mayorga, V., Lin, W., Schürings, M.-P., Demco, D. E., Böker, A., Winnik, M. A., Pich, A., 2013. Copolymer microgels by precipitation polymerisation of *N*-vinylcaprolactam and *N*-isopropylacrylamides in aqueous medium. *Colloid Polym. Sci.* 291 (1), 21–31.
- Buback, M., Gilbert, R. G., Russell, G. T., Hill, D. J. T., Moad, G., O’Driscoll, K. F., Shen, J., Winnik, M. A., 1992. Consistent values of rate parameters in free radical polymerization systems. II. Outstanding dilemmas and recommendations. *J. Polym. Sci., Part A: Polym. Chem.* 30 (5), 851–863.
- Hoare, T., McLean, D., 2006a. Kinetic prediction of functional group distributions in thermosensitive microgels. *J. Phys. Chem. B* 110 (41), 20327–20336.
- Hoare, T., McLean, D., 2006b. Multi-component kinetic modeling for controlling local compositions in thermosensitive polymers. *Macromol. Theory Simul.* 15 (8), 619–632.
- Janssen, F. A. L., Kather, M., Kröger, L. C., Mhamdi, A., Leonhard, K., Pich, A., Mitsos, A., 2017. Synthesis of poly(*N*-vinylcaprolactam)-based microgels by precipitation polymerization: Process modeling and experimental validation. *Ind. Eng. Chem. Res.* 56 (49), 14545–14556.
- Kröger, L. C., Kopp, W. A., Leonhard, K., 2017. Prediction of chain propagation rate constants of polymerization reactions in aqueous NIPAM/BIS and VCL/BIS systems. *J. Phys. Chem. B* 121 (13), 2887–2895.
- Meyer-Kirschner, J., Kather, M., Ksiazkiewicz, A., Pich, A., Mitsos, A., Viell, J., Submitted. Monitoring microgel synthesis by copolymerization of *N*-isopropylacrylamide and *N*-vinylcaprolactam via in-line Raman spectroscopy and Indirect Hard Modeling.
- Meyer-Kirschner, J., Kather, M., Pich, A., Engel, D., Marquardt, W., Viell, J., Mitsos, A., 2016. In-line monitoring of monomer and polymer content during microgel synthesis using precipitation polymerization via Raman spectroscopy and Indirect Hard Modeling. *Appl. Spectrosc.* 70 (3), 416–426.
- Pich, A., Richtering, W., 2011. Microgels by precipitation polymerization: Synthesis, characterization, and functionalization. In: Pich, A., Richtering, W. (Eds.), *Chemical Design of Responsive Microgels*. Vol. 234 of *Adv. Polym. Sci.* Springer, Berlin, Heidelberg, pp. 1–37.
- Storti, G., Carrà, S., Morbidelli, M., Vita, G., 1989. Kinetics of multimonomer emulsion polymerization. The pseudo-homopolymerization approach. *J. Appl. Polym. Sci.* 37 (9), 2443–2467.

Towards predictive models for organic solvent nanofiltration

Rebecca Goebel^a, Tobias Glaser^a, Ilka Niederkleine^a and Mirko Skiborowski^{a,*}

^a*Laboratory of Fluid Separations, TU Dortmund University, Emil-Figge-Str. 70, 44227 Dortmund, Germany*
Mirko.Skiborowski@tu-dortmund.de

Abstract

Organic solvent nanofiltration (OSN) is a promising technology for an energy-efficient separation of organic mixtures. However, due to the lack of suitable models that allow for a quantitative prediction of the separation performance in different chemical systems OSN is rarely considered during conceptual process design. The feasibility of OSN is usually determined by means of an experimental screening of different membranes. Further experiments are conducted for a selected membrane in order to determine membrane specific parameters for a model-based description of the separation performance for a specific mixture. Obviously, this classical approach is experimentally demanding. The effort in identifying a suitable membrane in the first step could be significantly reduced if a theoretical evaluation of the separation performance was possible. The current article proposes an automatic method for the determination of a suitable predictive model for a given membrane, taking into account a limited set of experimental data. Specially, the rejection of different solutes in a specific solvent is modeled based on a set of physical and chemical descriptors. The proposed approach is based on a combination of genetic programming and global deterministic optimization, allowing for the identification of innovative models, including non-linear parameter regression. The predictive capability of the generated models is validated on a separate data set. The identified models were able to predict the rejection of different components in the considered case studies with a deviation from the experimental values below 5%.

Keywords: organic solvent nanofiltration, model identification, data-driven approach, prediction

1. Introduction

Separation processes in the chemical industry are commonly dominated by energy-intensive thermal separations like distillation (Sholl and Lively (2016)). Especially pressure-driven membrane processes, such as organic solvent nanofiltration (OSN), offer a high potential for significantly improving the energy efficiency, since phase transitions and high operating temperatures are avoided (Marchetti et al. (2014)). Recent developments in solvent stable polymeric membranes allow for the application of OSN in a variety of industrial sectors, ranging from pharmaceuticals to petrochemicals and food industry (Lutze and Górak (2016)). However, despite the large prospect of OSN, it is rarely considered during conceptual process design as reliable predictions of the separation performance in different chemical systems are not available yet. In order to facilitate an effective consideration during conceptual design, a model-based description of the separation characteristics of the membrane is indispensable. Common models for OSN separation are solution-diffusion or pore-flow models (Marchetti et al. (2014)). However, these models require experimentally determined model parameters for each component in the system. Hence, the implementation of OSN is often linked to expensive and time-consuming screening experiments. Moreover, some

experimental results comply best with the pore-flow model, whereas others can be described better by solution-diffusion models or a combination of both (Marchetti et al. (2014)). Thus, it is not possible to determine which model type is more suitable for OSN in general. Obviously, a general mechanistic model would be desirable for the prediction of the separation performance. However, such an approach is yet a long-range target that is extremely challenging, due to the strong interactions between the solute(s), the solvent(s) and the membrane material.

In order to allow for a predictive description of the membrane performance, Bhanushali et al. (2001), Geens et al. (2006) and Darvishmanesh et al. (2009) developed different models to describe the permeation of a pure solvent, each based on a number of molecular descriptors, such as the viscosity or the surface tension. These models allow for the evaluation of the solvent flux. A prediction of the separation performance, especially the rejection of different solutes, was not reported so far. Furthermore, the proposed models are based on a fixed structure and membrane-specific parameters, resulting in strong variations in the quality of the prediction for different membranes.

Since the number of available polymeric membranes for OSN is yet limited, tailored model structures for each membrane type are a feasible option. However, the complexity of determining an optimal model structure and parametrization represents a much more complicated problem than a mere parameter identification for a fixed model. In order to solve this problem, an optimization-based data-driven approach is proposed. The method utilizes a combination of genetic programming (GP) and deterministic global optimization for the identification of optimal parameters, in order to automatically identify models with linear as well as nonlinear parameters. While the capability of the method to identify predictive models for pure solvent flux was demonstrated in a previous work (van den Bongard et al. (2017)), the current work illustrates that also models for the separation performance can be derived by such an approach.

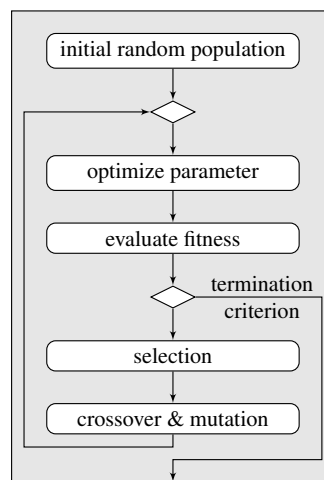


Figure 1: Structure of the GP approach

2. Optimization-based approach for model identification

The optimization-based approach for model identification utilizes a combination of GP and global deterministic optimization in order to derive a model structure and the corresponding parametrization, which reproduces a set of experimental data in the best way. For modeling OSN rejection, different descriptors that account for physical and chemical properties of the solutes and the solvent are correlated, taking into account experimentally measured rejection data of different components solved in the same solvent. The identification of the best parameter values for each model candidate is performed by means of global deterministic optimization. As measures for the mutual solubility descriptors based on the Hansen and Hildebrand solubility parameters of the components are used, since these were identified as suitable measures (Darvishmanesh et al. (2011); Zeidler et al. (2013)). As descriptors for physical and chemical properties of the solute and the solvent different parameters like molar mass, viscosity, density and surface tension are used which were found to be useful in different investigations (Bhanushali et al. (2001); Darvishmanesh et al. (2011)). In total 34 different descriptors for each solute-solvent combination are considered.

The GP approach is used for the identification of the model structure and it builds on the work of Madár et al. (2005). The different steps of the algorithm, which are implemented in Matlab[®], illustrated in Figure 1, are explained in further detail in the following subsections. An important feature of the current approach, which stands out in comparison to other automated model learning

algorithms, like the ALAMO approach of Cozad et al. (2014), is the ability to generate models that are nonlinear in the parameters. Therefore, a differentiation between linear and nonlinear regression models is considered in the embedded parameter optimization step, which utilizes a global deterministic solver in case of a nonlinear regression problem. The quality of the model candidates is evaluated based on an information criterion, rather than the least squares functional and the identifiability of the parameters is evaluated in a final postprocessing step.

2.1. Model representation in GP

The structure of each model candidate is represented by a tree with a predefined maximum tree depth. Figure 2 illustrates the basic structure of a tree with a maximum tree depth of 3. Each node of a tree represents either a function or a descriptor. However, the bottom positions in the tree (position 4, 5, 6 and 7 in figure 2) have to represent a descriptor. Besides the previously described descriptors a number of user-defined functions are available ($+$, $-$, $*$, $/$, exp , log , $\sqrt{\quad}$), allowing for the construction of linear and nonlinear models. The trees are translated to a single-equation model for which parameters are introduced for every node that represents a function. However, additional restrictions directly eliminate obviously correlated parameters. Finally, an additional parameter is added to the model as a constant. For models with only linear parameters additional restrictions are considered for the integration of parameters.

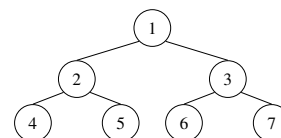


Figure 2: Tree with tree depth 3

2.2. Initial population

For all model candidates in the initial population and each type of node a random selection between the sets of descriptors and functions is performed. The final depth of the tree for each of these model candidates may therefore be smaller than the maximum depth, since nodes below a descriptor position do not contribute to the final model. In order to enforce a subset of models with maximum trees depth, 10% of the model candidates in the initial population are completely filled with functions and descriptors are only allowed for the bottom layer of the tree. The size of the initial population was set to 500 individuals.

2.3. Parameter optimization

Depending on the type of model either a linear or nonlinear parameter regression needs to be performed. The optimal parameter values for a linear regression problem are determined directly in Matlab[®] evaluating the first order optimality condition for the sum of squares functional by means of the matrix inversion. For a nonlinear regression problem, a global optimization problem has to be solved. Therefore, the model structure as well as the corresponding values of the included descriptors and the experimental data are passed from Matlab[®] to the general algebraic modeling system GAMS, where the nonlinear regression problem is solved to global optimality applying the solver ANTIGONE. In general, the parameter regression is performed only for a subset of the available experimental data. The remaining data is allocated as a test data set and a validation data set, which are not used for the parameter regression, but for fitness evaluation and the subsequent model validation.

2.4. Evaluation of fitness

In order to obtain reliable and useful models for performance prediction in OSN, two aspects are important. First, the experimental data has to be reproduced such that the goodness of fit is an important criterion. Second, an accurate fit of the model parameters is also important to

avoid overfitting with too many parameters. Thus, the fitness function should account for the quality of the fit as well as the number of parameters. Consequently, an information criterion is considered and in specific, the Akaike information criterion (AIC) is used in this work (Burnham and Anderson (2004)). The fitness function is evaluated for the training as well as the test data set, which provides also information about the predictive quality of the model.

2.5. Selection of Individuals

Based on the fitness evaluation, the GP continues with the generation of a new population, starting with the selection of model candidates that are considered for the application of reproduction, crossover and mutation operators. In order to preserve the best model structures, the best 10% of the current generation are passed to the next generation. The remaining 90% of the next generation are filled with new model structures created by crossover and mutation, whereas the parents for the new individuals are selected based on the tournament method (Affenzeller et al. (2009)). This method randomly selects two individuals out of the current population and the individual with the better fitness is selected as a parent. Consequently, the method is applied once for mutation and twice for crossover.

2.6. Crossover and mutation

For the generation of new model candidates crossover and mutation operators are applied with predefined probabilities. Here, a mutation probability of 80% for the second generation was specified, which further decreases for each generation until reaching a constant level of 20%. The crossover operator is applied opposed to the mutation operator, such that the probability always adds to a total of 100%. A variable mutation probability was used to ensure an exploration phase in the beginning, with a focused exploitation phase in the end. Both operators consider only active nodes in the tree, since nodes on a branch below a descriptor do not contribute to the model. Furthermore, the use of crossover is limited, as it requires trees with corresponding relevant nodes. In that case one of the nodes is randomly selected and the complete branch below that node is replaced by the corresponding branch of the other tree and vice versa. For mutation, again one of the identified nodes is randomly selected and one of the following two options is performed. Either the type of node at the selected position is changed from function to descriptor or vice versa, or it remains the same. Anyhow, the specific type of function or descriptor is modified and selected randomly.

2.7. Termination criterion

The GP approach terminates if the fitness of the best model candidate does not improve for a certain number of consecutive generations, or in case a predefined maximum number of generations has been evaluated. Here, a number of 25 generations was chosen for the evaluation of continuing progress, while the maximum number of generations was set to 75. However, none of the runs reached the maximum number of generations.

2.8. Postprocessing for potential model reduction

While the AIC, which is used as fitness function, already accounts for the number of parameters and avoids overfitting to some extent, it does not guarantee a high parameter precision. In order to evaluate the identifiability of the parameters, a post-processing step is performed for the best identified model after the GP stopped. In this step, the 95% confidence intervals of the parameter estimates are computed and an eigenvalue analysis of the Hessian matrix of the least squares functional is performed (Quaiser and Mönnigmann (2009)). Parameters which are not identifiable based on the given data or which are strongly correlated are eliminated from the model and the remaining model parameters are optimized again, with a subsequent evaluation of the AIC. The postprocessing is repeated until the parameter identifiability is satisfying.

3. Case Study

The proposed optimization-based method was used to identify predictive models for the rejection of different solutes in either toluene or isopropanol (IPA) for a PuraMem® S600 membrane manufactured by Evonik Resource Efficiency GmbH. A data set with 18 solutes for toluene as well as 16 solutes for IPA were considered, including a homologous series of even numbered alkanes, a branched isomer and different aromatic components. Besides the solubility of the solutes in the specific solvent a preferably wide distribution of the property values in terms of the considered descriptors was taken into account. For each of the solvent-solute combinations lab-scale experiments were conducted in a membrane test plant and the permeate and feed compositions were determined by means of gas chromatography. The rejection R was subsequently calculated based on the permeate and feed concentration of the solute according to

$$R = 1 - \frac{c_{\text{Permeate}}}{c_{\text{Feed}}}$$

On the basis of error propagation the relative measurement error of the determined rejections was generally below 2%, whereas the deviation of two consecutive experiments was below 8%. In order to successfully apply a data-driven modeling approach it is indispensable to warrant a good distribution of the data points. Therefore, the allocation of the data points to the training set was not performed randomly, but a high degree of variation, taking into account all descriptors was warranted.

For toluene the training data set consisted of 9 substrates, while 4 additional substrates were allocated to the test and the remaining 5 to the validation data set. For the smaller IPA data set the training, test and validation data set included 8, 4 and 4 substrates respectively.

A maximum tree depth of 3 was found to be sufficient, since a larger tree depth did not improve the results. In order to evaluate the stochastic nature of the GP approach 20 consecutive runs were performed for each solvent. Furthermore, additional 20 runs were performed with a restriction to model structures that are linear in terms of the parameters. A comparison of the results of the different runs showed that models, which are linear in the parameters, were sufficient for the prediction of the rejection in the investigated cases. For toluene the reproducibility of the results by repeated runs was also satisfying, producing most of the times model candidates with an equivalent fitness. However, especially for the case of the rejection in IPA different models were identified in various runs with fluctuating fitness. Consequently, the optimization-based approach still needs improvement in order to consistently identify the best model candidate. Nonetheless, the best identified models are able to describe the experimental data in all three data sets for both solvents with very high accuracy. The excellent agreement between the best models and the experimental data is illustrated in the parity plots in Figure 3 and 4. Herein, the training data is represented by circles, the test data by squares and the validation data by triangles. The dashed lines indicate an absolute deviation of 5% between experimental and calculated value. For both solvents only for one component out of each validation data set (deviation of 9 – 11%) a deviation of 5% is exceeded. For the best model candidates a sufficient parameter precision was validated, based on the confidence intervals and eigenvalue information, taking into account only the training data. The best model for the rejection in toluene

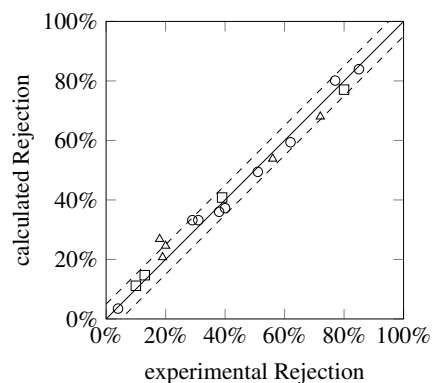


Figure 3: Rejection toluene

$$R_{\text{toluene}} = -52091.29(\pm 4681.91) \cdot \frac{d_{\text{eq,Solute}}}{M_{\text{Solute}} + M_{\text{Solvent}}} + 193.21(\pm 13.37)$$

includes only descriptors for the size of the solvent and solute molecule, i.e. the equivalent molecular diameter d_{eq} and the molar mass of the corresponding molecule M . Besides the determined model parameters, also the information on the 95% confidence interval is listed in the brackets.

4. Conclusion

The current article proposed an optimization-based approach for a systematic model identification and its application to organic solvent nanofiltration. For the first time rejection models are generated and the results are very promising, showing a high degree of accuracy when compared to the experimental data for two investigated solvents with a broad range of different solutes. These models can further be used to evaluate the applicability of the given membrane for the rejection of specific solutes in the considered solvents. Further work will aim at the extension of the approach towards solvent independent models and the improvement of the optimization approach.

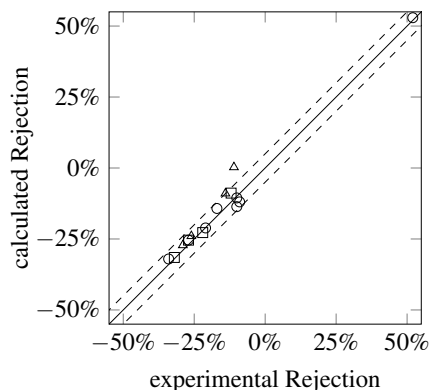


Figure 4: Rejection isopropanol

5. Acknowledgement

Financial support by the Federal Ministry for Economic Affairs and Energy under project number 03ET1279F is gratefully acknowledged.

References

- Affenzeller, M., Wagner, S., Winkler, S., Beham, A., 2009. Genetic algorithms and genetic programming: modern concepts and practical applications. CRC Press.
- Bhanushali, D., Kloos, S., Kurth, C., Bhattacharyya, D., 2001. Performance of solvent-resistant membranes for non-aqueous systems: solvent permeation results and modeling. *Journal of Membrane Science* 189 (1), 1–21.
- Burnham, K. P., Anderson, D. R., 2004. Multimodel inference. *Sociological Methods and Research* 33 (2), 261–304.
- Cozad, A., Sahinidis, N. V., Miller, D. C., 2014. *AIChE J.* 60 (6), 2211–2227.
- Darvishmanesh, S., Buekenhoudt, A., Degève, J., Van der Bruggen, B., 2009. Coupled series–parallel resistance model for transport of solvent through inorganic nanofiltration membranes. *Separation and Purification Technology* 70 (1), 46–52.
- Darvishmanesh, S., Vanneste, J., Tocci, E., Jansen, J. C., Tasselli, F., Degève, J., Van der Bruggen, B., 2011. Physicochemical characterization of solute retention in solvent resistant nanofiltration: the effect of solute size, polarity, dipole moment, and solubility parameter. *Journal of Physical Chemistry B* 115 (49), 14507–14517.
- Geens, J., der Bruggen, B. V., Vandecasteele, C., 2006. Transport model for solvent permeation through nanofiltration membranes. *Separation and Purification Technology* 48, 255–263.
- Lutze, P., Górák, A. (Eds.), 2016. *Reactive and Membrane-Assisted Separations*. De Gruyter Textbook. Berlin.
- Madár, J., Abonyi, J., Szeifert, F., 2005. Genetic programming for the identification of nonlinear input–output models. *Industrial and Engineering Chemistry Research* 44 (9), 3178–3186.
- Marchetti, P., Solomon, M. F. J., Szekely, G., Livingston, A. G., 2014. Molecular Separation with Organic Solvent Nanofiltration: A Critical Review. *Chemical Reviews* 114, 10735–10806.
- Quaiser, T., Mönnigmann, M., 2009. Systematic identifiability testing for unambiguous mechanistic modeling–application to jak-stat, map kinase, and nf- κ b signaling pathway models. *BMC Systems Biology* 3 (50).
- Sholl, D. S., Lively, R. P., 2016. Seven chemical separations: to change the world: purifying mixtures without using heat would lower global energy use, emissions and pollution–and open up new routes to resources. *Nature* 532 (7600), 435–438.
- van den Bongard, R., Larysz, P., Skiborowski, M., 2017. A new tool for prediction of solvent permeance. Presentation at 6th international Conference on organic solvent nanofiltration, St. Petersburg, Russia.
- Zeidler, S., Kätzel, U., Kreis, P., 2013. Systematic investigation on the influence of solutes on the separation behavior of a pdms membrane in organic solvent nanofiltration. *Journal of Membrane Science* 429, 295–303.

COSMO-derived descriptors applied in ionic liquids physical property modelling using machine learning algorithms

Ismael Díaz^{a,*}, Manuel Rodríguez^a, María González-Miquel^{a,b} and Emilio J. González^a

^a*Dpt. Ingeniería Química Industrial y del Medio Ambiente, ETSI Industriales, Universidad Politécnica de Madrid, Madrid 28006, Spain*

^b*School of Chemical Engineering and Analytical Science, The University of Manchester, Manchester M13 9PL, United Kingdom*
ismael.diaz@upm.es

Abstract

An application of machine learning algorithms for the prediction of physical properties of ionic liquids is presented herein. Molecular descriptors obtained from quantum-chemistry calculations (COSMO theory (Klamt, 2004)) containing both structural and energetic information are used as input parameters. In this sense, a set of COSMO-based descriptors is proposed by reduction of the original σ -profile (51 descriptors reduced to 9 bins). A critically evaluated set of viscosity data is used for a large number of ionic liquids (159). Artificial neural networks are then trained for the correlation of liquid viscosity and compared with available tools (QSPR).

Keywords: COSMO descriptors, ionic liquids, viscosity, artificial neural networks

1. Motivation

One of the latest paradigms in chemical engineering science has been product design. In the last decades the number of new specialized chemical products offering new solutions (health care, environmental, process industry. . .) has drastically grown. New promising computer tools have also been developed for the specific task of finding the best molecule for every application (Fung et al., 2016; Gani and Ng, 2015) in the context of Process System Engineering.

Any approximation for chemical products design relies on good physical properties predictions. Many of the current computer-aided process engineering (CAPE) use group contribution methods, specifically developed to estimate from individual to mixture properties. Some examples are Joback model for ideal gas heat capacity, Li-Ma model for vapor pressure of single components, Orrick-Erbar model for liquid viscosity or the well-known UNIFAC model for individual activity coefficients in a liquid mixture.

On the other hand, many efforts have also been made in the field of quantum mechanics in pursuing new procedures and methods for physical properties predictions computationally affordable in chemical engineering applications. The well-known COSMO-RS/SAC (Klamt, 2004; Lin and Sandler, 2002) models founded on the COSMO theory developed by A. Klamt and co-workers are good examples of well-established tools. These methods involves quantum chemical followed by statistical mechanics calculations to compute both pure and mixture thermodynamic properties. In the middle of the procedure, each molecule is characterized through the so-called σ -profile.

This σ -profile or derived properties (COSMO descriptors) have been successfully used in literature (figure 1) as inputs of different quantitative structure property relationships (QSPR) or artificial

neural network (ANN) models for the correlation and prediction of pure thermodynamic properties (i.e. Hansen solubility parameters (Járvás et al., 2011), heat capacities (Zhao et al., 2015) or densities (Palomar et al., 2008)), mixture thermodynamic properties (i.e. activity coefficients (Gonfa et al., 2016), vapor-liquid equilibrium (Bouza et al., 2016) or partition coefficients (Palomar et al., 2008)), and others (i.e. viscosity (Mehrkes and Karunanithi, 2016) or toxicity (Ghanem et al., 2017)). The use of ANN for the correlation of viscosity data from COSMO descriptors as proposed in this work has not been performance until now.

However many efforts have been done to develop good estimation models to predict ILs viscosity (figure 2). Between them, we can find property-based group contribution (GC) models such as the Gardas-Coutinho (Gardas and Coutinho, 2008) model which estimates viscosity from an Orrick-Erbar type equation combining some property information (density and molecular weight) and a GC-based estimation of parameters. On the other hand, the great amount of works in this topic are grounded on pure GC approximation using different kind of models (multilinear regression, support vector machines or artificial neural networks).

None of the previous approximations uses COSMO information as descriptors. Therefore, the main objective of our work is the development of different estimation methods for the prediction of both thermodynamic and transport properties of pure ILs. These methods will all start from a small set of shared molecular descriptors (derived from the σ -profile of the components) which allows for the design of molecules by the solution of the non-linear optimization problems where the properties are part of the objective functions and the σ -profiles descriptors the design variables.

In this first work, we use a reduced version of the σ -profile as the input of an artificial neural networks model for the correlation and prediction of pure IL viscosity. This reduction in the number of descriptors is required to decrease the number of fitting parameters in the model.

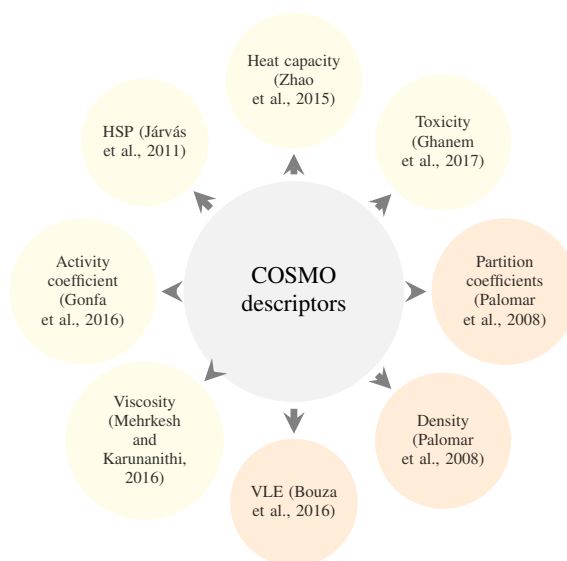


Figure 1: Literature use of COSMO descriptors in QSPR (yellow) and ANN (orange) models for ionic liquids property estimations

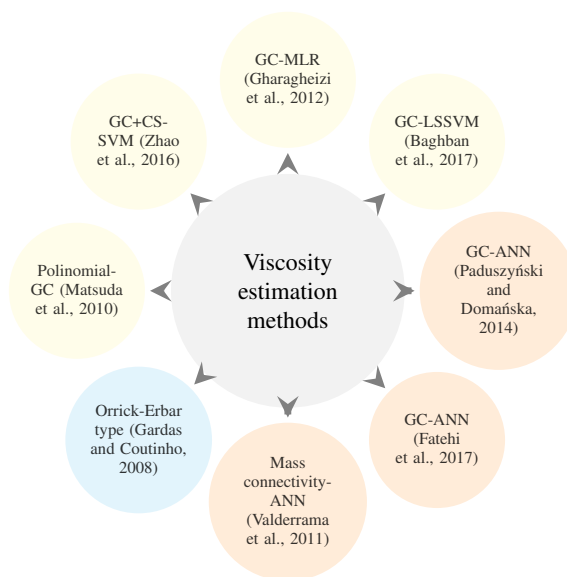


Figure 2: Literature methods for ionic liquids viscosity estimation. SVM-MLR based (yellow), physical property based (cyan), ANN based (orange)

2. Data obtention and ANN training

2.1. Viscosity dataset

The viscosity of ILs is a complicated property to predict because of the high discrepancy between existing data. We can find in literature both intracomponent discrepancy (different values for the same component) and intercomponent discrepancy (incoherent values for a family of compounds) (Valderrama et al., 2011). These highly different values of viscosity have motivated the development of a reliable database named ILUAM (Ferro et al., 2018) where all the available viscosity data was mined, critically evaluated and finally implemented in a commercial process simulation tool (AspenOne). The ILUAM database contains information of both σ -profile of ILs and a set of thermodynamic and transport properties of ILs statistically curated for a large number of compounds.

Thus, ionic liquids viscosity dataset is obtained from the extended version of the ILUAM database (ILUAM01-(CA)-RB). In this database all the experimental viscosity data for regressing the parameters (A and B) of the Andrade equation were obtained from the NIST Standard Reference Database ILthermo (NIST). All the data collected were filtered prior to the statistical fitting in order to ensure information of liquid phase measurements in a pressure range between 50 and 150 kPa (almost atmospheric pressure). All the IL data included in ILUAM01-(CA)-RB have been previously curated, ensuring enough viscosity data for each compound (minimum number of viscosity points = 5) and coherence between them (minimum fitting quality of $R^2=0.98$). In this work, only the viscosity information at 303 K is taken. A total number of 159 ILs viscosity points are used (the subset of ILs whose σ -profile was also available). The dataset was then divided into train (75%) and test (25%) sets.

2.2. COSMO descriptors

An increase in the number of descriptors used in the model results in a higher number of weights to be fitted (each descriptor is connected to each neuron in the hidden layer so an increase in one

descriptor involves an increase of # neurons weights to fit). Therefore, the ILs σ -profiles contained in the ILUAM01-(CA)-RB database were discretized reducing the number of descriptors from 51 (one $P(\sigma)$ for each screening charge σ) to 9 bins (figure 3) as proposed by Palomar et al. (2008).

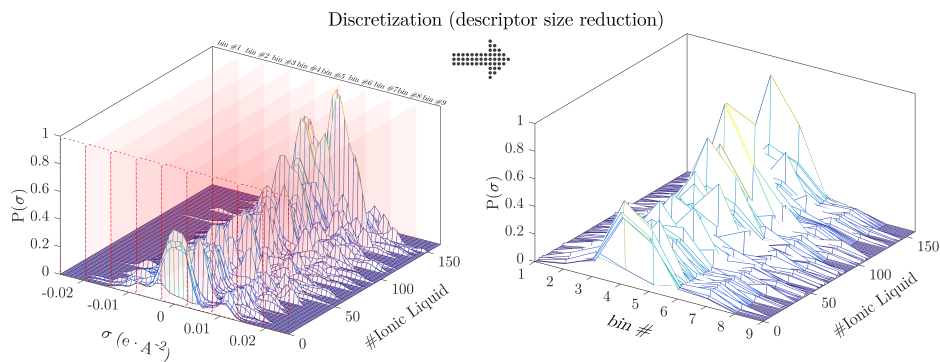


Figure 3: σ -profile information used as descriptors. Left, original information with 51 descriptors. Right, bin discretization with 9 descriptors

2.3. Artificial neural network

A typical feed forward structure (figure 4) is considered as proposed by other authors in similar works (Valderrama et al., 2011; Fatehi et al., 2017; Padaszyński and Domańska, 2014). A \tanh activation function is used in all the neurons. The size of the hidden layer is determined by using k-fold cross validation and preliminar trainings.

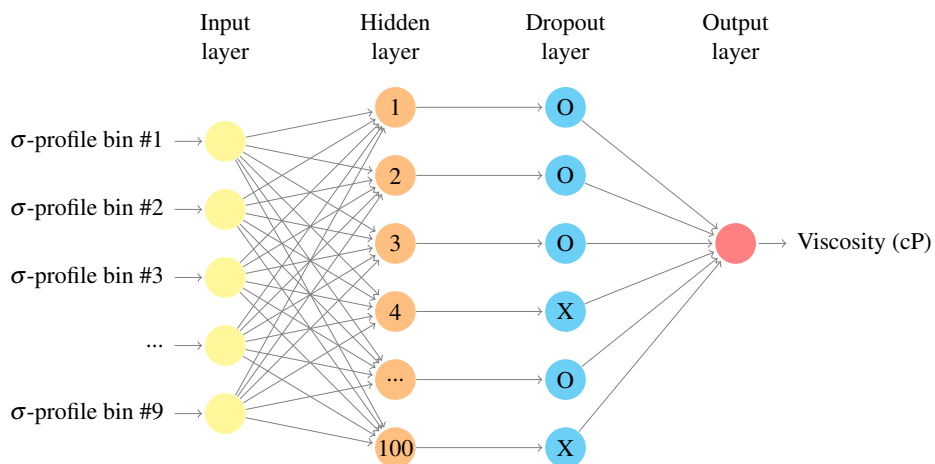


Figure 4: Feed forward ANN structure proposed

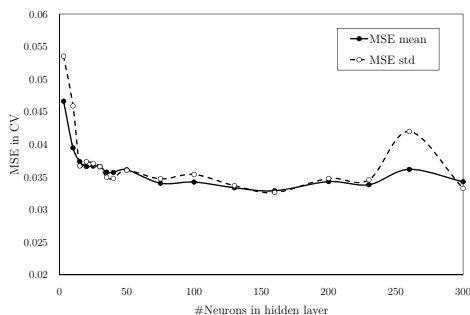


Figure 5: k-fold cross validation results

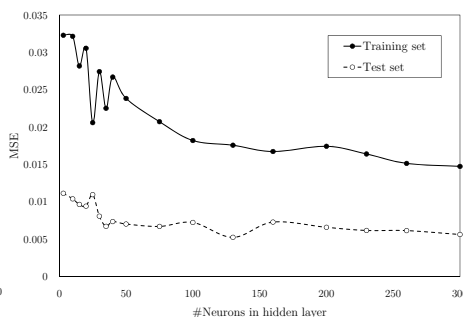


Figure 6: ANN preliminary training

2.4. Training

Once input-output data have been taken, the ANN model was trained using Tensorflow under Keras. Every ANN was trained using the Adam optimizer (Kingma and Ba, 2014) which is a gradient-based optimizer based on adaptive estimation of moments. Overfitting is minimized by using dropout fraction of the units to drop equal to 0.3.

In figure 5 the mean squared error (MSE) of the test set averaged over the 10 folds is depicted. In our case, 10 folds were chosen not showing better results in layers bigger than 100 neurons. By training individual ANNs in the range 3-300 neurons (weight initialized randomly 100 times) during 10^5 epochs, we obtained similar results. The calculated MSE of both training and test sets (figure 6) suggested no improvements for hidden layers with more than 100 neurons.

The weights of the 100 neurons ANN were randomly initialized 100 times. For the best initial point, we trained the ANN during 10^6 epochs. The results of the ANN performance are shown in figure 7 (MSE training set 0.00724, MSE test set 0.00725). For comparison, the estimation of the viscosity of 50 ILs was also carried out with the QSPR model (using COSMO-derived descriptors) available in the COSMOTermX (COSMOTerm, 2017) package.

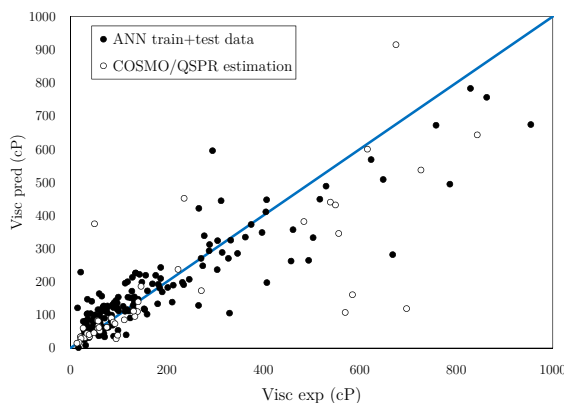


Figure 7: Ionic liquids viscosity modelling using ANNs

3. Conclusions

ANN and COSMO descriptors have been successfully used to fit and predict ILs viscosities. Accuracy was checked by comparing with existing QSPR tools. The final ANN model showed no overfitting and low deviations in terms of MSE.

4. Acknowledgement

The authors are grateful to the Com. de Madrid (project S2013-MAE-2800) for financial support.

References

- Baghban, A., Kardani, M. N., Habibzadeh, S., 2017. Prediction viscosity of ionic liquids using a hybrid LSSVM and group contribution method. *Journal of Molecular Liquids* 236, 452–464.
- Bouza, P., Díaz, I., Rodríguez, M., Palomar, J., Haug-Warberg, T., 2016. Prediction of co2physical solubility in ionic liquids using artificial neural networks and cosmo sigma-moments. In: *Innovations of Green Process Engineering for Sustainable Energy and Environment 2016 - Topical Conference at the 2016 AIChE Annual Meeting*. pp. 101–117.
- COSMOTerm, 2017. COSMOlogic GmbH Co KG.
- Fatehi, M., Raeissi, S., Mowla, D., 2017. Estimation of viscosities of pure ionic liquids using an artificial neural network based on only structural characteristics. *Journal of Molecular Liquids* 227, 309–317, cited By :1.
- Ferro, V., Moya, C., Moreno, D., Santiago, R., de Riva, J., Pedrosa, G., Larriba, M., Díaz, I., Palomar, J., 2018. Enterprise ionic liquids database (ILUAM) for its use in aspen one programs suite with cosmo-based property methods. *Industrial & Engineering Chemistry Research* 57, 980–989.
- Fung, K. Y., Ng, K. M., Zhang, L., Gani, R., 2016. A grand model for chemical product design. *Computers & Chemical Engineering* 91 (Supplement C), 15–27.
- Gani, R., Ng, K. M., 2015. Product design – Molecules, devices, functional products, and formulated products. *Computers & Chemical Engineering* 81 (Supplement C), 70–79.
- Gardas, R. L., Coutinho, J. A., 2008. A group contribution method for viscosity estimation of ionic liquids. *Fluid Phase Equilibria* 266 (1-2), 195–201.
- Ghanem, O., Mutalib, M., Lévêque, J.-M., El-Harbawi, M., 2017. Development of qsar model to predict the ecotoxicity of vibrio fischeri using cosmo-rs descriptors. *Chemosphere* 170, 242–250, cited By 1.
- Gharagheizi, F., Ilani-Kashkoul, P., Mohammadi, A. H., Ramjugernath, D., Richon, D., 2012. Development of a group contribution method for determination of viscosity of ionic liquids at atmospheric pressure. *Chemical Engineering Science* 80, 326–333.
- Gonfa, G., Bustam, M., Shariff, A., Muhammad, N., Ullah, S., 2016. Quantitative structure–activity relationships (qsars) for estimation of activity coefficient at infinite dilution of water in ionic liquids for natural gas dehydration. *Journal of the Taiwan Institute of Chemical Engineers* 66, 222–229, cited By 3.
- Járvás, G., Quellet, C., Dallos, A., 2011. Estimation of hansen solubility parameters using multivariate nonlinear qspr modeling with cosmo screening charge density moments. *Fluid Phase Equilibria* 309 (1), 8–14, cited By :23.
- Kingma, D. P., Ba, J., 2014. Adam: A method for stochastic optimization. *CoRR* abs/1412.6980.
- Klamt, A., 2004. *COSMO-RS, From Quantum Chemistry to Fluid Phase Thermodynamics and Drug Design*. Elsevier, Amsterdam.
- Lin, S.-T., Sandler, S. I., mar 2002. A Priori Phase Equilibrium Prediction from a Segment Contribution Solvation Model. *Industrial & Engineering Chemistry Research* 41 (5), 899–913.
- Matsuda, H., Yoji, T., Kurihara, K., Tochigi, K., 2010. Prediction of Thermophysical Properties Using Polynomial Expansion Equation and Genetic Algorithm. *J. Res. Inst. Sci. Tech.* (129), 1–10.
- Mehrkes, A., Karunanithi, A. T., 2016. New quantum chemistry-based descriptors for better prediction of melting point and viscosity of ionic liquids. *Fluid Phase Equilibria* 427, 498–503.
- Paduszyński, K., Domańska, U., 2014. Viscosity of ionic liquids: An extensive database and a new group contribution model based on a feed-forward artificial neural network. *Journal of Chemical Information and Modeling* 54 (5), 1311–1324, cited By :40.
- Palomar, J., Torrecilla, J. S., Ferro, V. R., Rodríguez, F., 2008. Development of an a priori ionic liquid design tool. 1. integration of a novel cosmo-rs molecular descriptor on neural networks. *Industrial and Engineering Chemistry Research* 47 (13), 4523–4532, cited By :56.
- Valderrama, J. O., Muñoz, J. M., Rojas, R. E., 2011. Viscosity of ionic liquids using the concept of mass connectivity and artificial neural networks. *Korean Journal of Chemical Engineering* 28 (6), 1451–1457.
- Zhao, Y., Huang, Y., Zhang, X., Zhang, S., 2015. Prediction of heat capacity of ionic liquids based on cosmo-rs σ -profiles. *Computer Aided Chemical Engineering* 37, 251–256, cited By 1.
- Zhao, Y., Zhang, X., Deng, L., Zhang, S., 2016. Prediction of viscosity of imidazolium-based ionic liquids using MLR and SVM algorithms. *Computers and Chemical Engineering* 92, 37–42.

A CFD investigation of the effect of particle sphericity on wellbore cleaning efficiency during oil and gas drilling

Emmanuel I. Epelle, Dimitrios I. Gerogiorgis*

School of Engineering (IMP), University of Edinburgh, Edinburgh, EH9 3FB, UK

D.Gerogiorgis@ed.ac.uk

Abstract

In all drilling operations in the oil and gas industry, the generation and eventual distribution of formation rock cuttings along the wellbore constitutes a major concern to operational feasibility and profitability. The nature of the annular geometry/wellbore trajectory, rheological properties of the non-Newtonian carrier fluid and physical properties of the cuttings are also very important to consider, particularly in the design stage. Cuttings encountered in practical operations are hardly of a perfectly spherical geometry; however, the ease of mathematical description due to this simplifying assumption is prevalent in most CFD modelling studies. This decreases the accuracy of simulated flow behaviour as far particle-particle and particle-fluid interactions are concerned. We address this challenge by modifying the Syamlal-O'Brien (SO) interphase exchange coefficient in the Eulerian-Eulerian model. This modification yields a better representation of the actual flow dynamics during cuttings transport. Our results show increased transport velocity of non-spherical particles compared to particles of perfectly spherical shape. The relatively complex wellbore geometry (in deviated drilling) considered reveals a key finding: there is greater particle deposition at the inclined-to-vertical (upper) bend, relative to other sections in the CFD flow domain.

Keywords: Computational Fluid Dynamics (CFD), sphericity, drag, drill cuttings.

1. Introduction

It is vital to understand the flow behaviour of drill cuttings carried by a non-Newtonian fluid in an annular geometry for successful design, efficient operation, and optimisation of the drilling process (Gerogiorgis et al, 2015). Drillers often control variables such as the penetration rate, fluid velocity and inner pipe rotation to obtain the best possible transport conditions; however, the application of advanced CFD methods for flow prediction guarantees better informed decisions. Although several experimental (Han et al, 2010; Osgouei, 2010) and computational (Rooki et al, 2015; Epelle and Gerogiorgis, 2017) efforts have sought to understand the impact of these factors on the overall transport efficiency, a widely recognised difficulty in particle transport modelling that has not been adequately addressed is the concept of particle sphericity. The assumption of perfectly spherical particles in most CFD models could yield inaccuracies in the predicted cuttings transport efficiency. In this work, this challenge is addressed by accounting for the particle sphericity as a means of increasing modelling accuracy. A modified interphase momentum exchange coefficient is implemented to better capture the particle-fluid interactions using the Eulerian-Eulerian model; thus, providing further insight into the actual dynamic particle behaviour during wellbore drilling and cleaning.

2. Drag Modification

Very few empirical correlations exist for the drag coefficient on a non-spherical single particle as well as multi-particle suspension systems. They are usually formulated either from experiments or Direct Numerical Simulations. However, our modification of the Syamlal-O'Brien drag model involves a re-definition of the particle diameter (in terms of the sphericity) in the interphase exchange coefficient. A direct application of the sphericity to the exchange coefficient ensures the particle shape is considered at conditions of high particle concentration (Gidaspow, 1994, Sobieski, 2011). The relative ease of implementation of this modification (Eq. 2 & 5) in the SO model influenced our choice of model relative to that of Gidaspow. Essentially, the need of a switch/blending function to ensure a smooth transition between conditions of high and low particle concentration is not necessary when using the SO model.

$$K'_{sl} = \eta K_{sl} \quad (1) \quad \text{Re}_s = \frac{\rho_l d_s |\vec{v}_s - \vec{v}_l|}{\mu_l} \quad (6)$$

$$d_p = \psi d_s \quad (2) \quad A = \alpha_l^{4.14} \quad (7)$$

$$\eta = \frac{1}{\psi} \quad (3) \quad C_D = \left(0.63 + \frac{4.8}{\sqrt{\text{Re}_s / v_{r,s}}} \right) \quad (8)$$

$$K_{sl} = \frac{3\alpha_s \alpha_l \rho_l}{4v_{r,s}^2 d_s} C_D \left(\frac{\text{Re}_s}{v_{r,s}} \right) |\vec{v}_s - \vec{v}_l| \quad (4) \quad \begin{array}{l} \text{for } \alpha \leq 0.85 \\ B = 0.8\alpha_l^{1.28} \end{array} \quad (9)$$

$$K'_{sl} = \frac{3\alpha_s \alpha_l \rho_l}{4v_{r,s}^2 d_p} C_D \left(\frac{\text{Re}_s}{v_{r,s}} \right) |\vec{v}_s - \vec{v}_l| \quad (5) \quad \begin{array}{l} \text{for } \alpha > 0.85 \\ B = 0.8\alpha_l^{2.65} \end{array} \quad (10)$$

$$v_{r,s} = 0.5(A - 0.06 \text{Re}_s + \sqrt{(0.06 \text{Re}_s)^2 + 0.12 \text{Re}_s (2B - A) + A^2}) \quad (11)$$

In this CFD model summary, K_{sl} and K'_{sl} denote the actual and modified interphase exchange coefficients of the SO model, respectively (Fluent, 2017), v_s and v_l are the velocities of the solid and liquid phases, α_s and α_l are the volume fractions of the solid and liquid phases, and ρ_s and ρ_l are the solid and liquid phase densities, respectively. Moreover, η is the drag modification factor, ψ is the particle sphericity (the ratio of the surface area of a sphere with the same volume as the particle, to the surface area of the actual particle), d_s is the volume-equivalent diameter (the diameter of a sphere having the same volume as the non-spherical particle), d_p is the modified particle diameter, Re_s is the relative Reynolds number, $v_{r,s}$ is the solid phase terminal velocity, μ_l is the liquid phase viscosity, and C_D the drag coefficient as per the definition of Dalla Valle (1948).

3. Simulation Parameters and Annular Flow Geometry

Table 1. Simulation input parameters

Drill pipe diameter, d_{pipe} (m)	0.113
Wellbore diameter, d_{wb} (m)	0.180
Computational length, L (m)	2.340
Cuttings diameter, d_s (m)	0.002 and 0.008
Cuttings density, ρ_s ($\text{kg}\cdot\text{m}^{-3}$)	2800
Sphericity, ψ	0.5, 0.75, 1.0
Drilling mud composition	0.5% CMC Solution
Drilling mud density, ρ_l ($\text{kg}\cdot\text{m}^{-3}$)	1000
Consistency index, K ($\text{Pa}\cdot\text{s}^n$)	0.5239
Flow behavior index, n	0.60
Fluid circulation velocity, v_l ($\text{m}\cdot\text{s}^{-1}$)	0.8
Cuttings inlet velocity, v_s ($\text{m}\cdot\text{s}^{-1}$)	0.5
Flow regime	Laminar – Unsteady state
Drill pipe rotation, Ω (rpm)	100
Hole eccentricity, e	0.6

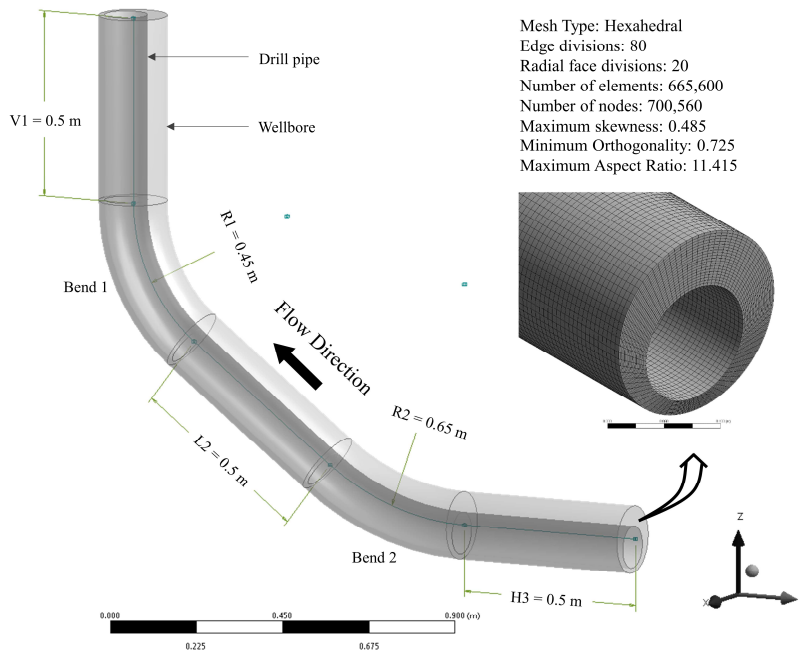


Figure 1. Dimensions of annular flow geometry with mesh properties adopted.

Transient simulations were run using the finite volume formulation with a time step of $5 \cdot 10^{-4}$ and a tolerance factor of 10^{-4} in the Ansys Fluent solver (17.1). Statistical averages of flow properties were performed over the entire converged time steps. Total simulation run time was approximately 8 days using the University of Edinburgh's high performance computing facility (Eddie mark 3 – Scientific Linux 7 Operating System)

with 32 CPU cores (2.4GHz Intel®-Xeon® CPU processor) and 64GB of RAM. The geometry is shown in Figure 1.

4. Results and Discussion

The particle velocity, pressure drop and volume fraction profiles averaged over the entire flow domain for a simulation period of 5 seconds are shown in Figure 2.

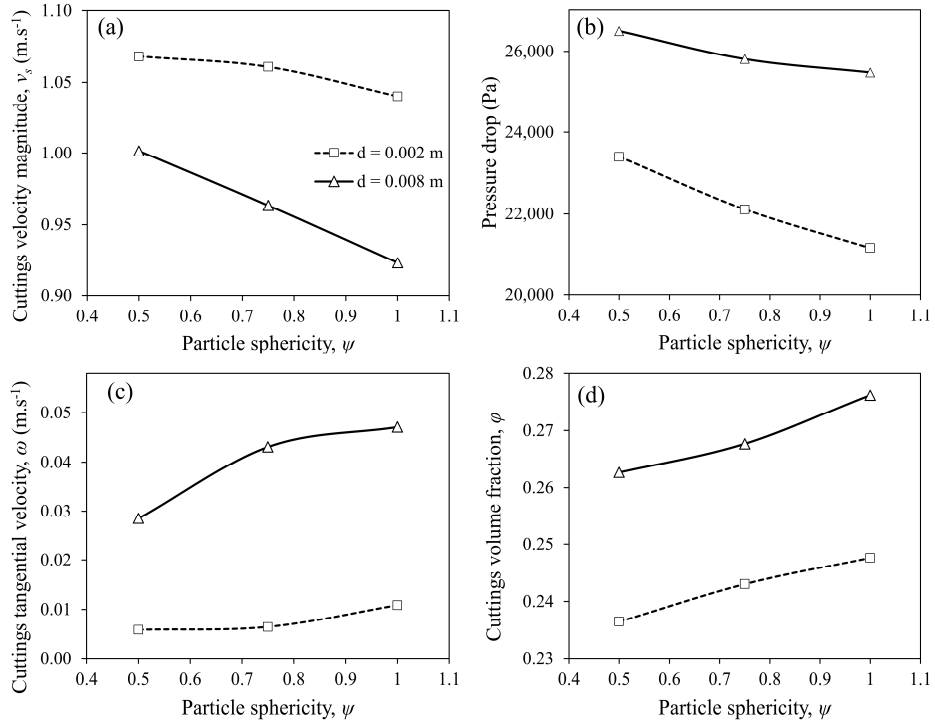


Figure 2. Cuttings velocity, pressure drop and volume fraction for variable sphericity.

It has been shown that non-spherical particles undergo a secondary oscillatory motion when transported in a fluid (Mandø et al. 2007). This tends to reduce its settling velocity compared to perfectly spherical particles (Byron, 2015). The higher settling velocity of spherical particles in the partially inclined geometry considered, is the most probable reason for the increased deposition (volume fraction – Figure 2d) and the reduced velocity in the direction of bulk flow (Figure 2a). Furthermore, spherical particles will tend to roll against the flow direction during transport; the results obtained show that these combined phenomena exhibited by spherical particles, are superior to the frictional resistance posed by the non-spherical particles (due to increased contact area).

Cuttings with diameter of 0.002 m generally travel faster in the annulus than those of 0.008 m (Figure 2a). However, larger particles exhibit stronger tangential motion compared to the smaller particles (Figure 2c). This occurs as a result of the rotating drillpipe which has a higher impact on spherical particles compared to non-spherical particles (Figure 2c). Spherical particles will more readily rotate along the axis of the drillpipe compared to non-spherical particles with a more chaotic flow character.

Interparticle collisions of non-spherical particles coupled with the increased drag forces are the most likely reasons for the higher pressure drop noticed with the non-spherical particles (Figure 2b). Additionally, larger particles will require more transport energy; hence the higher pressure drop and volume fractions (Figure 2d) observed. The impact of drillpipe rotation on the larger particles is further demonstrated in Figure 3 (d-f) and Figure 4. While the 0.002 m particles tend to settle at the lower section of the eccentric annulus, larger 0.008 m particles clearly experience an asymmetric deposition pattern.

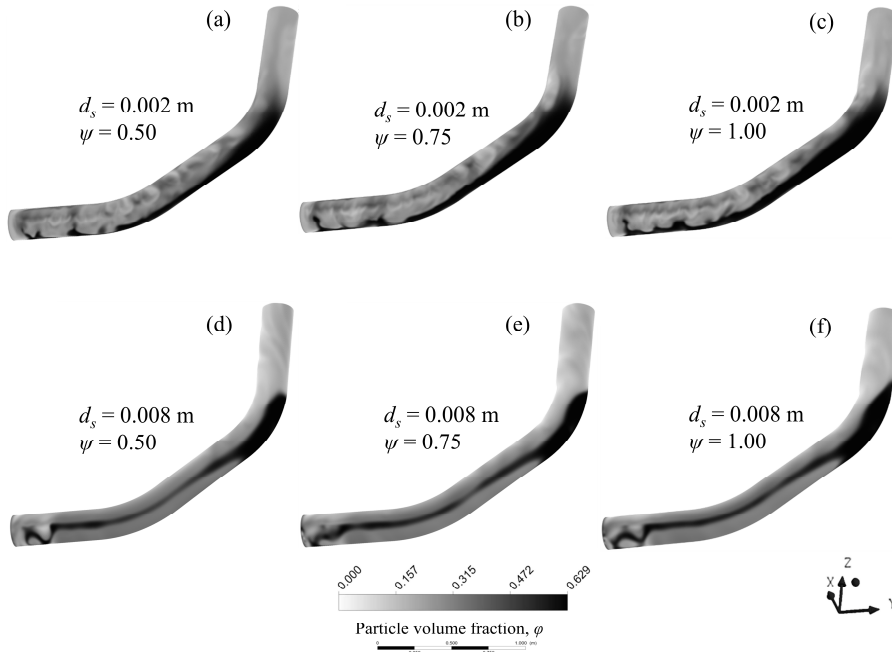


Figure 3. Impact of particle diameter and sphericity on solid volume fraction at bends.

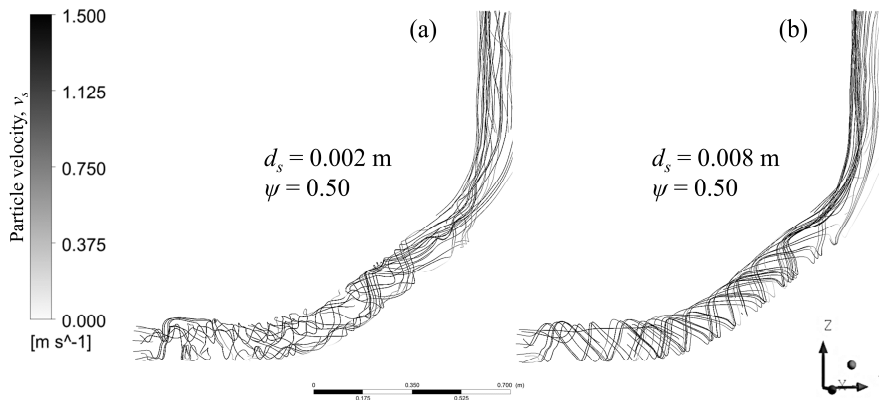


Figure 4. Annular flow velocity streamlines for two particle sizes at given sphericity.

The particle streamlines shown in Figure 3 (a & b) indicate that the impact of drill pipe rotation on particle motion in the vertical section of the annulus is much lower compared to the inclined and horizontal sections respectively. This effect was noticed for all particle sphericities considered. Furthermore, this reduced impact of drillpipe rotation due to the transition in the annular geometry coupled with the eccentric configuration of flow are the major reasons for increased particle deposition noticed around the bend (inclined-to-vertical) compared to other areas of the flow domain.

5. Conclusions

By incorporating the particle sphericity into the interphase momentum exchange coefficient of the Syamlal-O'Brien model, we have studied the impact of particle shape on the multiphase flow of drill cuttings in irregular annular geometries. The obtained results show a 5% reduction in cuttings volume fraction between particles of lowest sphericity (0.5) and perfectly spherical particles for both particle diameters considered. As far as the cuttings transport velocity is concerned, the shape of the particle is more influential on larger cuttings compared to smaller-sized cuttings. We also discover that the inclined-to-vertical (upper bend) is the most susceptible location for particle deposition. Drillpipe rotation is seen to have a more pronounced effect on larger particles, especially in the horizontal and inclined regions of the annulus. In the vertical section, the effect of rotation is low; we infer that this phenomena, alongside increased gravitational resistance are the main reasons for increased deposition in the upper bend.

6. Acknowledgements

Mr. Emmanuel Epelle gratefully acknowledges the financial support of the University of Edinburgh via the PhD fellowship awarded by the School of Engineering (IMP).

References

- D.I. Gerogiorgis, C. Clark, Z. Vryzas, V. Kelessidis, 2015, Development and parameter estimation for a multivariate Herschel-Bulkley rheological model of a nanoparticle-based smart drilling fluid, *PSE2015-ESCAPE25*, 271.
- D. Gidaspow, 1994, Multiphase flow and fluidization: continuum and kinetic theory descriptions. Academic press, New York.
- E.I. Epelle, D.I. Gerogiorgis, 2017, A multiparametric CFD analysis of multiphase annular flows for oil and gas drilling applications, *Comput. Chem. Eng.*, 106, 645-661.
- Fluent, Ansys. 18.1, 2017, Theory Guide. *Ansys Inc.*
- J.M. Dalla Valle, 1948, Micromeritics the Technology of Fine Particles. Pitman Publishing Corporation, New York.
- M.L. Byron, 2015, The rotation and translation of non-spherical particles in homogeneous isotropic turbulence, *University of California, Berkeley, USA.*
- M. Mandø et al., 2007, On the modelling of motion of non-spherical particles in two-phase flow, *6th International Conference on Multiphase Flow, ICMF*, 9-13.
- R.E Osgouei, 2010. Determination of cuttings transport properties of gasified drilling fluids, *Middle East Technical University, Turkey.*
- R. Rooki, F.D. Ardejani, A. Moradzadeh, M. Norouzi, 2015, CFD simulation of rheological model effect on cuttings transport, *J. Dispersion Sci. Technol.*, 36(3), 402-410.
- S.M Han, Y.K. Hwang, N.S. Woo, Y.J. Kim, 2010, Solid-liquid hydrodynamics in a slim hole drilling annulus, *J. Pet. Sci. Eng.*, 70(3), 308-319.
- W. Sobieski, 2010, Drag coefficient in solid-fluid system modelling with the Eulerian multiphase model, *Drying Technol.*, 29(1), 111-125.

Process network modelling for the assessment of environmental impacts

Raul Calvo-Serrano^a, Gonzalo Guillén Gosálbez^{a*}

^a*Centre for Process Systems Engineering, Imperial College of Science, Technology and Medicine, South Kensington Campus, London SW7 2AZ, UK*

g.guillen05@imperial.ac.uk

Abstract

Environmental databases have recently become an essential instrument in the sustainability evaluation of products. Unfortunately, these repositories still contain a limited number of chemicals and are based on fixed mass flows reflecting static industrial settings that might poorly reflect the characteristics of the facilities one wishes to analyse. To overcome these limitations, we propose a methodology to quantify the life cycle assessment (LCA) impact of chemicals based on a mathematical model of the petrochemical industry coupled with linear programming and allocation methods. Our approach was applied to a network comprising 178 processes and 144 products, generating results consistent with those available in the Ecoinvent database for widely used impact indicators such as Global Warming Potential (GWP) and ReCiPe methodology score. Our method provides estimates of the life cycle impact embodied in chemicals under varying yields and demands, even for products that are missing in standard repositories. Overall, this tool should complement existing databases, extending their capabilities and boosting the widespread use of LCA in the chemical industry by simplifying its application.

Keywords: Process Networks, Life Cycle Assessment, Linear programming

1. Introduction

The chemical industry is currently committed to achieve cleaner and more sustainable standards, a trend that has led to a plethora of environmental evaluation methodologies. Among them, Life Cycle Assessment (LCA) has become the prevalent one, due to its holistic view and versatility as applied to a wide range of processes (Azapagic, 1999; Guillen-Gosalbez et al., 2007). LCA is based on a detailed analysis of all the mass and energy flows exchanged with the environment in all the stages in the life cycle of a product, from the extraction of resources to its final disposal. Unfortunately, this requires large amounts of data, which hampers the application of LCA in cases where such information is hard to gather. Streamlined LCA (SLCA) approaches (Hunt et al., 1998; Wernet et al., 2008) have been proposed to simplify the data required by a standard LCA. The most of them are based on the use of information retrieved from an LCA database as proxy of the “true” data needed. LCA repositories (e.g. Ecoinvent3.3 (Swiss Centre For Life Cycle Inventories, 2017)) have experienced a widespread growth in the recent past. They contain LCA results for a wide variety of products and chemicals that comes from full LCA studies of real facilities while considering their geographical and temporal context. In practice, these results replace the missing data in a LCA study under the

assumption that the databases' references are similar to the ones of the studied process. The use of data from repositories as proxy data presents two main limitations.

First, repositories currently only contain a few hundred chemicals, being possible that the required one may not be available. This is especially true for novel or specialised products and processes. The second limitation is that databases are based on fixed flows and specific processes that might be quite different from the ones implemented by the suppliers in the product's supply chain. To circumvent this limitation, LCA databases tend to rely on uncertainty modelling, mainly by using Pedigree matrices in their different versions (Lewandowska et al., 2004; Weidema and Wesnaes, 1996). These are well-established LCA methodologies that characterize the uncertainty associated with the LCI entries in the database (i.e. feedstocks, emissions and wastes) via probability distributions that depend on the degree of similarity (in terms of geographical, technological and temporal context) between the process under study and the data present in the database and its quality. This approach is therefore based on qualitative items that do not cover the entire range of uncertainties encountered in the chemical industry.

Here, we propose a method to estimate the LCA impact of chemical production processes that aims to overcome the two limitations mentioned above. Our strategy combines a network-based model of the petrochemical industry with mathematical programming and allocation methods. This approach not only relies on a more detailed description of the chemical industry, but also is able to model uncertainties through sensitivity analysis, considering a set of plausible scenarios of the chemical industry. To demonstrate the capabilities of our approach we have assembled a network of petrochemical processes encompassing 178 processes and 144 chemical products, using data gathered from the literature (Rudd et al., 1981).

2. Methods

Our methodology relies on optimising a network of processes so as to generate mass flows consistent with a given industrial production scenario. These flows are later on used to allocate the total impact among the final products. The methodology can be divided into four steps: i) building a process network of the chemical industry; ii) optimising the process network to generate mass flows consistent with a given demand pattern, costs and environmental data; iii) allocating of the network impacts among its products considering the flows generated in step one; and iv) assessing the uncertainty of the results generated in previous steps. These steps are described in detail in the ensuing sections.

2.1. Step 1: Building a process network of the chemical industry

The network contains two types of nodes: technologies (j) and products (i). For simplicity, all the utilities are expressed in Fuel Oil Equivalent Tonnes (FOET) following the original work by Rudd et al. (1981). Technology nodes are modelled as black boxes, each described by mass yields (μ_{ij} , kg of i /kg processed by j), utilities consumption rates (u_j , FOET/kg processed by j) and maximum operational capacity (cap_j , kg processed by j). These parameters are complemented by the utilities' cost (uc , \$/FOET) and their environmental impacts embodied ($LCIA^u$, units of the analysed impact indicator/FOET). Product nodes model inputs and outputs of products. Products can either be feedstocks (FS , inputs not produced by any technology), final products (FP , outputs not consumed by any technology) or intermediates (consumed and produced by one or more technologies in the network).

2.2. Step 2: Deriving a mathematical model based on the network

The network previously assembled is used to assess the LCA impacts of the products involved. To this end, we first determine the optimal production pathways (and thus the mass flows exchanged between technologies) by solving an optimisation model M1. This model seeks to minimise the total production cost (TC) while satisfying a set of product demands (d_i). While other optimisation objectives can be established, here we assume that the minimal production cost pathway is the closest scenario to the current global production pathways. The main decision variables of the model are the mass flow rates of main products in each technology (W_j , kg processed by j). Model M1 is described in the following equations (Eqns.(1 to 5)).

$$\text{Min } TC = \sum_i P_i pc_i + \sum_j W_j u_j uc \quad (1)$$

$$P_i + \sum_{j \in OUT(i)} W_j \mu_{ij} = \sum_{j \in IN(i)} W_j \mu_{ij} + S_i, \forall i \quad (2)$$

$$P_i = 0, \forall i \notin FS \quad (3)$$

$$S_i \geq d_i, \forall i \quad (4)$$

$$W_j \geq cap_j, \forall j \quad (5)$$

$$W_j, P_i, S_i \geq 0$$

In model M1, the objective function (Eq.(1)) minimises the total production cost defined as the addition of all the individual processing costs and all the feedstocks purchased (where pc_i represents the purchasing cost for feedstock i , \$/ kg of i). In the previous formulation, note that the main source of processing cost is the utilities consumption. The mass balance of products is defined in Eq.(2), which enforces to consider the structure of the network via the sets $OUT(i)$ and $IN(i)$. $OUT(i)$ contains the processes j that produce product i , while set $IN(i)$ contains the processes that consume product i . The remaining equations force some logical limitations, such that only feedstocks can be purchased (Eq.(3)), that a demand of final products has to be satisfied (Eq.(4)) and that processes have to operate below their maximum capacity (Eq.(5)). Note that this model can accommodate different objective functions as well as additional constraints in order to reflect the specific details of an industrial setting.

2.3. Step 3: Allocating impacts based on mass flows

With the solution of model M1 (i.e. mass flows W_j^*, P_i^*, S_i^*) it is possible to calculate and allocate the LCA impact values ($LCIA_i^{ln}$) to the different products. These LCIA values are obtained by solving model M2, defined in the following equations (Eqns.(6 to 8)). Note that, if both models M1 and M2 were solved together, the combined model would be non-linear. This would not only translate into higher difficulty to obtain solutions (requiring more computational time), but also lower confidence over the results obtained as global optimality is not always ensured by non-linear model solvers.

$$\sum_{i \in IN^P(j)} \mu_{ij} W_j^* LCIA_i^{In} + u_j W_j^* LCIA^u = \sum_{i \in OUT^P(j)} \mu_{ij} W_j^* LCIA_{ij}^{Out}, \forall j \quad (6)$$

$$P_i^* LCIA_i^{fs} + \sum_{j \in OUT^P(i)} \mu_{ij} W_j^* LCIA_{ij}^{Out} = \sum_{j \in IN(i)} \mu_{ij} W_j^* LCIA_i^{In} + S_i^* LCIA_i^{In}, \forall i \quad (7)$$

$$LCIA_{ij}^{Out} = LCIA_{i'j'}^{Out}, \forall j, \forall i, i' \in OUT^P(j), i \neq i' \quad (8)$$

Model M2 is based on the impact balances in processes (Eq.(6)) and in products (Eq.(7)), where feedstocks ($LCIA_i^{fs}$) and utilities are considered the main source of environmental impact. As previously, the structure of the network is satisfied by using sets $IN^P(j)$ and $OUT^P(j)$ (which include all the products i being consumed and produced by a process j , respectively). In order to allocate the generated impact, here we assume that impact values are proportional to the mass flow of each product. This is satisfied with Eq.(8), which enforces all products generated in a process to have the same relative impact values ($LCIA_{ij}^{Out}$).

2.4. Step 4: Modelling uncertainty

The uncertainty associated to the obtained results is obtained through a sensitivity analysis in some network parameters. More in detail, the considered varying parameters in M1 are the product demands (d_i), utility consumption rates (u_j), and process mass yields of main products (μ_{ij} such that i is the main product of process j). In order to generate coherent uncertainties, these changing parameters are assumed to follow specific probability distributions instead of totally random values.

3. Results and discussion

We illustrate the capabilities of our approach by assessing 15 final products included in the network. As well, we focus on 3 environmental impact indicators: Cumulative Energy Demand (CED, energy consumption), Global Warming Potential (GWP, emission of greenhouse gases), and ReCiPe. Note that, while CED and GWP represent specific environmental footprints, ReCiPe evaluates the total environmental impact. When trying to assess these essentially different indicators with the presented method it is possible to characterise its suitability for different kinds of environmental impact indicators. Following the previous methodology, all the parameters values in M1 (i.e. technology utility consumption rates, u_j , and main yields, μ_{ij}) are obtained from Rudd et al. (1981) for the 178 technologies in the network. The feedstocks purchase cost (pc_i) and the final products' demands (d_i) have been obtained from a wide variety of sources, adapting them for the UK and the year 2016. Regarding the maximum capacities (cap_j), these have been set so the demand can be fully met. The impact embodied in the utilities and feedstocks are retrieved from the Ecoinvent3.3 database accessed via SimaPro8.1 (Pre Consultants, 2014). Considering this data, model M1 contains 406 equations and 458 continuous variables and was implemented in GAMS 24.4. The model was solved in 0.016 CPU seconds with the solver CPLEX 12.6 on an Intel Core i5-4570 3.20 GHz computer. Model M2 features 322 variables and the same number of independent linear equations, being solved with GAMS and CPLEX. Regarding the uncertainty calculation, each uncertain parameter (d_i , u_j and main μ_{ij}) is assigned a specific probability distribution. The demands of the final products are assumed to

follow a normal distribution to account for different market demand patterns. The normal distributions use the demands' nominal values as their mean and standard deviations of 30% of the nominal value in all cases). The utility consumptions are uniformly distributed between 0.75 and 1 times their nominal values, while the main product yields vary between 1 and 1.25 times the nominal product yields. These improvements on the processes' performances is done to compensate potentially outdated parameter values from Rudd et al. (1981) when compared to Ecoinvent3.3.. Uncertainties are quantified via 2,000 random scenarios generated via Monte Carlo sampling on the previously defined probability distributions. Models M1 and M2 are recalculated for each scenario. The obtained results and uncertainties are compared with those available in Ecoinvent3.3 (original values). For each scenario, we then compare the values provided by M2 and the ones from Ecoinvent3.3 in order to finally calculate a relative difference between both. Figure 1 displays the calculated and original impact values (as the mean values obtained from the uncertainty analysis) and their uncertainties as well as the relative difference between both original and calculated results. In all cases, the uncertainties are expressed as 25th and 75th percentiles.

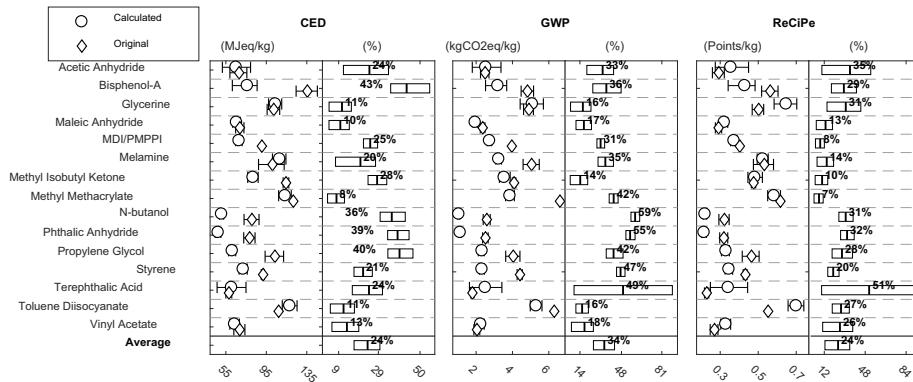


Figure 1, Calculated and original impact values and uncertainties (left) and their relative distances (average and 25th and 75th percentiles, right). Labels indicate the average relative differences.

Three indicators are considered to assess the quality of the results: average relative difference (the lower the better), width of the confidence interval of the difference (the smaller the better), and whether the confidence intervals of the two impact values overlap. In Figure 1, the calculated and original values agree reasonably, with 20-30 % average relative differences. However, since the original values consider additional impact sources and steps in the life cycle, the calculated results tend to be lower than the original values. Also, for some products, the processes selected by the assembled network were different to those considered in Ecoinvent3.3, obtaining notoriously discrepant impact values (as is it the case for Terephthalic Acid or N-butanol). This demonstrates how critical is to have a process network as complete as possible to evaluate as many alternatives as possible and therefore be able to better assess impact values. Looking at the confidence interval of the relative differences, their width is generally proportional to the expected error, with low errors having small uncertainty ranges. Concerning the overlap between confidence intervals, only 18 calculated results match (partially or completely) with their original counterparts.

4. Conclusions

Here we propose a methodology to calculate the life cycle impacts of chemicals based on the use of a petrochemical process network modelled via mathematical programming tools. This approach allows filling data gaps in LCA repositories, potentially producing better estimates based on a detailed and flexible representation of the industry underpinned by a mathematical model based on first principles. This methodology has been applied to a petrochemical network containing 178 processes and 144 products. The results obtained are in good agreement with the ones available in LCA databases, with the error of the estimate varying significantly depending on the product and impact indicator. In the future we aim to update and increase the process network data as well as to consider alternative optimisation objectives and allocation methods, then being possible to study how the changes in the global market may affect the petrochemical production pathways and also their environmental performance. This work has the potential to open up further research on methods for complementing LCA repositories based on a deep knowledge of an industrial sector.

References

- Azapagic, A., 1999. Life cycle assessment and its application to process selection, design and optimisation. *Chem. Eng. J.* 73, 1–21. [https://doi.org/10.1016/S1385-8947\(99\)00042-X](https://doi.org/10.1016/S1385-8947(99)00042-X)
- Guillen-Gosalbez, G., Caballero, J.A., Esteller, L.J., Gadalla, M., 2007. Application of life cycle assessment to the structural optimization of process flowsheets. *Comput. Aided Chem. Eng.* 24, 1163–1168. [https://doi.org/10.1016/S1570-7946\(07\)80218-5](https://doi.org/10.1016/S1570-7946(07)80218-5)
- Hunt, R.G., Boguski, T.K., Weitz, K., Sharma, A., 1998. Case studies examining LCA streamlining techniques. *Int. J. Life Cycle Assess.* 3, 36–42. <https://doi.org/10.1007/BF02978450>
- Lewandowska, A., Foltynowicz, Z., Podlesny, A., 2004. Comparative lca of industrial objects part 1: lca data quality assurance — sensitivity analysis and pedigree matrix. *Int. J. Life Cycle Assess.* 9, 86–89. <https://doi.org/10.1007/BF02978567>
- Pre Consultants, 2014. SimaPro Tutorial Colophon 89.
- Rudd, D.F., Fathi-afshar, S., Treviño, A.A., Stadtherr, M.A., 1981. *Petrochemical Technology Assessment*. Wiley.
- Swiss Centre For Life Cycle Inventories, 2017. Ecoinvent Data V3.3. Ecoinvent Cent., 2017. Ecoinvent 3.3 [WWW Document]. URL <https://www.ecoinvent.org/home.html> (accessed 5.20.17).
- Weidema, B.P., Wesnaes, M.S., 1996. Data quality management for life cycle inventories—an example of using data quality indicators. *J. Clean. Prod.* 4, 167–174. [https://doi.org/10.1016/S0959-6526\(96\)00043-1](https://doi.org/10.1016/S0959-6526(96)00043-1)
- Wernet, G., Hellweg, S., Fischer, U., Papadokostantakis, S., Hungerbühler, K., 2008. Molecular-Structure-Based Models of Chemical Inventories using Neural Networks. *Environ. Sci. Technol.* 42, 6717–6722. <https://doi.org/10.1021/es7022362>

Data-driven degradation model for batch processes: a case study on heat exchanger fouling

Ouyang Wu^{a,b,*}, Ala E.F. Bouaswaig^a, Stefan M. Schneider^a, Fernando Moreno
Leira^a, Lars Imsland^b and Matthias Roth^a

^a*Automation Technology, BASF SE, 67056 Ludwigshafen, Germany*

^b*Department of Engineering Cybernetics, NTNU, 7491 Trondheim, Norway*

ouyang.wu@ntnu.no

Abstract

In this paper, we present an industrial case study of a batch process; the degradation effect is fouling in heat exchangers which impedes heat transfer and fluid flow during batch production. The degradation increases from batch to batch until the batch reactor is shut down for a scheduled maintenance. That is, there is a periodic pattern in the batch-to-batch data as a result of the degradation. We propose a novel data-driven modeling technique for predicting the evolution of a batch degradation key performance indicator (KPI). This method extends existing algorithms (based on partial least squares, PLS) for the treatment of within-batch data to the present batch-to-batch degradation problem. An existing missing data algorithm for PLS models is employed to predict degradation in future batches. The proposed approach is then applied to the case study, and predicts the evolution of the fouling KPI with respect to the production planning under predefined process operations, which is a basis for optimal scheduling of batch production and maintenance.

Keywords: fouling, batch process, degradation evolution, unfolding approach, multiway PLS

1. Introduction

The performance and efficiency degradation of industrial equipment and assets is inevitable in their life cycles. The assessment of process condition provides information of degradation, and the following optimization of process operations is meant to mitigate the influence of degradation. In some cases, it is necessary to shut down the plant and carry out the maintenance operation for restoration when the degradation reaches a certain degree. Human experience-based maintenance scheduling is not necessarily optimal on account of degradation in production along with other physical and logistical constraints. However, optimal scheduling asks for information about future degradation evolution. Therefore, the development of a predictive degradation model plays a significant role in plant performance optimization in consideration of degradation effects.

A batch reactor is a multi-purpose unit operation that is widely used in process industry to manufacture diverse products. The flexibility of batch processes is the major reason for its popularity in the chemical industry. By using batch production plants industry can easily adapt to market fluctuations and extend their product portfolio to react to customer needs. A multi-product batch process runs in a finite time period. It includes several stages: the raw materials are charged and the initial conditions are set according to the recipe; then the reaction starts and lasts for some time; the product is transferred into a storage tank and the product final quality variables are recorded at the end of this batch. During the batch running period, the process variables such as temperature, pressure, etc. are measured in real-time, and their profiles are called trajectories. These trajectory data are presented in three-way form with time $t = 1, 2, \dots, T$, variable $k = 1, 2, \dots, K$ and batch

$n = 1, 2, \dots, N$, while the initial condition variables and the final quality variables are in two-way form with batch $n = 1, 2, \dots, N$ and variable $k = 1, 2, \dots, K$ (Nomikos and MacGregor, 1994). In comparison with continuous processes, monitoring, control and optimization of batch processes are more challenging. These challenges arise from the problems that are associated with batch processes: absence of steady state (wide operating range) and presence of constraints, irreversible behavior, repetitive nature (Bonvin et al., 2006). In the presented case study, the reaction heat is removed by pumping the reactant through the heat exchangers (HE), and the fouling in the heat exchangers impedes the fluid flow and leads to the increase of the pressure drop across the heat exchanger during the reaction period. As a result, the pressure drop of the heat exchanger is chosen as a fouling indicator for the process (see figure 1). However, the contribution of the fouling towards the real-time pressure drop measurement is hidden and the increasing trend of fouling is masked in the individual batch duration, which results from the variant batch operation conditions. To deal with this problem, the pressure drop measured under selected operation conditions (at the start of the reaction) is considered as the fouling KPI (red star) for each individual batch as figure 1 illustrates. The fouling evolution from batch to batch is then indicated by the fouling KPIs.

As for the degradation prediction in continuous process, a variety of degradation examples using different data-driven modeling approaches (such as support vector machine, neural network, etc.) are found in literature (Sun et al., 2008; Aminian and Shahhosseini, 2008; Riverol and Napolitano, 2005). Due to the characteristic of the batch processes (Bonvin et al., 2006), these approaches do not deal well with the multi-dimension batch data structure. On the other hand, the multiway approach was proposed to solve batch data structure problems by transforming three-dimension data into batch-wise unfolded data, and the multiway PLS approach is then employed in the within-batch modeling to predict the final quality of the individual batches (Nomikos and MacGregor, 1994; García-Muñoz et al., 2003; Wold et al., 2010). As to degradation in batch production, unlike final quality variables barely affected by previous batches, degradation grows from batch to batch. Moreover, degradation prediction usually means to predict degradation evolution in next N batches, and the time horizon for prediction can be longer than one month, while the application of the multiway PLS approach using the within-batch model is only available to predict the final degradation in a single batch.

In this paper, a novel data structure called “campaign” is proposed for the analysis of degradation evolution from batch to batch. A data-driven model is developed based on the unfolded campaign data. Finally, an application of the PLS method and its missing data estimation algorithm enable the prediction of degradation evolution. The paper structure is presented as follows: the proposed approach details are presented in Section 2; the corresponding application on the case study and its results are showing in Section 3; finally, Section 4 draws the conclusions.

2. Method

2.1. The campaign concept in batch processes

In some cases, the batch degradation KPI presents periodic nature as maintenance is carried out to restore its degradation state regularly (see Figure 2). The figure shows the evolution of the fouling KPI in the heat exchanger. Each point represents the fouling degree in an individual batch, and the color and symbol together denote the batch product type from P1 to P9. The product order is planned ahead of time and flexible to modify as necessary. The period between two

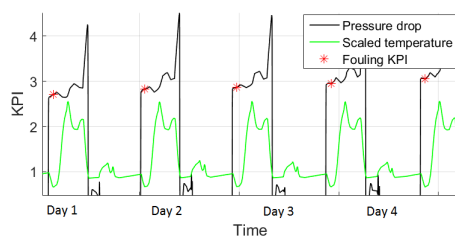


Figure 1: Fouling indication by the pressure drop across the heat exchanger

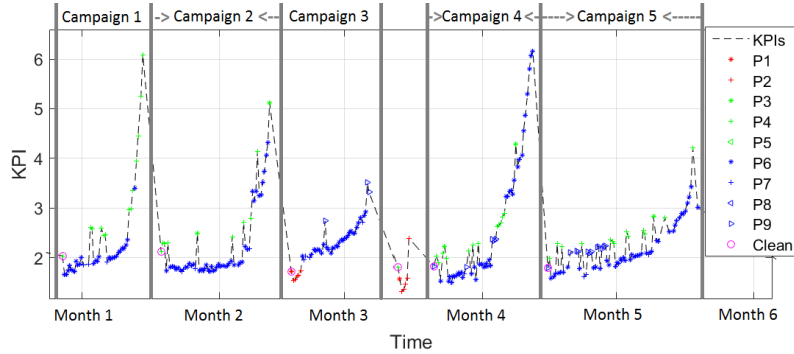


Figure 2: Heat exchanger fouling evolution in batch process and campaigns

maintenance operations is named campaign, which contains a series of batches. The idea of the campaign concept is to capture the dynamics of the degradation evolution. To make effective use of campaign data, further data structure analysis is necessary. The structure of campaign data includes individual batch data firstly, where batch trajectory data have three dimensions: batch, time and variable. Secondly, campaign is a “batch” consisting of a series of batches connected by the degradation evolution.

2.2. Campaign PLS approach and campaign data unfolding method

As one campaign consists of a series of batches, the campaign data structure has four dimensions (campaign, batch, variable and time). The modeling approaches for continuous processes are not applicable to the multi-dimension campaign process, and it requires an unfolding method to transform the multi-dimension campaign data into two-dimension data. In the multiway analysis, the batch-wise unfolding method is developed to transform the three-dimension batch data into two-dimension unfolded data: batch data are extracted horizontally in a time-wise fashion and each batch becomes a single row of data (Nomikos and MacGregor, 1994; García-Muñoz et al., 2003; Wold et al., 2010):

$$X_{batch}^m = [x_{i1}, x_{i2}, \dots, x_{iki}, x_{t1}^1, x_{t2}^1, \dots, x_{tT}^1, x_{t1}^2, x_{t2}^2, \dots, x_{tT}^2, \dots, x_{t1}^{kt}, x_{t2}^{kt}, \dots, x_{tT}^{kt}] \quad (1)$$

where, X_{batch}^m is the unfolded batch data of the m th batch, which includes initial conditions and unfolded trajectories: the initial condition variables x_{ik} , $k = 1, 2, \dots, ki$ is the index of initial condition variables; trajectory data $x_{t_k}^k$, $k = 1, 2, \dots, kt$ is the index of trajectory variables, $t = 1, 2, \dots, T$ is the time index in a single batch.

In a similar methodology, a campaign unfolding method is proposed to obtain 2-dimension unfolded campaign data. The variable and time dimensions are unfolded firstly to obtain the unfolded batch data X_{batch}^m using the batch-wise unfolding method. Then the three-dimension campaign data is unfolded as Figure 3 illustrates, where the campaign data are extracted horizontally in a batch-wise fashion and each campaign becomes a single row of different unfolded batch data. For simplicity, unfolded batch data are presented with the index $k = 1, 2, \dots, K$. Further, the unfolded campaign data are employed for the degradation modeling. To build a degradation model based on campaign data, the outputs are the evolution of degradation KPIs, and the inputs are the unfolded campaign data which contain control and process information of a single campaign.

In this section, PLS is employed for the campaign-based degradation modeling due to its advantage in dealing with a large number of correlated predictor variables and avoiding over-fitting problem. In PLS, the highly correlated data in the input and output space are modeled separately with orthogonal principal components based on multivariate statistical projection, and linear regression

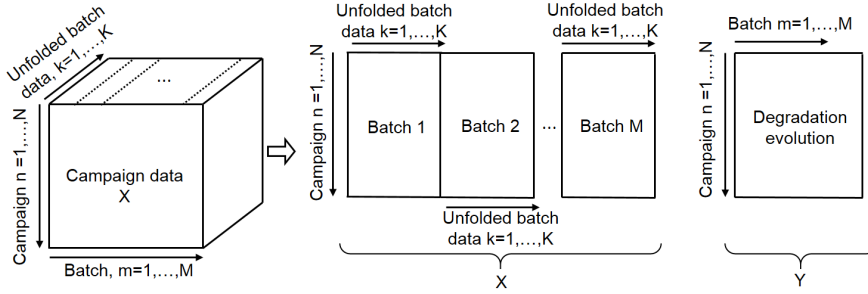


Figure 3: Campaign data structure and unfolding method

is employed on those dimension-reduced principal components (Geladi and Kowalski, 1986; Abdi, 2010). The campaign-based PLS model is:

$$\begin{aligned} X_n &= T_n P^T + E_n, & X_n &= [X_1^n, X_2^n, \dots, X_M^n], & X_m^n &= [x_1^m, x_2^m, \dots, x_{k_1}^m, z_1^m, z_2^m, \dots, z_{k_2}^m] \\ Y_n &= T_n C^T + F_n, & Y_n &= [y_1^n, y_2^n, \dots, y_M^n] \end{aligned} \quad (2)$$

where, $X_n \in \mathbb{R}^{1 \times M(k_1+k_2)}$ is the n th unfolded campaign; the m th unfolded batch data from the n th campaign $X_m^n \in \mathbb{R}^{1 \times (k_1+k_2)}$ are divided into manipulated data z_k^m , $k = 1, 2, \dots, k_2$ and process data x_k^m , $k = 1, 2, \dots, k_1$, while k is the corresponding index; the output $Y_n \in \mathbb{R}^{1 \times M}$ is a series of degradation KPI in a campaign, and the element y_m^n is the degradation KPI of m th batch in n th campaign; $T_n \in \mathbb{R}^{1 \times L}$ is the score of the n th campaign projecting on the principal component, while L is the dimension; $P \in \mathbb{R}^{M(k_1+k_2) \times L}$ and $C \in \mathbb{R}^{M \times L}$ are the model parameters, called loading matrix, which can be estimated through the NIPALS algorithm (Geladi and Kowalski, 1986).

The campaign-based PLS model can be used to estimate the evolution of batch degradation from the known input observations (historical process data and the manipulated data). In the batch fouling example, the manipulated data are exclusively the production planning, that is, the planned production schedule shows which products are going to be produced and the production order. Given the current batch K , the known data X_n^* are $\{X_{1:K}^n, x_{1:k_2}^{K+1:M}\}$, and missing data $X_n^\#$ are $\{x_{1:k_1}^{K+1:M}\}$. The future batch degradation indicators of interest are $\{y_{K+1:M}^n\}$. The missing data estimation approaches for PLS models such as the trimmed score regression (TSR) are meant to provide estimation of final score \hat{T}_n with the known samples X_n^* (the information update to K), and then output \hat{Y}_n is calculated from the estimated score \hat{T}_n . TSR algorithm is proved to be effective in multiway PLS applications (Arteaga and Ferrer, 2002; Nelson et al., 1996; Keivan Rahimi-Adli, 2016).

3. Case study

3.1. Case study description

The case study presents an example of heat exchanger fouling in a polymerization batch process (see the process schematic in Figure 4). This batch process produces multiple water and paper treatment chemicals. The polymerization starts when initiators are added into monomer emulsion in the reactor. The recirculation system works during the reaction, and two parallel heat exchangers help to cool down the reactor. The emulsion flow results in polymer residues depositing in the reactor and the heat exchangers. The fouling in heat exchanger impedes the flow and can even lead to a blockage, and it also decreases the cooling efficiency and prolongs batch duration with less production capacity. Therefore, the cleaning is required to remove the residues in the heat exchanger after running certain number of batches. We focus on the fouling in heat exchangers as it is the short-board of the process.

3.2. Multi-product effects on fouling KPIs

Multiple products in batch process add more complexity to degradation prediction. Different products mean different batch recipes, such as ratios of raw materials, additives and operation conditions, which results in disturbances to fouling KPIs. In figure 2, the fouling KPIs from batch to batch show an increasing trend between two cleanings, especially for the same product type. KPIs with different product type show some biases among them, for example, the green KPIs are relatively larger than the blue KPIs. This is not due to fouling evolution, and it brings more disturbances in degradation modeling. To avoid this, the product biases are calculated by comparing KPIs to some fitted curves of the main product KPIs (P6), and the bias correction is carried out by adding the product-based biases to the KPIs (see the smoothed KPIs in Figure 5).

3.3. Results

The factors that contribute to fouling evolution in heat exchangers include the product recipes and trajectory process variables like temperature, pressure, flowrate, etc. The pressure drop across the heat exchanger is employed as a batch fouling KPI, and the multi-product biases are excluded to obtain smooth increasing fouling KPIs with less disturbances. To model the fouling KPI evolution in the heat exchanger, the unfolded campaign data is obtained using the proposed method. An equally long campaign is a prerequisite for the PLS model, hence the last 30 batches of one cleaning period are collected as one campaign, which includes the dynamics of the fouling evolution. The collected historical data for modeling includes 20 campaigns. 23 input variables are selected from the unfolded batch data, which are production planning variables, landmarks of trajectory data and batch quality data (Wold et al., 2010). The output vector for each campaign includes 30 batch fouling KPIs. The unfolded campaign data X has a row of 460 input variables. The heat exchanger fouling campaign PLS model is developed based on the historical data (20 campaigns), where several campaigns are excluded for cross validation purpose. Based on this model, we can predict fouling evolution in upcoming campaigns of batches by using the missing data estimation method TSR as explained above. We illustrate this using two campaign examples in Figure 6, where three predictions are given using the data up to different stages of the campaign, and compared to the actual fouling KPIs. The first case is $K=1$, which means given observation data up to Batch 1 and the production planning for the whole campaign, one needs to predict the fouling evolution in the remaining 29 batches. Similar for $K=10$ and $K=20$. The fouling KPI predictions in Figure 6 follow the actual KPIs with a smooth increasing curve.

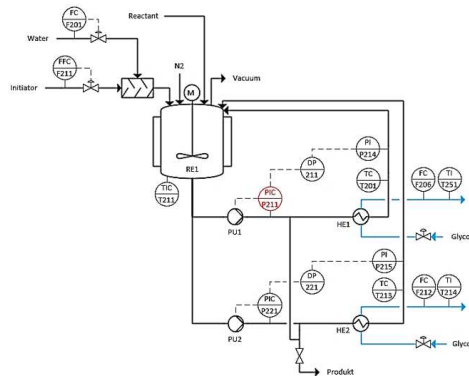


Figure 4: Case study process schematic

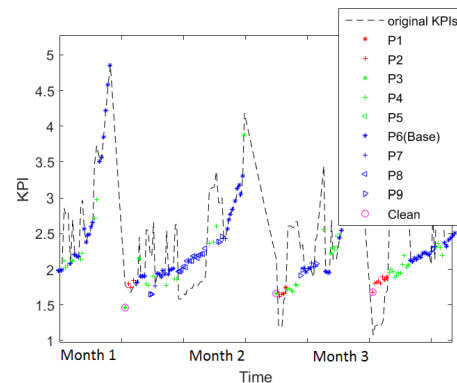


Figure 5: Bias corrected fouling indicators

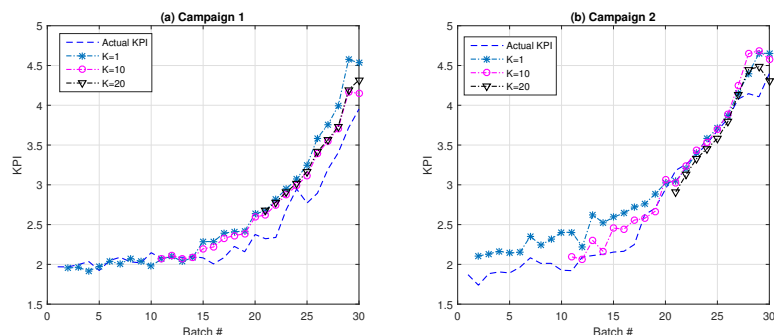


Figure 6: Two fouling KPIs campaign predictions: given information up to Batch $K = 1, 10, 20$

4. Conclusions

This paper focuses on degradation prediction for batch processes with heat exchanger fouling as the case study. To solve the degradation prediction problem, a new “campaign” concept is proposed to structure the batch degradation evolution. Furthermore, an unfolding method is proposed to transform the four-dimension data into two-dimension unfolded campaign data for PLS modeling. The campaign-based PLS approach is then applied in the case study, and the missing data estimation method TSR is employed for the degradation prediction. The validation result illustrates the effectiveness of the proposed campaign PLS approach in predicting heat exchanger fouling evolution, and this fouling predictions can provide further information for better production scheduling and maintenance planning.

Acknowledgments: Financial support is gratefully acknowledged from the Marie Skłodowska Curie Horizon 2020 EID-ITN project “PROcess NeTwork Optimization for efficient and sustainable operation of Europe’s process industries taking machinery condition and process performance into account PRONTO”, Grant agreement No 675215.

References

- Abdi, H., 2010. Partial least squares regression and projection on latent structure regression (PLS Regression). Wiley Interdisciplinary Reviews: Computational Statistics 2 (1), 97–106.
- Aminian, J., Shahhosseini, S., may 2008. Evaluation of ANN modeling for prediction of crude oil fouling behavior. Applied Thermal Engineering 28 (7), 668–674.
- Arteaga, F., Ferrer, A., 2002. Dealing with missing data in MSPC: Several methods, different interpretations, some examples. Journal of Chemometrics 16 (8–10), 408–418.
- Bonvin, D., Srinivasan, B., Hunkeler, D., 2006. Control and optimization of batch processes: Improvement of process operation in the production of specialty chemicals. IEEE Control Systems 26 (6), 34–45.
- García-Muñoz, S., Kourti, T., MacGregor, J. F., Mateos, A. G., Murphy, G., 2003. Troubleshooting of an industrial batch process using multivariate methods. Industrial & engineering chemistry research 42 (15), 3592–3601.
- Geladi, P., Kowalski, B. R., 1986. Partial least-squares regression: a tutorial. Analytica Chimica Acta 185 (C), 1–17.
- Keivan Rahimi-Adli, 2016. Grey-box modeling, state estimation and optimization of a semi-batch reactor. Master’s thesis, TU Dortmund University, Dortmund, Germany.
- Nelson, P. R. C., Taylor, P. A., MacGregor, J. F., 1996. Missing data methods in PCA and PLS: score calculations with incomplete observations. Chemometrics and Intelligent Laboratory Systems 35, 45–65.
- Nomikos, P., MacGregor, J. F., 1994. Monitoring batch processes using multiway principal component analysis. AIChE Journal 40 (8), 1361–1375.
- Riverol, C., Napolitano, V., may 2005. Estimation of fouling in a plate heat exchanger through the application of neural networks. Journal of Chemical Technology & Biotechnology 80 (5), 594–600.
- Sun, L., Zhang, Y., Zheng, X., Yang, S., Qin, Y., 2008. Research on the fouling prediction of heat exchanger based on support vector machine. In: Intelligent Computation Technology and Automation (ICICTA), 2008 International Conference on. Vol. 1. IEEE, pp. 240–244.
- Wold, S., Kettaneh-Wold, N., MacGregor, J., Dunn, K., 01 2010. Batch process modeling and mspc. In: Comprehensive Chemometrics. Vol. 2. Elsevier, pp. 163–197.

Applying New Sustainability Metric in Different Natural Gas Liquid (NGL) Recovery Configurations to Extend Investment Decision and Incorporate Sustainability Analysis

Saad A. Al-Sobhi,* Ahmed AlNouss

Chemical Engineering Department, College of Engineering, Qatar University. Doha, Qatar

saad.al-sobhi@qu.edu.qa

Abstract

Sustainable design is considered as one of emerging research area in process system engineering (PSE) society. It extends the investment decision that focuses mainly on profitability analysis to consider other aspects such as the environmental impact and safety aspects. The sustainability dimensions such as the economic and environmental impact are considered to assess the natural gas liquids (NGL) recovery process using a new sustainability metric referred as the sustainability weighted return on investment metric (SWROIM). It extends return on investment (ROI) concept and makes use of the augmented sustainability metrics and process integration targeting (benchmarking) approaches. We adapted a sequential strategy to assess different NGL configurations. The turbo-expanding separation method and its consequent configurations, the most applicable separation technology in today's gas industry were considered to process 84000 kg/h of natural gas. We used ASPEN HYSYS V9 to simulate six NGL flowsheet configurations. Other ASPEN products such as ASPEN Energy Analyser were utilized to perform other energy saving activities to improve the design of baes case. Considering the economic evaluation first, and using the ROI analysis, IPSI-1 and GSP are competing with the original ISS configuration with 44% and 40% as estimated rate of investment, respectively. After the incorporation of the sustainability metric with some weights (e.g. 0.07 for thermal saving via heat integration and 0.3 for CO₂ emission reduction) as relative importance to economic profit, both IPSI-1 and GSP configurations improved in SWROIM analysis with 47% and 42%, respectively. However, IPSI-2 showed to be promising with 10 %, a percentage incremental in SWROIM analysis in comparison to 8 % in IPSI-1 configuration for 0.45 as CO₂ emission reduction relative importance.

Keywords: Process Systems Engineering (PSE), Natural Gas Liquid (NGL), Process Simulation, Heat integration, Sustainability.

1. Introduction

Recently, sustainable design is considered as one of emerging research area in process system engineering (PSE) society. The sustainable design of industrial processes is the one that leads to economic growth, environmental protection and social prosperity. Many definitions are available to define sustainability. However, the most widely known definition of sustainable development, which has been used as the basis for

many definitions, is that given in the Brundtland Report (Brundtland, 1987): ‘Sustainable development is development which meets the needs of the present population without compromising the ability of future generations to meet their own needs’. Traditionally, chemical engineers are known for designing and operating processes with the focus on material utilization, cost and safety. For over a couple of decades, chemical engineers have been incorporating environment concerns into process design and operation in terms of sustainability (Batterham, 2006). Sustainability has been gaining popularity in chemical engineering education and practice. Figure 1 shows the uptrend in terms of the number of publications from 1999 to 2016 when we consider “chemical engineering design and sustainability” as key words in the search engine Scopus with 329 as a total number of documents.

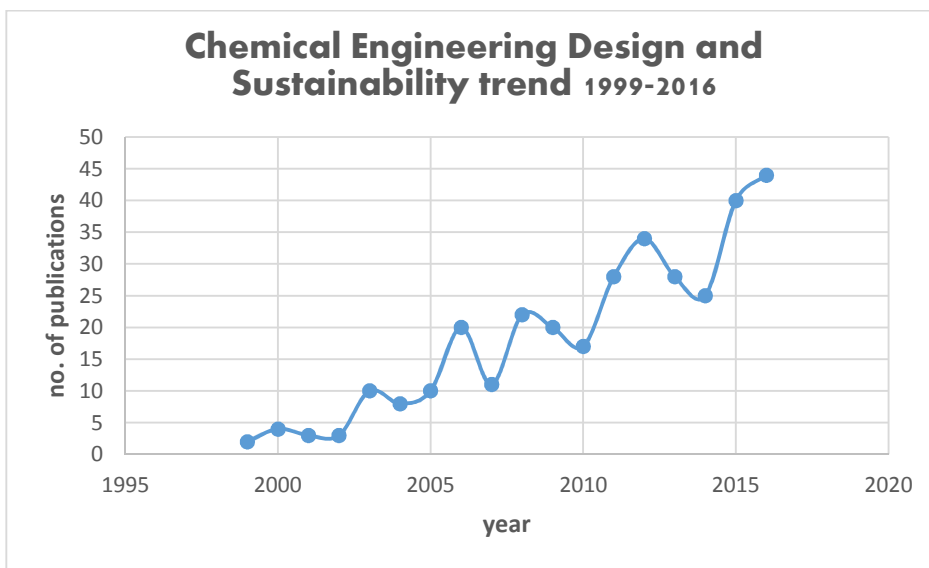


Figure 1 Uptrend in the number of publications addressing sustainable chemical engineering design from 1999 to 2016.

To extent our previous work, (Al-Nouss et al., 2017) and incorporate the sustainability analysis, we were motivated by the new metric referred to as the sustainability weighted return on investment metric (SWROIM) introduced recently by El-Halwagi (2017). It extends the Rate of Investment (ROI) concept and makes use of the augmented sustainability metrics and process integration targeting (benchmarking) approaches. The new metric was applied on different NGL recovery configurations. The main purpose of NGL recovery unit in gas processing facility is to recover the heavy hydrocarbons to satisfy pipeline gas specifications, safety and operational issues such as these heavier may result in the pipeline blockage when cooled. The advancements in turbo-expansion technology that can recover high values of ethane and propane made it a viable choice in today’s gas plants. Considering the simplest turbo expander scheme for NGL extraction, in this technology the feed gas is cooled in a series of heat exchangers by exchanging heat with residual gas and de-methanizer side stream and bottom reboiler. The partially condensed gas feed is then sent to a high pressure separator. The vapor is

expanded through a turbo-expander to obtain low temperatures, which makes the ethane less volatile, and larger amount of ethane can be recovered at the bottom of the de-methanizer. The expander shaft, which rotates during gas expansion, is coupled with the compressor shaft to utilize the expansion work while simultaneously producing a cooling effect. With the low temperatures at the de-methanizer top, carbon dioxide icing remains a problem. The ISS operational limitation had led to more advances schemes such as Cold residue gas-recycle (CRR), Gas sub-cooled process (GSP), Recycle split-vapor process (RSV), Enhanced NGL recovery process (IPSI-1), Internal refrigeration for enhanced NGL recovery process (IPSI-2). Basically, the GSP, CRR and RSV process schemes focus on improvements at the top side of the demethanizer column and IPSI-1 and IPSI-2 schemes focus on the improvements at the bottom side of the demethanizer column. Therefore, the industry standard single stage (ISS) and its consequently improved configurations are considered for simulation and sustainability analysis.

2. Overall Methodology

The sequential strategy consists mainly of five majors steps.

Step One: Process Simulation: steady state simulation of six NGL process schemes/configurations using ASPEN HYSYS V9 under different operating conditions to estimate material and energy requirements. ASPEN HYSYS, a powerful simulation package, it is used to estimate the material balance and energy balances and help to address what-if analysis and carry out sensitivity analysis.

Step Two: Economic Evaluation: estimate the capital, operational costs using ASPEN Economic Evaluation tool and perform profitability by calculating the total Annualized Cost and ROI as shown in Eq. (1).

$$ROI_p = \frac{AEP_p}{TCI_p} \quad (1)$$

Where AEP is the annual net economic profit and TCI is the total capital investment.

Step Three: Environmental Impact Assessment: estimate the annual carbon emissions in kg/h and the reduction targets in all recovery configurations using ASPEN software embedded CO₂ estimation algorithm.

Step Four: Process Integration and Improvements: perform heat integration techniques to estimate potential energy savings using ASPEN Energy Analyzer. It is an energy management software for performing optimal heat exchanger network design to minimize process energy. Also, the energy intensity before and after heat integration can be estimated.

Step Five: Sustainability Incorporation and Analysis: apply the sustainability metric with some weights as relative importance as ratio to economic profit as shown in Eq. (2).

$$SWROI M_p = \frac{AEP_p \left[1 + \sum_{i=1}^{N_{Indicators}} w_i \left(\frac{Indicator_{p,i}}{Indicator_i^{Target}} \right) \right]}{TCI_p} \quad (2)$$

where i is an index for the different sustainability indicators (other than the annual net economic profit with $i=1,2,\dots,N_{indicators}$). The weighing factor w_i is a ratio representing the relative importance of the i^{th} sustainability indicator compared to the annual net economic profit. The term $Indicator_{p,i}$ represents the value of the i^{th} sustainability indicator associated with the p^{th} project and the term $Indicator_i^{Target}$ corresponds to the target value of the i^{th} sustainability indicator (obtained from process integration benchmarking or taken as the largest value from all projects, or set by the company as a goal).

3. Case Study: Results and discussions

The selected process schemes namely, ISS, GSP, CRR, RSV, IPSI-1 and IPSI-2 were simulated in steady state mode using ASPEN HYSYS V9. Peng Robinson was considered as it is the recommended property fluid package for hydrocarbon system. For brevity, we present the simulated flowsheet for IPSI-1 configurations as shown in Figures (2). All other simulated configurations can be found in our recent work (AlNouss et. al., 2017). After the development of the flowsheets in ASPEN HYSYS, the six different process schemes were assessed based on the economic metric. After obtaining the recoveries values for sales gas, NGL product and the utility requirements using the steady state simulation mode, we activated Aspen process Economic Analyzer (APEA) to estimate the capital cost and annual operational cost in US dollars. By considering the raw materials and products prices, revenues were calculated to estimate

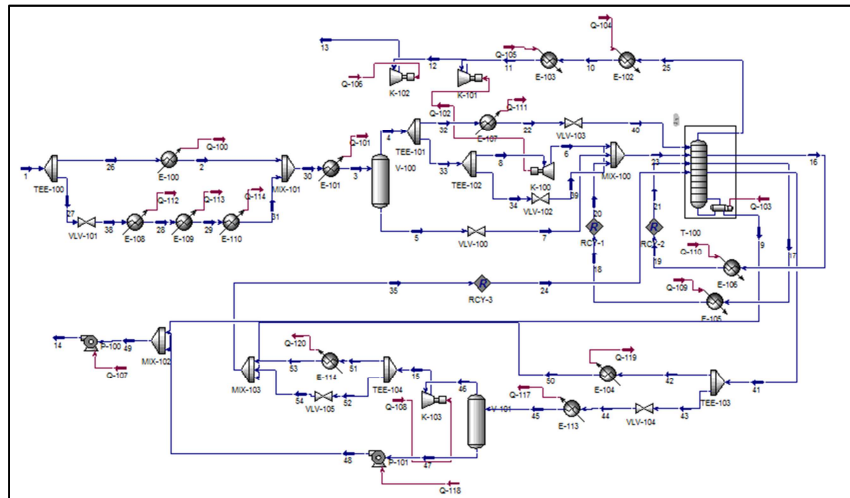


Figure 2 IPSI-1 ASPEN HYSYS flowsheet simulation.

ROI using Eq. (1) to perform the profitability analysis. Table 1 summarizes different economic, energy, and environmental parameters and values after activating the APEA and AEA components. Table 2 presents the targets and relative importance of sustainability indicators for IPSI-1 configuration.

Table 1 Main results from ASPEN Plus, ASPEN Process Economic Analyzer, and ASPEN Energy Analyzer.

	ISS	GSP	CRR	RSV	IPSI-1	IPSI-2
Economic Evaluation						
Capital Cost (\$), TCI	15,702,200	18,062,300	21,920,800	24,874,300	20,460,700	21,161,800
Operational Cost (\$/y)	7,992,220	9,651,420	10,451,300	15,376,300	8,015,280	8,802,430
Total Annualized Cost (\$/y)	13,242,717	15,691,087	17,781,171	23,693,761	14,856,923	15,878,506
NG Feed Cost (\$/y)	103,127,601	103,127,601	103,127,601	103,127,601	103,127,601	103,127,601
Sales Gas Revenue (\$/y)	106,472,976	106,180,124	106,247,075	105,686,056	107,053,414	105,549,166
NGL Revenue (\$/y)	13,583,693	13,877,814	13,833,235	13,961,024	13,003,539	14,506,638
AEP	8,936,848	7,278,918	6,501,409	1,143,179	8,914,072	8,125,772
Energy and Environmental Assessment						
Carbon Emissions Simulation (kg/h/y)	3,524	3,602	1,985	8,726	3,807	4,042
Total Utilities (kJ/h)	63,071,487	64,464,166	82,600,648	156,100,000	68,114,674	72,324,363
Available Energy Savings (kW)	58,555,830	58,935,652	42,054,692	142,800,000	55,538,358	71,860,137
Target Carbon Emissions [kg/h]	252.15	308.81	974.32	742.70	702.61	25.75
Sales Gas recovery, %	92.51	92.19	92.34	91.64	93.05	91.58
NGL recovery, %	7.49	7.81	7.68	8.00	6.94	8.42

Table 2 Targets and Relative Importance of sustainability indicators for IPSI-1 NGL configuration case study

Sustainability indicator (i)	Target $Indicator_i^{Target}$	Unit	Relative importance as a ratio to economic profit (w_i)
Thermal energy savings (via heat integration)	55,538,358	KW	0.07
CO ₂ emission reduction	702.61	Kg/h	0.30

By using Eq. (2), for all configurations and considering the targets and relative importance of sustainability indicators (e.g. 0.07 for thermal saving via heat integration and 0.3 for CO₂ emission reduction) relative importance as ratio to economic profit, the SWROIM % values are calculated and presented in Figure 3.

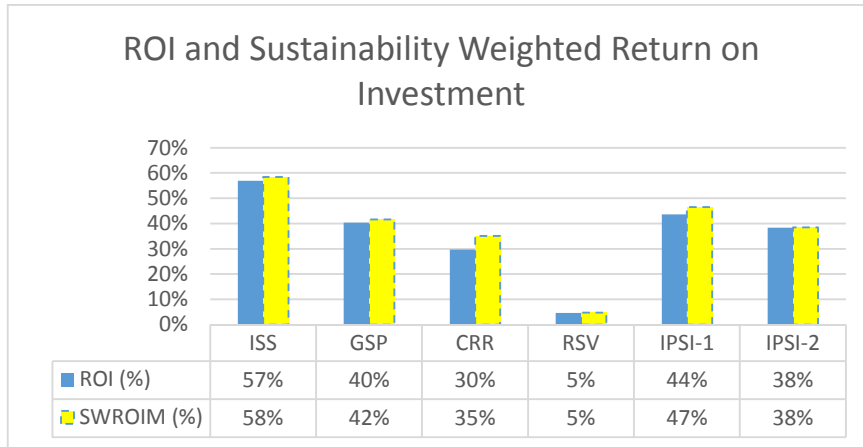


Figure 3 ROI and SWROIM for all NGL configurations.

4. Conclusions

The new sustainability metric was applied on different NGL recovery configurations. When considering only the economic factors and profitability criteria, IPSI-1 showed to be the most attractive configuration with 44 % as the highest ROI % next to ISS configuration. However, after incorporating the sustainability aspect, some configurations showed to be promising with 3, 2, 5 %, a higher incremental in SWROIM % analysis in comparison to profitability analysis in the case of GSP, IPSI-1, and CRR configurations, respectively for 0.3 for carbon emission relative importance. For a higher ratio as carbon emission relative importance such as 0.45, IPSI-2 showed a higher incremental percentage in SWROIM analysis to 48 % next to ISS with 69 %.

References

- Ahmed AlNouss, Mohamed Ibrahim, Saad A. Al-Sobhi, (2017). Potential energy savings and greenhouse gases (GHGs) emissions reduction strategy in natural gas liquid (NGL) recovery: process simulation and economic evaluation (submitted)
- Batterham, (2006). Sustainability-The next chapter. Chemical Engineering Science. Volume 61, 13, 4188-4193
- El-Halwagi, M.M., (2017). A return on investment metric for incorporating sustainability in process integration and improvement projects. Clean Technologies and Environmental Policy. 19, 611-617.

Identification of Mass Flow Dynamics in a Pretreatment Continuous Tubular Reactor

Ismael Jaramillo^{a*} and Arturo Sanchez^a

^aLaboratorio de Futuros en Bioenergía

Centro de Investigación y de Estudios Avanzados del IPN Unidad Guadalajara (CINVESTAV)

Av. del Bosque #1145, Zapopan, CP 45019, Jalisco, México

ijaramillo@gdl.cinvestav.mx

Abstract

Pretreatment is one of the most important stages for producing advanced bioethanol and bioproducts from lignocellulosic biomass in biochemical-platform biorefineries. Continuous pretreatment using tubular reactors is gaining importance at industrial scale. Mass flow represents a crucial variable to accurately predict pretreatment yields. In order to study realistic flow dynamics, a pilot-scale continuous tubular reactor was designed and built. In this work, a discrete-time surrogate model for the mass flow dynamics is presented. Flow data was carefully acquired for two types of biomass. The model accurately predicts the experimental data.

Keywords: mass flow, residence time, pretreatment, discrete-time modelling, lignocellulosic biomass

1. Introduction

Lignocellulosic biomass (LB) is currently considered as an important material source worldwide and is used for the bioethanol, bioproducts, power and heat production processes (Gupta and Verma, 2015). The bioethanol production process consists on four stages: pretreatment, enzymatic hydrolysis, sugar fermentation and product recovery (Saini et al., 2015). The pretreatment is considered as one of the most challenging stages and its task is to destroy the cellulose lignin matrix to reduce cellulose crystallinity and increase the fraction of amorphous cellulose as shown in Figure 1.

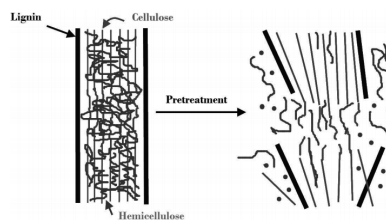


Figure 1: Pretreatment effect over LB (Mosier et al., 2005).

There are several technologies to carry out the pretreatment process depending on the LB's properties. Autohydrolysis has become popular due to its low environmental impact and has been widely

studied to find its optimal operation conditions (Kim et al., 2001; Shekiri III et al., 2014). One of the key variables for predicting autohydrolysis yields using kinetic models (Sidiras et al., 2011) is the mass flow output. According to Roberts (1999), the mass flow output is affected by geometric features of the continuous tubular reactor (CTR), transport phenomena such as backmixing flow or bulk sticking (Nachenius et al., 2015) and the LB's mechanical properties. Several authors have reported different approaches to identify the mass flow inside CTRs. Wan and Hanley (2004) presented a flow pattern prediction method to depict LB behavior inside the CTR. Owen and Cleary (2009) simulated the particles dynamics within the CTR by the discrete element method. In general, these two approaches use LB parameters that are either not reported in the literature or very difficult to measure in a CTR.

2. Equipment Description

The pilot-scale pretreatment CTR of the Energy Futures Laboratory of CINVESTAV Guadalajara served as a platform for carrying out the identification experiments using two biomass types with different physical properties: wheat straw (WS) and corn stover (CS). The CTR schematic diagram is shown in Figure 2. The main equipment parts involved in the pretreatment process are labeled with circled numbers and referenced in Table 1. The CTR task is divided into three phases, each one performing a different type of pretreatment: extrusion (parts 1, 2 and 3), autohydrolysis (parts 4, 5 and 6) and steam explosion (parts 7 and 8).

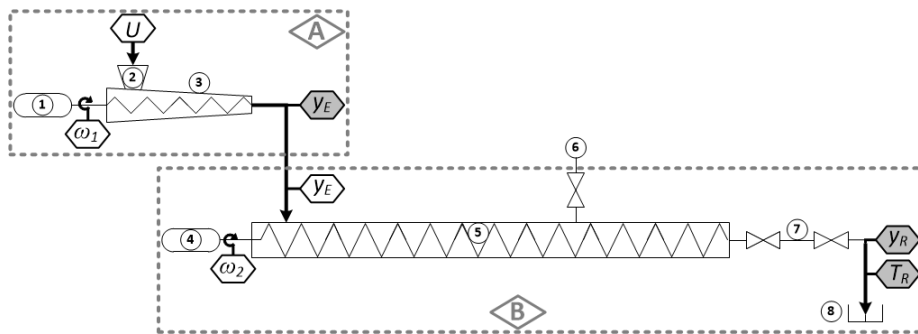


Figure 2: CTR schematic diagram.

Table 1: Process components from Figure 2.

ID	Device
1	Extruder screw
2	Hopper
3	Extruder's body
4	Screw conveyor
5	CTR body
6	Steam input
7	Discharge valves
8	Discharge box

LB was grinded and soaked before each experiment to improve the mechanical properties of the particles. The prepared LB was fed (by hand) through the hopper into the extruder's body. Flow input data U was acquired by measuring the time it takes to feed a fixed amount of biomass.

The extruder screw conveys and compresses the LB inside the extruder's body as it rotates at a fixed speed ω_1 . The LB filling time is termed cone filling delay (CFD) and represents the delay between LB input and output from the extruder. The extrusion phase aim is to create a dense biomass body in the CTR input to avoid steam from escaping the CTR. Extruder mass output y_E enters the CTR body directly. Once inside, it is transported by the rotation of the screw conveyor at a fixed speed ω_2 which determines the LB residence time (RT) T_R . Finally, LB reaches the discharge point where the discharge valves execute a predefined sequence of opening and closing with a fixed time interval so the biomass is expelled to the receiver box by the pressure difference between the CTR interior and the environment (steam explosion). Mass flow output samples y_R were collected, weighed and registered with a constant sample time T_s . Input and output LB moisture was measured at fixed time intervals.

3. System modelling

Identification runs were carried out and analyzed off-line. Experiments were executed first for the extrusion phase only. Then, experiments were carried out in the complete CTR (three phases) and consisted on registering the system response to an impulse feed of tracer (variables shown in Figure 2). Extrusion and reaction phases were modelled with discrete-time equations due to the sampling procedure according to the areas A and B shown Figure 2, respectively. The light and dark hexagonal blocks represent the corresponding input and output variables, respectively.

The extrusion model was proposed as a second order overdamped discrete transfer function as shown in Eq. (1). Additionally, the CFD phenomenon was considered by including a gain K_1 in the system's output Eq. (2) which depends on the total LB fed $\sum_0^k U(k)$ and the extruder's mass capacity C_e . For the reaction phase model, the CTR body was modelled as a series of n identical continuous stirred tank reactors (CSTR) (Fogler et al., 1999), with $n = 14$ due to the mechanical and geometric CTR characteristics as seen in Figure 3. Each CSTR (i.e. subreactor) mass flow output x_{iR} was modelled as a first order discrete transfer function described by Eqs. (3). The extruder output y_E is the first CSTR input, the first CSTR output x_{1R} is the second CSTR input, and so on. The output of the 14th CSTR x_{14R} is the system output y_R shown in Eq. (4). The total T_R is also divided in 14 equal CSTR delays δ_2 as seen in Eq. (5).

$$x_E(k+1) = \theta_1 x_E(k) - \theta_2 x_E(k-1) + \theta_3 U(k) - \theta_4 U(k-1) \quad (1)$$

$$y_E(k) = K_1(k) x_E(k) \quad (2)$$

$$x_{1R}(k+1) = \theta_5 x_{1R}(k) + \theta_6 y_E(k - \delta_2)$$

$$x_{2R}(k+1) = \theta_5 x_{2R}(k) + \theta_6 x_{1R}(k - \delta_2)$$

$$\vdots$$

$$x_{14R}(k+1) = \theta_5 x_{14R}(k) + \theta_6 x_{13R}(k - \delta_2) \quad (3)$$

$$y_R(k) = x_{14R}(k) \quad (4)$$

$$T_R(k) = \delta_2(k-14) + \delta_2(k-13) + \dots + \delta_2(k-1) \quad (5)$$

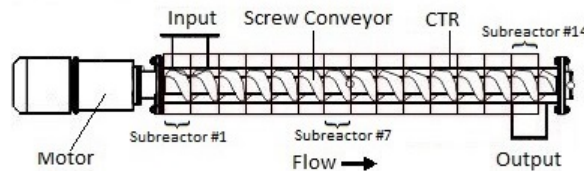


Figure 3: CTR body analysis.

Model parameters θ_1 , θ_2 , θ_3 and θ_4 depend on T_s as well as the damping ζ and natural frequency ω_n of the extrusion phase system, while θ_5 and θ_6 are explicit functions of T_s and the reaction phase time constant τ_2 . Expressions for the model parameters θ_i and gain K_1 are given in Appendix A. All parameters were estimated with a PSO algorithm (Liu et al., 2008) to reduce the mean squared error between real data and the model output. For the extrusion model the PSO algorithm was utilized to find the values of ω_n corresponding to a fixed $\zeta = 1.001$ (overdamped) so the system poles produced an output that reproduced experimental results for both LB (WS and CS) as shown in Figure 4. The CTR parameter estimation was divided in two tasks: first, a) parameters ω_{n2} and ζ_2 from an approximation function $\hat{x} = f(\omega_{n2}, \zeta_2, T_s)$ similar to Eq. (1) (second order overdamped transfer function) were estimated to fit the identification experimental data (Figure 5a). Then, b) the 14 τ_2 and δ_2 parameters in Eqs. (3) were estimated to fit the \hat{x} behavior (Figure 5b).

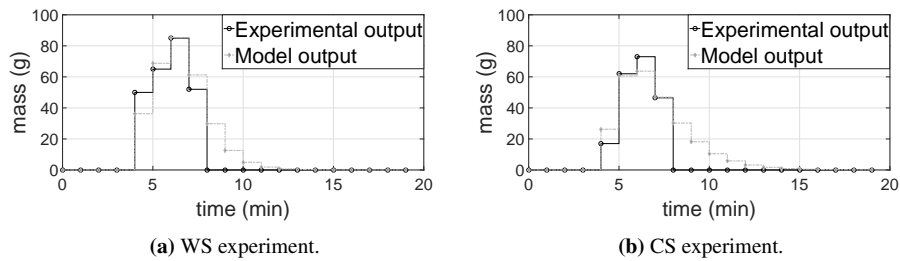


Figure 4: Extrusion phase tracer experiments predictions.

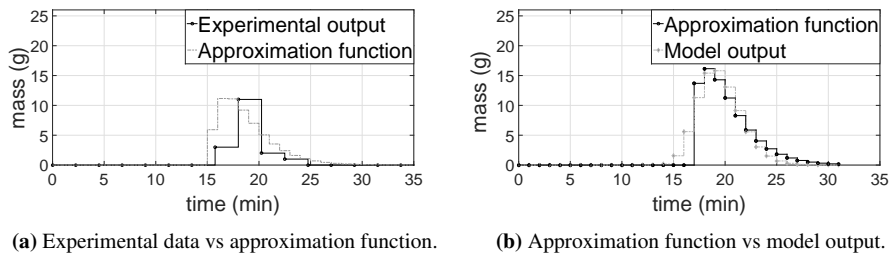


Figure 5: Reaction phase tracer experiment approximation and modelling.

4. Validation results

Figures 6 and 7 show: a) the acquired input signal and b) the comparison between experimental output data and the model output for two typical experiments using WS and CS, respectively. The error signal was analyzed with the method proposed by Zekki et al. (1999), which led to the conclusion that the model is adequate to reproduce experimental behavior in steady conditions.

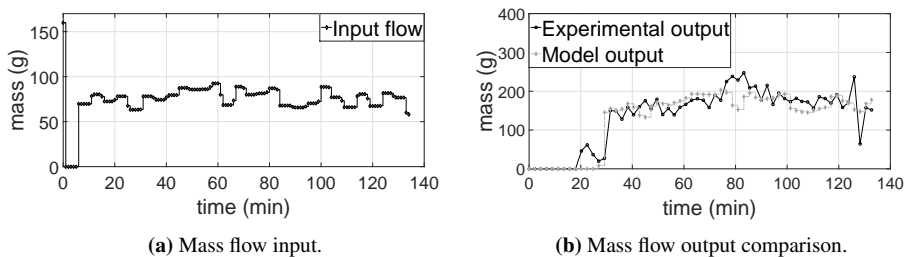


Figure 6: WS experiment.

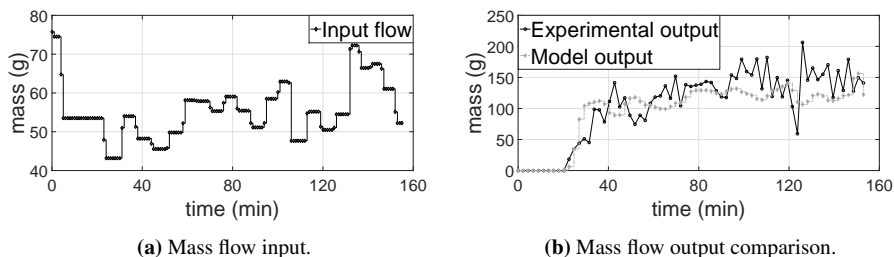


Figure 7: CS experiment.

5. Conclusion

Mass transport inside a CTR is a difficult phenomenon to describe. The identification experiments in a pilot-scale CTR showed that an important variable for mass flow prediction is the input flow. This input flow directly affects the extruder and CTR mass flow output and defines its erratic behavior in steady state conditions. The accurate acquisition of LB input flow allowed to reproduce the mass flow dynamics correctly. Different behaviors occurred for each LB when subjected to the extrusion phase only, but similarities were observed when both LB were subjected to the complete pretreatment conditions (high pressure and temperature). The modeling approach and experimental validation resulted in a set of equations that allow to predict the mass flow in the CTR explicitly. Future work will focus on the effects of different conditions of ω_2 over the mass flow and RT.

6. Acknowledgements

Financial support is kindly acknowledged from the Energy Sustainability Fund 2014-05 (CONACYT-SENER, Mexico) Grants 245750 and 249564 (Mexican Bioenergy Innovation Center, Bioalcohols Cluster). I.J. acknowledges financial support from CONACYT, Mexico in the form of MSc scholarship number 589640.

References

- H. S. Fogler, et al., 1999. Elements of Chemical Reaction Engineering. Prentice-Hall International London.
- A. Gupta, J. P. Verma, 2015. Sustainable bio-ethanol production from agro-residues: a review. *Renewable and Sustainable Energy Reviews* 41, 550–567.
- K. H. Kim, M. P. Tucker, F. A. Keller, A. Aden, Q. A. Nguyen, 2001. Continuous countercurrent extraction of hemicellulose from pretreated wood residues. *Applied Biochemistry and Biotechnology* 91 (1), 253–267.
- L. Liu, W. Liu, D. A. Cartes, 2008. Particle swarm optimization-based parameter identification applied to permanent magnet synchronous motors. *Engineering Applications of Artificial Intelligence* 21 (7), 1092–1100.

- N. Mosier, C. Wyman, B. Dale, R. Elander, Y. Lee, M. Holtzapple, M. Ladisch, 2005. Features of promising technologies for pretreatment of lignocellulosic biomass. *Bioresource Technology* 96 (6), 673–686.
- R. Nachenius, T. Van De Wardt, F. Ronsse, W. Prins, 2015. Residence time distributions of coarse biomass particles in a screw conveyor reactor. *Fuel Processing Technology* 130, 87–95.
- P. Owen, P. Cleary, 2009. Prediction of screw conveyor performance using the discrete element method (dem). *Powder Technology* 193 (3), 274–288.
- C. L. Phillips, H. T. Nagle, 2007. *Digital Control System Analysis and Design*. Prentice Hall Press.
- A. Roberts, 1999. The influence of granular vortex motion on the volumetric performance of enclosed screw conveyors. *Powder Technology* 104 (1), 56–67.
- J. K. Saini, R. Saini, L. Tewari, 2015. Lignocellulosic agriculture wastes as biomass feedstocks for second-generation bioethanol production: concepts and recent developments. *3 Biotech* 5 (4), 337–353.
- J. Shekro III, E. M. Kuhn, N. J. Nagle, M. P. Tucker, R. T. Elander, D. J. Schell, 2014. Characterization of pilot-scale dilute acid pretreatment performance using deacetylated corn stover. *Biotechnology for Biofuels* 7 (1), 23.
- D. Sidiras, F. Batzias, R. Ranjan, M. Tsapatsis, 2011. Simulation and optimization of batch autohydrolysis of wheat straw to monosaccharides and oligosaccharides. *Bioresource Technology* 102 (22), 10486–10492.
- Y. Wan, T. R. Hanley, 2004. Computational fluid dynamics simulation and redesign of a screw conveyor reactor. In: *Proceedings of the Twenty-Fifth Symposium on Biotechnology for Fuels and Chemicals Held May 4–7, 2003*, in Breckenridge, CO. Springer, pp. 733–745.
- H. Zekki, C. Gary, A. Gosselin, L. Gauthier, 1999. Validation of a photosynthesis model through the use of the co 2 balance of a greenhouse tomato canopy. *Annals of Botany* 84 (5), 591–598.

Appendix A

Expressions (6)–(15) were obtained from the Z-transform table (Phillips and Nagle, 2007) when discretizing with the zero order holder method. Parameter τ_2 in Eqs. (10)–(11) and, ζ and ω_n in Eqs. (12)–(15) were estimated by using 100 particles and 1000 iterations within the PSO algorithm. Gain K_1 shown in Eq. (16) was experimentally proposed as a sigmoid function to emulate the CFD influence over the extruder output. Raising parameter m was set to 0.2 for both LB.

$$\theta_1 = e^{T_s r_1} + e^{T_s r_2} \quad (6)$$

$$\theta_2 = e^{T_s (r_1 + r_2)} \quad (7)$$

$$\theta_3 = (r_3/r_1) (1 - e^{T_s r_1}) + (r_4/r_2) (1 - e^{T_s r_2}) \quad (8)$$

$$\theta_4 = (r_3/r_1) (1 - e^{T_s r_1}) (e^{T_s r_2}) + (r_4/r_2) (1 - e^{T_s r_2}) (e^{T_s r_1}) \quad (9)$$

$$\theta_5 = e^{-T_s/\tau_2} \quad (10)$$

$$\theta_6 = 1 - e^{-T_s/\tau_2} \quad (11)$$

$$r_1 = -\zeta \omega_n + \sqrt{\zeta^2 \omega_n^2 - \omega_n^2} \quad (12)$$

$$r_2 = -\zeta \omega_n - \sqrt{\zeta^2 \omega_n^2 - \omega_n^2} \quad (13)$$

$$r_4 = \omega_n^2 / (r_1 - r_2) \quad (14)$$

$$r_3 = -r_4 \quad (15)$$

$$K_1(k) = 1 / (1 + e^{-m(\sum_0^k U(k) - C_c)}) \quad (16)$$

Exploiting meta-modeling approach to investigate the effect of oil characteristics on the optimal operating conditions and biodiesel properties

P. Chhabra^a, L. Zhou^a, I. A. Karimi^{a,*} and M. Kraft^{b,c}

^a*Department of Chemical & Biomolecular Engineering, National University of Singapore, 4 Engineering Drive 4, Singapore 117576, Singapore*

^b*Department of Chemical Engineering & Biotechnology, Philippa Fawcett Drive, Cambridge, CB3 0AS, UK*

^c*School of Chemical & Biomedical Engineering, 62 Nanyang Dr, Singapore 637459
cheiak@nus.edu.sg*

Abstract

We investigate the influence of the biodiesel feedstock on the optimal operating conditions of the reactor and the properties of biodiesel produced at those conditions. To this end, we employ a generalized kinetic model to find optimal operating conditions for 4,500 different blends of six major oils *viz.*, Jatropha, Linseed, Olive, Palm, Rapeseed, and Sunflower oil. We then develop meta-models with the characteristics of the different feedstocks as input variables and the solution of the optimization problems as the output variables. We employ Regression tree ensembles in MATLAB to develop these meta-models. Finally, we use these meta-models for predicting the various properties of biodiesel to find the best blend of the considered oils in order to obtain the premium quality biodiesel as per both European (EN 14214) and American (ASTM D6751) standard specifications. We evaluate the weight distribution of these blends for a variety of scenarios. We observe that the optimal oil blend may vary a lot depending on the specifications we impose, thereby emphasizing the significance of such a study in our efforts to bridge the gap between academic research and commercialization of biodiesel.

Keywords: Biodiesel, Feedstock, Kinetics, Meta-model, Optimization

1. Introduction

The hunt for an assortment of energy sources is just about as old as humanity's need for energy. This search has been escalated by an expanding industrialization since the 19th century. The internal combustion engine is a prime example. Even though fuels obtained from fossil sources have been a prime choice since the onset of these engines, biofuels specially biodiesel have also found some interest. This interest has particularly gained momentum in the past few decades due to rapidly increasing energy demand and depletion in fossil fuel resources.

Biodiesel is a non-toxic, biodegradable, and environmentally benign fuel that can be used in diesel engines. The most commonly used method for the production of biodiesel is transesterification. It involves the reaction of the oil with an alcohol in the presence of a catalyst to form fatty acid alkyl ester (biodiesel) and glycerol. Although biodiesel is a promising alternative fuel, its production poses significant challenges due to its higher production costs compared to the petroleum-based diesel. Therefore, it becomes crucial to model and optimize the biodiesel production process to lower costs while meeting the desired property specifications.

The literature is replete with the studies about modelling and optimization of transesterification (Singh et al. (2008); Yang et al. (2016)). It is generally believed that reaction temperature, catalyst concentration, alcohol to oil molar ratio, and reaction time are the significant factors that impact the yield. Recently, statistical methods such as response surface methodology (RSM) (Pinzi et al. (2011b)), Taguchi method (Kumar et al. (2015)), *etc.* have been employed to optimize these factors and study their interactions. However, there is a notable divergence in the optimization results reported in the literature. This further leads to uncertainties in properties of the biodiesel produced at those conditions, thereby making these results unreliable. All this is primarily due to substantial variation in the composition of biodiesel feedstock. Although, a few comparative studies have been reported in the literature, all of them focus on static optimization, thereby neglecting the kinetics of biodiesel production.

The purpose of this study is to investigate the influence of the chosen biodiesel feedstock on the optimal operating conditions of the reactor and the quality of biodiesel. To this end, we use a generalized kinetic model in order to find those optimal conditions with 4,500 different blends of six major oils *viz.*, Jatropha, Linseed, Olive, Palm, Rapeseed, and Sunflower oil as feedstock. We employ three different objective functions to solve these optimization problems. We then develop meta-models with the solutions of these optimization problems as output variables and the characteristics of the feedstocks as the input variables. Finally, we employ these meta-models to identify the best possible blend of the considered oils which is required to obtain the premium quality biodiesel. Overall, the objectives of the current study are as follows,

1. Find optimal operating conditions of the reactor for biodiesel production using different vegetable oils as feedstock.
2. Develop meta-models outlining the effect of different vegetable oils/their blends on the optimal operating conditions of the reactor.
3. Develop meta-models depicting the effect of the different vegetable oils/their blends on the properties of the biodiesel produced using these feedstocks.
4. Use the developed meta-models to find the best possible blend.

The outline of the paper is as follows. In Section 2, we explain the details regarding the kinetic model employed in this study and also provide a brief account of the approximation technique *i.e.* Regression trees ensembles. We explain the methodology adopted for the current study in Section 3. We discuss the results in Section 4. Finally, we present our conclusions in Section 5.

2. Theoretical Background

2.1. Kinetic Model Description

A huge variety of vegetable oils can be used to produce biodiesel. However, most oils consist of 95 - 98 % of triglycerides (TG) with traces of diglycerides (DG), monoglycerides (MG), water, and free fatty acids (FFA). A triglyceride is an ester formed from one molecule of glycerol and three fatty acids. Considering the large variety of fatty acids, these can lead to the formation of a wide range of triglycerides. In our previous study (Chhabra et al. (2017)), we developed a generalized kinetic model based on the reaction scheme of all the glycerides formed by the combination of the five most common fatty acids present in oils *i.e.* oleic, linoleic, linolenic, palmitic, and stearic. Since any vegetable oil can be represented by an arbitrary mixture of these glycerides, our model can be adopted to investigate the product distribution with a vast variety of vegetable oils as feedstocks. We have validated our model for a variety of experimental datasets from the literature. In this study, we employ it to find the optimal operating conditions of

the reactor along with the properties of biodiesel developed at those conditions. The correlations employed to calculate the properties based on the distribution of various ester components in biodiesel have been taken from Pinzi et al. (2011b).

2.2. Regression tree ensembles

The idea of simple regression as a way of making quantitative predictions is well known. In simple regression, a dependent variable, \hat{y} is modeled as a function of multiple independent variables, $x_1, x_2, x_3, \dots, x_N$, where ε is a random noise,

$$\hat{y} = \beta_0 + \beta^T x + \gamma x x^T + \varepsilon \quad (1)$$

However, the number of parameters increases exponentially with increasing number of independent variables. Furthermore, strong nonlinearities among the independent variables enhance the complexity of the problem. Simple regression involves a single predictive formula that holds over the entire data-space. However, in case of large number of independent variables which interact in complex non-linear ways, assimilating a global model can be strenuous. Therefore, an alternative approach is to partition the entire space into small regions, where the interactions are easier to comprehend. The partitioning is continued till we reach a space where we can fit simple models to them. The regression tree ensembles, which are a variant of the decision trees, are based on this principle. There are several advantages associated with them, *i.e.*, the predictions are faster, it is easier to understand which variables are important (by simply looking at the tree structure), and there exist reliable algorithms to implement them. One may refer to Breiman et al. (1984) for a detailed discussion on the same.

3. Methodology

As stated earlier, our aim is to develop meta-models that can help us to comprehend the effect of the feedstock on a) the optimal operating conditions of the reactor, and b) the quality of biodiesel produced at those conditions. To this end, we have employed a three step methodology (as shown in Figure 1). We start with the collection of data to develop these meta-models. In order to achieve that, we solve an optimization problem for a blend from a pool of 4500 blends. This amounts to total 4500 optimization problems. As mentioned in Section 2.1, we employ the generalized kinetic model for performing the optimization. We chose three different objective functions to solve the optimization problems *i.e.* maximization of biodiesel yield, minimization of a property based

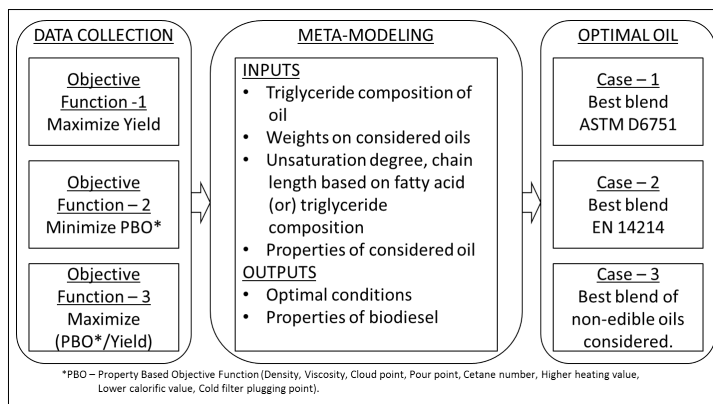


Figure 1: Adopted Framework for the current study.

objective function (considering density, viscosity, cold point, pour point, cetane number, higher heating value, lower calorific value, and cold filter plugging point), and a combination of the two, which is to minimize the ratio of the property based objective function and the yield. We solve each optimization problem by using the "fmincon" function in MATLAB. The computational time for each optimization problem is approximately 100 seconds. We use multiple MATLAB sessions to enhance the computation speed. The decision variables are reaction temperature (293.15 K to 343.15 K), catalyst concentration based on oil (0.2 wt.% to 2.0 wt.%), alcohol to oil molar ratio (2 to 12), and reaction time (2 minutes to 120 minutes). The bounds on the variables are chosen based on the results reported in the literature for optimization of base catalyzed transesterification over the past decade.

Once we obtain the solutions of these optimization problems we move to the second step, which is to develop the meta-models that can predict the effect of a feedstock on the operating conditions of the reactor and the quality of biodiesel obtained using that feedstock. The solution of the optimization problems refer to the set of dependent variables. For the set of independent variables, we need to characterize the feedstock in order to observe their effect on the set of dependent variables. In the past this has been done using the average chain length and the unsaturation degree of the fatty acids that constitute the oil (Giakoumis (2013)). Hence, we use this as one approach to characterize the feedstock. Additionally, we propose four different approaches to achieve the same *viz.* a) triglyceride composition (number of dimensions (N) = 34), b) average chain length, weighted unsaturation degree calculated based on the triglyceride composition of oil (N = 2) c) weights on the considered oils for the different blends (N = 6), and d) properties of oils, *i.e.* viscosity, density, heat capacity, enthalpy of vaporization, and vapor pressure calculated based on the triglyceride composition of oil (Zong et al. (2009)) (N = 5). We develop meta-models for each set of input-output pair and compare the performance on the basis of a normalized error metric, primarily the ratio of the percentage average absolute error in approach "i" to the minimum of the percentage average absolute error. The meta-models are developed using regression tree ensembles in MATLAB R2016b.

Finally, we employ the meta-models developed for predicting the properties of biodiesel to find the best possible blend (or) biodiesel feedstock that can provide the premium quality biodiesel *i.e.* it meets the standard specifications as stated by both Europe (EN 14214) and the United States of America (ASTM D6751).

4. Results & Discussions

The meta-models are as good as the data used to develop them. Therefore, in this study, we ensure that we examine the feedstock composition space as uniformly as possible. In order to achieve this, we consider a significantly high number (4500) of vegetable oil blends for collecting the data. Furthermore, as stated above, we choose three different objective functions for solving the optimization problems with the vegetable oil blends as feedstock. We observe that in the case of maximization of biodiesel yield (Objective Function - 1), the cold flow properties, specifically the Cold point and Pour point of biodiesel calculated at the obtained set of optimal conditions are very different from the standard specification of most of the countries. Similar problems persist in the case of minimization of the ratio of yield to property based objective function (Objective Function - 3). However, in the case of just the property based objective function (Objective Function - 2) we observe that even though the biodiesel yield drops for some of the considered blends, there is a notable improvement in the cold flow properties of the final product. Since the cold flow properties play a vital role in deciding the quality of biodiesel, we adopt the data generated by the latter case for developing the required meta-models.

Once we collect the set of output variables, our next task is to characterize the feedstock in order to obtain the set of input variables. As we discussed in Section 3, we employ five different ways to

Table 1: Error metric comparing the performance of different feedstock characterization approaches(A,B,C,D: Proposed in this study; E: From past studies in the literature).

Response	PAAE = $\frac{AAE}{AR} \times 100$				
	A	B	C	D	E
Reaction temperature, T (K)	1.74	2.14	1.71	2.05	2.12
Density, ρ (g/cc)	0.03	0.08	0.06	0.04	0.09
Viscosity, μ (mm ² /s)	0.91	1.88	0.97	1.46	2.40
Cloud point, CP (K)	0.40	0.74	0.46	0.65	0.74
Pour point, PP (K)	0.46	0.83	0.55	0.73	0.84
Cetane number, CN	0.96	1.82	1.08	1.42	2.55
Higher heating value, HHV (MJ/kg)	0.06	0.14	0.07	0.11	0.17
Lower calorific value, LCV (MJ/kg)	0.06	0.12	0.07	0.10	0.14
Cold filter plugging point, CFPP (K)	0.21	0.43	0.24	0.35	0.53

Table 2: Weight fraction of different oils in the optimal blend.

	Jatropha	Linseed	Olive	Palm	Rapeseed	Sunflower
Case-1	0.0454	0.0159	0.0851	0.6442	0.0115	0.1979
Case-2	0.2074	0.0462	0.0939	0.0828	0.4620	0.1077
Case-3	0.9059	0.0941	0.00	0.00	0.00	0.00

characterize the feedstock (or) Vegetable oil blends. We split the data into two parts, whereby 70% of the data is used for training, while the remaining 30% of it is used for validation of the model. Table 1 shows the percentage average absolute error (PAAE) for the optimal operating conditions and the biodiesel properties.

$$PAAE = \frac{\text{Average Absolute Error (AAE)}}{\text{Average Response (AR)}} \times 100 \quad (2)$$

where $AAE = \frac{1}{1350} \left(\sum_i |y_i - \hat{y}_i| \right)$ and $AR = \frac{1}{1350} \left(\sum_i y_i \right)$. We observe a minimum error of 1.74% in the prediction of reaction temperature. However, no strong correlation was observed for the set of other operating conditions *i.e.* catalyst concentration, alcohol to oil ratio, and reaction time. This may be because the reaction temperature is more significant than any of the other three decision variables. This is in accord with the findings reported in the past (Pinzi et al. (2011a)). We notice a sound agreement between the predictions made by the original model and the meta-models developed for predicting the biodiesel properties (Table 1), which is an excellent result.

Finally, we employ the meta-models developed for predicting the properties of biodiesel to find the optimal blend of the considered vegetable oils in order to produce the premium quality biodiesel. We achieve this optimization using genetic algorithm. The objective is to minimize the property based objective function. The decision variables are the weights on the considered oils. We evaluate the optimal weight distribution for three different scenarios. In the first case, we identify the optimal oil blend needed to produce biodiesel that satisfies the less stringent American specifications (ASTM D6751). In the second case, we identify the optimal oil blend required to produce biodiesel that satisfies the more stringent European specifications. Finally, since there has been lot of opposition against the use of edible oils for the production of biodiesel, we evaluated a scenario where we assume the non-availability of the edible oils. Hence, we aim to determine an optimal blend of Linseed and Jatropha oils in order to produce biodiesel that would meet both American and European specifications. Table 2 shows the optimal distribution of weights whereas Table 3 lists the property values of biodiesel produced using the suggested blends. We observe that the optimal blend obtained for the first case contains around 64% palm oil. Since the biodiesel formed

Table 3: Properties of biodiesel produced using the optimal blends as feedstock.

	ρ (g/cc)	μ (mm ² /s)	CP (K)	PP (K)	CN	HHV (MJ/kg)	LCV (MJ/kg)	CFPP (K)
Case-1	0.87	5.52	273.52	266.38	67.10	42.40	37.66	279.91
Case-2	0.88	5.00	271.24	264.36	58.54	42.08	37.54	271.43
Case-3	0.88	5.00	270.61	263.41	58.24	42.08	37.54	271.46

using palm oil has higher cetane number, the same is reflected in the properties of biodiesel produced using the first blend. However, since the viscosity of biodiesel formed using palm oil is comparatively higher, it fails to meet the specification imposed by EN 14214 (3.5 to 5.0 mm²/s). Therefore as we impose tighter constraints as in Case-2, we record a sharp decrease in the amount of palm oil suggested in the optimal blend, thereby leading to a marked reduction in the Cetane number as well. As per the results of Case-3, the properties of biodiesel are quite similar to the properties of biodiesel obtained using the blend for Case-2. This suggests that it is possible to produce premium quality biodiesel even without the consumption of edible oils. This will definitely bolster the efforts for commercialization of biodiesel production as the use of non-edible oils can significantly reduce the costs associated with the biodiesel production process.

5. Conclusions

In this study, we develop meta-models describing the effect of the characteristics of different feedstock on the optimal operating conditions of the biodiesel reactor and the quality of biodiesel produced at those conditions. We also demonstrate the application of these meta-models in finding an ideal feedstock for the production of premium quality biodiesel and evaluated the solution for a variety of pragmatic scenarios.

6. Acknowledgements

This project is funded by the National Research Foundation (NRF), Prime Ministers Office, Singapore under its Campus for Research Excellence and Technological Enterprise (CREATE) programme.

References

- L. Breiman, J. Friedman, C. J. Stone, R. A. Olshen, 1984. Classification and regression trees. CRC press.
- P. Chhabra, S. Mosbach, M. Kraft, I. A. Karimi, 2017. A generalized kinetic model for transesterification and saponification. URL <https://aiche.confex.com/aiche/2017/meetingapp.cgi/Paper/500597>
- E. G. Giakoumis, 2013. A statistical investigation of biodiesel physical and chemical properties, and their correlation with the degree of unsaturation. Renewable Energy 50, 858–878.
- R. S. Kumar, K. Sureshkumar, R. Velraj, 2015. Optimization of biodiesel production from manilkara zapota (L.) seed oil using taguchi method. Fuel 140, 90–96.
- S. Pinzi, L. Gandia, G. Arzamendi, J. Ruiz, M. Dorado, 2011a. Influence of vegetable oils fatty acid composition on reaction temperature and glycerides conversion to biodiesel during transesterification. Bioresource technology 102 (2), 1044–1050.
- S. Pinzi, D. Leiva, G. Arzamendi, L. Gandia, M. Dorado, 2011b. Multiple response optimization of vegetable oils fatty acid composition to improve biodiesel physical properties. Bioresource technology 102 (15), 7280–7288.
- V. Singh, K. Solanki, M. N. Gupta, 2008. Process optimization for biodiesel production. Recent patents on biotechnology 2 (2), 130–143.
- J. Yang, T. Astatkie, Q. S. He, 2016. A comparative study on the effect of unsaturation degree of camelina and canola oils on the optimization of bio-diesel production. Energy Reports 2, 211–217.
- L. Zong, S. Ramanathan, C.-C. Chen, 2009. Fragment-based approach for estimating thermophysical properties of fats and vegetable oils for modeling biodiesel production processes. Industrial & engineering chemistry research 49 (2), 876–886.

Mixed-integer multiparametric Metamodeling: A machine learning tool applied to reactive scheduling

Gicela Lupera^a, Ahmed Shokry^a, Georgios M. Kopanos^b, Antonio Espuña^{a,*}

^a*Center for Process and Environmental Engineering-CEPIMA, Av. Eduard Maristany
16, Barcelona 08019, Spain*

^b*Cranfield University, School of Water, Energy and Environment, Bedfordshire
MK430AL, United Kingdom*

antonio.espuna@upc.edu

Abstract

Reactive Scheduling is a dynamic and stochastic process, where changing circumstances continually force the reconsideration and revision of pre-established plans. The use of rolling horizon frameworks to exploit multiparametric programming techniques has been proposed, in which the optimal decisions are obtained as simple explicit functions of the uncertainty parameters, thus avoiding the need for repetitive solving the optimization problem. However, the main limitation of the proposed method is the increasing computational burden for solving big multiparametric programming problems (e.g., problems with many state variables and/or long prediction horizons). Recently the mixed-integer multiparametric approach based on machine learning has been proposed to solve optimization problems in a faster way. The objective of this work is to investigate the extension of mixed-integer multiparametric technique based in machine learning to deal with both uncertainties and optimal solutions with discrete behaviour and show its application to reactive scheduling problem with bounded uncertainty parameters. The results showed that the proposed methodology is capable of obtaining high accurate estimated optimal solutions, reducing the complexity of the solution procedure and scaling down the computational burden.

Keywords: Reactive Scheduling, Metamodel, Machine Learning.

1. Introduction

In highly dynamic production environments, Reactive Scheduling (RS) seeks to update production decisions in order to improve the profitability through the quick reaction to unexpected events or changes. Therefore, it is very important to consider how uncertainty is coupled with the scheduling process, since many of the parameters that are associated with the scheduling (demand, prices, machine reliability) vary with respect to time and are often subject to unexpected deviations (Li & Ierapetritou, 2007).

The Rolling Horizon (RH) method is commonly used to address RS problems: the involved optimization problem is solved sequentially over successive time intervals, in order to find the optimal decisions to be applied considering the uncertainty that may affect the system over this specific time interval. Recently Kopanos and Pistikopoulos, (2014) have introduced a multiparametric programming Rolling Horizon framework

(mp-RH) for the reactive scheduling problem of systems involving Uncertain Parameters (θ s), considering the θ s space divided by critical regions. Moreover, the Meta-Multiparametric (M-MP) approach has been proposed by (Shokry and Espuña, 2015) in order to solve optimization problems subjected to θ s in much simpler way. Recently, (Lupera, Shokry, Medina-González, Vyhmeister, & Espuña, 2018) have successfully proposed a mixed-integer multiparametric Metamodel (mi-mpM) technique based on machine learning techniques in order to handle general mixed integer optimization problems involving θ s. The objective of this work is to investigate the extension of mi-mpM technique to deal with both θ s and optimal solutions with discrete behaviour.

The rest of the paper will first revise the steps of proposed methodology, and then illustrate its application details to a reactive scheduling problem of a network of combined heat and power units. Then the discussion of the results will be addressed, to end with some concluding remarks.

2. Methodology

Taking in account a system that would involve discrete behaviour of some bounded θ s and the possible existence of mixed integer optimal solutions, the mi-mpM technique based on machine learning is proposed, Figure 1. A detail of the development of this methodology can be found in (Lupera et al., 2018).

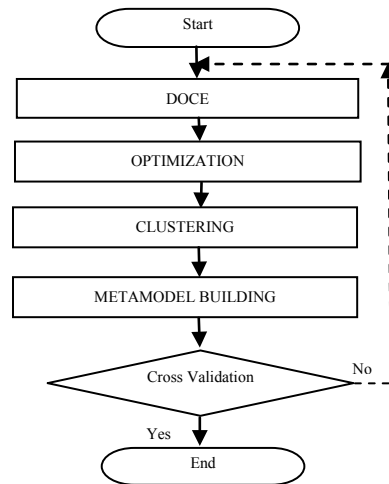


Figure 1. mi-mpM technique flowchart based in Machine Learning

Design of Computer Experiments (DOCE), is an important aspect to be considered when applying mi-mpM, in order to generate N combinations of θ s values. The designs should provide information about all portions of the experimental region. After analyzing several techniques like: Latin Hypercube, Hammersley sequencing, Monte Carlo, Full factorial design. A hybrid technique of Monte Carlo and full factorial design is proposed to ensure that all the portions are included representatively in the experimental region.

3. Case-study (Problem Statement)

This part illustrates the application of the proposed methodology in detail, through its application to a case-study (Kopanos, et al., 2014). This example considers the reactive scheduling problem of an energy system consisting of a CHP unit and a heat storage tank - as shown in Figure 2- over a certain period prediction horizon. The energy system can trade electricity with the main electrical grid, or even receive heat from external sources. More details about this problem can be found in Kopanos and Pistikopoulos (2014).

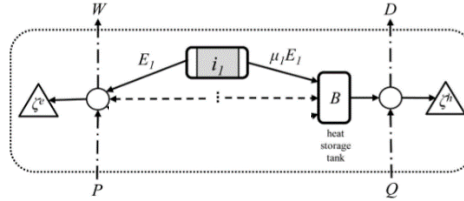


Figure 2. Representative structure of the energy network.

The resulting scheduling problem under consideration is formally defined in terms of the following items:

- (i) A given scheduling prediction horizon which is divided into a set of uniform time intervals $t \in T: = \{1, \dots, \tau\}$. Time interval t starts (ends) at time point $t - 1$ (t).
- (ii) A set of CHP units $i \in I$ having a ramp up limit ρ_i^+ (>0), a ramp down limit ρ_i^- (<0), a minimum (maximum) electricity production capacity ε_i^{min} (ε_i^{max}), a minimum running (shutdown) time δ_{iup} (δ_{idn}), and a known heat to electricity production ratio μ_i .
- (iii) The CHP units are connected to a heat storage tank with a known heat loss rate η , and minimum and maximum heat storage capacity levels λ_{min} and λ_{max} , respectively.
- (iv) At each time interval $t \in T$, the energy network is characterized by a total heat ζ_h and electricity demand ζ_e , which are considered as uncertain parameters with known bounds.
- (v) Economic parameters, which include the starting up (shutting down) cost ϕ_i (π_i) for each CHP unit $i \in I$, the (penalty) price for acquiring heat ζ_i from external sources, and the electricity purchased (selling) price ψ_i (v_i) from (to) external sources (e.g., main electrical grid). Additionally, α_i and β_i represent the fixed and variable energy production cost coefficients for every CHP unit $i \in I$, respectively.

In this study, we consider that there is an administrator that centrally controls the CHP unit. For every time interval $t \in T$, the key scheduling decisions to be made involve:

- (i) The operating status (startup $S_{(i,t)}$, shutdown $F_{(i,t)}$, in operation $X_{(i,t)}$) of CHP
 - $S_{(i,t)} = 1$, if CHP unit startups at the beginning of time interval $t \in T$; i.e., $X_{(i,t-1)} = 0$ and $X_{(i,t)} = 1$
 - $F_{(i,t)} = 1$, if CHP unit shutdowns at the beginning of time interval $t \in T$; i.e., $X_{(i,t-1)} = 1$ and $X_{(i,t)} = 0$
 - $X_{(i,t)} = 1$, if CHP unit is operating in time point $t \in T$
- (ii) The electricity production level $E_{(i,t)}$ of the CHP unit. If CHP unit is operating (i.e., $X_{(i,t)} = 1$), the upper and lower bounds on $E_{(i,t)}$ parameter are given by:
 - $E_{(i,t)max} = \varepsilon_{i,max}$, and $E_{(i,t)min} = \varepsilon_{i,min}$, respectively. Obviously, if $X_{(i,t)} = 0$, $E_{(i,t)} = 0$ and vice versa.

(iii) The total electricity purchases P_t and sales W_t , and

(iv) The total heat received from (disposed to) external sources Q_t (D_t).

B_t represent the heat storage level before the beginning of time interval $1 \leq t \leq \tau + 1$

$$\begin{aligned} \text{Objective Function} = & \underbrace{\sum_{i \in I} \sum_{t \in T} (\alpha_i X_{(i,t)} + \beta_i E_{(i,t)})}_{\text{energy production cost}} + \underbrace{\sum_{i \in I} \sum_{t \in T} (\phi_i S_{(i,t)} + \pi_i F_{(i,t)})}_{\text{switch on and off cost}} \\ & + \underbrace{\sum_{t \in T} (\psi_t P_t - v_t W_t + \xi_t Q_t + \omega_t D_t)}_{\text{energy purchases and sales}} + \underbrace{\sum_{t \in T} \gamma_{t+1} B_{t+1}}_{\text{inventory cost}} \end{aligned} \quad (1)$$

The total electricity and heat demand of the energy network at every time interval must be fully satisfied, and the optimization goal involves the minimization of total costs for producing and trading energy, as given by equation (1).

4. Illustrative Example

For simplicity and presentation purpose a single CHP unit and single-period prediction horizon, is considered. The parameters about the problem are showed in Table 1.

Table: 1 Data for the CHP Units.

θ_s	range	μ	ε_i^{\min}	ε_i^{\max}	ρ_i^+	ρ_i^-	δ_{iup}	δ_{idn}	Initial conditions
ζ_e	$0 \leq \zeta_e \leq 9$	2.5	2.00	8.00	2.880	-3.600	2	2	$E_{\theta} = 320$
ζ_h	$0 \leq \zeta_h \leq 20$	β	ϕ_t	π_t	λ_{\min}	λ_{\max}	η	α_i	$B_i = 3$
E_{θ}	$E_{\theta} = 0, 2 \leq E_{\theta} \leq 9$	2.226	34	17	0	30	0.05	37.0	$S_{(0,0)} = 1$

According to the proposed methodology, an hybrid technique (Monte Carlo & full factorial design) was used to generate the θ_s domain (ζ_e , ζ_h , E_{θ}) and the optimization problem was solved N times (1500) to obtain the optimal variable (E_t , P_t^* , W_t^* , Q_t^* , D_t^* , B_t^*) and the objective function (Optimum trading cost). The S and F are considered as additional θ_s . As a result, the problems must be solved for all possible combinations of the initial state binary decision (S=0, F=0; S=1, F=0; S=0, F=0; S=0, F=1), which were defined for each optimization. Each θ_s and their corresponding optimal solution form an instance I, and the set of instances make up a database of 831 training instances (I_t) and 669 validation instances (I_v). Based on the optimization results, the E_0 , B_0 and E_1 variables have a discrete behavior in addition to the binary variables (S, F).

5. Results and discussion

Therefore, once the proposed methodology was applied, 3 clusters (A, B, C), 3 metamodels based on optimization to predict the optimal values and 2 classification metamodels were determined. The metamodels' validation results and their corresponding interpolation time to determine a new instance are shown in the Table 2.

Table 2. mi-mpM results.

Metamodel	μ	σ^2	θ_1	θ_2	θ_3	θ_4	RMSE	I_t	Interpolation time (s) per instance
Cluster A	5.95	0.78	16.60	8.53	17.66	8.80	0.065	575	0.0002
Cluster B	8	0	2	2	2	2	0.000	50	0.0002
Cluster C	2.88	3.42E03	1.50	1.90	1.89	-	0.001	206	0.0002

The Figure 3 displays comparative results of the optimum electricity generation and the accumulated trading cost between mp-RH and mi-mpM for 20 consecutive instances of reactive scheduling. Observe that with mi-mpM, the predicted value (E1) have a difference, which have been quantified between 0% and 0.5% respect to mpRH. For other hand, when the objective function (accumulated optimum trading cost) is predicted with mi-mpM, there is a difference of 0.8% with respect to accumulated value obtained with mp-RH. The total execution time per iteration is 0.0002s, the same problem has been solved in 0.0003s by using mp-RH.

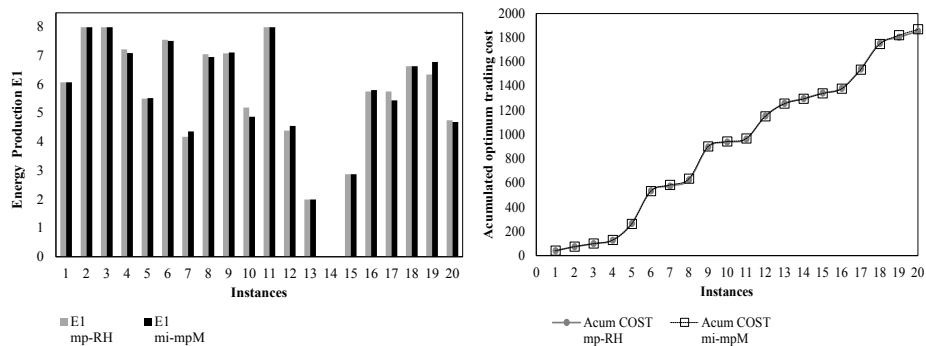


Figure 3. Detailed schedule per time interval using mp-RH and M-miMP.

6. Conclusions

The proposed methodology mi-mpM would address the reactive scheduling problems which involve discrete behaviour, with accuracy and computational efficiency.

Acknowledgements:

Financial support received from the Spanish "Ministerio de Economía, Industria y Competitividad" and the European Regional Development Fund, both funding the research Project AIMS (DPI2017-87435-R) and the Government of Ecuador through the National Secretary of Higher Education, Science, Technology and Innovation is fully acknowledged.

References

- Kopanos, G. M., & Pistikopoulos, E. N. (2014). Reactive Scheduling by a Multiparametric Programming Rolling Horizon Framework : A Case of a Network of Combined Heat and Power Units.

- Li, Z., & Ierapetritou, M. G. (2007). A New Methodology for the General Multiparametric Mixed-Integer Linear Programming (MILP) Problems.
- Lupera, G., Shokry, A., Medina-González, S., Vyhmeister, E., & Espuña, A. (2018). Ordinary Kriging: A machine learning tool applied to mixed-integer multiparametric approach. In ESCAPE 28. Graz.

Resolved Numerical Analysis of Drying on a Vibrating Grate

Bernhard Peters^{a,*}, Mohammad Mohseni^a, Marc Demouling^b and Thorsten Kläs^b

^a*University of Luxembourg, 6 rue Coudenhove-Kalergi, Luxembourg, 1359 Luxembourg*

^b*Soil-Concept S.A., B.P. 139, Friedhaff, 9378 Luxembourg*

bernhard.peters@uni.lu

Abstract

Biomass materials are initially wet containing with a moisture content of app. 25 - 65% which requires a thermal pre-treatment to reduce the moisture to app. 10% and increase the quality of a biofuel. Understanding and optimizing the heat transfer is important in order to decrease the cost of running the equipment. Due to the complexity of moving bed reactors, heat transfer is mainly assessed through experiments and derived empirical correlations that obviously depend on the operating conditions and include a degree of uncertainty. Therefore, the objective of this study is a drying analysis of wet woody particles on a vibrating grate using a DEM-CFD coupling method referred to as eXtended Discrete Element Method (XDEM). In this approach, the particles are resolved as a discrete phase and coupled via heat, mass and momentum transfer to the surrounding gas phase. Thus, the dynamics and thermodynamic behavior of biomass particles during drying is analyzed in detail when exposed to a hot gaseous environment and transported by the vibrating motion of a grate. An outstanding feature of the numerical concept is that each particle in addition to its position and orientation in time and space is described by its thermodynamic state e.g. temperature and reaction progress. Available positions of particles allow determining contact areas between particles and walls for heat transfer. Validation is carried out with experimental data taken from an industrial-scale facility on a vibrating grate dryer in Soil-Concept company in Luxembourg. Under these circumstances, different sizes of particles are employed to predict the final moisture content and density to compare with experiment and show a good agreement between measurements and predicted results. In addition, the influence of inlet gas temperature and velocity, heated-up device temperature and vibrating grate motion on the particle bed mean temperature and moisture content, drying rate and residence time is investigated. At the end, the surface temperature distribution of particles in different instances during drying is visually demonstrated.

Keywords: multi-scale, multi-physics, modeling, renewable energy

1. Introduction

In this DEM-CFD coupling module, all processes inside each particle are described by one dimensional and transient conservation equations of mass and energy. With summing up individual particle processes, the total process is established for the packed bed of particles. The arrangement of particles within the surrounding gas is expressed as void space. In this case, the flow through the void space of the packed bed is modeled as the flow through a porous medium with considering the interaction between the solid-gas phases by heat, mass and momentum transfer (Mahmoudi et al., 2014). Generally, there are three transport phenomena inside a dryer that take place simultaneously during drying as *i*) heat transfer between particle and gas; *ii*) particle transportation; and

iii) water vapor transportation from particle to gas. The heat and mass transfer during transportation of particles inside a dryer highly depends on the surface area and the contact time between particles and gas phase (Mujumdar (2006)).

The vibrating grate dryers studied in this work are a combination of conveying and fluidized bed dryers. That is, the transportation of particles from inlet to outlet is added to fluidization with a gas phase. This enables the vibrating grate dryers to be efficient and powerful drying facilities in the industrial applications. Also the entrainment phenomenon could happen when the grate motion and the gas flow rate are relatively high. In a typical vibrating dryer, the particles are transferred to the dryer where the bottom grate has an oscillatory motion in both vertical and horizontal directions. Simultaneously, the particles face the drying medium which leads to fluidisation and move the particles forward until exiting from the system. Whereby, the particles and gas phase mix properly leading to better heat transfer and consequently better drying. The presented DEM-CFD approach is used to analyze drying of biomass particles on a vibrating grate in this study. Also the motion of particles inside the vibrating grate dryer is modeled in which the particles move forward inside the dryer by oscillatory motion of vibrating grate plate as well as drag force by gas medium.

2. Mathematical modeling

Since the experiment is highly effortful and costly to realize the complex processes in the multi-phase flow systems, a full scale numerical simulation is desired to investigate the solid-gas behavior. In multiphase systems where the particles interact with fluid flow, there are two approaches to describe the behavior of different phases as Eulerian and Lagrangian. The Eulerian approach considers the flow as continuous while the Lagrangian approach tracks the properties of each particle as it traverses in the flow (Faghri and Zhang (2010)). Apart from compatibility with an Eulerian approach for fluid flow, employing this approach for solid phase leads to miss particulates properties during simulation which decreases the accuracy of results. The advantage of XDEM is resolving the continuous fluid phase with Eulerian approach with employing OpenFOAM tool, while Lagrangian approach is implemented to track each entity of the granular material. Fig.1 describes the schematic DEM-CFD coupling modules. The detailed description of mathematical modeling is presented in (Mohseni and Peters (2016)).

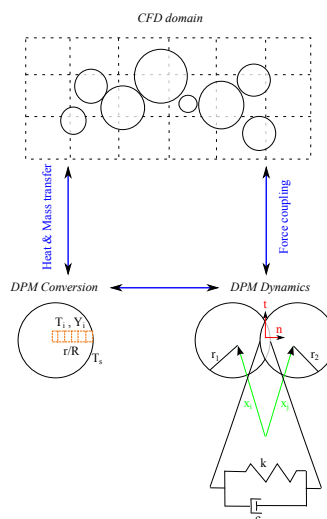


Figure 1: Schematic DEM-CFD modules

3. Result and discussion

Fig.2 shows the industrial scale vibrating grate dryer including the solid-gas inlets and outlets where the system is properly isolated. To heat up the system before drying, the steam is injected into the dryer until the gas temperature inside the dryer exceeds $100\text{ }^{\circ}\text{C}$. Then the biomass feeding starts using a screw feeder which transports the biomass into the dryer with the rate of 100 t/h for 5 s . The feedstock is forest residues. Dryer geometry in *length*, *width* and *height* directions are 7 , 1.5 and 2.2 m , respectively. The case study used for the simulations has the same geometry as the experimental facility except *width* direction. This is to reduce the running time of the simulation, since the temperature gradient is constant in *width* direction, thereby one slice of the dryer (as 0.1 m) is performed in this side. However, two periodic boundary walls are considered to predict the motion of particles properly. The particles are transported through the horizontal axis due to the vibrating motion of the grate and the gas flow drag force. The gas phase medium is the superheated steam which is in direct contact with the particles. The superheated steam enters the dryer and encounters the wet particles. And after heat exchange with particles, the cooled air exits the dryer through two upper outlets. The simulation domain with boundary specifications are illustrated in fig.3. To evaluate the effect of particle size distribution in accordance with the experimental test; and for tracking each particle size to investigate the density and moisture content variation, five different sizes as $5, 10, 15, 20, 25\text{ mm}$ are considered for simulations. This is according to the measured experimental size distribution. For validation, fig.4 compares the mean moisture content of three experiments with simulation prediction. The measurements are carried out in four points at four instances during the experiments. It can be seen that the moisture content values are in a good agreement between experimental and numerical predictions.

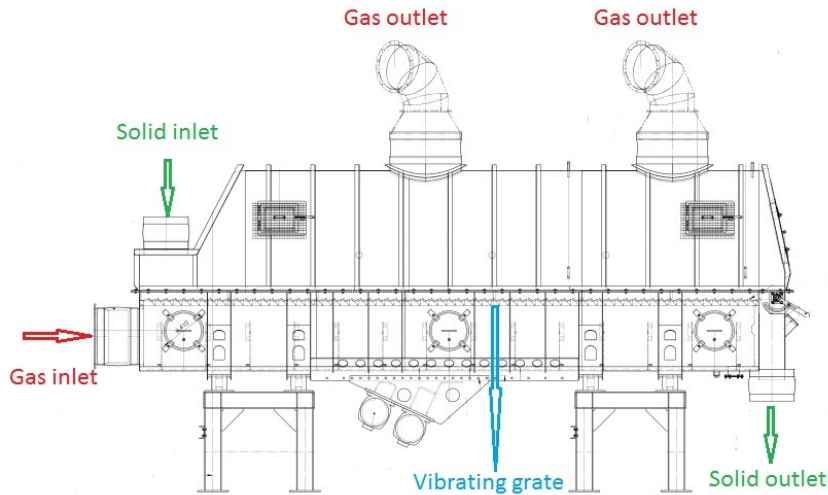


Figure 2: Schematic vibrating grate dryer

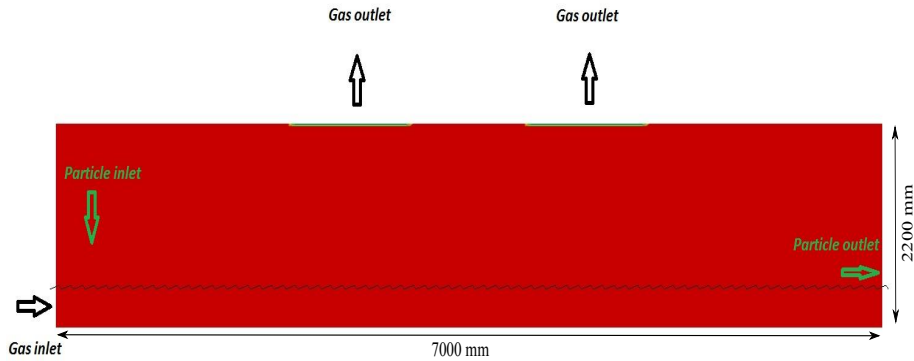


Figure 3: The simulation domain of vibrating fluidized bed dryer

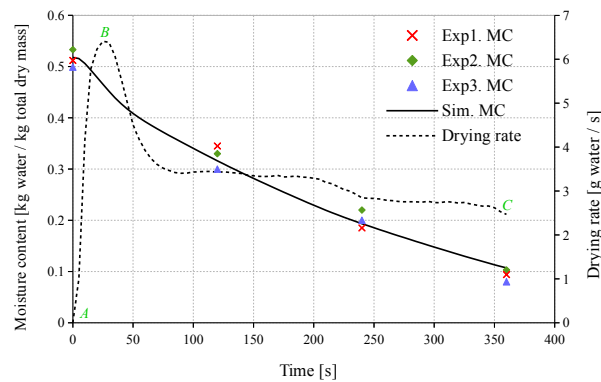


Figure 4: Validation of moisture content with experiment vs. drying rate

3.1. Instantaneous particle temperature

To evaluate the effect of particle size distribution during drying, the temperature distribution of particles is visually shown in fig.5 at five instances 5, 30, 120, 240, 360s. Fig.5(a) shows the particles falling down onto the grate after 5s. Initial gas temperature inside the dryer is 100 °C and with feeding the particles, inlet gas with temperature 210 °C is injected. With facing the hot gas (210 °C) with fed particles (with 95 °C), the bed temperature starts to increase. And since the particles at the bottom of the bed are in direct contact with the hot gas, the temperature rises faster than the particles through the bed. After 30s shown in fig.5(b), the bed height becomes uniform and the smallest particles move up further due to lower weight. In this moment, the surface temperature of particles reach the saturation status and the smallest particles specially before 1m in the system are dried. Fig.5(c) shows the system at 120s. In this moment, some particles left the dryer in saturation status. This is in accordance with the scope of the experiment as reaching the total moisture under 10 %wb. While at the middle of the vibrating dryer between 3 – 4m, the temperature of small particles reach the gas temperature. Most of the particles after 240s left the domain which is shown in fig.5(d). The particles inside the system still receive energy and the temperature continues increasing. It is clear that only small particles reach the gas temperature. This is due to the smaller size that leads to faster heat transfer from the surface to center of particles. In contrast, the large particles at the end of dryer are dried but the temperature is still under gas temperature.

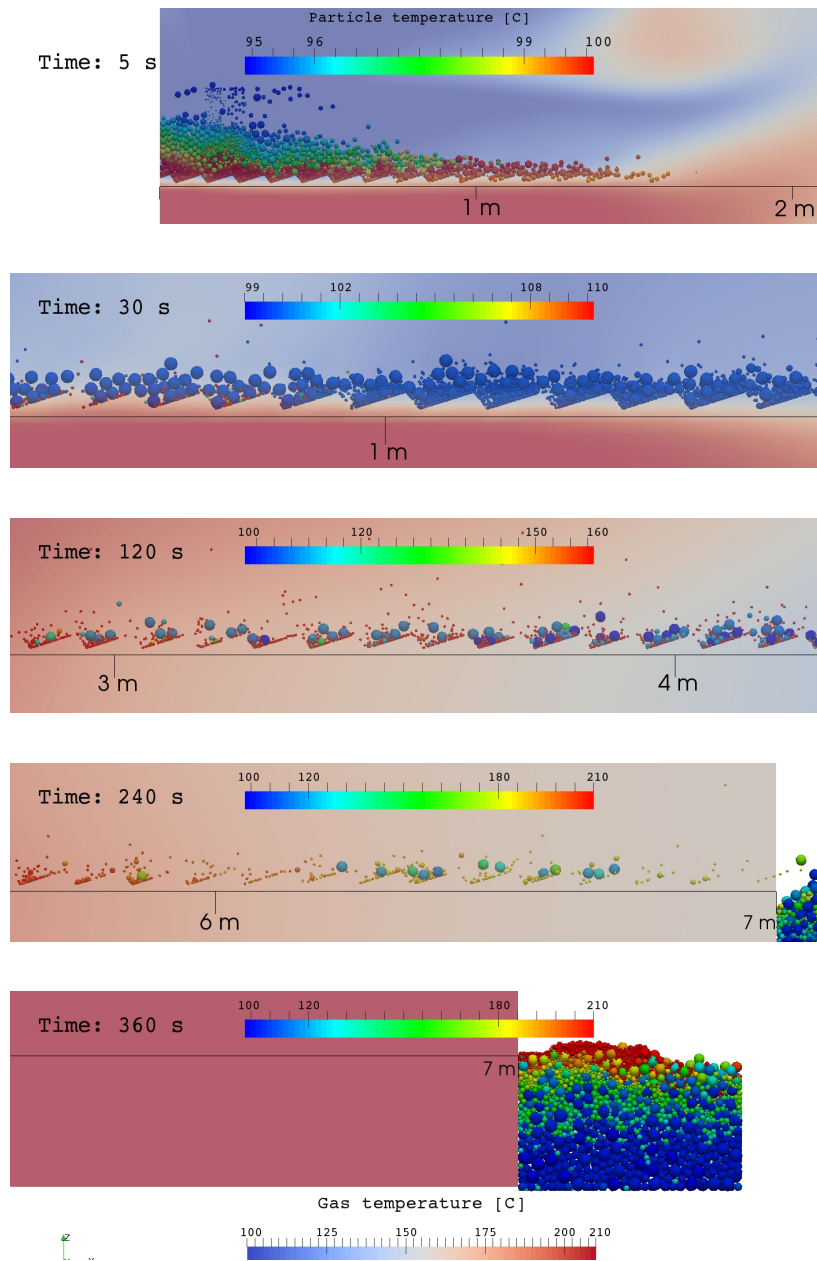


Figure 5: Temperature distribution of particles at different instances in zoomed view

At the end of simulation (360s) shown in fig.5(e), all particles are out of the dryer domain. And the gas temperature is uniformly 210 °C since there is no more solid element for heat transfer. With looking at the exterior bed, it is obvious that the temperature of upper part is close to the gas phase 210 °C while the bottom part has the saturation temperature (100 °C). This is explained as the particles at the top had more residence time and consequently the temperature exceeded the saturation status.

4. Conclusion

In this study, a DEM-CFD coupling approach is applied to evaluate drying of beechwood in a vibrating fluidized bed dryer. The particles are modeled based on discrete element method coupled to the continuous gas phase via heat, mass and momentum transfer using OpenFOAM as a computational fluid dynamics tool. To evaluate the numerical simulation, the experimental work is done via collaborating with Soil-Concept company in Luxembourg. The experiments are carried out in the industrial scale vibrating dryer to measure the moisture content, density and size distribution of materials. The comparison of moisture content at different instances as well as total residence time between experiment and simulation reveal a good agreement. The instantaneous temperature distribution of particles and gas phase are visually presented to examine the effect of size distribution on drying process. It is shown that the small particles are dried faster than large particles since heat is transferred from the surface to core of small particles faster.

References

- A. Faghri, Y. Zhang, 2010. *Transport Phenomena in Multiphase Systems*. Elsevier Academic Press.
- A. H. Mahmoudi, F. Hoffmann, B. Peters, 2014. Application of xdem as a novel approach to predict drying of a packed bed. *International Journal of Thermal Sciences* 75, 65–75.
- M. Mohseni, B. Peters, 2016. Effects of particle size distribution on drying characteristics in a drum by xdem: A case study. *Chemical Engineering Science* 152, 689–698.
- A. S. Mujumdar, 2006. *Handbook of Industrial Drying* 4th Ed. CRS Press.

Assessing the Performance of Industrial Ethanol Fermentation Unit Using Neural Networks

Rauber D. Pereira^a, Alberto C. Badino^a, Antonio J. G. Cruz^{a*}

^a*Chemical Engineering Graduate Program, Federal University of São Carlos, São Carlos, CEP 13565-905, Brazil.*

ajgcruz@ufscar.br

Abstract

The Brazilian sugarcane ethanol plays an important role in the country fuel market. It also presents a better strategic position to get the environmental targets established by Brazil at COP21 (in Paris). To reach these targets, the biofuel production needs to be improved to reach ca 50 billion liter of ethanol until 2030. Nowadays, the Brazilian mills seek for increasing the fermentation process efficiency from 83 % to values close to 90 %, making the ethanol raising production feasible. In this context, the present work aims to model the industrial ethanol fermentation unit using a feedforward neural network. A set of industrial data was used for training and validating the neural network. The backpropagation algorithm was used for training the network. It was possible to identify the variables that had a direct impact on the process performance. The better network configuration was able to attain a correlation coefficient value (R-value) of 0.84. Efficiency fermentation values were predicted by the network with good precision during stable process operation. From this information, it is possible to come up with new process modifications which will contribute towards the increase in industrial fermentation efficiency.

Keywords: Neural network, ethanol, fermentation, process efficiency.

1. Introduction

Bioethanol production has become more important not only in national discussions about biofuels but also worldwide once Brazil is committed to reducing greenhouse gas emissions. In Brazil, bioethanol production is a long-established process. Its production process is primarily based on the sugar fermentation (mainly sucrose) from sugarcane juice. After the launch of the Brazilian Alcohol Program (Proalcool, in Portuguese) in 1975, ethanol production increased considerably, from 600 million liter in 1975 to 11.8 billion liter of ethanol in 1986. In harvest 2016/2017, Brazil produced 27.2 billion liter of ethanol (UNICA, 2017). To reach a target established by Brazil at COP 21 in Paris, ca 50 billion liter of ethanol until 2030, several options exist: expansion of cultivation area, improvement in agricultural or in industrial yields, introduction of new industrial processing pathways which include improvements in first (sugars conversion) or second generation (lignocellulosic biomass conversion) ethanol industrial processing (Jonker et al., 2015).

Ethanol can be produced in fed-batch or continuous operation modes with cell recycle (Melle-Boinot process). A typical Brazilian distillery is divided into sectors or units which include: (1) an upfront section, named extraction unit, composed by cleaning and extraction juice; (2) treatment unit, composed by sedimentation and concentration processes to eliminate impurities and adjust the sugar concentration in the juice; (3)

fermentation unit, composed by a set of fermenters, centrifuges and distillation columns, and (4) heat and power unit, composed by the boilers and turbines which produces energy (vapour and electricity to the process). A simplified block diagram illustrating these main process units is illustrated in Figure 01.

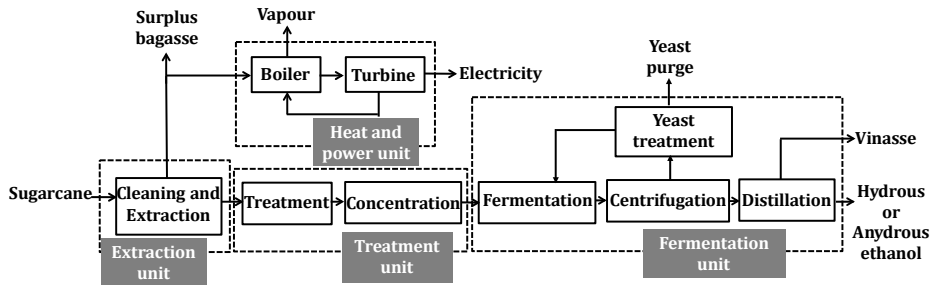


Figure 1. Block diagram illustrating the main process units in ethanol production.

Regarding ethanol production process there are in literature many works that focus on describing the fermentation process. Several kinetics models (Oliveira et al., 2017) together with mass balances equations can be used to describe the fermentation process, which means, to describe the profiles of cell, substrate, and product inside the bioreactor throughout the fermentation. The kinetic models seek to describe the inhibitory effects due to substrate, product, and biomass concentrations, common phenomena present in industrial process production. Other models can also include the effect of the medium temperature on kinetic parameters, which brings additional information for better process description. Models based on neural networks have also been used to describe the fermentation process (Mantovanelli et al., 2007). Fonseca et al. (2017) have modelled and simulated the entire fermentation unit which comprises the fermentation vessels, centrifuges, and distillation columns. The fermentation process, operated in fed-batch or continuous mode, was represented by both stoichiometric and kinetic-based fermentation models. There are advantages in using the first one approach instead of that involving reaction kinetics, such as fast convergence and simplicity of modelling and optimization, since dynamic fed-batch models require specialized optimization algorithms (Roubos et al. 1999). However, stoichiometric models typically do not incorporate the aforementioned inhibition effects that could hinder the product output of the reaction. Instead, they rely on previously known information on the substrate conversion rate. The use of neural networks to model the fermentation unit can overcome this difficulty. Using this approach, at the same time that important process variables are introduced into the model (as inputs to the network), the model can be easily solved making it more desirable for use in optimization problems.

The aim of this paper was to model an industrial fermentation unit using neural network approach. The objective is to estimate the process fermentation efficiency based on a set of variables.

2. Methodology

The data released by the industry (a mill located in the São Paulo state, Brazil) comprised 142 operation days from March to September of 2015. A set of 17 variables were monitored daily. These variables were used as input to the network. The selected variables were grouped in sub-sets named: molasse variables (1-total reducing sugars-TRS (%); 2-total soluble solids ($^{\circ}$ Brix); 3-molasse acidity (%); 4-molasse purity), wine variables (5-ethanol titer ($^{\circ}$ GL); 6-yeast concentration (% v/v), 7-wine bacterial contamination (FCU/ml); 8-cell viability (%); 9-residual reducing sugar (%)), fermentation variables (10-waiting time for wine centrifugation (hour); 11-molasse feeding time (hour); 12-fermentation temperature ($^{\circ}$ C); 13-standard deviation of molasse feeding time), and inoculum variables (14-pH of inoculum; 15-yeast treatment time (hour); 16-standard deviation of yeast treatment time; 17-inoculum ethanol titer ($^{\circ}$ GL)).

Figure 02 shows a schematic diagram of the industrial fermentation unit layout. The unit is composed by six fermentation tanks (650 m³ working volume), six pre-fermentation tanks (100 m³ working volume), and three centrifuges (100 m³/h of nominal flow rate). The fermentation unit has a nominal ethanol production of 700 m³ per day.

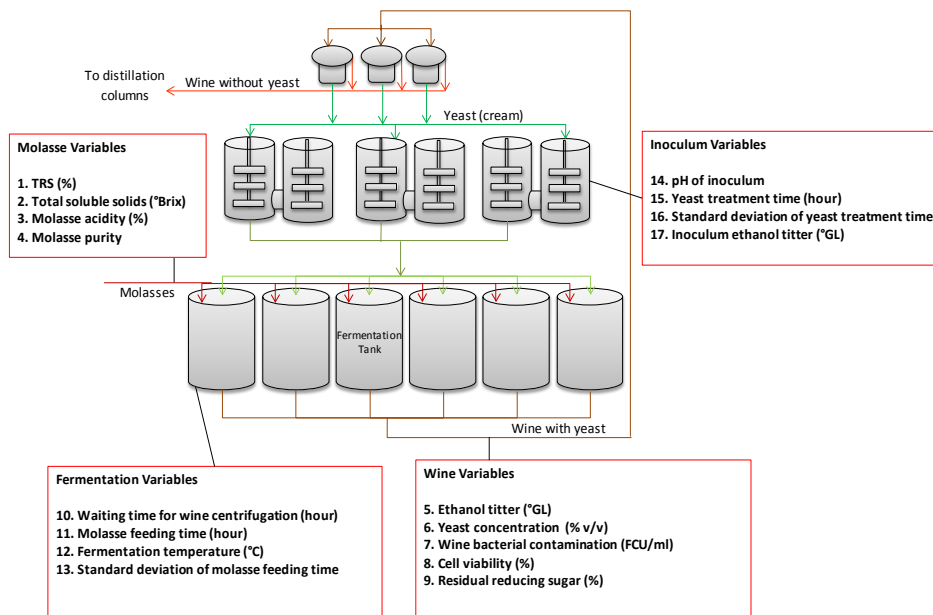


Figure 2. Schematic illustration of the industrial fermentation unit.

A feedforward neural network with one hidden layer was used throughout this work. The log-sigmoid transfer function was employed in the hidden layer neurons. The linear transfer function was used in the output layer. The Levenberg-Marquardt algorithm was used for training the neural network. Before starting the training step, the algorithm randomly distributed the data points into three data sets: training, validating and testing. Then, random initial weights for each network connection are attributed. Each network architecture was trained from different initial condition 2,100 times to assure that a global minimum was found during the training step. All the input data values were

normalized between -1.0 and 1.0. All the steps carried out to find the best neural network architecture was performed taking into account to avoid network overfitting. The mean squared error and the correlation coefficient were the parameters used to choose the best network configuration.

Different sets of input variables and different number of neurons in the hidden layer were evaluated. The best net configuration had eight input variables and seven neurons in the hidden layer. The following variables were used as input: total reducing sugar (TRS, %), ethanol titer ($^{\circ}$ GL) from wine, yeast concentration (% v/v) from wine, wine bacterial contamination (FCU/ml), waiting time for wine centrifugation (hour), molasse feeding time (hour), fermentation temperature ($^{\circ}$ C), and inoculum ethanol titer ($^{\circ}$ GL). Figure 03 illustrates the architecture of the feedforward network used in this work.

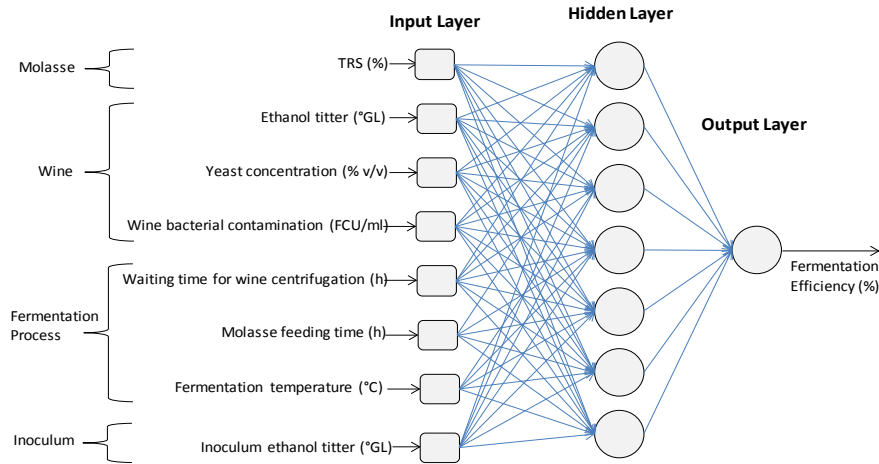


Figure 3. Neural network architecture implemented for simulation of the industrial fermentation unit. The network output is the fermentation efficiency (%).

3. Results and Discussion

Figure 4 illustrates the regression plot of the targets (experimental fermentation efficiency) and the neural network output (estimated fermentation efficiency). It can be seen that the neural network was able to predict with good precision the fermentation efficiency (correlation coefficient, $R = 0.84$). It must be considered that the variables used to estimate fermentation efficiency comprises effects of previous days of operation. It occurs because the industrial fermentation is a continuous process of molasses input and wine output, once there are several fermentation tanks operating in fed-batch mode in synchronized cycles. The correlation coefficient of 0.84 reached for a static neural network could be increased if it was considered a dynamic network with time delay in the input layer.

Figure 5A shows predict and experimental efficiency fermentation values in chronological order of the operation days, from March to September 2015. The relative error is shown in Figure 5B. It can be seen that the mean of the relative error decreases from 72nd to 141st day (1.5 %) when compared to the same value calculated from the

beginning of the harvest (1st to 71st day, 2.9 %). The dry weather (72nd to 141st day) allowed more stable operations. As a consequence, the network gave more accurate responses. Despite this, in this period some points reached relative errors above 5 % due to the occasional breakdown of equipment.

Process variables are collected on the shop floor and analyzed in the laboratory. When process instabilities occur due to rainy days or equipment breakdowns these samples are no longer representative as the sampling procedure was developed for steady state process operation.

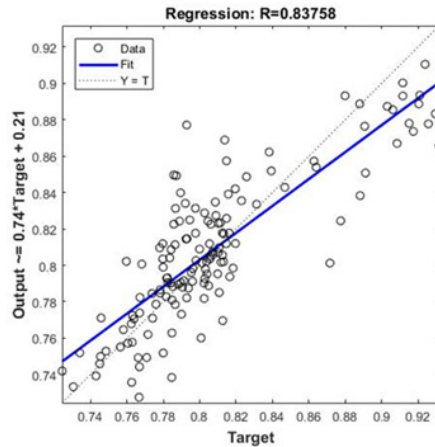


Figure 4. Regression plot between the industrial fermentation efficiency values (targets) and the network output.

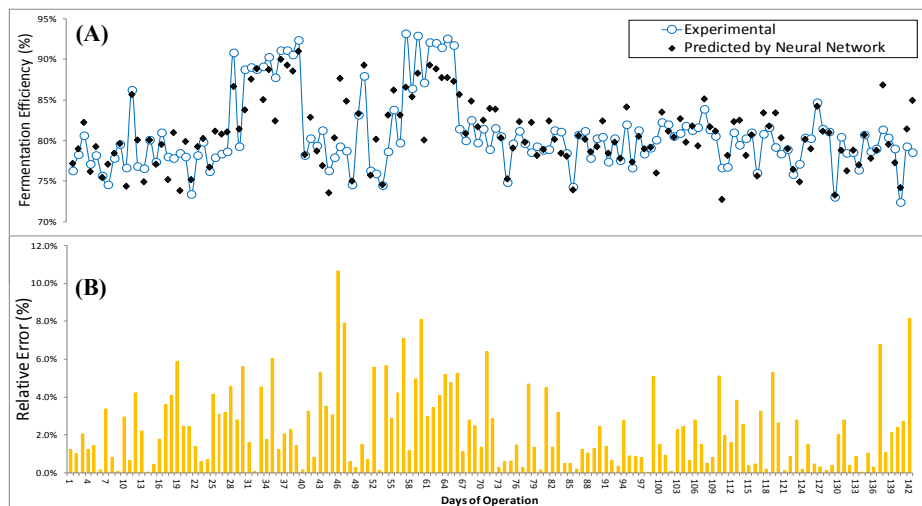


Figure 5. (A) Fermentation efficiency values (experimental and predicted by the network) in chronological order of the operation days; (B) Error plot between industrial fermentation efficiency values and the network outputs.

4. Conclusions

The neural network was able to model the fermentation unit providing with good precision fermentation efficiency values during stable process operation. This approach showed to be a promising way to circumvent the difficulty in using phenomenological models for process optimization studies. Actually, the decision on the level of model complexity to be used will be a trade-off between modeling effort, quality and quantity of available information and the application of the model.

Once the industrial process variables comprise features from the previous days of operations, the next step to this work would be to evaluate the performance of a dynamic network with time delay in the input layer.

Acknowledgements

The authors thank CAPES, CNPq, FAI-UFSCar for the financial support.

References

- G. C. Fonseca; C. B. B. Costa; A. J. G. Cruz, 2017. Comparing a Dynamic Fed-Batch and a Continuous Steady-State Simulation of Ethanol Fermentation in a Distillery to a Stoichiometric Conversion Simulation. *Brazilian Journal of Chemical Engineering* 34(4), 1121-1131.
- J. G. G. Jonker; F. van der Hilst; H. M. Junginger; O. Cavalett; M.F. Chagas; A. P. C. Faaij. 2017. Outlook for ethanol production costs in Brazil up to 2030, for different biomass crops and industrial technologies. *Applied Energy* 147, 593–610.
- I. C. C. Mantovanelli; E. C. Rivera; A. C. Costa; R. Maciel Filho, 2007. Hybrid Neural Network Model of an Industrial Ethanol Fermentation Process Considering the Effect of Temperature. *In: Mielenz J.R., Klasson K.T., Adney W.S., McMillan J.D. (eds). Applied Biochemistry and Biotechnology. ABAB Symposium. Humana Press*
- S. C. Oliveira; D. P. Stremel; E. C. D.; F. M. Pereira, 2017. Kinetic Modeling of 1-G Ethanol Fermentations. *Intech*. DOI: 10.5772/65460
- J. A. G. Roubos; G. Van Straten; A. J. B. Van Boxtel, 1999. An evolutionary strategy for fed-batch bioreactor optimization; concepts and performance. *Journal of Biotechnology*, 67(2): 173-187.
- UNICA, 2017. União da Indústria de cana-de-açúcar (in Portuguese). <<http://www.unica.com.br>>.

Thermal and hydraulic performance of pillow-plate heat exchangers

Olga Arsenyeva^{a,b,*}, Julian Tran^a, Eugeny Y. Kenig^a

^a Paderborn University, Chair of Fluid Process Engineering, Paderborn, Germany

^b National Technical University “Kharkiv Polytechnic Institute”, Ukraine

olga.arsenyeva@upb.de

Abstract

Pillow-Plate Heat Exchangers (PPHEs) represent an innovative equipment type, with space-effective, light and pressure-resistant construction. In this work, an experimental study of air cooling by water in small-scale pillow plates was carried out and an analysis of the hydraulic resistance and heat transfer inside the PPHEs was performed based on the experimental data. The correlations for friction factor and heat transfer in PPHEs channels were proposed and validated by the measurements of small-scale PPHEs. The correlation for the heat transfer coefficients in the channel with hot heat carrier is based on the modified Reynolds analogy between heat and momentum transfer; it is valid for fully developed turbulent flow with the Reynolds numbers between 2,000 and 20,000. The deviation of the data predicted by the proposed correlations from the experimental results is within $\pm 10\%$. The experimental data processing was realised using the developed software. The proposed correlations can be applied for the mathematical modelling of PPHE design parameters.

Keywords: pillow-plate heat exchangers, friction factor, thermo-hydraulic performance, heat transfer coefficient.

1. Introduction

Implementation of novel-type heat exchangers in industry requires design approaches based on reliable models for thermo-hydraulic performance. One of the innovative types of heat exchangers is the so-called *pillow-plate heat exchanger* (PPHE). Heat transfer in PPHEs is realised in channels with complex geometry, which are formed by spot-welding of two metal sheets, according to a particular welding spot pattern, and by subsequent expansion using hydroforming. PPHEs show enhanced heat transfer characteristics while keeping pressure loss on the product media side low (Tran et al., 2015). The ease of the production process as well as space-effective, light and pressure-resistant construction characterises this equipment as promising for implementation in industry. However, no reliable models for the heat transfer efficiency estimation in small-scale PPHEs are available.

The previous results on thermal and hydraulic performance of pillow plates available in the literature are given for turbulent flow in large-scale pillow plates with particular geometries, both for inner pillow-plate channel (Tran et al., 2015) and for outer pillow-plate channel (Piper et al., 2016). The data published for the outer channels formed between the pillow plates is limited to only one pillow plate geometry. The data transferability between different pillow-plate geometries is also uncertain. The present

tendency towards compact equipment makes investigation of hydraulic performance of small-scale pillow plates interesting for industrial application. Above all, the correlations for the friction factor and heat transfer coefficients are required. Only based on these correlations, the thermal and hydraulic performance of PPHEs can be determined in line with their geometrical design parameters. We developed an experimental set-up for the determination of pressure drop and heat transfer coefficients in the inner and outer channels of the small-scale PPHEs. Measurements were carried out and the obtained experimental data were analysed and validated using the developed software in Mathcad, which enables numerical evaluation of the obtained set of experimental data as well as determination of the friction factor and heat transfer coefficients for each set. The obtained results allowed the general correlation for heat transfer coefficient and friction factor in the outer pillow-plate channel to be developed using the least square method.

2. Description of experimental set-up

To study the pressure drop in the inner and outer channels of a PPHE, the experimental set-up shown schematically in Fig. 1 was developed. It consists of two cycles, one for water and one for dry air. Water was heated in the thermostat up to 20 °C and pumped to the inner channel of the PPHE. The water flow rate was varied during the experiments between 130 and 900 kg/h and measured using the Coriolis flow and density meter CMF025M (G2). To measure pressure drop in the inner pillow plate channel for water, sensors were installed in the inlet and outlet pipes of the pillow plate. The pressure drop measurements were made using the Rosemount pressure transmitter 3051CD (ΔP_2).

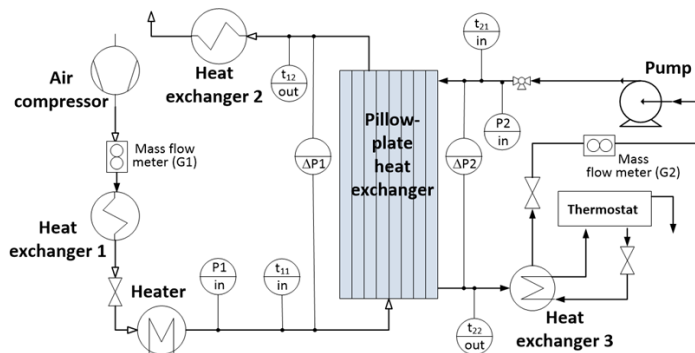


Figure 1. Experimental set-up

Dry air with the temperature varied from 20 to 325 °C was directed to the outer pillow plate channels by an air compressor. The flow rate of the air varying from 40 to 105 kg/h was measured using the Rosemount 8800D vortex flowmeter (G1). The pressure drop was determined with the Rosemount pressure transmitter 3051 (ΔP_1), using sensors installed at the inlet and outlet of the channel. Calibrated B-type thermocouples were used to measure the temperatures of air and water at the inlet and outlet. The total accuracy of the pressure drop experimental measurements was estimated as $\pm 0.10\%$ for water side and $\pm 0.50\%$ for air. The accuracy of flow rate

measurements was $\pm 0.50\%$ and $\pm 0.80\%$ for water and air, correspondingly. To decrease the uncertainty of air flowmeter data, non-ideal gas behaviour was taken into account, and the dry air thermo-physical properties were estimated for each specific gas flow measured. The data acquisition system based on PC running LabVIEW software together with sensors and digital multiplexers was used to process the measured data.

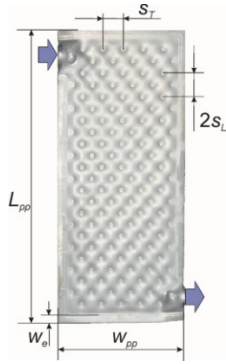


Figure 2. Dimensions of the studied small-scale pillow plate

Table 1. The geometrical parameters of investigated pillow plates

Parameter	Value, mm
d_{ws}	6
h_i	3.5
$2s_L$	42
s_T	36
w_{pp}	230
L_{pp}	530
w_e	30

A specific PPHE sample was manufactured by BUCO Laserplate GmbH (Germany). It consists of two small-scale pillow plates like one shown in Fig. 2. They are made of AISI 304 stainless steel, with the thickness of metal plate equal to 0.8 mm. The main geometrical parameters of the investigated small-scale pillow plates are presented in Fig. 2 and Table 1. The inner-plate expansion of both pillow plates (h_i) was 3.5 mm. The pillow plates were assembled together to compose a heat exchanger with one outer-plate channel for air and two inner-plate channels for water. The distance between the pillow plates (h) was equal to 12 mm. Water was directed inside pillow plate channels. For a better flow distribution inside this small-scale pillow plate, the entrance to the pillow plate was made at the plate side, while the outlet was placed diagonally opposite at the other side (see Fig. 2). The inner diameters of the entrance and outlet tubes were 24.9 mm. Water flowed through two inner pillow plate channels and air through the outer channel in a counter-current mode.

3. Heat transfer coefficients and hydraulic resistance in the PPHE

The thermal and hydraulic performance of PPHE can be estimated using the overall heat transfer coefficient, which can be determined as follows:

$$\frac{1}{U} = \frac{1}{h_1} + \frac{1}{h_2} + \frac{\delta_w}{\lambda_w} + R_f \quad (1)$$

where h_1 and h_2 are the heat transfer coefficients for air and water side of the PPHE, R_f is the thermal resistance of the fouling deposit on the heat transfer surface, δ_w is the thickness of the plate metal, λ_w is the heat conductivity of the plate material.

Eq. (1) can only be applied, if the correlations for both heat transfer coefficients are known. They depend on the fluid physical properties, friction factor and channel

geometry (Klimes et al., 2015). The friction factor in the PPHE channels is determined based on experimental data on pressure loss according to the following relationship:

$$\zeta = \frac{\Delta P \cdot 2 \cdot d_e}{\rho \cdot w^2 \cdot L_{EF}} \quad (2)$$

where d_e and L_{EF} are the characteristic lengths in tangential and longitudinal directions, correspondingly.

The friction factors for hot and cold channels, as well as corresponding heat transfer coefficients were analysed based on the experimental data for the small-scale PPHE with the geometrical parameters of channels, presented in Table 1.

3.1. Friction factor and heat transfer coefficient for the inner pillow-plate channel

The correlation for the friction factor in inner pillow-plate channels, proposed by Arsenyeva et al. (2017), was used:

$$\zeta = 8 \cdot \left[\left(\frac{12 + p2}{\text{Re}} \right)^{12} + \frac{1}{(A+B)^{\frac{3}{2}}} \right]^{\frac{1}{12}}; \quad A = \left[p4 \cdot \ln \left(p5 \sqrt[3]{ \left(\frac{7 \cdot p3}{\text{Re}} \right)^{0.9} + 0.27 \cdot 10^{-5} } \right) \right]^{16}; \quad B = \left(\frac{37530 \cdot p1}{\text{Re}} \right)^{16} \quad (3)$$

where $p1$ to $p5$ are parameters depending on the channel form and determined as follows:

$$\begin{aligned} p1 &= 1,439 \cdot c_1^2 + 256,900 \cdot c_2^2 - 38,450 \cdot c_1 \cdot c_2 - 775.9 \\ p2 &= (2.171 \cdot c_1 + 66.605 \cdot c_2)^{1.077} - 7.868 & p4 &= (0.508 \cdot c_1 + 7.169 \cdot c_2)^{-2.468} + 0.237 \\ p3 &= ((1.239 \cdot c_1)^{-2.284} + 1.109 \cdot c_2) - 0.188 & p5 &= (0.323 \cdot c_1 + 2.646 \cdot c_2)^{14.03} + 4.59 \end{aligned} \quad (4)$$

Here, c_1 is the ratio of the longitudinal distance between the adjacent welding spots to the transversal distance, without considering the welding spot diameter: $c_1 = (2s_L - d_{ws}) / (s_T - d_{ws})$, c_2 is the ratio of the inner expansion of the pillow plate h_i to the diagonal distance between the adjacent welding spots δ : $c_2 = h_i / \delta$.

The heat transfer coefficient was calculated using the dependence suggested by Tran et al. (2015) for the large-scale pillow-plate:

$$\text{Nu}_2 = 0.067 \text{Re}^{0.774} \text{Pr}^{0.338} \quad (5)$$

The characteristic parameters (d_{e1} , f_{CHI} and L_{EF}) in Eqs. (2)-(4) for the inner pillow-plate channel are determined using the relations given in (Tran et al., 2015) and specific geometrical values of the investigated pillow plate (Table 1).

3.2. Friction factor and heat transfer coefficient for the outer pillow-plate channel

The experiments with the outer pillow-plate channel were first carried out at a constant temperature of water and air equal to 20 °C. Afterwards, dry air temperature was varied to estimate the heat transfer coefficients for the outer PPHE channel. The experimental data for different Reynolds numbers are shown in Figure 3. For accurate estimation of the heat transfer and hydraulic parameters in the outer pillow-plate channel at varied dry air temperature and pressure along the channel length, the relations for dry air thermo-

physical properties were taken from the literature, namely, the correlation for density from Picard et al. (2008), the correlation for viscosity from Lemmon and Jacobsen (2004) and the air heat capacity and heat conductivity from Melling et al. (1997).

The obtained experimental data for friction factor and heat transfer were compared with those for tubes (Fig. 3a, line 2). The Blasius equation for the friction coefficient in a turbulent flow inside a smooth pipe was used:

$$\zeta = 0.3164 \cdot \text{Re}^{-0.25} \tag{6}$$

The experimental results on the hydraulic resistance obtained at constant temperature are in good agreement with Eq. (6) (Fig. 3a, line 2). The experimental data in the outer PPHE channel at varied temperature can be approximated using the following correlation:

$$\zeta = 0.7155 \cdot \text{Re}^{-0.361} \tag{7}$$

The data for the large-scale outer pillow-plate channel both for friction factor and heat transfer coefficient from Piper et al. (2016) are presented by line 1 in Fig. 3a. The heat transfer coefficients in tubes were determined using the Sieder and Tate equation (see Green and Perry, 2008):

$$\text{Nu} = 0.027 \cdot \text{Re}^{0.8} \cdot \text{Pr}^{1/3} \tag{8}$$

For the prediction of heat transfer in the outer PPHE channel, the following heat and momentum analogy is proposed (Fig. 3b, line 3):

$$\text{Nu} = 2.187 \cdot \text{Re}^{-0.356} \cdot \text{Pr}^{0.4} \tag{9}$$

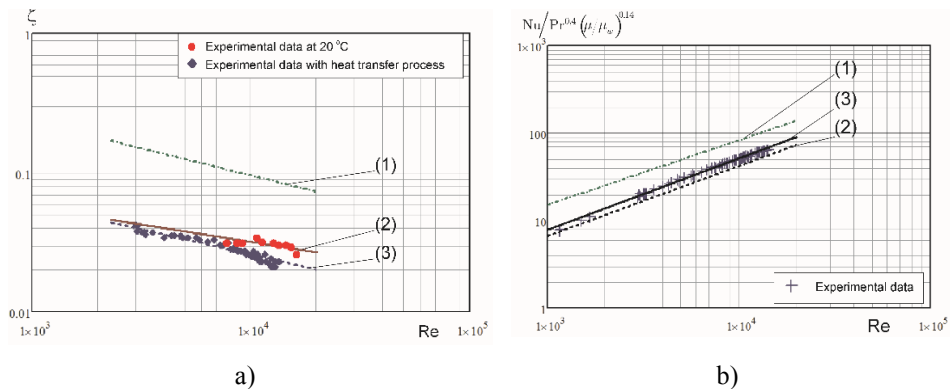


Figure 3. Measurements of friction factor (a) and heat transfer coefficients (b) in the outer pillow-plate channel: (1) – data for the large-scale pillow-plate channel investigated by Piper et al. (2016); (2) – data for tubes according to Eqs. (6),(8); (3) – predicted values according to Eqs. (7),(9)

Values calculated according to Eqs. (7),(9) differ from experimental data by less than $\pm 10\%$ and are valid in the range of Reynolds numbers between 2,000 and 20,000, what corresponds to fully developed turbulent flow in the PPHE channels. The analysis of the obtained experimental data revealed that the friction factor in the small-scale outer PPHE channel is 70 % lower than in the large-scale channel investigated by Piper et al. (2016), while the heat transfer coefficient is 40 % lower. It demonstrates a significant

influence of the channel geometry on thermal and hydraulic behaviour of the PPHE unit. The experimental results for friction factor were obtained both for the isothermal case and for varied temperature. For the isothermal case, they are in good agreement with the Blasius equation for tubes (Eq.(6)), whereas for varied temperature, a deviation is visible, and at high Reynolds numbers, about 20 % lower friction factor is obtained (Fig. 3a). This decrease could be caused by the change of the dry air temperature and pressure along the pillow plate. For a certain conclusion, further investigations are necessary. The heat transfer coefficients in small-scale PPHE outer channel (Eq. (9)) are 17 % higher than in tubes (Eq. (8)).

4. Conclusions

The experimental data for small-scale PPHE were analysed using the developed software. The correlations for friction factor and heat transfer in PPHEs channels were obtained and validated, with the deviation from experimental results within $\pm 10\%$. They are reliable for fully developed turbulent flow with the Reynolds numbers varying from 2,000 to 20,000. More detailed investigations of heat transfer processes in outer PPHE channel are needed. Nevertheless, the obtained low friction factor together with the high heat transfer coefficients for the studied geometrical pillow-plate parameters appear promising and allow to consider this equipment type interesting for implementation in process industries.

Acknowledgement

Olga Arsenyeva is grateful to the Alexander von Humboldt Foundation for the financial support.

References

- O. Arsenyeva, A. Zibart, J. M. Tran, M. Piper, E. Y. Kenig, and P.O. Kapustenko, 2017, Friction Factor Correlation in Small-Scale Pillow-Plate Heat Exchangers for Low-Grade Heat Utilization, In: 12th Conference on Sustainable Development of Energy, Water and Environmental Systems, Dubrovnik, Croatia.
- D.W. Green and R.H. Perry, 2008, Perry's Chemical Engineers Handbook. 8th ed. New-York, USA, McGraw-Hill.
- J.J. Klemes, O. Arsenyeva, P. Kapustenko, and L. Tovazhnyansky, 2015, Compact Heat Exchangers for Energy Transfer Intensification: Low Grade Heat and Fouling Mitigation, CRC Press, Boca Raton.
- E. W. Lemmon and R. T. Jacobsen, 2004, Viscosity and Thermal Conductivity Equations for Nitrogen, Oxygen, Argon, and Air, 25(1), 21-69.
- A. Melling, S. Noppenberger, M. Still, and H. Venzke, 1997, Interpolation Correlations for Fluid Properties of Humid Air in the Temperature Range 100 °C to 200 °C, Journal of Physical and Chemical Reference Data, 26 (4),1111-1123.
- A. Picard, R. S. Davis, M. Gläser, and K. Fujii, 2008, Revised Formula for the Density of Moist Air (CIPM-2007), Metrologia, 45 (2), 149-155.
- M. Piper, J.M. Tran, and E.Y. Kenig, 2016, A CFD Study of the Thermo-Hydraulic Characteristics of Pillow-Plate Heat Exchangers, Heat Transfer Summer Conference, 1, doi:10.1115/HT2016-7176.
- J.M. Tran, S. Sommerfeld, M. Piper, and E.Y. Kenig, 2015, Investigation of Pillow-Plate Condensers for the Application in Distillation Columns, Chemical Engineering Research and Design, 99, 67-74.

Predicting Research and Motor Octane Numbers based on Near Infrared Spectroscopy: Models based on Partial Least Squares Regression and Artificial Neural Networks

Ana L. Leal,^{a,b,c} Jorge C. Ribeiro,^b Artur M. S. Silva,^a F. G. Martins,^{c,*}

^a*QNOPNA, Department of Chemistry, University of Aveiro, Campus Universitário de Santiago, 3810-193 Aveiro, Portugal*

^b*Petrogal, s.a., Refinaria de Matosinhos, Laboratório, Rua Belchior Robles, 4451-852 Leça da Palmeira, Portugal*

^c*LEPABE, Chemical Engineering Department, Faculty of Engineering, University of Porto, Rua Dr. Roberto Frias, 4200-465 Porto, Portugal*

fgm@fe.up.pt

Abstract

This work focuses on the prediction of research and motor octane numbers of gasolines throughout multivariate statistical analysis, which may significantly increase the celerity of the quality control process. The aim of this work is to compare the performance of two different multivariate models, based on partial least squares regression and artificial neural networks. The results show that both models predict octane numbers with accuracy, presenting coefficients of determination above 0.95 for the calibration data set. For the test data set, partial least squares model is more accurate, which might indicate the existence of linear correlations between spectral data and octane numbers. The statistical parameters also show that the research octane number prediction is more accurate than the motor octane number.

Keywords: near infrared spectroscopy, partial least squares, artificial neural networks, octane numbers

1. Introduction

Due to the advances in technology, petroleum industry is facing one of the most transformative periods in its history. New energy sources are arising, especially in developed countries and now, more than ever, it is imperative to be more energy-cost-efficient, doing it right at first time and making products expeditiously available.

Petroleum products, namely gasolines, should meet several specifications, being conventional analytical techniques for their analysis very time consuming. Conversely, spectroscopic techniques are fast, and their implementation on products characterization, in combination with multivariate statistical models such as partial least squares (PLS) and artificial neural networks (ANN), represent powerful tools for industrial quality control and process monitoring. Research (RON) and motor (MON) octane numbers are two of the main parameters used for quality control of gasoline,

showing a significant impact on engine performance. Therefore, they were chosen for this case study.

Although petrochemical industry is a mature industry with much knowledge and improvement accumulated since its foundation, process improvements and safety enhancements are still possible, and spectroscopic methods such as near infrared (NIR) spectroscopy are tools that can be helpful.

1.1. NIR spectroscopy

Near infrared spectroscopy is a fast and non-destructive (vibrational spectroscopy based) technique for studying many multi-constituent chemical systems, namely for gasoline. It covers the wavelength range adjacent to the mid-infrared and extends up to the visible region (4000 to 12500 cm^{-1}). The adsorption bands presented in NIR spectra occur mainly due to the vibration of three functional groups, i.e., -CH, -NH and -OH (Reich 2005). Figure 1 depicts the NIR spectrum of a gasoline considered for the case study as well as the relative peak positions for prominent near infrared absorptions.

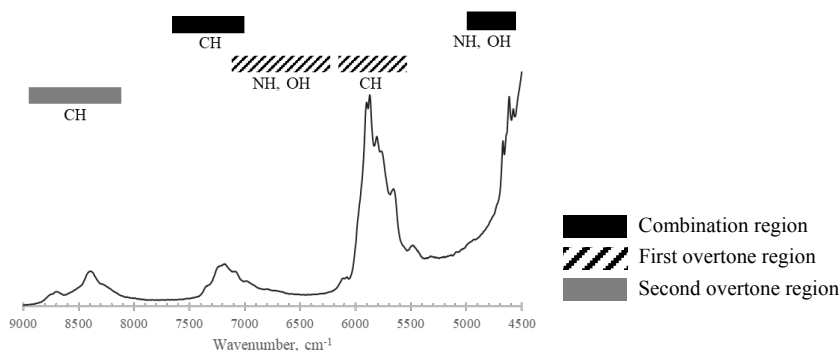


Figure 1. NIR spectrum of a gasoline.

The main advantages of NIR are little or no sample preparation, real-time data, and its immunity to thermal noise caused by internal electronic components. NIR instrumentation is simple to operate and no chemicals are used or generated (Andrade 2007). On the other hand, the presence of overtones makes NIR spectral data complex and not directly interpretable. Thus, it requires chemometric techniques to extract meaningful information from the spectra. In this work, two different multivariate calibration methods, PLS and ANN, were tested with the aim of comparing the predictive capacity for the determination of the octane numbers of gasoline.

1.2. Multivariate calibration analysis

The data obtained via spectroscopic analysis is a type of data that often presents the number of variables much higher than the number of objects and the variables are highly correlated. Thus, this type of data requires multivariate calibration.

PLS is one of the most frequently used methods for quantitative NIR analysis (Varmuza *et al.*, 2008). PLS is a multivariate linear regression method that finds the directions of greatest variability by comparing both spectral and target property information with the new axes, named PLS components. They represent the best correlation with the target property values, which are previously measured by conventional techniques.

ANN are learning methods that work in a way analogous to the neurons in the brain. The variables are presented to an input layer and processed by one or more intermediate layers, producing one or more outputs (Miller *et al.*, 2010). This method is particularly useful when there is no knowledge about the mathematical structure of the model.

2. Methodology

2.1. Experimental procedures

2.1.1. Standard method for RON and MON determination

Research and motor octane numbers provide a measure of the knock characteristics of motor fuels in automotive engines under mild and severe conditions of operation, respectively. The standard methods EN ISO 5164 and EN ISO 5163 were used for RON and MON determination, respectively.

2.1.2. Spectroscopic experiments

The NIR spectra were recorded with a NR800 Fourier Transformed Near-Infrared Analyzer equipped with a NIR fiber-optic probe, an interferometer, an InGaAs detector, and a halogen lamp as beam source. The FT-NIR spectrometer has a spectral range of 11000 to 4000 cm^{-1} with a resolution of 4 cm^{-1} . The software SPECTLAND 2 was used for the recording of NIR spectra.

2.2. Model calibration

The PLS and ANN models for the prediction of RON and MON of gasoline were developed using 70 samples of two different kinds of gasoline, covering a spectral range of 4500 – 9500 cm^{-1} . The data included RON values ranging from 91.7 to 99.8 and MON values ranging from 83.2 to 89.0.

The data was divided into three different groups: training, validation and test data sets. The training dataset was used for calibration, the validation data set was used to find the optimum dimensionality of the multivariate model, avoiding overfitting, and the test dataset was used to evaluate the models' performance when applied to a new dataset. This splitting is crucial for models with application in process control because the developed model must be valid not only for the overall dataset, but also for new samples. The approach used in this study considered that the three subsets had data points of the all range of the output data. The data division and the PLS regressions were performed in Microsoft® Excel using Visual Basic for Applications (VBA). The ANN models were developed in MATLAB® software.

The performance of the developed models was evaluated through the calculation and analysis of two statistical parameters, the coefficient of determination (R^2) and the root mean squared error-observations standard deviation ratio (RSR), which are presented in Table 1. A practical way of evaluating the developed models is to assign them a qualitative classification. Therefore, a qualitative classification was attributed as

follows: Very Good - If RSR is lower than 0.5; Good – If RSR is lower than 0.6; Satisfactory – If RSR is lower than 0.7

Table 1. Statistical parameters for model evaluation

Parameter	Expression	Definition
R^2	$R^2 = \frac{\sum_{i=1}^n (y_i - \bar{y})^2 - \sum_{i=1}^n (y_i - \hat{y}_i)^2}{\sum_{i=1}^n (y_i - \bar{y})^2}$	Variability of the model results compared with the observed data. High values of R^2 indicate small errors in variances.
RSR	$RSR = \frac{\sqrt{\sum_{i=1}^n (y_i - \hat{y}_i)^2}}{\sqrt{\sum_{i=1}^n (y_i - \bar{y})^2}}$	RSR is the ratio between root mean squared error-observations and the standard deviation of the measured data and is a valuable parameter once it integrates the benefits of error index statistics and a normalization factor.

Note: y_i = output value; \hat{y}_i = model output; \bar{y} = average of the output variable; n = number of predictions

3. Results and discussion

Figure 2 shows the NIR spectra of three gasoline samples with RON numbers of 91.7, 96.6, and 99.8. Due to structural similarities, the spectral features of the three samples are very similar, and there are only slight differences in some regions of the spectrum. These differences are the basis for the multivariate analysis to build models with capability to predict the properties in study. The full wavenumber range shown in Figure 2 was used for calibration.

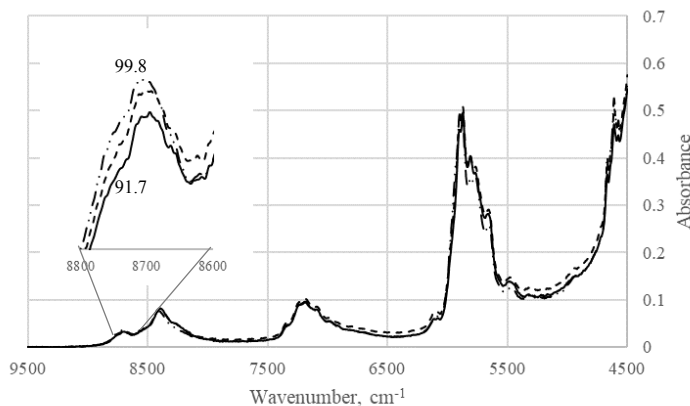


Figure 2. NIR spectra of three gasoline samples with different research octane numbers.

Tables 2 and 3 present the performance results of the developed models for RON and MON determination, respectively. Both methods present very good results for the training and validation data sets. For the test data set, PLS model is more accurate, which might indicate the existence of linear correlations between spectral data and octane numbers. In most cases, the ANN models are more suitable for situations with

nonlinear correlations (Geladi *et al.* 2017). Furthermore, the statistical parameters values show that the models, both PLS and ANN, predict RON with better accuracy than MON.

Table 2. Models' performance results for RON determination

	PLS			ANN		
	RSR	R ²	Classification	RSR	R ²	Classification
Training	0.120	0.986	Very Good	0.186	0.966	Very Good
Validation	0.372	0.862	Very Good	0.260	0.932	Very Good
Test	0.276	0.924	Very Good	0.335	0.888	Very Good

Table 3. Models' performance results for MON determination

	PLS			ANN		
	RSR	R ²	Classification	RSR	R ²	Classification
Training	0.093	0.991	Very Good	0.167	0.972	Very Good
Validation	0.315	0.901	Very Good	0.204	0.958	Very Good
Test	0.431	0.814	Very Good	0.514	0.736	Good

Figures 3 and 4 show the research and motor octane numbers predicted by the model plotted against the values determined by the standard method.

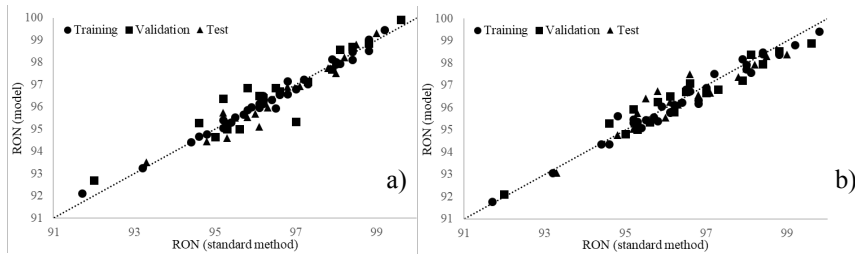


Figure 3. RON predicted by the developed model versus RON determined by the standard method: a) PLS; b) ANN.

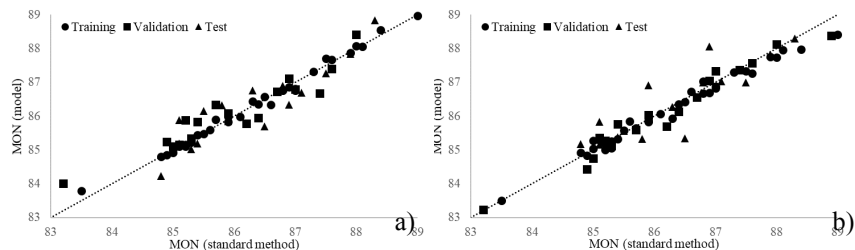


Figure 4. MON predicted by the developed model versus MON determined by the standard method: a) PLS; b) ANN.

4. Conclusions

Research and motor octane numbers have been successfully predicted from NIR spectra of gasolines via partial least squares and artificial neural network models without sample conditioning and data pre-processing. The values obtained for the statistical parameters R^2 and RSR indicate good agreement for both RON and MON prediction, which means that both methodologies can be implemented as a rapid and convenient alternative to the standard experimental method. PLS regression was slightly more accurate than ANN on predicting new samples.

5. Acknowledgements

This work was financially supported by the project POCI-01-0145-FEDER-006939 (Laboratory for Process Engineering, Environment, Biotechnology and Energy – UID/EQU/00511/2013) funded by the European Regional Development Fund (ERDF), through COMPETE2020 - Programa Operacional Competitividade e Internacionalização (POCI) and by national funds, through FCT - Fundação para a Ciência e a Tecnologia, and by QOPNA research project (FCT UID/QUI/00062/2013) financed by national funds and when appropriate co-financed by FEDER under the PT2020 Partnership Agreement.

Research Grant of A. L. Leal, financially supported from FCT Doctoral Program PD00158/2012, Ref: PD/BDE/128624/2017 and Galp Energia is also acknowledged.

References

- Andrade, L. A., 2007. Characterization of Flavour Delivery Systems by NMR. University of Nottingham, UK
- Geladi, P., Dãbakk, E., 2017. Computational Methods and Chemometrics in Near Infrared Spectroscopy, Encyclopedia of Spectroscopy and Spectrometry, 350-355
- Miller, J. N., Miller, J. C., 2010. Statistics and Chemometrics for Analytical Chemistry, Sixth Edition, Pearson, Essex, England
- Reich, G. 2005. Near-infrared spectroscopy and imaging: Basic principles and pharmaceutical applications, Advanced Drug Delivery Reviews, 55(8):1109-43
- Varmuza, K., Filzmoser, P., 2008. Introduction to Multivariate Statistical Analysis in Chemometrics, CRC Press, Boca Raton

Modeling of an air quality monitoring network with high space-time resolution

Daniele Sofia^{a,*}, Aristide Giuliano^a, Filomena Gioiella^a, Diego Barletta^b, Massimo Poletto^{b,*}

^a*Sense Square srl, Piazza Vittorio Emanuele 11, Fisciano (SA) 84084, Italy*

^b*University of Salerno, Via Giovanni Paolo II 132, Fisciano (SA) 84084, Italy*

info@sensesquare.eu

Abstract

With regard to pollution produced in urban areas, low-cost sensors offer the possibility to collect temporal and spatial data and they have a great potential to change the way to monitor the exposure of the population to the atmospheric pollution. However, one of the challenges associated with data coming from this kind of sensors is to try to make them more significant by combining sensors in network. In this work a dispersion model is used to test the distribution of dust (10 μm) measured by individual points of the network. The monitoring area considered is within a seaside town in southern Italy. The monitoring network is made of three sensors placed in points sensitive for the anthropic activity. We have applied an interpolation model to determine the areas of greatest pollution concentration within the monitored area. The model simulated the pollution movements at the level of the individual monitoring points taking into account the weather conditions.

Keywords: air quality, forecast models, monitoring, pollution, particulate matter.

1. Introduction

In urban agglomerations, it is increasingly usual to find in the atmosphere pollutants able to cause damage to human health. Pollutants are defined as any substance causing the alteration of air composition. They are continuously produced by human activities and therefore are localized mainly in metropolitan areas. Small particulates are among the substances responsible of direct damages to human health with particular reference to particulates with size less than 10 μm , PM 10, and less than 2.5 μm , PM 2.5. The main particulate sources are the road traffic, industrial plants and building heating. Accurate measurements of the concentrations of these pollutants are important not only from an environmental point of view, but also for economic reasons, since a part of taxation may be dependent on the emission values (Salehi et al., 2015; Steffens, 2009). Jerrett et al. (2005) reviewed some models for assessing into city environment exposure including: (i) proximity-based models, (ii) interpolation models, (iii) land use regression models, (iv) line dispersion models, (v) integrated emission-meteorological models, and (vi) hybrid models. These latter combine personal or household exposure monitoring with one of the previous methods. Unfortunately, the development of air quality monitoring networks is hindered by the high costs and large dimensions of nodes (monitoring stations) that make impossible to install them in all the critical locations (such as densely populated urban centers). Consequently, the reduced number of data makes the forecasting models more generic for large areas, losing the details of air pollution distribution on the land. Recent advances of tunable all solid state laser sensors and

Lidar technique (Light Detection and Ranging) opened new perspectives in the monitoring and 3D-analysis of atmospheric pollution dynamics. In fact, 3D mappings of concentrations of pollutants have been obtained, allowing a direct access to the physical and chemical dynamics of air pollution (Frejafon et al. 1998). Besides the detection, these species have to be tracked in their movement towards neighboring areas by the use of dispersion models (Steffens, 2009). Low-cost sensors offer the ability to collect highly resolved temporal and spatial data and they have a great potential to revolutionize the way to monitor the exposure of the population to the atmospheric pollution (Tianxing Caia et al., 2014). In this work a dispersion model of pollutions was proposed in order to validate the results obtained with a monitoring of 10 μm particulates in a seaside town of South Italy (Salerno). The monitoring network composed by three sensory systems is located in some relevant points for anthropic activity (Barnard et al., 2001). The first objective is to examine the monitoring area in terms of PM 10 concentration in order to obtain the areas exposed to higher concentrations and to find the sources of pollution. The second objective is to understand the combined effects of distributed and concentrated sources.

2. Materials and Methods

2.1. Monitoring stations

The monitoring stations are composed by sensors for the detection of fine particles at low concentrations (PM 10). They are combined with temperature, humidity, pressure and wind direction sensors in order to better support the elaboration of pollution dispersion model. In particular, fine powders sensors are based on the use of a laser source that crosses an air stream sampling the outside atmosphere. The air stream is conveyed by to the measuring chamber by suction system of the external air. When a particle in this stream crosses the laser beam, scatters this light with a pattern in which intensity and direction distribution depend on the particle size.

2.2. Sensor Networks

The sites interested by installation of the monitoring station have been selected in areas that are heavily affected by human activity. In particular, the three selected points are (as shown in Figure 1): Teatro Verdi (1), Duomo (2), Portanova (3). They are chosen in pedestrian areas just to assess the population's exposure to PM10. The software R was used with the statistical model, called Kriging is a method of interpolation for which the interpolated values are modeled by a Gaussian process governed by prior covariances, as opposed to a piecewise-polynomial spline chosen to optimize smoothness of the fitted values, in order to evaluate the distributions of dusts in the selected periods.



Figure 1: Installed monitoring network.

2.3. Model description

In this work, the Operational Street Pollution Model (OSPM) was used in order to test the possibility to successfully apply it in single monitored streets (J. Silver et al. 2013). Briefly, the main components of the OSPM are summarized as follows. For the pollutant PM 10, the concentrations are modeled as:

$$C = C_{bg} + Q_{trf} (C_{dir}^* + C_{rec}^*) \quad (1)$$

where:

- C is the concentration at the receptor point ($\mu\text{g m}^{-3}$);
- C_{bg} is the background concentration ($\mu\text{g m}^{-3}$);
- Q_{trf} are the emissions from traffic per street length ($\mu\text{g m}^{-1} \text{s}^{-1}$);
- C^* is a function determining the persistence of pollutant including the effect of meteorology, traffic speed and volume and street geometry (units: s m^{-2}). It is composed of a direct, C_{dir}^* , and a recirculation, C_{rec}^* , component.

The concentrations of PM 10 mainly includes the pollutants emitted by vehicles and combustion processes (industrial or house-heating combustion emissions). In the C^* function the C_{dir}^* term is calculated assuming a Gaussian plume, while a box model is used to calculate the contribution from the recirculation vortex (C_{rec}^*). In particular, the recirculation vortex only forms under certain conditions, governed by the wind speed and direction, as well as the canyon geometry. Meteorological parameters as the wind speed and direction are used to determine the size of the recirculation zone. The wind direction and speed are considered in the following way. On the windward side, C^* includes only the recirculating component (possibly with a contribution from the direct component, depending on the length of the recirculation zone) while on the leeward side C^* is the sum of the direct and recirculating components. Both sides account for the urban background. The function C^* includes also the contribution from the turbulence produced by the vehicular traffic, which depends on the speed and the intensity the traffic, as well as from the frontal area of the vehicles. Meandering of the wind direction is also accounted for in C^* , as the wind direction is not expected to remain constant during the 24 h time steps.

2.4. Model inputs

The number of cars, vans, trucks and buses (for km^2) were available for three points for each hour of all days. We also considered the proportion of cold starts and the mean travel speeds at each hour of the day. Vehicle emission factors and vehicle fleet composition are based on the European COPERT IV emission model (EEA, 2009). The temperature, humidity and pressure are considered into the model in order to evaluate the pollution dispersion. In particular, these parameters are included into the model using data from the previous year referred to the monitored area (Salerno). The estimated horizontal dispersion coefficient in an urban environment takes into account the turbulent effects of the highest temperature.

3. Results

Below we report the experimental results related to the anthropic activities in the monitored area. The monitoring campaign lasted two months overall. Some of these results are reported below. In particular, the reported results refer to the most useful days with the sensor networks mentioned above. As shown in Figure 2a (corresponding to a day of the weekend) most of the PM 10 mass would seem to come from the south-

east of the city centre. In Figure 2b (corresponding to a midweek working day) no PM 10 accumulation is found in any part of the monitored territory.

The maximum-recorded concentration is equal to $38 \mu\text{g m}^{-3}$. Compared to a midweek day, it is clear that the intense anthropic activity of the weekend connected to traffic and tourist arrivals increases the average concentration across the analyzed zone. In particular, the maximum concentration in the midweek day is 73% lower than in the weekend. These results demonstrated the good feasibility of OSPM model used in other works (Silver et al., 2013) to compare air quality in shorter periods (weeks). In general, the emissions from buildings must be considered but in the specific case for the particular conformation of the monitored area the effect of point sources of emissions was marginal. From the obtained results the higher contribution of pollution is due to a greater number of vehicles circulation demonstrating a marginal effect of domestic heating.

In Figure 3 a, b, c a concentration profiles of PM 10 in three selected points is shown. Concentrations of PM 10 are recorded every 2 minutes in a time frame from 11 a.m. to 11 p.m. The three graphs show a concentration decrease of particulates during the night period, a peak corresponding to the beginning of the anthropic activities. A reduction of PM 10 concentration is recorded during the morning working hours and subsequently a progressive increase due to the vehicular traffic is registered at the end of the working hours. More in detail, in Figure 3 a in addition to the maximum peak we also note a higher concentration of the PM 10 probably due to the urban orography of the monitored point.

In Figure 3 d, e, f, the daily average values of PM 10 concentration levels measured in the three station points is compared with the OSPM predicted values. The model is able to predict concentration trends of PM 10 in all three monitoring points. In particular, in Duomo monitoring station (Figure 3 d) the model is able to predict all the experimental points while in Portanova monitoring station (Figure 3 e) the lack of correspondence between the model and the experimental data is limited to some days. Probably the reason is a variation between the ratio of the distributed and the concentrated sources.

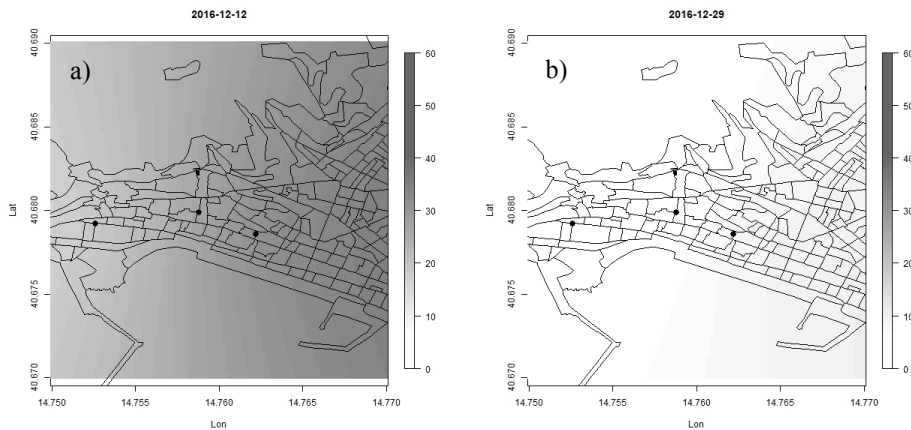


Figure 2: PM 10 concentrations in a weekend (a) and weekday (b).

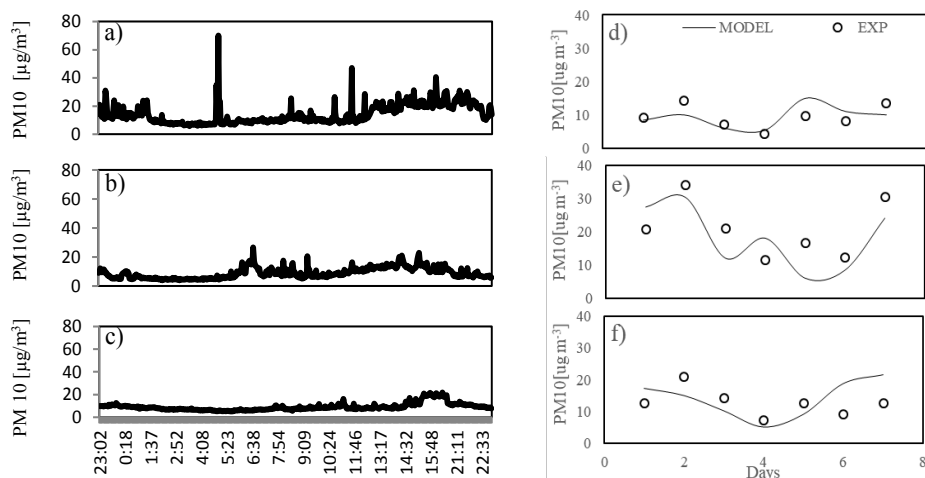


Figure 3: PM 10 concentration profile in Duomo (a), Portanova (b) and Teatro Verdi (c) recorded on Sunday 18th of December. Comparison of experimental and modelled results of PM 10 concentrations in Duomo (d), Portanova (e) and Teatro Verdi (f) monitoring stations.

4. Conclusions

A statistic model was used in order to compare the traffic effects on PM 10 concentration between mid-week and weekend days. In particular, the average concentration is higher in weekends, as expected, due to an increase in anthropic activities. The point of greatest concentration is almost always the Portanova monitoring station. A methodology is proposed to employ OSPM for the prediction of PM 10 concentrations in the town of Salerno. Applying the dispersion model to the experimental data, we can see how the model is able to predict the trend based on the hypotheses carried out mainly in the case of Duomo and Portanova monitoring stations but less in the case of Teatro Verdi station. The reason is probably due a variation of the ratio between distributed and concentrated sources of pollutants.

The successful application of the methodology is confirmed by the fairly good comparison between calculated results with measurements.

In the future in order to further improve the model it would be necessary to increase the number of monitored points and to have more data in the history.

Reference

- J.P. Barnard, C. Aldrich, 2001, Modelling of air pollution in an environmental system by use of non-linear independent component analysis, *Computer Aided Chemical Engineering*, Volume 9, Pages 81-86.
- T. Caia, S. Wang, Q. Xu, 2014, Air Quality Considered Site Selection for New Chemical Plants, *Computer Aided Chemical Engineering*, Volume 34, Pages 273-278.
- EEA, 2009, EMEP/CORINAIR Atmospheric Emissions Inventory Guidebook, Chapter on Exhaust Emissions from Road Transport, Version June 2009, Methodology for COPERT 4. Technical Report, European Environmental Agency, p. 128.

- E. Frejafon, J. Kasparian, P. Rambaldi, B. Vezin, V. Boutou, J. Yu, M. Ulbricht, D. Weibauer, B. Ottobriani, E. de Saeger, B. Kramer, T. Leisner, P. Rairoux, L. Woste, J.P., Wolf, 1998, Laser applications for atmospheric pollution monitorin. *The European Physical Journal D*, Volume 4, Pages 231-238.
- M. Jerrett, A. Arain, P. Kanaroglou, B. Beckerman, D. Potoglou, T. Sahsuvaroglu, J. Morrison, C. Giovis, 2005, A review and evaluation of intraurban air pollution exposure models, *Journal of Exposure Analysis and Environmental Epidemiology*, Volume 15, Pages 185-204.
- K. Klein, P. Plate, 1999, Wind-tunnel study of concentration fields in street canyons, *Atmospheric Environment*, Volume 33, Pages 3973-3979.
- C. A. McHugh, D. J. Carruthers, H. A. Edmunds, 1997. ADMS and ADMS-Urban. *International Journal of Environment and Pollution*, Volume 8, Pages 438-440.
- H. K. Salehi, D. Sofia, D. Barletta, M. Poletto, 2015, Dust Generation in Vibrated Cohesive Powders, *Chemical Engineering Transactions*. Vol. 43. Pag.769-774.
- J. D. Silver, M. Ketznel, J. Brandt, 2013, Dynamic parameter estimation for a street canyon air quality model, *Environmental Modelling & Software*, Volume 47, Pages 235-252.
- J. Steffens, E. Landulfo, R. Guardani, C. N. Oller, A. Moreira, 2009, Measurements of Air Quality Using Lidar System *Computer Aided Chemical Engineering*, Volume 27, Pages 1443-1448.

Modelling of biomass residence time distribution and xylan depolymerization kinetics analysis in a Pilot-Scale Pretreatment Continuous Tubular Reactor

Felicia Rodríguez^a, Arturo Sánchez^{a*}

^a*Laboratorio de Futuros en Bioenergía, Centro de Investigación y de Estudios Avanzados del IPN Unidad Guadalajara, Av. Del Bosque # 114, CP 45019, Jalisco, México*

arturo@gdl.cinvestav.mx

Abstract

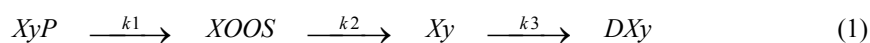
An empirical mathematical model to describe the xylan depolymerisation in a pilot-scale pretreatment continuous tubular reactor (PCTR) is presented. The proposed model involves depolymerization kinetics and mass flow dynamics. Although the reactor was modelling as a set of reactors in series, typical impulse response delays, kinetic behaviours and disturbances in the initial concentration of xylans were successfully simulated with low computational cost. Tracer injection method and experimental runs using corn stover at different PCTR operational conditions were used for experimental validation. Additionally, the accuracy of the proposed model and the classic modelling method were compared.

Keywords: Residence time distribution, continuous reactor, pretreatment, parameters estimation, autohydrolysis.

1. Introduction

Pretreatment is one of the most important steps in the biorefining of lignocellulosic biomass (LCB) to bioethanol and high value-added products. Among pretreatments, autohydrolysis followed by a sudden decompression (steam explosion) is gaining importance at industrial scale due to its high hemicelluloses release yield and increments in cellulose availability with low environmental impacts and acceptable CAPEX and OPEX. Previous studies indicate that hemicellulose depolymerization is due to autohydrolysis reaction (induced by water, organic acids and temperature witch the biomass is subjected before the decompression); while the sudden depressurization has a minimum contribution (Rodríguez et al., 2017).

Xylan is the main component in the hemicelluloses of different LCB sources, such as wheat straw, cane bagasse, corn stover, and agave bagasse. Besides increasing the bioethanol production yields, others different high added-value products can be also obtained from LCB xylan release. The simplest xylan autohydrolysis description is the set of simultaneous reactions described by Eq. (1), where XyP are polymeric xylan,



XOOS are short xylooligosaccharide chains, *Xy* is xylose and *DXy* are degraded xylans. k_1 , k_2 and k_3 are reaction rate constants of pseudo first order kinetics with Arrhenius temperature dependence. Therefore, temperature and residence time can be employed as control variables in order to produce maximum amounts of oligosaccharides and monomers as well as minimum degradation compounds. Temperature and residence time dependence of xylan depolymerization by autohydrolysis have been widely reported in batch reactors at laboratory scales. However transport phenomena (e.g. mass flows) also influence the kinetics in continuous reactors.

Analysing tubular reactor as a set of subsystems is a common technique for modelling the flows patters. According to Fogler (1999), experimental measurement of residence time distribution (RTD) using tracer injection and exit age density function ($E(t)$) provide valuable information to improve continuous reactor modelling. Mean residence time (t_m), variance (σ^2) and the number of tanks in series needed to describe the RTD (n) can be calculated from experimental results.

However, previous analysis of isothermal autohydrolysis kinetics in experimental runs in a pilot-scale PCTR showed that effects of biomass rheological characteristics (e.g. elasticity, flowability, viscosity and density) and mechanical reactor components must be taken into consideration on reaction models. Both items produce non ideal flows inside the reactor and therefore they influence in the particles age.

In this work an empirical mathematical model of xylan depolymerization in a 5 kg/h PCTR is proposed that may serve as the basis for designing control strategies.

2. Pretreatment continuous tubular reactor description

LCB is exposed to 3 pretreatments in the PCTR: extrusion, autohydrolysis and steam explosion (See Figure 1). Extrusion is carried out in the feeding section, where biomass is placed in the reactor body by a 4:2 extruder. Autohydrolysis is carried out while the LCB is transported along the reactor by a speed controlled screw conveyor. Water and thermal energy required for the reaction are provide by a steam supply. At the end, two globe valves open asynchronously producing steam explosion and consequently biomass output.

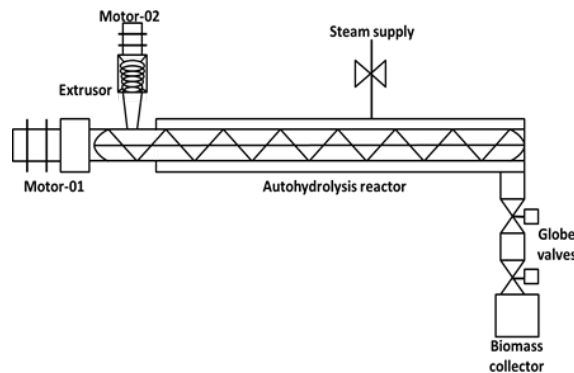


Figure 1: Pretreatment continuous tubular reactor (PCTR) diagram.

3. Experimental and simulated data

3.1. Experimental runs

Biomass pretreatment was carried out in the PCTR at 150 psi (180 °C approx.). Measured wet corn stover was manually fed in the hopper extruder. The extruder motor speed (Motor-02) remained constant throughout the experiment. The tested screw conveyor speeds (CS) were 100, 75, 50 and 33% of the nominal motor speed. The reactor operating conditions were constants for at least 2 hr in order to achieve the mechanical and chemical steady state (SS). After the system reached the SS a synthetic polymer tracer was fed in the PCTR. Valves opening frequency was fixed every minute and the biomass collection each 2 minutes.

3.2. Xylan depolymerization modelling

The effects of the PCTR on the biomass composition are synergy of individual contributions of extrusion, autohydrolysis and steam explosion phenomena. However, Rodriguez et al. (2017) showed that sudden changes of pressure from 150 psi to atmospheric pressure do not contribute significantly in the xylans depolymerization. Therefore, in this work xylan depolymerization yields were described using autohydrolysis variables. The autohydrolysis reaction was modelled as a first order reaction based on the reaction scheme of Eq. (1). The PCTR was approximated to a set of reactors in series with variable volume. Each screw conveyor vane was considered as a subreactor (r), so that the PCTR was modelled as 14 subreactors. Concentration of xylan in each subreactor ($[XyP]_r$) can be calculated from Eq. (2) and (3):

$$\frac{d[XyP]_r}{dt} = \frac{F_{r-1}}{m_r} [XyP]_{r-1} - \frac{F_r}{m_r} [XyP]_r - k[XyP]_r - \frac{[XyP]_r}{m_r} \frac{dm_r}{dt} \quad (2)$$

$$\frac{dm_r}{dt} = F_{r-1} - F_r \quad (3)$$

Where m_r is the mass in each subreactor, F_{r-1} and F_r are the input and output mass flow in the subreactor, respectively. Reaction rate constant (k) was estimated from experimental data using Particle Swarm Optimization (PSO) method (Rodríguez, 2014).

3.3. Mass flow modelling

Rheological characteristics of the biomass and mechanical components of the PCTR as well as operational conditions are important factors influencing biomass flows. Jaramillo (2017) developed an empirical model described by Eqs. (4) to (7) to estimate the biomass flow based on switched systems theory. In this model, the reactor was divided in 2 sections. The first part involves the extrusion step (Eq. (1) and (2)) where F_0 is the biomass extruder output, which depends on flow rate input (U), extruder fill delay (K_1) and biomass type dependent constants that describe the behaviour of the flow after a change in the motor speed (θ_1 to θ_4). In the second part, the model considers the reactor body as a set of subreactors in series with delay (δ_2). θ_5 and θ_6 are sampling period constants.

$$x_E(k+1) = \theta_1 x_E(k) - \theta_2 x_E(k-1) + \theta_3 U(k) - \theta_4 U(k-1) \quad (4)$$

$$F_0(k) = K_1(k)x_E(k) \quad (5)$$

$$x_r(k+1) = \theta_5 x_{nr}(k) + \theta_6 x_{(n-1)r}(k - \delta_2) \quad (6)$$

$$F_r(k) = x_r(k) \quad (7)$$

In this work, the proposed model incorporates Eqs. (2) and (7) in order to accurately describe the xylan depolymerization rate with low computational cost. Additionally, simulations using number of reactors (n) calculated from moments of RTD curves (Eq. (8)) at constant t_m and biomass flow (F_r) were analysed for comparative purposes. These assumptions are referred in the text as RTD-t.

$$n = \frac{t_m^2}{\sigma^2} \quad (8)$$

4. Results

4.1. Experimental and simulated RTD's curves

Figure 2 shows normalized concentration of tracer at four CS. As shown in the “RTD 100% curve” (screw conveyor is working at 100% of its nominal speed), the impulse responses are at least 16 min delayed and the spread across the reactor is more than 9 min. Delay time increased indirectly proportional to the CS in a non-linear way. The four experimental RTD's curves were used to estimate parameters of Eq. (4) to (6) by PSO and then, mass flows from Eq. (7). Simulation of “RTD 100%” using the proposed model is depicted in the continuous line (curve 14) of Figure 3. Response delay and the mass dispersion were satisfactorily approximated.

A total of 115 subreactors in series are required when Eq. (2) under RTD-t assumptions is applied to describe dispersive effects of the biomass inside the reactor. Simulations of “RTD 100%” using 14 and 115 subreactors with RTD-t characteristics are shown in the dotted (14 RTD-t) and dashed (115 RTD-t) lines in Figure 3, respectively. 115 subreactors in series describe in a correct manner the RTD curve. Actually the mean square error is 25 % less than the simulation of the proposed model. However, as shown in Eq. (1), xylan depolymerization reactions must be described for four equations in each subreactor, thus computational cost increases significantly when 115 subreactors are used. Therefore, using Eq. (7) for mass flow estimation we can save the computational cost up to 87% without significantly increasing the error in the estimation of t_m and σ^2 values.

4.2. Experimental depolymerization data

Experimental fraction of unreacted xylan from pretreated corn stover at 100, 50% and 33% of CS are shown in Figure 4 with black circles. Vertical semicontinuous lines show the time when changes were made in the CS set point.

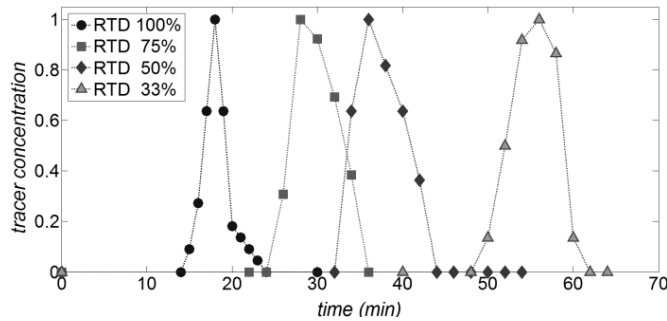


Figure 2: Tracer RTD curves at four screw conveyor speeds (CS).

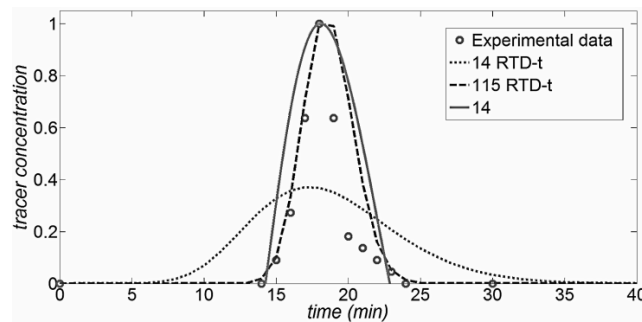


Figure 3: Experimental data and simulation of RTD using reactor in series technique.

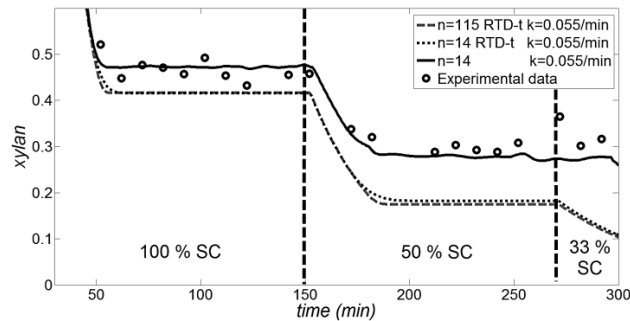


Figure 4: Experimental data and simulation of xylan depolymerization.

Two SS can be identified in the time interval of 60 to 150 min and 215 and 250 min, that corresponding to the operation of the screw conveyor at 100 and 50% of its nominal speed, respectively. Results show that t_m increases proportionally when the CS decrease to 50% and the reaction yield increase from 53 to 70%.

4.3. PCTR simulations

Black line represents the simulation of Eq. (2) using Eq. (7) to estimate the mass flow in Figs. 4 and 5. Dotted and dashed lines are the simulation of 14 and 115 reactors under RTD-t conditions. Experimental data were fitted to the proposed model in order to estimate k by PSO method, whose value is 0.055/min. As shown in fig 4, the proposed model describes the behaviours of the autohydrolysis reaction in the stationary states as well as during the transient states due to CS decreasing. Simulations under RTD-t assumptions with the CS working at 100% could be acceptable, however the simulation

error increase by decreasing the CS to 50%. The estimated value of k from RTD-t conditions is 0.0475/min. Region 1 and 2 (R1 and R2) of Figure 5 show that RTD-t simulation only converges with the proposed model when the CS is 100%.

4.4. Simulation of initial concentration changes

Figure 5 shows the simulation of impulse responses to changes in the initial concentration of xylan in the biomass at two CS (100 and 50%). The proportion of xylan in the hemicelluloses chains decreased from 100 to 50% in the region bounded by vertical dotted lines. The magnitude of the impulse response at 100% of the CS was equal in the 3 cases. However, the proposed model really involved the responses delay observed on the RTD curves (Figure 3). Also, the ability of the proposed model to describe the response delay was more evident when the CS was at 50%, since the SS was reached 10 minutes after that the simulation with 115 subreactors.

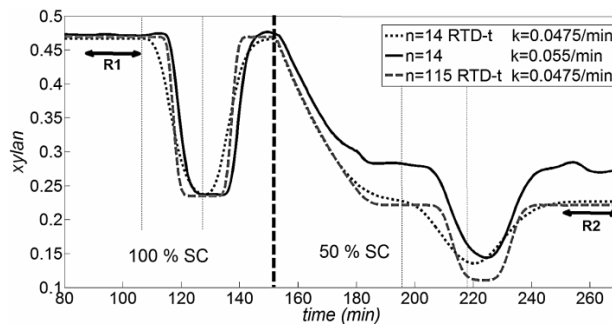


Figure 5: Simulation of xylan depolymerization with disturbances.

5. Conclusions

Results show that biomass transfer phenomena should not be omitted in the pretreatment process modelling, especially impulse response delay. The PCTR can be described by 14 subreactors in series using an accurate model to describe the mass flow rates, as the selected model does. Experimental residence time distribution and xylan depolymerization behaviours were successfully simulated from the proposed model and estimated autohydrolysis kinetic parameters. This model can be used as an important tool to control the of xylan depolymerization cascade reactions inside the PCTR with low computational cost.

References

- H.S. Fogler, 1999, Models for nonideal reactors, Elements of chemical reaction engineering, 3ed ed., pp 893-900, United States.
- F. Rodríguez, A. Sánchez, 2014, Particle swarm optimization (PSO): A method to improve kinetic parameters estimation of lignocellulosic biomass autohydrolysis, 3th Symposium on Biotechnology applied to lignocelluloses, October 26-29, Concepción, Chile,
- F. Rodríguez, A. Sanchez, C. Parra, 2017, Role of Steam Explosion on Enzymatic Digestibility, Xylan Extraction, and Lignin Release of Lignocellulosic Biomass, Sustainable Chemistry and Engineering, Volume 5 (6), pp 5234–5240, DOI:10.1021/acssuschemeng.7b00580.
- I. Jaramillo, 2017, Modelado del flujo másico y control de tiempo de residencia en un reactor tubular continuo de pretreatmento, Master's thesis (in spanish), CINVESTAV UGdl, México.

Simulation and Analysis of Indian Residential Electricity Consumption Using Agent-Based Models

Sohini Dhar¹, Babji Srinivasan² and Rajagopalan Srinivasan^{3*}

¹*Department of Electrical Engineering, Indian Institute of Technology Gandhinagar, Gandhinagar, 382355, India*

²*Department of Chemical Engineering, Indian Institute of Technology Gandhinagar, Gandhinagar, 382355, India*

³*Department of Chemical Engineering, Indian Institute of Technology Madras, Chennai-600 036, India*

babji.srinivasan@iitgn.ac.in, raj@iitm.ac.in

Abstract

The increasing demand of residential consumption and the integration of renewable energy sources have motivated researchers to develop grid simulations for testing energy management strategies. Agent-based modelling is one such methodology with the capability of mimicking the emergent and complex behaviour of grids over time. Thus, we have utilized this concept to model and predict the energy consumption of a house. Results from the simulation indicate the proposed approach closely mimics the fine-grained energy data obtained from the residential unit in India. This model possesses the flexibility to be extended to estimate the electricity demand of different localities in India and, in step, to understand the behaviour of the agent with the integration of low carbon technology.

Keywords: agent-based simulation, energy demand modeling, domestic sector, residential consumption.

1. Introduction

Domestic Sector in India accounts for 22% of the current electrical consumption which has increased from 80 TWh in 2000 to 186 TWh in 2012 (Rawal et al., 2014). It is predicted that the energy consumption in the domestic sector will increase by more than eight times by 2050. In order to manage the unsustainable energy demand, we need to focus on energy efficient management strategies and integration of Renewable Energy Sources (RES). Applications like demand side management (DSM), battery integration and micro grid with self-sustaining capabilities can help in efficiently utilizing the increased generation from RES for household energy consumption (Palensky et al., 2011). In order to plan and invest in better residential grid management strategies, it is essential to develop models of electricity consumption in the residential sector.

One of the approaches to model the behaviour of grid is by considering any of house, distribution sub-station, generator, humans, etc. as an agent, called agent-based modelling (Phelan and Scholl, 2004). It has the capability to model emergent behaviour of interactions by changing agent's behaviour and characteristics with time. This property of ABM can efficiently model the behaviour of a complex socio-technical system arising in biological, economic, engineering and social sciences (Alexrod et al., 1997). ABM approaches rely on the statistical data collected through audits for both model development and validation of residential consumption. Our work deals with collection of appliance level data from an Indian household and using the same to

develop fine-grained model of the residential grids. Results from our study show the distinct behaviour of Indian household over weekdays and weekends by modelling each major power consuming appliance. The behaviour of each appliance is validated with actual data and the errors in modelling are presented.

The paper is organized as follows: Section 2 summarizes the techniques used for modeling residential grids. Section 3 deals with agent based models in residential grids. A case study to validate our method is presented in Section 4. The article ends with a few concluding remarks.

2. Models for Residential Grids

Top-down and bottom-up are two distinct approaches used for modelling residential grids. Top down models “treats the residential sector as an energy sink and does not distinguish energy consumption due to individual end-uses”. In contrast, bottom up approaches extrapolates the residential consumption of individual sectors to estimate the energy demand of the whole residential grid. If the construction of any house is increased to 10% of the units, it will be difficult for the top-down approach to show its consequences in terms of increased demand as the vintage distribution of the housing stock would be changed significantly. Also, the reliance on historical data is a major drawback for these models as they have no capability of extrapolating discontinuous advances in technology, whereas, bottom up modelling takes into account the details of climate properties, indoor temperatures, occupancy schedules, equipment use etc. Although the simulation techniques become complex with this intricate level of modelling, yet the errors are highly minimized as compared to top-down approach (Swan and Ugursal, 2009).

Top down models are depended on statistical data and economic theory. A model for residential energy use in New Zealand uses this top-down approach (Saha and Stephenson, 1980). It describes the energy use at the national level for four types of fuels (electricity, oil, gas, and “others”). This study separately analyses the consumption due to end uses like space heating, domestic hot water, cooking which is then aggregated to obtain the annual energy consumption. This model predicts the consumption over 1960s and 1970s very well but since it does not take into account the shifts in home insulation levels, there is a mismatch between the actual and predicted results towards the end of 1970s. Their approach cannot estimate the city or further more segregated levels of consumption.

In contrast, the bottom-up approach identifies the contribution of each end-use towards the aggregate energy consumption value. It takes into account the electricity consumption at a much more ground level and then aggregates the total consumption to obtain the annual electricity consumption for the domestic sector. A case study in Chongqing (Yang et al., 2015) uses a bottom up model. Here, the residential household appliances are hourly monitored for a week. Based on this data certain rules are created to estimate the hourly energy consumption, running time, usage frequency and power of household appliances. The results are validated by the actual energy consumption value of residential building of a university in Chongqing. A deviation of 22.4% was established between the residential model and its true values. This study lacked the granularity of appliance level consumption in terms of time and power which can be addressed by monitoring the consumption at higher frequencies (in terms of minutes or

seconds). One of the bottom-up approaches which have recently been used to incorporate the emergent behavior of residential grids is agent based modelling.

3. Agent Based Models

Agent-Based Modelling and Simulation (ABMS) has been extensively used to study electricity systems integrated in an economic, technical and social context. In particular the dynamics of smart grid transitions require appropriate modelling approaches to understand such a complex model. The main focus of these modelling approaches lies in dealing with concepts related to demand response, distributed generation, intermediaries and their interactions with prosumers (active electricity consumers- who consume as well as produce electricity) as well as local markets and their integration in centralized markets. These approaches allow simulating in detail the behaviour of particular agents and observing an emergent development on system level by letting agents decide individually, cooperatively or competitively. Despite being a promising approach to increase the flexibility of modelling electricity systems, the reviewed literature struggles with well-known challenges of agent-based models concerning model description, calibration, verification, validation, and publication. However, studying smart grids with ABMS models is young and, therefore, a limited field of research and much work needs to be done in this field (Ringler et al., 2016).

A case study of London simulates the residential electricity and heat demands in urban areas using agent based approach (Bustos-Turu et al., 2016). It considers the humans living in these areas as agents. The data is calculated from seven boroughs in London covering an area of 175 km². Here, each borough or zone is simulated separately to understand the differences by taking into account factors like urban layout, land-use, socio demographic characteristics, energy infrastructure access, conversion technologies and user behaviour which affect the electricity profiles. The difference in statistical data and model was found to be 14.9% on an average. This study does not take into account the appliance level data or electricity consumption of individual buildings of each borough considered.

In this paper, we propose an agent based model to estimate the power consumption trend of a house and validate the same using information obtained from our NILM algorithm (Patel et al., 2016). Electricity data is collected at 1 Hz frequency from an Indian household and application of NILM algorithm (on this data) provides the electricity consumption profile (function of time) of various appliances. This information is used to model individual appliances in agent based simulation. The simulation studies takes into account factors like weather variations, the working status of the members of the household, the appliances present in their home, their consumption pattern and usage frequency that influences the residential energy consumption based on a local survey.

4. Case Study

The agent in our study is a house whose attributes are the appliances it contains. House consists of the following major power consuming appliances: refrigerator, television, washing machine, water purifier, dishwasher, air conditioner and rice cooker. All these appliances have distinct power consumption pattern. In our approach we model each appliance by splitting the consumption pattern based on their statistical characteristics. Each interval of the consumption pattern that has same statistical properties across

multiple runs is considered as a region. For example, appliances with motor element have an initial spike region before consumption settles to form a steady state region. In our study, this peak and the following steady part are modelled as two distinct regions.

Table 1: Refrigerator model parameters

Regions	Power ($\mu \pm \sigma$) (W)	Slope	Intercept	Duration ($\mu \pm \sigma$)(s)
Peak region	740.73 \pm 370.15	-	-	2 \pm 0
Slope region	139.40 \pm 4.63	-0.01	147.43	1238 \pm 30
Off region	1.84 \pm 0.52	-	-	3423 \pm 238

Each region is modelled by extracting following characteristics from the training data: mean power (P), slope (m) and intercept (c) of the region, variance (σ^2) of the fluctuations observed in the region and the duration of the region. Let us consider refrigerator as an example. As shown in Fig.1a the refrigerator (manufacturer-Whirlpool) has three regions: the peak region, the slope region and the OFF region. This pattern is repeated throughout the day. The refrigerator's pattern is modelled using the data of 15 patterns. We used 15 such patterns to train the parameters for each region. The parameters obtained from the training data are shown in Table 1. Five patterns are used as test data to calculate the error in our model. All other appliances like dishwasher, rice cooker, television, air conditioner, washing machine and water purifier are modelled in a similar manner. Every region in their power pattern is modelled separately. We validate our results by calculating the Percentage Error (PE) between our model and the test data.

$$PE = \frac{1}{n} \sum_{k=1}^n \frac{|P[k] - \hat{P}[k]|}{\max(P[k])} \quad (1)$$

Here, $P[k]$ is the actual power consumption and $\hat{P}[k]$ is the estimated consumption of an appliance at instant k . The results of our analysis are presented in Table 2.

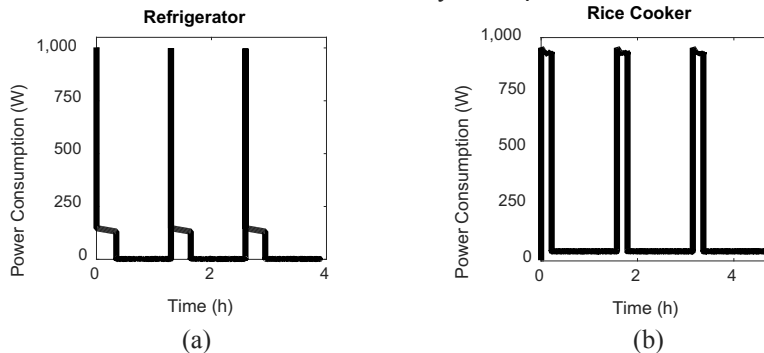


Fig. 1a : Behaviour of Refrigerator cycles; 1b: Behaviour of Rice Cooker cycles

Based on the survey of the usage time and frequency of each appliance we build a probabilistic model of the house. The rules for the agent are determined from the survey data obtained from the house being modelled. For example, refrigerator operates throughout the day so its pattern is repeated continuously, a TV operates approximately between 12pm-3pm on a weekend, we define a rule in which the model randomly chooses a turn on time between 12pm-12:30pm and also a duration of 2 $\frac{1}{2}$ -3hours

between which the TV is on. Similarly all other rules are laid down for each appliance. In this way house agent is modelled by integrating the region based model of each appliance with survey data containing information about time and its usage to estimate the consumption of the major appliances in the house. The consumption of entire house is obtained by aggregating the consumption of each appliance.

The behaviour across weekdays and weekends show a distinct pattern. Fig. 2a and Fig.2b shows the average consumption over a period of twenty days for the house during weekdays and weekends.

Table 2: MAPE of appliances

Sl. No.	Appliances	Regions of Appliances	Training Error (%)	Test Error (%)
1	TV	Region 1(on)	7.15	7.38
2	Rice Cooker	Region 1(Slope)	0.05	0.06
		Region 2(Steady State)	0.30	0.31
		Region 3(Fan Area)	0.52	0.56
3	Washing Machine	Region 1(rinse: on)	3.50	4.30
		Region 2(rinse: off)	5.70	6.40
		Region 3(heat: on)	0.38	0.49
		Region 4(heat: off)	0.30	0.45
4	AC	Region 1(temp 20°C: on)	0.83	0.97
		Region 2(temp 20°C : off)	9.70	10.00
		Region 1(temp 25°C : on)	1.72	1.80
		Region 2(temp 25°C : off)	9.03	9.31
5	Water Purifier	Region 1(Peak)	0.36	1.43
		Region 2(Slope)	0.01	2.83
		Region 3(Steady State)	2.85	2.94
6	Dish Washer	Region 1(65°C Wash-heat)	0.71	0.79
		Region 2(65°C Wash-rinse)	3.87	5.10
		Region 3(Intermediate-heat)	0.70	0.73
		Region 4(Intermediate-rinse)	2.95	5.00
		Region 5(Hot-heat)	0.78	0.85
		Region 6(Hot-rinse)	6.04	6.46

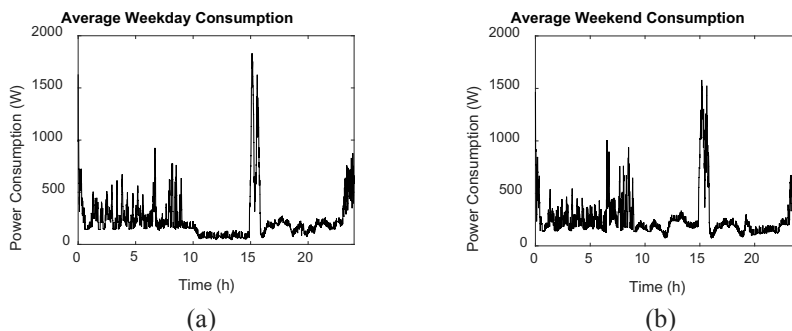


Fig. 2a: Average Weekday Consumption; 2b: Average Weekend Consumption

It is visible from Fig. 2a that there is minimum consumption for weekdays around 10am-3pm where usually the working members are not at home. The highest peak occurs between 3pm-4pm which indicates the dishwasher is being operated regularly. The behaviour of AC is visible during the early morning and late night period. The other appliances like washing machine are usually operated four to five times a week in the morning period. The weekend afternoons show the operation of TV in Fig.2b.

5. Conclusions

In this work, an agent based simulation model is developed to estimate the electricity consumption in the residential sector. The model is tested to mimic the power consumption trend of a house based in Gandhinagar; and the results are compared with the appliance level data obtained from the house which is expected to increase the accuracy of our predictions. This work also takes into account an almost exact user behaviour to arrive at the results which show that the behaviour of the house can actually be reproduced by understanding the consumption pattern and usage frequency.

Since this model takes into account the individual appliance level data, it ensures granularity but also consumes time. Future work will be to develop a model using ABM to mimic a residential colony. Also if we are able to collect the actual data containing details about base and peak loads of consumption throughout the day, it would help us in estimating the total power consumption of the house with minimal errors. This approach can then be validated to estimate the power consumption variation in places having a completely different weather conditions, user behaviour and socio economic factors which will then help to model the Indian domestic sector. We can then model our grid with the integration of renewable resources in order to look for ways to curb the increasing power demand.

References

- Axelrod, R. M. *The complexity of cooperation: Agent-based models of competition and collaboration*. Princeton University Press, 1997.
- Bustos-Turu, G., K.H.V. Dam, S. Acha, C.N. Markides, N. Shah "Simulating residential electricity and heat demand in urban areas using an agent-based modelling approach." *Energy Conference (ENERGYCON), 2016 IEEE International*. IEEE, 2016.
- Palensky, P., and D. Dietrich. "Demand side management: Demand response, intelligent energy systems, and smart loads." *IEEE transactions on industrial informatics* 7.3 (2011): 381-388.
- Patel, N., B. Srinivasan, and R.Srinivasan. "Non-intrusive appliance load monitoring for electric energy systems simulation and analysis—a case study in India." *European Symposium on Computer Aided Process Engineering*, 2016.
- Phelan, Steven E. "Using Integrated Top-down and Bottom-up Dynamic Modeling for Triangulation and Interdisciplinary Theory Integration", 2004.
- Rawal, R., and Y. Shukla. *Residential buildings in India: energy use projections and savings potentials*. Global building performance network (GBPN). technical report, 2014.
- Ringler, P., D. Keles, and W.Fichtner. "Agent-based modelling and simulation of smart electricity grids and markets—a literature review." *Renewable and Sustainable Energy Reviews* 57 (2016): 205-215.
- Saha, G. P., and J. Stephenson. "A model of residential energy use in New Zealand." *Energy* 5.2 (1980): 167-175.
- Swan, L. G., and V.I. Ugursal. "Modeling of end-use energy consumption in the residential sector: A review of modeling techniques." *Renewable and sustainable energy reviews* 13.8 (2009): 1819-1835.
- Yang, Q., M. Liu, C. Huang, Y.Min, Y. Zhong. "A model for residential building energy consumption characteristics and energy demand: a case in Chongqing." *Procedia Engineering* 121 (2015): 1772-1779.

Dull or bright you still get electric delight: A new approach to the design of all-weather panels

Sahar Hajizeinalibioki, Daniel Sebastia Saez, Oleksiy V. Klymenko, Harvey Arellano-Garcia*

Department of Chemical and Process Engineering, University of Surrey, Guildford GU2 7XH, UK

h.arellano-garcia@surrey.ac.uk

Abstract

Modern renewable energy sources have a great disadvantage of being intermittent. Harvesting solar energy directly using photovoltaic panels is one of the most promising renewable energy technologies. While this allows electricity generation during daytime when the sky is clear, at night there is no production at all and it is greatly diminished in cloudy or rainy conditions. Recently a concept of all-weather solar cells was proposed by Q. Tang et al. (*Angew. Chem. Int. Ed.* 55(17) (2016) 5243-5246) in which a solar panel was covered with a layer of graphene. This allows collecting energy from falling raindrops containing dissolved salts through charging and discharging of an electrical double layer at the water-graphene interface, which acts as a pseudocapacitor. Although this setup allows harvesting both direct solar radiation and some of the kinetic energy of falling rain drops, the output is low for realistic salt concentrations while the graphene layer diminishes the solar-to-electric conversion rate.

In this work, we propose a different approach to the same problem. Instead of relying on a sufficient concentration of salts in rain water, we propose to convert the mechanical energy delivered by drop impacts directly into electrical energy by supporting a thin-layer solar panel with an array of piezo crystals. The advantage of this setup is that the solar-to-electric performance of such a panel is not affected by the added piezoelectric support. However, only a fraction of the kinetic energy of the falling rain drops can be converted due to the energy dissipation within the material of the thin-layer panel. We have conducted detailed modelling of kinetic energy harvesting process from the drop impact and spreading to the dissipation of mechanical strain through the panel to the generation of piezoelectric potential. The results illustrate the viability of this concept, but they are still to be confirmed experimentally and require an economic feasibility analysis to be performed.

Keywords: renewable energy, rain energy, all-weather panels, piezoelectric energy harvester

1. Introduction

The development of cheap, efficient and reliable ways of harvesting energy from renewable sources is key to the solution of a number of global challenges such as providing power to an estimated 1.2 billion people (World Energy Outlook, 2016) who currently live without access to electricity, and combating climate change by substituting fossil fuels used for power generation. Renewable energy generation from all sources has been growing at a staggering rate of over 14% over the last 10 years,

however its share is still low relative to fossil fuels. Among the renewable sources, wind and solar generation are developing most rapidly. The former benefits from relatively high energy density of wind so large amounts of energy can be harvested from a relatively small area. The main disadvantage of wind power though is that the efficiency of generation increases with increasing turbine size, so substantial capital investment is required for efficient generation, which may be a limiting factor in poor or sparsely populated areas. On the other hand, the efficiency of harvesting solar energy using photovoltaic (PV) cells (which is the main type of solar panels) is independent of scale making it a more flexible and affordable (at least at small-to-medium scale) energy source. Moreover, the efficiency of the PV cells has increased dramatically over the last two decades with commercial panels achieving over 22% efficiency in commercially available panels and up to 46% efficiency in experimental solar cells. The main issue with the solar energy is its variability and intermittency due to the diurnal and annual cycles as well as the effects of cloud cover, snow, fog or dust. In fact, the solar energy is nearly zero 65-70% of the hours of the year.

There is, however, a largely overlooked renewable source available throughout at least 2/3 of land on Earth. This resource is rain. We already make use of hydroelectric power which utilises the potential energy of precipitation collected in a reservoir located at high altitude versus a lower reservoir. However, the enormous amounts of kinetic energy carried by raindrops as they fall to the ground are simply dissipated into the environment. Capturing this kinetic energy as the raindrops approach the ground would provide an additional contribution without affecting the output of hydroelectric generation. Combining raindrop kinetic energy harvesting with PV generation is also expected to reduce somewhat the intermittency of electricity generation since raindrop energy would partially compensate for the diminished solar irradiation in rainy conditions.

The amount of energy in question is indeed non-negligible. It has been estimated that in a country like Malaysia the annual average kinetic energy of rainfall is around 0.4 kWh/m²/day compared with ~5 kWh/m²/day of solar irradiance (Chua et al., 2016). This prompted a number of investigations into the possibility of harvesting this energy (Chua et al., 2016; Ilyas and Swingler, 2015; Wong et al., 2015; Zheng et al., 2014). The main approaches described in the literature include various applications of the piezoelectric effect to convert the mechanical strain caused by falling drops or collected rainwater (Guigon et al., 2008; Wong et al., 2015) as well as collecting the electrostatic energy of raindrops (Zheng et al., 2014) and using an electrochemical method relying on the effect of charging-discharging of the electrical double layer when a raindrop containing NaCl moves along a graphene-coated surface (Tang et al., 2016; Zhang et al., 2016). Despite the apparent simplicity of the latter approach the amount of energy generated is strongly dependent on the concentration of the salt, and it is low even for unrealistically high concentrations of NaCl (~3 orders of magnitude higher than the natural levels).

The use of the piezoelectric effect, on the other hand, is seen as a viable method of converting the kinetic energy of raindrops into mechanical deformations and vibrations of a piezoelectric material, which are in turn converted into electric potential. Piezoelectric energy harvesting (PEH) technologies have been widely used to convert vibrations and motions from any movements to electricity. Low cost of fabrication, simple structure and ease of application make them an affordable solution for many situations (Kumar et al., 2015; Wong et al., 2015). Although the concept of combined solar and piezoelectric energy harvesting has been around for some time, the existing contributions have not

offered a thorough computational framework instead limiting themselves to experimental measurements, quantitative estimations of energy output or partial modelling of the complex process of energy conversion inside such hybrid devices.

The aim of this study is to offer the first comprehensive modelling approach considering all the steps in detail: from the impact and spreading of raindrops on the surface of the panel, deformation and ensuing vibrations of the panel due to the pressure exerted by the spreading drop, and the electric potential ensuing from the ensuing compression of the piezoelectric crystals. This new model will then be used in an optimisation framework to design all-weather panels with maximum overall performance.

2. Modelling methodology

Falling raindrops are affected by drag and gravitational forces. For simplicity, in the following we assume that there is no side wind so that both forces act along the vertical axis. Provided the drop is not overly large (i.e., up to 5 mm in diameter), drag eventually equilibrates the gravitational pull due to the transfer of momentum from the drop to the surrounding air through eddies, and the drop reaches a terminal velocity, which determines its kinetic energy when it hits the ground. For drops ranging from 0.5 mm to 4 mm in diameter their terminal velocities lie between 2.06 m/s and 8.83 m/s. On the other hand, larger drops tend to flatten, become unstable and break up into smaller near-spherical ones (Ilyas and Swingler, 2015). Since heavy rain would naturally generate more energy, we focus here on the larger raindrops 4 millimeters in diameter with the terminal velocity at 8.83 m/s. This is a realistic value for the average drop diameter during a typical tropical thunderstorm.

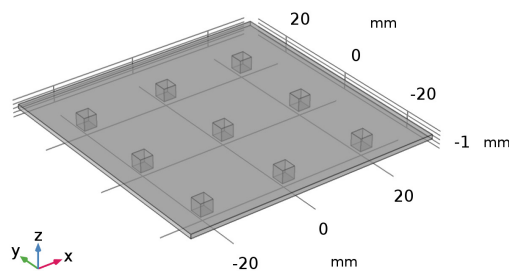


Fig. 1. Geometry of the hybrid solar-piezo panel

The solar panel-piezoelectric crystals assembly considered in this work is shown in Fig. 1. The panel is assumed to be horizontal with raindrops falling strictly vertically. The panel is supported by a square array of piezo crystals represented by small cubes underneath the solar panel. Note that the impact probability is uniform throughout the surface of the all-weather panel.

Before the piezoelectric response of the hybrid panel to raindrop impacts can be simulated the impact itself and the subsequent spreading of the drop over the panel surface must be well understood quantitatively. We simulated this process using the volume of fluid (VOF) method in ANSYS 15 software by assuming the panel to be completely rigid. The fact that fluid-solid interaction was ignored is not expected to introduce a significant error in the simulations since the panel deformation as a result of the impact is negligible compared to the size of the drop. Additionally, any changes in air pressure, temperature and density were also ignored. A surface tension of 0.072 M/m and the contact angle of 70 degrees have been adopted (Manzello and Yang, 2002).

As a result of these simulations the time-dependent distribution of pressure over the affected area of the panel was obtained for the given raindrop size (see Fig. 2). The impact centre experiences the highest pressures in the initial moments after the impact, after

which the drop quickly spreads with the bulk of it forming an expanding ring which exerts an ever diminishing pressure on the affected area of the panel. The whole process takes not more than about 3 ms and the drop spreads over an area in excess of 3 cm in diameter.

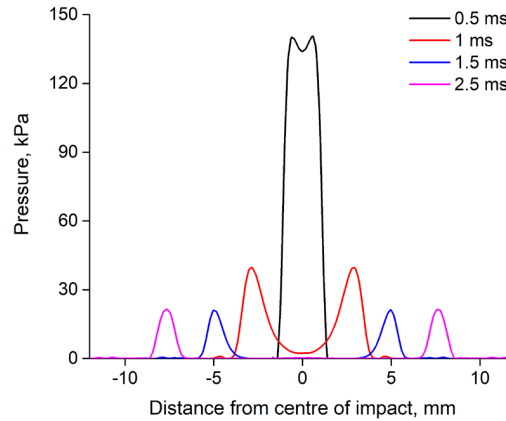


Fig. 2. Pressure distribution resulting from the impact of a 4mm diameter drop

The pressure distributions in Fig. 2 were approximated using analytical expressions and used as an input in coupled structural mechanics and piezoelectric simulations performed in COMSOL Multiphysics v. 5.2 (<https://www.comsol.com/>). The solar panel material was taken to be polycrystalline Si, due to its widespread use and superior performance (Zheng et al., 2015), with the thickness of 1 mm.

Similarly, Polyvinylidene Fluoride (PVDF) has been adopted as the piezoelectric material owing to its widespread use in PEH technologies (Ilyas and Swingler, 2015; Wong et al., 2015; Guigon et al., 2008). PVDF has a number of advantageous properties such as high flexibility, low density, non-toxicity, low-cost, sensitivity to mechanical strain and high optical transparency. In addition, under otherwise equal conditions, PVDF generates higher voltage and power in comparison with other piezoelectric materials.

In order to achieve realistic results for the strain and oscillations of the solar panel as a result of raindrop impacts, the panel dimension was taken to be significantly higher than the spread drop, i.e. 60 mm \times 60 mm. This model panel was supported from the bottom by nine cubic PVDF crystals with the edge length of 3 mm located 20 mm apart (centre to centre distance). The bottom faces of the cubic piezo crystals were assumed to be fixed to a substrate and therefore immobile. Finally, the location of the impact was varied to study the effect of stress wave attenuation on the harvested electrical energy.

3. Results

A drop impact causes a stress wave to spread from the point of contact throughout the panel. As it reaches the PVDF crystals, their top surfaces begin to oscillate together with the panel causing the crystals to expand and contract alternately. Typical simulation results from COMSOL Multiphysics corresponding to the drop impact at the midpoint between four piezo crystals of the array are illustrated in Fig. 3 showing a) the pressure distribution from spreading drop over the panel surface at $t = 1$ ms, b) voltage distribution throughout the piezo crystals at 0.4 ms, c) surface total displacement at 1

ms, and d) surface stress at 0.2 ms. These distributions demonstrate the complexity of the interplay between the external stimulation from fallen drop, the structural mechanics of the panel-piezocrystals assembly and the piezoelectric energy generation.

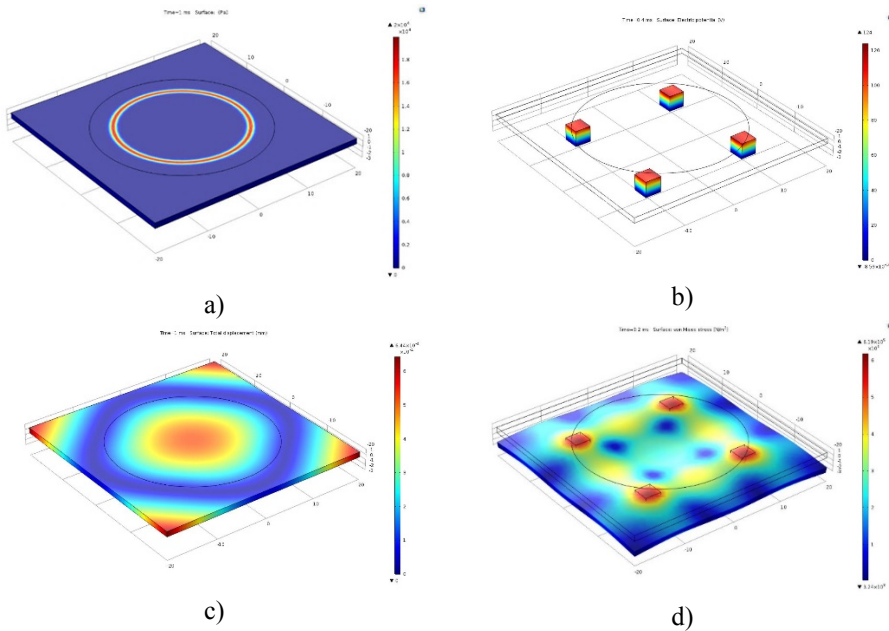


Figure 3. Distributions of a) pressure at 1ms, b) voltage at 0.4 ms, c) surface displacement at 1 ms, and d) stress at 0.2 ms.

As mentioned above, a raindrop hits any point on the panel with the same probability. However, different impact locations lead to different variations of the generated voltage depending on the propagation of the ensuing deformations in the panel (Fig. 4).

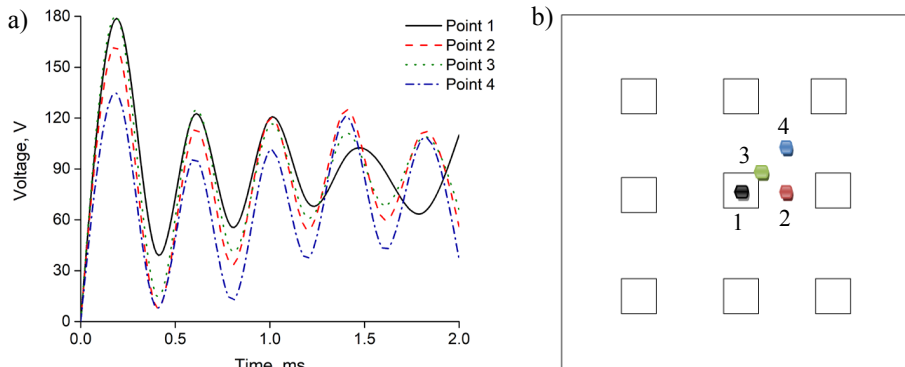


Figure 4. Open-circuit voltage generated by the all-weather panel (a) corresponding to drop impacts at different locations relative to the piezoelectric crystals (b).

Fig. 4a displays the simulated voltages corresponding to four impact points shown in Fig. 4b. Note that, if the size of the panel is sufficiently large, the triangle formed by

these four points represents the smallest tessellation unit for the square arrangement of the piezoelectric crystals. Therefore simulations of impacts within this triangle are representative of the whole panel. For the given sizes and relative distances between the PVDF crystals, there is no significant difference between voltages produced by impacts at different locations. Note that the electric potentials shown are open-circuit, and further work is being undertaken to extend the simulation to include an interfacing circuit and a load to obtain power characteristics.

4. Conclusions

Combining the capabilities of power generation from solar irradiation and kinetic energy of raindrops appears to be an appealing concept capable of enhancing the electricity production while also reducing its intermittency. This work offers a novel configuration of a hybrid all-weather panel consisting of a solar cell resting on an array of piezoelectric crystals. In rainy conditions, drop impacts cause transient vibrations of the panel that lead to the generation of piezoelectricity owing to the contraction-expansion of the piezoelectric elements. In order to achieve maximum efficiency of this setup in both modes of operation, a thorough modelling framework has been proposed that allows for the detailed simulation of raindrop impacts through CFD to be coupled with the structural mechanics and piezoelectric models to yield accurate distributions of pressure, stress, strain and power. The present model is key to accurate model-based optimisation of all-weather panels to yield maximum performance.

A thorough economic analysis must also be performed in order to ascertain the economic feasibility of combined solar-rain energy generation. It is clear, however, that hybrid solar panel designs like the one considered here, would be most efficient in areas with large amounts of both sunshine and rainfall, such as the tropical and equatorial zones.

References

- K.G. Chua, Y.F. Hor, H.C. Lim, 2016, Raindrop Kinetic Energy Piezoelectric Harvesters and Relevant Interface Circuits: Review, Issues and Outlooks, *Sensors&Transducers*, 200(5), 1-15.
- M.A. Ilyas, J. Swingler, 2015, Piezoelectric energy harvesting from raindrop impacts. *Energy*, 90, 796-806.
- R. Guigon, J.J. Chaillout, T. Jager, G. Despesse, 2008, Harvesting raindrop energy: theory. *Smart Material Structure*. 17, 1-8.
- S. L. Manzello, J. C. Yang, 2002, An experimental study of a water droplet impinging on a liquid surface, *Experiments in Fluids*, 32, 580-589.
- C.N. Kumar, 2015, Energy collection via Piezoelectricity, *J. Phys.: Conf. Ser.* 662 012031.
- Q. Tang, X. Wang, P. Yang, B. He, 2016, A solar cell that is triggered by sun and rain, *Angew. Chem. Int. Ed.*, 55(17), 5243-5246.
- C.-H. Wong, Z. Dahari, A.A. Manaf, M.A. Miskam, 2015, Harvesting Raindrop Energy with Piezoelectrics: a Review, *J. Electron. Mater.*, 44(1), 13-21.
- World Energy Outlook, 2016, International Energy Agency.
- Y. Zhang, Q.Tang, B. Hea, P. Yang, 2016, Graphene enabled all-weather solar cells for electricity harvest from sun and rain. *J. Mater. Chem. A*, 4, 13235-13241.
- L. Zheng, Z.-H. Lin, G. Cheng, W. Wu, X. Wen, S. Lee, Z.L. Wang, 2014, Silicon-based hybrid cell for harvesting solar energy and raindrop electrostatic energy, *Nano Energy*, 9, 291-300.

Direct Reduction of Iron-Ore in Fluidized Beds

M. Efe Kinaci^{a,*}, Thomas Lichtenegger^{b,c} and Simon Schneiderbauer^{a,c}

^a*Christian Doppler Laboratory for Mutli-Scale Modelling of Multiphase Processes, Johannes Kepler University, 4040 Linz, Austria*

^b*Linz Institute of Technology (LIT), Johannes Kepler University, 4040 Linz, Austria*

^c*Department of Particulate Flow Modelling, Johannes Kepler University, 4040 Linz, Austria*
mustafa_efe.kinaci@jku.at

Abstract

In order to carry out investigations of one of the most advantageous direct reduction processes, the fluidized bed reactors, computational tools need to be utilized. One such tool is the Computational Fluid Dynamics - Discrete Element Method (CFD-DEM) method. In this work, two of the most common types of models that represent the reactions between solid particles and fluids are implemented into the CFD-DEM library. Levenspiel (1999) describes these models as the Shrinking Particle Model (SPM), where the solid particle reacts with the fluid and changes its size, and the Unreacted Shrinking Core Model (USCM), where after reacting a product layer is formed around the layer that impedes the reaction rate. The SPM is used to verify communication between the CFD and DEM sides, whereas the USCM is used to represent the reduction of iron-ore.

The USCM is validated with a case that considers only a single iron-ore particle that reacts with a gas mixture of CO and N₂. The results are then compared with available experimental data that uses the ISO 4695 conditions at 950 °C and 50 Nl/min. We investigate possible parameters that influence the reduction process such as the particle porosity and pore diameter. Also, the reaction parameters such as the frequency factor, activation energy and the equilibrium constants are investigated by comparing the fractional reduction rates of simulations with experiments. These outcomes give us insight about the total reduction process.

Keywords: CFD-DEM, iron-ore modelling, particle shrinkage, unreacted core model, chemical-reaction kinetics

1. Introduction

The research on the reduction of iron ore has received much attention in the past few decades as a result of the increasing cost and low availability of raw materials. The reduction of gaseous emissions and the search for low-cost alternatives to traditional routes has also boosted the investigations for reduction processes (Plaul et al., 2009).

Currently the dominating process for the iron-ore reduction is the blast furnace (BF) technology. These furnaces consist of a moving bed reactor with a counter-current flow of the solid reactants against a reducing gas. Not only are the energy costs relatively high for these blast furnaces the pollution problems can also be quite severe. The iron-ore fines that enter the BF need to go through a pelletizing and sintering process. In other cases, such as the smelting reduction (SR) processes that use the fluidized bed technologies the iron-ore fines can directly be charged into the reduction process making it highly advantageous. Such fluidized bed reactors are used in the pre-reduction stage of the FINEX[®] process (Habermann et al., 2000). The FINEX[®] process, which was jointly developed by POSCO (Korea) and Primetals Technologies (Austria), produces

hot metal in the same quality as traditional blast furnaces. The iron-ores that are charged into the process go through fluidized bed reactors where they are heated and reduced to Direct Reduced Iron (DRI). The DRI is then charged into the melter gasifier where the final reduction and melting as well as the production of reducing gas by gasification of coal with oxygen takes place (Schenk, 2011).

To improve these processes computational tools such as the CFD-DEM method, which uses the coupling of CFD for the continuous fluid phase (i.e. the reduction gas) and DEM for the discrete particles such as iron-ore and coal, can be utilized. In this work, we are using the CFD-DEM coupling approach based on the open source software packages OpenFOAM and LIGGGHTS (Goniva et al., 2012). The Eulerian field follows a continuum approach and volume-averaged continuity equations are used to describe the behavior of the flow. The discrete particles are described by Newton's equations of motion. More information about the CFD-DEM system can be found in the works of Zhou et al. (2010). In this case, the DEM provides an easy way to evaluate the per-particle chemistry such as the shrink/growth of particles due to reactions. Other tools such as the Two-Fluid Model (TFM), can also be used. However, this model lacks the proper representation of particle size description and the related physical phenomena. Another method that can be thought of would be the hybrid Lagrangian-Eulerian model that combines the Lagrangian Discrete Phase Model (DPM) and a coarse-grained TFM such as in the works of Schneiderbauer et al. (2016).

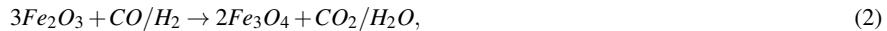
2. Reaction Kinetics

A general type of non-catalytic reaction may be represented by



where gas A is reacting with solid particle B to produce a gaseous product C and a solid product D . For gasification processes, one might consider v_D as zero. For modelling the general reactions two of the most common types is the Shrinking Particle Model (SPM) and the Unreacted Shrinking Core Model (USCM). In the SPM, the particle reacts with the gas and shrinks whilst the product gas diffuses to ambient fluid, such as the gasification of coal. However, in the USCM a product layer is formed around the core as the reaction proceeds, which eventually impedes the reactant gas as it has to diffuse through this newly formed layer.

The main reactions for the direct reduction of iron with a gaseous reductant, CO/H_2 , can be expressed in three reaction steps as



In the topochemical reduction of iron oxide, firstly the reducing gas is transported through the gas film onto the particle surface. Afterwards, the gas diffuses through the porous iron layer where it partially reacts with wustite at the wustite/iron interface producing iron and a gaseous product. The rest gas diffuses through the wustite layer until the wustite/magnetite interface and a portion of the gas reacts with magnetite producing wustite and a gaseous

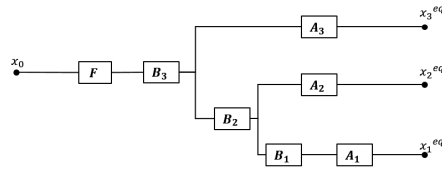


Figure 1: Resistance network diagram that illustrates the resistance of an iron-ore pellet that goes through in the reduction process.

product. The balance gas diffuses through the magnetite layer onto the magnetite/hematite interface. Chemical reaction of the leftover gas occurs at the hematite core and produces magnetite and a gaseous product. Eventually, the gaseous product diffuses outwards through the pores of the pellet (Tsay et al., 1976).

Each step poses a resistance to the completion of the chemical reaction. Therefore, a resistance network can be constructed as illustrated in Figure 1. If one of these steps is so slow that the others become insignificant, this step is considered to be the rate-controlling or rate-limiting step. The combined solution of this network leads to the chemical reaction rates, which are used to determine the mass source terms and can be calculated as

$$\begin{aligned} \dot{Y}_w = & \left([(A_1 + B_1)(A_2 + B_2 + B_3 + F) + A_2(B_2 + B_3 + F)](x_0 - x_{CO,3}^{eq}) \right. \\ & - [A_2(B_3 + F)](x_0 - x_{CO,1}^{eq}) \\ & \left. - [(A_1 + B_1)(B_3 + F)](x_0 - x_{CO,2}^{eq}) \right) \frac{1}{W}, \end{aligned} \quad (5)$$

$$\begin{aligned} \dot{Y}_m = & \left([(A_1 + B_1 + B_2)(A_3 + B_3 + F) + A_3(B_3 + F)](x_0 - x_{CO,2}^{eq}) \right. \\ & - [B_2(A_3 + B_3 + F) + A_3(B_3 + F)](x_0 - x_{CO,1}^{eq}) \\ & \left. - [(A_1 + B_1)(B_3 + F)](x_0 - x_{CO,3}^{eq}) \right) \frac{1}{W}, \end{aligned} \quad (6)$$

$$\begin{aligned} \dot{Y}_h = & \left([A_3(A_2 + B_2 + B_3 + F) + (A_2 + B_2)(B_3 + F)](x_0 - x_{CO,1}^{eq}) \right. \\ & - [A_3(B_2 + B_3 + F) + B_2(B_3 + F)](x_0 - x_{CO,2}^{eq}) \\ & \left. - [A_2(B_3 + F)](x_0 - x_{CO,3}^{eq}) \right) \frac{1}{W}, \end{aligned} \quad (7)$$

in which the term A_j represents the chemical reaction resistance term that is determined by

$$A_j = \frac{1}{(1 - f_j)^{\frac{2}{3}}} \frac{1}{k_j \left(1 - \frac{1}{Keq_j} \right)}. \quad (8)$$

The k_j is the reaction rate constant for layer j and is determined with the Arrhenius Equation of $k_j = k_0 \exp(-E_a/(RT))$, where k_0 is the frequency factor, E_a is the activation energy. The values for the frequency factor and activation energy for the reduction reaction can be found in the works of Negri et al. (1995), Tang et al. (2012) and Valipour (2009). R is the universal gas constant and T is the temperature. f_j represents the local fractional reduction rate that is determined with

$$f_j = 1 - \left(\frac{r_j}{r_{particle}} \right)^3. \quad (9)$$

Keq_j represents the reaction equilibrium constant. A wide range of correlations for the equilibrium constant is available in literature, however in this work we are using the correlation proposed by Valipour (2009). The diffusivity resistance term B_j can be calculated for the inner layers of magnetite and wustite as

$$B_j = \frac{(1 - f_{j+1})^{\frac{1}{3}} - (1 - f_j)^{\frac{1}{3}}}{(1 - f_{j+1})^{\frac{1}{3}} (1 - f_j)^{\frac{1}{3}}} \frac{r_g}{D_j^{eff}}, \quad (10)$$

and for the iron shell as

$$B_j = \frac{1 - (1 - f_j)^{\frac{1}{3}}}{(1 - f_j)^{\frac{1}{3}}} \frac{r_g}{D_j^{eff}}, \quad (11)$$

in which D_j^{eff} represents the effective diffusion coefficient of the relative layer. This is the combination of binary molecular diffusion, calculated with the Fuller-Schettler-Giddings correlation (Fuller et al., 1966), and the Knudsen pore diffusion. The term F in the chemical reaction rate equations represents the resistance generated by the gas mass transfer to the particle surface that can be determined by the Sherwood and Reynolds numbers as it can be found in the works of Valipour (2009) and Nouri et al. (2011).

3. Results and Discussions

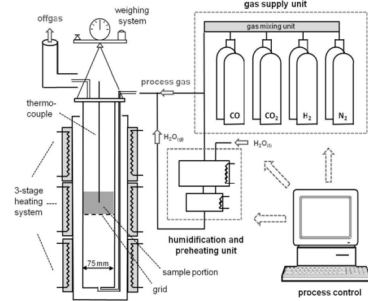


Figure 2: Schematic representation of the lab experimental setup used in the investigation of reduction processes for various iron-oxide ores (Martina Hanel, 2014).

ert gas and a total inlet velocity of 0.011 m/s has been used. The initial particle is taken as the limonitic-ore, which is more porous than hematite. Therefore, we set the initial porosity as 15% and calculated the other layer porosities accordingly using the correlation proposed by Tsay et al. (1976). The tortuosity in this case is taken as 3. The mean pore diameter is not exactly defined with the experiments therefore we have carried out investigations for a range of pore diameters varying from $4e - 5$ to $4e - 7$ m, which is illustrated in Figure 3, in which the overall fractional reduction from the simulations are compared with the available experimental data for limonitic- and hematitic-ores. The simulation is run for 7500 seconds, with a CFD time step of 1 and DEM time step of 0.01 resulting in a computational run time on two-cores of approximately 1 hour.

It can be seen in Figure 3 that the simulation results get really close to the experimental outcomes, especially for the pore diameter of $4 - 5 \mu\text{m}$. Even though the simulation reduces the iron-ore faster than the experiment, they both reduce 80% of ore almost at the same amount of time. Evidently, as the pore diameter gets smaller, the reduction speed gets slower. This effect is to be expected since the diffusion gets slower which makes the diffusion resistance higher thereby reducing the reaction speed. Another parameter that we looked at was the initial porosity value of the particle. Experimentally the particles were said to have a porosity of 15%, however we have carried out investigations in order to see the effects of increasing and decreasing the porosity had on the overall reduction. This effect is illustrated in Figure 4. It is clear that decreasing the porosity

We have taken the experimental work from the Dissertation of Martina Hanel (2014) as a basis to validate our simulation results. In the experimental setup a vertical reduction aggregate with an inner diameter of 75 mm has been used. The setup is schematically represented in Figure 2 as it was used in the lab. In the test case, first N_2 was blasted into the aggregate with a volumetric flow of 50 NI/min for 60 minutes. The temperature was then increased to 950 °C and the gas composition was changed to 60% N_2 and 40% CO , with the relative flow rates being 30 NI/min to 20 NI/min.

For the numerical simulation, the convective and diffusive terms are discretized using a central differencing scheme. The pressure-velocity coupling is achieved through a PIMPLE (PISO + SIMPLE) algorithm as in OpenFoam (2011). A computational domain has been built that represents the aggregate, where a single iron ore particle was placed into the middle of the volume. First step of N_2 blasting was neglected, as it is an in-

reduces the reduction rate. This is also an effect of diffusion term, since the particle becomes denser the resistances are higher. The values for separate resistance terms are plotted as a function of time in Figure 5. According to the works of Kawasaki et al. (1962), Bonalde et al. (2005) and Melchiori and Canu (2014), if the USCM is used at the beginning of the reaction the chemical reaction resistances are dominant, whereas afterwards the diffusion resistances become the rate limiting step. If we take a closer look at the first 300 seconds of Figure 5, we can also realize that the resistance due to chemical reaction kinetics is higher than the diffusion resistances, but in overall development the diffusion resistances are dominant.

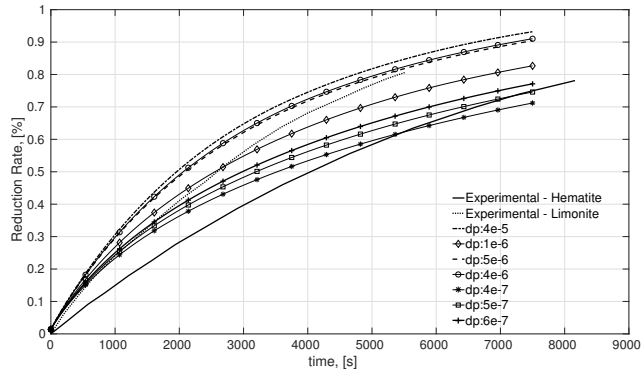


Figure 3: The overall reduction rate of experiments for limonitic- and hematitic-ores compared with the reduction rate of numerical simulations using various pore diameters.

4. Conclusion and Outlook

Through literature research, available models that represent the solid-fluid chemical reactions have been determined and implemented into the CFDEM coupling library, which can be used to investigate the reduction of iron-ores inside the fluidized bed reactors. Simulations have been carried out that investigate the different properties affecting the reduction process. The outcomes of these simulations are then compared with available experimental work. With the current comparison, it can be seen that the implemented mathematical model provides reasonable results for the reaction resistance terms and also the general reduction rate is in an acceptable agreement with experimental data. However, improvements are necessary in order to minimize the deviation between the experimental and simulation results. These deviations might be due to the solid properties and the effect that ongoing reaction has on it, such as the porosity values and each layers molar densities are definitive reduction effecting points that one should consider. Further investigations will cover other methods of calculating porosity and also using a time dependent pore diameter, in order to achieve results with less deviation.

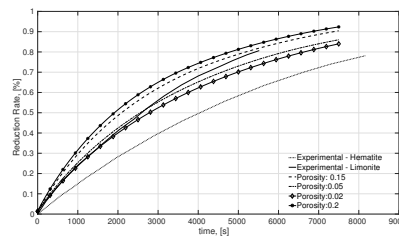


Figure 4: The overall reduction rate for different particle porosities, compared with the experiments.

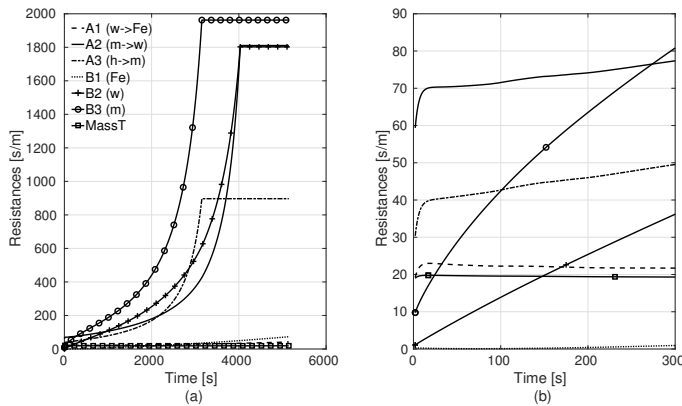


Figure 5: The reaction resistance terms A_j , B_j and F that define the chemical reaction rate dependent on time, on the left side (a) is the total development of the resistance values, on the right side (b) the first 300 seconds of the development of resistances confirming that the chemical reaction resistance is higher.

References

- A. Bonalde, A. Henriquez, M. Manrique, 2005. Kinetic Analysis of the Iron Oxide Reduction Using Hydrogen-Carbon Monoxide Mixtures as Reducing Agent. *ISIJ International* 45 (9), 1255–1260.
- E. N. Fuller, P. D. Schettler, J. C. Giddings, 1966. A new method for prediction of binary gas-phase diffusion coefficients. *Industrial and Engineering Chemistry* 16 (10), 551.
- C. Goniva, C. Kloss, N. G. Deen, J. A. Kuipers, S. Pirker, 2012. Influence of rolling friction on single spout fluidized bed simulation. *Particuology* 10 (5), 582–591.
- A. Habermann, F. Winter, H. Hofbauer, J. Zirngast, J. L. Schenk, 2000. An Experimental Study on the Kinetics of Fluidized Bed Iron Ore Reduction. *ISIJ International* 40 (10), 935–942.
- E. Kawasaki, J. Sanscranite, T. J. Walsh, 1962. Kinetics of reduction of iron oxide with carbon monoxide and hydrogen. *AIChE J* 8 (1), 48–52.
- O. Levenspiel, 1999. *Chemical Reaction Engineering*.
- Martina Hanel, 2014. Char. of Ferrous Burden Material for Use in Ironmaking Technologies. Ph.D. thesis.
- T. Melchiori, P. Canu, 2014. Improving the quantitative description of reacting porous solids: Critical analysis of the shrinking core model by comparison to the generalized grain model. *Industrial and Engineering Chemistry Research* 53 (22), 8980–8995.
- E. D. Negri, O. M. Alfano, M. G. Chiovetta, 1995. Moving-bed reactor model for the direct reduction of hematite - parametric study. *Industrial & Eng. Chem. Res.* 34, 4266–4276.
- S. M. M. Nouri, H. Ale Ebrahim, E. Jamshidi, 2011. Simulation of direct reduction reactor by the grain model. *Chemical Engineering Journal* 166 (2), 704–709.
- C. OpenFoam, 2011. Openfoam programmer's guide. OpenFOAM Foundation 2 (0).
- F. J. Plaul, C. Böhm, J. L. Schenk, 2009. Fluidized-bed technology for the production of iron products for steelmaking. *Journal of the Southern African Institute of Mining and Metallurgy* 109 (2), 121–128.
- J. L. Schenk, 2011. Recent status of fluidized bed technologies for producing iron input materials for steelmaking. *Particuology* 9 (1), 14–23.
- S. Schneiderbauer, S. Pirker, S. Puttinger, P. Aguayo, V. Touloupidis, A. Martínez Joaristi, 2016. A Lagrangian-Eulerian Hybrid Model for the Simulation of Poly-disperse Fluidized Beds: Application to Industrial-scale Olefin Polymerization. submitted to *Powder Technology*.
- H. Tang, Z. Guo, K. Kitagawa, 2012. Simulation study on performance of Z-path moving-fluidized bed for gaseous reduction of iron ore fines. *ISIJ International* 52 (7), 1241–1249.
- Q. T. Tsay, W. H. Ray, J. Szekeley, 1976. The modeling of hematite reduction with hydrogen plus carbon monoxide mixture. *AIChE J* 22 (6), 1064–1076.
- M. S. Valipour, 2009. Mathematical Modeling of a Non-Catalytic Gas-Solid Reaction : Hematite Pellet Reduction with Syngas. *Chemical Engineering* 16 (2), 108–124.
- Z. Y. Zhou, S. B. Kuang, K. W. Chu, A. B. Yu, 2010. Discrete particle simulation of particle-fluid flow: Model formulations and their applicability. *Journal of Fluid Mechanics* 661, 482–510.

Experiments and Direct Computer Mapping Based Model for Photo-Fenton Process

Francesca Audino,^a Mónica Varga,^b Montserrat Pérez-Moya,^a Moisès Graells,^a
Antonio Espuña,^a and Béla Csukás^{b*}

^a*Chemical Engineering Department, Universitat Politècnica de Catalunya, Spain*

^b*Research Group on Process Network Engineering, Kaposvar University, Hungary*

csukas.bela@ke.hu

Abstract

The photo-enhanced Fenton process has proved to be an effective alternative to conventional treatment processes that have shown to be unable to remove Contaminants of Emerging Concern (CECs). A great experimental effort and several modelling approaches have been proposed. Despite of this, the major challenge still remains the identification of an approximately unified, causally established coupling between the general photo-Fenton system and the decontamination of the arbitrarily chosen organic compounds. In the present work, Direct Computer Mapping based Programmable Structures was applied for modelling and simulation based analysis of the experimental results of photo-enhanced decomposition of the paracetamol (PCT). A design of experiments was performed in a 15-L pilot plant, consisting of an annular photo-reactor. A simplified first principles model (FPM), based on the well-known Fenton and photo-Fenton kinetics, and on our suggested idea of consecutive breakage steps, depending on the number of carbon atoms in the molecule to be decomposed, was proposed. This model allowed the fast, approximate combination of the simplified photo-Fenton core with the simplified decomposition reactions of the actual target.

Keywords: photo-Fenton, paracetamol, design of experiments, first principles model, programmable structures

1. Introduction

The photo-Fenton process is an Advanced Oxidation Process (a group of processes based on the formation of highly reactive free radicals, mainly HO[•]) that represents an extension of the Fenton process. By using a UV-VIS light source at wavelengths > 300 nm, it increases the production of HO[•] radicals by Fe³⁺ initiated photolysis of water that leads to a strong increase of the degradation rate of organic pollutants. In the last years, the photo-Fenton process has received a notable attention since it has proved to be an effective alternative to conventional treatment processes for the removal of the Contaminants of Emerging Concern (CECs). CECs are a group of chemicals that may be included in future environmental regulations depending on the results of the investigations on their effects on human health and the environment. Despite the great experimental effort and regardless to the available first principles (Ortiz de la Plata et al., 2010), empirical/heuristic (Pérez-Moya et al., 2008) and data analysis based (Shokry

et al., 2015) solutions, the model based support to develop photo-enhanced Fenton process for the effective decomposition of CECs is still facing the major challenge of finding an approximately unified, causally established coupling between the general photo-Fenton system and the decontamination of the arbitrarily chosen, and quite different organic compounds.

Direct Computer Mapping (DCM; Csukas et al., 2013) based Programmable Structures (Varga and Csukas, 2017a, 2017b; Varga et al., 2017) was applied for modelling and simulation based analysis of the experimental system. The non-conventional computational methodology allows the easy generation of various model structures from the description of a network and from two general functional meta-prototypes. The main feature of this technique consists of building the process model from unified, state (describing the actual state of the process) and transitions (describing the actual transformations, transportations and rules) building elements, executing the local programs, described by the respective prototype elements.

In the present work, DCM is coupled with a design of experiments technique, based on the selection of paracetamol ($C_8H_9NO_2$) as model pollutant. Paracetamol was selected because it is one of the most widely used antipyretics and analgesics. The aim was to propose a novel modelling approach of medium complexity that can be able to find a causally interpretable and generalizable solution for the possible single and multiple targets.

2. Experimental: Design of Experiments

Fenton and photo-Fenton assays (dark and irradiated conditions, respectively) were performed in batch mode with recirculation (recycling flow rate = 12 L min^{-1}), under optimal pH (2.8) and at a temperature of $25 \text{ }^\circ\text{C} \pm 2^\circ\text{C}$. The 15-L pilot plant consists of a 9-L glass reservoir tank and a 6-L glass annular photo-reactor with an irradiated volume of 1.5 L. The latter is equipped with an Actinic BL TL-DK 36 W/10 ISL lamp (UVA-UVB).

The performed experimental design was obtained by changing the initial concentration of H_2O_2 ($C_{H_2O_2}^0$) between half and two times (94.5 and 378 mg L^{-1} respectively) the stoichiometric dose (189 mg L^{-1}) to achieve total mineralization. The initial concentrations of Fe^{2+} ($C_{Fe^{2+}}^0$) were 5, 7.5 and 10 mg L^{-1} , being the latter the maximum legal value in wastewaters in Spain. The initial value of PCT concentration (C_{PCT}^0) was the same (40 mg L^{-1}) in each case, because, although higher than that found in wastewaters and surface waters, it allowed simplifying the monitoring of the contaminant and Total Organic Carbon (TOC) concentrations along the treatment span. Measurements of PCT, TOC, H_2O_2 , and iron species (Fe^{2+} , Fe^{3+} , Fe^{10T}) concentrations were performed using a HPLC Agilent 1200 series with UV-DAD, a Shimadzu VCHS/CSN TOC analyser and a Hitachi U-2001 UV-VIS spectrophotometer, respectively. Especially, PCT measurement method is the one described by Yamal-Turbay et al. (2012). For H_2O_2 and iron species measurement, the spectrophotometric technique described by Nogueira et al. (2005) and the 1, 10-phenanthroline method following ISO 6332:1998 were adopted, respectively. Also, a set of blind experiments (disregarding one or more components from amongst PCT, Fe^{2+} , H_2O_2 and light, alternatively) were also performed to filter the experimental errors, as well as for the better understanding of production and elimination of free radicals in the core model.

3. Modelling and Simulation: Programmable Structures

The Programmable Structure of the process model was generated from the transition based declaration of the (optionally four compartments) process network and from one state and one transition defining meta-prototypes, automatically. The locally executable actual program prototypes, extended by the case specific declarative (Prolog) programs were prepared in the editable GraphML format, as the extension of the automatically generated structure. Having declared the parameters and initial values of actual state and transition elements, the dynamic databases of the declarative model were generated and executed by the general purpose kernel program. Considering the experimental setup, a four compartments loop model was generated, supporting the future scaling up. To avoid the infeasible fast startup, we initialized the model by a perfectly mixed condition, except for H₂O₂ that was added during a period of 5 s, mixed with the recycling.

In the first modeling and simulation trials we started from the elementary kinetic model, suggested by Conte et al. (2012) for the degradation of 2,4-dichlorophenoxyacetic acid (2,4-D). Especially, the 2,4-D specific equations were removed and the remaining 10 Fenton/photo-Fenton related reactions were tested with the knowledge of the set of kinetic parameters collected by Namgoo et al. (2002). This set of elementary transitions was extended by the model reaction of photochemical HO[•] radical production, based on Cabrera Reina et al. (2012), as well as by the consideration of the H₂O dissociation at the controlled pH = 2.8. This initial model seemed to be extremely stiff, as well as very sensitive to the applied kinetic parameters. In addition, a rough estimation of some missing and infeasible parameters was needed.

Turning to the decomposition of the target compound, a detailed qualitative knowledge of the PCT decomposition pathways is available (Villota et al., 2017). However, the comprehensive identification of the respective kinetic model would need enormous efforts with uncertain success. Conversely, the key issue was to find a causally interpretable, but generalizable solution of medium complexity, considering the possible set of single and multiple targets. Accordingly, a simplified first principles model (FPM) has been developed, consisting of three parts, as follows:

1) Simplified free radical production was described by i) oxidization of Fe²⁺ by H₂O₂, generating Fe³⁺ and HO[•], ii) reduction of Fe³⁺ by H₂O₂, resulting in Fe²⁺ and HO₂[•], iii) in case of the additional photo-catalytic process, the reaction of Fe³⁺ with H₂O, producing Fe²⁺ and HO[•] free radicals and H⁺ ion, as well as iv) H₂O dissociation equilibrium, according to the controlled pH (2.8).

2) For the approximate description of the degradation kinetics of target molecule, the hypothesis of a consecutive breakage of the target into fragments and of the produced fragments into smaller fragments, was done. We assumed the approximately identical, halved carbon content of fragments, implemented in the series of kinetic equations with a temperature dependent, target specific parameter k (approximately the same for each steps), as follows:

$$M_i + R \rightarrow 2M_{i+1} \quad \frac{dc_i}{dt} = k \cdot (2 \cdot c_{i-1} \cdot c_R - c_i \cdot c_R) \quad i = 1, 2, \dots, N; \quad c_0 \equiv 0$$

where $i=1$ refers to the targeted compound (M_1) with a non-zero initial concentration of c_1^0 . N refers to the number of consecutive breakage steps that can be estimated from the number of carbon atoms in the molecule to be decomposed (i.e. $N=4$). The possible

reactants R are the pool of the free radicals (mainly $R = \text{HO}^\bullet$ as well as optionally HO_2^\bullet), and H_2O_2 itself.

3) Finally, the third part of the model consists of a simplified elimination scheme of free radicals, producing directly H_2O and O_2 , which competes with the useful consumption of the free radicals.

4. Results and discussion

The behavior of Fenton and photo-Fenton system can be analyzed taking into account the PCT and TOC conversion values that can be obtained for the various studied experimental conditions.

The paracetamol total remediation was achieved under all investigated conditions within a maximum time of 900 s and a minimum time of 150 s. Particularly, by doubling the value of $C_{\text{Fe}^{2+}}^0$, a 67% and a 75% increase of the process performance, in terms of PCT total remediation time, was achieved in case of dark and irradiated conditions, respectively.

Regarding TOC conversion (e.g. the mineralization level), the use of radiation improved the TOC conversion of about 34% and 77% when the lowest and the highest values of $C_{\text{H}_2\text{O}_2}^0$ and $C_{\text{Fe}^{2+}}^0$ were set, respectively. Finally, a 19% and a 33% enhancement of the TOC conversion was obtained by increasing $C_{\text{Fe}^{2+}}^0$ from 5 to 7.5 and from 5 to 10 mg L^{-1} , respectively.

Blank experiments without PCT helped to check the simplified free radical production and elimination model. Blank experiments with PCT, but without Fe^{2+} showed a decrease of H_2O_2 with no TOC decrease, which suggested a H_2O_2 initiated first breakage of PCT. This is in accordance with the very fast decrease of H_2O_2 in all experiments.

In the case of PCT, radical HO^\bullet proved to be the major decomposing agent. The decontamination was modelled by three breakage steps, in line with the number of carbon atoms (i.e. 8). Considering the fast initial decomposition of H_2O_2 , as well as the results of the blank experiments (with PCT and without Fe^{2+}) we assumed also a possible slower direct reaction of PCT with H_2O_2 producing C_4 fragments.

Some of the experimental values are compared with the results of the simulations in Figure 1. a), b), and c) for TOC, PCT and H_2O_2 respectively. This figure illustrates the cases of the worst (lowest initial concentrations of the catalyst and the oxidant, under dark conditions) and the best (highest initial concentrations of the catalyst and the oxidant, under irradiated conditions) performance. Particularly, in the worst case, a mineralization level of 30% was attained and PCT total remediation was obtained after 900 s. Conversely, the best performance was characterized by a 70% of TOC conversion and by a total PCT remediation after 150 s. Concerning H_2O_2 , the total consumption of the oxidant was observed for the irradiated case, while a decreasing small concentration was shown under dark conditions.

The model, developed from a representative part of experiments, predicted the results of the remaining set of experiments (including the "worst" and "best" performing extreme cases). As an error measure, we calculated Normalized Root Mean Square Error values as follows:

$$NRMSE = \frac{\sqrt{\frac{\sum_{i=1}^n (X_i^{measured} - X_i^{simulated})^2}{n}}}{\max(X^{measured}) - \min(X^{measured})}$$

NRSME for simulated data were 23% for PCT, 23% for TOC, and 27% for H₂O₂.

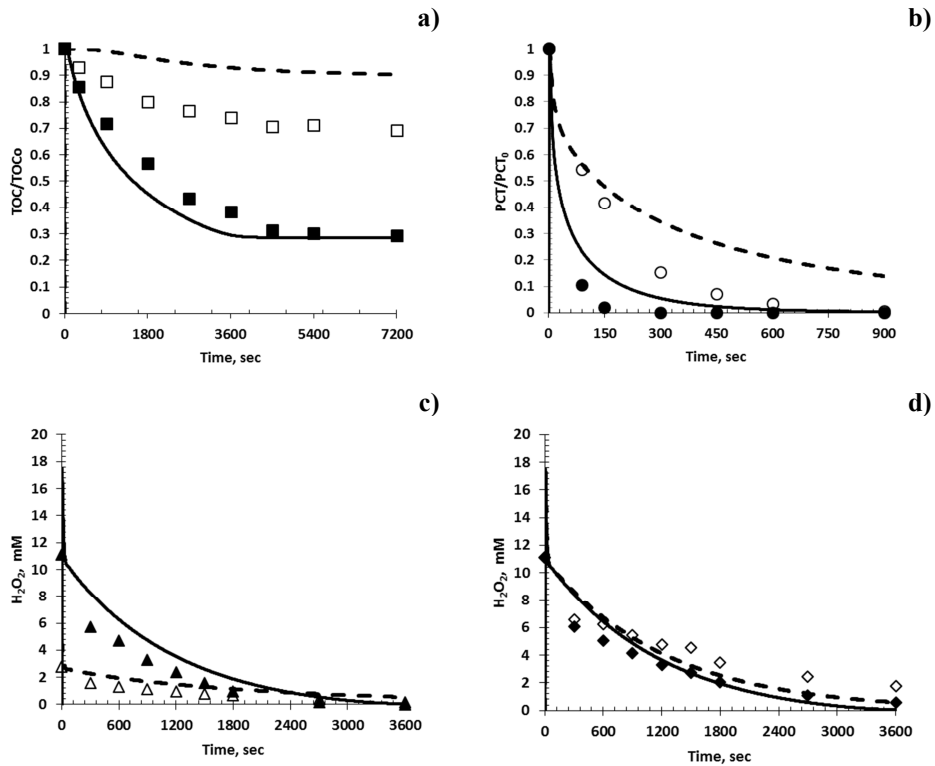


Figure 1. a), b) and c) show the experimental concentrations of TOC (\square), PCT (\circ), and H₂O₂ (Δ) versus predicted concentrations (--- , ---), in case of using $C_{PCT}^0=40 \text{ mg L}^{-1}$, $C_{Fe^{2+}}^0=5.00 \text{ mg L}^{-1}$ and $C_{H_2O_2}^0=94.50 \text{ mg L}^{-1}$ under dark conditions ($\square, \circ, \Delta, \text{---}$) and in case of using $C_{PCT}^0=40 \text{ mg L}^{-1}$, $C_{Fe^{2+}}^0=10.00 \text{ mg L}^{-1}$ and $C_{H_2O_2}^0=378.00 \text{ mg L}^{-1}$ under irradiated conditions ($\blacksquare, \bullet, \blacktriangle, \text{---}$). Fig. 1 d), shows the experimental (\diamond) versus predicted concentrations (--- , ---) of H₂O₂ for $C_{PCT}^0=0 \text{ mg L}^{-1}$, $C_{Fe^{2+}}^0=10.00 \text{ mg L}^{-1}$ and $C_{H_2O_2}^0=378.00 \text{ mg L}^{-1}$ under dark ($\diamond, \text{---}$) and irradiated conditions ($\blacklozenge, \text{---}$). TOC and PCT are normalized concentrations while H₂O₂ is a molar concentration (mM=mmol/L). In order to appreciate the different trends between the various investigated case studies, Figure 1. b) is plotted for the first 900 sec (maximum time at which the total removal of PCT occurs) while Figure 1. b) and c) are represented for the first 3600 sec (time at which the H₂O₂ is almost totally consumed).

5. Conclusions

First of all, it was concluded that it may be impossible to develop a detailed, but general first principles kinetic model, considering the possible reactions of the free radicals, as well as the alternative decomposition pathways for the various actual compounds to be decomposed. Also, the most detailed elementary reactions of the free radicals in the

photo-Fenton core may not be independent from actual targets. Consequently, they cannot be identified correctly, without the intimately coupled actual decomposition reactions. Another issue is that the kinetics of the detailed mechanism involving free radicals is stiff, and accordingly it is very sensitive for the individual parameters. To avoid "being penny wise and pound foolish", we tried to find a causally right, but simplified model of medium complexity, which makes the fast combination of the simplified photo-Fenton core with the simplified decomposition reactions of the actual target possible. The suggested simplified first principles model consists of three major parts i) a photo-enhanced Fenton core, ii) a simplified decomposition scheme of the organic target compounds (actually PCT) and iii) a simplified elimination scheme of free radicals. The photo-enhanced Fenton process produces more radicals, however it is accompanied by an increased H_2O_2 consumption. Considering the spontaneous elimination of the radicals, instead of a higher initial H_2O_2 concentration, the stepwise fed-batch supply of additional amounts seems to be an advantageous strategy to decrease the decontamination. Considering the applied novel methodology, Direct Computer Mapping based Programmable Structures showed the following advantages: i) it helped the easy generation and configuration of various model structures from the description of a network and from two functional meta-prototypes, ii) it supported the easy and local modification of the locally executable declarative programs associated with the state and transition prototypes, and iii) it allowed the switching on/off as well as the easy monitoring of the elementary processes through the transition based model representation. The application of the methodology is to be tried and refined for other target compounds in further work.

Acknowledgements

Financial support received from the Spanish "Ministerio de Economía, Industria y Competitividad" and the European Regional Development Fund, both funding the research Project AIMS (DPI2017-87435-R) is fully acknowledged. Hungarian authors acknowledge the support of EFOP-3.6.2-16-2017-00018. Francesca Audino, particularly acknowledges the MINECO for the PhD grant (BES-2013-065545).

References

- Cabrera Reina A et al., 2012. *Applied Catalysis B* 119-120: 132-138.
- Conte LO et al., 2012. *Ind. Eng. Chem. Res.* 51: 4181-4191.
- Csukas B et al., 2013. *Fuel Process. Technol.* 106: 186-200.
- Namgoo K et al., 2002. *Chemosphere* 47: 915-924.
- Nogueira RF et al., 2005. *Talanta* 66: 86-91.
- Ortiz de la Plata G et al., 2010. *Appl. Catal. B* 95: 14-25.
- Pérez-Moya M et al., 2008. *Appl Catal B, Environmental* 84: 313-323.
- Shokry A et al., 2015. *Proc. of 12th PSE and 25th ESCAPE Copenhagen*.
- Varga M, Csukas B, 2017a. *Proc. of AIChE Annual Meeting, Paper #448e*.
- Varga M et al., 2017. *BioSystems*, 152: 24-43.
- Varga M, Csukas B, 2017b. *Ecol. Model.* 364: 25-41.
- Villota N et al., 2017. *Chem Eng.*, 4(2): 1054.
- Yamal-Turbay E et al., 2012. *Environ sci Pollut res* DOI 10.1007/s11356-014-2990-9.

Surrogate-based modeling in flotation processes

Achref Rabhi^{a,b}, Abdellah Chkifa^a, Saad Benjelloun^a, Abderrazak Latifi^{a,b}

^a*Université Mohammed VI Polytechnique, Lot 660 - Hay Moulay Rachid, Benguerir, Morocco*

^b*Laboratoire Réactions et Génie des Procédés, ENSIC–CNRS –Université de Lorraine, Nancy, France*
Abderrazak.Latifi@univ-lorraine.fr

Abstract

In this paper, the objective was to develop surrogate models for a flotation process. A CFD model taking into account several complex phenomena involved in the flotation was first developed and simulated using COMSOL Multiphysics software. The approach of high dimension adaptive hierarchical polynomial interpolation was then used to develop simple surrogate models. The results show that the resulting models are accurate and fast to integrate compared to the original CFD ones. Their incorporation within an optimization algorithm to improve the flotation performances will be straightforward.

Keywords: Flotation processes, CFD simulation, Surrogate models, Hierarchical polynomial interpolation

1. Introduction

Flotation is a separation technique based on differences in the hydrophobicity of the surfaces of the particles to be separated. It is a kinetic process involving three phases, i.e. solid (fine particles), liquid (water) and gas (air). Its principle is based on the capture of particles (e.g. gangue minerals) suspended in a pulp to be treated, by means of floating collectors (air bubbles). If the particles brought into contact with the bubbles are captured by the latter, they rise to the surface of the flotation cell where these agglomerates are retained in foam which is then evacuated from the cell (Blazy, 1970). Flotation is considered to be the best available process for recovering fine ores. However, despite its widespread, especially in the recovery of phosphates, the flotation processes are still not well understood and the design and mastering of their operations still pose problems mainly due to the complexity of the phenomena involved. Understanding these phenomena is therefore of utmost importance in order to better model the processes and correctly predict the performances for their better optimization. In this work, a 3D transient CFD model was developed and solved under COMSOL Multiphysics modeling software. It takes into account several complex phenomena involved in the flotation process. However, taking into consideration all the mechanisms in the CFD model is computationally intensive. This makes the approach nonviable for repeated computational techniques such as iterative optimization algorithms or Monte Carlo sampling methods. Simple and accurate surrogate models are therefore necessary. The objective of this paper is to develop a flotation process surrogate model that relies on an efficient interpolation procedure that estimates the quantity of interest using a sampled data set. Each sample typically corresponds to an instance of the solution of the

CFD model. The approach of adaptive hierarchical polynomial interpolation will be particularly outlined.

2. Process model

Many research contributions have been recently devoted to CFD simulation of flotation processes with an emphasis on specific phenomena (Koh and Schwarz, 2008; Liu and Schwarz, 2009; Schwarz et al, 2016; Sarhan et al, 2017ab). The process model developed here is inspired from these contributions and involves three phases, i.e. liquid (continuous phase), particles (dispersed solid phase) and bubbles (dispersed gas phase). It is an Eulerian model that takes into account several complex phenomena involved in the flotation process. The governing equations consist of mass and momentum balance equations, turbulent kinetic energy and its dissipation rate. They have similar structure and are given as follows (for the lack of space, neither the $k - \varepsilon$ turbulence equations nor the initial and boundary conditions are presented):

- Mass balance equations:

$$\frac{\partial}{\partial t}(\rho_i \alpha_i) + \nabla(\rho_i \alpha_i U_i) = S_i \quad i = g, l, s \quad (1)$$

- Momentum balance equations:

$$\frac{\partial}{\partial t}(\rho_l \alpha_l U_l) + \nabla(\rho_l \alpha_l U_l U_l) = -\nabla p + \nabla \tau_l + \rho_l \alpha_l g + F_{lg} + F_{ls} \quad (2)$$

$$\frac{\partial}{\partial t}(\rho_g \alpha_g U_g) + \nabla(\rho_g \alpha_g U_g U_g) = -\nabla p + \nabla \tau_g + \rho_g \alpha_g g - F_{lg} \quad (3)$$

$$\frac{\partial}{\partial t}(\rho_s \alpha_s U_s) + \nabla(\rho_s \alpha_s U_s U_s) = -\nabla p + \nabla \tau_s + \rho_s \alpha_s g - F_{ls} \quad (4)$$

- The volume fractions should sum up to 1 as:

$$\alpha_l + \alpha_g + \alpha_s = 1 \quad (5)$$

where ρ_i , α_i , U_i , S_i and τ_i are density, volume fraction, velocity vector, mass source term (e.g. a source of air) and Reynolds stress tensor of phase i respectively. p is the pressure and g the specific gravity. F_{lg} and F_{ls} represent the interphase forces between liquid and gas phases, and liquid and solid phases respectively. All other forces including body, lift and virtual forces are neglected.

It is noteworthy that the resulting process model is quite complex and computationally intensive. Simple and accurate surrogate models will therefore be developed in §4. The next section will focus on the definition of the surrogate model problem.

3. Problem definition

One of the most relevant phenomena that influence the forces involved in equations (2-4), is the bubble-particle collision phenomenon. It is mainly controlled by the following mechanisms: (i) interception, (ii) inertia, (iii) gravitation, (iv) turbulence, and (v) Brownian diffusion.

The problem considered in this work dealt with the analysis of the bubble-particle collision phenomenon through the determination of the collision probabilities. More specifically, the influence of three parameters, i.e. bubble diameter, particle diameter and particle density, on the probabilities was investigated.

The model equations (1-5) were thus implemented and solved within COMSOL Multiphysics software (Rabhi et al, 2017). The computed collision probabilities were then compared to the literature results and showed that the model is quite accurate. The latter can therefore be used in optimization of the process performances. However, the computation time is so costly that the use of the model equations (1-5) within an optimization algorithm would not be an easy task and should be avoided. Simple and accurate alternatives are therefore needed. The next section is devoted to the development of surrogate models that will enable to compute the bubble-particle collision probability \mathbf{P}_c as a function of the aforementioned parameters, i.e. bubble diameter, \mathbf{d}_B , particle diameter, \mathbf{d}_p and particle density, ρ_p .

4. Development of surrogate models

The surrogate models developed are based on the approach of high dimension hierarchical polynomial interpolation (Chkifa et al 2014). We let $R = (r_j)_{j \geq 0}$ be a sequence of mutually distinct abscissas in $[-1, 1]$. We denote by $R_k := (r_0, \dots, r_{k-1})$ the subset of R formed by the first k abscissas of R and for a continuous function f in $\mathcal{C}([-1, 1])$, we denote $I_{k-1}[f]$ the polynomial of degree at most $k-1$ interpolating f at the k points $(r_0, f(r_0)), \dots, (r_{k-1}, f(r_{k-1}))$. We introduce the increment (or update) notation $\Delta_0[f] = I_0[f] \equiv f(r_0)$ and $\Delta_j[f] = I_j[f] - I_{j-1}[f]$ for $j \geq 1$. In view of the interpolation definition, $\Delta_j[f]$ is a polynomial of degree at most j , equal to 0 at r_0, \dots, r_{j-1} and equal to $f(r_j) - I_{j-1}[f](r_j)$ at r_j . Therefore, $\Delta_0[f] = f(r_0)h_0$ and $\Delta_j[f] = (f(r_j) - I_{j-1}[f](r_j)) h_j$ for $j \geq 1$ where $(h_j)_{j \geq 0}$ is the family of the so-called Newton polynomials defined here over $[-1, 1]$ by $h_0 \equiv 1$ and for $j \geq 1$ by

$$h_j(t) = \frac{\omega_j(t)}{\omega_j(r_j)}, \quad \omega_k(t) := (t - r_0) \dots (t - r_{j-1}) \quad (6)$$

The polynomials $I_k[f]$ can thus be computed using the hierarchical procedure

$$I_k[f] = \sum_{j=0}^k \Delta_j[f] = \sum_{j=0}^k c_j h_j \quad (7)$$

where the coefficients c_j are computed according to the recursion $c_0(f) := f(r_0)$ and

$$c_j(f) := f(r_j) - \sum_{i=0}^{j-1} c_i h_i(r_j) \quad (8)$$

This hierarchical procedure can be generalized to high dimensions using a technical tensor construction. We let $d \geq 1$ be an integer, $U := [-1, 1]^d$ the hypercube in dimension d and denote by $\mathcal{C}(U)$ the space of scalar valued d -variate continuous functions over U . We again let $R = (r_j)_{j \geq 0}$ be a sequence of mutually distinct abscissas in $[-1, 1]$. The goal is to build approximations to $f \in \mathcal{C}(U)$ using the interpolation of f at well-chosen nodes picked in the predefined grid $R^d \subset U$. The hierarchical feature of the scheme entails a certain structure on the nodes which we shall make clear. We let \mathbb{N}^d the set of multi-indices in dimension d . For $n := (n_1, \dots, n_d) \in \mathbb{N}^d$, we denote by y^n the d -variate monomial, i.e.

$$y^n := y_1^{n_1} \cdot y_2^{n_2} \cdot \dots \cdot y_d^{n_d} \quad (9)$$

and introduce the tensor product operator notation Δ_n by

$$\Delta_n := \Delta_{n_1} \otimes \dots \otimes \Delta_{n_d} \quad (10)$$

The definition of Δ_n uses standard of tensorization, see (Chkifa et al 2014). In other words, for a continuous function $f \in \mathcal{C}(U)$ we use the recursion

$$\Delta_n[f] = \Delta_{n_1} [t \rightarrow \Delta_{(n_2, \dots, n_d)}[f(t, \dots, \cdot)]] \quad (11)$$

We note however that we will not rely on (11). We recall that for $k \in \mathbb{N}$, $\Delta_k[\cdot]$ belongs to \mathbb{P}_k the space of univariate polynomials of degree at most k . We define over \mathbb{N}^d the order \leq by $m := (m_1, \dots, m_d) \leq n := (n_1, \dots, n_d)$ if and only if $m_1 \leq n_1, \dots, m_d \leq n_d$ and introduce for $n \in \mathbb{N}^d$ the rectangular block notation $\mathcal{B}_n := \{m \in \mathbb{N}^d : m \leq n\}$. Since every $\Delta_{n_j}[\cdot]$ belongs to \mathbb{P}_{n_j} , then $\Delta_n[f]$ belongs to $\mathbb{P}_{\mathcal{B}_n} := \text{span}\{y^m : m \in \mathcal{B}_n\}$ the space of d -variate polynomials of degree at most n_j in variable y_j for $j = 1, \dots, d$. For a set of multi-indices $\Lambda \subset \mathbb{N}^d$, we introduce the notation $\mathcal{J}_\Lambda[f]$ by

$$\mathcal{J}_\Lambda[f] = \sum_{n \in \Lambda} \Delta_n[f] \quad (12)$$

The d -variate polynomial $\mathcal{J}_\Lambda[f]$ is a sum of polynomials each belonging to $\mathbb{P}_{\mathcal{B}_n}$. We say that $\Lambda \subset \mathbb{N}^d$ is downward closed if and only if

$$n \in \Lambda \Rightarrow \mathcal{B}_n \subset \Lambda \quad (13)$$

This notion is central in the present framework. It implies in particular that if Λ is downward closed then $\mathcal{J}_\Lambda[f]$ belongs to

$$\mathbb{P}_\Lambda := \text{span}\{y^n : n \in \Lambda\} \quad (14)$$

In fact, in this case it is easy to verify, see (Chkifa et al 2014), that $\mathcal{J}_\Lambda[f]$ interpolates f at the node of the sparse high dimensional grid

$$\Gamma_\Lambda := \{r_n := (r_{n_1}, \dots, r_{n_d}) : n \in \Lambda\} \quad (15)$$

We observe that there exists a one-to-one correspondence between downward closed sets Λ , the polynomial spaces \mathbb{P}_Λ and the high dimensional grids Γ_Λ . In particular, the introduced scheme is hierarchical. Given $\Lambda \subset \mathbb{N}^d$ downward closed and $n \in \mathbb{N}^d$ such that $\Lambda' = \Lambda \cup \{n\}$ is also downward closed and having $\mathcal{J}_\Lambda[f]$ computed, we only need a single extra evaluation $f(r_n)$ to compute $\mathcal{J}_{\Lambda'}[f]$. The computation of $\mathcal{J}_{\Lambda'}[f]$ can be performed using a Newton like formula as in the one dimension setting. Indeed,

$$\mathcal{J}_{\Lambda'}[f] = \mathcal{J}_\Lambda[f] + \Delta_n[f] = \mathcal{J}_\Lambda[f] + (f(r_n) - \mathcal{J}_\Lambda[f](r_n)) h_n \quad (16)$$

where now $(h_n := \otimes_{j=1}^d h_{n_j})_{n \in \mathbb{N}^d}$ is the family of d -variate polynomials indexed in \mathbb{N}^d and obtained by tensor product from the family of univariate Newton polynomials $(h_k)_{k \in \mathbb{N}}$, i.e. $h_n(y) = h_{n_1}(y_1) \cdot h_{n_2}(y_2) \dots h_{n_d}(y_d)$. As mentioned earlier, we do not need to compute $\Delta_n[f]$ using the tensor product in (10) but we rely on this recursive formula. The hierarchical nature of the procedure can naturally be coupled with an adaptive strategy where the downward closed sets are enriched adaptively by adding one index n at a time according to a given criterion.

For example, we consider the following algorithm :

Algorithm: Adaptive hierarchical polynomial interpolation

Input: Integer $d \geq 1$, function $f \in \mathcal{C}(U)$ and a solver giving f for any query $y \in U$.

Parameter: N the total number of interpolation points, also the size of the set Λ .

Initialization: $i = 1, \Lambda := \{(0, \dots, 0)\}$ and $J_\Lambda[f] = c_0 \mathbf{1}$, with $c_0 = f(r_0, \dots, r_0)$.

Loop: while $i < N$:

- compute $\mathcal{N}(\Lambda) := \{n \notin \Lambda: \Lambda \cup \{n\} \text{ downward closed}\}$.
- for each $n \in \mathcal{N}(\Lambda)$, compute $f(r_n)$, $J_\Lambda[f](r_n)$ and $c_n := f(r_n) - J_\Lambda[f](r_n)$.
- find $n \in \mathcal{N}(\Lambda)$ with the largest update $\Delta_n[f] = c_n h_n$, in norm $|c_n| \sup_{y \in U} |h_n(y)|$.
- update $\Lambda \rightarrow \Lambda \cup \{n\}$ and $J_\Lambda[f] \rightarrow J_\Lambda[f] + c_n h_n$.
- update $i \rightarrow i + 1$.

Output: Downward closed set $\Lambda \subset \mathbb{N}^d$ of cardinality N and associated polynomial approximation $J_\Lambda[f] = \sum_{n \in \Lambda} c_n h_n$.

The stability and numerical behavior of this algorithm is studied in (Chkifa et al, 2014). The importance of the sequence R is in particular stressed. In our numerical experiment, we use the so-called \mathfrak{R} -Leja sequence (Chkifa et al, 2014) for which the stability was demonstrated.

5. Results and discussion

In the case study considered here, the parameters d_B , d_p and ρ_p vary in the intervals $[a_1 = 0.1, b_1 = 10]$ mm, $[a_2 = 40, b_2 = 125]$ μm and $[a_3 = 2000, b_3 = 10^4]$ kg/m³ respectively. They are then transformed into three variables y_1 , y_2 and y_3 defined in the unit interval $[-1, 1]$. The following affined function defined as: $\psi_{a,b}: x \mapsto \frac{a-b}{2}x + \frac{a+b}{2}$ allows to map linearly the unit interval $[-1, 1]$ to the intervals $[a_i, b_i]$, $i = 1, 2, 3$. The surrogate model for the prediction of the bubble-particle collision probability P_c is then defined over $[-1, 1]^3$ as:

$$P_c(y_1, y_2, y_3) = f(\psi_{a_1, b_1}(y_1), \psi_{a_2, b_2}(y_2), \psi_{a_3, b_3}(y_3)) \quad (17)$$

The algorithm described above was implemented using Python and allowed to compute the polynomials of the surrogate models. The main results are presented in figures 1 and 2. Figure 1 shows the variations of the collision probability P_c as a function of the bubble diameter for a fixed value of the particle diameter and for two different values of the particle density. Moreover, the figure compares the results obtained by CFD simulations (+ and \times) and by surrogate models computations (– – and – –).

It can be seen that as expected the probability decreases with the bubble diameter (Schwarz et al, 2016) and is lower when the particle density decreases for the same particle diameter. Furthermore, the resulting surrogate model predicts the computed CFD results with high accuracy which is exhibited in Figure 2 where the prediction absolute error, decreases with N the number of collocations points (also the dimension of the polynomial space where the surrogate is considered). Finally, we highlight one of the most important features of the surrogate models, i.e. their negligible CPU time compared to the CFD model computational load. For a fixed particle density ρ_p corresponding to phosphates particles, we could run a global optimization algorithm on the two decision parameters d_B and d_p . The evaluation of the probability of collision from the polynomial surrogate model permits to avoid the time consuming evaluations through CFD computations.

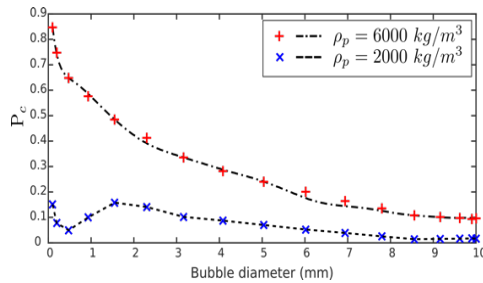


Figure 1 : Bubble-particle collision probability P_c vs bubble diameter d_b for $d_p=121\ \mu\text{m}$ and $N=650$.

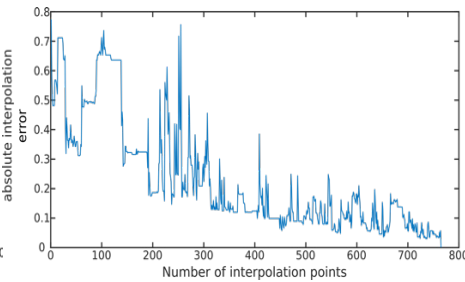


Figure 2 : Prediction absolute error vs N , the size of Δ .

6. Conclusion

The method of high dimension adaptive hierarchical polynomial interpolation developed in this work has proven to be a powerful approach in surrogate models building for complex processes and/or computationally intensive CFD models. The approach favors a sparsity based reconstruction which is particularly emphasized since this explains the sparsity of effects observed for the mechanisms pertaining the bubble-particle collision phenomenon. The results obtained are very interesting and encouraging; they show that the surrogate models developed are very accurate with negligible CPU time. Further works will focus on the use of the resulting surrogate models in optimal design and operation of the whole flotation process.

References

- P. Blazy, 1970, La valorisation des minerais, Presses Universitaires de France.
- A. Chkifa, A. Cohen, C. Schwab, 2014, High-dimensional adaptive sparse polynomial interpolation and applications to parametric PDEs, *Foundation of Computational Mathematics*, 14, 601 – 633.
- P.T.L. Koh, M.P. Schwarz, 2008, Modelling attachment rates of multi-sized bubbles with particles in a flotation cell, *Minerals Engineering*, 21, 989–993.
- T.Y. Liu, M.P. Schwarz, 2009, CFD-based multiscale modelling of bubble–particle collision efficiency in a turbulent flotation cell, *Chemical Engineering Science*, 64, 5287–5301.
- A. Rabhi, 2017, Modélisation et simulation multi-échelle des procédés de flottation, Internal Report, Université Mohammed VI Polytechnique, Benguerir, Morocco.
- A.R. Sarhan, J. Naser, G. Brooks, 2017a, CFD modeling of three-phase flotation column incorporating a population balance model, *Procedia Engineering*, 184, 313 – 317.
- A.R. Sarhan, J. Naser, G. Brooks, 2017b, CFD analysis of solid particles properties effect in three-phase flotation column, *Separation and Purification Technology*, 185, 1 – 9.
- M.P. Schwarz, P.T.L. Koh, D.I. Verrelli, Y.Feng, 2016, Sequential multi-scale modelling of mineral processing operations, with application to flotation cells, *Minerals Engineering*, 90, 2 – 16.
- S.A. Smolyak, 1963, Quadrature and interpolation formulas for tensor products of certain classes of functions, *Soviet Mathematics Doklady*, 4, 240 –243.

From Process Graph to Process Simulation with Proper Model Documentation

Arne Tobias Elve^{a,*} and Heinz A Preisig^a

^a*Norwegian University of Science and Technology, Department of Chemical Engineering, Trondheim, Norway*
arne.t.elve@ntnu.no

Abstract

This paper presents a new modelling framework called the *Process Modeller Suite*, which combines ontologies and graph-based modelling to do automatic code generation for models. The process models are represented by a process graph where the graph components capture system knowledge in the ontology in a systematic manner. The result is a software tool that promotes correct model formulation, interoperability between different modelling environment and reusability of the models and also generates a proper model documentation.

Keywords: Model Documentation, Graph-based Modelling, Automatic Code Generation, Customised Modelling

1. Background

Generating process models is a key activity When maintaining a process model, complete and up-to-date documentation is needed. This model documentation must outline the model structures, attributes, assumptions and constraints. Furthermore, up-to-date documentation for the process model is crucial for the maintenance, further development, system quality and communication with domain experts (Shafiee et al., 2017). Our objective is to construct a generic modelling framework that produces executable model code for essentially any targeted language with the models being synthesised from the ontology (Preisig and Elve, 2016) and also provide proper model documentation.

The modelling framework builds on the principles of a generic approach to modelling, with the objectives of generating consistent models (Preisig, 2010), produce complete models, using a canonical representation and include parser and compiler for the output language. We meet these objectives by synthesising knowledge captured in the ontology into modelling objects that are consecutively generated in a graph-based modelling environment. The modelling objects distribute the knowledge, captured by the ontology, over to the model by constituting the nodes and arcs in the directed graph. This graph captures the structure of the model and represents the topology. The nodes of the directed graph represent the capacitive elements, and the arcs, the communication elements. The model knowledge from the ontology in combination with the topology represented by the directed graph is used to generate executable Python-code automatically.

This approach to modelling is inspired by (Fedorova et al., 2015) and MOSAICmodeling (Kraus et al., 2014) which use templates for model generation. However, we separate from the template approach since we use an ontology to build our modelling objects. Hence we are conceptually closer to (Brandt et al., 2008), (Koo et al., 2017) and (Heitzig et al., 2014) since we use knowledge based systems for the generation models.

2. The Modelling Framework

We are developing a new modelling framework called the *ProcessModellerSuite* implementing modelling language, described in (Elve and Preisig, 2017), to a graph-based modelling environment. An illustration of the different components in the ProcessModellerSuite is provided in fig. 1.

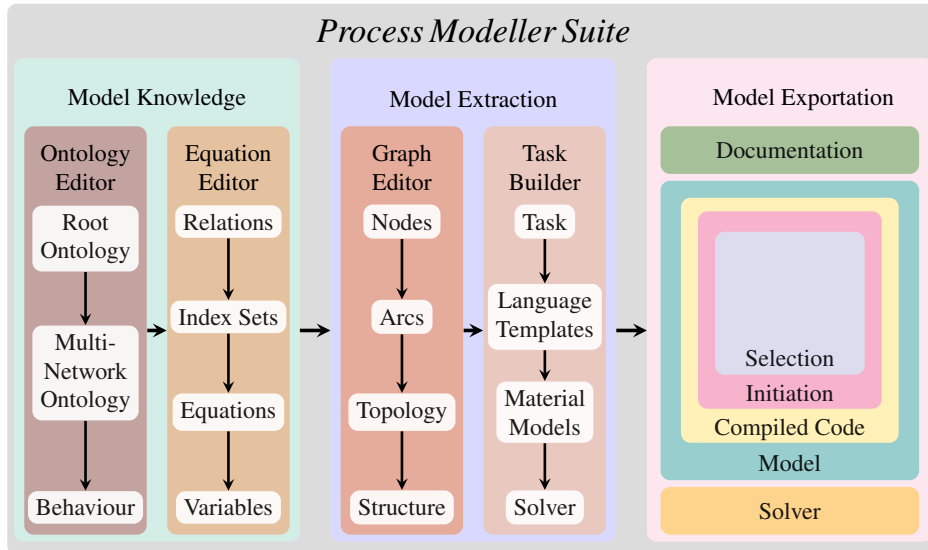


Figure 1: Illustration of the workflow for generating models. The user provides input to the different boxes which combined generate the model with full model documentation. The white boxes inside editors indicate what parts of the model are provided into the editors.

The framework is divided into three segments, following a sequential model implementation. In the first segment, we generate the model knowledge capturing what the model represents and the mathematical representation. The first editor constructs the ontology, which is the foundation for the rest of the modelling. We define an ontology to be the naming and definition of “things”, properties and relations that exist for a particular domain. The ontology captures all the model knowledge and provides the vocabulary that is used later when formulating the process models explaining the behaviour of these things. We start off by defining a root ontology describing basic terms and opening for definition into the graph-based modelling environment by defining the basic model components for a graph being nodes and arcs. The root ontology is then successively refined by adding properties specific to modelling domains, determining the behaviour of the produced model. In the equation editor, we define the relations for these “things” we are modelling. The relations describe how “things” are related, and adds the context to the graph by specific index sets adding the relations to specific sets model components in the graph. The equations capture the relations and are stored into variables, which are integrated as the mathematical description of the behaviour in the ontology.

In the next segment, we extract information based on the generated model knowledge and merge the knowledge to form a model. The central design tool in this software is the graph editor, which allows for a hierarchical representation of the model in the form of a topology. The topology has two components, the nodes representing capacities, and the arcs representing interactions that characterise these capacities, collectively the nodes and the arcs represent the structure of the model. Having the fundamental structure, we start preparing for the output generation. This

preparation happens in the task builder where the application is selected, and solver and solver properties are provided and linked up to any material models. The model is written out in the correct calculation sequence to the desired output format using specific language templates that translates the equations from the equation editor to the output language.

Based on the user input from the different editor, the software will produce a process model with attached documentation and solver. The model consists of an interface where the modeller can do selections of equations to be a part of the model, an initiation procedure for the state and constants variables and compiled model code, written out in executable form in the output language. The model is wrapped the specific task selected for the model. The model documentation is written out to pdf-file, containing all the important information for the model.

2.1. Equations

Equations are the relations of the ontology, and a set of equations describe how things are related. An equation is a recipe describing how to calculate a variable based on other variables and operators. Other equations can again describe these variables and so on. Together this forms a tree of altering equations and variables. Our model formulation is state-based with the state describing how “things” from the ontology behaves. In the equation tree, the state of the system is at the top, and the latent variables are below. Figure 2 illustrates an example of a small equation tree, where the yellow rectangles are equations and the circles are variables. A is the state variable, which is transmitted down the equation tree. Based on other constants defined in the leaves (B, C), the time (t) and the initial state value (A^o) we integrate a new state value at next time step and so on. D is the variable holding an equation used in the integration. This equation tree is automatically assembled and used by the framework to determine what equations from the ontology will be a part of the final model. By assembling the equation tree and checking for closure, the framework guarantee that the model can be computed.

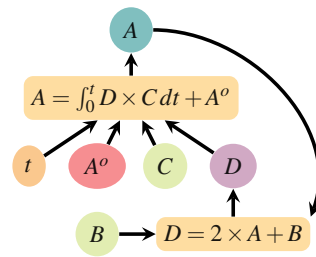


Figure 2: Illustration of equation tree.

3. A process graph for a mixing tank

To help us explain the concepts we present a case study of the construction of a dynamic model for a mixing tank in the *Process Modeller Suite*. The physical outline of the modelled mixing tank is illustrated in fig. 3. The tank consists of a liquid phase and a gas phase open to the surroundings. A stirrer ensure that the liquid phase is properly mixed. The liquid phase has a stirrer, which means that we can assume lumped behaviour. There are two feeds into the tank and one outlet. One of the inlets is an acidic solution, and the other inlet is basic. All of the inflows and outflows have a valve with adjustable opening. The valves for the inlets will be set to a fixed position, while the valve for the outlet is used to control the liquid level in the tank. In this model, we do not consider any interactions between the liquid and the gas phase to be of importance. The presence of gas phase implies that we can assume constant pressure in the tank equal to the surrounding pressure, but we do not assume any mass transfer and such. We, therefore, do not have to include the gas phase in the model.

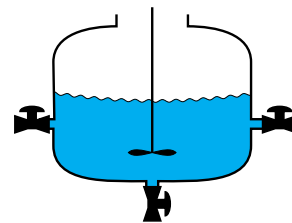


Figure 3: Illustration of the mixing tank.

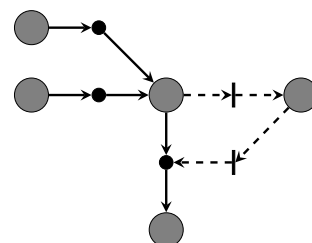


Figure 4: Skeleton of the topology of the mixing tank.

We initiate the modelling by generating a skeleton representing the different parts and their interactions, as illustrated in fig. 4. The grey circles represent capacities, and the small black circles represent the valves that manipulate the flows. The bars represent interfaces between the physical system and the control system, where properties can be transacted between two networks. The solid black arrows are physical flows while the black dashed arrows represent the transaction of the properties between different networks. In this skeleton, we have only considered the liquid phase and the control to be a part of the model. The steel construction of the tank itself and the effects of the surround gas phase is considered to be constant throughout the simulations and are captured as constants into the model.

Having the skeleton of the topology, we can start assigning the different model components with properties from the ontology. First, we define that there are two different networks in the model, a control network and a liquid network. Hence we use two different layers of the ontology for the description of model components. In addition we have an interface between the two networks, which is a transaction network. For the inlets into the tank, we define them to have constant compositions and pressures, which means that we can assign them as reservoirs. We label the two inlets with “A” for acidic and “B” for basic. The flow between the inlets and the tank is defined to be unidirectional volumetric mass transfer. In the tank, we can assume uniform property distributions due to the stirrer, but we neglect the work the stirrer provide to the liquid. The composition of the tank will change throughout the simulation, so we select the state to be the amount of moles of the different components, and we label this node with “L”. For the control network, we measure the level within the tank. This measurement is compared to a set-point within the control system, and we calculate a control input that will steer the level in the tank closer to the set-point based on a feedback loop. The controller input is transacted back to the physical network and then used to update the valve position of the outflow from the tank. In the outlet, we assume constant pressure and denote the outlet with “D”. The full topology of the mixing tank is illustrated in fig. 5.

3.1. Species propagation and reaction network selection

Having constructed the process graph it is time to populate it. We have implemented the rule that chemical species can be injected into mass reservoirs. From the reservoirs, the species propagate throughout the graph. New a species can appear in a node if a chemical reaction is defined and all the reactants are present in the node. A species library with reaction networks is defined. For the example of the mixing tank, we start off by injecting water denoted by “w” and acid, denoted by “a”, into “A” and water and a base, “b”, into “B”. From the inlets, the species propagate into “L” which is a dynamic node. The *Process Modeller Suite* then suggests reaction networks relevant to the current species. If more than one alternative reaction network, the user has to select what networks that should be used in the current model. For the mixing tank, we select a reaction network with buffer effects in a set of new species, “c”, which then appears in “L” and propagates further. The propagation of the species is illustrated in fig. 6. Due to the unidirectional flow from the inlets, the species from the tank does not propagate back into the inlets. If we used modelled the flow as bi-directional flow, the species would also propagate back to the reservoirs. The process graph is generated and stored in a JSON-file.

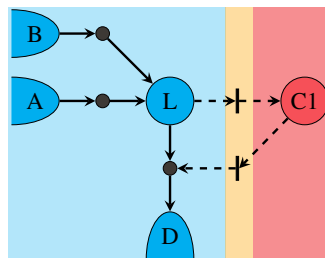


Figure 5: Illustration of the topology of the mixing tank with networks.

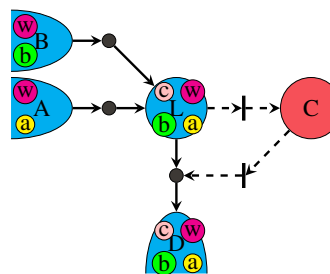


Figure 6: Species propagation. The small circles are species that propagates through the process graph.

4. Generating the model

Having established the process graph, we can start selecting the application. In principle, the process graph can be implemented into any application. Presently we have implemented a dynamic simulator environment in Python, but we are planning to design other applications for optimisation and process design and adding more languages. For the simulation of the mixing tank, we select to use Runge-Kutta as integrator and let the simulation run for 100 seconds.

4.1. Manual equation selections and initialisation

The task builder knows based on the process graph what states need to be calculated. It then starts rendering an equation tree similar to the equation tree illustrated in fig. 2. Based on the assumptions made when constructing the process graph, the model factory can eliminate a lot of equation alternatives. For example in the case of our mixing tank, we only have uniform conditions in the tank. We can, therefore, eliminate all equations written for distributed conditions. In some cases, the user has to select what equations will have to be used. An example from our mixing tank is what kind of controller will be used to calculate the controller output:

$$u(t) = K_p e(t)$$

$$u(t) = K_p e(t) + K_i \int_{t_0}^t e(t) dt + K_d \frac{de(t)}{dt}$$

Both the alternatives calculate the same property with the same units. The difference is that the first equation is based on a P-controller, and the second equation is the control equation for a PID-controller. For the mixing tank example, it was sufficient to use a P-controller.

After the selection, the states and the constants need to be given initial conditions and values. For the mixing tank example, we need to set compositions of species and pressure in the inlets. For the flows into the tank, we need to set valve openings and the cross-sectional area for the pipes. For the tank, we have to give pressure, the amount of moles of each of the species and the geometry of the tank. For the control system we to give a set-point for the level. The outflow requires a cross-sectional area, and the outlet needs pressure. Also, we can select the variables we want to be logged into a log file. For the mixing tank, we want to log the pH in the outflow.

4.2. Model documentation

The generation of the model documentation follow a similar approach to the generation of the executable code as described in (Elve and Preisig, 2017), the difference is that now the output language is L^AT_EX which again is compiled to generate a PDF-file. All documentation produced by the *Process Modeller Suite* is initiated with a presentation of the ontology used for generating the model including the domains and the properties that are part of this ontology and a user-defined description of the ontology. In addition, does all documentation includes a description of the mathematical operators that are implemented in the targeted language. The specific model documentation for the dynamic model of the mixing tank is initiated with the topology of the model, similar to the topology presented in fig. 5. This includes a description of all the nodes and arcs summarising the properties selected from the ontology, list of the variables calculated for that node, and initial state values, and specific constants for that model component. We also include a description of the reactions that are part of the model, with properties, and the species propagation. For the variables, we use templates describing how the output format of that variable is in the output format. This template includes physical units and index sets describing where in the topology the variable is used. The equations are written out also using templates for the representation of the equation with the variables and operators in the output language and the equation tree describing the closure of the model. The simulator environment is also described by a description code of the simulator including the solver and the solver properties. The documentation for the mixing tank includes full description of 5 nodes, 5 arcs, 46 variables (with constants) and 13 equations.

4.3. Simulation results of the mixing tank

We initiated the mixing tank with three different initial conditions and ran three simulations. In the first simulation, we defined the initial composition of the tank to have pH = 10 and then closing the valve from the basic reservoir, meaning that we only have inflow from the acidic reservoir. For the second simulation we set the initial composition of the tank equivalent to a pH = 4 and then closed the valve from the acidic reservoir and opened the valve from the basic reservoir. Then only adding base to the tank. The last simulation we set the initial composition of the tank to have a pH of 4 and then add equal amounts of from both A and B. Figure 7 illustrates how the pH changes during the simulations for the three different cases.

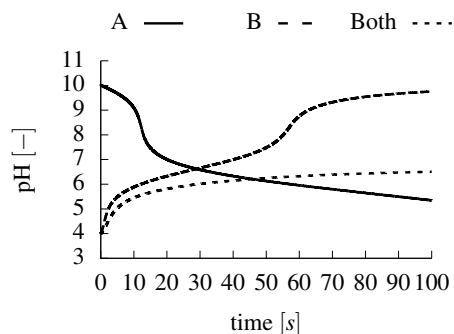


Figure 7: Simulation results. The lines plots the pH in the tank over the simulation time.

5. Conclusions

Proper model documentation is essential for maintainance, reusability and further development of process models. We are currently developing a new modelling framework called the *Process Modeller Suite*, that aids the modeller securely through the modelling and then automatically generates code with proper model documentation. This automatic code and documentation generation is made possible by employing a structure modelling methodology based on ontologies, which defines the vocabulary for expressing the process models in the context of a process graph representing the topology of the model. This process graph expresses the distribution of the properties from the ontology, and from there it is quite easy to generate code and documentation automatically. The *Process Modeller Suite* was applied in a case study of the generation of a dynamic model of a mixing tank where we generated a process graph and then wrapped the graph into a simulation environment. The generated code was well documented and produced a dynamic simulation, automatically.

References

- S. C. Brandt, J. Morbach, M. Miatidis, M. Theißen, M. Jarke, W. Marquardt, 2008. An ontology-based approach to knowledge management in design processes. *Computers & Chemical Engineering* 32 (12), 320–342.
- A. T. Elve, H. A. Preisig, jan 2017. From Ontology to Executable Program Code. *Computer Aided Chemical Engineering* 40, 2317–2322.
- M. Fedorova, G. Sin, R. Gani, 2015. Computer-aided modelling template: Concept and application. *Computers & Chemical Engineering* 83, 232–247.
- M. Heitzig, A. A. Linninger, G. Sin, R. Gani, 2014. A computer-aided framework for development, identification and management of physiologically-based pharmacokinetic models. *Computers & Chemical Engineering* 71, 677–698.
- L. Koo, N. Trokanas, F. Cecelja, 2017. A semantic framework for enabling model integration for biorefining. *Computers and Chemical Engineering* 100, 219–231.
- R. Kraus, S. Fillinger, G. Tolksdorf, D. H. Minh, V. A. Merchan-Restrepo, G. Wozny, 2014. Improving Model and Data Integration Using MOSAIC as Central Data Management Platform. *Chemie Ingenieur Technik* 86 (7), 1130–1136.
- H. A. Preisig, 2010. Constructing and maintaining proper process models. *Comput. Chem. Eng.* 34, 1543–1555.
- H. A. Preisig, A. T. Elve, 2016. Ontology construction for multi-network models. *Computer Aided Chemical Engineering* 38, 1087–1092.
- S. Shafiee, L. Hvam, A. Haug, M. Dam, K. Kristjansdottir, apr 2017. The documentation of product configuration systems: A framework and an IT solution. *Advanced Engineering Informatics* 32, 163–175.

Graph-Based Modelling with Distributed Systems

Heinz A Preisig^a and Arne Tobias Elve^a

^a*Norwegian University of Science and Technology, Dept of Chem Eng, 7491 Trondheim, Norway*
Heinz.Preisig@chemeng.ntnu.no

Abstract

The importance of explicitly discussing the effects of assumptions when modelling is being put on the stage. Starting with a completely distributed system asking for simplifications puts the assumptions right in top of the table. Every assumption on transfer rates, capacity effects and what is considered and what not comes very visible with visual modelling starting with distributed systems.

Keywords: Ontology, computer-aided modelling, multi-scale modelling, modelling framework

1. Background

Visual modelling allows the person generating the model, we call this person "the modeller", to be creative, to experiment with the fundamental structures of physical systems containing chemical and biological systems, which together form what we call a "process". We use the term "model" for a mathematical description of a process. On the basis, we insist on a "mechanistic" description, a model based on the conservation principles of physics, thus a "white-box" model in contrast to an empirical or black box model. Though the latter is not quite that hard, as there are nearly always some black-box or grey-box components in a mechanistic description, which also most commonly can be seen as crude mechanistic models. This reflects the fact that one often lacks in parts a precise description and one has to compromise for semi-empirical descriptions.

Given the task to model a system, one has to go through a number of steps. 1) Break the process down into sub-processes. This is done recursively yielding the basic spacial domains, the primitive systems, for which one has a basic description. 2) The conservation principles applied to the primitive systems provide the mathematical behaviour of the dynamics. 3) The interactions between the different subsystems are to be identified next and for each a mathematical description must be provided in terms of the conserved quantities being transferred. 4) Chemical or biological species are introduced expanding the mass conservation into species mass balances, which incorporate production rates representing the conversion of materials. 5) The remainder is to "close" the equation set by adding material models and geometrical relations together as well as auxiliary relations and definitions. 6) Control is plugged in via measurements and manipulating transfers.

We have worked on this problem for some time with the objective to provide a modelling suite, that constructs complex models based on an ontology. As part of the suite, the equation/variable bipartite graph is constructed on the background of the ontology. Given an ontology, the "modeller" has no direct contact with the mathematical model. Instead, the model is designed using a graphical interface supporting the construction of a hierarchical directed graph representing the topology of the process and the control system. This *ModelComposer* uses a ontology-derived automaton imposing the structural construction rules and the objects defined in the equation/variable system. Compilation to code and splicing into software components is to be done automatically. Different target languages and solver environments are supported. Whilst one obviously cannot cover

all existing simulation environments, the software is structured to make it easy to implement and connect to a new one in a short time. The ontology-based approach eliminates equation/variable-based modelling errors. It also leads to a centralised code for the basic models. The remainder is a book-keeping problem, which is handled by the *ModelComposer* and the application factory.

On the project's history: whilst it started with flow sheeting activities, the first project work was done on life support systems (Makela et al., 1988; Preisig et al., 1989, 1990) which after several iterations yielded a commercial product aiming at a generic chemical engineering domain (Westerweele, 2003; Westerweele and Laurens, 2008). The concepts were extended since then considering time-scale assumptions (Preisig and Westerweele, 2003; Preisig, 2004, 2008) and multi-network representation (Preisig and Elve, 2016), which is strongly linked to a Framework 7 EC project (Karoliuss et al., 2016, 2017). The project was related to other similar projects in Preisig (2010).

The overall objective is to enable the modeller to interact with the software on a more conceptual level, namely on the level of defining the structure of the model, whilst another person can provide the description of the various involved mechanisms and models. Thus the separation is essential. The latter results in defining a set of ontologies that can be linked together, where the term "ontology" is here used as a representation of the structure of the knowledge associated with a particular subject domain augmented with a precise mathematical representation of the modelled phenomenon (Elve and Preisig, 2017; Preisig and Elve, 2016).

Whilst the earlier papers dealt mostly with lumped systems, here we extend to networks of distributed systems and add the multi-scale aspect by enabling the computation of material properties from lower-scale models, such as what is usually referred to as meso-scale or the molecular scale.

2. Multi-networks for multi-scale systems

2.1. Concepts forming the ontology

To reach the current level of constructing the ontology is the result of an evolutionary process. It leads to the construction of a program set that allows us to define a very minimal basic ontology, which captures all the structural elements on which the lower-triangular equation system is constructed. The ontology is also used to define the graphical elements for the graphics driven model composer as well as the automaton controlling its interface. Finally the ontology supplemented with the equations and variable supergraph, facilitates the basics for the compilation into an executable task/application.

The key elements in the ontology are **structure**, which acknowledges the view that all systems can be represented as a directed graph rather independent of their nature: *physical systems* are networks of capacities and connecting transfers for the extensive quantities mass, energy and momentum, whilst *control* has dynamic and static blocks with signals connecting them. Or in *economical systems* it is money that flows from account to account.

Graphs may be typified or more detailed by adding classifying attributes such as liquid, solid and gas. With the nodes representing the material/mass capacities and the arcs the transfers of extensive quantities. Since transfer can be due to different mechanisms, such as heat conduction, radiation or mechanical work, arcs are equipped with corresponding attributes.

Capacities may be of different nature, like distributed or lumped. Transfer between neighbouring capacities occurs through the common interface, for which equilibria and flux conditions apply.

An abstraction can be achieved by defining communicating networks, where the interfaces are special trans-network graph components representing behaviours of phase boundaries or measurements/manipulation. Tokens generalise what is present in the graph, in physical systems the conserved quantities, in control information. This allows the concept to be expanded in almost all scientific and associated domains.

In earlier publications we reported the compact representation of lumped systems (Preisig, 2010). The conservation principles then read $\underline{\Phi} = \underline{\mathbf{F}} \underline{\Phi}$. For distributed systems we start with the integral balance:

$$\int_V \frac{\partial \underline{\Phi}}{\partial t} dV = - \int_S \underline{\hat{\Phi}}^T \underline{\mathbf{n}} dS \quad \left\{ \begin{array}{l} \underline{\Phi} \text{ density extensive quantity} \\ \underline{\hat{\Phi}} \text{ flux extensive quantity} \\ S \text{ surface} \\ \underline{\mathbf{n}} \text{ normal direction} \end{array} \right.$$

$$= - \int_V \frac{\partial}{\partial \underline{\mathbf{r}}} \underline{\hat{\Phi}} dV \quad \text{Gauss theorem}$$

$$\underline{\Phi} = - \sum_i \int_{S_i} \underline{\hat{\Phi}}_i^T \underline{\mathbf{n}}_i dS_i := - \sum_i \hat{\Phi}_i$$

which for a network of distributed systems also takes the form $\underline{\Phi} = \underline{\mathbf{F}} \underline{\Phi}$. With the "internals" obviously being the the integral of the left-hand-side of the partial differential equation representing the behaviour of the respective distributed system. Namely $\int_V \frac{\partial}{\partial \underline{\mathbf{r}}} \underline{\hat{\Phi}} dV$. The flows between distributed systems will in general be of distributed nature – the flux is a function of the position on the surface. In some cases though, a one or two dimensional distributed system is appropriate for the description of the physical system. Flows that cross the systems boundary orthogonal to the distribution direction, are uniform over the surface.

2.2. An example: tubular heat exchanger

The example was used to demonstrate model reduction in the frequency domain (Ma, 1993; Ma and Preisig, 1994a). The hot and the cold flows are modelled as 1-D systems and so is the wall but in orthogonal direction. The hot fluid transfers heat to the wall, whilst the cold receives heat from the wall.

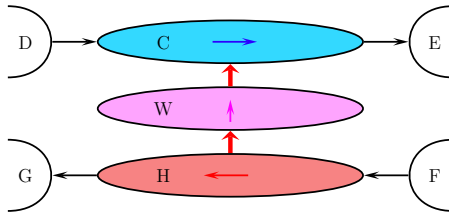


Figure 1: Topology heat exchanger

the isotropic linear heat transfer law : $\frac{\partial}{\partial \underline{\mathbf{r}}} \underline{\hat{\Phi}} := -k^q \frac{\partial T}{\partial \underline{\mathbf{r}}}$ which when substituted results in Fourier's heat diffusion equation.

The network equations then write:

$$\dot{H}_C = - \int_{V_C} \frac{\partial}{\partial \underline{\mathbf{r}}_C} \underline{\hat{\Phi}}_C dV_C = \hat{Q}_C + \hat{H}_{D|C} - \hat{H}_{C|E}$$

$$\dot{H}_H = - \int_{V_H} \frac{\partial}{\partial \underline{\mathbf{r}}_H} \underline{\hat{\Phi}}_H dV_H = -\hat{Q}_H + \hat{H}_{F|H} - \hat{H}_{H|G}$$

$$\dot{H}_W = - \int_{V_W} \frac{\partial}{\partial \underline{\mathbf{r}}_W} \underline{\hat{\Phi}}_W dV_W = \hat{Q}_H - \hat{Q}_C$$

Whilst the above network representation looks simple, the reader should be aware that the solu-

These heat flows are orthogonal to the fluid flow and thus the convective energy flow. For simplicity reasons, we assume constant mass flow and properties. The partial differential equations describing the fluids and the wall may be derived through the shell-balance mechanism. For the fluids the flow of enthalpy density $\hat{H} := \hat{m} c_p T$ which is to be normed by the volume to form the density. The term $\frac{\partial}{\partial \underline{\mathbf{r}}} \underline{\hat{\Phi}} := \hat{m} c_p V^{-1} \frac{\partial T}{\partial \underline{\mathbf{r}}}$ with \hat{m} the mass flow, c_p the specific heat capacity, thus the heat capacity per kg and K, V , the volume, T the temperature and $\underline{\mathbf{r}}$ the spatial coordinates. For the wall the simplest version is

The connections in the liquid streams are mass flows, whilst the ones to the wall are heat flows. One thus can split the network into two, namely a mass flow network and a heat flow network.

$$\underline{\dot{H}} = \underline{\mathbf{F}}^m \underline{\hat{H}} + \underline{\mathbf{F}}^q \underline{\hat{Q}}$$

tion of these three coupled partial differential equations is by no means trivial. They can be solved readily in the Laplace domain, given the assumptions (Ma, 1993), which can also be taken as the starting point for a model reduction, which is of particular interest for control applications (Ma and Preisig, 1994b; Preisig and Ma, 1995). In the time domain, this calls for numerical solutions, thus approximations are being made. With networks of control volumes being our core approach, we have a brief look on how such approximation institute themselves shown as topologies.

2.3. Approximations

The division into control volumes is in computational fluid dynamics referred to as gridding or meshing, which implies to superimpose a mesh of lines extending into intersecting surfaces thereby defining a block of non-overlapping control volumes. Whilst the gridding results in an exact representation of the space, the interactions are subject to approximations, as during the integration process one only gets information about each control volume as a whole, whilst for the transfer, the conditions at the common boundary should be known. The subject cannot be discussed in detail, but what comes out clearly in a topology representation is the question on how the interfaces are being defined. Gridding methods using block gridding for example require procedures to match the grids at the surface, either by design or by interpolations.

We give two simple approximations below and demonstrate that we can use the graphical representation to visualise different approximations.

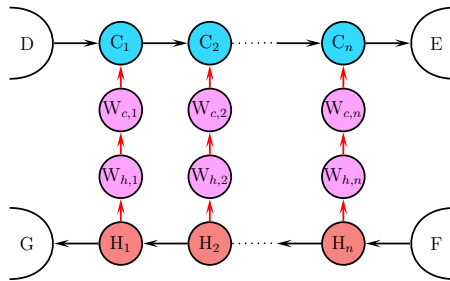


Figure 2: Topology lumped heat exchanger

If one approximates the distributed behaviour by a series of lumped systems, thus "slices" the heat exchanger. One defines a network of lumps and connections. One thus can split the network again into two, namely a mass flow network and a heat flow network.

$$\begin{aligned}\dot{\mathbf{H}} &= \underline{\mathbf{F}}^m \hat{\mathbf{H}} + \underline{\mathbf{F}}^q \hat{\mathbf{q}} \\ &= \underline{\mathbf{F}}^m_i \hat{\mathbf{H}}_i + \underline{\mathbf{F}}^m_e \hat{\mathbf{H}}_e + \underline{\mathbf{F}}^q_i \hat{\mathbf{q}}_i\end{aligned}$$

where the index i indicates the internal flows, whilst the e labels the external flows. An alternative would be to eliminate all capacitive elements in the wall by adding a time-scale assumption, namely that the heat transfer in the wall is instantaneous compared to the rest of the plant's dynamics of interest (Preisig,

2004). This results in the well-known overall-heat transfer model for the heat transfer between the two fluid bodies. The approximation with two lumps in the wall is a very interesting one as it requires the same number of parameters as its simpler non-capacity model, namely the three transfer coefficients film, wall, film. In contrast though, it does not neglect the capacity effect of the wall and thus is definitely a much better choice.

2.4. Dynamic splitting

The typical process model can be split into two dynamic regions, a fast one for the momentum distribution, as the pressure wave moves at the speed of sound, and the mass / energy transport, which is order of magnitudes slower. This time-scale separation is applicable for most processes but certainly excluding the description of explosions, detonations or any other process, where "things" happen at speed of sound.

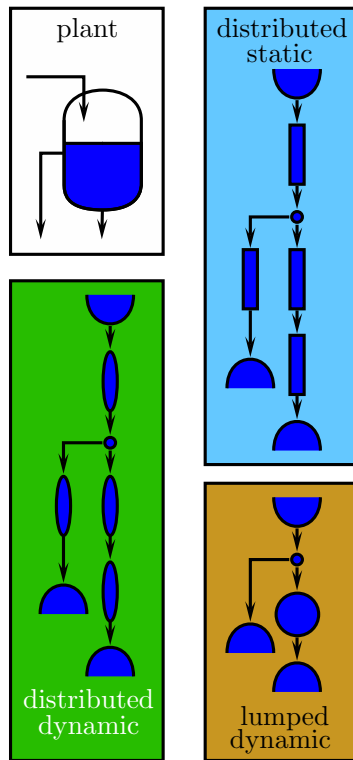


Figure 3: Topology lumped heat exchanger

A typical process that exhibits this behaviour is a tank with inlets and outlets. We show a tank with one inlet on the top and one on the side and another one on the bottom. The first model we generate is a distributed one - the green box. The liquid is fed on the top from a reservoir through a pipe, which we do not model. If included it would be a one-dimensional-along-the-pipe distributed system. The fluid above the side outlet though is modelled as a distributed system and the one below the outlet as well. The two outlet pipes are modelled as one-dimensional-along-the-pipe distributed system. In order to compute the pressure distribution in the plant, which we require to compute the outlets' volumetric flows, a stationary assumption is made about all parts yielding the model in the blue box on the right upper corner.

For the mass transfer we require the volumetric flow in the pipes, thus the pressures at the point of the side outlet, the bottom of the tank and the two receiving reservoirs. The representation of the fluid in the tank is also simplified. It is assumed to be ideally mixed and that the fluid body above the location of the side outlet is negligibly small which for an overflow is the most common assumption made even though that fluid level is a direct function of the outflow rate as constituted by what is often referred to as the weir equation.

3. Mechanics

Considering the mechanics of nature, modelling using distributed systems is the most natural approach, at least for macroscopic systems where the particular nature of matter is not of relevance. Since the world is not uniform, and process need to operate between two domains of systems that are not in equilibrium, distributed systems is the first thing to consider. Coupling occurs through the joint interfaces, the boundaries, which also are distributed. For the formulation of the model, one requires the description of the coupling between the adjacent distributed system, which in each point of the surface are equilibrium conditions with respect to the generalised forces, also called the effort variables, which are the conjugates to the potentials driving the flow of volume by pressure difference, mass through diffusion by a difference in the chemical potential, and conductive heat transfer through a temperature difference, to mention the most common transfers describing industrial processes. The second condition derives from the statement that the boundary has no capacity thus cannot accumulate extensive quantity. (Note - charge can be seen as an exception.) This implies that the flow of extensive quantity into the boundary must come out again, thus making the influx identical to the outflux.

Establishing the model based on distributed systems is thus rather straightforward. At this point one can start to implement a set of assumptions. Probably the first one is to assume that the pressure propagation is very fast, in comparison with the rest of the plant it is so fast, that it can be

assumed to be instantaneous thus of event dynamic nature. The second set of assumption may then be about mixing dynamics, thus time-scale separation between mixing and other dynamic effects, like reactions. The latter may or may not be a good assumption and mixing-controlled selectivity is not necessarily an exception (Bourne, 2003).

Many assumptions are implicitly applied by "modellers". One of the most common ones are heat transfer modelled by and "overall heat-transfer". They assume not only fast heat transfer in the complete assembly of the transfer system, which is of distributed nature but also as a consequence eliminates and thus ignores the capacity effects of the transfer system itself. The latter may be rather significant if one thinks of the construction of a vessel, for example.

4. Conclusions

Process modelling should start with distributed systems, and then assumptions should be applied. The model itself does not necessarily have to be established in algebraic form, but visual modelling offers a powerful tool to discuss and derive simple models from distributed and complicated ones. This makes it visible on where assumptions are made about the relative size of the capacities, relative transfer rates, relative time constants, distribution effects and neglecting parts of the system completely, besides the nature of the environment, which always drives the overall process.

References

- J. R. Bourne, 2003. Mixing and the selectivity of chemical reactions organic process. *Research & Development* 7, 471–508.
- A. T. Elve, H. A. Preisig, 2017. From ontology to executable program code. *Computer Aided Chemical Engineering* 40, 2317–2322.
- S. Karolius, H. A. Preisig, H. Rusche, 2016. Multi-scale modelling software framework facilitating simulation of inter-connected scales using surrogate models. *Computer Aided Chemical Engineering* 38, 463–468.
- S. Karolius, H. A. Preisig, H. Rusche, 2017. Sequential multi-scale modelling concepts applied to the polyurethane foaming process. *Computer Aided Chemical Engineering* 27, 487–492.
- Ma, 1993. Dynamic modelling, simulation and control of heat exchanger. Ph.D. thesis, UNSW, Sydney, Australia.
- X. H. Ma, H. A. Preisig, 1994a. Dynamic modelling and simulation of heat exchangers - what is available? *PSE* 94, 327–332.
- X. H. Ma, H. A. Preisig, 1994b. Model-supported control of heat exchangers. *CHEMECA* 94.
- M. Makela, A. D. Whittacker, H. A. Preisig, M. Holzapple, F. Little, 1988. Object-oriented model of a closed loop life support system. *Life Support Systems*.
- H. A. Preisig, 2004. Gymnastic exercises with topologies relating to time-scale assumptions. *ESCAPE* 14 (2004), 1105–1110.
- H. A. Preisig, 2008. Three principle model reductions based on time-scale considerations. *ESCAPE* 18.
- H. A. Preisig, 2010. Constructing and maintaining proper process models. *Comp & Chem Eng* 34(9), 1543–1555.
- H. A. Preisig, A. T. Elve, 2016. Ontology construction for multi-network models. *Computer-Aided Chemical Engineering* 39, 1087–1092.
- H. A. Preisig, T. Y. Lee, F. Little, 1990. A prototype computer-aided modelling tool for life-support system models. 20th ICES ISSN 0148-7191 (901269), 10.
- H. A. Preisig, T. Y. Lee, M. Makela, A. D. Whittacker, F. Little, 1989. On the representation of life-support system models. 19th ICES ISSN 0148-7191 (891479), 13.
- H. A. Preisig, X. H. Ma, 1995. Modellgestützte regelung von wärmeaustauschern. *Chemical Engineering Technology*, 1.
- H. A. Preisig, M. R. Westerweele, 2003. Effect of time-scale assumptions on process models and their reconciliation. *ESCAPE* 13 (2003), 875–880.
- M. R. Westerweele, 2003. Five septs for building consistent dynamic process models and their implementation in the computer tool modeller. Ph.D. thesis, The Netherlands: Eindhoven University of Science and Technology.
- M. R. Westerweele, J. Laurens, 2008. Mobatec modeller - a flexible and transparent tool for building dynamic process models. *ESCAPE* 18.

Closure Development for Multi-Scale Fluidized Bed Reactor Models: A CLR Case Study

Stefan Radl,^{a*} Federico Municchi,^a Schalk Cloete,^b Henrik Cloete,^b Stefan Andersson,^b Joana Francisco Morgado,^c Thomas Gurker,^d Rosa Quinta-Ferreira,^e Christoph Kloss,^f Christoph Goniva,^f Shahriar Amini^b

^a*Graz University of Technology, Institute of Process and Particle Engineering, Inffeldgasse 13/III, 8010 Graz, Austria*

^b*SINTEF, S.P. Andersens vei 15 B, 7031 Trondheim, Norway*

^c*Norwegian University of Science and Technology, Dept. of Energy and Process Engineering, Kolbjørn Hejes v 1B, 7491 Trondheim, Norway*

^d*Andritz AG, Stattegger Strasse 18, 8045 Graz, Austria*

^e*University of Coimbra, Dept. of Chemical Engineering, 3030-790 Coimbra, Portugal*

^f*DCS Computing GmbH, Industriezeile 35, 4020 Linz, Austria*

radl@tugraz.at

Abstract

Chemical looping reforming (CLR) processes offer textbook examples for challenges in chemical engineering with respect to transport limitations. Phenomena that potentially need to be considered in a rigorous reactor model include (i) diffusion in solids and nanometer-scale pores, (ii) heat and mass transfer between suspended particles and the ambient gas, (iii) meso-scale phenomena such as clustering, as well as (iv) large-scale phenomena such as particle and gas-phase dispersion in the reactor's axial direction. Here we summarize key scientific advances made in the "NanoSim" project, which established a computational platform that enables modelling a large range of these phenomena. Specifically, we show that already at the particle scale significant uncertainties are introduced when modelling chemical reactors in very detail. This is due to the nature of gas-particle flow, i.e., the spontaneous formation of heterogeneities (i.e., so-called meso-scale structures) that impact flow, species transport and reactions. The key finding is that these heterogeneities must be accounted for in typical CLR applications to correctly predict reaction rates in an industrial-scale reactor.

Keywords: fluidized bed, computational fluid dynamics, multi-scale model, chemical looping reforming, process intensification

1. Introduction

1.1. Context of the Present Models with Chemical Looping Technology

Chemical looping (CL) technology often uses dual fluidized beds (FBs) to circulate oxygen-carrier (OC) particles. The OC particles provide oxygen for the (partial) combustion of a fuel. In CL reforming (CLR), the focus is on the production of syngas, e.g., via partial oxidation of methane on catalytically-active OC particles. Nanostructuring such OC particles offers a potential to greatly increase their reactivity, mainly by increasing the surface area. In our present contribution we focus on FB technology applied to CLR.

Understanding the flow and conversion of particles in FB reactors offers another potential, namely for the intensification of CL processes. However, considering all relevant phenomena in FBs typically requires a “zoo” of models and software tools. The present study employs a multi-scale modelling approach (see Figure 1, panel a) involving scales spanning from the atomistic to the reactor level. Our ultimate aim is to quantify the process intensification benefit when using nano-structured OC particles for syngas production.

1.2. Scope and Overview of Scales

As an example for an important chemical looping reforming reaction, the partial oxidation of CH_4 over an iron oxide is considered. Specifically, we will focus on equipment-scale simulations (i.e., level 2 in Figure 1) that account for all relevant phenomena on the scales below (i.e., scales 3 to 6). With respect to the latter, reaction rates for (i) a nano-structured, and (ii) a standard OC materials were determined via atomistic modelling. An intra-particle diffusion model is used to account for particle-scale diffusion resistances. On modeling level 2, a filtered Two Fluid Model-based approach (fTFM; see Section 2 for details) is used to model the reactor. The fTFM accounts for the effect of nano-sized grains by a larger reaction rate (see Eqns. 2 and 3, as well as accompanying text). In the context of an fTFM, filtering refers to the spatial averaging of results from more detailed flow simulations. In addition to classical transport mechanisms (i.e., convection and diffusion), fTFMs account for transport limitations imposed by meso-scale structures (i.e., fluctuations of the local particle concentration; see Figure 1, panel b, for an illustration).

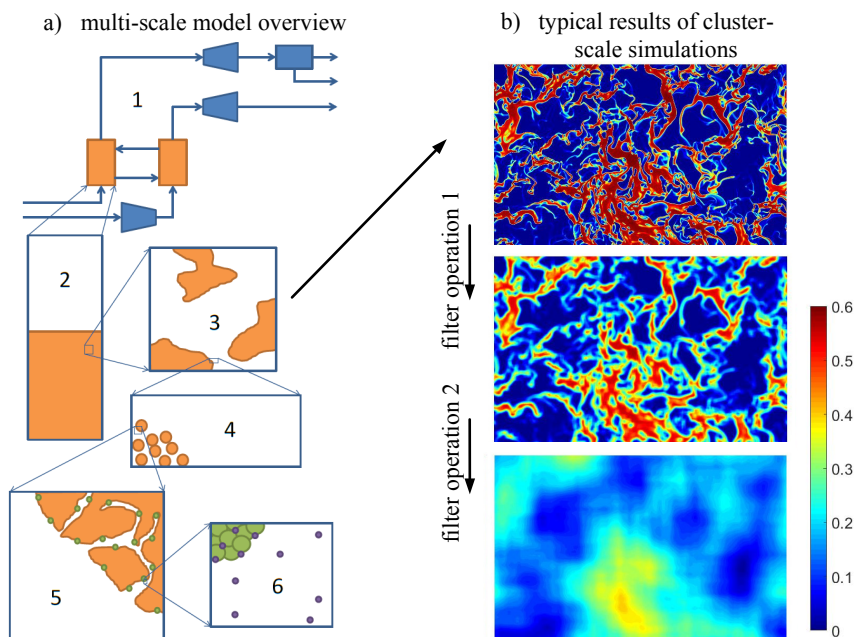


Figure 1. Overview of the multi-scale models (panel a; 1: system scale, 2: equipment scale, 3: cluster scale, 4: particle scale, 5: intra-particle pore scale, 6: atomistic scale), as well as a typical result of a cluster scale simulation (panel b; the colorbar illustrates the particle volume fraction).

2. Comprehensive Fluidized Bed Reactor Model

The reactor simulations were completed using the fTFM approach (Igci *et al.*, 2008) with closures derived from computationally expensive resolved simulations. These closures were developed by us, including verification and validation, during the past three years within the “NanoSim” project (<http://www.sintef.no/projectweb/nanosim>). The fTFM approach allows for the use of much larger computational cells than would normally be required. Therefore, this approach can be used to describe industrial-scale reactors with high accuracy and at moderate computational cost. The two most important fTFM closures were included in the present fTFM simulations: drag (similar to Igci *et al.*, 2008), and the effective reaction rate (Cloete, Cloete, Radl and Amini, 2017). The latter is expressed via the factor η_{meso} , see Section 2.2.

2.1. Case Description

Simulations were completed in a simple cylindrical geometry, 1 m in diameter and 5 m in height. The geometry was meshed with structured hexahedral elements using the cut-cell method. A mesh resolution of 6 cm (typical for industrial-scale CFD simulations) was used, leading to approximately 20,000 cells. A mass flow inlet was specified feeding pure methane at various flow rates. Partial slip wall boundary conditions were employed (Johnson and Jackson, 1987) with a specular coefficient of 0.1. A pressure outlet was used with a backflow solids volume fraction of 0.1 to ensure that the entire geometry contains particles (thus, the simulated geometry can be seen as a representative element of a larger system). The porous oxygen carrier particles were assumed to have a density of 4,000 kg/m³ and a particle size of 100 μ m. An operating pressure of 20 bar was selected with the gas density and viscosity/diffusivity determined via the ideal gas law and kinetic theory of gases, respectively. fTFM Simulations were carried out using ANSYS FLUENT (significantly extended by user-defined functions), with 2nd order spatial, and 1st order temporal discretization.

2.2. Reaction and Closure for the Reaction Rate

Partial oxidation of methane over an iron-based oxygen carrier was simulated in the present study. This CLR reaction can be described with:



Atomistic modelling (using the tool “REMARC”) was used to determine intrinsic reaction kinetics for this reaction for (i) a porous OC particle consisting of nano-size grains (10 nm in diameter), and (ii) a regular OC particle consisting of “standard” 1 μ m grains. The local (effective) reaction rate was modeled based on the local particle volume fraction α_s , the methane and iron oxide concentrations (i.e., C_{CH_4} , $C_{Fe_3O_4}$), the effectiveness factors η_{pore} and η_{meso} , as well as a temperature-dependent reaction rate constant k (E_A was fixed to 1.32 $\cdot 10^5$ J/mol):

$$R = \alpha_s k C_{CH_4} C_{Fe_3O_4} \eta_{pore} \eta_{meso} \quad (2)$$

$$k = A \exp\left[-E_A / (RT)\right] \quad (3)$$

In the above rate law, the pre-exponential factors for the nano-sized and standard grains are $A_{nano} = 1.17 \cdot 10^5$ cm³/mol/s and $A_{standard} = 2.23 \cdot 10^4$ cm³/mol/s. An intra-particle diffusion model (Yang, Cloete and Amini, 2016) is employed to consider intra-particle transport limitations, i.e., to calculate η_{pore} .

3. Key Results and Discussion

Simulations were carried out using a range of gas feed rates (i.e., 0.2-3 kg/s) for both OC materials. Simulations were run for at least 60 s, while collecting the outlet methane flow rate (in order to calculate methane slip) and the overall solids holdup in the geometry (to calculate the mass of OC in the system). These measures were averaged over the last 30 s of simulation time (i.e., after reaching a steady-state). For the ease of comparison, the reactor temperature and the Fe_3O_4 mass fraction were fixed at 900 °C and 0.15, respectively. Key results are shown in Figure 2, as well as Figure 3.

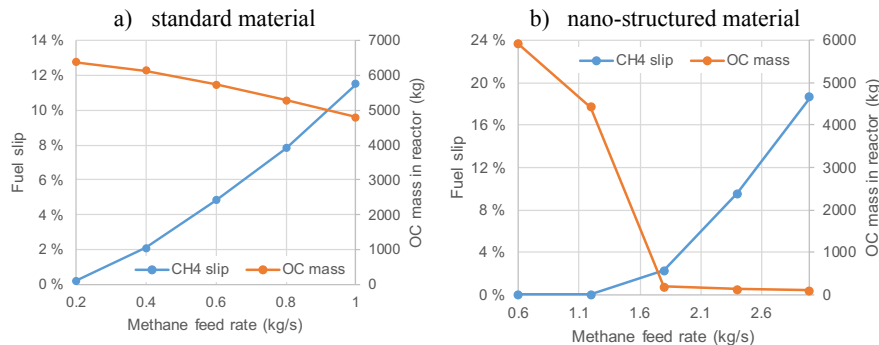


Figure 2: Reactor performance with the standard (panel a) and nano-structured (panel b) OCs (fuel slip is defined as one minus methane conversion, and illustrates reactor performance).

Clearly, the nano-structured oxygen carrier (10 nm grains) allows for much higher gas throughputs and lower oxygen carrier loadings than the standard (1 μm grains) oxygen carrier. From the results in Figure 2, it can be estimated that 99% methane conversion (i.e., 1% fuel slip) can be achieved with a flow rate of 0.3 kg/s and 6100 kg for the standard oxygen carrier. In contrast, the nano-structured oxygen carrier allowed for a flow rate of 1.4 kg/s (i.e., 4.7 times higher!) with only 2500 kg of OC required for the same methane conversion. It is also interesting to note that there is a sharp reduction of oxygen carrier loading for fuel flow rates of 1.8 kg/s and above. This is the result of the average solids loading becoming too low for dense solids clusters to form in the reactor. As a result, individual particles are easily swept upwards by the gas, whereas particle clusters forming at lower CH_4 feed rates (i.e., lower gas speed) can be retained in the reactor.

The superior performance of the nano-structured OC may be expected given that it has a 50 times faster intrinsic reaction rate constant than the standard OC. However, the increased reactivity is compensated to some degree by intra-particle and meso-scale transport limitations in the fluidized bed reactor: (i) intra-particle mass transfer limitations (expressed by η_{pore}) are often negligible for the small particles employed in typical FB applications. This is even the case for the highly reactive nano-structured OC particles (effectiveness factor 0.97). (ii) As shown in Figure 3 (panels iii) the mass transfer resistance imposed by the meso-scale phenomena (i.e., clustering) can be very large, resulting in effectiveness factors (defined as the ratio of the observed reaction rate to that without clustering) as low as 0.05. Clearly, not accounting for clustering on the reaction rate would lead to unrealistic predictions of the methane conversion rate, and ultimately an incorrect sizing of the reactor.

Despite the large meso-scale mass transfer limitations, the nano-structured oxygen carrier still enables a large degree of process intensification: In this case, a 5 m tall reactor achieving 99% methane conversion of a feed of 1000 MW_{th} methane would need to be 8.2 m in diameter with the standard OC, but only 3.8 m in diameter with the nano-structured OC (reactor volume reduction of -79%). The OC requirements for these two cases would be 407 tons and 36 tons (i.e., -91%), respectively, leading to respective pressure drops of 0.76 bar and 0.31 bar. Even though the nano-structured OC will be significantly more expensive to produce than the standard OC, these large process intensification benefits are likely to result in significant overall cost savings.

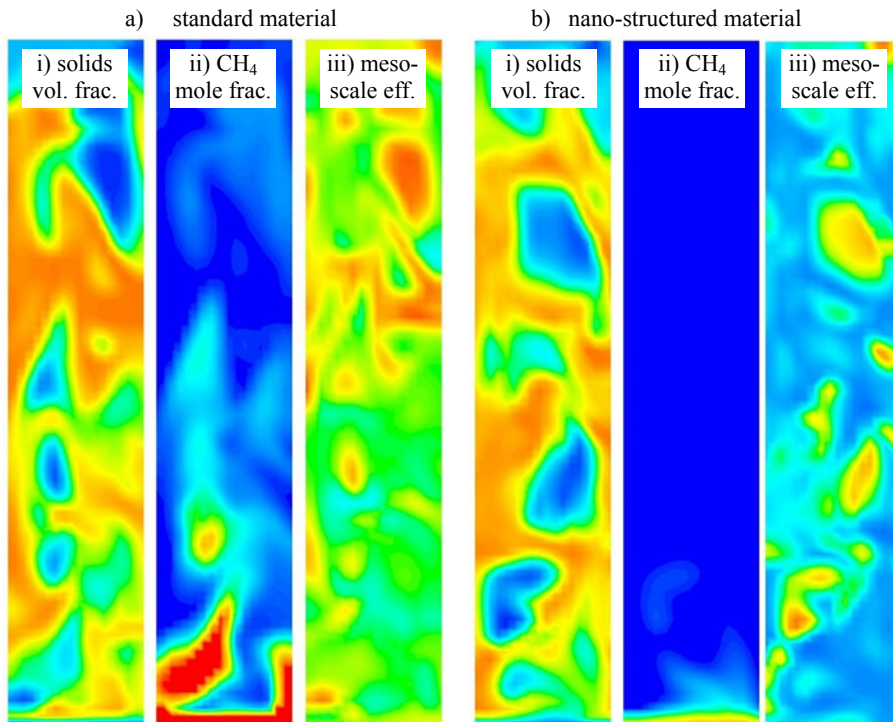


Figure 3: Snapshots of the instantaneous distribution of solids volume fraction (panels i, range 0-0.6), methane mole fraction (panels ii, range 0-0.2), as well as the meso-scale effectiveness factor (panels iii, range 0-1) for standard and nano-structured oxygen carrier particles (panel a and b, respectively); the colors indicate the range from low (blue) to high (red); 0.6 kg/s methane feed).

4. Conclusions

Our present contribution focused on a fully mechanistic description of an FB reactor as an alternative to simplified models often used on the system level (i.e., in the context of flow sheeting models). The presented hierarchy of models is especially interesting for the development of new processes (e.g., process intensification studies) and new materials. Furthermore, “virtual testing” of materials, as well as data generation to support simplified device models (e.g., 1D and compartment models, see (Morgado *et al.*, 2017)) is possible with the developed simulation platform.

The focus of our efforts was on establishing a new generation of closure models that account for both particle-scale (i.e., how fluid flow around individual particles affects

heat and mass transfer, see Municchi and Radl, 2017) and meso-scale phenomena (i.e., clustering and bubble formation in fluidized beds; see, e.g., Radl and Sundaresan, 2014). We have highlighted here one selected result, i.e., the importance of accounting for the meso-scale effectiveness factor when calculating effective reaction rates. The development of such meso-scale closures is of current interest, and was greatly accelerated by novel data filtering tools developed by us (Municchi, Goniva and Radl, 2016). While a rigorous experimental validation was not done in the present study, we speculate that these closures enable significantly more reliable simulations of reactive fluidized beds at industrial scale.

Finally, one should not forget about phenomena on other scales: (i) per-particle variations of drag, heat and transfer coefficients (Municchi and Radl, 2017), (ii) intra-particle (i.e., pore scale) transport, or (iii) diffusion through the metal (oxide) product layer on a sub-pore scale may play a decisive role in other types of reactors. The open-source multi-physics simulator “COSI” developed by us integrates the tools ParScale, CFDEM® (Hager *et al.*, 2014), and LIGGGHTS® (for download see <https://github.com/CFDEMproject>). COSI enables direct simulation of the above mentioned phenomena for small systems made up by $O(10^5)$ individual particles.

Acknowledgement

This work was funded by the European Commission under the NanoSim grant (project number: 604656).

References

- Cloete JH, Cloete S, Municchi F, et al.: The sensitivity of filtered Two Fluid Model to the underlying resolved simulation setup, *Powder Technol* 316:265–277, 2017.
- Cloete JH, Cloete S, Radl S and Amini S: Verification of filtered Two Fluid Models for reactive gas-solid flows, in Olsen, J. E. O. and Johansen, S. T. (eds.) 12th Int Conf CFD Oil Gas, Metall Process Ind. Trondheim, Norway, SINTEF, Norway, 2017.
- Hager A et al.: Parallel Resolved Open Source CFD-DEM: Method, Validation and Application, *J Comput Multiph Flows* 6(1):13–28, 2014.
- Igci Y et al.: Filtered Two-Fluid Models for Fluidized Gas-Particle Suspensions, *AIChE J* 54(6):1431–1448, 2008.
- Johnson PC and Jackson R: Frictional–collisional constitutive relations for granular materials, with application to plane shearing, *J Fluid Mech* 176:67–93, 1987.
- Morgado JF et al.: Modelling study of two chemical looping reforming reactor configurations: looping vs. switching, *Powder Technol* 316:599–613, 2017.
- Municchi F, Goniva C and Radl S: Highly efficient spatial data filtering in parallel using the opensource library CPPPO, *Comput Phys Commun* 207:400–414, 2016.
- Municchi F and Radl S: Consistent closures for Euler-Lagrange models of bi-disperse gas-particle suspensions derived from particle-resolved direct numerical simulations, *Int J Heat Mass Transf* 111:171–190, 2017.
- Radl S and Sundaresan S: A drag model for filtered Euler-Lagrange simulations of clustered gas-particle suspensions, *Chem Eng Sci* 117:416–425, 2014.
- Yang W, Cloete S and Amini S: An Effective Reaction Rate Model for Gas-Solid Reactions with High Intra-Particle Diffusion Resistance, *Int J Chem React Eng* 14(1):331–342, 2016.

Life Cycle Assessment of calcium carbonate loop CO₂ capture technology for brown coal power plant unit of the Czech Republic

Kristína Zakuciová^{a,b,*}, Vladimír Kočí^a, Karel Ciahotný^a, Ana Carvalho^c, Jiří Štefanica^d, Jana Smutná^d

^a *University of Chemistry and Technology, Prague, Technická 5, 165 00 Prague, the Czech Republic*

^b *Research Centre Řež s.r.o, Hlavní 120, Husinec-Řež, the Czech Republic*

^c *CEG-IST, Instituto Superior Técnico, Universidade de Lisboa, Portugal*

^d *ÚJV Řež a.s, Hlavní 120, Husinec-Řež, the Czech Republic*

* *Kristina.Zakuciova@cvrez.cz*

Abstract

The carbon capture technology is the new concept for cleaner energy production in the Czech Republic. In order to comply with sustainability requirements, this paper summarizes the analysis of carbonate loop technology (CaO looping) from environmental aspect by the Life Cycle Assessment (LCA) method by two main methodologies CML and ReCiPe. Two general scenarios were considered for evaluation – 250MWe Czech power unit based on brown coal combustion without (Scenario 1) and with carbonate loop (Scenario 2). Scenario 2 is further divided in three sub-scenarios with different source of energy for carbonate loop operation. LCA study was performed in different evaluation stages of characterization level, normalization level and pareto analyses of identifying the most significant environmental categories. Results are showing the significant reduction in scenario 2 in environmental categories of acidification, ozone formation and global warming potential. On the other hand, scenario 1 results in better values for abiotic depletion levels. Sub-scenarios of scenario 2 are showing, that the most optimistic is scenario 2.3 manifesting utilization of steam from carbonation process as the energy source. The most pessimistic is scenario 2.1 focusing on combustion of brown coal and no further utilization of energy from carbonation process. Environmental impacts are connected with the processes of brown coal mining and processing and with the subsequent thermal energy production. Thus, suggested scenarios are focused on the elimination of the impacts connected with mentioned processes even though brown coal is the primary source of energy in the energy mix of the Czech Republic.

Keywords: Life Cycle Assessment, carbon dioxide capture, carbonate loop.

1. Introduction

Life Cycle Assessment (LCA) is a suitable tool to assess CCS technologies in order to achieve sustainable goals in socio-economic and environmental pillars (Carvalho et al., 2014). LCA studies require understanding material and energetic inputs and outputs in order to create comprehensive model. LCA results are essential to point out the bottleneck of the technologies in order to diminish and minimize environmental impacts. The majority of the LCA studies were already performed specifically for post-

combustion capture using monoethanolamine (MEA) as a sorbent. Considering the other solvents, the CaO looping is one of the main research current focuses. Further research in CaO looping was made by Perejón et al. (2016). The main focus was on the possibility of integrating CaO looping in pre-combustion systems in order to reduce the energy demand. In the field of LCA and CaO looping, the comparative assessment of CaO looping and amine-based absorption was performed and discussed by Clarens et al. (2016). The study is confirming the assumption that the CaO looping is a viable alternative to amine based systems and it presents a 73% reduction in the climate change category. Based on the previous studies it is possible to confirm that LCA analyses for CO₂ capture technologies are in a rapid progress. CaO looping systems seem to be currently new area in the research of LCA and CO₂ capture technology. In this paper we will show, that it is necessary to analyze the final model by two considered LCA methods. The present paper aims to contribute with the following aspects:

- Two different LCA methods are applied in the study (CML and ReCiPe), leading to more robust conclusions and comparisons;
- Several different environmental impact categories are assessed, which provides a detailed assessment of the whole system.
- The LCA assessment will be performed in various scenarios at different LCA decision levels (characterization, normalization and identification of most contributing potential environmental impacts);

The recent studies, model development and its implementation were performed for the real case study of the brown coal power unit in the Czech Republic.

2. Methods

In order to build up and evaluate the LCA model of the case study, it is necessary to follow the methodological steps according to ISO 14044 (ISO, 2006), which specifies requirements for LCA. The LCA methodology consists of four steps, which include: 1) definition of the goal and scope of the LCA; 2) the life cycle inventory analysis (LCI); 3) the life cycle impact assessment (LCIA); 4) the life cycle interpretation and reporting. The goal of the study is to build a model to assess the environmental impact of capturing CO₂ by CaO looping process in a connection with an existent Czech power unit, of gross capacity 250 MWe, which is based on brown coal as source of energy. To define correctly the LCA model and to compare the results a functional unit, compatible for considered scenarios, should be defined. In this case, the functional unit is the nominal power output 250MWe, which is the same for all scenarios. Boundaries of the system considerate the power plant and carbonate loop chain from raw materials extraction through power generation to the final emissions treatment and CO₂ capture. Boundaries are excluding CO₂ transportation and final storage. Therefore, this approach is considered as “cradle to gate”. The phase of LCI involves the compilation and quantification of input and output flows for the system under the considered boundary (ISO, 2006). The aim of this step is to collect all the data required to develop LCA model. Data for the Czech power unit was collected from its annual operations’ report (Štefanica, et al., 2016). LCIA aims to understand and evaluate the magnitude and significance of the potential environmental impacts of a system. This phase is divided into 4 steps. The first two steps are classification and characterization, where impact potentials are calculated based on the LCI results. The next steps are normalization and pareto analyses. Normalization provides a basis for comparing different scenarios

according to regional (European) standardization of environmental impact categories. In order to define the most significant impact categories, pareto analyses was performed. The step of characterization and interpretation is based on evaluation of the computed environmental impacts and results. Results are characterized as potential environmental impact. Also, the final conclusions, limitations or recommendations are involved in the interpretation phase. According to ISO 14044 (ISO, 2006), normalization, in the context of LCA, is an optional step of Life Cycle Impact Assessment (LCIA) which allows to express results after the characterization step using a common reference impact. The normalization factors is showing the total impact occurring in a reference region for a certain impact category (e.g. climate change, eutrophication, etc.) in a reference year (Benini et al., 2014). The results of the normalized impact categories are further assessed by Pareto analyses in order to identify the most relevant impact categories. Pareto's rule, or the 80/20 rule, states that 20% of the all impact categories is causing 80 percent of environmental impacts (Carvalho et al., 2014).

3. Considered Scenarios

Two basic scenarios are considered for LCA evaluation. Scenario 1 represents the Czech power unit (PU) with the nominal power output 250MWe, in which the primary fuel is brown coal. This scenario represents the real power unit characterized by operational data (Štefanica, et al., 2016). Scenario 2 represents the modelled carbonate loop connected to the real power unit. Under scenario 2, three more sub-scenarios are considered:

Scenario 2.1 - Assessment of PU + CaO loop, where CaCO₃ is heated by combustion of lignite and thermal energy from the carbonation process is not used.

Scenario 2.2 - Assessment of PU+ CaO loop, where CaCO₃ is heated by combustion of natural gas and thermal energy from the carbonation process is not used.

Scenario 2.3 - Assessment of PU+ CaO loop, CaCO₃ heated by combustion of lignite + thermal energy from carbonation process is used in a steam form for CaO loop heating.

The high temperature carbonate loop is based on two crucial reactions of carbonation and calcination process. Carbonation process represents chemisorption of CO₂ on CaO, which is operating in the presence of high temperatures between 450-750 °C and is an exothermic reaction. Regeneration of the sorbent is performed by heating up on temperatures, which are exceeding the heat stability limit of actual carbonate (800-900 °C) where the thermic decomposition of produced carbonates is raised. The reaction is the calcination which is an endothermic reaction. Sulphates are not decomposed by these temperatures, thus it is necessary to separate them and substitute by a new sorbent. SO₂ is also reacting in a carbonation process with metal oxides and provides desulphurization of flue gases. The advantage of the carbonate looping is the high capacity sorption of CaO sorbent for CO₂. This process takes place usually in fluidized bed reactors, the carbonator and the calciner. The reactors are providing intensive circulation of materials and heat which contributes to high CO₂ capture from flue gases. Another advantage is the parallel desulphurization of flue gases. CaO looping system connected to the power unit is illustrated in the Figure 1.

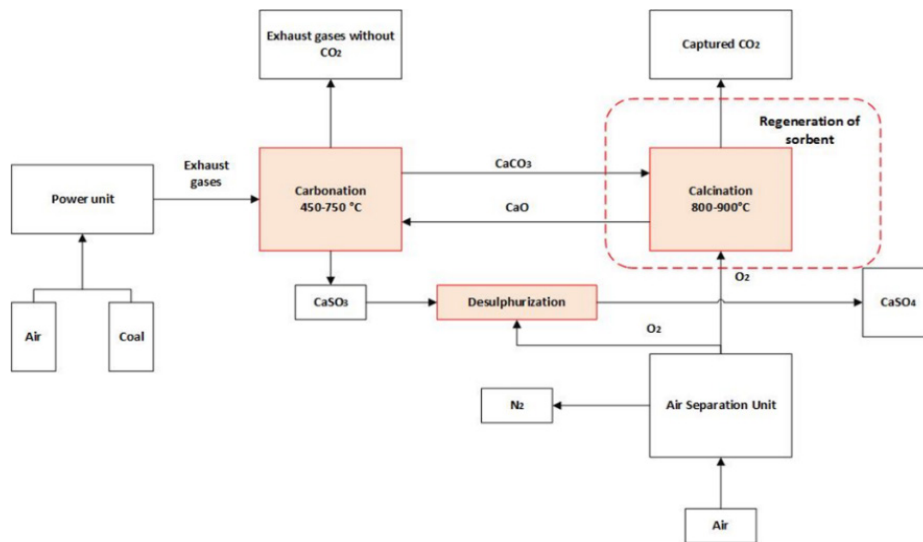


Figure 1 Scheme of CaO looping system with power unit connection

4. Results and discussion

The following table (Table 1) is summarizing normalized values for both methods ReCiPe and CML. The comparison of each scenario is showing for both methods the same result. However, values for both methods in the same scenario differs significantly (Table 1), because of different normalization coefficients for each LCA method. Scenario 1 has the highest contribution to the sum of environmental impacts, while scenario 2.3 is showing the lowest environmental impacts. Table 2 is providing a detailed look for comparison of scenario 1 and 2.3. The most significant is the depletion of climate change (CC) environmental category from $1.65\text{E}+05$ in scenario 1 to $1.94\text{E}+00$ in scenario 2.3. Moreover, another depletion occurs in categories such as fossils depletion (FD), terrestrial acidification (TA) and particulate matter formation (PMF). The depletion of TA is the consequence of utilization of carbonate loop as desulphurization unit. Moreover, TA potential depletion is caused by utilization of steam as the source of energy for CaO loop. Therefore, there is no need for additional combustion of brown coal or natural gas for heating. Particulate matter is the sum of all solid or liquid particles suspended in air and can cause several health issues. In a case of power unit, high concentration of SO_2 and CO_2 in the air increases PMF impact category. Pareto analyses shows that FD and CC contribute in 80% to the sum of all environmental impacts. Although, carbonate loop is assuming to capture 90% - 99% of CO_2 from exhaust gases, it still contributes to CC environmental impact due to combustion of lignite for thermal energy production in power unit but also for the carbonate loop operation. Another minor contribution is coming from CO_2 emissions, which were released to air through chimney. However, utilization of the energy is increasing, because of the carbonate loop operation energy requirements. Carbonate loop demands the energy for heating of fresh calcium carbonate from outdoor-air temperature to calcination temperature, which is 950°C . For 250 MWe nominal power, utilization of 240 t/h of brown coal is required in the current state of the Czech Republic

energy mix. If the primary source of energy for carbonate loop heating would be changed to natural gas (scenario 2.2), results will show slightly lower values (Table 1) in comparison with scenario 2.1. However, the best option would be to decrease FD by utilization of waste heat in the form of steam for carbonate loop heating (scenario 2.3). It would lead to the environmental credit for the whole system.

Table 1 Sum of environmental categories normalized values for CML and ReCiPe methods

Methods	Scenario 1	Scenario 2.1	Scenario 2.2	Scenario 2.3
CML	1.65E-06	9.59E-08	7.74E-08	6.09E-08
ReCiPe	7.34E+02	4.65E+01	3.73E+01	2.97E+01

Table 2 Normalized values for significant environmental category for Scenario 1 and Scenario 2.3

	Scenario 1	Scenario 2.3
FD	3.67E+04	2.32E+01
CC	1.65E+05	1.94E+00
TA	1.58E+04	1.20E+00
PMF	3.15E+03	1.06E+00
POF	1.29E+03	4.95E-01

5. Conclusions

Technology of CaO loop has potentially high importance in lowering the level of CO₂ in flue gases produced by brown coal combustion in the Czech Republic. LCA is a tool which provides environmental results and can lead to the further steps or scenarios towards the innovation. By LCA we could compare not only basic concepts of power unit with and without capture unit, but also different scenarios within carbonate loop implementation. The scenarios were mainly focused on the source of energy for the carbonate loop because it determines the main environmental problem in the frame of Czech energy mix. The results from the used LCA analyses based on two major methodologies ReCiPe and CML are showing significantly lower environmental harm in the scenarios with implemented carbonate loop. It is namely, depletion of climate change and terrestrial acidification. Carbonate loop technology contributes to depletion of CO₂ levels but also contributes as a desulphurization unit in depletion of SO₂ levels from flue gases. But in the whole life cycle of the power unit with carbonate loop, brown coal production and combustion creates the most significant problem. That is why the choice of the other energy source for CaO loop supply of heating, as is natural gas, could be the potential possibility for the environmental cost reduction. Another potential can be seen in the effective utilization of the steam from the waste heat which also could contribute to the overall environmental impacts reduction. The CaO loop technology is seen as a relatively cheap and environmentally very promising technology for the region of the Czech Republic. In the future, further analysis of the transportation infrastructure and final CO₂ storage from life cycle view has to be done. The complication is occurring with the pilot concepts of extensive infrastructure and potential storage sites which are currently investigated from geological and geomorphological conditions and their suitability in the Czech Republic.

Acknowledgements

The presented work was financially supported by the Ministry of Education, Youth and Sport Czech Republic - project LQ1603 Research for SUSEN. This work has been realized within the SUSEN Project (established in the framework of the European Regional Development Fund (ERDF) in project CZ.1.05/2.1.00/03.0108 and of the European Strategy Forum on Research Infrastructures (ESFRI) in the project CZ.02.1.01/0.0/0.0/15_008/0000293, which is financially supported by the Ministry of Education, Youth and Sports - project LM2015093 Infrastructure SUSEN.

References

- Benini, L., Mancini, L., Sala, S., Schau, E., Manfredi, S., & Pant, R. (2014). Normalisation method and data for Environmental Footprints, 113. <https://doi.org/10.2788/16415>
- Carvalho, A., Mimoso, A. F., Mendes, A. N., Matos, H. A., (2014). From a literature review to a framework for environmental process impact assessment index. *J.Clean. Prod.* 64, 36–62. doi:10.1016/j.jclepro.2013.08.010
- Clarens, F., Espí, J. J., Giraldi, M. R., Rovira, M., & Vega, L. F. (2016). Life cycle assessment of CaO looping versus amine-based absorption for capturing CO₂ in a subcritical coal power plant. *International Journal of Greenhouse Gas Control*, 46, 18–27. <https://doi.org/10.1016/j.ijggc.2015.12.031>
- International Organization for Standardisation. (2006). IS/ISO 14044 (2006): Environmental Management-Life Cycle Assessment-Requirements and Guidelines. ISO 14044.
- Perejón, A., Romeo, L. M., Lara, Y., Lisbona, P., Martínez, A., Valverde, J. M., (2016). The Calcium-Looping technology for CO₂ capture: On the important roles of energy integration and sorbent behavior. *Appl. Energy* 162, 787–807. doi:10.1016/j.apenergy.2015.10.121
- Štefanica, J., Smutná, J., Kočí, V., Macháč, P., Pilař, L., (2016). Environmental gains and impacts of a CCS technology Case study of post-combustion CO₂ separation by ammonia absorption. *Energy Procedia* 86, 215–218. doi:10.1016/j.egypro.2016.01.022

Computer-Aided Simulation of the Volumetric Efficiency of a 2 MW Gas Engine

Guillermo E. Valencia,^{a,*} Franklin E. Consuegra,^b Marisol Osorio^c

^a*Faculty of Engineering Universidad del Atlantico, km 7 antigua via Puerto Colombia, Barranquilla 080001, Colombia*

^b*Mechanical Engineering Department Universidad del Norte, km 5 antigua via Puerto Colombia, Barranquilla 080001, Colombia*

^c*Faculty of Electric and Electronic Engineering, Circular 1 No. 73-34, Medellin 050001, Colombia*

guillermoevalencia@mail.uniatlantico.edu.co

Abstract

In a mean value thermodynamic model of an internal combustion engine, operational parameters such as volumetric efficiency have a significant effect on the thermal performance of the engine, for example the combustion process inside the cylinder depends on the air-fuel ratio, large amounts of air are introduced to the combustion chamber require and consequently more fuel it is needed, which traduces in a higher output engine torque and electrical power. The air-fuel flow in the admission line has an appreciable inertia due to the turbocharged operation, but the intake manifold, the admission valves and the throttle act as an obstruction for the air-natural gas. Considering everything considered before, this paper proposes a model for the volumetric efficiency on the 2 MW Jenbacher Gas Engine, which is the capacity of the engine to fill the available geometric volume of the engine with a new charge of the air-fuel mix. A thermodynamic model was introduced to study the ratio between the real volume of air drawn off the cylinder, concerning the theoretical geometric volume of the cylinder based on a typical day of operation of the thermal power plant. Finally, to show the impact of the volumetric efficiency on the model results, a regression as a function of the intake manifold temperature and pressure, the volumetric gas flow and the engine revolutions was proposed. This allows to estimate the engine volumetric efficiency with a quadratic accumulated error ranging from 5.65 (when the volumetric efficiency model depends only on the air-gas mixture pressure) to 1.94 (when the model was correlated as a function of the pressure and temperature of the inlet manifold, motor angular speed, and the volumetric natural gas flow). The study gives evidence about a successful simulation of a Natural Gas Engine thermodynamic model built in Matlab due to the similarity found between the simulated results and the experimental data obtained from the data acquisition software installed on the equipment, obtaining in most cases a good accuracy to predict the effective efficiency and the electric power under different operation conditions.

Keywords: computer-aided simulation, volumetric efficiency, thermodynamic model, gas engine.

1. Introduction

Energy Sustainability (ES) in power generation systems has become a priority issue in the international research agenda (Omer, 2008), due to its close relationship with climate change, the rational use of energy and the fast increasing energy demand (Lima et al., 2017, Morales-Acevedo, 2014). The operational efficiency of systems and processes is one of the main ways to promote energy sustainability and eventually reduce greenhouse gas emissions, highlighting thermal generation engines as an alternative solution of distributed generation (DG) outstanding to the crisis energy (Jain et al., 2017). DG is defined by the IEEE as generation of energy through facilities smaller than the central generation, when interconnection with the network is provided, and supplying power to other facilities (Ackermann and Andersson, 2001).

The generation of electric power from the Internal Combustion Engines (ICE) has played a leading role in DG, to obtain lower operating costs and energy consumption (Dunia and Qin, 1998). This objective implies an effort to obtain higher performance in the machine improving volumetric and effective efficiency. For these parameters there are mathematical models intended for different applications.

Ahmed et al. (2013, 2011, 2010) has worked on the subject. Those works showed that the parameters that allow studying the performance of an engine, which is difficult or impossible to measure, such as the volumetric efficiency, can be estimated using observers. Another approach for estimating volumetric efficiency is the use of linear regressions (De Nicolao et al., 1996), which through multiple linear combinations of different variables, obtains statistical expressions that describe the behavior of the variable.

The previous developed search shows the importance that has an operative parameter such as volumetric efficiency at time of diagnosis the performance of an internal combustion engine. Taking into account the aforementioned, the main objective of this paper is to offer a comparative study of the simulated results of some thermodynamic models for the volumetric efficiency of the 2 MW Jenbacher Gas Engine as function real operation condition for 31 days, which can be used for control and observation of the engine.

2. Methodology and Experimental Set Up

In order to identify and generate an easy and reliable expression for the volumetric efficiency, as first step was needed to study the engine performance during normal and abnormal operation, and also must be known in general the engine parts, type of fuel and the operational regime. Second, a thermodynamic analysis of the different variables that participates in the behaviour of the volumetric efficiency was developed and finally a statistical expression was proposed.

As for subsequent control and observation of the engine, it is important to rely on a precise model to describe it; it is possible to obtain tuned equations using the real-time sensors values. The studied J612 Jenbacher gas engine offers high levels of fuel consumption due to a combustion technology according to the world quality standards. The engine reaches 2004 kW of electrical output at 1,500 rpm, under a thermal efficiency (i.e., a fuel to power efficiency) of 42.9%. Figure 1a shows the industrial plant and Figure 1b the schematic diagram of the air admission system to the engine

including the turbocharger, which is used to obtain more power output with the same size of the engine. As seen before, it is important to estimate the volumetric efficiency. To obtain a reliable estimator for this variable, the mathematical equations that describe the dynamic behavior of admission air system are needed.

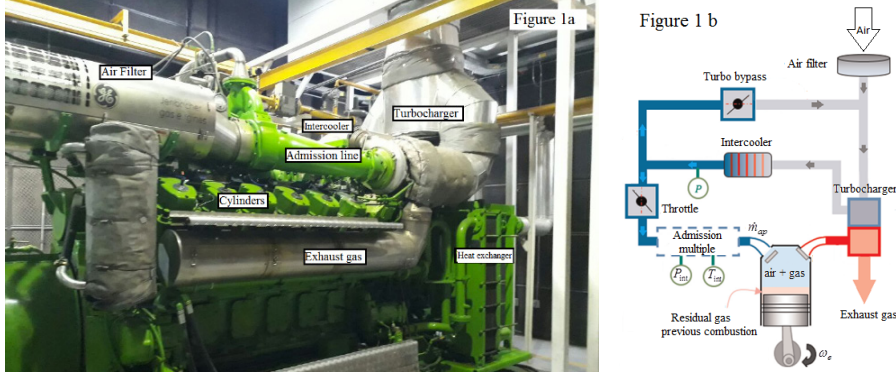


Figure 1. J612 Jenbacher gas engine a) Industrial plant, b) Schematic diagram.

The pressure (P_{int}) and temperature (T_{int}) in the intake manifold were considered constant due to engine control unit, allowing to calculate the inlet air mass to the cylinder (\dot{m}_{ap}) as Eq. (1).

$$\dot{m}_{ap} = \frac{\omega_e V_d \eta_v P_{int}}{120 R_{air} T_{int}}, \quad (1)$$

Where ω_e is the engine angular speed in rpm, V_d is the displacement volume in the cylinders (m^3), \dot{m}_{ap} is the air mass flow that enters the cylinders in kg/s , P_{int} is the intake manifold pressure in kPa, T_{int} is the intake manifold temperature in K, R_{air} is the ideal gas constant for air in $kPa m^3/kg K$, and η_v is the volumetric efficiency (dimensionless). In addition, the fuel mass flow is computed as function of the air mass flow as Eq. (2).

$$\lambda = \frac{1}{\alpha_s} \frac{\dot{m}_{ap}}{\dot{m}_f}, \quad (2)$$

Where λ is the air/fuel ratio, and α_s is the stoichiometric coefficient with a value of 17.2 for the natural gas. Finally, the volumetric gas flow measurement should be corrected with the gas density to obtain the mass flow under the Eq. (3).

$$\dot{m}_f = \frac{P_f V_f}{R_f T_f} \quad (3)$$

With (2) and (3), the volumetric efficiency can be calculated according to Eq. (4).

$$\eta_v = \frac{\lambda \alpha_s \dot{m}_f 120 R_{air} T_{int}}{\omega_e V_d P_{int}} \quad (4)$$

Finally, four linear regressions were proposed using the volumetric efficiency equation (Eq. (4)) and the real data operation condition for 31 days (T_{int} , \dot{m}_f , ω_e , P_{int} and λ are the

real data operation condition used), allowing to estimate the quadratic accumulated error for each model suggested as a function of the intake manifold temperature and pressure, the volumetric gas flow and the engine revolutions. The linear least squares approach fitting in Matlab® was used to determine the parameters of the statistical models.

3. Results and Discussion

From the operational database of the engine, the resulting fitted models were used to predict the volumetric efficiency values as shown in Table 1, with the respective sum of squared residuals (SSR).

Table 1. Proposed linear models for the volumetric efficiency

Proposed linear models	SSR = $\sum e^2$
Eff Vol1(T_{int}) = $-0.37212 + 0.0029436 \times T_{int}$	5.6507
Eff Vol2(P_{int}, T_{int}) = $0.055047 + 3.5993 \times 10^{-5} \times P_{int} + 0.0016411 \times T_{int}$	5.5829
Eff Vol3($P_{int}, T_{int}, \omega_e$) = $0.51079 + 5.5385 \times 10^{-5} \times P_{int} - 0.0009234 \times T_{int} + 0.0002695 \times \omega_e$	4.5892
Eff Vol4($P_{int}, T_{int}, \omega_e, \dot{V}_f$) = $0.24354 - 0.001371 \times P_{int} + 0.00035484 \times T_{int} + 0.00013084 \times \omega_e + 5.1829 \times \dot{V}_f$	1.9497

The best regression is the fourth one, reaching an SSR of 1.9497, which can be explained due to the fact that the volumetric gas fuel was considered in the model. The remaining regressions have a good performance, but due to limitations in their capability of prediction when the gas flow change, they presented a high SSR. The variables were separately simulated for 6 hours to have a full understanding of the accuracy of each model. Figure 2 shows the case of the first model. In it, the intake manifold temperature does not have a severe impact on the behavior of the volumetric efficiency. Also, the Figure 2 shows that at 0.025 hours of operation, 330 K were obtained for the intake manifold temperature, 1482 kW for the electric power and 0.441 for the volumetric efficiency. This behavior implies a relative error of 28.21 % comparing to the response obtained with the fourth model as shown in Figure 3, which means that this regression does not take into account some effect of other influencing variables on the engine operation and could be improved.

Analyzing the behavior of the volumetric efficiency for all the proposed models as shown in Figure 3, it is important to highlight that the third regression although has an abnormal behavior in the first operation hours, with the lower SSR in comparison with the first and second regressions.

An abnormal behavior in the third regression of the volumetric efficiency, which does not consider the effects of the gas volume, is presented in Figure 3. A relative error during the first 0.03 hours of operation of 62.29 % was obtained compared to the fourth model, revealing the importance of the gas flow variable. For the case of the other models that do not consider the gas flow, the linear combination effect of their variables does not generate a big impact on the volumetric efficiency estimation. This situation could be justified by the values of the relative errors of 4.32 % and 1.819 % for the first and second regression, respectively. These results were obtained from the values of 0.588, for the first regression, and 0.604 for the second, at 0.025 hours, as shown on Figure 3. Then, a good behavior in the volumetric efficiency, due to the correct lineal interaction, is observed, as shown in Figure 4.

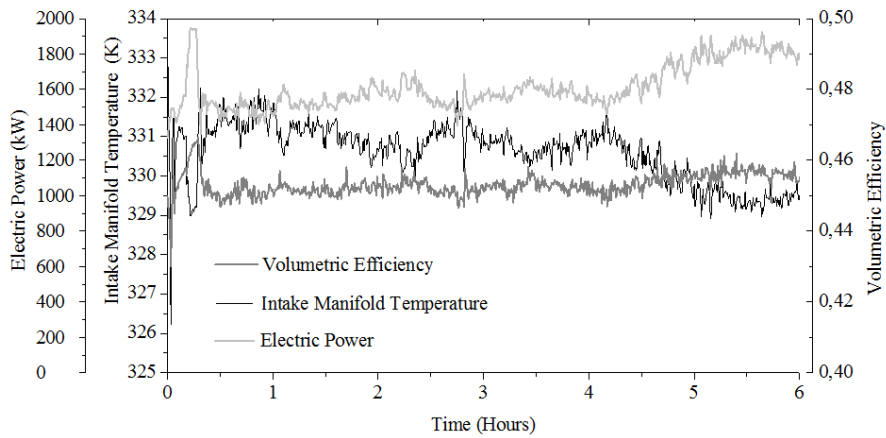


Figure 2. Respond of the volumetric efficiency using the first model.

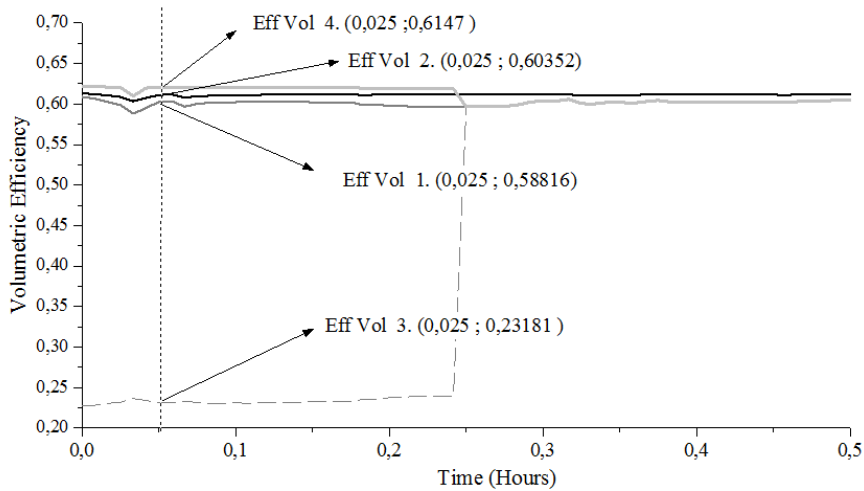


Figure 3. Comparative responds of the volumetric efficiency models.

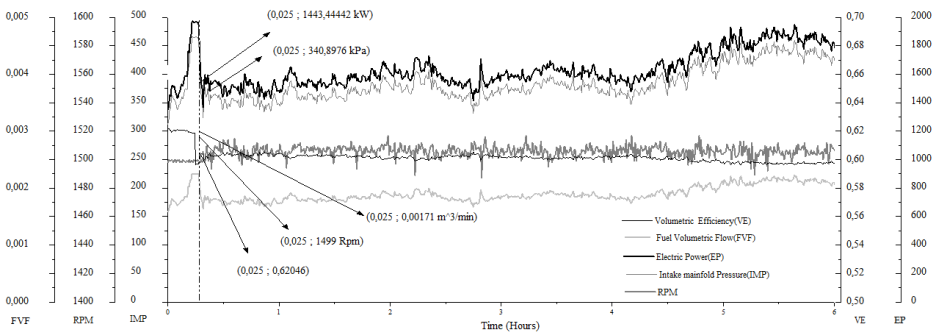


Figure 4. Respond of the volumetric efficiency using the fourth model.

4. Conclusions

Based on the simulated results obtained from the different model proposed for the volumetric efficiency of the natural gas generation engine, we conclude that both the angular speed of the engine and its volumetric fuel flow have an important impact on the volumetric efficiency of the engine, moreover the volumetric flow of fuel, as observed in the Table. 1 in term of the sum of squared residuals obtained respect to real data. Also, the effects of the temperature and the pressure of the intake manifold should not be despised, since they directly define variables associated with the volumetric efficiency, such as the density of the new charge of the combustion chamber. Finally, as expected, a proportional linear relation between the power generated by the gas engine and the volumetric efficiency was identified. Since this parameter indicates that the load was renewed inside the cylinders, directly affecting its performance, results that confirm the correct behavior of the proposed modeling and simulation.

References

- M. Omer, 2008, Energy, environment and sustainable development, *Renew. Sustain. Energy Rev.*, vol. 12, no. 9, pp. 2265–2300.
- D. A. Lima, 2017, R. C. Perez, and G. Clemente, A comprehensive analysis of the Demand Response Program proposed in Brazil based on the Tariff Flags mechanism, *Electr. Power Syst. Res.*, vol. 144, pp. 1–12.
- A. Morales-Acevedo, 2014, Forecasting future energy demand: Electrical energy in Mexico as an example case, *Energy Procedia*, vol. 57, pp. 782–790.
- S. Jain, S. Kalambe, G. Agnihotri, and A. Mishra, 2017, Distributed generation deployment: State-of-the-art of distribution system planning in sustainable era, *Renew. Sustain. Energy Rev.*, vol. 77, no. September 2015, pp. 363–385.
- S. L. Ackermann T, Andersson G, 2001, Distributed generation: a definition, *Electr Power Syst Res*, pp. 195–204.
- R. Dunia and S. J. Qin, 1998, Joint diagnosis of process and sensor faults using principal component analysis, *Control Eng. Pract.*, vol. 6, pp. 457–469.
- Q. Ahmed, A. Iqbal Bhatti, M. Abbas Rizvi, and M. Raza, 2013, Gasoline engine air filter health monitoring by second-order sliding modes, *Int. J. Adapt. Control Signal Process.*, vol. 27, no. 6, pp. 447–461.
- Q. Ahmed and A. I. Bhatti, 2011, Estimating SI engine efficiencies and parameters in second-order sliding modes, *IEEE Trans. Ind. Electron.*, vol. 58, no. 10, pp. 4837–4846.
- Q. Ahmed and A. I. Bhatti, 2010, Second order sliding mode observer for estimation of SI engine Volumetric Efficiency and Throttle Discharge Coefficient, *Var. Struct. Syst. (VSS)*, 2010 11th Int. Work., pp. 307–312.
- G. De Nicolao, R. Scattolini, and C. Siviero, 1996, Modelling the volumetric efficiency of ic engines: parametric, non-parametric and neural techniques, *Control Eng. Pract.*, vol. 4, no. 10, pp. 1405–1415.

The Ordinary Kriging in Multivariate Dynamic Modelling and Multistep-Ahead Prediction

Ahmed Shokry^{a,b}, Antonio Espuña^a

^a*Department of Chemical Engineering, Universitat Politècnica de Catalunya, EEBE – Eduard Maristany, 14, 08019 Barcelona – SPAIN*

^b*Department of Mechanical Design and Production Engineering, Faculty of Engineering, Zagazig University, Zagazig, Egypt.
Antonio.espuna@upc.edu, ahmed.shokry@upc.edu*

Abstract

This paper investigates the data-driven MultiVariate Dynamic Modelling (MVDM) and MultiStep-Ahead Prediction (MSAP) of nonlinear systems based on the Ordinary Kriging (OK) metamodel. The OK is used to build a set of Nonlinear Autoregressive models with Exogenous inputs (NAREX), able to approximate the system future outputs as a function of previous inputs and outputs considering a specific delay. Then, these OK-based dynamic models are used in a recursive interactive interpolations scheme to predict the process outputs over several time steps. The capabilities of the OK-based dynamic models are compared to other leading techniques, via their application to benchmark cases. The application results reveal the OK promising and competitive capabilities for MVDM of nonlinear systems, in terms of prediction accuracy and prediction time horizon.

Keywords: Multivariate dynamic modelling, Multistep-ahead prediction, Complex Nonlinear processes, Surrogate Models, Ordinary Kriging, ANNs, Gaussian models.

1. Introduction

In the process system engineering area, a considerable attention has been directed to the use of Ordinary Kriging metamodels, due to their potential capabilities for approximating complex highly nonlinear systems. These capabilities stem from the OK ability to combine global modelling through estimating a general trend of the system, and local modelling through its correlation function. However, almost all the OK usages and developments are concentrated in the approximation and modelling of “static” systems. So few works (Hernandez and Gallivan 2008; Boukouvala et al. 2011) have explored the OK capabilities in dynamic modelling and simulation, where the OK has been used to describe the dynamic system future outputs as a function of the current inputs and outputs. However, these works assumed simplified Markovian dynamic processes with no delayed behaviour. Besides, they have considered significantly simple dynamic profiles of the control inputs. Additionally, they have assumed the habitual availability of a First Principle Model (FPM) that can be combined with a proper design of computer experiments techniques, in order to generate optimal training datasets. However, in real engineering applications, only input-output data signals measured from the process may be available. Moreover, the comparison of these methods with the other existing state of the art proposals is not sufficiently illustrated.

This work presents a generic and robust data-driven method for the MultiVariate Dynamic Modelling (MVDM) and MultiStep-Ahead Prediction (MSAP) based on the OK metamodels. The method is aimed at approximating general real-world nonlinear dynamic processes, providing dynamic models able to predict the process future outputs for any change in the inputs, over relatively large time horizons, and also to accommodate delayed behaviours of the processes. The proposed method trains a set of OK metamodels to approximate the system future outputs -over a constant time step- as a function of previous inputs and outputs. The fitted OK-based dynamic models are then used in a recursive interactive interpolation scheme to predict the system outputs over several time steps. Within the proposed MVDM approach, the OK capabilities are compared to other pioneer techniques as Artificial Neural Networks (ANNs) and Gaussian Process (GP) models, through their application to benchmark case studies. The results show the OK promising capabilities for the MVDM of nonlinear systems.

2. Compared modelling techniques (data-based models)

2.1. Ordinary Kriging (OK)

Given a set of input-output training data $[x_i, y_i]$, $i=1,2,\dots,n$, $x \in R^k$, $y \in R$, the OK assumes a predictor $\hat{y}(x) = \mu + Z(x)$ that is composed by a constant term μ , and a deviation $Z(x)$ from that term. The deviation $Z(x)$ is considered as a stochastic Gaussian process with expected zero value, $E(Z(x))=0$, and a covariance between two points x_i , x_j as $cov(Z(x_i), Z(x_j)) = \sigma^2 R(x_i, x_j)$, being σ^2 the process variance, $R(x_i, x_j) = \exp(-\sum_{l=1}^k \theta_l |x_{i,l} - x_{j,l}|^{p_l}) + \delta_{ij} \lambda$, a correlation function, δ_{ij} the Kronecker delta and λ a regularization constant. The parameters $[\mu, \sigma^2, \theta_l, p_l, \lambda]$ are estimated via maximizing the likelihood function of the observed data $[Y]_{n \times 1}$. Then, the OK final predictor is obtained as $\hat{y}(x^*) = \mu + r^T R^{-1}(Y - 1\mu)$, where x^* is a new interpolating point, and r is the $n \times 1$ vector of correlations $R(x_i, x^*)$ between the n training data and the new point x^* . For this work, a specific Matlab implementation of this OK formulation has been used.

The OK is considered as a specific form of the general class of the GP models. Although of the quite similarity between them, still each one attracting different audiences.

2.2. Gaussian Process (GP) models

Within a Bayesian modelling framework, and assuming an unknown relation $y(x) = f(x) + \varepsilon$, where $\varepsilon \sim \mathcal{N}(0, v_o)$ is a white noise, the GP approach places a Gaussian prior probability distribution over the space of the observed unknown function (Rasmussen, 2006). This prior is considered as a collection of random functions having a joint zero-mean multivariate Gaussian distribution; $y_1, \dots, y_i \dots y_n \sim \mathcal{N}(0, \mathcal{R})$, being $\mathcal{R}(y_i, y_j) = v e^{-\sum_{l=1}^k \varpi_l |x_{i,l} - x_{j,l}|^2} + \delta_{i,j} v_o$ the covariance between the observed functions, $\varpi_l, l = 1, 2, \dots, k$ the set of hyper-parameters of the covariance function, and v a parameter controlling the covariance magnitude. The GP model provides the predictive distribution of \hat{y} corresponding to a new input point x^* as $\hat{y}(x^*) = r(x^*)^T \mathcal{R}^{-1} Y$. The function “fitrgp” included in the Matlab statistical toolbox is used in this work to construct GP models.

2.3. Artificial Neural Networks (ANNs)

ANNs are efficient data-driven modelling tools widely used for nonlinear systems dynamic modelling and identification, due to their universal approximation capabilities

and flexible structure that allow to capture complex nonlinear behaviors. Feed-forward multi-layer perceptron ANNs type is frequently used in engineering applications (Nagy, 2007). In this work, the Matlab ANNs toolbox and the function “*feedforwardnet*” have been used to create a feed forward ANNs; the number of neurons and layers, and the training algorithm (“*trainbr*”- Levenberg-Marquardt optimization method) were selected to balance simplicity and accuracy.

3. Multivariate dynamic modelling and multistep-ahead prediction

Considering a dynamic system or process having the inputs $U(t) \in R^{D_u}$ and the outputs $Y(t) \in R^{D_y}$, which are assumed to be either measured from a real process or simulated using a complex FPM over discrete and equal time steps $T_0, T_1, T_2, \dots, T_j, \dots, T_{q-1}, T_q$. Then, $U(t) = [U_{T_0}, U_{T_1}, \dots, U_{T_j}, \dots, U_{T_q}]$ and $Y(t) = [Y_{T_0}, Y_{T_1}, \dots, Y_{T_j}, \dots, Y_{T_q}]$, and the sampling time step is $\Delta t = (T_j - T_{j-1})$. Using this input-output training signal/data, the OK is employed to construct a set of D_y NAREX models (Eq.(1)) where each model f_i approximates the future value of one process output $\hat{y}_i(t + 1)$ as a function of the process previous inputs and outputs $[Y_{T_j}, U_{T_j}]$, considering a specific delay L .

$$\hat{y}_i(t + 1) = f_i [\hat{Y}(t), \dots, \hat{Y}(t - L), U(t), \dots, U(t - L)], i = 1, 2 \dots D_y \quad (1)$$

Once the set of the OK-based dynamic models – one step-ahead models- are trained, it will be possible to emulate or predict the dynamic evolution of the system outputs over larger time domain through the MSAP. This is accomplished via recursive interactive interpolation, where the initial conditions of the outputs $Y_{T_0}^v$, and the new inputs scenario $U^v(t) = [U_{T_0}^v, U_{T_1}^v \dots U_{T_j}^v, \dots, U_{T_{w-1}}^v, U_{T_w}^v]$ are given (the superscript v refers to “validation”). Considering zero lag ($L=0$) dynamic models (for simplicity of illustration), the recursive interpolation starts using the known interpolation inputs $[Y_{T_0}^v, U_{T_0}^v]$ to predict the values of the outputs at next time step $\hat{Y}_{T_1}^v$. The predicted output values $\hat{Y}_{T_1}^v$ are fed back to the models together with the new control values, representing the new interpolation inputs $[\hat{Y}_{T_1}^v, U_{T_1}^v]$ for the new time step prediction, in order to estimate the values of the outputs $\hat{Y}_{T_2}^v$, and so on until the last time step, in which the interpolation inputs $[\hat{Y}_{T_{w-1}}^v, U_{T_{w-1}}^v]$ are used to predict the outputs $\hat{Y}_{T_w}^v$. Hence, an accuracy measure (e.g. Normalized Root Mean Square Error (NRMSE)) can be calculated by comparing the real and the estimated values of the output signal. During the recursive interactive interpolation, each dynamic model f_i contributes with its prediction \hat{y}_i^v to compose the outputs $\hat{Y}_{T_j}^v = [\hat{y}_1^v, \hat{y}_2^v, \dots, \hat{y}_i^v, \dots, \hat{y}_D^v]$, which at the same time, represent the inputs for the dynamic models in the next step, so each model exploits the information provided by the other dynamic models in the previous time step.

4. Applications

4.1. Continuous Stirred Tank Reactor (CSTR)

A benchmark model (Eqs.(2)) for a CSTR (Bequette, 1998) is used to evaluate the proposed method, and to compare different metamodels types. The model describes the evolution of the reactant concentration C_A ($kgmol/m^3$) and the reactor temperature T_r (K), which are affected by the three control variables: the inlet feed concentrations C_F , the inlet feed temperature T_F and the water jacket temperature T_{jck} . The model parameters can be found also in the Matlab system identification toolbox. In this study, the values of C_F and T_F are kept constants ($10 kgmol/m^3$, and $298.15 K$), while the water

jacket temperature can be manipulated within the range $250\text{ K} \leq T_{jck} \leq 310\text{ K}$. The model is just considered here as the process plant, from which input-output data are measured (i.e. simulated), considering a sampling period of 1 hour. The goal is to construct a set of multivariate dynamic models (Eqs.(3)).

$$\left. \begin{aligned} \dot{C}_A &= -\frac{F}{V}(C_F - C_A) + k_0 \exp\left(-\frac{E}{R T_r}\right)C_A \\ \dot{T}_r &= -\frac{F}{V}(T_F - T_r) - \frac{H}{C_p Rho} k_0 \exp\left(-\frac{E}{R T_r}\right)C_A - U A \frac{(T_r - T_{jck})}{C_p Rho V} \end{aligned} \right\} \quad (2)$$

A random training signal of the process input-output variables $[T_{jck}(t), C_A(t), T_r(t)]$ is generated. Thus, a piecewise-constant signal of the input $T_{jck}(t)$ is synthesized (Figure 1-(a)) by random changes of its amplitude values within the allowable control limits (each step change holds for several (20) sampling periods, in order to capture the whole dynamic behavior of the outputs in response to each step change).

$$\left. \begin{aligned} \hat{C}_A(t+1) &= f_1 [C_A(t), \dots, C_A(t-L), T_r(t), \dots, T_r(t-L), T_{jck}(t), \dots, T_{jck}(t-L)] \\ \hat{T}_r(t+1) &= f_2 [C_A(t), \dots, C_A(t-L), T_r(t), \dots, T_r(t-L), T_{jck}(t), \dots, T_{jck}(t-L)] \end{aligned} \right\} \quad (3)$$

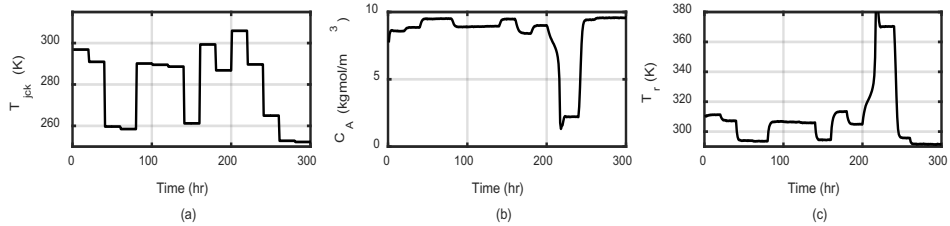


Figure 1. Random training signal (CSTR).

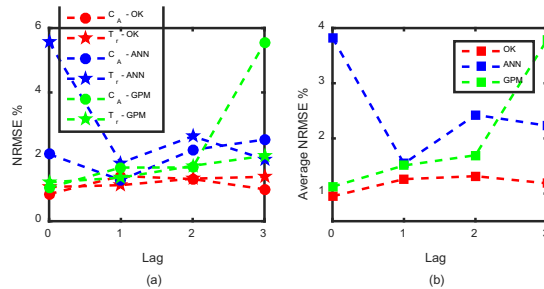


Figure 2. NRMSE of the dynamic models prediction (CSTR).

The input signal is simulated by the process model (Eqs.(2)) in order to obtain the corresponding outputs (Figure 1-(b, c)). Gaussian noise is added to each output (C_A and T_r) with a zero mean and a standard of deviation of 0.00075% of their variation range. This input-output random signal is used to train the dynamic models (Eqs.(3)) based on the OK, GP and ANNs considering different model orders/lags ($L=0, 1, 2, 3$). In order to validate the fitted dynamic models, a random validation signal is generated (Figure 3) as previously mentioned. The dynamic models are harnessed to predict the reactant concentration C_A and the reactor temperature T_r over 500 time steps, corresponding to the validation input signal (Figure 3-(a)) through the recursive interactive interpolation

fashion (section 2). Figure 2-(a,b) shows the prediction accuracy of the output signals in terms of the NRMSE for each metamodel type (OK, ANNs, GP) with the different lags. Figure 3-(b, c) shows the prediction of C_A and T_r using the best dynamic models (with lag achieving the lowest NRMSE, see Table 1).

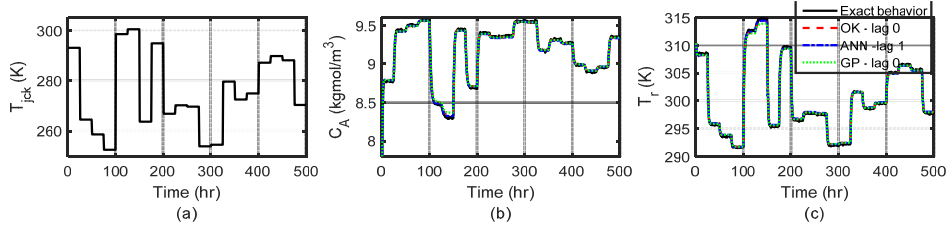


Figure 3. Random validation signal (CSTR), and the multivariate dynamic model predictions.

4.2. Fed-batch Fermentation reactor

This case considers a common nonlinear model (Eqs.(4)) of a yeast fermentation fed-batch reactor (Galvanin et al., 2007). In the model, C_m is the biomass concentration (g/L), C_s is the substrate concentration (g/L), $U1$ is the dilution factor (h^{-1}), and $U2$ is substrate concentration in the feed (g/L). Besides, some operating limits should be considered. The process variables are measured each 15 minutes along the batch run of 40 hr.

$$\left. \begin{aligned} \dot{C}_m &= (r - U1 - 0.05)C_m \\ \dot{C}_s &= -\frac{r C_m}{0.55} + U1(U2 - C_s), \quad r = \frac{0.31 C_s}{0.18 + C_s} \\ 1 \leq C_m(0) \leq 20, C_s(0) &= 0.01, 0.05 \leq U1 \leq 0.15, 15 \leq U2 \leq 30 \end{aligned} \right\} \text{* MERGEFORMAT} \quad (4)$$

In order to construct a set of multivariate dynamic models ((Eqs.(5)), the same procedure is applied here also: a random signal of the process inputs and outputs [$U1(t)$, $U2(t)$, $C_m(t)$, $C_s(t)$] is generated (Figure 4) and used to train the dynamic models based on the different metamodels and lags L .

$$\left. \begin{aligned} \widehat{C}_m(t+1) &= f_1[C_m(t), \dots, C_m(t-L), C_s(t), \dots, C_s(t-L), U1(t), \dots, U1(t-L), U2(t), \dots, U2(t-L)] \\ \widehat{C}_s(t+1) &= f_2[C_m(t), \dots, C_m(t-L), C_s(t), \dots, C_s(t-L), U1(t), \dots, U1(t-L), U2(t), \dots, U2(t-L)] \end{aligned} \right\} \quad (5)$$

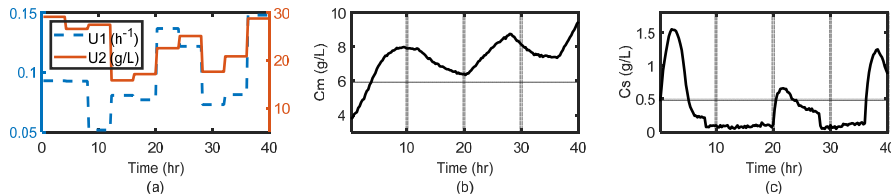


Figure 4. Random training signal (fed-batch).

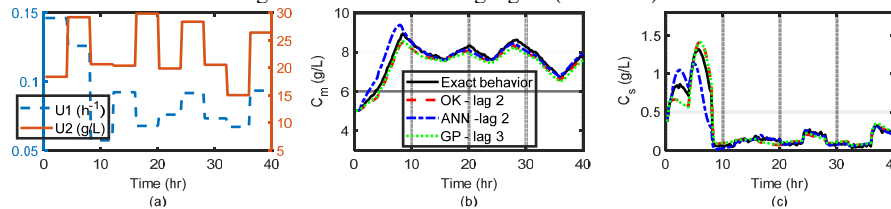


Figure 5. Random validation signal (fed-batch).

Similarly, a random validation signal (Figure 5) is used to assess the dynamic models, which are harnessed to emulate the biomass and substrate concentrations over 160 time steps (Figure 5-(b,c)).

Table 1. NRMSE (%) of the best dynamic models for both application cases.

	Lag	Case 1: CSTR			Lag	Case2: fed-batch		
		\widehat{C}_A	\widehat{T}_r	Average		\widehat{C}_m	\widehat{C}_s	Average
OK	0	0.8	1.1	0.95	2	5.8	5.8	5.80
GP	0	1.0	1.2	1.10	3	6.9	5.7	6.30
ANNs	1	1.3	1.8	1.55	2	8.3	10.6	9.45

5. Conclusions

The paper presents a robust and generic method for the data-driven MVDM and MSAP based on metamodels, which has not been investigated before. The method employs metamodels to construct a set of NAREX models, which are then used in a recursive interactive interpolation scheme, in order to predict the process outputs over several time steps. The method is applied to two multi-input/multi-output nonlinear dynamic processes showing promising capabilities: high prediction accuracy, large prediction time horizon, high flexibility to simulate complex dynamic profiles of the inputs and ability to model the delayed behaviour of the system. The method is also able to model both continuous and batch processes, although the later shows extra challenges (higher NRMSE), due to the higher nonlinearity often inherent to these processes. Within the proposed MVDM and MSAP method, the OK is compared with other leading techniques as ANNs and GP models: the OK shows better characterises in dynamic modelling, not only in terms of higher prediction accuracy, but more importantly, easier and more flexible tuning of parameters. The work also opens several novel application areas for the OK models, as model predictive control, dynamic soft sensing (Shokry et al., 2017(b)) and monitoring studies (Shokry et al., 2017(a)).

Acknowledgements: Financial support received from the Spanish "Ministerio de Economía, Industria y Competitividad" and the European Regional Development Fund, both funding the research Project AIMS (DPI2017-87435-R) is fully acknowledged.

References

- A. F. Hernandez, M. G. Gallivan, 2008, An Exploratory Study of Discrete Time State-Space Models using Kriging, American Cont. Conf., Washington, USA, June 11-13.
- A. Shokry, M.H. Ardakani, G. Escudero, M. Graells, A. Espuña, 2017a, Dynamic Kriging based Fault Detection and Diagnosis Approach for Nonlinear Noisy Dynamic Processes, Comput. & Chem. Eng., 106, 758-77.
- A. Shokry, M. P.-Moya, M. Graells, A. Espuña, 2017b, Data-Driven Dynamic Modeling of Batch Processes Having Different Initial Conditions and Missing Measurements. Computer Aided Chemical Engineering, 40, 433-438.
- B.W. Bequette, 1998, Process Dynamics: Modeling, Analysis and Simulation, Prentice.
- F. Boukouvala, F. J. Muzzio, M. G. Ierapetritou, 2011, Dynamic Data-Driven Modeling of Pharmaceutical Processes, Ind. Eng. Chem. Res., 50, 6743–6754.
- F. Galvanin, S. Macchietto, F. Bezzo, 2007, Model-Based Design of Parallel Experiments Ind. Eng. Chem. Res., 46, 871-882.
- K. Azman, J. Kocijan, 2007, Application of Gaussian processes for black-box modelling of biosystems, ISA Transactions, 46, 443–457.

Modelling and advanced dynamic optimisation strategies for hydrological and water quality management in continental water bodies

A.G. Siniscalchi^(a), L. Fritz^(b), C. Garcia Prieto^(a), V. Estrada^(a), M. Hoffmeyer^(b), R.J. Lara^(b), M.S. Diaz^{(a)*}

^a *Planta Piloto de Ingeniería Química (Universidad Nacional del Sur-CONICET), Camino la Carrindanga Km 7, Bahía Blanca 8000, Argentina*

^b *Instituto Argentino de Oceanografía (IADO-CONICET), Camino La Carrindanga Km7,5, Bahía Blanca 8000, Argentina*

sdiaz@plapiqui.edu.ar

Abstract

In this work, we propose mechanistic models for water quality and hydrological management in freshwater and saline lakes within a dynamic optimisation framework. We formulate management problems as optimal control problems for two case studies corresponding to water bodies located in Buenos Aires Province, Argentina. The hydrological model is used to address flooding and salinity issues in salt lakes. The water quality model allows dealing with eutrophication problems in freshwater reservoirs. The proposed optimization models provide decision-making tools to plan management actions for different objectives and under different scenarios, as well as to evaluate their effects.

Keywords: Dynamic Optimisation, Lake Management, Hydrological Mathematical Model, Eutrophication

1. Introduction

During the last decades, much work has been devoted to modelling of water bodies with different objectives and approaches. The identification of meteorological, hydrological and ecological components and driving forces behind problems as eutrophication, floods and salinisation in water bodies is the first step to develop useful tools for decision-making in the management of lakes and reservoirs. Barjas Blanco et al. (2010) and Uysal et al. (2016) proposed hydrological models for flood management in freshwater reservoirs for short-term operations. Estrada et al. (2011) formulated a mechanistic model within a dynamic optimization framework to control algal blooms in water bodies. Di Maggio et al. (2015) proposed the integrated management of lakes and artificial wetlands through the application of dynamic optimization strategies. A recent review on main ecological simulation models was carried out by Anagnostou et al. (2017), focusing on the understanding of eutrophication processes. However, these authors do not address hydrological and ecological models formulated within an optimization approach.

In this work, we formulate optimal control problems to plan management strategies in lakes and reservoirs, based on ecohydrological models represented by differential

algebraic equation systems that include mass balances, evaporation, kinetic equations, etc. In the first case, the objective is to avoid flooding of a nearby village and tourist facilities and to keep salinity at appropriate levels for fish reproduction within a salt lake. In a second case study, we address control of algal blooms in a reservoir that provides drinking water to two cities, by considering reduction of external nutrient charge to the water body (control variable: fraction of nutrient rich water stream that is diverted through an artificial wetland) and fish removal strategies (control variable: fish removal rate). Dynamic optimization problems are formulated within a control vector parameterization framework in gPROMS (PSEnterprise, 2017). Numerical results provide control variables profiles to plan restoration actions and their ecological and hydrologic effects.

2. Model description

2.1 Hydrological Model

In the hydrological model for a salt lake, the dynamic water mass balance is as follows:

$$\frac{dm}{dt} = \left[Q_{pp}(t) \left(\frac{V}{h} \right) + Q_{river}(t) + Q_{gw} - Evap(t) \left(\frac{V}{h} \right) \right] \delta_w / 1000 \quad (1)$$

where m is total mass in the lake (kg); δ_w , is water density (kg. m⁻³), which is assumed constant; V corresponds to lake volume and h is average depth. Q_{pp} (L.day⁻¹.m⁻²) corresponds to precipitations, Q_{river} (L.day⁻¹) is tributary river flowrate, Q_{gw} (L.day⁻¹) is groundwater flowrate and $Evap$ (L.day⁻¹.m⁻²) corresponds to evaporation per unit area in the lake. Bathymetric information is used to assess lake volume at the beginning of the integration horizon. Evaporation is calculated taking into account energy and momentum balances (Penman 1948):

$$Evap = \frac{10}{\lambda v} [W Rn(t) + (1 - W) F_{wind} (T_{vap0} - T_{vap})] \quad (2)$$

where W is a weighting factor of the radiation effects on evaporation; $Rn(t)$ is net radiation (ly.d⁻¹), F_{wind} is a wind function that expresses wind effects as available energy to evaporate water (km.d⁻¹) and $(T_{vap0} - T_{vap})$ is a vapour saturation deficit. Additional algebraic equations include latent heat of vaporization for water and forcing functions, represented by Fourier series, including tributary and groundwater flowrate, air temperature, relative humidity, solar radiation, mean wind rate and related meteorological variables. As salt concentration in both groundwater and the tributary is negligible, we assume that salt mass is constant within the lake. Therefore, salt concentration (C_s) is calculated as:

$$\frac{dC_s}{dt} = - \frac{C_s}{V} \left[Q_{pp}(t) \left(\frac{V}{h} \right) + Q_{river}(t) + Q_{gw} - Evap(t) \left(\frac{V}{h} \right) \right] \delta_w / (\delta \cdot 1000) \quad (3)$$

Furthermore, we include a water mass balance for an artificial reservoir of fixed area, located upstream of the tributary, to which a fraction of the tributary can be diverted for lake management purposes:

$$\frac{dhm}{dt} = [Q_{pp}(t) + Q_{out}(t)/A - Evap(t)] / 1000 \quad (4)$$

where hm is water column height, Q_{pp} corresponds to rainfall over the reservoir, Q_{out} is the diverted fraction flowrate. The model has 3 differential and 23 algebraic equations.

2.2 Water Quality Model

A water quality model for a freshwater reservoir has been previously proposed (Estrada et al., 2009; 2011). Based on experimental evidence from a monitoring program that is being carried out by our group since 2013, the model has been extended to include piscivorous fish dynamics due to the control that this predator exerts on the lower trophic level (zooplanktivorous fish). The extended model includes mass balances for the main components of the trophic chain of the Reservoir, represented by:

nutrients \rightarrow phytoplankton (Diatoms, Chlorophytes, Cyanobacteria) \rightarrow zooplankton (Copepoda and Cladocera) \rightarrow zooplanktivorous fish (three sizes of *Odontesthes bonariensis*) \rightarrow piscivorous fish (two sizes of *Oligosarcus jenynsii*).

Algebraic equations stand for forcing functions profiles, such as solar radiation, temperature, tributaries inflows and their associated nutrient concentrations, as well as the generation/consumption rates for each ecological state variable. The model takes into account concentration gradients along the water column through two horizontal layers; horizontally averaged concentrations, constant water density and constant lake transversal area are assumed. The entire model has 42 differential and 110 algebraic equations.

2.3 Dynamic Optimisation Model

We formulate management problems for water bodies as optimal control problems subject to the differential algebraic equation (DAE) systems described in the preceding sections. In the first case, the goal is to keep salt concentration in the lake (C_s) around a desired value of 23 kg.m^{-3} within a wet climate scenario, considering the flowrate fraction of the tributary that is diverted (Q_{out}) as the control variable. In the second case, the inclusion of the main variables controlling the phytoplankton growth in the freshwater reservoir model, allows the formulation control problems to evaluate optimal restoration strategies. Table 1 shows both problems formulation.

Table 1. Optimal control problems for hydrological management (Case 1) and eutrophication control (Case 2)

Case 1	Case 2
Control Variable	Control Variables
Fraction of tributary diverted to an artificial water reservoir for salinity control with ecological/commercial purposes and to avoid flood	Fraction of tributary stream diverted to an artificial wetland for nutrient removal Removal rate for each of three zooplanktivorous fish size classes ($m = S1, S2, S3$)
$\min Z = \int_0^{t_f} (C_s(t) - 23)^2 dt$ s.t.	$\min Z = 0.7 \int_0^{t_f} (C_{phyto}(t) - 0.2)^2 dt + 0.3 \int_0^{t_f} (C_p(t) - 0.02)^2 dt$ s.t.
DAE Hydrological Model	DAE Water Quality Model
$C_s(0) = C_s^0, V(0) = V^0$	$C(0) = C^0$
$C_s^L \leq C_s \leq C_s^U$	$C^L \leq C \leq C^U$
$V^L \leq V \leq V^U$	$0 \leq F_{wetland} \leq 0.5 F_{El\ Divisorio}$
$Q_{river} = Q_{in} + Q_{out}$	$S_i R^L \leq S_{m,removal} \leq S_i R^U$
	$r_{im} = R_{im,pred} - R_{im,bm} - R_{im,recruit} + R_{im,spaw} - S_{m,removal}$

We include two restoration methodologies: 1) the reduction of external loading of nutrients to achieve bottom-up control of algae blooms (Di Maggio et al. 2015), and 2) a top-down control strategy, based on the food chain manipulation (Jeppesen, 2012; Estrada et al., 2011). This technique consists in the removal of the zooplanktivorous fish biomass to increase the grazing pressure of zooplankton over the phytoplankton community. Both control problems (Case 1 and 2) were implemented within a control vector parameterization framework in gPROMS (gPROMS, PSEnterprise, 2017).

3. Results and Discussion

3.1. Case 1. Salinity and flood control in Chasicó Lake

In this case, we address salinity and flood control in Chasicó Lake, a salt lake located in Argentina (38°38' S; 63°03' W). This water body belongs to an endorheic basin and has one tributary (Chasicó River). The lake has undergone salinity variations ranging from 17 to 100 g.L⁻¹, during the last fifty years (Lara, 2006). The hydrologic regime of this basin is closely related to climatic conditions, with decadal dry and humid cycles. Floods and droughts have brought devastating consequences in the regional economy, damaging productive fields, sports fishing of silverside (*Odontesthes bonariensis*) and touristic activities (Kopprio et al., 2014). The hydrological model has been calibrated and validated with collected salinity data throughout the last ten years (Siniscalchi et al., 2017). Chasicó Lake groundwater flowrate is estimated as 24% of the local rainfall. Figure 1 shows Chasicó River and the diverted stream (Q_{out}) flowrate profiles for two control interval lengths, 30 and 15 days, with a time horizon of two years within an extended a wet period. Similar results are obtained for either length of the control interval, keeping salinity and volume lake, around the proposed objective for salinity (23 kg.m⁻³) and volume (480 Hm³), as can be seen in Fig. 2a. The accumulated water volume diversion is 63.4 Hm³ during the period, taking into account evaporation and rainfall within the artificial reservoir (Fig. 2b).

3.2. Case 2. Eutrophication control in Paso de las Piedras Reservoir

In this case study, we focus on the restoration of Paso de las Piedras Reservoir, a eutrophic freshwater reservoir, located in Argentina (38° 22'S;61°12'W) that supplies drinking water to more than 450,000 inhabitants of two cities and for industrial purposes at a petrochemical complex nearby. It has two tributaries that run through an important agricultural area in the country, with a drainage basin area of 1620 km². The lake has a surface area of 36 km², while its mean depth is 8.2 m and its retention time is 4 years. The eutrophic characteristic of the reservoir is mainly caused by the external discharge of nutrients (mainly phosphorus and nitrogen). This fact causes recurrent algal blooms, which produce several problems in the potabilization process, affecting humans and in the natural ecosystem. The high concentration of cyanobacteria within the blooms raises concerns on the potential production of cyanotoxins, harmful for human and animal health. Optimal preliminary profiles for the restoration strategies are obtained based on the extended water quality model calibrated with data from 2015. Tributary diversion to an artificial wetland for nutrient removal is at its upper bound throughout the entire time horizon. Figures 3 (a) and (b) show fish biomass and removal rate profiles for a two-year horizon for size S1 (0-100 mm) and Size S2 (100-200 mm) of the zooplanktivorous fish *O. bonariensis*, respectively. Gut content studies (data not shown) show that zooplankters copepoda and cladocera (which in turn graze on phytoplankton) are the

main items in *O. bonariensis* diet, supporting the biomanipulation strategy. Preliminary numerical results indicate a substantial increase in zooplankton biomass after fish removal (Figure 4 (a)) and subsequent decrease in phytoplankton biomass (Figure 4 (b)). The inclusion of mass balances for a predator of *O. bonariensis* (two sizes of *O. jenynsii*) provides more realistic insights on restoration actions.

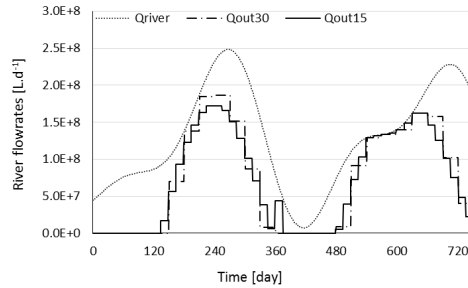


Figure 1: Chasicó River flowrate without control (dotted line) and River diversion (Q_{out}). Interval controls for river diversion: 15 and 30 days

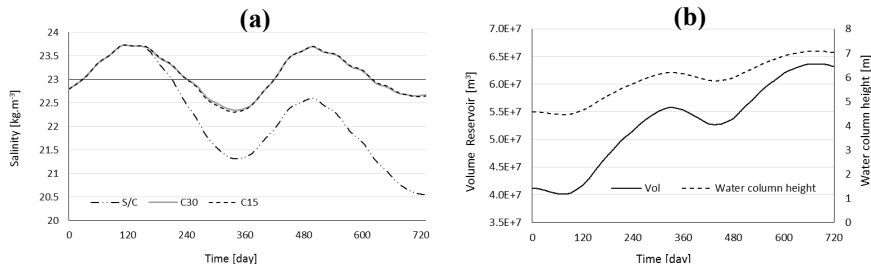


Figure 2. (a) Optimal salinity profiles with control intervals of 15 and 30 days and without control (S/C); (b) Water column height and volume profile in artificial reservoir with management actions

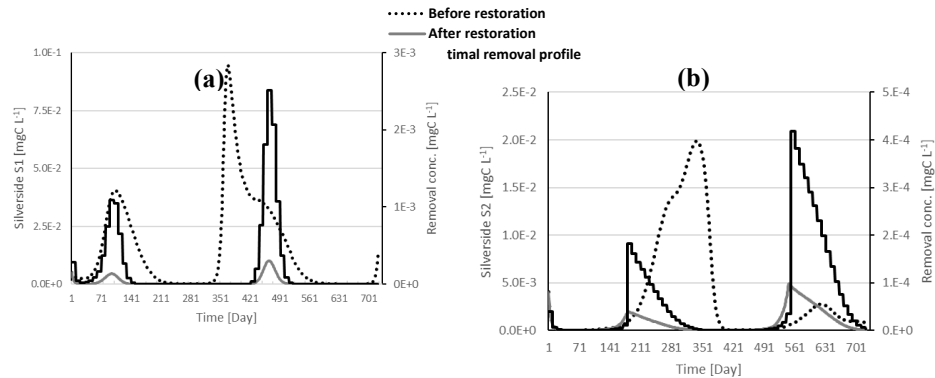


Figure 3. Zooplanktivorous fish sizes S1 (a) and S2 (b) concentration profiles before and after fish removal (left axis) and optimal removal rate (right axis)

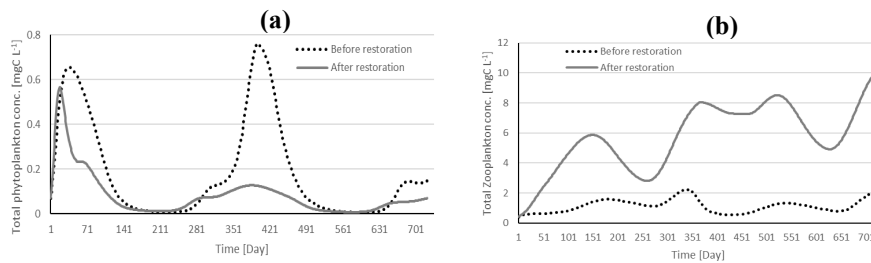


Figure 4. Total phytoplankton (a) and zooplankton (b) concentration profiles before and after fish removal and diversion of tributary to an artificial wetland

4. Conclusions

In this work, we propose detailed mechanistic models of lakes and reservoirs as constraints for optimal control problems to provide useful tools in planning water bodies management and exploring the associated effects. In Case 1, we study a salt lake. Numerical results show the optimal profile for the tributary fraction that should be diverted to an artificial water reservoir to avoid flood events and keep salt concentration at the physiological optimum for a high-commercial value fish. In Case 2, we address algae bloom control in a freshwater reservoir. Numerical results show the need for tributary diversion to an artificial wetland for nutrient removal, as well as zooplanktivorous fish removal, to keep phytoplankton concentration under eutrophication limits.

References

- E. Anagnostou, A. Gianni, I. Zacharias, 2017, Ecological modeling and eutrophication-A review, *Natural Resource Modeling*, e12130.
 - T. Barjas Blanco, P. Willems, P.K. Chiang, N. Haverbeke, J. Berlamont, B. De Moor, 2010, Flood regulation using nonlinear model predictive control, *Control Engineering Practice*, 18: 1147-1157
 - J. Di Maggio, V. Estrada, M.S. Diaz, 2015, Water resources management with dynamic optimization strategies and integrated models of lakes and artificial wetlands, *Computer Aided Chemical Engineering*, 37: 2543-2548.
 - V. Estrada, E. Parodi, M.S. Diaz, 2009, Middle term optimal control problem in eutrophic lakes through advanced mathematical programming approaches, *Computer Aided Chemical Engineering*, 26: 1153-1158
 - V. Estrada, J. Di Maggio, M.S. Diaz, 2011, Water Sustainability: A process systems engineering approach to the restoration of eutrophic lakes, *Comput. Chem. Eng.*, 35: 1598-1613.
 - E. Jeppesen, Søndergaard, Lauridsen, Davidson, Liu, Mazzeo, Trochine, Özkan, Jensen, Trolle, Starling, Lazzaro, Johansson, Bjerring, Liboriussen, Larsen, Landkildehus, Egemose, Meerhof, 2012, Biomanipulation as a restoration tool to combat eutrophication: recent advances & future challenges, *Adv.Ecol.Res.*, 47:411-488.
 - G. Kopprio, R. Freije, M. Arias-Schreiber, R.J. Lara, 2014, An ecohydrological adaptive approach for a salt lake in semiarid grasslands of Argentina, *Sustain. Sci*, 9: 229-238.
- Process Systems Enterprise, 2017, gPROMS, www.psenderprise.com/gproms.

- R.J. Lara, 2006, Climate change, sea-level rise and the dynamics of South American coastal wetlands: case studies and the global frame, In *Wissenschaftliche Zusammenarbeit mit Argentinien: Begrenzung und Zuversicht Arbeits und Diskussionspapier* (Frühwald, ed.), Bonn: Von Humboldt Foundation 40-50.
- A.G. Siniscalchi, A. Raniolo, G. Kopprio, E. Gomez, M.S Diaz, R.J. Lara, 2017, Hydrological modeling and management of a salt lake with dynamic optimization strategies, WCCE 2017, 1-5 Oct 2017, Barcelona, Spain.

Recursive Model Estimation for the Plasma Parameters Quality Control

Junmo Koo^a, Damdae Park^a, Sangwon Ryu^b, Gon-Ho Kim^b, Youn-Woo Lee^{a,*}

^a*School of Chemical and Biological Engineering, Seoul National University, Build. 302, 1, Gwanak-ro, Gwanak-gu, Seoul (08826), Republic of Korea*

^b*Department of Nuclear Engineering, Seoul National University, Build. 30, 1, Gwanak-ro, Gwanak-gu, Seoul (08826), Republic of Korea*

ywlee@snu.ac.kr

Abstract

In recent years, plasma etching process has been considered important because it is one of the most critical processes in semiconductor manufacturing. Numerous research results have been presented in relation to the plasma etch processes, especially plasma parameters control. Although the above results are expected to bring about positive effects in various fields, they do not consider the variability of the system. In this paper, we performed the recursive model estimation of which the model structure is ARX considering the time delay. The recursive algorithm contains the Kalman filter interpretation to the model parameters. We have confirmed that the system model updated in real-time by our recursive model estimation algorithm continuously calculates the model parameters that predict the output variable precisely. Through these results, we expect the better performance of MPC control using the recursive model estimation

Keywords: Online System Identification, Recursive Normalized Model Estimation, Plasma Parameter Control, Real Time Control

1. Introduction

Due to Moore's law, the higher quality control is demanded in the semiconductor industry as well as the semiconductor manufacturing process has also been regarded as a very important issue because of the development of AI. There have been many studies about the plasma etch process the most important processes in the semiconductor manufacturing process in various forms. Also, our research group has presented a paper about successful multivariable plasma parameters control in real-time using optical emission spectroscopy (OES).

Though previous studies have shown good results, it is difficult to apply them directly to the current semiconductor manufacturing environment for a variety of reasons. One of the reasons is that the monitoring of the plasma parameters must be done in real-time because of the high sensitivity of the plasma. In addition, online model estimation is indispensable because of the characteristics of the plasma parameters control process, in which the system model changes not only in different batches but also in the same batch. This is even more essential in the case of using model predictive control (MPC)

the default control technique in current semiconductor manufacturing process because of the high model dependency of MPC. The last important reason is that no other studies using online parameter estimation in plasma parameters control process normalized their variables though the normalized variables have a large impact on system control and the performance.

In this paper, we performed the recursive normalized model estimation, a form of online system identification, for realizing the plasma parameter system. We utilized an OES based single input single output (SISO) plasma parameter controller. OES, a non-invasive tool and the default plasma monitoring sensor for every plasma reactor, has the advantages of less impact on the system than other invasive sensors such as hairpin probe and no concern about installation.

This paper is organized as follows. In Section 2, the monitoring of the plasma parameter through OES is explained briefly. In Section 3, the theoretical backgrounds of recursive model estimation including the normalized model estimation are explained. In Section 4, the results of the recursive normalized model estimation are illustrated

2. Plasma Parameter Estimation by OES

It is important to control plasma parameters in plasma etch processes such as electron density, electron temperature and so on. As mentioned in section 1, many studies and literature about the control of plasma parameters have been presented and our research group have also published the study of the control of plasma parameters monitored by OES. Optical fiber attached on the chamber viewport measures the plasma emission. An emission intensity from p^{th} state to k^{th} state is described as

$$\Phi_{pk} = n_0 n_e \int_{E_{thr}}^{\infty} \sigma_{pk}(E) \left(\frac{2E}{m_e} \right)^{\frac{1}{2}} f(E) dE \quad (1)$$

where n_0 is the number density of ground state atoms, n_e is the electron density, $\sigma_{pk}(E)$ is the excitation cross section from level p into level k as a function of electron energy E , $f(E)$ is the electron energy distribution function (EEDF), m_e is the electron mass.

In order to compute the plasma parameters by OES, we utilized the ratio of several emission lines based on the separate line-ratio techniques that is only a function of the electron density (J. B. Boffard et al., 2004).

We used a capacitively coupled plasma reactor illustrated in Figure 1. It carries 300mm wafer and is powered by three radio frequency (RF) generators. The gap between top and bottom electrodes is 25 mm. For the definition of plasma system, the input variable is 60 MHz RF power and the output variable is electron density measured through Eq. (1) with OES.

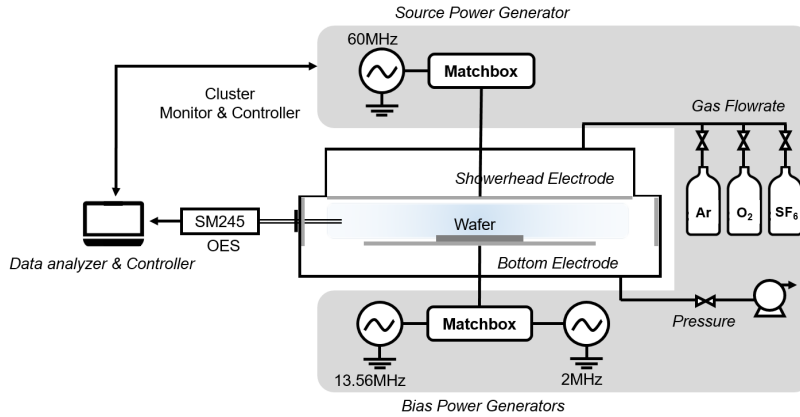


Figure 1. Schematic of capacitively coupled plasma reactor and plasma sensors used in this study.

3. Recursive Model Estimation

3.1 Recursive model estimation algorithm with forgetting factor

As mentioned earlier, online model estimation is essential when controlling a sensitive system such as a plasma related system. It is even more so for MPC controller which has high model dependency. Recursive model estimation is one form of the online model estimation algorithms. It uses the estimated model parameter,

$$\hat{\theta}_t = \underset{\theta}{\operatorname{argmin}} \sum_{k=1}^t \beta(t, k) [y(k) - \varphi^T(k)\theta], \quad (2)$$

which minimizes the weighted error criterion where $y(k)$ is the measured output, $\varphi(k)$ is the regression vector, θ is the present model parameter and $\beta(t, k)$ is the weighting sequence which has the following property:

$$\beta(t, k) = \lambda(t)\beta(t-1, k), \quad 0 \leq k \leq t-1$$

$$\beta(t, t) = 1 \quad (3)$$

where $\lambda(t)$ is the forgetting factor the value of which is recommended to be from 0.98 to 0.995. Solving Eq. (2), we have

$$\hat{\theta}_t = \hat{\theta}_{t-1} + \bar{R}^{-1}(t)\varphi(t)[y(t) - \varphi^T(t)\hat{\theta}_{t-1}] \quad (4.a)$$

$$\bar{R}(t) = \lambda(t)\bar{R}(t-1) + \varphi(t)\varphi^T(t) \quad (4.b)$$

where

$$\bar{R}(t) = \sum_{k=1}^t \beta(t, k) \varphi(k)\varphi^T(k). \quad (5)$$

3.2 Recursive model estimation algorithm with Kalman filter interpretation

The other methodology is not using the forgetting factor but utilizing the Kalman filter interpretation. That is,

$$\begin{aligned}\theta(t+1) &= \theta(t) + w(t) \\ y(t) &= \varphi^T(t)\theta(t) + v(t)\end{aligned}\quad (6)$$

with $Ew(t)w^T(t) = R_1(t)$, and $E v(t)v^T(t) = R_2(t)$. Then the expectation and covariance of $\hat{\theta}_t$ as

$$\hat{\theta}_t = \hat{\theta}_{t-1} + L(t)[y(t) - \varphi^T(t)\hat{\theta}_{t-1}] \quad (7.a)$$

$$L(t) = \frac{P(t-1)\varphi(t)}{R_2(t) + \varphi^T(t)P(t-1)\varphi(t)} \quad (7.b)$$

$$P(t) = P(t-1) - \frac{P(t-1)\varphi(t)\varphi^T(t)P(t-1)}{R_2(t) + \varphi^T(t)P(t-1)\varphi(t)} + R_1(t). \quad (7.c)$$

The initial parameter covariance matrix and the process noise covariance should be set by engineers. Engineers set these based on the system condition and experience.

3.3 Normalization of the system for robustness

The sizes of matrix $R_1(t)$ and $R_2(t)$ inflict on $\hat{\theta}_{t-1}$. Normally, the difference between the sizes of variables of plasma parameters control system is large enough. Therefore, normalization is essential for more accurate recursive model estimation. The normalization can also affect MPC design, so that when designing a controller, the normalization should be considered. In our study, all variables were gathered through normalization process, and the model parameters calculated through normalized Eq. (6)~(7) are parameters of the normalized system.

4. Results and Discussion

The performance of the recursive model estimation algorithm with Kalman filter interpretation was evaluated by the control results data that was previously performed. The control results had been done by MPC controller performing a setpoint tracking test of electron density.

The system input (manipulated variable for MPC) is 60 MHz RF power and system output (controlled variable for MPC) is electron density which is measured in real-time by OES and Eq. (1).

The chosen model structure is a linear, time-varying, discrete-time autoregressive exogenous model (ARX),

$$A(z)y(k) = B(z)u(k) + e(k), \quad (8)$$

where

$$A(z) = a_1 + a_2z^{-1} + \dots \quad (9.a)$$

$$B(z) = b_1 + b_2z^{-1} + \dots \quad (9.b)$$

where a_1 is always 1, b_1 is always 0, $u(k)$ is the input variable, 60MHz RF power, $y(k)$ is the output variable, electron density, $e(k)$ is a zero-mean, white noise with variance σ^2 and $A(k, z)$ and $B(k, z)$ are model parameters which are calculated in real-time based on Eq. (7). The model parameters are calculated in real-time based on Eq. (2) ~ (5).

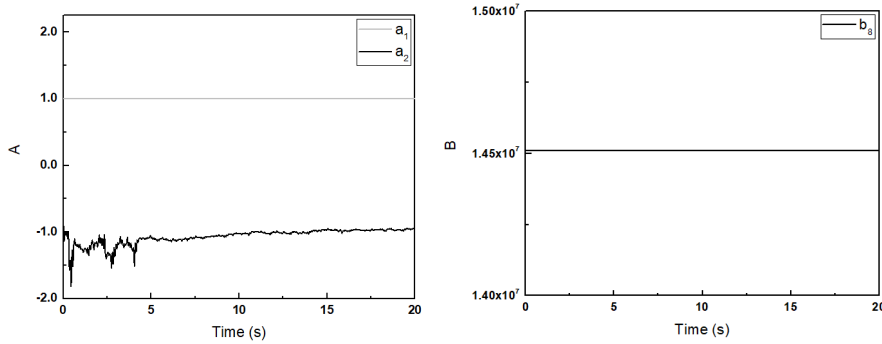


Figure 2. The model parameters, $A(k, z)$ and $B(k, z)$, composing the ARX model structure.

Figure 2 shows the recursive model estimation results. The recursive model estimator needs the initial parameter values, A_0 and B_0 , which can be set from the original model structure which had been performed at the setpoint tracking control test. The initial parameter covariance and the process noise covariance in Eq. (7.c), R_1 , were set previously and R_2 was set as 1. It shows some changes in various time which means that the model estimation could develop the performance when it is applied to adaptive MPC.

In figure 3, the comparison of the estimated electron density calculated by the recursive model estimator and the measured electron density are illustrated.

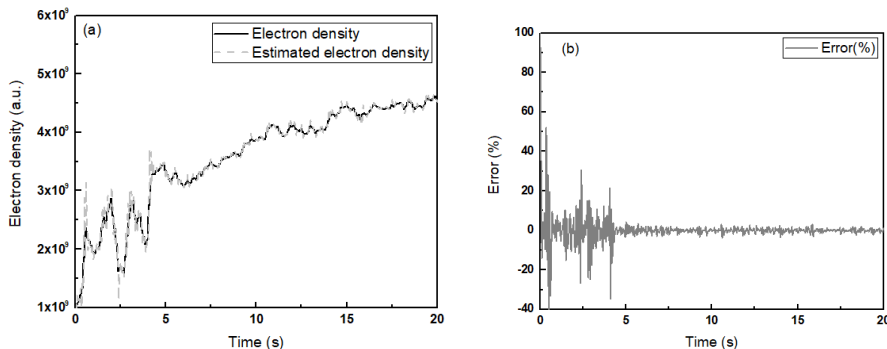


Figure 3. (a) The measured electron density and the estimated electron density calculated by the recursive model estimator and (b) error percentage.

As shown in figure 3, the estimated electron density suits well to the measured electron density. The error percentage is within 2% after 4.6s. These guarantee that the recursive model estimator conducted the estimation successfully and it has the potential of better performance in control strategy.

5. Conclusions

We conducted the recursive model estimation of the plasma parameter system of which the final goal is to get the best control results. Because the plasma parameter control system has very sensitive characteristics which means the model might be changed and the better MPC requires the better fitted model. The recursive model estimation simulation of ARX model structure shows successful performance which has only 2% error between the estimated electron density and the measured electron density. We hope that these results will contribute to maximize the performance of plasma parameter control process.

6. Future Work

In this study, the normalization of the system and the recursive model estimator and the experimental results using them are omitted. Our future studies will contain the results of the normalized estimation experiment. Also, the optimization problem of the initial parameter covariance and the process noise covariance is also well worth considering.

References

- D. E. Seborg, T.F. Edgar, D.A. Mellichamp, 2004, *Process Dynamics and Control*, 2nd ed., John Wiley & Sons
- H.J. Rho, Y.J. Huh, H.K. Rhee, 1998, Application of adaptive model-predictive control to a batch MMA polymerization reactor, *Chemical Engineering Science*, 53(21), 3729-3739
- J. B. Boffard, C.C. Lin, C.A. DeJoseph Jr, 2004, Application of excitation crosssections to optical plasma diagnostics, *J. Phys. D: Appl. Phys.* 37, R143.
- J. Koo, D. Ha, D. Park, H. Roh, S. Ryu, G. Kim, K.H. Baek, C. Han, 2017, Design of optical emission spectroscopy based plasma parameter controller for real-time advanced equipment control, *Computers & Chemical Engineering*, 100, 38-47
- L. Ljung, 1999, *System Identification: Theory for the User*, 2nd ed., Upper Saddle River, NJ, USA: Prentice-Hall.
- L. Ljung, 2009, Experiments with identification of continuous time models. *IFAC Proceedings Volumes*, 42(10), 1175-1180

Model transformations and integration for process plant simulation, optimization and visualization

Manuel Rodriguez^a, Ismael Diaz^a

^a *Universidad Politecnica de Madrid, Dpt. Of Chemical Engineering, C/ Jose Gutierrez Abascal 2, 28006 Madrid, ES*

manuel.rodriguez@upm.es

Abstract

Industry is in constant evolution. Nowadays we are in what is called the fourth industrial revolution (called Industry 4.0 or connected industry). Its target is to make more efficient and flexible plants, reduce times and costs of projects and products lifecycle. It is an integrated engineering approach where different software tools are interconnected during the whole lifetime of the project, reducing inconsistencies and developing times.

To have a central neutral model of a process plant that is available during the whole lifecycle of the system (process + product) and that can be transformed automatically to specific models suited for different applications.

To achieve this goal we use a Model Based Systems Engineering approach, starting from the model requirements and covering the whole lifecycle of the project. This central model is specified using the Systems Modelling Language (SysML). This language is a profile of the Unified Modelling Language (UML developed by the Object Management Group) that is neutral and domain free. The developed model is partially generated in SysML and partially constructed using existing specific models. Having a single central model guarantees the consistency and allows for traceability at any stage of the lifecycle.

First, we present the architecture developed to implement this system. After, we create a SysML model of a process plant (the production of ethylbenzene) starting with the requirements. This model includes the behavioural (block definition and activity diagrams) and structural (internal and block definition diagrams) aspects of the model. Once the model is created automatic transformations (bidirectional) from it to some applications are performed. The applications are:

- Process design . Transformation to a steady state model used (specifically an Aspen Plus model) in a process simulation environment(Previous work presented in other conferences).
- Risk assessment. Transformation to a functional model to perform risk analysis (HAZOP).
- Process optimization . Automatic generation of the objective and constraints. We use Melody to integrate the SysML with the optimization model. In this

case Matlab is being used for the optimization (Previous work presented in other conferences).

- Process visualization. Transformation from the 3D model to SysML. We use Syndeia to achieve the integration. The 3D models are done using PTCreo.

In this work we will put more focus on the development of the 3D modelling integration in the proposed architecture.

This work shows the potential of having models at design time, central and consistent and coherent models. Industry trends look for models that generate virtual plants that can be “operated” and that allow to discover design mistakes at early design phases. Thus providing, when constructed, more robust, consistent and efficient plants. Model development effort is reduced and data exchange between different applications is facilitated keeping a central and consistent model.

Keywords: energy integration, Distillation, Process control

Property Prediction of Pharmaceuticals for Designing of Downstream Separation Processes

Getachew S. Molla^a, Lukasz Ruszczynski^a, Jens Abildskov^a, Gürkan Sin^a

^a*Technical University of Denmark, 2800 Kgs. Lyngby, DK*

gsmo@kt.dtu.dk

Abstract

Downstream processing of pharmaceuticals is often a complex and expensive process section in pharmaceutical industry. The separation and purification cost of small to medium-sized active pharmaceutical ingredients (APIs) can be up to 70-90% of the total production cost. Designing a downstream processing includes selection, arrangement and rigorous evaluation of various unit operations such as crystallization and extraction. Solvent screening and selection is a critical step in designing such unit operations. The solubility of APIs is a major property for solvent screening and selection. Solubility can either be determined experimentally or by using predictive thermodynamic models. However, experimental solvent screening is most often expensive and laborious, or sometimes simply not possible due to the lack of sufficient amount of an API. Moreover, designing some unit operations; for example, crystallization further requires solubility property of an API as a function of temperature, solvent composition and pH for cooling, antisolvent and reactive crystallization, respectively, or any combination thereof.

In this work, different predictive thermodynamic models such as COSMO-SAC, COSMO-RS, NRTL-SAC and UNIFAC were applied for solubility prediction of a large molecular weight steroid-like structure antibiotic. The predicted solubility data were compared with experimental solubility data in a set of various solvents representative of wide solvent properties. Therefore, a model which gives more accurate solubility prediction can be selected. For this specific case study, the root mean square errors (RMSEs) of COSMO-SAC, UNIFAC, COSMO-RS and NRTL-SAC are 54.3%, 51.8%, 34.3% and 4.8%, respectively. NRTL-SAC was selected as a property prediction tool for solvent screening and selection as well as for further designing and optimization of crystallization unit operation. Moreover, global sensitivity and uncertainty analyses of the predictive thermodynamic model parameters were performed in order to identify sources of uncertainty and evaluate their influence.

Keywords: Crystallisation, Solubility prediction, Solvent screening

Incorporating fouling model in plate heat exchanger modelling and design

Olexiy Demirskyy^a, Petro Kapustenko^a, Olga Arsenyeva^b, Olexandr Matsegora^c,
Pavlo Arsenyev^a, Vladimir Tovazhnianskyi^a, Alisher Khusanov^d

^a*National Technical University "Kharkiv Polytechnic Institute", ITPA, 21 Frunze Street, 61002, Kharkiv, UA*

^b*Paderborn University, Chair of Fluid Process Engineering, Pohlweg 55, 33098 Paderborn, DE*

^c*Ao Spivdruzhnist-T, R&D, 2 Chervonoprapornyy prov, 19, 61002, Kharkiv, UA*

^d*M.Auezov South Kazakhstan State University, Dpt. of Chemical Engineering, Taukehana Avenue, 160012 Shymkent, KZ*

o.p.arsenyeva@gmail.com

Abstract

Efficient heat recuperation is of primary concern in resolving the problem of optimal energy usage. To achieve best results it requires the use of efficient compact heat exchangers among which Plate Heat Exchanger (PHE) is one of the most promising types. Its flexibility allows finding economically viable solutions in different processes of heat utilisation. But the fouling formation on surfaces of plates can lead to energy losses, additional power consumption and the costs of cleaning. This practical operational problem is a significant challenge in the progression towards sustainable development.

The traditional two approaches to account for fouling in heat exchanger design are (1) to increase heat transfer surface by employing fixed fouling thermal resistance or (2) by introducing margin for heat transfer surface area. However the reliable data on fouling factors for different streams in PHEs are limited and both approaches can lead to significant errors in estimation of required heat transfer area in PHE, the increase of which can lead to lower flow velocities and higher fouling tendencies. The method of PHE based on the mathematical model accounting for local process parameters distribution along heat transfer surface is proposed. It is incorporating earlier developed fouling model (Arsenyeva et al., 2013). It requires the data of fouling monitoring for any heat exchanger working with considered streams to identify model parameters. Having these data the method can be used for design of new PHEs or for retrofitting the existing PHEs on considered enterprise for optimal performance.

The applicability of the method is demonstrated with a case study for PHE working in food industry application. The PHE (290 plates) with heat transfer area 259.2 m² was initially designed to heat glucose solution by another stream of glucose solution coming with 140 °C. The heavy fouling was observed, which required cleaning after one week of operation due to drop in heat transfer load and increase in pressure drop up to 1 bar. The redesigning of PHE with the proposed method has shown the possibility to decrease

heat transfer area to 137.7m² (155 plates) of the PHE by rearranging plates with different corrugation geometry and reducing their number on the same frame. The monitoring of PHE performance during one year of operation have shown that the same drop in heat transfer load and increase in pressure drop was observed only after a month of operation, the cleaning during that period was not required. It has reduced the capital cost of PHE, operating cost for cleaning and prolonged the service life time of rubber gaskets. The case study demonstrated the ability of the proposed method of PHE design to optimise the PHE performance with proper selection of PHE plates and complete use of available pressure drop to mitigate fouling formation.

Keywords: energy efficiency improvement, Industrial application, thermo-hydraulic model, heat exchanger design, fouling

Acknowledgement

The support of Grant of Education and Science Ministry of the Republic Kazakhstan in state program “Grant funding for research” is sincerely acknowledged. Olga Arsenyeva is grateful to the Alexander von Humboldt Foundation for the financial support.

References

Arsenyeva O. P., Crittenden B., Yang M., Kapustenko P. O. (2013). Accounting for the thermal resistance of cooling water fouling in plate heat exchangers. *Applied Thermal Engineering*, 61(1), 53-59.

Multi-scale modelling and simulation of Ca-looping cycle process for CO₂ post-combustion capture

Carla I.C. Pinheiro^a, Rui Filipe^b, Miguel Abreu Torres^a, João M. Silva^b,
Henrique A. Matos^a

^a*Instituto Superior Técnico, Universidade de Lisboa, PT*

^b*Instituto Superior de Engenharia de Lisboa, Instituto Politécnico de Lisboa, PT*

carla.pinheiro@tecnico.ulisboa.pt

Abstract

The present work focuses on one of the more promising new post-combustion technologies using calcium-based materials, known as the “Ca-looping cycle” process, which endeavors to scrub CO₂ from flue gases and syngases by using natural lime-based sorbents and which appears to potentially offer limited CO₂ capture costs. So, the major driving force is to improve overall efficiency, reduce the cost, and minimize adverse environmental impacts of post-combustion Ca-looping cycle CO₂ capture, as compared to more conventional technologies (e.g., amine-based solvent scrubbing). There is a large energy penalty with amine scrubbing, the closest to market technology.

The main objective of this work is to develop a first principles model to simulate different natural sorbents looping cycle performance in a fixed bed reactor laboratory scale system.

A rigorous non-linear dynamic model of the looping cycle process was developed in gPROMS, based on the multiscale concept. The multiscale modeling is an emerging technique, where the characteristic length for each phenomena that occurs is taken into consideration, leading to a set of submodels with different scale lengths. These submodels when coupled together allow the simulation of a macrosystem (Hangos and Cameron, 2001). After the identification of the characteristic dimensions involved in the models, the first step is the development of a single particle model, which takes into account the energy and material transport, undergoing reactions (carbonation and calcination) and structural changes inside the particle. The material and heat transport inside the particle take into account the structural changes. Detailed models of single particle undergoing cycles of calcination and carbonation are developed. An improved decay approach is introduced in the model for those sorbents exhibiting carbonation decay with the number of cycles. The experimental characterization of the samples gave vital information on the physicochemical changes occurring during testing that need to be described in the model in the carbonation decay function. The conversion decay does not only depend on the number of cycles, but also on the conditions of the previous cycles, temperature, pressure, gas phase composition and characteristics of the material used for the carbonation. Model parameters are estimated from experimental results obtained for different sorbents tested (Santos et al., 2012)(Pinheiro et al., 2016). Several simulations for different sorbents and operating conditions were performed and the

model was validated with experimental data obtained in a fixed bed reactor. It was also important to ensure that the model is numerically stable within a large range of values.

Keywords: simulation, CO₂ capture, Calcium Looping, Carbon emissions reduction, Multi-scale modelling

Acknowledgement

The authors gratefully acknowledge the financial support by the Portuguese Foundation for Science and Technology (Fundação para a Ciência e Tecnologia), through Research Projects Nos. UID/QUI/00100/2013 and PTDC/AAG-MAA/6195/2014.

References

- K.M. Hangos, I.T. Cameron, "Process modelling and model analysis", Academic Press, 2001.
- E.T. Santos, C. Alfonsin, A.J.S. Chambel, A. Fernandes, A.P.S. Dias, C.I.C. Pinheiro, and M.F. Ribeiro, "Investigation of a stable synthetic solgel CaO sorbent for CO₂ capture", *Fuel*, vol. 94, pp.624-628, 2012.
- C.I.C. Pinheiro, A. Fernandes, C. Freitas, E.T. Santos, and M.F. Ribeiro, "Waste Marble Powders as Promising Inexpensive Natural CaO-Based Sorbents for Post-Combustion CO₂ Capture", *Ind. Eng. Chem. Res.*, vol.55, pp.7860-7872, 2016.

Good modelling practice for process engineering: pitfalls and requirements to develop fit for purpose models

Ingmar Nopens^a

^a*Ghent University, BIOMATH – Department of data analysis and mathematical modelling, Coupure Links 653, 9000 Gent, BE*

ingmar.nopens@ugent.be

Abstract

Many process industries are yearning for more detailed process knowledge mainly envisioning process optimization, both in terms of operation and design. Most processes are complex in nature (physical-chemical and kinetic processes involving multiple phases and in a heterogeneous environment due to process scale) and cannot be optimized using experimentation only. The last decades have proven that mathematical models are powerful tools to achieve this goal. However, many physical-based modelling frameworks of different levels of complexity are at hand and many pitfalls exist in the model building process. It is therefore crucial that Good Modelling Practice (GMP) is applied in any modelling study in order to get the most out of models, i.e. ensuring they are reliable and have a sufficient predictive power. This is crucial to convince people that models are a necessity for any process optimization and worth investing in. Consecutive steps in a model building exercise according to GMP are: objective definition, state of the art, experimental data collection (including optimal experimental design-OED), framework definition, parameter estimation and model selection and model validation.

Within GMP, the goal or objective is probably the most important decision as it significantly impacts the subsequent steps such as the framework choice and data collection. In many cases the objective is process optimization, either at unit process level (operational and design) or at process train level (mostly operational). In any case, a model for optimization should have a sufficient predictive power if one wants to use it in decision making, which means it should be validated up to a certain accuracy level (defined in the objective). The latter is not yet common practice for a variety of reasons: insufficient data quality and/or quantity, lack of availability of tools to verify calibration quality, model overparameterisation, insufficient model complexity. In most cases, this leads to uncertainties in inputs and parameters that result in model output uncertainty. One should therefore strive for this as part of the modelling exercise and be self-critical about the real usefulness of a model rather than being pleased by calling a model prediction “quite good”.

The uncertainties mentioned are mostly related to insufficient process knowledge. In order to increase process knowledge, one needs to move to more complex models that aim to describe processes in more detail (e.g. CFD, PBM, DEM). This comes at a significant cost as it requires significantly higher computational effort as well as more tedious data collection. Probably the latter is even most often the problem and is a clear

point of attention. Another issue is the fact that many model analysis tools such as sensitivity analysis, global optimization, uncertainty analysis and optimal experimental design require a vast number of model simulations which become hard or even impossible when model structures are too complex. The avenue to go here is to translate the obtained knowledge at the complex model scale to models at intermediate complexity scale such as compartmental models (CM). Those models should be less uncertain given the extra knowledge they contain which will reflect in less need for calibration and, hence, a higher predictive power yielding better decisions for operational optimization. When it comes to design optimization, the developed complex models are now a good reference to evaluate where improvement is possible. However, using these models is also not straightforward as they are computationally intensive and there is a myriad of options to alter a design. There is clearly a need for a sound methodology that could also be based on CMs. Alternatively, we need to investigate scale-up vs numbering up and think out of the box.

In this contribution I would like to touch on some of these aspects by means of examples.

Keywords: Uncertainty, population balance, optimization

Efficient simulation of ion exchange chromatography with application to bioseparations

Marcus Fechtner^{a,*}, Malte Kaspereit^b and Achim Kienle^{a,c}

^a*Otto-von-Guericke-Universität Magdeburg, Chair for Automation and Modelling, Universitätsplatz 2, 39106 Magdeburg, Germany*

^b*Friedrich-Alexander-Universität Nürnberg-Erlangen, Chair for Separation Science and Technology, Egerlandstrae 3, 91058 Erlangen, Germany*

^c*Max Planck Institute for Dynamics of Complex Technical Systems, Process Synthesis and Process Dynamics, Sandtorstrae 1, 39106 Magdeburg, Germany*
fechtner@ovgu.de

Abstract

Recently, we developed an approach for the efficient simulation of packed bed adsorbers accounting for equilibrium models with any kind of implicit adsorption isotherm. Application was demonstrated for stoichiometric ion exchange with constant solution normality (Fechtner and Kienle, 2017) and later on for the ideal adsorbed solution theory (Fechtner and Kienle, 2018). In this paper, the extension to stoichiometric ion exchange with variable solution normality and its application to salt gradient elution is presented. Further, the approach is also extended to the steric mass action law, which is frequently applied to protein separation.

Keywords: Adsorption, Differential algebraic systems, Stoichiometric ion exchange, Steric mass action law, Protein separation

1. Introduction

Mathematical modeling of spatially distributed packed bed adsorbers leads to systems of partial differential equations. An important class of models assume thermodynamic equilibrium between the fluid and the solid phase (Rhee et al., 1986, 1989). Besides explicit isotherms also implicit formulations are quite common to describe the adsorption equilibrium. Typical examples are stoichiometric ion exchange (Tondeur, 1969; Helfferich and Klein, 1970) and the ideal as well as real adsorbed solution theory approaches (Ruthven, 1984). These are computationally much more difficult to treat due to the implicit phase equilibrium. Usually some challenging implicit analytical or numerical differentiation of the equilibrium relations is required to calculate the capacity matrix of the model equations (Kaczmarski and Antos, 1999; Landa et al., 2013). Recently, we developed an approach for the efficient simulation of packed bed adsorbers with implicit adsorption isotherms (Fechtner

parameter	value	description
L [m]	5.0	column length
N_z [-]	1000	number of grid points
v [$\frac{m}{s}$]	1.0	interstitial velocity
ε [-]	0.5	void fraction
q_{tot} [$\frac{mol}{T}$]	2.0	exchanger capacity
K_{13} [-]	8.0	equilibrium constant
K_{23} [-]	1.905	equilibrium constant
v_1 [-]	2	stoichiometric factor
v_2 [-]	1	stoichiometric factor
v_3 [-]	1	stoichiometric factor

Table 1: Parameters of the step gradient example.

and Kienle, 2017). The resulting system of partial differential and algebraic implicit equations is reformulated such that explicit differentiation of the isotherm is avoided. Using the method of lines (Schiesser, 1991), the resulting differential algebraic equations (DAE) can be solved simultaneously using standard software. Application was demonstrated for stoichiometric ion exchange with constant solution normality. In this paper, the extension to systems with variable solution normality is presented. This extension allows to consider a large variety of additional processes like salt gradient elution and / or protein separation (Carta and Jungbauer, 2010). In the present paper, application to step gradient elution (Karkov et al., 2013) with stoichiometric ion exchange and linear gradient elution (Gallant et al., 1995) with steric mass action law (Brooks and Cramer, 1992) for protein separation is demonstrated.

2. Modeling

2.1. Adsorber dynamics

In this paper focus is on the equilibrium dispersive model to describe the dynamics of a fixed bed adsorber (Guiochon and Lin, 2003). All dispersive effects that cause band broadening are lumped together in a single parameter, namely the apparent dispersion coefficient D_a . The model exploits a set of simplifying assumptions that are justified for many different applications (Guiochon et al., 2006). This set includes isothermal operation, thermodynamic equilibrium between solid and fluid phase, a constant mobile phase velocity u as well as a constant void fraction ε . Thus, the adsorber dynamics accounting for N adsorbable components with fluid phase concentration \mathbf{c} and solid phase concentration \mathbf{q} , respectively, are described by the following system of N partial differential equations (PDEs)

$$F \frac{\partial \mathbf{q}(\mathbf{c})}{\partial t} + \frac{\partial \mathbf{c}}{\partial t} + u \frac{\partial \mathbf{c}}{\partial z} = D_a \frac{\partial^2 \mathbf{c}}{\partial z^2}, \quad \mathbf{c}, \mathbf{q} \in \mathbb{R}^N, \quad (1)$$

with time t and spatial coordinate z . Parameter $F = \frac{1-\varepsilon}{\varepsilon}$ denotes the volumetric phase ratio. For constant solution normality only $N - 1$ equations are required. In contrast to this for variable solution normality an additional material balance has to be taken into account. For the solution of Eq. (1), further N boundary conditions $\mathbf{c}(z = 0, t) = \mathbf{c}_{feed}(t)$ and initial conditions $\mathbf{c}(z, t = 0) = \mathbf{c}_{init}(z)$ as well as the adsorption isotherm model represented by $\mathbf{q}(\mathbf{c})$ are required.

2.2. Mass action laws

In ion exchange chromatography, the stoichiometric ion exchange is a classical problem formulation, which has been treated first by Tondeur (1969) and Helfferich and Klein (1970). The corresponding mass action law

$$K_{iN} = \left(\frac{q_i}{c_i} \right)^{v_i} \left(\frac{c_N}{q_N} \right)^{v_N} = const, \quad \forall i \in \{1, \dots, N-1\}, \quad (2)$$

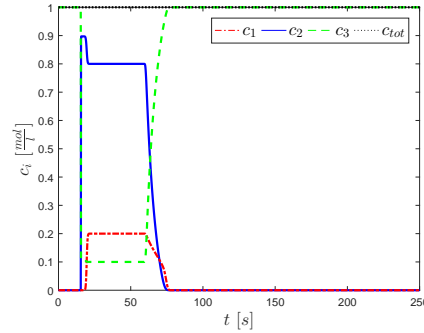


Figure 1: Chromatographic cycle with constant solution normality $c_{tot} = 1 \frac{mol}{l}$.

is also valid for formulation with variable solution since the N -th algebraic relation is defined by the constant exchanger capacity

$$q_{tot} = \sum_{i=1}^N \frac{q_i}{\nu_i} = const. \quad (3)$$

and does not require a constant solution normality. Parameters K are the equilibrium constants of the ideal mass action law, and the ν variables denote the reciprocal valences of the ionic species.

Protein separation can also be realized through ion exchange chromatography (Carta and Jungbauer, 2010). In this case, the equilibrium relation can be expressed by the steric mass action (SMA) law (Brooks and Cramer, 1992), which can be summarized by the following algebraic equations

$$K_{iN} = \left(\frac{q_i}{c_i}\right)^{\mu_i} \left(\frac{c_N}{q_N}\right)^{\mu_N} = const, \quad \forall i \in \{1, \dots, N-1\}, \quad (4)$$

$$q_{tot} = \sum_{i=1}^N \frac{1 + p_i \mu_i}{\mu_i} q_i = const. \quad (5)$$

Eq. (4) has the same structure as (2), but therein the $\mu \in \mathbb{R}_+$ denote the reciprocals of characteristic charges of the proteins with μ_N being typically the only ionic charge related to the salt. For classical SMA, $\mu_N = 1$ is assumed. The feature of the SMA is given by the steric factors p_i that account for the steric hindrance of the proteins. This hindrance is based on the assumption that large adsorbed proteins block a certain amount of the active surface of the ion exchanger. Accordingly, for the salt, $p_N = 0$ applies.

3. Simulation

Since the adsorber dynamics are based on the equilibrium dispersive model, and the algebraic equations (2,3) as well as (4,5) can be easily rewritten into the form

$$\mathbf{0} = \mathbf{f}(\mathbf{q}, \mathbf{c}), \quad (6)$$

the methodology presented in Fechtner and Kienle (2017) can be also applied here. In particular, we introduce the joint capacity

$$\mathbf{v} = \mathbf{c} + F\mathbf{q}, \quad (7)$$

to avoid explicit differentiation of the adsorption isotherms. For simplicity, axial dispersion is neglected here in a first step. This allows us to rewrite the PDAE system (1,6) into the general form

$$\mathbf{0} = \frac{\partial \mathbf{v}}{\partial t} + u \frac{\partial \mathbf{c}}{\partial z}, \quad \mathbf{c}, \mathbf{v} \in \mathbb{R}^N \quad (8)$$

$$\mathbf{0} = \mathbf{f}(\mathbf{q} = \frac{\mathbf{v} - \mathbf{c}}{F}, \mathbf{c}). \quad (9)$$

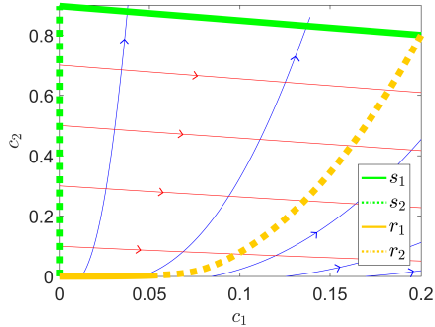


Figure 2: Hodograph for chromatographic cycle with $c_{tot} = 1 \frac{mol}{l}$ including numerical concentration profile (green and orange).

A corresponding DAE system is obtained from (8,9) by applying the method of lines (Schuesser, 1991). Resulting ODEs from (8) and the AEs (9) can be solved simultaneously for \mathbf{v} and \mathbf{c} using standard DAE numerics such as DASSL (Brenan et al., 1989), LIMEX (Deuffhard et al., 1987), or ODE15s (The MathWorks, 2016). In the present paper the latter is used. For demonstration purposes, simple spatial discretization is realized through first order backward differences on an equidistant grid. However, application of more advanced discretization techniques (LeVeque, 1992) is straight forward. Step gradient as well as linear gradient elution use typically piecewise initial conditions based on an equilibrated column. Hence, consistent initial conditions for the initialization of the DAE numerics can be easily obtained offline by solving (9) once for given $\mathbf{c}_{init}(z)$. Compared to the approach in Fechtner and Kienle (2017), a PDE corresponding to an arbitrary component 'i' in (8) can be replaced by the PDE for the total solution normality $c_{tot} = \sum_{i=1}^N \frac{c_i}{v_i}$, which can be easily derived using the adsorber dynamics (1) together with (3) or (5)

$$\frac{\partial c_{tot}}{\partial t} + u \frac{\partial c_{tot}}{\partial z} = \mathbf{0}. \quad (10)$$

For simulation purposes, either the total material balance (7) in combination with $N - 1$ component material balances or alternatively N component material balances can be used. Computational times are similar in both cases. Since Eq. (7) is linear, it also can be solved separately with an analytical approach, which is then used afterwards for the numerical solution of the remaining component material balances. However, effect of such an analytical approach on computational costs for the overall solution is small. Additionally, its implementation is much more involved. Therefore, simultaneous numerical solution of Eq. (1) is done in the remainder.

4. Applications

4.1. Step gradient elution

The first application is to step salt gradient elution with stoichiometric ion exchange. Focus is on the extension of the numerical approach to systems with variable solution normality. The associated additional degree of freedom allows to change one component in order to improve the ad-/desorption of the other components. For this purpose, a ternary example is considered where the component with the lowest affinity is used to specifically affect the adsorption of the other two components. Corresponding parameters can be found in Tab. 1. Two different chromatographic cycles are considered.

First, the column is equilibrated with $1 \frac{\text{mol}}{\text{l}}$ salt (c_3), i.e. $\mathbf{c}_{init} = [0, 0, 1]^T$. The feed composition is set to $\mathbf{c}_{feed} = [0.2, 0.8, 0.1]^T$ for the loading step and is maintained for 50 s. Afterwards, the feed is changed back to $\mathbf{c}_{feed} = [0, 0, 0.1]^T$ for the regeneration of the other two components. As a result, the solution normality $c_{tot} = \sum_{i=1}^N \frac{c_i}{v_i}$ with v_i according to Tab. 1 is kept constant during the complete cycle. Corresponding simulation results can be found in Fig. 1. The numerical solution in Fig. 1 is validated with theoretical prediction from equilibrium theory in Fig. 2 (Fechtner and Kienle, 2017; Mazzotti and Rajendran, 2013).

For the second chromatographic cycle, the initial condition of the column is $\mathbf{c}_{init} = [0, 0, 0.1]^T$, again, containing salt (c_3) only. The same feed $\mathbf{c}_{feed} = [0.2, 0.8, 0.1]^T$ as in the first cycle is

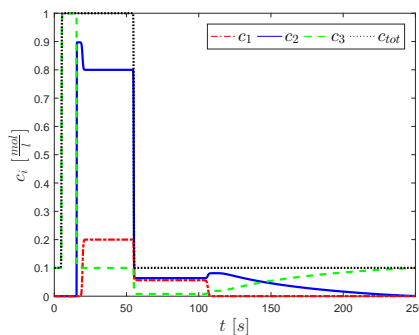


Figure 3: Chromatographic cycle with constant $0.1 \frac{\text{mol}}{\text{l}}$ salt but variable solution normality.

used also here for the loading step. After 50 s the feed is changed to $\mathbf{c}_{feed} = [0, 0, 0.1]^T$ for the regeneration keeping the salt concentration c_3 constant but not the total solution normality. Simulation results can be seen in Fig. 3.

Comparing Figures 1 and 3, the following can be observed. The first chromatographic cycle consists of four transition in total, two shocks during the loading step and two rarefaction waves during the regeneration, which is in agreement with Fig. 2. The second chromatographic cycle, however, consists of six transitions in total. Here, the loading step consists of a contact discontinuity and two shocks, while the regeneration consists of a contact discontinuity followed by a shock and afterwards a rarefaction wave. The following can be deduced from these observations. The variable solution normality in the second chromatographic cycle increases the number of transitions. In particular it allows for two contact discontinuities at 5 s and 55 s in Fig. 3 with a change of the solution normality c_{tot} . This was already deduced from Eq. (10). Furthermore, the variable solution normality also changes the type of one of the transitions in the regeneration step from rarefaction wave (first cycle at 60 s) to a shock (second cycle at 105 s). A more detailed theoretical investigation revealed a selectivity reversal, which is not present for constant solution normality as in the first example (see Fig 2 without reversed direction on neither blue nor red curves). The last fact is supported by Fig. 2, which shows clearly no selectivity reversal. Finally, the first cycle is much shorter with approximately 80 s compared to the second cycle with approximately 250 s. The reason is obviously the significantly different regeneration behavior. In the first cycle the regeneration uses an increased salt concentration by the factor of ten, while the salt concentration is kept constant for the second cycle. The example demonstrates, how the present approach can be used to study systematically the effect of step salt gradients on separation performance. Furthermore, it could also be used to optimize the separation, which however is beyond the scope of the present paper.

4.2. Linear gradient elution

The second application is concerned with linear gradient elution with steric mass action law. It demonstrates the applicability of the numerical approach to feed conditions that are not piecewise constant. A quaternary example, which is taken from Gallant et al. (1995) with parameters in Tab. 2, is considered. The objective of this example is the separation of three proteins. For this purpose, a column is equilibrated with 30 mM of the salt (NaCl). A feed is injected containing 30 mM sodium and 0.2 mM of each protein (chymotrypsinogen A, cytochrome c, lysozyme) for 254.47 s. The feed is then changed to contain sodium only. In addition to the 30 mM NaCl, a linear gradient of $0.19649 \frac{mM}{s}$ further increases its feed concentration over time. The separation result is shown in Fig. 4. Comparison with Fig. 1b in Gallant et al. (1995) shows good agreement of our simulation results and verifies the extension of the presented numerical approach to protein separation based on the steric mass action law.

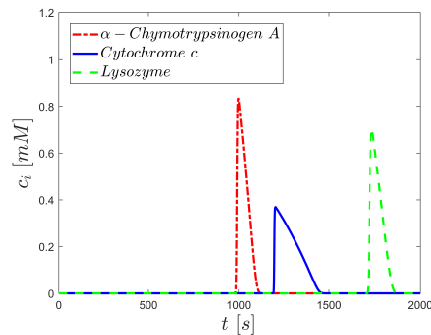


Figure 4: Protein separation with linear salt gradient $0.19649 \frac{mM}{s}$.

5. Conclusion

In this paper, the numerical approach for implicit adsorption isotherms presented in Fechtner and Kienle (2017) was successfully extended to applications with variable solution normality and vari-

able feed conditions. Again, the system of partial differential and algebraic implicit equations is reformulated such that explicit differentiation of the isotherm is avoided. Using the method of lines, the resulting DAEs can be solved simultaneously using standard software. In particular, the applicability to step and linear gradient elution, which are standard process operations for bio separations, were demonstrated. Further, some additional features of Riemann experiments with variable solution normality were observed, namely the occurrence of contact discontinuities and the associated existence of selectivity reversals. A detailed discussion with equilibrium theory was beyond the scope of the present paper and will be the subject of future work.

6. Acknowledgments

The financial support by the International Max Planck Research School for Advanced Methods in Process and Systems Engineering - IMPRS ProEng is greatly acknowledged.

References

- K. E. Brenan, S. L. Campbell, L. R. Petzold, 1989. Numerical Solution of Initial Value Problems in Differential-Algebraic Equations. North Holland & Elsevier Science Publishing Company.
- C. Brooks, S. Cramer, 1992. Steric mass-action ion exchange: Displacement profiles and induced salt gradients. *AIChE Journal* 38(12), 1969–1978.
- G. Carta, A. Jungbauer, 2010. Protein Chromatography. Vol. 1. WILEY-VCH Verlag GmbH & Co. KGaA, Weinheim.
- P. Deuffhard, E. Hairer, J. Zugck, 1987. One-step and extrapolation methods for differential-algebraic systems. *Numerische Mathematik* 51, 501–516.
- M. Fechtner, A. Kienle, 2017. Efficient simulation and equilibrium theory for adsorption processes with implicit adsorption isotherms – mass action equilibria. *Chemical Engineering Science* 171, 471–480.
- M. Fechtner, A. Kienle, 2018. Efficient simulation and equilibrium theory for adsorption processes with implicit adsorption isotherms – ideal adsorbed solution theory. *Chemical Engineering Science*.
URL <https://doi.org/10.1016/j.ces.2017.11.028>
- S. Gallant, S. Vunnum, S. Cramer, 1995. Optimization of preparative ion-exchange chromatography of proteins: linear gradient separations. *Journal of Chromatography A* 725, 295–314.
- G. Guiochon, A. Felinger, D. G. Shirazi, A. M. Katti, 2006. Fundamentals of Preparative and Nonlinear Chromatography. Vol. 2. Elsevier Academic Press, San Diego.
- G. Guiochon, B. Lin, 2003. Modeling for Preparative Chromatography. Vol. 1. Elsevier Academic Press, San Diego.
- F. G. Helfferich, G. Klein, 1970. Multicomponent Chromatography. Theory of Interference. M. Dekker, New York.
- K. Kaczmarski, D. Antos, 1999. Calculation of chromatographic band profiles with an implicit isotherm. *Journal of Chromatography A* 862, 1–16.
- H. Karkov, L. Sejergaard, S. Cramer, 2013. Methods development in multimodal chromatography with mobilephase modifiers using the steric mass action model. *Journal of Chromatography A* 1318, 149–155.
- H. O. R. Landa, D. Flockerzi, A. Seidel-Morgenstern, 2013. A method for efficiently solving the IAST equations with aq application to adsorber dynamics. *AIChE Journal* 59, 1263–1277.
- R. J. LeVeque, 1992. Numerical Methods for Conservation Laws. Birkhäuser Verlag, Basel.
- M. Mazzotti, A. Rajendran, 2013. Equilibrium theory-based analysis of nonlinear waves in separation processes. *Annual Review of Chemical and Biomolecular Engineering* 4, 119–141.
- H.-K. Rhee, R. Aris, N. R. Amundson, 1986. First-Order Partial Differential Equations: Volume I – Theory and Application of Single Equations. Prentice Hall, New Jersey.
- H.-K. Rhee, R. Aris, N. R. Amundson, 1989. First-Order Partial Differential Equations: Volume II – Theory and Application of Hyperbolic Systems of Quasilinear Equations. Prentice Hall, New Jersey.
- D. M. Ruthven, 1984. Principles of Adsorption and Adsorption Processes. John Wiley & Sons.
- W. E. Schiesser, 1991. The Numerical Method of Lines Integration of Partial Differential Equations. Academic Press, San Diego.
- I. M. The MathWorks, 2016. Version 9.0.0.341360 (R2016a). Birkhäuser Verlag, Natick, Massachusetts, USA.
- D. Tondeur, 1969. Theorie des colonnes d'change d'ions. Ph.D. Thesis, Universite de Nancy.

Virtual splitting of shared resource networks for price-based coordination with portfolio tariffs

Simon Wenzel^{a,*}, Lukas Samuel Maxeiner^a and Sebastian Engell^a

^a*Process Dynamics and Operations Group, Department of Biochemical and Chemical Engineering, TU Dortmund, Emil-Figge Straße 70, 44227 Dortmund, Germany*
E-mail: {simon.wenzel;lukas.maxeiner;sebastian.engell}@tu-dortmund.de

Abstract

In the process industries, the optimal allocation of shared resources among physically coupled units or plants is key to an efficient operation of the overall site. If the units or plants have a certain degree of autonomy or it is desired to preserve confidentiality of the detailed operation and performance of the plants, price-based coordination can be employed where an independent system operator (ISO) iteratively adjusts transfer prices for the shared resources until the demand and the supply match, i. e., the shared resource networks are balanced. In this contribution, a modified subgradient price update scheme is presented, which can be used for systems that are connected to external resources, e. g., via pipelines, so that certain amounts of these resources can be exchanged at prices that are fixed in portfolio tariffs. The approach virtually splits the shared resource networks to account for the different price regimes in the available tariff. The principle is illustrated in a simulation study of a production site with three production plants that are connected to an external distribution grid.

Keywords: Demand-side response; Price-based coordination; Lagrangian decomposition; Resource allocation; Resource efficiency; Energy tariffs

1. Introduction

Increasing the efficiency and sustainability in the process industries is not only beneficial with respect to plant economics, but also necessary to fulfill environmental regulations from the government (Sirola and Edgar, 2012). One important handle is the time-varying optimal allocation of shared resources such as electricity, steam at different pressure levels, heating gas, or intermediates in a system. Distributed price-based optimization techniques based on Lagrangian relaxation or ADMM (Boyd, 2010) can be used to determine the optimal allocation of shared resources in systems of systems that consist of physically coupled subsystems, while preserving a certain level of autonomy and confidentiality (Wenzel et al., 2016). Large production sites in the process industries that consist of many production plants—possibly belonging to different business units or companies are examples of such systems of systems (Engell and Sonntag, 2016). In addition to the side-wide networks, there are usually connections to external (smart) grids (Samad and Kiliccote, 2012) as illustrated in Figure 1, through which resources can be bought or sold. This can be managed by grid tariffs that range from simple to highly sophisticated constructs (Braithwait, 2010) (e.g., see Figure 2). Especially, when there is shortage or surplus of the shared resources in the networks, price-based coordination algorithms lead to transfer prices that can exceed or be below the market prices of the external resources by far. Thus, it is beneficial for the site to buy or sell certain amounts of resources externally to cope with such shortage or surplus.

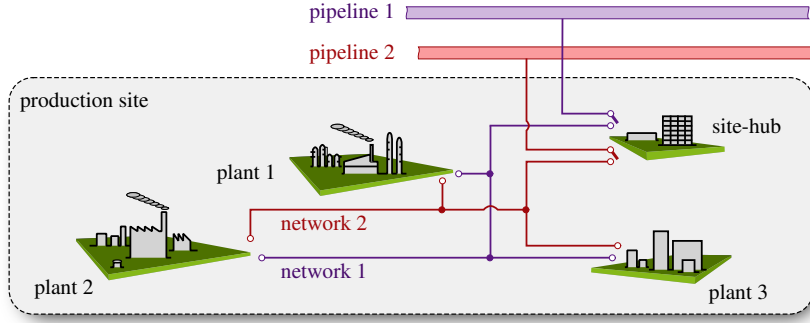


Figure 1: Site-wide optimization problem with external pipeline connections.

In this contribution, we study such a situation and propose a price-based coordination scheme that is aware of the portfolio tariffs for the external pipeline systems or grids. The networks for the shared resources on site are virtually split according to the contract structure and the coordinating entity on site can decide to buy or sell certain amounts of shared resources. We illustrate the principle of the coordinator update by a simulation study using three production plants that are internally connected by two networks on site and externally connected to two pipelines for which a portfolio tariff with three different price regimes has been negotiated. The rest of the paper is structured as follows: First, the site-wide optimization problem is stated. Then the modeling of the virtual networks for the price-based coordination in the presence of portfolio tariffs is introduced. A tariff-aware coordinator update is proposed and tested in a simulation study and finally a brief outlook on future research is given.

2. Problem description

The topology of an industrial production site that consists of (partially) autonomous subsystems (plants) that are physically connected by networks for shared resources is depicted in Figure 1. The internal networks are connected to the pipelines via the site hub. The site-hub manages a surplus of demand or supply of a particular resource by buying or selling resources. This resource allocation in the presence of different price regimes can be formulated as an optimization problem. It is assumed that the site-hub can acquire limited amounts of shared resources at different rates. A possible tariff structure that reflects the amounts and prices that are available from the pipeline is shown in Figure 2. The optimization problem of the site can be formulated as follows

$$\max_{\mathbf{u}_i, \mathbf{r}_i, \forall i} \sum_{i=1}^n \mathbf{p}_{i,\text{prod.}}^\top \mathbf{y}_i - \mathbb{1}^{(1 \times m)} (\mathbf{P} \circ \mathbf{R}_P) \mathbb{1}^{(s \times 1)}, \quad (1a)$$

$$\text{s. t. } \sum_{i=1}^n \mathbf{r}_i - \mathbf{R}_P \mathbb{1}^{(s \times 1)} = \mathbf{0}, \quad \mathbf{R}_P \in \mathcal{R}_P, \quad (1b)$$

$$\mathcal{F}_i(\mathbf{u}_i, \mathbf{r}_i) := \{\mathbf{u}_i, \mathbf{r}_i | \mathbf{y}_i = \mathbf{f}_i(\mathbf{u}_i), \mathbf{r}_i = \mathbf{g}_i(\mathbf{u}_i, \mathbf{y}_i), \mathbf{u}_i \in \mathcal{U}_i\}, \forall i, \quad (1c)$$

where it is assumed that the site strives for a maximization of the sum of the individual objectives (here, product sales $\mathbf{p}_{i,\text{prod.}}^\top \mathbf{y}_i$) under the consideration of the additional costs or benefits that are caused by interfacing the pipelines with the constrained resource amounts given in \mathbf{R}_P . We denote $\mathbf{A} \circ \mathbf{B}$ as the Hadamard product (element-wise multiplication) and $\mathbb{1}^{(s \times 1)}$ as a column vector with s identity entries. The matrix $\mathbf{P} \in \mathbb{R}^{(m \times s)}$ contains the individual prices for m resources and s price regimes in the tariff (cf. Figure 2) and $\mathbf{R}_P \in \mathbb{R}^{(m \times s)}$ is the amount of resources that is exchanged with the pipelines for each resource at each price. The overall costs

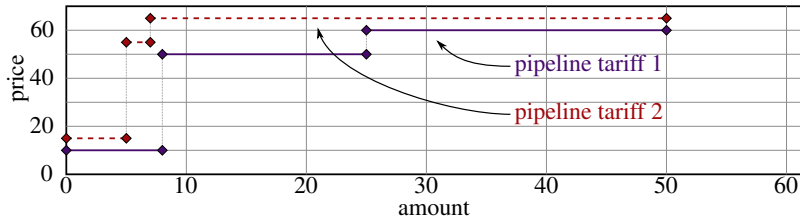


Figure 2: Portfolio tariff with different price regimes.

or benefits are then computed as $\mathbf{P} \circ \mathbf{R}_p$. The constraints are on the one hand the network balance Eq. (1b), which should be closed at any time and on the other hand the individual constraint sets \mathcal{F}_i for each subsystem $i = 1, 2, \dots, n$ that result from technical limitations. In the site-wide formulation, the contribution of the subsystem i to the network balance is given by a vector $\mathbf{r}_i \in \mathbb{R}^{(m \times 1)}$ that indicates the demand or supply, which is computed based on a tariff-independent model and where positive numbers indicate demands and negative numbers supplies. If the optimization problem is decomposed by Lagrangian relaxation to set up a price-based coordination algorithm (Bertsekas and Tsitsiklis, 1997), a single vector of Lagrange multipliers with a single multiplier for each resource is not sufficient, since the site-hub can buy and sell resources at different rates depending on the amount that is taken from or sent to the pipelines. This leads to the following modeling approach.

3. Virtual splitting of the networks on the subsystem level

A standard Lagrangian relaxation of the problem stated in Eq. (1) can be written as the following optimization problem that needs to be solved by each subsystem i

$$\max_{\mathbf{u}_i, \mathbf{r}_i} \mathbf{p}_{i,\text{prod}}^\top \mathbf{y}_i - \boldsymbol{\lambda}^\top \mathbf{r}_i, \quad (2a)$$

$$\text{s. t. } \mathcal{F}_i(\mathbf{u}_i, \mathbf{r}_i), \quad (2b)$$

where $\boldsymbol{\lambda}$ is the vector of Lagrange multipliers, which can be interpreted as the vector of prices that are associated with the demand or supply of the shared resources given by \mathbf{r}_i that depends on the degrees of freedom \mathbf{u}_i . To account for different price regimes in the portfolio contract, the constraints of the individual systems have to be extended. To model the different price regimes in a tariff, the networks can be split into *virtual networks*, i. e., each of the m resource networks is split into s virtual networks of the same resource. Here, without the loss of generality, we assume that for each resource s price regimes exist. This results in the following formulation ($r_{i,j,l} \in \mathbb{R}$)

$$\mathbf{r}_i = \begin{pmatrix} r_{i,1} \\ \vdots \\ r_{i,m} \end{pmatrix} = \begin{pmatrix} \sum_{l=1}^s r_{i,1,l} \\ \vdots \\ \sum_{l=1}^s r_{i,m,l} \end{pmatrix} = \mathbf{R}_i \mathbf{1}^{(s \times 1)} = \begin{pmatrix} r_{i,1,1} & \cdots & r_{i,1,s} \\ \vdots & \ddots & \vdots \\ r_{i,m,1} & \cdots & r_{i,m,s} \end{pmatrix} \mathbf{1}^{(s \times 1)}. \quad (3)$$

The optimization problems for each subsystem are changed such that for each resource j only one virtual network is allowed to be active. This is realized by a constraint adaptation, announced by the site-coordinator. The reasoning behind this is as follows: If the internal price of a shared resource exceeds the next higher external price (pipeline price in the tariff), the coordinator buys an amount of resource from the pipeline and allocates it to the internal shared resource network. From this point in time on, the subsystems that demanded shared resources receive an allocated amount of resource for the particular network. Afterwards, the

amount they received is fixed and the cost is stored at the rate of the pipeline price. The next virtual network is activated for the next price coordination round. The reformulation involves the following constraint adaptation, where the resources from the preceding price regimes ($t_j - 1$, with \mathbf{t} as a vector storing the index of active price regimes $(1, 2, \dots, s)$ for each resource j) are frozen and the succeeding virtual networks, i. e., for $t_j < l$, are set to zero

$$r_{i,j,l} \in \mathcal{R}_{i,j,l}^{(\mathbf{t})}, \quad \mathcal{R}_{i,j,l}^{(\mathbf{t})} = \begin{cases} \mathbb{R} & t_j = l \\ 0 & l > t_j, \\ \hat{r}_{i,j,l} & \text{else} \end{cases} \quad (4)$$

where $\hat{r}_{i,j,l}$ is the amount of the resource that has been bought during the last price regime by the coordinator and that has been assigned proportionally to the demanded amount of every subsystem. Further, the modeling involves the matrix $\mathbf{F}^{(\mathbf{t})}$, $f_{j,l} \in [0, 1]$, which activates the respective virtual networks. The optimization problems for the subsystems are changed to

$$\begin{aligned} \max_{\mathbf{u}_i, \mathbf{R}_i, \forall i} \quad & \mathbf{p}_{i,\text{prod}}^\top \mathbf{y}_i - \mathbf{1}^{(1 \times m)} (\mathbf{\Lambda} \circ \mathbf{R}_i) \mathbf{1}^{(s \times 1)} & (5a) \\ \text{s. t.} \quad & \left. \begin{aligned} & \mathcal{F}_i(\mathbf{u}_i, \mathbf{r}_i), \\ & \mathbf{r}_i - \mathbf{R}_i \mathbf{F}^{(\mathbf{t})} \mathbf{1}^{(s \times 1)} = \mathbf{0} \\ & r_{i,j,l} \in \mathcal{R}_{i,j,l}^{(\mathbf{t})}, \forall j, l \end{aligned} \right\} \text{individual constraints,} & (5b) \end{aligned}$$

where the manipulated variables of the subsystem are the vector \mathbf{u}_i and the matrix \mathbf{R}_i . The vector of Lagrange multipliers $\boldsymbol{\lambda}$ is extended to the matrix of prices $\mathbf{\Lambda} \in \mathbb{R}^{(m \times s)}$.

4. Proposed coordination scheme

The proposed update scheme is formulated for buying resources only. The formulation for selling resources to external resources can be formulated analogously. The proposed coordination scheme receives the planned amounts of consumed and produced shared resources from the subsystems as input (see Algorithm 1). After a convergence check, the network balance is evaluated and it is checked whether the Euclidean norm of the balance is below a threshold ε . The coordinator evaluates whether one of the internal prices exceeds the next higher pipeline price that is offered to buy additional quantities of resources. If the coordinator decides to buy additional resources at the pipeline price, the subsystems are queried again for the exact pipeline price, since $\boldsymbol{\Lambda}_{j,t_j}$ can be higher than the pipeline price \mathbf{P}_{j,t_j} , before the bought amount is assigned to the subsystems. The assigned quantities are calculated based on the demands of the receiving plants only, i. e., a producing plant is not assigned any resource. If the internal price is lower than the next higher price in the tariff, a normal subgradient update is performed. Whenever the coordinator buys an amount for a specific network, the virtual networks that are linked to the lower-priced tariff regimes are “frozen”, i. e., the Lagrange multipliers in $\mathbf{\Lambda}$ and the received quantities $r_{i,j,l}$ are fixed (see constraint in (4)).

5. Case study

The optimization problem is given in Eq. (5). The manipulated variables of each plant are limited to lie between 0 and 1 (lower and upper bound on the load). The numerical values for

Algorithm 1 Price-based coordinator update with constraint adaption.

```

1: procedure COORDINATORUPDATE( $[\mathbf{R}_1, \dots, \mathbf{R}_n]$ )                                ▷ Input: responses of the subsystems
2:    $\mathcal{G} \leftarrow \sum_{i=1}^n \mathbf{R}_i - \mathbf{R}_P$                                           ▷ Subgradient evaluation
3:   if  $\|\mathcal{G}\|_2 < \varepsilon$  then
4:     return;                                                                    ▷ Convergence achieved (Eukledian norm)
5:   end if
6:   for  $j = 1, 2, \dots, m$  do                                                  ▷ Do for all shared resource networks
7:     if  $\Lambda_{j,t_j} \geq \mathbf{P}_{j,t_j}$  then                                       ▷ If price exceeds pipeline price
8:        $\Lambda_{j,t_j} \leftarrow \mathbf{P}_{j,t_j}$                                        ▷ Assign the pipeline price
9:        $\mathcal{G} \leftarrow \sum_{i=1}^n \mathbf{R}_i(\Lambda) - \mathbf{R}_P$                                ▷ Reevaluation with new price
10:       $r_{j,t_j} \leftarrow \min(\mathcal{G}_{j,t_j}, \bar{r}_{j,t,p})$                                ▷ Buying from the pipeline
11:      for  $i = 1, 2, \dots, n$  do                                             ▷ Do for all subsystems
12:         $\hat{r}_{i,j,t_j} \leftarrow (r_{i,j,t_j} \div \sum_{i=1}^n \max(r_{i,j,t_j}, 0)) \times r_{j,t_j}$    ▷ Allocate bought quantities
13:      end for
14:       $t_j \leftarrow t_j + 1$                                                   ▷ Update price regime
15:       $\mathbf{F}_{j,t_j} \leftarrow 1$                                               ▷ Update activation matrix
16:    else
17:       $\Lambda_{j,t_j} \leftarrow \Lambda_{j,t_j} + \mathbf{S}\mathcal{G}$                                ▷ Normal subgradient update
18:    end if
19:  end for
20: end procedure

```

the tariff are given in Figure 2. The model equations for the three plants are:

$$\mathbf{f}_1(\mathbf{u}_1) = \begin{bmatrix} 32u_{1,1}^2 + 8u_{1,1} \\ 24u_{1,2}^2 + 3u_{1,2} \end{bmatrix}, \mathbf{g}_1(\mathbf{u}_1) = \begin{bmatrix} 60u_{1,1} + 20 \\ 40u_{1,2} + 35 \end{bmatrix}, \mathbf{p}_{1,prod.} = \begin{bmatrix} 5.4 \\ 2.1 \end{bmatrix}, \quad (6a)$$

$$\mathbf{f}_2(\mathbf{u}_2) = \begin{bmatrix} 35u_{2,1}^2 + 15u_{2,1} \\ 37u_{2,2}^2 + 10u_{2,2} \end{bmatrix}, \mathbf{g}_2(\mathbf{u}_2) = \begin{bmatrix} 50u_{2,1} + 10 \\ 45u_{2,2} + 2 \end{bmatrix}, \mathbf{p}_{2,prod.} = \begin{bmatrix} 1.5 \\ 2.6 \end{bmatrix}, \quad (6b)$$

$$\mathbf{f}_3(\mathbf{u}_3) = \begin{bmatrix} 25u_{3,1} + 15 \\ 30u_{3,2}^2 + 8 \end{bmatrix}, \mathbf{g}_3(\mathbf{u}_3) = \begin{bmatrix} -25u_{3,1} - 15 \\ -20u_{3,2} + 20 \end{bmatrix}, \mathbf{p}_{3,prod.} = \begin{bmatrix} 1.5 \\ 3.2 \end{bmatrix}. \quad (6c)$$

The results of the simulation study using Algorithm 1 with $s_{i,j=i} = 0.7, s_{i,j \neq i} = 0, s_{i,j} \in \mathbf{S}$ are shown in Figure 3 and Figure 4. It can be seen that when for a particular resource network the price-based coordination leads to a price that is higher than the next higher pipeline price (diamond symbols in Figure 3), the coordinator buys the necessary (less or equal to the available) amount from the pipeline for this price (see vertical bars in Figure 4). The network imbalance at these events is reduced until finally the network imbalance is below the threshold. Upon convergence of the algorithm the final cost a subsystem has to pay is the summation of the costs from each virtual network, i. e., the cost for a particular resource is determined from the amounts that are bought and received externally at different price regimes and the amount that is traded at the equilibrium price on site.

6. Conclusion and outlook

The problem of portfolio tariffs with different price regimes depending on the quantity of shared resource that is retrieved from the pipeline network has been studied and a price-based coordinator update that is aware of the tariff has been proposed. The simulation results show that the coordinator is able to react to the situation by buying optimal amounts of shared resources at fixed rates. The coordination strategy converges to a solution that is feasible for the two networks and that finds the equilibrium price by employing a subgradient-based update step for the investigated case study. The optimality of the found solution cannot be

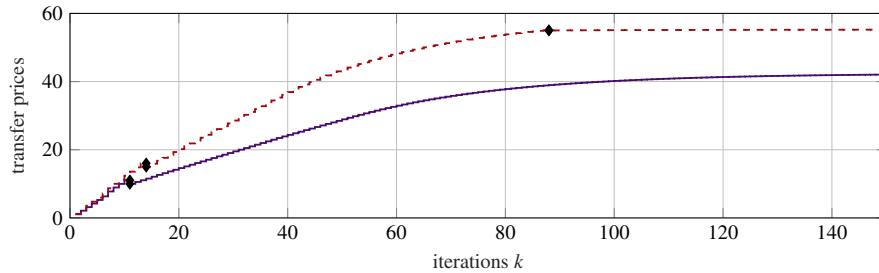


Figure 3: Transfer prices against the number of iterations.

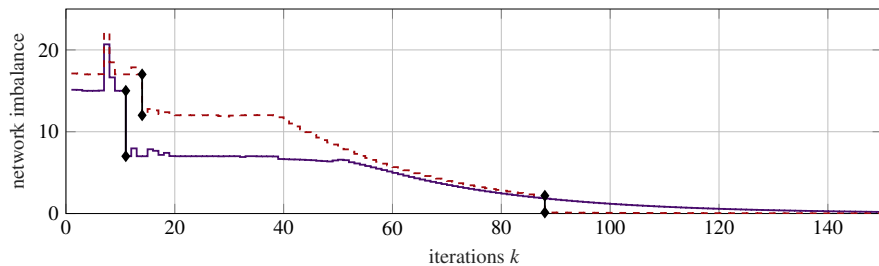


Figure 4: Network resource balance against the number of iterations.

ensured in general. However, the strength of the proposed approach is its transparency with respect to the different price regimes, i. e., each subsystem has consistent information how its overall cost function is computed. The advantage of price-based coordination is kept and thus, the individual cost functions remain private. Future research should be devoted to higher degrees of interactions between the different shared resource networks, which are usually coupled through the plant models, e. g., by a joint demand of steam and electricity.

Acknowledgment

The project leading to this publication has received funding from the European Union's Horizon 2020 research and innovation programme under grant agreement No 723575 (CoPro, spire2030.eu/copro) in the framework of the SPIRE PPP.

References

- D. P. Bertsekas, J. N. Tsitsiklis, 1997. *Parallel and Distributed Computation: Numerical Methods*. Athena Scientific, Belmont.
- S. Boyd, 2010. Distributed Optimization and Statistical Learning via the Alternating Direction Method of Multipliers. *Found. Trends Mach. Learn.* 3 (1), 1–122.
- S. Braithwait, May 2010. Behavior Modification. *IEEE Power and Energy Magazine* 8 (3), 36–45.
- S. Engell, C. Sonntag (Eds.), 2016. Proposal of a European Research and Innovation Agenda on Cyber-physical Systems of Systems, 2016-2025. CPSoS EU Project.
- T. Samad, S. Kiliccote, Dec. 2012. Smart grid technologies and applications for the industrial sector. *Computers & Chemical Engineering* 47 (2012), 76–84.
- J. Siirola, T. Edgar, Dec. 2012. Process energy systems: Control, economic, and sustainability objectives. *Computers & Chemical Engineering* 47, 134–144.
- S. Wenzel, R. Paulen, G. Stojanovski, S. Krämer, B. Beisheim, S. Engell, Jan. 2016. Optimal resource allocation in industrial complexes by distributed optimization and dynamic pricing. *at - Automatisierungstechnik* 64 (6), 428–442.

Ensuring $(n - 1)$ -reliability in the optimal design of distributed energy supply systems

Dinah Elena Hollermann^a, Dörthe Franzisca Hoffrogge^a, Maike Hennen^a and André Bardow^{a,b,*}

^a*Institute of Technical Thermodynamics; RWTH Aachen University; Aachen, Germany*

^b*Institute of Energy and Climate Research (IEK-10); Forschungszentrum Jülich; Jülich, Germany*

andre.bardow@ltt.rwth-aachen.de

Abstract

For distributed energy supply systems, reliability is important but still often neglected during design. We present a rigorous design approach which ensures the exact supply of all energy demands during the failure of one arbitrary component at any time. Since this $(n - 1)$ -reliable approach leads to high computational effort, we propose an alternative inexact approach with reduced computational effort. This so-called $(n - \max)$ -reliable approach also ensures sufficient energy supply but allows overproduction. An industrial real-world case study shows that both reliability approaches reduce both investment costs as well as total annualized costs significantly for a reliable design compared to current practical heuristics.

Keywords: Optimization, energy systems, synthesis problem, reliability, MILP

1. Introduction

For the design of distributed energy supply systems (DESS), mathematical optimization is a well suited tool (Frangopoulos et al., 2002). However, the resulting optimal design depends on many uncertainties. Uncertain input parameters, such as demand and price data, have been integrated into the optimal design using robust optimization approaches (e. g., based on Γ -robustness (Akbari et al., 2014) or strict robustness (Majewski et al., 2017)).

However, uncertainty also arises from the availability of energy components. Availability describes the probability that an item delivers its required function during a certain time period (Aguilar et al., 2008). Despite uncertain availability, DESS need to ensure high system reliability—the probability that a system is able to provide a required function. In practical applications, system reliability is often enhanced by installing additional units following rules of thumb (Aguilar et al., 2008). Such heuristics usually result in a sub-optimal design since the additional components are not part of the optimization. Thus, developing optimization approaches for reliability is an important task. In literature, the application of stochastic optimization approaches is popular to achieve reliable designs (e. g., Abdollahzadeh and Atashgar (2017); Andiappan and Ng (2016)). However, employing stochastic approaches cannot guarantee 100% security of energy supply since only probabilities are regarded in the optimization. To circumvent the dependence on probabilities, scenario-based approaches have been proposed (Caserta and Voß, 2015; Aguilar

et al., 2008). However, considering scenarios also cannot guarantee 100% reliable supply since selecting scenarios becomes crucial.

We present a rigorous approach which identifies 100% reliable designs for DESS: The so-called $(n-1)$ -reliable approach depends neither on the selection of failure scenarios nor on failure probabilities. The approach allows for failure of 1 arbitrary component at any time and thus ensures that all energy demands can still be covered exactly during failure of 1 component or maintenance. Since applying the $(n-1)$ -reliable approach increases the computational effort remarkably, we propose an inexact but computationally efficient approach: The $(n-max)$ -reliable approach ensures sufficient energy supply during the failure of 1 arbitrary component at any time while allowing overproduction.

2. Reliable design of distributed energy supply systems

Reliability of distributed energy supply systems (DESS) is crucial in practical applications to ensure security of energy supply and to enable maintenance of components. To illustrate our approach, we focus on reliable tri-generation systems covering heating, cooling, and electricity demands. In Section 2.1, we introduce the optimization problem for DESS without failure of components. In Section 2.2, two new reliability approaches are presented.

2.1. The nominal design model

The model of industrial DESS optimization is formulated as a mixed-integer linear program (MILP) (Voll et al., 2013). In the following, we call this model nominal. In the nominal model, no failure of components is taken into account; and thus, no reliability can be ensured. To optimize DESS, we choose the total annualized costs as objective function (Pintaric and Kravanja, 2006). Instead of the total annualized costs, any other objective function can be chosen since the proposed reliability approaches only affect the constraints, i. e., the energy balances:

$$\sum_{k \in K} \dot{V}_{kt} = \dot{E}_t \quad \forall t \in T. \quad (1)$$

Here, the supplied energy flow of component k is given by \dot{V}_{kt} ; K and T denote the set of all components k and all time steps t , respectively. \dot{E}_t represents the energy demand in time step t . In each time step t , the energy demand \dot{E}_t comprises the heating demand \dot{E}_t^h , cooling demand \dot{E}_t^c , and electricity demand \dot{E}_t^e . Here, the heating demand \dot{E}_t^h already includes the heating required for running absorption chillers AC , besides the heating demand of the considered industrial site $\dot{E}_t^{h,s}$:

$$\dot{E}_t^h = \dot{E}_t^{h,s} + \sum_{k \in AC} \dot{E}_{kt}^h. \quad (2)$$

2.2. An exact approach for $(n-1)$ -reliable design

The idea of the $(n-1)$ -reliable approach is adapted from electrical network planning where any component out of n components might fail at any time—but only 1 at the same time (Wiest et al., 2018). To obtain a reliable design based on this idea, we need additional energy balances to capture the potential failure of each component of the implemented system and the resulting lack in supply. Thus, every potentially failing component $k' \in K$ leads to a new set of energy balances:

$$\sum_{k \in K \setminus \{k'\}} \tilde{V}_{kt}^{k'} = \dot{E}_t \quad \forall t \in T \quad \forall k' \in K. \quad (3)$$

Here, we introduce new operation variables \tilde{V}_{kt}^k which specify the adapted output of component k in time step t if component k' fails. The new operation variables are determined such that the demands can still be covered exactly with the remaining components $K \setminus \{k'\}$. The number of additional constraints is proportional to the product of the number of time steps and potentially installed components which might result in high computational times. As a result, the $(n-1)$ -reliable approach might be unsuitable for large-scale design problems. Thus, as an alternative, we propose a computationally fast but inexact reliability approach.

2.3. $(n-max)$ -reliability: Optimal design ensuring sufficient energy supply

$(n-max)$ -reliability ensures sufficient energy supply during the failure of 1 arbitrary component at any time while allowing overproduction. If overproduction is allowed, only failure of the largest component has to be considered since a larger component can always replace a smaller component. Here, we focus on supplying heating demands \dot{E}_t^h and cooling demands \dot{E}_t^c since we assume that electricity demands can always be covered by the electricity grid. Instead of considering all occurring heating demands \dot{E}_t^h and cooling demands \dot{E}_t^c in each time step t , it is sufficient to consider only peak demands ($\dot{E}^{h,max}$ and $\dot{E}^{c,max}$, respectively). This is due to the fact that all inequalities including smaller demands are redundant if overproduction is allowed. As a result, we only obtain the additional inequalities

$$\sum_{k \in K^{h/c}} \dot{V}_k^N - \dot{V}_{K^{h/c}}^{max} \geq \dot{E}^{h/c,max} \quad (4)$$

where the set of all heating and all cooling components is given by K^h and by K^c , respectively. \dot{V}_k^N is the installed thermal power of component k and $\dot{V}_{K^{h/c}}^{max}$ represents the maximal deficit in energy (heating/cooling) supply for 1 failing component. The maximal heating and cooling deficit $\dot{V}_{K^{h/c}}^{max}$ is defined as the installed heating/cooling power of the largest component:

$$\dot{V}_{K^{h/c}}^{max} := \max \left\{ \dot{V}_k^N \mid k \in K^{h/c} \right\}. \quad (5)$$

The impact of a failing heating component on the cooling circuit is taken into account by considering the required heating of the absorption chillers AC in the heating demand \dot{E}_t^h (Eq. (2)).

Eq. (5) can be replaced by the following constraints in order to keep an MILP formulation:

$$\dot{V}_{K^h}^{max} \geq \dot{V}_k^N \quad \forall k \in K^h \quad (6)$$

$$\dot{V}_{K^c}^{max} \geq \dot{V}_k^N \quad \forall k \in K^c. \quad (7)$$

The number of additional constraints in Eq. (4), (6), and (7) depends on the number of potentially installed components $|K|$ but does not depend on the number of time steps $|T|$. Thus, the advantage of $(n-max)$ -reliability compared to $(n-1)$ -reliability is that the number of additional constraints is only proportional to the number of potentially installed components. Therefore, the expected increase in computational time is low compared to the nominal problem. Further details can be found in Hollermann et al. (2017).

3. Case Study

We consider a real-world example of an industrial park. The case study is based on a nominal design problem of a DESS published by Voll et al. (2013). All problems are implemented in GAMS 24.7.3 and solved with CPLEX 12.6.3.0 to machine accuracy on a computer with 64 GB RAM and 3.24 GHz employing 4 threads.

3.1. Description of the industrial real-world example

We consider an industrial park with time-varying heating, cooling, and electricity demands (Voll et al., 2013). Beside peak demands, we consider time-aggregated demands based on k -means aggregation with 5 time steps leading to a high accuracy for the full time series (Bahl et al., 2017). The cooling demands are supplied by two separated circuits (Site A and B) while the heating grid is connected. We assume that the industrial site is a “green field” with no existing components. However, the proposed approach can also be employed for the optimal retrofit of reliable DESS.

3.2. Reliable designs for the distributed energy supply system

To benchmark the approaches introduced in Section 2.2 and 2.3, we employ a rule of thumb for reliability from engineering practice: Based on the nominal optimal design, the largest component in each supply circuit is installed twice to ensure reliability of the DESS while allowing overproduction. We call this approach ($2 \times \max$)-reliability.

Computational times for calculating optimal solutions vary from less than 18 seconds for the calculation of the nominal, the ($2 \times \max$)-reliable, and the ($n - \max$)-reliable design up to 15 minutes for the calculation of the ($n - 1$)-reliable design.

The costs for the nominal problem without considering reliability aspects and the costs for the three reliability approaches are compared in Figure 1.

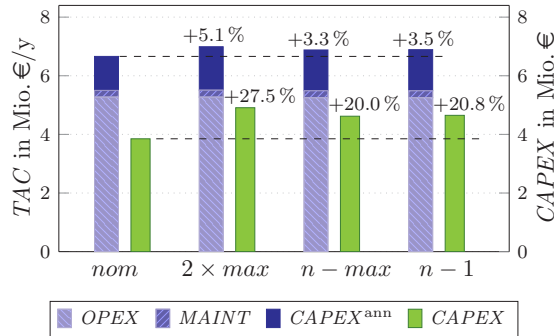


Figure 1: Total annualized costs TAC , operational costs $OPEX$, maintenance costs $MAINT$ and (annualized) investment costs $CAPEX^{(ann)}$ of the nominal problem (nom) and the reliability approaches

The total annualized costs for the ($2 \times \max$)-reliable design are the highest, 5.1% above the costs for the nominal design, whereas the total annualized costs for the ($n - \max$)-reliable design and the costs for the ($n - 1$)-reliable design are only 3.3% and 3.5% higher, respectively. The operational costs $OPEX$ are nearly identical for all approaches with only 2% variation around 5.20 Mio. €/y. Differences can be observed in the investment costs (Figure 1): The nominal design leads to 3.85 Mio. € investment costs; investment costs for the the ($2 \times \max$)-reliable design are 1.06 Mio. € higher which corresponds to an increase of 27.5%. In contrast, the ($n - \max$)-reliable design and the ($n - 1$)-reliable design involve only low additional investment costs compared to the nominal design, i. e., 0.77 Mio. € and 0.80 Mio. €, corresponding to an increase of 20.0% and 20.8%, respectively. Therefore, the ($n - \max$)-reliable approach and the ($n - 1$)-reliable approach save 35.4% and 32.5% of additional investment costs compared to the heuristic ($2 \times \max$)-reliable approach, respectively.

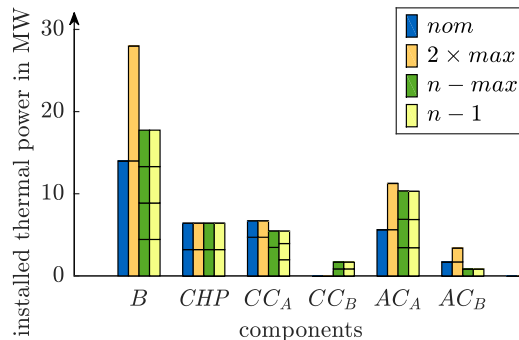


Figure 2: Installed components and their installed thermal capacities for each approach: components of nominal design (nom), of reliable designs ($2 \times max$), ($n - max$), and ($n - 1$) for each technology from left to right; B boiler, CHP combined heat and power engine, CC_A and CC_B compression chillers, and AC_A and AC_B absorption chillers installed on Site A and Site B, respectively

Despite high investment costs, the ($2 \times max$)-reliable design cannot cover the required demands exactly if one component fails and leads to overproduction of up to 55.5%. The ($n - max$)-reliable design comprises smaller and more components compared to the ($2 \times max$)-reliable design (Figure 2). But still, the ($n - max$)-reliable design might also lead to overproduction: If the smallest compression chiller on Site A (CC_A) fails, the minimal part load of the replacing compression chillers and absorption chillers (AC_A) is too high to cover the minimal cooling demand exactly. However, the resulting overproduction is only 83.7kW (= 13.8%) during one time step. This overproduction can be avoided by running 1 absorption chiller in part load with 17.6% of the nominal installed power instead of the allowed minimum of 20%. In emergencies, such a slight adaption or a slight overproduction for a short time will often be justifiable. For higher system flexibility, the ($n - 1$)-reliable design comprises even smaller and more absorption chillers on Site A. The results of the case study show that reliable design options can be identified at low additional costs with both proposed reliability approaches. However, there remains a trade-off between ($n - 1$)-reliability and ($n - max$)-reliability regarding solution quality and computational time.

4. Conclusions

In the design of distributed energy supply systems (DESS), reliability is crucial. We propose an exact approach to identify $(n - 1)$ -reliable designs for DESS. The approach does not require selection of scenarios or probabilities. Our approach ensures reliable energy supply during the failure of 1 arbitrary component at any time and thus also enables to maintain components at any time when no failure occurs simultaneously. However, the exact approach might involve high computational effort. For this reason, we propose an inexact but computationally efficient approach, called $(n - max)$ -reliability which ensures sufficient energy supply if 1 component fails but allows overproduction. An industrial real-world example shows that pragmatic heuristics from industry applications, such as installing redundant components by rules of thumb, lead to unnecessary high investment costs. Applying the proposed reliability approaches reduces the investment costs for a reliable design up to 35.4% compared to a pragmatic heuristic. The total annualized costs increase only by 3.5% compared to the original problem without considering reliability. Thus, our proposed reliability approaches identify reliable designs for distributed

energy supply systems at low additional costs. The exact $(n - 1)$ -reliable approach ensures reliability while $(n - \max)$ -reliability is easy to implement and identifies computationally efficiently an inexact but well-performing design.

5. Acknowledgments

This work was supported by the Helmholtz Association under the Joint Initiative Energy System 2050—A Contribution of the Research Field Energy. Furthermore, we acknowledge the support of Fabian Mayer in automating the computational test framework and we thank Maren Ihlemann for scrutinizing our approaches.

References

- H. Abdollahzadeh, K. Atashgar, 2017. Optimal design of a multi-state system with uncertainty in supplier selection. *Comput Ind Eng* 105, 411–424.
- O. Aguilar, J.-K. Kim, S. Perry, R. Smith, 2008. Availability and reliability considerations in the design and optimisation of flexible utility systems. *Chem Eng Sci* 63 (14), 3569–3584.
- K. Akbari, M. M. Nasiri, F. Jolai, S. F. Ghaderi, 2014. Optimal investment and unit sizing of distributed energy systems under uncertainty: A robust optimization approach. *Energy Build* 85, 275–286.
- V. Andiappan, D. K. Ng, 2016. Synthesis of tri-generation systems: Technology selection, sizing and redundancy allocation based on operational strategy. *Comput Chem Eng* 91, 380–391.
- B. Bahl, A. Kümpel, M. Lampe, A. Bardow, 2017. Time-series aggregation for synthesis problems by bounding error in the objective function. *Energy* 135, 900–912.
- M. Caserta, S. Voß, 2015. An exact algorithm for the reliability redundancy allocation problem. *Eur J Oper Res* 244 (1), 110–116.
- C. A. Frangopoulos, M. R. von Spakovsky, E. Sciubba, 2002. A brief review of methods for the design and synthesis optimization of energy systems. *Int J Appl Thermodyn* 5 (4), 151–160.
- D. E. Hollermann, D. F. Hoffrogge, M. Hennen, A. Bardow, 2017. Optimal design of $(n - 1)$ -reliable distributed energy supply systems, Submitted.
- D. E. Majewski, M. Lampe, P. Voll, A. Bardow, 2017. TRusT: A two-stage robustness trade-off approach for the design of decentralized energy supply systems. *Energy* 118, 590–599.
- Z. N. Pintaric, Z. Kravanja, 2006. Selection of the economic objective function for the optimization of process flow sheets. *Ind Eng Chem Res* 45 (12), 4222–4232.
- P. Voll, C. Klaffke, M. Hennen, A. Bardow, 2013. Automated superstructure-based synthesis and optimization of distributed energy supply systems. *Energy* 50, 374–388.
- P. Wiest, K. Rudion, A. Probst, 2018. Efficient integration of $(n-1)$ -security into probabilistic network expansion planning. *Int J Electr Power Energy Syst* 94, 151–159.

Integrating Real-time Operational Constraints in Planning of Water and Energy Supply

Negar Vakilifard*, Parisa A. Bahri, Martin Anda, Goen Ho

School of Engineering and Information Technology, Murdoch University, 90 South Street, Murdoch, Perth, Western Australia 6150, Australia

n.vakilifard@murdoch.edu.au

Abstract

Given increasing urban population, environmental issues and limited natural resources, long-term planning of water supply systems driven by renewable energies is the only way towards affordable secure and sustainable water and energy future. In this context, daily surplus output from grid-connected rooftop photovoltaics (PVs) is a promising clean energy source to be considered in urban water-related energy mix. In this paper, we address the optimal strategic investment decisions of an urban desalination-based water supply system driven by grid electricity and surplus PVs output, considering real-time operational constraints. The model is formulated as a two-level mixed integer linear programming (MILP) problem. The real-time operational constraints associated with water production, storage and transfer are integrated with yearly planning constraints corresponding to desalination plants, storage tanks and pipeline capacities and locations. The optimal decisions are obtained such that the operation of the water supply system has the most compatibility with available renewable energy. The capabilities of the proposed model are tested through a case-study from north-western corridor of Perth, Western Australia.

Keywords: Desalination, rooftop photovoltaics, long-term planning, optimisation

1. Introduction

Urban areas are responsible for high level of water and energy consumptions as a result of being the centres of population and economic development. Supplying increasing urban water and energy demand given the diminishing natural resources and environmental concerns highlights the importance of an analytical long-term planning to address water security and clean energy.

In land-restricted cities located in arid regions, daily surplus output from residential grid-connected rooftop photovoltaics (PVs) is a clean energy source that can be potentially allocated to energy-intensive water supply technologies. This source of energy is the result of the mismatch between load and PV output during the day and due to its intermittency, is a limiting factor for connection of greater number of these systems to the existing electrical grid. Hence, using it for meeting the water-related electricity demand, not only aligns with the sustainable future water supply but can also enable higher level of PV installations in urban areas.

In our previous study (Vakilifard et al., 2017), we addressed the optimal operation of the urban desalination-based water supply system driven by grid electricity and surplus PV output such that it resulted in the highest compatibility with available renewable energy. In the current study, we extend the mathematical model to a long-term planning of such system and include more detailed modelling of some system components (such

as pipeline network) as well as detailed financial analysis of the water supply system. The model is formulated as a two-level mixed integer linear programming (MILP) problem combining yearly constraints of long-term planning of water supply system with real-time (hourly) operational constraints. Three tools of geographical information system (GIS), system advisor model (SAM) and Excel analysis are used to provide some of the main model parameters. Accordingly, while the discounted total cost of the water supply system is minimised, the model gives the optimal strategic investment decisions such as the capacities and locations of desalination plants, storage tanks and pipeline as well as optimal operational scheduling of the system including desalinated water production, storage and transfer, such that it has the most compatibility with available renewable energy. A case study from north-western corridor of Perth, Western Australia is then considered to show the application of the model.

2. Methodology

2.1. Problem statement

1. The temporal aspect of the problem is captured considering a planning horizon of 20 years (begins from 2017), two seasons of summer and winter and 24 time blocks representing hours of a day.
2. Four zones are considered in the case-study area using ArcGIS 10 and Excel tools. The zones boundaries were determined based on our previous study (Vakilifard et al., 2017). In each zone and time period, water demand is supplied by desalination-based water supply system. Considering the annual water demand and population growth rate, we used a simple unit loading method (Walski et al., 2003) to forecast water demand in each zone till the end of 20 years. We assumed the constant water demand during all hours of a day.
3. Total water demand is supplied by a decentralised seawater reverse osmosis (SWRO) water supply system composed of desalination plants, storage tanks and a pipeline network. For a given zone, a desalination plant design capacities are selected from 7 discrete values (from 20,000 to 140,000 m³/day) considering the plant factor of 0.85. Their potential locations were considered to be next to the ocean. For those zones equipped with a desalination plant, a storage tank can potentially be located in the relative population center to store extra produced water. The design capacities of storage tanks are chosen from 3 different values (5000, 10,000 and 20,000 m³).
4. Desalinated water can be transferred between any two adjacent zones. The maximum water that can be transferred is ascertained based on the capacity of the associated pipeline. In this study, we considered a modular design for pipeline network where the design capacity is standard for a flow of 80,654 m³/day. Additional capacity can be added to the infrastructure annually, as needed.
5. The capital costs and the average operational and maintenance (O&M) cost for different desalination plants capacities were estimated based on (Watson et al., 2003). The capital cost of storage tanks and average O&M cost of storing per unit of desalinated water were determined according to (T&ES, 2015). The capital cost per unit length of pipeline was estimated based on (Shahabi et al., 2017). The operational cost of transferring water was calculated based on the electricity cost of water pumping. All cost data have been adjusted to 2017 Australian dollars (\$).
6. Seasonal residential electricity demand and water-related electricity demand are met by electricity sources consisting of residential rooftop PVs output and grid electricity. The maximum grid electricity that can be transferred to each zone is limited by the

maximum capacity of the associated substations. Using SAM tool, the maximum possible PV output for each zone is determined based on Perth's weather file (from the solar resource library of the model) as well as PV installation density in each zone.

8. The grid electricity price follows the time of use (TOU) tariff structure for residential and business sectors. For surplus PV output usage, variable electricity charge is implemented based on the net feed in tariff (FiT). All electricity price data was taken from Synergy, the electricity retailer of Perth.

9. Discount factors for business and residential sectors are calculated based on the discount rates adopted from (WCWA, 2012) and (AEC, 2017), respectively.

Accordingly, the model gives the optimum solution for the following decision variables:

1. The design capacities of water supply system components as well as their locations on yearly basis

2. Real-time scheduling of desalinated water production, storage and transfer

Such that the most compatibility with available surplus PV output is achieved while the discounted total cost of the water supply system is minimised.

2.2. Mathematical formulation

In line with our previous study (Vakilifard et al., 2017), we formulated the problem as a two-level MILP model. The first level objective function concerns the minimisation of the discounted residential electricity cost during planning horizon (z1). The output of this stage is stored in an auxiliary parameter used in the second level of optimisation to calculate the surplus PV output in each time period that can be assigned to both electricity demand of households not equipped with PV systems as well as water supply system. The objective function at this level is discounted total cost of water supply system (z2) minimised over the planning horizon. The main model constraints are given by Eqs.(1)-(21) as follows:

$$z_1 : \text{Min} \sum_t DF_t^r \cdot \sum_s nd_s \cdot \left[Cfe_t^r + \sum_i \sum_b Ce_{t,s,b}^r \cdot P_{t,i,s,b}^r \right]$$

$$z_2 : \text{Min} \sum_t DF_t^{bi} \cdot \sum_s nd_s \cdot \left[Cfe_t^{bi} + \sum_i \sum_b Cr_t^{bi} \cdot RE_{t,i,s,b}^w + Ce_{t,s,b}^{bi} \cdot P_{t,i,s,b}^w + COM_t \cdot Q_{t,i,s,b} + Cs_t \cdot V_{t,i,s,b} \right]$$

$$+ \sum_t DF_t^{bi} \cdot \sum_i \left[\sum_c Cap_{t,c}^{DP} \cdot XW_{t,i,c} + \sum_m Cap_{t,m}^{STT} \cdot X_{t,i,m} \right]$$

$$+ \sum_t DF_t^{bi} \cdot \left[\sum_{(i,j) \in \{AL_{i,j} | i=j\}} Cap_{t,i}^{PI} \cdot np_{t,i} \cdot L_{i,j} \cdot convf_2 + \sum_{(i,j) \in \{AL_{i,j} | i \neq j\}} Cap_{t,i}^{PI} \cdot np_{t,i} \cdot L_{i,j} \cdot convf_2 \right]$$

$$\text{Residential energy balance (with PVs):} \quad P_{t,i,s,b}^r + RE_{t,i,s,b}^r = k_1 \cdot D_{t,i,s,b} \quad (1)$$

$$\text{Residential energy balance (without PVs):} \quad P_{t,i,s,b}^m + RE_{t,i,s,b}^m = (1 - k_1) \cdot D_{t,i,s,b} \quad (2)$$

$$\text{Water-related energy balance:} \quad P_{t,i,s,b}^w + RE_{t,i,s,b}^w = Q_{t,i,s,b} \cdot De^{DP} + \quad (3)$$

$$\sum_{j:(i,j) \in \{PL_{i,j} | i=j\}} WTC_{t,i,s,b} \cdot De_{i,j}^{PI} + \sum_{j:(i,j) \in \{PL_{i,j} | i \neq j\}} WT_{t,i,j,s,b} \cdot De_{i,j}^{PI}$$

$$\text{PV share constraints:} \quad RE_{t,i,s,b}^m + RE_{t,i,s,b}^w \leq \text{Surp}_{t,i,s,b}; RE_{t,i,s,b}^r \leq \text{MaxR}_{t,i,s,b} \quad (4),(5)$$

$$\text{Grid share constraint:} \quad P_{t,i,s,b}^r + P_{t,i,s,b}^m + P_{t,i,s,b}^w \leq \text{dur}_b \cdot \text{MaxPS}_{t,i} \quad (6)$$

$$\text{Water balance:} \quad WQ_{t,i,s,b} + WV_{t,i,s,b} + \sum_{j:(i,j) \in \{AL_{i,j} | i \neq j\}} WT_{t,j,i,s,b} = Dw_{t,i,s,b} \quad (7)$$

$$\text{Plant capacity:} \quad DQ_{t,i} = DQ_{t-1,i} + \sum_c AC_c \cdot XW_{t,i,c} \cdot ; \sum_c XW_{t,i,c} \leq 1 \quad (8),(9)$$

$$\text{Storage capacity:} \quad SN_{t,i} = SN_{t-1,i} + \sum_m ST_m \cdot X_{t,i,m} ; \sum_m X_{t,i,m} \leq \sum_c XW_{t,i,c} \quad (10),(11)$$

$$\text{Pipeline capacity within zone:} \quad DTW_{t,i} = DTW_{t-1,i} + MaxTW \cdot np_{t,i} \quad (12)$$

$$\text{Pipeline capacity between zones:} \quad DTWIJ_{t,i,j} = DTWIJ_{t-1,i,j} + MaxTW \cdot npIJ_{t,i,j} \quad (13)$$

$$\text{Max. water desalinated:} \quad \sum_s nd_s \cdot \sum_b Q_{t,i,s,b} \leq PF \cdot \sum_s DQ_{t,i} \cdot nd_s \quad (14)$$

$$\text{Total and Max. water pushed for storage:} \quad WTC_{t,i,s,b} = Q_{t,i,s,b} - WQ_{t,i,s,b} - \sum_{j:(i,j) \in \{AL_{i,j} | i \neq j\}} WT_{t,i,j,s,b} \quad (15)$$

$$WTC_{t,i,s,b} \leq convf_1 \cdot DTW_{t,i} \cdot dur_b \quad (16)$$

$$\text{Total and Max. water stored:} \quad V_{t,i,s,b} = V_{t,i,s,b-1} + WTC_{t,i,s,b} - WV_{t,i,s,b} \quad (17)$$

$$V_{t,i,s,b} \leq SN_{t,i} \quad (18)$$

$$\text{Max. water transferred between zones:} \quad WT_{t,i,j,s,b} \leq convf_1 \cdot DTWIJ_{t,i,j} \cdot dur_b \quad (19)$$

$$\text{Max. water distributed from the storage tank:} \quad WV_{t,i,s,b} \leq V_{t,i,s,b-1} \quad (20)$$

$$\text{Unused surplus energy:} \quad Surp_{t,i,s,b} - RE_{t,i,s,b}^m - RE_{t,i,s,b}^w \cong 0 \quad (21)$$

2.3. Results and discussion

The two-level MILP model consists of 117,960 constraints and 97,774 variables (including 1,006 binary variables). The model was run in GAMS 24.3.1 software and solved by CPLEX 12.6.

The optimal result gives the accumulated total cost of \$ 3,003,833,149 for investment and operation of the desalination-based water supply system. As shown in Figure 1, the optimal investment solution considers desalination plants in all zones in year one, which will be then expanded once in zone 2 and twice in zone 4 during the planning horizon. Except for zone 1, all other zones are equipped with storage tanks to store extra water produced. In zone 1, the whole water demand is met by desalinated water directly assigned from the desalination plant during the planning horizon.

The optimal operational scheduling (on hourly basis) of the system during summer, for a representative zone 3 and year 2023 is presented in Figure 2(A) and 2(B). As expected, the business TOU tariff is not the only affecting factor on the operational scheduling of the system but the availability of renewable energy also plays a significant role. Accordingly, despite the high electricity rate, the highest level of production and hence the water storage occurs during peak electricity period due to the availability of the surplus PV output that can be assigned to water-related electricity demand. The stored water is then used to satisfy the demand for later hours of the peak electricity pricing period when there is no availability of surplus PV output. This is in agreement with our previous study (Vakilifard et al., 2017) where similar operational behaviour was observed for the hybrid energy scenario, in which both grid electricity and PV output were considered to meet the demand.

For off-peak periods, the production of the desalinated water is limited to the water demand directly assigned from the desalination plant. It is also notable that the amount of water transfer obtained is negligible for all zones during the planning horizon. This is because of the fixed installation density assumed for all zones during the planning horizon as well as the necessity of using all surplus PV output. Consequently, in the

optimal solution all zones are equipped with a desalination plant and hence there is no need for water transfer. This limitation will be addressed in the future work.

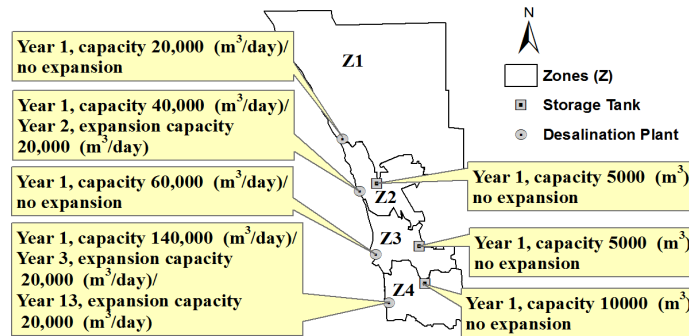


Figure 1: Optimal capacities and locations of desalination plants and storage tanks

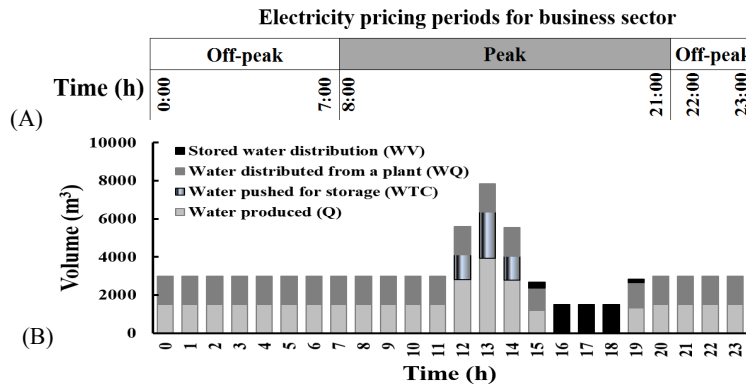


Figure 2: (A) Electricity pricing periods for business sector; (B) Optimal operation of desalination-based water supply system during summer in the representative zone 3 and year 2023

3. Conclusion

In this paper, we addressed long-term planning of a desalination-based water supply system integrated with real-time operational constraints. The model has been formulated as a two-level MILP to give the optimal strategic investment decisions as well as real-time operational scheduling of the water supply system based on availability of the renewable energy and discounted total cost of the system over the planning horizon. The results of applying the model to an urban area located in the north-western corridor of Perth, shows a multi-stage construction and expansion planning as an optimal solution for long term sustainable demand supply.

Nomenclatures

Sets:

AL, PL = allowable zones for water transfer and where pumping is needed, respectively
c = discrete points of plant capacities

Parameters (cont'd):

Cr = renewable electricity cost (\$/kWh)
Cs = O&M cost of water storage (\$/m³)
D = residential energy demand (kWh)

i, j = zone	De = water-related electricity demand (kWh/m ³)
m = discrete points of storage tank capacities	DF = discount factor
t, s, b = planning horizon, season and time block, respectively	dur = duration of the time block (h)
Continuous variables:	Dw = residential water demand (m ³)
DQ = capacity of a plant (m ³ /day)	k_l = PV installation density (%)
$DTW, DTWIJ$ = capacity of pipeline (m ³ /day)	L = distance (m)
P = share of grid electricity (kWh)	$MaxPS$ = Max. substation capacity (kW)
Q = desalinated water produced (m ³)	$MaxR$ = Max. PV output (kWh)
RE = share of renewable energy (kWh)	$MaxTW$ = Max. pipeline capacity (m ³ /day)
SN = capacity of the storage tank (m ³)	nd = number of days (day)
V = existing water storage (m ³)	PF = plant factor
WQ = water distributed from a plant (m ³)	ST = size of storage tank with m element (m ³)
WT = desalinated water transferred (m ³)	$Surp$ = surplus PV output (kWh)
WTC = water pushed for storage (m ³)	Integer variables:
WV = stored water distribution (m ³)	$np, npIJ$ = capacity multiplier of pipeline
Parameters:	Binary variables:
AC = design capacity of plant with c element (m ³ /day)	X, XW = decisions for storage tank size and plant capacity, respectively
Cap = capital cost for plant and storage tank (\$) and for pipeline (\$/km)	Superscripts associated with:
Ce = variable grid electricity cost (\$/kWh)	bi = business sector (water supplier)
Cfe = fixed grid electricity cost (\$/day)	DP = plant
COM = plants O&M cost (\$/m ³)	PI = pipeline
$convf_1, convf_2$ = conversion factors, (day/h) and (km/m), respectively	r, rn = households with and without PVs, respectively
	STT = storage tank
	w = water

References

- AEC, 2017, Australian Energy Council, Solar report, https://www.energycouncil.com.au/media/9932/australian-energy-council-solar-report_september-2017.pdf, [accessed 11.01.18].
- M. P. Shahabi, A. McHugh, M. Anda, G. Ho, 2017, A framework for planning sustainable seawater desalination water supply, *Science of The Total Environment*, 575, 826-835.
- T&ES, 2015, Department of Transportation and Environmental Services, city of Alexandria, CSS long term control plan, alternatives evaluation: storage tanks, <https://www.alexandriava.gov/uploadedFiles/tes/oeq/info/LTCPU%20Storage%20Alternative-FINAL.pdf>, [accessed 09.07.17].
- N. Vakilifard, P. A. Bahri, M. Anda, G. Ho, 2017, Water security and clean energy, co-benefits of an integrated water and energy management, 27th European symposium on computer aided process engineering, 40, 1363-1368.
- T. M. Walski, D. V. Chase, D. A. Savic, W. Grayman, S. Beckwith, E. Koelle, 2003, Advanced water distribution modeling and management, Haestad press, Waterbury, CT.
- I. C. Watson, O. Morin Jr., L. Henthorne, 2003, *Desalting Handbook for Planners*, United States Department of the Interior, Denver.
- WCWA, 2012, Water Corporation of Western Australia, Economic regulation authority inquiry into the efficient costs and tariffs of the Water Corporation, Aqwest and Busselton Water Board (submission in response to the draft report), <https://www.erawa.com.au/cproot/10903/2/20121024%20-%20D97720%20-%20Water%20Corporation%20Response%20to%20ERA%20Draft%20Report%202012.pdf>, [accessed 09.07.17].

Leveraging the Power of Big Data Analytics for Process Scheduling under Uncertainty using a Stochastic Robust Optimization Approach

Chao Ning, Fengqi You

Cornell University, Ithaca, New York, 14853, USA

Abstract

This paper is concerned with the multipurpose batch process scheduling problem under uncertainty. A novel process scheduling model is developed using a data-driven stochastic robust optimization approach to hedge against uncertainty. Labeled multi-class uncertainty data collected in batch productions are modelled with machine learning methods including Dirichlet process mixture model and maximum likelihood estimation. A stochastic robust process scheduling modelling framework is further proposed based on the data-driven uncertainty model through a bi-level optimization structure. The outer optimization problem follows a two-stage stochastic programming approach to optimize the expected profit obtained from the scheduling horizon over different data classes; adaptive robust optimization is nested as the inner problem to ensure the robustness of the process schedule while maintaining computational tractability. A case study on batch process scheduling under processing time and product demand uncertainties is presented to demonstrate the effectiveness of the proposed scheduling framework.

Keywords: big data, scheduling, uncertainty, stochastic robust optimization

1. Introduction

In recent years, the area of batch process scheduling under uncertainty has attracted immense attention from both academia and industries (Wassick et al., 2012; Chu and You, 2015). Since deterministic schedule could become suboptimal or even infeasible with parameter variations, operators in batch plants need to account for various uncertainties when making a production schedule. Risk management of batch process scheduling was investigated using a stochastic programming approach (Bonfill, 2004). To immune against demand uncertainty, a multi-period scheduling model was developed based on a stochastic programming approach (Balasubramanian and Grossmann, 2004). Stochastic programming method focuses on the expected performance of a solution by leveraging the scenarios of uncertainty realization and their probability distribution (Birge and Louveaux, 2011). However, these scheduling model requires accurate information on the probability distribution, and the resulting optimization problem could become computationally challenging as the number of scenarios increases. As an alternative paradigm, robust optimization could effectively tackle process scheduling under uncertainty (Bertsimas et al., 2011). Recently, adaptive robust optimization (ARO) was employed for batch process scheduling in which some decisions can be made in a “wait-and-see” mode based upon uncertainty realizations (Shi and You, 2016). Nevertheless, robust scheduling models do not take advantage of available probability distribution information, and its solution usually suffers from the

conservatism issue. The state-of-the-art approaches for optimization under uncertainty leverage the synergy of different optimization methods to inherit their corresponding strengths and complement respective weaknesses (Yue and You, 2016). In this work, we propose a novel data-driven stochastic robust process scheduling model that makes the most of uncertainty data for batch operations.

2. Data-Driven Stochastic Robust Scheduling Model

We adopt a continuous-time process scheduling model as the deterministic scheduling model (Méndez et al., 2006), shown as follows:

$$\begin{aligned}
\max \quad & \text{Profit of selling products minus the purchasing and operating cost} & (1) \\
\text{s.t.} \quad & \text{Mass balance constraints} & (2) \\
& \text{Batch size constraints} & (3) \\
& \text{Inventory constraints} & (4) \\
& \text{Demand satisfaction constraints} & (5) \\
& \text{Processing time constraints} & (6)
\end{aligned}$$

which is formulated as a mixed-integer linear programming problem. Based on the deterministic model (1)-(6), we propose a two-stage data-driven stochastic robust scheduling model in its compact form, denoted as DDSRO, which is presented in (7). The first-stage decisions include task sequencing variables, whereas the second-stage decisions are continuous variables including timing of tasks, batch sizes, inventory levels. Notice that the second-stage decisions are made after the uncertainty is realized.

$$\begin{aligned}
\min_{\mathbf{x}} \quad & \mathbf{c}^T \mathbf{x} + \mathbb{E}_{s \in \Xi} \left[\max_{i \in \{1, \dots, m(s)\}} \max_{\mathbf{u} \in U_{s,i}} \min_{\mathbf{y}_s \in \Omega(\mathbf{x}, \mathbf{u})} \mathbf{b}^T \mathbf{y}_s \right] \\
\text{s.t.} \quad & \mathbf{A}\mathbf{x} \geq \mathbf{d}, \quad \mathbf{x} \in R_+^{n_1} \times Z^{n_2} & (7) \\
& U_{s,i} = \left\{ \mathbf{u} \mid \mathbf{u} = \boldsymbol{\mu}_{s,i} + \kappa_{s,i} \boldsymbol{\Psi}_{s,i}^{1/2} \boldsymbol{\Lambda}_{s,i} \mathbf{z}, \|\mathbf{z}\|_{\infty} \leq 1, \|\mathbf{z}\| \leq \Phi_{s,i} \right\} \\
& \Omega(\mathbf{x}, \mathbf{u}) = \left\{ \mathbf{y}_s \in R_+^{n_3} : \mathbf{W}\mathbf{y}_s \geq \mathbf{h} - \mathbf{T}\mathbf{x} - \mathbf{M}\mathbf{u} \right\}
\end{aligned}$$

where \mathbf{x} represents the task assignment decision, and \mathbf{y} includes other decisions, such as timing and batch size decisions. \mathbf{u} is the uncertainty vector. Notice that \mathbf{x} is made “here-and-now”, whereas \mathbf{y} is made in a “wait-and-see” manner. $\Xi = \{1, 2, \dots, C\}$ is the set of data classes, C is the total number of data classes, $m(s)$ is the total number of mixture components for data class s .

In the following, we build an uncertainty model. We consider the multi-class uncertainty data with labels $\left\{ \mathbf{u}^{(i)}, c^{(i)} \right\}_{i=1}^L$, where $\mathbf{u}^{(i)}$ is i th uncertainty data point, $c^{(i)}$ is its corresponding label, and L is the total number of uncertainty data. The uncertainty information on the probability of different data classes can be extracted from labeled uncertainty data by leveraging their label information. The occurrence probabilities of data classes are modeled with a multinoulli distribution. The probability of each data class can be calculated through maximum likelihood estimation, as given by Eq. (8),

$$p_s = \frac{\sum_i \mathbb{I}(c^{(i)} = s)}{L} \quad (8)$$

where p_s represents the occurrence probability of data class s , $c(i)$ is the label associated with the i th uncertainty data point, $c(i)=s$ indicates that the i th uncertainty data point is from data class s , and $\mathbb{I}(c^{(i)}=s)$ is an indicator function. The second part of the uncertainty modelling is the construction of data-driven uncertainty sets from uncertainty data in the same data class. Based on the extracted information from Dirichlet process mixture model, we construct a data-driven uncertainty set for data class s using both l_1 and l_∞ norms (Ning and You, 2017a), as presented in Eq. (9).

$$U_s = \bigcup_{i: \gamma_{s,i} \geq \gamma^*} U_{s,i} = \bigcup_{i=1}^{m(s)} \left\{ \mathbf{u} \mid \mathbf{u} = \boldsymbol{\mu}_{s,i} + \kappa_{s,i} \boldsymbol{\Psi}_{s,i}^{1/2} \Lambda_{s,i} \mathbf{z}, \|\mathbf{z}\|_\infty \leq 1, \|\mathbf{z}\|_1 \leq \Phi_{s,i} \right\} \quad (9)$$

where $\gamma_{s,i}$ is the weight of the i th component data class s ,

$$\gamma_{s,i} = \frac{\tau_{s,i}}{\tau_{s,i} + \nu_{s,i}} \prod_{j=1}^{i-1} \frac{\nu_{s,j}}{\tau_{s,j} + \nu_{s,j}}, \quad i = 1, \dots, M-1 \quad \text{and} \quad \gamma_{s,M} = 1 - \sum_{i=1}^{M-1} \gamma_{s,i} \quad (\text{Campbell and$$

How, 2015). The weight $\gamma_{s,i}$ indicates the probability of the corresponding mixture component. γ^* is a threshold value. Variational inference algorithm is employed for the Dirichlet process mixture model. $\tau_{s,i}$, $\nu_{s,i}$, $\boldsymbol{\mu}_{s,i}$, $\kappa_{s,i}$, $\boldsymbol{\Psi}_{s,i}$ are the inference results of the i th component using the variational inference algorithm. $\Lambda_{s,i}$ is a scaling factor, and $\Phi_{s,i}$ is an uncertainty budget. Other data-driven methods, such as kernel learning (Shang et al., 2017) and kernel smoothing (Ning and You, 2017b) techniques, can also be used to derive the data-driven uncertainty set for robust optimization.

3. An Industrial-Scale Application

Process scheduling plays a critical role in process systems engineering, and attracts immense attention. The case study is originated from an industrial multipurpose batch process in The Dow Chemical Company (Chu et al., 2013), and the network is shown in Figure 1. This multipurpose batch process has one preparation task, three reaction tasks, two packing tasks and two drumming tasks. The equipment units include one mixer, two reactors, one finishing system and one drumming line (Yue and You, 2013).

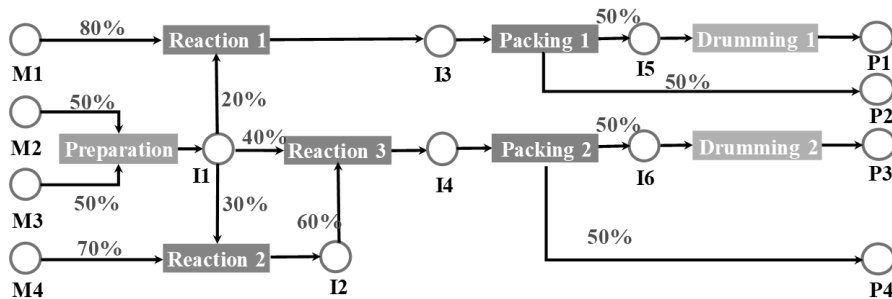


Figure 1. The state-task network of the multipurpose batch process.

In this case study, the processing times of all reaction tasks and demands of all final products are subject to uncertainty. The uncertainty sets are directly constructed from data via the variational inference algorithm. Due to different set points of temperature and pressure, the reaction tasks are performed under multiple operating modes. Therefore, class labels for batch processing time in this case study are various operating

modes. To demonstrate the superiority of the proposed approach, the deterministic optimization method and ARO with budgeted uncertainty set are also implemented for comparisons. In the deterministic scheduling model, the processing times and the demands are set to be their mean values of the corresponding uncertainty data. Without leveraging the label information, the ARO with budget based uncertainty set treats all these uncertainty data as a whole.

The computational experiments are implemented on a computer with an Intel (R) Core (TM) i7-6700 CPU @ 3.40 GHz and 32 GB RAM, and a Windows 10 64-bit operating system. The optimization models and the solution algorithm are coded in GAMS 24.7.3. Since both the master problem and the sub-problems are MILP problems, we solve them using CPLEX 12.6.3 with an optimality tolerance of 0. We set the relative optimality gap for the solution algorithm to be 0.1%.

Figure 2 shows the Gantt chart of the deterministic scheduling approach. Although this schedule generates a high profit, it becomes infeasible when processing times deviate from their nominal values. For example, when the processing time for Reaction 1 performed in Reactor 2 in the 3rd time slot becomes longer than the nominal value, there are some overlaps between Reaction 1 and Reaction 2 in the same equipment unit. However, it is impractical to perform these two reaction tasks in the same reactor simultaneously. Consequently, the scheduling result determined by the deterministic optimization approach becomes infeasible when the processing time varies.

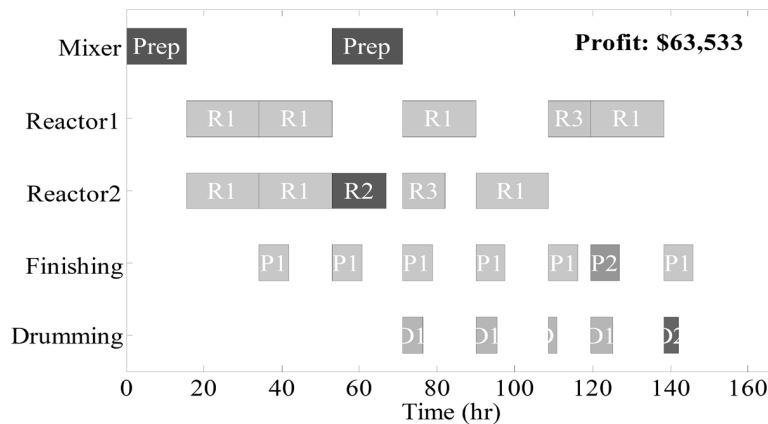


Figure 2. Gantt chart determined by the deterministic scheduling model.

Figure 3 demonstrates the Gantt chart determined by the ARO with a budget based uncertainty set. Since this method hedges against the uncertainty in processing times, the time allocations for reaction tasks tend to be longer than those of the deterministic method. Therefore, the scheduling solution remains feasible when the processing times are subject to uncertainty. For the ARO with budgeted uncertainty set method, it ensures the robustness of the operation at the expense of optimality.

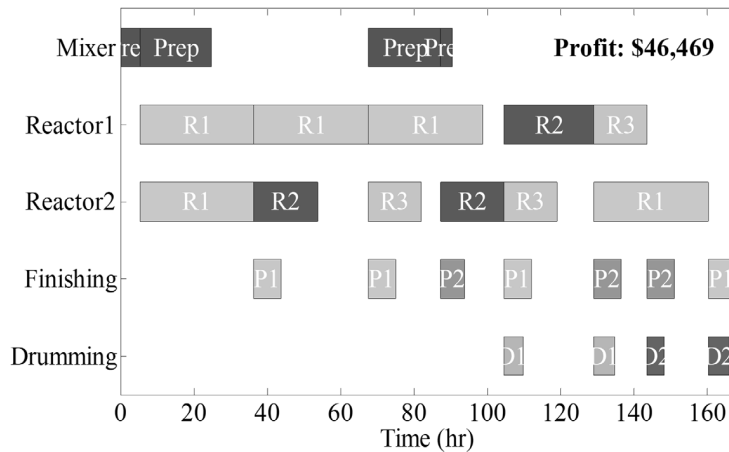


Figure 3. Gantt chart determined by the conventional ARO with budgeted uncertainty set.

The Gantt chart determined by the proposed approach is shown in Figure 4. As can be observed, one more Reaction 3 task is performed in the optimal solution determined by the DDSRO approach. Compared with the deterministic scheduling method, the ARO and the DDSRO approach perform more Reaction 2, Reaction 3, Packing 2 and Drumming 2 to manufacture sufficient amount of product 3 and product 4 for satisfying the demands. The deterministic scheduling method tends to manufacture relatively expensive products, i.e., products 1 and 2. However, it cannot fulfill the demands for other final products when their required amounts increase.

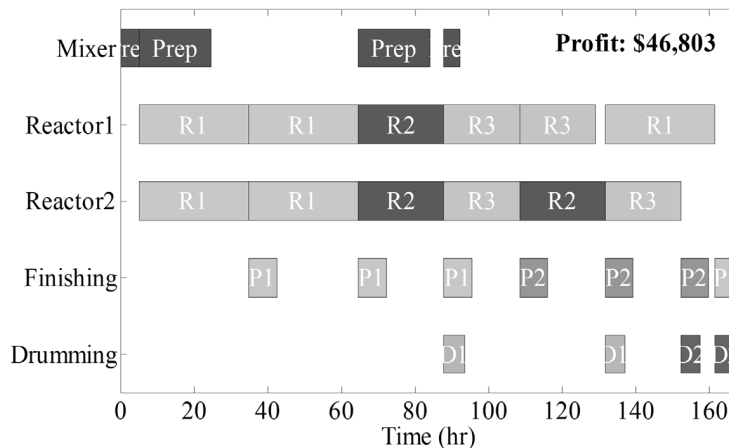


Figure 4. Gantt chart determined by the proposed approach.

In terms of computational time and results, we can see that the computational times of the ARO approach and the proposed scheduling approach are longer than that of the nominal deterministic method. Compared with ARO with budget based uncertainty set, the proposed approach is less conservative by generating more profits while ensuring that the schedule remain feasible under uncertain processing times and demands.

4. Conclusions

A novel data-driven stochastic robust scheduling model was proposed that explicitly accounted for the label information in the proposed multi-level optimization model. Probability distribution for data classes was learned from uncertainty data through maximum likelihood estimation. A group of Dirichlet process mixture models was used to construct uncertainty sets for each data class. The proposed robust process scheduling framework leveraged the advantages of two-stage stochastic programming approach and robust optimization, and at the same time exploited the value of big data. We presented an application on multipurpose batch process scheduling. The results showed that the proposed approach was advantageous over the conventional robust scheduling method in handling uncertainty with historical data, and was more computationally efficient.

References

- J. Balasubramanian, I. E. Grossmann, 2004, Approximation to multistage stochastic optimization in multiperiod batch plant scheduling under demand uncertainty, *Industrial & Engineering Chemistry Research*, 43, 3695-3713.
- D. Bertsimas, D. B. Brown, C. Caramanis, 2011, Theory and applications of robust optimization, *SIAM Review*, 53, 464-501.
- J. R. Birge and F. Louveaux, 2011, *Introduction to stochastic programming*: Springer Science & Business Media.
- A. Bonfill, M. Bagajewicz, A. Espuña, L. Puigjaner, 2004, Risk management in the scheduling of batch plants under uncertain market demand. *Industrial & Engineering Chemistry Research*, 43, 741-750.
- T. Campbell, J. How, 2015, Bayesian nonparametric set construction for robust optimization, In *Proceedings of the American Control Conference (ACC)*, Chicago, USA, 4216-4221.
- Y. Chu, J.M. Wassick, F. You, 2013, Efficient scheduling method of complex batch processes with general network structure via agent-based modeling, *AIChE Journal*, 59, 2884-2906.
- Y. Chu, F. You, 2015, Model-based integration of control and operations: Overview, challenges, advances, and opportunities, *Computers & Chemical Engineering*, 83, 2-20.
- C.A. Méndez, J. Cerdá, I.E. Grossmann, I. Harjunkoski, M.Fahl, 2006, State-of-the-art review of optimization methods for short-term scheduling of batch processes, *Computers & Chemical Engineering*, 30, 913-946.
- C. Ning, F. You, 2017a, Data-driven adaptive nested robust optimization: General modeling framework and efficient computational algorithm for decision making under uncertainty. *AIChE Journal*, 63, 3790-3817.
- C. Ning, F. You, 2017b, A data-driven multistage adaptive robust optimization framework for planning and scheduling under uncertainty. *AIChE Journal*, 63, 4343-4369.
- C. Shang, X. Huang, X., F. You, 2017, Data-Driven Robust Optimization Based on Kernel Learning. *Computers & Chemical Engineering*, 106, 464-479.
- H. Shi, F. You, 2016, A computational framework and solution algorithms for two-stage adaptive robust scheduling of batch manufacturing processes under uncertainty, *AIChE Journal*, 62, 687-703.
- J.M. Wassick, A. Agarwal, N. Akiya, J. Ferrio, S. Bury, F. You, 2012, Addressing the operational challenges in the development, manufacture, and supply of advanced materials and performance products, *Computers & Chemical Engineering*, 47, 157-169.
- D. Yue, F. You, 2013, Sustainable Scheduling of Batch Processes under Economic and Environmental Criteria with MINLP Models and Algorithms. *Computers & Chemical Engineering*, 54, 44-59.
- D. Yue, F. You, 2016, Optimal supply chain design and operations under multi-scale uncertainties: Nested stochastic robust optimization modeling framework and solution algorithm, *AIChE Journal*, 62, 3041-3055.

A hierarchical approach for solvent selection based on successive model refinement

Kai Fabian Kruber^a, Jan Scheffczyk^b, Kai Leonhard^b, André Bardow^b, Mirko Skiborowski^{a*}

^a*TU Dortmund University, Faculty of Chemical and Biochemical Engineering, Laboratory of Fluid Separations, Emil-Figge-Straße 70, 44227 Dortmund, Germany*

^b*RWTH Aachen University, Institute of Technical Thermodynamics, Schinkelstraße 8, 52062 Aachen, Germany*

mirko.skiborowski@tu-dortmund.de

Abstract

Liquid-liquid extraction has widespread use in industry, e.g., for separation of highly diluted components from fermentation broths. Feasibility and economic operation of the extraction processes depend critically on the selection of a suitable solvent. While the choice for an optimal solvent inherently depends on the overall process performance, common methods for solvent selection focus on much simpler performance indicators which can lead to suboptimal solutions. In order to improve solvent selection, we present a hierarchical approach with successive model refinement. The approach builds on the prediction of thermodynamic properties by COSMO-RS, avoiding the need for experimental data in early conceptual design phase. In the approach, advanced pinch-based shortcut models are combined with rigorous superstructure optimization to determine promising solvent candidates. The approach allows for an evaluation of several thousand potential solvents and identifies highly promising solvents based on the evaluation of process economics for an optimized process. The approach is illustrated for the extraction of γ -valerolactone from an aqueous feed stream.

Keywords: Optimization, Solvent, Screening, Extraction, Distillation

1. Introduction

Liquid-liquid extraction is one of the most promising techniques for the separation of components with similar molecular sizes, boiling and melting points (Skiborowski et al., 2013). Furthermore, the separation of azeotropic and highly diluted mixtures can effectively be addressed. Therefore, liquid-liquid extraction is of specific importance for the processing of bio-renewables, e.g., highly diluted aqueous streams such as fermentation broths. For liquid-liquid extraction, the solvent has a considerable impact on the economic and environmental performance of the final process. Thus, one of the first and usually most important steps in designing a liquid-liquid extraction process is selecting a suitable solvent. However, solvent selection is usually based on heuristic guidelines, expert knowledge and simplified process performance indicators such as distribution coefficients, as well as the selectivity and the capacity of the solvent (Gmehling and Schedemann, 2014). These simplified process performance indicators are usually combined to characterize the performance of solvents (Hampe, 1985). To identify solvents with the best performance indicators, computer-aided molecular design (CAMD) methods can automatically design solvent candidates (Harper et al., 1999).

However, the use of process performance indicators in CAMD implies a strong simplification of the separation performance which is usually maximized by a certain trade-off between different indicators. E.g., efficient extraction requires a high affinity of the solute to the solvent, whereas a low affinity helps to reduce the energy for solvent recovery by distillation (Papadopoulos and Linke, 2006).

To overcome heuristic weighting of multiple performance indicators, solvent candidates should be evaluated based on a performance evaluation on the process level, preferably taking into account process economics. In order to accomplish this and enable CAMD based on process performance, a variety of approaches have been proposed for integrated solvent and process design in the last fifteen years (for details see the excellent review by Austin et al. (2016)). For the design of liquid-liquid extraction processes especially the works of Kim and Diwekar (2002), Papadopoulos and Linke (2006), as well as Karunanithi et al. (2005) are of interest. These approaches are usually based on group-contribution models which need experimental data for parameterization. To avoid also the limitations of group-contribution based CAMD models, some of the present authors recently proposed a new method for an automated solvent screening for hybrid extraction–distillation processes (Scheffczyk et al., 2016). The approach builds on the prediction of thermodynamic properties by COSMO-RS, a semi-empirical model based on quantum mechanical (QM) calculations without substance-specific parameters. The predicted thermodynamic models enable an automated evaluation of the process performance based on thermodynamic sound pinch-based process models. While this approach already provides an efficient evaluation of the process performance on the basis of the required energy demand, this work expands the scope to integrate economics in the screening and add subsequent rigorous superstructure optimization of the hybrid process based on equilibrium-stage models in combination with sizing and costing equations. The resulting approach facilitates the efficient selection of a solvent for an extraction–distillation hybrid process with a hierarchical model refinement to manage the trade-off between detailed results and minimal effort.

2. Methodology

The methodology can be divided into four subsequent stages according to Figure 1. A thorough discussion of the first three stages is presented in the work of Scheffczyk et al. (2016). The following subsections provide a brief summary of these steps, with a focus of integrated economic aspects already in the target function for solvent performance in the rapid shortcut-based screening. Finally, a rigorous optimization of the process is performed for the most promising solvents from the preceding shortcut screening.

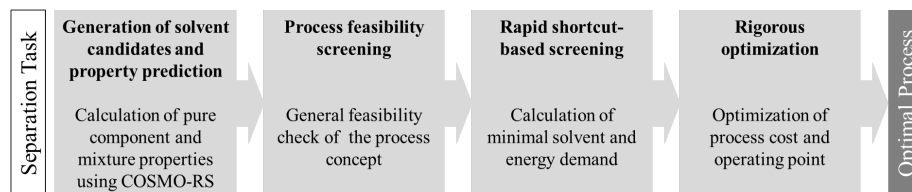


Figure 1: Schematic representation of hierarchical design approach

2.1. Generation of solvent candidates and property prediction (first stage)

In order to evaluate the process performance of different solvent candidates thermodynamic models for various properties are required. To overcome the need for

experimentally determined interaction parameters, recent solvent selection approaches propose the use of QM-based approaches, which are, however, computationally demanding (Struebing et al., 2013). In this work, COSMO-RS (Klamt et al., 2001) is used as a prediction tool. A large-scale database is employed which contains several thousand solvents. This database is evaluated with COSMO-RS, providing property predictions for pure components and mixtures. While the available database allows for a large-scale screening, the generation of new molecules is a potential extension that was already investigated by Scheffczyk et al. (2017). Thus, the presented framework could be extended towards integrated process and molecular design.

2.2. Process feasibility screening (second stage)

Prior to the evaluation of the process performance, the general feasibility of the process concept is evaluated for each solvent. At first, the existence of a miscibility gap between the solvent and the carrier is evaluated, based on binary liquid-liquid equilibrium (LLE) calculations. Furthermore, the existence of any azeotropes between solvent and solute is checked, based on vapour-liquid equilibrium (VLE) calculations. Additional constraints on thermodynamic properties may be employed to further limit the number of feasible solvent candidates. E.g., constraints on the boiling point of the solvent ensure liquid state of the solvent at ambient conditions (cf. Scheffczyk et al. (2016) for details).

2.3. Rapid shortcut-based screening (third stage)

All of the solvent candidates, which are feasible according to the previous step, are passed to the shortcut-based process screening. For an accurate evaluation of the process performance, the use of advanced pinch-based shortcut models allows for the consideration of non-ideal thermodynamics, which is a necessary prerequisite for the application to non-ideal systems such as those considered whenever dealing with liquid-liquid extraction processes. The evaluation of the minimal solvent demand in the extraction process is performed by the shortcut method of Redepinning et al. (2016), while the minimal energy demand for the solvent recovery is subsequently performed by the rectification body method (Bausa et al., 1998). Both are computationally highly efficient, allowing for the evaluation of more than thousand solvents within few hours of computational time (Scheffczyk et al., 2016). In the previous work of Scheffczyk et al. (2016), the optimal solvent choice was determined based on the minimal energy demand for solvent regeneration ($Q_{b,\min}$), being a good indicator of the operating costs, which usually dominate the overall separation process costs. However, preliminary results of the subsequent rigorous process evaluation indicated a significant effect of the solvent loss on the overall process costs depending on the specific solvent. Thereby, we adapted the target function for the screening by integrating solvent loss into the estimate for operating costs (C_{op}). Solvent loss in the raffinate phase was considered with a fixed price of the benchmark solvent, and the costs for fresh solvent were added to the utility costs for the distillation column. This adjustment reflects the actual costs more closely and results in a much better agreement with the subsequent economic optimization.

2.4. Rigorous optimization (fourth stage)

Despite the adaption of the target function for the shortcut-based screening, pinch-based process models only provide an estimate of the process costs since they are based on simplified models leading e.g. to sharp separation splits. The final cost of the process can only be calculated accurately with detailed models and especially a simultaneous process optimization, which considers the aggregation of all processing steps and closed recycle streams with finite purities. Therefore, the last step in the described approach

(Fig. 1) is the application of a rigorous process optimization based on detailed equilibrium-based superstructure models for the most promising solvent candidates. The optimization approach builds on the model description and the solution approaches described by Skiborowski et al. (2015).

The superstructure model of the hybrid extraction-distillation process is shown in Figure 2. Compared to the process structure for the shortcut-based screening, two additional heat exchangers are considered for preheating the feed to the distillation column and cooling the top product stream prior to the decanter, in order to get a more accurate estimation for the process cost. Furthermore, the recycle

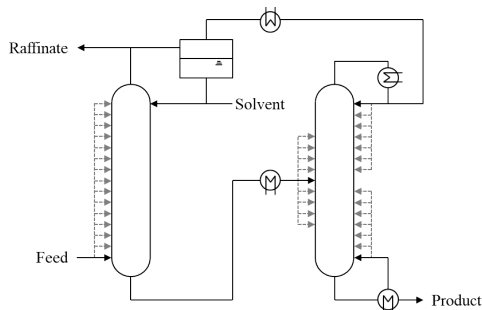


Figure 2: Superstructure of the hybrid process

stream coming from the decanter considers the finite purities in the rigorous optimization. While this recycle can be negligible in some cases, it can result in drastic changes of the operation point of the whole process. The extraction column is operated in counter-current mode and the number of equilibrium stages in the extraction and the distillation column are degrees of freedom in the optimization. This superstructure model provides the trade-off calculation between operational and investment cost. Investment cost are estimated using the method of Guthrie (1969).

While the full process optimization has a significant number of benefits compared to the shortcut-based screening, the computational effort is much higher and the approach is not directly applicable to the large number of feasible solvents from the second step (Fig. 1). The proposed hierarchical combination therefore allows for screening the full solvent database and subsequent detailed investigation of the process performance for the most promising candidates only.

3. Case study – purification of γ -Valerolactone

The proposed approach is applied to the purification of the platform chemical γ -Valerolactone (GVL) from a fermentation broth. GVL is a bio-based platform chemical and a promising preliminary product in the synthesis of bio-based fuel or commodity chemicals (Alonso et al., 2013). This case study is also presented in the publication of Scheffczyk et al. (2016) where the first two stages of the approach have already been performed. This work therefore focuses on the changes of the results in step three due to the modified target function and the results of the rigorous process costs evaluation for an evaluation based on the process costs. A feed stream of 100 mol/s is considered that consists of 5 mol% GVL and 95 mol% water. All equipment is operated at a pressure of 1 atm, while the temperature for extraction and decantation is 25 °C. The desired purity for GVL is 99.99 mol% and water in the raffinate is limited to 0.001 mol%.

The process feasibility screening and the rapid shortcut-based screening is performed for a database with 4600 solvent candidates. The results for stage 1 and 2 are summarized in the article of Scheffczyk et al. (2016). From these candidates, we consider five solvents for further evaluation in the rigorous design optimization: n-Butylacetate as benchmark solvent, toluene as a common industrial solvent and three different furane molecules (furane (FUR); 2-methyl-furane (2MFUR); 3-methyl-furane

(3MFUR)). Furane molecules are among the best in the shortcut-based screening, both in terms of energy demand $Q_{b,\min}$ and estimated operating costs C_{op} . Further solvents, mainly diols, are found to be superior in terms of process energy demand but the chemical stability of these molecules stands to question. These molecules are thus excluded from further consideration.

Table 1 lists the ranking of the selected molecules in terms of the shortcut screening ranking with energy demand $Q_{b,\min}$ and the adapted target function integrating solvent cost C_{op} , as well as the results of the rigorous economic process optimization for each of the five solvent candidates. Additionally, the total annual cost (TAC) and operating cost (TOC) are listed along with the amount of fresh solvent S_{fresh} , the composition of the recycled solvent x_S and the energy demand in the reboiler of the distillation Q_b .

Table 1: Results of the cost optimization with fixed superstructure

Solvent	Ranking		$S_{fresh} /$ $\text{mol}\cdot\text{s}^{-1}$	$x_{S,GVL} /$ $\text{mol}\%$	$x_{S,W} /$ $\text{mol}\%$	$Q_b /$ MW	TOC / $\text{k}\text{€}\cdot\text{y}^{-1}$	TAC / $\text{k}\text{€}\cdot\text{y}^{-1}$
	$Q_{b,\min}$	C_{op}						
3MFUR	18	28	0.050	0.0001	1.03	0.49	262	340
2MFUR	30	37	0.044	0.0000	0.92	0.59	269	354
TOL	211	54	0.011	0.0014	0.53	1.03	346	465
FUR	11	219	0.165	0.0000	1.20	0.44	421	490
nBAC	161	380	0.090	0.0000	21.01	1.14	623	738

As indicated by the positions listed in Table 1 the ranking of all investigated solvents changes already on shortcut level depending on whether cost C_{op} or energy $Q_{b,\min}$ is used as target function. In particular, a switch occurs in the order of nBAC and TOL. For both molecules, a significant amount of solvent is lost in the raffinate stream, which indicates a strong influence of solvent loss on the overall process performance. This importance of solvent loss is further highlighted for FUR where costs for fresh solvent exceed the operating costs of the distillation column by almost a factor of three. Thus, solvent loss needs to be already considered on pinch-based process level by cost C_{op} .

Using cost C_{op} as target function, the ranking of the shortcut-based screening is in excellent agreement with economic optimization for the five considered solvents. Thus, the general concept of the presented approach allows for a reliable ranking of the solvents on pinch-based level and detailed evaluation of a few promising candidates. This final evaluation is still required to capture all effects on the process performance. E.g., the simultaneous optimization of the full process for nBAC reveals that the recycled solvent stream to the extraction column contains about 20 mol% water. This solvent dilution reduces the solvent make-up demand in closed recycle streams in comparison to sequential pinch-based evaluation. Such effects are successfully captured by the hierarchical design approach presented in this work.

4. Conclusion

The current article presents a systematic approach for an elaborate and efficient solvent selection based on advanced property prediction and hierarchical model refinement. For the investigated case study, more than 4600 solvent candidates are evaluated. The results of the revised screening and rigorous optimization demonstrate the capability of the approach to determine a cost-optimal solvent based on the overall process design. In particular, a process using the solvent 2- or 3-methylfurane can reduce the total annual cost by more than 50% compared to the benchmark solvent n-butylacetate. The results

also illustrate the importance of an appropriate target function for the screening of suitable solvents. The presented approach is highly flexible and computationally efficient and thus the application to other solvent-based separation processes and more complex process configurations will be subject to future work.

Acknowledgements

The work of the authors from RWTH Aachen University was performed as part of the Cluster of Excellence ‘Tailor-Made Fuels from Biomass’, which is funded by the Excellence Initiative by the German federal and state governments to promote science and research at German universities.

References

- D. M. Alonso, S. G. Wettstein, J. A. Dumesic, 2013, Gamma-valerolactone, a sustainable platform molecule derived from lignocellulosic biomass, *Green Chem.*, 15, 3, p. 584
- N. D. Austin, A. P. Samudra, N. V. Sahinidis, D. W. Trahan, 2016, Mixture design using derivative-free optimization in the space of individual component properties, *AIChE J.*, 62, 5, p. 1514–1530
- J. Bausa, R. v. Watzdorf, W. Marquardt, 1998, Shortcut methods for nonideal multicomponent distillation: I. Simple columns, *AIChE J.*, 40, 10, p. 2181–2198
- J. Gmehling, A. Schedemann, 2014, Selection of Solvents or Solvent Mixtures for Liquid–Liquid Extraction Using Predictive Thermodynamic Models or Access to the Dortmund Data Bank, *Ind. Eng. Chem. Res.*, 53, 45, p. 17794–17805
- K. M. Guthrie, 1969, Capital cost estimating, *Chem. Eng. Tech.*, 76, 6, p. 114–142
- M. J. Hampe, 1985, Lösungsmittel-Auswahl bei der Flüssig/Flüssig-Extraktion unter physikalisch-chemischen Aspekten, *Chem. Ing. Tech.*, 57, 8, p. 669–681
- P. M. Harper, R. Gani, P. Kolar, T. Ishikawa, 1999, Computer-aided molecular design with combined molecular modeling and group contribution, *Fluid Phase Equilibr.*, 160, p. 337–347
- A. T. Karunanithi, L. E. K. Achenie, R. Gani, 2005, A new decomposition-based computer-aided molecular/mixture design methodology for the design of optimal solvents and solvent mixtures, *Ind. Eng. Chem. Res.*, 44, 13, p. 4785–4797
- K. J. Kim, U. M. Diwekar, 2002, Efficient combinatorial optimization under uncertainty. 2. Application to stochastic solvent selection, *Ind. Eng. Chem. Res.*, 41, 5, p. 1285–1296
- A. Klamt, F. Eckert, M. Hornig, 2001, COSMO-RS: A novel view to physiological solvation and partition questions, *J. Comput. Aided Mol. Des.*, 15, p. 355–365
- A. I. Papadopoulos, P. Linke, 2006, Multiobjective molecular design for integrated process-solvent systems synthesis, *AIChE J.*, 52, 3, p. 1057–1070
- C. Redepenning, S. Recker, W. Marquardt, 2016, Pinch-based shortcut method for the conceptual design of isothermal extraction columns, *AIChE J.*, 63, 4, p. 1236–1245
- J. Scheffczyk, L. Fleitmann, A. Schwarz, M. Lampe, A. Bardow, K. Leonhard, 2017, COSMO-CAMD: A framework for optimization-based computer-aided molecular design using COSMO-RS, *Chem. Eng. Sci.*, 159, p. 84–92
- J. Scheffczyk, C. Redepenning, C. M. Jens, B. Winter, K. Leonhard, W. Marquardt, A. Bardow, 2016, Massive, automated solvent screening for minimum energy demand in hybrid extraction–distillation using COSMO-RS, *Chem. Eng. Res. Des.*, 115, p. 433–442
- M. Skiborowski, A. Harwardt, W. Marquardt, 2013, Conceptual design of distillation-based hybrid separation processes, *Annu. Rev. Chem. Biomol. Eng.*, 4, p. 45–68
- M. Skiborowski, A. Harwardt, W. Marquardt, 2015, Efficient optimization-based design for the separation of heterogeneous azeotropic mixtures, *Comput. Chem. Eng.*, 72, p. 34–51
- H. Struebing, Z. Ganase, P. G. Karamertzanis, E. Sioukrou, P. Haycock, P. M. Piccione, A. Armstrong, A. Galindo, C. S. Adjiman, 2013, Computer-aided molecular design of solvents for accelerated reaction kinetics, *Nat. Chem.*, 5, 11, p. 952–957

Optimal synthesis of mass exchange networks through a state-task representation superstructure

Miguel Ángel Velázquez-Guevara,^{a*} Agustín Ramón Uribe-Ramírez,^a
Fernando Israel Gómez-Castro,^a Juan Gabriel Segovia-Hernández,^a Salvador
Hernández,^a José María Ponce Ortega^b

^a*Departamento de Ingeniería Química, División de Ciencias Naturales y Exactas,
Campus Guanajuato, Universidad de Guanajuato, Noria Alta S/N, Guanajuato, Gto.,
36050, México*

^b*División de Estudios de Posgrado, Facultad de Ingeniería Química, Universidad
Michoacana de San Nicolás de Hidalgo, Francisco J. Múgica S/N, Morelia, Mich.,
58060, México*

guevaraf@ugto.mx

Abstract

The use of mass exchange networks is a strategy that allows the recovery and reuse of dangerous components from effluents of industry, reducing, or even avoiding, the pollution derived from the release of such components to the environment. The most common strategy for the synthesis of mass exchange networks involves the use of analogies to the pinch point method for heat exchange networks, and some approaches have been reported on the use of mathematical methods to solve the synthesis problem following a super-structure based on stages. Nevertheless, such super-structure requires deciding the proper number of stages. In this work, a superstructure is proposed to represent the synthesis of a mass exchange network for the recovery of copper in an etching process. The superstructure is developed following a state-task representation, using the concepts of transfer units for the design of the mass exchangers. This representation allows obtaining a wide search space, with no need of assuming additional parameters related to the formulation. The disjunctive mathematical model is developed and its MINLP equivalent is obtained through the convex hull strategy. The MINLP is then solved using the DICOPT solver of GAMS.

Keywords: mass exchange networks, state-task representation, mathematical programming

1. Introduction

Mass exchange networks are structures with many direct-contact mass transfer units, on which waste process streams (so-called rich streams) are treated to remove pollutants. This removal task is usually performed through external mass separation agents (so-called poor streams). The selection of which rich streams must exchange mass with which poor streams is one of the main challenges in the design of mass exchange networks. One of the first methodologies to synthesize mass exchange networks has been proposed by El-Halwagi and Manousiouthakis (1989), where the minimum capital cost is obtained through heuristics. The use of superstructures to represent the set of

possible configurations for the network has been widely developed in the last years. Chen and Hung (2005) proposed a synthesis methodology based on the design of heat exchange networks. On the other hand, Isafiade and Fraser (2008) used a superstructure based on intervals of composition. Liu et al. (2013) reported a superstructure for the synthesis of mass exchange networks, involving the recovery of multiple components. Isafiade and Short (2016) proposed the use of more rigorous cost functions to solve the synthesis problem of mass exchange networks. Ghazouani et al. (2017) proposed a superstructure for the simultaneous design of mass and heat exchange networks, with a simplified model, obtaining a MILP problem. Other design approaches have been also reported, based on graphical methods and the pinch point analysis (Gadalla, 2015).

Most of the previously mentioned works report the use of a stage-based superstructure. Nevertheless, an important parameter to choose when obtaining such a superstructure is the number of stages, whose proper value is unknown at the beginning of the solution, although some approaches have been reported to this end (Chen and Hung, 2005). An alternative way to propose the superstructure is through the development of a state-task-network based superstructure. In this approach, the tasks (physical or chemical transformations) and the states (properties for the streams) are defined, while the assignation of equipment is unknown. In this work, a state-task-network based superstructure is developed for a classic mass exchange network synthesis problem. The problem is modelled through general disjunctive programming, relaxed into a MINLP and solved with the software GAMS. The non-linear terms are involved mainly in the design equations for the mass transfer units.

2. Case study

The design of a mass exchange network for the removal of copper in an etching plant is studied (Chen and Hung, 2005). This problem involves the integration between two rich streams and two poor streams. Figure 1 shows a simplified representation of the network. Stream R_1 is a solution with ammonia, while stream R_2 comes from a washing stage. Both, R_1 and R_2 , have a high concentration of copper, so they must be treated to reach the environmental regulations with little affection to the process economy.

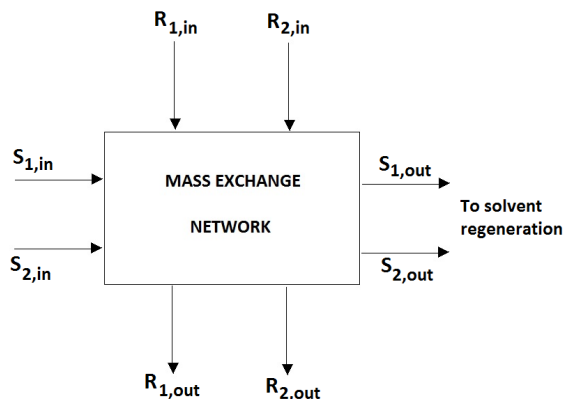


Figure 1. Simplified representation of the mass exchange network.

R_1 has a flowrate of 0.25 kg/s, with initial composition of copper of 0.13. On the other hand, flowrate for R_2 is 0.10, with initial composition of copper of 0.06. It is desired to reach compositions of 0.10 and 0.02 for streams R_1 and R_2 , respectively. To perform this task, there are two external mass separation agents, S_1 and S_2 , where S_1 has a unitary cost of 58,680 USD/kg·y, while the unitary cost of S_2 is 704,160 USD/kg·y (Papalexandri et al., 1994).

3. Superstructure and mathematical modelling

Figure 2 shows the superstructure representing the feasible combinations between streams and equipment. Such superstructure is based on a state-task-network representation. In Figure 2, the circles are units for mixing or separation of streams, which allows to split a single stream and treat its sub-streams in different equipment, or mixing to streams to be treated in a single equipment. Units 1 and 3 are trayed columns, while Units 2 and 4 are packed columns. Variables written in capital letters (Q_i , R_i , S_i and T_i) are mass flowrates, while variables in lowercase letters (x_i , y_i , z_i) are mass compositions. The superstructure is arranged in a way to allow parallel and serial arrangements, or combinations of both. Moreover, as abovementioned, this superstructure allows the split of the streams, which is one of the major advantages of this approach.

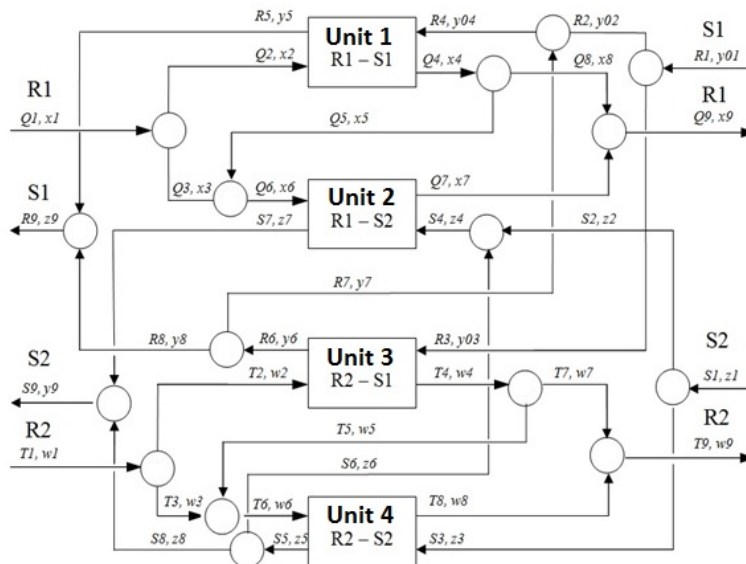


Figure 2. State-task-network based superstructure.

The mathematical model for the superstructure includes the mass balances in the nodes, the mass balances in the separation units, relationships for thermodynamic equilibrium, equations for dimensioning of the mass exchangers, disjunctions and logical

propositions, and equations for the calculation of total annual cost. The mass balances in the nodes are applied in each point where streams are mixed or split. The bilinear terms in these balances contribute to the non-convexity of the model. The mass balances in the separation units are applied for each component. The relationships for thermodynamic equilibrium are used to establish the feasibility for mass transfer in each exchange. Here, a minimum allowed difference in composition is used to ensure a finite number of stages in the trayed columns and/or a finite packing height in the packed columns. In the case of the dimensioning of the mass exchangers, the Kremser equation with the approximation of Chen has been used for the trayed columns. As aforementioned, for the packed columns, the concept of height of transfer unit is used. The logical propositions are established to allow independence between the mass exchangers, i.e., the selection of one unit does not affect the possibility of selection or not selection of a second unit. The objective function for the optimization is given by the minimization of the total annual cost, which is the sum of the annualized capital costs and the operational costs. For this network, the operational costs are given by the solvents. The disjunctions have been relaxed through the convex hull strategy, and the resulting MINLP model is solved using the DICOPT solver of GAMS.

4. Results

The MINLP model to be solved has 93 continuous variables, 4 binary variables and 148 equations. Figure 3 shows the resulting network. The numbers in the rectangles with dotted lines represent the quantity of mass transferred in each unit. The exchanges R1-S1 and R2-S2 have parallel arrangement, while the exchanges R2-S1 and R2-S2 have a serial arrangement. From Figure 3, it can be seen that the stream S1 is divided, so a fraction of S1 exchanges mass with R1, while the other fraction performs the exchange with R2. The total annual cost for the network is 50,855 USD/y, where 63% of the total annual cost is given by the operational costs.

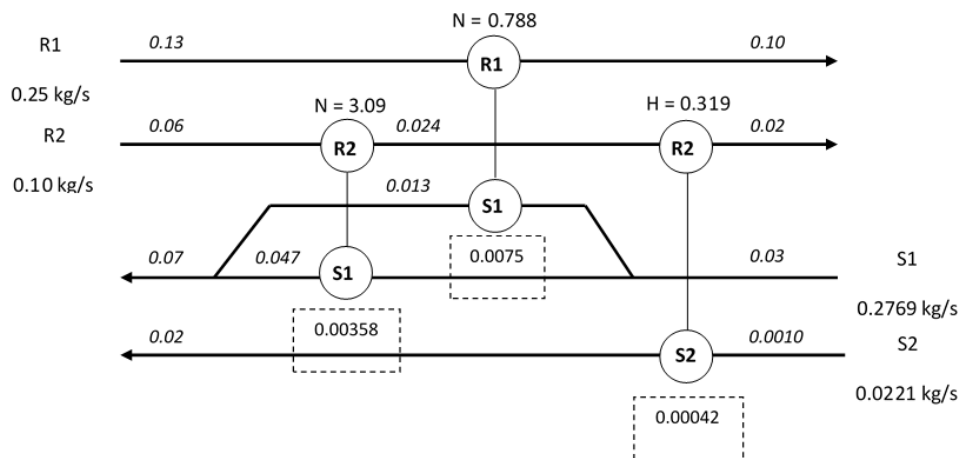


Figure 3. Optimal mass exchange network.

Table 1. Comparison of the results with a previous work.

	S1 (kg/s)	S2 (kg/s)	TAC (USD/y)
This work	0.2769	0.0221	50,855
Chen and Hung (2005)	0.276	0.023	52,300

The obtained solution has been compared with that reported by Chen and Hung (2005), this comparison is shown in Table 1. In terms of the use of solvent, the results for the base work are very similar to those obtained by the proposed alternative. Nevertheless, the total annual cost obtained through the method reported here is around 3% lower than that obtained by Chen and Hung (2005). Thus, the state-task-network based superstructure has allowed obtaining a similar solution to that previously reported for the same case study, with a lower total annual cost and making use of the possibility of split streams.

5. Conclusions

A state-task-network based superstructure has been proposed to solve the synthesis problem of a mass exchange network. This approach opens the possibility of split for a given stream to exchange mass with more than one stream. Moreover, the dimensioning of the columns is performed through semi-rigorous approaches, namely the Kremser equation and the high of transfer unit concept. This allows obtaining proper designs of the mass transfer equipment. The superstructure has been modelled through general disjunctive programming, and relaxed to a mixed-integer non-linear problem through the convex hull method. The proposed superstructure has been applied to a classic problem for the removal of copper in an etching facility. The relaxed problem has been solved using the software GAMS, with a proper selection of the initial values for the degrees of freedom, obtaining a solution similar to that reported in the literature. Moreover, the resulting network makes use of the split of one of the solvent streams to satisfy the requirement of one of the rich streams.

References

- C.C. Chen, P.S. Hung, 2005, Simultaneous synthesis of mass exchange networks for waste minimization, *Computers & Chemical Engineering*, 29, 7, 1561-1576.
- M.M. El-Halwagi, V. Manousiouthakis, 1989, Synthesis of mass exchange networks, *AIChE Journal*, 35, 8, 51-59.
- M.A. Gadalla, 2015, A new graphical-based approach for mass integration and exchange network design, *Chemical Engineering Science*, 127, 239-252.
- S. Ghazouani, A. Zoughaib, S. Le Bourdieu, 2017, An MILP model for simultaneous mass allocation and heat exchange networks design, *Chemical Engineering Science*, 158, 411-428.
- A.J. Isafiade, D.M. Fraser, 2008, Interval based MINLP superstructure synthesis of mass exchange networks, *Chemical Engineering Research and Design*, 86, 8, 909-924.

- A.J. Isafiade, M. Short, 2016, Synthesis of mass exchange networks for single and multiple periods of operations considering detailed cost functions and column performance, *Process Safety and Environmental Protection*, 103, Part B, 391-404.
- L. Liu, J. Du, M.M. El-Halwagi, J.M. Ponce-Ortega, P. Yao, 2013, Synthesis of multi-component mass exchange networks, *Chinese Journal of Chemical Engineering*, 21, 4, 376-381.
- K.P. Papalexandri, E.N. Pistikopoulos, C.A. Floudas, 1994, Mass exchange networks for waste minimization: a simultaneous approach, *Chemical Engineering Research and Design*, 72, 3, 279-294.

Optimization of Cryogenic Carbon Capture and LNG process by Mathematical programming

Orakotch Padungwatanaroj,^a Kitipat Siemanond^{a*}

^a *The Petroleum and Petrochemical College, Chulalongkorn University 254 Soi Chulalongkorn 12, Phayathai, Bangkok and 10330, Thailand*

*Kitipat.S@chula.ac.th

Abstract

Cryogenic processes are industrial processes of sub-ambient or low temperature, used for freezing or liquefaction of gas. The cryogenic condition is done by the refrigeration system with compressors and condensers consuming high operating costs of shaft work, and condenser duty, therefore mathematical programming; GAMS, is applied as a tool to optimize the energy efficiency of the refrigeration system. In this work, cryogenic carbon capture and LNG processes (Fazlollahi, 2015) was applied as a base case for improving energy efficiency by reducing shaft work and energy duty at compressors and condensers. The concept of energy-optimization model was from Non-Linear Programming model (NLP) (Colmenares and Seider, 1989). The base-case process was simulated by software Aspen plus V8.8. Representing economic change, scenarios of different operating costs were applied. Two energy-optimization models of simple and cascade refrigeration systems; under two scenarios of shaft-work cost dominance and condenser-duty cost dominance, were developed. Under shaft-work cost dominance, the simple-refrigeration model saved 72.68% and 56.12 % in shaft-work and condenser-duty costs, respectively, compared to the base case. Cascade-refrigeration model saved 48.53% and 64.77 % in shaft-work and condenser-duty costs, respectively. Under condenser-cost dominance, the simple refrigeration model saved 65.12 % and 57.73 % in shaft-work and condenser-duty costs, respectively. Cascade refrigeration model saved 8.12 % and 62.1 % in shaft-work and condenser-duty costs, respectively. As a result, cascade refrigeration model gave lower condenser-duty cost in both scenarios. However, the cascade refrigeration model had constraints to prevent negative temperature approach in condensers and constraints not to allow shaft work at compressors reach the lowest value. Simple refrigeration model gave a better design solution for only shaft-work reduction. However, cascade refrigeration model gave higher energy efficiency for both condenser-duty and shaft-work costs reductions.

Keywords: mathematical programming model, non-linear programming, cryogenic process, optimization.

1. Introduction

Low-temperature process is the process mainly dealing with refrigeration system. The problems of this process is high energy requirement from both shaft work and cold utility. Therefore, plant manager can save energy usage by several methods. Mathematical programming is an optimization method for improving the energy efficiency of refrigeration system. The energy optimization model by NLP (Colmenares and Seider, 1989) has its objective function of minimum shaft-work and cold-utility costs in

refrigeration system. The solution is the optimal cryogenic process design. In this research, cryogenic process and carbon capture process (Fazlollahi, 2015) were chosen as a base cases. Cryogenic carbon capture and liquefied natural gas (LNG) processes used integrated refrigeration systems. Natural gas is utilized as a refrigerant for process capturing carbon dioxide (CO_2) from flue gas of power plant. Heat exchanger network (HEN) in refrigeration system of the base case was simulated by ASPEN plus 8.8 program and optimized by GAMS software. Therefore, the objective of this research is to improve the process for saving shaft-work and cold-utility costs in the refrigeration system.

2. Simulation of Base-case Cryogenic Carbon Capture and LNG processes

Base-case cryogenic carbon capture and LNG processes have been simulated using commercial software Aspen plus V8.8. The fluid package of thermodynamics properties is Peng Robinson equation of state. The ambient conditions are assumed at 25°C (298.15 K) and 1 bar. Its process flow diagram is shown in Figure 1. According to simulation, it consumes 3,121.41 kW of shaft work and cold utility or 32,662.65 \$/hr. The energy load is high at loop 4; the biggest loop of refrigeration system. Therefore, loop 4 is focused for improvement.

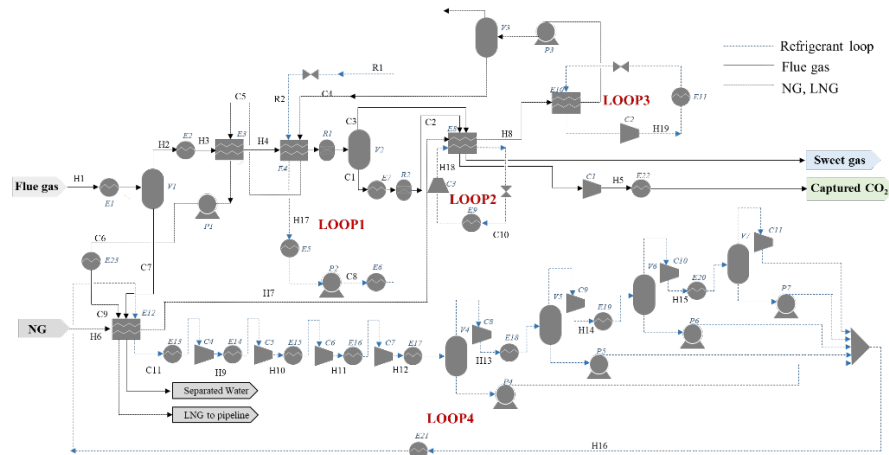


Figure.1 Process flow diagram of cryogenic carbon capture and LNG processes

3. Model and Equations

There are two models of refrigeration loop design in this research; simple and cascade refrigeration model. Both of model was non-linear programming model (NLP) set to minimize shaft-work and cold-utility costs under equality and inequality constraints. To formulate NLP model, these following definitions and equations must be defined.

i { i i is hot process stream }	TRI_k Inlet evaporator temperature refrigerant k
k { k k is cold process stream }	TRO_k Outlet evaporator temperature refrigerant k
W_k Shaft work of compressor	TRCO_k Inlet condenser temperature refrigerant k
J Interval	TRCDO_k Outlet condenser temperature refrigerant k
n Number of Interval	h_{BC_k} Enthalpy of refrigerant before compressor
$S_{i,k,J}$ Heat exchanged in stream	h_{AC_k} Enthalpy of refrigerant after compressor
$R_{i,J}$ Heat load in each interval J	PRI_k Refrigerant pressure entering to compressor

$D_{i,j}$ Heat of hot stream flowing between intervals	PRO_k Refrigerant pressure leaving from compressor
Q_k^c Heat condenser of refrigerant k	PR_k Compression ratio of compressor
Q_k^e Heat evaporator of refrigerant k	Le_k Latent heat of refrigerant at evaporator
CpR_k Heat capacity flow rate of refrigerant k	Lc_k Latent heat of refrigerant at condenser
FR_k Flow rate of refrigerant k	C_w Cost of work
	C_c Cost of condenser duty

The main objective function is Eq. (1)

$$\text{Minimize (WCT)} = \sum_{k=1}^n C_w W_k + \sum_{k=1}^n C_c Q_k^c \quad (1)$$

Calculation of condenser duty is

$$Q_k^c = FR_k(CpR_k(TRCDO_k - TRCO_k) + Lc_k) \quad (2)$$

and evaporator duty for simple refrigeration model is

$$Q_k^e = FR_k(CpR_k(TRI_k - TRO_k) + Le_k) \quad (3)$$

For cascade refrigeration model, evaporator equation is added with logical function which are divided into 4 stages of refrigeration.

$$\text{Stage 1: } Q_{ref1'}^e = -S('H_1', 'ref1', 'J_0') \quad (4)$$

Stage

$$2: Q_{ref2'}^e =$$

$$-S('H_1', 'ref2', 'J_1') +$$

$$\left[\text{bool_or} \left[\text{floor} \left(\frac{Q_{ref3'}^c + 1}{10} \right), \text{floor} \left(\frac{S('H_1', 'ref2', 'J_1') + 1}{10} \right) \right] \times Q_{ref3'}^c \right] +$$

$$\left[\text{bool_and} \left[\text{bool_not} \left(\text{floor} \left(\frac{Q_{ref3'}^c + 1}{10} \right), \text{floor} \left(\frac{Q_{ref2'}^c + 1}{10} \right) \right) \times Q_{ref4'}^c \right] \right] \quad (5)$$

Stage3:

$$Q_{ref3'}^e =$$

$$-S('H_1', 'ref3', 'J_2') + \left[\text{bool_or} \left(\text{floor} \left(\frac{10}{Q_{ref4'}^c + 10} \right), \text{floor} \left(\frac{Q_{ref3}^c + 1}{10} \right) \right) \times Q_{ref4'}^c \right]$$

$$\text{Stage 4: } Q_{ref4'}^e = -S('H_1', 'ref4', 'J_0'); \quad (6)$$

For outlet refrigerant temperature of evaporator and compressor, Eq (7) and (8) are applied.

$$\left(\frac{Q_k^e}{FR_k CpR_k} \right) + TRI_k = TRO_k \quad (7)$$

$$TRCO(k) = TRO(k) \left(1 + \frac{PRO_k^{k-1}}{PRI} - 1 \right) \quad \text{which } k = Cp/C_v \quad (8)$$

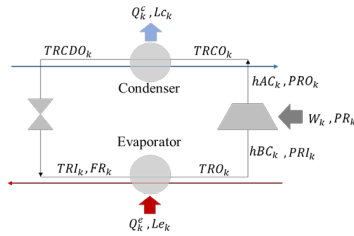
and η is an isentropic efficiency = 0.9

From energy balance of hot and cold stream I in interval J, Eq. (9) and (10) are represented, respectively.

$$D(I, J_n) - D(I, J_{n-1}) + \text{SUM}(K, S(I, K, J_n)) = R(I, J_n) \quad (9)$$

$$\text{SUM}(I, S(I, K, J_n)) = P(K, J_n) \quad (10)$$

Properties equations in this model which are enthalpy, latent heat and bubble point equation come from data simulation in aspen Hysys V.8.8. Moreover, logical function (Bool_not(x)) must be applied to the GAMS model in a part of outlet enthalpy calculation due to varied compression ratio. Constraints of positive-temperature-approach is for heat exchanger design and controlling temperature of hot and cold streams which are added to both models.



Shaft work (\$/kWh)	Cold utility1 (\$/kWh)	Cold utility 2 (\$/kWh)
0.08	1.8051	2.7341

Figure 2 Simple-refrigeration model

Table 1 Cost of shaft work and cold utilities

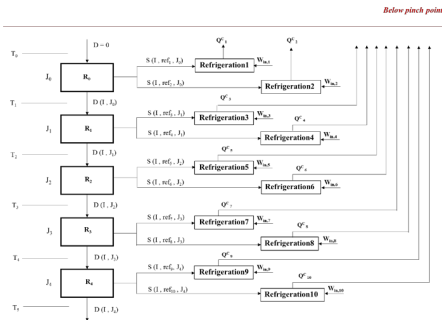


Figure 3 Simple refrigeration model

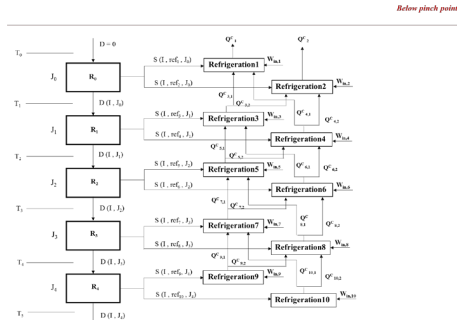


Figure 4 Cascade refrigeration model

4. Results and discussion

According to simulation result, the modification of refrigeration occurs at unit E12 due to the highest shaft work loaded. So E-12 unit which is one-stage refrigeration was improved. Model was achieved under these assumptions: (1) Constant heat capacity flow rate (2) EMAT(Exchanger minimum approach temperature) lower than 10 °C (3) Refrigerant pressure inlet of evaporator = 1 bar and vapor fraction = 0.1 (4) Layout and pressure drop costs are neglected. Variables in this program are $S_{I,K,J}$, $D_{I,J}$, FR_K , TRO_K and PR_K . These variables are varied until the lowest cost of shaft work and cost of utility are achieved. The optimal solutions are represented in two scenarios which are more significant on cold utility cost (scenario1) and more significant on shaft work (scenario2). Cost of shaft work was assumed as an electricity cost of Thailand. For cold utility, there are only 2 types which are listed in Table1. The optimal solutions from GAMS are validated by Aspen plus simulation before analyses the result.

4.1. Simple-refrigeration model

In scenario 1, cost of cold utility is higher than cost of shaft work. An optimal refrigeration system at scenario 1, as shown in Figure. 5a, is two-stage refrigeration which reduces cold

utility cost 57.73 % and shaft work 65.12 % comparing to the base case (3,121.41 kW of total shaft work and 32,662.65 \$/hr cost of cold utility), as shown in Table 2. The model selected process with high loaded compressors to design two-stage refrigeration. In scenario 2, cost of shaft work is higher than cost of cold utility about 5 times. Therefore, four-stage refrigeration was applied to design the optimal refrigeration system, as shown in Figure. 5b. The more stage of refrigeration system, the more shaft work reduction. The energy saving results of refrigeration system at scenario 2 are shown in Table 2.

Table 2 Simple refrigeration model results

Scenario 1		Scenario 2	
% Shaft work reduction	% Cost of cold utility reduction	% Shaft work reduction	% Cost of cold utility reduction
65.12	57.73	72.68	56.12

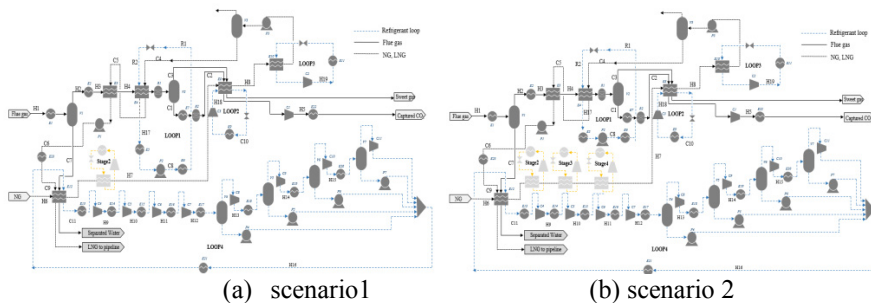


Figure. 5 Improved refrigeration systems using simple refrigeration model

However, simple refrigeration model still shows high amount of cold utility cost. Then, cascade refrigeration model was applied to improve process by optimizing both of condenser and shaft work, simultaneously.

4.2. Cascade-refrigeration model

Cascade-refrigeration model is another kind of refrigeration system used in this work. Heat from condenser at lower stage (n) is sent to a higher stage (n-1) in order to reduce condenser duty at very low temperature which consumes higher cost. All of definitions and equations are the same as simple-refrigeration model except equation of heat of evaporator listed in Eq. (4)-(6). Scenario 1 has cold-utility-cost dominance. The condenser in process was improved by changing temperature level of cold utility to higher one which consumes the lower price of utility. The result shows that cascade-refrigeration model can eliminate condenser operated at very low temperature by using higher-temperature-stage condenser. The improved refrigeration system is three-cascade-refrigeration system applied to the base case. However, shaft work of this case is saved only 8.2 % as shown in Table 3, due to small cost of shaft work in objective function. For scenario 2 which is shaft-work-cost dominance, this model is to minimize shaft work, significantly. By using cascade-refrigeration model, cold utility is reduced 64.77 %, as shown in Table 3, which is lower than one from simple-refrigeration system at scenario 2. Moreover, shaft work is decreased around 48.53 % higher than one from simple-refrigeration model. This model has more constraint equations of temperature controller. Therefore, the compression ratio was limited by positive temperature approach constraint (hot stream temperature must be higher than cold stream at least EMAT of 10 °C)

Table 3 Cascade refrigeration model results

Scenario 1		Scenario 2	
% Shaft work reduction	% Cost of cold utility reduction	% Shaft work reduction	% Cost of cold utility reduction
8.2	62.10	48.53	64.77

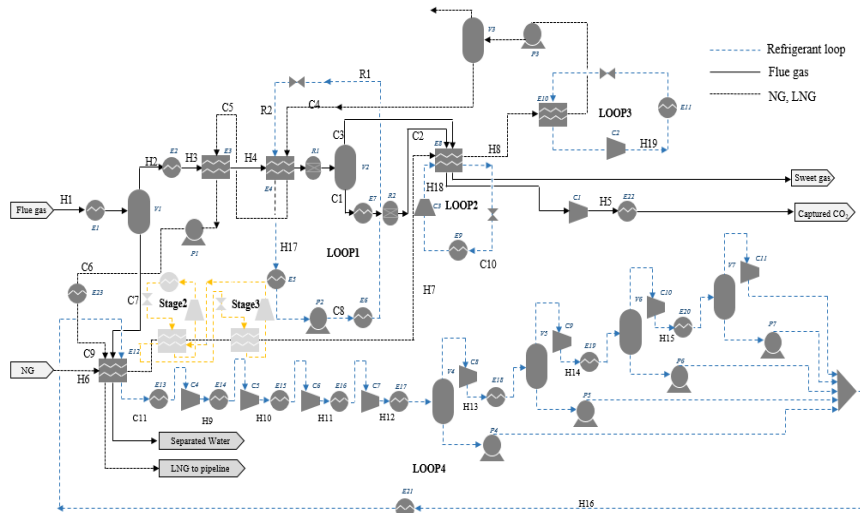


Figure. 6 Improved refrigeration system by cascade-refrigeration model at scenario 1 & 2

According to the result, cold-side condenser temperature at scenario 1 is increased from -67.21 to 35.73 °C having lower cold-utility cost than one at scenario 2 increased from -88.94 to 29.95 °C having higher cold-utility cost at scenario 2. Table 3 shows higher cold-utility-cost reduction at scenario 2 than one at scenario 1.

5. Conclusions

Mathematical programming method shows a potential improvement for the base-case process on energy efficiency. The best improved case for cryogenic carbon capture and liquefied natural gas (LNG) processes depends on requirement of process. For the lowest shaft-work consumption, simple-refrigeration model under both scenarios gives the best refrigeration system design. For the lowest condenser-duty cost, cascade-refrigeration model gives the best alternative design.

Acknowledgements

Authors would like to express our gratitude to Government budget for funding support.

References

- F. Fazlollahi, A. Bown, E. Ebrahimzadeh, L.L. Baxter, 2015, Design and analysis of the natural gas liquefaction optimization process- CCC-ES (energy storage of cryogenic carbon capture), *Energy*, 90, 244-257
- T.R. Colmenares, W.D. Seider, 1989, Synthesis of cascade refrigeration systems integrated with chemical processes, *Computers chem. Eng.*, 13, 247-258

A methodology of a hybrid hydrogen supply network (HHSN) under alternative energy resources (AERs) of hydrogen footprint constraint for sustainable energy production (SEP)

Soonho Hwangbo,^a ChangKyoo Yoo^{a,*}

*^aDepartment of Environmental Science and Engineering, Kyung Hee University, 1732 Deogyong-daero Giheung-gu, Yongin-si Gyeonggi-do, 17104, the Republic of Korea
ckyoo@khu.ac.kr*

Abstract

We aim to suggest a methodology of a smart hybrid hydrogen supply network based on diverse alternative energy resources of hydrogen footprint constraint. To date, hydrogen production has been mostly dependent on fossil fuels. However, future hydrogen would be harnessed contingent on eco-friendly energy resources to support environmentally benign hydrogen economy. In this study, a smart hybrid hydrogen supply network is designed considering hydrogen production from solar energy, wind energy and wastewater and hydrogen distribution by using reinforcement learning. A mathematical model is divided into two phases. First phase is a stochastic programming under demand uncertainty, where multi objective functions are to minimize the total annual costs and environmental costs, respectively. Second phase is a heuristic optimization problem based on Q-learning which is one of the reinforcement learning algorithms. The suggested model is applied to Gyeongsang province in the Republic of Korea as a case study. Alternative energy resources are selected considering regional characteristics. We verify possibilities for construction of a smart future hydrogen supply network based on various feasible scenarios, where can propose the best hydrogen network to decision-makers.

Keywords: Smart hybrid hydrogen supply chain network, renewable energy resource, stochastic programming, reinforcement learning.

1. Introduction

Hydrogen production in industries has continuously increased and the role of hydrogen as a promising energy carrier has explicitly been highlighted. Research on hydrogen production, storage and distribution have been broadly studied and changes from fossil fuels to hydrogen energy based on hydrogen economy concept have been suggested (Marbán and Valdés-Solis 2007). To date, hydrogen production processes have mostly been dependent on fossil fuels such as natural gas and great amounts of hydrogen have been generally harnessed by steam methane reforming. Recently, eco-friendly hydrogen production methods using renewable resources have been studied and commercialized (Figure 1) (Nikolaidis and Poullikkas 2017). Even though hydrogen production from renewable resources has several drawbacks a financial point of view comparing to existing hydrogen production processes, hydrogen price is expected to converse toward a suitable price range through the technical advance and political support such as a subsidy. One of the biggest advantages of hydrogen is that hydrogen is able to be stored

as a fuel cell and converted into electricity. Therefore, the way to hydrogen storage would be one of the crucial components to construct a hydrogen economy. Lastly, proper distribution of hydrogen between various sink companies and source companies has to be designed. The idea of supply chain network has been applied to hydrogen transfer (Hwangbo, Lee et al. 2017). In spite of the evaluation of case studies, geometric barriers between a sink company and a source company has not been taken into account because, in the case of the consideration of those barriers, a number of variables and nonlinear equations would be generated and also it is almost impractical that all constraints are formulated within one mathematical model.

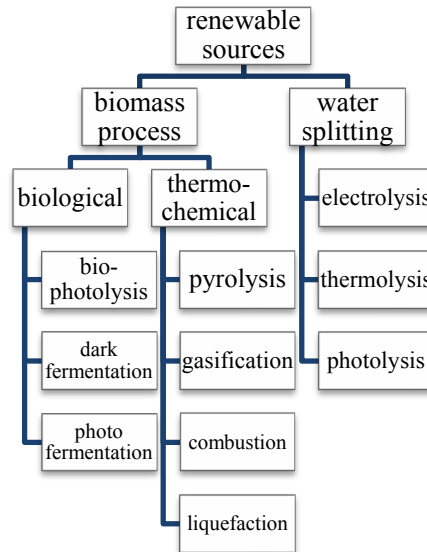


Figure 1. Hydrogen production methods utilizing renewable resources.

Therefore, this study proposes a methodology of the construction of a smart future hydrogen supply network dividing hydrogen production, storage and distribution into two phases. Hydrogen production and storage using alternative energy resources are conducted based on a stochastic programming under hydrogen demand uncertainty and smart distribution of hydrogen is performed by reinforcement learning. A case study of Gyeongsang province in the Republic of Korea was applied to the proposed methodology and the possibilities of this study were confirmed according to the results

2. Problem statement

The expected amounts of future hydrogen demands are illustrated showing different values depending on into various reports or papers. However, the common ground is that hydrogen demand will increase and the range of hydrogen utilization will be extended. Moreover, hydrogen world will go away from hydrogen production from fossil fuels, toward hydrogen production from renewable resources which hardly emit carbon emissions. Storage systems in this study are assumed to operate existing storage systems because the qualities of hydrogen from fossil fuels and renewable resources are usually identical.

2.1. Algorithm

Figure 2 depicts an algorithm of the proposed model. Firstly, hydrogen demands by region are calculated and a two-stage stochastic programming model considering hydrogen demand uncertainty is constructed. The type of objective function is able to be selected depending on a situation. Costs can be optimized by using a simple single objective function and environmental costs or risk as well as costs are able to be minimize by multi objective functions. In the case of multi objective optimization, ϵ -constraint method as a typical algorithm to solve multi objective problems is generally employed. Pareto analysis is performed based on Pareto sets of the above procedure and feasible scenarios are created. Regions for hydrogen production from renewable resources and a quantity of produced hydrogen are determined and capital and operating costs of needed facilities or processes are decided. In Phase B, smart distribution for hydrogen transfer is designed contingent on the results from Phase A. As aforementioned, the development of global environmental model considering all components in detail is normally impossible because there exist diverse sink and source companies in different regions and many barriers are located in between. Therefore, reinforcement learning is selected to find an optimal route without knowing an environmental model. This study uses Q-learning among several algorithms in reinforcement learning because four results from a value function at regions where are divided by a grid can be illustrated by Q-table. The optimal pathway from a source company to a sink company is suggested by following the maximum value among the results. Finally, a smart hydrogen supply network is developed by phases A and B.

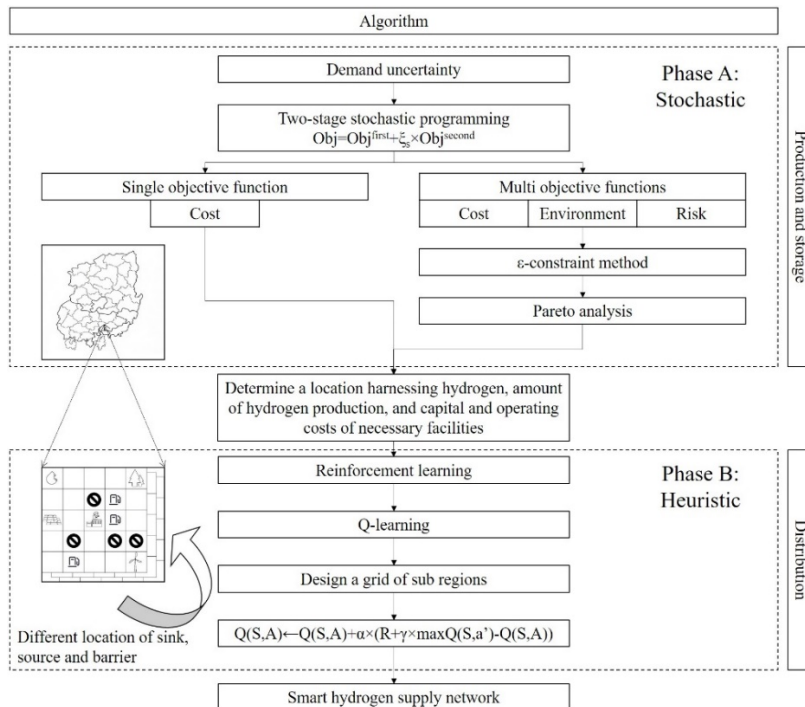


Figure 2. An algorithm of two-phase optimization problem for construction of smart hydrogen supply network.

3. Mathematical model

A stochastic programming used in phase A is a mixed-integer linear programming and multi objective functions concerning costs and environmental costs are formulated (Eq. (1)). Phase B is constructed by environment and agent. Sink, source and barrier in each region are encompassed in environment and agent performs the state and action forward the direction having the biggest reward value which is obtained by Q-learning. The reward value of a source company is assigned as a positive value on the other hand the reward value of barriers where are allocated in many places is designated as a negative value. The total 1,000 episodes are generated. Agent initially acts random exploration, as time goes by, agent finds an optimal route to a source company because Q-function is updated when an episode ends up (Eq. (2)).

Phase A :

$$\min Total_Cost = Cost^{First} + \sum_s \{ \zeta_s \times Cost_s^{Second} \} \quad \forall s \quad (1)$$

$$\min Downside_Risk = \sum_s \{ \zeta_s \times Index_s \} \quad \forall s$$

Phase B :

$$Q(S_t, A_t) \leftarrow Q(S_t, A_t) + \alpha \times \left\{ R_{t+1} + \gamma \times \max_{a'} Q(S_{t+1}, a') - Q(S_t, A_t) \right\} \quad (2)$$

The first stage total cost of the total costs in phase A $Cost^{First}$ is the term which is not affected by demand uncertainty and generally includes facility capital costs. The second stage total cost of the total costs in phase A $Cost_s^{Second}$ is the term which is directly affected by demand uncertainty and normally contains facility operating costs. The probability considering demand uncertainty ζ_s has in general the value that 1 is divided by the number of scenarios. Q-function $Q(S_t, A_t)$ is consistently updated according to the nearest state and action. Learning rate α is constant and assists that Q-function is converged. Reward R_{t+1} is able to be constant or formulated as a function. This study takes into account that a barrier has a negative value and a source company has a positive value. Discount factor γ presents the difference between Q-function values from the initial state to the final state based on the number of steps.

4. Results and discussion

A case study of Gyeongsang province of the Republic of Korea is simply applied to the proposed method. According to regional characteristics of Korea, renewable energy production using wind power and solar power are mainly conducted and a future renewable energy roadmap is expected to focus on those energy systems. Regions for large-scale wind and solar power systems where have been already installed or are anticipated to be built in the future are allocated in four and five places, respectively. And, industry complexes including a huge petrochemical industry are located in four regions. All regions underpin wastewater treatment plants where are able to produce

biogas. This study assumes that wind power and solar power are necessarily integrated into a smart hydrogen supply network. Results from multi objective problems in phase A by using a moderate epsilon value show that 13 regions among the total 42 regions construct and operate waste biogas production processes in order to harness hydrogen (Figure 3). The developed hydrogen supply network in this study covers above the half of the total hydrogen demand which were fulfilled by hydrogen production from fossil fuels. The total costs increase 19% otherwise the amounts of carbon emissions decrease 26% compared to the base case. A smart distribution by reinforcement learning for hydrogen transfer results from phase B. In the case of the previous hydrogen transfer model, a number of variables and nonlinear equations were created because a mathematical model was formulated by applying Euclidean distance calculation between a sink company and a source company, and it would result in infeasible solutions and the consideration of a barrier was rarely conducted (Figure 4(a)). However, in the case of Q-learning which does not request a mathematical model for the environment, an optimal route avoiding barriers is suggested.

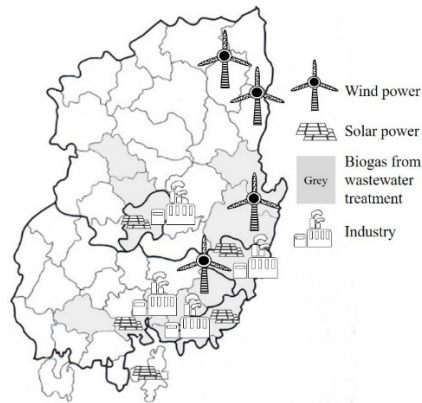


Figure 3. A case study of Gyeongsang province in the Republic of Korea.

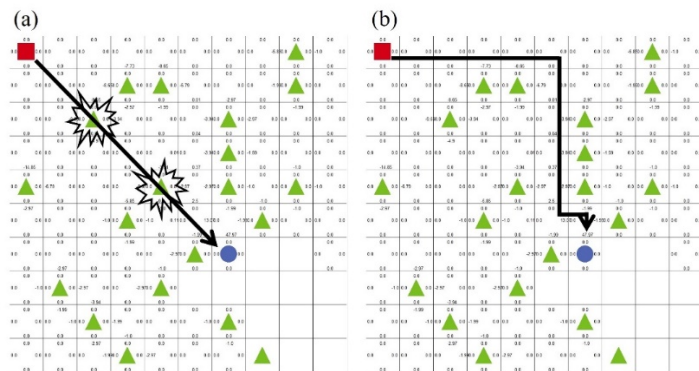


Figure 4. A result example from Q-learning; (a) existing pathway using Euclidean distance; (b) modified pathway using reinforcement learning; rectangle: source, circle: sink and triangle: barrier.

5. Conclusions

This study suggested a novel methodology for the development of a smart future hydrogen supply network. The proposed model was divided into two phases in order to separate hydrogen production/storage and distribution. We verified the reasonable smart distribution of hydrogen without the design of a specific mathematical model by employing reinforcement learning. We believe that the results from this study can propose the feasibilities of the efficient construction of a hydrogen economy or a hydrogen infrastructure.

Acknowledgement

This work was supported by the National Research Foundation of Korea (NRF) grant funded by the Korea government (MSIP) (No. 2017R1E1A1A03070713).

References

- Hwangbo, S., S. Lee and C. Yoo (2017). "Optimal network design of hydrogen production by integrated utility and biogas supply networks." *Applied Energy* 208: 195-209.
- Marbán, G. and T. Valdés-Solis (2007). "Towards the hydrogen economy?" *International Journal of Hydrogen Energy* 32(12): 1625-1637.
- Nikolaïdis, P. and A. Poullikkas (2017). "A comparative overview of hydrogen production processes." *Renewable and sustainable energy reviews* 67: 597-611.

Kinetic Modeling of Plastic Waste Pyrolysis in a Laboratory Scale Two-stage Reactor

Zoltán Till,^{a,*} Tamás Varga,^a János Sója,^b Norbert Miskolczi,^b Tibor Chován^a

^a*University of Pannonia, Department of Process Engineering, 10, Egyetem Street, H-8200 Veszprém, Hungary*

^b*University of Pannonia, MOL Department of Hydrocarbon and Coal Processing, 10, Egyetem Street, H-8200 Veszprém, Hungary*

tillz@fmt.uni-pannon.hu

Abstract

Pyrolysis of waste polymers looks attractive way for their transforming into valuable hydrocarbons. Due to the high number of reactions, the detailed kinetic modeling of the pyrolysis process is often not feasible. Hence the so-called lumping technique is often used to study these complex systems. In this study, the pyrolysis reactions were modeled in a two stage laboratory scale batch reactor using five component lumps. For pyrolysis the mixtures of real plastic waste were used. Kinetic parameters were identified and the model results were compared to the experimental results. It was found that the suggested model can properly describe the dynamic behavior of the reactor under semi batch conditions.

Keywords: discrete lumping, energy from waste, fuel production, kinetic identification, recycling

1. Introduction

Pyrolysis has growing interest in terms of waste recycling. Both biomass (Kim-orba et al., 2015) and petroleum based polymer waste can be transformed into valuable feedstocks for petrochemical sector and refinery. Pyrolysis is a versatile process with a wide product range that can be easily varied with reaction temperature and residence time (Onwudili et al., 2009).

Kinetic modeling of pyrolysis can be challenging due to the various composition of feedstocks and the high complexity of decomposition reactions. The complex network approach is a more sophisticated method to analyze the pyrolysis process. Given that sufficient a priori information is available, the detailed reaction network can be generated automatically; nevertheless the kinetic parameter identification requires some simplification in the model (e.g. the assumption that similar reactions have similar rate coefficients) (Zang et al., 2015). The incremental model identification (IMI) approach can also be applied when the model has a high number of parameters to be identified in case of that the main problem is decomposed into a sequence of subtasks easier to handle individually; for example determine the extent of each reaction in a tubular reactor first then identify the relevant kinetic parameters in each section (Bhatt and Visvanathan, 2015). However, to use this method, concentrations of all components need to be measured along reactor length.

Discrete lumping is a straightforward yet powerful method to analyze complex processes and identify reliable kinetic parameters for a specific process. There are

numbers of previous studies (e.g. Ding et al., 2012, Artetxe et al., 2014) dealing with discrete lumping methods, yet the majority of these solutions deal with batch reactors that are extensively used extensively in laboratory scale. Therefore the potential application of discrete lumping for semi batch processes has been investigated. The aim of our study is to identify the kinetic parameters of a lumped reaction network suitable for the thermal pyrolysis of real plastic waste.

2. Experimental setup

Plastic waste pyrolysis was carried out in a laboratory scale two-stage reactor at atmospheric pressure. 50 g of shredded and crashed real plastic waste was charged into the 1st reactor. To ensure inert atmosphere nitrogen was used. Temperature was maintained at 425/455/485 °C in the 1st reactor and at 395 °C in the 2nd reactor. The mixture of decomposed hydrocarbons obtained from 2nd reactor was driven through a water cooled tube-in-tube heat exchanger, where condensable was transformed into liquid phase. During the pyrolysis, samples of liquid products were collected at given intervals, and then were analyzed by gas chromatography. The volume of gaseous products was measured using a gas flow meter.

3. Reactor model

For kinetic studies, a reaction network was proposed consisting five lumps and nine first-order reactions (Figure 1). The model was developed using a discrete lumping approach. Plastic waste feedstock (P) decomposes into lighter pseudocomponents, namely heavier liquid (L+), lighter liquid (L-) and pyrolysis gas (G). These lumps were characterised based on the average carbon number of the compounds forming them (L+: 15-30, L-: 6-15, G: 0-6). The coke is formed during the decomposition of the feedstock and the L+/L- lumps as well. At the high temperature of the first reactor, P and C are considered to be quasi solid (immobile) and the other pseudocomponents as gaseous (mobile). The mass transfer between the two phases were regarded as instantaneous, in other words, L+, L- and G are only present in gas phase while P and C form the solid phase. Nitrogen from reactor flush was considered as a standalone component aside from pyrolysis gas.

The rate of the i^{th} reaction in the j^{th} reactor is described as a function of the mass concentration of the reactant (with the weight of the specific pseudocomponent divided by the volume of the appropriate phase) (Eq (1)). Reaction rate coefficients were assumed to have Arrhenius-type temperature dependencies (Eq (2)).

$$r_i^j = k_i(T^j) \cdot \frac{m_r^j}{V_p^j} \quad (1)$$

$$k_i = k_{0,i} \cdot \exp\left(-\frac{E_{a,i}}{R \cdot T^j}\right) \quad (2)$$

Component sources were calculated from reaction rates and the stoichiometric matrix of the reaction network (Eq (3)). In order to maintain the mass balance, reaction rates were multiplied by the volume of the phase in that the reaction takes place (Eq (4)).

$$\underline{R}^j = \underline{\nu} \cdot \underline{r}^{j'} \quad (3)$$

$$r_i^j = V_p^j \cdot r_i^j \quad (4)$$

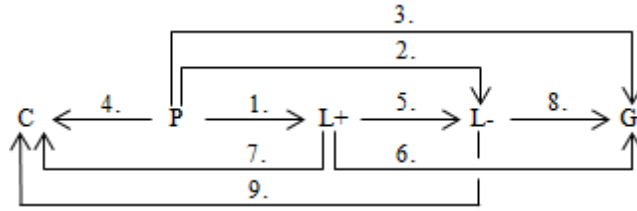


Figure 1. Suggested reaction network consisting five component lumps and nine lumped reactions.

Both reactors were considered to be ideally mixed given the small volumes and low residence time. The change in mass of component c is the result of the difference between the inflow and outflow rates as well as its source from Eq (3):

$$\frac{dm_c^j}{dt} = m_c^{j,in} - m_c^{j,out} + R_c^j \quad (5)$$

For components P and C, flow rate calculation can be omitted because of immobility. In case of the 1st reactor, gaseous component inflow rates are equal to zero except for the nitrogen flush while the inlet of the 2nd reactor is equal to the outlet of the 1st vessel. Reactor outflow (Eq (6)) is a result of three independent phenomena:

- components are formed or depleted in the reactor;
- component mass is increased because of inflow;
- gas phase volume increases with the decrease of the solid phase.

$$m_{c,g}^{j,out} = \left(\sum_k \frac{R_k^j}{M_k} + \sum_k \frac{m_k^{j,in}}{M_k} + \frac{dn_g^j}{dt} \right) \cdot x_{c,g}^j \cdot \bar{M}_c \quad (6)$$

Assuming that the behavior of gaseous phase follows the ideal gas law, at constant pressure and temperature the molar mass of substance changes with the gas phase volume as described in Eq (7):

$$\frac{dn_g^j}{dt} = -\frac{p}{R \cdot T^j} \cdot \left[\frac{d}{dt} \left(\frac{m_p}{\rho_p} \right) + \frac{d}{dt} \left(\frac{m_c}{\rho_c} \right) \right] \quad (7)$$

The aim of our study is to determine the reaction kinetic parameters defined in Eq (2) to model and predict thermal degradation of polymer waste. The objective is to minimize the difference between measured and calculated weight fractions (Eq (8)), in that square error between measurement (m) and calculation (c) is summarized for three temperature (T) levels, five pseudocomponents ($comp$) and all measurement points (p) (one for P, C and G; four to six for L+ and L-):

$$f(x^n) = \sum_T \sum_{comp} \sum_p (w_m - w_c)^2 \quad (8)$$

Decision variables in Eq (8) are expressed in Eq (9-10) and include the pre-exponential factors and activation energies for each reaction, normalized between 0 and 1 for better convergence. Values of lower and upper bounds summarized in Table 2 were chosen as

a result of a set of preliminary studies regarding the values of rate coefficients at individual temperature levels.

$$\mathbf{x}^n = \left[\left(k_0^n \right)^T \quad \left(E_a^n \right)^T \right]^T \quad (9)$$

$$\mathbf{x}^{act} = \mathbf{x}^n \cdot (\mathbf{u}_b - L_b) + L_b \quad (10)$$

The dynamic model of the laboratory scale two-stage pyrolysis reactor was implemented and solved in MATLAB R2011b. The reactor model was solved using the variable-step, variable-order (VSVO) solver based on the numerical differentiation formulas called ode15s (Shampine and Reichelt, 1997). For solving the optimization problem, the NOMAD software package was used that implements the Mesh Adaptive Direct Search (MADS) algorithm and is a well suited solver for derivative-free optimization (Le Digabel, 2011). It also has a MATLAB interface available that can be called directly from the OPTI Toolbox (Currie and Wilson, 2012).

4. Results and discussion

Measured and calculated mass fractions are shown in Figure 2 as a function of time. In case of liquid and gas products (L+, L- and G) the mass fraction was calculated as a quotient of the amount that has left the 2nd reactor and the initial charge; while in case of P and C, the amounts inside the two reactors were taken into consideration. The resulting curves appear to indicate that the suggested reaction network can properly describe the concentration changes taking place during polymer waste pyrolysis. Curve fitting for both liquid fractions are mostly the same and is acceptable within reason. The model predicts the final mass of G and C accurately, while predicted remaining P amount is fairly high.

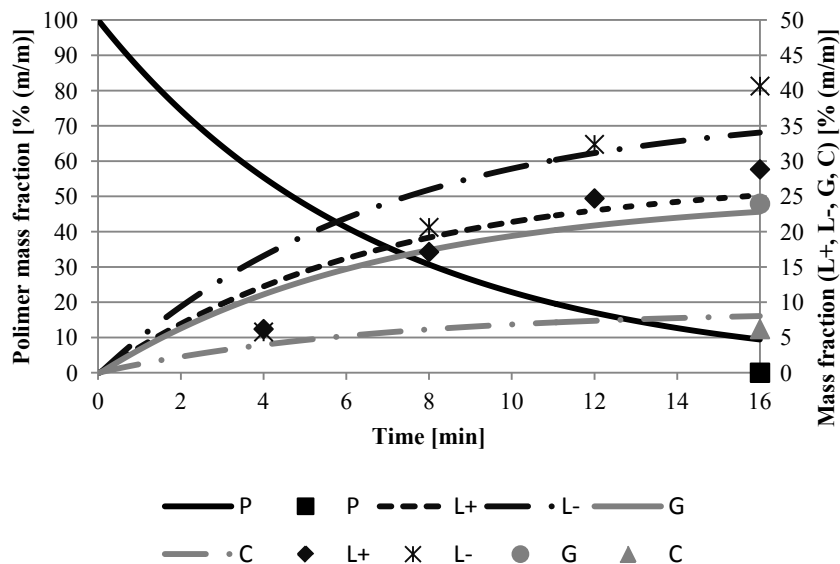


Figure 2. Pseudocomponent mass fractions at 455 °C – experimental (markers) and model (lines)

Table 1. Root-mean-square error (RMSE) between measured and calculated data

	P	L+	L-	G	C	Lump aggregated
425 °C	7.0 %	1.9 %	2.6 %	2.8 %	0.9 %	2.8 %
455 °C	9.4 %	3.8 %	6.9 %	1.1 %	1.9 %	5.6 %
485 °C	5.3 %	3.2 %	3.8 %	1.3 %	0.2 %	3.4 %
Temperature aggregated	7.4 %	2.9 %	4.5 %	1.9 %	1.2 %	4.0 %

To express the reliability of the identified kinetic parameters quantitatively, the root of mean square errors between measured data and model results for each lump and the complete data set were calculated and are listed in Table 1. Overall, the lowest values were obtained for 425 °C reactor temperature. The identified model gives reasonable estimation for G and C; on the other hand, it tends to overestimate the remaining amount of P at the end of the run. Estimated values of L+ and L- are in reasonable agreement with the measured data; however, as shown in Figure 2, the actual formation of these components is slightly slower at the beginning than predicted.

The identified kinetic parameters for the suggested reaction network as well as the values of reaction rate coefficients at 455 °C are listed in Table 2. It is visible that the rate coefficients for the first four reactions are significantly higher than for the latter five; this could indicate that the formation of products during polymer waste pyrolysis happens simultaneously rather than following a consecutive pattern. This is also supported by reaction networks suggested previously in literature (Ceamanos et al., 2002, Al-Salem and Lettieri, 2010).

Table 2. Lower and upper bounds, identified kinetic parameters and reaction rate coefficients for the specified reactions

Reaction	k_0 [s^{-1}]			E_a [$kJ\ mol^{-1}$]			k at 455 °C [s^{-1}]
	l_b	l_b	actual	l_b	u_b	actual	
P → L+	$1.00 \cdot 10^{16}$	$1.00 \cdot 10^{16}$	$1.23 \cdot 10^{16}$	10.0	500	268.37	$6.87 \cdot 10^{-4}$
P → L-	$1.00 \cdot 10^{19}$	$1.00 \cdot 10^{19}$	$7.62 \cdot 10^{19}$	10.0	500	319.40	$9.31 \cdot 10^{-4}$
P → G	$1.44 \cdot 10^2$	$1.44 \cdot 10^2$	$9.94 \cdot 10^2$	10.0	500	86.46	$6.24 \cdot 10^{-4}$
P → C	$1.20 \cdot 10^{12}$	$1.20 \cdot 10^{12}$	$1.07 \cdot 10^{13}$	10.0	500	232.67	$2.18 \cdot 10^{-4}$
L+ → L-	$1.44 \cdot 10^{-2}$	$1.44 \cdot 10^{-2}$	$1.24 \cdot 10^{-1}$	17.3	864	229.71	$4.10 \cdot 10^{-18}$
L+ → G	$1.66 \cdot 10^{-1}$	$1.66 \cdot 10^{-1}$	1.18	14.4	720	386.17	$2.34 \cdot 10^{-28}$
L+ → C	$7.68 \cdot 10^{-4}$	$7.68 \cdot 10^{-4}$	$1.37 \cdot 10^{-3}$	14.4	720	215.74	$4.57 \cdot 10^{-19}$
L- → G	$6.40 \cdot 10^{-1}$	$6.40 \cdot 10^{-1}$	3.94	14.4	720	208.21	$4.56 \cdot 10^{-15}$
L- → C	1.15	1.15	6.95	17.3	864	393.89	$3.85 \cdot 10^{-28}$

5. Conclusions and future work

In this work, kinetic parameters of a lumped reaction system consisting five pseudocomponents and nine reactions were identified from experimental data obtained

in a laboratory scale two-stage semi batch reactor. In general, the proposed model can effectively describe the concentration changes in the system, while also fast and slow reaction routes can be distinguished; this fact might give room for further model reduction. Future work may consider the non-isothermal behaviour of the reactor, i.e. taking the heat-up period of measurements into consideration. The proposed method can be applied for catalytic pyrolysis as well, for instance the effect of different catalysts on individual reactions can be investigated.

Acknowledgements

We acknowledge the financial support of Széchenyi 2020 under the GINOP-2.3.2-15-2016-00053. János Sója and Norbert Miskolczi acknowledge for the financial support of Széchenyi 2020 under the EFOP-3.6.1-16-2016-00015.

References

- S. M. Al-Salem and P. Lettieri, 2010. Kinetic study of high density polyethylene (HDPE) pyrolysis, *Chemical Engineering Research and Design*, 88 (12), 1599–1606.
- M. Artetxe, G. Lopez, M. Amutio, J. Bilbao, M. Olazar, 2014. Kinetic modelling of the cracking of HDPE pyrolysis volatiles on a HZSM-5 zeolite based catalyst, *Chemical Engineering Science*, 116 (Suppl. C), 635–644.
- N. Bhatt and S. Visvanathan, 2015. Incremental Kinetic Identification based on Experimental data From Steady-state Plug Flow Reactors, in K. V. Gernaey, J. K. Huusom, és R. Gani, (Eds), *Computer Aided Chemical Engineering*, 37 (Suppl. C), 593–598, Elsevier, 2015.
- J. Ceamanos, J. F. Mastral, A. Millera, M. E. Aldea, 2002. Kinetics of pyrolysis of high density polyethylene. Comparison of isothermal and dynamic experiments, *Journal of Analytical and Applied Pyrolysis*, 65 (2), 93–110.
- J. Currie and D. Wilson, 2012. OPTI: Lowering the Barrier Between Open Source Optimizers and the Industrial MATLAB User, In *Foundations of Computer-Aided Process Operations*, Savannah, GA, USA, Jan. 8–13, 2012., N. Sahinidis, J. Pinto (Eds), Elsevier: Toronto, 2012.
- F. Ding, L. Xiong, C. Luo, H. Zhang, X. Chen, 2012. Kinetic study of low-temperature conversion of plastic mixtures to value added products, *Journal of Analytical and Applied Pyrolysis*, 94 (Suppl. C), 83–90.
- Z. Fang, T. Qiu, B. Chen, 2015. Analyzing and Modeling Ethylene Cracking Process with Complex Networks Approach, in K. V. Gernaey, J. K. Huusom, és R. Gani (Eds), *Computer Aided Chemical Engineering*, 37 (Suppl. C), 407–412, Elsevier, 2015.
- K. Im-orba, L. Simasatitkul, A. Arpornwichanop, 2015. Performance Analysis and Optimization of the Biomass Gasification and Fischer-Tropsch Integrated Process for Green Fuel Productions, in K. V. Gernaey, J. K. Huusom, R. Gani (Eds), *Computer Aided Chemical Engineering*, 37 (Suppl. C), 275-280, Elsevier, 2015.
- S. Le Digabel, 2011. Algorithm 909: NOMAD: Nonlinear optimization with the MADS algorithm, *ACM Transactions on Mathematical Software*, 37 (4), 44.
- J. A. Onwudili, N. Insura, P. T. Williams, 2009. Composition of products from the pyrolysis of polyethylene and polystyrene in a closed batch reactor: Effects of temperature and residence time, *Journal of Analytical and Applied Pyrolysis*, 86 (2), 293–303.
- L. Shampine and M. Reichelt, 1997. The MATLAB ODE Suite, *SIAM Journal on Scientific Computing*, 18 (1), 1–22.

Experimentally Driven Guaranteed Parameter Estimation: a Way to Speed up Model-Based Design of Experiments Techniques

Arun Pankajakshan,^a Marco Quaglio,^a Federico Galvanin^{a,*}

^a*Department of Chemical Engineering, University College London, London, WC1E 7JE, United Kingdom*

f.galvanin@ucl.ac.uk

Abstract

Parameter estimation in modelling reaction kinetics is affected by the prior knowledge on the domain of variability of model parameters which can be very limited at the beginning of model building activities. In conventional parameter estimation approaches a reasonably wide domain of variability for kinetic parameters is initially assumed, but this uncertainty on domain definition might deeply affect the efficiency of model-based experimental design techniques for model validation. In this work, we propose the use of binary classification techniques to define a feasible parametric region of parameter variability satisfying a set of user-defined model-based constraints. The proposed approach is illustrated in a case study of consecutive reactions in a plug flow reactor.

Keywords: Support vector machine, guaranteed parameter estimation, model-based design of experiments

1. Introduction

Mathematical models are an approximation of the real system, limited by the knowledge and understanding of the dynamics from experimental observations (Box, 1976). First-principles-based models have been used to represent nonlinear dynamic systems, but the major challenge involved with the use of such models is the precise estimation of large numbers of model parameters (Prasad and Vlachos, 2008). Modelling the kinetics of chemical reactions represents a typical example of such complex nonlinear systems. Recently, model-based design of experiments (MBD_{oE}) techniques have emerged as powerful tool for the rapid development and refinement of reaction kinetic models from flow data (Galvanin et al., 2016). However, in the conventional MBD_{oE} framework proposed in Asprey and Macchietto (2000), the model building procedure might become time-consuming and computationally expensive because the robustness of experimental design is critically affected by the presence of parametric uncertainty (Asprey and Macchietto, 2002). As an alternative method to the conventional MBD_{oE} using Fisher information matrix (FIM) Mukkula and Paulen (2017) used guaranteed parameter estimation (GPE) technique in the optimal design of dynamic experiments. In the optimal experiment design using GPE, the knowledge on measurement error is limited to error bounds. In comparison to MBD_{oE} using FIM, MBD_{oE} using GPE is computationally expensive. Both the methods assume an initial admissible parameter space containing the prior estimate and are critically affected by its definition. In the present work, we propose a computationally fast methodology to identify a feasible parametric space without any knowledge on measurement error and prior estimate. In

the proposed approach, bounds on a set of user defined characteristic variables are used to obtain the prior admissible parameter set. Characteristic variables are either derived from experimental observations or obtained from experimenter's intuition on the process. In this way, the experimenter's knowledge on the process can be exploited to obtain a robust prior parametric space before performing any experiments. The proposed methodology is implemented as a two-step binary classification procedure using support vector machine (SVM) and can be used with both FIM based and GPE based optimal design approaches. The method is applied to a simulated case study for the identification of the domain of variability of kinetic parameters in reaction systems.

2. Problem statement

We assume that a process model is described by a set of differential and algebraic equations (DAEs) in the form

$$\mathbf{f}(\dot{\mathbf{x}}(z, t), \mathbf{x}(z, t), \mathbf{u}(z, t), \mathbf{w}, \boldsymbol{\theta}, t, z) = 0 \quad (1)$$

$$\hat{\mathbf{y}}(z, t) = \mathbf{h}(\mathbf{x}(z, t), \mathbf{u}(z, t), \mathbf{w}, \boldsymbol{\theta}, t, z) \quad (2)$$

where $\mathbf{x}(z, t) \in \mathbf{R}^{N_x}$ is the time and space dependent vector of state variables (i.e. for example time and space dependent concentrations in a flow reactor), $\mathbf{u}(z, t) \in \mathbf{R}^{N_u}$ is the vector of control variables (manipulated inputs) whereas $\mathbf{w} \in \mathbf{R}^{N_w}$ represents the vector of constant controls, $\boldsymbol{\theta} \in \mathbf{R}^{N_\theta}$ is the set of unknown model parameters to be estimated within a continuous realisable set Θ which is unknown and to be identified in the present problem, $\mathbf{y}(z, t) \in \mathbf{R}^{N_y}$ is the set of response variables (i.e. state variables that are measured in the process) and $\hat{\mathbf{y}}(z, t)$ represents the corresponding values of response variables predicted by the model, t is the time and z is the axial domain.

3. Methodology

The procedure involved in the proposed approach is illustrated in Figure 1. First step in the proposed approach is the generation of model-based constraints using support vector machine (SVM) classifiers. The experimenter's intuition and understanding about the process is used to define a set of constraints. These constraints are defined by the expected limits of variability of a set of characteristic variables identified by the experimenter to provide a quantitative description of the process. In the second step, a region of parametric space satisfying these constraints (feasible parametric space) is identified using binary classification technique carried out with SVM. The two stage classification procedure is implemented as a standalone module in Python and can be easily integrated to the MBDoE module built in Python.

3.1. Generation of model-based constraints and classification criteria

The model-based constraints are defined by a set of characteristic variables $\boldsymbol{\psi}(\mathbf{u}, \mathbf{y}, \mathbf{w}, z, t) \in \mathbf{R}^{N_\psi}$ identified by the experimenter (these can be for example yield, conversion or concentrations) and correspond to the extreme model responses at given experimental conditions. For the generation of model-based constraints, the set $\boldsymbol{\Psi}$ is enforced on the model by using a set of functional relationships \mathbf{g} between $\boldsymbol{\Psi}$ and $\hat{\mathbf{y}}(z, t)$ at specific experimental conditions $\mathbf{u}(z, t)$ and \mathbf{w} in the form

$$\boldsymbol{\psi}(z, t) = \mathbf{g}(\hat{\mathbf{y}}(z, t), \mathbf{u}(z, t), \mathbf{w}). \quad (3)$$

It is assumed that the input from the experimenter is in the form of maximum expected variability range $\psi^- \leq \psi \leq \psi^+$, where ψ^- and ψ^+ respectively denotes the lower/upper bounds of the variable ψ .

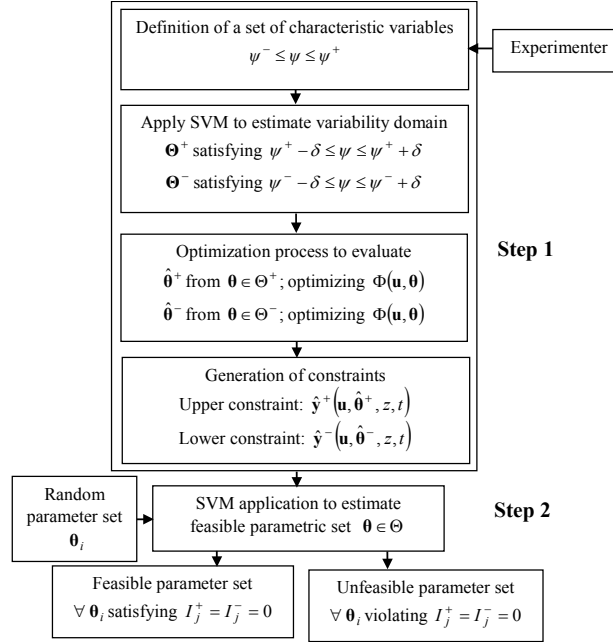


Figure 1. Proposed framework for the identification of feasible region of model parameters

Once the set Ψ is known, binary classification using SVM is applied to identify the parameter domains Θ^+ and Θ^- corresponding to a small variability range for upper limit ψ^+ defined as $(\psi^+ - \delta, \psi^+ + \delta)$ and that for lower limit ψ^- defined as $(\psi^- - \delta, \psi^- + \delta)$ respectively, where δ is a small number; Θ^+ and Θ^- are the parametric domains enclosing all set of parameters for which the predicted responses give ψ in the range $(\psi^+ - \delta, \psi^+ + \delta)$ and $(\psi^- - \delta, \psi^- + \delta)$ respectively. In the next procedure, an optimization problem is formulated within the domains Θ^+ and Θ^- to compute the desired set of parameter values $\hat{\theta}^+$ and $\hat{\theta}^-$ generating the upper and lower bounds for the model given by $\hat{y}^+(\mathbf{u}, \hat{\theta}^+, z, t)$ and $\hat{y}^-(\mathbf{u}, \hat{\theta}^-, z, t)$ respectively. The objective function $\Phi(\mathbf{u}, \theta)$ depends on the process and can be generally represented as

$$\hat{\theta}^+ = \arg \min_{\theta \in \Theta^+} \Phi(\mathbf{u}, \theta) \quad \text{and} \quad \hat{\theta}^- = \arg \min_{\theta \in \Theta^-} \Phi(\mathbf{u}, \theta) \quad (4)$$

In the second step of the proposed procedure, SVM is applied to estimate a feasible parametric domain Θ of model parameters from any random set such that the predicted responses for the feasible set of parameters are always constrained within the constraints generated in the first part. Mathematically this is formulated based on the following criteria

$$I_j^+ = \int_0^\tau \min(0, y_j^+(\mathbf{u}, \hat{\theta}^+, t) - \hat{y}_j(\mathbf{u}, \theta_i, t)) dt \quad i=1, \dots, N_s; \quad j=1, \dots, N_y \quad (5)$$

$$I_j^- = \int_0^\tau \min \left(0, \hat{y}_j(\mathbf{u}, \boldsymbol{\theta}_i, t) - y_j^-(\mathbf{u}, \hat{\boldsymbol{\theta}}^-, t) \right) dt \quad i=1, \dots, N_s; \quad j=1, \dots, N_y \quad (6)$$

where N_s and N_y denotes the number of random parameter sets and the number of model responses respectively, I_j^+ and I_j^- respectively denotes the integral of minimum deviation between model response for j -th response variable and the upper and lower constraint at any parameter set $\boldsymbol{\theta}_i$.

3.2. Application of support vector machine

SVM is capable of learning the decision function with appropriate training data to determine the optimum hyperplane that separates the given samples into feasible and unfeasible sets. In the present problem, the training set for SVM is represented as $(\boldsymbol{\theta}_i, Y_i)$, where $Y_i \in \{-1, 1\}$; -1 for feasible parameters and 1 for unfeasible parameters (binary classification). SVM classifier seeks to maximize the width of the largest margin separating the sample $\boldsymbol{\theta}_i$ into two classes and can be formulated as a convex optimization problem (Cortes and Vapnik, 1995):

$$L = \sum_{i=1}^n \alpha_i - \frac{1}{2} \sum_{i=1}^n \sum_{j=1}^n \alpha_i \alpha_j Y_i Y_j k(\boldsymbol{\theta}_i \cdot \boldsymbol{\theta}_j) \quad \text{s.t. } \boldsymbol{\Lambda} \geq 0 \text{ and } \boldsymbol{\Lambda}^T \mathbf{Y} = 0 \quad (7)$$

Where L is the Lagrangian form of the objective function, $\boldsymbol{\Lambda}^T = (\alpha_1, \dots, \alpha_n)$ is the n -dimensional vector of Lagrange multipliers, $\mathbf{Y}^T = (Y_1, \dots, Y_n)$ is the n -dimensional vector of labels which is either -1 or 1, k is the kernel function which is a measure of similarity between two samples $\boldsymbol{\theta}_i, \boldsymbol{\theta}_j$ to be classified. In the present study, the Gaussian radial basis function (RBF) kernel was selected over linear and polynomial kernels based on accuracy of classification of the training set. The two parameters C and γ of the RBF kernel were optimized using grid search cross validation scheme reported in Scholkopf and Smola (2002).

4. Case study

We demonstrate the proposed approach to identify the feasible region of reaction rate constants for a series of consecutive reactions in a plug flow reactor in the form: $A \xrightarrow{k_1} C \xrightarrow{k_2} D$. Assuming power law type kinetic model, the reaction system is described by the following set of DAEs:

$$\frac{-V_{in}}{A_c} \frac{dC_i}{dz} + \sum_{j=1}^{N_{rean}} \nu_{ij} r_j = 0 \quad i=1, \dots, N_{comp}; \quad j=1, \dots, N_{rean} \quad (8)$$

$$r_j = f(k_j, C_i) \quad ; \quad k_j = k_{0j} \cdot \exp(-Ea_j/R \cdot T) \quad i=1, \dots, N_{comp}; \quad j=1, \dots, N_{rean} \quad (9)$$

In Eq. (8), C_i is the concentration (mol/L) of the i -th component, r_j and ν_{ij} are respectively, the j -th reaction rate and the stoichiometric coefficient of the i -th species in the j -th reaction, V_{in} is the inlet volumetric flowrate of reactant A (ml/min), A_c is the reactor cross sectional area (here assumed 2 cm²), z is the axial coordinate along the

reactor length, l is the length of reactor channel (25 cm), u is the vector of control variable consisting of initial concentration of reactant A (1.5 mol/L), reaction temperature T (353 K) and the inlet volumetric flowrate of reactant A (5 ml/min), i.e. $\mathbf{u} = [1.5, 353, 5]$. In Eq. (9), the temperature dependency of reaction rate is described using Arrhenius law, where k_j denotes the reaction rate constant for the j -th reaction (min^{-1}), k_{0j} the frequency factor (min^{-1}) and Ea_j the activation energy (J/mol). The four model parameters $\boldsymbol{\theta} = [k_{01}, Ea_1, k_{02}, Ea_2]$ were normalised with respect to the set $\boldsymbol{\theta}^0 = [50, 10000, 80, 20000]$. The normalised parameters $\boldsymbol{\theta}^n$ defined as $\boldsymbol{\theta}^n = \boldsymbol{\theta}/\boldsymbol{\theta}^0$ were randomly varied from a uniform distribution with range (0, 2) and the corresponding values of parameters ($\boldsymbol{\theta}$) were used to compute the two reaction rate constants k_1 (min^{-1}) and k_2 (min^{-1}) which were actually used as the training set for the classifier. Thus the four model parameters were varied to obtain the corresponding rate constants which were used for the classification. The characteristic variables with suitable ranges provided by the experimenter are: (i). Conversion of reactant A: (80 – 100 %), (2). Yield of product C: (20 – 40 %), (3). Yield of product D: (60 – 80 %). In this work, constraints on yield of product C was used for generating the model-based constraints with $(\psi^+ - \delta, \psi^+ + \delta) = (38\%, 42\%)$ and $(\psi^- - \delta, \psi^- + \delta) = (18\%, 22\%)$. The time t_{\max} at which the intermediate product C reaches the maximum concentration, calculated as $t_{\max} = \ln(k_2/k_1)/(k_2 - k_1)$ (Fogler, 2006), was chosen to be the objective function $\Phi(\mathbf{u}, \boldsymbol{\theta})$ in Eq. (4). The parameter set $\hat{\boldsymbol{\theta}}^+$ (defining the upper bound of variability) was estimated from the domain Θ^+ by minimizing t_{\max} which corresponds to the fastest reaction (comparing the model responses for C for all $\boldsymbol{\theta}_i \in \Theta^+$). Similarly, $\hat{\boldsymbol{\theta}}^-$ was estimated from the domain Θ^- maximizing t_{\max} which corresponds to the slowest reaction for the formation of C.

5. Results

Following the procedure for the generation of model-based constraints explained in Section 3.1, the parameter sets corresponding to upper and lower constraints were estimated to be $\hat{\boldsymbol{\theta}}^+ = [2.52, 0.09]$ and $\hat{\boldsymbol{\theta}}^- = [0.17, 0.24]$ and corresponding constraints are given in Figure 2a. In the figure, the thick dashed line represents the upper constraint which is the concentration profile of product C at the parameter set $\hat{\boldsymbol{\theta}}^+ = [2.52, 0.09]$ calculated from Eq. (4). Similarly, the thick dotted line represents the lower constraint which is the concentration profile of C at the parameter set $\hat{\boldsymbol{\theta}}^- = [0.17, 0.24]$ calculated from Eq. (4). Due to small misclassification, it can be seen that some of the generated profiles violates the constraints. Figure 2b shows the feasible parametric space identified by the trained classifier for a random parametric domain of variability (0, 2). In the figure, the dotted white space shows the feasible parametric region and the plane area represents the unfeasible region. Each point within the feasible space (except the misclassified parameter sets shown in white circle) represents a feasible parameter set for which the concentration profile of product C is within the constraints (these profiles are shown in thin dotted lines in Figure 2a). The approach provides a narrow feasible parametric domain (the white area) for any random set of model parameters where the model identification techniques such as MBDoE for parameter estimation can be applied in a more robust and effective way. The whole procedure is computationally very fast and consumed a total CPU time of approximately 5 seconds on an Intel® Xenon® E5-1650, 3.5 GHz, RAM 32 GB.

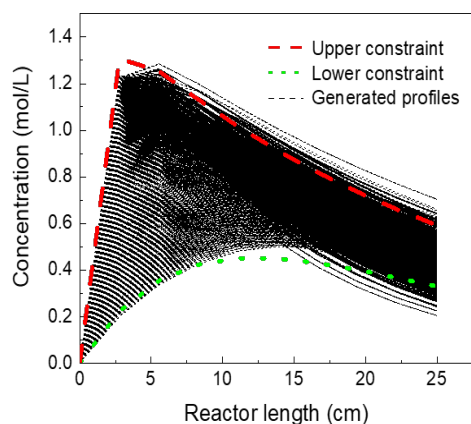


Figure 2a. The upper and lower constraint defined for the process in terms of concentration of product C

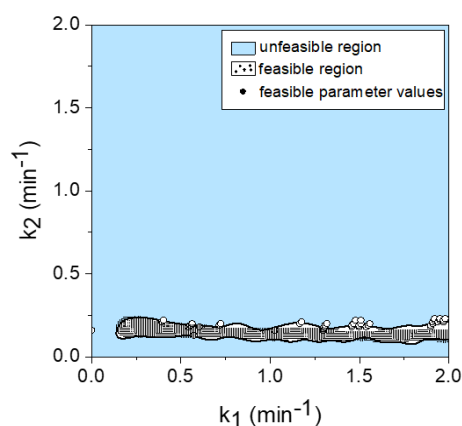


Figure 2b. Feasibility region for parameters k_1 and k_2 (dotted white area) separated from the unfeasible region (plane area)

6. Conclusions

A general method is proposed in this paper to estimate the domain of variability of model parameters satisfying a set of model-based constraints whose definition can be obtained from user-defined information on the experimental system. Support vector machine (SVM) methods were used for both defining the set of constraints and for obtaining the feasibility region of model parameters. Results from the case study show how even limited preliminary information on conversion and yield can significantly reduce the expected uncertainty domain of model parameters. The method provides a narrow feasible region of model parameters where identifiability analysis can be targeted to obtain a reliable parametric uncertainty region in estimation problems. In the resultant narrow parametric space, MBDoE techniques can be effectively applied for the quick development and validation of deterministic process models.

References

- G. E. P. Box, 1976, *J. Am. Stat. Assoc.* 71, 791-799
- V. Prasad, D. G. Vlachos, 2008, *Ind. Eng. Chem. Res.* 47, 6555-6567
- F. Galvanin, E. Cao, N. Al-Rifai, A. Gavriilidis, V. Dua, 2016, *Comput. Chem. Eng.* 95, 202-215
- S. P. Asprey, S. Macchietto, 2000, *Comput. Chem. Eng.* 24, 1261-1267
- S. P. Asprey, S. Macchietto, 2002, Designing robust optimal dynamic experiments, *J. Process Contr.* 12, 545-556
- A. R. G. Mikkula, R. Paulen, 2017, *Comput. Chem. Eng.* 99, 198-213
- C. Cortes, V. Vapnik, 1995, *Machine Learning*, 20, 273-297
- B. Scholkopf, A. J. Smola, 2002, *Learning with kernels: Support Vector Machines, Regularization, Optimization and Beyond*, MIT Press
- S. H. Fogler, 2006, *Elements of Chemical Reaction Engineering*, 4th Ed., Prentice Hall

Optimal Design of a Dividing Wall Column for The Separation of Aromatic Mixtures using the Response Surface Method

Pedro Barbosa de Oliveira Filho^a, Marcio Luis Ferreira Nascimento^a, Karen Valverde Pontes^{a,*}

^a*Industrial Engineering Graduate Program (PEI), Polytechnic School of the Federal University of Bahia Address, Salvador, 40210-630, Brazil*

**karenpontes@ufba.br*

Abstract

Dividing wall columns (DWC) are the industrial implementation of the Petlyuk configuration in a single shell. The optimal design of dividing wall columns is a multivariable, mixed-integer and non-linear problem with a non-convex optimization function presenting several local optima. The response surface method (RSM) associated with the steepest descent method offers a practical approach to optimize the DWC design. In the present study, a central composite design is carried out to obtain and validate the response surface for a DWC performing an aromatic ternary separation. The resulting aromatic DWC system presented a better optimal design compared with previous work and energy savings by 44% compared with a conventional two-column configuration (C2C) typically used for aromatic separation. The method is able to systematically solve the problem while minimizing simulation effort and optimizing the DWC design parameters.

Keywords: Dividing wall columns, Optimization, Response surface method, Distillation process.

1. Introduction

Distillation has been the most commonly used process for the separation of liquid mixtures and one of the most studied unit operations in the history of chemical engineering (Li et al., 2016). Despite its wide industrial application, distillation technology has drawbacks related to its high operational and implementing costs. In conventional two-column (C2C) sequences the natural presence of flow remixing in the columns sections results in energy inefficiency. This remixing is inherent in any separation involving the presence of a component with intermediate volatility at high concentrations (Hernández et al. 2006). An alternative configuration which is more energy efficient is a fully thermally coupled (FTC) configuration, called the Petlyuk configuration (Figure 1a). In this configuration, the vapor and liquid streams emerging from the first column (pre-fractionator) are directly coupled to the second column (main column). The Petlyuk configuration has higher thermal efficiency compared to the C2C configurations due to the decrease in the remixing effect, providing considerable energy savings, approximately 30% (Petlyuk, 2004).

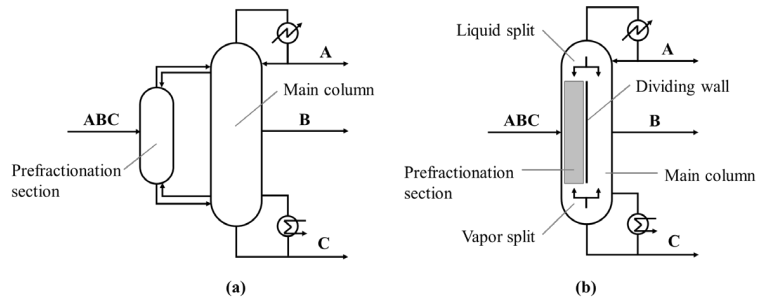


Figure 1 – (a) Petlyuk column and (b) Dividing-wall column.

The dividing-wall column (DWC), depicted in Figure 1b, is the industrial implementation of the Petlyuk column in a single shell, generating greater integration and cost reduction. Besides the greater energy efficiency, the DWC offers a further advantage, compared to conventional columns, of producing high purity side products and separating several pure components in a single unit (Dejanović et al., 2010).

Authors have developed different conceptual design methods for FTC columns, such as the Petlyuk and the DWC, and reported gains in energy efficiency compared to conventional distillation column sequences. Halvorsen and Skogestad (2003) developed the V-min Diagram Method for the minimization of energy requirement in multicomponent distillation systems. The method is based on the Underwood equations, considering constant molar flows, an infinite number of theoretical stages and constant relative volatilities. The authors have shown that the FTC configuration always presents a lower energy consumption, when compared to the C2C configuration, for the separation of an N-component mixture. The V-min Diagram Method can be summarized in a graphical representation, which is a useful tool for the conceptual design of FTC configurations. Dejanović et al. (2011) developed a method, based on the V-min Diagram (Halvorsen and Skogestad, 2003), to determine the optimal number of stages and reflux ratio of a DWC for a three-product separation. The authors reported a 43% reduction in energy consumption using the DWC compared to a conventional indirect sequence.

Although many conceptual design methods have been developed, the design and optimization of an FTC multicomponent distillation column is a non-linear, multivariable and mixed-integer problem with a non-convex objective function with several local optimums (Vazquez-Castillo et al., 2009). Gómez-Castro et al. (2008) studied the design and optimization of dividing wall columns using a genetic algorithm. The objective function was evaluated using Aspen PlusTM process simulator which was coupled with MatlabTM for solving the optimization problem. The authors report that the method appears to be suitable for the design of dividing-wall columns. This optimization method, however, have drawbacks related to implementation complexities. Thus, the development of a straightforward optimization method for DWCs would be useful.

Statistical approaches have been shown to be promising for process optimization studies (Van Duc Long and Lee, 2012). Response surface method (RSM) is a collection of statistical techniques used for studying the relationships between measured responses and independent input variables. In the present paper, RSM is used for the optimization

of the main design parameters of a DWC aiming lower energy and investment costs. The separation of a benzene, toluene and p-xylene ternary mixture (BTX) in a DWC investigated by Premkumar and Rangaiah (2009) is used as a case study.

2. Simulation model and optimization method

2.1. Simulation

A shortcut design method is essential for ascertaining reasonable estimates for more precise simulations. The V-min diagram method proposed by Halvorsen and Skogestad (2003) calculates the minimum vapor and liquid flows required to perform all binary separations on a given mixture, assuming an infinite number of stages. The V-min diagram method will be used as a shortcut method for ascertaining the initial guess for the rigorous simulation.

The DWC can be simulated in Aspen PlusTM through a thermodynamically equivalent configuration using one to four columns. The four-column model (Dejanović et al., 2011) is usually harder to initialize and converge, however, offers more flexibility when performing process optimization (Nguyen et al., 2016). The rigorous model calculation was performed by a RadFrac four-column model in Aspen PlusTM. The number of stages in each column, products flows rates, reflux ratio, boil-up ratio and liquid and vapor feed flows to the pre-fractionator were set according to the V-min diagram. For simplification purposes, the column pressure was maintained constant at 10 bar. The Reflux ratio, side-product flow and boil-up ratio were set as variables for the design specification for the top, middle and bottom products, respectively.

The case study is the separation of a hydrocarbon mixture (benzene, toluene, p-xylene), as proposed by Premkumar and Rangaiah (2009). Feed conditions are set at 100 kgmol/h of saturated liquid at 10 bar. Molar feed composition is 33% benzene, 33% toluene and 34% p-xylene. The top, middle and bottom products specifications are 99.5% benzene, 91% toluene and 92% p-xylene, respectively. The UNIQUAC method was used for vapor-liquid equilibrium calculations.

2.2. Optimization

The main design parameters for the DWC are the number of stages in the top (NC1), bottom (NC22), and pre-fractionator (NC1) sections and the internal vapor (VFC1) and liquid (LFC1) flows to the pre-fractionator. For simplification purposes, the number of stages at the two sides of the partitional wall were considered the same. The simple yet effective objective function $\Phi = N_T(R + 1)$, where N_T is the total number of stages and R is the reflux ratio, was suggested by Dejanović et al. (2011) for measuring the optimal relation between stage and reflux requirements for the DWC.

Design of experiments (DOE) was used as part of the RSM sequential procedure for identifying the DWC optimal design region. For the first factorial design, factor levels were chosen by single-factor testing (Van Duc Long and Lee, 2012). As the V-min diagram method considers an infinite number of theoretical stages, the method of steepest descent was used next to move sequentially in the direction of the minimum response, based on the statistically significant effects computed by the first DOE. Then, factorial and central composite designs are performed sequentially at the new region to fit first and second order models, so that an optimal response can be reached. All experimental designs and ANOVA analysis were performed using the MinitabTM software.

3. Results and discussions

For the first design of experiments, a 2^5 complete factorial design with one central point was carried out. The maximum values of the design parameters were taken from the V-min diagram and the minimum values by single-factor testing. All main design parameters were considered statistically significant at a 95% confidence level. The path of steepest descent was calculated based on the design parameters main effects and levels. A minimum response in the path was identified and a new full factorial design was performed at the minimum response region as the central point. Factor levels for all design parameters are presented in Table 1 (design # 1). The summarized results for design no. 1 are presented in Table 2. The ANOVA analysis was carried out using a 95% confidence level to evaluate the significance of the design parameters. One can notice that the liquid and vapor flows to the pre-fractionator are only significant as interaction effects. This finding is in accordance with Dejanović et al. (2011), who identified a flat region around the optimal point, indicating that the objective function is not sensible to these two main effects. The low F-Value (11.04) for this model indicates that a first-order model is not suitable for the DWC. From this point, a central composite design will be used attempting to fit a second-order model. As the number of stages in the top section (NC21) and the internal vapor (VFC1) and liquid (LFC1) flows to the pre-fractionator are no longer statistically significant to the model, they were held constant at the central values of 17 stages, 72.3 kgmol/h and 118.4 kgmol/h, respectively. The factor levels for this central composite design is summarized in Table 1 (design # 2).

Table 1 – Parameters design levels.

Design #	Design type	Design parameters	Coded levels		
			Low (-1)	Center (0)	High (1)
1	Factorial	NC1	36	46	56
		NC21	12	17	22
		NC22	21	26	31
		LFC1/kgmol.h ⁻¹	62.3	72.3	82.3
		VFC1/kgmol.h ⁻¹	108.4	118.4	128.4
2	Central composite	NC1	25 (-1.414)	46	67 (-1.414)
		NC22	12 (-1.414)	26	40 (-1.414)
3	Central composite	NC1	24 (-1.414)	31	38 (-1.414)
		NC22	4 (-1.414)	11	18 (-1.414)

Table 2 – Summarized results from ANOVA analysis for fitted models.

Model	Order	No. of simulations	Significant factors			F-Value
			Linear	Interaction	Square	
1	first	33	NC1	NC21*VFC	-	11.04
			NC22	LFC1*VFC1		
2	second	13	NC1	-	NC1 ²	174.59
			NC22			
3	second	13	NC1	NC1*NC22	NC1 ²	1256.30
			NC22			

A 2^2 ($\alpha = 1.414$) central composite design was performed for fitting a second-order model. Table 2 shows that model 2 is significant with an F-Value of 174.59. The contour plot in Figure 2a indicates that, although the model is significant, it is still not in the optimal response region. Therefore, to approximate the model to the optimal response region, a second steepest descent is performed using the minimum values from the contour plot in Figure 2a to redefine factor levels. The factor levels for the new central composite design are shown in Table 1 (design # 3). The summary results for the new second-order model is shown in Table 2 (model 3). The large F-Value (1256.30) indicates that the model is statistically significant. The new contour plot in Figure 2b shows that the steepest descent method was able to move the model in the direction of the minimum response of -0.1571 (≈ 32 stages) for NC1 and 0.6143 (≈ 15 stages) for NC22.

Table 3 compares the C2C and DWC configuration investigated by Premkumar and Rangaiah (2009) and the new DWC configuration optimized using the RSM. The new DWC configuration presents a lower number of stages and slightly lower energy requirements than the DWC suggested by Premkumar and Rangaiah (2009), which means savings in operating and capital costs. Those savings are probably possible due to better values for the vapor and liquid internal flows to the pre-fractionator, which were not informed by Premkumar and Rangaiah (2009). Compared to the C2C configuration, the new DWC shows savings about 44% in reboiler and condenser duties, confirming the reduction in energy consumption while ensuring the same product quality.

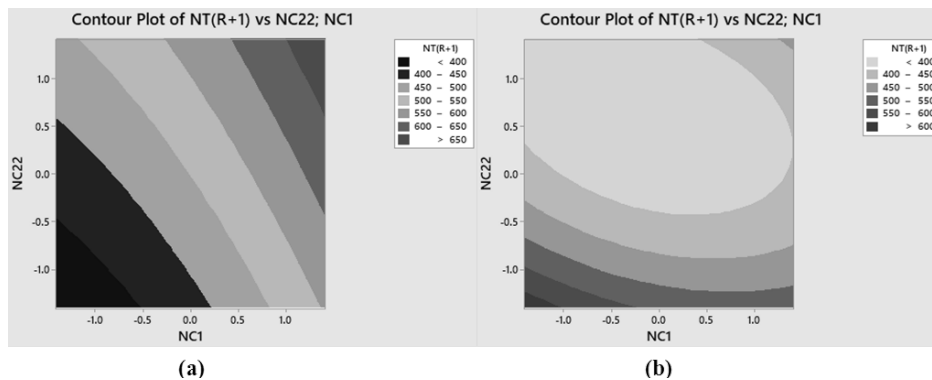


Figure 2 – Contour plots for models (a) 2 and (b) 3.

Table 3 – Comparison between C2C and DWC configuration.

Design parameters	C2C configuration ^a			DWC ^a	DWC (RSM)
	C1	C2	Total		
No. of stages	31	40	71	68	62
No. of stages (top, middle, bottom)	-	-	-	17, 35, 16	17, 31, 14
Condenser duty / kW	1,476	876	2,352	1,306	1,296
Reboiler duty / kW	1,508	890	2,398	1,355	1,345

^aPremkumar and Rangaiah (2009)

4. Conclusions

A straightforward method for design and optimization of a DWC using the DOE and RSM was presented in this paper. The steepest descent method was proven efficient for moving sequentially in the direction of the minimum response by changing the main parameters values according to their effects and factor levels. The final second-order model was statistically significant and the optimization of the final two main design parameters resulted in a DWC six-stage lower than the one reported in the literature with savings of 44% in reboiler and condenser duties compared to the C2C configuration for the same aromatic separation. This work shows the systematics, low computational effort and simplicity of the RSM for optimizing the DWC design.

References

- Dejanović, I., Matijašević, L., Olujić, Ž., 2011. An effective method for establishing the stage and reflux requirement of three-product dividing wall columns. *Chem. Biochem. Eng. Q.* 25, 147–157.
- Dejanović, I., Matijašević, L., Olujić, Ž., 2010. Dividing wall column-A breakthrough towards sustainable distilling. *Chem. Eng. Process. Process Intensif.* 49, 559–580. <https://doi.org/10.1016/j.cep.2010.04.001>
- Gómez-Castro, F.I., Segovia-Hernández, J.G., Hernández, S., Gutiérrez-Antonio, C., Briones-Ramírez, A., 2008. Dividing wall distillation columns: Optimization and control properties. *Chem. Eng. Technol.* <https://doi.org/10.1002/ceat.200800116>
- Halvorsen, I.J., Skogestad, S., 2003. Minimum Energy Consumption in Multicomponent Distillation. 2. Three-Product Petlyuk Arrangements. *Ind. Eng. Chem. Res.* 42, 605–615.
- Hernández, S., Gabriel Segovia-Hernández, J., Rico-Ramírez, V., 2006. Thermodynamically equivalent distillation schemes to the Petlyuk column for ternary mixtures. *Energy.* <https://doi.org/10.1016/j.energy.2005.10.007>
- Li, H., Wu, Y., Li, X., Gao, X., 2016. State-of-the-Art of Advanced Distillation Technologies in China. *Chem. Eng. Technol.* 39, 815–833. <https://doi.org/10.1002/ceat.201500656>
- Nguyen, T.D., Rouzineau, D., Meyer, M., Meyer, X., 2016. Design and simulation of divided wall column: Experimental validation and sensitivity analysis. *Chem. Eng. Process. Process Intensif.* 104, 94–111. <https://doi.org/10.1016/j.cep.2016.02.012>
- Petlyuk, F.B., 2004. Distillation Trajectories in Infinite Complex Columns and Complexes. *Distill. Theory Its Appl. to Optim. Des. Sep. Units* 170–217.
- Premkumar, R., Rangaiah, G.P., 2009. Retrofitting conventional column systems to dividing-Wall Columns. *Chem. Eng. Res. Des.* 87, 47–60. <https://doi.org/10.1016/j.cherd.2008.06.013>
- Van Duc Long, N., Lee, M., 2012. Dividing wall column structure design using response surface methodology. *Comput. Chem. Eng.* 37, 119–124. <https://doi.org/10.1016/j.compchemeng.2011.07.006>
- Vazquez-Castillo, J.A., Venegas-Sánchez, J.A., Segovia-Hernández, J.G., Hernández-Escoto, H., Hernández, S., Gutiérrez-Antonio, C., Briones-Ramírez, A., 2009. Design and optimization, using genetic algorithms, of intensified distillation systems for a class of quaternary mixtures. *Comput. Chem. Eng.* 33, 1841–1850. <https://doi.org/10.1016/j.compchemeng.2009.04.011>

Simulation/optimization of bio-hydrogenated diesel process with techno-economic analysis

Pooreerat Tawai^a, Kitipat Siemanond^{a*}

^aThe Petroleum and Petrochemical College, Chulalongkorn University, 254 Soi Chulalongkorn 12, Phayathai road, Bangkok 10330, Thailand;
Pooreerat.t@gmail.com, Kitipat.s@chula.ac.th

Abstract

In this study, Pro II and general algebraic modeling system (GAMS) software were applied to synthesize and optimize the Bio-hydrogenated diesel (BHD) process. This research had been divided into three main parts. The first part was focused on conceptual process simulation of BHD process. The operating condition analysis method represented operating parameters at 325°C, 500 psig with NiMo/Al₂O₃ catalyst. The final commercial products were n-hexadecane and n-octadecane. The input information such as reaction conditions, conversion of each reaction, production yield and products purity were provided by petrochemical industry in Thailand. The second part was concentrated on process improvement in energy efficiency by mathematical programming which was used for designing heat exchanger network (HEN) or heat integration of the process. It decreased operating cost and saved hot and cold utility usages. In final part, techno economic analysis was a key factor that played an important role on investment decision by using economic parameters of net present value (NPV), internal rate of return (IRR) and payback period (PBP). The BHD plant capacity was 10,000 Liters/day which used palm oil as feedstock. The energy consumption was optimized by HEN designed by GAMS programing. The simulation result showed the production rate was 12,374.09 Liters/day, the conversion of biodiesel range was 99.83%, and product yield and purity of commercial product were 79.89 and 99.92% respectively. BHD process required 7 heat exchangers resulting in the reduction of energy consumption on heater from 1,335,233 kJ/h to 655,905 kJ/h or heating utility was saved about 50%. Moreover, BHD process made profit over 45.67 million Baht with PBP of 9.4 years and IRR at 25.40%.

Keywords: Palm oil, Bio-hydrogenated diesel, Techno-economic, Simulation

1. Introduction

Nowadays, consumption of energy from fossil is increasing the growth of transportation and population. Most of automobiles use diesel engine. Using diesel produced from non-renewable resource. Therefore, it is necessary to find a new energy resource that can supply the global energy demands. One of the most important renewable energies is bio-hydrogenated diesel (BHD) which has a similar properties as diesel where the main composition is C₁₄-C₂₂ and it can be produced from vegetable oil (palm, soybean, and jatropa), animal oil and waste cooking oil. Bio-hydrogenated diesel or (BHD) is produced by triglyceride reacting with hydrogen. Reaction of bio-hydrogenated diesel (BHD) consists of 3 main reactions. First is decarboxylation reaction (DCO₂), where carbon dioxide is removed with endothermic reaction. Second is decarbonylation reaction (DCO), where this reaction is also endothermic reaction for carbon monoxide and water removal. Last is hydrogenation (HDO) which is exothermic reaction. This

reaction eliminates oxygen to form water and produce the same number of carbon atom as reactant (Mathias Snare et al., 2006).

In industrial process, the simulation software was the most popular method for designing and developing process because almost industrial process had to spend a lot of money on investment cost such as processing equipment, operating cost, raw materials and transportation. Therefore, it was essential to estimate the process expense and revenue by using techno economic analysis before investment decision. The purposes of this work were to provide the appropriate product to meet the operating plan, to minimize energy consumption by HEN, and to estimate profitability project.

1.1 Properties and Specification

The main feedstock of palm oil was 500 Kg/h. The properties of feedstock were shown in Table 1.

Table 1. Properties of palm oil feed at condition 25.00 °C and 500 psig

Palm oil	
Component	%wt
Linoleic	100
Oleic	200
Palmitic	300

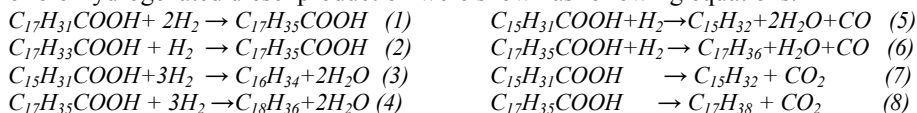
Table 2. Properties of BHD product

BHD Product			
Component	% wt	Component	% wt
LINOLEIC	0.0041	CO	0.0044
H ₂	0.0965	CO ₂	0.0271
STEARIC	0.0106	PALMITIC	0.1328
OLEIC	0.0014	NC17	4.2742
NC16	156.74	NC15	2.7533
H ₂ O	0.0355	NC18	235.7

The process simulation results showed the BHD production rate was 12,374.09 Liters/day, the conversion of biodiesel, product yield, and purity of commercial product were 99.83%, 79.89%, and 99.92% respectively. The product specifications were shown in Table 2.

1.2 BHD reactions

Bio-hydrogenated diesel (BHD) was from exothermic reaction between triglyceride and hydrogen. The operating parameters were 325°C and 500 psig with NiMo/Al₂O₃ catalyst. The final commercial or BHD products were n-hexadecane (NC16) and n-octadecane (NC18). The conversion of biodiesel was at 95.00%. The overall reactions of bio-hydrogenated diesel production were shown as following equations.



2. Methodology

This step had been divided into three main parts. The first part was the process simulation of a base-case BHD process from petrochemical industry in Thailand including feedstock composition and thermodynamic properties. The second part was energy efficiency improvement by using GAMS for heat exchanger network (HEN) design. The final part was techno-economic analysis for overall process.

2.1 Process simulation

The BHD process had been divided in three parts which were conversion reactor, separation product and product storage. The base case of the BHD production process which used palm oil as a raw material was simulated by simulation software (Pro II). For the thermodynamic model of biodiesel production, NRTL-RK model was applied due to the BHD process was operated under severe condition. In addition, chemicals component in BHD process were non-ideal liquid-liquid mixtures (A. Kantama et al.,

2015). This process started from preheated palm oil at 325 °C and 500 psig. Compressed hydrogen at 500 psig which was mixed together with palm oil were fed to reactor requiring only conversion of palm oil at suitable condition (325°C, 500 psig). The products from the conversion reactor were sent to flash drum for separating water and gas. Hydrogen from gas products was recycled to the reactor. The liquid products were sent to the distillation column to separate hydrocarbons C₁₅-C₁₈ from BHD at the top of column and unreacted palm oil at the bottom. Then unreacted palm oil was recycled to the reactor.

2.2 Heat integration

HEN was designed for reducing heating and cooling utilities of the base case. This HEN model by GAMS was based on the minimum temperature approach (ΔT_{min}) at 10°C. The base case consisted of five hot and three cold streams. The base case consumed the hot and cold utilities about 1,335,233 and 679,317.9 kJ/h respectively as shown in Figure 1.

2.3 Techno economic analysis

The overall concept of techno economic analysis consisted of two main parts. The first part was process simulation. This part started from process design diagram by using palm oil at 500 kg/h as feedstock. After that, the process would be modified by applying heat exchanger network (HEN) for reducing operating cost. The second part which was techno-economic for capital and operating cost calculation. The modified process would be evaluated by cash flow diagram (profitability analysis) and sensitivity analysis.

3. Result and discussion

3.1 Process simulation

The simulation result showed that this process converts 500 kg/h of palm oil to 12,374.09 liters/day of BHD products. The conversion of biodiesel was 99.83%, yield and commercial product purity were 79.89 and 99.92% respectively.

3.2 BHD improvement process

The base case consumed the hot and cold utility about 1,335,233 and 679,317.9 kJ/h respectively. The modified BHD required 655,905 kJ/h and no requires cold utility as shown in Table 3. The modified BHD process with HEN was shown in Figure 2.

Table 3. Heating and cooling utilities saving

	Heating utility (KJ/Hr)	Cooling utility (KJ/Hr)
Base case without HEN	1,335,233	679,317.90
Modified case with HEN	655,905	0
Saving (%)	50.88	100

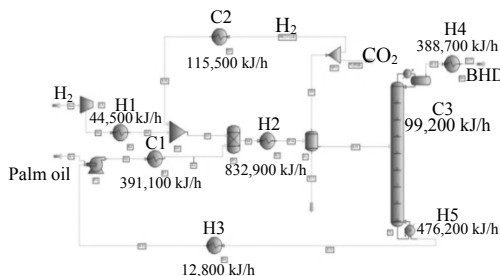


Figure 1. Base case of BHD process

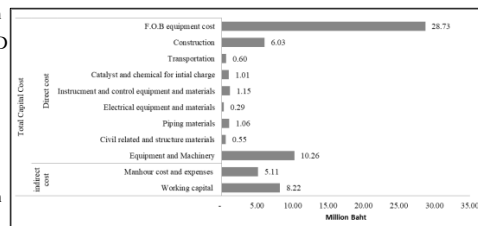


Figure 3. Total capital cost of BHD process

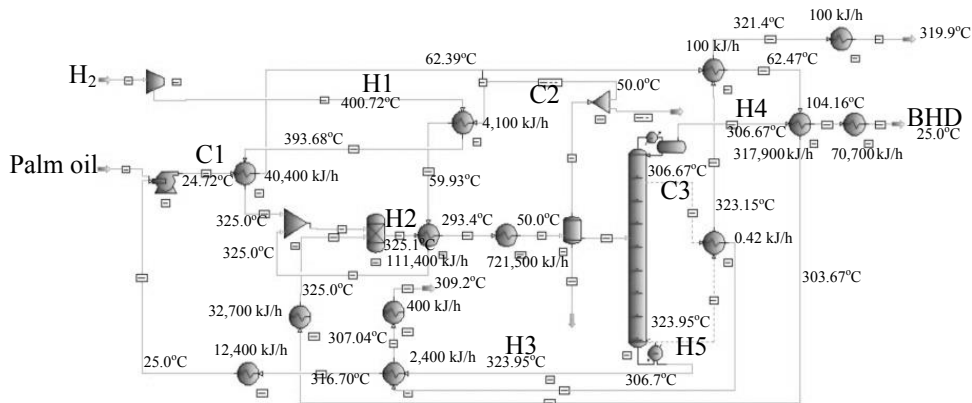


Figure 2. The modified process with HEN

3.3 Techno economic analysis

Equation 1 was applied for calculating the chemical Engineering Plant Cost Index (CEPCI) by updating the equipment costs to the year 2017.

$$\text{Present cost} = \frac{\text{Capital cost index in 2017}}{\text{Capital cost index in 2000}} \times \text{previous cost} \quad (9)$$

3.3.1 The total capital cost (CAPEX)

Each of processing equipment was designed based on mass and energy balance for calculating the purchased cost. The installation cost of BHD process and the laborer wage were included with the total capital cost. This process investment cost was around 63 million Baht. The result showed that F.O.B equipment cost was the largest fraction of overall capital cost at 28.73 million Baht whereas the lowest capital cost was electrical equipment and materials at 0.29 million Baht. There was only a 2 million Baht different between working capital equipment and machinery at 8.22 and 10.26 million Baht respectively as shown in Figure 3.

3.3.2 Total expense cost (OPEX)

The total expense cost was around 117 million Baht/year which was evaluated to cover on general expense, indirect expense, operating cost and variable cost. The annual operating cost which was calculated based on daily operating cost was 0.67 million Baht/year. The BHD process was operated 24 h for 350 days/year and there were 3 shifts which are 7am-3pm, 3pm-11pm and 11pm-7am per day (k.W.Cheah et al., 2017) so this process investors had to hire labor 3 persons/shift for controlling all equipment. For the total expense cost, it showed that raw material which was the highest proportion of overall expense cost was equal 97.44 million Baht/year. Another part that affected to the total expense cost was utility cost (9.59 million Baht). The laboratory charge which was the least fraction of total expense cost was 0.07 million Baht/year as shown in Figure 4.

3.3.3 Total revenue

Commercial product of this process was biodiesel. The capacity of process was 12,374.09 Liters/day by assuming operating time 350 days/year so total revenue was equal 136.42 million Baht/year as shown in Table 4.

Table 4. Total revenue of BHD

Commercial product	quantity(l/day)	price (baht/l)	baht/year
BHD	12,374.09	31.5	136,424,342.25

3.3.4 Cash flow analysis

Evaluated economic information which was shown in Table 5 was used for designing cash flow diagram. From Figure 5, the cash flow diagram presented data relating to level of BHD process finance from the process started up at first year to the end of process at eleventh year. It could be clearly seen that the BHD process finance dramatically decreased in both rate of return which were 10 and 15% in the first four year because this process was under construction and testing period in first year and the revenue of process had to pay tax so cash flow diagram showed negative value. After that the BHD process finance significantly increased from the fifth year to the end of process because this process could make profit from selling commercial product which was biodiesel. The economic analysis was evaluated the overall profits of BHD process in term IRR, NPV and PBP by assuming rate of return at 10 and 15% as shown in Table 6. The result from rate of return at 10% indicated that this process would obtain profit in 9.5 year (PBP) with NPV 45.47 million Baht and IRR 25.01%. Similarly to rate of return at 10%, the rate of return at 15% illustrates that this process had NPV 25.59 million Baht, PBP 10.8 year and IRR 25.01%.

3.3.5 Sensitivity analysis

In this study, the uncertain variables of BHD process were analyzed by sensitivity method for finding variables that had influence on BHD production cost. All uncertain parameters were varied in ranging 10% (price increasing and decreasing up to 10%). From sensitivity analysis data it could be concluded that biodiesel price had a largest impact on BHD production whereas the lowest impact on BHD production was total capital cost as represented in Figure 6.

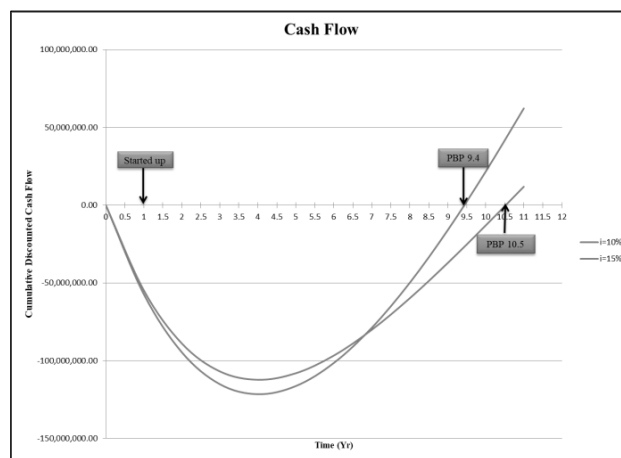


Figure 5. Cash flow analysis of BHD process

Table 5. Evaluated economic information

Process information	Baht
Total capital cost	54,787,127.39
Working capital (15%)	8,218,069.11
Depreciation (10%)	5,478,712.74
Total expense	117,144,152.86
Total revenue	136,424,342.25

Table 6. Overall profits of BHD process

Rate of return	IRR	NPV (Baht)	PBP (year)
10%	25.40%	46,725,489.37	9.4
15%	25.40%	26,620,795.71	10.5

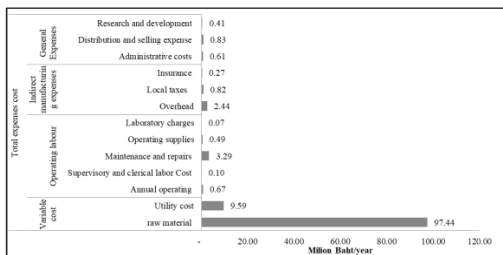


Figure 4. Total expense cost

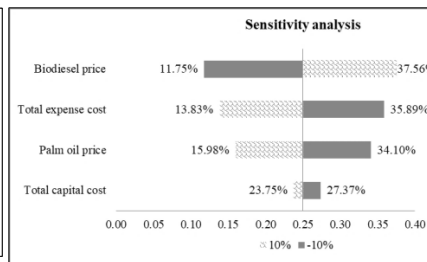


Figure 6. Sensitivity analysis of BHD process

Conclusion

BHD process could be produced from palm oil with conversion reactor at 325°C and 500 psig. The process simulation result represented conversion, yield and purity at 99.83, 79.89 and 99.92% respectively. After that the modified process with HEN could reduce hot utility for 50% requirement. Final part, techno-economic analysis at 10% rate of return shows that, NPV was equal 45.67 million Baht, PBP 9.4 year and IRR 25.40%. At the same way, this process had 25.59 million Baht of NPV, PBP 10.5 year and IRR 25.40% at 15% rate of return. Additional, NPV was positive value therefore BHD process was worth for investment.

Acknowledgements

Authors would like to express our gratitude to The Petroleum and Petrochemical College, Chulalongkorn University, National Centre of Excellence for Petroleum, Petrochemicals and Advanced Materials (PETROMAT), Governing budget and The PTT Public Company Limited (PTT) for funding and industrial data support.

References

1. Kin Wai Cheah, Suzana Yusup, Haswin Kaur Gurdeep Singh, Yoshimitsu Uemura and Hon Loong Lam, "Process simulation and techno economic analysis of renewable diesel production via catalytic decarboxylation of rubber seed oil – A case study in Malaysia." *Journal of environmental Management* (2017) 1-12
2. Angsana Kantama, Phavane Narataruksa, Piyapong Hunpinyo and Chaiwat Prapainainar, "Techno-economic assessment of a heat-integrated process for hydrogenated renewable diesel production from palm fatty acid distillate." *Biomass and Bioenergy* (2015) 83 448-459
3. Mathias Šnãre and Iva Kubic'kova, "Heterogeneous Catalytic Deoxygenation of Stearic Acid for Production of Biodiesel", *Industrial & Engineering Chemistry Research* (2006) 45 5708-5715

A Bilevel Decomposition Method for the Simultaneous Synthesis of Utility Systems, Rankine Cycles and Heat Exchanger Networks

Cristina Elsido,^a Emanuele Martelli,^{a*} Ignacio E. Grossmann^b

^a *Politecnico di Milano, Dipartimento di Energia, Via Lambruschini 4, Milano, IT*

^b *Department of Chemical Engineering, Center for Advanced Process Decision-Making, Carnegie Mellon University, Pittsburgh, PA, USA*

emanuele.martelli@polimi.it

Abstract

This work tackles the simultaneous optimization of utility systems, Rankine cycles and heat exchanger networks (HEN). Thanks to the combination of two superstructures (Rankine cycle and HEN), all heat integration options between heat sources/sinks and Rankine cycle can be considered, and the trade-off between efficiency and plant costs is optimized. On the other hand, the resulting MINLP is extremely challenging due to its large number of binary variables and bilinear terms. We present an ad-hoc bilevel decomposition algorithm based on the McCormick relaxation with reinforcement constraints, piecewise linearization of the cost functions and “nested” integer cuts. The algorithm is applied to literature and real-world case studies to show its effectiveness compared to commercial MINLP solvers and metaheuristic algorithms.

Keywords: nonconvex MINLP, bilevel decomposition, McCormick relaxation, utility systems, Rankine cycle superstructure.

1. Introduction

The heat integration problem involves the design and synthesis of the Heat Exchanger Network (HEN) and the utility systems necessary to provide thermal, refrigeration, mechanical and electric power to the process units of energy systems and chemical processes. A key role is often played by steam cycles and, in general, Rankine Cycles, because of their capability of converting waste heat into useful mechanical power and/or achieving high efficiency by cogenerating heat/steam and power for the plant. Several authors, for instance (Papoulias & Grossmann, 1983; Bruno et al., 1998), proposed approaches to improve the design of steam cycles and steam networks. However, the optimization of the steam generator layout (pre-heating, evaporation and superheating) and of the possible integration options with the process heaters/coolers is not dealt with. Previous studies mainly focus either on the design of utility systems or on the synthesis of HEN, and the two problems are carried out sequentially. Only a few studies tackle both problems together: (Marechal & Kalitventzeff, 1998), (Mian et al. 2016), (Duran & Grossmann, 1986), (Hipólito-Valencia et al., 2013) and (Yu et al., 2017), adapted the sequential framework for HEN synthesis while, more recently, (Martelli et al. 2017) and (Elsido et al., 2017a) proposed a simultaneous approach.

In this work, we present an ad hoc bilevel decomposition to tackle the general model proposed by (Martelli et al., 2017) and extended by (Elsido et al., 2017a) for the

simultaneous optimization of utility systems, Rankine cycles and heat exchanger networks. The model enables the automated generation of Rankine cycles (e.g., Steam Cycles, Organic Rankine Cycles, Heat pump cycles), recovering heat from one or more heat sources, and the HEN of the overall heat integration (i.e., considering also the internal heat exchanger arrangement of the boilers).

2. Mathematical model

The problem of simultaneous optimization of utility systems, Rankine cycles and HEN can be stated as follows: “Given the set of hot and cold streams of the process (i.e., heat sources/sinks), the process needs of hot water/liquid and steam/vapor, the technical limitations (e.g., forbidden/forced matches, no stream splitting, etc.) and economic data (e.g., price of fuels, price of electricity, cost models of process units, etc.), determine the optimal configuration of the Rankine Cycle, the mass flow rates and the optimal HEN.”

The model is based on the SYNHEAT superstructure (Yee & Grossmann, 1990) for the optimal design of heat exchanger networks. The SYNHEAT model is extended to include the streams of the heat recovery cycle, with variable mass flow rate.

The thermodynamic cycles are modelled with a very general “ p - h superstructure” (Elsido et al., 2017a, 2017b), capable of reproducing many configurations of Rankine cycles, both power cycles and inverse cycles (refrigeration cycles or heat pumps), steam cycles or Organic Rankine Cycles (ORC), with single or multiple pressure levels, as well as heat/steam distribution networks. A schematic representation of the Rankine cycle superstructure proposed to tackle the heat recovery steam cycle design problems proposed in this work is represented in Fig. 1. The steam cycle can be designed with up to three levels of pressure. Cycle pressures and temperatures are not optimized. All components have a binary activation variable (ν). Economizers, evaporators, superheaters, reheaters, and condensers are also part of the HEN (i.e., they are streams with variable flow rates).

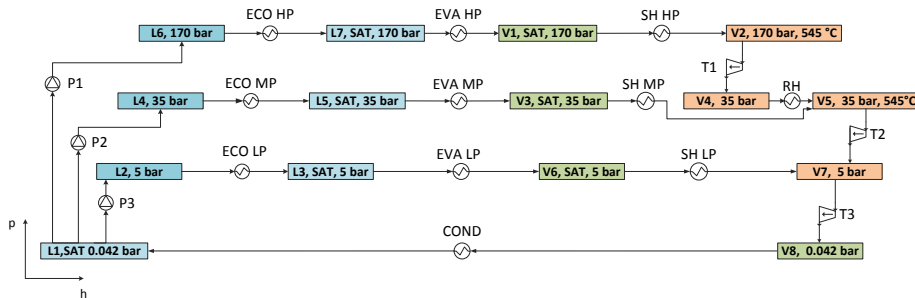


Figure 1: The steam cycle “ p - h superstructure” with three levels of pressure used in this work.

The main constraints are: overall heat balance for each stream (Eq.1); heat balance for stage for non-isothermal streams (Eq.2); feasibility of temperatures (Eq.3); calculation of approach temperature differences (Eq.4); logical constraints such as upper bounds on heat loads, existence of components, no stream splitting, forced and forbidden matches; mass and energy balances on components (Eq.5 and Eq.6). The objective function is the Total Annual Cost (TAC) of the overall plant including HEN, utilities and Rankine cycle, minus revenues (Eq.7). The extended model is a challenging nonconvex Mixed Integer NonLinear Program (MINLP), because of the logarithmic mean temperature difference (LMTD) terms in the objective function (Eq.7) and the bilinear products in the energy balances of the streams with variable mass flow rate (Eq.2).

$$(Tin_i - Tout_i) \cdot F_i \cdot Cp_i = \sum_k \sum_j q_{ijk} + qcu_i, \forall i \quad (1)$$

$$(Tout_j - Tin_j) \cdot F_j \cdot Cp_j = \sum_k \sum_i q_{ijk} + qhu_j, \forall j$$

$$(t_{i,k} - t_{i,k+1}) \cdot F_i \cdot Cp_i = \sum_j q_{ijk}, \forall i, k \quad (t_{j,k} - t_{j,k+1}) \cdot F_j \cdot Cp_j = \sum_i q_{ijk}, \forall j, k \quad (2)$$

$$t_{i,k} \geq t_{i,k+1}, \forall i, k \quad t_{j,k} \geq t_{j,k+1}, \forall j, k \quad (3)$$

$$dt_{ijk} \leq t_{i,k} - t_{j,k} + \Delta T_{ij,max} (1 - z_{ijk}), \forall i, j, k \quad (4)$$

$$\sum_{in} F_{c,in} - \sum_{out} F_{c,out} = 0, \forall c \quad (5)$$

$$\sum_{in} F_{c,in} h_{c,in} - \sum_{out} F_{c,out} h_{c,out} + Q_{c,in} - Q_{c,out} - P_{c,out} = 0, \forall c \quad (6)$$

$$TAC = \sum_c FC_c y_c + \sum_{ijk} FC_{ij} z_{ijk} + \sum_c VC_c F_c^\alpha + \sum_{ijk} VC_{ij} \left(\frac{q_{ijk}}{U_{ij} LMTD_{ijk}} \right)^\beta - R \quad (7)$$

3. Bilevel decomposition

While (Mistry & Misener, 2016) proposed an outer approximation algorithm for the global solution of a similar problem with bilinear terms and LMTD, this work proposes a bilevel decomposition. In the first stage (i.e., the “master” problem), a linearized and relaxed version of the original problem (MILP) is solved, then, in the second stage, for fixed binary variables, the continuous variables are re-optimized solving a nonconvex nonlinear program (NLP). Two nested loops of integer cuts allow exploring different system configurations very efficiently.

3.1. Master problem

The master problem includes all the linear constraints of the full MINLP problem while the bilinear terms ($F_i t_{i,j,k}$) in the energy balance constraints in Eq.2 (due to the variable mass flow rates of utility streams, F) are linearized with McCormick relaxations (McCormick, 1976), as shown in Eq.8. Since for each utility component the lower bound of F is zero when the component is not selected ($y = 0$) and F^L when it is selected ($y = 1$), the auxiliary variable θ is needed to replace the product between t and y .

$$\begin{aligned} Ft &\geq Ft^L + F^L \theta - F^L yt^L & Ft &\geq F^U t + Ft^U - F^U t^U \\ Ft &\leq Ft^U - F^L yt^U + F^L \theta & Ft &\leq F^U t + Ft^L - F^U t^L \\ \theta &\geq yt^L & \theta &\geq t + yt^U - t^U & \theta &\leq yt^U & \theta &\leq t + yt^L - t^L \end{aligned} \quad (8)$$

Since the relaxation of the energy balance equations of temperature stages (Eq.2) overestimates the availability of high temperature heat, the heat cascade (Papoulias & Grossmann, 1983) constraints (i.e., the linear heat balance constraints for each temperature zone defined by the inlet temperature of streams) are included in the MILP. These constraints guarantee heat transfer feasibility and tighten the relaxation.

The nonlinear terms for the calculation of the areas of the heat exchangers, using Chen approximation (Chen, 1987) for the LMTD, are linearized with first order Taylor's series expansions. The exponential expression of the costs of components, such as heat exchangers and turbines, are linearized with piecewise linearization.

3.2. NLP subproblem

In the second stage, the binary variables from the solution of the master problem (i.e., the plant configuration and heat exchangers layout) are fixed. The continuous variables of the nonlinear subproblem are optimized with a nonlinear optimization algorithm, with the TAC as objective function. The solution of the subproblem yields a valid upper bound for the problem.

3.3. Nested integer cuts and termination criterion

In each iteration, the MILP master problem and the NLP subproblem are solved in sequence, and integer cuts are added to the master level at each iteration to exclude the binary solutions already evaluated. Fig. 2 shows the scheme of the algorithm. Two types of integer cuts are added in nested loops: the outer loop adds "utility cuts" on the binary selection variables of the utilities and Rankine cycle components (y), while the inner loop, for fixed utility selection/cycle configuration, adds "HEN cuts" on the selection of heat exchangers (z). "HEN cuts" are added at each iteration, while "utility cuts" are added after $N_{I,MAX}$ iterations without solution improvement. The algorithm stops after $N_{TOT,MAX}$ iterations without solution improvement.

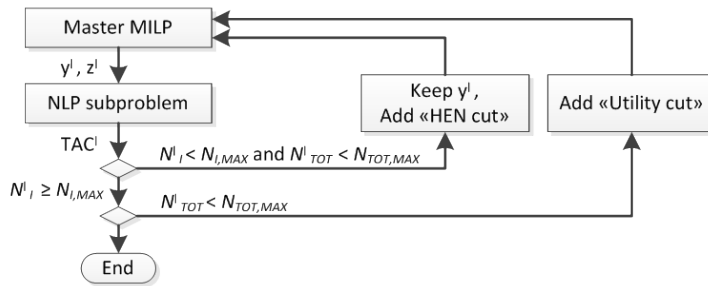


Figure 2: Scheme of the algorithm. For each iteration l , N^l_I and N^l_{TOT} count the number of iterations with no solution improvement respectively in the inner loop and overall.

4. Test cases

The methodology is used to optimize the design and the HEN of three different real-world test cases reported in literature.

- Design and HEN of a Heat Recovery Steam Cycle (HRSC) of a Combined Cycle (Martelli et al., 2017). The only hot process stream is the stream of flue gases of a gas turbine. The steam cycle superstructure is represented in Fig.1. The full MINLP problem has 2,060 variables (446 binaries) and 4,245 equations.
- Design and HEN of a geothermal Organic Rankine Cycle (ORC). The only hot process stream is represented by geothermal hot water. The ORC superstructure, with pentane as working fluid, and the data for the problem are described in (Elsido et al., 2017b). The full MINLP problem has 1,231 variables (270 binaries) and 2,371 equations.

- Design of HRSC and HEN of an Integrated Gasification Combined Cycle (IGCC) plant (Martelli et al., 2017) with 9 hot process streams and 4 cold process streams in addition to the streams of the superstructure. The steam cycle superstructure is the same as for the Combine Cycle test case. The full MINLP problem has 8,608 variables (1,999 binaries) and 15,737 equations.

For all test cases, Rankine cycle pressures and temperatures have not been optimized. The proposed bilevel decomposition algorithm is solved using CPLEX as solver for the MILP master problem and the Sequential Quadratic Programming algorithm of SNOPT for the NLP subproblem. The results are compared with two alternative solution strategies: direct solution of the nonconvex MINLP problem with the global MINLP solver BARON (Tawarmalani & Sahinidis, 2005), and a meta-heuristic two-stage algorithm, consisting of the Variable Neighbourhood Search (VNS) in the first stage for the binary variables and SNOPT for the real variables, as described in (Martelli et al., 2017). Computational results are reported in Table 1.

Table 1. Computational results of the test problems.

	BARON	Two-stage (Martelli et al. 2017)	Bilevel (this work)
Combined Cycle			
Best solution found, M\$/y	-37.0	-42.8	-42.8
Computational time, s	20,000 (limit)	6,000	120
Number of iterations		50,000	50
ORC			
Best solution found, M\$/y	-0.277	-0.321	-0.357
Computational time, s	20,000 (limit)	4,000	41
Number of iterations		20,000	48
IGCC			
Best solution found, M\$/y	No feasible sol.	-86.7	-88.5
Computational time, s	20,000 (limit)	6,000	2,000
Number of iterations		10,000	60

It should be noticed that a negative value of the objective function represents a revenue. In all cases, BARON has the worst performances in solving the challenging nonconvex MINLP problem among the three methods. Indeed, it reaches suboptimal solutions for the Combined Cycle and the ORC cases and not even finding a feasible solution for the IGCC test case. On the other hand, the bilevel decomposition method is very effective, finding the best solutions in all cases (16-29 % better objective values than BARON) with a computational time up to 2 orders of magnitude shorter than to the other two approaches.

5. Conclusions

We presented an ad-hoc bilevel decomposition method to solve complex optimization problems for the simultaneous design of utility systems, Rankine cycles and HEN. The literature and real-world case studies proved that the bilevel decomposition method, compared to commercial MINLP solver and meta-heuristic two-stage algorithm, is the most effective both in terms of computational time and quality of the solutions found.

Nomenclature

Indices

i, j hot/cold process or utility stream
 k index for temperature stage
 c component of Rankine cycle
 in input, out output
 L, U lower/upper bound
Parameters
 C_p heat capacity
 T_{in}, T_{out} inlet/outlet temperature
 U heat transfer coefficient
 ΔT_{max} upper bound for temp. difference
 h enthalpy
 FC fixed cost for component/exchanger
 VC flow/area cost coefficient
 α, β exponent for component/area cost

Binary Variables

z existence of heat exchanger
 y existence of utility/Rankine cycle component

Continuous variables

F mass flow rates of streams (fixed for process streams)
 t temperature of streams at a stage
 dt approach temperature difference
 $LMTD$ log mean temperature difference
 q, q_{cu}, q_{hu} heat exchanged
 Q thermal power
 P electric power
 R revenues from electricity selling
 TAC Total Annual Cost
 θ auxiliary variable for McCormick relaxations

References

- J. Bruno, F. Fernandez, F. Castells & I.E. Grossmann, 1998. A rigorous MINLP model for the optimal synthesis and operation of utility plants. *Trans IChemE*, 76(A), 246–258.
- J. Chen, 1987. Letter to the editors: comments on improvement on a replacement for the logarithmic mean. *Chemical Engineering Science*, 42, 2488–2489.
- M.A. Duran & I.E. Grossmann, 1986. Simultaneous optimization and heat integration of chemical processes. *AIChE J.* 32 (1), 123–138.
- C. Elsidó, A. Mian, F. Marechal & E. Martelli, 2017a. A general superstructure for the optimal synthesis and design of power and inverse Rankine cycles. *Computer Aided Chemical Engineering*, 40, 2407–2412.
- C. Elsidó, A. Mian & E. Martelli, 2017b. A systematic methodology for the techno-economic optimization of Organic Rankine Cycles. *Energy Procedia*, 129, 26–33.
- B.J. Hipólito-Valencia et al., 2013. Optimal integration of organic Rankine cycles with industrial processes. *Energy Conversion & Management*, 73, 285–302.
- F. Marechal & B. Kalitventzeff, 1998. Process integration: Selection optimal utility system. *Computers & Chemical Engineering*, 22, S149–S156.
- E. Martelli, E. Amaldi & S. Consonni, 2011. Numerical optimization of heat recovery steam cycles: Mathematical model, two-stage algorithm and applications. *Computers & Chemical Engineering*, 35(12), 2799–2823.
- E. Martelli, C. Elsidó, A. Mian & F. Marechal, 2017. MINLP Model and two-stage Algorithm for the Simultaneous Synthesis of Heat Exchanger Networks, Utility Systems and Heat Recovery Cycles. *Computers & Chemical Engineering*, 106, 663–689.
- G.P. McCormick, 1976. Computability of global solutions to factorable nonconvex programs: Part I – Convex underestimating problems. *Mathematical Programming*, 10(1):147–175.
- A. Mian, E. Martelli & F. Marechal, 2016. Framework for the Multiperiod Sequential Synthesis of Heat Exchanger Networks with Selection, Design, and Scheduling of Multiple Utilities. *Industrial & Engineering Chemistry Research*, 55, 168–186.
- M. Mistry & R. Misener, 2016. Optimising heat exchanger network synthesis using convexity properties of the logarithmic mean temperature difference. *Comp. & Chem. Eng.*, 94, 1–17.
- S.A. Papoulias & I.E. Grossmann, 1983. A structural optimization approach in process synthesis - II Heat Recovery Networks. *Computers & Chemical Engineering*, 7(6), 707–721.
- M. Tawarmalani & N.V. Sahinidis, 2005. A polyhedral branch-and-cut approach to global optimization. *Mathematical Programming*, 103(2), 225–249.
- T. Yee & I.E. Grossmann, 1990. Simultaneous optimization models for heat integration—II. Heat exchanger network synthesis. *Computers & Chemical Engineering*, 14(10), 1165–1184.
- H. Yu et al., 2017. Simultaneous heat integration and techno-economic optimization of Organic Rankine Cycle (ORC) for multiple waste heat stream recovery. *Energy*, 119, 322–333.

Energy and exergy analysis for cryogenic process design/retrofit

Nattawat Threerachannarong^a, Kitipat Siemanond^{a*}

^a*The Petroleum and Petrochemical College, Chulalongkorn University, Bangkok, Thailand*

kitipat.s@chula.ac.th

Abstract

While the oil price has been decreasing dramatically, downstream petrochemical industries using by-products from upstream process such as methane, ethane, and others are still growing due to demand of domestic products e.g., plastic and resin. The downstream process like LNG production or Gas separation processes needs refrigeration system for cooling the natural gas to reach the proper condition which requires high energy consumption of compressor work, evaporator and condenser. To gain more benefit, reduction of utilities are the main goal. For this purpose, exergy analysis has been applied with pinch analysis called Extended Pinch Analysis and Design (ExPANd) (Aspelund et al., 2007) to reduce that work by adjusting the pressure and temperature. Besides that, graphical and mathematical models have been used to identify efficient condition by using the exergetic temperature concept (Marmolejo-Correa et al., 2012) which is the energy quality parameter. This parameter can be used to conduct the $T^{E^T} - \dot{E}^T$ diagram (Exergetic composite curves) defining the utility consumption that should be reduced by exergy target.

Keywords: Energy analysis, Exergy analysis, Cryogenic process, Optimization

1. Introduction

Low-temperature process which is refrigeration system requires high energy usages for cooling from shaft-work required at compressors and utilities. Consequently, many industrial processes have been improved to gain more profit. In the past, many methodologies to reduce utility consumption and work consumption are proposed such as Pinch Analysis using recovery energy and required energy from steams in process to identify new heat exchanger network (HEN). Although, Pinch Analysis (PA) (Linnhoff and Hindmarsh, 1983) is useful to reduce utility's usage by heat integration, this technic uses only temperature as design variable but pressure is not considered. Therefore, Exergy Analysis (EA) (Linnhoff and Dhole, 1992) was combined with PA to minimize energy consumption by including pressure as design variable. EA has been integrated with the traditional Pinch Analysis, which is called Extended Pinch Analysis and Design (ExPANd) (Aspelund et al., 2007). This method has potential to synthesize the improved design of compressor and expander sequence in term of utility's consumption if the existing plant still has expansions or compressors available. In addition, Exergetic temperature (Marmolejo-Correa et al., 2012) which is the energy quality parameter for identifying the exergy target (exergy loss) and utility's usage in the process is applied in ExPANd. In this research, the case study of liquefied natural gas (LNG) production with refrigeration system; from Pro/II's tutorial as shown in Fig. 1 is used to study optimization of energy consumption.

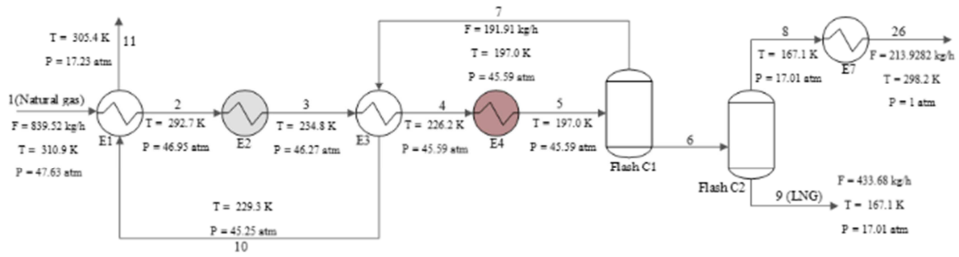


Figure 1: (a) Flowsheet of LNG production from Pro/II's tutorial

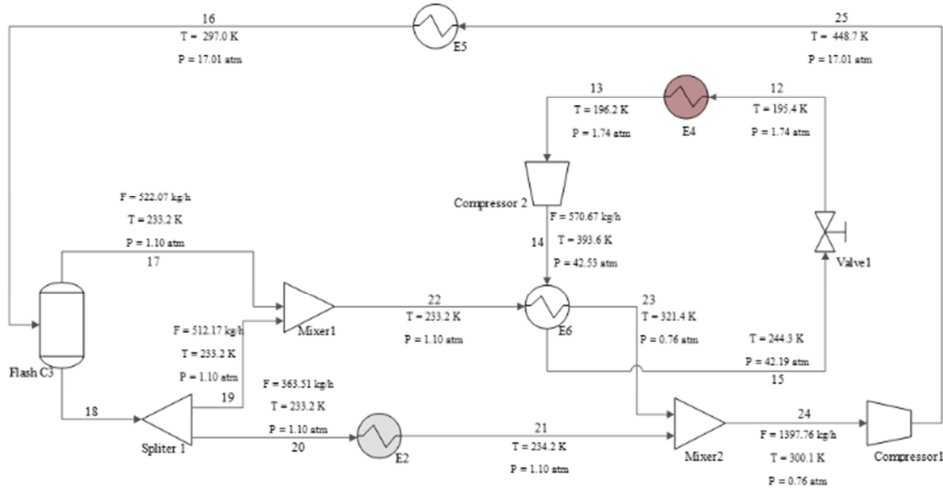


Figure 1: (b) Flowsheet of Base-case refrigeration system

2. Methodology

2.1. Extended Pinch Analysis and Design (Aspelund et al., 2007)

A general methodology is used for designing process by manipulating process streams to reduce utility usage and optimize shaft-work. This methodology is powerful to identify the suitable pressure and temperature for streams, this solution becomes very complex when process has many streams and units operations. Thus, there are heuristic rules to find the favourable ways for manipulating pressure and make the suitable decision for complex design. For example; one of favourable rule, the supply pressure is higher than the target pressure for a cold stream, the available expander should be added in that stream to obtain cold utility and shaft-work from expander when Composite curves requires cold utilities. Other rule is for hot gas or dense fluid with target pressure equal to the supply pressure be compressed to above the pinch point, and cooled to near the pinch point for increasing hot duty. After that, expander will be added in the same stream to adjust pressure to target pressure, besides, this expander generates the additional work and the cold duty. This model consists of four parts: the pinch operator, pressure operator, exergy operator and objective function is shown Fig. 2.

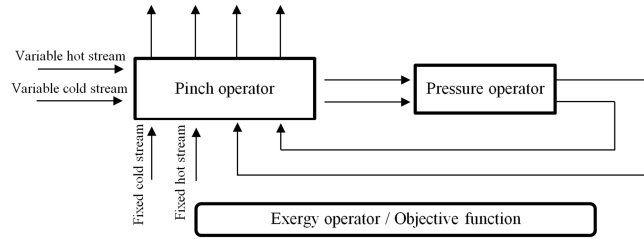


Figure 2: Diagram of identifying the proper state for adding compressor or expander (Aspelund et al., 2007)

The pinch operator is the heart of the optimization model because all streams must be concerned in this operator. Therefore, this model will create a lot of temperature intervals to support varied temperature from calculation and create the new Composite curves to define utility consumption. The pressure operator defines the appropriate compressors or expanders and the proper outlet pressure of these units by using the reversible and adiabatic compression or expansion of an ideal gas that can be formulated as followings:

$$\frac{T_S}{T_1} = \left(\frac{P_2}{P_1}\right)^{\frac{K-1}{K}} \text{ or } (K-1) \ln P_1 + K \ln T_S = (K-1) \ln P_2 + K \ln T_1 \quad (1)$$

$$(T_1 - \tilde{T}_S) = (T_1 - T_S)\eta_c \quad (2) \quad (T_1 - \tilde{T}_S)\eta_e = (T_1 - T_S) \quad (3)$$

$$W_c = Fc_p(\tilde{T}_S - T_1) \quad (4) \quad W_e = Fc_p(T_1 - \tilde{T}_S) \quad (5)$$

The exergy operator's main purpose is to calculate of the exergy of process streams formulated as follows:

$$Ex_{hu} = Q_H \left(1 - \frac{T_0}{T_H}\right) \quad (6) \quad Ex_{cu} = Q_C \left(\frac{T_0}{T_C} - 1\right) \quad (7)$$

Lastly, the objective function is minimization of the combination of results from pinch operator, pressure operator and exergy operator.

$$\text{Objective function} = \text{Min}(Ex_{hu} + Ex_{cu} + W_c + W_e) \quad (8)$$

2.2. Exergetic temperature (T^{ET}) (Marmolejo-Correa et al., 2012)

The exergetic temperature is the energy quality parameter to propose the $T^{ET} - \dot{E}^T$ diagram that plots exergy sources and exergy sinks by defining reference temperature (T_0). Especially, this diagram is proposed parallel with traditional composite curves (CCS). The exergy deficit and surplus are the utility's usage for upper and lower exergy pinch point, respectively. The exergy destruction can be defined by the boundary temperature of hot stream and cold stream form composite curves into the $T^{ET} - \dot{E}^T$ diagram. Moreover, the exergy targets are used for synthesis process by manipulating operating condition as follows: minimum exergy requirement, minimum exergy rejection, minimum exergy destruction and maximum exergy recovery.

$$T^{ET} = \left[T_0 \left(\frac{T_2 - T_1}{T_0} - \ln \frac{T_2}{T_1} \right) \right] \quad (9)$$

$$\dot{E}_{\text{Requirement, min}} = \dot{E}_{\text{Deficit, min}} + \dot{E}_{\text{Destruction, min}} \quad (10)$$

$$\dot{E}_{\text{Rejection, min}} = \dot{E}_{\text{Surplus, min}} - \dot{E}_{\text{Destruction, min}} \quad (11)$$

3. Results

According to the Fig. 1, this LNG production consists one hot stream (Natural gas) and two cold refrigerants (Ethane and Propane). ExPANd model is applied to indicate the proper sequence of adding expander or compressor. The exergetic temperature concept is used to conduct the $T^{E^T} - \dot{E}^T$ diagram for manipulating the appropriate condition to improve the utility consumption using the exergy targets (Eq.9 to11).The model formulations (Eq.1 to8) are used to find the minimum utility. The efficiency factors for work by compressor and expander (η_c and η_e) are constant at 0.8. Moreover, the constraints for pressure and temperature can be defined between the supply value and the target value. Eq. 1 to 3 are used to define the intermediated temperature after passing through turbo machines (compressor or expander). Eq.4to5 are used to calculate work output from turbo machines. Eq.6to7 are used to identify exergy energy for hot and cold utilities. Furthermore, Eq.8 is the objective function in optimization model. Considering the base case, there are compressor work as 155.41 kW, no hot utility and the cold utility as 232.85kW. For overall process, the exergy requirement and rejection are -56.52 kW and 0 kW, respectively. Hence, two cold streams are necessary used as variable stream (10 to 11 and 8 to26). For the first cold stream, $F_{c_p}=0.14$ kW/K, $T_{in}=229.3$ K, $T_{out}=305.4$ K, $P_{in}=45.25$ atm, $P_{out}=17.23$ atm and $\kappa=1.65$. For the other, $F_{c_p}=0.15$ kW/K, $T_{in}=167.1$ K, $T_{out}=298.2$ K, $P_{in}=17.01$ atm, $P_{out}=1.0$ atm and $\kappa=1.55$. When assuming flow rates and heat capacities constant, six available turbo machines can be added in this process to gain better profits.

In case 1, this process added five expanders, three expanders are located between stream No.10 and 11 and the others are located between stream No. 8 and 26. In term of energy, the cold utility is around 175 kW and the produced work is 39 kW.

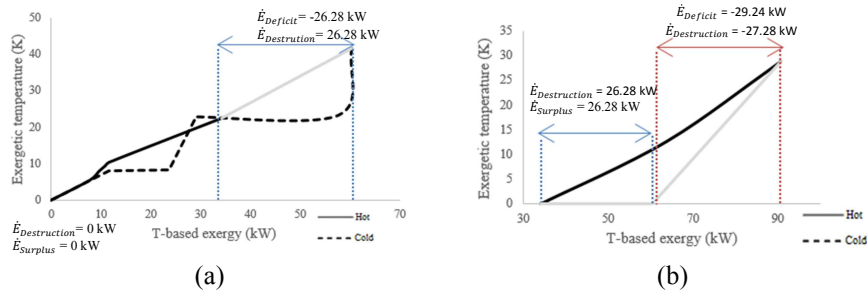


Figure 3: $T^{E^T} - \dot{E}^T$ diagram for Base case (a) below T_0 , and (b) above T_0

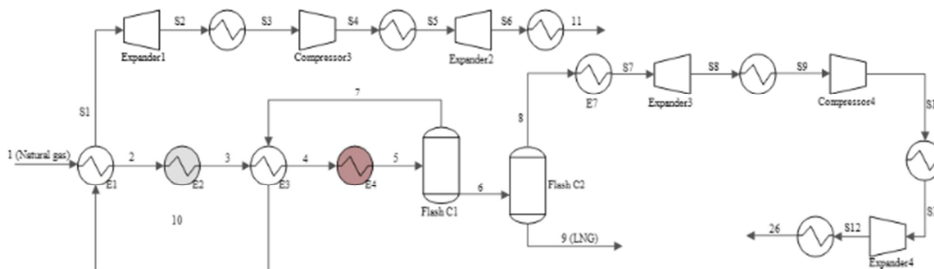


Figure 4: LNG production for Case 3

Table 1: Results for temperature and pressure at heat exchangers

Case1	T _{in} (K)	T _{out} (K)	P (bar)	Case2	T _{in} (K)	T _{out} (K)	P (bar)
10 → S1	229.26	305.37	45.85	10 → S1	229.26	293.55	45.85
S2 → S3	244.26	305.37	26.05	S2 → S3	244.44	302.41	28.84
S4 → S5	297.04	229.26	24.28	S4 → S5	321.36	229.26	33.64
S6 → 11	200.23	305.37	17.24	S6 → 11	176.06	305.37	17.24
8 → S7	167.12	298.15	17.24	8 → S7	167.12	297.97	17.24
S8 → S9	224.60	298.15	7.74	S8 → S9	244.28	298.15	9.83
S10 → 26	145.16	298.15	1.01	S10 → S11	244.26	298.15	5.60
				S12 → 26	162.81	298.15	1.01

Case3	T _{in} (K)	T _{out} (K)	P (bar)	Case4	T _{in} (K)	T _{out} (K)	P (bar)
10 → S1	229.26	305.37	45.85	10 → S1	229.26	305.37	45.85
S2 → S3	239.09	305.37	24.67	S2 → S3	231.87	305.37	22.83
S4 → S5	352.70	305.37	35.54	S4 → S5	360.01	305.37	34.63
S6 → 11	229.48	305.37	17.24	S6 → 11	231.82	305.37	17.24
8 → S7	167.12	298.15	17.24	8 → S7	167.12	298.15	17.24
S8 → S9	171.86	298.15	3.63	S8 → S9	213.64	298.15	6.72
S10 → S11	352.70	298.15	5.84	S10 → S11	213.64	298.15	2.62
S12 → 26	160.37	298.15	1.01	S12 → 26	212.98	298.15	1.01

In case 2, this process added five expanders and one compressor, two expanders and one compressor are located between stream No.10 and 11 and the others are located between stream No. 8 and 26. The improved process uses only the hot utility is around 77kW without the cold utility.

In case 3, no utility consumption is included as the constraint to optimize. This process added four expanders and two compressors. Two compressors and one expander are added in each stream. The diagram of improved LNG production is shown Fig.4.

Lastly, in case 4, the exergetic concept is applied in the ExPANd model using the same six available turbo-machines and $T_0 = 298.15$ K. The new sequence is similar to the case2 but the operating conditions are different. Below T_0 , there are no both of exergy requirement and exergy rejection. Above T_0 , The exergy requirement and exergy rejection are 0 kW. The $T^{E^T} - \dot{E}^T$ diagram is shown Fig. 5. The results of temperature and pressure for these units are shown in Table1. The saving of utilities consumption and shaft-work is shown Table2.

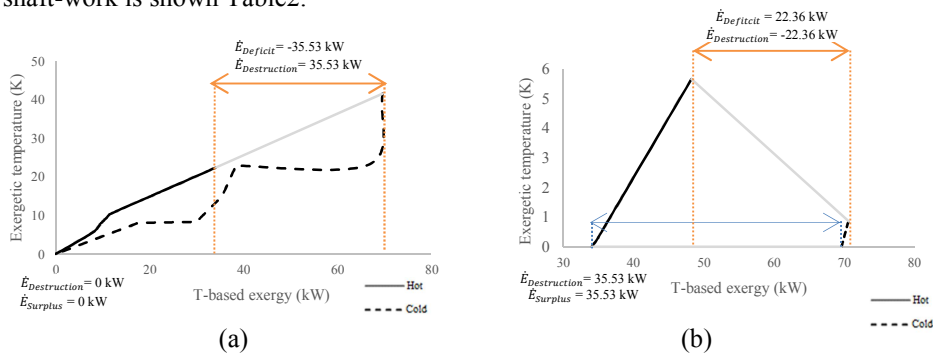


Figure 5: $T^{E^T} - \dot{E}^T$ diagram for Case 4 (a) below T_0 , and (b) above T_0

Table 2: Saving utility results

Case	W_c (kW)	W_e (kW)	Hot utility (kW)	Cold Utility (kW)	Overall saving
Base case	0	0	0	232.85	0
Improved case 1	0	39.00	0	174.75	97.1
Improved case 2	3.15	41.01	77.05	0	193.66
Improved case 3	18.76	48.14	0	0	262.23
Improved case 4	9.80	47.51	0	0	270.56

4. Conclusions

In this study, the synthesis for heat integration with the turbo-machine can be used to reduce the utility consumption. The energy and exergy analysis can be defined the new operating condition and synthesis for the process having the available turbo-machines. Although this methodologies can improve the utility consumption, the calculation of pressure operator is not more accurate. Because the equations are used for the ideal gas. For the optimization, the objective function is the minimum of energy consumption or maximum saving energy usage without concerning the capital cost. The results show the case 4 is the optimal solution because it does not use the utilities and the generated work of the expander overcomes the required work of compressor. In addition, this process can be still improved. For example, the variable stream can change to the others and the operating conditions of refrigeration system are manipulated.

Notation

c_p	heat capacity, kJ/kg K	Q_H	hot utility used, kW
$\dot{E}_{Deficit}$	exergy deficit rate, kW	T_0	ambient temperature, K
$\dot{E}_{Destruction}$	exergy destruction rate, kW	T_1	temperature of inlet streams, K
$\dot{E}_{Rejection}$	exergy rejection rate, kW	T_2	temperature of outlet streams, K
$\dot{E}_{Requirement}$	exergy requirement rate, kW	T_s	temperature of exiting a ideal turbo machine, K
\dot{E}^T	exergy flow based temperature, kW	\tilde{T}_s	temperature of exiting a turbo machine, K
$Excu$	exergy of cold utility, kW	T_U^C	temperature of cold utility, K
$Exhu$	exergy of hot utility, kW	T_U^H	temperature of hot utility, K
F	molar flow rate, kmol/h	T^{E^T}	temperature base exergy, K
H_l	enthalpy at bubble point, kW h / kmol	W_c	work required by compressor, kW
H_v	enthalpy at dew point, kW h / kmol	W_e	work generated by compressor, kW
P_1	pressure of inlet streams, bar	η_c	isentropic efficiency of the compressors
P_2	pressure of exiting a turbo machine, bar	η_e	isentropic efficiency of the expanders
p^{sat}	pressure at saturated, atm	K	polytropic exponent
Q_c	cold utility used, kW		

References

- Aspelund, A., et al. (2007). "An Extended Pinch Analysis and Design procedure utilizing pressure based exergy for subambient cooling." *Applied Thermal Engineering* 27(16): 2633-2649.
- Wechsung, A., et al. (2011). "Synthesis of heat exchanger networks at subambient conditions with compression and expansion of process streams." *AIChE Journal* 57(8): 2090-2108.
- Marmolejo-Correa, D. and T. Gundersen (2012). "A new graphical representation of exergy applied to low temperature process design." 31: 1180-1184.

Ammonia/Urea Production Process Simulation/Optimization with Techno-Economic Analysis

Jiranart Jeenchay^a, Kitipat Siemanond^{a*}

^aThe Petroleum and Petrochemical College, Petroleum Technology, 254 Soi
Chulalongkorn 12 Phayathai road, Bangkok 10300, Thailand
email: jiranart.jeenchay@hotmail.com^a, Kitipat.S@chula.ac.th^{a}*

Abstract

Currently, the global ammonia/urea productions are continuously increasing. Since the demand of crops has been increased, production of fertilizer seems to be suitable for Thailand, a country with primary agricultural development. The purposes of this work are to design conceptual processes of ammonia/urea plants and to do economic analysis and feasibility study. This paper consists of two main parts; simulation of ammonia/urea plants and techno economic analysis. First, the simulation software PRO/II is used to simulate the base-case process. From the base-case studies the principal route of urea production is originally from carbon dioxide and ammonia, which are produced from nitrogen and hydrogen. All conditions and input parameters are obtained from petrochemical industry in Thailand. Finally, techno economic analysis is a key of feasibility study to estimate investment cost and the profitability of project. This technique represents the capital expenditure, the operating expenditure, net present value, payback period, and return of investment. Economic evaluation of the process represented core factors that affect the economic feasibility which are production rate, the conversion of methane to hydrogen, feed temperature of individual reactors, conversion ratio of each reactions, operating pressure, feed temperature to the ammonia/urea synthesis reactors and energy management. The results are expected to be conceptual manufacturing processes of ammonia with the capacity of 3,264 ton per day and urea with the capacity of 2,000 ton per day by using methane as feedstock.

Keywords: Ammonia, Urea, Techno-economic, Simulation

1. Introduction

Ammonia is colourless, pungent gas and a weak alkaline which is very soluble in water. It consisted of nitrogen and hydrogen with formula NH_3 . Ammonia is manufactured by mainly nitrogen and hydrogen in an industrial process called the Haber process. Ammonia is the initial chemical material for several industries. Approximately 88% of apparent ammonia consumption was for fertilizer production, including the manufacture of synthetic fibers and coolers etc. Urea (NH_2CONH_2) is an organic compound of nitrogenous compound containing a carbonyl group attached to two amine groups. It is solid odourless white crystals and non-combustible. Urea is mainly used to produce fertilizer as well. During the production, a lot of money is invested on feedstock, utilities, chemicals, equipment, operating cost and treatment unit in order to produce marketable process industry products on time. Techno-economic analysis is significant

financial decision that can help to estimate the total investment cost and the profitability of this project.

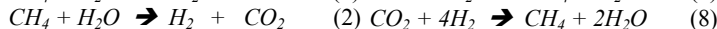
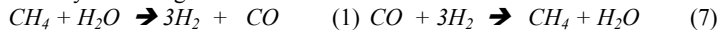
1.1. Properties and Specification

The main feedstock of natural gas is 152 ton/h. The properties of feedstock are shown in Table 1. The ammonia production is 3,264 ton/day of 99.95% purity ammonia. The ammonia product specifications are shown in Table 2. The urea production is capable of processing 2,000 ton/day of 99.99% purity urea. The product specifications are shown in Table 3.

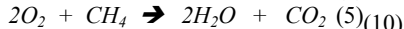
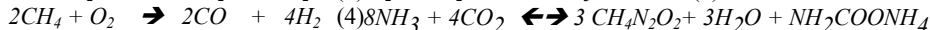
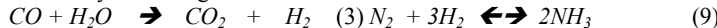
1.2. Ammonia synthesis reactions

Ammonia is produced from nitrogen and hydrogen. Hydrogen is obtained by natural gas (methane) reacting with steam. Nitrogen is obtained by burning hydrogen in air. The operating condition use high temperature about 450-500°C and high pressure about 80-90 bar. The reaction mixture is cooled so that the ammonia is liquefied and removed. The remaining nitrogen and hydrogen are recycled. The overall reaction of ammonia production is shown as following equations.

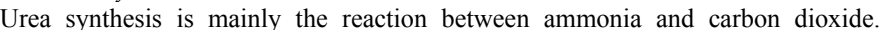
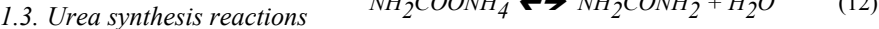
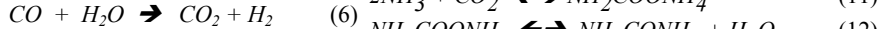
Primary reforming:



Secondary reforming:



Shift conversion:



Carbon dioxide removal:



Ammonia converter:



1.3. Urea synthesis reactions

Urea synthesis is mainly the reaction between ammonia and carbon dioxide. The operating condition use high pressure 20-25 bar with temperature 150-220°C. The overall reaction of urea production is shown as equation 10 -12.

Table 1. Compositions of natural gas feed at condition 15.556°C and 340 psig.

Natural Gas Feed	
Component	% mole
Carbon dioxide	0.028496
Nitrogen	2.105208
Methane	97.471142
Ethane	0.394549
Propane	0.000605
Flowrate (kg-mol/h)	4,238

Table 5. Overall energy consumption of ammonia, urea and sweetening processes.

Process	Energy Consumption		
Ammonia Manufacturing process	Stage 1	1379.3058 x 10 ⁶	kJ/h
	Stage 2	1034330 x 10 ⁶	kJ/h
	Stage 3	252.0069 x 10 ⁶	kJ/h
	Stage 4	5293.1366 x 10 ⁶	kJ/h
	Total	1041260 x 10 ⁶	kJ/h
Urea Manufacturing process	Total	1945.5431 x 10 ⁶	kJ/h
	Total	3791.5721 x 10 ⁶	kJ/h

Table 2. Ammonia product specification

Ammonia Product Specification	
Ammonia purity (% mole)	99.95 %
Flowrate (kg mol/h)	7,243
Temperature (°C)	57.08
Pressure (psig)	350

Table 3. Urea product specification		Table 4. Parameters for economic evaluation	
Urea Product Specification		Parameter	Values
Urea purity (% mole)	99.99%	Base year	2017
Flowrate (kg-mol/h)	1,301	Exchange Rate	32.68 ₺ = 1\$
Temperature (°C)	93.33	Plant lifetime	11 years
Pressure (psig)	0.304	Operating days per year	365
		Interest rate (% per year)	10%, 15%
		Urea processing capacity (tons/day)	2,000
		Urea price (₺/tons)	9,744
		Annual urea capacity (tons/year)	730,000
		Ammonia processing capacity (tons/day)	3,264
		Ammonia price (₺/tons)	9397.5
		Annual ammonia capacity (tons/year)	1,191,360

1.4. Techno Economic Analysis

Techno Economic Analysis is to estimate costs of investment and the profitability of project. This cost assessment technique represents the capital expenditure, the operating expenditure, net present value, pay-back period, and return of investment. These data are used to design and to develop the final ammonia/urea process. For cost indexes the most common one is from IHS CERA index. The equipment costs were estimated by using a guide to chemical engineering process design and economics book shown as equation 13.

$$\text{Present cost} = (\text{capital cost index in 2017} / \text{capital cost index in 2000}) \times \text{previous cost} \quad (13)$$

1.5. Sensitivity Analysis

For ammonia and urea processes, these variables help to identify the main factors affecting the plant feasibility; (a.) Production Rate: varied to keep the feed rate of natural gas as low as possible. (b.) Stream/methane Ratio: varied to maximize the conversion of methane to hydrogen. (c.) Feed Temperatures of the Shift Reactors: varied to control the conversion of CO to CO₂. CO is converted to methane because of carbon dioxide removal reaction leading to high inert CH₄ concentration in the synthesis loop and decreasing profitability. (d.) Air/methane Ratio: varied to maximize methane conversion to hydrogen where H₂/N₂ ratio is 3:1. (e.) Synthesis Loop Pressure: varied to the appropriate pressure for ammonia/urea synthesis reaction. (f.) Feed Temperature to the Ammonia Reactor: varied to lowest temperature. (g.) Conversion percentage: varied to reach optimal condition in each reaction.

2. Methodology

Methodology consists of three parts: simulation of ammonia and urea processes and techno-economic analysis.

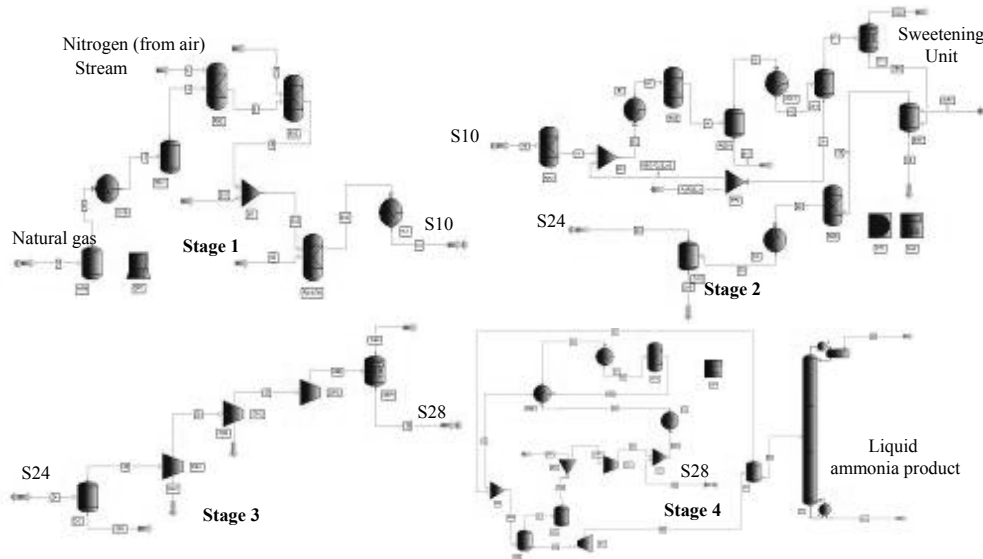


Figure 1. The simulation of ammonia production

This simulation contains three sections: ammonia manufacturing, urea manufacturing, and sweetening process sections.

2.1 Process flow diagram (PFD) – A conceptual design of ammonia production

This ammonia producing process has been simulated by commercial software PRO/II program version 9.4 using SRK thermodynamic model to achieve the ammonia specification. The ammonia plant has production capacity 3,264 ton per day shown in Figure 1. The ammonia manufacturing process is divided into four stages: stage 1 catalytic reforming to produce hydrogen from natural gas containing methane and steam, stage 2 shift conversion and methanation units to purify syngas by removal of carbon dioxide and carbon monoxide, stage 3 compression unit to increase required pressure of syngas, and stage 4 the ammonia conversion.

2.2 Process flow diagram (PFD) - A conceptual design of urea production

The urea plants are capable of producing 2,000 ton per day. The urea producing process has been simulated using NRTL thermodynamic model. This process is to convert CO₂ and synthetic ammonia with high pressure form into urea which is shown in Figure 2.

2.3 Process flow diagram (PFD) - A conceptual design of sweetening process

The objectives of this section are to eliminate carbon dioxide from the ammonia production and to ensure the specification of carbon dioxide is about 0.005-0.2 mole%. AMINE thermodynamic model was used to eliminate impurities. The sweetening unit is displayed in Figure 3.

3. Result and discussion

3.1 Energy requirement of processes

For ammonia plant, total energy consumption in stage 1, stage 2, stage 3, and stage 4 are shown in Table 5. Stage 2 consumes largest amount of energy of 1.03433×10^{12} kJ/h. Cooler (E-3) consumes energy about 50% and the rest 50% is heater (E-5). For urea plant, Urea production consumes energy about 1945.5431×10^6 kJ/hr. Cooler consumes

energy about 81% from overall, the second is reactor “RX2” with 8% including 11% of other units (2% of flash drum, 2% of reactor RX3, 3% of crystalizer, 2% of dryer DR1 and 2% of freezer). Basically, sweetening plant consists of absorber and regenerator columns, a valve, an exchanger and two expander vessels. This process consumes energy about 3791.5721×10^6 kJ/h where reboiler, condenser and cooler (E1) consume energy of 52%, 31%, and 17%, respectively.

3.2 Project economic assessment

Summation of parameters for economic assumptions used to evaluate the techno-economic models are given in Table 4. The cash flow statement summarizes the overall cash flows of both income and outcome of the project as a result of operating activities, investments and financing activities. To maximize profits of this project, there are significant factors are shown in Table 6 which impact on project cash flows. Economic evaluation is set by 10% and 15% of interest rate. Net Present Value (NPV) is analysis of the sum of the present values of future cash flows that invest on project. For urea plant, calculation of equipment cost is based on material and energy balance, operating condition, material handling. Due to the total capital investment (CAPEX) evaluation, F.O.B equipment cost have the biggest impact on capital investment. It's about 415.72 million Baht for urea manufacturing. Total production cost (OPEX) evaluation shows that raw material cost is the largest value about 4.97 billion Baht per year. As a result of the total capital investment (CAPEX) evaluation for ammonia manufacturing, F.O.B equipment cost have a huge investment reached 47.160 billion Baht. In term of total production cost(OPEX), raw material cost is the largest value about 54.926 billion Baht per year.

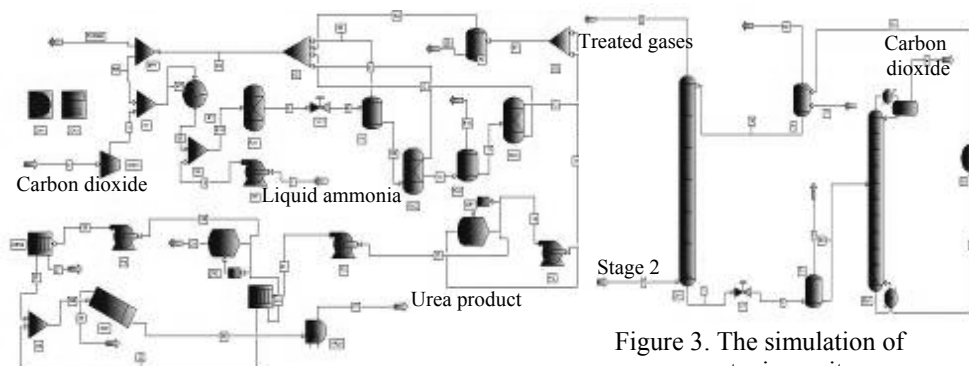


Figure 2. The simulation of urea production

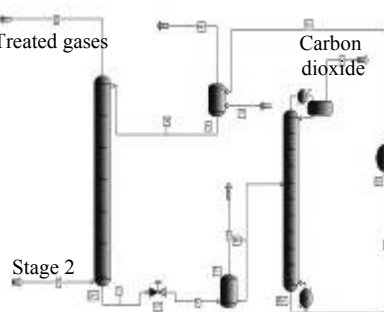


Figure 3. The simulation of sweetening unit

4. Conclusion

Ammonia production is significant material to produce urea. The mainly route of ammonia production was done by Haber process. In this paper, PROII was used to simulate ammonia and urea processes. The capacity of ammonia process is 3,264 ton per day by using natural gas as feedstock. Urea process has the capacity of 2,000 ton per day. The financing decision data for urea manufacturing represented in Table 6. Economic evaluation of urea manufacturing found that NPV is positive value and payback period within 2.75 years. This project is acceptable. In consequence of the total capital investment (CAPEX) evaluation for ammonia manufacturing have a huge investment reached 47.160 billion Baht. Now that total expense is more than total

revenue cost and NPV value is negative. Therefore, ammonia plant is not worth to investment. For the final investment decision, there are 2 cases; Case I: Ammonia and Urea project and Case II: Urea project. By solving an unprofitable project, in this case the major source of ammonia is made from natural gas as the result of high cost of raw materials price so it could end up with investing on only urea project and imported ammonia instead of building the new ammonia plant. Since urea manufacturing is more attractive to invest and high profit. Improvement steps for heat exchanger network will be represented in the future work. Reduction of energy consumption of hot and cold utilities will be considered including the modified heat exchanger investment cost.

Table 6. Technical information and key process parameters in each project.

No.	Description	Urea plant	Ammonia plant
1	Plant capacity, MTPD	2,000	3,264
2	Raw material	Ammonia and Carbon dioxide	Hydrogen is from natural gas
3	Overall energy consumption, kJ/hr	$1,945.5431 \times 10^6$	1.041260×10^{12}
4	Product quality and specification	Urea for 99.99% purity	Ammonia for 99.95% purity
5	CAPEX, ฿	415,716,675	47,160,124,275
6	Working capital cost, ฿	62,357,501	7,074,018,641
7	OPEX, ฿/year	4,973,100	54,926,180
8	Total expenses, ฿	5,016,418,457	61,839,574,139
9	Total revenue, ฿	7,113,237,923	11,195,209,920
10	Financing decision	I = 10%, PBP= 2.75 yrs, NPV= ฿ 5,714,614,708	I = 10%, NPV= ฿ - 195,339,062,737
		I = 15%PBP= 2.75 yrs, NPV= ฿6,170,951,940	I = 15%, NPV= ฿ - 132,539,668,331

Acknowledgements

Authors would like to express our gratitude to The Petroleum and Petrochemical College, Chulalongkorn University, National Centre of Excellence for Petroleum, Petrochemicals and Advanced Materials (PETROMAT) and The PTT Public Company Limited (PTT) for funding and industrial data support.

References

1. Abdolaziz Edrisi et al. "Urea synthesis using chemical looping process – techno-economic evaluation of a novel plant configuration for a green production." *International Journal of Greenhouse Gas Control*, 44 (2016) 42–51.
2. Kin Wai Cheah et al. "Process simulation and techno economic analysis of renewable diesel production via catalytic decarboxylation of rubber seed oil- A case study in Malaysia." *Journal of Environmental Management*, (2017)1-12.
3. Yee, T.F. and Grossmann, I.E.(1990), Simultaneous optimization models for heat integration- II.Heat exchanger network synthesis.*Computers & Chemical Engineering* 10(14),1165-1184

Towards a Quantitative Food-Energy-Water Nexus Metric to Facilitate Decision Making in Process Systems: A Case Study on a Dairy Production Plant

Styliani Avraamidou^{a,b}, Aaron Milhorn^{a,c}, Owais Sarwar^{a,d}, Efstratios N. Pistikopoulos^{a*}

^a*Texas A&M Energy Institute, Artie McFerrin Department of Chemical Engineering, Texas A&M University, College Station TX, 77843, U.S.A.*

^b*Centre of Process Systems Engineering, Department of Chemical Engineering, Imperial College London, London, SW7 2AZ, U.K.*

^c*Department of Systems Science and Engineering, Cornell University, Ithaca, NY, 14850, U.S.A.*

^d*Department of Chemical Engineering, Carnegie Mellon University, Pittsburgh, PA, 15213 U.S.A.*

stratos@tamu.edu

Abstract

While the importance of the Food-Energy-Water Nexus (FEW-N) has been widely accepted, a holistic approach to facilitate decision making in FEW-N systems, along with a quantitative index assessing the integrated FEW-N performance is rather lacking. In this work, we propose a FEW-N metric along with a framework to facilitate decision making for FEW-N process systems through a FEW-N integrated approach.

The framework and metric are illustrated through a case study on a dairy production and processing plant. The dairy industry is a significant user of water and energy, with water being a top issue for most dairy industries and organizations worldwide. Following the framework, we develop a mixed-integer scheduling model, with alternative pathways, that faithfully replicated the major food, energy, and water aspects of a real cottage-cheese production plant. Using the developed FEW-N metric we were able to optimize the cottage-cheese plant process and observe different trade-offs between the FEW-N elements.

Keywords: Food-Energy-Water Nexus, Multi-Objective Optimization.

1. Introduction

The Food-Energy-Water Nexus (FEW-N) is becoming an increasingly significant and active area of research in Process Systems Engineering. Elements of the FEW-N are tightly interlinked and interdependent. For example, 70% of global water use and 30% of global energy use goes towards food production (Garcia and You, 2016).

However, interactions and trade-offs between FEW elements, as well as trade-offs with factors relevant to a decision maker (e.g. Profit), remain difficult to quantify. From a process systems engineering perspective, this makes it very challenging to account for the trade-offs between elements when designing optimized process systems.

The goal of this work is to provide ideas and analysis towards the development of a FEW-N metric, and develop a methodology that will account for the interactions between elements in the FEW-N in a manner that is specific enough to be used in process optimization.

2. FEW-N metric

2.1. Elements and Dependencies of the FEW-N metric

The FEW-N metric can be decomposed into dimensions, indicators, and indexes. In our case-study for example, a dimension we consider is the “Water Dimension.” Indicators for the “Water Dimension” include the amount of water used for cleaning and water used for pasteurization. These “Water Indicators” are then normalized to develop a “Water Index.” This index is then aggregated with the other indices to form a metric.

To develop and analyse a FEW-N metric, we have firstly detailed its components and aggregated their dependencies, illustrated in Table 1.

Table 1 Components and dependencies of the FEW-N metric

Dimensions	<ul style="list-style-type: none"> • FEW elements (produced or used) • Dimensions can include any other decision elements that are relevant to the decision maker (e.g. profit)
Indicators	<ul style="list-style-type: none"> • The method used to measure/quantify each dimension element • The boundary definition of the process system
Dimensional Index	<ul style="list-style-type: none"> • Normalization scheme • Mathematical Form of the metric
Composite Metric	<ul style="list-style-type: none"> • Weight assigned to each index • Mathematical Form of the metric

All dependencies must be developed through extensive research and analysis for each particular process system, therefore a single metric for all FEW Nexus systems is unlikely. Therefore, a methodology for developing such a metric for FEW-N systems will be presented.

The FEW-N metric developed in this work is meant to be used as an ‘optimizable’ measure of a process system’s impact on the FEW-N. The purpose of the metric is not to describe the system relative to other completely different process systems, but to compare the system to other iterations or alternatives of the same system.

2.2. Mathematical Form of the metric

We have tested four different mathematical forms for aggregating FEW elements along with any other element that interest the decision maker (e.g. cost, safety, environmental impact) into one composite metric. For all methods, the objective is to maximize the metric. Metrics include: i) linear average (LA), ii) bilinear average (BA), iii) trilinear average (TA) and iv) quadrilinear average (QA). Metrics are all determined using Eq. 1.

$$r^{\text{th}} \text{ order average} = \frac{\text{Sum of all } r^{\text{th}} \text{ order multiplicative combinations of decision indexes}}{C_r^n} \quad (1)$$

where C_r^n is the total number of possible r^{th} order combinations of n decision indexes. In our study, each index is given the same weight.

2.2.1. Linear average (LA)

The mathematical form of this metric is the simple arithmetic mean of the dimension indexes. Emphasis can be placed on one or more elements by multiplying the element index by a weighting factor. The key property of LA is that it implies perfect substitutability between the elements of the FEW-N. That means that an improvement in one area can be neutralized by proportional worsening in another area.

2.2.2. Higher order averages (BA, TA, QA)

Weighting for those mathematical forms is done by raising the indexes to the power of the weight factor. With increasing order of the average the substitutability between dimensions is decreasing, until the order is equal to the number of dimension elements, where it allows for the least substitutability, and gives the greatest implicit weight to elements that are low in value.

2.3. Normalization scheme

The decision indexes are normalized to values between 0 and 1. The normalization is based upon the maximum and minimum values of each element index that are possible in the process system under investigation. A value of 1 represents the ‘best-case’ scenario (e.g. minimum energy, maximum food, etc.) for the element in the process system.

The proposed metrics were applied to the cottage cheese plant case-study to determine the effect of the mathematical form of the metric on the optimal solution.

3. Case study: Cottage cheese plant

To develop and test our metric and methodology, we used a cottage cheese plant (CCP) case study taken largely from the work of Stefanis et al. (1997). We made considerable additions to Stefanis’ model to better represent the FEW-N trade-offs.

The dairy industry consumes a huge amount of energy and water. In the United States alone, there are over 5,000 dairy plants that discharge over 200 billion liters of waste – water. This waste water is high in Biological Oxygen Demand and contains harmful pollutants and suspended solids and therefore must be treated in energy intensive processes. Still, roughly 40% of this wastewater is discharged directly into bodies of freshwater (Northwest Food Processor Association, 2017).

Cottage cheese in particular requires a large amount of water to be produced, somewhere between 0.8 and 12.4 kg of water per kg of milk processed (Northwest Food Processor Association, 2017). For these reasons, a cottage cheese plant is an excellent case study to observe the FEW Nexus interactions.

3.1. Process description

The process is largely taken from Stefanis et al. (1997), and modifications were made to introduce energy and water elements in the process. The plant specifications are kept the same as in Stefanis et al. (1997), with the required production of cheese being 137.7 t over 5508 h/y production time. Skimmed milk is fed to the process and after pasteurization, is mixed with culture in up to three vat processors with different design specifications for 240 minutes to produce curd and whey. Optionally, the curd is stored before further processing.

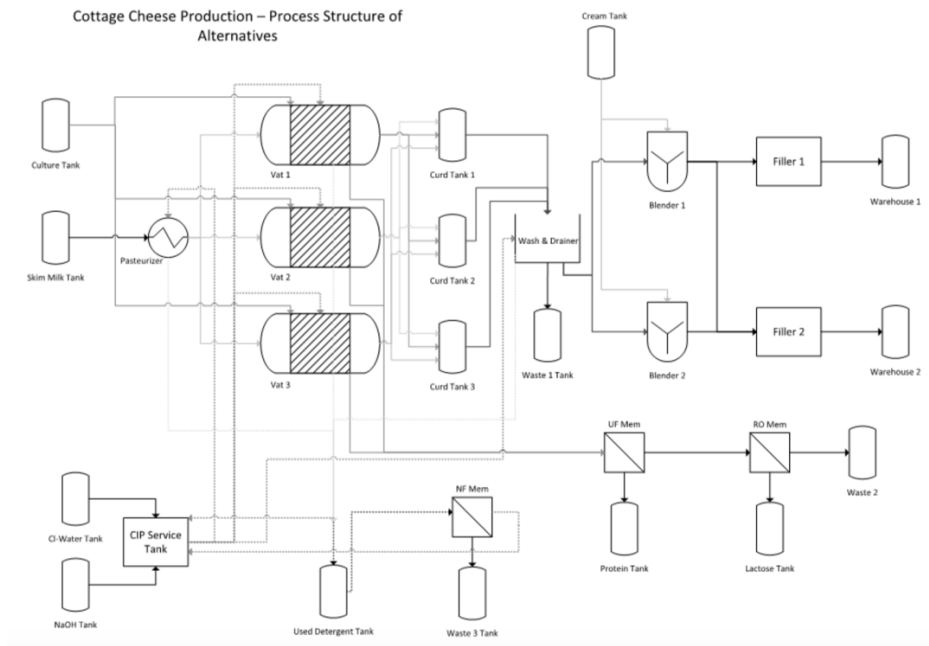


Figure 1 Flowsheet of the Cottage Cheese Plant

The curd is then drained (30 min) and the solidified curd is blended with cream for 60 minutes to produce cottage cheese which is then filled into different size containers (Fillers 1 and 2). The final products are then stored in warehouses for delivery.

The whey by-product is further processed to recover the concentrated protein and lactose (sold as by-products) in two membrane separation stages: the ultrafiltration stage (240 min) and the reverse osmosis stage (60 min). For constant recovery, the ultrafiltration stage is maintained at 4 atm pressure drop while protein by-product recovery and waste generation depend on the operating pressure of the reverse osmosis unit (1.7 - 3.8 atm).

Cleaning-in-Place (CIP) is an essential part of dairy plant operation. All units that involve heating of milk must be cleaned after each use. For this case study, this means that the Pasteurizer, all Vats, and the Drainer must all be cleaned.

Cleaning takes 30 minutes and uses 100 kg of detergent. Detergent is made in the CIP Tank by mixing chlorinated water with NaOH to form a 0.5% NaOH solution. After cleaning, roughly half of the detergent can be recycled. Used detergent is then either stored or sent to nanofiltration (60 minutes) for 90% recovery of clean detergent.

3.1.1. Food aspect of the CCP

The food aspect of the process does not only include the cheese produced, that is constant at 137.7 t per year of operation, but also includes the protein and lactose by-products. Although the amount of cheese and protein produced never varies, there is variability in the amount of lactose that is produced. This variability stems from the pressure of the reverse osmosis unit. At higher pressures, more lactose is produced at increased economic and energy cost.

3.1.2. Energy aspect of the CCP

The energy required to operate the ultrafiltration, nanofiltration, and reverse osmosis units was taken into consideration the same way as in Stefanis et al. (1997). The energy required to raise the cleaning water from room temperature to 50°C was also accounted for and the higher the amount of cleaning, the more energy required (Clark and Potter, 2007). Moreover, we included the energy required to refrigerate the stored milk, cheese, curd, and cream in their respective storage tanks (Sun et al., 2017). These calculations all assumed a constant value for the amount of energy lost per unit time and a coefficient-of-performance for refrigeration. Finally, the amount of energy required to operate the pasteurizer as a function of throughput was accounted for.

3.1.3. Water aspect of the CCP

The water aspects of the process included the steam used for pasteurization, the water used for cleaning, the water used for washing curd (roughly 2.5 times the amount of milk processed) (Clark and Potter, 2007), and the waste water generated by the process. The amount of Waste 2 generated varied with the amount of lactose produced. The more lactose produced, the lower the amount of Waste 2, at the expense of higher energy and operating costs.

The developed scheduling model was implemented in GAMS and consisted of 4,096 equations, 1,241 integer variables and 2,518 continuous variables. The detailed model was excluded here due to page restrictions but can be provided upon request.

4. Optimal solutions

The dimension elements of the FEW-N metric for the case study included the three FEW-N elements and the profit element (Revenue – Operating/Fixed Cost). For each FEW-N metric an optimization problem was formed with objective to maximize each the metric subject to the constraints of the CCP schedule model. For comparison purposes, another four optimization problems were formed and solved to maximize profit and food produced, and minimize energy used and water used.

All optimization problems were solved to 2% optimality using global optimization solvers (BARON and ANTIGONE) for mixed-integer non-linear optimization problems.

The numerical solutions for of each problem created from the metrics are presented in Table 2 and are compared with the value of each metric for various objectives that a decision maker may consider. Objectives included: maximize profit, maximize food production, minimize energy use, and minimize water use. The solution schedule for the LA metric is presented in Fig.2. The full detailed numerical solutions, along with the schedules for BA, TA and QA FEW-N metrics were excluded from the document due to page limitations but can be provided upon request.

Table 2 FEW-N metric value

	Optimal	Maximum Profit	Maximum Food	Minimum Energy	Minimum Water
LA	0.823	0.598	0.598	0.378	0.765
BA	0.660	0.297	0.297	0.085	0.567
TA	0.496	0.098	0.098	0	0.405
QA	0.345	0	0	0	0.279

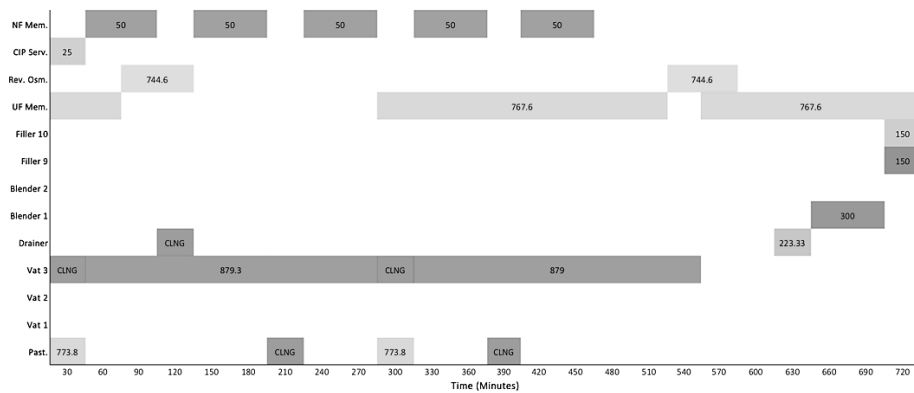


Figure 2 Optimal Schedule for maximum LA FEW-N metric

5. Conclusions

In this work, we were able to define a framework for the development of a quantitative index assessing the integrated FEW-N performance of different process systems that can be used to facilitate decision making in process optimization. The metrics developed were able to accurately quantify the impact of the CCP system on the FEW-N and are general enough that they can be adjusted and applied to a wide variety of process systems while considering any number of decision elements. For the CCP process, it was observed that using any of the mathematical forms of the FEW-N metric we were able to get much better FEW-N solution that optimizing different FEW-N elements individually.

6. Acknowledgement

We are grateful to NIEHS Superfund Research Program (P42 ES027704), Texas A&M Superfund Research Center, Texas A&M University and Texas A&M Energy Institute for the financial support. We are also grateful to the Department of Chemical Engineering of Imperial College London for an EPSRC-funded Doctoral Training Partnership (DTP) studentship.

References

- D. J. Garcia, F. You, 2016, The water - energy - food nexus and process systems engineering: A new focus, *Computers and Chemical Engineering*, Volume 91.
- S.K. Stefanis, A.G. Livingston, E.N. Pistikopoulos, 1997, Environmental impact considerations in the optimal design and scheduling of batch processes, *Computers & Chemical Engineering*, Volume 21, Issue 10.
- Northwest Food Processors Association, 2017, Dairy Processing - Wastewater Management, Accessed Online in June 2017.
- S. Clark, D.E. Potter, 2007, Handbook of Food Products Manufacturing edited by Y. H. Hui, Cottage Cheese. Chapter 26.
- A. Sun, D. Reindl, D. Reinemann, Energy Use in Wisconsin's Dairy Industry and Options for Improved Energy Efficiency. Accessed Online in June 2017.

Numerical Evaluation of Different Turbulence Models for Single-Phase Flow in the Outer Pillow-Plate Channel

Marco Vocciante^{a,b}, Mark Piper^c, Alexander Zibart^b, Eugeny Y. Kenig^{b,d,*}

^a*DCCI, Dipartimento di Chimica e Chimica Industriale, Università degli Studi di Genova, Via Dodecaneso 31, Genova 16146, Italy*

^b*Chair of Fluid Process Engineering, Paderborn University, Pohlweg 55, Paderborn 33098, Germany*

^c*FloCess, Garage 33, Technologiepark 8, Paderborn, 33100 Germany*

^d*Gubkin Russian State University of Oil and Gas, Moscow, Russian Federation.
eugeny.kenig@upb.de (E.Y. Kenig)*

Abstract

Pillow-plate heat exchangers (PPHE) are fabricated as stacks of pillow plates with alternating inner and outer channels. In this contribution, we show results of a numerical investigation of the turbulent single-phase flow ($3000 \leq Re \leq 8000$) in the outer channels performed with the aid of the OpenFOAM[®] simulation software. Several turbulence models based on different approaches (RANS, DES, LES) were tested. The simulation results were compared with pressure loss measurements conducted earlier by our group. Despite inherent simplifications, some advanced RANS models are capable of adequately capturing the complex fluid dynamics in the outer pillow-plate channels, showing results comparable to those of the more time-consuming LES simulations.

Keywords: Pillow plates, Computational Fluid Dynamics, Numerical simulations, Turbulent transport, Heat exchanger.

1. Introduction

Pillow-plate heat exchangers (PPHE) represent an innovative and promising alternative to conventional equipment. The waviness of the pillow plates promotes lateral mixing and turbulence, which results in a good thermo-hydraulic performance, offering a significant energy-saving potential. However, the implementation of PPHE is still limited due to the lack of comprehensive data and publicly available proven design methods, while the range of applicability of existing correlations has not yet been fully determined. To overcome this problem, our group has been intensively studying this equipment type over the past years, using both theoretical and experimental methods. In this contribution, we consider the turbulent single-phase flow ($3000 \leq Re \leq 8000$) in the outer channels formed when several pillow plates are arranged in parallel to stacks.

Nowadays, the range of turbulence models available within modern CFD codes is large illustrating the fact that no single model is suitable for all scenarios. Apart from the Direct Numerical Simulation (DNS), traditionally, two families of models exist: i) SRS (Scale Resolving Simulation) in the form of Large Eddy Simulation (LES) resolve the largest turbulent scales within a flow; ii) RANS (Reynold Averaged Navier Stokes), or URANS (Unsteady-RANS) eddy-viscosity models, which compute mean flow with no attempt to resolve spatial or temporal scales. In recent years, Hybrid SRS/URANS

models have started to appear within codes, such as detached eddy simulation (DES), which combines LES with the use of economical well-tuned URANS in the simulation of near wall flows. Using an appropriate turbulence model is necessary for obtaining reliable results. For this reason, we tested several turbulence models based on different approaches (RANS, DES, LES) with the aid of the open source OpenFOAM® (OF) simulation software. The main objective of this paper is the performance evaluation of simpler turbulence models, including URANS and hybrid SRS, when describing the complex flow in the outer channel of a pillow plate in comparison with LES simulations.

2. Materials and Methods

2.1. Geometry creation and discretization

The genuine pillow-plate geometry has been obtained using forming simulations (Piper et al. 2015), an approach which adequately imitates the hydroforming process during the real manufacturing of pillow plates and thus permits an accurate reconstruction of the wavy pillow-plate channels for all possible variations of the geometric parameters. The computational domain has been defined by exploiting all the existing symmetry planes and the periodicity of the flow to reduce the computational effort. For the domain discretization, a structured body-fitted grid has been adopted. This grid type is ideal for wavy surfaces, since the cells align with the geometry contours, and this property leads to high-quality cells favourable for numerical accuracy and convergence. The grid has been generated by using the commercial software STAR-CCM[†]. Afterwards, the grids have been properly converted for the use in OF release 4.1. The meshes obtained had over 6 million cells. Thanks to the significant refinements applied to the walls, it was possible to reach y^+ values below unity in all the cases simulated in this study.

2.2. Numerical setup

The resolution of transient flow has been achieved with the prebuilt Eulerian solver *pisFoam*, which is the transient solver for incompressible flows using the well-established predictor–corrector PISO (pressure implicit with splitting of operators) algorithm for pressure-velocity decoupling. All diffusive and advection terms were approximated with a second-order accuracy, while a blended first/second order implicit scheme (Crank-Nicolson) was used for time integration. The time step has been varied to assure a maximum Courant number less than 1 for all simulations performed. In our study, the Reynolds number is defined by using the mean stream velocity and the hydraulic diameter, evaluated as the quadruple ratio of the total domain volume and the wet surface given by the two domain walls.

2.3. Turbulence modelling

Since flow separation is expected to occur in the pillow-plate outer channels, it is extremely important to appropriately resolve the velocity boundary layer. The use of standard wall functions (SWF) is expected to be invalid here, because of flow separation and recirculation. On the contrary, Low-Reynolds-number (LRN) turbulence models do not require the specification of the wall-functions for the near-the-wall region treatment, but require a finer mesh for the near-wall region, resulting in higher computational costs. In the LES framework, the ‘unresolved’ turbulent viscosity relates directly to the sub-grid scales (SGS). The Smagorinsky (1963) eddy viscosity is one of the simplest SGS models, but several alternatives exist, a promising one being the WALE (Nicoud and Ducros, 1999), which represents a good compromise between accuracy and computational cost.

Considering advantages and disadvantages of the methods mentioned, in the present work, both RANS and LES were compared. The adopted turbulence treatments are listed in Table 1.

Table 1. Applied turbulence models.

Family	Model	Wall	Notes
RANS	R k- ϵ	SWF	two-equation k- ϵ with realizable option (Shih et al., 1995)
	RNG k- ϵ	SWF	two-equation k- ϵ with renormalization group (Yakhot et al., 1992)
	SA	LRN	one-equation Spalart and Allmaras (1992)
	LL k- ϵ	LRN	two-equation k- ϵ Lien and Leschziner (1993)
	k-kL- ω	LRN	three-equation k-kL- ω (Walters and Cokljat, 2008)
URANS	k- ω SST	LRN	two-equation k- ω with shear stress transport (Menter, 1994)
SRS-	DES k- ω	---	k- ω SST Detached Eddy Simulation (Menter et al., 2003)
URANS	SST		
SRS	LES (SM)	---	Smagorinsky (1963) constant coefficient sub-grid
	LES	---	Wall Adapting Local Eddy Viscosity sub-grid (Nicoud and Ducros, 1999)
	(WALE)		

2.4. Boundary conditions

To reduce the computational effort, we used periodic boundary conditions in the problem under study. However, a specified pressure gradient is needed to drive the flow. This means that the values of pressure on the left and right edges of the domain must be different, and thus, applying periodic boundary conditions directly on the pressure is not possible. An easy strategy to overcome this problem is to split the local pressure into two parts: a linearly-varying component and a residual component, $p = P + p'$. In this way, it is possible to fix the applied pressure gradient (the gradient of the linearly-varying component), which is constant and can be interpreted as a source term, $-\partial P/\partial y = F$, and numerically resolve only the perturbations in pressure, represented by the residual component $\partial p'/\partial y$. In addition, the source term introduced, which acts as a volume force in every point of the domain, can easily be tuned to suitably change the flow conditions. In particular, for each turbulent model investigated, this parameter has been progressively increased from a certain starting condition, verifying the convergence of the system at each of the assumed values. Thus, each simulation is initialised with a velocity field very similar to the sought solution, and in this way, instability and convergence problems are reduced.

2.5. Code validation

In Figure 1, the specific pressure loss determined by CFD simulations is validated using the data obtained from experiments performed by our group (Piper et al. 2016). The numerical results agree well with the experiment over the entire range of Reynolds numbers investigated here (3000-8000). The best fit shows a relative error around 5 % for the DES simulation, whereas for the other cases, the deviation varies from 10 to 20%. Surprisingly the k- ω SST model exceeds 50% deviation from the expected values. This means inadequacy with regard to the phenomenon in question. It is interesting to note that the LES approach with SM sub-grid model also fails, at least in the configuration adopted in the present study, in evaluating pressure losses along the outer channel, with an overprediction of more than 20%, whereas the simplest model, SA, yields just around 10% underestimation.

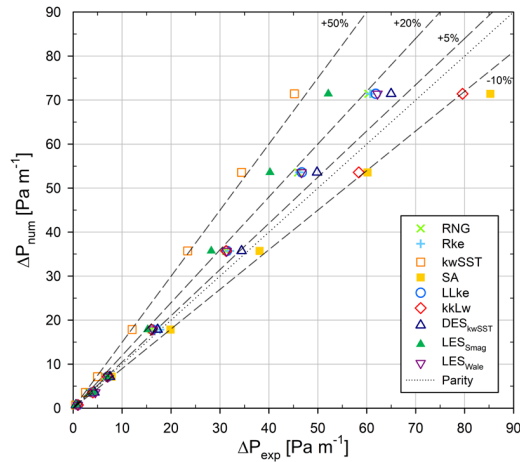


Figure 1. Comparison of numerical and experimental results for pressure loss in the outer pillow-plate channel for $3000 \leq Re \leq 8000$.

3. Results and Discussion

Figure 2 qualitatively shows the vortex structures arising upstream of the welding spots. They result from the significant cross-section variation in stream-wise direction of the outer channel, which leads to an adverse pressure gradient and causes boundary layer separation. The fluid located in the vortices is transported spirally outwards away from the troughs; it is then directed diagonally into the next downstream trough.

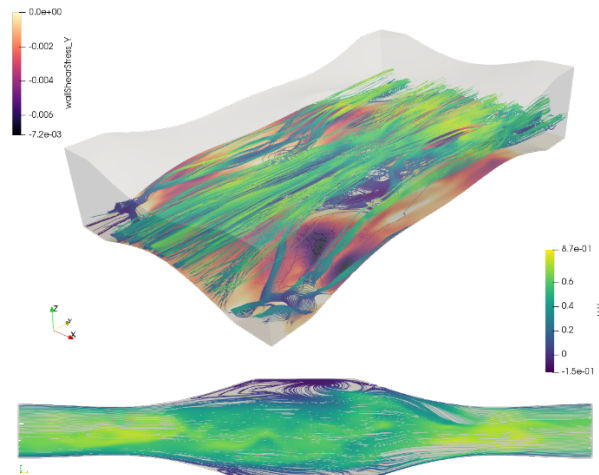


Figure 2. Illustration of the characteristic flow pattern in the outer pillow-plate channel, with vortex structures (represented by streamlines) arising near the welding spots ($Re=8000$).

The size of these vortices can be evaluated more clearly by the regions of negative wall shear stress τ_w in Figure 3, indicating recirculation of the flow. The recirculation zones cause form drag, which contributes approximately 50% of the Darcy friction factor. After boundary layer re-attachment, the flow is re-accelerated out of a trough.

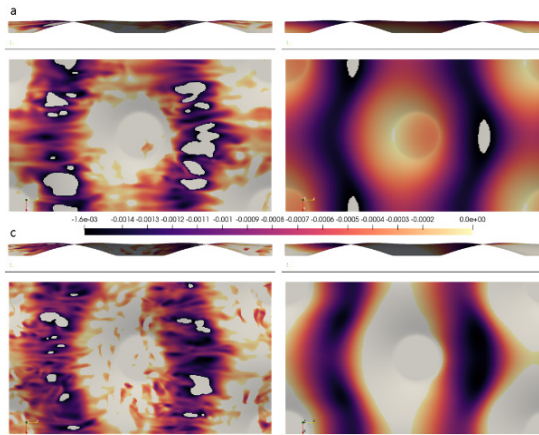


Figure 3. Comparison of shear stress profiles at inferior wall for $Re=5000$. a) DES $k-\omega$ SST; b) $k-\omega$ SST; c) $k-kL-\omega$; d) SA. Size of recirculation zones is represented by $\tau_w, \leq 0$. τ_w [$m^2 s^{-2}$] is rescaled by dividing by the density of the fluid (water at 25 °C).

We also investigated the evolution of the Darcy friction factor $\zeta_{\Delta p}$ in the range $3000 \leq Re \leq 8000$. Based on previous studies, the best fit for the Darcy friction factor for the outer channel is represented by $\zeta_{\Delta p} = 3.46Re^{-0.39}$ with a maximum deviation of 2% (Piper et al. 2016). This relation has been employed as reference in Figure 4, where the $\zeta_{\Delta p}$ prediction by all the investigated turbulence models are compared. Similar results to what seen for Δp can be drawn for the prediction of $\zeta_{\Delta p}$, with $k-\omega$ SST model giving the worst performance (over 50% deviation from the expected value). Nevertheless, all the other models, regardless of their prediction capacity on pressure losses, are able to adequately capture the trend of the coefficient and provide values very close to the expected ones. Also in this case, the best fit is given by the DES $k-\omega$ SST model.

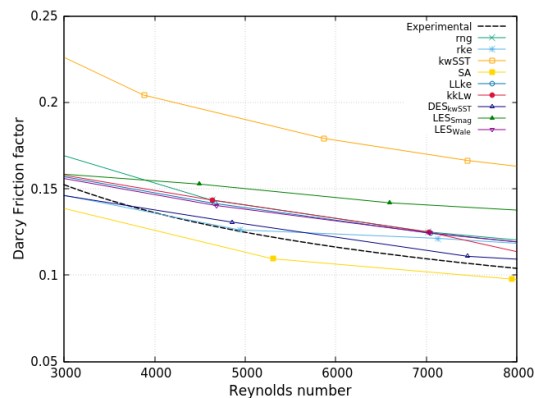


Figure 4. Evolution of the Darcy friction factor in the outer pillow-plate channel as a function of the Reynolds number.

4. Conclusions

The turbulent single-phase flow in the outer channel of a pillow plate was investigated using OpenFOAM[®]. Several turbulence models were tested. DES $k-\omega$ SST seems to be

an optimal approach: it provides the best agreement with experiments, has lower computational costs and is easier to configure compared to LES simulation. Some advanced RANS models are also capable of adequately capturing the complex flow in the outer pillow-plate channels, showing results comparable to those of the more time-consuming LES simulations. In particular, k - kL - ω ensure a reasonable fit to experiments, thanks to the improved wall treatment, whereas SA shows the ability to catch the average characteristics of the flow in a very satisfactory way considering its inherent simplicity, and certainly, it is a choice to be preferred for general studies. On the contrary, k - ω SST seems to be inadequate in our case, despite that it is known to be a well performing model for the simulation of flows subject to separation.

Acknowledgement

Marco Vociante sincerely acknowledges the financial support of the German Academic Exchange Service (DAAD).

References

- F.S. Lien, M.A. Leschziner, 1993, A pressure-velocity solution strategy for compressible flow and its application to shock/boundary-layer interaction using second-moment turbulence closure, *J. Fluids Eng.* 115(4), 717-725.
- F.R. Menter, 1994, Two-equation eddy-viscosity turbulence models for engineering applications. *AIAA Journal* 32(8), 1598-1605.
- F.R. Menter, M. Kuntz, R. Langtry, 2003, Ten Years of Industrial Experience with the SST Turbulence Model, *Turbulence, Heat and Mass Transfer 4*, ed: K. Hanjalic, Y. Nagano, M. Tummers, Begell House, Inc., 625-632.
- F. Nicoud, F. Ducros, 1999, Subgrid-scale stress modelling based on the square of the velocity gradient tensor, *Flow Turbul. Combust.* 62(3), 183-200.
- M. Piper, A. Olenberg, J.M. Tran, E.Y. Kenig, 2015, Determination of the geometric design parameters of pillow-plate heat exchangers, *Appl. Therm. Eng.* 91, 1168-1175.
- M. Piper, J.M. Tran, E.Y. Kenig, 2016, A CFD study of the thermo-hydraulic characteristics of pillow-plate heat exchangers, *Proc. ASME 2016 Heat Transfer Summer Conference*, Washington, D.C. (USA).
- T.H. Shih, W. Liou, A. Shabbir, Z. Yang, J. Zhu, 1995, A new k - ϵ eddy-viscosity model for high Reynolds number turbulent flows – model development and validation, *J. Comput. Fluids* 24(3), 227-238.
- J. Smagorinsky, 1963, General circulation experiments with the primitive equations: I. the basic experiment. *Mon. Weather Rev.* 91, 99-164.
- P.R. Spalart, S. Allmaras, 1992, A one equation turbulence model for aerodynamic flows. In: 30th aerospace sciences meeting & exhibit, Reno, NV, 1992.
- D.K. Walters, D. Cokljat, 2008, A three-equation eddy-viscosity model for Reynolds-averaged Navier–Stokes simulations of transitional flow, *J. Fluids Eng.* 130(12), 121401.
- V. Yakhot, S.A. Orszag, S. Thangam, T.B. Gatski, C.G. Speziale, 1992, Development of turbulence models for shear flows by a double expansion technique, *Phys. Fluids A: Fluid Dynamics* (1989-1993), 4(7), 1510-1520.

Improving Convergence Behavior of Nonlinear Equation Systems in Intensified Process Models by Decomposition Methods

Saskia Bublitz^{a,*}, Erik Esche^a, Gregor Tolksdorf^a and Jens-Uwe Repke^a

^a*Process Dynamics and Operations Group, Technische Universität Berlin, Sekr. KWT 9, Str. des 17. Juni 135, D-10623 Berlin, Germany*

saskia.bublitz@tu-berlin.de

Abstract

The two decomposition methods Dulmage-Mendelsohn (DM) decomposition and bordered block transformation (BBTF) have been examined on their capabilities to eliminate convergence problems during the iteration of large, nonlinear equation systems as they occur frequently in process modeling. They both divide the overall system into lower dimensional subsystems, which can be solved separately in sequence. Exemplarily these methods were applied on the model of a reactive distillation column, where the decomposed systems show a higher robustness with respect to systematically selected initial points compared to the original system. Nevertheless, the improvement in DM seems small since a large subsystem with 576 of the 664 model equations remains. The convergence result from the iteration of the BBTF decomposed system depends a lot on the initial values for certain strongly coupled variables called tearing variables. In future, methods will be investigated and may also be developed to further reduce the dimension of the subsystems in DM and provide accurate initial values for the tearing variables in BBTF.

Keywords: Numerical methods, Efficiency, Robustness, Condition number

1. Introduction and Motivation

In order to enhance the economic potential of processes in chemical industry their concepts become steadily more complex due to the increasing usage of recycles or multiple operations within one apparatus as in process intensification. The occurring interrelations cause difficulties for both physical modeling and the applied numerical algorithms to solve the equation system. In this contribution, the focus is laid on the numerical aspects of the process model solution.

A strategy to overcome the convergence problems is to subdivide the overall system into subsystems, which can be solved independently in sequence. Two of these decomposition methods, the Dulmage-Mendelsohn (DM) decomposition and the bordered block transformation (BBTF) are examined here. In the worst case, each subsystem is theoretically as ill-conditioned as the original system. Consequently, for most cases the condition number of the subsystems will improve significantly. Apart from that, the computational effort is reduced due to solving lower dimensional systems in sequence. Two decomposed versions of a reactive distillation column will exemplarily be investigated based on these assertions.

2. Solving Nonlinear Equation Systems

The solution of nonlinear systems is divided among three different classes of algorithms: Direct substitution methods (e.g. Wegstein, Dominant Eigenvalue) typically suffer from stability issues in case of ill-conditioned systems; residual minimization techniques (e.g. MATLAB's `fsolve`) face issues with the nonuniqueness of solutions of squared nonlinear systems. Next to those, the (quasi-)Newton-type class of algorithms combined with globalizing line search techniques is the workhorse for many difficult nonlinear systems. They solve equation systems of the form:

$$0 = F(x) \tag{1}$$

by calculating a Newton step Δx_k to the next iteration point x_{k+1} via:

$$J(x_k) \cdot \Delta x_k = -F(x_k) \tag{2}$$

While the various Newton implementations differ in how the Jacobian matrix J is computed (e.g. Broyden's approximation, analytic Jacobian) and whether the full Newton step is performed (dampening and line search techniques), they almost all have to solve a linear system for each Newton step. Therefore, well-known techniques, which improve the condition of linear systems such as row and column scaling or those which reduce numerical costs by permuting rows and columns can also enhance the iteration performance of Newton-type algorithms.

In this study, the numerical performance is evaluated by the number of equation calls also called function count until a solution is found and the condition of the initialized system is measured by the condition number based on the Euclidean norm.

2.1. Decomposition Techniques

The core of most decomposition methods is the permutation of columns and rows. During the solution of a nonlinear systems the row and column order of the Jacobian matrix J is rearranged for the solution of each linear Newton step. Given that J contains the first derivatives of all equations with respect to all variables a permutation of the rows implies a rearrangement of the equations and a permutation of columns changes the order of all variables.

2.1.1. Dulmage-Mendelsohn Decomposition

In DM the original Jacobian is converted to an upper block triangular matrix by maximizing the number of blocks along the diagonal. Dulmage and Mendelsohn (1958) explain this procedure in detail. Fig. 1 shows the incidence matrix of the Jacobian belonging to a tray-based column model. Starting from the first block on the bottom right of J the blocks are solved in sequence. Already calculated variables from former blocks act as constants values in the following. Thus, all entries above the diagonal are previously determined quantities. The number of variable dependencies within the equations increases from the bottom right to the top left, causing highly dependent equations to be solved last.

2.1.2. Bordered Block Transformation

In contrast to DM, BBTF turns the Jacobian to a lower block triangular form as shown in Fig. 1 for the examined example. Erisman et al. (1985) present the principle of the method in more detail. During the restructuring highly linked variables called "tearing variables" are separated and shifted to the right of J . Hence, the dimension of the blocks can be further reduced. The solution process is divided into an inner and an outer loop. It starts with the inner iteration from the block in the

upper left corner of J . All blocks are then solved in sequence for a constant set of tearing variables. During the outer iteration the tearing variables are iterated within the “tearing equations”, wherein all other variables from the inner loop are kept constant. The algorithm converges on satisfying a certain tolerance for the outer loop.

3. Decomposition of a reactive distillation model

Representatively a model for the production of Methyl-Tert-Butylether (MTBE) in a reactive distillation column has been built and used for investigations on both decomposition methods.

MTBE appears as additive in fuels and as solvent or extracting agent in the chemical industry. As discussed by Taylor and Krishna (2000) the conventional process requires a reactor followed by three extraction columns to cope with the arising azeotropes of the reaction mixture. Through the combination of reaction and distillation the extend of the process reduces to only one column. Nevertheless this leads to a more complex process model and a higher challenge in solving the related equation system.

3.1. Model description

MTBE is synthesized by the reaction of Methanol with Isobutene at the presence of another olefin, which is N-Butene in this case. Neglecting the side reactions, the reaction:



is considered in the liquid phase of the model. Amberlist 15 acts as a solid caterlyst in the reactive part of the column.

The classical equilibrium stage approach is applied which involves thermal, mechanical and chemical equilibrium between liquid and vapor phase on all stages. Nevertheless the reaction kinetics are considered in the liquid phase based on data from Rehfinger and Hoffmann (1989) and Sundmacher and Hoffmann (1994). The real fluid behavior of the liquid phase is described by UNIFAC, while the vapor phase is assumed to behave as ideal gas. All thermo-physical and component-dependent properties are taken from CHEMCAD (2017). The whole process is modeled as steady-state.

Since the focus of this work is the observation of the decomposition methods the model validation through experimental data is not amplified here. Beside this the model consists of only two rectifying and one reactive stage to keep the restructuring comprehensible. More complex reactive distillation models that can also describe the dynamic behavior of those processes were set up and experimentally validated by Reepmeyer et al. (2004) and Forner et al. (2006). The entire model encompasses 664 nonlinear algebraic equations. It has been implemented in our department's modeling and code generation software MOSAICmodeling, that is presented by Merchan et al. (2016). Both decomposition methods are already integrated in MOSAICmodeling and were used on the test system. Subsequently, the original and decomposed versions were exported to MATLAB and iterated with the Netwon-based Trust-region-dogleg-solver.

3.2. Observation of the decomposed systems

Fig. 1 presents the incidence Jacobian matrices of the original and the decomposed systems. The DM decomposition retains a quite large block with a dimension of 576 equations and variables. This block contains the whole UNIFAC-model and conservation balances which are both strongly coupled through the mole fractions and stage temperatures.

The BBTF identifies the mole fractions of all three components that take part in the reaction referring to eq.3 and the stage temperatures as tearing variables. This sums up to 12 tearing

variables. As a result the block dimension along the diagonal can be drastically reduced to a dimension of 3 at maximum.

3.3. Test methods and results

Starting at one solution of the equation system each iteration variable is separately varied between ± 5 and 30 % while keeping the other variables at their solution value. This is done for the original and the decomposed systems to generate the same set of initial points. For each equation system a total number of 5312 iterations was performed. Fig.2 shows the ratio of successful runs to performed runs over the perturbation of the variables for all three systems. Since the number of converging iterations does not differ much between increasing and decreasing the variable values by a certain percentage (the maximum difference is five iterations), only the average value is shown.

BBTF features the best convergence performance in this case. The ratio of successful iterations stays constant at 98 % in the examined range. The number of failed iterations refers to the perturbation of the tearing variables. Even for a perturbation of 5 % these iterations do not succeed. In contrast the perturbation of all other variables does not influence the convergence result at all. Hence the convergence of a BBTF decomposed system highly depends on the initial guess of the tearing variables, while the initial guess of the remaining variables can be arbitrary.

As expected, the number of successful iterations decreases with higher perturbations for the other two systems. The DM seems to be a bit more robust than the original system. Interestingly in both versions the perturbation of certain variables leads to failing iterations for all tested perturbation values. These variables can be identified as quantities of the UNIFAC model, to be exact they are the van der Waals volumina and surfaces that determine the combinatorial component of the activity coefficient. Per definition they are both related to the molar fractions that were identified as highly linked variables and could spread any deviation directly into other parts of the equation system. On top they occur in exponential expressions that are strongly non-linear and obviously not well described by any linear approximation of a Newton-based algorithm.

Next to the convergence performance the computational effort to iterate the three systems has been investigated. Therefore, all variables were perturbed at once by ± 3 %. Subsequently the systems were solved with the same solver settings (maximum number of function calls per block: 30000, Step size tolerance: 10^{-6} , function tolerance: 10^{-10}). During iteration the function calls have

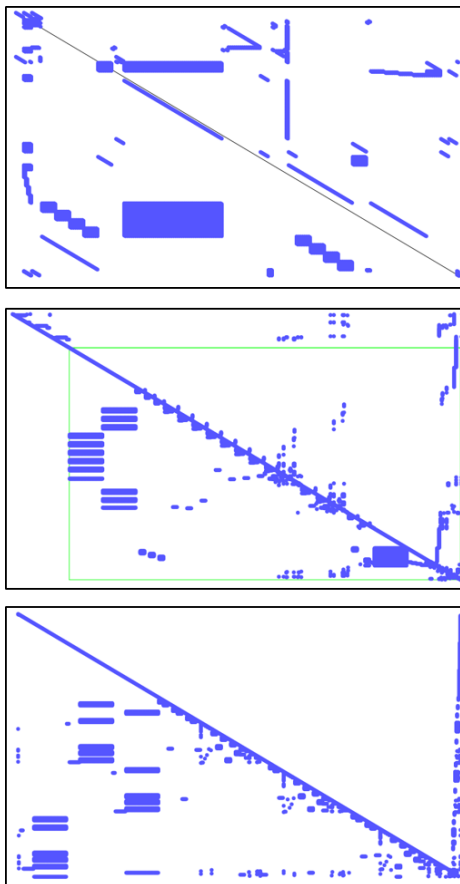


Figure 1: Incidence Jacobian matrices of the original equation system (top), the DM decomposed system (center) and the BBTF decomposed system (bottom)

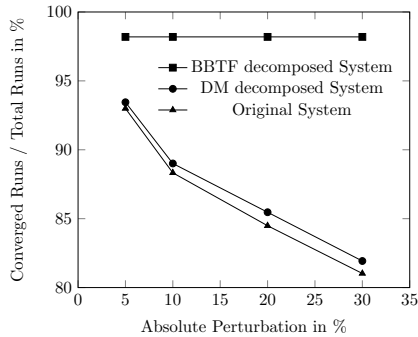


Figure 2: Ratio of converged to total iterations by variable wise perturbation at the initial point

Table 1: Function counts to solver termination at 3% perturbation of all variables

System	Function Counts		Solved
	(+3%)	(-3%)	
BBTF	in: > 10 ⁶ out: 693	in: > 10 ⁶ out: 1078	no
BBTF (TV=const.)	in: 303054 out: 110	in: 121265 out: 44	yes
DM	14254	13094	yes
Original	15960	15295	yes

been tracked to finally calculate the total function count until the solver terminates. The results are presented in Table 1.

Although the residual series of the BBTF decomposed system seemed to converge, it could not be properly reduced after more than one million function calls within the inner iterations. Both outer iterations ($\pm 3\%$ perturbation) were terminated by deceeding the set step size tolerance. When keeping the tearing variables at their solution values the solver needed a total sum of 303164 function calls to succeed at a perturbation of +3 % and less than half the number at a perturbation of -3 %. Hence in BBTF both the convergence and the efficiency of the solving procedure depend a lot on values of the tearing variables.

The best performance shows the DM decomposed system closely followed by the original system. Presumably the performance of the decomposed system would be much better in a more decoupled system. For this example, 97 % of the function counts are used within the large block with its 576 equations.

Finally, the conditions of the systems along their iteration trajectories are examined by recording their condition numbers. It is started from the initial point where all variables exceed their solution by 3 %. Surprisingly, the condition number of the original and the decomposed system differ only marginally for their first 17 iteration steps. This encourages the suspicion that the DM decomposition cannot efficiently uncouple the overall system into lower dimensional blocks in this case. Hence the problematic terms causing the high condition numbers are probably still part of the large block. The number of iterations until a solution is found equals 23 for both systems, although less function calls are necessary to solve the lower dimensional large block of the decomposed system. From iteration step 17 to 23 the condition numbers vary by roughly $2 \cdot 10^{18}$. This could be the result of slightly differing final values of the iteration variables. Using the same solver settings the original version might be more accurate since both iterations finish by deceeding the function tolerance. In the iteration of

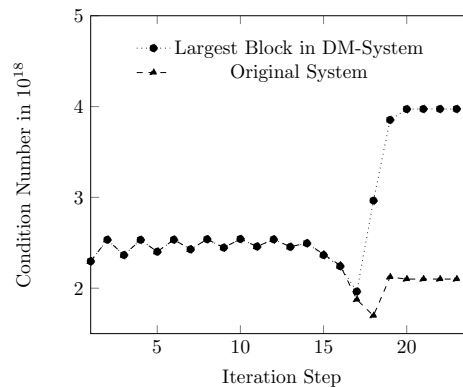


Figure 3: Condition numbers along iteration trajectories of the original system and the largest blocks of the DM decomposed system

From iteration step 17 to 23 the condition numbers vary by roughly $2 \cdot 10^{18}$. This could be the result of slightly differing final values of the iteration variables. Using the same solver settings the original version might be more accurate since both iterations finish by deceeding the function tolerance. In the iteration of

the original system the quadratic sum of more function residuals has to fulfill this criterion.

The condition numbers of the outer iteration of the BBTF decomposed system do not change much and lie all within the range $4.879 \pm 0.0005 \cdot 10^{13}$. This is the best conditioned system of the three examined versions. The condition numbers of the inner blocks are negligibly small.

4. Conclusion and Outlook

The effect of the Dulmage-Mendelsohn decomposition and bordered block transformation on a nonlinear algebraic equation system referring to a stationary reactive distillation model has been examined concerning convergence, computational effort and conditioning.

The results show that the DM decomposed system features a small improvement to the original system regarding the convergence behavior and the decrease in numerical costs during iteration. Nevertheless, a large block remains, that probably hinders the efficiency to be further increased. This block is caused by the used UNIFAC model where mole fractions and temperatures induce a strong coupling between the equations in the system. A concept to eliminate this problem is to decompose the large block by DM as well and solve it in an inner iteration. This will be part of our future investigations.

For known solutions of the tearing variables the BBTF seems to be quite robust to any perturbation of the inner iteration variables. Due to the low dimensional blocks the condition can be improved by five orders of magnitude to the original system. Still the numerical costs are quite high. Even when the tearing variables are initialized with their solution values the solver requires roughly 20 times more function calls than the other system modifications. This is the result of a very low rate of convergence. When the tearing variables differ only slightly from their solution the low convergence velocity can lead to a stagnating minimization of the function residuals. The BBTF gives a better numerical performance in systems with a smaller number of tearing variables as discussed in Bublitz et al. (2017). Further test cases will be performed to identify a limit for the number of tearing variables where the numerical costs are still reasonably low. Besides, methods as the one of Baharev et al. (2017) which systematically generate initial values close to the solution will be examined in order to provide a sufficient set of initial values for the tearing variables and achieve a certain level of efficiency during the iteration of a BBTF decomposed system.

References

- A. Baharev, F. Domes, A. Neumaier, 2017. A robust approach for finding all well-separated solutions of sparse systems of nonlinear equations. *Num. Algo.* 76, 163–189.
- S. Bublitz, E. Esche, G. Tolksdorf, V. Mehrmann, J.-U. Repke, 2017. Analysis Decomposition for Improved Convergence of Nonlinear Process Models in Chemical Engineering. *Chem. Ing. Tech.* 89, 11503–1514.
- CHEMCAD, 2017. CHEMCAD Component Database.
URL www.chemstations.com
- A. Dulmage, N. Mendelsohn, 1958. Coverings of bipartite graphs. *Canad. J. Math* 10, 517–534.
- A. Erisman, R. Grimes, J. Lewis, W. Pool, 1985. A structurally stable modification of Hellerman-Raricks P4 algorithm for reordering unsymmetric sparse matrices. *SIAM J. Anal.* 22, 369–385.
- F. Forner, M. Meyer, M. Dker, J.-U. Repke, J. Gmehling, G. Wozny, 2006. Comparison of the Startup of Reactive Distillation in Packed and Tray Towers. Vol. 21 of *Computer Aided Chemical Engineering*, pp. 137–142.
- V. A. Merchan, E. Esche, S. Fillinger, G. Tolksdorf, G. Wozny, 2016. Computer-Aided Process and Plant Development. A Review on Common Software Tools and Methods and Comparison against an Integrated Collaborative Approach. *Chem. Ing. Tech.* 88, 50–69.
- F. Reepmeyer, J.-U. Repke, G. Wozny, 2004. Analysing the Start Up of Reactive Distillation Columns. *IFAC Proceedings Volumes* 37, 731–736.
- A. Rehfinger, U. Hoffmann, 1989. Kinetics of Methyl Tertiary Butyl Ether Liquid Phase Synthesis Catalyzed by Ion Exchange Resin-I. Intrinsic Rate Expression in Liquid Phase Activities. *Chem. Eng. Sci.* 45, 1605–1617.
- K. Sundmacher, U. Hoffmann, 1994. Macrokinetic Analysis of MTBE-Synthesis in Chemical Potentials. *Chem. Eng. Science* 49, 3077–2089.
- R. Taylor, R. Krishna, 2000. Modelling Reactive Distillation. *Chem. Eng. Sci.* 55, 5183–5229.

Optimizing Decolorization Efficiency of Methylene Blue by Photo-Fenton Process over Fe-Diatomite using Central Composite Design

Pongsert Sriprom^a, Varocha Champa^b, Prakob Kitchaiya^b,
Pornsawan Assawasaengrat^{b,*}

^a*Program of Food Processing Engineer, Faculty of Agro-Industry, King Mongkut's Institute of Technology Ladkrabang, Bangkok 10520, Thailand*

^b*Department of Chemical Engineering, Faculty of Engineering, King Mongkut's Institute of Technology Ladkrabang, Bangkok 10520, Thailand*
pornsawan.as@kmitl.ac.th

Abstract

The methylene blue was degraded by photo-fenton over Fe-diatomite prepared by dry impregnation method. The characterizations of catalyst were studied by XRD, XRF and BET surface area. The photo-fenton reaction conditions were studied as parameters of the H₂O₂ concentration, the amount of Fe-diatomite, the initial concentration of methylene blue and the initial pH of solution, which were designed by central composite design (CCD) based on response surface methodology (RSM) to accomplish the optimal condition. The results showed that the optimum condition was at the initial H₂O₂ concentration of 116 mg/L, the Fe-diatomite of 1 g/L, the initial MB concentration of 200 mg/L and the pH of 5.8. It could predict the decolorization value of 100% and reduce the total organic carbon (TOC) to 72.3%. Finally, the validation was tested in 5 runs at the optimization about 99.2±0.2% which implied that the regression model is in a good agreement.

Keywords: Central Composite Design (CCD), Photo-fenton, Methylene blue, Fe-diatomite, Heterogeneous catalyst.

1. Introduction

Dyes, which usually contaminate in the effluent, are non-degradable and toxic, and have the carcinogenic nature. Thus, dye-contaminated wastewater should be treated before being discharged into environmental. Methylene blue (MB), a kind of dye, is commercially amiable which is always released from the washing process.

Therefore, MB contaminated in wastewater must be worried. Photo-fenton is one of advanced oxidation processes (AOPs) which can treat the pollutants into green products with smaller molecules. Heterogeneous catalysts used in Photo-fenton process are interested because they are easier to be separated after reactions than homogeneous catalysts. Diatomite is mainly composed of silica and some irons which would enable it to use as a photo-fenton catalyst (Khraisheh et al., 2005)

Response surface methodology (RSM) is a statistically method widely used to design an experiment, explain the main and interaction effects of the independence variables, and determine the optimal condition with a limited number of experiments (Song et al., 2014). Along with RSM, central composite design has been applied to design the experiments using statistical software. In AOPs, central composite design has been used to identify the factors to be studied with methylene blue removal (Mazaheri et al., 2016)

Finally, central composite design was used in this study to identify the optimum condition in photo-fenton using Fe-diatomite to remove colour from the synthetic dye wastewater. Also, response surface methodology was applied to estimate their optimal value. Knowing the optimal condition using statistical computer software can help, and make it easy, to determine the main and interaction effects.

2. Experimental

2.1 Catalyst Preparation and Characterization

A natural diatomite from Lampang (Thailand) was chosen as the raw material. FeSO₄ of 0.02 mole was dropped into diatomite by using dry impregnation method. The chemical compositions of Fe-diatomite were analyzed by X-ray fluorescence (a Bruker S1 Turbo SD, Germany) with CuK α radiation. The crystalline structures of diatomite and Fe-diatomite were characterized by X-ray diffraction (XRD; Bruker AXS-D8; Karlsruhe, Germany) using CuK α radiation ($\lambda = 15406 \text{ nm}$) with an anode current of 30 mA and an accelerating voltage of 40 kV. The samples were scanned from 5 degree to 80 degree (2 theta) in the scanning step of 0.02 degree at a rate of 5 degree per min. The surface area, pore volume and average pore diameter were determined by nitrogen adsorption-desorption measurements (BET method).

2.2 Experimental Design

Methylene blue (C₁₆H₁₈ClN₃S, MW 319.85 g/mol) purchased from Sigma Aldrich (Germany) was chosen as the synthetic model dye. All other analytical grade chemicals were purchased from UNILAB (Thailand) and LABSCAN (Thailand). The experimental design and data analysis were carried out using the software MINITAB version 16.0. The experimental was designed by central composite design at four-factor (X_1 : the H₂O₂ concentration, X_2 : the amount of Fe-diatomite, X_3 : [MB]₀ and X_4 : the initial pH) and three-level (low, medium, high) as shown in Table 1. The total numbers of 31 experimental runs were conducted to assess the effects of independent variable on the efficiency of photo-fenton process. The decolorization efficiency (%) in Eq.(1) as a response function was optimized to achieve a desire value by response optimizer.

$$\% \text{ Decolorization Efficiency} = \left(\frac{c_0 - c_t}{c_0} \right) \times 100 \quad (1)$$

where c_0 is the initial concentration and

c_t is the measured MB concentration after 30 min of reaction.

2.3 Experimental Run

The photo-fenton oxidation condition from CCD was carried out in a 500-mL batch stirrer photo reactor and the catalyst was added to the 300 mL of methylene blue solution. The sample was stirred about 10 min in the dark for adsorption process, and then the samples were collected, and the initial methylene blue concentrations were analyzed. After that, the amount of H₂O₂ was added into the sample, and the solution was stirred for 30 min. Then, the samples were collected, and the concentrations of methylene blue were analyzed at the end of run. The maximum wavelength of 464 nm was applied for the UV detector.

Table 1 The central composite design of photo-fenton process

Factors		Level		
		-1	0	1
Initial H ₂ O ₂ concentration (mg/L)	X ₁	50	75	100
Fe-Diatomite (g/L)	X ₂	0.4	0.6	0.8
initial MB concentration (mg/L)	X ₃	300	400	500
pH	X ₄	3	5	7

3. Results and Discussion

3.1 Characteristic of Fe-Diatomite Catalyst

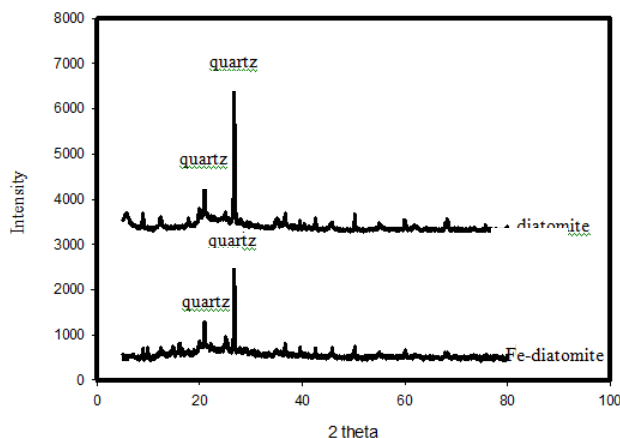


Figure. 1 The XRD pattern of Fe-diatomite

From X-ray fluorescence analysis, the results showed that Fe-diatomite had 66.9%wt silica as its main constituents. The iron oxide was 7.48 %wt upon the impregnation of Fe ions in diatomite. The XRD pattern for Fe-diatomite was showed in Figure.1. The XRD pattern evidenced the presence of quartz with $2\theta = 20.86, 26.64$ (JCPDS: 46-1045) (Inchaurredo et al., 2017) and did not show the peak related to iron oxides. Diatomite is naturally-occurring clay in the earth crust. It typically consists of silica as the main component and a small amount of iron oxide. The BET surface area of Fe-diatomite was 20.40 m²/g. The pore volume and average pore diameter were 0.071 ml/g and 12.9 nm, respectively.

3.2 Response Surface Methodology and Optimization

The results of decolorization of methylene blue in photo-fenton process of all conditions designed by central composite technique were estimated by least-square technique to determine the regression quadratic equation as shown in Eq.(2):

$$Y = \beta_0 + \sum_{i=1}^4 \beta_i X_i + \sum_{i=1}^4 \beta_i^2 X_i^2 + \sum_{i=1}^3 \sum_{j \neq i}^4 \beta_{ij} X_i X_j \pm \varepsilon \quad (2)$$

where Y is the response (decolorization efficiency, %) $\beta_0, \beta_i, \beta_i^2$ and β_{ij} are the constant coefficients, X is the independence variable that X_1, X_2, X_3 and X_4 are the H_2O_2 concentration, the amount of Fe-diatomite, the initial methylene blue concentration and the initial pH, respectively, and ε is the experimental error. The regression quadratic equation was resulted in Eq.3:

$$Y = 25.81 + 1.05X_1 + 12.01X_2 - 0.08X_3 + 4.53X_4 - 0.00420X_1^2 - 0.370X_4^2 \quad (3)$$

The predicted results can be calculated by Eq.(1). Then, the internal standard residual was applied to check how well the model satisfies the assumption of the analysis of variance (ANOVA).

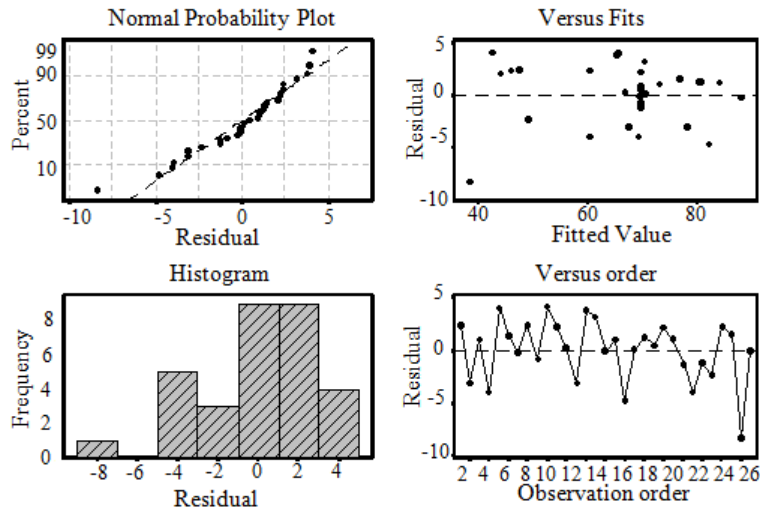


Figure.2 Internal standard residual plots versus normal probability, histogram, fit and order.

As illustrated in Figure.2, a normal probability plot of standard residual from least-square-fit plot showed the data along a straight line. The frequency of residual in normal distributions was shown in the histogram. The residual versus the fitted value showed randomly scattered around the zero line, which recommend that the data seemed to show the relatively-constant variance across the predicted value and had no outliers or influential observations (Sriprom, 2015). In addition, the standard residuals versus observation showed fluctuation around the center line, indicating that the data were distributed well (Wantala, 2013).

A good agreement has been achieved between the predicted results and the experimental results with R^2 of 95.17% as shown in Figure.3. This observation indicated that the purposed model showed adequate approximation of main variable effect on methylene blue removal with a difference of about 5%.

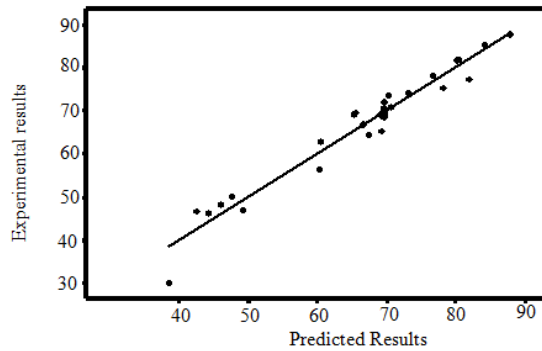
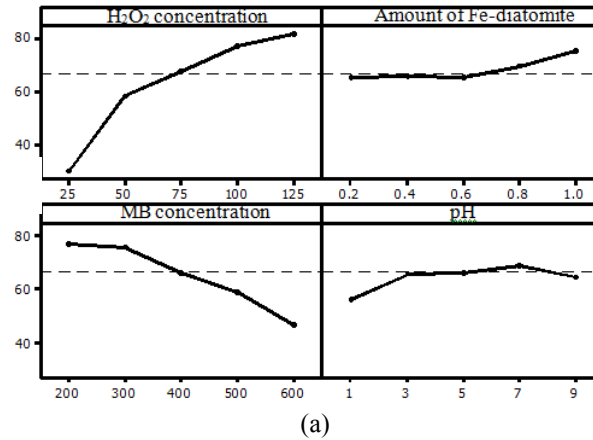
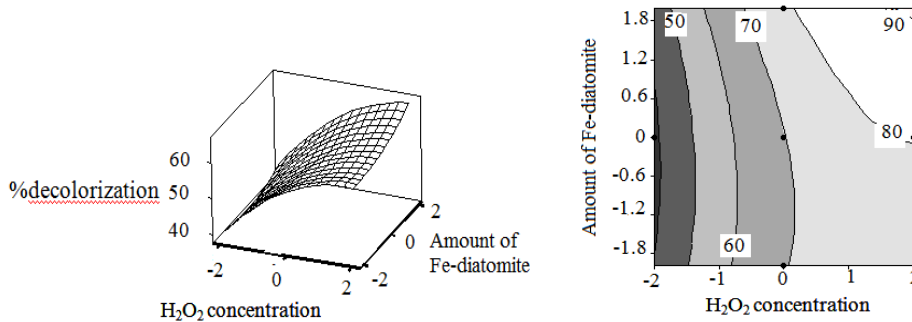


Figure. 3 The observed value (%) plotted against the predicted values (%)

At 95% confidence, the independence variable of H₂O₂ concentration, the amount of Fe-diatomite, the initial methylene blue concentration and the initial pH are the significant effects on percent decolorization of methylene blue ($P_{\text{value}} < 0.05$).



(a)



(b)

(c)

Figure. 4 The percent depolarization of main effects (a) surface plot (b) and contour plot (c)

The main effects were shown in Figure 4(a) indicating that the H₂O₂ concentration, the amount of Fe-diatomite and the initial pH were increased with increasing decolorization

efficiency. However, decolorization efficiency was decreased with the increasing initial concentration of methylene blue. As depicted in Figure. 4(b) and 4(c), the percent of methylene blue removal increased clearly as the H₂O₂ concentrations and the amounts of Fe-diatomite increased.

Finally, MINITAB 16.0 software was used to optimize the model for the maximum % decolorization of methylene blue. The results showed that the optimum condition was found at the initial H₂O₂ concentration of 116 mg/L, the Fe-diatomite of 1 g/L, the initial MB concentration of 200 mg/L and the pH of 5.8. It can predict the value of 100% decolorization and reduce the total organic carbon to 72.3%. The prediction of model was verified by additional 5 runs under the optimum condition, resulting in a color removal of 99.2±0.2%. It can be seen that experimental value closely agrees with the predicted values of 100%, showing that RSM was an effective and reliable method for estimating the optimum condition.

4. Conclusion

In this study, the Fe-diatomite prepared by dry impregnation method in high Fe content could be applied in photo-fenton process to decolourize the synthetic dye wastewater containing methylene blue. It was seen from the results that the H₂O₂ concentration and the amount of Fe-diatomite were shown in the significant terms on the decolourization percent of dye in synthetic wastewater. The optimum condition was found at the initial H₂O₂ concentration of 116 mg/L, the Fe-diatomite of 1 g/L, the initial MB concentration of 200 mg/L and the pH of 5.8. It can predict the value of 100% decolorization and reduce the total organic carbon to 72.3%. In the future, this optimum condition can be used with the actual dye wastewater treatment.

References

- C. Song, Y. Kitamura, S. Li, 2014, Optimization of a novel cryogenic CO₂ capture process by response surface methodology (RSM), *Journal of the Taiwan Institute of Chemical Engineers*, 45, 1666-1676
- H. Mazaheri, M. Ghaedi, A. Asfaram, S. Hajat, 2016, Performance of CuS nanoparticle loaded on activated carbon in the adsorption of methylene blue and bromophenol blue dyes in binary aqueous solutions: Using ultrasound power and optimization by central composite design, *Journal of Molecular Liquids*, 219, 667-676
- K. Wantala, P. Sriprom, N. Pojananukij, A. Neramittagapong, S. Neramittagapong, P. Kasemsiri, 2013, Optimal decolorization efficiency of reactive red 3 by Fe-RH-MCM-41 catalytic wet oxidation coupled with Box-Behnken Design, *Key Engineering Material*, 545, 109-114
- M.A.M. Khraisheh, S.J. Al-Ghouti, M.N. Ahmad, 2005, Effect of OH and silanol groups in the removal of dyes from aqueous solution using diatomite, *Water Research*, 39, 5, 922-932
- N. Inchaurredo, C.P. Ramos, G. Žerjav, J. Font, A. Pintar, P. Haure, 2017, Modified diatomites for Fenton-like oxidation of phenol, *Microporous and Mesoporous Materials*, 239, 396-408
- P. Sriprom, S. Neramittagapong, C. Lin, K. Wantala, A. Neramittagapong, N. Grisdanurak, 2015, Optimizing chemical oxygen demand removal from synthesized wastewater containing lignin by catalytic wet-air oxidation over CuO/Al₂O₃ catalysts, *Journal of the air and waste management association*, 65:7, 828-836

An optimization method to estimate the SOFC market in waste water treatment

Sonja Sechi,^{a,b} Sara Giarola,^{a*} Andrea Lanzini,^b Marta Gandiglio,^b Gbemi Oluleye,^a Massimo Santarelli,^b Adam Hawkes^a

^a*Imperial College London, London, SW7 2AZ, UK*

^b*Politecnico di Torino, Corso Duca degli Abruzzi, 24, 10129 Turin, Italy*

s.giarola10@imperial.ac.uk

Abstract

Wastewater treatment plants (WWTP) are one of the most energy intensive public utilities. The valorization of the biogas produced from the sludge in combined heat and power (CHP) systems allows important energy and emissions reduction, particularly if highly efficient engines, like solid-oxide fuel cells (SOFCs) are used.

This paper proposes a two-stage stochastic optimization approach to assess the market potential for SOFCs in WWTPs in Europe. Despite the biogas availability is a challenge to guarantee continuity of operation, the results show that the WWTP is a promising market to pave the way for SOFC cost reduction and further technological learning.

Keywords: solid-oxide fuel cells, stochastic optimization, wastewater treatment, biogas.

1. Introduction

SOFCs are one of the most promising options in the technological transition of the energy systems towards a carbon-constrained world because of the high efficiencies at which they can operate. They play an important role within the decarbonisation strategies in Europe. In particular, when fueled with WWTP-biogas, they would operate at zero net emissions (EC, 2017). Currently, the high investment costs of SOFCs are the major limitation to the deployment of the technology.

The technical and economic feasibility of SOFC integration into WWTPs also relates to the biogas availability on a daily and seasonal basis (Giarola et al. 2017). Optimization approaches have proven to be necessary to determine the optimal SOFC operations within large systems (Hawkes et al. 2009). In particular, the optimal generator dispatch can effectively be assessed using stochastic optimization when uncertainty on key inputs is considered (Nowak and Römisch, 2000, Ramadhani et al, 2017).

This work proposes a two-stage stochastic MILP (Mixed Integer Linear Programming) optimization model which aims to minimize the expected total system costs of a SOFC-energy provision system integrated with WWTPs, and determine the optimal system dispatch. The deterministic model proposed in (Giarola et al., 2017), later extended to a stochastic approach in (Sechi et al., 2017) is further developed to include a Pareto frontier optimisation with respect to the number of modules. The model is iteratively applied to a set of case studies, corresponding to the typical WWTP capacity ranges in Europe and builds a Pareto frontier of two competitive variables, the SOFC utilization factor and the number of modules installed. In doing so, it determines the optimal number of modules corresponding to each plant size accounting for uncertainty in the biogas availability.

2. Methods

The model here described proposes a generic framework to determine the optimal size as well as dispatch of a biogas-fed SOFC CHP system integrated to a WWTP. It extends the stochastic model proposed in (Sechi et al., 2017) to a Pareto approach, where the number of generators is optimised *a posteriori*, compromising the technology utilization and the biogas exploitation rate. The system refers to a generic plant with the layout of Fig.(1).

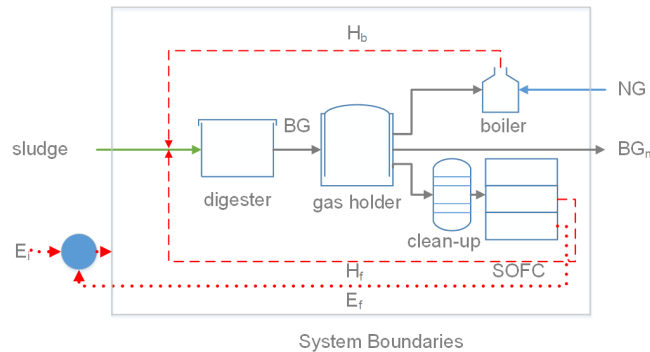


Figure 1. WWTP layout including the SOFC installation in the energy provision system. E_i and NG are the electricity and natural gas from the grid, BG and BG_n are the biogas produced from the anaerobic digester and the unexploited one, H_f and E_f represent the heat and electricity produced by the SOFC-CHP system.

The objective function in Eq.(1) is the minimization of the total costs: the expected operational costs OP_s depending on the scenario s of biogas availability; fixed costs (annualised capital costs, CC , and yearly maintenance costs, MC) dependent on the number of modules; start-up and shut-down costs (FC_t) of each module.

$$\min \sum_s p_s \cdot OP_s - CC - MC - \sum_t FC_t \quad (1)$$

The first stage of the stochastic model include not only the binary variable to set the on/off status of each generator at time t but also the electrical and thermal output. In the second stage, the recourse variables are the natural gas and the electricity bought from the grid, the biogas storage level, the amount of biogas unexploited. The number of SOFCs to install is set as a parameter in the model and the optimization is sequentially performed for each one of these configurations. The Pareto front approach is adopted as two conflicting objectives are involved: the total costs of the SOFC-CHP plant and its utilization factor, i.e. the actual number of operating hours of the system.

Further constraints involve the limit on nameplate capacity of the generators, on the capacity of the boiler as well as operational regimes for each SOFC module (i.e. nominal and partial load). Constraints regarding maximum ramp-rates, minimum duration of shut-downs and start-ups have been imposed to avoid thermal cycling and rapid damage of the device. Finally, a periodic boundary condition between begin and end of a year on the gas holder levels were set to extend the yearly optimization to multiple years.

3. Bottom-up approach to the estimate of the market potential

Figure 2 summarizes the approach used to extend the optimisation of specific case studies to the European scale. A set of representative case studies was defined corresponding to five capacity ranges of WWTP selected according to a statistical analysis of a WWTP Database (EC, 2016), the Waterbase-UWWTD. The database is conceived to contain the data of quality and quantity of the sludge collected as well as of the discharge of waste water of the WWTPs present in Europe. Although the source is quite fragmented, plants are always characterized by the number of people equivalent (P.E.), as a measure of the plant capacity. From the original set of plants, a first discriminant was applied to define the economic feasibility of the anaerobic digestion process; in Europe, the minimum size is typically 20,000 P.E.. Moreover, only plants equipped with a secondary treatment, which is fundamental to perform the stabilization of the sludge and the production of biogas, were considered for the integration with SOFCs. In total, the number of suitable plants was around 6,400.

A subdivision of the plants was performed to identify different segments of the potential market for the SOFCs. Five case studies or WWTP capacity ranges were selected: extra-small (XS), small (S), medium (M), large (L) and extra-large (XL). The capacity corresponding to the median of each interval, was used in the optimization of the number of modules. Also, each WWTP capacity range, was characterized by a suitable nameplate capacity of the SOFC module. For example, for the M case the SOFC size used was 58.3 kW as in DEMOSOFC project. SOFC techno-economic characteristics were defined within the framework of the DEMOSOFC project (DEMOSOFC, 2016).

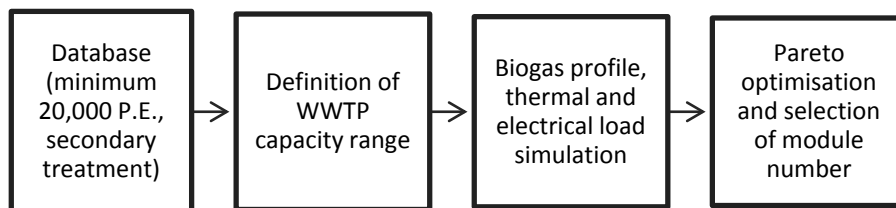


Figure 2. Methodology to the case study definition

3.1. Monte Carlo scenario generation, thermal and electric WWTP load

A Monte Carlo simulation integrated in a random walk algorithm was developed in MATLAB® (Sechi et al, 2017) to develop the scenarios of daily biogas profiles. A statistical analysis was applied to an industrial datasets of biogas daily flows spanning 3 years (SMAT, 2017). The seasonal probability profiles of biogas were regressed using daily biogas flow values disaggregated into seasons. 200 Monte Carlo simulations were performed using an average value of seasonal production and a standard deviation as percentage of the average production and the ratio of seasonal production.

The average value of biogas production of the most productive season was calculated from the number of person equivalent provided by the UWWTD assuming a constant specific biogas production (10 litres/P.E./day). In fact, the person equivalent unit is legally a measure of the maximum organic load produced by the WWTP during a year.

The archetypal profile for the XS, S and M capacities were defined using standard deviation and seasonal ratios as calculated from the industrial data provided by the SMAT Collegno plant (180,000 P.E.); while for the larger capacities, L and XL, the characteristics of the Castiglione Torinese plant (Italy) were set.

The data for the electric load (Table 1) were selected from the statistical surveys performed in the framework of a European project (Enerwater, 2017). The median value of the consumption corresponding to the appropriate WWTP capacity range was used and fixed as constant during all the operating hours in a year.

Table 1. Size and specific electricity consumption of the WWTP case studies (i.e. capacity ranges)

Case study	Case studies, P.E.	SOFC nameplate capacity, kW	Electric Consumption, kWh/P.E./day
XS	30,000	10	48
S	90,000	10	42.3
M	210,000	58.3	37.6
L	450,000	100	37.6
XL	1,100,000	150	37.6

3.2. Natural Gas and Electricity Prices

Industrial electricity and natural gas prices were obtained from Eurostat as a function of the annual electricity and heat consumption. The values used in the model were the average prices over the 28 European countries.

3.3. Bottom-up approach to SOFC market potential estimate

Finally, for the assessment of the maximum SOFC capacity that could be potentially installed in Europe, the optimal number of modules was linearly extrapolated from the case study to each WWTP capacity range selected from the UWWTD database, and later multiplied by the market share of each capacity range.

4. Results and discussion

The two-stage stochastic model for the Pareto front optimization was solved using CPLEX in GAMS[®].

The results in terms of technology utilization (i.e. number of operating hours to total hour in a year), operating costs, total costs (including maintenance and clean-up costs) are presented for the medium capacity case study (M) in Figure 3. It can be noted that there is a minimum of costs when the number of cells is between 3 and 4, and keep increasing where a bigger number of modules is installed. It appears from the cost trends, that the marginal improvement due to the introduction of a new module becomes negative and the benefits of the co-generation cannot compensate the incurred fixed costs. From the technical prospective, the minimum costs configuration, represents also the maximum utilization ratio of the available biogas in the SOFC system, which is around 1 % (not shown here).

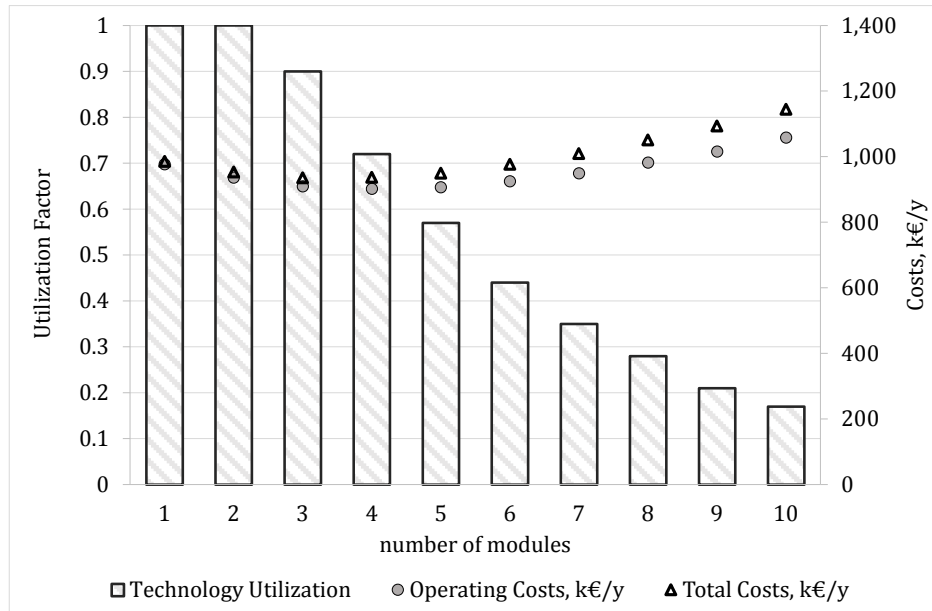


Figure3: Optimal cells number for the medium WWTP size (M)

Table 2. Results of the Pareto front optimization. The table reports: the total installed capacity (Total SOFC capacity), the number of modules and the nameplate capacity of the modules used in each case study (XS, S, M, L, XL) as well as the technology utilization ratio.

Case study	Median WWTP size (P.E.)	SOFC nameplate capacity, kW	Optimal Number of SOFC	Total SOFC capacity, kW	Technology utilization, %
XS	30,000	10	3	30	80
S	90,000	58.3	2	117	59
M	210,000	58.3	3-4	233	72
L	450,000	100	6	600	77
XL	1,100,000	150	10-11	1,500-1,650	77-66

For the M (medium size) case study, the Pareto frontier optimization results were consistent with the results of the deterministic study conducted for the Collegno plant, (Giarola et al. 2017). While according to the deterministic study, 3 modules were needed for the minimum operating costs of the plant, the stochastic study gave an optimal number of modules between 3 and 4 depending on the biogas fluctuations.

The market potential in Europe was determined correlating the optimal number of modules with the WWTP capacity range. The results extended to a European level show that the potential for SOFC in the niche market of WWTPs, could be in the range of 400 and 800 MW, depending on the biogas availability.

Table 3. Results of the regression analysis: potential SOFC capacity to install for each WWTP capacity range

Case study	Capacity range, P.E.	Total SOFC Potential capacity, MW
XS	20,000-60,000	135
S	60,001-150,000	164
M	150,001-350,000	136
L	350,001-750,000	144
XL	750,000- greater than 1,100,000	226

5. Conclusions

This work has proposed a bottom-up approach to estimate the market potential of solid oxide fuel cells integrated in waste water-treatment plants in Europe. In doing so, the model optimizes the expected total cost of the system and the optimal number of modules to be installed accounting for a notable source of uncertainty, the daily biogas fluctuations. The results suggest that an overall SOFC capacity between 417 and 800 MW could be installed in Europe. This value would correspond to a cumulative number of 58.3 kW - units greater than 10,000 which would enable capital cost reduction of more than 60 % (Ammermann et al., 2015) on the current capital costs and would pave the way for further technology deployment.

Acknowledgements

This research was carried under the H2020 grant agreement number 671470-DEMOSOFC'

References

- Ammermann, H., Hoff, P., Atanasiu, M., Aylor, J., Kaufmann, M., & Tisler, O., 2015, Advancing Europe's energy systems: Stationary fuel cells in distributed generation. Technical Report Fuel Cells and Hydrogen Joint Undertaking
- DEMOSOFC, 2016. www.demosofc.eu.
- EC, 2016. <https://ec.europa.eu>
- Enerwater, 2017. www.enerwater.eu
- S. Giarola, Forte O., Lanzini A., Gandiglio M., Santarelli M. Hawkes A., 2017, Applied Energy. 211, 689–704.
- A.D. Hawkes, D.J.L. Brett and N.P. Brandon, 2009, Int J Hydrogen Energy, 34, 9545–9557.
- F. Ramadhani, Hussain M., Mokhlis H., Hajimolana S., 2017, Renew Sustain Energy Rev, 76, pp. 460–484
- Römisch, M. Nowak and W., 2000, Annals of Operations Research, 100, 251 - 272.
- S. Sechi, Giarola S., Lanzini A., Gandiglio M., Oluleye G., Santarelli M., Hawkes A., 2017. Proceedings of 27th Symposium on Computer Aided Process Engineering.
- SMAT, 2016, <http://www.smatorino.it>

Optimal Chemical Grouping and Sorbent Material Design by Data Analysis, Modeling and Dimensionality Reduction Techniques

Melis Onei^{a,b}, Burcu Beykal^{a,b}, Meichen Wang^c, Fabian A. Grimm^c, Lan Zhou^d,
Fred A. Wright^e, Timothy D. Phillips^c, Ivan Rusyn^c, Efstratios N.
Pistikopoulos^{a,b,*}

^a *Artie McFerrin Department of Chemical Engineering, Texas A&M University, College Station, TX, 77843, USA*

^b *Texas A&M Energy Institute, Texas A&M University, College Station, TX, 77843, USA*

^c *Department of Veterinary Integrative Biosciences, Texas A&M University, College Station, TX, 77843, USA*

^d *Department of Statistics, Texas A&M University, College Station, TX, 77843, USA*

^e *Bioinformatics Research Center, North Carolina State University, Raleigh, NC, 27695-7566, USA*
stratos@tamu.edu

Abstract

The ultimate goal of the Texas A&M Superfund program is to develop comprehensive tools and models for addressing exposure to chemical mixtures during environmental emergency-related contamination events. With that goal, we aim to design a framework for optimal grouping of chemical mixtures based on their chemical characteristics and bioactivity properties, and facilitate comparative assessment of their human health impacts through read-across. The optimal clustering of the chemical mixtures guides the selection of sorption material in such a way that the adverse health effects of each group are mitigated. Here, we perform (i) hierarchical clustering of complex substances using chemical and biological data, and (ii) predictive modeling of the sorption activity of broad-acting materials via regression techniques. Dimensionality reduction techniques are also incorporated to further improve the results. We adopt several recent examples of chemical substances of Unknown or Variable composition Complex reaction products and Biological materials (UVCB) as benchmark complex substances, where the grouping of them is optimized by maximizing the Fowlkes-Mallows (FM) index. The effect of clustering method and different visualization techniques are shown to influence the communication of the groupings for read-across.

Keywords: Clustering, dimensionality reduction, predictive modeling, read-across.

1. Introduction

Climate change has become one of the major risk factors for chemical contamination events. Therefore, precise and rapid examination of the complexity of the hazardous chemical exposures is essential to identify the potential adverse health impacts, and subsequently to provide immediate solutions and/or prevent further catastrophic events. At Texas A&M Superfund Research Program (TAMU SRP), we aim to develop

comprehensive tools and models for addressing exposure to unknown chemical mixtures, and accordingly design solutions for the community during environmental emergency-related contamination events (TAMU Superfund Research Center, 2017). In this paper, we present two applications where data analysis, modeling and dimensionality reduction techniques guide experimental design and decision-making in biomedical and environmental areas.

First, we aim to design a framework for optimal grouping of unknown chemical mixtures based on their multi-dimensional analytical chemistry and bioactivity profiles. Detailed chemical characterization of a chemical mixture is challenging due to the variation in chemical composition during environmental emergencies. To provide rapid solutions, grouping an unknown chemical mixture to a group of well-studied, “known”, chemicals is critical. Here, the hypothesis is that, once an unknown chemical mixture is grouped into a cluster of known chemicals, read-across between cluster members would bridge the gap between data-poor and data-rich chemical substances. To do this, we use an integrated data analysis framework with dimensionality reduction and clustering techniques. Furthermore, we optimize the clustering structures by incorporating the Fowlkes-Mallows (FM) index, a measure for comparative assessment of clustering quality. Secondly, the environmental chemical contaminants can easily get mobilized, subsequently contaminate soil, and threaten the safety of the municipal water and food supply during environmental emergencies. In order to minimize the adverse health effects of chemical exposures, we aim to identify and develop novel broad-acting, high-capacity sorbents, enterosorbents, which can be implemented in diets to reduce the bioavailability of chemical mixtures. Here, the selection of the optimal sorption material for a given chemical mixture is a challenging and iterative task, where the chemical-sorbent property space needs to be explored iteratively to fine-tune and guide the experimental designs. Therefore, we perform predictive modeling of sorption activity of materials via regression techniques.

2. Data Acquisition

2.1. Derivation of Analytical Chemistry and Bioactivity Profiles of Complex Substances

In order to explore a more suitable clustering algorithm that may be used to establish the chemical and biological similarity between complex substances or mixtures, we use several recent examples of substances of Unknown or Variable composition Complex reaction products, and Biological materials (UVCB substances) as a benchmark. These include CON01-CON05 as Straight Run Gas Oils (SRGO); CON12-CON18, CON20 as Vacuum & Hydro-treated Gas Oils (VHGO); A083/13, A087/13, A092/13 as Heavy Fuel Oils (HFO), and CON07, CON09 as Other Gas Oils (OGO). These are complex petroleum substances that are products of oil refining that contain hydrocarbons in the range from C9-C25, C13-C30, C20-C50, and C10-C27 respectively (Grimm et al., 2016). Categorization of petroleum substances is based on the manufacturing process and physico-chemical properties. Petroleum substances are highly complex and may be variable in composition, hence they are excellent examples of UVCBs that present a major challenge in terms of substance identification, classification and grouping. In addition, gaps in available toxicity data create challenges for regulatory decision-making on these substances. In this study, a measure of chemical composition of the reported UVCB substances was derived using Ion Mobility Mass Spectrometry (IM-MS) analysis (Grimm et al., 2017). IM-MS analysis provides chemical fingerprint of

substance complexities by yielding the m/z (mass divided by charge number), drift time (time for each ion to traverse within a homogeneous electric field in the ion mobility spectrometer) and abundance. Here, the IM-MS data involves information on the sample-specific heteroatom class distribution based on relative abundance of individual features yielding 82 unique heteroatom classes as features. In addition, the bioactivity characteristics of the selected UVCB substances are derived from *in vitro* models. Specifically, the dimethyl sulfoxide (DMSO)-soluble extracts of UVCB substances are exposed to induced pluripotent stem cell-derived cardiomyocytes and hepatocytes. The resulting concentration-response curves are used to derive ToxPi scores, which serve as the final bioactivity data with 16 features (Grimm et al., 2016).

2.2. Characterization of Broad-Acting Enterosorbents for Mitigation of Chemicals

Several different sorbent materials (e.g., activated carbon and processed sorbent material) are experimentally tested and characterized for various hazardous chemicals. For each sorbent material, equilibrium isothermal analysis has been performed by fitting the experimental data to multiple isotherm equations. This analysis enables the calculation of various material-toxin properties including, binding affinity (K_d), capacity (Q_{max}) and relative surface binding in water. These material-toxin properties are previously found to be the most important features for identifying optimal binding *in vivo* (Phillips, 2008) and can be used to build predictive models which will guide the selection of toxin binders for future testing. In this study, we use the first set of experimental data on the aforementioned sorbent materials with following chemicals: pentachlorophenol (PCP), benzo(a)pyrene (BaP), lindane, diazinon, zearalenone, aldicarb, 2,4-Dinitrophenol (DNP) and aflatoxin (only with processed sorbent material). The data includes information on chemical binding capacity (Q_{max}) and logP, which characterizes the difference in solubility of a solute in two immiscible phases at equilibrium (i.e. octanol and water). As water and octanol being polar and nonpolar solvents, respectively, the logP value provides a measure for the hydrophobicity or hydrophilicity of the substance.

3. Methodology

3.1. Clustering of Complex Substances

In this study, we use hierarchical clustering with 3 distinct agglomeration methods, i.e. Ward's method, average linkage, and complete linkage along with 3 different correlation metrics, namely Kendall, Pearson, and Spearman correlations. This yields 9 different clustering algorithms for testing. Furthermore, an integrated dimensionality reduction and clustering analysis is performed to assess the effect of principal components analysis (PCA) on the clustering results. For each principal component subset, clustering is performed iteratively using all listed algorithms. The quality of the clustering structure is optimized by maximizing the FM index. FM index provides a measure of similarity between two clustering trees, between clustering trees generated based on 9 aforementioned algorithms and a reference categorization of the complex substances based on their manufacturing streams (i.e. HFO, SRGO, etc.). The optimal clustering tree and corresponding algorithm are reported when the highest FM index is achieved. In future studies, we aim to utilize Support Vector Machine-based feature selection algorithm as an alternative dimensionality reduction technique, which has been successfully applied in bioinformatics (Kieslich et al., 2016).

3.2. Predictive Modeling of Material Sorption Activity on Chemicals

We implement linear and nonlinear regression techniques (Boukouvala and Floudas, 2017) to postulate a surrogate model that will guide iterative experimental design for maximizing the sorption activity of broad-acting materials. Regression is performed by minimizing the least-squares error between the actual experimental values and model predictions. In this study, linear, general quadratic, and signomial function of order 1 are investigated as candidate surrogate models to predict relative sorption level of the material. The goodness-of-fit for each model is assessed using coefficient of determination (R^2), and root-mean-square error (RMSE).

4. Results

4.1. Optimal Clustering of Complex Substances based on Chemical and Biological Data

We present feature intensity maps of 18 tested complex substances using their relative abundance of heteroatom class distributions in Figure 1A. Intensity map highlights the most informative features that separate the substances into categories by providing qualitative and quantitative compositional comparison. The results show that N1 heteroatom class is the most predominant feature with 33.41% presence among all substances. This is followed by N1 S1, O1, N2 S1, and N1 13C1 heteroatom classes with 13.53%, 8.29%, 6.76, and 3.76% occupancy. Relative occupancy of the 5 most descriptive heteroatom classes within each substance category is presented in Table 1.

Table 1. Identification of the top 5 descriptive features (heteroatom classes) for each category.

Substance Category	Heteroatom Class	Relative Occup. (%)	Substance Category	Heteroatom Class	Relative Occup. (%)
HFO	N1	32.57	VHGO	N1	33.66
	N1 S1	10.03		N1 S1	13.49
	N2 S1	9.32		O1	8.22
	N2	8.40		N2 S1	7.11
	N1 13C1	6.99		N1 O1	3.49
OGO	O1	34.48	SRGO	N1	45.50
	O1 13C1	7.61		N1 S1	20.29
	N2 O1 S2	7.38		N2 S1	6.56
	N1 O1	5.81		O1 S2	6.00
	N2 O1 S1	4.12		N1 13C1	4.24

Among all the clustering algorithms, highest FM index (0.669) is achieved with the integrated PCA - hierarchical clustering with complete linkage using Kendall correlation. The same clustering algorithm without dimensionality reduction (82 features) reveals the FM index of 0.325 (Figure 1A). Similarly, bioactivity profiles obtained from two cell types, namely cardiomyocytes and hepatocytes, are depicted via feature intensity map in Figure 1B. Figure 1B demonstrates that the most distinctive biological features of HFO category result from 4 hepatocyte phenotypes, e.g. mitochondrial integrity intensity, viability, mitochondrial integrity, and total area of live cells. Moreover, the top informative features for VHGO category belong to 2 cardiomyocyte phenotypes, e.g. peak amplitude and mitochondrial integrity. OGO and SRGO categories reveal similar biological features that are mostly part of

cardiomyocyte phenotypes, where OGO diverges with the lack of 2 hepatocyte phenotypes, e.g. mitochondrial integrated intensity and total area of live cells, as well as 3 cardiomyocyte phenotypes e.g. mitochondrial integrity, nuclei count, and viability. In clustering analysis, highest FM index (0.805) is achieved with the integrated PCA - hierarchical clustering with 4 features through complete and average linkage using Spearman correlation. On the other hand, the same clustering algorithm without dimensionality reduction generates FM index of 0.768 with 16 features (Figure 1B).

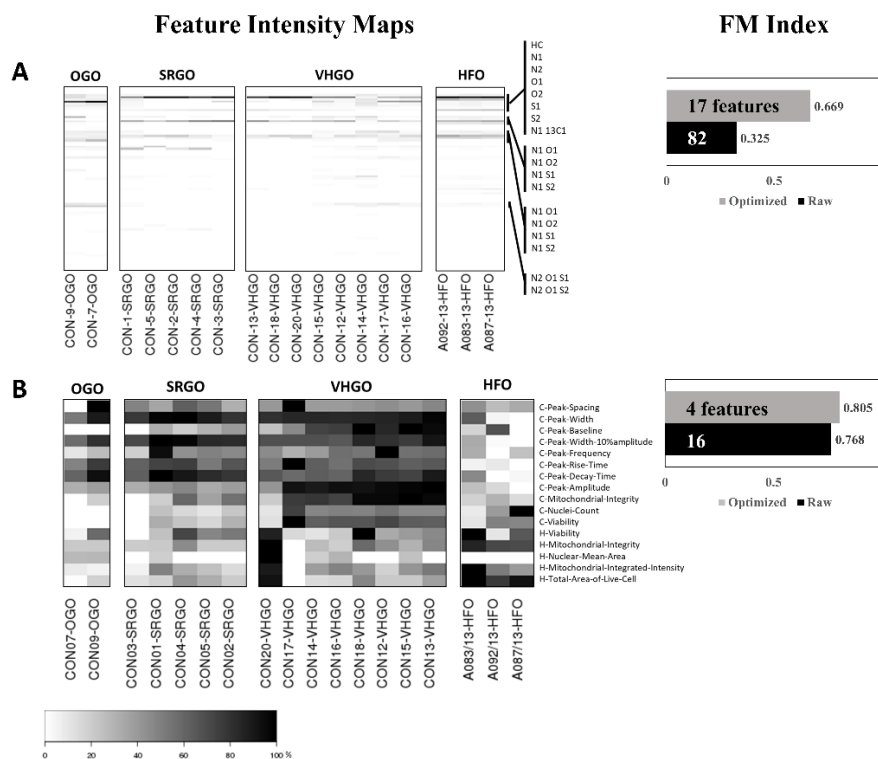


Figure 1. (A) Chemical and (B) bioactivity profiling and cluster analysis of UVCB substances based on IM-MS and human induced pluripotent stem cell analysis data set, respectively. Feature intensity maps (informative features are provided in the side bar; features starting with “C-“ and “H-“ belong to cardiomyocyte and hepatocyte phenotypes, respectively). FM index from clustering studies are provided in bar plots before and after dimensionality reduction.

4.2. Surrogate Modeling for Sorbent Materials

In order to perform predictive modeling of sorption activity of two sorbent materials based on Q_{\max} and $\log P$, we have used 3 different surrogate model types, namely linear, general quadratic, and signomial of order 1. Table 2 and 3 demonstrate the surrogate model parameters along with the corresponding coefficient of determination (R^2), and root-mean-square error (RMSE). Complex surrogate models are avoided to prevent overfitting in the regression analysis. The results show that quadratic functional forms perform better than the others, where the goodness-of-fit should be improved with additional experimental data. The analysis presented here is performed first on mono-constituent chemicals that are anticipated to be part of environmental mixtures and serves as an initial starting point of an iterative data-driven procedure which aims to maximize sorbent activity by

providing feedback for future experiment designs. Here, by locating and reporting the sample space spanned by Q_{\max} and $\log P$, where maximum sorption activity is achieved with the best surrogate models (i.e. quadratic functions), we provide feedback to experimental collaborators to design further set of experiments. In the future studies, more chemical properties such as chemisorption indices, specificity, affinity, capacity, and enthalpy will be included in characterization of chemical-sorbent relationship along with designable (morphological and functional) properties of the sorbent material. Then, predictive modeling of the interconnected relationship between the various sorbent properties and sorbent activity will facilitate the exploration of the large chemical-sorbent property space and guide future experimental designs to maximize sorption. Finally, for a mixture of chemicals, % binding can be estimated by analyzing; (i) fraction of each compound in mixture, and (ii) Q_{\max} of each compound in mixture. These will be used to generate predictive models for mixture of chemicals in solution.

Table 2. Surrogate models for sorption activity of activated carbon using Q_{\max} and $\log P$.

Model Type	R ²	RMSE	Surrogate Model Form, y=%bound
Linear	0.472	0.282	$y = 0.070 + 0.761Q_{\max} + 0.210 \log P$
Quadratic	0.872	0.139	$y = -3.480 + 11.714Q_{\max} + 7.904 \log P - 7.044Q_{\max}^2 - 6.188Q_{\max} \log P - 4.787 \log P^2$
Signomial Order 1	0.498	0.275	$y = 1.010Q_{\max}^{0.574} \log P^{0.090}$

Table 3. Surrogate models for sorption activity of processed sorbent material using Q_{\max} and $\log P$.

Model Type	R ²	RMSE	Surrogate Model Form, y=%bound
Linear	0.546	0.204	$y = 0.248 + 0.576Q_{\max} - 0.132 \log P$
Quadratic	0.627	0.185	$y = -0.253 + 1.279Q_{\max} + 1.576 \log P - 0.269Q_{\max}^2 - 0.923Q_{\max} \log P - 1.121 \log P^2$
Signomial Order 1	0.516	0.211	$y = 0.715Q_{\max}^{0.619} \log P^{-0.049}$

5. Conclusions

Here, we present an application of data analysis, modeling, and dimensionality reduction techniques in biomedical and environmental setting. Our analysis provides comprehensive data-driven tools for (i) optimal grouping of an “unknown” mixture with “known” chemicals that enables read-across, thus rapid decision-making during environmental emergencies, and (ii) guide experimental setups to achieve optimal entero-sorbent material designs that can mitigate the adverse effects of the chemical exposure. This research was funded by U.S. National Institute of Health grant P42 ES027704.

References

- Boukouvala, F and Floudas CA. Optimization Letters (2017), 11, 895-913.
 CONCAWE, REACH-Analytical Characterisation of Petroleum UVCB Substances (2012).
 Fowlkes, EB, Mallows, CL. Journal of the American Statistical Association (1983), 78, 553-569.
 Grimm, FA, et al. Green Chemistry (2016), 18, 4407-4419.
 Grimm, FA, et al. Environmental Science & Technology (2017), 51, 7197-7207.
 Kieslich CA et al. PLoS One (2016), 11, DOI: 10.1371/journal.pone.0148974.
 Phillips TD et al. Food Additives & Contaminants Part A (2008), 25, 134-45.
 TAMU Superfund Research Center (2017). <https://superfund.tamu.edu/> (accessed 18 Dec 2017).

Solution of the Population Balance Equation by the Meshless Moving Particle Method (MMPM)

Menwer Attarakih,^{a,b,*} Hans-Jörg Bart,^b

^a*Department of Chemical Engineering, University of Jordan, Amman 11942, Jordan*

^b*Chair of Separation Science and Technology, TUK, Kaiserslautern 67653, Germany*

m.attarakih@ju.edu.jo

Abstract

In this contribution we deal with a critical problem in the numerical modelling of the dispersed phase flow systems using population balances. To solve this problem, we derived a Meshless Moving Particle Method (MMPM) which is based on coupling information and function approximation theories to recover the complete particle size distribution in a grid free environment. The particles, which adapt their positions according to population integral properties, are allowed to propagate using a few number of ODEs. These particle positions are found exactly the same as those predicted by the Chebyshev-QMOM; however, without iterative eigenvalue calculations. The overall complexity of the method is $O(N)$ where N is the number of moving particles. The MMPM is validated using many test cases with known analytical solutions including microbial cell dynamics in a constant abiotic environment. The sequence of the continuous approximations of the number concentration function is found to converge with an order $O(1/N^c)$ with $c > 1$.

Keywords: Meshless Methods, Moving Particles, Population Balances, Modelling.

1. Introduction

The population balance equation (PBE) which governs the space-time evolution of discrete phase systems, at micro or macro state levels, finds numerous applications including inanimate particles and animate cells (Ramkrishna and Sing, 2014). The complexities in the solution of the PBE are twofold: The latent functional in the integral source term and its spatial geometrical dependencies in practical cases. Since its first appearance in the early of sixties, it has received a great attention by researchers as well as practitioners both on mathematical and numerical modelling levels where latest reviews are found in Ramkrishna and Sing (2014) and Ferreira et al. (2017). In spite of the intensive research in the last decades, which is concerned with fast numerical solvers based on the moment methods, numerical solutions which are able to conserve particle integral properties suffer from losing the particle size distribution. The latter is required in industrial particulate systems where it is used to determine mechanical and physiochemical system properties, for online control purposes (Attarakih et al., 2012), to evaluate the negative particle fluxes at zero particle size as in the case of droplet evaporation (Vie et al., 2013) and to accommodate time varying boundary conditions in age-structured models of hematological disease (Foley and Mackey, 2009). In the present work, we overcome the lost size distribution problem, while estimating accurately the required particle mean properties, by introducing a unique converging

sequence of continuous approximations to the PBE on moving particles. The moving particles become a necessity when fixed discretization of the particle phase space requires a huge number of grid points due moving distribution functions.

2. The Meshless Moving Particle Method (MMPM)

Given $f(\zeta, t)$ as a number concentration function in a homogenous space with particle property phase space ζ , the PBE for growth, breakage and aggregation is written as:

$$\frac{\partial f(\zeta, t)}{\partial t} + \frac{\partial [G(\zeta, S)f(\zeta, t)]}{\partial \zeta} = L\{f\} \quad (1)$$

In the above equation, particles are allowed to grow or shrink due to mass transport to or from its continuous surrounding phase through the variable S at a rate $G(\zeta, S)$ at any given instant t . The volumetric source term $L\{f\}$ represents the loss and formation of particles due to instantaneous breakage and aggregation events. Eq.(1) can be solved using the moment methods with QMOM as a closure rule because of the general dependencies of the interaction frequencies in $L\{f\}$ on ζ . The popularity of these methods results from the non-stiff ODEs in terms of $f(\zeta, t)$ moments and the accuracy of the moving Gauss quadrature used to integrate the source term. As discussed in section 1, the moment methods destroy the number concentration $f(\zeta, t)$ due to moment construction over the particle phase space. The reconstruction of this function from its low-order moments faces the uniqueness and stability problems and often results in assuming parametrized distribution like the generalized lambda distributions. Since the objective is to reconstruct a unique and non-negative number concentration function, the maximum entropy functional is the ideal choice (Attarakih and Bart, 2014). This results in a number distribution that is statistically most likely to occur with Lagrange multipliers in terms of its moments. This method still suffers from averaging the spatial velocity in the convective term and hence prevents its dependence on particle size which is required for momentum balances in multifluid models. Moreover, the number of low-order moments is increased for accurate reconstruction of asymmetric and bimodal number concentration functions. These problems arise due to ignorance of local information about the number concentration function. In this regard, Attarakih and Bart (2017) introduced a novel maximum entropy solution by maximizing the Shannon maximum entropy subject to the available local information of $f(\zeta, t)$:

$$f(\zeta, t) = \exp \left(\sum_{j=0}^{N-1} \alpha_j(t) Le_j(\zeta) \right) \quad (2)$$

In this work, the resulting continuous Lagrange multiplier is expanded by a complete set of orthogonal Legendre basis functions Le_j with a closed set of expansion coefficients α_j . This solution is consistent with the expected values $E\langle Le_j, f \rangle$ with respect to $f(\zeta, t)$ and satisfies the positivity condition imposed on $f(\zeta, t)$. Instead of using fixed sampling (collocation) points to calculate α_j , we introduce the essence of the MMPM by discretization of the initial particle phase space ζ into an ordered particle positions $\Xi_0 = \{\zeta_0 < \zeta_1 \dots < \zeta_{N-1}\}$ which should be consistent with at least $N+1$ low-order moments of the initial particle distribution. These positions are found by using the recently developed Chebyshev-QMOM algorithm which is more robust than the PD algorithm (Attarakih et al., 2017). Now, the coefficients $\alpha_j(t)$ are calculated from the function

values $f(\zeta, t)$ by applying the orthogonal collocation method in a moving sense where Eq.(1) is transformed into a system of ODEs that are exactly satisfied at a moving set of moving particles $\Xi_t = \{\zeta_0(t) < \zeta_1(t) \dots < \zeta_{N-1}(t)$ and is given by:

$$\frac{df(\zeta_i(t), t)}{dt} + \left[\gamma_i(t)[Le'(\zeta)]^T \alpha(\zeta, t) + \frac{dG(\zeta_i(t), S)}{d\zeta} \right] f(\zeta_i(t), t) = L\{f(\zeta_i(t)), \zeta_i(t)\} \quad (3)$$

$$\gamma_i(t) = G(\zeta_i(t), S) - \frac{d\zeta_i(t)}{dt} \quad (4)$$

Where γ_i represents the net growth velocity which is a contribution of physical particle growth ($G(\zeta, S)$) and the moving particle velocity $d\zeta/dt$. Note that $Le'(\zeta)$ is a column vector of Legendre polynomial derivatives. The gradient of $f(\zeta, t)$ due to growth is computed by exact differentiation of Eq.(2). This is an exact meshless moving differential quadrature (DQ) which alleviates the problem of FDS's that require a huge number of grid points. To calculate the moving particle velocity $d\zeta/dt$ we employed the inversion of a few number of low-order moments using the Chebyshev-QMOM algorithm. However, for pure particle growth, Eq. (4) is reduced exactly to:

$$\frac{d\zeta_i(t)}{dt} = G(\zeta_i(t), S) \quad (5)$$

Where ζ obtained from this equation is exactly the same as that computed from the Chebyshev-QMOM algorithm. This implies that the moving particles speed cannot be less or greater than their growth velocity. This elegant mathematical and physical consistency persists irrespective of the functional form of the growth function and is valid for multidimensional PBEs with pure growth. Moreover, since particle growth conserves the total number of particles, the moving quadrature weights are constant. Using Eqs.(3) and (4 or 5) the elements of $\alpha(t)$ in Eq.(2) are found from:

$$\alpha_j(\zeta(t)) = \frac{2N+1}{2} \sum_{m=0}^{N-1} \omega_m Le_j(\chi_m) \ln[f(\zeta(\chi_m(t)))]], j = 0, 1, \dots, N-1, \quad (6)$$

Note that $\zeta(\chi(t)) = \zeta_0(t) + ((\zeta_{N-1}(t) - \zeta_0(t))/2)(\chi + 1)$ and $\chi \in (-1, 1)$, $m = 0, 1, \dots, N$ are the moving roots of the shifted Legendre polynomials and χ and ω are the fixed Gauss-Legendre quadrature nodes and weights respectively. On the other hand, in the absence of growth from Eq.(3), the moving particles feels a negative particle growth (evaporation) in case of particle aggregation and positive growth (condensation) due to particle breakage. This growth term act as a buffer which resists the changes in the source term and hence keeps the functional profiles ($f(\zeta, t)$) smooth w.r.t. time. It is interesting to note in cases of equal binary particle breakage and growth rates and in case of equal breakage and aggregation rates the particles velocity will be reduced to zero. It is clear from this brief discussion that source terms of aggregation and breakage mechanisms can be modelled as a positive and negative growth terms respectively. This lead us to unify our solution framework and think of finding characteristic (eigenvalues) lines similar to that of pure growth. Since Eqs.(5) reproduce exactly the set of the eigenvalues predicted by the Chebyshev-QMOM algorithm, the reverse is correct when dealing with the PBE with source term. In this case, the eigenvalues produced by the Chebyshev-QMOM algorithm are the characteristic lines of the PBE in the presence of source term. Therefore, the moving particle velocities $d\zeta_i/dt$ are derived from the slopes of the eigenvalues calculated by the Chebyshev-QMOM algorithm.

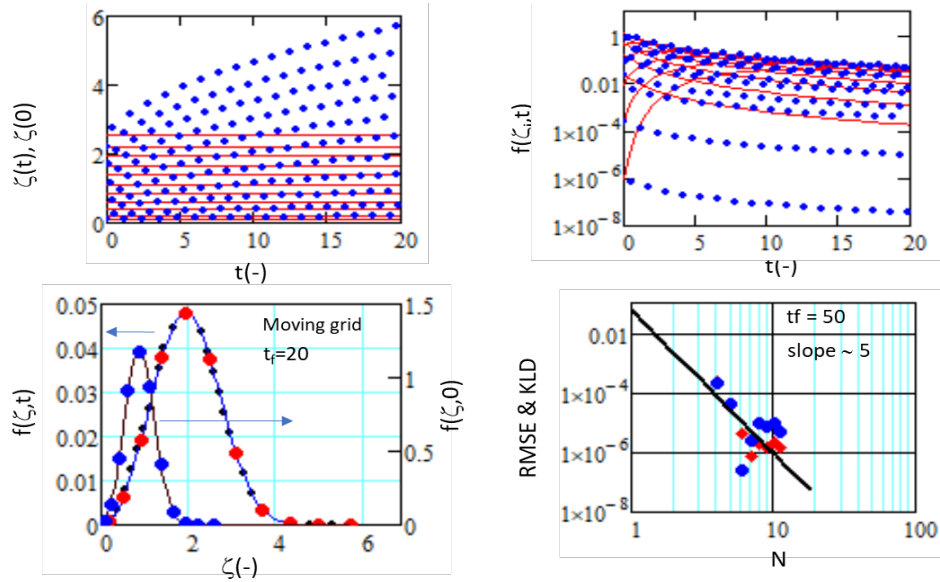


Figure (1): Solution of the PBE with constant particle aggregation using the moving and fixed particle trajectories with their function values (filled circles on moving particles).

After careful analysis of this algorithm, the velocity of the moving particles is given by:

$$\frac{d\zeta_i(t)}{dt} = \zeta_i(0)\eta(\mu_0(t), \mu_1(t), \dots), \quad i = 0, 1, \dots, N - 1 \quad (7)$$

The function η is expressed in terms of low-order moments of $f(\zeta, t)$ using the Chebyshev-QMOM. Our undergoing research shows that the space of the moments can be reduced where simple expressions for $\eta(\mu_0, \mu_1, \dots)$ is derived. The set of Eqs.(2) to (7) defines completely the numerical model for the MMPM for the solution of the PBE.

3. Numerical Results and Discussion

3.1. Numerical Analysis

The proposed MMPM is first validated against analytical solution of the PBE for constant kernel aggregation in closed homogeneous space. This is used to explore the numerical features of the MMPM on moving and fixed particles. The eleven initial moving particles were generated from the initial condition $(3\zeta^2 \exp(-\zeta^3))$ using the Chebyshev-QMOM (Attarakih et al., 2017) with 22 low-order moments without placing bounds on the minimum and maximum particle sizes. These particles are shown on the upper panel (left) of Figure (1) as solid lines while the moving particles are shown as small filled circles. The velocities of these moving particles are estimated from Eq.(7). Also, these initial positions along with the tabulated values of Gauss-Legendre quadrature's weights and nodes are used to calculate the coefficients of the Legendre polynomials from Eq.(6). It is clear that the fixed grid has two drawbacks: The first one is its inability to accommodate the newly born particles after $t \sim 5$, and the second one is the departure of the characteristic particles away from the fixed ones as time increases.

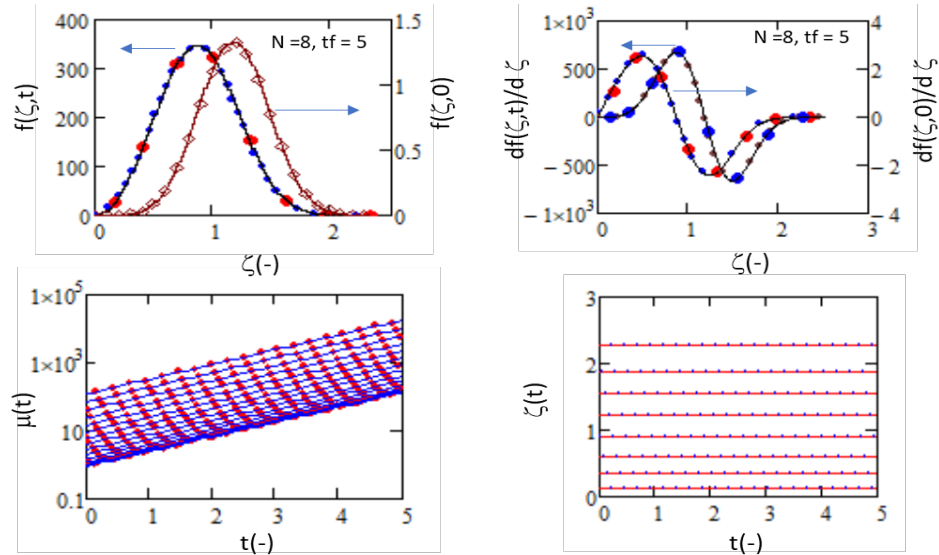


Figure (2): Microbial cell dynamics with binary division and growth using the MMPM as compared to analytical solution (solid line).

This results in discretization inconsistency unless suitable algorithm is used to conserve the desired particle integral properties. On the other hand, the moving particle trajectories conserve exactly $2N$ low order integral properties since particle positions are determined based on these moments. The sampled values of $f(\zeta_i, t)$ are calculated on these moving particles using Eq.(3). The evolution of these values in time are shown in Figure (1) upper panel (right) as compared to the fixed particle trajectories. It is clear that the sampled values at moving particles are evolved smoothly compared to that of fixed particles. This makes efficient use of the ODE solvers and reduces the CPU time by a factor of order 5. The reconstructed continuous functional at $t = 20$ is shown in Figure (1) bottom panel (left) along with the analytical solution (solid line). It is clear that the numerical solution at the moving particles (filled large circles) and the interpolated ones (small filled circles) are indistinguishable from the analytical solution using only 11 particles. The remarkable convergence of the continuous solutions is supported by the rapid error decrease based on the root mean square error (RMSE) and Kullback-Leibler divergence (KLD) (Attarakih and Bart, 2014) as shown in Figure (1) lower panel (right) where the slope of the convergence line is ~ 5 .

3.2. Case study: Microbial cell dynamics in constant abiotic environment

This case describes simultaneous cell growth and division. It presents microbial cell dynamics in abiotic environment with a constant quantity of substrate (S). To allow for an analytical solution, an isothermal batch chemostat, constant abiotic environment, single cell growth rate is proportional to its mass, and dividing cells partition their material uniformly to the two daughter cells, were assumed. The intercellular state is represented here by the cell size (ζ). The cell mass is transformed into cell diameter (ζ) with an assumed spherical shape where analytical solution was derived in Attarakih et al. (2015). This analytical solution is compared to the MMPM as shown in Figure (2) upper panel (left) which shows the dynamic evolution of the microbial cell population under simultaneous growth and division. It is evident that the MMPM follows with a high accuracy the evolution of the population dynamics using only 8 particles. Actually,

since the rate of growth equals the rate of particle loss by division, an equilibrium is achieved between growth and particle division. This results in stationary particle diameter as shown in the lower panel of Figure (2) (right). Actually, all mean cell lengths (ζ_{10} , ζ_{30} , ζ_{32} ... etc.) are constant as function of time. From this one can calculate $\zeta(t)$ and particle weight without resorting to the Chebyshev-QMOM algorithm. Finally, the numerical derivative of $f(\zeta,t)$ required for the evaluation of the growth source terms is calculated using the DQ and the results are compared to the analytical values as shown in Figure (2) upper panel (right) thanks to the orthogonal expansion of the maximum entropy functional and its exact derivative.

4. Summary and Conclusions

A MMPM is derived and validated for the solution of PBE with particle growth, breakage and aggregation. The MMPM is validated using cases with known analytical solutions. The sequence of the continuous approximations is found to converge in terms of the Kullback-Leibler distance and the RMSE with order $O(1/N)$. As a case study, the MMPM is applied to simulate the microbial cell dynamics which includes simultaneous cell growth and division in a constant abiotic environment. The results show that the MMPM tracks the dynamic evolution of the microbial cell population using only 8 moving particles with the conservation of the first 16 population low-order moments.

Acknowledgment

This work has been carried out during sabbatical leave granted to the author Professor Menwer Attarakih from the University of Jordan during the academic year 2017/2018.

References

- M. Attarakih, A. Hasseine and H.-J. Bart, 2017, On the Solution of the PBE by Orthogonal Expansion of the Maximum Entropy Functional. *Comp. Aided Chem. Eng.*, 40, 2053-2058.
- M. Attarakih, A. Hasseine H.-J. Bart, 2015, A meshfree maximum entropy method for the solution of the population balance equation, *Comp. Aided Chem. Eng.*, 37, 197-202.
- M. Attarakih and H.-J. Bart, 2014, Solution of the population balance equation using the differential maximum entropy method (DMaxEntM): An application to liquid extraction columns. *Chem. Eng. Sci.*, 108, 123-133.
- M. Attarakih, H. B. Jildeh, M. Mickler and H. J. Bart, 2012, The OPOSPM as a nonlinear autocorrelation population balance model for dynamic simulation of liquid extraction columns. *Comp. Aided Chem. Eng.*, 31, 1216-1220.
- G. G. S. Ferreira, P.L. Lage and L. F. L. R. Silva, 2017, Extension and convergence analysis of the univariate direct quadrature spanning tree method. *Powder Tech.*, 322, 301-313.
- C. Foley and M. C. Mackey, 2009, Dynamic hematological disease: A review. *J. Math. Biol.*, 58, 285-322.
- D. Ramkrishna and M. R. Singh, 2014, Population Balance Modeling: Current Status and Future Prospects, *Annu. Rev. Chem. Biomol. Eng.*, 5, 123-146.
- A. Vie, F. Laurent and M. Massot, 2013, Size-velocity correlations in hybrid high order moment/multi-fluid methods for polydisperse evaporating sprays: Modeling and numerical issues. *J. Comp. Phys.*, 237, 177-210.

Multi-objective optimization of a CO₂-EOR process from the sustainability criteria

Juan Pablo Gutierrez^{a,*}, Eleonora Erdmann^b, Davide Manca^c

^a*Instituto Tecnológico de Buenos Aires (ITBA), CONICET, Av. Eduardo Madero 399, Buenos Aires, C1106ACD, Argentina.*

^b*ITBA, Av. Eduardo Madero 399, Buenos Aires, C1106ACD, Argentina.*

^c*PSE-Lab, CMIC Department, Politecnico di Milano, P.zza Leonardo da Vinci 32, Milano, 20133, Italia.*

jgutierrez@itba.edu.ar

Abstract

Aim of this article is to estimate and discuss the economic and environmental impacts for the obtainment of CO₂ in such conditions to be injected as enhanced oil recovery (EOR) fluid. Particularly, this study focuses on the compression sector design needed to process the CO₂ coming from an already existing absorption plant. Currently, 18.68 kmol/h of a high-purity CO₂ stream may be used for injecting and increasing the production of a pilot crude oil well near the location of the industrial plant. However, it is still necessary to perform an economic evaluation to quantify the investment and the operating costs that the compression involves.

An optimization problem for minimizing the energy consumption of the new sector while increasing the pressure of the stream is solved. It has been found that the conditions to obtain the lower energy requirement are a 4-stage compressing layout with a pressure ratio equal to 4 and intercooling units of 41.73 °C. After discussing these results, an economic assessment to estimate investment, operating and utility costs is presented. Although the installation cost for the additional sector is more than 3000 kUSD, the investment might be compensated with the increasing production of the well under study. In addition to this, the development of EOR projects could create a market in a region where the technology is still not considered.

In the final part of the article, CO₂, CH₄, H₂O wastes and combustion gases emissions are calculated. As expected, almost the total amount of the vented CO₂ can be captured for this double-purpose technology, increasing the total incomes while geologically confining large-volumes of this pollutant and greenhouse gas.

Keywords: Sustainability, Economic assessment, Environmental impact, CO₂ EOR, CO₂ absorption process.

1. Introduction

Several industrial processes produce highly concentrated streams of carbon dioxide (CO₂) as a by-product (Herzog, 2011). For instance, the absorption of CO₂ from natural gas by using alkanolamines produces a high purity CO₂ stream, with a molar concentration over 87 % in most of the cases (Peters et al., 2011; Ahmad et al., 2012; Banat et al., 2014; Al-Lagtah et al., 2015; Gutierrez et al., 2016; Gutierrez et al., 2017).

As it can be inferred, this large amount of CO₂ produced continuously may be used for improving the crude oil production, during the stage of enhanced oil recovery (EOR). In this regard, the CO₂ for EOR has already demonstrated to be a technical and economic success in different locations for a number of years (Khan et al., 2013). Having a paramount potential for carbon dioxide capture and storage (CCS), the CO₂ EOR significantly increases the production of mature wells while decreasing the greenhouse gas emissions on a large-scale (Brush et al., 2000; Peters et al., 2011).

Different studies have assessed the economics involved in the installation of a CO₂ absorption for EOR purposes (Peters et al., 2011; Mazzetti et al., 2014; Kazemi et al., 2014; Suleiman et al., 2016). Peters et al. (2011) developed an economical model to calculate the capital investment and the gas processing cost of an amine-based process. To assess the economics, they performed a simulation model in Aspen HYSYS, where they assumed a molar concentration above 90 % CO₂ in the acid gas.

Mazzetti et al. (2014) estimated the costs of CO₂ removal from natural gas with subsequent geological storage by using a suitable simulation model. Particularly, they estimated the total capital cost to obtain CO₂ for EOR in North Europe, with an MDEA-based absorption process. From the economic viewpoint, they stated that large-scale EOR projects could cover the necessary expenditures to improve remote fields' production.

Kazemi et al. (2014) simulated an alkanolamine process with Aspen HYSYS and performed an economic assessment with Aspen Economic Analyser. Based on a typical gas produced in Iran, they compared the performance of the process with three other technologies in regard to their capital and annual costs, for different sour gas molar flows.

Suleiman et al. (2016) evaluated two absorption processes using a feed flow of 1245 kmol/h to produce a clean natural gas with purity of 99 %. Those authors used simulation models to define stream properties, heat duties, power requirements and equipment sizes. For the economic assessment, they introduced suitable raw material costs, working capital, capital of investment, and total annual incomes.

With reference to previous works, the alkanolamine process to clean the natural gas while obtaining a side-product CO₂ stream has been extensively studied worldwide. However, the economic assessment performed by the predecessors consider the units of absorption and regeneration only, and exclude the conditioning of the CO₂ to be used in different applications. This paper presents and discusses the optimal design, the economic evaluation, and the environmental impact to condition CO₂ for EOR. Although the costs of CO₂ obtainment and storage appear to be high, we discuss the sustainability and the effect of the investment in the region under study.

2. Location and process description

The southern Neuquén basin (NQNB) of Argentina is the location selected because its crude oil chemical properties favor the implementation of CO₂-EOR (Gallo and Erdmann, 2017). Large-scale volumes of CO₂ are emitted throughout this area from gas & oil processing industries, mining companies and power generation plants. Particularly, CO₂ coming from natural gas absorption plants is of special interest in this work for their permanent availability.

This typical CO₂ absorption process features two main operations. In the former, the acid gases of the natural gas are chemically absorbed by an alkanolamine liquid stream. In the latter, that rich amine leaving from the bottom of the absorption tower is sent to a stripping column, where the CO₂ is recovered at higher purity.

3. Methodology

Initially, the steady-state of the process to remove CO₂ from a natural gas stream is simulated in Aspen HYSYS (Aspen Tech., 2012). In the simulation model, a combination of the Non-Random Two-Liquid method for electrolytes (eNRTL) and the Peng- Robinson Equation of State for vapor phase is applied for the prediction of the thermodynamic properties (Song and Chen, 2009). Material streams, flowrates, compositions and conditions are taken from an existing MDEA-based absorption plant in Argentina (Figure 1).

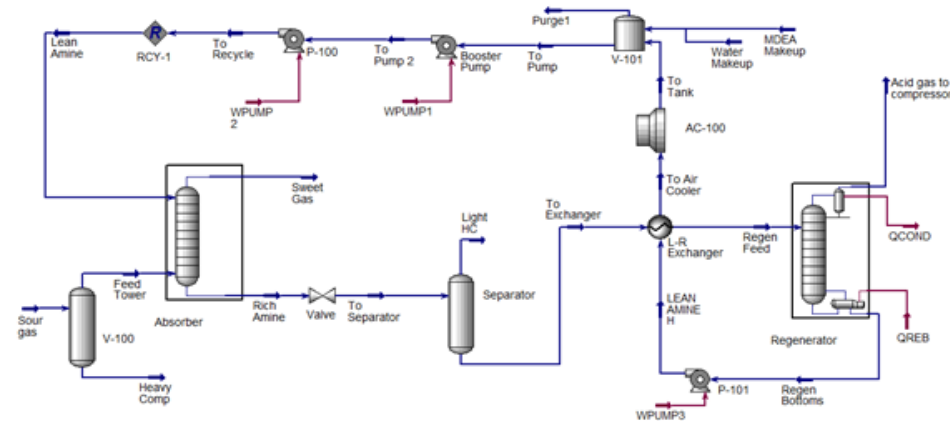


Figure 1. MDEA-based absorption plant for removing CO₂ from natural gas.

18.68 kmol/h of acid gas at 47.27 °C are obtained from the top of the stripping column, composed by CO₂ (87.93 mol%), water (9.32 mol%), methane (1.33 mol%), and heavy hydrocarbons. However, the pressure of the stream is considerably low (14.50 psia) and thus a subsequent compressing system should be design to properly dispose this high purity CO₂ stream.

According to empirical considerations, a 4-stage compression system might be implemented to increase the pressure of the acid gas leaving the plant. In the sector to be designed, the available variables are the temperature of the intercooling stages and the pressure ratio of each compressor. Centrifugal compressors with 75 % adiabatic efficiency are assumed and logical operators (SET and ADJUST) are used to unify the compression ratios and the cooling temperatures (Figure 2).

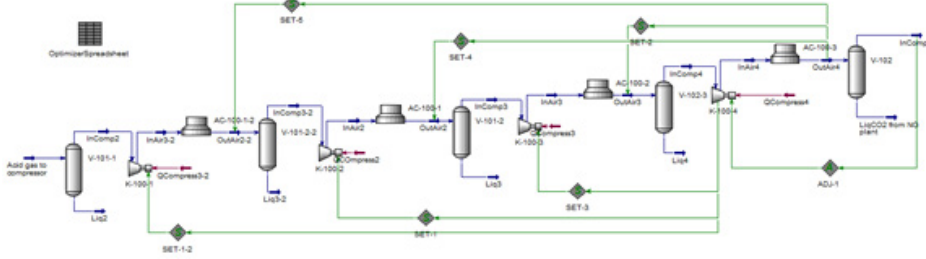


Figure 2. Compression and intercooling of 4-stages for CO₂ conditioning.

After modelling the compression sector, we propose a minimization problem to define the optimal conditions. Eq. (1) summarizes the mathematical expression representing the minimum problem to solve.

$$\begin{aligned}
 & \min_{u_1, u_2} (Q_{Total}) \\
 & \text{s. t.:} \\
 & 2 \leq u_1 \leq 10; \\
 & 25 \leq u_2 \leq 55; \\
 & y_{CO_2}^{Prod} > 0.87 \\
 & P_{CO_2}^{Prod} > 6,000 \text{ kPa}
 \end{aligned} \tag{1}$$

Where $Q_{Total} = Q_{Compressing} + Q_{Cooling}$ (MJ/h) is the duty needed for the compression and the cooling stages. u_1 represents the pressure ratio for each centrifugal compressor, u_2 the temperature after the cooling units (°C), $y_{CO_2}^{Prod}$ and $P_{CO_2}^{Prod}$ the purity and the pressure of the CO₂ product stream.

Similar to Kazemi et al. (2014), we employ Aspen Economic Analyser to estimate capital costs, operating costs and utility costs of each process. Using Aspen Energy Analysis and material balances, we also estimate the greenhouse gases emissions (GHG) particularly CO₂, H₂O, and CH₄ for the studied alternative.

4. Results and discussion

In Table 1, the values of optimal Q_{Total} , u_1 , and u_2 are shown. As it can be seen, the compression ratio remains equal to 4 for design purposes, and the temperature of the intercooling stages slightly under the initial acid gas temperature.

Table 1. Optimal values of Q_{Total} , u_1 , u_2 , $y_{CO_2}^{Prod}$, and $P_{CO_2}^{Prod}$ for the 4-stage process design.

Q_{Total} (MJ/h)	u_1	u_2 (°C)	$y_{CO_2}^{Prod}$	$P_{CO_2}^{Prod}$ (kPa)
639.85	3.849	41.73	0.9777	6,865

A total equipment cost of 3,828 kUSD is estimated for this design, distributed in accordance with the Figures 3 (a) and (b). Concerning the distribution of the investment cost, the compressors represent 86 % of the total investment.

Figure 4(a) shows the total operating and utility costs. The values observed might be attributed to the significant consumption of electricity.

Figure 4(b) presents the distribution of the energy consumption. Contrary to the expected, the highest consumption corresponds to the air-cooling system due to temperature drops of around 40°C.

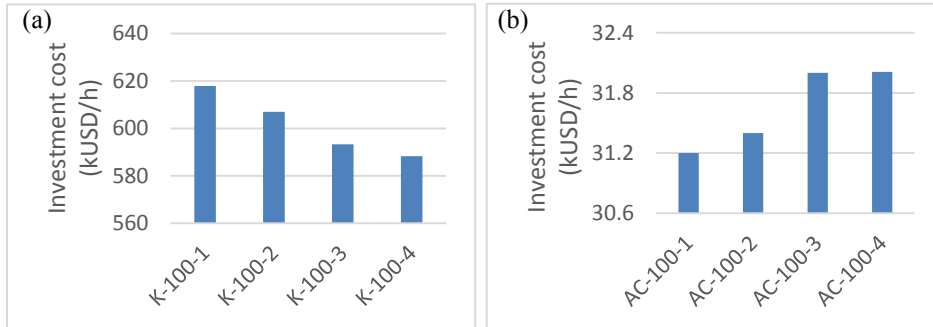


Figure 3. Investment cost (kUSD) per each (a) compressor, and (b) cooling unit of the 3 and 4- Stages system.

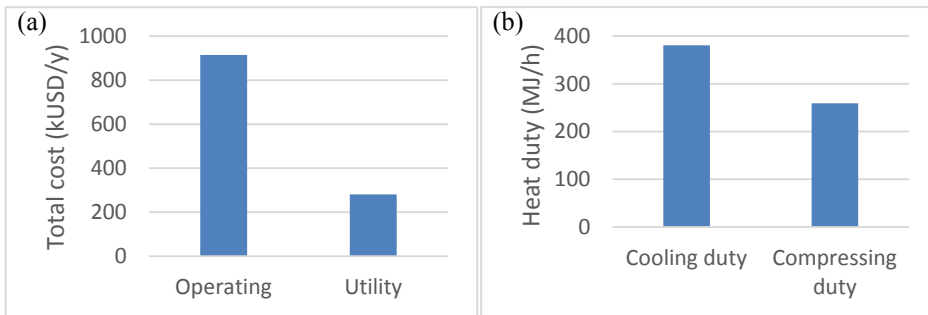


Figure 4.(a) Operating and utility costs (kUSD/y); (b) Distribution of the heat duty (MJ/h).

Even though the total cost for including the compression section falls in the order of million USD, the income for the industry should also increase. Gallo and Erdmann (2017) estimate a production of more than 2 bbl of crude oil per CO₂ ton, injected in a sample well of the NQNB.

Figure 5 shows the leaks to the environment. Molar flows (kmol/h) of CO₂, H₂O, CH₄, and other GHG are plotted. Respect to the combustion GHG emissions, they were estimated assuming hot oil burning in the stripping column. As it can be observed, the CO₂ wastes remain almost negligible with the addition of the compression section.

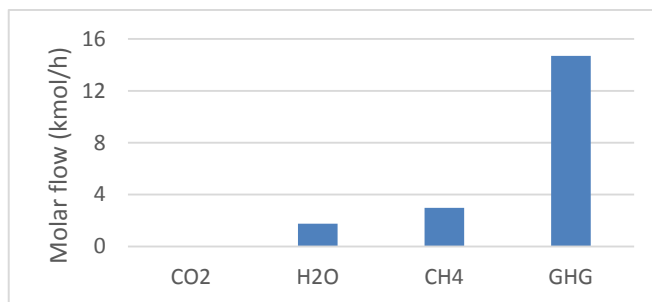


Fig. 5. Comparison of gases leaks (kmol/h).

5. Conclusions

An optimal design to condition CO₂ for EOR purposes is presented. According to the study, a total amount of 18.26 kmol/h of high purity CO₂ at 6865 kPa can be obtained from an already existing gas plant for improving crude oil production. Although the investment for the additional sector to start is over 3,000 kUSD, the investors should also take into account that not only the CO₂ emissions are almost reduced to zero but also that the EOR may start a market in the NQNB where this technology is not still exploited.

References

- F. Ahmad, K. Lau, A. Shariff, G. Murshid, 2012, Process simulation and optimal design of membrane separation system for CO₂ capture from natural gas. *Computers & Chemical Engineering* Volume, 36, Pages 119–128.
- N. Al-Lagtah, S. Al-Habsi, S. Onaizi, 2015, Optimization and performance improvement of Lekhwair natural gas sweetening plant using HYSYS. *J. of Nat. Gas Sci. and Eng.*, 26, 367-381.
- Aspen Technology, 2012, Aspen HYSYS Thermodynamics COM Interface V8.3. MA, USA.
- F. Banat, O. Younas, I. Didarul, 2014, Energy and exergical dissection of a natural gas sweetening plant using methyldiethanol amine (MDEA) solution. *J. of Nat. Gas Sci. and Eng.*, 16, 1-7.
- R. Brush, H. Davitt, O. Aimar, J. Arguello, J. Whiteside, 2000, Immiscible CO₂ flooding for increased oil recovery and reduced emissions. In *SPE/DOE Improved Oil Recovery Symposium*. Society of Petroleum Engineers.
- G. Gallo, E. Erdmann, 2017, Simulation of viscosity enhanced CO₂ nanofluid alternating gas in light oil reservoirs. In *SPE Latin America and Caribbean Petroleum Engineering Conference*. Society of Petroleum Engineers.
- J. Gutierrez, E. Ale Ruiz, E. Erdmann, 2017. Energy requirements, GHG emissions and investment costs in natural gas sweetening processes. *J. of Nat. Gas Sci. and Eng.*, 38, 187-194.
- J. Gutierrez, L. Benitez, E. Ale Ruiz, E. Erdmann, 2016, A sensitivity analysis and a comparison of two simulators performance for the process of natural gas sweetening. *Journal of Natural Gas Science and Engineering*, 31, 800-807.
- H. Herzog, 2011, Scaling up carbon dioxide capture and storage: From megatons to gigatons. *Energy Economics*, 33(4), 597-604.
- A. Kazemi, M. Malayeri, A. Shariati, 2014, Feasibility study, simulation and economical evaluation of natural gas sweetening processes—Part I: A case study on a low capacity plant in iran. *Journal of Natural Gas Science and Engineering*, 20, 16-22.
- C. Khan, R. Amin, G. Madden, 2013, Carbon dioxide injection for enhanced gas recovery and storage (reservoir simulation). *Egyptian Journal of Petroleum*, 22(2), 225-240.
- L. Peters, A. Hussain, M. Follmann, T. Melin, M. Hägg, 2011, CO₂ removal from natural gas by employing amine absorption and membrane technology—a technical and economical analysis. *Chemical Engineering Journal*, 172(2), 952-960.
- Y. Song, C. Chen, 2009, Symmetric Electrolyte Nonrandom Two-Liquid Activity Coefficient Model, *Ind. Eng. Chem. Res.*, 48, 7788-7797.
- B. Suleiman, A. Abdulkareem, Y. Abdulsalam, U. Musa, A. Kovo, I. Mohammed, 2016, Thermo-economic analysis of natural gas treatment process using triethanolamine (TEA) and diethanolamine (DEA) as gas sweeteners. *J. of Nat. Gas Sci. and Eng.*, 36, 184-201.

A software tool for optimizing intra-logistic activities

Dimitrios Poulimenos^{a*}, Dimitrios Bechtsis^a, Dimitrios Vlachos^a, Eleftherios Iakovou^b

^a*Aristotle University of Thessaloniki, Department of Mechanical Engineering, Laboratory of Statistics and Quantitative Analysis Methods, P.O. Box 461, 54124 Thessaloniki, Greece*

^b*Department of Engineering Technology and Industrial Distribution, Texas A&M University, College Station, TX 77843-3367, United States*

poulimeno@meng.auth.gr

Abstract

Digital manufacturing promotes the use of innovative technologies in the global market landscape and provides effective and efficient Supply Chain Management Systems. The purpose of this research is to contribute to the automation of an industrial warehouse by elaborating a novel software simulation tool for solving a classical NP-hard optimization problem, the Capacitated Vehicle Routing Problem with Multiple Trips (CVRPMT). The software tool promotes the use of Automated Guided Vehicles (AGVs) in industrial facility layouts and is based on an existing software framework, developed in the C# programming language. At this study we first formulate the mathematical model for the CVRPMT, we implement a hybrid metaheuristic Ant Colony Optimization (ACO) algorithm and develop a friendly Graphical User Interface (GUI) for scheduling and monitoring the AGVs' activities.

Keywords: Ant Colony Optimization (ACO), Metaheuristic, Software Tool, C#, CVRP.

1. Introduction

The Vehicle Routing Problem (VRP) is a well-documented and widely discussed NP-hard problem. The question in hand considers the optimal route for visiting a predefined number of customers under the constraint that the total travelled distance is minimized. Among a great deal of variations, we could distinguish the Capacitated Vehicle Routing Problem (CVRP) which extends the basic scheme by identifying the vehicle's capacity and the customer's demand. For solving the VRP we focus on the Ant Colony Optimization (ACO) algorithm, taking into consideration its swarm intelligence features and its correspondence with modern agent based architectures.

Mazzeo and Loiseau (2004) elaborated on an ACO algorithm for the CVRP, and identified the optimal route based on transitional rules. They presented the pheromone levels for reducing the number of ants used, as well as heuristics for confronting problems with more than 50 nodes. Gajpal and Abad (2009) presented an Ant Colony System (ACS), and implemented local search methods for solving the VRP namely: Simultaneous Pick-Up and Delivery (VRPSD), Backhauls and Mixed loads. The final algorithm uses a step-oriented scheme for optimizing the final solution (2-opt): (i)customer insertion/interchange, and (ii)sub-path exchange multi-route scheme.

Moreover, they provide a detailed explanation of the ACS for VRPSD and use the elitist ants' solution for updating the ant trails. Skinderowicz (2017) used Simulated-Annealing (SA) as a local search method to improve his results, and presented (i)SA with ACS, (ii)enhanced ACS and (iii)Sequential Ordering Problem -3-exchange. Based on a known solution, which may not be the best, the algorithms continuously optimize the results, improve the quality of the final solution and are very efficient. Finally, Ismkhan (2016) handles large-scale optimization problems, that confront issues regarding optimal memory usage, time complexity constraints and total performance. The author proposed efficient methods, for redefining the levels of pheromone and speeding up ACO in a local level.

Literature review provided an insight to the work of other researchers and motivated us to develop the proposed algorithm and the software tool. Our scope is to create an open source software simulation framework with a user-friendly Graphical User Interface (GUI) for optimizing intralogistics, using swarm optimization techniques. The presented work is motivated from ACO methods to simulate the pick-up and delivery of goods in a warehouse and optimize the AGVs' schedule (De Santis et al., 2017) and even the use of time windows in order picking (Sholz et al., 2017). The remainder of the manuscript is organized as follows. In Section 2 the Mathematical Model is presented, in Section 3 we explain the ACO, in Section 4 we present the proposed extensions and finally in Section 5 we conclude with computational results, conclusions and future research work.

2. Formulating the mathematical model

The first step in our research was the implementation of the CVRPMT's mathematical model. Given a complete graph $G=(B,A)$, where $B=\{0, \dots, N+1\}$ is the vertex set with 0 being the starting station and $N+1$ the exit station for all AGVs and A the arc set, we identify the optimal freight transport sequence. Our scope is to minimize the total distance travelled while picking loads from the shelves (loading nodes) of a warehouse and transferring them to the exit station using $v=\{1,2, \dots, V\}$ AGVs, while each AGV makes $t=\{1,2, \dots, T\}$ trips (Toth and Vigo 2001). A trip is a complete AGV's route from the starting to the exit station after it has visited the required loading nodes, for picking the total number of loads (demand). The total number of trips from all the available AGVs is called a tour. The model could be considered as CVRP taking into consideration that (i) vehicles have two distinct nodes a starting and an exit station (the starting and ending nodes are not the same) and (ii) each vehicle can be used in more than one trips.

3. Ant colony optimization algorithm

ACO is a metaheuristic, probabilistic algorithm proposed by Dorigo (1992) and is based on the behaviour of real ants trying to find the shortest path to gather their food supplies. Dorigo and Gambardella (1997) proposed a modified ACO version the Ant Colony System (ACS) that includes two main procedures (i) the tour construction, and (ii) the pheromone update. In the tour construction each ant selects the next loading node based on the transition probability Eq. (1) incase node $j \in N_i$, otherwise $p_{ij} = 0$ (Dorigo and Gambardella, 1997; Yousefi khoshbakht and Sedighpour, 2011). N_i is the set of all the feasible nodes (ants can visit them), τ_{ij} is the amount of pheromone deposited on arc (i,j) , η_{ij} is a visibility term calculated as the inverse of the distance

between node i and node j Eq. (2), γ_{ij} is the savings algorithm Eq. (3) and finally the heuristic parameters α , β and λ are the values for the pheromone concentration, the ant's visibility and the distance savings. Furthermore, in ACS the ant selects the next visiting node, following a state transition rule, based on a uniformly distributed variable q $[0,1]$, while the ant selects either the typical exploration rule or the greedy choice. If $q > q_0$ the transition probability for the exploration rule is selected otherwise the ant visits the next available node from Eq. (4). The pheromone values update considers both the global and the local pheromone update rule. The global pheromone update rule force updates only to the arcs that belong to the best solution found using Eq. (5) where L^{best} is the length of the best-known tour T^{best} and ρ is the global pheromone decay parameter. In our algorithm the global decay parameter is not constant, but it's calculated according to Eq. (6). The local pheromone update rule is activated whenever an ant finishes a tour and the visited arcs pheromone level is updated according to Eq. (7), where ξ is the local pheromone decay parameter and τ_0 is the initial pheromone value. Eq. (8) indicates the value of τ_0 where L^{NB} is the length of the tour constructed by the Nearest Neighbor algorithm and $Size$ is the total number of loading nodes to be visited including the starting and ending stations.

$$p_{ij} = \frac{\tau_{ij}^{\alpha} \eta_{ij}^{\beta} \gamma_{ij}^{\lambda}}{\sum_{l \in N_i} \tau_{il}^{\alpha} \eta_{il}^{\beta} \gamma_{il}^{\lambda}} \quad (1)$$

$$\eta_{ij} = \frac{1}{c_{ij}} \quad (2)$$

$$\gamma_{ij} = c_{i0} + c_{0j} - c_{ij} \quad (3)$$

$$j = \arg \max_{z \in N_i} \tau_{iz}^{\alpha} \eta_{iz}^{\beta} \gamma_{iz}^{\lambda} \quad (4)$$

$$\tau_{ij} = (1 - \rho) \tau_{ij} + \rho \left(\frac{1}{L^{best}} \right) \quad \forall (i, j) \in T^{best} \quad (5)$$

$$\rho = \frac{\tau_{ij}}{\tau_{\min} + \tau_{\max}} \quad (6)$$

$$\tau_{ij} = (1 - \xi) \tau_{ij} + \xi \tau_0 \quad (7)$$

$$\tau_0 = \frac{1}{L^{NB} Size} \quad (8)$$

4. The proposed hybrid ACO algorithm for the CVRPMT

Both ACO and ACS provide near to optimal solutions to the CVRPMT for a certain complexity level. The accuracy of the algorithm is decreased as the number of loading nodes and AGV's increase. Therefore, we implemented a hybrid version for confronting specific drawbacks of ACO and provide reliable results. To begin with, ACO is easily trapped on a local minimum, thus we used local search algorithms. The 2-opt local search solves the Traveling Salesman Problem (TSP). In CVRPMT each trip can be considered as an individual TSP, and that improves the overall performance by terminating the procedure when it fails to come up with an optimized solution after 500 consecutive iterations. While 2-opt is a very powerful algorithm that produces very promising results it has a major drawback; it can be applied on an individual trip and not to the whole tour. To overcome this problem, two common CVRP algorithms have been implemented: (i) the loading node insertion and (ii) the swapping local search (Abdulkader et al. 2015). The loading node insertion algorithm detaches a node from a vehicle's trip and it attaches on it another available one taking into consideration the capacity constraints. Otherwise, the algorithm swaps this node with another one, belonging to any other trip. This procedure continues until the algorithm finds no improvement for 20 consecutive iterations. Furthermore, to overcome the pheromone over-concentration, we implemented the MAX-MIN Ant System (Stützle and Hoos, 2000) where we set upper and lower limits for the pheromone levels of each arc. Finally, to increase accuracy, we implemented the SA algorithm (Skinderowicz, 2017) where the active solution technique is used in global pheromone update rule. The initialization of the algorithm requires a matrix of every node's real distance from all the other nodes calculated using the k-star algorithm, a matrix that stores the demand of every loading node and finally the values of all the parameters. The algorithm calculates the number of vehicles for keeping up with the total demand, the nearest neighbour solution, the visibility and saving parameters of every arc and the initial pheromone levels. Then it calculates the temperature value for the SA with random solutions. In the proposed algorithm every ant represents the whole fleet of vehicles and starts from node 0 (starting station) selecting randomly the next loading node. The total load of the ant's first vehicle is updated, while the ant continues to the next loading node using the state transition rule, taking into consideration the vehicle's capacity constraint. When the vehicle meets its capacity, it travels to node N+1 (exit station) and the second vehicle begins from node 0 following the same process. Multiple trips are required in case all vehicles have been used, and in this case vehicles use node N+1 as the starting station. The process terminates when all the loads are transferred. When the first ant finishes its tour the local pheromone levels are updated. When all the ants create a complete tour the algorithms swap and insertion, as well as 2-opt local search are used in the best solution found by them. Finally, the best improved solution is used by the SA technique to update the global pheromone levels completing the first iteration. The best solution is proposed when all the iterations are over.

5. Results and Conclusions

As identified from the literature review, the majority of the available benchmarks are using the CVRP algorithm (not the CVRPMT), and therefore the authors adjusted the proposed model, in order to compare the outcome of their algorithm to the CVRP benchmark results. Each benchmark was tested with the proposed ACO algorithm and after multiple executions of our model for every benchmark; the mean values of the

results are presented in Table 1. The results indicate that the model is well suited even for large scale problems and provides effective and efficient solutions. It must be stated that the authors identified specific parameter values that provide optimized results for all the benchmarks (Table 2).

Table 1 Algorithm's Results

Benchmark	Number of Vehicles	Number of Nodes	Best Known Solution	Proposed Model Results	Dev%
E-n22-k4	4	22	375	375	0.00%
B-n31-k5	5	31	672	672	0.00%
A-n39-k5	5	39	822	822	0.00%
A-n45-k6	6	45	944	944	0.00%
E-n51-k5	5	51	521	521	0.00%
A-n53-k7	7	53	1010	1016	1.58%
P-n55-k7	7	55	568	577	1.58%
P-n76-k4	4	76	593	611	3.04%
P-n101-k4	4	101	681	719	5.58%

Table 2 Optimized parameter values

a	b	γ	ξ	q0	M	MaxIterations
1	2	2	0,1	0.9	10	3000

Finally, the authors present a software tool (Figure 1) that uses the optimized parameter values and is based on an open source framework developed in the C# programming language (Bechtis et al., 2018). The framework enables practitioners and academics to design the facility layout of a plant by loading an image of the layout and further importing all the appropriate entities (boundaries, shelves and loads, obstacles and compartment dividers, the vehicles' and their starting position, the exit station). Load entities are considered as Pick Up and Delivery (P/D) nodes and vehicles navigate in the facility and pick up loads under specific capacity requirements. In order to calculate the distances in the facility layout the framework uses the A* algorithm and calculates the shortest path taking into consideration the P/D nodes, the vehicles' starting node, the vehicles exit station, the obstacles and the compartment dividers. The implemented ACO algorithm is integrated with the framework and executed in order to determine the total trips travelled by each vehicle. In the ACS window we can define all the required parameters (from Section 4) and run the simulation. As a last step, a schedule of the vehicles' trips is presented to the end user.

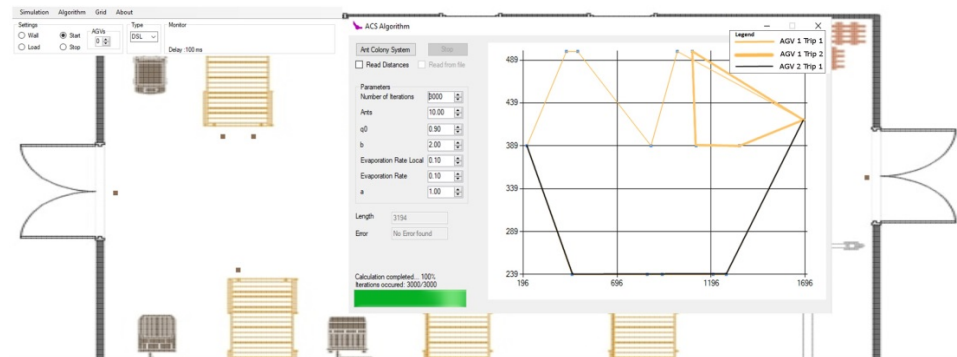


Figure 1 Overview of the GUI with the ACS module

As an extension for future research work, the authors will consider to integrate the algorithm to a software tool for last-mile logistics, taking into account predefined time windows. The implementation could use GPS data and travel distances from real Case Studies.

References

- A. Scholz, D. Schubert, G. Wäscher, 2017, Order picking with multiple pickers and due dates – Simultaneous solution of Order Batching, Batch Assignment and Sequencing, and Picker Routing Problems, *European Journal of Operational Research*, 263, 461-478
- D. Bechtsis, N., Tsolakis, D., Vlachos, J.S., Srari, 2018, Intelligent Autonomous Vehicles in digital supply chains: A framework for integrating innovations towards sustainable value networks, *Journal of Cleaner Production*, 181, 60-71.
- H. Ismkhan, 2016, Effective heuristics for ant colony optimization to handle large-scale problems, *Swarm and Evolutionary Computation*, 32, 140-149.
- M. Abdulkader, Y. Gajpal, T. Y. ElMekkawy, 2015, Hybridized and colony algorithm for the Multi Compartment Vehicle Routing Problem, *Applied Soft Computing*, 37, 196-203.
- M. Dorigo, G. Di Caro, 1999, The ant colony optimization meta-heuristic, *New Ideas in Optimization*.
- M. Dorigo, L. M. Gambardella, 1997, Ant Colony System: A Cooperative Learning Approach to the Traveling Salesman Problem, *Transactions on evolutionary computation*, 1,1.
- M. Yousefi khoshbakht, M. Sedighpour, 2011, An optimization Algorithm for the Capacitated Vehicle Routing Problem Based on Ant Colony System, *Australian Journal of Basic and Applied Sciences*, 5, 12, 2729-2737.
- P. Toth, D. Vigo, 2001, *The Vehicle Routing Problem*, SIAM Monographs on Discrete Mathematics and Applications.
- R. De Santis, R. Montanari, G. Vignali, E. Bottani, 2017, An adapted ant colony optimization algorithm for the minimization of the travel distance of pickers in manual warehouses, *European Journal of Operational Research* (2017), <https://doi.org/10.1016/j.ejor.2017.11.017>
- R. Skinderowicz, 2017, An improved Ant Colony System for the Sequential Ordering Problem, *Computers & Operations Research*, 86, 1-17, 10.1016/j.cor.2017.04.012.
- S. Mazzeo, I. Loiseau, 2004, An Ant Colony Algorithm for the Capacitated Vehicle Routing Problem, *Electronic Notes in Discrete Mathematics* 18, 181–186.
- T. Stützle, H. H. Hoos, 2000, MAX-MIN Ant System, *Future Generation Computer Systems*, 16, 889–914.
- Y. Gajpal, P. Abad, 2009, An Ant Colony System (ACS) for vehicle routing problem with simultaneous delivery and pickup, *Computers&OperationsResearch*, 36, 3215-3223.

Electricity mix assessment of the EU member countries using DEA and EffMixF

Patricia Zurano-Cervelló^a, Carlos Pozo^b, Josep María Mateo-Sanz^a, Laureano Jiménez^a, Gonzalo Guillén-Gosálbez^{a,b*}

^a*Departament d'Enginyeria Química, Universitat Rovira i Virgili, Av. Paisos Catalans 26, 43007 Tarragona, Spain*

^b*Centre for Process Systems Engineering, Department of Chemical Engineering, Imperial College London, South Kensington, London SW7 2AZ, UK*

g.guillen05@imperial.ac.uk

Abstract

The assessment of the sustainability level achieved by electricity mixes is a crucial step in the change towards a more sustainable energy system. Here we assess the three dimensions of sustainability -the economic, environmental and social performance- of the 28 EU members electricity mix in 2015 by combining life cycle assessment, data envelopment analysis (DEA) and mathematical programming tools. Our method encompasses three main steps: i) the efficiency assessment of the electricity portfolios of the 28 EU countries via DEA ii) the optimization of inefficient countries portfolios by means of solving the EffMixF model that we pose in this work, and iii) the efficiency evaluation of the optimized electricity portfolios obtained in STEP 2. The EffMixF model takes into account the main technical constraints involved in electricity generation within each country, complementing standard DEA in order to extend previous research and obtain more realistic information for policy-making. We find that 12 countries are inefficient, being United Kingdom, Lithuania and Italy the ones with the lowest efficiency. In our main findings, we determine that inefficient countries have to reduce the non-renewable electricity sources by 10% (with respect the total electricity production) in order to become efficient.

Keywords: Optimization, Sustainability, DEA, Electricity mix, Eco-efficiency

1. Motivation

The transition to a more sustainable energy production is one of the foremost challenges in our era. The sustainability concept includes economic, environmental and social aspects, where each of them can be quantified by an extensive diversity of indicators. Finding a way to combine all these metrics into a unique score in an objective and systematic method is the main difficulty when assessing the sustainability level of a system. In this respect, DEA arises as a promising methodology. This method, evaluates the relative efficiency of a set of options (called decision making units, DMUs) by using a large number of indicators (inputs and outputs) (Cooper et al., 2011). The DMUs deemed efficient are the vertices of an efficient frontier. Furthermore, DEA provides improvement targets for inefficient DMUs that, if attained, would make them efficient. These targets are obtained by projecting each inefficient DMU to the efficient frontier,

being each projection the linear combination of the reference set –i.e., efficient DMUs of the facet where the inefficient one is projected-. However, the practical feasibility of DEA targets is controversial among the scientific community.

In this work, we extend previous research by suggesting a new approach where standard DEA is supplemented with a novel projection step using optimization tools. In particular, we assess the 28 EU members efficiency in 2015 taking into account eight sustainability indicators covering the economic, environmental and social dimensions. Then, we study if DEA targets are indeed attainable and propose a best-scenario electricity mix for each inefficient country. With this purpose, we pose and solve the EffMixF optimization problem which considers real potentials for the renewable sources as well as techno-economic constraints and the reliability of the supply. This model allows projecting inefficient DMUs towards the more fitting point of the efficient facet (rather than a particular point of it, as in standard DEA), thus granting higher chances to achieve efficiency.

2. Methods

2.1. Data used

We use the electricity portfolio data of the 28 EU countries in 2015 from the Eurostat Energy Statistics -energy datasheets- (European Union, 2016). These datasheets disaggregate the electricity production into 12 energy sources, from which we consider nine: the most representative technology for each energy source (see Table 1). Then, we calculate the environmental, economic and social performance of each country's mix (i.e., inputs and outputs) using indicator coefficients for each technology, see Table 2.

Table 1. Technologies and assumptions used in our study.

Name used ^{a,b}	Technology
Gases	Natural gas CCGT plant
Nuclear	Pressure water reactor
Petroleum Products	Petroleum, heavy fuel oil
Solid Fuels	Coal plant
Biomass and Renewable wastes	Biomass CCGT plant
Geothermal	Deep geothermal
Hydro	Run-of-river
Solar	Photovoltaic open ground installation
Wind	Onshore wind

a) In bold dispatchable technologies (DP). b) In gray shade, renewable technologies.

Table 2. Environmental, economic and social indicators considered.

Indicator name	Abbreviation	Unit	Source
Climate change	GWP100	kg CO _{2e} /kWh	(Wernet et al., 2016)
Fossil depletion	FDP	kg Oil _e /kWh	(Wernet et al., 2016)
Human toxicity	HTPinf	1,4-DCB _e /kWh	(Wernet et al., 2016)
Ozone depletion	ODPinf	kg CFC-11 _e /kWh	(Wernet et al., 2016)
Total land occupation	TLOP	m ² /yr/kWh	(Wernet et al., 2016)
Water depletion	WDP	m ³ /kWh	(Wernet et al., 2016)
Levelized cost of electricity	LCOE	USD/MWh	(NEA et al., 2015)
Total job-years	Job-yr	Job-yr/GWh	(Wei et al., 2010)

In our study, we take into account the country potentials for the renewable electricity sources except for biomass -embedded in set *RP*- (Eea, 2009; EREC, 2011; Pirker et al., 2011), as well as the capacity factors for all the technologies (NEA et al., 2015).

2.2. Step 1: DEA model

In Step 1, we assess the electricity mix efficiency of each EU member through DEA, a methodology that evaluates the relative performance of a set of DMUs translating multiple inputs into multiple outputs. We therefore consider each country as a DMU consuming seven inputs and producing one output. With the given data, DEA determines an efficiency score for each DMU (θ), which is expressed as the weighted sum of outputs divided by the weighted sum of inputs. This θ is assessed by optimizing the weights attached to each input and output. In particular, we use the Variable Returns-to-Scale (VRS) input-oriented model (Cooper et al., 2011). Additionally, DEA provides the improvement targets required by the inefficient DMUs to become efficient as the difference between their initial inputs and outputs and the values attained when radially projected on the efficient frontier.

2.3. Step 2: EffMixF model

The EffMixF model -defined for each inefficient country i - contains two sets of equations: (i) those related with electricity generation; and (ii) those related with the DEA targets we aim to achieve.

2.3.1. Electricity generation

The total electricity generated (E_{Gen}) in each country i must be preserved. For this, we define an electricity mix merging standard (Mix^{ST}) and back-up (Mix^{BU}) generation using the existing technologies j . Note that we do not consider electricity trade among countries, as we aim to improve the efficiency of the electricity generated rather than consumed.

$$\sum_j (Mix_{ij}^{ST} + Mix_{ij}^{BU}) = E_{Gen}_i \quad (1)$$

We ensure the reliability of the supply via Eq. 2, where we use the back-up parameter (Gross et al., 2006) ($BUP=50\%$) to indicate the capacity of dispatchable (DP) sources required to holdup each unit of non-dispatchable installed.

$$\sum_{j \in DP} Cap_{ij}^{BU} \geq BUP \sum_{j \in DP} Cap_{ij}^{ST} \quad (2)$$

Cap^{ST} and Cap^{BU} are the capacities installed for standard and back-up technologies. Note that only the dispatchable technologies can participate as back-up sources.

The amount of electricity generated for both standard and back-up purposes are given by the product between the corresponding installed capacities, the capacity factor (Cf) and the total number of hours in a year (H).

$$Mix_{ij}^{ST} = Cap_{ij}^{ST} Cf_{ij} H \quad \forall j \quad (3)$$

$$Mix_{ij}^{BU} = Cap_{ij}^{BU} Cf_{ij} H \quad \forall j \quad (4)$$

Additionally, we consider the potential available (PT_{ij}) for electricity generation in each renewable source included in the set RP , preventing unrealistic solutions (Eq. 5).

$$Mix_{ij}^{ST} + Mix_{ij}^{BU} \leq PT_{ij} \quad \forall j \in RP \quad (5)$$

We impose that the nuclear electricity produced cannot be higher than the existing due to the nuclear energy policy reversal of some EU countries (Müller and Thurner, 2017).

2.3.2. *DEA linkers*

The equations in this section connect the electricity mixes modeled via Eq. 1 to 5 with the DEA targets from STEP 1. First of all, we force inputs z and outputs y to be equal or better than the initial ones (Imp_{iz} and Out_{iy}):

$$\sum_j (CT_{ijz}^{INP} (Mix_{ij}^{ST} + Mix_{ij}^{BU})) \leq Imp_{iz} EGen_i \quad \forall z \tag{6}$$

$$\sum_j (CT_{iyy}^{OUT} (Mix_{ij}^{ST} + Mix_{ij}^{BU})) \geq Out_{iy} EGen_i \quad \forall y \tag{7}$$

Being CT_{ijz}^{INP} and CT_{iyy}^{OUT} the inputs and outputs coefficients for each country/technology.

In Eqs. 8-10 we assess the distance (in the space of inputs and outputs) between the efficient DEA facet and the inputs and outputs attained with the new Suggested mix:

$$\sum_{i \in RS_i} (\lambda_i Imp_{i,z}) EGen_i + S_z^N = \sum_j (CT_{ijz}^{INP} (Mix_{ij}^{ST} + Mix_{ij}^{BU})) \quad \forall z \tag{8}$$

$$\sum_{i \in RS_i} (\lambda_i Out_{i,y}) EGen_i - S_y^P = \sum_j (CT_{iyy}^{OUT} (Mix_{ij}^{ST} + Mix_{ij}^{BU})) \quad \forall y \tag{9}$$

$$\sum_{i \in RS_i} \lambda_i = 1 \tag{10}$$

Where λ_i is the linear coefficient for countries i' belonging to the reference set of country i (RS_i), and S_z^N and S_y^P are the inputs (z) and outputs (y) slacks for country i . Note that here λ_i is a decision variable (and not the value provided by DEA in STEP 1), thus allowing EffMixF to project inefficient countries onto a whole efficient facet.

In Eq. 11, we present the overall model, which guarantees the electricity supply whilst approaching as much as possible the efficient facet provided by the original DEA.

$$\begin{aligned} \text{minimize} \quad ObjFun_i &= \sum_z (S_z^N / Imp_{iz}) + \sum_y (S_y^P / Out_{iy}) \\ \text{s.t. Eqs 1-10} & \\ Mix_{ij}^{ST}, Mix_{ij}^{BU}, Cap_{ij}^{ST}, Cap_{ij}^{BU}, S_z^N, S_y^P, \lambda_i &\geq 0 \quad \forall y, z, j \end{aligned} \tag{11}$$

3. Results and Discussion

Firstly, in STEP 1 we obtain the efficiency for each EU country using the VRS method. These efficiencies (see Table 3) range from 0.8 to one, and reveal that 12 out of the 28 countries analyzed are inefficient ($\theta < 1$), being United Kingdom, Lithuania and Italy, the ones presenting the lowest efficiency (0.84, 0.86 and 0.89 respectively).

Table 3. Efficiencies of the 28 EU member countries given by ISO 3166-2 code.

Code	Efficiency	Code	Efficiency	Code	Efficiency	Code	Efficiency
AT	1.00	EE	0.99	HU	0.93	NL	1.00
BE	0.96	ES	0.95	IE	1.00	PL	1.00
BG	1.00	FI	0.90	IT	0.89	PT	0.96
CY	1.00	FR	1.00	LT	0.86	RO	1.00
CZ	0.98	GB	0.84	LU	1.00	SE	1.00
DE	1.00	GR	1.00	LV	0.92	SI	1.00
DK	1.00	HR	1.00	MT	1.00	SK	0.92

Pie charts in Fig. 1 compare the Current (internal ring) and Suggested mixes (external ring) for each inefficient country (STEP 2). Broadly speaking, non-renewable electricity sources continue being the biggest part of the mix (mean of 58%), regardless of being displaced in part by renewable sources (10% of electricity production).

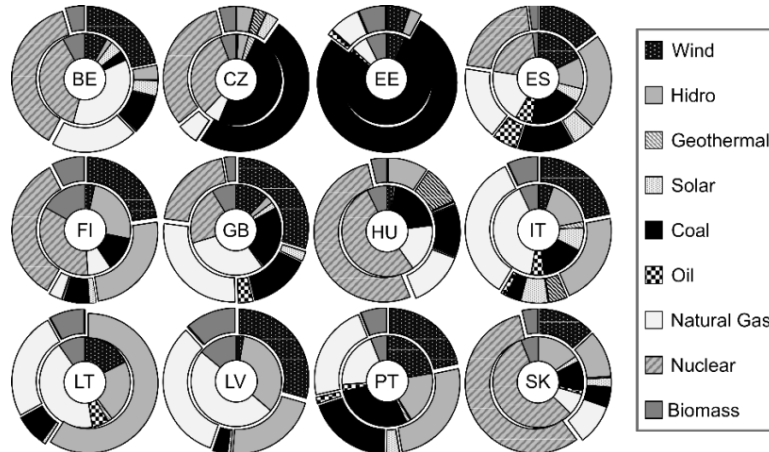


Fig. 1. Current (internal rings) and Suggested (external) electricity portfolios.

As a general trend, we found that hydropower and wind are the technologies that need to be promoted in order to improve the environmental impact. On the other hand, coal is the one to be used to improve the economic performance (LCOE), and solar the social one, as is the one that more jobs-year generates.

To conclude, we use DEA to assess again the efficiency of the 28 EU countries (STEP 3) using, on the one hand, the Current mixes for the countries deemed efficient in STEP 1 and the Suggested mixes for the inefficient ones (STEP 2). We find that all the efficiencies were improved in the Suggested mixes (see Table 4). More specifically, five out of the 12 countries originally found inefficient in STEP 1 were found weakly efficient when their Suggested mixes were considered. The reason for this is that, even though their efficiency is one, they cannot achieve an *ObjFun* of zero -they present slacks- indicating they cannot attain the strongly efficient frontier.

Table 4. Efficiencies of the Suggested electricity mixes of the inefficient EU countries.

Code	Efficiency	Code	Efficiency	Code	Efficiency	Code	Efficiency
BE	0.99	ES	1.00	HU	0.94	LV	0.97
CZ	1.00	FI	1.00	IT	1.00	PT	1.00
EE	0.99	GB	0.92	LT	0.96	SK	0.99

4. Conclusions

We posed and solved a new approach that combines a VRS DEA model with an optimization problem (EffMixF) that takes into account exhaustive techno-economic features. We used this approach to study the 28 EU members electricity mix for the year 2015 covering the three sustainability pillars: the economic, environmental and social.

Firstly, we applied DEA to the EU countries, finding 12 of them inefficient. Then, we posed and solved the EffMixF model to obtain new portfolios enhancing inefficient

countries. This model considers the key technical constraints needed when modeling the electricity generation within each country (renewable sources potentials, capacity factors, reliability of the supply). We found that none of the inefficient countries reached the strong frontier, which demonstrates that the original targets given by DEA are not attainable. The reason for this is the limited availability of intermittent sources, which makes it necessary to use a certain percentage of dispatchable sources, as well as the constraints that prevents the worsening of any indicator with respect to the Current values. Nevertheless, the efficiencies obtained with the Suggested mixes are in all the cases higher than with the Current ones, as verified in the second DEA assessment.

Finally, it is significant to note that the efficiency scores and portfolios attained depend completely on the indicators considered. However, our framework is flexible enough to incorporate diverse indicators and/or constrains, providing in all the cases feasible and sensible solutions. Therefore, the methodology we propose can be used to guide policy makers, as it indicates which technologies should be boosted (or hindered) to improve the sustainability efficiency of each inefficient country.

Acknowledgements

Laureano Jiménez and Gonzalo Guillén-Gosálbez thank the Spanish Ministry of Education and Competitiveness (CTQ2016-77968-C3-1-P, MINECO/FEDER) for the financial support. Gonzalo Guillén-Gosálbez wishes to acknowledge financial support from the EPSRC - Engineering & Physical Science Research Council (project P65819).

References

- Eea, 2009, Europe's onshore and offshore wind energy potential. EEA Technical report, Vol. 6.
- EREC, 2011, Mapping Renewable Energy Pathways towards 2020. EREC, 28.
- European Union, 2016, EU energy in Figures, Statistical pocketbook.
- G. Wernet, C. Bauer, B. Steubing, J. Reinhard, E. Moreno-Ruiz, B. Weidema, 2016, The ecoinvent database version 3 (part I): overview and methodology.
- M. Wei, S.Patadia, D.M. Kammen, 2010, Putting renewables and energy efficiency to work: How many jobs can the clean energy industry generate in the US? *Energy Policy*, 38(2), 919–931.
- NEA, IEA, & OECD (Eds.), 2015, Projected Costs of Generating Electricity. OECD Publishing.
- O. Pirker, I. Argyrakis, V. Babkin, M. Chudy, G. Crosnier, N. Dahlback, M. Timm, 2011, Hydro in Europe: Powering renewables. *Renewable Action Plan*, 66.
- R. Gross, T. Green, M. Leach, J. Skea, P. Heptonstall, D. Anderson, 2006, The Costs and Impacts of Intermittency: An assessment of the evidence on the costs and impacts of intermittent generation on the British electricity network.
- W. C. Müller & P. W. Thurner, 2017, *The Politics of Nuclear Energy in Western Europe*, OUP.
- W.W. Cooper, L.M. Seiford, J. Zhu, 2011, Data envelopment analysis: History, models, and interpretations. *ISOR*, Vol. 164, pp. 1–39.

CFD modelling of pulsed sieve plate liquid extraction columns using OPOSPM as a reduced population balance model: hydrodynamics and mass transfer

Samer Alzyod,^b Menwer Attarakih,^{a,b} Hans-Jörg Bart^b

^a*Department of Chemical Engineering, University of Jordan, Amman 11942, Jordan*

^b*Chair of Separation Science and Technology, TU Kaiserslautern, Kaiserslautern 6765, Germany*

bart@mv.uni-kl.de

Abstract

A reduced coupled 2D-CFD and Population Balance Model (PBM) framework (Alzyod et al., *Comput. Aided Chem. Eng.*, 40, 61-66) is extended to model the mass transfer behaviour of pulsed sieve plate liquid extraction columns. The Euler-Euler approach is used to model the two phase flow inside the column, while the One Primary One Secondary Particle Method (OPOSPM), the simplest form of SQMOM, is utilized as a reduced population balance solver. The proposed framework is numerically tested and the results are compared with the published experimental data. The required breakage and coalescence parameters to perform the 2D-CFD simulation are estimated using PPBLab software, where a 1D-CFD simulation using a multi-sectional grid is performed. A very good agreement is obtained at the experimental and the numerical validation levels.

Keywords: 2D-CFD, OPOSPM, PPBLab, Population balances, Pulsed columns.

1. Introduction

Pulsed liquid extraction columns have the advantage over the other extraction equipment, where they find many applications in chemical, biochemical and pharmaceutical industries. Unlike the agitated extraction equipment, pulsed sieve plate extraction columns provide a wider operational range and require less maintenance efforts (Haverland and Slater, 1994). The applied pulsation intensity characterizes the flow patterns inside the column and increases the available interfacial area, which enhances the column efficiency. The available lumped correlations and mixture models are still insufficient to describe the actual behaviour of the dispersed phase, where they ignore the droplet-droplet and the interphase interactions (Attarakih et al., 2015). These interactions include: breakage, coalescence and interphase mass transfer. To take all of these interactions into account, a coupled PBM and CFD framework can be used. The required information about the velocity field and energy dissipation is provided by the CFD solver, while the droplet-droplet interactions are taken into account using the PBM. In this regard, OPOSPM is considered as an attractive reduced PBM in terms of simplicity and computational cost. OPOSPM is the simplest special case of the general Sectional Quadrature Method Of Moments (SQMOM), where it directly conserves the zero moment and third moment of the droplet size distribution (Attarakih et al., 2009;

2016). In contrast to the moments based methods, OPOSPM avoids the divergence problems arise when applying the classical inversion algorithms to close the source terms, which makes it a stable framework. A first attempt to couple OPOSPM and CFD solvers was done by Drumm et al., (2010) to model a lab scale RDC liquid extraction column. In the same direction, Jaradat et al. (2011) simulated a pulsed sieve plate column using the LLECMOD software and Attarakih et al., (2015) implemented OPOSPM to simulate the hydrodynamics and mass transfer behaviour of a pilot plant RDC column. In a recent work, Alzyod et al., (2017) presented a coupled OPOSPM-CFD framework for modelling the hydrodynamics behaviour of a pulsed sieve plate extraction column. In this contribution, we extended this work to model the mass transfer behaviour of pulsed sieve plate liquid extraction columns. The proposed framework is tested and the results are compared with the published experimental data by Garthe (2006). The required breakage and coalescence parameters to perform the 2D-CFD simulation are estimated using PPBLab software (Attarakih et al., 2012; 2017). A positive validation at the numerical and experimental levels is obtained.

2. Coupled OPOSPM-CFD framework

The two phase flow inside the column is modelled using Euler-Euler approach. The continuity transport equation for the i^{th} phase is given by (Drumm et al. 2010):

$$\partial_t (\alpha_i \rho_i) + \nabla \cdot (\alpha_i \rho_i u_i) = 0 \quad (1)$$

Where α_i and u_i are the volume phase fraction and the velocity of the i^{th} phase respectively. The momentum balance equation for the i^{th} phase is given as follows:

$$\partial_t (\alpha_i \rho_i \bar{u}_i) + \nabla \cdot (\alpha_i \rho_i \bar{u}_i \bar{u}_i) - \nabla \cdot \tau_i = -\alpha_i \nabla p + \alpha_i \rho_i g + F_i \quad (2)$$

In Eq.(2), τ_i is the stress tensor, p is the pressure shared by all phases, g is the gravitational acceleration vector, and F_i represents the interphase forces. In this work, only the drag force is taken into account as recommended by Drumm et al., (2010). Based on this, the interphase momentum exchange coefficient is given by:

$$K_{ij} = 3\alpha_i \alpha_j \rho_j C_D |u_i - u_j| (u_i - u_j) / 4d_{30} \quad (3)$$

Where, d_{30} is the mean droplet diameter, and C_D is the drag coefficient, which is given by Kumar and Hartland (1985). The turbulence flow is modelled using the mixture $\kappa - \varepsilon$ model. Moreover, the required droplet diameter (d_{30}) to close Eq.(3) is obtained by solving the total number balance equation coupled with Eq.(1). The total number balance equation of the dispersed phase is given by (Attarakih et al., 2016):

$$\partial_t (\alpha_d \rho_d N) + \nabla \cdot (\alpha_d \rho_d u_d N) = \alpha_d \rho_d [(\mathcal{G} - 1)\Gamma(d_{30})N - 0.5\omega(d_{30}, d_{30})N^2] \quad (4)$$

Here, N is the total number concentration of the droplets, \mathcal{G} is the number of daughter droplets produced due to the breakage events, and Γ and ω are the breakage and coalescence kernels respectively. The mean mass droplet diameter is given by:

$$d_{30} = \sqrt[3]{6\alpha_d/\pi N} \quad (5)$$

In this work, the required breakage and coalescence kernels to close Eq.(4) are given by Coualoglou and Tavlarides (1977) as follows:

$$\Gamma = c_1 \frac{\varepsilon^{1/3}}{d^{2/3}(1+\alpha_d)} \exp\left(-\frac{c_2\sigma_d(1+\alpha_d)^2}{\rho_c \varepsilon^{2/3} d^{5/3}}\right) \quad (6)$$

$$\omega = c_3 \frac{\varepsilon^{1/3}}{1+\alpha_d} (d+d')^2 (d^{2/3} + d'^{2/3})^{1/2} \exp\left(\left(-\frac{c_4\eta_c\rho_c\varepsilon}{\sigma_d^2(1+\alpha_d)^3}\right)\left(\frac{dd'}{d+d'}\right)\right)^4 \quad (7)$$

The parameters c_i appearing in Eqs.(6 & 7) are fitting parameters. More information concerning the parameters estimation procedure is given in the numerical and experimental validation section. Here, σ_d is the dispersed phase interfacial tension, and ε is the energy dissipation. The required energy dissipation correlation to perform the 1D-CFD simulation, as implemented in PPB Lab software, is given by Milot et al., (1990):

$$\varepsilon = C_5 (Af)^3 / H_c \quad (8)$$

Where, c_5 depends on the column geometry, and H_c is the compartment height. The solute mass transfer conservation equation for the i^{th} phase is given by (Attarakih et al., 2015):

$$\partial_t (\alpha_i \rho_i c_i) + \nabla \cdot (\alpha_i \rho_i u_i c_i) = \rho_i \zeta a_p K_{od} (m c_c - c_d) \quad (9)$$

Where, c_i is the solute concentration in the i^{th} phase, a_p is the available interfacial area ($a_p = 6\alpha_d/d_{30}$), and K_{od} is the overall mass transfer coefficient. The factor ζ appears in Eq.(9) has a value of -1 and 1 for the continuous and dispersed phases respectively. The overall mass transfer coefficient is given by:

$$k_{od} = (m/k_c + 1/k_d)^{-1} \quad (10)$$

Where m is the solute distribution coefficient, k_c and k_d are the individual mass transfer coefficients of the continuous and dispersed phases respectively. More information concerning the individual mass transfer coefficients is given in the numerical and experimental validation section.

3. Computational domain and boundary conditions

In this work, FLUENT 18.2 is utilized, where Eqs.(3-7) and Eqs.(9-10) are implemented as user defined functions. The column used in simulation is a pilot plant sieve plate liquid-liquid extraction column based on the experimental work of Garthe (2006). The detailed dimensions are shown in Table (1). In the present work, only the active height of the column is considered, where an axisymmetric grid is used to model the active

height as shown in Figure (1). To reflect the actual column geometry, the sieve plate hole diameter is kept constant and the pitch diameter is varied to achieve the experimental free area value.

Table (1): Sieve plate liquid extraction column geometry (all dimensions are in m)

Column active height	Column diameter	Hole diameter	Free area
2.95	0.08	0.002	20%

A velocity inlet boundary is used at the bottom of the column, while a pressure outlet boundary condition is used at the top. Moreover, a sinusoidal pulsed velocity is used at the bottom of the column to take the pulsation effect in to account as follows:

$$u(t) = u_c + \left(d_p^2/d_c^2\right)A \sin(2\pi Ft) \quad (11)$$

Where d_p and d_c are the piston and the column diameters respectively, A is the pulsation amplitude, and F is the pulsation frequency.

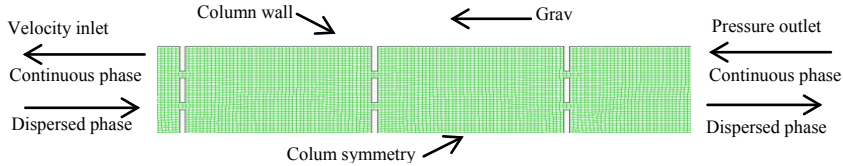


Figure (1): Part of the computational domain and the implemented boundary conditions.

4. Numerical and experimental validation

The 2D-CFD framework prediction is validated using the published experimental data by Garthe (2006) using toluene (d)/acetone/water chemical system. The dispersed and continuous phases inlet velocities are 40 and 48 litter/h respectively. The pulsation intensity is fixed at a value of 2 cm/s. The inlet dispersed phase solute concentration is 0.4 kg/m^3 , while the inlet continuous phase solute concentration is 53.5 kg/m^3 . The initial conditions are zero for both droplets number and the dispersed phase volume fraction, while the initial concentration is the same as in the continuous phase inlet feed. The coalescence and breakage kernels parameters are estimated using PPBLab software, where the parameters values are estimated by matching the 1D-CFD simulation hydrodynamics predictions with the experimental data. The obtained breakage and coalescence kernels are given by: $c_1 = 0.001$, $c_2 = 100 \text{ m}^{-2}$, $c_3 = 0.05$, and $c_4 = 1.33 \times 10^{10} \text{ m}^{-2}$ respectively. Figure (2.A) shows a comparison between the predicted average energy dissipation by the 2D-CFD model and the predicted values using Eq.(8). It is clear that the correlation of Milot et al., (1990) shows a good agreement with the 2D-CFD result. Indeed, this is a substantial validation step because the estimated breakage and coalescence models parameters using PPBLab software, as a 1D-CFD simulation environment, depend on the energy dissipation. Figure (2.B) shows a comparison between the simulated mean droplet diameter and the experimental data, where a very good agreement is obtained using both simulation tools. Here, a multi-sectional grid (w.r.t. droplet diameter and solute concentration) is used to perform the 1D-CFD simulation to numerically validate the 2D-CFD simulation results. Figure (3.A) depicts a comparison between the simulated light phase solute concentration profiles and the

experimental data. In this work, the continuous phase mass transfer coefficient is given by Heertjes (1954), while the dispersed phase mass transfer coefficient is given by Kronig and Brink (1950) respectively. Both CFD simulation tools show a very good agreement with the experimental data. However, a better prediction using PPBLab software is observed at the bottom of the column. This is because PPBLab's software PBM solver has the advantage as a detailed multi-sectional numerical solver. Figure (3.B) depicts the effect of the solute mass transfer process on the dispersed phase interfacial tension, where the interfacial tension is decreasing along the column height. Therefore, the droplet breakage is enhanced and the droplet size is shifted toward smaller values.

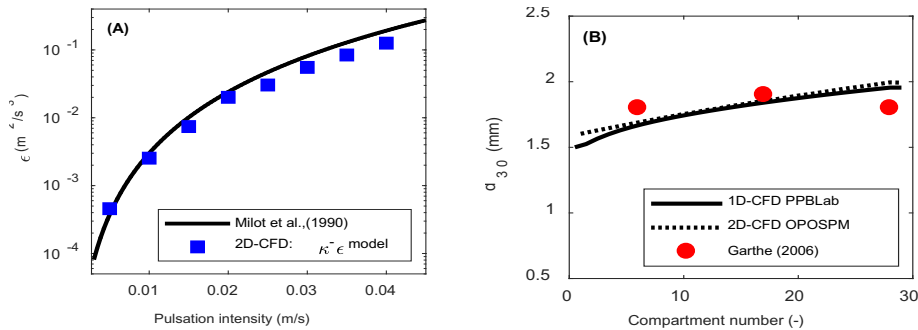


Figure (2): A) Comparison between the simulated average energy dissipation using 2D-CFD model and the predicted values using the correlation of Milot et al., (1990). B) Comparison between the simulated mean droplet diameter values and the experimental data (Garthe, 2006).

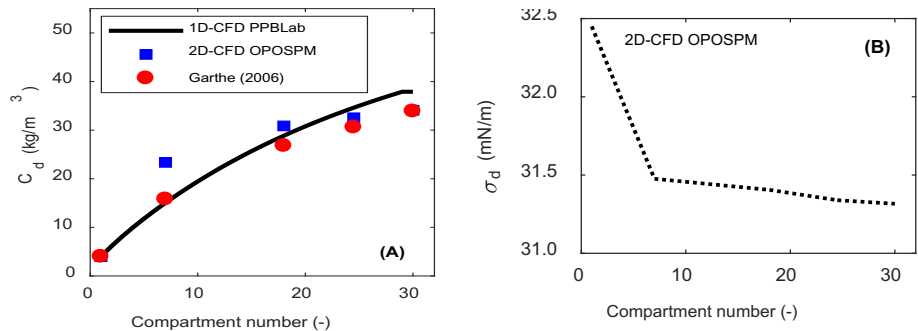


Figure (3): A) Comparison between the simulated light phase solute concentration profiles and experimental data (Garthe, 2006). B) Effect of the solute mass transfer process on the light phase interfacial tension along the column height.

5. Conclusions

In this work, a 2D OPOSPM-CFD framework is extended to model the mass transfer behaviour of pulsed sieve plate liquid extraction columns. To perform the 2D-CFD simulation, PPBLab software, as a 1D-CFD model, is used to estimate the required breakage and coalescence kernels parameters. Both simulation frameworks are able to predict the hydrodynamics and the mass transfer behaviour as compared with the published experimental data. In this regard, PPBLab software has the advantage in terms of CPU time and the grid generation.

Acknowledgment

The authors would like to acknowledge the financial support of the DFG-GrK 1932 “Stochastic Models for Innovations in the Engineering Sciences”. This work has been carried out during sabbatical leave granted to the author Professor Menwer Attarakih from the University of Jordan during the academic year 2017/2018.

References

- S. Alzyod, M. Attarakih, A. Housseine and H.-J. Bart, 2017, CFD modelling of pulsed sieve plate liquid extraction columns using OPOSPM as a reduced population balance model, *Comput. Aided Chem. Eng.*, 40, 61-66.
- M. Attarakih, S. Alzyod and A. Fricke, 2017, Population balance modelling of pulsed packed bed extraction columns using PPBLab software, *Comput. Aided Chem. Eng.*, 40, 67-72.
- M. Attarakih, A. Housseine and H.-J. Bart, 2016, CFD Modelling of Bubbly Gas Flow using coupled OPOSPM two-fluid model. *Comput. Aided Chem. Eng.*, 38, 403-408.
- M. Attarakih, M. Hlawitschka, M. Abu-Khader, S. Alzyod, H.-J. Bart, 2015, CFD-population balance modeling and simulation of coupled hydrodynamics and mass transfer in liquid extraction columns, *Appl. Math. Model.*, 39, 5105–5120.
- M. Attarakih, M. Jaradat, C. Drumm, H.-J. Bart, S. Tiwari, V. K. Sharma, J. Kuhnert and A. Klar, 2009, Solution of the population balance equation using the One Primary and One Secondary particle Method (OPOSPM), *Comput. Aided Chem. Eng.*, 26, 1333-1338.
- M. Attarakih, S. Al-Zyod, M. Abu-Khader and H.-J. Bart, 2012, PPBLAB: A New Multivariate Population Balance Environment for Particulate System Modelling and Simulation, *Procedia Eng.*, 42, 1445-62.
- C. Coualaloglou, L. Tavlarides, 1977, Description of interaction processes in agitated liquid-liquid dispersions, *Chem. Eng. Sci.*, 32(11), 1289-97.
- C. Drumm, M. Attarakih, M. W. Hlawitschka and H.-J. Bart, 2010, One-group reduced population balance model for CFD simulation of a pilot-plant extraction column, *Ind. Eng. Chem. Res.*, 49, 3442–3451.
- D. Garthe, 2006, Fluidynamics and mass transfer of single particles and swarms of particles in extraction columns, Published Dissertation, Technische Universität München, Germany.
- H. Haverland and M.J Slater, 1994, Population balance based modelling, In: Slater, Godfrey (Ed.), *Liquid-liquid extraction equipment*, John Wiley and Sons, New York, 278-305.
- P. Heertjes, W. Holve, H. Talsma, 1954, Mass transfer between isobutanol and water in a spray column, *Chem. Eng. Sci.*, 3, 122-142.
- M. Jaradat, M. Attarakih and H.-J. Bart, 2011, Population balance modeling of pulsed (packed and sieve-plate) extraction columns: Coupled hydrodynamic and mass transfer, *Ind. Eng. Chem. Res.*, 50, 14121-14135.
- R. Kronig and J. Brink, 1950, On the theory of extraction from falling droplets, *Appl. Sci. Res.*, A2, 142-154.
- A. Kumar and S. Hartland, 1985, Gravity Settling in Liquid/Liquid Dispersions, *Can. J. Chem. Eng.*, 63, 368-376.
- J. Milot, J. Duhamet, C. Gourdon and G. Casamatta, 1990, Simulation of a pneumatically pulsed liquid-liquid extraction column, *Chem. Eng. J.*, 45, 111-122.

Systematic generation of insulation materials via DEA and Building modelling

A. Torres-Rivas^a, C. Pozo^b, A. Ewertowska^a, D. Boer^{c*} and L. Jiménez-Esteller^a

^a *Department of Chemical Engineering, Universitat Rovira i Virgili, Paisos catalans, 26, Tarragona 43005, Spain*

^b *Department of Chemical Engineering, Imperial College London, South Kensington, London SW7 2AZ, United Kingdom*

^c *Department of Mechanical Engineering, Universitat Rovira i Virgili, Paisos catalans, 26, Tarragona 43005, Spain*

dieter.boer@urv.cat

Abstract

Policies are encouraging to reduce emissions in all sectors, due to the high energy demand during the life cycle of the processes. Constructions are not an exception and policies are encouraging to reduce energy demand in buildings. Although new constructions are reducing their energy demand according to new directives, without interventions in the actual building stock, the European goals proposed for 2050 cannot be achieved.

Insulation is known to achieve an important reduction in the energy demand in the operation phase of the buildings. Despite that, this implementation carries out an initial investment in both, cost and impact, which suggest that using low embodied materials, such as bio-based materials, could improve this solution. Despite their good thermal properties, these new materials are not arriving at the actual market for insulators. In order to improve this scalability, an evaluation of the efficiency of different materials is carried out, with a following combination of the efficient materials in order to generate new hybrid solutions. These hybrid materials cope to simplify the applicability of bio-based materials, generating sandwich panels or combined mats to generate materials similar to the commercialized ones which have an increasing market nowadays.

The methodology presented combines Data Envelopment Analysis (DEA) and Building modelling simulation. Using thermal simulations of EnergyPlus and the evaluation of efficiency and further projections of DEA.

Seven bio-based materials and polyurethane for comparison have been studied, with a thickness that varies from 1 cm and 26 cm in increments of 5 cm. DEA analysis is used to quantify the efficiency score of the different thicknesses of the materials. The non-efficient materials are projected to this frontier, achieving a combination of materials. Those combinations have been analysed in order to model only the feasible solutions, which have proved to achieve efficiency in all the combinations proposed.

Keywords: DEA, life cycle assessment, bio-based materials, buildings, thermal insulation

1. Introduction

Reducing the primary energy consumption seems one of the rows to achieve a sustainable development, so focusing in one of the main consumers of this energy is essential. In Spain, buildings represent a 32% of this primary energy demand, which main consumption is done in conditioning the building. Insulation of the building has been proved to achieve an important reduction in this consumption. Despite that, this implementation should be carried out in a sensible way, as in the majority of the cases the materials used are high embodied energy materials which can counter-effect the improvements achieved counting the whole life cycle of the solution.

To skip this trade-off, bio-based materials may represent an important alternative, as their thermal and acoustic properties are really competitive comparing with commercial ones. Despite that, the commercial scalability of those materials is growing slowly what suggest that a major boost for trade is required. Taking into account this fact and the high demand for sandwich panels in the building sector, a hybrid generation of insulation materials could generate a change in the actual commercial tendency of bio-based materials.

Previous research has been carried out combining Data Envelopment Analysis (DEA) and LCA, but only a little research has been carried out in the building sector and only one has combined LCA+DEA with the evaluation of the efficiency of constructions sets (Iribarren (2015)).

A systematic methodology to evaluate the ecoefficiency of these materials and a further generation of hybrid combinations is proposed via a Data Envelopment Analysis (DEA). This methodology consists in a benchmarking of the different solutions against predefined inputs and outputs. The main goal of this research is focused on the opportunity for the non-efficient solutions, which can be projected to the efficient frontier generating hybrid combinations of different materials in order to control their properties and achieve new materials.

2. Methodology

The methodology we propose allows assessing the ecoefficiency of candidate alternatives (i.e., materials and thicknesses) and systematically generate ecoefficient materials combinations from inefficient ones. This strategy comprises three main steps and integrates energy simulations, life cycle cost and impact as well as DEA.

The first step corresponds to the data generation, where each alternative is simulated in a building model providing the energy requirements. These requirements are then used to calculate the total life-cycle cost and impact associated with each alternative. The second step consists in an objective reduction, which is carried out in order to simplify subsequent calculations by ruling out of the analysis redundant indicators. In the third step, which is the core of our methodology, we apply DEA to benchmark the efficiency of the different alternatives. To this end, each alternative is modelled as a decision-making unit (DMU) whose performance is evaluated from the cost and impact indicators determined in step one and retained after step two. The efficient alternatives (efficiency score of 1), would be saved as a reference. Conversely, the non-efficient would be used to systematically identify hybrid materials potentially ecoefficient (see further details in section 2.3). Finally, these hybrid candidates would be simulated in the

cubicle model and a second DEA would be used to compare their performance with that of the ecoefficient alternatives already identified in step three.

2.1. Model definition, energy simulation and cost and environmental evaluation

To analyse the performance of the different materials, a cubicle-like building has been modelled in EnergyPlus. In energy terms, this software includes the equations set which define the energy consumption of the building taking into account the climate conditions and the heat and mass transfer balances. This simulation provides the energy demand during a specific time period (1 year). This energy demand and the materials stock of the building are used to evaluate the environmental impact associated with each category and the total cost of the different solutions to evaluate. The different impact categories and the cost would be different inputs of our model, while the output selected is an output dummy that quantifies if the solution achieves the defined conditions of the building (1 fulfilled, 0 not fulfilled). Finally, the impacts and cost associated with each combination of material and thickness correspond to a DMU in DEA.

To quantify the inputs of each DMU, 2 different databases have been used, in order to quantify the cost and the environmental impact of the solutions. On the first hand, for the total cost of the solutions, iTEC database has been used to achieve the price of all the conventional construction materials, whereas, for the bio-based materials, their cost has been extracted directly for different suppliers. The total cost of the materials used (Menoufi (2012)) is supposed to be invested during the first year of the insulation of the building. Furthermore, the electricity price has been extracted from iTeC, in this case, the cost of energy is paid each year with an annual increment of 5%.

On the other hand, for the environmental impact, each material has been evaluated with all the impact categories of Ecoindicator99; each one has been calculated based on the mass used. The impact of the electricity has been evaluated with the impact of low voltage electricity of the Spanish mix for 1 kWh.

2.2. Objective Reduction

In order to eliminate the redundant objectives, a dimensionality reduction analysis is carried out. This analysis can be done in the inputs, outputs or both, in this methodology it has been carried out only in the inputs. The different inputs may differ in the magnitude order between them, in order to solve the problems originated by the nature of the data; each input and output is normalized between 0 and 1.

Seven of the total inputs have been extracted from the further analysis due to their redundancy with the other inputs. The final objectives chosen are Land Occupation, Ozone layer depletion, Fossil Fuels, Mineral extraction and Total cost.

2.3. DEA application

A combined method of LCA + DEA is applied in this research; the main reason for the inclusion of DEA methodology is due to the necessity to implement its projection method. Despite that, it is also a beneficial methodology in order to quantify the efficiency of the different insulation materials and thicknesses.

Due to the nature of our inputs and outputs, an input-oriented method is required, which determines the proportional reduction in inputs required by an inefficient solution in order to become efficient, while the output is constant. The model used corresponds to BCC model (Cook (2009)).

Once identified the efficient frontier with the efficient solutions, all the inefficient solutions are projected to the frontier with a Radial Projection (Cook (2009)). Each non-efficient DMU projected to the efficient frontier achieves a combination of different DMUs, with a specific material and thickness.

After this combination, a deeper analysis has to be done in order to verify the manufacturing possibility of mixing the different DEA suggested materials. The different restrictions applied are shown on the following list:

- PU used for comparative; PU mixings are excluded from the following steps.
- Cellulose installation method is not compatible with other materials.
- Natural fibres can be combined in order to produce mats with other materials.
- Wood and cork can be used as external layers of sandwich panels.
- Not more than 3 materials combined would be used as hybrid solutions.

Finally, the proposed combinations are evaluated in order to verify their efficiency.

3. Results and discussion

We next present and discuss the results of the applying methodology to seven bio-based materials and polyurethane. For each material, six different thicknesses have been analysed, 0.01, 0.06, 0.11, 0.16, 0.21 and 0.26 cm. The first analysis corresponds to the efficiency of the different solutions, as it is shown in figure 1, 21 solutions are efficient, against 27 non-efficient ones.

As it is shown, wool is efficient in five out of six thicknesses, this is due to its thermal properties and its low cost which helps to achieve the efficiency. On the other hand, cork does not achieve efficiency in any of its solutions. This can be explained because their properties are really similar to wood and hemp but with a higher price and impacts.

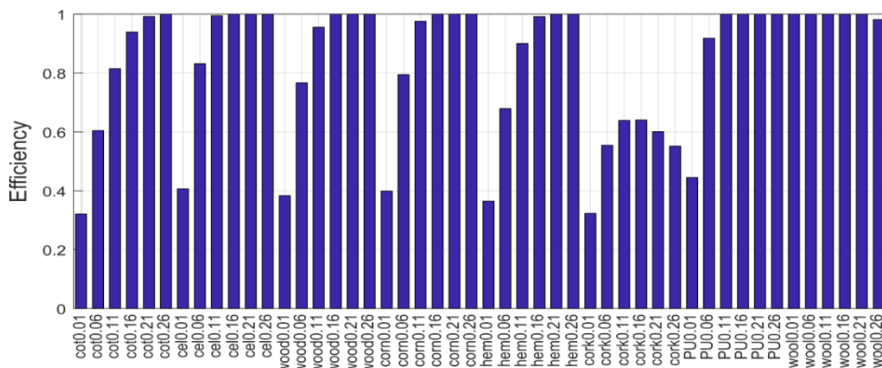


Figure 1: Efficiency score of the different insulation layers.

We can also see that thicker insulation layers achieve better efficiencies than lower ones. This can be explained because thicker layers require less energy demand and the electricity mix in Spain is expensive and dependent on fossil fuels, which tends to penalize those solutions with higher energy demand. When we take into account the projected solutions, 27 different combinations are achieved, mixing between two and four different materials as it is shown in figure 2. If the restrictions proposed in section 2.3 are considered, only seven combinations are feasible, which correspond to different thicknesses combining cotton and hemp.

The most used solutions with a higher percentage of material used correspond to cellulose and hemp. PU is also used in a lot of combinations, but the percentage used is lower than in the cellulose and hemp. Those two materials are more widely used due to their good properties and the low cost and environmental impact. On the other hand, wool solutions despite being efficient in the majority of its thickness is not a reference set of nearly any solutions. This is due to that wool solutions are in the extremes of the efficient frontier and radial projections hardly ever project in this section.

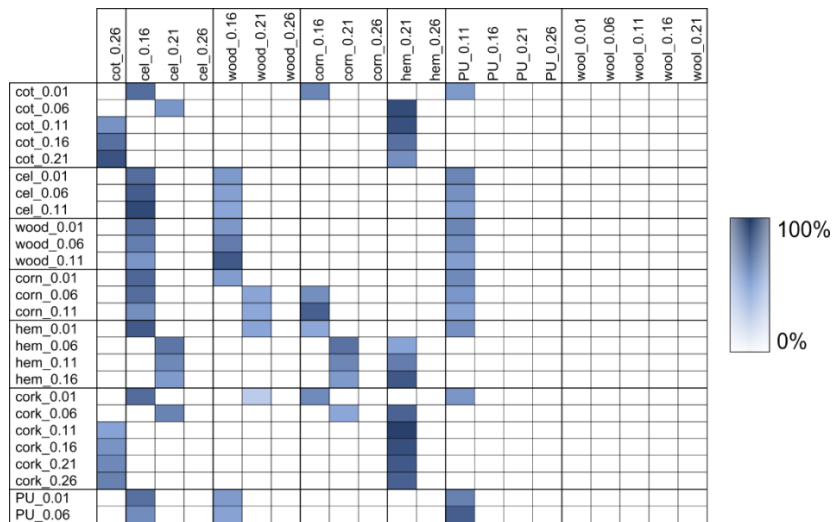


Figure 2: Projected combinations of the non-efficient solutions against efficient ones.

Once the solutions are selected, the thicknesses of each material are achieved with the combination of the percentage of the materials and the thickness of the selected DMU, achieving the following hybrid materials:

Table 1: Combination materials and thicknesses.

Hybrid Materials	Total Thickness (cm)
6cm Cotton + 17cm Hemp	23
13cm Cotton + 11cm Hemp	24
20cm Cotton + 5cm Hemp	25
2cm Cotton + 19cm Hemp	21
5cm Cotton + 17cm Hemp	22
8cm Cotton + 15cm Hemp	23
9cm Cotton + 13cm Hemp	22

All the thickness vary between 21 and 25cm, this higher thickness minimizes the energy consumption. These values are achieved due to the low impact of those materials and the reasonable cost of them, which penalize the energy consumption against the installation of thicker layers of insulation.

Finally, figure 3, shows that all the solutions suggested by our model achieve an efficiency score of 1. This proves that our methodology can generate hybrid combinations which achieve efficiency but with more balanced properties due to the mix of different materials.

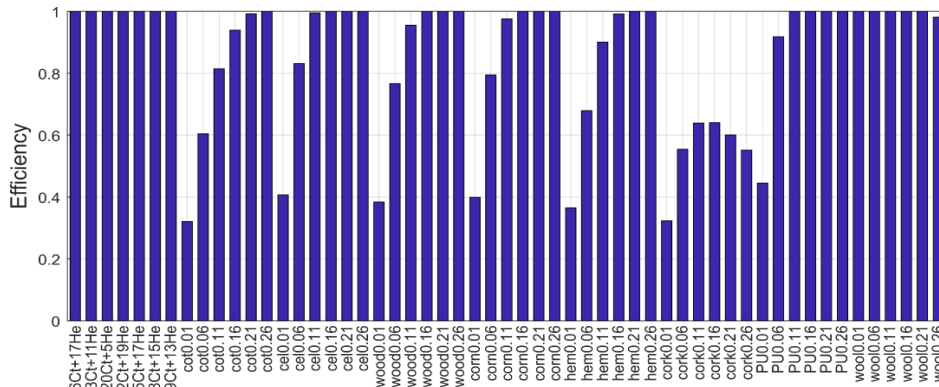


Figure 3: Final efficiency scores for all the insulation layers.

4. Conclusions

A methodology which systematically provides combinative solutions of insulation materials have been proposed and proved its results in a modelled building. The objective reduction proposed has been able to reduce 7 inputs out of 12, this has helped to eliminate redundant solutions that do not provide new information compared to the actual results.

A total of 21 out of 48 solutions have achieved an efficiency score of 1 without requiring to be combined with other materials. Thick insulation layers are requested in order to achieve efficiency in the majority of the solutions, this proves that reducing the energy demand with insulation achieves lower costs and impacts according to the eco-efficiency score obtained.

Only 7 from 21 hybrid combination were feasible solutions due to the restrictions of the model. More similar materials should be applied in order to increase the number of applicable solutions. Extracting PU would also help to find more applicable solutions. All the 7 hybrid combinations have been able to achieve an efficiency score of 1, providing new materials which could be implemented as insulation layers.

References

- D. Iribarren, A. Marvuglia, P. Hild, M. Guiton, E. Popovici, E. Benetto, Life cycle assessment and data envelopment analysis approach for the selection of building components according to their environmental impact efficiency: a case study for external walls J. Clean. Prod., 87 (2015), 707-716
- K. Menoufi, A. Castell, L. Navarro, G. Pérez, D. Boer, L.F. Cabeza, Evaluation of the environmental impact of experimental cubicles using Life Cycle Assessment: A highlight on the manufacturing phase, Appl. Energy. 92 (2012) 534–544.
- W.D. Cook, L.M. Seiford, Data envelopment analysis (DEA) – Thirty years on, Eur. J. Oper. Res. 192 (2009) 1–17.

Simulation-Based Optimization of Chemical Processes Using the Extended Cutting Plane Algorithm

Juan Javaloyes-Antón^{a,*}, Jan Kronqvist^b, José A. Caballero^a

^a*Institute of Chemical Process Engineering. Universito of Alicante, Alicante, Spain.*

^b*Process and System Engineering. Åbo Akademi University, Turku, Finland.*

javaloyes.anton@ua.es

Abstract

In this work, we study the performance of the mixed-integer nonlinear programming solver extended cutting plane (ECP) for solving simulation-based optimization problems. This solver, unlike other commercial derivative-based solvers such as the ones based on the branch and bound or outer approximation algorithms, does not require solving a nonlinear programming problem in each major iteration. This is an important feature of the ECP solver, since solving simulation-based nonlinear programming problems is a complex task due to the absence of accurate derivatives. The approach has been applied in the economic optimization of a rigorous tray-by-tray distillation column.

Keywords: Simulation-based optimization, MINLP, extended cutting plane, Aspen Hysys.

1. Introduction

Sequential modular flowsheeting programs are widely used by chemical engineers for the design and test of chemical processes, both in research and industry. These software packages include thermodynamic libraries and tailored numerical models for a variety of unit operations that lead to accurate predictions for the simulated processes. However, regards to optimization, in particular with problems involving both discrete and continuous decision variables, modular process simulators have not reached the same degree of maturity. This short of optimization problems, called mixed-integer nonlinear programming (MINLP) problems, are the most general, and also the most common in process system engineering.

Significant research efforts for overcoming this weakness or lack of robust and reliable optimization tools embedded in the modular process simulators is currently underway. In essence, in simulation-based optimization, the key issue is how to tackle the optimization of a black-box function.

There are two main approaches to address this problem. We can try to tackle the problem directly and connect the process simulator with an external solver taking advantage of the connectivity capabilities of some modular process simulators. Derivative-based or derivative-free optimization (DFO) solvers can be used. In addition to the difficulties related to the optimization of nonlinear and non-convex problems (intrinsic to some unit operations and the thermodynamic models), the following main

challenges arise. One of the major difficulties is related to the inherent numerical noise of some unit operations. From the simulation point of view, this noise is completely negligible, but in optimization we need accurate derivatives. In a modular process simulator, the only way of getting derivative information of the objective and/or constraint functions is by numerical differentiation, which limits the accuracy and effectiveness of derivative-based solvers.

This problem can be overcome by using derivative-free optimization solvers, since they only require the values of the objective function. Of course, there are significant drawbacks of not having derivative information, and we cannot expect the same performance of the derivative-based methods. The size of the problem that can be efficiently solved by DFO solvers does not exceed a few tens of variables. In addition, these methods do not guarantee the optimality of the solution found. They require a large number of function evaluations, and they exhibit poor performance in highly constrained systems. Despite these difficulties, derivative-based and derivative-free solvers have been employed successfully. For example, Navarro et al. (2014) developed a modelling system that integrates Aspen Hysys with the MINLP logic based outer approximation algorithm. The particle swarm optimization (PSO) algorithm has been used by Javaloyes et al. (2013) for the economic optimization of different distillation processes. And most recently, Ibrahim et al. (2017) used Aspen Hysys and the genetic algorithm for the optimization of crude oil distillation units.

The second approach is based on building a hybrid model replacing the most complex unit operations or set of unit operations by analytically tractable and computationally cheap surrogate models. Then, the subsequent optimization of the resulting model (involving unit operations at the level of the process simulator and explicit surrogate models) can be done using conventional MINLP solvers. For example, Henao and Maravelias (2011) replaced complex unit operations with neural networks models. Then, they use commercial MINLP solvers for solving different chemical process synthesis problems. Quirante et al. (2015) used Kriging surrogate models and derivative-based solvers for the economic optimization of different distillation processes.

The objective of this work is to study the performance of the MINLP derivative-based extended cutting plane (ECP) solver (Westerlund and Pettersson, 1995) for solving simulation-based optimization problems. Despite the challenges related with the calculation of the derivatives, it has been proven that derivative-based solvers can be employed. However (as far as the authors are aware), the proposed approaches do not exploit the main features of the ECP. The ECP solver does not require solving a nonlinear programming (NLP) problem in each major iteration as other state-of-the-art solvers, such as the branch and bound or outer approximation. Solving simulation-based NLP problems is a nontrivial task due to challenges related to the calculation of the derivatives commented above. Thus, finding a solution that satisfies the KKT conditions might be difficult. In addition, the integer/binary variables represent logic decisions, and they represent the structure of the flowsheet for the simulated process. For such variables, it is not possible to run the simulator with non-integer values, and therefore, it is not possible to use a standard branch and bound or outer approximation method for solving the simulation-based problem. The application of the proposed approach to the optimization of a rigorous tray-by-tray distillation column is discussed in this work. The results are compared with the solution found by the derivative-free PSO algorithm.

2. Basics of the Extended Cutting Plane

The ECP method was originally presented as a method for solving convex MINLP problems. The MINLP problems considered here are non-convex, which will require extra attention. The MINLP problems considered here can be formulated as follows

$$\begin{aligned} & \min f(\mathbf{x}) \\ \text{s.t. } & g_j(\mathbf{x}) \leq 0 \quad \forall j = 1, \dots, m, \\ & \mathbf{x} \in \mathbb{R}^N, \text{ some } x_i \in \mathbb{Z}. \end{aligned} \quad (1)$$

Here some of the constraints functions and/or the objective function will be considered as black box functions, and the functions values are given by the process simulator. The main idea behind the ECP method is to construct a linear approximation of problem (1). At iteration k , a linear approximation of MINLP problem (1) is given by

$$\begin{aligned} z^k &= \min \mu \\ \text{s.t. } & f(\mathbf{x}^i) + \nabla f(\mathbf{x}^i)^T (\mathbf{x} - \mathbf{x}^i) \leq \mu \quad \forall i = 1, \dots, k-1, & \text{MILP} \\ & g_j(\mathbf{x}^i) + \nabla g_j(\mathbf{x}^i)^T (\mathbf{x} - \mathbf{x}^i) \leq 0 \quad \forall j \in A_i, \forall i = 1, \dots, k-1, & \text{master} \\ & (\mathbf{x}, \mu) \in \mathbb{R}^{N+1}, \text{ some } x_i \in \mathbb{Z}, \end{aligned} \quad (2)$$

where \mathbf{x}^i are the trial solutions obtained in previous iterations and A_i contains the indexes of the violated constraints at iteration i . By solving problem (MILP master) we obtain a new trial solution \mathbf{x}^k . For convex problems, we know that in case all constraints are satisfied within the desired tolerance and

$$f(\mathbf{x}^k) - z^k \leq \varepsilon, \quad (3)$$

then the solution \mathbf{x}^k is optimal. In case the criteria are not met we continue and the next MILP problem will then contain more linearizations or so called cutting planes. For convex problems the linearizations will underestimate the real functions, which guarantee that no feasible solutions are excluded from the search space, and after some iterations the procedure will converge to the optimal solution.

3. Using the Extended Cutting Plane method for non-convex problems

Since the problems we consider here are non-convex we cannot guarantee that we will find the global optimal solution, and the goal will be to obtain a good feasible solution without having to evaluate the black box function too many times. The main difficulty when applying a linearization based method such as ECP to a non-convex problem is the fact that the linearizations are not necessarily underestimating the real functions. Therefore it is possible that the optimal solution is excluded from the search space by one of the cutting planes. Even worse, it is possible that all feasible solutions are excluded from the search space and that there are no solutions that satisfies problem (MILP master). For the optimization problems considered here we noticed that this issue does occur, and the problem (MILP master) becomes infeasible. This is a known problem, and to handle this issue we use an approach where we solve an optimization problem to restore feasibility of the MILP master problem. If the MILP master problem becomes infeasible, we solve the following feasibility problem

$$\begin{aligned}
& \min \sum_j \sum_i w_i r_{j,i} \\
& \text{s.t. } f(\mathbf{x}^i) + \nabla f(\mathbf{x}^i)^T (\mathbf{x} - \mathbf{x}^i) \leq \mu \quad \forall i = 1, \dots, k-1, \\
& \quad g_j(\mathbf{x}^i) + \nabla g_j(\mathbf{x}^i)^T (\mathbf{x} - \mathbf{x}^i) - r_{j,i} \leq 0 \quad \forall j \in A_i, \forall i = 1, \dots, k-1, \\
& \quad (\mathbf{x}, \mu) \in \mathbb{R}^{N+1}, r_{j,i} \in \mathbb{R}_+, \text{ some } x_i \in \mathbb{Z},
\end{aligned} \tag{4}$$

where $r_{j,i}$ is a new variable which allows a violations of the cutting planes. By solving problem (4), we find the minimum modification of the cutting planes needed in order to make problem (MILP master) feasible. The objective of problem (4) is given by the sum of the residuals $r_{j,i}$ with weights w_i . The weights are used to penalize the residual of the cutting planes differently. Here we have chosen the weights as follows

$$w_i = i^2, \tag{5}$$

where i is the iteration index. By this approach, we allow for larger modifications of the cutting planes added in early iterations compared to the cutting planes added in the later iterations. By solving problem (4) we obtain the minimum residuals $r_{j,i}^*$, and we modify the cutting planes in the problem (MILP master) according to

$$g_j(\mathbf{x}^i) + \nabla g_j(\mathbf{x}^i)^T (\mathbf{x} - \mathbf{x}^i) - 1.5 \cdot r_{j,i}^* \leq 0 \quad \forall j \in A_i, \forall i = 1, \dots, k-1. \tag{6}$$

The cutting planes are relaxed by a factor 1.5 times the minimum modification to further extend the search space, and avoid running into an infeasible MILP problem in the next iteration. The weights of the residuals in problem (4) are introduced to reduce the change of cycling. Without the weights it would be possible to add several cutting planes in one iteration and basically remove them in the next iteration. As for the penalty approach used in DICOPT, we cannot guarantee that this technique will find a solution to non-convex MINLP problems, but for the problems considered here it worked well.

4. Simulation-based optimization approach

A scheme of the proposed approach is shown in Figure 1. The first step is to build a superstructure that includes all the alternatives of interest of the process that we want to optimize. Once the flowsheet is implemented at the level of the process simulator, the objective function must be defined. Typical objective functions such as the total annual cost (TAC), net profit or energy costs can be used according to our main interest. The objective function, as well as the optimization solver, the interface module, and all the auxiliary files are implemented in Matlab. The interface module is a key file in the

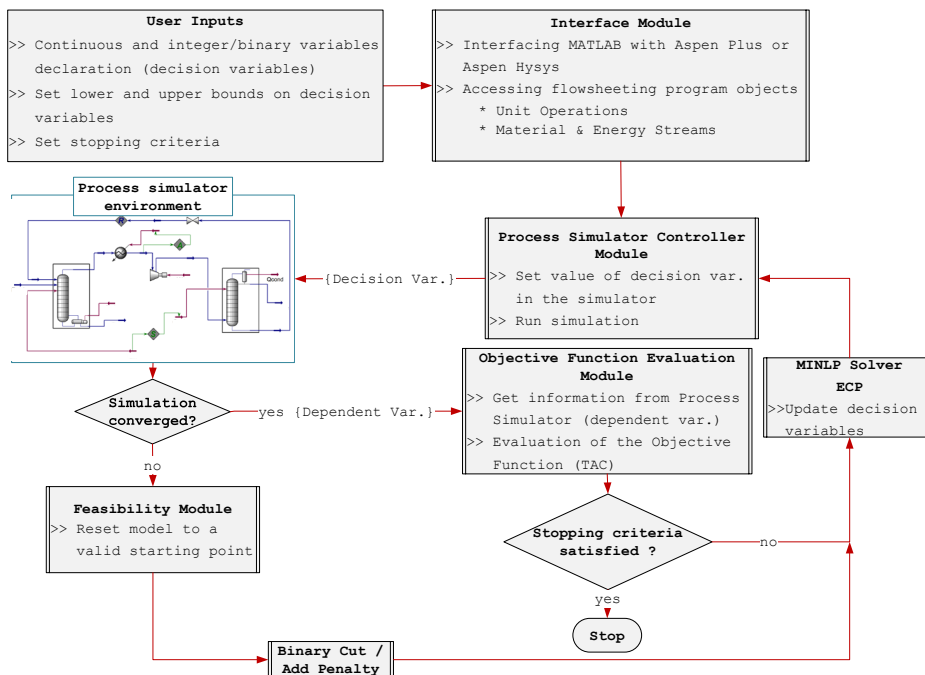


Figure 1. Algorithm flowchart for the simulation-based optimization processes using the ECP.

approach. Sequential modular process simulators such as Aspen Hysys or Aspen Plus can be accessed from external programs via the binary-interface standard Component Object Model (COM), by Microsoft. Thus, we can modify the flowsheet topology and operating conditions of our superstructure according to the values of the decision variables.

After the interface module and objective function have been implemented in Matlab, the algorithm can be executed. First of all, it is necessary to set the upper and lower bounds on the decision variables as tight as possible to avoid convergence problems. Then, the solver is initialized and the values of the decision variables are sent to the process simulator. At this point, the flowsheet is automatically updated and converged. The process simulator returns all the dependent variables needed for computing the objective function and constraints. New values of the decision variables are calculated by the MINLP solver.

5. Case Study

In this work, we consider the economic optimization of a conventional distillation column. The problem can be stated as follow. Given is the feed with known composition and the required purity of the products (distillate and residue). The objective is to determine the optimal number of trays and feed location, as well as the operating conditions that minimizes the total annual cost (TAC). The TAC comprises the annualized investment cost (or capital cost) of the main equipment, and the most relevant operating cost

$$TAC\left(\$/y\right) = C_{op} + FC_{cap}, \quad (7)$$

where C_{op} is the operating cost in (\$/y), C_{cap} is the total cost of installed equipment in (\$), and F is the annualization factor for the capital cost, which can be obtained from Eq. (8), and takes into account the fractional interest rate per year, i , and the years over which the capital is to be annualized, n .

$$F = \frac{i(1+i)^n}{(1+i)^n - 1} \quad (8)$$

The equipment cost (distillation column and heat exchangers) is based on the cost correlations given by Turton et al. (2008). Steam and cooling water are the main utilities considered in the calculation of the operating costs, based on 8,000 operating hours per year. Figure 2 shows the superstructure implemented in the process simulator. The optimal number of trays and feed location are given by the number of active trays in the rectifying (NR) and stripping (NS) section. The problem formulation is also shown in Figure 2. The decision variables are the number of active trays in the rectifying, and stripping section, which are integer variables, and the reflux ratio, RR , boilup ratio, BR , and top pressure, P_{top} , which are continuous variables. The function f_{CDC} refers to the implicit block in the process simulator that contains the set of equations describing the behaviour of the distillation column.

5.1. Results

The results of the optimization of the proposed case study are summarized in Table 1. We solved the problem using the ECP solver and the PSO. Since the PSO is a stochastic DFO algorithm, we run the problem several times. The solution shown in Table 1 is the best one found so far. ECP gave both a better solution and with less function evaluations.

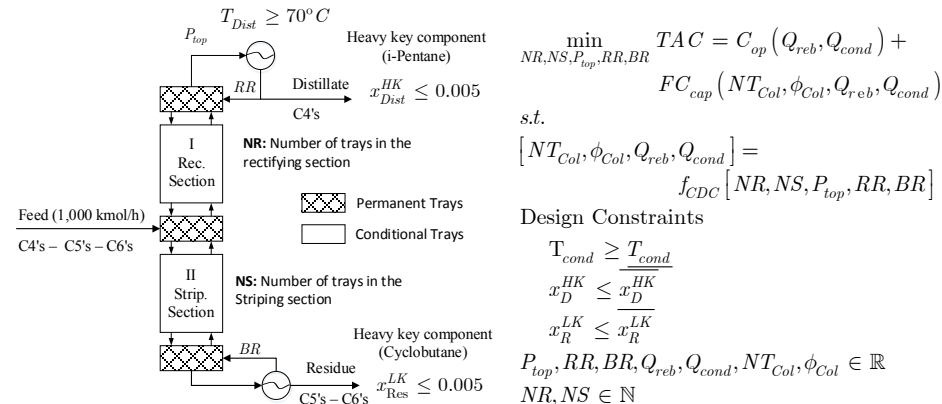


Figure 2. Superstructure representation for the optimal number of trays, feed location and operating conditions of a conventional distillation column, and problem formulation.

Table 1. Results for the optimization of a distillation column using the ECP and PSO algorithms.

Solver	TAC (MM\$/y)	NR	NS	RR	BR	P (bar)	No. Iter.	No. Fun. eval.	Time (s)
ECP	3.185	26	29	2.56	1.70	9.25	88	528	407
PSO	3.334	25	25	2.92	1.87	10.9	160	1600	830

6. Conclusions

Here we have studied the performance of the ECP algorithm for solving a bench mark simulation-based optimization problem. The results are encouraging. Further examples comprising complex flowsheets with recycle streams and large number of unit operations must be done in future work to test the robustness of the proposed approach.

Acknowledgments.

The authors gratefully acknowledge the financial support by the Spanish Ministry of Economy, Industry and Competitiveness CTQ2016-77968-C3-02P, FEDER, UE.

References

- Henao, C.A., Maravelias, C.T., 2011. Surrogate-Based Superstructure Optimization Framework. *AICHE J.* 57, 1216–1232.
- Ibrahim, D., Jobson, M., Guillén-Gosálbez, G., 2017. Optimization-Based Design of Crude Oil Distillation Units Using Rigorous Simulation Models. *Ind. Eng. Chem. Res.* 56.
- Javaloyes-Antón, J., Ruiz-Femenia, R., Caballero, J.A., 2013. Rigorous Design of Complex Distillation Columns Using Process Simulators and the Particle Swarm Optimization Algorithm. *Ind. Eng. Chem. Res.* 52, 15621–15634.
- Navarro-Amorós, M. a., Ruiz-Femenia, R., Caballero, J. a., 2014. Integration of modular process simulators under the Generalized Disjunctive Programming framework for the structural flowsheet optimization. *Comput. Chem. Eng.* 67, 13–25.
- Quirante, N., Javaloyes, J., Caballero, J.A., 2015. Rigorous design of distillation columns using surrogate models based on Kriging interpolation. *AICHE J.* 61, 2169–2187.
- Turton, R., Baile, R.C., Whiting, W.B., 2008. *Analysis, synthesis and design of chemical processes*. Pearson Education.
- Westerlund, T., Pettersson, F., 1995. An extended cutting plane method for solving convex MINLP problems. *Comput. Chem. Eng.* 19, 131–136.

Towards a Methodology for Reusable Ontology Engineering: Application to the Process Engineering Domain

Nikolaos Trokanas^{a*}, Linsey Koo^b, Franjo Cecelja^{b,*}

^a*CLMS UK Ltd, London, UK*

^b*PRISE Group, University of Surrey, Guildford, GU2 7XH, UK*
n.trokanas@clmsuk.com

Abstract

This paper proposes a methodology for ontological engineering with an aim to develop reusable ontologies. The proposed methodology combines experience of developing ontology engineering using a ‘good’ practice with established methodologies and concomitantly implementing reusability in the eSymbiosis ontology.

Keywords: Ontological Engineering, Methodology, Ontology Reuse.

1. Introduction

Existing methodologies in ontology engineering focus on good practice of ontology development with primary aim in developing a consistent ontology with a complete description of the domain by following certain and established principles. To our knowledge, the existing methodologies do not appear to consider reusability as a main objective during the process of developing an ontology. Although the main objective of ontology engineering is and should remain to create ontologies which represent knowledge in the domain and which is useful for respective purposes, we argue that a higher level of reusability could be achieved by considering and following comparatively simple steps in ontology design. The proposed methodology, the MetROn, is a result of the experience gained in the course of the eSymbiosis project (Cecelja et al. 2013, Trokanas et al. 2013, Trokanas et al. 2012). The proposed methodology does not intend to dictate how to develop a correct ontology, rather than how to correctly develop an ontology.

2. Reusability characteristics

Representing knowledge is undoubtedly the most important aspect of ontology; there is no point in putting an extra effort in trying to assure reusability of an ontology that is irrelevant to the domain. Existing systems, such as ontology matching, alignment or evaluation, work under an assumption that the ontologies are somehow suitable for the task at hand. Apart from representing the appropriate knowledge, there are various aspects of an ontology that support in facilitating the reusability aspect.

2.1. Modularisation

Modularisation (Morbach, Wiesner & Marquardt 2009, Doran, Tamma & Iannone 2007) extends in three dimensions of the ontology: i) domain, ii) level, and iii)

properties. Domain modularisation refers to the creation of different modules at the domain level. The main criteria are the knowledge representation and the intended use of the ontology in domain modularisation. By using different and more importantly modules representing distinct parts of the domain, the ontology can be reused as a whole, but also in parts, as demonstrated by the example of eSymbiosis ontology in Figure 1, where distinct segments of the domain refer to processing technologies, materials, description of the process using attributes, and description of participants.

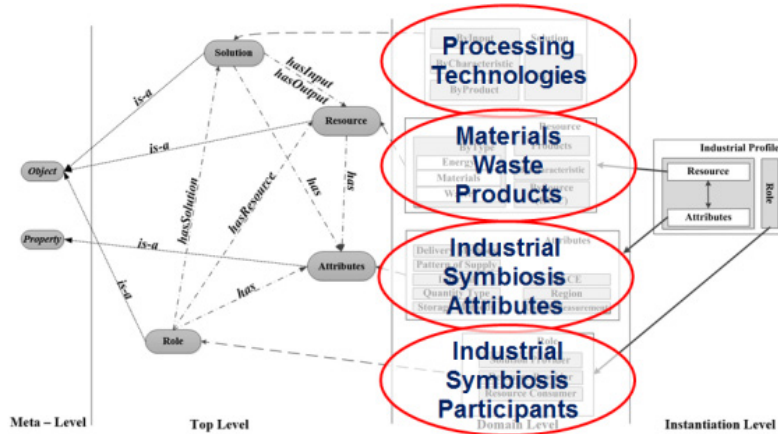


Figure 1 eSymbiosis ontology domain modularisation

Level modularisation serves a similar purpose as the domain modularisation (Figure 2); it is used to differentiate the whole level of abstraction instead of distinct knowledge segments. It is more useful for the reuse of top-level and meta-level ontologies, which usually consist of fewer classes and properties in comparison to the domain level.



Figure 2 eSymbiosis ontology level modularisation

As with concepts, modularisation of the properties in the ontology is also possible and useful. Properties can be grouped along their range, their function, or both. Grouping along the range supports reusability of separate modules of the ontology while grouping along the function supports the reusability of the ontology as a whole, but it also supplements the represented knowledge, as it enables the use of these properties in an application in a more structured approach aiding specific functionalities of the user requirements.

2.2. Naming conventions

Although ontologies are tools for semantic representation, syntactic information still plays an important role in comparing, reusing and generally managing ontologies. It is therefore important for the ontology developers to use consistent terminology and natural language in general; i.e. interchangeably using spellings of both British English and American English can cause discrepancies at large scales. Moreover, naming conventions to improve the readability of an ontology from consistent use of capitalisation for the concept name containing more than one word, as well as use of prefix “has” for properties are known as a good practice that can help towards more accurate similarity calculation and, more importantly, make the ontology more comprehensible (Noy, McGuinness 2001).

2.3. Coherent modelling

Coherent modelling (Fernández-López, Gómez-Pérez & Juristo 1997) has a certain overlap with naming conventions; besides the language used for modelling, it is also important to be consistent with the encoding of the ontology. Here, encoding refers to the use of data types (integers, floats etc.), to the use of external resources, to the use of inverse properties, and also to the modelling of restrictions on properties. For example, an ontology will be inconsistent if a float type is inserted in a slot which has been defined as the integer. The use of unnecessary external resources limits similarity calculations in the process of reusability.

2.4. Detailed annotations

Annotations are key to manual reuse of an ontology (Trokanas, Cecelja & Raafat 2014). They are very helpful to provide definitions, comments and explanations and they can also provide synonyms helping towards better syntactic similarity without the use of external lexicons and vocabularies. Annotations are also used for multilingual modelling.

2.5. Minimum restrictions

Restrictions on properties are application specific. It is therefore good practice to keep them to a minimum when publishing an ontology for reuse. By only defining restrictions at a high level, each module of the ontology is easier to reuse.

3. The MetROn methodology

The proposed metROn methodology combines steps from established methodologies in ontology engineering and experience from developing and implementing the eSymbiosis ontology (Trokanas et al. 2013, Trokanas, Cecelja & Raafat 2014).

3.1. Define domain and application of the ontology

Most of the existing methodologies agree upon the importance of the first step, which is the domain and application of the ontology should be clearly defined. This might include competency questions, market research, user interaction or contribution from domain experts or stakeholders. Competency questions are although useful in ontology

engineering, they are generally replaced by the user requirements if the ontology is developed with a specific application in mind.

3.2. Consider reusing existing ontologies

Redundant efforts can be saved by identifying existing ontologies in the same or complementary domains. As a matter of guidance, existing ontologies are available from the literature as well as from a number of libraries, such as Watson and Swoogle. Reusing of ontologies is a demanding and troublesome task primarily because of the fact that many of the ontologies described in literature are not publicly available, but also often inconsistent. Finally, ontologies that are not updated become more difficult to reuse mainly due to the unavailable repositories (external resources).

3.3. Identify existing classifications, vocabularies and standards

Along with the ontologies suitable for reusability, other sources of useful and structured information can be used. These include existing classifications (e.g. European Waste Catalogue), domain vocabularies (e.g. WordNet), industrial standards (e.g. ISA88) and mark-up language specifications (e.g. B2MML).

3.4. Identify terminology

Terminology of the identified from the source described in 3.3, but also from other sources such as literature, reports, white papers etc. Term identification is performed either manually or automatically with the use of term extraction tools such as TerMine which provide links to ontology editors such as Protégé.

3.5. Define the classes

Once terminology has been defined, concepts representing classes should be organised into groups and respective hierarchy (Figure 3). In consequence, the initial structure of the ontology is formed with distinct modules. There are four suggested approaches for this step.

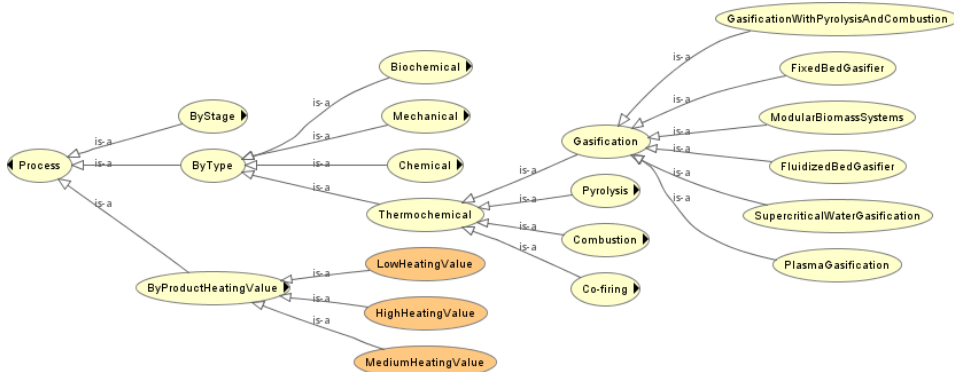


Figure 3 Organising taxonomical structure

The top-down approach begins with the modelling of the high-level concepts first (more general), i.e. Process, ByType, and then moving onto the more detailed concepts, i.e. Thermochemical, Pyrolysis etc. The bottom-up approach is the opposite to top-down; it begins with the modelling of the more specific concepts, i.e. PlasmaGasification,

FixedBedGasifier, which are subsequently organised in more general concepts, i.e. Gasification, Thermochemical. The middle-out approach is usually the first step in ontology design and it begins with modelling concepts which are not categorised as top or bottom level concepts. Still, following middle-out approach is problematic, since it requires knowledge of the ontology structure. The most realistic approach in ontology development, however, is the combination of all the approaches (hybrid). The actual approach the developer will use is dictated by the available knowledge for the domain. Modelling begins from the concepts that are supported by established knowledge and expertise and moves organically to either more detailed or more general concepts.

3.6. Define properties

Properties are derived from the identified terms and are generally dictated by the application requirements in the domain. The definition of properties should start from the top level of the ontology taking advantage of inheritance, therefore reducing the required effort and following good practice.

3.7. Consider reusing existing ontologies

At this stage, reusing existing ontologies step is revisited. This time the aim is not to find ontologies that represent the domain in question, but to identify supplementary ontologies instead. For the case of eSymbiosis ontology, this refer to ontologies representing units of measurement, geographical information etc.

3.8. Create namespaces

Ontologies that are being reused should have meaningful namespaces and the same principle applies for the developed modules of the ontology. The use of meaningful namespaces makes the ontology more comprehensible and serves the very practical purpose of modelling. To explain, the ontology engineer will have to type concept names extensively while modelling properties and restrictions on properties are still in place. As a result, using meaningful namespaces reduces the required effort significantly.

3.9. Define restrictions

Restrictions on properties are application specific. Restrictions are essential in applications that require inference of the ontology. Modelling restrictions at the highest level possible is not only good practice but it also allows for easier manipulation of the restrictions for reuse purposes.

3.10. Annotate the ontology

Annotation of the ontology has a two-fold purpose. Annotation are application specific, i.e. concept names and application information, but it can also be very helpful for reuse, i.e. by providing synonyms and explanations for concepts.

4. Conclusions

MetROn is a methodology for ontology engineering that focuses on developing ontologies that can be reused without compromising the usability of the ontology. The proposed methodology is a result of the experience gained through the development of the eSymbiosis ontology. It has also been validated through the development of another ontology the BiOnto, an ontology for biomass and bioprocessing technologies.

References

- Cecelja, F., Trokanas, N., Raafat, T. & Kokossis, A. 2013, "Ontology Engineering for the Development of Industrial Symbiosis Networks", 2013 AIChE Annual Meeting
- Doran, P., Tamma, V. & Iannone, L. 2007, "Ontology module extraction for ontology reuse: an ontology engineering perspective", Proceedings of the sixteenth ACM conference on Conference on information and knowledge management ACM, pp. 61.
- Fernández-López, M., Gómez-Pérez, A. & Juristo, N. 1997, "Methontology: from ontological art towards ontological engineering".
- Morbach, J., Wiesner, A. & Marquardt, W. 2009, "OntoCAPE—A (re) usable ontology for computer-aided process engineering", Computers & Chemical Engineering, vol. 33, no. 10, pp. 1546-1556.
- Noy, N.F. & McGuinness, D.L. 2001, "Ontology development 101: A guide to creating your first ontology".
- Trokanas, N., Raafat, T., Cecelja, F. & Kokossis, A. 2013, "OFIS – Ontological Framework for Industrial Symbiosis", Computer Aided Chemical Engineering, vol. 32, no. 23rd European Symposium on Computer Aided Process Engineering, pp. 523-528.
- Trokanas, N., Raafat, T., Cecelja, F., Kokossis, A. & Yang, A. 2012, "Semantic Formalism for Waste and Processing Technology Classifications Using Ontology Models", Manuscript submitted for publication to Escape.
- Trokanas, N., Cecelja, F. & Raafat, T. 2014, "Towards a Re-Usable Ontology for Waste Processing", Computer Aided Chemical Engineering, vol. 33, no. 0, pp. 841-846.

Simultaneous Optimization for Integrated Cooling Water System with Chemical Processes

Fei Song^{a,b}, Nan Zhang^b, Robin Smith^b, Yujiao Zeng^a, Jie Li^b, Xin Xiao^{a*}

^a *Institute of Process Engineering, Chinese Academy of Sciences, Division of Environment Technology and Engineering, Beijing, 100190, China*

^b *Centre for Process Integration, School of Chemical Engineering and Analytical Science, The University of Manchester, M13 9PL, UK*

xxiao@ipe.ac.cn

Abstract

Cooling water from the cooling water system is frequently used to reject process heat in chemical industries. The performance of chemical processes could be greatly affected by varying conditions of cooling water. Therefore, there is a need of integration between chemical processes and cooling water system for effective use of cooling water and improve the performance of chemical processes. In this work, a nonlinear programming formulation is developed for operational optimization of integrated recirculating cooling water system and chemical processes. The model is solved to local optimality using CONOPT in GAMS. The results demonstrate the total profit can be significantly improved by 337 k£/y through integration compared to that without integration.

Keywords: optimisation, integration, cooling water, nonlinear programming

1. Introduction

The recirculating cooling water system consisting of cooling towers, cooler network and piping network is widely used to reject process heat in chemical industries in order to keep chemical processes working efficiently and safely. The performance of chemical processes could be greatly affected by varying conditions of cooling water, resulting in a trade-off between process economics and the operating cost of the cooling water system (Song et al., 2017). Therefore, integration of the cooling water system and chemical processes is substantial to improve the overall economics.

Previous studies mainly focused on operational optimization of the cooling water system without integration of chemical processes. For instance, Castro et al. (2000) developed a model for the cooling water system based on the regression model of cooling towers. Modelling cooler network only involves energy balance without considering heat transfer. Cortinovis et al. (2009) proposed a model for the cooling water system where the cooling tower is modelled based on simple mechanism. Modelling the cooler network considered both energy balance and heat transfer. Song et al. (2017) developed a nonlinear model for the cooling water system. When modelling cooling tower, water evaporation was related to both water conditions and ambient air conditions. The cooler network in series and parallel configurations were taken into account, which are not addressed in Castro et al. (2000) and Cortinovis et al. (2009).

There were also some studies on optimization or analysis of integrated cooling towers and condensing turbines without simultaneous optimization. Barigozzi et al. (2014) proposed a modular-based optimization method for integrated cooling tower and condensing turbines to maximize the net power output. Laković et al. (2015) analyzed the effect of ambient air conditions on the energy efficiency of power plants having cooling towers and condensing turbines.

To the best of our knowledge, simultaneous optimization of integrated cooling water system with chemical processes has not been addressed. In this paper, we develop a nonlinear programming model for simultaneous optimization of integrated cooling water system with chemical processes. The model for the cooling water system from Song et al. (2017) is used to determine optimal water and air flowrate to each cooling tower and water distribution in chemical processes. The computational studies demonstrate the total profit can be significantly improved by 337 k£/y through simultaneous optimization compared to separate optimization of the cooling water system and chemical processes.

2. Problem statement

Figure 1 shows a simplified integrated cooling water system with chemical processes including a condensing turbine in a refinery. There are i ($i = 1, 2, \dots, J$) chemical processes and J ($j = 1, 2, \dots, J$) cooling towers. The chemical processes whose economics is affected by operating conditions of the cooling water system are included in the set \mathbf{I}_p . The temperature of a chemical process i after cooling must satisfy some limit. While each chemical process has its own cooler or condenser, each cooling tower has one corresponding fan and pump. In other words, there are also J fans and J pumps. The water fed into a cooler can be from a cooling tower or at least one of other coolers.

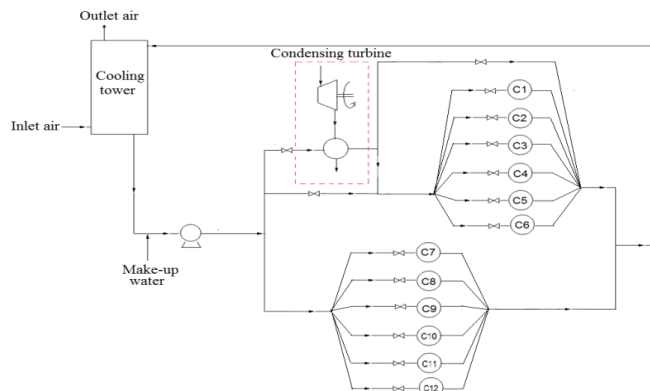


Figure 1 A simplified integrated cooling water system with a condensing turbine in a refinery

Given: characteristics of cooling towers, ambient air conditions, process specifications, cooler configurations and pipe specifications, temperature limit for chemical processes after cooling. *Determine:* cooling water flowrate in individual coolers and towers, air flowrate in individual towers, cooling water temperature produced by towers, the performance of processes, the overall economic performance of integrated cooling water system and processes. *Assumptions:* (i) uniform cross-sectional area of towers; (ii) no supersaturated air from towers; (iii) the properties of cooling water related to

temperature are calculated at the mean temperature of inlet and outlet of individual coolers; (iv) heat loss to the environment is negligible; (v) heat transfer coefficient of processes is constant.

The objective is to maximize the overall profit which is calculated as the revenue from chemical processes minus the operating cost of cooling water systems.

3. Mathematical formulation

3.1. Objective function

The objective function is to maximize total profit, which is represented by eq. (1).

$$TP = \sum_i EP(i) - C1 \cdot \sum_j m_m(j) - C2 \cdot \sum_j [P_p(j) + P_f(j)] \quad (1)$$

where, $m_m(j)$ is make-up water consumption in cooling tower j , $P_p(j)$ is power consumption by pump j , $P_f(j)$ is power consumption by fan j , $C1$ is unit cost of make-up water and $C2$ is unit cost of power, $EP(i)$ is the economic profit from chemical process i , which is influenced by its mass flowrate [$m_p(i)$], the temperature before cooling [$t_{pi}(i)$] and after cooling [$t_{po}(i)$]. The detailed model for process economics very depends on what the process is used for. Therefore, the general formulation is expressed for all the processes with cooling demand as eq. (2). A detailed process economic model for condensing turbines is developed and presented in Appendix.

$$EP(i) = f[t_{po}(i), m_p(i), t_{pi}(i)] \quad (2)$$

3.2. Cooling water system modelling

The model for the cooling water system from Song et al. (2017) is used as follows.

3.2.1. Cooling tower modelling

The temperature of water leaving cooling towers is calculated by eq. (3).

$$t_{wo}(j) = t_{wi}(j) - \gamma1 \cdot NTU(j)^{\gamma2} \cdot m_{wi}(j)^{\gamma3} \cdot m_a(j)^{\gamma4} \cdot (t_{wi}(j) - t_{wbi})^{\gamma5} \quad (3)$$

where, NTU is the characteristics of cooling tower j , $m_{wi}(j)$ is the mass flowrate of cooling water fed to tower j , $m_a(j)$ is dry air mass flowrate, $t_{wi}(j)$ and $t_{wo}(j)$ are cooling water inlet and outlet temperature of tower j respectively, t_{wbi} is ambient wet bulb temperature and $\gamma1$ - $\gamma5$ are coefficients.

The humidity of air leaving towers [$w_o(j)$] is calculated by eq. (4). The water evaporation rate [$m_e(j)$] is predicted by the mass balance, which is expressed as eq. (5). The water consumption [$m_m(j)$] is calculated by eq. (6).

$$w_o(j) = (\beta1 + \beta2 \cdot (t_{wi}(j) - t_{wo}(j)) + \beta3 \cdot (t_{abi} - t_{wbi}) + \beta4 \cdot (t_{wi}(j) - t_{wbi})) \cdot m_{wi}(j)^{\beta5} \cdot m_a(j)^{\beta6} + \beta7 \cdot w_i \quad (4)$$

$$m_e(j) = m_a(j) \cdot (w_o(j) - w_i) \quad (5)$$

$$m_m(j) = \frac{cc \cdot m_e(j)}{cc - 1} \quad (6)$$

where, w_i is ambient air humidity ratio, t_{dbi} is ambient temperature, cc is the cycles of concentration, defined as the ratio between the concentration of dissolved solids in the circulating water and in makeup water, and β_1 - β_7 are coefficients.

Note that the coefficients in eqs. (3) - (6) are regressed using the least square method with the measured data or the operating data.

3.2.2. Cooler network modelling

Energy balance and heat transfer equations for coolers are used to calculate the temperature of water and processes leaving coolers. The heat transfer coefficient of water flowing in the tube side is calculated by the equation from Wang et al. (2012), and that of processes is set to be constant as the flowrate of processes is constant. Cooler network in both parallel and complex configurations are modelled by mass and energy balance.

3.2.3. Piping network modelling

Piping network models are developed by mechanical energy conservation to predict water distribution in chemical processes and power consumption of pumps.

3.3. Chemical processes modelling

The temperature of processes after cooling impacts the thermal and economic performance of processes. Although the detailed model for the calculation of the temperature depends on whether there is a phase change during heat transfer, the elements that influence the temperature are clear, including the water mass flowrate used to cool down process i [$m_c(i)$], the supply temperature of water to cool down process i [$t_{ci}(i)$], the heat capacity flowrate of process i [$CP_p(i)$] and the temperature of process i before cooling [$t_{pi}(i)$]. Generally the temperature of process i after cooling [$t_{po}(i)$] is given by,

$$t_{po}(i) = T[m_c(i), t_{ci}(i), CP_p(i), t_{pi}(i)] \quad (7)$$

The entire model is nonlinear programming (NLP) optimization model, which is solved to local optimality using the solver CONOPT in the software GAMS.

4. Case studies

We use the proposed model to solve three cases involving a forced draft wet cooling tower, a condensing turbine and 12 processes with corresponding coolers, as shown in Figure 1. While in case 1, the operating cost of the cooling water system is minimized without considering the power profit from the condensing turbine, the power generation from the condensing turbine is maximized without considering the operating cost of the cooling water system in case 2. In case 3, the overall profit of the cooling water system and the condensing turbine is maximized. The computational results are listed in Table 1.

From Table 1, it can be clearly observed that there is a trade-off between the cooling water system and the condensing turbine. When the power from the condensing turbine is maximized without considering the operating cost of the cooling water tower, it led to the highest operating cost of the cooling tower. This is similar for case 1 where the

operating cost of the cooling tower is minimized only, resulting in the lowest power generation from the condensing turbine. After simultaneous optimization of the integrated cooling water system and the condensing turbine, the maximum profit of 8,743 k£/y is achieved, which is improved by 337 k£/y compared to case 2. Although there is little difference of the overall economics between case 1 and case 3, the optimal circulating cooling water flowrate in case 3 is about 6416 t/h, which is 367 t/h more than that of 6047 t/h in case 1.

5. Conclusions and future work

In this paper, an equation-based NLP optimisation model was successfully developed for the integrated cooling water systems and chemical processes with cooling demand to improve the overall process economics. The proposed NLP model is solved to local optimality using the solver CONOPT in GAMS. The computational studies demonstrate the total profit can be significantly improved by 337 k£/y through simultaneous optimization compared to separate optimization of the cooling water system and chemical processes. Future work is to investigate integration of the cooling water system with other processes such as compressor inter-cooling, condensation of light components for distillation, and pre-cooling for compression refrigeration.

Table 1 Comparative results for cases 1-3

Units	Results	Base case	Case 1	Case 2	Case 3
Cooling water system	Circulating water flowrate (t/h)	7,560	6,047	9,000	6,414
	Air flowrate (t/h)	8,237	7,267	12,053	7,258
	Operating cost (£/y)	2,012k	1,813k	2,416k	1,844k
Condensing turbine	Inlet cooling water mass flowrate (t/h)	5,287	3,908	6,796	4,246
	Condensate temperature from the condenser (°C)	48.8	50.9	46.7	50.4
	Power generation (kW)	13,360	13,190	13,528	13,234
	Profit from power generation (£/y)	10,688k	10,552k	10,822k	10,587k
Total profit (£/y)		8,676k	8,739k	8,406k	8,743k

Appendix

The detailed model between a cooling water system and condensing turbines is described as heat transfer in condensers

$$Q_{ds}(i) + Q_{cn}(i) = m_c(i) \cdot C_{pw}(i) [tco(i) - tci(i)] \quad (\text{A.1})$$

$$A(i) = \frac{Q_{ds}(i)}{U_{sd}(i) \Delta t_{dsm}(i)} + \frac{Q_{cn}(i)}{U_{cn}(i) \Delta t_{cnm}(i)} \quad (\text{A.2})$$

where $m_c(i)$ is mass flowrate of cooling water in condenser i , $C_{pw}(i)$ is specific heat capacity of cooling water in condenser i , $A(i)$ is the area of the condenser i , $Q_{ds}(i)$ and

$Q_{cn}(i)$ are the cooling duty of the desuperheating and condensing zones in condenser i respectively, $U_{sd}(i)$ and $U_{cn}(i)$ are the overall heat transfer coefficient of the desuperheating and condensing zones respectively, $\Delta t_{dsm}(i)$ and $\Delta t_{cmm}(i)$ are the logarithmic mean temperature of the desuperheating and condensing zones respectively.

$$\Delta t_{dsm}(i) = \frac{[T_{out}(i) - tco(i)] - [T_{cc}(i) - tcc(i)]}{\ln\left\{\frac{[T_{out}(i) - tco(i)]}{[T_{cc}(i) - tcc(i)]}\right\}} \quad (\text{A.3})$$

$$\Delta t_{cmm}(i) = \frac{[T_{cc}(i) - tcc(i)] - [T_{cc}(i) - tci(i)]}{\ln\left\{\frac{[T_{out}(i) - tco(i)]}{[T_{cc}(i) - tcc(i)]}\right\}} \quad (\text{A.4})$$

where, $tci(i)$ and $tcc(i)$ are the inlet and outlet cooling water temperature of the condensing zone, $tco(i)$ is the outlet cooling water temperature of the desuperheating zone, $T_{out}(i)$ is the temperature of the steam leaving turbine i , $T_{cc}(i)$ is the saturated temperature of the steam at the vacuum pressure in condenser i .

The enthalpy of the steam leaving turbine i is calculated by,

$$H_{out}(i) = H_{in}(i) - (H_{in}(i) - H_{is}(i))\eta_{is}(i) \quad (\text{A.5})$$

where $H_{in}(i)$ and $H_{out}(i)$ is specific enthalpy of steam entering and leaving turbine i respectively, $H_{is}(i)$ is specific enthalpy of steam at the outlet pressure having the same entropy as the inlet steam in turbine i , $\eta_{is}(i)$ is the isentropic efficiency of turbine i . The expressions for the relationship among the temperature, pressure and specific enthalpy of steam in IAPWS-IF 97 (2007) are employed to calculate $H_{in}(i)$, $H_{out}(i)$, $H_{is}(i)$ with the temperature and pressure of steam in the corresponding condenser.

Power generation of condensing turbine i ($W_t(i)$) is calculated by Eq. (13).

$$W_i(i) = m_s(H_{in}(i) - H_{out}(i))\eta_m(i) \quad (\text{A.6})$$

where $m_s(i)$ is the mass flowrate of steam into turbine i , $\eta_m(i)$ is the mechanical efficiency of turbine i .

References

- G. Barigozzi, A. Perdichizzi and S. Ravelli, 2014, Performance Prediction and Optimization of a Waste-To-Energy Cogeneration Plant with Combined Wet and Dry Cooling System, Applied Energy, 115, pp. 65–74.
- M.M. Castro, T.W. Song and J.M. Pinto, 2000, Minimization of Operational Cost in Cooling Water Systems, Trans IChemE, 78 (part A), pp. 192-201.
- G.F. Cortinovia, J.L. Paiva, T.W. Song and J.M. Pinto, 2009, A Systemic Approach for Optimal Cooling Tower Operation, Energy Conversion and Management, 50, pp. 2200-2209.
- M. Laković, M. Banjac and M. Jovic, 2015, Improving the Energy Efficiency of the Coal Fired Power Plant by Adjusting the Hydraulic Load of the Cooling Tower System, Sci-Afric J. Sci. Issues. Res. Essays, 3(12), pp. 873-880.
- F. Song, N. Zhang and R. Smith, 2017, Chapter 3 Operational Optimisation of Recirculating Cooling Water Systems, PhD thesis, the University of Manchester.
- Y.F. Wang, M. Pan, I. Bulatov, R. Smith and J.K. Kim, 2012, Application of Intensified Heat Transfer for the Retrofit of Heat Exchanger Network, Applied Energy, 89, pp.45–59.

Parameter Estimation of Biosurfactant Production from Agro-industrial Waste Using Genetic Algorithm

Ana Luiza Campos^a, Júlia Nogueira^a, Filipe A. Coelho^b, Brunno F. Santos^{*a}

^a *Department of Chemical and Materials Engineering, Pontifical Catholic University of Rio de Janeiro (PUC-Rio), Rua Marquês de São Vicente, 225, Gávea, Rio de Janeiro, RJ 22452-900, Brazil.*

^b *School of Chemical Engineering (FEQ), Department of Chemical Systems Engineering (DESO), University of Campinas (UNICAMP). Rua Albert Einstein, 500 – Cidade Universitária, Campinas – SP, 13083-852, Brazil.*

bsantos@puc-rio.br

Abstract

Although various kinds of kinetic models were proposed to describe the dynamic behaviour of biologically reacting systems, very little studies have been carried about biosurfactant formation. Its sustainable production, in renewable culture medium, is even more complex. In this sense, emerges the Genetic Algorithm (GA), an effective stochastic global search algorithm inspired in the evolution theory that has been showing a great potential to find optimal solutions in complex systems. This work aims to evaluate the GA's estimation of parameters involved in biosurfactant production from agro-industrial waste using *Bacillus subtilis*. Three different models were proposed to describe biomass growth, substrate consumption, biosurfactant synthesis and dissolved oxygen in the medium. The technique's quality was evaluated by the sum of squared errors (SSE) and correlation coefficient (R^2). The results indicated that the best model to describe the system's dynamics obtained SSE lower than 1 and R^2 superior to 0.97 for almost all the variables.

Keywords: Genetic Algorithm; Biosurfactant Production; Agro-industrial Waste.

1. Introduction

Biosurfactants are surface active molecules that have several applications in petrochemical, food and cosmetics industries, besides an important role in environmental protection, oil spills control, biodegradation, and detoxification of oil contaminated industrial effluents and soil (Khopade et al., 2012). Multiple microorganisms are capable to synthesize biosurfactants from renewable sources that includes agro-industrial wastes such as wheat bran, glycerol from biodiesel synthesis, corn steep liquor and potato peels (Amodu et al., 2016).

Even though many studies have been reported about biosurfactant synthesis, very restricted information is available with respect to its kinetic production, as well as renewable substrate's consumption. This knowledge is essential to optimize and economically favour biosurfactant production in industrial scale, still considered an expensive process.

However, math modelling is complicated once it deals with the metabolism of living organisms, which makes system's behaviour slightly predictable. In these cases,

numerical methods based on gradient are not applied because they often get stuck at local minima. On the other hand, Artificial Intelligence is employed to model and optimize high complexity systems, such as biochemical processes, where the use of exact methods are considerably limited (Link & Weuster-Botz, 2006, Pappu & Gummadi, 2017, Dhanarajan et al., 2017). Stochastic approaches, as Genetic Algorithm, are appreciably strong and effective for its purpose. They are considered the most proper way to find the optimal solution since they are based on probability rules (Chowdhury & Garai, 2017).

This work aims to find the best kinetic model to describe substrate consumption, biomass growth, product formation and dissolved oxygen concentration of a biosurfactant production process performed by *Bacillus subtilis* in renewable medium. The model that best represent the set of variables had its parameters estimated using GA as the global optimum search mechanism.

2. Process Description

The experimental procedure was developed by Santos (2015) and the data was used to model and optimize system's behaviour. The fermentation was carried by *Bacillus subtilis* in a residual glycerine and peel beet broth medium for 24 h. The computational method was realized in MATLAB R2017a with the aid of Global Optimization Toolbox. The optimization function pursues the minimization of the sum of quadratic errors between the experimentally determined concentrations and those obtained through the GA. The tested models were adapted from Monod's (1942), Ghose-Tyagi's (1979) and Megee's et al. (1972) original proposals. At the end of the simulation, the code exhibits the optimized parameters, variable's graphical trend, SSE and R².

2.1 General Equations

The mass balance equations in batch bioreactor that describe the biomass growth, substrate consumption, and dissolved oxygen are listed by Eq. (1) to Eq. (4).

$$\frac{dX}{dt} = \mu_x X \quad (1)$$

$$\frac{dS}{dt} = -\mu_S X + \frac{1}{2} k_1 S_C^k - \mu_{mO_2} S P^n \quad (2)$$

$$\frac{dC_{O_2}}{dt} = k_L a (C_{O_2s} - C_{O_2}) - Q_{O_2} X \quad (3)$$

$$Q_{O_2} = m_o + \frac{\mu_x}{Y_o} \quad (4)$$

where X, S and P are biomass, substrate and biosurfactant concentrations (g L⁻¹), respectively. Additionally, μ_x and μ_S are the specific growth and substrate rates (h⁻¹), S_C is the sucrose concentration (g L⁻¹), μ_{mO_2} is the maximum oxygen consume rate (h⁻¹) and n, k and k_1 are kinetic parameters. The variable $k_L a$ refers to oxygen's volumetric transfer coefficient (h⁻¹), C_{O_2s} is the saturated oxygen concentration (g L⁻¹), Q_{O_2} is the specific consumption rate (g_{O₂} g_{cells}⁻¹ h⁻¹), m_o is the gas' maintenance coefficient (g_{O₂} g_{cells}⁻¹ h⁻¹) and Y_o is the conversion factor to cells (g_{O₂} g_{cells}⁻¹).

2.2 Individual Model Equations

As this paper works with different proposals for microorganism behaviour, the particular equations of each model are exhibited in Table 1. Monod indicated that

specific growth rate depends only on substrate concentration while Ghose-Tyagi suggested that the reaction product could be an inhibitory factor and Megee proposed that the microorganism may consume two different substrates.

Table 1. Individual equations for each tested model.

	Monod	Ghose-Tyagi	Megee
μ_x	$\mu_m \frac{S}{(K_S + S)}$	$\mu_m \frac{S}{(K_S + S)} (1 - \frac{P}{K_p})$	$\mu_m \frac{S_1 S_2}{(K_{S1} + S_1)(K_{S2} + S_2)}$
μ_s	$Y_{xs} \mu_{O_2} \frac{S}{(m_S + S)}$	$Y_{xs} \mu_{O_2} \frac{S}{(m_S + S)}$	$\frac{\mu_x}{Y_{xs}} + m_s$
μ_{O_2}	$\frac{C_{O_2}}{(K_{O_2} + C_{O_2})}$	$\frac{C_{O_2}}{(K_{O_2} + C_{O_2})}$	-
$\frac{dP}{dt}$	$\mu_{O_2} k_3 e^{-m} S^N X - k_2 S P^N$	$k_3 \mu_x X - k_2 S P^N$	$\mu_{O_2} k_3 e^{-m} S^N X - k_2 S P^N$

Notice that μ_m is the maximum specific growth rate (h^{-1}), Y_{xs} is the theoretical biomass yield and K_S and m_S are the saturation constant and maintenance coefficient for substrate (gL^{-1}). The variable μ_{O_2} is the oxygen consumption rate (h^{-1}), K_{O_2} is the oxygen's saturation constant ($g L^{-1}$) and C_{O_2} refers to its concentration ($g L^{-1}$). Finally, k_2 , k_3 , m and N are kinetic parameters and K_p is the inhibition product constant ($g L^{-1}$).

3. Results and Discussion

The kinetic performance of each model for substrate consumption, product formation, cell growth and dissolved oxygen can be measured by R^2 and SSE between the experimental and simulated data. Both decisive criteria are displayed in Table 2. The graphical results for dissolved oxygen and biosurfactant concentrations are exhibited in Figure 1 and Figure 2, respectively. The asterisks represent the experimental values, measured by Santos (2015), and the curves show the dynamic trend calculated by GA.

Once the substrate is consumed by the microorganism, glucose concentration experimental data presented a decrease tendency over 24 h. Ghose-Tyagi's and Megee's models performed the expected decay, stabilizing close to zero in the end of the experiment. The latter best illustrated glucose pattern, achieving $R^2 = 0.9718$. In contrast, Monod's equation did not show the awaited conduct and neither match the experimental data.

The rise and stability of cell concentration during the experiment, was observed in all the simulated models. However, Monod's model was not capable to recognize the existence of an inflection point around 12 h, caused by reduction in growth velocity. On the other hand, both Ghose-Tyagi's and Megee's equations showed trends very near to reality, designing almost perfectly the exponential and stationary phases of biomass growth curve. Yet, R^2 reveals that Megee reached better results.

Every tested model presented a decline pattern for dissolved oxygen in medium. This conduct is expected once biosurfactant is produced by an aerobic route. Although Monod's and Megee's models attained R^2 values close to 1, both reached zero around

10 h of experiment, which do not agree with experimental data. Therefore, neither of them described the awaited behaviour. Ghose-Tyagi's was the only model to correctly predict dissolved oxygen's evolution, obtaining $R^2 = 0.9898$.

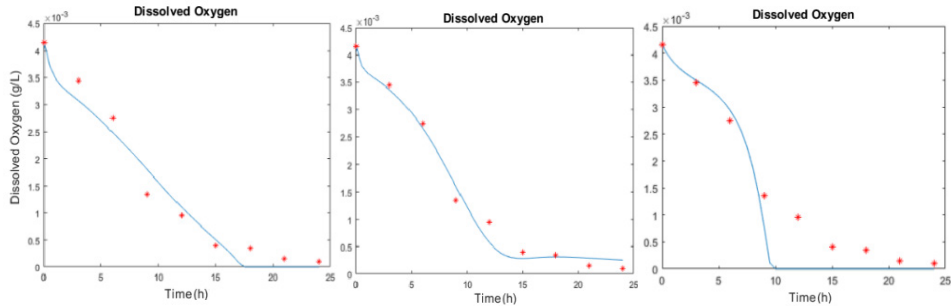


Figure 1. Dissolved oxygen results for Monod, Ghose-Tyagi and Megee models.

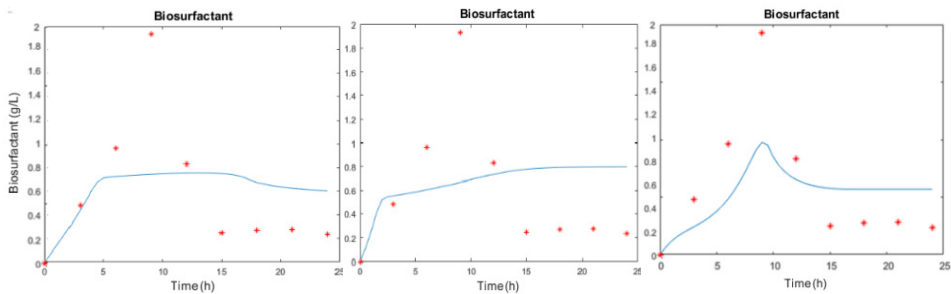


Figure 2. Biosurfactant results for Monod, Ghose-Tyagi and Megee models.

In respect of biosurfactant production, any of the tested models were able to represent the real trend. Experimental data reveals that biosurfactant production initially increases, but around 9 h it switches the behaviour, exhibiting a fall followed by stability. Monod's and Ghose-Tyagi's models were able to keep up only with the firsts experimental points. On the other hand, Megee's model indicated proper conduct, producing a peak right where the experimental data also presented the maximum point. In addition, it shows the subsequent stabilization approximately at the same time as the experimental data.

Considering the system's complexity, little understanding of microorganism metabolism and lack of knowledge about biosurfactant synthesis kinetics, there are great difficulties to express mathematically the process' behaviour. In addition, renewable media are natural sources that have multiple components in different concentrations. The amount and proportion of these substances are not well known and can influence the development of the microorganisms.

Despite the challenge, Megee's model has proved to be promising to further studies in the area. Although improvements in the equations are crucial to achieve better R^2 , the model's ability to represent the product curve similarly to experimental trend is a notable indication that future in-depth analysis should have optimistic results.

Table 2. R² and SSE for each model.

	Monod	Ghose-Tyagi	Megee et al.	
R ²	Glucose	0.7329	0.9521	0.9718
	Biosurfactant	0.2849	0.0399	0.4162
	Biomass	0.7655	0.9885	0.9941
	Dissolved Oxygen	0.9709	0.9898	0.9705
SSE	1.7021	0.8442	0.6059	

The simulations, as well as SSE and R², indicated that, among all the tested models in this work, Megee’s is the most suitable model to portray *Bacillus subtilis*’ biosurfactant production in agro-industrial waste medium. It presented the higher R² for three of the four variables studied and values greater than 0.97 for almost all of them. Moreover, the SSE is the closest to zero of all models. The optimum parameters calculated by GA for Megee’s model are shown in Table 3.

Table 3. Optimum parameters calculated by GA for Megee’s model.

k ₁	k _L a	Y _{xs}	m _S	K _S	μ _{mO2}	K _{O2}	μ _m	k ₃
0	0.9151	6.75	0.0528	0.2695	0.4179	0.0152	10.50	43.90
m _o	Y _o	N	K	k ₂	K _p	N	M	
0.0083	32.96	0.7828	17.67	0.2651	23.07	1.739	0.1625	

4. Conclusion

Computer simulations are essential to optimize and reduce the costs of biosurfactant production in industrial scale. In this sense, Artificial Intelligence methods such as GA are usually applied. In this paper, three different kinetic models were tested for biosurfactant synthesis from *Bacillus subtilis* in agro-industrial waste growth medium through optimization strategy. Glucose, biomass and dissolved oxygen concentrations had great fitting values in all models. In contrast, the lack of knowledge about biosurfactant production kinetics together with the unpredictability of microorganism metabolism causes great obstacles for math modelling this variable’s behaviour. Still, Megee’s model showed to be promising to further studies. Despite the complexity, the simulations showed optimistic results: SSEs for all models were below 2, implying the errors were acceptable, and most R² near to 1, emphasising the ability to anticipate the experimental data. Although further studies are necessary to better understand the microorganism metabolism in complex growing medium and improvements in the equations are vital, Genetic Algorithm as optimization strategy was satisfactory to provide the model parameters.

References

O. Amodu, T. Ojumu, S. Ntwampe, 2016, Kinetic Modelling of Cell Growth, Substrate Utilization, and Biosurfactant Production from Solid Agrowaste (*Beta vulgaris*) by *Bacillus licheniformis* STK 01, The Canadian Journal of Chemical Engineering, 94, 2268-2275.

- B. Chowdhury, G. Garai, 2017, A review on multiple sequence alignment from the perspective of genetic algorithm, *Genomics*, 109, 419-431.
- G. Dhanarajan, V. Rangarajan, C. Bandi, A. Dixit, S. Das, K. Ale, R. Sen, 2017, Biosurfactant-biopolymer driven microbial enhanced oil recovery (MEOR) and its optimization by an ANN-GA hybrid technique, *Journal of Biotechnology*, 256, 46-56.
- T. Ghose, R. Tyagi, 1979, Rapid ethanol fermentation of cellulose hydrolysate - Product and substrate inhibition and optimization of fermentor design. *Biotechnology and Bioengineering*, 21, 1401-1420.
- A. Khopade, B. Ren, X. Liu, K. Mahadik, L. Zhang, C. Kokare, 2012, Production and Characterization of Biosurfactant from Marine *Streptomyces* species B3, *Journal of Colloid and Interface Science*, 367, 311-318.
- H. Link, D. Weuster-Botz, 2006, Genetic algorithm for multi-objective experimental optimization, *Bioprocess and Biosystems Engineering*, 29(5-6), 385-390.
- R. Megee, J. Drake, A. Fredrickson, H. Tsuchiya, 1972, Studies in intermicrobial symbiosis *S. cerevisiae* and *L. casei*. *Canadian J. Microbiol.*, 18, 1733-1742.
- J. Monod, 1942, *Recherches sur la Croissance des Cultures Bacteriennes*, Hermann & Cie., Paris.
- S. Pappu, S. Gummandi, 2017, Artificial neural network and regression coupled genetic algorithm to optimize parameters for enhanced xytol production by *Debaryomyces nepalensis* in bioreactor, *Biochemical Engineering Journal*, 120, 136-145.
- B. Santos, 2015, Study of biosurfactant production using agro-industrial waste with development of statistical models and soft sensor by artificial neural network. Doctoral Thesis– University of Campinas. Campinas/SP-Brazil.

Comparison of reformulations of the Duran-Grossmann model for Work and Heat Exchange Network (WHEN) synthesis

Haoshui Yu, Matias Vikse, Truls Gundersen*

*Department of Energy and Process Engineering, Norwegian University of Science and Technology, Kolboern Hejes v. 1A, NO-7491 Trondheim, Norway
truls.gundersen@ntnu.no*

Abstract

Work and Heat Exchange Networks (WHENs) have received increasing attention from both researchers and engineers during the last 5-10 years. The Duran-Grossmann model (Duran and Grossmann, 1986) can deal with heat integration problems with variable process streams. In WHENs, however, the identity of streams (hot/cold) can also change. Therefore, a revised Duran-Grossmann model applied to WHENs without knowing the identity of streams a priori is proposed. The revised Duran-Grossmann model consists of both binary variables and non-smooth functions. To facilitate the solution of the model, the non-smooth functions (max operators) can be reformulated in three ways. The first method is to reformulate the max operator using a Smooth Approximation (Balakrishna and Biegler, 1992). This function incorporates a small parameter, which may lead to either an ill-conditioned approximation or loss of accuracy if poorly chosen. The second method is using Explicit Disjunctions based on principles of the Duran-Grossmann model (Grossmann et al., 1998). To avoid using a max operator, disjunctions explicitly revealing the relationship between the stream inlet/outlet temperatures and pinch candidate temperatures are applied. The last method reformulates the max operator with Direct Disjunctions (Quirante et al., 2017). The max operator picks up the maximum value of two variables, thus it can be straightforward reformulated by a disjunctive programming approach. Even though these three reformulations of the Duran-Grossmann model have been previously investigated, considering uncertain stream identities applied to WHENs has not yet been reported. In this study, all the reformulations and models are implemented in the GAMS (Brooke et al., 1998) modelling framework. For a case study without isothermal streams, Smooth Approximation performs better than the other two formulations.

Keywords: Duran-Grossmann Model, Reformulations, Work and Heat Exchange Networks, Disjunctive Programming, MINLP

1. Introduction

Heat integration focusing on reducing hot/cold utilities is an important technique because thermal energy contributes significantly to the total cost of a process (Huang and Karimi, 2013). If heat integration and process optimization are performed simultaneously, more benefits can be obtained. Duran and Grossmann proposed a mathematical model for simultaneous process optimization and heat integration (Duran and Grossmann, 1986). The Duran-Grossmann model is a powerful tool to solve the heat integration problem with variable process streams. This model has been

successfully applied to organic Rankine cycles system recovering low-temperature waste heat (Yu et al., 2017a), processes for liquefaction of natural gas (Wechsung et al., 2011), and fuel cell systems (Marechal et al., 2005).

Temperature and pressure are both important parameters in the chemical industry. If the pressure is considered while designing Heat Exchange Networks (HENs), the new topic Work and Heat Exchange Networks (WHENs) arise. Pressure specifications on the process streams make the problem more challenging compared with conventional HENs. Holiastos and Manousiouthakis (2002) proposed a mathematical model minimizing hot/cold/work utility cost for HENs. They proposed the term “work utility”, which refers to the generation or consumption of work (electricity or shaft work). Fu and Gundersen (2015a) presented a systematic graphical design procedure for integration of compressors in HENs above ambient temperature. They concluded that compression should be performed at pinch or ambient temperature to achieve minimum exergy consumption. Fu and Gundersen also studied the integration of expanders into heat exchanger networks above (Fu and Gundersen, 2015b) and below (Fu and Gundersen, 2015c) ambient temperature. These studies have similar conclusions about how to optimally integrate pressure changing streams into a background process with minimum exergy consumption. Wechsung et al. (2011) combined Pinch Analysis, Exergy Analysis, and Mathematical Programming to synthesize HENs below ambient temperature with compression and expansion of process streams. The pinch operator is based on the simultaneous heat integration and process optimization idea proposed by Duran and Grossmann (1986).

Since the thermodynamic path and the identity (hot/cold) of process streams are uncertain in WHENs, classical heat integration methods cannot be applied. **In addition**, the identity of streams can also temporarily change in WHENs. This paper mainly applies a revised Duran-Grossmann model to WHENs without knowing the identity of streams a priori. There are three different reformulations for the revised Duran-Grossmann model. This study mainly focuses on the effect of reformulation on revised model.

2. Mathematical model

The WHENs problem can be stated as follows: Given a set of process streams with supply state and target state (temperature, pressure), as well as hot, cold and power utilities; design a network consisting of heat transfer equipment such as heat exchangers, heaters and coolers, and pressure manipulation equipment such as expanders, compressors, pumps and valves with minimum Exergy Consumption or Total Annual Cost.

Since the identity of streams in the WHEN is unknown a priori, the Duran-Grossmann model cannot be applied directly and is extended to a new model using binary variables to denote the identity of streams. In the extended Duran-Grossmann model, separate sets of hot and cold streams no longer exist. Binary variables are used to distinguish hot and cold streams automatically in the model. The extended Duran-Grossmann model is formulated as follows.

Min obj = Exergy Consumption

$$\text{s.t. } h(\omega, x) = 0 \quad (1)$$

$$g(\omega, x) \leq 0 \quad (2)$$

$$T_s^p = T_s^{in} + y_s \cdot HRAT \quad (3)$$

$$QSOA(x)^p = \sum_{s \in S} (1 - y_s) FCp_s \left[\max \{0, T_s^{in} + y_s \cdot HRAT - T^p\} - \max \{0, T_s^{out} + y_s \cdot HRAT - T^p\} \right] \quad (4)$$

$$QSIA(x)^p = \sum_{s \in S} y_s \cdot FCp_s \left[\max \{0, T_s^{out} + y_s \cdot HRAT - T^p\} - \max \{0, T_s^{in} + y_s \cdot HRAT - T^p\} \right] \quad (5)$$

$$Z_H^p(x) = QSIA(x)^p - QSOA(x)^p \quad (6)$$

$$Z_H^p(x) \leq Q_{HU} \quad (7)$$

$$\Omega(x) + Q_{HU} - Q_{CU} = 0 \quad (8)$$

$$\Omega(x) = \sum_{s \in S} (1 - y_s) FCp_s (T_s^{in} - T_s^{out}) - \sum_{s \in S} y_s \cdot FCp_s (T_s^{out} - T_s^{in}) \quad (9)$$

x represents the flow rates and temperatures of the streams involved in heat integration. ω represents all other process variables. Eqs. (1) and (2) denote the process constraints. y_s is a binary variable to denote the identity of any stream $s \in S$, where $y_s = 1$ is used for cold streams. $QSOA$ and $QSIA$ denote the heat load of hot and cold streams above each pinch candidate $p \in P$. $Z_H^p(x)$ is heat deficit above each pinch candidate. $\Omega(x)$ is the heat load difference between hot and cold streams. $HRAT$ denotes the heat recovery approach temperature. The objective function is minimizing the exergy consumption of the system. A detailed model description is beyond the scope of this paper and will be presented as an extended journal publication.

3. Model reformulation

The new model incorporates max operators in Eqs. (4) and (5), which result in non-differentiabilities at T^p . Max operators represent a challenge for deterministic solvers and have to be removed before solving the model. In this study, three methods are proposed to reformulate the model.

3.1. Smooth Approximation

A method using smooth approximations is proposed by Balakrishna and Biegler (1992). Yu et al. (2017b) applied this smooth approximation to design an ORC system recovering waste heat. The max operator is smoothed by the approximation shown in Eq. (10), which can be used to replace the max operators in Eqs. (4) and (5).

$$\max \{0, x\} \cong \frac{1}{2} (x + \sqrt{x^2 + \varepsilon}) \quad (10)$$

ε is a small constant, typically between 10^{-3} and 10^{-6} .

3.2. Explicit Disjunction

To remove the nonsmooth max operator in the Duran-Grossmann model, Grossmann et al. (1998) proposed a disjunctive formulation. The key idea of the disjunctive formulation is the explicit treatment of three possibilities for process stream temperatures: a process stream is totally above, totally below or across the pinch

candidate temperature. As a result, the disjunctions in Eq. (11) can be applied to replace the max operators in Eqs. (4) and (5). R is a large enough parameter to relax the corresponding constraints for hot or cold streams.

$$\left[\begin{array}{c} Y1_{sp} \\ T_s^{in} + y_s \cdot HRAT \geq T^p \\ T_s^{out} + y_s \cdot HRAT \geq T^p \\ T_s^{in,p} = T_s^{in} + y_s \cdot HRAT - T^p \\ T_s^{out,p} = T_s^{out} + y_s \cdot HRAT - T^p \end{array} \right] \vee \left[\begin{array}{c} Y2_{sp} \\ T_s^{in} + y_s \cdot HRAT \geq T^p - y_s \cdot R \\ T_s^{out} + y_s \cdot HRAT \geq T^p - (1 - y_s) \cdot R \\ T_s^{in} + y_s \cdot HRAT \leq T^p + (1 - y_s) \cdot R \\ T_s^{out} + y_s \cdot HRAT \leq T^p + y_s \cdot R \\ T_s^{in,p} = (1 - y_s)T_s^{in} - (1 - y_s)T^p \\ T_s^{out,p} = y_s \cdot T_s^{out} + y_s \cdot HRAT - y_s \cdot T^p \end{array} \right] \vee \left[\begin{array}{c} Y3_{sp} \\ T_s^{in} + y_s \cdot HRAT \leq T^p \\ T_s^{out} + y_s \cdot HRAT \leq T^p \\ T_s^{in,p} = 0 \\ T_s^{out,p} = 0 \end{array} \right] \quad (11)$$

$$QSOA(x)^p = \sum_{s \in S} (1 - y_s) FCP_s(T_s^{in,p} - T_s^{out,p}); \quad QSLA(x)^p = \sum_{s \in S} -y_s \cdot FCP_s(T_s^{in,p} - T_s^{out,p})$$

The disjunctive model can be reformulated by the Big-M method or convex hull method. In this study, LogMIP (Vecchietti and Grossmann, 2004), a specially designed program for disjunctive programming, is adopted as the solver.

3.3. Direct Disjunction

Recently, Quirante et al. (2017) proposed a novel robust alternative disjunctive reformulation. This reformulation shows better relaxation gaps and reduced number of equations and variables. The max operator is directly replaced by a disjunction without physical insights. This reformulation has fewer Boolean variables compared with the previous disjunctive reformulation by Grossmann et al. (1998). The max operator is expressed as follows:

$$\phi = \max(0, c^T x)$$

To avoid using max operators and smooth approximations, the direct disjunctive model is proposed as follows:

$$\left[\begin{array}{c} Y \\ c^T x \geq 0 \\ \phi = c^T x \end{array} \right] \vee \left[\begin{array}{c} -Y \\ c^T x \leq 0 \\ \phi = 0 \end{array} \right]$$

$$Y \in \{True, False\}$$

Then the above disjunction is applied to Eqs. (4) and (5) in the model. The resulting disjunctions are shown in Eq. (12). The Direct Disjunction model is formulated with Eq. (12) to replace the max operators in the model, and it is also solved by LogMIP.

$$\left[\begin{array}{c} Y_{in} \\ T_s^{in} + y_s \cdot HRAT - T^p \geq 0 \\ \phi_{in} = T_s^{in} + y_s \cdot HRAT - T^p \end{array} \right] \vee \left[\begin{array}{c} -Y_{in} \\ T_s^{in} + y_s \cdot HRAT - T^p \leq 0 \\ \phi_{in} = 0 \end{array} \right]$$

$$\left[\begin{array}{c} Y_{out} \\ T_s^{out} + y_s \cdot HRAT - T^p \geq 0 \\ \phi_{out} = T_s^{out} + y_s \cdot HRAT - T^p \end{array} \right] \vee \left[\begin{array}{c} -Y_{out} \\ T_s^{out} + y_s \cdot HRAT - T^p \leq 0 \\ \phi_{out} = 0 \end{array} \right] \quad (12)$$

$$QSOA(x)^p = \sum_{s \in S} (1 - y_s) FCP_s(\phi_{in} - \phi_{out}); \quad QSLA(x)^p = \sum_{s \in S} -y_s \cdot FCP_s(\phi_{in} - \phi_{out})$$

4. Case study

This case study is adopted from the study by Fu and Gundersen (2015a). The stream data is listed in Table 1. C1 needs to be compressed from 100 kPa to 300 kPa. The hot and cold utilities are supplied at 400°C and 15°C respectively. The model proposed in this study can determine the optimal temperature of C1 before compression. The results are consistent with the study by Fu and Gundersen (2015a). For detailed results, please refer to their study (Fu and Gundersen, 2015a). It should be noted that disjunctive programming models can be reformulated into MINLP models by the Big-M or convex hull methods with LogMIP as the solver for the Explicit and Direct Disjunction models. BARON (Tawarmalani and Sahinidis, 2005) is adopted as the MINLP solver.

Table 1. Stream data for the case study

Stream	T^{sup} (°C)	T^{or} (°C)	FCp (kW/°C)	ΔH (kW)	P^{sup} (kPa)	P^{or} (kPa)
H1	300	50	4	1000	-	-
H2	120	40	4	320	-	-
C1	70	380	3	930	100	300
C2	30	180	3	450	-	-

Table 2 shows the computational performance of each reformulation. It is clear that Smooth Approximation performs much better than the other two reformulations in this case. Smooth Approximation has fewer continuous variables and significant fewer binary variables. The computation time is also considerably less than the other two reformulations. The Direct Disjunction model has more disjunctions and continuous variables but fewer binary variables compared with the Explicit Disjunction model. The convex hull reformulation is better than the Big-M method in this study for both Explicit and Direct Disjunction. This case is a simple and small size problem and only non-isothermal streams are considered. It should be emphasized that the Smooth Approximation might cause numerical problems when isothermal streams or multiple utilities are involved. For cases without isothermal streams, Smooth Approximation performs better than other reformulations. More examples will be tested in future work.

Table 2. Computational results for the case study

Items	Smooth Approximation	Explicit Disjunction		Direct Disjunction	
		Big-M	Convex hull	Big-M	Convex hull
Disjunctions	-	49	49	98	98
Continuous Variables	168	411	908	462	994
Binary Variables	4	151	151	102	102
CPU time (s)	17.5	207.3	196.3	76.6	61.2

5. Conclusions

An extended Duran-Grossmann model is applied to WHENs in this study. Three different reformulations of the model are presented. Even though these three reformulations have been investigated before, reformulations considering uncertain stream identities applied to WHENs have not yet been reported. The computational efforts and results of different reformulations have been compared. For the case study, the results show that the Smooth Approximation outperforms the other two reformulations. However, this case study represents a small size problem. Large problems will be tested in future work. Isothermal process streams and multiple utilities

should also be considered. The small parameter ε in the smooth approximation and the Big-M value in the disjunctive programming models have significant influence on the solution of the problems. More detailed investigations will be performed in future work.

Acknowledgments

This publication has been funded by HighEF-Centre for an Energy Efficient and Competitive Industry for the Future. The authors gratefully acknowledge the financial support from the Research Council of Norway and user partners of HighEFF, an 8 year Research Centre under the FME-scheme (Centre for Environment-friendly Energy Research, 257632/E20).

References

- S. Balakrishna, L.T. Biegler, 1992, Targeting strategies for the synthesis and energy integration of nonisothermal reactor networks, *Industrial & Engineering Chemistry Research*, 31(9), 2152-2164.
- A. Brooke, D. Kendrick, R. Raman, 1998, GAMS: A User's Guide, release 2.50, Washington DC: GAMS Development Corporation.
- M.A. Duran, I.E. Grossmann, 1986, Simultaneous optimization and heat integration of chemical processes, *AIChE Journal*, 32(1), 123-138.
- C. Fu, T. Gundersen, 2015a, Integrating compressors into heat exchanger networks above ambient temperature, *AIChE Journal*, 61(11), 3770-3785.
- C. Fu, T. Gundersen, 2015b, Integrating expanders into heat exchanger networks above ambient temperature, *AIChE Journal*, 61(10), 3404-3422.
- C. Fu, T. Gundersen, 2015c, Sub-ambient heat exchanger network design including expanders, *Chemical Engineering Science*, 138, 712-729.
- I.E. Grossmann, H. Yeomans, Z. Kravanja, 1998, A rigorous disjunctive optimization model for simultaneous flowsheet optimization and heat integration, *Computers & Chemical Engineering*, 22, S157-S164.
- K. Holiastos, V. Manousiouthakis, 2002, Minimum hot/cold/electric utility cost for heat exchange networks, *Computers & Chemical Engineering*, 26(1), 3-16.
- K.F. Huang, I.A. Karimi, 2013, Simultaneous synthesis approaches for cost-effective heat exchanger networks, *Chemical Engineering Science*, 98, 231-245.
- F. Marechal, F. Palazzi, J. Godat, D. Favrat, 2005, Thermo-Economic Modelling and Optimisation of Fuel Cell Systems, *Fuel Cells*, 5(1), 5-24.
- N. Quirante, J.A. Caballero, I.E. Grossmann, 2017, A novel disjunctive model for the simultaneous optimization and heat integration, *Computers & Chemical Engineering*, 96, 149-168.
- M. Tawarmalani, N.V. Sahinidis, 2005, A polyhedral branch-and-cut approach to global optimization, *Mathematical Programming*, 103(2), 225-249.
- A. Vecchiotti, I.E. Grossmann, 2004, Computational experience with LogMIP solving linear and nonlinear disjunctive programming problems. In *Proc. Foundation on Computer Aided Process Design, FOCAPD*, Princeton, NJ.
- A. Wechsung, A. Aspelund, T. Gundersen, P.I. Barton, 2011, Synthesis of heat exchanger networks at subambient conditions with compression and expansion of process streams, *AIChE Journal*, 57(8), 2090-2108.
- H. Yu, J. Eason, L.T. Biegler, X. Feng, 2017a, Process integration and superstructure optimization of Organic Rankine Cycles (ORCs) with heat exchanger network synthesis, *Computers & Chemical Engineering*, 107, 257-271.
- H. Yu, J. Eason, L.T. Biegler, X. Feng, 2017b, Simultaneous heat integration and techno-economic optimization of Organic Rankine Cycle (ORC) for multiple waste heat stream recovery, *Energy*, 119, 322-333.

Semantic Networking Facility for the Biorefining Community

Edlira Kalemi^a, Linsey Koo^a, Franjo Cecelja^a

*^aProcess & Information Systems Engineering Research Centre, University of Surrey,
Guildford, Surrey, GU2 7XH, United Kingdom.*

e.kalemi@surrey.ac.uk

Abstract

Biorefining is a dynamic field with ever growing number of computer models developed, heterogeneous data acquired and generally new knowledge generated in large volumes, all to serve functions at different scales and for different purposes. Sharing and reusing of these resources, especially models and data, inherently saves developing time, but also enables solving ever more complex problems and addressing ever more complex functions. This, in turn, necessitates efficient networking tool to allow for publishing, discovery, but also inferring new knowledge and integration of resources, dominantly computer models.

This paper introduces a semantic networking facility developed to enable an efficient reuse and sharing of knowledge and resources in the domain of biorefining. This networking facility, which is built around model integration platform, allows for knowledge and other resources in the domain of biorefining to be accessible by humans, but also by agents and services. It is organised as a collaborative, WiKi like platform, aiming to facilitate collaboration and to bring biorefining community together by sharing knowledge and resources. The operation of the proposed facility is supported by a biorefining domain ontology, but also by Semantic Media Wiki extension. The features of the Biorefining Semantic Wiki include semantic repository of the biorefining models, model discovery and integration tool, supply chain networking and demonstration, documentation, including published article repository and discovery, forum for the community and with active social media of the biorefining community. The operation of Biorefining Semantic Wiki has been implemented as a semantic web service and its operation verified in practice.

Keywords: wiki, semantic technologies, biorefining community, knowledge sharing

1. Introduction

There is lack of online knowledge sharing and collaboration environments in the domain of biorefining despite the fact that the benefits of these have been widely acknowledged. The field of biorefining comes with a vast amount of heterogeneous models and data in different formats and produced by different developments and for different purposes, which have potential to be available to share and reuse. To this end, we propose a semantic networking facility developed to enable an efficient reuse and sharing resources whilst providing access to the knowledge in the domain of biorefining to both humans and machines. The operation of the proposed facility is supported by the biorefining domain ontology (Koo et al., 2017b), Web Ontology Language Semantic Mark-Up for Services (OWL-S) framework and Media Wiki extended by Semantic

Media Wiki which annotates the pages with machine processable information. Main services include i) semantic repository for biorefining datasets and models, ii) model and data discovery and integration tool, iii) repository of publications and recorded documentation and respective discovery facility, iv) repository of practical experimentation, implementation and case studies, and v) forum for the community including active social media of the biorefining community (Figure 1). Implemented as a multilingual web service, the proposed facility serves different categories of users; i) administrator ensuring a smooth operation, ii) editor auditing contributions and changes, iii) publications authors, iv) contributor of datasets and other resources, and v) subscribers benefiting directly from the facility.

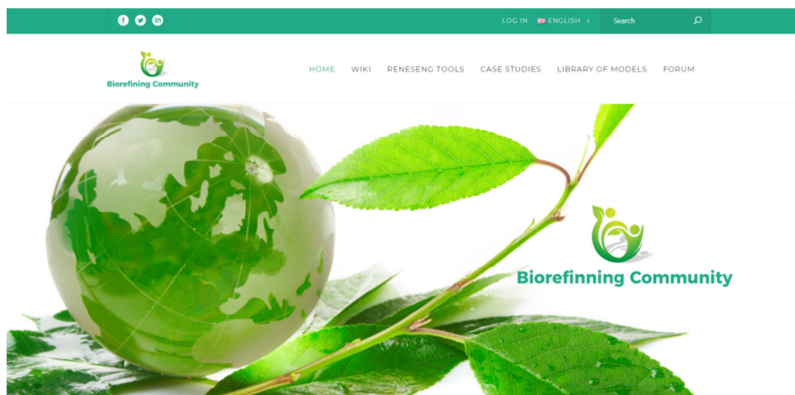


Figure 1 Homepage of the Semantic Networking Facility.

2. The Architecture and Features

2.1. Semantic repository of biorefining models

Important component of this facility is the biorefining dataset and model repository at different scales. The repository is populated by users the biorefining community members, who want to share model(s) or data. Each model and dataset is considered as a web service and is semantically described in terms of its functionality, inputs required for a successful execution, outputs generated in the course and after the execution, and preconditions for the model to run. This knowledge is acquired through a registration phase where model descriptions are registered as the ontology instances. The actual models and datasets remain with the owner and assuring a full ownership hence further motivating sharing with no risk of losing the respective intellectual proprietary or commercial value. In terms of technology this is accomplished by using OWL-S framework (Martin et al. 2007), a set of interlinked ontologies for semantically describing web services and combined with the biorefining domain ontology InterCAPEmodel (Koo et al., 2017a). To this end the InterCAPEmodel ontology provides i) classification and relations for semantically describing datasets and models for the purpose of registration, and ii) common vocabulary for model and dataset discovery and integration (Koo et al., 2017a).

2.2. Model discovery and integration tool

Efficient discovery and integration of biorefining models and data remain to be a challenging task due to the large amount as well as the heterogeneity. The process has

been developed by the CAPE-OPEN standard which supports model reusability and interoperability (Braunschweig et al., 2004). Still, efficiency and flexibility in model and data discovery and hence integration remains a challenge primarily because the model interface semantics are implicit, understandable by humans, but difficult to allow for automation controlled by machines. In order to automate model discovery and subsequently model integration, we propose a semantic service which annotates biorefining models with a machine readable description. To this end, models and data are semantically described using the key parameters and during the registration stage when the semantic repository is populated. The discovery process is supported by the well-established OWL-S framework and relies on the semantic annotation of models and data, and the input/output matching approach introduced by Cecelja et al. (2015). Here, the input/output matching is a two-stage matching process including i) matching the tacit properties established by calculating similarity measures which define the level of compatibility between the requesting and candidate models and data ii) matching the explicit properties by input/output property matching, and iii) ranking of the candidate models by their similarity measure. A dedicated Input/Output matchmaker is developed in JAVA performing matching and ranking by the level of semantic similarity.

2.3. Biorefining Semantic Wiki

Wikis are a very popular collaboration tool operation on the web and many online communities employ wikis to exchange knowledge. Wiki manage online content in a quick and easy way, mainly as plain text. Best known example of Wiki is Wikipedia. In terms of technology and implementation Wikipedia is powered by Media Wiki engine, open software initially developed for Wikipedia and later on used by many wiki projects. Although the data in this Wikis is structured, it is unclear to computers because it is not represented in a machine-processable way. Users can easily link between two articles in wikis to indicate a relationship but not so to indicate the nature of that relationship in a way that is computationally accessible to the system or to external developers. To improve this a wiki can use the Semantic Media Wiki (SMW) extension which enables to semantically annotate wiki pages with explicit, machine-readable information, based on which the wiki contents can be browsed, searched, and reused in novel ways. The representation difference between a wiki and a semantic wiki is illustrated in Figure 3 with the case of an article about London (Figure 2) and giving specific information about it as area and population. Annotation of pages in SMW is established using properties and types. Properties are used to express binary relationships between one semantic entity (as represented by a wiki page) and some other such entity or data value (Krötzsch et al., 2007).



The image shows a screenshot of a Semantic Media Wiki (SMW) page for "London". The page is titled "London" and includes a navigation menu on the left with options like "Main Page", "People", "Events", "Help", "browse", "RDF Feeds", and "Recent changes". The main content area displays a paragraph: "London is the capital of [England](#) and of the [UK](#). As of [2005](#), the total resident population of London was estimated [7,421,328](#). Greater London covers an area of [609 square miles](#)." Below this, there is a "Facts about London" section with a table of properties and values:

Property	Value
Area	1.5773e+9 m ² (157,730.276 ha, 1,577.303 km ² , 609 miles ²)
Capital of	England, and United Kingdom
Population	7,421,328

The "Category" is listed as "City". The page also includes a "Log in / create account" link in the top right corner and tabs for "article", "discussion", "edit", and "history".

Figure 2 A semantic view of London from Krötzsch et al 2007.

A semantic wiki is set up and integrated with the proposed facility where experts of the domain can use this dedicated online space to publish the output of their work in the form of scientific articles, case studies or other forms, participate in discussions and contribute in or benefit from the advancement of the biorefining field.

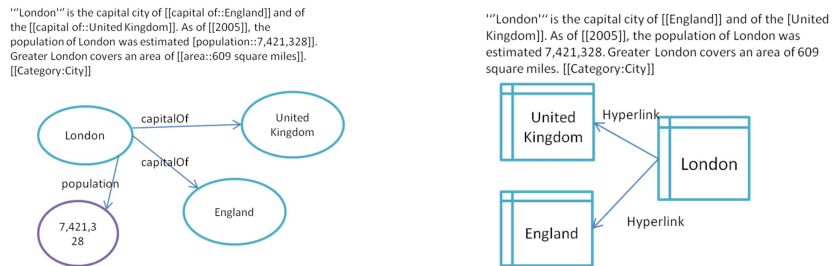


Figure 3 A page about London in MediaWiki (right) and in SMW (left).

The use of semantic annotation becomes beneficial when exploiting the semantics described in those annotations. SMW offers several features for that. In the example of London from Figure 2 is shown also a section called *Factbox* which summarises the given annotations *area*, *capital of* and *population*. The *Factbox* supports browsing the wiki based on its semantic content by showing the annotations (reference) in that page, all annotations where the given page is used as value and performing an inverse search for all pages with similar annotations by using the magnifier icon behind each value (Figure 2). The *RDF Feed* link in the *Factbox* allows exporting data in RDF format.

SMW includes as well a query language to access the wiki knowledge and the possibility to map all formal semantics of annotations to the OWL DL ontology language. SMW query language can be used to directly query the wiki, or to add the answer to a page by creating an inline query. In the OWL DL mapping all normal pages correspond to abstract individuals, properties correspond to OWL properties, categories correspond to OWL classes, and property values can be abstract individuals or typed literals using appropriate URIs as identifiers to prevent confusion with URLs of the wiki's HTML documents.

All together and with the compatibility to both OWL and RDF this enables a maximal reuse of SMW's data.

2.4. Forums and social profiles

The forum for sharing knowledge, ideas and solutions to different problems that the individuals of the community face in their research is part of the semantic networking facility in a dedicated area. The forum is managed and maintained by an administrator but the users are free to share their opinions and to create new topics for discussion or to ask for help and support from experts of the biorefining domain.

Social profiles of Facebook, Twiteer and LinkedIn are integrated with the semantic publishing facility and the biorefining community can easily share the contents of the biorefining domain with other networks. Further, if the users own an FOAF ("friend of a friend") (Kalemi and Martiri 2011) profile or would like to use the FOAF ontology to say thing about people of the community and their relation with other people or objects, they can accomplish this by importing the ontology in the semantic wiki. FOAF is ontology to describe people and their social network in a semantic way. FOAF could get used within many wikis for annotating user pages, or describing articles about people.

3. Use Cases

3.1. Discovering models

The following is a use case of model discovery for the purpose of model integration. As the first step (Figure 4, Step 1) the user defines the request which contains the functionality of the requesting model, the characteristics and the inputs that it needs.

Step 1

HOME MODEL REGISTRATION REPOSITORY MODEL DISCOVERY

OWL Tree

- Model By Functionality
 - Functionality For Process Level
 - Conversion Process
 - Thermochemical Process
 - Biochemical Conversion Process
 - Fermentation
 - C6 Fermentation
 - Chemical Conversion Process
 - Combined Conversion Process
 - Separation Process
 - Prefermentation Process

C6 Fermentation

Total Row(s): 50000 Temp: 34 Pressure: 101 Brand Fraction: 0.075

Complexity: Equation Form Scale Modeling Type Modeling Scope

SEARCH FOR MODEL

Step 2

Offered Models

Model	Similarity	Cosine Similarity	Euclidean Similarity	Property Similarity	Aggregated Similarity	Details
MODEL3	0.800	1.000	0.315	0.658	0.729	DETAILS
MODEL3	1.000	1.000	0.988	0.979	0.990	DETAILS
MODEL2	1.000	1.000	0.000	0.900	0.790	DETAILS
MODEL7	0.800	1.000	0.275	0.637	0.718	DETAILS
MODEL3	0.800	1.000	0.416	0.700	0.764	DETAILS
MODEL5	1.000	1.000	0.639	0.820	0.910	DETAILS

Figure 4 Demonstrating model discovery and integration functionality.

As a second step (Figure 4, step 2) a list of candidate models will be listed, ranked based on the quantified semantic relevance between the requesting model and the candidate models that have been previously stored in the repository. Based on this result and other details that come with each candidate model, the user can choose the model that will be integrated with the requesting model.

3.2. Populating the semantic wiki

In this use case we demonstrate how we create a page containing information about a journal article titled “A semantic framework for enabling model integration for biorefining”, define the authors, say thing about the authors using the FOAF ontology terms. In Figure 5 is given the code behind the wiki page that the user sees in Figure 6. Properties as *Has author*, *Has Doi* are self defined and the properties *name*, *mbox* and *homepage* are imported from FOAF ontology.

```

***A semantic framework for enabling model integration for biorefining***<br>
Authors [[Has author:Lineay Roo]] [[Has author:Rikolase Toomas]] [[Has author:Franjo Ceelja]]<br>
[[Has doi:http://dx.doi.org/10.1016/j.comchem.2017.02.004]]<br>
***Abstract***<br>
This paper introduces a new paradigm for establishing a framework that enables interoperability between process models and datasets using ontology engineering. <br>
Semantics are used to model the knowledge in the domain of biorefining including both tacit and explicit knowledge, which supports registration and instantiation of the models and datasets. <br>
Semantic algorithms allow the formation of model integration through input/output matching based on semantic relevance between the models and datasets. In addition, partial matching is employed to facilitate flexibility to broaden the horizon to find opportunities in identifying an appropriate model and/or dataset. The proposed algorithm is implemented as a web service and demonstrated using a case study.<br>
***About authors***<br>
[[foaf:name:Franjo Ceelja]] has email [[foaf:mbox:fr.ceelja@surrey.ac.uk]] and homepage [[foaf:homepage:http://www.surrey.ac.uk/cpe/people/franjo_ceelja/]].

__SHOWFACTBOX__
[[Category:Model Integration]]
[[Category:Person]]
[[Category:FOAF]]
[[Category:Journal Article]]

```

Figure 5 Source code of the wiki text for the Model Integration page.

All the properties and their values are nicely summarised in the Factbox by allowing further browsing of all the information summarized there.

Model Integration

A semantic framework for enabling model integration for biorefining

Authors Linsey Koo Nikolaos Trokanas Franjo Cecelja

<https://doi.org/10.1016/j.comchemeng.2017.02.004>

Abstract

This paper introduces a new paradigm for establishing a framework that enables interoperability between process models and datasets using ontology engineering.

Semantics are used to model the knowledge in the domain of biorefining including both tacit and explicit knowledge, which supports registration and instantiation of the models and datasets.

Semantic algorithms allow the formation of model integration through input/output matching based on semantic relevance between the models and datasets. In addition, partial matching is employed to facilitate flexibility to broaden the horizon to find opportunities in identifying an appropriate model and/or dataset. The proposed algorithm is implemented as a web service and demonstrated using a case study.

About authors

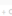
Franjo Cecelja has email f.cecelja@surrey.ac.uk and homepage https://www.surrey.ac.uk/ice/people/franjo_cecelja/.

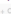
Categories: [Model Integration](#) | [Person](#) | [Foaf](#) | [Journal Article](#)


Facts about "Model Integration"

RDF feed 

Foaf mbox: f.cecelja@surrey.ac.uk 

Foaf homepage: https://www.surrey.ac.uk/ice/people/franjo_cecelja/ 

Foaf name: [Franjo Cecelja](#) 

Has DOI: <https://doi.org/10.1016/j.comchemeng.2017.02.004> 

Has author: [Linsey Koo](#)  , [Nikolaos Trokanas](#)  and [Franjo Cecelja](#) 

Figure 6 View of Model Integration page.

4. Conclusions

A semantic publishing facility has been introduced to bring together the biorefining community. Through this platform the members of biorefining community at different level of expertise can share the results of their work in various formats, models and data, as well as successful case studies. The benefit of using the tools offered by the platform and the solutions are provided from other experts through forums and discussion pages. As future work we plan to improve and add more tools to our list, to enrich the repository of model and article and to motivate the community to be active in all collaborative activities that the platform offer.

Acknowledgements

The authors wish to acknowledge the financial support by the Marie Curie Initial Training Networks Program, under the RENESING project (FP7-607415).

5. References

- B.Braunschweig, E.Fraga, Z.Guessoum, W.Marquardt, O.Nadjemi, D.Paen, , D.Pinol, P.Roux, S.Sama, M.Serra, I.Stalker, A.Yang, 2004. CAPE web services: the COGents way, *Comput. Aided Chem. Eng.*, 18 (C) , pp. 1021–1026
- L.Koo, N.Trokanas, F.Cecelja, 2017b. A semantic framework for enabling model integration for biorefining. *Computers & Chemical Engineering*. Vol. 100, pp. 219
- D.Martin, M.Burstein, O.Lassila, M.Paolucci, T.Payne, S.McIlraith, 2004. Describing Web Services using OWL-S and WSDL. <http://www.daml.org/services/owl-s/1.1/owl-s-wsdl.html>
- M.Krötzsch, D.Vrandecic, M.Völkel, H.Haller, R.Studer, 2007. Semantic Wikipedia. In *Journal of Web Semantics* 5/2007, pp. 251–261. Elsevier.
- F. Cecelja, N. Trokanas, T. Raafat, M. Yu, 2015. Semantic algorithm for Industrial Symbiosis network synthesis. *Computers & Chemical Engineering*, Online.
- E. Kalemi, E. Martiri, 2011. FOAF-Academic Ontology: A Vocabulary for the Academic Community. In *Proceedings of the 2011 Third Int. Conf. on Intelligent Networking and Collaborative Systems (INCOS '11)*. IEEE Computer Society, Washington, DC, USA, 440-445.
- L.Koo, N.Trokanas, A.Panteli, E.Kalemi, N.Shah, M.Bussemaker, F.Cecelja, 2017a. Integration of CAPE Models and Data for the Domain of Biorefining: InterCAPEmodel Ontology Design, *Computer Aided Chemical Engineering*, Vol. 40, pp. 2323

Economic and environmental benefits of waste-based energy closed-loop integration in process industries under uncertainty

Shabnam Morakabatchiankar^a, Kefah Hjaila^b, Fernando D. Mele^c,
Moisés Graells^a, Antonio Espuña^a

^a *Chemical Engineering Department, Universitat Politècnica de Catalunya, EEBE. Av. Eduard Maristany, 10-14, Edifici I, Planta 6, 08019 Barcelona, Spain*

^b *Gaza, Palestine*

^c *Departamento de Ingeniería de Procesos, FACET, Universidad Nacional de Tucuman (UNT), Avenida Independencia 1800, S. M. de Tucumán T4002BLR, Argentina*

shabnam.morakabatchiankar@estudiant.upc.edu

Abstract

In this work, the effects of waste-based energy closed-loop integration under internal energy demand uncertainty on the multi-objective optimization of supply chains (SC) is analysed and compared. The proposed approach is based on developing a waste-based closed-loop energy integration MOO model to optimize the strategic and tactical decisions of country-size SCs in the presence of conflicting objectives. A stochastic multi-scenario mixed-integer linear program (MILP) is proposed and the capabilities of the approach are illustrated through a case study from a Sugar cane industry reported by Mele, et al. (2011). Additionally, this approach enables to consider and manage the financial risk associated to the different strategic/tactical decisions, resulting in a set of Pareto optimal solutions. It is shown that the stochastic solution improves the economic performance of the SC in comparison with the deterministic one at any level of the environmental impact. In fact, the stochastic approach optimizes the conflicting objectives as well as improves the whole system robustness compared to the deterministic one and should be therefore the preferred choice in practice.

Keywords: waste-based energy, multi objective optimization, risk management, Optimization under uncertainty, closed-loop energy integration

Introduction

Waste-based energy integration provides an effective solution for both problems; it increases the waste valorisation while cogenerating energy. Optimization of waste-based energy generation supply chains has recently received much attention. In this regard, several models have been proposed as decision support tools for strategic analysis, along with tactical planning of bio-energy SCs.

Perez-Fortes et al., (2014) and recently Cambero, et al., (2016) proposed Multi objective models focused on proposing an optimal design/planning of a biomass conversion system along with optimizing economic benefits environmental impacts associated with all the SC stages. However, these authors have not proposed a closed-loop energy integration model within multi objective optimization framework for a generic SC.

Regarding uncertainty management, extensive studies have been done focusing on demand in SCs (Ruiz-Femenia et al. 2013), but to the best knowledge of the authors,

only the works by Sabio et al. (2014), and Guillen-Gosalbez & Grossmann (2009 & 2010) have studied the effect of uncertainties in the environmentally conscious SCs. These authors introduced a multi objective mixed-integer linear program that explored a simultaneous optimization the economic and environmental performance of the SC under uncertain conditions. However, and further investigation opportunities cannot be taken into account, demand uncertainty in energy closed-loop integration SCs has not been targeted in their models. Accordingly, the proposed approach is to merge generic SCs with biomass SCs and develop a waste-based closed-loop energy integrated MOO model considering energy demand uncertainty to optimize the strategic and tactical decisions of country-size SCs in the presence of conflicting objectives.

Problem statement

According to the approach previously outlined, the proposed model determines a generic waste-based energy integration SC network that is illustrated in Fig. 1. The goal of the study is to determine solutions associated with structural and operational decisions that can be considered more reliable. These decisions include the number, location and capacity of the process plants (including the technologies selected in each of them); warehouses and cogeneration units to be set up, and their capacity expansion policy; and the transportation links between the SC entities. The operational decisions are the cogeneration level, the production rate at the plants in each time period, the flows of materials between plants, warehouses and product markets, and the sales of final products and excess energy.

The SC configurations obtained by means of deterministic mathematical programming can be compared with those determined by different stochastic scenarios representing different approaches to face uncertainty. Additionally, this approach enables to consider and manage the financial risk associated to the different design options, resulting in a set of Pareto optimal solutions that can be used for decision-making.

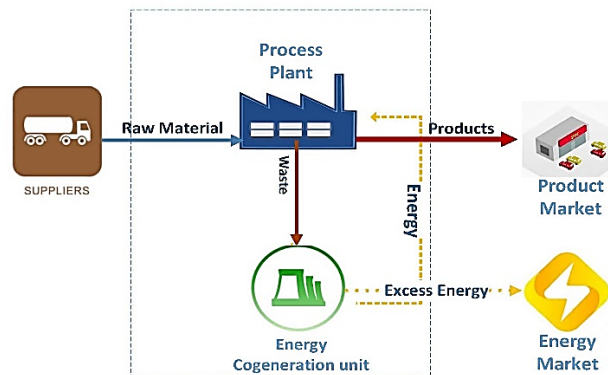


Fig 1. Waste-based Energy closed loop Integration SC

The result of the model provides sets of Pareto solutions to be used by the decision maker in order to take the optimum tactical/strategical decision.

Multi objective stochastic Model

The proposed approach relies on a two-stage Stochastic Mixed Integer Linear Programming (MILP) to incorporate the uncertainty associated to the energy demand. In

this line, the uncertainty is represented by a set of scenarios with given probability of distribution and the mathematical formulation of such model is described as following.

A stochastic programming MILP model based on the one introduced by Mele et al. (2011) is proposed. The model equations are classified into four main blocks: mass balance equations and capacity constraints of the production process section, mass/energy balance equations and capacity constraints of the energy cogeneration section and objective function equations.

3.1 Energy cogeneration section

The amount of cogenerated energy ($Qe_{g,t,sc}$) in region g time period t for scenario sc is less than the energy amount produced from the wastes of process plants ($w_{g,t,sc}$) (Eq. 1). ρ is energy output per metric unit of the waste mass (Illukpitiya et al. 2013).

$$Qe_{g,t,sc} \leq \rho \times w_{g,t,sc} \quad \forall g, t, sc \quad (1)$$

The total amount of energy generated ($Qe_{g,t,sc}$) is also limited by the internal energy demand ($ED_{g,t,sc}$) (Eq. 2)

$$Qe_{g,t,sc} \geq ED_{g,t,sc} \quad \forall g, t, sc \quad (2)$$

and the cogeneration unit capacity ($CogenCap_{g,t}$) (Eq. 3).

$$Qe_{g,t,sc} \leq CogenCap_{g,t} \quad \forall g, t, sc \quad (3)$$

The operational cost ($OprCost_{t,sc}$) associated to each cogeneration unit is determined for each time period (Eq. 4). CE is defined as the cost of producing a unit of energy.

$$OprCost_{t,sc} = \sum_g Qe_{g,t,sc} \times CE \quad \forall t, sc \quad (4)$$

The excess energy is marketed and the associated revenue ($Rev_{t,sc}$) is given in Eq. 5.

$$Rev_{t,sc} = \sum_g (Qe_{g,t,sc} - ED_{g,t,sc}) \times EPrice \quad \forall t, sc \quad (5)$$

3.2 Objective functions

The whole SC system whose model has been described before must attain two targets: the economic objective is represented by the NPV whereas environmental concerns are quantified by the global warming potential (GWP).

3.2.1 Expected Net present value

Different NPV values are obtained for each scenario under study (NPV_{sc}) once the uncertainty is unveiled. The model described before must account for the maximization of the expected value ($E[NPV]$) of the resulting NPV distribution, which can be computed by performing an average of the aforementioned NPVs as stated by Eq. (6):

$$E[NPV] = \sum_{sc} Prob_{,sc} \times NPV_{sc} \quad (6)$$

3.1.1.1 Financial risk

For the two-stage stochastic problem, the financial risk associated with the economic objective is determined with the help of the following constraints:

$$DRisk = \sum_{sc} Prob_{,sc} \times \delta_{sc} \quad (7)$$

$$\delta_{sc} \geq \Omega - NPV_{sc} \quad \forall sc, \delta_{sc} \geq 0 \quad (8)$$

The resulting objective functions are finally expressed as follows:

$$\text{Min}\{-E[NPV]; GWP\} \quad \text{S.t. constraints 1-8 and the constraints proposed by (Mele et al., 2011)} \quad (9)$$

The solution of this problem consists of a set of Pareto optimal SC configurations. These are obtained in this work by applying the ε -constraint method.

Case Study

It is revisited herein the first example introduced by Mele et al., (2011) that addresses the optimal retrofit of an existing sugar cane industry established in Argentina. There are 5 different technologies available to manufacture 2 main products: ethanol and sugars. Nominal capacity of the sugar mill and distillery plants are 350 and 300 thousand tons per year. A time horizon is divided into a set of time periods, and a specific geographic area is divided into a set of regions where the facilities of the SC can be configured. Each region has an associated supply (sugar cane crop) capacity in every time interval. The by-product (bagasse) is supposed to be sent to cogeneration units to generate electricity as added-value product. Energy demand uncertainty is represented by 3 scenarios. On the basis of Illukpitiya et al. (2013) assumptions, the estimated total electricity requirement for internal use in the processing plants is 160 kJ per kg of cane. It is assumed that the nominal capacity of the power plant is 8.33 MW and the power generation is available on a continuous basis for at least 7800 h annually. The electricity market price and the operational cost of electricity generation are 0.15USD/kWh and 0.08USD/kWh respectively.

Results

Figure 2 compares the results obtained by the deterministic and stochastic approaches. Not only the deterministic model exhibits less $E[NPV]$, but it also presents higher probabilities of low profits. For instance, the deterministic solution exhibits a 10% probability of NPV below 3M\$, while the stochastic configuration yields only a 1.5%. In addition, in Fig. 2, both solutions are compared under the same CO2 emissions level.

The associated operative Pareto curves show how the stochastic solution performs better than the deterministic one for the entire range of CO₂ emissions levels. It is also interesting to point out that, for the same cogeneration capacity of 8.33MW (Fig.3), the stochastic solution allows operating at most for energy demand so that leads to involve more regions in generating waste-based energy and using waste as bio energy. In other words, cogenerated energy in the whole SC not only meets the internal energy demand but also the excess energy can be marketed to increase NPV by 10%.

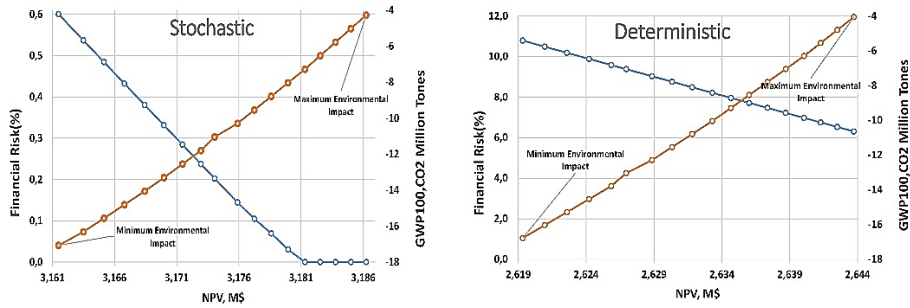


Fig. 2 Pareto set of solutions GWP100 vs NPV and associated Financial Risk

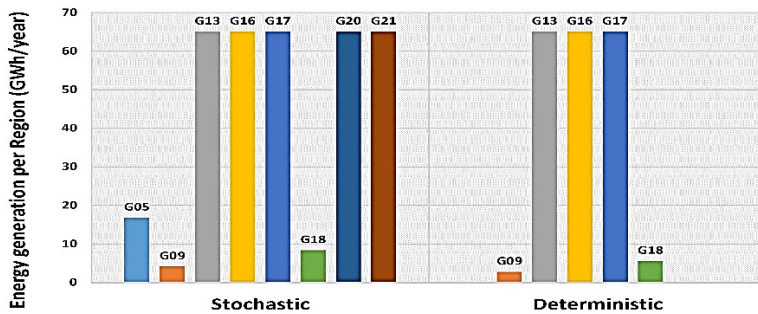


Fig. 3 Energy generation per Region in Deterministic and Stochastic solutions

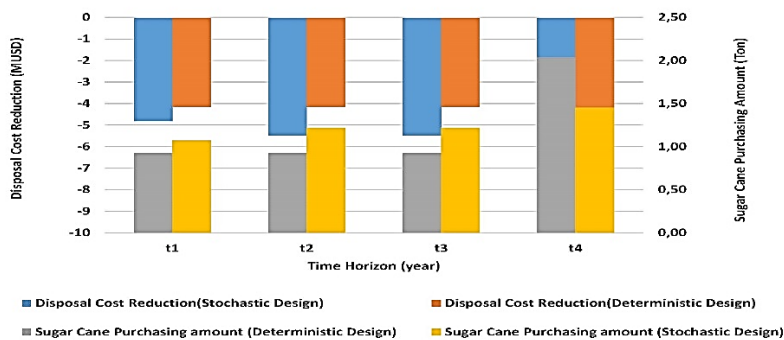


Fig. 4 Disposal Cost Reduction vs Sugar Cane Purchasing Amount

The results show (Fig. 4) that the stochastic energy demand scenarios lead to overall disposal costs decrease 3.1% in the stochastic solution while only by 12% increase in

purchasing amount of sugar cane not only the energy demand can be satisfied but also it can be marketed by adding 97.5 Million USD to the annual revenue.

Conclusions

This work has addressed the optimal design and planning of waste-based energy integrated SC under uncertainty. In order to discover further investigation opportunities, the problem is mathematically formulated as a bi-criterion stochastic MILP that accounts for the maximization of the expected NPV and minimization of the environmental impact (in terms of GWP). The effects of this uncertainty are accounted as a risk associated to the NPV, which has been introduced as an additional constraint into the model. Then, this risk can be managed to reduce the probability of having low profit. The capabilities of the model were highlighted through its application to a case study. The proposed stochastic approach maximizes the expected profit while satisfying at the same time a minimum environmental impact. Numerical results show that the stochastic solutions improves the deterministic one and should be therefore the preferred choice in practice. The optimal solutions are obtained according to the amount of waste used to cogenerate energy, which is directly related to the objectives. The interaction between the design objectives has been shown. This way of generating different possible configurations will help the decision-maker to determine the best design according to the selected objectives.

Acknowledgements

Authors fully appreciate financial support from the Spanish Ministry of Economy and Competitiveness and the European Regional Development Fund, both funding Projects AIMS (DPI2017-87435-R).

References

- Camero, C., Sowlati, T. & Pavel, M., 2016. Economic and life cycle environmental optimization of forest-based biorefinery supply chains for bioenergy and biofuel production. *Chem. Eng. Res. Des.*, 107, pp.218–235.
- Guillén-Gosálbez, G. & Grossmann, I., 2010. A global optimization strategy for the environmentally conscious design of chemical supply chains under uncertainty in the damage assessment model. *Comput. Chem. Eng.*, 34(1), pp.42–58.
- Guillen-Gosalbez, G. & Grossmann, I.E., 2009. Optimal Design and Planning of Sustainable Chemical Supply Chains Under Uncertainty. *Comput. Chem. Eng.*, 55(1), pp.99–121.
- Illukpitiya, P. et al., 2013. Sugar-ethanol-electricity co-generation in Hawai'i: An application of linear programming (LP) for optimizing strategies. *Biomass Bioenergy*, 48, pp.203–212.
- Mele, F.D. et al., 2011. Multiobjective Model for More Sustainable Fuel Supply Chains. A Case Study of the Sugar Cane Industry in Argentina. *Ind. Eng. Chem. Res.*, 50(9), pp.4939–4958.
- Perez-Fortes, M. et al., 2014. Optimization of pre-treatment selection for the use of woody waste in co-combustion plants. *Chem. Eng. Res. Des.*, 92(8), pp.1539–1562.
- Ruiz-Femenia, R. et al., 2013. Multi-objective optimization of environmentally conscious chemical supply chains under demand uncertainty. *Chem. Eng. Sci.*, 95, pp.1–11.
- Sabio, N. et al., 2014. Multiobjective optimization under uncertainty of the economic and life-cycle environmental performance of industrial processes. *AIChE J.*, 60(6), pp.2098–2121.

Minimum Entropy Based PFR Analysis

David Rosa^{a*}, Paulo Goes^a, João Manzi^a

^aFederal University of Campina Grande, Chemical Engineering Department, Av. Aprígio Veloso 882, Bodocongó, 58429-900, Campina Grande – PB, Brazil

david.rosa@eq.ufcg.edu.br

Abstract

This paper is concerned with assessing the behaviour of entropy, or the production of entropy, when analysing the performance of a reactive system in which Plug Flow Reactors (PFR) are used. To describe the process properly when using this type of reactor, the well-known balances of mass and energy have been turned to, besides the balance of entropy as its set is more appropriate for describing the processes with constraints of Nature, which they normally undergo. The strategy adopted consisted of minimizing entropy production. The aim was to keep the correlations of force between energy and entropy, given by the Gibbs energy, in balance with a minimal disturbance in the level of organization of the reactive system. A simple exothermic reactive system was evaluated for several wall temperatures. For the conditions analysed, no significant difference was noted between the entropy production profile and its minimum. Moreover, the results indicate a positive correlation with the wall temperature either of conversion or of the entropy production rate throughout the length of the reactor. The conclusion that can be drawn reveals that the reactive system operates under the minimum entropy condition and that the analysis developed, based on entropic modelling, succeeded in presenting essential and decisive details for assessing and improving the performance of a PFR either from a design or from an operational point of view.

Keywords: minimum entropy, optimization, PFR, thermodynamics

1. Introduction

The chemical industry is continually faced with an aggressive market, and constantly needs to upgrade processes, to reduce systemic costs and additionally to comply with increasingly severe, new environmental regulations.

To deal more appropriately with the aforementioned problems, the authors of this study considered that the following statement of O'Connell (2017) was worth further examination, namely that there seems to be less exploration of entropy generation in chemical process systems, where chemical reactions and diffusive mass transfer are involved, especially in reaction-separation.

Therefore, this paper focuses on the analysis of entropy in seeking a solution for these problems in the context of the author's research interest, which is as follows: given that Plug Flow Reactors (PFRs) are among the most used models in the industrial sphere, mainly for chemical reactions in the gas phase, it is vital to analyse them so as to tackle the above-mentioned problems. To describe the process properly using this type of reactor, the well-known balances of mass and energy have been systematically used,

based on First Principles. Although the First Law of Thermodynamics can result in an energy balance *par excellence*, it does not deal adequately with the constraints of Nature which the processes undergo, and this may generate sub-optimal results (Manzi and Carrazoni, 2008). Since the description of the general problem cannot be appropriate, then the introduction of the entropy balance can make the approach more realistic. In reactive systems the correlations of force between energy and entropy expressed by Gibbs free energy, $g = h - Ts$, plays a pivotal role from either the thermodynamic or economic point of view (Andresen, 2011).

Given that the classical methodologies for designing reactive systems have sought to lead the process to a minimum energy condition (Bejan, 1996) and considering that the natural tendency for increasing entropy is always present, it is desirable to reduce the energy bound together with the increase in entropy because this will make the process more spontaneous. On the other hand, an increase in entropy can be sufficiently high for it to affect the level of organization of the reactive system. Consequently, this will generate an undesirable large number of by-products. Because such by-products should be removed, treated and disposed of, the overall energy cost can be very high.

Thus, the aim of this paper is to assess the behaviour of entropy, or particularly, the production of entropy, when analyzing the performance of a reactive system. The strategy adopted for minimizing the entropy production rate was developed considering that concentration can be expressed as a function of temperature, which makes the implementation of the procedure straightforward. A simple exothermic reactive system was evaluated for several wall temperatures, aiming at also the generation of concentration and temperature profiles. Moreover, the area depicted under the profile of the entropy production has been considered for analysis with the wall temperature and conversion throughout the length of the reactor.

2. Theoretical Background

A PFR can be represented by a set of partial and differential equations of mass and energy along the length of the reactor. Some assumptions on the modelling are made: radial gradients are neglected, the volumetric flow rate is constant, the diffusion terms are negligible, which is valid when the linear velocity is high, and the drop in pressure does not generate external heating, cooling or even work.

The mathematical modeling is given by:

$$\frac{\partial C_i}{\partial t} + \frac{\partial C_i}{\partial z} v_z = -r_i \quad (1)$$

$$\rho c_p \frac{\partial T}{\partial t} + \rho c_p \frac{\partial T}{\partial z} v_z = \Delta H_R (-r_i) \pm \dot{Q} \quad (2)$$

where r_i is the reaction rate based on the Arrhenius equation.

Additionally, the entropy balance is embedded in the model and this results in:

$$\frac{\rho c_p}{T} \frac{\partial T}{\partial t} + \frac{\rho c_p}{T} \frac{\partial T}{\partial z} v_z = \frac{\dot{Q}}{T} + \dot{\sigma} \tag{3}$$

in which $\dot{\sigma}$ denotes the entropy production rate.

As the main purpose is to minimize the entropy production rate, some aspects should be observed. According to Hardy (2014), the idealization of a reversible process is regarded as useful because almost all real processes are irreversible. Thus, the minimization leads the system for reversibility, which is associated with a steady state. This is the reason why only Eqs. (1), (2) and (3) in their particular steady states will be considered in this paper. Making use of such a consideration, as well as of the equations given above, the relationship that represents the entropy production rate can be found as follows:

$$\dot{\sigma} = \frac{\Delta H_R}{T} (-r_i) \tag{4}$$

Considering the PFR is in a certain number of blocks or sections, the balance equations can be applied in each of these blocks. For each block, the values for concentration (C) and temperature (T) can be found, thus generating profiles of concentration and temperature throughout the length of the reactor.

Since the minimum entropy rate is a function of temperature and concentration, to make the minimization procedure easier, Eq. (4) must be re-arranged so that it becomes dependent only on a single variable. By solving jointly Eqs. (1) and (2), a temperature/concentration pair is generated for each section, and so it is not difficult to find the functional relationship between temperature and concentration. By choosing a small interval for the section, it is easier to find one variable as a function of the other by linear interpolation. Such a procedure ensures that the linearization does not have large deviation values. What remains to be done is to consider the classical criterion for establishing the minimum, that is, to express Eq. (4) as a function either of temperature or concentration, and to apply the derivative related to the chosen variable, making it equal to zero. The strategy is shown in Fig. 1

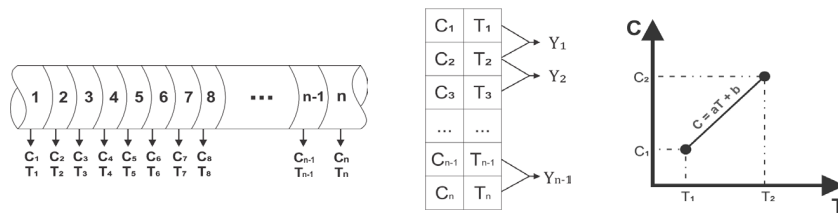


Figure 1: Sequential pairs (C_i, T_i) generated along the length of the reactor and pairs used for the interpolation procedure.

3. Results and Discussion

A case study, based on the classical work of Bilous and Amundson (1956), is presented which applies the methodology shown in this paper. A simple reaction $A \rightarrow B$, first order and exothermic, is carried out in an unpacked PFR that is submitted to several

constant wall temperatures. Some details, kinetics and thermodynamics, about simulation are presented in Table 1.

Table 1: Nominal operating conditions and kinetic parameters for the PFR

E	$9.405 \times 10^7 \text{ J/(kg.mol)}$	M	$0.0073 \text{ (m}^3.\text{K)/mol}$
k_0	$6.566 \times 10^{10} \text{ s}^{-1}$	N	$3.33 \times 10^{-3} \text{ s}^{-1}$
R	$8.314 \text{ cal/(mol.K)}$	C_0	$2 \times 10^{-4} \text{ mol/m}^3$
T_0	340 K		

The parameters M and N refer to simplified terms in the energy balance where

$$M = -\frac{\Delta H_R}{\rho c_P} \quad \text{and} \quad N = \frac{2h}{r \rho c_P}.$$

Fig. 2 shows the profiles of concentration and temperature found by simulating several wall temperatures. Some of these profiles present a peak, indicating that the reaction is completed at this point.

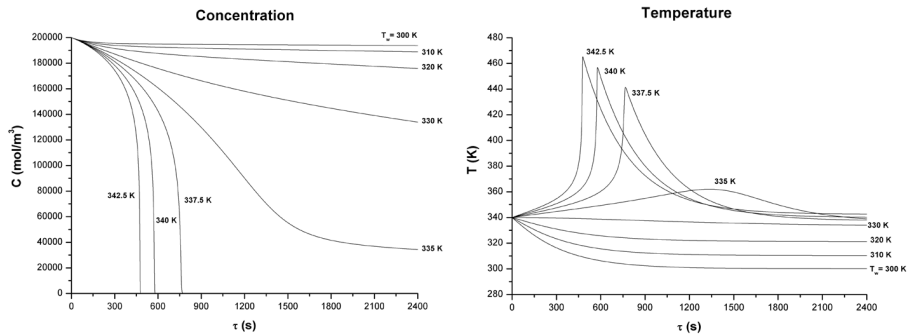


Figure 2: Concentration and temperature profiles submitted to several wall temperatures

Fig. 3 shows the behaviour of the rate of entropy production, its minimum value and the areas corresponding to the entropy production for some temperatures. The area under the curve of the entropy production rate denotes the entropy production throughout the length of the reactor.

By analysing jointly the conversion given in Fig. 2 and the entropy production rate profiles in Fig. 3, it is easy to verify that an increase in the wall temperature generates a desired increase in the conversion but an undesired increase in the entropy production, throughout the length of the reactor.

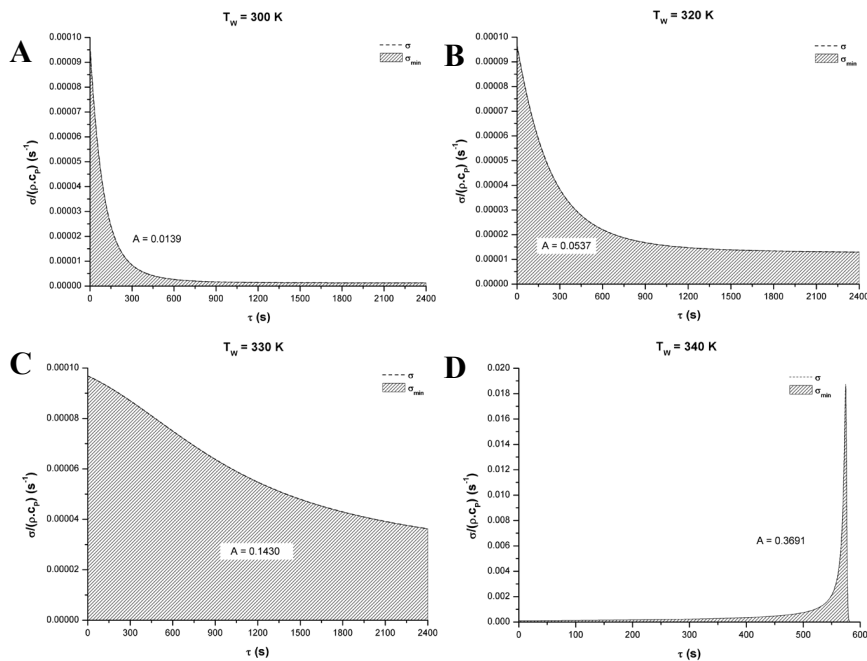


Figure 3: Entropy production and the behavior of the entropy production rate and their minimum values for some wall temperatures. A) $T_w = 300\text{K}$ B) $T_w = 320\text{K}$ C) $T_w = 330\text{K}$ and D) $T_w = 340\text{K}$.

In this case, the profiles of the entropy production rates and their minimum values have followed the same trajectory, indicating that such systems work close to reversibility, thus yielding their best performances. For the sake of clarity, to understand for what reasons the entropy production rate has the same behavior as its minimum value, the following should be taken into account. The velocity of the fluid or of the energy associated with it has been considered constant with a little dispersion, along the length of the reactor, which is quite reasonable. This means that the energy spectrum or the probability density function for the energy is substantially closed. Thus, the change in the kinetic energy that corresponds to the magnitude of the work available for breaking the chemical bonds desired is very appropriate, because this generates collisions and complete ruptures between molecules, which can lead to yielding the desired product. In other words, the work is very close to the energy required to break the chemical bonds. From this, it can be inferred that the question of selectivity is directly involved in the energy distribution function and that the ratio of the sections of the energy distribution function can provide a good approximation of the degree of selectivity.

Since concentration and the entropy production have been shown to have significant and particular correlations with the wall temperatures for the reaction type considered, then such a feature can give rise to an economic analysis that depends on each process type as well as on the constraints imposed by the *modus operandi*. This must be carried out by assuming a trade-off between conversion and the entropy production in order to yield the most favourable cost-benefit ratio, the aim of which is to extract the best operating conditions and configuration for the process.

4. Conclusions

In this paper, model-building has been presented for a PFR, which takes into account both Laws of Thermodynamics, including the entropy balance, besides kinetic concepts. Some simplifications have been considered by neglecting mainly the radial gradients and the diffusion terms. These assumptions are valid when the linear velocity is high enough. Such an approach has enabled the entropy production rate to be derived.

A strategy was developed for obtaining the profiles of conversion, temperature and for the minimum entropy production rate, in which linearization and optimization procedures were introduced as a subroutine in the main scheme of the optimizer.

The results showed that the profiles for the minimum entropy production rate and its minimum follow the same trajectory, indicating that PFRs work under the minimum entropy conditions and this is strongly desired.

Finally, the conclusion that can be drawn is that the methodology developed, based on modelling entropy, proved to have a significant analytical potential, which presents essential and decisive details for assessing and improving the performance of a PFR either from a design or an operational point of view. What remains to be done is to undertake an economic analysis for each process considered and to assume that a trade-off between conversion and the entropy production will result in the best cost-benefit.

References

- Andresen, B. 2011. Current Trends in Finite-Time Thermodynamics. *Angewandte Chemie* 50, 2690-2704.
- Bejan, A. 1996. Entropy generation minimization: The new thermodynamics of finite-size devices and finite-time processes. *J. Appl. Phys* 79, 1191-1218.
- Bilous, O. Amundson, N. R. 1956. Chemical Reactor Stability and Sensitivity – II. Effect of Parameters on Sensitivity of Empty Tubular Reactors. *A.I.Ch.E Journal* 2, 117-126.
- Hardy, R. J. Binek, C. 2014. *Thermodynamics and Statistical Mechanics: an integrated approach*. John Wiley & Sons.
- Johannessen, E., & Kjelstrup, S. 2005. A highway in state space for reactors with minimum entropy production. *Chemical Engineering Science* 60, 3347-3361.
- Manzi, J., & Carrazzoni, E. 2008. Analysis and Optimization of a CSTR by Direct Entropy Minimization. *Journal of Chemical Engineering of Japan* 3, 194-199.
- O'Connell, J. P. 2017. Chemical process systems analysis using thermodynamic balance equations with entropy generation. *Computers and Chemical Engineering* 107, 3-15.

Exergy Analysis of an Extractive Distillation Column for Reducing Energy Consumption in a Bioethanol Production Process

J. Cristóbal García-García^a, Danahe Marmolejo-Correa^{a*}, J. Carlos Cárdenas-Guerra^a, Ricardo Morales-Rodríguez^b

^a*División de Ciencias e Ingenierías Universidad de Guanajuato, Loma del Bosque 103, León, Guanajuato. MX 37150, México*

^b*División de Ciencias Naturales y Exactas Universidad de Guanajuato, Noria Alta s/n, Guanajuato, Guanajuato. MX 36050, México*

d.marmolejocorrea@ugto.mx

Abstract

This work focuses on the exergy analysis of an extractive distillation column in the second-generation bioethanol production process. The study of the exergy performance of the separation and purification section is relevant from a thermodynamic point view due to the large amount of the energy consumed by their unit operations. A sensitivity analyses of the separation section, the location of the feeding stages for the solvent and the ethanol-water azeotropic mixture, the reflux ratio and solvent/feed ratio were performed for obtaining the minimum energy consumption in the column reboiler. Finally, the profiles of exergy components, irreversibilities and the exergy efficiency for the base case and enhanced case were compared. The results show a 29.21 % decrease on the irreversibilities and a corresponding increase of 22.82 % in the exergy efficiency for the separation section. The simulation as well as the sensitivity analyses were done using a connection between the process simulator Aspen Plus v 8.8 and Excel.

Keywords: Exergy analysis, bioethanol, sensitivity analysis, extractive distillation.

1. Introduction

Bioethanol is an organic biofuel that has been identified and utilized as an alternative fuel to reduce the fossil fuels usage. The production of bioethanol consists of numerous unit operations that allow obtaining high-purity grade ethanol from lignocellulosic biomass that constitutes a renewable substrate that may contribute to environmental sustainability. This raw material can be obtained from agricultural residues at low-cost and high availability and its main constituents are cellulose, hemicellulose and lignin (Limayem and Ricke, 2012).

Despite the advantages of second-generation bioethanol, the high energy consumption in pretreatment, fermentation and separation sections have limited its industrialization to only a few countries like Brazil or USA (Waldron, 2010). These countries are developing research with the aim of maximizing process efficiency. Exergy analysis is a powerful tool that allows evaluating and analyzing processes by identifying their imperfections due to thermodynamic irreversibilities.

Therefore, the objective of this work is to perform an efficiency analysis that provides exergy profiles within the purification section and to present opportunities for improvements in the design of an Extractive Distillation Column (EDC). The aim is to reduce energy consumption in a bioethanol production process by using a computer-aided based approach.

2. Exergy Analysis

Exergy is the maximum theoretical work that can be obtained from a system when it is brought to thermal, mechanical and chemical equilibrium with an environmental state of reference. Exergy content in open systems can be classified by its origin: a) exergy accompanying energy flows and b) exergy accompanying material flows. For material flows, exergy can be further divided into: thermo-mechanical or physical exergy and chemical exergy (Marmolejo-Correa and Gundersen, 2015).

Thermo-mechanical exergy in Eq. (1) is defined by differences in enthalpy ($H-H_0$) and entropy ($S-S_0$) from the current conditions of the system (T, P) to the ambient conditions (T_0, P_0). Where T and P stand for temperature and pressure, respectively.

$$E^{ph} = H - H_0 - T_0(S - S_0) \quad (1)$$

Chemical exergy for a non-ideal mixture is shown in Eq. (2) and proposed by Szargut (1989), where x_i are mole fractions, ε_i are the standard chemical exergy and γ_i are the activity coefficient of each component.

$$E^{ch} = \sum_{i=1}^n (x_i \varepsilon_i + x_i \ln \gamma_i x_i) \quad (2)$$

The irreversibility rate (I) in the EDC is calculated developing an exergy balance as shown in Eq. (3), where, E_{IN} and E_{OUT} are the total exergy rates entering and exiting the column, respectively. $\sum E^Q$ is the total exergy flow accompanying the heat entering in reboiler and exiting condenser of the column.

$$E_{IN} - E_{OUT} + \sum E^Q = I \quad (3)$$

The rational efficiency defined by Kotas (1995) is shown in Eq. (4).

$$\psi = \frac{E_{IN} - E_{OUT}}{\sum E^Q} \quad (4)$$

Exergy analysis applied in bioethanol production processes, (Ojeda et al., 2011; Silva Ortiz and de Oliveira Jr, 2014) usually reports overall analyses to the complete processes. However, these studies do not include a stage-by-stage analysis for the EDC. The standard chemical exergy of the components present in the study are shown in Table 1.

Table 1 Standard Chemical Exergy (ϵ), MJ/kmol of the Main Components.

Component	Standard chemical exergy	Component	Standard chemical exergy
Water	3.12	Cellulose	3,404.40
Ethanol	1,364.56	Xylan	3,449.50
Glucose	2,793.20	Lignin	3,449.50
Xylose	1,835.30	Ash	0.00
Arabinose	2,328.08	Enzyme	145.60
CH ₃ COOH	908.00	CaSO ₄	4.30
H ₂ SO ₄	108.60	Ca(OH) ₂	62.50
DAP	220.98	Glycerol	1,999.27
Protein	145.60	<i>Z. mobilis</i>	540.47
CO ₂	19.09		

The standard chemical exergy of ethanol, water, CO₂, calcium sulphate (CaSO₄), calcium hydroxide (Ca(OH)₂), H₂SO₄ and CH₃COOH were obtained from Kotas (1995). For the components enzyme, glucose, cellulose, xylose and lignin the used values were the reported by Ojeda et al. (2011). The values of diammonium phosphate (DAP), arabinose, glycerol and *Zymomonas mobilis* were obtained by using Eq. (5), where, [C], [H], [O] and [N] are the atomic fractions for each element in the evaluated component.

$$\epsilon = 4.19 \left\{ \begin{array}{l} 8177.8[C] + 5.25[N] + 27892.6[H] - 3173.7[O] \\ + 0.15[O](7837.7[C] + 33888.9[H] - 4236.1[O]) \end{array} \right\} \quad (5)$$

3. Description of Bioethanol Production Process

The second-generation bioethanol production plant was simulated employing the Aspen Plus v 8.8 process simulator and divided into five stages: pretreatment, overliming, saccharification, fermentation and separation (Sánchez et al., 2013). The analysis was carried out taking wheat straw as raw material with a mass flowrate of 7,752.13 kg/h with composition in mole fraction of 0.47 of water, 0.34 of cellulose, 0.15 of xylan, 0.05 of lignin and traces of ash. In the saccharification section, the cellulose that cannot be dehydrated during the pretreatment section is converted into glucose with the help of enzymes that favor its reaction. During fermentation the fermentable sugars presents in the stream are converted into ethanol by *Z. mobilis*.

The ethanol purity obtained after fermentation must be raised up to 99.6 % to be utilized as a fuel. The latter is accomplished by setting a series of distillations columns as shown in Figure 1. The first column is called concentration column and it is used to increase the ethanol concentration in the product stream by eliminating the solids and low volatility compounds. The outlet stream of the concentration column contains ethanol at 80 % in mole base. Next, an EDC is used. In this, both, product and solvent streams are fed to the column. The solvent (in this case glycerol) breaks the azeotrope between ethanol and water by lowering the volatility of the water favoring the separations and high ethanol purity in the distillate stream. The molar based purity of the ethanol is 99.6%.

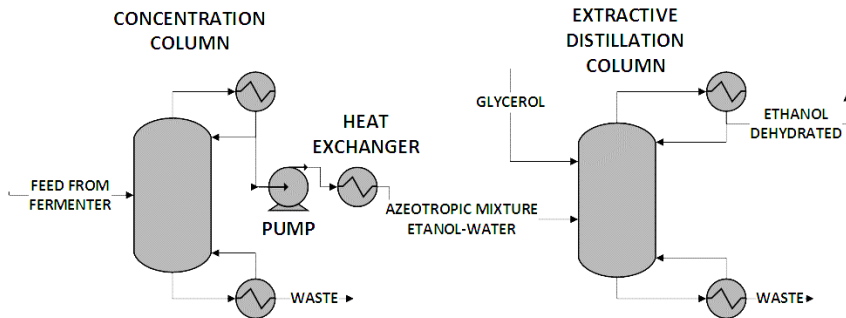


Figure 1. Separation Section on Bioethanol Production Plant.

The EDC was further analyzed through sensitivity analysis to obtain better operating conditions that allow lower energy consumption. Exergy analyses for comparing the exergy efficiency of base case and enhanced case were also performed.

4. Computer-Aided Tools Integration for Exergy Analysis

The simulator Aspen Plus v 8.8 has a shortcoming regarding exergy calculations, because it does not calculate chemical exergies of process streams. It only calculates physical exergies. In this work interconnections between the Aspen Plus and spreadsheets in Microsoft Excel were used for calculating chemical exergies of the material streams and irreversibilities in unit operations. The variables such as, H , S , x_i , mole flows (n), T and heat duty (Q) were imported to spreadsheets for further use in chemical exergy calculations. Figure 2 shows the six stages of the methodology used for exergy calculations inside the EDC. This methodology is used for the rest of the material streams and unit operations of the total bioethanol processes.

5. Results

The search range for the feed location of azeotropic mixture and solvent varied from stage 2 to stage 19, the molar reflux ratio (RR) from 0.10 to 10.00 and the solvent to feed molar ratio (S/F) from 0.10 to 5.00. Table 2 shows the results obtained in this study. Figure 3a and 3b shows the results of the sensitivity analysis. It is observed that feeding stages for the solvent and azeotropic mixture in stages 4 and 12, respectively, the energy rate is reduced from 1.81 MW to 1.75 MW in the reboiler. This energy rate is the lowest for a fixed RR of 0.5 and S/F ratio of 0.45, these ratios are obtained from sensitivity analysis showed in Fig 3b. Figures 3c and 3d show the physical and chemical exergy profiles, respectively.

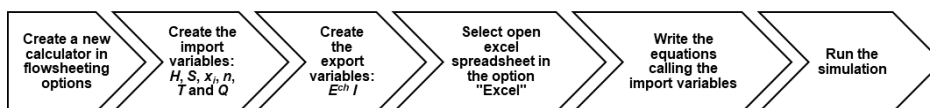


Figure 2. Systematic Methodology to Integrate the Calculations of E^{ch} and I .

Table 2. Results of Exergy and Sensitivity Analysis in the Both Cases Studied.

Results	Base case	Enhanced case
Solvent feed location	2	4
Azeotropic mixture feed location	10	12
RR	0.50	0.50
S/F	1.00	0.45
Reboiler heat duty, MW	1.81	1.75
Irreversibility, MW	0.35	0.25
Rational efficiency, %	1.18	24.00

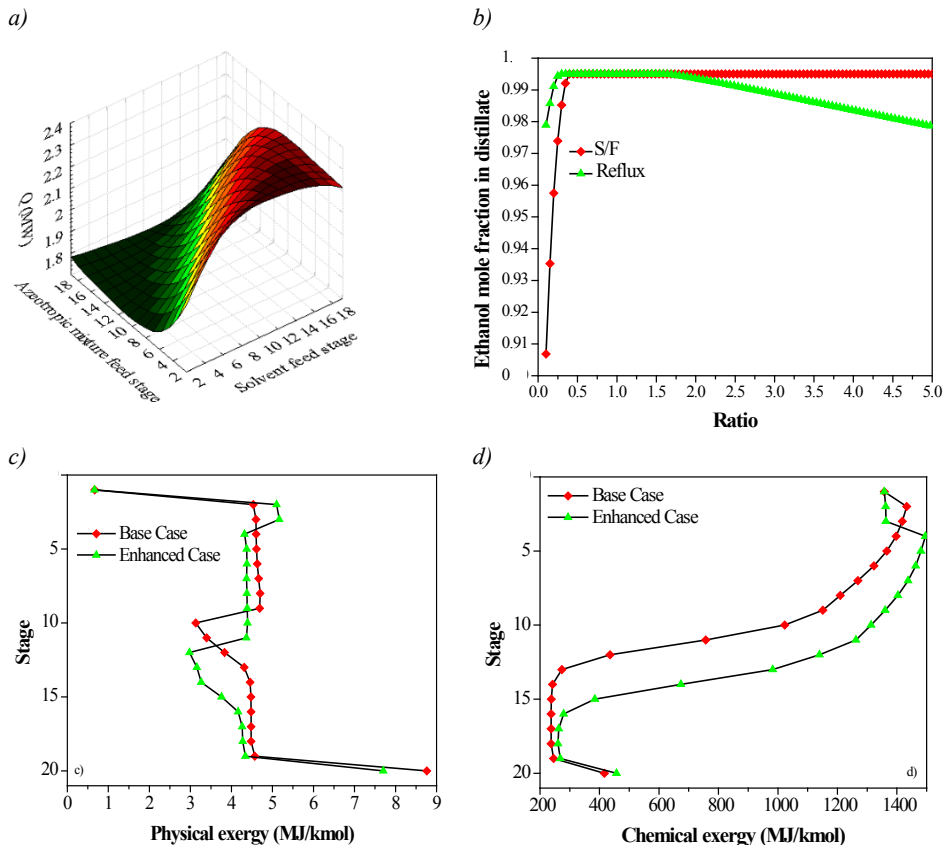


Figure 3. Results of the sensitivity analysis: a) feed location and b) reflux and S/F ratios. Exergy profiles: c) physical exergy profile and d) chemical exergy profile.

The chemical exergy profiles have a kink in the solvent feeding stage where the maximum chemical exergy is visible. Because of these stages, the greatest glycerol concentration is located, and the standard chemical exergy of this solvent is greater than that of ethanol and water. One can also note that in Figure 3c both curves start and end at

the same points, meaning that the chemical exergies of the top and bottoms are the same for ethanol and water/glycerol mixture standard chemical exergies, respectively.

The increase in total exergy in the enhanced case means that the capacity of obtain power of the product stream of the EDC increased after the sensitivity analysis increasing the efficiency of the column. This efficiency was calculated using Eq. (4), obtaining a value of 1.18 % and 24.01 % in the case base and enhanced case, respectively. The irreversibility was also calculated in both cases using Eq. (3) obtaining a reduction from 0.35 MW to 0.25 MW in the case base and enhanced case, respectively.

6. Conclusions

The extractive distillation column increases its efficiency in 22.82 % from the conditions reported by Gil et al. (2012) to the propose operating conditions by this work. This proposal does not increase the number of stages and decreases the energy consumption in the reboiler. Additionally, the incorporation of rigorous calculations of chemical exergies in Aspen Plus v 8.8 helped to perform the exergy analysis of the complete plant that will be shown in further publications.

Acknowledgments

The authors acknowledge the partial financial support by the Mexican Bioenergy Innovation Centre, Bioalcohols Cluster (249564) and the Universidad de Guanajuato for the development of this project

References

- I. D. Gil, J. M. Gómez and G. Rodríguez, 2012, Control of an extractive distillation process to dehydrate ethanol using glycerol as entrainer, *Computers and Chemical Engineering*, pp. 129-142.
- T. J. Kotas, 1995, Chemical exergy and enthalpy devaluation (appendix A), *The Exergy Method of Thermal Plant Analysis*, pp. 236-262. Florida, USA.
- A. Limayem and S. C. Ricke, 2012, Lignocellulosic biomass for bioethanol production: current perspectives, potential issues and future prospects, *Progress in Energy and Combustion Science*, 38, pp. 449-467.
- D. Marmolejo-Correa and T. Gundersen, 2015, A new efficiency parameter for exergy analysis in low temperature processes, *International Journal of Exergy*, 17, pp. 135-170.
- K. Ojeda, E. Sánchez and V. Kafarov, 2011, Sustainable ethanol production from lignocellulosic biomass - application of exergy analysis. *Energy*, 36, pp. 2119-2128
- A. Sánchez, V. Sevilla-Güitrón, G. Magaña and L. Gutierrez, 2013, Parametric analysis of total cost and energy efficiency of 2G enzymatic ethanol production. *Fuel*, 113, pp. 165-179
- P. Silva Ortiz and S. de Oliveira Jr., 2014, Exergy analysis of pretreatment processes of bioethanol production based on sugarcane bagasse, *Energy*, 76, pp. 130-138.
- J. Szargut, 1989, Chemical Exergies of the Elements, *Applied Energy*, 32, pp. 269-286.
- K. Waldron, 2010, Separation and purification processes for lignocellulose-to-bioalcohol production, *Bioalcohol production. Biochemical conversion of lignocellulosic biomass*, pp. 246-277. New, York, USA.

A Relaxed Knapsack-Problem Based Decomposition Heuristic for Large-Scale Multistage Stochastic Programs

Zuo Zeng, Selen Cremaschi*

*Department of Chemical Engineering, Auburn University, Auburn, AL 36849, USA
selen-cremaschi@auburn.edu*

Abstract

Most optimization problems with endogenous uncertainty can be modelled as multistage stochastic programs (MSSPs). The MSSPs grow exponentially with the increase in the numbers of scenarios and time periods, and quickly become computationally intractable for real-world sized problems. This paper presents a Relaxed Knapsack-problem based decomposition Algorithm (RKDA) to efficiently generate tight dual bounds for large-scale MSSPs. The algorithm builds upon the Knapsack-problem based Decomposition Algorithm (KDA) (Christian and Cremaschi, 2015), which generates feasible solutions for MSSPs with endogenous uncertainty by decomposing the original multi-period MSSP into a series of knapsack problems and by solving these problems at appropriate decision points of the planning horizon. The new approach, RKDA, employs KDA to solve a relaxed version of the original MSSP. The relaxed MSSP is obtained by removing its resource constraints. We applied KDA and RKDA to generate initial primal and dual bounds for the pharmaceutical clinical trial planning problem with two-, three-, four-, five-, six-, seven- and ten-products and three clinical trials with different planning horizon lengths. The results revealed that the initial relative gaps ranged from 2.10% to 4.66%, and KDA and RKDA yielded these gaps in 0.1 to 2377.0 CPU seconds.

Keywords: stochastic programming, endogenous uncertainty, knapsack-problem based decomposition heuristic, primal and dual bounds

1. Introduction

Optimization problems with decision-dependent, i.e., endogenous, uncertainty are commonly observed in process industry, e.g., R&D pipeline management (Colvin and Maravelias, 2010), synthesis of process networks with uncertain process yields (Tarhan and Grossman, 2008), and artificial lift infrastructure planning (Zeng and Cremaschi, 2017). In these problems, decisions may impact the resolution time (Type II) and/or the probability distributions of the uncertain parameters (Type I) (Apap and Grossmann, 2017). This paper restricts its scope to optimization problems with Type II uncertainty.

One approach to address these problems is multistage stochastic programming, which is a scenario-based method that considers decisions and recourse actions in multiple stages as uncertainty is realized. Each scenario defines a unique set of realizations for all uncertain parameters. In MSSP formulations of problems with endogenous uncertainty, decision variables are defined independently for each scenario. To prevent decision variable values that anticipate future outcomes of uncertain parameters, non-anticipativity constraints (NACs) are explicitly incorporated to MSSP formulations. Size of decision variables and

NACs grow exponentially as the number of uncertain parameters and the number of outcomes for each uncertain parameter increase. This growth results in both space and time complexities for solving MSSPs for real-world sized problems. In general, the solution approaches for large-scale MSSPs with endogenous uncertainty rely on heuristic, approximation, and decomposition methods, such as sample average approximation algorithm (Solak et al., 2010), improved Lagrangean decomposition framework (Gupta and Grossmann, 2014), sequential scenario decomposition approach (Apap and Grossmann, 2017), a branch and bound algorithm (Christian and Cremaschi, 2017) and a rolling-horizon heuristic approach (Colvin and Maravelias, 2009). It has been shown that moderate-size problems can be solved to optimality.

Here, we presents a Relaxed Knapsack-problem based Decomposition Algorithm (RKDA) to generate tight dual bounds for large-scale MSSPs with endogenous uncertainty. The algorithm builds upon the KDA (Christian and Cremaschi, 2014). Instead of enumerating all uncertain parameter space as scenarios, the KDA decomposes the original multi-period MSSP into a series of knapsack problems and solves these problems at appropriate decision points of the planning horizon. It provides tight primal bounds for the original problem, and generates these bounds several orders of magnitude faster than solving the original MSSP. The RKDA generates a tight dual bound by employing a relaxed version of the KDA to solve a relaxed version of the original MSSP. The relaxed MSSP is obtained by removing its resource constraints. The application of RKDA is demonstrated by solving instances of clinical trial planning problem, which is introduced in Section 2. Then, we describe KDA and RKDA (Section 3). In Section 4, we apply KDA and RKDA to different instances of the clinical trial planning problem with scenarios ranging from 64 up to 1,048,576. Finally, the concluding remarks are summarized in Section 5.

2. Clinical Trial Planning Problem and its MSSP formulation

The goal of the clinical trial planning problem is to identify the schedule of clinical trials for a set of candidate drugs, $i \in \mathbf{I} = \{1, 2, \dots, |\mathbf{I}|\}$, that maximizes the expected net present value (ENPV) of the clinical trial pipeline. The outcomes of the clinical trials for each drug are uncertain and decision-dependent, because the outcome of a clinical trial can only be realized once the trial is completed. A drug has to complete three clinical trials in order ($j \in \mathbf{J} = \{PI, PII, PIII\}$), and it can either pass (P) a clinical trial or fail (F) it. A drug that has failed a trial cannot continue to the subsequent clinical trial(s). Let θ_i be the uncertain parameter associated with this uncertainty for drug i . We then define the realizable values of this uncertain parameter with set $\Theta_i = \{PI(F), PII(F), PIII(F), PIII(P)\}$, where $PIII(P)$ corresponds to the outcome that drug i passes trials PI, PII , and $PIII$. The scenarios for the MSSP model are constructed as Cartesian product of uncertain parameter outcomes. Therefore, the total number of scenarios for a clinical trial planning problem with $|\mathbf{I}|$ drugs each of which should complete all three clinical trials is $|\mathbf{S}| = 4^{|\mathbf{I}|}$, where \mathbf{S} is the scenario set.

The planning horizon is defined as $t \in \mathbf{T} = \{1, 2, \dots, |\mathbf{T}|\}$ (period t starts at time $t-1$ and ends at time t). Each drug has a known cost C_{ij} , required resources ρ_{ijr} (where $r \in \mathbf{R} = \{1, 2, \dots, |\mathbf{R}|\}$), and fixed duration of τ_{ij} for each clinical trial. After successfully completing all clinical trials, the revenue from drug i is realized. Potential revenue is defined using the maximum revenue, rev_i^{max} , associated with drug i . Patent life of a drug is assumed to starts shrinking

once the drug enters the pipeline, and associated losses are represented by two penalty terms: γ_i^D (loss of market share) and γ_i^L (loss of patent life).

A slightly revised version of the MSSP formulation by Colvin and Maravelias (2010) is given in Figure 1. The decision variable $X_{i,j,t,s}$ is equal to one if clinical trial j of drug i is started at time t in scenario s . Equations 2-5 calculate the ENPV. Equations 6-8 are sequencing constraints. Per Colvin and Maravelias (2010), a clinical trial j' of drug i cannot be started at time t in scenario s , (1) if drug i fails a prerequisite trial ($j < j'$) in scenario s , and (2) if $t \leq \sum_{j=1}^{j'-1} \tau_{ij}$. We define set \mathbf{N} to include trial j' of drug i that cannot be started at time t in scenario s , and set decision variables associated with these (drug, clinical trial) pairs for these time periods and scenarios equal to zero by Eq. 8. Equation 9 enforces the resource limitations. The NACs are given in Eq. 10 for the first time period, and Eq. 11 for $t > 1$. For Eq. 11, we define the subset \mathbf{B} of $\mathbf{S} \times \mathbf{S}$ as scenarios s and s' , which are distinguishable in the outcome of one (drug, clinical trial) pair $(i^{s,s'}, j^{s,s'})$.

$$\max ENPV \tag{1}$$

$$\text{s.t. } ENPV = \sum_s p_s (Rev_s + FRev_s - Cst_s) \tag{2}$$

$$Rev_s = \sum_i \sum_t \left\{ rev_{i,j,t,s}^{max} X_{i,PIII,t,s} - \gamma_i^D \sum_{j=PII,PIII} (-X_{i,j,1,s} + \sum_{t' > \tau_{ij}-1} X_{i,j-1,t'-\tau_{ij}-1,s} - \sum_{t' \leq t} X_{i,j,t',s}) - \gamma_i^L (t + \tau_{i,PIII}) X_{i,PIII,t,s} \right\} \quad \forall s \tag{3}$$

$$FRev_s = \sum_i \sum_{j \neq PI} rev_{i,j}^{open} f_{i,j} (-X_{i,j,1,s} + \sum_{t' > \tau_{ij}-1} X_{i,j-1,t'-\tau_{ij}-1,s} - \sum_{t' \leq |T|} X_{i,j,t',s}) + \sum_i rev_{i,PI}^{open} f_{i,PI} (1 - \sum_{t' \leq |T|} X_{i,PI,t',s}) + \sum_i \sum_{j \in \{PI,PIII\}} \sum_{t > |T| - \tau_{ij}} rev_{i,j,t}^{run} f_{i,j+1} X_{i,j,t,s} \quad \forall s \tag{4}$$

$$Cst_s = \sum_{i,j,t} cd_t C_{i,j} X_{i,j,t,s} \quad \forall s \tag{5}$$

$$\sum_t X_{i,j,t,s} \leq 1 \quad \forall i, j, s \tag{6}$$

$$\sum_{t'} X_{i,j,t',s} \leq \sum_{t'} X_{i,j-1,t',s} \quad \forall i, j > 1, t', s \tag{7}$$

$$X_{i,j,t,s} = 0 \quad \forall (i, j, t, s) \in \mathbf{N} \tag{8}$$

$$\sum_i \sum_j \sum_{t' > t - \tau_{ij}} \sum_{t' \leq t} \rho_{i,j,t'} X_{i,j,t',s} \leq \rho_r^{max} \quad \forall r, t, s \tag{9}$$

$$X_{i,j,1,1} = X_{i,j,1,s} \quad \forall i, j, s \tag{10}$$

$$\left[\begin{array}{c} \sum_{t' \leq p - \tau_{i^s, s'}, j^s, s'} Y_{i^s, s', j^s, s', t', s} \\ X_{i,j,t,s} = X_{i,j,t,s'} \end{array} \right] \vee \left[\sum_{t' \leq t - \tau_{i^s, s'}, j^s, s'} Y_{i^s, s', j^s, s', t', s} \right] \quad \forall i, j, t \geq 1, (s, s') \in \mathbf{B} \tag{11}$$

Figure 1. An MSSP formulation for the clinical trial planning problem

3. Proposed Heuristic Algorithms

3.1. Knapsack-problem based decomposition algorithm (KDA)

The KDA generates and solves a series of $|\mathbf{R}|$ -dimensional 0-1 knapsack problems based on the realizations of uncertainty. The KDA uses the concept of eligible item set \mathbf{K} , where items $k \in \mathbf{K}$ are created by enumerating all allowable decisions associated with endogenous uncertain parameters at time period t according to the logic of the sequencing constraints. Each item has a value, V_k , and weight(s), W_k^r , associated with it. Item values and weight(s) are estimated using expected gains and resource requirements, respectively.

Suppose that a clinical trial planning problem only includes two drugs (A and B). The KDA starts by generating the eligible item set at $t=1$, the root node. The eligible items are (A, PI) and (B, PI) , and they are determined using the logic of sequencing constraints (Eqns. 6-8). Next, item values and weights are calculated. The value for (A, PI) is the expected value of its revenue assuming all remaining clinical trials are completed continuously, and it is calculated via Eqns. 12 and 13. Note that $t=1$ for Eq. 12. The item values approximate the impact of starting the drug, clinical trial pair at the current time period would have on objective function value of the original MSSP (Eqns. 2-5). Equation 12 reduces the potential revenue, rev_A , due to loss of active patent life for the total duration of the current and remaining clinical trials. The potential revenue is calculated by deducting the linearly depreciated clinical trial costs $C_{A,j'}$ from the maximum revenue rev_A^{max} (Eq. 13). Item weights for (A, PI) are equal to $\rho_{A,PI,r}$. The $|\mathbf{R}|$ -dimensional capacity vector $\{W_r^{max}\}$ contains the available resources for investment, ρ_r^{max} .

$$V_{(A,PI)} = E[rev_A - \gamma_A^L(t + \sum_{j' \geq PI} \tau_{A,j'} + 1)] \quad (12)$$

$$rev_A = rev_A^{max} - \sum_{j' \geq PI} C_{A,j'} \left(1 - 0.025 \sum_{j'' > PI} \tau_{A,j''} - 1\right) \quad (13)$$

The knapsack problems that are generated and solved are given in Eqns. 14-16. The objective is to maximize the total value (Eq. 14), and the weight constraints (Eq. 15) are equivalent to the resource constraints of the original MSSP (Eq. 9).

$$\max \sum_{k \in E} V_k y_k \quad (14)$$

$$\text{s.t. } W_{k,r} y_k \leq W_r^{max} \quad \forall r \in \mathbf{R} \quad (15)$$

$$y_k \in \{0, 1\} \quad \forall k \in \mathbf{K} \quad (16)$$

Once the root node knapsack problem is solved, the number of new knapsack problems generated and their generation times are based on the outcomes of the root node knapsack problem solution. For our example, if the solution selects (A, PI) and (B, PI) , time period is set to $\max(\tau_{A,PI}, \tau_{B,PI})$ and $2^2=4$ additional knapsack problems are generated. These problems correspond to the four possible outcomes: (1) drugs A and B pass clinical trial PI , (2) drug A fails PI while drug B passes it, (3) drug A passes trial PI while drug B fails it, and (4) both drugs fail trial PI . For each knapsack problem, the algorithm updates set \mathbf{K} and calculates corresponding item values and weights at the corresponding time period. The item values are updated based on the realizations of uncertainties that correspond to each individual knapsack problem. The algorithm continues to solve and generate new child knapsack problems until the end of the planning horizon or no eligible items remain. The KDA yields a feasible solution, and hence, generates a primal bound for the MSSP. Detailed discussions of KDA can be found in Christian and Cremaschi (2015, 2017).

3.2. Relaxed knapsack-problem based decomposition approach (RKDA)

The RKDA generates a valid dual bound for the original MSSP by solving a relaxed version of the original MSSP to optimality. The original MSSP is relaxed by removing the resource constraints (Eq. 9). We refer to this relaxed MSSP formulation as RMSSP. The optimal solution of RMSSP provides a dual bound for the original MSSP.

The weight constraints of the knapsack problems in the KDA are equivalent to the resource constraints of the MSSP. Therefore, to solve the RMSSP, the weight

constraints of the knapsack problems are removed yielding the relaxed knapsack problems given in Eqns. 17-18. The original KDA is modified to generate and solve the relaxed knapsack problems every time period at which the outcome of an uncertain parameter is realized. We refer to this modified KDA as relaxed KDA (RKDA). The solution obtained by RKDA to the RMSSP satisfies the sequencing constraints (Eqns. 6-8) and the NACs (Eqns. 10-11) of the RMSSP, and recommends starting all eligible clinical trials at the earliest time allowable. Therefore, the RKDA yields the optimal solution of the RMSSP, which is a tight dual bound for the original MSSP.

$$\max \sum_{k \in E} V_k y_k \quad (17)$$

$$\text{s.t. } y_k \in \{0, 1\} \quad \forall k \in \mathbf{K} \quad (18)$$

4. Results and Discussion

We applied KDA and RKDA to generate initial primal and dual bounds for the clinical trial planning problem with two-, three-, four-, five-, six-, seven- and ten-products and three clinical trials with different planning horizons. We also solved the original MSSPs of these problems to 0.1% optimality gap when possible. The models and algorithms were implemented in Pyomo and solved using CPLEX 12.6.3 on a standard node of Auburn University Hopper Cluster. Problem data are available upon request.

Number of trials, time periods, and scenarios for the problems are summarized in Table 1 along with the optimum ENPVs and the MSSP solution times for the problems that were solved to optimality. As expected, the MSSP solution times grow exponentially with the number scenarios. For example, CPLEX 12.6.3 required more than 30 hours to solve the six-product problem. The MSSP enumerates all scenarios, and quickly becomes computationally intractable due to its space and time complexity. Therefore, the MSSP formulations of seven- and ten-product problems cannot be generated in RAM and hence cannot be solved using CPLEX 12.6.3 due to their space complexities.

Table 1. Main characteristics and the MSSP solutions of the problems

Case Name	Number of Trials	Number of Time Periods	Number of Scenarios	ENPV (\$M)	MSSP Solution Time (CPUs)
2-prod	2	5	9	1104	0.1
3-prod	3	12	64	1189	4
4-prod	3	6	256	1696	7
5-prod	3	6	1,024	2082	185
6-prod	3	6	4,096	2450	29,357
7-prod	3	8	16,384	--	--
10-prod	3	10	1,048,576	--	--

Primal and dual bounds obtained for the problems using KDA and RKDA are compiled in Table 2. An initial relative gap for each problem is calculated using the primal and dual bounds. The gaps ranged between 2.10% and 4.66% (Table 2). The KDA and RKDA yielded these relative gaps very quickly, in 0.1 to 2377 CPU seconds. The Pearson correlation coefficient between the total solution time and number of scenarios is 1.00, revealing the strong linear relationship between them. It is worth noting that KDA and RKDA are able to generate a feasible solution and quantify its quality for even the ten-product problem under one CPU hour.

5. Conclusion

This paper discussed decomposition based heuristic algorithms, KDA and RKDA, to quickly obtain a feasible solution, a primal and a dual bound for large scale MSSP problems with endogenous uncertainty. Unlike the deterministic equivalent of MSSP formulations, the KDA and RKDA do not suffer from space complexity, and hence, can be used to generate a feasible solution and to obtain its solution quality for problems that are currently computationally intractable. Furthermore, the proposed algorithms is an initial step towards optimally solving large-scale MSSP for real-world sized problems.

Table 2. Primal and dual bounds, relative gap, and solution times for the KDA and RKDA

Case Name	KDA Primal Bound (\$M)	RKDA Dual Bound (\$M)	Relative Gap	Solution Time (CPUs)
2-prod	1097	1120	2.10%	0.1
3-prod	1178	1221	3.65%	2
4-prod	1677	1721	2.62%	3
5-prod	2052	2127	3.65%	7
6-prod	2407	2516	4.53%	18
7-prod	2874	3008	4.66%	69
10-prod	4078	4237	3.90%	2377

References

- Apap, R. M., & Grossmann, I. E. (2017). Models and computational strategies for multistage stochastic programming under endogenous and exogenous uncertainties. *Computers & Chemical Engineering*, 103, 233-274.
- Christian, B., & Cremaschi, S. (2014). A Quick Knapsack Heuristic Solution for Pharmaceutical R&D Pipeline Management Problems. *Computer-Aided Chem Engineering*, 33, 1285-1290.
- Christian, B., & Cremaschi, S. (2015). Heuristic solution approaches to the pharmaceutical R&D pipeline management problem. *Computers & Chemical Engineering*, 74, 34-47.
- Christian, B., & Cremaschi, S. (2017). Variants to a knapsack decomposition heuristic for solving R&D pipeline management problems. *Computers & Chemical Engineering*, 96, 18-32.
- Christian, B., & Cremaschi, S. (2017). A branch and bound algorithm to solve large-scale multistage stochastic programs with endogenous uncertainty. *AIChE Journal*, DOI 10.1002/aic.16019.
- Colvin, M., & Maravelias, C. T. (2009). Scheduling of testing tasks and resource planning in new product development using stochastic programming. *Computers & Chemical Engineering*, 33(5), 964-976.
- Colvin, M., & Maravelias, C. T. (2010). Modeling methods and a branch and cut algorithm for pharmaceutical clinical trial planning using stochastic programming. *European Journal of Operational Research*, 203, 205-215.
- Gupta, V., & Grossmann, I. E. (2014). A new decomposition algorithm for multistage stochastic programs with endogenous uncertainties. *Computers & Chemical Engineering*, 62, 62-79.
- Solak, S., Clarke, J. P. B., Johnson, E. L., & Barnes, E. R. (2010). Optimization of R&D project portfolios under endogenous uncertainty. *European Journal of Operational Research*, 207(1), 420-433.
- Tarhan, B., & Grossmann, I. E. (2008). A multistage stochastic programming approach with strategies for uncertainty reduction in the synthesis of process networks with uncertain yields. *Computers & Chemical Engineering*, 32(4), 766-788.
- Z. Zeng, & S. Cremaschi (2017) Artificial lift infrastructure planning for shale gas producing horizontal wells. *FOCAPO/CPC*, Tuscan, AZ.

A Time-series-based approach for robust design of multi-energy systems with energy storage

Paolo Gabrielli^a, Florian Furer^a, Portia Murray^{b,c}, Kristina Orehounig^{b,c},
Jan Carmeliet^{b,c,d}, Matteo Gazzani^c and Marco Mazzotti^{a,*}

^a*Institute of Process Engineering, ETH Zurich, Sonneggstrasse 3, 8092 Zurich, Switzerland*

^b*Chair of Building Physics, ETH Zurich, Stefano-Franscini-Platz 5, 8093 Zurich, Switzerland*

^c*Laboratory for Urban Energy Systems, EMPA, Dübendorf, Switzerland*

^d*Laboratory for Multiscale Studies in Building Physics, EMPA, Dübendorf, Switzerland*

^e*Copernicus Institute of Sustainable Development, Utrecht University, Heidelberglaan 2, 3584 CS Utrecht, The Netherlands*

marco.mazzotti@ipe.mavt.ethz.ch

Abstract

This work proposes a mixed-integer linear program approach to consider the uncertainty of input data in the optimal design of distributed multi-energy systems involving both conventional and renewable-based conversion technologies, as well as storage units. The design procedure determines the minimum-cost combination of technology selection, size and operation. Traditionally, distributed multi-energy systems are designed using deterministic optimization methods, implying that the input data are known when the system optimization is performed. However, such input data are commonly affected by significant uncertainty, making the deterministic solution possibly suboptimal or even unfeasible. Recently, both robust and stochastic optimization have been applied to the optimal design of multi-energy systems. Nevertheless, when including energy storage in the analysis, the traditional techniques are complicated by the short- and long-term evolution of the input data of the underlying optimization problem, as well as their complex interactions. Moreover, the analysis of the uncertainties characterizing such input data for the optimal design of multi-energy systems, as well as the evaluation of their impact on the system design, have been investigated in little details. The approach proposed in this work is based on the analysis of the historical time-series representing the input data of the mixed-integer linear program for different years. First, the most important input data in terms of optimality and robustness of the system design are identified. Moreover, the most relevant features of the corresponding time-series are determined and assessed. Then, this information is used to build a custom set of input data which translates into a system design able to guarantee both security of supply and cost optimality.

Keywords: Multi-energy systems, time-series analysis, MILP, stochastic optimization, energy storage

1. Introduction

The necessity of reducing the environmental impact of the current energy system has led to the development and deployment of conversion technologies based on renewable energy sources, storage systems to compensate for the resulting intermittent generation, as well as novel paradigms to design the future energy system, International Energy Agency (2016). Within this framework, distributed multi-energy systems (MES) integrating multiple energy carriers (e.g. electricity, heat,

natural gas, hydrogen) with high fractions of renewable energy and storage technologies, are promising options to cope with this challenge, Mancarella (2014). Within the analysis and optimization of MES, mixed integer linear program (MILP) has been particularly favored as optimization framework since it well catches the features of such systems with a reasonable computational complexity, Allegrini et al. (2015).

Traditional MILP approaches for the design of distributed multi-energy systems use deterministic optimization, implying that the boundary conditions of the optimization problem, i.e. weather conditions, energy prices and demands, are known with certainty when the optimization is performed, e.g. Weber and Shah (2011); Gabrielli et al. (2017a). However, the aforementioned input data are commonly affected by considerable uncertainty, making the deterministic solution possibly suboptimal or even infeasible, Ben-Tal et al. (2009). Recently, robust and stochastic MILP methods have been proposed to tackle the data uncertainty so as to guarantee the feasibility of the solution, which translates into security of energy supply under different operating conditions. In fact, both approaches have been investigated in literature. During his thesis, Mavromatidis (2017) investigated the optimal design of distributed urban energy systems under uncertainty. He compared a stochastic formulation, the traditional robust formulation by Soyster (1973), the robust optimization with uncertainty budget proposed by Bertsimas and Sim (2004), and the finely adjustable robust optimization introduced by Ben-Tal et al. (2004). Another approach was proposed by Majewski et al. (2017), who proposed a two-stage robust optimization considering at the same time the average and the worst-case scenarios and applied it to the optimal design of an industrial park. They found that robustness and optimality are not mutually exclusive, as the robust design itself is not more expensive, but the cost of the system increases only when worst-case operation occurs. Furthermore, Billionnet et al. (2016) have considered the design of a stand-alone energy system under uncertainty pertaining to both energy demands and solar and wind generation, whereas Zatti et al. (2017) proposed a three-stage stochastic integer programming model accounting for the uncertainty in the short-term forecast, the day-ahead electricity bidding, the day-ahead scheduling of large power plants and the possibility of real-time scheduling adjustment of flexible energy systems (through integer recourse). Despite these previous works, the analysis of the uncertainties characterizing the boundary conditions for the optimal design of distributed multi-energy systems, as well as the evaluation of their impact on the system design, have been investigated in little details. Moreover, when considering energy storage, traditional robust and stochastic optimization techniques are further complicated by the short- and long-term evolution of the input data, as well as their interactions. Indeed, large optimization problems can result from stochastic optimization due to the creation of a large number of scenarios, or from robust optimization due to the adoption of large uncertainty sets. Here, a three-stage procedure is developed based on the analysis of the historical time-series of the input data of a MILP problem aimed at determining the optimal combination of technology selection, size and operation in terms of total annual cost of the system. First, the optimal deterministic system design is determined for several sets of input data from different years. Next, each of the resulting designs, corresponding to a given year, is tested by operating it for all the other years. Within this phase, every design is evaluated in terms of cost optimality and robustness. Finally, the most relevant inputs, as well as the most important features of the time-series, are identified and assessed to build a custom year which ensures both cost optimality and robustness. A Swiss case-study is considered.

2. Problem formulation and system description

The multi-energy system (MES) considered in this study has the primary scope of supplying electricity and heat to a defined user. The MES is connected to the electrical grid and is composed of a set of conversion and storage technologies. A deterministic MILP is formulated to determine the

optimal system design. It can be written in the general form as

$$\begin{aligned}
 & \min_{\mathbf{x}, \mathbf{y}} (\mathbf{c}^T \mathbf{x} + \mathbf{d}^T \mathbf{y}) \\
 & \text{s.t.} \\
 & \mathbf{Ax} + \mathbf{By} = \mathbf{b} \\
 & \mathbf{x} \geq \mathbf{0} \in \mathbb{R}^{N_x}, \mathbf{y} \in \{0, 1\}^{N_y}.
 \end{aligned} \tag{1}$$

Inputs to the optimization problem are the (i) electricity price, (ii) end-users energy demands, (iii) weather conditions (ambient temperature and solar radiation), and (iv) set of available technologies with the corresponding performance and cost coefficients. Outputs of the optimization problem are the design and operation strategy which yield to the minimum total annual cost. In particular, the following decision variables are returned: (i) the size of the installed technologies, (ii) the scheduling (on/off) status of the conversion units, (iii) the input/output energy of both conversion and storage technologies, (iv) the amount of energy in the storage units, (v) the imported/exported energy from/to the electricity grid. The objective function of the optimization problem is the total annual cost of the system, given by the sum of capital, operation and maintenance contributions. The constraints of the optimization problem include the (i) energy balances within the multi-energy system, and (ii) performance of conversion and storage technologies. The former require that the sum of imported and generated power equals the sum of exported and used power for all the involved energy carriers. The latter describe the behavior of the conversion and storage units. Affine and piecewise affine descriptions of conversion and storage technologies are implemented to correlate the output power to the input power and to the unit size, as indicated in Gabrielli et al. (2018). The optimization framework implements the time-series aggregation method M2 introduced by Gabrielli et al. (2017b) to consider the entire year with hour resolution as the time horizon at reduced computation complexity. Overall, a detailed description of the optimization framework can be found in Gabrielli et al. (2017b).

2.1. Modeling the uncertainty

The input data (i)-(iii) are time-dependent profiles for one year with hourly resolution, based on historical realizations for a neighborhood in Zurich, Switzerland. Such input data are calculated and discussed by Murray et al. (2017). The proposed design approach is based on the following three-stage procedure:

- First, the MILP discussed above, given by Eq. 1, is applied to obtain the optimal deterministic design for the aforementioned multi-energy system for different sets of input data describing different years.
- Next, each of the resulting designs is tested by operating it on all the other years. At this stage, every design is evaluated in terms of cost optimality and robustness. In specific, an optimality index O is introduced for every year i :

$$O_i = \frac{1}{N} \left(\sum_{j=1}^N \frac{c_{jj}}{c_{ij}} \right) \tag{2}$$

where N is the number of considered years and $c_{i,j}$ the total annual cost (in /yr) obtained by operating on year j the design determined with year i . Similarly, a robustness index R is introduced for every year i :

$$R_i = 1 - \frac{1}{v_{\max} N} \left(\sum_{j=1}^N v_{ij} \right) \tag{3}$$

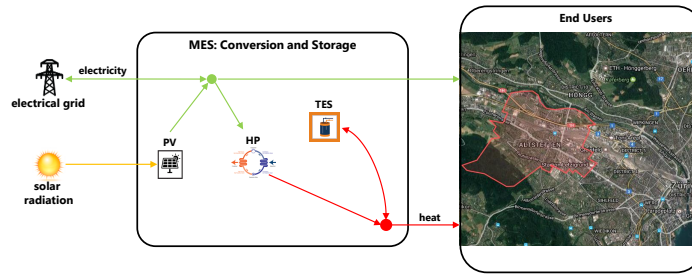


Figure 1: Schematic representation of the investigated multi-energy system.

where v_{ij} is the thermal demand not delivered (in kWh/yr) when operating on year j the design determined by using year i and v_{\max} is the maximum registered violation. Note that the decision of defining the robustness index based on the thermal demand (instead of the electrical or the total demand) stems from the consideration that, in this work, the electrical demand can always be satisfied by purchasing electricity from the grid.

- Finally, the most relevant inputs, as well the most important features of the time-series, are identified and assessed to build custom years ensuring both cost optimality and robustness at design level.

2.2. Case study

The proposed methodology is applied to the simple multi-energy system illustrated in Fig. 1, composed of photovoltaic (PV) panels, electricity-driven heat pump (HP), and hot water sensible thermal storage (TES). The system is connected to the electricity grid and provides electricity and heat to a neighborhood requiring a peak electrical and thermal demands of 0.42 MW and 2.01 MW, respectively. Here, we consider a single energy hub that satisfies the heat and electricity demands; therefore, the energy is converted and stored in a central node and then delivered to the buildings (see Gabrielli et al. (2017b)). Moreover, a constraint of 260 ton/yr is imposed on the maximum amount of CO₂ emissions. Such constraint corresponds to a 50% emission reduction with respect to the worst possible value for all the years. Such a limit is imposed to force the installation of PV panels, so to account for the solar radiation within the analysis.

3. Results

Some preliminary results are presented in this section, by using four different years including extreme high weather conditions (ambient temperature and solar radiation), extreme low weather conditions, and average weather conditions for two different years. Figure 2 shows the robustness-optimality Pareto front for the investigated years, where the color code indicates either the total electrical and thermal annual demand (left-hand side) or the 5-day peak thermal demand (right-hand side). The 5-day peak thermal demand is the largest thermal demand during a sequence of five days for all the considered years (integral value). For the considered pool of years, the analysis suggests that this is a good indicator of the robustness of the system design. Similarly, the total electrical and thermal annual demand is found to be a good indicator of the system optimality. Indeed, the left-hand side of Fig. 2 shows that an increase in optimality is observed when decreasing the total annual demand. Thus, the year 1 is the most optimal year, but the least robust one. Moreover, the right-hand side of the figure shows that an increase in robustness is observed when increasing the 5-day peak thermal demand. Therefore, the year 4 is the most robust year, but the

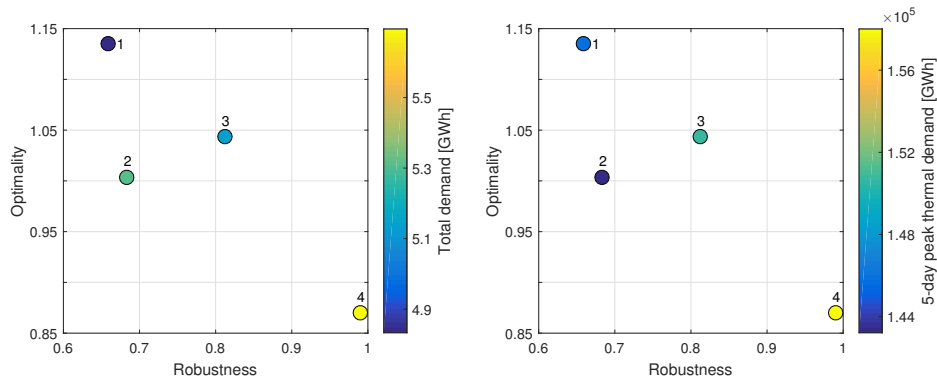


Figure 2: Robustness-optimality Pareto front for the four considered years. The color code indicates the total electrical and thermal annual demand (left) and the 5-day peak thermal demand (right).

least optimal one. The years 2 and 3 are located in the middle of the robustness-optimality plane, with year 2 being dominated by year 3.

Following these considerations, a custom year is built by replacing the five days of year 4 where the peak thermal demand occurs within the year 1, characterized by the lowest total demand. Such a custom year is reported on the robustness-optimality Pareto front in Fig. 3. One can note that the custom year improves the optimality by about 15% while reducing the robustness of only 0.7%. This suggests that starting from favorable conditions and adding an extreme event translates into an optimal and robust system design. Note that, in addition to providing a method to increase optimality and robustness at the same time, a quantitative evaluation of indicative extreme events can provide relevant insights (i) from a robust optimization perspective, e.g. indications for choosing suitable uncertainty sets; (ii) in terms of most suited clustering features for modeling the time horizon. Indeed, the investigated application highlights the necessity of detecting sequences of day, in this case a five-day sequence of high thermal demand, when applying clustering techniques

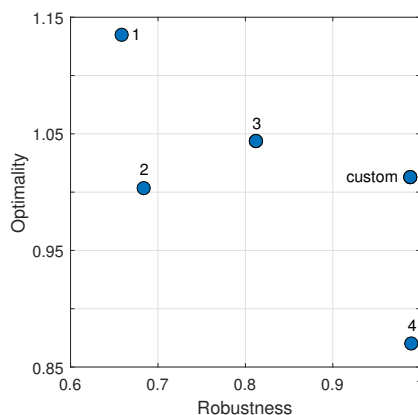


Figure 3: Robustness-optimality Pareto front for the four considered years and the custom year built by combining the total demand of year 1 and the 5-day peak thermal demand of year 4.

on the time horizon.

4. Conclusions

This work proposes a MILP approach to consider the uncertainty of the input data in the optimal design of distributed multi-energy systems involving both conventional and renewable-based conversion technologies, as well as storage units. A three-stage procedure is developed, based on the analysis of the historical time-series of the input data characterizing the underlying optimization problem. First, the optimal deterministic system design is determined for several sets of input data describing different years. Next, each of the resulting designs, corresponding to a given year, is tested by operating it on all the other years. Within this phase, every design is evaluated in terms of cost optimality and robustness. Finally, the most relevant inputs, as well the most important features of the time-series, are identified and assessed to build a custom year ensuring both cost optimality and robustness of the design. Findings show that the total electrical and thermal annual demand is an important indicator of the system optimality, whereas a five-day sequence of peak thermal demand is found to be a good indicator of the system robustness. A custom year built by accounting for both these features is found to ensure optimality and robustness at the same time.

Acknowledgment

This work was supported by the Swiss National Science Foundation (SNF) under the National Research Program Energy Turnaround (NRP70), grant number 407040-153890 (IMES project).

References

- J. Allegrini, K. Orehounig, G. Mavromatidis, F. Ruesch, V. Dorer, R. Evins, 2015. A review of modelling approaches and tools for the simulation of district-scale energy systems. *Renewable and Sustainable Energy Reviews* 52, 1391–1404.
- A. Ben-Tal, L. El Ghaoui, A. Nemirovski, 2009. *Robust Optimization*. Princeton University Press.
- A. Ben-Tal, A. P. Goryashko, A. Nemirovski, 2004. Adjustable robust solutions of uncertain linear programs. *Mathematical Programming* 99, 351–376.
- D. Bertsimas, M. Sim, 2004. The Price of robustness. *Operations Research* 52 (1), 35–53.
- A. Billionnet, M.-C. Costa, P.-L. Poirion, 2016. Robust optimal sizing of a hybrid energy stand-alone system. *European Journal of Operational Research* 254 (2), 565–575.
- P. Gabrielli, M. Gazzani, E. Martelli, M. Mazzotti, 2017a. A MILP model for the design of multi-energy systems with long-term energy storage. In: A. Espuña, M. Graells, L. Puigjaner (Eds.), *Computer aided chemical engineering*. Vol. 40. Elsevier, Amsterdam, Netherlands, pp. 2437–2442.
- P. Gabrielli, M. Gazzani, E. Martelli, M. Mazzotti, 2017b. Optimal design of multi-energy systems with seasonal storage. *Applied Energy*.
- P. Gabrielli, M. Gazzani, M. Mazzotti, 2018. Electrochemical conversion technologies for optimal design of decentralized multi-energy systems: modeling framework and technology assessment. International Energy Agency, 2016. *Energy, Climate Change & Environment: 2016 Insights*. Tech. rep.
- D. E. Majewski, M. Lampe, P. Voll, A. Bardow, 2017. TRusT: A Two-stage Robustness Trade-off approach for the design of decentralized energy supply systems. *Energy* 118, 590–599.
- P. Mancarella, 2014. MES (multi-energy systems): An overview of concepts and evaluation models. *Energy* 65, 1–17.
- G. Mavromatidis, 2017. Model-based design of distributed urban energy systems under uncertainty. Ph.D. thesis, ETH Zurich.
- P. Murray, A. Omu, K. Orehounig, J. Carmeliet, 2017. Power-to-gas for Decentralized Energy Systems : Development of an Energy Hub Model for Hydrogen Storage. In: *Building Simulation Conference*. San Francisco.
- A. L. Soyster, 1973. Convex programming with set-inclusive constraints and applications to inexact linear programming. *Operations research* 21 (February 2015), 1154–1157.
- C. Weber, N. Shah, 2011. Optimisation based design of a district energy system for an eco-town in the United Kingdom. *Energy* 36 (2), 1292–1308.
- M. Zatti, E. Martelli, E. Amaldi, 2017. A three-stage stochastic optimization model for the design of smart energy district under uncertainty. In: *Computer aided chemical engineering*. Elsevier, pp. 2389–2394.

Ordinary Kriging: A machine learning tool applied to mixed-integer multiparametric approach

Gicela Lupera^a, Ahmed Shokry^a, Sergio Medina-González^a, Eduardo Vyhmeister^b, Antonio Espuña^{a*}

^a*Center for Process and Environmental Engineering-CEPIMA, Av. Eduard Maristany 16, Barcelona 08019, Spain.*

^b*Universidad Central de Chile, Toesca 1783, Chile.*

antonio.espuna@upc.edu

Abstract

The complexity of optimization problems of optimization problems increases along with the dimensions, non-linearity, and/or the required accuracy of the model constraints and objective functions. Additionally, for mixed-integer multiparametric problems, the discreet and uncertain nature of the variables and parameters to be considered, affect the complexity further more. Recently, machine learning or data-driven techniques have been proposed as alternatives for the solution of complex multiparametric programming problems. However, those methods presents as a main limitation its very high prediction error in variables that show discrete behavior and on the limits of the critical/local regions. This work extends this investigation line via proposing a novel machine learning method for solving these kind of problems based on an iterative process that use Ordinary Kriging as supervised learning tool to classify and model data. Furthermore, Ordinary Kriging can be also used, as an unsupervised tool to cluster data. The proposed methodology is applied to a benchmark case-study and the numerical results exhibits a significant improvements, up to 65% based on the normalized root-mean-square error, compared with reported information that used other modeling techniques.

Keywords: Machine learning tool, classification, clustering, metamodeling.

1. Introduction

Given the fact that the complexity of today's optimization and simulation problems increases (Qiu, Xu, Gao, Li, & Chi, 2016), Metamodel Based Optimization (MBO) is one of the first-choice methodologies employed in the industrial sector. This can be seen as the most efficient technique for addressing complex optimization problems that cannot be managed using classical /mathematical optimization methods, due to the models high nonlinearity, complexity, dimensionality and/or complicated structure (Bartz-Beielstein & Zaefferer, 2017). The idea behind the MBO is to replace the complex and/or computationally-expensive algorithm with a simpler computationally-cheap data-driven model. These models, also called surrogates models or metamodels, can use different modelling techniques, such as Response Surface Methodology (RSM), Support Vector Machine, Radial Basis Function, Artificial Neural Network, and Gaussian Process Model or Kriging Model (Bartz-Beielstein & Zaefferer, 2017). Among the different metamodeling techniques RSM and Kriging are the most widely used given their prediction accuracy and tuning flexibility (Wang, Li, Li, & Zhong, 2008). Basically a Kriging model is composed of a polynomial term, $f(x)$ which

approximates the global trend of the system, plus a spatial deviation model, $Z(x)$. This model allows Kriging to represent non-linear behavior with high fidelity; Where Z is a stochastic Gaussian process, that represent the uncertainty of the mean of $y(x)$ with expected value zero $E(Z(x))=0$ and covariance for two points $(x_i, x_j) : cov(Z(x_i), Z(x_j)) = \sigma^2 R(x_i, x_j)$. Here σ^2 is a scale factor known as process variance that can be tuned to the data and $R(x_i, x_j)$ is the spatial correlation function (SCF). There are many choices for the SCF, but the most common used in kriging models is the exponential function Eq. (1) (Caballero & Grossmann, 2008).

$$R(x_i, x_j) = \exp\left(-\sum_{l=1}^d \Phi_l |x_{i,l} - x_{j,l}|^{P_l}\right), \quad \Phi_l \geq 0; \quad 0 \geq P_l \leq 2 \quad (1)$$

If $x_i = x_j$, then the SFC is one, and tends to zero as the difference between both points increases. In other words, the influence of the sampled data point on the point to be predicted becomes weaker as the distance among them increases. The value of Φ_l indicates how fast the correlation goes to zero as we move in the l^{th} coordinate direction. For large values of Φ_l , only the data points very close to each other are well correlated. Parameter P_l is a measure of the smoothness of the function. The response becomes smoother as the value for P_l increases. To estimate the values of μ , σ , Φ_l , P_l , the log-likelihood function Eq. (2) is maximized. The final predictor of the kriging method is given by equations (3).

$$\max_{\Phi_l, P_l} -\frac{n}{2} \ln(\sigma^2) - \frac{1}{2} \ln(|R|), \quad \sigma^2 = \frac{(y-1\mu)^T R^{-1} (y-1\mu)}{n} \quad (2)$$

$$\hat{y}(x^{\text{new}}) = \mu + r^T R^{-1} \cdot (y - 1\mu), \quad \mu = \frac{1^T R^{-1} y}{1^T R^{-1} 1} \quad (3)$$

In these equations r is the $n \times 1$ vector of correlations $R(x^{\text{new}}, x_i)$ between the point to be correlated and the sample design points. We are more confident in the prediction if the new point is near a sampled/training point, since then the error drops to zero in all sampled points. A detail of the development of the calculations can be found in (Sasena, 2002).

Recently, (Lupera Calahorrano, Shokry, Campaña, & Espuña, 2016) have successfully proposed a Meta-MultiParametric (M-MP) algorithm for the solution of multiparametric mixed-integer nonlinear problems, through the combination of metamodeling with clustering and classification techniques. However, these techniques are limited to consider continuous optimization problems/variables, because their approach showed a remarkable limitation associated to the very high prediction error of the metamodels at the limits of the critical/local uncertain regions and in the presence of variables with discrete behaviors. Therefore, the contributions to the discrete domain are still an open challenge.

In this work we show a methodology to solve multiparametric mixed-integer nonlinear problems. The methodology proposed is based on a machine-learning procedure, using Ordinary Kriging (OK) as a supervised learning tool to classify the data (e.g., feasible, unfeasible). Also, OK is used as an unsupervised learning tool to identify clusters. Lastly, OK is used for modelling the data of each cluster in order to specify the metamodel that would be used to evaluate the optimal solutions (Z^* , x^* and y^*) with continuous and discrete behavior as a function of the uncertain parameters (θ 's) (Eq. (4)).

$$Z_p^* = f_p(\theta), \quad x_{i,p}^* = f_{i,p}(\theta), \quad y_{j,p}^* = f_{j,p}(\theta) \quad (4)$$

$i = 1, 2, \dots, K_{\text{cnt}}, \quad j = 1, 2, \dots, K_{\text{int}}, \quad p = 1, 2, \dots, P, \quad \theta_{lb^p} < \theta_p < \theta_{ub^p}$

In Eq. (4) Z_p^* is the objective function, θ represents the bounded uncertainty, y is a vector of integer/binary variables, x is a vector of continuous variables.

The proposed methodology is evaluated by applying it to a benchmark case–study (Dua & Pistikopoulos, 1999), later used by Shokry et al., (Shokry, Medina-González, & España, 2017) applying neural networks and K-means techniques to classify and cluster data. Therefore, comparative results with Shokry’s investigation are reported.

2. Methodology

Figure 1, shows a flowchart of the proposed methodology which is briefly explained as follows:

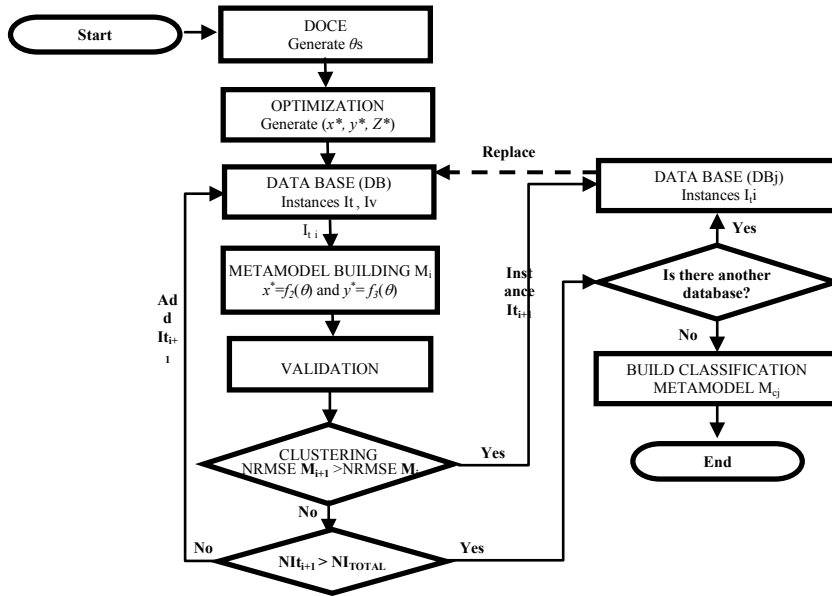


Figure 1. MBO Methodological Flowchart

Design of Computer Experiments (DOCE): Used for generate N combinations of the θ 's values. The design should provide information about all portions of the θ 's space. In the present work, a hybrid sampling technique of Hammersley sequence and full factorial design is used for selecting both the inputs of the training and validation data.

Optimization: Once the θ 's values were defined with DOCE, the mp-MINLP problem was solved to obtain a set of optimal solutions $(x^*, y^*$ and $Z^*)$.

Metamodel building: The metamodel based on OK was built. Since some variables could have a discrete or high nonlinearity behavior, the possibility of the P_l values to be between 0 and 2 during the maximization process of the log-likelihood was considered Eq. (2). This is done to have a wider representation of the smoothness of spatial correlation function.

Clustering: Considering the existence of discrete behaviors of some variables inside the optimization problem, the need to include a clustering technique was identified. Because

the proposed clustering algorithm is an iterative data process: two Data Bases (DB) are formed during the process being DB and DB_j. The starting DB consists of *N* instances (each instance is composed of the θ 's and their corresponding optimal values x^*, y^*, Z^*), both of the set of training instances (I_t) used to build the metamodel and a set of validation instances (I_v) used to validate it metamodel. DB_j is generated in the clustering process.

To begin the clustering process, a metamodel is built with a first set of instances (I_t ∈ DB), that was selected based on the proximity among them (Euclidean distance). Then, through an iterative process, the instances were added one by one to build a metamodel of each variable. After each metamodel is formed as the instances are added, a validation process is performed (base on NRMSE). The modeling and validation is made until completing the total amount of instances of the DB. The instances that produce a NRMSE smaller or equal to the previous one are sent to a primary cluster (DB_j with *j*=1 for the first iteration). Similarly, those that produce a greater NRMSE are sent to a secondary cluster (e.g. DB_j with *j*=2 in the first iteration). Once the original set of instances is completely analyzed, the process is repeated again with the instances not included in the first cluster (DB_j), and the process is repeated until no more clusters are detected.

Classification Metamodel building: The primary and secondary training clusters are used to construct a Classification Metamodel (M_c) based on OK. Where, the desired solutions are fed to the algorithm as labels (e.g.: primary cluster = 1, secondary cluster = 0). Once the M_c is trained, it is used to classify the original validation set I_v, and it will use to identify the cluster of a new instance. Those classified I_v, that belong the validation primary cluster are used to validate the corresponding cluster model. Those classified I_v, that belong the validation secondary cluster are used for next clustering analysis.

Validation: The validation data set is used for the metamodel assessment. The corresponding instances (I_v) were used in order to calculate the NRMSE for each built metamodel. Additionally, once classifying and integer variables models are built, the F₁-score, a measure of a test's accuracy in analysis of binary classification is evaluated to test of accuracy.

3. Case study and Results

With the objective to illustrate the proposed methodology capabilities, the case study proposed by (Dua & Pistikopoulos, 1999) has been used. The basic process scheme and model are illustrated in Figure 2.

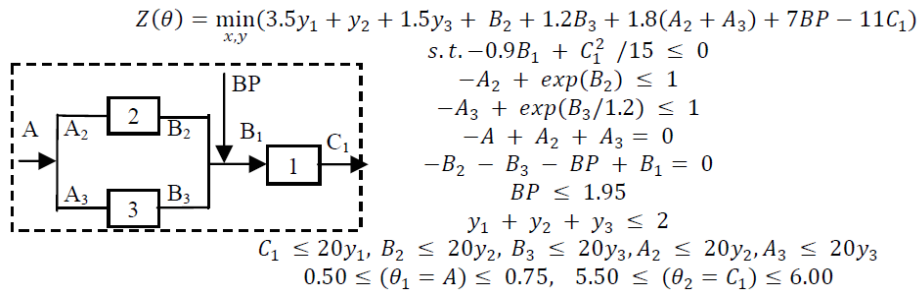


Figure 2. Case-study illustration and model

According to the methodology, a total of 650 samples for the first iteration (as shown in Table 1) has been generated in order to model the θ 's domain $[\theta_1, \theta_2]$. Those samples are used to solve the optimization problem N times and, ultimately, to obtain the optimal value of the main variables and objective function $[A^*, B^*, BP^*, C_1^*, A_2^*, A_3^*, B_2^*, B_3^*, Z^*, y_1^*, y_2^*, y_3^*]_n$. The optimization model has been written in GAMS 23.8.2 and solved using a CEPLEX11.0 on a PC (Intel (R) Core (TM) i7-4790 processor, 3.60 GHz, 16.0 GB RAM).

Table 1. Sample/iteration

No. Instances	Clustering		Metamodel's validation	Classification Metamodel
	I_c	I_v	I_v	I_c
DB	250	400	23	8
DB ₁	242	377	55	40
DB ₂	202	322	322	-

Once the proposed methodology based in OK is applied, the unfeasible region and 3 clusters have been identified in the feasible region (Figure 3). Therefore, 39 MBOs and 2 M_C have been built to resolve the case study. The results of 39 metamodels validation (based on NRMSE/ F_1 -score) together with the computational effort to build the models are summarized in Table 2. With the objective to compare techniques, the validation results of 13 MOBs based on OK and a single cluster per variable, are presented in Table 3. Finally, Table 4 show the results of MOBs' validation, which were based on Artificial Neural Network (ANN) to classification, K-means to clustering and OK to modelling, obtained in previous research realized by Shokry et al., (Shokry et al., 2017).

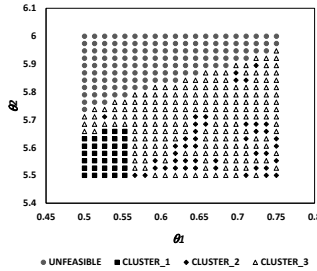


Figure 3. MOB clusters

Table 2. Results of MBO based on OK, (classification, clustering, metamodeling)

Cluster	NRMSE (%)									F ₁ -score (%)			
	A*	A ₂ *	A ₃ *	B ₁ *	B ₂ *	B ₃ *	BP*	C ₁ *	Z*	y ₁ *	y ₂ *	y ₃ *	F*
C1	0.2	0.1	0.0	0.4	0.1	0.0	0.3	0.1	0.0	100	100	100	100
C2	0.1	7.0	5.7	0.1	6.9	5.9	0.2	0.1	0.0	100	100	100	100
C3	1.1	14.0	11.9	0.1	13.4	12.2	4.4	0.1	0.5	100	98	97	99
CPU time (s)	Classifiers			1.8	Clustering		1952.0	Metamodels		19.6			

Table 3. Results of MBO based on OK (1 cluster)

Cluster	NRMSE (%)									F ₁ -score (%)			
	A*	A ₂ *	A ₃ *	B ₁ *	B ₂ *	B ₃ *	BP*	C ₁ *	Z*	y ₁ *	y ₂ *	y ₃ *	F*
C1	1.4	18.2	17	1.1	18.2	17.6	5.2	0.2	0.9	100	100	100	100
CPU time (s)	Classifiers			--	Clustering		--	Metamodels		68.1			

Table 4. Results of MBO based on OK (modeling), ANN (classification), K-Means (clustering)

Cluster	NRMSE (%)									F ₁ -score (%)			
	A [*]	A ₂ [*]	A ₃ [*]	B ₁ [*]	B ₂ [*]	B ₃ [*]	BP [*]	C ₁ [*]	Z [*]	Y ₁ [*]	Y ₂ [*]	Y ₃ [*]	F [*]
1	1.2	0.4	0.4	1.1	0.0	0.0	4.8	0.1	0.5	100	98.5	97	99
2	-	21.5	20.7	-	17.0	20.1	-	-	-				

(Shokry, Medina-González, & Espuña, 2017)

These results show that the proposed MBO technique allows reductions from 15% and up to 65% in the worst NRMSE values (34% in the average worst case), compared with a MBO built with one cluster. On the other hand, when the results now proposed are compared with previous research using artificial neural network and k-mean as techniques for classification and clustering, the proposed MBO methodology allows significant reductions. In particular, the average worst NRMSE values was improved in 24% in the average worst case (from 1% and up to 64%) and a more comprehensive treatment of the information (same clusters for all variables).

4. Conclusions

The OK can be used as an effective machine learning tool for classifying, clustering and modelling based in data. The proposed MBO methodology allows addressing mp-MINL problems satisfactorily obtaining reduction up 65% of NRMSE values compared with previous research and when it is built with a MBO. The same clusters for each variable were identified in all domain of problem, evidencing with this result the interrelation between the variables in the system.

Acknowledgements:

Financial support received from the Spanish "Ministerio de Economía, Industria y Competitividad" and the European Regional Development Fund, both funding the research Project AIMS (DPI2017-87435-R), the Mexican council of science and technology (CONACyT) and the Government of Ecuador through the National Secretary of Higher Education, Science, Technology and Innovation is fully acknowledged.

References

- Bartz-Beielstein, T., & Zaefferer, M. (2017). Model-based methods for continuous and discrete global optimization. <https://doi.org/10.1016/j.asoc.2017.01.039>
- Caballero, J. A., & Grossmann, I. E. (2008). An algorithm for the use of surrogate models in modular flowsheet optimization. <https://doi.org/10.1002/aic.11579>
- Dua, V., & Pistikopoulos, E. N. (1999). Algorithms for the Solution of Multiparametric Mixed-Integer Nonlinear Optimization Problems. <https://doi.org/10.1021/ie980792>
- Lupera Calahorrano, G. J., Shokry, A., Campanya, G., & Espuña, A. (2016). Application of the Meta-Multiparametric methodology to the control of emissions in the industry under continuous and discrete uncertain parameters. <https://doi.org/10.1016/j.cherd.2016.09.006>
- Qiu, H., Xu, Y., Gao, L., Li, X., & Chi, L. (2016). Multi-stage design space reduction and metamodeling optimization method based on self-organizing maps and fuzzy clustering. <https://doi.org/10.1016/j.eswa.2015.10.033>
- Sasena, M. J. (2002). Flexibility and Efficiency Enhancements for Constrained Global Design Optimization with Kriging Approximations. <https://doi.org/10.1.1.2.4697>
- Shokry, A., Medina-González, S., & Espuña, A. (2017). Mixed-Integer MultiParametric Approach based on Machine Learning Techniques. *Computer Aided Chemical Engineering*, 40, 451–456. <https://doi.org/10.1016/B978-0-444-63965-3.50077-5>
- Wang, H., Li, E., Li, G. Y., & Zhong, Z. H. (2008). Development of metamodeling based optimization system for high nonlinear engineering problems. <https://doi.org/10.1016/j.advengsoft.2007.10.001>

Assessment of technology portfolios with enhanced economic and environmental performance for the energy, water and food nexus

Rajesh Govindan^{a*}, Tareq Al-Ansari^a, Anna Korre^b, Nilay Shah^c

^a*Division of Sustainable Development, College of Science and Engineering, Hamad Bin Khalifa University, Qatar Foundation, Doha*

^b*Department of Earth Science and Engineering, Royal School of Mines, Imperial College, London SW7 2BP, U.K.*

^c*Department of Chemical Engineering, Imperial College, London SW7 2AZ, U.K.*

*rgovindan@hbku.edu.qa

Abstract

In modern day sustainable development, it has become necessary to apply integrated approaches that aid in the understanding of the synergies and trade-offs between various systems and processes which co-exist and utilizing the resources in the energy, water and food nexus has become necessary. The research presented in this paper discusses a probabilistic risk-based approach to assess the diversification of the energy economy, which would particularly play an important role in the enhancement of food security in the State of Qatar. The modern portfolio theory was adopted for this purpose and was used to evaluate energy portfolios with enhanced economic and environmental performance, when compared to the constituent power generation assets. The results obtained thus far demonstrate that a symbiosis between the industries related to energy and biomass waste utilisation could simultaneously help tackle the problem of environmental deterioration and mitigate economic risks, primarily caused by the variabilities in the natural gas and CO₂ prices.

Keywords: Food Security, Portfolio Theory, Stochastic Processes.

1. Introduction

The growth in global population and rapid urbanization pose significant stresses on the Earth's natural resources. Recent research efforts focusing on sustainable development have increasingly placed an emphasis on the importance of assessing the energy, water and food (EWF) nexus to gain a deeper understanding of the intricate relationships that exist between the processes that utilize the EWF resources. There exists a significant body of literature that discusses the application of the Life Cycle Assessment (LCA) methodology which enables a holistic understanding of the interactions between industrial processes, product cycles, and value-chain accounting (e.g. Al-Ansari et al., 2014; 2015; 2016; 2017). Al-Ansari et al. (2014) presented a LCA modelling framework of the EWF system, implemented for a case study of domestic food production intensification set in the State of Qatar aiming to deliver a hypothetical pre-specified crop profile that represents 40% of the total food requirement. Multiple technological configurations were assessed, and their environmental impacts were

quantified within the EWF nexus. It was recognized that opportunities to reduce the net impact on the environment could be sought by focusing on the integration of technologies to capture CO₂ emissions and recycle biomass waste for energy production. However, such portfolios are exposed to potential risks and uncertainties, e.g. fluctuations in fuel prices; innovations in renewable energy technologies, which influence their capital and operating cost competitiveness against fossil fuel-based technologies; compliance requirements in the ever-changing national and international regulatory environments; and geopolitical risks. To the best of the authors' knowledge, the current literature does not include a robust approach for accounting the economic risks in technology portfolios which could be used to assess the sustainable development of energy sub-systems in the EWF nexus.

The objective of the work presented in this paper is to develop a methodology focusing on the techno-economic assessment of EWF sub-systems, including the probabilistic modelling of tangible risks that are associated with them. The individual levelized energy costs under uncertainty were estimated for the different power generation assets, namely conventional natural gas-fuelled combined cycle (CCGT) power plants; biomass integrated gasification combined cycle (BIGCC) power plants; CCGT and BIGCC power generation with the integration of post-combustion carbon capture (PCC) technology; and harnessing solar power using photovoltaic cells. The important risks considered in this study include the natural gas and CO₂ price variations that were modelled using some of the well-known stochastic processes, namely mean-reverting jump diffusion and geometric Brownian motion. Modern portfolio theory (MPT) was implemented for assessing the energy sub-systems under twelve EWF scenarios that serve a 40% food production increase for the State of Qatar. The aim is to develop an understanding of energy diversification that can be used to deliver food security in Qatar in an economically and environmentally sustainable manner.

2. Cost of electricity generation

2.1. Natural gas combined cycle power plant

Natural gas-fired plants have become a mainstay of the power generation industry, with a share of about 20% of the global electricity production and which is expected to rise owing to its low investment costs, high thermal efficiencies, high reliability and high flexibility (Italiana, 2012). The US Electric Power Research Institute (EPRI) has estimated that the expected value of capital costs would lie in the range of \$1,060 - \$1,150 per kW for CCGT plants without carbon dioxide capture, against a higher range of \$1,600 - \$1,900 per kW for CCGT plants with carbon dioxide capture (EPRI, 2011). The main problem, however, with natural gas-based power generation is the volatility of gas price, which could have a damaging effect on economic growth in countries that rely heavily on gas-fired power generation.

2.2. Biomass-based power generation

One of the solutions proposed in the literature is to utilize the carbon-neutral energy locked within biomass (from the syngas produced) for co-firing with natural gas. This can be controlled in providing reliable power following the variable load by means of a co-firing process called the Biomass Integrated Gasification Combined Cycle (BIGCC). A problem, however, is related to uncertainties in the economics of power generation

using biomass, and under most circumstances it is not very favourable due to the high capital costs incurred in the short-term, primarily owing to significant differences in the composition of natural gas and syngas. It is therefore recognized that the co-firing using the mixture of natural gas and biomass gas could reduce the costs of electricity from biomass by bringing about economies of scale (Faaij et al., 1998). An indicative capital cost requirement for retrofitting biomass co-firing to an existing coal-fired power plant is in the range of \$50 - \$500 per kW of biomass generating capacity in the United States depending on the type of boiler; the prices are likely to be similar in Europe (Breeze, 2014).

2.3. Solar power using photovoltaic cells

Solar energy is one of the vital resources that is freely available and sustains all forms of biomass on the Earth's surface. In many parts of the world where there is a good solar resource, high levels of sunlight can provide synchronized peak power with demand, particularly in the form of rooftop solar panels. Solar-generated electricity was generally considered as an expensive source of electricity, particularly from photovoltaic cells relative to electricity derived from fossil fuels. However, there now exists a noticeable fall in the costs owing to technological advances and economies of scale due to the rise in production volumes (Breeze, 2014). Moreover, there has been fierce competition from the photovoltaic manufacturers in China by undercutting the prices of traditional manufacturers in the United States and Europe. The cost of a crystalline silicon solar cell in Europe in 2009 was \$2,620 per kW, but by the beginning of 2013 the cost had fallen to \$790 per kW (Breeze, 2014). A similar price trend is also true for other solar cell types, such as the cadmium-telluride thin films. This is beginning to make solar photovoltaics competitive with fossil fuel-based power generation technologies today, even without government subsidies, depending on location.

3. Methodology

The Levelized Cost of Electricity (LCOE) in Eq. (1) was adopted in the current work since it allows for the direct comparison of the costs of electricity generation projects with unequal economic life, capital costs, risks and returns, capacity factor, efficiencies, and fuel costs. It is defined as:

$$LCOE = \frac{\text{Capital Investment} + \sum_{n=1}^N \frac{O \& M \text{ Costs}}{(1 + DR)^n}}{\sum_{n=1}^N \frac{\text{Net Annual Energy Generated} (1 - DF)^n}{(1 + DR)^n}} \quad (1)$$

where DF is the degradation factor, which considers the deterioration of performance of CCGT; and DR is the discount rate, which allows the consideration of the time value of money and O&M stand for operating and maintenance costs. Some of the key economic risks were modelled by simulating the stochastic paths for both natural gas and CO₂ prices using market parameters available in the literature that were calibrated using historical price movements (Lucheroni and Mari, 2017). The stochastic behaviour of price paths for fossil fuels, such as natural gas, is described using the mean-reverting jump diffusion process, given by:

$$dX_t = (\alpha - \kappa X_{t-1}) dt + \sigma dW_t + J_t(\mu_J, \sigma_J) d\pi_t(\lambda_J) \quad (2)$$

where X is the (log) price value; α and κ are mean reversion parameters; σ is the price volatility; W is a standard Brownian motion (or Weiner process); J is the jump amplitude, with normally distributed mean μ_j and standard deviation σ_j ; and π is a Poisson process with constant intensity λ_j . This scheme captures the economic logic of considering large variations in price owing to unexpected events/shocks or abnormal arrival of news and information. An additional source of risk for power generation using fossil fuels also comes from the fluctuations in nominal carbon prices. The carbon price path evolution is usually represented with a simpler model, such as the geometric Brownian motion, given by:

$$dX_t = \mu X_{t-1} dt + \sigma X_{t-1} dW_t \quad (3)$$

where X is the (log) price value; μ is the percentage drift expected per annum, normally assumed to be associated with the inflation rate; σ is the daily volatility expected in the prices; and W is a Weiner process. In the case of BIGCC, BECCS (BIGCC integrated with carbon capture) and PV technologies, however, only systematic risks or volatilities were assumed, and thus explicit modelling of other potential risk factors was not considered in this study. Finally, the estimated values were used to implement the MPT theory (Markovitz, 1952) to assess the economic performance of different energy portfolios that cater for the resource requirements in the EWF nexus to meet the stated target of 40% in the annual domestic food production in the State of Qatar (see Table 1).

Table 1. Power generation portfolios considered in this study.

Scenario	a	b	c
1 Conventional mode	CCGT is used to power the water and food sub-systems.	PV is integrated with the water sub-system.	PV is integrated with the water and food sub-systems.
2 Integration of BIGCC	<i>BIGCC power is distributed amongst the water and food sub-systems.</i>		
	CCGT is used to power the water and food sub-systems.	PV is integrated with the water sub-system. The food sub-system is powered by the CCGT.	PV is integrated with the water and food sub-systems.
3 Integration of PCC	Same as scenario 1(a).	PCC is integrated with the CCGT powering the water sub-system.	PCC is integrated with the CCGT powering the water and food sub-systems.
4 Integration of PV and BECCS (BIGCC + PCC)	<i>BIGCC power is distributed amongst the water and food sub-systems.</i>		
	Same as scenario 2(a).	PV is integrated to power the water sub-system. The food sub-system is powered with the CCGT integrated with PCC.	PV is integrated to power the water and food sub-systems. The BIGCC is integrated with PCC.

4. Results and discussion

Fig 1(a) illustrates selected examples of histograms of the LOCE for the cases 1a and 3a, using CCGT based power generation in the conventional mode and one that includes CO₂ capture respectively. For both the cases, in general, Monte Carlo simulations were performed by drawing 10,000 price paths for both natural gas and CO₂ prices, and computing the corresponding LCOE distributions. Whilst the contributions from the volatilities of the natural gas and CO₂ prices towards the O&M costs are represented in 1a, only that of natural gas is represented in 3a. Meanwhile, a noticeable increase in the average LCOE exists owing to the capital cost of PCC integration. It was also estimated that there is an increase of 7-8% in levelized energy cost with a 10% increase in the cost of natural gas. Fig 1(b) illustrates the results obtained for the estimated LCOE generated by a given portfolio against the corresponding risk level that the costs are subjected to under uncertainty. It was assumed that there exists no correlation between the assets in terms of their capital and operating costs. Interestingly, four distinct clusters arise in the cost and risk structure based on the MPT evaluation, as follows:

- low levelized costs and intermediate risks (2a and 4a) - these portfolios are predominantly driven by power generation using BIGCC;
- intermediate levelized costs and high risks (1a, 3a, 3b and 3c) - these portfolios are purely driven by power generation using CCGT; albeit the increased environmental performance, it is noted that the integration of PCC technology further increases the economic risk owing to the increase in natural gas utilization;
- high levelized costs and low risks (1b and 1c) - these portfolios are predominantly driven by power generation using PV; and
- intermediate levelized costs and intermediate risks (2b, 2c, 4b and 4c) - these portfolios represent the trade-off between the costs and associated risks for power generation using CCGT, BIGCC and photovoltaics, including the integration of PCC technology; based on the current assumptions used in the calculations and scenarios assessed thus far, 4b represents an optimal portfolio, both in terms of its economic and environmental performance.

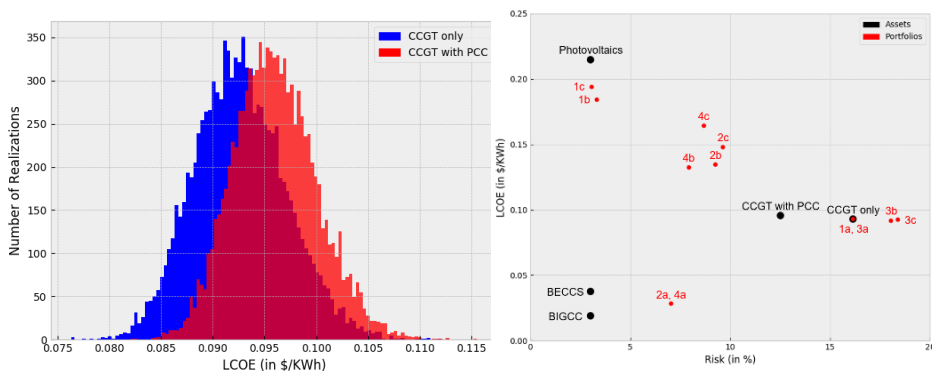


Fig 1. (a) Histograms of the stochastic LCOE values for conventional CCGT and CCGT with CO₂ capture technology integration; (b) Expected LCOE values and associated risk levels for the different portfolios considered in this study.

5. Conclusions

This paper presents a portfolio assessment methodology used to assess the economic risks for a variety of power generation technology portfolios that serve the same food security target within a EWF nexus framework developed for the State of Qatar. Whilst the current results indicate that energy mixes involving conventional CCGT exhibit variability in terms of economic risks, this is readily minimized by the introduction of BIGCC/BECCS technologies, as indicated by the cluster representing the intermediate levelized costs and risks. In addition, the inclusion of photovoltaics further diversifies the mix and hedges against the potential risks owing to the fluctuations in natural gas prices and carbon tax. Moreover, in accordance with the principles of economy of scale and learning curves, a general tendency now exists for the lowering of capital costs, which is expected to make photovoltaics a more competitive form of power generation in the future.

With regards to the drawbacks identified in the proposed methodology, there is a need for an extension to include a detailed consideration of other potential risk factors that have been assumed to be absent in the current assessment, particularly in the cases of renewable energy sources. Moreover, the authors acknowledge that a more rigorous time-dependent stochastic optimization framework with predictive capabilities could be implemented by including the levelized costs of other technologies that participate in the sustenance of the nexus, namely those related to the water and food sectors, and the associated value chains.

References

- Al-Ansari, T., Korre, A., Nie, Z. and Shah, N., 2014. Development of a life cycle assessment model for the analysis of the energy, water and food nexus. In *Computer Aided Chemical Engineering* (Vol. 33, pp. 1039-1044). Elsevier.
- Al-Ansari, T., Korre, A., Nie, Z. and Shah, N., 2015. Development of a life cycle assessment tool for the assessment of food production systems within the energy, water and food nexus. *Sustainable Production and Consumption*, 2, pp. 52-66.
- Al-Ansari, T., Korre, A., Nie, Z. and Shah, N., 2016. Integration of Biomass Gasification and CO₂ Capture in the LCA Model for the Energy, Water and Food Nexus. In *Computer Aided Chemical Engineering* (Vol. 38, pp. 2085-2090). Elsevier.
- Al-Ansari, T., Korre, A., Nie, Z. and Shah, N., 2017. Integration of Greenhouse Gas Control technologies within the Energy, Water and Food Nexus to enhance the environmental performance of food production systems. *Journal of Cleaner Production*, 162, pp. 1592-1606.
- Breeze, P., 2014. *Power generation technologies*. Newnes.
- Electric Power Research Institute, 2011. *Program on Technology Innovation: Integrated Generation Technology Options*, Technical Update, June 2011 (EPRI reference 1022782).
- Faaij, A., Meuleman, B., Turkenburg, W., van Wijk, A.D., Bauen, A., Rosillo-Calle, F. and Hall, D., 1998. Externalities of biomass based electricity production compared with power generation from coal in the Netherlands. *Biomass and Bioenergy*, 14(2), pp.125-147.
- Italiana, F.W., 2012. *Operating flexibility of power plants with CCS*. IEA GHG Report (June 2012).
- Lucheroni, C. and Mari, C., 2017. CO₂ volatility impact on energy portfolio choice: A fully stochastic LCOE theory analysis. *Applied Energy*, 190, pp.278-290.
- Markowitz, H., 1952. Portfolio selection. *The Journal of Finance*, 7(1), pp.77-91.

Multi-objective Optimization for Plant Design via Tabu Search

Faiz Mandani^a, Kyle Camarda^{a,*}

^a*University of Kansas, Department of Chemical & Petroleum Engineering, Eaton Hall,
1520 W 15th St, Lawrence, KS 66045, United States of America*

f088m502@ku.edu and camarda@ku.edu

Abstract

Multi-objective optimization algorithms are employed in chemical process engineering to simultaneously model objectives related to profit, emissions, and safety. The challenge in generating trade-off curves for these problems comes from the nonlinearity and complexity of plant design models, so stochastic optimization techniques are considered in this work to compute Pareto-optimal surfaces. The purpose of this research is to investigate the efficacy and capabilities of the Tabu search algorithm for multi-objective optimization, specifically for plant design models. Traditional Tabu search algorithms have three key characteristics: local intensification, diversification, and the utilization of a Tabu list to apply adaptive memory to guide the search. Local intensification serves to ensure that search areas with several good solutions are searched thoroughly. Diversification allows access to wider regions of the search space.

In this work, a Tabu Search algorithm is developed to solve plant design models for multiple objectives. An alkylation process was investigated in order to maximize the profit while simultaneously minimizing the byproduct formation. This is significant as energy requirements decrease with decreasing byproduct formation. Pareto-optimality curves were generated, and results show how tuning the parameters of the algorithm leads to more efficient determination of the Pareto surface, for highly nonlinear plant design models. While the Tabu search algorithm allows for the generation of Pareto-optimality curves, it is limited for larger problems by its lack of directionality in search. Therefore, the implemented multivariable Tabu search algorithm utilizes a greedy heuristic in determining the next region of the search space to investigate. A bounding component was introduced which progressively tightens of bounds, leading to smaller search regions and improving computational efficiency of the algorithm. Results show the efficacy of the novel approach.

Keywords: Multi-objective Optimization, Tabu Search, Plant Design

1. Introduction

Optimization within plant design enables the determination of operating conditions which produce the most profit, minimize environmental impact, or reduce safety concerns (Kalyanmoy, 2013). Often it is desirable to simultaneously optimize multiple objectives including profit, and environmental impact (Acevedo & Pistikopoulos, 1997). Realistic plant design models are normally formulated as mixed-integer nonlinear programs (MINLPs). When these models are solved while optimizing multiple objectives, the goal becomes the determination of a Pareto-optimal set of solutions. A solution can be classified as Pareto-optimal if one of the objectives cannot be improved without worsening another objective (Rangiah, 2017) The value of the

Pareto-optimal solution set lies in the fact that a process designer can use it to consider trade-offs. For example, a process can be design to operate with lower risk, but at a higher cost. Due to the nonlinearities in the problem formulations, deterministic algorithms often fail to find Pareto-optimal points; therefore, stochastic algorithms are utilized. While other stochastic methods such as genetic algorithms have been used for multi-objective optimization (Fonseca 1995), Tabu search has many advantages which allow an efficient determination of the Pareto-optimal solution set.

Tabu search is a stochastic algorithm developed in 1989 that uses the search history to guide the algorithm (Glover, 1989). Tabu search has been used for job-shop scheduling (Dell'Amico & Trubian, 1993), plant layout problems (Kaku & Mazzola, 1997), and molecular design (McLeese *et al*, 2010). Traditional Tabu search for single variable optimization exhibits three key characteristics: local intensification diversification, and the use of a Tabu list (Glover, 1989).

2. Methods: Multi-objective Tabu Search

To simultaneously optimize two objectives via Tabu search, the first objective is optimized, then the second objective is optimized while holding the first objective within a variable tolerance of the maximum value. Both loops utilize Tabu search with local intensification, diversification, and bound strengthening. Local intensification is a technique applied to promising regions of the feasibility space to ensure that they are more thoroughly searched. A region of the search space may be classified as promising if it contains a solution set for which the objective value exceeds a user-defined benchmark or is within a certain tolerance of a current Pareto-optimal solution. Local intensification reduces the step size of changes to independent variables, ensuring a finer search is conducted in regions containing good solution sets.

A search space is deemed promising if the successive addition of a directional step change, h_1 , to one of the independent variables increases the investigated objective function. Local intensification occurs after the objective function no longer increases with the addition of the step change to the independent variable. Subsequently, the directionality of the step change is reversed and divided by a positive integer, η , such that: $h_2 = -\frac{h_1}{\eta}$, where h_2 is an integer. This increases the efficacy of the algorithm as only promising search areas are tested with small sequential step changes to the independent variables. This process is repeated until the objective function no longer increases, at which point diversification is enabled.

After local intensification, the candidate solution set of the investigated search space is evaluated against other local optima. If the objective value of the candidate solution vector is greater than the objective value of the previously determined 'best' solution vector, then the candidate solution vector becomes the 'best' solution vector and is added to the Tabu list. Figure 1 shows the details of local intensification and the tuning of the step size within the developed multi-objective Tabu search algorithm.

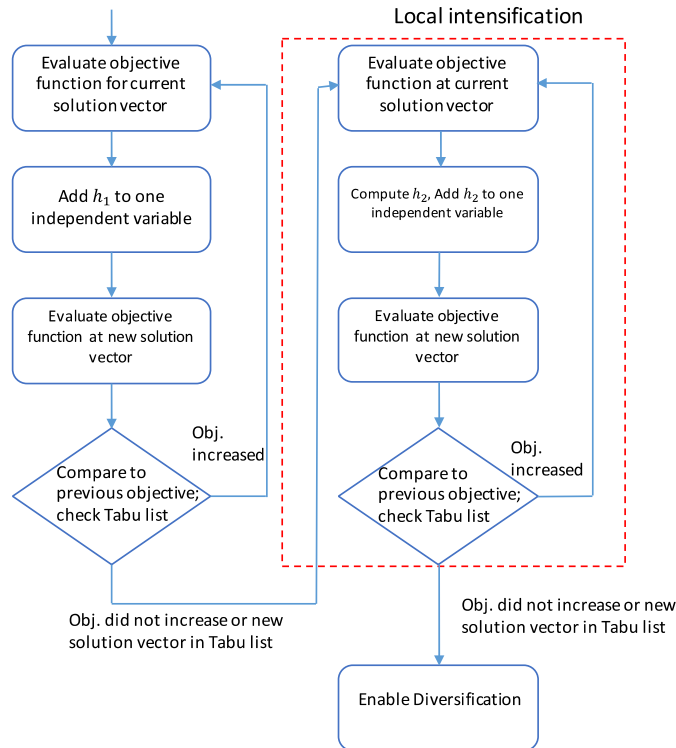


Figure 1: Flowchart showing the structure for varying an independent variable with the addition of a step to find a locally Pareto-optimal solution, $h_1 = \text{step change}$, $h_2 = -\frac{h_1}{\eta}$ where η is an integer.

Diversification is a technique that is employed after the algorithm has completed local intensification, determined that the solution vector is Pareto-optimum, or has encountered a solution vector on the Tabu list. Modifications are made to the solution set to move the next candidate solution set to a new area of the search space. For this algorithm, after a candidate solution set is evaluated against the best candidate solution set, the next candidate solution set is filled from the possible values of the independent variables. This enables a shallow search of many regions quickly to determine which ones are promising and should be investigated with more rigor.

A greedy heuristic is utilized in the determination of the candidate solution set by selecting the neighbor, in the investigated direction, of the current candidate solution vector that has the greatest objective value. Note that if the next candidate solution vector is on the Tabu list, then the next candidate solution set is determined through diversification. To reduce the search space that must be investigated, the bounds of the independent variables are tightened. The bounds of the independent variables are: the modified upper bound is a fixed value greater than the respective variable value within the ‘best’ solution vector, the modified lower bound is another fixed value less than the respective variable value with the ‘best’ solution set. The modified lower and upper bounds cannot be greater or lesser, respectively, than the original constraints on the independent variables.

In order to optimize two variables simultaneously, an inner and outer loop structure was utilized. Within the inner loop the first objective function was optimized using single variable Tabu search. The optimized value of the first objective, and the corresponding ‘best’ solution set are subsequently utilized as the starting point for the outer loop. Within the outer loop, the second objective is optimized using Tabu search, while the first objective is maintained within a tolerance of the optimized value of the inner loop. This is treated as a constraint that must be satisfied in order to replace the outer ‘best’ solution vector for that iteration. This process is repeated while the tolerance increases with each iteration. As can be seen in Figure 2, at the end of each iteration, the outer ‘best’ solution vector should correspond to a value of the first objective that is within the tolerance of the inner loop valve, while the second objective is maximized with respect to the constraints.

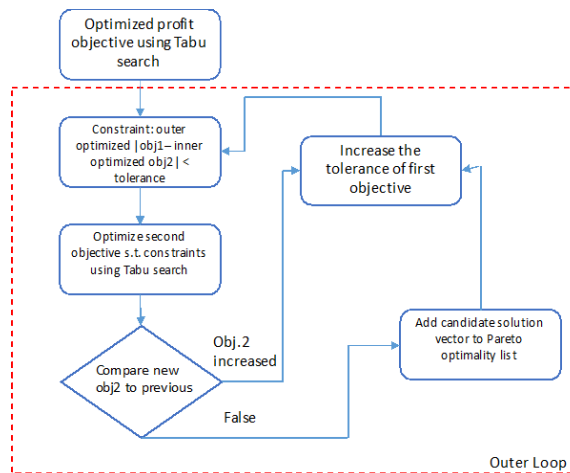


Figure 2: Flowchart showing the structure of the inner and the outer loop of the multi-objective Tabu search algorithm

3. Problem Formulation

To evaluate the effectiveness of the novel algorithm, the following example was obtained from Rangiah (2016). This example shows the capacity of the algorithm to determine Pareto-optimal points for highly nonlinear problem formulations with multiple degrees of freedom, and objectives. The formulation is sufficiently generic as to be applicable to specific industrial settings without requiring large modifications.

Table 1: Variables in the example formulation and their physical meaning

Variables:	Physical Representation:	Units:
x_1	Olefin Feed Flowrate	Barrels/day
x_2	Isobutane Recycle Flowrate	Barrels/day
x_3	Acid Addition Rate	Thousand pounds/day
x_4	Alkylate Production Rate	Barrels/day
x_5	Isobutane Feed Flowrate	Barrels/day
x_6	Spent Acid Strength	Weight Percent
x_7	Octane Number	N/A

x_8	Isobutane to Olefin Ratio	N/A
x_9	Acid Dilution Factor	N/A
x_{10}	F-4 Performance Number	N/A

Objectives:

$$\text{Max Profit} = 0.063x_4x_7 - 5.04x_1 - 0.035x_2$$

$$\text{Max isobutane: olefin ratio} = x_8$$

Bounds on Variables:

$$0 \leq x_1 \leq 2,000$$

$$90 \leq x_7 \leq 95$$

$$3 \leq x_8 \leq 12$$

$$0 \leq x_4 \leq 5,000$$

$$0 \leq x_5 \leq 2,000$$

$$0 \leq x_2 \leq 16,000$$

$$85 \leq x_6 \leq 93$$

$$145 \leq x_7 \leq 162$$

$$1.2 \leq x_9 \leq 4$$

$$0 \leq x_3 \leq 120$$

Constraints:

$$x_4 = x_1(1.12 + 0.13167x_8 - 0.006667x_8^2)$$

$$x_5 = 1.22x_4 - x_1$$

$$x_2 = x_1x_8 - x_5$$

$$x_{10} = -133 + 3x_7$$

$$x_9 = 35.82 - 0.222x_{10}$$

$$x_3 = 0.001 \frac{(x_4x_6x_9)}{98 - x_6}$$

4. Results

The example problem formulation is solved with our multi-objective Tabu search algorithm, and the Pareto-optimal points shown in Figure 4 were generated. A modified Tabu search which includes an additional bounding technique which reduces the search region, by constricting the bounds of the manipulated variables was utilized to generate Figure 3.

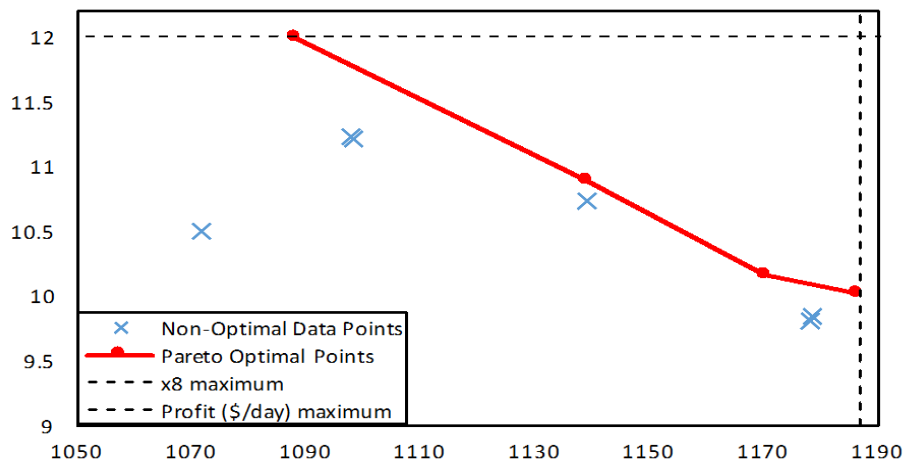


Figure 3: Pareto-optimality curve for the alkylation problem, the profit is on the x-axis, while the isobutane:olefin ratio is on the y-axis

It was determined that the utilization of the designed Tabu search algorithm is successful in determining Pareto-optimality points. The points classified as Pareto-optimal are those for which the profit cannot be improved without worsening the isobutane to olefin ratio, or vice versa. The points were shown to be locally Pareto-optimal via comparison with the solution vector's corresponding neighboring points. The maximum profit was determined by conducting a single variable optimization with profit serving as the sole objective and the maximum isobutane to olefin ratio was determined via the constraints. For the example presented, the novel method finds the Pareto-optimality frontier efficiently and the Pareto-optimal points generated are in agreement with those presented in Rangiah 2017.

5. Conclusions

In this work, a novel multi-objective Tabu search optimization technique is presented. Additionally, a bounding technique was applied which increases the efficacy of the algorithm by reducing the search space, through tightening of constraints. It was determined that it is feasible to generate a Pareto-optimality curve for plant design problems utilizing multi-objective Tabu search. The advantage of utilizing Tabu search for multivariable optimization stems from its ability to be easily modified for various problem formulations and its ability to be solved in parallel. For the implemented algorithm, and Tabu search holistically, the structure of the search technique allows it to be easily modified to solve different problem formulations. As the algorithm can search different regions of the feasibility space independently, the search space can be partitioned, allowing for the problem to be solved in parallel. The use of the Tabu list also prevents cycling issues between near Pareto-optimal solutions. Most importantly, because of local intensification ensuring a thorough search, diversification ensuring a broad search, and the Tabu list with bound modification driving the direction of search, the algorithm is able to converge on Pareto-optimal solutions efficiently.

6. References

- C. M. Fonseca, *Multiobjective Genetic Algorithms with Application to Control Engineering Problems*. PhD thesis, University of Sheffield, 1995.
- B. K. Kaku & J. B. Mazzola (1997). A Tabu-search heuristic for the dynamic plant layout problem. *INFORMS Journal on Computing*, 9, 374-384.
- F. Abedin, B. Roughton, Q. Ye, P. Spencer & K. Camarda (2017). Computer-aided molecular design of water compatible visible light photosensitizers for dental adhesive. *Chemical Engineering Science*, 159, 131-139
- S. E. McLeese, J. C. Eslick, N. J. Hoffmann, A. M. Scurto, K. V. Camarda (2010). Design of ionic liquids via computational molecular design. *Computers and Chemical Engineering*, 34, 1476-1480
- J. Acevedo & E. N. Pistikopoulos (1998). Stochastic optimization based algorithms for process synthesis under uncertainty. *Computers and Chemical Engineering*, 22, 647-671
- M. Dell'Amico & M. Trubian (1993). Applying Tabu search to the job-shop scheduling problem. *Annals of Operations Research*, 4, 231-252
- F. Glover (1989). Tabu search – Part 1, *ORSA Journal on Computing*, 1, 190-206
- B. Lin & D.C. Miller (2004). Tabu search for chemical process optimization, *Computers & Chemical Engineering*, 28, 2287-2306

Alternative mixed-integer reformulation of Generalized Disjunctive Programs

Miloš Bogataj ^{a,*}, Zdravko Kravanja ^a

^a*Faculty of Chemistry and Chemical Engineering, University of Maribor, Smetanova 17, SI-2000 Maribor, Slovenia*

milos.bogataj@um.si

Abstract

In this work, we propose an alternative mixed-integer (MI) reformulation of Generalized Disjunctive Programs (GDP) and compare its efficiency against the Big-M and hull reformulation (HR). We show that the reformulation yields a continuous relaxation equal to the HR for linear GDPs and comparable to the one obtained by HR for nonlinear GDPs. A particular advantage of the proposed reformulation is that the usage of the perspective function can be avoided when reformulating nonlinear GDPs. The reformulation is validated on a set of numerical examples using Branch and Bound algorithm. Results obtained thus far indicate that the proposed reformulation represents a promising alternative to the established ones.

Keywords: Disjunctive Programming, Mixed-Integer Programming, Big-M Relaxation, Hull Relaxation.

1. Introduction

A common approach to process synthesis is usually based on a superstructure representation of competitive/plausible alternatives. The most intuitive way for representing it in a mathematical language is the one in the form of GDP (Raman and Grossmann, 1994; Türkay and Grossmann, 1996). While, among other advantages, the GDP framework facilitates the modelling stage, solving these problems is not a straightforward task. In most cases, a GDP problem is reformulated to an MI problem and then solved using the established solvers.

The GDP problems can be formulated as mixed-integer (non)linear problems (MI(N)LP) in different ways. This, however, leads to models of different sizes (in a number of variables and constraints) and of different tightness (i.e. relation of the feasible region of a problem to the feasible region of its continuous relaxation). Therefore, the efficiency of the solvers to solve these problems depends on the type of the reformulation.

Several procedures can be utilized to achieve the MI formulation - the most instinctual being the Big-M relaxation (Nemhauser and Wolsey, 1988). While it produces small-sized models, its relaxation strongly depends on the selection of Big-M parameters. Often, even when the smallest Big-M parameters are selected, the Big-M reformulation results in a weak continuous relaxation. Recently, an improved Big-M reformulation for GDP has been presented by Trespalacios and Grossmann (2015). In contrast to the traditional one, the latter uses multiple Big-M parameters for each constraint. Consequently, it produces tighter continuous relaxations and reduces the computational effort needed to solve discrete-continuous optimization problems.

To obtain tighter relaxations, Lee and Grossmann (2003) proposed an HR for (non)linear convex GDPs. It produces at least as tight relaxation as the Big-M reformulation, however, it requires additional variables and constraints. It has been shown that HR, although it produces larger-sized models, dominates the Big-M reformulation in the majority of cases, primarily because of the tight relaxation it produces. The concept of HR in process synthesis problems was utilized and further developed by Ropotar and Kravanja (2009). The authors presented an HR based on MI translation of variables. The reformulation tends to exploit the benefits of the fact that the variables in engineering problems are often bounded by nonzero positive lower and upper bounds. For additional insights into a hierarchy and advances in relaxations and reformulations for GDPs, the reader is referred to Sawaya and Grossmann (2012), and Ruiz and Grossmann (2012).

The remainder of the manuscript is organized as follows. In section 2 we present an overview of a GDP model and present the alternative MI reformulation. In section 3 we present an illustrative example. Section 4 is dedicated to testing of the proposed reformulation on a set of process synthesis examples and presentation of the results.

2. Alternative MI reformulation of GDP

Consider the general GDP presented as follows:

$$\begin{aligned}
 \min Z &= \sum_{ik} c_{ik} + f(x) \\
 \text{s.t.} \quad & h^g(x) \leq 0 \\
 & \bigvee_{i \in D_k} \begin{bmatrix} Y_{ik} \\ g_{ik}(x) \leq 0 \\ c_{ik} = \gamma_{ik} \end{bmatrix} \quad k \in K \quad (\text{GDP}) \\
 & \bigvee_{i \in D_k} Y_{ik} \quad k \in K \\
 & \Omega(Y) = \text{True} \\
 & x \in \square^n, c_{ik} \in \square, Y_{ik} \in \{\text{True}, \text{False}\}
 \end{aligned}$$

In (GDP) the objective is a function of continuous variables, $h^g(x) \leq 0$ are global (non)linear constraints, which must hold true regardless of the discrete decision. Each of the disjunctions $k \in K$ contains disjunctive terms D_k , linked by an OR operator (\vee). A Boolean variable Y_{ik} is assigned to each of the disjunctive terms, which contain a set of local (non)linear constraints ($g_{ik}(x) \leq 0$) describing the alternatives. The local constraints within a given term are only enforced when a corresponding Boolean variable takes a value of *True*. On the other hand, if the Boolean variable equals *False*, the local constraints are ignored. $\Omega(Y) = \text{True}$ represents a set of logical propositions.

The proposed MI reformulation of (GDP) based on MI translation of variables is given by (AMI). Similar to the HR presented by Lee and Grossman (2003), the Boolean variables in (AMI) are transformed into 0-1 variables y_{ik} , the continuous variables x disaggregated into variables x_{ik}^D and the logical propositions reformulated into a set of linear constraints $Ey \leq e$. The main difference between the reformulations is that the disaggregated variables x_{ik}^D are not required to be forced to 0 when $y_{ik} = 0$.

$$\begin{aligned}
\min Z &= \sum_{ik} y_{ik} \gamma_{ik} + f(x) \\
\text{s.t.} \quad & h^g(x) \leq 0 \\
x &= \sum_{i \in D_k} x_{ik}^D - (1 - y_{ik}) x_{ik}^F & k \in K \\
g_{ik}(x_{ik}^D) - (1 - y_{ik}) g_{ik}(x_{ik}^F) &\leq 0 & i \in D_k, k \in K \\
x_{ik}^D &\geq x_{ik}^{D,LO} y_{ik} + (1 - y_{ik}) x_{ik}^F & i \in D_k, k \in K \quad (\text{AMI}) \\
x_{ik}^D &\leq x_{ik}^{D,UP} y_{ik} + (1 - y_{ik}) x_{ik}^F & i \in D_k, k \in K \\
Ey &\leq e \\
\sum_{i \in D_k} y_{ik} &= 1 & k \in K \\
x^{LO} &\leq x \leq x^{UP}, y_{ik} \in \{0, 1\}
\end{aligned}$$

Instead, they are forced to arbitrary fixed values x_{ik}^F (vanishing points -VPs), which are usually chosen between nonzero lower and upper bounds of variables x_{ik}^D . For additional explanation of the reformulation based on MI translation of variables, the reader is referred to Ropotar and Kravanja (2009). In their work, the authors have shown that if local constraints ($g_{ik}(x) \leq 0$) are reformulated using the perspective function i.e.

$y_{ik} (g_{ik}((x_{ik}^D - (1 - y_{ik}) x_{ik}^F) / y_{ik})) \leq 0$, the above reformulation produces relaxation identical to HR. If local constraints in (GDP) are linear, it can be easily shown that $y_{ik} (g_{ik}((x_{ik}^D - (1 - y_{ik}) x_{ik}^F) / y_{ik})) = g_{ik}(x_{ik}^D) - (1 - y_{ik}) g_{ik}(x_{ik}^F)$. Therefore, the reformulation as given by (AMI) is a hull relaxation for GDPs containing linearly constrained disjunctive feasible regions. If the local constraints are nonlinear or combination of linear and nonlinear constraints, the relaxation of (GDP) as given by (AMI) is generally weaker as the one produced by the HR. However, using an initialization procedure, described in section 2, the relaxation obtained by (AMI) is expected to be considerably tighter than the one obtained by the Big-M reformulation.

3. Illustrative example

We illustrate the proposed reformulation on an example taken from Trespalacios and Grossmann (2015). The example deals with optimization of linear objective function over a set of disjoint circles. Its GDP representation is given by (1). The optimal solution of the example is $Z = -9.472$, $Y = (\text{False}, \text{False}, \text{True})$, $x = (5.789, 2.106)$. If we apply the (AMI) model to (1) we obtain the MINLP reformulation (2). The solution of the relaxed MINLP, assuming the VPs are the centers of the circles (i.e. (0,0), (1,5) and (4,3)), is $Z^R = -9.816$, $y = (0.027, 0.038, 0.935)$ and $x = (5.859, 1.902)$. The continuous relaxation is stronger as the one obtained by the Big-M reformulation ($Z^R = -10.493$) and slightly weaker than the one obtained by the improved Big-M reformulation ($Z^R = -9.735$). However, if we select the VPs as (0.680, 1.934), (1.372, 4.431) and (5.788, 2.015), the relaxation is identical to the one obtained by the HR and relaxed MINLP problem produces integer solution: $Z^R = Z = -9.472$, $y = (0, 0, 1)$, $x = (5.789, 2.106)$. It is evident that the selection of VPs in (AMI) plays an important role in providing tight continuous relaxations when the constraints in the disjunctions are nonlinear.

$$\begin{aligned}
\min \quad & Z = \sum_{v \in V} c_v x_v \\
& \bigvee_{i \in D_k} \left[(x_1 - a_i)^2 + (x_2 - b_i)^2 - r_i \leq 0 \right] \\
& \bigvee_{i \in D_k} Y_i = \text{True} \\
& -1 \leq x_1 \leq 6, -1 \leq x_2 \leq 7; \\
& c = (-2, 1), a = (0, 1, 4), b = (0, 5, 3), r = (1, 2, 4)
\end{aligned} \tag{1}$$

$$\begin{aligned}
\min \quad & Z = \sum_{v \in V} c_v x_v \\
x_v &= \sum_{i \in D_k} x_{v,i}^D - (1 - y_i) x_{v,i}^F \quad v \in V \\
& (x_{1,i}^D - a_i)^2 + (x_{2,i}^D - b_i)^2 - r_i - (1 - y_i)((x_{1,i}^F - a_i)^2 + (x_{2,i}^F - b_i)^2 - r_i) \leq 0 \quad i \in D_k \\
& x_{v,i}^D \geq x_{v,i}^{D,LO} y_i + (1 - y_i) x_{1,i}^F \quad v \in V, i \in D_k \\
& x_{v,i}^D \leq x_{v,i}^{D,UP} y_i + (1 - y_i) x_{1,i}^F \quad v \in V, i \in D_k \\
& \sum_{i \in D_k} y_i = 1 \\
& x_{v,i}^{D,LO} = (-1, -1), x_{v,i}^{D,UP} = (6, 7) \quad v \in V, i \in D_k \\
& c = (-2, 1), a = (0, 1, 4), b = (0, 5, 3), r = (1, 2, 4)
\end{aligned} \tag{2}$$

3.1. Algorithm for selection of VPs

To study the effect of how the selection of VPs affects the continuous relaxation of (2), we have generated 500 random VPs within each of the disjoint feasible regions. The results show the average value of $Z^R = -10.542 \pm 0.764$ to be approximately 10 % weaker than the one obtained by the HR. Nevertheless, we have observed that the relaxed problem does produce relaxation identical to the HR in several instances. Currently, the theoretical background for whether there always exists a set of VPs that guarantees as tight continuous relaxation as the one obtained by the HR and, if it does, how to determine such VPs is still under investigation. However, what has shown to be a promising path is to first solve a reduced version of (AMI) and set the optimal values of disaggregated variables as VPs for (AMI). The reduced model (redAMI) is given as follows:

$$\begin{aligned}
\min \quad & Z = \sum_{i,k} f(x_{ik}^D) \\
\text{s.t.} \quad & g_{ik}(x_{ik}^D) \leq 0 \quad i \in D_k, k \in K \\
& x_{ik}^{D,LO} \leq x_{ik}^D \leq x_{ik}^{D,UP}
\end{aligned} \tag{redAMI}$$

By solving (redAMI), we optimize the continuous part of the objective function over the feasible region constrained solely by local constraints. Note that the only type of variables present in the model is the disaggregated continuous variables. Testing the procedure on the 500 randomly generated VPs has revealed that in all the instances (redAMI) produces VPs that lead to the tightest possible continuous relaxation. We must note that solving (redAMI) introduces another step into the optimization

procedure; however, since the model is significantly smaller, the impact of solving (redAMI) on the solution time is expected to be low. As a final note, the effect of VPs on the tightness of the continuous relaxation is only present if the disjunctions contain nonlinear or combination of linear and nonlinear constraints.

4. Process Synthesis Examples

In this section, we compare the efficiency of the proposed reformulation against Big-M and HR reformulation. The process network synthesis is a classical optimization problem in which the goal is to select a process network that maximizes profit while considering the costs of raw materials and the cost of the process units. The numerical examples Proc8, Proc10 and Proc12 are variations of the example introduced by Turkey and Grossmann (1996). A general GDP model is described by (3). The examples were solved using SBB solver. The results for the three instances are given in Tables 1-2.

$$\begin{aligned}
 \min Z &= \sum_i c_i + \sum_j p_j x_j + \gamma \\
 \text{s.t. } &\sum_j r_{j,n} x_j \leq 0 \quad \forall n \in N \\
 &\left[\begin{array}{c} Y_i \\ \sum_j d_{i,j} (e^{x_j/t_{i,j}} - 1) - \sum_j s_{i,j} x_j \leq 0 \\ c_i = \gamma_i \end{array} \right] \vee \left[\begin{array}{c} -Y_i \\ x_j = 0, j \in J^i \\ c_i = \gamma_i \end{array} \right] \quad (3) \\
 \Omega(Y) &= True \\
 x_j, c_i &\geq 0, Y_i \in \{True, False\}
 \end{aligned}$$

Table 1: Comparison of relaxations and total computational times.

Ex./N _{bins}	Opt.	Big-M ^a		HR ^b		redAMI + AMI	
		LB	t _{CPU} /s	LB	t _{CPU} /s	LB	t _{CPU} /s
Proc8/8	68.01	-829.88	0.23	67.7334	0.13	67.7334	0.11
Proc10/10	-27.93	-1146.88	0.84	-40.1313	0.16	-40.1314	0.14
Proc12/12	-69.21	-894.52	2.01	-73.8895	0.14	-73.8895	0.09

a – Value of 50 was used for all the Big-M parameters. | b – In the HR reformulation, value of 1e-6 was used for ε.

Table 2: SBB solver statistics.

Ex.	Big-M			HR			redAMI + AMI		
	Iter	Nds	t _{NLP} /s	Iter	Nds	t _{NLP} /s	Iter	Nds	t _{NLP} /s
Proc8	801	34	0.23	117	1	0.12	53	1	0.09
Proc10	2820	205	0.84	236	4	0.15	78	5	0.05
Proc12	7347	463	1.97	174	3	0.14	99	3	0.08

As can be seen in Table 1, the HR and the proposed approach (redAMI +AMI) produce significantly tighter relaxations than the Big-M reformulation in all the instances. Both the HR and the proposed reformulation exhibit faster computational times. The proposed approach produces equally tight continuous relaxations as HR in two instances (Proc8 and Proc12), while the relaxation of Proc10 is slightly weaker, consequently causing an increase in the number of nodes searched to find the optimal solution. Interestingly, the proposed approach requires the least computational time to find optimal solutions and the least solver iterations (Table 2).

5. Conclusions

Over the last decades, a number of reformulation strategies for obtaining tighter continuous relaxations of discrete-continuous problems have been proposed. In this work, we present a reformulation that utilizes MI translation of variables and avoids the usage of the perspective function. When dealing with nonlinear GSPs and their MINLP representations, the first property, as suggested by Ropotar and Kravanja (2009), tends to reduce the search space of nonlinear subproblems. The second property might be important for producing more robust nonlinear subproblems as the proposed reformulation does not introduce additional nonlinearities to the model. Based on the results presented in this work, we can conclude that the proposed reformulation provides results comparable to those obtained by the HR, both in terms of tightness of continuous relaxation as well as of the computational effort needed to obtain optimal solutions. Future work will focus on research dedicated to providing the answers regarding the procedures for obtaining VPs, and testing of the proposed reformulation on large-scale synthesis problems. We believe that the findings of the future work will enable us to fully evaluate the benefits as well as drawbacks of the proposed reformulation.

References

- S. Lee, I. E. Grossmann, 2003, Generalized Convex Disjunctive Programming: Nonlinear Convex Hull Relaxation. *Computational Optimization and Applications*, 26 (1), 83–100.
- G. L. Nemhauser, L. A. Wolsey, 1988, *Integer and combinatorial optimization*. Wiley-Interscience, Wiley.
- R. Raman, I. E. Grossmann, 1994, Modeling and Computational Techniques for Logic Based Integer Programming. *Computers and Chemical Engineering*, 18 (7), 563–578.
- M. Ropotar, Z. Kravanja, 2009, Translation of Variables and Implementation of Efficient Logic-Based Techniques in the MINLP Process Synthesizer MIPSYN, *AIChE Journal*, 55 (11), 2896–2913.
- J. P. Ruiz, I. E. Grossmann, 2012, A hierarchy of relaxations for nonlinear convex generalized disjunctive programming, *European Journal of Operation Research*, 218, 38–47.
- N. Sawaya, I. E. Grossmann, 2012. Reformulations, relaxations and cutting planes for linear generalized disjunctive programming. *European Journal of Operational Research* 216, 70–82.
- F. Trespalacios, I. E. Grossmann, 2015, Improved Big-M reformulation for generalized disjunctive programs. *Computers and Chemical Engineering*. 76, 98–103.
- M. Türkay, I. E. Grossmann, 1996, Logic-Based Algorithms for the Optimal Synthesis of Process Networks. *Computers and Chemical Engineering*, 20 (8), 959–978, 1996.

LES of particle collision and agglomeration in vertical channel flows

T. Ogholaja*, D.O. Njobuenwu, M. Fairweather

School of Chemical and Process Engineering, University of Leeds, Leeds LS2 9JT, UK

**pm09ito@leeds.ac.uk*

Abstract

Large eddy simulation in a four-way coupled system is used to simulate particle collisions and agglomeration in turbulent vertical channel flows. The particle phase is modelled using Lagrangian particle tracking, ensuring that individual particle behaviour is effectively monitored by solving the particle equation of motion. Particle collisions are described using the hard-sphere collision model, with agglomeration tested based on the pre-collision kinetic energy, restitution coefficient and the van der Waals interactions between particles. The conditions influencing collision and agglomeration are studied for a fluid of $Re_\tau = 300$ with $125 \mu\text{m}$ spherical particles at volume fraction $\phi_v \sim O(10^{-3})$. Comparing flows in upward and downward directions reveals the influence of the various forces acting on the particles, with the drag and lift forces being dominant in both flows, although the latter is found to govern particle behaviour in downflow, driving the particles towards the wall regions where increased collisions and agglomeration occur. The particle distribution in upflow is more symmetric, with fewer collisions and agglomerations, due to the increased effects of drag. The fluid flow is also slightly modified by the presence of the particles.

Keywords: Eulerian-Lagrangian, particles, collision, agglomeration, vertical channel

1. Introduction

Particle collision and agglomeration can occur in a wide range of industrial applications where particle-laden flows are being transported. Instances of such behaviour are found in the nuclear industry during the mobilisation and transport of waste materials, in the pharmaceutical industry where fine chemicals are continuously being processed, and in the oil and gas industry during the exploration and processing of crude oil. In these applications, as well as in many others, it is important to gain an understanding of the rheological behaviour of such flows, particularly in terms of the impact of particle agglomeration which can lead to particle deposition and ultimately flow blockage. Numerical models are frequently used in evaluating particle-laden flows since they can generate understanding that is often impossible to gain through experimental means. The Reynolds-averaged Navier-Stokes (RANS) computational fluid dynamic approach is most commonly used in industry due to its relatively modest computational requirements, although large eddy simulation (LES) and direct numerical simulation (DNS) provide far more accurate turbulent flow predictions, and do not require the case-by-case adjustments necessary when using RANS techniques. LES is preferred in this study given that it is a compromise between the more accurate but computationally expensive DNS, and the relatively low computational cost but lower precision RANS approach.

The current study combines LES with a Lagrangian particle tracking (LPT) approach to improve the accuracy of turbulent two-phase flow predictions over those based on RANS techniques through the time and spatial resolution of the motion of large turbulent eddies, with individual particle motion tracked. Only a few studies of particle agglomeration in wall-bounded flows exist, with most investigations focussing on the dynamics of particles within a flow and their resulting effect on the flow structure. Relevant studies include those of Afkhami et al. (2015) and Njobuenwu et al. (2017) who both used LES as the basis for predicting particle agglomeration, although particle behaviour was modelled using the discrete element method and Lagrangian particle tracking, respectively. Almohammed et al. (2016) compared energy-based and momentum-based agglomeration models, whilst Sommerfeld et al. (2017) introduced a novel agglomerate structure model. Overall, however, our understanding of particle agglomeration remains poor, particularly for the case of wall-bounded flows. Building on previous work (Ogholaja et al., 2017), this study aims at improving our understanding of these flows by extending the investigation to vertical channels, where fluid flow with and against the direction of gravity is expected to lead to contrasting collision and agglomerate formation processes. In particular, the type and number of agglomerates formed in these flows, their local concentrations and their impact on the flow are considered. The understanding gained is of value in improving our ability to predict particle deposition that may lead to flow restrictions.

2. Numerical Simulation

Fluid flow predictions were derived based on solutions of the time-dependent Navier-Stokes equations for an incompressible Newtonian fluid. The BOFFIN-LES simulation code was employed (Bini et al., 2008), which uses a top-hat technique to filter the governing equations of motion. A dynamically calibrated version of the Smagorinsky model was used in computing the resulting sub-grid scale tensor, while the influence of the unresolved velocity fluctuations on particle motion was modelled using a stochastic Markov technique. The code is based on a finite-volume approach, having a co-located grid arrangement and using an implicit low-Mach number formulation. A two-step approximate factorisation pressure correction method is applied to ensure mass conservation, with the time step chosen to ensure the maximum Courant number lies between 0.1 and 0.3. More details of the mathematical model and numerical solution method can be found in Bini et al. (2008) and Ogholaja et al. (2017).

Integration of the particle equation of motion was performed within the LPT code, with the particle velocity and location computed using a fourth-order Runge-Kutta integration method, given initially random particle positions and velocities set equal to those of the fluid. The study considered all the significant forces acting on the particles, namely drag, gravity/buoyancy, added mass, shear lift and pressure gradient forces. The simulation was four-way coupled, ensuring particle-particle and particle-fluid interactions. The deterministic hard-sphere collision model (Breuer and Alletto, 2012) was employed in the prediction of particle interactions, with agglomeration modelled using the approach proposed by Breuer and Almohammed (2015).

The number of grid nodes used in the x , y and z directions of the channel was $129 \times 128 \times 128$, respectively, corresponding to the wall normal, spanwise and streamwise

directions. For both fluid and particles, periodic boundary conditions were imposed in the y and z directions, whilst in the x direction, fixed boundaries with no-slip conditions for the fluid velocity and elastic particle collisions were assumed. The flow considered was of shear Reynolds number $Re_\tau = u_\tau h/\nu = 300$, based on the channel half height, h , the shear velocity, u_τ , and the kinematic viscosity, $\nu = 10^{-6} \text{ m}^2 \text{ s}^{-1}$. The continuous phase density was that of water, $\rho = 10^3 \text{ kg m}^{-3}$. The particles were assumed spherical and of equal diameter, $d_p = 125 \text{ }\mu\text{m}$, and density, $\rho = 2710 \text{ kg m}^{-3}$, with a particle volume fraction $\phi_v \sim O(10^{-3})$. The minimum particle contact distance δ_0 was $3.36 \times 10^{-10} \text{ m}$, the mean yield stress σ was $3.0 \times 10^8 \text{ Pa}$, and the Hamaker constant H set to $3.8 \times 10^{-20} \text{ J}$, with the normal restitution coefficient $e_n = 0.4$ being representative of calcite (a frequently used simulant in nuclear waste studies). Simulations were performed for flows in both upward and downward directions, given the anticipated differences in particle behaviour. In order to isolate these effects, a number of assumptions were made: particle-particle collisions are binary; no agglomerate break-up due to turbulence; minimal particle deformation post-collision; and particle agglomeration based on the pre-collision particle energy, restitution coefficient and van der Waals interactions.

3. Results and Discussion

Results from both single- and two-phase channel flow simulations were first validated against direct numerical simulation-based predictions, see Ogholaja et al. (2017), with good agreement found.

For the upward and downward channel flows, Fig. 1(a) compares the total number of particle collisions, N_{col} , and agglomerations, N_{agg} , for both flows up to a simulation time of $t^+ = 1000$. Both flows show increases in N_{col} and N_{agg} with time, and it is clear that not all collisions result in agglomeration. Both flows initially show a sharp increase in the number of collisions and agglomerations, although with time the rate of increase of both reduces. Unlike for the upflow, however, N_{col} and N_{agg} continue to increase with time in the downflow, and do not asymptote to an approximate steady state. This is as a result of the lift effect which enhances particle migration into regions of high turbulence near the channel walls, consequently increasing particle interactions. This is confirmed by the particle concentration profiles in Fig. 1 which clearly indicate particle migration towards the wall regions in the downflow, whilst the bulk of the particle concentration for the upflow remains evenly distributed across the channel, although depleted in the near-wall regions. Also shown in Fig. 1(b) is the rate of depletion of the primary single particles with time, and the corresponding evolution of multi-sized particle agglomerates, for the two flow cases. In both flows, two-particle agglomerates form fairly rapidly early in the simulation, after which larger agglomerates form through collisions between single primary particles and larger agglomerates, and also between the agglomerates themselves. These results also show that the formation of agglomerates is more prevalent in downflow, with agglomerates consisting of up to five primary particles forming over the time period considered, which contrasts with the upflow case which has a maximum of three particle agglomerates. Again, the increased number of multi-sized particle agglomerates in downflow is a result of more collision events occurring in near-wall regions within the flow where particle concentrations are high due to effect of the lift force on the particles.

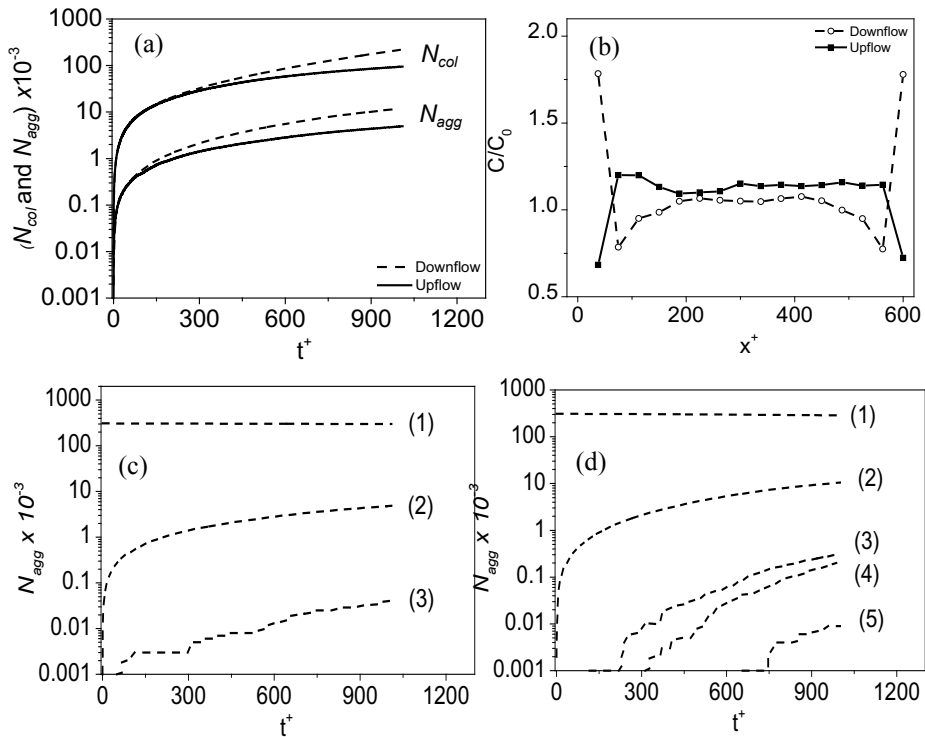


Figure 1. (a) Total number of collisions and agglomerates with time, (b) particle concentration profiles across the channel, and (c, d) agglomerate formation with time for upflow and downflow, respectively. Line numbers: single particle (1), double particle (2), etc.

Figure 2 provides more detail on the collision and agglomeration distribution across the channel width. Results are shown for the cross-stream domain divided into 16 regions in the wall-normal direction at $t^+ = 1000$, although results are averaged over $t^+ \pm 500$ about this time to provide a sufficiently large statistical sample. In upflow, the number of collisions and agglomerations are roughly constant, although there are slightly more collisions in the near-wall regions of the flow where turbulence levels are high. In downflow, the trends are noticeably different, with collision and agglomeration reaching maximum levels in the two wall regions due to the migration of particles from the bulk flow towards the walls. As already noted, the lift force is responsible for the continuous increase in particle concentration in the wall regions where turbulence levels are high, consequently promoting more collisions and agglomerations. This is confirmed in the plots that give the forces acting on the particles in the wall-normal direction in the same figure. In these plots, only one half of the channel is shown as the results show identical behaviour in both halves. The lift and drag forces are clearly dominant, and act on the particles in opposite directions, whilst all other forces are insignificant. In upflow, these two forces are almost balanced, explaining why collision and agglomeration events across the channel are nearly symmetric, although there is a slight migration of particles towards the wall owing to the more dominant lift force. In downflow, this imbalance is more pronounced, with the more dominant lift force pushing the particles at a faster rate towards the two wall regions.

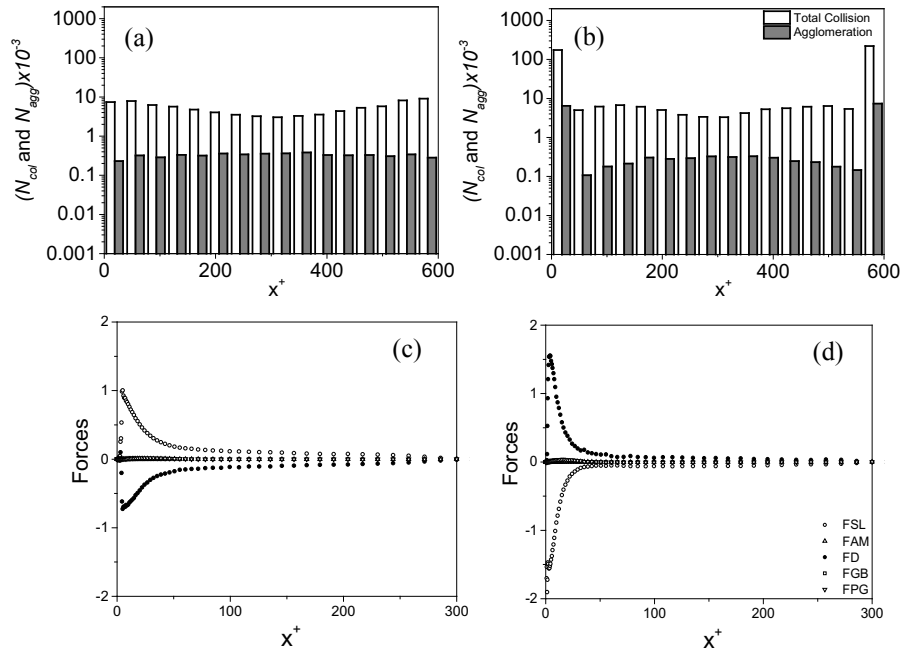


Figure 2. Distribution of particle collisions and agglomerations across the channel for (a) upflow and (b) downflow, and (c, d) forces in $(N \text{ kg}^{-1})$ acting on the particles at $t^+ = 1000$ for upflow and downflow, respectively (FSL = shear lift, FAM = added mass, FD = drag, FGB = gravity/buoyancy, FPG = pressure gradient).

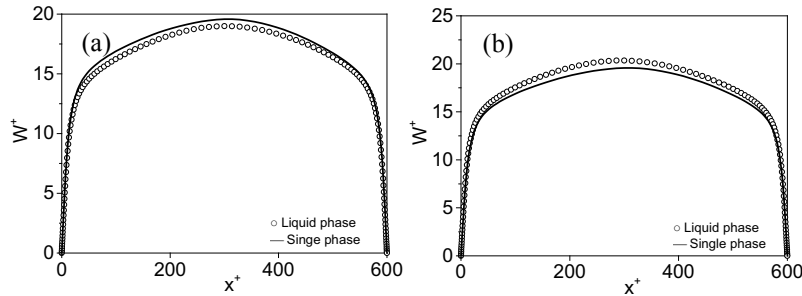


Figure 3. Continuous phase streamwise mean velocity in (a) upflow and (b) downflow.

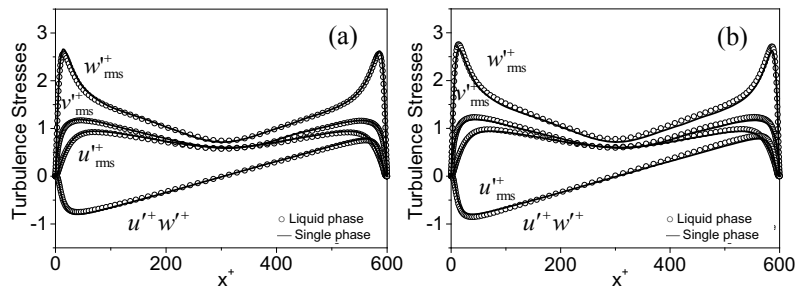


Figure 4. Continuous phase normal and shear stresses in (a) upflow and (b) downflow.

Lastly, the effect of particles on the fluid flow is considered in Figs. 3 and 4, again at $t^+ = 1000$, where single-phase flow predictions are compared with liquid phase results for flows including particles. In upflow, the fluid mean streamwise velocity is suppressed due to the increased drag on the fluid, and enhanced in downflow where drag forces are less influential. Additionally, in Fig. 4 a very slight decrease in the upflow stresses is apparent, whilst the opposite is the case in downflow. These differences are, however, almost negligible.

4. Conclusions

LES coupled with a Lagrangian particle tracking technique has been employed to predict particle collision and agglomeration in turbulent vertical channel flows. Collision and agglomeration increase with time, although at a much higher rate for a downward flow where particles are observed to migrate towards the wall regions, where turbulence levels are high, owing to the dominant lift force effect on the particles. The particle distribution in upflow is more symmetric, with fewer collisions and agglomerations, due to the increased effect of drag. Only slight changes to the velocity field of the continuous phase are predicted due to the presence of the particles, although some slight enhancement is evident in downflow, with the opposite the case in upflow.

Acknowledgements

T.O. would like to thank the Nigerian Government for their financial support of the work described.

References

- M. Afkhami, A. Hassanpour, M. Fairweather, D.O. Njobuenwu, 2015, Fully coupled LES-DEM of particle interaction and agglomeration in a turbulent channel flow, *Comput. Chem. Eng.*, 78, 24-38.
- N. Almohammed, M. Breuer, 2016, Modeling and simulation of agglomeration in turbulent particle-laden flows: A comparison between energy-based and momentum-based agglomeration models, *Powder Technol.*, 294, 373-402.
- M. Bini, W.P. Jones, 2008, Large-eddy simulation of particle-laden turbulent flows, *J. Fluid Mech.*, 614, 207-252.
- M. Breuer, M. Alletto, 2012, Efficient simulation of particle-laden turbulent flows with high mass loadings using LES, *Int. J. Heat Fluid Fl.* 35, 2-12.
- M. Breuer, N. Almohammed, 2015, Modeling and simulation of particle agglomeration in turbulent flows using a hard-sphere model with deterministic collision detection and enhanced structure models, *Int. J. Multiphase Flow*, 73, 171-206.
- D.O. Njobuenwu, M. Fairweather, 2017, Simulation of deterministic energy-balance particle agglomeration in turbulent liquid-solid flows, *Phys. Fluids*, 29, 083301.
- T. Ogholaja, D.O. Njobuenwu, M. Fairweather, 2017, Particle size effects on collision and agglomeration in turbulent channel flows, 27th European Symposium on Computer Aided Process Engineering, A. Espuña, M. Graells, L. Puigjaner (Eds.), Elsevier, 79-84.
- M. Sommerfeld, S. Stübing, 2017, A novel Lagrangian agglomerate structure model, *Powder Technol.*, 319, 34-52.

Improved modeling of membrane separation in integrated hybrid processes

Bettina Scharzec^a, Mirko Skiborowski^a

^a *TU Dortmund University, Faculty of Biochemical and Chemical Engineering, Emil-Figge-Str. 70, 44227 Dortmund, DE*

bettina.scharzec@tu-dortmund.de

Abstract

Membrane processes reportedly provide a tremendous potential for improving separation performance and energy efficiency compared to thermal separation processes (Sholl and Lively, 2016). However, the benefits of membrane processes, as e.g. the ability to overcome limitations of other separation techniques introduced by azeotropes or eutectic points, are exploited best when integrated in hybrid processes (Skiborowski et al., 2013). Nevertheless, industrial applications are still limited due to a lack of reliable models that allow for an accurate description of the separation performance of the membrane. Process design approaches oftentimes neglect limiting effects, such as pressure drop, or concentration and temperature polarization. However, the impact of ignoring these limitations was recently demonstrated by Micovic et al. (Micovic et al., 2014) for modeling organic solvent nanofiltration. Additionally, the correct consideration of the flow pattern, such as co- and counter-current as well as cross flow, can have an equally significant impact on the accuracy of the model. However, the consideration of cross flow requires a two dimensional discretization resulting in a more complicated model compared to co- or counter-current flow.

In order to consider all these complex effects in a simultaneous process optimization an efficient model reduction without sacrificing model accuracy has to be performed. In this respect, Skiborowski et al. (Skiborowski, 2014) proposed to model a pervaporation-assisted distillation process, using an orthogonal collocation on finite elements (OCFE) for accurately modeling a co-currently operated membrane module, while applying external functions for computing thermodynamic properties. However, only temperature polarization was considered.

The current work extends this approach by implementing concentration polarization and pressure drop computations. Furthermore, modifications of the OCFE approach towards the alternative flow patterns are investigated and comparisons with simple discretization schemes are presented. The results indicate the benefits of the efficient model reduction by OCFE in order to allow for the consideration of more accurate modeling of the membrane process.

Keywords: optimization, membrane processes, hybrid processes, flow pattern

References

- Sholl, D.; Lively, R.: Seven chemical separations to change the world: purifying mixtures without using heat would lower global energy use, emissions and pollution and open up new routes to resources. *Nature*, 2016, 532, p. 435-438.
- Skiborowski, M.; Harwardt, A.; Marquardt, W.: Conceptual design of distillation-based hybrid separation processes. *Annual Review of Chemical and Biomolecular Engineering*, 2013, 4, p. 45-68.
- Micovic, J.; Werth, K.; Lutze, P.: Hybrid separations combining distillation and organic solvent nanofiltration for separation of wide boiling mixtures. *Chemical Engineering Research and Design*, 2014, 92, p. 2131-2147.
- Skiborowski, M.; Wessel, J.; Marquardt, W.: Efficient Optimization-Based Design of Membrane-Assisted Distillation Processes. *Industrial & Engineering Chemistry Research*, 2014, 53, p. 15698-15717.

Ontology engineering approach to support process of model integration

Linsey Koo^a, Edlira Kalemi^a, Nikolaos Trokanas^a, Franjo Cecelja^a

^a*University of Surrey, Guildford, GU2 7XH, GB*

f.cecelja@surrey.ac.uk

Abstract

Process modelling and simulation is a vital tool to plan, evaluate, assess, and develop different alternatives for the design of products and processes. The complexity of problems as well as heterogeneity of modelling methods make process modelling and simulation challenging, time consuming and often tedious process requiring a wide range of expertise. Inconsistencies in model development are the main cause for redundant work. Models remain implicit to the engineers who have built them, which further limits the potential of reusability. The only model integration framework in use, the CAPE-OPEN, addresses the issue of standardisation of interfaces to enable interoperability between simulator software components from different sources. It is the framework built around a middleware, the Common Object Request Broker Architecture (CORBA) that hosts communication between unit operations defined for a specific function and the process modelling environments. The standard specification is defined as a property package which is needed for a thermodynamic or physical property calculation. The interoperability of models, such as model selection, parameter identification, and experimental work is enabled through the connection related to the unit operations and physical properties. It is not necessary to match all parameters in order to facilitate Input-Output (I-O) matching. However, the shortcoming of the CAPE-OPEN is in the need for identifying key variables for each unit operation.

In this paper a new approach for model integration is proposed which builds upon the CAPE-OPEN framework and proposes the use of ontology and replaces the object bus with more flexible semantic repository (Koo, Trokanas and Cecelja, 2017). Models are described by Semantic Web Services (SWS) using Ontology Web Service Description (OWL-S) as an enabler of web services through service discovery, selection, composition, and execution stages (Figure 1). The discovery stage allows formation of an integrated model through matching requests from a public repository(ies). The best match that satisfy the requestor's functionality is selected in the model selection stage. The model composition stage then formulates the chain of integrated models and execution of integrated model takes place during the execution stage. This paper focuses on the matching parameters related to the domain of process system engineering, with emphasis placed on the role of physical properties and unit operation. Each model representing a device (e.g. unit operations, flowsheets, subflowsheets etc.) is semantically described in domain ontology including domain assumptions and descriptions of the functionality of the model. The domain ontology guides the process of registering models and instantiation of ontology through ontology parsing, which makes the model and data explicit and sharing terminology in domain ontology

improves consistency. The devices in a process are connected via streams that transmit information through multiple inlets and outlets from one unit to the other. The connection between devices are described in ontology by introducing the concept of 'ports' and 'connections'. The 'ports' generally describe inlets and outlets of devices and three different types of streams are distinguished: material, energy, and information, which are further described by objective properties. The 'connections' are the object that is responsible for establishing a link between two ports, which contains information regarding methods, types, quantities, and units of streams.

Keywords: modelling, Ontology, Semantic

References

Koo, L., N. Trokanas, et al. (2017). "A semantic framework for enabling model integration for biorefining." *Computers & Chemical Engineering* 100: 219-231

Approximation Algorithms for Process Systems Engineering

Dimitrios Letsios^a, Georgia Kouyialis^a, Ruth Misener^a

^aImperial College London, Department of Computing, South Kensington Campus, SW7 2AZ, GB

r.misener@imperial.ac.uk

Abstract

Approximation algorithms offer heuristics with performance guarantees for difficult mixed integer linear optimization problems. In this presentation, we consider two major problems in process systems engineering, heat exchanger network synthesis and re-optimization after an unexpected system fail.

Heat exchanger network synthesis exploits excess heat by integrating process hot and cold streams and improves energy efficiency by reducing utility usage. Determining provably good solutions to the minimum number of matches is a bottleneck of designing a heat recovery network using the sequential method. This subproblem is an NP-hard mixed-integer linear program exhibiting combinatorial explosion in the possible hot and cold stream configurations. We explore this challenging optimization problem from a graph theoretic perspective and correlate it with other special optimization problems such as cost flow network and packing problems. In the case of a single temperature interval, we develop a new optimization formulation without problematic big-M parameters. Numerical results from a collection of 51 instances substantiate the method.

Unexpected system failures may confront a decision-maker. For example, a machine in an industrial system may unexpectedly fail, a client may suddenly cancel a job, or a machine may complete a job significantly earlier than expected. In these circumstances, re-optimization is essential.

Our work studies a fundamental parallel machine-scheduling problem, which is part of several complex problems, e.g. manufacturing production planning. We show that the recovery problem is strongly NP-hard, at least as hard as the planning problem. Thus, combining planning and recovery does not mitigate the problem's computational complexity. But, if the initially planned solution is produced using lexicographic optimization, we prove a positive performance guarantee of the recovered solution for every input realization. Lexicographic optimization becomes a powerful tool towards efficient re-optimization under uncertainty. In addition to its significance in scheduling problems, our contribution can be extended to uncertain min-max partitioning problems with more general cost functions and other major applications, e.g. facility location and network communications. The novel lexicographic optimization method strengthens solutions obtained with our approach. This method and its underlying components are also of independent interest to other fields in the scope of lexicographic optimization including multi-objective optimization and fairness.

We close with an outlook on the possible applications of approximation algorithms to process systems engineering.

Keywords: optimization, Heat Exchanger Network, multiobjective optimization

Alternative processes for obtaining solar grade silicon

César Ramírez-Márquez,^a Marta Vidal Otero,^b José Antonio Vázquez-Castillo,^c
Mariano Martín,^b Juan Gabriel Segovia-Hernández.*^a

^a *Universidad de Guanajuato, Campus Guanajuato, División de Ciencias Naturales y Exactas, Departamento de Ingeniería Química, Noria Alta S/N, 20256, Guanajuato Gto., México*

^b *Universidad de Salamanca, Departamento de Ingeniería Química. Pza. Caidos 1-5, 37008 Salamanca, España.*

^c *Universidad Autónoma de Chihuahua, Facultad de Ciencias Químicas, Circuito Universitario 8, Campu UACH II, 31125, Chihuahua Chih., México.*

gsegovia@ugto.mx

Abstract

In this work we have developed and analyzed two alternative $\text{Si}_{(\text{SG})}$ production processes using a stochastic optimization scheme within ASPEN PLUS. The first one is an intensified Fluidized Bed Reactor (FBR) process using a reactive distillation column. The second process is a hybrid process combining both the Siemens and the conventional FBR processes. The base case is the optimized Siemens process. The optimized processes show savings in the TAC of 53.28%, 67.65% and 62.58% for Siemens, Intensified FBR and Hybrid process, respectively. Siemens process is the one with the lowest TAC. However, it has the lowest silicon production rate, 0.47 kt/y. The Intensified FBR Union Carbide Process turns out to be the most expensive of the three, but with a large production of $\text{Si}_{(\text{SG})}$, 1.49 kt/y. However, it is the hybrid process which shows the larger yield by far, with a production of 1.89 kt/y of $\text{Si}_{(\text{SG})}$ and TAC of 1.95 M\$/y, showing the highest profit from sales of the three, 40.47 M\$/y. From the environmental point of view, the Siemens process shows the lowest environmental impact based on the eco-indicator 99, while the Hybrid process is the second best.

Keywords: Silicon, Alternative processes, Optimization, TAC

1. Introduction

For years, microelectronic industry has been an important source of polysilicon. In that industry, ultrapure Si, 9N or $\text{Si}_{(\text{EG})}$, is required. The waste of Si remaining in the melting units as well as the pieces of waffles that do not reach the proper purity are typical sources of solar grade Si (Braga et al., 2008). However, the development of the solar sector has increased the demand for solar grade Silicon and the scraps from microelectronic industry are no longer enough to meet the needs of PV industry. Therefore, there is a need to improve the production processes from polysilicon to reduce their cost. The cost shares per Watt Peak of polysilicon solar systems are roughly as follows: Solar grade silicon ($\text{Si}_{(\text{SG})}$): 20%; ingot and wafer production: 28%; solar cell processing: 13%; solar module processing: 9%; installation of the PV-system including converter costs: 30% (Sadique, 2010). There are two main opportunities to reduce the

panels cost since approximately half of it is due to the materials, bulk silicon production and wafer manufacturing (Müller et al., 2006). Thus, the development of optimized processes for production of cheap $\text{Si}_{(\text{SG})}$ feedstock material can help reduce PV power production costs

Solar grade silicon can be produced from quartz following a two-stage process consisting of the production of metallurgic silicon and its further purification up to solar grade quality. The two most used processes are Siemens and Fluidized Bed Reactor, FBR, from Union Carbide. Siemens process was patented by Siemens Corporation in the 1950's. Its main feature is the Siemens or Bell reactor where 6N silicon is produced by Si deposition on a silicon pole (Payo, 2009). However, this alternative shows a large energy consumption and a number of waste streams. On the other hand, Union Carbide's process uses silane as a raw material for the production of Si. It was developed in the 1970s (Erickson and Wagner, 1952). Even though the yield of this alternative is larger than the one provided by Siemens process, the conversion from silane is larger than that from trichlorosilane and the operating conditions are more difficult to achieve.

Due to the high production cost of PV panels, the aim of this work is to reduce the production costs of $\text{Si}_{(\text{SG})}$ by developing more efficient processes. In particular two novel processes have been developed in this paper. The first one corresponds with an intensified FBR's process by substituting the conventional reactors and separation stage with a reactive distillation column (RD) intensifying the process. Furthermore, this configuration improves the yield, because products alone are withdrawn from the reactive zone while reactants remain inside the reactive zone for further reaction. This reactive distillation section has been reported previously in the work of Ramírez-Márquez et al. (2016). The second alternative process is a novel process that is based on both, the Siemens and the FBR attempting to reduce the use of raw material (Vidal and Martín, 2014). The three simulated processes were optimized for a consistent comparison of their in their Total Annual Cost (TAC) and in their production capacity of solar grade silicon.

2. Methodology

We first simulate the all three processes rigorously in Aspen Plus V8.4. To predict the thermodynamic of the system, we used the thermodynamic package Peng-Robinson, and 'Solids' property method for solids components. To meet the typical production capacity of around 2000 t/y, the processes are fed with the components and quantities with 532.32 kg/h of SiO_2 and 369.84 kg/h of Carbon. The simulation was carried out through the use of various Aspen modules. In the case of reactors, the stoichiometric module was mainly used, in the chlorosilanes synthesis reactors, the combination of two reactors had to be considered, because the software did not allow the sequential reaction of the components in a single reactor. Something similar happened with the carboreduction and deposition of silicon, where the reactor is essentially an oven, where the reactor was used with an oven to achieve the simulation. The 'RadFac' module was used for rigorous conventional distillation columns and for reactive distillation. A conventional set of modules was also used to implement the separators, pumps, compressors and exchangers, always trying to take care of each of the processes. Note that implementing solid compounds in Aspen is an arduous task. Next, we perform a

stochastic based optimization to decide on the column design and the operating conditions for each process.

Furthermore in this work we have added the calculation of the environmental impact which is measured through the Eco-indicator 99, a cradle to gate methodology, which reflects the advances in the damage-oriented method recently developed for Life Cycle Impact Assessment (LCA), as show Guillén-Gosálbez et al., (2008). The Eco-indicator 99 was chosen, since it is one of the most widely used impact assessment methods in LCA, and for the purposes of this work it is indicated, because allows the environmental load of a product to be expressed in a single score. Three different processes are proposed for obtaining the $Si_{(SG)}$, such is the case of the a) Siemens Process, b) the Enhanced FRB Process and c) the Hybrid Process (See Figure 1).

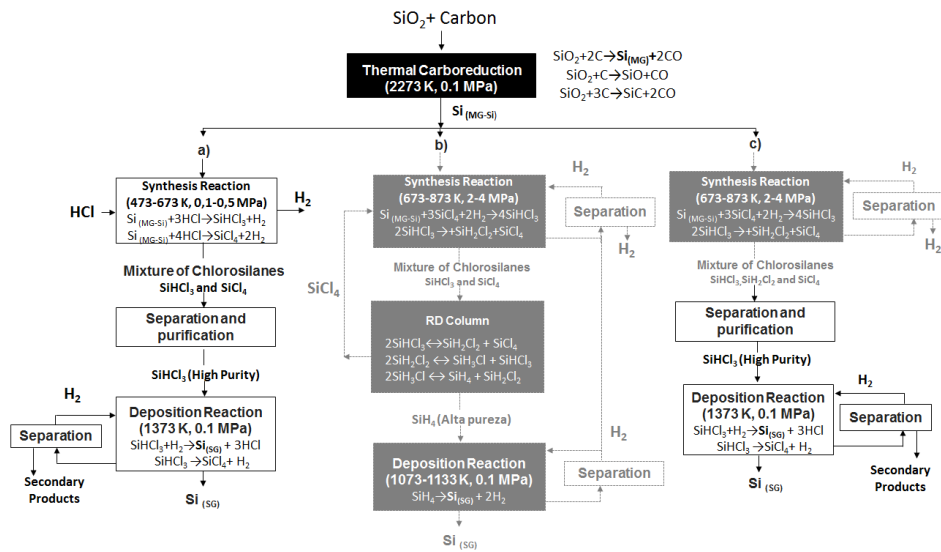


Figure 1. Scheme of the $Si_{(SG)}$ production processes. a) Siemens process, b) FBR Union Carbide with RD column process, c) Hybrid process.

The first case is the Siemens Process, which consists of a carboreduction section, followed by a chlorosilanes synthesis reactor using HCl as a precursor. Next, the mixture is separated in a conventional distillation column, to finish with the Siemens deposition reaction to produce solar grade silicon. The second process called intensified FRB, begins also with quartz carboreduction. Next, chlorosilanes are produced using $SiCl_4$ as a precursor. Subsequently, the separation process consists of two conventional separation columns, and two reactive distillation columns to obtain silane before moving on to the silicon deposition reaction. The last process is the one named as the Hybrid Process. It consists basically of the combination of the two previous ones. The first part of the process, until the separation, corresponds to the FRB Process. Then in the separation, two conventional columns are used, and the part of the deposition reaction, similar to the Siemens Process. Each process is optimized separately. Note that the design and the optimization of the processes are highly nonlinear problems involving continuous and discrete design variables. Furthermore, the objective function is potentially non-convex, with the possibility of finding local optimum and being subject to constraints.

In order to optimize the three processes, we used a stochastic hybrid optimization method due to the model is highly non-linear, potentially non-convex and with a large amount of local minimums, also the model is not explicitly stated. The use of stochastic optimization methods is a good alternative; several reports have proved the successful application in cases of study with those already mentioned characteristics. The stochastic hybrid optimization is called differential evolution with tabu list (DETL) (Srinivas and Rangaiah, 2007). The implementation of this optimization approach was made using a hybrid platform including Microsoft Excel, Aspen Plus and Matlab. The vector of decision variables (i.e., the design variables) are sent to Microsoft Excel to Aspen Plus using DDE (Dynamic Data Exchange) through a COM technology. In Microsoft Excel, these values are attributed to the process variables that Aspen Plus needs. After the simulation, Aspen Plus returns to Microsoft Excel the resulting vector. Those values are sent from Microsoft Excel to Matlab where the objective functions are calculated. Finally Microsoft Excel suggests new values of decision variables according to the used stochastic optimization method.

For this study, the following parameters have been used for the DETL method: 200 generations, 200 individuals, a tabu list size of 100 individuals, a tabu radius of $2.5 \cdot 10^{-6}$, Crossover fractions (Cr): 0.8, Mutation fractions (F): 0.6, respectively. The parameters were obtained via preliminary calculations, as shown in the methodology of Srinivas and Rangaiah, (2007a). The objective function used is shown in equation (1).

$$TAC = \frac{\text{Capital Cost}}{\text{Payback time}} + \text{Operating cost} \quad (1)$$

The payback time of the plant is considered to be five years, and 8400 hours of annual operation for each process are assumed. In each of the iterations we calculate the TAC of units such as the vessel of the reactor, furnaces, separators, mixers, heat exchangers, pumps and compressors. The units cost depend on their size and operating cost.

3. Results

In this section we present the results of the optimization of each of the processes including the iteration results to show that a plateau is reached and the operating and design variables. Thus, we first show a Figure of the iterations vs TAC obtained for each case will be shown. The TAC decreases over the iterations and a good value is achieved for 40,000 iterations. This is taken to be a valid solution since there is not a significant decrease in the last evaluations. This demonstrates the robustness of the DETL method, showing the convergence and results corresponding to good solutions.

All the runs to carry out the optimization were performed on an Intel (R) Core TM i7-4790 CPU @ 3.6 GHz, 16 GB computer, the computing time for obtaining the optimal solutions was different according to the complexity of each process: The Siemens process required 28.2 hours, the FBR Union Carbide Process required 125.6 hours, and the Hybrid process required 127.2 hours. In the case of the Siemens configuration, it is possible to observe that only the optimization of a single conventional column and the fresh feed of HCl to initiate the reaction of the reactor producing the silanes are performed. These parameters represent substantial economic savings in the process, since the separation section always represents a high cost in any chemical process, and that the right amount of reactant represent large savings in the actual operation of the

process. In the optimization of the Siemens Process, the initial configuration has a TAC of 1.08 M\$/y, ending with a TAC of 0.50 M\$/y, representing savings of 53.28%.

The Intensified FBR Union Carbide Process has the highest number of decision variables to optimize. For the Siemens Process infers the manipulation of 7 decision variables among continuous and discrete variables for each route process. The Intensified FBR Union Carbide Process implies the manipulation of 29 variables among continuous and discrete variables for each route process. And for the Hybrid Process infers the manipulation of 13 continuous and discrete variables for each route process. The optimization was carried out in two conventional columns, two reactive distillation columns, and the fresh feed stream of SiCl_4 . The TAC of the initial configuration of the Intensified FBR Union Carbide is 7.95 M\$/y and ending with 2.57 M\$/y, saving 67.65%. The Hybrid Process shows the optimization of two conventional columns, and the fresh SiCl_4 feed. The initial configuration has a TAC of 5.21 M\$/y, ending with 1.95 M\$/y, saving 62.58%. Table 1 shows, for all sequences, the capital cost, the TAC, the energy required and the products. Note the comparison between the TAC and the amount of products, mainly with the produced $\text{Si}_{(\text{SG})}$.

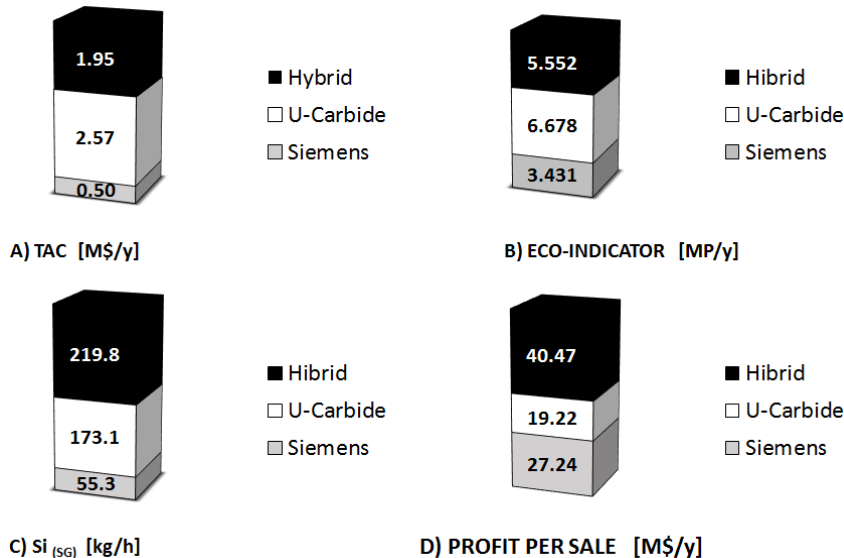


Figure 2. Results of TAC, ECO-99, amount of solar grade silicon, and profit per sale of all configurations.

Table 1. Comparative results for all process.

	Q [kW]	TAC [\$/y]	$\text{Si}_{\text{S-G}}$ [ton/y]	H_2 [ton/y]	SiH_2Cl_2 [ton/y]	SiCl_4 [ton/y]	HCl [ton/y]
Siemens	58,963	506,790	477.4	185.2	N/A	7807.9	N/A
FBR	63,042	2,573,400	1,495.9	221.0	1,237.2	N/A	N/A
Hybrid	64,344	1,951,075	1,899.0	260.1	1,335.1	5762.9	1643.5

The least expensive process is the Siemens one. However, it also shows the minimum annual production of $\text{Si}_{(\text{SG})}$. The Intensified FBR Union Carbide Process turns out to be the most expensive of the three proposed, with a large production of $\text{Si}_{(\text{SG})}$, but it is not

the best in this way. The Hybrid Process shows the highest production of $\text{Si}_{(\text{SG})}$, at a higher cost compared to the Siemens process, but lower than the Intensified FBR Union Carbide process. Figure 2 shows the potential of the hybrid process with the most important items. Performing the analysis of the results the potential of the Hybrid Process could be observed, which could represent an incentive for the silicon industry. It is known that the processes Siemens and FBR Union Carbide, are technologies that have matured over time and are the ones usually used in the production of $\text{Si}_{(\text{SG})}$, but the $\text{Si}_{(\text{SG})}$ industry could benefit from novel alternatives such as the Hybrid Process.

4. Conclusions

In this work, we have developed intensified and optimized processes for the production of $\text{Si}_{(\text{SG})}$. The results show that the Siemens process presented the smallest TAC, but with the lowest production of $\text{Si}_{(\text{SG})}$. The Intensified FBR Union Carbide Process, showed the largest TAC due to the capital cost of the equipment and the heat duty for $\text{Si}_{(\text{SG})}$ purification. Finally, the Hybrid Process exhibited a large production of $\text{Si}_{(\text{SG})}$, with a TAC between the one of the Siemens process and that of the Intensified FBR Union Carbide. However, evaluating the TAC vs production of $\text{Si}_{(\text{SG})}$, it turned out that the Hybrid Process was the best of the three. In addition to the above, the Hybrid Process shows the largest gains from the sale of the multiple products resulting, with earnings of 40.47 M\$/y. It is expected that with this type of research can be made more competitive the technology based on $\text{Si}_{(\text{SG})}$, lowering the costs for the industry of solar panels.

5. References

- M. Bououdina, 2014. Handbook of research on nanoscience, nanotechnology, and advanced materials. IGI Global, 119-126.
- A. F. B. Braga, S. P. Moreira, P. R. Zampieri, J. M. G. Bacchin, P. R. Mei, 2008. New processes for the production of solar-grade polycrystalline silicon: A review. *Sol. Energ. Mat. Sol. C*, 92(4), 418-424.
- C. E. Erickson, and G. H. Wagner, 1952. U.S. Patent No. 2,595,620. Washington, DC: U.S. Patent and Trademark Office.
- G. Guillen-Gosalbez, J. A. Caballero, L. Jimenez, 2008. Application of life cycle assessment to the structural optimization of process flowsheets. *Industrial & Engineering Chemistry Research*, 47(3), 777-789.
- A. Müller, M. Ghosh, R. Sonnenschein, P. Woditsch, 2006. Silicon for photovoltaic applications. *Mat. Sci. Eng. B*, 134(2), 257-262.
- M. J. R. Payo, 2009. Purificación de triclorosilano por destilación en el proceso de obtención de silicio de grado solar. PhD Thesis. Universidad Complutense de Madrid.
- C. Ramírez-Márquez, E. Sánchez-Ramírez, J.J. Quiroz-Ramírez, F.I. Gómez-Castro, N. Ramírez-Corona, J.A. Cervantes-Jauregui, J.G. Segovia-Hernández, 2016. Dynamic behavior of a multi-tasking reactive distillation column for production of silane, dichlorosilane and monochlorosilane. *Chem. Eng. Process.*, 108, 125-138.
- S. E. Sadique, 2010. Production and Purification of Silicon by Magnesiothermic Reduction of Silica Fume. MSc Thesis. University of Toronto.
- Solar Market Insight Report, 2016. <http://www.seia.org/research-resources/solar-market-insight-report-2016-q2>.
- M. Srinivas, G.P. Rangaiah, 2007. Differential Evolution with Tabu List for Solving Nonlinear and Mixed-Integer Nonlinear Programming Problems. *Ind. Eng. Chem. Res.*, 46, 7126-7135.
- M. Vidal, M. Martín, 2014. Planta de producción de silicio para módulos fotovoltaicos. *Era Solar. Fototérmica y Fotovoltaica*. 180, Año XXXII. 24-35.

An Engineering Tool to Screen and Integrate Biomass Valorization Paths in Multiple-Feedstock Biorefineries

Konstantinos A. Pyrgakis, Antonis C. Kokossis

School of Chemical Engineering, National Technical University of Athens, Iroon Polytechniou 9, Athens, GR-15780, Greece

kpyrg@mail.ntua.gr

Abstract

Biorefineries are the most promising route for the sustainable exploitation of lignocellulosic biomass sources into a wide range of fuels and materials. Value chains include all potential processing routes from raw materials to intermediate and end-chemicals that are possible to enter the biorefinery site. In this scope, process integration techniques are required to evaluate all potential biorefinery structures and reveal promising multiple-product biorefinery solutions with high efficiencies in use of energy and materials. Provided that biorefinery operations subject to seasonal availability of biomass varieties, the design problem additionally requires screening and planning of appropriate biorenewable feedstocks. This work introduces new concepts and representations that incorporate processes and feedstocks as additional degrees of freedom in integration. The proposed methodology investigates synergies among candidate processes, which benefit the biorefinery instead of operating individually, as well as schedules multiple-feedstock operations. A biomass representation maps all process synthesis options along value chains, while a cascade representation is proposed to simultaneously model direct (heat source-to-sink) and indirect (via steam generation-reuse) integration among involved processes of under-construction site. The proposed model (MILP) is explained through real-life biorefinery cases, which involve 15 candidate biorefinery paths and 6 candidate biomass varieties. The model reveals high efficiency biorefining routes and examines preferences on the use of multiple feedstocks minimizing the annual energy cost of under-construction biorefineries.

1. Introduction

Biorefineries are mainly related with the use of cheap and abundant lignocellulosic material that consists of sugars and lignin. Lignocellulosic sources are met in agricultural and forestry residues as well as in pulp industry wastes. A range of novel chemistries have been revealed over the recent years that upgrade lignocellulosic biomass into commodity and chemical specialties like polymers, solvents, lubricants, pharmaceuticals, nutraceuticals, cosmetics, surfactants, animal feed and fuels (Hughes et al., 2013). Figure 1 shows a typical lignocellulosic value chain with multiple choices for biomass feedstocks and chemical products that may enter upcoming biorefineries. Since there are not clear technical, commercial and environmental evidences for the selection of biomass varieties and chemistries, engineering tools are required to systematically screen benefits from integration of different processes across same site and detect biomass mixtures that maximize efficiencies in use of energy and materials.

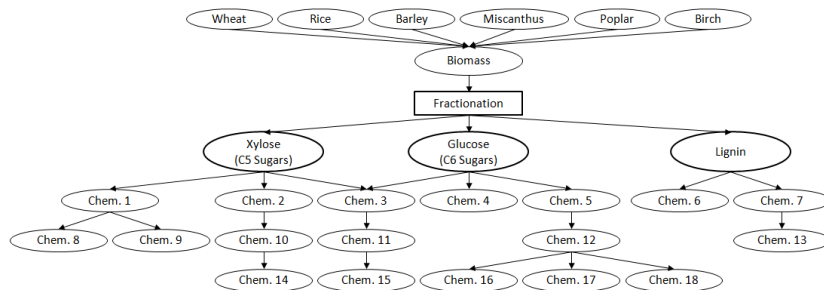


Figure 1. Illustrative biorefinery value chain.

2. Problem description

Process integration techniques are used to estimate cost savings by exchanging materials and energy among processes instead of operating individually. Energy integration searches for heat source-to-sink matches maximizing heat recovery within each process. At a next level, Total Site Analysis (TSA) applies for the integration of different processes and estimates steam targets by means of graphical and numerical tools based on the concept of Site Sources and Sinks Profiles (SSSPs). Though there is extensive literature for steam targeting in sites, the conventional concepts appear inefficient to apply for the design of biorefineries, since processes and operations are not fixed and known beforehand; namely, SSSPs cannot directly apply for the infinite candidate sites that emerge through value chains. Beyond selection of processes to integrate, the problem also brings questions about operations and capacities of involved processes, which subject to seasonal availability and variability of biomass. There are several literature studies focusing on the optimization of biomass supply chains (Yue et al., 2014) and planning energy systems (Varbanov and Klemeš, 2011); however the approaches are limited by the use of graphical tools that exclusively address particular synthesis applications and scenarios. The design of sustainable biorefineries requires for multiple processes and products that properly integrate within sites as well as planning of multiple-feedstock operations over the year. Therefore, integration thermodynamics should be combined with mathematical programming to systematically assess energy targets of all potential process combinations so as to maximize benefits from process-to-process integration. Fundamentals of this concept has been recently presented by Kokossis et al. (2015). This work further presents systems representations that map value chain synthesis options and integration thermodynamics to develop a comprehensive optimization model that can be widely used as a engineering tool for synthesis, integration and planning problems in existing or upcoming industries.

3. Methodology

The conventional Total Site integration tools assume given processes that exchange energy via steam production and reuse. When the case includes candidate processes and infinite combinations to integrate, the graphical tool appears inefficient to estimate steam targets; steam sources and sink profiles would actually behave as variable curves that vary according to process selections and capacities along value chains each time. Kokossis et al. (2015) originally introduced an integration concept that addresses processes as additional variables in integration generating value chain paths combinations assuming paths as binary options. This paper further establishes a cascade

representation that lets processes and their capacities get combined in any way; namely, competitive processes may exist in the design for sake of improved energy targets. Synthesis options for storing and biomass pre-treatment (drying) are also introduced in the process synthesis representation to enable switching and combining biomass feedstocks as well as to plan multiple-feedstock operations over the year.

Process portfolios are developed by means of a Biomass Bipartite graph Representation (BBR) that enables the development of mass balances along value chains considering seasonal changes in biomass feedstocks. Heat contents of sources (hot streams) and sinks (cold streams) vary according to selections made by BBR. A Total Site Representation (TSR) that is based on common sense of heat cascading but formulated by means of an extended transshipment model enables recording energy balances among candidate process hot/cold streams and utility levels. The proposed Total Site Cascade is configured by combining temperature intervals of all individual heat cascades - each related with a candidate process - along a super-interval cascade that is used for direct and indirect integration purposes of variable processes. Heat contribution to cascade intervals is adjusted by decisions made by BBR. Direct heat source-to-sink integration (within each process) is described quite similarly to conventional integration at each interval of the proposed cascade that is configured according to minimum temperature difference (ΔT_{min}). Indirect integration refers to heat exchange among processes via steam production-reuse and is described by translating excess heat of intervals into generated steam and transferring that energy, through cross-interval heat flows, to lower temperature intervals according to minimum temperature difference of the site, $\Delta T_{min}^{site} = 2 \cdot \Delta T_{min}$, where $1 \cdot \Delta T_{min}$ accounts for steam generation and $1 \cdot \Delta T_{min}$ for steam reuse. Hot streams and utilities residuals of the proposed Total Site Cascade can be used to reproduce the sources and sinks profiles of regular SSSPs.

Synthesis of paths also copes with matching steam-source with steam-sink processes improving steam savings due to overlap of generated and demanded steam. Processes may act as steam source or sink or both according to processes portfolio in which they are integrated with. While Total Site cascade evaluates steam savings under steady-state biorefinery operations, biomass seasonality imposes changes on process capacities and energy efficiencies in time, since each variety features with different organic content and yields in sugars and lignin capacities; these constitute the main intermediates in lignocellulosic biorefineries (Figure 1) and rule all downstream process capacities.

Biomass seasonality and the use of multiple feedstocks are incorporated by letting input chemicals flows related with chemicals stored in previous seasons. Storage and drying facilities have been employed (i) to store biomass feedstocks for seasons with biomass shortage as well as to compose biomass mixtures that improve biorefinery efficiencies and (ii) to dry woody biomass before entering the biomass fractionation process, which constitutes the core process in lignocellulosic biorefineries (Figure 1). Changes in biomass feedstocks naturally result in changes of intermediates yields, downstream process capacities and process streams heat contents. As a result, selections on biomass varieties have an apparent impact on energy savings and the selection of steam-source/sink-process portfolios. Steam savings are also affected by the number and the temperature levels of applied utilities along the cascade. The size and complexity of the combined process synthesis and integration problem require the use of mathematical programming to optimize multiple-product biorefinery structures and plan multiple-feedstock operations. Portfolios made by BBR are integrated and evaluated by TSR. Mass (BBR) and energy (TSR) balances are constructed as an optimization model

(MILP) that makes selections on processes, biomass mixtures and utilities and plans the annual biorefinery operation to minimize the energy cost of the under-construction site.

4. Systems representations

BBRs (Figure 2.a) employ product nodes, units and interconnections to translate unclear value chains into superstructure-like representations for optimization purposes. So, let $P=\{p|p=1,NP\}$ and $PR=\{pr|pr=1,NPR\}$ be the process units and product nodes assigned to each path and chemical of the value chain; $T=\{t|t=1,NT\}$ be the interconnections that make connections among nodes (pr) and units (p); $B=\{b|b=1,NB\}$ be the biomass varieties and $SE=\{se|se=se1,\dots,se4\}$ be the seasons of the year for biorefinery operation. Also, let variable F_t be the chemical flowrate of interconnection t . Storing in BBRs is dedicated to interconnections that transfer chemicals from one season to next one. Storing in facilities protected from environmental conditions is also capable to secure drying of woody biomass (50% w/w moisture content) at the rate of 5% w/w per season. For this reason, storages $p1-p4$ denote (Figure 2.a) free of energy cost drying in storage facilities for seasons $se1-se4$, respectively; drying in storages cannot reduce moisture lower than 30% w/w. Drying units $p6-p9$ are next applied to further dry biomass exiting units $p1-p4$ down to the limit of 15% w/w that is required for operation of the core biomass fractionation process; drying is not required for non-woody biomass, whose moisture content is below this limit. Mass balances are recorded using flowrates, F_t , of input-output interconnections at each product node and process unit. Logical constraints are also required to limit intense and impractical fluctuations of process capacities over the year due to equipment sizing and instrumental design limitations. The heat contents of contributed process streams are linearly estimated by the selected operation capacities (flowrates of process input interconnections) and the known (estimated by process simulations) heat contents of streams per product flowrate.

For the development of TSR (Figure 2.b), let C_p be the cascade of each candidate process p . Also, let $QS_m^{C_p}$, $QW_n^{C_p}$ and QS_m^{TS} , QW_n^{TS} be the heat loads of hot, cold utilities of cascade C_p and the Total Site. The Total Site Cascade (TSC) is formulated by the temperature intervals of all candidate cascades. Energy balances are formulated using an extended transshipment model that uses detailed heat exchange options among hot-cold streams and utilities at each interval. Heat flows referring to direct integration of streams of different processes are fixed to zero. Thus, the TSC incorporates all debottleneck problems of candidate processes without affecting each other; accordingly, the utility demands of the TSC correspond to the demands of all individual cascades. A Utility Storages System (USS) has been also set-up to supervise the utilities demands of the TSC. Excess heat from the TSC is extracted by cold utilities and next sent to lower-temperature intervals replacing external steam demands. The excess heat is transferred via energy bridges that pass through the USS, which estimates the energy overlap between generated-demanded steam and thus, minimizes the external utilities needs.

5. Case studies

5.1. Case 1

The biorefinery value chain of Figure 3 involves 6 candidate biomass varieties (wheat straw, rice, barley, miscanthus, softwood and hardwood) and 17 chemical products that need to be examined in order to reveal energy promising biorefinery solutions. Each

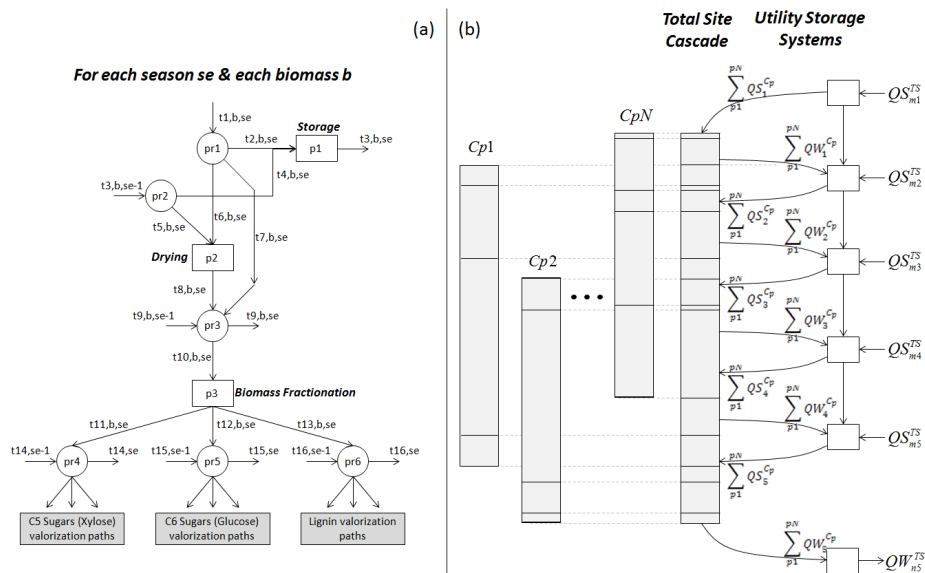


Figure 2. Systems Representations of BBR (a) and TSR (b).

path from one chemical to another denotes a chemical process. The paths have been optimized in the course of a biorefinery study in Hungary based on real-life seasonality data. Hungary offers options for wheat, barley and hardwood. The biorefinery size is bounded by the installation capacity of the biomass fractionation process at 22.500 kg/hr of dry matter. Wheat straw was preferred instead of barley and hardwood due to its low sugars content, which result in lower operation capacities and energy cost for the energy intensive sugar-based paths compared to the lower energy intensive lignin-based paths. Barley is used at wheat depletion completing the annual biomass needs, while hardwood is excluded. The biorefinery includes the biomass fractionation process as well as the xylitol, isoprop./butanol and poly-urethanes production processes. The utilities are estimated to 58 MW (hot) and 40 MW (cold), while the generated steam replaces 6.5% of external steam demands. In Case 2, the proposed model was applied to examine preferences on biomass varieties in building biorefinery efficiencies.

5.2. Case 2

The model was applied for multiple times by additionally using inter-cut equations to constrain selections about biomass varieties by excluding each time the varieties that selected in previous runs. Table 1 presents the results according to the preferences obtained for the varieties. Miscanthus has been selected as the prime biomass variety for minimizing energy cost, while softwood holds the last position. High trends have been obtained for xylitol, isoprop./butanol and poly-urethanes production processes, while itaconic acid enters the biorefinery site sharing the xylose (C6 sugars) intermediate with isoprop./butanol process at the use of rice or barley. The percentages reflect to the selected process operation capacities on the basis of their maximum capacities. The maximum capacities account for operations, when processes do not share upstream (input) chemicals with other competitive processes. Drying facilities are also included at the use of woody biomass. The results of Table 1 could play a significant role in making quick decisions on selecting and planning production lines and multiple-feedstock operations according to biomass availability at each season.

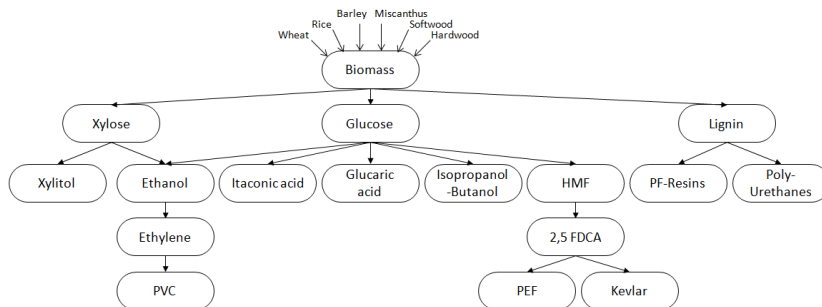


Figure 3. Understudied biorefinery value chain.

Table 1: Ranking of biomass varieties with respect to energy cost

Ranking biomass varieties	Dryers	Splitting intermediates among competitive products			
		Biomass to Fractionation process	Xylose to Xylitol	Glucose to Itaconic acid	Lignin to Poly-Urethanes
(1)Miscanthus	-	100%	100%	100%	100%
(2)Rice	-	100%	100%	13%	100%
(3)Wheat	-	100%	100%	100%	100%
(4)Barley	-	100%	100%	13%	100%
(5)Hardwood	100%	100%	100%	100%	100%
(6)Softwood	100%	100%	100%	100%	100%

6. Conclusions

This paper presents systems representations to model process-to-process integration and select biorefinery portfolios that subject to seasonal availability of biomass varieties. Total Site integration is re-stated as a process synthesis tool that addresses processes and biomass feedstocks as additional degrees of freedom in integration procedure. A biomass representation maps all value chain process synthesis options and the use of multiple feedstocks, while an extended transshipment model is used to evaluate energy savings from process-to-process integration. The proposed methodology was used to reveal high energy efficient process portfolios, assess preferences on biomass varieties and plan multiple-feedstock operations minimizing the annual biorefinery energy cost.

Acknowledgments

The authors acknowledge joint financial support by Alexander S. Onassis Public Benefit Foundation (Greece) and the FP7 KBBE Grant BIOCORE (FP7-241566).

References

- Hughes SR, Gibbons WR, Moser BR, Rich JO., InTech, 2013, <http://dx.doi.org/10.5772/54804>.
- Kokossis AC, Tsakalova M, Pyrgakis K., Computers & Chemical Engineering, 2015, 81, 40-56.
- Yue D, You F, Snyder SW., Computers & Chemical Engineering, 2014, 66, 36-56.
- Varbanov PS, Klemeš JJ., Computers & Chemical Engineering, 2011, 35, 1815-1826

Processes Separation to Furfural, Design and Optimization Involving Economical, Environmental and Safety Criteria

G. Contreras-Zarazúa^a, E. Sánchez-Ramírez^a, J.A. Vázquez-Castillo^b, C. Ramírez-Márquez^a, J.G. Segovia-Hernández^{a*}

^a*Department of Chemical Engineering University of Guanajuato, Noria Alta S/N, Guanajuato, Gto., 36000, Mexico.*

^b*Faculty of Chemical Sciences Autonomous University of Chihuahua, Circuito Universitario 8, Campus II, Chihuahua, Chih. 31125, Mexico*

g_segovia@hotmail.com

Abstract

In this work is presented the simultaneous design and optimization of three alternatives of azeotropic distillation processes to purify Furfural by the mathematical technique called Differential Evolution with Tabu List (DETL), having as objective functions economic, environmental and safety criteria to the processes were evaluated. The schemes here studied are: conventional Quaker Oats process to purification of Furfural (CQO), an azeotropic distillation process with heat integration through vapour recompression (DHI) and dividing wall azeotropic distillation column (DWC). The results of the simultaneous optimization show that the intensification processes DHI and DWC have important reduction on the cost and environmental impact, with respect to conventional process (CQO). However, the increase in operative pressures in the case of DHI process and the increase of internal flows and the size of equipment in DWC process cause an increment of the risk, despite of the risk increment in DWC it is considered the best option to furfural purification due reductions mainly on TAC and Eco99 that mean important savings in a long-term.

Keywords: Furfural, Optimization Process, Multi- Objective Optimization, Process Intensification, Bio-Refinery.

1. Introduction

The depletion of sources energy, greenhouse effect and the high environmental impact, are some problems of using petroleum. Thus the efforts in recent years have been focused on developing of alternative renewable resources that can replace to derivate petroleum products like fuels, plastics among others. The biomass is considered the most important among the renewable resources due to is the most abundant feedstock in the planet (Long et al. 2016). The US National Renewable Energy Laboratory (NREL) gave himself to the task to identify the chemicals from biomass and listed 30 potential chemical from biomass that could compete and replace the chemical from petroleum. Furfural stands out in this list with a wide range of applications that go from extracting for the refinement of lubricating oils, as a fungicide, nematocide and as a raw material (up to 65% of all furfural produced), to furfural alcohol production and other important products like levulinic acid (Long et al. 2016).

The furfural is produced from biomass rich in pentoses like corn cobs, oat hulls, sugar cane bagasse to name a few. The first process production of furfural was Quaker Oats process established in 1921 and it remains as the most used today. This process has had few changes since 1921, the Quaker Oats consists mainly of two steps, which are a reaction and distillation steps respectively. At the reaction step, the biomass is pretreated and subsequently it is introduced in a reactor with diluted sulphuric acid where the biomass is degraded in a hydrolysis reaction into furfural, methanol and acetic acid. The stream from the reactor has a composition in mass fraction of 6% furfural, 4% of methanol and acetic acid and 90% of water (Zeitsch; 2000). As almost all bio-refinery process, the low composition of the main product (in this case furfural) conditions us to high separation costs, in the case of furfural purification these costs are even higher due the formation of azeotropes between the organic components with the water. For this reason in this work are studied three different azeotropic distillation process to purify Furfural; conventional Quaker Oats process purification of Furfural (CQO) and two intensified processes, an azeotropic distillation process with heat integration through vapour recompression (DHI) and dividing wall azeotropic distillation column (DWC). Due the bio-refineries need to be the most profitable and cheap, with less environmental impact and with the safest operating conditions, the design and optimization of the three distillation process were realized in order to minimize these aspects.

2. Methodology

The three different schemes studied in this work are showed on the Figure 1, compositions and flows were taken by Long et al. 2016. The CQO and DHI processes consist in an azeotropic column (C1) that breaks the azeotrope furfural-water, a mixture rich in water and acetic-acid leaves the bottom of this column, whereas from the top of the azeotropic column a stream rich in water and methanol leaves the column, which is then separated in a conventional distillation column (C2), also a side stream is withdrawn between the top and bottom of C1, this stream contains a mixture rich in water and furfural which is sent to a decanter where the organic phase rich in furfural is purified in a third column (C3). On the other hand the DWC process, the C1 and C2 have been integrated in only one column with a dividing wall.

The three distillation schemes were designed and simulated using ASPEN PLUS™ to obtain purities of 99.2% and 99.5% mass fraction of methanol and furfural respectively. The vapor-liquid equilibrium can be predicted by NRTL-HOC model, which includes the Hayden- O'Connell equation, which can predict reliably the solvation of polar compounds and dimerization in the vapor phase, which occurs with mixtures containing carboxylic acids (Long et al. 2016).

The total annual cost (TAC), Eco-indicator 99 (Eco99) and individual risk (IR) were chosen as the objective function to be minimized. TAC was calculated through the Guthrie method, all the parameters for the equipments were taken from Turton et al. 2008, carbon steel was the assumed as the construction material for all the equipments, and the time of investment was considered ten years. The trays selected to the columns were the type Sieve with spacing between trays of 2 ft. The operating costs included cooling utilities, heating utilities, and 8500 hours of yearly operation for each configuration were defined. The operating costs were taken of Turton et al. 2008.

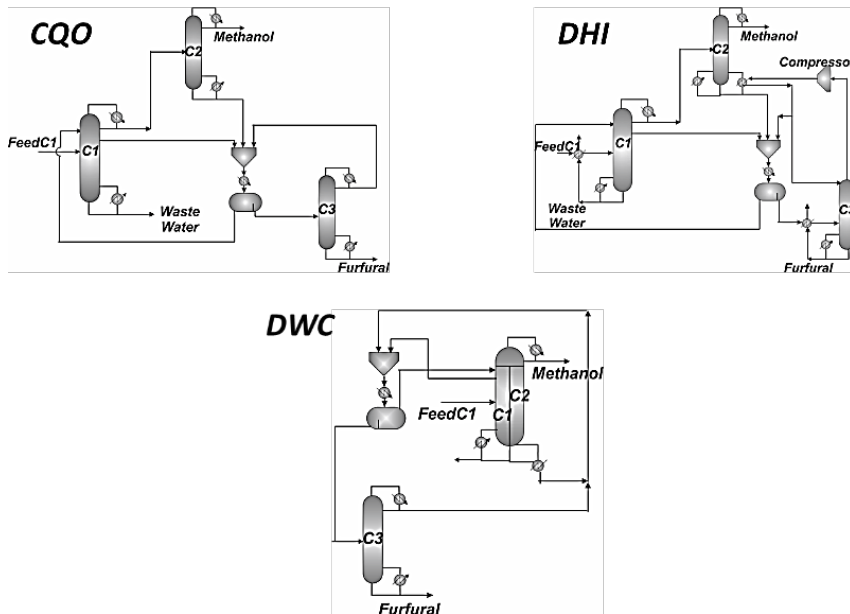


Figure 1. Azeotropic Distillation schemes to furfural purification

The Eco99 was used to evaluate the sustainability of the processes, this methodology is based on lifecycle analysis of different categories where individual scores are assigned depending on the categories, three impact categories (steel, electricity, and vapor) were considered according to work presented by Errico et al. 2016 where this indicator has been utilized to quantify the environmental impact in some chemical processes. In the case of the safety, the individual risk was calculated through quantitative risk analysis technique, which is a methodology of inherent safety where the main objective is to evaluate the frequency and probability of death or injury due to accidents like explosions or toxic release. This methodology has been successfully used to evaluate the risk on chemical process (American Institute of Chemical Engineers 2000), the equations and procedure was realized to a distance of 50 m from the equipments according to reported by American Institute of Chemical Engineers, 2000.

In this work, it has been used the Differential Evolution with Tabu List Algorithm which is a multi-objective optimization method proposed by Sharma and Rangaiah 2010. The DETL has four basic steps: generation of initial population, mutation, crossover, a selection of the best solutions, each one of these steps require of some parameters that need to be determined by a tuning process where is evaluate the ability of the algorithm the algorithm's ability to find solutions that meet all constraints. The value of required parameters to the DETL algorithm determine by tuning process are the following: Population size (NP): 120 individuals, Generations Number (GenMax): 834, Tabu List size (TLS): 60 individuals, Tabu Radius (TR): 0.01, Crossover fractions (Cr): 0.8, Mutation fractions (F): 0.3. The implementation of the multi-objective optimization strategy involved a hybrid platform, which linked Aspen Plus™, Microsoft Excel™. The decision variables for each reactive distillation configuration are reported in Table 1. Finally, the multi-objective optimization problem can be expressed mathematically as in Eq. (1) and Eq. (2):

$$\min Z = \{TAC; Eco99; IR\} \quad (1)$$

$$\text{Subject to: } \begin{aligned} y_{i,PC} &\geq x_{i,PC} \\ w_{i,FC} &\geq u_{i,FC} \end{aligned} \quad (2)$$

Table 1. Decision variables of the reactive distillation configurations.

Decision Variables	Continuous	Discrete
Number of stages, C1		X
Number of stages, C2		X
Number of stages, C3		X
Feed stage recycle of C1		X
Feed stage, C1		X
Stage of side stream C1		X
Feed stage C2		X
Feed stage C3		X
Reflux ratio of C1	X	
Reflux ratio of C2	X	
Reflux ratio of C2		
Heat duty of C1, kW	X	
Heat duty of C2, kW	X	
Heat duty of C3, kW		
Diameter of C1, m	X	
Diameter of C2, m	X	
Diameter of C2, m	X	
Discharge pressure of compressor(Comp), atm	X	
Interlinking flow, Kg h ⁻¹	X	

The objective function is restricted to the accomplishment of the purity vectors, and the mass flowrate vectors for the components in the mixture. For example, the values of the purities for the components obtained during the optimization process $y_{i,PC}$ must be either greater or equal to the specified values of purities for the component $x_{i,PC}$. Furthermore, the mass flowrates obtained $w_{i,PC}$ must also be either greater or equal to the specified values of the mass flowrate $u_{i,PC}$.

3. Results

The optimal design parameters, design specifications, and values for the objective functions for all the studied sequences are offered in Table 2. Figure 2 shows the Pareto charts of the DWC process, the DHI and CQO keep the same tendency.

The results show that the DHI process does not provide a big saving of TAC and the values of Eco99 and IR are bigger than the values of the CQO process. The reason of these results is because the energy savings in DHI are very low compared to conventional process, the addition of more equipment such as heat exchangers and compressors directly affects steel category on Eco99 and the probability of an accident to occur increases due IR value is bigger than CQO.

Table 2. Optimal design parameters for the sequences.

Design Variables	CQO	DHI	DWC
Number of stages, C1	50	51	70
Number of stages, C2	9	33	72
Number of stages, C3	6	8	12
Feed stage recycle of C1	14	19	5
Feed stage, C1	30	29	37
Stage of side stream C1	12	13	30
Feed stage C2	8	20	-----
Feed stage C3	4	7	6
Reflux ratio of C1	22.95	2.93	-----
Reflux ratio of C2	0.203	1.25	25.09
Reflux ratio of C3	1.564	0.28	0.273
Heat duty of C1, kW	20018	19519	19131
Heat duty of C2, kW	773	882	320
Heat duty of C3, kW	604	566.246	715
Diameter of C1, m	1.396	0.86	-----
Diameter of C2, m	0.524	0.80	1.535
Diameter of C3, m	0.380	1.13	0.321
Discharge pressure of compressor(Comp), atm	-----	1.29	-----
Interlinking flow, kg h ⁻¹	-----	-----	25887
TAC (\$/yr)	9,383,987	9,318,611	9,179,222
Eco99 (Eco-points)	4,344,805	4,546,195	4,299,778
IR (1/yr)	2.734x10 ⁻⁴	2.850x10 ⁻⁴	5.371 x10 ⁻⁴

In the case of DWC this process has savings of TAC and low Eco99 value with respect to CQO process due there are less equipment because of the thermally coupling. This process presented an important reduction in the side of the divided wall column that corresponding to column C2 in the conventional process, however the column C3 has an increment in the energy consumption of around 100 KW with respect to the C3 column of CQO process. The azeotropic column is the equipment that contributes with the greatest amount of energy in the CQO process, the DWC has a reduction near 900 KW it indicates that TAC and Eco99 reductions are due the lessening of steel category because of the integration of C1 and C2 columns in only one equipment and it is not for energy savings. The IR presents increment in DWC process with respect to CQO, the increment of risk is mainly due the increment of the size and the amount of material of dividing wall column. The IR is dependent of the size of equipment, bigger distillation columns imply that there is more mass inside the columns from which like explosions can derivate in a greater range of damage , and due DWC is used to purify methanol, a big column represents more flammable material inside it, then the potential of a more destructive accident increases. It has traditionally been thought that dividing wall columns provide more secure process due to the reduction of equipment reduce the probability of accident, nevertheless, the results obtained in this work indicate that this affirmation may not be met in all cases.

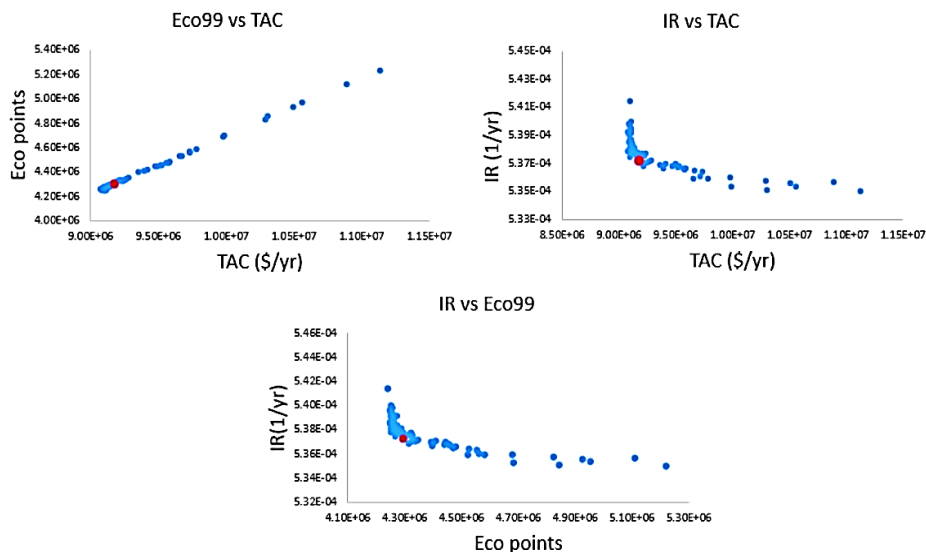


Figure 2. Pareto Fronts to DWC process

4. Conclusions

In this work was realized the simultaneous design and optimization of three alternatives to purification of furfural, the application of the quantitative risk analysis represents an additional selection criterion that can help to take measures to a safe operation of these processes. The results indicate that the DHI does not provide reductions on TAC, Eco99 and IR compared to CQO processes thus DHI is not considered a good option to purify furfural. The DWC processes has an increment in the value of IR compared with CQO mainly to increase in size of dividing wall column, we considered that IR of DWC process is not enough large to a dangerous. Therefore, DWC is considered the best option to furfural purification due reductions mainly on TAC and Eco99 that significates important savings in a long-term.

References

- American Institute of Chemical Engineers. Guidelines for chemical process quantitative risk analysis; Wiley & Sons: New York, NY, USA. 2000
- Errico, M., Sanchez-Ramirez, E., Quiroz-Ramirez, J. J., Segovia-Hernandez, J. G., & Rong, B. G. (2016). Synthesis and design of new hybrid configurations for biobutanol purification. *Computers & Chemical Engineering*, 84, 482-492.
- Long, N. V. D., Kim, S., & Lee, M. (2016). Design and optimization of intensified biorefinery process for furfural production through a systematic procedure. *Biochemical Engineering Journal*, 116, 166-175.
- Rangaiah, G. P. (2010). *Stochastic global optimization: techniques and applications in chemical engineering*. World Scientific.
- Turton, R., Bailie, R. C., Whiting, W. B., & Shaeiwitz, J. A. (2008). *Analysis, synthesis and design of chemical processes*. Pearson Education.
- Zeitsch, K. J. (2000). *The chemistry and technology of furfural and its many by-products (Vol. 13)*. Elsevier.

Techno-economic assessment of a lignocellulosic biorefinery co-producing ethanol and xylitol or furfural

Aristide Giuliano^a, Diego Barletta^{a,*}, Isabella De Bari^b, Massimo Poletto^a

^a*Department of Industrial Engineering, University of Salerno, Via Giovanni Paolo II, 132, 84084 Fisciano (SA), Italy*

^b*ENEA, Italian National Agency for New Technologies, Energy and Sustainable Economic Development, S.S. 106 Ionica, km 419+500, Rotondella, MT, Italy*

dbarletta@unisa.it

Abstract

The economic sustainability of lignocellulosic biorefineries can be significantly improved by co-producing added value chemicals together with common biofuels like ethanol. In this work a techno-economic analysis of a multiproduct biorefinery was carried out by means of process simulations, cost and profitability analysis. Alternative process flowsheets including the co-production of xylitol or furfural from C₅ sugars deriving from biomass hydrolysis were assessed and compared with the ethanol base case. A comparison between the purchase of enzymes and the on-site production of enzymes was also addressed. The lowest Payback Selling Price of ethanol was obtained for the case of xylitol co-production thanks to its higher added value.

Keywords: lignocellulosic biorefinery, multi-product, xylitol, ethanol, furfural.

1. Introduction

The strong dependence of modern society on fossil fuels derives from the intensive use and consumption of petroleum products. To reduce the dependence on oil and to limit simultaneously the effects on climate change, it is necessary to make changes in transport and in chemical sector, where new production processes are needed (Conde-Mejía et al., 2016). The National Renewable Energy Laboratory of US listed the 12 chemical compounds more easily obtainable from lignocellulosic biomass by industrial biorefineries (Bozell and Petersen, 2010). They are value-added chemicals or precursors of other chemicals in common use. However, the commercialization of conversion technologies has been hindered by several factors including the unavailability of reliable feedstock supply systems (Galanopoulos et al., 2017), the seasonality of biomass production (Giuliano et al., 2016b) and conversion systems non-fully mature. Besides these, integrated process layouts enabling the optimized exploitation of the feedstock are necessary to make the biorefinery sustainable. For the latter issue, the optimization by process synthesis and integration methods can help to identify the optimal pathways to increase the biobased products profitability. Few studies reported in the literature addressed the optimization of the biomass allocation among alternative pathways for a biorefinery co-producing several compounds (Giuliano et al., 2014) such as alcohols like ethanol or/and butanol (Ségolène et al., 2016), high-value chemicals like succinic acid and levulinic acid (Giuliano et al., 2016a). Significant improvements in the techno-

economic feasibility can be also obtained by applying the biorefinery cascade approach in which the process by-products/secondary streams can be thermally valorised to bioenergy (da Silva et al., 2017).

The aim of this paper is to analyze the technical-economic feasibility of a lignocellulosic biorefinery converting the cellulose into ethanol and the hemicellulose into xylitol or furfural. This analysis is performed by process simulation tools. Material and energy balances were solved. Reactors and separation units were sized. The profitability of alternative process flowsheets was assessed by calculating the cumulated cash flows and by computing the payback selling price of ethanol provided the price of by-products.

2. Biorefinery process description

The process simulation of the biorefinery was carried out through the implementation of a process flowsheet in Aspen Plus (version 8.6). Figure 1 reports the general simplified biorefinery Block Flow Diagram (BFD) including all the possible process pathways. Each block corresponds to an Aspen Plus *hierarchy*, containing a specific process section of the plant. Solid line streams and blocks refer to the base case process (E and E_s), while dashed line streams and blocks refer to optional pathways considered for alternative cases (EX and EF).

The wet biomass is first processed in the steam explosion section where it is pretreated by the steam explosion technology. Steam pretreated pulp can be further fractionated into its main components or sent directly to the enzymatic hydrolysis. (De Bari et al., 2014). Pretreated biomass is sent to the enzymatic hydrolysis section, where the polysaccharides, namely cellulose and hemicellulose, are converted into C6 and C5 sugars. Two scenarios were analysed: 1) cellulase enzymes are purchased (case E), they are produced on site by using part of the pretreated feedstock (case E_s). C6 and C5 sugars are then fermented to ethanol. Ethanol separation and purification is performed by distillation and molecular sieves. The exhausted hydrolysis cake containing lignin and residual cellulose and hemicellulose is sent to the thermal section where is burnt to produce heat and electricity. Biogas generated through the anaerobic digestion of liquid waste streams is also converted to energy.

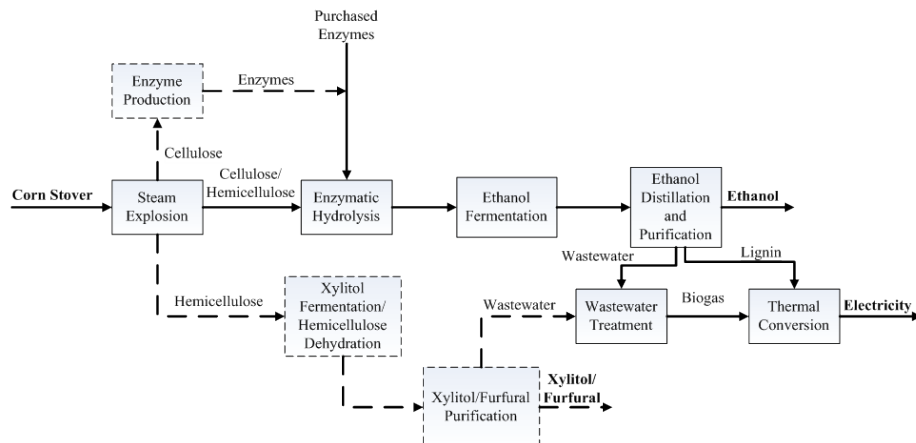


Figure 1: General Flowsheet of the multi-product lignocellulosic biorefinery.

Table 1: Corn stover data, conversion data and economic parameters of process simulations.

Feedstock data		
Feedstock flowrate (t_{WET}/h)	33	
Water ($\%_{WET}$)	17.0	
Cellulose ($\%_{DRY}$)	42.8	
Hemicellulose ($\%_{DRY}$)	17.7	
Lignin ($\%_{DRY}$)	31.5	
Other compounds ($\%_{DRY}$)	8.0	
Reactors data	conversion (%)	residence time (h)
Xylose to ethanol	70	18
Glucose to ethanol	93	18
Xylose to xylitol	69	30
Xylose to furfural	70	1
Economic data		
Plant Life (y)	20	
Xylitol Price (€/kg)	3.50	
Furfural Price (€/kg)	1.10	
Biomass Price (€/t)	60	
Discount Rate (%)	5	
Enzyme cost (€/kg)	3	
Electricity cost (€/MWh)	94	
Electricity selling price (€/MWh)	150	

In two alternative cases the hemicellulose leaving the Steam Explosion section is separated and sent to dedicated conversion units to produce xylitol (case EX) *via* fermentation or furfural (case EF) *via* sugars dehydration. The production of xylitol (case EX) occurs in a bioreactor where xylose is transformed to xylitol. The broth is sent to a purification section where 99% pure xylitol is recovered by a sequence of a flash, an activated coal adsorption unit and a crystallizer. In the case of furfural production (case EF), dehydration of the hemicellulose takes place and xylose is transformed to furfural in a reactor. Reaction products are sent to the purification section consisting in sequence of distillation, column, decanter and distillation column to obtain a 99% pure furfural product.

Table 1 reports the data of the biomass feedstock, corn stover, main economic data and reactor data assumed from previous simulation results on enzymatic hydrolysis and ethanol fermentation (Giuliano et al., 2015) and from literature data. Unit sizing was carried by shortcut methods based on the residence time. More accurate evaluations were performed for the sizing of distillation columns by means of rigorous stage-to-stage methods.

3. Economic Analysis

Economic analysis of the several cases was performed by estimating capital and operating costs. Capital cost were estimated by power law correlations based on unit capacity. Data relevant to biorefinery sections were taken from the literature (Hamelinck et al., 2005). The factorial method was applied to obtain the total investment cost. Operating costs are mainly given by raw materials. In particular, a 60 €/t purchase cost for corn stover and 3 €/kg purchase cost for enzymes were assumed. Moreover, the costs of inoculum, NaOH, SO₂ and water required for pretreatment and hydrolysis were also accounted for. In addition, the costs of salaries, maintenance, and insurance were assessed by the factorial method.

Revenues consists in the sales of the products (ethanol, xylitol and furfural) and of electricity. Linear depreciation was assumed. A discounted cash flow analysis was carried out to obtain the Payback Selling Price (PSP) of ethanol provided the price of the other possible by-products. The PSP was calculated as the value that makes the Net Present Value equal to zero after a 20 years plant life.

4. Results

Results reported in Figure 2 show that the total mass yield to products was almost equal for all the case studies and it was about 25%. In fact, ethanol yield was 25% for the case E and 18% for cases EX and EF. Xylitol and furfural yield was about 8% for the EX and the EF cases, respectively. The ethanol yield for the case E_s was slightly lower (24%) than for the case E due to the partial consumption of cellulose for the enzymes production on site.

The electricity produced by the plant was significantly higher for the production of ethanol only (cases E and E_s) than for the multiproduct cases (case EX and EF), as shown in Figure 2. This is due to two reasons: 1) the inlet stream to the thermal treatment section for the cases EX and EF has a lower organic content, and thus a lower heating value, which reduces the energy yield; 2) the co-production of xylitol or furfural requires more steam. In particular, the higher energy demand is for the xylitol crystallizer and for the distillation columns of furfural.

Table 2 reports the economic analysis results for all the cases in terms of investment costs for each plant section, operating costs and Payback Selling Price (PSP) of ethanol. For the production of ethanol only, as expected, the Total Investment Cost for the plant with the on site enzymes production (case E_s) is higher than that for the plant with the purchased enzymes (case E). On the other hand, lower operating costs are necessary for the case E_s than for the case E due to the avoided purchase cost of the enzymes. On the whole, the two opposite effects tend to counterbalance each other and result in similar PSP values.

The multiproduct cases require on the one hand additional investment cost for the process section transforming the C5 sugars into xylitol or furfural, but on the other hand lower cost for a smaller size section for the enzymatic and the ethanol fermentation.

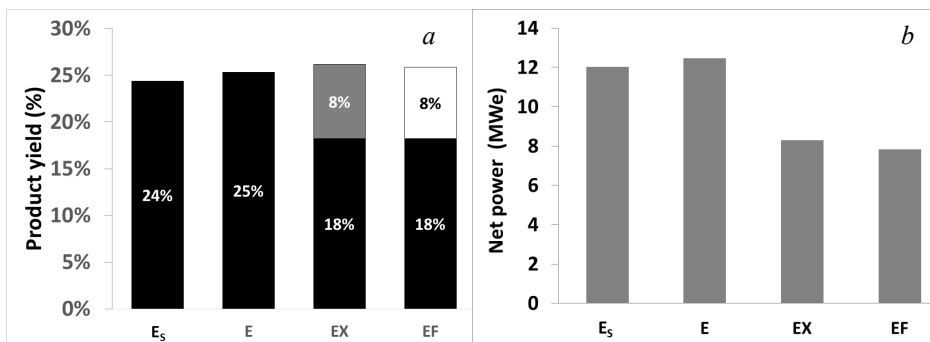


Figure 2. *a*: Product yields for 4 biorefineries. Black bar is the ethanol yield, dark grey bar is the xylitol yield, blank bar is the furfural yield. *b*: net power for 4 biorefineries.

Table 2: Economic results for 4 biorefinery cases.

	E _s	E	EX	EF
<i>Total Investment Cost (M€)</i>	184.4	153.1	144.9	130.9
Steam Explosion	11.4	11.4	11.4	11.4
Enzymatic Hydrolysis & Ethanol Fermentation	23.7	24.1	19.6	19.6
Xylitol Fermentation	-	-	6.7	-
Hemicellulose Dehydration	-	-	-	3.7
Ethanol Distillation & Purification	11.9	12.0	11.3	11.3
Xylitol Purification	-	-	2.2	-
Furfural Purification	-	-	-	1.3
Wastewater Treatment	20.7	20.7	22.1	19.0
Thermal Conversion	82.6	84.5	71.6	64.4
Enzyme Production	34.1	-	-	-
<i>Operating costs (M€/y)</i>	85.3	89.5	89.9	90.0
<i>Revenues (M€/y)</i>	94.6	97.6	97.3	96.9
Ethanol	85.6	88.3	31.0	72.8
By-product (Xylitol or Furfural)	-	-	60.1	18.2
Electricity	9.0	9.3	6.2	5.8
<i>Payback Selling Price of Ethanol (€/kg)</i>	1.62	1.61	0.79	1.85

Significantly lower cost is necessary for the thermal conversion due to the lower production of electricity. On the whole, the Total Investment Cost for the case EX and the case EF is lower than for case E by 5% and 14%, respectively. Instead, operating costs are equivalent for the three cases E, EX and EF. As mentioned above, the yield values to ethanol and the yield values to the other by-product (xylitol or furfural) are very similar for the cases EX and EF. As a result, since the xylitol price is three times the furfural price, the by-product revenues for the case EX is about three times those for the case EF. Consequently, since also the ethanol production is comparable, the PSP of ethanol for the case EF is about twice the PSP of ethanol for the case EX. Furthermore, the PSP for the case EX is slightly higher than the PSP for the case E.

5. Conclusions

A techno-economic analysis on a biorefinery processing corn stover to obtain ethanol as main product was carried out. Similar mass yield and Payback Selling Price of ethanol were obtained for the case with purchased enzymes and for the case with enzymes produced on site. We are aware that this result might be significantly affected by the plant size or the production rate of the biorefinery and deserves a sensitivity analysis, which will be addressed in future works.

Alternative process flowsheets including the co-production of xylitol or furfural from C₅ sugars deriving from biomass hydrolysis were assessed and compared with the ethanol base case. A constant total mass yield to products of the biorefinery, about 25%, was obtained for all the cases with different biomass yield values to single products in

multiproduct cases. The electricity produced by the plant decreases by about 30% if xylitol or furfural is produced together with ethanol.

From the profitability point of view, xylitol coproduction appears more convenient than both the co-production of furfural and the production of ethanol alone. This result is due to the significantly higher selling price of xylitol which prevails by means of higher revenues, despite the 10% higher total investment cost than that for the co-production of furfural.

References

- Bozell, J.J., Petersen, G.R., 2010. Technology development for the production of biobased products from biorefinery carbohydrates—the US Department of Energy’s “Top 10” revisited. *Green Chem.* 12, 539.
- Conde-Mejía, C., Jiménez-Gutiérrez, A., Gómez-Castro, F.I., 2016. Purification of Bioethanol from a Fermentation Process: Alternatives for Dehydration. *Comput. Aided Chem. Eng.* 38, 373–378.
- da Silva, A.R.G., Errico, M., Rong, B.-G., 2017. Evaluation of organosolv pretreatment for bioethanol production from lignocellulosic biomass: solvent recycle and process integration. *Biomass Convers. Biorefinery*. <https://doi.org/10.1007/s13399-017-0292-4>
- De Bari, I., Cuna, D., Di Matteo, V., Liuzzi, F., 2014. Bioethanol production from steam-pretreated corn stover through an isomerase mediated process. *N. Biotechnol.* 31, 185–195.
- Galanopoulos, C., Odierna, A., Barletta, D., Zondervan, E., 2017. Design of a wheat straw supply chain network in Lower Saxony, Germany through optimization. *Comput. Aided Chem. Eng.* 40, 871–876.
- Giuliano, A., Cerulli, R., Poletto, M., Raiconi, G., Barletta, D., 2016a. Process Pathways Optimization for a Lignocellulosic Biorefinery Producing Levulinic Acid, Succinic Acid, and Ethanol. *Ind. Eng. Chem. Res.* 55, 10699–10717.
- Giuliano, A., Cerulli, R., Poletto, M., Raiconi, G., Barletta, D., 2014. Optimization of a Multiproduct Lignocellulosic Biorefinery using a MILP Approximation. *Comput. Aided Chem. Eng.* 1423–1428.
- Giuliano, A., Poletto, M., Barletta, D., 2016b. Process optimization of a multi-product biorefinery: The effect of biomass seasonality. *Chem. Eng. Res. Des.* 107, 236–252.
- Giuliano, A., Poletto, M., Barletta, D., 2015. Process Design of a Multi-Product Lignocellulosic Biorefinery. *Comput. Aided Chem. Eng.* 1313–1318.
- Hamelinck, C.N., Van Hooijdonk, G., Faaij, a. P.C., 2005. Ethanol from lignocellulosic biomass: Techno-economic performance in short-, middle- and long-term. *Biomass and Bioenergy* 28, 384–410.
- Ségolène, B., Ludovic, M., Stéphane, N., Serge, D., 2016. Design of a Multiproduct Lignocellulosic Biorefinery through the Process Modelling of a Feasible Superstructure. *Comput. Aided Chem. Eng.* 38, 595–600.

Endpoint-oriented Life Cycle Optimization Models for Sustainable Design and Operations of Shale Gas Supply Chains with Modular Manufacturing

Jiyao Gao, Fengqi You

Cornell University, Ithaca, New York, 14853, USA

Abstract

Modular manufacturing is identified with great potential in the exploitation of shale gas resource. In this work, we propose a novel mixed-integer nonlinear fractional programming model, where design and operational decisions regarding both the conventional processing plants and modular manufacturing devices are considered. The allocation, capacity selection, installment, moving, and salvage decisions of modular manufacturing devices are modeled with corresponding integer variables and logic constraints. To systematically evaluate the full spectrum of environmental impacts, an endpoint-oriented life cycle optimization framework is applied that accounts for up to 18 midpoint impact categories and three endpoint impact categories. Total environmental impact scores are obtained to evaluate the comprehensive life cycle environmental impacts of shale gas supply chains. A tailored global optimization algorithm is also presented to efficiently solve the resulting computationally challenging problem. To illustrate the applicability of proposed modeling framework and tailored global optimization algorithm, a case study of a well-to-wire shale gas supply chain based on Marcellus Shale is considered. Based on the optimization results, the application of modular manufacturing helps achieve the lowest LCOE of \$59.4/MWh and the smallest ReCiPe endpoint environmental impact score per MWh electricity generation as 64.5 points/MWh.

Keywords: Endpoint, life cycle optimization, modular manufacturing, shale gas

1. Introduction

In recent years, the rapid expansion of shale gas industry leads to continuing growth in shale gas production (Cafaro and Grossmann, 2014). However, the lack of midstream infrastructure impedes the exploitation of shale gas resources (Gao and You, 2017). Modular manufacturing has been proposed as a viable approach to address this issue (Tan and Barton, 2015). Modular manufacturing devices are small-scale, highly mobile process units that are produced as individual modules and shipped to the sites of interest for quick assembling (Stewart, 2015). Compared with the conventional shale gas processing plants, the modular manufacturing devices have the potential of reducing the capital expenditures, improving the accessibility of shale gas energy resource, and mitigating the life cycle environmental impacts through process intensification (Gong et al., 2017). To systematically investigate the economic and environmental implications of shale gas modular manufacturing, it is imperative to account for and optimize relevant modular manufacturing options in shale gas supply chain design and operations for better economic and environmental sustainability (Gao and You, 2015).

In this work, we propose a novel mixed-integer nonlinear fractional programming (MINLFP) model. Moreover, a general endpoint-oriented LCO framework is developed that can quantify the full spectrum of environmental impacts in the optimal design and operations of shale gas supply chains. An endpoint-oriented LCIA method ReCiPe is adopted, which comprises of 18 midpoint impact categories and three endpoint impact categories (Goedkoop et al., 2009). This endpoint-oriented LCIA approach is further integrated into a functional-unit-based multiobjective LCO framework to connect the optimization decisions with their environmental impact scores. To illustrate the applicability of proposed modeling framework, a case study of a well-to-wire shale gas supply chain based on Marcellus Shale is considered.

2. Problem Statement

This LCO framework accounts for the well-to-wire life cycle of shale gas, which starts with the well drilling at shale sites and ends with the electricity generation at NGCC power plants (Laurenzi and Jersey, 2013). Corresponding to the well-to-wire life cycle of shale gas, we employ a functional unit of generating one MWh of electricity (DOE/NETL, 2011). Accordingly, both the economic and environmental performances are evaluated based this functional unit. The main data sources of this basic LCI are the most up-to-date LCA studies on shale gas and the Ecoinvent database v3.3 (Laurenzi and Jersey, 2013; Stamford and Azapagic, 2014; "Ecoinvent database v3.3," 2017). We choose the endpoint-oriented LCIA approach ReCiPe to quantify the full spectrum of life cycle environmental impacts (Goedkoop et al., 2009).

We consider a planning horizon consisting of a set of time periods with identical intervals. There are a set of shale sites. Each shale site allows multiple wells to be drilled. The raw shale gas produced at shale sites is either sent to conventional processing plants or transported to modular LNG plants for processing (He and You, 2014, 2016). Once a modular LNG plant is constructed, it can be disassembled and moved to another location at any time. The sales gas from the conventional processing plants is sent to a set of NGCC power plants with known electricity generation efficiency. LNG produced at modular plants, on the other hand, can be sent to a set of storage facilities for temporary storage or transported to a NGCC power plant directly for electricity generation. Based on the given information, the objective of this LCO problem is to simultaneously optimize the economic and comprehensive environmental performances of the shale gas supply chain with modular manufacturing devices by optimizing the following decisions: (1) Drilling schedule, production profile, and water management strategy at each shale site; (2) Construction and capacity choices of conventional processing plants, locations and specs of modular manufacturing devices, moving schedule of modular manufacturing devices, and production planning; (3) Installment and capacity selection of gathering pipeline networks, planning of transportation activities, and storage inventory management;

In accordance with the predefined well-to-wire system boundary and the functional unit of one MWh of electricity generation, we consider the following objective functions:

- Minimizing the LCOE generated from shale gas, which is formulated as the total net present cost divided by the total amount of electricity generated.
- Minimizing the endpoint environmental impact score associated with producing one MWh of electricity.

3. Model Formulation and Solution Algorithm

According to the problem statement in the previous section, a multiobjective MINLFP model is proposed to address the endpoint-oriented LCO of shale gas supply chains with modular manufacturing devices. The economic objective is to minimize the LCOE generated from shale gas, denoted as $LCOE$ and formulated as the total net present cost (TC) divided by the total amount of electricity generation (TGE). The environmental objective is to minimize the endpoint environmental impact score per MWh electricity generation, denoted as UE and formulated as the total environmental impact score (TE) divided by the total amount of electricity generation (TGE). The total environmental impact score accounts for the full spectrum of environmental impacts associated with water management (E_{water}), shale well drilling, stimulation, and completion (E_{drill}), shale gas production (E_{prod}), shale gas processing (E_{proc}), transportation (E_{trans}), LNG storage (E_{stor}), and electric power generation (E_{power}).

$$\min LCOE = \frac{C_{proc}^{CAPEX} + C_{trans}^{CAPEX} + \sum_{t \in T} \left[\frac{C_{water,t}^{OPEX} + C_{drill,t}^{OPEX} + C_{prod,t}^{OPEX} + C_{proc,t}^{OPEX} + C_{trans,t}^{OPEX} + C_{stor,t}^{OPEX} + C_{power,t}^{OPEX}}{(1+dr)^t} \right]}{\sum_{g \in G} \sum_{t \in T} GE_{g,t}} \quad (1)$$

$$\min UE = \frac{TE}{TGE} = \frac{E_{water} + E_{drill} + E_{prod} + E_{proc} + E_{trans} + E_{stor} + E_{power}}{\sum_{g \in G} \sum_{t \in T} GE_{g,t}} \quad (2)$$

- s.t. Economic Constraints (3)
- Environmental Constraints (4)
- Mass Balance Constraints (5)
- Capacity Constraints (6)
- Bounding Constraints (7)
- Logic Constraints (8)

The resulting multiobjective MINLFP problem is computationally challenging to be optimized globally. Based on the problem structure, we apply a tailored global optimization algorithm integrating the parametric algorithm (Zhong and You, 2014) with a branch-and-refine algorithm to tackle this computational challenge.

4. Application to a Well-to-Wire Shale Gas Supply Chain

To illustrate the applicability of the proposed endpoint-oriented LCO model of shale gas supply chains with modular manufacturing devices, we consider a case study of a well-to-wire shale gas supply chain based on Marcellus Shale. A total of 12 shale sites are considered, among which six shale sites are existing ones with active wells and six shale sites are potential ones to be developed. Each shale site allows for drilling of up to four to eight shale wells. There are two existing and one potential conventional shale gas processing plants. Up to six locations are considered for the modular LNG plants. There are three capacity levels for the modular LNG plants, corresponding to 25 kgal, 50 kgal, and 100 kgal maximum LNG production per day, respectively. Relevant process-level data are taken from recent literature (Stewart, 2015; Tan and Barton, 2015; Yang and You, 2018; Gong and You, 2018). There are two LNG storage facilities where LNG products can be temporarily stored before being sent to the market. In this well-to-wire shale gas supply chain, there are three NGCC power plants with combined cycle gas turbines, and the average efficiency is 50% on a lower heating value (LHV) basis. A 10-year planning horizon is considered. The planning horizon is divided into 20 time

periods, and each time period represents half a year. The resulting MINLFP problem has 4,012 integer variables, 13,767 continuous variables, and 9,556 constraints. All the models and solution procedures are coded in GAMS 24.7.3 on a PC with an Intel® Core™ i7-6700 CPU and 32GB RAM.

The resulting MIBLFP problem is solved using the presented tailored global optimization algorithm and a Pareto-optimal curve consisting of 13 Pareto-optimal solutions is shown in Figure 1. The x -axis represents the ReCiPe endpoint environmental impact score per MWh electricity generation from shale gas. The y -axis represents the LCOE in the shale gas supply chain.

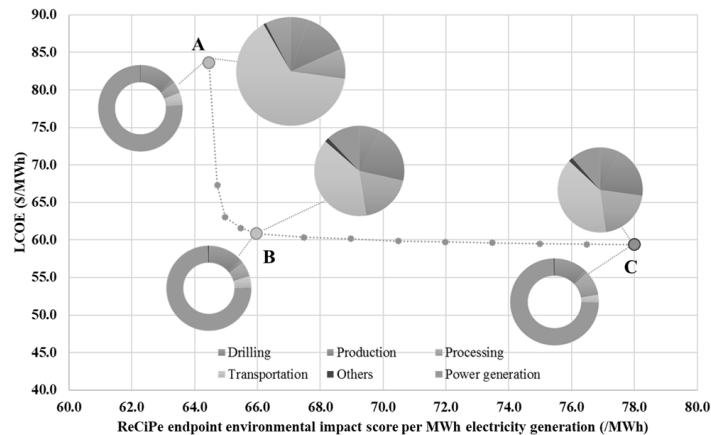


Figure 1. Pareto-optimal curve illustrating the trade-offs between LCOE and ReCiPe endpoint environmental impact score per MWh electricity generation with breakdowns.

Along this Pareto-optimal curve, we choose 3 solution points from point A to point C for comparison. Their corresponding LCOE breakdowns are presented with pie charts above the curve, and the breakdowns of environmental impact score per MWh electricity generation are demonstrated with the donut charts below the curve. The sizes of these charts are proportional to the absolute values of total net present cost and total environmental impact score. From point A to point C, the portion of environmental impact score associated with processing activities increases, and the portion associated with transportation activities decreases accordingly for the similar reason as discussed above on the LCOE breakdowns.

In Figure 2 we present the detailed design and planning decisions for modular LNG plants in different Pareto-optimal solutions. As can be seen, there are four modular LNG plants in the optimal solution of point A. In addition to the existing modular plants, a capacity of 25 kgal LNG/day is installed at location 1 in the beginning. Relocation of modular LNG plants is observed in the optimal solutions of point C. Specifically, for point C, the modular plant at location 5 with a capacity of 25 kgal LNG/day is moved to location 6 three years later, and the modular plant at location 6 with a capacity of 50 kgal LNG/day is moved to location 5 half a year later. Such an exchange of modular LNG plants matches the varying demand of processing capacity at different regions. The moving option of modular LNG plants offers more flexibility in the operations of a shale gas supply chain, and the overall economic performance can be improved. Nevertheless, the moving activities of modular plants incur extra environmental

impacts, such as land use change, energy consumption, and emissions. Thus, the relocation of modular plants may not be preferred when minimizing the comprehensive environmental impacts is the main objective.

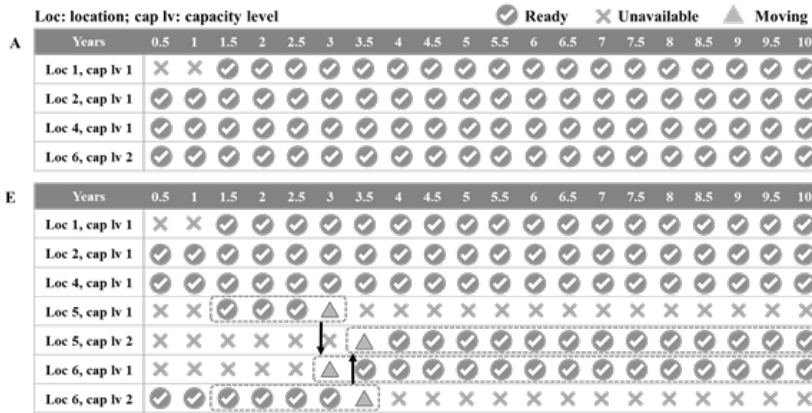


Figure 2. Design and planning decisions for modular LNG plants.

The detailed midpoint environmental impact score breakdowns associated with Pareto-optimal solutions A and E are presented in Figure 3. The impacts of climate change to human health and climate change to ecosystems stand out as two major contributors especially in the life cycle stages of shale gas production, LNG storage, and power generation. Fossil depletion is one of the major midpoint impact categories in water management, drilling, shale gas processing, and transportation, which are all energy-intensive processes. The human toxicity is another key midpoint impact category especially in water management and drilling phases, when large amounts of chemicals and additives are used in drilling and fracturing fluids. The different wastewater treatment strategies also result in disparate environmental performance. We identify RO technology for onsite treatment as the optimal wastewater treatment technology in point A. Nevertheless, in point C, all the wastewater is treated by remote CWT facilities.

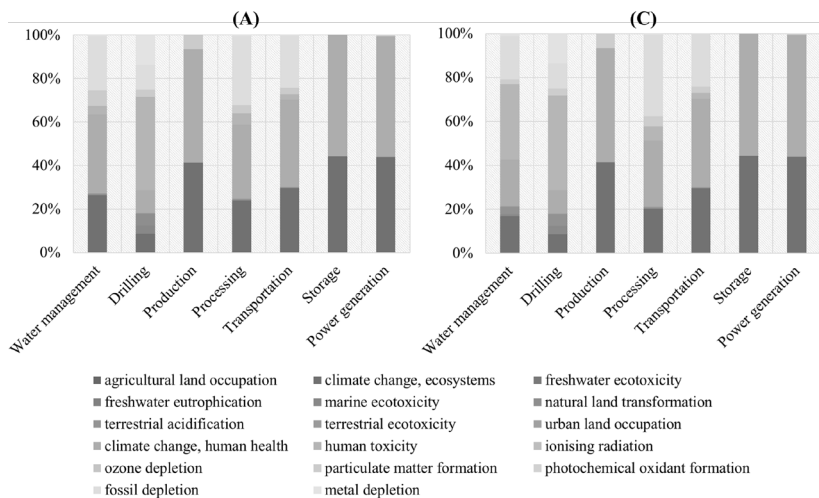


Figure 3. Midpoint environmental impact score breakdowns.

5. Conclusions

A novel endpoint-oriented LCO model was proposed to investigate the economic and environmental implications of incorporating modular manufacturing devices in the optimal design and operations of shale gas supply chains. The applicability of proposed endpoint-oriented LCO framework was illustrated by a well-to-wire shale gas supply chain based on Marcellus Shale. Through a detailed analysis and discussion, we conclude that the application of modular manufacturing devices could improve the economic performance of a shale gas supply chain.

References

- D. C. Cafaro, I. E. Grossmann, 2014, Strategic planning, design, and development of the shale gas supply chain network, *AIChE Journal*, 60, 2122–2142.
- DOE/NETL, 2011, Life cycle greenhouse gas inventory of natural gas extraction, delivery and electricity production.
- Ecoinvent database v3.3, 2017, <http://www.ecoinvent.org>. (accessed May 2017).
- J. Gao, F. You, 2015, Shale gas supply chain design and operations toward better economic and life cycle environmental performance: MINLP model and global optimization algorithm, *ACS Sustainable Chemistry & Engineering*, 3, 1282–1291.
- J. Gao, F. You, 2017a, Design and optimization of shale gas energy systems: Overview, research challenges, and future directions, *Computers & Chemical Engineering*, 106, 699–718.
- J. Gao, F. You, 2017b, Game theory approach to optimal design of shale gas supply chains with consideration of economics and life cycle greenhouse gas emissions, *AIChE Journal*, 63, 2671–2693.
- M. Goedkoop, R. Heijungs, M. Huijbregts, A. De Schryver, J. Struijs, R. van Zelm, 2009, ReCiPe 2008-a life cycle impact assessment method which comprises harmonised category indicators at the midpoint and the endpoint level.
- J. Gong, M. Yang, F. You, 2017, A systematic simulation-based process intensification method for shale gas processing and NGLs recovery process systems under uncertain feedstock compositions, *Computers & Chemical Engineering*, 105, 259–275.
- J. Gong, F. You, 2018, A new superstructure optimization paradigm for process synthesis with product distribution optimization: Application to an integrated shale gas processing and chemical manufacturing process, *AIChE Journal*, 64, 123–143.
- C. He, F. You, 2014, Shale Gas Processing Integrated with Ethylene Production: Novel Process Designs, Exergy Analysis, and Techno-Economic Analysis, *Industrial & Engineering Chemistry Research*, 53, 11442–11459.
- C. He, F. You, 2016, Deciphering the true life cycle environmental impacts and costs of the mega-scale shale gas-to-olefins projects in the United States, *Energy & Environmental Science*, 9, 820–840.
- I. Laurenzi, G. Jersey, 2013, Life cycle greenhouse gas emissions and freshwater consumption of marcellus shale gas, *Environmental Science & Technology*, 47, 4896–4903.
- L. Stamford, A. Azapagic, 2014, Life cycle environmental impacts of UK shale gas, *Applied Energy*, 134, 506–518.
- M. Stewart, 2015, LNG on the Go: GE's Modular Liquefied Natural Gas Facility Offers Field Flexibility, GE.
- S. Tan, P. Barton, 2015, Optimal dynamic allocation of mobile plants to monetize associated or stranded natural gas, part i: Bakken shale play case study, *Energy*. 93, Part 2, 1581–1594.
- M. Yang, F. You, 2018, Modular Methanol Manufacturing from Shale Gas: Techno-economic and Environmental Analyses of Conventional Large-scale Production versus Small-scale Distributed, Modular Processing, *AIChE Journal*, 2, 495–510.
- Z. Zhong, F. You, 2014, Globally convergent exact and inexact parametric algorithms for solving large-scale mixed-integer fractional programs and applications in process systems engineering, *Computers & Chemical Engineering*, 61, 90–101.

Surrogate-based Optimization Approach to Membrane Network Synthesis in Gas Separation

Jos E.A. Graciano^{a,b}, Rita M.B. Alves^b and Benot Chachuat^{a,*}

^a*Department of Chemical Engineering, Centre for Process Systems Engineering, Imperial College London, UK*

^b*Department of Chemical Engineering, Escola Politécnica da Universidade de So Paulo, Brazil*

**b.chachuat@imperial.ac.uk*

Abstract

This paper is concerned with the synthesis of membranes networks for gas separation using a surrogate-based optimization approach. The developed methodology accounts for the main sources of non-ideality in membrane processes based on a mechanistic model. These non-idealities are typically neglected in membrane network synthesis formulations, which often results in inaccurate predictions. The optimization proceeds by a trust-region algorithm and relies on grey-box surrogates that combine a shortcut model with response surface models. The methodology is applied to a case study in natural gas sweetening, where it is shown that the surrogate predictions are within 0.1% of the mechanistic model upon convergence of the trust-region algorithm. Comparisons with classical, constant-permeability surrogates confirm the benefits of the proposed approach.

Keywords: membrane network, process synthesis, surrogate-based optimization, natural gas sweetening

1. Introduction

Over the last few decades, membranes have proved to be a viable technology for the separation of gas mixtures. Due to lack of selectivity however, single-stage membrane modules are often not able to meet high purity targets in terms of contaminant concentrations and meanwhile achieve a large enough product recovery. Instead, a gas mixture can be processed using multiple modules and passes, namely a membrane network or cascade arrangement (Agrawal, 1996).

The problem of determining the optimal design and operation of a membrane network in terms of capital and operating costs, subject to a given purity target, as received attention in the literature. Qi and Henson (2000) formulated a mixed-integer nonlinear programming (MINLP) model for the synthesis of membranes cascades with applications to natural gas (NG) sweetening, whereby the differential equations describing a membrane module are discretized into a set of algebraic equations using a Runge-Kutta scheme. Uppaluri et al. (2004) used a discretized membrane model within a superstructure optimization problem for membrane network synthesis. Alshehri et al. (2013) modelled a membranes permeator in a sequential modular process simulator, where a numerical solution of the differential equations is computed using Gears method, while the membrane network is designed based on a simplified superstructure optimization problem. A common trait among the abovementioned studies is the use of simplified models to describe the performance of individual membrane modules, namely the assumption of a constant permeability for the various gas species through the membrane. The recent review Khalilpour et al. (2015)

emphasizes the need for more accurate models, which can account for the main sources of non-ideality for more reliable membrane network synthesis and design.

It is noteworthy that high-fidelity, mechanistic models for predicting the behavior of membrane permeators have become available in recent years (Bounaceur et al. (2017); Scholz et al. (2013)), and they can be interfaced with commercial process simulators, e.g., via the CAPE-OPEN standard. Such models may be embedded into systematic optimization procedures based on mathematical programming for the design and optimization of a given membrane network. However, they remain too complex for use in a generic superstructure optimization approach in order to determine an optimal network configuration using state-of-the-art MINLP methods.

The main contribution in this paper is the development and application of a surrogate-based modelling approach to enable a more rigorous optimization of membrane networks in gas separation. The surrogates are constructed from data generated using the mechanistic model by Scholz et al. (2013), which accounts for a number of non-ideal effects, in a given trust-region. The mechanistic model is implemented using Aspen Custom Modeler (ACM), while the surrogate-based superstructure model is implemented in GAMS, and the update/refinement of the surrogates is performed using Matlab. Using a case study in NG sweetening, we show that the surrogate models enable the solution of the superstructure optimization subproblems to optimality as part of the trust-region algorithm. The benefits of the proposed methodology are also illustrated by comparing the optimized membrane network with networks designed using constant-permeability membrane models.

2. Superstructure Modelling of Gas Membrane Network

The optimization methodology developed herein relies on a superstructure model, which accounts for all the equipment in the membrane network system and describes the mass and energy balances thereof. It is inspired from the model described in Qi and Henson (2000), where the binary variables describing the existence of interconnections and other logical decisions have been removed, converting the original MINLP into an NLP. The basic set of equipment comprises of the permeators, compressors, stream mixers and stream splitters. In order to enable non-isothermal process operations, heaters are included in every retentate recycle stream. The role of such heaters is to compensate for the Joule-Thomson effect (described in the mechanistic permeator model) by providing sufficient energy to maintain the feed temperatures of the permeator modules at their optimal levels.

Both a mechanistic membrane model (Sec. 2.1) and a grey-box surrogate membrane model (Sec. 2.2) are used to describe the membrane permeators with different accuracies within the superstructure optimization methodology. The surrogates are embedded in the superstructure NLP problem for computational tractability, whereas the mechanistic model is used to generate data points in order to train and refine the surrogates.

2.1. Mechanistic Membrane Model

The mechanistic model of a hollow fiber membrane module developed by Scholz et al. (2013) has been used in this work. The sources of non-ideality captured by this model include: concentration polarization, Joule-Thomson effect, pressure drops (on both sides of the membrane module), and real gas behavior. This model has been implemented in ACM in order to take advantage of the thermo-physical property packages and the numerical integration schemes available therein (a detailed description this model can be found in the original work). Furthermore, the model has been adapted to a NG sweetening application by considering a gas mixture comprised of five species: CH_4 , CO_2 , C_2H_6 , C_3H_8 and H_2S . The permeabilities for CO_2 and CH_4 are computed for a polyimide membrane in function of the pressure and temperature based on the equations proposed

by Safari et al. (2009), and fitted with experimental data provided by Chung et al. (2004). The permeabilities of the other three species are calculated by assuming a constant selectivity of each component with respect to CH_4 , equal to 16, 0.4 and 0.1 for H_2S , C_2H_6 , C_3H_8 , respectively.

Overall, the numerical simulation of this mechanistic membrane model requires the specification of 9 inputs or parameters (flow rate, temperature, pressure and composition of the feed; pressure of the permeate stream; and membrane area), denoted collectively by v_{in} thereafter. The differential equations are discretized using a 2nd-order orthogonal collocation method, resulting in a system of 13,602 algebraic equations that are solved using a Newton-like iterative approach.

2.2. Grey-Box Surrogate Membrane Model

The use of grey-box surrogate models is advantageous compared to completely black-box models, as it often offers a reduction in the number of nonlinear terms needed to accurately fit a set of experimental or in-silico data. The grey-box surrogate in Eqs. (1) to (6) combines a shortcut model with several response surface models:

$$F_i^f = F_i^r + F_i^p \quad (1)$$

$$F_i^p = K_i A p_i \quad (2)$$

$$\Delta p_i^{0.3275} = 0.5(p_i^f - p_i^p)^{0.3275} + 0.5(p_i^r)^{0.3275} \quad (3)$$

$$K_i = a_i + 0.5b_i(T^f + T^r) + c_i p^f \quad (4)$$

$$T^r = T^r(v_{in}) \quad (5)$$

$$T^p = T^p(v_{in}) \quad (6)$$

The shortcut model in Eqs. (1) and (2) is based on an analogy with counter-current heat exchangers as developed by Pettersen and Lien (1994). Here, F_i denotes the molar flow rate for species i , in the feed (f), retentate (r) and permeate (p), K_i the permeability for species i , Δp_i the driving force for species i , and A the membrane area. Note that in the original shortcut model the driving force Δp_i is represented by the logarithmic mean of the partial pressures p_i , whereas this term has been replaced by Chens approximation in Eq. (3), in order to avoid numerical difficulties. The permeabilities K_i in Eq. (4) consist of a 1st-order approximation in terms of the feed and retentate temperatures (T^f , T^r) and the total pressure (p^f), with a_i , b_i and c_i as adjustable parameters (see Step 3 of Algorithm in Sec. 3). An important physical mechanism in the NG sweetening process is the Joule-Thomson effect, mainly due to the presence of CO_2 and the large pressure drop across the membrane. To account for this effect, the retentate and permeate temperatures were approximated by 2nd-order polynomials in terms of all nine inputs / parameters v_{in} in Eqs. (5) and (6).

3. Surrogate-based Superstructure Optimization Algorithm

The proposed superstructure optimization algorithm is inspired by the trust-region (TR) method developed by Eason and Biegler (2016). It comprises the following steps:

Step 1 Initialization

1.1 - Solve the superstructure NLP model using the grey-box model in Eqs. (1) to (6) with fixed values for the permeabilities (K_i) and temperatures (T^r and T^f).

1.2 - Initialize the TR around the initial superstructure given by Step 1.1, e.g. by incorporating a priori knowledge about the problem in order for grey-surrogate to provide a good fit of the mechanistic membrane model predictions within the TR.

Step 2 Generate data from the mechanistic model

2.1 - Obtain a sample set within the current TR, and then simulate the mechanistic model of Sec. 2.1 at each sampling point.

Step 3 Train the surrogate model in Eqs. (1) to (6)

3.1 - Update the quadratic approximations for T^r and T^f in Eqs. (5) and (6) using data at the input values v_{in} for the sample set of Step 2. Here, we apply a model reduction and parameter estimation algorithm based on partial least squares (PLS) regression as proposed by Graciano et al. (2018).

3.2 - Update the linear approximations for the permeabilities K_i in Eq. (4) using the updated surrogates for T^r and T^f in Step 3.1. Here, the parameters a_i , b_i and c_i are determined using least-squares error minimization between Eq. (4) and the mechanistic model predictions on the sample set of Step 2.

Step 4 Solve the superstructure optimization model to optimality

4.1 - Solve the superstructure NLP model, by minimizing the economic objective function, within the current TR and using the updated grey-box surrogate in Step 3.

4.2 - If the NLP problem is infeasible, interpolate a point in-between the last to feasible solutions, and return to Step 2.

Step 5 Termination

5.1 - If the solution in Step 4.1 is on the boundary of the current TR, check the surrogate accuracy against the mechanistic model at this point. If the error between the surrogate and mechanistic model predictions is less than 2%, increase the TR by 30%, and center the TR at the new point. If the error is greater than 5%, reduce the TR by 30%, and then center the TR at the new point. Return to Step 3.

5.2 - If the solution in Step 4.1 is in the interior of the current TR, also check the surrogate accuracy against the mechanistic model at this point. If the error between the surrogate and mechanistic model predictions is less than 0.1%, terminate the search. Otherwise, reduce the TR by 30%, and return to Step 3.

Upon termination, the algorithm will normally reach a neighborhood of a local optimum of the superstructure optimization problem. A formal analysis of the convergence conditions is currently under investigation.

4. Case Study in Natural Gas Sweetening

The superstructure optimization problem consist of minimizing the total annualized cost of a gas membrane network subject to a maximum CO_2 concentration of 2%vol in the NG product stream; refer to Qi and Henson (2000) for more details about the formulation of the economic objective function. Two membrane modules are considered next in this case study.

The results of the surrogate-based superstructure optimization algorithm are shown in Figure 1 (top). This approach determines a simple network structure, where the first module is responsible for the main separation, so that the NG stream meets the 2%vol specification; whereas the second module enable methane recovery for the permeate of the first module. In the convergence, the grey-box surrogate presents a maximum error of 0.058% with respect to the mechanistic model. It is important to reiterate that the synthesis problem accounts for the main process non-idealities; for instance, the feed temperature is reduced to its lower bound so as to increase the selectivity between CO_2 and CH_4 (Safari et al., 2009).

Next, the results obtained by the surrogate modelling approach are compared with the synthesis of a membrane cascade using simplified models, which do not account for the non-idealities observed in the process. Specifically, the superstructure is optimized using the simplified model in Eqs. (1) to (6), now with fixed permeabilities and temperatures (step 1, section 3). For validation purposes, the mechanistic model is simulated using the specifications determined by the simplified model. The results are shown in Figure 1 (bottom).

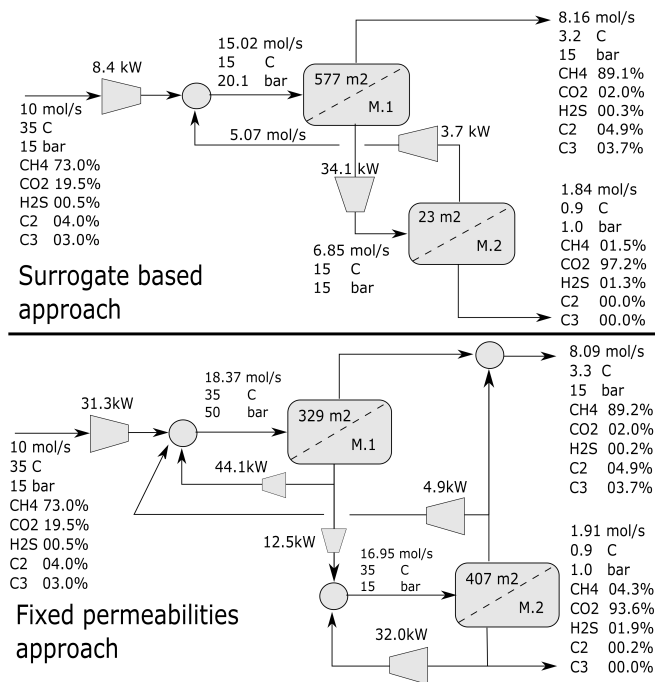


Figure 1: Comparison between the results obtained by the surrogate modeling approach and the fixed permeabilities model.

Large discrepancies are observed between the surrogate model using fixed permeabilities and the mechanistic model (maximum error of 200% for the predicted CO_2 concentration in retentate

stream). In order to compensate for the model mismatch and satisfy the 2%vol CO_2 specification in the product stream, the optimized membrane network presents a large number of recycle streams, which results in extra capital and operational costs.

5. Conclusion

This paper has presented a strategy for the synthesis of membrane networks using a surrogate modeling-based approach. The main objective is to design reliable membrane cascades taking into account the main sources of non-ideality present in this process. A mechanistic model is used to train a surrogate, which is embedded into a superstructure optimization problem and updated using a trust-region like approach. The results show that the algorithm can obtain a reliable cascade structure with errors smaller than 0.1%, whilst the network synthesis based on simplified models (with fixed permeabilities) can result in suboptimal networks to compensate for the mismatch between the simplified and mechanistic models.

Acknowledgements: The authors would like to thank the sponsorship of Shell and FAPESP through the Research Centre for Gas Innovation - RCGI (FAPESP Proc. 2014/50279 – 4), hosted by the University of Sao Paulo, and the strategic importance of the support given by ANP (Brazil National Oil, Natural Gas and Biofuels Agency) through the R&D levy regulation, as well the fellowship from Conselho Nacional de Desenvolvimento Científico e Tecnológico (CNPq Proc. 200470/2017 – 5).

References

- R. Agrawal, Jan 1996. Membrane Cascade Schemes for Multicomponent Gas Separation. *Industrial & Engineering Chemistry Research* 35 (10), 3607–3617.
- A. Alshehri, R. Khalilpour, A. Abbas, Z. Lai, 2013. Membrane Systems Engineering for Post-combustion Carbon Capture. *Energy Procedia* 37, 976–985.
- R. Bounaceur, E. Berger, M. Pfister, A. A. Ramirez Santos, E. Favre, Feb 2017. Rigorous variable permeability modelling and process simulation for the design of polymeric membrane gas separation units: MEMSIC simulation tool. *Journal of Membrane Science* 523, 77–91.
- T.-S. Chung, C. Cao, R. Wang, Jan 2004. Pressure and temperature dependence of the gas-transport properties of dense poly[2,6-toluene-2,2-bis(3,4-dicarboxylphenyl)hexafluoropropane diimide] membranes. *Journal of Polymer Science Part B: Polymer Physics* 42 (2), 354–364.
- J. P. Eason, L. T. Biegler, Sep 2016. A trust region filter method for glass box/black box optimization. *AIChE Journal* 62 (9), 3124–3136.
- J. Graciano, R. Giudici, R. Alves, B. Chachuat, 2018. A Simple PLS-based approach for the construction of compact surrogate models, preprint.
- R. Khalilpour, K. Mumford, H. Zhai, A. Abbas, G. Stevens, E. S. Rubin, Sep 2015. Membrane-based carbon capture from flue gas: a review. *Journal of Cleaner Production* 103, 286–300.
- T. Pettersen, K. Lien, May 1994. A new robust design model for gas separating membrane modules, based on analogy with counter-current heat exchangers. *Computers & Chemical Engineering* 18 (5), 427–439.
- R. Qi, M. A. Henson, Dec 2000. Membrane system design for multicomponent gas mixtures via mixed-integer nonlinear programming. *Computers & Chemical Engineering* 24 (12), 2719–2737.
- M. Safari, A. Ghanizadeh, M. M. Montazer-Rahmati, Jan 2009. Optimization of membrane-based CO_2 -removal from natural gas using simple models considering both pressure and temperature effects. *International Journal of Greenhouse Gas Control* 3 (1), 3–10.
- M. Scholz, T. Harlacher, T. Melin, M. Wessling, Jan 2013. Modeling Gas Permeation by Linking Nonideal Effects. *Industrial & Engineering Chemistry Research* 52 (3), 1079–1088.
- R. V. S. Uppaluri, P. Linke, A. C. Kokossis, Jul 2004. Synthesis and Optimization of Gas Permeation Membrane Networks. *Industrial & Engineering Chemistry Research* 43 (15), 4305–4322.

Balancing Costs, Safety and CO₂ Emissions in the Design of Hydrogen Supply Chains

Anton Ochoa Bique^{a,*}, Leonardo K. K. Maia^a, Fabio La Mantia^b, Davide Manca^c, Edwin Zondervan^a

^a*Laboratory of Process Systems Engineering, Department of Production Engineering, Universität Bremen, Leobener Str. 6, 28359 Bremen, Germany*

^b*Energy storage and conversion systems group, Department of Production Engineering, Universität Bremen, Wiener Str. 12, 28359 Bremen, Germany*

^c*Process Systems Engineering Laboratory, Dipartimento di Chimica, Materiali e Ingegneria Chimica "Giulio Natta", Politecnico di Milano, P.zza Leonardo Da Vinci, 32, 20133 Milano, Italy*

antchoa@uni-bremen.de

Abstract

In this work, a novel strategy for the design of a hydrogen supply chain (HSC) network for Germany is presented for minimum daily supply costs, minimum mitigation costs of CO₂ and maximum network safety. The proposed model is a mixed integer linear program that is solved with the Advanced Integrated Multidimensional Modeling System (AIMMS). The model is solved as a multi-criterion decision making problem, where three objectives (costs, safety and environmental impact) are balanced. The results show that hydrogen as type of fuel has potential to replace carbon-based fuels in the near future. Implementation of decentralized hydrogen production plant based on water electrolysis may compete with coal-based dominant technology.

Keywords: Hydrogen supply chain design, Mixed integer linear programming, fuel infrastructures, Multi-objective optimization, AIMMS.

1. Introduction

The transportation sector plays a crucial economic role in the world. The main transportation fuels currently in use come from non-renewable fossil sources. Moreover, being the main fossil fuel consumer, the transportation sector is the second largest contributor of CO₂ emissions worldwide, which is one of the causes of global warming. The vehicle industry has been working on the improvement of fuel efficiency and the reduction of greenhouse gas emissions. The use of different types of fuel such as biodiesel, methanol, hydrogen, is considered a promising alternative. Being the most abundant element in the universe, hydrogen is regarded as a suitable energy carrier for mobility and stationary fuel cell systems applications. The challenge of developing a successful hydrogen infrastructure stands behind the development of a hydrogen supply chain (HSC) considering safety, economic and environmental impact issues.

In this work, a model of the HSC network is developed for the transport sector in Germany considering a significant fuel cell electrical vehicles penetration into customer market. The model is solved using a deterministic Mixed Integer Linear Programming

(MILP) approach and implemented in AIMMS/CPLEX for multiple objectives: costs, safety and environmental impact are balanced via the epsilon constraint method to generate the Pareto front. The sampling grid of this three-dimensional window is created by a surface response methodology. The aim of the current work is to identify the best hydrogen infrastructure pathways while taking into account local factors such as the location of the hydrogen supply and demand, and distribution between the hydrogen production location and hydrogen demand points. Two types of technologies to produce hydrogen are evaluated, namely coal gasification and water electrolysis.

2. Methodology

2.1. Problem Description

Given are the location and capacity of energy source suppliers, capital and operating costs for a large-scale hydrogen production plants, transportation modes and storage facilities of the network, under the conditions that:

1. locations of storage facilities are fixed;
2. the relative risk of production plants, storage facilities and transportation modes are expected not to change under the various demand scenarios;
3. electricity is the main energy source to power rail freight transport;
4. electricity price is based on industrial electricity price for Germany.

Each facility of the HSC includes: a technological option, a capacity, a location. The problem is concerned with finding the number and locations of the production facilities for a given demand, considering the minimum total operating cost, the minimum safety risk and the minimum environmental impact of HSC network.

2.2. Formulation of the HSC

The model consists of a set of grid points g (each grid point represents a German state), energy sources e , different transportation modes t , different hydrogen production p and storage facilities s . As hydrogen might be generated by different production technologies p (i.e. coal gasification, water electrolysis), it may be transported into two forms f (i.e. liquid or gaseous), which determines the transportation mode that will be used. In the following subsections, each component of the HSC model will be described in more detail.

2.2.1. Grid

In this study, the landscape of Germany is divided into 16 grid points, each of these grid points represents a German region. Moreover, the region's largest city is taken as the potential centre for a hydrogen production facility and for a storage facility to satisfy the local demand and further product distribution to another region. The total hydrogen demand was estimated based on the fuel cell electric vehicles (FCEVs) penetration rate of 10% of the total number of passenger transports (public buses, light motor vehicle) available by 2030. 2015 was used as the reference year for the calculations.

2.2.2. Primary energy sources

The primary energy resource availability at each grid point plays an important role in defining the type and location of production technologies. Moreover, the main problem of a domestic production facility is concerned with finding an appropriate energy source supplier. There are three opportunities related with the energy source consumption from i) a domestic grid point or ii) supply from neighbouring grid points or iii) import from abroad.

2.2.3. Hydrogen production

Two types of technologies to produce hydrogen were included in model: coal gasification and water electrolysis. Each facility has fixed capital and operational costs. The main decisions to be made are: the type, location and number of production facilities. Each facility carries out large-scale hydrogen production (960 ton per day).

2.2.4. Hydrogen physical form

Hydrogen can be carried in two physical forms: liquid and gaseous. The hydrogen form plays an important role in defining which transportation mode and storage facilities should be used. These decisions affect the final costs of the HSC network.

2.2.5. Transportation mode

The transportation mode is related to the hydrogen form. The main decision is to define the transportation mode and its number of vehicles used to deliver the final product from production point to storage point. Each transportation mode has a specific capacity, capital cost, operating cost and delivery distance. It is noted that the operating cost is associated with the delivery distance (including fuel, labour, maintenance and general expenses).

2.2.6. Storage facility

The storage facility, just like the transportation mode, is linked to the hydrogen form. Each type has a specific capacity, capital and operating cost. Storage facilities are installed at each grid point to satisfy the local hydrogen demand. Storage facilities could be located next to production plant or away from it.

2.3. Mathematical formulation

This proposed model must meet three target requirements:

- Minimize the total cost of the HSC network
- Minimize environmental impact
- Minimize the total relative risk of the network.

2.3.1. Total daily cost

The first objective function is the total daily cost (*Total*) of HSC network. It consists of the production, storage and transportation capital and operating costs and expenses of energy sources as follows:

$$\text{Total} = \text{PC} + \text{SC} + \text{TS} + \text{ESC} \quad (1)$$

$$\text{PC} = \sum_{p,f,g} \left(\frac{\text{PCC}_{p,f} \text{NPF}_{p,f,g} \text{AF}_p}{\text{OP}} + \text{HP}_{p,g,f} \text{POC}_{p,f} \right) \quad (2)$$

$$\text{SC} = \sum_{f,s,g} \left(\frac{\text{SCC}_{s,f} \text{NSF}_{s,f,g} \text{AF}_s}{\text{OP}} + \text{SOC}_{p,f} \left(\text{HP}_{g,f} + \sum_{t,g'} \text{HI}_{g',g,t,f} \right) \right) \quad (3)$$

$$\text{TC} = \sum_{f,t,g,g'} \left(\frac{\text{TCC}_{t,f} \text{NTF}_{f,t,g,g'} \text{AF}_t}{\text{OP}} + \text{FC} + \text{LC} + \text{MC} + \text{GC} \right) \quad (4)$$

$$\text{ESC} = \sum_{g'',g,p,e} \left(\text{PESN}_{g'',g,p,e} \text{ESDis}_e \text{Dis}_{g'',g} + \text{PESAv}_{g'',g,p,e} \text{ESCost}_e + \text{PESIm}_{g,p,e} \text{ESICost}_e \right) \quad (5)$$

where PC (production cost), SC (storage cost), TC (transportation cost), ESC (energy sources cost), PCC (production capital cost), SCC (storage capital cost), TCC (transport capital cost), POC (production operating cost), SOC (storage operating cost), NPF(number of production facilities), NSF(number of storage facilities), NTF (number of transportation mode), AF (annual capital charge factor), OP (operating period) HP (domestic produced hydrogen), HI (imported hydrogen from neighbouring grid points), FC (fuel cost), LC (labour cost), MC (maintenance cost), GC (general cost), PESAv (the amount of available domestic energy sources), PESN (the amount of energy source supplied from neighbouring grid points), PESIm (the amount of imported energy sources), ESDis (the delivery price for energy source), ESCost (energy source price), ESICost (energy source import price), Dis (distance between grid points).

2.3.2. Total environmental impact

Based on the work of Almaraz (De-León Almaraz et al., 2013), the total daily greenhouse gas (GHG) emission is associated with GHG in production, storage sites and transportation of HSC network as indicated by:

$$\text{TotalCO}_2 = \text{PCO}_2 + \text{SCO}_2 + \text{TCO}_2 \quad (6)$$

$$\text{PCO}_2 = \sum_{p,g,f} \text{HP}_{p,g,f} \text{GEP}_{p,f} \quad (7)$$

$$\text{SCO}_2 = \sum_{p,g,f} \text{HP}_{p,g,f} \text{GES}_f \quad (8)$$

$$\text{TCO}_2 = \sum_{g,g',t,f} 2\text{Dis}_{t,f,g,g'} \text{NTF}_{g,g',t,f} \text{GET}_t \quad (9)$$

where TotalCO₂ (total daily amount of realized GHG in HSC network), PCO₂ (daily GHG emissions from production sites), SCO₂ (daily GHG emissions from storage sites), TCO₂ (daily GHG emissions during hydrogen delivery), GEP (kg GHG emissions per kg H₂ produced), GES (kg GHG emissions per kg H₂ in storage side), GET (kg GHG emissions per km).

2.3.3. Total relative risk

Based on the work of Kim (Kim and Moon, 2008), the total relative risk consists of total relative risk of production, storage sites and total relative risk of transportation as given by:

$$\text{TotalRisk} = \text{TotalPRisk} + \text{TotalSRisk} + \text{TotalTRisk} \quad (10)$$

$$\text{TotalPRisk} = \sum_{p,f,g} \text{NPF}_{p,f,g} \text{PRisk}_p \text{PW}_g \quad (11)$$

$$\text{TotalSRisk} = \sum_{s,f,g} \text{NSF}_{s,f,g} \text{SRisk}_s \text{PW}_g \quad (12)$$

$$\text{TotalTRisk} = \sum_{g,g',f,t} \text{NTF}_{g,g',f,t} \text{DRisk}_{t,f,g,g'} \text{TRisk}_t \quad (13)$$

where: TotalRisk (total relative risk), TotalPRisk (total risk of production facilities), TotalSRisk (total risk of storage facilities), TotalTRisk (total risk associated with hydrogen distribution between grid points), PRisk (risk level of the production facility), SRisk (risk level of the storage facility), TRisk (risk level of the transportation mode), DRisk (road risk level between grids), PW (population weight factor).

2.4. Multi-objective problem

The tri-objective optimization problem is solved by implementing epsilon constraint method. The HSC design problem in this work is given as follows:

$$\min\{\text{Total}, \text{TotalCO}_2, \text{TotalRisk}\} \quad (14)$$

3. Results and Discussion

The model is formulated as a mixed integer linear programming model and has 2508 constraints, 5498 continuous variables and 2177 integer variables. AIMMS is used as optimization platform and CPLEX 12.6.3 is selected as the preferred solver. A three dimensional pareto front is created using the epsilon constraint method. The sampling grid of this three-dimensional window is created by a surface response methodology. The German government targets to reduce GHG emissions up to 20% by 2050, this work considers two types of hydrogen production technologies: water electrolysis and coal gasification. A case study of Germany threatened by Almansoori (Almansoori and Betancourt-Torcat, 2016) shows the benefit of coal gasification based HSC as compared to the network based on other types of hydrogen production technologies such as steam methane reforming, biomass gasification. This result has also been considered to illustrate capabilities of the proposed work.

In our work there are 4 cases, which will be analysed and compared to each other. Each case consists of a minimization target. Three objectives were optimized separately to analyse how their optimal values decrease when making a multi-objective optimization. The results of each optimization cases can be seen in Table 1.

Table 1 – Results of optimization among treated cases

	Total cost (M\$ d ⁻¹)	Relative risk (units)	CO ₂ gas emission (10 ³ t CO ₂ d ⁻¹)
Min Total Cost (case 1)	9.6 (59.1%)	5072 (-36.4%)	102.9 (27.7%)
Min Total CO ₂ (case 2)	148.9 (-84.2%)	1993 (41.5%)	83.3 (38.2%)
Min risk (case 3)	29.8 (-21.3%)	5058 (-38.2%)	15.6 (89%)
Multi-objective optimization (case 4)	23.5	3225	142.4

The results obtained for Case 1 are in agreement with the base case Almansoori (Almansoori and Betancourt-Torcat, 2016) and reasonable with the average hydrogen cost expected for Europe in the 2030 (i.e. around 3.2). A minimum number of 3 production plants is obtained with coal gasification technology. The number of storage facilities is 62 adopting for projected hydrogen demand and storage period of 10 days. The total cost of the HSC is 9.6 M\$ involving 201 transportation vehicles to cover the demand between grids. Case 2 minimizes the total relative risk. In this case, there is environmental benefit of 20% as compared to case 1. The total cost of the HSC is 148.9 M\$ involving 115 transportation vehicles. As in Case 1, the number of storage facilities adopted for a storage period of 10 days. In Case 3, there is a high risk of accidents, but reduced costs for HSC network as compared to Case 2. The total cost of the HSC is 29.8 M\$ involving 228 transportation vehicles. For cases 2 and 3 hydrogen is produced in liquid form via water electrolysis, this explains a high price of the HSC network for both cases. The optimal configuration of the HSC for Case 4 involves 6 production plants with coal gasification technology. The total HSC network costs are 23.5 M\$ per day and 308.1 kt CO₂-equiv per day involving 169 transportation vehicles. The analysis of the network is quite different from other cases. Table 2 shows that the best value obtained for the total costs in Case 4 is higher (by 59.1%) than Case 1. Moreover, the CO₂ emissions increased by 27.7%, but the risk improved by 36.4%. The total costs decrease by 84.2 % in Case 4 as compared to Case 2 while the CO₂ emissions increase by 41.5% and risk by 38.2%. The HSC network costs decrease by 21.1% in Case 4 and risk by 36.2% but CO₂ emissions are increased by 89% as compared with Case 3. Finally, the hydrogen production costs vary between 3.4 and 8.43 \$ per kg for cases 1

and 4. It can be concluded that the costs of the HSC are still high, and technological improvements are needed: the modification of conventional methods or development of innovative technologies are necessary for reduction of conversion losses and capital costs investment. The model consider centralized hydrogen production. Due to centralized production guarantees more financial benefits with less safe and environmental friendly construction, decentralized production needs to take into account in future work (Han et al., 2013).

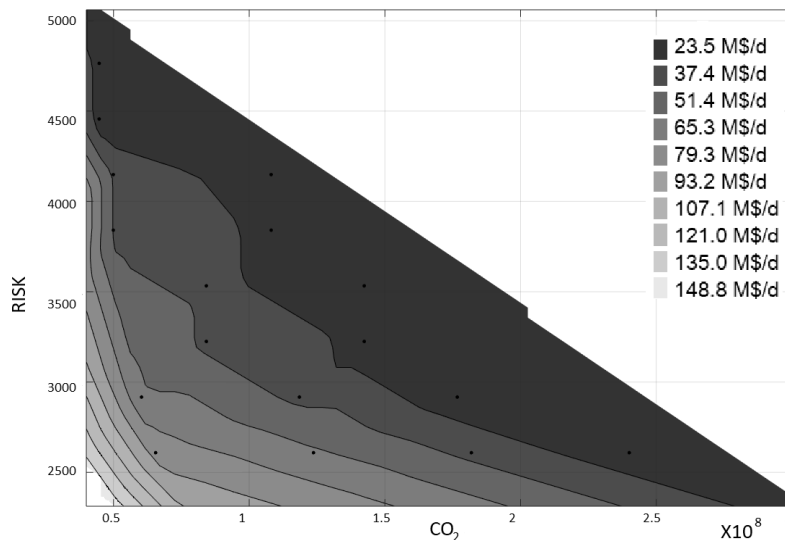


Figure 1 – Contour plot of three dimensional pareto front (Cost vs Emissions, Risk)

4. Outlook and Conclusions

In this work, multi-criterion optimization for development of sustainable HSC network is done. Main objectives are cost, safety and environmental impact. This study shows that coal gasification is the most economic method, but it emits considerable amounts of CO₂. Otherwise, for safety and environmental purposes, water electrolysis technology is more suitable. To develop a sustainable HSC network based on water electrolysis, considering supply cost, safety and mitigation cost, decentralized H₂ production configuration needs to be taken into account, due to the reason it may guarantees a safer and more environment friendly HSC.

References

- A. Almansoori, A. Betancourt-Torcat, 2016, Design of optimization model for a hydrogen supply chain under emission constraints - A case study of Germany, *Energy*, 111, 414–429
- S. De-León Almaraz, C. Azzaro-Pantel, L. Montastruc, L. Pibouleau, O.B. Senties, 2013, Assessment of mono and multi-objective optimization to design a hydrogen supply chain, *Int. J. Hydrogen Energy*, 38, 14121–14145
- J.H. Han, J.H. Ryu, I.B. Lee, 2013, Multi-objective optimization design of hydrogen infrastructures simultaneously considering economic cost, safety and CO₂ emission, *Chem. Eng. Res. Des.*, 91, 1427–1439
- J. Kim, I. Moon, 2008, Strategic design of hydrogen infrastructure considering cost and safety using multiobjective optimization, *Int. J. Hydrogen Energy*, 33, 5887–5896

Process Integration as an Effective Route Towards Sustainable Oil Refinery Development

Poland Jelihi,^{a,*}, Timo Wasserman,^b, Edwin Zondervan,^a

^a*University of Bremen, Leobener Straße 6, Bremen 28359, Germany*

^b*FG Resiliente Energy Systems, Enrique-Schmidt-Str. 7, 28359 Bremen, Germany*

pjelihi@uni-bremen.de

Abstract

In this paper, the process integration of a conventional oil refinery hydrotreatment unit and renewable hydrogen production is proposed. This might lead to reductions in the need for energy and greenhouse gas emissions. First a conventional hydrotreating process is modeled and simulated with the flowsheeting package Unisim Design R450 (Honeywell). Secondly an exergy analysis for identification and quantification of thermodynamic inefficiencies is accomplished with Aspen Plus V10. To complement the exergy analysis, the evaluation of environmental impact is with a life cycle assessment (LCA) tool (Eco-indicator 99) is done.

Keywords: Oil refinery, hydrotreating unit, renewable hydrogen, exergy analysis, life cycle assessment

1. Introduction

An atmospheric residue desulphurization (ARDS) hydrotreater is applied in oil refineries for the purpose of residue upgrading. This highly exothermic process unit allows a purification from sulfur, nitrogen, oxygen, chlorine and metal impurities as well as the cracking of heavy hydrocarbons, prior to downstream processing.

This catalytic pretreatment step is basically implemented by application of hydrogen at high temperature and pressure. Currently, the hydrogen used for hydrotreatment in a refinery is obtained from light hydrocarbons through the conversion stages of synthesized gas in steam methane reforming or pressure swing adsorption to produce a final product with purity ranges between 70 to 80 %. The consumption of hydrogen during this treatment process ranges from 0.6 kg hydrogen per ton of light distillates to 10 kg hydrogen per ton for vacuum distillates (Fahim et al. 2010a).

Renewable hydrogen production via electrolysis from a hybrid system that combines wind and solar energy has become attractive due to installation flexibility, increasing performance efficiency and large scale production capability. In this study we propose the possibility to integrate the renewable hydrogen with the modified ARDS system.

2. Theory & definitions

A sustainable refinery needs to be energy efficient and environmentally friendly. An exergy analysis according to second law thermodynamics provides measures in quantifying the actual energy consumption, energy destruction rate, location of losses

and real efficiency that considers the energy losses in the system. Additionally, an environmental impact assessment is an essential indicator to operational sustainability.

2.1 Exergy, exergy destruction and exergy efficiency

Exergy is defined as the maximum amount of work obtained as the process changes reversibly from the given state to a state of equilibrium with the environment. Alternatively exergy can be defined as the maximum work that can be obtained from any quantity of energy (Kotas, 1995). Physical exergy is the work obtainable by taking the substance through a reversible process from its initial state (T, P) to the state of the environment (T_0, P_0). The specific physical exergy is written as:

$$ex_j^{phy} = ex_i - ex_o = (h_i - h_o) - T_0(s_i - s_o) \quad (1)$$

here the enthalpy, h_i and entropy, s_i are the independent thermodynamic state functions. h_o and s_o denote the variables at a reference condition. Unless otherwise, the reference temperature and pressure are 298.15 K and 1.013 kPa respectively.

Chemical exergy is the maximum extractable work when a substance is brought from the reference environment state to the dead state (T_0, P_0, μ_0) by a process including heat transfer and the exchange of substances only with the reference environment (Dincer and Rosen, 2013a). The chemical exergy in the process stream can be determined from the standard molar chemical exergy of all components in the stream as given by Moran (1999):

$$ex_j^{chem} = \sum_{i=1}^j y_i \bar{e}_i^{ch} + RT_0 \sum_{m=1}^j y_m \ln y_m \quad (2)$$

y_i is the component fraction, R is universal gas constant and \bar{e}_i^{ch} is the standard molar chemical exergy of the components. The specific total exergy is the summation of physical and chemical exergy neglecting the potential and kinetic exergy terms.

$$ex_j^{total} = ex_j^{phy} + ex_j^{chem} \quad (3)$$

The exergy rate of a stream is calculated as the product of the mass flow of material j and the total exergy:

$$\dot{E}x_j = \dot{m}_j ex_j^{total} \quad (4)$$

Exergy destruction or irreversibility is the magnitude of exergy loss as a result of the entropy generated in the system. The losses can occur internally due to irreversibility within the system or externally due to wastes to environment. Exergy destruction is determined by the Gouy-Stodola theorem:

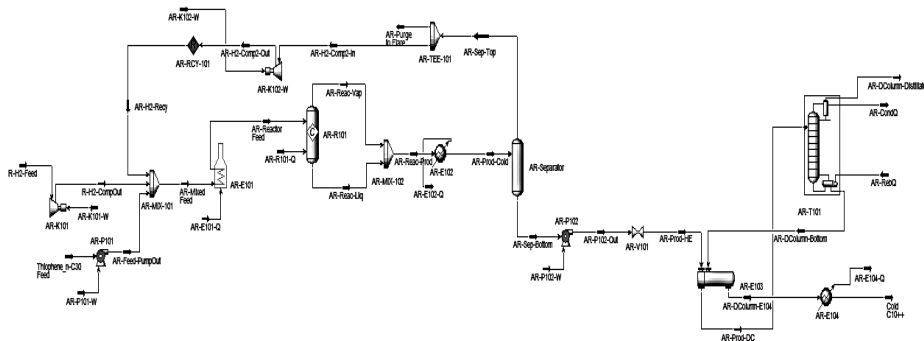
$$E_d = \sum E_{x_{input}} - \sum E_{x_{output}} \quad (5)$$

Exergy efficiency of the unit and system are calculated respectively (Dincer and Rosen 2013b):

$$\psi_{unit} = \frac{\sum \dot{E}x_{product}}{\sum \dot{E}x_{source}} \quad (6)$$

$$\psi_{overall} = \frac{\sum \dot{E}x_{outlet}}{\sum \dot{E}x_{inlet}} \quad (7)$$

Figure 1 : The ARDS hydrotreating modelled and simulated in UniSim Design R450



2.2 Environmental impact analysis

As defined in the ISO Standard 2006, LCA refers to the evaluation of the total energy and material used and the waste released to the environment throughout the full life cycle of the products and processes (Elzakker et al. 2017). A quantitative aggregated indicator LCA tool, the Eco-indicator 99 is chosen as method for this purpose because the outcome can be translated into a singular accumulated metric point. The damage oriented approach is used to determine the environmental impact based on the damage to human health, resource and ecosystem (Pré Consultants, 2000).

3. Modelling and Simulation

3.1 ARDS process description

The process flow diagram of the ARDS hydrotreating is shown in Figure 1. Data input and process flow are adapted from Fahim et al. (2010b) and Parkash & Parkash (2003). This process is required to remove undesired sulphur in the form of thiophene and at the same time cracks the heavy hydrocarbon component *n*-C30 into lighter components *n*-C20, *n*-C10 and *n*-C4. Operation are assumed at the steady state condition. The feed stream contains the mixed components of *n*-C30 and thiophene and are pumped at 455 kg mole/h at 38 °C and 820 kPa. The thiophene fraction is 1 % of the feed. This feed stream is then mixed with the (renewable) hydrogen at a flowrate of 560 kg mole/h at 65 °C and 1,380 kPa. Subsequently, the stream is heated to 370 °C and 10.35×10^3 kPa in the fired heater and enter the conversion reactor. The sequential reactions involved in the reactor are shown in Table 1. Products from reactor are then cooled to 92 °C by the cooler and conveyed to the gas-liquid separator. An amount of 126.5 kg mole/h of hydrogen with small trace of hydrogen sulphide H₂S is splits from the gas stream from the top separator stream and recycled to reactor to maintain the partial pressure and compensate the amount consumed. The remaining amount of top product is purged in a flaring system. Liquid products at bottom are then transferred and expanded by a valve to reduce the pressure to 1,780 kPa. The stream is then heated to 105°C in a shell and tube heat exchanger using the hot product stream from bottom of the distillation column. In the distillation column, the stream is distilled to produce top distillates and bottom products. The top distillates contain mostly light hydrocarbon gas, hydrogen and trace amounts of other components are sent to the next processing unit. At the bottom, the cracked hydrocarbons are cooled to 38 °C and 400 kPa. It is noted that the process also simulated in Aspen Plus V10 to compare the results and calculate the exergy efficiencies.

Table 1 Reaction in the hydrotreating reactor

No	Reactions	Reactor type	Percent Conversion
1	$C_4H_4S + 4H_2 \rightarrow C_4H_{10} + H_2S$	Conversion	100
2	$C_{30}H_{62} + H_2 \rightarrow C_{20}H_{42} + C_{10}H_{22}$	Conversion	70

3.2 LCA analysis using Eco-indicator 99

The input and output streams for the environmental impact analysis is based on the process flow diagram of Figure 1. The input streams include the feed and the utilities such as hydrogen, heat, electricity and the fuel gas combusted for the heater and reboiler. The output products are the CO₂ and SO₂ emissions during the operation.

In this study, the goal of analysis is to evaluate the environmental impacts of ARDS hydrotreating process and products. The impacts includes two components, the utilities consumed and the emissions by the products burning. Three damage categories are considered as specified in the Eco-indicator 99 manual; the ecosystem, human health and resources. Each of the categories are determined by a total of ten respective impacts categories such as ecotoxicity, carcinogens and respiratory effects. In the analysis, the relevant input and outputs mass and energy associated with the process are used to calculate the environmental impacts. The life cycle inventory (LCI) of utilities and pollutants impact factor values are gained from the Eco-indicator 99 database (Pré Consultants, 2000). The damage in each of the impact categories is calculated from the life cycle impact categories as:

$$IMP_{j,u} = \sum_i m_u LCI_{i,u} \quad \forall_j \quad (8)$$

where $IMP_{j,u}$ is the impact factor in Pt /kg or Pt /kWh, j and i represent the damage category and impact category respectively, m_u denotes the consumption or emission of utilities or pollutants in kg /h or kW /h and $LCI_{i,u}$ is the impact factor of utilities and pollutants, in Pt /kg or Pt /kWh. The impact categories are then aggregated into three damage categories and integrated into a single environmental metric: the environmental impact of process and products as in the following equations:

$$DAM_u = \sum_j IMP_{j,u} \quad (9)$$

$$EI = \left(\sum_u DAM_u \right) \cdot t \quad (10)$$

where DAM_u denotes the damage factor of utilities and pollutants, in Pt /kg or Pt /kWh and EI is the environmental impact in Pt /year. The t is annual operating time in hours which is assumed equivalent to 8,400 hours a year in this study.

The data and calculation for fuel gas consumption, m_{fg} for furnace and boiler are taken from Wu & Liu (2016). The furnace and boiler have 6,485 kW and 24,462 kW power ratings respectively with similar efficiencies, 93.8 %. The high calorific value of the fuel gas from the diesel oil used is 44,800 kJ /kg. The calculated m_{fg} is 2,651.19 kg /h. The (renewable) hydrogen consumption, in kg /h, the heat flows and electricity to drive pumps and compressors, in kWh are taken from simulation results.

CO₂ and SO₂ are two important output parameters released by the burning fuel gas. The emission of CO₂ is determined from

$$m_{CO_2} = \frac{44}{12} \times m_{fg} w_{fg,c} \quad (11)$$

where m_{CO_2} is the mass of CO₂ emitted in kg /h, 44 and 12 are the molecular weights of CO₂ and carbon, in kg /kmol, m_{fg} is the fuel gas consumption, in kg /h and $w_{fg,c}$ is the carbon content in fuel gas, in %. The m_{fg} is 2,651.19 kg /h from the previous calculation and the carbon content is 66.3% (Wu and Liu 2016). Therefore, m_{CO_2} is 6,445.03 kg /h. The SO₂ emission in fuel gas and flaring system is determined as:

$$m_{SO_2} = \frac{64}{32} \times (m_{fg} w_{fg,s} + m_{H_2S} w_{H_2S,s}) \quad (12)$$

where $w_{fg,s}$ and $w_{H_2S,s}$ are the sulphur contents which both are assumed as 18.8 ppm referred to Parkash & Parkash (2003) and $w_{H_2S,s}$ is the purge gas flow rate to the flaring system obtained from the simulation. The calculated m_{SO_2} from the fuel gas is 0.05 kg /h and from burning H₂S is 0.004 kg /h.

4. Results and Discussion

In the reactor, thiophene is totally removed from the mixed feed stream in the conversion reactor. There are no traces of thiophene found in the subsequent streams. Approximately, 41.5 % of the top product from the separator which mostly contains hydrogen and a small trace of H₂S is purged from the system to maintain the partial pressure in the reactor. The balance is compressed and recycled with the new *n*-C30 and hydrogen feed to the reactor. In the distillation column, 460 kg mole/h and 451 kg mole/h distillates and bottom products are produced respectively. The distillate consists of 314.1 kg mole/h of *n*-C10, 137.2 kg mole/h of hydrogen and small amounts of *n*-C4 and H₂S. The bottom distillation product contains the cracked amount of *n*-C30 at 135.13 kg mole/h, *n*-C20 at 315.31 kg mole/h and at *n*-C4 at 1.17 kg mole/h. Approximately 3.64 kg renewable hydrogen is used to produce a ton of distillation product in this simulation. This equivalent to 63.3 percent reduction as only hydrodesulphurization and cracking reactions involved.

The input and results from Unisim Design R450 are further processed with Aspen Plus V10 and Microsoft Excel to determine the exergy destruction rate, E_d and exergy efficiency for each equipment in the ARDS hydrotreating unit. The highest exergy loss rates occur in the reactor at 1,100 MW, followed by the distillation column at 599 MW and the separator at 334 MW. For the other equipment, the exergy losses are less than 14 MW. The exergy destruction rates are proportionally related to the changes in chemical exergy of the streams. For example, in the reactor AR-R101, the chemical exergy changed from 1703 MW to 603 MW due to reactions in desulphurisation of thiophene and crackings *n*-C30 to *n*-C20 and *n*-C10. In the distillation column, these chemical exergy transformed from 909 MW at the inlet to the 473 MW and 1047 MW at the distillates and bottom products. The lower exergy efficiencies occur in pumps at less than 20 %, coolers and heaters between 21- 42.2 % and for the reactor and distillation column at 36.4 % and 36.6 % respectively. Compressors, separator and valve retains efficiencies above 64 %. Coolers and heater efficiencies are depending on the amount of heat used for the cooling and heating requirements of process streams. In the distillation column a large amount of heat at 12,106 kW is removed via the condenser to obtain the distillates while at the bottom reboiler uses a huge amount of heat at 84,025 kW for reboiling the bottom liquid products.

The input utilities consumed have a greater damage impact than output products i.e. the emissions of gas CO₂ and SO₂. The damage impact to human health are high as compared to ecosystem quality and resources. Input utilities of heat consumed gives the highest points for all damage categories at 2.9897 x10⁹, 3 x10¹⁰ and 2.491 x10⁷ point per year respectively. Electricity and fuel gas have approximately equivalent impacts while there is only a minor effect from the use of make-up hydrogen. The damage impact in the output to human health, ecosystem quality and resources are at 9.5301 x10⁵, 1.5745 x10⁵ and 9.5301 x10⁵ point per year respectively. Most of the impact can be attributed to the emission of CO₂ and SO₂ due to the burning of fuel gas for fired heater and reboiler. The calculated impact of SO₂ emission from the top purged gas in the flaring system is very limited due to small fraction of H₂S in the purging amount.

5. Outlook and Conclusions

Integration of renewable hydrogen in the hydrotreating process yields potential reductions in the energy consumption and environmental impact. Approximately 3.64 kg of hydrogen is used to produce a ton of distillate products in this simulation considering the thiophene desulphurization and *n*-C30 cracking.

The exergy analysis shows that reactor, distillation column and separator have large energy losses between 334 -1,100 MW. The lower exergy efficiency occurs in pumps, heat exchangers, reactor and distillation column in the range of 10.9 - 42.4 %. Life cycle analysis through Eco indicator-99 method reveals the apparent damage effects to human health of greenhouse gases emission from burning fuel gas for fired heater and reboiler. This is corresponding to 9.5301 x10⁵ point per year. The impact of SO₂ emission from burning excess H₂S in the flaring system to atmosphere is minor and can be neglected.

References

- I. Dincer and M A. Rosen, 2013a, Chemical Exergy, *Exergy, 2nd Ed.*, 31- 49
- I. Dincer and M.A. Rosen. 2013b, Exergy and Energy Analyses, *Exergy, 2nd Ed.* , 21-30
- L. Wu and L. Yongzhong, 2016, Environmental Impacts of Hydrotreating Processes for the Production of Clean Fuels Based on Life Cycle Assessment, *Fuel*, 164, 352-60
- M.A. Fahim, A. A. Taher and E. Amal, 2010a, Hydrogen Production, *Fundamentals of Petroleum Refining*, 285-302
- M.A. Fahim, A.A.Taher and E. Amal, 2010b, Hydroconversion, *Fundamentals of Petroleum Refining*, 153-98
- M.J. Moran, 1999, Engineering Thermodynamics, Mechanical Engineering Handbook, CRC Press LLC, Boca Raton, 1-89
- Pré Consultants, 2000, Eco-Indicator 99 Manual for Designers, *Ministry of Housing, Spatial Planning and the Environment*
- S. Parkash and S. Parkash. 2003, Treating Processes, *Refining Processes Handbook*, 210-219
- T.J. Kotas, 1995, The Exergy Method of Thermal Plant Analysis, 2nd ed., Krieger Publishing Company, Florida, USA, 29-51
- V.M.A.H. Elzakkher, L.K.K. Maia, I.E. Grossmann and E. Zondervan, 2017, Optimizing Environmental and Economic Impacts in Supply Chains in the FMCG Industry, *Sustainable Production and Consumption*, 11, 68 -79

Experimental Study of a Biomass Downdraft Gasifier with Multi-tube Gas Outlets to Improve Synthesis Gases Quality

Ajaree Suwattthikul and Paisan Kittisupakorn*

Department of Chemical Engineering, Chulalongkorn University, Bangkok 10330, Thailand

paisan.k@chula.ac.th

Abstract

A downdraft gasifier is favored due to its easy fabrication and due to low tar content in the synthesis gas. This work presents a designed and experimental results of downdraft gasifier. The throat, the smallest cross-sectional area, is approximately 175 millimeters. The gasifier is divided into 2 pieces (top and bottom) for easy fabrication and cleaning of the internal parts. The top is a fuel chamber while the bottom is a reaction and ash chamber. This gasifier was made of carbon steel inserting multi-tube (12) carbon steel of 1 inch diameter to be outlets of synthesis gas. These tubes were returned back to drying and pyrolysis zones of the top chamber as a heat source to wood pellets. The gasification was carried out under atmospheric pressure with ambient air as gasifying agent. Experimental results showed that average volumetric percentage in the synthesis gas were 39.71 % CO, 16.48 % CO₂, 36.26 % H₂ and 7.55 % CH₄. The gasification efficiency of this work of 40.47 % can be achieved.

Keywords: Design, Experiment, Biomass, Downdraft, Gasifier

1. Introduction

Gasification is a thermo-chemical process which converses organic material with partial oxidation to generate synthesis gas (mixture of CO, CO₂, CH₄ and H₂). The synthesis gas can be used as fuel in the internal combustion engine in order to produce electricity. A 25 kWe downdraft gasifier was presented by Ladpala et al. 2007. The fuel consumption rate was 50 kg/h and the heating value of synthesis gas was 4.5 MJ/ m³. The gasification efficiency of 66 % was achieved. Ma et al. 2012 designed a 190 kWe biomass fixed bed gasification. The overall height and effective inner diameter were 6205 mm and 1154 mm, respectively. The gasifier was made from steel (A105, ASTM) that was lined by refractory and insulated by ceramic fibers. The upper part was an air jacket for preheating the air agent. The lower part was a water jacket with an aim to reduce the charcoal's temperature as much as possible. This gasifier was a double air stage to reduce the tar level considerably and increase the heating value of the synthesis gas. A primary air supply located at the top section and a secondary air supply located at the middle section. Wood chips were used as feedstock with the consumption rate 250 kg/h. The heating value of 5.25 MJ/Nm³ and the gasification efficiency of 53 % were achieved. A small downdraft gasifier was presented by Chawdhury and Mhkamov 2011. The main body of the gasifier was divided into 3 sections. These three sections were top cylinder (fuel chamber), middle cylinder (reaction chamber) and bottom cylinder (ash

chamber). The top cylinder (pyrolysis zone) was made of 6.3 mm thick, 219 mm outer diameter and 272 mm length stainless pipe. Middle part (the oxidation zone and the throat section) was made of 6.3 mm thick, 219.1 mm outer diameter and 320 mm long stainless steel pipe. Inside this chamber there was a slab of thermal resistant concrete to provide insulation around hot zone. There were 4 holes in middle of the slab for the air supply nozzles. The bottom chamber (ash zone) was made of 219.1 mm diameter and 325 mm long cylinder. The consumption rate of wood chips and wood pellets were 3.1 and 2.9 kg/h, respectively. The heating value of synthesis gas was 4424 - 5007 kJ/m³ and the gasification efficiency was 62.5- 69.4 %.

The objective of this work is to experimentally study a downdraft gasifier with multi-tube gas outlets using wood pellets as feedstock. The performance of the downdraft gasifier is evaluated in terms of the synthesis gas composition, the heating value (LHV) and the gasification efficiency.

2. Design of downdraft gasifier

In this work, the gasifier is divided into 2 pieces (top and bottom) for easy fabrication and cleaning of the internal parts. The top is a fuel chamber while the bottom is a reaction and ash chamber as shown in Figure 1. The total height of the gasifier is 1.8 m with the inside diameter 700 mm. The throat, the smallest cross-sectional area, is approximately 175 mm. This gasifier was made of carbon steel and lined by refractory. The inserting multi-tube (12) were made of carbon steel of 1 inch diameter to be outlets of synthesis gas. These tubes were returned back to drying and pyrolysis zones of the top chamber as a heat source to wood pellets.

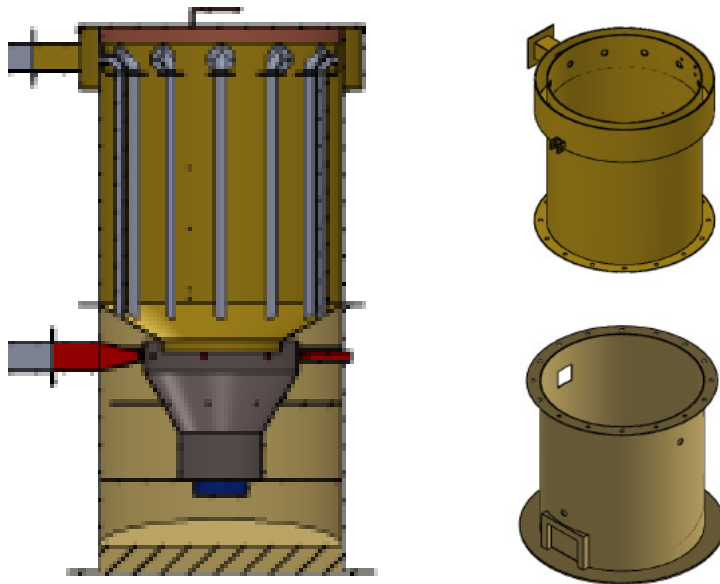


Figure 1 The schematic of the downdraft gasifier with multi-tube gas outlets.

3. Experimental setup

The experimental setup is shown in Figure 2. To control the gasification, air supply is designed to be adjusted by a damper. Air is fed into the gasifier from the center air distribution nozzle which then is allocated throughout the chamber via seven air nozzles. An air blower of 1 Hp motor with variable air flow rates is used to provide sufficient quantity of air for combustion. The wood pellets in the reduction zone are supported by a fixed grate at the bottom of the gasifier. The remaining ash is collected in the bottom. To measure the temperature of various zones in the gasifier, thermocouples are placed inside the gasifier at different locations. Temperatures along the gasifier are monitored every 10 minutes by type K thermocouples located at 0.11, 0.50, 0.73, 0.88 and 1.30 m above of the grate and another at the synthesis gas exit.



Figure 2 The experimental setup of the downdraft gasifier

4. Experimental procedure

The wood pellets of 100 kg were fed into the gasifier, afterwards, the gasifier was ignited at the ignition starting hole, which was installed at the combustion zone. After ignition, the hole was closed and air was supplied by the blower through the air inlet pipe. A gas analyser was used to measure the composition of the gas. The temperatures in the gasifier were measured using six thermocouples and recorded using a data logger and computer. The gasification was carried out under atmospheric pressure with ambient air as a gasifying agent.

5. Experimental results

5.1. Effect of air flow rate on the synthesis gas composition

The effect of air flow rate on synthesis gas consumption rate is shown in Figure 3. In this experimental study, air flow rate is varied from 95 to 120 m³/h and biomass consumption rate is then varied correspondingly from 20 to 22 kg/h. It was found that an increase in the air flow rate lead to the increase in biomass consumption rate. This is because the increase in the air flow rate will provide more oxygen to oxidize and higher amount of biomass will get combusted.

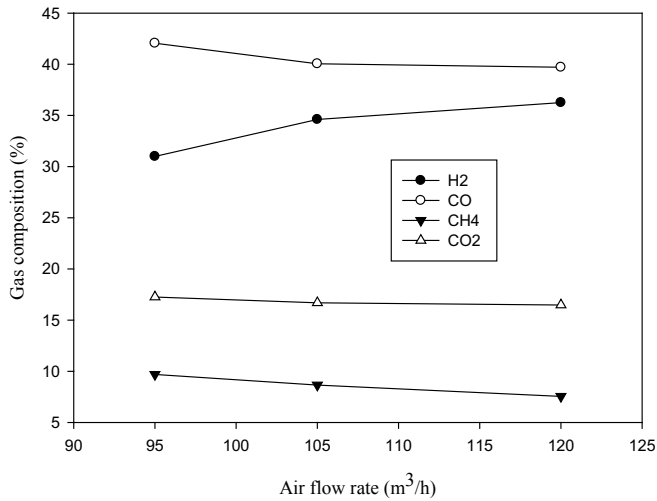


Figure 3 Effect of air flow rate on the synthesis gas composition

Figure 4 shows the temperature readings from T1 to T6 located as described above during the 3 h experimental run. T1 and T2 represent the temperatures at reduction and combustion zones, respectively. It can be seen that the highest T1 of 350 °C can be achieved at 50 minute, then it slightly decreases to 280 °C at the end. T2 reaches 280 °C at 20 minute, then it increases to the maximum of 760 °C at 170 minute and decreases to 600 °C at the end.

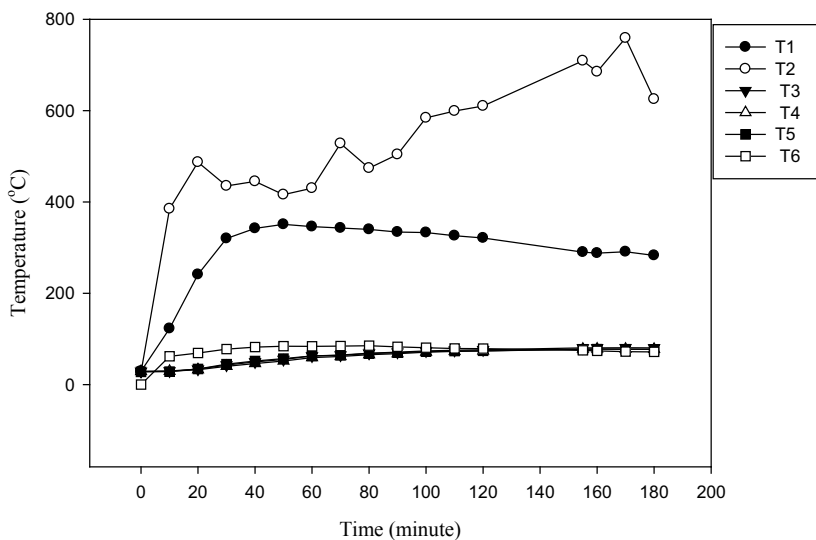


Figure 4 The temperature profiles of T1 to T6 at air flow rate 105 m³/h

5.2. Effect of air flow rate on LHV and gasification efficiency

The gasification efficiency is defined as the ratio between the energy content of the synthesis gas (in terms of LHV) and the energy content of the biomass (in terms of HHV) (Azzone et al. 2012). The gasification efficiency is calculated as below:

$$\eta = \frac{LHV_g \times Q_g}{HHV_b \times M_b} \times 100\% \quad (1)$$

Q_g is volumetric flow rate of the synthesis gas (Nm^3/h). M_b is biomass consumption rate (kg/h). LHV_g is heating value of the synthesis gas (MJ/Nm^3). HHV_b is the heating value of the biomass (kJ/kg). The heating values of typical gases are obtained from the standard gas tables as $10.1 \text{ MJ}/\text{Nm}^3$ for hydrogen, $12.64 \text{ MJ}/\text{Nm}^3$ for carbon monoxide and $38 \text{ MJ}/\text{Nm}^3$ for methane (Keche et al. 2015). The following equation is used to calculate the gas heating value:

$$LHV_g = \frac{10.1V_{H_2} + 12.64V_{CO} + 38V_{CH_4}}{100} \quad (2)$$

The effect of air flow rate on the heating value (LHV) of the synthesis gas is illustrated in Figure 5. When the air flow rate increases from 95 to $120 \text{ m}^3/\text{h}$, the LHV of the synthesis gas decreases. This is because the content of CH_4 is relatively low at high air flow rate. According to Eq. (2), the LHV of CH_4 is $35.814 \text{ MJ}/\text{Nm}^3$, which is more than three times as the LHV of H_2 ($10.788 \text{ MJ}/\text{Nm}^3$). Therefore, a small change of the CH_4 content will lead to large decrease in the LHV of the synthesis gas.

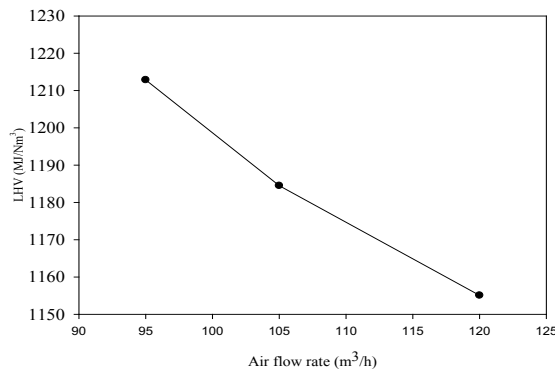


Figure 5 Effect of air flow rate on the LHV of the synthesis gas

Figure 6 shows the effect of air flow rate on the gasification efficiency. It was found that the increase in the air flow rate lead to the increase in gasification efficiency. The maximum gasification efficiency take place at the air flow rate of $120 \text{ m}^3/\text{h}$. Eq. (2) shows that the gasification efficiency is determined by the LHV, biomass consumption rate and the volumetric flow rate of synthesis gas. The results show that the gasification efficiency of the gasifier is directly proportional to the volumetric flow rate of synthesis gas; the change in the volumetric flow rate of synthesis gas has more impact on the gasification efficiency than the heating value and the biomass consumption rate.

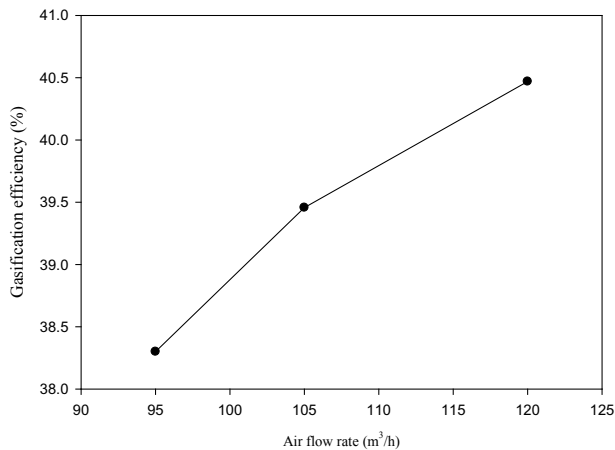


Figure 6 Effect of air flow rate on the gasification efficiency

6. Conclusions

This work presents a designed and experimental results of a downdraft gasifier with multi-tube gas outlets. When the air flow rate increases from range 95 to 120 m³/h, the heating value decreases (from 1212.86 to 1155.06 MJ/Nm³) while the gasification efficiency increases (from 38.30 to 40.47 %). The maximum gasification efficiency, 40.47 %, take place at the air flow rate of 120 m³/h. The volumetric percentage of the synthesis gas composition of 39.71 % CO, 16.48 % CO₂, 36.26 % H₂ and 7.55 % CH₄ can be achieved.

Acknowledgments

Financial of this research was supported by the Thailand Research Fund (TRF) under Grant Number PHD57I0054.

References

- S. Ladpala, et al. (2007). "Performance evaluation of a 25 kWe biomass power generation system prototype for community in Thailand." *International Journal of Renewable Energy*, 2, 53-62.
- Z. Ma, et al. (2012). "Design and experimental investigation of a 190 kWe biomass fixed bed gasification and polygeneration pilot plant using a double air stage downdraft approach." *Energy*, 46, 140-147.
- M. A. Chawdhury, and K. Mahkamov (2011). "Development of a small downdraft biomass gasifier for developing countries." *journal of scientific research*, 3, 51-64.
- E. Azzone, et al. (2012). "Development of an equilibrium model for the simulation of thermochemical gasification and application to agricultural residues." *Renewable Energy*, 46, 248-254.
- A. J. Keche, et al. (2015). "Simulation of biomass gasification in downdraft gasifier for different biomass fuels using ASPEN PLUS." *Clean Technologies and Environmental Policy*, 17(2), 465-473.

Design and Optimisation of Novel Cascade Refrigeration Cycles for LNG Production

Fernando Almeida-Trasvina and Robin Smith*

Centre for Process Integration, School of Chemical Engineering and Analytical Science, The University of Manchester, Manchester M13 9PL, UK.

robin.smith@manchester.ac.uk

Abstract

LNG production involves the use of large, complex and energy-intensive refrigeration cycles. The costs associated with the energy for refrigerant compression (shaft work energy) dominates the overall operating costs of the refrigeration cycles. In this work, a novel cascade refrigeration cycle is presented, as an alternative option for large scale LNG production, which is competitive in terms of energy-efficiency with the commercial cascade cycles: propane precooled mixed refrigerant (C₃MR) cycle, dual mixed refrigerant (DMR) cycle and Phillips Cascade cycle. In a case study, the novel and the commercial cascade cycles are optimised to minimise shaft work consumption for a given liquefaction duty. A stochastic search optimisation (Genetic Algorithm) is firstly applied in order to avoid local optima, and the best solution found with the Genetic Algorithm is used as the starting point for a deterministic optimisation (SQP). The optimised novel cascade cycle ('CryoMan Cascade' cycle) is able to achieve energy savings of around 5 % when compared to the optimised DMR cycle, which is the most energy-efficient commercial cascade cycle.

Keywords: LNG production, cascade refrigeration cycle, design and optimisation.

1. Introduction

Complex cascade refrigeration cycles are usually employed for the large-scale production of liquefied natural gas (LNG), i.e. for production rates above 2.5 million t per annum (MTPA). The multistage compressors used for refrigerant compression heavily influence the capital cost of the refrigeration cycle. The corresponding shaft work energy demand for refrigerant compression strongly dominates the operating costs of these cascade refrigeration cycles. Thus, minimising the total shaft work demand in a given refrigeration cycle configuration leads to minimise operating costs. Intercooling after each compression stage reduces the volumetric flow rate of the refrigerant stream fed into the next compression stage, hence reducing the overall shaft work energy demand. Therefore, the number of compression stages and associated intercoolers significantly affects the performance of the refrigeration cycles.

The commercially-established refrigeration cycles are the propane precooled mixed refrigerant (C₃MR) cycle, dual mixed refrigerant (DMR) cycle and Phillips Cascade cycle. Previous work studied the energy efficiency (in terms of shaft work demand) of the commercial cascade cycles for the production of LNG. However, the resulting performance indicators are difficult to use for comparisons because i) the configuration of the cascade cycles (number of compression stages) are often different across the

literature; ii) the natural gas feed flow rates and compositions also vary; iii) different modelling assumptions are made (minimum temperature approach in heat exchangers, compression efficiencies, etc.) across the publications; and iv) some of the reported energy efficiencies of the cascade cycles are values from simulations rather than values from optimised scenarios. Furthermore, from the open research literature it is evident that the development of novel cascade refrigeration cycles for large-scale LNG production is not a research focus.

In this work, a novel cascade cycle is developed – The CryoMan Cascade cycle – which is competitive in terms of energy efficiency with those commercially-established. The commercial cascade cycles are firstly modelled and fully optimised so as to have relevant benchmarks for comparing the novel cascade cycle. The cascade cycles are evaluated for the same basis of natural gas liquefaction duty and under the same modelling assumptions (e.g. minimum temperature approach in heat exchangers, compression isentropic efficiencies, etc.). Additionally, an effort is made in order to keep a similar configuration in terms of the number of compression stages across the cascade cycles. The novel cascade cycle is based on the CryoMan process (Figure 1), which is a single mixed refrigerant cycle for small scale production of LNG (Kim and Zheng, 2011).

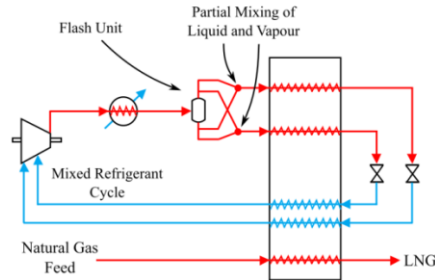


Figure 1. The CryoMan process (Kim and Zheng, 2011).

2. Configuration of the commercial cascade refrigeration cycles

An effort is made to define the configuration of the commercial cascade cycles to have a similar number of compression stages. The cascade refrigeration cycles are modelled using Aspen HYSYS v8.2 (Aspen Technology Inc., 2013). The models of the commercial cascade cycles have been verified after simulating various examples from the open literature (since real operational data is not available for model validation).

The configuration of the C_3MR cycle (Figure 2a) consists of three cooling stages in the (propane) precooling cycle and so three refrigerant compression stages. Propane is the refrigerant and kettle-type heat exchangers are used in the precooling cycle. In the liquefaction cycle, the mixed refrigerant is composed of $C_1 - C_3$ and N_2 , and multi-stream heat exchangers (MSHEs) are employed. Refrigerant compression is carried out in three compression stages. Overall, the C_3MR cycle has six compression stages. The model of the C_3MR cycle has been verified by simulating examples published by Fahmy et al. (2016a) and by Wang et al. (2012) for the propane cycle and the mixed refrigerant cycle, respectively.

The configuration of the DMR cycle (Figure 2b) consists of a precooling cycle in which cooling is provided at two pressure levels, and MSHEs are employed. The heavy mixed refrigerant comprises C_2 to C_4 . Refrigerant compression is carried out in three compression stages. In the liquefaction cycle, the light mixed refrigerant consists of C_1 to C_3 and N_2 . Cooling is provided in MSHEs and refrigerant compression takes place in three compression stages. Overall, the DMR cycle has six compression stages. The model of the DMR cycle has been verified after simulating the example published by Hwang et al. (2013).

In the Phillips Cascade cycle (Figure 2c), the propane precooling cycle provides cooling in three stages and the refrigerant is compressed in three compression stages. In the ethylene cycle, refrigerant compression is performed in two compression stages. In the ‘methane’ open-loop cycle, the natural gas stream is flashed at three expansion pressure levels and cooled in two MSHEs. Compression of the ‘methane’ refrigerant is carried out in three compression stages. Overall, the Phillips Cascade cycle has eight compression stages, which is due to the nature of the process – having three refrigeration cycles. The model of the Phillips Cascade cycles has been verified by simulating the example presented by Fahmy et al. (2016b).

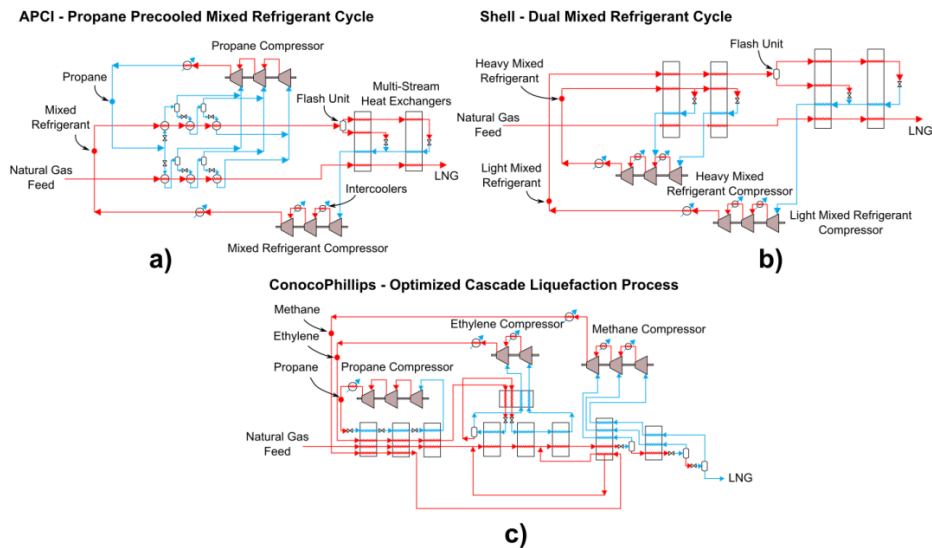


Figure 2. Configuration of the commercial cascade refrigeration cycles: a) C_3 MR cycle; b) DMR cycle; c) Phillips Cascade cycle.

3. Configuration of the novel CryoMan Cascade cycle

For the configuration of the novel cascade cycle, the CryoMan process is used as the liquefaction cycle within the cascade, since the liquefaction cycle usually has a larger cooling duty than the precooling cycle, and so the potential energy savings would be more evident. For the precooling cycle, a mixed refrigerant cycle is employed.

So, in the configuration of the novel CryoMan Cascade cycle (see Figure 3) the heavy mixed refrigerant in the precooling cycle consists of C_2 to C_4 . Cooling is provided at two pressure levels using MSHEs. Refrigerant compression is performed with three compression stages. In the liquefaction cycle, the light mixed refrigerant is comprised of

C₁ to C₃ and N₂. Cooling is provided in MSHEs at two pressure levels. Refrigerant compression is carried out in three compression stages. Overall, the novel CryoMan Cascade cycle has six compression stages.

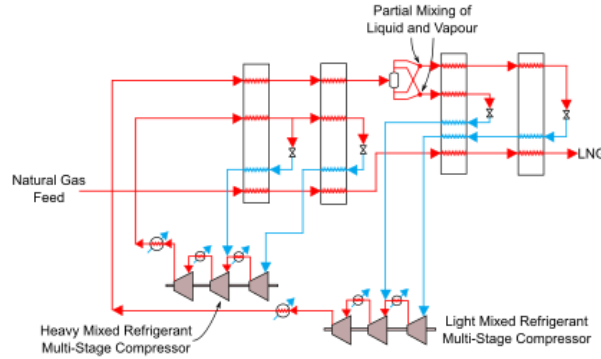


Figure 3. The novel CryoMan Cascade cycle.

4. Optimisation strategy and case study

All the commercial cycles (C₃MR, DMR and Phillips) and the novel CryoMan Cascade cycle are evaluated using the same optimisation strategy, and for the same liquefaction case study. The case study consists in fully liquefying a natural gas stream (see Table 1) for producing 5.6 MTPA of LNG – data based on that from (Fahmy et al., 2016a) – while minimising the total shaft power demand for refrigerant compression. The minimum temperature approach is assumed as 2 °C for the MSHEs and 5 °C for the kettle-type heat exchangers. Intercooling is available after each compression stage to cool down the refrigerant stream to 30 °C. Compression isentropic efficiency is assumed as 80 %. The maximum compression ratio (outlet to inlet pressures) in any compression stage is defined as 3.5. Peng–Robinson equation is used for calculating thermodynamic and physical properties (e.g. enthalpies, temperatures, etc.) of the refrigerant streams.

The cascade refrigeration cycles are modelled in Aspen HYSYS and the optimisation is performed using MATLAB (The MathWorks Inc., 2013). The objective function of the optimisation is to minimise the specific shaft work demand for refrigerant compression in each cascade refrigeration cycle, i.e. the total shaft work demand per unit production of LNG, according to Eq.(1).

$$\frac{W^{Total}}{\dot{m}_{LNG}} = \sum_{i=1}^n \frac{W_i^{Stg}(\phi)}{\dot{m}_{LNG}} \quad (1)$$

A stochastic search algorithm (Genetic Algorithm) is applied in order to avoid local optima. The set of random initial conditions is generated in MATLAB and each vector of random conditions is simulated in HYSYS. The performance of the simulations is continuously evaluated in MATLAB as the optimisation progresses. Once the stochastic optimisation terminates, the best solution found is used as the starting point for a deterministic optimisation (using *fmincon*) to refine further the final solution.

For each cascade cycle, the degrees of freedom to be optimised include the refrigerant flow rates, refrigerant compositions, expansion pressure levels, outlet temperatures of each stream in each MSHE, compression ratio of relevant compression stages, and refrigerant split fractions (where applicable), for both precooling and liquefaction cycle within a cascade cycle. During the optimisation process, penalties are applied if practical constraints are not met, such as having infeasible heat transfer in any MSHE, a compression ratio above 3.5 in any compression stage, or wetness at the inlet of any compression stage.

Table 1. Natural gas data for the case study.

Flow rate [$\text{kg}\cdot\text{s}^{-1}$]	177.59
Inlet pressure [bar]	63.0
Inlet temperature [$^{\circ}\text{C}$]	25.0
Outlet temperature [$^{\circ}\text{C}$]	-161.0
Composition [mole fraction]	
Methane	0.98385
Ethane	0.01070
Propane	0.00090
<i>n</i> -Butane	0.00020
CO ₂	0.00005

The optimised shaft work demand value for each cascade cycle is shown in Table 2. Energy and associated operating cost savings of each cascade cycle, also shown in Table 2, are relative to the C₃MR cycle which is the commercially dominant cascade cycle. The unit shaft work energy cost is taken as £0.0976 per kWh (U.K. Department of Energy & Climate Change, 2017).

Table 2. Optimised performances and comparison between cascade refrigeration cycles.

	C ₃ MR Cycle	DMR Cycle	Phillips Cascade	CryoMan Cascade Cycle
Compression stages	6	6	8	6
Initial specific shaft work [MW/MTPA LNG]	38.48	33.48	38.52	29.01
Optimised specific shaft work [MW/MTPA LNG]	30.09	27.32	34.80	25.97
Energy savings [%]	—	+ 9.20 %	-15.65 %	+ 13.71 %
Annual operating cost savings	—	+ £13.26 million	- £2.98 million	+ £19.75 million

The DMR cycle is the most energy-efficient amongst the commercial cascade cycles (27.32 MW/MTPA LNG), achieving 9.2 % savings in shaft work compared to the C₃MR cycle (30.09 MW/MTPA LNG). The Phillips Cascade resulted as the cascade cycle with the lowest energy-efficiency (34.80 MW/MTPA LNG) despite having two additional compression stages compared to the rest of the cascade cycles.

The optimised CryoMan Cascade cycle yielded 25.97 MW/MTPA LNG, which means shaft work savings of around 13.7 % when compared to the C₃MR cycle. Moreover, the

specific shaft work demand achieved with the CryoMan Cascade cycle is also equivalent to shaft work savings of around 5 % when compared to the DMR cycle, which is the most energy-efficient commercial cascade cycle.

In terms of the operating variables, the light mixed refrigerant flow rate (in liquefaction cycle) of the CryoMan Cascade cycle increases from 334.4 kg/s to 407.1 kg/s when compared to that in the DMR cycle. However, the composition of the light mixed refrigerant in the CryoMan Cascade cycle is heavier (ethane mole fraction increases from 0.3189 to 0.3513, and propane mole fraction from 0.2012 to 0.2213). A refrigerant stream with a relatively heavy composition requires less shaft work energy for compression than a refrigerant stream with a lighter composition. Thus, partial mixing the flash outlet streams of the liquefaction cycle allows manipulating the composition of the refrigerant streams, and so the CryoMan Cascade cycle is able to work with a heavier refrigerant stream, which helps reducing the overall shaft work demand, while still meeting the cooling demand. Furthermore, the operating cost savings achieved by the CryoMan Cascade cycle come as the expense of relatively minor increase in complexity and associated capital costs when compared to the DMR cycle.

5. Conclusions

A novel cascade refrigeration cycle is presented, which is competitive in terms of energy efficiency with the commercial cascade cycles. The novel cascade cycle and the commercial cycles are optimised to liquefy a given natural gas stream while minimising the specific shaft power demand. The models of the commercial cascade cycles have been verified by simulating examples published in the open research literature. From the case study presented, around 5 % savings in shaft work energy are achieved by the CryoMan Cascade cycle when compared to the DMR cycle, which is the most energy-efficient commercial cycle.

References

- Aspen Technology Inc. (2013). Aspen HYSYS v8.2. Bedford, USA.
- Fahmy, M. F. M., Nabih, H. I. & El-Aziz, M. R. A. (2016a). Investigation and Performance Improvement of the Propane Precooling Cycle in the Propane Precooled Mixed Refrigerant Cycle Liquefaction Process. *Industrial & Engineering Chemistry Research*, 55(10), 2769-2783.
- Fahmy, M. F. M., Nabih, H. I. & El-Nigeily, M. (2016b). Enhancement of the efficiency of the Open Cycle Phillips Optimized Cascade LNG process. *Energy Conversion and Management*, 112, 308-318.
- Hwang, J.-H., Roh, M.-I. & Lee, K.-Y. (2013). Determination of the optimal operating conditions of the dual mixed refrigerant cycle for the LNG FPSO topside liquefaction process. *Computers & Chemical Engineering*, 49(0), 25-36.
- Kim, J.-K. & Zheng, X. (2011). *Refrigeration process*. The University of Manchester. PCT/GB2011/050617.
- The MathWorks Inc. (2013). MATLAB Version 2013a. Natick, USA.
- U.K. Department of Energy & Climate Change. (2017). *International industrial energy prices* [Online]. Available: <https://www.gov.uk/government/statistical-data-sets/international-industrial-energy-prices> [Accessed 05 September 2017].
- Wang, M., Zhang, J. & Xu, Q. (2012). Optimal design and operation of a C3MR refrigeration system for natural gas liquefaction. *Computers & Chemical Engineering*, 39(0), 84-95.

Method of Removing water from Products of Dehydration Reaction of 3-hydroxypropionic acid in Acrylic acid Process

Jae-Hyeon Yang ^a, Chul-Jin Lee ^{a,*}

^{a,*}*School of Chemical and Materials science Chung-Ang University, 84 Heukseok-ro, Dongjak-gu, Seoul, 06980, Republic of Korea.*

cjlee@cau.ac.kr

Abstract

The present predominant resource of acrylic acid is formed partial oxidation of propene, produced as a by-product from industrial production of ethylene and gasoline. This process depends on the processing of petrochemicals as raw material, resulting in resource depletions and many environmental problems. Therefore, biomass technology has been introduced to reduce the disadvantages of existing conventional process. The proposed process is composed of a bio-fermentation reactor, a catalytic dehydration reactor, a quencher, and an acrylic acid purification unit. Among them, it focuses on the quencher process. Recently, most of the research is currently focused on microorganisms in fermentation reaction and developing catalysts in dehydration reaction. However, this technology also remains a problem that a large quantity of water is required in the bio-fermentation and dehydration reactors. In this paper, we focus on the after the dehydration of 3-hydroxypropionic acid to produce acrylic acid about the method of efficient removal of water. To solve this problem, we introduced a quencher using solvent to remove water and improve the efficiency of the process. It is essential to remove water in order to obtain high purity of the acrylic acid.

We designed the process using Aspen Plus v8.8 simulator. Approximately 76.0 wt% of water, 22.6 wt% of acrylic acid, 1.4wt% 3-hydroxypropionic acid were fed to quencher. The results from the simulation show that 64.2 wt% of water was removed and 47.5 wt% of total flow was saved. The elimination of water reduces the overall flow rate, resulting in reduced equipment size of the process. Therefore, we expect that the use of this method will reduce the capital cost and operating cost of the acrylic acid purification process.

Keywords: Biomass. Acrylic acid. Quencher. 3-Hydroxypropionic acid. Removal of water.

1. Introduction

Acrylic acid is an important polymer as raw material for many industrial and consumer products. It can numerous to apply for surface coatings, textiles, adhesives, paper treatment, baby diapers, feminine hygiene products detergents and super absorbent polymers as known (Danner et al., 1998). Currently, most acrylic acid is obtained from the catalytic partial oxidation of propene which is a by-product of ethylene and gasoline production. In this two-step oxidation reaction via acrolein is usually preferred, achieving about 90 % overall yield (Lin, 2001; Straathof et al., 2005). However, this conventional process affects global CO₂ emissions: 175 kg/ton of CO₂ has been released in converting propene to acrylic acid (Segawa, 2014) and petrochemical carbons sources are limited and not renewable. The global acrylic acid market sizes is growing. Because acrylic acid demands for super absorbent polymers is expected the growth (Research, 2016). This process feedstock, propene, is related to volatile crude oil prices. Therefore, alternative methods have been studied such as biomass resources. It is encouraging to find renewable alternatives to produce acrylic acid in more environmentally friendly and economical way. Most of the feedstock for producing the acrylic acid, the quantitative conversion to lactic acid would open a new market for renewable resources (Danner et al., 1998). There are recent advances in the research and development of acrylic acid via the fermentation of renewable sources using microorganisms that ferment the 3-hydroxypropionic acid that is then dehydrated to from acrylic acid. In this paper, we focus on the process after the dehydration of 3-hydroxypropionic acid to produce acrylic acid. We conducted simulations and designed proposed model using commercial simulators that referred as the patent product components. This process introduced a quencher using solvent to cool the main stream in order to separate water in extractor unit and to avoid acrylic acid polymerization. It remove water from fermentation reaction of biomass and catalytic dehydration reaction of 3-HP. By first removing water from the quencher through solvent, the initial investment cost and the operating cost of the separation process can be reduced.

2. Process description

2.1. Propene based conventional process

Acrylic acid is used a precursor to a wide variety of chemicals in the polymer and textile industries. There are several chemical pathways to produce acrylic acid but the most common one is via the partial oxidation of propene. The usual mechanism for producing acrylic acid utilizes a two-step process in which propene is first oxidized to acrolein (1) and the further oxidized to acrylic acid (2). Each reaction step usually takes place over a separate catalyst and at different operating conditions (Turton et al., 2013).



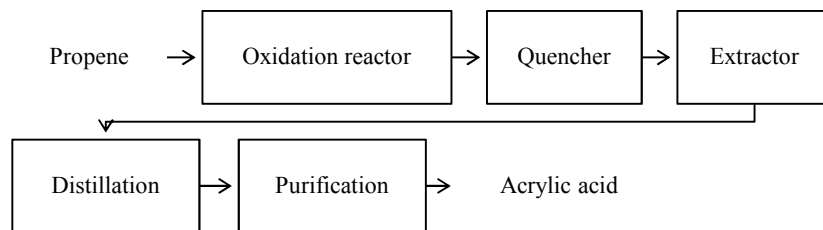


Figure 1 Propene based conventional process flow diagram

The conventional process based on propene overall flow diagram is shown in Figure 1. First, propene flows to the oxidation reactor. In this reactor, a proprietary catalyst is used to eliminate the production of intermediates such as acrolein and acetic acid. After the reaction, it is essential to cool the products to avoid further oxidation reactions and to achieve rapid quenching of the reactor effluent with a cool recycle. This is combined with the liquid phase to form the feed to the extractor unit. In the liquid-liquid extraction step, the acid fraction is preferentially removed from the water prior to purification. There are many possible solvents that can be used as the organic phase in the separation: high solubility for acrylic acid and low solubility for water are desirable. Some examples include ethyl acetate, isopropyl acetate, ethyl acrylate, methyl isobutyl ketone, toluene, and xylene, which are used in the extraction unit (Alvarez et al., 2007). The organic phase is sent to a solvent recovery column where the solvent is recovered overhead and returned to the extractor. The bottom stream of the extractor product is sent to the purification column. Thereafter, acrylic acid is obtained as a product of high purity. However, the conventional process depends heavily on the processing of petrochemicals as the base raw material. Also, it includes problems with limited fossil fuel resources and environmental issues related to CO₂ emissions.

2.2. Biomass based proposed process

The pathway from biomass procedure is provided below. Beginning with a source of glycerol, a special strain of *Escherichia coli* produces 3-hydroxypropionic acid via a biosynthetic pathway (3). It can be dehydrated with a phosphoric acid catalyst to form acrylic acid (4).



The Figure 2 is acrylic acid manufacturing proposed process based on glycerol overall flow diagram. This process has been divided into a fermentation reactor, a dehydration reactor, a quencher, an extraction, a distillation, and a purification unit. In order to successfully produce acrylic acid from glycerol, first glycerol is converted to 3-hydroxypropionic acid via the aerobic fermentation of *E. coli*. This concentrated 3-hydroxypropionic acid stream flows through a reactor with phosphoric acid. This acid acts as a catalyst in the dehydration reaction, converting 3-hydroxypropionic acid to acrylic acid in roughly 30% yield. Through the bio-fermentation reaction, a large quantity of water and acrylic acid are produced through a gaseous phase dehydration reaction. It requires high energy to separate the generated water and acrylic acid (Bebensee et al.,

n.d.). Therefore, we focus on quencher, the between dehydration of 3-hydroxypropionic acid and distillation, to produce acrylic acid about the method of efficient removal of water using solvent.

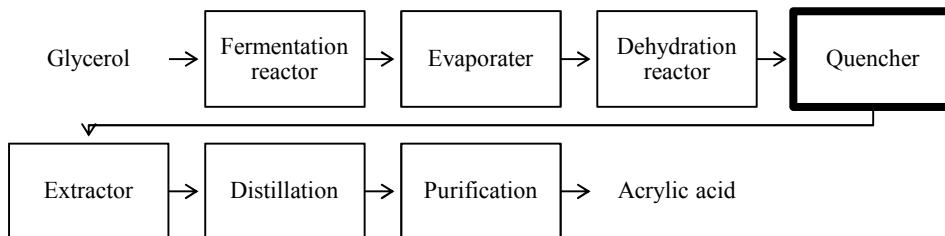


Figure 2 Glycerol based proposed process flow diagram

3. Proposed process modeling methodology

The simulated proposed process is shown Figure 3. We applied a NRTL-HOC thermodynamic package model for this model, in order to select the proper physical property methods of the simulation (Carlson, 1996). The effluent through dehydration is based on the experimental data provided in a BASF patent (Bebensee et al., n.d.). In this model, the products of the dehydration reaction stream (1000) and solvent (2000) is entered into a quencher column. The preceding dehydration is a 350 °C high temperature dehydrating reaction, and the temperature should be lowered to 40 °C for the extraction process of water and acrylic acid. However, the heat exchanger should be minimized considering that the acrylic acid is easily polymerized. This is because it should not take longer to stay in high temperature at 90°C. Hence, 170 °C of stream generated through a single heat exchanger is sent into the quencher. The gaseous phase stream (1000) and solvent (2000) is formed azeotropic conditions. The vapor stream (1001) withdrawn from the top is condensed and fed to a decanter (1002) in which organic and aqueous phases are formed. The organic phase (1003) is recycled to a quencher column while part of the aqueous phase is separated (1005). The solvent selection is important to this process. Toluene is ultimately selected as the most appropriate solvent. Because toluene can form azeotrope composition 52.3 mol% with water and have stable azeotropic temperature at 85 °C in order to avoid acrylic acid polymerization (Gmehling et al., 1996). The azeotrope properties of toluene are shown in Table 1. Also, the toluene used in this process should be the same as the solvent used for the extractor unit.

Table 1 Characteristics of toluene used as a solvent (Horsley, 1962)

Component, <i>i</i>	Normal B.P., (°C)	Azeotropic Temp, (°C)	Azeotropic Comp, (mol %)
Toluene	110.6	85.0	52.3

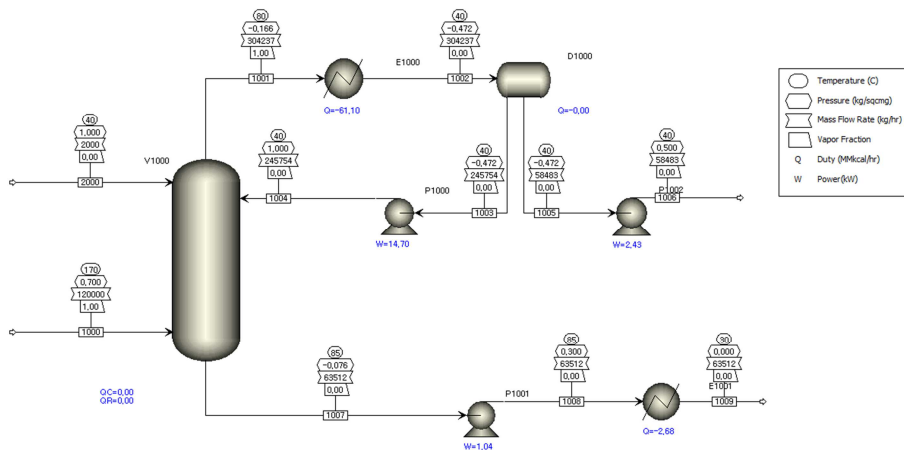


Figure 3 Flow diagram of the quencher

Table 2 Simulation results

	Inlet	2000	Outlet
Stream name	1000	2000	1009
Temperature (°C)	170.0	40.0	30.0
Pressure (Bar)	1.70	1.99	1.01
Total mass flow rate (kg/hr)	120,000	2,000	63,517
Component mass flow rate			
Water	91,030	0	32,587
Acrylic acid	27,128	0	27,128
3-hydroxypropionic acid	1,842	0	1,842
Toluene	0	2,000	1,960
Total mole flow rate (kmole/hr)			
Component mole flow rate			
Water	5,454.9	21.7	2,232.0
Acrylic acid	5,052.9	0	1,808.8
3-hydroxypropionic acid	376.4	0	376.4
Toluene	25.5	0	25.5
	0	21.7	21.2

4. Results and conclusion

The manufacturing process of biomass based acrylic acid occurred to overcome the environmental limitations of the existing propene based process. There is a problem with the amount of water droplets in bio-fermentation and dehydration reaction. It is necessary to undergo and extraction process to separate water and acrylic acid and that is decreased to the proper temperature using quencher. In this research, we designed

through the quenching from 3-hydroxypropionic acid of dehydration reaction product. It has the effect of removing the amount of water with additional solvent. We conducted commercial simulation using 3-hydroxypropionic acid dehydration reaction data onto patent. As a result, the total flow rate can be reduced from 120 ton/hr to 63 ton/hr, 47.5 wt% decreased. And water flow rate reduced from 91 ton/hr to 32.6 ton/hr, 64.2 wt% decreased without loss of acrylic acid. As the overall flow rate reduce after an extractor, a distillation and a purification unit size will be decreasing. This proposed process as using biomass can solve the environmental and price volatility of conventional. This process, which has been limited to a large quantity of water, can increase efficiency using quencher with toluene. Furthermore, the study will complete the post purification acrylic acid model and apply it to overall process to evaluate the economy.

Reference

- Alvarez, M.E.T., Moraes, E.B., Machado, A.B., Filho, R.M.I., Wolf-Maciel, M.R., 2007. Evaluation of liquid-liquid extraction process for separating acrylic acid produced from renewable sugars, in: *Applied Biochemistry and Biotechnology*. pp. 451–461. doi:10.1007/s12010-007-9071-1
- Bebensee, R.H., Zajackowski-fischer, M., Veronika wloka, n.d. WO 2016026761 A1.
- Carlson, E.C., 1996. Don't gamble with physical properties for simulations. *Chem. Eng. Prog.* 92, 35–46.
- Danner, H., Urmös, M., Gartner, M., Braun, R., 1998. Biotechnological production of acrylic acid from biomass. *Appl. Biochem. Biotechnol.* 70–72, 887–894. doi:10.1007/BF02920199
- Gmehling, J., Menke, J., Krafczyk, J., Fischer, K., Fontaine, J., Kehiaian, H. V., 1996. Azeotropic Data for Binary Mixtures. *Handb. Chem. Phys.* 6-210-6–228.
- Horsley, L.H., 1962. Azeotropic Data — Ii. *Adv. Chem. Ser.* doi:10.1021/ba-1962-0035
- Lin, M.M., 2001. Selective oxidation of propane to acrylic acid with molecular oxygen. *Appl. Catal. A Gen.* 207, 1–16. doi:10.1016/S0926-860X(00)00609-8
- Research, G.V., 2016. *Acrylic Acid Market Analysis, By Product (Acrylate Esters, Glacial Acrylic Acid), By End-Use (Surfactants and Surface Coatings, Organic Chemicals, Adhesives, Textiles, Water Treatment, Personal Care Products), Bio Acrylic Acid Downstream Potential And Seg 120.*
- Segawa, K., 2014. *Catalyst Technology for Green and Sustainable Chemistry.* JCCP.
- Straathof, A.J.J., Sie, S., Franco, T.T., van der Wielen, L.A.M., 2005. Feasibility of acrylic acid production by fermentation. *Appl. Microbiol. Biotechnol.* 67, 727–734. doi:10.1007/s00253-005-1942-1
- Turton, R., Bailie, R.C., Whiting, W.B., Shaeiwitz, J.A., Bhattacharyya, D., 2013. *Analysis, Synthesis, and Design of Chemical Processes, Fourth Ed.* ed. PEARSON.

Multi-floor process plant layout using mixed-integer optimisation

Jude O. Ejeh^a, Songsong Liu^b and Lazaros G. Papageorgiou^{a,*}

^a*Centre for Process Systems Engineering, Department of Chemical Engineering, UCL (University College London), London WC1E 7JE, United Kingdom;*

^b*School of Management, Swansea University, Bay Campus, Fabian Way, Swansea SA1 8EN, United Kingdom;*

Abstract

Techniques to address the process plant layout problem have gone from an engineering judgement-based approach prior to the late 90s, to a more systematic means - through mathematical programming, simulated annealing and a range of other techniques. Over the past 20 years, factors such as the connectivity costs, pumping costs, cost of safety device installations, pipe routing, multi-floor arrangements, etc., have all been included as constraints in a mathematical programming model to determine predominantly, the most cost effective and safe means for plant layouts.

This work proposes a mixed integer linear programming (MILP) model to include more realistic considerations for the multi-floor process plant layout problem - specifically tall process plant units with heights well above the typical floor height - which are common in most process plants but have not been given considerable attention in previous works. The model accounts for floor construction costs, area-dependent land use costs, pumping costs (upwards and within the same floor), connection costs by pipes as well as variable connection points along the heights of process units. The proposed optimisation approach has been applied successfully to an industry-relevant examples of 17 processing units with satisfactory computational results.

Keywords: multi-floor plant layout; optimisation; MILP

1. Introduction

The practice of process plant layout dates as early as process plant design, but systematic approaches were not employed until the late 90s. The layout design of a process finds the spatial arrangement of process equipment with interconnections in order to achieve a balance in safety requirements within and without the plant, economics, construction, maintenance, operation as well as the need for future expansions (Moran, 2016). In chemical process plants, these interconnections are mostly by pipes.

Earlier works in the area of mathematical programming techniques applied to process plant layout predominantly sort to minimise a cost function, and have remained so till date with slight variations. Penteado and Ciric (1996) proposed a mixed integer non-linear programming (MINLP) model to minimise the total layout cost - piping, land allocation, as well as financial risk and safety costs. Georgiadis and Macchietto (1997) included pumping and floor construction costs, but excluded financial risk and safety in a discretized spatial domain in a mixed integer linear programming (MILP) model. Papageorgiou and Rotstein (1998) solved the layout problem over a continuous spatial domain preventing equipment overlap for a single floor case with production

sections and then a multi-floor case (Patsiatzis and Papageorgiou, 2003). Scenarios with different inputs and outputs for each equipment, irregularly shaped equipment, safety and operability factors and a 3D representation was modelled by Barbosa-Póvoa et al. (2002). In each of these formulations, case studies with more than 11 units could not be handled in reasonable computational time to a global optimum. Patsiatzis and Papageorgiou (2003); Xu and Papageorgiou (2009) proposed successful algorithms for larger case studies, but global optima could not be guaranteed in all cases. Apart from a cost minimisation objective, other factors such as safety and risk assessment (Jung, 2016), area minimisation (Ku et al., 2013), routing and layout of pipes (Guirardello and Swaney, 2005), etc., have also been researched; with varying solution techniques (Xin et al., 2016). The work seeks to build upon previous research whilst addressing two key deficiencies: the scalability of exact model solutions, and the modelling of more realistic considerations within process plants. It extends the work of Patsiatzis and Papageorgiou (2003), proposing an model to address the multi-floor process plant layout problem with additional considerations for long-length equipment - equipment that exceed the typical height of a floor. Ku et al. (2013) previously proposed an MINLP model with a hybrid solution technique to handle this consideration, but a more efficient MILP will be proposed to handle larger case studies. Varying connection points between equipment will also be considered for a more realistic consideration.

In the rest of the paper, a process plant layout problem is described in detail in section 2. The mathematical programming model is proposed in section 3, and its computational performance is shown with a relevant case study in section 4. Final remarks and areas for future considerations are then given in section 5.

2. Problem Description

A description of the multi-floor process plant layout problem and the underlying assumptions made in the mathematical formulation are given in this section. In the mathematical formulation, equipment items are approximated as having a rectangular geometry, with rectilinear distances taken between equipment geometrical centres in the x-y plane. Vertical distances/connections are taken from a predefined point along the equipment height based on conditions unique to the problem being solved. Each equipment is allowed to rotate in 90° angles in the x-y plane, and must start from the base of each available floor. The floor height is fixed across all floors and if an equipment exceeds such height, it is allowed to extend through successive available floors.

The problem description is as follows:

Given:

- a set of N process plant equipment items, i, j , and their dimensions (length, α_i , breadth, β_i , and height, γ_i);
- the connections amongst each equipment;
- a set of K available floors for layout with floor height, FH ;
- connection, C_{ij}^c , pumping (horizontal, C_{ij}^h , and vertical, C_{ij}^v), land purchase (LC) and construction ($FC1$, $FC2$) cost data;
- space and equipment allocation limitations; and the minimum safe distances between equipment items;

determine

- the total number of required floors for layout;
- spatial equipment allocation to floors; and

- floor area;

so as to minimise the total plant layout cost.

3. Mathematical Formulation

The mathematical formulation to address the multi-floor process plant layout problem is outlined in this section. It constitutes an extension of the model initially proposed by Patsiatzis and Papageorgiou (2003).

First, every equipment is assigned to an equivalent number of floors based on its height, M_i :

$$\sum_k V_{ik} = M_i \quad \forall i \quad (1)$$

where V_{ik} is binary variable that determines if an equipment i is assigned to floor k . A binary variable, N_{ij} , is introduced to determine if two equipment i and j are assigned to the same floor k :

$$n_{ijk} \geq V_{ik} + V_{jk} - 1 \quad \forall i = 1, \dots, N-1, j \neq i, k = 1, \dots, K \quad (2)$$

$$N_{ij} \geq n_{ijk} \quad \forall i = 1, \dots, N-1, j \neq i, k = 1, \dots, K \quad (3)$$

Multi-floor equipment are assigned successive floors, starting from any available floor:

$$\sum_{\theta=1}^{M_i-1} v_{i,k+\theta} \geq (M_i - 1) \cdot (V_{ik} - V_{i,k-1}) \quad \forall i, k \quad (4)$$

Each of these available floors should only be considered for construction ($W_k = 1$) if an equipment starts on it, and not just passes through it.

$$S_{ik}^s \leq W_k \quad \forall i, k \quad (5)$$

where S_{ik}^s , the starting floor k of an equipment i , is defined by eq. 6 and must only occur on one floor (eq. 7), with each floor existing only if the preceding floor is occupied (eq. 8):

$$-V_{ik} + V_{i,k-1} + S_{ik}^s \geq 0 \quad \forall i, k \quad (6)$$

$$\sum_k S_{ik}^s = 1 \quad \forall i \quad (7)$$

$$W_k \leq W_{k-1} \quad \forall k = 2, \dots, K \quad (8)$$

The total number of floors (NF) required is then determined by eq. 9:

$$NF \geq \sum_k W_k \quad (9)$$

Every equipment is allowed a 90° rotation only in the x-y plane, as otherwise is unrealistic. Connections between equipment are assumed to originate from the mid point of equipment (x_i, y_i) , and these equipment are placed within the boundaries ($[0, 0]$ and $[X^{max}, Y^{max}]$) of the floor area. Each of these constraints is as defined in Patsiatzis and Papageorgiou (2003). Each equipment is placed at the base of each floor assigned (eq. 10).

$$\gamma_i = h_i \quad \forall i \quad (10)$$

The horizontal, vertical and total distances between connected equipment is defined by eqs. 11 - 13, and is taken from the mid-points of equipment in the x-y plane, and from pre-specified heights,

OP_{ij} and IP_{ij} , from equipment i to equipment j , in the z plane respectively:

$$R_{ij} - L_{ij} = x_i - x_j \quad \forall(i, j) : f_{ij} = 1 \quad (11)$$

$$A_{ij} - B_{ij} = y_i - y_j \quad \forall(i, j) : f_{ij} = 1 \quad (12)$$

$$U_{ij} - D_{ij} = FH \sum_k (k-1) (S_{ik}^s - S_{jk}^s) + OP_{ij} - IP_{ij} \quad \forall(i, j) : f_{ij} = 1 \quad (13)$$

$$TD_{ij} = R_{ij} + L_{ij} + A_{ij} + B_{ij} + U_{ij} + D_{ij} \quad \forall(i, j) : f_{ij} = 1 \quad (14)$$

where R_{ij} , L_{ij} , A_{ij} , and B_{ij} are the relative distances between equipment i and j , if i is to the right, left in x coordinates; above, below in y coordinates; higher, lower in z coordinates; of j , respectively, and are connected ($f_{ij} = 1$). These equipment, connected or not, are prevented from overlapping if they are on the same floor as described in Patsiatzis and Papageorgiou (2003). The total area FA is defined from a set of predefined sizes, s , by a binary variable Q_s and is determined by eqs. 15 - 18:

$$FA = \sum_s AR_s Q_s \quad (15)$$

$$\sum_s Q_s = 1 \quad (16)$$

$$X^{max} = \sum_s \bar{X}_s Q_s \quad (17)$$

$$Y^{max} = \sum_s \bar{Y}_s Q_s \quad (18)$$

A new term NQ_s is introduced in order to linearise the cost term associated with the area of floors ($FC2 \cdot FA \cdot NF$) in the objective function.

$$NQ_s \leq K Q_s \quad \forall s \quad (19)$$

$$NF = \sum_s NQ_s \quad (20)$$

The objective function which minimises the total floor construction (fixed and area dependent), land area, pumping and connection cost is given by:

$$\begin{aligned} \min \sum_i \sum_{j \neq i: f_{ij}=1} [C_{ij}^c TD_{ij} + C_{ij}^v D_{ij} + C_{ij}^h (R_{ij} + L_{ij} + A_{ij} + B_{ij})] \\ + FC1.NF + FC2 \sum_s AR_s.NQ_s + LC.FA \end{aligned} \quad (21)$$

The multi-floor process plant layout model can then be summarized as the minimisation of the total layout cost (eq. 21), *subject to* floor constraints (eqs. 1 - 3, 5 - 9), multi-floor equipment constraint (eq. 4), distance constraints (eqs. 10 - 14), area constraints (eqs. 15 - 20), equipment orientation, non-overlapping and layout constraints (Patsiatzis and Papageorgiou, 2003).

4. Case study

For the case study, a Crude Distillation plant with preheating train (CDU plant) was simulated with Aspen HYSYS® v8.0. It consisted of a total of 17 units, 5 of which - pre-flash drum (unit 5), atmospheric distillation tower (unit 7), fired heaters 1 and 2 (unit 6 and 12), and debutaniser (unit 15) - exceeded the floor height of 5m. The process flow diagram of the plant is shown in Figure 1 and data on the equipment dimensions, connectivity and construction costs were evaluated from results from the simulation. 7 floors (K) were made available for layout, with land cost LC , fixed

floor construction cost $FC1$ and area dependent cost $FC2$ as 666rmu^1 , $3,330\text{rmu}$ and 33.3rmu respectively. All multi-floor equipment were made to start from the ground floor as such represents a realistic representation from a construction point of view. The summary of the model statistics and computational performance is shown in Table 1 and the optimal layout in Figure 2.

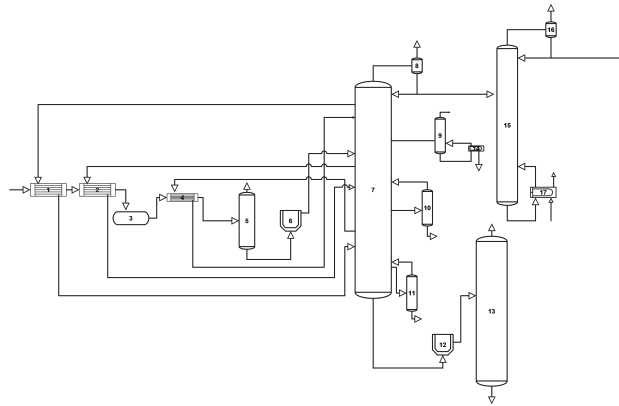


Figure 1: Flow diagram of Crude Distillation Plant with Preheating train

Table 1: Summary of model statistics and computational performance

CDU Plant (17 units)	
Total cost (rmu)	749,690
CPU (s)	105.0
Number of binary variables	568
Number of continuous variables	1,388
Number of equations	2,993

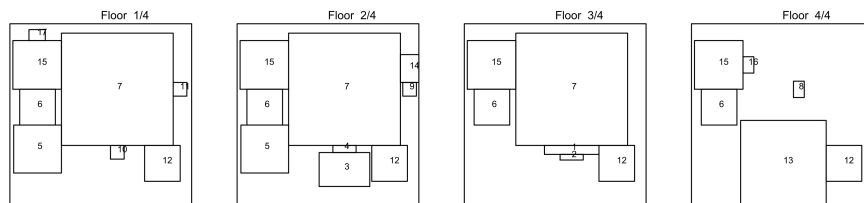


Figure 2: Optimal layout results

The results obtained gave a total of 4 floors, out of an available 7, with each measuring $20\text{m} \times 20\text{m}$ (Figure 2). A total cost of $749,690\text{rmu}$ was obtained (Table 1) - 6% attributed to connection costs, 50% pumping costs and 44% construction costs - consistent with previous observations (Patsiatzis and Papageorgiou, 2003). As all the multi-floor equipment (5, 6, 7, 12 and 15) starting floors were predefined, they all started from the first floor through the number of floors required based on their height. It is worthy of noting that although equipment 14 required 5 floors based on

¹relative monetary units

its height, a total of 4 floors was decided. This is because the construction of a fifth floor was deemed unnecessary as no other equipment other than equipment 14 was to be located on such floor in order to obtain an optimal solution, and the additional construction cost for a fifth floor was eliminated. So, although a multi-floor equipment can span a specified number of floors based on its height, not every one of those floors need to be constructed. Practical examples include multi-floor layouts about fired heaters with long stacks, distillation columns and flare stacks.

5. Concluding remarks

The process plant layout MILP model by Patsiatzis and Papageorgiou (2003) was extended to address a larger problem scale with multi-floor equipment in chemical process plants having varying connection points along their height. The new model proposed allowed multi-floor equipment start on a floor to be determined and span successive floors equivalent to the height of the equipment. Connection points on each equipment were at heights unique to the problem being solved. The model was validated with a CDU plant case study and model performance noted. The CDU plant had a total of 17 major equipment with 5 multi-floor units, and 7 floors made available for layout. A global optimum was achieved in 105s selecting 4 out of 7 floors with a floor area of 20mx20m. The model successfully handled multi-floor equipment, allowing their placement in successive floors equivalent to their height. Each floor was constructed on the basis of its use by non-multi-floor equipment, as such is obtainable in practice. Further work will entail model validation with larger case studies and the development of decomposition techniques.

Acknowledgement

JOE gratefully acknowledges the financial support of the Petroleum Technology Development Fund (PTDF); and the Centre for Process Systems Engineering.

References

- A. P. Barbosa-Póvoa, R. Mateus, A. Q. Novais, 2002. Optimal 3D layout of industrial facilities. *International Journal of Production Research* 40 (7), 1669–1698.
- M. C. Georgiadis, S. Macchietto, 1997. Layout of Process Plants: Approach A Novel. *Computers & Chemical Engineering* 21, 337–342.
- R. Guirardello, R. E. Swaney, 2005. Optimization of process plant layout with pipe routing. *Computers & Chemical Engineering* 30 (1), 99–114.
- S. Jung, 2016. Facility siting and layout optimization based on process safety. *Korean Journal of Chemical Engineering* 33 (1), 1–7.
- N.-K. Ku, J.-H. Hwang, J.-C. Lee, M.-I. Roh, K.-Y. Lee, 2013. Optimal module layout for a generic offshore LNG liquefaction process of LNG-FPSO. *Ships and Offshore Structures* 9 (3), 311–332.
- S. Moran, 2016. *Process Plant Layout*. Butterworth-Heinemann.
- L. G. Papageorgiou, G. E. Rotstein, 1998. Continuous-domain mathematical models for optimal process plant layout. *Industrial & Engineering Chemistry Research* 37 (9), 3631–3639.
- D. I. Patsiatzis, L. G. Papageorgiou, 2003. Efficient Solution Approaches for the Multifloor Process Plant Layout Problem. *Industrial & Engineering Chemistry Research* 42, 811–824.
- F. D. Penteado, A. R. Ciric, 1996. An MINLP Approach for Safe Process Plant Layout. *Industrial & Engineering Chemistry Research* 35 (4), 1354–1361.
- P. Xin, F. Khan, S. Ahmed, 2016. Layout Optimization of a Floating Liquefied Natural Gas Facility Using Inherent Safety Principles. *Journal of Offshore Mechanics and Arctic Engineering* 138 (4), 041602.
- G. Xu, L. G. Papageorgiou, 2009. Process plant layout using an improvement-type algorithm. *Chemical Engineering Research and Design* 87 (6), 780–788.

Feasibility study of using reactive distillation for the production of renewable aviation fuel

Maritza Lisette Soria-Ornelas^a, Claudia Gutiérrez-Antonio^{a*}, Fernando Israel Gómez-Castro^b, Salvador Hernández^b

^a*Facultad de Química, Universidad Autónoma de Querétaro, Cerro de las Campanas s/n, Las Campanas, Querétaro, Querétaro, 76010, México*

^b*Departamento de Ingeniería Química, División de Ciencias Naturales y Exactas, Campus Guanajuato, Universidad de Guanajuato, Noria Alta s/n, Guanajuato, Guanajuato, 36050, México*

claugtez@gmail.com

Abstract

The forecast indicates that aviation sector will grow 4.8% each year, until 2036; which means that more fuel will be required and more carbon dioxide will be released. Therefore, the International Air Transport Association has identified the renewable aviation fuel as the most promissory alternative for the sustainable development of the sector. The renewable aviation fuel can be obtained by triglycerides hydroprocessing, which consists on deoxygenation, cracking/isomerization and purification. Regarding this process, researchers have been focused on the determination of the yield to biojet fuel of different raw materials, the development of more selective and multifunctional catalysts, and the proposal of strategies to reduce energy consumption. In particular, the decreasing in energy consumption has been addressed through energy integration and thermally coupled distillation sequences. However, one alternative that remains as an opportunity area is the use of reactive distillation. Therefore, in this work the feasibility of using this intensified strategy in the hydrotreating process is presented. The design of the reactive distillation column is performed through recursive simulation, since the reactive system is multicomponent and multireaction. The conventional hydrotreating process is compared with the intensified one, in terms of total annual costs, CO₂ emissions and biojet fuel price. Results show that renewable aviation fuel can be produced through reactive distillation, with a slightly increasing of 1% in the yield and a decreasing of 87% in the operation pressure, in comparison with the conventional process. Also, the profitability of the process can be increased in 7,188 USD/year, due to the electricity required in the process is generated along with an excess.

Keywords: reactive distillation, biojet fuel, hydroprocessing.

1. Introduction

Aviation sector is forecasted to grow up at 4.8% per year until 2036 (Gutiérrez-Antonio et al., 2016a); this will mean at least doubling the fuel requirements in 2036, and also an increasing in CO₂ emissions. In this context, the International Air Transport Association has identified the renewable aviation fuel as the best alternative to significantly reduce the CO₂ emissions of aviation sector (IATA, 2009). Renewable aviation fuel, or biojet fuel, consists of hydrocarbons in the boiling point range of C₈-C₁₆, including paraffinic and naphthenic compounds. It can contain aromatic compounds, depending of the

production process; the absence of these compounds does not affect the properties of the fuel, but may cause leaks from the fuel tanks. Thus, the standard ASTM D7566 (2016) establishes the use of biojet fuel in mixtures until 50% in volume. Biojet fuel can be obtained from any type of biomass for different processing routes (Gutiérrez-Antonio et al., 2017). One of the most advanced and mature technologies is the hydroprocessing of triglyceride feedstock, which consists on hydrodeoxygenation, followed by hydroisomerization and hydrocracking (McCall et al., 2009). As result, light gases, naphtha, biojet fuel and green diesel are obtained. These renewable hydrocarbons are separated through distillation. Several works have studied the reduction in energy consumption of hydroprocessing. Thermally coupled distillation columns with energy integration have been proposed considering *jatropha curcas*, castor and microalgae oils (Gutiérrez-Antonio et al., 2013; 2015, 2016a, 2016b). Recently, reactive distillation for green diesel production has been reported (Perez-Cisneros et al., 2017); however, the use of reactive distillation columns for biojet fuel production remains as an opportunity area. Therefore, in this work the use of reactive distillation is proposed to intensify the hydrotreating process; *jatropha curcas* oil is used as renewable raw material. Conventional and intensified biojet fuel production processes are compared in terms of total annual costs, CO₂ emissions and biojet fuel price.

2. Modelling of conventional hydrotreating processes

The conventional hydroprocessing consists of hydrodeoxygenation reactor, hydroisomerization/hydrocracking reactor and purification train. The modelling of this process was presented by Gutiérrez-Antonio et al. (2016a), and the reported results are taken as baseline for comparison. A brief description of the modelling is presented. A flow stream of 100 kg/h of *jatropha curcas* oil is considered, which composition in %wt is: triolein (42), trilinolein (44), tripalmitin (11) and tristearine (3%) (Herrera, 2007). Moreover, a hydrogen flow of 1500 mL NPT H₂/mL of vegetable oil is used, in order to avoid coke formation (McCall et al., 2009). The hydrodeoxygenation reactions are described with the kinetic model reported by Sharma et al. (2012), at 320 °C and 80 bar:

$$C_L = \frac{-k_1}{k'} C_{tg0} (e^{-k't} - 1) \rightarrow \frac{dC_L}{dt} = -k_1 C_{tg} \quad (1)$$

$$C_J = \frac{-k_2}{k'} C_{tg0} (e^{-k't} - 1) \rightarrow \frac{dC_J}{dt} = -k_2 C_{tg} \quad (2)$$

$$C_H = \frac{-k_3}{k'} C_{tg0} (e^{-k't} - 1) \rightarrow \frac{dC_H}{dt} = -k_3 C_{tg} \quad (3)$$

$$C_P = \frac{-k_4}{k'} C_{tg0} (e^{-k't} - 1) \rightarrow \frac{dC_P}{dt} = -k_4 C_{tg} \quad (4)$$

Where C_{tg} , C_{tg0} , C_L , C_J , C_H and C_P are the concentration of triglycerides, initial triglycerides, light compounds (C5–C8), intermediate compounds (C9–C14), heavy compounds (C15–C18), and oligomerized compounds (>C18), respectively; the values of the kinetic constants are k' (14.35), k_1 (0.04), k_2 (0.11), k_3 (1.24) and k_4 (13.25). The effluent of the first reactor is hydrocracked and hydroisomerized at 480 °C and 80 bar. For the hydrocracking we used the kinetic model developed by Shayegh et al. (2012):

$$\frac{dC_{VGO}}{dt} = -k_{12}C_{VGO}^2 - k_{13}C_{VGO}^2 \quad (5)$$

$$\frac{dC_{gasoline}}{dt} = -k_{12}C_{VGO}^2 - k_{23}C_{gasoline} \quad (6)$$

$$\frac{dC_{GL}}{dt} = -k_{13}C_{VGO}^2 - k_{23}C_{gasoline} \quad (7)$$

Where C_{VGO} , $C_{gasoline}$ and C_{GL} are the concentration of vacuum gas oil (C19–C21), n and iso-paraffins (C5–C11), and light gases (C1–C4), respectively; k_{12} (16,401,205,675), k_{13} (33,040,947,364), and k_{23} (74.13) are the values of the kinetic constants. For the hydroisomerization, the kinetic modeling of Calemma et al. (2000) is considered:

$$\frac{dC_{isoparaffins}}{dt} = k_2 C_{paraffins} \quad (8)$$

Where $C_{isoparaffins}$ and $C_{paraffins}$ are the concentrations of isoparaffins and paraffins, respectively; and k_2 (0.00239 min^{-1}) is the kinetic constant. Both reactors are modeled in the RPlug module of Aspen Plus. The kinetic constants values are reported at a fixed temperature, where the maximum yield to biojet fuel is obtained; also, kinetic models are used in the form reported by their authors (Sharma et al., 2012; Shayeg et al., 2012, Calemma et al., 2000). From the reactive zone, light gases, naphtha, biojet fuel and green diesel are obtained, which are separated through a direct conventional distillation sequence, since it presented the lower energy consumption (Gutiérrez-Antonio et al., 2016a). The design is performed with DSTW module, with recoveries of 99% of the key components. The distillation scheme is simulated in Radfrac module assuming equilibrium stages. Additionally, the conditioning of both reactants is performed through pump, compressor and heat exchangers in order to be fed to the first reactor; the effluent of the second reactor is conditioning with a turbine to generate electricity in the process. Figure 1 shows the conventional hydrotreating process.

3. Modelling of intensified hydrotreating process

As mentioned before, the intensification between the isomerization/cracking reactor is proposed in this work, and the kinetic models described in section 2 are used. Since we have a multicomponent system with multiple reactions, recursive simulations are used. Manipulated variables were operation pressure, number of reactive stages, number of separation stages, reflux ratio, feed stage of reactants, condenser type and temperature of feed flow streams. Figure 2 shows the intensified hydrotreating process. Both hydrotreating processes are compared in terms of three parameters. The first one is the total annual cost, where capital costs are calculated with the Guthrie method (Turton et al., 2008):

$$\text{Total annual cost (TAC)} = \text{Annual operating cost} + \text{Annual capital cost} \quad (9)$$

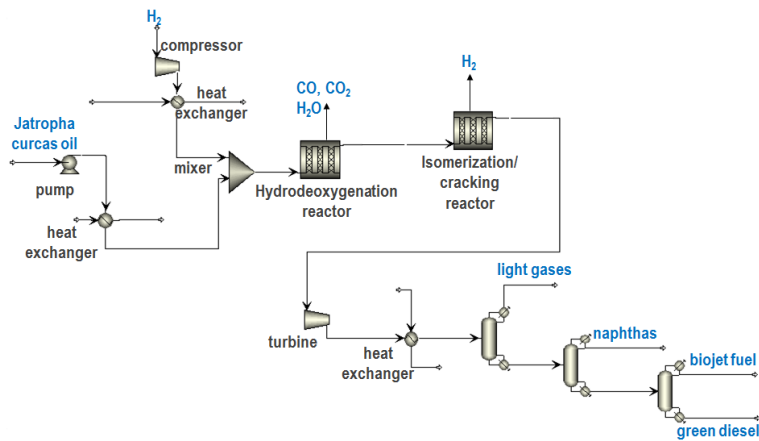


Figure 1. Conventional hydrotreating process to produce biojet fuel

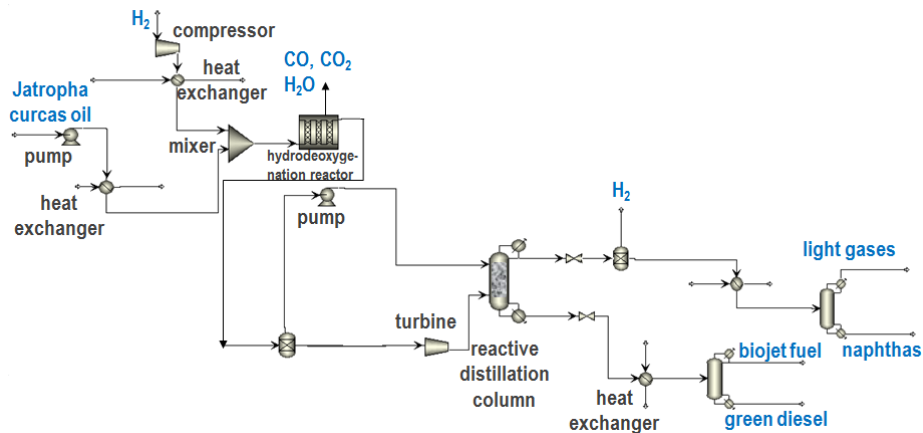


Figure 2. Intensified hydrotreating process to produce biojet fuel

The second parameter is given by the CO₂ emissions due to steam and electricity generation, which are calculated with emission factors and the amount of used fuel. The emission factor for steam production is 2.15 kg CO₂/kg burned fuel, while for electricity generation is 0.166 kg CO₂/kWh (Gutiérrez-Antonio et al. 2016a). Finally, the estimation of the price of the products is realized with the methodology proposed by Gutiérrez-Antonio et al. (2016b), where the mass fraction of each product along with its price and density are employed.

4. Analysis of results

In this section the analysis of the results is presented. Table 1 shows the total annual costs, and biojet fuel prices, while Table 2 presents the CO₂ emissions for both conventional (CHP) and intensified (IHP) hydrotreating processes. The raw material cost is 4,470,116.82 USD/year for both hydrotreating processes.

Table 1. Equipment, services, electricity and total annual costs (TAC), USD/year, and biojet fuel price (BJ price), USD/L, for both hydrotreating processes.

Process	Equipment	Services	Electricity	Excess energy	TAC	BJ price
CHP	234,017.41	27,670.93	2,087.39	0	4,751,742.59	0.689
IHP	191,115.13	359,712.31	0	5,101.03	5,020,944.16	0.728

Table 2. CO₂ emissions (kg/year) in hydrotreating processes.

Process	Emissions due to vapour generation	Emission due to electricity	Total generated emissions	Saved emissions
CHP	286,458,714.13	8,692.48	286,467,406.6	0
IHP	295,031,520.66	0	295,031,520.66	6,037.73

According to Table 1 we can observe that the total annual cost of the conventional processes is 5.3% lower than the one of the intensified process; as consequence, a similar difference can be found in the biojet fuel price. However, an interesting finding is that the intensified process is self-sufficient with respect to the electricity required. Indeed, an excess of energy is produced, which can be sold generating a potential gain of 5,101.03 USD/year. Also, it can be noted that CO₂ emissions are lower in the conventional process, in spite that the excess energy allows avoiding the emission of 6,037.73 kg CO₂/year. Nevertheless, according to the simulation data the reactive distillation column operates at 10 atm, which means a significantly decreasing with respect to the pressure in the second reactor of the conventional process. Other authors have reported processes in which reactive distillation schemes are integrated operate at lower pressures compared to conventional processes (Rosales-Quintero et al., 2008). However, this result is obtained in a simulation environment; therefore, experimental validation is required. Also, an increase of 1% in the yield to biojet fuel was observed when the reactive distillation column is used. The reactive distillation column includes a total condenser, 13 total stages with a reactive section of 7 stages.

5. Conclusions

A feasibility study for the intensification of the hydrotreating process between the isomerization/cracking reactor and the first distillation column of the separation train has been presented. The intensified process is compared with the conventional one. Results shows that is feasible to perform the intensification of the hydroprocessing through reactive distillation; however, from the economic and environmental point of view the conventional hydroprocessing is slightly better, in spite of excess electricity is generated.

Acknowledgments

Financial support provided by CONACyT, grants 239765 and 279753, is acknowledged.

References

- ASTM Standard D7566, 2016, Standard Specification for Aviation Turbine Fuel Containing Synthesized Hydrocarbons, DOI: 10.1520/D7566-14A, www.astm.org
- V. Calemma, S. Peratello, C. Perego, 2000, Hydroisomerization and hydrocracking of long chain n-alkanes on Pt / amorphous SiO₂ – Al₂O₃ catalyst, *Applied Catalysis*; 190, 207–218.
- C. Gutiérrez-Antonio, F. I. Gómez-Castro, J. G. Segovia-Hernández, and A. Briones-Ramírez, 2013, Simulation and optimization of a biojet fuel production process, *Computer Aided Process Engineering*, 32, 13-18.
- C. Gutiérrez-Antonio, F. I. Gómez-Castro, S. Hernández, and A. Briones-Ramírez, 2015, Intensification of a hydrotreating process to produce biojet fuel using thermally coupled distillation, *Chemical Engineering and Processing: Process Intensification*, 88, 29–36.
- C. Gutiérrez-Antonio, F.I. Gómez-Castro, A.G. Romero-Izquierdo, S. Hernández, 2016a, Energy integration of a hydrotreating process for the production of biojet fuel, *Computer Aided Process Engineering*, 38, 127–132.
- C. Gutiérrez-Antonio, A.G. Romero-Izquierdo, F.I. Gómez-Castro, S. Hernández, A. Briones-Ramírez, 2016b, Simultaneous energy integration and intensification of the hydrotreating process to produce biojet fuel from *Jatropha curcas*, *Chemical Engineering and Processing: Process Intensification*, 110, 134–145.
- C. Gutiérrez-Antonio, F.I. Gómez-Castro, J.A. de Lira-Flores, S. Hernández, 2017, A review on the production processes of renewable jet fuel, *Renewable and Sustainable Energy Reviews*, 79, 709–729.
- J. Herrera-Martínez, 2007, Experiencia con *Jatropha Curcas* L. en México, IPN.
- International Air Transport Association, 2009, A global approach to reducing aviation emissions – First step: carbon neutral growth from 2020, 8 pp, www.iata.org
- M.J. McCall, T.L. Marker, R.E. Marinangeli, J.A. Kocal, 2009, Production of aviation fuel from renewable feedstocks, Patent No. US 8,039,682 B2.
- E. S. Perez-Cisneros, M. Sales-Cruz, R. Lobo-Oehmichen, T. Viveros-García, 2017, A reactive distillation process for co-hydrotreating of non-edible vegetable oils and petro-diesel blends to produce green diesel fuel, *Computers and Chemical Engineering*, 105, 105-122.
- A. Rosales-Quintero, F. D. Vargas-Villamil, E. Arce-Medina, 2008, Sensitivity analysis of a light gas oil deep hydrodesulfurization process via catalytic distillation, *Catalysis Today*, 130, 509-518.
- R. K. Sharma, M. Anand, B.S. Rana, R. Kumar, S.A. Farooqui, M.G. Sibi, A.K. Sinha, 2012, *Jatropha*-oil conversion to liquid hydrocarbon fuels using mesoporous titanasilicate supported sulfide catalysts, *Catalysis Today*, 198(1), 314–320.
- F. Shayegh, A. Farshi, A. Dehghan, 2012, A Kinetics Lumped Model for VGO Catalytic Cracking in a Fluidized Bed Reactor, *Petroleum Science Technology*, 30(9), 945–957.
- R. Turton, R. Bailie, W. Whiting, J. Shaeiwitz, 2008, *Analysis, Synthesis and Design of Chemical Processes*, Prentice Hall International Series, 4th Edition.

Extended Value Chain Synthesis towards the Design of Multi-Feedstock Algae Biorefineries

Melina Psycha, Maria Kapnisi, Antonis C. Kokossis

School of Chemical Engineering, National Technical University of Athens, Zografou Campus, 9, Iroon Polytechniou Str., GR-15780 Athens, Greece

akokossis@mail.ntua.gr

Abstract

The work focuses on broadening the scope beyond the state-of-the-art and deals with more complicated concepts in the field of algae biorefineries. A general methodology is analyzed targeting the design of multi-feedstock biorefineries, thus providing flexibility in terms of feedstock and products. For this purpose, three microalgae are introduced as potential feedstock (Dunaliella, Nannochloropsis and Haematococcus), which individually are commercialized for the unique high-value compounds they have to offer (β -carotene, ω -3 fatty acids and astaxanthin respectively). The integration of their value chain identifies the similarities and differences between these microalgae in terms of prospective compounds rendering the formulation of the product portfolio an important degree of freedom.

Keywords: flexible biorefineries, value chain, synthesis, algae, design.

1. Introduction

The merits of microalgae as an alternative source of biomass are well established over the years, especially because of their versatility in terms of products. This potential in addition to the utilization of carbon dioxide, which microalgae need for their growth, render the development of a large-scale application extremely promising either as a standalone venture or in integration with other plants. Specifically, the co-production of specialty chemicals from microalgae is gaining ground as the related markets expand and profit margins grow (García Prieto et al., 2017; Psycha et al., 2014)). A plethora of microalgae has been studied and researched, especially for applications in the pharmaceutical, nutraceutical and cosmetic sector (Chua and Schenk, 2017; Panis and Rosales Carreon, 2016).

The challenges related to the design of algae-based systems are numerous which are enhanced by the lack of industrial applications in this field. The present work focuses on broadening the scope beyond the state-of-the-art and addresses the challenges of designing multi-feedstock microalgae biorefineries by capitalizing on previous research on single-feedstock microalgae biorefineries (Psycha and Kokossis, 2016, 2017). This paper proposes a flexible microalga biorefinery to deal with more complicated concepts in this field (competitive chemistries between microalgal species, seasonality for cultivation, advanced technologies, volatile markets for specialty chemicals).

2. Methodology

2.1. Formulation of value chains

The selection of suitable algae strains is a challenging task that requires extensive knowledge and/or research regarding the respective value chains. The different strains must share characteristics and properties in terms of treatment and group of products. For instance, the production of biodiesel from algae requires fundamentally unlike processing than the recovery of chemicals (commodity and specialty). Specifically, the recovery of specialty chemicals of high market value has already been highlighted in this paper and constitutes a significant criterion for the presented methodology. Figure 1a illustrates two value chains of microalgae A and B as a generic approach to the problem.

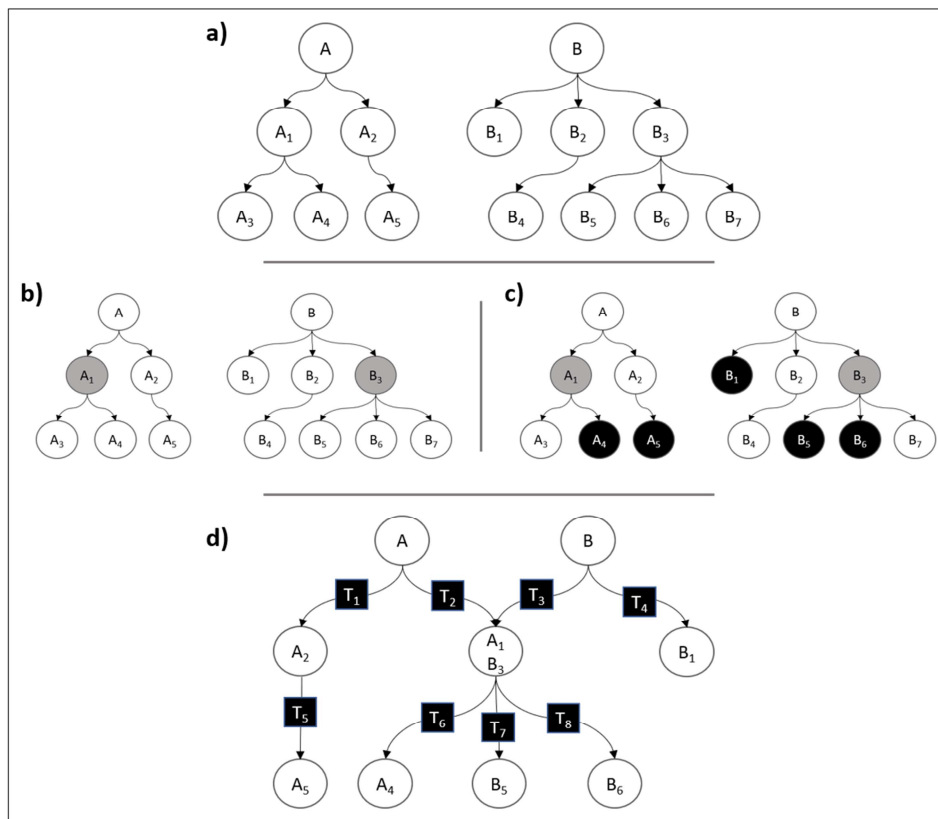


Figure 1: Graphical representation of general methodology

2.2. Identification of common fractions

The fractions are directly extracted from the cells and each fraction represents a group of products and/or a single product. For instance, the fraction of carotenoids can be further divided into carotenes and xanthophylls, while the fraction of glycerol is a product by itself. Depending on the synthesis of the product portfolio, one can set as

end-product any intermediate of the value chain. These intermediates are considered mixtures of chemicals which are further separated into pure end-products.

The main fractions are proteins, lipids, carbohydrates and carotenoids. A plethora of components can be found in each fraction and they vary depending on the algal strain. Thus, different products can be recovered from the same fraction among different strains. Figure 1b shows the identification of the common fractions among algae A and B and demonstrates the variety of end-products from the same fraction.

2.3. Product portfolio customization

The finalization of the product portfolios requires knowledge regarding yields and market prices of the potential end-products. The product portfolios are formulated for each strain separately, since the need for mutual products among the strains is not important, which is not the case for the fractions as explained in the previous section. Thus, the product selection has to be carried out with respect to every single strain and the number of products is a matter of synthesis decision. Figure 1c shows the selection of the final products for each value chain with three of these products deriving from the indicated common fraction (A_4 , B_5 and B_6).

2.4. Integrated value chain

The final step is the combination of the different value chains into one integrated value chain. As depicted in Figure 1d, only the selected fractions and products are incorporated into the final value chain. For instance, the product A_3 is not included, since it was not selected; the fraction A_2 is part of the integrated value chain, even though it was not characterized as a common fraction because product A_5 (deriving from fraction A_2) is part of strain A product portfolio as shown in Figure 1c. Consequently, suitable technologies need to be used for the extraction of fractions from the algal cells and for further separating these fractions into the desired products.

3. Comparison study

3.1. Biorefineries of single strains

Three algae strains have been selected in the context of this study, *Dunaliella*, *Haematococcus* and *Nannochloropsis*. All are characterized by a target product and include high-value specialty chemicals in the value chain. Specifically, *Dunaliella* is well established for its β -carotene production, *Haematococcus* for the production of astaxanthin and *Nannochloropsis* for the accumulation of large amounts of lipids. Additional products are taken into account for each case and the corresponding flowsheets of the three biorefineries are shown in Figure 2.

Table 1 lists the costs (capital and operating) as well as the revenue for each plant. The costing estimations derive from a combination of known costing equations (Lang, 1947) and the commercial software Aspen Process Economic Analyzer v8.4, which offers valuable information regarding the sizing of equipment. The target products play the leading role in the revenue of the biorefinery; β -carotene corresponds to 94% of the revenue, astaxanthin to 80%, whereas in the case of *Nannochloropsis*, proteins and violaxanthin correspond to 90% in total. It is worth mentioning that lipids from *Nannochloropsis* do not yield high revenue and render that biorefinery less promising as observed by the numbers in Table 1.

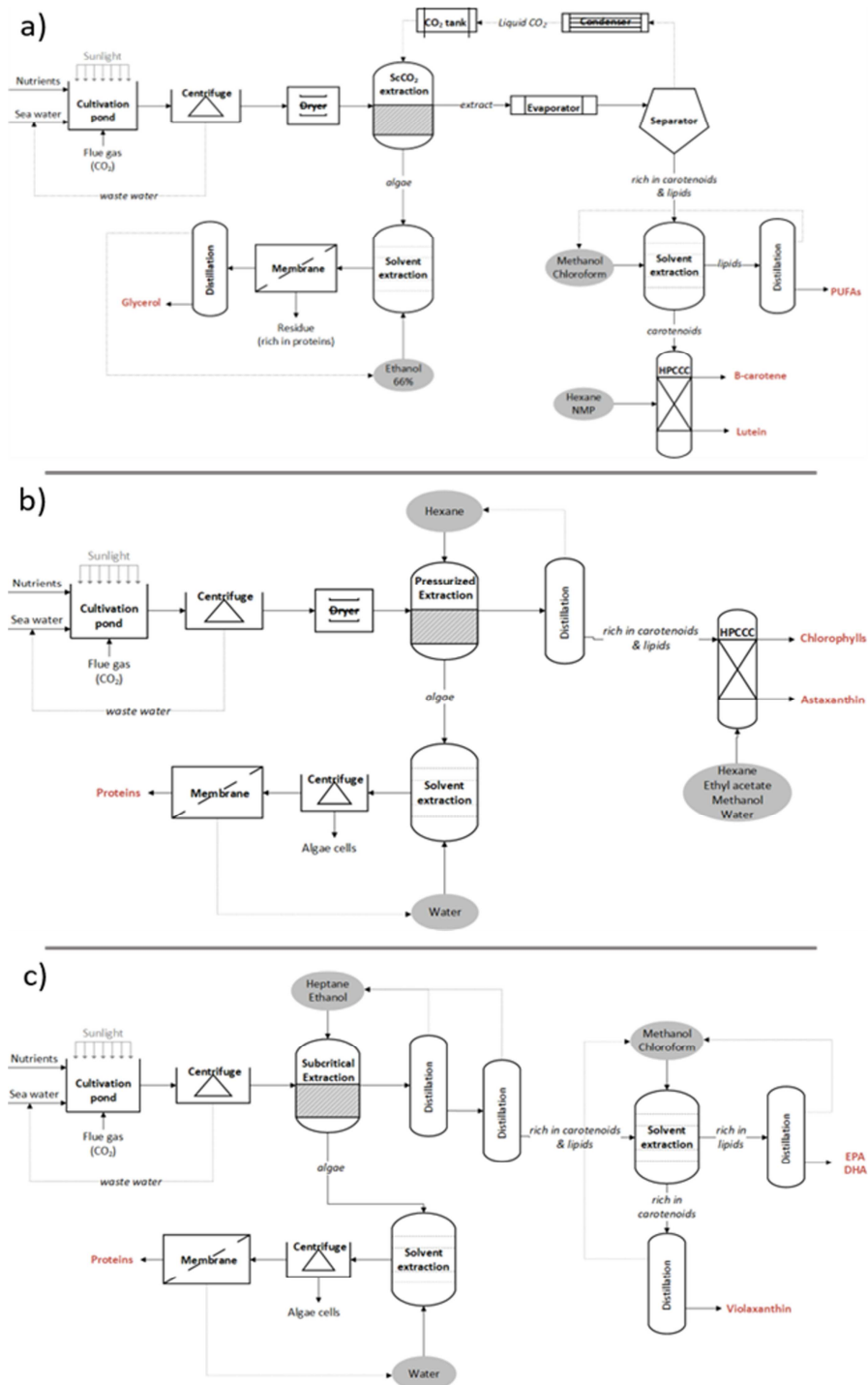


Figure 2: Conceptual flowsheets of three plants – a) *Dunaliella* biorefinery; b) *Haematococcus* biorefinery; c) *Nannochloropsis* biorefinery

Table 1: Economics of the three biorefinery plants

	Dunaliella biorefinery	Haematococcus biorefinery	Nannochloropsis biorefinery
Capital cost (M\$)	89	80	96.7
Operating cost (M\$/y)	31.2	25.7	35.1
Revenue (M\$/y)	126.6	108	44.2
Number of products	4	3	3

3.2. Flexible biorefinery of multiple strains

Following the methodology presented in this paper, the integrated value chain of Figure 3 is constructed, which relates to the three algal strains studied in the previous section (Dunaliella, Haematococcus, Nannochloropsis). The final products are indicated and derive from the common fractions of the different strains. As shown in Figure 3, proteins are produced by both Haematococcus and Nannochloropsis and it is considered the only mutual product in this case.

The biorefinery presented in Figure 4 is characterized by flexibility in terms of feedstock and products, thus attempting to overcome difficulties related to market uncertainties. The proposed flexible biorefinery has the potential of minimum 10 products and the employed technologies overlap by 83% compared to the single-feedstock biorefineries. The capital investment of such a venture is estimated at 128 M\$, a small increase considering the enhancement of the biorefinery potential. Especially in the case of microalgae biorefineries, CAPEX holds a predominant place, as reported by Psycha and Kokossis (2017). By integrating three candidate plants, the proposed biorefinery copes with high CAPEX demands and introduces the concept of flexibility in the field of microalgae biorefineries.

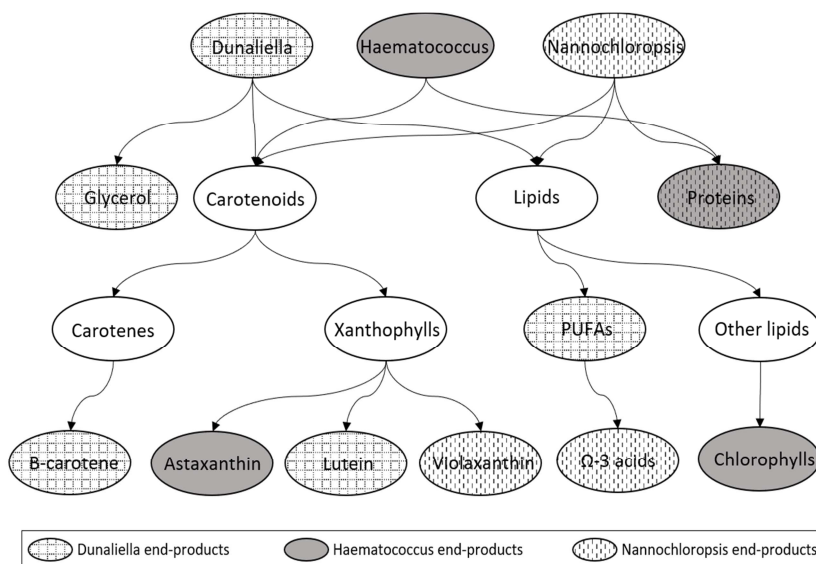


Figure 3: Integrated value chain of a multi-feedstock biorefinery

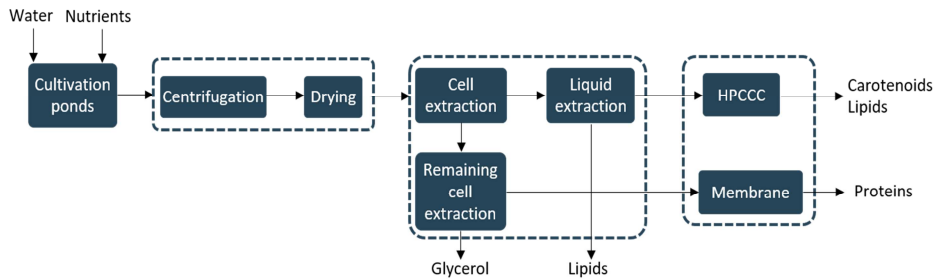


Figure 4: Processing stages of the flexible algal biorefinery

4. Conclusions

The present work attempts to address challenges related to the design of algae biorefineries by introducing the novel concept of the flexible alga biorefinery. A generic methodology for the development of integrated value chains is analysed, and three algae strains are used as a case study. With a process overlap of 83%, the resulting biorefinery is flexible in terms of feedstock and products and overcomes difficulties related to market uncertainties. Furthermore, the biorefinery potential enhances with a small increase in total investment. More research is required focusing on the predictability of operation and the study of different strains and potential products.

References

- C.V. García Prieto, F.D. Ramos, V. Estrada, M.A. Villar, M.S. Diaz, 2017, Optimization of an Integrated Algae-based Biorefinery for the Production of Biodiesel, Astaxanthin and PHB, *Energy*, 139, 1159-1172
- E.T.Chua, P.M. Schenk, 2017, A Biorefinery for Nannochloropsis: Induction, Harvesting, and Extraction of EPA-rich Oil and High-value Protein, *Bioresource Technology*, 244, 2, 1416-1424
- G. Panis, J. Rosales Carreon, 2016, Commercial Astaxanthin Production Derived by Green Alga *Haematococcus pluvialis*: A Microalgae Process Model and a Techno-economic Assessment all through Production Line, *Algal Research*, 18, 175-190
- H.J. Lang, 1947, Cost Relationships in Preliminary Cost Estimation, *Chemical Engineering*, 54, 117-121
- M. Psycha, A.C. Kokossis, 2016, Synthesis and Optimization of Microalgae Biorefineries, *Computer Aided Chemical Engineering*, 38, 325-330
- M. Psycha, A.C. Kokossis, 2017, Techno-economic Evaluation of an Integrated Microalga Biorefinery Targeting the Co-production of Specialty Chemicals, *Computer Aided Chemical Engineering*, 40, 1981-1986
- M. Psycha, K. Pyrgakis, A.C. Kokossis, 2014, Process Design Analysis for the Valorization and Selection of Integrated Micro-algae Biorefineries, *Computer Aided Chemical Engineering*, 33, 1543-1548

Selection of fractionation pathways and intermediates for mixed consumer products

Alberto Castiglioni^a, Jochem Jonkman^{a,*}, Renzo Akkerman^a, Albert van der Padt^{b,c}

^a *Operations Research and Logistics Group, Wageningen University, P.O. Box 8130, 6700 EW, Wageningen, The Netherlands*

^b *Food Process Engineering Group, Wageningen University, P.O. Box 8129, 6700 EV, Wageningen, The Netherlands*

^c *FrieslandCampina, Stationsplein 4, 3818 LE, Amersfoort, The Netherlands*

jochem.jonkman@wur.nl

Abstract

Mixed consumer products, such as cosmetics and foods, normally consist of a mixture of intermediates. Most of these intermediates are currently produced by fractionation, a rather complex process where multiple intermediates are obtained from a single raw material, often focused on high purity. These intermediates can subsequently be combined to satisfy demand and quality requirements. The chemical purity of intermediates is, however, not always necessary, and mild fractionation of raw materials is often sufficient. Therefore, we propose an optimization-based decision support framework to select cost-efficient fractionation pathways and intermediates. We illustrate our approach for the processing of lupin seeds and yellow peas, and investigate mild fractionation as a more resource-efficient way of producing intermediates for mixed consumer products. The results show that, if only few intermediates are used, high purity is needed to comply with the quality requirements of a broad range of final applications. If more intermediates can be used, mildly refined intermediates can be selected to cover the demand of a part of the products with resource savings. In our illustrative case, using eight instead of four intermediates leads to water and energy reduction of about 29 % and 28 %, respectively. In general, our results indicate that using fractionation pathways leading to intermediates with lower purity provides opportunities for more resource-efficient production, and similar opportunities are expected to exist in integrated product and process design for other mixed consumer products.

Keywords: optimization, product selection, mild fractionation, process selection

1. Problem description

Consumer products such as cosmetics and foods are often a blend of intermediates. The production of these intermediates can be resource intensive due to a focus on purity, with the aim to guarantee a standard quality and broad applicability (van der Goot et al., 2016). Generally, there is a reduction in yield and an increase in the resources required to refine a raw material into intermediates with a higher degree of purity (Tamayo Tenorio et al., 2017). However, the purity of intermediates is often not required for application in mixed products. The functionality of products does not only depend on a single pure component, but is expressed in the complex composition of different

components with their native functionality (Geerts et al., 2017). Therefore, applying mild fractionation and using less-refined intermediates could improve resource efficiency (Berghout et al., 2015).

However, for an intermediate producer, the selection of the set of intermediates is not straightforward. Intermediates to produce a variety of mixed products, need to be selected in such a way that these products could be made while minimising costs and resource consumption. Additionally, the divergent nature of fractionation pathways inherently leads to the production of multiple intermediates that all have to be valorized (Jonkman et al., 2015).

This paper provides an optimization-based decision support framework for the selection of raw materials, fractionation pathways, as well as its associated intermediates. Producers of intermediates can use this framework to improve their integrated product and process design.

2. Decision support framework

A producer of intermediates has to decide how to meet customer demands based on product specifications resulting from the final application in which the intermediate is used. The intermediate producer must select the materials and the fractionation pathways required to produce intermediates that can be used to make products according to customer requirements. Intermediates can be used directly in the fulfillment of customer requirements, but can also be blended. Figure 1 illustrates the producer's decision problem.

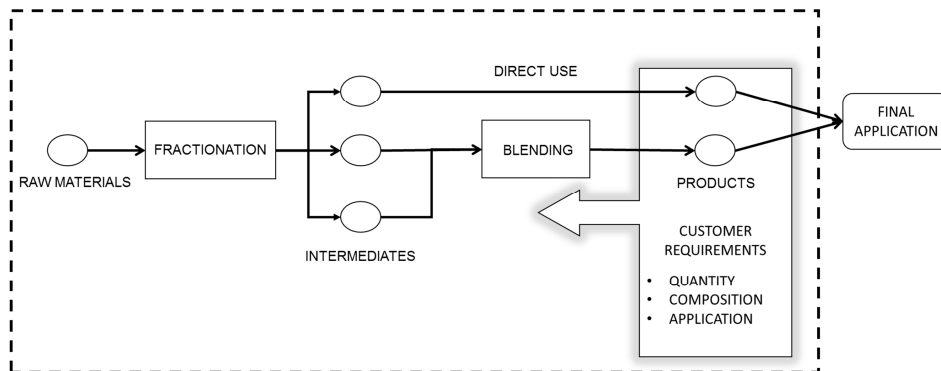


Figure 1. Fractionation system with boundaries for the intermediates producer

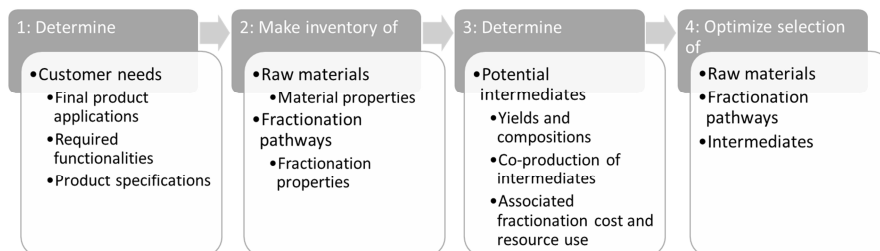


Figure 2. Decision support framework

To support this decision, we propose the approach as presented in Figure 2. The first stage of the approach is focussed on determining the needs of the different customers and should lead to insight in the final application of the intermediate, the required functionality, and a description of the properties the intermediate should have. In the second stage, the intermediate producer has to create an inventory of the possible raw materials and fractionation pathways to use, and identify the properties of these materials and pathways. This information is combined in the third stage, leading to a set of potential intermediates with associated properties, co-production relationships, and fractionation costs. In the fourth stage, an optimization model is used to select the combination of raw materials, fractionation pathways, and intermediates that satisfies the demand of the customers, while minimizing the total raw material and production (i.e. fractionation and blending) costs.

The formulation of the optimization model used in the fourth stage is based on the work of Akkerman et al. (2010). Due to space limitations, we do not include our complete model, but limit ourselves to a brief discussion of the changes we made to the original model. Their model is extended to allow for (i) the selection of different fractionation pathways; (ii) the consideration of co-production of intermediates in intermediate portfolios, including related material balance relationships; and (iii) the consideration of the resource consumption of water and energy.

3. Case study

In this section, we illustrate our decision support framework with an example from the food industry. We use the illustration to investigate the potential benefits of selecting mild-refined intermediates. Our case considers an intermediate producer conventionally focused on producing protein-rich intermediates for its customers, using yellow peas (*Pisum sativum*) and lupin seeds (*Lupinus angustifolius*) as raw materials.

3.1. Description and data

The customers demand protein-rich intermediates for applications in products that can be grouped into categories, such as solid and liquid foods, nutraceuticals and supplements, and non-food applications. Although the conventional high-purity intermediates meet the customers' demand, the first stage of the decision support framework leads to the insight that the different product categories do not strictly need high-purity protein intermediates. For example, in the category of solid foods are pasta or pasta-like products. Pasta enriched with vegetable protein targets the need for protein supplement in vegan or similar diets (Duranti, 2000), while also containing other components. In liquid foods, protein-rich drinks require the addition of protein without negatively affecting the viscosity of the drink by adding too much fibre. Supplements like protein powders for athletes, on the other hand, do require a higher degree of protein purity. Non-food applications, such as livestock feed, do not have strict targets on the presence of other components besides protein. The quality requirements for the product categories are summarized in Table 1.

For the second and third stages of the framework, the intermediate producer knows that conventional and mild fractionation pathways can be used to produce a variety of intermediates with different degrees of purity from yellow peas (Pelgrom *et al.*, 2014) and lupins (Berghout *et al.*, 2015). Yellow peas are pulses rich in starch and protein, whereas lupins are oilseed legumes with a protein content similar to soy but with a

lower oil content. They are two types of potential raw materials to obtain intermediates suitable for the applications described above.

Table 1. Quality bounds for the product according to the final applications

Product description	Quality requirement
Pasta enriched with veg-protein	Min 55 % protein content.
Protein-rich drink	Max 5 % fibre content and low viscosity.
Nutraceuticals (e.g. protein powders)	High purity and low moisture.
Non-food application	Flexible, no restrictions.

Four fractionation pathways are considered: conventional, aqueous, dry, and a combination of dry and aqueous. However, only aqueous and dry are applicable to fractioning yellow peas. Each fractionation pathway leads to a specific portfolio of intermediates, i.e. producing one intermediate from the portfolio implies co-producing the other intermediates, for a total of eighteen intermediates in the case study. The yield of each intermediate and its composition are given in Table 2. Moreover, the use of each fractionation pathway implies a certain resource consumption, in terms of water and energy usage, and production costs.

3.2. Optimizing the selection of fractionation pathways and intermediates

The problem is optimized subject to a set of constraints in the fourth stage. The quality constraints, such as a minimum percentage of protein are defined as in Akkerman *et al.* (2010), with upper and lower bounds for each quality parameter of the product, defined according to the final application requirements. Balance constraints are used to ensure that demand of the customers was met according to the product formulation. Operational constraints are added to regulate the maximum number of intermediates that could be selected, the maximum number of intermediates allowed to blend to satisfy a customer's demand, and the possibility to use an intermediate to cover demand for a product. Demand for products is fixed and blending capacity is set at a non-binding value.

Table 2. Intermediate portfolios produced per raw material and fractionation pathway. Yields and composition are reported as 'x(a:b:c:d)', where x is the intermediate yield per kg of processed raw material, and (a:b:c:d) represents the ratio of fibre, protein, sugars, and fat, respectively (w/w%), multiplied by ten for readability. Water use (kg) and energy use (MJ) are reported per kg of processed raw materials (Berghout et al., 2015; Geerts et al., 2017; Pelgrom et al., 2014).

	Conventional	Aqueous	Dry	Combined
Lupin	0.27 (0:8.3:1:0)	0.29 (0:8:0:0.7)	0.33 (0:4.9:3.5:0.7)	0.14 (0:8:0:0.7)
	0.37 (6.8:2.3:0:0)	0.46 (6.5:1.2:0:1.6)	0.67 (3.7:3.2:1.4:0.6)	0.11 (4.7:2:0:2.6)
	0.27 (0:2.8:5.9:0)	0.20 (0:3.7:5:0)		0.07 (0:6.4:2.2:0)
	0.07 (0:0:0:10)			0.67 (3.7:3.2:1.4:0.6)
Pea		0.66 (2.5:0.4:6.6:0)	0.32 (3.8:3.9:0.2:0.3)	
		0.24 (3:5.3:0.3:0.9)	0.68 (1.9:0.7:6:0.1)	
		0.10 (2.9:5.1:0.2:1)		
Water	51.00	51.00	0.00	35.40
Energy	9.99	10.50	0.52	3.88

3.3. Selected case results: Resource efficiency

The number of intermediates used affects the resource efficiency and operational complexity for the intermediate producer. Using more intermediates leads to an increase in operational complexity, while allowing for application specific intermediates that could improve resource efficiency. Therefore, we investigate the trade-off between operational complexity and resource savings. By varying the maximum number of selected intermediates, we obtain an overview of the raw material, water, and energy use, defined as the total kg of raw materials, the kg of water, and the MJ of energy required to produce all the needed intermediates (Figure 3).

If 4 or 5 intermediates are allowed, conventional fractionation is selected because it leads to more purified intermediates that can cover demand for all products. It is possible to cover demand using the 3 intermediates from the aqueous fractionation pathway, however the lower yield of the pure protein intermediate in the process requires more materials to be processed, and consequently leads to higher resource use. When the number of selected intermediates is equal to or above 6, the mild fractionation pathways dry and combined are selected to process part of the raw materials. However, the production of conventional intermediates remains necessary for those applications that require high-purity protein intermediates. When the maximum number of intermediates is equal to 8, there is a water use reduction of about 29 % and energy savings of about 28 %. Selecting more than 8 intermediates does not lead to additional cost and resource savings in the illustrative case.

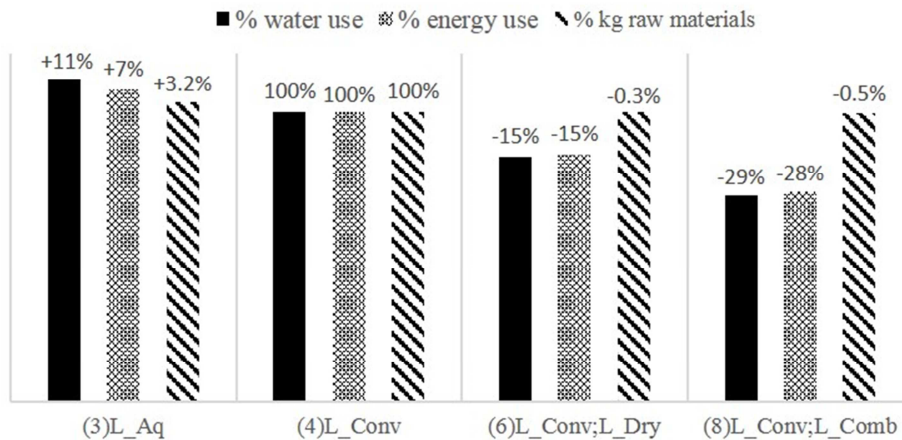


Figure 3. Water and energy use for different maximum numbers of intermediates. Conventional is set to 100%. L=Lupin; Aq=Aqueous; Conv=Conventional; Comb=Combined dry and aqueous.

4. Discussion and conclusions

This paper presents an optimization-based decision support framework for the selection of raw materials, fractionation pathways, as well as intermediates, which can be used to support integrated product and process design for mixed consumer products. The application in a case study illustrated the applicability of the proposed framework. The results also indicate that mild fractioned intermediates could lead to more resource-efficient production of mixed consumer products. However, there is an added complexity in handling the number of intermediates by the intermediate producer, and there has to be more collaboration between the intermediate producer and its customers producing the final mixed consumer products. Additionally, certain customer requirements are not translatable to chemical composition only (Bongers, 2009; Dubbelboer et al., 2015). Therefore, extending the scope of the approach to include functionality on top of chemical composition will lead to additional value.

References

- R. Akkerman, D. van der Meer, D.P. van Donk, 2010. Make to stock and mix to order: choosing intermediate products in the food-processing industry. *Int. J. Prod. Res.* 48, 3475–3492. <https://doi.org/10.1080/00207540902810569>
- J.A.M. Berghout, P.J.M. Pelgrom, M.A.I. Schutyser, R.M. Boom, A.J. Van Der Goot, 2015. Sustainability assessment of oilseed fractionation processes: A case study on lupin seeds. *J. Food Eng.* 150, 117–124. <https://doi.org/10.1016/j.jfoodeng.2014.11.005>
- P.M.M. Bongers, 2009. Process and Equipment Design Optimising Product properties and attributes. *Computer Aided Chemical Engineering* 26, 225–230. [https://doi.org/10.1016/S1570-7946\(09\)70038-0](https://doi.org/10.1016/S1570-7946(09)70038-0)
- A. Dubbelboer, J. Janssen, A. Krijgsman, E. Zondervan, J. Meuldijk, 2015. Integrated Product and Process Design for the Optimization of Mayonnaise Creaminess, *Computer Aided Chemical Engineering* 37, 1133–1138. <https://doi.org/10.1016/B978-0-444-63577-8.50034-6>
- M. Duranti, 2000. Pasta enriched with vegetable proteins. *EP 0 997 078 A2*, 2000
- M.E.J. Geerts, E. Mienis, C. V. Nikiforidis, A. van der Padt, A.J. van der Goot, 2017. Mildly refined fractions of yellow peas show rich behaviour in thickened oil-in-water emulsions. *Innov. Food Sci. Emerg. Technol.* 41, 251–258. <https://doi.org/10.1016/j.ifset.2017.03.009>
- J. Jonkman, J.M. Bloemhof, J.G.A.J. Vorst, A. van der Padt, 2015. A Sustainability Driven Methodology for Process Synthesis in Agro-Food Industry. *Computer Aided Chemical Engineering* 37, 1289–1294. <https://doi.org/10.1016/b978-0-444-63577-8.50060-7>
- P.J.M. Pelgrom, R.M. Boom, M.A.I. Schutyser, 2014. Functional analysis of mildly refined fractions from yellow pea. *Food Hydrocoll.* 44, 12–22. <https://doi.org/10.1016/j.foodhyd.2014.09.001>
- A. Tamayo Tenorio, R.M. Boom, A.J. van der Goot, 2017. Understanding leaf membrane protein extraction to develop a food-grade process. *Food Chem.* 217, 234–243. <https://doi.org/10.1016/j.foodchem.2016.08.093>
- A.J. van der Goot, P.J.M.M. Pelgrom, J.A.M.M. Berghout, M.E.J.J. Geerts, L. Jankowiak, N.A. Hardt, J. Keijer, M.A.I.I. Schutyser, C. V. Nikiforidis, R.M. Boom, 2016. Concepts for further sustainable production of foods. *J. Food Eng.* 168, 42–51. <https://doi.org/10.1016/j.jfoodeng.2015.07.010>

Sustainable Optimal Strategic Planning for Shale Water Management

Alba Carrero-Parreño^a, Rubén Ruiz-Femenia^a, José A. Caballero^a, Juan A. Reyes-Labarta^a, Ignacio E. Grossmann^b

^a*Institute of Chemical Process Engineering, University of Alicante, Ap. Correos 99, Alicante 03080, Spain*

^b*Department of Chemical Engineering, Carnegie Mellon University, Pittsburgh, PA 15213, U.S.A.*

alba.carrero@ua.es

Abstract

In this work, we introduce a non-convex MINLP optimization model for water management in shale gas production. The superstructure includes: reuse/recycle in the same or neighboring wellpad, treatment in mobile units or in centralized water treatment (CWT) facility, or transport to Class II disposal wells. We consider four different water qualities: flowback water, impaired water, desalinated water and freshwater. Additionally, water blending ratios are unrestricted and friction reducers expenses are calculated accounting for impaired water contamination. The objective is to optimize the fracturing schedule, the number of tanks needed in each time period, flowback destination (reuse, treated or disposal), and fracturing fluid composition by maximizing the “sustainability profit” (Zore et al., 2017). The problem is tackled in two steps. First, we solve an MILP model based on McCormick relaxations. Second, a smaller MINLP is solved in which some binary variables are fixed. The capabilities of the proposed mathematical model are validated against long-time horizon scenario from historical data of the Marcellus Shale play.

Keywords: shale gas, water management, sustainability profit, optimization, mixed-integer nonlinear programming

1. Introduction

The development of new additives in the shale gas industry, which tolerate the use of high Total Dissolved Solids (TDS) base fluid, has allowed reusing the wastewater in the drilling of subsequent wells (U.S. Environmental Protection Agency, 2016). This practice is currently the most popular and cost-effective option for shale gas water management. Although it minimizes freshwater consumption, producers should take into consideration possible long-term issues and challenges. For instance, the TDS concentration will increase significantly, around 2-3 times, which can represent a cost barrier to reuse the water for fracturing operations. Besides, as the number of drilled wells decrease this practice becomes less attractive. Specifically, the volume of fracturing fluid required to fracture new wells may be less than the volume of water generated by producing wells in the area.

Currently, several works have been reported on the optimization of shale gas water management (Gao and You, 2015; Yang et al., 2015; Lira-Barragán et al., 2016). However, most of the works published in the literature consider that the water blending

ratio is restricted or the return to pad operations are not allowed. Drouven and Grossmann (2017) assume that the water-blending ratio is unrestricted, they over-estimate the friction reducers expenses. The MILP model that they proposed does not account the salt concentration of impaired water. Moreover, they only distinguish between two types of water: impaired water and freshwater. Hence, the model cannot handle any water management option when drilling operation decrease.

In this work, we propose a mixed-integer non-linear programming (MINLP) model considering the TDS concentration of wastewater and different water treatment solutions. We estimate the friction reducers expenses as a function of TDS concentration to determine if the level of TDS in impaired water is an impediment to reusing it in fracturing operations. Moreover, the model distinguishes between four types of water: impaired water, flowback water, desalinated water and freshwater. The objective is to maximize the “sustainability profit” in order to obtain a compromise solution between economic, environmental and social aspects. Only a single objective function is necessary since all the indicators are expressed in monetary terms (Zore et al., 2017).

2. Problem statement

The superstructure proposed for water management in shale gas operations is shown in Figure 1. The water management system comprises wellpads p , shale gas wells in each wellpad w , centralized water treatment technologies (CWT) k , freshwater sources f , fracturing crews c , and disposals wells d .

After hydraulic fracturing, a portion of water called flowback water returns to the wellhead. The flowback water is stored in fracturing tanks (FT) onsite before basic treatment (pre-treatment) in mobile units or transport to CWT facility, Class II disposal or neighboring wellpad. Pre-treatment includes technologies to remove suspended solids, oil and grease, and bacteria, certain ions that can cause the scale to form on equipment and interfere with fracturing chemical additives. After pre-treatment, the water can be used as a fracturing fluid in the same wellpad, or can be desalinated in the onsite TDS removal technologies. The flowback water reused for fracturing operations is called impaired water. Several desalination technologies can be selected such as multi-stage membrane distillation (MSMD), multi-effect evaporation with mechanical vapor recompression (MEE-MVR) or forward-reverse osmosis (FO-RO) hybrid. We consider that the outflow brine salinity in the onsite treatment is close to salt saturation conditions to achieve zero liquid discharge (ZLD) operation. Cost and salinity levels restrict the type of desalination unit that can be used for TDS removal. The onsite desalinated water can also be used as a fracturing fluid in the same wellpad, transported to the next wellpad or discharge for other usages. The flowback water can also be transported and treated in CWT plants. Desalinated water from CWT plants can select the same routes as the desalinated water in onsite technologies. Natural freshwater is obtained from an uninterrupted fresh water source. Desalinated water and freshwater are stored in freshwater tanks (FWT) and/or water impoundment. Transportation of freshwater, impaired water, flowback water and desalinated water can only be through trucks. Storage tanks and mobile treatment are assumed to be leased.

The problem is to determine: (1) wellpad fracturing start date (fracturing schedule), (2) number of tanks leased at each time period, (3) number of trucks needed in each time period, (4) flowback destination, reuse (impaired water), treatment (onsite or offsite) or disposal, and (5) quality of water used to fracture each well.

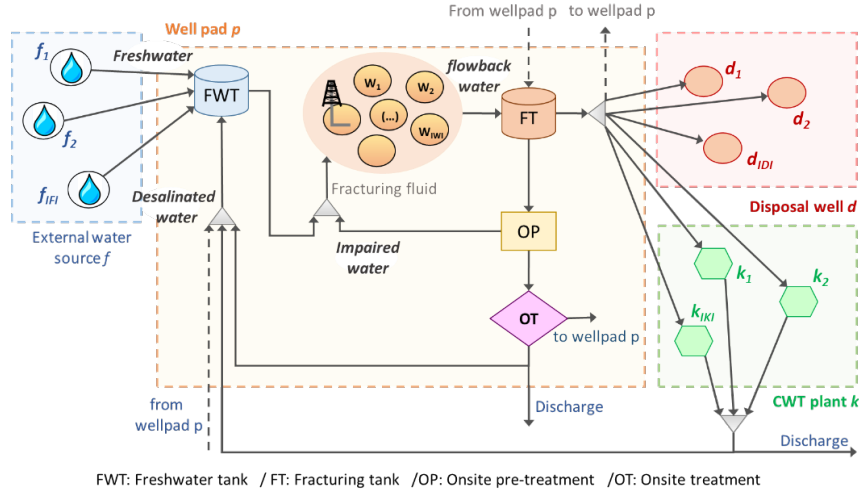


Figure 1. General superstructure of shale gas water management operations

3. Problem formulation

The optimization problem is formulated as an MINLP model that includes: assignment constraints, material balance in storage tanks, mixer and splitters, logic constraints and an objective function. Salt material balances are modeled using total flows and salt composition as variables (bilinear terms). An advantage of using this representation is that the variables involved in the bilinear terms are well bounded, allowing us to define tight under and over estimators. A brief outline of some of these equations is next given.

3.1. Assignment constraints

Eq. (1) ensures that in each time period only one well can be fractured by one of the available fracturing c. $y_{t,p,w,c}^{hf}$ indicates the beginning of stimulating each well.

$$\sum_{t \in T} \sum_{c \in C} y_{t,p,w,c}^{hf} \leq 1 \quad \forall w \in W, p \in RPW \quad (1)$$

Eq. (2) guarantees there is no overlap in the hydraulic fracturing operations between different wells. τ_w^{hf} is the time required to fracture well w with fracturing crew c.

$$\sum_{p \in RPW} \sum_{w \in W} \sum_{t=t-\tau_w^{hf}+1}^t y_{t,p,w,c}^{hf} \leq 1 \quad \forall t \in T, c \in C \quad (2)$$

3.2. Storage balance

Flowback water, impaired water and freshwater is storage in portable leased tanks at a wellpad. Eq. (3) describes the storage balance of tank s in wellpad p in time period t.

$$n_{t,p,s} = n_{t-1,p,s} + n_{t,p,s}^{ins} - n_{t,p,s}^{unins} \quad \forall t \in T, p \in P, s \in S, \quad (3)$$

where $n_{t,p,s}$ is a total number of tanks, $n_{t,p,s}^{ins}$ and $n_{t,p,s}^{unins}$ represents the number of tanks installed or uninstalled in a specific time period.

The amount of water stored $ST_{t,p,s}$ is bounded by the capacity of one tank CST_s and the number of tanks installed. As time is discretized into weeks, the storage tank should

handle the inlet water that comes from one day. Therefore, $\theta_{t,p,s}$ represents the inlet water in the storage tank divided by the number of days in a week.

$$ST_{t,p,s} + \theta_{t,p,s} \leq CST_s \cdot n_{t,p,s} \quad \forall t \in T, p \in P, s \in S \quad (4)$$

$$y_{t,p,s}^{st} \cdot N_s^{LO} \leq n_{t,p,s}^{ins} \leq N_s^{UP} \cdot y_{t,p,s}^{st} \quad \forall t \in T, p \in P, s \in S \quad (5)$$

N_s^{LO} and N_s^{UP} are lower and upper bounds of a number of tanks installed. $y_{t,p,s}^{st}$ indicates the occurrence of installation tanks for each tank s at each time period t .

3.3. Objective function

The objective function to be maximized is defined as the sum of economic profit ($P^{Economic}$), eco-profit (P^{Eco}) and social profit (P^{Social}).

$$\max SP = P^{Economic} + P^{Eco} + P^{Social} \quad (6)$$

Economic profit includes revenues from natural gas minus the sum of the following expenses: wastewater disposal cost, storage tank cost, freshwater cost, friction reducer cost, wastewater and freshwater transport cost and onsite and offsite treatment cost.

Eco-profit distinguishes between eco-benefit (raw material and products that unburden the environment) and eco-cost (raw material and products that burden the environment). Both terms are calculated by using eco-cost coefficients (Delft University of Technology, 2017). In our problem, impaired water and desalinated water used to fracture a neighboring well exhibit unburdening effect on the environment. However, natural gas, freshwater withdrawal, disposal and transportation burden the environment.

Social profit includes social security contributions paid for the employed people to fracture a well, plus the social transfer by hiring people, minus social cost. We only take into account the numbers of jobs on a fracturing crew and the time that they are working to fracture a specific well. Once the well is completed, the number of jobs generated by truck drivers or maintenance team are not considered.

4. Case study

The proposed model is applied to a case study in Marcellus Play with 3 wellpads and 20 wells, one year discretized at one week per time period, four interruptible sources of fresh water, three class II disposal wells, two CWT plants and one fracturing crew.

The MINLP problem consists of 3,117 binary variables, 13,463 continuous variables and 10,297 constraints. In order to treat the presence of bilinear terms, which are non-convex, we apply the following decomposition strategy:

- The original MINLP is relaxed using under and over estimators (McCormick convex envelopes), obtaining an MILP. The solution of this problem yields an upper bound (UB) to the MINLP.
- The binary variables which determine the fracture schedule ($y_{t,p,w,c}^{hf}$) are fixed into the original MINLP, resulting in a smaller MINLP.

The model is implemented in GAMS 25.0.1. The relaxed MILP problem is solved with Gurobi 7.5.2 and the MINLP problem with DICOPT 2 using CONOPT 4 to solve the

NLP sub-problems. Although DICOPT cannot guarantee a global solution, we calculate the optimality gap to obtain the deviation of this solution with respect to the global optimum. The decomposition strategy applied for bilinear non-convex MINLP models solves the problem within 0.1% optimality gap in 1904 CPUs.

The sustainable profit of the optimal solution is equal to k\$ 767, where the economic profit and social profit are equal to k\$ 16,910, and k\$ 1,469 million, respectively. However, the eco-profit component is negative equal to k\$ -17,611.

The solution of the model shows that the capabilities to reuse impaired water to fracture other wells is the best economic and environmental practice for shale gas water management. Figure 2 displays the fracturing schedule for each wellpad. The producer would spend k\$171 on tolerant additives. Overestimating the price of the friction reducers this cost would rise to k\$270, decreasing the total profit to k\$668. It is important to highlight that in Marcellus play, only 10-40% of the water injected is recovered. For that reason, although 92,700 m³ are recirculated, 124,300 m³ of fresh water are still necessary to complete all candidate wellpads.

The solution also provides an effective storage water management strategy to minimize the total storage cost and maximize the impaired water. We consider that operators lease fracturing tanks with 60 m³ of capacity. The total cost of storage is equal to \$363,000. Figure 3 (a) shows the number of tanks required in each wellpad along time horizon. Figure 3 (b) displays the blending ratio - impaired water used compared to water demand required to fracture each well - over the time.

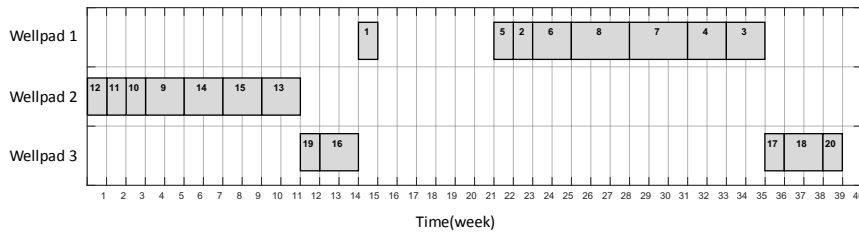


Figure 2. Fracturing schedule.

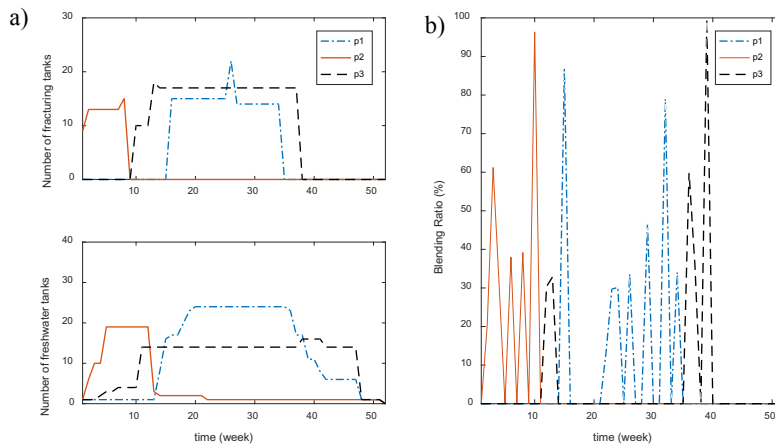



Figure 3. Results for the case study: a) Number of fracturing tanks (FT) and freshwater tanks (FWT) and b) Blending ratio over time for each wellpad.

As commented in the introduction section, it is important to figure out the water management option when all candidates wells are completed. The practice selected by the model is desalinate the water onsite using membrane distillation treatment. Finally, although transportation cost decreases reusing the wastewater, it still represents a high contribution to the final water management cost equal to \$806,000.

5. Conclusion

An MINLP model has been proposed for economic and environmental decisions in shale gas water management. The new measure expressed in monetary value helps the producers to make sustainable, viable and economic decisions. The model, which can be effectively solved with the proposed decomposition technique, reveals that the level of TDS in impaired water is not an obstacle to reusing it for fracturing purposes. Also, it has been shown that onsite desalination treatment can be cost-effective for operators once no more wells to fracture are available. Further development of this work includes the analysis of different sources of uncertainty of some inlet parameters as gas and wastewater production.

Acknowledgements

 This project has received funding from the European Union's Horizon 2020 Research and Innovation Program under grant agreement No. 640979 and from the Spanish «Ministerio de Economía, Industria y Competitividad» CTQ2016-77968-C3-02-P (FEDER, UE).

References

- Delft University of Technology, 2017. The Model of the Eco-costs/Value Ratio (EVR). URL <http://www.ecocostsvalue.com> (accessed 12.1.17).
- Drouven, M.G., Grossmann, I.E., 2017. Optimization models for impaired water management in active shale gas development areas. *J. Pet. Sci. Eng.* 156, 983–995.
- Gao, J., You, F., 2015. Shale Gas Supply Chain Design and Operations toward Better Economic and Life Cycle Environmental Performance: MINLP Model and Global Optimization Algorithm. *ACS Sustain. Chem. Eng.* 3, 1282–1291.
- Lira-Barragán LF, Ponce-Ortega JM, Serna-González M, El-Halwagi MM. Optimal Reuse of Flowback Wastewater in Hydraulic Fracturing Including Seasonal and Environmental Constraints. *AIChE J.* 2016;62(5).
- U.S. EPA, 2016. Technical Development Document For Effluent Limitations Guidelines and Standards for the Oil and Gas Extraction Point Source Category. Washington, DC.
- Yang, L., Grossmann, I.E., Mauter, M.S., Dilmore, R.M., 2015. Investment optimization model for freshwater acquisition and wastewater handling in shale gas production. *AIChE J.* 61, 1770–1782.
- Zore, Ž., Čuček, L., Kravanja, Z., 2017. Syntheses of sustainable supply networks with a new composite criterion – Sustainability profit. *Comput. Chem. Eng.* 102, 139–155.

Compact and Multi-Stream Heat Exchanger Design

Somei Hayashi^a, Kitipat Siemanond^{a,*}

^a*The petroleum and petrochemical college, Chulalongkorn University, 254 Phayathai road, Patumwan sub-district, Bangkok 10330, Thailand*

kitipat.s@chula.ac.th

Abstract

Energy recovery has been playing a major role in most of chemical industries and related fields. A conventional heat recovery system or heat exchanger network (HEN) is usually composed of lots of exchangers. This may lead to extra costs in operation and construction. Thus, this work focuses on designing, optimizing, and applying multi-stream plate-fin heat exchangers (PFHEs) into a HEN to reduce a number of exchangers and costs. The process of doing so starts with synthesis of a conventional HEN. The process stream data used as the case study in this work is taken from a gas separation plant in Thailand. Such network is recognized as the based case which will be improved by replacing some exchangers with PFHEs. The improved network is recognized as the improved case which provides less annual cost than the conventional one around 3 times.

Keywords: multi-stream, plate-fin, heat exchanger, design, techno-economic study

1. Introduction

Heat exchanger networks (HENs) are imperative for utility saving because they help recovering heat from hot streams to others leading to a reduction in utility requirement. A common type of exchanger used worldwide is shell-and-tube heat exchanger (STHE) which has a limit to facilitate exchange of heat from two streams, one hot and one cold. Thus, Most of HENs must contain lots of STHEs leading to high expenses. A STHE requires a large area for installation and a great robust supporter for holding it, thus it is not suitable for application where the area is limited like vehicles and offshore platforms. Compact heat exchangers are considered to resolve such problems. A PFHE is classified as one type of compact heat exchangers having area density more than 700 m²/m³ which is extremely greater than A STHE. At the beginning, Kays and London (1984) published their work concerning compact heat exchangers. They presented the basic fundamental principles, correlations, and behaviours of frictional and thermal performances of many secondary surfaces of a PFHE from experiment. Then, Picón-Núñez (2002) proposed a thermal design of a multi-stream plate-fin heat exchanger by using the pinch technology, thermo-hydraulic model. Their methodology considers a maximum pressure drop of a critical stream as the design objective. Recently, Nassim and Samira (2013) developed some parts of Picon's work to make it more accurate and reliable. They introduced the temperature correction factor parameter (ζ) to correct the value of physical properties of fluids changed across a heat exchanger.

2. Intensification process of a heat exchanger network (HEN)

A heat exchanger network normally consists of a large number of exchangers leading to many consequences. A possible way to reduce a number of exchangers is to applying multi-stream heat exchanger into a HEN. The process starts off the following steps.

2.1. Generation of a conventional shell-and-tube heat exchanger network (HEN)

A conventional HEN is generated by using the grassroots technique or stage-model presented by Grossmann et al. (1990). The exchanger minimum approach temperature (EMAT) used to generate the network is assumed to 1 °C. After finishing generating the HEN, heat load, utility consumption, inlet and outlet temperatures, area, volume, and cost of each exchanger are determined and recognized as the base case.

2.2. Design of a multi-stream plate-fin heat exchange (PFHE)

The network generated from the previous step is redesigned by removing all exchangers that have small approach temperature difference, around 5 °C, and all groups of exchangers performing exchange of heat from split streams and then replacing with PFHEs. The design process of a PFHE starts with collecting inlet and outlet temperatures of streams of such exchangers and then constructing composite curves to calculate heat load per interval, stream population, and inlet and outlet temperatures. After that, dimensions (length, height), heat transfer coefficient, and pressure drop of each exchanger is calculated by guessing fin type, width, and number of passages. Heat transfer coefficient of each stream is calculated by the equation (1) below

$$h = \frac{am^{1-b}\mu^b c_p}{d_h^b Pr^{2/3}} \times \left(\frac{1}{A_c}\right)^{1-b} \quad (1)$$

where h is the heat transfer coefficient, a and b are constants in the correlation between Colburn factor and Reynolds number provided by Kay and London (1984), m is the mass flow rate per passage, μ is the fluid's viscosity, C_p is the specific heat capacity, d_h in the hydraulic diameter of the secondary surface, Pr is the Prandtl number, A_c is the cross sectional free flow area. Then, volume of two passages that are adjacent is calculated by the equation (2)

$$V_i = \frac{Q}{\Delta T_{lm}} \left[\frac{1}{\eta_1 \alpha_1} \left(\frac{1}{h_1} + R_{f,1} \right) + \frac{1}{\eta_2 \alpha_2} \left(\frac{1}{h_2} + R_{f,2} \right) + R_w V_i \right] \quad (2)$$

Where Q is the heat load per passage, ΔT_{lm} is the logarithmic mean temperature difference, η is the surface efficiency which is assumed to one, α is area density faction calculated by equation (3), R_f is the fouling factor that is negligible in this design step, and R_w is the thermal resistance which is normally close to zero if the wall thickness is really thin. For the total volume of a PFHE can be estimated by equation (4)

$$\alpha_1 = \frac{\beta_1}{\beta_1 + \beta_2} \quad (3)$$

$$V_T = \sum_i V_i \quad (4)$$

After that, length of a PFHE is easily estimated by the equation (5). For pressure drop can be calculated by the equation (6)

$$L = \frac{V_T}{A_{fr}} \quad (5)$$

$$\Delta P = \frac{2xm^{2-y}\mu^y}{d_h^{1+y}\rho} L \left(\frac{1}{A_c}\right)^{2-y} \quad (6)$$

Where A_{fr} is the frontal area of a PFHE estimated by the equation (7), and β is the area density between plates, x and y are the constants in the correlation between friction factor and Reynolds number, ρ is the fluid density.

$$A_{fr} = \sum \frac{4A_c}{\beta d_h} \quad (7)$$

The height (H) of a PFHE is estimated by the equation (8) and the heat transfer area is calculated by the equation (9)

$$H = \frac{v_T}{L \times W} \quad (8)$$

$$A = \sum_{i=1}^n [W \times L \times \delta \times N \times \beta]_i \quad (9)$$

Where W is the width which is guessed, δ is the plate spacing, N is the number of passages.

2.3. Cost estimation

Costs of a heat exchanger whether they are operation or construction are necessary to estimate because they are a useful economic factor for investment decision. The capital expenditure of an exchanger in this work is known as CAPEX while OPEX is referred to operating expenditure of an exchanger. CAPEX and OPEX are estimated from equations (10) and (11).

$$CAPEX = C_1 \frac{I_2}{I_1} \frac{Q}{\Delta T_{min}} \quad (10)$$

Where C_1 is the cost per unit of $Q/\Delta T_{lm}$ of a certain year in the past, and I_2 is the cost index of the same year as C_1 while I_1 is of the current year. Value of C_1 of different type of exchanger will be different and can be found in several literature such as Hewitt et al. (2007) and Hesselgreaves et al. (2017)'s work. The unit of equations (10) is Baht but the unit of OPEX is Baht/y, thus equation (10) has to be multiplied by the capital recovery factor $\left(\frac{i(1+i)^n}{(1+i)^n - 1}\right)$, where i and n are the interest rate and operating period assumed to 10 % a year and 10 years, respectively.

$$OPEX = \text{pumping or compressing cost} + \text{maintenance cost} \quad (11)$$

$$\text{Pumping cost} = \frac{1}{\varepsilon} \dot{V} \Delta P \times AH \times f_e \quad (12)$$

$$\text{Compressing cost} = \frac{n_c}{n_c - 1} \frac{P_{in} \dot{V}_{in}}{\eta_p} \left[1 - \frac{P_{out}}{P_{in}} \frac{n_c - 1}{n_c} \right] \times AH \times f_e \quad (13)$$

Where ε is the pump's efficiency assumed to 80 %, \dot{V} is the volumetric flow rate, ΔP is the pressure drop, AH is the annual hour of operation assumed to 7200 h/y, f_e is the electrical cost that is 1.666 Baht/kWh, η_p is the polytropic efficiency and n_c is the polytropic coefficient.

$$n_p = 0.017 \ln(\dot{V}) + 0.7 \quad (14)$$

$$n_c = \frac{\gamma n_p}{\gamma n_p - \gamma + 1} \quad (15)$$

$$\frac{P_{out}}{P_{in}} = \frac{P_{in} + \Delta P}{P_{in}} \quad (16)$$

Maintenance cost of each exchanger is assumed to 10 % of its annualized CAPEX. Total annual cost (TAC) is the summation of annualized CAPEX and OPEX.

2.4. Optimization process of a PFHE

The objective function for optimizing a PFHE is TAC of itself. The optimization process is performed by minimizing TAC by varying a number of passages and width under following constrains: a number of passages are integers and range between 1 and 200, width ranges from 0.5 to 2 meters, height is not exceed 3 meters, and length is set to 0.2 meter at least.

3. Case study

Stream data used as a case study in this work is from a gas separation plant in Thailand. Such process stream data is taken to generate a conventional HEN by grassroots technique and shown as a grid diagram in the Figure 1(a). The number of exchangers in the network is 19. Calculated area, EMAT, volume, and cost of each individual are

shown in Table 1. From the grid diagram of a conventional HEN, exchanger no. 2, 3, 5, 8, and 9 facilitate exchange of heat from split streams leading to the more number of exchangers exists in the network which is undesirable. Thus, exchanger no. 2, 3, and 5 will be replaced with a single unit of PFHE, exchanger no. 8 and 9 are also replaced with a PFHE. Moreover, exchanger no. 1, 4, 7, 12, 13, 17, and 19 have small EMAT which is impractical for STHE, thus such exchangers are replaced with PFHEs as well. The total number of PFHEs to be designed for this network is 9. Detailed design of each PFHE is shown in Table 2. For the fin type of all PFHE is plain-fin 15.08. The improved network is shown in Figure 1(b). The cost analysis of the improved case, shown in Table 3, shows that TAC is lower than up to 3 times a conventional HEN.

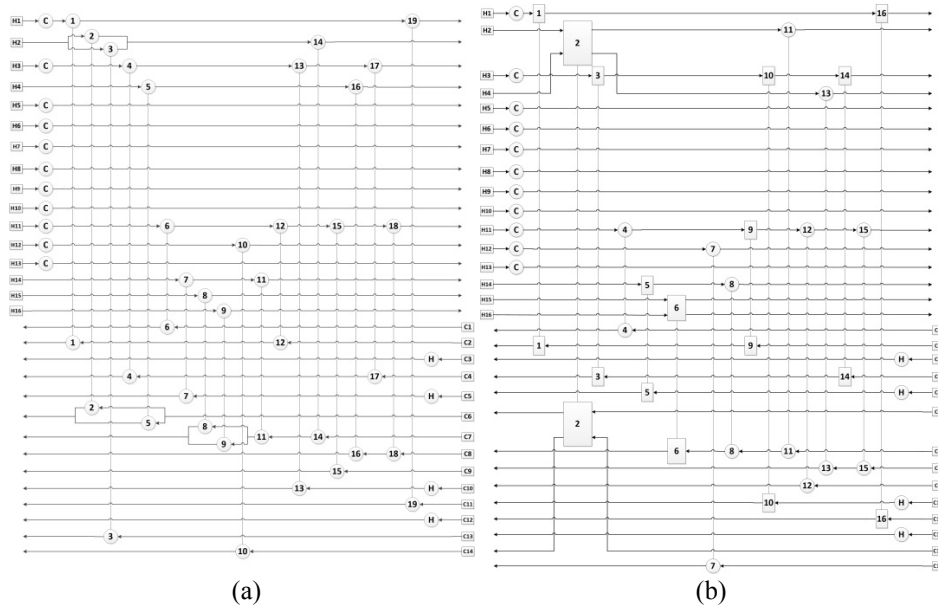


Figure 1: Grid diagram of the base case (a), Grid diagram of the improved case (b)

Table 1: EMAT, area, volume, and costs of exchangers of the base case

No.	EMAT (°C)	A (m ²)	V (m ³)	Annualized CAPEX (MB/y)	OPEX (MB/y)		TAC MB/y
					Pump./Comp.	Maint.	
1	4.12	36,417.39	523.91	13.17	4.83	1.32	19.32
2	17.40	1,570.74	22.60	0.20	144.59	2.02E-02	144.81
3	16.60	2,119.80	30.50	0.11	140.42	1.07E-02	140.54
4	6.55	16,227.24	233.45	6.80	2.06	0.68	9.54
5	16.70	4,223.65	60.76	0.47	133.88	4.73E-02	134.41
6	14.28	2,157.95	31.04	0.17	20.31	1.72E-02	20.50
7	1.20	3,539.97	50.93	6.19E-02	6.76E-04	6.19E-03	0.07
8	25.36	470.45	6.77	0.05	0.10	4.60E-03	0.15
9	21.21	127.77	1.84	1.25E-02	0.09	1.25E-03	0.10
10	10.41	1,537.31	22.12	0.09	1.00	9.11E-03	1.10

Table 1: EMAT, area, volume, and costs of exchangers of the base case (continued)

No	EMAT (°C)	A (m ²)	V (m ³)	Annualized CAPEX (MB/y)	OPEX (MB/y)		TAC (MB/y)
					Pump/Comp	Maint	
11	48.55	367.74	5.29	1.58E-02	1.25E-05	1.58E-03	0.02
12	1.00	2,358.67	33.93	0.77	20.21	0.08	21.06
13	1.00	15,026.32	216.17	5.37	1.09	0.54	7.00
14	46.32	579.98	8.34	0.08	159.09	7.65E-03	159.18
15	76.70	510.63	7.35	0.08	23.83	7.64E-03	23.91
16	70.88	57.40	0.83	6.52E-03	202.02	6.52E-04	202.03
17	1.00	34,992.19	503.41	12.13	4.00	1.21	17.34
18	104.49	635.20	9.14	0.11	23.27	1.11E-02	23.39
19	4.33	1,482.98	21.33	0.35	2.27	3.47E-02	2.65
To tal		124,403.38	1,789.7 0	40.05	883.07	4.01	927.12

Table 2: Detailed design of all PFHEs

PFHE	W (m)	L (m)	H (m)	Interval	Stream	N	h (w/m ² k)	ΔP (kPa)
1	2.00	4.69	2.99	1	H1	141	1,456.08	238.56
					C2	141	408.97	607.15
2	2.00	0.93	2.99	1	H4	141	131.08	12.38
					C6	141	218.66	2.51E-01
				2	H4	140	131.58	6.29
					C6	120	238.33	1.35E-01
					C13	20	161.58	1.12E-01
				3	H2	69	193.64	123.70
					H4	69	191.98	125.29
					C6	115	243.81	2.11
					C13	23	149.96	1.64
				4	H2	141	132.21	2.31E-02
C13	141	56.95	2.06E-04					
3	2.00	2.49	2.99	1	H3	141	1,389.11	109.56
					C4	141	399.97	305.54
4	2.00	0.24	2.99	1	H14	141	29.84	1.03E-02
					C5	141	1,127.06	14.80
5	1.96	0.20	0.08	1	H16	3	468.96	0.24
					C7	3	2.43E-01	1.62E-01
				2	H15	4	413.94	6.70E-01
					C7	4	1,693.91	3.59E-01
6	2.00	0.56	2.99	1	H11	141	253.00	19.70
					C2	141	408.97	72.91
7	2.00	2.30	2.9	1	H3	141	1,389.11	101.16
					C10	141	328.43	4.36
8	2.00	4.44	2.99	1	H3	141	1,389.11	195.42
					C4	141	399.97	544.99
9	2.00	0.19	2.99	1	H1	141	1,456.08	9.91
					C11	141	234.84	2.31E-01

Table 3: Area, volume, and costs of exchangers of the improved case

No.	Type	A (m ²)	V (m ³)	Annualized CAPEX (MB/y)	OPEX (MB/y)		TAC MB/y
					Pump/Comp	Maint.	
1	PFHE	38,182.81	28.11	22.28	40.07	2.23	64.57
2	PFHE	7,429.96	5.57	1.31	56.52	0.13	57.95
3	PFHE	20,268.08	14.92	11.50	24.88	1.15	37.54
4	STHE	2,157.95	31.04	0.17	20.31	1.72E-02	20.50
5	PFHE	1,977.92	1.46	0.11	0.09	1.05E-02	0.21
6	PFHE	41.95	3.33E-03	0.10	5.42E-03	9.85E-03	0.11
7	STHE	1,537.31	22.12	0.09	1.00	9.11E-03	1.10
8	STHE	367.74	5.29	0.02	1.25E-05	1.58E-03	0.02
9	PFHE	4,585.08	3.38	1.31	9.74	0.13	11.19
10	PFHE	18,714.71	13.78	9.08	0.49	0.91	10.49
11	STHE	579.98	8.34	0.08	1.25E-05	7.65E-03	0.08
12	STHE	510.63	7.35	0.08	20.21	7.64E-03	20.29
13	STHE	57.40	0.83	0.01	1.09	6.52E-04	1.10
14	PFHE	36,152.22	26.62	20.52	36.06	2.05	58.63
15	STHE	635.20	9.14	0.11	23.27	1.11E-02	23.39
16	PFHE	1,585.82	1.17	0.59	0.06	0.06	0.70
Total		134,784.8	179.14	67.34	233.80	6.73	307.9

4. Conclusions

PFHEs are an alternative for HEN because PFHEs have enough potential to handle exchange of heat from process streams at small EMAT. From the results, area of the improved case is more than the base case about 13,381.42 m² (8.34 % increase) while its total volume is less about 1610.56 m³ (899.05 % reduction). This means a PFHE provides a large heat transfer area with small volume compared to a STHE. Moreover, the number of exchangers of the improved case is reduced and TAC is much less around 3 times. Anyway, cost, pressure drop, and heat transfer coefficient of a PFHE are directly affected from changes of values of width, length, height, and fin type. This work does not cover the fin selection, thus the optimum fin is not presented here.

References

- I.E. Grossmann, T.F. Yee, 1990, Simultaneous Optimization Models for Heat Integration II-Heat Exchanger Network, *Computers and Chemical Engineering*, 14, 10, 1165-1184
- J.E. Hesselgreaves, R. Law, D.A. Reay, 2017, Chapter 2 – Industrial Compact Exchangers, *Compact Heat Exchangers 2nd*, 35-89
- G.F. Hewitt, S.J. Pugh, 2007, Approximate Design and Costing Methods for Heat Exchangers, *Heat Transfer Engineering*, Butterworth-Heinemann, 28, 2, 76-86
- W.M. Kays, A.L. London, 1984, Chapter 10 – Heat Transfer and Flow-Friction Design data, *Compact Heat Exchangers 3rd*, McGraw-Hill, 186-279
- M. Medina-Flores, M. Picón-Núñez, G.T. Polry, 2002, Thermal Design of Multi-Stream Heat Exchangers, *Applied Thermal Engineering*, 22, 14, 1643-1660
- T. Nassim, M.Samira, 2013, Pressure Drop Optimisation in Design of Multi-Stream Plate-Fin Heat Exchangers, *Considering Variable Physical Properties*, 91, 10, 1650-1659

Optimal design of biogas supply chains

Grégoire Alain Chomette^a, Theodoros Damartzis^{a*}, François Maréchal^a

^a *Industrial Process and Energy Systems Engineering (IPESE), Ecole Polytechnique Federale de Lausanne (EPFL) Valais, 1951, Sion, Switzerland*

theodoros.damartzis@epfl.ch

Abstract

The current work addresses a methodology for the optimal design of biogas supply chains based on anaerobic digestion of animal manure. The problem formulation allows the utilization of optimized processing plants that have been previously designed within a generic superstructure-based optimization problem. The definition of the plant capacity is performed based on the raw biomass availability as well as the demand profiles. Thus, these plants, carrying information on their capacity, investment and operating costs as well as their energetic input and outputs can be used as building blocks within an MILP optimization framework that aims to optimally place the plants with respect to total cost minimization. The latter is subject to constraints related to the application domain, biomass availability and end products demand. The spatial identification of the processing plants is performed taking into account the potential synergies between them, in the form of energy exchanges between the units as well as the consideration of storage locations.

Keywords: supply chain design, biogas, biomass conversion, animal manure

1. Introduction

Recent fluctuations in the prices of fossil fuels as well as the overall shift towards renewable energy have led to the intensification in the design and employment of biomass-based conversion technologies. Animal waste in the form of manure is a great source of biogenic carbon, exploitable for the production of biofuels as well heat and power cogeneration. Especially in agricultural countries such as Switzerland where the sustainable potential of animal manure amounts to 9.9 PJ per year out of which only 9.6 % is currently exploited (Thees et al., 2017), there appears to be a promising potential to enhance the role of biomass in the modern energy mix.

The swift introduction of such technologies in the market, however, necessitates not only the robust design of the conversion process itself but also the consideration of the entire supply chain that introduces the link between raw materials, conversion technologies and end services. To this end, the integration of process design with the supply chain will highlight the benefits and reveal potential synergies between the various steps of the path from raw materials to services. Further, it will bridge the current design methodologies and set the transition from process design level to national design level, while considering the economies of scale.

Numerous studies regarding the design of biomass supply chains based on manure and bio-SNG exist in the recent literature. Balaman and Selim (2014) used a fuzzy multi-objective optimization to design the supply chain of anaerobic digestion based

bioenergy. Recently, Calderón et al. (2017) present an optimization framework for bio-SNG supply chain design. Their work encompasses a generic spatially explicit multi-period MILP optimization scheme that is able to investigate different design scenarios. Svanberg et al. (2017) analyzed the potential of horse manure in waste to energy supply chains exploring the parameters that affect their efficient design. Ghaderi et al. (2016) provide a comprehensive review of the design of biomass supply chains. Their work compares the approaches of a large number of published works revealing a large diversity in the modeling approaches and at the same time providing a good insight on the current state-of-the-art.

Although most works focus on the design of the supply chain itself, aiming at the minimization of the transportation costs and the identification of the facility locations, few address the problem of integrating the factors affecting the design of the conversion plants themselves. To this end, this work proposes a methodology for the optimal design of a supply chain addressing the conversion of cow manure into biogas through anaerobic digestion, upgrading into bio-SNG and subsequent conversion to heat and power. The design of the conversion plants on the process level is performed using a generic framework that utilizes a process superstructure approach to represent the possible pathways as well as their synthesis from a list of available conversion and intermediate processes that act as building blocks. The combination of these optimally designed plants in a similar optimization framework that addresses the possible spatial correlations and connectivity patterns between the various raw material supply points, conversion plants, as well as the end use locations will determine the optimal allocation strategy in the form of spatial identification of the supply chain components. The efficient design of the supply and conversion chain is achieved using a MILP optimization approach that aims to minimize the total cost. By using the above formulation, not only the spatial allocation is possible, but also the potential synergies between neighboring facilities can be identified, allowing for an integrated approach that considers the minimization of energy losses and the effective utilization and distribution of the end products.

2. Methodology

2.1. Biomass conversion to fuels, heat and power

Animal manure, as most wet biomass types can be converted to biogas through anaerobic digestion, a biochemical process that is used to break the biogenic carbon and transform it to a mixture of methane and carbon dioxide through a complex series of chemical reactions. In practice, anaerobic digestion is often preceded by a pre-treatment step that aims to increase the rates of the chemical reactions through mechanical, thermal, chemical or biochemical processing. On the other hand, biogas, consisting of approximately 55-65 % CH₄ and 35-45 % CO₂ as well as traces of other impurities like H₂S, NH₃, siloxanes etc., can either be utilized as it is or undergo an upgrading process to increase its methane content, thus creating a stream of bio-SNG. The latter is achieved either by CO₂ separation or conversion of the contained CO₂ to additional CH₄. Lastly, the upgraded or non-upgraded biogas can be used to produce heat, power or fed to cogeneration units for CHP production. Bio-SNG can be directly injected to the gas grid, provided that it fulfills the corresponding criteria. Particular care also has to be given to the treatment of digested manure. Indeed, when the digested matter is

removed from the reactor (generally around 70% of the initial manure), it can either be transported back to the farms to be used as a fertilizer, or go through additional processes, such as hydrothermal gasification, for carbon acquisition. The latter is a high pressure catalytic treatment that allows the transformation of organic matter into methane in the presence of moisture, resulting in an extra methane stream as well as the reclaiming of useful concentrated nutrients. Obviously, the large number of possible options when considering manure-to-services leads to structural and operational decisions that have to be taken *a priori*, during the process design stage. The multiple design paths arising from this complexity are depicted in Figure 1 in the form of a generalized process superstructure that accounts for the different possible conversion and treatment pathways.

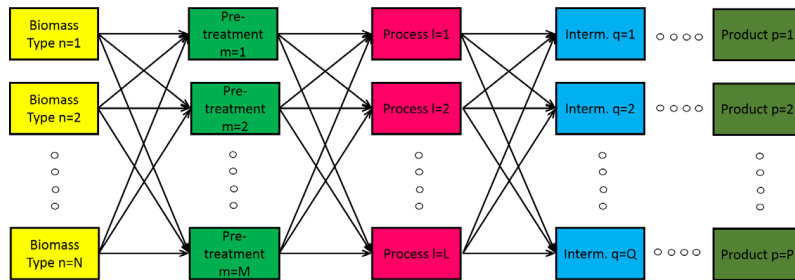


Figure1. Generalized plant design superstructure.

2.2. Formulation of the biomass supply chain

The definition of the supply chain is based on the identification and spatial placement of the biomass processing units based on a set of pre-defined criteria. In this case, an economic criterion is used, encompassing both the investment and operating costs of the conversion plants (CAPEX and OPEX) and the transportation costs between the sources, plants and end users as well as the net revenues from the sales of the end products. Thus, the economic objective becomes the basis of multi-parametric optimization problem, the solution of which will define the optimal locations of the biomass conversion facilities.

As previously described, the conversion of manure to services requires four main steps: pre-treatment, biomass conversion, biogas upgrading and conversion to services that can be either electricity, heat, or bio-SNG meeting the grid requirements. A generic formulation of the supply chain problem should account for the disconnection of the above conversion chains, leading to the consideration of biomass processing at different spatial locations (e.g. pre-treatment at different locations but digestion in a large centralized plant). The latter results in the formulation of sub-chains including biomass processing plants that account for the spatial diversity. Some of the arising possibilities are schematically depicted in Figure 2. Suitable intermediate storage facilities should also be considered to account for the potential centralized distribution.

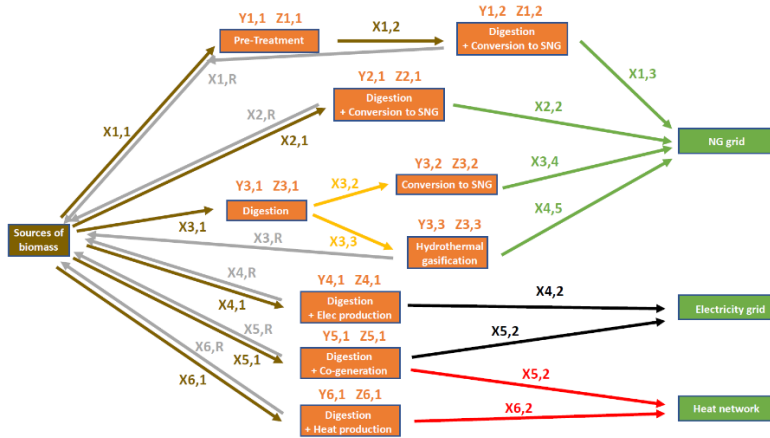


Figure 2. Schematic representation of indicative biomass supply chains

On the other hand, a crucial parameter in the design of biomass the supply chains is the identification of the plant sizes. The classification of the various plants based on their capacity is performed by the assessment of the regional supply and demand profiles so that sensible size selections are used. To this end, the process design problem illustrated in Figure 1 is used to generate solutions based on known biomass supply and demand that will be used during the determination of the plant locations. This results in a catalogue of pre-optimized plants of known size and functionality that are used as building blocks in a mixed integer linear (MILP) optimization problem. Each of these solutions carries the information of plant capacity as well as associated total annualized cost, together with the energetic demands and output. The latter is the necessary link between the various plants, enabling the accounting of energy exchanges that will help explore potential plant synergies during the design of the supply chains.

3. Mathematical approach

3.1. Objective function formulation

The mathematical formulation of the problem is based on a linearized objective function that aims to minimize the expenses throughout the supply chain. It is composed of four main terms namely the revenues from the sales of the end products, the investment and operating costs of the plants as well as the transportation costs within the design space as seen in Eq. 1:

$$\min J = -\sum P + \sum_{i=1}^{np} C_{CAPEX} + \sum_{i=1}^{np} C_{OPEX} + \sum tc \quad (1)$$

3.2. Linearization of the transportation costs

For large scale problems like the one addressed here, mathematical simplifications that ensure the acquisition of fast and reliable solutions are imperative. Although the nature

of the three first terms in Eq. (1) is linear based on the original process design problem (Gassner and Maréchal, 2009), the transportation costs are essentially non-linear. The last term can be linearized over a spatial domain (x,y) containing n_L+1 and n_H+1 discretization points for the x and y directions respectively. The linearized transportation cost between a plant of type l (e.g. pre-treatment, conversion etc.) and another plant of random type m , is given by an expression of the form:

$$\sum_{i=1}^{n_s} \sum_{j=1}^{n_L+1} \sum_{k=1}^{n_H+1} \sum_{l=1}^{n_1} \sum_{\substack{m=1 \\ m \neq l}}^{n_1} tc_{l,m} X_{i,j,k,l} \sqrt{(sx_i - dx(j-1))^2 + (sy_i - dy(k-1))^2} \quad (2)$$

where sx_i and sy_i denote the spatial coordinates of the supply point of biomass type i that has to be transported to a location defined by (dx, dy) . $tc_{l,m}$ expresses the transport cost between a plant of type l and a plant of type m , while $X_{i,j,k,l}$ stands for the transported biomass quantity.

Similarly, the transport costs between all combinations of adjacent units including the initial supply positions as well as the end use locations are discretized in a fashion similar to Eq. 2. The objective function (Eq. 1) is solved with respect to constraints describing the continuity of biomass flows through a plant m , as well as inequalities that ensure that the transported flows remain within the bounds set by the end products demand (sq_i) and also remain below the pre-defined capacity limit (cap_i) of each processing unit (Eqs. 3, 4 and 5 respectively):

$$\sum_{j=1}^{n_L+1} \sum_{k=1}^{n_H+1} \sum_{l=1}^{n_1} \sum_{\substack{m=1 \\ m \neq l}}^{n_m} X_{i,j,k,l,m} = \sum_{j=1}^{n_L+1} \sum_{k=1}^{n_H+1} \sum_{\substack{m=1 \\ m \neq l}}^{n_m} \sum_{\substack{p=1 \\ p \neq l,m}}^{n_p} X_{i,j,k,m,p} \quad (3)$$

$$\sum_{j=1}^{n_L+1} \sum_{k=1}^{n_H+1} \sum_{l=1}^{n_1} \sum_{\substack{m=1 \\ m \neq l}}^{n_1} X_{i,j,k,l,m} \leq sq_m \quad (4)$$

$$\sum_{j=1}^{n_L+1} \sum_{k=1}^{n_H+1} \sum_{l=1}^{n_1} \sum_{\substack{m=1 \\ m \neq l}}^{n_1} X_{i,j,k,l,m} \leq cap_m \quad (5)$$

Furthermore, binary variables Y and Z associated with the existence of each unit in the design problem as well as along the spatial coordinates, respectively, are used. For the binary variables, Y , the following constraint holds, expressing the permissibility of the link between the mass streams in plant locations l and m :

$$\sum_{i=1}^{n_s} \sum_{j=1}^{n_L+1} \sum_{k=1}^{n_H+1} X_{i,j,k,l,m} - M_l Y_{l,m} \leq 0, \quad \forall l, m = 1 \dots, n_1, \quad l \neq m \quad (6)$$

with M_l representing the maximum biomass capacity that can be transferred between locations l and m , while the Z binary variables are subject to:

$$\sum_{j=1}^{n_l+1} \sum_{k=1}^{n_{ll}+1} Z_{j,k,l} \leq 0, \quad \forall l = 1 \dots, n_l \quad (7)$$

The mathematical system of Eqs. (1-7) can be solved using conventional MILP solvers, provided that the biomass availability and end products demand profiles as well as the plant sizes and spatial application domain are known.

4. Conclusions

A comprehensive methodology for the design of biogas supply chains was presented here. The approach involves the use of pre-designed processing plants representing the main steps of the biomass-to-services conversion chain. Such plants of assigned capacity, configuration and operation are then used within a MILP optimization framework that identifies their spatial locations accounting for the raw biomass availability, end products demand, as well as the possible energetic exchanges between the plants in an effort to minimize the total supply chain expenses. The latter are defined as the sum of the plants' investment and operating costs and the linearized transportation costs between the supply chain's components, also considering the annualized total revenues from the satisfaction of the energetic demands within the applied domain.

Acknowledgements

This research project is financially supported by the Swiss Innovation Agency Innosuisse and is part of the Swiss Competence Center for Energy Research SCCER BIOSWEET.

References

- S. Y. Balaman, H. Selim, 2014, A fuzzy multiobjective linear programming model for design and management of anaerobic digestion based bioenergy supply chains, *Energy*, 74, 928-940.
- A. J. Calderón, P. Agnolucci, L. G. Papageorgiou, 2017, An optimisation framework for the strategic design of synthetic natural gas (BioSNG) supply chains, *Applied Energy*, 187, 929-955.
- M. Gassner, F. Maréchal, 2009, Methodology for the optimal thermo-economic, multi-objective design of thermochemical fuel production from biomass, *Computers and Chemical Engineering*, 33, 769-781.
- H. Ghaderi, M. S. Pishvaei, A. Moini, 2016, Biomass supply chain network design: An optimization-oriented review and analysis, *Industrial Crops and Products*, 94 (30), 972-1000.
- M. Svanberg, C. Finnsgård, J. Flodén, J. Lundgren, 2017, Analyzing animal waste-to-energy supply chains: The case of horse manure, *Renewable Energy*, In Press, doi: 10.1016/j.renene.2017.04.002
- O. Thees, V. Burg, M. Erni, G., Bowman, R. Lemm, 2017, Biomass potenziale der Schweiz für die energetische Nutzung, *WSL Berichte*, Heft 57.

Retrofit of mass exchange networks using a reduced superstructure synthesis approach

Adeniyi J. Isafiade

^aDepartment of Chemical Engineering, University of Cape Town, 7701, South Africa

Aj.isafiade@uct.ac.za

Abstract

This paper presents a new methodology for the retrofit of mass exchanger networks using the reduced superstructure synthesis approach. The new method entails two steps. In the first step, the retrofit problem specification is first solved for a grass-root scenario using the mass exchange network synthesis equivalent of the stage-wise superstructure synthesis method. The mass exchange units selected in the solution of the first step are then used to generate a reduced superstructure in the second step. This reduced superstructure is initialised using a combination of the matches selected in the first step and the existing matches of the original network. This ensures that much of the existing units in the original network are utilized in the retrofitted network so as to reduce additional capital investment. The reduced superstructure is then solved as a mixed integer non-linear model so as to obtain an optimal retrofitted network. One of the major benefits of this synthesis approach is that the resulting reduced superstructure of the second step is less computationally intensive in terms of its solution generation process due to the presence of fewer binary variables. The result of the method of this paper gives better payback period when compared with those in the literature.

Keywords: retrofit, mass exchange network, superstructure.

1. Introduction

The rising concerns over the emissions of pollutants into the environment by process plants has necessitated the need for mass exchange network synthesis (MENS) which was first presented by El-Halwagi and Manousiouthakis (1989). The authors drew analogies from pinch technology as applied to heat exchanger network synthesis (HENS), for the synthesis of mass exchange networks. Hallale and Fraser (2000a) improved on the synthesis method of El-Halwagi and Manousiouthakis (1989) by developing capital cost targeting methods as well as pinch design methods for mass exchanger networks. Mathematical programming based synthesis methods have also found applications in MENS. Some of these applications include the approach of Sztikai et al. (2006), which is a MENS equivalent of the stage-wise superstructure (SWS) of Yee and Grossmann (1990) where rich and lean streams are made to participate in intervals of a superstructure for the purpose of mass exchange. The method presented by Azeez et al. (2013) is also a stage-wise superstructure based approach, however the stages are defined based on the supply compositions of the participating rich and lean streams in the problem. Another mathematical based synthesis approach was presented by Papalexandri et al. (1994) where a simultaneous approach was used. Further extensions to MENS in the aspect of multi-period operations was presented by Isafiade and Fraser (2009) while the aspect of accounting for more detailed mass exchanger

designs in MENS was presented by Isafiade et al. (2016) using the supply based superstructure of Azeez et al. (2013).

It is worth stating at this point that the MENS methods reviewed so far have mostly involved grass-root scenario, whereas some existing plants whose designs are not optimal in terms of usage of mass separating agents (MSAs) need to be optimally retrofitted so as to minimise operating costs. In the aspect of retrofitting of process plants, HENS has received more attention with very few papers presented for mass exchanger network (MEN) retrofit. One of the earliest papers presented on MEN retrofit is the work of Fraser and Hallale (2000) where pinch technology was adopted. The method entails three steps which are, setting of utility savings targets and investment targets, construction of a savings investment curve for a range of minimum composition differences and the generation of designs that meets the set targets. Alfadala et al. (2001) used a two-stage approach for the synthesis of retrofit MENS. The first step entails identifying potentially optimal configurations through heuristics, while the next step involves the development of a new mass pinch analysis approach which aims at maximising the use of existing equipment and minimising newly added capital. Chen and Hung (2005) were the first to adopt a simultaneous mathematical programming approach for the retrofitting of MENS. The technique used by the authors is based on the stage-wise superstructure (SWS) for MENS. To the best of the knowledge of the current author, only the work of Chen and Hung (2005) has adopted a simultaneous mathematical programming approach to the retrofit of MENS. Hence this paper is presented so as to further develop this field of process synthesis by proposing a method that uses a simultaneous synthesis approach that has the ability to generate cost effective retrofit networks with relatively low payback periods. The solution generation of the new method is also less computationally intensive due to the adoption of the reduced superstructure synthesis approach which was first presented for multi-period HENS by Isafiade et al. (2015).

2. Problem statement

The problem addressed in this paper can be stated as follows: Given an existing MEN having the following: a set of mass exchangers of known sizes and location in the network, a set of rich and lean process streams with supply compositions, target compositions, flowrates and their pairings within each unit of the existing network. Also given are available external MSAs, as well as their supply and target compositions and unit costs, cost per equilibrium stage for newly added trays and reassignment of tray in staged columns. It is desired to minimize the total annual cost of the retrofitted MEN in terms of MSA consumption while ensuring that existing mass exchanger stages are used as much as possible so that only minimal trays/columns would be added to the network if needed.

3. Methodology

The first step entails extracting the process data from the existing MEN and solving it for a grass-root scenario using the SWS model for MENS presented by Sztikai et al. (2006). The capital cost function used in the objective function of the superstructure model at this stage are those earmarked for new mass exchangers that may need to be installed. The stream matches selected in the optimal solution of this step are identified and used as the set of initialising binary variables for the reduced superstructure of the

next step. The second step is where the reduced superstructure is generated and solved. The process adopted entails constructing the reduced superstructure using two sets of matches as initialising binary variables. The first set entails the matches selected in the solution of the grass-root model of step 1 while the second set involves the set of matches that existed in the original unretrofitted network. Matches that are common to these two sets of matches are only represented once in the reduced superstructure. This reduced superstructure at this stage is still constructed using the SWS model with the same number of stages as used in step 1. The superstructure is also solved as a mixed integer non-linear program (MINLP) model because the final optimal retrofitted network may need fewer number of units compared to that of the reduced superstructure. Another reason the reduced superstructure is solved as a MINLP model is to make provision for a scenario where the designer may want to explore the possibilities of getting a better retrofitted network by including other promising matches that may not have been among the selected matches in the grass-root network solution of step 1. The model in this step is called a reduced superstructure because the number of participating binary variables in the superstructure is fewer than what obtains for the grass-root superstructure of step 1. The capital cost component in the objective function of the resulting reduced superstructure needs to be adjusted for the purpose of accommodating new exchangers. These new exchangers are those that were not present in the original network. They also include those exchangers present in the original network that may need to be reused or have their sizes increased through addition of extra stages. It should be known that the detailed model equations for step 1 of the newly presented synthesis method of this paper are the same as those of Szitkai et al. (2006). These same set of model equations are used in step 2 but with fewer number of binary variables. However, the objective function of this new method, and its associated equations (i.e. Equations 1 and 2 shown in section 4), are newly presented in this paper.

4. Model equations

Equation 1 illustrates the number of stages $N_{i,j,k}^{Select}$ selected after solving the reduced superstructure. In this equation, Δy^n is the rich stream concentration difference, Δy^{*n} is the lean stream equilibrium concentration difference, Δy_1^n is the rich end of the exchanger driving force, Δy_2^n is the lean end of the exchanger driving force, n is defined as 1/3 by Underwood (1970).

$$N_{i,j,k}^{Select} = \left[\frac{\Delta y^n + \Delta y^{*n}}{\Delta y_1^n + \Delta y_2^n} \right]^{1/n} \quad (1)$$

In Equation 2, subscript i represents index for rich stream, subscript j represents index for lean stream, subscript k represents index for stages in the superstructure, $N_{i,j,k}^{Exist,orig}$ is the number of stages in each of the existing mass exchangers in the original network while $N_{i,j,k}^{New}$ is the difference in number of stages between $N_{i,j,k}^{Select}$ and $N_{i,j,k}^{Exist,orig}$. In order to further illustrate the model equations adopted, consider a case where mass exchanger $N_{2,4,3}^{Select}$ is selected after solving the reduced superstructure as presented in step 2. If that same exchanger, i.e. $N_{2,4,3}^{Exist,orig}$ existed in the original network, then the difference in the number of stages between $N_{2,4,3}^{Select}$ and $N_{2,4,3}^{Exist,orig}$ determines the number of stages of $N_{i,j,k}^{New}$. This $N_{i,j,k}^{New}$ is the number of stages that is then costed as part of the capital equipment that would be paid for as illustrated in the objective function shown in Equation 3. On the other hand, if $N_{i,j,k}^{Select}$ was selected in the second step but

$N_{2,4,3}^{Exist,orig}$ did not exist in the original network, then the implication of this is that a completely new mass exchanger, represented as $N_{i,j,k}^{New}$ will be included as part of the capital cost in the objective function.

$$N_{i,j,k}^{New} = N_{i,j,k}^{Select} - N_{i,j,k}^{Exist,orig} \quad (2)$$

If $N_{i,j,k}^{Select}$ is less than $N_{i,j,k}^{Exist,orig}$, then the difference between the two can be systematically reassigned for use in some other location in the network. Although considering the way the model is set up, i.e. $N_{i,j,k}^{Exist,orig}$ being included as part of the initializing binary variables of the reduced superstructure, then $N_{i,j,k}^{Exist,orig}$ is most likely going to be selected and fully utilized most of the time. This implies that fewer new exchangers would be need to be included in the retrofitted network.

$$TAC = \min \left(\sum_{j \in S} CUL_j \cdot L_j + \sum_{i \in R} \sum_{j \in S} \sum_{k \in K} CF_{i,j} \cdot z_{i,j,k} + ACT_{i,j} \cdot \sum_{i \in R} \sum_{j \in S} \sum_{k \in K} N_{i,j,k}^{New} \right) \quad \forall i \in R; j \in S; k \in K \quad (3)$$

In Equation 3, CUL_j is the cost per unit of lean stream j , L_j is the flowrate of lean stream j , R represents set of rich streams, S represents set of lean streams, K represents set of stages in the superstructure, $CF_{i,j}$ represents installation cost for mass exchangers, $z_{i,j,k}$ represents the binary variable in the reduced superstructure, $ACT_{i,j}$ is the annual cost per stage. General Algebraic Modelling System (GAMS), version 24.2.3 (Rosenthal, 2012), is used as the solver environment for the models of this paper. The machine used operates on Microsoft® Windows 7 Enterprise™ 64 bit, Intel® Core™ i5-3210M processor running at 2.50 GHz with 4 GB of installed memory. CPLEX and CONOPT, in conjunction with DICOPT, were used as the solvers for the MILP and NLP sub-problems respectively.

5. Example

The example considered in this paper, which is a coke-oven gas sweetening process was first presented by El-Halwagi and Manousiouthakis (1989). The grass-root design presented for this problem by Papalexandri et al. (1994) is used as the original network to be retrofitted. Also, the capital cost presented by the authors (\$4552 per stage per year with an annualisation period of 5 years) is adopted. This same original network shown in Figure 1 has been retrofitted by very few authors which are Fraser and Hallale (2000) and

Table 1: Stream data for the coke-oven gas sweetening process

Rich streams	G_i (kg/s)	Mass fraction		Lean streams	L_j^c (kg/s)	Mass fraction		Annual cost (\$/y)/(kg/s)
		Y^s	Y^t			X^s	X^t	
R_1 Coke-oven gas	0.9	0.07	0.0003	S_1 Aqueous NH_3	2.3	0.0006	0.031	117,360
R_2 Claus tail gas	0.1	0.051	0.0001	S_2 Chilled methanol	∞	0.0002	0.0035	176,040

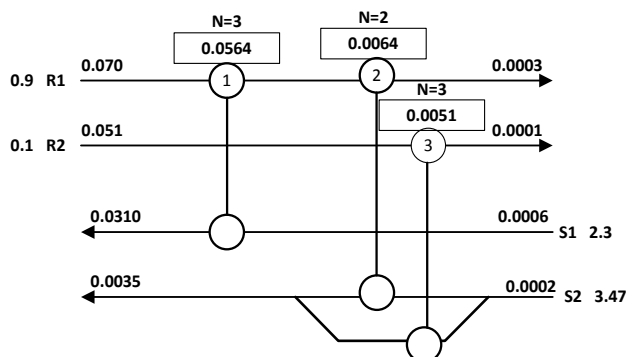


Figure 1: Original network for the coke-oven gas process

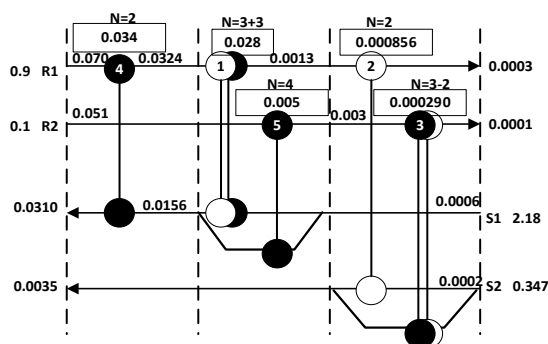


Figure 2: Retrofit network of the coke-oven gas process using proposed method

Chen and Hung (2005). The stream data for the problem is shown in Table 1. The equilibrium constants for the lean streams are: $S_1: y = 1.45x_1$; $S_2: y = 0.26x_2$. Applying step 1 of the newly developed method of this paper gives a structure with 5 matches which are (R1,S1,1); (R1,S2,3); (R2,S2,3); (R1,S1,2); (R2,S1,1). Three of these matches (i.e. R1,S1,2; R1,S2,3; R2,S2,3) exist in the original network, hence the reduced superstructure of step 2 was constructed using the five matches selected in step 1. Solving the reduced superstructure gives the solution shown in Figure 2. This solution has an objective value of \$477,833 for the first year which is about 13.3% less than the objective value presented by Chen and Hung (2005). The \$477,833 cost of this paper involves an annual operating (AOC) cost of \$318,513 and \$159,320 as the cost of network modification in the first year. The AOC saved is $\$881,463 - \$318,513 = \$562,950$. This savings corresponds to a payback period of $159,320/562,950 = 0.28$ year. This is lower than the payback time of Chen and Hung (2005) which is 0.33 year. In Figure 2, exchangers 1, 2 and 3 exist in the original network. Exchanger 2 is fully utilised as it was in the original, exchanger 1 is increased by 3 stages while exchanger 3 is decreased by 2 stages. Exchangers 4 and 5 are newly added exchangers.

6. Conclusions

A new method for retrofitting MENs has been presented in this paper. The method entails generating a reduced superstructure from a combination of the set of matches existing in the original network and those selected when the problem data is solved as a

grass-root model. An example from the literature was considered and the solution obtained compares favourably with those in the literature. The method presented in this paper has only been applied to staged mass exchangers, however it can easily be extended to continuous contact columns as well.

Acknowledgement

This study is supported by the National Research Foundation of South Africa (Grant number: 85536) and the Research Office of the University of Cape Town, South Africa. The funds are gratefully acknowledged.

References

- A.J.W. Underwood, 1970, Simple formula to calculate mean temperature difference, *Chemical Engineering* 77: 192.
- A. J. Isafiade, M. Short, Z. Kravanja, K. Moller, 2016, Synthesis of mass exchange networks using mathematical programming and detailed cost functions, *Computer Aided Chemical Engineering*, 38, 1875 - 1880.
- A. Isafiade, M. Bogataj, D. Fraser, Z. Kravanja, 2015, Optimal synthesis of heat exchange networks for multi-period operations involving single and multiple utilities, *Chemical Engineering Science*, 127, 175-188.
- A. Isafiade, D. Fraser, 2009, Interval based MINLP superstructure synthesis of multi-period mass exchange networks, *Computer Aided Chemical Engineering*, 26, 877 - 881.
- C-L. Chen, P-S. Hung, 2005, Retrofit of mass exchange networks with superstructure based MINLP formulation, *Industrial and Engineering Chemistry Research*, 44(18), 7189 – 7199.
- D.M. Fraser, N. Hallale, 2000, Retrofit of mass exchange networks using pinch technology, *AIChE Journal*, 46(10), 2112 – 2117.
- H.E. Alfadala, A.K. Sunol, M.M. El-Halwagi, 2001, An integrated approach to the retrofitting of mass exchange networks, *Clean Products and Processes*, 2(4), 236 – 247.
- K.P. Papalexandri, E.N. Pistikopoulos, C.A. Floudas, 1994, Mass exchange networks for waste minimization: A simultaneous approach, *Trans IChemE*, 72, 279 - 294.
- M.M. El-Halwagi, V. Manousiouthakis, 1989, Synthesis of Mass Exchange Networks, *AIChE Journal*, 35(8), 1233-1244.
- N. Hallale, D.M. Fraser, 2000, Capital and total cost targets for mass exchange networks, Part 2: Detailed capital cost models, *Computers & Chemical Engineering*, 23, 1681-1699.
- O.S. Azeez, A.J. Isafiade, D.M. Fraser, 2013, Supply-based superstructure synthesis of heat and mass exchange networks, *Computers and Chemical Engineering*, 56, 184-201.
- R.E. Rosenthal, 2012, *GAMS - A User's Guide*, Washington, DC, USA: GAMS Development Corporation.
- T. Yee, I. Grossman, 1990, Simultaneous Optimization Models for Heat Integration—II. Heat Exchanger Network Synthesis. *Computers & Chemical Engineering*, 14(10), pp. 1165-1184.
- Z. Sztikai, T. Farkas, Z. Lelkes, Z. Fonyo, Z. Kravanja, 2006, Fairly linear mixed integer nonlinear programming model for the synthesis of mass exchange networks, *Industrial Engineering Chemistry Research*, 45, 236-244.

Optimization-Based Process Synthesis for Integrated Crystallizer-Wet Mill System for Improved Crystal Shape Control

Botond Szilagyí^{a,b}, Zoltan K. Nagy^{a,b,*}

^a *Department of Chemical Engineering, Loughborough University, Loughborough, LE11 3TU, UK;*

^b *Davidson School of Chemical Engineering, Purdue University, West Lafayette, IN 47907-2100, USA*

zknagy@purdue.edu

Abstract

The simultaneous control of crystal size and shape is particularly important in fine chemical and pharmaceutical crystallization. These two quantities not only influence significantly the dissolution rate and bioavailability of final drug products, but also contribute to the manufacturability and efficiency of downstream operations. The manipulation of crystal shape, however, is difficult since it requires the decoupled growth rate control of individual crystal faces. The supersaturation and solvent system dependency of these rates are often not strong enough to enable impactful crystal shape control through temperature and/or solvent composition variation.

The aim of this work is to analyse and evaluate the control possibilities of bivariate size distribution (which by definition involves crystal size and shape information) of high-aspect ratio crystals in an integrated crystallizer-external wet mill system. The crystallizer is modelled by primary and secondary nucleation, crystal growth and dissolution along the length and width axes, whereas in the wet mill – in addition to the aforementioned sub-processes - fragmentation and attrition are also considered. The advanced hydrodynamic description enables the direct implication of stirrer revolution speed in the model. The generated system of hyperbolic partial differential and ordinary differential equations is solved by the fully discretized high-resolution finite volume method, involving graphical processing unit acceleration, which brings significant – generally two orders of magnitude - speed-up. The dynamic optimization of wet-mill rotation speed, crystallizer temperature and recirculation flowrate revealed that the target bivariate crystal size distribution can be achieved much better with the integrated system than manipulating only the temperature profile of the batch crystallizer.

Keywords: crystallization, crystal breakage, integrated system, population balance, shape control

1. Introduction

Batch crystallization is one of the most efficient and economic separation and purification technique available in the fine chemical and pharmaceutical industry. It is also significant from the particle formation point of view, as during the batch the crystal size distribution (CSD) can be adjusted, although within a certain domain determined by supersaturation and crystallization mechanisms that occur during the batch. There are

many techniques to broaden the achievable crystal size domain, which is desired for quality reasons as well as for good operation of downstream processes, from optimal dynamic seeding (Aamir et al. 2010) through application of growth rate modifiers in tailored quality and quantity (Jones & Ogden 2010). A recently proposed system involves an external wet mill through a recirculation loop (Yang et al. 2015), which was shown to increase simultaneously the overall system flexibility and achievable crystal size domain (Vetter 2016).

In the last decades it was revealed that, in addition to the crystal size, the crystal shape also impacts the drug-substance relevant properties (Ma et al. 2002). After this discovery the interest turned into the direction of understanding and controlling simultaneously the crystal size and shape during crystallization (Nagy et al. 2013). The shape control is more challenging than the size control as the supersaturation generally has significantly lower impact on the crystal shape than on the size. The growth rate modifiers are known to be effective tools when comes to shape control, which has the strongest impact on the crystal habit (Klapwijk et al. 2016; Borsos et al. 2016). Mechanical methods, such as breakage, are also applicable and its effect on crystal shape was analysed in detail (Szilágyi & Lakatos 2017). This work shows that the optimal operation of crystallizer-wet mill integrated system is able to improve tremendously the CSD in terms of target satisfaction (Szilágyi & Nagy 2017).

A work that employs external wet-milling during crystallization for simultaneous crystal size and shape control for the best knowledge of authors has not been published yet. In this study we attempt to fill this gap by developing a two-dimensional population balance model for the crystallization of rod-like crystals, which is often encountered amongst active pharmaceutical ingredients, in integrated batch crystallizer-wet mill system. Using the process model the integrated system operation, including the crystallizer temperature profile, circulation flowrate and wet-mill impeller speed, are optimized. It was shown that the integrated system could approximate significantly better the target 2D CSD than the crystallizer-only setup. The optimal operation strongly relied on powerful milling in the wet-mill and fines dissolution at the end of the batch.

2. Process model development

The supersaturation and temperature dependencies of growth rates along the length and width axes leads to particulate systems in which the crystal shape may exhibit complex habit variations during the crystallization process. Consequently, the crystal must be characterized with two independent size variables, namely the crystal length and width (L_1, L_2) $\rightarrow \mathbf{L}$. For the characterization of particle population the bivariate size density function $n(\mathbf{L}, t)d\mathbf{L}$ is introduced, which gives the number of crystals within the $(L_1, L_1+dL_1) \times (L_2, L_2+dL_2)$ size domain in t time moment. The process model is developed for the integrated system presented (Figure 1a) by taking into account the assumptions:

- The crystallizer and wet mill are perfectly mixed
- There is no transport delay and no crystallization occurs in the circulation lines
- Primary nucleation, growth and dissolution occurs in the crystallizer
- Primary nucleation, growth, dissolution, attrition and fragmentation takes place in the wet-mill

Then, the population balance equation (PBE) for the crystallizer takes the form:

$$\frac{\partial n_c(\mathbf{L}, t)}{\partial t} + \sum_{i=1}^2 G_i \frac{\partial n_c(\mathbf{L}, t)}{\partial L_i} = B\delta(\mathbf{L} - \mathbf{L}_n) + \frac{n_{wm}(\mathbf{L}, t) - n_c(\mathbf{L}, t)}{\tau_c} \quad (1)$$

With the initial and boundary conditions:

$$\begin{aligned} n_c(\mathbf{L}, t=0) &= n_{c,0}(\mathbf{L}) \\ n_c(\mathbf{L} = \infty, t) &= 0 \end{aligned} \quad (2)$$

Where the initial condition gives the seed distribution whereas the boundary condition expresses that the crystals must have finite size. The first term in Eq.(1) gives the temporal evolution of 2D CSD, the second term is for the growth, whereas the left hand side is the nucleation and feed/discharge streams. The PBE for the wet-mill is:

$$\frac{\partial n_{wm}(\mathbf{L}, t)}{\partial t} + \sum_{i=1}^2 G_i \frac{\partial n_{wm}(\mathbf{L}, t)}{\partial L_i} = B\delta(\mathbf{L} - \mathbf{L}_n) - S(\mathbf{L})n_{wm}(\mathbf{L}, t) + \iint b(\mathbf{L}|\mathbf{Y})S(\mathbf{Y})n_{wm}(\mathbf{Y}, t)d\mathbf{Y} + \frac{n_c(\mathbf{L}, t) - n_{wm}(\mathbf{L}, t)}{\tau_{wm}} \quad (3)$$

The Eq.(2) boundary conditions are valid. The second and third term in the right hand side of Eq.(3) express the sink and birth functions of crystal breakage. The kinetic equations of the nucleation, growth and dissolution are described by the trivial power-law functions of supersaturation. The temperature dependency of solubility is approximated with Apelblat equation. These are well-known equations, thus, for brevity, are not given here. In order to complete the model, mass balances are required for the crystallizer and wet mill, which, assuming $L_n = 0$ nucleon size, have the form:

$$\begin{aligned} \frac{dc_c}{dt} &= -k_v\rho_c \left(\iint G_1 L_2^2 n_c(\mathbf{L}, t) d\mathbf{L} + 2 \iint G_2 L_1 L_2 n_c(\mathbf{L}, t) d\mathbf{L} \right) + \frac{c_{wm} - c_c}{\tau_c} \\ \frac{dc_{wm}}{dt} &= -k_v\rho_c \left(\iint G_1 L_2^2 n_{wm}(\mathbf{L}, t) d\mathbf{L} + 2 \iint G_2 L_1 L_2 n_{wm}(\mathbf{L}, t) d\mathbf{L} \right) + \frac{c_c - c_{wm}}{\tau_{wm}} \end{aligned} \quad (4)$$

With the initial conditions:

$$c_c(t=0) = c_{c,0}; \quad c_{wm}(t=0) = c_{wm,0} \quad (5)$$

The wet-mill is a complex crystallization system. Figure 1b illustrates a snapshot from the continuous mill operation, governed by Eq.(4), in which the effects of crystallization

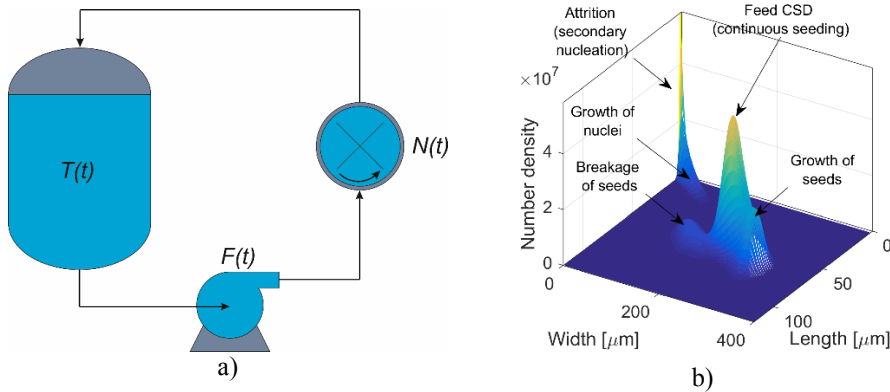


Figure 1. a) Scheme of the integrated crystallizer-wet mill system with the most important design parameters; b) the effects of simultaneously ongoing mechanisms on the crystals population in the wet-mill

mechanisms can be distinguished clearly. This figure also highlights the importance of full PBM solution when comes to distribution shaping control, over calculating and

controlling just the mean crystalline properties. The wet-mill energy balance, taking into account the effects of inlet-outlet streams, impeller energy and heat of crystallization is:

$$\frac{dT_{wm}}{dt} = \frac{P_{stirr}(N)}{V_{wm}c_{p,sol}\rho_{sol}} - \frac{k_v\rho_cH_c}{c_{p,sol}\rho_{sol}} \left(\iint G_1L_2^2n_{wm}(\mathbf{L},t)d\mathbf{L} + 2\iint G_2L_1L_2n_{wm}(\mathbf{L},t)d\mathbf{L} \right) + \frac{T_c - T_{wm}}{\tau_{wm}} \quad (6)$$

where P_{stirr} denotes the impeller stirring power, which is a function of impeller revolution speed. The initial condition for Eq.(6) is:

$$T_{wm}(t=0) = T_{wm,0} \quad (7)$$

Since the crystallizer temperature is a manipulated variable, the crystallizer energy balance is not written up. In the partial and ordinary differential model equations the nucleation and growth rates are calculated for the temperature and concentration of the modelled sub-system. In this context, the growth rates in the crystallizer and wet mill equations have the same notations but they may represent different values.

3. Process simulations and optimizations

The model Eq.(1)-(7) were solved by a full-discrete implementation of the high resolution finite volume method (HR-FVM). The algorithm contains many parallelizable operations, such as the integral calculations, breakage selection and daughter distribution function calculations as well as the HR-FVM operations, which are time consuming if solved serially. To boost the simulation time, these operations were passed to the graphical processing unit (GPU) of the computer, which has massive parallel hardware architecture thus it is natively well-suited for the execution of parallel tasks. Due to the brevity, the numerics is not presented, but the GPU acceleration brings two orders of magnitude speed-up compared to the compiled serial C code.

The existence of a high-performance system alone is not a guarantee of quality, that economic and ecologic related constraints will all be satisfied. The system operation needs to be fine-tuned. In this work, the temperature (T), circulation flowrate (F) and wet mill impeller revolution speed (N) profiles have been optimized, which in fact represents the synthesis of an integrated system operation. The objective function:

$$SSE(T, F, N) = \iiint \left(\frac{n_c(\mathbf{L}, t=t_{final}) - n_{ref}(\mathbf{L})}{n_{ref}(\mathbf{L})} \right)^2 d\mathbf{L} dt + w_1 \int N(t) dt + w_2 \int F(t) dt \quad (8)$$

The first part of Eq.(8) minimizes the difference between the target and product CSD whereas the last two terms minimize the wet-mill and pump usage. Thus, the system is supposed to produce the target CSD with minimal equipment (which translates to energy) utilization. The optimization was solved in Matlab environment using the evolution strategy with covariance matrix adaptation (CMA-ES) global optimization algorithm. Both systems involve a final cooling for fines dissolution. The optimal circulation ensures both the optimal transport of crystals and the optimal temperature and concentration conditions in the wet-mill. The crystallizer-only configuration cannot even approximate the target CSD – despite it favors width growth significantly, which highlights the importance of controlled breakage through the wet-mill. The target CSD can be approximated better by enabling longer batch time and/or giving more weight to the CSD part in the objective function. This optimization itself demonstrates clearly the high potential of the presented integrated system for simultaneous size/shape control.

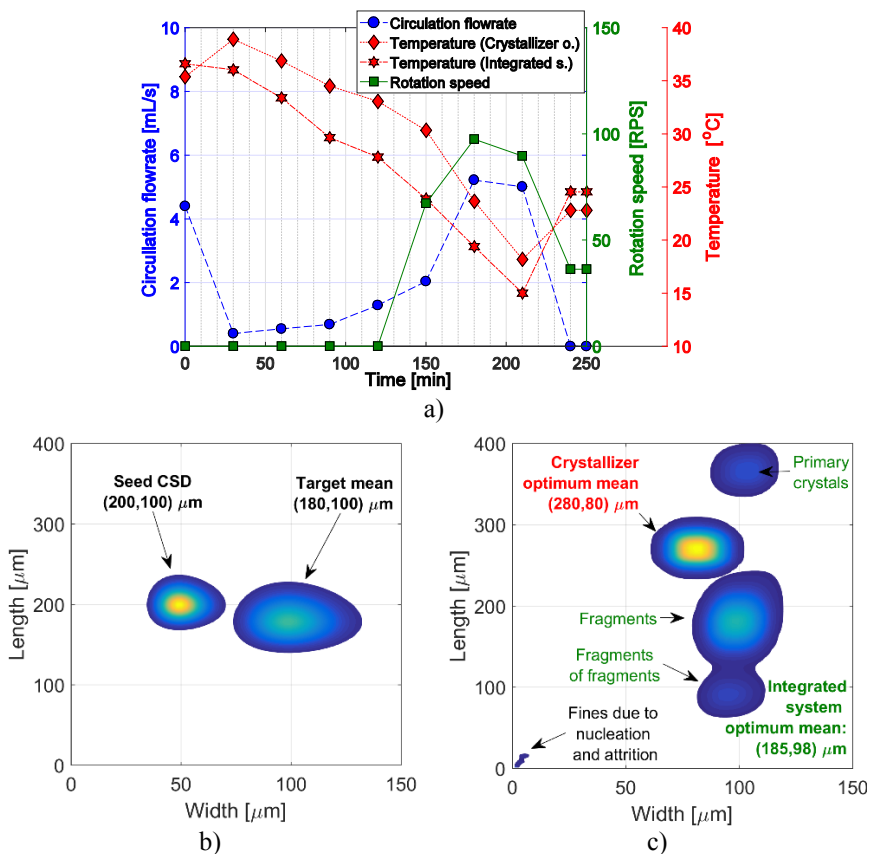


Figure 2. a) Optimal profiles for the integrated system and for the crystallizer-only configuration; b) initial and target CSD; c) CSD realized by the crystallizer-only configuration and by the integrated system

4. Conclusions

In this study the concept of simultaneous size and shape control of high aspect ratio crystals was evaluated in an integrated crystallizer-wet mill system based on mathematical modeling and simulation. The population balance model involves primary nucleation, growth and dissolution along the length and width faces in the crystallizer but for a more realistic wet-mill description, next to the attrition (collision generated secondary nucleation) and binary breakage, primary nucleation, crystal growth and dissolution mechanisms were also included, as well as the impeller heating effect.

The model-equations were solved by a full-discrete implementation of the high-resolution finite volume method (HR-FVM). For simulation time improvement the graphical processing unit (GPU) was also implied for the execution of parallel operations (such as breakage, HR-FVM and integral calculations), which leads to two orders of magnitude speedup compared to the serial C implementation.

The dynamic optimization was carried out based on evolutionary global optimization algorithm and it revealed that the wet-mill is indispensable for the production of low

aspect ratio product of material with high length-growth kinetics directly in the crystallization step. The optimal system operation involves both cooling (for crystal growth) and heating (for fines dissolution) stages in the crystallizer as well as variable circulation flowrate and wet-mill rotation speed. Further investigations are required to clarify the individual role of crystallization mechanisms in the crystallizer and wet mill under optimal conditions as well as to find economically advantageous operations. However, the current work demonstrates clearly the high potential of the integrated system for efficient and elegant crystal shape control.

5. Acknowledgements

The financial support of the International Fine Particle Research Institution is acknowledged gratefully. Funding from the European Research Council under the European Union's Seventh Frame-work Programme (FP7/2007-2013)/ERC grant agreement No. [280106-CrySys] is also acknowledged.

6. References

- Aamir, E., Nagy, Z.K. & Rielly, C.D., 2010. Optimal seed recipe design for crystal size distribution control for batch cooling crystallisation processes. *Chemical Engineering Science*, 65(11), 3602–3614.
- Borsos, A., Majumder, A. & Nagy, Z.K., 2016. Multi-Impurity Adsorption Model for Modeling Crystal Purity and Shape Evolution during Crystallization Processes in Impure Media. *Crystal Growth & Design*, 16(2), 555–568.
- Jones, F. & Ogden, M.I., 2010. Controlling crystal growth with modifiers. *CrystEngComm*, 12(4), 1016–1023
- Klapwijk, A.R., Simone, E., Nagy, Z.K., Wilson, C., 2016. Tuning Crystal Morphology of Succinic Acid Using a Polymer Additive. *Crystal Growth & Design*, 16(8), 4349–4359.
- Ma, D.L., Tafti, D.K. & Braatz, R.D., 2002. High-Resolution Simulation of Multidimensional Crystal Growth. *Industrial & Engineering Chemistry Research*, 41(25), 6217–6223.
- Nagy, Z.K., Fevotte, G., Kramer, H., Simon, L.L., 2013. Recent advances in the monitoring, modelling and control of crystallization systems. *Chemical Engineering Research and Design*, 91(10), 1903–1922
- Szilágyi, B. & Lakatos, B.G., 2017. Model-based analysis of stirred cooling crystallizer of high aspect ratio crystals with linear and nonlinear breakage. *Computers & Chemical Engineering*, 98, 180–196
- Szilágyi, B. & Nagy, Z.K., 2018, Population balance modeling and optimization of an integrated batch crystallizer – wet mill system for crystal size distribution control, *Crystal Growth & Design*, DOI: 10.1021/acs.cgd.7b01331
- Vetter, T., 2016. Attainable Regions of Particle Sizes for Continuous Milling-Crystallization Processes. In *AIChE Annual Meeting*.
- Yang, Y., Song, L., Gao, T., Nagy, Z.K., 2015. Integrated Upstream and Downstream Application of Wet Milling with Continuous Mixed Suspension Mixed Product Removal Crystallization. *Crystal Growth and Design*, 15(12), 5879–5885.

Mathematical Modeling and Simulation in Natural Flavors and Fragrances Bioproduction Intensification

Ivan Červeňanský^a, Mario Mihal^{pa}, Jozef Markoš^{a*}

*^aInstitute of Chemical and Environmental Engineering, Slovak University of
Technology in Bratislava, Radlinského 9, 812 37 Bratislava, Slovak Republic
jozef.markos@stuba.sk*

Abstract

Production intensification is nowadays done using mathematical models and universal process simulators, where modeling of specific biocatalytic kinetics can be difficult because often such models are simply not available. For the study of parametric influence on the system or for intensification tasks, specific biocatalytic kinetics has to be programmed individually. An example of such kinetics is also the bioproduction of 2-phenylethanol from L-phenylalanine by yeasts *Saccharomyces cerevisiae*. For the subsequent separation of 2-phenylethanol from the fermentation medium, membrane processes (microfiltration and membrane extraction) are applied, models of which are also missing in universal process simulators. Therefore, mathematical models of biotransformation and separation steps were developed and a model library with individual unit operations (bioreactor, microfiltration, membrane extraction, distillation) was assembled in this work. Description of the mathematical models is given and the approach towards the development of a custom simulation tool is presented. The finalized tool can simulate bioproduction of 2-phenylethanol in the batch mode as well as in a hybrid production system with continuous product removal. Simulation results can be used to study the production system as well as to master intensification tasks.

Keywords: process intensification, 2-phenylethanol, hybrid system, bioreactor, modeling.

1. Introduction

The past decade has shown that consumers search for the label natural, especially in food and cosmetic products, for which they are willing to pay higher prices. Flavors and fragrances are widely used in the food and cosmetic industry and, according to legislation, a product can be labeled as natural only if the substrate used for the production process is of natural origin (Etschmann et al., 2002). Many natural aromas can be produced in a biotechnological way via enzymatic and microbial processes but a common hindrance of more effective bioproduction is the toxicity of the precursor or the product. In case of precursor toxicity, the enhancement in production can be achieved by gradual precursor addition to the bioreactor; in case of product toxicity, production can be intensified by integration of the bioreactor and continuous product removal techniques thus creating a hybrid system (Krishna, 2002). Extensively used separation techniques in the design of biotechnological hybrid systems are membrane separations, which operation currently cannot be simulated in the universal process simulators. Also, biocatalytic reactions often have very specific kinetics which is not

easily implemented into these simulation environments. In general, sophisticated models not only of biotechnological hybrid systems but also of highly integrated configurations of classical separation processes (e.g. divided wall columns) are missing in the universal process simulators (Waltermann et al., 2017). In such cases, custom made mathematical models of hybrid systems have to be individually programmed to provide a tool for the study of the variety of parameters influencing the behavior of the whole hybrid system. After the verification of the mathematical models used, these custom tools can be applied for intensification tasks. In this work, mathematical models of different hybrid systems for biotechnological production of 2-phenylethanol (PEA), which is an important aroma with characteristic rose-like fragrance, were programmed. Computational tool with graphical user interface was created facilitating the study of hybrid systems and for the use in further intensification tasks.

2. Bioproduction of 2-phenylethanol

Biocatalytic production of PEA runs according to the Ehrlich metabolic pathway, where the precursor L-phenylalanine (Phe) is transformed to PEA. When the amino acid is the sole nitrogen source available, many yeast strains utilize the Ehrlich pathway for its metabolization and *Saccharomyces cerevisiae* provide high production yields (Etschmann et al., 2003). Production of PEA is growth related and since *Saccharomyces cerevisiae* are also used as a producer of other important products, mathematical models of their growth are available in literature. Published mathematical models differ in complexity depending on the structure or segregation of the model. Currently, universal process simulators have been successfully used in the development of unstructured and unsegregated models for *Shimwellia blattae* growth on specific substrates (Rodriguez et al., 2017). However, more complex kinetic models are still programmed individually using various computational software. *Saccharomyces cerevisiae* can exhibit diauxic growth when their overall growth is dependent on three metabolic pathways where two substrates are utilized. Such growth can be described by structured and unsegregated model proposed by Di Serio et al. (2001), where the optimal metabolic path is chosen at any moment in order to maximize the growth rate. This model consists of eight ordinary differential equations (balancing the biomass, glucose, ethanol, dissolved oxygen, enzymes for glucose oxidation and fermentation, enzymes for ethanol oxidation and volume of the fermentation medium) and provides information about the influence of the operation condition on the growth, which is very useful in case of further optimization of the conditions. However, the kinetic model by Di Serio et al. (2001) does not consider the inhibition of biomass growth induced by ethanol or PEA. Both inhibitors are able to stop the biomass growth but at different concentrations in the fermentation medium. For ethanol, total growth inhibition occurs at about 70 g/L and biomass growth is influenced by ethanol concentration of above 15 g/L. But ethanol formation in the fermentation medium can be limited employing a good strategy of glucose feeding, developed by the kinetic model of biomass growth involving the inhibition aspects. For comparison, total inhibition of the biomass growth occurs at much lower PEA concentration in the fermentation medium, of about 4 g/L, and first signs of growth inhibition can be observed at 0.6 g/L. Therefore, inhibition aspects of both products in PEA biocatalytic production have to be included in the mathematical model describing the biomass growth kinetics. Mathematical model of the inhibition by ethanol and PEA was presented by Strak et al. (2003), where the inhibition extent is calculated from the actual concentration of the respective inhibitor which is then applied

to the specific growth rate of biomass. Since the model by Di Serio et al. (2001) does not consider consumed Phe and produced PEA, these equations were added to the model by Mihal' et al. (2012). Production of 2-phenylethanol runs at aerobic conditions and more intensive aeration during the bioproduction increases the capacity of oxidative metabolism, which is in favor of more intensive growth of biomass. Also, ethanol can be stripped in the gaseous phase used for the aeration and leave the bioreactor in the off-gas stream. The second effect of intensive aeration is also in favor of more intensive biomass growth since the inhibitor is stripped from the reactor. This phenomenon can be described by adding the expression for mass transfer of ethanol to the gaseous phase to the ethanol balance in the kinetic model by Di Serio et al. (2001). Also, the ethanol balance in the gaseous phase with the expression for mass transfer has to be added to the mathematical model. The mathematical model described above consist of 11 differential equations balancing the main components of the production system and eight more equations for the calculation of parameters in the actual time of simulation. This complex model was firstly assembled in the work of Mihal' et al. (2012), where it was also verified by experimental results of PEA production proving an acceptable agreement with experiments. Because of the specific kinetics of the model it is not possible to assemble it in a process simulator, therefore, graphical user interface (GUI) was built in MATLAB for the PEA biotransformation model.

3. Separation of 2-phenylethanol

Effectivity of the separation has a significant role in overall production economics with respect to the selection of suitable separation steps as well as the scale of used equipment. Many separation techniques have been examined for possible PEA separation from the fermentation medium e.g. adsorption, absorption, extraction. These techniques were mainly studied for in situ product removal to effectively reduce the strong inhibitory effect of PEA, which leads to significant intensification of its overall productivity. Mathematical models of PEA continuous separation from the fermentation medium were published only by Mihal' et al. (2012), where microfiltration and membrane extraction coupled with distillation were used. Mathematical model of microfiltration consists of steady-state flux through membrane calculation based on the biomass concentration, experimentally obtained at the transmembrane pressure of 20 kPa. The calculated flux through the membrane is then used in the balances of individual fermentation medium components and volume. In membrane extraction, hollow fibers were considered as the membrane module construction material and film theory was applied for the mass transfer description. According to the film theory, the solute of interest passes three resistances in a series when it is transferred from the aqueous to the organic phase: the aqueous phase boundary layer, membrane, and the organic phase boundary layer. The membrane module was divided into the shell side and the fiber side, which were both fractionated into 100 ideally mixed tanks in series in the mathematical description of the transported component. These models were verified by experimental data with acceptable agreement and they can be used for the study of the whole hybrid system for PEA production as well as for the intensification tasks and scale up of the system. Also, the models can be used to simulate and design batch PEA production after including changes in equations expressing mutual connections of the separation processes. To develop a complex tool for the study and design of PEA production, verified mathematical models of microfiltration, membrane extraction and distillation were programmed in MATLAB and they were connected to a biotransformation model through GUI.

3.1. Batch production

Batch production starts with the biotransformation of Phe to PEA in a bioreactor. The production ends when the PEA concentration of 4 g/L is reached in the fermentation medium since it is not continuously removed during the process. The bioreactor is emptied after the biotransformation and the fermentation medium is transported to the accumulation tank. The separation part of the technology starts with microfiltration, in which cell free fermentation medium is obtained in the permeate stream. The next separation step is membrane extraction, where heptane is used as an organic solvent. In case of the presence of unreacted Phe in the fermentation medium, heptane provides selective PEA separation due to the Phe insolubility in heptane. Membrane extraction is coupled with a distillation column for heptane regeneration from which regenerated heptane is recycled back to the membrane extraction unit. The described production procedure in the batch configuration can be simulated in GUI.

3.2. Hybrid systems

Continuous PEA removal reduces its inhibitory effect on the biomass growth; therefore, creating a hybrid system with a bioreactor interconnected with a separation system enables the intensification of the whole production process (Červeňanský et al., 2017). In the hybrid production of PEA, the bioreactor is connected to a microfiltration unit in which cell free fermentation medium is obtained and the retentate stream is recycled back to the bioreactor. Permeate from the microfiltration is then led to the hollow fiber membrane extraction module, where PEA from the medium is transported to the organic phase. Heptane is used as an extractant in which Phe is insoluble; thus, heptane provides selective PEA separation. Fermentation medium from the membrane extraction is recycled back to the bioreactor and heptane is led to the distillation unit for its regeneration. Regenerated heptane is recycled back to the membrane extraction module. Bioproduction and separation processes used in the hybrid system are mathematically described by the models presented above but their mutual interaction has to be added to the already prepared model equations. Equations describing individual components of the hybrid system and those describing their mutual interactions are solved simultaneously, thus equation-oriented approach is applied in the modeling of hybrid systems. Prepared GUI can be used for the study and design of hybrid systems with the same user dependent parameters as described in the batch production system. The presented hybrid system corresponds to only one possible configuration of hybrid system, but also other configurations can be simulated with the prepared GUI.

4. Graphical user interface and results from simulations

Mathematical models of bioproduction and all used separation processes as well as the GUI were programmed in MATLAB. Graphical user interface is divided into five main sections: Options, Fermentation, Microfiltration, Extraction and Distillation and its outline is presented in Figure 1. In Options, the user can choose whether the batch production or hybrid production should be applied for the simulation. The user can also choose what separation processes are applied in either production mode. In this section, also changes in the glucose and Phe feed can be specified. In the Fermentation section, the user can change the initial conditions of the system as well as important parameters (volumetric mass transfer or yield coefficients). There is a possibility to enable or disable the ethanol stripping phenomenon with additional information needed for the calculation. In the Microfiltration section, the main design parameter is the membrane

area. Design parameters in the Extraction section are connected to the geometry of the selected hollow fiber membrane module (e.g. number of fibers, length of the module, fibers dimension) and also to the user dependent parameters (time of membrane extraction, volume of organic phase used, volumetric flow rates on shell and fiber side). Distillation coupled with membrane extraction is defined in the Distillation section, where the main design parameter is the delivered heat. Found optimal conditions in the Batch or Hybrid production can be saved through the interface and loaded for future work.

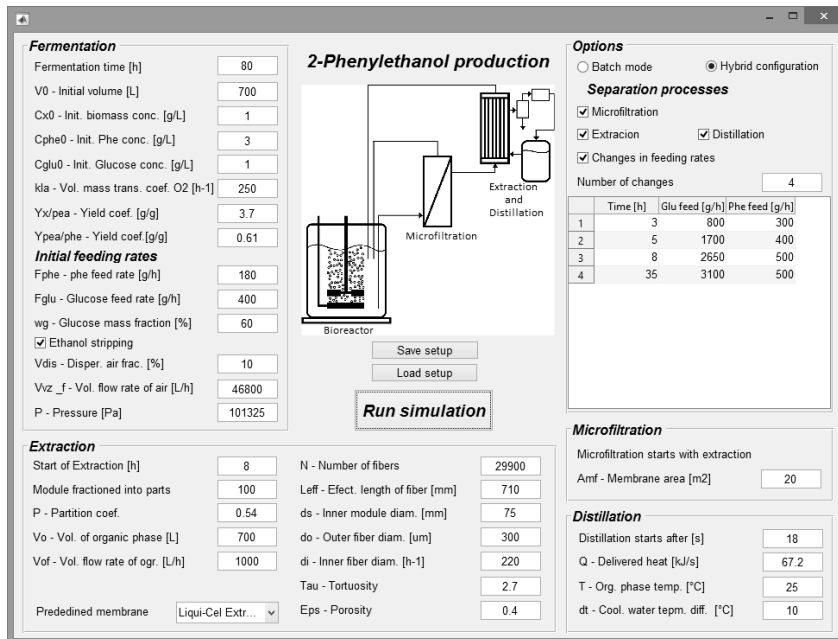


Figure 1. GUI for the simulation of PEA production in batch and in hybrid system configuration.

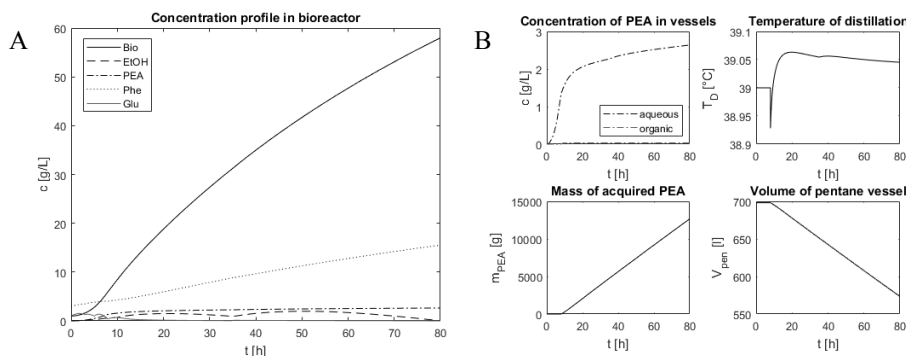


Figure 2. Results of the simulation from GUI for PEA production in hybrid system. A – concentration profiles in the bioreactor, B – result of membrane extraction coupled with distillation.

Results of the fermentation simulation are presented in form of graphs with concentration changes of biomass, ethanol, glucose, Phe and PEA in time. Results of the

separation processes simulation are time dependent concentration profiles of PEA in connected accumulation tanks. In case distillation is a part of the system, also information about separated PEA and distillation temperature are provided.

5. Conclusions

Mathematical modeling has currently an irreplaceable position in process intensification but its application in biocatalytic production of natural flavors and fragrances is difficult mainly because of very specific kinetics of the biotransformation process. Such specific kinetics cannot be easily implemented into universal process simulators which are often used for the search of optimal working conditions. Also, mathematical models of membrane separation processes are not developed in process simulators. Therefore, in these cases the only way of using mathematical modeling for the search of optimal working conditions is creating a custom program tool. In this work, such a tool has been created for the bioproduction of PEA, which is an important natural flavor. The developed program tool combines mathematical models of bioproduction, microfiltration, membrane extraction and distillation which can work in batch configuration or as one hybrid system with continuous product removal. This tool can be used to compare batch and hybrid systems or to study and intensify PEA bioproduction.

Acknowledgements

This work was supported by the Slovak Scientific Agency, Grant No. VEGA 1/0687/16, and Slovak Research and Development Agency under the contract No. APVV-16-0111.

References

- I. Červeňanský, M. Mihal', J. Markoš, 2017, Modelling and Intensification of Biocatalytic Production of Natural Compounds Performed in Hybrid Systems, *Comp. Aided Chem. Eng.* 40, 1039–1044.
- M. Di Serio, R. Tesser, E. Santacesaria, 2001, A kinetic and mass transfer model to simulate the growth of baker's yeast in industrial bioreactors, *Chem. Eng. J.* 82, 347–354.
- M.M.W. Etschmann, W. Bluemke, D. Sell, J. Schrader, 2002, Biotechnological production of 2-phenylethanol. *Appl. Microbiol. Biotechnol.* 59, 1–8.
- M.M.W. Etschmann, D. Sell, J. Schrader, 2003, Screening of yeasts for the production of the aroma compound 2-phenylethanol in a molasses-based medium, *Biotechnol. Lett.* 25, 531–536
- R. Krishna, 2002, Reactive separations: More ways to skin a cat, *Chem. Eng. Sci.* 57, 1491–1504.
- M. Mihal', R. Vereš, J. Markoš, 2012, Investigation of 2-phenylethanol production in fed-batch hybrid bioreactor, *Sep. Purif. Technol.* 95, 126–135.
- M. Mihal', R. Vereš, J. Markoš, V. Štefuca, 2012, Intensification of 2-phenylethanol production in fed-batch hybrid bioreactor, *Chem. Eng. Process. Process Intensif.* 57–58, 75–85.
- A. Rodriguez, M. Wojtusik, F. Masca, V.E. Santos, F. Garcia-Ochoa, 2017, Kinetic modeling of 1,3-propanediol production from raw glycerol by *Shimwellia blattae*: Influence of the initial substrate concentration, *Biochem. Eng. J.* 117, 57–65.
- D. Stark, D. Zala, T. Münch, B. Sonnleitner, I.W. Marison, U. von Stockar, 2003, Inhibition aspects of the bioconversion of l-phenylalanine to 2-phenylethanol by *Saccharomyces cerevisiae*, *Enzyme Microb. Technol.* 32, 212–223.
- T. Waltermann, D. Münchrath, M. Skiborowski, 2017, Efficient optimization-based design of energy-intensified azeotropic distillation processes, *Comp. Aided Chem. Eng.* 40, 1045–1050.

Simulation and economic evaluation of NO_x removal in wet scrubbers of low-speed two-stroke vessels using H₂O₂ as a replacement for conventional EGR

Yeongryeol Choi^{a,b}, Junghwan Kim^{a,*}

^a*Ulsan Regional Division, Korea Institute of Industrial Technology, Ulsan, South Korea*

^b*School of Energy and Chemical Engineering, UNIST, Ulsan, South Korea*

kjh31@kitech.re.kr

Abstract

NO_x is one of the major pollutants present in the exhaust gas of marine diesel engines. Normally, NO_x is difficult to remove using scrubbers because NO, which accounts for 90 % of NO_x, has very low water solubility. However, if NO is oxidized to other highly soluble nitrogen oxides, the removal efficiency of NO_x in a wet scrubber can be greatly improved. In this study, we estimated the efficiency of NO_x removal from the exhaust gas of a 50 MW diesel engine using H₂O₂ solution. Then, we compared the results with the removal efficiency of a conventional exhaust gas recirculation (EGR) system. The amount of H₂O₂ consumption varied from 0 to 760.30 kg/h to satisfy emission regulations, depending on the amount of NO_x input in the scrubber. In this study, we conducted an economic evaluation of the operation costs of NO_x removal using H₂O₂, considering other parameters affecting the operation cost and by comparing the results with that of the conventional EGR system. The results of the economic evaluation show that the use of EGR in ECAs was 2.307 M\$/y, which is more economical than that of H₂O₂, and the use of H₂O₂ in non-ECAs was 1.044 M\$/y, more economical than that of EGR. If the ECA ratio is less than 31.5%, the operation cost of using H₂O₂ is lower than using EGR.

Keywords: NO_x removal, EGR (Exhaust Gas Recirculation), H₂O₂, Low-speed diesel engine.

1. Introduction

With increasing awareness on the global environment, the International Maritime Organization (IMO) has further enforced stronger regulations on the emissions of SO_x and NO_x from the exhaust gases of ships since 2016 (Figure 1). While SO_x, which is

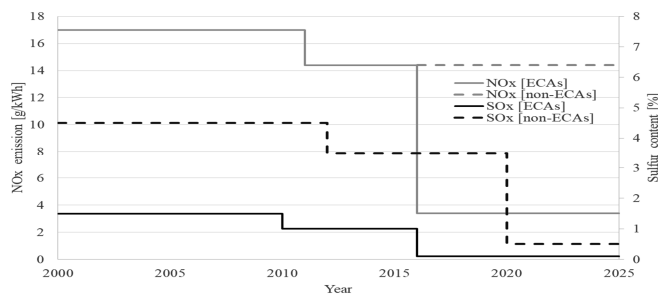


Figure 1. IMO regulation: NO_x emission and fuel sulfur contents.

water soluble, can be easily removed by using a wet scrubber, NO, which accounts for 90 % of NO_x, has very low water solubility and is difficult to remove through a wet scrubber. Many technologies for NO_x removal exist including selective catalytic reduction (SCR), EGR, oxidizing agents.

Although SCR can effectively remove NO_x, the equipment is large and heavy and the installation cost is high; as a result, installation on large ships would not be economically feasible. In contrast, the equipment size for EGR is smaller and the installation cost is lower than those for SCR. However, EGR is disadvantageous in that it can remove only 80 % of NO_x. Moreover, it also leads to fuel penalty as the fuel consumption rate increases, along with the increase in the release of other harmful substances. Among the oxidizing agents used for NO, H₂O₂ can oxidize NO and other substances, has a simple reaction mechanism, and does not generate secondary pollutants.

There are two methods for NO oxidation using H₂O₂. In the first, H₂O₂ is decomposed into OH radicals by UV to react with NO. However, this method is difficult to use on large ships that have a high emission of NO_x because the number of UV lamps required increases as the amount of NO_x increases. The second method is to initiate a reaction between NO and H₂O₂. This method does not require any additional equipment other than the H₂O₂ storage tank, which is available on large ships and takes up lesser space than that required with other technologies. This study developed a model for the NO_x removal process for low-speed two-stroke ships using H₂O₂. Furthermore, this study simulated the model by using Aspen Plus and performed an economic evaluation in comparison with the EGR process without using H₂O₂.

2. Simulation

2.1. Process flow diagram (PFD)

Exhaust gas from the engine enters the bottom of the scrubber, and H₂O₂ and water enter the top and flow downward in the scrubber. In the wet scrubber, the gas that has been cleaned through the reaction in the gas-liquid phase is discharged from the top of the scrubber into the air, and the dirty water is released from the bottom (Figure 2).

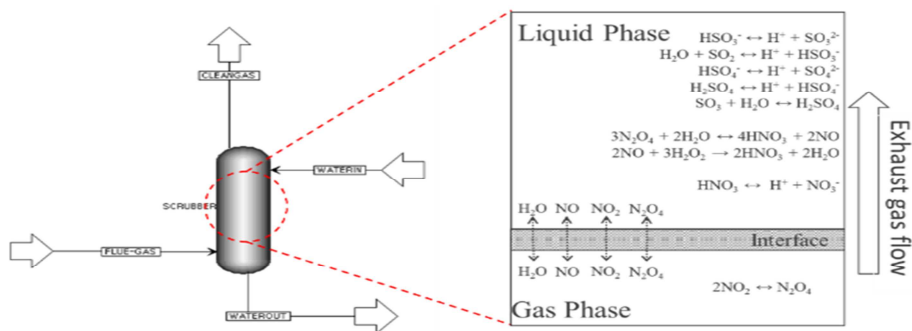


Figure 2. Process flow diagram (PFD) in Aspen plus and details.

Table 1. Engine data for simulation.

Item	Data
Engine model	11S90ME-C V9.2
100 % load	53,250 kW(81 rpm)
Experiment load (75 %)	39,938 kW(73.6 rpm)
Exhaust gas temperature	365 °C
Before turbine temperature	342 °C
After turbine temperature	193 °C
NOx	15.79 g/kWh

Table 2. Gas composition data.

Component	Typical	Calculated
N ₂	75.80 %	88.52 kg/s
O ₂	13.00 %	15.18 kg/s
H ₂ O	5.35 %	6.25 kg/s
CO ₂	5.20 %	6.07 kg/s
SO _x	0.06 %	0.07 kg/s
NO _x	0.15 %	0.18 kg/s
etc.	-	-
Total.	99.56 %	116.27 kg/s

2.2. Engine specification and exhaust gas composition

Engine data such as NO_x emissions, temperature, power, and rpm used for the simulation were based on the data from a master's thesis (Kim, 2014) of Ulsan University. Table 1 shows the exhaust gas emissions and other components of the exhaust gas calculated in reference to the exhaust gas composition (Woodyard D., 2004) of a typical low-speed two-stroke vessel (Table 2). In this study, typical compositions such as N₂, O₂, H₂O, CO₂, SO_x, and NO_x were included as the exhaust gas, and other substances such as PM and hydrocarbon (HC) were not considered. The simulation was performed by normalizing the major components based on the NO_x emission data.

Table 3. Reaction kinetics

	Reactions	Reference
1	$2\text{NO} + 3\text{H}_2\text{O}_2 \rightarrow 2\text{HNO}_3 + 2\text{H}_2\text{O}$	Baveja et al., 1979
2	$2\text{NO}_2(\text{g}) \leftrightarrow \text{N}_2\text{O}_4(\text{g})$	Yang, 1994
3	$3\text{N}_2\text{O}_4 + 2\text{H}_2\text{O} \leftrightarrow 4\text{HNO}_3 + 2\text{NO}$	Thiemann et al, 2002
4	$\text{HNO}_3 + \text{H}_2\text{O} \leftrightarrow \text{NO}_3^- + \text{H}^+$	Haunstetter and Weinhart, 2015
5	$\text{H}_2\text{O} + \text{SO}_2 \leftrightarrow \text{H}^+ + \text{HSO}_3^-$	Haunstetter and Weinhart, 2015
6	$\text{HSO}_3^- \leftrightarrow \text{H}^+ + \text{SO}_3^{2-}$	Haunstetter and Weinhart, 2015
7	$\text{HSO}_4^- \leftrightarrow \text{H}^+ + \text{SO}_4^{2-}$	Haunstetter and Weinhart, 2015
8	$\text{H}_2\text{SO}_4 \leftrightarrow \text{H}^+ + \text{HSO}_4^-$	Haunstetter and Weinhart, 2015
9	$\text{SO}_3 + \text{H}_2\text{O} \leftrightarrow \text{H}_2\text{SO}_4$	Haunstetter and Weinhart, 2015

2.3. Scrubber model

2.3.1. Reaction kinetics

The reaction kinetics used are shown in Table 3. HNO₂, which is the product of the reaction between H₂O₂ and NO, is an unstable intermediate product that exists only for a very short time. Thus, the simulation was performed by using the integrated reaction

equation. To identify the removal rate of ρ in the scrubber, the SO_x reaction equation in the liquid phase was used and it was assumed that other substances do not react.

2.3.2. Scrubbing water input

As the amount of water entering the scrubber increases, the removal rate of SO_x increases. Thus, in this study, the amount of water that removes 99 % of SO_x was set as a fixed variable when the amount of SO_x was the greatest. The removal rate of SO_x was the highest when EGR was 0 %. The removal rate of SO_x was 99 % when the ratio of water to gas entering the scrubber was 0.398 L/m³.

3. Simulation results

3.1. EGR ratio and H₂O₂ consumption according to NO_x removal

3.1.1. Case study

In this study, the simulation was performed by dividing cases according to the EGR ratio and the emission control areas (ECAs) to identify the consumption of H₂O₂, depending on the specific removal amount of NO_x.

- i) Case 1–5: H₂O₂ consumption according to the EGR ratio in ECAs.
- ii) Case 6–7: H₂O₂ consumption and EGR ratio in non-ECAs.

Table 4. Simulation result for NO_x removal with H₂O₂ and EGR.

ITEM	Unit	In ECAs					In non-ECAs	
		1	2	3	4	5	6	7
Case								
EGR ratio	%	0.00	20.76	31.34	34.31	34.50	0.00	4.90
Fuel Penalty	%	0.00	2.09	3.80	4.36	4.40	0.17	0.45
NO _x removal	%	0.00	-33.30	-66.67	-76.07	-76.67	0.00	-1.05
NO _x outlet	g/kWh	3.40	3.40	3.40	3.40	3.40	14.40	14.40
H ₂ O ₂ consumption	kg/h	760.30	428.42	98.77	3.78	0.00	10.37	0.00
H ₂ O ₂ cost	\$/h	532.21	299.89	69.14	5.82	0.00	7.26	0.00
Fuel cost	\$/h	2488.78	2540.77	2540.77	2597.39	2598.34	2488.78	2500.00
Total cost	\$/h	3020.98	2840.66	2840.66	2601.46	2598.34	2496.03	2500.00

3.1.2. Case study result

The amount of H₂O₂ necessary to satisfy the emission regulations without using EGR was 760.30 kg/h in ECAs and 10.37 kg/h in non-ECAs. Furthermore, as the EGR ratio increases, the H₂O₂ consumption to remove NO_x decreased. The NO_x removal rate and fuel penalty according to the EGR ratio were based on the results obtained from other studies. (S. I. Raptotasios et al., 2014). The EGR ratios required to satisfy the emission regulations were 34.5 % and 4.9 % in ECAs and non-ECAs, respectively. The cost of each case was calculated considering H₂O₂ and Fuel. Cost of H₂O₂ 50 % solution is 350 \$/t and Cost of IFO380 (Intermediate Fuel Oil 380) which is commonly used for fuel oil for large marine vessels is 360 \$/t. (table 4).

3.2. Parameters affecting cost

As shown in Table 4, the parameters affecting cost are the consumption of H₂O₂ as well as the fuel penalty according to the EGR ratio. When considering only two parameters,

it is cheaper to use EGR in ECAs and H₂O₂ in non-ECAs. But there are many parameters exists in real operation, like maintenance cost, power consumption, etc. The results of this study and other parameters affecting operating costs were used to evaluate the economics of the NOx removal method using H₂O₂.

4. Economic evaluation

4.1. Assumptions and parameters

- i) CAPEX was not considered because it depends on the ship size and ship manufacturer. Only the operation cost was compared. Although the capex of EGR and scrubber is shown table 5, it is just used for calculation of maintenance cost.
- ii) The ship considered uses IFO380 for fuel and uses the scrubber to remove SOx.
- iii) The evaluation was conducted for each NOx removal technology separately in both ECAs and non-ECAs.
- iv) NaOH is used in order to neutralize the sulfuric acid in scrubber and protect the engine components for corrosion. (Kotakis NK, 2012) We assumed that NaOH is consumed only EGR-method because the side-reactions of H₂O produce the OH- which can neutralize the solution. (Liu Y xian and Zhang J, 2011)
- v) The evaluation parameters include power consumption of the EGR and scrubber system, NaOH price in EGR, maintenance, and fuel and H₂O₂ solution prices. The operating costs, which included the fuel and H₂O₂ prices, were based on the results of this study, and other parameters were in reference to other studies. (J.P. Hansen et al., 2014), (M. Jeppesen, 2016), (E. den boer and M. Hoen, 2015) (Table 5).

Table 5. Operation cost parameters.

Item	Value
Maintenance of EGR	3.20\$/MWh
Maintenance scrubber	1.11\$/MWh
NaOH	350 \$/t
H ₂ O ₂ (50 % solution)	350 \$/t
IFO380	360 \$/t
Power	0.1098 \$/kWh

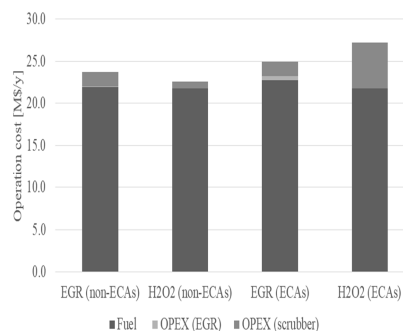


Figure 3. Annual operation cost.

4.2. Results

The most important parameters were H₂O₂ cost and power consumption according to the EGR ratio. As shown in Figure3, The operation cost was lowered by 1.044 M\$/y when H₂O₂ was used in non-ECAs, and by 2.307 M\$/y when EGR was used in ECAs (Table 6). Because the ratio of ECAs differs according to each ship type, route and loop in the actual operation, calculations were performed by adjusting the costs of the method using H₂O₂ as equal according to the ratio of ECAs. As a result, when the ratio of ECAs was approximately 31.5 % or less, the operating cost of H₂O₂ was advantageous, and when it was 31.5 % or more, and the operating cost of EGR was advantageous.

5. Conclusions

1. H_2O_2 is a powerful oxidizing agent that can effectively remove NOx. The results of this study show that 760.30 kg/h and 10.37 kg/h of H_2O_2 were consumed in ECAs and non-ECAs, respectively, to satisfy the emission regulations.
2. The factors significantly affecting the operation cost were fuel penalty according to the EGR rate and cost based on H_2O_2 consumption. The results of the economic evaluation show that the use of EGR in ECAs was 2.307 M\$/y, which is more economical than that of H_2O_2 , and the use of H_2O_2 in non-ECAs was 1.044 M\$/y, more economical than that of EGR.
3. The operation costs for the EGR and H_2O_2 were calculated according to the ratio of ECAs, and it was observed that the operation cost of the method using H_2O_2 was equal to that of the method using EGR when the ratio of ECAs was approximately 31.5 %.

References

- C.-L. Yang, 1994, Aqueous Absorption of Nitrogen Oxides Induced by Oxychlorine Compounds: A Process Development Study for Flue Gas Treatment, Ph.D. diss., New Jersey Institute of Technology
- E. den Boer, M. Hoen, 2015, Scrubbers - An Economic and Ecological Assessment, Delft, CE Delft, March, 15.4F41.20
- J. Kim, 2014, A Parametric Study and Design Optimization to Reduce BSFC and NOx of the 2-Stroke Low-Speed Marine Propulsion Diesel Engine by Using GT-Power, M.S. Thesis, University of Ulsan
- J. Haunstetter, N. Weinhart, 2015, Evaluation of a Novel Concept for Combined NOx and SOx removal, M.S. Thesis, Chalmers University of Technology, Gothenburg, Sweden
- J. P. Hansen, J. Kaltoft, F. Bak, J. Gørtz, M. Pedersen, C. Underwood, 2014, Reduction of SO₂, NOx and Particulate Matters from Ships with Diesel Engines. Miljøstyrelsen, 978-87-93026-57-5
- K. Baveja, D. Subba Rao, M.K. Sarkar, 1979, Kinetics of Absorption of Nitric Oxide in Hydrogen Peroxide Solutions, Journal of Chemical Engineering of Japan, 12, 4, 322-332
- Koch-Glitsch, 2010, Intalox Packed Tower Systems IMTP High Performance Packing, USA
- M. Jeppesen, Greener Shipping Summit 2015, MAN Diesel&Turbo
- M. Thiemann, E. Scheibler, K. W. Wiegand, 2002, Nitric Acid, Nitrous Acid, and Nitrogen Oxides, Ulmann's Encyclopedia of Industrial Chemistry, Wiley-VCH Verlag GmbH & Co. KGaA, 177-122
- S. I. Raptosios, N. F. Sakellaridis, R. G. Papagiannakis, D. T. Hountalas, 2015, Application of a Multi-Zone Combustion Model to Investigate the NOx Reduction Potential of Two-Stroke Marine Diesel Engines Using EGR, Applied Energy, 157, 814-823
- Kotakis NK, 2012, Cost comparative assessment study between different retrofit technologies applied on model ship to conform to IMO MARPOL 7/78, ANNEX VI, REG. 14. Master's thesis. University of Greenwich
- Liu Y xian, Zhang J., 2011, Photochemical Oxidation Removal of NO and SO₂ from Simulated Flue Gas of Coal-Fired Power Plants by Wet Scrubbing Using UV/H₂O₂ Advanced Oxidation Process. Industrial & Engineering Chemistry Research
- Woodyard D., 2004, Pounder's Marine Diesel Engines and Gas Turbines. Elsevier.

Comparative Performance Analysis of Industrial Scale Catalytic Steam Reformer with Membrane Steam Reformer

Arun Senthil Sundaramoorthy.,^a Arun Prem Anand Natarajan.,^a
Sundaramoorthy Sithanandam^{b,*}

^a *Department of Chemical Engineering, Sri Venkateswara College of Engineering, Sriperumbudur, 602117, India*

^b *Department of Chemical Engineering, Pondicherry Engineering College, Puducherry, 605014, India*

ssm_pec@pec.edu

Abstract

The objective of this work is to develop a framework to compare the performance of an industrial scale Catalytic Steam Reformer (CSR) with that of a Membrane Steam Reformer (MSR) and to decide on the choice of MSR as a viable alternative to CSR for production of hydrogen. For this purpose, a mathematical model is developed in this work to represent the industrial scale operation of MSR. Using the mathematical models, operations of CSR and MSR are optimized to achieve maximum methane conversion. The advantage of higher methane conversion achieved in MSR as compared to CSR has to be weighed against the additional cost of Pd membrane used in MSR. A mathematical equation is presented in this work to calculate and compare the unit costs of hydrogen as a function of optimal values of various operating parameters obtained for CSR and MSR.

Keywords: Process intensification, Process design, Process optimization, Membrane steam reforming, Techno-economic analysis

1. Introduction

With increasing demand for hydrogen as a clean fuel and with abundant availability of natural gas resources across the globe, Catalytic Steam Reforming of methane is gaining prominence as the most attractive process for production of hydrogen. In a conventional CSR, the maximum achievable conversion of methane is limited to equilibrium conversion. Whereas, in a MSR, the equilibrium is shifted in favour of higher methane conversion by letting the hydrogen produced in the reactor to permeate out through a Pd membrane. Although a number of studies have been reported (Silva et al, 2016) on laboratory scale MSR, there is no evidence of any industrial application of MSR technology. This is mainly due to enormous cost of preparation of Pd membranes (Criscuoli et al., 2001), which is expected to decrease in future with growing number of industrial applications of MSR.

The present work addresses the need to develop a mathematical model to appropriately represent the industrial scale operation of MSR and evaluate the economic feasibility of replacing the existing CSR technology by MSR technology. For this purpose, the design

of industrial scale side fired CSR reported in Rajesh et al. (2000) is taken and is suitably altered to represent the industrial scale MSR. A mathematical model for the MSR is developed by modifying the model equations for CSR reported in Rajesh et al. (2000) to account for transport of hydrogen through Pd membrane. A systematic comparative analysis of optimum performances of CSR and MSR is carried out for various surface areas of Pd membrane tubes used in MSR. An equation for calculating the unit production cost of hydrogen as an explicit function of optimal values of feed and operating parameters of CSR and MSR is presented in this work for the purpose of economic feasibility analysis.

2. Process Description of CSR and MSR

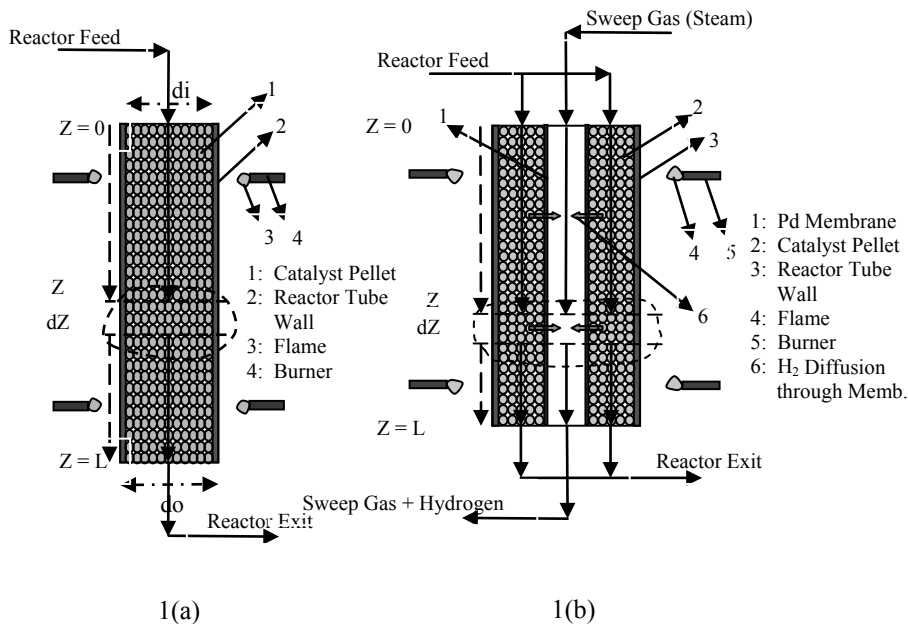
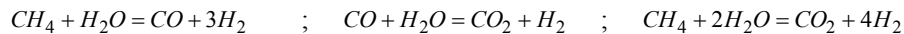


Figure 1: (a) Single reactor tube in a CSR (b) Single reactor tube in a MSR

Three chemical reactions listed below take place in the Catalytic Steam Reformer:



Kinetic rate equations reported by Xu and Froment (1989) are used in this work. Industrial scale side fired CSR (Fig.1a) reported in Rajesh et al. (2000) is taken in this study. CSR contains $n_t = 176$ numbers of catalyst filled reactor tubes (outer diameter $d_o = 102$ mm, inner diameter $d_i = 79.5$ mm, length $L = 11.95$ m) placed in a refractory lined furnace. The catalyst is Ni on Al_2O_3 pellet of diameter $D_p = 17.4$ mm. The furnace has 112 burners. The feed gas is a mixture of CH_4 , H_2O , CO_2 , H_2 and N_2 . F_{CH_4} is the molal feed rate of methane. S/C, H/C, D/C and N/C are respectively the molar ratios $\text{H}_2\text{O}/\text{CH}_4$, H_2/CH_4 , CO_2/CH_4 and N_2/CH_4 in the feed gas.

The design of CSR (Fig.1a) is altered into a MSR as shown in Fig.1b. In MSR, each reactor has two concentric tubes. Inner empty tube (radius r_o) is made of Pd membrane of thickness $\delta = 7.5 \mu m$ through which a sweep gas (steam) is passed. Annular section is the reactor packed with catalyst pellets through which feed gas is sent. H_2 permeates through Pd membrane wall into the inner tube at a molar flux of J_{H_2} (Sieverts law)

$$J_{H_2} = \frac{Q_o}{\delta} \exp\left(-\frac{E_p}{RT}\right) \left(P_{H_2}^{0.5} - P_{H_2p}^{0.5}\right) = \frac{Q_o}{\delta} \exp\left(-\frac{E_p}{RT}\right) \left((P y_{H_2})^{0.5} - (P_p y_{H_2p})^{0.5}\right) \quad (1)$$

P_p is the permeate pressure and y_{H_2p} is mole fraction of hydrogen in permeate. Values of parameters Q_o and E_p are taken from Johannessen et al. (2005)

3. Mathematical Modelling of CSR and MSR

In this work, one dimensional mathematical model for side fired industrial scale CSR reported in Rajesh et al. (2000) is adapted with some modifications. Further, a model is developed to represent the industrial scale side fired MSR by suitably modifying the model equations of CSR to account for flux of hydrogen through the Pd membrane. The model equations for CSR and MSR are combined using a switching parameter α which takes a value $\alpha = 1$ for MSR and $\alpha = 0$ for CSR.

Model Equations for Catalytic Reactor Section of CSR and MSR:

Over all mass balance equation is

$$\frac{dG}{dz} = -\alpha \left[\left(\frac{4\pi r_o L}{A_c} \right) J_{H_2} \right] \quad (2)$$

Component molal balance equation is written in terms of $x_i = \frac{y_i}{M}$ as

$$\frac{dx_i}{dz} = \frac{L \rho_b \eta_i R_i}{G} + \alpha(1 - \beta) \left[\frac{x_i}{G} \left(\frac{4\pi r_o L}{A_c} \right) J_{H_2} \right] + \alpha \beta \left[\frac{(2x_i - 1)}{G} \left(\frac{2\pi r_o L}{A_c} \right) J_{H_2} \right] \quad (3)$$

$i = CH_4, H_2O, CO, CO_2, H_2$

Over all heat balance equation is

$$\frac{dT}{dz} = \frac{L}{GC_{pg}} \left[\left(\alpha \left(\frac{\pi D_i U}{A_c} \right) + (1 - \alpha) \left(\frac{4U}{d_i} \right) \right) (T_{wi} - T) + \rho_b \sum_{j=1}^{III} \eta_j r_j (-\Delta H_j) - \alpha \left(\frac{U_m (2\pi r_o)}{A_c} \right) (T - T_p) \right] \quad (4)$$

Pressure drop in reactor channel is calculated using Kozney – Karman equation

$$\frac{dP}{dz} = -\frac{1.75 L G^2 (1 - \varepsilon_b)}{\varphi_s D_p \varepsilon_b^3 \rho_g} \quad (5)$$

A_c : cross sectional area of the reactor channel, y_i : mole fraction, \bar{M} : average molecular weight, R_i : rate of formation of chemical species, G : mass velocity of gas, β : switching parameter ($\beta=1$ for $i=H_2$ and $\beta=0$ for $i \neq H_2$), η_i : catalyst effectiveness factor (equal values of 0.03 assigned for all three reactions as reported in E. Johannessen et al. 2005), C_{pg} : specific heat capacity of gas, T : gas temperature, T_{wi} : inner tube wall temperature, U : catalyst bed side heat transfer coefficient, T_p : permeate gas temperature, U_m : overall heat transfer coefficient across the membrane.

Model Equations for Permeate Tube Section of MSR:

Hydrogen mole balance, Heat balance and Pressure drop equations are as follows,

$$\frac{dy_{H_2p}}{dz} = \left(\frac{2\pi r_o L (1 - y_{H_2p})}{G_p} \right) J_{H_2} \quad ; \quad \frac{dT_p}{dz} = \left(\frac{(2\pi r_o L) U_m}{G_p C_{pp}} \right) (T - T_p) \quad ; \quad \frac{dP_p}{dz} = - \frac{4fL}{d_p} \left(\frac{v_p^2}{2g} \right)$$

(6), (7), (8)

G_p : molal flow rate of permeate gas per unit area, G_{pp} : specific heat capacity of the permeate gas, f : friction factor, v_p : gas velocity, d_p : permeate tube diameter

4. Simulation and Optimization of CSR and MSR operations

The main objective of this work is to quantify the improvement in performance of MSR over CSR when the surface area (A_m) of Pd membrane is increased. For this purpose, identical tube lengths (L) and catalyst bed volumes are taken for both MSR and CSR and A_m is varied by changing the inner membrane tube radius r_o . To accommodate equal catalyst bed volumes in CSR and MSR, the inner diameter D_i of the outer tube of MSR is increased as $D_i = \gamma d_i$. By changing the value of parameter $\gamma > 1$, the values of r_o and A_m are changed respectively as $r_o = \frac{d_i}{2} \sqrt{\gamma^2 - 1}$ and $A_m = \pi d_i \sqrt{\gamma^2 - 1} L n_t$.

Matlab®R2015a was used to simulate CSR and MSR models. Simultaneous stiff ordinary differential equations (Eq. 2-8) were solved using function subroutine *ode15s* to obtain the profiles of mole fractions, temperature and pressure for different feed and operating conditions. Factors that influence CH_4 conversion (M_c) in CSR are feed temperature T_i , feed pressure P_i , furnace gas temperature T_g , S/C and H/C. In addition to all these factors listed for CSR, conversion of CH_4 in MSR is also influenced by permeate feed temperature T_{pi} , permeate feed pressure P_{pi} and sweep ratio S_r which is the ratio of feed rate of sweep gas (steam) to the feed rate of methane.

In this work, CSR and MSR operations were optimized to achieve maximum CH_4 conversion (M_c) for fixed values of $F_{CH_4} = 1000$ kmol/h, $D/C = 0.091$ and $N/C = 0.02$, subject to operational constraints and bounds (Rajesh et al. 2000) listed here, $T_{wo} \leq 1200$ K, $F \leq 5000$ kmol/h, $725 \leq T_i \leq 900$ K, $2400 \leq P_i \leq 3000$ kPa, $2.0 \leq S/C \leq 6.0$, $0.01 \leq H/C \leq 0.5$, $1375 \leq T_g \leq 1650$ K, $1.0 \leq S_r \leq 3.0$, $600 \leq T_{pi} \leq 800$ K, $200 \leq P_{pi} \leq 300$ kPa. MSR is optimized for different values of γ varying between 1.15 and 2. The constrained optimization problem is solved using *fmincon* optimization routine of Matlab® R2015a.

5. Results and Discussion

Optimal values of feed and operating variables and the corresponding values of methane conversion (M_c), H_2 production rate (P_{H_2}) and CO_2 production rate (P_{CO_2}) are reported in Table 1. In CSR, an optimal methane conversion of only 49% was achieved, whereas 99.9% conversion was achieved in MSR for $\gamma = 2$. Although methane conversion increases steadily with increase in γ , the increase is not very significant for $\gamma > 1.75$ suggesting that $\gamma > 1.75$ is not economical. Further, optimal operation of MSR requires the feed gas to be at a higher pressure P_i and furnace gas to be at a higher temperature T_g compared to CSR in order maintain a higher hydrogen concentration gradient across the Pd membrane.

Table 1: Comparison of Key Optimum Performance indices of CSR and MSR

Operating Parameters	CSR	MSR					
		$\gamma = 1.15$	$\gamma = 1.30$	$\gamma = 1.40$	$\gamma = 1.65$	$\gamma = 1.75$	$\gamma = 2.00$
T_g (K)	1,575.5	1,644.5	1,650.0	16,50.0	1,643.2	1,630.4	1,606.7
T_i (K)	900.0	878.8	891.8	900.0	900.0	900.0	900.0
P_i (kPa)	2,400.0	2,505.6	3,000.0	3,000.0	2,519.4	2,988.5	2,539.7
S/C	3.879	3.879	3.879	3.878	3.877	3.863	3.647
S_r	-	2.998	3.000	2.595	3.000	2.971	3.000
T_{pi} (K)	-	800.0	800.0	800.0	800.0	799.6	793.1
P_{pi} (kPa)	-	200.0	200.0	200.0	200.0	200.0	200.0
P_{H_2} (kmol/h)	1,817.9	3,039.3	3,497.1	3,668.0	3,891.8	3,945.2	3,938.0
P_{CO_2} (kmol/h)	346.7	712.6	836.2	876.7	925.7	951.4	940.3
M_c (%)	49.0	77.6	88.7	93.0	98.9	99.8	99.9

The economics of choice of MSR over CSR has to take into account influence of various parameters listed in Table 1 on the fixed and operating costs of steam reformer.

In this work, an explicit equation (Eq. 9) is derived to calculate the unit cost of production of hydrogen C_{PH} as a function of these parameters (Table 1)

$$C_{PH} = \frac{C_{RM} + C_{FR} + C_{SP} + C_{OT} + C_{OC}}{\bar{P}_{H_2}} \quad (9)$$

$$C_{RM} = C_M \left(\frac{M_C}{100} \right) \bar{F}_{CH_4} + C_{H_2O} (S/C + \alpha S_r) \bar{F}_{CH_4} \quad ; \quad C_{FR} = C_R \bar{F}_{CH_4} + \alpha C_{P_d} \left(\pi d_i \sqrt{\gamma^2 - 1} L n_t \right)$$

$$C_{SP} = C_{MS} \left(1 - \frac{M_C}{100} \right) \bar{F}_{CH_4} + (C_{CS} - C_{CO_2}) \bar{P}_{CO_2} + C_{HS} \bar{P}_{H_2} \quad ; \quad C_{OC} = c_1 (\bar{F}_{P_i})^{d_1} + \alpha \left[c_2 (S_r \bar{F}_{CH_4} P_{P_i})^{d_2} \right]$$

$$C_{OT} = a_1 (\bar{F}_{T_i})^{b_1} + a_2 (T_f)^{b_2} + \alpha \left[a_3 (S_r \bar{F}_{CH_4} T_{P_i})^{b_3} \right]$$

Here, C_M , C_{H_2O} , C_{CO_2} : unit costs of methane, steam, carbon dioxide, C_R : annualized fixed cost of catalytic reactor tubes per unit kmole of methane processed, C_{P_d} : annualized fixed cost of palladium membrane tubes per unit area, C_{MS} , C_{CS} , C_{HS} : annualized fixed and operating costs of separators for methane, carbon dioxide hydrogen per unit kmole of separation, a_i , b_i , c_i , d_i : coefficients of empirical cost correlations for C_{OT} cost for thermal heating and C_{OC} cost for feed gas compression.

By comparing the unit production costs of hydrogen C_{PH} calculated for CSR and MSR for different values of γ , one can make a decision on the choice of MSR over CSR and the value of γ at which the cost is minimum.

6. Conclusions

In this paper, a mathematical model has been developed to represent the industrial scale operation of a side fired Membrane Steam Reformer (MSR). The mathematical models of CSR and MSR are used to compare their optimal performances and to evaluate the suitability of MSR over CSR. The economics of choice of MSR in place of CSR is to be evaluated by taking in to account a number of cost factors. A frame work is developed in this paper to calculate the unit cost of production of hydrogen by representing various cost factors as functions of optimal feed and operating parameters.

References

- A. Criscuoli, A. Basile, E. Drioli, O. Loiacono, 2001, An economic feasibility study for water gas shift membrane reactor, *Journal of Membrane Science* 181, 21-27
- E. Johannessen, Kristin Jordal, 2005, Study of a H₂ separating membrane reactor for methane steam reforming at conditions relevant for power processes with CO₂ capture, *Energy Conversion and Management*, 46, 1059-1071
- J.K. Rajesh, S. K. Gupta, G.P. Rangaiah, A. K. Ray, 2000, Multiobjective optimization of steam reformer performance using genetic algorithm, *Ind. Eng. Chem. Res.*, 39, 3, 706-717
- J. D. Silva, Cesar Augusto Moraes de Abreu, 2016, Modelling and simulation in conventional fixed-bed and fixed-bed membrane reactors for the steam reforming of methane, *International Journal of Hydrogen Energy*, 41, 27, 11660-11674
- J. Xu, G.F. Froment, 1989, Methane steam reforming, methanation and water-gas shift: I. Intrinsic kinetics, *AIChE Journal*, 35, 1, 88-96

Towards the synthesis of modular process intensification systems with safety and operability considerations - application to heat exchanger network

Yuhe Tian^a, M. Sam Mannan^{a,b}, Zdravko Kravanja^c, Efstratios N. Pistikopoulos^{a,d*}

^a*Artie McFerrin Department of Chemical Engineering, Texas A&M University, College Station, TX 77843, United States*

^b*Mary Kay O'Connor Process Safety Center, Artie McFerrin Department of Chemical Engineering, Texas A&M University, College Station, TX 77843, United States*

^c*Faculty of Chemistry and Chemical Engineering, University of Maribor, Maribor, SI-2000, Slovenia*

^d*Texas A&M Energy Institute, Texas A&M University, College Station, TX 77843, United States*

stratos@tamu.edu

Abstract

In this work, we present a systematic framework for the synthesis of safely operable process intensification systems. Herein, intensified designs are automatically generated by using phenomena-based Generalized Modular Representation Framework, while their safety and operability performances are guaranteed by incorporating: (i) flexibility analysis and multiperiod design, (ii) inherent safety analysis utilizing quantitative risk assessment, and (iii) multi-parametric model predictive control strategies developed via the PAROC framework. As an example from a broader set of intensified systems, the proposed framework is applied to heat exchanger network synthesis for thermal intensification, demonstrating its capability on enhancing safety and operability at early design stage.

Keywords: Process intensification, flexibility analysis, quantitative risk assessment, multi-parametric Model Predictive Control, heat exchanger network

1. Introduction

Modular process intensification provides opportunities for drastic process improvement to meet the increasing demands for sustainable production through the integration, or enhancement, of operations, functions, and phenomena (Lutze et al., 2010). However, these schemes are often highly integrated due to the maximization of synergy effects, thus resulting in a loss of degrees of freedom for safe operation and process control (Baldea, 2015). In recent years, despite increasing efforts towards a systematic synthesis strategy to generate novel intensified processes from phenomena level (Demirel et al., 2017), there is a lack of approach to simultaneously assess process operability, control,

and safety at the synthesis stage to ensure the expected functionality of the derived intensified structures under varying conditions.

To address the aforementioned challenges, this work introduces a systematic framework, which utilizes the phenomena-based Generalized Modular Representation Framework (GMF) to discover intensification opportunities from process fundamentals, and also embeds flexibility analysis, inherent safety analysis, and controller design to guarantee expected operability performance. The full framework (Figure 1a) and its detailed methodologies (Figure 1b) are described on a step-by-step basis in section 2. In section 3, the proposed framework is applied to a heat exchanger network (HEN) synthesis problem for thermal intensification.

2. Framework Description

As shown in Figure 1a, this framework comprises three interactive toolboxes (i.e., process intensification/synthesis toolbox, process simulation/optimization toolbox, and process operability/control/safety toolbox). Each toolbox is open to different techniques implemented in multiple software environments, thus rendering this framework a desirable flexibility and opening up the potential to deliver multiple design alternatives. By interconnecting steady-state synthesis, dynamic analysis, and operability assessment, this framework allows for the systematic identification of verifiable and operable process intensification designs. The stepwise procedure for this purpose and the techniques employed in the current work are described as follows (Figure 1b).

Step 1: Process Intensification/Synthesis Representation – The phenomenological representation of chemical processes is achieved via the Generalized Modular Representation Framework (Papalexandri and Pistikopoulos, 1996). Built on aggregated multifunctional mass/heat exchange modules and pure heat exchange modules, GMF discloses intensification possibilities by optimizing mass and heat transfer performances based on Gibbs free energy (Ismail et al., 2001).

Step 2: Process Optimization – A superstructure formulation is developed based on GMF without any pre-postulation of plausible unit operations or flowsheets. This results in a mixed integer nonlinear programming (MINLP) problem to be solved in GAMS.

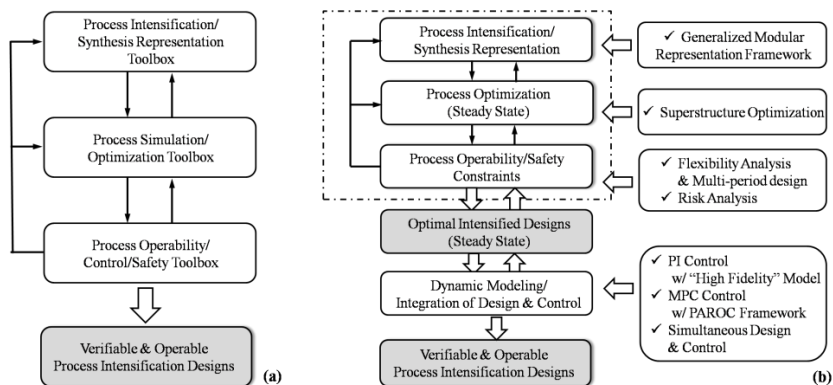


Figure 1. Proposed framework for the synthesis of operable intensification systems
(a) The systematic framework, (b) Methodology flow

Step 3: Process Operability/Safety Assessment – The initial design from previous steps is tested with feasibility analysis to evaluate system performance against uncertain parameters. If any critical operation point is detected, a multiperiod MINLP model is reformulated to accommodate uncertainty. Meanwhile, risk assessment (Nemet et al., 2017), which accounts for equipment failure frequency and consequence severity, is incorporated as a constraint into the synthesis model to derive inherently safer designs.

Step 4: Optimal Intensified Steady-state Designs – At the exit of Step 3, the derived intensified designs with enhanced flexibility and safety performance are fully analyzed with steady-state simulation tools.

Step 5: Dynamic Modelling/Integration of Design and Control – “High fidelity” dynamic models are then developed to validate the intensified designs. This task takes place in gPROMS® Process Systems Enterprise (1997-2017). Two approaches, with different computational complexity in control strategy and model fidelity, are investigated to integrate design and control via the formulation of a (mixed-integer) dynamic optimization (DO) problem, namely: (i) simultaneous design and PI control using “high fidelity” model, and (ii) multi-parametric model-based predictive controller (mp-MPC) design via the PAROC framework (Pistikopoulos et al., 2015) followed by a further simultaneous design and control step (Diangelakis et al., 2017).

Step 6: Verifiable and Operable Process Intensification Designs – Closed-loop validation is finally performed to ensure the consistency throughout the framework, after which verifiable and operable intensification designs are ready to be delivered.

3. Heat Exchanger Network Synthesis

As an example from a broader set of process intensification systems, the proposed framework is applied to a heat exchanger network synthesis problem for thermal intensification. The case study aims to demonstrate the steps of the proposed framework and its capability to incorporate operability assessment at synthesis stage.

3.1. Problem Description

This HEN problem to be addressed here considers two hot streams, two cold streams, and one hot utility. Given are: (i) stream flowrate data (Kotjabasakis and Linnhoff, 1987); (ii) uncertain heat transfer coefficients (U_{H1-C1}) within a specific range, which arouses flexibility concerns; (iii) disturbance and control objective, for which controller design is essential; and (iv) stream toxicity data (LC_{50}) and equipment data for four types of heat exchanger (HE), namely: double pipe HE (DP), plate and frame HE (PF), fixed plate shell and tube HE (SF), and U-tube shell and tube HE (UT), which necessitates inherent safety evaluation (Nemet et al., 2017). The objective is to synthesize a HEN with minimized total annual cost and desired operability.

3.2. Steady-state Synthesis with Flexibility and Safety Considerations

The superstructure-based optimization problem for steady-state HEN synthesis is formulated based on the pure heat exchange module representation in GMF. A nominal HEN design without flexibility or safety considerations is first performed to obtain a reference network (Figure 2a). Feasibility analysis identifies two periods of operation characterized by the extreme values of U_{H1-C1} . To obtain an inherently safer design, the overall HEN toxicity risk is constrained to be 25 % less than that of the nominal design.

This results in the change of H1-C2 exchanger type from SF to UT (Figure 2b), as UT has much higher area density to significantly reduce the amount of hazards contained in the equipment. However, as the individual risk of H1-C2 HE takes up more than 75 % of the overall process risk in this case, the risk tolerance is further decreased by constraining individual HE toxicity risk to be less than 50% of overall risk. As a result, a different network configuration is synthesized in order to render H1-C2 HE a lower risk level by relieving its heat exchange burden (Figure 2c). These two safely operable HENs are exported as Candidate 1 and 2 for the next dynamic analysis.

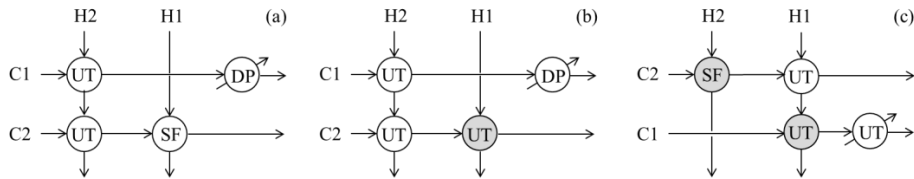


Figure 2. Topology of HEN at different operability level:
(a) Nominal design, (b) Candidate 1, (c) Candidate 2

3.3. "High Fidelity" Modelling and Dynamic Analysis

The dynamic HEN is described by a Partial Differential Algebraic Equation (PDAE) model based on gPROMS® Process Model Library for Heat Exchange (PSE, 1997-2017). To ensure the consistency between steady-state synthesis and dynamic simulation, the dynamic model is validated to match its steady-state synthesis analogue.

The controller design, as well as the simultaneous design and control, takes place for the two candidates individually under the schemes of PI control and mp-MPC control. In each case, the network configuration is fixed as per Figure 2b or 2c and heat exchanger areas are used as design variables. The bypass flowrate and the heat utility duties are the degrees of freedom, and the outlet temperature of stream H1 and C1 are the system outputs. The inlet temperature of stream H2 is treated as a disturbance to the operation. The dynamic optimization problem is formulated and solved to minimize the sum of the total annual cost and scaled deviation penalty, the latter term of which minimizes error with respect to controller design.

3.4. Design and PI Control Optimization

Decentralized PI control structure is implemented for operation. The pairing scheme is chosen based on the following HEN heuristics (Luyben, 2010): (i) manipulate utility stream flowrate to control a process temperature; and (ii) bypass the stream whose outlet temperature is to be controlled. With the selected control structure, DO is performed to optimize the design of the heat exchangers and the gains of the controllers using the "high fidelity" model. As the outcomes, the controller parameters are reported in Table 1, while the optimal design variables and costs are summarized in Table 2.

Table 1. PI controller configuration for HEN candidates

Candidate	Controller	K _p	K _i
1	Bypass	9481.6	5101.2
	Utility	9958.0	10000
2	Bypass	9647.2	5335.1
	Utility	10000	10000

3.5. Design and mp-MPC Control Optimization

The mp-MPC controller is designed following the PAROC framework (Pistikopoulos et al., 2015). Each mp-MPC problem is formulated using corresponding linear state-space model approximated by the System Identification Toolbox of MATLAB®. Via POP® toolbox in MATLAB®, the problem of Candidate 1 is solved for an output horizon of 2 and a control horizon of 2 resulting in 118 critical regions in solution map, while that of candidate 2 is solved for an output horizon of 2 and a control horizon of 1 resulting in 89 critical regions.

Given random disturbances deviating within ± 10 K per second, the designed controllers are tested against the “high fidelity” model but at fixed design configurations for closed-loop validation. With these validated mp-MPC controllers, the dynamic optimization step is implemented to determine the optimal design variables as shown in Table 2. The corresponding output profile at the optimal design configuration is shown in Figure 3, indicating the agreement between the outputs and setpoints.

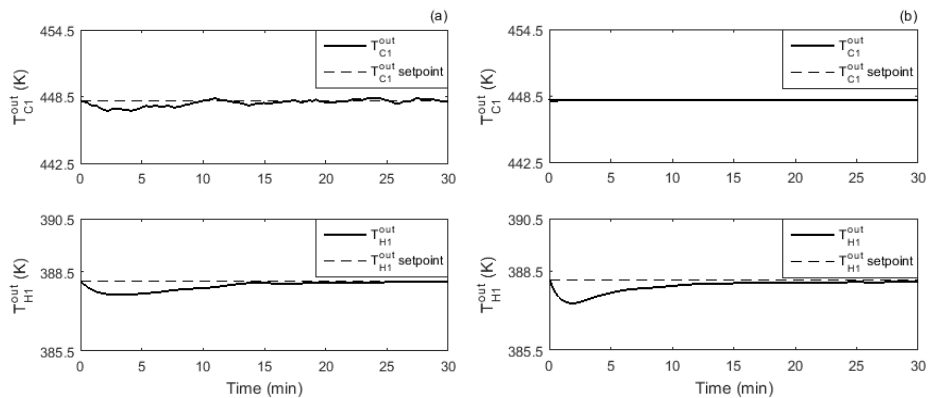


Figure 3. mp-MPC output profiles at optimal design configurations
(a) Candidate 1, (b) Candidate 2

Table 2. Dynamic optimization results for HEN synthesis

HEN Candidate	Control Strategy	HE Area (m ²)				Investment Cost (k\$)	Operating Cost (k\$/y)
		H1 – C1	H1 – C2	H2 – C1	H2 – C2		
1	PI	/	585.0	138.7	106.3	530.0	6911.4
	mp-MPC	/	604.4	125.6	99.9	528.4	7357.0
2	PI	210.5	518.6	/	167.1	553.8	8885.9
	mp-MPC	221.4	522.2	/	165.7	557.4	8593.9

3.6. Verifiable and Operable Intensified HEN Designs

Up to this point, several HEN candidates have been delivered as design alternatives with desired flexibility, increasing level of inherent safety, and different control strategies. In this context, this framework opens up the potential for comparison of various operable design alternatives. As the benefit, the final construction decision will enjoy a much larger freedom to investigate the trade-off between desired operability behavior and economic performance.

4. Conclusions

In this paper, we present an integrated framework, which embeds inherent safety, flexibility, and controllability analysis within a phenomenological Generalized Modular Representation Framework to derive intensified designs with guaranteed safety and operability performance. The framework is demonstrated by a heat exchanger network synthesis problem to achieve thermal intensification. Ongoing work focuses on further developing and demonstrating the framework to general process intensification problems, such as reactive separations and other hybrid processes (Tian et al., 2018).

5. Acknowledgements

Financial supports from Texas A&M Energy Institute, Shell, and RAPID SYNOPSIS Project are gratefully acknowledged.

References

- Baldea, M. 2015. From process integration to process intensification. *Computers & Chemical Engineering*, 81, 104-114.
- Demirel, S. E., Li, J. and Hasan, M. F. 2017. Systematic process intensification using building blocks. *Computers & Chemical Engineering*, 105, 2-38.
- Diangelakis, N. A., Burnak, B., Katz, J., and Pistikopoulos, E. N. 2017. Process Design and Control optimization: A simultaneous approach by multi-parametric programming. *AIChE Journal*, DOI: 10.1002/aic.15825.
- Ismail, S. R., Proios, P. and Pistikopoulos, E. N. 2001. Modular synthesis framework for combined separation/reaction systems. *AIChE Journal*, 47(3), 629-649.
- Kotjabasakis, E., and Linnhoff, B. 1987. Flexible Heat Exchanger Network Design: Comments on the Problem Definition and on Suitable Solution Techniques. In *ICHEME Symposium" Innovation In Process Energy Utilization*, 1-17.
- Lutze, P., Gani, R. and Woodley, J. M. 2010. Process intensification: a perspective on process synthesis. *Chemical Engineering and Processing: Process Intensification*, 49(6), 547-558.
- Luyben, W. L. 2010. Heat-exchanger bypass control. *Industrial & Engineering Chemistry Research*, 50(2), 965-973.
- Nemet, A., Klemeš, J. J., Moon, I. and Kravanja, Z. 2017. Safety Analysis Embedded in Heat Exchanger Network Synthesis. *Computers & Chemical Engineering*, 107, 357-380.
- Papalexandri, K. P. and Pistikopoulos, E. N. 1996. Generalized modular representation framework for process synthesis. *AIChE Journal*, 42(4), 1010-1032.
- Pistikopoulos, E. N., Diangelakis, N. A., Oberdieck, R., Papathanasiou, M. M., Nascu, I. and Sun, M. 2015. PAROC—An integrated framework and software platform for the optimisation and advanced model-based control of process systems. *Chemical Engineering Science*, 136, 115-138.
- Process Systems Enterprise, 1997-2017. gPROMS.
URL <http://www.psenderprise.com/gproms/>
- Tian, Y., Mannan, M. S. and Pistikopoulos, E. N. 2018. Towards a systematic framework for the synthesis of operable process intensification systems. 13th International Symposium on Process Systems Engineering, *Computer Aided Chemical Engineering*, Submitted.

Design, Control and Economics of a Process for Isobutyl Acrylate Production

Mihai Daniel Moraru^{1,2,*}, Diana Adela Berinde², Costin Sorin Bildea²

^a*Hexion, Department of Process Technology and Development, Seattleweg 17, Pernis, 3195 ND, The Netherlands*

^b*University Politehnica of Bucharest, Department of Chemical and Biochemical Engineering, 1-7 Polizu, Bucharest, 011061, Romania*

mihai.moraru@hexion.com

Abstract

Isobutyl acrylate (*i*-BA) can be produced by direct esterification of acrylic acid with isobutanol using solid-based catalysts. The novelty of this work consists in developing a process for *i*-BA production, for which design, control and economic evaluation studies have not been reported in literature. The reaction is performed in a multitubular fixed-bed reactor, while the separation system employs conventional distillation equipment. The difficult separation between the acrylate and acid (close boiling and maximum temperature homogeneous azeotropy at 1.013 bar) is achieved by vacuum distillation, condition at which the relative volatility increases and the azeotrope disappears. The process is controllable, the control system showing robustness when production capacity and reactor temperature change. The economic evaluation shows attractive key economic indicators in terms of revenues, and capital and utility costs.

Keywords: acrylic acid, *i*-butanol, esterification, reaction-separation-recycle

1. Introduction

Isobutyl acrylate (*i*-BA) is used as precursor in the production of coatings, adhesives, and polyethylene plastics (Karakus et al., 2014). Being considered a higher-acrylate, *i*-BA is preferably produced batchwise by esterification of acrylic acid (AA) with isobutyl alcohol (*i*-BuOH) in presence of an organic solvent as entrainer and sulfuric acid as homogeneous catalyst (Ohara et al., 2003). To overcome corrosion, eliminate catalyst separation problems and prevent environmental issues with catalyst disposal, this esterification reaction was studied using solid-based catalysts (Karakus et al., 2014).

To the best of our knowledge, process development studies for *i*-BA production processes using solid catalysts have not been reported in literature. In this work, we present the design, control and economic evaluation of a reaction-separation-recycle process for production of 20.5 kt/y of *i*-BA at 99.6 %mass purity. Aspen Plus and Aspen Plus Dynamics are used as CAPE tools to support the analysis.

2. Thermodynamics and reaction kinetics

The pure component physical properties are available in the Aspen databanks. The UNIQUAC model is selected to model the phase equilibria, using two sets of binary interaction parameters. One set calculates the VLE, while the other calculates the LLE. The parameters for water/AA and water/*i*-BuOH are available in Aspen, for both VLE

and LLE applications; for water/*i*-BA, the parameters are estimated with UNIFAC-LL group contribution method, while for the remaining three pairs *i*-BuOH/*i*-BA, *i*-BuOH/AA and *i*-BA/AA, the UNIFAC method is used.

Equation (1) represents the liquid phase esterification reaction of AA and *i*-BuOH with formation of *i*-BA and water. The course of reaction under catalytic conditions (Amberlyst 131) can be described by the LHHW kinetic model given by equations (2)-(5), taken from recent literature (Karakus et al., 2014). The parameters for the adsorption constant equation are regressed using the data presented in the same reference. These are shown in Table 1.



$$r = \frac{k_f K_{acid} K_{alcohol} (a_{acid} a_{alcohol} - (1/K_{eq}) a_{ester} a_{water})}{(1 + K_{acid} a_{acid} + K_{alcohol} a_{alcohol} + K_{ester} a_{ester} + K_{water} a_{water})^2} \quad (2)$$

$$k_f / [\text{kmol}/(\text{kg}_{cat} \cdot \text{s})] = 2.526 \cdot 10^8 \exp\left(-\frac{76015.7}{8.314T}\right) \quad (3)$$

$$K_{eq} = \exp(1972.6/T - 1.5134) \quad (4)$$

$$\ln(K_i) = A_i + B_i/T, \quad i = \text{acid, alcohol, water, ester} \quad (5)$$

Table 1. Regression parameters *A* and *B* of the adsorption constant equation

Parameter	Acid	Alcohol	Water	Ester
<i>A</i>	-7.6835	-8.5882	-1.8902	-2.16
<i>B</i> / [K]	2753.6	2380.3	1215.6	738.67

Figure 1 shows the *x*-*y* diagrams for key binary systems; *i*-BuOH/*i*-BA diagram (left) suggests a good separation of the acrylate from a mixture with alcohol at atmospheric pressure, while the AA/*i*-BA diagram (right) shows that the acrylate separation from a mixture with acid is favoured at vacuum conditions. Figure 2 shows ternary diagrams of the four component system. For the three systems in which water is present, large immiscibility areas are observed. Water and acid are fully miscible; the ternary system of the organic components presents no immiscibility area. The binary systems water/*i*-BuOH and water/*i*-BH, and the ternary water/*i*-BuOH/*i*-BA present minimum boiling heterogeneous azeotropy.

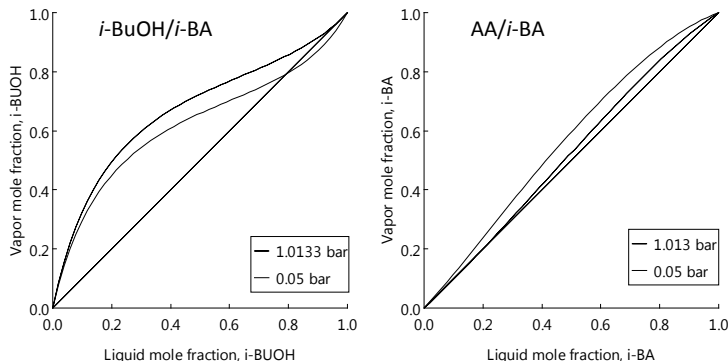


Figure 1. Selected *x*-*y* diagrams: *i*-BuOH/*i*-BA (left) and AA/*i*-BA (right)

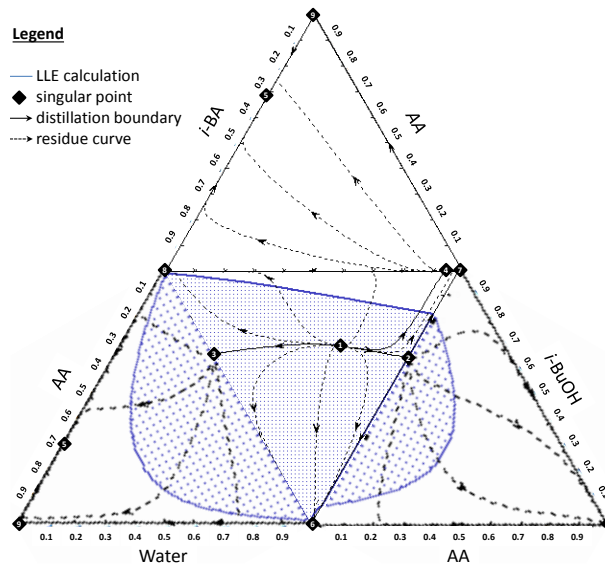


Figure 2. Ternary diagrams (mass based): liquid-liquid equilibrium at 30 °C and 1.013 bar and residue curve maps for the system water/*i*-BuOH/*i*-BA/AA; Boiling temperature of singular points (no./°C): (1/89.7), (2/90.3), (3/93.3), (4/107.7), (5/141.6), (6/100), (7/107.7), (8/137.0), (9/141.2)

3. Analysis of the reaction-separation-recycle system

The first analysis investigates the influence of conversion (X_{AA}) on the recycle flow rates of acid ($F_{AA,RCY}$) and alcohol ($F_{i-BuOH,RCY}$), and on the required mass of catalyst (m_{cat}) of the Reactor-Separation-Recycle process. The structure of the process, together with the results, is shown in Figure 3-left (top-right corner). The fresh ($F_{AA,0}$, $F_{i-BuOH,0}$) and recycled reactants are mixed and fed to a fixed-bed tubular reactor (PFR) operated adiabatically. The reactor is modeled using the kinetic model. The separation section (SEP) distributes the inlet components at given separation factors β_i . In this analysis perfect separation is assumed, the products being completely removed from the system ($\beta_{i-BA} = 1$, $\beta_{Water} = 1$) while the reactants completely recovered ($\beta_{i-BuOH} = 0$, $\beta_{AA} = 0$) and recycled to the reaction section as two separate streams. This structure with two recycles is possible since the boiling points are $T_{B,Water} < T_{B,i-BuOH} < T_{B,i-BA} < T_{B,AA}$. Low X_{AA} means large recycles (i.e. high separation costs), while high X_{AA} leads to a large amount of catalyst (i.e. high reaction cost). Thus, a preliminary X_{AA} interval of interest is 0.5-0.9.

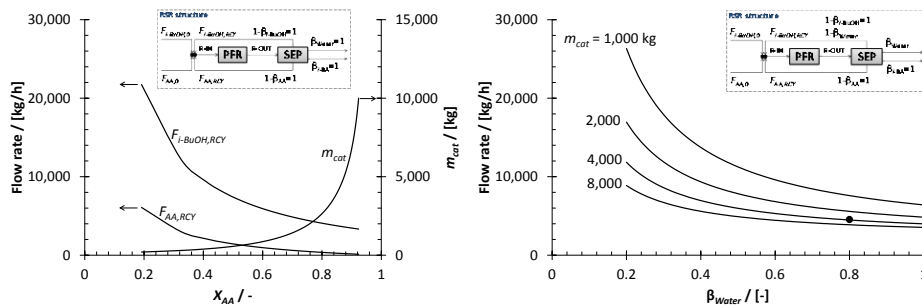


Figure 3. Effect of conversion (left) and water separation (right) on recycle and mass of catalyst

The second analysis investigates the influence of water separation (β_{water}) on the recycle flow rates, at various amounts of catalyst. The structure of the process (Figure 3-right (top-right corner)) is identical with the previous one, except that the water separation factor is not fixed (i.e. $\beta_{water} < 1$), water being allowed to return to the reactor. As more and more water is returned to the reaction, the (sum of the) recycle flow rates increase, and more catalyst is required to reduce this effect. For β_{water} in the interval 0.6-1, low catalyst amounts (1,000-2,000 kg) show high sensitivity to water recycle, while more than 4,000 kg do not give a significant reduction in the recycle flow rate.

4. Process design

Based on the previous analyses, a catalyst amount of 4,000 kg is selected. This operating point is shown in Figure 3-left (black dot). The structure of the separation system is developed starting with the composition of the reactor outlet, and making use of thermodynamic insights. The heterogeneous azeotropes containing large amounts of water can be obtained as vapour, condensed and phase split. *i*-BuOH/*i*-BA diagram suggests that the acrylate can be separated from a mixture with alcohol at atmospheric pressure, while the AA/*i*-BA diagram suggests the separation of acrylate from a mixture with acid at vacuum conditions due to increase in relative volatility at lower pressures.

The process flow diagram, together with a mass balance, is shown in Figure 4. The two-recycle structure previously proposed is preserved. Water is removed first; the heterogeneous azeotropes containing large amounts of water are obtained as vapour distillate (C-1, atmospheric), condensed (COND-1), and phase separated (V-3); the aqueous phase containing alcohol is flashed (V-4) to recover the reactant and to eliminate water from the system (99.1 %wt). The bottom stream of C-1 is distilled (C-2, atmospheric) obtaining the alcohol as distillate, which is recycled to the reaction section. The bottom stream of C-2 is further distilled (C-3, vacuum), obtaining the acrylate product as distillate, while the acid is recovered as bottoms and recycled.

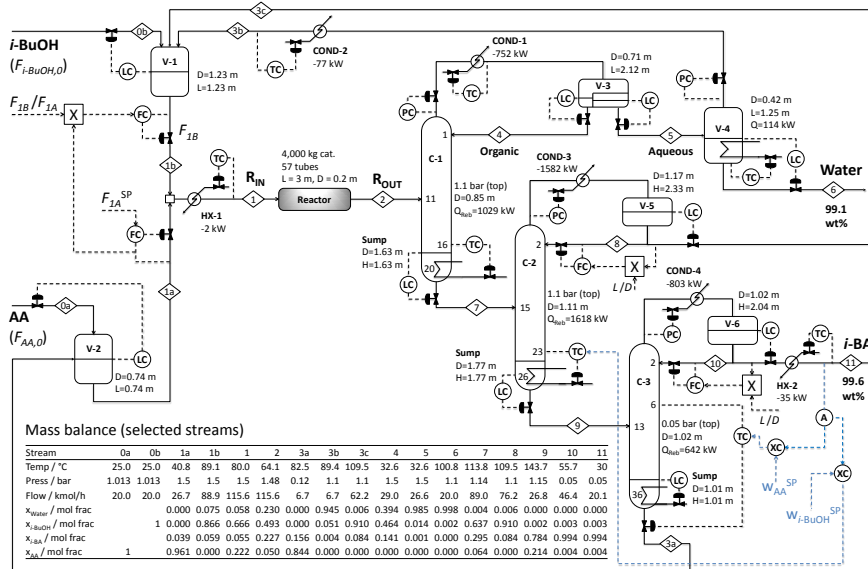


Figure 4. Process flow diagram, mass balance, main equipment sizes and plantwide control

5. Plantwide control

The plantwide control structure, shown in Figure 4, is typical to systems involving two reactants which are distinctly recycled (Bildea et al., 2004). It fixes the reactor-inlet flow rate of the limiting reactant (AA) and the ratio of reactants ($i\text{-BuOH}/\text{AA}$) at reactor inlet. The fresh reactants are fed on level control. In this way, the control structure ensures that the amounts of reactants brought in the process match the amounts of reactants consumed in the reactor. The distillation columns C-1 and C-2 are controlled using standard pressure, level and temperature control loops. The product column C-3 operates at high boilup ratio. Therefore, the reboiler duty is used to control the sump level, while the bottom flow rate controls one temperature in the column (LB configuration). PI controllers tuned by the direct synthesis method were used.

Figure 5 presents dynamic simulation results. The top diagrams show the flow rates of fresh reactants and products, and the products purity, when the reactor-inlet flow of the limiting reactant ($F_{I,A}$) is changed by $\pm 25\%$. The production rate changes by roughly $+10\%$ and -18% , respectively. The dynamics is rather slow, a new steady state being reached in several hours. The purity of the water product is practically constant. However, the purity of the $i\text{-BA}$ product drops significantly when control of the column C-3 uses only temperature control loop. Therefore, two concentration control loops are introduced (dashed lines in Figure 4), using the set-points of the temperature controllers of columns C-2 and C-3. In this way, the impurification of the product (continuous line in Figure 5) with alcohol or acid, respectively, is prevented (dashed line in Figure 5).

The bottom diagrams show the response of the plant for $\pm 10^\circ\text{C}$ changes of reactor-inlet temperature. The production rate changes by roughly $+14\%$ and -18% , respectively. The dynamics is comparable with the previous case. Again, concentration control is necessary in order to ensure product purity.

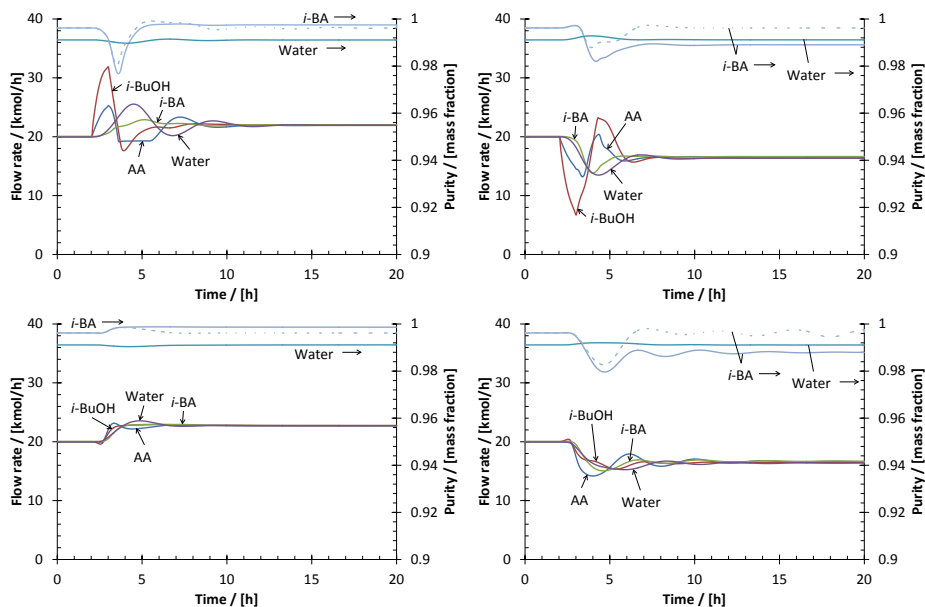


Figure 5. Dynamic simulation results (flow rates and products purity) at various process changes: $\pm 25\% F_{AA,I}$ (left/right top diagrams) and $\pm 10^\circ\text{C}$ reactor inlet (left/right bottom diagrams)

6. Economic evaluation

The economics of the process is evaluated using the annual economic potential (i.e. revenues), $EP = C_{\text{prod}} - (C_{\text{react}} + C_{\text{OpEx}} + C_{\text{CapEx}}/3)$. The cost of product and raw materials are taken from www.icis.com, a large source that shares chemical prices. The total investment costs (C_{CapEx}) include the reactor, heat exchangers, distillation columns and flashers, mixers and decanters. A payback period of 3 years is used, with 8000 hours/year operating time. For calculating the operating costs (C_{OpEx}), the heating, cooling and waste water treatment costs considered are standard: LP steam (6 bar, 160 °C, \$7.78/GJ), cooling water (25 °C, \$0.72/GJ), and bio-treatment of waste water (500 \$/t of organics and 27 \$/t of waste water).

The product sales bring 38,427,000 \$/y, while the overall production costs are 34,424,000 \$/y, thus annual revenues of 4,000,000 \$. The largest share of the production costs is attributed to the cost of reactants with 32,014,000 \$/y, followed by the cost of amortization with 1,531,000 \$/y, and the cost of utilities with 879,000 \$/y. A breakdown of the amortization cost shows that 38.3 % is taken by columns, 42.4 % by heat exchangers, 16.1 % by the reactor, and 3.2 % by other vessels. For utilities, 85.8 % is paid for steam, 10.4 % for waste water treatment, and 3.8 % for cooling water.

7. Conclusions

i-BA production at the industrial scale using Amberlyst 131 as solid catalyst is feasible. 20.5 kt/y are achieved in a RSR process using an adiabatic multitubular reactor and conventional distillation equipment. The required 4000 kg of catalyst is arranged in 55 tubes, each of 0.2 m diameter and 3 m length. The separation equipment has reasonable sizes and energy requirements (3400 kW heating, 2470 kW cooling). The difficult separation between *i*-BA and AA is achieved by vacuum distillation, condition at which the relative volatility increases and the binary azeotrope disappears. The process shows attractive economic indicators: annual revenues around 4,000,000 \$, for 34,424,000 \$/y production costs (raw materials, equipment amortization and utilities). The process is controllable, the plantwide control structures achieving a smooth transition to the new operating points for large throughput and reactor inlet temperature changes. To achieve tight control of the acrylate purity, two concentration control loops are required.

Acknowledgement

C.S. Bildea gratefully acknowledges the financial support of the European Commission through the European Regional Development Fund and of the Romanian state budget, under the grant agreement 155/25.11.2016 (Project POC P-37-449, acronym ASPiRE).

References

- C.S. Bildea, A.C. Dimian, S.C. Cruz, P.D. Iedema, Design of Tubular Reactors in Recycle Systems, *Comp. & Chem. Eng.* 2004, 28, 63-72.
- S. Karakus, E. Sert, A.D. Buluklu, F.S. Atalay, Liquid Phase Esterification of Acrylic Acid with Isobutyl Alcohol Catalyzed by Different Cation Exchange Resins, *Ind. Eng. Chem. Res.* 2014, 53, 4192-4198.
- T. Ohara, T. Sato, N. Shimizu, G. Prescher, H. Schwind, O. Weiberg, K. Marten, H. Greim, Acrylic acid and derivatives. *Ullmann's Encyclopedia of Industrial Chemistry*, Wiley, 2003.

Optimization based design of an industrial cluster for economic and environmental benefits

D. Varshney^a, P. Mandade^a, Yogendra Shastri^{a*}

*^aDepartment of Chemical Engineering, Indian Institute of Technology Bombay, Mumbai, India - 400076
fenila@iitb.ac.in, *yshastri@che.iitb.ac.in*

Abstract

This work proposes an optimization model for the design of an industrial cluster based on sugarcane bagasse in the Indian context. Three different products, namely, ethanol, electricity, and pellets, along with the possibility of selling raw bagasse and burning it in boiler are considered. An economic optimization model to maximize the net present value of the cluster is formulated. Simultaneously, a multi-objective optimization model to minimize the environmental impacts is formulated. The model was applied to a case of a sugar mill processing 181 Mg/h sugarcane. Economic optimization recommended electricity production as the optimal option at the current product prices. This was also desirable from the GHG emission reduction standpoint. However, electricity production led to highest water footprint. Ethanol price has to increase by 100% over the target price for economic feasibility. Pelletization was preferred only from a water footprint perspective.

Keywords: Bagasse, Industrial Ecology, Optimization, India, Ethanol

1. Introduction

Sugarcane bagasse is a highly promising source of biomass in the Indian context for the establishment of a bio-based economy. Bagasse can be used to produce a number of value added products such as pellets, electricity, ethanol, paper board, and specialty chemicals such as vanillin. Each of these products varies in terms of costs, technology readiness level, per unit revenue, and market capacity. Moreover, the environmental impacts of these alternatives also vary considerably. Utilization of sugarcane bagasse, therefore, poses a sustainability challenge with food, energy and water nexus. Region specific factors are critical and must be considered in the analysis. Such studies have been reported in literature for some sugar producing countries (Furlan et al, 2012, Ensinas et al, 2013). However, such an analysis has not been conducted in the Indian context. This work addresses this knowledge gap by proposing an industrial ecology approach and optimizing the design of an industrial cluster based on sugarcane bagasse. An existing sugar refinery providing a fixed quantity of bagasse is considered. Three different products of bagasse, namely, pellets, electricity, and ethanol, are considered. An economic optimization model is formulated to understand the profitable products and the sensitivity of those results to product market prices. Simultaneously, the global warming potential (GWP) and water footprint for the same products are calculated to understand the environmental trade-offs.

The article is arranged as follows. The optimization model formulation is given in Section 2. Section 3 discusses the key results from the simulation studies, and the important conclusions are summarized in Section 4.

2. Optimization model formulation

An existing sugar mill with a boiler to provide process heat in the form of steam is assumed. The procurement of sugarcane to the facility and the operations part of the conventional sugar mill are not considered since it is assumed that those are already set-up and operational. Similarly, transportation of products produced from bagasse (or bagasse as a product) is not the part of the system boundary. For a fixed capacity of the sugar mill, the bagasse availability is also known.

Bagasse generated can potentially be split into five streams, three of which include further processing to produce value added products, namely, ethanol, pellets, and electricity (Fig. 1). Of the remaining two streams, one stream goes to the boiler to meet the energy demand of the mill as well as various production processes within the industrial cluster. This ensures that the industrial cluster is energy self-sufficient. The second stream represents bagasse that is directly sold in the market without any processing. The energy production operations in the clusters (boiler and electricity) are further supported by trash collected from sugarcane farms as feedstock. It is assumed that only the trash on farms supplying sugarcane to the mill is available, which sets an upper bound on the total trash that can be utilized.

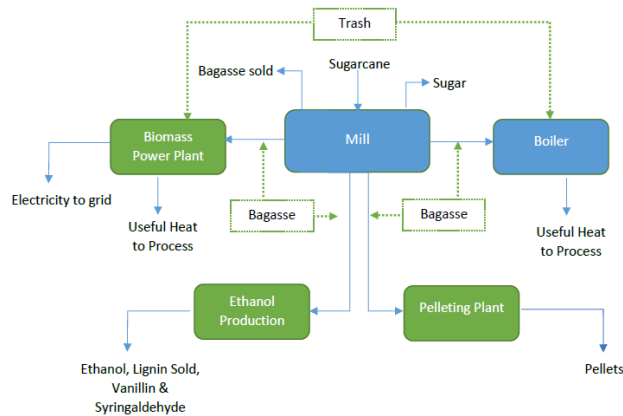


Figure 1: Alternatives for the utilization of bagasse and trash considered in the cluster. Blue boxes indicate existing facilities in the sugar mill while green boxes indicate new facilities

The ethanol production process uses the organosolvent pretreatment, which produces relatively pure lignin that can be used as feed to the boiler. The cellulose and hemicellulose separated after pretreatment are used for ethanol production. Pelletization involves three major steps: drying (up to 10% on wet basis), grinding (size reduction) and densification (Mani *et al.*, 2006). Individual pellet density ranges from 1000 to 1200 kg/m³ whereas the bulk density of pellets is 600 to 700 kg/m³. Pellets coming out of pellet mill (at about 70°C to 90°C) are cooled, packaged and sold. Biomass Integrated Gasification Combined Cycle (BIG-CC) configuration is considered for electricity production using bagasse and trash as the feedstock. Combustion gases drive the gas turbine to generate electricity through generator. The exhaust gases from gas turbine are used to generate steam in Heat Recovery Steam Generator. The steam drives

the steam turbine to generate more electricity and useful heat, which can be delivered to other processes of the facility (Ensinas *et al.*, 2007).

Two different optimization models have been formulated, capturing the economic and environmental impact associated with the proposed industrial cluster. These models are explained in the following sections.

2.1. Economic optimization model formulation

The model constraints include the mass and energy balances relevant to each unit process/operation described in the previous section. These constraints are formulated by considering the performance data from literature. Only selected constraints are reported here for brevity. A key mass balance constraint is the distribution of bagasse to five possible routes as shown in Fig. 1, which is modeled as follows:

$$total_{bagasse} = bgs_{eth} + bgs_{elec} + bgs_{pel} + bgs_{boiler} + bgs_{market} \quad (1)$$

where, $total_{bagasse}$ is the total available bagasse (Mg/h) obtained after sugarcane juice extraction, bgs_{eth} is the amount of bagasse (Mg/h) sent to ethanol production, bgs_{elec} is the amount of bagasse (Mg/h) sent to the electricity generation unit, bgs_{pel} is the amount of bagasse (Mg/h) sent to the pelleting plant, bgs_{boiler} is the amount of bagasse (Mg/h) sent to the boiler, and bgs_{market} is the amount of bagasse (Mg/h) that is directly sold in the market. Additional key constraint is the distribution of collected trash to electricity generation unit and the sugar mill boiler:

$$total_{trash} = trash_{elec} + trash_{boiler} \quad (2)$$

where, $total_{trash}$ is the total trash collected and transported (Mg/h) to the integrated facility, $trash_{elec}$ is the amount of trash (Mg/h) sent as a feed to electricity generation unit, and $trash_{boiler}$ is the amount of trash (Mg/h) sent to the boiler. Another important energy constraint is the overall heat demand of the facility:

$$C_{p,bagasse} * bgs_{boiler} + C_{p,lignin} * lignin_{boiler} + C_{p,trash} * trash_{boiler} + heat_{useful,elec} \geq heat_{mill} * Feed + bgs_{eth} * heat_{ethanol} \quad (3)$$

where, $C_{p,i}$ is the specific heat of combustion of material i (bagasse, trash, or lignin), $heat_{useful,elec}$ is the heat supplied by the power plant, $heat_{mill}$ is the heat demand of existing sugar mill, $heat_{ethanol}$ is the heat demand of ethanol generation facility, bgs_{boiler} is the amount of bagasse sent to boiler, $lignin_{boiler}$ is the amount of lignin sent to boiler, $trash_{boiler}$ is the amount of trash sent to boiler, and $Feed$ is the amount of sugarcane processed in the facility. The capital and operating costs for each of these processes are considered, and the corresponding cost functions constitute another important set of constraints. The key decision variables are the distribution of bagasse and trash to the various streams, as described the constraints in Eq. 1-3. The objective function is the maximization of Net Present Value (NPV) of the integrated facility where the NPV equation is linearized. This is a Mixed Integer Linear Programming (MILP) problem with 144 continuous variables, 4 binary variables

(selection of processing options), and 144 constraints. The model is formulated in GAMS[®] (General Algebraic Modelling System) solved using the CPLEX[®] solver.

2.2. Environmental optimization model formulation

The multi-objective optimization problem considering two environmental impact categories, namely, net greenhouse gas emissions (GHG) and water footprint, is formulated. Only the direct water footprint is considered. The model also considered the avoided GHG emission due to replacement effect, such as the replacement of petroleum based gasoline with ethanol from bagasse. Since the overall GHG emissions and water footprint numbers for all the processing options are directly used, a detailed mass balance for each step is not necessary. This model, therefore, is much simpler than the economic optimization model previously described. It is linear programming model with the decision variables as the amount of bagasse diverted to each of the five streams. ϵ constraint method is used to solve the problem and obtain the Pareto front. The model is not discussed here for brevity.

3. Results and discussion

The model was applied to a case of sugar refinery processing 181 Mg/h of sugarcane. 50% retention of trash on farm was assumed as base case. The selling prices for electricity (₹6/kWh) and pellets (₹10/kg) were as per the market values while the selling price of ethanol (₹39 /l) was as per the target price set by the government (₹ represents Indian Rupees). The pelletization rate was 4 Mg/h and a minimum size of 6.5 MW power plant was enforced. The prices of various chemicals and inputs were taken from literature. Table 1 shows the values of GHG emissions and water requirement for various products, including GHG offset due to replacement of an existing product.

Table 1: Life cycle input data for the different products produced from bagasse (adapted from different sources in literature)

Products	Bagasse requirement (kg)	GHG emissions; GHG offset (kg of CO ₂ /unit of Product)	Water requirement (lit /unit of Product)
Ethanol (lit)	6.046	0.562; 0.357	231
Electricity (kw)	2.394	0.0685; 0.81	224
Pellets (kg)	1.8	0.221; 0	65

3.1. Economic optimization

The model was first used to determine the Break Even Selling Price (BESP) for all the three commodities individually when integrated with the existing sugar mill. BESP of ethanol, pellets and electricity was ₹64/l, ₹9/kg, and ₹3/kWh, respectively. This indicated that ethanol production was not profitable. In contrast, electricity production was profitable; primarily due to the consideration that bagasse (feedstock) was free.

When the optimization model was solved considering all potential uses of bagasse, electricity generation was recommended as the optimal solution and no other processing route was chosen. With the feed rate of 181 Mg/h and 50% trash retention, all of the 22.17 Mg/h available bagasse and 12.62 Mg/h trash was sent to the power plant facility.

Boiler got no feed of bagasse and trash as the heat generated by the power plant was enough to meet the energy demands. The size of the plant was 37.84 MW and hence capable of providing around 281 million units (kWh) of electricity annually to the grid generating revenues of ₹169 crores at an initial investment of ₹712.6 crores with annual profit of ₹105.75 crores (1 crore is equal to 10 Million, and 1 ₹ is about 0.015 USD)

The sensitivity of the result to the market prices of various products was studied. Electricity market is well established and therefore the prices are relatively stable. Therefore the cost of electricity was fixed at the base value. The selling prices of ethanol and pellet were varied and the resulting optimal product portfolio was determined. The results (Fig. 2) indicated that ethanol production became profitable only if the selling price was more than ₹76/l. Similarly, pelletization became profitable if the selling price was more than ₹14/kg. Note that since there was an upper cap on the pellet market, electricity was still produced for a pellet price higher than ₹14/kg.

Trash retention is often recommended as a sustainable farming practice since it reduces the requirement of chemical fertilization and increases yield due to natural soil enrichment. Therefore, a scenario with 100% trash retention on farm was studied. This reduced the availability of trash. The results (Table 2) indicated that the optimal strategy in such a case was to use bagasse in the boiler to meet the energy demands of the mill and sell the remaining bagasse directly to the market. Production of any of the processed products was economically infeasible. This indicated the importance of trash collection and utilization for this system. Cases for various trash retention values between 0% and 100% were simulated and the results are not reported here.

Fig. 3 shows the results of the environmental impact optimization model. There was a strong trade-off between water footprint and net GHG emission. For minimum water footprint, pelletization was the only product produced. However, greater importance to GHG emission resulted in the production of ethanol and then electricity. This was primarily due to the avoided GHG emissions of conventional products (gasoline and coal based electricity). For minimum GHG emission, only electricity production was recommended

Table 2: Impact of trash retention on optimal industrial cluster design

Variable	Base Case	100% trash retention
Feed	181 Mg/h	181 Mg/h
Sugarcane yield	72.4 Mg/ha	82.9 Mg/ha
Bagasse processing route	Power Plant (37.84 MW)	Market & Boiler
Net Present Value (NPV)	₹366.06 crores	₹104.24 crores
Net annual profit	₹105.75 crores	₹10.22 crores

4. Conclusions

This work developed an optimization model to design an industrial cluster based on sugarcane bagasse in India. The economic optimization results indicated that electricity production was the most profitable option for a sugar mill processing 181 Mg/h sugarcane. Trash availability from sugarcane farms was important to achieve economic feasibility of the electricity production option. Ethanol and pellet market prices needed to increase significantly to achieve economic feasibility of those products from bagasse. The net GHG emission and water footprint had a trade-off and the desirable products

changed with varying weights given to each of these two objectives. The ongoing work is focusing on integrating the economic and environmental impact optimization problems. Although results presented here provide some insights into the trade-offs, the integrated problem will provide quantitative results.

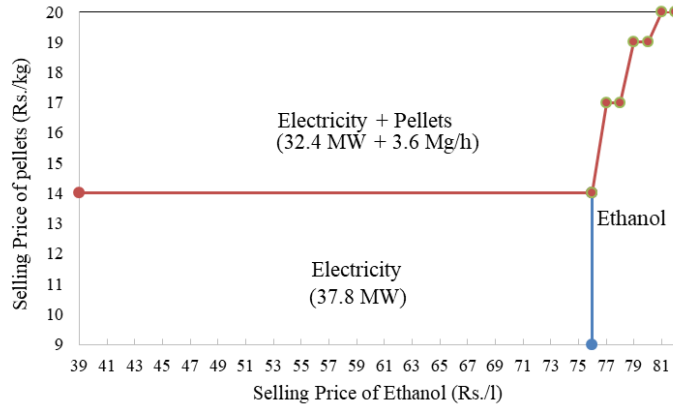


Figure 2: Impact of product prices on optimal product portfolio of the industrial cluster. Points on orange line indicate electricity+pellets region and points on blue line indicate ethanol region

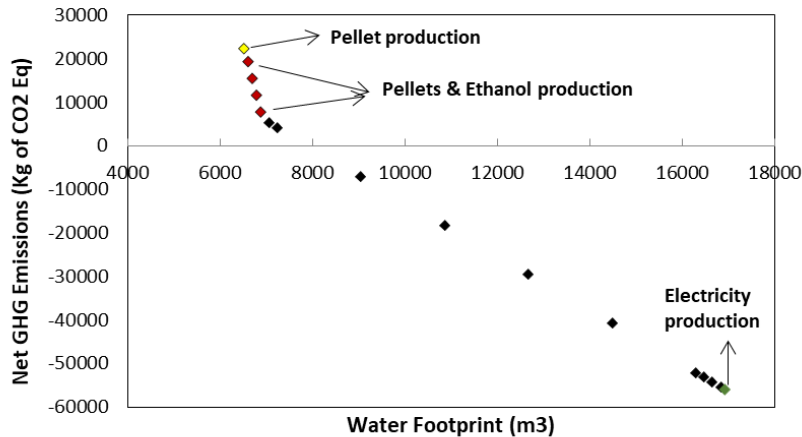


Figure 3: Net GHG emission and water footprint trade-off and the product portfolio. For the intermediate points (black), electricity and ethanol are produced in varying proportions

References

- A.V. Ensinas, S.A. Nebra, M.A. Lozano, and L.M. Serra, 2007, Energy Conversion and Management, 48, 2978–2987
- A.V. Ensinas, V. Codina, F. Marachal, J. Albarelli, and M.A. Silva, 2013, Chemical Engineering Transactions, 35, 523–528.
- F. Furlan, C. Costa, G. Fonseca, R. Soares, A. Sechhi, A. Cruz, and R. Giordano, 2012, Comput. Chem. Eng., 43, 1–9.
- S. Mani, S. Sokhansanj, X. Bi, and A. Turhollow, 2006, Applied Engineering in Agriculture, 22(3), 421–426.

Process Simulation and Optimization of 10-MW EFB Power Plant

Jaechan Han^{a,b}, Junghwan Kim^{a,*}

^a*Ulsan Regional Division, Korea Institute of Industrial Technology, Ulsan, South Korea*

^b*Department of Applied Chemical Engineering, Korea University of Technology and Education, Cheonan, 31253, South Korea*

*kjh31@kitech.re.kr**

Abstract

Empty fruit bunch (EFB) is a kind of biomass formed during the production process of palm oil. EFB that used to be disposed of as waste has recently been used as fuel as quantities have increased. EFB commonly has a high moisture content, which lowers the combustion temperature and reduces energy efficiency. Therefore, a drying process should be incorporated when designing an EFB power plant. In this study, we simulated a process that includes the drying process for a 10-MW power plant and compared the optimized energy efficiency with an existing process. We found the optimum moisture content of EFB considering the temperature, time, flow rate, and critical moisture content of the drying process. At the optimum point, the moisture content of EFB was 7.79 %, and the efficiency was increased by 14.29 %.

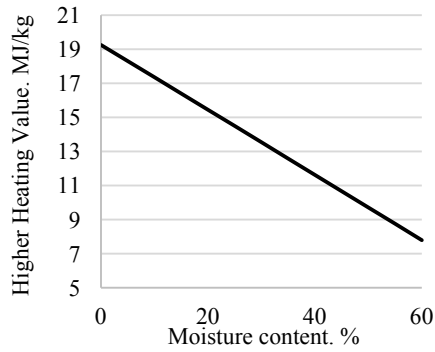
Keywords: Biomass, Empty Fruit Bunch (EFB), EFB Power Plant, Moisture Content

1. Introduction

Empty fruit bunch (EFB) comprises 20 % of the byproducts produced during palm oil production. In Indonesia, the world's largest producer of palm oil, an enormous amount of EFB is produced every year, and the process of disposing of the EFB has led to significant costs and environmental pollution (Abdullah and Sulaiman, 2013). As the demand for electricity has increased due to rapid economic growth, Indonesia is planning to build biomass power plants for a smooth electricity supply (Differgroup, 2012). If EFB is used as fuel for a power plant, EFB would solve both environmental pollution and electric power supply problems. A drying process is essential to use EFB as fuel for a power plant.

Table 1. Properties of EFB.

Fuel analysis	EFB
Proximate analysis (wet basis)	wt. %
Volatile matter	67.4
Fixed carbon	9.8
Ash	2.8
Moisture	20
Ultimate analysis (dry basis)	
C	45.9
H	6.1
N	0.43
S	0.13
O	47.44
HHV (MJ/kg, MC 20 %)	15.5

**Figure 2. HHV vs Moisture content.**

was set as 400 °C, which is the optimum drying temperature for typical rotary dryers (Li et al., 2012). The residence time of the EFB was set so as not to exceed the average residence time of a typical rotary dryer of 17.5 min (Girovich, 1996).

2.2. Drying kinetics

The factors required for drying kinetics modeling in Aspen Plus are heat transfer coefficient (α_G) and mass transfer coefficients (β_G), critical moisture content (X_c) of the material, equilibrium moisture content, and the drying curve of a falling-rate drying period. Heat transfer and mass transfer coefficients were calculated from Eqs. (1) and (2) (Gunter Brenn and Helfried Steiner, 2014), (Sattler and Feindt, 2008). To calculate Le , Sc , and Re , vapor diffusion coefficient (δ_G), drying gas velocity (u_G), density (ρ_g), dynamic viscosity (η_g), specific heat ($C_{p,g}$), and thermal conductivity (λ_G) were obtained by using the stream analysis of Aspen Plus. The diameter, L , required to calculate the mass transfer coefficient and Reynolds number was replaced with the Sauter mean diameter (d_{32}) and median particle diameter (d_p) of EFB. As shown in Eqs. (1) ~ (6), the higher the velocity and temperature of the drying gas, the smaller the particle size, the higher the heat and mass transfer coefficients, and the better the drying process. The velocity of the drying gas for calculation of heat and mass transfer (typical range: 0.5 m/s to 2.5 m/s) was selected as the average value of 1.5 m/s (Saravacos and Kostaropoulos, 2002).

$$\beta_G = \frac{Sh * \delta_G}{d_{32}} \quad (1)$$

$$\alpha_G = \beta_G * \rho_G * C_{p,G} * Le^{1-n} \quad (2)$$

$$Sh = \sqrt{Sh_{laminar}^2 + Sh_{turbulent}^2} \quad (3)$$

$$Sh_{laminar} = 0.664 * \sqrt{Re} * \sqrt[3]{Sc} \quad (4)$$

$$Sh_{turbulent} = \frac{0.037 * Re^{0.8} * Sc}{1 + 2.443 * Re^{-0.1} * (Sc^{\frac{2}{3}} - 1)} \quad (5)$$

$$Re = \frac{u_G * d_p * \rho_G}{\eta_G}, Sc = \frac{\eta_G}{\delta_G * \rho_G}, Le = \frac{\lambda_G}{C_{p,G} * \rho_G * \delta_G} \quad (6)$$

The critical moisture content varies depending on the material, and it is further related to velocity and temperature. Because many factors affect the critical moisture content, we used the average value of the critical moisture content shown in Table 2 (Hasibuan and Wan Daud, 2007). The temperature and relative humidity of the drying gas significantly affect the equilibrium moisture content, which is different depending on the material. At a high drying temperature and low relative humidity, the equilibrium moisture content becomes close to zero. The drying rate starts to decrease after passing the critical moisture content, and the moisture is no longer evaporated when reaching the equilibrium moisture content. The drying curve of a falling-rate drying period given in Eq. (7) was used (Hasibuan and Wan Daud, 2007). $\frac{X}{X_c}$ refers to normalized moisture content, and $\frac{R}{R_c}$ refers to normalized drying rate.

$$\frac{R}{R_c} = [1 - (1 - \frac{X}{X_c})^{1.506}] \quad (7)$$

2.3. Boiler and steam cycle model

In the steam cycle shown in Figure 1, the pressure of the feed water increases to 2 atm by Pump 1. The feed water entering the deaerator is further preheated to 127 °C by the steam at 159 °C and 6 atm coming from the turbine extraction valve. The pressure of the preheated feed water rises to 67 atm by Pump 2. In the boiler, due to the heat obtained by burning the EFB, the water becomes steam at 433 °C and 60 atm. After heating the water, the temperature of flue gas is assumed to be 200 °C. High pressure steam generates 10-MW of electricity through the turbine, and the steam is discharged as low-pressure steam at 47 °C and 0.105 atm. The low-pressure steam entering the condenser is fully condensed and circulated by Pump 3.

2.4. Thermal efficiency of the boiler

The thermal efficiency of the boiler depends on the moisture content of EFB. Aspen Plus reflected the thermal efficiency of the boiler according to the moisture content of wood (Dzurenda and Banski, 2017).

$$y = -0.0025 x^2 + 0.0145 x + 84.612, R^2 = 0.9941 \quad (8)$$

2.5. Net power generation

The remainder after subtracting the work energy to generate from the power generation is called the net power generation.

$$W_{net} = W_{turbine} - (W_{boiler} + W_{pump 1} + W_{pump 2} + W_{pump 3}) \quad (9)$$

3. Results

3.1. Case study

A case study was conducted to examine the power generation efficiency by using the dried EFB. When the EFB was not dried, the base case was set to produce 10-MW of electric power by using EFB with a 60% moisture content. The amount of EFB required to produce the same power and the amount of fuel consumed in the drying process were calculated according to the flow rate of drying gas at 400 °C. The following constraints were applied to all cases to discover the optimum point while varying the flow rate. 1) The relative humidity of the drying gas exiting the dryer cannot exceed 95 %, as the

Table 2. Critical moisture content.

NO.	Xc	T(°C)	V(m/s)
T1	0.84	200	0.89
T2	0.62	220	0.89
T3	0.68	240	0.89
T4	0.7	260	0.89
T5	0.63	280	0.89
V1	0.7	200	0.79
V2	0.77	200	0.89
V3	0.82	200	0.99
V4	0.95	200	1.09
AVG	0.745	-	-

Table 3. Simulation conditions.

Parameter	Value
Drying gas temperature	400 °C
Drying gas velocity	1.5 m/s
Mass transfer coefficient	0.1405 m/s
Heat transfer coefficient	0.068 kW/sqm-K
Outlet drying gas RH	≤ 95 %
Residence time	≤ 17.5 min
Particle size	5 mm
Excess air ratio	1.6

moisture can condense in the dryer. 2) The particle size of EFB is 5 mm. 3) The excess air ratio close to complete combustion was 1.6. 4) EFB with a moisture content of 60% was used as fuel in the burner for better comparison of the results with those obtained when kerosene, diesel, or natural gas are used. The simulation conditions are summarized in Table 3.

3.2. Case study result

The calculation results from the case study are shown in Table 4. Figure 3 shows the graph of the moisture content and total fuel consumption according to the flow rate. In the base case, there was no fuel used for the burner because EFB was not dried and 22,483 kg/h of wet EFB was required to generate 10-MW. Even without the energy for the drying process, the pump work required to operate the steam cycle basically was 101 kW. In Case 1, when the residence time of EFB is longer, the relative humidity of the drying gas exceeds 95 %. Thus, the residence time is extremely short compared with other cases. In Cases 2, 3, and 4, although the maximum residence time of the solids was reached, the relative humidity was much less than 95 % due to the high flow rate of the drying gas. Case 2 showed the maximum efficiency. The efficiency increased by 14.29 % compared with the base case, the moisture content was 7.79 %, and the drying gas flow rate was 58,477 kg/h. The efficiency gradually decreased from Case 3, which passed the optimum point, and the efficiency for Case 4 was -0.71 %, which was lower than that without drying.

Table 4. Result of case studies.

Parameter	Unit	Base	Case 1	Case 2	Case 3	Case 4
Moisture content of dried EFB	%	60	38.91	7.79	0.32	0.29
Drying gas	kg/h	0	41,355	58,477	69,891	112,693
Residence time	min	0	1.31	17.5	17.5	17.5
Relative humidity	%	0	94.95	92.07	23.98	1.51

Fuel for burner (①)	kg/h	0	2,902	4,105	4,907	7,913
$W_{\text{blower}}+W_{\text{pump}}$	kW	101	113	115	117	125
Wet EFB (②)	kg/h	22,483	17,536	15,164	14,887	14,730
Dried EFB	kg/h	22,483	11,482	6,577	5,974	5,910
Quantity of evaporation	kg/h	0	6,054	8,587	8,913	8,820
Total fuel consumption (①+②)	kg/h	22,483	20,438	19,269	19,794	22,643
Turbine work	kW	10,101	10,113	10,115	10,117	10,125
Net power generation	kW	10,000	10,000	10,000	10,000	10,000
Relative efficiency	%	-	9.09	14.29	11.96	-0.71

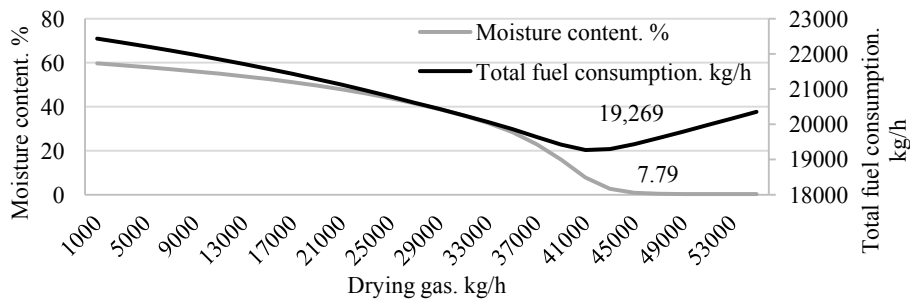


Figure 3. Moisture content and Total fuel consumption vs Drying gas.

4. Conclusion

This study modeled and optimized a 10-MW power plant by using Aspen Plus. The drying process was modeled with a typical rotary dryer. As the heating value of EFB increases with drying, the amount of EFB required to produce 10-MW is reduced. However, the fuel consumption of burner also increases. We conducted the case study considering the EFB heating value and fuel consumption of burner to find optimum point. The results of the case study showed that less total fuel was required when some of the wet EFB was used for drying than when using the whole wet EFB as the fuel for a power plant. In Case 2, which is the optimum point, when EFB was dried to 7.79 %, the efficiency increased by 14.29 % compared with the base case without drying. When the drying was continued beyond the optimum point, the efficiency gradually decreased, and the efficiency of the drying gas was -0.71 % at the rate of 112,693 kg/h, and the drying became infeasible. Utilizing this process modeling, the optimum point can be easily and quickly obtained even under various conditions such as changing particle size or temperature of drying gas.

5. References

- Abdullah, N., & Sulaiman, F. (2013). The oil palm wastes in Malaysia. In *Biomass Now-Sustainable Growth and Use*. InTech.
- Amos, W. A. (1999). Report on biomass drying technology (No. NREL/TP-570-25885). National Renewable Energy Lab., Golden, CO (US).
- Differgroup. (2012). The Indonesian electricity system - a brief overview. Storgata 26, 0184 Oslo, Norway. http://www.differgroup.com/Portals/53/images/Indonesia_overall_FINAL.pdf, 7.

- Dzurenda, L., & Banski, A. (2017). Influence of moisture content of combusted wood on the thermal efficiency of a boiler. *Archives of Thermodynamics*, 38(1), 63-74.
- Gebreegiabher, T., Oyedun, A. O., Luk, H. T., Lam, T. Y. G., Zhang, Y., & Hui, C. W. (2014). Design and optimization of biomass power plant. *Chemical Engineering Research and Design*, 92(8), 1412-1427.
- Girovich, M. J. (1996). *Biosolids treatment and management: Processes for beneficial use*. CRC Press, 284.
- Gunter Brenn., Helfried Steiner. (2014). TRANSPORT PROCESSES 1 AND 2. Institute of Fluid Mechanics and Heat Transfer, Graz University of Technology. https://www.tugraz.at/fileadmin/user_upload/Institute/ISW/Lehre/Downloads/Mat_TP_english.pdf, 34.
- Hasibuan, R., & Wan Daud, W. R. (2007). Through drying characteristic of oil palm empty fruit bunch (EFB) fibers using superheated steam. *Asia-Pacific Journal of Chemical Engineering*, 2(1), 35-40.
- Li, H., Chen, Q., Zhang, X., Finney, K. N., Sharifi, V. N., & Swithenbank, J. (2012). Evaluation of a biomass drying process using waste heat from process industries: A case study. *Applied Thermal Engineering*, 35, 71-80.
- Mujumdar, A. S. (Ed.). (2014). *Handbook of industrial drying*. CRC press, 425.
- Saravacos, G. D., & Kostaropoulos, A. E. (2002). *Handbook of food processing equipment*. Springer Science & Business Media, 392.
- Sattler, K., & Feindt, H. J. (2008). *Thermal separation processes*. John Wiley & Sons, 333.

Dimethyl Carbonate Production Process from Urea and Methanol

Daniel Vázquez^{a,b*}, Juan Javaloyes-Antón^a, Juan D. Medrano-García^a, Rubén Ruiz-Femenia^a, José A. Caballero^a

^a *Institute of Chemical Processes Engineering, University of Alicante. P.O. 99, E-03080, Alicante, Spain*

^b *Departament d'Enginyeria Química, Universitat Rovira i Virgili, Av. Països Catalans 26, 43007 Tarragona, Spain*

danielvazquez150791@gmail.com

Abstract

In this paper, we aim to provide a feasible flowsheet of the process of dimethyl carbonate (DMC) production from urea and methanol. We use Aspen Plus for the simulation and we perform an economic and energetic study of the process. We also remark which process variables and units affect the design the most. The results prove the viability of this synthesis route, which for a production of 74 kt/y of DMC, grants a 21.1 MMS/y of profit, as long as a proper catalyst is employed in the synthesis.

Keywords: DMC, Aspen Plus, Techno-economic Analysis, Simulation.

1. Introduction

Dimethyl carbonate stands out as one of the key chemicals in the Green Chemistry approach thanks to its versatile uses as a safe, non-toxic, green reagent. Among its uses, its capability of replacing dimethyl sulfates and methyl halides in methylation reactions, as well as replacing phosgene in the production of polycarbonates, must be highlighted. It is also being considered as a component of reformulated fuels due to its high oxygen content, having as much oxygen as three times the amount in methyl-tert-butyl ether (MTBE), and good blending properties (Pacheco & Marshall, 1997). Its molecule is shown in Figure 1.

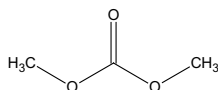


Figure 1. Dimethyl carbonate molecule.

Despite being able to be synthesized by numerous routes, DMC is only industrially produced by three different routes: liquid phase oxidative carbonylation of methanol, vapor phase oxidative carbonylation of methanol and transesterification of ethylene carbonate with methanol.

Traditionally, DMC was prepared by phosgenation of methanol, but that route is being gradually abandoned due to the environmental, safety and economic drawbacks that it entails. This, and a review of all the processes, can be found in Keller et al. (2010).

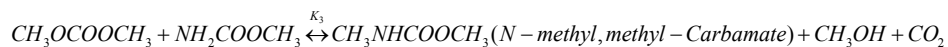
Focusing on the objective of the paper, the urea route allows the production of DMC using only urea and methanol as raw materials, which are comparatively abundant and

have a low price (Lin et al., 2004). It also avoids the use of phosgene, carbon monoxide, nitric oxide and ethylene oxide, which are present in the other routes. In addition, it also provides the perfect opportunity for the integration of both the fuel industry and the fertilizer industry, since urea production is comparable to the environmental gasoline oxygenates demand (Pacheco & Marshall, 1997).

As such, this route seems very attractive for the industry. It has however some drawbacks in which this paper dwells on.

2. Reaction mechanism

There are several studies of the synthesis of DMC from urea and methanol in literature. From these works, the following mechanism can be established:



In the first reaction, urea and methanol react to form methyl carbamate (MC), a reaction intermediate in this process, and ammonia. During the second reaction, MC reacts further with methanol to produce dimethyl carbonate (DMC) and more ammonia. This is the main reaction process, common in all the studies.

The third reaction is considered as the main side reaction. DMC and MC react between them to produce the by-product, N-methyl,methyl-carbonate (NMMC), methanol and carbon dioxide. Its extent is around 2 – 4 % of MC conversion.

The first reaction is thermodynamically favorable, while the second is not (Wang et al., 2007). In addition, the first reaction equilibrium is favored towards the products, thus favorable to the production of MC, while the second reaction is heavily favored towards the reactants, hindering the production of DMC, as shown in Table 1.

In the work by Wang et al. (2007), it is also noted that the first reaction is also remarkably fast, with urea reaching a high conversion to MC in a consistent residence time. Due to the equilibrium of the second reaction, that cannot be said for this step. As such, it is necessary to perform this second step, if not both at the same time, in a reactive distillation column adding a catalyst and removing the ammonia while it is being produced.

Table 1. Equilibrium data.

T(K)	Reaction 1		Reaction 2	
	$\Delta_r G(kJ \cdot mol^{-1})$	K	$\Delta_r G(kJ \cdot mol^{-1})$	K
300	-13.26	203.88	15.41	2.08×10^{-3}
350	-13.95	120.88	15.85	4.30×10^{-3}
400	-14.82	86.07	16.41	7.20×10^{-3}
450	-15.91	70.27	17.08	1.04×10^{-2}
500	-17.21	62.74	17.84	1.37×10^{-2}
550	-18.60	58.40	18.73	1.66×10^{-2}
600	-20.23	57.65	19.72	1.82×10^{-2}

Kinetic data for a heterogeneous catalyst of $ZnO - Al_2O_3$ are presented in the work of Zhao et al. (2012). The first and main problem of this route arises here, which is the kinetics. A representation of the amount of DMC and NMMC produced per amount of MC introduced at different temperatures in a plug flow reactor without taking into account the reverse reaction is shown in Figure 2. It can be seen that even at very high temperatures (~ 220 °C), the residence time for a significant yield of DMC is more than 5 h. This residence time is unobtainable in a continuous reactive distillation column. The process here is simulated considering the equilibrium is reached, and as such acts as an upper bound for the possible real process, once the catalysts reach satisfactory reaction rates.

In Figure 2 it can be also appreciated that when working at high temperatures, the amount of NMMC produced starts to overshadow the DMC, and thus working at extreme temperatures and pressures is not a solution. Additional research on the catalyst is required to obtain a viable conversion under a realistic operating time.

Therefore, we perform a curve fitting in order to use the kinetic parameters shown in Table 1. The equation has the form shown in Eq.(1) where the temperature (T) is in Kelvin. The results of the curve fitting can be seen in Table 2.

$$\ln K_{eq} = A + B / T + C \ln(T) + DT \quad (1)$$

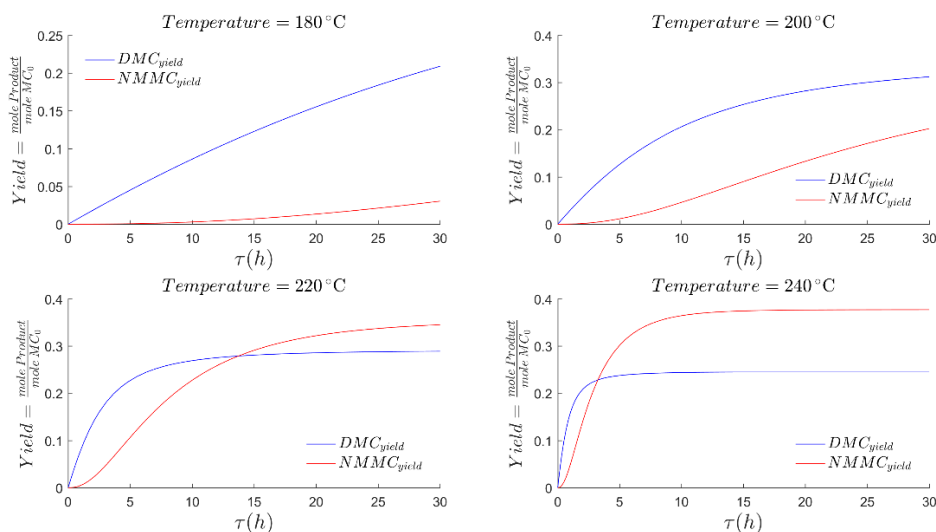


Figure 2. Kinetic of reactions 2 and 3 at different temperatures.

Table 2. Curve fitting for the equilibrium of reactions 1 and 2.

	A	B	C	D	R^2
Reaction 1	-14.48	2020	2.188	0.001952	0.9999
Reaction 2	-38.53	-521.3	6.543	-0.01077	0.9999

3. Simulation and results

The simulation is performed in a similar flowsheet to the one represented in the patent by Ryu and Gelbein (2002), with the following changes:

- In order to use the kinetic rate for the formation of NMMC, instead of the homogeneous catalyst Triglyme, we use a heterogeneous catalyst based on ZnO.
- While in the patent all the reactions are performed in a single reactive distillation column, in this simulation reaction 1 is carried out in a previous plug flow reactor, in order to remove the greatest possible amount of ammonia before entering the reactive distillation column where the second and third reaction occur.

The simulation, with a yearly production of 74 kt/y of DMC, is divided in the following three sections.

3.1. Section 1

In this first section (Figure 3), the stored urea and methanol are mixed, pumped and heated up to the conditions of the first reactor (R-101) which works at 155 °C and 9.3 bar. Here, the first reaction occurs, whose products are MC and ammonia. Ammonia is then removed in a flash separation unit (S-101) and the remaining MC, alongside the excess methanol, continues to Section 2.

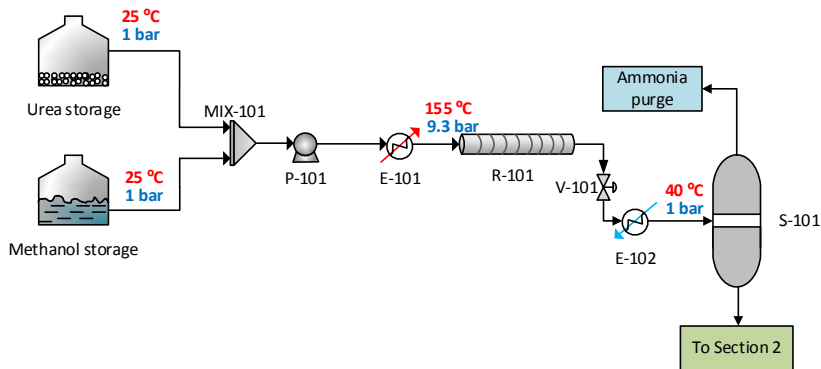


Figure 3. First reaction step and separation of ammonia (Section 1)

3.2. Section 2

In the second section (Figure 4), the stream from the first section is mixed with a recycle stream from the end of the current section containing the heavy components, where MC is recycled. Then it is pumped and heated up to the entry conditions of the reactive distillation column (R-201). It is introduced in the fifteenth stage, while at the bottom of the column, in the reboiler, a stream of methanol make-up, mixed with a recycle from the third section, composed mostly by methanol, is introduced. The DMC is extracted from both the distillate and the bottoms of the column and thus it must be further separated. The distillate is introduced into another column (S-201), where the remains of ammonia are removed and DMC exits as the bottom product. The bottoms enter column S-202 where the heaviest components (mainly NMMC and MC) are recycled into the reactive distillation column. In addition, a purge avoids the NMMC build-up and helps with the convergence of the model in Aspen Plus. The DMC, alongside most of the methanol, continues to the third section.

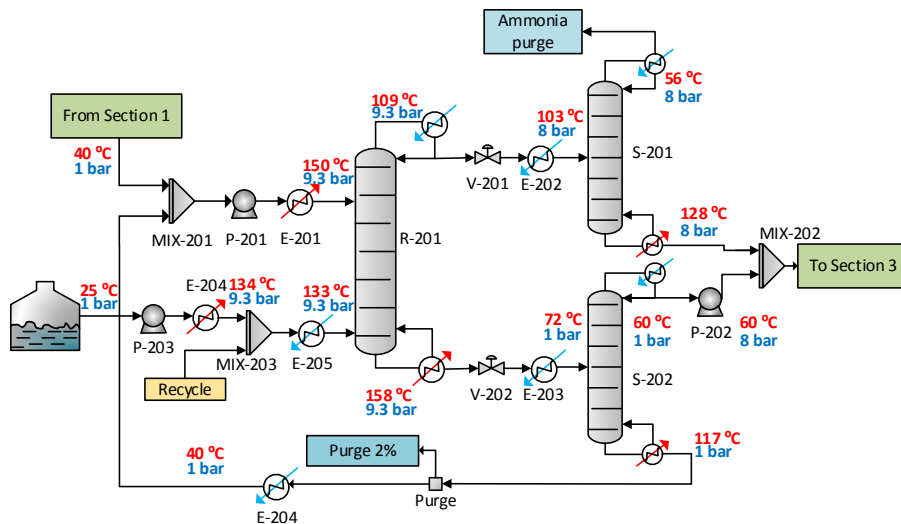


Figure 4. Reaction and initial separation of the product (Section 2)

3.3. Section 3

In the third section (Figure 5), the separation of the pair DMC / methanol is performed. This is a difficult step, since a binary azeotrope affects what otherwise would be an easy separation. Due to this, the stream from the second section is pressurized to 16 bar, where the azeotrope has a molar fraction of ~97 % of methanol, and heated up to its saturation temperature. The pair of columns S-301 and S-302 are utilized to separate this azeotrope. The distillate of these columns is composed of mostly methanol, with the molar fraction previously mentioned, while the bottom stream of S-302 has more than a 99 % of DMC molar fraction.

The distillate of this pair of columns is then mixed and sent back to section 2, where it is mixed with make-up methanol from storage and enters the reactive distillation column R-201. The DMC product is then prepared for storage and sale.

3.4. Results

The yearly results, considering 8000 h/y of operation, is shown in Table 3. Only the operation costs are taken into account for this study.

Table 3. Results of the simulation

MATERIALS	Price (\$/t)	Amount (t/y)	ENERGY	Price (\$/kWh)	Amount (kWh/y)
Urea	250	50,185	Cooling Water	0.0013	234,364,824
Methanol	330	58,234	Refrigeration Water	0.0159	24,766,786
Dimethyl Carbonate	820	74,079	Medium pressure steam	0.0534	128,024,146
			High pressure steam	0.0637	3,372,372
			Electricity	0.0600	1,831,176
PROFIT (\$/y)					21,121,739

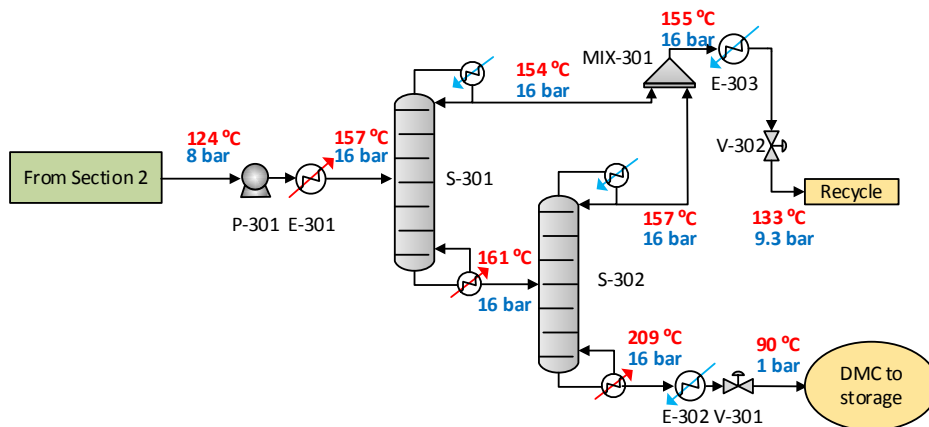


Figure 5. Separation of the azeotrope and the final product (Section 3)

4. Conclusions

The urea route for the synthesis of dimethyl carbonate (DMC) stands out as a promising alternative to the actual non-environmentally friendly processes. The results show that DMC could be synthesized with an annual production of 74 kt and profit of 21 M\$. Furthermore, the ammonia obtained as a byproduct could be integrated with a urea production plant to further increase the benefits, both economic and environmental.

However, overcoming the kinetic barrier with an adequate catalyst is the key to the rise of this technology. At this moment, with the studied catalysts, it is not possible to maintain a continuous production of DMC in a realistic time slot with this route. Hopefully, the progress in the development of the catalyst will reach a point where this route emerges as the most profitable and green method to synthesize DMC.

Acknowledgements

The authors acknowledge financial support from the Spanish “Ministerio de Economía, Industria y Competitividad” (CTQ2016-77968-C3-02-P, FEDER, UE).

References

- Keller, N., Rebmann, G., & Keller, V. (2010). Catalysts, mechanisms and industrial processes for the dimethylcarbonate synthesis. *Journal of Molecular Catalysis A: Chemical*, 317, 1-18.
- Lin, H., Yang, B., Sun, J., Wang, X., & Wang, D. (2004). Kinetics studies for the synthesis of dimethyl carbonate from urea and methanol. *Chemical Engineering Journal*, 103, 21-27.
- Pacheco, M. A., & Marshall, C. L. (1997). Review of Dimethyl Carbonate (DMC) Manufacture and Its Characteristics as a Fuel Additive. *Energy & Fuels*, 11, 2-29.
- Ryu, J. Y., & Gelbein, A. P. (2002). Process and catalyst for making dialkyl carbonates. US Patent, 6392078.
- Wang, M., Wang, H., Zhao, N., Wei, W., & Sun, Y. (2007). High-Yield Synthesis of Dimethyl Carbonate from Urea and Methanol Using a Catalytic Distillation Process. *Industrial and Engineering Chemistry Research*, 46, 2683-2687.
- Zhao, W.-b., Han, B., Zhao, N., Xiao, F., & Wei, W. (2012). Macro kinetics for synthesis of dimethyl carbonate from urea and methanol on Zn-containing catalyst. *Journal of Central South University*, 19, 85-92.

Design and Analysis of Edible Oil Processes Containing Lipids

Olivia A. Perederic^a, Sten Appel^b, Bent Sarup^b, John M. Woodley^a, Georgios M. Kontogeorgis^a, Rafiqul Gani^{a,c}

^a*Department of Chemical and Biochemical Engineering, Technical University of Denmark, DK-2800 Kgs. Lyngby, Denmark*

^b*Vegetable Oil Technology Business Unit, Alfa Laval Copenhagen A/S, DK-2860 Søborg*

^c *Current address: PSE for SPEED, Skyttemosen 6, DK-3450 Allerød, Denmark*
gk@kt.dtu.dk

Abstract

Edible oil processing showed an increase interest in the last years as a result of new applications and improved product quality requirements. Recent developments in lipid pure compounds and mixtures property modelling allow the use of computer aided methods and tools for the edible oil industry. In this work, Shea oil solvent fractionation is designed and analysed using a systematic approach involving four steps: (1) process data collection, (2) process modelling, design and simulation, (3) process performance analysis (e.g.: energy, economic and environmental analysis), (4) process hot-spots identification and retrofit solutions. SPEED lipids database is used to provide pure compound and mixture property models, which includes the special lipids developed parameters for a wide range of UNIFAC models.

Keywords: lipids, process synthesis and design, solvent fractionation, Shea oil, UNIFAC model.

1. Introduction

Increasing consumer demands, lead to the expansion of many industries, one of them being the vegetable oils (lipids) industry, with both edible and non-edible applications, e.g.: food, pharma, bio-fuels, lubricants, paints, energy storage materials. For many years, the lipids related industries have been using empirical methods for developing their processes because of insufficient data and models to describe this type of compounds and their mixtures. However, improvements in lipids property modelling allowed the use of computer aided tools and methods for exploring, improving and developing lipids related processes.

The new systematic identification method for data analysis and phase equilibria applied for lipids systems (Perederic et al., 2018) provides a new set of parameters for group contribution type of models dedicated to lipids systems. The lipids parameters (Damaceno et al., 2018; Perederic et al., 2018) are available for following variants of the UNIFAC model: Original (Fredeslund et al., 1975), Linear (Hansen et al., 1992), Modified (Larsen et al., 1987) and Dortmund UNIFAC (Weidlich et al., 1987). The new sets of parameters improve phase equilibria description for lipids related systems, and

the predictive capacities of UNIFAC models allows a broader application, making feasible the synthesis, design and analysis of lipids related processes.

One such example is the fractionation of edible oils used in the food and pharmaceutical industries. Through dry or solvent fractionation (Kellens et al., 2007), added value products with specific characteristics (different melting curves and composition) can be obtained. The process is applied to cocoa butter equivalents (CBEs) production, which are used as replacements for cocoa butter within confectionary products. The need of CBEs has emerged as a result of increasing chocolate consumption and cocoa prices. Shea stearin and Palm mid fraction are used together as CBEs, and both can be obtained through fractionation of Shea and Palm oil, (V. K. S. Shukla., 2005). Shea oil is one of the most important natural sources for symmetrical stearic rich triacylglycerols (e.g.: Stearic-Oleic-Stearic triacylglycerol) which are exhibiting very closed properties (e.g.: melting point), making solvent fractionation the only feasible solution for separation. The solvent is used to lower the viscosity of the melted raw material, in order to have a faster crystallization process and a better selectivity (fractions with higher purity and sharper melting curves). The most commonly used solvents are hexane and acetone, and their selection depends on the composition of the Shea oil.

In this work, Shea oil fractionation using acetone is presented and analysed using a method consisting of four steps, as presented in following section. The work has been performed in collaboration with Alfa Laval, which has provided most of the process related data. For confidentiality reasons, a simplified PFD of the process is presented herein (Figure 1). The aim of the work was to analyse and improve the Shea oil fractionation process. Additionally, the performance of the SPEED Lipids Database, which includes lipids based parameters for Original UNIFAC model, can be validated within a process context.

2. Process and method description

The proposed process, acetone fractionation of Shea oil, consists of mixing the melted Shea oil with cooled solvent in the crystallizer. The crystals are separated by filtration and they are washed with fresh solvent. The solvent is recovered from the two products, Shea stearin and Shea olein, through a series of multiple effect evaporators followed by a steam stripping step for product finishing. Since both products are used in edible and/or cosmetics applications, the solvent has to be completely removed from the products. The solvent is recycled within the process directly, or after a purification step for water removal. The simplified process flow diagram (PFD) is presented in Figure 1.

The process of Shea oil solvent fractionation is modelled and analysed through a method consisting of four steps: (1) process data collection, (2) process modelling, design and simulation, (3) process performance analysis (e.g.: energy, economic and environmental analysis), (4) process hot-spots identification and retrofit solutions (Gani and Cameron, 2011). These steps are covering the design stage, stage two, within the three stage approach for synthesis and design (Bertran et al., 2017). The aim of this work is to improve the process performance, such as product quality, energy consumption, and environmental impact through a systematic approach.

2.1 Process data collection

Once the process is established by defining the problem to be solved, the required data is collected. The information for all process parameters is collected from the literature

and industrial data, and includes following type of information: feed composition, solvent-to-oil ratio, separation factors, and product specification. SPEED Lipids Database (Perederic et al., 2018) is used to provide all the necessary thermo-physical property data (e.g.: vapour pressures, melting points, phase equilibria behaviour) for all the compounds involved. The database provides also the lipids based group interaction parameters for the Original UNIFAC model (Perederic et al., 2018) for activity coefficient calculation.

2.2 Process modelling, design and simulation

The process model is developed in PRO/II by using the design data collected from Step 1. SPEED Lipids Database is linked to PRO/II, providing easy access to all the thermo-physical data necessary to perform the simulation. Simulation results are further used to perform equipment sizing (Biegler et al., 1999).

2.3 Process performance analysis

In this step, the process performance analysis is carried out. Energy requirements, economic analysis and life cycle assessment are used to determine economic, sustainability and environmental impact indicators. The computer-aided tools used to perform the evaluation are: ECON (Saengwirun, 2011) for economic analysis and LC Soft (Kalakul et al., 2013) for the life cycle (LC) assessment.

2.4 Process hot-spots identification and retrofit solutions

Using the results from the previous step, the process hot spots are identified and tackled for improvement through optimisation and process integration. After all the improvement solutions are implemented, the economic analysis and life cycle assessment are performed for the new case, and the results are compared with the ones from the base case (Step 2).

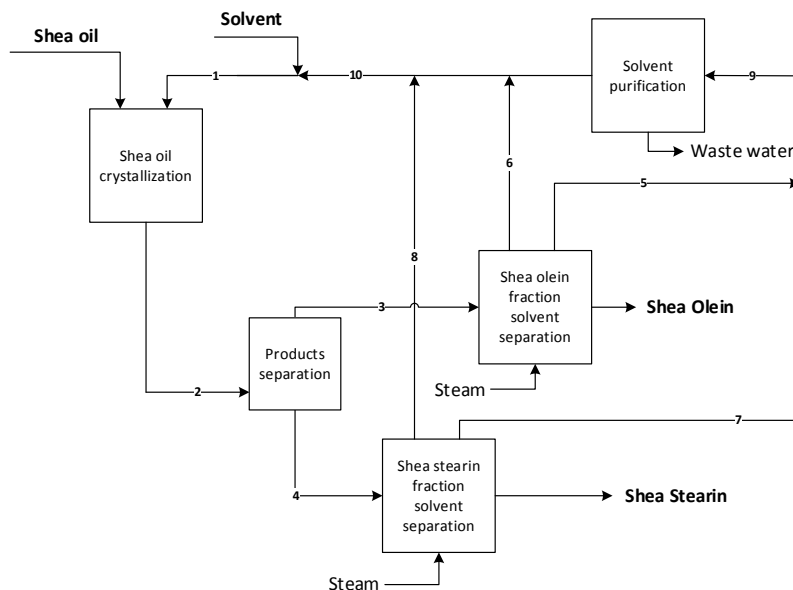


Figure 1. PFD of Shea oil solvent (acetone) fractionation.

3. Results

3.1. Process data collection

The aim is to design the process for a 2000 kg/h of Shea oil feed. The feed and products specifications (Shea olein and Shea stearin) are provided by Alfa Laval (see Table 1). The ratio between Shea oil and acetone is 1:4. High solvent purity is required, since water or other impurities can affect the crystallization process. It is assumed that the oil is dried before entering the process.

3.2. Process modelling, design and simulation

Short cut models are used for modelling of the crystallizer and the filter, while detailed models are employed for the solvent separation which consists of several evaporators modelled as flash units, stripping columns, a distillation column for acetone-water separation and several heat exchangers. The details for most important process streams for the base case as named in Figure 1 are given in Table 1. The products yield is 53% for Shea olein, and 47% for Shea stearin. Process utility requirements are 1.65 MW for cold utilities, and 1.68 MW for hot utilities. The results from the equipment sizing are used further to perform the economic analysis.

Table 1. Base case stream results.

Stream	Shea Oil	Solvent	3	4	Shea Olein	Shea Stearin	Waste Water
T, K	300	293	268	268	303	303	303
Flowrate, kg/h							
TAGs	1768.9	0.0	871.8	897.2	897.2	871.8	<10 ⁻⁴
DAGs	1.6	0.0	0.8	0.8	0.8	0.8	<10 ⁻⁴
MAGs	20.0	0.0	10.6	9.4	9.4	10.6	<10 ⁻⁴
FFAs	200.0	0.0	171.8	28.2	28.2	171.8	<10 ⁻⁴
Minor components	8.5	0.0	4.5	4.0	3.5	3.9	<10 ⁻⁴
Water	1.0	<10 ⁻⁴	0.5	0.5	0.7	1.0	12.1
Acetone	0.0	<0.1	7060.0	940.0	<10 ⁻⁴	<10 ⁻⁴	<10 ⁻⁴

TAGs – triacylglycerides, DAGs – monoacylglycerides, MAGs – monoacylglycerides, FFAs – free fatty acids, Minor components: sterols and tocopherols.

3.3. Process performance analysis

The economic analysis using ECON gives the following results: total capital investment is 2.8 M€, the operating cost is 24.5 M€/year, and the payback period is 3 years. Feasibility of the process is dependent by the product-raw material price balance, to which the process is highly sensitive. The biggest cost impact is given by the acetone-water separation column and the crystallizer, 30% of total capital investment. Regarding the utility consumption, the highest consumption belongs to the heat exchanger for heating up the Shea olein-solvent fraction resulted after the filtration step, and which consist of \approx 80% acetone.

For the LC analysis, all output streams were considered within the analysis (Shea stearin, Shea olein - products, waste water – waste stream) along with the utilities generation (natural gas is considered as fuel). The main impact indicators provided by the LC analysis are given in Table 2.

Table 2. Base Case main environmental impact indicators.

Indicator	HTPI	HTPE	ATP	GWP	PCOP	AP	HTC
Unit	1/LD ₅₀	1/TWA	1/LC ₅₀	kg CO ₂ eq	C ₂ H ₂ eq	H+ eq.	kg benzene eq
Value	6.1E-05	4.2E-04	3.2E-03	3.5E+02	3.0E-01	2.5E+01	1.4E+00

HTPI – human toxicity potential by ingestion, HTPE – human toxicity by exposure, ATP – aquatic toxicity potential, GWP – global warming potential, PCOP – photochemical oxidation potential, AP – acidification potential, HTC – human toxicity carcinogenic.

3.4. Process hot-spots identification and retrofit solutions

The hot-spots identified based on the results from Step 3 are presented in Table 3. The results indicate a necessity of heat integration to reduce the utility consumption. Moreover, an optimization of the flash units temperature in both stearin and olein fraction solvent separation sections could be performed in order to allow a higher energy recovery through heat integration. The improvements of process indicators after performing the heat integration are presented in Figure 2. Total capital investment increase with 0.13 M€, while the operation cost decrease with 0.23 M€ for the improved case. The LCA analysis show improvements in all environmental indicators as well. The global warming potential of the process drops from 350.9 CO₂ equivalent (eq.) to 61.9 CO₂ eq.

Table 3. Shea oil acetone fractionation process hot-spots.

Hot-Spots	Design targets	Improvement solution
High utility consumption in heat exchanger for olein fraction heating	Reduction of utility consumption	Optimization of flash temperature to allow energy recovery and better separation
High utility consumption for evaporators (flash units)		Heat integration

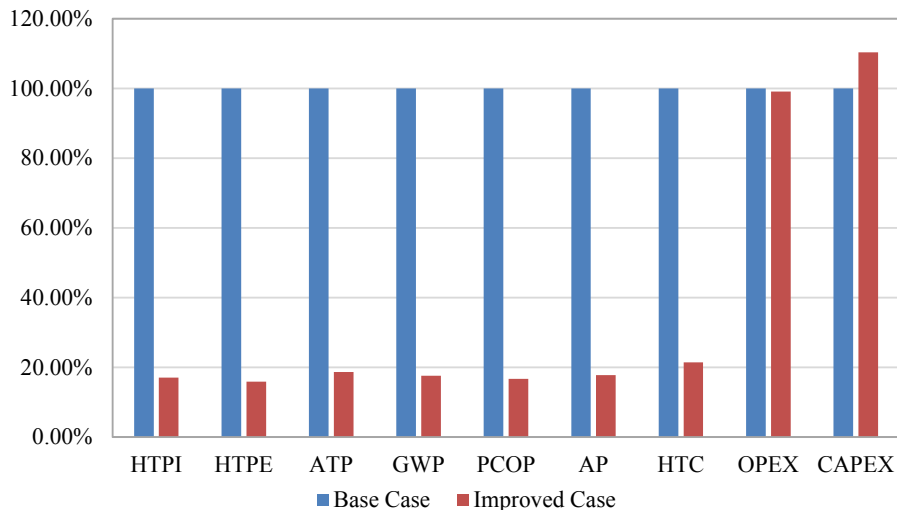


Figure 2. Process performance indicators variation reported to the base case.

4. Conclusions

A systematic analysis of Shea oil acetone fractionation process is presented. SPEED Lipids database using lipids based interaction parameters for Original UNIFAC model is used to provide all the thermo-chemical data necessary to perform the simulation. The process data is collected from literature and industrial data. The process modelling, design and simulation is performed in PRO/II. Economic and LCA analysis results are used to identify process hot-spots and to propose retrofit solutions. Process performance parameters of the base case were improved after heat integration was applied. In future work, the base case will be further improved by applying simultaneous process optimization and integration techniques.

References

- M.-O. Bertran, R. Frauzem, A.S. Sanchez-Arcilla, L. Zang, J. M. Woodley, R. Gani, 2017, *Computers and Chemical Engineering*, 106, 892–910.
- L.T. Biegler, I.E. Grossmann, A.W. Westerberg, *Systematic methods of chemical process design*, Prentice Hall PTR, 1999, New Jersey, USA.
- D. Damaceno, O.A. Perederic, R. Ceriani, G.M. Konogeorgis, R. Gani, 2018, *Fluid Phase Equilibria*, doi: 10.1016/j.fluid.2017.12.009.
- A. Fredenslund, R. Jones, J.M. Prausnitz. *AIChE J.* 21 (1975). pp. 1086–1099.
- H. K. Hansen, B. Coto, and B. Kuhlmann, 1992, UNIFAC with linearly temperature-dependent group interaction parameters. Internal report. 1992.
- M. Kellens, V. Gibon, M. Hendrix, and W. De Greyt, 2007, *European Journal of Lipid Science and Technology*, 109, 4, 336–349.
- S. Kalakul, P. Malakul, K. Siemanond, R. Gani, 2014, *Journal of Cleaner Production*, 71, 98-109
- B. Larsen, P. Rasmussen, A. Fredenslund. *Ind. Eng. Chem. Res.* 26 (1987). pp. 2274–2286.
- O.A. Perederic, L.P. Cunico, S. Kalakul, B. Sarup, J.M. Woodley, G.M. Kontogeorgis, R. Gani. 2018, *Journal of Chemical Thermodynamics*, doi: 10.1016/j.jct.2018.02.007.
- P. Saengwirun, 2011. *ECON: A Software for Cost Calculation and Economic Analysis*, MSc Thesis. Chulalongkorn University, Bangkok, Thailand.
- Analysis, MSc Thesis. Chulalongkorn University, Bangkok, Thailand.
- F. Shahidi, Ed., 2005, *Bailey's Industrial Oil and Fat Products*, 6th ed. New Jersey, USA: John Wiley & Sons, Inc.
- U. Weidlich and J. Gmehling. *Ind. Eng. Chem. Res.* 26 (1987). pp. 1372–1381.
- V. K. S. Shukla., 2005, *Confectionery Lipids*, *Bailey's Industrial Oil and Fat Products*, Vol. 6, Sixth Edition, 159-175.
- Z. Zahng, X. Ma, H. Huang, Y. Wang, 2017, *LWT – Food Science and Technology*, 86, 492-500.

Multi-objective optimization of sustainability criteria in the design of chemical plants

Federico Scotti, Nicola Fabricatore, Davide Manca*

*PSE-Lab, Process Systems Engineering Laboratory
Dipartimento di Chimica, Materiali e Ingegneria Chimica “Giulio Natta”
Politecnico di Milano – Piazza Leonardo da Vinci 32, 20133 Milano, Italy
davide.manca@polimi.it*

Abstract

Assessing and enhancing the sustainability of chemical processes is a key challenge for chemical engineering. Sustainability is usually conjugated in three distinct but interconnected dimensions or *pillars*: economic, environmental, and social. In order to develop a sustainable process, the three pillars should be harmonized. In most cases, these pillars conflict with each other and a compromise may be found by solving a multi-objective optimization (MOO) problem. This paper proposes a solution strategy for the MOO of sustainability in the conceptual design of chemical plants. Two different approaches are analyzed and discussed, based on Pareto’s fronts analysis and scalarization technique.

Keywords: sustainability, process design, multi-objective optimization, Pareto front, scalarization

1. Introduction

The concept of sustainability embraces the economic, environmental, and social aspects of most human activities. In a nutshell, a sustainable process is the one that “*constrains resource consumption and waste generation to an acceptable level, makes a positive contribution to the satisfaction of human needs, and provides enduring economic value to the business enterprise*” (Bakshi and Fiksel, 2003). According to this definition, in order to be sustainable, an industrial process must be feasible and profitable from the economic point of view and, at the same time, must harmonize with both environmental and the societal matters.

This article embraces the detailed modelling and simulation of a chemical process, specifically the cumene production plant. Cumene is an important commodity derived from benzene, with a worldwide production of 16 million tons in 2016. It is produced through the Friedel-Crafts alkylation of benzene with propylene, followed by several undesired side-reactions of further alkylation to form p-diisopropylbenzene (PDIB) and heavier species (PIBs). For the sake of simplicity, our case study considers only the benzene alkylation and its main side reaction to PDIB. In conventional cumene plants, PDIB is converted back to cumene by a transalkylation reactor to recover valuable product. The present conceptual design is based on the flowsheet of Pathak et al. (2011). The second step consists in assigning the degrees of freedom of the optimization problem, *i.e.* the variables that mostly affect the process performance. Such dominant variables are the reactor inlet temperature and the reactor tube length. The Grid-Search algorithm was selected to optimize the plant because of its robustness and exhaustiveness. In fact, it evaluates all the possible plant configurations, which for the inlet temperature fall in the

300-350 °C range (with a discretization interval of 5 °C) and for the reactor length belong to the 4-12 m range (with a discretization interval of 0.5 m).

2. Formulation of the MOO problem: Sustainability criteria

As far as the economic sustainability is concerned, several economic assessment (EA) techniques have been developed in the literature. The most important milestone in this field is represented by “Conceptual Design” (Douglas, 1988), which entails a systematic methodology to assess the economic feasibility of a chemical process in the preliminary design stage. Starting from Douglas’ approach, Manca (2015) introduced a novel methodology that also accounts for the price fluctuations of raw materials, products, and utilities, christened “Predictive Conceptual Design” (PCD). The PCD concept has been applied successfully to different case studies (Barzaghi et al., 2016; Sepiacci et al., 2017; Scotti et al., 2017) and in this work the Dynamic Economic Potential of fourth level (Manca, 2015) is adopted as the economic sustainability objective function:

$$DEP_{4k} = \frac{\sum_{i=1}^{nMonths} (Revenues_{4i,k} * nHpM)}{nMonths/12} - \frac{\sum_{e=1}^{nEquip} (IC_e)}{nMonths/12} \quad (1)$$

With:

$$Revenues_{4i,k} = \max \left[0, \sum_{products} C_{i,k} F_p - \sum_{raw} C_{i,k} F_r - \sum_{utility} C_{i,k} F_u - \sum_{EE} C_{i,k} W_{EE} \right] \quad (2)$$

Where F_x [kmol/h] is the flowrate of products (p), raw materials (r), utilities (u), and W_{EE} is the electric energy (EE) consumption [MWh]. $C_{i,k}$ [€] is the price at month i and scenario k . The CAPEX terms are included in the installation costs (IC) of the equipment and $nHpM$ is the number of working hours of the plant per month.

Concerning the assessment of the environmental sustainability of a process, several methodologies are available in the literature. For the sake of plant optimization, a proper methodology should adopt a gate-to-gate approach, *i.e.* it should consider as boundaries of the system the battery limits of the plant and neglect the rest of the life cycle of the product and its corresponding physical and geographical spheres of influence. The Waste Reduction Algorithm (Young and Cabezas, 1999) is a valid candidate (see also Sepiacci et al. (2017) and Scotti et al. (2017) for further details). Thus, the Potential Environmental Impact (PEI) implements the following formulation:

$$PEI_{tot}^{out} = \sum_j^{st} M_j^{out} \sum_k^{cp} x_{kj} \sum_z^{ca} \alpha_z \psi_{kz} \quad (3)$$

where M_j^{out} is the mass flow rate of output stream j , x_{kj} is the mass fraction of species k in stream j . ψ_{zk} is the specific PEI for species k for the impact category z and α_z is the corresponding weighing factor for category z .

The objective function for the environmental sustainability is the normalized PEI, *i.e.* the PEI for unit of mass of product:

$$normalized\ PEI = \frac{PEI_{tot}^{out}}{F_{cumene}^{out}} \quad (4)$$

Where F_{cumene}^{out} is the cumene productivity in kg_{cumene}/h .

Eventually, social sustainability is the least defined, discussed, and understood dimension of sustainability. According to the context of this work, it can be stated in terms of “inherent safety” of the process, as proposed by Kletz (2013). Based on this philosophy, a proper methodology for the estimation of the inherent safety is required. For this purpose, the Hazard Identification and Ranking (HIRA) methodology (Khan and Abbasi, 1998) can be tailored for the optimization of the social sustainability of chemical plants (Scotti et al., 2017). Finally, the social sustainability objective function is the overall Hazard Potential (HP), calculated as follows:

$$\text{Overall HP} = \sum_{j=1}^{N \text{ units}} HP_j \quad (5)$$

Where HP_j is the Hazard Potential of the j-th unit.

3. Pareto's fronts analysis

The first solution approach is based on the analysis of the Pareto fronts and consists in identifying the trade-offs between each couple of objective functions. By doing so, the original MOO problem is decomposed into three two-objective optimization problems and the most relevant trade-offs are outlined. When pair-wise comparisons of the objective functions are involved, the problem can be dealt with by visualizing the Pareto front, which provides detailed information about objectives trade-off. This concept, introduced by the Italian economist Vilfredo Pareto (Pareto, 1897), defines as “Pareto optimal solutions” (also known as “dominant” or “non-dominated” solutions) those points within the decision space, whose corresponding objective functions cannot be all simultaneously improved. Starting from the whole set of possible combinations (named as Pareto curve, Fig. 1), the Pareto optimal solutions can be found numerically by means of some specific algorithm. The present work employs the algorithm reported in Mishra and Harit (2010). Three different Pareto fronts are reported in Figs 2-4, each accounting for a pair-wise comparison among the three objective functions (*i.e.* DEP4/PEI, DEP4/HP, and PEI/HP).

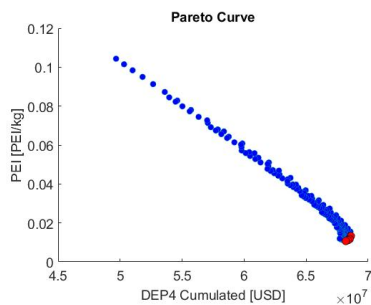


Figure 1: Pareto curve DEP4 vs PEI

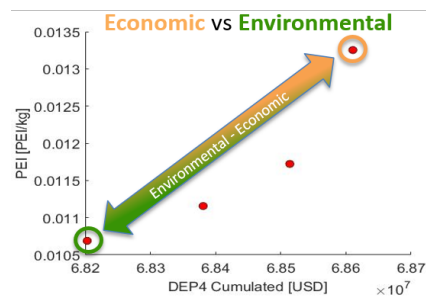


Figure 2: Pareto front DEP4 vs PEI

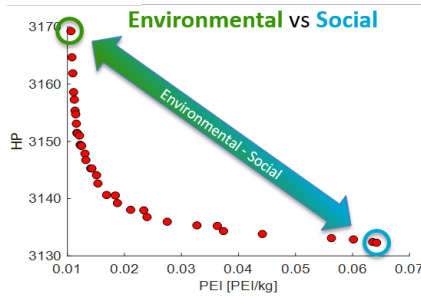


Figure 3: Pareto front PEI vs PEI

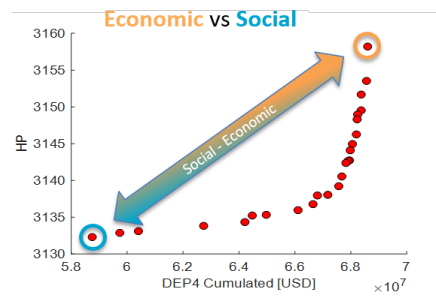


Figure 4: Pareto front DEP4 vs HP

A closer look to Figs 1-2 allows identifying four dominant solutions, whose values are quite close. Indeed, the present case study does not exhibit any actual conflicts between the economic and environmental sustainability criteria. On the other hand, Figs 3-4 show evident trade-offs between those two and the social one.

4. Scalarization

As already outlined, Pareto fronts provide the final decision maker with some useful bits of information about the main trade-offs among the objective functions and identify a set of potential solutions of the overall MOO problem. However, when dealing with more than three objective functions, this approach can be confusing and sometimes misleading.

An interesting technique that can be applied for solving the Sustainability MOO problem is scalarization. This consists in transforming a MOO problem into a single-objective optimization problem by collecting all the conflicting criteria in a single objective function. The scalarization of an objective function essentially consists in normalizing it and make it comparable with other scalarized objective functions. Different scalarization methods can be adopted and the choice is usually arbitrary. In the present case, i.e. the MOO of sustainability criteria, each objective function is normalized in order to assume a value of 1 for the “most sustainable” solution and 0 for the unsustainable one(s).

As far as the economic sustainability of the process is concerned, a value of 1 is assigned to maximum DEP4, and a value of 0 to DEP4 equal to zero. This index, ranging from 0 to 1, is christened Economic Sustainability Index (EcSI), and is expressed as:

$$EcSI_i = \begin{cases} \frac{DEP4_i}{\max(DEP4)} & \text{if } DEP4_i > 0 \\ 0 & \text{if } DEP4_i \leq 0 \end{cases} \quad (6)$$

Where $DEP4_i$ is the value of DEP4 for configuration i , and $i = 1, \dots, NC$ with NC the number of process configurations (equal to 187). EcSI becomes equal to 0 when the process is unsustainable, i.e. when the DEP4 is zero or negative.

The same reasoning is followed for the expression of the Environmental Sustainability Index (EnSI), which assumes a value of 1 when PEI is minimum and 0 when PEI is greater than $0.15 \text{ PEI/kg}_{cumene}$. Indeed, this value can be considered as a threshold value above which the process becomes unsustainable from the environmental point of view. EnSI is formulated as:

$$EnSI_i = \begin{cases} \frac{(0.15 - PEI_i)}{(0.15 - \min(PEI))} & \text{if } PEI \leq 0.15 \\ 0 & \text{if } PEI > 0.15 \end{cases} \quad (7)$$

As far as the social sustainability is concerned, no threshold values are provided for the overall Hazard Potential in order to discriminate between sustainable and unsustainable processes. Hence, a possible way to normalize HP is to assign 1 to the lowest value, and 0 to the highest value. The Social Sustainability Index (SoSI) of the process is expressed as:

$$SoSI_i = \left\{ \frac{(\max(HP) - HP_i)}{(\max(HP) - \min(HP))} \right. \quad (8)$$

Finally, the objective function of the scalarized MOO problem is simply the weighted sum of the Economic, Environmental, and Social Sustainability indexes. Each of them is properly weighted, according to the relative importance of the three pillars of Sustainability. In the present work, the hierarchy of importance that is here proposed considers the economic aspect of sustainability as predominant, followed by environmental sustainability, and eventually by social sustainability. Therefore, a value of 0.5 is assigned to the economic pillar, and values of 0.3 and 0.2 to the environmental and social ones, respectively. The scalarized objective function is christened as Normalized Process Sustainability (NPS), and the scalarized MOO problem undertakes the following formulation:

$$\max_{T,L} NPS = \{w_{Ec} * EcSI + w_{En} * EnSI + w_{So} * SoSI\} \quad (9)$$

Where the degrees of freedom are T , the reactor inlet temperature, and L , the reactor tube length. w_{Ec} , w_{En} and w_{So} are the weighting factors for the economic, environmental, and social sustainability indexes, respectively.

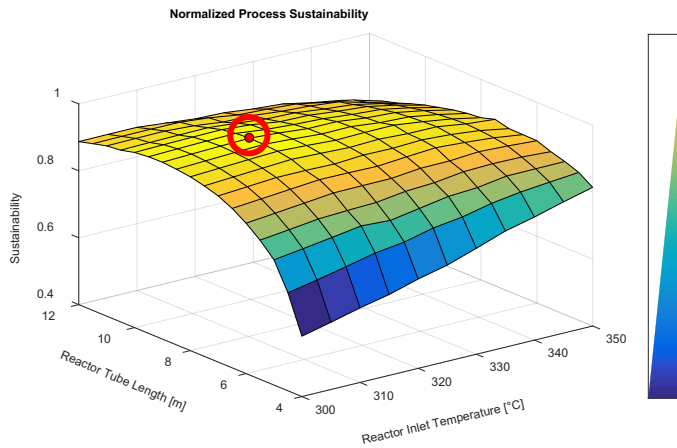


Figure 5: 3D plot of the Normalized Process Sustainability

Fig. 5 shows the 3D plot of the NPS function for the cumene case study. According to its definition, it ranges from 0 to 1, where 0 corresponds to completely unsustainable solutions and 1 to ideal sustainability, i.e. all the three indexes are maximized

simultaneously. The red circle identifies the optimal solution characterized by a NPS value of 0.938. This configuration corresponds to an inlet temperature of 315 °C and a reactor length of 9 m.

5. Conclusions

The cumene production process was adopted as a case study to perform a multi-objective optimization of economic, environmental, and social sustainability criteria. A proper objective function was formulated to assess each pillar of sustainability. The MOO problem was assigned and solved by means of two different approaches. The Pareto fronts analysis allowed identifying the relevant trade-offs among the three criteria and showed to be a valid support for the decision maker, even though it does not provide a univocal solution. The second approach to MOO involves scalarizing the problem and converting it to a single-objective optimization problem. The new objective function was defined as the weighted sum of the three criteria properly normalized. The values of the weighting factors were assigned to highlight a hierarchy among sustainability criteria. As far as the cumene case study is concerned, the optimal solution represents a good trade-off configuration, whose values of the objective functions are all close to their respective optimum values: its DEP4 is 67.58 MUSD (98.5% of the maximum), while its environmental (EnSI = 0.942) and social (SoSI = 0.813) indexes show that both PEI and HP approach their minimum (*i.e.* optimal) values.

References

- Bakshi, B.R., Fiksel, J., 2003. The quest for sustainability: Challenges for process systems engineering. *AIChE J.* doi:10.1002/aic.690490602
- Barzaghi, R., Conte, A., Sepiacci, P., Manca, D., 2016. Optimal design of a styrene monomer plant under market volatility, in: *Computer Aided Chemical Engineering*. pp. 1653–1658. doi:10.1016/B978-0-444-63428-3.50280-0
- Douglas, J.M., 1988. *Conceptual design of chemical processes*. McGraw-Hill, New York.
- Khan, F.I., Abbasi, S.A., 1998. Multivariate hazard identification and ranking system. *Process Saf. Prog.* 17, 157–170. doi:10.1002/prs.680170303
- Kletz, T., 2013. What you don't have, can't leak. *Inst. Chem. Eng.* 43–47.
- Manca, D., 2015. Economic Sustainability of Products and Processes. *Comput. Aided Chem. Eng.* doi:10.1016/B978-0-444-63472-6.00025-2
- Mishra, K.K., Harit, S., 2010. A Fast Algorithm for Finding the Non Dominated Set in Multi objective Optimization. *Int. J. Comput. Appl.* 1, 35–39. doi:10.5120/460-764
- Pareto, V., 1897. The New Theories of Economics. *J. Polit. Econ.* 5, 485–502. doi:10.1086/250454
- Pathak, A.S., Agarwal, S., Gera, V., Kaistha, N., 2011. Design and control of a vapor-phase conventional process and reactive distillation process for cumene production. *Ind. Eng. Chem. Res.* 50, 3312–3326. doi:10.1021/ie100779k
- Scotti, F., Fabricatore, N., Sepiacci, P., Manca, D., 2017. A MOO approach towards sustainable process design: integrating the three pillars of sustainability. *Proc. 27th Eur. Symp. Comput. Aided Process Eng. – ESCAPE 27*.
- Sepiacci, P., Depetri, V., Manca, D., 2017. A systematic approach to the optimal design of chemical plants with waste reduction and market uncertainty. *Comput. Chem. Eng.* 102, 96–109. doi:10.1016/j.compchemeng.2016.11.032
- Young, D.M., Cabezas, H., 1999. Designing sustainable processes with simulation: The waste reduction (WAR) algorithm. *Comput. Chem. Eng.* 23, 1477–1491. doi:10.1016/S0098-1354(99)00306-3

Evaluating the effect of separation and reaction systems in industrial symbiosis

Ana Somoza-Tornos, Moisès Graells, Antonio Espuña*

Universitat Politècnica de Catalunya, Department of Chemical Engineering, Campus Diagonal-Besòs, Eduard Maristany, 16, 08019 – Barcelona (Spain)

antonio.espuna@upc.edu

Abstract

Considering chemical transformation, separation and/or reaction, is still a pending issue in the optimization of industrial symbiosis networks. This work aims to provide an optimization approach to determine the best network configuration by analysing the available separation and reaction alternatives. The model has been tested on an academic case study. Results show that the tool developed provides the best routes to convert waste into raw materials and gives rise to new possible synergies that could remain unnoticed without the use of a systematic tool. It is also highlighted that reaction plays a vital role in increasing the potential recycle of resources and closing material loops.

Keywords: Sustainability, Industrial Symbiosis, Material Exchange, Optimization, Superstructure.

1. Introduction

The first concerns on the problems generated by the degradation of the ecosystems date back to the last century (Hardin, 1968). This degradation is caused not only by the excessive consumption of resources but also due to the corresponding increase in waste accumulation. Industrial symbiosis offers a way to address both problems by providing an alternative to disposal of waste and reducing the amount of resources that are exploited. In this light, the focus of recent research has been on finding systematic methods to identify the best alternatives for establishing synergies.

Recent works are related to the building of superstructures that increase the opportunities of resources exchange (Boix et al., 2017). These benefits are increased if transformation opportunities are analysed as a way to convert waste into new profitable materials (Boix et al., 2015). There have been some attempts to solve the design of separation-reaction systems, but always applied to a single supply chain (Kong and Shah, 2016). Previous works address the development of superstructures for separation and the targeting of reaction systems (Somoza-Tornos et al., 2017; Giraldo-Carvajal et al., 2017). However, there is still the need of an integrated framework that considers separation and reaction opportunities in the decision-making process of industrial symbiosis systems.

The aim of this work is to extend the existing models to develop an optimization tool that integrates separation and reaction opportunities to increase the extent of material exchanges in industrial symbiosis. While common approaches focus on finding global solutions (i.e. a regulating administration), the novelty of this approach consists on addressing the problem from the point of view of a transformation company that seeks

maximizing its particular profit by closing the loop between waste producers (suppliers) and resource necessities (customers).

The system is modelled as a process superstructure in order to identify the best process configuration, selecting among the different available alternatives of separation and reaction steps.

2. Problem statement

The operation problem addressed can be posed as follows: Given are a set of waste streams i with known composition of products n coming from different industries, and a set j of resources needed by the same or other companies. Given are also a set of available treatment technologies k . They are modelled as separators ($k \in SE$) or reactors ($k \in RE$) with different operation modes m and associated cost parameters (γ_{km}). The different outlets of a transformation unit are represented in set l . Decisions include amounts of waste sent to disposal, reuse or recycling; the way to satisfy the demand of raw materials (with recycled or fresh inlets) and which transformation units are active. Thus, the optimal configuration of the system has to be determined.

The different alternatives are analyzed through the definition of a superstructure as the one shown in Figure 1. Waste streams are divided by the first set of splitters (S1) and may then by-pass the transformation units or enter in transformation stages. A first set of mixers (M1) concentrate all the flows entering the same treatment unit k of the set TU. After transformation, a second set of splitters (S2) divide the flow in the part that is recycled to other treatment units, the part that is valuable as raw material, and the part sent to disposal (D).

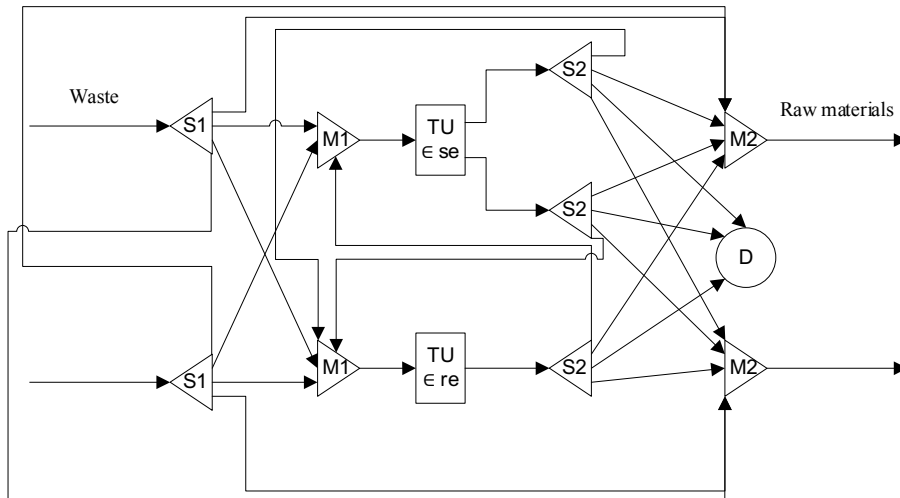


Figure 1. Superstructure for two waste streams, two treatment units (TU, a separator and a reactor) and two raw material streams.

3. Mathematical formulation

The proposed MINLP problem formulation associated to the problem statement extends a version in a previous work (Somoza-Tornos et al., 2017) to consider reaction and more general separation systems with l outlets instead of two.

3.1. Waste inlet

Eq. (1) defines the amount of waste from a supplier (W_{in}) that is acquired by the transformation company (a_{in}). It is calculated through fraction pa_i , which maintains composition constant. In Eqs. (2-4), this amount is divided in two parts, the one that is directly by-passed to the outlet streams (continuous variable p_{ijn} and 0-1 fraction $S1p_{ij}$) and the one sent to the transformation units (continuous variable f_{ikn} and 0-1 fraction $S1f_{ik}$). (Somoza-Tornos et al., 2017)

$$a_{in} = pa_i \cdot W_{in} \quad \forall in \quad (1)$$

$$p_{ijn} = a_{in} \cdot S1p_{ij} \quad \forall ijn \quad (2)$$

$$f_{ikn} = a_{in} \cdot S1f_{ik} \quad \forall ikn \quad (3)$$

$$\sum_j S1p_{ij} + \sum_k S1f_{ik} = 1 \quad \forall i \quad (4)$$

3.2. Treatment units

e_{kn} denotes the inlet of component n to treatment unit k and is calculated considering direct waste coming from inlet i and recycled streams from outlet l of treatment unit k' . Eqs. (6-7) express the constraints on the flow to be treated and its inlet concentration, which must be satisfied.

$$e_{kn} = \sum_i f_{ikn} + \sum_{k'l} g_{klkn} \quad \forall kn \quad (5)$$

$$\sum_m (tmin_{km} \cdot X_{km}) \leq \sum_n e_{kn} \leq \sum_m (tmax_{km} \cdot X_{km}) \quad \forall k \quad (6)$$

$$\sum_m (ctmin_{kmn} \cdot X_{km}) \leq \frac{e_{kn}}{\sum_n e_{kn}} \leq \sum_m (ctmax_{kmn} \cdot X_{km}) \quad \forall kn \quad (7)$$

In these equations, X_{km} represents the operation mode m that is active in treatment unit k . Separators can operate under a single mode at the same time (Eq. (8)), while reactors can have simultaneous modes, if several reactions occur at the same time (Eq. (9)).

$$\sum_m X_{km} \leq 1 \quad \forall k \in SE \quad (8)$$

$$\sum_m X_{km} \geq 0 \quad \forall k \in RE \quad (9)$$

The outlet flow l of component n after treatment unit k under operation mode m is stored in variable o_{kln} . It is then split into three streams: the one sent to outlet j (t_{jkl} denotes the amount and $S2t_{jkl}$ the fraction), the one recycled to treatment unit k' ($r_{klk'n}$ and $S2r_{klk'}$), and the disposed amount (d_{kln} and $S2d_{kl}$). The corresponding balances are given by Eqs. (10-13).

$$t_{jkl} = o_{kln} \cdot S2t_{jkl} \quad \forall jkln \quad (10)$$

$$g_{klk'n} = o_{kln} \cdot S2g_{klk'} \quad \forall klk'n \quad (11)$$

$$d_{kln} = o_{kln} \cdot S2d_{kl} \quad \forall kln \quad (12)$$

$$\sum_j S2t_{jkl} + \sum_{k'} S2g_{klk'} + S2d_{kl} = 1 \quad \forall kl \quad (13)$$

The next subsections present the specific equations for separation units and reactors.

3.2.1. Separation units

The outlet of each separation unit o_{kln} is given by Eq. (14), in which parameter xt_{kmln} denotes the recuperation of each component n in outlet l after treatment in unit k under separation mode m .

$$o_{kln} = e_{kn} \cdot \sum_m (xt_{kmln} \cdot X_{km}) \quad \forall l, n, k \in SE \quad (14)$$

3.2.2. Reaction units

The model for reaction units has been adapted from Kong and Shah (2016).

The reactor outlet Eq. (15) is a function of the inlet, the stoichiometric coefficient (sc_{kmn}) and the reaction extent (rx_{km}). The reactor outlet is constrained by Eqs. (16-17), so that the inlet of reactant cannot exceed the reactant required by the reaction and that it is bounded by a maximum value, respectively.

$$\sum_l o_{kln} = e_{kn} + \sum_m (sc_{kmn} \cdot rx_{km}) \quad \forall n, k \in RE \quad (15)$$

$$e_{kn} + \sum_m \frac{sc_{kmn} \cdot rx_{km}}{xc_{km}} \geq 0 \quad \forall n, k \in RE \quad (16)$$

$$0 \leq rx_{km} \leq X_{km} \cdot rx^{max} \quad \forall n, k \in RE \quad (17)$$

3.3. Demand constraints

c_{jn} denotes the amount of component n supplied as raw material j and can be calculated through bypassed and transformed streams as in Eq. (18). It cannot exceed the total demand of raw material R_j and should satisfy the range of concentration for each component (Eqs. (19,20)).

$$c_{jn} = \sum_i p_{ijn} + \sum_{kl} t_{jkl} \quad \forall jn \quad (18)$$

$$\sum_n c_{jn} \leq R_j \quad \forall j \quad (19)$$

$$Pmin_{jn} \geq \frac{c_{jn}}{\sum_n c_{jn}} \geq Pmax_{jn} \quad \forall jn \quad (20)$$

3.4. Objective function

Eq. (21) shows the objective function to be minimized. It consists of an economic balance taking into account the income from selling raw materials j (α_j), the economic value of using waste i from a producer company (β_i), the cost of transforming waste into raw materials (γ_k) the cost of disposal (δ_n). Note that α_j and β_i are aggregated parameters that include acquisition/selling and transportation costs.

$$OF = \sum_j (\alpha_j \cdot \sum_n c_{jn}) - \sum_i (\beta_i \cdot \sum_n a_{in}) - \sum_k (\gamma_k \cdot \sum_n e_{kn}) - \sum_n (\delta_n \cdot \sum_k d_{kn}) \quad (21)$$

3.5. MINLP model

The resulting model for the industrial symbiosis superstructure can be posed as follows:

$$\begin{aligned} \text{Sym} \quad & \min [\text{OF}] \\ \text{s.t.} \quad & \text{Eqs. (1)-(21)} \end{aligned}$$

4. Case study

An academic case study has been defined for the sake of comparison. It considers 4 available waste streams and 3 required resource streams composed by 3 components, which we may call A, B and C. The transformation company owns two distillation columns (one that separates A from B and the other that separates B from C) and a reactor where the reaction $A + B \rightarrow C$ can take place. Three different scenarios are analysed: 1) no transformation units are available, thus only direct synergies are feasible; 2) distillation columns are active but no reactors can be used; 3) all transformation units are available.

5. Results

Figure 2.a depicts the solution for the first scenario, in which the only possible connections are those between compatible waste and raw material streams. The higher purity of W1 leads to a higher acquisition cost than W2, but it is compensated by a lower transportation cost for its closeness to the transformation company. In the second scenario (represented in Figure 2.b), separation of waste streams can be considered, which results in an increase of the amount of waste that is recycled and the percentage of demand that is satisfied. This situation is even increased when reaction takes part.

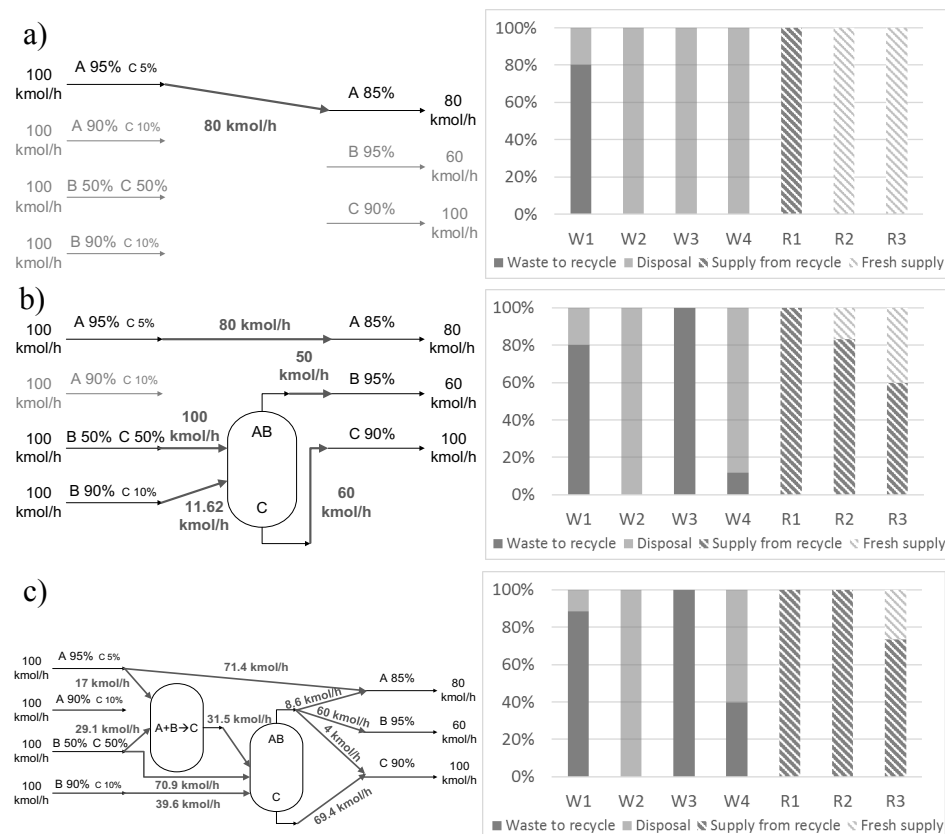


Figure 2. Network configuration and fraction of waste recycled and supply covered from it for a) scenario 1, b) scenario 2 and c) scenario 3.

(Figure 2.c). In this case, the amount of recycled material is 2.9 times higher than in the first scenario. It is achieved without the total coverage of the demand of R3, as it would lower the purity of B, resulting in an incompatibility with R2.

All the alternatives proposed are increasingly profitable for the transformation company, which by discovering these business opportunities contributes to integrating different supply chains and consolidating industrial symbiosis.

6. Conclusions

This study has focused on the development of an optimization model to detect new possible synergies in industrial symbiosis by considering separation and reaction. The approach is based on addressing the problem from the point of view of a transformation company that seeks maximizing its particular profit and contributes the consideration of specific transformation processes such as separations and reactions. Results show that the more transformation processes are involved the further extent of material reuse is achieved. Furthermore, the proposed model gives rise to new possible synergies that could remain unnoticed without the use of a systematic tool. Thus, it allows broadening the current limits of industrial symbiosis, moving towards a more sustainable use of resources, and expanding the lifespan of materials by identifying and assessing the business opportunities that transformation companies may take advantage of within the circular economy. Based on the promising findings, future work will address the multi-objective optimization of the system, taking into account sustainable criteria and considering the effect of negotiation between the different actors.

Acknowledgements

Financial support received from the Spanish "Ministerio de Economía, Industria y Competitividad" and the European Regional Development Fund, both funding the research Projects AIMS (DPI2017-87435-R) and PCIN-2015-001/ELAC2014/ESE0034 is fully acknowledged.

Ana Somoza-Tornos thankfully acknowledges financial support received from the Spanish Ministry of Education, Culture and Sport (Ayuda para la Formación de Profesorado Universitario - FPU15/02932).

References

- M. Boix, L. Montastruc, C. Azzaro-Pantel, S. Domenech (2015). Optimization methods applied to the design of eco-industrial parks: A literature review. *J. Clean. Prod.* 87, pp. 303-317.
- M. Boix, L. Montastruc, M. Ramos, O. Gentilhomme, S. Domenech (2017). Benefits analysis of optimal design of eco-industrial parks through life cycle indicators. *Comp. Aided Chem. Engng.*, 40-B, pp. 1951-1956.
- V. Giraldo-Carvajal, A. Somoza, M. Graells, A. Espuña (2017). Evaluating the effect of separation and reaction systems in industrial symbiosis. 10th World Congress of Chemical Engineering. Barcelona, 4/10/2017.
- G. Hardin (1968). The tragedy of the commons. *Science* 162-3859, pp. 1243-1248.
- Q. Kong, N. Shah (2016). An optimization-based framework for the conceptual design of reaction-separation processes. *Chem. Eng. Res. Des.*, 113, pp. 206-222.
- A. Somoza-Tornos, M. Graells, A. Espuña (2017). Systematic Approach to the Extension of Material Exchange in Industrial Symbiosis. *Comp. Aided Chem. Engng* 40-B, pp.1927-1932.

A framework for optimised sustainable solvent mixture and separation process design

Eduardo Sánchez-Ramírez, Jaime D. Ponce-Rocha, Juan G. Segovia-Hernández, Fernando I. Gómez-Castro, Ricardo Morales-Rodríguez*

Departamento de Ingeniería Química, División de Ciencias Naturales y Exactas, Campus Guanajuato, Universidad de Guanajuato, Noria Alta S/N, Guanajuato, Gto. 36050, México.

ricardo.morales@ugto.mx

Abstract

The design of optimal product, mixtures and processes must be performed relying on systematic steps. For example, the separation and purification of the acetone-butanol-ethanol (ABE) from a fermentation broth is still a challenge to overcome. A feasible process configuration that includes the use of liquid-liquid extraction (LLE) and distillation, requires the design/selection of the extracting agent/solvent and the equipment design in order to overcome the azeotropes in the ABE mixture. Therefore, this study proposes and implements a framework consisting of organized steps combining methods and tools, using as a case study the ABE separation from water and the purification of ABE compounds. The LLE unit included in the process allowed the solvent design, the formulation and evaluation of a mixture of extracting agents with the required characteristics for the extraction; followed by the process design of the equipment, and finally the optimisation step using a hybrid stochastic optimisation method, differential evolution with tabu list. The optimal design of the mixture of extracting agents converged in mass fraction values of 0.3799 for n-hexyl-acetate and 0.6201 for n-heptyl acetate, which allowed to reduce the total annual cost by 78 % and the environmental impact by 79 % relying on the eco-indicator, compared with base case scenario.

Keywords: molecular design, mixture design, heptyl acetate, hexyl acetate, ABE.

1. Introduction

The production of chemicals implies different tasks where the separation and purification processes (SPP) are important to obtain the desired product quality in terms of purity and quantity. There are some SPP that include the use of solvents or mixtures, for example, the crystallization process (Karunanithi and Achenie, 2007) and the liquid-liquid extraction (LLE) employ the use of extracting agents/solvents, where the selection of the compounds to perform the tasks is fundamental. Hence, the use of computer-aided molecular/mixture design (CAMD) becomes important since assisting to obtain tailor-made compounds and compositions for mixtures (Harper et al., 1999). According to the state of the art, there is still an opportunity to improve the design of processes (such as, LLE) that involve solvent and mixture design for SPP combining different computer-aided tools. Thus, the objective of this work is to present a systematic framework for the optimised design of solvent mixtures (to be used as

extracting agent) and SPP relying on sustainability metrics. The proposed framework is assessed employing the ABE fermentation broth composition for the SPP case study, where an important hurdle is the presences of two azeotropes in the ABE mixture. Thereby, it is necessary to include a LLE process that requires the design of the extracting agent that could be a sole solvent or a suitable mixture of solvents, its feasibility has been previously analysed in terms of cost and environmental impact (Errico et al., 2015)

2. A framework for optimised sustainable mixture and rigorous separation process design

The framework for optimized sustainable solvent-process design shown in Figure 1, may be summarized and explained as follow: 1) the data collection and state of art analysis related with LLE; 2) the product design task, aiming to find the potential extracting agents with tailor-made characteristics, employing a computer-aided molecular design software (CAMD) that is based on functional groups to build the molecules (Harper et al., 1999); 3) selection of the extracting agents based on the cost, market availability and toxicity, and the thermodynamic model suitable for the mixture to separate; 4) evaluation of extracting agents candidates in a simulation tool (Aspen plus, PRO II, etc); 5) comparison of the evaluated solvent with the base case (BC) in order to determine its performance and continue with the design of the subsequent equipment, whether the performance of the candidate is worse than the BC scenario in terms of selected criteria, it is possible to return to step number 3 to select another candidate, otherwise, just continue with the next step; 6) the potential candidates can be identified in order to formulate possible extracting agents mixtures, it is very important to perform a physicochemical properties analysis, since the selected compounds must have similar boiling points to facilitate their recovery, otherwise, the separation task could generate the introduction of an extra separation unit; 7) process design employing shortcut methods followed by a sensitivity analysis to refine the process specification, and finally, the selection of configurations with better performance based on product recovery, purity and operating cost, whether the mixture is not suitable it is possible to return to step 6 to formulate a new mixture of solvents or go back to step 3 for finding new potential individual extracting agents; 8) multi-objective optimization employing an stochastic hybrid method, differential evolution with tabu list (DETL), minimizing the total annual cost (TAC) and the environmental impact (EI) calculated with the Eco-indicator 99; and finally the selection of the best configuration based on a Pareto front. Please note that the solvent design includes only the first 6 steps, the process design steps 7-8 and the extracting agent's mixture design the steps from 3 to 8.

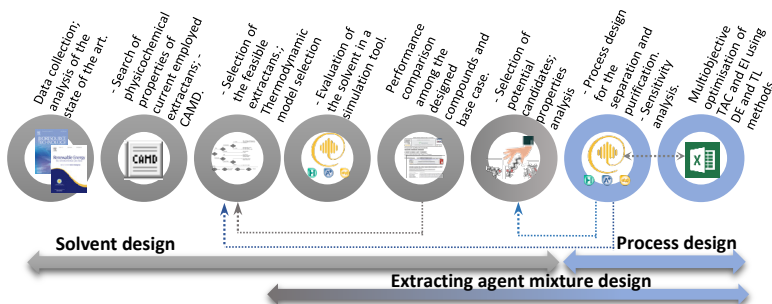


Figure 1. Framework for optimized sustainable mixture and rigorous separation process design.

3. How the framework for optimised sustainable mixture design works.

The framework used as case study the separation of a fermentation broth containing ABE, water, carbon dioxide and hydrogen, since the residual sugars such as glucose and xylose are separated in distillation column before entering to the LLE unit.

3.1. Data collection and state of the art analysis.

The implementation of LLE includes the selection of extracting agent. In a previous work Kraemer et al. (2010) employed 1,3,5-trimethylbenzene (mesitylene). Moreover, Morales-Espinosa et al. (2017) employed hexyl acetate (HEX) as extracting agent having better results than using mesitylene. In any case, it is still required to look for an environmentally friendlier and economic extracting agent substitute.

3.2. Solvent design by a computer-aided molecular design.

The potential molecules to be employed as extracting agents can be designed relying on CAMD principles (using molecular functional building blocks). Thereby, it is necessary to list the desired characteristics of the reference solvent (in this case mesitylene), such as, partition coefficient, water solubility, vapour pressure, not azeotrope creation with the present compounds, etc. That information is specified in the Pro-CAMD that is available in the ICAS software. The Pro-CAMD designed a number of candidates that were reduced by manipulating the lower and upper limit values of the desired characteristics. The software provided 846 compounds as potential extracting agents.

3.3. Selection of the potential candidate to be used as extracting agents and the thermodynamic model.

The discrimination to determine the final list of possible candidates was obtained checking the existence or availability of the compound in the market, and also the commercial prices compared with the reference compound. The heptyl acetate (HEP), HEX among others was found as the most promising substitutes for the mesitylene. HEX was already analysed as extracting agent in a previous study (Morales-Espinosa et al., 2017), while the implementation of the HEP is still in progress. In any case, both seem to be feasible for their implementation as extracting agents separately or together like a mixture. The thermodynamic model selected for the LLE unit was NRTL, while the liquid phase and vapour phase in the DC were the predicted using NRTL model and Hayden O'Connell equation of state, respectively.

3.4. Evaluation of the potential extracting agents/solvents candidates.

The HEX, HEP and mesitylene were tested in a LLE unit with the same number of stages (5), process conditions ($T = 35\text{ }^{\circ}\text{C}$ and $P = 1\text{ atm}$) and molar-based feeding ratio (1:0.84, ABE-water and extracting agents, respectively), just with the end of comparing and evaluating the performance of the extracting agents at the same circumstances.

3.5. Comparison of the potential candidates vs case base of extracting agent

The results employing HEX and HEP had similar ABE recovery. In addition, the commercial price of mesitylene compared with HEX and HEP prices were 1.62 and 2.62 times higher, respectively. Thereby, finding the HEX and HEP as feasible candidates in terms of economy.

3.6. Selection of potential candidates and property analysis.

The HEX and HEP are from the same organic family and differ by 1 and 2 carbon and hydrogen atoms, respectively. The boiling points of both compounds are higher for more than 50°C compared with butanol, which is the compound with higher boiling point present in the mixture to be separated.

3.7. Process design for separation and purification.

The process synthesis was done relying in heuristic rules, then the equipment design was done using shortcut methods for the DC and a sensitivity analysis to improve the LLE design and the DC. Once, the design is gotten a rigorous simulation is performed using EXTRACT unit for LLE and RADFRAC for DC in Aspen plus (AP). The process configuration is shown in Figure 2.

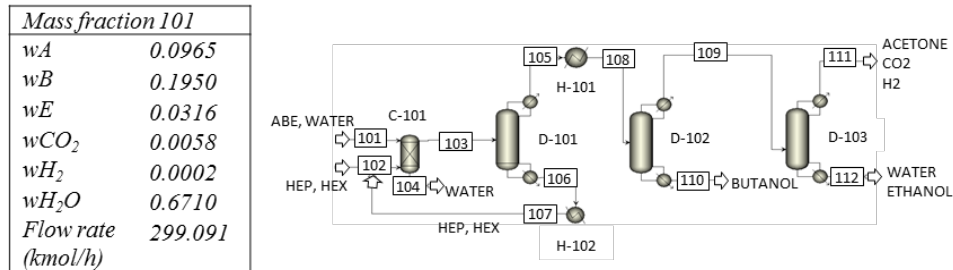


Figure 2. Configuration for the ABE separation using HEX-HEP mixture as extracting agent.

3.8. Multiobjective optimisation

The optimal mixture compositions of the extracting agent and the process design is performed simultaneously through the last step.

3.8.1. Objective Function

The objective function included the simultaneous minimization of the TAC and the eco indicator 99. The minimization of these objectives was subject to the required recoveries and purities in each product stream (see Equation 1).

$$\text{Min}(TAC, \text{Eco } 99) = f(N_m, M_{in}, N_{fn}, R_m, F_m, D_{cn}), \text{ subject to } y_m \geq x_m \quad (1)$$

where N_m are total column stages in LLE column and DCs, M_{in} is the mixture of the extracting agents feeding flowrate to the LLE, N_{fn} is the feed stage of all streams in columns, R_m is the reflux ratio, F_m is the distillate fluxes and D_{cn} is the column diameter, y_m and x_m are vectors of obtained and required mass purities (95%, 99.5% and 83% for ABE) with the mass recoveries (98%) for the m components, respectively. Moreover, note the variable M_{in} involves both the amount of mass in the feed stream and the mass fraction for the case of a mixture of the extracting agents. This minimization implied the manipulation of 18 continuous and discrete variables. The TAC calculation was performed as it is shown in Equation 2.

$$TAC = \frac{\text{Capital Cost}}{\text{Payback period}} + \text{Operative cost} \quad (2)$$

On the other hand, the environmental indicator was measured through the eco-indicator 99 based on the methodology of the life cycle analysis (Geodkoop and Spriensma, 2001). In the eco-indicator 99 methodology, 11 impact categories were considered, aggregated into three major damages categories: (1) human health, (2) ecosystem quality, and (3) resources depletion.

3.8.2. Global stochastic optimisation strategy

To optimize the process route for biobutanol production, a stochastic optimisation method, Differential Evolution with Tabu List (DETL) was used, which have shown being robust to optimize intensified separation systems. Srinivas and Rangaiah (2007) showed that the use of some concepts of the metaheuristic tabu can improve the performance of DE algorithm. The implementation of this optimisation approach was made using a hybrid platform where the DETL was coded using Microsoft Excel (ME) and the separation process was rigorously simulated using Aspen plus. For the optimisation of process routes analysed in this study, the following parameters for DETL method were used: 200 individuals, 300 generations, a tabu list of 50% of total individuals, a tabu radius of 0.0000025, 0.80 and 0.6 for crossover and mutation fractions, respectively.

4. Results

The results of the optimisation are illustrated in Figure 3. The possible optima are illustrated inside the oval. The point (a) which considers the use of a HEX-HEP mixture as extracting agent was determined as the optimal point, with a mass fraction in the feed stream of 0.3799 for n-hexyl-acetate and 0.6201 for n-heptyl. The TAC was equal to 2,956,262 US\$/year and eco indicator = 1,013,908 points/year. The comparison between the optimal scenarios for TAC and eco-points with the base case (BC) point scenarios for HEX (b), HEP (c), and the mixture HEX-HEP (d) indicated that the BC points were 2.3, 3 and 4.6 time higher for the TAC and 2.7, 3.1 and 4.8 times higher for the eco-indicator, respectively. The results showed an improvement in the terms of the economic and environmental because of reduction in the amount of extracting agent. In other words, the best points for each case were obtained using 22,938.57 kg/h in comparison with 39,040.8 and 77,646.9 kg/h for HEP and HEX respectively. Thus, the optimisation task undoubtedly achieved its objectives.

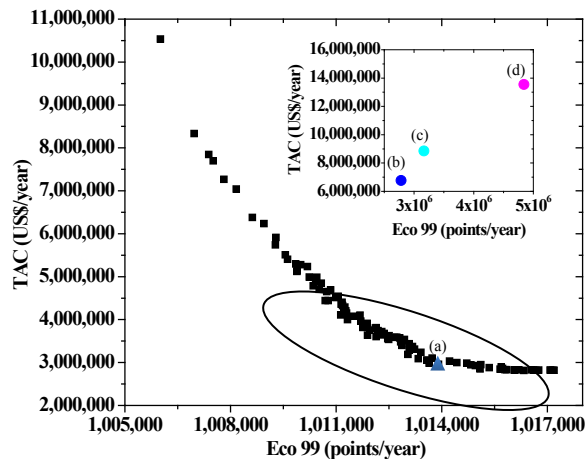


Figure 3. Pareto Chart for determining the optimal process design in terms of economic and environmental aspects.

Table 1 shows the optimal (Opt) specifications compared with the BC scenario. The results showed the D-101 and D-103 units are shorter, and the reflux ratio was highly decreased. The reflux ratio in D-103 was reduced several times that results on the reduction of the operation cost because of the heat duty decrease.

Table 1. Specifications of the unit operations included in the downstream section.

Unit	Base case	Optimal design
C-101	NS=5; P=1 atm; ABE-water/HEX-HEP =1.60; TT= 21.5°C; BT= 24°C	NS=7; P=1 atm; ABE-water/HEX-HEP =1.9; TT= 21.6°C; BT= 24.3°C
D-101	NS=37; RR=0.2; DR=130.75 kmol/h; FS=27; P=1 atm; TT=100°C; BT=180.5°C	NS=31; RR=0.1974; DR=130.75 kmol/h; FS=21; P=1 atm; TT=100°C; BT=182.6°C
H-101	T=35°C; P= 1 atm	T=35°C; P= 1 atm
D-102	NS=37; RR= 0.3; BR=52 kmol/h; FS=18; P=1 atm; TT=78.7°C; BT=117.3°C	NS=38; RR=0.29; BR=51.98 kmol/h; FS=12; P=1 atm; TT=78.8°C; BT=117.3°C
D-103	NS=37; RR=22; DR=28.7 kmol/h; FS=14; P=1 atm; TT=54°C; BT=81°C	NS=49; RR=3.26; DR=28.8 kmol/h; FS=38; P=1 atm; TT=54.4°C; BT=81°C

NS: number of stage; P: pressure; ABE/HEX-HEP ratio in molar base; TT: top temperature; BT: bottom temperature; RR: reflux ratio; BR: bottom rate; FS: Feed stage; T: temperature; DR: Distillate rate.

5. Conclusion

This study proposed a framework for the simultaneous design of the mixture of extracting agents employed in the LLE process, as well as the process design of the required equipment in the separation and purification process for ABE. The framework was possible due to the combination of different methods and computer-aided tools. The results showed an improved design by reducing the TAC and the eco-indicator 78% and 79%, respectively, because of the reduction in the amount of extracting agent. The enhancement was achieved due to the optimal and rigorous mixture and molecular design that provided the appropriate composition for the mixture of the extracting agents in the LLE unit, which had better performance as previous solvents used before.

Acknowledgments

Dr. Morales-Rodríguez acknowledges the partial financial support by the Mexican Bioenergy Innovation Centre, Bioalcohols Cluster (249564) and the Universidad de Guanajuato for the development of this project.

References

- M. Errico, E. Sanchez-Ramirez, J.J. Quiroz-Ramírez, J.G. Segovia-Hernandez, B.-G. Rong, 2015, Alternative Hybrid Liquid-Liquid and Distillation Sequences for the Biobutanol Separation. *Comput.-Aided Chem. Eng.*, 37, 1127-1132.
- M. Geodkoop, R. Spriensma, 2001, The eco-indicator 99. A damage oriented for life cycle impact assessment. Methodology report and manual for designers, Technical report, PRe Consultants, Amersfoort, The Netherlands.
- P.M. Harper, R. Gani, P. Kolar, T. Ishikawa, 1999, Computer-Aided Molecular Design with combined molecular modelling and group contribution, *Fluid Phase Equilib.*, 158-160, 337-347.
- A.T. Karunanithi, L.E.K. Achenie, 2007, Solvent design for crystallization of pharmaceutical products, *Comput-Aided Chem Eng*, 23, 115-147.
- N. Morales-Espinosa, E. Sánchez-Ramírez, J.J. Quiroz-Ramírez, J.G. Segovia-Hernández, F.I. Gómez-Castro, R. Morales-Rodríguez, 2017, A Framework for an Optimized Sustainable Product and Process Design: Acetone-Butanol-Ethanol Separation and Purification, *Comput.-Aided Chem. Eng.*, 40, 697-702.
- M. Srinivas M., G.P. Rangaiah, 2007, Differential Evolution with Tabu List for Solving Nonlinear and Mixed-Integer Nonlinear Programming Problems, *Ind. Eng. Chem. Res.*, 46, 7126-7135.

Optimal Design and Operation of Hybrid Osmosis Processes for Simultaneous Production of Water and Power under Different Demand Conditions

Jyh-Cheng Jeng^{*}, Heng-Yi Chu

National Taipei University of Technology, Taipei 10608, Taiwan

jcjeng@ntut.edu.tw

Abstract

This study investigates the optimal design of hybrid osmosis process systems for simultaneous seawater desalination and power production under different demand conditions. Optimization of four serial configurations that connect the RO, PRO, and FO processes with different order (i.e., RO-PRO, PRO-RO, FO-RO-PRO and PRO-FO-RO) are conducted by minimizing the total annual cost (TAC). The results show that the configurations with FO process are not cost-effective. The PRO-RO system is more favorable when the water demand is relatively large compared to the power demand and when higher water quality is demanded. Furthermore, a general RO/PRO structure that involves more flexible connection of streams is developed and optimized. Compared with the serial configurations, the optimal general structures allow reductions of TAC up to 35%, depending on the demand scenarios. The results also reveal that there exists an optimal concentration of water permeate under a specific demand condition. The proposed model of process integration is effective for designing hybrid osmosis process systems to simultaneously produce water and power on demand.

Keywords: Process optimization, Reverse osmosis, Pressure retarded osmosis, Forward osmosis, Seawater desalination.

1. Introduction

It is recognized that potable water and energy are gradually insufficient for human needs. To exploit sustainable resources, technologies have been developed to desalinate seawater and produce power using salinity gradient. Reverse osmosis (RO) is one of the major technologies for desalinating seawater, while pressure retarded osmosis (PRO) is a promising technology for power production. Therefore, the hybridization of RO and PRO processes enables the build of dual-purpose desalination/power plants (Almansoori and Saif, 2014). Senthil et al. (2016) modelled six hybrid RO-PRO structures to minimize the net specific energy consumption (NSEC). The results showed that NSEC could be lowest when PRO draw solution entirely recycled to RO feed with an energy recovery device. However, there will be no power generation. Furthermore, forward osmosis (FO) can be used as a pre-treatment process of RO to reduce the extensive energy consumption required in RO process. Blandin et al. (2015) studied the energy consumption and economic evaluation of FO-RO hybrid. They reported that FO-RO hybrid can be beneficial for high energy costs and/or substantial operational cost savings. Altee et al. (2015) studied the impact of the draw and feed solutions' flow rate

and the impaired water TDS on the performance of three design configurations, PRO-RO, FO-RO, and RO-PRO.

In this study, we focus on the optimal design and operation of the hybrid osmosis systems that integrate the RO, PRO, and FO stages for power production and seawater desalination. The most efficient configuration of the hybrid likely depends on the demand conditions of water and power. Design configurations of four serial structures and a more flexible structure are proposed and the optimizations are carried out by minimizing the total annual cost (TAC). The effects of the demand conditions on the optimal structure and operation of the hybrid osmosis systems are investigated.

2. Configurations of hybrid osmosis process

Figure 1 shows four structures that connect the osmosis processes in series (i.e., RO-PRO, PRO-RO, FO-RO-PRO, and PRO-FO-RO). The seawater (TDS 35000 ppm) can be chosen entering any osmosis processes, serving as the RO feed or as the draw solution of FO and PRO. The leaving stream of a preceding osmosis process can be partly discharged before entering the next osmosis process. The feed solution of FO and PRO are municipality water (TDS 2000 ppm). The pressure exchanger (PX) is an energy recovery device that transfers pressure from a high-pressure stream to a low-pressure one. Hydro-turbine generates power when PRO draw solution partly passed it.

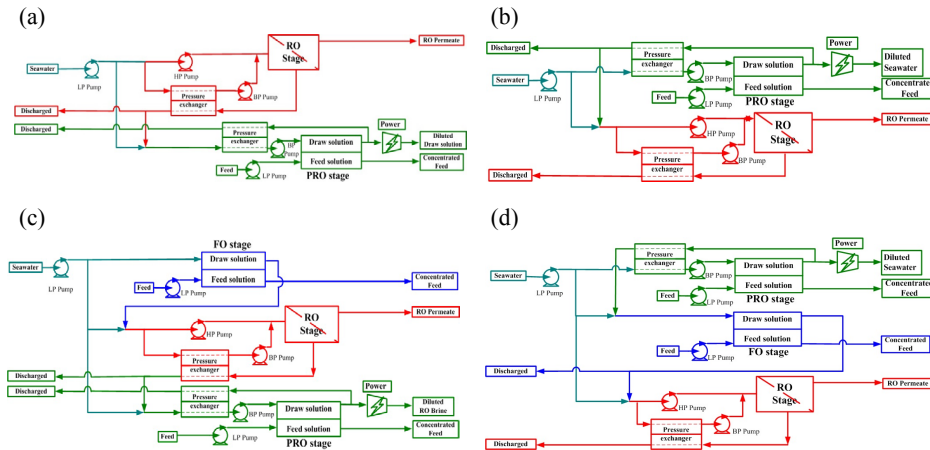


Figure 1. Four serial configurations of hybrid osmosis processes. (a) RO-PRO; (b) PRO-RO; (c) FO-RO-PRO; (d) PRO-FO-RO.

3. Optimization model

The MINLP optimization model describes the design and operation of the hybrid osmosis systems. The mathematical programming equations involve the mass balance for the mixing/splitting points and the model equations for the osmosis stages. Binary variables define the number of pressure vessels and number of membrane modules in a pressure vessel for each osmosis stage. Continuous variables define the flow rate, concentration, and pressure in the system. The model equations for RO, PRO, and FO stages have been given by Almansoori and Saif (2014) and Blandin et al. (2015). The characteristics of the membrane for RO, PRO, and FO are shown in Table 1.

Table 1. Characteristics of RO, PRO, and FO membrane (Almansoori and Saif, 2014; Blandin et al., 2015).

	RO	FO	PRO
active area (m ²)	37.2	37.6	37.6
length of the element (m)	0.88	2.25	2.25
feed channel equivalent diameter (m)	0.0008126	0.0025	0.0025
feed flow rate range (kg/s)	0.22-4.5	0.22-4	0.22-4
feed cross-section open area (m ²)	0.0147	0.0097	0.0097
void fraction of the spacer	0.9	0.8	0.8
maximum operating pressure (Mpa)	8.3	1	2
water permeability (kg/m ² · s · Mpa)	0.0035	0.013	0.012
TDS permeability (kg/m ² · s)	0.000032	0.00012	0.000457
structural parameter (m)	1000	0.00000346	0.00000034

The objective function for minimization is the total annual cost (TAC) which is defined as the sum the annualized total capital cost (ATCC) and annual operation cost (AOC). The TCC comprises the capital costs (CC) of pressure vessels and membranes, seawater and municipality water intake/pretreatment equipments, booster and high pressure pumps, pressure exchangers, and hydro-turbine:

$$ATCC = 0.071 \left(\sum_i CC_i^{PV} + \sum_i CC_i^{SWIP} + \sum_j CC_j^{MWIP} + \sum_k CC_k^{BP} + CC_{RO}^{HPP} + \sum_k CC_k^{PX} + CC_{PRO}^{HT} \right) \quad (1)$$

$$\begin{aligned} CC_i^{PV} &= C_i^{Mem} (NE_i \times NPV_i) + C_i^{PV} NPV_i; \quad CC_i^{SWIP} = C_i^{SWIP} (F_i^{SWIP})^{0.8}; \quad \forall i \in RO, PRO, FO \\ CC_j^{MWIP} &= C_j^{MWIP} (F_j^{MWIP})^{0.8}; \quad \forall j \in PRO, FO \\ CC_k^{BP} &= C_k^{BP} F_k^{BP} \Delta P_k^{BP}; \quad CC_k^{PX} = C_k^{PX} (F_k^{PX})^{0.58}; \quad \forall k \in RO, PRO \\ CC_{RO}^{HPP} &= C_{RO}^{HPP} F_{RO}^{HPP} \Delta P_{RO}^{HPP}; \quad CC_{PRO}^{HT} = C_{PRO}^{HT} F_{PRO}^{HT} \Delta P_{PRO}^{HT} \end{aligned} \quad (2)$$

where C_i^{Mem} is the capital cost of a membrane, NE_i is the number of membranes in a pressure vessel, NPV_i is the number of the pressure vessels, C is the capital cost coefficient, F is the mass flow rate, ΔP is the pressure difference, and 0.071 is the annualized factor. The AOC comprises the operation cost (OC) of pressure vessels, seawater and municipality water pretreatment, booster and high pressure pumps, equipment insurance, maintenance, chemical usage, and labor:

$$AOC = \sum_i OC_i^{PV} + \sum_i OC_i^{SWIP} + \sum_j OC_j^{MWIP} + \sum_k OC_k^{BP} + OC_{RO}^{HPP} + \sum_i OC_i^{ins} + \sum_i OC_i^{maint} + OC_{RO}^{chem} + OC_{RO}^{lab} \quad (3)$$

$$\begin{aligned} OC_i^{PV} &= O_i^{PV} CC_i^{PV}; \quad OC_i^{SWIP} = O_i^{SWIP} \frac{F_i^{SWIP} \Delta P_i^{SWIP}}{\eta^{SWIP} \eta_{MOTOR}}; \quad \forall i \in RO, PRO, FO \\ OC_j^{MWIP} &= O_j^{MWIP} \frac{F_j^{MWIP} \Delta P_j^{MWIP}}{\eta^{MWIP} \eta_{MOTOR}}; \quad \forall j \in PRO, FO \\ OC_{RO}^{HPP} &= O_{RO}^{HPP} \frac{F_{RO}^{HPP} \Delta P_{RO}^{HPP}}{\eta^{HPP} \eta_{MOTOR}}; \quad OC_k^{BP} = O_k^{BP} \frac{F_k^{BP} \Delta P_k^{BP}}{\eta_{BP} \eta_{MOTOR}}; \quad \forall k \in RO, PRO \\ OC_i^{ins} &= O_i^{ins} \times TCC_i; \quad OC_i^{maint} = O_i^{maint} \times TCC_i; \quad \forall i \in RO, PRO, FO \\ OC_{RO}^{chem} &= O_{RO}^{chem} F_{RO}^{FEED}; \quad OC_{RO}^{lab} = O_{RO}^{lab} F_{RO}^{PERM} \end{aligned} \quad (4)$$

where O is the operation cost coefficient and η is the efficiency factor. The parameters and cost coefficients for calculation are shown in Table 2.

Table 2. The parameters and cost coefficients for calculation (Almansoori and Saif, 2014).

$C_{RO}^{Mem} / C_{PRO}^{Mem} / C_{EO}^{Mem}$ (\$)	1200/1000/1500	O_i^{PV} (yr^{-1})	0.2
C_i^{PV} (\$)	1000	O_i^{SWIP} , O_i^{MWIP} ($\text{kW}\cdot\text{yr}^{-1}$)	946
C_i^{SWIP} , C_i^{MWIP} ($\text{\$ (kg/s)}^{-0.8}$)	35300	O_{RO}^{HPP} , O_{RO}^{HPP} ($\text{\$ (kW}\cdot\text{yr)}^{-1}$)	946
C_k^{PX} ($\text{\$ (kg/s)}^{-0.58}$)	6590	O_i^{ins} (yr^{-1})	0.005
C_{RO}^{HPP} , C_k^{BP} , C_{PRO}^{HT} ($\text{\$ (kg/s}\cdot\text{Mpa)}^{-1}$)	187	O_i^{main} (yr^{-1})	283.8
η^{HPP} , η^{BP} (%)	75	O_{RO}^{chem} ($\text{\$ (kg/s}\cdot\text{yr)}^{-1}$)	638.6
$\eta^{PX} / \eta^{HT} / \eta^{MOTOR}$ (%)	95/90/98	O_{RO}^{lab} ($\text{\$ (kg/s}\cdot\text{yr)}^{-1}$)	283.8

The water production in the RO stage and the power production in the PRO stage should meet the designer-specified water and power demands, respectively. In addition, the quality (concentration) of product water should meet the designer-specified specification.

4. Results and discussion

4.1. Results for the serial configurations

To investigate the effect of demand conditions on the optimized hybrid osmosis system, three water demands (50, 150, and 250 kg/s) and three power demands (50, 150, and 250 kW), with a total of nine cases, are considered for the optimization. Furthermore, two specifications of product water concentration, i.e., 250 and 500 ppm, are considered.

The MINLP problems were solved using the GAMS software. Table 3 shows the best configuration that has the lowest TAC among the four configurations for each of the demand scenarios. The results show that the configurations with FO stage are not cost-effective in all the cases. Compared the FO-RO-RPO with the RO-PRO system, the use of FO stage can be beneficial for RO stage, while it has a negative impact on the PRO stage for power production. Compared the PRO-FO-RO with the PRO-RO system, the advantage of using FO stage becomes minor because the seawater has been diluted by the PRO stage that results in a low salinity gradient for the FO stage.

For the systems without FO stage, the PRO-RO system is more favourable when the water demand is relatively large compared to the power demand because the seawater feeds to the RO stage has a lower salinity. On the contrary, the RO-PRO system is suitable for large power demand because a higher salinity gradient becomes available for the PRO stage. Furthermore, the PRO-RO system tends to be more effective when a higher water quality (lower water concentration) is demanded.

Table 3. The configuration that has the lowest TAC for each of the demand scenarios.

Demand	250 ppm			500 ppm		
	50 kg/s	150 kg/s	250 kg/s	50 kg/s	150 kg/s	250 kg/s
50 kW	PRO-RO	PRO-RO	PRO-RO	RO-PRO	PRO-RO	PRO-RO
150 kW	RO-PRO	PRO-RO	PRO-RO	RO-PRO	RO-PRO	PRO-RO
250 kW	RO-PRO	RO-PRO	PRO-RO	RO-PRO	RO-PRO	RO-PRO

4.2. A more general RO/PRO hybrid structure

In addition to the configurations that connect the osmosis process in series, we further develop a more flexible structure that involves the recirculation of the stream leaving

the last stage. The recirculation of stream has the advantage of reducing pre-treatment cost and environmental impact. Because systems with FO stage are not cost-effective, only the RO and PRO stages are considered in the general structure. Figure 2 shows the general structure where the leaving stream from one stage can be recycled as the feed of the other stage.

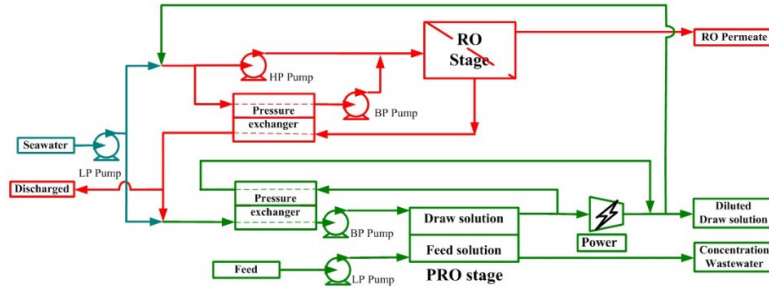


Figure 2. General structure of hybrid osmosis system of RO and PRO stages.

The minimum TAC for the general structure as well as those for the previous four serial structures under different demand conditions are presented in Figure 3. The general structure can be solved with the lowest TAC among the five structures for all the demand conditions. Compared with the optimal serial structure, the general structure allows a more than 25% improvement of TAC for most of the cases, with a maximum of 35% for the case of 250 kg/s (250 ppm) water and 50 kW power. In three cases (50 kg/s & 150 kW, 50 kg/s & 250 kW, and 150 kg/s & 250 kW), the TAC of the optimized general structure is close to that of the optimal serial structure. The optimization results indicate that the recirculation ratio of PRO draw solution is much lower in these three cases so that a large flow rate of seawater enters the system. This is because large draw solution recirculation would diminish the stream salinity in the system and, therefore, causes the PRO stage inefficient in the case of low water and high power demand.

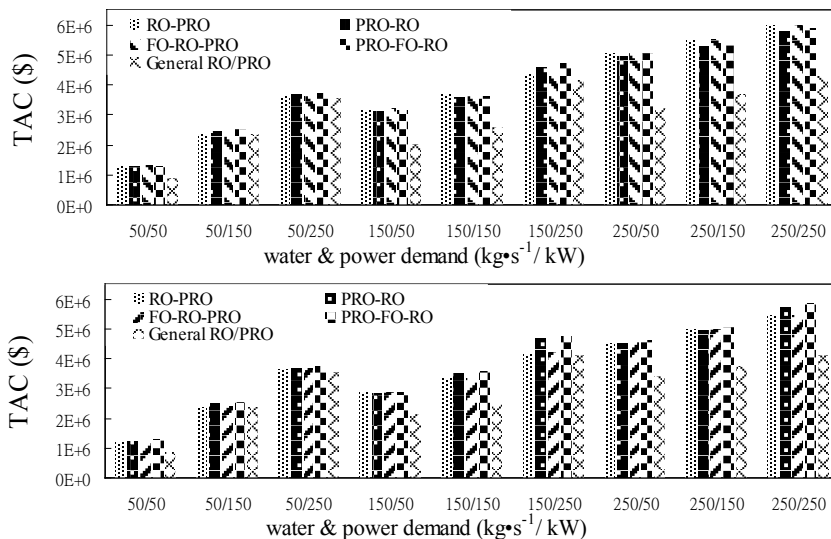


Figure 3. Minimum TAC for different demand conditions with product water TDS 250 ppm (up) and 500 ppm (down).

The effect of target product water concentration on the minimum TAC is also investigated. Figure 4 shows the minimum TAC of the general structure for the demand conditions of 150 kg/s & 50 kW with various target product water concentrations. The minimum TAC is identified at the product water concentration of 257 ppm. A higher product water concentration (lower RO brine TDS) may reduce the RO cost for water production but the PRO cost for power production is increased. On the other hand, the RO cost is increased for a lower product water concentration but the resulting higher RO brine TDS is advantageous for the PRO power production. Therefore, specifying a product water concentration greater than the optimal value should be avoided.

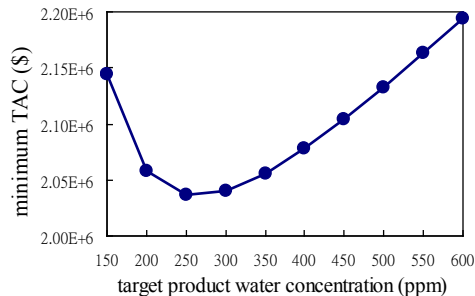


Figure 4. Minimum TAC of the general structure for the demand condition of 150 kg/s & 50 kW.

5. Conclusions

In this study, the optimizations of hybrid osmosis processes for simultaneous production of water and power under different demand conditions are presented and the results are analyzed. It is found that the use of FO as the pre-treatment unit for the RO stage is not cost-effective in the dual-purpose desalination/power plants. This is due to not only the extra capital cost of FO stage but also the insufficient salinity gradient in the PRO stage. For the systems with serial connection of RO and PRO stages, the favorable structure depends on the demand conditions and the target product water concentration. An efficient system is that the stage producing the major product follows the other stage. The proposed optimization model of the general structure can provide an effective RO/PRO integrated system for simultaneously producing water and power on demand.

Acknowledgement

The authors thank the support from MOST of Taiwan under grant 106-2221-E-027-115.

References

- A. Almansoori and Y. Saif, 2014, Structural Optimization of Osmosis Processes for Water and Power Production in Desalination Applications, *Desalination*, 344, 12-27.
- A. Altaee, A. Sharif, G. Zaragoza and A. F. Ismail, 2015, Evaluation of FO-RO and PRO-RO Designs for Power Generation and Seawater Desalination using Impaired Water Feeds, *Desalination*, 368, 27-35.
- G. Blandin, A.R.D. Verliefe, C.Y. Tang, P. Le-Clech, 2015, Opportunities to Reach Economic Sustainability in Forward Osmosis–Reverse Osmosis Hybrids for Seawater Desalination, *Desalination*, 363, 26-36.
- S. Senthil and S. Senthilmutugan, 2016, Reverse Osmosis–Pressure Retarded Osmosis Hybrid System: Modelling, Simulation and Optimization, *Desalination*, 389, 78-97.

Superstructure optimization (MINLP) within ProSimPlus Simulator

Qiao Zhao^{a,b}, Thibaut Neveux^b, Mounir Mecheri^b, Romain Privat^a, Philippe Guittard^c, Jean Noël Jaubert^{a*}

^a*LRGP-CNRS, 1 Rue Grandville, 54000 Nancy, France*

^b*EDF R&D, 6 quai Watier 78401 Chatou, France*

^c*PROSIM SA, 51, RUE AMPERE 31670 Labège France*

Jean-Noel.Jaubert@univ-lorraine.fr

Abstract

Although the methodologies of optimization-based process synthesis have evolved significantly during the last thirty years, the ability to robustly and accurately solve industrially-relevant global flowsheet problems remains limited. Engineering expertise and simulation-based sensitivity analysis still remain an essential guide for system alternatives generation and key devices selection.

The purpose of this study is to provide a superstructure mixed-integer nonlinear programming (MINLP) optimization within the commercial simulator ProSimPlus. The entire optimization loop is directly managed by the simulator and both continuous variables and discrete integer variables are optimized simultaneously by an external metaheuristic optimizer called MIDACO (Mixed Integer Distributed Ant Colony Optimization).

Keywords: Superstructure, Optimization, Process Simulator, MINLP, Ant Colony Optimization

1. Introduction

Thanks to the advances made in artificial intelligence and mathematical programming, the computer-aided approaches in process synthesis (e.g., superstructure optimization) have evolved significantly during last thirty years (Voll et al., 2013). Nevertheless, low disseminations of such optimization into the industrial community are noticed because that real-world industrial studies are complex non-linear and non-convex problems (Barnicki and Sirola, 2004; Quaglia et al., 2015).

One of the widely applied approach is the equation-based optimization, yet there is a known compromise on solution quality obtained (i.e., rigorousness) since linear approximation or surrogate models are frequently applied (Chen and Grossmann, 2017). On the other hand, simulator-based optimization approach has been received more attention recently since it can benefit directly from the reliability and rigor of process simulator. Regarding this topic, studies have been carried out in different applications such as distillation systems (Bravo-Bravo et al., 2010; Leboreiro and Acevedo, 2004; Caballero et al., 2005; Corbetta et al., 2016), chemical processes retrofit, (Diwekar et al., 1992; Gross and Roosen, 1998; Brunet et al., 2012; Chen et al., 2015) as well as

energy conversion system application (Wang et al., 2014). The MINLP optimizations carried out within process simulator (Flowtran, Aspen Plus, Aspen Hysys, PRO/II or Epsilon Professional) require an additional interface (i.e., GAMS, C++), requiring tedious supporting tool construction.

In this work, a superstructure MINLP optimization of SC-CO₂ Brayton cycle is brought out with ProSimPlus, a commercial simulator. Unlike researches cited above, our strategy is to use ProSimPlus as main (and the only) interface to both manage the graphical representation of the superstructure as well as the MINLP optimizer. An external solver MIDACO (Schluter et al., 2009), an Ant Colony Optimization (ACO) metaheuristic algorithm is applied for the MINLP problem discussed in this paper. The rigorous models for unit operations implemented in ProSimPlus are directly used during the MINLP optimization without approximation.

2. Methodology

2.1. Metaheuristic optimization with MIDACO

The motivation of using metaheuristic optimizer MIDACO in this study is its black-box and stochastic probabilistic nature. The first property allows to optimize non-convex MINLP problem without explicit expression of the objective and constraint functions. Secondly, the stochastic nature of ACO makes it possible to selectively search a much smaller fraction of the solution space thus reduces the computational time efforts.

2.2. Optimization unit in ProsimPlus

The link with an external optimizer is made possible in ProSimPlus thanks to predefined communication interfaces that are implemented in the ProSimPlus standard optimization unit.

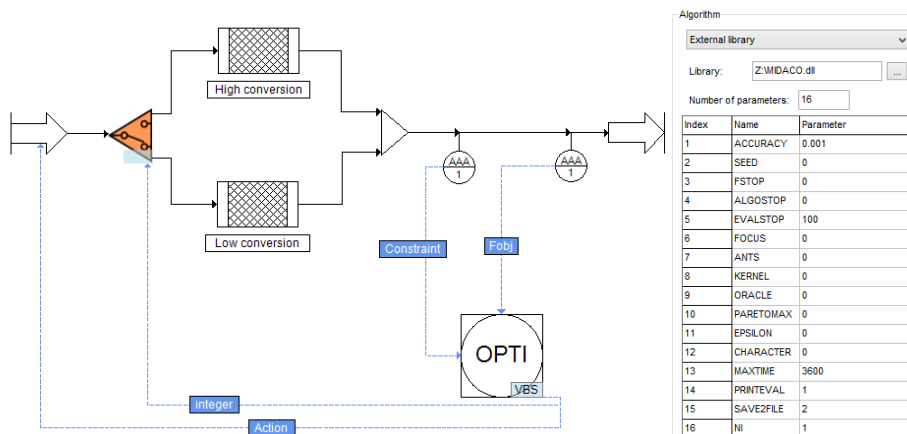


Figure 1 Illustration superstructure graphic representation (left) and optimization unit (right) in ProSimPlus, case of a Two Reactors Problem (blue dashed lines are information streams: 1 objective function, 1 constraint, 1 integer decision and 1 continuous variables)

If a user does not want to use the native stochastic optimization (genetic algorithm) or the default nonlinear programming optimization algorithm (based on a SQP method), it

is possible to select an external dynamic library which implements these communication interfaces and is statically or dynamically linked with the external algorithm.

When the external solver is provided as a dynamic link library, a wrapper dll is needed to perform the communication between ProSimPlus and the external algorithm.

The value of the objective function as well as the values of the equality and inequality constraints are automatically passed to the external dynamic library to make them available to the external algorithm, which calculates the new values of the optimization variables.

A customizable table of parameters, available in the graphical user interface of the optimization unit, allows to access to the parameters of the external algorithm, see the example in Figure 1 for a simple two reactors problems (such as in Diwekar et al., 1992).

2.3. Formulation strategy in process simulator

2.3.1. Superstructure connectivity

Defining the component connection in superstructure is to characterize the existence of component and to remove the redundant component when it is not used. For our superstructure formulation in this study, redundant component is only virtually removed by simply setting their flow rate to zero.

A multipath (2 or more) logical switch is coded in ProSimPlus. The switch level y_i is thus defined as the integer decision variable in the superstructure optimization and enables to select a specific path between all possible alternatives.

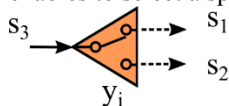


Figure 2 Logic switch defined in this study

2.3.2. Other rules in formulation stage

The result of a MINLP optimization is known to be strongly influenced by the formulation of the problem and the selection of variables. It is thus important to formulate the problem in the way that allows fast and easy convergences of the process simulator flowsheet with all the values in the range between lower and upper bounds (Corbetta et al., 2016). Several rules are set in this paper:

- a) Tear Stream. When the superstructure involves a closed loop or recycle loop, it is necessary to choose tear stream(s) in the simulator (both *feasible path* and *infeasible path* approaches can be used).
- b) Fictive unit. Components situated in the middle of a simulation sequence need to be combined with a fictive unit if the component is to be optimized with constraints along with dependency of other optimized variable. The fictive unit will only be activated if the evaluated scenario is infeasible. When it is active, the work (or heat) consumed by the entire fictive unit need to be considered in the objective function. Consider turbine outlet pressure optimization as an example: its fictive unit is composed of a fictive compressor and a fictive cooler in order to avoid infeasible engineering scenario (when the ratio is smaller than 1). It is preferred to have fictive units than additional inequality constraints (force the pressure ratio greater than 1) since the latter case introduces more non-convexity to the optimization problem.
- c) Counter-current exchangers' separation. The counter-current exchangers used in the superstructure optimization should be divided into two simple parts: a heater and a

cooler. This modification avoids additional simulation iterations inside the counter-current exchanger and reduces the possible divergent cases. The optimization itself benefits faster iteration from the relaxation of counter exchangers.

3. Application examples

3.1. Case study: SC-CO₂ Brayton cycle superstructure optimization

The fundamental aspects of supercritical CO₂ (SC-CO₂) Brayton cycle are under worldwide development, hence importance of optimization. Current optimizations of SC-CO₂ Brayton cycle have only been done to maximize the cycle efficiency with parametric optimization with fixed process topology (cycle configuration). However, an optimal-synthesis searching for the most energy efficient cycle layout can further reveal its real potential in its future deployment.

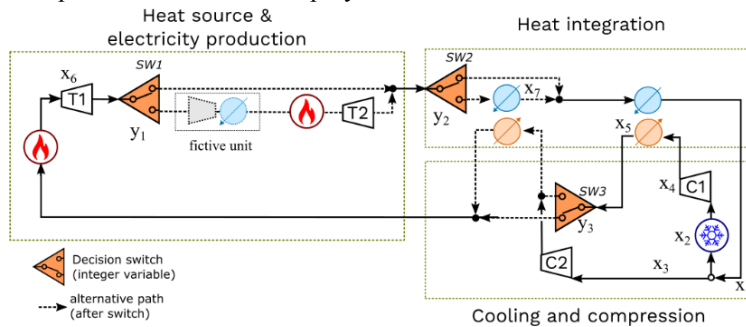


Figure 3 Superstructure of SC-CO₂ Brayton cycle with fictive unit ($2^3=8$ structural alternatives)

The superstructure in Figure 3 integrates some configurations based on previous experiences as well as some innovative design solutions created by the combination. Note that the rules described in section 2.3.2 are respected and a fictive unit is implemented after turbine T1.

The indicator of the energy performance, cycle efficiency, is seen as the objective function. 10 variables (3 integer variable y_1, y_2, y_3) are to be optimized in this MINLP problem.

3.2. Results and discussion

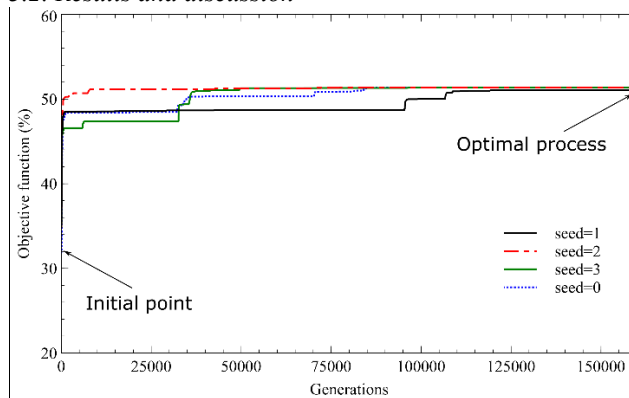


Figure 4 Optimization progress of four runs with different random seeds

Four different optimization runs are carried out with four different pseudo random number (seed) in MIDACO, Figure 4. Note that different random seed has indeed diverse progress of optimization, different corresponding populations are generated.

Moreover, at the end of 6 hours evaluation (up to 16,000 generations), the structural result of the best individual is identical (i.e., identical set of $\{x,y\}$), which also confirms that this layout is the best known solution to the defined optimization problem.

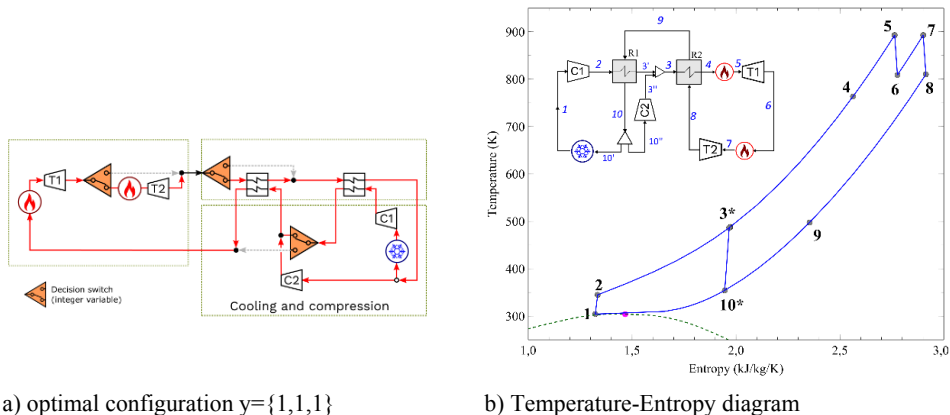


Figure 5 Process synthesis result: optimal flowsheet for the SC-CO₂ Brayton cycle

This optimal process layout with cycle net efficiency as high as 51.4 % is composed of two compressors, two recuperators, and one reheat (thus two turbines). Compared with the initial proposal of SC-CO₂ Brayton cycle by Feher, 1967 and Angelino, 1969, the optimal process configuration has an enforced heat integration. Figure 5 indicates all the exchangers have a minimal accepted thermal pinch (10 K). Furthermore, entropy loss is avoided at mixer since stream 3' and 3'' have the identical temperature and pressure (iso-entropy) before mixing.

4. Conclusion

In this work, we presented a simulator-based approach for superstructure optimization in process simulator ProSimPlus. Compared with other simulator-based optimization methods, the proposed superstructure optimization approach is more general on terms of component and optimizer. Any component available in the simulator can be used in the superstructure generation and external optimizers can be linked with ProSimPlus through its optimization unit.

Furthermore, this paper illustrated how the simulator enables to manage the entire optimization loop while both continuous variables and discrete integer variables are optimized simultaneously by MIDACO.

The case study carried out in this paper illustrate the above advantages of the presented optimization strategy. The obtained results are the best known optimal design for both application studies. In addition, the formulation rules provided in this paper guarantees the convergence of simulation which helps to reduce the infeasible region search while optimizing both continuous and integer variables.

References

G. Angelino, 1969, Real gas effects in carbon dioxide cycles, ASME Paper No. 69-GT-103, 1-12

- S. D. Barnicki, J. J. Siirola, Process synthesis prospective, 2004, *Computers & Chemical Engineering* 28 (4) 441-446
- C. Bravo-Bravo, J. G. Segovia-Hernandez, C. Gutierrez-Antonio, A. L. Duran, A. Bonilla-Petriciolet, A. Briones-Ramrez, 2010, Extractive Dividing Wall Column: Design and Optimization, *Industrial & Engineering Chemistry Research* 49 (8) 3672-3688
- R. Brunet, J. A. Reyes-Labarta, G. Guillén-Gosálbez, L. Jiménez, D. Boer, 2012, Combined simulation optimization methodology for the design of environmental conscious absorption systems, *Computers & Chemical Engineering* 46, 205-216
- J. A. Caballero, D. Milan-Yanez, I. E. Grossmann, 2005, Rigorous Design of Distillation Columns: Integration of Disjunctive Programming and Process Simulators, *Industrial and Engineering Chemistry Research* 44 (17) 6760-6775
- Q. Chen, I. Grossmann, 2017, Recent Developments and Challenges in Optimization-Based Process Synthesis, *Annual Review of Chemical and Biomolecular Engineering*, 249-283
- Y. Chen, J. C. Eslick, I. E. Grossmann, D. C. Miller, 2015, Simultaneous process optimization and heat integration based on rigorous process simulations, *Computers & Chemical Engineering* 81, 180-199
- M. Corbetta, I. E. Grossmann, F. Manenti, 2016, Process simulator-based optimization of biore_ery downstream processes under the Generalized Disjunctive Programming framework, *Computers & Chemical Engineering* 88, 73-85
- U. M. Diwekar, I. E. Grossmann, E. S. Rubin, 1992 An MINLP process synthesizer for a sequential modular simulator, *Industrial & Engineering Chemistry Research* 31 (1) 313-322
- E. Feher, 1967, The supercritical thermodynamic power cycle Douglas Paper No.4348, in: *Proceedings of the Intersociety Energy Conversion Engineering Conference*, 13-17
- B. Gross, P. Roosen, 1998, Total process optimization in chemical engineering with evolutionary algorithms, *Computers & Chemical Engineering* 22, S229-S236
- J. Leboeiro, J. Acevedo, 2004, Processes synthesis and design of distillation sequences using modular simulators: a genetic algorithm framework, *Computers & Chemical Engineering* 28 (8) 1223-1236
- A. Quaglia, C. L. Gargalo, S. Chairakwongsa, G. Sin, R. Gani, 2015, Systematic network synthesis and design: Problem formulation, superstructure generation, data management and solution, *Computers & Chemical Engineering* 72, 68-86
- M. Schluter, J. A. Egea, L. T. Antelo, A. A. Alonso, J. R. Banga, An Extended Ant Colony Optimization Algorithm for Integrated Process and Control System Design, *Industrial & Engineering Chemistry Research* 48 (14) (2009) 6723-6738,
- M. Schluter, M. Gerdts, 2010, The oracle penalty method, *Journal of Global Optimization*, 293-325
- M. C. Tayal, Y. Fu, U. M. Diwekar, 1999, Optimal Design of Heat Exchangers: A Genetic Algorithm Framework, *Industrial & Engineering Chemistry Research* 38 (2) 456-467
- P. Voll, C. Klffke, M. Hennen, A. Bardow, 2013, Automated superstructure-based synthesis and optimization of distributed energy supply systems, *Energy* 50, 374- 388
- L. Wang, Y. Yang, C. Dong, T. Morosuk, G. Tsatsaronis, 2014, Parametric optimization of supercritical coal-fired power plants by MINLP and di_ifferential evolution, *Energy Conversion and Management* 85, 828-838

Sustainable Supply Chain: Monetization of Environmental Impacts

Cátia da Silva^{a*}, Ana Paula Barbosa-Póvoa^a, Ana Carvalho^a

^a*CEG-IST, University of Lisbon, Av. Rovisco Pais, 1049-001 Lisboa, Portugal*

catia.silva@tecnico.ulisboa.pt

Abstract

Taking into account the increase of business competitiveness and legislation compliance faced by industry's SC, environmental SC problems became a reality that companies have to deal with. This work is developed along this line and proposes a mixed integer linear programming model (MILP) that accounts for the economic and environmental pillars in the same objective function by monetizing environmental impacts. Economic and environmental performances are taking into account in the same unit allowing a single optimum solution. Conclusions can be drawn on how monetization can support decision maker's decision. To show model applicability a real-based SC is studied.

Keywords: supply chain, sustainability, monetization, design and planning

1. Introduction

Supply chain (SC) is an essential system in any organization, which has been studied for several years due to its importance in both research and industrial communities. Taking into account the increasing organizational competitiveness and governmental pressures, SC has expanded its main focus on economic profits to include environmental and social concerns as well (Barbosa-Póvoa et al., 2017). In addition, SC encompasses several complex decisions related to the number of products, entities, and variables involved. Thus, managing sustainable supply chains (SSC) towards efficient and sustainable objectives is a challenge, especially if this management encompasses the design and planning of the chain. Most SSC design and planning approaches have employed multi-objective methods to optimize the SC. In fact, the majority of real-world decision problems involve the optimization of more than one objective at the same time. As an example, considering the concern and awareness towards sustainability issues, stakeholders want to optimize companies' environmental performance, while accounting for economic issues. Therefore, multi-objective optimization methods are needed to analyze trade-offs between environmental and economic performances. However, the adequate weighting of such objectives is still a problem to be solved. In fact, these methods require a subjective weighting factors assignment for objectives by decision makers (Lim et al., 2013). In this context, the need to develop a mathematical optimization model with a single objective function for the economic and environmental pillars of sustainability becomes clear. One way to achieve this is by monetizing environmental impacts. According to Herendeen (1998), monetization is helpful to understand the cost of environmental impacts. For this reason, we intend to perform a monetization of environmental impacts of a real SC. Conclusions can be drawn on how these two pillars of sustainability can influence the SC design and planning decisions, and on how monetization can support decision maker's decision.

2. Environmental monetization methodologies

Diverse methods for assessing environmental impacts are available. Life cycle assessment (LCA) is one of the most used methodologies, which is composed by four main phases. The first one includes the goal and scope definition, where the context of the study is set out. This is a key phase that has to be clearly defined and consistent with the intended application as ISO standards require. The second phase is related to inventory analysis, which involves creating flows' inventory from and to nature for a system. These inventory flows can include inputs of water, energy, raw materials, releases to air, land, and water, and include the activities that are going to be assessed in the SC. The third step is the life cycle impact assessment (LCIA) phase that aims to evaluate the significance of potential environmental impacts based on the life cycle inventory flow results. This is a controversial phase because it encompasses the assignment of weighting factors by decision-makers and the difficult choice of the best methodology to use. The fourth phase is the life cycle interpretation that allows the identification, quantification, check and evaluation of the information from the LCA results. On the LCIA phase monetization is one methodology that can be used. Three monetization methods have been used to convert environmental impacts into monetary units (Chen and Holden, 2018), namely EPS, Eco-cost and Stepwise. According to the European Commission, EPS 2000 is a quite complete method and it has the uncertainties fully specified when compared to other LCIA methods. Thus, in this work, monetization is performed by using EPS. The environmental impacts are quantified in a monetary unit through EPS, which is mainly derived from the willingness-to-pay (WTP). The WTP values resulted from academic knowledge to proactively reduce environmental impacts (Steen, 1999).

3. Problem description and model characterization

The problem in study considers the SC design simultaneously with all the associated planning activities. The generic SC considered is represented in Figure 1, where raw materials flow from suppliers to factories and final products are obtained. Then, these final products flow to warehouses or directly to markets. End-of-life products can be recovered at the markets and sent to warehouses or directly to factories, where they are remanufactured. Transportation between SC entities can occur by unimodal or intermodal transportation. Thus, the problem under study can be defined as: given, the possible set of locations of SC entities, production and remanufacturing technologies, possible transportation modes between entities, and products within the SC; the goal is to obtain: the SC network structure, supply and purchase levels, entities' capacities, transportation network, production, remanufacturing and storage levels, supply flow amounts, and product recovery levels; in order to: maximize profit, and minimize environmental impacts.

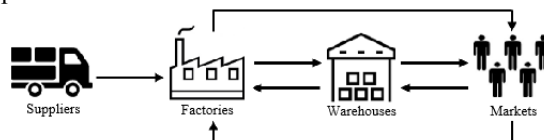


Figure 1. Scheme of SC network

To solve the above problem a Mixed Integer Linear Programming (MILP) model is developed considering as basis the formulation from Mota et al. (2017). The economic

and environmental performances are considered independently and simultaneously in the objective function.

The economic objective function is obtained from the maximization of the Net Present Value (NPV), see Eq. (1). This is assessed through the sum of the discounted cash flows (CF) in each period at a given interest rate. These CF are obtained from the net earnings, which are given by the difference between incomes and costs. The costs include raw material costs, production/remanufacturing operating costs, product recovery costs, transportation costs, handling costs at the hub terminal, contracted costs with airline or freight, inventory costs, and labor costs. Also, for the last time period, it is considered the salvage values of the SC (FCI³). The environmental impact is obtained using EPS 2015, which is an updated version of EPS 2000. Considering the SC as a functional unit, LCA is performed on the transportation modes and on entities installed in the SC boundaries. The Life Cycle Inventory is retrieved from the Ecoinvent database (assessed through SimaPro 8.4.0 software). From these results, an inventory list is obtained, and knowing the corresponding quantities, it is determined the environmental impact of each activity (transport and installation of entities). The results are expressed in Environmental Load Units (ELU) and used as input data in Eq. (2), namely the environmental impact of transportation (first term) and environmental impact of entity (second term). Finally, Eq. (3) reflects the objective function that is obtained through maximization of the difference between NPV and environmental impact (EnvImpact).

$$\max \text{NPV} = \sum_{t \in T} \frac{CF_t}{(1 + ir)^t} - \sum_{\gamma} FCI_{\gamma} \quad (1)$$

$$\min \text{EnvImpact} = \sum_{\substack{t \in T \\ (a,m,i,j) \in \text{NetP}}} ei_{ac} pw_m d_{ij} X_{majt} + \sum_{i \in I_f \cup I_w} ei_{ic} YC_i \quad (2)$$

$$\max \text{NPV} - \text{EnvImpact} \quad (3)$$

4. Case study

To show the applicability of the proposed methodology a case-study of a real SC based in Italy, already addressed by Mota et al. (2017) is considered. The company's suppliers are located in Verona. Currently, the company owns a factory and a warehouse in Verona with sufficient capacity to meet the demand of their existing clients. These clients are located in three main markets: Spain, Italy, and Germany. Currently, the SC capacity cannot meet a demand increase and four new potential clients induce the company's decision-makers to study different SC possibilities of expansion. Given the locations of the clients, Leeds and Hannover are possible locations for installing new factories, which may lead to significant changes in the transportation modes, especially for clients that are located outside Europe. Also, other possible warehouse locations are to be considered namely in Hannover, Leeds, Zaragoza, Lisbon, São Paulo and Recife, being these close to the markets. In addition, Budapest and Sofia are also possible considerations, given the economic and social attractive features.

Regarding SC products, there are two types of products (fp1 and fp2) that are currently being produced in Verona through technologies gp1 and gp2, respectively. However, there are two new technologies (gp1alt and gp2alt) available to produce the referred products. Final product fp1 can be obtained either through technology gp1 or gp1alt. In

the same way, final products fp2 can be obtained through technologies gp2 and gp2alt. End-of-life products can be recovered, being referred as rp1 and rp2. These can be remanufactured into final products through remanufacturing technology gr1 and gr2.

Related to transportation, there are two available options, namely unimodal and intermodal that can be performed only by road or through a combination of road, air and sea transportation modes, respectively. In addition, transportation by road implies investment in trucks. There are two types available (Truck1 and Truck2) that vary in terms of capacity, investment costs, depreciation rate, variable costs, and vehicle consumption.

Based on the SC reality, three scenarios are designed to understand the different decisions that can be made, regarding design and planning of the SC. These are:

Scenario A: studies the solution with the optimum economic performance as main target;

Scenario B: studies the solution with the optimum environmental performance as main target, assessed using two different methods: EPS and ReCiPe;

Scenario C: studies the solution with the optimum balance between economic and environmental performances (the later assessed using EPS).

5. Results

Table 1 shows the total environmental impact and the NPV obtained in each scenario. Comparing all scenarios, it can be seen that scenario A has the highest NPV associated, resulting from the maximization in its objective function. On the other hand, scenario B, which minimizes the environmental impact has the lowest NPV value independently of the environmental method used. When using the ReCiPe methodology (as described in Mota et al., 2017) the environmental impact is translated into 389,238.00 points (Pts), while when using the EPS methodology the environmental impact corresponds to 508,676,145.00 €. Finally, scenario C represents the maximization of the difference between NPV and environmental impact costs, which can only be performed due to the monetization of environmental impact, performed through the EPS method.

Table 1. Results for the economic (NPV) and environmental (EPS and ReCiPe) performances.

	Scenario A	Scenario B		Scenario C
	-	EPS	ReCiPe	EPS
Objective function	Max. NPV	Min. EnvImpact		Max. (NPV-EnvImpact)
NPV	1,280,985,986.00 €	878,621,338.00 €	832,789,347.00 €	1,279,892,213.00 €
Environmental impact	110,483,902,918.00€	508,676,145.00 €	389,238.00 Pts	516,848,072.00 €

Thus, comparing scenario A with C, it is possible to say that the SC global profit is reduced in 1 million euros, but the environmental impact improved almost 110 billion euros, which is only possible to achieve with a single objective function. Moreover, between scenario B and C, we can note that global profit increased more than 400 million euros, while environmental impact is worst at almost 8 million euros.

Table 2 shows SC structure decisions considering the objectives explained in Table 1. It can be seen that there are some variations across the scenarios studied. In addition to the already existent Verona factory, all scenarios suggest that two other factories should be installed, namely Hannover and Leeds. On the warehouses, the results of all scenarios show that there is a need to increase global capacity by opening new warehouses. Scenario A and C have a warehouse located in Sofia, which is justified by the smaller

construction costs. On the other hand, scenario B has warehouses located in different places, which is a result of environmental impacts' balance between both entities installation and transportation.

Table 2. Summary of the SC decisions considering the different scenarios

	Scenario A		Scenario B		Scenario C
	-		EPS	ReCiPe	EPS
Factories			Verona, Hannover, and Leeds		
Warehouses	Verona and Sofia		Verona Lisbon	and Verona, Leeds and São Paulo	Verona and Sofia
Suppliers	Verona and Leeds		Verona, Hannover, and Leeds		
Suppliers allocation	Verona supplies factories in Verona and Hannover. Factory in Leeds is supplied by Verona and Leeds		Factories are supplied in totally by closest supplier		
Production	Most production of fp1 is in Verona				
	Most production of fp2 is divided between Hannover and Leeds				
Remanufacturing	Most remanufacturing of fp1 is performed in Leeds. Most remanufacturing of fp2 is performed in Hannover		Mostly performed in Leeds. The remaining is divided between Verona and Hannover		Mostly performed in Verona. The remaining is divided between Hannover and Leeds
Product recovery	Minimum possible				
Inventory	fp1 and fp2 divided between Verona and Sofia		fp1 divided between Verona and Lisbon; and most inventory of fp2 kept in Verona	Most fp1 kept in Leeds and São Paulo; and fp2 divided between Verona and São Paulo	fp1 divided between Verona and Sofia; and most inventory of fp2 kept in Verona
Transportation	Road	8 Truck1 and 15 Truck2	6 Truck1 and 22 Truck2	1 Truck1 and 24 Truck2	3 Truck1 and 18 Truck2
	Air	Not used	Used for some transportation	intracontinental	Not used
	Sea		Used in all cases		

Regarding suppliers' choice and suppliers' allocation it can be seen that in scenario B and C (where environmental impacts are considered), the results reveal that 100% of the needs of each factory are met to the closest supplier of the installed factories and the allocation follows the same principle. This can be explained by the minimization of environmental impact of transportation. On the other hand, in scenario A, the maximization of the NPV leads to a balance between lower costs of raw materials and fewer transportation costs. On the transportation, the truck with more capacity (Truck2) is preferred in scenarios where environmental impacts are accounted for since this has a lower environmental impact. However, in scenario A, the choice between truck types is more balanced due to both lower investment and lower transportation costs of Truck1. Regarding intermodal transportation, sea option is preferred in all scenarios. Finally, air transportation is preferred in scenario B since it has a higher capacity compared with trucks, which compensate in terms of environmental impact. On the other hand, in scenarios A and C, the higher cost of this transportation mode justifies the preference to alternative transportation modes.

Looking closer to all scenarios, it can be seen that the network structure of scenario C is similar to scenario A since both SC entities and transportation modes are the same, with only some differences in the capacities involved and in the flows between entities. This fact added to the values obtained for NPV and environmental impact of these two scenarios leads to the conclusion that there is a huge benefit to the environment with a

low variation of NPV when environmental performance and profit are considered in the same objective function (scenario C).

6. Conclusions

This work aimed to understand how monetization can improve decisions related to design and planning of SSC. Overall, we note that different optimization objectives result in different decisions. In the same way, according to the results, all decisions are interconnected with each other, because a given decision implies that the other SC levels have to adapt. Considering the monetization approach, we are able to quantify the environmental impacts in a monetary unit (€). This process of monetization allows a better comprehension of environmental impacts, particularly for decision-makers, who are accustomed to perceive financial impacts on their SC. Thus, this work intends to provide a financial value for something that is commonly described in the literature as a score helping the decision process. In this way, it is possible to provide a solution that contemplates both economic and environmental performances in the same objective function. When comparing to the most used multi-objective approaches such methodology allows a variety of options for decision makers by comparing the financial and environmental performances. However, decision-makers are often more sensible to analyze decisions evolving monetary units, which can only be achieved by this monetization approach. To conclude, regarding economic and environmental performances, instead of comparing euros with points they can compare euros with euros, respectively supporting as already said a more informed decision.

As future work, some aspects are important to mention. Further research should be done on this topic to evolve monetization approaches in order to be a reliable alternative for multi-objective optimization approaches, particularly in assessing weighting factors. Also, an extension of this work should account for the need of monetizing social impacts considering the three pillars of sustainability in the same unit of analysis.

7. Acknowledgements

This work was supported by Portugal 2020, POCI-01-0145-FEDER-016418 by UE/FEDER through the program COMPETE2020.

References

- A.P. Barbosa-Póvoa, C. da Silva, A. Carvalho, Opportunities and Challenges in Sustainable Supply Chain: An Operations Research Perspective, *European Journal of Operational Research* (2017), <http://doi.org/10.1016/j.ejor.2017.10.036>
- W. Chen, N. M. Holden, 2018, Bridging environmental and financial cost of dairy production: A case study of Irish agricultural policy, *Science of the Total Environment*, 615, 597-607
- R. A. Herendeen, 1998, Monetary-costing environmental services: nothing is lost, something is gained, *Ecological Economics*, 25, 29-30
- S. R. Lim, Y. R. Kim, S. H. Woo, D. Park, J. M. Park, 2013, System optimization for eco-design by using monetization of environmental impacts: a strategy to convert bi-objective to single-objective problems, *Journal of Cleaner Production*, 39, 303-311
- B. Mota, M. I. Gomes, A. Carvalho, A. P. Barbosa-Póvoa, Sustainable supply chains: An integrated modelling approach under uncertainty. *Omega* (2017), <http://doi.org/10.1016/j.omega.2017.05.006>
- B. Steen, 1999, A systematic approach to environmental priority strategies in product development (EPS), Version 2000 – General system characteristics, CPM Report 1999:4 CPM, Chalmers University of Technology, Goteborg, Sweden

Design of Biotechnological Production of 2-Phenylethanol

Peter Vargai^a, Ivan Červeňanský^a, Mário Mihal^a, Jozef Markoš^{a,*}

^aInstitute of Chemical and Environmental Engineering, Slovak University of Technology in Bratislava, Radlinského 9, 812 37 Bratislava, Slovak Republic

jozef.markos@stuba.sk

Abstract

Biocatalytic production of many natural compounds is usually connected with strong inhibition effect of the product; therefore, an innovative process, where reaction and separation steps are integrated into one operational unit, has been developed. There are no general rules for optimal hybrid system design and final decision is made after the economic analysis of different production alternatives (Krishna, 2002). In this paper, the comparison of different process configurations for biotechnological production of 2-phenylethanol from L-phenylalanine by yeasts *Saccharomyces cerevisiae* with strong inhibitory effect on the production strain is presented. Classical fed-batch fermentation and two different hybrid systems were simulated using appropriate mathematical models and compared considering: overall production rate of target product, performance cost of proposed technology, investment cost, energy consumption, waste production. It has been shown that the hybrid system with in-situ product removal using an immersed extractive hollow fibre membrane module with continuous regeneration of organic solvent provides better results in 2-phenylethanol production compared to traditional batch technology.

Keywords: 2-phenylethanol, batch system, hybrid system, bioreactor, membrane extraction.

1. Introduction

In the recent years, the innovations in natural aromas and flavours produced by biotechnological route have been on the rise. One of those flavours is 2-phenylethanol (PEA), an aromatic alcohol with rose-like aroma, widely used in cosmetics, pharmaceuticals or food industry. Nowadays, natural PEA is produced via transformation of L-phenylalanine (PHE) in a bioreactor using yeasts *Saccharomyces cerevisiae*. Process is strongly aerobic and product formation is directly connected to yeast growth. PEA concentrations above 2 g/L severely inhibit yeasts' growth and concentrations above 4 g/L are fatal for the yeasts (Hua and Xu, 2011). Additionally, side product of the growth, ethanol, can produce synergistic inhibitory effect with PEA (Wang et al., 2011). Therefore the usual production time of conventional batch system is 24 h (Červeňanský et al., 2017). In order to prolong the production time and maximize product yield, systems, in which reaction and separation steps are integrated into one operation unit (so called hybrid systems) have been studied and developed (Krishna, 2002).

This work focuses on comparison by means of mathematical modelling of three PEA production alternatives – traditional batch production, and two hybrid systems for in situ PEA removal from fermentation broth. Mathematical models were developed, described and compared with experiments in our previous papers Mihal' et al., 2014, Červeňanský, 2017.

2. System design

2.1. Simulation constraints

For the sake of comparability, basic constraints were set for each of the systems. Based on these constraints, reaction and separation were simulated and the results were used to propose the equipment, design time schedule and calculate capital and operating costs. General constraints applying to all systems are: volume of the bioreactor is 10 m³, final product as 40 wt. % PEA in organic solvent (pentane), initial yeasts concentration in fermentation medium is 3.143 g/L. Furthermore, each system has its own subset of additional constraints, such as fermentation time, based on the characteristics of the system, (Červeňanský et al., 2017).

2.2. Batch system

Based on the results from the simulations, the batch system for PEA production and separation was proposed, as seen in Figure 1. The production starts with filling the bioreactor with glucose, PHE, yeasts and water and Glucose tank (GT) with glucose solution. When the fermentation is done, fermentation broth is transported to Fermentation broth tank (FBT) and subsequently should undergo separation: by microfiltration (MF) biomass is removed and PEA from permeate is extracted in hollow fibre membrane extractive module (E) into organic solvent. Solvent is regenerated in Rectification column (RC), distillate stream contains practically pure pentane and is recycled back to Pentane tank (PT). Product – 40 wt. % PEA solution leaves the column in the bottoms. Time schedule of each unit is shown in Figure 2, the results are summarized in Table 1.

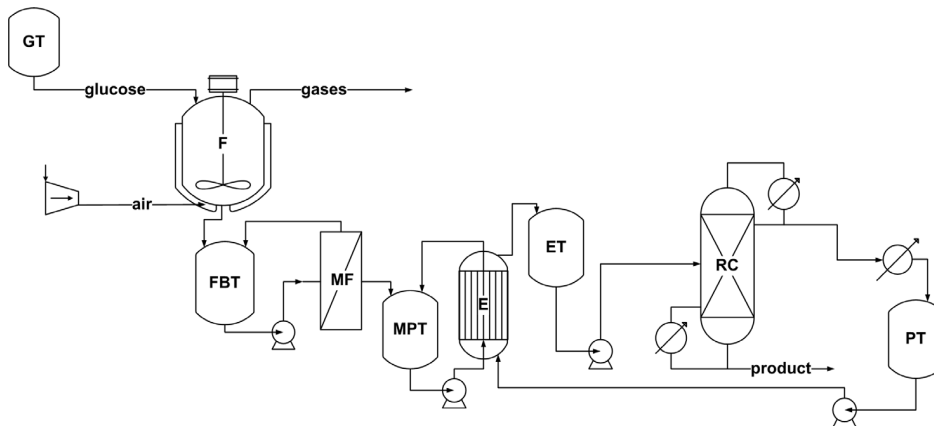


Figure 1 Scheme of proposed Batch system: bioreactor followed by separation steps.

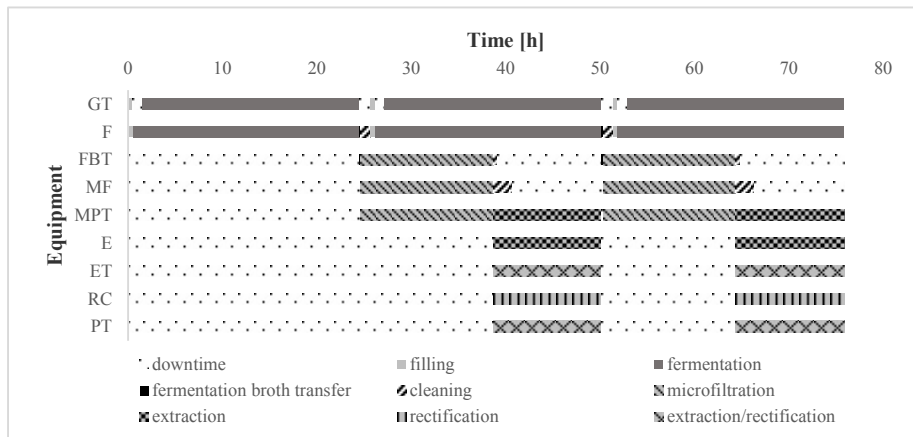


Figure 2 Time schedule of each unit for Batch system.

2.3. Hybrid system I

Hybrid system I integrates bioreactor with separation part (MF with E and RC) resulting in elimination of PEA inhibitory effects, prolonging the fermentation time and keeping PEA concentration below 2 g/L. Figure 3 and Figure 4 show simple process scheme and time schedule of each unit, respectively. In-situ product removal is activated 5 h after the fermentation starts. Fermentation broth is circulated through MF. Retentate is led back into the reactor and permeate is led through Microfiltration permeate tank (MPT) into the E. There, PEA is extracted into pentane and the mixture then continues into Extraction tank (ET). The retentate from extraction is pumped back into the reactor. PEA-pentane mixture from ET is separated in RC, from which distillate is recycled into the PT and bottoms is the desired product.

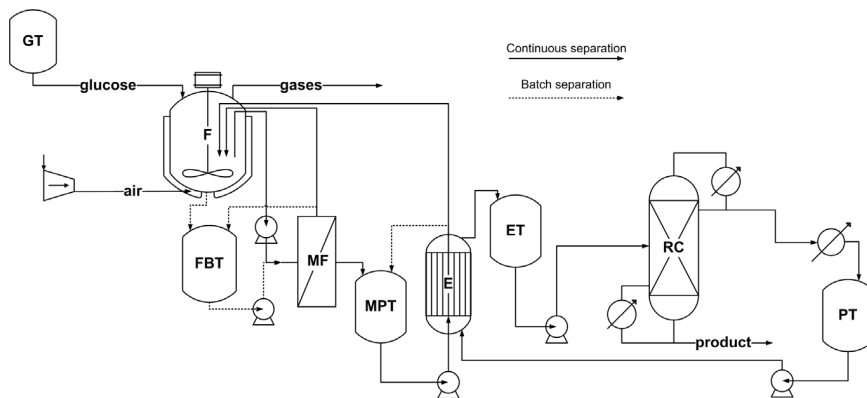


Figure 3 Scheme of proposed Hybrid system I.

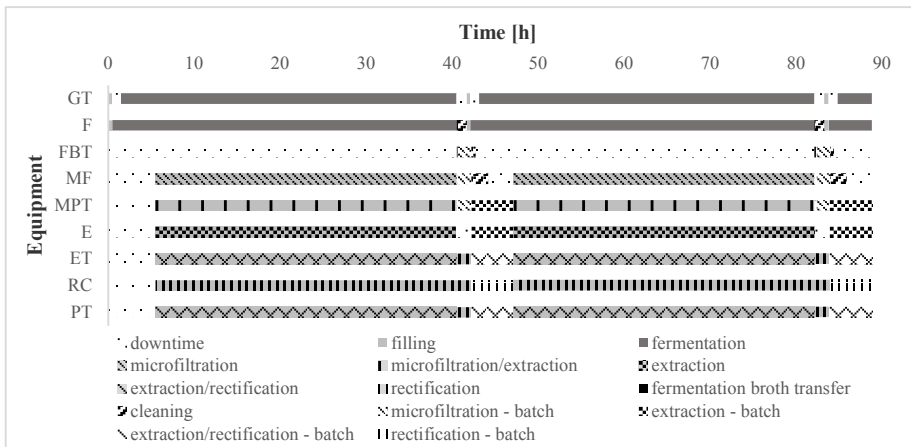


Figure 4 Time schedule of each unit in Hybrid system I.

2.4. Hybrid system II

The weakest link in previous Hybrid system I is microfiltration because of membrane fouling at high biomass concentrations. The removal of microfiltration membrane and immersing hollow fibre extraction module into bioreactor (FIEM) leads to lengthening the fermentation time up to 70 h. After 6 h, the extraction starts, and PEA is continually removed directly from the reactor. Similar to Batch and Hybrid system I, PEA is extracted into pentane, then led through ET into the RC. Bottoms is the desired product and distillate is pure pentane, which is recycled into PT. Figure 5 and Figure 6 show overall process scheme and time schedule of equipment.

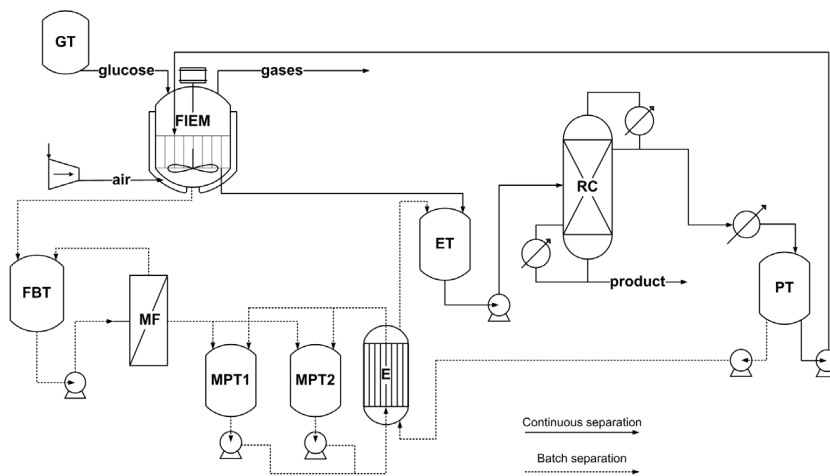


Figure 5 Scheme of proposed Hybrid system II.

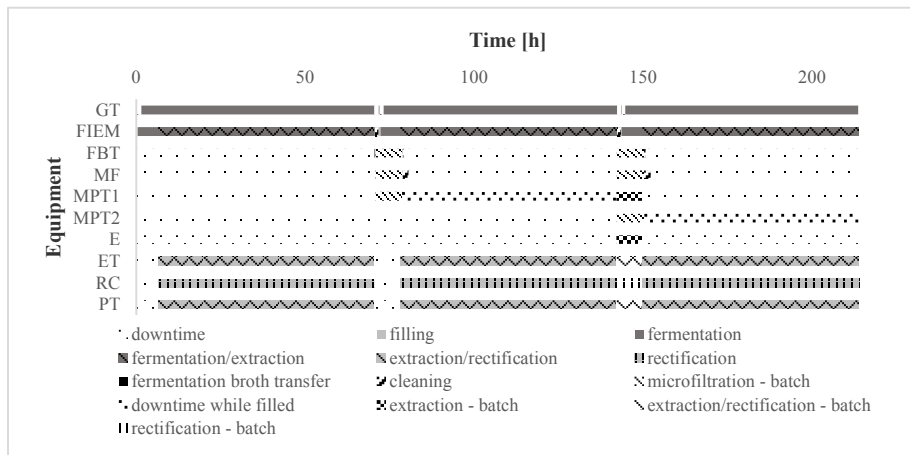


Figure 6 Time schedule of each unit in Hybrid system II.

3. Comparison of proposed systems

The summary of compared parameter for each system is shown in Table 1. The highest amount of acquired PEA is via Hybrid system II, even more than two times the amount of PEA acquired via Batch system. Naturally, the profit from product sales is the highest for this production alternative. The price used for this comparison was 830 \$ per 1 kg of PEA. Investment costs were calculated based on their size or power using simple increment method (Woods, 2007). Higher investment costs in hybrid systems are caused by the requirement of equipment with large effective surface (namely microfiltration membrane) in Hybrid system I and the custom-made, more expensive immersed extraction module in Hybrid system II. Operating costs consist of costs for electricity, water, heat and raw materials. The lowest operating costs are in Hybrid system II, which is related to the fact that in-situ product removal lengthens the fermentation time. This means that there is overall less downtime for the bioreactor and separation units and raw materials are being used more efficiently.

4. Conclusion

Three configurations of biocatalytic 2-phenylethanol production using *Saccharomyces cerevisiae* as a production strain were proposed – traditional batch production, hybrid system with microfiltration and organic solvent extraction, and hybrid system with immersed hollow fibre extraction module. Using appropriate mathematical models and simulations the three systems were designed and compared. The results show that via hybrid system, approximately two times more 2-phenylethanol can be acquired compared to batch system while operating costs of hybrid system are lower than operating costs of batch system.

Hybrid system II promises the best results out of the three compared alternatives. During fermentation, there is no microfiltration membrane used, which allows longer fermentation time and saving of raw materials, thus reducing operating costs. The main disadvantage of Hybrid system II is that the immersed extraction module has to be made

Table 1 Comparison of proposed systems.

	Batch system	Hybrid system I	Hybrid system II
Time of one cycle (h)	25.7	40.7	70
Cycles per year	308	190	110
PEA removed during fermentation (kg)	-	81.34	166.83
PEA removed from FB after fermentation (kg)	27.11	9.58	6.04
Total amount of PEA per year [kg]	8,350	17,275	19,016
Annual sales profit (after 20 % taxes) [mil. \$]	5.54	11.47	12.62
Investment costs [mil. \$]	3.72	5.79	5.21
Operating costs [mil. \$]	2.86	2.34	1.89
Investment return rate [y]	1.33	0.62	0.48

specifically for the given type of bioreactor. Moreover, for the final separation of the fermentation broth, separate microfiltration membrane and extraction module have to be used, which on the one had increases the amount of acquired 2-phenylethanol, but on the other hand it also increases overall investment costs. But in any case, comparing data from Table 1, Hybrid system II exhibits the best alternative for PEA production.

Acknowledgements: *This work was supported by the Slovak Scientific Agency, Grant No. VEGA 1/0687/16 and Slovak Research and Development Agency under the contract No. APVV-16-0111.*

Abbreviations

E	Extraction module	MF	Microfiltration membrane
ET	Extraction tank	MPT	Microfiltration permeate tank
F	Bioreactor (fermenter)	PEA	2-phenylethanol
FBT	Fermentation broth tank	PHE	L-phenylalanine
FIEM	Bioreactor with immersed extraction module	PT	Pentane tank
GT	Glucose tank	RC	Rectification column

References

- I. Červeňanský, M. Mihal', J. Markoš, 2017, Modelling and intensification of biocatalytic production of natural compounds performed in hybrid systems, *Comp. Aided Chem. Eng.* 40, 1039–1044.
- D. Hua, P. Xu, 2011, Recent advances in biotechnological production of 2-phenylethanol, *Biotechnol. Adv.* 29, 654–660.
- R. Krishna, 2002, Reactive separations: More ways to skin a cat, *Chem. Eng. Sci.* 57, 1491–1504.
- M. Mihal', R.F. Goncalves, J. Markoš, 2014, Intensive 2-phenylethanol production in hybrid system combined of stirred tank reactor and immersed extraction membrane module, *Chem. Pap.* 68, 1656–1666
- H. Wang, Q. Dong, A. Guan, C. Meng, X. Shi, Y. Guo, 2011, Synergistic inhibition effect of 2-phenylethanol and ethanol on bioproduction of natural 2-phenylethanol by *Saccharomyces cerevisiae* and process enhancement, *J. Biosci. Bioeng.* 112, 26–31.
- D.R. Woods, 2007, *Rules of Thumb in Engineering Practice*.

Process Innovation through bio-inspired design

Anne Marie Barthe-Delanoë^a, Stéphane Négny^{a*}, Jean Marc Le Lann^a

*^aUniversité de Toulouse, Laboratoire de Génie Chimique UMR 5503 INPT-CNRS-UPS,
4 Allée Emile Monso, 31 432 Toulouse, France*

stephane.negny@ensiacet.fr

Abstract

In process system engineering, we often adopt a constructivist approach to answer the question “How can we go from parts to a whole system?” To answer to this question we need to propose approach that, based on the knowledge of phenomena at small-scale, allows going up the different scales in order to design process but also to innovate thanks to the creation of new knowledge. In this paper, a bio inspired design approach is presented. It is based on two main principles which intervene repetitively to understand and analyze the passage between scales for living organisms: the juxtaposition of foundational blocks that assemble, and then differentiation. The goal of this paper is to demonstrate that these principles can find a more widespread use and in particular they can be integrated into a process system engineering constructivist approach for innovative design. After defining the fundamental building blocks to initiate the process of juxtaposition and integration, an example on distillation and reactive distillation is used to illustrate the method capabilities in process synthesis.

Keywords: Process Innovation, Bio inspiration, Constructivist approach, Process synthesis.

1. Introduction

Process engineering is becoming more and more complex as our analyses become more efficient. Process engineering has evolved over time through instrumental and modelling developments that have made our capabilities for observations and analysis more efficient. But in his approach for problem solving, engineer tends to divide a problem into levels of understanding. For example the process engineering offers a broad set of methods and tools for efficient problem solving for different scales: molecular, phase and transport, unit operation, process, industrial parks... Similarly, in the manner of nested dolls, life is organised on scales of increasing complexity ranging from the cellular organelle to the eco-system, via the cell, the tissue, the organ, the organism, the population. Figure 1 illustrates this parallel between the decomposition and hierarchization of scales between living organisms and process engineering. But, it is important to keep in mind that any division or hierarchization is arbitrary and offers only an ease of analysis. Therefore, any fragmented analysis of a living or technological system does not make it possible to understand it in details. Indeed, in this approach we isolate the parts, as a consequence we do not consider exchanges between scales and thus we reduce the understanding of the problem.

Multi scale approaches try to restore this dialogue in order to have a better understanding of the system under study. Despite the important advances of these

approaches and therefore the improvement of processes, most of the time we reach only incremental innovation. The aim of this paper is to propose a new way to analyse, integrate and cross the scales with a bio inspired approach as the nature is constantly obliged to innovate. The goal is to demonstrate that the physical processes and the principles that appear in the evolution of the living organisms are relevant to be used in the design of new process, and could lead to solutions with a higher level of innovation.

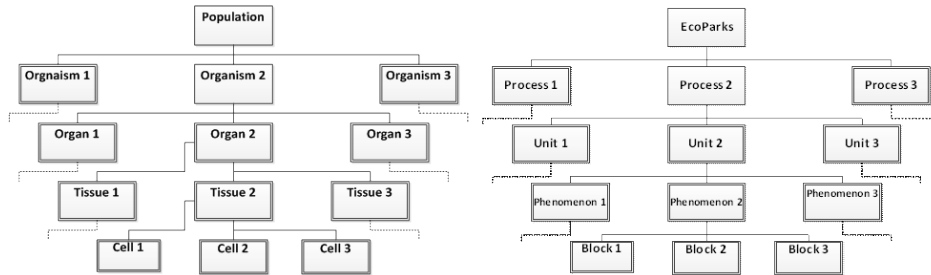


Figure 1 Comparison of scales hierarchization between living organism and process synthesis

2. Backgrounds

Most of the research works in process engineering are based on a reductionist approach, which consists of understanding the fundamental phenomenon. Analyzing a system by focusing on one element moves away from the overall understanding of this system. Thus, focusing on parts takes away from a global vision. Conversely in process system engineering, we often adopt a constructivist approach to answer the question “How can we go from parts to a whole system?” Thus it is easy to understand the difficulty encountered by the process designers: without multiscale integration and systemic approach, the vision of the whole makes the complexity and the relations between the parts invisible. A process (or even at the macroscopic a supply chain) can be seen as a set of nested structures, made up with distinct elements, which juxtapose but which cannot be simply explained by summing the elements. As a result, a process encompasses different scales, each as its own “world” and it is constituted with all those of lower ranks and with which it shares some properties. Thus the elements of a scale serve to constitute the next higher scale. All this leads to the emergence of the complexity, i.e. we cannot reduce the behavior of a scale to the simple addition of those of lower levels. As a result, the large-scale organization comes from a hierarchy of assembly from the smallest to the largest and the interdependence where large scales require smaller ones. The complexity is due to the fact that on the one hand the connections between elements are multiple and that everything is linked, and on the other hand to the passage from one scale to another sometimes accompanied by a paradigm shift. Addressing this complexity and offering systematic solution is the heart of process systems engineering. In conclusion, to have a whole vision of a system, it is necessary to understand what is happening at smaller scales. So, with a constructivist approach, the question that arises is how to do this upscaling.

To continue the parallel with the nature, a starting point for answering to this question was the analysis of complexity of living things made by (Chapoutier and Kaplan, 2011). In the emergence of the complexity for living organisms two main principles seem to intervene repetitively to understand and analyze the passage between scales: the

juxtaposition of foundational blocks that assemble, and then differentiation. The two fundamental principles are the juxtaposition of entities of the same order of complexity (and thus of the same scale) and then modification (mutation) of these entities in higher level structures. For example, cells juxtapose then mute to form a tissue, or at a different scale organisms to form a population. Figure 2 gives a schematic interpretation of these principles for two successive scales. Even if theoretically these steps can be repeated indefinitely, in nature they rarely exceed 5 to 6 levels of complexity: from the cell to the animal population.

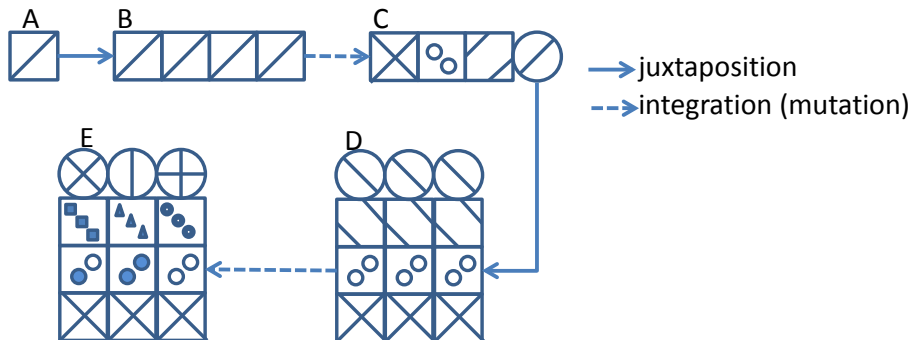


Figure 2 juxtaposition and integration principles (Chapoutier, 2001).

In figure 2, the juxtaposition of element A gives B, where elements do not interact with each other. The integration leads to C where the interaction appears while elements preserve a certain autonomy. Then the process is repeated with the juxtaposition of C to create D and then E by mutation.

For process synthesis, as a first approximation, the juxtaposition can be done linearly and sequentially by appealing not only to elements of the same level of complexity but also to strictly identical elements. Then we find more integrated entities, sometimes more intensified in engineering processes, to form more complex structures. This step is important because in the design of a process, one seeks the maximum efficiency that leads to specialization, which implies to accentuate the integration and the interactions between elements. The purpose is to optimize the transfers, the weight, the form, to make it as compact as possible ... and most often to operate each part to its limits, i.e. to its maximum constraints.

It must be also emphasized that the evolution of living organisms is based on the integration of elements within higher-level elements. The main reasons for the diversification of life and its hierarchical organization are these mutations of individualities at all levels that we have mentioned. As a result, the application of this principle to process synthesis may lead to enhancement of the process performances but also to innovative solutions.

The next step is to identify the initial blocks, i.e. leafs of the tree of figure 1, for process synthesis, which will allow scaling up through the successive repetition of the principles of juxtaposition and integration (also named mutation).

3. Knowledge representation: building blocks

All living organisms are deduced from a four-letters alphabet that are the four nitrogen-containing nucleobases (cytosine [C], guanine [G], adenine [A] or thymine [T]) of the DNA molecule. In the same way as for DNA, it is necessary to determine the constitutive elements that have many degrees of freedom that will thus offer more efficient and sustainable alternatives, but also immense potentialities that can lead to innovations. For process synthesis, these elements must be based on the current process engineering knowledge. Furthermore the knowledge representation chosen must be compatible with the constructivist approach previously mentioned. The fundamental building blocks representation, recently proposed by (Demirel et al., 2017) and (Babi et al., 2015), seems to be a relevant way to represent knowledge. For the former, a bloc is an abstract module that represents a fundamental constituent of a unit operation, which can host single or multiple phenomena. For the latter, a block gathers only one phenomenon. This last definition is well suited for our approach and compatible with the two principles. Relying on the work of (Babi et al., 2015), as most of processes combine, mass, energy, and momentum phenomena, a first set of building blocks could be mixing (M), two phases mixing (2phM), cooling (C), heating (H), reaction (R), phase contact (PC), phase transition (PT), phase separation (PS). These building blocks can be associated with different levels of scale and complexity: process phenomena, tasks, unit operation, etc. In the previous studies, these building blocks are used to formulate a mixed integer nonlinear optimization model to identify process alternatives. Even if some innovative solutions could be reached with this approach, to go deeper in the innovation process, i.e. to find solutions with a higher level of inventiveness, we must propose new principles for the construction. Indeed, there are missing laws to explain consciousness and tacit knowledge.

Let's take the example of (Babi et al., 2015) to detail the proposed approach. The figure 3 depicts the juxtaposition and mutation principles to represent different phenomena and unit operations. First, different building blocks can be juxtaposed in order to generate a feasible phenomenon, e.g. figure 3 is the association of mixing, phase contact, and phase separation. From this point, a first option consists in designing a specific unit where this phenomenon can occur, for the previous example the phenomena can be interpreted as a flash if there is a liquid and a vapor phase. A second option consists in a juxtaposition of the same phenomena. In this configuration if the two phases are liquid then we would find a liquid-liquid extraction. On the other hand, if there is a liquid phase and a vapor phase, i.e. the succession of the same phenomena as the flash vessel, no known unit operation appears clearly. Then the mutation principle can be applied as for example with the addition of cooling and heating at both ends to represent a condenser and a reboiler in order to generate a distillation column. From this point, we can go further in the mutation by adding a reaction block as reaction and separation can occur simultaneously. The reaction block is not added to all the previous blocks but only to some of them, because the mutation does not necessarily apply to all blocks present. This second mutation (or deeper mutation) enables to find the reactive distillation unit operation.

In the same way, at the unit level (figure 1), juxtaposition and integration of unit operations lead to the design of a process alternatives. Indeed, for example the purification section of a process is often composed by successive separation units (juxtaposition). Sometimes this can be improved by the external integration if two

different types of separators to fulfil one purification also known as hybrid separation in process intensification (e.g. distillation and membrane, distillation and crystallization). As a result, another strength of the proposed approach is to make more systematic the best process intensification option at the different scales.

It can be also noticed that instead of relying on phenomenon, building blocks could be atoms to generate new groups and then molecules. As a result, the proposed approach is also relevant for computer aided design molecules.

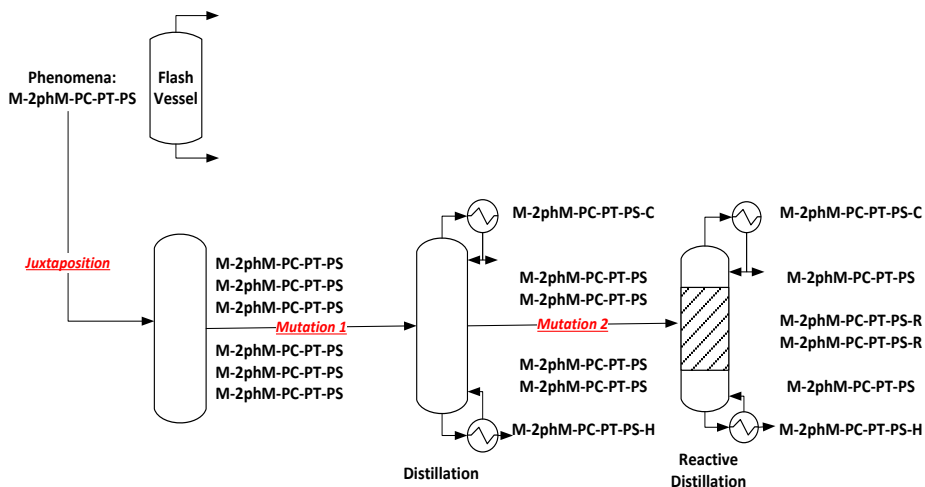


Figure 3: Example of juxtaposition and mutation based on the case study of (Babi et al., 2015)

4. Discussion

In most cases, living organisms are made up of many characteristic units, i.e. cells, so they are in their vast majority multicellular. The objective of the successive integrations of these different cells is also to create specialized structures with particular functions, e.g. heart, liver, nervous system ... for the organs. Likewise, at the same hierarchical level as the organs but on the process engineering side (figure 1), the unit operations also consist of several blocks in order to achieve at least one function. However, a current trend in process engineering is to design multifunctional devices, but this aspect is less present in living organisms. As demonstrated by the example of reactive distillation, more advanced mutations on the process engineering side make it possible to produce multifunctional devices (and more generally more intensified processes and for all scales). But in return, the direct consequence of a further mutation is an increase in the number of possibility of juxtaposition and mutation as the scales rise. As a result, the problem becomes highly combinatory.

Indeed, when dealing with innovation, the search for a solution requires exploring the space of solutions in its entirety, so we must test all possible combinations. For example, during juxtaposition, the number and the type of entity to be juxtaposed are not predefined. When an entity is repeated multiple times, it is difficult to establish when the completion is reached. Moreover, the juxtaposition can be operated with similar or different entities as we have seen in the previous examples. The combinatorial

aspect also comes from the principle of mutation. As we demonstrated in the example on reactive distillation, the mutation does not necessarily concern all entities on the one hand, we can also delete, add or replace one or several entities on the other hand. Therefore, all these mutations offer a lot of possibilities. Moreover, for each juxtaposition or mutation, we must verify if the proposed solution is feasible or not. In the previous example, we underline that the multiple repetitions of the phenomenon can lead to none feasible solution when we have a liquid and vapor phases. For living organisms, this question of feasibility does not arise because naturally the steps of juxtaposition and mutation do not allow the creation of non-viable entities. Another direct consequence of this natural selection is the decrease of the combinatorial aspect. For process synthesis, one way to proceed to avoid this drawback could be to define and to use predefined combination rules. Unfortunately, this strategy of adding predefined knowledge would have the detrimental effect of diminishing the innovation potential of the approach. A more relevant solution would be to refine the definition of blocks by adding functional, financial, regulatory etc. aspects. This strategy would also have the advantage of integrating these dimensions from the initial design of the process.

Another crucial point is that we propose only theoretical reflection, strongly supported by examples, but experimental studies should also be proposed to validate the future alternatives created.

5. Conclusions

In this paper, we propose bio-inspired design approach for process synthesis. Nature often evolves and innovates according to a mosaic organization, by using two fundamental principles *juxtaposition* of entities of the same order of complexity and then *modification* of these entities in higher level structures. These two principles permit to understand and to explain the passage between two successive spatial scales. As a result, this vision of mosaic complexity emerging from life, compatible with Darwinian evolution but proposing general principles of progress towards complexity and diversity. The goal of this paper is to demonstrate that these principles can find a more widespread use and in particular they can be integrated into a process system engineering constructivist approach for innovative design in process engineering. After defining the fundamental building blocks to initiate the process of juxtaposition and integration, an example on flash vessel, distillation and reactive distillation is used to illustrate the method capabilities in process synthesis. The main drawback on this approach is that it is highly combinatorial. As a result, it is impossible to explore all the possibilities offered. A future perspective of this work would be to incorporate design constraints to limit the space of solutions to feasible alternatives.

References

- Babi, D., Holtbruegge, J., Lutze, P., Gorak, A., Woodley, J., Gani, R., 2015. *Comp. & Chem. Eng.*, 81, 218-244.
- Chapoutier, G., 2001. Odile Jacob, Paris.
- Chapoutier, G., Kaplan, F. 2011. CNRS Editions.
- Demirel, S., Li, J., Hasan, M., 2017. *Comp. & Chem. Eng.*, 105, 2-38.

Heat pump assisted azeotropic DWC for enhanced biobutanol separation

Iulian Patraşcu,^a Costin Sorin Bildea,^a Anton A. Kiss,^{b,c*}

^a *University “Politehnica” of Bucharest, Polizu 1-7, RO-011061 Bucharest, Romania. E-mail: s_bildea@upb.ro*

^b *The University of Manchester, School of Chemical Engineering and Analytical Science, Sackville Street, The Mill, Manchester M13 9PL, United Kingdom. E-mail: tony.kiss@manchester.ac.uk*

^c *University of Twente, Sustainable Process Technology, PO Box 217, 7500 AE Enschede, The Netherlands. E-mail: a.a.kiss@utwente.nl*

Abstract

Biobutanol is a renewable fuel produced nowadays from waste biomass feedstocks. It features low water miscibility, flammability, corrosiveness, with the additional advantage that it can replace gasoline in cars, without any engine modifications. The butanol obtained after the fermentation step has a low concentration (typically less than 3 %wt) that leads to high energy requirements for conventional downstream separation. To overcome this issue, we propose here a novel hybrid separation process based on a heat pump assisted azeotropic dividing-wall column (A-DWC). CAPE tools and Pinch analysis have been used for the process synthesis, design and optimization of the process. The plant capacity considered here is 40 ktpy butanol (99.4 %wt). Remarkably, the energy requirement for butanol separation using heat integration and vapour recompression assisted A-DWC is reduced by 58 % from 6.3 to 2.7 MJ/kg butanol.

Keywords: Azeotropic dividing-wall column, distillation, heat pump, energy efficiency

1. Introduction

In the fermentation process of acetone-butanol-ethanol (ABE), biobutanol is obtained in diluted form, typically less than 3 %wt concentration. The low concentration of butanol obtained by fermentation leads to high energy requirements for downstream processing, in the range of 14.7-79.05 MJ/kg butanol (Patrascu et al., 2017). A higher butanol yield is achieved in fermentation using anaerobic bacteria as *Clostridium acetobutylicum* and *Clostridium beijerinckii* (Tashiro et al., 2013). Moreover, the ABE concentration can be further increased by gas stripping technology to 4.5 %wt acetone, 18.6 %wt butanol and 0.9 %wt ethanol (Xue et al., 2013). On the other hand, the productivity, yield and concentration can be also improved by genetic engineering, which is a longer-term goal. This has an important impact on the cost of the separation, which needs to be significantly reduced. Numerous separation techniques are available for ABE separation, such as distillation, reverse osmosis, adsorption, liquid-liquid extraction and others (Abdehagh et al., 2014; Sanchez-Ramirez et al., 2017). This work develops a new hybrid separation sequence combining distillation and vapour recompression (Kiss et al., 2013). The azeotropic DWC combines three distillation columns into one unit and reduces the energy used for separation by employing a heat pump and heat integration.

2. Problem statement

The conventional separation sequence using three distillation columns along with one decanter (Figure 1, left) requires 6.3 MJ/kg butanol. By using heat integration and combining two columns into a dividing-wall column (Figure 1, right), a reduction of 29 % of the energy requirement was achieved (Patrascu et al, 2017). This is a significant reduction of the energy requirements, but can the energy savings be pushed any further?

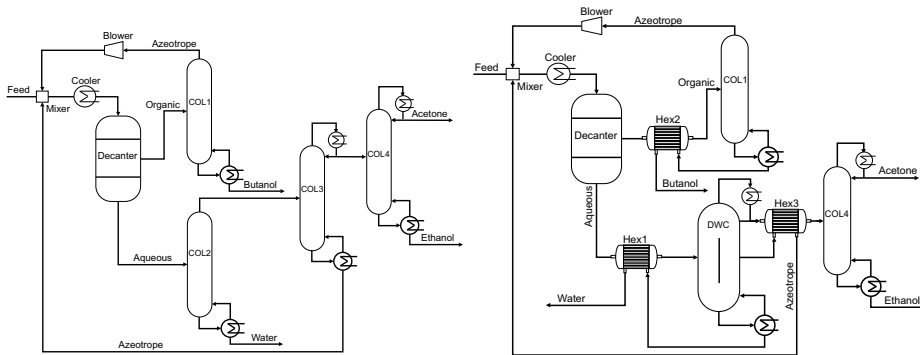


Figure 1. Process flowsheet of ABE downstream separation sequences (Patrascu et al., 2017)

To achieve more savings, a novel process is proposed in this work. The decanter is not used here as the first separation unit, as the organic phase (rich in butanol) has a high impact on reboiler duty for butanol purification and makes the heat pump extremely inefficient. Note that the temperature of the compressed vapour is limited to 150 °C, and the temperature in the reboiler is around 127 °C. High energy usage occurs under 120 °C for vapours condensation. By using a highly integrated azeotropic dividing-wall column (A-DWC) assisted by vapour recompression (VRC) technology the energy savings can be increased by another 39 % as described hereafter.

3. Modelling approach

The process is simulated in Aspen Plus, using the NRTL as suitable property model. In Figure 1 the fourth column (COL-4) separates only the light components (acetone and ethanol) hence it is not considered in the energy requirement for butanol separation. To account for a realistic composition of the ABE mixture, impurities are taken into account: 0.1 %wt. CO₂, as well as small amounts of acetic acid and butyric acid.

Several basic assumptions and design specifications are used for the optimization and heat integration: butanol purity is 99.4 %wt.; each side of the dividing wall has the same number of stages; feed streams are preheated to 97 °C; product streams are cooled to 25 °C; the (left) side reboiler is not considered in optimization process of A-DWC because will be replaced with a heat exchanger.

Pinch analysis provides understanding of the energy targets and subsequent design of the optimal heat exchange network. The investment and operation costs of the complete process are evaluated in order to show the advantages of this design (Dimian et al., 2014). The coefficient of performance (COP) is used for evaluating the feasibility of using a heat pump, while also accounting the additional costs and the payback time.

4. Results and discussion

4.1. Heat integration analysis

Figure 2 shows the composite curves that reveal the energy targets. The left side of Figure 2 shows that heat integration may lead to important reduction of heating and cooling requirements. However, the energy savings are rather small compared to previous separation sequences (Figure 1). In particular, the vapour stream from the top of the A-DWC cannot be used for heat integration due to its low temperature. But, by recompression to 5.8 bar, it can be heated to 150 °C, which is useful for heat integration. The suitability of using VRC is evaluated by using the COP as given by:

$$COP = Q/W = 1/\eta = T_c/(T_r - T_c) > 10 \quad (1)$$

where Q = reboiler duty, W = work provided, η = Carnot efficiency, T_r = reboiler temperature, and T_c = condenser temperature (Plesu et al., 2014). If the Q/W ratio is lower than 5, using a heat pump (HP) brings no benefits, but if it exceeds 10 then a HP should be considered. The maximum energy savings are given by (Blahusiak et al., 2018):

$$Max.savings(\%) = 100 \cdot (Q_{reb} - HR \cdot Q_{reb} / COP) / Q_{reb} \quad (2)$$

Figure 2 (right) shows that, for a Q/W ratio of 7.43, the heat pump helps to reduce the heating and cooling requirement by about 50 % (equivalent to 2.7 MJ/kg butanol).

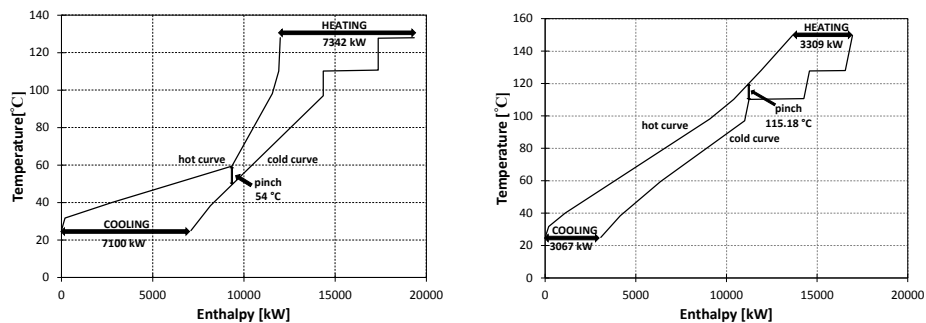


Figure 2. Composite curve for simple heat integration (left) and heat pump assisted (right)

Figure 3 shows the dependence on pressure of the LMTD and compressor power. The compressor outlet temperature is max. 150 °C for safety reasons: at higher temperatures the system may fail from worn rings, acid formations, oil breakdown (Luo et al., 2015).

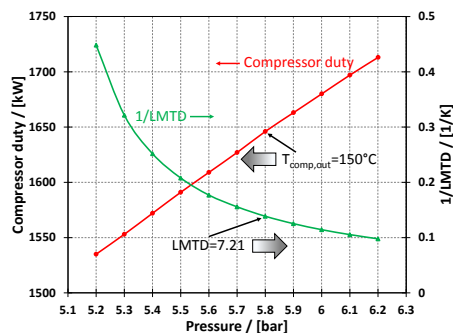


Figure 3. Dependence of compressor duty and the long-mean temperature difference (LMTD) on the pressure

4.2. Heat pump assisted azeotropic dividing-wall column design

Figure 4 presents the process flowsheet, including the key design parameters. The column has a total of 45 stages, 13 stages for the fractionation section and 32 stages for stripping sections. Butanol and water are the bottom products, while acetone and ethanol with some water (AEW) are obtained as distillate. The ABE feed and the aqueous phase recycled from the decanter are fed on 1st stage of the stripping section (14th stage of A-DWC), which separates water as bottom product. The top vapour stream is compressed to 5.8 bar (150 °C), provides heat to the (left) side reboiler (HEX1), preheats the diluted ABE feed (HEX2) and is finally condensed. The liquid flowing down the column is routed to the right stripping section. From the 13th stage, a mixture close to the azeotropic composition is withdrawn as side stream, cooled, and sent to liquid-liquid separation. The organic phase is recycled on 2nd stage of the right stripping section (15th stage of A-DWC), from which butanol is obtained as bottom product. The aqueous phase is recycled to the left stripping section. Additional heat is recovered by using the water product stream to preheat the aqueous and organic phases (HEX3, HEX4).

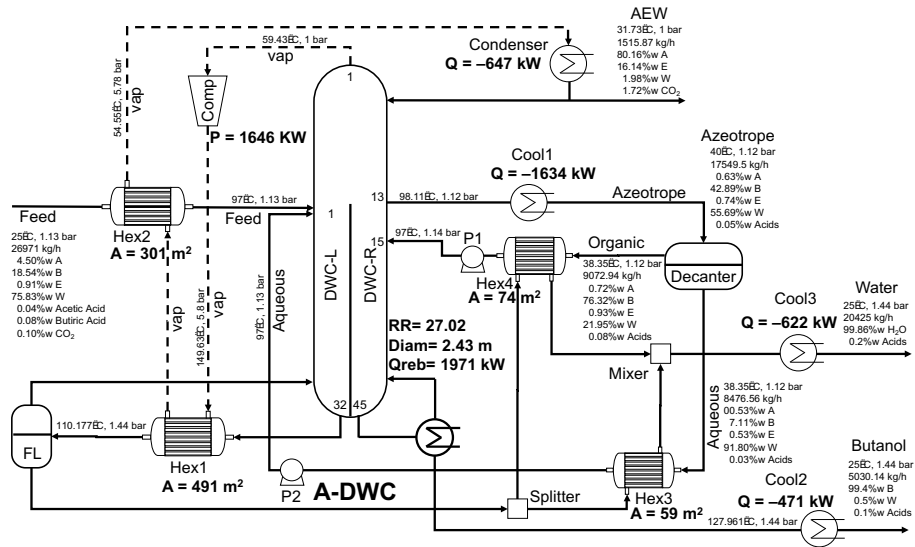


Figure 4. Process flowsheet of the new downstream separation process based on A-DWC

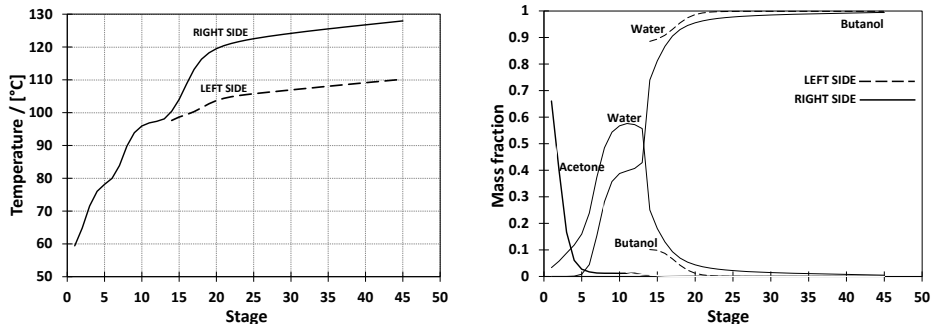


Figure 5. Temperature and mass composition profiles along the A-DWC unit

5. Process evaluation

The process is optimized using the total annual cost (TAC) as the objective function to be minimized: $TAC = OpEx + CapEx / 3$. The design parameters (e.g. number of trays, feed tray) are used as decision variables in the optimization (Patrascu et al., 2017).

The total investment costs (CapEX) include the heat exchangers, coolers, heat pump, flash unit, distillation column, and the decanter. The equipment cost is evaluated at 5,250 k\$/year. A payback period of 3 years is used, with 8000 hours/year operating time. The heating and cooling costs considered are standard: LP steam (6 bar, 160 °C, \$7.78/GJ), cooling water (25 °C, \$0.72/GJ) and chilled water (5 °C, \$4.43/GJ). The compressor power cost taken into account is 15.5 \$/GJ power. The minimized operating cost is 1,435 k\$/year, including also the cooling of the products.

Table 1. Economic evaluation of the heat pump assisted A-DWC for butanol recovery

Item description (unit)	DWC	Decanter	Coolers	Exchangers	Flash &Comp
Shell / [10^3 US\$]	718.1	71.6	-	-	1618.9
Trays / [10^3 US\$]	94.6	-	-	-	-
Condenser / [10^3 US\$]	266.7	-	1,179.5	-	-
Reboiler / [10^3 US\$]	497.8	-	-	803.4	-
Heating / [10^3 US\$/year]	441.8	-	-	-	737.3
Cooling / [10^3 US\$/year]	82.5	-	173.2	-	-
TAC / [10^3 US\$/year]	1,050.0	23.9	566.4	267.8	1,276.8

Figure 6 shows a comparison of the energy efficiency. Note that the energy required for heating without any heat integration and no heat pump assistance is 8.78 MJ/kg butanol, which exceeds 6.3 MJ/kg butanol for the conventional separation sequence. The heat pump assisted A-DWC design requires only 2.7 MJ/kg butanol (58 % less than in conventional separation sequence). But using a heat pump increases the capital cost due to the expensive compressor (1,581.5 k\$). Considering the energy savings (1.69 MJ/kg butanol) evaluated at 1,893 k\$/year, the payback time is about 10 months.

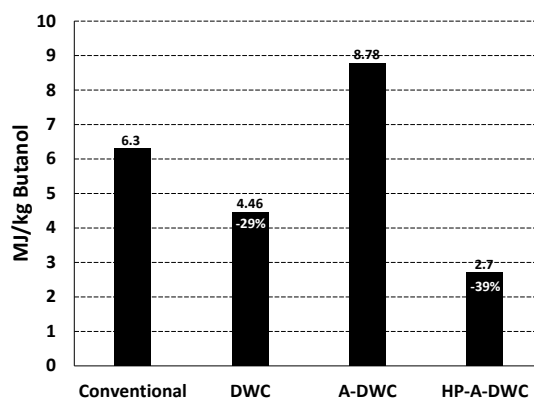


Figure 6. Energy efficiency for the new vs previous butanol downstream processes

6. Conclusions

The biobutanol recovery from the ABE mixture obtained by fermentation can be efficiently achieved in just a few separation units: three classic distillation columns are combined in one azeotropic dividing-wall column (A-DWC) and one decanter is used for the liquid-liquid split of the heterogeneous azeotrope. The novel process proposed was designed, optimized, and heat integrated. The economic evaluation proves that it is feasible. The energy requirement is drastically reduced by applying heat integration and vapour recompression technology. The investment cost of the process (40 ktpy capacity) is $5,250 \cdot 10^3$ US\$, and the operating cost is $1,434 \cdot 10^3$ US\$/year. Although, the cost of the heat pump is high ($1,581.5 \cdot 10^3$ US\$), the payback period is only 10 months. The highly integrated A-DWC system reduces the energy requirement for butanol separation to only 2.7 MJ/kg butanol, a reduction of 58 % as compared to a conventional design.

Acknowledgment

Financial support of the European Commission through the European Regional Development Fund and of the Romanian state budget, under the grant agreement 155/25.11.2016 Project POC P-37-449 (ASPiRE) is gratefully acknowledged. AAK gratefully acknowledges the Royal Society Wolfson Research Merit Award.

References

- N. Abdehagh, F. H. Tezel, J. Thibault, 2014, Separation techniques in butanol production: Challenges and developments, *Biomass and Bioenergy*, 60, 222-246.
- M. Blahusiak, A. A. Kiss, K. Babic, S. R. A. Kersten, G. Bargeman, B. Schuur, 2018, Insights into the selection and design of fluid separation processes, *Separation and Purification Technology*, 194, 301-318.
- A.C. Dimian, C.S. Bildea, A.A. Kiss, 2014, *Integrated design and simulation of chemical processes*, 2nd Edition, Elsevier, Amsterdam.
- A. A. Kiss, 2013, *Advanced distillation technologies - Design, control and applications*, Wiley, Chichester, UK.
- H. Luo, C. S. Bildea, A. A. Kiss, 2015, Novel heat-pump-assisted extractive distillation for bioethanol purification, *Industrial & Engineering Chemistry Research*, 54, 2208-2213.
- I. Patrascu, C. S. Bildea, A. A. Kiss, 2017, Eco-efficient butanol separation in the ABE fermentation process, *Separation and Purification Technology*, 177, 49-61.
- V. Plesu, R. A. E. Bonet, J. Bonet, J. Llorens, 2014, Simple equation for suitability of heat pump use in distillation, *Computer Aided Chemical Engineering*, 33, 1327-1332.
- E. Sanchez-Ramirez, J. J. Quiroz-Ramirez, S. Hernandez-Castro, J. G. Segovia-Hernandez, A. A. Kiss, 2017, Optimal hybrid separations for intensified downstream processing of biobutanol, *Separation and Purification Technology*, 185, 149-159.
- Y. Tashiro, T. Yoshida, T. Noguchi, K. Sonomoto, 2013, recent advances and future prospects for increased butanol production by acetone-butanol-ethanol fermentation, *Engineering in Life Sciences*, 13, 432-445.
- C. Xue, J-B. Zhao, F-F. Liu, C-G. Lu, S-T. Yang, F-W. Bai, 2013, Two-stage in situ gas stripping for enhanced butanol fermentation and energy-saving product recovery, *Bioresource Technology*, 135, 396-402.

Optimization based design of a resilient biomass to energy system

Ashish Soren^a, Yogendra Shastri^{a*}

^a*Department of Chemical Engineering, Indian Institute of Technology, Bombay-400076, India*

yshastri@che.iitb.ac.in

Abstract

An optimization model for the supply chain design of biomass to energy system considering potential biomass supply disruption scenarios has been proposed. The model includes farms/supply points, regional biomass processing depots (RBPD), and biorefinery. Disruption is modelled as loss of biomass availability at farms, with each farm assigned a specific disruption probability and level of disruption. Shortfall in fuel production as well as short-term feedstock procured during disruption is penalized. The objective function to minimize the total production cost considering disruption. The model was applied to a case of 452 farms distributed over a region of covering 202,500 km². For base case with shortfall penalty of \$ 335/Mg and short-term procurement penalty of 50% over the base value, the proposed model led to a 6.9% reduction in the total production cost as compared to a model ignoring the disruptions. The penalty on shortfall was varied from \$ 320-375/Mg to understand their impact on the design decisions as well as total cost.

Keywords: Optimization, supply chain, resiliency, biofuel, disruption

1. Introduction

Biomass-to-energy systems require an efficient supply chain of biomass feedstock due to the highly distributed availability of low density material. As a result, biomass supply chain optimization has emerged as a key research area. However, biomass based systems are highly susceptible to natural disruptions such as droughts, floods, and pest attacks, which significantly affect the availability of biomass. These disruptions must be considered at the supply chain design stage to improve the resiliency of the system. Maheshwari et al. (2017) developed an optimization model considering potential disruptions and illustrated that ignoring the effect of these disruptions led to sub-optimal designs. This work extends their formulation to make it more comprehensive and realistic. Firstly, the possibility of unmet biomass demand at the biorefinery is included (Poudel et al., 2016). Moreover, the possibility of replacement feedstock during disruption being available at a higher price is modelled. The model is then applied to a case study considering supply of corn stover from 452 farms randomly distributed over a given region. The results are compared with those obtained using a model that completely ignores the possibility of disruption.

The paper is arranged as follow. The next section discusses the components of the supply chain and summarizes the optimization model formulation. Section 3 describes

the case study, while section 4 presents the base case as well as sensitivity results. Section 5 provides the conclusions.

2. Optimization model formulation

The biomass to energy system considered in this paper includes three components: farms/supply points, regional biomass pre-processing depots (RBDs), and biorefineries. The farms are considered to provide low density chopped biomass which can be pelletized at the RBDs to improve storage and transport efficiencies. The biomass from farms can also be sent directly to the biorefineries. Storage facilities are available at both RBD and biorefinery since no storage is assumed at farms. The farm sizes are known, which decides the maximum availability of biomass from each farm. All the farm locations also serve as the potential RBD and biorefinery locations. The biorefinery has a fixed monthly demand of biomass and converts it into ethanol. The transportation is assumed to be via trucks. Maheshwari et al. (2017) explain the basic version of the optimization model in detail. The constraints of the model relate to the mass balance of biomass from farms to the biorefinery. This includes supply constraints at each farm, storage and capacity constraints at the RBD and biorefinery, and demand constraints at the biorefinery. In reality, the disruptions are stochastic in nature, and stochastic programming problem is necessary. However, stochastic programming problems are computationally highly challenging. Therefore, this work considers scenario based optimization, where the design is optimized over a selected number of scenarios. Multiple disruption scenarios model loss of biomass at the farms due to a natural event. The probability of disruption captures the likelihood of disruption affecting the farm in a given year (based on historical data), while the level of disruption decides the extent of losses incurred by the farm. Each farm is assumed to have a predefined probability and level of disruption. Moreover, those are uncorrelated with each other since farms may have varying capacities to handle disruptions. The design problem considers an ideal scenario without disruption as well as multiple scenarios with disruption. Disruption scenarios may require procurement of additional feedstock from farms not considered in the ideal scenario. Such feedstock is considered to be available at a premium price by considering a penalty. This is possible since such farms may not be contracted and hence may charge a higher price. The penalized feed quantity is calculated as shown in Eq. 1 and is weighted over by the probability of the disruption scenario.

$$B_{\text{penalized}}(i, es) = \max(0, B_{\text{Total}}(i, es) - B_{\text{Total}}(i, ei)), \quad \forall i, es \quad (1)$$

where, set i indicates a farm, and sets es and ei indicates disrupted and non-disrupted (ideal) scenarios, respectively, which are a subset of total scenarios represented by set e . However, production cost increases with an increase in the cost of biomass or for a very low availability of biomass during disruption. In such cases, biorefineries may prefer to not procure biomass and instead prefer to pay a penalty for not meeting contractual obligation regarding the supply of fuel. This is modelled by enabling the biorefineries to have an unmet demand ($B_{\text{Unmet}}(n, e)$), in addition to the biomass processed at the biorefinery ($C_{\text{OP}}^B(k, n, e)$), to meet the total demand ($D(n, e)$) as shown in Eq. 2.

$$D(\mathbf{n}, \mathbf{e}) = \sum_k C_{OP}^B(k, \mathbf{n}, \mathbf{e}) + B_{Unmet}(\mathbf{n}, \mathbf{e}), \quad \forall \mathbf{n}, \mathbf{e} \quad (2)$$

where, \mathbf{k} is the set of biorefineries and \mathbf{n} is the set of months. The cost functions of all the operations, including transportation, storage, pelletization, and processing are the additional set of model constraints. In addition, operational decisions such as flow of biomass along the various links are also optimized. The decision variables include design decisions such as locations of farms to be contracted, RBDs and biorefineries, as well as the capacities of RBDs and biorefineries. The objective function is to minimize the total cost (TC) for a specific target ethanol (fuel) production target, which is the weighted sum of the cost for ideal (\mathbf{ei}) as well as each disruption scenarios (\mathbf{es}).

$$\text{Min } TC = \sum_e P(\mathbf{e}) * (G_{SC}(\mathbf{e}) + G_U(\mathbf{e})) + \sum_{es} P(\mathbf{es}) * (G_{FP}(\mathbf{es})) \quad (3)$$

Here, $G_{SC}(\mathbf{e})$ and $G_U(\mathbf{e})$ are the total cost of production in the supply chain, and the penalty due to unmet demand, respectively. $G_{FP}(\mathbf{es})$ is the penalty on additional biomass procured during disruption scenario. This model is termed as the resiliency model in further discussion. A base model that ignores the disruption is also solved for comparison. This model is a subset of the resiliency model with only one scenario (\mathbf{ei}) without any disruption. The model simulation and decision making horizon is one year, and operational decisions are optimized on a monthly basis. The objective function considers the total annual operating costs as well as the capital costs that are annualized. The detailed mathematical formulation is not reported here for brevity. It is a mixed integer linear programming (MILP) model, which is programmed in GAMS and solved using the CPLEX[®] solver.

3. Case study details

The proposed model was applied to a case study considering 452 farms randomly distributed over a 450 km x 450 km grid (Fig. 1). For computational efficiency, the region was divided into 16 square sub grids, and one of the central farms in each grid was considered as the potential RBD locations (stars in Fig. 1, 16 potential locations). Similarly, five farms, roughly distributed in the central part of the region, were considered as potential biorefinery locations (red square in Fig. 1). The biomass feed considered was corn stover which was assumed to be available for three months in a time horizon of 12 months. The probability of disruption was assumed to be uniformly distributed between 0-30%. The disruption level was normally distributed with a mean of 50% and a standard deviation of 15.4% (minimum of 12% and maximum of 99%). The disruption scenarios included disruptions in each of the 16 grids independently, thereby generating 17 scenarios including the ideal scenario. Simultaneous disruption in multiple grids was not considered. The probability of disruption and the level of disruptions for each of these farms was fixed and randomly sampled from the mentioned range. Farm size was normally distributed with a mean of 58.66 ha. Corn stover yield was 6.9 Mg/ha (Maheshwari et al., 2017) and 70% of stover was available for use. The unit feed cost was \$ 40/Mg. The capital cost at RBD was scaled using CEPCI for 2016 using a base value of \$ 269,000/y for a capacity of 45,000 Mg/y (Mani et al., 2006). The operating cost at RBD was considered to be \$ 21.16/Mg (Mani et al., 2006). Biorefinery costs were also obtained using CEPCI considering capital cost of \$ 357,203,083/y for a capacity of 772,000 Mg/y and operation cost of \$ 49.49/Mg (Humbird et al., 2011). Variable component of transportation cost was \$ 0.13/Mg-km for chopped biomass and \$ 0.047/Mg-km for pelletized biomass. The fixed component

of transportation cost was \$ 12/Mg for chopped biomass and \$ 2.8/Mg for pelletized biomass. RBPDS and biorefineries were assumed to have a collection radius of 90 km and 75 km, respectively. A demand of 89,378 Mg/y of ethanol was assumed at the biorefinery, which account for 80% of feed available in an ideal (non-disruption) scenario. Shortfall penalty for unmet demand was \$ 335/Mg of biomass and penalty on additional feedstock was 50% of the base value. The model includes 1,982,711 variables (42 discrete variables) and 1,874,511 constraints.

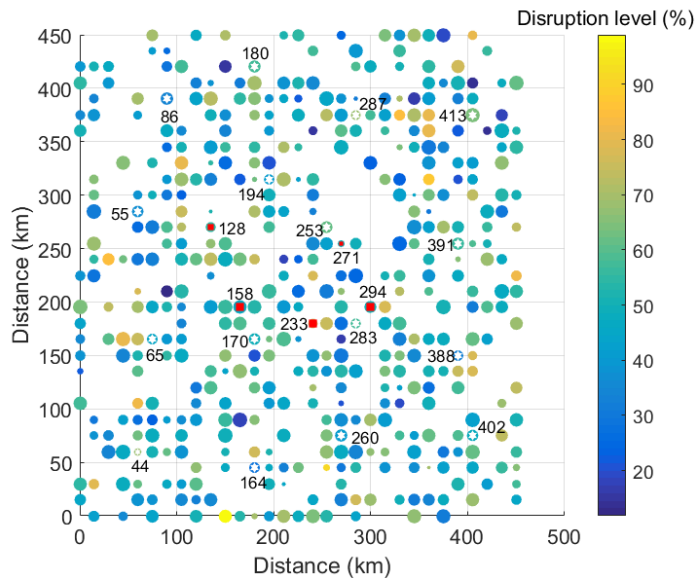


Figure 1: Farm location with disruption level. Size of the dot represents relative size of the farms and colour represents the level of disruption

4. Result and discussion

The base case results are first discussed, followed by the sensitivity analysis with respect to the two penalty factors.

4.1 Base case

For the base case, it was observed that the resiliency model recommended 11 RBPDS and a central biorefinery at the 294th location. The biorefinery had a design capacity of 89,378 Mg/y and a total of 36,707 Mg/y of demand was left unmet. This was due to the fact that procuring replacement feed was costlier than paying the penalty for unmet demand. In contrast, only 8 RBPDS were recommended for the base model (ideal scenario only). The biorefinery was proposed at the 294th location with a capacity of 88,825 Mg/y. In addition to the difference in the number of RBPDS, it was observed that the capacities of the RBPDS also differed significantly (Fig. 8). For example, instead a large RBPDS of 40,760 Mg/y capacity at location 55 for the base model, two smaller RBPDS were selected at locations 65 and 86 for the resiliency model (Fig. 2). It was also observed that grids with lower average probability of disruption were preferred for procurement. The benefit of the resiliency model was quantified by optimizing the resiliency model again but with the design decisions fixed to those proposed by the base model. It was observed that the resiliency model solution reduced the total cost by \$

242,782/y on a total annual cost of \$ 31,032,304/y for the base model solution. This emphasized the importance of considering disruptions in the design stage.

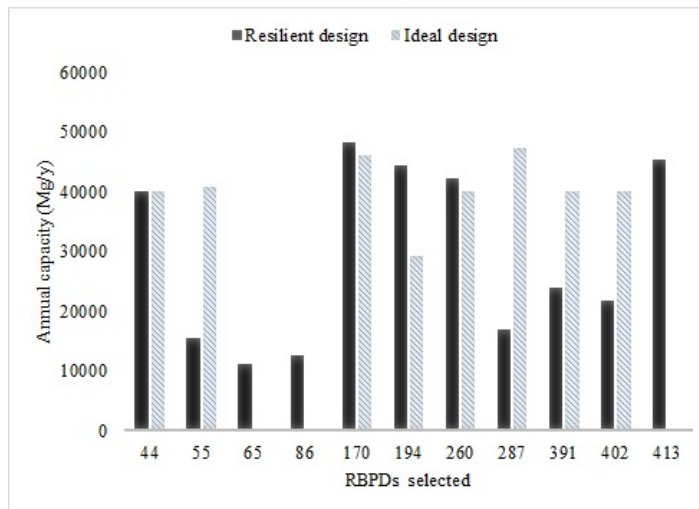


Figure 2: RBPDs selected in resilient and ideal design for a shortfall penalty= \$ 335/Mg and 50% penalty on additional feedstock

4.2 Variation in penalty on supply shortfall

For this case, the results of the base case simulation were compared with the results when shortfall penalty was equal to \$ 320/Mg and \$ 375/Mg. The penalty on short-term feedstock via penalty factor was fixed to 50% for both these simulations. It was observed that for a smaller shortfall penalty of \$ 320/Mg, the complete demand was left unmet by a resiliency model solution, thus resulting in 6.9 % lower total cost as compared to base model solution. However, with an increase in the shortfall penalty to \$ 375/Mg, where production at biorefinery is an economically beneficial option, a reduction in the unmet demand was observed. The unmet demand quantity reduced from 36,707 Mg/y to 33,581 Mg/y and an additional RBPD was set-up at the 388th location as per the resiliency model solution. The optimal biorefinery location also changed to 233 as compared to the base model solution which is indicated in black hexagon (Fig. 3a, 3b). While base model solution did not change the location and capacities of RBPDs for both penalty values, the resiliency model recommended an additional RBPD as well as reduction in long distance collection of biomass. A major change was observed for RBPDs at 44th and 65th location with new design capacities of 14,671 Mg/y and 50,095 Mg/y, respectively. The annual total cost also showed a 1.1 % reduction to \$ 31,097,077/Mg as compared to a base model solution. The change in penalty on additional feedstock would also effect the design decisions such as the facility location, and capacity, which would be discussed in subsequent studies.

5. Conclusions

A novel formulation to design optimal biomass to energy supply chains considering potential disruptions at the design stage was proposed. The possibility of demand being unmet as well as replacement biomass being available at a higher cost was incorporated. Farms/supply points were effected by disruption where the probability and extent of

loss due to drought were non-uniform. The supply chain was optimized to minimize the overall cost across all potential disruption scenarios in addition to the ideal scenario. The results indicated that for an increase in the shortfall penalty from \$335 to \$ 375/Mg a change in the biorefinery to 233rd location was observed for a 50% penalty factor. An additional RBPB established at 388th location to improve the transportation efficiency of the biomass. These results also showed notable benefits of the proposed resiliency model as compared to the base model without considering disruptions.

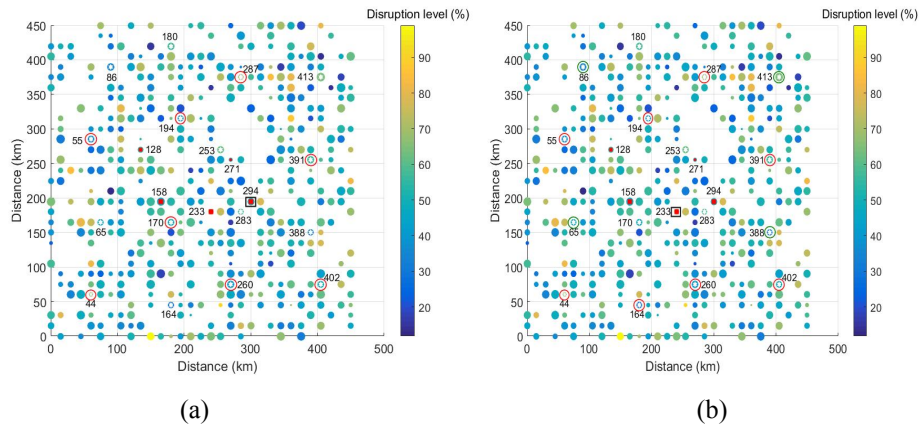


Figure 3: RBPB and biorefinery location for shortfall penalty = \$ 375/Mg and penalty factor = 50% for: (a) Ideal design; (b) Resilient design

References

- Maheshwari, P., Singla, S., Shastri, Y., 2017. Resiliency optimization of biomass to biofuel supply chain incorporating regional biomass pre-processing depots. *Biomass and Bioenergy* 97, 116–131. <https://doi.org/10.1016/j.biombioe.2016.12.015>
- Mani, S., Sokhansanj, S., Bi, X., Turhollow, A., 2006. Economics of producing fuel pellets from biomass. *Appl. Eng. Agric.* 22, 421–426. <https://doi.org/10.13031/2013.20447>
- Poudel, S.R., Marufuzzaman, M., Bian, L., 2016. Designing a reliable bio-fuel supply chain network considering link failure probabilities. *Comput. Ind. Eng.* 91, 85–99. <https://doi.org/10.1016/j.cie.2015.11.002>
- Humbird, D., Davis, R., Tao, L., Kinchin, C., Hsu, D., Aden, A., 2011. Process Design and Economics for Biochemical Conversion of Lignocellulosic Biomass to Ethanol. *Renew. Energy* 303, 147. <https://doi.org/10.2172/1013269>

Optimal on-grid hybrid power system for eco-industrial parks planning and influence of geographical position

Florent Mousqué^{a*}, Marianne Boix^a, Stéphane Négny^a, Ludovic Montastruc^a,
Louis Genty^a, Serge Domenech^{a*}

^a*Université de Toulouse, Laboratoire de Génie Chimique, UMR 5503 Toulouse INP-CNRS-UPS, 4, Allée Emile Monso, 31432 Toulouse, France*

florent.mousque@ensiacet.fr

Abstract

Nowadays, many Eco-Industrial Parks (EIP) are emerging all around the world. In these eco-industrial parks, industries gather to share several streams like energies, water, resources, and wastes in order to realise economic benefits while lowering their environmental impact. However, most of the time, these EIP are historically constituted and therefore sub-optimal. To really observe the sought gains, exchange networks need to be optimally designed. This article aims to develop a methodology for a grassroots design of hybrid power system (HPS) based on multi-objective optimization to supply an EIP. Overhang of this study is multi-objective (MO) approach which aims to minimize energy cost for project lifespan and to minimize environmental impact of energy production to supply EIP demand. This last criterion is evaluated by a life cycle assessment (LCA) on each sources. Another advantage is that geographical influence on HPS design is taken into account to evaluate climate effect on RE production and LCA impact depending on selected position for the EIP. A case study compares single objective and MO optimization and geographical influence on designed HPS for the same EIP, in two countries, Malaysia and in Germany. Results shows that a big reduction on environmental impact (above 70%) thanks to a little invest (cost increased about 10%) can be reached. Also, compared with different geographic positions, designed solution is really contrasted according to cost, environmental impact and selected RE sources.

Keywords: eco-industrial parks, renewable energies, multi-objective optimization, environmental assessment

1. Introduction

In recent years, at climate conference of the UNO (COP23 in 2017) important measures have been taken to fight against climate change and global warming, and to reduce human footprint on his environment. In this aim, to reduce extraction of raw materials and to limit amount of generated wastes, industrial ecology proposes to industries to gather within eco-industrial parks (EIP) to exchange energies and resources. Thereby, the main opportunity for companies is to reduce their environmental impact while increasing their competitiveness by making economic gains. In their review (Boix et al., 2015) have analysed methods applied to design and to optimize networks and streams in

EIP. Previous studies have been mainly focused on water and materials networks, while there is already a little number of publication dealing with energy networks for EIP. However to supply energy demand while reducing its environmental impact an EIP could produce its own local energy by using a renewable energy hybrid power system (HPS). An HPS is an energy network where several renewable energy sources are available also called RE-HPS. Lee et al. (2014) developed an LP optimization model to minimize energy loss of a RE-HPS. More recently, Theo et al. (2016) have completed this study by introducing an MILP model to minimize operating and investment costs and to select storage technologies.

The aim of this paper is to develop an on-grid HPS model to optimize energy planning to supply an EIP. MO optimization method is driven by both antagonist criteria: economic and environmental. To measure geographical impact of the location, the same HPS is optimized in different countries (Malaysia, Germany) using the same EIP demand, regardless of HPS technologies. Moreover, this model for the grassroots design of an EIP allows to optimize energy storage size, and renewable energy power rating (for wind Turbines, photovoltaic panels and biomass combustion) in order to provide known energy demand of EIP's processes.

2. Methodology and model formulation

The first step of this methodology is to define a model representing HPS. To this end, a superstructure has been developed, in which are represented links between sources and power demand (each company owns a number of process units representing sinks). Scheme of this superstructure is illustrated in figure 1.

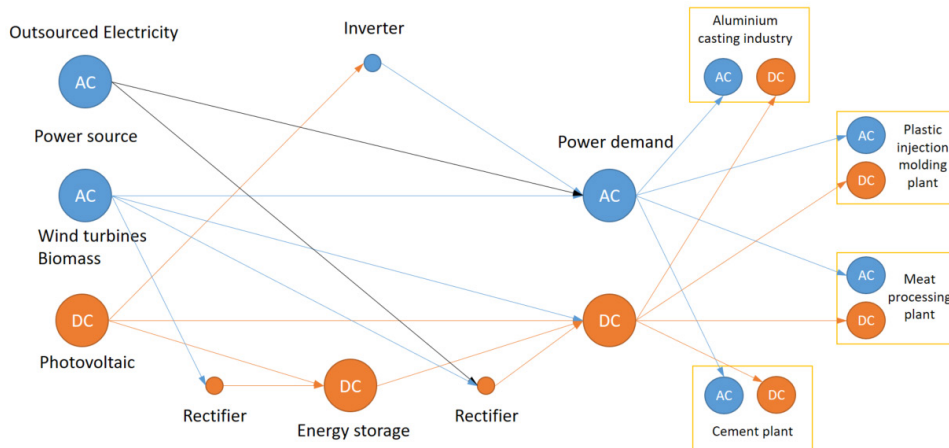


Figure 1: Superstructure of the HPS model

In this HPS, the renewable energy Alternative Current (AC) power sources are Wind Turbines, Biomass and Direct Current (DC) one is Photovoltaics panels. It is also possible to buy AC outsourced electricity (OE) from grid. To convert AC or DC electric current, rectifier and inverter are available. Due to the intermittency of renewable energy production, it is a dynamic model, in which time is discretized by hour, at any hour of the horizon time.

The EIP consists in 4 industries composed of AC or DC process to supply. While it is a theoretical EIP, energy demands are those of real process industries, in order to represent a complex demand, with many variations over time. Indeed in the aluminium casting industry works as a batch production (most of energy demand is between 7AM and 6PM) while the other industries works continuously. The cement plant is the biggest consumer (above 75% of the consumption) due to processes like raw-mill driver, cement mill driver and conveyor system. Moreover, renewable energy production can be stored in DC energies storage which is lead-acid batteries technology due to their best price capacity ratio to make profitable storage use.

The main mathematical constraints are energy balances at power source which is supplied directly to the power demand or charged into storage. This constraint is available for each power source and for each type of electrical current. Concerning the demands, the power demand must be satisfied by equivalent power of sources or batteries multiplied by potential energy loss if it has to be converted or discharged. Any loss corresponds to charging efficiency (90%) and converter efficiency (95%).

Energy balance for the storage system is also considered, i.e. the total amount of energy stored at the end of a time slice is the sum of the initial amount of energy stored and the net difference of charging and discharging. Additional constraints are added in order to limit converter and batteries capacities to maximal values observed throughout the duration time of the simulation. Furthermore, the geographical influence is considered through input model parameters. These parameters are outsourced electricity (OE) price, wind and solar power, and environmental impact of each renewable energy sources. The parameters related to geographical position are external electricity price, impact of sources, wind speed and solar irradiation.

The variables are the power rate of each renewable energy source, power capacity of converter (inverter and rectifier), the storage capacity and the amount of OE purchased.

A multi-objective optimization model is solved with an economic and an environmental criteria. The economic criteria to minimize is defined as the total Net Present Value of HPS over its lifetime, including capital investment, maintenance cost, operational expenditure for designed decision variable which are renewable energy sources, lead-acid batteries, and convertors. Finally cost of purchased OE from external network is taken into account. The environmental objective is based on a LCA approach (cradle-to-grave), for each source (renewable energy and outsourced electricity) producing 1 kWh, the impact is quantified through SIMAPRO® software. This value depends on the country where energy is produced. The function to minimize is calculated by adding total impact produced by each source.

The resulting optimization model is an LP model able to find a global optimal solution and it has been solved with IBM ILOG CPLEX Optimizer.

3. Case study

In this case study, Malaysian data are taken from a previous work so that the model can be validated (Theo et al., 2016). The second location, i.e. Germany, is chosen to be very different from the first one because they have adopted a policy to promote renewable energy sources, favourable to renewable energy HPS implantation. Germany is a windy country with an important potential for wind turbines and low solar potential while

Malaysia is sunnier. Furthermore, in Germany, impact of RE sources is globally really lower than in Malaysia (Figure 2).

To get reliable data, horizon time of this simulation is set at 4 days, one per season, which allows to consider annual climate changing. Indeed, while Malaysia is near from equator with low seasonal impact, in Germany huge variations can be noted between seasons.

Solar information, are obtained with PVGIS® tool from the European commission. On the other hand wind speed for Malaysia comes from Theo et al. (2016) and for Germany from Fraunhofer ISE European research institute (2014). Outsourced electricity price used in this model is the average for industries in Malaysia: 0.078 USD/kWh (Theo et al., 2016) and in Germany: 0.103 USD/kWh according to Clean Energy Wire (2015).

The different sources taken into account in this model and their impact are shown in figure 2, for Malaysia and Germany. Values come from SIMAPRO® software, using Ecoinvent® database and Impact 2002+ method. It allows to propose an aggregated indicator, gathering 4 damage categories: Human health, Ecosystem quality, Climate change and Resources. The unity of this unique indicator is the mean environmental impact of a European during a year.

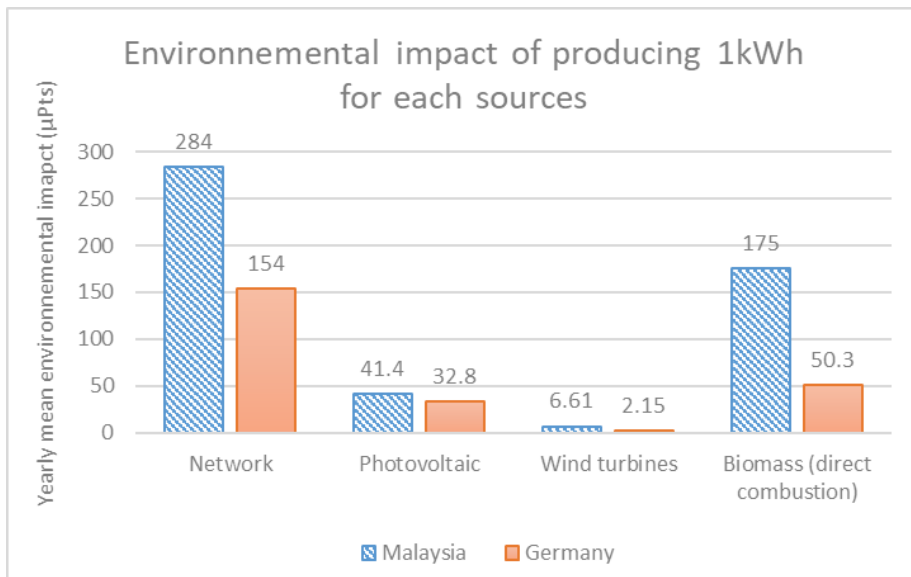


Figure 2 Environmental impact data collected for each country

4. Results and discussion

This section highlights the differences between mono and multi-objective optimization and also investigates the influence of geographical position. Figure 3 shows the Pareto front solutions obtained for Malaysia (MY) and Germany (GE). In addition, detailed results for designed HPS are presented in Table 1 where the geographic influence between Malaysia and Germany can be clearly highlighted.

According to these results, it can be noticed that these criteria are antagonist (when cost increases, environmental impact (ENV) decreases) what justifies the choice to use a MO

analysis. As a result, the MO approach epsilon-constraint is retained to obtain the Pareto front illustrated in figure 3. Multi-criteria decision analysis (MCDA) tool TOPSIS gives a solution among optimal ones, this solution is the nearest from the best value for each criteria and the farthest from worst ones.

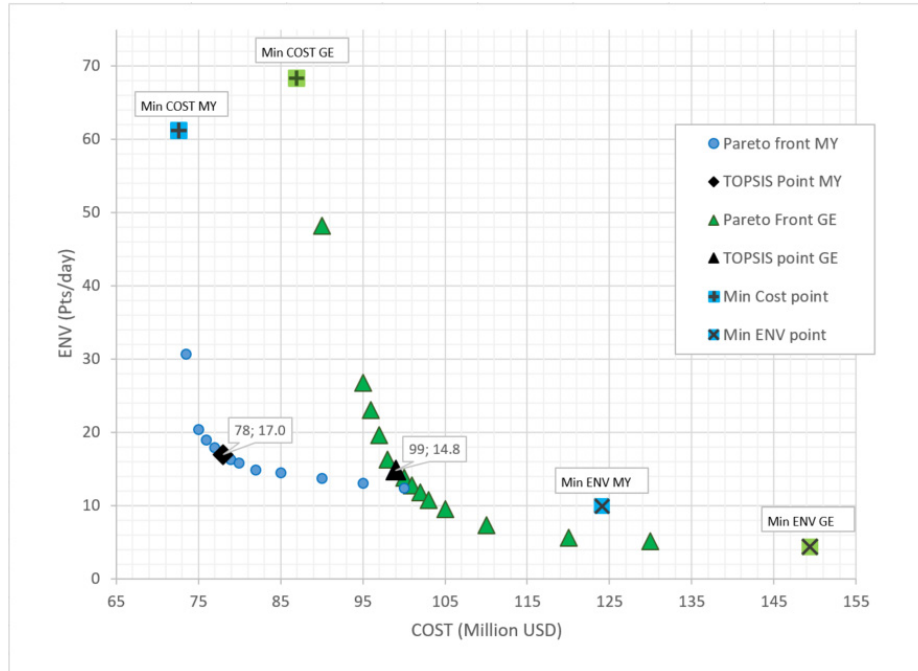


Figure 3 Pareto fronts and optimal points for Malaysian and German HPS implantation

Compared to the minimal cost point (Min COST), the TOPSIS multi-criteria solution observes a project cost 7% higher but a decrease of 72% on environmental impact for Malaysia. In Germany, it is also significant with a cost 14% higher and an ecological effect 78% lower. These results emphasize the importance of using a MO optimization because it shows that a little invest can have a big effect on environmental impact. One can also observe that when cost is minimized (min COST), compared to Malaysia, the German project is more expensive (+20%) and environmental impact also (+12%). This is mostly due to the higher price of OE which favours biomass. The latter gets a bigger impact than wind turbines used in Malaysian case.

Then, when environmental impact is minimized (min ENV), the German case observes a lower impact than Malaysia (-56%) that can be attributed to lower LCA impact of German RE sources (Figure 3). Lastly, with comparison of TOPSIS, the values obtained show a higher cost and a lower environmental impact. In both cases, wind turbines are essentially used. To conclude about geographic influence, this comparison between countries implantation shows some important differences on the respective solutions. This can be explained by (i) price for OE, (ii) impact for renewable energy sources, and (iii) by weather conditions, like seasonal influence (Germany is far from equator while Malaysia has a more regular climate). Regarding the types of renewable energy sources used, no solution proposes the solar one, it can be explained by an important investment cost and its high environmental impact (mainly due to the step of production of

photovoltaic panels) (cf. figure 2). Simulating in a more sunny country and including government helps should promote this technology. Biomass can be chosen, depending on countries, indeed, in Germany its impact is really low. At last, due to its low impact on environment, wind turbines appear to be the most used solution in this design.

		Cost (M USD)	ENV (Pts/day)	Cost storage (M USD)	Cost OE (M USD)	Wind Power rated (kW)	Biomass Power rated (kW)	Solar Power rated (kW)
Min COST	Malaysia (MY)	72,6	61,2	2,7	18,4	8764	2262	0
	Germany (GE)	86,9	68,4	6,6	8,6	0	13497	0
	Comparison GE/MY (%)	20%	12%	142%	-53%	-100%	497%	-
Min ENV	Malaysia (MY)	124,1	9,9	35,1	0	14717	0	0
	Germany (GE)	149,4	4,3	42,8	0	16578	0	0
	Comparison GE/MY (%)	20%	-56%	22%	-	13%	-	-
TOPSIS	Malaysia (MY)	78	17,0	8,0	9,1	12545	0	0
	Germany (GE)	99	14,8	10,4	33,3	9027	0	0
	Comparison GE/MY (%)	27%	-13%	30%	267%	-28%	-	-

Table 1 Detailed results for each designed solution

5. Conclusion

In support of a framework for energy supply of an eco-industrial park, we have presented a generic methodology to optimize the renewable energy sources with a MO optimization approach. Using this methodology, we can determine, economic cost and environmental impact of such a solution but also the corresponding size for storage batteries. It also allows to determine the most profitable RE sources for a given geographic position. An interesting perspective, after this design of the EIP depending on its geographic implantation is to achieve a sensibility analysis. To go further future improvements for this model can be to allow it to select between several technological alternatives for RE sources or storage, due to its genericity it can be done easily by transforming it into an MILP. Finally because an EIP is constantly evolving, by using a multi-period approach, future research may make possible to modify network over time to adapt it to its moving context.

References

- Boix, M., Montastruc, L., Azzaro-Pantel, C., & Domenech, S. (2015). Optimization methods applied to the design of eco-industrial parks: A literature review. *Journal of Cleaner Production*, 87(1), 303–317.
- Clean Energy Wire (2015). Report on Industrial power prices and the Energiewende. <https://www.cleanenergywire.org/> Last access on November 2017.
- Fraunhofer IWES (2014). Fraunhofer Institute for Wind Energy and Energy System Technology. <https://www.iwes.fraunhofer.de/en.html> Last access on November 2017.
- Lee, J.-Y., Chen, C.-L., & Chen, H.-C. (2014). A mathematical technique for hybrid power system design with energy loss considerations. *Energy Conversion and Management*, 82(Supplement C), 301–307.
- Theo, W. L., Lim, J. S., Wan Alwi, S. R., Mohammad Rozali, N. E., Ho, W. S., & Abdul-Manan, Z. (2016). An MILP model for cost-optimal planning of an on-grid hybrid power system for an eco-industrial park. *Energy*, 116(Part 2), 1423–1441.

Life cycle assessment of pulp and paper production – A Portuguese case study

Andreia Santos,^{a,*} Ana Barbosa-Póvoa,^a Ana Carvalho^a

^a*CEG-IST, Avenida Rovisco Pais, 1049-001 Lisbon, Portugal*

andreia.d.santos@tecnico.ulisboa.pt

Abstract

Life Cycle Assessment (LCA) is the most used methodology to assess the environmental impacts of supply chains. Despite being the most used methodology, LCAs studies regarding forest wood supply chains considering an exhaustive Life Cycle Impact Assessment (LCIA) approach are still lacking with the majority choosing a small subset of impact categories and indicators. This work aims to develop a comprehensive Life Cycle Assessment considering two different LCIA methodologies (IMPACT 2002+ and ReCiPe 2008) to the pulp and paper supply chain to identify possible alternatives that would allow a better environmental impact based on the identification of the most critical impact categories through the Pareto principle. A Portuguese company from the pulp and paper industry is used as an illustrative case study.

Keywords: Life cycle assessment, ReCiPe 2008, IMPACT 2002+, Paper industry, SimaPro

1. Introduction

The forest sector is responsible for the transformation of a very important renewable resources into various products vital to human well-being such as furniture, lumber, energy in all its forms (heat, electricity, and fuels), newsprint and hygienic papers (World Wildlife Fund, 2000). Portugal in the European and even international context is a country specialized in this industry which is responsible for 2% of the gross domestic product, 10% of exports and for the creation of 92,000 (Instituto da Conservação da Natureza e das Florestas, 2017). It was on the forest sector that the concept of sustainability was first introduced at the beginning of the 18th century (Carlowitz, 1713). Since then, the sustainability concept has evolved with the economic, environmental and social areas being identified as equally important pillars (Department of Economic and Social Affairs, 1992). In relation to the environmental pillar, Life Cycle Assessment (LCA) has been the most used methodology to estimate the environmental impacts of different products and processes and was also identified by the European Commission as the best framework to do so (Mimoso, et al., 2015). There are several Life Cycle Impact Assessment (LCIA) methods that can be used when conducting an LCA and these methods consider different impact categories to assess the environmental impacts which can have distinct names and can be express using different units. This diversity of methods makes the decision on the best method to use harder. By using an illustrative case study of a Portuguese company from the forest sector, particularly the pulp and paper industry, and the SimaPro software, this study compares two LCIA methods, namely IMPACT 2002+ and ReCiPe 2008, in terms of the single score obtained and the critical impact categories considered by each method.

These critical categories were identified by conducting a Pareto's analysis. In Section 2 the methodology followed in this study is explained and in the following section the case study is presented. Section 4 presents the results' analysis. In the last section the main conclusions and limitations of the study are given along with suggestions for future lines of research.

2. Methodology

The LCA methodology consists of four main steps including Goal and Scope Definition, Inventory Analysis, Impact Assessment, and Results Interpretation (ISO, 2006). These steps are presented in Figure 1.



Figure 1 - Methodology followed in this study.

A brief explanation of each step is given below (ISO, 2006):

Goal and Scope Definition – where the main objectives of the study, functional units and boundaries of the system are defined. The functional unit is a representative element of the system being study and is the basis from which all inputs and outputs are calculated. The inputs and outputs to be considered depend on the boundary defined.

Inventory Analysis or Life Cycle Inventory (LCI) – consists in the calculation/collection of all the flows of materials/energy and processes needed for the functional unit. The materials and processes to be considered depend on the goals and system boundaries defined in the previous step. This step is also known as.

Impact Assessment or Life Cycle Impact Assessment (LCIA) – where the environmental impact of the inventory listed in the preceding step is measured. The inventory values are converted into impact category indicators at the midpoint level using characterisation factors. Depending on the LCIA method used, these midpoint categories can be aggregate into fewer categories of damage (endpoint categories). Different LCIA methods will consider different midpoint and endpoint categories. The endpoint categories can then be normalised using a normalisation factor. The normalised results can be multiplied by a weighting factor (assigned to each impact category based on their relative importance) and the weighted results can be added up to calculate one single score (SS).

Results Interpretation – consists in analysing and interpreting the results of the three previous steps to identify the hotspots of the system being studied and suggest possible improvements. Pareto analysis can be used to identify the critical impact categories.

In the next section the case study and the results of applying the LCA methodology to this case study are presented in terms of the first three steps. The last step is presented in Section 4.

3. Case Study

The Portuguese company from the pulp and paper industry used as a case study is integrated in a supply chain illustrated in Figure 2. This company produces and sells to the domestic and European markets three products: pulp, UWF (uncoated wood free) printing and writing paper, and tissue paper.

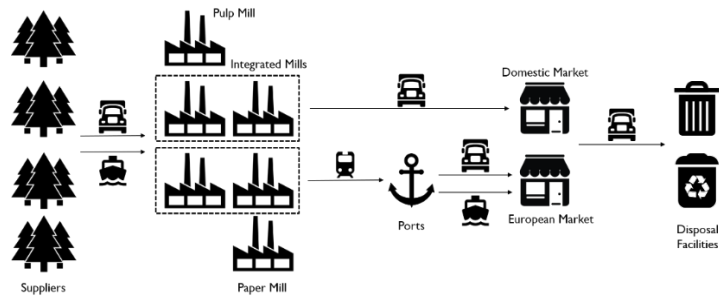


Figure 2 - Case study's supply chain.

Following the methodology presented in the previous section:

Goal and Scope Definition – the main objective of this study is to assess the environmental impacts of a forest wood supply chain, particularly a paper supply chain, to identify the critical processes (hotspots) and give improvement suggestions. A Cradle-to-Grave boundary was considered which includes all stages of the products' life cycle starting with growing and harvesting trees and finishing with products' disposal. The functional unit selected was 1 hectare of trees harvest which allows the production of approximately 25 t of pulp, 27 t of UWF printing and writing paper, and 716 kg of tissue paper.

Inventory Analysis or Life Cycle Inventory (LCI) – Table 1 presents the results of the LCI step considering the functional unit and system boundary defined, the flow between different entities of the supply chain and a paper recycling rate of 72 %.

Table 1 – Life cycle inventory and selected SimaPro references.

Life Cycle Stage	SimaPro Process	Quantity	Unit
Pulp Production	Sulfate pulp {GLO} market for	25076.4379	kg
UWF Paper Production	Paper, woodfree, uncoated {RoW} paper production, woodfree, uncoated, at integrated mill	27072.3177	kg
Tissue Paper Production	Tissue paper {GLO} production, virgin Conseq, U	716.4697	kg
Road Transportation	Transport, freight, lorry, unspecified {RER} transport, freight, lorry, all sizes, EURO5 to generic market for	24160.1270	tkm
Rail Transportation	Transport, freight train {Europe without Switzerland} market for	5420.0682	tkm
Maritime Transportation	Transport, freight, sea, transoceanic ship {GLO} processing	67898.5670	tkm
Products' Disposal	Paper (waste treatment) {GLO} recycling of paper Conseq, U	72	%
	Waste graphical paper {Europe without Switzerland} treatment of waste graphical paper, sanitary landfill Conseq, U	28	%
	Waste paper, sorted {RER} tissue paper production Conseq, U	100	%

Impact Assessment or Life Cycle Impact Assessment (LCIA) – The IMPACT 2002+ and ReCiPe 2008 methods were selected. SimaPro was the chosen software to help assess the environmental impact of the supply chain studied. Table 1 also shows the references used to create a model in this software that best represents the case study. When using SimaPro, the hierarchist perspective was selected for the ReCiPe 2008 method. After implementing the case study in the SimaPro software, the results can be analysed.

4. Results and Discussion

An overall environmental impact of 28.7 Pt and 8.83 kPt was obtained using the IMPACT 2002+ and ReCiPe 2008 methods, respectively. Looking at these results, it was possible to conclude that in both LCIA methods the production and usage phase of the products (Market for All Products) contribute the most to the overall environmental impact as can be seen in Figure 3. Furthermore, it is the production and usage of UWF Paper (Market for UWF Paper) that most contributes to this result as represented in Figure 4. The impact of the Market for UWF Paper is higher when using the IMPACT 2002+ method while the impact of the Market for Pulp is higher when using the ReCiPe 2008 method.

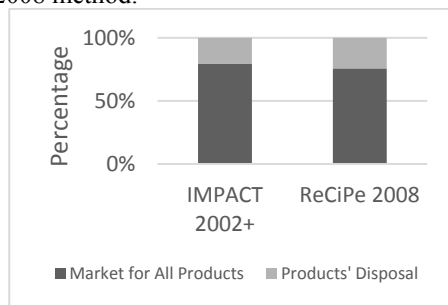


Figure 3 - Life Cycle

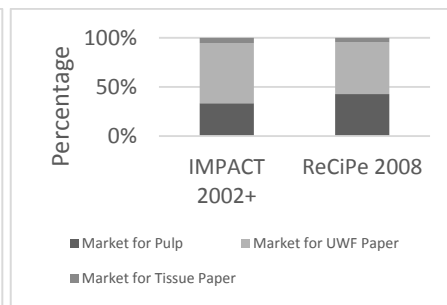


Figure 4 - Market for All Products

The process that most contributes to the impact of the Market for UWF Paper is UWF Paper Production in both LCIA methods considered as represented in Figure 5.

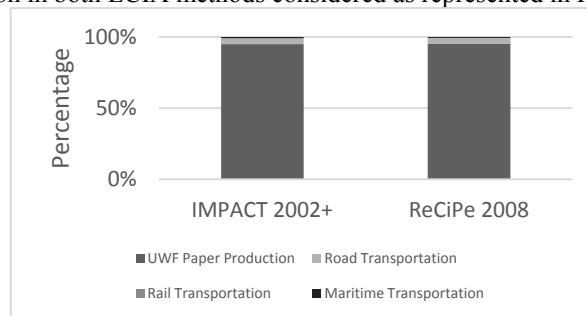


Figure 5 - Market for UWF Paper

A Pareto analysis was performed to identify the most critical impact categories regarding the UWF Paper Production process. The results are illustrated in Figure 6 for the IMPACT 2002+ and ReCiPe 2008 methods. From Figure 6 it is possible to conclude that four midpoint categories (respiratory inorganics, terrestrial ecotoxicity, global

warming, and non-renewable energy) are responsible for 84 % of the environmental impact related to UWF Paper Production when considering the IMPACT 2002+ method. It is also possible to conclude that three midpoint categories (agricultural land occupation, climate change and fossil depletion) are responsible for 85 % of the environmental impact related to UWF Paper Production when considering the ReCiPe 2008 method.

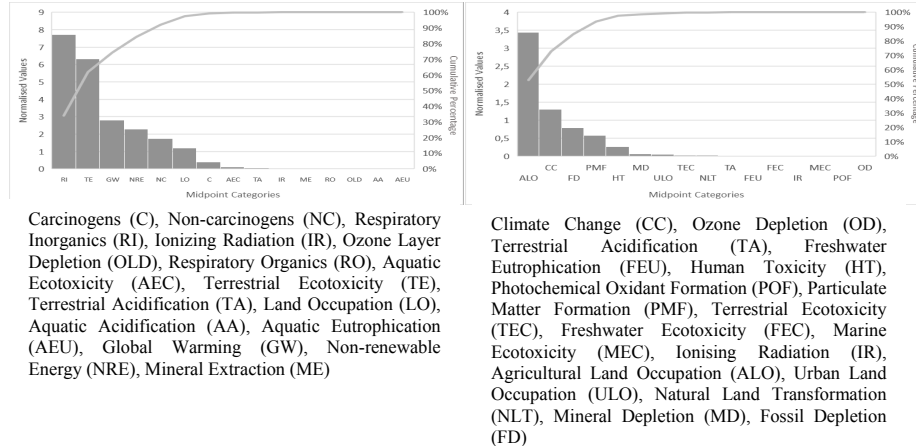


Figure 6 - Pareto Analysis (IMPACT 2002+ on the left and ReCiPe 2008 on the right)

The inputs of the UWF Paper Production process that most contribute to the critical impact categories identified previously are illustrated in Figure 7 for both LCIA methods. From the analysis of Figure 7 it is possible to conclude that electricity is the input that most contributes to three of the four critical impact categories identified with IMPACT 2002+ with the exception being the terrestrial ecotoxicity where the input that most contributes is wood ash mixture. Similarly, electricity is the input that most contributes to two of the three critical impact categories identified with ReCiPe 2008 with the exception being agricultural land occupation where the input that most contributes is pulpwood. For these reasons and to minimize the environmental impacts of the supply chain studied, a switch in the sources of electricity could be made by switching from non-renewable sources to renewable sources of energy such as biomass.

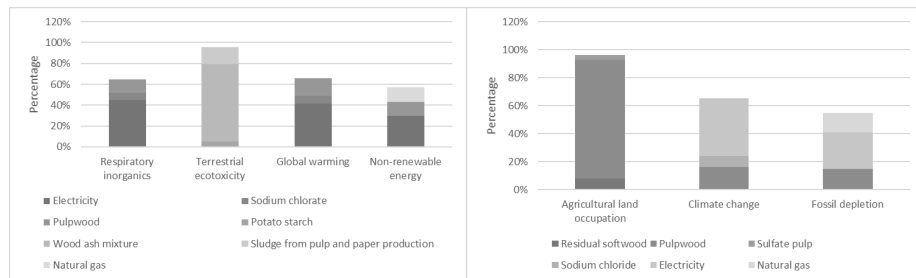


Figure 7 - Main Inputs of the UWF Paper Production (IMPACT 2002+ on the left and ReCiPe 2008 on the right)

The comparison of the two methods allows the following conclusions to be drawn:

- 1- Both methods pointed out the same process as the bottleneck of the life cycle and therefore the confidence in this conclusion is high.

2- In terms of the most relevant impact categories the results are not the same. This reinforces the problem of standardization in LCA, where the same bottleneck influences different impact categories.

3- It is not possible to recommend the best method to apply, but it is possible to recommend that bottlenecks' identification in terms of processes and environmental impacts, should be done through the application of several methods, in order to strength the robustness of the conclusions.

4 – When making comparison amongst systems, in our case supply chain, the same method should always be used so as to avoiding unfair comparisons, but as mentioned in point 3 the usage of different methods reinforce the bottlenecks' identification.

5. Conclusions

A comparative analysis of two LCIA methods, IMPACT 2002+ and ReCiPe 2008, was proposed. These methods were applied to a case study, a Portuguese company from the pulp and paper industry, which was implemented in the SimaPro software. The LCA methodology revealed to be useful for identifying the most impactful processes from an environmental point of view. With this information, improvement suggestions could be made. The study presented in this paper should be extended to include more LCIA methods to make the conclusions more robust. Furthermore, other case studies could be analysed to identify similarities between different industries in the forest sector.

Acknowledgements

The authors grateful acknowledge the project funding (POCI-01-0145-FEDER-016733).

References

- Carlowitz, H. C. v., 1713. *Sylvicultura oeconomica*. s.l.:s.n.
- Department of Economic and Social Affairs, 1992. *United Nations Conference on Environment & Development*, Rio de Janeiro: United Nations Sustainable Development.
- Instituto da Conservação da Natureza e das Florestas, 2017. *Fileiras Florestais*. [Online] Available at: <http://www.icnf.pt/portal/florestas/fileiras/econ>[Accessed 07 December 2017].
- ISO, 2006. *International Organization for Standardization*. [Online] Available at: www.iso.org[Accessed 04 December 2017].
- Mimoso, A. F., Carvalho, A., Mendes, A. N. & Matos, H. A., 2015. Roadmap for Environmental Impact Retrofit in chemical processes through the application of Life Cycle Assessment methods. *Journal of Cleaner Production*, Volume 90, pp. 128-141.
- World Wildlife Fund, 2000. *The Forest Industry in the 21st Century*, Surrey: WWF's Forests for Life Campaign.

Modelling and Analysing Supply Chain Resilience Flow Complexity

João Pires Ribeiro^{a,*} and Ana Barbosa-Póvoa^a

^a*CEG-IST, Instituto Superior Técnico, University of Lisbon, Av. Rovisco Pais, 1049-001 Lisboa, Portugal*
pires.ribeiro@tecnico.pt

Abstract

Globalization has increased the exposure of Supply Chains (SC) to higher uncertainties that call for adequate strategies, thus supporting the creation of SC Resilience. There is, however, no absolute strategy that decision makers can follow to guarantee such resilience and the knowledge on how to characterise SC resilience (SCR) is still an open issue. This work focuses on a strategic level of decision and analyses the relationship between SCR and SC complexity, aiming to conclude how SC flow complexity reflects SCR. The design and planning of a multi-product, multi-period SC are addressed through a Mixed Integer Linear Programming (MILP) model where demand uncertainty is considered. A set of disruptions is studied for different SC structures and as main conclusions, it can be stated that SC flow complexity leads to an increase in SC resilient performance and appears as a good indicator of SCR.

Keywords: Supply Chain Resilience, Quantitative models, Flow Complexity; Design and Planning

1. Introduction

The concept of Supply Chain Management was for the first time introduced in the XX century by Oliver et al. (1982) and since then has evolved. The need to guarantee competitiveness in a global market has lead SC to expand geographically and consequently, SC structures have been facing an increased exposure to risks due to a larger set of uncertainties that they have to deal with. This has created the necessity of deeply analysing the concept of SC resilience as a way to deal with such uncertain context. This is critical in the case of process supply chain as this type of systems are frequently global chains, whose business spreads around the globe, and whose products with great importance to society have to be continuously available, as is the case of pharmaceuticals, food, chemicals, energy, amongst others (Barbosa-Póvoa, 2014).

SCR is one of the newer concepts in SC and it comes as a need to better prepare SC for challenges brought by global SC operations. As stated by Ribeiro and Barbosa-Povoia (2018) in a recent review on the topic, “A resilient supply chain should be able to prepare, respond and recover from disturbances and afterwards maintain a positive steady state operation in an acceptable cost and time”.

In such setting, the interest in a sound understanding of SCR has led academics and companies to pursuit efforts regarding such objective (Tang, 2006; Kamalahmadi and Parast, 2016). It is on the best interest of real SC the increase in knowledge in SCR as it is fundamental to better understand not only the resilience concept but also how this can help SC to deal with disruptive events that can endanger their steady-state operation (Cardoso et al., 2015). Several authors have been recently

studying SCR but there is still a lack of understanding on how to quantify SCR (Ribeiro and Barbosa-Póvoa, 2018). Cardoso et al. (2015) studied SCR and proposed a set of SC indicators that could be used to analyse SCR. SC flow complexity was identified as one of the most promising indicators and further studies on this should be performed to confirm such result.

Based on these results, the present work focus on the design and planning of SC where decisions taken on the SC network structure are analysed. A design and planning multi-product, multi-period MILP model is developed where demand uncertainty is considered. Five different supply chain structures are analysed and the associated complexity optimized. The resulted SC structures are subject to a set of disruptive events and their resilience is analysed.

2. Problem and Model Description

In order to be able to discuss how different SC networks behave towards resilience, a five echelons supply chain was considered, where reverse flows are also possible to occur. Such SC involves: Raw Material Suppliers; Plants that can also function as Disassembling Centres with end of life products; Warehouses with added value activities as reconditioning non-conforming products; Outsourcing contractors as an alternative to plants production and finally Markets. In the plants and warehouses, technologies can be installed, which influence production, assembly and disassembly processes. These technologies can be fitted to the entities, or upgraded, to provide better performance.

Based on this generic SC structure five different SC cases are studied where different SC structures are considered and allow to compare and construe results on SC resilience: Case A - a forward supply chain; Case B - similar to A, but now integrating also reverse flows between consecutive echelons; Case C - similar to B, but plants and markets can directly exchange products, thus bypassing the warehouses; Case D - similar to B, but with the possibility of transshipment at plants, disassembling centres and warehouses; Case E - the most general case, encompassing all the previous ones, forming a closed-loop supply chain where plants send directly products to markets and can also receive directly from markets the end-of-life products. Transshipment is allowed at plants, warehouses and disassembling centres.

The MILP model developed by Cardoso et al. (2015) is taken as a base and was adapted to this work goals, providing a new objective function and a set of constraints to study SC flow complexity. Uncertainty was considered in the SC demand and on Disruptions. A scenario tree is constructed combining the two sources of uncertainty. Demand variability is introduced by generating a scenario on each period from a set of three possibilities (Pessimistic, Realistic or Optimistic). The result probabilistic nodes are then combined with the variability from the disruption that can only assume two options, or it occurs or it does not occur on a specific time period to consider. With this, each scenario probability is given by the probabilities of the path, with all stages, between the root node and each final leaf node.

2.1. Objective Function

Two objective functions are studied, Equations 1 and 2. A first one considers the maximization of the network flow complexity (Equation 1), as this would return a network configuration with maximum flow complexity (FC) under the feasibility space generated by problem constraints, being FC_t the summation of all positive flows present in the SC for each time period.

$$\text{Max} \sum_t FC_t \quad (1)$$

This model formulation, although returning a SC with the maximum amount of feasible possible flows does not take into consideration economic concerns, leading to solutions that may have a

low performance in financial terms. This issue can, however, be tackled by setting additional constraints in the model, as is the case of establishing a minimum profit that must be obeyed. However, this method was not followed due to two reasons. First, restrictions had to apply to all cases and scenarios, which involve setting up conditions that cannot interfere with the feasibility of the model. Second, by setting up new conditions there is the possibility of endangering the established relationship and compatibility with the original model.

Therefore, a two-step approach is followed. Primarily the model is run based on Equation 1 to retrieve the SC with maximum flow complexity within the model feasibility. The second step is used to retrieve the obtained network configuration and then study how much such network configuration maximizes the economic return. The economic return is based on the Expected Net Present Value, Equation 2 (where CF stands for the Cash flow for each scenario and time period, and ir for a defined interest rate). Through this method it is ensured a network with maximum flow complexity and with the most advantageous economic performance to the company.

$$MaxENPV = \sum_s pb_s \times NPV_s \quad pb_s = \text{Probability scenarios} \quad NPV_s = \sum_t \frac{CF_{st}}{(1+ir)^t} \quad (2)$$

By fixing the network configuration there is no capability for the SC network to change, however, it can adapt to the variability introduced in each situation by investing in new technologies, or upgrades to the existing facilities as well as optimize the supply chain flows.

3. Case Study

The presented model is tested in a Case Study of an European Chemical Process SC. The values associated are scaled down, due to confidentiality reasons. The initial SC configuration comprises a set of European locations, with one plant in Hamburg, one warehouse in Munich, four raw materials suppliers, 3 suppliers of final products and 18 European cities as markets. In broad terms, the company is studying the existent SC in order to assess the investment necessary in technologies for current entities, or the implementation of new facilities, to improve the SC's resilient capability. Four operational conditions are studied; one reference case with perfect operational conditions and three examples of disruptions. The disruptions were chosen following failure modes defined by Rice and Caniato (2003). **Disruption 1** (Production Facilities)- "100% decrease in the production capacity of the most important plant (plant P13), in time period 2, caused, for example, by a major natural catastrophe". **Disruption 2** (Supply)- "The most important raw materials suppliers (s3, s5, s8, s9 and s10) have their supply suspended in time period 2, due to an assumed industrial action". **Disruption 3** (Transportation)- "The 3PL hired to operate those transportation links, between plants and warehouses, that carry the highest quantity of products (links between P13 and warehouses W1, W2 and W4), goes out of business in time period 2". The scenario tree responsible for the uncertainty in the demand is built based on the assumption that the demand in the beginning is known and that there are three possible branches for time period 2 and 3, with the same probability in both periods; Optimistic 0.25, Realistic 0.5 and Pessimistic 0.25. (Time period 2: Optimistic with an increase of 10%; Realistic with an increase of 3%; Pessimistic with a decrease of 2%. Time period 3: Optimistic with an increase of 5%; Realistic with an increase of 2%; Pessimistic with a decrease of 2%)

For each SC case, two configurations are established based on the SC network provided by the two objective functions: maximization of ENPV and maximization of flow complexity, when there is no disruption. These network designs are then subject to the disruptions and the results are analysed and discussed. The MILP model is developed using the GAMS software. The results when applying a network configuration for ENPV maximization can be seen in Table 1, whereas the results for a SC with its flow complexity maximized are presented in Table 2.

Table 1: Combined results for ENPV Maximization

Case A	Complexity	ENPV	FCI	Investment	Inventory	Purchases	Sales	ECSL
Reference	46	1.96E+07	7.61E+05	7.32E+05	1450.707	342670	50563000	85.7%
Disruption 1	46	1.65E+07	8.10E+05	7.81E+05	1084.072	356550	43821000	63.3%
Disruption 2	44	1.78E+07	1.06E+06	1.03E+06	1231.576	373537.712	47473000	72.1%
Disruption 3	44	1.83E+07	7.80E+05	7.52E+05	1278.613	313616.662	48435000	75.7%
Case B	Complexity	ENPV	FCI	Investment	Inventory	Purchases	Sales	ECSL
Reference	89	1.91E+07	7.65E+05	7.20E+05	1449.68	334490	50548000	85.6%
Disruption 1	84	1.64E+07	7.99E+05	7.56E+05	1091.136	346070	44301000	63.8%
Disruption 2	87	1.77E+07	1.04E+06	9.92E+05	1229.269	302462.827	47672000	72.0%
Disruption 3	87	1.79E+07	7.89E+05	7.45E+05	1301.026	304995.435	48744000	77.0%
Case C	Complexity	ENPV	FCI	Investment	Inventory	Purchases	Sales	ECSL
Reference	110	2.05E+07	8.45E+05	7.90E+05	913.478	380870	52937000	99.4%
Disruption 1	109	1.66E+07	9.58E+05	9.03E+05	791.844	377550	45538000	83.4%
Disruption 2	108	1.45E+07	9.84E+05	9.30E+05	720.256	374369	40396400	71.8%
Disruption 3	108	1.84E+07	9.31E+05	8.77E+05	885.054	457070	51674000	98.4%
Case D	Complexity	ENPV	FCI	Investment	Inventory	Purchases	Sales	ECSL
Reference	90	1.91E+07	7.65E+05	7.20E+05	1452.711	334880	50586000	85.8%
Disruption 1	83	1.55E+07	8.28E+05	7.86E+05	1123.564	266442.058	42559300	65.5%
Disruption 2	89	1.77E+07	1.04E+06	9.95E+05	1227.958	302704.653	47651000	72.0%
Disruption 3	88	1.79E+07	7.88E+05	7.44E+05	1301.334	304860.924	48747000	77.0%
Case E	Complexity	ENPV	FCI	Investment	Inventory	Purchases	Sales	ECSL
Reference	106	2.05E+07	8.46E+05	7.91E+05	913.478	380670	52940000	96.4%
Disruption 1	102	1.64E+07	9.68E+05	9.14E+05	796.152	379080	45463000	83.7%
Disruption 2	104	1.65E+07	1.00E+06	9.47E+05	805.425	348862.167	44065000	77.8%
Disruption 3	104	1.84E+07	9.31E+05	8.77E+05	885.033	4,55E+05	51674000	98.4%

3.1. Case A

Case A represents a simple SC structure allowing only forward flows. One relevant analysis can be made regarding the delta of ENPV value between the two options, maximizing ENPV versus maximizing complexity. Comparing the results from both configurations, respectively in Tables 1 and 2 it can be seen an increase in service quality (ECSL) and that the loss in ENPV by incrementing complexity (-0.01E7€) is easily compensated by the gains in disruption 1 and 2 (0.15E7€ and 0.1E7€), representing gains of 9% and 5% respectively. During Disruption 3 the leaner SC network is able to provide the same economic return than the network with increased complexity, however, it does so with a decreased service quality.

3.2. Case B

Case B represents a SC structure where reverse flows are allowed between consecutive echelons adding complexity to the operation. It is expected an increase in flow complexity in order to cope with such requirement. The SC configuration with ENPV maximization has an increased impact from disruptions causing a decrease in ENPV of 14%, 7% and 6% for disruptions 1, 2 and 3 respectively. When no disruption is present a variation of -0.03E7€ in ENPV is expected, when the SC shifts to a more complex network the ENPV variation are positive, with a gain more than the double of the cost if no disruption is present. The service quality is also impacted by a more complex configuration with improvements of 21%, 15% and 7% for disruptions 1, 2 and 3 respectively.

3.3. Case C

Case C introduces a different kind of flexibility to the network, it allows the same flows as Case B and also allows for plants and markets to exchange products without any warehouse intervention. There is an increased susceptibility to Disruption 2 in Case C and this is much related with the non-existence of transshipment between entities in the same echelon. The leaner SC has a decrease in ENPV of 19%, 30% and 10% for disruptions 1, 2 and 3 respectively, while the more complex

Table 2: Combined results for Complexity Maximization

Case A	Complexity	ENPV	FCI	Investment	Inventory	Purchases	Sales	ECSL
Reference	156	1.95E+07	8.30E+05	7.32E+05	1451.691	342800	50572000	85.8%
Disruption 1	156	1.80E+07	9.54E+05	8.56E+05	1305.564	316095.608	48831000	76.9%
Disruption 2	151	1.88E+07	9.56E+05	8.61E+05	1409.266	333077.386	50058000	83.1%
Disruption 3	154	1.83E+07	8.78E+05	7.81E+05	1392.458	328540	49883000	82.2%
Case B	Complexity	ENPV	FCI	Investment	Inventory	Purchases	Sales	ECSL
Reference	346	1.89E+07	9.01E+05	7.19E+05	1451.139	334770	50564000	85.7%
Disruption 1	343	1.75E+07	1.01E+06	8.30E+05	1320.152	310323.917	49012000	76.9%
Disruption 2	341	1.83E+07	1.03E+06	8.47E+05	1409.159	324379.133	50053000	83.1%
Disruption 3	344	1.78E+07	9.41E+05	7.61E+05	1390.301	320275.72	49855000	82.1%
Case C	Complexity	ENPV	FCI	Investment	Inventory	Purchases	Sales	ECSL
Reference	495	2.03E+07	1.05E+06	7.90E+05	914.547	381050	52933000	99.4%
Disruption 1	495	1.89E+07	1.22E+06	9.59E+05	915.528	364530	52193000	95.1%
Disruption 2	491	1.83E+07	1.29E+06	1.03E+06	918.789	345240	51382000	90.1%
Disruption 3	493	1.94E+07	1.09E+06	8.29E+05	914.66	378400	52886000	98.9%
Case D	Complexity	ENPV	FCI	Investment	Inventory	Purchases	Sales	ECSL
Reference	376	1.89E+07	9.21E+05	7.20E+05	1456.127	335370	50607000	85.9%
Disruption 1	373	1.75E+07	1.03E+06	8.28E+05	1355.382	314110.778	49432000	79.9%
Disruption 2	372	1.82E+07	1.07E+06	8.75E+05	1381.246	316696.483	49723000	81.5%
Disruption 3	374	1.78E+07	9.59E+05	7.59E+05	1391.087	319616.258	49853000	82.1%
Case E	Complexity	ENPV	FCI	Investment	Inventory	Purchases	Sales	ECSL
Reference	525	2.03E+07	1.07E+06	7.89E+05	915.493	380820	52933000	99.4%
Disruption 1	516	1.89E+07	1.23E+06	9.51E+05	916.495	365270	52210000	95.2%
Disruption 2	520	1.92E+07	1.25E+06	9.80E+05	975.706	354997.874	51803000	92.8%
Disruption 3	523	1.94E+07	1.10E+06	8.26E+05	915.648	377860	52886000	99.0%

SC shows improvements of 14%, 27% and 5% for disruptions 1, 2 and 3 respectively. In terms of service quality it is perceptible an increase in ECSL for the more complex structure, maintaining levels of above 90% even during disruptions.

3.4. Case D

Case D allows forward and reverse flows between consecutive echelons and adds a new set of possibilities by allowing transshipment at plants, disassembling centres and warehouses. Applying the leaner configuration, disruptions cause an ENPV decrease of 19%, 7% and 6% for disruptions 1, 2 and 3 respectively. These results can be improved by 13% and 3% for disruptions 1 and 2 respectively, if a more complex network is deployed. In terms of ECSL the leaner configuration leads to a decrease of 24%, 16% and 10% for disruptions 1, 2 and 3 respectively, the more complex network allows for a steady service level of around 80%, improving the alternative configuration by 22%, 13% and 7% for disruptions 1, 2 and 3 respectively.

3.5. Case E

Case E represents a network that includes all the possibilities from previous cases. This closed loop SC can perform transshipment at all levels, except for markets, and flows bypassing intermediate entities are also allowed. ENPV variations between steady-state operation and disruptive scenarios are visible, resulting in a decrease of 20%, 20% and 10% for disruptions 1, 2 and 3 respectively on the network provided by the ENPV maximization. On the other hand, applying the more complex network the results of ENPV during the disruptive events are improved by 15%, 16% and 5% for disruptions 1, 2 and 3 respectively. With the maximization of complexity, the SC can return ECSL higher than 90% in all scenarios, even when a disruption does occur. When a leaner network is implemented disruptive scenarios cause a decrease in service level of 13% and 19% for disruptions 1 and 2 respectively. Applying the network with a higher amount of permitted flows leads to an improvement of 14%, 19% and 1% for disruptions 1, 2 and 3 respectively.

4. Conclusions and Discussion

From the above study, it can be concluded that the obtained results vary not only with the SC complexity but also with the SC structure (e.g. forward or closed-loop) as well with the different types of disruptions. Different disruptions cause different results and so decision makers should have enough information to make the most acceptable decision considering model results and available information. It is in this line that, studying SC Resilience factors gain importance, as it allows the development of better models to aid decision making.

Considering the behaviour on ENPV caused by the increased complexity, when no disruption occurs, is observed an increment on costs, due to the obligations that come from opening and maintaining more facilities and flows. However, if disruptions occur, there is an evident benefit of operating a more complex SC. The difference in ENPV in disruptive scenarios between the more complex and a leaner SC is always positive, in comparison with not investing in preventive strategies.

There is a more evident benefit from deploying a more complex SC in terms of ECSL. The notable shift is made possible by the increased flexibility and redundancy allowed by the higher amount of entities and flows involved resulting in an increased SC responsiveness. The investment made in increasing complexity is completely overcome by the resilience created in the supply chain structures as they are able to better react to disruptions guaranteeing higher service levels and higher profit values. However, this characteristic should be always met by a specific analysis of each SC and to its, perceptible, vulnerabilities.

As a final analysis, it is relevant to compare the results of this paper with those from the original publication of Cardoso et al. (2015), aimed at maximizing ENPV for each SC structure and scenario. As expected, our results produce a network with lower ENPV but with a trade-off for better ECSL.

As main conclusions, it can be said that investing in proactive resilient Supply Chain Design can reduce losses, generate value to companies and reduce the need for reactive strategies, in case of facing a disruptive event. With this work, we are also capable of attesting the positive correlation between the increased SC complexity with a positive outcome in case of some disruptions, as suggested by Cardoso et al. (2015) in their study.

Acknowledgements

The authors acknowledge the project DPI2015-67740-P (MINECO/FEDER)

References

- A. P. Barbosa-Póvoa, 2014. Process supply chains management - where are we? where to go next? *Frontiers in Energy Research* 2, 23.
URL <https://www.frontiersin.org/article/10.3389/fenrg.2014.00023>
- S. R. Cardoso, A. P. Barbosa-Póvoa, S. Relvas, A. Q. Novais, 2015. Resilience metrics in the assessment of complex supply-chains performance operating under demand uncertainty. *Omega* 56, 53–73.
- M. Kamalahmadi, M. M. Parast, 2016. A review of the literature on the principles of enterprise and supply chain resilience: Major findings and directions for future research. *International Journal of Production Economics* 171, 116–133.
- R. K. Oliver, M. D. Webber, et al., 1982. Supply-chain management: logistics catches up with strategy. *Outlook* 5 (1), 42–47.
- J. P. Ribeiro, A. Barbosa-Póvoa, 2018. Supply Chain Resilience: Definitions and quantitative modelling approaches - A literature review. *Computers & Industrial Engineering* 115, 109 – 122.
URL <https://www.sciencedirect.com/science/article/pii/S0360835217305272>
- J. B. Rice, F. Caniato, 2003. Building a secure and resilient supply network. *Supply Chain Management Review*, V. 7, No. 5 (Sept./Oct. 2003), P. 22-30: III.
- C. S. Tang, 2006. Perspectives in supply chain risk management. *International Journal of Production Economics* 103 (2), 451–488.

A model-based approach to design miniaturised structured packings for highly efficient mass transfer in gas/liquid multiphase flows

Daniel Sebastia-Saez and Harvey Arellano-Garcia*

Department of Chemical and Process Engineering, University of Surrey, Stag Hill Campus, Guildford GU2 7XH, United kingdom

**Corresponding author: Professor Harvey Arellano-Garcia (h.arellano-garcia@surrey.ac.uk)*

Abstract

Fractals are the evolutionary answer that Nature has developed to provide highly packed structures for mass and heat transfer. In this work, a computational fluid dynamics model will be presented to gain insight on the multiphase flow characteristics within fractal geometries. A substantial increment of the gas-liquid interface area with the fractal dimension of the particular geometry being tested is expected. This will allow the implementation of more compact designs, i.e. with greater specific area, than the conventional structured packings currently used for gas separation. More compact designs also mean less solvent used for the same gas absorption rate, reducing the heat duty of solvent regeneration. The next steps of this research will include the use of 3D printing techniques to reproduce fractal geometries to be tested in an experimental set-up, and the study of the interaction between nature-inspired gas absorbers and the rest of the carbon emitting facility through process simulations.

Keywords: CFD, fractals, biomimetics, structured packing, gas separation.

1. Biomimetics and the need for a new generation of structured packings

Nature has provided some of the most ingenious and elegant solutions to complex engineering challenges over millions of years of evolution. On different scales and in various scenarios, many living creatures have encountered similar design problems than humans, such as drag reduction or the need for efficient heat and mass transfer. Biomimetics consists on the replication of systems found in Nature to solve complex engineering situations. The design of Japan's bullet trains is an example. At high speeds, the blunt nose of the train would create a sonic boom upon exiting tunnels far exceeding environmental noise standards. By mimicking the geometry of the kingfisher beak, engineers were able to develop a more silent high speed train, which was also 10% faster and used 15% less electricity. Replication of the microscale patterns of shark skin to be applied to marine vessels and planes is another example of biomimetics. Shark scales possess a geometry that prevents the formation of microorganisms, and also reduces the overall hydrodynamic drag making swimming less energy consuming. It has since been applied to airplanes, marine vessels, and high-performance swimsuits. The application of biomimetics to improve chemical engineering equipment has not been however, so extensively explored to date. This work aims to investigate the

application of nature-inspired fractal geometries to improve structured packings (SPs) for gas separation. The purpose of SPs is to increase gas separation efficiency by providing high specific area. They consist of a sequence of parallel corrugated sheets with a purpose-built embossed surface texture to allow maximum spreading of a given solvent, hence maximizing the gas-liquid contact area. SPs are ubiquitous in industry, being distillation, air separation, and the production of chemicals some of their applications. Carbon capture and storage (CCS) is another remarkable field of recent development where SPs have been utilized. Proof of the importance of SPs in industry is the estimation from the CCS Association, which foresees that CCS could create 100,000 jobs across the UK by 2030, contributing £6.5 billion to the UK's economy (IME), and that the CCS industry could be as big as the North Sea oil industry, taking a significant share of a £5 trillion global CCS business by 2050 (AEA). The UK, with the plus of having an adequate storage capacity, will have a unique opportunity to benefit from this emerging sector. Given their widespread use, an improvement in the design of SPs would result in an enormous impact in the UK's chemical sector. One of the drawbacks of gas separation processes is the regeneration of the effluent solvent from the absorption column, which constitutes the greatest energy penalty of the process. To tackle this issue, the underlying hypothesis of this work lies in that a significant reduction of the regeneration cost could be achieved by reducing the volume of solvent circulated within the CCS facility, the key to achieve that goal being a dramatic increase in the process intensification. The results of the literature research conducted suggest that the application of microfluidics and fractal geometries increase the specific gas-liquid contact area, resulting in a significant reduction in the amount of solvent and the subsequent heat duty, and opening the gates towards economically attractive CCS. The results are transferrable to other chemical engineering sectors such as petrochemical, pharmaceutical, etc., which are fundamental to the UK's economy. The design of the novel breed of SPs is supported by recently developed fields such as microfluidics, fractal geometries, the application of externally generated turbulence, and rapid prototyping, the relation between them and the objectives of the project being depicted in Figure 1.

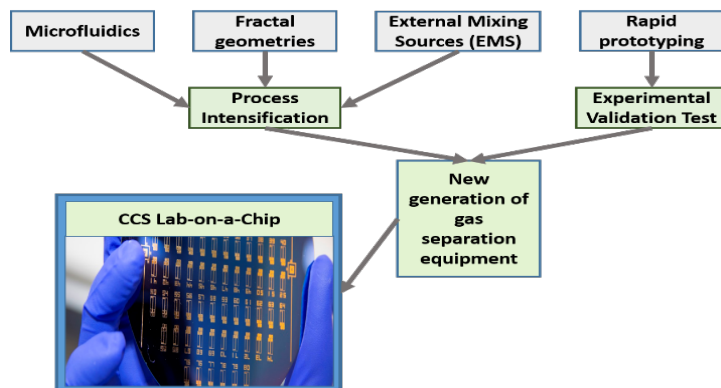


Figure 1 Relation between the novel concepts introduced in the design process and the objectives of this research

A substantial gain in intensification, determined by the use of fractal shapes and the scaling of the geometry down to the microscale, is thus envisaged. As laminar flows are encountered in microfluidic devices owing to the low Reynolds numbers, mixing is to be improved with the use of external sources of turbulence, namely electrophoresis, ultrasonic fields, etc. The partial objectives of this research are thus to determine the intensification capabilities of the application of the three above mentioned technologies, and the use of rapid prototyping, i.e. 3D printing techniques, to overcome past difficulties encountered in the manufacturing process of such complex geometries. Rapid prototyping will allow reducing any delay between the CFD-based analysis and the experimental confirmation of the resulting models. The whole design process is framed in a modelling approach that consists in multi-scale CFD analysis of the multiphase flow within fractal geometries to accelerate the validation of shapes tested numerically and the analysis of the performance of the new shapes in a process modeling environment.

2. Microfluidics, the concept of fractals and their application to the design of gas separation systems

Fractal shapes appear regularly in Nature in a variety of places and for many purposes. Snowflakes, blood vessels, plant root systems and DNA are just some of the numerous examples. Fractal shapes consistently appear in situations which require mass or heat transfer throughout a large space, such as blood vessels transporting blood to extremities of the body. The reason they are so common is how effectively they can use a given space to its maximum potential by spreading in a repetitive and consistent pattern. Tatsumi et al. (1989) demonstrated that a number of trees and plants used fractal root systems to gather nutrients. Rather than just growing in one long bending root, the roots split and spread to be able to gain more nutrients from the same volume of soil. This characteristic of optimal spreading and transfer throughout a space is of particular interest for heat and mass transfer devices. A fractal-shaped gas separation device would be potentially more compact than current SP designs and as a result, less solvent would be needed for the same gas absorption rate, reducing the heat duty for regeneration.

Repetitive patterns were first investigated in the 17th century, but little was understood until two centuries later when mathematician Karl Weierstrass demonstrated the first function that later would be defined as a fractal. A number of mathematicians followed on from Weierstrass' work and studied the geometry of fractals, being Sherman's functional relationship between the diameter of the branches and a number of flow characteristics including pressure gradient, wall shear stress, velocity gradient, Reynold's number, volumetric flow and average linear velocity of the flow (Sherman, 1981) one of the key achievements. Fractals had been recognized as appearing frequently in nature, but a holistic theory was not developed until 1982 by Mandelbrot, who investigated the fractal structures of coastlines, snowflakes, clouds, galaxy clusters, and other various naturally-occurring shapes, and defined the concept of fractal dimension as a measure of their space-filling capacity. The application of fractals to

improve fluid dynamic designs started when West derived a general model for minimising the work flow for bulk fluid transport through a network of branching tubes (West et al., 1997). To date, evidence has been reported in the literature as to the underlying phenomena which explains the available space exploitation provided by fractal shapes, as well as better pressure drop characteristics with respect to regular cylindrical geometries. Alharbi et al. (2004) demonstrated that the pressure drop through a fractal-like network is 50% less than that through a straight channel network. This difference is attributed to a local pressure recovery at each bifurcation. Fractal shapes provide thus a means to maximise the exploitation of the space available with more favourable pressure drop conditions than that found in geometries used in current SP designs.

3. Objectives

The general objective of this research is the design of a novel CCS technology in which the amount of solvent is drastically reduced compared to current SP designs, giving as a result a smaller heat duty at the solvent-recovery stage of the facility. A step-change in the performance of PCC facilities is therefore needed to accomplish the above-mentioned goal, which will eventually lead to a significant reduction of the volume of solvent used and a lower heat duty in the regeneration column. The general objective of this research is thus to take advantage of the high specific area of fractal geometries so as to investigate its application to gas absorption processes in order to reach high intensification. Further process intensification will be achieved through the scale of those geometries down to the characteristic size of microfluidic devices by imitation of natural structures, such as ramifications in blood vessels and other fractal structures, both at the level of the channel network and the wall roughness inside the channel. A new generation of small-scale PCC facilities with low heat duty and pressure loss will be obtained as a result. Since laminar flow characterises is encountered in microfluidic channels owing to their small diameter, external mixing sources (EMS) such as the application of electrophoresis, magnetic and ultrasonic fields, are to be investigated to improve mixing by inducing turbulence to obtain high performance designs in terms of separation efficiency.

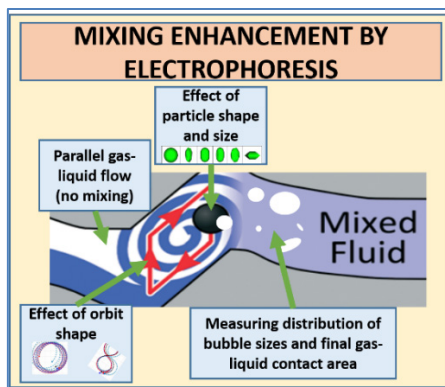


Figure 2 Illustration of the application of electrophoresis for mixing enhancing in microchannels.

Figure 2 shows a schematic of the mixing enhancement based on electrophoresis. The direction of the flow is from the left (where laminar flow is encountered owed to the small Reynolds number) to the right-hand side. The momentum exchange between the particles, which owe their movement to the external electric field, and the fluid result in enhanced mixing, thus opening the door towards even smaller structured packing geometries. Several parameters might affect the final degree of mixing, namely the particle size and the shape of both the particle and its trajectory within the microchannel.

Finally, experimental testing of the resulting prototypes will be possible by using rapid prototyping, i.e. 3D printing. The study is firstly focused on CCS applications, and therefore the main two columns which form such a facility (the absorption column and the stripper) are the primary object of this research. The regeneration of the solvent accounts for as much as 70% of the total opex cost for carbon capture and is the main target, although it should be noted that the findings can be extrapolated to the absorption column, and to any unit operation in a chemical plant involving gas separation. The specific key objectives of the project are summarised as follows:

- To tackle the problem of the high cost of solvent regeneration by achieving a critical reduction in the volume of solvent used within the post-combustion CCS facility. The latter implies the reduction of the heat duty in the stripping process, which is the main energy penalty.
- To characterise the hydrodynamics of multiphase flows within a ramified network of vessels in terms of reactor volume and pressure drop.
- To reach an unprecedented reduction in the size of the equipment needed for CCS, owing to the combination of the use of microfluidics with specifically built shapes, and EMSs.
- To explore the capabilities of rapid prototyping to create fast experimental fractal-like samples to be validated.
- To find the trade-off between the increase in specific surface resulting from the use of fractal shapes and the extra pressure drop expected from the scale-down to microfluidic characteristic lengths.
- To investigate the effect of the EMSs in the increase of mixing and, ultimately, their capability to provide extra intensification.

The design of the final unit capable of treating the entire amount of exhaust gases produced in a large carbon dioxide source, i.e. a power plant, is envisaged with the application of experimental validation and process simulations to check the interaction with the rest of the plant. The final unit will be formed of smaller lab-on-a-chip (LOC) modules in either cascade or parallel disposition, or a combination of both. Modularity is expected to help with adapting the size of the final unit to the amount of exhaust gas to be treated, which can vary with the source power output. The intensification potential resulting from the application of the fractal vessel network will determine the volume of exhaust gas that can potentially be treated with each LOC module and its nominal size. The basic configuration of the final LOC module design will therefore consist in the fractal vessel network, the external turbulence source equipment and the auxiliary control and instrumentation equipment. Replication of the basic LOC module will result in the final design being adaptable to the gas separation requirements at hand.

4. Conclusions

Although being a long-standing and mature technology, with not much evolution in the last decades, there is still room for improvement in the field of structured packings. Its matureness has actually resulted in a widespread use in almost any field of the chemical industry in which gas separation is needed, yet their efficiency has proved insufficient in the field of carbon capture and storage, owing to the high heat duty of the solvent recovery unit. This leads to the need for seeking a new paradigm in the design of structured packing geometries.

An improvement of the overall efficiency of the carbon capture process is envisaged in this work by implementing a radical change in the design of mass transfer equipment. This paradigm shift is based on the imitation of naturally occurring fractal-like geometries, and the use of micro fluidics to boost the specific area and thus reduce the amount of solvent to be regenerated for a given carbon removal rate.

Computational fluid dynamics are to be used to explore the intricacies of the multiphase flow within such complex geometries, saving the hurdles posed by experimental work in this aspect. The experimental work is reserved for the final testing of 3D printed prototypes resulting from the numerical investigation. The link between absorption columns filled with the new breed of packings and the carbon producing facility will be explored by using process simulations.

References

- AEA, Future value of coal carbon abatement technologies to UK industry for the Department of Energy and Climate Change, December 2008;
- A.Y. Alharbi, D.V. Pence and R.N. Cullion, 2004, Thermal characteristics of microscale fractal-like branching channels, *Journal of Heat Transfer*, 126(5), pp. 744–752.
- Institution of Mechanical Engineers (IME). UK becomin an also-ran' in carbon capture and storage race. *PE Magazine – ImechE*. 17th October 2012
- B.B. Mandelbrot, 1983, *The fractal geometry of Nature*, W.H. Freeman, San Francisco, CA.
- T.F. Sherman, 1981, On connecting large vessels to small. The meaning of Murray's law, *Journal of General Physiology*, 78(4), pp. 431–453.
- J. Tatsumi, A. Yamauchi and Y. Kono, 1989, Fractal analysis of plant root systems, *Annals of Botany*, 64(5), pp. 499–503.
- G.B. West, J.H. Brown and B.J. Enquist, 1997, A general model for the origin of allometric scaling laws in biology, *Science*, 276, 122–126.

Preliminary economic ranking of reactive distillation processes using a navigation method

Rahma Muthia,^a Aloijsius G. J. van der Ham,^a Anton A. Kiss^{a,b*}

^a*Sustainable Process Technology, Faculty of Science and Technology, University of Twente, PO Box 217, 7500 AE Enschede, The Netherlands*

^b*School of Chemical Engineering & Analytical Science, The University of Manchester, Sackville St, Manchester, M13 9PL, United Kingdom*

a.a.kiss@utwente.nl, tony.kiss@manchester.ac.uk

Abstract

Evaluating the applicability of reactive distillation (RD) is an important stage in the conceptual design phase, when RD is considered as a promising process intensification option. However, performing that task may be both time consuming and difficult due to the complexity of the models and the detailed data required. To solve this problem, this study presents a quick approach to perform a preliminary economic ranking of RD using a navigation method. This method works like a global positioning system (GPS) in which pre-defined maps (i.e. the plot of reflux ratio vs number of stages) are used to charting the applicability of RD. Together with the pre-defined maps, the data of RD configurations (i.e. number of rectifying, reactive, stripping stages) are generated. By using the navigation method, this study checks the applicability of RD for quaternary reversible reaction systems ($A+B=C+D$) with different boiling point orders. The result of a preliminary economic assessment is given as RD cost ranking which can be used as a valuable pre-screening prior to performing any detailed economic analysis. Therefore a full assessment requiring a long time can be avoided. With a fair comparison in terms of relative volatilities, the system with mid-boiling reactants generates the lowest cost, whereas the system with mid-boiling products requires the most expensive RD setup.

Keywords: reactive distillation, navigation method, conceptual design.

1. Introduction

Multifunctional reactors are essential components of process intensification, which integrate reaction and at least another function into a single unit operation (Stankiewicz, 2003). These technologies offer major benefits in reducing costs and saving energy (Castillo-Landero et al., 2017). Among the available multifunctional reactors, reactive distillation (RD) has become one of the most recognized and attractive units in chemical processing. The RD operation is promising for various types of reactions, e.g. (trans)esterification, hydrolysis and isomerization. In the RD application, optimum conversion and selectivity are attainable (Kiss 2003a), the separation limitation due to azeotropes can be prevented (Kaymak, 2017), a better plant environment (in terms of emission reduction and safety improvement) can be obtained (Shah et al., 2012). Considering the encouraging pathway of RD utilization, the primary evaluation of the RD applicability in the phase of conceptual design is important. However, performing that assessment may be both time consuming and difficult due to the detailed data,

complexity of the models and the lengthy algorithms required for optimal design (Segovia-Hernandez et al., 2015). Moreover, in many cases the result of the evaluation of RD application is unfortunately economically infeasible. In other words, the amount of time allocated to investigate the RD application and the results of the RD evaluation are unbalanced. To overcome this problem, this study presents a quick approach to perform an early economic ranking of RD using a navigation method. Using the proposed approach, the outcome is expected to be the first consideration of selecting chemical systems which might benefit from using RD as an intensified process.

2. Modelling approach

The navigation method used in this study has been introduced in our previous work (Muthia et al., 2018). The main objective of the method is to predict the RD applicability to real (non-ideal) chemical systems based on generic (ideal) cases. In this work, the only focus is applying the method to perform preliminary economic ranking for the RD application. For the sake of clarity in this study, the generic cases of quaternary systems ($A+B=C+D$) with different boiling point orders were assessed. Using pre-defined maps (i.e. the plot of reflux ratio (RR) vs number of stages (NTS), see Figure 1), this GPS-like method navigates the applicability of RD. Next to the pre-defined maps, the data of RD configurations (i.e. number of rectifying, reactive, stripping stages) are presented. To generate the pre-defined maps, ideal generic cases were used and few basic (constant) parameters were required, i.e. relative volatility values (α) and chemical equilibrium constants (K_{eq}).

For consistency, the groups naming of the quaternary systems used in this study follows the rules proposed by Luyben and Yu (2008). A fair comparison of the relative volatilities was determined in which the α_{AB} and α_{CD} values were specified (Table 1). Only the specified variables in the group I_r are different from those in the other groups since the boiling points order gives no opportunity to obtain the specified α_{AB} and α_{CD} at 2 and 6, respectively. The groups with either the heaviest reactants (group II_p , i.e. $T_{b,C} < T_{b,D} < T_{b,A} < T_{b,B}$) or the lightest reactants (group II_r , i.e. $T_{b,A} < T_{b,B} < T_{b,C} < T_{b,D}$) are excluded because, from a thermodynamic viewpoint, collecting either the lightest or the heaviest products from equimolar reactants would be almost impossible.

Using the proposed method, a preliminary cost ranking was obtained for these quaternary systems. The cost relation can be obtained because NTS directly represents the height of column and gives an estimation of the investment cost. RR is proportional to the column diameter and is associated with the energy requirements (Kiss, 2013b). Using NTS and RR as indirect cost parameters for equipment and energy, in this study there was no explicit cost formula. The outcome of the preliminary cost ranking was then compared with the results reported by Luyben and Yu (2008) who generated the economic estimation data by performing detailed simulations with only a fixed K_{eq} .

Table 1. Groups of quaternary systems based on boiling points orders

Group	A + B \rightleftharpoons C + D, T_b orders	Specified variables		Set variables	
		α_{AB}	α_{CD}	α_{CA}	α_{BD}
I_p	C < A < B < D	2	6	2	1.5
I_r	A < C < D < B	6	2	0.6	0.6
III_p	C < A < D < B	2.1	6	4	0.7
III_r	A < C < B < D	2.1	6	0.7	4

All the simulations were performed using the Aspen Plus (v8.6) process simulator. The feed streams of pure A and B (saturated liquid) in a stoichiometric ratio were fed to a RD column operating at an atmospheric pressure. The light reactant was introduced into the column at the bottom part of the reactive section and the heavy reactant was fed at the top part of the reactive section, therefore resulting in a counter current flow along the reactive part of the RD column. There were two important design criteria specified: a) 99 mol% bottom product purity, and b) 0.5 mol/mol bottom-to-feed ratio. Having set these two criteria, the minimum overall conversion was always 99 mol%.

3. RD applicability space

Figure 1 (left) presents an illustrative applicability space of RD for a certain chemical system. The dotted line indicates the boundary of the RD applicability space which separates the “applicable” and “not-applicable” areas. Exactly on the boundary line and inside the “applicable” area, the product purity is equal to or larger than the minimum criterion. For the sake of presenting clear results in this study, the applicability space is shown with the maximum scale of 100. The NTS_{min} is specified as NTS with $RR=100$ and the RR_{min} is defined as the lowest RR in case $NTS=100$. From the bottom-left to the top-right inside the “applicable” area, the colour shifts from white to light grey to darker grey, which indicates that the lighter colour is the preferred region for the RD operation.

The vertical orange line shows an example of a NTS with multiple RD configurations which have different RR values. Point 1 highlights the lowest RR and point 2 gives a higher RR with another RD configuration. Selecting point 1 with the lowest RR may be preferred in terms of the energy use. However, it is essential to also consider other points, such as point 2, since some configurations could be more beneficial and gives less capital investment (e.g. less number of reactive stages).

Figure 1 (right) presents an example of a plot of RR vs number of reactive stages for the illustrative applicability space in Figure 1 (left) at $NTS=40$, which indicates multiple RD configurations available with the RR values slightly higher than the lowest RR at point 1. In practice, the very marginal difference of RR values (e.g. in two decimal places) is negligible. Therefore, in this study it seems logic to consider the RD configurations with the RR values within the 3% range of the lowest RR, e.g. 20 reactive stages for the lowest RR value as shown in Figure 1 (right).

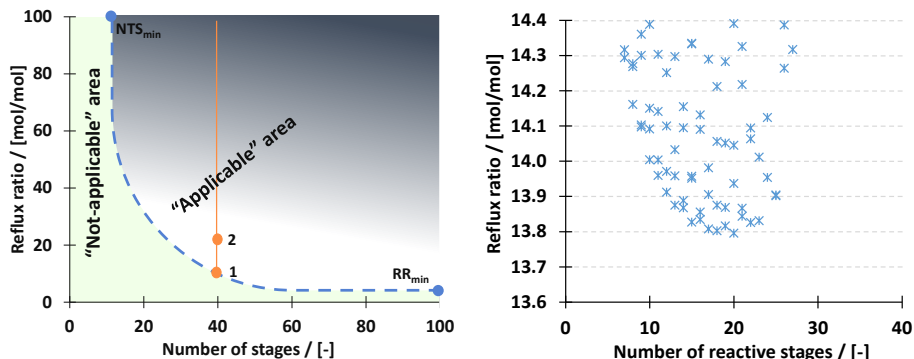


Figure 1. An illustrative applicability space of RD (left) and multiple RD configurations available inside the applicability space at $NTS = 40$ (right) (Muthia et al., 2018)

4. Preliminary economic ranking of RD

For the preliminary economic ranking of RD configurations, the applicability spaces and the configurations of RD are presented. Figure 2, Figure 3 and Figure 4 on the left show the RD applicability spaces for groups I_p, III_p, III_r, respectively. In the cases of groups I_p and III_p, the boundary lines of $K_{eq}=0.01-10$ are obtained for $NTS \leq 100$ and $RR \leq 100$. For group III_r, the boundary line of $K_{eq}=0.01$ is outside the applicability space and might still be obtained if $NTS \geq 100$ and $RR \geq 100$. All the groups (I_p, III_p, III_r) show the same trend of the RD applicability spaces in response to the increasing K_{eq} . For a higher K_{eq} , the applicability space is always larger since a higher K_{eq} gives a better conversion, which implies a lower RR required for a certain NTS.

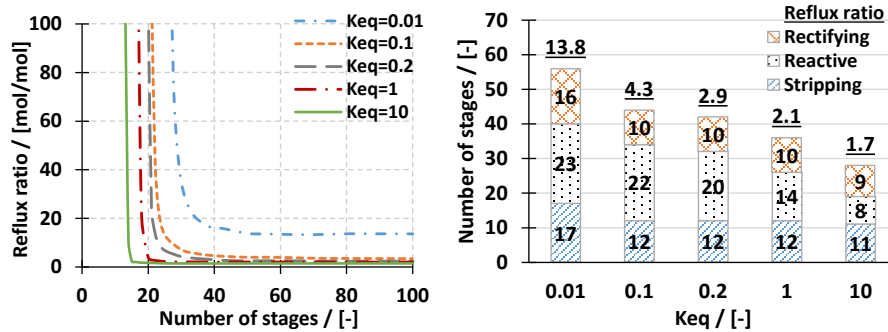


Figure 2. RD applicability spaces (left) and configurations (right) at $NTS=2 \cdot NTS_{min}$ for group I_p

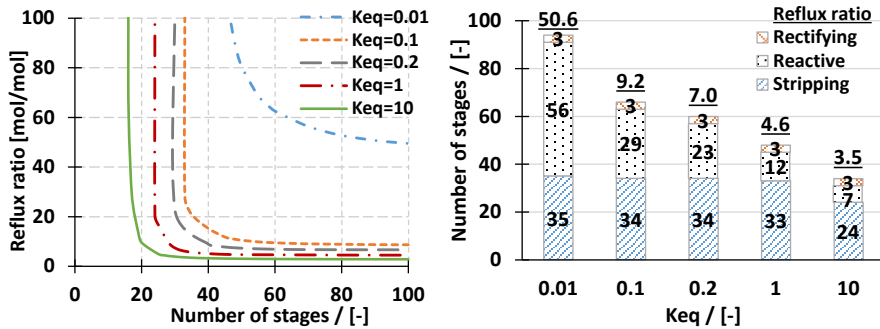


Figure 3. RD applicability spaces (left) and configurations (right) at $NTS=2 \cdot NTS_{min}$ for group III_p

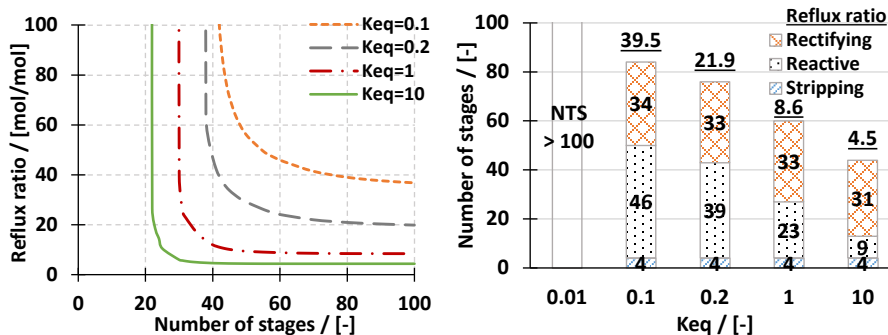


Figure 4. RD applicability spaces (left) and configurations (right) at $NTS=2 \cdot NTS_{min}$ for group III_r

For group I_r , a single RD column is not applicable since the simulations of the generic cases with $K_{eq}=0.01-10$ did not meet the required product purity and the bottom-to-feed ratio. Obtaining mid-boiling products from the lightest and the heaviest reactants might need an RD set-up with side-draw product stream(s). In that case, at least one additional normal distillation is required to purify the desired products (Luyben and Yu, 2008). As another option, a reactive dividing wall column can be considered. Due to its complexity, group I_r results in the most expensive RD set-up of all the categories.

Figure 2, Figure 3 and Figure 4 on the right show the RD configurations for groups I_p , III_p , III_r , respectively, in response to varying K_{eq} . The underlined numbers in the plots show reflux ratios. The presented plots are based on the lowest RR at $NTS=2 \cdot NTS_{min}$ in the RD applicability spaces. Selecting this NTS is only based on design rules for conventional distillation columns. Alternatively, other NTS values, such as the NTS at $1.2 \cdot RR_{min}$, can also be selected. For a higher K_{eq} , the number of reactive stages and RR are always smaller due to the better reaction performance. The number of rectifying and stripping stages stays more or less the same but the separation can be done with less reflux ratio RR since the reactants are converted to a larger extent in the reactive section, therefore making the separation easier.

The RD configurations of the various groups presented in Figure 2, Figure 3 and Figure 4 (all plots on right) are then analyzed for a uniform K_{eq} . The NTS and RR values increase from group I_p , III_p , to III_r which are also in an agreement with the increase in the number of reactive stages. The increase of NTS and RR clearly indicate the cost ranking of these three groups – I_p , III_p , III_r – from the lowest to the highest cost respectively. The comparison of the RD configurations at the same K_{eq} also suggests the RD column design as shown in Figure 5. This suggestion is in accordance with the results obtained by Luyben and Yu (2008).

If group III_p is compared to group I_p , a larger reactive section is needed to convert reactant B and to avoid B reaching the stripping section. Besides, the number of stripping stages of the group III_p is bigger than the stripping section of the group I_p because the separation between reactant A and product D is more difficult to achieve ($\alpha_{AD}=3$ for group I_p and $\alpha_{AD}=1.5$ for group III_p). The number of rectifying stages of the group III_p is smaller because the separation, mainly between reactant B and product C, is easier than the group I_p ($\alpha_{CB}=4$ for group I_p and $\alpha_{CB}=8.4$ for group III_p).

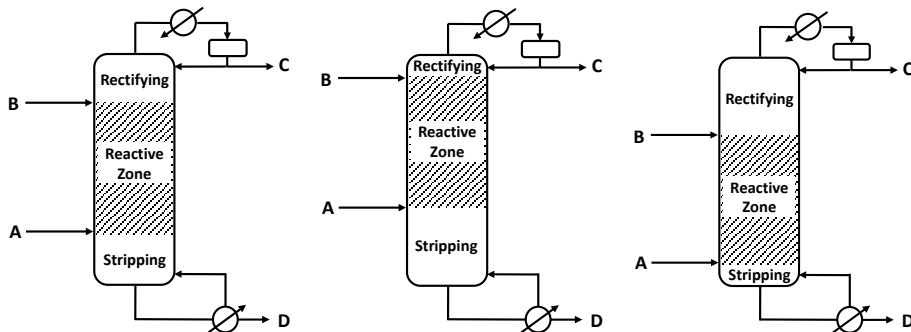


Figure 5. Proposed RD configurations for groups I_p (left), III_p (center), and III_r (right)

Considering the relative volatilities listed in Table 1, the RD configurations of group III_r were expected to be the mirror of the RD column set-up of group III_p. However, the results show that a larger reactive section and a larger RR are required for group III_r in comparison to group III_p. A larger reactive section is required to convert reactant A and avoid it reaching the rectifying section. This reaction task is more challenging than the one in group III_p since the reactant A is easily vaporized, therefore interfering with the desired purity of product C. Correspondingly, a higher reflux ratio is needed to condense it back to the liquid phase.

5. Conclusions

The investigation of the quaternary systems with various boiling point orders and a fair comparison of the relative volatilities (based only on the outcome of RD configurations for the generic cases) gives a first overview of the cost ranking – group I_p, III_p, III_r – from the lowest to the highest cost. A single RD column is not applicable for group I_r in which a RD followed by a conventional distillation or a reactive dividing wall column can be considered. In this respect, group I_r leads to the most expensive RD set-up. The GPS-like navigation method was successfully applied to perform preliminary economic ranking of RD for different generic cases of the quaternary systems, and this quick approach holds the promise to be used in a real system. Prior to implementing that task, the RD applicability for a real system can be quickly evaluated by the navigation method, as provided in our previous work (Muthia, et al. 2018).

References

- A. Castillo-Landero, A. Jiménez-Gutiérrez, R. Gani, 2017, Development of an Intensified Reactive Distillation Process for the Synthesis of Dioxolane Products, *Computer Aided Chemical Engineering*, 40, 1081-1086.
- D. B. Kaymak, 2017, Design and Control of a Separation Process for Bioethanol Purification by Reactive Distillation, *Computer Aided Chemical Engineering*, 40, 1075-1080.
- A. A. Kiss, 2013a, *Advanced Distillation Technologies - Design, Control, and Applications*, John Wiley & Sons, Ltd., UK.
- A. A. Kiss, 2013b, Novel applications of dividing-wall column technology to biofuel production processes, *Journal of Chemical Technology and Biotechnology*, 88, 8, 1387-1404.
- W. L. Luyben and C. C. Yu, 2008, *Effect of Boiling Point Rankings on the Design of Reactive Distillation*, *Reactive Distillation Design and Control*, John Wiley & Sons, Inc, USA.
- R. Muthia, A. G. T. Reijneveld, A. G. J. van der Ham, A. J. B. ten Kate, G. Bargeman, S. R. A. Kersten, A. A. Kiss, 2018, Novel method for mapping the applicability of reactive distillation, *Chemical Engineering and Processing: Process Intensification*, Submitted for publication.
- M. Shah, A. A. Kiss, E. Zondervan, A. B. de Haan, 2012, A systematic framework for the feasibility and technical evaluation of reactive distillation processes, *Chemical Engineering and Processing: Process Intensification*, 60, 55-64.
- J. G. Segovia-Hernandez, S. Hernandez, A. Bonilla Petriciolet, 2015, Reactive distillation: A review of optimal design using deterministic and stochastic techniques, *Chemical Engineering and Processing: Process Intensification*, 97, 134-143.
- A. Stankiewicz, 2003, Reactive separations for process intensification: an industrial perspective, *Chemical Engineering and Processing: Process Intensification*, 42, 3, 137-144.

Multi-scale system modelling under circular bioeconomy

Miao Guo*

Department of Chemical Engineering, Imperial College London, SW7 2AZ, UK

miao.guo@imperial.ac.uk

Abstract

Waste sector is expected to play significant roles in the evolving circular bioeconomy in the coming decades. Considerable amount of carbon-containing and nutrient-rich wastewater and organic solid waste resources are generated every year globally. In the UK, wastewater is estimated as 16 billion litre per day, which together with annual production of over 100 million tonnes of carbon-containing solid biowaste (e.g. biodegradable fraction municipal solid waste (BFMSW)), above 14 million tonnes of forestry and agricultural residues and large amount of other waste provide significant opportunities (BIS 2015). They could be converted via various routes to bioenergy or other value-added products such as bioenergy, biofuels, bio-plastics and fertilisers, which shift us to a resource-circular bioeconomy. In this study, a multi-scale system modelling approach is presented to investigate the holistic economic and environmental profiles of alternative resource recovery methods integrated into wastewater and organic waste treatment systems, and bring such sustainability criteria into the process synthesis and value chain optimisation. By introducing game theory into the multi-objective optimisation model and formulating the interactions between multi-level nodes involved in the supply chain, our modelling toolkit offers the functionality to account for both macro-level economy performances and micro-level individual stakeholder benefits. The modelling methodology has been applied to two case studies - wastewater and lignocellulosic waste resource recovery. Our results suggest that ion exchange is a promising technology showing high nitrogen and phosphorus removal and recovery efficiency from municipal wastewater and delivering competitive sustainability scores; whereas the integrated thermochemical and biochemical routes are favourable options for lignocellulosic resources. Current study also demonstrates such multi-scale modelling toolkit can support decision-making on optimal or equilibrium solutions for the waste bioconversion process design and waste recovery supply chain strategy at temporal-spatial scales, which are the key elements in building a sustainable circular economy.

Keywords: Waste resource recovery, process design, sustainability, optimisation.

1. Introduction

Bioeconomy has made substantial contribution to the global socio-economic growth; in the UK, it injected over £200 billion gross value into British economy and supported 5 million jobs by 2014 (Bauen et al. 2016). The predominant role of waste market has been highlighted in the UK and beyond. Considerable amount of carbon-containing and nutrient-rich wastewater and organic solid waste resources are generated every year globally. As estimated by Green Investment Bank, UK waste capacity by 2020 could

bring £5 billion investment opportunity. UK wastewater estimated as 16 billion litre per day, together with annual production of over 100 million tonnes of carbon-containing solid biowaste (e.g. BFMSW) above 14 million tonnes of forestry and agricultural residues and large amount of other waste provide significant opportunities (BIS 2015). They could be converted via various routes to bioenergy or other value-added products shifting us to a resource-circular bioeconomy. By far the most widespread recovery technology in the wastewater treatment and bio-based solid sectors is anaerobic digestion (AD). The generated biogas i.e. carbon recovery is often used for onsite combined-heat-and-power generation, but may as well be upgraded and injected into the natural gas grid or compressed as transport fuels, or used for methanol and biodegradable plastic production (such as PHA) (Science and Technology Committee 2014; Karthikeyan et al. 2015) or reformed to hydrogen for microbial single cell protein production (Matassa et al. 2015). In the UK, AD has been promoted as an environmentally favourable option for waste carbon recovery, undergoing significant development since 2011 when Anaerobic Digestion Strategy and Action Plan was launched (DEFRA 2011, 2015). By end of 2016, there were 540 operational AD facilities in the UK with a total capacity of 708 MW (equivalent to powering 850,000 households); over 90 AD plants injected bio-methane into the natural gas grid, accounting for 2.2% UK gas consumption (Anaerobic Digestion & Bioresources Association 2016). Despite of the fact that nutrient-rich waste recovery (e.g. struvite recovery) is in particular of interests due to the dominancy of fossil fuel in nutrient production (e.g. energy-intensive Haber-Bosch process for nitrogen fertiliser production), and depleting non-renewable mineral deposit (e.g. phosphorus), the value and cycling of nutrients resulted from AD (e.g. nitrogen and phosphorus) are often overlooked. Much concerns have been also raised regarding the over capacity issues and the fact that the energy-focused incentive strategies could hinder the penetration of other, potentially more environmentally favourable, resource recovery options. Such risks could be mitigated via AD-based bioconversion systems integrating advanced C conversion with other technology options for N/P and wider resource recovery e.g. AD integration with nature-based remediation solutions (Lee et al. 2018). However, such paradigm shift requires an understanding of the process configuration and whole resource-waste system design, but also the stakeholders (e.g. technology developers and operators, feedstock suppliers, finance systems, policy-makers) involved to achieve optimal or equilibrium solutions for the entire value chains, considering the environmentally sustainable and economically viable development of waste bioresource sectors. Despite of the advances in mathematical modelling, waste-treatment process synthesis e.g. (Puchongkawarin et al. 2015; Puchongkawarin et al. 2016), and sustainability evaluation and optimisation, research gaps emerge in the integrative system modelling approach that links the inherently waste recovery sub-systems with value chains complexity and wider ecosystem and natural capital variables (e.g. land, water). This study aims to contribute to the modelling advancement by proposing a multiple-scale modelling tool, which combines biogeochemical and process simulation, sustainability evaluation and multi-objective optimisation to bring environmental and economic criteria into optimal and equilibrium solutions and bridge process synthesis and whole-system level design. In particular, under the modelling framework, the interconnection of bio-waste with wider resources and ecosystem drivers has been addressed; multi-scale decision spaces involved in the waste resource management have been considered.

2. Methods

As presented in Fig 1, the modelling framework is underpinned by a closed-loop concept for resource-waste-land-water nexus under circular bioeconomy. The proposed modelling framework is presented in Fig 2, where the resource-waste-land-water nexus are captured by the integrative approach incorporating biogeochemical simulation, process-based waste recovery into optimization tools. Multi-scale (i.e. operational and tactical and strategic decision) and multi-echelon (resource supply, technology, distribution) complexity involved in the nexus are reflected in the model; ecosystem drivers and various conversion technologies (centralized vs. decentralized) and sustainability matrix and multi-stakeholders involved in the decision making are formulated. Under the framework, the combined reaction kinetic and equilibrium modelling approaches are employed to configure the process and operation and simulate the technical performances of diverse waste resource recovery to derive process flowsheet. This has been achieved by combining Aspen Plus and a state-of-the-art wastewater treatment simulator (GPS-X). The input-output flowsheet predicted was used to represent process performance; by applying CapdetWorks in conjunction with GPS-X and Economic Analyser embedded in AspenTech, the costing flows were obtained. As formulated in Eq. (1), a life cycle sustainability assessment (LCSA) approach was adopted as a systematic and rigorous evaluation tool to account for holistic sustainability (economic and environmental perspectives). The cradle-to-grave LCSA was performed on Simapro[®] platform.

$$EI_{kpi} = \sum_r \sum_s EI_{r,kpi}^{in} F_{r,s}^{in} X_{r,s}^{in} + \sum_c \sum_s EI_{c,kpi}^{out} F_{c,s}^{out} X_{c,s}^{out} \quad (1)$$

Where the variable EI_{kpi} denotes the total impacts of a given process (per functional unit) expressed as key sustainability performance indicator kpi . EI_{kpi} is determined by the characterisation impact factors for input resource r ($EI_{r,kpi}^{in}$) or emitted compound c ($EI_{c,kpi}^{out}$) input-output flows ($F_{r,s}^{in}$ or $F_{c,s}^{out}$) and concentration ($X_{r,s}^{in}$ or $X_{c,s}^{out}$) at stage s .

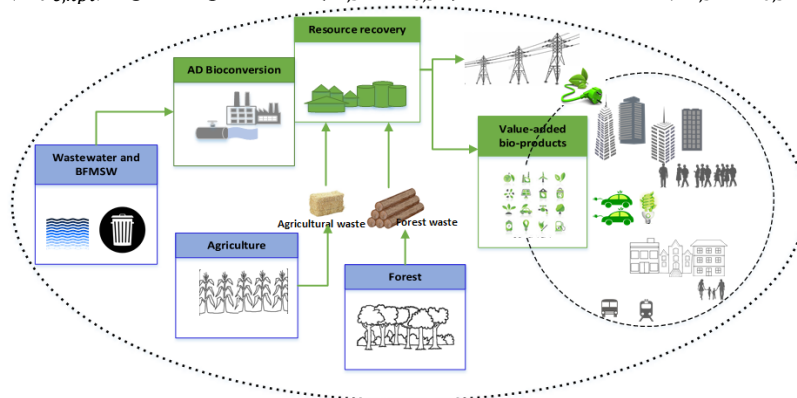


Figure 1 Waste resource recovery under circular bioeconomy

A mixed integer linear programming (MILP) optimisation model was developed to explore the temporal-spatial solutions for waste recovery system design (e.g. AD-based bioconversion) under circular bio-economy, where nonzero-sum, non-cooperative games were modelled to explore equilibrium solutions. As the modelling concept demonstrated in the Fig 1, different stakeholders involved across supply chain echelons were captured in the equilibrium model, including the feedstock suppliers, existing technology (e.g. AD) operators, new bioconversion technology developers and operators, distribution centres, investors and finance systems, policy-makers and regulators. The government is modelled as system regulator defining the marco-economy boundary conditions and implementing

policies, where the deployment policies were grouped into seven schemes and formulated in the model. A flexible echelon structure was simulated; whereas the model was further configured to consider the natural capital resource competition issues e.g. land-competition between the agricultural waste as feedstock and the bioenergy crops (e.g. miscanthus) exclusively grown for waste resource recovery processes.

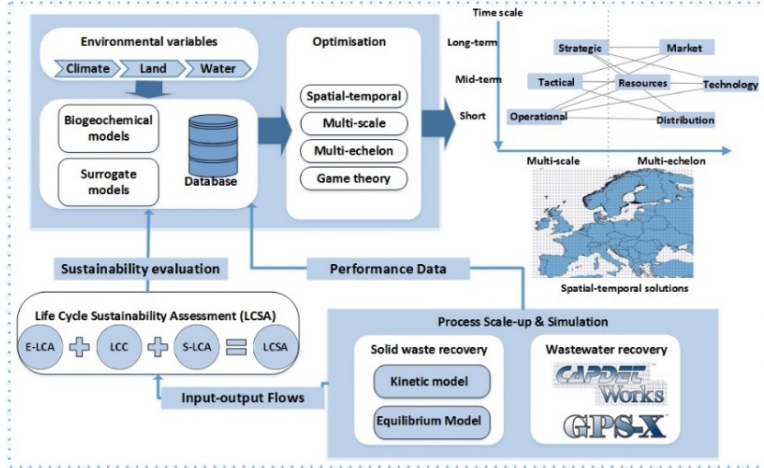


Figure 2 Multi-scale modelling framework for circular bioeconomy

Under decentralised optimisation mode, objective function (Eq. (2)) is to achieve Nash equilibrium solution for the multi-echelon waste-recovery value chains where the stakeholders involved in are expressed as nodes n_1, n_2, \dots . Each node n has a status quo point (\widehat{TI}_n), which reflects the acceptable profitability threshold of the investment on node n . The Nash solution is TI_n , where $TI_n \geq \widehat{TI}_n$ and future economic impacts are discounted back to the present values. ε_n represents the negation power of the node n . The higher negotiation power indicator is, the more advantage the node n has in profit allocation. The variable TI_n (Eq.(3)) is determined by the income of node n from trading in market and with other nodes n' over time period t ($SALEI_{n,t}$), government subsidy during time period t ($SUBSIDY_{n,t}$), tax paid by node n ($TAX_{n,t}$), loan interest over time period t ($Interest_{n,t}$), capital investment with bank loan decision (binary parameter $Equity_n$), Insurance cost for n ($Insure_{n,t}$), and impacts caused by process operation ($OPEX_{n,kpi,t}$), transport ($TRI_{n,kpi,t}$), capital inputs ($CAPEX_{kpi,n}$) as well as the discount rate over time t (Dis_t). Two key performance indicators (kpi) were accounted for i.e. economic and greenhouse gas (GHG). The impacts of GHGs have been monetarised by introducing a weighting factor $WeightF_{kpi,t}$, where the market price for traded C emissions is applied (£/kg CO₂ equivalence). A user defined parameter $\theta_{kpi,t}$ scopes whether policy instrument for emission trading is included (1=inclusion; 0=exclusion).

$$\max Obj = \prod_n (TI_n - \widehat{TI}_n)^{\varepsilon_n} \quad (2)$$

$$TI_n = \sum_t ((SALEI_{n,t} + SUBSIDY_{n,t} - TAX_{n,t} - Interest_{n,t} Equity_n - Insure_{n,t} - \sum_{kpi} (OPEX_{n,kpi,t} + TRI_{n,kpi,t} - Cap_{kpi \in EPI,n,t}) WeightF_{kpi,t} \theta_{kpi,t}) \times \frac{1}{(1+Dis_t)^t} - \sum_{kpi} CAPEX_{kpi,n} \quad (3)$$

Based on the IRN, IPCC, IE renewable deployment policy reports (IEA 2011), key renewable deployment policies have been classified and generalised into seven schemes

(Eq.(4)). By incorporating such schemes, model could address a range of questions e.g. how the system performs in response to the different government incentive strategies.

$$SUBSIDY_{n,t} = \sum_{sub} (In_{sub,n,t} + ProPay_{sub,n,t} + TaxRed_{sub,n,t} + LoanSUB_{sub,n,t} + TarrifSUB_{sub,n,t} + BuySUB_{sub,n,t} + CertiTrade_{sub,n,t}) \tau_{sub,n,t} \pi_{sub,t} \quad (4)$$

Where $\pi_{sub,t}$ is a user-defined parameter (1= policy *sub* is implemented; 0= exclusion of policy *sub*) and binary variable $\tau_{sub,n,t}$ represents the choice of node *n* in terms of their participation in government subsidy scheme *sub*. The following seven schemes have been taken into account -

Scheme 1 lump-sum direct subsidy $In_{sub,n,t}$ e.g. grant, premium payment, rebate;

Scheme 2 revenue support for bio-products *r* produced (e.g. energy production payment), where variable $ProPay_{sub,n,t}$ is determined by Eq. (5);

Scheme 3 government tax reduction variable $TaxRed_{sub,n,t}$ (Eq.(6)) depending on the revenues e.g. tax credit, tax reduction, accelerated depreciation schemes

Scheme 4 continuous variable $LoanSUB_{sub,n,t}$ (Eq. (7)) representing the government financing provided to nodes in return for a loan as investment;

Scheme 5 deployment policies to guarantee node with priority access and dispatch by setting a fixed tariff per unit bio-product *r* delivered ($TarrifSUB_{sub,n,t}$, Eq. (8))

Scheme 6 as formulated in Eq.(9), government green product purchasing schemes regulate the supply of green product purchase beyond obligations (e.g. green energy purchasing); the variable $BuySUB_{sub,n,t}$ depends on the regulated rate $BuySUBR_{sub,r,t}$ and bio-product purchase and consumption.

Scheme 7 certificate trading gain under quota mandate scheme. Variable $CertiTrade_{sub,n,t}$ Eq.(10) is determined by the purchased or consumed bioproducts, obligation threshold for bioproducts and price under certificate trading scheme.

$$ProPay_{sub,n,t} = \sum_{mr} \sum_c \sum_m \sum_p ReS_{sub,mr,t} Con_{mr,p,m} Pro_{p,m,c,n,t} \quad \text{if } Con_{r,p,m,n} > 0 \quad (5)$$

$$TaxRed_{sub,n,t} = NRev_{n,t} TaxRRate_{sub,t} \quad (6)$$

$$LoanSUB_{sub,n,t} = SubIntR_{sub,t} Loan_n \quad (7)$$

$$TarrifSUB_{sub,n,t} = \begin{cases} 0 & \text{if } FixedTarrif_{sub,r,t} \leq P_{r,t} \\ \sum_{mr} (FixedTarrif_{sub,mr,t} - P_{mr,t}) Sale_{mr,n,t} & \text{if } FixedTarrif_{sub,r,t} > P_{r,t} \end{cases} \quad (8)$$

$$BuySUB_{sub,n,t} = \sum_{mr} BuySUBR_{sub,mr,t} (Purchase_{n,mr,t} - Mandate_{mr,t}) \quad (9)$$

$$CertiTrade_{sub,n,t} = \sum_{mr} Certificate_{sub,mr,t} (- \sum_c \sum_m \sum_p Con_{mr,p,m} Pro_{p,m,c,n,t} - Mandate_{mr,t}) \epsilon_{sub,t} \quad \text{if } Con_{r,p,m,n} < 0 \quad (10)$$

The non-linear equations in the model (e.g. Eq.(4)) were converted to linear formulations. Objective function (Eq. (2)) is non-linear and non-convex, which was transformed into a logarithmic formulation Eq. (11). The derived mixed integer non-linear programming can be converted to MILP using the algorithm proposed by You and Grossmann (2011).

$$\max Obj' = \sum_n \epsilon_n \ln(TI_n - \widehat{T}I_n) \quad (11)$$

3. Results

The modelling methodology has been applied to two case studies - wastewater and lignocellulosic waste resource recovery. In case study 1, the chemical and biological

pathways and ion exchange pathways for phosphorus (P) and nitrogen (N) removal and recovery were simulated using ManTIS 3 built in GPS-X. These include three N removal and recovery routes (i.e. conventional nitrification/denitrification, Anammox, and an anaerobic route with ion exchange), three P removal and alternative recovery routes (struvite, ferric & phosphate recovery and hydroxyapatite recovery). Overall the ion exchange route performs best for N removal, with a superior costing profile, and environmental advantages on most impact categories except for its high eutrophication burdens. Under multiple sustainability criteria, chemical pathway outperformed biological routes and ion exchange for P removal whereas the struvite is shown as a promising P recovery route in terms of environmental footprint. In case study 2 the integrated thermochemical and biochemical routes were indicated as favourable options for lignocellulosic waste resource recovery. The process design and sustainability performance results were fed into MILP model and solved in AIMMS 4.0 using CPLEX 12.6 solver on a 3.4 GHz (2 processor) 96GB RAM computer (results not shown here). Via two case studies, this research highlights the insights the proposed framework could generate for multi-scale value chain design for waste recovery at spatial and temporal scales and to explore trade-offs between economic targets and environmental issues involved in the waste resource recovery systems in the coming decades. The model can be extended to include other technologies for generating other high-value products from bio-waste and used to address a range of research questions e.g. how the circular bioeconomy system and individual stakeholder would perform in response to the different government incentive schemes and what would be the most effective approach (e.g. incentives) to achieve innovative waste recovery technology deployment.

References

- Anaerobic Digestion & Bioresources Association. 2016. ADBA Market & Policy Reports 2016
- Bauen, A., G. Chambers, M. Houghton, B. Mirmolavi, S. Nair, L. Natrass, J. Phelan, and M. Pragnell. 2016. "Evidencing the Bioeconomy."
- BIS. 2015. "Building a high value bioeconomy: opportunities from waste."
- DEFRA. 2011. "Anaerobic Digestion Strategy and Action Plan."
- IEA. 2011. 'Deploying Renewables 2011'.
- Karthikeyan, O. P., K. Chidambarampadmavathy, S. Cires, and K. Heimann. 2015. 'Review of Sustainable Methane Mitigation and Biopolymer Production', *Critical Reviews in Environmental Science and Technology*, 45: 1579-610.
- Lee, Jongkeun, Ki Young Park, Jinwoo Cho, and Jae Young Kim. 2018. 'Releasing characteristics and fate of heavy metals from phytoremediation crop residues during anaerobic digestion', *Chemosphere*, 191: 520-26.
- Matassa, Silvio, Damien J. Batstone, Tim Hülsen, Jerald Schnoor, and Willy Verstraete. 2015. 'Can Direct Conversion of Used Nitrogen to New Feed and Protein Help Feed the World?', *Environmental Science & Technology*, 49: 5247-54.
- Puchongkawarin, C., C. Gomez-Mont, D. C. Stuckey, and B. Chachuat. 2015. 'Optimization-based methodology for the development of wastewater facilities for energy and nutrient recovery', *Chemosphere*, 140: 150-58.
- Puchongkawarin, C., Y. Vaupel, M. Guo, N. Shah, D. Stuckey, and B. Chachuat. 2016. 'Towards the Synthesis of Wastewater Recovery Facilities using Enviroeconomic Optimization.' in *The Water-Food-Energy Nexus: Processes, Technologies and Challenges*.
- ScienceandTechnologyCommittee. 2014. "Waste or resource? Stimulating a bioeconomy "
- You, Fengqi, and Ignacio E. Grossmann. 2011. 'Stochastic inventory management for tactical process planning under uncertainties: MINLP models and algorithms', *AIChE Journal*, 57: 1250-77.

An Integrated Reactive Separation Process for Co-Hydrotreating of Vegetable Oils and Gasoil to Produce Jet Diesel

Miriam García-Sánchez^b, Mauricio Sales-Cruz^a, Teresa López-Arenas^a, Tomás Viveros-García^b, Alberto Ochoa-Tapia^b, Ricardo Lobo-Oemichen^b and Eduardo S. Pérez-Cisneros^{b*}

^a*Departamento de Procesos y Tecnología, Universidad Autónoma Metropolitana-Cuajimalpa, Avenida Vasco de Quiroga No.4871, Colonia Santa Fe, Delegación Cuajimalpa de Morelos, Ciudad de México, C.P. 05300, México*

^b*Departamento de Ingeniería de Procesos e Hidráulica, Universidad Autónoma Metropolitana-Iztapalapa, Av. San Rafael Atlixco No. 186, Col. Vicentina, Ciudad de México, C.P. 09340, México*

espc@xanum.uam.mx

Abstract

An integrated reactive separation process for the production of jet diesel from vegetable oils and gasoil mixture has been developed. The integrated reactive separation process consider three interconnected sections: 1) a triglyceride hydrolysis section consisting of a catalytic heterogeneous reactor which is used to transform the triglycerides of the vegetable oils or animal fats to the corresponding fatty acids and a coupled decanter-distillation column to separate the fatty acids from glycerol and water; 2) a co-hydrotreating section where a reactive distillation column is proposed to perform the deep hydrodesulfurization (HDS) of gasoil and the hydrodeoxygenation (HDO) and the decarbonilation of the fatty acids simultaneously and 3) a isomerization section where a catalytic reactor is used to produce the jet diesel with the appropriate fuel properties. Through intensive simulations the effect of the different operating variables of the three sections were studied. Results show that for the first section the water excess and the operating pressure are key variables for the transformation of the triglycerides. For the reactive distillation column for the HDS of gasoil and HDO of the fatty acids, it is very important to maintain the hydrogen excess in the feed with a low reflux ratio to allow the release of the light gases produced and, to guarantee the deep HDS of gasoil and the complete transformation of the vegetable oils. Finally, the isomerization reactor must be carefully operated with respect to the amount of light hydrocarbons compounds allowed in the mixture to be cracked and isomerized.

Keywords: Jet diesel, co-hydrotreating, reactive distillation.

1. Introduction

The emergence of new economies where energy demand is increasing exponentially is forcing the petroleum-based fuels consumer countries to redefine their energy strategies.

Such concerns have promoted much research on reliable alternatives to conventional fuels. In this way, a renewable diesel or Jet diesel has emerged as a substitute for mineral diesel fuels. Its production is not limited to seed oils, but it is flexible in that it can use a number of different feedstocks. Renewable or Jet diesel can be produced by hydrotreating (HDT) of vegetable oils, whereby the oxygenates in bio-feedstocks are hydrogenated into hydrocarbons. HDT may take place in existing diesel hydrotreaters reactors in a co-processing scheme, where the bio-feed component is deoxygenated and the fossil diesel component is simultaneously desulphurised, or it can take place in a standalone unit processing 100% bio-feed. In both cases, conversion occurs over HDT catalysts and in conditions similar to those used in hydrotreaters. Recently, Pérez-Cisneros et al (2017) proposed a reactive distillation process for the co-hydrotreating of sulfured diesel and triglycerides and fatty acids. They conclude that the hydrodesulfurization reactions are mainly affected by introducing larger amounts of triglycerides while these are not affected when only fatty acids are considered. Therefore, in this work, a novel integrated technological approach for producing Jet diesel considering a previous step of triglycerides conversion to fatty acids is included. Thus, the integrated process considers: 1) a triglyceride hydrolysis section consisting of a catalytic heterogeneous reactor which is used to transform the triglycerides of the vegetable oils or animal fats to the corresponding fatty acids and a coupled decanter-distillation column to separate the fatty acids from glycerol and water; 2) a co-hydrotreating section where a reactive distillation column is proposed to perform the deep hydrodesulfurization (HDS) of gasoil and the hydrodeoxygenation (HDO) and decarbonilation of the fatty acids simultaneously and 3) an isomerization section where a catalytic reactor is used to produce the jet diesel with the appropriate fuel properties required by the international standards.

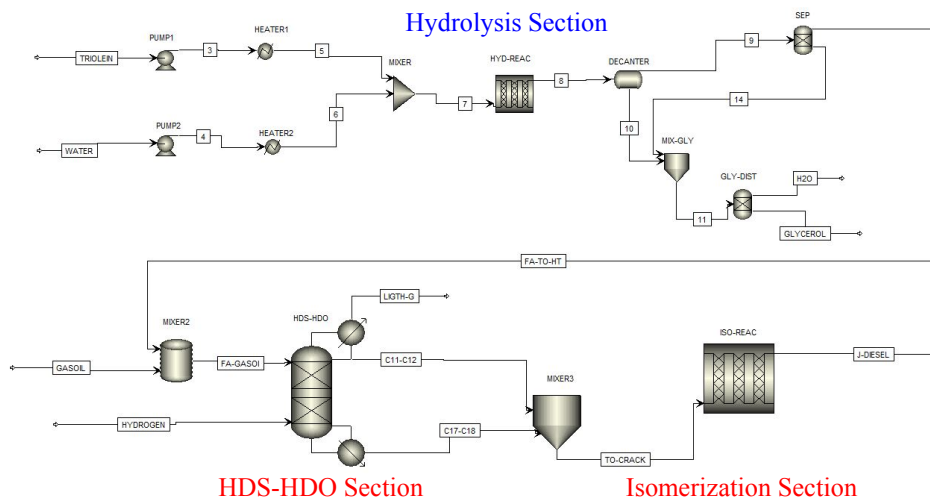


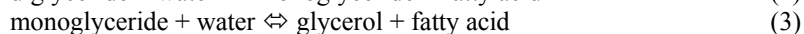
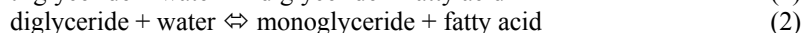
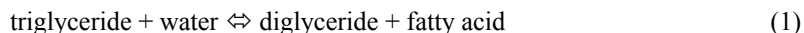
Figure 1. Simplified integrated co-hydrotreating reactive separation process for jet diesel production from vegetable oils and sulphured gasoil

2. The integrated reactive separation process

Figure 1 shows the integrated reactive separation process flowsheet. The first section (hydrolysis) considers two pumps where the pressure of the exit streams is 30 atm and two heaters where the temperature of the streams entering to the mixer is 180 C. The fixed bed hydrolysis reactor operates at moderated pressure (30 atm) and it consists of 2 tubes with 0.5 m of diameter and 25 m length. Next, a decanter tank is used to separate the glycerol water mixture followed by two distillation columns where the pure fatty acid is separated from a low concentration glycerol-water mixture and a second distillation column where pure glycerol is produced. The second section (HDS-HDO) considers a reactive distillation column (RDC) where a mixture of sulphured gasoil and fatty acid is fed at the top of the RD column and hydrogen is fed in excess at the bottom. The light gases leave the RDC from the vapour-liquid condenser and a liquid mixture of C₁₁-C₁₂ linear hydrocarbon chains are mixed with the hydrodesulphurized gasoil compounds and the C₁₇-C₁₈ hydrocarbons produced by the HDO reactions. The third section considers a fixed bed hydrocracking-isomerization reactor where the C₁₁-C₁₂ hydrocarbons and the C₁₁-C₁₈ hydrocarbons mixture is cracked and isomerized to obtain the jet diesel.

2.1 The triglycerides hydrolysis section

Fatty acids are major components and presursors for a great variety of products such as soaps, detergents, pharmaceuticals, etc. In general, at moderate temperatures, the hydrolysis of vegetable oils reactions can be described as follows:

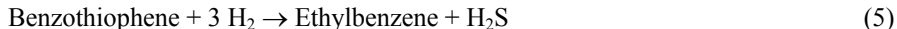


Currently, fatty acids are obtained commercially from the reaction of vegetable oils and/or animal fats with superheated steam. Conventionally, the reaction is carried out at 100-260 °C and 100-7000 kPa using a 0.4-1.5 wt % water-to-oil ratio. Different variations of this technology have been used by industry (e.g., the Twitchell process, the Colgate-Emery synthesis, and the Eisenlohr process). These processes are normally referred to as fat splitting. In the present work the reaction kinetics reported by Ngaosuwan et al (2009) are used for the fixed-bed reactor simulation considering a tungstated zirconia (WZ) and the solid composite SAC-13 as catalyst.

2.2 The HDS-HDO section

Hydrotreating (HDT) of vegetable oils has previously been used to produce straight chain alkanes ranging from *n*-C₁₅-*n*-C₁₈, from a fatty acid fraction of tall oil, and other vegetable oils. The aim of the hydrodeoxygenation (HDO) process is to upgrade vegetable oils by removing the oxygen content as water. The process includes treatment of vegetable oils at high pressures and moderate temperatures over heterogeneous catalysts. The use of vegetable oils, mainly non-edible vegetable oils, as feedstock for the HDO process is highly favorable because their hydrocarbon content is in the same range as that of fossil fuels, such as kerosene and diesel. The fatty acids in vegetable oils are composed of straight chains of carbon atoms, and HDO produces *n*-alkanes as the primary products. Thus, fatty acids in the vegetable oils are transformed into alkanes with water as by-product. Carbon dioxide or carbon monoxide is also obtained as by-products when the reaction follows decarboxylation and decarbonylation under HDO

conditions. The reactions considered for the HDS of the sulphured gasoil can be written in a simplified form as:



It should be noted that Eq. 6 only considers the hydrogenolysis reaction pathway. For the HDO of fatty acids the simplified reactions are:



Kinetic expressions for the HDS reactions are taken from Perez-cisneros et al (2017) and, due to the lack of information about the kinetics of the complex HDO reactions, a conversion of 99% of fatty acids was considered for the numerical simulations.

2.3 The hydrocracking-isomerization section

The hydrocracking reactions of the larger normal hydrocarbons produced in the HDS-HDO section can be written in simplified form as:



and the isomerization reactions as:



It should be noted that the cracking reactions produce n-butane, which it is further separated in the gas phase. The yield of cracking and isomerization was taken from Yeob-Kim et al (2017) where a Pt supported on nanocrystalline large-pore BEA zeolite is used as catalyst.

3. Simulation of the integrated reactive-separation process

3.1. Hydrolysis section

Several amounts of triglycerides were used for intensive simulation of the integrated process. Due to space reasons only the results for the production of 70 kmol/h of fatty acid are reported here. Table 1 shows the simulation results for the hydrolysis section considering the production of 70 kmol/h of oleic acid (fatty acid) using ASPEN-PLUS. It can be observed that a complete conversion of triolein is achieved at 453 K and water in excess (150 kmol/h). The decanter and the distillation column for glycerol separation operate at 1 atm and 278 K. Also, it must be considered that a reliable thermodynamic model to treat the polar reactive mixture. In this work the RK-ASPEN has been applied for the hydrolysis section.

Table 1. Simulation results of the Triglycerides hydrolysis section

Stream	TRIOLEIN	WATER	7	8	11	GLYCEROL	FA-TO-HT
Mole Flow kmol/h							
TRIOLEIN	23,35	0	23,35	0	0	0	0
OLEIC-Ac	0	0	0	70,050	1,03E-18	0	70,050
WATER	0	150	150	79,949	79,9499	0,00247	2,07E-07
GLYCEROL	0	0	0	23,350	23,350	23,3499	4,97E-05
Mass Fraction							
TRIOLEIN	1	0	0,8844	0	0	0	0
OLEIC-Ac	0	0	0	0,8464	8,13E-20	0	0,99999
WATER	0	1	0,1156	0,0616	0,4011	2,08E-05	1,89E-10
GLYCEROL	0	0	0	0,0919	0,5988	0,9999	2,31E-07
Total Flow kg/h		2702,29					
Temperature K	20675,238	2	23377,530	23377,544	3590,729	2150,453	19786,820
Pressure atm	298,15	298,15	449,79	453,15	298	557,93	513
	1	1	30	30	1	1	30

3.2. HDS-HDO section

Table 2 shows the simulation results for the HDS-HDO section considering a mixture of oleic acid and gasoil of 70 and 100 kmol/h, respectively. The hydrogen feed was set to 400 kmol/h in order to achieve complete conversion of the fatty acid. The Reactive distillation column consists of 14 stages with two reactive stages sections (5-7, 9-11) operating at 30 atm. It can be noted in Figure 2a that the composition of the C11-C12 stream contains mainly *n*-undecane and *n*-dodecane hydrocarbons and stream C17-C18 carried the heavier hydrocarbons (C_{16} - C_{18}). On the other side, Figure 2b shows that the LIGTH-G stream is rich in the light gases produced by the HDS and HDO reactions (i.e., CO , CO_2 , H_2 , H_2S , H_2O , etc). It should be noted that the temperature of the C11- C12 stream (185 C) is different from the C17-C18 stream (473 C), thus a extra heater must be considered to heat the C11-C12 stream before mix it with the heavier hydrocarbons. PC-SAFT EoS was used for the simulation of this section. The gasoil feed composition and temperature condition was taken from Pérez-Cisneros et al (2017).

3.3. Isomerization section

Finally, Table 3 shows the final composition of the jet diesel obtained in the hydro cracking and isomerization reactor. It should be clear that the exit stream from this reactor should be flashed in order to eliminate the hydrogen and butane present in the final mixture. The specific kinetics and reactor configuration were established considering the information given by Yeob-Kim et al (2017).

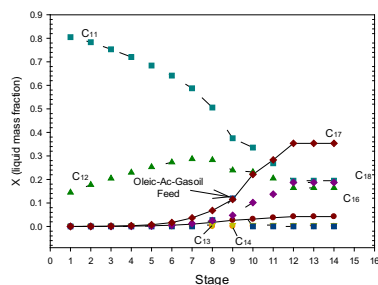


Figure 2a. Liquid profile in the HDS-HDO RD column

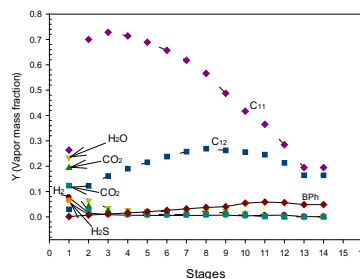


Figure 2b. Vapor profile in the HDS-HDO RD Column

Table 3. Simulation results of the cracking-isomerization section

Stream	TO-CRACK	J-DIESEL
Mass Flow (kg/h)	3,0294E+04	4,3419E+03
Mass Frac		
<i>n</i> -C11	2,1024E-01	5,9269E-02
<i>n</i> -C12	1,7289E-01	6,9593E-02
<i>n</i> -C13	5,3954E-03	2,5800E-02
<i>n</i> -C14	9,8195E-04	1,7533E-02
<i>n</i> -C16	4,4027E-02	2,2512E-02
<i>n</i> -C17	3,7044E-01	2,4435E-01
<i>n</i> -C18	1,9602E-01	1,6085E-01
<i>n</i> -BUTANE	0,0000E+00	5,1456E-04
<i>iso</i> -HEXA	0,0000E+00	2,0084E-02
<i>iso</i> -HEPTA	0,0000E+00	2,1498E-01
<i>iso</i> -OCTA	0,0000E+00	1,6400E-01
H ₂	0,0000E+00	5,1374E-04
Temperature K	7,4415E+02	5,4815E+02

It can be observed in Table 3 that the jet-diesel produced contains mainly *n*-C₁₇ and *n*-C₁₈ linear hydrocarbons with their corresponding isomers *i*-C₁₇ and *i*-C₁₈. Also, the presence of the light linear hydrocarbons *n*-C₁₁ and *n*-C₁₂ gives the appropriate final jet fuel properties.

4. Conclusions

An integrated co-hydrotreating reactive separation process for the production of jet diesel from mixtures of fatty acids and sulphured gasoil, is proposed. From the simulation results it can be concluded that the key operating parameters for the production of the jet diesel are the water excess and the total pressure for the hydrolysis reactor and the non presence of light compounds (H₂S, CO₂, CO) in the feed stream for the cracking-isomerization reactor. Finally, it is mandatory to have more reactive stages at the HDS-HDO RD column in order to achieve an ultra-clean (no-sulphur) diesel at the bottom of the column. Work considering the controllability of the integrated process and its economic evaluation is currently done.

References

- E. S. Perez-Cisneros, M. Sales-Cruz, R. Lobo-Oehmichen, T. Viveros-García, 2017, A reactive distillation process for co-hydrotreating of non-edible vegetable oils and petro-diesel blends to produce green diesel fuel, *Comp. & Chem. Eng.*, [http:// dx.doi.org/10.1016/j.compchemeng.2017.01.018](http://dx.doi.org/10.1016/j.compchemeng.2017.01.018).
- K. Ngaosuwan, E. Lotero, K. Suwannakarn, J.G. Goodwin, P. Praserttham, 2009, Hydrolysis of Triglycerides using Solid Acid Catalysts, *Ind. Eng. Chem. Res.*, 48, 4757-4767
- M. Yeob Kim, Jae-Kon Kim, Mi-Eun Lee, Songhyun Lee, Minkee Choi, 2017, Maximizing Biojet Fuel Production From Triglyceride: Importance of the Hydrocracking Catalyst and Separate Deoxygenation/Hydrocracking Steps, *ACS Catalysis*, 7, 6256-6267.

Understanding the dynamic behaviour of semicontinuous distillation

Pranav Bhaswanth Madabhushi^a, Edgar Iván Sánchez Medina^b and Thomas Alan Adams II^{a,*}

^a*McMaster University, Main St. W., Hamilton, Ontario L8S 4L8, Canada*

^b*Universidad Nacional Autónoma de México, University City, Mexico City, CDMX, 04510, Mexico*
tadams@mcmaster.ca

Abstract

Semicontinuous, ternary distillation was first envisioned using a single distillation column and a middle vessel (MV) in the seminal work by Phimister and Seider. In the “sequential design methodology” introduced by Pascall and Adams for semicontinuous distillation, firstly, a steady state side-stream column that only meets the distillate and bottoms product purity specification is designed. Then by recycling the side-stream to the MV, the system is forced to move away from the steady state (initial state). Through repetitive input actions the system becomes periodic.

The objective of the current study is to understand the effect of changing the above initial state on the nature of the periodic orbit; specifically, its period. The initial state is changed by varying the values of the internal column recycle rates and also the external recycle rate. The periods of the converged periodic orbits are remarkably lower (almost 18 %) when compared to the base case design. Results revealed that the sequential design methodology is inherently sub-optimal. In conclusion, a rigorous design procedure that searches the space of initial states to reach an economically optimal periodic orbit is essential.

Keywords: Dynamic system analysis, design procedure, periodic orbits, semicontinuous process.

1. Introduction

Distillation systems are ubiquitous to chemical process industries. A significant portion of the total process industry’s energy demand and therefore, a major portion of the operational costs of the plant can be attributed to these systems (Halvorsen and Skogestad, 2011). Semicontinuous distillation is aimed to be the best design for industries that are slowly transitioning from low to high production rates, which are currently being operated within intermediate production ranges (Adams and Pascall, 2012). It is an intensified process that has a forced cyclic operating policy to separate multicomponent mixtures using a single distillation column and a number of tightly integrated middle vessels (MVs). The number of MVs required are decided based on the number of intermediate boiling components in the mixture to be separated. For example, to separate an imaginary ternary mixture A, B, and C, where ‘B’ is the intermediate boiling component, one middle vessel and one distillation column is required. In this study, the focus is on separation of ternary mixtures. A single semicontinuous cycle is demarcated based on the concentration of intermediate boiling component ($x_{MV,B}(t)$) and the height of liquid in the MV ($h_{MV}(t)$) into three modes of operation: the separating mode, the discharging mode, and the charging mode. Discrete input actions on the flow control valves on streams associated with the MV, trigger these mode changes when the algebraic states of the system: $h_{MV}(t)$, $x_{MV,B}(t)$, reach pre-specified values.

1.1. Ternary semicontinuous distillation: Process Description

In a typical semicontinuous ternary distillation process, the feed flow to the column from the MV ($F(t)$), the distillate flow rate ($D(t)$), the bottoms flow rate ($Bo(t)$) and the side stream recycled to the MV ($S(t)$) are all continuous functions of the independent variable, time (t). The MV has two inlet streams and two outlet streams. Based on the mode of operation, the number of functional inlet streams that supply liquid material and the number of outlet streams that draw from the MV varies. In the “separating mode”, the MV has only one functioning liquid inlet ($S(t)$) and one liquid outlet ($F(t)$) stream. The side stream is drawn from a location in the column that has high intermediate boiling component mole fraction when compared with the contents in the MV and therefore, the liquid in the MV gets gradually concentrated in component ‘B’. Once the desired purity of component ‘B’ in the MV is reached, the contents of the middle vessel are discharged through a middle vessel discharge stream ($F_{dis}(t)$) by fully opening the discharge valve. This discrete input action marks the end of the separating mode and the beginning of the “discharging mode”. During this mode, liquid is drawn from the middle vessel through two outlet streams: $F(t)$, $F_{dis}(t)$ and enters the MV through one inlet stream ($S(t)$). The discharge valve is fully closed when $h_{MV}(t)$ reaches a pre-specified lower limit while the charging valve is opened fully immediately, which controls the supply of liquid feed to be separated to the system ($F_{char}(t)$). Through these discrete input actions, a mode transition to the “charging mode” is signified. In this mode, the MV has two inlet streams ($S(t)$, $F_{char}(t)$) feeding liquid and one outlet stream ($F(t)$) drawing liquid from the MV. Liquid feed is fed to the MV until the liquid height in the MV reaches a pre-specified upper limit, delineating the end of the charging mode. The end of this mode also simultaneously demarcates the end of the cycle and a new cycle begins. During a cycle, because of the input actions the system is forced to move away from any steady states.

1.2. Ternary semicontinuous distillation: Control structure

Because of the concentration dynamics in the feed to the column, the process is not self-regulating, and therefore controllers are used for maintaining the distillate and bottoms purities at the desired values. The Distillate-Bottoms (DB) control configuration is used for this purpose (Figure 1). This control configuration was shown to be capable of handling off-spec products, because, in a total reflux condition, the MV prevents the preservation of liquid inventory within the column (Phimister and Seider, 2000). The control topology suggested by Pascall and Adams (2013) is typically used to regulate the reflux drum level, the sump level, and the column pressure along with the low and high volatile component concentrations in the distillate and bottoms streams. The semicontinuous ternary distillation

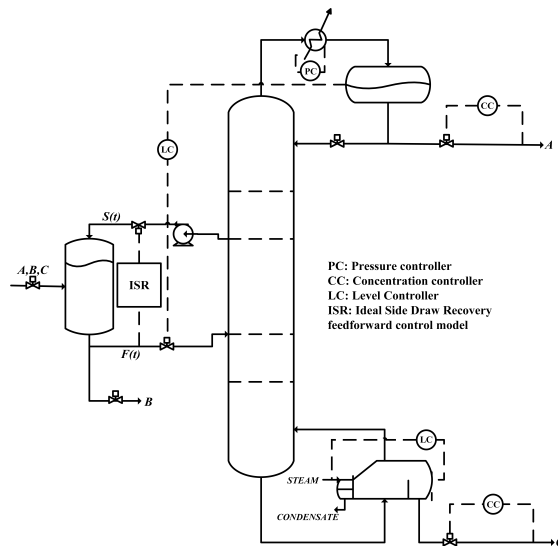


Figure 1: Semicontinuous Ternary Distillation Process

process has seven degrees of freedom out of which five are used as control inputs in the suggested multi-loop control structure. They also recommended the use of a model-based control of the side stream flow rate to address the issue reducing the loss of intermediate boiling component

through the distillate and the bottoms streams. The model used was first derived by Adams and Seider (2008) by assuming that the column is operated at pseudo steady state and that the side stream is a 100 % pure in component ‘B’. The model:

$$S(t) := F(t)x_{MV,B}(t) \quad (1)$$

was nomenclated as the “ideal side draw recovery” control law (ISR). The remaining degree of freedom, which is the reflux rate ($L(t)$) is fixed at the initial steady state value (\bar{L}) throughout the process.

1.3. Ternary semicontinuous distillation: The initial state

In simulation studies that ensued the seminal work on semicontinuous ternary distillation, the initial state was chosen to be a “hypothetical” steady state of a continuous side stream column, where the distillate and bottoms products are separated to the desired purity continuously. The steady state reflux rate (\bar{L}) and the steady state reboil rate (\bar{V}) are varied for a chosen steady state side stream flow rate (\bar{S}) to achieve the desired degree of low and high volatile product separation (Pascall and Adams, 2013). Therefore, different steady states can be generated by choosing a different value of ‘ \bar{S} ’. This design procedure will be henceforth referred to as the “sequential design methodology”. The semicontinuous system evolves from the chosen initial steady state (or initial condition) after recycling the side stream flow rate, and through repetitive state dependent input actions it converges to a periodic orbit in the n-dimensional phase space; the operating locus of the semicontinuous distillation process described in section 1.1.

Pascall and Adams (2013) briefly mentioned the effect that ‘ \bar{S} ’ has on the cycle time (or period of the converged periodic orbit) (T) of the semicontinuous distillation operation when using the sequential design methodology. However, there is no reason stated in the literature for choosing the initial condition of the dynamical system as a steady state where the distillate and bottoms products are separated at the desired purity. From an economic point of view, a steady state must be chosen from the space of initial conditions such that the converged periodic orbit has the minimum possible separation cost (defined as the total annualized cost per kmol of feed/product processed) subject to system constraints. The focus of this study is not to solve this general optimization problem, but to analyze the effect that the initial condition has on the system dynamics and to motivate research on proposing better algorithms to find the optimal designs of semicontinuous distillation of zeotropic mixtures.

2. Methodology

The cycle time (T) is a composition of the time taken to complete each of the three operating modes. The separating mode is completed when the concentration of intermediate boiling component in the middle vessel reaches the desired purity. Therefore, to reduce the separating time, the rate at which this component is concentrated in the MV has to be increased. From the dynamic component mass balance and the total mass balance of the MV during the separating mode:

$$\frac{dx_{MV,B}(t)}{dt} = \frac{S(t)}{M(t)}(x_{S,B}(t) - x_{MV,B}(t)) \quad (2)$$

where, $M(t)$ is the total molar holdup of liquid in the middle vessel, and $x_{s,B}(t)$ is the mole fraction of component B in the side stream recycled to the MV; in the time period close to the initial time ($t = 0$), it can be inferred that for the left hand side of Eq.(2). to be large for a given non-zero value of $M(t) \approx \bar{M}$ and $x_{MV,B}(t) \approx \bar{x}_{MV,B}$, both the values of $S(t)$ and $(x_{S,B}(t) - \bar{x}_{MV,B})$ have to be large. However, $S(t)$ is controlled using the ISR control law, and because $F(t)$ is the manipulated variable for controlling the reflux drum level, the reflux rate ($L(t) \equiv \bar{L}$) should also have an effect on the

rate at which the intermediate boiling component is concentrated in the middle vessel although they are spatially separate. Thus, the chosen steady state value of reflux rate has an effect on cycle time. However, since the mathematical analysis of the differential equation (Eq.(2).) for all time is not straightforward, numerical simulation experiments were conducted in this study. Similar dynamical equations can be written for the discharging and charging modes of a cycle.

The high purity (99 mol%) semicontinuous separation of a near-equimolar mixture (33-33-34 mol%) of benzene, toluene, and o-xylene (B-T-X) was chosen as the simulation example since it is an industrially significant and an almost ideal ternary mixture (Ling and Luyben, 2009). The design data required to simulate the steady state initial point were taken from Ling and Luyben (2009), and Meidanshahi and Adams (2015). The column was designed to have 40 stages with the feed stream location “above stage 25” and the side stream location “on stage 14”. The column diameter was chosen to be 1.3716 m so that flooding within the column can be avoided at all points during the cycle. In the present study, the sequential design methodology was adopted for simulating the BTX semicontinuous separation system. The thermodynamic properties are computed using the Non-random Two-Liquid (NRTL) activity coefficient model (Ling and Luyben, 2009), which was shown to match well with experimental data for the isobaric state of 101.325 kPa (R^2 value of approximately 0.99 for each binary interaction); experimental data was obtained from Gupta and Lee (2012, 2013).

A condenser pressure of 0.37 atm with a stage pressure drop of 0.0068 atm was chosen by Ling and Luyben (2009) such that cooling water and low pressure steam can be used as condenser and reboiler utilities respectively. Since a very similar configuration was adopted by Meidanshahi and Adams (2015) to simulate a steady state continuous side stream column, and because a rigorous procedure was applied to obtain the location of the feed stream, side stream and the number of stages, the design data from this study was used. The MV, which is an essential part of semicontinuous separation was sized using the heuristics that were used in the case studies from Pascall and Adams (2013), to have total molar hold-up of 200 kmol of liquid feed, by using a length to diameter ratio of three and 90 % of its volume filled with liquid at the end of each charging mode.

All valves were sized to accommodate a 3 atm pressure drop except the distillate and the bottoms flow control valve, which were sized to have a 0.1 atm pressure drop keeping the operating pressure of the column in mind. The reflux drum and the sump were sized according to the design heuristics of Luyben (2013). The control configuration using the ISR feedforward control model for side stream molar flow control was used. A proportional controller (P) was used for reflux drum level, sump level, and side stream flow rate control and a proportional-integral (PI) controller was used to control the remaining outputs similar to the study by Meidanshahi and Adams (2015).

3. Results and Discussion

The base case was chosen as the case where \bar{L} , \bar{V} were found such that the desired degree of benzene and o-xylene separation was achieved. The value of \bar{S} for the base case can be chosen to be $\bar{F}\bar{x}_{MV,B}$ according to the ISR control law. However, at this value of the side stream flow rate, the steady state column used as initial state was found to operate beyond the flooding limit. Therefore, a slightly higher value was chosen to avoid flooding in the column. Two sets of experiments were performed: constant internal column recycle rates (\bar{L} , \bar{V}), and constant external recycle rate (\bar{S}).

In the first set of experiments, the ratio of side stream molar flowrate to the feed molar flow rate to the column was varied from the base case value in increments of 0.05 until a value of 0.65 in one set of numerical simulation experiments. Beyond the value of 0.65, the magnitude of bottoms flow rate was found to be small enough that it is impractical to control the bottoms product concentration by manipulating it using a controller. The reflux rate and the boilup rate were not changed from the base case value, and therefore the distillate and bottoms product purities were not maintained at the desired values. The results are presented in Table 1:

Table 1: Results of constant reflux and reboil rates experiments ($\bar{F} = 100$ kmol/h)

	Base Case	Case 1	Case 2	Case 3	Case 4	Case 5
Steady State: Specified						
$\frac{\bar{L}}{\bar{F}}$	0.106	0.106	0.106	0.106	0.106	0.106
$\frac{\bar{V}}{\bar{F}}$	0.117	0.117	0.117	0.117	0.117	0.117
$\frac{\bar{S}}{\bar{F}}$	0.396	0.45	0.5	0.55	0.6	0.65
Steady State: Calculated						
$\bar{x}_{D,B}$	0.99	0.976	0.954	0.932	0.911	0.892
$\bar{x}_{Bo,B}$	0.99	0.999	0.999	0.999	0.999	0.999
$\bar{x}_{S,B}$	0.82	0.72	0.634	0.565	0.507	0.459
Column flooding	No	No	No	No	No	No
Periodic Orbit: Calculated						
T (h)	16.60	14.96	13.64	12.65	12.03	12.40
Column flooding	No	No	No	No	No	No

Consider for example “Case 2”, the $\frac{\bar{S}}{\bar{F}}$ ratio of the steady state point used as the initial state was changed from the base case value by 25 %. At this steady state, the distillate mole fraction is less than the desired purity by 3.6 %. When the base case was used to simulate the dynamic behaviour, the cycle time was observed to be around 16.6 h. By choosing the $\frac{\bar{S}}{\bar{F}}$ ratio to be 0.5 and using the sequential design methodology ($\bar{x}_{D,B} = 0.99$ and $\bar{x}_{Bo,B} = 0.99$ are specified at steady state) resulted in a periodic orbit of cycle time of approximately 16.47 h (result not presented in the table). However, when the steady state presented in the table was used as the initial condition for dynamic simulation, the cycle time dropped to 13.64 h; an approximate 18 % drop. Furthermore, from the table we can infer that “Case 4” has the lowest possible cycle time when compared to the rest of the cases in the first set of experiments. The reason for the observed differences in cycle time can be attributed to the contrasts in the behaviour of the individual controllers after the side stream is recycled to the MV because of the differences in initial state. Similar results were observed (although not of the same magnitude) when one of the internal column recycle rates - reflux rate (\bar{L}) is maintained constant and the $\frac{\bar{S}}{\bar{F}}$ ratio is varied. For the sake of brevity these results are not presented in this article.

Since reflux rate is a degree of freedom that is maintained at a constant value \bar{L} during the semicontinuous distillation operation, its effect on cycle time was also studied. This investigation resulted in the next set of experiments using a constant external recycle rate (\bar{S}); results are presented in Table 2. The reflux rate was increased from the base case value of 106.34 kmol/h to 140 kmol/h. Increasing this value further resulted in column flooding at steady state. In these set of experiments, the bottoms concentration was not changed from the desired value at steady state. Although reflux rate has an influence on cycle time, its effect is not as significant when compared to the previous set of experiments. In practice, ideally the optimal values of \bar{L} , \bar{V} , and \bar{S} (or the optimal initial condition) has to be found, which results in the optimum separating cost.

4. Conclusion

The sequential design methodology that was historically used to converge to a periodic orbit can result in sub-optimal periodic orbits as demonstrated using the simulation experiments. The space of initial conditions from which the system can reach a stable periodic orbit has expanded to include more steady states than previously imagined. From the numerical simulation experiments, for the equimolar separation of BTX, a case was found where an approximate 18 % decrease

Table 2: Results of constant side draw flow rate experiments ($\bar{F} = 100$ kmol/h)

	Base Case	Case 1	Case 2	Case 3
Steady State: Specified				
$\bar{x}_{Bo,B}$	0.99	0.99	0.99	0.99
$\frac{\bar{L}}{\bar{F}}$	0.106	0.12	0.13	0.14
$\frac{\bar{S}}{\bar{F}}$	0.396	0.396	0.396	0.396
Steady State: Calculated				
$\bar{x}_{D,B}$	0.99	0.994	0.995	0.996
$\frac{\bar{V}}{\bar{F}}$	0.117	0.129	0.137	0.146
$\bar{x}_{S,B}$	0.82	0.821	0.821	0.822
Column flooding	No	No	No	Close
Periodic Orbit: Calculated				
T (h)	16.60	16.35	16.18	16.03
Column flooding	No	No	No	Yes

in cycle time was observed while operating without violating the column hydraulic constraints. Although this initial state is “hypothetical”, a start-up procedure for semicontinuous zeotropic separation can be devised where this steady state is first reached before allowing the system to converge to a periodic orbit. An alternate optimization based design methodology is thus required to search through the space of steady states and choose the optimal steady state. This methodology should also incorporate the other decision variables, like for example, the controller tuning parameters, to ensure that the control inputs are optimal. A dynamic optimization based procedure that considers all the above requirements would be ideal. Research in this area is currently in progress.

5. Acknowledgements

Support for this research is made possible through funding from the McMaster Advanced Control Consortium (MACC) and MITACS Globalink Program.

References

- T. A. Adams II, A. Pascall, 2012, Semicontinuous thermal separation systems, *Chemical Engineering & Technology* 35, 1153-1170.
- T. A. Adams II, W. D. Seider, 2008, Semicontinuous distillation for ethyl lactate production, *AIChE journal* 54, 2539-2552.
- B. S. Gupta, M. Lee, 2012, Isobaric vaporliquid equilibrium for the binary mixtures of nonane with cyclohexane, toluene, m-xylene, or p-xylene at 101.3 kpa, *Fluid Phase Equilibria* 313, 190-195.
- B. S. Gupta, M. Lee, 2013, Isobaric vapor-liquid equilibrium for binary systems of toluene+o-xylene, benzene+o-xylene, nonane+benzene and nonane+heptane at 101.3kpa, *Fluid Phase Equilibria* 352, 86-92.
- I. J. Halvorsen, S. Skogestad, 2011, Energy efficient distillation, *Journal of Natural Gas Science and Engineering* 3, 571-580.
- H. Ling, W. L. Luyben, 2009, New control structure for divided-wall columns, *Industrial & Engineering Chemistry Research* 48, 6034-6049.
- W. L. Luyben, 2013, *Distillation design and control using Aspen simulation*, John Wiley & Sons.
- V. Meidanshahi, T. A. Adams II, 2015, A new process for ternary separations: Semicontinuous distillation without a middle vessel, *Chemical Engineering Research and Design* 93, 100-112.
- A. Pascall, T. A. Adams II, 2013, Semicontinuous separation of dimethyl ether (DME) produced from biomass, *The Canadian Journal of Chemical Engineering* 91, 1001-1021.
- J. R. Phimister, W. D. Seider, 2000, Semicontinuous, middle-vessel distillation of ternary mixtures, *AIChE journal* 46, 1508-1520.

Integrated Solvent-Membrane and Process Design Method for Hybrid Reaction-Separation Schemes

Yuqiu Chen,^a Evangelia Koumaditi,^a John Woodley,^{a*} Georgios Kontogeorgis,^a
Rafiqul Gani^{a,b}

^a*KT Consortium, Department of Chemical Engineering, Technical University of Denmark, Building 229, DK-2800 Lyngby, Denmark*

^b*Current address, PSE for SPEED, Skyttemosen 6, DK-3450 Allerød, Denmark*

jw@kt.dtu.dk

Abstract

Hybrid process schemes, which combine processing units operating at their highest efficiencies to perform one or more process tasks, are increasingly being considered as promising innovative and sustainable processing options. The objective of this paper is to present an integrated design method for solvent-membrane screening with energy efficient and/or high product yield hybrid processing schemes. Application of the method is illustrated through two case studies. Case-1 involves a highly energy intensive distillation operation that is replaced by a combination of distillation and membrane or solvent based extraction. Case-2 involves simultaneous reaction-separation to increase the product yield through a hybrid scheme.

Keywords: Hybrid reaction-separation schemes, Ionic liquids, Membrane, Computer-aided molecular design (CAMD), Energy intensive processes.

1. Introduction

Solvents and membranes are widely used in many applications in chemical and related industries. For example, solvents have a multipurpose role in chemical and pharmaceutical processes since different solvents can be used in different processing steps, such as chemical reaction and separation. In these processes, a reaction step often takes place in one solvent and the separation step for product recovery requires another solvent or membrane. In bio-processes, downstream separations are usually very difficult (Woodley et al., 2017), while in petrochemical and chemical processes, most vapor-liquid separations are energy intensive (Tula et al., 2017). For all these processes, hybrid schemes are able to significantly reduce the complexity (for biochemical processes) and/or reduce energy consumption.

Together with organic chemicals, Ionic liquids (ILs) are receiving attention as solvents for use in hybrid schemes replacing energy intensive processes. Unlike volatile organic chemicals (VOCs) that easily escape into the atmosphere because of their high volatility, ILs possess attractive features like almost negligible vapor pressure, low-melting point, and high thermal and chemical stability (Rogers et al., 2003). IL based extraction is an alternative to energy intensive volatile organic solvent based extractive distillation (Lei et al., 2014) and Fang et al., (2016) proposed a molecular designed method based on COSMO-SAC for using IL as solvent in some extractive distillation

processes. For the same reason, membrane-based separations are also promising processing options (Drioli et al., 2011). However, both IL based extraction as well as membrane based separation are limited to low flux operations due to operational and economic constraints. Therefore, combinations of processing units operating at their highest efficiencies in hybrid schemes are promising options.

The objective of this paper is to introduce hybrid schemes that have potential to satisfy the demands of lower energy consumption, reduced waste as well as satisfying process specifications. As successful application of the hybrid schemes depends on the appropriate choice of the solvents and/or membranes for the schemes considered in this work, a screening method is integrated with the design of the hybrid scheme. As proof of concept, results from two case studies are presented.

2. Generation of Hybrid Scheme

2.1. Flow-sheet of hybrid processing schemes

The generation of hybrid schemes is based on the method developed by Babi et al., (2015). Based on identified “hot-spots” of a process, design targets for improvement that overcomes the “hot-spots” are set. Different hybrid schemes are generated to test if any match the targets while also satisfying the process specifications. In addition to the six hybrid schemes proposed by Babi et al., (2015), two new schemes are proposed in this paper. In scheme-1 (see Figure 1), a conventional energy intensive distillation operation is replaced by a combination of not energy intensive distillation operation with a membrane or IL-based extraction. The result is same separation obtained at much lower cost, better environmental impact and reduced waste. In scheme-2 (see Figure 2), a typical bioreactor operation is combined with solvent-based product removal giving a higher yield and avoiding catalyst (enzyme) inhibition.

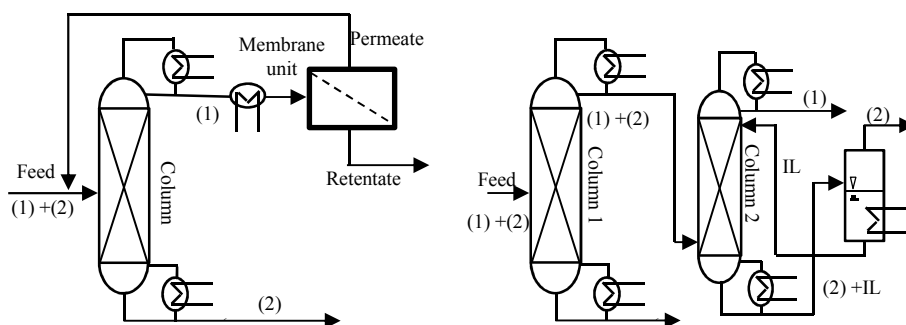


Figure 1a: Hybrid distillation with membrane Figure 1b: Hybrid distillation with IL

2.2. Solvent (IL) and membrane screening method

A large collection of organic solvents (Kalakul et al., 2017) and ILs (Chen et al., 2017) is available. Also, a database of known membranes used for specific separation tasks is under development. These databases have a search-retrieve engine where given the target properties for the solvents and or membranes, the sets of feasible solvents or membranes are generated. The most appropriate solvent or membrane is then selected

by ordering the results according to a performance indicator, such as solubility versus selectivity (for solvents) or permeability versus selectivity. The organic solvents database has around 2000 organic chemicals; the IL database has 4960 ILs, out of which around 300 have been reported to exist.

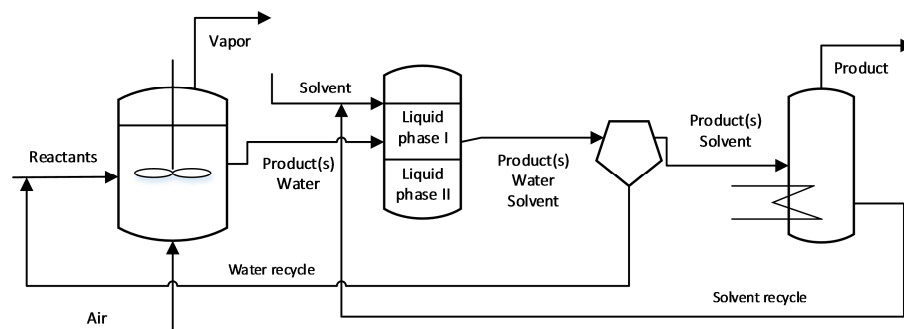


Figure 2: Reaction-separation scheme

3. Case studies

In this paper two proof of concept case studies are presented. Case-1: Methanol dehydration; and Case-2: Bio-oxidation of alcohols

3.1. Methanol dehydration

Separation of aqueous solutions is widely encountered in industries, such as in methanol dehydration process, the energy input increases rapidly with respect to the recovery of methanol from 0.98 to 0.995 (shown in Figure 3). Therefore, a sustainable hybrid design for methanol dehydration is a promising alternative for this separation process.

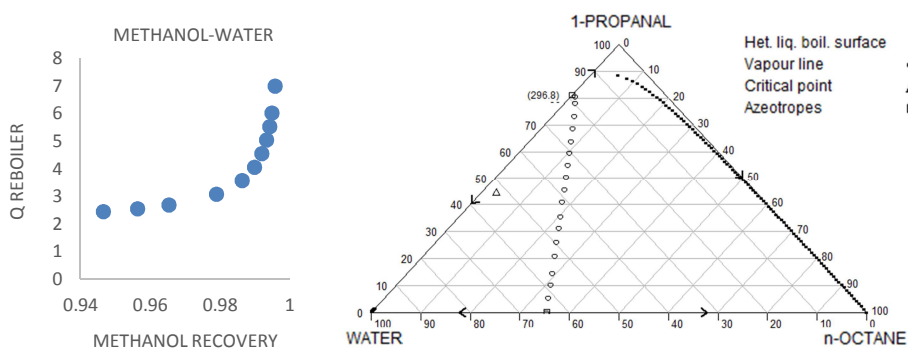


Figure 3: Energy consumption distribution Figure 4: Ternary plot

In this hybrid schemes, IL-based extractive distillation is considered to perform the separation work with the recovery from 0.98 to 0.995. 1-dodecyl-3-methylimidazolium tetrafluoroborate ($[C_{12}MIm][BF_4]$) is selected as the entrainer based on the CAMD method (Gani, 2004; Chen et al., 2017). This hybrid scheme is verified through simulation with AspenPlus and the results are given in Table 1. Compared with the traditional distillation process that required heat duty of 6027 KW, clearly the hybrid

process design proposed in this work has a better energy performance. The hybrid scheme-1 with membranes (see Fig 1a) has also been verified and the energy consumption (recovery from 0.98 to 0.995) by around 50% can be reduced.

Table 1: Fixed parameters and optimization results of the methanol dehydration process

Fixed parameters	Value	
Column operating pressure	1 atm	
Feed rate and composition	500 kmol/h, (0.5 CH ₃ OH, 0.5 H ₂ O)	
Purification of product	0.995 CH ₃ OH	
Optimal variables	Hybrid design	Traditional distillation
Solvent (IL)	[C ₁₂ MIm] [BF ₄]	
Solvent flow rate	10 kmol/h	
Heat duty (recovery from 0.5-0.98)	3103 KW	3103 KW
Heat duty (recovery from 0.98-0.995)	1108 KW	2924 KW
Heat duty (IL recycle)	15 KW	
Total heat duty	4226 KW	6027 KW

3.2. Bio-oxidation of alcohols

Dehydrogenation of alcohols is a widely used method for the synthesis of aldehydes in industries. In this work, the proposed hybrid reaction-separation scheme (see Figure 2) is applied to bio-oxidation of alcohols (see Table 2). Six primary alcohols (1-propanol, 1-butanol, 1-pentanol, 1-hexanol, 1-heptanol and benzyl alcohol) are considered as reactants to produce six corresponding aldehydes in this application.

Table 2: Information of the studied bio-oxidation of alcohols

Reaction scheme	$A + B \longrightarrow C + D$
Reaction class	Oxidation
Reactants	Primary alcohol, oxygen
Products	Aldehyde, water
Reaction class form	$R-OH + O_2 \longrightarrow R-CHO + H_2O$
Catalyst	Galactose oxidase

Table 3 summarizes the process conditions and the kinetic data (adopted from Toftgaard et al., 2015) needed to perform the calculations. The operating conditions for the reactor are the same for all the six reactions.

For steady state, the objective is the separation of the diluted aldehyde from water. The design methodology includes also a methodology for solvent selection, since the separation technique is liquid-liquid extraction. Following the method for solvent screening and by using the tool Pro-CAMD, heavy organic solvents were identified. The evaluation of the separation feasibility with the identified solvent is performed by the ternary plots for system of water + aldehyde + solvent. Simulations of the reactor for all the case studies are run in PRO/II and the NRTL is employed for the liquid-liquid equilibrium calculations. Results of the hybrid scheme simulation (Bio-oxidation of 1-propanol) are given in Table 4. The product is to be recovered from the liquid outlet.

The solvent used for this process is n-octane and the ternary plot for water+1-propanal+n-octane is presented in Figure 4, from which the feasibility of the 1-propanal separation from water is validated, since the phase split occurs.

Table 3: Important data used in the present work

Kinetic parameters			
Parameters	Value	Parameters	value
K_{cat} (kmol/kg CFE)	0.066	C_E (kg/m ³)	0.0011
K_{mS} (kmol/m ³)	0.051	C_O (kg/m ³)	0.5
K_{IP} (kmol/m ³)	0.0017	C_S (kg/m ³)	0.265
Reactor conditions			
T (°C)	25	$C_{alcohol}$ (kmol/m ³)	0.05
P (atm)	1	Aeration (vvm)	0.5

Table 4: Mass balance in the reactor – Bio-oxidation of 1-propanol

Component	Inlet (kmol/h)	Vapor outlet (kmol/h)	Liquid outlet (kmol/h)	% vapor loss
1-propanol	0.05	0	0	-
1-propanal	0	4.0190E-03	0.046	8.04
Water	55.4537	0.0403	55.4634	0.073
Oxygen	0.2659	0.2407	2.4054E-04	
Nitrogen	1.0004	0.9999	5.0907E-04	

For the dynamic state, the objective is to increase the reaction yield. The simulation is performed in MOT (Fedorova et al. 2015) and the molar composition in the reactor with respect to time is calculated based on the kinetic parameters presented in Table 3.

The results of the batch simulation are compared with the results of simulations for continuous product removal. Figure 5 illustrate the product yield, Y and reaction rate, R between batch operation and continuous product removal. Clearly the hybrid scheme of continuous product removal has a better reaction and yield performance than the batch operation.

In addition, for the cases of heavy aldehydes, heavier and non-volatile compounds would be required. A solution to that might be the use of hydrophobic ionic liquids. The difficulty of finding the appropriate solvent is due to the similarities between alcohol and aldehydes, which make them miscible to the same substances

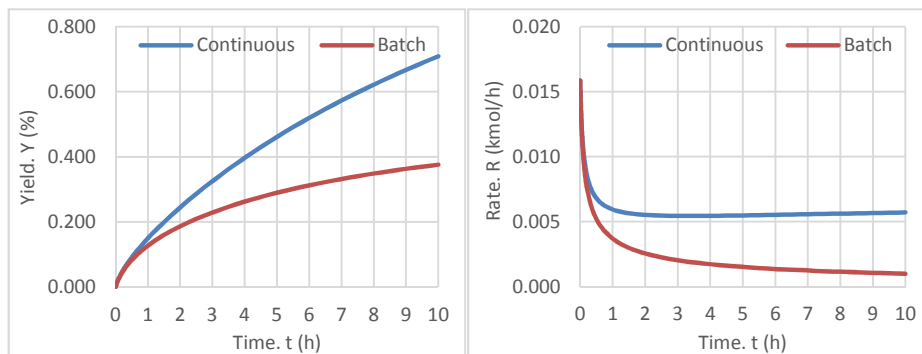


Figure 5: Comparison between batch operation and continuous product removal

4. Conclusions

Hybrid schemes that have potential to satisfy the demands of lower energy consumption, reduced waste as well as satisfying process specifications have been proposed in this work. Case studies involving methanol dehydration and bio-oxidation of alcohols have been presented to highlight the hybrid schemes in this work. Future work is to expand the method into a generalized one covering a wide range of applications, integrated with a collection of tools consisting of, for example, databases, models and design strategies for hybrid schemes.

References

- D.K. Babi, J. Holtbruegge, P. Lutze, A. Grak, J.M. Woodley, R. Gani, 2015, *Computers & Chemical Engineering*, 81, 218-244.
- Y. Chen, J.M. Woodley, G. Kontogeorgis, R. Gani, 2017, 13th International Symposium on Process Systems Engineering, Elsevier B.V., San Diego, California, USA, Accepted.
- E. Drioli, A.I. Stankiewicz, F. Macedonio, 2011, *Journal of Membrane Science*, 380, 1-8.
- J. Fang, R. Zhao, W. Su, C. Li, J. Liu, B. Li, 2016, *AIChE Journal*, 62, 2853-2869.
- M. Fedorova, G. Sin, R. Gani, 2015, *Computers & Chemical Engineering*, 83, 232-247.
- R. Gani, 2004, *Chemical Engineering Research and Design*, 82, 1494-1504.
- S. Kalakul, M.R. Eden, R. Gani, 2017, *Computer Aided Chemical Engineering*. 40, 979-984.
- Z. Lei, C. Dai, J. Zhu, B. Chen, 2014, *AIChE Journal*, 60, 3312-3329.
- R.D. Rogers, K.R. Seddon, 2003, *Science*, 302, 792-793.
- A. Toftgaard Pedersen, W.R. Birmingham, G. Rehn, S.J. Charnock, N.J. Turner, J.M. Woodley, 2015, *Organic Process Research & Development*, 19, 1580-1589.
- A.K. Tula, B. Befort, N. Garg, K.V. Camarda, R. Gani, 2016, *Computers & Chemical Engineering*. 105, 96–104.
- J.M. Woodley, 2017, *Computers & Chemical Engineering*. 105, 297-307.

Exergy efficiency based design and analysis of utilization pathways of biomasses

Hongliang Qian,^{a,b} Weiwei Zhu,^b Chang Liu,^c Xiaohua Lu,^c Georgios M. Kontogeorgis,^{a,*} Rafiqul Gani^{a,d}

^a Department of Chemical and Biochemical Engineering, Technical University of Denmark, DK-2800 Kgs. Lyngby, Denmark;

^b Department of Pharmaceutical Engineering, China Pharmaceutical University, Nanjing 210009, China;

^c State Key Laboratory of Materials-Oriented Chemical Engineering, Nanjing Tech University, Nanjing 210009, China

^d Current address: PSE for SPEED, Skyttemosen 6, DK-3450 Allerød, Denmark
gk@kt.dtu.dk

Abstract

The utilization of biomasses has advantages with respect to energy conservation, emission reduction and resource utilization. In this paper, the concept of functional exergy efficiency is extended as a unified approach for evaluating the effective utilization of energy in three utilization pathways of biomasses; pyrolysis, gasification and anaerobic digestion. Based on our prediction model for higher heat value (*HHV*) of biomass, it has been shown that the Gibbs energy minimization method can be used to simulate the pyrolysis and gasification processes of biomasses. Biogas data of anaerobic digestion process is obtained through the practical biochemical methane potential (PBMP) model. Based on our chemical exergy prediction model of biomass, functional exergy efficiencies of utilization processes of biomasses (three kinds of straws and three kinds of manures) are evaluated. It is found that the functional exergy efficiencies of gasification process of manures and straws are all greater than those of the pyrolysis process at different temperatures, and compare with pyrolysis and gasification processes after 850 °C, the functional exergy efficiencies of anaerobic digestion are the lowest.

Keywords: Biomass utilization, Process simulation, Process evaluation, Exergy efficiency

1. Introduction

The chemical conversion technologies for utilizing biomass can be separated into three basic categories: direct combustion processes, thermochemical processes (pyrolysis process, gasification process and direct liquefaction), biochemical processes (anaerobic digestion and alcoholic fermentation). Biomass resources include wood and wood wastes, agricultural crops and their waste by-products, municipal solid wastes, animal wastes, wastes from food processing and aquatic plants and algae (Demirbaş, 2001). From the proximate analysis or ultimate analysis of biomass, the composition and moisture of biomasses are varied depending on the kind of biomasses considered and even for the same kind of biomass it may vary at different regions and reasons. Different utilization pathways and various types of biomasses lead to issues such as the lack of unified approach to evaluate the biomass utilization. In this study, we focus on how to evaluate utilization pathways of biomasses with respect to energy utilization. The purpose is, thus, to simulate different utilization pathways and then to evaluate the effective utilization of energy based on the simulation results.

At present, there is no general method in the literature to analyse and compare the efficient utilization of energy for the utilization pathways of biomasses. For thermochemical processes, the main criteria of the effective use of energy efficiency are the loss of exergy (Ex_{loss}) and exergy efficiency. Therefore, current energy use in thermochemical conversion processes for biomass are analysed via exergy analysis (Peters et al., 2015). However, for the biochemical utilization of biomasses in order to obtain biogas, any exergy analysis is basically not considered because of the difficulty to determine the exergy of broth, biogas slurry and biogas residue. Therefore, output to input ratio of energy efficiency is selected as an effective indicator of energy use (Havukainen et al., 2014). Since the energy efficiency is based on the first law of thermodynamics, so it cannot truly reflect the utilization of energy. In the field of power plants, exergy efficiency can be divided into two different approaches (A brute-force or functional exergy efficiency), compare with brute-force exergy efficiency, a functional exergy efficiency for any system is defined as the ratio of the exergy associated with the desired energy output to the exergy associated with the energy expended to achieve the desired output (DiPippo, 2004).

The main objective of this study is to compare utilization pathways of biomasses. It should be mentioned that both process simulation and energy evaluation are based on experimental thermodynamic data of biomass in the literature. As the type and composition of biomasses vary, it is necessary to predict their thermodynamic data in order to compare utilization pathways of biomasses via the composition of biomasses. The innovative aspects of this study are related to the following two points: (1) The functional exergy efficiency concept was extended to evaluate utilization pathways of biomasses; (2) Process simulation and energy evaluation are based on the prediction model of HHV (Qian et al., 2016) and chemical exergy (Qian et al., 2017) of biomass from our previous studies. Thus, with the help of ultimate analysis and proximate analysis of biomasses, utilization pathways of biomasses can be simulated and evaluated.

2. Material and methods

2.1 System boundary and definition of functional exergy efficiency

Forming system boundaries around a system is a method to examine the input and outputs from this system. In this study, system boundaries (the dashed box) of pyrolysis, gasification and anaerobic digestion processes were shown in Figures 1-3, respectively. It should be mentioned that the mass of wet biomass was taken as 100 g in different utilization pathways to compare the energy utilization better.

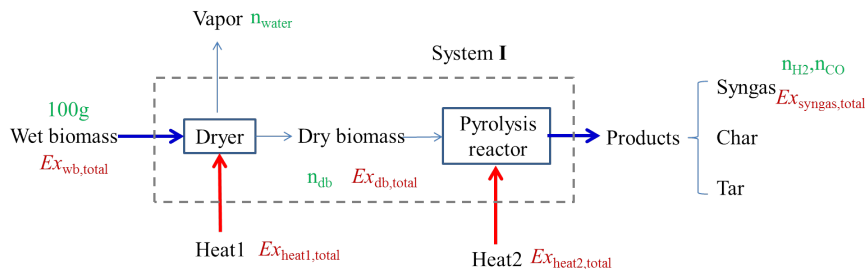


Figure 1 Schematic diagram of the pyrolysis process of biomass

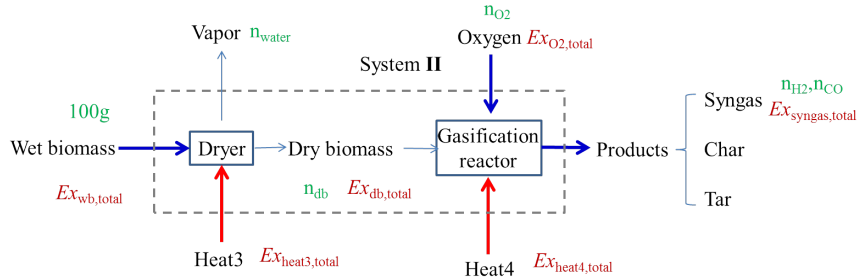


Figure 2 Schematic diagram of the oxygen gasification process of biomass
System III

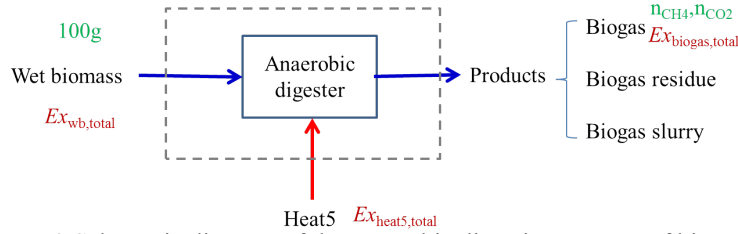


Figure 3 Schematic diagram of the anaerobic digestion process of biomass

Based on the system boundaries, the functional exergy efficiencies of pyrolysis, gasification and anaerobic digestion processes were defined, respectively, as follows:

$$\eta_I = \frac{Ex_{\text{syngas,total}}}{Ex_{\text{wb,total}} + Ex_{\text{heat1,total}} + Ex_{\text{heat2,total}}} \quad (1)$$

$$\eta_{II} = \frac{Ex_{\text{syngas,total}}}{Ex_{\text{wb,total}} + Ex_{\text{O}_2,\text{total}} + Ex_{\text{heat3,total}} + Ex_{\text{heat4,total}}} \quad (2)$$

$$\eta_{III} = \frac{Ex_{\text{biogas,total}}}{Ex_{\text{wb,total}} + Ex_{\text{heat5,total}}} \quad (3)$$

2.2 Thermodynamic data prediction

The value of energy change of combustion reaction in oxygen bomb calorimeter is *HHV*:

$$-0.001M \times HHV = x\Delta_f H_{m,\text{CO}_2} + \frac{y}{2}\Delta_f H_{m,\text{H}_2\text{O}(l)} + \frac{a}{2}\Delta_f H_{m,\text{N}_2} + b\Delta_f H_{m,\text{SO}_2} - \Delta_f H_{m,\text{C}_x\text{H}_y\text{O}_z\text{N}_a\text{S}_b} - (x + \frac{y}{4} - \frac{z}{2} + b)\Delta_f H_{m,\text{O}_2} \quad (4)$$

where M is molecular weight of **dry biomass**, $100\text{g}\cdot\text{mol}^{-1}$. With the help of a prediction model of *HHV* proposed in our previous study (Eq. (5)) (Qian et al., 2016), the final calculation equation of standard molar enthalpy of formation of dry biomass was obtained (Eq.(6)).

$$HHV = 874.08\left(\frac{1}{3}C + H\right) \text{ kJ}\cdot\text{kg}^{-1} \quad (5)$$

$$\Delta_f H_{m,\text{C}_x\text{H}_y\text{O}_z\text{N}_a\text{S}_b}^\circ = -32.762C - 141.781H - 9.258S + 0.874M\left(\frac{1}{3}C + H\right) \text{ kJ}\cdot\text{mol}^{-1} \quad (6)$$

Standard molar entropy S_m° (Song et al., 2011) and heat capacity C_p (Rath et al., 2003) of dry biomass were predicted via Eq. (7) and Eq.(8), respectively.

$$S_m^\circ = M \times (0.0055C + 0.0954H + 0.0096O + 0.0098N + 0.0138S) \text{ J}\cdot\text{mol}^{-1}\cdot\text{K}^{-1} \quad (7)$$

$$C_p = 0.001Mc_p = 0.001M(-212.928 + 4.8567T) \text{ J}\cdot\text{mol}^{-1}\cdot\text{K}^{-1} \quad (8)$$

2.3 Process simulation

Thermochemical processes were simulated via Gibbs energy minimization (Shabbar & Janajreh, 2013) and the final equation was shown as follows:

$$\Delta_f H_{m,i}^o + \int_{298.15}^T C_{p,i} dT + T \left(S_{m,i}^o + \int_{298.15}^T \frac{C_{p,i}}{T} dT \right) + RT \ln \left(\frac{n_i}{n_{total}} \right) + \sum_k \lambda_k a_{ik} = 0 \quad (9)$$

According to Eq. (9), with $\Delta_f H_m^o$, S_m^o and C_p of biomass, the equilibrium composition (n_i) of the system at given temperature and pressure is received.

Anaerobic digestion processes of biomass were simulated via the PBMP model (Liu et al., 2016) in order to obtain the volume of biogas.

$$V_{CH_4} = 100 \times \text{PBMP} (\text{mL CH}_4 / \text{g wb}) \\ = (80.4 - 2.70 \text{Lignin}) \% \times 22400 \text{TS} \% \times (C/24 + H/8 - O/64 - 3N/112) \text{ mL} \quad (10)$$

2.4 Calculation of exergy

In order to obtain the functional exergy efficiencies, exergies of wet biomass, syngas, biogas, drying process, and reactor were calculated based on process simulation and thermodynamic data prediction and the results are listed in Table 1.

Table 1 Exergy calculated in the utilization pathways of biomasses

	Pyrolysis	Gasification	Anaerobic digestion
Wet biomass (wb)	$Ex_{db} = 92.072 (\frac{1}{3}C + H) \text{ kJ} \cdot \text{mol}^{-1}$ (Qian et al., 2017) $Ex_{wb, total} = n_{wb} Ex_{db} + n_{water} Ex_{H_2O}$ $= (TS/100) Ex_{db} + ((100 - TS)/18) Ex_{H_2O}$ $= 92.072 (\frac{1}{3}C + H) \times TS \% + 5.278 \times (1 - TS \%)$		
Dryer	$Ex_{heat1, total} = n_{water} Ex_{heat1}$ $= 5.556(1 - TS \%)(1 - \frac{T_0}{T_{Dry}}) \left(\int_{T_0}^{373.15} 0.001 C_{p, H_2O} dT + 40.668 \right)$ $Ex_{heat3, total} = Ex_{heat1, total}$		
Reactor	$Ex_{heat2, total}$ $= TS \% \times (1 - \frac{T_0}{T_I}) \times \int_{T_0}^{T_I} 0.001 C_{p, db} dT$	$Ex_{heat4, total} = Ex_{heat4, O_2, total} + Ex_{heat4, db, total}$ $= TS \% \times (1 - \frac{T_0}{T_{II}}) \int_{T_0}^{T_{II}} 0.001 C_{p, db} dT$ $+ TS \% \times (1 - \frac{T_0}{T_{II}}) \int_{T_0}^{T_{II}} 0.001 C_{p, db} dT$	$Ex_{heat5, total} = m_{ad} e_{heat5}$ $= 0.027S \times (1 - \frac{T_0}{T_{III}}) \times 4.2 \times (T_{III} - T_0)$
Gas product	$Ex_{syngas, total} = Ex_{total}^{ph} + Ex_{total}^{ch} = (n_{H_2} Ex_{H_2}^{ph} + n_{CO} Ex_{CO}^{ph})$ $+ (n_{H_2} (e_{H_2}^{ch} + RT_0 \ln x_{H_2}) + n_{CO} (e_{CO}^{ch} + RT_0 \ln x_{CO}))$		$Ex_{biogas, total} = n_{total} Ex^{ch}$ $= n_{CH_4} e_{CH_4}^{ch}$

2.5 Biomass scenarios

We selected straws (3 types) and manures (3 types) to compare utilization pathways of biomasses. The physical and ultimate analysis results are listed in Table 2.

Table 2 Physical and ultimate analysis of biomass (Li et al., 2013)

Wet biomass	TS%	VS%	VS/TS%	Lignin	Ash	C	H	O	N
Chicken manure	25.9	19.5	75.3	1.6	24.7	35.9	5.1	30.5	3.4
Dairy manure	38.5	28.8	74.8	17.4	25.2	37.6	5.1	28.9	2.8
Swine manure	30.4	22.0	72.4	4.3	27.6	34.8	4.7	30.3	2.2
Corn stover	84.9	76.9	90.6	10.3	9.4	43.2	5.9	40.2	0.8
Wheat straw	90.5	77.9	86.1	7.6	13.9	39.9	5.7	39.6	0.4

Rice straw	92.9	81.6	84.6	10.8	15.4	39.7	5.4	38.2	0.9
------------	------	------	------	------	------	------	-----	------	-----

3. Results and discussion

The exergy efficiencies of pyrolysis of six wet biomasses at different temperatures are shown in Figure 4. For the same type of biomasses, the exergy efficiencies increase with increasing pyrolysis temperature. In general, the exergy efficiencies of straws are higher than that of manures at different pyrolysis temperatures. At 950 °C, the exergy efficiencies of manures can reach about 0.6, while that of straws can reach about 0.7.

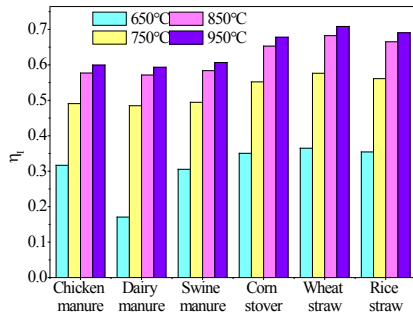


Figure 4 Exergy efficiencies of pyrolysis of six wet biomasses at different temperatures

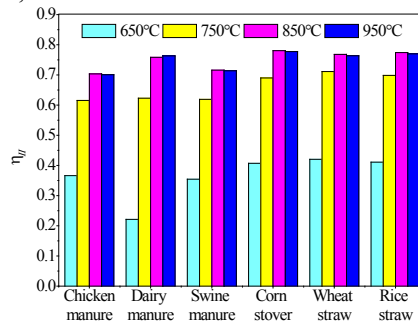


Figure 5 Exergy efficiencies of oxygen gasification of six wet biomasses at different temperatures

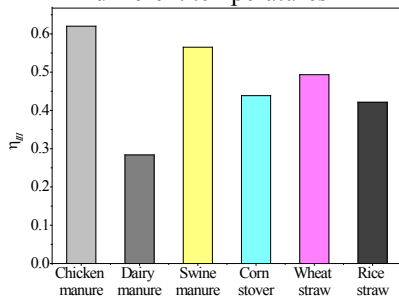


Figure 6 Exergy efficiencies of anaerobic digestion of six wet biomasses

The exergy efficiencies of oxygen gasification for six wet biomasses at different temperatures are shown in Figure 5. The higher the gasification temperature is, the greater are the exergy efficiencies for the same type of biomasses. However, the picture changes little after 850 °C, and the exergy efficiency slightly decreases at 950 °C, which is different to the pyrolysis process. This is mainly due to the increase of the available energy required for heating the oxygen added at 950 °C. Unlike what was the case with the pyrolysis process, the exergy efficiencies of dairy manure at 850 and 950 °C are the lowest in the pyrolysis process but the highest in the gasification process, this is due to the relative high carbon content in dairy manure, which leads to increase of CO generated. Exceeding 850 °C, compared with the pyrolysis process, the exergy efficiencies of the manures have increased, close to those of straws.

The exergy efficiencies of anaerobic digestion processes of six wet biomasses are shown in Figure 6. Compared with thermochemical processes, the exergy efficiencies of the anaerobic digestion process of most manures, except for the dairy manure (due to its high lignin content (no degradable)), are higher than that of straws. The highest exergy efficiency is chicken manure (0.6). The exergy efficiencies of anaerobic digestion are

lower than that of thermochemical processes while the temperature exceeds 850 °C for the organic matter (includes lignin) entering the biogas residue.

4. Conclusions

(1) Pyrolysis process: the functional exergy efficiencies of manures are about 0.6 and generally lower than that of straws (0.7), and the higher the temperature (<950 °C), the greater are the exergy efficiencies;

(2) Gasification processes: the functional exergy efficiencies of manures (>0.7) and straws (maximum 0.77) are all higher than that of pyrolysis process. Below 850 °C, the higher the temperature, the greater the exergy efficiencies, after 850 °C, a slight downward trend is observed;

(3) Anaerobic digestion process: the functional exergy efficiencies of straws are generally lower than that of manures.

Compared with the pyrolysis and gasification processes, although the functional exergy efficiencies of the gas products of anaerobic digestion are low (< 0.6), anaerobic digestion has received increasing attention due to its economic, agronomic, and environmental advantages. Therefore, an important task of the anaerobic digestion process is to improve its biogas production rate such as via pre-treatment to reduce the lignin content.

References

- Demirbaş, A. 2001. Biomass resource facilities and biomass conversion processing for fuels and chemicals. *Energy Conversion and Management*, **42**(11), 1357-1378.
- DiPippo, R. 2004. Second law assessment of binary plants generating power from low-temperature geothermal fluids. *Geothermics*, **33**(5), 565-586.
- Havukainen, J., Uusitalo, V., Niskanen, A., Kapustina, V., Horttanainen, M. 2014. Evaluation of methods for estimating energy performance of biogas production. *Renewable Energy*, **66**, 232-240.
- Li, Y., Zhang, R., Liu, G., Chen, C., He, Y., Liu, X. 2013. Comparison of methane production potential, biodegradability, and kinetics of different organic substrates. *Bioresource Technology*, **149**(7), 565-569.
- Peters, J.F., Petrakopoulou, F., Dufour, J. 2015. Exergy analysis of synthetic biofuel production via fast pyrolysis and hydrouprgrading. *Energy*, **79**, 325-336.
- Qian, H., Guo, X., Fan, S., Hagos, K., Lu, X., Liu, C., Huang, D. 2016. A Simple Prediction Model for Higher Heat Value of Biomass. *Journal of Chemical & Engineering Data*, **61**(12), 4039-4045.
- Qian, H., Zhu, W., Fan, S., Liu, C., Lu, X., Wang, Z., Huang, D., Chen, W. 2017. Prediction models for chemical exergy of biomass on dry basis from ultimate analysis using available electron concepts. *Energy*, **131**, 251-258.
- Li, Y., Zhang, R., Liu, G., Chen, C., He, Y., Liu, X. 2013. Comparison of methane production potential, biodegradability, and kinetics of different organic substrates. *Bioresource technology*, **149**(7), 565-569.
- Liu, C., Wang, J., Ji, X., Qian, H., Huang, L., Lu, X. 2016. The biomethane producing potential in China: A theoretical and practical estimation. *Chinese Journal of Chemical Engineering*, **24**(7), 920-928.
- Rath, J., Wolfinger, M., Steiner, G., Krammer, G., Barontini, F., Cozzani, V. 2003. Heat of wood pyrolysis. *Fuel*, **82**(1), 81-91.
- Shabbar, S., Janajreh, I. 2013. Thermodynamic equilibrium analysis of coal gasification using Gibbs energy minimization method. *Energy conversion and management*, **65**(3), 755-763.
- Song, G., Shen, L., Xiao, J. 2011. Estimating specific chemical exergy of biomass from basic analysis data. *Industrial & Engineering Chemistry Research*, **50**(16), 9758-9766.

Systematic tool for sustainable synthesis and design of flexible processes and supply chains under uncertainty

Klavdija Zirngast, Žan Zore, Lidija Čuček, Zorka Novak Pintarič*, Zdravko Kravanja

University of Maribor, Faculty of Chemistry and Chemical Engineering, Smetanova ulica 17, 2000 Maribor, Slovenia

zorka.novak@um.si

Abstract

This contribution presents a methodological tool for synthesis and design of sustainable processes and supply chains under uncertainty. The methodology decomposes the problem into two main parts where firstly the first-stage variables are derived, and in the next step, the second-stage variables are determined followed by the generation of the probability functions of decision criterion. Main advantage of the proposed approach is that the exponential growth of the optimization models while increasing the numbers of uncertain parameters is avoided by using “as low as practically reasonable” number of scenarios, thus providing useful information at sufficient level of confidence. Sustainability of processes and supply chains is accounted for by using composite sustainability objective functions that combine the economic, environmental and social objectives. Proposed methodology is demonstrated on two case studies, i) synthesis of flexible heat exchanger network, and ii) complex biogas supply network, that demonstrate the potential of the methodology for solving more challenging problems.

Keywords: sustainable processes and supply chains, flexibility, uncertainty, mathematical programming, synthesis and design

1. Introduction

Optimization under uncertainty has been an active area of research in different fields over the last decades (Grossmann et al., 2015). Over the years several barriers have been identified, such as availability of data in terms of uncertainty, the nature of uncertainties, selection of strategy for solving uncertain systems, large computational expense and difficulties regarding interpreting the results (Grossmann et al., 2015). On the other hand, there are several typical uncertain parameters relating to synthesis and design of flexible processes and supply chains, such as product demands, prices, product yields, sizes of equipment, technical parameters (Grossmann et al., 2016), parameters related to political and cultural context (Martín and Martínez, 2015) and other.

Despite the importance of uncertainty in synthesis and design of processes and supply chains, the uncertainty analyses are still uncommon (Moret et al., 2016). Even less research is performed relating to uncertainty of systems including different sustainability objectives, despite growing awareness relating to more sustainable systems (Tsao et al., 2018). This contribution presents a methodology for decision-making regarding sustainable design of processes and supply chains with larger numbers of uncertain data.

Methodology is based on several steps in order to produce flexible process/supply chain designs with a manageable number of scenarios which enables solving problems of any complexity. Sustainability is incorporated into decision-making process by using objective functions that combine economic, environmental and social criteria on a monetary basis within a single-objective optimization (Zore et al., 2017).

2. Methodology

The proposed methodology is intended to handle large-scale problems with great numbers of uncertain input data. It consists of several steps described below.

2.1. Nominal process flowsheet

The main goal of this step is to obtain a process structure at the nominal values of uncertain parameters, which would serve as a good starting point for generation of flexible process flowsheet in the second step. Initial process structure is generated by solving one-scenario Mixed Integer Linear or Nonlinear Programming problem (MILP or MINLP, Eq. (1)).

$$\begin{aligned}
 Z^N &= \min(c^T y^N + f(d^N, x^N, z^N, \theta^N)) \\
 \text{s.t.} \\
 h(d^N, x^N, z^N, \theta^N) &= 0 \\
 g(d^N, x^N, z^N, \theta^N) + B y^N &\leq 0 \\
 d^N &= g_d(x^N, z^N, \theta^N) \\
 A y^N &\leq a \\
 d^N, x^N, z^N &\geq 0, y^N \in \{0, 1\}
 \end{aligned} \tag{1}$$

where Z is a scalar objective variable, c fixed costs of alternatives, f variable cost function, y binary variables, d design variables, x operating variables, z control variables, h equality constraints, g inequality constraints, g_d design expressions, θ uncertain parameters, and A , B and a are the matrices and vectors of constants. Superscript N denotes the nominal values. The result of this step is an optimal nominal process flowsheet which is most likely inflexible for deviations of uncertain parameters from their nominal values.

2.2. Flexible process flowsheet

The main goal of this step is to determine first-stage variables, i.e. the topology binary variables (y) and the sizes of process units (d) for feasible operation within specified deviations of uncertain parameters. This step starts with the initial nominal process flowsheet and is performed by solving sequentially two-scenario MINLP problems, see Eq. (2). The first scenario corresponds to the nominal point (θ^N) while the second one stands for a randomly selected extreme point (θ_s). Those binary variables that obtained unity values at previous iterations are fixed to 1, while the remaining binary variables are optimized either to 1 or 0. Design variables are limited downwards by the optimal values obtained at previous iterations (d_{s-1}). In this way, already selected topology options (e.g. process units) are forced to increase their design variables (sizes) as much as possible, while the new alternatives are included into the flowsheet only if required for feasibility.

$$\begin{aligned}
Z_s &= \min \left(c^T (y_s \setminus y_{s-1}^1) + f(d_s, x^N, z^N, \theta^N) \right) \\
\text{s. t. } & h(d_s, x^N, z^N, \theta^N) = 0 & h(d_s, x_s, z_s, \theta_s) = 0 \\
& g(d_s, x^N, z^N, \theta^N) + B y_s \leq 0 & g(d_s, x_s, z_s, \theta_s) + B y_s \leq 0 & \forall s \in S_{\text{RSV}} \\
& d_s \geq g_d(x^N, z^N, \theta^N) & d_s \geq g_d(x_s, z_s, \theta_s) \\
& d_s \geq d_{s-1}, \quad A y_s \leq a & y_s = \begin{cases} 1 & \text{if } y_s \in y_{s-1}^1 \\ \{0,1\} & \text{otherwise} \end{cases} \\
& d_s, x_s, z_s, x^N, z^N \geq 0
\end{aligned} \tag{2}$$

where s is an index of random vertex scenarios within the set S_{RSV} , and y_{s-1}^1 is a vector of binary variables that obtained unity values at previous iterations.

The model shown in Eq. (2) is solved by successively adding the new vertex points to the nominal point until the new topology options are added into the flowsheet and/or the design variables increase. It is assumed that flexible structure is achieved when the flowsheet structure and the values of design variables stop changing. The results of this step are the values of the first-stage variables that are most likely flexible for prescribed variations of uncertain parameters.

2.3. Flexibility index and stochastic Monte Carlo optimization

The flexibility index of process flowsheet structure and design variables obtained in previous step is determined by maximizing scaled deviations of uncertain parameters from their nominal values towards the extreme values in positive and negative directions (Swaney and Grossmann, 1985). Nonlinear programming (NLP) one-scenario problems are solved over a randomly selected set of vertex directions. Flexibility of the first-stage variables is confirmed if the minimum scaled deviation is greater than or equal to one.

In the next step stochastic Monte Carlo optimizations are performed in order to determine the values of the second-stage, i.e. the operating and control variables (x and z). Single-scenario problem shown in Eq. (3) is solved within a loop for a set of randomly selected points from the intervals of uncertain parameters at the fixed values of binary and design variables (y_{opt} and d_{opt}).

$$\begin{aligned}
Z_s &= \min \left(c^T y_{\text{opt}} + f(d_{\text{opt}}, x_s, z_s, \theta_s) \right) \\
\text{s. t. } & h(d_{\text{opt}}, x_s, z_s, \theta_s) = 0 \\
& g(d_{\text{opt}}, x_s, z_s, \theta_s) + B y_{\text{opt}} \leq 0 & \forall s \in S_{\text{MC}} \\
& d_{\text{opt}} \geq g_d(x_s, z_s, \theta_s) \\
& A y_{\text{opt}} \leq a, \quad x_s, z_s \geq 0
\end{aligned} \tag{3}$$

where S_{MC} is a set of randomly-selected points from the intervals of uncertain parameters. If the sample size is large enough, it could be assumed that the objective variable is normally distributed, and the expected value could be expressed as the mean value of the objective values Z_s obtained at the selected scenarios.

2.4. Derivation of probability functions

Finally, based on the results of the stochastic Monte Carlo optimizations the interval of the objective values obtained is divided into a specified number of subintervals, following by the generation of frequency and cumulative distribution functions for

optimal flexible process flowsheet or supply chain. These curves provide the insights into the distribution of the decision criteria, and represent the tools for the efficient decision-making process.

2.5. Sustainability objective function for multi-objective decision-making

Sustainability objective functions incorporate economic, environmental and social aspects, and are defined as single-objective optimization criteria to avoid generation of multiple Pareto solutions. Sustainability profit (SP) from the macro-economic perspective is used as optimization criterion (Zore et al., 2017). SP is a composite measure of sustainability expressed in monetary terms and is defined as the sum of the economic profit (P^{Economic}), eco-profit (P^{Eco}), and social profit (P^{Social}), see Eq. (4).

$$SP = P^{\text{Economic}} + P^{\text{Eco}} + P^{\text{Social}} = \left(R - E - \frac{I^{\text{Economic}}}{t_d} \right) + (EB - EC) + (SS + SU - SC) \quad (4)$$

where R represents the revenue (€/y), E the expenditure (€/y), t_d depreciation period (y), I^{Economic} capital investment (€), EB eco benefit (€/y) arising e.g. from using waste as raw material or by replacing the existing products with ‘greener’ ones, EC is the eco-cost (€/y) representing the pollution prevention cost, SS the social security payments (€/y), SU unburdening of social funds due to new jobs (€/y), and SC the social cost (€/y). For more details relating to SP the readers are referred to the literature (Zore et al., 2017).

3. Examples

3.1. Synthesis of flexible Heat Exchanger Network

Heat Exchanger Network (HEN) consisted of 6 hot and 3 cold streams, see Figure 1. Supply temperatures of all streams were assumed to deviate for ± 10 K from the nominal values. The flowsheet obtained at the nominal point is shown in Figure 1, and included 6 process-to-process matches (No. 1-6), two coolers (No. 7 and 8) and two heaters (No. 9 and 10).

In the second step, a set of random vertices was generated, and the MINLP problems were solved while sequentially adding vertices to the nominal point. At each iteration the sizes of the existing heat exchange units were allowed to increase and/or the additional heat transfer units can be added into the network.

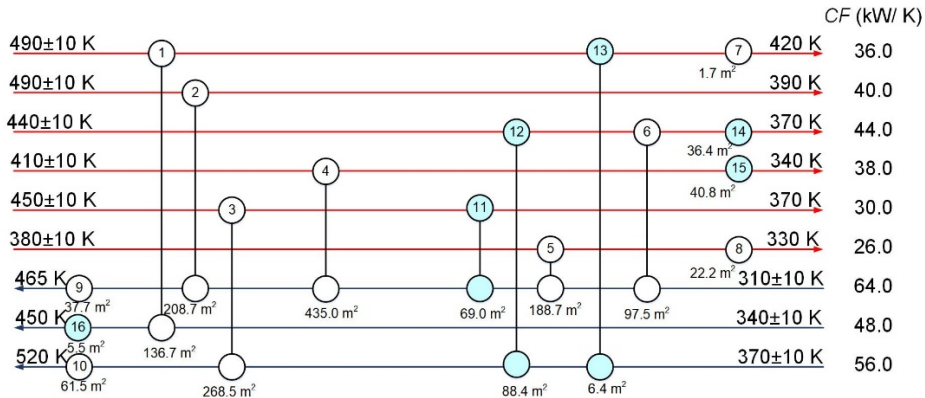


Figure 1: Nominal HEN structure (units 1 to 10) and flexible structure (units 1 to 16)

After 240 iterations, HEN structure and the areas of heat exchangers stopped to change, and the final HEN consisted of nominal units (No. 1-10) plus three additional heat exchangers, two coolers and one heater (No. 11-16).

The flexibility of determined HEN structure was confirmed over 12,000 randomly selected vertices. Stochastic Monte Carlo optimization over 12,000 randomly selected points provided the expected Total Annual Cost (TAC) of 1.308 M\$/y. Cumulative probability and frequency functions (Figure 2) were derived in the final step yielding the information about distribution of decision criterion.

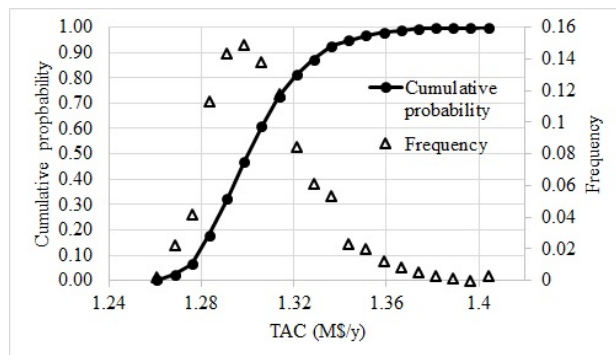


Figure 2: Frequency and cumulative distribution functions of TAC in flexible HEN

3.2. Synthesis of a biogas supply network

The second example was a synthesis of supply network for electricity production from biogas (modified from Egieya et al., 2018 and simplified from Egieya et al., 2017). A multi-period (monthly-based) mixed integer linear programming (MILP) model could choose up to 6 locations for biogas facilities, 15 input substrates, and 2 transportation modes for delivering substrates to biogas plants (road transport or pipeline). Substrates could be selected within the radius of up to 9 km from biogas facilities in 5 locations, and digestate could be used in 5 locations. 18 uncertain parameters were defined that varied $\pm 10\%$ from their nominal values: availability of poultry manure and grass silage in 5 locations, dry matter content of poultry bedding and grass silage, methane content of poultry manure and poultry bedding, and prices of digestate, electricity, grass silage and wheat silage. Objective function was defined as the sum of the economic and eco-profit. The latter included the unburdening effects of the manures, slurries and bedding, the substitution of electricity mix from the grid with the biogas-based one, and inorganic fertilizers with the organic one. Burdening effects originated from cultivation of silages, straws and grains, production of electricity, utilization of fertilizers, use of water, and from transportation.

Optimal solution under nominal conditions included four biogas plant locations with the total capacity of 3.3 MW, 16.2 M\$ of capital investment, and 1.51 M\$/y of annual composed profit. Selected raw materials were poultry and cattle manures, poultry bedding, poultry slurry, and various types of silages transported by road trucks and tanks. After including the deviations of uncertain parameters, the total capacity increased to 3.8 MW at the total capital cost of 17.6 M\$, while the expected profit decreased to 1.37 M\$/y. The same substrates were selected as in nominal solution while additionally a small quantity of glycerol was chosen using the same transportation mode. Flexibility of supply chain was confirmed over 1000 randomly selected vertices.

4. Conclusions

This work presented a new general methodology for the synthesis of flexible process flowsheets and supply chains having larger numbers of uncertain parameters. The methodology consists of several steps that gradually lead from generally inflexible flowsheet obtained at the nominal conditions to the generation of flexible process structure, and to the final optimization of the second-stage variables and generation of decision criteria distribution functions.

The main advantage of the proposed approach is that the model size does not increase with the number of uncertain parameters, but instead the single- or two-scenario problems are solved in the loops yielding the optimal flexible solutions at the specific level of confidence which is suitable for quality decision-making in practice.

Acknowledgments

The authors acknowledge financial support from the Slovenian Research Agency (PhD research fellowships MR-39209, MR-37498, project L2-7633, and programs P2-0032 and P2-0377), Perutnina Ptuj and the SCOPES joint research project CAPE-EWWR ‘Computer Aided Process Engineering Applied to Energy, Water and Waste Reduction During Process Design and Operation’.

References

- J. Egieya, L. Čuček, A. Isafiade, Z. Kravanja, 2017, Synthesis of Supply Networks over Multiple Time Frames: A Case Study of Electricity Production from Biogas, in: A. Espuña, M. Graells, L. Puigjaner (Eds.), *Computer Aided Chemical Engineering*, 40, 1447-1452
- J. Egieya, L. Čuček, K. Zirngast, A. Isafiade, Z. Kravanja, 2018, Biogas supply chain optimisation considering different multi-period scenarios, submitted to 21st Conference Process Integration, Modeling and Optimisation for Energy Saving and Pollution Reduction - PRES 2018, Prague, Czech Republic
- I. E. Grossmann, R. M. Apap, B. A. Calfa, P. Garcia-Herreros, Q. Zhang, 2015, Recent Advances in Mathematical Programming Techniques for the Optimization of Process Systems under Uncertainty, in: K.V. Gernaey, J.K. Huusom, R. Gani (Eds.), *Computer Aided Chemical Engineering*, 37, 1-14.
- I. E. Grossmann, R. M. Apap, B. A. Calfa, P. Garcia-Herreros, Q. Zhang, 2016, Recent advances in mathematical programming techniques for the optimization of process systems under uncertainty. *Computers & Chemical Engineering*, 91, 3-14.
- M. Martín, A. Martínez, 2015, Addressing Uncertainty in Formulated Products and Process Design, *Industrial & Engineering Chemistry Research*, 54, 5990-6001.
- S. Moret, M. Bierlaire, F. Maréchal, 2016, Strategic Energy Planning under Uncertainty: a Mixed-Integer Linear Programming Modeling Framework for Large-Scale Energy Systems, in: Z. Kravanja, M. Bogataj (Eds.), *Computer Aided Chemical Engineering*, 38, 1899-1904.
- R. E. Swaney, I. E. Grossmann, I. E., 1985, An index for operational flexibility in chemical process design, Parts I and II. *AIChE Journal*, 31 (4), 621-641.
- Y.-C. Tsao, V.-V. Thanh, J.-C. Lu, V. Yu, 2018, Designing sustainable supply chain networks under uncertain environments: Fuzzy multi-objective programming, *Journal of Cleaner Production*, 174, 1550-1565.
- Ž. Zore, L. Čuček, Z. Kravanja, 2017, Syntheses of sustainable supply networks with a new composite criterion - Sustainability profit, *Computers & Chemical Engineering*, 102, 139-155.

Processing Systems Synthesis with Embedded Reliability Consideration

Akos Orosz^a, Zoltan Kovacs^b, Ferenc Friedler^{b,*}

^a*Department of Computer Science and Systems Technology, University of Pannonia, H-8200 Veszprém, Egyetem u. 10. Hungary*

^b*Center for Process Systems Engineering and Sustainability, Pázmány Péter Catholic University, H-1088 Budapest, Szentkirályi u. 28, Hungary*

friedler.ferenc@itk.ppke.hu

Abstract

Reliability is one of the most important properties of processing systems, still there is no general method that is able to simultaneously considering the reliability during the design procedure. The proposed method is capable of synthesizing processing networks simultaneously taking into account reliability constraints or generating all Pareto optimal solutions for cost vs. reliability. The method is based on structural examinations and P-graph algorithms

Keywords: Reliability, P-graph, Process synthesis

1. Introduction

Process systems design and reliability engineering are based on different types of mathematical modeling tools that makes their simultaneous consideration difficult. While process systems design is traditionally solved as mixed-integer optimization, reliability engineering is primarily based on probability theory and combinatorial mathematics.

There are only few major contributions in this area. In designing a batch plant, Pistikopoulos et al. (1996) optimized the redundancy of the equipment units. Terrazas-Moreno et al. (2010) considered both reliability and flexibility in optimizing the production capacities, the intermediate storages, and the redundancy on the production units. Goel et al. (2002) retrofitted a HDA process with additional structural options.

For the simultaneous consideration of reliability in process design, a general modeling technique is required that can conveniently represent the two areas.

In the present work, it has been shown that the formerly developed axioms based combinatorial approach to process network synthesis (PNS), the so-called P-graph framework (Friedler et al. 1992b), can conveniently cover and integrate these two areas. The interface between the synthesis and the reliability analysis of process systems design is established on the basis of the axioms of structurally feasible processing networks. Since the structural feasibility of the synthesis procedure and the structural operability of the reliability engineering are closely related terms, they can simultaneously be considered in an integrated procedure.

P-graph framework is based on the fundamental combinatorial properties of feasible process networks. Since these properties are general and independent of the types of mathematical models of the operating units, the framework is also general and independent of these mathematical models. For this reason, the current work will be

shown for the simplest type of mathematical models of the operating units, it can simply be extended to other types of models. The key point of the development of the integrated procedure is the combinatorial interface between the two areas, this is the focus of the paper. It is supposed that the failures of operating units in a system are independent and time invariant. An operating unit is either functional or non-functional, the probability of the functionality of an operation is given as its reliability.

2. Main components of the P-graph framework

The P-graph framework represents a processing network by a directed bipartite graph of the operating units and the materials. A PNS problem is given by the sets of operating units, raw materials, and products. The optimal solution of the problem is to be given as a subset of the set of operating units that represents the related P-graph as the network of the process. Naturally, the set of operating units of a feasible process, including the optimal process, must satisfy certain structural (combinatorial) properties. For example, each product must be produced by at least one operating unit from this set of operating units. Also, if a material is consumed by at least one operating unit and not produced by any of them from this set, this material must be a raw material. In the P-graph framework, these types of combinatorial properties of the feasible process networks are collected and formally identified as set of five axioms. Networks of operating units satisfying the five axioms are called combinatorially feasible networks. Therefore, the network of each feasible process must be combinatorially feasible. Consequently, the search for the optimal network can be reduced to the set of combinatorially feasible networks. In practice, the set of combinatorially feasible networks is a small subset of all sets of networks. There are algorithms exploiting this property of networks resulting in a big acceleration in the search for the optimal network.

Algorithm MSG (Friedler et al. 1992a) is for generating the so-called maximal network (super-structure) that is the minimal among networks that include all combinatorially feasible networks. Algorithm SSG (Friedler et al. 1992a) is capable of generating the whole set of combinatorially feasible networks, while algorithm ABB (Friedler et al. 1996) is an accelerated branch-and-bound algorithm for generating the optimal network. These algorithms are the building blocks of process network synthesis simultaneously considering reliability constraints.

3. Reliability formula for processing systems

Though it is easy to determine the reliability of specific systems, e.g., for series or parallel systems (Biroliini 2007), no formula is known for general, highly interconnected processing systems that may include several loops.

Suppose that there are n operating units on the maximal network numbered from 1 to n . Each operating unit has a binary state, which determines if it is functional or not. Binary vector $X=(x_1, x_2, \dots, x_n)$, describe the functionality of the operating units where x_i is 1 if unit i ($i= 1, 2, \dots, n$) is functional, otherwise it is 0. The functional operating units represented in X describe a network of units that is a subnetwork of the maximal network. The operability of the network of functional operating units is to be determined next. Since the structural properties of the networks are considered here and no mathematical models of the units are given, structural operability will be defined. A network is considered to be structurally operational if it has a combinatorially feasible subnetwork. Naturally, any operational network is also structurally operational. This property can easily be tested by algorithm MSG. Therefore, set U of operational

networks can be determined by selecting the operational networks from all binary n -vectors.

Unit failures are supposed to be independent. The reliability of unit i is given by p_i , ($i=1, 2, \dots, n$). The probability of the occurrence of subnetwork given by binary vector (b_1, b_2, \dots, b_n) is determined by Formula (1), where P denotes the probability of an event.

$$P((x_1, x_2, \dots, x_n) = (b_1, b_2, \dots, b_n)) = \prod_{i=1}^n p_i^{b_i} (1-p_i)^{(1-b_i)} \quad (1)$$

The reliability of the network of operating units is the sum of the probabilities of the structurally operational networks in set U as determined by Formula (2).

$$P(U) = \sum_{(x_1, x_2, \dots, x_n) \in U} \prod_{i=1}^n p_i^{x_i} (1-p_i)^{(1-x_i)} \quad (2)$$

Once set U is determined for a process network, the reliability formula gives the reliability of the process for any values of p_i , ($i=1, 2, \dots, n$). Naturally, this general formula is also valid for specific process networks e.g., for parallel and sequential networks.

4. Synthesis with Reliability Consideration

The previous section summarized the method to determine the reliability of any system represented by P-graph. We can integrate this procedure into algorithm SSG of the framework to create a method capable of solving process network synthesis problems with reliability considerations.

The network of the operating units given in the input is represented as a P-graph, then, algorithm MSG generates the maximal network by eliminating those units that cannot be involved in any feasible process. It is followed by algorithm SSG for generating all combinatorially feasible networks. Naturally, the optimal solution of the PNS problem with required level of reliability is one of the elements of this set of networks (if it exists). For the determination of the optimal solution, each combinatorially feasible network must be evaluated for its costs and reliability. Then, the optimal solution or solutions can simply be selected.

The cost of a combinatorially feasible network is to be determined by an available process systems analysis technique or simulation program. The reliability of a network is given as far as it is shown at the reliability formula.

Note that the procedure for determining the optimal solution of a PNS problem that satisfies reliability requirements is general, e.g., no limitations applied for the number of nodes, the level of interconnections, the number of loops or any other structural property.

5. Case study

The structure of the case study is given by the maximal network shown in Figure 1, it was generated by algorithm MSG. The simplest model is considered here for each operating unit, therefore, it is assumed that the cost of a unit is constant, and the cost of a process is the sum of the costs of its units. It is also assumed that the reliability of a unit is constant and time-independent. The reliabilities and costs of the operating units of the case study are given in Table 1. Operating units O1A and O1B are considered as alternatives. Unit O1B has higher reliability with higher cost than that of unit O1A.

Similarly, for units O2A and O2B. Material flows, and material costs are not considered in this example.

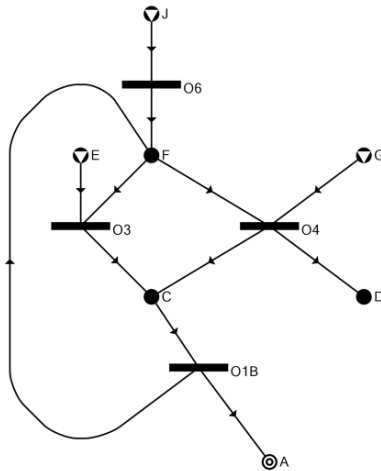


Figure 1: Maximal network of the case study

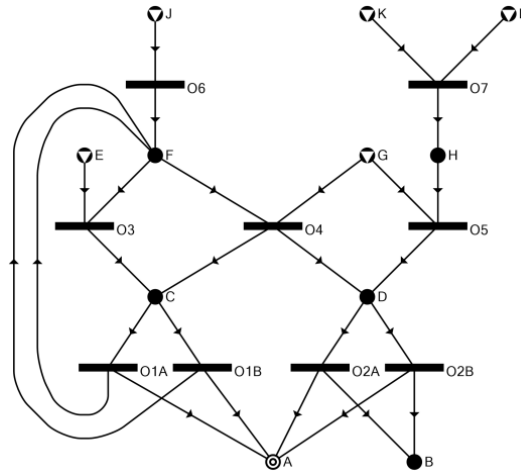


Figure 2: Network #12 as one of the 58 combinatorially feasible networks of the case study.

Table 1: Reliabilities and costs of the operating units

Unit	Reliability	Cost
O1A	0.99900	10
O1B	0.99995	16
O2A	0.99900	12
O2B	0.99995	20
O3	0.99990	5
O4	0.99990	6
O5	0.99950	4
O6	0.99950	3
O7	0.99950	5

There are 58 combinatorially feasible networks for the case study. For each of these networks, the cost and reliability are determined. This is illustrated by analyzing network #12 (from the 58 networks), it is shown on Fig. 2. This network has 4 operating units, thus, $2^4=16$ networks are tested by algorithm MSG. Six of the 16 networks are structurally operational, these networks are shown in Fig. 3.

The probability of the occurrence of each subnetwork is determined next. The sum of these probabilities gives the reliability of the network, it is 0.99994999. The cost of network #12 is the sum of the costs of its operating units, i.e., it is 30.

For illustration, the costs vs probabilities of failures for all 58 combinatorially feasible networks are shown on Fig. 4 on logarithmic scale, where the probability of failure of a network is 1 minus its reliability. There are 8 Pareto-solutions; these solutions are listed in Table 2. Each solution is given with its reliability, cost, probability of failure, and the number of structurally operational subnetworks.

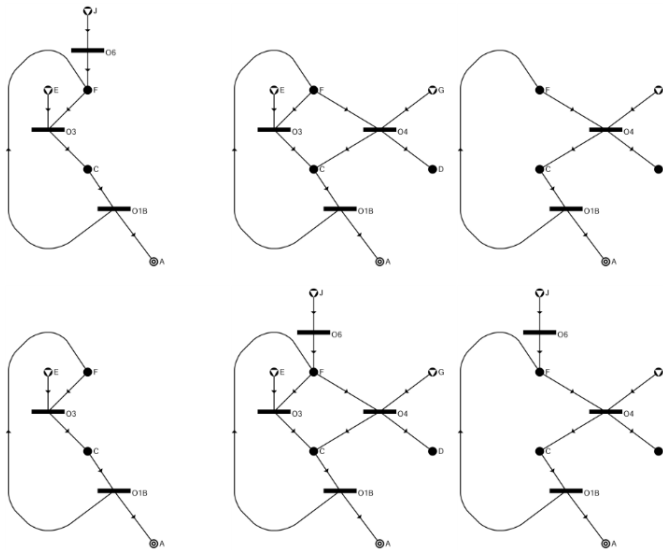


Figure 3: Structurally operational subnetworks of network #12.

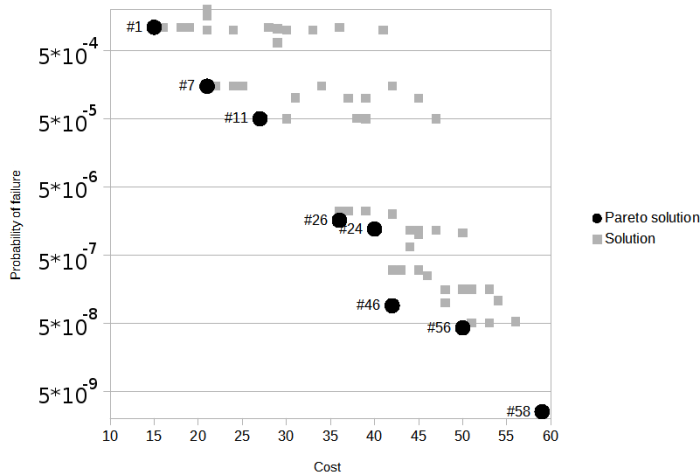


Figure 4: Combinatorially feasible networks shown as cost vs. probability of failure.

6. Note on nonlinear models of the operating units

In the present work, the integration of PNS and reliability analysis is primarily based on combinatorial properties of process networks. The proposed procedure is independent of the types of the mathematical models of the operating units. In chapters 4 and 5, the simplest model has been shown. In practice, more realistic models are to be used for the selection of the best network in terms of cost and reliability.

Suppose that the operating units are described by simulation program modules. Then, the procedure given in this paper is to be extended as follows. Algorithm SSG generates the combinatorially feasible networks as given in chapter 4. Each of these networks must be tested for feasibility by the simulation program. For each feasible network, the

structurally operational subnetworks must be tested for feasibility by the simulation program. Then, the reliabilities of only the feasible networks are determined as far as it has been given in formula (2).

Table 2: Costs and reliabilities for the Pareto-solutions

Network	Operating units in the network	Reliability	Cost	Probability of failure	Number of structurally operational subnetworks
#1	O1A, O3	0.9989001000	15	0.0010999000	1
#7	O1B, O3	0.9998500050	21	0.0001499950	1
#11	O1B, O3, O4	0.9999499900	27	0.0000500100	3
#24	O1A, O2A, O4, O5, O6, O7	0.9999987997	40	0.0000012003	23
#26	O1A, O2A, O3, O4, O6	0.9999983907	36	0.0000016093	14
#46	O1B, O2A, O3, O4, O6	0.9999999100	42	0.0000000900	14
#56	O1B, O2B, O3, O4, O6	0.9999999575	50	0.0000000425	14
#58	O1B, O2B, O3, O4, O5, O6, O7	0.9999999975	59	0.0000000025	64

7. Concluding remarks

A general procedure has been introduced to perform process network synthesis simultaneously taking into account reliability. The procedure is general and capable of effectively designing complex, highly interconnected processing networks. A by-product of the present work is the launch of the formerly unavailable reliability formula of processing networks. It has been shown that the P-graph framework is capable of effectively integrating structurally related design problems for their simultaneous solution.

References

- Birolini A., 2007, Reliability engineering. Heidelberg: Springer
- Friedler F, Tarjan K, Huang YW, Fan LT., 1992a, Combinatorial algorithms for process synthesis. Computers & chemical engineering. 16 pp. S313-20.
- Friedler F, Tarjan K, Huang YW, Fan LT., 1992b, Graph-theoretic approach to process synthesis: axioms and theorems. Chemical Engineering Science. 47(8) pp. 1973-88.
- Friedler F, Varga JB, Feher E, Fan LT., 1996, Combinatorially accelerated branch-and-bound method for solving the MIP model of process network synthesis. In: State of the Art in Global Optimization (pp. 609-626). Springer US.
- Goel, H.D., Grievink, J., Herder, P.M. and Weijnen, M.P., 2002. Integrating reliability optimization into chemical process synthesis. Reliability Engineering & System Safety, 78(3), pp.247-258.
- Pistikopoulos, E.N., Thomaidis, T.V., Melin, A. and Ierapetritou, M.G., 1996. Flexibility, reliability and maintenance considerations in batch plant design under uncertainty. Computers & chemical engineering, 20, pp.S1209-S1214.
- Terrazas-Moreno, S., Grossmann, I.E., Wassick, J.M. and Bury, S.J., 2010. Optimal design of reliable integrated chemical production sites. Computers & Chemical Engineering, 34(12), pp.1919-1936.

A Multi-stage and Multi-level Computer Aided Framework for Sustainable Process Intensification

Nipun Garg^{a*}, Georgios M. Kontogeorgis^a, John M. Woodley^a, Rafiqul Gani^{a,b}

^a*Department of Chemical and Biochemical Engineering, Technical University of Denmark, Søtofts Plads, DK-2800 kgs. Lyngby, Denmark*

^b*Current address: PSE for SPEED, Skyttemosen 6, DK-3450 Allerød, Denmark*

nipgar@kt.dtu.dk

Abstract

Ensuring sustainability during production of chemicals and related products has become an ever-growing challenge due to rising demand for sustainability. Thus, there is a need to look for innovative solutions that are not only economic and efficient but also sustainable. Process intensification as an integrated part of process synthesis & design has the potential to determine more sustainable and innovative solutions. In this paper, a multi-stage and multi-level computer aided framework to perform sustainable process synthesis, design and intensification is presented. The framework employs a phenomena-based technique, which is capable of generating innovative, more sustainable and non-trade off solutions for any existing process flowsheet or a totally new process. In this paper, the framework is further extended in terms of application range validated through a case study for production of bio (enzyme-based conversion) succinic acid from multiple feed options. The case study highlights the generation of a novel superstructure of alternatives, from which an optimal processing route under different scenarios is determined. This optimal processing route is further improved through phenomena-based technique to generate innovative, more sustainable and intensified alternatives for the production of bio succinic acid.

Keywords: process intensification, computer-aided framework, sustainable solutions.

1. Introduction

Sustainable solutions refer to those design alternatives that correspond to improved values of a set of targeted performance parameters related to economic, social and environmental factors. Process Intensification (PI) is defined as improvements of a process at unit operational, functional and/or phenomena levels that can be obtained by integration of unit operations, integration of functions and phenomena's or targeted enhancement of the phenomena for a set of target operations (Lutze et al., 2013). The conventional approach for process synthesis design operating at unit operation (Jakslund et al., 1995) and functional level (Jakslund et al., 1995, Siirola, 1996) has been further extended by incorporating a lower scale phenomena level (Babi et al., 2015). At the phenomena level, one can investigate underlying driving forces associated with unit operations (unit-ops) to generate new unit-ops that lead to innovative flowsheet alternatives. At the highest level of aggregation, process flowsheets options in terms of unit-ops are synthesized and/or evaluated. These flowsheet options correspond to acceptable designs matching the process specifications and represent the "base case" design. However, at this level, only known unit-ops are considered and thus the search space is limited. This search space can be

further increased by operating at a lowest scale of aggregation, i.e. phenomena level (Papalexandri et al., 1996, Lutze et al., 2013). At this level, the phenomena involved in performing specific tasks are identified and are recombined using a systematic and generic approach such that they perform the same tasks, while not only matching the original process specifications but also satisfying a set of design targets. This leads to the generation of more sustainable and non-trade-off alternatives compared to the base case and measured in terms of a set of performance criteria.

In this work, the phenomena based synthesis approach is extended by expanding the database and algorithms to identify phenomena building blocks (PBB's) and generation of new basic structures translating to unit-ops. In its application, the superstructure-based optimization is performed for various scenarios to consider the influence of different parameters on the optimization, for example by varying the objective function, varying the prices of material and utilities according to different locations etc., to obtain corresponding optimal processing routes, which are further developed in the design and innovation stages of the framework.

2. Multi-stage framework for sustainable process synthesis-intensification

An overview of the multi-stage and multi-level computer aided framework for sustainable process synthesis-intensification is shown in figure 1. This framework is based upon a generic 3-stage approach for sustainable process design (Babi et al., 2015). The computer-aided tools used at different stages of the framework are also highlighted. Note that entry to a problem can be at any stage, depending on the available input information, for example, if a process flowsheet already exists, entry is at stage 2.

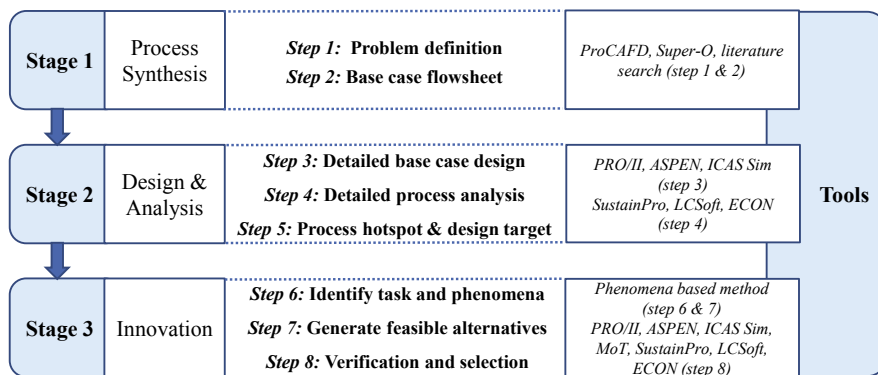


Figure 1: Overview of multi-stage framework for sustainable process synthesis-intensification

The objective of stage 1 is to identify the optimal process flowsheet. In stage 2, the detailed design and analysis for the selected flowsheet is performed to identify the process “hot-spots” and set design targets for improvement. In stage 3, these targets are achieved by applying phenomena based intensification. The detailed steps of the framework are not explained here, as they are available in Garg et al. (2018).

3. Case study

The case study involves the application of the framework for production of bio succinic acid. Succinic acid is a potential precursor to produce a wide range of chemicals, which

have great industrial significance in the food, pharma and chemical sectors (Song et al., 2006). Thus, the main objective of this case study is to identify more sustainable and intensified alternatives for the production of bio succinic acid under different scenarios not reported earlier.

3.1. Stage 1: Synthesis

The main objective of the synthesis problem is to find the optimal processing route for the production of bio succinic acid with a purity of at least 99.9%. Glucose, glycerol, maltose and sucrose along with CO₂ have been considered as the raw materials. On basis of selected raw materials, reaction paths with different bacterial and yeast strains are identified from literature along with required reaction data (step 1). To solve the synthesis problem, the superstructure-based optimization is employed (step 2). The superstructure describing the network of configurations for different processing routes has 8 processing steps and 33 processing intervals excluding raw material and product steps (see figure 2). Then the superstructure-based optimization problem is set up in Super-O (Bertran et al., 2017), where it is solved to determine the optimal processing route. The optimization problem is solved for different scenarios, which are described below.

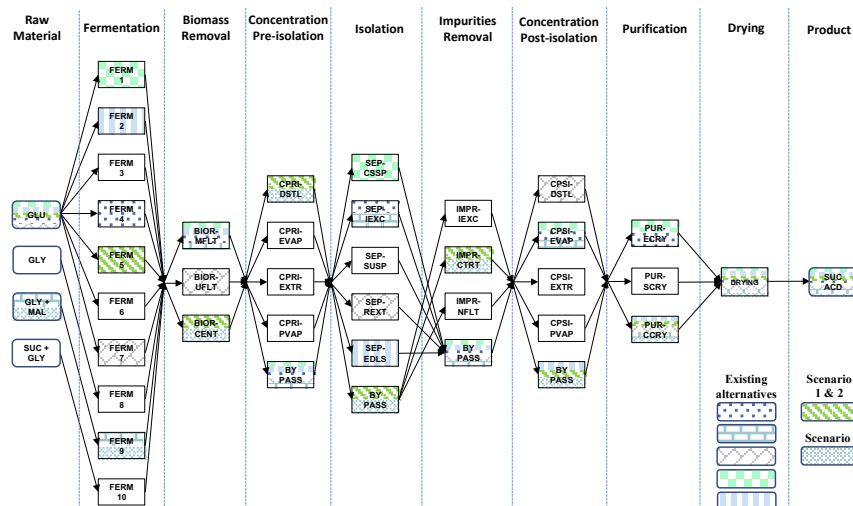


Figure 2: Superstructure of alternatives for the bio succinic acid case study

Optimization scenarios: The first scenario involves optimization to find the processing route corresponding to maximizing sales profit of the product considering raw material cost, chemical cost and product cost in USA. The optimal route for this scenario is shown in figure 2. In the second scenario, the objective is again to maximize the sales profit of the product, but in this case, the operational costs are also considered with same location as scenario 1. Considering the operational cost, the optimal solution remains the same with the same fermentation model and downstream separation route. In the third scenario, the optimization is performed considering scenario 2 but by changing the raw material, chemical and utility prices to another country, for example, Thailand. Owing to lower raw material prices, the optimal processing route changes as compared to scenario 1 and 2. Here the optimal route goes through the interval with fermentation model 9 while downstream separation intervals are the same as scenario 1 and 2. The problem type for all the scenarios is MILP and the solver used is CPLEX. Other model statistics for the three scenarios are listed in table 1.

The optimal process flowsheet alternatives obtained from the three scenarios are novel processing routes while five other existing routes reported in the literature, for example, by Glassner et al. (1992) are also identified (see figure 2). Thus, potentially from this superstructure 2604 novel and existing feasible process flowsheets alternatives can be generated for the production of bio succinic acid.

Table 1: Superstructure-based optimization statistics for different scenarios

Superstructure parameter	Scenario 1	Scenario 2	Scenario 3
Location	USA	USA	Thailand
Objective function	Sales	Sales-OPEX	Sales-OPEX
Number of equations	989,003	989,003	989,003
Number of variables	973,451	973,451	973,451
Number of discrete variables	164	164	164
Execution time (seconds)	2.50	2.52	2.56
Objective function (MM USD/y)	42.56	30.91	40.72

3.2 Stage 2: Design and analysis

The optimal processing route, which is same for the first and second scenario, is considered for stage 2. Here, the basic design information, like reaction conversion, operating conditions, distillation column stages and reflux ratios, feed and product material information, is obtained from literature, databases or design calculations. Using this basic information, the base case process is designed and simulated (PRO/II) to get the base case design (step 3). Then from the simulation results, the detailed mass and energy balance data is extracted to perform process analysis (step 4) in terms of sustainability, life cycle analysis and economics using the in-house tools SustainPro (Carvalho et al., 2013), LCSOFT and ECON (Kalakul et al., 2014). The sustainability analysis indicates loss of product and raw material in open path (in-out streams) containing crystallizer. The economic analysis shows high utility costs related to distillation operation in one open-path. Further, the LCA analysis confirms the high carbon footprint for the reboiler of the same distillation column. Based on the above analysis, process hot-spots (inefficient operations) are identified that are translated into design targets for improvement (step 5). The identified process hotspots are high energy consumption and/or demand for succinic acid recovery and loss of product in the above mentioned open paths. Their translations to design targets are reduction of energy demand, increase in product recovery, reduction in number of unit operations and improvement in sustainability and LCA factors.

3.3 Stage 3: Innovation (Phenomena based intensification)

The base case flowsheet based on unit-ops is first represented in terms of separation and reaction tasks. These tasks are further represented in terms of phenomena constituting the initial search space. The identified PBB's are R (reaction), M (mixing), 2pM (two phase mixing), PC(VL), PT(VL), PS(VL), PC(LS), PT(LS), PS(LS), H (heating) and C (cooling) where, PC is phase contact; PT is phase transfer and PS is phase separation; while V, L and S represent vapor, liquid and solid phases. Here, the tool library to identify the PBB's has been extended in order to incorporate wider search space. The pure component and mixture property analysis is performed using ICAS (Gani et al., 1997), which identified one azeotrope between water and ethanol. As in this case study, the main objective is to get pure succinic acid, the separation of water and ethanol is not considered in further

steps. Thus, using process hot-spots, additional list of PBB's are identified and added to the existing list leading to an increase of search space. The new list consists of 20 PBB's where PT(PVL), PT(VV), PS(VV), PC(LL) and PS(LL) are additional PBB's. The total number of possible combinations of these PBB's to form simultaneous phenomena building blocks (SPB's) are 519,252. However, not all combinations are feasible. Thus, using connectivity rules, 244 SPB's are found to be feasible.

The identified feasible SPB's are combined to form basic structures. These basic structures are formed in a way that they satisfy the identified reaction and/or separation tasks. These combinations of basic structures are then translated to unit-ops and thus three intensified flowsheet alternatives are generated, as shown in figure 3.

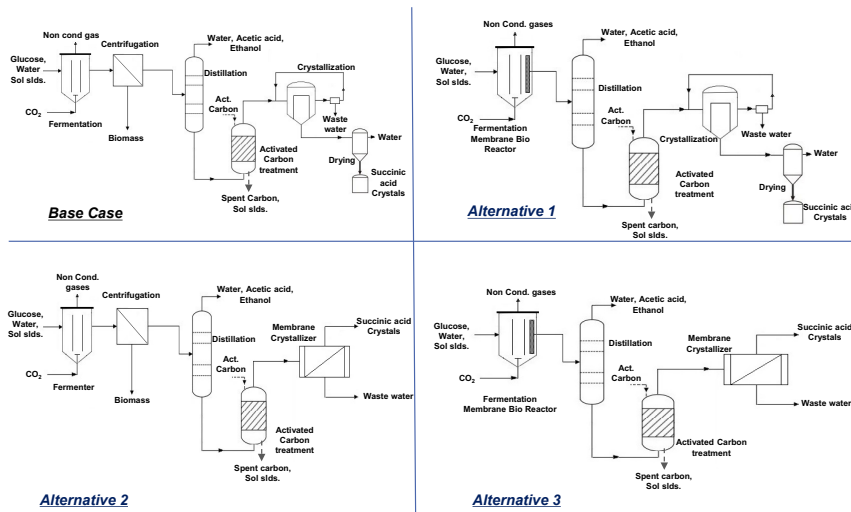


Figure 3: Base case and intensified flowsheet alternatives for bio succinic acid

In alternative 1, starting with the first task of reaction, the second task, which is biomass separation could be combined to obtain a new basic structure of phenomena's consisting of reaction (R) and separation PS(LS) phenomena. This combination of basic structure is then translated into a membrane bioreactor. In this unit operation, the fermentation broth is clarified, i.e., the reaction product is removed continuously and the cell culture remains in the bioreactor leading to increase in cell concentration and high product yield, also observed by Wang et al. (2014). In alternative 2, the integration of basic structures for the last two separation tasks is considered. This is possible as both separation tasks involve SPB involving separation of crystalline product from the liquid phase. Thus, a basic structure having phenomena PT(LS) and PS(LL) is selected. Additional PBB's like cooling, heating and mixing can also be added to the selected SPB's. Thus, in flowsheet alternative 2 the combined basic structure is translated to membrane crystallizer to obtain higher recovery and desired purity of succinic acid. Alternative 3 is a combination of alternative 1 and 2 including both membrane bioreactor and membrane crystallizer.

The radar plot (see figure 4) confirm that the intensified alternatives are more sustainable and non-trade-off, in terms of the selected performance criteria. Here, the outer boundary of the plot represents the base case design while all the more sustainable intensified alternatives should be within the boundary. The values are calculated by taking percentage ratios of different factors with respect to the base case (except profit

where inverse ratio has been taken). Note that the base case and all alternatives also satisfy the process objectives.

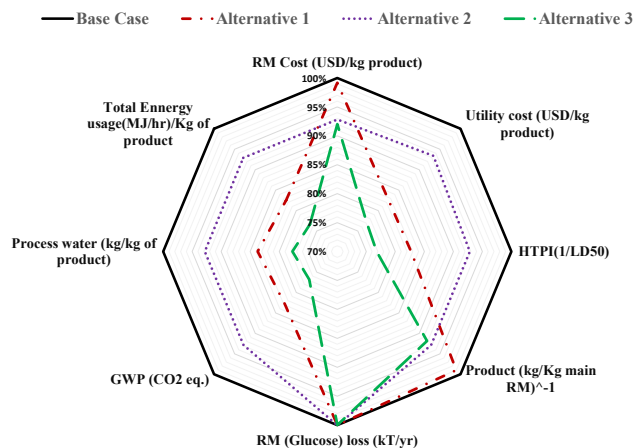


Figure 4: Comparison of intensified alternatives relative to the base case design (HTPI: Human toxicity potential by ingestion, GWP: Global warming potential)

4. Conclusions

An overview of multi-stage and multi-level framework for process synthesis–design and intensification has been presented. The application of the extended framework is illustrated through the bio succinic acid case study where, different scenarios have been analysed using the superstructure-based optimization approach, generating more than 2600 alternatives at the synthesis stage. However, by applying the phenomena based method, three intensified and more sustainable alternatives, compared to the base case, have been determined. Current and future work is extending the phenomena based approach and its implementation in the ProCAFD tool (Tula et al., 2017).

References

- D. K. Babi, J. Holtbruegge, P. Lutze, A. Gorak, J. M. Woodley, R. Gani, 2015. *Comput. Chem. Eng.*, 81, 218-244.
- M. O. Bertran, R. Frauzem, A. S. Arcilla, L. Zhang, J. M. Woodley, R. Gani, 2017, *Comput. Chem. Eng.*, 106, 892-910.
- A. Carvalho, H. A. Matos, R. Gani, 2013, *Comput. Chem. Eng.*, 50, 8-27.
- R. Gani, G. Hytoft, C. Jaksland, A. K. Jensen, 1997, *Comput. Chem. Eng.*, 21, 1135-1146.
- N. Garg, G. M. Kontogeorgis, J. M. Woodley & R. Gani, provisionally accepted at *Process Systems Engineering Conference 2018*, San Diego, USA.
- D. A. Glassner, R. Datta, 1992, U.S. Patent 005,143,834 A.
- C.A. Jaksland, R. Gani, K.M. Lien, 1995, *Chem Eng Sci.*, 50, 511-530.
- S. Kalakul, P. Malakul, K. Siemanond, R. Gani, 2014, *Journal of Cleaner Production*, 71, 98-109.
- P. Lutze, D. K. Babi, J. M. Woodley, R. Gani, 2013, *Ind. Eng. Chem. Res.*, 52, 7127-7144.
- K.P. Papalexandri, E.N. Pistikopoulos, 1996, *AIChE Journal*, 42, 4, 1010-1032.
- J. J. Siirola, 1996. *Comput. Chem. Eng., Supplement 2*, 20, S1637-S1643.
- H. Song, S. Y. Lee, 2006, *Enzyme and Microbial technology*, 39(3), 352-361.
- A. K. Tula, D. K. Babi, J. Bottlaender, M. R. Eden & R. Gani, 2017, *Comp. Chem. Eng.*, 105, 74-95.
- C. Wang, W. Ming, D. Yan, C. Zhang, M. Yang, Y. Liu, Y. Zhang, B. Guo, Y. Wan, J. Xing, 2014, *Bioresource technology*, 156, 6-13.

Thermodynamic Network Flow Approach for Chemical Process Synthesis

Georg Liesche^a, Dominik Schack^a, Karsten Hans Georg Rätze^a and Kai Sundmacher^{a,b,*}

^a*Max Planck Institute for Dynamics of Complex Technical Systems, Sandtorstr. 1, D-39106 Magdeburg, Germany*

^b*Otto-von-Guericke-University Magdeburg, Universitätsplatz 2, D-39106 Magdeburg, Germany*
Sundmacher@mpi-magdeburg.mpg.de

Abstract

A thermodynamic network flow approach (TNFA) is proposed for the purpose of process synthesis. Firstly, the feasible region of the thermodynamic state space (T, p, x) is analyzed wherein the optimal process route should be identified. Within this region, we define elementary directions into which the matter elements can be moved by manipulation of mass and energy fluxes. Secondly, we discretize the feasible region along the elementary directions such that a grid of thermodynamic state points is obtained. The grid points form the nodes of a directed 'thermodynamic graph'. To each graph edge, a cost contribution is attributed. Thirdly, a network flow problem is formulated based on the graph representation in order to determine the optimal flow distribution at minimal cost. By defining a linear cost function in terms of the network flows, due to the fact that the nodes of the graph have fixed thermodynamic coordinates, the flow problem results in a purely linear programming (LP) problem. The TNFA methodology is demonstrated with two case studies: i) the feed compression section and ii) the reactor section of the methanol synthesis process. With these examples, a proof of concept of the TNFA is given highlighting the versatility of the proposed methodology.

Keywords: Process Design, Process Optimization, Network Flow Problem, Methanol Synthesis

1. Introduction

The synthesis of highly efficient chemical production processes remains one of the most important tasks in Process Systems Engineering. In a previous work, we have sketched a novel approach to process design, named 'Elementary Process Functions (EPF) methodology' (Freund and Sundmacher, 2008). The key idea of this EPF approach is to track matter elements over time and to identify an optimal route in the thermodynamic state space as a basis for the subsequent technical realization by use of modular functional devices. So far, the EPF approach was successfully demonstrated for the design of catalytic gas phase reactors (Peschel et al., 2010) and multiphase reactors (Kaiser et al., 2017). The motivation for the present work is to extend the EPF approach for designing complete chemical production systems consisting of multiple processing steps, including the feed pretreatment, reactor section, separation of the product from non-converted reactants, and the final product purification. In order to account for different process unit types, the EPF methodology is modified: the step-wise approach starting from an ideal thermodynamic pathway towards real process units is replaced by a directed graph representing the discretized thermodynamic state space where edges denote elementary process functions. The subsequent process design task is then formulated as a flow optimization problem.

2. Method

Chemical processes are inherently nonlinear due to a strong temperature, pressure and composition dependence of the underlying elementary operations. Therefore, the optimization of such processes leads to nonlinear programming (NLP) formulations. Despite of the availability of very efficient NLP-solvers, a large number of decision variables increases the computational effort significantly, requires good initializations and may attain only local optima (Biegler and Grossmann, 2004).

In this contribution, we propose a novel optimization approach that decouples the nonlinear build-up of the solution space and the linear mass- and energy flux optimization. By discretizing the thermodynamic state space (Figure 1), the chemical process is divided into elementary steps, such as conversion, heating or cooling. Suitable nonlinear models are used to simulate each discrete elementary step. In this way, a graph of nodes and edges is created. The nodes represent discrete state points which are connected by a single elementary step, representing an edge.

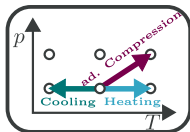
The derived graph of discrete state points serves as a superstructure of numerous possible pathways from an initial state towards a final state. In order to identify the optimal pathway, a linear programming problem (LP) is formulated. The previously identified key information are used to relate each elementary edge with a certain cost level. In this way, each edge shows a different impact on the objective function.

$$\begin{aligned} \min_{\mathbf{x}} \quad & f(\mathbf{x}) = \mathbf{c}^\top \mathbf{x} \\ \text{s.t.} \quad & \mathbf{A}\mathbf{x} \leq \mathbf{b} \\ & \mathbf{lb} \leq \mathbf{x} \leq \mathbf{ub} \end{aligned} \quad (1)$$

Eq. (1) shows the general form of a LP. Herein, f is the objective function and $\mathbf{x} = (\dot{\mathbf{N}}, \dot{\mathbf{\Gamma}}, \dot{\mathbf{Q}}, \dot{\mathbf{W}})^\top$ denotes the vector of all decision variables, namely the mass fluxes $\dot{\mathbf{N}}$, the heat $\dot{\mathbf{Q}}$ and work fluxes $\dot{\mathbf{W}}$ and the unit scaling factors $\dot{\mathbf{\Gamma}}$. The influence of the decision variables on the objective function is determined by the cost vector $\mathbf{c} = (\mathbf{c}_N, \mathbf{c}_\Gamma, \mathbf{c}_Q, \mathbf{c}_W)$. The cost vector \mathbf{c} , the coefficient matrix \mathbf{A} and the solution vector \mathbf{b} as well as the lower \mathbf{lb} and upper bounds \mathbf{ub} vary depending on the chosen application.

In this contribution, the validity and versatility of the TNFA are illustrated using two examples: a compressor cascade and the methanol synthesis reaction. In the following sections, both case studies are introduced with their respective balance equations as well as possible objective functions. Afterwards, optimal pathways for different objective functions are presented and discussed for both example processes.

2.1. Case Study 1: Compressor Cascade



In the first case study, the TNFA is illustrated for the pretreatment compression cascade of Lurgi's methanol synthesis where the directed graph is best illustrated using a p - T grid (Ott et al., 2012). Three possible edges result from this node formulation for the compressor cascade: heating, cooling and isentropic compression. Pressures are linked by either single stage compression – i.e. compression to the adjacent grid point – or multiple compression stages – i.e.

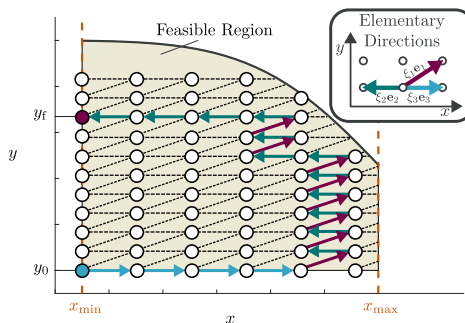


Figure 1: Illustration of the optimal path in state-space for an arbitrary process based on fixed thermodynamic state points (nodes). The elementary directions define feasible transitions between nodes.

connection of non-neighbouring grid points.

Heating and cooling duties $q^{\text{hcu,ext}}$ are derived from the energy balance of the heating/cooling unit (hcu). Enthalpies are obtained from the Shomate equation (Burgess, n. d.)

$$0 = (h_{\text{in}}^{\text{hcu}} - h_{\text{out}}^{\text{hcu}}) + q^{\text{hcu,ext}}. \quad (2)$$

In order to generate the isentropic compression edges, outlet temperatures of the compression $T_{\text{out}}^{\text{comp}}$ and the necessary technical work w_t^{comp} are calculated for the predefined pressure grid:

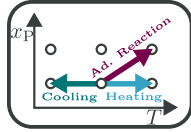
$$T_{\text{out}}^{\text{comp}} = T_{\text{in}}^{\text{comp}} \left(\frac{P_{\text{in}}^{\text{comp}}}{P_{\text{out}}^{\text{comp}}} \right)^{\frac{1-\kappa}{\kappa}}, \quad w_t^{\text{comp}} = (h_{\text{out}}^{\text{comp}} - h_{\text{in}}^{\text{comp}}). \quad (3)$$

Optimizations are performed using two different objective functions: the first optimization (I) serves as an identification of the compression route which requires minimal technical work (Eq. 4a). In contrast to the first objective function, the second optimization (II) identifies the minimum capital cost via an estimation of the relative equipment cost (Eq. 4b) (Peters et al., 2004).

$$C^{\text{I}} = \sum_{i=1}^{N_{\text{comp}}} W_i = \mathbf{c}_W^{\top} \mathbf{W} \quad \text{with} \quad \mathbf{c}_W := \mathbf{1}, \quad \mathbf{c}_N, \mathbf{c}_T, \mathbf{c}_Q := \mathbf{0}, \quad (4a)$$

$$C^{\text{II}} = \sum_{i=1}^{N_{\text{comp}}} C_{\text{scale},i} = \mathbf{c}_T^{\top} \mathbf{T} \quad \text{with} \quad c_{T,i} := \left(\frac{\Delta p_i}{\Delta p_0} \right)^{0.69}, \quad \mathbf{c}_N, \mathbf{c}_Q, \mathbf{c}_W := \mathbf{0}. \quad (4b)$$

2.2. Case Study 2: Reactor Design



The second case study is a methanol synthesis reactor design study illustrating the versatility of the proposed concept. Instead of pressure in the compressor example, the product mole fraction of methanol is considered on the ordinate. Therefore, adiabatic reactor edges are defined instead of compressors in order to move from lower to higher product mole fractions in the thermodynamic state space. The adiabatic reactor edge is defined as a discrete step in the product mole fraction which is reformulated as a conversion of the reactant CO and a single reaction equation:



By introducing the conversion $X_{\text{CO}} = 1 - \frac{\dot{N}_{\text{CO,out}}}{\dot{N}_{\text{CO,in}}}$, the adiabatic temperature difference is obtained from

$$\Delta T_{\text{ad}} = \frac{-\Delta_R H(T_{\text{in}})}{-v_{\text{CO}}} \cdot \frac{\dot{N}_{\text{CO,in}}}{\sum_i \bar{N}_i c_{p,i}(T_{\text{in}})} \cdot X_{\text{CO}}, \quad (5)$$

where \bar{N}_i is the arithmetic average molar flux of component i along an adiabatic reactor edge. Acquiring an energy optimal solution is not relevant since the major part of the enthalpy change originates from the reaction enthalpy. Instead, an exergetically optimal pathway (III) is derived by minimizing exergy losses due to cooling. In a second optimization, the reactor volume is minimized which is achieved via maximization of the reaction rates. For this purpose, the adiabatic reactor edges are priced with kinetic rate expressions obtained from the kinetic model 2 for CH_3OH synthesis by Villa et al. (1987)

$$C^{\text{III}} = \sum_{i=1}^{N_{\text{hcu}}} E_{L,i} = \mathbf{c}_Q^{\top} \mathbf{Q} \quad \text{with} \quad c_{Q,i} := \left(1 - \frac{T_{\text{env}}}{T_i} \right), \quad \mathbf{c}_W, \mathbf{c}_T, \mathbf{c}_N := \mathbf{0}, \quad (6a)$$

$$C^{\text{IV}} = - \sum_{i=1}^{N_{\text{reac}}} R_i = -\mathbf{c}_T^{\top} \mathbf{R} \quad \text{with} \quad c_{T,i} := r_i, \quad \mathbf{c}_Q, \mathbf{c}_W, \mathbf{c}_N := \mathbf{0}. \quad (6b)$$

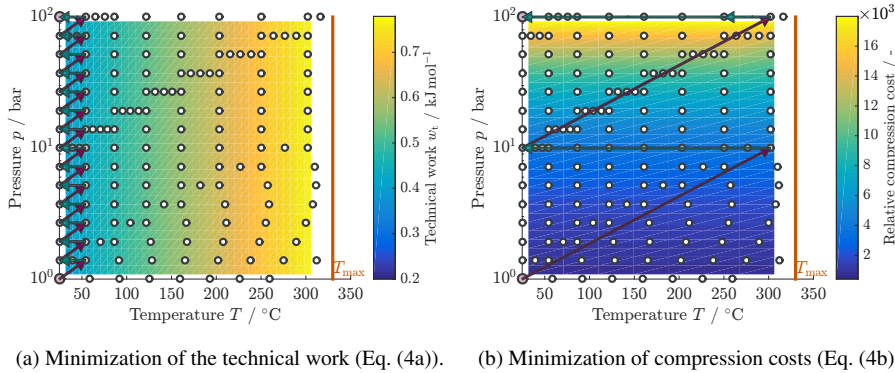


Figure 2: Thermodynamically attainable region and optimization result of the TNFA applied to a compressor cascade of Lurgi's methanol synthesis.

3. Results & Discussion

3.1. Optimal Compression Cascade

Results of the compressor cascade optimization are illustrated in Figure 2 in a semilogarithmic plot. The case study is a synthesis gas compression from 1 to 100 bar with in- and outlet flows at ambient temperature. A logarithmically equidistant pressure grid is applied and a maximum temperature of 330 °C is assumed as the upper temperature limit at the outlet of the compressor. Figure 2a shows the minimization of technical work as formulated in Eq. (4a). A colormap in the background illustrates the technical work required for compression at each compressor edge mean temperature. The energy minimal pathway climbs up to the required pressure in as many single steps as possible because compression work increases with temperature and this pathway is closest to the ideal case of a reversible isothermal compression. The second optimization scenario that takes only relative compressor costs into account (Eq. (4b)) results in the minimum number of compressor units and a maximum compression duty – i.e. combination of single edges to multiple edges – in each unit while fulfilling the temperature constraint.

The results of both optimizations are summarized in Table 1 representing the extreme cases: purely variable and purely fixed cost minimization. However, the real compressor cost are strongly loca-

Table 1: Compressor cascade optimization results.

Scenario	Technical work / kW	Relative capital cost / -
Energy minimization (Eq. (4a))	11.9	$1.3 \cdot 10^5$
Investment cost minimization (Eq. (4b))	16.2	$7.6 \cdot 10^4$

tion dependent due to a regional variability in capital and operational cost. As a consequence, a worldwide optimum is thus not sensible. The generic formulation proposed here allows to identify the best technical approximation and forms the foundation for decision making in specific cost scenarios.

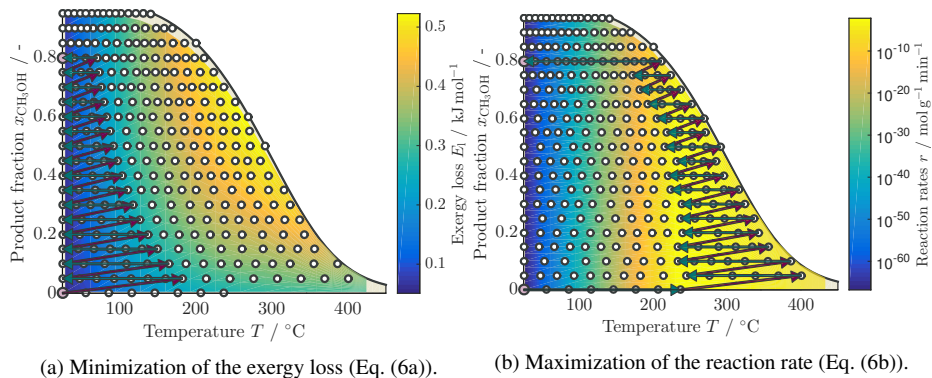


Figure 3: Thermodynamically attainable region and optimization result of the TNFA applied to the methanol synthesis reaction.

3.2. Optimal Reaction Pathway

The results of the reactor optimization for both objective functions (Eqs. (6a) and (6b)) are illustrated in Figure 3. In both cases, the reactor feed is a stoichiometric mixture of CO and H₂ at a temperature of 25 °C under isobaric conditions at 150 bar. At the reactor outlet, the molar flux is desired to contain 80 % of CH₃OH. The feasible region is bounded by the chemical equilibrium line which is obtained by Gibbs energy minimization and the thermodynamic state points are computed by means of Eq. (5). First, the results of the exergetic optimization (Eq. (6a)) are shown in Figure 3a. There, the background colormap denotes the exergy loss due to cooling to ambient temperature at each state point which increases with higher temperatures. The exothermic reaction is favored at low temperatures according to Le Chatelier's principle and requires therefore intermediate cooling. Consequently, the exergy optimal reaction pathway is found at low temperatures even though low reaction rates are present in this regime.

Figure 3b illustrates the optimization results for the kinetic rate maximization (Eq. (6b)). In contrast to the exergetic optimization, the reactants are preheated first. Due to the heat production during the reaction, the reactor still has to be cooled in order to stay within the feasible region. Considering the technical realization, the obtained pathway leads to a compact construction of the reactor since a pathway along maximum reaction rates is directly linked to a minimum reactor volume. The optimization results of both cases are summarized in Table 2. The kinetic optimization

Table 2: Methanol reactor optimization results.

Scenario	Exergy loss / kW	Reaction rate / mol g ⁻¹ min ⁻¹
Exergetic optimization (Eq. (6a))	$10.3 \cdot 10^3$	$9.9 \cdot 10^{-43}$
Kinetic optimization (Eq. (6b))	$47.8 \cdot 10^3$	$5.4 \cdot 10^{-3}$

leads to 4-5 times higher exergy losses due to cooling while increasing the reaction rates significantly. Therefore, the methanol synthesis process is typically carried out at temperatures between 250 °C to 300 °C (Ott et al., 2012) in industrial plants. Once more, both examined scenarios have to be regarded as extreme cases which were selected in order to demonstrate the applicability of our proposed method for reactor design purposes.

4. Conclusion

In this contribution, a novel thermodynamic network flow approach for the optimization of chemical processes is proposed. In this method a generalized matter element in the thermodynamic state space under the action of mass and energy fluxes is considered. By evaluating the thermodynamic potential of every discretized state point and evaluating the elementary steps in terms of heat, work and mass fluxes required for the node-to-node transition, the nonlinearities are decoupled effectively from the optimal network flow problem, which is purely linear if linear cost functions are chosen. The methodology is successfully validated and illustrated with two processes, a compressor cascade and the methanol synthesis reaction.

Since the decoupled linear optimization is solvable efficiently for a high number of decision variables – while preserving uniqueness and global optimality – and the required nonlinear computations can be carried out a priori, the proposed method is well suited for application to complex processes. Furthermore, the number and complexity of elementary process steps is easily adjustable due to the decoupling and modular build-up of the state point grid. Especially for industrial applications, it seems to be favorable that the formulation of the objective functions is highly versatile and enables numerous optimization scenarios depending on the application priorities as shown with the two case studies.

However, it should be mentioned that the accuracy of the optimization results depends strongly on the grid spacing in the state space. Finer grids require higher computational cost for the formulation of the constraint matrix. Finally, the novel proposed methodology should be benchmarked in terms of efficiency with well established nonlinear mixed integer approaches.

Acknowledgements

This research is supported by a research grant of the "International Max Planck Research School (IMPRS) for Advanced Methods in Process and System Engineering (Magdeburg)".

References

- L. T. Biegler, I. E. Grossmann, 2004. Retrospective on optimization. *Computers and Chemical Engineering* 28 (8), 1169–1192.
- D. R. Burgess, n. d. Thermochemical data. In: E. P. Linstrom, W. Mallard (Eds.), *NIST Chemistry WebBook: NIST Standard Reference Database Number 69*. Gaithersburg MD, 20899.
- H. Freund, K. Sundmacher, 2008. Towards a methodology for the systematic analysis and design of efficient chemical processes. Part 1. From unit operations to elementary process functions. *Chemical Engineering and Processing: Process Intensification* 47 (12), 2051–2060.
- N. M. Kaiser, M. Jokiel, K. McBride, R. J. Flassig, K. Sundmacher, 2017. Optimal Reactor Design via Flux Profile Analysis for an Integrated Hydroformylation Process. *Industrial & Engineering Chemistry Research* 56 (40), 11507–11518.
- J. Ott, V. Gronemann, F. Pontzen, E. Fiedler, G. Grossmann, D. B. Kersebohm, G. Weiss, C. Witte, 2012. Methanol. In: *Ullmann's Encyclopedia of Industrial Chemistry*. Wiley-VCH Verlag GmbH & Co. KGaA, Weinheim, Germany.
- A. Peschel, H. Freund, K. Sundmacher, 2010. Methodology for the design of optimal chemical reactors based on the concept of elementary process functions. *Industrial and Engineering Chemistry Research* 49 (21), 10535–10548.
- M. Peters, K. Timmerhaus, R. West, 2004. *Plant Design and Economics for Chemical Engineers*. College Ie. McGraw-Hill, Singapore, pp. 169–170.
- P. Villa, P. Forzatti, G. Buzzi-Ferraris, 1987. Response to comments on "synthesis of alcohols from carbon oxides and hydrogen. 1. kinetics of the low-pressure methanol synthesis". *Industrial Engineering Chemistry Research* 26 (2), 401–402.

A General Model-based Methodology for Chemical Substitution

Spardha Jhamb^{a*}, Xiaodong Liang^a, Rafiqul Gani^{a,b}, Georgios M. Kontogeorgis^a

^aDepartment of Chemical and Biochemical Engineering, Technical University of Denmark, DK-2800, Kgs. Lyngby, Denmark

^bCurrent address: PSE for SPEED, Skyttemosen 6, DK-3450 Allerød, Denmark
spajha@kt.dtu.dk

Abstract

The paper presents a general methodology for model-based chemical substitution, which considers different problem definitions depending on the objective for substitution. The developed methodology makes use of validated property models and modeling tools, thus avoiding the resource intensive and time-consuming experimental procedures during the initial stages. First, data and the property models are used to identify the chemicals present in a product that do not satisfy the regulatory property (EH&S: environmental, health and safety) bounds. Next, candidate molecules are generated and evaluated in order to identify those that can serve as safe substitutes and which are compatible with the original product or process function. Practical examples on substitution of chemicals used in processes and products in various sectors like automobiles, coatings and solvents, and polymers have been solved (Jhamb et al., 2017). In this paper we illustrate the methodology with an example concerning the substitution of a solvent, which is toxic to the aquatic environment (Eurochlor.org, 2015) but commonly used for dissolution of ultrahigh molecular weight - polyethylene (UHMW-PE), in its gel spinning process.

Keywords: property models, chemical substitution, general methodology.

1. Introduction

The regulatory authority on the safety of chemicals, the European Chemical Agency (Echa.europa.eu, 2007), has a goal to advance the safe use of chemicals for the benefit of the environment and human-health in the European Union (EU). One of the ways in which they strive to achieve this mission is by implementing the REACH regulation, which compels companies operating in the EU to stop the use of hazardous substances and replace them with environmentally benign and safe chemicals without disturbing the product function. However, in order to perform this task in a versatile manner, a systematic, model-based methodology can help to find the substitutes, as a first estimate, in a fast and reliable way, before focused experiments to validate the results are carried out.

Consumer-oriented chemical-based products are generally structured product formulations and they are composed of a set of chemicals, which due to their useful properties have brought substantial benefits to human lives and health. Besides these, single molecule products used in processes as working fluids, like solvents and refrigerants are also essential and have significantly contributed to the needs of our society. However, some chemicals constituting these products can be damaging to

human health and destructive for the environment due to their hazardous EH&S properties. Also, there are many more chemicals, which have not been evaluated due to lack of sufficient resources for experiments and paucity of reliable estimation methods (Hukkerikar *et al.*, 2012). Hence, there is an urgent need to efficiently identify substitute chemicals that will not be dangerous to the environment and/or toxic to human health while allowing the smooth functioning of the eco-system.

The objective of this paper is to present a chemical substitution methodology that can quickly and reliably identify promising candidates for substitution through model-based techniques that can later be verified through experiments. In this way, the experimental resources are used for verification rather than the time-consuming, trial-and-error search for alternatives. The very large search space, depending on the problem and the range of chemicals to-be considered, is reduced by employing a reverse design approach (Gani, 2004). That is, predictive property models are used to find alternative chemicals by matching the desired properties of the original product and avoiding the undesired EH&S properties of the 'compound to-be substituted'. The developed methodology can be used to systematically identify safe and environmentally compatible alternatives to the chemicals of concern. Note also that safe chemical product formulations with the same or better product performance as well as processes that make use of less hazardous chemicals, can be designed through this methodology.

2. A Generic Framework for Model-based Chemical Substitution

A systematic and generic framework, which incorporates model-based methods and tools that is able to solve a wide range of chemical substitution problems, is presented here. The framework contains a comprehensive property model library, EH&S property database, and a chemical properties database. A workflow diagram for the methodology for substitution of hazardous chemicals available through the framework is shown in Figure 1 (adopted from Jhamb *et al.*, 2017).

It should be noted that while solving any chemical substitution problem, if after the problem formulation step, it is recognized that the necessary property models or data are not available, then they will need to be added to the framework first. GC models for the required properties can then be quickly developed through the property modeling toolbox in ProCAPD (Kalakul *et al.*, 2017) by regressing the group contribution parameters.

3. Application of the Methodology

Case-study 1: The application of the methodology is highlighted through a case study involving the substitution of a single molecule solvent used in a UHMW-PE polymer spinning process (Fang *et al.*, 2016). UHMW-PE can yield fibers with high mechanical strength after extrusion in a gel-spinning process. However, due to its high melt viscosity it cannot be directly extruded. Therefore, it needs to be dissolved in a solvent before it passes through the extruder and is spun into fibers. Typically, 1,2,4-trichlorobenzene is used as a solvent for the dissolution of this polymer. In a post-extrusion step, an extraction solvent, n-hexane is used to remove the solvent from the polymer gel fibers. However, 1,2,4-trichlorobenzene appears on the REACH restricted substance list and it therefore needs to be replaced by another acceptable solvent.

3.1. Task 1: Identification of Problem Type

Firstly, the problem type, that is, the objective for substitution and function of the 'compound to-be substituted' in the original product or process, is identified. In this case, 1,2,4-trichlorobenzene is the solvent currently being used for UHMW-PE. The -

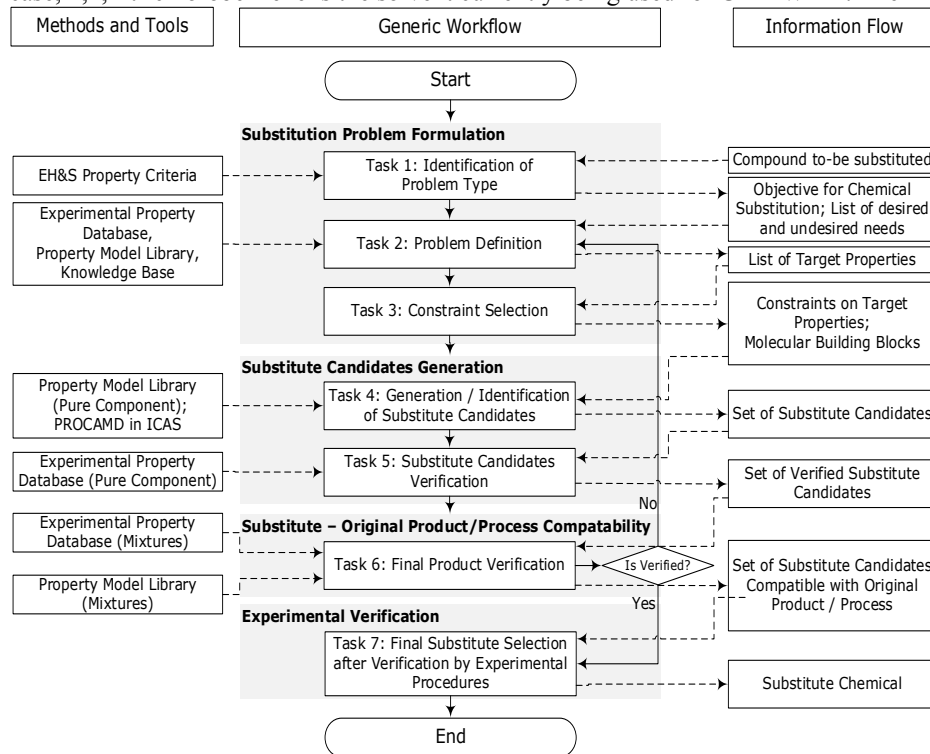


Figure 1: Workflow diagram for the methodology for chemical substitution

$\log(\text{LC}_{50})$ measured for fathead minnow (FM) – a freshwater fish, is 4.7 for this solvent (Eurochlor.org, 2015). For compliance with REACH regulations, solvents with values of $-\log(\text{LC}_{50})$ less than 3.5 and molecular weights in the range of 100 to 300 g/mol (Fisk, 2004) need to be used.

3.2. Task 2: Problem Definition

With the desired and undesired needs identified, they are converted to target pure component and mixture properties as given in Table 1 using a special knowledge base developed for the methodology.

3.3. Task 3: Constraint Selection

The constraints on the desired properties like normal melting point, normal boiling point, vapour pressure, viscosity, etc., associated with the function and performance of the solvent, are selected as close as possible to those of 1,2,4-trichlorobenzene, while the $-\log(\text{LC}_{50, \text{FM}})$ should be at least lower than the regulatory limit.

3.4. Task 4: Generation of Substitute Candidates

Since Group Contribution (GC) based models for the prediction of the pure component properties (Marrero and Gani, 2001) are available in the property model library for this problem, Computer Aided Molecular Design (CAMD) is used to generate substitute candidates with the tool, ProCAMD in ICAS (Gani et al., 1997). For this case-study, the

molecular building blocks of carbocyclic compounds are chosen because these are similar to the repeating unit of the polymer to be dissolved. The building blocks of aromatic compounds are not used to avoid hazardous properties associated with these structures. Four compounds are found to satisfy the pure component physicochemical

Table 1: Needs, Target Properties and Constraints for Example

Need	Target Property	Target Property Constraints
Ability to dissolve UHMW-PE at operating temperature	Solubility Parameter (δ_{Hild})	$16 \text{ MPa}^{1/2} < \delta_{Hild} < 18 \text{ MPa}^{1/2}$
Total Miscibility with the extraction solvent (n-hexane)	Gibbs Energy of Mixing (ΔG^{mix})	$\Delta G_{mix}/RT < 0$
Low volatility	Vapor Pressure (VP)	$0.0003 \text{ bar} < VP < 0.0012 \text{ bar}$
Not too viscous to allow flowability	Viscosity (η), Density (ρ)	$\eta < 1.65 \text{ cP}, \rho < 1.5 \text{ g.cm}^{-3}$
Liquid phase at operating temperature	Normal Melting Point (NMP), Normal Boiling point (NBP)	$NMP < 293.2 \text{ K}$ $475.2 \text{ K} < NBP < 600 \text{ K}$
Non-toxic to aquatic environment	Lethal Concentration ($LC_{50,FM}$)	$-\log LC_{50,FM} < 3.5 \log(\text{mol.L}^{-1})$

target properties. Out of these only one with building groups: CH_3 (1), CH_2 (10), CH (1) that is, methyl cycloundecane (CAS: 13151-44-5), satisfies the EH&S property constraint.

3.5. Task 5: Substitute Compound Verification

Since, the average absolute error in the $-\log(\text{LC}_{50, FM})$ property prediction model is 0.48 (Hukkerikar et al., 2012), this property needs to be verified experimentally for the identified substitute solvent. At this stage, the properties of methyl cycloundecane are also compared with other similar solvent candidates reported in the literature. Decalin, which is a carbocyclic compound with two rings, has satisfactory functional properties for the process considered here (Schaller et al., 2015). However, it is toxic to the aquatic environment ($-\log(\text{LC}_{50, FM})$ is 4.8) and highly volatile.

3.6. Task 6: Final Product Verification

Lastly, it is required that the generated candidate is compatible with the other chemicals used in the original process. This is done using appropriate mixture property models. Since, the extraction solvent used to remove the solvent from the extruded polymer is n-hexane, the miscibility of the recognized substitute solvent with n-hexane is checked by calculating the Gibbs energy of mixing using Eq. (1). Here, the activity coefficient (γ_i) is estimated using the original UNIFAC model. The Gibbs energy of mixing (ΔG_{mix}) at 298.2 K is found to be negative for all molar compositions of the methyl cycloundecane and n-hexane mixture (Figure 2), suggesting total miscibility.

$$\frac{\Delta G_{mix}}{RT} = \sum_i^{NC} x_i \ln(x_i) + \sum_i^{NC} x_i \ln(\gamma_i) < 0 \quad (1)$$

Besides this, the trend in the activity of methyl cycloundecane with increasing molar fraction in its mixture with UHMW-PE is checked, by using the UNIFAC-FV activity coefficient model (Oishi and Prausnitz, 1978). It is seen that the activity monotonically

increases (Figure 3), hence ensuring the solubility of the polymer in methyl cycloundecane.

3.7. Task 7: Final Substitute Selection after Verification by Experimental Procedures

Here, all the target properties of the methyl cycloundecane are verified through appropriate experiments before it is finally selected as the replacement solvent. This

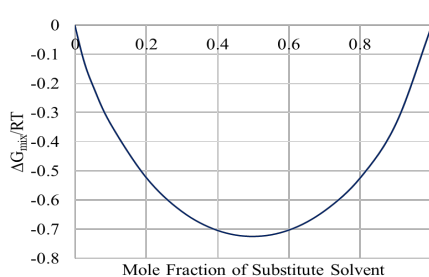


Figure 2: Gibbs energy of mixing for methyl cycloundecane-n-hexane mixture

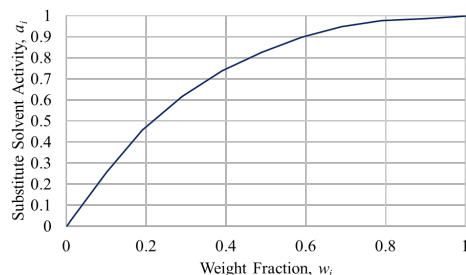


Figure 3: Methyl cycloundecane activity in methyl cycloundecane-polymer mixture using UNIFAC-FV model

step, however, is not performed in this case study.

Other case studies: The methodology has been successfully applied to substitution of hazardous and/or unsafe compounds from single-phase liquid formulated products. The classes of product (Gani and Ng, 2015) for which these substitution problems have been solved along with the function of the ‘compound to-be substituted’ are shown in Figure 4 and a summary of the results obtained is given in Table 2.

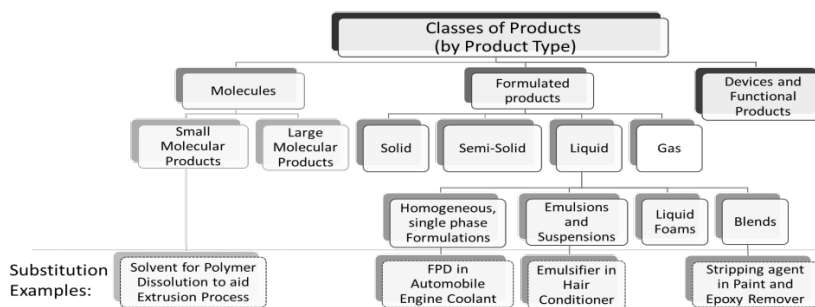


Figure 4: Class of products for which substitution problems are solved using the developed methodology

Table 2: Summary of results for solved substitution problems from chemical-based products

Compound to-be Substituted	Function of the Compound	Reason for Substitution	No. of properties compared	Substitute candidates recognized
Ethylene glycol	Freezing point depressant (FPD) in automobile engine coolant	Toxicity to mammals	1 EH&S + 8 physico-chemical properties	Propylene glycol

Methylene chloride	Stripping agent in paint and epoxy remover	Moderate aquatic toxicity	1 EH&S + 8 physico-chemical properties	2-propanone
Cetrimonium bromide	Surfactant in hair conditioner	High aquatic toxicity, Low biodegradability	2 EH&S + 4 physico-chemical properties	CAM (N _α -acyl-arginine methyl ester, n=8)

Specifically, for the case of cetrimonium bromide substitution, the amino acid based surfactant, CAM (Pérez et al., 2002) is identified as a substitute by means of a database search due to lack of GC-based models for EH&S and surface-active properties for amino acids and their derivatives.

4. Conclusion and Future Work

A systematic model-based methodology for chemical substitution has been developed and its application is illustrated via an example to substitute an environmentally hazardous single molecule solvent from a polymer spinning process. The methodology has also been used to find substitutes to environmentally unfriendly and/or unsafe chemicals used in single-phase liquid product formulations from various industrial sectors. The challenges and opportunities for chemical substitution in other classes of products like devices, solid-state products, polymers and plastics still need to be evaluated. While some of the missing property models have been developed and validated, for instance, the GC models for predicting normal melting point, water solubility and octanol water partition coefficient for the amino acid class of compounds (Jhamb et al., 2018), the development of many more property models is necessary for expanding the scope, significance and range of applicability of model based methodologies like these.

References

- A.S. Hukkerikar, S. Kalakul, B. Sarup, D.M. Young, G. Sin and R. Gani, 2012, *Journal of Chemical Information and Modeling*, 52, 11, 2823–2839
- Echa.europa.eu., 2007, REACH Legislation - ECHA. [online] Available at: <https://echa.europa.eu/regulations/reach/legislation> [Accessed 10 Dec. 2017]
- Eurochlor.org., 2015, Available at: http://www.eurochlor.org/media/49375/8-11-4-19_marine_ra_124_trichlorobenzene.pdf [Accessed 10 Dec. 2017]
- J. Marrero and R. Gani, 2001, *Fluid Phase Equilibria*, 183-184, 183-208
- L. Pérez, M.T. García, I. Ribosa, M.P. Vinardell, A. Manresa and M.R. Infante, 2002, *Environmental Toxicology and Chemistry*, 21, 6, 1279-1285
- P. Fisk, 2004, In: *Chemical Risk Assessment: A Manual for REACH*, John Wiley & Sons, Ltd, 317 – 339. Available at: <http://onlinelibrary.wiley.com/book/10.1002/9781118683989>
- R. Gani, G. Hytoft, C. Jakslund and A.K. Jensen, 1997, *Computers and Chemical Engineering*, 21, 10, 1135–1146
- R. Gani, 2004, *Computers and Chemical Engineering*, 28, 12, 2441-2457
- R. Gani and K. Ng, 2015 *Computers and Chemical Engineering*, 81, 70–79
- R. Schaller, K. Feldman, P. Smith and T. Tervoort, 2015, *Macromolecules*, 48, 24, 8877-8884
- S. Jhamb, X. Liang, G.M. Kontogeorgis and R. Gani, Submitted to: *13th International Symposium on Process Systems Engineering*. 2018. San Diego: Elsevier B.V.
- S. Jhamb, X. Liang, R. Gani, A.S. Hukkerikar, 2018, *Chemical Engineering Science*, 175, 148-161
- T. Oishi, and J. Prausnitz, 1978, *Industrial & Engineering Chemistry Process Design and Development*, 17, 3, 333-339
- X. Fang, T. Wyatt, Y. Hong and D. Yao, 2016, *Polymer Engineering & Science*, 56, 6, 697-706

Synthesis, design and analysis of energy efficient sustainable process alternatives

Rafiqul Gani^{a*}, Ramsagar Vooradi^b, Sarath Babu Anne^b

^a*PSE for SPEED, Skyttemosen 6, DK-3450 Allerød, Denmark (rgani2018@gmail.com)*

^b*Department of Chemical Engineering, National Institute of Technology Warangal, Telangana – 506004, India*

Abstract

This paper gives a brief review of the available energy sources for consumption, their effects in terms of CO₂-emission and its management, and sustainable chemical processing where energy-consumption, CO₂-emission, as well as economics and environmental impacts are considered. Analysis of the data indicate that not all available energy sources are being utilized efficiently, while, the energy sources causing the largest emissions of CO₂ are being used in the largest amount. Sustainable alternatives are defined as those where the energy consumption – CO₂ emission are addressed such that the net CO₂ emission is significantly reduced while still satisfying the energy demand. Different schemes for generating these sustainable alternatives are highlighted in this paper. These examples highlight issues of energy related to CO₂ neutral design; sustainable conversion; retrofit design, and process intensification.

Keywords: energy sources, energy consumption, CO₂ emission & management, sustainable alternatives

1. Introduction

Among the challenges we are facing today, one of the most important concerns is energy as it effects directly and/or indirectly most of the other challenges related to water, food and environment. Energy is needed in some form for almost all our activities within sectors such as transportation, commercial, industrial and residential. The energy needs (demands) for the different sectors are met through different sources of energy that is dependent on geographical location, availability, cost of harnessing it as well as environmental effects. Availability of the energy sources is not uniform through-out the earth, neither are costs or needs. The sources of energy can be broadly classified as conventional and unconventional. Conventional sources of energy are the natural energy resources (coal, oil, natural gas, wood, etc.), which are generally accepted as fuel to produce heat, light, food and electricity. Unconventional energy sources are classified as solar, wind, biological wastes, hot springs, tides, etc., that may be used also to generate heat and power. Unlike the conventional energy sources, which are non-renewable, limited in terms of availability and cause pollution (for example, emits CO₂ to the atmosphere), the unconventional energy sources are renewable, are present in abundance in nature and also generally pollution free.

Energy consumption per capita is an important parameter to assess the quality of life of the population of a country. Thus, sustainable harnessing of the available energy resources with a view to meet the necessities of increasing world population, to ensure a

safe and healthy living of the present as well as the future generations on earth, is an essential ingredient of all governmental planning (Brundtland Commission, 1987). With the rapid industrialization and growth in population, the demand for energy is increasing continuously. However, because of the cost and availability, the most used source of energy is non-renewable, which also has the largest effect on the environment because of the emission of CO₂.

Depending on the specific application, these sources of energy are converted into potential energy (any type of stored energy, for example, chemical, nuclear, gravitational, or mechanical) and/or kinetic energy, which is related to movement (for example, electricity is the kinetic energy of flowing electrons between atoms (does not release CO₂). Note that the kinetic energy that help the wheels to turn in a car is the transformed potential energy trapped in gasoline, for example and results in CO₂ emission. Another common example of transformation of energy from one form to another is a power plant. However, power plants using non-renewable energy sources (coal, natural gas, oil, wood) transform the chemical potential energy trapped in the fossil fuels to electricity (releasing, thereby, CO₂); while nuclear power plants change the nuclear potential energy of uranium or plutonium also into electricity, wind turbines change the kinetic energy of air molecules in wind into electricity, hydroelectric power plants transform the gravitational potential energy of water as it falls from the top of a dam to the bottom into electricity. Initiatives to capture the released CO₂ is therefore similar to trying to “cure” the pollution problem. As the amount and source of energy used effects our environment and thereby, our sustainability, to meet demand for energy, the conventional resources need to be supplemented with the unconventional resources such that CO₂ emission could be managed together with energy utilization.

The objective of this paper is to present a brief analysis of the available energy resources for consumption and their effects in terms of sustainable development. Recently, Vooradi, et al. (2017) provided a detailed overview of the different types of energy resources and their current consumption. In this paper, we further extend the analysis of Vooradi, et al. (2017) with additional data, new analysis together with new developments related to generation of more sustainable alternatives, that aims to prevent the pollution problem rather than curing it after it has occurred. That is, “prevent” the pollution problem through alternatives that are sustainable.

2. Energy resources, their consumption and CO₂ emission – current status

The distribution of energy consumption in the OECD and non-OECD countries is shown in Fig 1a, while the distribution of the total energy in different regions of non-OECD countries is shown in Fig 1b and distribution of total energy in terms of sectors is shown in Fig 1c. It can be noted that the biggest increase in 2040, compared to 2015, will be in non-OECD countries (in Asia) and in terms of sectors, in the industrial sector (see Fig 1c). The question, however, is which energy resources should be used to meet this increased energy demand? Figure 2 shows the distribution of energy sources to generate electricity (Fig 2a), while Figs 2b-2e show the energy resources consumed by different sectors. If we combine this data with the data from Table 1, where the three most used conventional fuels are analyzed, we can see that we will have a major ‘curing’ the pollution problem. Clearly, this is not sustainable! Figures 3a-3c, however, show a positive trend. Some countries have managed to reduce their overall CO₂ emission, China has managed to stabilize its CO₂ emission by reducing the consumption of coal and a few countries have increased their CO₂ emission, but their contribution

compared to the total is quite small. This indicates that re-allocation of energy resources to tackle the energy consumption – CO₂ emission is already going on and needs to be further advanced.

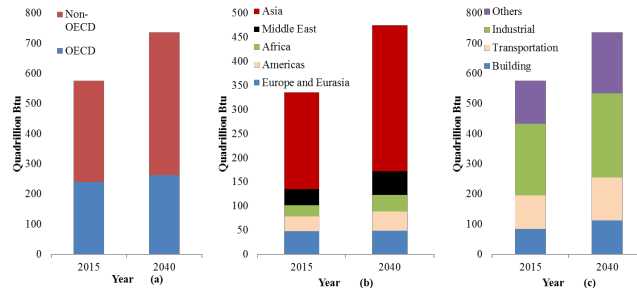


Figure 1: Energy consumption a) Total energy b) Total energy in Non-OECD c) Sector wise (Data Source: The International Energy Outlook, 2017).

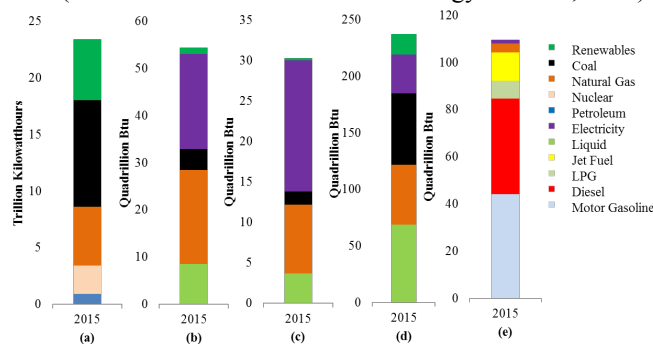


Figure 2: Different forms of energy (a) Net electricity generation by fuel; Energy consumptions (b) in Residential sector, (c) in Commercial sector (d) in Industrial sector (e) in Transportation Sector. Data Source: The International Energy Outlook, 2017.

Table 1: Fossil energy information for the year 2016 (Statistical review of world energy, 2016; GES Yearbook, 2017)

Energy	Reserves	Consumption	CO ₂ Emission	Remarks
Oil	1706.7 Bb	35.40 Mb/year	10.7 Bt	Accounts for nearly 1/3 of global energy consumption.
Natural Gas	186.6x10 ³ Bcm	3550 Bcm	6.93 Bt	World consumption increased by 63 Bcm (1.5%).
Coal	1139.3 Bt	3.75 Btoe	13.84 Bt	World consumption is showing a decreasing trend, which is 0.053 Btoe (1.7%).

Units: Bb-Billion barrels, Bt-Billion Tons, Bcm- Billion cubic meter, Btoe-Billion Tons of Oil Equivalent

2.1 Perspectives

The above analysis points to the need for re-allocation of energy resources to meet the energy demands. While the trend is an increased energy demand, significant effort is needed to meet these demands through unconventional energy resources, such as biomass, solar, wind, etc., especially in the transportation and residential sectors. At the

same time, the design and operation of energy intensive processes need to be revised so that new, more sustainable and innovative designs can be found (see section 3 on sustainable alternatives).

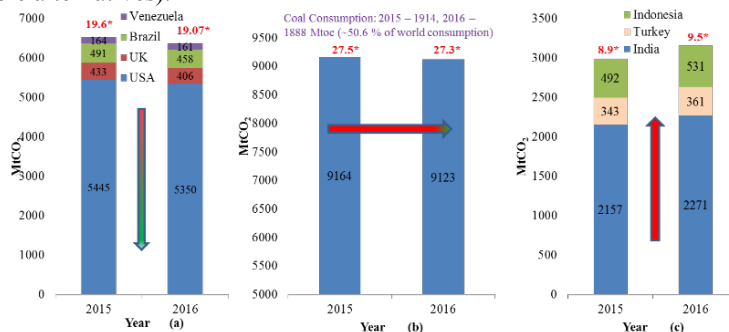


Figure 3: CO₂ emissions a) Countries with decreasing trend b) China c) Countries with increasing trend. World CO₂ emissions: 2016 – 33432 MtCO₂; 2015 – 33304 MtCO₂; 2014 – 33342 MtCO₂; * Percent of total world emission (GES Yearbook, 2017).

3. Sustainable alternatives

Examples of energy consumption -CO₂ emission management are highlighted below for selected cases involving the industrial sector (chemical and related processes).

3.1 Energy-CO₂ neutral process design

This option is not really preventing the pollution problem but it nevertheless promises the potential to significantly reduce the CO₂ emission as well as points to issues that need to be resolved if the energy consumption - CO₂ emission management should find a sustainable solution. Roh, et al. (2015) and more recently Bertran, et al. (2017) have shown that the CO₂ released from power plants can be captured with the currently available technologies and converted to chemicals such as methanol, dimethyl ether, dimethyl carbonate, succinic acid and many more with a net CO₂ emission of zero or negative (CO₂ released – CO₂ utilized). The problem, however, is that the demands for the chemicals produced are currently so low that the CO₂ captured from a few power plants of standard size is enough to cover these demands. Note that this is a pollution “curing” problem after it has occurred, making it more difficult to solve. To make a significant impact, the demands for the chemicals need to increase or the power plants need to switch from fossil to unconventional resources, thereby, preventing the pollution problem.

3.2 Energy-process intensification (use of solar energy as source)

The development and implementation of alternative energy conversion techniques using solar energy, prominent due to its abundance, has been reported by Gencer and Agrawal (2017). More specifically, they introduced a process design concept to synthesize Solar Electricity, Water, Food and Chemical (SEWFAC) processes by optimally utilizing solar energy. The objective is the development of coproduction processes around the clock on an as-needed basis. Application of this interesting concept is illustrated through the design of efficient solar thermal hydrogen production. The underlying principle is to maximize solar energy conversion via coproduction of hydrogen and electricity and an efficient way to supply the required electricity demand is by cogenerating from incident solar energy. Much more work, however, is needed to establish this interesting concept, especially related to sizing of the plant, material of

construction, high temperature of operation and heat integration issues. The scope and significance of final integrated process will be able to significantly reduce the size of the power generation unit of the plant for the same overall output. Other intensification options to generate more sustainable energy efficient alternatives have been reported by Babi, et al. (2015).

3.3 Energy – sustainable conversion of biomass

Biomass chemical conversion processes allow the production of solid, liquid and gaseous biofuels, which can substitute almost any kind of fossil fuel and reduce the associated greenhouse gas emissions. Three interesting recent works are highlighted here. Bertran. et al. (2017) recently reported the development of a systematic method for conversion of biomass into useful chemicals, including biofuels, taking into account the biomass location, amount available, chemical (product) demand, and transportation costs. Through the developed method and associated computer aided tools, it is possible to identify more sustainable alternatives to convert a given biomass at a specific geographical location to a set of desired products at other locations, according to their demand. Note that production of chemicals reduces the use of non-renewable resources for their production, thereby making the bio-conversion route more sustainable. Girones, et al. (2017) proposed a biomass gasifier to convert lignocellulosic biomass such as wood into syngas, which can be used in Solid Oxide Fuel Cell (SOFC) to produce heat and electricity. Also, Sharma, et al. (2017) compared many biomass conversion options taking into account the complete energy conversion pathway, from the resource to the supply of energy services. The comparison (includes 56 scenarios) is performed by evaluating the CO₂ abatement potential of integrating these different pathways into a national energy system. Results show that biofuels can allow for an overall better performance in terms of avoided CO₂ emissions compared to direct combustion of biomass. To exploit this potential, however, it is necessary to link the production of biofuels to a wider deployment of the corresponding efficient end-use technologies. Biomass is an attractive renewable and stored energy that can be converted to transportation fuels, chemicals and electricity using bio-chemical and 5hermos-chemical conversion routes. Notably, biofuels have relatively lower greenhouse gas emissions compared to the fossil fuels. A biomass gasifier can convert lignocellulosic biomass such as wood into syngas, which can be used in Solid Oxide Fuel Cell (SOFC) to produce heat and electricity. SOFC has very good thermodynamic conversion efficiency for converting methane or hydrogen into electricity, and integration of SOFC with gasifier gives heat integration opportunities that allow one to design systems with electricity production efficiencies as high as 70%. Generally, process design and operational optimization problems have conflicting performance objectives, and Multi-Objective Optimization (MOO) methods are applied to quantify the trade-offs among the objectives and to obtain the optimal values of design and operating parameters. This study optimizes biomass gasifier and SOFC plant for annual profit and annualized capitalBiomass is an attractive renewable and stored energy that can be converted to transportation fuels, chemicals and electricity using bio-chemical and 5hermos-chemical conversion routes. Notably, biofuels have relatively lower greenhouse gas emissions compared to the fossil fuels. A biomass gasifier can convert lignocellulosic biomass such as wood into syngas, which can be used in Solid Oxide Fuel Cell (SOFC) to produce heat and electricity. SOFC has very good thermodynamic conversion efficiency for converting methane or hydrogen into electricity, and integration of SOFC with gasifier gives heat integration opportunities that allow one to design systems with electricity production efficiencies as high as 70%. Generally, process design and operational optimization problems have conflicting performance

objectives, and Multi-Objective Optimization (MOO) methods are applied to quantify the trade-offs among the objectives and to obtain the optimal values of design and operating parameters. This study optimizes biomass gasifier and SOFC plant for annual profit and annualized capital

3.4 Energy-retrofit design

Application of the energy efficient hybrid separation scheme proposed by Tula, et al. (2017) is highlighted here for the energy intensive separation of two azeotropic mixtures, namely benzene-cyclohexane and acetonitrile-water. In the separation scheme for benzene-cyclohexane mixture, membrane unit is used to enrich the cyclohexane product purity. In the second example, the mixture at the azeotropic composition is separated by using membrane. The proposed schemes are associated with the additional capital cost due to the inclusion of the membrane module. However, the hybrid schemes result in significant operational (energy) savings. The economics of the proposed designs are investigated by calculating the payback period for the additional capital investment using the operational savings (selected results are given in Table 2).

Table 2: Economics of the hybrid schemes

Calculation details	Benzene-cyclohexane	Acetonitrile-water
Membrane considered	carboxymethyl cellulose (Kuila and Ray, 2014)	SiO _x modified Al ₂ O ₃ ceramic membrane (Kolsch, et al. 2002)
Base case utility need	43.5 Gcal/h	0.045335 Gcal/h
Base case (Opex)	1456.032 €/h	1.517472 €/h
Hybrid case utility need	17.042 Gcal/h	0.037978 Gcal/h
Hybrid case (Opex)	905.14 €/h	1.272 €/h
Membrane area	19942 m ²	40.9411 m ²
Membrane Capex	10649028 €	3302.31 €
Operational savings	550.9 €/h	0.2461 €/h
Payback period	193330.24 h (2.2 years)	13418.5 h (1.53 years)

4. Conclusion and Future Work

The grand challenges of energy, water, food and health facing current and future societies can be addressed through sustainable development (Negro, et al. 2017). For the next 25 years, renewables as well as unconventional (solar, wind, and nuclear) are projected to be the world's fastest-growing energy sources. Current research on energy storage technologies is in tune with the recent developments in renewable energy harvesting technologies, so as to ensure an uninterrupted power supply. For the next few decades, fossil fuels are still projected to be the main energy source for the base load power supply. Hence these processes need to be integrated with CCS and CCU for sustainable development with the objective of net CO₂ emission reduction. Also, re-allocation of energy sources needs to be made so that unconventional sources not emitting CO₂ is consumed in a bigger amount together with better design of energy intensive processes. Superstructure based optimization techniques successfully being applied in process synthesis can be adopted for optimal energy source allocation matching various forms of energy demands at reduced CO₂ emission. That is, given a set of energy sources, a set of energy demands, select a set of appropriate energy efficient technologies to match the sources-demands such that the CO₂ emission is

significantly lower and sustainable. Uncertainties in data and location dependence of energy sources and/or demands may also be included in the problem formulation. Collection of data and development of appropriate models is a good starting point.

References

- Babi, D. K., Holtbruegge, J., Lutze, P., Gorak, A., Woodley, J. M., Gani, R., 2015, *Computers & Chemical Engineering*, 81, 218-244.
- Bertran, M. O., Frauzem, R., Sanchez-Arcilla, A. S., Zhang, L., Woodley, J. M., Gani, R., 2017, *Computers & Chemical Engineering*, 106, 892-910.
- Brundtland Commission, 1987. Report of the World Commission on Environment and Development: Our Common Future. Oxford University Press.
- Gençer, E., Agrawal, R., 2017, *Computers & Chemical Engineering*, 105, 328-347.
- Girones, V. C., Moret, S., Peduzzi, E., Nasato, M., Marechal, F., 2017, *Energy*, 137, 789-797.
- Global Energy Statistical (GES) Yearbook 2017, CO₂ emissions from fuel combustion, <https://yearbook.enerdata.net/> (Accessed: 14.02.2018).
- Kolsch, P., Sziladi, M., Noack, M., Caro, J., Kotsis, L., Kotsis, I., Sieber, I., 2002, *Chemical Engineering & Technology*, 25(4), 357-363.
- Kuila, S.B., Ray, S. K., 2014. *Separation and Purification Technology*, 123, 45–52.
- Roh, K., Frauzem, R., Gani, R., Lee, J.H., 2016, *Chem. Eng. Res. Des.*, 116, 27-47.
- Negro, C, Garcia-Ochoa, F, Tanguy, P, Ferreira, G, Thibault, J, Yamamoto, S, Gani, R, 2018, *Chemical Engineering Research & Design*, 129, A1-A2
- Sharma, S., Celebi, A. D., Merechal, F, 2017, *Energy*, 137, 811-822.
- Statistical review of world energy, 2016, Energy economics, <https://www.bp.com>. (Accessed: 15.02.2018).
- The international energy outlook, 2017, U.S. Energy Information Administration. www.eia.gov/forecasts/ieo. (Accessed: 14.02.2018).
- Tula, A.K., Befort, B., Garg, N., Camarda, K.V., Gani, R., 2017, *Computers & Chemical Engineering*, 105, 96-104.
- Vooradi, R., Bertran, M. O., Frauzem, R., Anne, S. B., Gani, R., 2017, Sustainable chemical processing and energy-carbon dioxide management: Review of challenges and opportunities, *Chem. Eng. Res. Des.*, <https://doi.org/10.1016/j.cherd.2017.12.019>.

Process synthesis and optimization of membrane systems with superstructure approach for the mitigation of CO₂ emissions from a coal-fired power plant

Sunghoon Lee^a, Jin-Kuk Kim^a

^a*Hanyang University, Dpt. of Chemical Engineering, 222 Wangsimni-ro, Seongdong-gu, Seoul 04763, KR*

jinkukkim@hanyang.ac.kr

Abstract

Greenhouse gases emissions to the atmosphere has become a crucial cause to the climate change. As, CO₂ accounts for about 90% of emissions in volume, various separation technologies, such as absorption, adsorption, and membrane etc. have been studied for CO₂ removal. In particular, the membrane for CO₂ capture is regarded as a promising solution, due to clear advantages i.e. small foot print, easy installation, fast membrane development and flexibility in hybrid process. Furthermore, coal-fired plant contributes almost 46 % of global CO₂ emission (IEA, 2016), and its dominance is expected to be remained for the near future. Hence, the introduction of CO₂ capture systems to the coal-fired power plant has been considered to achieve cost-effectiveness of CO₂ capture process.

Here, we first developed in-house mathematical model for single-stage membrane in MATLAB® of which accuracy has been validated with literature. It is accepted that only single membrane process is limited to achieve both high purity and recovery for CO₂ product simultaneously from low CO₂ concentration of the feed flue gas. The multi-stage membrane is widely adopted in separation fields. The modeling framework for membrane is expanded to consider multi-stage networks, and a superstructure approach is applied for the process-synthesis of membrane systems which can evaluate all the possible configurations with various combinations of the pressure controllers, in a systematic manner. Furthermore, the optimization framework is developed, such that rigorous economic trade-off is systematically evaluated with capital expenditure (compressor, membrane etc.) and main operating expenditure of factors (power usage). Genetic Algorithm (GA) is adopted as an optimization solver to identify optimal operating conditions and membrane configurations.

With the developed automated tool for membrane system, design complexity in multi-stage configurations can be readily dealt with, while system-wide design interactions can be fully exploited in confidence. Sensitivity analysis of key design variables was carried out, with which conceptual understanding and design guidelines for membrane-based CO₂ capture systems are obtained. In particular, techno-economic impacts on the systems are investigated when membrane performance (permeance and selectivity) are varied. This provides practical guidelines for future membrane development in the CO₂ capture process. Case study is presented to demonstrate the applicability of

superstructure-based optimization method and illustrate the effectiveness in identifying the most appropriate membrane network, subject to process constraints and other practical limitations.

Keywords: optimization, Superstructure, membrane process

Acknowledgement

This research was supported by the Korea Carbon Capture & Sequestration R&D Center (KCRC) through the National Research Foundation of Korea (NRF) funded by the Ministry of Science, ICT (NRF-2014M1A8A1049338)

References

CO₂ emissions from fuel combustion highlights (2016, Ed.), International Energy Agency(IEA), p. 11

Semantically-enabled CAPE platform: Towards a generic and dynamic formulation for the synthesis and optimisation of value chains

Eirini Siouγκrou^a, Foteini Barla^a, Antonis Kokossis^a

^a *National Technical University of Athens, Chemical Engineering, 9 Heroon Polytechniou Street, 157 80 Athens, GR*

esiouγκrou@mail.ntua.gr

Abstract

In an attempt to link, manage and put in new-use the large amount of dispersed and heterogeneous CAPE data and models, a dynamic platform is developed able to offer high-throughput discovery and analysis of information for a wide range of users based on ontology engineering. Ontological modelling capabilities have recently attracted a lot of attention in process systems community for managing, querying and enriching knowledge. The services that have been designed for the platform consider a range of user roles, including three main categories of services. (a) Basic services, such as search and upload of conversion pathways and models, (b) integration with external tools and databases, and (c) custom-made services that include synthesis and optimisation of value chains. The basic services include models, which are of varied scale and describing diverse systems. The scale of a technology model could range from a detailed equation-based model or a conceptual flowsheet to a black box with some composition data, and all these developed in different design tools. A corresponding range can also be found for physical property, cost and LCA models.

The developed platform supports the integration of models, such as property or data models (e.g. LCA models, cost models). Not only will the user be able to get information about these models but also apply them to data from the database or personal data. Furthermore, a data mining approach has been used to implement the link to external databases service.

For the custom-made services, the technology models could be interlinked, according to their input and outputs, establishing value chains. The service enables the automatic design of value chains by semantic querying and retrieval algorithms. Further, the value chains could be assessed for economic and environmental feasibility through means of mathematical optimisation. Building on previous works (Barla et al., 2016; Siouγκrou & Kokossis, 2016), the platform is further developed to enable a customised formulation for the optimisation of the value chains. A general formulation of the model equations is introduced, where each process unit is considered to be a black box described by inlets, outlets and generic functions that define the relationship between inlets and outlets, e.g. mass balances, energy requirements, cost functions, etc.. The user can define the form of the model equations in the ontology and then the model equations are transferred from the ontology to a mathematical form through a disjunctive programming formulation. Design constraints, such as product requirements

and feedstock availability, can also be added to the optimisation formulation in a similar manner. Piecewise interpolation is applied to any non-linear model equations, to produce a final Mixed Integer Linear Programming formulation which is then solved with the GAMS software. The generic optimisation formulation and the ontological representation of the model equations render the formulation dynamic and completely flexible to the user's needs.

Representative services of the semantic platform are illustrated as alternative cases of possible users, demonstrating platform's ability to integrate information of varied origin and type using synthesis analysis, produce and assess metadata via reasoning and optimisation, and enabling to reach a wider audience, thus achieving to develop an expandable open CAPE platform.

Keywords: Optimisation, synthesis, value chain, ontology engineering

A novel Graphical Gibbs Energy-Driving Force Method for the Optimal Design of Non-reactive and Reactive Distillation Columns

Mauricio Sales-Cruz^a, Rafiqul Gani^b, Eduardo Perez-Cisneros^c

^a *Universidad Autónoma Metropolitana – Cuajimalpa, Departamento de Procesos y Tecnología, Avenida Vasco de Quiroga 4871, Col. Santa Fe Cuajimalpa, Delegación Cuajimalpa de Morelos, C.P. 05348, Ciudad de México, MX*

^b *PSE for SPEED Company Ltd., Skyttemosen 6, DK 3450 Allerød, Denmark*

^c *Universidad Autónoma Metropolitana, Ingeniería de Procesos e Hidráulica, Av. San Rafael Atlixco 186, C.P. 09340, Ciudad de México, MX*

espc@xanum.uam.mx

Abstract

A simple Gibbs-Driving force method for designing non-reactive and reactive distillation columns (non-RDC and RDC respectively) has been developed. Based on the binary driving force diagrams (Gani and Bek-Pedersen, 2000)(Pérez-Cisneros and Sales-Cruz) coupled with the equilibrium Gibbs energy plots a systematic graphical method for the design of non-RDC and RDC is proposed. The design method exploits the connection between the driving force values and the equilibrium Gibbs energy to determine the number of stages, the optimal feed location, the heat required at the reboiler and condenser and the minimum reflux ratio. The final design guarantee an optimal operation since the global minimum of the equilibrium Gibbs energy is achieved. The above optimal criteria is equivalent to the maximum entropy condition required for a stable operation of the distillation columns. The method has been applied for the design of two non-reactive systems: a) Benzene-Toluene ideal system and b) propanol-water non-ideal system as well as, two reactive systems: a) isomerization of n-butane and b) the MTBE production. The final designs of the non-RDC and RDC were validated through intensive simulation, showing that the designs obtained correspond to the minimal energy requirements for the separation.

Keywords: Uncertainty, population balance, optimization

References

- R. Gani and E. Bek-Pedersen, "Simple New Algorithm for Distillation Column Design," *AIChE Journal*, 46(6), 2000 pp. 1271–1274.
- E. Pérez-Cisneros and A. Sales-Cruz. Thermodynamic Analysis of the Driving Force Approach: Non-reactive systems. *Computers & Chemical Engineering*. .
10.1016/j.compchemeng.2017.06.021



28TH EUROPEAN SYMPOSIUM ON COMPUTER AIDED PROCESS ENGINEERING

PART B

Edited by
ANTON FRIEDL, JIŘÍ J. KLEMEŠ, STEFAN RADL,
PETAR S. VARBANOV AND THOMAS WALLEK



COMPUTER-AIDED CHEMICAL ENGINEERING, 43

28TH EUROPEAN SYMPOSIUM ON
COMPUTER AIDED PROCESS
ENGINEERING

PART B

28TH EUROPEAN SYMPOSIUM ON COMPUTER AIDED PROCESS ENGINEERING

PART B

Edited by

Anton Friedl

*Institute of Chemical, Environmental and Bioscience Engineering, TU Wien
Getreidemarkt 9/166, A-1060 Vienna*

Jiří J. Klemeš

*NETME Centre, Faculty of Mechanical Engineering, Brno University of Technology
Technická 2896/2, 616 69 Brno*

Stefan Radl

*Institute of Process and Particle Engineering, Graz University of Technology
Inffeldgasse 13/III, A-8010 Graz*

Petar S. Varbanov

*NETME Centre, Faculty of Mechanical Engineering, Brno University of Technology
Technická 2896/2, 616 69 Brno*

Thomas Wallek

*Institute of Chemical Engineering and Environmental Technology
Graz University of Technology
8010 Graz, Inffeldgasse 25/C/II*



ELSEVIER

Amsterdam – Boston – Heidelberg – London – New York – Oxford
Paris – San Diego – San Francisco – Singapore – Sydney – Tokyo

Elsevier
Radarweg 29, PO Box 211, 1000 AE Amsterdam, Netherlands
The Boulevard, Langford Lane, Kidlington, Oxford OX5 1GB, UK
50 Hampshire Street, 5th Floor, Cambridge, MA 02139, USA

Copyright © 2018 Elsevier B.V. All rights reserved.

No part of this publication may be reproduced or transmitted in any form or by any means, electronic or mechanical, including photocopying, recording, or any information storage and retrieval system, without permission in writing from the publisher. Details on how to seek permission, further information about the Publisher's permissions policies and our arrangements with organizations such as the Copyright Clearance Center and the Copyright Licensing Agency, can be found at our website: www.elsevier.com/permissions.

This book and the individual contributions contained in it are protected under copyright by the Publisher (other than as may be noted herein).

Notices

Knowledge and best practice in this field are constantly changing. As new research and experience broaden our understanding, changes in research methods, professional practices, or medical treatment may become necessary.

Practitioners and researchers must always rely on their own experience and knowledge in evaluating and using any information, methods, compounds, or experiments described herein. In using such information or methods they should be mindful of their own safety and the safety of others, including parties for whom they have a professional responsibility.

To the fullest extent of the law, neither the Publisher nor the authors, contributors, or editors, assume any liability for any injury and/or damage to persons or property as a matter of products liability, negligence or otherwise, or from any use or operation of any methods, products, instructions, or ideas contained in the material herein.

British Library Cataloguing in Publication Data

A catalogue record for this book is available from the British Library

Library of Congress Cataloging-in-Publication Data

A catalog record for this book is available from the Library of Congress

ISBN (Part B): 978-0-444-64238-7

ISBN (Set): 978-0-444-64235-6

ISSN: 1570-7946

For information on all Elsevier publications visit our website at <https://www.elsevier.com/>



Working together
to grow libraries in
developing countries

www.elsevier.com • www.bookaid.org

Publisher: Joe Hayton

Acquisition Editor: Kostas Marinakis

Editorial Project Manager: Emily Thomson

Production Project Manager: Paul Prasad Chandramohan

Designer: Greg Harris

Typeset by SPi Global, India

Contents

Process Operation and Control

160. A heuristic neighbourhood search-based algorithm for the solution of resource-task network scheduling problems
Giancarlo Dalle Ave, Xing Wang, Iiro Harjunkoski and Sebastian Engell 907
161. Robust Process Scheduling under Uncertainty with Regret
Chao Ning, Fengqi You 913
162. Process Scheduling under Ambiguity Uncertainty Probability Distribution
Chao Shang, Fengqi You 919
163. Mixed Integer Linear Programming Formulation for Sensible Thermal Energy Storages
Martin Koller and René Hofmann 925
164. Scheduling of a Multiproduct and Multiple Destinations Pipeline System with Repumping Operations
William Hitoshi Tsunoda Meira, Leandro Magatão, Susana Relvas, Lúcia V.R. Arruda, Flávio Neves Jr. and Ana Paula Barbosa-Póvoa 931
165. Data-based modelling for predicting the completion time of batch processes
Shao-Heng Hsu, Yao-Chen Chuang, Tao Chen, Yuan Yao 937
166. Sequential Bayesian Experimental Design for Process Optimization with Stochastic Binary Outcomes
Martin F. Luna, Ernesto C. Martínez 943
167. Oil product distribution planning via robust optimization
Camilo Lima, Susana Relvas, Ana Paula Barbosa-Póvoa, Juan M. Morales 949
168. A Discrete-time Scheduling Model for Continuous Power-intensive Processes Considering Fatigue of Equipment
Andreas Obermeier, Christoph Windmeier, Erik Esche and Jens-Uwe Repke 955
169. Multivariable Robust Model Predictive Control of a Laboratory Chemical Reactor
Juraj Oravec, Monika Bakošová, Linda Hanulová and Alajos Mészáros 961

170. Improvement of Synergistic Extraction of Neodymium Ions via Robust Model Predictive Control <i>Paisan Kittisupakorn, Wasamon Konaem, Ajaree Suwatthikul</i>	967
171. New continuous-time scheduling formulation for multilevel treelike pipeline systems <i>Pedro M. Castro, Hossein Mostafaei</i>	973
172. Tackling the complexity of designing multiproduct multistage batch plants with parallel lines: the application of a cooperative optimization approach <i>Floor Verbiest, Trijntje Cornelissens and Johan Springael</i>	979
173. Customized detailing of plant simulations with regard to different applications <i>Florian Pöllabauer, Gerald Bachmann and Thomas Wallek</i>	985
174. Risk assessment for the design and scheduling optimization of periodic multipurpose batch plants under demand uncertainty <i>Miguel Vieira, Helena Paulo, Corentin Vilard, Tânia Pinto-Varela, Ana Paula Barbosa-Póvoa</i>	991
175. Dynamics and MPC of an Evaporative Continuous Crystallization Process <i>Marcellus G. F. de Moraes, Maurício B. de Souza Jr., Argimiro R. Secchi</i>	997
176. Learning operation strategies from alarm management systems by temporal pattern mining and deep learning <i>Gyula Dörög, Peter Pigler, Mate Haragovics, Janos Abonyi</i>	1003
177. A two-stage stochastic programming approach to integrated day-ahead electricity commitment and production scheduling <i>Egidio Leo and Sebastian Engell</i>	1009
178. Changing between Active Constraint Regions for Optimal Operation: Classical Advanced Control versus Model Predictive Control <i>Adriana Reyes-Lúa, Cristina Zotică, Tamal Das, Dinesh Krishnamoorthy and Sigurd Skogestad</i>	1015
179. Health-Aware Operation of a Subsea Compression System Subject to Degradation <i>Adriaen Verheyleweghen, Julie Marie Gjøby and Johannes Jäschke</i>	1021

180. Application of CFD modelling to external nuclear reactor vessel cooling
Marco Colombo, Michael Fairweather 1027
181. New approaches for scheduling of multitasking multipurpose batch processes in scientific service facilities
Nikolaos Rakovitis, Jie Li, Nan Zhang 1033
182. Incorporating Systems Structure in Data-Driven High-Dimensional Predictive Modeling
Marco P. Seabra dos Reis 1039
183. Dynamic Real-time Optimization of Batch Membrane Processes using Pontryagin's Minimum Principle
Radoslav Paulen, Ayush Sharma and Miroslav Fikar 1045
184. An Integrated Medium – Term Energy Planning Model For Interconnected Power Systems
Apostolos P. Elekidis, Nikolaos E. Koltsaklis, Michael C. Georgiadis 1051
185. Multi-period multi-time optimisation of CO₂ based district energy systems
Raluca Suciu, Paul Stadler, Luc Girardin and François Maréchal 1057
186. Data-driven water-efficient production scheduling in the food industry
Sai Jishna Pulluru, Renzo Akkerman 1063
187. Online Quantification of the Concept Drift Using Incremental Learned Classifier and Non-automatic Clustering
Mohammad Hamed Ardakani, Ahmed Shokry, Gerard Escudero, Moises Graells, Antonio Espuna 1069
188. Production Scheduling of Multi-Stage, Multi-Product Food Process Industries
Georgios P. Georgiadis, Chrysovalantou Ziogou, Georgios Kopanos, Manuel Garcia, Daniel Cabo, Miguel Lopez, Michael C. Georgiadis 1075
189. A Proposal to Include the Information of Disturbances in Modifier Adaptation Methodology for Real Time Optimization
Daniel Navia, Antonio Puen, Paulina Quintanilla, Luis Bergh, Luis Briceño, César De Prada 1081
190. Towards the cooperative-based control of chemical plants
Bogdan Dorneanu, Evgenia Mechleri, Harvey Arellano-Garcia 1087

191. A multiparametric analysis of molecular complexities vs. economic data towards the continuous pharmaceutical manufacturing (CPM) of antibiotics
Mabel E. Ellerker, Samir Diab, Dimitrios I. Gerogiorgis 1093
192. Combined Use of Bilevel Programming and Multi-objective Optimization for Rigorous Analysis of Pareto Fronts in Sustainability Studies: Application to the Redesign of the UK Electricity Mix
Phantisa Limleamthong, Gonzalo Guillén-Gosálbez 1099
193. An effect of explosion venting panel using CFD in low pressure hydrogen facilities
Seungsik Cho, Jaewon Lee, Sunghyun Cho, Hyungjoon Yoon, and Il Moon 1105
194. Control of the Steady-State Gradient of an Ammonia Reactor using Transient Measurements
Harro Bonnowitz, Julian Straus, Dinesh Krishnamoorthy, Esmaeil Jahanshahi and Sigurd Skogestad 1111
195. A Simultaneous Parameter and State Estimator for Polymerization Process Based on Molecular Weight Distribution
Jiayuan Kang, Zhijiang Shao, Xi Chen, Lorenz T. Biegler 1117
196. Unsupervised Automatic Updating of Classification Models of Fault Diagnosis for Novelty Detection
Mohammad Hamed Ardakani, Ahmed Shokry, Gerard Escudero, Moisés Graells, Antonio Espuña 1123
197. Development of a fuzzy system for dissolved oxygen control in a recombinant *Escherichia coli* cultivation for heterologous protein expression
Rafael A. Akisue, Antonio C. L. Horta, Ruy de Sousa Jr 1129
198. Logistics optimization for dispositions and depooling of distillates in oil-refineries: closing the production scheduling and distribution gap
Brenno C. Menezes, Jeffrey D. Kelly, Ignacio E. Grossmann 1135
199. Multi-objective Optimization of the Energy System in an Iron and Steel Plant for Energy Saving and Low Emission
Yujiao Zeng, Xin Xiao, Jie Li, Fei Song 1141

200. Dynamic process simulation based process malfunction analysis <i>Alex Kummer, Tamás Varga</i>	1147
201. Virtual inflow estimation with simplified tuning using cascaded and Kalman-like least squares observers <i>Christoph Josef Backi and Sigurd Skogestad</i>	1153
202. Smarter process engineering across the plant life-cycle: CAPE 4.0 in industrial practice <i>David Elixmann, Michael Imle, Markus Feist, Rolf-Dieter Becher</i>	1159
203. Network formulations for the design and scheduling of multiproduct batch plants with parallel lines <i>Floor Verbiest, Tânia Pinto-Varela, Trijntje Cornelissens and Ana Barbosa-Povoa</i>	1165
204. Fault detection of fermentation processes <i>Ernie Che Mid, Vivek Dua</i>	1171
205. Nonlinear model predictive control application for gas-lift based oil production <i>Simone C. Miyoshi, Matheus Nunes, André Salles, Argimiro R. Secchi, Mauricio B. de Souza Jr., Amanda L. Brandão</i>	1177
206. System identification for a system subjected to persistent disturbances <i>Roberto Mei, Massimiliano Grosso, Federico Desotgiu, Stefania Tronci</i>	1183
207. Towards Obviating Human Errors in Real-time through Eye Tracking <i>Mohd Umair Iqbal, Babji Srinivasan, Rajagopalan Srinivasan</i>	1189
208. Online Monitoring of an Enzymatic Reactor based on Density Measurements <i>Emilio Granada-Vecino, Mauricio Sales-Cruz, Teresa Lopez-Arenas</i>	1195
209. Optimal Strategic Planning of Integrated Petroleum and Petrochemical Supply Chain <i>Rahayu Ginanjar Siwi, Furqan Aljumah, Jie Li, Xin Xiao</i>	1201
210. Real-Time Nonlinear State Estimation in Polymerization Reactors for Smart Manufacturing <i>Santiago D. Salas, Jorge Chebeir, Stefania Tronci, Roberto Baratti, José A. Romagnoli</i>	1207

211. Optimisation of water supply systems in the water – energy nexus: Model development and implementation to support decision making in investment planning <i>Christiana M. Papapostolou, Emilia M. Kondili, Georgios Tzanes</i>	1213
212. Planning the Drilling Rig Activities – Routing and Allocation <i>M. Sadegh Tavallali, Marzieh Zare</i>	1219
213. Decision support platform based on intelligent mathematical modeling agents <i>Edrisi Muñoz, Elisabet Capón-García, Luis Puigjaner</i>	1225
214. Leak Detection Modeling Of A Pipeline Using Echo State Neural Networks <i>Alexandre M. Ribeiro, Caroline D. Grossi, Brunno F. Santos, Rejane B. Santos, Ana M. F. Fileti</i>	1231
215. Economic Model Predictive Control of a Wastewater Treatment Plant using Neural and Fuzzy models <i>Silvana Revollar, Hernán Álvarez, Rosalba Lamanna, Pastora Vega, Alejandro Goldar</i>	1237
216. Bayesian estimation of product attributes from on-line measurements in a dropwise additive manufacturing system <i>Andrew J. Radcliffe, Gintaras V. Reklaitis</i>	1243
217. Data Driven Reduced Order Nonlinear Multiparametric MPC of Large Scale Systems <i>Panagiotis Petsagkourakis, Constantinos Theodoropoulos</i>	1249
218. Model-based real-time prediction of corrosion in heat exchangers <i>Günther Holzer, Thomas Wallek</i>	1255
219. Control strategy for the Super Heat Integrated Distillation Column <i>Manuel Rodriguez, Ismael Diaz</i>	1257
220. Dynamic simulation and process control study for enhancing operability of small-scale BOG (Boil-off gas) re-liquefaction process in LNG-fueled ship <i>Hyunsoo Son, Jin-Kuk Kim, Dong-Hun Kwak</i>	1259
221. Global Optimization Algorithm for Multi-period Design and Planning of Centralized and Distributed Manufacturing Networks <i>Cristiana Lara, Ignacio Grossmann</i>	1261

Environment and Energy

222. Optimal Integrated Facility for Waste Processing
Edgar Martín-Hernández, Apoorva M. Sampat, Victor M. Zavala, Mariano Martín 1263
223. Assessing Energy and CO₂ Emission Reduction from Ammonia Production by Chemical Looping as Innovative Carbon Capture Technology
Dora-Andreea Chisalita, Letitia Petrescu, Ana-Maria Cormos, Calin-Cristian Cormos 1269
224. Use of excess heat from ethylene recycling in a low-density polyethylene production plant
Rodolfo D.C. Matos, Isabel M. João, João M. Silva 1275
225. Flexible Hydrogen and Power Co - generation based on Dry Methane Reforming with Carbon Capture
Szabolcs Szima, Ana-Maria Cormos, Calin-Cristian Cormos 1281
226. Parameter estimation for modelling of organophilic pervaporation
Andras Jozsef Toth, Eniko Haaz, Szabolcs Solti, Nora Valentinyi, Anita Andre, Daniel Fozer, Tibor Nagy, Peter Mizsey 1287
227. Simultaneous Optimization of Multistream Heat Exchangers and Processes
Yingzong Liang, Keat Ping Yeoh, Ergys Pahija, Pui Ying Lee, Chi Wai Hui 1293
228. Population Balance Equation Applied to Microalgae Harvesting
Pui-Ying Lee, Ergys Pahija, Ying-Zong Liang, Keat-Ping Yeoh, Chi-Wai Hui 1299
229. Total Site Utility Systems Structural Design Considering Environmental Impacts
Timothy G. Walmsley, Xuexiu Jia, Petar S. Varbanov, Jiří J. Klemeš, Yutao Wang 1305
230. Decarbonisation of the Industrial Sector by means of Fuel Switching, Electrification and CCS
Sandro Luh, Sara Budinis, Thomas J. Schmidt and Adam Hawkes 1311

231. Solvent use optimization on polyphenols extraction from grape marc involving economical aspects
R. de Mattos, B. Zecchi, P. Gerla, A. Ferrari 1317
232. Integrated Process Design and Optimization of a Nitrogen Recovery in Natural Gas Processing with Varying Feed Composition
Yongseok Lee, Youngsub Lim, Chonghun Han 1323
233. Sequential Flowsheet Optimization: Maximizing the Exergy Efficiency of a High-Pressure Water Scrubbing Process for Biogas Upgrade
Alberto Penteadó, Jan C. Schöneberger, Erik Esche, Hamid R. Godini, Günter Wozny, Jens-Uwe Repke 1329
234. Extensions for Multi-Period MINLP Superstructure Formulation for Integration of Thermal Energy Storages in Industrial Processes
Anton Beck, René Hofmann 1335
235. Dynamic simulation of a post-combustion CO₂ capture pilot with assessment of solvent degradation
Hana Benkoussas, Grégoire Léonard, Madalina Ioana Burca, Ana-Maria Cormos 1341
236. A computer-aided analysis on regional power and heat energy systems considering socio-economic aspects: A case study on an isolated island in Japan
Yasunori Kikuchi, Yuko Oshita, Miwa Nakai, Aya Heiho, Yasuhiro Fukushima 1347
237. Simulation-based Analysis of Sewage Sludge Treatment Considering Regional, Social, and Technological Characteristics
Akinori Shimizu, Tatsuya Okubo, Yasunori Kikuchi 1353
238. Increasing Energy Efficiency in Pulp and Paper Production by Employing a New Type of Latent Heat Storage
Christoph Zauner, Rene Hofmann, Bernd Windholz 1359
239. The role of CCS and biomass-based processes in the refinery sector for different carbon scenarios
Julia Sachs, Sukma Hidayat, Sara Giarola, Adam Hawkes 1365
240. Modelling and optimization of a geotextile dewatering tubes process
Franco Mangone, Jimena Ferreira, Adrián Ferrari, Soledad Gutiérrez 1371

241. Innovative Temperature Swing Adsorption Simulation Model for Biogas Upgrading
Hannes Vogtenhuber, Elisabeth Sonnleitner, Franz Helming, René Hofmann, Gerhard Schöny, Veronika Wilk, Michael Lauer, Andreas Werner and Hermann Hofbauer 1377
242. Reduced Model Describing Efficient Extraction of Hydrogen Transported as Co-Stream in the Natural Gas Grid
Werner Liemberger, Martin Miltner and Michael Harasek 1383
243. Packed bed sorption enhanced methane reforming on CaO/CuO/Al₂O₃(NiO) catalyst
Giuseppe Diglio, Piero Bareschino, Erasmo Mancusi, Francesco Pepe, Dawid Hanak, Vasilije Manovic 1389
244. A Heat Load Distribution Method for Retrofitting Heat Exchanger Networks
Hür Bütün, Ivan Kantor, Alberto Mian, François Maréchal 1395
245. Combining Biomass, Natural Gas and Carbonless Heat to Produce Liquid Fuels and Electricity
Leila Hoseinzade, Thomas A. Adams II 1401
246. Optimisation of Wastewater Treatment and Recovery Solutions in Industrial Parks
Edward O'Dwyer, Hongcheng Wang, Ai-jie Wang, Nilay Shah and Miao Guo 1407
247. Integration of carbon dioxide and hydrogen supply chains
Anton Ochoa Bique, B.H. Nguyen, Grazia Leonzio, Christos Galanopoulos, Edwin Zondervan 1413
248. Multi-objective Optimization of a Carbon Dioxide Utilization Superstructure for the Synthesis of Formic and Acetic Acid
Juan D. Medrano-García, Rubén Ruiz-Femenia, José A. Caballero 1419
249. Concentrating High Purity CO₂ from Syngas after Oxy-fuel Combustion by Pressure Swing Adsorption Process
Cheng-Tung Chou, Bi-Ching Wu, Tien-Lin Wu, Hong-Sung Yang, Chia-Hsuan Shen 1425

250. Flow diagram of waste double base propellant treatment including fluidized bed reactor
Raymoon Hwang, Jiheon Lee, Inkyu Lee, Hyunsoo Kim, Jungsoo Park, Oh Min, Il Moon 1433
251. Integration of Renewable Resource into Petroleum Refining
Mohamed Al Jamri, Robin Smith, Jie Li 1439
252. Simulation of CO₂ Geological Storage Together with a Water Alternating Gas Process for Oil Production in Fang Oilfield (Thailand)
Kreangkrai Maneeintr, Hutthapong Yoosook 1445
253. A Multi-period Mixed Integer Linear Program for Assessing the Benefits of Power to Heat Storage in a Dwelling Energy System
Gbemi Ohuleye, John Allison, Nick Kelly, Adam Hawkes, 1451
254. Numerical Representation for Heat Exchanger Networks Binding Topology and Thermodynamics
Petar S. Varbanov, Timothy G. Walmsley, Michael Walmsley, Jiří J. Klemeš, Zdravko Kravanja 1457
255. Optimisation of Integrated Bioenergy and Concentrated Solar Power Supply Chains in South Africa
Massimo Liu, Koen H. Van Dam, Antonio M. Pantaleo, Miao Guo 1463
256. Use of Artificial Intelligence to Experimental Conditions Identification in the Process of Delignification of Sugarcane Bagasse from Supercritical Carbon Dioxide
Isabelle C. Valim, Artur S.C. Rego, Alex Queiroz, Vinnicius Brant, Antônio A. F. Neto, Cecília Vilani, Brunno F. Santos 1469
257. Including Agricultural and Organic Waste in Food-Water-Energy-Waste Nexus Modelling and Decision-Making
Daniel J. Garcia and Fengqi You 1475
258. Optimum Utilization of Biomass for the Production of Power and Fuels using Gasification
Ahmed AlNouss, Gordon Mckay, Tareq Al-Ansari 1481
259. An energy, water and food nexus approach aiming to enhance food production systems through CO₂ fertilization
Tareq Al-Ansari, Rajesh Govindan, Anna Korre, Zhenggang Nie, Nilay Shah 1487

260. Energy and water integration for the design of sustainable total textile waste refinery
Athanassios Nikolakopoulos, Antonis Kokossis 1493
261. The potential for carbon dioxide capture and utilization within the State of Qatar.
Ali Attiq Al-Yaeshi, Tareq Al-Ansari, Rajesh Govindan 1499
262. Optimization of Batch Heteroazeotropic Distillation Operational Strategies with Entrainer Recycle
Laszlo Hegely, Peter Lang 1505
263. Energy Efficient Design of Ionic Liquid based Gas Separation Processes
Xinyan Liu, Xiaodong Liang, Xiangping Zhang, Suojiang Zhang, Georgios M. Kontogeorgis, Rafiqul Gani 1513
264. Techno-Economic Analysis of CO₂ Capture Processes from Coal-fired Power Plants
Seokwon Yun, Sunghoon Lee, Jin-Kuk Kim 1519
265. Process design of absorption-membrane hybrid CO₂ capture systems for coal-fired power plant
Mun-Gi Jang, Sunghoon Lee, Seokwon Yun, Jin-Kuk Kim 1521
- Bioresources, Bioprocesses, and Biomedical Systems**
266. Feasibility of energy integration for high-pressure biofuels production processes
Luis Alberto Villegas-Herrera, Fernando Israel Gómez-Castro, Araceli Guadalupe Romero-Izquierdo, Claudia Gutiérrez-Antonio, Salvador Hernández 1523
267. Design of a low-cost process for the production of biodiesel using waste oil as raw material
Roberto Gasca-González, Fernando Israel Gómez-Castro, Araceli Guadalupe Romero-Izquierdo, Eric Zenón- Olvera, Claudia Gutiérrez-Antonio 1529
268. Energetic assessment of lignin extraction processes by simulation
Javier Fernández-Rodríguez, María González Alriols, Fabio Hernández Ramos, Jalel Labidi 1535

269. Retro-Techno-Economic-Environmental Analysis (RTEEA) from the cradle: a new approach for process development
Andrew M. Elias, Felipe F. Furlan, Marcelo P. A. Ribeiro, Roberto C. Giordano 1541
270. Dynamic Modeling of Butanol Production from Lignocellulosic Sugars
Cansu Birgen and Heinz A. Preisig 1547
271. Enzymatic keratin hydrolysis: Dynamic modelling, parameter estimation and validation
Alistair Rodman, Francesco Falco, Dimitrios I. Gerogiorgis, Krist V. Gernaey 1553
272. Adaptation of a Monte Carlo method to the hydrotreating of bio-oil model compounds
Ana R. Costa da Cruz, Jan Verstraete, Nadège Charon, Jean-François Joly 1559
273. Ontology Modelling for Lignocellulosic Biomass: Composition and Conversion
Madeleine Bussemaker, Nikolaos Trokanas, Linsey Koo, Franjo Cecelja 1565
274. Optimization of Cellulose Hydrolysis in a Non-ideally Mixed Batch reactor
F. Fenila, Yogendra Shastri 1571
275. Combined basic and fine chemical biorefinery concepts with integration of processes at different technology readiness levels
Sara Badr, Jane Yee Yap, Jully Tan, Matty Janssen, Elin Svensson, Stavros Papadokonstantakis 1577
276. CFD modelling of organosolv lignin extraction in packed beds
Michael Harasek, Bahram Haddadi, Christian Jordan, Anton Friedl 1583
277. Pyrolysis Kinetics of Genetically Engineered Hybrid Poplars for Bio-Oil Production
Vo The Ky, Jinsoo Kim 1589
278. Model-based Fed-batch Algal Cultivation Strategy for Enhanced Starch Production
Gonzalo M. Figueroa-Torres, Jon K. Pittman, Constantinos Theodoropoulos 1595

Food, (Bio-)Pharma, and Fine Chemicals

279. Model-based process development for a continuous lactic acid bacteria fermentation
Robert Spann, Anna Eliasson Lantz, Christophe Roca, Krist V. Gernaey and Gürkan Sin 1601
280. A Global State Feedback Linearization and Decoupling MPC of a MIMO Continuous MSMR Cooling Crystallization Process
Ravi Parekh, Brahim Benyahia, Chris D. Rielly 1607
281. Models for Designing Hydrogen Peroxide Decontamination Processes in Sterile Drug Product Manufacturing
Keisho Yabuta, Haruka Futamura, Koji Kawasaki, Masahiko Hirao, Hirokazu Sugiyama 1613
282. Multi-flowrate Optimization of the Loading Phase of a Preparative Chromatographic Separation
Anton Sellberg, Mikael Nolin, Anton Löfgren, Niklas Andersson and Bernt Nilsson 1619
283. Mathematical modelling of moisture migration in confectionery multicomponent food systems
Paschalia Mavrou, Rex Thorpe, William Frith, Guoping Lian, Tao Chen 1625
284. Model predictive control for automated anesthesia
Adriana Savoca, Jessica Barazzetta, Giuseppe Pesenti, Davide Manca 1631
285. Process modelling, design and technoeconomic evaluation for continuous paracetamol crystallisation
Hikaru G. Jolliffe, Dimitrios I. Gerogiorgis 1637
286. Process modelling, simulation and technoeconomic optimisation for continuous pharmaceutical manufacturing of (S)-warfarin
Samir Diab, Dimitrios I. Gerogiorgis 1643
287. Dynamic modelling and simulation of reactive transport phenomena in an amperometric blood glucose biosensor
Fergus McIlwaine, Dimitrios I. Gerogiorgis 1649
288. Industrial Scale Experiments towards the Development of Process Evaluation Models for Continuous Pharmaceutical Tablet Manufacturing
Kensaku Matsunami, Takuya Nagato, Koji Hasegawa, Masahiko Hirao, Hirokazu Sugiyama 1655

289. A Process System Approach to Nose-to-Brain Delivery of Biopharmaceutics <i>Costas Kiparissides, Aleck H. Alexopoulos, Philippos Karageorgos, Athina Vasileiadou and Vassilis Bourganis</i>	1661
290. Artificial vision system for the online characterization of the particle size distribution of bulk materials on conveyor belts <i>Mario Soprana, Andrea C. Santomaso, Pierantonio Facco</i>	1667
291. Automatic controller failure detection with application in model based control of an <i>E. coli</i> fed-batch <i>Sophia Ulonska, Julian Kager and Christoph Herwig</i>	1673
292. A Novel Dynamic Model of Plate Heat Exchangers Subject to Fouling <i>Shunfeng Guan, Sandro Macchietto</i>	1679
293. Risk based approach for batch release <i>Linas Mockus, Gintaras Reklaitis, Kenneth Morris, David LeBlond</i>	1685
Open Science Movement and Education	
294. Computational Improvements for the Eddy Dissipation Concept by Operator Splitting and Tabulation <i>Eva-Maria Wartha, Markus Bösenhofer and Michael Harasek</i>	1687
295. Active Learning of Process Control <i>Manuel Rodríguez, Alberto Prada, Ismael Díaz, Emilio Gonzalez, María González-Miquel</i>	1693
296. Combining Open Source and Easy Access in the field of DEM and coupled CFD-DEM: LIGGGHTS®, CFDEM@coupling and CFDEM@workbench <i>Dr. Alice Hager, Dr. Christoph Kloss and Dr. Christoph Goniva</i>	1699
297. Open-use and community-based tools for education in process system engineering: industrial applications from decision automation to data analytics <i>Brenno C. Menezes, Jeffrey D. Kelly</i>	1705
298. An interactive virtual laboratory for process engineering education <i>Diana Ibet Roman-Sanchez, Teresa Lopez-Arenas, Mauricio Sales-Cruz</i>	1707
Author Index	1709

A heuristic neighbourhood search-based algorithm for the solution of resource-task network scheduling problems

Giancarlo Dalle Ave^{a,b}, Xing Wang^{a,c}, Iiro Harjunkski^{a,*} and Sebastian Engell^b

^aABB AG Corporate Research Center, Wallstadter Str. 59, 68526 Ladenburg, Germany

^bProcess Dynamics and Operations Group, Department of Biochemical and Chemical Engineering, Technische Universität Dortmund, Emil-Figge-Str. 70, 44221 Dortmund, Germany

^cBusiness School University of Mannheim, Schloss Schneckenhof Ost SO 230, 68131 Mannheim, Germany

Iiro.Harjunkski@de.abb.com

Abstract

There are many challenges facing the widespread industrial deployment of scheduling solutions. These include to find a generic scheduling model that can be applied to a broad variety of scenarios, and to design algorithms that can provide good quality solutions in industrially relevant time frames. The discrete-time Resource-Task Network (RTN) is a generic scheduling framework that has been successfully applied to many different problems. However, RTN models can quickly become intractable as problem size increases. In this work, an iterative neighbourhood-search based algorithm is developed in order to speed-up the solution of RTN scheduling models. The speed-up is achieved by limiting the binary variables of a subproblem to a specific neighbourhood in a way that allows the algorithm to iteratively move towards better solutions. Results show that this approach is able to tackle problems that are intractable for a full-space model while still finding near optimal solutions.

Keywords: Resource-task network (RTN), Heuristic, Neighbourhood search, Iterative scheduling algorithm

1. Introduction

Some of the challenges facing the use of scheduling in industry are: to find a generic scheduling framework and efficient solution algorithms, which can provide good quality solutions that can be used in practice (Harjunkski et al. (2014)). The discrete-time Resource-Task Network (RTN) formulation has been shown to be applicable to various industrial applications with small application-specific configuration effort required. Such applications include, stainless steel-making (Castro et al. (2013)), thermo-mechanical pulping (Hadera et al. (2015)), and petrochemical production (Wassick and Ferrio (2011)). In the direction of deploying industrial scheduling solutions, Harjunkski and Bauer (2014) suggested the use of the ISA-95 standard as a way to efficiently communicate between the layers of the so-called automation pyramid.

The advantages of the RTN formulation and of mixed-integer linear programming (MILP) scheduling solutions in general are that they provide optimal solutions to problems with complex objective functions. The downside of MILPs is that solution time often increases dramatically with problem size, to the point where even a feasible solution cannot be guaranteed. Conversely, constructive

scheduling heuristic algorithms have fast execution times and scale very well with problems size; however, they give no indication of optimality and cannot handle competing objectives.

It is therefore desirable to combine the speed and scalability of heuristics with the mathematical rigor of MILPs. Works in this area include the sequential updating procedures proposed by Roslöf et al. (2001) which updates an initial heuristic-based solution by iteratively releasing a set of jobs and optimally inserting them into the existing job sequence. Other options include the use of pre-ordering rules to eliminate sequencing variables (Méndez and Cerdá (2002)) or to use heuristics to limit the search space of a problem and to use that solution to initialize a full-space model as in Panek et al. (2005). Alternatively, Castro et al. (2011) proposed a greedy algorithm to insert orders into a schedule a few jobs at a time, while allowing for partial rescheduling at each iteration.

In this work, an algorithm is proposed that takes advantage of heuristics to assist RTN-based scheduling solutions to find good solutions with comparatively small computational effort. This is accomplished by combining the two approaches of MILP and heuristic solutions in a novel iterative neighbourhood-based approach. In this algorithm, a heuristic is used to provide an initial feasible solution which is then used to constrain the binary variables of RTN scheduling models in a way that greatly reduces the computation time of the MILP, while still allowing it to move towards better solutions.

2. RTN Formulation

The proposed approach is based on the discrete-time RTN framework to make it generic and easy to adapt to various applications. This section will briefly present the RTN-scheduling model as well as specific modeling constraints and scenarios that are necessary to make the model even more flexible, at the expense of computational efficiency.

The RTN formulation is generic as it represents the entire scheduling model as a set of resources (R) and tasks (I). In this formulation, tasks consume and produce sets of resources. Examples of resources include raw materials, final products, and processing units. In the discrete-time RTN formulation, the scheduling horizon H is divided into a set of δ sized intervals T . Tasks ($i \in I$) are characterized by two sets of variables, the binary variable $N_{i,t}$ and the continuous variable $\xi_{i,t}$. The binary variable identifies that task i starts at time point $t \in T$ while the continuous variable indicates the amount of a resource handled by the task. The parameter τ_i is the duration of task i and $\mu_{i,r,\theta}$ and $\nu_{i,r,\theta}$ represent the interaction of task i on resource r based on the occurrence (defined by $N_{i,t}$) and continuous (defined by $\xi_{i,t}$) extent of the task respectively. The resource consumption over the time horizon is tracked by the excess resource balance given in Equation (1).

$$R_{r,t} = R_{r,t-1} + \sum_i \sum_{\theta=0}^{\tau_i} (\mu_{i,r,\theta} N_{i,t-\theta} + \nu_{i,r,\theta} \xi_{i,t-\theta}) + \pi_{r,t} \quad \forall r \in R, t \in T \quad (1)$$

Equations (2) and (3) limit the excess resources and the continuous extent of a task respectively.

$$R_{r,t}^{\min} \leq R_{r,t} \leq R_{r,t}^{\max} \quad \forall r \in T, t \in T \quad (2)$$

$$V_{i,r}^{\min} N_{i,t} \leq \xi_{i,t} \leq V_{i,r}^{\max} N_{i,t} \quad \forall r \in T, r \in R^{eq}, i \in I \quad (3)$$

2.1. Problem Specific Considerations

In order to meet typical requirements the base RTN model needs to be modified. The first modification is related to product-specific batch-tracking. This means that a specific batch or order can be tracked at each stage of production with a unique batch identifier. In the base RTN model, tasks belonging to the same family are aggregated to reduce model size. To meet the batch-tracking requirement, these variables need to be disaggregated. This means that a unique task and resource needs to be associated with each stage of production for a product. This requirement aligns the

RTN formulation with the ISA-95 standard (as each order corresponds to a specific OperationsRequest) and is a scenario often found in industry. An example of this can be found in stainless steel making, where a specific batch needs to be tracked to ensure that sequencing constraints are met throughout the production process. This leads to the assumption of a fixed-batch size; since each batch needs to be specifically tracked it is assumed that the size of the batch is determined elsewhere. Thus, the continuous extent variable $\xi_{i,t}$ and Eq (3) are not considered in this RTN formulation.

Other simplifications that are often made when using RTN models are to aggregate parallel equipment, and to use simplified transfer times between the stages. In this work, a separate resource is defined for each parallel equipment at each stage of production (corresponding to a specific ISA-95 Equipment definition). This enables the consideration of machine-specific transfer tasks. This greatly expands the size of the model as a new $N_{i,t}$ variable is required for each pair of equipment between two subsequent stages as well as resources to distinguish between an intermediate product that is ready for transport or that already has been transported.

Another important feature to consider is sequence dependent changeovers. To model these, a new task is needed which ‘consumes’ a piece of equipment in a specific operation mode and ‘produces’ the same piece of equipment but in a different mode. A sample RTN containing all of the aforementioned features is shown in Figure 1.

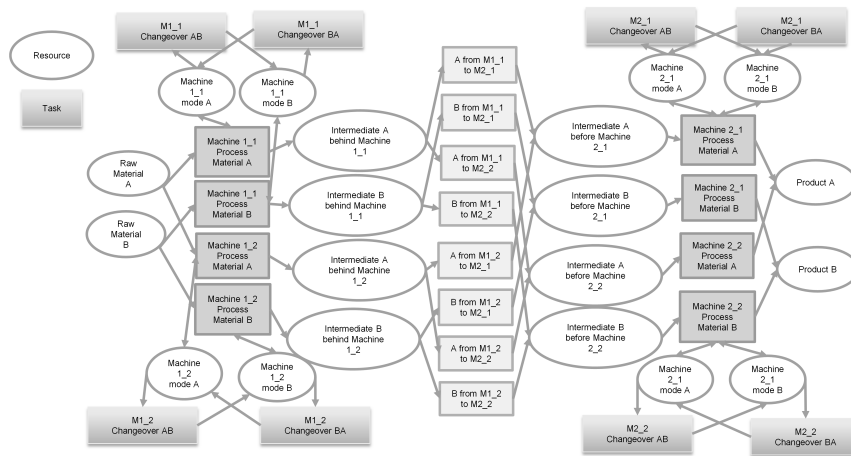


Figure 1: Example RTN of a two-stage batch process considering all the problem features.

While these specific features add flexibility to the RTN model, and conform to the ISA-95 standard proposed for scheduling, they add considerable complexity to the formulation. This provided the motivation to investigate new solution algorithms for such problems.

3. Proposed Algorithm

The proposed iterative algorithm uses a constructive heuristic to provide an initial feasible solution. Pseudocode for the constructive heuristic can be viewed below in Figure 2. The algorithm is initialized with the set of all jobs that needs to be scheduled. For example, job A needs to be processed on Stages 1,2, and 3, and a job is created for the processing of A at each stage. The next job to be scheduled is selected according to some sequencing rule. In this work an As Soon As Possible (ASAP) rule was used, but the algorithm can be applied to any sequencing heuristic. The last step of the algorithm is to greedily schedule that job to a machine based on its required

resource availability. This is performed until all jobs have been scheduled and a complete feasible solution is obtained.

```

I ← set of jobs to be scheduled
while I ≠ ∅ do
  | Select i ∈ I according to some sequencing rule (e.g. As Soon As Possible)
  | Greedily schedule i as soon as possible based on its resource availability
end

```

Figure 2: Pseudocode for the constructive scheduling heuristic

The next step of the algorithm is to match the continuous-time starting times of each of the jobs to the discrete-time grid used by the RTN. This can be done using Eq.(4) where $ST_{m,i}$ is the start time of job i on machine m as given by the heuristic and t_i is the corresponding start time interval in the discrete time RTN formulation.

$$t_i = \left\lceil \frac{ST_{m,i}}{\delta} \right\rceil \quad (4)$$

3.1. Neighbourhood Definition

The heuristic solution is then saved as the best solution which then can then be used to define a subset of the original domain where a better, or even optimal, solution could be located. This neighbourhood is defined based on the start times of adjacent jobs relative to the current task. A job is constrained to start between the start times of the W jobs preceding it (the W^{th} neighbour) on the current machine and the start time of the W^{th} neighbour following it. The neighbourhood of times when a job can start is then given by Equations (5) and (6), where $ST_{m,i}^{early}$ is the earliest time a task can start and $ST_{m,i}^{late}$ is the latest a task can start.

$$ST_{m,i}^{early} = ST_{m,i-W} \quad (5)$$

$$ST_{m,i}^{late} = ST_{m,i+W} \quad (6)$$

If the W^{th} neighbour of a job does not exist, the corresponding bound is not constrained. The earliest and latest possible start times can then be mapped to the discrete time intervals. A similar approach to define the window can be followed if the job start times are already in a form matching the RTN intervals. The binary start variable $N_{i,t}$ can then be constrained to this interval which greatly reduces the number of binary variables (and thus the computation time) of the RTN model while still allowing the jobs the flexibility to switch sequencing positions with their W adjacent neighbours. Note that this applies to the binary variables related to all parallel machines, so a job may be shifted to a different parallel machine. A diagram of the neighbourhood definition can be viewed in Figure 3. In this diagram, job A1 is constrained to start in the neighbourhood defined by the start time of jobs B1 and C2. The binary variables for the processing of job A1 outside of this interval on all machines are set to zero. Once the binary variables of the RTN model have been constrained to their respective neighbourhoods, the optimization problem can be run with the current best solution providing an initial feasible point. The solution from the optimization problem can be saved as the best solution, which then can be used to initialize the next iteration. This process can be performed iteratively until one of three stopping criteria are met. The stopping criteria are: maximum computation time, maximum number of iterations, or a convergence criterion. The convergence criterion checks if the optimal value from the previous iteration and the current iteration are the same. If they are, no further improvement can be made within this given neighbourhood meaning that further iterations would yield no improvement. The downside of the heuristic nature of the algorithm is that it is unable to guarantee global optimality. The complete algorithm flowchart can be seen in Figure 4.

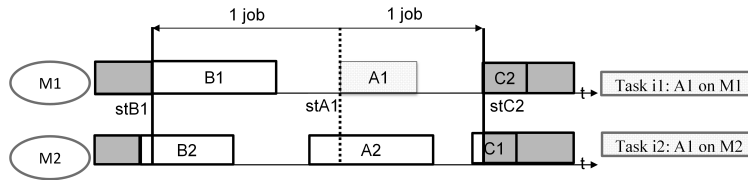


Figure 3: An example neighbourhood for job A1 where $W = 1$.

4. Results and Discussion

The proposed algorithm was tested on a four stage batch process with two parallel machines at each stage. The problem considers six product types with four orders per type. The algorithm was tested against a full-space RTN, however for all cases the full-space model was unable to return a solution within the allotted time of 10,000 seconds. To provide an optimal reference point, an RTN which aggregates the products by type (by considering only one binary per product type which executes multiple times) provides an exact optimal value. This is an exact aggregation, however it violates the specific batch tracking requirements of the problem. The optimization problems were solved using GAMS 24.7.4/CPLEX 12.6.3.0. The algorithm was tested for three objective functions: makespan (min), electricity cost (€, with hourly prices), and inventory minimization. For the inventory objective, the goal is to minimize the waiting times of products between stages. Note that the objective function only applies to the MILP in the algorithm, as only an ASAP heuristic was considered in this work. All problems were run with neighbourhood sizes of one, two, and three jobs (denoted $W1$, $W2$, and $W3$ respectively). The results are presented in Table 1.

The results indicate that the iterative algorithm is able to find near optimal, or optimal solutions, in orders of magnitude less time than the full-space model would require. For the makespan objective, both the $W2$ and $W3$ configurations were able to find the optimum solution in less than half the time it took to solve the aggregate problem. For the electricity cost objective, none of the scenarios were able to find the optimum, however, they all got to within 0.5% of it. For this case the $W2$ and $W3$ scenarios both took longer to solve than the aggregated model, due to the fact that they had more binary variables per iteration. For the inventory objective the algorithm was able to find the optimal value of zero for all cases. It is interesting to observe that for all objectives the $W2$ scenario took longer than the $W3$ scenario as it was difficult for this configuration to close the optimality gap. For all objectives the $W1$ case took less than four minutes but was able to get to within 2.2% of the true optimum.

5. Conclusion

In this work a novel iterative neighbourhood search-based algorithm was proposed for the solution of RTN scheduling models. The algorithm reduces the search space of the original RTN problem by limiting the task start times to a neighbourhood in a way that greatly reduces the number of

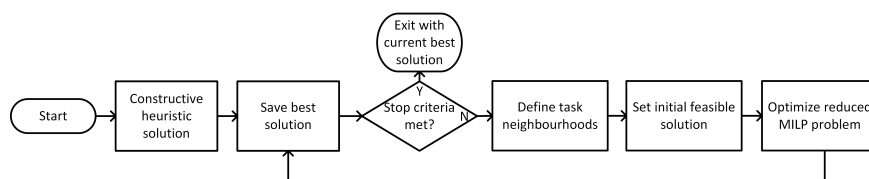


Figure 4: Algorithmic flowchart of the proposed iterative neighbourhood search algorithm

binary variables while still allowing the schedule to move towards better solutions. This procedure is repeated iteratively until the stopping criteria are met. Results show that the novel approach is able to tackle problems that are intractable for the full-space RTN in industrially relevant time frames while sacrificing optimality. Future work includes combining this approach with a rolling horizon scheme in order to deal with very large problems.

Table 1: Results from the test cases. Objective MS = Makespan, Inv = Inventory holding cost, El = Electricity cost

Algorithm	Objective	Best Solution	Improvement from Heuristic (%)	Gap From Optimal (%)	Number of Iterations	Computation Time (s)
ASAP	MS	1620	0	18.7	N/A	<5
Agg. RTN	MS	1365	18.7	0	N/A	7,871
Iter. W1	MS	1395	13.9	2.2	4	215
Iter. W2	MS	1365	18.7	0	4	2,796
Iter. W3	MS	1365	18.7	0	2	1,166
ASAP	El	105,114	0	4.6	N/A	<5
Agg. RTN	El	100,293	4.6	0	N/A	1,243
Iter. W1	El	100,658	4.2	0.4	7	121
Iter. W2	El	100,646	4.3	0.4	4	3091
Iter. W3	El	100,393	4.5	0.1	4	2003
ASAP	Inv	206	0	100	N/A	<5
Agg. RTN	Inv	0	100	0	N/A	439
Iter. W1	Inv	0	100	0	4	200
Iter. W2	Inv	0	100	0	3	222
Iter. W3	Inv	0	100	0	2	131

6. Acknowledgements

Financial support is gratefully acknowledged from the Marie Skłodowska Curie Horizon 2020 EID-ITN project “PRONTO” (Grant agreement No 675215). The authors also greatly appreciate many scientific discussions with Pedro Castro.

References

- P. M. Castro, I. Harjunkoski, I. E. Grossmann, 2011. Greedy algorithm for scheduling batch plants with sequence-dependent changeovers. In: *AIChE Journal* 57, 373–387.
- P. M. Castro, L. Sun, I. Harjunkoski, 2013. Resource-task network formulations for industrial demand side management of a steel plant. *Industrial and Engineering Chemistry Research* 52, 13046–13058.
- H. Hadera, P. Wide, I. Harjunkoski, J. Mäntysaari, J. Ekström, G. Sand, S. Engell, 2015. A Mean Value Cross Decomposition Strategy for Demand-side Management of a Pulping Process. In: *European Symposium on Computer Aided Process Engineering - 12th International Symposium on Process Systems Engineering*, Copenhagen Denmark, 31 May - 4 June.
- I. Harjunkoski, R. Bauer, 2014. Sharing data for production scheduling using the ISA-95 standard. *Frontiers in Energy Research* 2, 44.
- I. Harjunkoski, C. T. Maravelias, P. Bongers, P. M. Caster, S. Engell, I. E. Grossmann, J. Hooker, C. Mendez, G. Sand, J. Wassick, 2014. Scope for industrial application of production scheduling models and solution methods. *Computers and Chemical Engineering* 62, 161–193.
- C. A. Méndez, J. Cerdá, 2002. An MILP Framework for Short-Term Scheduling of Single-Stage Batch Plants with Limited Discrete Resources. In: *European Symposium on Computer Aided Process Engineering* 12, 721–726.
- S. Panek, S. Engell, C. Lessner, 2005. Scheduling of pipeless multi-product batch plant using mixed-integer programming combined with heuristics. In: *European Symposium on Computer-Aided Process Engineering* 15, 29 May - 1 June 2005, Barcelona Spain, 1570–1575.
- J. Roslöf, I. Harjunkoski, J. Björkqvist, S. Karlsson, T. Westerlund, 2001. An MILP-based reordering algorithm for complex industrial scheduling and rescheduling. *Computers and Chemical Engineering* 25, 821–828.
- J. M. Wassick, J. Ferrio, 2011. Extending the resource task network for industrial applications. *Computers and Chemical Engineering* 35, 2124–2140.

Robust Process Scheduling under Uncertainty with Regret

Chao Ning, Fengqi You

Cornell University, Ithaca, New York, 14853, USA

Abstract

In this paper, we address multipurpose batch process scheduling under uncertainty problems. A novel adaptive robust process scheduling model is proposed that effectively incorporates the minimax regret criterion. In batch process scheduling, regret is defined as the deviation of profit obtained over the scheduling horizon from the perfect-information schedule. The regret arises due to the limited knowledge on realized uncertainty, and serves as an important evaluation metric for decision making on process scheduling. In addition to the conventional robustness criterion, the proposed multi-objective scheduling model also simultaneously optimizes the worst-case regret to push the performance of the schedule towards the utopia one under perfect information. Two case studies on multipurpose batch process scheduling under product demand uncertainty are presented.

Keywords: batch process scheduling, uncertainty, robust optimization, regret

1. Introduction

Multipurpose batch plants play a critical role in producing high-value-added products, such as food, semiconductors and pharmaceuticals (Wassick et al., 2012). Batch process scheduling allocates limited resources to different tasks over the scheduling horizon for a higher production efficiency and more profit. Therefore, scheduling of multipurpose batch process has attracted tremendous attention from both academia and industry (Chu and You, 2015). A large amount of literature is devoted to deterministic scheduling models which assume all the involved parameters are known for certainty (Méndez et al., 2006). However, in real practice, operators in batch plants need to make a schedule in the face of various uncertainties. As an inherent characteristic of batch processes, uncertainty could render the deterministic schedule suboptimal or even non-implementable. To this end, extensive research efforts have been made towards the development of systematic methodologies for handling uncertainty in batch process scheduling. Balasubramanian and Grossmann (2004) proposed a multistage stochastic optimization approach to address batch scheduling problems. To hedge against uncertainty, a proactive scheduling strategy was developed based on robust optimization and multiparametric programming (Wittmann-Hohlbein and Pistikopoulos, 2013). Adaptive robust optimization (ARO) was applied for process scheduling such that some decisions can be made in a “wait-and-see” mode based upon uncertainty realizations through a data-driven robust optimization framework (Ning and You, 2017a). Although conventional ARO based scheduling model has a number of attractive features, it does not account for an important evaluation metric, known as regret (Dunning, 2016), in decision-making theory (Bell, 1982). In this work, we propose a novel adaptive robust batch process scheduling model explicitly accounting for regret.

2. Bi-Criterion Adaptive Robust Scheduling Model

In this section, we propose a bi-objective adaptive robust scheduling model with regret based on a deterministic scheduling model (Méndez et al., 2006; Yue and You, 2013):

$$\begin{aligned}
\max \quad & \text{Profit of selling products minus the production cost} & (1) \\
\min \quad & \text{Regret over the scheduling horizon} & (2) \\
\text{s.t.} \quad & \text{Mass balance constraints} & (3) \\
& \text{Batch size constraints} & (4) \\
& \text{Inventory constraints} & (5) \\
& \text{Demand satisfaction constraints} & (6) \\
& \text{Timing constraints} & (7)
\end{aligned}$$

The resulting batch process scheduling model is formulated as a bi-objective adaptive robust mixed-integer program. The task assignment decision is made “here-and-now”, while other decisions, including continuous decisions on batch sizes, inventory levels, and timings of tasks, are made in a “wait-and-see” manner (Shi and You, 2016). The compact form of the scheduling model, denoted as (BCARO), is presented in (8).

$$\begin{aligned}
\min_{\mathbf{x}} \quad & \text{Worst-case cost} = C^w(\mathbf{x}) \\
\min_{\mathbf{x}} \quad & \text{Worst-case regret} = R^w(\mathbf{x}) \\
\text{s.t.} \quad & \mathbf{Ax} \geq \mathbf{d}, \quad \mathbf{x} \in R_+^{n_1} \times Z^{n_2} \\
& C^w(\mathbf{x}) = \max_{\mathbf{u} \in U} \min_{\mathbf{y} \in \Omega(\mathbf{x}, \mathbf{u})} [\mathbf{c}^T \mathbf{x} + \mathbf{b}^T \mathbf{y}] \\
& R^w(\mathbf{x}) = \max_{\mathbf{u} \in U} \min_{\mathbf{y} \in \Omega(\mathbf{x}, \mathbf{u})} [\mathbf{c}^T \mathbf{x} + \mathbf{b}^T \mathbf{y} - \Pi(\mathbf{u})] \\
& \Omega(\mathbf{x}, \mathbf{u}) = \{\mathbf{y} \in R_+^{n_3} : \mathbf{Wy} \geq \mathbf{h} - \mathbf{T}\mathbf{x} - \mathbf{Mu}\} \\
& \Pi(\mathbf{u}) = \min_{\hat{\mathbf{x}}, \hat{\mathbf{y}}} \mathbf{c}^T \hat{\mathbf{x}} + \mathbf{b}^T \hat{\mathbf{y}} \\
& \text{s.t.} \quad \mathbf{A}\hat{\mathbf{x}} \geq \mathbf{d}, \quad \hat{\mathbf{x}} \in R_+^{n_1} \times Z^{n_2} \\
& \quad \quad \mathbf{W}\hat{\mathbf{y}} + \mathbf{T}\hat{\mathbf{x}} \geq \mathbf{h} - \mathbf{Mu}, \quad \hat{\mathbf{y}} \in R_+^{n_3}
\end{aligned} \tag{8}$$

where \mathbf{x} represents the task assignment decision, and \mathbf{y} includes other decisions, such as timing and batch size decisions. Notice that \mathbf{x} is made “here-and-now”, whereas \mathbf{y} is made in a “wait-and-see” manner. $\Pi(\mathbf{u})$ is the best objective value that could be achieved by assuming that all the decisions are made in a “wait-and-see” mode.

We could further reformulate the worst-case regret to reduce the number of levels, shown in Eq. (9).

$$\begin{aligned}
R^w(\mathbf{x}) &= \max_{\mathbf{u} \in U} \min_{\mathbf{y} \in \Omega(\mathbf{x}, \mathbf{u})} [(\mathbf{c}^T \mathbf{x} + \mathbf{b}^T \mathbf{y}) - \Pi(\mathbf{u})] \\
&= \max_{\mathbf{u} \in U} \min_{\mathbf{y} \in \Omega(\mathbf{x}, \mathbf{u})} \left[(\mathbf{c}^T \mathbf{x} + \mathbf{b}^T \mathbf{y}) - \min_{\hat{\mathbf{x}}, \hat{\mathbf{y}} \in \Xi(\mathbf{u})} (\mathbf{c}^T \hat{\mathbf{x}} + \mathbf{b}^T \hat{\mathbf{y}}) \right] \\
&= \mathbf{c}^T \mathbf{x} + \max_{\hat{\mathbf{x}}, \hat{\mathbf{y}} \in \Xi(\mathbf{u}), \mathbf{u} \in U} \min_{\mathbf{y} \in \Omega(\mathbf{x}, \mathbf{u})} [\mathbf{b}^T \mathbf{y} - (\mathbf{c}^T \hat{\mathbf{x}} + \mathbf{b}^T \hat{\mathbf{y}})]
\end{aligned} \tag{9}$$

where $\Xi(\mathbf{u}) = \{\hat{\mathbf{x}} \in R_+^{n_1} \times Z^{n_2}, \mathbf{y} \in R_+^{n_3} : \mathbf{A}\hat{\mathbf{x}} \geq \mathbf{d}, \mathbf{W}\hat{\mathbf{y}} + \mathbf{T}\hat{\mathbf{x}} \geq \mathbf{h} - \mathbf{Mu}\}$.

By explicitly incorporating the minimax regret criterion, it pushes the performance of the resulting solution towards the utopia schedule under perfect information. We further propose a unified optimization model (BCARO- λ) shown in (10).

$$\begin{aligned}
& \min_{\mathbf{x}} \left[(1-\lambda) \cdot C^w(\mathbf{x}) + \lambda \cdot R^w(\mathbf{x}) \right] \\
& \text{s.t. } \mathbf{Ax} \geq \mathbf{d}, \quad \mathbf{x} \in R_+^{n_1} \times Z^{n_2} \\
& \quad C^w(\mathbf{x}) = \max_{\mathbf{u} \in U} \min_{\mathbf{y} \in \Omega(\mathbf{x}, \mathbf{u})} \left[\mathbf{c}^T \mathbf{x} + \mathbf{b}^T \mathbf{y} \right] \\
& \quad R^w(\mathbf{x}) = \mathbf{c}^T \mathbf{x} + \max_{\hat{\mathbf{x}}, \hat{\mathbf{y}} \in \Xi(\mathbf{u}), \mathbf{u} \in U} \min_{\mathbf{y} \in \Omega(\mathbf{x}, \mathbf{u})} \left[\mathbf{b}^T \mathbf{y} - (\mathbf{c}^T \hat{\mathbf{x}} + \mathbf{b}^T \hat{\mathbf{y}}) \right] \\
& \quad \Omega(\mathbf{x}, \mathbf{u}) = \left\{ \mathbf{y} \in R_+^{n_3} : \mathbf{Wy} \geq \mathbf{h} - \mathbf{T}\mathbf{x} - \mathbf{Mu} \right\}
\end{aligned} \tag{10}$$

where λ is a parameter ranging from 0 to 1. (BCARO- λ) could provide a wide spectrum of solutions by changing the value of λ from 0 to 1. Specifically, it reduces to the conventional ARO model when λ equals to 0, and it becomes the ARO with minimax regret criterion when λ equals to 1. If the value of λ is chosen between 0 and 1, the proposed model makes a trade-off between the conventional robustness and minimax regret criteria.

We develop (BCARO- ε) in (11) by transforming the objective on the worst-case regret into an extra constraint that specifies the upper bound of $R_w(\mathbf{x})$. Similarly, (BCARO- ε) can reveal the trade-offs between the conventional robustness and minimax regret criteria in the scheduling problem.

$$\begin{aligned}
& \min_{\mathbf{x}} C^w(\mathbf{x}) \\
& \text{s.t. } R^w(\mathbf{x}) \leq \varepsilon \\
& \quad \mathbf{Ax} \geq \mathbf{d}, \quad \mathbf{x} \in R_+^{n_1} \times Z^{n_2} \\
& \quad C^w(\mathbf{x}) = \max_{\mathbf{u} \in U} \min_{\mathbf{y} \in \Omega(\mathbf{x}, \mathbf{u})} \left[\mathbf{c}^T \mathbf{x} + \mathbf{b}^T \mathbf{y} \right] \\
& \quad R^w(\mathbf{x}) = \mathbf{c}^T \mathbf{x} + \max_{\hat{\mathbf{x}}, \hat{\mathbf{y}} \in \Xi(\mathbf{u}), \mathbf{u} \in U} \min_{\mathbf{y} \in \Omega(\mathbf{x}, \mathbf{u})} \left[\mathbf{b}^T \mathbf{y} - (\mathbf{c}^T \hat{\mathbf{x}} + \mathbf{b}^T \hat{\mathbf{y}}) \right] \\
& \quad \Omega(\mathbf{x}, \mathbf{u}) = \left\{ \mathbf{y} \in R_+^{n_3} : \mathbf{Wy} \geq \mathbf{h} - \mathbf{T}\mathbf{x} - \mathbf{Mu} \right\}
\end{aligned} \tag{11}$$

where ε is a parameter which bounds the worst-case regret from above.

3. Applications

We consider two batch scheduling problems in section to illustrate the proposed methodology. The state-task-network of the first batch process is shown in Figure 1. This batch process involves one heating task, three reaction tasks, and one separation task (Kondili et al., 1993). This network involves three raw materials (A-C), four intermediates (Hot A, Impure E, and I1-I2) and two products (P1-P2). There are four equipment units: one heater, two reactors, and one separator.

The scheduling results are shown in Figure 2. By comparing the two Gantt charts, we can observe that the assignment decisions determined by the two approaches are different. Specifically, Reaction 3 starts at a unique time point in the scheduling solution determined by the conventional robustness criterion, while Reaction 3 shares the same starting time point with Reaction 1 in the scheduling solution determined by the minimax regret criterion.

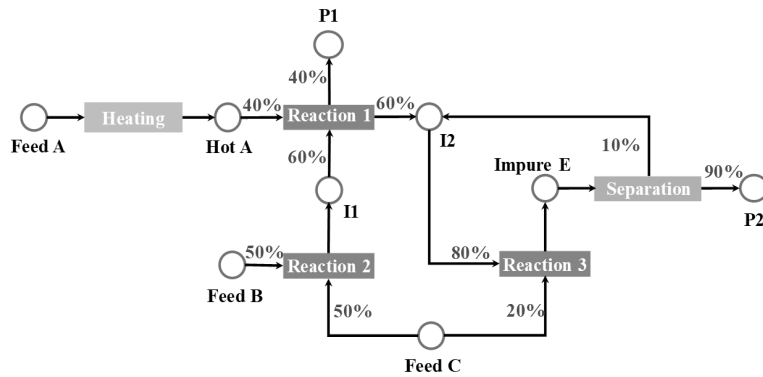


Figure 1. State-task network of the multipurpose batch process in case study 1.

The values of worst-case profit and regret are listed in Figure 2. The scheduling solution determined by the minimax regret criterion has the lowest worst-case regret of \$13.6, and only decreases the worst-case profit by 0.3% compared with solution under the conventional robustness criterion.

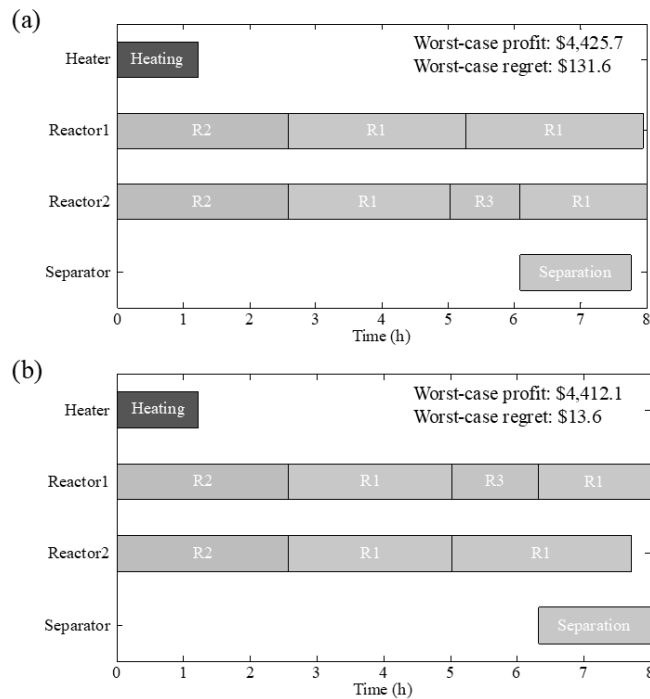


Figure 2. Gantt charts determined by (a) the conventional robustness criterion, and (b) the minimax regret criterion in case study 1.

We then apply the proposed scheduling approach to another process scheduling problem (Ning and You, 2017b). This case study is originated from an industrial multipurpose

batch process in The Dow Chemical Company (Chu et al., 2013), and the network is shown in Figure 3. This multipurpose batch process has one preparation task, three reaction tasks, two packing tasks and two drumming tasks. The equipment units include one mixer, two reactors, one finishing system and one drumming line (Chu et al., 2013). The scheduling horizon is one week, i.e. 168 hours, and there are 11 time points.

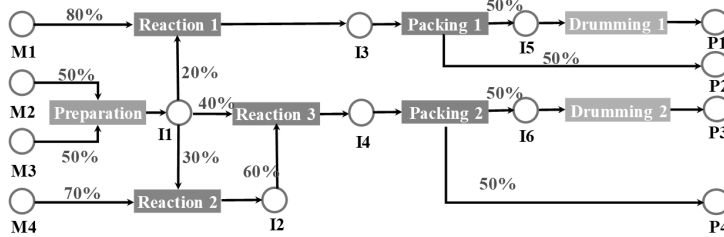


Figure 3. The state-task network of the multipurpose batch process in case study 2.

We solve the resulting scheduling problems with different values of parameter λ . The Gantt charts of the ARO solutions under the conventional robustness criterion and the minimax regret criterion are shown in Figure 4 (a) and (b), respectively. From the Gantt chart, we can observe that the assignment decisions are different, but the worst-case profit and regret remain unchanged for the two solutions. This is because of a different problem setup from Case study 1.

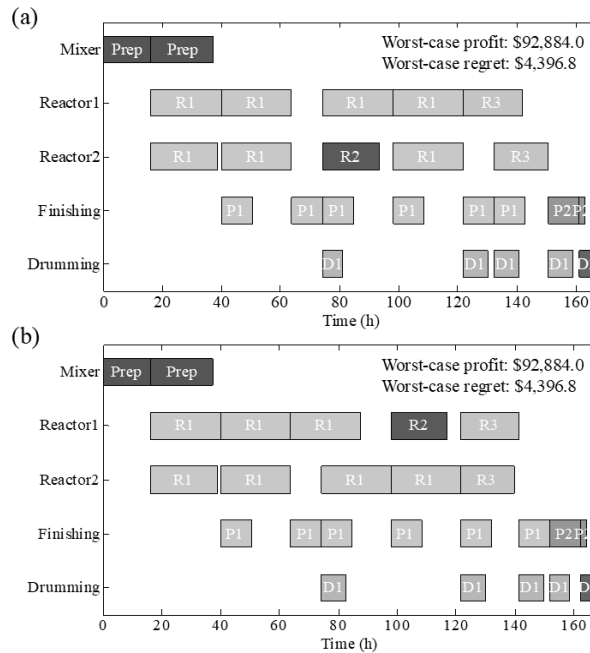


Figure 4. Gantt charts determined by (a) the conventional robustness criterion, and (b) the minimax regret criterion in case study 2.

4. Conclusions

In this paper, a novel multi-objective robust batch process scheduling model was proposed to account for the minimax regret criterion. Apart from the conventional robustness criterion, the worst-case regret was introduced as another objective to minimize the deviation of profit from the perfect-information schedule. A set of Pareto-optimal schedules was generated to reveal the systematic trade-offs between the conventional robustness and minimax regret criteria. The results of two case studies showed that the proposed scheduling decision could make a systematic trade-off between the conventional robustness criterion and minimax regret criterion.

References

- J. Balasubramanian, I. E. Grossmann, 2004, Approximation to multistage stochastic optimization in multiperiod batch plant scheduling under demand uncertainty, *Industrial & Engineering Chemistry Research*, 43, 3695–3713.
- D. Bell, 1982, Regret in decision making under uncertainty, *Operations Research*, 30, 961-981.
- A. Ben-Tal A. Nemirovski, 2002, Robust optimization, *Mathematical Programming*, 92, 453-480.
- D. Bertsimas, D. B. Brown, C. Caramanis, 2011, Theory and applications of robust optimization, *SIAM Review*, 53, 464-501.
- Y. Chu, J.M. Wassick, F. You, 2013, Efficient scheduling method of complex batch processes with general network structure via agent-based modeling, *AIChE Journal*, 59, 2884-2906.
- Y. Chu, F. You, 2013, Integration of Scheduling and Dynamic Optimization of Batch Processes under Uncertainty: Two-stage Stochastic Programming Approach. *Industrial & Engineering Chemistry Research*, 52, 16851-16869.
- Y. Chu, F. You, 2015, Model-based integration of control and operations: Overview, challenges, advances, and opportunities, *Computers & Chemical Engineering*, 83, 2-20.
- I. R. Dunning, 2016, Advances in robust and adaptive optimization: algorithms, software, and insights, Massachusetts Institute of Technology, Massachusetts, USA.
- E. Kondili, C. C. Pantelides, and R. W. H. Sargent, 1993, A general algorithm for short-term scheduling of batch operations," *Computers & Chemical Engineering*, 17, 211-227.
- C.A. Méndez, J. Cerdá, I.E. Grossmann, I. Harjunkoski, 2006, State-of-the-art review of optimization methods for short-term scheduling of batch processes, *Computers & Chemical Engineering*, 30, 913-946.
- C. Ning, F. You, 2017a, A data-driven multistage adaptive robust optimization framework for planning and scheduling under uncertainty. *AIChE Journal*, 63, 4343-4369.
- C. Ning, F. You, 2017b, Data-driven adaptive nested robust optimization: General modeling framework and efficient computational algorithm for decision making under uncertainty. *AIChE Journal*, 63, 3790-3817.
- C. Shang, X. Huang, X., F. You, 2017, Data-Driven Robust Optimization Based on Kernel Learning. *Computers & Chemical Engineering*, 106, 464–479.
- H. Shi, F. You, 2016, A computational framework and solution algorithms for two-stage adaptive robust scheduling of batch manufacturing processes under uncertainty, *AIChE Journal*, 62, 687-703.
- J.M. Wassick, A. Agarwal, N. Akiya, J. Ferrio, S. Bury, F. You, 2012, Addressing the operational challenges in the development, manufacture, and supply of advanced materials and performance products, *Computers & Chemical Engineering*, 47, 157-169.
- M. Wittmann-Hohlbein, E.N. Pistikopoulos, 2013, Proactive scheduling of batch processes by a combined robust optimization and multiparametric programming approach, *AIChE Journal*, 59, 4184-211.
- D. Yue, F. You, 2013, Sustainable Scheduling of Batch Processes under Economic and Environmental Criteria with MINLP Models and Algorithms. *Computers & Chemical Engineering*, 54, 44-59.

Process Scheduling under Ambiguity Uncertainty Probability Distribution

Chao Shang, Fengqi You

Cornell University, Ithaca, New York, 14853, USA

Abstract

Distributionally robust optimization (DRO) has been gaining increasing popularity in decision-making under uncertainties due to its capability in handling ambiguity of distributions. However, it is a nontrivial task to approach the scheduling problem within the DRO framework. In this paper, we propose a novel DRO scheduling model under uncertain demand. We adopt max-out moment functions to characterize the ambiguity set, which includes a variety of distributions. In addition, we take into account recourse decisions made after random demands become known. In this way, a two-stage distributionally robust scheduling model can be developed, which can be approximately solved by linear decision rules. Applications in industrial-scale batch process scheduling show that, the proposed approach can leverage empirical data information with effect, better hedge against the inexactness of uncertainty distributions, and bring more profits.

Keywords: Distributionally robust optimization, decision-making under uncertainty, process planning, big data

1. Introduction

Process scheduling is an important control problem that has already been extensively investigated in process system engineering in the past two decades (Grossmann et al., 2016; Chu and You, 2015). The general purpose of a scheduling problem is to manufacture a series of products by optimally assigning limited resources at hand. Typical production objectives include maximizing the profit, minimizing the makespan, etc., which induces deterministic mixed-integer linear program (MILP) models.

However, deterministic scheduling models cannot handle uncertainties that are ubiquitous in real world. Therefore, stochastic programming (SP) and robust optimization (RO) have been extensively adopted in process planning and scheduling for better immunization against uncertainties (Balasubramanian and Grossmann, 2004; Shi and You, 2016). As an intermediate approach between SP and RO, distributionally robust optimization (DRO) is paving a new way for addressing uncertainties in optimization problems, and has received immense attentions in operations research community (Delage and Ye, 2010; Goh and Sim, 2010). DRO can be considered as optimizing the worst-case expected performance on a set constituted by a variety of distributions, which is termed as the ambiguity set and can be developed based on data. In this way, DRO could hedge against the ambiguity of probability distribution.

Nevertheless, process scheduling has not been benefited from recent advances in DRO. The orientation of this work is hence to fill in this gap by developing a novel DRO method for process scheduling applications. By considering uncertainties revealed sequentially and some adjustable wait-and-see decisions to be implemented after uncertainties are unfolded, we develop a two-stage DRO model. The linear decision rule

(LDR) approximation is adopted to provide a tractable, albeit conservative solution towards two-stage DRO problems. which enjoys considerable computational convenience in practice. An application in multi-purpose batch process scheduling demonstrates that the two-stage DRO model bears clear statistical interpretations and the conservatism of solutions can be significantly ameliorated. This highlights massive data as an asset for advancing decision-making in process scheduling.

2. Distributionally Robust Scheduling Model

Here we adopt the global event-based, continuous-time process scheduling model developed by Castro et al. (2004) as the deterministic model:

$$\begin{aligned}
 \max \quad & \text{Profit of selling products minus the purchasing cost and running cost} & (1) \\
 \text{s.t.} \quad & \text{Mass balance constraints} & (2) \\
 & \text{Batch size constraints} & (3) \\
 & \text{Inventory constraints} & (4) \\
 & \text{Demand satisfaction constraints} & (5) \\
 & \text{Processing time constraints} & (6)
 \end{aligned}$$

which is typically cast as an MILP. Let us further suppose that the product demands are random, whose exact distribution is unknown but belongs to an ambiguity set. We fix all binary sequencing variables and initial purchasing amount as first-stage decisions, while regarding continuous variables pertaining to batch sizes, inventory levels, and timings of all periods as second-stage decisions made after the demands are known. Therefore, the problem is cast in a two-stage setting. Therefore, based on the deterministic model (1)-(6), we can arrive at a succinct expression of the two-stage distributionally robust scheduling model:

$$\begin{aligned}
 \min_x \quad & \mathbf{c}^T \mathbf{x} + \sup_{\mathbb{P} \in \mathcal{D}} \mathbb{E}_{\mathbb{P}} \{L(\mathbf{x}, \boldsymbol{\xi})\} & (7) \\
 \text{s.t.} \quad & \mathbf{A}\mathbf{x} \leq \mathbf{b}
 \end{aligned}$$

Here \mathbf{x} includes both continuous and binary variables. The second-stage cost is given by:

$$L(\mathbf{x}, \boldsymbol{\xi}) = \begin{cases} \min_y \mathbf{d}^T \mathbf{y} \\ \text{s.t. } \mathbf{T}(\boldsymbol{\xi})\mathbf{x} + \mathbf{W}\mathbf{y} \leq \mathbf{h}(\boldsymbol{\xi}) \end{cases} \quad (8)$$

In this work, we adopt the following formulation of ambiguity sets:

$$\mathcal{D} = \left\{ \mathbb{P}_{\boldsymbol{\xi}} \in \mathcal{M}_+^M \mid \mathbb{P} \{ \boldsymbol{\xi} \in \Xi \} = 1, \mathbb{E}_{\mathbb{P}} \{ g_i(\boldsymbol{\xi}) \} \leq \gamma_i, i = 1, \dots, I \right\} \quad (9)$$

Here we use upper and lower bounds to specify the support of uncertainties $\Xi = \{ \boldsymbol{\xi} \mid \boldsymbol{\xi}_{\min} \leq \boldsymbol{\xi} \leq \boldsymbol{\xi}_{\max} \}$. The second constraint in (9) characterizes moment information of uncertainties via I functions $\{g_i(\cdot)\}$, and enforces the generalized moment $\mathbb{E}_{\mathbb{P}} \{ g_i(\boldsymbol{\xi}) \}$ cannot exceed a given threshold γ_i . In this work, we use the max-out function as moment functions:

$$g_i(\boldsymbol{\xi}) = \max \{ \mathbf{f}_i^T \boldsymbol{\xi} - q_i, 0 \}, i = 1, \dots, I \quad (10)$$

which can be conceived as the tail expectation along a certain direction f_i truncated at q_i . In fact, D can be rewritten as the projection of a lifted ambiguity set \bar{D} by introducing auxiliary random variables φ :

$$\bar{D} = \left\{ \mathbb{Q}_{\xi, \varphi} \mid \mathbb{P}\{(\xi, \varphi) \in \bar{\Xi}\} = 1, \mathbb{E}_{\mathbb{Q}}\{\varphi\} \leq \gamma \right\}, \quad (11)$$

and the lifted support is given by

$$\bar{\Xi} = \left\{ (\xi, \varphi) \mid \xi \in \Xi, g_i(\xi) \leq \varphi_i \right\}. \quad (12)$$

It turns out that the introduction of φ is particularly beneficial for deriving a desirable reformulation of the DRO problem. Note that the ambiguity sets could be derived from historical data using data-driven methods such as kernel learning (Shang et al., 2017).

3. Approximated Solution Algorithm with Linear Decision Rules

In a two-stage setting, deriving an explicit expression of optimal recourse policy and calculating the worst-case expectation are intractable (Bertsimas et al., 2010). A practical strategy is to adopt the well-known LDR, which assumes the recourse decision y to be affinely varying with the uncertainties (Ben-Tal et al., 2004; Chen et al., 2008; Ning and You, 2017a):

$$y(\xi, \varphi) = y^0 + Y^\xi \xi + Y^\varphi \varphi \quad (13)$$

By substituting the LDR approximation for the decision policy, a conservative approximation to the two-stage DRO problem can be derived:

$$\begin{aligned} \min_x \min_{y(\xi, \varphi)} c^T x + \sup_{\mathbb{P} \in \mathcal{D}} \mathbb{E}_{\mathbb{P}} \{d^T y(\xi, \varphi)\} \\ \text{s.t. } Ax \leq b \\ T(\xi)x + Wy(\xi, \varphi) \leq h(\xi), \forall (\xi, \varphi) \in \bar{\Xi} \end{aligned} \quad (14)$$

Here, coefficients of LDR can be regarded as first-stage variables, thereby resulting in a single-stage optimization problem. Then we concentrate on the inner problem, which can be explicitly expressed as:

$$\begin{aligned} \sup_{\mathbb{Q}} \int_{\bar{\Xi}} p(\xi, \varphi) d^T y(\xi, \varphi) d\xi d\varphi \\ \text{s.t. } \int_{\bar{\Xi}} p(\xi, \varphi) d\xi d\varphi = 1, \int_{\bar{\Xi}} p(\xi, \varphi) \varphi d\xi d\varphi \leq \gamma \end{aligned} \quad (15)$$

By adopting the conic duality, (15) can be translated into the following RO problem by introducing Lagrange multipliers (Shapiro, 2001):

$$\begin{aligned} \min_{\eta, \beta} \eta + \gamma^T \beta \\ \text{s.t. } \beta \geq 0 \\ \eta + \varphi^T \beta \geq d^T y(\xi, \varphi), \forall (\xi, \varphi) \in \bar{\Xi} \end{aligned} \quad (16)$$

Therefore, (14) could be also cast as a trivial RO problem. We can then leverage duality to translate infinite-dimensional constraints into their robust counterparts. Specifically, if we use classic uncertainty sets in RO such as the box and polyhedral sets to describe

the uncertainty support, a tractable MILP reformulation of the two-stage distributionally robust scheduling problem can be attained, which can be easily handled using CPLEX.

4. An Industrial-Scale Application

4.1. Problem Setup

The proposed DRO model is applied to an industrial multi-purpose pharmaceutical batch production process in The Dow Chemical Company (Chu et al., 2013). It includes one mixer, two reactors, one finishing system and one drumming line to accomplish one preparation task, six reaction tasks, two packing tasks and two drumming tasks (Chu et al., 2014). The actual demand fluctuations are supposed to follow a truncated Gaussian distribution around their nominal values. Accordingly, 500 data samples are collected in total. We developed the deterministic model, the two-stage DRO, and two-stage ARO models taken from Ning and You (2017b), all of which can be transformed into MILPs. In two-stage ARO, the box uncertainty set is adopted with its size estimated with 500 available samples. In two-stage DRO, we adopt principal component analysis to estimate projection directions f_i in moment functions from 500 data samples, and then set several truncation points q_i evenly on each principal axis.

We plot Gantt charts of scheduling decisions under nominal values of demands in Figure 1. Under the nominal case the deterministic model yields the highest profits, while the ARO model gives the lowest profits. This is due to the different optimization criteria adopted. In addition, it can be observed that DRO schedules more tasks than the other two methods, which allow for more flexibility to adjust batch sizes for a high profit under demand uncertainties, since more tasks can afford heavier manufacturing workload. The sequencing decisions attained by the deterministic approach may become infeasible when demands exhibit randomness, thereby lacking robustness.

Next we further examine performances of different approaches by resorting to Monte Carlo simulations. There are 1,000 random samples collected in total, and we first solve the problems of two-stage DRO and ARO and derive first-stage decisions. Then for each sample, we solve the second-stage problem by fixing first-stage decisions, and calculate the second-stage cost. By summarizing results over all random samples, we can empirically compute the mean value of total profits. In this way, we can arrive at a fair comparison between DRO and ARO. By varying the value of G , we obtain results under different magnitudes of uncertainties, as reported in Table 1.

Table 1. Expected Profits (\$) Based on Monte Carlo Simulations

G	5		10		20	
Profit	DRO	ARO	DRO	ARO	DRO	ARO
Total	2,416	2,416	2,222	2,131	1,959	1,470
1 st -Stage	-10,241	-10,240	-10,434	-10,386	-10,633	-10,247
2 nd -Stage	12,657	12,656	12,656	12,517	12,592	11,717

We can see that in the case of large magnitude of uncertainties ($G = 20$), DRO has significant advantages over ARO. In the case of small magnitude ($G = 5$), DRO and ARO yield nearly identical expected profits. This bears rationality since the worst-case realization that ARO hedges against is not sufficiently extreme.

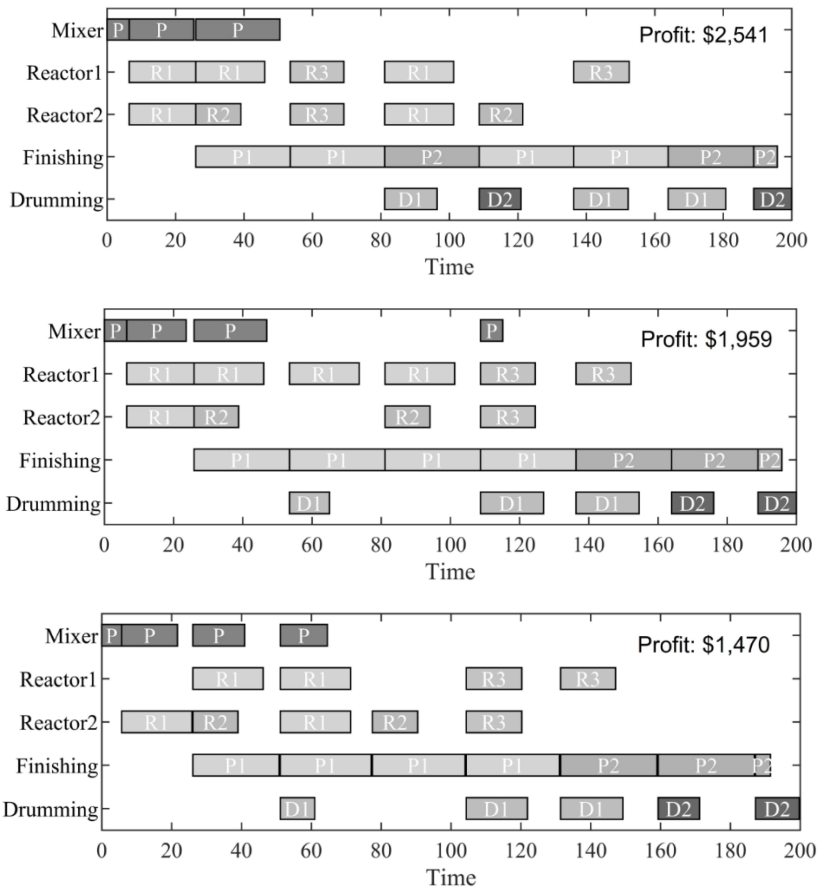


Figure 1. Gantt charts of scheduling results of deterministic scheduling (top), two-stage DRO (middle) and two-stage ARO (bottom)

Notice that decisions made by DRO invest more in the first-stage. This is also implied by Gantt charts and the purchase amounts in Table 2, which shows that more initial materials, especially M1, are bought by DRO. Such a high investment finally turns out to be beneficial in obtaining higher second-stage profits as well more total profits on average. By contrast, the ARO-based approach tends to take conservative first-stage decisions, which finally exert significant influences on the overall profits. In this sense, by extracting useful statistical information from data, the two-stage DRO approach leads to less conservative solutions and achieves better expected performance in comparison with classic ARO-based approach.

Table 2. Purchase Amounts (kg) of Initial Materials as First-Stage Decisions

G	5		10		20	
	DRO	ARO	DRO	ARO	DRO	ARO
M1	608.00	608.00	608.00	601.60	608.00	571.18
M2	198.76	198.74	203.73	203.70	211.98	211.40
M3	198.76	198.74	203.73	203.70	211.98	211.40
M4	177.80	177.76	186.16	186.10	202.90	202.77

5. Conclusions

In this paper, a novel DRO-based strategy is proposed to solve process scheduling problems under uncertainties. The worst-case expected performance on the ambiguity set is optimized, thereby providing protection against the inexactness of probability distributions. We develop two-stage DRO models by including second-stage decisions made after uncertainty realizations, and adopt LDR approximations to derive tractable solutions. An industrial-scale application demonstrates that the proposed approach can effectively hedge against distributional ambiguity, and bring more profits under stochastic demands in comparison with classic RO-based approaches.

References

- A. Ben-Tal, A. Goryashko, E. Guslitzer, A. Nemirovski, 2004, Adjustable robust solutions of uncertain linear programs, *Mathematical Programming*, 99, 351-376.
- J. Balasubramanian, I. E. Grossmann, 2004, Approximation to multistage stochastic optimization in multiperiod batch plant scheduling under demand uncertainty, *Industrial & Engineering Chemistry Research*, 43, 3695-3713.
- D. Bertsimas, X.V. Doan, K. Natarajan, C.P. Teo, 2010, Models for minimax stochastic linear optimization problems with risk aversion, *Mathematics of Operations Research*, 35, 580-602.
- P. M. Castro, A. P. Barbosa-Pvoa, H. A. Matos, A. Q. Novais, 2004, Simple continuous-time formulation for short-term scheduling of batch and continuous processes, *Industrial & Engineering Chemistry Research*, 43, 105-118.
- X. Chen, M. Sim, P. Sun, J. Zhang, 2008, A linear decision-based approximation approach to stochastic programming, *Operations Research*, 56, 344-357.
- Y. Chu, J. M. Wassick, F. You, 2013, Efficient scheduling method of complex batch processes with general network structure via agent-based modeling, *AIChE Journal*, 59, 2884-2906.
- Y. Chu, F. You, J. M. Wassick, 2014, Hybrid method integrating agent-based modeling and heuristic tree search for scheduling of complex batch processes. *Computers & Chemical Engineering*, 60, 277-296.
- Y. Chu, F. You, 2015, Model-based integration of control and operations: Overview, challenges, advances, and opportunities. *Computers & Chemical Engineering*, 83, 2-20.
- E. Delage, Y. Ye, 2010, Distributionally robust optimization under moment uncertainty with application to data-driven problems, *Operations Research*, 58, 595-612.
- J. Goh, M. Sim, 2010, Distributionally robust optimization and its tractable approximations, *Operations Research*, 58, 902-917.
- I. Grossmann, R. Apap, B. Calfa, P. García-Herreros, Q. Zhang, 2016, Recent advances in mathematical programming techniques for the optimization of process systems under uncertainty, *Computers & Chemical Engineering*, 91, 3-14.
- C. Ning, F. You, 2017a, A data-driven multistage adaptive robust optimization framework for planning and scheduling under uncertainty. *AIChE Journal*, 63, 4343-4369.
- C. Ning, F. You, 2017b, Data-driven adaptive nested robust optimization: General modeling framework and efficient computational algorithm for decision making under uncertainty. *AIChE Journal*, 63, 3790-3817.
- C. Shang, X. Huang, X., F. You, 2017, Data-Driven Robust Optimization Based on Kernel Learning. *Computers & Chemical Engineering*, 106, 464-479.
- A. Shapiro, 2001. On duality theory of conic linear problems, in: *Semi-Infinite Programming*, Springer, 135-165.
- H. Shi, F. You, 2016, A computational framework and solution algorithms for two-stage adaptive robust scheduling of batch manufacturing processes under uncertainty, *AIChE Journal*, 62, 687-703.
- J. M. Wasick, A. Agarwal, N. Akiya, J. Ferrio, S. Bury, F. You, 2012, Addressing the Operational Challenges in the Development, Manufacture, and Supply of Advanced Materials and Performance Products," *Computers & Chemical Engineering*, 47, 157-169.

Mixed Integer Linear Programming Formulation for Sensible Thermal Energy Storages

Martin Koller^a and René Hofmann^{a,*}

^a*TU Wien, Institute for Energy Systems and Thermodynamics, Getreidemarkt 9, Vienna 1060, Austria*
rene.hofmann@tuwien.ac.at

Abstract

In order to model the charging and discharging power of sensible thermal energy storages for the unit commitment problem with mixed integer linear programming more precisely, two extended formulations are proposed in this work. To this end, simulation data of a detailed simulation model, derived from measurement data of a fixed bed regenerator test rig, were investigated in order to determine the actual charging and discharging power of the storage in highly dynamic operation. The two formulations were derived from an original MILP storage model with fixed maximum charging and discharging power. The first proposed formulation adds linear constraints for charging and discharging power depending on the fill level. The second proposed formulation introduces auxiliary variables, taking into account the fill level at the end of the previous charging or discharging phase. The predicted operation for a test case of the original and the two proposed mixed integer linear formulations are compared with the achieved operation of the detailed simulation model. While the original formulation allows infeasible predictions for the storage operation, the two proposed formulations are able to describe the real operating behavior more detailed, therefore decreasing the infeasible predictions for operation as well as increasing the overall system performance.

Keywords: Unit Commitment, Mixed Integer Linear Programming, Sensible Thermal Energy Storage, Industrial Processes, Smart Energy Systems

1. Nomenclature

ABBREVIATIONS			INDICES AND SETS	
CHP	Combined Heat and Power		<i>ch</i>	Charging
HTF	Heat Transfer Fluid		<i>chp</i>	CHP unit
MILP	Mixed Integer Linear Programming		<i>dis</i>	Discharging
SM	Storage Medium		<i>htf</i>	Heat transfer fluid
STES	Sensible Thermal Energy Storage		<i>k</i>	1D-element, from 1 to <i>K</i>
UC	Unit Commitment		<i>sm</i>	Storage medium
PARAMETERS			<i>t</i>	Time step, from 1 to <i>T</i>
c_p	[kJ/kg]	Specific heat capacity	<i>w</i>	Wall
m	[kg]	Mass	VARIABLES	
q	[MWh]	Heat demand	<i>S</i>	[MWh] Storage fill level
$\hat{\delta}_t$	[MWh]	Storage fill level	<i>H</i>	[MWh] Auxiliary variable
Δt	[s]	Time step size	<i>B</i>	[-] Commitment variable
ϑ	[°C]	Temperature	\dot{Q}	[MW] Power (heat flow)

2. Introduction

In Europe's changing energy system, industrial processes play a future key role with a share of the total energy consumption of 25.3 % according to eurostat (2017). By interconnection of electricity, heat and gas networks to a smart grid and by flexibilization of energy supply systems of industrial processes in such smart grids, the increasing share of volatile wind and solar energy can be supported and the occurring surpluses and shortages can be counteracted. To this end, important topics are the integration of energy storages and optimal control concepts to exploit the gained flexibility. The result is a smart energy system with a high share of renewable energy sources, as proposed in Lund et al. (2016).

The optimal control of energy supply systems is obtained by solving the corresponding unit commitment (UC) problem. There are several approaches to solve the UC problem in the literature, as listed in Padhy (2004). To this end, mixed integer linear programming (MILP), as proposed in Carrion and Arroyo (2006), is well suited. Some examples are studies on tighter and more compact MILP formulations (Morales-Espana et al. (2013)), minimal uptime and downtime formulations (Rajan and Takriti (2005)), intraperiod load gradient changes (Correa-Posada et al. (2017)) or different approaches for the modeling of start-up costs (Silbernagl et al. (2016)). Hardly any studies consider more detailed formulations of thermal energy storages. To the authors knowledge, MILP formulations for thermal energy storages are implemented mostly by storage energy balances with fixed maximum charging and discharging power, which is appropriate to model e.g. warm water storages in district heating networks. In Baeten et al. (2015) several more detailed formulations for model predictive control were compared, including slow accurate non-convex, fast suboptimal linear and iterative linear formulations for stratified hot water tank. In Steen et al. (2015) a storage model for improved tracking of losses is presented. Zachar and Daoutidis (2016) present a formulation for an electric battery storage that has a similar methodology as model B presented in this paper with maximum charging/discharging power depending on the fill level.

In reality, thermal energy storages often have more complex characteristics, like sensible thermal energy storages (STES). An example is that the charging and discharging power of these storages is dependent on the temperature spread of the in- and out-flowing heat transfer fluid (HTF). The temperature spread for STES typically decreases during a charging or discharging phase, which does not match the often assumed fixed maximum charging and discharging power in common MILP models. To address this problem, two formulations for more detailed modeling of a STES for MILP-UC are presented in this paper.

3. Methodology

The presented MILP models were developed based on simulation data of a 1D-model of a fixed bed regenerator that was validated by measurement data of a test rig. In the following the test rig, simulation model and data are briefly discussed, followed by the MILP formulation and comparison of the developed STES models. For both, MILP and simulation models, MATLAB[®] was used as modeling framework. Gurobi[™] was used as MILP solver.

3.1. STES Test Rig, Simulation Model and Data

The fixed bed regenerator presented in Mayrhuber et al. (2017) is a STES with gravel as storage medium (SM) and air as HTF with a steel casing (wall). These three components are considered for the developed first principle 1D-model for detailed simulations. This model was validated by measurement data of a test rig in the laboratories of TU Wien, see Figure 1. In Figure 2 a scheme of the 1D-model is depicted. The three components wall, SM and HTF each were modeled as discrete 1D-elements with heat transfer between the components for each discrete 1D-element and heat conduction for all components and convective transport of the HTF along the 1D-axis.

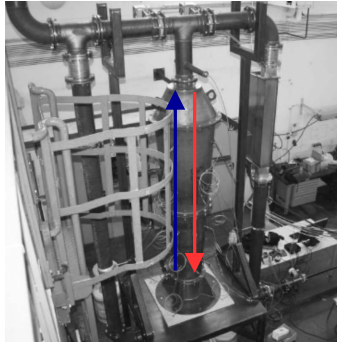


Figure 1: Fixed bed regenerator test rig without insulation

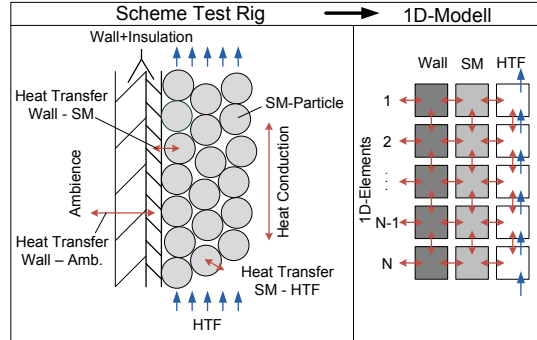


Figure 2: Realistic scheme and 1D-model of the regenerator

To facilitate the analysis of the storage characteristics, the model was slightly adjusted by choosing a cylindrical instead of the actual conic shape and neglecting thermal losses, so that the charging and discharging behavior is identical. With this simulation model, highly dynamic operation with non-complete charging and discharging cycles was simulated. Charging and discharging temperatures and mass flow of the HTF are fixed values, but the duration of charging and discharging phases was randomly chosen during the simulation to cover all possible operating states. The total simulated time is 5,000 hours with a time step size of 30 seconds. The model consists of $K = 48$ discrete elements along the 1D-axis for each component (SM, HTF and Wall).

In Figure 3 and Figure 4 simulation data of complete cycle operation and highly dynamic operation are shown. The plots show the parameters storage fill level, charging and discharging power (actually temperature spread of the in- and out-flowing HTF, but since the mass flow is fixed, this corresponds directly to the storage power, which is of interest in this paper) and an auxiliary parameter, representing the reached storage fill level of the previous charging or discharging phase. The arrows represent the trajectories for charging and discharging phases. The storage fill level is calculated according to Eq.(1) and represents the sensible heat.

$$\hat{s}_t = \sum_{k=1}^K m_{sm,k} \cdot c_{p,sm,k} \cdot \vartheta_{sm,k,t} + m_{htf,k} \cdot c_{p,htf,k} \cdot \vartheta_{htf,k,t} + m_{w,k} \cdot c_{p,w,k} \cdot \vartheta_{w,k,t} \quad (1)$$

For complete cycle operation the charging and discharging power depends on the storage fill level. For highly dynamic non-complete cycle operation, the charging and discharging power is also depending on the reached fill level at the end of the previous charging or discharging phase. If the STES is almost full or empty, a short discharging or charging phase leads again to a high charging or discharging power for the following charging or discharging phase respectively, despite the correlation of power and fill level of complete cycle operation.

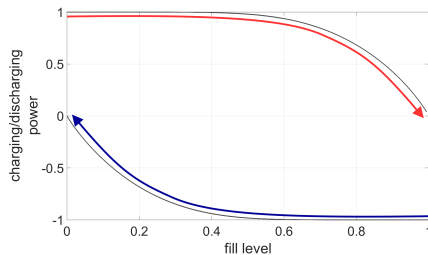


Figure 3: Simulation of complete cycles

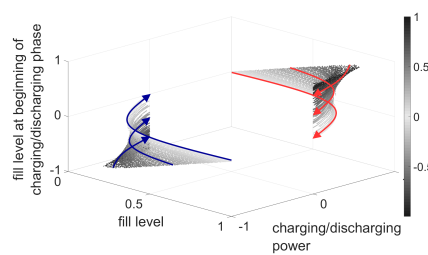


Figure 4: Dynamic simulation (non-complete cycles)

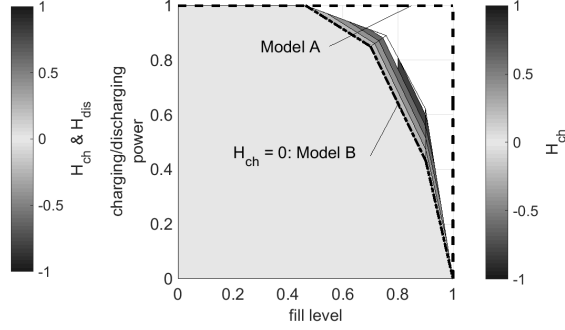
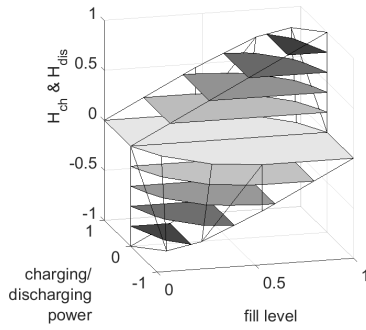


Figure 5: Model C: Operating planes for different values of the auxiliary variables H_{ch} and H_{dis}

Figure 6: View from below of Figure 5 (charging part) with feasible areas of model A and B

3.2. MILP Model Formulation

In order to integrate a STES model with the shown system behavior in a MILP-UC, two extended formulations (models B and C) for the original MILP model (model A) were developed. The shown bounds of the actual feasible operation space in Figure 4 have a non-convex hyperbolic shape, yet this is approximated by two convex solution spaces for charging and discharging (model C) or one convex area (model B). A visualization of model C is shown in Figure 5 and Figure 6.

Typical models include energy balances for the system and the storage with given heat demand:

$$(\dot{Q}_{chp,t} + \dot{Q}_{dis,t} - \dot{Q}_{ch,t}) \cdot \Delta t = q_t \quad (2) \quad S_{t+1} = S_t + (\dot{Q}_{ch,t} - \dot{Q}_{dis,t}) \cdot \Delta t \quad (3) \quad 0 \leq S_t \leq S_{max} \quad (4)$$

$$\dot{Q}_{ch,t} \leq \dot{Q}_{ch,max} \quad (5) \quad \dot{Q}_{dis,t} \leq \dot{Q}_{dis,max} \quad (6)$$

Model A: The above balance Eq.(2) and Eq.(3) and the constraints for maximum charging and discharging power Eq.(5) and Eq.(6) describe the original energy storage formulation. Note that storage losses can be modeled by adding coefficients to the terms in Eq.(3) for losses relative to the fill level, conversion losses or fixed losses. Model A has a fixed normalized maximum charging and discharging power ($\dot{Q}_{ch,max}$ and $\dot{Q}_{dis,max}$) of 1 in comparison to the varying maximum values for model B and C, see Figure 6.

$$\dot{Q}_{ch,t} \leq a + b \cdot S_t \quad (7) \quad \dot{Q}_{dis,t} \leq a + b \cdot (S_{max} - S_t) \quad (8)$$

Model B: Model A is extended by one or multiple instances of Eq.(7) and Eq.(8). These equations decrease the maximum charging power with increasing fill level and the maximum discharging power with decreasing fill level. The equations are a linear approximation of the real bounds, see Figure 3. Therefore the feasible area is enclosed smoother with an increasing number of constraints. This formulation ensures feasible charging and discharging power. Although the possible higher power output according to the investigation of simulation data is neglected as well. This model extension preserves the convexity of model A and therefore only slightly increases the computational effort, since there are just additional linear constraints, but no additional variables needed. The feasible solution space of model B equals model C with $H_{ch} = 0$ and $H_{dis} = 0$ in Figure 5 and Figure 6.

$$\dot{Q}_{dis,t} \leq a + b \cdot (S_{max} - S_t) + c \cdot H_{dis,t} \quad (9) \quad \dot{Q}_{ch,t} \leq a + b \cdot S_t + c \cdot H_{ch,t} \quad (10)$$

$$0 \leq H_{ch} \leq S_t \leq S_{max} \quad (11) \quad 0 \leq H_{dis} \leq S_{max} - S_t \leq S_{max} \quad (12)$$

$$H_{ch,t+1} \leq H_{ch,t} + B_{dis,t} \cdot S_{max} \quad (13) \quad H_{dis,t+1} \leq H_{dis,t} + B_{ch,t} \cdot S_{max} \quad (14)$$

$$H_{ch,t+1} \leq H_{ch,t} + e \cdot \dot{Q}_{dis,t} \quad (15) \quad H_{dis,t+1} \leq H_{dis,t} + f \cdot \dot{Q}_{ch,t} \quad (16)$$

$$0 \leq \dot{Q}_{ch,t} \leq \dot{Q}_{ch,max} \cdot B_{ch,t} \quad (17) \quad 0 \leq \dot{Q}_{dis,t} \leq \dot{Q}_{dis,max} \cdot B_{dis,t} \quad (18) \quad B_{ch,t} + B_{dis,t} \leq 1 \quad (19)$$

Model C: Model B is extended by two continuous auxiliary variables H_{ch} and H_{dis} as well as two binary variables B_{ch} and B_{dis} . The auxiliary variables are necessary to model the higher power due to non-complete cycles according to Figure 4. The auxiliary variables are represented in Figure 5 by the positive Z-axis for H_{ch} and the negative Z-axis for H_{dis} and determine the feasible operating area during the current charging or discharging phase. Eq.(9) and Eq.(10) describe inequality constraints representing the bounding planes. The binary variables define the current phase: Charging ($B_{ch} = 1$), discharging ($B_{dis} = 1$) or neither of both ($B_{ch} = 0$ and $B_{dis} = 0$). Only one of the two binary variables is allowed to be 1 in each time step according to Eq.(19). In Figure 5 several operating areas for different values of H_{ch} and H_{dis} are shown. To model the non-convexity of the simulation data even more detailed, additional binary variables can be introduced to split up the feasible space into multiple convex subspaces, although this increases the needed computational effort further. In this work, the operating range was approximated with just one convex subspace for both charging and discharging, still violating the convex model formulation of the original model A and the proposed model B. Since model C introduces two additional continuous and two binary variables for each time step, the needed computational effort increases. Coefficients a , b , c , d and e in the above equations emerge from the chosen bounding planes and will not be further discussed in this work.

4. Comparison and Discussion

The three models were tested by simulation of a test case over a duration of 30 days with a time step size of 15 minutes with receding horizon and a prediction horizon of 24 hours to simulate online scheduling. The case consists of a combined heat and power (CHP) unit and a STES, represented by the models A, B and C with given heat load that has to be satisfied. The fuel price for the CHP is assumed to be constant, electricity prices are taken from historic spot market prices and are given as well.

In each optimization step of the receding horizon the solutions of the optimization models A, B and C provide a prediction. Then the STES simulation model tries to operate according to the predicted STES operation from the optimization models. The fill level of the optimization models at the beginning of the prediction horizon is set to the real fill level achieved by the simulation model for each step of the receding horizon. If there is an infeasible prediction, the simulation model is not able to exactly match the predicted operation. In order to investigate the impact of this prediction error, the cost function values with the corrected storage operation are calculated. The resulting corrected cost function value is worse than the original and the difference of the two values indicates the impact of the prediction error. In Table 1 the original and corrected cost function values (normalized to the corrected value of model A), the relative infeasibility ($\frac{\sum |Predicted Power - Achieved Power|}{\sum Predicted Power}$) and the average computation time (Intel Xeon E5-1650 @3.5 GHz, 16 GB RAM) of each optimization step are shown for each model. The values depend on the chosen case and may differ for other cases.

The maximum power of model A is the least constrained, therefore the original cost function value is the lowest. Due to the assumed fixed maximum power, infeasible operation occurs, leading to high prediction errors. The maximum power of model B is the most constrained, therefore having the worst original cost function value, but the relative infeasibility is low. The original cost

Table 1: Comparison between models A, B and C of the relative infeasibility, the original and corrected cost function values and the average computation time

	Rel. Infeasibility	Cost Func. Value	Corr. Cost Func. Value	Av. Comp. Time
Model A	21.05 %	92.05 %	100.00 %	0.44s
Model B	3.91 %	96.57 %	96.69 %	1.59s
Model C	5.96 %	94.92 %	96.48 %	3.68s

function value and infeasibility of model C lies between the values of model A and B. Despite having the best original cost function value, model A has the worst corrected value, due to the high prediction error, resulting in the worst system performance. The corrected cost function value of model B is almost the same as the original, due to the low prediction error. Model C has the best corrected value, due to the compromise of feasibility and constraining, resulting in the best system performance. The average computation time for model A is lower than for model B. Due to the additional binary variables in model C the average computation time is clearly higher.

These models are still energy balance models, but the presented modeling approach can be used e.g. to satisfy temperature requirements.

5. Conclusion

A detailed simulation model validated by measurement data of a fixed bed regenerator was used to develop two extended MILP-UC models B and C based on an original model A. The optimization models A, B and C were tested with a test case and the predicted operation was checked by the STES simulation model to quantify the prediction error due to simplifications of the MILP optimization models. Models B and C both perform better than model A, regarding feasibility and corrected cost function value, whereas model B has less computational effort and less infeasible operation than model C, but model C reaches a better overall system performance than model B.

6. Acknowledgment

This work was initiated by the endowment professorship of the Technical University of Vienna (TUW), Institute for Energy Systems and Thermodynamics - Industrial Energy Systems, and the Austrian Institute of Technology (AIT) - Center for Energy - Energy in Industries. The authors want to thank the institute's department Thermodynamics and Thermal Engineering (TUW) for providing the measurement data of the fixed bed regenerator test rig (GSG, FFG-Project 836636).

References

- Baeten, B., Rogiers, F., Patteeuw, D., Helsen, L., 2015. Comparison of optimal control formulations for stratified sensible thermal energy storage in space heating applications. The 13th International Conference on Energy Storage.
- Carrion, M., Arroyo, J. M., 2006. A computationally efficient mixed-integer linear formulation for the thermal unit commitment problem. *IEEE Transactions on Power Systems* 21 (3), 1371–1378.
- Correa-Posada, C. M., Morales-Espana, G., Duenas, P., Sanchez-Martin, P., 2017. Dynamic ramping model including intraperiod ramp-rate changes in unit commitment. *IEEE Transactions on Sustainable Energy* 8 (1), 43–50.
- euostat, 2017. Consumption of energy.
URL http://ec.europa.eu/eurostat/statistics-explained/index.php/Consumption_of_energy#Further_Eurostat_information
- Lund, H., Østergaard, P. A., Connolly, D., Ridjan, I., Mathiesen, B. V., Hvelplund, F., Thellufsen, J. Z., Sorknæs, P., 2016. Energy storage and smart energy systems. *International Journal of Sustainable Energy Planning and Management* 11, 3–14.
- Mayrhuber, F., Walter, H., Hameter, M., 2017. Experimental and numerical investigation on a fixed bed regenerator. 10th International Conference on Sustainable Energy and Environmental Protection.
- Morales-Espana, G., Latorre, J. M., Ramos, A., 2013. Tight and compact milp formulation of start-up and shut-down ramping in unit commitment. *IEEE Transactions on Power Systems* 28 (2), 1288–1296.
- Padhy, N. P., 2004. Unit commitment—a bibliographical survey. *IEEE Transactions on Power Systems* 19 (2), 1196–1205.
- Rajan, D., Takriti, S., 2005. Minimum up/down polytopes of the unit commitment problem with start-up costs. IBM Research Report RC23628.
- Silbernagl, M., Huber, M., Brandenberg, R., 2016. Improving accuracy and efficiency of start-up cost formulations in mip unit commitment by modeling power plant temperatures. *IEEE Transactions on Power Systems* 31 (4), 2578–2586.
- Steen, D., Stadler, M., Cardoso, G., Groissböck, M., DeForest, N., Marnay, C., 2015. Modeling of thermal storage systems in milp distributed energy resource models. *Applied Energy* 137, 782–792.
- Zachar, M., Daoutidis, P., 2016. Dynamic real-time optimization of microgrids with day-ahead commitments for external power exchange. In: 26th European Symposium on Computer Aided Process Engineering. Vol. 38 of Computer Aided Chemical Engineering. Elsevier, pp. 103–108.

Scheduling of a Multiproduct and Multiple Destinations Pipeline System with Repumping Operations

William Hitoshi Tsunoda Meira^{a*}, Leandro Magatão^a, Susana Relvas^b, Lúcia V. R. Arruda^a, Flávio Neves Jr.^a and Ana Paula Barbosa-Póvoa^b

^a*CPGEI-UTFPR - Graduate Program in Electrical and Computer Engineering, Universidade Tecnológica Federal do Paraná, 80230-901 Curitiba, Paraná, Brazil*

^b*CEG-IST - Centre for Management Studies, Instituto Superior Técnico, Lisbon University, 1049-001 Lisbon, Portugal*
williammeira@gmail.com

Abstract

In the oil supply chain, products transportation by pipelines is the most used distribution modal, justified by its high volume capacity, reliability, and safety compared to the other transportation modes. The scheduling of pumping and delivery operations in pipelines is a complex problem. Thus, a better usage of the involved resources calls for the existence of tools that can help the associated decision-making process. This work explores this need and proposes a decomposition approach that integrates Mixed Integer Linear Programming models and heuristics to solve the scheduling of a single-source and multiple distribution centers (DCs) pipeline network, where a repumping DC operation, not yet considered in the literature in the area, is often used in practice. This operation corresponds to a situation where the repumping DC acts as the final DC of the network, receiving all batches arriving and, at the same time, operates as a source node. The DC repumps products previously received in tanks to attend the demand of downstream DCs. In this case, the storage profile has to be carefully controlled in order to perfectly manage the involved operations. A real-world Brazilian network, where such operation can be executed for the transport into the last segment, is used to validate the proposed approach. The approach solves the case where the repumping DC attends a single downstream destination. Scheduling results with and without the repumping operation active are presented. The obtained results translate valid operational solutions in a reasonable CPU time for both executions.

Keywords: Multiproduct pipeline, Scheduling, Repumping Operation, Mixed integer linear programming

1. Introduction

Transportation of crude oil and its derivatives is one of the main problems faced by oil companies. Different transportation modes exist involving different stages of the oil supply chain: from oil terminals to refineries, from refineries to distribution centers (DCs), and among other segments until the client. The operation is carried out mainly by trucks, trains, vessels, and pipelines. However, for many countries, pipelines are the most used mode due to their high volume capacity, reliability, economy, and safety compared to the other modals (Sasikumar et al., 1997). The high cost associated in building a new pipeline network motivates oil companies to develop strategies and tools to aid the scheduling of pumping and delivery activities in the installed network with the purpose to optimize and improve the decision-making process of the system.

Often these networks involve multiproduct pipelines that allow the transportation of more than one product through the same pipeline and connect a single or multiples sources to one or more destinations. The disposition of the network sources, destinations and pipelines define the topology of the system and may consist of a straight pipeline or form complex structures, such as tree-structures, and mesh-structures. This work focuses on straight multiproduct pipeline networks connecting a single-source (a refinery) to multiples DCs. A typical transport operation in this network consists in allocating and sequencing batches of products to be pumped from the refineries, and scheduling delivery activities to attend the local demand of each DC. The problem involves many operational constraints, such as inventory management, demand attendance, flow rate limits, batch restrictions, tank and pipeline maintenance periods. Several approaches have been studied to solve this topology based on mathematical programming using mixed integer linear programming (MILP) (Zaghian and Mostafaei, 2016), mixed integer non-linear programming (MINLP) (Cafaro et al., 2015) and based on heuristics (Sasikumar et al., 1997). Research in such approaches has been exploring the introduction of new characteristics or more detailed operations in order to approximate the proposed approaches to the real-world pipeline networks where the complexity of the problem becomes a challenge. To overcome this problem, decomposition strategies have been also proposed by the academic community. For instance, Cafaro et al. (2012) developed a two-level hierarchical decomposition: aggregate planning with rolling horizon (sequence of the batches and aggregate deliveries) and detailed scheduling (temporization, when the deliveries should occur). Meira et al. (2018) also proposed a decomposition framework using heuristics and MILP models to solve the scheduling of a real-world multiproduct pipeline network with a refinery and multiples DCs. In this work, an extension of this framework is studied to consider a particular real type of operation, the so-called “repumping”.

The remainder of this work is organized as follows. Section 2 describes the problem and the repumping operation. Section 3 explains the decomposition approach. In section 4, we discuss the results of a case study of a real-world pipeline network. Section 5 presents the conclusions and future work.

2. Problem Definition

The problem considers a real-world straight multiproduct pipeline that connects a single-source (refinery) and multiple destinations (DCs), where the repumping operation is possible for the upstream DC of the last segment. Repumping operations are justified as they add some flexibility to the network and may avoid costs involved with shortage or surplus of inventory. In a repumping DC, the inventory capacity is usually higher in order to store more products and attend the downstream DCs whenever necessary. As this DC has no production, its operation requires a proper inventory management since its stock depends on having products received previously from the refinery. Additionally, it may happen that, simultaneously, the repumping DC may be receiving from the refinery and repumping to the downstream destination. The repumping option is decided by the operations managers when scheduling the pipeline operation, as this may be required to avoid extra costs of not supplying the necessary products to the destinations.

In this context, the objective is then to schedule the sequence of batches (product, start-end times, volume, flow rate) to be pumped by the refinery and the delivery operations in each DC during the established time horizon, while minimizing surplus or shortage of inventory for each product in each DC, flow rate variations in each segment, and the number of product interfaces. The solution has also to respect operational constraints, such as flow rate limits (pumping, repumping if active, delivery, and pipeline segment); inventory limits; batch size constraints; forbidden sequences of batches; pipeline and tank maintenance periods.

The developed approach relies on the following assumptions: (1) batches flow unidirectionally from the refinery to the downstream DCs; (2) the pipeline is always full of incompressible prod-

ucts, an input operation propagates instantaneously through the network and the same amount of volume is removed; (3) refinery has sufficient product to attend all the network demand; (4) tanks of the same product in a DC are aggregated; (5) simultaneous deliveries of products in two or more terminals are allowed; (6) repumping operation is possible on the upstream DC of the last segment; (7) inventory management is based on Magatão et al. (2012), also taking into account two intermediate ranges (target range and acceptable operational range), besides physical maximum capacity and empty status limits, to better control the inventory and obtain an operationally viable solution.

3. Decomposition Approach

The proposed approach is an extension of the framework introduced by Meira et al. (2017) and extended in Meira et al. (2018). Figure 1 shows the flowchart of the decomposition strategy, which combines heuristics and MILP models. The novelty is the introduction of the “Repumping Module” as an alternative for the last segment iteration of the Scheduling Module (SM) that is executed when the parameter “repumping” is set on.

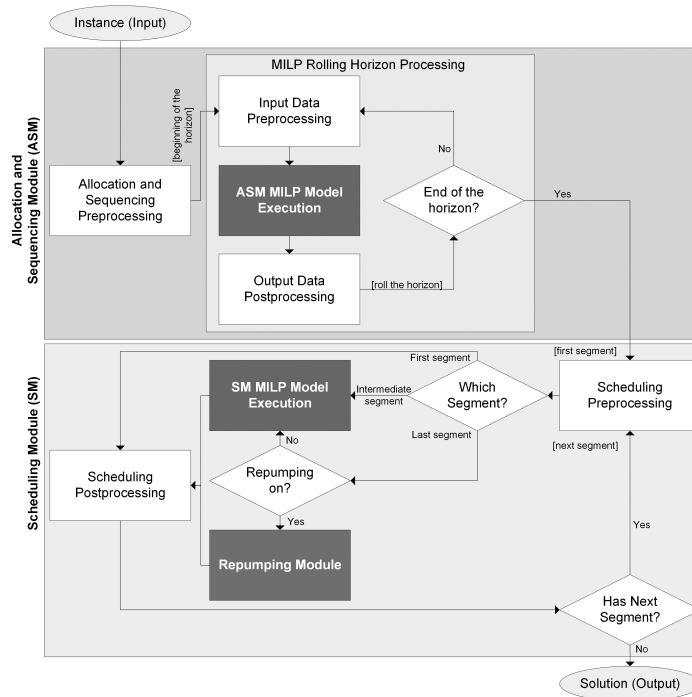


Figure 1: Flowchart of the developed decomposition approach

As input data we have the network information (terminals, pipeline, tanks, and products); demand for the considered time horizon; initialization batches; initial inventory; inventory ranges in each terminal; scheduled maintenance periods; and configuration parameters. The decomposition approach is executed and the output solution contains all the pumping, repumping (when active), and receiving operations to be performed during the considered time horizon. The decomposition approach involves two main modules: Allocation and Sequencing Module (ASM) and Scheduling Module (SM). First, the Allocation and Sequencing Module (ASM) is responsible to allocate the

volume, flow rate, product, and sequence of the batches to be pumped from the refinery during the time horizon. The ASM module receives the data, applies some heuristics in the preprocessing, and proceeds to the rolling horizon process solving part of the time horizon at each iteration by the ASM MILP model. Then, the Scheduling Module (SM) is executed taking as input the plan for the pumping operations from the ASM module and determines the detailed scheduling of all the delivery operations to be performed at each DC. The SM module applies a structural decomposition, solving one pipeline segment per iteration. Each iteration determines the receiving of the upstream DC of the segment being considered. The execution flow depends on the actual segment. The first segment goes directly to the postprocessing since it is the refinery input segment. Intermediate segments execute the SM MILP model and the last segment may execute the same SM MILP model or the Repumping Module depending on the repumping parameter.

3.1. Repumping Module

The proposed Repumping Module solves the allocation and sequencing of the batches to be pumped into the last segment from its upstream DC. The flow process is similar to the ASM MILP rolling processing part (without ASM preprocessing heuristics), where the goal is to allocate volume, flow rate, product, and sequence of batches. However, for this particular case, it allows us to study the problem as a single-source and single-destination straight pipeline topology. The Repumping MILP model considers a discrete-time for the repumping operations and demand due dates; batch constraints (size, forbidden sequences); batches tracking inside the pipeline segment; and inventory is managed for the upstream (source) and downstream DC (destination), where all the batches arriving at the upstream DC are directly received in a tank. These products' receiving are input data of the Repumping Module. Every SM postprocessing calculates the timings of batches arriving at the upstream DC of the next segment. For the long-term scheduling, a rolling horizon strategy may also be considered as in the ASM.

4. Results and Discussion

A real-world straight multiproduct pipeline network with repumping operation was considered in our case study. The considered network distributes products to part of the southeast and central-west regions of Brazil. The total pipeline length is 964 km with 164,374 m³ of internal volume. Figure 2 illustrates the considered case study. The volume dimension of each pipeline segment (S1-S5) is available. Also, the gray dashed line indicates the volumetric coordinate of each DC (DC1-DC5) in relation to the refinery. As illustrated, repumping operation is possible on DC4 to attend the demand of the last DC (DC5). Another detail is that pipeline segments S1-S4 have 20" (50.8 cm) of diameter and S5 has just 12" (30.48 cm), which makes the maximum flow rate in S5 (450 m³/h) lower than the others (1,200 m³/h). The network transports 3 products (P1-P3), where due to high contamination a batch of P3 is transported between batches of P1.

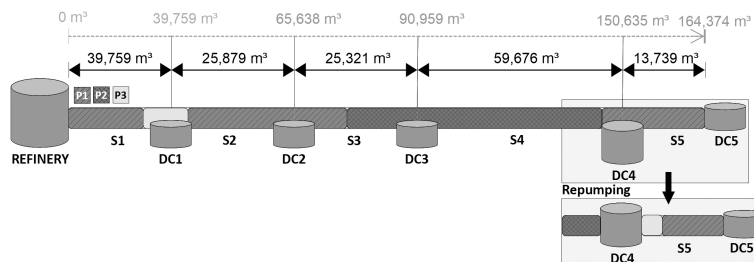


Figure 2: Real-world pipeline network in study

Although repumping operation is costly, operation managers have the possibility of using it in order to avoid possible inventory shortages or surpluses of product that, as a consequence, may decrease service level (e.g. not attending a demand) or add an even higher cost (e.g. the use of different modals, such as trucks to compensate a shortage of inventory).

The proposed approach was developed using Java programming language and IBM ILOG CPLEX Optimization Studio 12.6. Results were obtained on a PC platform with Intel i7-6500 2.5 GHz and 16 GB RAM using Windows 10 64-bits as the operational system. We solved a case of the studied network considering both flow alternatives, repumping off and on.

For a 30-day time horizon, the first execution without repumping took 308 s and the second execution with repumping took 905 s. Since the difference was only in the last segment execution, the solution for the ASM module is equal for both; in addition, the first 3 DCs have also the same solution. The Repumping Module demanded a computational time relatively higher, but the obtained solution was considerably better than the obtained in the first execution, mainly, due to the initial status of the instance. The inventory profiles of P3-DC5 of Figure 3 show the main difference between solutions. As highlighted, the SM model could not avoid a $-1,117 \text{ m}^3$ violation of the empty status in the first execution. Also, notice in Figure 2 that an initialization batch of product P3 is passing by DC1 at the beginning of the horizon, its head volumetric coordinate is $120,115 \text{ m}^3$ far from DC5. Even if a maximum flow rate ($1,200 \text{ m}^3$) is applied, which is only possible if no receiving happens upstream the P3 batch during this period, the DC5 would start receiving P3 only close to the 100 h point. Hence, it is not possible to avoid inventory shortage. In this case, operation managers would need to act in order to avoid such problem. One solution is repumping operations as shown in Figure 3(b) since DC4 has a considerable amount of P3 in stock (80 % of inventory capacity). Predicting the possibility of a shortage of P3-DC5, the Repumping Module scheduled a batch of P3 as the first to be repumped to DC5, thus, avoiding the problem. For both executions, no further inventory problem in DC4 and DC5 was observed during the entire time horizon.

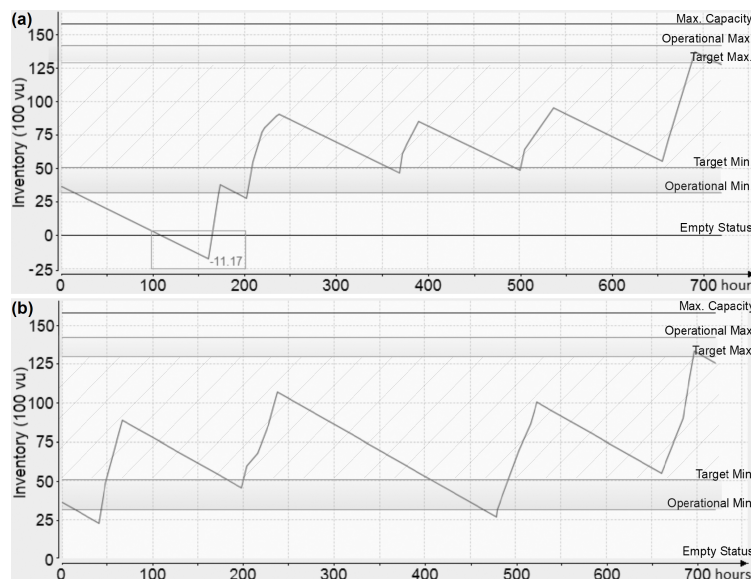


Figure 3: Inventory profile of P3-DC5 with repumping off (a) and on (b)

From these results, it can be seen that repumping operation is an alternative to avoid situations where inventory problems may arise. The cause for such need may be related, for example, to unforeseen demand changes and/or unexpected events. The flexibility added from the repumping operation has a high cost involved when active for a long period. Short-term solutions may be applied, alternating between repumping on and off as necessary.

5. Conclusions

This work proposed an extension of the framework in Meira et al. (2017) and considered repumping operations as an alternative to better manage inventory levels, avoiding shortage of products. A Repumping Module was proposed using a MILP model with rolling horizon. To validate the use of repumping operation, we executed the approach considering repumping off and on in a real-world Brazilian pipeline network. As the main result, the repumping operation was effective in solving a particular inventory problem, which justifies its usage in practice.

As this is the first attempt to model repumping in a pipeline network more work can still be developed. For instance, the current Repumping MILP formulation relies on discrete-time representation, then a continuous-time approach could be explored. The proposed approach could also be extended so as to allow the application of the repumping operation in different segments of the network. Another improvement would be the proposed approach to automatically decide when to repump or not during the complete time horizon.

6. Acknowledgments

The authors acknowledge the Erasmus Mundus SMART² support (Project Reference: 552042-EM-1-2014-1-FR-ERA MUNDUS-EMA2) coordinated by CENTRALESUPLEC. The authors would also like to acknowledge financial support from the Brazilian Oil Company PETROBRAS (grant 0050.0066666.11.9 and 5850.0102354.16.9), CAPES - DS and CNPq (grants 305816/2014-4, 309119/2015-4, and 406507/2016-3).

References

- V. G. Cafaro, D. C. Cafaro, C. A. Méndez, J. Cerdá, 2012. Detailed scheduling of single-source pipelines with simultaneous deliveries to multiple offtake stations. *Industrial and Engineering Chemistry Research* 51 (17), 6145–6165.
- V. G. Cafaro, D. C. Cafaro, C. A. Méndez, J. Cerdá, 2015. MINLP model for the detailed scheduling of refined products pipelines with flow rate dependent pumping costs. *Computers and Chemical Engineering* 72, 210–221.
- S. N. B. Magatão, L. Magatão, H. L. Polli, F. Neves-Jr, L. V. R. Arruda, S. Relvas, A. P. F. D. Barbosa-Póvoa, 2012. Planning and sequencing product distribution in a real-world pipeline network: An MILP decomposition approach. *Industrial and Engineering Chemistry Research* 51 (12), 4591–4609.
- W. H. T. Meira, L. Magatão, S. Relvas, A. P. Barbosa-Póvoa, F. Neves-Jr, L. V. R. Arruda, 2018. A matheuristic decomposition approach for the scheduling of a single-source and multiple destinations pipeline system. *European Journal of Operational Research*, doi.org/10.1016/j.ejor.2018.01.032.
- W. H. T. Meira, L. Magatão, S. Relvas, A. P. F. D. Barbosa-Póvoa, F. Neves-Jr, 2017. A decomposition approach for the long-term scheduling of a single-source multiproduct pipeline network. In: *Operational Reserach, IO 2017, Valença do Minho, Portugal, Springer Proceedings in Mathematics*. Springer, pp. 1–14, doi.org/10.1007/978-3-319-71583-4_16.
- M. Sasikumar, P. Ravi Prakash, S. M. Patil, S. Ramani, 1997. PIPES: A heuristic search model for pipeline schedule generation. *Knowledge-Based Systems* 10 (3), 169–175.
- A. Zaghian, H. Mostafaei, 2016. An MILP model for scheduling the operation of a refined petroleum products distribution system. *Operational Research* 16 (3), 513–542.

Data-based modelling for predicting the completion time of batch processes

Shao-Heng Hsu,^a Yao-Chen Chuang,^a Tao Chen,^b Yuan Yao^{a*}

^a*Department of Chemical Engineering, National Tsing Hua University, Hsinchu, Taiwan 30013. ROC*

^b*Department of Chemical and Process Engineering, University of Surrey, Guildford GU2 7XH, United Kingdom*

* yyao@mx.nthu.edu.tw

Abstract

Batch processing is a widely used method in process industry for its flexibility in manufacturing low-volume and high-value-added products. Due to inter-batch variations, the batch duration often varies, which may cause difficulties in operation scheduling and decision-making. The capability of predicting batch completion time offers valuable information to improved capacity utilisation, reduced workload, and reduced operating cost. To this end, several data-driven modelling methods have been reported. However, the uncertainty of the predicted completion time has not been well explored in previous research. In this paper, the challenges for batch-end prediction are discussed by stressing the importance of prediction uncertainty. This has been demonstrated by the application of probabilistic principal component analysis (PPCA) and quantitative sensitivity analysis to two batch processes. The prediction uncertainty tends to increase substantially, when the variable defining the completion time changes slowly towards the end of batch. Under such situations, we argue that the uncertainty should always be considered along with the mean prediction for practical use.

Keywords: batch process modelling, batch-end prediction, probabilistic principal component analysis, sensitivity analysis, prediction uncertainty.

1. Introduction

In today's process industry, batch processing has been widely used as it is flexibility in manufacturing low volume and high value-added products. Although often considered to be repetitive, a batch process often has variable durations due to inter-batch variations. This may cause difficulties in operation scheduling and decision-making (Li and Ierapetritou, 2008; Méndez et al., 2006). It is desired to develop mathematical models that can predict the batch completion time during the operation. Such prediction can be used to enable reactive scheduling. In practice, even if no rigorous scheduling is implemented (which is still the case in many plants), the capability of predicting batch end time still offers valuable information to help the operators make empirical decisions, which may lead to improved capacity utilisation, reduced expected workload, and overall reduced operating cost. In addition, such predictions can also be used in model-based optimisation and control of the process, for example to optimise the product quality while minimising the processing time.

In batch processes, a batch is usually considered complete when the value of the variable of primary interest reaches a predetermined threshold. Modelling with the aim to predict batch completion time has received significant interest in both academia and

industries. Generally, the prediction methods can be divided into two classes: those based on the fundamental (i.e. first-principal) models (Michaud et al., 2008) and those who are empirical (i.e. data-driven) (Montague et al., 2008). In this work, we focus on the empirical method because it has a minimum requirement on mechanistic understanding of the target process and can be established in an efficient manner. There have been a number of research efforts aimed at solving related problems. For example, Montague et al. (2008) adopted a pattern-based method named case-based reasoning (CBR) to achieve fermentation operational decision making. In CBR, the variable trajectory in the current batch is compared with the historical data. Then, the future behaviour prediction of the current batch can be made based on the pattern discovered in the most similar historical case.

Despite the achievements made to date, the existing methods only provide point estimation and ignore the uncertainty associated with the estimates. The practical goal that motivates this research is to develop a method to reveal the challenges for batch-end prediction by stressing the importance of prediction uncertainty. In detail, probabilistic principal component analysis (PPCA) (Tipping and Bishop, 1999) is adopted to predict the future batch trajectory during the operation, according to which the completion time of each batch can be inferred and the quantitative sensitivity analysis is realized. Although PPCA has been implemented in many other applications, such as process monitoring (Chen and Sun, 2009), this is the first time that it has been used for batch-end prediction. The cause studies show PPCA achieves a comparative prediction accuracy to the existing methods, such as CBR, but provides additional information about the prediction uncertainty which is useful in decision-making.

2. Probabilistic principal component analysis

Principal component analysis (Jolliffe, 2002) is a multivariate statistical projection technique for dimensionality reduction. The core idea of PCA is to project the original d -dimensional data vector, \mathbf{x} , onto a space where the variance is maximized:

$$\mathbf{x} = \mathbf{W}\mathbf{t} + \boldsymbol{\mu} + \mathbf{e} \quad (1)$$

Here \mathbf{W} refers to the eigenvector of the sample covariance matrix corresponding to the q ($q \leq d$) largest eigenvalues, \mathbf{t} is the q -dimensional score vector, $\boldsymbol{\mu}$ is the mean of the entire data set, and \mathbf{e} is the noise term.

In 1999, Tipping and Bishop (1999) proposed a probabilistic formulation of PCA from the perspective of a Gaussian latent variable model. The noise is reasonably assumed to be Gaussian distributed, i.e. $\mathbf{e} \sim G(\mathbf{0}, \sigma^2 \mathbf{I})$, which implies $\mathbf{x} | \mathbf{t} \sim G(\mathbf{W}\mathbf{t} + \boldsymbol{\mu}, \sigma^2 \mathbf{I})$. Furthermore, by adopting a Gaussian distribution assumption for the scores, i.e. $\mathbf{t} \sim G(\mathbf{0}, \mathbf{I})$, the marginal distribution of the original data is also Gaussian: $\mathbf{x} \sim G(\boldsymbol{\mu}, \mathbf{C})$, where the covariance matrix \mathbf{C} can be represented as $\mathbf{C} = \mathbf{W}\mathbf{W}^T + \sigma^2 \mathbf{I}$. Hence, the corresponding log-likelihood is

$$L = \sum_{n=1}^N \ln(p(\mathbf{x}_n)) = -\frac{N}{2} (d \ln(2\pi) + \ln|\mathbf{C}| + tr(\mathbf{C}^{-1}\mathbf{S})) \quad (2)$$

where $\mathbf{S} = \frac{1}{N} \sum_{n=1}^N (\mathbf{x}_n - \boldsymbol{\mu})(\mathbf{x}_n - \boldsymbol{\mu})^T$, N is the total number of observations, and n is the observation index. The model parameter \mathbf{W} , $\boldsymbol{\mu}$ and σ^2 can then be obtained by using the maximum likelihood (ML) or expectation maximization (EM) algorithm.

PPCA offers a natural way to handle the batch process data with uneven batch durations. Without loss of generality, suppose \mathbf{x} is data vector of the variable of primary interest and the maximum length of a batch is m . For each batch with the length smaller than m , the data vector can be divided as $\mathbf{x}^T = [\mathbf{x}_o^T \quad \mathbf{x}_u^T]$, where the sub-vectors \mathbf{x}_o and \mathbf{x}_u consist of the observed and unobserved data, respectively. In such cases, the model parameters can also be obtained by applying the EM algorithm. In the E-step, the distribution of \mathbf{x}_u is calculated based on \mathbf{x}_o and the current estimates of the parameters. In the M-step, the missing data \mathbf{x}_u are imputed by the mean and covariance of \mathbf{x}_u obtained from the E-step, while the log-likelihood function is maximised to update the parameter estimates.

In online implementation, the conditional distribution of the future measurements given the available measurements, which is Gaussian, can be predicted during the process operation. Accordingly, the batch completion time is estimated by comparing the predicted trajectory to a predetermined threshold. The performance of the prediction model is evaluated through leave-one-out cross-validation (LOOCV) and quantified using the root mean squared error (RMSE). Here, two different RMSE indices are considered, including the average RMSE for the prediction of future variable trajectory and the RMSE for the prediction of batch completion time.

3. Sensitivity analysis

Sensitivity analysis is a technique used to reveal how an output of a system is impacted by the uncertainty in the inputs (Saltelli, 2002), which is adopted in this work to illustrate that fundamentally when x does not vary significantly with respect to time around the threshold x_h , it is very difficult to predict the batch end-point. Here, x is the variable of primary interest in the investigated batch process, and the corresponding threshold is x_h . A batch is considered to be complete when the value of x is beyond the threshold. The corresponding time point is denoted as t_h .

According to PPCA, the prediction of x at any time point t can be expressed by a normal distribution with a mean value \bar{x}_t and a variance σ_t^2 where \bar{x}_t is the mathematical expectation of the estimated value and σ_t^2 indicates the uncertainty (or error) in the prediction. Around a small neighbourhood of t_h , the relationship between x and t can be well approximated by a straight line with a slope a and an offset b : $x_t = at + b$, by utilising for example the Taylor expansion. Correspondingly, the predicted time is also approximately normally distributed, i.e. $t \sim N((\bar{x}_t - b)/a, \sigma_t^2/a^2)$. Clearly, the uncertainty of the predicted t , indicated by the variance, depends on the slope term $a = dx/dt$. When a is large and thus x varies with time substantially, the prediction uncertainty is small; otherwise the estimation of time is sensitive to small change in x , and thus the predicted batch end-point carries substantial uncertainty. This conclusion seems straightforward. However, with the help of PPCA prediction, the prediction uncertainty can be evaluated in a quantitative manner. Such information can help the operators to assess the confidence and potential risk in decision-making.

4. Case studies

4.1. Beer fermentation

The first case study is a beer fermentation process in which the wort is mixed with yeast to initiate the production of alcohol. The end-point of this process can be determined by the present gravity (PG) which measures the alcohol content of the brew. As the fermentation progresses, the sugars in the wort are converted to alcohol, while the density of the brew decreases. The process is complete when all of the sugars have been consumed. In this case study, the end-point is set at gravity = 13.

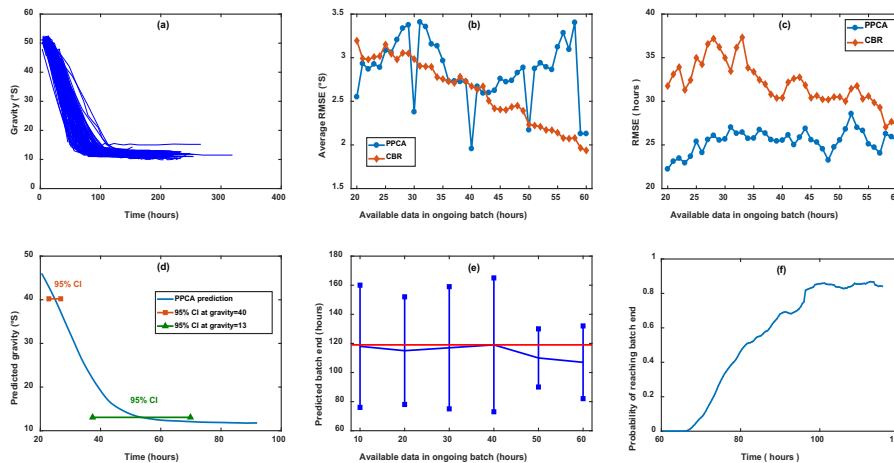


Figure 1. (a) Trajectories of present gravity, (b) average RMSE for prediction of future variable trajectory, (c) RMSE for prediction of batch completion time, (d) 95% CIs corresponding to different batch-end settings, (e) 95% CIs vs. available data points in ongoing batch, and (f) probability of reaching batch end.

Figure 1(a) shows the gravity trajectories recorded in 100 batches, from which significant inter-batch variations can be observed. For comparison, PPCA and CBR were used in the predictions. In Figure 1(b), the average RMSE for the prediction of future variable trajectory is plotted, which was calculated based on LOOCV. In this figure, the x-axis indicates the amount of the available data points in the ongoing batch when the prediction was made. In this particular case, there is no significant trend observed in the values of the average RMSE derived from the PPCA prediction results, while the performance of CBR improves with the increase of the amount of the available measurements. Figure 1(c) depicts the RMSE for the prediction of batch completion time. Here, PPCA outperforms CBR. Figure 1(d) shows the PPCA predictions of the gravity in a single batch in which the actual completion time is about the 119th hour. These results were obtained at the 20th hour of the ongoing batch. The 95% confidence intervals (CIs) of the predictions of the batch completion time are also plotted in the same figure. For the end-point at gravity = 13, the CI is plotted in green. For comparison, the CI is recalculated by assuming the end-point is set at gravity = 40 (although such an end-point selection is not practical), which is plotted in red. It is observed that the uncertainty increases when the variable trajectory turns to be flat, as verified by Figure 1(e). In Figure 1(e), the predicted values of the batch end-point are

plotted, together with the corresponding CIs. The x-axis has a similar meaning to that in Figures 1(b) and 1(c). It is noted that the prediction uncertainty does not reduced significantly with the increase of the observed data points in the ongoing batch. In addition, the probability for each time point of reaching the batch-end can be easily derived from the PPCA prediction result. The results shown in Figure 1(f) are based on the PPCA prediction made at the 60th hour in the ongoing batch. The probability for the batch to be complete at the 119th hour is larger than 50%. CBR and other conventional methods cannot provide information as in Figures 1(d)-(f), because they only make point estimations.

4.2. Rapid gravity filter

The second illustrative case is a rapid gravity filter where wastewater passes through granular materials to remove suspended particles and other impurities. In order to maintain the filter efficiency, backwashing needs to be done routinely. In some contexts, this process behaves like a batch process, where the duration between two times of backwashing can be regarded as a batch. The batch completion time, i.e. the time for backwashing, can be determined according to the solid concentration in the outlet flow. In this case study, when the concentration is larger than 0.2 mg/L, the backwashing should be carried out.

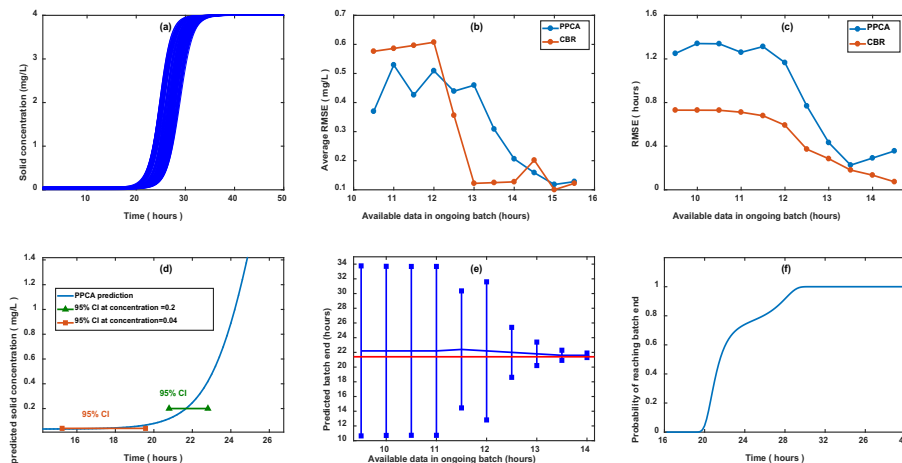


Figure 2. (a) Trajectories of concentration, (b) average RMSE for prediction of future variable trajectory, (c) RMSE for prediction of batch completion time, (d) 95% CIs corresponding to different batch-end settings, (e) 95% CIs vs. available data points in ongoing batch, and (f) probability of reaching batch end.

Figure 2(a) shows the simulated data of the solid concentration collected in 100 batches. The average RMSE values for the prediction of future variable trajectory are plotted in Figure 2(b), while the comparison results of the RMSE for the prediction of batch completion time are shown in Figure 2(c). In both figures, there is a shift in the prediction performance around the 13th hour. Such results are reasonable, because the trajectory of the solid concentration is very flat and contains little prediction information before the time close to the batch end. In addition, CBR, which is an inherently nonlinear method, outperforms the linear PPCA in this case. The possible reason is that this process is highly nonlinear. Figure 2(d) shows the PPCA predictions

of the solid concentration obtained at the 14th hour of an ongoing batch. The 95% CIs of the batch completion time predictions are plotted in the same figure, where the batch-end is set at 0.2 mg/L and 0.04 mg/L, respectively. Figure 2(e) plots the predicted batch completion time together with the CIs, which were calculated along the running time of the batch. The actual end time of this batch (corresponding to solid concentration = 0.2 mg/L) is around the 21.4th hour. A shift in the prediction uncertainty can be observed, which confirms the finding in Figures 2(b) and 2(c). Figure 2(f) shows the probability of each time point of reaching the batch end, which is calculated based on the PPCA predictions made at the 15th hour. It is noted that there is an obvious change in the probability value around the actual completion time.

5. Conclusions

In this work, the problem of batch-end prediction is studied. A PPCA-based scheme is proposed. Comparing to the conventional methods, such as CBR, PPCA provides comparative prediction accuracy and additional information of prediction uncertainty. Through sensitivity analysis, it is proved that when the variable of interest does not vary significantly with respect to time around the threshold, it is fundamentally very difficult to predict the batch end-point. Such a conclusion is verified with the experimental results. Furthermore, the case studies show the capability of PPCA to present the prediction uncertainty in a quantitative manner. The confidence intervals and the probability information can be very useful in industrial applications.

Acknowledgement

This work was supported in part by Ministry of Science and Technology, ROC under Grant No. MOST 106-2622-8-007-017.

References

- A. Michaud, R. Peczalski, J. Andrieu, 2008, Optimization of crystalline powders vacuum contact drying with intermittent stirring, *Chemical Engineering Research and Design*, 86, 606-611.
- A. Saltelli, 2002, Sensitivity analysis for importance assessment, *Risk Analysis*, 22, 579-590.
- C. A. Méndez, J. Cerdá, I. E. Grossmann, I. Harjunkoski, M. Fahl, 2006, State-of-the-art review of optimization methods for short-term scheduling of batch processes, *Computers & Chemical Engineering*, 30, 913-946.
- G. Montague, E. Martin, C. O'Malley, 2008, Forecasting for fermentation operational decision making, *Biotechnology Progress*, 24, 1033-1041.
- I. Jolliffe, 2002, *Principal Component Analysis* (2nd ed.), New York: Springer.
- M. E. Tipping, C. M. Bishop, 1999, Probabilistic principal component analysis, *Journal of the Royal Statistical Society: Series B (Statistical Methodology)*, 61, 611-622.
- T. Chen, Y. Sun, 2009, Probabilistic contribution analysis for statistical process monitoring: A missing variable approach, *Control Engineering Practice*, 17(4), 469-477.
- Z. Li, M. Ierapetritou, 2008, Process scheduling under uncertainty: review and challenges, *Computers & Chemical Engineering*, 32, 715-727.

Sequential Bayesian Experimental Design for Process Optimization with Stochastic Binary Outcomes

Martin F. Luna, Ernesto C. Martínez*

INGAR (CONICET-UTN), Avellaneda 3657, Santa Fe S3002 GJC, Argentina
ecmarti@santafe-conicet.gov.ar

Abstract

For innovative products, the issue of reproducibly obtaining their desired end-use properties at industrial scale is the main problem to be addressed and solved in process development. Lacking a reliable first-principles process model, a Bayesian optimization algorithm is proposed. On this basis, a short of sequence of experimental runs for pinpointing operating conditions that maximize the probability of successfully complying with end-use product properties is defined. Bayesian optimization is able to take advantage of the full information provided by the sequence of experiments made using a probabilistic model (Gaussian process) of the probability of success based on a one-class classification method. The metric which is maximized to decide the conditions for the next experiment is designed around the expected improvement for a binary response. The proposed algorithm's performance is demonstrated using simulation data from a fed-batch reactor for emulsion polymerization of styrene.

Keywords: Bayesian optimization, end-use product properties, Gaussian processes, one-class classification, scale-up.

1. Introduction

For innovative products, the issue of reproducibly obtaining their desired end-use properties is the main problem to be addressed in process development (Colombo et al., 2016). For example, emulsion polymerization processes are well-known examples of the importance of guaranteeing reproducibility of end-use properties such as tensile strength and melt index by properly choosing the operating policy (Valappil and Georgakis, 2002). Similar problems are encountered in production of high-quality graphene sheets, single-walled carbon nanotubes and functionalized polymer nanofibers. The main drawback in the development of this type of innovative, high-value products is lacking a reliable first-principles model to predict the binary outcome (success/failure) of a production run for a given setting of the controlled variables in the face of variability due to the effect of uncontrolled factors on end-use properties. Also, even at bench scale, experiments are time consuming and/or expensive, which demand fast pinpointing operating conditions where the probability of success is maximum.

The problem of sequential experimental design for process optimization with stochastic binary outcomes is addressed by combining one-class classification with Gaussian processes (Xiao et al., 2015) and Bayesian optimization (Shahriari, et al., 2016). It is assumed that errors (failures) incurred in the sequence of runs are not punished, but instead it is of major concern the final recommendation for operating conditions once the available budget (in time and/or money) for experimental optimization is over.

2. Problem statement

Given an initial Region of Interest (ROI) $\mathbb{X} \subset \mathbb{R}^d$ for the controlled inputs, an unknown objective function $\pi: \mathbb{X} \rightarrow [0, 1]$ descriptive of the probability of complying with product end-use properties and a maximum budget of n experiments, the problem of sequentially making decisions $\mathbf{X}_i = [x_1, x_2, \dots, x_i]^T$ which are rewarded by a “success” with probability $\pi(x)$ and “failure” with probability $1 - \pi(x)$, is to recommend, after n experiments, the operating conditions x^* that maximizes π . Note that the choice of the operating conditions for each experiment x_i in the sequence is based solely on knowledge of the binary outcomes $\mathbf{y}_i = [y_1, y_2, \dots, y_i]^T$ from previous runs. The observations at x_i are considered to be drawn from a Bernoulli distribution with a success probability $p(y = 1|x_i)$. The probability of success is related to a latent function $f(x): \mathbb{R}^d \rightarrow \mathbb{R}$ that is mapped to a unit interval by a sigmoid transformation. The transformation used is the *probit* function $p(y = 1|x_i) = \Phi(f(x_i))$, where Φ denotes the cumulative probability function of the standard Normal density.

As there not exist correct examples of the success probability π over ROI but evaluative feedback from binary outcomes $\{-1, +1\}$, using Gaussian processes (GPs) for one-class classification is a more appropriate choice for probabilistic modelling of the objective function being maximized. At the observed inputs, the latent variables $\mathbf{f} = \{f(x_i)\}_{i=1}^n$ have a Gaussian prior distribution. Given a training set $D = (\mathbf{X}, \mathbf{y})$, the probabilistic model chosen $p(y_*|D, x_*)$ aims to predict the target value y_* for a new sample x_* by computing the posterior probability $p = (\mathbf{f}|\mathbf{X}) = N(\mathbf{f}|\mu, \mathbf{K}_{f,f})$, where $\mathbf{K}_{f,f}$ is the covariance matrix and μ is the mean function. Since neither of the class labels is considered more probable, the prior mean is often set to zero. As a GP generate an output z in the range $(-\infty, \infty)$, a monotonically increasing response function $\sigma(z)$ is used convert the GP outputs to values within $[-1, 1]$ which can be interpreted as class probabilities (Rasmussen and Williams, 2006). In particular, the latent GP \hat{f} defines a Gaussian probability density function p_f^x for an input $x \in \mathbb{X}$. At any given x , the corresponding probability density for the positive class (success) is defined as p_π^x .

The inference step for conditioning the posterior GP on sampled observations \mathbf{X} and \mathbf{y} require computing the following integral to determine the posterior \hat{f} at any x_* over \mathbb{X} :

$$p(\hat{f}_*|\mathbf{x}, \mathbf{y}, x_*) = \int p(\hat{f}_*|\mathbf{x}, \mathbf{y}, x_*) p(\mathbf{f}_*|\mathbf{x}, \mathbf{y}) d\mathbf{f}_* \quad (1)$$

In this equation, \mathbf{f}_* represents the GP prior on the latent function at x_* . The main idea is to use a mean of the prior with a smaller value than our positive class labels (i.e., $y=1$), such as a zero mean. This restricts the space of probable latent functions to those whose values gradually decrease when being far away from observed points. By choosing a smooth covariance function such as the simple squared exponential

$$k((\mathbf{x}_r, \mathbf{x}_m|\zeta, \ell)) = \zeta^2 \exp\left(-\frac{\|\mathbf{x}_r - \mathbf{x}_m\|^2}{2\ell^2}\right) \quad (2)$$

an important subset of latent functions is obtained. The parameter ℓ defines its characteristic length scale whose value must be optimized for improved discriminatory power, and ζ^2 is the magnitude parameter. The GP mean μ_* typically decreases for

inputs distant from the training data and can be directly utilized as a measure of membership for the positive class. Conversely, the variance σ_*^2 of the prediction is always increasing for distant inputs, which suggests that the negative variance value can serve as an alternative criterion for discriminating operating conditions for successes from those end-use properties are obtained. As it is shown by Rasmussen and Williams (2006), if σ is the Gaussian cumulative density function, the expected value of the probability of success (posterior) at x_* can be approximated by

$$\mathbb{E}[p_{\pi}^x] = \bar{\pi}(x) = \Phi\left(\frac{\mu_*}{\sqrt{1 + \sigma_*^2}}\right) \quad (3)$$

3. Bayesian optimization

Mathematically speaking, given the problem of finding a global maximum of the unknown objective function $\bar{\pi}$ over \mathbb{X} which is defined based on a priori knowledge

$$x_{best} = \arg \max \bar{\pi}(x), x \in \mathbb{X} \quad (4)$$

The sequential Bayesian experimental design algorithm in Fig. 1 selects, at each iteration i , the operating conditions x_{i+1} for the next experiment and observe the binary outcome y_{i+1} . After n experiments, the algorithm makes a final recommendation x^* which represents the algorithm's best estimate (based on the available experimental budget) of the operating conditions for which the probability of success is the global maximum.

The Bayesian optimization algorithm (see Fig. 1 for details) resorts to a selection metric (often known as *acquisition function*) that allows selecting the next experiment to be made using a trade-off between exploration and exploitation. In this work, the expected improvement for stochastic binary outcomes proposed by Tesch et al. (2013) is used. By querying the GP posterior at each point in \mathbf{X} , and letting

$$\tilde{\pi}_{max} = \max \bar{\pi}(x), x \in \mathbf{X} \quad (5)$$

The improvement I_{π} for stochastic binary outcomes at any $x \in \mathbb{X}$ is defined as follows

$$I_{\pi}(\pi(x)) = \max(\pi(x) - \tilde{\pi}_{max}, 0), x \in \mathbb{X} \quad (6)$$

The corresponding expectation for I_{π} over \mathbb{X} is

$$\mathbb{E}I_{\pi}(\tilde{\pi}_{max}) = \max \int_{\sigma^{-1}(\tilde{\pi}_{max})}^{\infty} (\sigma(z) - \tilde{\pi}_{max}) p_f^x(z) dz \quad (7)$$

4. Case study

4.1. Process description

The proposed methodology is tested by simulation of the emulsion polymerization of styrene. The reactor operates in fed-batch mode, with two inlets: the monomer feed (x_1) and the chain transfer agent (CTA) feed (x_2), both measured in mol/s. The reactor is initially charged with solvent and an initiator, and is seeded with particles of three

different sizes. As the monomer is fed, polymer chains growth unevenly, giving rise to a distribution of chain lengths (and molecular weights). The CTA modifies the length of the chains. The end-use properties of the product depend on the distribution of molecular weights, both in weight (MW_w) and in number (MW_n).

Algorithm: Bayesian optimization

- *Inputs:* $n_0, n, D_0 = \{\mathbf{X}_0, \mathbf{Y}_0\}$
- ▷ **For** $i = n_0 + 1$ to n **do**
 - Select new x_i by optimizing the expected improvement $EI_\pi(x)$

$$x_{i+1} = \arg \max EI_\pi(x, D_i), x \in \mathbb{X}$$
 - Do the next experiment at x_{i+1} and observe y_{i+1}
 - Augment dataset $D_{i+1} = \{D_i, (x_{i+1}, y_{i+1})\}$
 - Update statistical model \hat{f}
- ▷ **End for**
- $x^* = \arg \max \bar{\pi}(x), x \in \mathbf{X}_n$
- *Output:* x^*

Figure 1. Bayesian optimization algorithm for stochastic binary outcomes.

In this work, the melt flow index (MI) and the tensile strength (TS) are the end-use properties of interest. A batch is considered successful if both properties are kept within their desired intervals:

$$1.25 \times 10^{-4} < MI \leq 7.5 \times 10^{-4} [g/min]; 6900 < TS \leq 7200 [psi] \quad (8)$$

These end-use properties are correlated with the molecular weights as follows:

$$MI = \frac{30}{(MW_w^{3.4} \times 10^{-18} - 0.2)} \quad (9)$$

$$TS = 7390 - 4.51 \times 10^8 \left(\frac{1}{MW_n} \right) \quad (10)$$

The variability due to uncontrolled factors is introduced in the simulation as a 5% perturbation (normally distributed) in the initial charge of seeded particles and the initiator concentration. Details of the stochastic simulation model for the polymerization process can be found in Colombo et al. (2016). The contour lines for the probability of success in the ROI are shown in Fig. 2.

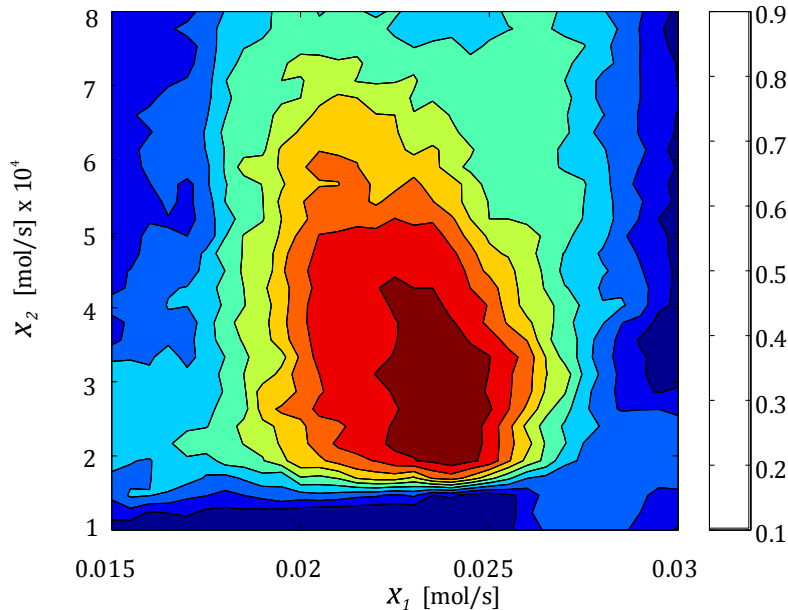


Figure 2. Contour plots for the probability of success in the case study.

4.2. Results

The proposed algorithm is tested for the case study described in Section 4.1 using the stochastic simulation model. In each trial, 50 experiments are performed before the method selects the optimal operation condition x^* that maximizes π . Experiments are divided between an initial sampling set (with n_0 points) and experiments designed based on Bayesian optimization. Thus, the algorithm in Fig. 1 is tested using 100 independent sequences generated from different number and selection of the initial experiments. The initial n_0 points were chosen using Latin hypercube sampling. A simple squared exponential covariance with fixed hyper-parameters (length scale of $e^{0.75}$ and signal variance of e^5) was used. Results obtained are shown in Table I.

Fig. 3 depicts the GP approximation $\bar{\pi}(x_1, x_2)$ of the probability of success, after 50 experiments in one of the independent trials made, obtained using the proposed algorithm in Fig. 1. It is worth noting that for the process simulation model the (assumed unknown) maximum probability of success is 0.97.

5. Concluding remarks

The role of Bayesian optimization in sequentially making decisions regarding operating conditions aiming at maximizing the probability of success in achieving the desired end-use properties has been discussed. The proposed algorithm is based on expected improvement for stochastic binary outcomes and one-class classification using Gaussian processes. Simulations results are promising bearing in mind the level of variability considered and that Bayesian optimization does not require a first-principles model.

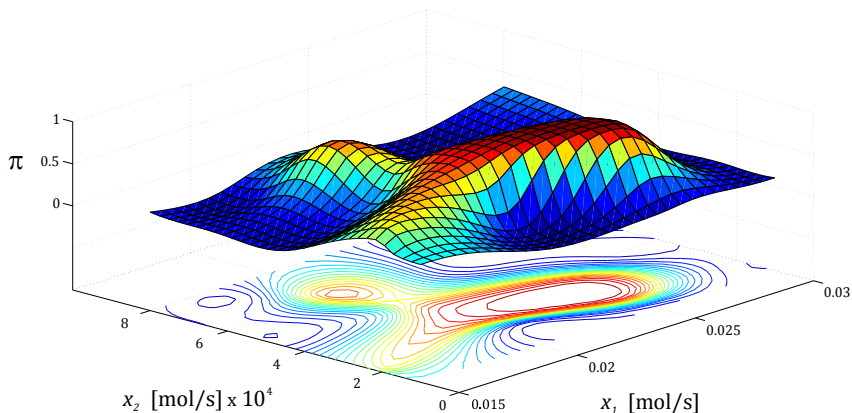


Figure 3. Response surface and contour plots for the estimated $\bar{\pi}(x_1, x_2)$ in a trial.

Table I. Bayesian optimization based on 100 independent trials of 50 runs.

n_0	\bar{x}_1^* [mol/s]	\bar{x}_2^* [mol/s] x 10^4	$\bar{\pi}$	$\sigma^2(\pi)$	$\pi(\bar{x}_1^*, \bar{x}_2^*)$
5	0,0229	3,679	0,860	0,015	0,927
10	0,0229	3,522	0,879	0,013	0,939
15	0,0230	3,602	0,867	0,018	0,930
20	0,0228	3,522	0,843	0,020	0,915
25	0,0227	3,630	0,840	0,024	0,915
30	0,0225	3,695	0,801	0,029	0,881
45	0,0229	3,840	0,812	0,037	0,916

References

- Colombo, E., M. F. Luna, M., E. C. Martínez, 2016, Probability-Based Design of Experiments for Batch Process Optimization with End-Point Specifications, *Ind. Eng. Chem. Res.*, 55, 1254–1265.
- C. E. Rasmussen , C. K. Williams, 2006, *Gaussian Processes for Machine Learning*, MIT Press.
- Shahriari, B. et al., 2016, Taking the Human Out of the loop: A Review of Bayesian Optimization, *Proceedings of the IEEE*, 104, 148-175.
- M. Tesch, J. Schneider, H. Choset, 2013, Expensive Function Optimization with Stochastic Binary Outcomes, *Proceedings of the 30th International Conference on Machine Learning*.
- J. Valappil, C. Georgakis, 2002, Nonlinear Model Predictive Control of End-Use Properties in Batch Reactors, *AIChE J.*, 48, 9, 2006-2021.
- Y. Xiao, H. Wang, W. Xu, 2015, Hyperparameter Selection for Gaussian Process One-Class Classification, *IEEE Trans. on Neural Networks and Learning Systems*, 26, 9, 2182-2187.

Oil product distribution planning via robust optimization

Camilo Lima^{a*}, Susana Relvas^a, Ana Paula Barbosa-Póvoa^a, Juan M. Morales^b

^a*CEG – IST, Instituto Superior Técnico, University of Lisbon, Av. Rovisco Pais, 1049-001 Lisboa, Portugal*

^b*Department of Applied Mathematics, University of Málaga, Málaga, Spain*

camilo.lima@tecnico.ulisboa.pt

Abstract

This paper approaches the tactical distribution planning in the downstream oil supply chain (DOSC) under uncertain market conditions by using robust optimization (RO). The tactical RO model makes use of general polyhedral uncertainty sets, which encompass the so-called ramping constraints. These restrain the maximum variation in the random parameters, so that the time correlation present in the input time series can be captured, as well as the level of conservatism of the robust solutions can be adjusted. Additionally, autoregressive integrated moving average (ARIMA) techniques and Monte Carlo simulation are used in order to determine the parameters of the uncertainty sets. An example based on the Portuguese DOSC is studied so as to confirm both the applicability and adequacy of the developed RO models to real-world problems.

Keywords: Robust optimization, Uncertainty, Downstream Oil Supply Chain.

1. Introduction

The oil supply chain (OSC) can be split up into an upstream segment, which comprises the oil production activities, a midstream segment, which encompasses the activities related to oil refining, and a downstream segment, which focuses on the distribution and marketing of oil products (Lima et al., 2016). The OSC aims to move crude oil from its reservoir, process it into refined products at oil refineries, and then deliver the oil products to the final consumers. Generally, the greatest part of oil products is majorly delivered using pipelines from oil refineries to storage depots, and by tanker trucks from these to the local markets.

Such complex supply chain is subject to uncertainties that may arise from many sources and interfere in its management. Essentially, uncertain market conditions take shape in oil production fluctuations, unsettled processing capacities, unstable prices and changeable demands. Usually, companies within this uncertain environment have imprecise information about their operation, even though they must make agile and proper decisions. A means to accomplish better performances is the optimization of the supply chain. Hence, efficient optimization tools need to be designed to further assist managers in making more robust decisions with regards to the diverse uncertainty sources inherent to the oil market.

This work follows this need and addresses the tactical problem in oil product distribution planning under exogenous uncertainties via RO. Therefore, uncertainties are introduced in price and demand for crude oil. Zugno and Conejo's robust formulation (Zugno and Conejo, 2015) is used to manage uncertainty in the random parameters by

way of budget uncertainty sets that can consider the time dependency of the input data. ARIMA models are adjusted to the input data, and then a systematic procedure to generate scenarios for the random parameters are created based on Monte Carlo simulation. Therefore, the parameters of the uncertainty sets are estimated from the simulated data.

The developed RO approach is applied to solve a real case study on the product distribution in Portugal.

2. Problem definition

The DOSC includes a set of oil companies, oil refineries, storage depots, retail service stations and transportation modes that aims to meet the oil product demands in a certain geographical area. Its planning problem under uncertainty can be stated as follows:

Given a vertically integrated DOSC, where an oil company controls the refining processes, logistics operations and trade of refined products;

Determine the optimal tactical planning, with uncertainties arising from oil demand and price, which consists of refinery production planning, distribution planning, inventory policies and customer fulfilment/satisfaction;

Subject to material balance, yield fractions, processing capacity, storage capacity and transportation capacity restrictions;

In order to maximize the total profit for the downstream oil supply chain.

3. Robust optimization approaches

Lima et al. (2018) developed a multistage stochastic programming to solve the distribution problem of refined products under different uncertainties in market conditions. The main drawback of this scenario-based approach was the great number of required scenarios to represent the random parameters over the time horizon, which lead to high problem solution times. However, the distribution planning based on a RO formulation avoids such increase in complexity and solution difficulties.

Here, the tactical DOSC problem is alternatively formulated as RO model based on the work developed by Zugno and Conejo (2015), considering the same sources of uncertainty, namely, demand and price for crude oil.

3.1. Overview of robust optimization

In RO, random parameters are described by uncertainty sets instead of using probability distributions like stochastic programming does. In general, a RO problem is formulated in order to provide the optimal solution for the worst possible value that the random parameter can take on within the established uncertainty set. In the following, the general RO formulation is presented, which considers the different uncertain parameters affecting constraints and/or objective function. Thus, a general RO problem without recourse takes the general form shown in (1) (Morales et al., 2013):

$$\begin{aligned} & \min_x \max_u \{f(x, u), u \in U\} \\ & \text{s.t. } g_i(x, u) \leq 0, \quad \forall i, \forall u \in U, \\ & \forall x \in X. \end{aligned} \tag{1}$$

Variable $x \in X$, which can be declared as continuous and/or discrete, refers to the decisions to be made before the realization of the random parameter $u \in U$. Note that u takes values within the uncertainty set U . f is a real-valued function to be minimized and $g_i, \forall i$, corresponds to a set of restrictions. Problem (1) can be rewritten as in (2):

$$\begin{aligned} & \min_{x,z} z \\ & \max_u \{f(x, u), u \in U\} \leq z, \\ & \max_u \{g_i(x, u), u \in U\} \leq 0, \quad \forall i, \\ & \forall x \in X. \end{aligned} \tag{2}$$

The unconstrained variable z represents a proxy for the objective function. Thus, the maximization of the real-valued function f over u does not exceed this new real-valued variable z , while all constraints $g_i, \forall i$, must be satisfied for all values assigned to u from within the uncertainty set U . A proper manner to solve Problem (2) is to transform this bilevel problem into a single-level problem by dualizing the lower level problems, if these u -problems are convex, and then incorporating the established dual problems to the upper level problem, the x -problem, provided that strong duality holds.

3.2. Uncertainty set definition

Assume that the uncertain parameters vary within convex and budget uncertainty sets, being defined by the following set of linear inequalities from Eq.(3) to Eq.(7):

$$\Delta u_t = \Delta u_t^+ - \Delta u_t^-, \quad \forall t \in T, \tag{3}$$

$$0 \leq \Delta u_t^+ \leq \Delta u_t^{max}, \quad \forall t \in T, \tag{4}$$

$$0 \leq \Delta u_t^- \leq \Delta u_t^{max}, \quad \forall t \in T, \tag{5}$$

$$\sum_t \frac{\Delta u_t^+ + \Delta u_t^-}{\Delta u_t^{max}} \leq \Gamma, \tag{6}$$

$$\frac{\Delta u_t}{\Delta u_t^{max}} - \frac{\Delta u_\tau}{\Delta u_\tau^{max}} \leq \rho_{t\tau}, \quad \forall t, \tau \in T. \tag{7}$$

Eq.(3) splits the deviation of the uncertain parameter Δu_t for any time point t into a positive component Δu_t^+ and a negative component Δu_t^- , which are both declared as positive variables. Eq.(4) and Eq.(5) define the lower bound (i.e., zero) and the upper bound Δu_t^{max} for both types of deviations, respectively. Eq.(6) assures that the sum of the normalized absolute values of both deviations, across all time points t , must not exceed the user-defined budget of uncertainty Γ . Eq.(7) enforces the temporal correlation between the realizations of the uncertain parameter Δu_t by limiting the difference between the normalized deviations for any two different time points (i.e., t and τ) to a given measure $\rho_{t\tau}$.

3.3. Robust optimization approach for oil demand and price uncertainties

The proposed RO model arises from a bilevel problem, whose lower-level problems aim to determine the most adverse values for the oil price and demand, and whose upper-level problem seeks to define an optimal solution even for the worst-case scenarios. The level of uncertainty is controlled by the budget of uncertainty Γ that provides a way to balance the level of conservatism of the robust solutions. After dualizing both inner problems and incorporating them into the outer max-problem (by appealing to strong

duality), a RO formulation that relies on Zugno and Conejo (2015) is established to deal with uncertainties in oil price and oil demand.

For the sake of brevity, the RO model is qualitatively stated by a description of the its objective function and its constraints. However, the objective function of the RO model comprises an unconstrained real-valued variable *Profit* that must be maximized, being subject to a constraint that enforces that the sum of margins and costs must remain below this variable *Profit*. The former comprises the margins of refineries, storage depots and retail market, while the latter includes the costs of exportation, importation, lost demand, primary and secondary transportation and oil and oil products inventories. In addition, a protection term is added to this prior constraint in order to provide the suitable protection against its violation when the oil price varies. Besides, some constraints must be defined in order to quantify the sensitivity of the system to variations in oil price. Also, the RO model is subject to the following set of network constraints: flow balance, inventory balance, oil procurement, flow capacity, storage capacity, refining capacity, yield fractions, nonnegative and integrity. The uncertainty regards the independent coefficients of the oil procurement constraint (right-hand-side), that is, the oil demands. Hence, an additional binary variable with fixed value of 1 is introduced into the model in order to include the oil demands into the coefficient matrix (left-hand-side) – see Li and Ierapetritou (2008). Additionally, the oil procurement constraint includes a buffer term to avoid violation due to variation in oil demand. Other constraints must be established to quantify the sensitivity of the system to changes in oil demands.

4. Case study

The case study is based on the Portuguese industry, which consists of two oil refineries (Sines and Matosinhos), three storage depots (Boa Nova, CLC, Mitrena), 278 local markets (i.e., all the Portuguese municipalities in mainland Europe), and four transportation modes: oil tanker, tank truck, tank wagon and pipeline. Crude oil is received at Sines and Matosinhos, which transform it into eight refined products, namely, butane, diesel, fuel oil, gas oil, gasoline 95, gasoline 98, jet fuel and propane. Both refineries supply storage depots and local markets and can export surplus of refined products abroad, while storage depots supply local markets and Mitrena depot may compensate the shortage of refined products by importing from overseas markets. The product distribution is undertaken by oil tanker, tank truck, tank wagon and pipeline for the primary distribution, and only by tank truck for the secondary distribution. The planning horizon covers six monthly cycles.

5. Results and discussion

The RO mixed integer linear programming (MILP) model was implemented in GAMS 24.5.6 and solved using CPLEX 12.6 on a processor Intel(R) Xeon(R) CPU E5-2660 v3 @ with 2.60 GHz (2 processors) and 64 GB RAM memory, for a 0% optimality gap.

5.1. Simulation study

As abovementioned, the oil demand and price are treated as stochastic processes that are characterized via ARIMA techniques. For this purpose, monthly time series for oil demand and price in Portugal from January 2008 to December 2016 are analyzed, addressing 108 observations for each time series. Through ARIMA fits, it is possible to represent the probability distributions of both random parameters through the generation of scenarios. In order to make this scenario generation process efficient and reproducible, a systematic procedure based on Monte Carlo simulation is established by replacing the

error terms ϵ_t^P and ϵ_t^D in the ARIMA fits, Eq.(8) and Eq.(9), by normal distributions with zero mean and constant variance – $N(0, \sigma_{\epsilon^P}^2)$ and $N(0, \sigma_{\epsilon^D}^2)$ distributions.

The ARIMA model below is used to generate scenarios to represent the crude oil prices for the six-month time horizon from January 2017 to June 2017:

$$\ln(y_t^P) = \ln(y_{t-1}^P) + \phi_1 \ln(y_{t-1}^P) - \phi_1 \ln(y_{t-2}^P) + \epsilon_t^P, \quad \forall t \in T, \quad (8)$$

where y_t^P represents the oil price stochastic process, ϕ_1 is the autoregressive parameter of order 1, whose value estimate is 0.401 at 5% significance level, and ϵ_t^P is a white noise.

Additionally, the next seasonal ARIMA model is employed to produce scenarios to represent the crude oil demands for the same six-month time horizon:

$$\ln(y_t^D) = \ln(y_{t-1}^D) + \ln(y_{t-12}^D) - \ln(y_{t-13}^D) + \epsilon_t^D - \theta_1(\epsilon_{t-1}^D) - \theta_1(\epsilon_{t-12}^D) + \theta_1\theta_1(\epsilon_{t-13}^D), \quad \forall t \in T, \quad (9)$$

where y_t^D is the oil demand stochastic process, θ_1 is the regular moving average parameter of order 1 and θ_1 is the seasonal moving average parameter of order 1, whose values are respectively -0.869 and -0.856 at 5% significance level, and ϵ_t^D is a white noise. For more details about the adjustment of these autoregressive models, the interested reader is referred to Lima et al. (2018).

After running 10000 simulations and, hence, 10000 scenarios are generated for oil price and demand, the nominal values and deviation amplitudes of the uncertainty sets are estimated from the simulated data, which correspond respectively to the forecast mean and maximum deviation for oil price and demand at each time point over the time horizon. In addition, the values for the budgets of uncertainty Γ^{price} and Γ^{demand} are also estimated from the simulated data as the average relative deviations. Thus, the budget of uncertainty Γ^{price} , which takes values within the range [0,6], is defined as 1.16, while the budget of uncertainty Γ^{demand} , which in turn assumes values within the range [0,1], is set as 0.20. However, the values of ρ_{tt}^{price} and ρ_{tt}^{demand} are estimated as the maximum total relative deviation between time points observed in the simulated data.

5.2. Comparison between robust and stochastic approaches

Compared to the scenario-based stochastic programming approach with 1024 scenarios and 1365 tree nodes (Lima et al., 2018), the robust optimization approach has the major benefit of not leading to a large optimization problem due to the number of random parameters and their possible realizations. Table 1 reports the statistics for both optimization models. Indeed, the case study solved by the stochastic programming (SP) model results in many more constraints and variables than the robust optimization (RO) model, even though this RO formulation comprises a binary variable. The computational effort to solve the SP model is extremely high when compared to the one needed to solve the RO model, as highlighted by the solution time required by the solver to settle the optimization problem.

Table 1: Model statistics

Cases	Scenarios	Tree nodes	Variables		Constraints	Profit (€)	Solution time (s)
			Binary	Continuous			
RO	1	-	1	336,550	159,914	2,613,704,721	7.937
SP	1,024	1,365	-	12,691,756	5,346,530	2,771,474,827	1,076.700

Table 2 breaks down the network profit for the RO and SP approaches into margins and costs components, while Table 3 presents the corresponding network plans that are described by the set of decision variables that control the network flows.

Table 2: Network profitability: objective function components in millions of €.

Cases	Margins			Costs			Transport costs		Inventory costs			Profit	
	Refinery	Depot	Retail	Export	Import	Lost	Primary	Secondary	Oil	Refinery	Depot		Retail
RO	1,076.274	1,007.517	1,332.961	3.159	442.293	3.149	94.351	142.811	10.579	6.222	2.144	2,987	2,611.864
SP	1,070.631	1,141.603	1,395.812	3.785	561.808	2.319	100.541	144.175	12.171	6.188	2.573	3.011	2,771.475

Table 3: Network planning: volumes traded in millions of cubic meters.

Cases	Volumes					Inventory volumes					
	Exported	Imported	Lost	Oil delivery	Processed	Primary	Secondary	Crude oil	Refineries	Depots	Markets
RO	1.238	0.793	1.501	6.091	7.117	6.055	4.111	0.576	0.301	0.073	0.079
SP	1.483	0.932	1.105	6.457	7.620	6.313	4.317	0.671	0.304	0.089	0.079

The composition of the network profit is closely linked to the established network planning as reported in Table 2 and Table 3. Overall, the SP approach outperforms the RO approach with regards to network profit by 6.11%. Specifically, the stochastic approach defines an expected profit and a flexible network planning that is balanced for all the considered scenarios, while the RO approach determines a total profit associated to a network plan that is based on the worst-case scenario for oil price and demand, in accordance with the levels of uncertainty that are adjusted by the budgets of uncertainty (i.e., $\Gamma^{price} = 1.16$ and $\Gamma^{demand} = 0.20$). In conclusion, the RO approach provides robustness of the established network planning by decreasing the network profit, while the level of conservatism of the robust solutions can be adjusted by the decision maker.

6. Conclusions

In this paper, a robust optimization model based on Zugno and Conejo (2015) is developed to cope with oil price and demand uncertainties, in the tactical management of the DOSC. The robust approach is also compared with its stochastic counterpart, and the results show that the robust model with well-defined budgets of uncertainty can adequately address oil price and demand uncertainties by generating robust planning and suitable profits, but both results are lower than the ones obtained for the stochastic model. As advantage, the robust approach avoids the computational burden inherent to the stochastic one. As future works, adaptive robust optimization and decomposition methods will be explored aiming to provide dynamic robust solutions for the studied problem, where a deeper comparison between robust and stochastic models will be performed.

References

- Z. Li, M.G. Ierapetritou, 2008, Robust optimization for process scheduling under uncertainty, *Industrial & Engineering Chemistry Research*, 47(12), 4148–4157.
- C. Lima, S. Relvas, A.P. Barbosa-Póvoa, 2016, Downstream oil supply chain management: A critical review and future directions, *Computers and Chemical Engineering*, 92, 78–92.
- C. Lima, S. Relvas, A.P. Barbosa-Póvoa, 2018, Stochastic programming approach for the optimal tactical planning of the downstream oil supply chain, *Computers and Chemical Engineering*, 108, 314–336.
- J.M. Morales, A.J. Conejo, H. Madsen, P. Pinson, M. Zugno, 2013, *Integrating renewables in electricity markets: operational problems* (Vol. 205), Springer Science & Business Media.
- M. Zugno, A.J. Conejo, 2015, A robust optimization approach to energy and reserve dispatch in electricity markets, *European Journal of Operational Research*, 247, 659–671.

A Discrete-time Scheduling Model for Continuous Power-intensive Processes Considering Fatigue of Equipment

Andreas Obermeier^{a,*}, Christoph Windmeier^a, Erik Esche^b and Jens-Uwe Repke^b

^a*Linde AG, Engineering Division, R&D Process Development, Dr.-Carl-von-Linde-Straße 6-14, D-82049 Pullach im Isartal, Germany*

^b*Process Dynamics and Operations Group, Technische Universität Berlin, Sekr. KWT-9, Str. des 17. Juni 135, D-10623 Berlin, Germany*

**andreas.obermeier@linde.com*

Abstract

In the light of the growing renewable energy generation, matching of electricity supply and demand has become increasingly challenging. By participating in demand side management programs, industry can contribute to counter this challenge. However, the frequent adjustment of operation conditions according to volatile electricity prices leads to additional dynamic loads for the equipment. In this work, a mixed-integer linear programming based discrete-time model is proposed for scheduling of a single air separation unit, explicitly considering fatigue of equipment occurring during transient operation. Besides constraints for describing the feasible region and the process dynamics, this model includes constraints for considering mechanical fatigue of some key equipment. The resulting model is applied to investigate the impact of mechanical constraints on the potentials of demand side management.

Keywords: Scheduling, Fatigue, Mechanical limitations, Air Separation, Demand Side Management

1. Introduction

Demand side management (DSM) has been recognized as one of the key enablers for a cost-efficient energy transition. Especially, energy-intensive industries can contribute to the energy transition by offering high potentials for grid stabilization in terms of DSM and at the same time mitigate their own economic risks related to volatility in energy supply. Depending on the electricity market the industry has various measures to participate in DSM programs, whereby the programs can be distinguished into two main DSM categories (Charles River Associates, 2005): Energy efficiency (EE) and demand response (DR). In the first category attempts are made to increase the efficiency of the industrial process and thus to reduce the energy consumption. The second category is focused on the load profile adjustment, driven by market incentives. A more detailed explanation of DSM as well as a comprehensive review of existing works on planning and scheduling for industrial DR is provided in the work of Zhang and Grossmann (2016). Here, contributions are listed which address the application of DR in various energy-intensive industries such as aluminum, cement, chlor-alkali, steel, and air separation.

In particular, the operational planning (scheduling) of cryogenic air separation units (ASUs) under time-sensitive electricity prices has gained considerable attention. As one of the first, the work of Daryanian et al. (1989) addressed the topic of DSM, using a simplified model. For a more accurate representation of an ASU, Ierapetritou et al. (2002) proposed the notion of operating

modes to take into account that one process may show operation regions with different configurations and states. In such a mode-based model, each operating mode is defined by a specific feasible region and the process can only operate in one of these operating modes in each time step (Zhang and Grossmann, 2016). Based on this model, Karwan and Kebulis (2007) as well as Mitra et al. (2012, 2013) further developed the concept of mode-based models. Moreover, Mitra et al. introduced additional constraints to better capture the process dynamics, plus addressing the uncertainty in forecast of electricity prices. The aspect of uncertainty related to electricity prices, product demand, and dispatchable DR is also investigated in other studies (Ierapetritou et al., 2002; Mitra et al., 2014; Zhang et al., 2015, 2016a). Once again based on the concept of mode-based models Mitra et al. (2014) described a multiscale capacity planning model for finding the optimal investment strategy for purchasing new components or upgrading existing components over a time horizon of multiple years. A further development of the mode-based modeling approach was proposed by Zhang et al. (2015), whereby each mode is specified by a Convex Region Surrogate (CRS) model according to Zhang et al. (2016b). In contrast to all aforementioned works Manenti and Rovaglio (2013) have increased the number of ASUs to investigate the optimization of gas supply networks, applying multiscale approaches to implement this so-called plant-wide or enterprise-wide optimization. The same topic was addressed in Zhang et al. (2016c) whereby the combination of mode-based modeling approach and CRS models is used to model a network of continuous power-intensive processes. A similar approach was applied by Zhou et al. (2017) to examine the optimal scheduling of a real-world production network.

As can be seen here, a great deal of effort has gone into the improvement of approaches for planning and scheduling power-intensive processes under time-sensitive electricity prices, whereby the plants (respectively process networks), the electricity markets with their energy contracts as well as uncertainties of input variables are described with increasing detail. However, the participation in DSM programs may be associated with frequent adjustment of operating conditions and thus triggers the necessity for a paradigm change in plant design and operating philosophies, away from static conditions towards transient operation. Consequently, process equipment is increasingly subjected to additional dynamic loads and the resulting stress is potentially reducing its lifetime. In order to ensure mechanical integrity of all plant components over the whole life span, the lifetime consumption due to transient operation has to be considered in both plant design and operations planning (scheduling).

2. Model formulation

In this work, a method is proposed for explicitly considering fatigue of equipment occurring during transient operation. In the following section, the method and the related optimization model is described in more detail.

Normally, a process is modeled by using detailed equations describing the heat and mass balance of each apparatus. However, the non-linear characteristic of these equations leads to a non-linear optimization model that is hard to solve in particular if the time horizon increases. For this reason, another approach is chosen. Similar to Mitra et al. (2012) the plant is described applying a data based surrogate model; more specifically, results from steady-state process simulations are used to represent the feasible region of the plant. In terms of the steady-state simulations, a highly detailed simulation model was applied to generate the data base for the surrogate model. For example, the simulation model does not only include equations for capturing the basic heat and mass balance but also detailed equations for describing the realistic behavior of the installed equipment in off-design, i.e., partial load and over load. More precisely, it covers inter alia: load-dependent efficiency and boundaries of the turbo compressors and turbines, load-dependent heat transfer, and hydraulic behavior of process equipment and piping. Consequently, by means of this detailed simulation model the steady-state behavior within the feasible region and its boundaries can be well described, but also a representative data base can be generated for the surrogate model. For

approximating the non-linear characteristic of this data base, a piecewise linear surrogate model is applied.

In a scheduling model, the time can generally be represented applying a discrete- or continuous-time formulation. Here, the optimization model is structured as discrete-time scheduling model, since in contrast to continuous-time models discrete-time model generally show better computational performance in terms of the application to large-scale problems. Castro et al. (2009) showed that only small-sized problems can be solved efficiently by continuous-time models, whereas comparable discrete-time models can handle large-scale problems.

2.1. Feasible region

Along the lines of aforementioned studies, this study also applies the approach of mode-based models, whereby a mode is defined as a set of operating points that show the same set of active discrete operating decisions (i.e., selection of running machines). By using this approach, discrete operating decisions of a plant can be distinguished by selecting various operating modes. But, within each mode the operating points vary only in terms of the continuous variables (i.e., flow rate of material). For capturing these variations each mode is separately described using the surrogate models as described above.

The focus of this study lies on investigating the impact of mechanical fatigue on optimal plant operation. For this reason, the feasible region of the plant is only considered in a reduced manner to keep the optimization model simple. More precisely, the feasible region of each mode $m \in M$ is spanned by several steady state operation points ($i \in I_m$) and the consecutive interpolation between two adjacent points results in a piecewise linear surrogate model. Note, that this surrogate model may be thought of as path of lines through the feasible region. In order to capture non-linear characteristics of various attributes within the region, the path can be easily adapted by adding further operation points within this subregion. Figure 1 illustrates such path/surrogate model in a two-dimensional product space with the products A and B .

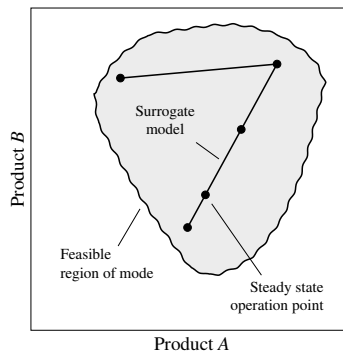


Figure 1: Visualisation of surrogate model within the feasible region of an arbitrary mode.

The plant is captured by the combination of several of these modes, whereby the feasible regions of the modes can overlap, but for each discrete time step $t \in T$ only one mode $m \in M$ can be selected.

2.2. Mass balance

A mass balance is implemented to capture the relationship between production, export and content in the storage facilities. The export EXP_c^t is defined by the demand of the respective product c .

Over the whole observation period, the production PRO_c^t must be equal to or higher than the total export to guarantee the demands of the customer. This relationship can be expressed for each product in the set C by

$$\sum_{t \in T} PRO_c^t \geq \sum_{t \in T} EXP_c^t \quad \forall c \in C. \quad (1)$$

The content CON_c^t of such storage facilities can be described by applying the mass balance:

$$CON_c^t = CON_c^{t-1} - EXP_c^t + PRO_c^t \quad \forall t \in T, \forall c \in C^{liq}, \quad (2)$$

$$CON_c^{min} \leq CON_c^t \leq CON_c^{max} \quad \forall t \in T, \forall c \in C^{liq}. \quad (3)$$

Additionally, the content must satisfy the technical requirements of the installed storage facility (CON_c^{min} and CON_c^{max}), whereby the Equation (2) is only valid for the reduced set of liquid products C^{liq} .

2.3. Transitions

The surrogate models only capture the plant itself – the steady-state behavior within the feasible region and its boundaries – but not process dynamics. However, a transient plant operation implies frequent transitions between several operating points and thus the introduction of representative transitional states and associated differential constraints is necessary to include the process dynamics in the scheduling model.

In a mode-based model all transitions can be distinguished in two major types: transitions between operating points which are assigned to one operation mode or transitions which are assigned to different operation modes. Transitions of the former type are basically dominated by a differential constraint that limits the change in power consumption within a defined time slot, whereas various logical constraints are used with respect to the second type of transitions to define permitted transitions as well as specific operation sequences.

2.4. Mechanical fatigue

As mentioned above, fatigue design is considered for some key equipment in order to ensure mechanical integrity over the whole plant lifetime. More specifically, the estimated life expectancy of machinery, e.g. compressors and of heat exchangers is integrated in the mixed-integer linear programming (MILP) problem by using equipment specific parameters. The concept may however easily be extended to other process components (e.g., piping).

The lifetime of compressors can be considered in a simplified way by limiting the number of starts according to the fatigue design of the compressor casings and the electrical drives. More precisely, the maximum number of starts per day is usually kept under a machine-specific limit following the recommendations of the machine manufactures. For integrating these recommendations binary variables and logical constraints are added to the MILP to count and limit the start per day and thus prevent excessive loads for the machines.

In terms of heat exchangers there are two aspects affecting its lifetime: Purely mechanical stress from pressure cycling and thermo-mechanical stress originating from transient temperature profiles. Similar to the previously outlined compressors, design numbers of pressure cycles at specified stress levels are specified during the fatigue design. By using this number as a reference, the lifetime consumption due to the first aspect can be described in a simplified way as a linear function of the number of pressure cycles. Lifetime consumption due to the second aspect is considered by implementing equipment-specific results of a thermo-mechanical stress analysis – generated by dynamic FEM simulations (finite element method) – in a piece-wise linear function. As worst-case scenario, both aspects can be captured by applying the approach of linear damage accumulation.

2.5. Electricity market

Specifics about energy markets are primarily dependent upon their geographical location and originate from differences in power generation technology portfolios, degrees of integration of local electric energy grids as well as regulatory background. The location of the plant and its associated energy market thus imply large impact upon the optimal operation strategy. Consequently, the energy market requires modeling in an adequate manner.

2.6. Objective function

As mentioned in section 1 the objective of DR is the load profile adjustment according to market incentives and thus the minimization of operational expenditure (OPEX). With regard to ASUs the OPEX is primarily characterized by energy costs, caused by the electric-driven machines of the compressors. Hence, the objective can be formulated as the sum of the product of the electrical power consumption and the corresponding electricity price for each time step.

3. Illustrative Examples

The above outlined model is used to generate illustrative examples investigating the impact of mechanical fatigue on the potentials of DSM, more precisely on the objective during the operation of a specific ASU.

The examples are performed using an air separation plant, which mainly produces two products, liquid oxygen (LOX) and liquid nitrogen (LIN). Each liquid product can be stored in a separate storage tank. Gaseous products like nitrogen are not considered as such to keep the example simple. Consequently, a merchant liquid plant is considered that supplies a local gas market without having on-site customers.

The demand of each liquid product and state of the storage facilities are described by applying the constraint (1) and (2), respectively. Since, the impact of technical limitations on the plant operation can be investigated independently of the fluctuating product delivery rate, a constant average demand is specified for each product.

The plant is described using this work's approach along with realistic constraints in order to capture its performance, dynamics and the fatigue design of its key equipment. More precisely, the maximum number of starts per day is specified for each machine as well as the design number of allowed pressure cycles and the equipment-specific results of thermo-mechanical stress analyses for heat exchangers. Note, that these results are specific to the installed type of heat exchanger and strongly depend on the assumed operation schemes for shutting down the plant, leaving it in cold standby, and restarting it.

For this study, the European Electricity Exchange (EEX) electricity market is considered, more precisely the hourly-based day-ahead prices of 2016 are applied for an integral period of 31 days (January 1, 2016 to January 31, 2016). The period is represented by using a moving horizon approach with 7 days forecast updated on a daily basis.

In order to investigate the impact of mechanical fatigue on the potentials of DSM, various cases with different fatigue specifications, regulatory constraints and tank volumes are defined. As a detailed discussion on all parameters is beyond the scope and will be supplied in future publications, only exemplary findings of a simplified reference scenario will be given at this point.

In this scenario, the consideration of mechanical fatigue during the operational scheduling leads to a modified operation profile. As a result, the plant is operated in a manner where the specified equipment lifetimes of 25 years can be met, whereas non-consideration would lead to the reduction of individual equipment lifetimes as much as one order of magnitude. However, the operation is

restricted by additional constraints and thereby is less optimal in terms of adjusting plant operation to the variations of the electricity market. In doing so, the objective function is increased only by about 2% maintaining the mechanical integrity of the plant on a long-term basis.

4. Conclusions & Outlook

This contribution demonstrates that the consideration of mechanical fatigue during operation scheduling is essential to avoid excessive stress on equipment as well as associated production losses due to damage driven down-times. Note, that equipment specific fatigue design may impact the potentials of scheduling of DSM strongly. Therefore, it is concluded that the proposed method allows the assessment of different equipment designs regarding their suitability for transient operation and thus allows for the optimization of plant designs for different energy market requirements.

In future work, the method shall be extended to include a more detailed description of the plant performance to exclude effects due to the reduced description of the feasible region.

5. Acknowledgements

The project on which this report is based was supported by funds from the German Federal Ministry of Education and Research, funding code 03SFK3X1. Responsibility for the content of this publication is assumed by the author.

References

- P. M. Castro, I. Harjunkoski, I. E. Grossmann, 2009. New continuous-time scheduling formulation for continuous plants under variable electricity cost. *Industrial & Engineering Chemistry Research* 48 (14), 6701–6714.
- Charles River Associates, 2005. Primer on demand-side management with an emphasis on price-responsive programs. Tech. rep., World Bank.
- B. Daryanian, R. E. Bohn, R. D. Tabors, Aug 1989. Optimal demand-side response to electricity spot prices for storage-type customers. *IEEE Transactions on Power Systems* 4 (3), 897–903.
- M. G. Ierapetritou, D. Wu, J. Vin, P. Sweeney, M. Chigirinskiy, 2002. Cost minimization in an energy-intensive plant using mathematical programming approaches. *Industrial & Engineering Chemistry Research* 41 (21), 5262–5277.
- M. H. Karwan, M. F. Kebblis, 2007. Operations planning with real time pricing of a primary input. *Computers & Operations Research* 34 (3), 848 – 867, *logistics of Health Care Management* Part Special Issue: *Logistics of Health Care Management*.
- F. Manenti, M. Rovaglio, 2013. Market-driven operational optimization of industrial gas supply chains. *Computers & Chemical Engineering* 56, 128 – 141.
- S. Mitra, I. E. Grossmann, J. M. Pinto, N. Arora, 2012. Optimal production planning under time-sensitive electricity prices for continuous power-intensive processes. *Computers & Chemical Engineering* 38, 171–184.
- S. Mitra, J. M. Pinto, I. E. Grossmann, 2014. Optimal multi-scale capacity planning for power-intensive continuous processes under time-sensitive electricity prices and demand uncertainty, part i: Modeling. *Computers & Chemical Engineering* 65, 89 – 101.
- S. Mitra, L. Sun, I. E. Grossmann, 2013. Optimal scheduling of industrial combined heat and power plants under time-sensitive electricity prices. *Energy* 54, 194 – 211.
- Q. Zhang, J. L. Cremer, I. E. Grossmann, A. Sundaramoorthy, J. M. Pinto, 2016a. Risk-based integrated production scheduling and electricity procurement for continuous power-intensive processes. *Computers & chemical engineering* 86, 90–105, druck-Ausgabe: 2016. - Online-Ausgabe: 2015.
- Q. Zhang, I. E. Grossmann, 2016. *Planning and Scheduling for Industrial Demand Side Management: Advances and Challenges*. Springer International Publishing, Cham, pp. 383–414.
- Q. Zhang, I. E. Grossmann, C. F. Heuberger, A. Sundaramoorthy, J. M. Pinto, 2015. Air separation with cryogenic energy storage: Optimal scheduling considering electric energy and reserve markets. *AIChE Journal* 61 (5), 1547–1558.
- Q. Zhang, I. E. Grossmann, A. Sundaramoorthy, J. M. Pinto, Jun 2016b. Data-driven construction of convex region surrogate models. *Optimization and Engineering* 17 (2), 289–332.
- Q. Zhang, A. Sundaramoorthy, I. E. Grossmann, J. M. Pinto, 2016c. A discrete-time scheduling model for continuous power-intensive process networks with various power contracts. *Computers & Chemical Engineering* 84, 382 – 393.
- D. Zhou, K. Zhou, L. Zhu, J. Zhao, Z. Xu, Z. Shao, X. Chen, 2017. Optimal scheduling of multiple sets of air separation units with frequent load-change operation. *Separation and Purification Technology* 172, 178 – 191.

Multivariable Robust Model Predictive Control of a Laboratory Chemical Reactor

Juraj Oravec^{a*}, Monika Bakošová^a, Linda Hanulová^a and Alajos Mészáros^a

^a*Slovak University of Technology in Bratislava, Faculty of Chemical and Food Technology, Institute of Information Engineering, Automation, and Mathematics, Radlinského 9, Bratislava 81237, Slovak Republic*

juraj.oravec@stuba.sk

Abstract

Optimal control of chemical reactors represents a challenging task, as their behaviour is non-linear, asymmetric, and highly affected by various uncertainties. The paper presents multivariable control of a laboratory chemical reactor, in which acetic acid reacts with sodium hydroxide and the neutralization process runs in the reaction mixture. The challenge is to optimize the set-point tracking of pH in the presence of parametric uncertainties. The control inputs are the volumetric flow rates of acid and base. The robust model predictive control was designed to fulfil the control task. To make the optimization problem more tractable, the LMI-based formulation of the convex optimization problem is implemented. The optimization problem has a special structure to ensure offset-free control performance and satisfaction of constraints on control inputs. Moreover, optimal control actions are calculated considering the multiple input system. As only the controlled output is measured, the state observer was designed and used. The main contribution of the paper is the experimental investigation of the LMI-based and state-observer-based robust model predictive control with integral action designed subject to input constraints. Control performance of the laboratory neutralization chemical reactor satisfies all control requirements.

Keywords: Robust control, model predictive control, chemical reactor, linear matrix inequalities.

1. Introduction

Continuous stirred-tank reactors (CSTRs) are frequently used plants in the chemical and food industries. Control of CSTRs is a challenging problem due to the non-linear behaviour, multiple steady-states, heat effect of the chemical reactions, time delay, and effect of various time-varying uncertainties, see (Luyben, 2007, chap. 1). The model predictive control (MPC) represents the state-of-art in the optimization-based control for complex systems (Maciejowski, 2000). The robust model predictive control optimizes control action according to the bounded uncertain parameters (Bemporad and Morari, 1999). LMI-based robust MPC represents an intensively developed class of control strategies, as it is handled via the convex optimization (Kothare et al., 1996). MPC requires the system model in the proper form. To find a suitable mathematical formulation for a complex system can be a challenging task. The model of monomer semi-batch emulsion copolymerization for MPC design was investigated in Chaloupka et al. (2017). The multi-parametric MPC enables to speed up the online evaluation of the complex controller, see Charitopoulos et al. (2017). Another perspective branch of predictive control, the economic MPC for an uncertain model of a heat exchanger was designed in Pour et al. (2017). The possibility to control a CSTR using the novel algorithm of hierarchical MPC providing the exact, global and multi-parametric solution of bi-level programming was investigated in Avraamidou and Pistikopoulos (2017). In Ho-

laza et al. (2018) an advanced reference-governor-based control of the chemical reactor was analysed. When comes to implementing the advanced control strategy, it is not straightforward to develop the software tool for the different groups of users, e.g., industrial users, technology developers, and researchers, see Varbanov et al. (2017). The software tool MUP for robust MPC design suitable for researchers is proposed in Oravec et al. (2017).

This paper presents particular results of our research focused on the advanced LMI-based robust MPC design for the chemical reactors. The work directly extends the results of previous work Oravec et al. (2017), where robust MPC was designed for the considered neutralization chemical reactor, but in the different control setup. In comparison to Oravec et al. (2017), the main contribution of this work originates in the investigation of the control performance by using two control inputs, i.e., the volumetric flow-rates of acid and base, respectively. The controlled output was pH of the solution in the outlet stream. As only the controlled output was measured, the state observer had to be used to estimate the system states. We redesigned the robust MPC subject to the extended vector of the system states and the integral action. The weighting matrices in the quadratic cost function optimizing the control performance were experimentally tuned. The paper demonstrates the benefits of the proposed robust MPC design strategy for set-point tracking problem.

2. Controlled Chemical Reactor

The controlled plant was a laboratory continuous stirred-tank reactor (CSTR) of Armfield PCT40. The main part of the chemical reactor is a reaction vessel that has volume $V = 1.5 \text{ dm}^3$. In the reaction vessel neutralization of sodium hydroxide (NaOH) and acetic acid (CH_3COOH) ran. The products of neutralization were sodium acetate (CH_3COONa) and water (H_2O). The chemical reaction is described as follows: $\text{NaOH}(\text{aq}) + \text{CH}_3\text{COOH}(\text{aq}) \rightarrow \text{CH}_3\text{COONa}(\text{aq}) + \text{H}_2\text{O}(\text{l})$. The controlled variable was pH (potential of hydrogen) of the outlet flow from the reaction vessel. The actual pH value was measured using a pH probe. Two retention tanks were used to store acid and base, and their volumes were $V_A, V_B = 100 \text{ dm}^3$, respectively. Two peristaltic pumps delivered solutions into the reaction vessel. Pump A ensured the required volumetric flow rate of acid and pump B dosed base into the reactor. Concentrations of input solutions were $c_A = 0.01 \text{ mol dm}^{-3}$ for acid, and $c_B = 0.01 \text{ mol dm}^{-3}$ for base. The volumetric flow rates of inlet streams were within $[0, 10] \text{ ml s}^{-1}$. The detail non-linear model of CSTR was derived in Holaza et al. (2018). For robust MPC design, the discrete-time domain of the uncertain controlled system was considered. Vertices of the controlled system were the linear state-space systems derived for all combinations of limit values of uncertain parameters. The set of uncertain controlled systems \mathbb{A} was represented by all systems lying in the convex hull of the vertices given by:

$$x(k+1) = A^{(v)}x(k) + B^{(v)}u(k), \quad x(0) = x_0, \quad y(k) = Cx(k), \quad (1a)$$

$$\left[A^{(v)}, B^{(v)} \right] \in \mathbb{A}, \quad \mathbb{A} = \text{convhull} \left(\left\{ \left[A^{(v)}, B^{(v)} \right], \forall v \right\} \right), \quad (1b)$$

where $k \geq 0$ is an element of the discrete-time domain, $x(k) \in \mathbb{R}^{n_x}$ is the real-valued vector of system states, $u(k) \in \mathbb{R}^{n_u}$ are control inputs, $y(k) \in \mathbb{R}^{n_y}$ are system outputs, x_0 is the measured or estimated vector of system initial conditions, $A \in \mathbb{R}^{n_x \times n_x}$ denotes the system-state matrix, $B \in \mathbb{R}^{n_x \times n_u}$ is the matrix of system inputs, $C \in \mathbb{R}^{n_y \times n_x}$ is the matrix of system outputs and $v = 1, \dots, n_v$. Parameter n_v represents the total number of uncertain system vertices. The matrix superscript (v) denotes the v -th vertex system of \mathbb{A} . Function convhull denotes the convex hull that maps original set to the smallest-volume convex set that includes the original set.

The system in (1) was normalized for the robust MPC design. The steady-state values were moved into the origin. The novelty of this experimental case study originates in using two actuators, i.e., the pump feeding the solution of acid and the pump dosing the solution of base into the reactor. The

vector of manipulated variables was defined as $u(k) = [q_A(k) - q_A^s, q_B(k) - q_B^s]^T$ and the vector of unmeasurable system states was $x(k) = [x_A(k) - x_A^s, x_B(k) - x_B^s]^T$. The measurable system output was $y(k) = [\text{pH}(k) - \text{pH}^s]$. The superscript s denotes the steady-state values that correspond with the operation point: $q_A^s = q_A = 5 \text{ ml s}^{-1}$ and $\text{pH}^s = 7$.

The experimental step-response-based identification of CSTR was performed to obtain the uncertain state-space system in (1) suitable for robust MPC design. The behavior of the chemical reactor was significantly non-linear and asymmetric and therefore the sets of upwards and downwards step responses were measured. As two actuators were considered, the step responses were measured as follows: (i) step changes of the volumetric flow rate of acid were done at the fixed volumetric flow rate of base, and (ii) step changes of the volumetric flow rate of base were done at the fixed volumetric flow rate of acid. The normalized step responses were identified to obtain two mathematical models:

$$G_A(s) = \frac{\Delta \text{pH}(s)}{\Delta q_A(s)} = \frac{Z_A}{T_A s + 1} e^{-D_A s}, \quad G_B(s) = \frac{\Delta \text{pH}(s)}{\Delta q_B(s)} = \frac{Z_B}{T_B s + 1} e^{-D_B s}, \quad (2)$$

where G_A, G_B are the transfer functions of the chemical reactor, Z_A, Z_B are the system gains, T_A, T_B are the time constants, and D_A, D_B are the time delays. The subscripts A, B denote the identification subject to the step changes of the volumetric flow rates of acid and base, respectively. The system parameters were identified in the form of interval uncertainties taking into account also the measurement noise to increase the robust control performance. The minimum, maximum and mean values of the parameter intervals are summarized in Tab. 1. The mean values represent the nominal system, i.e., an idealized system with no uncertain parameters. Without loss of the robustness guarantee, the time delays D_A, D_B were neglected, as their values were low in comparison with the associated time constants T_A, T_B . Finally, for the robust MPC design, the experimentally identified parameters of the transfer functions in (2) were transformed into the state-space system in the discrete-time domain (1) considering the sampling time $t_s = 10 \text{ s}$.

3. Robust MPC with Integral Action and State Observer

For robust MPC design, the neutralization chemical reactor was modelled using the state space system in (1). The task was to calculate the gain matrix $F \in \mathbb{R}^{n_u \times n_x}$ of the state-feedback control law: $u(k) = F(k)x(k)$, to ensure the robust stability of the closed-loop system. The feedback law is based on the values of the system states $x(k) \in \mathbb{R}^2$. We measured only one output $y(k)$, i.e., the actual pH value of the solution in the outlet stream. Therefore, the state observer had to be implemented. The Luenberger observer was designed to estimate the vector of system states in each control step. Based on the nominal model of CSTR, the LQR-based strategy was applied to evaluate the optimal matrix of the observer $L \in \mathbb{R}^{n_x \times n_y}$. The weighting matrices were tuned as follows: $Q_L = \begin{bmatrix} 0.5 & 0 \\ 0 & 1 \end{bmatrix}$, $R_L = [0.1]$, to calculate the matrix of the state observer $L = [-1.1646 \quad 2.3917]$. In contrast to the well-known LQG, H_2 and H_∞ -based strategies, the main advantage of the proposed LMI-based robust MPC approach lies in its possibility to respect the constraints on control

Table 1: Identified parameters of the system transfer functions.

value	Z_A [s/ml]	Z_B [s/ml]	T_A [s]	T_B [s]	D_A [s]	D_B [s]
minimum	-2.7	0.7	92.9	94.6	2.9	1.8
mean	-1.5	1.5	137.9	134.2	4.1	3.3
maximum	-0.6	2.3	182.8	174.0	5.3	4.7

inputs and system outputs: $-u_{\text{sat}} \preceq u(k) \preceq u_{\text{sat}}$, $-y_{\text{sat}} \preceq y(k) \preceq y_{\text{sat}}$, $\forall k \geq 0$, where $u_{\text{sat}} \in \mathbb{R}^{n_u}$ and $y_{\text{sat}} \in \mathbb{R}^{n_y}$ are the symmetric boundaries. Moreover, the robust MPC implemented in the receding horizon control fashion significantly reduces the process-model mismatch. Control performance was optimized subject to minimization of the LQR-based quadratic quality criterion $J_{0 \rightarrow n_k} = \sum_{k=0}^{n_k} J(k) = \sum_{k=0}^{n_k} \left(\|x(k)\|_Q^2 + \|u(k)\|_R^2 \right)$, where $Q \in \mathbb{R}^{n_x \times n_x} \succeq 0$, $R \in \mathbb{R}^{n_u \times n_u} \succ 0$ are the weighting matrices, and n_k is the total number of control steps. For the considered robust MPC design procedure, the future performance of the controlled plant was calculated considering the infinity prediction horizon, i.e., $n_k \rightarrow \infty$. The control task was to ensure the offset-free set-point tracking for pH value. Therefore, the state-space system was extended to implement the robust MPC with integral action. Hence, the vector of system states $z \in \mathbb{R}^{(n_x+n_y)}$ was in the form: $z(k) = [x(k) \quad \sum_{i=0}^k e(i)]^T$, where e is the control error given by: $e = w - y$, and $w \in \mathbb{R}^{n_y}$ is the reference value. The technical details how to extend system in (1) using an integrator are in Oravec et al. (2017). The quadratic criterion had to be updated subject to the extended vector z :

$$\tilde{J}_{0 \rightarrow n_k} = \sum_{k=0}^{n_k} \tilde{J}(k) = \left(\|z(k)\|_{\tilde{Q}}^2 + \|u(k)\|_R^2 \right), \quad (3)$$

where $R \in \mathbb{R}^{n_u \times n_u} \succ 0$ is the weighting matrix of the control inputs, i.e., the volumetric flow rates of acid and base, respectively. $\tilde{Q} \in \mathbb{R}^{(n_x+n_y) \times (n_x+n_y)} \succeq 0$ is the weighting matrix for the extended vector of states z , and has the form: $\tilde{Q} = \begin{bmatrix} Q & 0 \\ 0 & Q_I \end{bmatrix}$, where $Q \in \mathbb{R}^{n_x \times n_x} \succeq 0$ is the partial weighting of the proportional controller action and $Q_I \in \mathbb{R}^{n_y \times n_y} \succeq 0$ is the partial weighting of the integral action. From the implementation point of view, it is not the straightforward task to set the weighting matrices of robust MPC, as one needs to tune at least $(n_x + n_y + n_u)$ parameters of the principal diagonals of the matrices Q , Q_I , R in (3). In the considered case of robust MPC design for CSTR, five parameters had to be tuned. The robust MPC designed by Kothare et al. (1996) and extended subject to the integral action solves the following optimization problem in each control step:

$$\min_{\gamma, X, Y, U} \gamma \quad \text{s.t.:} \quad \begin{bmatrix} 1 & \star \\ z & X \end{bmatrix} \succeq 0, \quad \begin{bmatrix} X & \star \\ Y & U \end{bmatrix} \succeq 0, \quad U_{i,i} \leq u_{\text{sat},i}, \forall i \in \mathbb{N}_1^{n_u}, \quad (4a)$$

$$\begin{bmatrix} X & \star \\ \tilde{C}(\tilde{A}^{(v)}X + \tilde{B}^{(v)}Y) & y_{\text{sat}}^2 I \end{bmatrix} \succeq 0, \quad \begin{bmatrix} X & \star & \star & \star \\ \tilde{A}^{(v)}X + \tilde{B}^{(v)}Y & X & \star & \star \\ \tilde{Q}^{1/2}X & 0 & \gamma I & \star \\ R^{1/2}Y & 0 & 0 & \gamma I \end{bmatrix} \succeq 0, \quad (4b)$$

where $v = 1, 2, \dots, n_v$, $i = 1, 2, \dots, n_u$, and the decision variables are: $X \in \mathbb{R}^{n_x \times n_x}$, $Y \in \mathbb{R}^{n_u \times n_x}$, $U \in \mathbb{R}^{n_u \times n_u}$, and $\gamma \in \mathbb{R}^{1 \times 1}$. The matrices A , B , C of the system in (1) extended subject to the integral action were derived in Oravec et al. (2017). The symbol \star denotes the symmetric structure of the matrix. y_{sat}^2 denotes the element-wise power of 2. Technical details of the optimization problem are in Kothare et al. (1996). Then the state-feedback gain-matrix-controller of the control law is $F = YX^{-1}$. Although the nominal system was considered for the state estimation, the robustness of the control performance was ensured through the receding-horizon-based controller design, and the reference tracking was ensured by the integral action.

4. Results and Discussion

To obtain the results comparable to the results of the work Oravec et al. (2017), analogous setup of the robust MPC with integral action was considered, i.e., the laboratory chemical reactor of

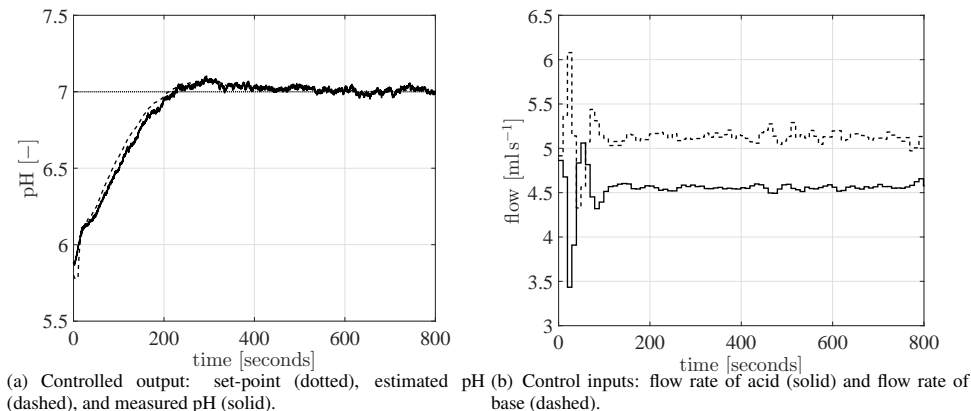


Figure 1: Set-point tracking: increasing step change of the set-point.

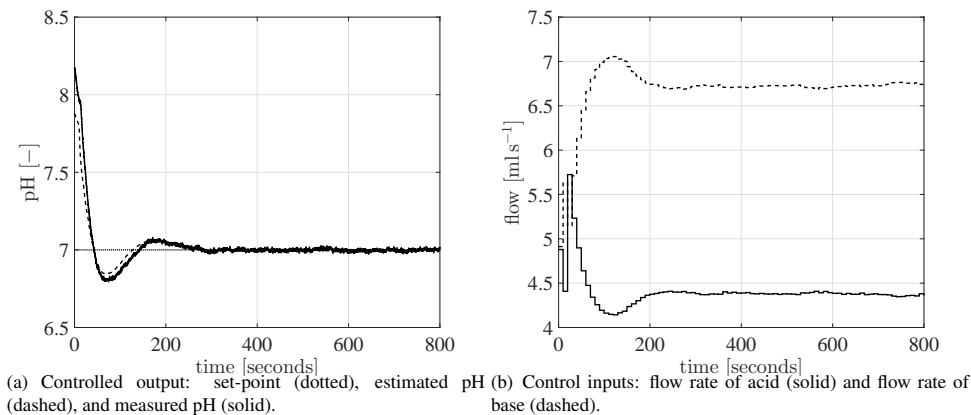


Figure 2: Set-point tracking: decreasing step change of the set-point.

Armfiled PC40 was controlled by CPU i7 3.4 GHz and 8 GB RAM. The robust MPC was implemented using MATLAB/Simulink R2012b environment, and the communication with the plant was ensured by the Real-Time Windows Target v4.1 toolbox. The robust MPC design was provided using MUP toolbox (Oravec et al., 2017), the optimization problem in (4) was evaluated via toolbox YALMIP (Löfberg, 2004), and solved by solver SeDuMi (Sturm, 1999). The sampling time of robust MPC was $t_s = 10.0$ s, meanwhile the plant-computer communication time was $t_c = 0.2$ s. The closed-loop control performance was investigated considering $t_{RMPC} = 800$ s, i.e., the $n_k = 80$ control steps. The matrices in the quadratic criterion in (3) were tuned subject to the matrices Q_L, R_L as follows: $Q = I, Q_I = 10, R = 10 \times I$ with appropriate dimensions, where I is the identity matrix. The constraints on the both manipulated variables and the system output were set to ensure the technical constraints in the controlled chemical reactor. The volumetric flow rates q_A, q_B were within the interval $[0, 10]$ ml s⁻¹, and the value of pH was within the interval $[0, 14]$. So, $u_{\text{sat}} = 5.0$ ml s⁻¹, $y_{\text{sat}} = 7.0$. The closed-loop set-point tracking was investigated for two control scenarios, see Figures 1–2. Figure 1(a) depicts the control performance of pH value for the increasing step change of the set-point value: $6 \rightarrow 7$, and Figure 2(a) shows the results for

the decreasing step change of the set-point value: $8 \rightarrow 7$. The associated control input trajectories are plotted in Figures 1(b), 2(b), respectively. In both control cases, the estimated pH tracks very well the measured pH, see Figures 1(a), 2(a) (dashed). Based on the estimated system states, robust MPC computed the optimal volumetric flow-rates of acid (Figures 1(b), 2(b), solid) and base (Figures 1(b), 2(b), dashed). It is seen in Figures 1–2 that the robust MPC with integral action ensured the offset-free control in both control cases. It has been observed, that for the same value of the set-point, various steady-state inputs were computed. This phenomenon could be caused by the real uncertainties that influence the dynamics of the laboratory reactor, as e.g. not exactly the same concentration of the acid and base solutions and not exactly the same laboratory conditions in different experiments.

5. Conclusion

The laboratory implementation of LMI-based multivariable robust MPC with integral action for the neutralization chemical reactor is presented in the paper. The state observer was used to solve the control task for the controlled process with two control inputs and one measured controlled output. The control performance of the complex non-linear CSTR with asymmetric behaviour was investigated in the set-point tracking problem. The next research is focused on the robust MPC design in economic fashion.

6. Acknowledgements

The authors gratefully acknowledge the contribution of the Scientific Grant Agency of the Slovak Republic under the grants 1/0403/15, 1/0112/16, and the Slovak Research and Development Agency under the project APVV-15-0007.

References

- S. Avraamidou, E. Pistikopoulos, 2017. A multi-parametric bi-level optimization strategy for hierarchical model predictive control. In: 27th European Symposium on Computer Aided Process Engineering. Barcelona, Spain, pp. 1591–1596.
- A. Bemporad, M. Morari, 1999. Robust Model Predictive Control: A Survey. In: Robustness in Identification and Control. Springer London, pp. 207–226.
- T. Chaloupka, A. Zubov, J. Kosek, 2017. Real-time hybrid monte carlo method for modelling of 4 monomer semi-batch emulsion copolymerization. In: 27th European Symposium on CAPE. Barcelona, Spain, pp. 259–293.
- M. Charitopoulos, V. Dua, L. Papageorgiou, 2017. Economic predictive control of a pasterization plant using a linear parameter varying model. In: 27th European Symposium on Computer Aided Process Engineering. Barcelona, Spain, pp. 1273–1278.
- J. Holaza, M. Klaučo, J. Drgoňa, J. Oravec, M. Kvasnica, M. Fikar, 4 January 2018. Mpc-based reference governor control of a continuous stirred-tank reactor. *Computers & Chemical Engineering* 108, 289–299.
- M. V. Kothare, V. Balakrishnan, M. Morari, 1996. Robust Constrained Model Predictive Control Using Linear Matrix Inequalities. *Automatica* 32, 1361–1379.
- J. Löfberg, 2004. YALMIP : A Toolbox for Modeling and Optimization in MATLAB. In: Proc. of the CACSD Conf. Taipei, Taiwan.
- W. L. Luyben, 2007. *Chemical Reactor Design and Control*. John Wiley & Sons, New Jersey, USA.
- J. Maciejowski, 2000. *Predictive Control with Constraints*. Prentice Hall, London.
- J. Oravec, M. Bakošová, L. Hanulová, M. Horváthová, 2017. Design of robust MPC with integral action for a laboratory continuous stirred-tank reactor. In: 21st International Conference on PC. Štrbské Pleso, Slovakia, pp. 459–464.
- F. Pour, V. Puig, O.-M. C., 2017. Closed loop integration of planning, scheduling and control via exact multi-parametric nonlinear programming. In: 27th European Symposium on CAPE. Barcelona, Spain, pp. 1573–1578.
- J. F. Sturm, 1999. Using SeDuMi 1.02, A Matlab toolbox for optimization over symmetric cones. *Optimization Methods and Software* 11, 625–653.
- P. Varbanov, J. Klemeš, F. Friedler, 2017. Challenges and potentials of modelling tools total site integration and utility system optimisation. In: 27th European Symposium on CAPE. Barcelona, Spain, pp. 2545–2550.

Improvement of Synergistic Extraction of Neodymium Ions via Robust Model Predictive Control

Paisan Kittisupakorn^{*}, Wasamon Konaem, Ajaree Suwatthikul

Department of Chemical Engineering, Chulalongkorn University, Bangkok 10330, Thailand

paisan.k@chula.ac.th

Abstract

A neodymium, a high value rare earth element (REE), is widely used as a rare earth magnet. Neodymium magnets (also known as NdFeB) are permanent magnets made of neodymium, iron and boron alloy. These magnets used in several products require low magnet mass or strong magnetic fields such as microphones, in-ear headphones, and computer hard disks. As neodymium is a precious metal, high purity separation of neodymium from low concentrate is required. A hollow fiber supported liquid membrane (HFSLM) is a viable technique for metal extraction at very low concentration because it has a larger mass transfer per unit surface area, high selectivity property, and low energy consumption. Moreover, the HFSLM consumes lower amount of extractant solution than conventional solvent extraction methods. This research is aimed at studying the extraction of neodymium ions Nd(III) through the HFSLM by mean of synergistic extraction systems to increase in extraction efficiency. The separation of Nd(III) in nitric solution is carried out by 0.5 M of di-2-ethylhexyl phosphoric acid (D2EHPA) and 0.5 M of trioctyl phosphine oxide (TOPO) in the liquid membrane, and 1 M of sulfuric acid in the stripping solution. To achieve good separation of the Nd(III) throughout the continuous process, a Model Predictive Control (MPC) technique is applied to control the concentration of extracted neodymium at a desired set point by manipulating the flow rate of feed solution and its control performance is compared with that of a Proportional Integral Derivative (PID) controller. Simulation study has shown that the optimum extraction of 94.5 % can be achieved and the MPC and PID controllers can control the concentration of neodymium ions at the desired set point. However, the MPC provides better control responses than the PID controller does in both nominal and parameter mismatch cases.

Keywords: Model predictive control, Neodymium ions, Synergistic, Hollow fiber supported liquid membrane

1. Introduction

Neodymium, one of rare earth elements, is the raw material used in high-strength permanent magnets (Nd–B–Fe). The separation and purification are hardly achieved because of similar chemical and physical properties of neighboring rare earth elements.

The technique employed in this study is separation via hollow fiber supported liquid membrane (HFSLM). It is the technique that has carrier-mediated transport through HFSLM where simultaneous extraction and stripping process of target ions occurs in a single step operation. The HFSLM process has several advantages, such as low energy

consumption and low amount of extractant solution used. It also has a larger mass transfer per unit surface area (Kittisupakorn et al. 2007, Pancharoen et al. 2010).

In this work, an extraction of neodymium ions by HFSLM that operated in a once-through-mode has been studied. Di-2-ethylhexyl phosphoric acid (D2EHPA) and trioctyl phosphine oxide (TOPO) are used as the mixtures of the synergistic extractant. Sulfuric acid is used as stripping solution. Model predictive control (MPC) is applied to determine the feed flow rate to achieve maximum extraction of the neodymium. Fluid-flow models describing the transport phenomena of neodymium ions at unsteady-state condition were solved by a developed software (Wongsawa et al. 2013).

2. Theory

2.1. Hollow Fiber Supported Liquid Membrane (HFSLM)

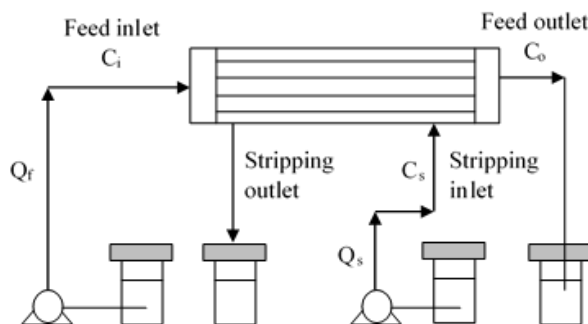


Figure 1 Schematic counter current flow diagram for once-through-mode operation in HFSLM.

The HFSLM system consists of a feed solution (containing metal ions) and a stripping solution. Both feed and stripping phases are separated by a supported liquid membrane embedded with one type of organic extractant or a mixture of two types of extractant to enhance the separation. Figure 1 shows the counter current flow pattern for once-through-mode operation in the hollow fiber supported liquid membrane. The mixture (Q_f) is fed at the feed inlet with the feed concentration (C_i) and the stripping mixture (Q_s) is fed counter-currently.

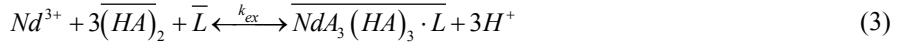
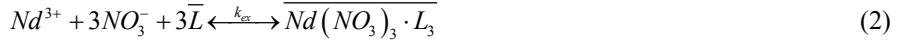
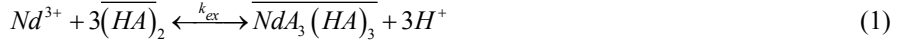
In this work, the liquid membrane phase consists of the mixture of D2EHPA and TOPO, and sulfuric acid is used as stripping solution. The feed solution containing neodymium ions and the stripping solution are generally fed counter-currently in the tube and shell of the hollow fiber module, respectively. The characteristics of the hollow fiber modules are referred to Wannachod et al. 2014.

2.2. Transportation Mechanism of Neodymium Ion in HFSLM

Neodymium ions in the feed solution is reacted with D2EHPA and TOPO (extractant) at the feed membrane interface to form complex substances. Subsequently, the neodymium complex substances diffuse across the liquid membrane to react with sulfuric acid (stripping solution) at the liquid membrane-stripping interface. Then, the neodymium complex substances are stripped into the stripping phase. Thus, neodymium ions can be extracted and stripped simultaneously in a single step, as shown in Figure 2.

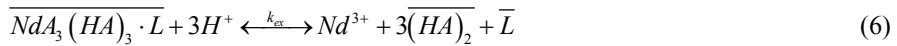
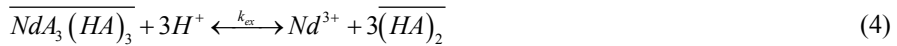
The driving force in this transportation mechanism is the concentration gradient of hydrogen ions, H^+ , between the feed and stripping phases.

Eqs. (1) – (3) show the extraction of Neodymium ions with D2EHPA, TOPO, and synergistic extractants (mixture of D2EHPA and TOPO), respectively.



where the overbar represents the species in the liquid membrane phase, $(HA)_2$ is the dimer form of D2EHPA and k_{ex} is the reaction rate constant of extraction. The neutral donor (L) captures the inorganic anion (NO_3^-) in the feed phase to form the second extractant. Subsequently, it reacts with Neodymium to produce complex ions ($Nd(NO_3)_3 \cdot L_3$).

The stripping reactions involved are summarized in Eqs. (4) – (6).



2.3. Transportation Mechanism of Neodymium Ion in HFSLM

The model in feed phase is developed referred to Wannachod et al. 2014 for predicting the outlet concentration of Neodymium at any time in the feed phase. The model equation was derived from mass conservation where the conventional as well as reaction flux was taken into account, as shown in Eq. (7).

[Rate of mass transport into the system by convection] - [Rate of mass transport out of the system by convection] + [Rate of mass transport through the system by diffusion] - [Rate of mass extracted by extraction reaction] = [Rate of mass accumulation within the system]

$$q_f C_{z-1,i}^k - q_f C_{z,f}^k + \frac{A_{c,f} D_f}{\Delta x} (C_{z,i}^k - C_{z-1,i}^k) - \Delta x A_{c,f} \langle r_{C_{z,i}^k} \rangle = \frac{\Delta x A_{c,f}}{\Delta t} (C_{z,i}^k - C_{z,i}^{k-1}) \quad (7)$$

2.4. Transportation Mechanism of Neodymium Ion in HFSLM

The percentage of Neodymium extraction from experiment can be calculated by Eq. (8).

$$\% \text{Extraction} = \frac{[Nd^{3+}]_{f,in} - [Nd^{3+}]_{f,out}}{[Nd^{3+}]_{f,in}} \times 100 \quad (8)$$

3. Controllers

The control objective is to control the concentration of neodymium ions extracted via the hollow fiber supported liquid membrane. The formulations of the PID and MPC are demonstrated below.

3.1. The concentration control of neodymium ions in feed solution by MPC controller

The basic idea of the MPC controller is to determine the manipulated input profile (q) by minimizing an objective function which is the sum of squares of the deviation of set point and predicted value on output and inputs over the next time step. The general structure of the MPC system is given in Equation (9) - (13).

$$\text{Objective function: } \min \int_0^{120} \left\{ W_1 \left([Nd^{3+}] - [Nd^{3+}]_{sp} \right)^2 + W_2 (\Delta q_f)^2 \right\} dt \quad (9)$$

Subject to

$$\text{State equations: } \dot{X} = f(X(t), U(t)) \quad (10)$$

$$\text{Bound on the manipulate variable: } 50 < q(t) < 300 \quad (11)$$

$$\text{Bound on the control variable: } 0 < [Nd^{3+}]_t < 100 \quad (12)$$

$$\text{Constraint: } [Nd^{3+}]_{(t+t_f)} = 4.12 \quad (13)$$

Where W_1 is a weighting matrix on outputs, W_2 is a weighting matrix on inputs and t_f is final time. The optimization problem is then formulated in the discrete-time via a simple Euler's approach with a step size of 0.01 minutes. Next, the problem is solved by minimizing a constrained nonlinear optimization problem using a MATLAB program.

4. Figures and tables

4.1. The response of the open-loop system

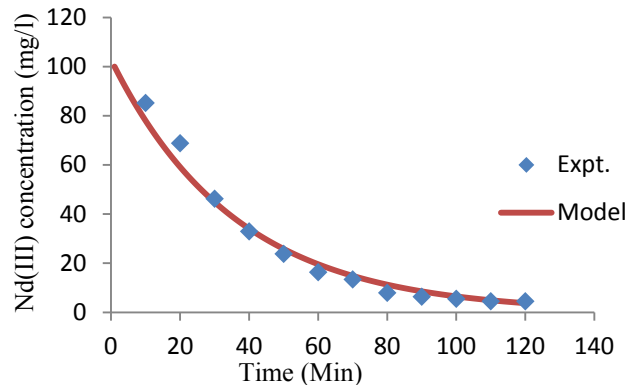


Figure 2 The concentration of neodymium ions in the feed solution at various times

Figure 2 shows the comparison of neodymium concentration in feed solution between experimental data by Wannachod et al. 2014 and simulation data based on the developed model. It was found that the developed model provides good estimates of the neodymium ions concentration in feed solution; the absolute error of 15.68 % is obtained and most discrepancy occurs in the early stages of operation.

4.2. The response of the closed-loop system

Figure 3 and 4 show the response of the process control by PID and MPC controllers respectively. The PID tuning parameters are determined by a Ziegler-Nichols method and then fine-tuned by a trial and error approach. It can be seen that the PID controller can control the concentration of neodymium ions at the set point with the IAE of 2069.5. The manipulated variable, feed flowrate, is adjusted and reduced to a constant value.

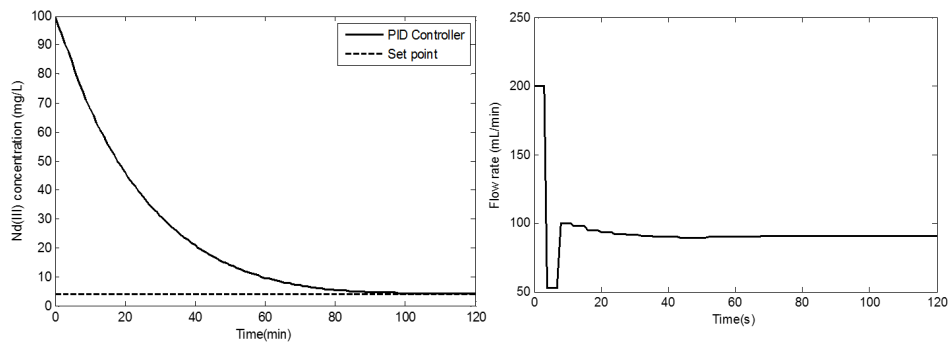


Figure 3 The neodymium ions concentration under the PID controller in the nominal case

The MPC controller can control the concentration of the extracted neodymium ions at the set point with the IAE of 1928.2. and can provide tracking of the set point faster than the PID does.

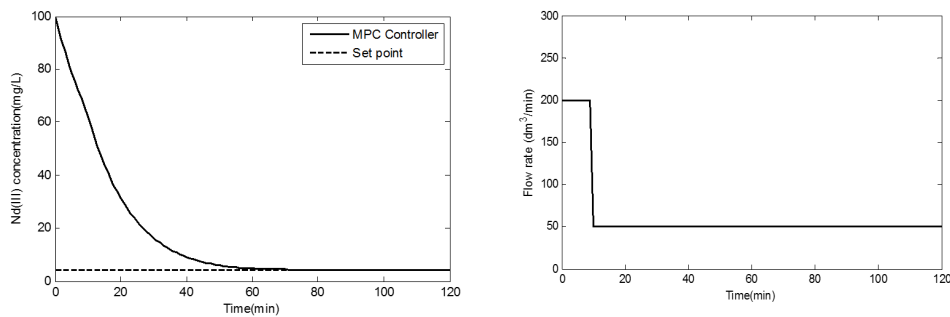


Figure 4 The neodymium ions concentration under the MPC controller in the nominal case

4.3. Effect of the volumetric flowrate in feed solution

The performance and robustness of each controller are evaluated in nominal and parameter mismatch cases. In parameter mismatch cases, three key parameters (cross

sectional area, A , reaction rate constant, k_{ex} , and diffusion coefficient, D_f) are changed of 20 % around the nominal value. It was found that the MPC controller gives better control performance than the PID in the nominal case and is robust in almost all cases as seen in Table 1.

Table 1 Integral Absolute Error of PID and MPC controllers in nominal and parameter mismatches

Case	Integral Absolute Error	
	PID	MPC
Normal case	2069.5	1928.2
A increase 20 %	2015.5	1905.9
A decrease 20 %	2893.0	2859.6
k_{ex} increase 20 %	1735.7	1850.5
k_{ex} decrease 20 %	2527.2	1909.9
D_f increase 20 %	2048.6	1928.2
D_f decrease 20 %	2069.5	1928.3

5. Conclusions

In this work, a hollow fiber supported liquid membrane system has been studied to provide the synergistic extraction of neodymium ions using 0.5M D2EHPA and 0.5M TOPO mixtures and once-through-mode operation. Simulation results of the developed systems are in good agreement with the experimental data reported. Model Predictive Control (MPC) has been applied to control the extracted neodymium at a desired set point and its control performance is compared with the PID one. It was found that both MPC and PID can control the concentration at the set point with achieved optimum extraction of 94.5 %. However, the MPC provides better control response than the PID in both nominal and parameter mismatch cases.

References

- P. Kittisupakorn, et al. (2007). "Modeling and simulation of copper-ion extraction with hollow fiber supported liquid membrane." *Journal of Industrial and Engineering Chemistry*, 13, 903-910.
- U. Pancharoen, et al. (2010). "Selective removal of mercury as $HgCl_4^{2-}$ from natural gas well produced water by TOA via HFSLM." *Journal of Alloys and Compounds*, 489, 72-79.
- T. Wannachod, et al. (2014). "Synergistic effect of various neutral donors in D2EHPA for selective neodymium separation from lanthanide series via HFSLM." *Journal of Industrial and Engineering Chemistry*, 20, 4152-4162.
- T. Wongsawa, et al. (2013). "Fluid-flow models operating on linear algebra for extraction and stripping of silver ions from pharmaceutical wastewater by HFSLM." *Chemical Engineering Journal*, 222, 361-373.

New continuous-time scheduling formulation for multilevel treelike pipeline systems

Pedro M. Castro^{a*}, Hossein Mostafaei^b

^a*CMAFCIO, Faculdade de Ciências, Universidade de Lisboa, Lisboa, Portugal*

^b*Dep. Applied Mathematics, Azarbaijan Shahid Madani University, Tabriz, Iran*

pmcastro@fc.ul.pt

Abstract

We propose a mixed-integer linear programming formulation for scheduling treelike systems with unidirectional flow. Refined products are converted to batches as they enter the pipeline so as to facilitate modeling the movement between pipeline segments. The novelty is the handling of multilevel branches, frequent in practice as illustrated with a real-life case study. Through the solution of three benchmark problems from the literature, we show that the new formulation is capable of finding better solutions in less time than a state-of-the-art product-centric formulation.

Keywords: Optimization; Petroleum industry; Iranian pipelines; Computational logistics.

1. Introduction

In the oil supply chain, refined petroleum products are frequently transported from refineries to distribution centers by pipeline. Multiproduct pipelines range from the simplest configuration with an input node at one extreme and an output node at the other, to complex treelike and mesh structures with multiple input and output nodes. Flow is typically unidirectional but systems with reversible flow can also be encountered. Batches pumped from a refinery take different routes, may increase/decrease in size while passing through input/output nodes, pipeline segments vary in diameter and some product sequences are forbidden. These features turn it into one of the most challenging scheduling problems.

Research on pipeline scheduling can be divided into product- (Rejowski and Pinto, 2003; Magatão et al., 2004) and batch-centric approaches (Cafaro and Cerdá, 2004; Relvas et al., 2006; MirHassani and Jahromi, 2011; Cafaro and Cerdá, 2011; Mostafaei and Ghaffari-Hadigheh, 2014; Mostafaei et al. 2016). Batch-centric models have the advantage of requiring fewer continuous-time slots to represent a schedule, a parameter strongly related to computational performance. It is because multiple batches/products can enter/leave a segment during a slot (Mostafaei and Castro, 2017) compared to just one product in the models by Castro and Mostafaei (2017) and Castro (2017). The disadvantages are that forbidden product sequences cannot be rigorously enforced, we need to postulate the total number of batches, and properly assign the initial products in the pipeline to batches, to avoid losing the optimal solution (Mostafaei and Castro, 2017). The latter is no longer an issue in systems without intermediate input nodes, like in the treelike configuration considered here.

In this work, we extend the batch-centric model for straight pipelines of Mostafaei and Castro (2017) to generic treelike systems. This is a modular and simpler approach than

other batch-centric models in the literature. The reason for returning to batch-centric models after developing the most general formulation for pipeline systems (Castro, 2017), is that the latter failed to solve in reasonable time, a treelike problem with eight segments, one refinery and six output nodes, a tractable problem with the formulation by Mostafaei et al. (2015), which however cannot handle systems with multilevel branches.

2. Motivating problem

The Tabriz-Urmia pipeline in Iran starts in Tabriz refinery (R1) and conveys three oil products (gasoline, kerosene and gasoil) to three cities, Maragheh (depot D1), Miandoab (D2) and Urmia (Figure 1). The 278-km trunk line connecting Tabriz to Urmia City (D3) is wider in diameter (10.8 inches) until Miandoab, decreasing to 8'' in the last 138 km. As a consequence, the operating flowrate range decreases from $[90, 164]$ to $[70, 120]$ m^3/h . The line has multiple branches, one to connect to Maragheh (through segment S2) and a two-level branch to connect to the power plant (D4) and petrochemical complex (D5) in Urmia. The pipeline is operated by the Iranian Oil Pipelines and Telecommunication Company (IOPTC), which delivered the volumes given in Table 1 in the first week of November 2017, except for D4. We added 1000 m^3 of gasoil to force the activation of segment S7 so as to validate our model for multilevel treelike systems.

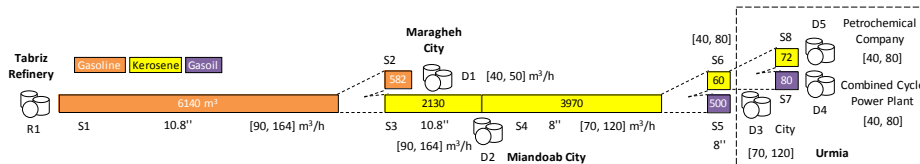


Figure 1. The Tabriz-Urmia Iranian pipeline.

Table 1. Problem data for motivating problem

Product/Destination	D1	D2	D3	D4	D5
Gasoline (P1)	800	2400	4600	-	-
Kerosene (P2)	900	2100	4000	-	1800
Gasoil (P3)	800	3000	3500	1000	-

The real-life problem was solved with the objective of minimizing makespan while respecting the flowrate bounds on the different segments. The schedule in Figure 2 considers $|T|=13$ event points and $|I|=6$ batches, and features a makespan of 161.405 h. Notice the simultaneous product delivery to two or more depots and that supply sometimes exceeds demand (e.g. 950.7 m^3 of P2 in D1). The schedule shows the refinery operating at the maximum flowrate of 164 m^3/h , during 80.9% of the time.

Unfortunately, this schedule cannot be implemented in practice since gasoil cannot immediately follow gasoline (check S2 during $[61.04, 74.27]$ h), i.e. P1-P3 (also P3-P1) are forbidden product sequences. The model given next, has a constraint to avoid forbidden sequences at injection points but they can still occur at delivery points.

3. Mathematical model

The mathematical formulation adopts a continuous-time representation with a single reference grid consisting of $|T|$ event points, i.e. $|T|-1$ time slots (Mostafaei and Castro,

2017). The makespan MS will be the absolute time of the last event point, Eq. (1), with Eq. (2) relating the absolute time (T_t) and slot duration variables (L_t).

$$\min T_{|T|} \quad (1)$$

$$T_{t+1} = T_t + L_t \quad \forall t \neq |T| \quad (2)$$

We consider a treelike system with a single input node and multiple output nodes. Let binary variable $X_{i,t}^R=1$ if the refinery is pumping batch i during slot t . Exactly one batch is injected during a slot, Eq. (3). Eq. (4) states that the injected volume $F_{i,t}^R$ must be within minimum and maximum values (given parameters). We also need to define disaggregated variables $F_{i,p,t}^{R,d}$ to relate batches with the actual products p , Eq. (5). Eq. (6) enforces the flowrate out of the refinery to be within given lower ($\rho_p^{R,\min}$) and upper bounds ($\rho_p^{R,\max}$), where h is the given time horizon (upper bound on the makespan). To save space, we do not show the depot constraints, which are similar to Eqs. (3)-(6).

$$\sum_i X_{i,t}^R = 1 \quad \forall t \neq |T| \quad (3)$$

$$f_p^{R,\min} X_{i,t}^R \leq F_{i,t}^R \leq f_p^{R,\max} X_{i,t}^R \quad \forall i, t \neq |T| \quad (4)$$

$$F_{i,t}^R = \sum_p F_{i,p,t}^{R,d} \quad \forall i, t \neq |T| \quad (5)$$

$$\sum_i \sum_p \frac{F_{i,p,t}^{R,d}}{\rho_p^{R,\max}} \leq L_t \leq \sum_i \sum_p \frac{F_{i,p,t}^{R,d}}{\rho_p^{R,\min}} + h \cdot (1 - \sum_i X_{i,t}^R) \quad \forall t \neq |T| \quad (6)$$

A batch needs to be linked to exactly one product, Eqs. (7)-(8). From the initial products in the pipeline, the user defines old batches (I^{old}) and parameters $y_{i,p}$ (e.g. $y_{I1,P3} = y_{I2,P2} = y_{I3,P1} = 1$, in Figure 1). The total number of batches specified by the user, $|I|$, will also include new batches I^{new} , with assignment variables $Y_{i,p}$. Assignment of a product to a batch needs to be associated to the injection of a minimum amount of product, to avoid dummy batches, see left side of Eq. (9). The delivery to depots in Eq. (10) only features the upper bound since we need to account for the possibility of the last injected batch(es) to not leave the pipeline. Notice the additional depot index d in disaggregated variables $F_{d,i,p,t}^{D,d}$.

$$\sum_p Y_{i,p} = 1 \quad \forall i \in I^{new} \quad (7)$$

$$Y_{i,p} = y_{i,p} \quad \forall i \in I^{old}, p \quad (8)$$

$$f_p^{P,\min} Y_{i,p} \leq \sum_{t \neq |T|} F_{i,p,t}^{D,d} \leq f_p^{P,\max} Y_{i,p} \quad \forall i, p \quad (9)$$

$$\sum_d \sum_{t \neq |T|} F_{d,i,p,t}^{D,d} \leq f_p^{P,\max} Y_{i,p} \quad \forall i, p \quad (10)$$

Forbidden sequences at the injection point can be avoided by Eq. (11), where $p' \in P_p$ indicates that p' cannot follow p . Since batches can take different routes, it is possible for batch $i+2$ featuring p' to immediately follow i (product p) at some delivery node d . Thus, forbidden sequences may still appear, e.g. I3 (P1) and I5 (P3) in Figure 2 ([61.04, 74.27]).

$$Y_{i,p} + \sum_{p' \in P_p} Y_{i+1,p'} \leq 1 \quad \forall i, p \quad (11)$$

We assume that the refinery is connected to the left of segment S1 (by convention, flow goes from left to right in the diagrams), and so the volume entering the segment ($F_{s,i,t}^{S,in}$) is equal to the volume leaving the refinery, Eq. (12). When branching, the volume leaving

segment s must be equal to the sum of the volumes entering the branches (and depot). In Eq. (13), subsets S_s and D_s hold respectively the segment branches of s and the depot located at its end. Eq. (14) ensures that if batch i is delivered to depot d during slot t ($X_{d,i,t}^D=1$), then i is the only batch leaving the segment during t ($X_{s,i,t}^{S,out} = 1$); otherwise multiple batches can leave. While multiple batches can enter a segment, we cannot allow this to happen simultaneously in branches s' and s'' originating from s . This is the same as saying that if batch i enters s' , no other batch i' can enter s'' , see Eq. (15).

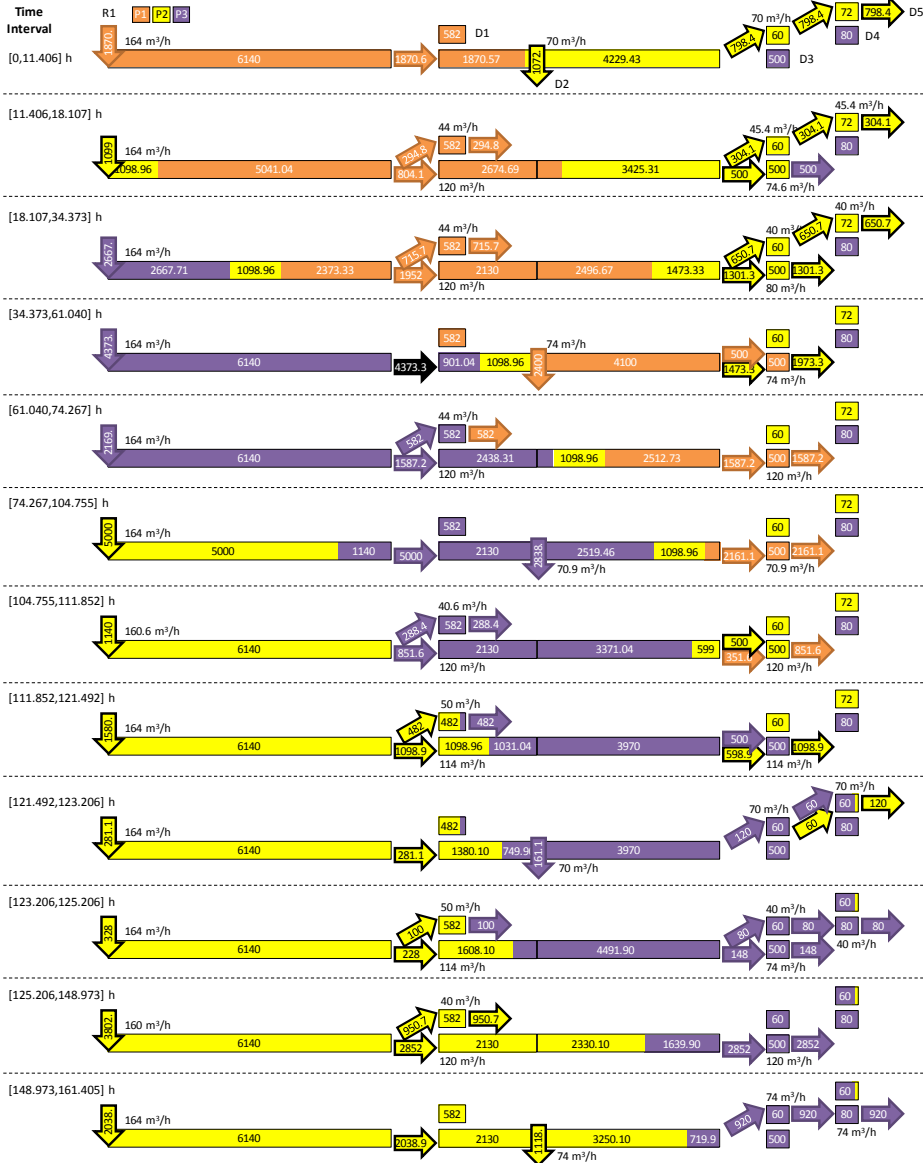


Figure 2. Best-found schedule for real-life motivating problem ($|T|=13$ and $|I|=6$).

$$F_{S_1,i,t}^{S,in} = F_{i,t}^R \quad \forall i, t \neq |T| \quad (12)$$

$$F_{S,i,t}^{S,out} = \sum_{s' \in S_s} F_{s',i,t}^{S,in} + \sum_{d \in D_s} F_{d,i,t}^D \quad \forall s, i, t \neq |T| \quad (13)$$

$$\sum_i X_{S,i,t}^{S,out} \leq 1 + (|I_s| - 1) \cdot (1 - \sum_i X_{d,i,t}^D) \quad \forall s, d \in D_s, t \neq |T| \quad (14)$$

$$X_{S,i,t}^{S,in} + X_{s',i',t}^{S,in} \leq 1 \quad \forall s, s' \in S_s, s'' \in S_s, s'' \neq s', i, i' \neq i, t \neq |T| \quad (15)$$

Other constraints are needed to model what goes on inside a pipeline segment. Since they are shared with Mostafaei and Castro (2017), they are omitted due to lack of space.

4. Computational results

The performance of the proposed batch-centric continuous-time formulation is evaluated on three benchmark problems from the literature involving single-level treelike systems (Mostafaei et al., 2015). It is compared to the product-centric formulation of Castro (2017), which is able to solve Ex1 and Ex2 in reasonable time but not the motivating problem neither Ex3, since it requires too many event points to represent the schedule (intractable problem). The new formulation was implemented in GAMS 24.9.2 and solved with CPLEX 12.7 running in parallel deterministic mode using up to eight threads. The termination criteria were either a relative optimality tolerance of 10^{-6} or a maximum wall time limit of 18,000 CPUs. The hardware consisted of a Windows 10, 64-bit desktop with an Intel i7-4790 (3.6 GHz) processor and 8 GB of RAM.

By allowing multiple products to enter/leave a segment during a time slot, our new batch-centric formulation generates at least the same solution as the product-centric formulation for a given number of event points ($|T|$), see results in Table 2. Since this a parameter strongly affecting computational time, it means we can further explore the solution space, ending up with better solutions for Ex1 and Ex2 (151.43 vs. 162 h). For Ex3, we even know that the solution is the global optimum, since the makespan of 125.25 h is equal to the value of the LP relaxation, which does not change with $|T|$. Our formulation does need an additional parameter, the total number of batches ($|I|$), but we found that it only affected solution quality until finding the first feasible solution. It is thus not as critical as for systems with multiple input nodes (Hosseini and Castro, 2017). Analysis of the schedules for Ex1-Ex3 did not show forbidden sequences in the pipeline system.

5. Conclusions

This paper has presented a new batch-centric continuous-time formulation for scheduling multilevel treelike systems with a single input and multiple output nodes, motivated by a real-life problem from the company responsible for operating the Iranian pipelines. We have shown that the new monolithic formulation can cope with a weekly demand plan but still requires additional constraints to enforce forbidden product sequences in all pipeline segments after the first. They will be part of the extended version of this paper. For this specific system configuration, it is significantly more powerful than the most general formulation for pipeline scheduling.

References

- D.C. Cafaro, J. Cerdá, 2004, Optimal Scheduling of Multiproduct Pipeline Systems using a Non-discrete MILP Formulation, *Comp. Chem. Eng.* 28, 2053.

- D.C. Cafaro, J. Cerdá, 2011, Optimal Scheduling of Multi-level Tree-structure Pipeline Networks, *Computer Aided Chemical Engineering* 29, 980.
- P.M. Castro, 2017, Optimal Scheduling of Multiproduct Pipelines in Networks with Reversible Flow, *Ind. Eng. Chem. Res.* 56, 9638.
- P.M. Castro, H. Mostafaei, 2017, Product-centric Continuous-time Formulation for Pipeline Scheduling, *Comp. Chem. Eng.* 104, 283.
- L. Magatão, L.V.R. Arruda, F. Neves Jr., 2004, A mixed Integer Programming Approach for Scheduling Commodities in a Pipeline, *Comp. Chem. Eng.* 28, 171.
- S.A. MirHassani, H.F. Jahromi, 2011, Scheduling Multi-product Tree-structure Pipelines, *Comp. Chem. Eng.* 35, 165.
- H. Mostafaei, A. Ghaffari-Hadigheh, 2014, A General Modeling Framework for the Long-Term Scheduling of Multiproduct Pipelines with Delivery Constraints, *Ind. Eng. Chem. Res.* 53, 7029.
- H. Mostafaei, P.M. Castro, 2017, Continuous-Time Scheduling Formulation for Straight Pipelines, *AIChE J.* 63, 1923.
- H. Mostafaei, P.M. Castro, A. Ghaffari-Hadigheh, 2015, Novel Monolithic MILP Framework for Lot-Sizing and Scheduling of Multiproduct Treelike Pipeline Networks, *Ind. Eng. Chem. Res.* 54, 9202.
- H. Mostafaei, P.M. Castro, A. Ghaffari-Hadigheh, 2016, Short-term Scheduling of Multiple Source Pipelines with Simultaneous Injections and Deliveries, *Comp. Oper. Res.* 73, 27.
- R. Rejowski, J.M. Pinto, 2003, Scheduling of a Multiproduct Pipeline System, *Comp. Chem. Eng.* 27, 1229.
- S. Relvas, H.A. Matos, A.P.F.D. Barbosa-Póvoa, J. Fialho, A.S. Pinheiro, 2006, Pipeline Scheduling and Inventory Management of a Multiproduct Distribution Oil System, *Ind. Eng. Chem. Res.* 45, 7841.

Table 2. Computational statistics

Model		This work				Castro (2017)*	
Problem	LP relaxation (h)	T	I	MS (h)	CPUs	MS (h)	CPUs
Motivating	151.83	12	6	190.75	15302	-	-
		13	6	161.41	18000	-	-
Ex1	135	10	7	140	264	Infeas.	306
		11	7	138.33	1955	138.33	704
		12	7	136.67	4969	138.33	11004
		13	7	136.67	12733	-	-
Ex2	145	10	7	170	250	Infeas.	1285
		11	7	160	851	162	3126
		12	7	155.71	15887	164.29	18000
		13	7	151.43	18000	-	-
Ex3	125.25	11	7	136.25	1578	-	-
		12	7	129.09	14639	-	-
		13	7	125.25	864	-	-

*CPLEX 12.6.3, Intel i7-6400K and same termination criteria.

Tackling the complexity of designing multiproduct multistage batch plants with parallel lines: the application of a cooperative optimization approach

Floor Verbiest^{a,*}, Trijntje Cornelissens^a and Johan Springael^a

^a*ANT/OR - Operations research group, Dpt. of Engineering Management, University of Antwerp, Prinsstraat 13, Antwerp 2000, Belgium
floor.verbiest@uantwerpen.be*

Abstract

Over the last decade, cooperative optimization approaches, that combine metaheuristics with exact methods, have been attracting a lot of interest to solve mixed integer linear programming (MILP) problems. In this paper, we present such a hybrid technique for the batch plant design problem with parallel production lines. The aim of this MILP problem is to minimize capital and setup costs through the optimization of 3 decisions: the number of lines to install on the plant, their design, and the assignment of products and production quantities to the installed lines. These different types of decisions lead to a natural separation of the global problem into subproblems, each of which can be solved with adequate solution methods. More specifically, we applied an iterative local search (ILS) metaheuristic for the discrete design decisions for every stage of every line, whereas the product-to-line assignments are optimized with an exact MILP solver. We present a case study of a lubricant plant to compare the performance of the proposed methodology to an exact method, and to illustrate its operation. We found that our cooperative optimization approach obtained very good solutions in significantly lower computing time.

Keywords: batch plant design, cooperative optimization, hybrid metaheuristics, parallel lines

1. Introduction

Over the past decades metaheuristics have been very successful in solving combinatorial optimization problems. Especially in real-life situations, where the dimensionality of the problem becomes too large to solve the problem by means of an exact method within a reasonable amount of time, metaheuristics have proven to be very powerful (Sörensen and Glover, 2013). Also for the multiproduct batch plant design problem successful metaheuristics such as e.g. simulated annealing (Patel et al., 1991) and genetic algorithms (Dedieu et al., 2003) were developed.

Although metaheuristics do exist to tackle optimization problems involving continuous variables (see e.g. Mladenović et al. (2008)), these methods are not so well adapted. On the contrary, exact methods perform extremely well for (linear) optimization problems involving no discrete variables. Hence, in case of a MILP, it could be rewarding to combine both techniques: a metaheuristic and an exact method. This is referred to as a cooperative optimization approach.

In this paper we present such a cooperative optimization approach for the batch plant design problem extended for parallel production lines as introduced in Verbiest et al. (2017). This optimization problem involves 3 decisions: number of lines to install, their design, i.e. number and size of equipment units at every stage (out of a discrete set of options), and assignment of products and produc-

tion quantities to the installed lines, where a product may be assigned to multiple lines (product duplication). The existence of these different types of decisions leads to a natural separation of the global optimization problem into subproblems. This is the main idea behind the cooperative approach presented here: to split the optimization problem into easier to solve subproblems and to exploit the characteristics of every subproblem. Indeed, we start with a metaheuristic framework to solve one of the subproblems. The hereby obtained solution is then used as an input to another subproblem, solved by an exact mathematical programming method. This results into another part of the global solution, which is fed back as a context to solve again the subproblem by means of a metaheuristic. This type of cooperative approach is called a (hierarchical) decomposition approach (Ball, 2011), of which the application in the context of the batch plant design problem is rather limited (Xi-Gang and Zhong-Zhou, 1997).

In Section 2 of this paper, a brief description of the multiproduct batch plant design problem with parallel lines is presented. In Section 3, the cooperative optimization approach, developed for this problem, is discussed. The performance of our approach is illustrated in Section 4 through a case study of a lubricant plant, and we end with some conclusions in the last section.

2. Problem formulation: design of a multiproduct batch plant with parallel production lines

We consider a multiproduct plant designed for a multistage process. More specifically, P products i are to be produced over J stages j , where every stage performs a batch operation. There is the possibility to install at most L production lines l on the production site, each consisting of the same stages J . The demand for every product and the total production horizon are known upfront, as well as the characteristic size factors and the fixed batch processing times. The main assumptions are: at most N identical parallel batch equipment per stage, operating out-of-phase; a discrete set of S equipment sizes for all stages to choose from and operation in single product campaign mode.

We formulated an MILP model to determine the optimal design of a plant that should be large enough to produce all products within the given horizon. The aim is to minimize the total cost, which consists of capital, startup and contamination costs. Due to space limitations, only the objective function is presented here (see Verbiest et al. (2017) for a description of the entire model):

$$\min \left[\sum_{l=1}^L \sum_{j=1}^J \sum_{n=1}^N \left(\sum_{s=1}^S c_{js} z_{ljn} u_{ljs} + \sum_{i=1}^P C_{start_i} z_{ljn} t_{li} + \sum_{f=1}^F C_{cont} b_{fl} g_l z_{ljn} \right) \right]$$

The first term defines the capital costs, with c_{js} the stage dependent cost coefficients for equipment of size s . The binary z_{ljn} indicates if unit n of stage j of line l exists and binary u_{ljs} defines if units of stage j of line l have size s . The second term represents the startup costs for preparing the equipment units at the start of every series of batches of product i . We assumed a given product dependent startup cost (C_{start_i}) and the binary t_{li} that indicates if product i is produced on line l . Finally, the last term is the contamination cost. Products with similar characteristics are often grouped into product families and the fixed contamination cost C_{cont} is a penalisation for producing multiple families on 1 line. Binary b_{fl} defines if product family f is produced on line l , and the binary g_l is introduced to avoid a contamination cost when there is a single family on a line. This nonlinear goal function is linearized using known techniques.

3. Overview of the cooperative optimization approach

As introduced, we have implemented a cooperative optimization approach, hereafter referred to as COA-design, in which the problem is decomposed into 3 subproblems: determining the number of lines to install, their design, and the assignment of products to the installed lines. Specific solution methods are applied to the different subproblems. More specifically, the COA-design proceeds

according to the following steps. At first, the number of lines is fixed in an incremental manner (from 1 to L) with after every incrementation an evaluation of the absolute lower bound in terms of costs, to exclude too large and thus too expensive plants. Next, for every feasible given number of lines, the optimal design and product-to-line assignments are determined by iteratively solving both problems, until an optimal combination is found.

More explicitly, for every given number of lines, a first product-to-line assignment is based on grouping products by product families, so as to minimize the contamination cost. After determining the optimal design for this first assignment, the product assignment is re-optimized by keeping this design fixed. This is repeated until an optimal combination is found, meaning that we can not find a new assignment or design anymore that lowers total costs. To escape from this (local) optimal combination, a perturbation step is performed in which a certain percentage of products are reassigned (via simple rules) to another line. With this new assignment, the iterative procedure is started again. After a certain number of perturbations, which is determined experimentally, without an improvement of the best solution for this number of lines, we compare this solution with the best solution found so far and, if needed, update the latter. Then, we increment the number of lines and restart the procedure.

The solution method applied for the product-to-line assignment subproblem for a fixed design, meaning binaries $z_{l,jn}$ and u_{ljs} are given, is an MILP calculation. On the contrary, to optimize the discrete design decisions when the product assignment is given, an iterated local search metaheuristic (ILS) is used (Lourenço et al., 2010). This ILS starts with a maximal plant layout as the initial solution, to ensure feasibility. This means that for every stage of every line the maximal number of units and the largest sizes are chosen. To improve this solution, two different move types are considered: for a specific stage, decrease the number of units with 1 or decrease the equipment size. The selection of the move type is done randomly, with a higher chance of decreasing the number of units (as this has the largest impact on the objective function). A steepest descent strategy is used to pick, out of all stages, the stage to perform the move on. When no more improvements can be made, a local optimal solution is found which is compared to the cheapest design found so far. To escape from this local optimum, a perturbation step is performed in which a certain percentage of stages get again the maximum number of units or largest sizes. The entire procedure is repeated until a certain number of perturbations is reached without an improvement of the best solution.

During the development of this COA-design, we noticed that when the assignment involves product duplication over the lines, the above ILS is not the most suitable technique to determine the design. Indeed, with product duplication, the constraint calculation, i.e. checking if the performed move, and thus new design, is feasible, is more complex and requires an LP-solver to determine the (continuous) amounts of these duplicated products for every line. Since a steepest descent strategy is used, the LP-solver is called for every stage before a move is made. In fact, the numerous number of calls made to the LP-solver takes longer than a 1-time call to solve the MILP problem exactly for a given product-to-line assignment (variable t_{li}). Hence, the use of ILS is less effective. Analogous conclusions can be drawn for the assignment problem: intuitively, one would expect the binary t_{li} to be determined heuristically. However, the number of product combinations, duplication yes or no and if yes, over how many lines, leads again to (too) many evaluations of new assignments, justifying the use of 1 MILP calculation. The iterative optimization procedure for a given number of lines, together with the eventual chosen solution methods to solve both subproblems, is visualized in Figure 1.

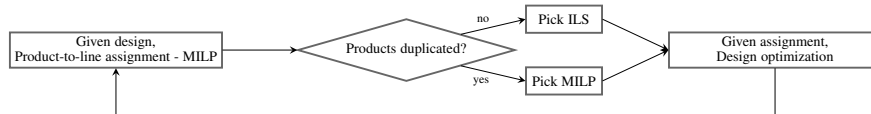


Figure 1: Iterative optimization procedure, and solution methods used, to determine the optimal assignment and design for a given number of lines

4. Case study: design of a lubricant plant

In this section, the performance and operation of the COA-design is discussed via an example of a lubricant plant.

4.1. Process description and solution

We assume a lubricant plant that has to produce the demand for 35 lubricants, belonging to 3 product families, within a given horizon. A single product campaign mode of operation is assumed. The production process consists of 5 stages, and equipment sizes can be chosen out of a discrete set of 5 options. The plant surface area allows for the installation of at most 6 parallel lines and 4 units per stage, operating out-of-phase. The main production data are summarized in Table 1.

Table 1: Main data case study - lubricant plant

Demand data (in kg): range between 3000 - 35,000 Horizon H (in h) = 6500
Cost coefficients: Capital costs: $\alpha_j = \{468, 357, 168, 402, 286\}$; $\beta_j = \{0.47, 0.49, 0.61, 0.43, 0.46\}$ Startup costs: 750 Contamination costs: 3000
Product families: 3 $Pf_1 = \{1, 3, 5, 9, 14, 16, 23, 25, 27, 28, 32, 35\}$ $Pf_2 = \{2, 4, 8, 11, 13, 17, 19, 20, 21, 26, 30, 33\}$ $Pf_3 = \{6, 7, 10, 12, 15, 18, 22, 24, 29, 31, 34\}$

We solved this example for the minimization of case (a) only capital costs, and case (b) capital and setup costs. Table 2 compares the results for an exact method and our COA-design. For the COA-design, we report the best solutions found over 10 runs, and the time needed. The exact solutions were found solving the entire MILP problem with Gurobi Optimizer 7.0 and are aborted after 24 h of CPU-time. In such a case, the best solution found so far is reported. As can be seen, the COA algorithm provides very good solutions in significantly lower computation time. For case (a) the exact solver could not solve the problem up to optimality after 24 h, and found the current best solution in 25,918 s (7 h). The same solution was found with our COA-design in only 2.5 % of the time (639.67 s). For case (b), the optimal solution was found by both methods, but again in significantly less time with the COA-design. The average gap, being the gap between the goal function value obtained by the exact method and its average over 10 runs of the COA-design, is in both cases small. This implies a low variation in solution quality. The last three columns of the table provide some details on the problem sizes.

Table 2: Results for minimization of (a) capital and (b) capital and setup costs

	Sol. Gurobi	CPU (s-Gurobi)	Sol. COA-design	avg.gap (%)	CPU (s-COA-design)	Vars.	Bin. Vars	Const.
(a) Capit.	116,708 (gap:12%)	24 h	116,708	0.8	639.67	13,410	1230	38,626
(b) Capit.Setup.	278,551	19,345	278,551	0.0	13.92	18,354	6174	44,188

All numerical results were obtained using an Intel(R) Core(TM) i7-4790 CPU, 3.60GHz and 16 GB of RAM

In Table 3 the chosen designs for the two cases are presented, and the corresponding product-to-line assignments are shown in Table 4. For case (a), it is optimal to install 2 parallel lines and there is product duplication for products 3 and 34. When including setup costs in case (b), it appeared optimal to install an extra production line so that product families can be grouped and a single line is used for every product. This is at the expense of a higher capital cost (+26 %).

Table 3: Solution at minimum (a) capital and (b) capital and setup cost

	(a) Capit. costs = 116,708		(b) Capit.Setup. costs = 278,551 (with Capit.:147,301)		
	line 1 size (numb)	line 2 size (numb)	line 1 size (numb)	line 2 size (numb)	line 3 size (numb)
stage 1	1000 (1)	1600 (1)	800 (1)	1000 (1)	1000 (1)
stage 2	1000 (1)	1800 (1)	1000 (1)	1000 (1)	800 (1)
stage 3	1200 (1)	1400 (1)	1000 (1)	1000 (1)	800 (1)
stage 4	1400 (1)	1800 (1)	1200 (1)	1400 (1)	1000 (1)
stage 5	1400 (1)	1800 (1)	1200 (1)	1200 (1)	800 (1)

Table 4: Product-to-line assignment for (a) capital and (b) capital and setup cost

Product assignment (a) capital costs	
line 1	2, 3, 4, 13, 14, 17, 18, 19, 20, 21, 22, 24, 28, 31, 32, 34
line 2	1, 3, 5, 6, 7, 8, 9, 10, 11, 12, 15, 16, 23, 25, 26, 27, 29, 30, 33, 34, 35
Product assignment (b) capital and setup costs	
line 1	2, 4, 8, 11, 13, 17, 19, 20, 21, 26, 30, 33
line 2	6, 7, 10, 12, 15, 18, 22, 24, 29, 31, 34
line 3	1, 3, 5, 9, 14, 16, 23, 25, 27, 28, 32, 35

4.2. Progress of the COA-design approach

The progress of our COA-design is presented in Figure 2 for the minimization of capital costs and in Figure 3 for the minimization of capital and setup costs. The blue crosses *perturbed-design* refer to the design solutions found after the initial product-to-line assignments based on product family grouping or after the perturbation step (shuffling of products over the lines). *MILP-design* are the solutions found for the design problem with the exact solver (Gurobi) whereas *ILS-design* refers to the design solutions found with the ILS metaheuristic. Finally, *MILP-assignment* stands for the optimal product-to-line assignments found with the exact solver. The figures show the total cost associated with every solution and the L-points mark the start of the iterative optimization procedure for every new (incremented) number of lines.

A first observation when comparing the two figures is the difference in total running time. In case (b), our COA-design reaches the stopping criterion after 13.92 s whereas in case (a), it takes 639.67 s. This is for a great extent due to the application of the ILS metaheuristic in case (b) to solve the design problems. Indeed, in case (a), it appeared that the optimal product-to-line assignment in every iteration has duplicated products. Hence, the design problem (MILP) is always (except for 1 time) solved using the exact solver. The horizontal distance between the *MILP-assignment* solution (red dots) and the *MILP-design* solution (green triangles) in Figure 2, so the time needed to solve the MILP-design problem, is on average larger than the distance between the *MILP-assignment* solution and the *ILS-design* solution (green squares) in Figure 3. Furthermore, case (a) and (b) stop after investigating respectively 2 and 3 lines. This means that for more lines the minimum costs associated with these plants would already be higher than the best cost found so far. Thirdly, it is apparent that the progress in case (b) is much more volatile than in case (a). After every product-to-line perturbation, a much worse solution is found and larger drops are achieved when optimizing the assignments. This indicates the influence of the setup costs on obtaining the optimal solution. When minimizing only capital costs, much more product combinations and possibilities for spreading production quantities over multiple lines can be considered.

Finally, from Figure 3, and verified by Table 4, it can be seen that the optimal solution is the one where products are grouped into product families on equipment. As after every line incrementation, this is the initial assignment to start the iterative procedure from, the first design found with this assignment (*perturbed-design*) when 3 lines are investigated is the optimal one.

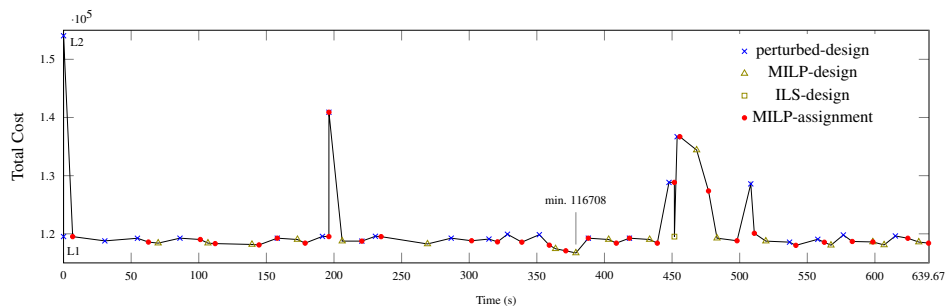


Figure 2: Case (a)-progress of COA-design for capital costs (best solution: 116,708)

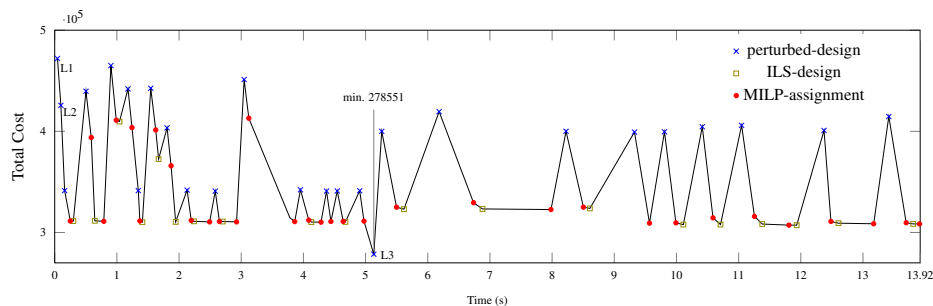


Figure 3: Case (b)-progress of COA-design for capital and setup costs (best solution: 278,551)

5. Conclusion

In this paper, we described a cooperative optimization approach for the batch plant design problem with parallel production lines. In this MILP problem, the decisions to optimize are 3-fold: number of lines to install, their design and the product-to-line assignment with corresponding production quantities. As this problem consists of different types of decisions, a cooperative optimization approach (COA-design), that separates the different decisions and exploits their individual characteristics, seemed a useful technique. More specifically, the first decision is to fix the number of lines in an incremental manner. Then, for every given number of lines, the design and assignment subproblems are iteratively solved, until an optimal combination is found. The solutions of the former are considered given in the latter, and vice versa. The solution methods applied for both subproblems are exact MILP calculations for the assignment problem and an exact MILP calculation and an ILS metaheuristic for the design problem. The performance of our proposed optimization approach is illustrated through a case study of a lubricant plant. From this example, we can conclude that our approach found very good solutions in significantly lower computation times. Moreover, also the search process of the COA-design was analyzed. This showed that the application of the ILS metaheuristic as well as a calculation reduction strongly contribute to the efficiency of our COA-design. Given the good performance of our approach, a possible progression of this work is to investigate its application for more extended batch plant design problems, such as e.g. considering multiple objectives.

6. Acknowledgements

This work was supported by the Research Foundation - Flanders (FWO).

References

- M. O. Ball, 2011. Heuristics based on mathematical programming. *Comput. Oper. Res. (SORMS)* 16 (1), 21–38.
- S. Dedieu, L. Pibouleau, C. Azzaro-Pantel, S. Domenech, 2003. Design and retrofit of multiobjective batch plants via a multicriteria genetic algorithm. *Comp. & Chem. Eng.* 27 (12), 1723–1740.
- H. R. Lourenço, O. C. Martin, T. Stützle, 2010. Iterated local search: Framework and applications. In: M. Gendreau, J.-Y. Potvin (Eds.), *Handbook of Metaheuristics*. Springer US, pp. 363–397.
- N. Mladenović, M. Dražić, V. Kovačević-Vujčić, M. Čangalović, 2008. General variable neighborhood search for the continuous optimization. *Eur. J. of Oper. Res.* 191 (3), 753–770.
- A. N. Patel, R. S. H. Mah, I. A. Karimi, 1991. Preliminary design of multiproduct noncontinuous plants using simulated annealing. *Comp. & Chem. Eng.* 15 (7), 451–469.
- K. Sörensen, F. W. Glover, 2013. *Metaheuristics*. Springer US, Boston, MA, pp. 960–70.
- F. Verbiest, T. Cornelissens, J. Springael, 2017. Design of a chemical batch plant with parallel production lines: Plant configuration and cost effectiveness. *Comp. & Chem. Eng.* 99, 21–30.
- Y. Xi-Gang, C. Zhong-Zhou, 1997. A hybrid global optimization method for design of batch chemical processes. *Comp. & Chem. Eng.* 21, Supplement, S685–S690, suppl. to 6th International Symposium on PSE and 30th ESCAPE.

Customized detailing of plant simulations with regard to different applications

Florian Pöllabauer^a, Gerald Bachmann^b and Thomas Wallek^{a,*}

^a*Graz University of Technology, Institute of Chemical Engineering and Environmental Technology, Inffeldgasse 25 C, 8010 Graz, Austria*

^b*OMV Refining and Marketing GmbH, Trabrennstraße 6-8, 1020 Vienna, Austria*
thomas.wallek@tugraz.at

Abstract

This paper emphasizes the use of graphs for model analysis and simplification within industrial flowsheet simulators. A procedure for developing a complexity measure for models based on weighted cycles and paths in attributed graphs is highlighted. This procedure uses an interface to the process simulator for graph generation. The novel complexity measure serves as the basis for a model reduction approach using attributed graphs and is applied to the real industrial example of an ethylene plant model.

Keywords: flowsheet simulation, model reduction, graph theory

1. Motivation

The use of commercial process simulation tools is state of the art in chemical engineering. Their applications range from simple mass balances in basic or conceptional design to real-time optimization during operation, case studies for retrofit of existing equipment or assessment of alternative operating modes of existing compound systems such as refineries. Because in every stage of chemical engineering projects simulation models are developed for a specific purpose, model reuse or integration of plant models into enterprise or site-wide models pose a challenge. Especially if utility supply is to be analyzed in addition to production plants, a holistic approach is required. By adding these additional points of consideration, the models themselves need to be simplified, which implies the question of how to conceptualize a model that is as accurate as required, but as simple as possible. This paper aims at systematically describing the impacts of severe model simplifications on prediction quality and proposes a novel decision support for model simplification based on graph theory.

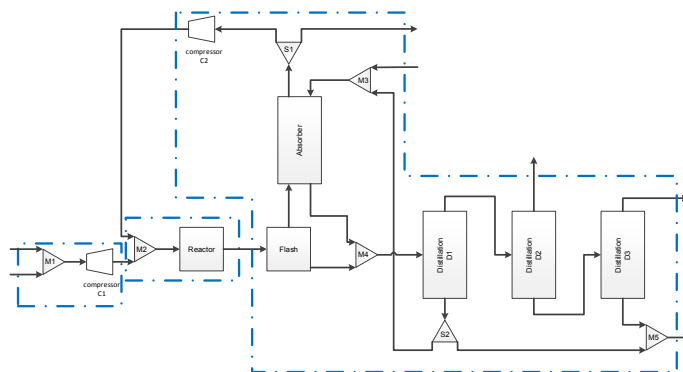
2. Graphs in chemical engineering

While graph or network theory is currently experiencing increasing popularity in connection with social networks (Barabasi (2016)), it has a long history with chemical engineering. The broad applicability of graphs in chemical engineering has been highlighted by Mah (1983). Surma and Braunschweig (1996) are using graph representations to develop similarity measures for flowsheets.

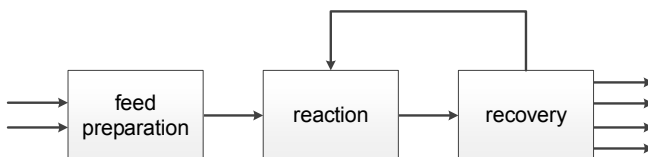
Graph theory has been applied for analysis of large scale systems in chemical industry with focus on mathematical modeling (Mangold et al. (2002)), visual modeling (Preisig (2014b)), Preisig

(2015)) or for closing mass and energy balances or describing pressure distribution in plant operation (Preisig (2007), Preisig (2014a)). In contrast, this work focuses on describing models of industrial flowsheet simulators.

Graphs and model simplification have been addressed by Dones and Preisig (2009) lumping trays in distillation columns in order to obtain a simplified model. This concept is extended to a lower level of detail where unit operations in a simulator may be lumped or neglected as illustrated by the example given in Biegler et al. (1997). For black box splitter models, the real system is decomposed into sub-systems. Figure 1a shows an example of a process consisting of a reactor, the feed preparation and the purification of the products.



(a) detailed flowsheet



(b) Block flow diagram

Figure 1: (a): Balance envelopes in the detailed flowsheet. (b): Block flow diagram. After Biegler et al. (1997)

These three main parts can be grouped to three blocks (see Figure 1b), as illustrated by the balance envelopes. In this case there is only one recycle stream, in contrast to the original representation with two recycles. This aggregation could even be further simplified to only one black box, the total process. In process simulation these blocks are commonly modeled using subflowsheets or even further simplified by black box components splitters. All three representations describe the same process but have different properties, which can easily be visualized and analyzed using graphs.

3. Approach

Previous work has developed a graph theoretic methodology for the reduction and optimization of the modeling depth of flowsheet models. Within the present paper this simplification strategy is extended and validated using the real industrial application of integrating an ethylene plant model into a refinery wide model. Graph theory provides a very general framework for the representation

of networks, in the present case applied to networks of unit operations in chemical plants. In this case all unit operations or aggregated black boxes are considered as nodes whereas any streams of mass, energy or information are regarded as links, as proposed by Gilles (1998). In contrast, the P-graph approach developed by Friedler et al. (1992) considers both operating units and process streams as nodes.

It is assumed that the setup of a model is mainly determined by

- the selection of representative sub-systems or elements of a model that can range from single molecules or phases over equilibrium stages to black box aggregations of unit operations or plants and
- the calculation method that is used to simulate these model elements, e.g. rigorous column, shortcut column or component splitter.

Each of these model elements interacts with another by exchanging streams of material, energy or information. As illustrated in Figure 2, this procedure results in a attributed graph (for basic examples see Bothorel et al. (2015)), that represents a meta-model (in terms of a model of a model) describing the flowsheet model in the process simulator.

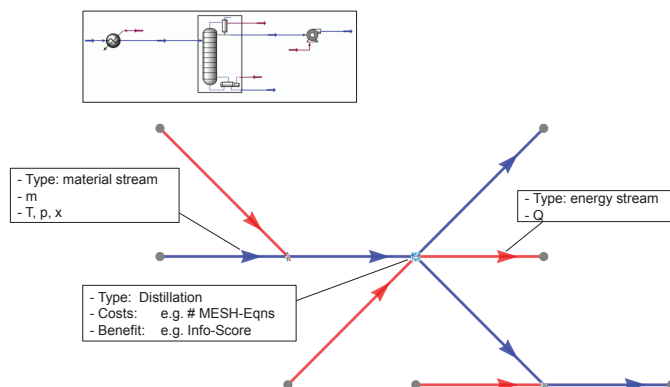


Figure 2: Attributed graph of a simple distillation flowsheet

Based on these graphs, different key figures are calculated and combined to a complexity measure that can be used as a target criterion of a simplification algorithm.

The term complexity is widely used in literature having many different meanings ranging from complex mixtures over complex column configurations to time and space complexity of algorithms. For the complexity and entropy of graphs, extensive reviews (Boccaletti et al. (2006), Costa et al. (2007)) and applications (Han et al. (2012), Holzinger et al. (2014), Kim and Wilhelm (2008), Dehmer and Mowshowitz (2011)) are available.

Common simplification strategies are based on aggregating nodes (unit operations) or identifying main links, that remain in a simplified graph. This can be achieved by

- using the mass flow as additional information as weight of edges and removing edges with a weight below a threshold value (see Fig. 3a, skeletal reduction),
- by weighting the edges according to their similarity to a reference main product of the plant (see Fig. 3b, main product cuts) or
- via searching graph communities or graph partitions and merge them to a black box.

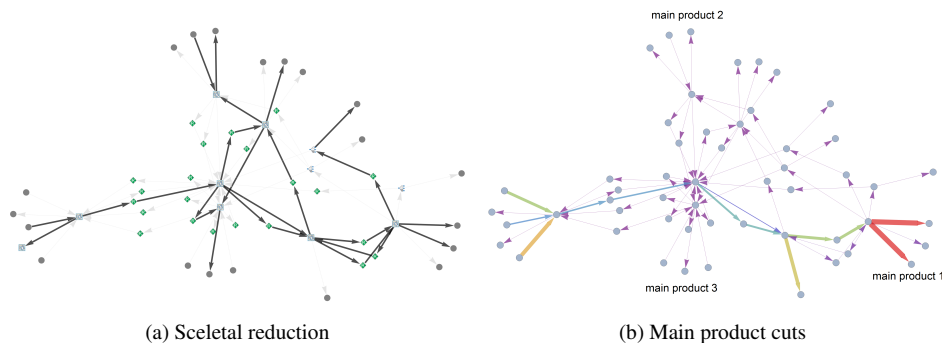


Figure 3: (a): Sceletal reduction of a flowsheet graph inspired from reaction mechanism reduction (Lu and Law (2005)). Gray links have a mass flow below threshold, black links remain in simplified graph. (b): Visualization of main product cuts in a graph. Link style indicates the contribution of the representing stream to a main product

4. Methodology

In order to rate modeling alternatives, representative sub-flowsheets are selected, for which all suitable permutations in the modeling concept of each unit operation (e.g. rigorous column, shortcut column or component splitter) and possible aggregations of multiple unit operations to a single black box component splitter are investigated. Within this procedure for generating modeling alternatives constant temperature and pressure or composition of the main products of each unit operation serve as constraints for changes in the calculation method.

For all these models j graphs are generated in Wolfram Mathematica using an interface to KBC Petro-SIMTM. In addition to calculating standard graph measures, cycles and paths are searched and categorized for each graph. Along these cycles and paths, statistics that rate unit operations according to costs (number of MESH-equations) and benefits (rating of information obtained) of the simulation are applied. This procedure yields a set of n graph measures m comprising standard graph measures and chemical engineering expert knowledge. Under the assumption that a linear combination of these measures

$$C_j = \sum_{i=1}^n m_{i,j} \cdot w_i \quad (1)$$

approximates the costs of solving the flowsheet, which are represented by the calculation time, the investigated models are compared manually according to the expected simulation costs. Within this assessment for every model a corresponding model is selected, that only differs in the simulation method of one unit operation (e.g. rigorous column or shortcut column), which implies the hypothesis that one model is more complex than the other.

The resulting set of inequalities, $C_j > C_{j+1}$, is then solved using linear programming. For each pair of models $\Delta m_{i,j,j+1} = m_{i,j} - m_{i,j+1}$ and a penalty variable $d_{j,j+1}$ is defined.

The linear program minimizes the sum of penalties

$$\sum_{j=1}^{p-1} d_{j,j+1} \quad (2)$$

constrained that

$$\begin{pmatrix} \Delta m_{1,1,2} & \Delta m_{2,1,2} & \dots & \Delta m_{n,1,2} & 1 & 0 & \dots & 0 \\ \Delta m_{1,1,3} & \Delta m_{2,1,3} & \dots & \Delta m_{n,1,3} & 0 & 1 & \dots & 0 \\ \vdots & \vdots & \ddots & \vdots & \vdots & \vdots & \ddots & \vdots \\ \Delta m_{1,p-1,p} & \Delta m_{2,p-1,p} & \dots & \Delta m_{n,p-1,p} & 0 & 0 & \dots & 1 \end{pmatrix} \cdot \begin{pmatrix} w_0 \\ w_1 \\ \vdots \\ w_n \\ d_{1,2} \\ d_{2,3} \\ \vdots \\ d_{p-1,p} \end{pmatrix} \geq \begin{pmatrix} 0 \\ 0 \\ \vdots \\ 0 \\ 0 \\ 0 \\ \vdots \\ 0 \end{pmatrix} \quad (3)$$

For validation a test sequence is carried out with all models, where the calculation time as well the deviation from real operating data is monitored. It is shown that a linear combination of graph measures is capable of predicting influences of model set up on calculation time and prediction quality. The effective use of the methodology is demonstrated by an exemplary model reduction tasks of an ethylene plant (Figure 4).

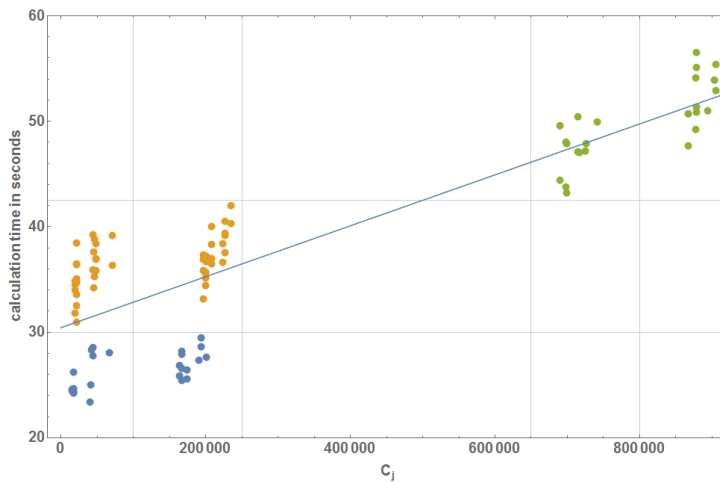


Figure 4: Calculation times of a feed variation test sequence for 96 modeling alternatives of a C3 splitter flowsheet plotted versus a complexity measure obtained from linear programming

The clusters in Figure 4 show that

- in the time-dimension on the ordinate: the real calculation time is determined by the model setup, as models within one clusters share the same simulation method for key unit operations
- in the complexity-dimension on the abscissa: the linear program successfully distinguishes between them.

5. Conclusions

The developed algorithm yields simplification proposals comparable to those of experienced professional engineers, providing a decision support for model set-up for large scale flowsheet models.

The authors admit that sophisticated knowledge management systems in process analysis, such as OntoCAPE developed by Morbach et al. (2007), cover even more information on models. However, the simple concept of unit operations connected by streams in a graph is easy to understand and visualize for application orientated software users that are not familiar with system theory or ontology.

In a next step the use of multiple linear regression for predicting the calculation time or deviations from real measurements is to be carried out as an alternative to linear programming.

References

- A.-L. Barabasi, 2016. *Network Science*. Cambridge University Press.
- L. T. Biegler, I. E. Grossmann, A. W. Westerberg, 1997. *Systematic Methods of chemical Process Design*. Prentice Hall PTR.
- S. Boccaletti, V. Latora, Y. Moreno, M. Chavez, D.-U. Hwang, 2006. Complex networks: Structure and dynamics. *Physics Reports* 424 (4-5), 175–308.
- C. Bothorel, J. D. Cruz, M. Magnani, B. Micenková, 2015. Clustering attributed graphs: Models, measures and methods. *Network Science* 3 (3), 408 – 444.
- L. d. F. Costa, F. A. Rodrigues, G. Traverso, P. R. Villas Boas, 2007. Characterization of complex networks: A survey of measurements. *Advances in Physics* 56 (1), 167–242.
- M. Dehmer, A. Mowshowitz, 2011. A history of graph entropy measures. *Information Sciences* 181 (1), 57 – 78.
- I. Dones, H. A. Preisig, 2009. Graph theory and model simplification. case study: distillation column. In: J. Jeowski, J. Thullie (Eds.), 19th European Symposium on Computer Aided Process Engineering. Vol. 26 of *Computer Aided Chemical Engineering*. Elsevier, pp. 767 – 772.
- F. Friedler, K. Tarjn, Y. Huang, L. Fan, 1992. Graph-theoretic approach to process synthesis: axioms and theorems. *Chemical Engineering Science* 47 (8), 1973 – 1988.
- E. D. Gilles, 1998. Network theory for chemical processes. *Chemical Engineering & Technology* 21 (2), 121–132.
- L. Han, F. Escolano, E. R. Hancock, R. C. Wilson, 2012. Graph characterizations from von neumann entropy. *Pattern Recognition Letters* 33 (15), 1958 – 1967, graph-Based Representations in Pattern Recognition.
- A. Holzinger, M. Hörtenhuber, C. Mayer, M. Bachler, S. Wassertheurer, A. J. Pinho, D. Koslicki, 2014. *On Entropy-Based Data Mining*. Springer Berlin Heidelberg, Berlin, Heidelberg, pp. 209–226.
- J. Kim, T. Wilhelm, 2008. What is a complex graph? *Physica A: Statistical Mechanics and its Applications* 387 (11), 2637 – 2652.
- T. Lu, C. K. Law, 2005. A directed relation graph method for mechanism reduction. *Proceedings of the Combustion Institute* 30 (1), 1333 – 1341.
- R. S. Mah, 1983. Application of graph theory to process design and analysis. *Computers & Chemical Engineering* 7 (4), 239 – 257.
- M. Mangold, S. Motz, E. Gilles, 2002. A network theory for the structured modelling of chemical processes. *Chemical Engineering Science* 57 (19), 4099 – 4116.
- J. Morbach, A. Yang, W. Marquardt, 2007. OntoCAPE - a large-scale ontology for chemical process engineering. *Engineering Applications of Artificial Intelligence* 20 (2), 147 – 161, special Issue on Applications of Artificial Intelligence in Process Systems Engineering.
- H. A. Preisig, 2007. A graph-theory-base approach to the analysis of large-scale plants. In: V. Plesu, P. S. Agachi (Eds.), 17th European Symposium on Computer Aided Process Engineering. Vol. 24 of *Computer Aided Chemical Engineering*. Elsevier, pp. 81 – 86.
- H. A. Preisig, 2014a. A graph approach to representing the pressure distribution in complex plants. In: J. J. Kleme, P. S. Varbanov, P. Y. Liew (Eds.), 24th European Symposium on Computer Aided Process Engineering. Vol. 33 of *Computer Aided Chemical Engineering*. Elsevier, pp. 865 – 870.
- H. A. Preisig, 2014b. Visual modelling. In: M. R. Eden, J. D. Siirola, G. P. Towler (Eds.), *Proceedings of the 8th International Conference on Foundations of Computer-Aided Process Design*. Vol. 34 of *Computer Aided Chemical Engineering*. Elsevier, pp. 729 – 734.
- H. A. Preisig, 2015. Model reduction in visual modelling. In: K. V. Gernaey, J. K. Huusom, R. Gani (Eds.), 12th International Symposium on Process Systems Engineering and 25th European Symposium on Computer Aided Process Engineering. Vol. 37 of *Computer Aided Chemical Engineering*. Elsevier, pp. 629 – 634.
- J. Surma, B. Braunschweig, 1996. Case-base retrieval in process engineering: Supporting design by reusing flowsheets. *Engineering Applications of Artificial Intelligence* 9 (4), 385 – 391.

Risk assessment for the design and scheduling optimization of periodic multipurpose batch plants under demand uncertainty

Miguel Vieira^a, Helena Paulo^{a,b}, Corentin Vilard^c, Tânia Pinto-Varela^{a*}, Ana Paula Barbosa-Póvoa^a

^a*CEG-IST, Instituto Superior Técnico, Universidade de Lisboa, Av. Rovisco Pais, 1, 1049-001 Lisboa, Portugal*

^b*ISEL, IPL, Rua Conselheiro Emídio Navarro, 1959-007 Lisboa, Portugal*

^c*INP-ENSIACET, Department of Chemical Engineering, 4, allée Emile Monso 31030 Toulouse, France*

**tania.pinto.varela@tecnico.ulisboa.pt*

Abstract

The aim of the present work is to provide an integrated decision support approach for the design and scheduling of multipurpose batch plants under demand uncertainty allowing the assessment of alternative risk profile solutions. Based on two-stage mixed integer linear programming (MILP) model, the goal is to maximize the annualized profit of the plant operation under a set of scenarios while minimizing the associated financial risk, evaluated by the Conditional Value at Risk (*CVaR*) using the augmented ε -constraint method. Considering a literature example, the conclusions highlight the advantages of the proposed approach for the decision-support in industrial plant design and scheduling solutions by considering the explicit risk measure assessment towards expected financial outcomes

Keywords: Multipurpose batch plants, risk assessment, conditional value-at-risk, stochastic programming, augmented ε -constraint method.

1. Introduction

One of the most important issues in the management of current industrial processes relates to the uncertainty level of most operational parameters. This uncertainty typically arises from the demand market variability, which impacts on the resources availability, equipment efficiency and capacity reliability (Shah, 2005). One of the major research topics relies in the complexity of industrial design and scheduling decisions, where several works have focused on optimal modelling solutions that can encompass the overall supply chain (Cardoso et al., 2016). The design flexibility of multipurpose batch plants in uncertain environments has also been addressed, as noted by Pinto-Varela et al. (2009), with the use of stochastic models to compare expected performance to a deterministic approach. However, most of these works do not provide the analysis of the alternative possible outcomes by assessing different risk management profiles, since stochastic models optimize the total expected performance assuming that the decision maker is risk-neutral. As one of few examples, the work by Bonfill et al. (2004) has addressed the short-term scheduling of batch plants incorporating the solution trade-offs between risk and profit at the decision level. By allowing to evaluate

alternative scheduling policies for different scenarios, it becomes a highly valuable tool to identify the best strategy according to the decision makers' attitude toward risk. A similar analysis has not yet been performed for the simultaneous design and scheduling of batch plants.

In this work, a modelling approach to the design and scheduling of multipurpose batch plants is simultaneously addressed considering demand uncertainty, where a risk measure optimization is evaluated against the annualized profit performance maximization. For the scope of this study, was find suitable the risk measure given by the Conditional Value at Risk (*CVaR*), which is explicitly modelled into the stochastic programming problem. A bi-objective model is formulated using the augmented ε -constraint method (Mavrotas, 2009) to generate an approximation to the Pareto-optimal curve and the obtained results for an industrial literature example are discussed.

2. Methodology

The problem under study consists in determining plant design and scheduling decisions at a project level, evaluating the risk associated to the demand uncertainty. Several methods exist to model with uncertainty, such as stochastic programming, fuzzy programming or robust optimization. In this study, we considered as baseline the stochastic two-stage mixed integer linear programming (MILP) model proposed by Pinto-Varela et al. (2009), based on the adapted Resource Task Network (RTN) framework with a discrete-time representation. This model was extended to consider simultaneously the two objective functions with augmented ε -constraint method, the maximization of the economic profit performance and the minimization of the financial risk. Given the plant and process data for a set of products, the model determines the plant configuration and process schedule with an optimal economic and risk performance for the planning horizon, suitable according to risk profile of decision-maker (for further model detail please check the seminal paper). In this two-stage stochastic optimization approach, each uncertain parameter is considered as a random variable with an associated probability distribution, and the decision variables are classified into two stages. In this case, the products demand is considered in a scenario tree which presents the advantage of allowing the discretization of the stochastic data and provide a flexible approach that can be adjusted during the planning horizon. In the scenario tree, a node represents a possible state and the arcs the different evolutions it may have, where each node has a specific probability (pb_s) for the corresponding state occurrence and the path from the root node to a leaf node represents a scenario.

To integrate the risk assessment in the model, and acknowledging that several measures could be considered, as noted by Conejo et al. (2010), for this study we have considered the *CVaR* as a coherent risk management approach. *CVaR* allows to evaluate the likelihood that a specific loss will exceed a certain value at risk (*VaR*), which is the minimum profit obtained for a given confidence level. Eq. (1) shows the objective function that describes the annualized profit performance (*PR*) deducting the plant costs, namely operating cost (*OC*), raw material costs (*RMC*) and capital cost ($CC*CCF$) over all of the scenarios for planning horizon *H* and cycle time *T*. For discrete distributions, *CVaR* is defined as the weighted average between *VaR* and the expected profit lower than *VaR*. Rockafellar and Uryasev (2002) defined the linear approximation of *CVaR* shown in Eq. (2), where *a* represents the confidence level between 0 and 1 defined by the decision maker, and δ_s measures the positive difference between the *VaR* and the profit obtained in each scenario.

$$Max Profit = (PR - OC - RMC) \cdot \frac{H}{T} - CC \times CCF \tag{1}$$

$$Min CVaR_a = Var + \frac{1}{1-a} \sum_s pb_s \times \delta_s \tag{2}$$

3. Case study

3.1. Problem definition

In order to apply the previously described methodology, the risk assessment to support the optimal design and scheduling of a multipurpose batch plant with a periodic mode of operation of an industrial example available from literature is solved, considering a horizon of 720 h with a cycle of 10 h. The objective is to define the optimal design and the operating schedule for a plant where five products (S5, S6, S9, S10, and S11) are produced using three raw materials (S1, S2, and S7) by the appropriate equipment, reactors (R) and storage vessels (V) accordingly to the product recipe illustrated on Figure 1, in order to maximize profit. The plant costs are defined by a fixed and variable terms and expressed in monetary units (c.u.), while the demand uses a maximum variable range in mass units (m.u.), and the design capacity is defined in terms of mass units per square meter (mu/ m²). Detailed information about the process data can be found in the seminal work by Pinto-Varela et al. (2009).

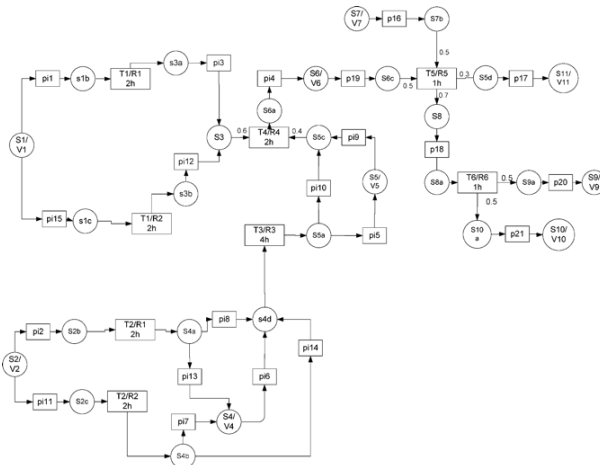


Figure 1. Products' recipe from Pinto-Varela et al. (2009)

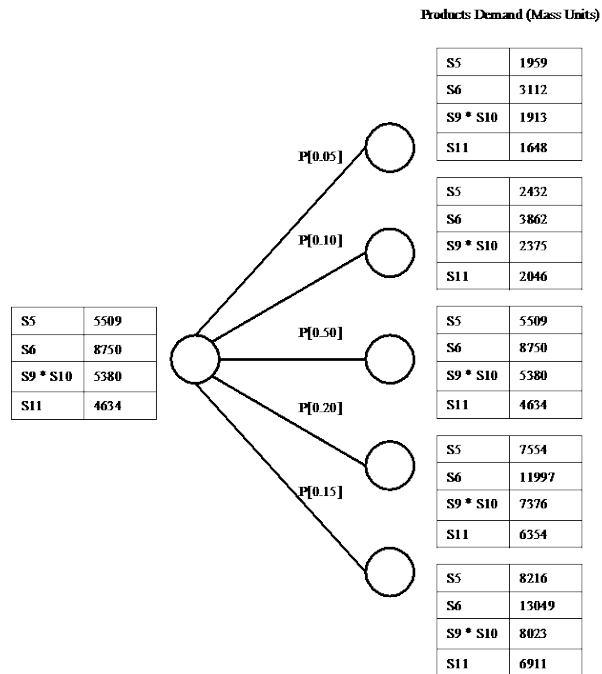


Figure 2. Scenario tree with demand uncertainty

For the given problem, the modelling approach describes the uncertainty in products demand as a scenario tree displayed in Figure 2. The uncertainty in demand is assumed

known for the actual market conditions and a total of five scenarios are considered as possible demand patterns for the next time period. The expected product demand for each scenario and respective probabilities were determined by discretizing a probability distribution function based on historical data to forecast the market trends.

Acknowledging the main objective of the proposed approach as to provide the decision maker with an enhanced decision assessment that enables the trade-off evaluation between risk and profit, the bi-objective model generates the Pareto optimal curve subject to the analysis of the alternative solution. The model was implemented in GAMS (24.5.6 ver.), using CPLEX (12.6.2 ver.) solver in an Intel(R) Xenon(R) CPU ES-2660v3 @2.60GHz with 64GB RAM and a 1% optimality gap as stopping criteria.

For the given illustrative example, three different cases are tested, analysed and compared: (1) one that considers the products demand as a deterministic information; (2) a second study that considers the demand uncertainty in a stochastic approach without considering a risk measure (risk-neutral); (3) and finally, a study that evaluates the results regarding the trade-off between the expected profits and the associated financial risk using *CVaR* as a risk measure, where two extreme scenarios are analysed in more detail: higher profit has a high risk (risk prone); and a lower profit has a lower risk (risk averse).

3.2. Results

In order to compare the results for each case, we focus on the analysis of the expected profit value (or profit value for the deterministic case) and the decision variables related with the equipment selection and capacity utilization. These results are summarized in Table 1. Due to the extent of problem example, in this study we focus only on the reactors design and capacities, given that only reactors R1 and R2 are multitask. Else, each storage vessel is dedicated to a single task and are always required to production, with a designed capacity that verifies the mass balance restrictions dedicated to storage of intermediate and final products produced in the different reactors.

Considering the deterministic approach, it is possible to observe a profit of 191 408 c.u. and a design structure that includes the installation of the reactor R1, R3, R4, R5, and R6. The stochastic problem (risk neutral), presents a value for the expected profit of 202 380 c.u., whereas some reactors are required to install considerable different capacities. The increase on the capacity for reactors R1 and R4 is, respectively, 61% and 49%, and the reduction for reactors R3, R5, and R6 is approximately 30%.

Now considering the integration *CVaR* to make possible to evaluate the likelihood of obtain a profit value lower than the *VaR*, i.e. the minimum expected plant profit for a given confidence level for a given time period. To obtain the *VaR*, it is necessary to compute the model for each scenario of demand and build the cumulative distribution function, as shown in Figure 2. It is noted that for scenario 1, that corresponds to the lower products demand, the profit is 65% lower than the deterministic solution, though in each demand scenario the profit exhibits steady variations from 67 410 to 285 103 c.u. For the given case with a confidence level of 95%, the determined *VaR* value is 83 856 c.u., meaning that, at the end of time horizon with a 95% of probability, the plant profit of the design and scheduling solution is going to be, at least, that value. Using this value, the Pareto-optimal curve using *CVaR* as a risk measure was obtained, shown in Figure 4.

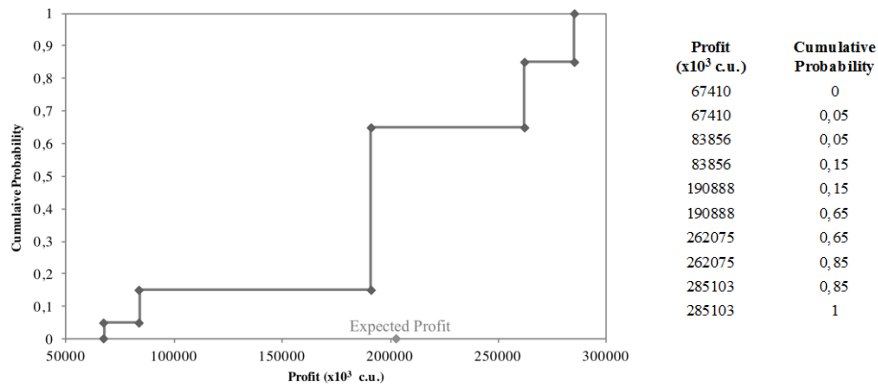


Figure 3. Cumulative distribution function to determine VaR

As expected, the results show that as the profit increases, so does the risk associated with that decision. However, the Pareto curve can provide the assessment of different solutions, from one extreme point where a low profit scenario has a low risk (risk averse), to the other extreme point where a higher profit has a higher risk (risk prone). As detailed in Table 1, significant design differences can be found when the extreme points of the Pareto curve are compared, not only in terms of expected profit but also in terms of equipment’s capacity. For a low profit - low risk scenario, the chosen reactors can differ from all the other solutions, with R2 elected instead of R1. Comparing the results for reactors R3 and R4, 29% and 52% lower capacities are used on the risk averse scenario. The results also generate different plant schedules for the two extreme points decisions, as shown in Figure 5. The multipurpose operation of reactors R1 and R2 is displayed in the scenarios of largest probability P[0.50], as only the high profit - high risk scenario is able to nearly fulfil the demand (99,5%) at the end of planning horizon (720h).

Table 1 – Summary of the results for optimal profit and equipment design

	Profit/ Expected Profit (c.u.)	Equipment capacity (mu/m ²)					
		R1	R2	R3	R4	R5	R6
Deterministic	191408.0	83.91	-	167.82	114.14	106.75	74.72
Stochastic (risk neutral)	202380.9	135.23	-	115.05	170.21	75.91	53.14
(CVaR) High Profit - High Risk	202839.9	125.14	-	83.91	170.21	79.59	55.71
(CVaR) Low Profit - Low Risk	154073.9	-	74.08	59.69	81.12	75.91	54.14

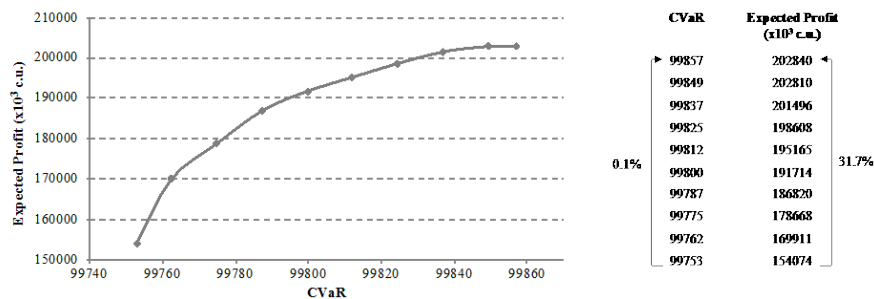


Figure 4 – Pareto curve using CVaR risk measure

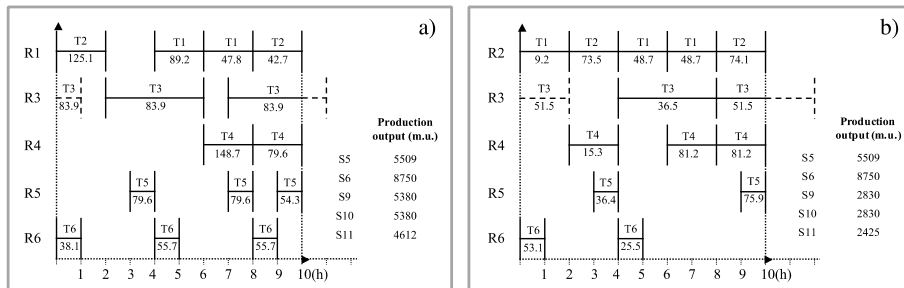


Figure 5 – Plant scheduling solutions for (a) High Profit - High Risk and (b) Low Profit - Low Risk for the scenario with $P[0.50]$

4. Conclusions

In this work, we have developed a modelling approach to provide decision-support on the design and scheduling of multipurpose batch plants, where the maximization of the economic plant profit was considered against the minimization of financial risk. In order to assess risk, the integration of *CVaR* risk measure in a bi-objective optimization framework was extended to a literature MILP model using the augmented ε -constraint method. The Pareto optimal curve enables the evaluation of the different solutions trade-offs, while considering the uncertainty in the products demand modelled through a scenario tree approach. From the results, it is clear that different risk strategies lead to different results and so the accountability of risk is very important in the management of batch plants. As future work, further analysis on the solution strategies derived from different risk measures and scenario trees to support robust decision-support in the optimization of design and scheduling industrial solutions.

Acknowledgments

The authors would like to acknowledge the financial support from Portugal 2020 project POCI-01-0145-FEDER-016418 by UE/FEDER through the program COMPETE2020.

References

- A. Bonfill, M. Bagajewicz, A. España, L. Puigjaner, 2004, Risk management in the scheduling of batch plants under uncertain market demand, *Ind Eng Chem Res*, 43(3), 741-750.
- A. J. Conejo, M. Carrión, and J M. Morales, 2010, *Decision Making Under Uncertainty in Electricity Markets (Vol. 1)*, New York: Springer.
- S. R. Cardoso, A. P. Barbosa-Póvoa, A. P., S. Relvas, 2016, Integrating financial risk measures into the design and planning of closed-loop supply, *Comput Chem Eng*, 85, 105-123.
- G. Mavrotas, 2009, Effective implementation of the ε -constraint method in multi-objective mathematical programming problems, *Ap Math Comp*, 213(2), 455-465.
- T. Pinto-Varela, A. P.F.D. Barbosa-Povoa, A. Q. Novais, 2009, design and scheduling of periodic multipurpose batch plants under uncertainty, *Ind Eng Chem Res*, 48, 9655-9670.
- R. Rockafellar, S. Uryasev, 2002, Conditional value-at-risk for general loss distributions, *Journal of Bank Finance*, 26(7), 1443-71.
- N. Shah, 2005, Process industry supply chains: Advances and challenges, *Comput Chem Eng*, 29(6), 1225-1235.

Dynamics and MPC of an Evaporative Continuous Crystallization Process

Marcellus G. F. de Moraes^{a,b*}, Maurício B. de Souza Jr.^{a,b}, Argimiro R. Secchi^a

^a *Chemical Engineering Program – COPPE – Universidade Federal do Rio de Janeiro, Av. Horácio Macedo, 2030, Centro de Tecnologia, Bloco G, Sala G115, CEP: 21941-914, Rio de Janeiro, RJ – Brazil*

^b *School of Chemistry, Universidade Federal do Rio de Janeiro, Av. Horácio Macedo, 2030, Centro de Tecnologia, Bloco E, CEP: 21941-914, Rio de Janeiro, RJ – Brazil*

* *marcellus@peq.coppe.ufrj.br*

Abstract

Only few applications of Model Predictive Control (MPC) for continuous crystallization processes are found in the open literature. A reason for this may be the nonlinear behaviour of this process. This work applies the MPC approach to improve the control of a Mixed Suspension – Mixed Product Removal (MSMPR) evaporative crystallizer. The modelling of the process was developed for potassium sulphate crystallization due to its well established kinetics for nucleation and growth. The model is described by six equations: the Population Balance Equations (PBE), integrated in moment equations; solute mass balance and the energy balance. The main objective was the regulatory control for the most common disturbances in the process: the feed solute concentration and the feed flowrate. The considered manipulated variables were temperature and steam outflow rate. The results showed that MPC is a feasible control strategy for the process. This is observed especially when the main interest is keeping under regulatory control more easily measured output variables, such as the second order momentum (related to the superficial area of crystals), the concentration, and the suspension temperature. The MPC controller was also compared to PI controllers, presenting better performance and desirable zero offsets for the outputs of greater interest.

Keywords: crystallization control, MPC, continuous crystallization, PBE, crystallization dynamics.

1. Introduction

Only few applications of Model Predictive Control (MPC) for continuous crystallization processes are found in the open literature. According to Kalbasenka et al. (2012), this scarcity is due to the nonlinear behaviour of this process. Rohami et al. (1999) showed that an offset-free control of the outputs was not possible to achieve using linear model-based MPC, attributing this shortcoming to possible model inaccuracies. Moreover, Moldoványi et al. (2005) have shown that a linear MPC was a capable and feasible controller for continuous Mixed Suspension – Mixed Product Removal (MSMPR) crystallizers, but the authors did not consider the energy balance in the model.

The online measurement of important variables, such as the solute concentration and the Crystal Size Distribution (CSD), make the MPC implementation viable. In addition to that, observers for unmeasured outputs are also robust enough to enable the MPC applications (DAMOUR et al., 2010; KALBASENKA et al., 2012).

In this work, the dynamic model of Andrade (1974) for a continuous MSMPR evaporative crystallizer was simulated. The potassium sulphate crystallization is considered due to the established kinetics for nucleation and growth of these crystals. Andrade (1974) had proposed the use of PI controllers to control the process. The MPC approach is presented here as a way to improve the process control of the crystallizer.

For the synthesis of MPC system, a multi-variable state space model was developed and the designed MPC controller was used to control both linear and nonlinear process models. The focus was in the regulatory control, evaluating the behaviour under unmeasured disturbances. The dynamics under PI and MPC controllers were then evaluated and compared.

2. Mathematical Modelling

The mathematical model was initially structured using the population balance of the crystals (ANDRADE, 1974). As the particle size distribution is difficult to observe, the transition to a macroscopic scale model can be performed using properties that can be measured in practice. As the first four moments have physical meaning, these moments were used to obtain the equations of the model: the zero order moment (μ_0) represents the total number of particles; the first order moment (μ_1) represents the sum of all characteristic lengths of the crystals; the second order moment (μ_2) is associated with the specific total area of the crystals; and the third order moment (μ_3) is associated with the specific total mass of the crystals – determined experimentally.

The moment equations (Equations 1-4) are obtained by performing the necessary integrations in the PBE.

$$\frac{d\mu_0}{dt} = \left(\frac{v_o}{\rho_w} - Q_i\right) \frac{\mu_0}{V} + B^0 \quad (1)$$

$$\frac{d\mu_1}{dt} = \left(\frac{v_o}{\rho_w} - Q_i\right) \frac{\mu_1}{V} + G^0(a\mu_0 + b\mu_1) \quad (2)$$

$$\frac{d\mu_2}{dt} = \left(\frac{v_o}{\rho_w} - Q_i\right) \frac{\mu_2}{V} + 2G^0(a\mu_1 + b\mu_2) \quad (3)$$

$$\frac{d\mu_3}{dt} = \left(\frac{v_o}{\rho_w} - Q_i\right) \frac{\mu_3}{V} + 3G^0(a\mu_2 + b\mu_3) \quad (4)$$

where V is the active volume inside the crystallizer; ρ_c and ρ_w are the specific mass of crystal and solvent (water), respectively; Q_i is the volumetric flow rate in the feed stream; v_o is the steam flow rate; B^0 is the nucleation rate; and G^0 is the initial growth rate. The mass balance of the solute is described by Equation 5.

$$\frac{dC_o}{dt} = \left(\frac{v_o}{\rho_w} - Q_i\right) \frac{C_o}{V} + \frac{Q_i C_i}{V} - \frac{1}{2} \rho_c k_A G^0 (a\mu_2 + b\mu_3) \quad (5)$$

where C_i and C_o is the solute concentration in the feed stream and in the suspended product stream, respectively. The energy balance was developed using the following assumptions: the accumulation of energy in the crystals and steam can be neglected; the sensible heat of the crystals is negligible compared to the sensible heat of the solution and produced steam; the steam is saturated, so that the enthalpy of vaporization is written as a function of temperature only. The energy balance yields the sixth equation of the model (Equation 6), in terms of the suspended product temperature T_o :

$$\frac{dT_o}{dt} = \frac{1}{(\rho_w + C_o)(a_1 - 2 a_2 T_o)} \left\{ \frac{Q_i}{V} (\rho_w + C_i) (h_i - h_o) + \frac{1}{2} \rho_c k_A G^0 (a \mu_2 \frac{v_o}{V} (h_o - H_{vap}) + b \mu_3) (h_o + \Delta H_{cryst}) \right\} \quad (6)$$

where $h_i = h_i(T_i, C_i)$, $h_o = h_o(T_o, C_o)$, $H_{vap} = H_{vap}(T_o)$ and $\Delta H_{cryst} = \Delta H_{cryst}(T_o, C_o)$ are mass based enthalpies.

3. Control Objectives and MPC Design

This work aims at the development of a strategy based on MPC for the multivariate process of the continuous crystallizer. The comparison of the MPC results with both conventional and optimal PI controllers was realized. The state variables, based on the model described in Section 2, are: $\mu_o, \mu_1, \mu_2, \mu_3, C_o$ and T_o . The variables T_i and v_o are manipulated variables. The disturbances are Q_i and C_i , assumed unmeasured. For the states variables, the vector of normalized state is defined $\mathbf{X} = [X_1 \ X_2 \ X_3 \ X_4 \ X_5 \ X_6]^T$. The vector \mathbf{U} represents the combined normalized manipulated (U_1 e U_2) and unmeasured disturbance (P_1 e P_2) vector ($\mathbf{U} = [U_1 \ U_2 \ P_1 \ P_2]^T$).

The regulatory control is applied to X_3, X_5 and X_6 (related to the superficial area of crystals, the suspension solute concentration and temperature, respectively), because they are possible to be directly measured in an easier way. The dimensionless time (t/τ) takes into consideration the normalization by the crystallizer residence time, τ .

The MPC formulation minimizes the process performance index J , the objective function of the problem (Equation 7). The MPC control horizon N_c was chosen as 5 and the prediction horizon N as 10 sampling intervals. The matrices \mathbf{Q} and \mathbf{R} are weighting matrices for the outputs and increment inputs, respectively; $\hat{\mathbf{y}}(k+j)$ is the predicted output and $\mathbf{y}_{ref}(k+j)$, its reference value. The decision variables of the optimization problem are the input control actions (\mathbf{u}). In the incremental formulation (Equation 7), $\Delta \mathbf{u}(k+j-1)$ is the vector of input increments (Equation 8).

$$J = \sum_{j=1}^N \left(\hat{\mathbf{y}}(k+j) - \mathbf{y}_{ref}(k+j) \right)^T \mathbf{Q} \left(\hat{\mathbf{y}}(k+j) - \mathbf{y}_{ref}(k+j) \right) + \sum_{j=1}^{N_c} \Delta \mathbf{u}(k+j-1)^T \mathbf{R} \Delta \mathbf{u}(k+j-1) \quad (7)$$

$$\Delta \mathbf{u}(k+j-1) = \mathbf{u}(k+j-1) - \mathbf{u}(k+j-2) \quad (8)$$

The rate weights for the inputs (U_1 e U_2), elements of \mathbf{R} , were maintained as 0.1. For the matrix \mathbf{Q} , since the main objective is the best performance for simpler direct measurable variables X_3, X_5 and X_6 , the results for the regulatory control were chosen with weights equal to 1 for these outputs. The variables were considered unconstrained in this study.

4. Results and Discussion

First, the linearization of the model was taken in the form of a state space model. The linear and nonlinear models were compared, for step responses. The linear model presents a good agreement with the nonlinear for the operation process transient

response and small steady-state errors. Figure 1 presents the results (X_2, X_4, X_5, X_6) for a 5% step in Q_i .

Table 1 presents the offset response values for -10% step in P_1 for the nonlinear plant model. The results allow the comparison of the MPC strategy with the continuous and discrete-time optimal PI controllers, as well as with the open-loop system. The tuning parameters for the PI controllers were: $K_{C_1} = 0.45$ and $\tau_{I_1} = 0.30$ for the first loop (v_o controlling C_o), using Ziegler-Nichols; $K_{C_2} = 15.0$ and $\tau_{I_2} = 0.026$ for the second loop (T_i controlling T_o), considering the closed-loop time as half of the residence time and the damping ratio equal to 0.3. For the discrete time controller, the dimensionless sampling time was 0.0333. The results show that the MPC presented the best performance.

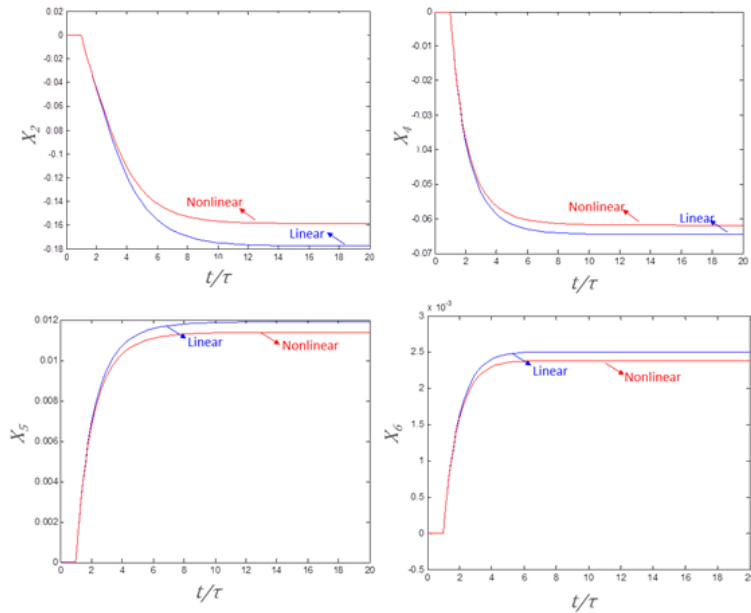


Figure 1 – Example of open-loop response for 5% step in Q_i ($P_i = 0,05$) for X_2, X_4, X_5 and X_6

Table 1- Comparison of offset for the negative step (-10%) in P_1

Variable	Offset			
	Open-Loop	Continuous PI	Discrete-time optimal PI	MPC
X_1	0,63	0,21	0,12	0,13
X_2	0,46	0,098	0,075	0,077
X_3	0,28	0,019	-0,020	0
X_4	0,157	-0,061	-0,078	-0,065
X_5	-0,026	0	0,0071	$5,4 \times 10^{-5}$

The output responses are shown in Figure 2, for a step disturbance in Q_i ($P_1 = -0.1$), using the nonlinear model as the plant model. Figure 3 shows the responses for a step disturbance in C_i ($P_2 = -0.1$).

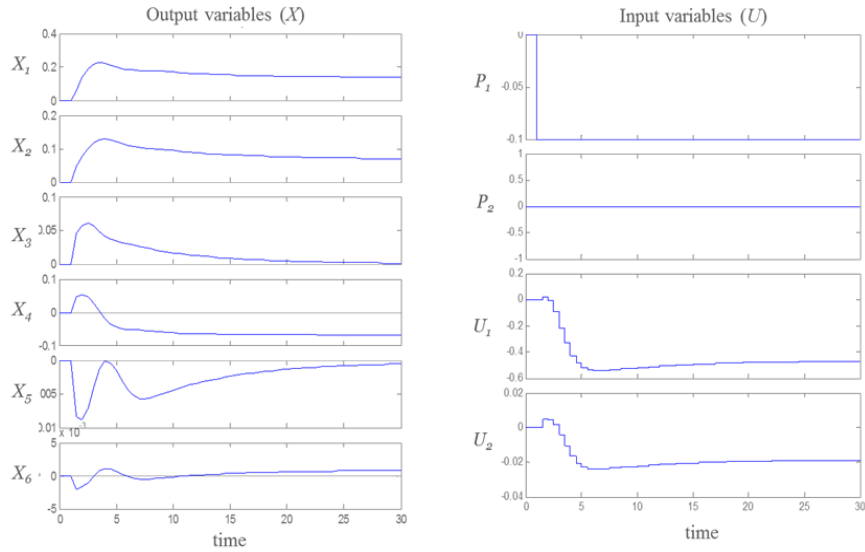


Figure 2 – MPC output responses and inputs for -10% step in Q_i ($P_1=-10\%$) for nonlinear plant model.

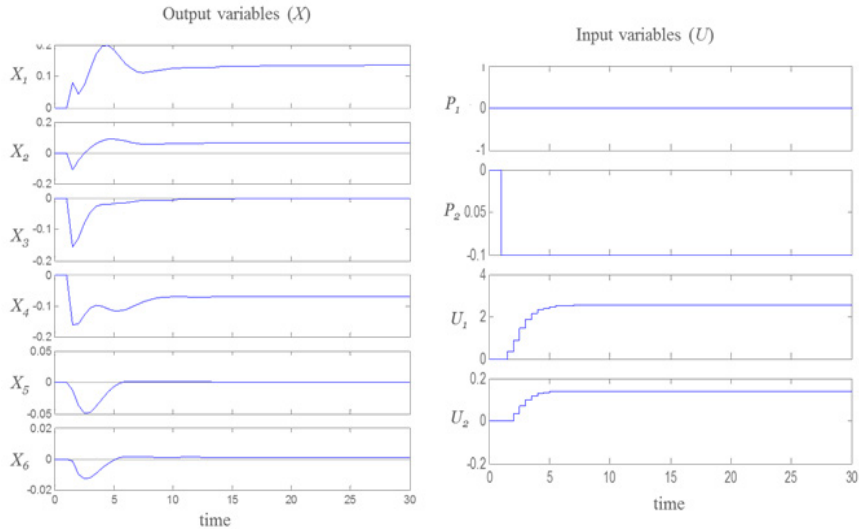


Figure 3– MPC output responses and inputs for -10% step in C_i ($P_2=-10\%$) for nonlinear plant model.

Preliminary evaluation using the linear plant model exhibits very close response to the observed in Figures 2 and 3, suggesting that the linearized plant model is The results prove the feasibility of MPC to control the variables X_3, X_5 and X_6 , in a regulatory system due to disturbances P_1 and P_2 . The variables X_1, X_2 and X_4 were not maintained in the exact original values (that is, in deviation, equal zero) but the changes and the offset for these variables are acceptable for the crystallization process. The successful

control results may be attributed to the good agreement between the nonlinear and linear models shown in Figure 1.

It is worth pointing out that some outputs are physically unmeasured in practice. If the outputs X_1 , X_2 and X_4 were declared as unmeasured, the obtained results (not shown due to lack of space), using a steady-state Kalman filter for state estimation in MPC, are very close to those pointed in Figures 1 and 2 for the same load perturbations.

5. Conclusion and prospects

In this work, an MPC was developed for a MSMMPR continuous crystallizer to improve the process control of this industrial process. The importance of the energy balance (that was not considered in the work of Moldoványi et al. (2005) to the mathematical model for the crystallizer is highlighted. In this sense, the open-loop dynamics of the input temperature of the solution is the most important one. This fact justifies the use of T_i as manipulated variable, being crucial for the control of the process.

The six state variables for the process were considered as possible to be directly measured. This is not easily achievable in practice due the difficulty in experimental determination of all moments. In order to solve this problem, the use of internal state observers in MPC formulation is a good strategy.

The MPC presented a better performance than PI controllers for most of the available cases. In some cases, it was possible to reach the desirable steady state values for the three outputs of greatest interest (X_3 , X_5 and X_6).

Moreover, it is suggested to incorporate feedforward actions to the MPC strategies, since the loads Q_i e C_i (P_1 and P_2 in normalized variables) can be measurable variables. The study of more complex models for the crystallization phenomena is interesting to be conducted with this MPC formulation, which can be a good alternative for the crystallization process control. For example, the description of crystals break and aggregation in PBE equations or the consideration of recycle of fine particles can be relevant to other models for crystallization process.

References

- ANDRADE, JOSÉ FLÁVIO M. Dinâmica, Controle Contínuo e Discreto de Cristalizadoros Contínuos, 1974. 105p. Dissertation (Master of Science) – Coordenação dos Programas de Pós-Graduação em Engenharia, Universidade Federal do Rio de Janeiro, Rio de Janeiro.
- DAMOUR, Cédric; Benni, Michel; Boillereaux, Lionel; Grondin-Perez, Brigitte; Chabriat, Jean-Pierre. NMPC of an industrial crystallization process using model-based observers, *Journal of Industrial and Engineering Chemistry* 16, p. 708-716, 2010.
- KALBASENKA, Alex N.; Huesman, Adrie E. M.; Kramer, Herman J. M. Model Predictive Control. *Industrial Crystallization Process Monitoring and Control*. Wiley-VCH, 2012.
- MOLDOVÁNYI. Nóra; Lakatos, Béla G.; Szeifert, Ferenc. Model predictive control of MSMMPR crystallizers. *Journal of Crystal Growth*, 275, p. e1349-1354, 2005.
- RAMKRISHNA, D. Population Balances - Theory and Applications to Particulate Systems in Engineering. Academic Press, 2000.
- ROHANI, S.; Haeri, M.; Wood, H. C. Modeling and control of a continuous crystallization process: Part 1: Linear and nonlinear modelling. *Computational Chemical Engineering*, 23, 263-377., 1999.

Learning operation strategies from alarm management systems by temporal pattern mining and deep learning

Gyula Dorgo^a, Peter Pigler^a, Mate Haragovics^b and Janos Abonyi^{a,*}

^a*MTA-PE Lendület Complex Systems Monitoring Research Group,
Department of Process Engineering, University of Pannonia,
Egyetem str. 10, Veszprém, H-8200, Hungary*

^b*MOL Danube Refinery, Olajmunkás str. 2., Százhalombatta, H-2443, Hungary
janos@abonyilab.com*

Abstract

We introduce a sequence to sequence deep learning algorithm to learn and predict sequences of process alarms and warnings. The proposed recurrent neural network model utilizes an encoder layer of Long Short-Term Memory (LSTM) units to map the input sequence of discrete events into a vector of fixed dimensionality, and a decoder LSTM layer to form a prediction of the sequence of future events. We demonstrate that the information extracted by this model from alarm log databases can be used to suppress alarms with low information content which reduces the operator workload. To generate easily reproducible results and stimulate the development of alarm management algorithms we define an alarm management benchmark problem based on the simulator of a vinyl acetate production technology. The results confirm that sequence to sequence learning is a useful tool in alarm rationalization and, in more general, for process engineers interested in predicting the occurrence of discrete events.

Keywords: alarm management, operator support system, recurrent neural networks

1. Introduction

Forecasting of discrete events has critical importance in process (safety) engineering (Baptista et al., 2018). In complex chemical production systems faults generate long sequences of alarm and warning signals. Although - according to alarm management guidelines - a single abnormal event should produce a unique and informative alarm, the high number of interacting components in modern production systems makes the co-occurring and redundant alarms almost inevitable (Mehta and Reddy, 2015). Since most of the signals are redundant, the handling of the malfunctions is a challenging task even for well-trained operators due to the unnecessarily high information overload. The concept of advanced alarm management is that the occurring alarms should be grouped and the prediction of future events should be used for the suppression of predictable, nuisance alarms.

The core concept of our methodology is based on the assumption of predictable alarms do not contain any novel information, so the state of the process can be already characterized based on the previously registered signals, so this information is enough to determine what operator actions are required in the given situation. As the efficiency of this approach relies on the performance of the model used for the prediction of the events, we selected the most advanced sequence to sequence deep learning neural network structure (Kiros et al., 2015) to realize our concept.

2. Methodology

2.1. Formulation of the sequence to sequence prediction problem

In process engineering practice, we frequently need to predict the occurrence of a discrete event. This task is highly relevant in alarm management, where the problem can be formulated as follows. Alarm and warning signals can be treated as *states* of the technology. Each state (denoted by s) is represented by $\langle pv, a \rangle$ data couples, where pv is the index of the process variable and a is the attribute showing the process variable's value related to the alarm and warning limits, such as $a \in \{Low A, Low W, High W, High A\}$, where A stands for Alarm and W stands for Warning. For example the description of a state can be represented as follows: $s_e := \langle Column Top Temperature, High A \rangle$. An *event* is the time interval in which the defined state occurs, denoted by e . We suppose that the $\Phi = (e_1, \dots, e_T)$ sequence of events (present and past alarms) defines the state of the process and we assume that based on this information we can predict the sequence of future events $\Phi \Rightarrow \hat{\Phi}$, where $\hat{\Phi} = (\hat{e}_1, \dots, \hat{e}_{\hat{T}})$. Therefore, we look for a $\hat{\Phi} = f(\Phi)$ model that efficiently handles this sequence to sequence modeling problem.

2.2. Encoder-decoder recurrent neural network based sequence prediction

The most advanced approach of sequence to sequence learning is based on deep learning neural networks. Although Nguyen et al. (2017) applied these models for event prediction, according to our knowledge, our work is the first example when it is used for the prediction of alarm and warning signals. The application of this unique recurrent neural network is not trivial, so in this section, we describe the proposed goal-oriented model structure (presented in Figure 1).

Forming the input of the model: Figure 1 highlights the important characteristics of the input sequences. As can be seen, an end-of-sequence (EOS) tag is appended to the sequence. To ensure fixed sequence length, we completed the sequences to the T -th element by adding padding symbols (PAD) after the EOS tag. Moreover, the order of the events in the input sequence is reversed, since Sutskever et al. (2014) found that the prediction accuracy improves when the beginning of the input sequence is "closer" to the beginning of the predicted sequence.

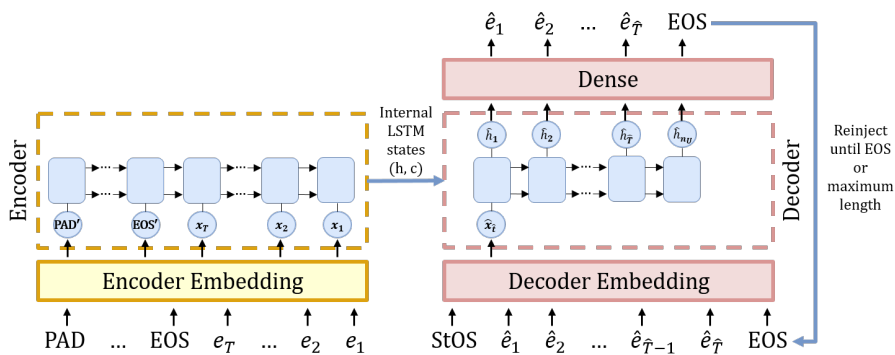


Figure 1: The schematic illustration of the proposed methodology. The encoder maps the input sequence into a fixed length vector representation. Using this vector as initial state the decoder layer determines the next event with the highest probability by the argmax function of the dense layer.

Embedding layer: To utilize the sequences of symbols as inputs of the neural network, we encode the symbols of the events as one-hot encoded vectors, \mathbf{oh}_t , where only one bit related to the encoded signal is fired among the n_d bits, where n_d represents the number of symbols. The embedding layer realises a $\mathbf{x}_t = \mathbf{W}_{emb} \mathbf{oh}_t$ linear transformation, which maps the one-hot encoded vectors into a lower (n_e) dimension of continuous values. Note that in Figure 1 the embedded form of the EOS and PAD symbols are represented as EOS' and PAD' respectively.

Encoder and decoder layers: The encoder LSTM layer maps the embedded input sequence into its internal states. The vector of the internal states and the activity values of the encoder layer are used for the conditioning of the LSTM units of the decoder layer, which means the transferring of information about what has happened in the process and what kind of prediction should the decoder layer generate. The decoder itself is trained to predict the next event of the predicted sequence, so the procedure is repeated until the prediction of an EOS signal or reaching the maximum sequence length.

Dense layer: The decoder layer maps the $\hat{\mathbf{x}}_t$ input event into a $\hat{\mathbf{h}}_t$ vector of real values represented as $\hat{\mathbf{h}}_t = [\hat{h}_1, \dots, \hat{h}_t^{n_U}]$ and used to calculate the probabilities of the occurrences of the events by the softmax activation function represented by the dense layer in Figure 1,

$$P(\hat{e}_{t+1} | \hat{\mathbf{x}}_t) = P(\hat{e}_{t+1} | \hat{\mathbf{h}}_t) = \frac{\exp(\hat{\mathbf{h}}_t^T \mathbf{w}_{s,j} + b_j)}{\sum_{j=1}^{n_d} \exp(\hat{\mathbf{h}}_t^T \mathbf{w}_{s,j} + b_j)} \quad (1)$$

where $\mathbf{w}_{s,j}$ represents the j -th column vector of the \mathbf{W}_s weight matrix of the output dense layer of the network, and b_j represents the bias.

Training: Deep learning requires a high number of training sequences which can be extracted from the log files of the process control system. When the malfunctions are also logged, special sequences can be defined that can be also used for fault classification (Dorgo et al., 2018). For the training of the model, we have to encode the input data to the one-hot vectorized form. The input data of the decoder is the one-hot vectorized form of the sequences that we want to predict. The decoder target data is also identical to the decoder input data, but it is shifted by one timestep since from the e_t event we would like to predict the e_{t+1} event. This training approach is referred as teacher forcing, which means that we use the expected future output from the training dataset at the current time step as input in the next time step, rather than the predicted output generated by the model, (J. Williams and Zipser, 1998). Using this technique, we train all of the layers (the two embedding, the encoder, the decoder and the dense layers) simultaneously.

Prediction: Prior to the prediction, we need to encode the sequence defining the internal state vector. The internal states of the encoder network are transferred to the decoder layer. The prediction starts with the start-of-sequence symbol (marked as StOS in Figure 1). The layer generates a prediction for the next event which will also be applied to the input of the next time step. The generated events are always appended to the predicted target sequence. This prediction process is repeated until the layer generates the end-of-sequence symbol or hit the previously set limit of the length of the predicted target sequence.

Evaluation: The evaluation of the model should be related to its intended application. Since we are focusing to build an alarm suppression algorithm, we defined two measures to evaluate the performance of the resulted models. Firstly, we defined val_1 as the percent of sequences having at least one well-predicted event, secondly, we calculate the percent of the well-predicted events (val_2).

3. Results

We present a reproducible benchmark example to ensure the comparability and reproducibility of our results. We extended the widespread dynamic simulator of a vinyl-acetate production system (VAC Chen et al. (2003)) to be able to serve case studies of alarm management and event analysis. The used dynamic simulator of the vinyl acetate (VAc) process contains 27 controlled and 26 manipulated variables, therefore it is complex enough to define alarm management problems. The model is available from the website of the authors (www.abonyilab.com). The extended simulator handles 11 malfunctions related to the fault of valves or actuators (see Figure 2). The events (alarms and warnings) were defined when the process variables exceeded certain threshold limits used to determine the normal operating range. The details of the alarms are given in our previous publication (Dorgo et al., 2018). In this study, the faults have lognormal time distribution, and their effects were simulated in 200 one-hour-long operating periods. A 100-minute time window was used to identify events that we consider as direct consequences of the malfunctions. We transformed these events into sequences based on their start time. The resulted sequences were filtered for the minimal length of five events, and the first half of the sequence was used as the encoder input sequence, and the rest of the sequence was used as the target sequence for prediction. From the originally generated 2200 sequences 1289 satisfied the minimal sequence length condition.

The simulation and the data preprocessing were carried out in MATLAB environment. Since we are interested in the development of open source and industrially applicable solutions, the deep neural network was identified and applied in Python/Keras using Tensorflow as backend. We trained the model using a Nvidia GeForce GTX 1060 6GB GPU with the application of CUDA. We selected the optimal model structure by 7-fold cross-validation experiments. The final model has an embedding dimension of 40. The number of LSTM units in both the encoder and decoder layer was 256. The number of epochs was set to 4000, with 256 as batch size using the RMSProp optimizer of Keras.

The performance of the resulted model is shown in Figure 3. As the 7-fold cross validation illustrates, the model has consistently excellent performance in case of all fault types.

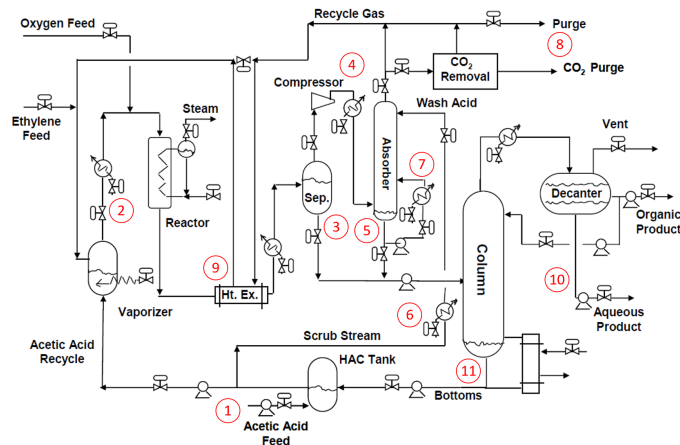


Figure 2: Flow chart of the vinyl acetate production technology (The numbers in circle (red) show the type of the implemented fault)

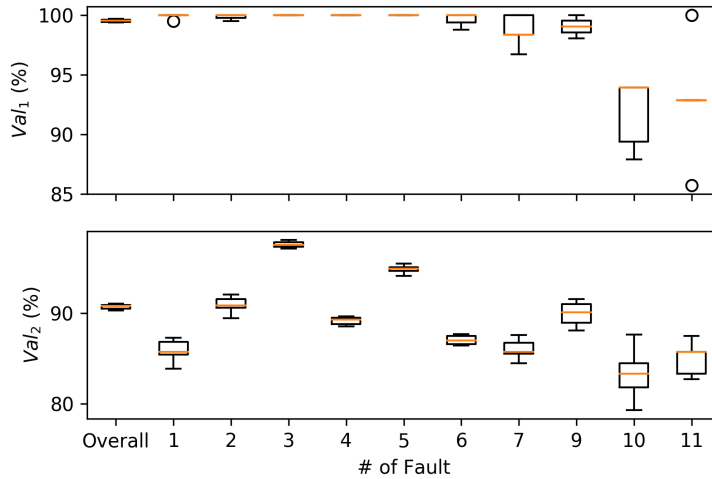


Figure 3: 7-fold cross validation of the prediction performance. Val_1 represents the percent of the sequences with at least one correctly predicted event, while Val_2 shows the average percent of the correctly predicted events. The first column shows the overall performance, while the other columns show the prediction power of the model in a given fault type.

Table 1 gives a didactic example for sequence prediction and for the evaluation process. In case of the first sequence two event tags, T_{14}^{LW} and Q_{20}^{HW} are correctly predicted, therefore $val_2 = 66\%$, while in the case of the second sequence, all of the events are predicted correctly (however, not in the correct order), therefore $val_2 = 100\%$.

Table 1: Illustration of the sequence prediction procedure. We denote the alarms by capital letters of T, Q and L to show the type of the measure variable, i.e. temperature, quality and level respectively. The letters L, H, W and A stand for low, high, warning and alarm respectively, and the numbers in lower script show the No. of the process variable. The prediction is based on input sequences used to represent the current operating state. To demonstrate how we evaluate the model performance the predicted and the logged sequences are also shown in two particular example.

Input Sequence					True Sequence					Predicted sequence								
T_{14}^{HA}	T_{14}^{LA}	T_7^{LW}	EOS		T_{14}^{LW}	Q_{20}^{HW}	L_{12}^{LW}	EOS		T_{14}^{LW}	Q_{20}^{HW}	L_{12}^{HW}	EOS					
L_3^{LW}	T_{16}^{HW}	T_{16}^{HA}	L_3^{LA}	T_{16}^{LA}	EOS		L_3^{LW}	T_{16}^{LW}	T_{16}^{HW}	L_{12}^{HW}	EOS		L_3^{LW}	T_{16}^{LW}	L_{12}^{HW}	T_{16}^{HW}	EOS	

4. Conclusions

We proposed a sequence to sequence learning based methodology to model the temporal patterns of discrete events related to the operation of complex chemical processes.

As we were interested in "translating" the sequence of past events that define the state of the technology and utilized operating strategy into the future sequence of events, the structure of the proposed recurrent neural network model has been inspired by the deep learning models used for language translation. The model consists of long short-term memory units which are specifically designed to handle long-term time-dependency, so ideal for the prediction of discrete events. The encoder layer maps the input sequence into a vector with fix length, while the decoder layer generates the next prediction based on the previously predicted elements. Both the inputs of the encoder and the decoder layer utilize embedding layers to map the set of discrete events into a lower dimension of continuous variables, while the prediction of the decoder layer is calculated by the argmax function of the dense layer.

We designed a benchmark simulation example to evaluate the effectiveness of alarm suppression algorithms. The results demonstrate the applicability of the proposed methodology for the extraction of useful operating patterns, which can be transformed to alarm suppression rules.

Acknowledgements

The research has been supported by the National Research, Development and Innovation Office NKFIH, through the project OTKA 116674 (Process mining and deep learning in the natural sciences and process development) and the EFOP-3.6.1- 16-2016- 00015 Smart Specialization Strategy (S3) Comprehensive Institutional Development Program.

References

- M. Baptista, S. Sankararaman, I. P. de Medeiros, C. Nascimento, H. Prendinger, E. M. Henriques, 2018. Forecasting fault events for predictive maintenance using data-driven techniques and arma modeling. *Computers and Industrial Engineering* 115 (Supplement C), 41 – 53.
URL <http://www.sciencedirect.com/science/article/pii/S036083521730520X>
- R. Chen, K. Dave, T. J. McAvoy, M. Luyben, 2003. A Nonlinear Dynamic Model of a Vinyl Acetate Process. *Industrial and Engineering Chemistry Research* 42 (20), 4478–4487.
URL <http://dx.doi.org/10.1021/ie020859k>
- G. Dorgo, P. Pigler, J. Abonyi, 2018. Understanding the importance of process alarms based on the analysis of deep recurrent neural networks trained for fault isolation. *Journal of Chemometrics*, to appear.
- R. J. Williams, D. Zipser, 09 1998. A learning algorithm for continually running fully recurrent neural networks 1.
- R. Kiros, Y. Zhu, R. Salakhutdinov, R. S. Zemel, A. Torralba, R. Urtasun, S. Fidler, 2015. Skip-thought vectors. *CoRR abs/1506.06726*.
URL <http://arxiv.org/abs/1506.06726>
- B. Mehta, Y. Reddy, 2015. Chapter 21 - alarm management systems. In: B. Mehta, Y. Reddy (Eds.), *Industrial Process Automation Systems*. Butterworth-Heinemann, Oxford, pp. 569 – 582.
URL <http://www.sciencedirect.com/science/article/pii/B9780128009390000218>
- D. Q. Nguyen, D. Q. Nguyen, C. X. Chu, S. Thater, M. Pinkal, 2017. Sequence to sequence learning for event prediction. *CoRR abs/1709.06033*.
URL <http://arxiv.org/abs/1709.06033>
- I. Sutskever, O. Vinyals, Q. V. Le, 2014. Sequence to sequence learning with neural networks. *CoRR abs/1409.3215*.
URL <http://arxiv.org/abs/1409.3215>

A two-stage stochastic programming approach to integrated day-ahead electricity commitment and production scheduling

Egidio Leo^{a*} and Sebastian Engell^a

^aProcess Dynamics and Operations Group, Department of Biochemical and Chemical Engineering, Technische Universität Dortmund, EmilFigge-Str.70, 44221 Dortmund, Germany

egidio.leo@tu-dortmund.de

Abstract

To ensure stability of the power grid, the electricity suppliers impose a daily day-ahead hourly electricity commitment to large consumers. In case the actual electricity consumption differs from the committed profile, the consumer is obliged to pay penalties. The challenge addressed in this work is to simultaneously determine the optimal day-ahead electricity commitment and the optimal production scheduling. Since the consumers have to commit themselves to the amount of energy they are going to purchase and use for a period of 24 hours one day before the actual electricity demand is realized, a major challenge lies in the uncertainty: equipment failures may reduce the production capacity and can make the actual electricity consumption drastically deviating from the day-ahead electricity commitment. For this purpose a two-stage stochastic mixed-integer linear programming model that considers equipment breakdowns is proposed. The application of the proposed approach to a continuous power intensive plant shows the improvement achieved by solving the stochastic model.

Keywords: Production scheduling, Two-stage stochastic programming, Demand Side Management, Load deviations, Conditional value-at-risk.

1. Introduction

Industrial Demand Side Response is a promising technology that is aiming at reducing operating costs for energy-intensive industries exploiting production flexibility to take advantage of time-sensitive electricity prices (Merkert et al., 2014). The volatility of the electricity prices, due to the availability of renewable energy sources, for electricity consumers constitutes a potential saving and for electricity suppliers an increased effort to match demand and supply. To ensure the stability of the power grid, the electricity suppliers impose a daily day-ahead hourly electricity commitment to large consumers and in case the actual consumption deviates from the pre-agreed values, financial penalties, which are often in the same range as the net electricity cost, are incurred. This is known in literature as the load-deviation problem. Nolde and Morari (2010) proposed a scheduling solution for electrical load tracking of a steel plant. The schedule is defined such that the total electricity consumption tracks the load curve as closely as possible while respecting all production constraints. In (Hadera et al., 2015), the authors take into account multiple electricity sources (Base load and Time-Of-Use (TOU) power contracts, day-ahead market, onsite generation) and the load deviation problem to determine the optimal production schedule. However, in these contributions the load

commitment decisions are assumed as given and are not optimized. In this work, we address the challenge of determining simultaneously the optimal day-ahead electricity commitment and the optimal production scheduling. Since decisions regarding the electricity commitment have to be made before the actual electricity demand is known for the time horizon of interest, it is crucial to account for uncertainties in the decision-making process. To this challenge we propose a two-stage stochastic programming approach (Birge and Louveaux, 2011). The first-stage variables represent the day-ahead electricity commitment decisions. The second stage faces plant capacity uncertainty and second-stage variables for each breakdown scenario are the plant operating decisions (production levels, inventories...) and the electricity consumption deviations from the day-ahead commitment. A similar approach has not been considered in this context before. In Section 2, the problem statement is presented highlighting the uncertainty modelling strategy and the proposed two-stage MILP. Section 3 applies the proposed framework to a power-intensive process and the results are summarized in terms of the Value of the Stochastic Solution (VSS) for risk-neutral and risk-averse optimization. The main insights from the results are discussed in Section 4 before providing some final conclusion in Section 5.

2. Problem statement

2.1. Uncertainty modeling strategy

To integrate day-ahead electricity commitment and production scheduling, we propose a two-stage stochastic programming approach (Birge and Louveaux, 2011). In two-stage stochastic programming (2SSP), uncertainty is represented by discrete scenarios, and decisions are made at two different stages which are defined by the realization of the uncertainty. Therefore we can divide the decision variables in two sets: here-and-now (or first-stage) decisions that have to be made at the beginning and cannot be changed over the scheduling horizon, and wait-and-see (or second-stage) decisions that can be adjusted after the realization of the uncertainty. In the proposed approach, we consider equipment breakdowns as source of uncertainty and three different levels of uncertainty—low, medium, and high. The low, medium and high uncertainty levels represent respectively 10, 30 and 40 percent reduction of the maximum plant production capacity. The production capacity reduction is modelled by 8 breakdown scenarios: in scenario 1 no breakdown occurs, whereas in Schemes 2–8 the breakdown occur in periods 1-4,...,22-24, respectively. The probabilities are 50% for scenario 1 and (50/7) % for scenarios 2–8.

2.2. Plant model

To demonstrate the main features of the proposed approach, we apply it to a continuous-production plant. The plant is the same as in (Zhang et al., 2016). In the proposed mathematical formulation *here-and-now* decisions have no scenario subscript and *wait-and-see* decisions have the scenario subscript s . The plant produces two products i ($P1$ and $P2$) and it can operate in three different modes m : *off*, *startup*, and *on*. The possible mode transitions are *off* to *startup*, *startup* to *on*, and *on* to *off* and they can happen only after fixed period of time that have been spent in the modes (*off*: 8 h, *startup*:2 h, *on*:6 h) (Eq.6). The transitions between the modes of operation and the relations with the active modes are modelled by Eq.(7). The binary variable (Eq.(4)) is 1 if mode m is selected in time period t of the horizon T . For each mode, the operating conditions are expressed as a convex combination of the extreme points v_{mjis} of the feasible region of

operation (Eq.(2)). Eq.(1)-(2) define the hourly production levels \overline{PD}_{mits} for each product i and operating mode m and the aggregated production PD_{its} .

$$PD_{its} = \sum_m \overline{PD}_{mits} \quad \forall i, t \in T, s \quad (1)$$

$$\overline{PD}_{mits} = \sum_j \lambda_{mjts} * v_{mjis} \quad \forall i, t \in T, m \in M, s \quad (2)$$

$$\sum_j \lambda_{mjts} = y_{mt} \quad \forall m, t \in T, s \quad (3)$$

$$\sum_m y_{mt} = 1 \quad \forall t \in T \quad (4)$$

$$EU_{ts} = \sum_m \left(\delta_m * y_{mt} + \sum_i \gamma_{mi} * \overline{PD}_{mits} \right) \quad \forall t \in T, s \quad (5)$$

$$\sum_{k=1}^{\theta_{mm'}} z_{mm't-k} \leq y_{m't} \quad \forall (m, m') \in M, t \in T \quad (6)$$

$$\sum_{m'} z_{m'm,t-1} - \sum_{m'} z_{mm',t-1} = y_{mt} - y_{m,t-1} \quad \forall m, t \in T \quad (7)$$

Eq. (8) defines the inventory level IV_{its} at time t as the sum of the inventory level at time period $t-1$ and the production at time t , PD_{its} , minus the amount of product sold, SL_{its} , and the amount of products wasted, PW_{its} , at time period t . Note that all these variables are *wait-and-see* variables and therefore they are defined for each scenario s . Eq. (9) sets upper and lower bounds of the inventory levels and Eq. (10) ensures that the demand of product i as the sum of the amount of product sold, SL_{its} , and the amount of products purchased from other sources, PC_{its} , is satisfied.

$$IV_{its} = IV_{i,t-1,s} + PD_{its} - SL_{its} - PW_{its} \quad \forall i, t \in T, s \quad (8)$$

$$IV_{it}^{min} \leq IV_{its} \leq IV_{it}^{max} \quad \forall i, t \in T, s \quad (9)$$

$$SL_{its} + PC_{its} = D_{it} \quad \forall i, t \in T, s \quad (10)$$

Eq. (11) - (14) provide the initial and final condition of the plant in terms of inventory levels and active operating modes.

$$IV_{i,0,s} = IV_i^{initial} \quad \forall i, s \quad (11)$$

$$y_{m,0} = y_m^{initial} \quad \forall m \quad (12)$$

$$IV_{i,t^{final},s} \geq IV_i^{final} \quad \forall i, s \quad (13)$$

$$z_{mm't} = z_{mm't}^{ini} \quad \forall (m, m') \in M, s, -\theta^{max} + 1 \leq t \leq -1 \quad (14)$$

2.3. Day-ahead electricity commitment

Eq. (15) defines the day-ahead electricity commitment, ES_t , the over-consumptions Δe_{ts}^+ and the under-consumptions Δe_{ts}^- . Since the consumers have to commit themselves to the amount of energy they are going to purchase for a period of 24 hours one day before the actual electricity demand is realized, the electricity commitment decisions are first-stage variables and the load deviations and the actual electricity consumptions are second stage variables.

$$EU_{ts} - ES_t = \Delta e_{ts}^+ - \Delta e_{ts}^- \quad \forall t \in T, s \quad (15)$$

2.4. Objective function

We solve the proposed stochastic formulation considering both risk-neutral and risk-averse optimization. The two approaches mainly differ in the objective functions. The

risk-neutral optimization minimizes the expected operating cost; the risk-averse optimization balances two conflicting objectives: the expected cost and the risk, defined as the expected cost over the worst scenarios.

2.4.1. Risk-neutral optimization

The model minimizes the total expected operating costs, z , defined in Eq.(16) as the first-stage cost of day-ahead electricity commitment and the expected second-stage cost of deviation penalties and purchasing of products on the market.

$$z = \sum_t \left(p_t^{\text{day-ahead}} ES_t + \sum_s \varphi_s \left(p_t^+ \Delta e_{ts}^+ + p_t^- \Delta e_{ts}^- + \sum_i p_i PC_{its} \right) \right) \quad (16)$$

where $p_t^{\text{day-ahead}}$, p_t^+ , p_t^- , p_i represent the day-ahead electricity price, the penalty cost for over consumption and under consumption and the product purchasing prices; φ_s denotes the probability of scenario s .

2.4.2. Risk-averse optimization

Different risk measures have been presented in the literature: value-at-risk (VaR), downside risk, Conditional value-at-risk (CVaR) (Rockafellar and Uryasev (2000)). We adopted the CVaR (Rockafellar and Uryasev (2000)), since it is a coherent risk measure (it preserves convexity) and it is able to consider the tail of the probability density function. The CVaR is defined by Eq.(17)-(18).

$$CV = k + \frac{1}{1 - \alpha} \sum_s \varphi_s \theta_s \quad (17)$$

$$\sum_t \left[p_t^{\text{day-ahead}} ES_t + p_t^+ \Delta e_{ts}^+ + p_t^- \Delta e_{ts}^- + \sum_i p_i PC_{its} \right] - k \leq \theta_s \quad \forall s \quad (18)$$

$$\min\{\delta * CV + (1 - \delta) * z\} \quad (19)$$

where k, θ_s are continuous variables with $k \in \mathbb{R}$ and $\theta_s \geq 0$. Eq. (19) defines the objective function as the weighted sum of the total expected cost and the CVaR ($\delta = 0.5$).

3. Results

To measure the improvement that can be achieved by solving the stochastic model instead of its deterministic counterpart, we compute the value of the stochastic solution (VSS). The VSS and the relative \overline{VSS} , defined in Eq.(20)-(21), show the impact of the uncertainty on the first-stage variables:

$$VSS = z_{det}^* - z_{stoc}^* \quad (20) \quad \overline{VSS} = \frac{z_{det}^* - z_{stoc}^*}{z_{det}^*} \quad (21)$$

where z_{stoc}^* is the optimal solution of the stochastic problem and z_{det}^* is the optimal solution of the stochastic problem with first-stage variables fixed to the values at the optimal solution of the deterministic problem. Table 1 shows the VSS for risk-neutral and risk-averse optimization: the VSS can be quite significant and that it grows with the uncertainty level. The high values of the VSS demonstrate that there is a significant benefit from considering breakdown uncertainty in the integrated day-ahead electricity procurement and production scheduling. The VSS obtained for the risk-averse optimization are considerably higher than those obtained in risk-neutral optimization. Each model has up to approximately 6,500 continuous variables, 209 binary variables, and 3,900 constraints. All models were solved to zero integrality gap in less than 10 s

on an Intel(R) Core(TM) i7-4790 machine at 3.60 GHz with eight processors and 16 GB RAM. All models were implemented in GAMS 24.7.4 (GAMS Development Corporation, 2015), and the MILPs were solved applying the commercial solver CPLEX 12.6.3.0.

Table 1 Value of the stochastic solution for risk-neutral and risk-averse optimization for different levels of uncertainty

Uncertainty level	Risk-neutral optimization		Risk-averse optimization	
	VSS [€]	\bar{VSS} [%]	VSS [€]	\bar{VSS} [%]
Low	84.4	2.8%	367.3	3.7%
Medium	214.6	6.4%	1029.5	10.6%
High	247.9	7.0%	1210.2	12.9%

4. Discussion

Fig.1 shows the electricity purchase profiles that were obtained solving the risk-neutral stochastic model and the deterministic model for the medium uncertainty level. Time-of-Use (TOU) and base load profiles represent the amount of energy purchased from the power contracts. TOU and base load profiles are supposed to be given and therefore not optimized since contract related decisions have to be made before the time horizon of interest (1 week before for the TOU contract and 1 year before for the base load contract). The comparison between the two solutions shows the impact on the day-ahead electricity commitment (first-stage variables) of accounting for other scenario besides the expected one. In the deterministic solution (Fig.1b) the day-ahead commitment depends exclusively on the day-ahead electricity price: in case of price peak (at 9-10 h and 20-21 h) the electricity purchase is drastically reduced and the production is shifted to time periods when the electricity price decreases. In the stochastic solution (Fig.1a), instead, during the price peaks more electricity is purchased in order to be able to compensate reductions of the production capacity. By doing so, lower penalties for deviating from the day-ahead commitment are incurred.

5. Conclusion

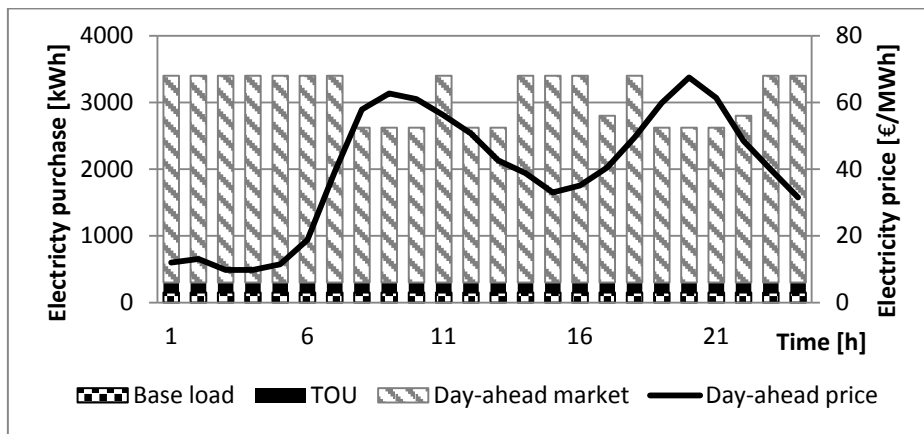
This work addresses the integrated day-ahead electricity commitment and production scheduling for continuous power-intensive processes. A two-stage stochastic programming approach is proposed to model uncertainty of equipment breakdowns. The application of the proposed approach to a power intensive plant shows the benefit of the stochastic model. Risk is taken into account by incorporating the CVaR into the optimization model.

Acknowledgements Financial support is gratefully acknowledged from the Marie Skłodowska Curie Horizon 2020 EID-ITN project “PROcess NeTwork Optimization for efficient and sustainable operation of Europe’s process industries taking machinery condition and process performance into account – PRONTO”, Grant agreement No 675215.

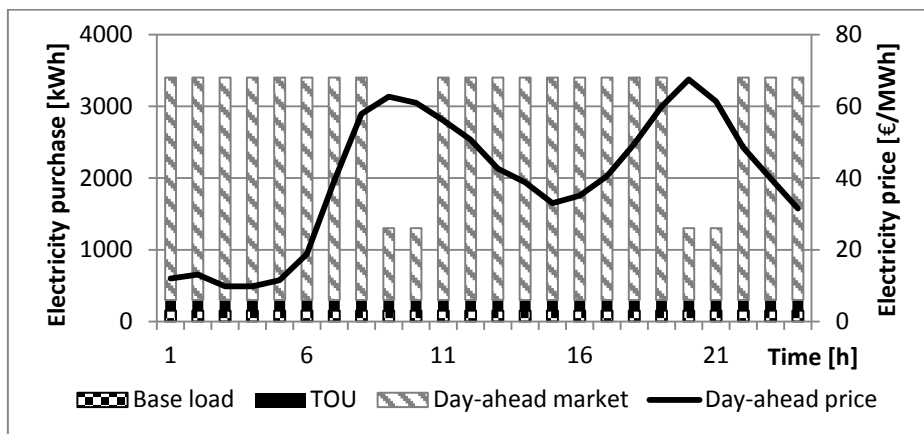
References

JR. Birge, F. Louveaux.2011, Introduction to stochastic programming, 2nd ed Springer Science+Business Media.

- H. Hadera, I.Harjunoski, G.Sand, I.E.Grossmann and S.Engell, 2015, Optimization of steel production scheduling with complex time-sensitive electricity cost, *Comput. Chem. Eng.*, 76, 117-136.
- L. Merkert, I.Harjunoski, A.Isaksson, S.Säynevirta, A. Saarela and G. Sand, 2014, Scheduling and energy – industrial challenges and opportunities, *Comput. Chem. Eng.*, 72, 183-198.
- K. Nolde, M. Morari, 2010. Electrical load tracking scheduling of a steel plant. *Comput. Chem. Eng.* 34 (11), 1899–1903.
- RT. Rockafellar, S. Uryasev. Optimization of conditional value-at-risk. *J Risk* 2000;2:21–42.
- Q. Zhang, L. Jochen, L. Cremer, I.E. Grossmann, A. Sundaramoorthy and J.M. Pinto, 2016, , Risk-based integrated production scheduling and electricity procurement for continuous power-intensive processes, *Comput. Chem. Eng.*, 86, 90-105.



a



b

Figure 1. Electricity purchase profiles obtained solving the stochastic model (a) and the deterministic model (b) for the medium uncertainty level.

Changing between Active Constraint Regions for Optimal Operation: Classical Advanced Control versus Model Predictive Control

Adriana Reyes-Lúa^a, Cristina Zotică^a, Tamal Das^a, Dinesh Krishnamoorthy^a and Sigurd Skogestad^{a*}

^a*Norwegian University of Science and Technology, Department of Chemical Engineering, Sem Sælands vei 4, 7491 Trondheim, Norway*

**sigurd.skogestad@ntnu.no*

Abstract

Control structures must be properly designed and implemented to maintain optimality. The two options for the supervisory control layer are Advanced Control Structures (ACS) and Model Predictive Control (MPC). To systematically design the supervisory layer to maintain optimal operation, the constraints that can be given up when switching active constraint regions should be prioritized. We analyze a case study in which we control the temperature and the flow in a cooler with two degrees of freedom (DOF) represented by two valves, one for each of the two streams. Either valve can saturate and make a constraint active, forcing other constraints to be given-up, and thus changing the set of active constraints. We show that optimal or *near*-optimal operation can be reached with both ACS and MPC. We do a fair comparison of ACS and MPC as candidates for the supervisory layer, and provide some guidelines to help steer the choice.

Keywords: Process control, supervisory control, PID control, MPC, optimal control, active constraints

1. Introduction

On a time-scale basis, the overall control problem of a process plant can be decomposed into different layers. The upper layers are explicitly related to slow time scale economic optimization, which sends economic setpoints to the lower and faster control layer. The control layer is divided into supervisory layer and regulatory layer. The latter follows the set-points given by the former and stabilizes the plant. Most process are operated under a set of constraints, which can be operational limitations, quality specifications, or safety and environmental requirements. “Active constraints” are related to variables that should be kept at their limiting value to achieve optimality. These can be either Manipulated Variables (MVs) or Controlled Variables (CVs). The MVs correspond to the dynamic (physical) DOF used by the control system, and a typical MV constraint is the maximum opening of a valve. An example of CV constraint is the maximum pressure in a distillation column. Every process is subject to disturbances, such as changes in feed rate or product specification. It is the task of the supervisory or “advanced” control layer to maintain optimal operation despite disturbances. The supervisory control layer has three main tasks (Skogestad, 2012):

1. Switch between the set of CVs and control strategies when active constraint changes occur due to disturbances.

2. Supervise the regulatory layer, avoiding saturation of the MVs used for regulatory control.
3. Follow economic objectives by using the setpoints to the regulatory layer as MVs .

The supervisory control layer could be designed using classical ACS with PID controllers, or using MPC, which achieves optimal operation and handles constraints and interactions by design. With ACS, we refer to PID-based structures such as split range control (SRC), input resetting (valve positioning), and use of selectors, to name a few.

2. Changes in active constraint regions and optimal operation

When a disturbance occurs, the process might start operating in a different active constraint region. If the supervisory layer is well-designed, it is possible to maintain optimal operation by using ACS with PID controllers, or by using MPC.

2.1. Optimal control in the presence of active constraint changes

Regardless of whether we choose ACS or MPC, the first step to systematically design the supervisory control layer is to identify and prioritize all constraints. It is useful to visualize how disturbances may cause new constraints to become active. In some cases, we can generate a plot showing the active constraint regions (optimal operation) as a function of variations in important disturbances by solving a series of optimization problems. This may be very time consuming and, in some cases, difficult due to the lack of an appropriate model. Moreover, it can also be difficult to visualize for more than two variables. Alternatively, we can use process knowledge and engineering insight to minimize the need for numerical calculations (Jacobsen and Skogestad, 2011). This information is useful regardless of the type of controller used in the supervisory layer.

Prioritization of constraints has been implemented in a few industrial MPC applications (Qin and Badgwell, 2003). Reyes-Lúa et al. (2018) propose a guideline to generate a priority list of constraints that can be used also for ACS. Under this scheme, the constraints with the lowest priority should be the first given-up when it is not feasible to fulfill all constraints. This way, controlling a high priority constraint will never be sacrificed in order to fulfill a low priority constraint.

2.2. Advanced control structures in the supervisory layer

ACS requires a choice of pairings, which can become challenging with changing active constraints. When implementing ACS, Reyes-Lúa et al. (2018) propose to start designing the control system for the nominal point, with few active constraints and with most of the priorities satisfied. Then, to minimize the need for reassignment of pairings when there are changes in active constraints, we should pair MVs with CVs according to the *Pairing Rule* (Minasidis et al., 2015): *An important controlled variable (CV) (which cannot be given up) should be paired with a manipulated variables (MV) that is not likely to saturate.*

When a disturbance occurs and the process starts operating in a different active constraint region, two types of constraints might be reached:

- MV constraint: we must give up controlling the corresponding CV. If the pairing rule is followed, this MV is paired with a low priority CV, which can be given-up. However, if it is not possible to follow the *pairing* rule, the high priority CV must be reassigned to an MV which is controlling a low priority CV. This requires the use of ACS such as input resetting (valve position control) or SRC combined with a selector block.
- CV constraint: we should give up controlling a CV with a lower priority. We can do this using a *min/max* selector.

2.3. Model predictive control in the supervisory layer

MPC uses an explicit process model to predict the future response of the plant and, by computing a sequence of future MV adjustments, optimizes the plant behavior. The first input of the sequence is applied to the plant, and the entire calculation is repeated at every sampling time (Qin and Badgwell, 2003).

The main challenge when using MPC is that expertise and a good model is required. This is either difficult to have ready at startup, or the modelling effort is too expensive. To achieve a truly optimal operation, the model would need to be perfect, and all the measurements would need to be available and reliable, which is unrealistic from a practical point of view. There are methods to circumvent this, but there is no universal solution and this analysis is out of the scope of this paper.

When an application lacks DOF to meet all control specifications, standard text-book MPC does not handle changes in active constraints effectively. The standard approach is to use weights in the objective function to assign the priorities. Having weights in the objectives function implies a trade-off between the control objectives. An optimal weights selection can assure that a CV is completely given-up, or that the solution will lie at the constraint, as explained in Section 3.4.2. However, there is no systematic way of choosing the weights, as there are no tuning rules for MPC, and this has to be done by trial and error.

An alternative approach consists of implementing a two-stage MPC with a priority list. The first stage has the purpose of finding the solution of a sequence of local steady-state optimization problems (LPs and/or QPs). In this sequence constraints are added in order of priority. The resulting information regarding feasibility is used in the formulation of the dynamic optimization problem for the MPC in the second stage (Qin and Badgwell, 2003).

3. Case study

We study a cooler in which the main control objective is to keep the outlet temperature in the hot stream to a desired setpoint ($T_H = T_H^{sp}$) by using cooling water (F_C). Additionally, the setpoint for the flow of the hot stream (F_H^{sp}) can be changed.

There are two MVs, one corresponding to the cooling water (F_C) and another to the hot stream (F_H). Desired operation is at maximum throughput, with $F_H^{sp} = F_H^{max}$. The primary input (F_C) may saturate for a large disturbance (T_c^{in}). This case is an extension of what is presented by Reyes-Lúa et al. (2018).

3.1. Process model

We consider a countercurrent cooler, represented by the dynamic lumped model in Eq. (1). The cooler is discretized in space into a series of $n = 10$ cells, as depicted in Fig. 1. Incompressible fluids and constant heat capacities are assumed. The boundary conditions are: $T_{H_0} = T_{H_{in}}$ for cell $i = 1$ (inlet), and $T_{C_{11}} = T_{C_{in}}$ for cells $i = 10$ (outlet). The energy balance for cell $i = 1 \dots n$ is:

$$\frac{dT_{C_i}}{dt} = \frac{F_C}{\rho_C V_{C_i}} (T_{C_{i+1}} - T_{C_i}) + \frac{UA_i(T_{H_i} - T_{C_i})}{\rho_C V_{C_i} c_{pC}} \quad (1a)$$

$$\frac{dT_{H_i}}{dt} = \frac{F_H}{\rho_H V_{H_i}} (T_{H_{i-1}} - T_{H_i}) + \frac{UA_i(T_{H_i} - T_{C_i})}{\rho_H V_{H_i} c_{pH}} \quad (1b)$$

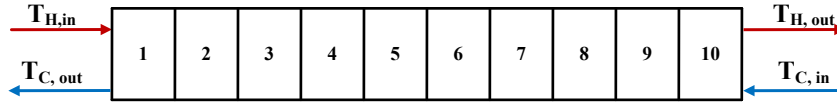


Figure 1: Lumped model for the studied cooler.

3.2. List of priorities

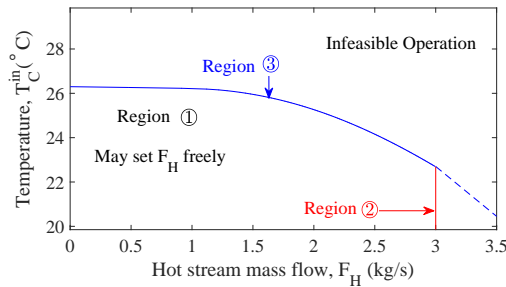
Table 1 shows the priority list of constraints for the cooler we are analyzing.

Table 1: Constraints for the studied cooler.

Priority level	Description	Constraints
1	MV inequality constraints which define the feasibility region	$F_H \leq F_H^{max}$ $F_C \leq F_C^{max}$
2	MV or CV equality constraints, which is the control objective	$T_H = T_H^{sp}$
3	Desired throughput	$F_H = F_H^{sp}$
4	CV inequality constraints or self optimizing variables	none

3.3. Active constraint regions for cooler

As we want to keep $T_H = T_H^{sp}$, this constraint is always active and only one DOF remains. With one DOF and three potential constraints we have three possible active constraint regions, which are shown as a function of the throughput (F_H) and the disturbance (T_c^{in}) in Fig. 2.



Active constraint in each region:

- Region 1: $F_H = F_H^{sp}$
- Region 2: $F_H = F_H^{max}$
- Region 3: $F_C = F_C^{max}$

Figure 2: Active constraint regions for the cooler

3.4. Design of the supervisory layer for the cooler

We consider nominal operation in Region 2 ($F_H^{sp} = F_H^{max}$). According to the priority list, when T_c^{in} is so high that $F_C = F_C^{max}$, the controller should give up controlling $F_H = F_H^{max}$ and reduce F_H to keep $T_H = T_H^{sp}$, thus switching to Region 1. We design both an ACS and an MPC for this case.

3.4.1. Classical advanced control structures for optimal operation

To design the supervisory layer using ACS, we implement SRC with a *min* selector block, as in Fig. 3. The controller is tuned by fitting a first order plus delay model obtained from the open-loop step response of the process, and applying the SIMC rule (Skogestad, 2003) with $\tau_c = 80$ s and $K_c = -0.06$. To account for the different gains that F_C (negative) and F_H (positive) have on T_H , the MVs were respectively multiplied with a gain of 1 and -2 .

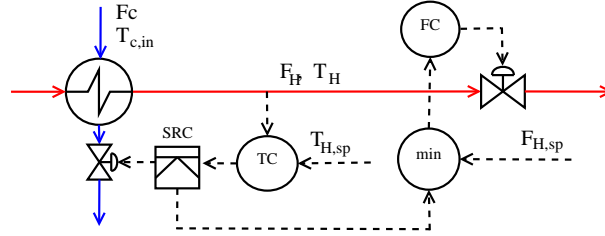


Figure 3: Split range control structure for cooler.

3.4.2. Model predictive control for optimal operation

The optimal control problem is discretized into a finite dimensional optimization problem divided into $N = 40$ control intervals. We use a third order direct collocation scheme for a polynomial approximation of the system dynamics for each time interval.

The dynamic optimization problem is setup in CasADi (Andersson, 2013), which is an algorithmic differentiation tool. According to Eq. 1, the dynamic model is non-linear. The resulting NLP problem is thus solved using IPOPT (Wächter and Biegler, 2005). The prediction horizon is set to 400 s with a sampling time of $\Delta t = 10$ s. We assume we have full state feedback and the disturbance, T_c^{in} , is measured.

In this paper, we chose to implement the standard MPC formulation given by Eq. 2, and to assign different weights for the two control objectives. A high weight is assigned to the high priority CV (T_H) and a low weight is assigned to the low priority CV (F_H). The values $\omega_1 = 3$ and $\omega_2 = 0.1$ are used. These were found by trial and error. In addition, the MVs are restricted to a rate of change of 10% of F_H^{max} and F_C^{max} respectively.

$$\begin{aligned}
 \min \quad & \sum_{k=1}^N \left(\omega_1 \| (T_{H_k} - T_H^{sp}) \|^2 + \omega_2 \| (F_{H_k}^{max} - F_{H_k}) \|^2 \right) \\
 \text{s.t.} \quad & \left. \begin{aligned}
 T_{k,i} &= f(T_{H_{k,i}}, T_{H_{k,i-1}}, T_{C_{k,i}}, T_{C_{k,i+1}}, F_{H_k}, F_{C_k}) \\
 0 &\leq F_{H_k} \leq F_H^{max} \\
 0 &\leq F_{C_k} \leq F_C^{max}
 \end{aligned} \right\} \quad \forall k \in \{1, \dots, N\} \\
 & \left. \begin{aligned}
 0 &\leq \Delta F_{H_k} \leq 0.1 F_H^{max} \\
 0 &\leq \Delta F_{C_k} \leq 0.1 F_C^{max}
 \end{aligned} \right\} \quad \forall k \in \{1, \dots, N-1\}
 \end{aligned} \tag{2}$$

where $\Delta F_k = F_k - F_{k-1}, \forall k \in \{1, \dots, N-1\}$. For $k = 1$, F_{k-1} represents the flow at the nominal operation point.

3.4.3. Simulation results

Fig. 4 shows the simulation results for the case study. T_H^{sp} is 26.3°C . MPC and SRC are tested for the same step disturbances in T_c^{in} : $+2^\circ\text{C}$ at $t = 10\text{s}$, and an additional $+4^\circ\text{C}$ at $t = 1000\text{s}$. Both MPC and SRC follow the priority list and reach optimal operation at steady state. Once $F_C = F_C^{max}$, the control structure gives-up controlling $F_H = F_H^{max}$, and F_H is used as MV to maintain $T_H = T_H^{sp}$.

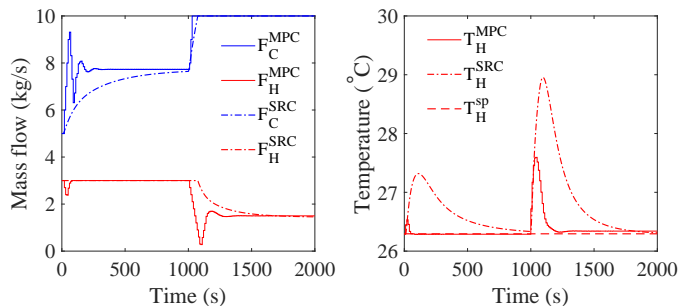


Figure 4: Simulation results for MPC and SRC.

4. Discussion and conclusion

The supervisory control layer can be designed using MPC or ACS. MPC uses the manipulated variables to achieve optimal operation by design, but it requires expertise and a model, which may be difficult to obtain. Well designed ACS can also maintain optimal operation, require much less model information, and are usually easier to implement and tune. In our example, SRC efficiently switches the MVs, achieving optimal operation. Compared to ACS, MPC implementation requires more effort as the tuning of weights in the objective function is more challenging because it is done by trial and error. As it is seen in Fig 4, for a short transient time during the first disturbance in the MPC implementation, $F_H \neq F_H^{max}$. This could be improved by increasing ω_2 relative to ω_1 . This would however be at the expense of having an offset for T_H from T_H^{sp} , as its weight in the objective function would be smaller. Therefore, we should point out that a different MPC implementation or tuning could have better performance, especially on the input usage.

We recommend to use priority lists as a tool for analyzing and designing the supervisory layer. Understanding the process is an important step to decide which controller should be implemented. Both ACS and MPC have advantages and disadvantages, and the designer of the control layer should be aware of these. While in simple cases such as the presented case study, ACS seems better fitted due to achieving optimality with less implementation effort, in multivariable systems with more interactions, MPC should be considered as the most convenient alternative.

5. Acknowledgements

This work was partly supported by the Norwegian Research Council under HighEFF (Energy Efficient and Competitive Industry for the Future) and SUBPRO (Subsea Production and Processing).

References

- J. Andersson, 2013. A General Purpose Software Framework for Dynamic Optimization. Phd thesis, KU Leuven.
- M. G. Jacobsen, S. Skogestad, 2011. Active Constraint Regions for Optimal Operation of Chemical Processes. *Industrial & Engineering Chemistry Research* 50 (19), 11226–11236.
- V. Minasidis, S. Skogestad, N. Kaistha, 2015. Simple Rules for Economic Plantwide Control. In: K. V. Gernaey, J. K. Huusom, R. Gani (Eds.), *PSE 2015 and ESCAPE-25*. Elsevier Science Direct, pp. 101–108.
- S. Qin, T. A. Badgwell, 2003. A survey of industrial model predictive control technology. *Control Engineering Practice* 11 (7), 733–764.
- A. Reyes-Lúa, C. Zotica, S. Skogestad, 2018. Optimal Operation with Changing Active Constraint Regions using Classical Advanced Control. In: 10th ADCHEM. IFAC, Shenyang, China.
- S. Skogestad, 2003. Simple analytic rules for model reduction and PID controller tuning. *Journal of Process Control* 13, 291–309.
- S. Skogestad, 2012. Economic Plantwide Control. In: G. P. Kariwala, Vinay Rangaiah (Ed.), *Plantwide Control*. Wiley, Ch. 11, pp. 229–251.
- A. Wächter, L. T. Biegler, Apr. 2005. On the implementation of an interior-point filter line-search algorithm for large-scale nonlinear programming. *Mathematical Programming* 106 (1), 25–57.

Health-Aware Operation of a Subsea Compression System Subject to Degradation

Adriaen Verheyleweghen^a, Julie Marie Gjøby^a and Johannes Jäschke^{a,*}

^a*Dept. of Chemical Engineering, NTNU, N-7491 Trondheim, Norway*
jaschke@ntnu.no

Abstract

We propose an health-aware operation approach for combining short-term control objectives with long-term profit and reliability targets. In particular, we present a hierarchical approach for operating a compressor subject to degradation. We consider a case study of a subsea compressor, where the goal is to maximize the gas throughput, while ensuring that the compressor can be operated continuously until a planned maintenance stop. In the top layer, we repeatedly solve a dynamic optimization problem to find the optimal long-term operation strategy, subject to load-induced compressor degradation. The supervisory control layer below receives the computed setpoints and operational parameters, and applies them in a self-optimizing control structure to ensure near-optimal operation in the presence of disturbances. The regulatory control layer in the bottom stabilizes operation in an otherwise unstable operating region (surge). We show the efficacy of our health-aware operation approach by comparing it to traditional control structures where the equipment health is not explicitly considered as part of the production optimization. Our approach results in higher average production, without jeopardizing the health of the system.

Keywords: Health-aware operation, Control, Reliability, Optimal Operation, Rotating Machinery

1. Introduction

Unplanned maintenance intervention of subsea systems are costly, so it is necessary to ensure that operation does not reduce the system reliability to unacceptable levels. Traditionally, this has been achieved by introducing large safety margins and enforcing conservative operational strategies. Better economical performance can be achieved by employing prognostics and health monitoring (PHM), which means that the system state is monitored and projected into the future. A natural extension of PHM is health-aware control, in which we combine control and reliability objectives, yielding a control structure that maximizes plant profitability while keeping the plant health within acceptable limits (Sanchez et al., 2015; Verheyleweghen and Jäschke, 2017).

Health-aware control is achieved by repeatedly solving a shrinking horizon dynamic optimization problem to find an operating strategy based on the current compressor health and its predicted development. The time horizon is from the present until the next planned maintenance intervention, and the objective is to maximize the profit subject to health constraints. The dynamics of this layer are on the time-scale of weeks to months. On a more frequent basis, disturbances are rejected by a supervisory control layer in order to keep operation close to the desired (optimal) operating point. We use self-optimizing control ideas (Skogestad, 2000) to achieve this. The lowest and fastest control layer is in charge of surge control. Surge is an unwanted mode of operation characterized by limit-cycle oscillations in flow and pressure, which can harm the internals of the compressor (McMillan, 1983). Traditionally, operation is restricted by a generous safety margin from the surge

line. However, it is often desirable to operate closer to the surge line, as this leads to increased efficiency and lower operating costs. An alternative to surge avoidance is active surge control. For this purpose, a close-coupled valve (CCV) is introduced to the system. Using the CCV, we can control the compressor characteristic, thereby stabilizing operation in an otherwise unstable region (Gravdahl and Egeland, 1999). A feedback linearizing controller proposed by Backi et al. (2016), is used for this purpose. An illustration of the proposed control structure is shown in Figure 1.

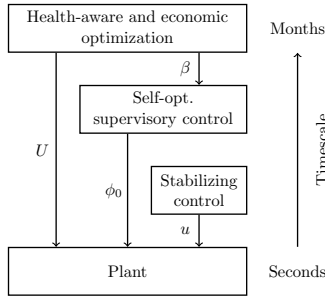


Figure 1: Multi-layer control structure for stable, health-aware operation.

of the non-dimensional compressor mass flow ϕ and the non-dimensional pressure rise across the plenum, ψ . A detailed description and derivation of the model is given in Gravdahl and Egeland (1999), but a summary is given below for completeness. An illustration of the system is given in Fig. 2. Three degrees of freedom are available for control in the system: the compressor speed, the CCV opening and the throttle opening.

The two-state Greitzer model is given as:

$$\dot{\hat{\phi}} = B [\hat{\Psi}_C(\hat{\phi}) - \hat{\psi} - u] \quad (1)$$

$$\dot{\hat{\psi}} = \frac{1}{B} [\hat{\phi} - \hat{\Phi}_T(\hat{\phi})], \quad (2)$$

where the ($\hat{\cdot}$)-symbol is used to denote deviation from the specified operating points, $\hat{\phi} = \phi - \phi_0$ and $\hat{\psi} = \psi - \psi_0$. (ϕ_0, ψ_0) is the specified operating point. In the above expression, B is the Greitzer parameter, which is proportional to the compressor blade tip speed U , $B = kU$, where k is a geometry-dependent constant. $\hat{\Psi}_C$ is the cubic approximation of the axisymmetric compressor characteristic, $\hat{\Phi}_T$ is the throttle characteristic, and the input u is the pressure drop across the CCV (as determined by its opening). The compressor and throttle characteristics is shown in Figure 3.

The compressor characteristic $\hat{\Psi}_C$ indicates the pressure rise for a given flow, and is unique for every compressor. The characteristic is approximated by the cubic

$$\hat{\Psi}_C(\hat{\phi}) = -k_3\hat{\phi}^3 - k_2\hat{\phi}^2 - k_1\hat{\phi}, \quad (3)$$

where $k_1 = \frac{3H\phi_0}{2W^2} \left(\frac{\phi_0}{W} - 2 \right)$, $k_2 = \frac{3H}{2W^2} \left(\frac{\phi_0}{W} - 1 \right)$ and $k_3 = \frac{H}{2W^3}$. H and W are equipment-specific parameters relating to the peak and valley points of the compressor characteristic. The peak point, $(\phi^*, \psi^*) = (2W, \psi^*)$, is assumed to be the surge point, with all points left of the peak being unstable.

The main contributions of this paper are the following: 1) We propose a three level control structure for health-aware control of a compression system. 2) We show that the method outperforms traditional control methods

2. Model description

2.1. Short timescale dynamics: Surge

The surge model used here is that of a centrifugal compressor with an added CCV for surge control, which as described by Simon (1993). We use the transformed version of the model presented by Gravdahl and Egeland (1999), by which the system can be described in terms

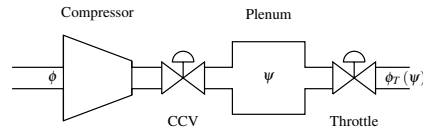


Figure 2: Flowsheet of the Greitzer compressor model

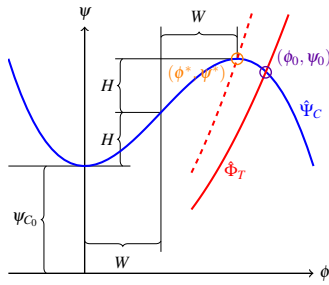


Figure 3: Cubic approximation of the axisymmetric compressor characteristic (blue) and the throttle characteristic (red). The operating point (ϕ_0, ψ_0) is shown in purple and the surge point $(\phi^*, \psi^*) = (2W, \psi^*)$ is shown in orange. The surge line (surge point at various compressor speeds) is shown as the dashed line.

The throttle characteristic is given as

$$\hat{\Phi}_T(\hat{\Psi}) = \frac{\phi_0}{\sqrt{\psi_0}} \left(\text{sign}(\psi) \sqrt{|\psi|} - \sqrt{\psi_0} \right). \quad (4)$$

The intersection between $\hat{\Psi}_C$ and $\hat{\Phi}_T$ gives the operating point (ϕ_0, ψ_0) , shown in purple in Figure 3.

2.2. Long timescale dynamics: Compressor degradation

Variations in pressure and flow rate (as caused by surge) lead to radial vibrations, axial thrust displacement and a large temperature rise. This will in turn damage bearings, blades and other internal components (McMillan, 1983). We lump the accumulated damage on all internal components into a health indicator state x , whose propagation is modeled as

$$\dot{x} = \mathbb{E} \left(p_1 \phi_0 + \int_0^\infty \left(p_2 |\hat{\phi}(d)| + p_3 |\hat{\psi}(d)| \right) dt \right), \quad (5)$$

where \mathbb{E} is the expected value operator, $d = [W \ H \ \psi_{C_0}]^\top$ are independently normal distributed disturbances and p_i are weights. The p_1 -term is the damage caused by regular operation, which is proportional with the throughput. The harder the compressor is run (in terms of throughput), the more rapidly it degrades. The p_2 -term is damage caused by oscillations in pressure and flow, caused by surge. The p_3 -term accounts for high-frequency oscillations, as these are thought to be more harmful to the compressor than low-frequency oscillations.

3. Hierarchical control structure for the subsea compressor

Due to the large difference in time scales for the problem, it is natural to divide it into several timescale-separated layers. The lowest layer stabilizes operation, the middle layer rejects disturbances, and the top layer is used to ensure reliable operation. Three degrees of freedom are available to achieve this: the pressure drop over the CCV, u , the blade tip speed, U , and the flow through the compressor, ϕ_0 , as determined by the throttle. The three layers are described in more detail in the following subsections.

3.1. Stabilizing control layer

The purpose of the lowest control layer is to stabilize the compressor beyond the surge line. For this purpose, we use a feedback linearizing controller which adjusts the CCV. Feedback linearizing control enables controlling non-linear systems with a linear control law, allowing for higher sampling frequencies due to the reduced computational complexity. Since the surge phenomenon happens on a short time scale, while simultaneously being non-linear, the use of feedback linearization is appropriate. We use the feedback linearizing controller presented by Backi et al. (2016). A full description and derivation of the control law is given there.

The proposed feedback linearizing controller for the CCV is:

$$u = \mu_1 \hat{\phi} + \mu_2 \hat{\psi}, \quad (6)$$

where u is the pressure drop across the CCV and μ_1 and μ_2 are controller tuning parameters.

3.2. Supervisory control layer (Local disturbance rejection: Self-optimizing control)

After stabilizing the system with the CCV, we can optimize operation by adjusting the flow through the system. The operational objective is to maximize the compressor efficiency, but operation too close to the surge point is penalized.

$$\min_{\phi_0, U} \quad J^{SOC} = -\eta(\phi_0) + \beta(2W - \phi_0). \quad (7)$$

In the above expression η is the efficiency and β is the penalty weight. Using self-optimizing control (Skogestad, 2000; Jäschke et al., 2017), we can keep the operation such that it is near optimal in the sense of (7) by controlling a combination of carefully chosen plant measurements y , to a predetermined set-point:

$$c = H^{SOC}y \quad (8)$$

In this case, the plant measurements are augmented by disturbance measurements, $d = [W \quad H \quad \Psi_{C_0}]^T$, such that $y = [\phi \quad \psi \quad d]^T$. A measurement combination matrix H^{SOC} that can be shown to minimize the average loss $L = J(\phi_0, d) - J^{opt}(\phi_0^{opt}, d)$ is (Yelchuru and Skogestad, 2010)

$$(H^{SOC})^T = (YY^T)^{-1}G^y, \quad (9)$$

where

$$Y = [FW_d \quad W_{n^y}], \quad (10)$$

and $G^y = \left. \frac{\partial y}{\partial \phi_0} \right|_{\phi_0^{nom}}$ is the linearized system model evaluated at the nominal operating point, $F = \frac{dy^{opt}}{dd}$ is the optimal sensitivity matrix, and W_{n^y} and W_d are diagonal matrices of appropriate sizes with the variances of the measurement errors / noise n^y and the variances of d .

3.3. Optimal economic and reliable operation

In the top control layer, we devise a dynamic real-time optimization (DRTO) scheme to calculate the optimal compressor speed U and penalty weight β for the SOC layer. The purpose of this layer is to adjust operation for the other layers to ensure both economic optimality and satisfaction of operational and reliability constraints. At each time step we solve the following dynamic optimization problem

$$\min_{\beta, U} \quad J^{DRTO} = -\int_0^{t_f} NPV(\phi_0)dt = -\int_0^{t_f} \frac{\phi_0}{(1+i)^t} dt \quad (11)$$

$$s.t. \quad x < x_{max} \quad (12)$$

$$\Psi_{out} > \Psi_{out, min}, \quad (13)$$

where NPV signifies the net present value with discount rate i and x is the degradation from (5). $\Psi_{out} = \hat{\Psi} + \psi_{res}$ is the outlet pressure from the compressor.

4. Simulations

The system described in Section 2 and the control structure described in Section 3, are implemented in MATLAB/Simulink and Casadi 3.0.0 (Andersson, 2013). IPOPT 3.12.3 (Wächter and Biegler, 2006) is used to solve the optimization problems (7) and (11).

4.1. Stabilizing control

Figure 4 shows the response of the system with the surge controller turned off (solid blue line) and with the surge controller turned on (dashed blue line) to a step change in ϕ_0 . After the step, the new set-point lies within the unstable operating region, causing the limit cycle behavior in the uncontrolled case.

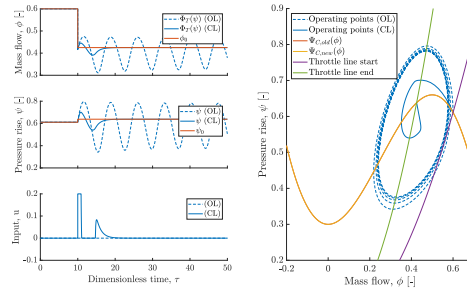


Figure 4: Closed-loop (CL) and open-loop (OL) responses to a set-point change in ϕ_0 into the unstable region.

4.2. Local disturbance rejection (Self-optimizing control)

Fig. 5 shows the response of the SOC structure (open loop (OL) and closed loop (CL)). As can be seen, the CL structure drives operation back to the optimal point. The OL structure, while stable thanks to the surge controller, does not. Operation continues at a sub-optimal operating point, resulting in higher cost. Note that for the simulated disturbance in H and ψ_{c0} , the steady state loss for the CL structure is higher than that of the OL structure. On the other hand, a step in W results in a lower loss, illustrating that it is the average loss that is minimized by (9), not the loss for each individual disturbance.

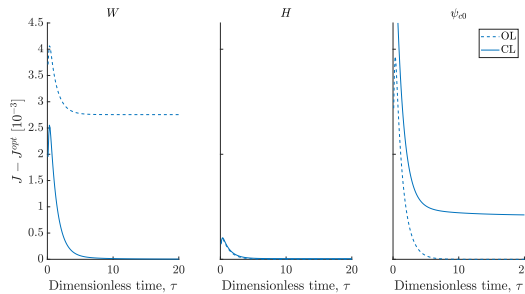


Figure 5: Open loop (OL) and closed loop (CL) losses for the SOC structure for the disturbances W , H and ψ_{c0}

4.3. Optimal economic and reliable operation

We consider three cases of DRTO. The DRTO1 and DRTO2 do not take the degradation constraint into account, and differ in terms of the maximum allowable shaft speed. DRTO1 allows higher shaft speed. DRTO2 is more conservative with a lower maximum allowable shaft speed. The DRTO3 is health-aware and does not have constraints on the shaft speed, but instead ensures that the degradation is not exceeded. The closed-loop responses of the DRTOs are shown in Fig. 6. It can be seen that operation is adjusted to maximize the NPV of the production in all three cases by gradually reducing the production over time. However, only the "conservative" DRTO2 with the lower maximum allowable speed and the health aware DRTO structures satisfy the reliability constraints. The non-health-aware DRTOs do not "see" the compressor degradation. The system is disturbed at around $t = 1.5$ and again at $t = 2.5$, by stepping first up, then down in the degradation speed, to show that the health-aware control structure takes into account the updated health information.

5. Concluding remarks and future work

We have proposed a control structure for a compression system subject to long-term load-induced degradation. By using time scale separation it is possible to counteract surge and reject disturbances, while also achieving long term optimality and satisfaction of reliability constraints. We have shown that the proposed method is better than a "regular" DRTO scheme, in which reliability considerations are not taken into account when planning future production.

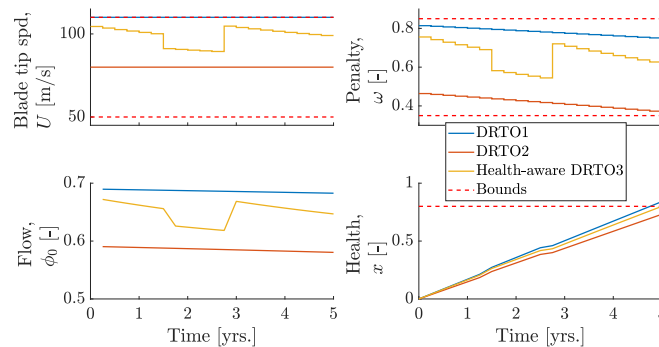


Figure 6: Closed loop responses of the regular DRTOs and the health-aware DRTO to disturbances in degradation speed.

Several assumptions have been made in this work: we assume perfect state feedback for the DRTO, meaning that we can measure the health indicator state directly and without errors. This is somewhat unrealistic. In practice, we need to estimate the health indicator from other measurements. In the DRTO, we did not use parameter estimation to adapt the model when the operating conditions changed. Finally, the DRTO has to be made robust towards model uncertainty by formulating a robust/stochastic optimization problem. This will be addressed in future work.

6. Acknowledgments

This work is funded by the SUBPRO center for research based innovation, www.ntnu.edu/subpro. Johannes Jäschke acknowledges support by DNV-GL.

References

- J. Andersson, October 2013. A General-Purpose Software Framework for Dynamic Optimization. PhD thesis, Arenberg Doctoral School, KU Leuven, Department of Electrical Engineering (ESAT/SCD) and Optimization in Engineering Center, Kasteelpark Arenberg 10, 3001-Heverlee, Belgium.
- C. J. Backi, J. T. Gravdahl, S. Skogestad, 2016. Robust control of a two-state Greitzer compressor model by state-feedback linearization. In: Control Applications (CCA), 2016 IEEE Conference on. IEEE, pp. 1226–1231.
- J. T. Gravdahl, O. Egeland, 1999. Compressor Surge and Rotating Stall: Modeling and Control. Advances in Industrial Control. Springer Science & Business Media.
- J. Jäschke, Y. Cao, V. Kariwala, 2017. Self-optimizing control—A survey. Annual Reviews in Control.
- G. K. McMillan, 1983. Centrifugal and Axial Compressor Control. Momentum Press.
- H. Sanchez, T. Escobet, V. Puig, P. F. Odgaard, 2015. Health-aware model predictive control of wind turbines using fatigue prognosis. IFAC-PapersOnLine 48 (21), 1363–1368.
- J. S. Simon, February 1993. Feedback Stabilization of Compression Systems. PhD thesis, Massachusetts Institute of Technology, Department of Mechanical Engineering, 77 Massachusetts Ave, Cambridge, MA 02139, USA.
- S. Skogestad, 2000. Plantwide control: The search for the self-optimizing control structure. Journal of Process Control 10 (5), 487–507.
- A. Verheyleweghen, J. Jäschke, 2017. Framework for Combined Diagnostics, Prognostics and Optimal Operation of a Subsea Gas Compression System. In: 2017 IFAC World Conference. Vol. 50. pp. 15916–15921.
- A. Wächter, L. T. Biegler, 2006. On the implementation of an interior-point filter line-search algorithm for large-scale nonlinear programming. Mathematical programming 106 (1), 25–57.
- R. Yelchuru, S. Skogestad, 2010. MIQP formulation for Controlled Variable Selection in Self Optimizing Control. IFAC Proceedings Volumes 43 (5), 61–66.

Application of CFD modelling to external nuclear reactor vessel cooling

Marco Colombo*, Michael Fairweather

School of Chemical and Process Engineering, University of Leeds, Leeds LS2 9JT, UK

**M.Colombo@leeds.ac.uk*

Abstract

In nuclear power plants, passive cooling can increase the safety of reactors whilst reducing costs and design complexity. However, the effectiveness of passive mechanisms needs to be carefully proved with reliable computational modelling. This work focuses on assessing the external reactor vessel cooling (ERVC) strategy by means of computational fluid dynamics (CFD). The accuracy of a two-fluid Eulerian-Eulerian CFD model with boiling capabilities is first assessed, as subsequently is its ability to predict ERVC. The CFD model described proves to be a valuable tool for predicting passive cooling by detecting local boiling incipience and providing three-dimensional vessel temperature distributions, as well as thermal stratification and velocity field predictions in the cooling pool. This work is part of a larger programme aimed at assessing CFD capabilities for predicting passive cooling strategies, with a quantitative assessment of ERVC currently ongoing.

Keywords: Computational fluid dynamics, natural convection, passive cooling, boiling

1. Introduction

Natural convection relies solely on naturally occurring phenomena, possibly lasting indefinitely without interruption, and does not require any active power or moving parts. Therefore, it is regarded as an efficient, cost-effective and reliable heat transfer mechanism and is used in numerous heat transfer applications (e.g. air ventilation and thermal storage). In the nuclear sector, there has been a gradual increase in reactor design reliance on passive cooling mechanisms. As the recent events in Fukushima have shown, there is a great benefit in ensuring that the necessary cooling of the reactor can be entirely provided by natural processes for a significant amount of time before any power intervention is needed. Because of this, many modern designs adopt the so-called external reactor vessel cooling (ERVC) strategy. In a severe accident scenario that involves damage to and melting of the fuel rods, the melted corium is retained inside the reactor vessel. After flooding the region outside the vessel, heat is removed passively by natural convection on the outside vessel wall (Kim et al., 2012). Boiling is also expected to occur on that wall, and the maximum amount of heat safely removable from the system is limited by the critical heat flux. This must not be exceeded to avoid overheating of the vessel to temperatures potentially well-beyond operating limits.

Although passive cooling may appear simple and reliable, there are many underlying complexities. Thermal and velocity fields are strongly coupled, and buoyancy effects may increase or suppress turbulence in the flow (Hanjalic, 2002). Buoyancy-driven flows are also often prone to flow instabilities (Basu et al., 2014) and thermal stratification may

prevent the required amount of heat being effectively removed (Minocha et al., 2016). Therefore, numerical tools of proven accuracy become essential in demonstrating that the required heat removal can always be guaranteed, and the design and engineering limits, which safeguard the safety and integrity of the reactor, met. With respect to more traditional one-dimensional approaches currently used in the industry, CFD can fully account for three-dimensional effects at a much finer space resolution, providing detailed temperature distributions as well as identifying higher thermal load regions and hot spots. However, CFD has not been extensively applied to ERVC and more generally to buoyancy-driven boiling flows, although boiling needs to be detected by any CFD model that aims at predicting ERVC. Krepper et al. (2002) used single-phase CFD to study thermal stratification of a condenser submerged in a pool. Minocha et al. (2016) also predicted the single-phase flow in an isolation condenser pool, with the same group also studying thermal stratification for a vertical rod submerged in a rectangular (Ghandi et al., 2013a) and a cylindrical (Ghandi et al., 2013b) pool with boiling at the wall.

In this paper, the predictive capabilities of a two-fluid Eulerian-Eulerian boiling CFD model are assessed. Initially, model results are compared against measurements for a submerged cylindrical heated rod (Ghandi et al., 2013b). Subsequently, the model is used to predict natural convection on the outside of a horizontal cylindrical vessel, scaled on the calandria vessel of the Indian pressurized heavy water reactor. Model capabilities to detect boiling and predict the distinctive features of ERVC are qualitatively assessed. The work is part of a larger programme aimed at proving that CFD approaches of this kind can be confidently used for the assessment of ERVC, and identifying and implementing any model improvements that might be required.

2. CFD Model

The Eulerian-Eulerian, two-fluid boiling model solves a set of mass, momentum and energy conservation equations for each phase. Because of averaging, closure models are required for mass, momentum and energy interphase transfers. In the continuous phase, buoyancy is accounted for in the gravitational term of the momentum equation, adopting the Boussinesq approximation, which is acceptable provided that changes in temperature and density are limited. Turbulence is solved in the continuous phase with a multiphase formulation of the standard k - ε model that also accounts for production of turbulence by buoyancy (CD-adapco, 2016). Previous studies reported how high-Reynolds wall treatments, and the logarithmic law of the wall, cease to be valid in natural convection boundary layers (Omranian et al., 2014). For this reason, the two-layer formulation proposed by Xu et al. (1998) for natural convection flows is employed. The model solves for the turbulence kinetic energy k , but prescribes algebraically the turbulence energy dissipation rate in the first computational cell near the wall using $\varepsilon = k^{3/2} / l_\varepsilon$. The length scale l_ε and the turbulent viscosity ratio are obtained from:

$$l_\varepsilon = \frac{8.8y}{1 + 10/y_v^* + 0.0515y_v^*} \quad \frac{\mu_t}{\mu} = \frac{0.544y}{1 + 50250y_v^{*1.65}} \quad (1)$$

In the previous equations, y is the normal distance from the nearest wall and y_v^* is a function of the wall normal stress $\overline{v\overline{v}}$, modelled as a function of the dimensionless wall distance $y^* = yk^{0.5} / \nu$, where ν is the kinematic viscosity (Xu et al., 1998). The turbulent heat fluxes are modelled by extending the eddy-viscosity approach (CD-adapco, 2016).

Heat flux from the wall, following the Rensselaer Polytechnic Institute (RPI) heat flux partitioning approach (Kurul and Podowski, 1990), is partitioned between convection to the single-phase liquid, evaporation and quenching. The evaporative contribution to the heat flux q_{ev} is equal to:

$$q_{ev} = Nf \left(\frac{\pi d_w^3}{6} \right) \rho_v h_{lv} \quad (2)$$

Active nucleation site density N is calculated from Hibiki and Ishii (2006), the bubble departure diameter d_w from Kocamustafaogullari (1983) and the bubble departure frequency f from Cole (1960). The average bubble diameter in the flow is related to the local subcooling (Kurul and Podowski, 1990), and evaporation/condensation in the bulk is evaluated using the Ranz and Marshall (1952) correlation.

Simulations were performed using the STAR-CCM+ code (CD-adapco, 2016). For the cylindrical rod submerged in a pool, a three-dimensional, 45° radial section of the geometry was employed with symmetry boundary conditions applied at the two ends. The no-slip boundary condition was imposed at the walls of the tank and the heated rod, which had an imposed temperature of 140° C. The simulation was run for a total of 200 s, starting from fluid initially at rest at 27°C. The fluid had a thermal expansion coefficient $\beta = 0.00068$ and a Rayleigh number $Ra = 5.9 \times 10^{11}$. A full three-dimensional horizontal cylindrical vessel submerged in a rectangular pool geometry was built for the calandria vessel case. No-slip boundary conditions were imposed on the walls. Vapour is not expected to reach the top of the pool but to entirely condense in the subcooled water. A radial decreasing heat flux distribution was imposed on the outside vessel wall. Values were selected to represent an experiment conducted on a similar geometry at the Bhabha Atomic Research Centre that is being used for an ongoing detailed quantitative assessment of the model. Time transients represent the timescale of the experiment, with the computed flow time reaching 3600 s. In both cases, sensitivity studies assured that the obtained solutions were grid independent.

3. Results and Discussion

A preliminary assessment of the model was made against the experimental data of Ghandi et al. (2013b). Some results are shown in Fig. 1 for the temperature distribution on a radial plane, and radial profiles of the vertical velocity at two different heights. Warm water flows upwards near the heated rod, reaches the free-surface and circulates back downward near the outside wall of the pool. The tank gradually heats up and thermal stratification increases with time. Temperature profiles were found to be in reasonable agreement with the experiment, although excessive stratification was predicted. This is most probably related to the heat flux turbulence modelling being limited to a gradient assumption at the present time (Colombo and Fairweather, 2017). Radial velocity profiles show good agreement with data, the main discrepancies being the underestimation of the extent of the downward flow at $z/H = 0.9$. The necessity for a near-wall model is confirmed by the majority of the flow being restricted to a very thin boundary layer region. Boiling at the wall was correctly detected, but the amount of vapour generated was minimal and almost entirely condensed in the subcooled liquid without reaching the free surface, in agreement with experimental observations.

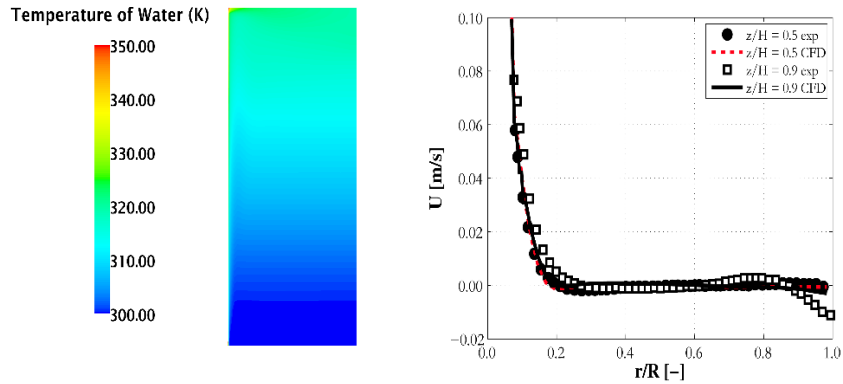


Figure 1. Temperature distribution in the pool (left) and comparison of radial velocity profiles against the experimental data of Ghandi et al. (2013a) (right).

In the calandria vessel case, to study the capabilities of CFD to detect local heat transfer and boiling conditions, the imposed heat flux distribution varies in space and time. In the context of ERVC, the heat to be removed is mainly due to radioactive decay and, consequently, decreases with time. External wall temperatures are given in Fig. 2 as a function of time and angle, where 0° is the bottom and 180° the top of vessel. Although the flow is mainly single-phase, subcooled boiling is observed on the bottom of the vessel for more than 30 minutes, as demonstrated by the flat temperature profile at 0° in Fig. 2.

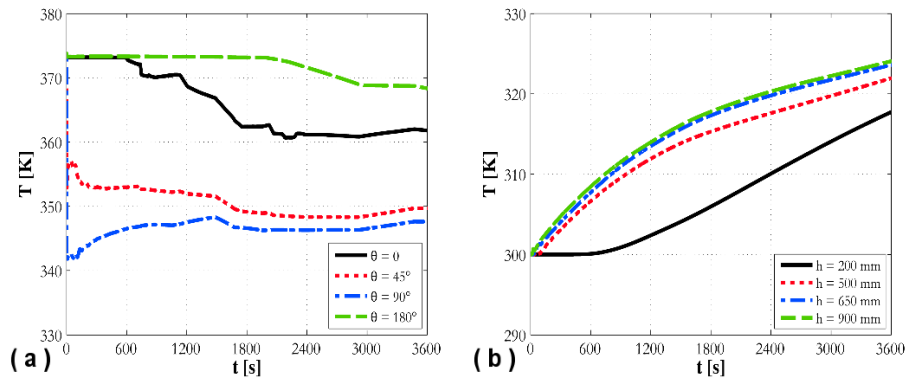


Figure 2. Behaviour with time of (a) the temperature on the outside wall of the vessel at different radial locations, and (b) of the temperature in the pool at different heights.

As the water in the external pool heats up, thermal stratification occurs (Fig. 2(b)). This is also evident in Fig. 3, which shows temperature and velocity fields inside the pool. Water heats up and flows upward, generating a plume above the cylindrical vessel and two large recirculation regions. Detailed heat transfer coefficient distribution can be obtained from the CFD (Fig. 4(a)). As shown, heat transfer is a maximum on the side of the vessel and, once boiling ends, a minimum at the top and bottom of the vessel. Although boiling was detected, boiling conditions were not sustained for the entire duration of the transient simulation. Therefore, a second simulation was undertaken with higher heat fluxes, greater than 85 kW m^{-2} at the beginning of the transient. In

these conditions, boiling lasts for the entire duration of the transient, as demonstrated by the wall temperatures remaining close to saturation in Fig. 4(b). Even if more sustained, boiling was still in the subcooled nucleate boiling regime and distant from film boiling or critical heat flux, and these conditions were successfully handled by the model.

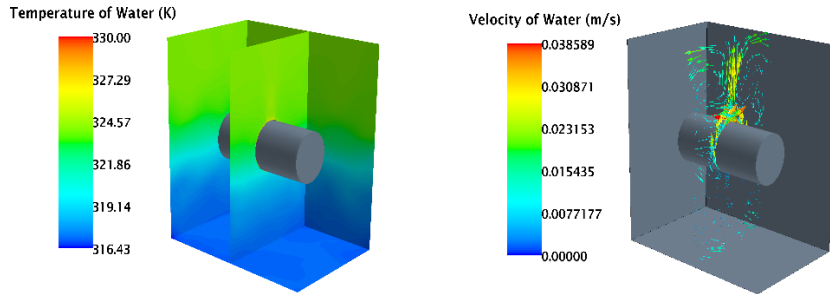


Figure 3. Temperature distribution (left) and velocity field (right) in the water pool of the calandria vessel.

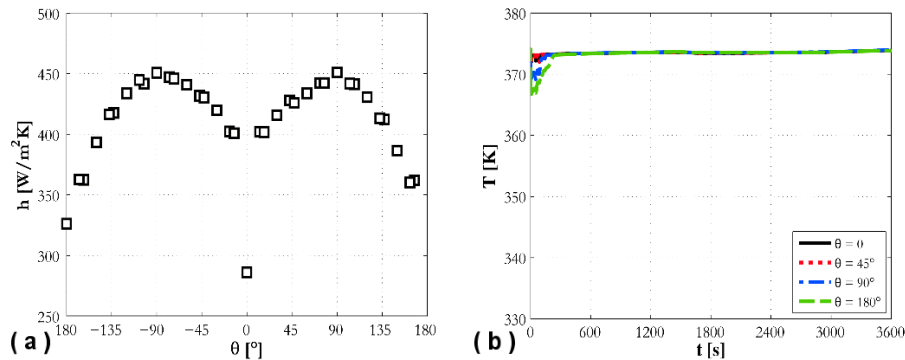


Figure 4. (a) Heat transfer coefficient distribution on the vessel external wall, and (b) time behaviour of the vessel wall temperature at higher heat flux.

4. Conclusions

The ability of a two-fluid Eulerian-Eulerian CFD boiling model to predict natural convection and boiling at a wall, as well as to assess the effectiveness of the ERVC strategy in nuclear reactors, has been studied. Comparison with experimental data for a heated cylindrical rod in a pool demonstrates that the model correctly predicts the onset of boiling and recirculation, and thermal stratification in the pool. The quantitative accuracy of these predictions are, however, likely to be improved by more advanced turbulent heat flux modelling. The qualitative features of an ERVC transient in a scaled cylindrical calandria vessel of the Indian pressure-tube type were also predicted. The model provides a detailed three-dimensional distribution of the vessel wall temperature and local boiling conditions, as well as recirculation and thermal stratification in the pool. These results confirm the capability of the present model to detect the distinctive features of ERVC and, therefore, to evaluate the effectiveness of the passive cooling. A detailed quantitative assessment against experimental data is currently ongoing.

Acknowledgements

The authors gratefully acknowledge the financial support of the EPSRC under grant EP/M018733/1, Grace Time, part of the UK-India Civil Nuclear Collaboration.

References

- D.N. Basu, S. Bhattacharyya, P.K. Das, 2014, A review of modern advances in analyses and applications of single-phase natural circulation loop in nuclear reactor thermal hydraulics, *Nuclear Engineering and Design*, 280, 326-348.
- CD-adapco, 2016, STAR-CCM+® Version 10.04 user guide.
- R. Cole, 1960, A photographic study of pool boiling in the region of the critical heat flux, *AIChE Journal*, 6, 533-538.
- M. Colombo, M. Fairweather, 2017, CFD simulation of single- and two-phase natural convection in the context of external reactor vessel cooling, 17th International Topical Meeting on Nuclear Reactor Thermal Hydraulics (NURETH-17), Xi'an, China, 3rd-8th September.
- M.S. Ghandi, J.B. Joshi, A.K. Nayak, P.K. Vijayan, 2013a, Reduction in thermal stratification in two-phase natural convection in rectangular tanks: CFD simulations and PIV measurements, *Chemical Engineering Science*, 100, 300-325.
- M.S. Ghandi, J.B. Joshi, P.K. Vijayan, 2013b, Study of two-phase thermal stratification in cylindrical vessels: CFD simulations and PIV measurements, *Chemical Engineering Science*, 98, 125-151.
- K. Hanjalic, 2002, One-point closure models for buoyancy-driven turbulent flows, *Annual Review of Fluid Mechanics*, 34, 321-347.
- T. Hibiki, M. Ishii, 2006, Active nucleation site density in boiling systems, *International Journal of Heat and Mass Transfer*, 46, 2587-2601.
- T.I. Kim, H.M. Park, S.H. Chang, 2012, CHF experiments using a 2-D curved test section with additives for IVR-ERVC, *Nuclear Engineering and Design*, 243, 272-278.
- G. Kocamustafaogullari, 1983, Pressure dependence of bubble departure diameter for water, *International Communications in Heat and Mass Transfer*, 10, 501-509.
- E. Krepper, E.F. Hicken, H. Jaegers, 2002, Investigation of natural convection in large pools, *International Journal of Heat and Fluid Flow*, 23, 359-365.
- N. Kurul, M.Z. Podowski, 1990, Multi-dimensional effects in sub-cooled boiling, 9th International Heat Transfer Conference, Jerusalem, Israel, 19th-24th August.
- N. Minocha, J.B. Joshi, A.K. Nayak, P.K. Vijayan, 2016, 3D CFD simulations to study the effect of inclination of condenser tube on natural convection and thermal stratification in a passive decay heat removal system, *Nuclear Engineering and Design*, 305, 582-603.
- A. Omranian, T.J. Craft, H. Iacovides, 2014, The computation of buoyant flows in differentially heated inclined cavities, *International Journal of Heat and Mass Transfer*, 77, 1-16.
- W.E. Ranz, W.R. Marshall, 1952, Evaporation from drops, *Chemical Engineering Progress*, 48, 141-146.
- W. Xu, Q. Chen, F.T.M. Nieuwstadt, 1998, A new turbulence model for near-wall natural convection, *International Journal of Heat and Mass Transfer*, 41, 3161-3176.

New approaches for scheduling of multitasking multipurpose batch processes in scientific service facilities

Nikolaos Rakovitis, Jie Li,* Nan Zhang

*School of Chemical Engineering and Analytical Science, University of Manchester,
Manchester M13 9PL, UK*

jie.li-2@manchester.ac.uk

Abstract

Scheduling of multitasking multipurpose batch industry has not gained adequate attention in the literature. In this work, two novel mathematical models for scheduling of multitasking multipurpose batch processes in scientific service facilities are developed. The first model is developed based on unit-specific event-based approach, while the second is based on task-specific event-based approach. By solving a number of examples with both proposed models and the existing ones in the literature, it seems that both proposed models reduce the model size. The proposed unit-specific event-based model is superior to others, significantly reducing the model size and requiring at least one order of magnitude less computational time to generate the optimum solution, especially for the case of makespan minimization.

Keywords: Scheduling, Multitasking, Scientific service facilities, Mixed-integer linear programming

1. Introduction

Scientific service facilities examine a number of samples from different customers for their physical and chemical properties using a number of units. Each unit can examine one property and process samples from more than one customer simultaneously due to its large capacity, which allows multitasking. Due to the high competitive market, scientific service seeks ways to minimize the use of units and raw materials.

Even though, process scheduling has been considered in the last three decades (Harjunkoski et al., 2014), most of the existing models only allow single tasking and they cannot be directly applied to this class of problem. Recently, Patil et al. (2015) developed a discrete-time model for scheduling scientific service facilities. Lagzi et al. (2017a) used the global event time approach for the same problem. However, both models require large amount of computational time due to their large model sizes.

The advantages of the unit-specific event-based approach have been well established in the literature (Shaik and Floudas, 2009; Li and Floudas, 2010), where the scheduling horizon is divided based on units. Although there are some models that divide the scheduling horizon based on tasks, they are also classified as unit-specific event-based models (Shaik and Floudas 2009), which are actually task specific.

In this work, two novel models based on unit-specific and task-specific event-based approaches are developed for this problem. Both models allow multitasking to take

place in a unit. New tightening constraints are developed for the task-specific event-based model. The computational results show that the proposed unit-specific event-based model is superior to the proposed task-specific event-based model and the existing ones (Patil et al., 2015; Lagzi et al., 2017a) with smaller model size and at least one magnitude less computational time to generate the optimum solution, especially for the case of makespan minimization.

2. Problem description

A scientific service facility (Figure 1) examines Pr ($Pr = 1, 2, \dots, Pr$) properties, using J ($J = 1, 2, \dots, J$) units. Each unit is able to process only one property denoted by a set J_{pr} . The facility has to examine m sample groups, each one for different properties. In each unit more than one groups can be processed simultaneously. Given the total sample groups, the number of samples in each group, the processing path, the scheduling horizon H , as well as the capacity and processing time of each unit, the scheduling problem is to determine the optimal production schedule, including batch sizes, allocations, sequences, timings on processing units. It is assumed that each unit requires a fix time to examine a property, regardless of the samples that are processed. Furthermore, unlimited storage capacity (UIS) for all samples is considered.

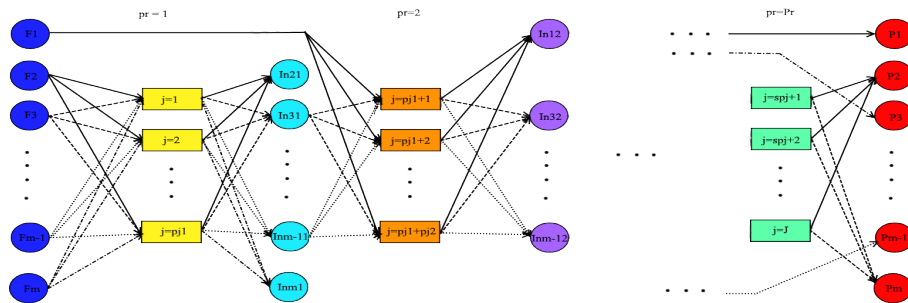


Figure 1 STN representation of scientific service facility

3. Mathematical formulations

3.1. Unit-specific event-based model

We first develop a novel unit-specific event-based model for scheduling multitasking batch processes.

3.1.1. Allocation constraints

A unit must start and end only at one event point.

$$\sum_{n-\Delta n \leq n' \leq n} \sum_{n \leq n' \leq n' + \Delta n} w_{j,n',n'} \leq 1 \quad \forall j, n, \Delta n > 0 \tag{1}$$

3.1.2. Capacity constraints

The total batch sizes taking place in a unit should be constrained at an event point.

$$\sum_{i \in I_j} b_{i,j,n,n'} \leq B_j^{\max} w_{j,n,n'} \quad \forall j, n, n \leq n' \leq n + \Delta n \tag{2}$$

3.1.3. Material balance constraints

$$ST_{s,n} = ST_{s,n-1} + \sum_{i \in I_s^c} \rho_{i,s} \sum_j \sum_{n-1-\Delta n \leq n' \leq n-1} b_{i,j,n',n-1} + \sum_{i \in I_s^c} \rho_{i,s} \sum_j \sum_{n \leq n' \leq n+\Delta n} b_{i,j,n,n'} \quad \forall s, n > 1 \quad (3)$$

$$ST_{s,n} = ST0_s + \sum_{i \in I_s^c} \rho_{i,s} \sum_j \sum_{n \leq n' \leq n+\Delta n} b_{i,j,n,n'} \quad \forall s, n = 1 \quad (4)$$

3.1.4. Duration constraints

The finish time of unit j must be after the start time of the unit at the same event point plus the processing time required to process task.

$$Tf_{j,n'} \geq Ts_{j,n} + \alpha_j w_{j,n,n'} \quad \forall j, n, n \leq n' \leq n + \Delta n \quad (5)$$

3.1.5. Time matching constraints

A state is available to be consumed after the finish time of the production task.

$$T_{s,n} \geq Tf_{j,n} - M \left(1 - \sum_{n-\Delta n \leq n' \leq n} w_{j,n',n} \right) \quad \forall s \in S^{in}, j, n, \sum_{i \in I_j} \rho_{i,s} > 0 \quad (6)$$

The start time of a unit, that consumes a state s at event point $n+1$, should be after the time that the state is available to be consumed at event n .

$$T_{s,n} \leq Ts_{j,n+1} + M \left(1 - \sum_{n+1 \leq n' \leq n+1+\Delta n} w_{j,n+1,n'} \right) \quad \forall s \in S^{in}, j, n < N, \sum_{i \in I_j} \rho_{i,s} < 0 \quad (7)$$

3.1.6. Sequencing constraints

The start time of unit j at event $n+1$ must be after the finish time at the event n .

$$Ts_{j,n+1} \geq Tf_{j,n} \quad \forall j, n < N \quad (8)$$

The time that a state is available at a time event point should be earlier that the time that the same state is available at the next event point.

$$T_{s,n} \leq T_{s,n+1} \quad \forall s \in S^{in}, n < N \quad (9)$$

3.1.7. Objective functions

Both maximization of productivity during a specific scheduling horizon and minimization of makespan have been considered.

$$z = \sum_s p_s \sum_{i \in I_s^p} \sum_j \sum_{n \leq n' \leq n+\Delta n} \rho_{i,s} b_{i,j,n,n'} \quad \forall s \in S^{in}, n < N \quad (10)$$

$$MS \geq Tf_{j,N} \quad \forall j \quad (11)$$

In the latter case all properties in all samples should be examined at the last event point

$$ST_{s,N} + \sum_{i \in I_s^c} \rho_{i,s} \sum_j \sum_{N-\Delta n \leq n' \leq N} b_{i,j,n',N} \leq D_s \quad \forall s \quad (12)$$

3.2. Task-specific event-based model

The task-specific event-based model of Shaik and Floudas (2009) for scheduling of single-tasking multipurpose batch processes was modified to consider multitasking. In this section, the modified constraints are only presented.

3.2.1. Allocation constraints

Shaik and Floudas (2009) introduced several allocation constraints where only one task is processed in a unit in event n . We replace these constraints with a new set of allocation constraints, which allows multitasking.

$$\sum_{n-\Delta n \leq n' \leq n} \sum_{n \leq n' \leq n' + \Delta n} w_{i,n',n} \leq 1 \quad \forall j, n, \Delta n > 0 \quad (13)$$

A binary variable $y_{j,n,n'}$ is defined as one if unit j is active from event n to n' .

$$y_{j,n,n'} \geq w_{i,n',n} \quad \forall i \in I_j, j, n, n \leq n' \leq n + \Delta n \quad (14)$$

$$y_{j,n,n'} \leq \sum_{i \in I_j} w_{i,n',n} \quad \forall j, n, n \leq n' \leq n + \Delta n \quad (15)$$

3.2.2. Capacity constraints

In multitasking, the summation of the batch sizes of all tasks that are able to be processed in a unit should be constrained.

$$\sum_{i \in I_j} b_{i,n,n'} \leq B_j^{\max} y_{j,n,n'} \quad \forall j, n, n \leq n' \leq n + \Delta n \quad (16)$$

3.2.3. Tightening constraints

The tightening constraints in Shaik and Floudas (2009) are only effective for single tasking in a unit. New tightening constraints below are introduced for multitasking.

$$Tj f_{j,n'} \geq Tj s_{j,n} + [\max_{i \in I_j} (\alpha_i)] y_{j,n,n'} \quad \forall j, n, n \leq n' \leq n + \Delta n \quad (17)$$

$$Tj s_{j,n+1} \geq Tj f_{j,n} \quad \forall j, n < N \quad (18)$$

4. Computational results

Five examples were solved using proposed models as well as the existing models of Patil et al. (2015) and Lagzi et al. (2017a). In example 1, a small-scale facility presented in Patil et al. (2015) was considered, while for the next 3 examples a random facility was generated. The last example uses a representation of an actual scientific service facility as presented by Lagzi et al. (2017b). Both maximization of productivity and minimization of makespan were considered as objective. All examples were solved in a machine using GAMS 24.6.1. CPLEX 12 in an Intel® Core™ i5-2500 3.3 GHz and 8 GB RAM running windows 7.

The comparative results with maximization of productivity are given on Table 1. Both proposed models require less number of event points, which decrease the model size.

However, the unit-specific event-based model leads to significantly smaller model size and therefore less computational time. The discrete-time model of Patil et al. (2015) also seems competitive due to the fact that it has the tightest relaxation. In cases of very detailed processing times, though such as example 4, the model size makes it infeasible to generate a feasible solution after one hour. By comparing continuous-time models, it seems that the proposed models improve the relaxation of the problem.

Table 1 Comparative results for examples 1-5 for maximization of productivity as objective

Ex.	Model	Event points	CPU time (s)	RMILP	MILP	Discrete Variables	Continuous Variables	Constraints
1	L ^a	8	3600 ^e	4822	3047 ⁱ	2196	2709	9402
	P ^b	96	0.826	3147	3147	5150	4417	5387
	T-S ^c	7	87.94	3424	3147	770	1219	5102
	U-S ^d	7	0.218	3424	3147	427	623	1211
2	L	8	162.0	1404	1254	540	585	2341
	P	480	2.886	1279	1254	6264	6721	10569
	T-S	7	4.602	1404	1254	154	337	672
	U-S	7	0.234	1404	1254	105	221	348
3	L	20	3600 ^f	3259	1194 ^h	6300	7350	26491
	P	480	217.6	2330	2330	32445	38401	45135
	T-S	17	3600 ^g	2744	2300 ^h	2312	4030	16946
	U-S	17	103.0	2744	2330	1275	2687	4715
4	L	6	2000	4495	3100	1456	3500	6424
	P	-	>3600	-	-	-	-	-
	T-S	5	10.12	3382	3100	460	1216	2730
	U-S	5	0.125	3382	3100	260	650	703
5	L	3	0.202	846	666	3744	4920	16330
	P	480	7.270	666	666	71220	64375	65850
	T-S	3	0.046	846	666	966	1768	4617
	U-S	3	0.094	846	666	702	669	2284

^a Lagzi et. al. 2017. ^b Patil et. al. 2015. ^c Task-specific model. ^d Unit-specific model. ^e Relative gap 36.8%. ^f Relative gap 63.4%. ^g Relative gap 16.2%. ^h Suboptimal solution

The results for the same examples using minimization of makespan as objective are presented on Table 2. In that case, the unit-specific event-based model is superior to others with smaller model size and tighter relaxation. Consequently, it generates the optimum solution in at least one order of magnitude less computational time. The superiority of the model is also illustrated in example 3, where the unit-specific event-based model generates the optimum solution in less than one minute, while reported models are not even able to generate a feasible solution after one hour. The task-specific event-based model has also a better relaxation and leads to smaller model sizes than the models previously reported in the literature.

5. Conclusions

In this work, two novel mathematical models, based on task-specific and unit-specific event-based approaches for scheduling of multitasking batch process in scientific service facilities were presented. Both mathematical models lead to smaller model size with less number of event points, variables and constraints than previous reported formulations. The unit-specific event-based model is superior model than other models

with significantly smaller model, much tighter relaxation and at least one magnitude less computational time to generate optimal solution, especially for the case of makespan minimization.

Table 2 Comparative results for examples 1-5 for minimization of makespan as objective

Ex.	Model	Event points	CPU time (s)	RMILP	MILP	Discrete Variables	Continuous Variables	Constraints
1	L ^a	8	3600 ^e	99.50	1065.0	2196	2709	9411
	P ^b	250	93.49	23.90	1065.0	14544	11501	25636
	T-S ^c	8	3600 ^f	125.13	1065.0	880	1393	5978
	U-S ^d	8	0.187	934.38	1065.0	488	717	1816
2	L	8	119.7	88.09	555.0	540	585	2343
	P	600	13.74	4.02	555.0	8064	6401	26642
	T-S	7	1.482	137.39	555.0	154	337	685
	U-S	7	0.219	307.50	555.0	105	221	403
3	L	-	>3600	-	-	-	-	-
	P	-	>3600	-	-	-	-	-
	T-S	52	3600 ^g	167.75	1966.0	7072	12325	53425
	U-S	52	27.58	1562.00	1696.0	3900	8357	18160
4	L	7	3600 ^h	95.15	1001.7	1664	4000	7364
	P	-	>3600	-	-	-	-	-
	T-S	6	2.325	223.50	1001.7	552	1459	3418
	U-S	6	0.281	840.56	1001.7	312	786	1128
5	L	13	3600 ⁱ	14.25	7431.0	13104	18340	59434
	P	-	>3600	-	-	-	-	-
	T-S	13	3600 ^j	169.00	5131.0	4186	7658	24112
	U-S	13	3600 ^k	624.38	5131.0	3042	3039	12581

^aLagzi et. al. 2017 with objective function $MS \geq T_N$. ^bPatil et. al. 2015 with objective function $MS \geq [(t - 1) + Tr(p) - 1] \cdot y_{j,t}$. ^c Task-specific model. ^d Unit-specific model. ^e Relative gap 25.9%. ^f Relative gap 25.6%. ^g Relative gap 89.6%. ^h Relative gap 19.0%. ⁱ Relative gap 99.7%. ^j Relative gap 78.9%. ^k Relative gap 62.5%.

References

- I. Harjunkoski, C. Maravelias, P. Bongers, P. Castro, S. Engell, I. Grossmann, J. Hooker, C. Méndez, G. Sand, J. Wassick, 2014, Scope for industrial application of production scheduling models and solution methods, *Computers and Chemical Engineering*, 62(5), 161-193
- S. Lagzi, R. Fukasawa, L. Ricardez-Sandoval, 2017a, A multitasking continuous time formulation for short-term scheduling of operations in multipurpose plants, *Computers & Chemical Engineering*, 97, 135-146
- S. Lagzi, D. Lee, R. Fukasawa, L. Ricardez-Sandoval, 2017b, A Computational Study of Continuous and Discrete Time Formulations for a Class of Short-Term Scheduling Problems for Multipurpose Plants, *Industrial & Engineering Chemistry Research*, 56(31), 8940-8953
- J. Li, C. Floudas, 2010, Optimal event point determination for short-term scheduling of multipurpose batch plants via unit-specific event-based continuous-time approaches, *Industrial & Engineering Chemistry Research*, 49(16), 7446-7469
- B. Patil, R. Fukasawa, L. Ricardez-Sandoval, 2015, Scheduling of operations in a large-scale Scientific services facility via multicommodity flow and an optimization-based algorithm, *Industrial & Engineering Chemistry Research*, 54(5), 1628-1639
- M. Shaik, C. Floudas, 2009, Novel Unified Modeling Approach for Short-Term Scheduling, *Industrial & Engineering Chemistry Research*, 48(6), 2947-2964

Incorporating Systems Structure in Data-Driven High-Dimensional Predictive Modeling

Marco P. Seabra dos Reis ^{a,*}

^a CIEPQPF – Department of Chemical Engineering, University of Coimbra, Rua Silvio Lima, 3030-790, Coimbra, Portugal

marco@eq.uc.pt

Abstract

Current predictive analytics approaches are strongly focused on optimizing accuracy metrics, leaving little room to incorporate a priori knowledge about the processes under analysis and relegating to a secondary concern the interpretation of results. However, in the analysis of complex systems, one of the main interests is precisely the induction of relevant associations and dependencies, in order to understand or clarify the way systems operate. On the other hand, there is often information available regarding the structure of the underlying processes, which could be used in benefit of the analysis and to enhance the interpretation of results. The importance of this issue was recognized and led to the development of multiblock approaches. In this paper, two classes of multiblock frameworks are addressed, that present interpretational-oriented features, while allowing components of the system's structure to be incorporated, maximizing the use of existing knowledge about the process. The two classes of methodologies are comparatively tested using a real world dataset. Their performance is also compared with their single-block counterparts, namely principal components regression and partial least squares. Results confirm the added value of adopting suitable multiblock predictive methodologies, when variables present a block-wise or network structure.

Keywords: Multiblock methods, Network-Induced Supervised Learning, Concatenated PLS, Multiblock PLS, Hierarchical PLS, Sequential Orthogonalised PLS.

1. Introduction

Modeling is a fundamental part of any workflow for process improvement, monitoring and control. With the increasing availability of data in the Big Data era and with the emergence of Industry 4.0, there is a strong emphasis in developing data-driven modeling approaches to address these tasks. In the domain of data-driven predictive frameworks, the mainstream methods tend to treat all variables *a priori* in the same way. The different methodologies vary according to the way variables are selected and/or combined in order to compound the final model. We call these methods “single-block”, as they treat all regressors equally in a first stage.

Taking a closer look to the recurrent structures found in data and to the way systems generating them actually work, one can notice that, most often, not all variables are actively contributing to the phenomenon under study (as assumed in multivariate methods) nor are they bringing independent and isolated pieces of information to the model (for which variable selection schemes would be adequate). Rather, the prevailing

structure seems to present the form of clusters of variables – modules – composed by sets of variables, where each cluster is relative to a given functional mechanism. Variables falling in the same cluster exhibit some degree of mutual correlation, and may be aggregated in a super level, in an hierarchical way (Clauset et al., 2008; Guimerà and Amaral, 2005; Newman, 2006; Ravasz et al., 2002). In this context, instead of multivariate or variable selection schemes for handling high-dimensional systems, methods should enable the definition and selection of clusters of variables that better reflect the system structure, which can then be selected for integrating the model according to their predictive power (Reis, 2013a, b). This setting calls for methods that are able to handle simultaneously several heterogeneous blocks of variables in their formulation, called hereafter as multiblock methods.

Upon a close analysis of the available literature, two classes of multiblock methods can be identified. On one side, there are methods where the blocks of variables are defined based on *a priori* knowledge about the system's structure, e.g., when variables regard different process units, arise from different analytical measurement sources or are related to distinct and identifiable functional modules of the system. On the other side, one can find methods where such knowledge is not explicitly known, but a modular structure is believed to exist, that must be inferred and extracted from the available existing data. It is the purpose of this work to briefly provide an overview of both classes of multiblock methods and to illustrate their application with resort to a real world case study.

This article is organized as follows. In the next section, the main representatives of the two classes of methods, that will also integrated the present work, are briefly presented. Then, in Section 3, the results obtained are presented and discussed. Section 4 concludes this paper, with an overview of its contents and some concluding remarks about the relevance of considering multiblock methods in the analysis of high-dimensional systems.

2. Multiblock methods for predictive analytics

Classical data analysis is focused on handling isolated variables, which should be selected and/or weighted differently, during the construction of predictive models. Multiblock methods, on the other hand, constitute a class of analytical methodologies that maintain the integrity of clusters of variables in the analysis. The objects of analysis are no longer isolated variables, but variable clusters. These clusters carry information about different phenomena, functions, process units, stages, etc., and therefore increase the interpretability of the models developed. There are two types of multiblock methods, depending on whether the clusters are formed using *a priori* knowledge, or they are inferred from data, i.e., extracted in a data-driven way.

2.1. Blocks known a priori

Belong to this class all multiblock methods that assume the composition of the different blocks to be known beforehand. This attribution is often possible to be made when there is sufficient knowledge about the system, and the way variables are naturally organized regarding how they contribute to the final outcome. Several multi- and megavariate methods fall in this category, and we will contemplate in this work the mainstream ones, namely, Concatenated PLS (CPLS), Hierarchical PLS (HPLS), Multiblock PLS

(MPLS), as well as recent advances in this field, such as Sequential and Orthogonalised PLS (SO-PLS).

In brief terms, Concatenated PLS (CPLS) consists in concatenating all blocks of variables in a single augmented matrix and perform the classical PLS method over the entire data array. The different blocks should be weighted before being used in the model in order to give equal importance to all or to increase/decrease the importance of a given block in the model. Typically, two block-scaling methods are described in the literature: soft block scaling and hard block scaling (Eriksson et al., 2006).

In Hierarchical PLS (HPLS), each data block is considered as a separate source of information and the multiblock model extracts the common structure for all the different blocks. This common structure forms the so-called super level of the model, combining information from all blocks of predictors at the lower levels. This means that block scores, loadings and weights for each separate block are available for interpretation in the lower level and super scores, loadings and weights are available in the super level for the interpretation of the global model.

Multiblock PLS (MBPLS) was proposed by Wold et al. (Wold et al., 1983) and later by Wangen and Kowalski (Wangen and Kowalski, 1988). Similarly to the HPLS method, this method also presents two levels: the super level with global information and the lower level with information from each block. The main difference between this method and HPLS is that the Y block is regressed on all descriptor X blocks, whereas in HPLS the Y block is only regressed on the super block, which means that the block scores are calculated in an unsupervised way. This causes the block scores to be different in these two methods.

Sequential and Orthogonalized Partial Least Squares (SO-PLS) was proposed by Naes et al. (2013) and is a methodology that incorporates several blocks of variables in the model, one at a time, while evaluating/interpreting the incremental or additional contribution of the different blocks for improving the model predictions. This capability is relevant when one wants to assess the gain of introducing an additional source of information. The sequential nature of SO-PLS implies that the order chosen for including the blocks in the model can influence the final result.

2.2. Blocks inferred from data

When the composition of the blocks is unknown, then it must be induced from data. Network Induced Supervised Learning Regression (NI-SL) is a method proposed by M. S. Reis (Reis, 2013a, b), with the goal of bringing interpretation features to the forefront of the analysis goals. The method is divided in two stages. The first stage (Network-Induced Clustering) aims at finding functionally related groups of variables (clusters), which form meaningful X blocks with predictive power for Y. The second stage consists in developing a predictive model, based on the variates (i.e., linear combinations) computed for the blocks induced in the first stage. For such, classical PLS models are developed separately between each X block and the Y response, and a predefined number of latent variables are retrieved from each block (in the present study five latent variables were retrieved from each block). These latent variables are gathered into a super block and a forward stepwise regression procedure is implemented to select the subgroup of latent variables leading to the best fit.

3. Measurement units, numbers

We illustrate the application of multi-block methodologies with resort to a real world case study taken from the food & drink industry: wine production. More specifically, this example is focused on the prediction of ageing time in Madeira wine, based on different analytical measurement sources: volatile profile (1st block), the polyphenols and two furanic compounds (2nd block), the organic acids quantification (3rd block) and the ultraviolet-visible spectra (4th block). The volatile profile was analysed by gas chromatography coupled to mass spectrometry (GC-MS), preceded by solid phase extraction; the second block of data was obtained by High-Performance Liquid Chromatography combined with Photodiode Array Detection (HPLC-DAD; direct injection); organic acids (the 3rd block of variables) were also quantified by Liquid Chromatography combined with Photodiode Array Detection; UV-Vis absorbance spectra (4th block of variables) was done in a Perkin-Elmer Lambda 2 spectrophotometer (Waltham, MA, USA). More information about the data used in the analysis of this case study is available in ref. (Campos et al., 2017).

A total of 26 samples were analysed, covering a range of 20 years (2-3 wine samples were taken per ageing year, with 2 year intervals). All samples correspond to wines produced from the same grape variety (Malvasia) and were supplied from the same Madeira wine producer.

In this paper, and due to space limitations, the analysis will be focused on the predictive capabilities of the methods, which is assessed in a robust way, according to the following protocol: 50 data sets are formed from the original dataset, through Monte Carlo random assignment of samples; for each Monte Carlo assignment, the dataset is randomly divided into a training set (80%) and a test set (20%); the training set is used to calibrate the models and to determine the respective hyper-parameters based on 10-fold cross validation method; this procedure originates 50 different models for each multiblock method (one for each randomly generated data set). The test sets are used for prediction based on which one computes the root mean square error of prediction (RMSEP), for each Monte Carlo run and for each method, using equation 1.

$$RMSEP = \sqrt{\frac{\sum_{i=1}^{n_{test}} (y_{pred,i} - y_{obs,i})^2}{n_{test}}} \quad (1)$$

The distribution of the RMSEP over the 50 trials characterizes the methods performance in terms of prediction accuracy and robustness. Moreover it can be used to compare different methods by evaluating the statistical significance of the difference between the prediction errors obtained under similar testing conditions.

Table 1. Average root mean square error of prediction and the respective interquartil range (IQR) obtained for the different multiblock methods tested in this paper.

Method	\overline{RMSE}	IQR (75%-25%)
Concatenated PLS (CPLS)	0.93	0.61
Hierarchical PLS (HPLS)	1.48	0.44
Multiblock PLS (MBPLS) - Block Scores deflation	1.36	0.58
Multiblock PLS (MBPLS) - Super Scores deflation	1.34	0.54
Network Induced Supervised Learning (NI-SL)	1.17	0.85
Sequential Orthogonal-Partial Least Squares (SO-PLS)	0.97	0.49

Table 2. Average root mean square error of prediction and the respective interquartil range (IQR) obtained in the Monte Carlo Cross-Validation for single block approaches.

Chemical Data	Method	\overline{RMSEP}
Polyphenol Content	PCR	1.18
	PLS	1.17
Volatile Composition	PCR	1.55
	PLS	1.43
UV-Vis	PCR	2.23
	PLS	2.86
Organic Acids	PCR	2.93
	PLS	2.86

Table 1 presents the mean RMSEPs obtained for the several multiblock methods studied in this article. The methods leading to better performance are CPLS (with a new scaling methodology developed by the authors; see ref. (Campos et al., 2017)) and SO-PLS, followed by NI-SL. The first two methods present superior predictive performances than the best linear multivariate methodologies applied to each block separately – see results for Principal Component Regression (PCR) and Partial Least Squares (PLS) in Table 2 (Rendall et al., 2017). These results indicate that it is possible to synergistically combine different sources of information for improving the predictive performance of the methods, even though the single-block methods based on the Polyphenol Content already lead to interesting predictive results. Moreover, the multiblock methodologies bring other interpretational dimensions to the analysis, namely regarding the importance of the different blocks for predicting the response and their redundancy or overlap, which are not addressed in this short article.

4. Conclusions

In this work, we illustrate the potential of using multiblock predictive methods in datasets composed by natural blocks of variables. The case study illustrates the advantage of using all blocks of variables simultaneously, in a structured way, rather than in an isolated fashion.

Even though multiblock methods represent constrained versions of their single-block counterparts, the predictive ability found may not be inferior. On the contrary, it was often found to be superior, which is due to their more parsimonious nature that leads to a more stable parameter estimation and finally to more accurate predictions (Reis, 2013a, b). If, on top of this, one considers the expected higher interpretability of the multiblock methods, one can easily conclude about the increasing interest in adopting this modeling formalism to address the analysis of data collected from complex processes and phenomena, a situation that will be increasingly frequent in the Industry 4.0 era.

References

- Campos, M.P., Sousa, R., Pereira, A.C., Reis, M.S., 2017. Advanced predictive methods for wine age prediction: Part II - a comparison study of multiblock regression approaches. *Talanta* 171, 121-142.
- Clauset, A., Moore, C., Newman, M.E.J., 2008. Hierarchical structure and the prediction of missing links in networks. *Nature* 453, 98-101.
- Eriksson, L., Johansson, E., Kettaneh-Wold, N., Trygg, J., Wikström, C., Wold, S., 2006. Multi- and Megavariate Data Analysis Part I – Basic Principles and Applications. Umetrics Inc, Umeå, Sweden.
- Guimerà, R., Amaral, L.A.N., 2005. Functional cartography of complex metabolic networks. *Nature* 433, 895-900.
- Naes, T., Tomic, O., Afseth, N.K., Segtnan, V., Måge, I., 2013. Multi-block regression based on combinations of orthogonalisation, PLS-regression and canonical correlation analysis. *Chemometrics and Intelligent Laboratory Systems* 124, 32-42.
- Newman, J.A.S., 2006. Modularity and Community Structure in Networks. *Proc. Natl. Acad. Sci. USA* 103, 8577-8582.
- Ravasz, E., Somera, A.L., Mongru, D.A., Oltvai, Z.N., Barabási, A.-L., 2002. Hierarchical Organization of Modularity in Metabolic Networks. *Science* 297, 1551-1555.
- Reis, M.S., 2013a. Applications of a new empirical modelling framework for balancing model interpretation and prediction accuracy through the incorporation of clusters of functionally related variables. *Chemometrics and Intelligent Laboratory Systems* 127, 7-16.
- Reis, M.S., 2013b. Network-Induced Supervised Learning: Network-Induced Classification (NIC) and Network-Induced Regression (NI-R). *AIChE Journal* 59, 1570-1587.
- Rendall, R., Pereira, A.C., Reis, M.S., 2017. Advanced predictive methods for wine age prediction: Part I - a comparison study of single-block regression approaches based on variable selection, penalized regression, latent variables and tree-based ensemble methods. *Talanta* 171, 341-350.
- Wangen, L.E., Kowalski, B.R., 1988. A multiblock partial least squares algorithm for investigating complex chemical systems. *Journal of Chemometrics* 3, 3-20.
- Wold, S., Martens, H., Wold, H., 1983. The multivariate calibration problem in chemistry solved by the PLS method, in: Kågström, B., Ruhe, A. (Eds.), *Matrix Pencils. Lecture Notes in Mathematics*. Springer, Berlin, Heidelberg.

Dynamic Real-time Optimization of Batch Membrane Processes using Pontryagin's Minimum Principle

Radoslav Paulen*, Ayush Sharma and Miroslav Fikar

*Faculty of Chemical and Food Technology, Slovak University of Technology in Bratislava,
Radlinskeho 9, Bratislava, 81237, Slovakia
E-mail: {Radoslav.Paulen, Ayush.Sharma, Miroslav.Fikar}@stuba.sk*

Abstract

This paper studies a dynamic real-time optimization in the context of model-based time-optimal operation of batch processes under parametric model mismatch. A class of batch membrane separation processes is in the scope of the presented applications. In order to tackle the model-mismatch issue, a receding-horizon policy is usually followed with frequent re-optimization. The main problem addressed in this study is high computational burden that is usually required by such schemes. We propose an approach that uses parametrized conditions of optimality in the adaptive predictive-control fashion. The uncertainty in the model predictions is treated explicitly using reachable sets that are projected into the optimality conditions.

Keywords: real-time optimization, Pontryagin's minimum principle, membrane processes, parameter estimation

1. Introduction

In this paper we consider a real-time implementation of a control policy that optimizes a process by assigning dynamic degrees of freedom such that a certain performance index is optimized:

$$\min_{u(t) \in [u_L, u_U], t_f} \mathcal{J} := \min_{u(t) \in [u_L, u_U], t_f} \int_0^{t_f} F_0(x(t), p) + F_u(x(t), p)u(t) dt \quad (1a)$$

$$\text{s.t. } \dot{x}(t) = f_0(x(t), p) + f_u(x(t), p)u(t), \quad x(0) = x_0, \quad x(t_f) = x_f, \quad (1b)$$

where t is time with $t \in [0, t_f]$, $x(t)$ is an n -dimensional vector of state variables, p is an m -dimensional vector of model parameters, $u(t)$ is a (scalar) manipulated variable, $F_0(\cdot)$, $F_u(\cdot)$, $f_0(\cdot)$, and $f_u(\cdot)$ are continuously differentiable functions, x_0 represents a vector of initial conditions, and x_f are specified final conditions. We note here that an inclusion of multi-input and/or state-constrained cases is a straightforward extension but it is not considered in this study for sake of simplicity of the presentation. We also note that the specific class of input-affine systems is a suitable representation for a large variety of the controlled objects (Hangos et al., 2006).

The presented problem was studied in many previous works using on-line or batch-to-batch adaptation of the optimality conditions (Francois and Bonvin, 2013) or by design of robust controller for tracking the conditions of optimality (Nagy and Braatz, 2003). Recently, several advanced robust strategies were presented in the framework of model predictive control (Lucia et al., 2013).

Acknowledgements: The research leading to these results has received funding from the Slovak Research and Development Agency under the project APVV 15-0007 and from the Scientific Grant Agency of the Slovak Republic under the grant 1/0004/17.

This paper proposes an adaptation of these approaches to the problem of dynamic real-time optimization of batch processes. This task is not straightforward because if one uses a preceding-horizon control strategy, the prediction horizons need to be quite long, because of the presence of terminal constraints, which might compromise the real-time feasibility of the scheme.

We base the presented methodology on parameterization of the optimal operation using the conditions of optimality given by Pontryagin's minimum principle. This makes the dynamic decision problem (1) to boil down to identification of switching times of the optimal control policy. Such approach reduces computational burden while allowing for the use of sufficiently long prediction horizons when projecting the parametric uncertainty in controller performance and feasibility, particularly w.r.t. terminal time conditions. Robustness w.r.t. parametric uncertainty is addressed by taking into account the imprecision of parameter estimates such that it is projected into the uncertainty of the switching times. In order to improve performance of such a controller, i.e., to reduce conservatism introduced by uncertain switching times, we use on-line parameter estimation.

2. Preliminaries

2.1. Conditions for Optimality

Pontryagin's minimum principle can be used (Srinivasan et al., 2003) to identify the optimal solution to (1) via enforcing the necessary conditions for minimization of a Hamiltonian

$$H := \mu_L(u_L - u) + \mu_U(u - u_U) + \underbrace{F_0 + \lambda^T f_0}_{H_0(x(t), \lambda(t), p)} + \underbrace{(F_u + \lambda^T f_u)u}_{H_u(x(t), \lambda(t), p)}, \quad (2)$$

where $\lambda(t)$ is a vector of adjoint variables, and $\mu_L(t)$ and $\mu_U(t)$ are corresponding Lagrange multipliers. The optimality conditions of (1) can then be stated as (Srinivasan et al., 2003): $\forall t \in [0, t_f]$

$$\frac{\partial H}{\partial u} := H_u(x(t), \lambda(t), p) - \mu_L(t) + \mu_U(t) = 0, \quad (3)$$

$$H(x(t), \lambda(t), p, u(t), \mu_L(t), \mu_U(t)) = 0, \quad H_0(x(t), \lambda(t), p) = 0, \quad x(t_f) - x_f = 0. \quad (4)$$

The condition $H = 0$ arises from the transversality, since the final time is free (Pontryagin et al., 1962), and from the fact that the optimal Hamiltonian is constant over the whole time horizon, as it is not an explicit function of time. The condition $H_0 = 0$ is the consequence of the former two conditions. Since the Hamiltonian is affine in input (see (2)), the optimal trajectory of control variable is either determined by active input constraints or it evolves inside the feasible region.

Assume that for some point t we have $H_u = 0$ and $u_L < u(t) < u_U$. It follows from (3) that the optimal control maintains $H_u(t) = 0$. Such control is traditionally denoted as singular. Further properties of the singular arc, such as switching conditions or state-feedback control trajectory can be obtained by differentiation of H_u with respect to time (sufficiently many times) and by requiring the derivatives to be zero. The time derivatives of H and H_0 must be equal to zero as well. Earlier results on derivation of optimal control for input-affine systems (Srinivasan et al., 2003) suggest that it is possible to eliminate $\lambda(t)$ from the optimality conditions and thus arrive at analytical characterization of switching conditions between singular and saturated-control arcs.

As the optimality conditions obtained by the differentiation w.r.t. time are linear in the adjoint variables, the differentiation of H_u (or H_0) can be carried out until it is possible to transform the obtained conditions to a pure state-dependent switching function $S(x(t), p)$. It is usually convenient to use a determinant of the coefficient matrix of the equation system $A\lambda = 0$ for this. The singular control $u_s(x(t), p)$ can be found from differentiation of switching function w.r.t. time as

$$\frac{dS}{dt} = \frac{\partial S}{\partial x^T} \frac{dx}{dt} = \frac{\partial S}{\partial x^T} (f_0 + f_u u_s) = 0 \quad \Rightarrow \quad u_s(x(t), p) = -\frac{\partial S}{\partial x^T} f_0 \Big/ \frac{\partial S}{\partial x^T} f_u. \quad (5)$$

The resulting optimal-control policy is then given as a step-wise strategy (Paulen et al., 2015) by

$$u^*(t, \pi) := \begin{cases} u_L, & t \in [0, t_1], S(x(t), p) > 0, \\ u_U, & t \in [0, t_1], S(x(t), p) < 0, \\ u_s(x(t), p), & t \in [t_1, t_2], S(x(t), p) = 0, \\ u_L, & t \in [t_2, t_f], S(x_f, p) < 0, \\ u_U, & t \in [t_2, t_f], S(x_f, p) > 0, \end{cases} \quad (6)$$

$$x_f = x(t_2) + \int_{t_2}^{t_f} f_0(x(t), p) + f_u(x(t), p)u^*(t) dt, \quad (7)$$

where $\pi := (p^T, t_1, t_2, t_f)^T$ is the vector that parameterizes the optimal control strategy. Note that the presented optimal-control strategy determines implicitly the switching times t_1 , t_2 and the terminal time t_f as functions of model parameters p .

2.2. Set-membership estimation

In order to estimate model parameters we will assume the model being linear in parameters as

$$\hat{y}(p) = c^T p, \quad (8)$$

where \hat{y} is the prediction of the plant output y and c is a so-called regressor vector. The linearity of the model in parameters is not restrictive, the presented methodology applies to systems that are non-linear in parameters too. We will further assume that the measurement noise is bounded with

$$|y - \hat{y}(p)| \leq \sigma. \quad (9)$$

Under these assumptions a recursive set-membership estimation scheme was presented in Fogel and Huang (1982), which over-bounds the set of all parameter values that satisfy (9) as an ellipsoid

$$(p - \hat{p})^T V^{-1} (p - \hat{p}) \leq 1, \quad (10)$$

where \hat{p} is the expected true value of the parameters and V is parameter covariance matrix. Upon receiving a new measurement y , \hat{p} and V are updated by

$$\hat{p}_+ = \hat{p} + \frac{\beta d}{1 + \beta g} V \tilde{c}, \quad V_+ = \left(1 + \beta - \frac{\beta d^2}{1 + \beta g}\right) \left(V - \frac{\beta}{1 + \beta g} V \tilde{c} \tilde{c}^T V\right), \quad (11)$$

where $\tilde{c} := c/\sigma$, $g := \tilde{c}^T V \tilde{c}$, $d := y/\sigma - \tilde{c}^T \hat{p}$. The parameter $\beta \in (0, 1)$ can be selected in order to minimize trace or determinant of the covariance matrix V (Fogel and Huang, 1982). The updated bounds of parameters (parameter confidence intervals) can be found via

$$P_+ := \left[\hat{p}_+ - \text{diag} \left(V_+^{\frac{1}{2}} \right), \hat{p}_+ + \text{diag} \left(V_+^{\frac{1}{2}} \right) \right]. \quad (12)$$

3. Dynamic real-time optimization

As the optimal control structure is a function of uncertain parameters, the uncertainty should be taken into account when devising a real-time implementation of the optimal control on the process. We will assume a bounded uncertainty $p \in P := [p^L, p^U]$ with a nominal realization $p_0 := \text{mid}(P)$.

Given the structure of the optimal-control policy (6) one can project the parametric uncertainty into uncertainty of the switching times and singular control as

$$t_i(p) \in [t_i^L(P), t_i^U(P)] := T_i, \quad \forall i \in \{1, 2, f\}, \quad (13)$$

$$u_s(t, p) \in [u_s^L(t, P), u_s^U(t, P)] := U^*(t), \quad \forall t \in [t_1(p), t_2(p)], \quad (14)$$

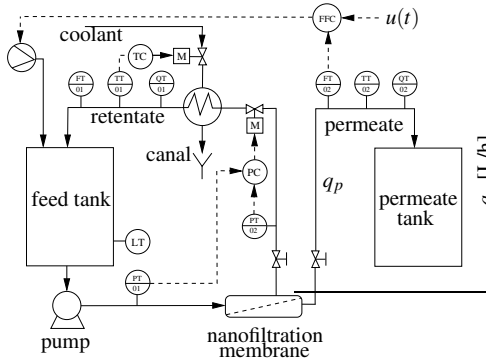


Figure 1: Diafiltration process scheme.

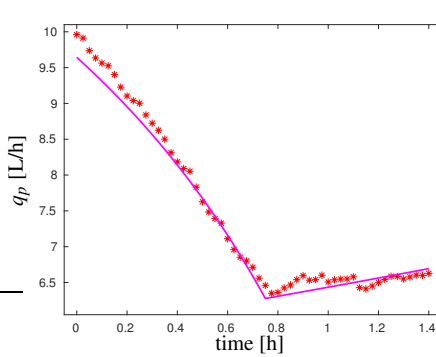


Figure 2: Comparison of data and model predictions.

using some set-theoretic technique for calculating reachable sets (Chachuat et al., 2015). Here a particular technical advantage can be exploited i.e., that the integration of in (7) can be done backwards in time from the final condition. As the batch processes exhibit inherently unstable dynamics, their backward integration is stable. Such a feature can readily be exploited by modern bounding approaches for parametric ordinary differential-algebraic equations.

The result (13) then in practice establishes a parametric solution to the real-time optimization problem. Its implementation can be performed in a robust fashion to determine the parameters of the optimal-control structure that lead to the best performance in the worst case. We can then solve

$$\min_{\substack{u_s(t,p) \in U^*(t), \forall t \in [t_1(p), t_2(p)] \\ t_i \in T_i, \forall i \in \{1, 2, f\}}} \max_{p \in P} \|\mathcal{J}(p) - \mathcal{J}(p_0)\|_2^2 \quad \text{s.t. (6), (7),} \quad (15)$$

for a given $x(0) = x_0$ and P , where we propose to minimize variance of the objective under the worst-case realization of $p \in P$.

In order to reduce conservatism of a robust scheme, parameter estimation can be used for exploitation of data gathered along the process run. The employed parameter estimation scheme should take into account noise in measurements and, if applied recursively for each newly gathered measurement set, it should result in a sequence of the confidence intervals

$$P_k \subseteq P_{k-1} \subseteq \dots \subseteq P_1 \subseteq P_0 \subseteq P. \quad (16)$$

The problem (15) can then be resolved with the initial state conditions $x(k) = x_k$ and with updated parameter bounds P_k in shrinking-horizon fashion. Once the optimal value of the objective function of (15) reaches $\|\mathcal{J}(P) - \mathcal{J}(p_0)\|_2^2 < \varepsilon$, the calculated control actions can be implemented, e.g., with a feedback scheme (Francois and Bonvin, 2013), until the terminal conditions are met. Note that due to the parametrization of the optimal-control policy, the re-estimation and re-optimization do not need to be run at every sampling time but on a much coarser time scale given by range of uncertainty in the sampling times T_i . Sophisticated strategies can then be used to evaluate the trade-off between real-time feasibility and performance.

4. Case study

We consider a case study of time-optimal control of a batch diafiltration process from Paulen et al. (2012). The scheme of the plant is shown in Fig. 1. The goal is to process a solution with initial volume (V_0) that is fed into the feed tank at the start of the batch and that comprises two solutes of initial concentrations $c_{1,0}$ and $c_{2,0}$. At the end of the batch, the prescribed final concentrations

$c_{1,f}$ and $c_{2,f}$ must be met. The transmembrane pressure is controlled at a constant value. The temperature of the solution is maintained around a constant value using a heat exchanger. The manipulated variable $u(t)$ is the ratio between fresh water inflow into the tank and the permeate outflow q_p that is given by

$$q_p = \gamma_1 \ln \left(\frac{\gamma_2}{c_1 c_2^{\gamma_3}} \right) = \gamma_1 (\ln(\gamma_2) - \ln(c_1) - \gamma_3 \ln(c_2)). \quad (17)$$

and is measured at intervals of one minute with the measurement noise that is determined experimentally and bounded by $\sigma = 0.5\text{L/h}$. The model of the permeate flux can be reduced to another widely used *limiting flux model* if $\gamma_3 = 0$, so this example offers to study both parametric and non-parametric plant-model mismatch. The measurement of q_p is used for inferring the values of the parameters $\gamma_1, \gamma_2, \gamma_3$. Note that this leads to linear parameter estimation problem with the regressor $c = (1, \ln(c_1), \ln(c_2))^T$ and parameters $\hat{p} = (\gamma_1 \ln(\gamma_2), \gamma_1, \gamma_1 \gamma_3)^T$, from which the values of $\gamma_1, \gamma_2, \gamma_3$ follow directly. Concentrations of both components $c_1(t)$ and $c_2(t)$, where the first component is retained by the membrane and the second one can freely pass through, are measured as well and filtered prior to estimation.

The objective is to find a time-dependent input function $u(t)$, which guarantees the transition from the given initial $c_{1,0}, c_{2,0}$ to final $c_{1,f}, c_{2,f}$ concentrations in minimum time. This problem can be formulated as:

$$\mathcal{J}^* = \min_{u(t) \in [0, \infty)} \int_0^{t_f} 1 \, dt, \quad (18a)$$

$$\text{s.t. } \dot{c}_1 = \frac{c_1^2 q_p}{c_{1,0} V_0} (1 - u), \quad c_1(0) = c_{1,0}, \quad c_1(t_f) = c_{1,f}, \quad (18b)$$

$$\dot{c}_2 = -\frac{c_1 c_2 q_p}{c_{1,0} V_0} u, \quad c_2(0) = c_{2,0}, \quad c_2(t_f) = c_{2,f}, \quad (18c)$$

$$q_p = \gamma_1 (\ln(\gamma_2) - \ln(c_1) - \gamma_3 \ln(c_2)). \quad (18d)$$

The parameters of the problem are $c_{1,0} = 50\text{g/L}$, $c_{1,f} = 110\text{g/L}$, $c_{2,0} = 5.3\text{g/L}$, $c_{2,f} = 1\text{g/L}$, $V_0 = 21\text{L}$. The extremal values of $u(t)$ stand for a mode with no water addition, when $u(t) = 0$ and pure dilution, i.e., a certain amount of water is added at a single time instant, $u(t) = \infty$.

The preliminary run of the laboratory apparatus with $u(t) = 0$ for 0.75 h and $u(t) = 1$ for 0.65 h was used to gathered data which were subsequently used in set-membership estimation to determine the confidence intervals of parameters as $\gamma_1 = [1.86, 3.91]\text{L/h}$, $\gamma_2 = [4.1163, 0.6589] \times 10^3\text{g/L}$, $\gamma_3 = [-0.11, 0.17]$. The value of β used for the estimation is 0.5. Particularly the value of lower bound of γ_3 points to a potentially strong structural plant-model mismatch. We note for completeness that the particular advantage of used the set-membership estimation is that the assumption γ_3 , which one might like to use in this case, could be easily incorporated in the estimation.

The nominal (parametrized) optimal control of this process can be identified using Pontryagin's minimum principle (Pontryagin et al., 1962) as (6) where the singular control and the respective switching function can be found explicitly (Paulen et al., 2012) as

$$u_s(x(t), p) := \frac{1}{1 + \gamma_3}, \quad S(x(t), p) := \gamma_1 (\ln(\gamma_2) - \ln(c_1) - \gamma_3 \ln(c_2) - \gamma_3 - 1). \quad (19)$$

For the given nominal parameters of the problem, the optimal control sequence is $u^* = \{0, 0.9333, \infty\}$ with switching times $t_f = 2.86\text{h}$. This operation is taken as a base case for evaluation of the discussed control schemes.

It is clear that the real-time optimality of the operation is strongly influenced by accuracy of the parameter estimates, mostly γ_2 and γ_3 since γ_1 can be factored out from $S(\cdot)$. Preliminary

numerical tests with optimal experiment design (OED) methodology (Gottu Mikkula and Paulen, 2017) showed that for the most accurate estimation of γ_2 the manipulated variable $u(t) = 0$ and, on the other hand, the best estimation accuracy of γ_3 is reached when $u(t) = 1$. This shows mutual benefit of the optimal control strategy $u^* = \{0, 0.9333, \infty\}$ and estimation of γ_2 , and a potential conflict of accurate estimation of γ_3 and the optimal control policy. This can also be seen from (17) and (18c), where it is clear that when a controller applies $u(t) = 0$, the parameter γ_3 is unidentifiable as the concentration $c_2(t)$ remains constant. The OED studies also showed that the best time to measure the plant outputs is in the beginning of the operation. This stems from the absolute error of the measurement (see (9)) and from the fact that the measured permeate flux is highest in the beginning of the operation and drops dramatically with the increase of $c_1(t)$.

The real-time optimal operation using on-line adaptation of parameters reached the final time of operation 2.87 h, which is practically the same performance as the optimal operation, while its counterpart without parameter estimation reached the operation time 4.23 h, which clearly too conservative. This result shows the significant benefits of the proposed scheme.

5. Conclusion

We have presented a methodology for dynamic real-time optimization of batch processes (with particular application to membrane systems) via parametrization of the optimal controller using Pontryagin's minimum principle. The employed parametrization greatly reduces the computational burden in order to guarantee feasibility of the operation. In order to address parametric plant-model mismatch issue, we have suggested a robust approach, which consisted in projection of the plant uncertainty into optimality conditions. This again greatly reduces computational burden. As the uncertainty in parameters can greatly affect the optimality of the batch, we have proposed an adaptive scheme that makes use parameter estimation and, as shown in the case study, can greatly assist in reducing conservativeness of the real-time scheme.

References

- B. Chachuat, B. Houska, R. Paulen, N. D. Perić, J. Rajyaguru, M. E. Villanueva, 2015. Set-theoretic approaches in analysis, estimation and control of nonlinear systems. *IFAC-PapersOnLine* 48 (8), 981–995.
- E. Fogel, Y. Huang, 1982. On the value of information in system identification bounded noise case. *Automatica* 18 (2), 229–238.
- G. Francois, D. Bonvin, 2013. Chapter one - measurement-based real-time optimization of chemical processes. In: S. Pushpavanam (Ed.), *Control and Optimisation of Process Systems*. Vol. 43 of *Advances in Chemical Engineering*. Academic Press, pp. 1–50.
- A. R. Gottu Mikkula, R. Paulen, 2017. Model-based design of optimal experiments for nonlinear systems in the context of guaranteed parameter estimation. *Computers & Chemical Engineering* 99, 198–213.
- K. M. Hangos, J. Bokor, G. Szederkényi, 2006. *Analysis and control of nonlinear process systems*. Springer Science & Business Media.
- S. Lucia, T. Finkler, S. Engell, 2013. Multi-stage nonlinear model predictive control applied to a semi-batch polymerization reactor under uncertainty. *J Process Contr* 23 (9), 1306–1319.
- Z. K. Nagy, R. D. Braatz, 2003. Robust nonlinear model predictive control of batch processes. *AIChE Journal* 49 (7), 1776–1786.
- R. Paulen, M. Fikar, G. Foley, Z. Kovács, P. Czermak, 2012. Optimal feeding strategy of diafiltration buffer in batch membrane processes. *Journal of Membrane Science* 411–412, 160–172.
- R. Paulen, M. Jelemenský, Z. Kovács, M. Fikar, 2015. Economically optimal batch diafiltration via analytical multi-objective optimal control. *Journal of Process Control* 28, 73–82.
- L. S. Pontryagin, V. G. Boltyanskii, R. V. Gamkrelidze, E. F. Mishchenko, 1962. *The Mathematical Theory of Optimal Processes*. John Wiley & Sons, Inc., New York.
- B. Srinivasan, S. Palanki, D. Bonvin, 2003. Dynamic optimization of batch processes: I. Characterization of the nominal solution. *Computers & Chemical Engineering* 27 (1), 1–26.

An Integrated Medium – Term Energy Planning Model for Interconnected Power Systems

Apostolos P. Elekidis^a, Nikolaos E. Koltsaklis^a, Michael C. Georgiadis^{a,*}

^a *Department of Chemical Engineering, Aristotle University of Thessaloniki, University Campus, Thessaloniki, 54124, Greece*

mgeorg@auth.gr

Abstract

This work presents a generic Mixed-Integer Linear Programming model that integrates a Mid-term Energy Planning model for the optimal integration of power plants into interconnected power generation systems. The time horizon consists of a representative day for each month of the year. The Unit commitment problem is modelled in details to optimally determine the optimal operational strategy in order to meet the electricity demand at a minimum total cost by utilizing the optimal combination of a set of available power generation plants. Furthermore, the model considers the possibility of building new units selected from a set of proposed ones, as well as expanding the capacity of existing renewable energy units. The possibility of expanding the existing interconnection capacity between systems is also considered. Environmental-related constraints for the production of CO₂, NO_x, SO_x and PM_x emissions are also taken into account. The main objective is the minimization of the total annualized cost. The applicability of the proposed model is illustrated in a case study including two interconnected power systems. Finally, a sensitivity analysis is performed in order to investigate the effect of key process parameters on the final power generation policies.

Keywords: Mid-term Energy Planning, Unit commitment problem, Transmission expansion planning, Mixed integer linear programming.

1. Introduction

In recent years, the problems of climate change and environmental pollution constitute a major concern for the global community. As a result, the fossil fuels usage is constantly decreasing while the percentage of Renewable Energy Sources (RES) penetration gets higher, in order to achieve lower emissions of key air pollutants. Furthermore, a number of other challenges are to be addressed, such as the constantly electricity demand increase, the variability of the fossil fuel prices and the transmission network safety (Koltsaklis et al, 2014). Under these challenges, power systems expansion planning is of paramount importance for an affordable, secure, and sustainable energy future. Focusing on the spatial characteristics of the power system, Koltsaklis et al., (2014), presented a generic multi-regional MILP model for the optimal generation expansion problem of a power system at a national and/or regional level, incorporating also energy resources management aspects. Sadeghi et al. (2017), provide a detailed review of the technical, regulatory, environmental, and economic aspects that influence the generation expansion planning (GEP) decisions, highlighting possible directions for future works. Furthermore, Denny et al. (2012), made use of a stochastic unit commitment model to

assess the influence of increased interconnection for the island of Ireland with high penetrations of wind generation. The findings indicate that increased interconnections can decrease average prices as well as their variability, while they can enhance power system security to a significant extent. Georgiou (2016), developed a mixed integer linear programming (MILP) model for the optimal generation expansion planning (GEP) of a power system incorporating possible interconnections between mainland and insular systems. The results indicate the potential benefits of such an interconnected power system, in terms of operational flexibility and environmental impact. This work utilizes a detailed and generic mixed-integer linear programming model for the optimal power systems expansion planning problem of interconnected systems. The results indicate the optimal type of power generation technologies of each system along with their daily operation, their capacity and location of new units under several technical, economic, regulatory, and environmental constraints.

2. Problem Statement

The problem under consideration is formally defined in terms of the following items. The period under consideration is annual and is divided into a set of monthly periods $m \in M$, through the introduction of specific representative days. The duration of each representative day of each month $m \in M$ (in days) is represented by the parameter DUR_m . A set of power generating units $i \in I$ are installed in each power system $s \in S$. The producing power generation of each unit is represented by the variable $P_{i,m,t}$. This set of power generating units can include thermal power units $th \in TH$, hydroelectric units $j \in J$, and renewable (except hydroelectric) units $ren \in REN$. The thermal units are described by their efficiency and their conversion factor of fuel to energy, given by the parameters EF_{th} and $HEATVALUE_{th}$, and they also have a fixed operating cost given by the parameter $OTHERS_{th}$, while there is also a minimum penetration level of renewable energy units $MINREN$ ($MAXREN$). Each renewable unit, $ren \in REN$, is characterized by a specific availability during each time interval $t \in T$ and month $m \in M$ given by $AV_{ren,m,t}$. The subset which includes the new candidates for construction units, is denoted by $n \in N$, while the binary variable UB_n is equal to 1 if a new unit is constructed. Furthermore, the capacity of the renewable units is able to be expanded up to an upper expansion limit represented by the parameter $MAXEXP_{ren}$. The expansion is given by the variable $PEXP_{ren}$. The new units are characterized by a specific investment cost INV_n (subject to a specific capital recovery factor CRF), as the expansion cost for the renewables is represented by $INVR_{ren}$. Each power system, $s \in S$, can be interconnected with other power systems ($s' \neq s$) $\in S$ according to a specific network structure. Each power system $s \in S$ is characterized by a certain electricity demand in each time period $t \in T$ and month $m \in M$ given by the parameter $D_{s,m,t}$. The transmitted power between interconnected power systems $s \in S$ and $s' \in S$, $s \neq s'$, given by the variable $CFL_{s,s',m,t}$. Each interconnector between the interconnected system is characterized by a specific ramp-up, CUP , and ramp-down, CDN , rate. Its transmission expansion cost is described by the parameter $TRANS_COST$, while the expansion level is given by the variable $COREX_{s,s'}$. There is also a maximum transmission capacity expansion value given by $MAXTRANSM$. Each power generating unit $i \in I$ is identified based on specific technical characteristics including technical minimum (maximum) of each power unit $i \in I$, $PMIN_i$ ($PMAX_i$). Emissions rate coefficients (COE_{th} , NOX_{th} , SOX_{th} and PM_{th}) describe the CO_2 , the NO_x the SO_x and the PM_x emissions as the CO_2 emission cost is described by the parameter $CCOST_{th}$.

Each thermal unit $th \in TH$ has a specific fuel cost $FCOST_{th}$. The environmental standards of the studied power system include: (i) Upper annual CO2 emissions limit $MAXCO2_{th}$, (ii) Upper annual NOX emissions limit $MAXNOX_{th}$, (iii) Upper annual SOX emissions limit $MAXSOX_{th}$, and (iv) Upper annual PMX emissions limit $MAXPM_{th}$.

3. Mathematical Formulation

The objective function (1) includes the operating costs of all production units and systems. In particular, the first term expresses the variable cost that depends on the output power of all thermal units over the examined period. The second term refers to the annualized construction cost of all the new units which are decided to be constructed. Similarly, the next term represents the annualized expansion cost of each RES power unit under expansion. The next two terms refer to the interconnection grid between the energy systems. The first term describes the total electricity flow between the energy systems and the last term quantifies the cost of the transmission grid expansion.

$$\begin{aligned} \min & \left[\left(\sum_{m \in M} \sum_{i \in I} \sum_{t \in T} \frac{FCOST_{th}}{HEATVALUE_{th} \cdot 0.277778 \cdot EF_{th}} + COE_{th} \cdot CCOST + OTHERS_{th} \right) P_{i,m,t} \cdot DUR_m \right. \\ & + CRF \cdot \left(\sum_{n \in N} UB_n \cdot INV_N + \sum_{ren \in REN} PEXP_{ren} \cdot INVR_{ren} \right) + \\ & \left. + \left(\sum_{s \in S} \sum_{s' \in S} (CFL_{s,s',m,t}) + \sum_{s \in S} \sum_{s' \in S} COREX_{s,s'} \cdot \frac{TRANS_COST}{2} \right) \right] \end{aligned} \quad (1)$$

$$\sum_{i \in IS} P_{i,m,t} + \sum_{s' \in INT} CFL_{s',s,m,t} = D_{s,m,t} + \sum_{s' \in INT} CFL_{s,s',m,t} \quad \forall s \in S, m \in M, t \in T, type_i \neq 4 \quad (2)$$

Constraint (2) quantify the energy balance of the problem. The first term is a sum referring to the total power output generated by all units at each time period $t \in T$, while the second sum refers to the total energy entering the system $s \in S$ from the all the other interconnected options. The third term is the demand of each system $s \in S$ at each time period $t \in T$, while the fourth term refers to the total energy exporting from a system $s \in S$ to the other interconnected power systems.

$$CEXP_{s,s'} \leq COREX_{s,s'} \cdot MAXTRANSM \quad \forall s \in S, s' \in S, s' \neq s \quad (3)$$

According to constraint (3), the expansion of the interconnection network $CEXP_{s,s'}$ has an upper limit, expressed by parameter $MAXTRANSM$. The binary variable $COREX_{s,s'}$ takes the value 1 if the transmission grid is decided to be expanded.

$$CFL_{s,s',m,t} - CFL_{s,s',m,t-1} \leq CUP \cdot CFL_{s,s',m,t-1} \quad \forall s \in S, s' \in S, m \in M, t \in T \quad (4)$$

$$CFL_{s,s',m,t-1} - CFL_{s,s',m,t} \leq CDN \cdot CFL_{s,s',m,t-1} \quad \forall s \in S, s' \in S, m \in M, t \in T \quad (5)$$

Constraints (4) and (5), indicate that both the increase and decrease of the transmitted power between two hours $CFL_{s,s',m,t}$, should be lower than the two percentages, expressed by parameters, CUP and CDN, respectively.

Additional constraints of the model include: (i) Units' power capacity constraints, (ii) power adequacy constraint, (iii) maximum and minimum penetration of RES constraints, (iv) new units construction and RES units expansion constraints, (v) hydroelectric units' constraints, (vi) environmental impact constraints and (vii) ramp-up and down limits of power units. The overall problem is formulated as an MILP problem, involving a cost minimization objective function and subject to the above constraints.

4. Case Study

The applicability of the proposed model is illustrated using a representative case study, in which the annual energy production of two interconnected systems, S1 and S2, is considered. Each system consists of a set of power generation units. These units are sorted into thermal units (lignite-fired and natural gas units), hydroelectric units and renewable energy sources (RES) units (solar and wind units). The possibility of building new units in system S1, selected from a set of proposed ones, as well as expanding the capacity of existing renewable energy units is also taken into account. The possibility of expanding the existing interconnection capacity between systems is also considered, as well as the air pollutants emissions and more specifically the emissions of CO_2 , NO_x , SO_x , and PM_x . The objective corresponds to the minimization of the total annualized cost. Figure 1 presents the total capacity per technology type in each power system.

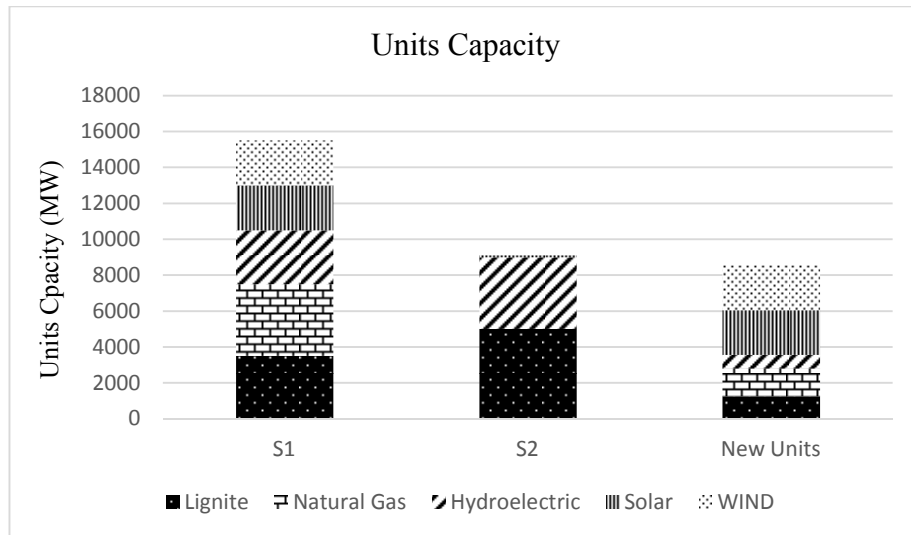


Figure 1: Total capacity per technology type in each power system (MW)

The parameters' values that have been used are based on data from the U.S. Energy Information Administration (U.S. Energy Information Administration, 2016)

5. Results

The problem has been solved to global optimality making use of the ILOG CPLEX 12.6.0.0 solver incorporated in the General Algebraic Modelling System tool (GAMS, 2017). An integrality gap of 1% has been imposed in all Scenarios.

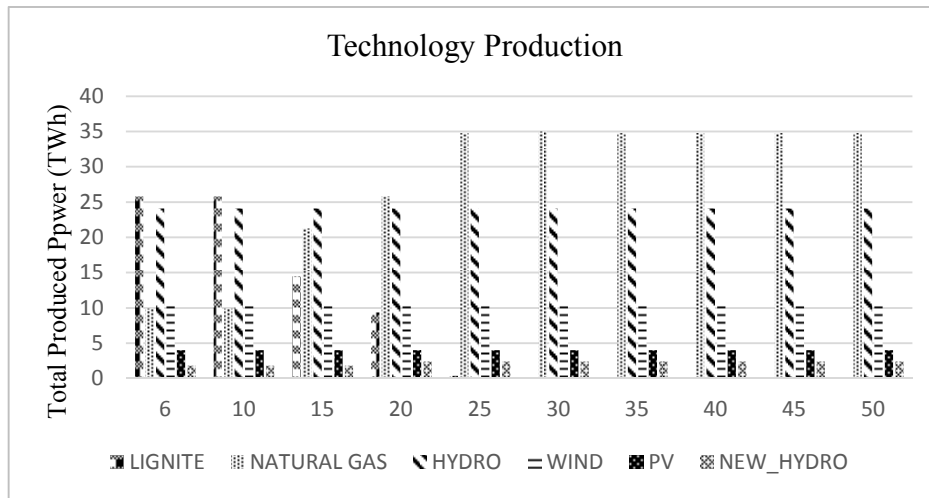


Figure 2: Annual production mix per selected Scenario (TWh)

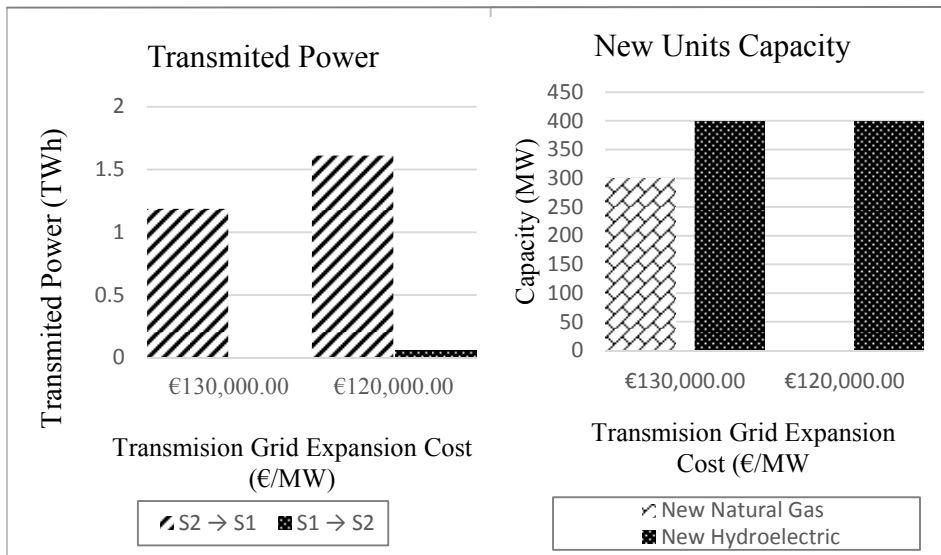


Figure 3: a) Total power flow between the two systems in each case (TWh) b) New units' capacity in each case by each technology type (MW)

The first sensitivity analysis bears upon the variation of the CO₂ emissions cost. Beginning with a reference value (6 €/tn), the price is firstly increased to 10 €/tn and then reaches gradually the value of 50 €/tn. Figure 2 presents the total production for each type of units in each case. It is clear that the gradual increase of the CO₂ emission value, causes a decrease in the total lignite units' production, while a remarkable

increase in the natural gas units' contribution also appears. More precisely, the annual production of lignite units is reduced from 25 TWh initially to the half, when the CO₂ cost is equal to 15 €/tn and it is going up to zero for higher CO₂ prices. On the contrary, the total annual production of natural gas units is doubled for a CO₂ cost value equal to 15 €/tn, and reaches an upper production limit of 35 TWh for a CO₂ cost price of 25 €/tn.

The marginal cost for the transmission grid expansion which connects the two systems is also studied. As shown in Figure 3(a), this cost is 120,000 €/MW. In case the expansion cost is higher than this marginal value, no extension of the interconnection grid takes place and the total transmitted power is lower, whereas the construction of an additional natural gas unit is decided, as illustrated in Figure (3b). On the contrary, for a transmission cost equal or lower than the marginal cost, the power unit is not built.

6. Conclusions

The main objective of the present work is the development of a mathematical model for the optimal mid-term power systems planning, which implements the generation and transmission expansion planning of interconnected power systems on an annual scale. The proposed model can be utilized by decision makers to take strategic decision-making such as the construction of new units, expansion of renewable ones, as well as the capacity of transmission lines between the interconnected power systems. Furthermore, the proposed approach incorporates several environmental constraints in terms of gaseous pollutants such as CO₂, NO_x, SO_x and particulate matter PM_x. In addition, the proposed model can be used in order to study two or more interconnected power systems which represent either individual power systems of a country or each system represents separately the overall power system of a country.

References

- E. Denny, A. Tuohy, P. Meibom, A. Keane, D. Flynn, A. Mullane, and M. O'Malley, 2010, The impact of increased interconnection on electricity systems with large penetrations of wind generation: a case study of Ireland and Great Britain, *Energy Policy*, vol. 38, pp. 6946–6954.
- Georgiou, P. N., A bottom-up optimization model for the long-term energy planning of the Greek power supply sector integrating mainland and insular electric systems. *Computers & Operations Research* 2016, 66, 292-312.
- Koltsaklis, N. E.; Dagoumas, A. S.; Kopanos, G. M.; Pistikopoulos, E. N.; Georgiadis, M. C., A spatial multi-period long-term energy planning model: A case study of the Greek power system. *Applied Energy* 2014, 115, 456-482.
- R. E. Rosenthal, 2017, *GAMS - A User's Guide*, GAMS Development Corporation, Washington, DC, USA.
- Sadeghi, H.; Rashidinejad, M.; Abdollahi, A., A comprehensive sequential review study through the generation expansion planning. *Renewable and Sustainable Energy Reviews* 2017, 67, 1369-1394.
- U.S. Energy Information Administration (US EIA), 2016, Capital Cost Estimates for Utility Scale Electricity Generating Plants. https://www.eia.gov/analysis/studies/powerplants/capitalcost/pdf/capcost_assumption.pdf (accessed Nov. 8, 2017).

Multi-period multi-time optimisation of CO₂ based district energy systems

Raluca Suciu^a, Paul Stadler^a, Luc Girardin^a and François Maréchal^a

^a*École Polytechnique Fédérale de Lausanne, Rue de L'industrie 17, Case Postale 440, Sion, CH-1951, Switzerland*
raluca-ancuta.suciu@epfl.ch

Abstract

Energy system design should take into account the hourly, daily and seasonal variations of both the energy demand and the considered utilities, and therefore requires a multi-time-resolution problem formulation. Multi-period / multi-time optimization is needed when a multi-time (e.g. hourly) optimization is performed inside another multi-period (e.g. typical day) optimization. However, optimizations over large temporal or spatial horizons tend to become computationally expensive, due to the large number of variables and constraints indexed over the times and over the periods. Employing typical operating periods (e.g. a number of typical operating days during the year) offers an interesting solution for problem size reduction. A variety of data clustering algorithms have been proposed in literature in order to select the best typical periods for different applications. This work uses a MILP formulation of a k-medoids based algorithm (PAM) in order to obtain typical operating periods which pass energy from one period to another, in view of performing long term energy storage. The algorithm is used coupled with an optimization of a CO₂ based district energy network in a typical urban center. The intra-daily resolution allows the exploration of short term energy storage in the form of batteries located in the medium and low voltage grid. Coupled with the seasonal resolution, it offers a better understanding of the impact of daily storage on the long term storage and on the total energy requirement. The results show that implementing short-term energy storage leads to reductions of 2% in the size of the long term storage tank and 7.5 - 7.8% in the size of the main energy providers (PV panels).

Keywords: multi-period optimization, short and long term energy storage, district energy networks, CO₂ network

1. Introduction and motivation

Multi-period models are used to optimize the design and operation scheduling of energy systems. Optimal operation scheduling has been extensively reviewed across different fields (Floudas and Lin, 2004; Méndez et al., 2006; Phanden et al., 2011; Maravelias, 2012). However, such optimizations have a large number of variables and are computationally expensive. Typical operating periods represent an efficient solution which reduces the number of variables. Indeed, appropriate typical operating periods allow to reduce the data, while keeping the key features of the different profiles and ensuring a proper sizing of the equipment. However, a trade-off between the desired precision and the quality of the results must be found.

Data clustering techniques were first introduced by Lloyd in 1957, and published in 1982 (Lloyd, 1982). These techniques have been used across different fields, such as machine learning, biomedical research (Xu and Wunsch, 2010), or energy system engineering (Fazlollahi et al., 2014; Bungener et al., 2013).

The selection of typical operating periods has been approached in different ways. (Fazlollahi et al., 2014) used a k-means algorithm (Seber, 1984) and ϵ -constraints (a parametric optimization which minimizes the number of operating periods while maximizing their quality (Steuer, 1989)). In the k-means algorithm, the yearly profile is grouped in clusters and the period closest to the center of each cluster is used as the typical period which represents the cluster. Peak load periods are added as isolated clusters to ensure that the system is able to operate at these conditions.

(Domínguez-Muñoz et al., 2011) proposed a k-medoids algorithm to select representative operating periods. The main difference with the previous approach is that k-medoids selects the center of the cluster using a data point from within the cluster, and that scaling factors are used on the cluster days in order to ensure the annual energy balance. Similar to k-means, the peak load periods are added manually.

Other approaches are present in the literature. (Marechal and Kalitventzeff, 2003) and (Bungener et al., 2013) used an evolutionary algorithm to select typical operating periods for industrial energy systems. (Ortiga et al., 2011) proposed a graphical algorithm to reduce the number of operating periods in order to reproduce heating and cooling load duration curves. (Lozano et al., 2009) used 24 typical operating days, 2 for each month: one using averaged data over the working days and one using averaged data over the weekends.

In this paper, a mixed integer linear programming (MILP) formulation of a k-medoids based algorithm is used in order to find typical operating periods for an urban energy system (Rager, 2015; Stadler et al., 2016). A typical urban center (Suciú et al., 2017) using a CO₂ based district energy network (DEN) is used as case study. CO₂ networks have already been integrated with power to gas (P2G) systems for long term energy storage (Suciú et al., 2017, 2016). However, the intraday resolution has not been addressed. In view of this the current study further integrates the system with batteries located in the medium and low voltage grids, in order to explore short-term energy storage and to better understand the impact of daily storage on the size of the long term energy storage tank and of the main energy providers (the PV panels).

2. Methodology

2.1. Selection of typical periods

Since the problem computational time increases drastically with the problem size (figure 1a), in this work a k-medoids based data clustering algorithm is used to reduce the complexity of the problem studied. This approach selects the cluster centers based on the smallest sum of distances within each cluster, while the cluster size is chosen based on a series of performance indicators (Stadler et al., 2016; Rager, 2015).

Two input parameters are considered for the clustering process, namely the ambient temperature (T_{ext}) and the global solar irradiation (GI). Other data such as consumption profiles and their corresponding temperatures of demand are defined based on the computed cluster centers. The k-medoids algorithm is run between 2 and 25 typical days. A maximum of 12% error in the load duration curve (ELDC) is set and consequently the number of typical days should be higher than 5 (figure 1b). In order to select the optimal number of typical days, the Davies-Bouldin (DB) index is used. The DB index is a measure of how good the clustering scheme is (Davies and Bouldin, 1979). It accounts for the separation between the clusters, which ideally has to be as large as possible, and the within cluster scatter, which has to be as low as possible. The index is defined as the ratio of the cluster separation and the within the cluster distance, and the lower the value, the better the separation of the clusters and the 'tightness' inside the clusters. As observed in figure 1c, for this problem the DB index has the lowest value for 7 typical days. Therefore, this value is used for further analysis.

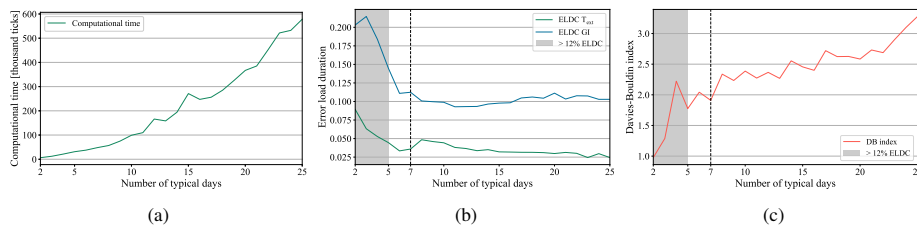


Figure 1. Computational time (a), error load duration curves (b), and Davies-Bouldin index (c) for different # of typical days

2.2. CO₂ based district energy networks

A detailed description of the refrigerant based network using CO₂ as the heat transfer fluid is given by (Weber and Favrat, 2007) and possible energy conversion technologies have been investigated by (Henchoz, 2011, 2016; Henchoz et al., 2015). The network has been integrated with electrolysis and methanation units to convert electricity to natural gas for energy storage and with co-generation solid oxide fuel cell (SOFC)-gas turbine units to convert natural gas back to electricity and heat (Suciu et al., 2017, 2016).

A typical urban area is studied (Suciu et al., 2017). The energy demands considered are heating in the form of space heating and domestic hot water, cooling in the form of air cooling and refrigeration, and the demand for electrical appliances (utilities) (figure 2b). The decentralized energy technologies used are: heat pumps for space heating and domestic hot water, heat exchangers for air cooling, and vapor compression chillers for refrigeration. The centralized energy technologies used are: a central plant which balances the network (in the form of a lake or geothermal wells), photo-voltaic (PV) panels, a solid oxide fuel cell (SOFC) - solid oxide electrolysis cell (SOEC) co-generation unit, and a boiler-steam network installed at the waste incinerator (figure 2a).

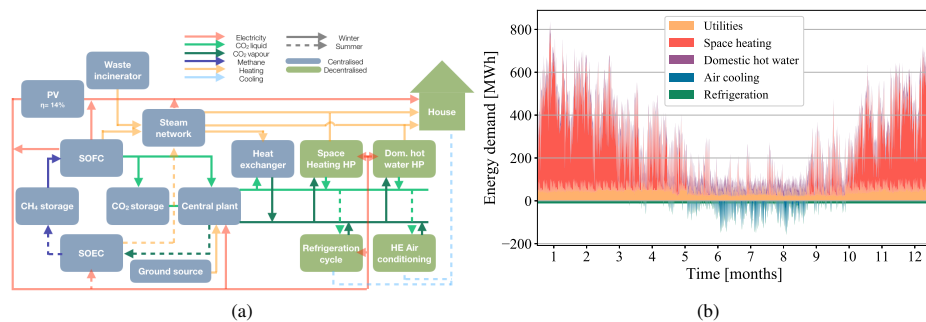


Figure 2. Schematic description of CO₂ DENs (a) and service energy demand (b)

Details on the models and cost parameters used can be found in (Suciu et al., 2017, 2016). The system is further integrated with batteries to explore the influence of daily storage on the size of the long term storage tank and of the PV panels. The problem uses a mixed integer linear programming (MILP) formulation based on optimal utility selection (Marechal and Kalitventzeff, 2003). The objective function is the minimization of the operating cost and the main constraints are the heat cascade equations and the resource balance equations. Additional constraints such as energy conversion technology sizing (and selection) apply.

3. Results and discussion

First, the impact of the short term energy storage on the size of the long term (methane) storage tank is shown. Figures 3 and 4 show the profile of the methane tank level for 7 typical days without and with short-term storage, respectively. When short term storage is used, the size of the methane tank reduces by approximately 2%, since the battery performs a peak load shifting during the day (see close-ups in figures 3 and 4).

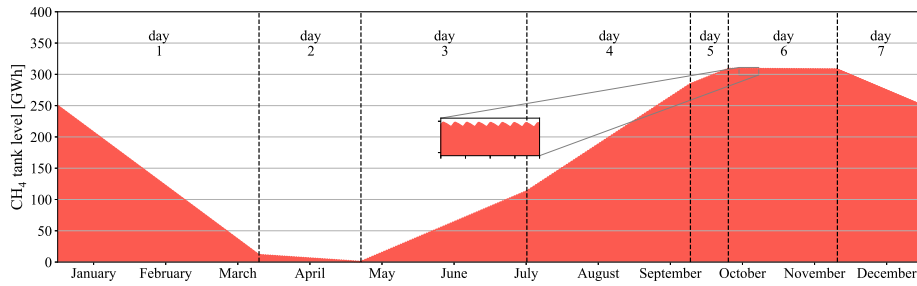


Figure 3. Long term energy storage level, 7 typical days

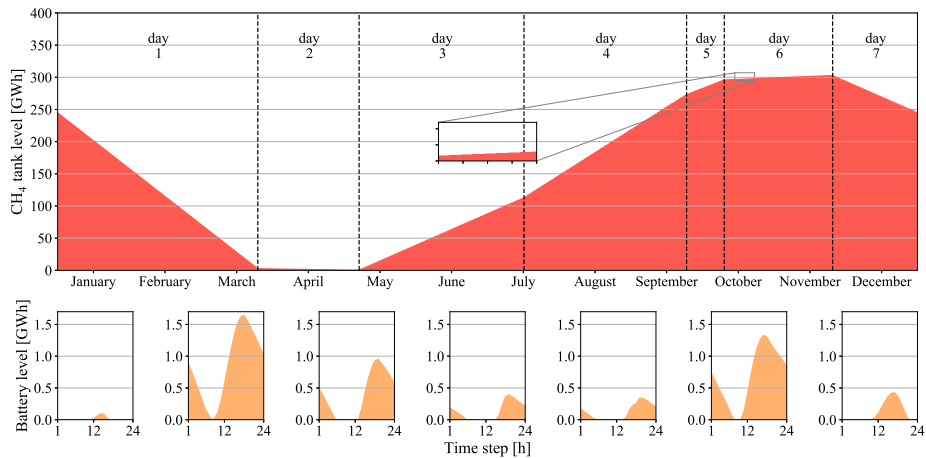


Figure 4. Long and short term energy storage levels, 7 typical days

Taking a closer look at the methane and battery storage levels, one can see that the methane tank charges during summer, when the solar irradiation is high and the excess electricity is used to produce methane and discharges in winter, when the heating demand is high and methane is consumed in the SOFC to produce electricity (for the heating heat pumps).

The short term storage has a few typical operating modes. In days 2, 3, 4, 5, and 6 the battery charges in the afternoon, when the global irradiation is high, and discharges during the night to provide energy services such as electricity for utilities, domestic hot water, or refrigeration. In this case the battery performs a load-shifting from day to night. Typical days 1 and 7 depict a load shifting during the afternoon. In these cases, the battery is charging in the early afternoon and discharging in the late afternoon.

Next, the economic impact of the solution is analyzed. Six cases are considered, 3 scenarios without short term energy storage (a) and their corresponding scenarios with short term energy storage (b). The first scenario (1) is the base case, in which the heat from the environment is provided by a lake, in the second scenario (2) the municipal solid waste produced in the area is valorised, and in the third scenario (3) the municipal solid waste is valorised and the heat from the environment is provided by geothermal wells.

Details on the costs of the different equipments can be found in (Suciu et al., 2017, 2016) and on the battery cost in (Nick et al., 2017). The breakdown of the investment cost for the different cases can be observed in figure 5 and the fixed and variable investment costs for the main contributors in table 1.

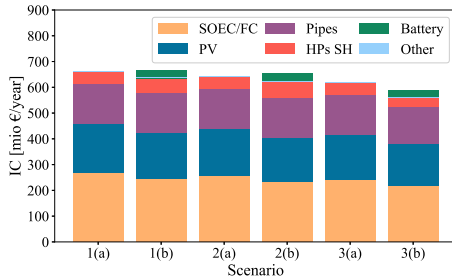


Figure 5. Investment cost breakdown

Table 1. Parameters for investment cost

Unit	Fixed cost	Var. cost	Attribute
SOEC/FC	-	4760 [€/kW]	\dot{E}_{SOEC}
PV	-	247 [€/m ²]	A_{PV}
HPs SH	5680 [€]	1240 [€/kW]	\dot{E}_{comp}
Pipes	5670 [€]	613 [€/m]	$d_{network}$
Battery	20000 [€]	200 [€/kW]	$\dot{E}_{Battery}$

When the waste incinerator-steam network provides part of the electricity, the PV panel size reduces by approximately 4.6%. When the heat from the environment is provided by geothermal wells, the overall electricity consumption decreases (Suciu et al., 2017, 2016) and therefore the size of the PV panels decreases further by 5.4%. When short term energy storage is considered, the PV panel size decreases by 7.5 - 7.8% for the different scenarios. The size of the co-generation unit also decreases, but the size of the SH HPs and the network pipe diameter increase, since less waste heat is available from the co-generation units. For scenarios (1) and (2) the savings in the investment cost of the PV panels and of the co-generation units are smaller than the investment cost of the battery, making the short-term storage implementation unattractive from an economic point of view. However, in scenario (3) the savings due to the use of short-term energy storage are higher than the investment cost of the batteries, making the use of batteries for intra-daily load shifting economically favorable.

4. Conclusion

This work uses a multi-period (7 typical days) multi-time (24 hours) resolution to optimize CO₂-based district energy networks. The intra-daily resolution offers a better understanding of the impact of daily electricity storage on the size of the long term energy storage tank and on the size of the main energy providers (the PV panels). When daily storage is used, the long term energy storage (methane) tank reduces by approximately 2%, since the batteries perform daily load-shifting.

The size of the PV panels is compared for 3 different scenarios, with and without short term energy storage. The size reduces by 4.6 % when waste is considered since the steam network satisfies part of the electricity demand and it reduces further by 5.4 % when geothermal wells are used since the overall electricity consumption decreases. The short term storage leads to reductions in the PV panel size of 7.6% for scenario (1), 7.5% for scenario (2), and 7.8% for scenario (3). While for scenarios (1) and (2) investing in short-term energy storage is not economically favorable,

in scenario (3) the savings in investment cost from using short-term storage are higher than the investment cost of the battery, making it a economically attractive solution.

5. Acknowledgements

This project is carried out within the frame of the Swiss Centre for Competence in Energy Research on the Future Swiss Electrical Infrastructure (SCCER-FURIES) with the financial support of the Swiss Innovation Agency (Innosuisse - SCCER program). The author would also like to acknowledge the financial support from EOS Holding.

References

- Bungener, S. L., Van Eetvelde, G., Marechal, F., 2013. A methodology for creating sequential multi-period base-case scenarios for large data sets 35, 1231–1236.
- Davies, D. L., Bouldin, D. W., 1979. A cluster separation measure PAMI-1 (2), 224–227.
- Domínguez-Muñoz, F., Cejudo-López, J. M., Carrillo-Andrés, A., Gallardo-Salazar, M., 2011. Selection of typical demand days for CHP optimization 43 (11), 3036–3043.
- Fazlollahi, S., Bungener, S. L., Mandel, P., Becker, G., Maréchal, F., 2014. Multi-objectives, multi-period optimization of district energy systems: I. selection of typical operating periods 65, 54–66.
- Floudas, C. A., Lin, X., 2004. Continuous-time versus discrete-time approaches for scheduling of chemical processes: a review 28 (11), 2109–2129.
- Henchoz, S., 2011. On a multi-service, CO₂ based, district energy system for a better energy efficiency of urban areas.
- Henchoz, S., 2016. Potential of refrigerant based district heating and cooling networks.
- Henchoz, S., Weber, C., Maréchal, F., Favrat, D., 2015. Performance and profitability perspectives of a CO₂ based district energy network in geneva's city centre 85, 221–235.
- Lloyd, S., 1982. Least squares quantization in PCM 28 (2), 129–137.
- Lozano, M. A., Ramos, J. C., Carvalho, M., Serra, L. M., 2009. Structure optimization of energy supply systems in tertiary sector buildings 41 (10), 1063–1075.
- Maravelias, C. T., 2012. General framework and modeling approach classification for chemical production scheduling 58 (6), 1812–1828.
- Marechal, F., Kalitventzeff, B., 2003. Targeting the integration of multi-period utility systems for site scale process integration 23 (14), 1763–1784.
- Méndez, C. A., Cerdá, J., Grossmann, I. E., Harjunkoski, I., Fahl, M., 2006. State-of-the-art review of optimization methods for short-term scheduling of batch processes 30 (6), 913–946.
- Nick, M., Cherkaoui, R., Paolone, M., 2017. Optimal planning of distributed energy storage systems in active distribution networks embedding grid reconfiguration, 1–1.
- Ortiga, J., Bruno, J., Coronas, A., 2011. Selection of typical days for the characterisation of energy demand in cogeneration and trigeneration optimisation models for buildings 52 (4), 1934–1942.
- Phanden, R. K., Jain, A., Verma, R., 2011. Integration of process planning and scheduling: a state-of-the-art review 24 (6), 517–534.
- Rager, J. M. F., 2015. Urban energy system design from the heat perspective using mathematical programming including thermal storage.
- Seber, G. A. F., 1984. *Multivariate Observations*. Wiley Series in Probability and Statistics. John Wiley & Sons, Inc., DOI: 10.1002/9780470316641.
- Stadler, P., Ashouri, A., Maréchal, F., 2016. Model-based optimization of distributed and renewable energy systems in buildings 120, 103–113.
- Steuer, R. E., 1989. *Multiple criteria optimization: theory, computation, and application*. Krieger.
- Suciú, R., Stadler, P., Ashouri, A., Maréchal, F., 2016. Towards energy-autonomous cities using CO₂ networks and power to gas storage.
- Suciú, R.-A., Girardin, L., Maréchal, F., 2017. Energy integration of CO₂ networks and power to gas for emerging energy autonomous cities in europe.
- Weber, C., Favrat, D., 2007. Conventional and advanced district energy systems 1, 517–524.
- Xu, R., Wunsch, D. C., 2010. Clustering algorithms in biomedical research: A review 3, 120–154.

Data-driven water-efficient production scheduling in the food industry

Sai Jishna Pulluru,^{a*} Renzo Akkerman^b

^a *TUM School of Management, Technische Universität München, Munich, Germany*

^b *Operations Research and Logistics group, Wageningen University, Wageningen, The Netherlands*

*pulluru.sai.jishna@tum.de

Abstract

Reuse and regeneration of water is becoming increasingly important in the food industry. Planning both water reuse and production while at the same time ensuring food safety is a challenge. We propose a novel scheduling methodology to simultaneously plan water reuse and production in food production processes utilizing real time water quality data. We develop a two-stage predictive scheduling and reactive scheduling approach taking into account the dynamic nature of water quality. Overall, our approach can prevent undesired contamination of food products due to reuse of water and achieve higher water efficiency.

Keywords: data driven approach, real-time scheduling, water efficiency, online water quality measurement, food industry.

1. Introduction

Increasing population, economic growth, and demographic changes have all contributed to an increased consumption of processed foods. Water is both an essential ingredient for food processing in its pure form, and an unwanted byproduct that poses significant financial and environmental burden. Many food processing plants are investing in advanced water treatment technologies to reuse wastewater streams in daily production and cleaning requirements. Ensuring that water of appropriate quality reaches a water-demanding process at the correct time is key to achieving efficient water reuse. As a result, managing water flows in food industries becomes inseparable from production planning and scheduling. Additionally, in order to ensure safe water reuse, real-time water quality monitoring technologies are also increasingly deployed. Such systems are often used to raise alarms in case of water quality abnormalities that require operator intervention. However, using such measurements to provide early warnings and make necessary operational decisions remains a challenge.

Integrated water minimization and production management in process plants is a relevant field of research in this context, and has been actively contributed to by both operations research and process systems engineering communities. Several mixed integer linear programming models have been developed in the last decade to integrate production scheduling with water network planning (Gouws et al. 2010). Recent works have also addressed aspects like water–production efficiency tradeoffs (Chaturvedi & Bandyopadhyay 2014, Pulluru & Akkerman 2017), sequence-dependent cleanings (Adekola et al. 2017), and water quality classifications (Pulluru & Akkerman 2017). A

major shortcoming of these works is that they assume either pre-determined water qualities or model ideal process systems. In practice, there is a high margin for error in these estimates, due to e.g. treatment equipment failures, temperature variations, non-ideal mixing, feed quality variations, or insufficient cleaning. Undesirable fluctuations from these estimates/assumptions can render carefully constructed water-efficient production schedules infeasible resulting in significant efficiency losses. Augmenting water-integrated production scheduling with real-time water quality data obtained from online monitoring systems is a potential way to tackle this problem.

In this paper, we present a two-stage scheduling approach capable of scheduling production and planning water reuse in multi-stage flow shops employing real-time water quality data collected from online monitoring systems. We apply statistical inferences to characterize fluctuations in the quality of water obtained from regeneration systems like reverse osmosis (RO) and predict the extreme behaviour of the process. We formulate a scheduling model to model production in multi-stage flow shops combining both discrete and continuous time representations in order to capture both timely water flows/inventories and quality fluctuation behaviour of water obtained from treatment equipment. Based on observed quality data during schedule execution, our approach is capable of making various rescheduling decisions such as cleaning/maintenance of potentially contaminated equipment, delaying of batches, usage of different water sources, or additional treatment of water. This leads to increased adherence to production and water efficiency targets, and safety standards for food production. We illustrate our approach using a case of cheese production with whey treatment as a source of regenerated water.

2. Intelligent water-efficient scheduling model

To include real-time water quality data in our scheduling approach, we use extreme value theory to analyse the extreme measurements of water quality arising from regeneration units. This results in suitable probability density function described by shape parameter ξ , scale parameter a , and location parameter b which is then used to predict the magnitude of extreme measurements, also known as return level x as a function of time T . These functions represent a performance decay process in which water quality fluctuation gradually increases over time. For more details on extreme value analysis, its development and applications, we refer to Gomes & Guillou (2015) and Skou et al. (2017).

Using these analyses, we developed a sensor-data-driven hybrid discrete-continuous time scheduling model to make decisions on reuse of treated water, and scheduling of production and cleaning activities in multi-stage flow shops. Due to space limitations, we only present the key model characteristics and illustrate this in Figure 1. We assume a lot-by-lot sequencing in our flow shop to reflect real-life practice of producing lots consisting of several identical batches of the same product. For simplicity reasons, we only model sequence-dependent and time-dependent cleanings. We use constraints similar to Stefansdottir et al. (2017) to model the time-dependent cleanings. However, in their formulation, modelling of sequence-dependent cleanings is not explicit due to the use of a global precedence relationship between tasks. As our work requires determination of exact start and finish times (to be able to track water production and consumption), we instead use an immediate precedence relationship to model the sequencing of product lots and batches in the flow shop.

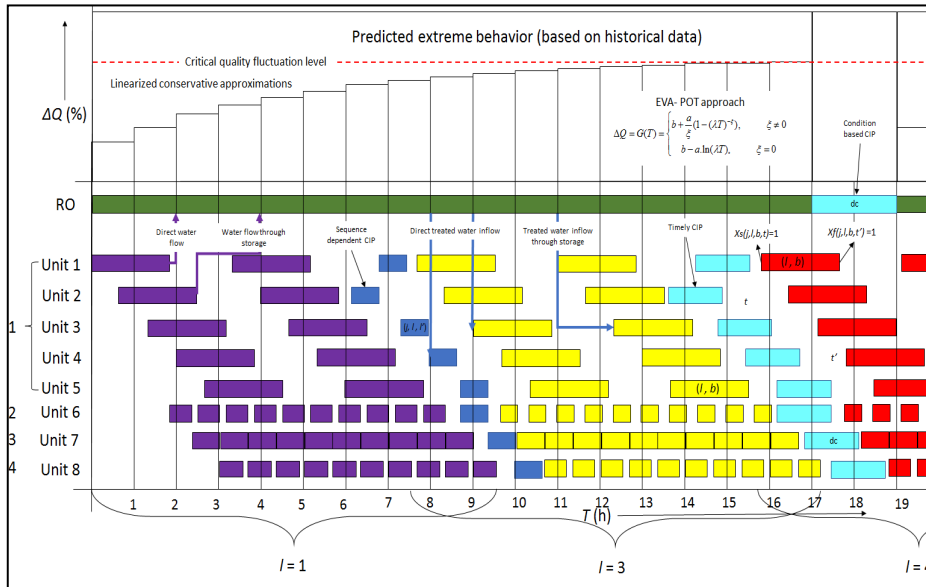


Figure 1: Illustration of the hybrid discrete-continuous-time scheduling model. Dynamic water quality degradation behaviour is used to determine treatment equipment cleaning and water reuse.

Another important decision that is crucial for our model is the sizing of lots. Usually, the number of lots to be produced for each product and the number of batches per lot is predetermined at a production planning level based on market demands (referred to as lot sizing). However, in case of water-integrated scheduling, moving the lot sizing decision to a production planning level may result in inflexible production schedules and suboptimal planning of water reuse. Therefore, we allow for calculation and recalculation of lot sizes based on water availability and other system characteristics encountered during both the scheduling and execution levels. This allows us to move batches between lots of the same product if that would benefit water or production efficiency.

Our water network has two key parts, exchange of water between cleaning-in place (CIP) operations and usage of treated water obtained from treatment of water-rich side streams. We model exchange of water between CIPs happening on different units at different times to capture the reuse of last flush effluent as an input for first flush. We further allow CIPs to use both treated water and fresh water for the first flush. However, use of treated water and CIP effluent for last flush is legally prohibited in most of the food industries, to prevent accumulation of contaminants in processing equipment. Therefore, we restrict such reuse in our model. Similarly, the requirement of water by processing tasks can either be met by fresh water or treated water.

In order to model treated water reuse and extreme water quality behaviour, we connect the continuous time scheduling model to a discrete time grid of fixed granularity. For this, we use grid connection variables that place task starts and finishes in relation to the discrete time grid. We use constraints similar to Hadera et al. (2015) to link the discrete time grid with continuous start and finish time variables. We model treatment equipment cleaning and other related decisions using the discrete time grid. This approach allows us to have both exact modelling of production and cleaning times and

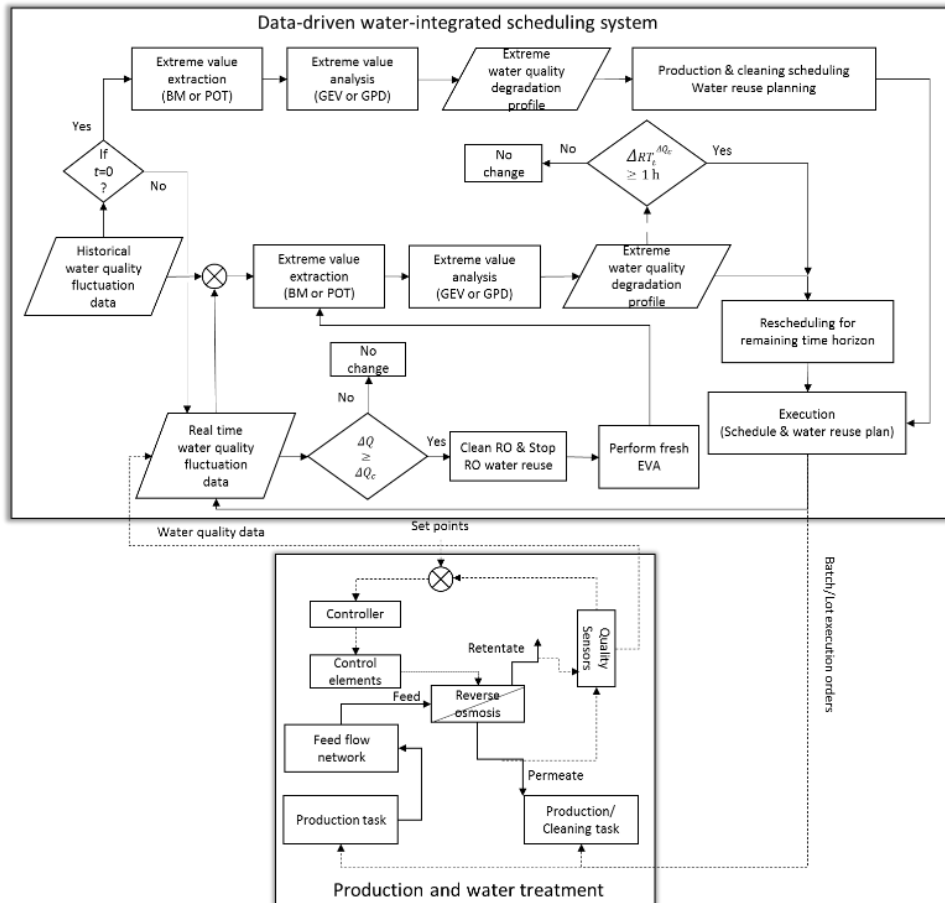


Figure 2: Data-driven water-integrated scheduling algorithm

also simplified representation of treated water withdrawal by production and cleaning tasks, extreme water quality behaviour, and water inventory. A piecewise linear approximation of the extreme water quality degradation is used to make cleaning decisions for treatment units.

Finally, for simplification of the problem, we use the constant batch ordering rule proposed by Marchetti & Cerda (2009). This concept relies on sequencing of lots on non-bottleneck stages based on the requirements of a bottleneck stage. We optimize our scheduling model to minimize total costs associated with fresh water usage and wastewater disposal. In case of rescheduling, we minimize deviation of the total cost from the minimal cost obtained during scheduling level.

3. Data-driven water-integrated scheduling algorithm

Based on the scheduling model and the production system characteristics described above, we propose a data-driven water-integrated scheduling algorithm that can use real-time water quality data from the online sensors. A schematic diagram of the algorithm is shown in Figure 2. At the start, relevant historical water quality data is

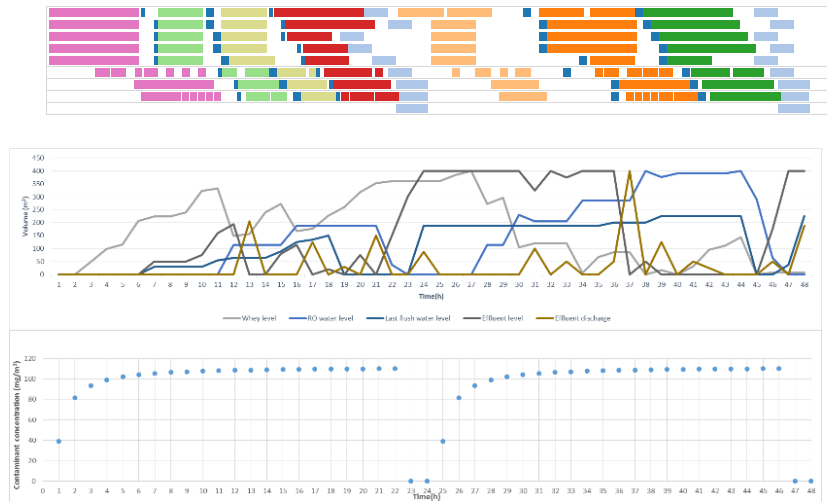


Figure 3: Illustrative water integrated production schedule, stored water/effluent levels and extreme water quality degradation behaviour of RO unit.

considered to generate extreme water quality fluctuation behaviour using EVA. Based on this predicted behaviour, a critical quality fluctuation level ΔQ_c is defined and the return time $RT^{\Delta Q_c}$ for corresponding quality fluctuation level is determined. This measure is then used to schedule timely cleanings on the water treatment equipment. It is assumed that all cleanings are perfect and restore the treatment unit to a return level of 0% and return time of 0 h after a cleaning. Similarly, production and cleaning tasks on other units are scheduled according to the treated water availability and extreme water quality behaviour. During execution of this schedule, water quality data obtained from various sensors is monitored and updates to the water quality data are made. Based on these updates, the extreme value behaviour curve of the system is constantly updated. Corrective rescheduling of production and water reuse is triggered based on two measures of system behaviour: the quality fluctuation level ΔQ_c and the change in return time $\Delta RT^{\Delta Q_c}$, calculated as the difference between currently calculated critical fluctuation return time $RT^{\Delta Q_c}$ from the value calculated immediately after last known treatment equipment cleaning. Rescheduling is done if (1) ΔQ_c exceeds a critical quality fluctuation level or (2) $\Delta RT^{\Delta Q_c}$ exceeds a specific limit. In the first case, treatment equipment is cleaned immediately, and production and cleaning tasks are rescheduled in view of this action. In the second case, rescheduling actions taken in this case are early cleaning of treatment equipment, and reorganization of processes as described earlier.

4. Illustrative results

In order to test our approach, we developed a problem instance resembling a typical cheese production setting. We assume a flow shop with five fermentation tanks feeding into prepressing, form filling, and postpressing. Equipment is cleaned on sequence changes and at the end of the day, requiring water. Further, water from the last CIP flush is used as an input to the first flush. Fermentation and prepressing operations result in whey that is treated in UF and RO units. RO permeates are reused to meet water requirements in production and cleaning operations. RO permeates may contain traces of undesired organic compounds. Presence of these compounds may cause the growth of microorganisms in the water and the product in which the water is used, resulting in safety

risks. We generate concentration fluctuation data with highly infrequent, randomly occurring extreme values resembling data collected from online quality sensors. Using the POT approach of EVA, we obtain shape, location, and scale parameters as inputs from the data and provide them as model inputs. For this, we set a threshold of 102 mg/m^3 for the contaminant under consideration. Similarly, we extract these parameters during execution of the data-driven real-time scheduling algorithm. For this, we set ΔQ_c equal to 110 mg/m^3 . The values we choose are illustrative; in real-life food production settings, these can be selected based on previous knowledge on the effect of water contamination levels on product quality. Figure 3 presents the resulting production schedule, together with water storage levels, effluent discharge, and extreme water quality behaviour of the RO units in one of the test instances. In this figure, the drop in contaminant concentration and resetting of the degradation behaviour results from cleaning of the RO units, which is done when the quality reaches a critical contamination value. A total water related cost of 6741.2 units was obtained for a 48h period, which improves a scenario with no water reuse with 62.45%. Further, safety of water reuse is ensured by only cleaning RO units when the prediction of extreme water quality exceeds a critical contamination limit.

5. Conclusions

To support food production plants in reusing wastewater streams in a safe and cost-effective manner, we developed an online water quality sensor-data-driven water-integrated scheduling algorithm. Using a hybrid discrete-continuous time scheduling formulation to capture scheduling, sequencing, water flow, and water quality aspects, our algorithm is capable of both scheduling and rescheduling production and cleaning operations both in a predictive and reactive manner. Despite the explicit modelling of quality, an important aspect of potential contamination of products due to reuse is not yet discussed in this paper. Further development requires integration of batch dispersion measures into the water-integrated scheduling model, and allocation of water streams to less risky products, when their contamination can be potentially high. Further, our model suffers from high integrality gaps due to a large number of binary variables and big-M constraints. Future research is then also directed towards computational improvements.

References

- Chaturvedi, N. D., & Bandyopadhyay, S. (2014). Simultaneously targeting for the minimum water requirement and the maximum production in a batch process. *Journal of Cleaner Production*, *77*, 105-115.
- Gomes, M. I., & Guillou, A. (2015). Extreme value theory and statistics of univariate extremes: a review. *International Statistical Review*, *83*(2), 263-292.
- Gouws, J. F., Majozi, T., Foo, D. C. Y., Chen, C. L., & Lee, J. Y. (2010). Water minimization techniques for batch processes. *Industrial & Engineering Chemistry Research*, *49*(19), 8877-8893.
- Marchetti, P. A., & Cerdá, J. (2009). An approximate mathematical framework for resource-constrained multistage batch scheduling. *Chemical Engineering Science*, *64*(11), 2733-2748.
- Pulluru, S. J., & Akkerman, R. (2017). Water-integrated scheduling of batch process plants: Modelling approach and application in technology selection. *European Journal of Operational Research*. <http://dx.doi.org/10.1016/j.ejor.2017.07.009>
- Skou P. B., Holroyd S., van den Berg, F. (2017), Tutorial—applying extreme value theory to characterize food-processing systems. *Journal of Chemometrics*, *31*:e2930.
- Stefansdottir, B., Grunow, M., & Akkerman, R. (2017). Classifying and modeling setups and cleanings in lot sizing and scheduling. *European Journal of Operational Research*, *261*(3), 849-865.

Online Quantification of the Concept Drift Using Incremental Learned Classifier and Non-automatic Clustering

Mohammad Hamed Ardakani^{a1}, Ahmed Shokry^a, Gerard Escudero^{b1}, Moisès Graells^{a1}, Antonio Espuña^{a1*}

^a *Department of Chemical Engineering, Universitat Politècnica de Catalunya, EEBE.*

^b *Department of Computer Science, Universitat Politècnica de Catalunya, EEBE.*

¹ *Av. Eduard Maristany, 10-14, Edifici I, Planta 6, 08019 Barcelona.*

antonio.espuna@upc.edu

Abstract

The Concept Drift (CD) effect is often involved in most of the chemical manufacturing processes, and could easily lead to the decay of the Fault Detection and Diagnosis (FDD) system performance. This paper proposes a methodology for the online quantification of the CD amount. The method is based on the combination of an incremental learned classifier (Hyperplane Distance- Support Vector Machines (HD-SVM)) and a non-automatic clustering method (K-means technique). The incremental learned classifier is employed to examine and characterized the classes (i.e. normal, fault-type 1, fault-type 2, etc.) of the measured online datasets. Then, the CD amount is tracked through the monitoring of the matching extent between the latent pattern of the online dataset (regarding each class) and the latent pattern extracted from a certain reference dataset (for the corresponding class). The results of the method application to a benchmark case study involving a Continuous Stirred Tank Reactor (CSTR) indicate promising capabilities for tracking the CD amount along the operating time.

Keywords: Fault detection and diagnosis, Incremental learning, Concept drift, Clustering

1. Introduction

Data-driven FDD approaches have gained a wide popularity due to their application flexibility and robustness. As these approaches neither require the process detailed analytical model nor a deep knowledge about the process units and structure. However, their main limitation is that their efficiency is strictly conditioned by the quality of the available process history data used for their training. But, chemical manufacturing processes habitually involve time varying behaviors, due to several reasons as the process aging, fouling and drifting, which is consequently reflected to the online recorded data, leading to what is called Concept Drift (CD). Widmer et al. (1996) have defined the CD as the change of the target concept that is caused by changes in some hidden context.

The CD is usually associated to online supervised machine learning, where the statistical properties of the observed variables change over the time. Consequently, this leads to the deterioration of the FDD system performance/accuracy as the time passes. Therefore, many methods have been developed for the continuous updating of the data driven FDD systems with information about the process new or changeable conditions, in order to maintain their performance efficiency. Among several updating methods that

deal with the CD, the incremental learning have been deeply investigated by several researchers. Especially the HD-SVM incremental learning technique (Li et al., 2009) is receiving a growing interest. Recently, Ardakani et al. (2016) have proposed a HD-SVM-based algorithm for updating the FDD system against the CD effects due to the reduction in heat transfer coefficient through the time. Their algorithm have been able to efficiently keep the FDD performance at constant high level. Although almost all the methods available for updating the data driven FDD systems are able to successfully keep the FDD system accuracy at acceptable range, however, they do not provide any information about amount of the CD affecting the process. The assessment of the CD amount is of essential importance, as the continuous blind updating of the FDD system, without any information about the CD amount could easily drive the process to an unsafe operating conditions.

This work presents a methodology for the online quantification/tracing of the CD amount using incremental learned classifier and non-automatic clustering techniques. The proposed method is applied to a benchmark case study of a CSTR. The results indicate the promising capabilities of the method to track the CD amount along the operating time.

2. Tools and techniques

2.1. Clustering techniques

Clustering is an unsupervised pattern recognition method, which characterizes the possible latent patterns in a set of observations. It divides a set of observations or samples into subsets (i.e. clusters), in such a way that samples of the same cluster are similar, while samples of different clusters are distinct according to a certain criterion (Ouyang et al., 2011). The K-means algorithm is a non-automatic clustering method that has been commonly used in different areas (Chen et al., 2014), because of its efficiency, flexibility and ease of implementations. The basic idea of this method is the initiation of a centroid for each one of the clusters. Then the samples are assigned to the clusters in such a way that minimizes a metric relate to the distance measures between each sample and its cluster centroid. The shape of the obtained clusters are affected by the selected metric and also the definition of distance measure (He et al., 2005). The main limitations of the K-means method are the selection difficulty of the most suitable number of clusters, and also the initialization of the clusters centroid. Besides, the algorithm may converge to a local minimum, but several runs of the algorithm can solve this weakness (Yin et al., 2012).

2.2. Hyper distance support vector machines (HD-SVM)

The Support Vector Machines (SVM) technique is a type of supervised pattern recognitions methods that has been widely used for the data-driven FDD. It is used to assign (i.e. classify) a new unknown sample into one of the predefined classes or labels. In order to adapt the SVM classification performance when it is applied for the FDD of processes involving time varying conditions, the incremental learned SVM has been proposed. It utilizes the arriving online samples to update the original support vectors, only if they violate the Karush-Kuhn-Tucker (KKT) conditions (Wang et al., 2014; Yin et al., 2014). Thus, new samples satisfying KKT conditions are supposed to have no influence for updating the hyperplane.

The HD-SVM (Li et al., 2009) algorithm is a development of the incremental learned SVM. The algorithm considers that in addition to the samples that violate KKT conditions, other samples could be treated as support vectors too, based on the geometric distance of each new sample from the center of each class and the separating hyperplane. In this work, the performance of the SVM is reported in term of the F1score (Eq. (1)). It is calculated as a weighted average of precision and recall, where the precision is the portion of retrieved samples that are relevant, and recall is the portion of relevant samples that are retrieved. The F1-score reaches its best value at 1 and worst value at 0 (Ardakani et al., 2016).

$$F1 = \frac{2 \times \text{Precision} \times \text{Recall}}{\text{Precision} + \text{Recall}} \quad (1)$$

3. Proposed methodology

The proposed method for the monitoring/quantifications of the CD amount involves two phases, including offline and online ones. The offline phase encompasses the training and validation of the classifier using the early or the initial dataset X^0 of the process measured variables. This initial dataset is assumed to be measured under the process nominal conditions and include all the possible information about the process classes (normal and different faulty situations). Thus, $X^0 = [x_{cl_1}^0, x_{cl_2}^0, \dots, x_{cl_i}^0, \dots, x_{cl_N}^0]$, where cl_i is the i^{th} class type, i could be normal or any of the $N-1$ possible fault types and each $x_{cl_i}^0$ may contain different number of observations.

In the online phase, the process measurements are assumed to be collected along the time over j discrete periods in the form of discrete datasets. Where, each online dataset X_j^{onl} includes the same number of samples and may contain any possible combination of the process aforementioned classes.

The first stage of the online phase is the FDD, which encompasses the application of the trained HD-SVM classifier in order to detect and diagnose the possible faults that may affect the process using the j^{th} arriving dataset X_j^{onl} . Thus, the outcome of this stage is the assignment of the samples of the dataset X_j^{onl} into specific class(es), i.e. $X_j^{\text{onl}} = [x_{j,cl_1}^{\text{onl}}, \dots, x_{j,cl_i}^{\text{onl}}, \dots]$.

The second stage of the online phase, is the tracing of the CD amount based on monitoring the extent of matching between the latent pattern(s) in each class of the online dataset and the corresponding class of the initial dataset. Accordingly, an augmented dataset X_{j,cl_i}^{aug} for each class must be synthesized, through combining the samples of the specific i^{th} class of the initial dataset as a first part, and the samples of the corresponding i^{th} class of the online dataset as a second part, thus $X_{j,cl_i}^{\text{aug}} = [x_{cl_i}^0, x_{j,cl_i}^{\text{onl}}]$. After that, the non-automatic clustering technique is used to cluster the samples of each augmented dataset (X_{j,cl_i}^{aug}) –independently– into two clusters. Finally, the matching between the pattern of the clusters included in the online dataset x_{j,cl_i}^{onl} and the pattern of the clusters in the initial data $x_{cl_i}^0$ is assessed. This task is achieved through the comparison of the clustering labels that the K-means algorithm has assigned to the online dataset samples x_{j,cl_i}^{onl} and the labels assigned to the initial dataset samples x_{j,cl_i}^0 . In more details, the label of the first sample in the online dataset is compared to the label of the first sample in the initial dataset, and so on.

A relative Matching Measure MM_{j,cl_i} is calculated for each augmented set X_{j,cl_i}^{aug} , where MM_{j,cl_i} equals to the number of the similar clustered samples of x_{j,cl_i}^{onl} relative to x_{j,cl_i}^0 , divided by the total number of samples of x_{j,cl_i}^{onl} . In other words, MM_{j,cl_i} is an index that expresses the matching between the clusters pattern of the online dataset x_{j,cl_i}^{onl} , and the clusters pattern of the initial dataset $x_{cl_i}^0$. Figure 1 illustrates the framework, considering only two classes of the process, including normal class cl_1 and faulty class cl_2 .

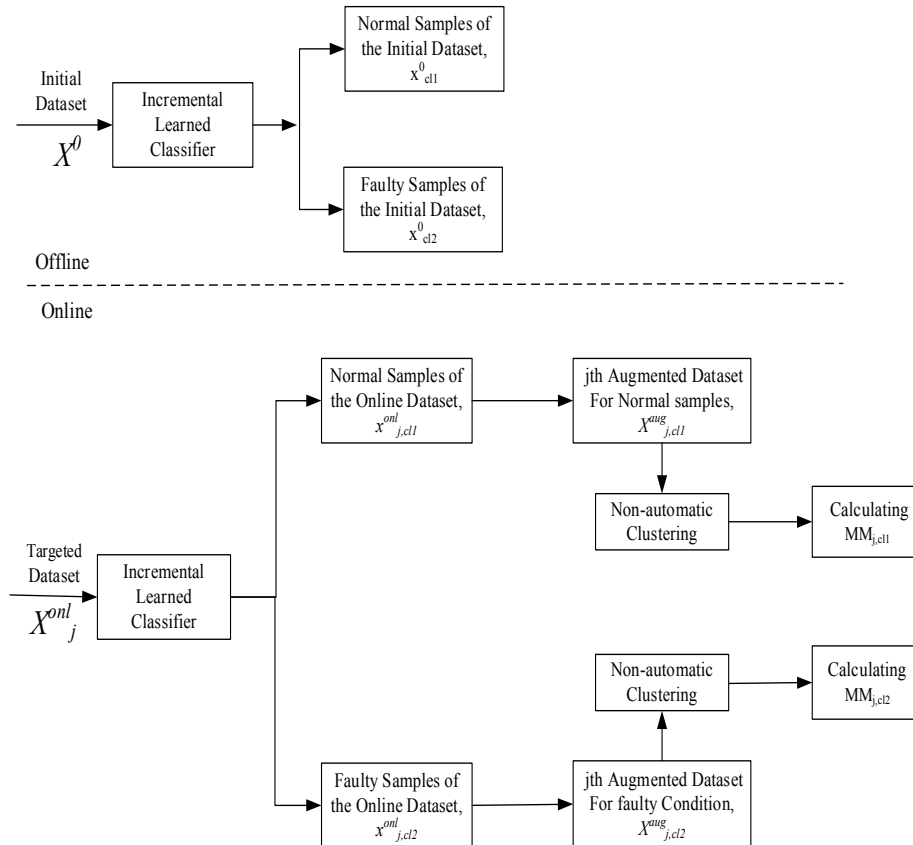


Figure 1. Proposed framework.

4. Case Study

The addressed case study involves a simulation model of a CSTR running the “Van der Vusse” reactions: $A \rightarrow B \rightarrow C$ and $2A \rightarrow C$ (Chen et al., 1995). The CSTR is used to produce cyclopentenol (desired product B) from cyclopentadienyl (reactant A) by mean of acid-catalysed electrophilic hydration in aqueous solution. Four process variables are assumed to be measured including the reactant concentration C_A , the product concentration C_B , the reactor temperature T_R and the cooling jacket temperature T_J . The nominal (normal) inlet concentration of the reactant equals to $5.1+v_o \text{ mol/L}$, where $v_o \approx \mathcal{N}(\mu = 0, \sigma = 0.045 \text{ mol/L})$ is a Gaussian white noise. In this work, one type of faults is considered to influence the process, which is defined as a step change in the

inlet concentration C_A from its predefined normal value to $5.13+v_o$ mol/L. The gradual change of the heat transfer coefficient through the time is treated as the source of the CD. Thus, the nominal/initial magnitude of the heat transfer coefficient ($k_w=4032$ KJ/hr.m².K) is linearly decreased over the time, so as to reach 95% of its nominal value at the end of the operating time.

5. Results

Along the total simulation/operation time, twelve datasets are collected in a successive way at discrete time intervals. The datasets have been collected with equal sizes (each dataset includes 4000 sample), assuming that the fault may take place at any time within any of the sets. The first/initial dataset measured at the earliest time of the process operation is used to train and validate the classifier (i.e. offline phase). Then, each of the subsequent eleven datasets is fed to the classifier and the clustering system in order to monitor the processes and to trace the CD amount (i.e. online phase).

For the sake of comparison, the FDD performance of the proposed framework based on the HD-SVM is compared to its performance when a classical SVM is used for classification, instead. The HD-SVM is able to maintain its high level of accuracy (F1 score of 94.89%) along the operating time and adapt its performance to the continuously changing conditions (heat transfer coefficient). In contrary, the SVM shows a decaying performance along the operating time, until it reaches to a very worthless performance (F1 score of 65.00%) at the last dataset.

Figure (2) displays the MM_{j,cl_i} of the online datasets. As previously mentioned in the methodology, the MM_{j,cl_i} has been calculated for each of the process classes independently (top plot for normal samples, and bottom plot for faulty samples). The figure also shows how the proposed algorithm is able to trace the involved CD in the process over the time. For normal samples, the matching measure drops from 99.0% in the second dataset ($j=2$) to 84.5% in the last dataset ($j=12$). While for the faulty samples, the matching measure decreases from 99.2% at in second dataset ($j=2$) to 68.7% in the last dataset ($j=12$). It can be noticed that after the 6th dataset, the MM of the faulty samples does not significantly change, which could be justified because of the limited number of faulty samples in those datasets.

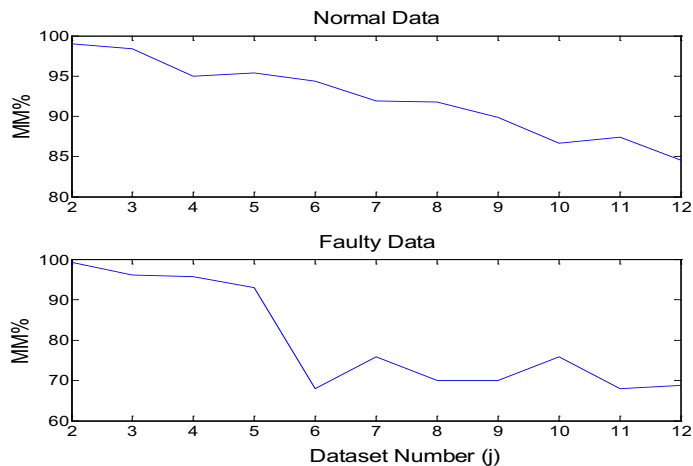


Figure 2. MM of the normal and faulty samples for the applied scenario.

6. Conclusions

Existing methods for updating supervised data-driven FDD systems do not provide any information about the amount of the CD influencing the process. This paper presents a data-driven methodology for the FDD of chemical processes involving time varying conditions, which relies on the combination of an incremental learned classifier and a non-automatic clustering technique. The methodology tracks the CD amount via monitoring the matching extent between the clusters pattern of the online datasets and a reference dataset. The application results of the method to a benchmark case study illustrate promising capabilities, as the method is able to maintain the FDD system performance over the operating time. More significantly, the method is able to provide valuable information about the CD amount along the time, which can be used to prevent the process to reach unsafe operating conditions. Although of the simplicity of the addressed case study, but it was sufficient for the initial assessment of this new method. The future work will consider the exploration of the method performance when handling more complex and realistic cases.

References

- M. Ardakani, M. Askarian, A. Shokry, G. Escudero, M. Graells, A. Espuña, 2016, Optimal Features Selection for Designing a Fault Diagnosis System, *Computer Aided Chemical Engineering*, 38, 1111–1116.
- M. Ardakani, G. Escudero, M. Graells, A. Espuña, (2016), Incremental Learning Fault Detection Algorithm Based on Hyperplane-Distance, *Computer Aided Chemical Engineering*, 38, 1105–1110.
- H. Chen, A. Kremling, F. Allgöwer, 1995, Nonlinear Predictive Control of a Benchmark CSTR, *Proc. of the European Control Conf.*, 1, 3247–3252.
- H. Chen, P. Tiño, X. Yao, 2014, Cognitive fault diagnosis in Tennessee Eastman Process using learning in the model space, *Computers and Chemical Engineering*, 67, 33–42.
- Q. P. He, S. J. Qin, J. Wang, 2005, A new fault diagnosis method using fault directions in Fisher discriminant analysis, *AIChE Journal*, 51(2), 555–571.
- C. Li, K. Liu, H. Wang, 2009, The incremental learning algorithm with support vector machine based on hyperplane-distance, *Applied Intelligence*, 34(1), 19–27.
- Z. Ouyang, Y. Gao, Z. Zhao, T. Wang, 2011, Study on the classification of data streams with concept drift. 2011 Eighth International Conference on Fuzzy Systems and Knowledge Discovery (FSKD), 3, 1673–1677.
- P. Wang, C. Yang, X. Tian, D. Huang, 2014, Adaptive Nonlinear Model Predictive Control Using an On-line Support Vector Regression Updating Strategy, *Chinese Journal of Chemical Engineering*, 22(7), 774–781.
- G. Yin, Y. Zhang, Z. Li, G. Ren, H. Fan, 2014, Online fault diagnosis method based on Incremental Support Vector Data Description and Extreme Learning Machine with incremental output structure, *Neurocomputing*, 128, 224–231.
- S. Yin, S. Ding, A. Haghani, H. Hao, P. Zhang, 2012, A comparison study of basic data-driven fault diagnosis and process monitoring methods on the benchmark Tennessee Eastman process, *Journal of Process Control*, 22(9), 1567–1581.

Production Scheduling of Multi-Stage, Multi-product Food Process Industries

Georgios P. Georgiadis^{a,b}, Chrysovalantou Ziogou^b, Georgios Kopanos^c,
Manuel Garcia^d, Daniel Cabo^e, Miguel Lopez^e, Michael C. Georgiadis^{a,b,*}

^a*Department of Chemical Engineering, Aristotle University of Thessaloniki, Thessaloniki 54124, Greece*

^b*Chemical Process and Energy Resource Institute (CPERI), Centre for Research and Technology Hellas (CERTH), PO Box 60361, 57001, Thessaloniki, Greece*

^c*Cranfield University, School of Energy, Environment & Agrifood, Bedfordshire MK43 0AL, United Kingdom*

^d*Frinisa del Noroeste S.A., Avenida Ramiro Carregal Rey – Parcela 29, Ribeira, La Coruña, Spain*

^e*ASM Soft S.L., Crta. De Bembrive 109, Vigo, Spain*

mgeorg@auth.gr

Abstract

The production scheduling of a real-life multi-product, mixed batch and continuous food industrial facility is considered in this work. More specifically, the scheduling of canned fish production in a large-scale Spanish industry is studied in detail. The deployment of an efficient solution strategy is proposed to handle the computationally challenging scheduling problem. In particular, a Mixed-Integer Linear Programming (MILP) model is used, in parallel with a decomposition technique. The problem under consideration focuses on two important stages of the plant, the sterilization and the packaging. The proposed strategy takes into account the specific characteristics of the canned fish production facility resulting in interesting results. It should be noted that the same methodology can be used with appropriate modifications in other food process industries with similar production characteristics.

Keywords: production scheduling, multistage, food industry, mixed integer programming, decomposition.

1. Introduction

The scientific community has widely recognised the importance of applying scheduling solutions to industrial cases which so far is not adequately applied in real-life plants (Harjunoski et al., 2014). Therefore, there is a growing interest in the theoretical implementation to industrial practice. Many challenges exist due to the complexity of such cases in terms of number of stages and their mode of operation, number of products and shared resources typically met in real-life processes. In this work the canned fish production is considered, which comprises of multiple batch and continuous production operations, thus working in a semicontinuous production mode. Numerous studies addressing batch or continuous production modes are found in literature (Mendez et al., 2006). Nevertheless, not much work has been done considering

semicontinuous processes, despite being very common in food industries. Amorim et. al (2011) developed a hybrid genetic algorithm, for the lot-sizing and scheduling problem of a dairy industry considering perishability issues. Kopanos et. al (2010) studied a real-life yoghurt production process and proposed a novel mixed discrete/continuous time representation. The problem was mainly focused on the packaging stage, since it was identified as the production bottleneck. The main challenge in the efficient scheduling of food process industries is the integrated modelling of all production stages. Optimizing all processing stages increases the plant production capacity by reducing unnecessary idle times and reduces the production cost of final products.

2. Problem Statement

This work considers the scheduling of canned fish production in a real-life industrial facility. In particular, the production process of FRINSA, one of the largest canned fish industries in Europe is investigated using realistic process data. The plant can produce more than 400 final products and has a production capacity of 3-4 million cans per day. Several stages, mixed batch and continuous, are required for the production of each can (Fig.1). Initially, the fish stored in blocks is unfrozen and then filled in cans along with the ingredients (e.g. oil, tomatoes, etc.) required by the recipe. The next stage is the sterilization which guarantees the microbiological quality of the product. Finally, the sterilized cans are packaged (labelling, packing into cartons, boxes etc.) into the final products.

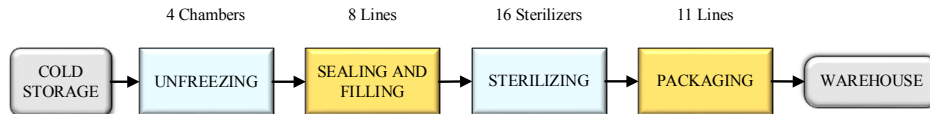


Figure 1: Canned fish production line layout

The plant is a multiproduct multistage facility combining both batch (unfreezing, sterilizing) and continuous (sealing and filling, packaging) processes with multiple parallel units. In general, the large production demand and high production flexibility (multiple units can process every single final product) increases significantly the complexity. The sterilization and packaging stages are the most intensive processes of the plant and they constitute the main production bottlenecks. The short-term scheduling horizon of interest is 5 days, whereas the sterilizers and packaging units are available 24 hours. Sequence-dependent changeovers and inventory limitations are considered. The salient characteristics of the scheduling problem is to take into account a large number of design and operating constraints while ensuring demand satisfaction. The overall production schedule is affected by rather conflicting goals such as the optimal use of resources, the minimization of makespan and the reduction of costs and optimal energy use.

3. MILP-based Solution Strategy

The key decisions to be made are related to: a) the required number of product batches to be scheduled, b) the allocation of batches to units in every stage, c) the relative sequence of product batches in each stage and d) the start and completion time of product batches in each stage. The proposed MILP-based solution strategy consists of: (i) a pre-optimization step, where the batching problem is solved, (ii) the MILP model which is used to optimize the schedule based on a specific objective and (iii) an order-

based decomposition technique, to split the initial problem into sets of tractable subproblems.

3.1. Pre-optimization step

In most food industries, such as the one studied in this work, the industrial practice imposes operations of the intermediate batch processes in their maximum capacity. The maximum utilization of the batch stage, allows for high production levels and minimization of changeovers between products. Hence the batching problem can be solved a priori. Constraints (1) define the minimum number of batches, β_p , to fully satisfy the demand based on the total demand, the capacity of sterilizers and storage limitations. Constraints (2) calculate the required time $t_{p,b}$ to process each batch in the packaging stage.

$$\beta_p^{\min} = \left(\frac{dem_p - s_p^{init} + s_p^{\min}}{BC_p} \right), \quad \forall p \tag{1}$$

$$t_{p,b}^{pack} = \frac{BC_p}{rate_p}, \quad \forall p, b \neq b_{last} \tag{2}$$

3.2. MILP model

The MILP model employed is based on an extension of a general precedence framework as developed in our previous work (Kopanos et. al, 2011). A brief description of the model follows due to the lack of space.

$$\sum_{j \in (J_p \cap J_s)} Y_{p,b,s,j} = 1, \quad \forall p, b \leq \beta_p^{\min}, s \tag{3}$$

$$L_{p,b,s} + t_p^{ster} = C_{p,b,s}, \quad \forall p, b \leq \beta_p^{\min}, s : s = 1 \tag{4}$$

$$L_{p,b,s} + t_{p,b}^{pack} = C_{p,b,s}, \quad \forall p, b \leq \beta_p^{\min}, s : s = 2 \tag{5}$$

$$L_{p,b,s} = C_{p,b,s-1}, \quad \forall p, b \leq \beta_p^{\min}, s : s = 2 \tag{6}$$

$$C_{p,b,s} = L_{p,b+1,s}, \quad \forall p, b \leq \beta_p^{\min}, s : s = 2 \tag{7}$$

$$L_{p',b',s} > C_{p,b,s} + ch_{p,p',j} - M * (1 - \bar{X}_{p,b,p',b'}) - M * (2 - Y_{p,b,s,j} - Y_{p',b',s,j}), \tag{8}$$

$$\forall p, b \leq \beta_p^{\min}, p', b' \leq \beta_{p'}^{\min}, s, j \in (J_p \cap J_{p'} \cap S_j) : p < p', s = 2$$

$$L_{p',b',s} > C_{p,b,s} + ch_{p,p',j} - M * (1 - X_{p,p'}) - M * (2 - Y_{p,b,s,j} - Y_{p',b',s,j}), \tag{9}$$

$$\forall p, b \leq \beta_p^{\min}, p', b' \leq \beta_{p'}^{\min}, s, j \in (J_p \cap J_{p'} \cap S_j) : p < p', s = 1$$

$$C_{max} > C_{p,b,s}, \quad \forall p, b, s : s = 2 \tag{10}$$

Constraints (3) ensure that each product batch p,b will go through one unit j in every stage s , utilizing the binary variable $Y_{p,b,s,j}$. The timing constraints (4) and (5) are imposed for a product batch in the same production stage. In particular, constraints (4) ensure that the completion time of a product batch in the sterilization stage $C_{p,b,s}$ is equal to the starting time of the process $L_{p,b,s}$ plus the required sterilization time t_p^{ster} for the specific product. Same holds for constraints (5), which express the connection between the start and finish of the packaging processes based on the required packing time for each product batch $t_{p,b}^{pack}$. Constraints (6) state that the packaging process of product batch starts exactly when the sterilization process is completed. A single production campaign policy is guaranteed by constraints (7). The sequencing constraints between product batches in both processing stages are portrayed in constraints (8) and (9). More specifically, constraints (8) enforce the starting time of a product batch p',b' to be greater than the completion time of a product batch p,b processed beforehand, plus the corresponding changeover time $ch_{p,p',j}$, when both batches are allocated to the same packing line. Similarly, constraints (9) define the sequencing of different products in the sterilization stage. Two general precedence binary variables are employed, $X_{p,p'}$, $\bar{X}_{p,b,p',b'}$, while M is a big-M parameter. The objective function of the model is expressed by constraints (10), which is the minimization of the total production makespan, C_{max} , hence it also considers the minimization of changeovers and unnecessary idle times.

3.3. Decomposition Strategy

The goal of the decomposition strategy is to split the initial problem into several tractable subproblems, which can be solved by the proposed MILP model in a reasonable time. In each subproblem a predefined number of products are scheduled. Basic parameters of the decomposition algorithm are the position of the last scheduled product z and the number of products scheduled at each iteration step.

Fig. 2. illustrates the flowchart of the solution strategy algorithm. Initially, the batching decisions are made in the preoptimization step. Afterwards, the decomposition algorithm parameters are defined and the subproblem is solved utilizing the aforementioned MILP model. Next, the derived decisions made for the specific subproblem are fixed and the algorithm continues to the next iteration. Finally, when all products are considered, the final schedule is generated.

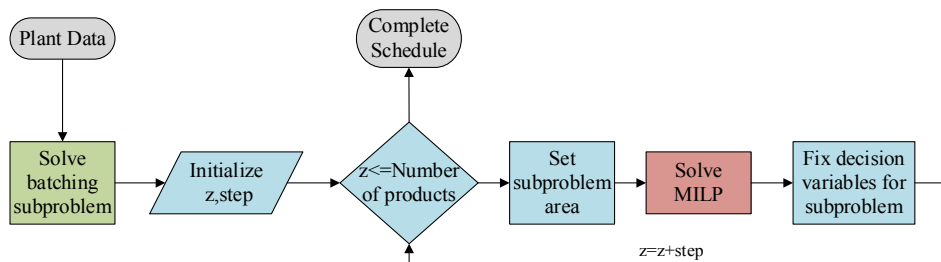


Figure 2: Solution strategy algorithm equivalent flowchart

4. Case study

An industrial case for the scheduling of 100 final products using realistic data from the FRINSA production plant is demonstrated. The preoptimization step calculates that 362 batches are required in total to satisfy the demand. Utilizing the proposed decomposition technique, 20 final products are scheduled in each iteration. The MILP model was implemented in GAMS 24.9 and solved using CPLEX 12.0. Optimality is reached for all iterations of the suggested solution strategy. Figure 3 illustrates the complete schedule generated for the sterilization units, while in figure 4 the corresponding schedule of the packaging units is depicted.

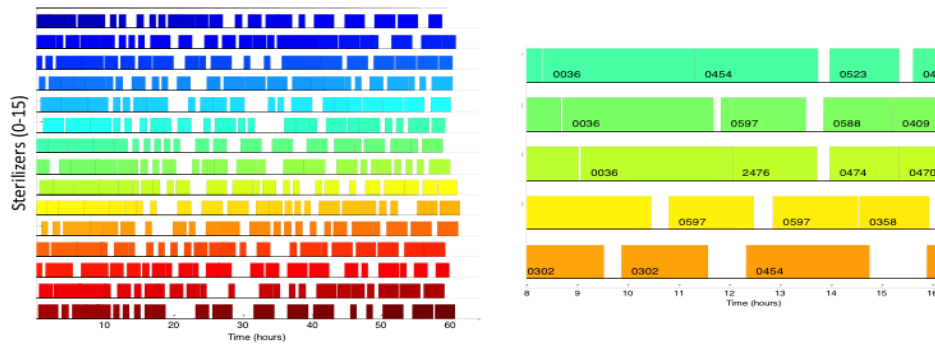


Figure 3: a) Gantt chart of the sterilization units, b) indicative schedule with product codes for the ST7-11 sterilization unit during 8hrs

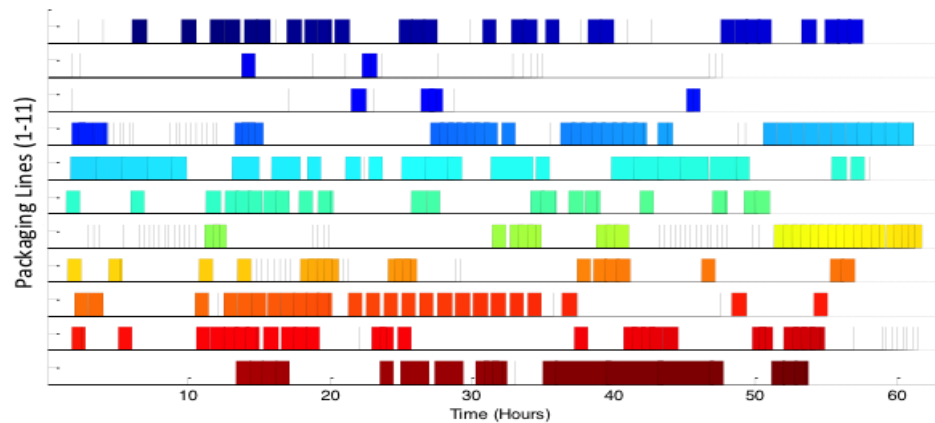


Figure 4: Gantt chart of the packaging units

It is evident from the Gantt charts (Fig. 3) that the sterilizers are more active than the packaging units. On the other hand, the utilization in the packaging stage depends on the demand profile, since each product can be processed only at specific packaging units, whereas all products can be processed in any sterilizer. Nevertheless, all packaging units are underutilized compared to the sterilizers. Hence, the sterilization stage is identified as the production’s bottleneck in line with conclusions made by the plan operators. This is also illustrated at Fig. 5, where the utilization of all units is illustrated.

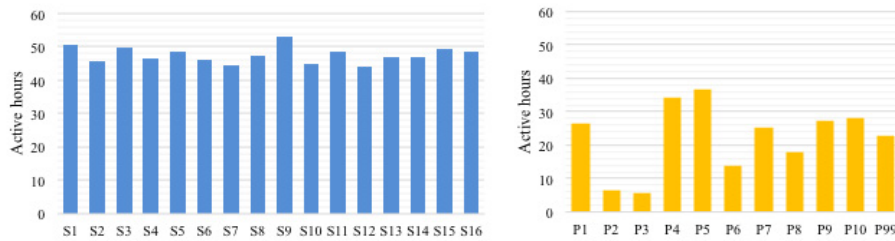


Figure 5: a) Utilization of sterilizers and b) packaging units

5. Conclusions

This work presents the production scheduling of a real-life industrial problem. More specifically, the sterilization and packaging stage of a canned fish production facility have been scheduled using recent advancements on mathematical programming-based scheduling. The aforementioned plant structure (a batch process followed by a packing stage) is typically met in many industries such as food and consumer packaged goods, hence, the applicability of the presented solution strategy can be implemented in other industrial problems. It was demonstrated, that the proposed MILP-based solution strategy can successfully solve a scheduling problem with significant degree of complexity in terms of number of products, shared resources, stages and multiple operational and quality constraints. The results illustrate that the sterilization stage is the main production bottleneck, an important conclusion for further investigation. As future steps, the integration of all production stages of the plant will be considered. Moreover, cost related objectives and the introduction of uncertainty in product orders will be considered in a rolling horizon scheduling framework.

Acknowledgements

The work leading to this publication has received funding from the European Union's Horizon 2020 research and innovation programme under grant agreement No 723575 (Project CoPro) in the framework of the SPIRE PPP.

References

- P. Amorim, C.H. Antunes, B. Almada-Lobo, 2011, Multi-objective lot-sizing and scheduling dealing with perishability issues, *Industrial & Engineering Chemistry Research*, 50, 6, 3371-3381
- I. Harjunkoski, C.T. Maravelias, P. Bongers, P. M. Castro, S. Engell, I. E. Grossmann, J. Hooker, C.Méndez, G. Sand, J. Wassick, 2014, Scope for industrial applications of production scheduling models and solution methods, *Computers & Chemical Engineering*, 62, 161-193
- G.M. Kopanos, L. Puigjaner, M.C. Georgiadis, 2010, Production scheduling and lot-Sizing in dairy plants: The yoghurt production line, *Industrial & Engineering Chemical Research*, 49, 2, 701-718
- G.M. Kopanos, L. Puigjaner, M.C. Georgiadis, P.M.M Bongers, 2011, An efficient mathematical framework for detailed production scheduling in food industries: The ice-cream production line, *Computer Aided Chemical Engineering*, Volume 29, 2011, Pages 960-964
- C.A. Méndez, J. Cerdá, I.E. Grossmann, I. Harjunkoski, M. Fahl, 2006, State-of-the-art review of optimization methods for short-term scheduling of batch processes, *Computer & Chemical Engineering*, 30, 6-7, 913-94

A Proposal to Include the Information of Disturbances in Modifier Adaptation Methodology for Real Time Optimization

Daniel Navia^{a*}, Antonio Puen^a, Paulina Quintanilla^a, Luis Bergh^a, Luis Briceño^b, César de Prada^c

^a*Dpto. de Ingeniería Química y Ambiental, Universidad Técnica Federico Santa María, Avda. Vicuña Mackenna 3939, San Joaquín, Santiago, Chile*

^b*Dpto. de Matemáticas, Universidad Técnica Federico Santa María, Avda. Vicuña Mackenna 3939, San Joaquín, Santiago, Chile*

^c*Dpt. of Systems Engineering and Automatic Control – University of Valladolid, Doctor Mergelina S/N, 47011, Valladolid, Spain*
daniel.navia@usm.cl

Abstract

This work presents an extension of the Modifier-Adaptation (MA) methodology for Real-Time Optimization (RTO), to include the available information of uncontrolled input variables in the estimation of plant gradients. The idea is to extend the applicability of this method for processes where disturbances affect the quantities involved in the necessary conditions of optimality of the process. The implementation was carried out in a simulated flotation column, including the effect disturbances coming from of contiguous units. The dual approach was used to estimate the process gradients. Results show that the system is able to follow the trajectory of the real optimum of the process under continuously changing scenario, unlike traditional MA.

Keywords: Real-Time optimization, Modifier adaptation, Disturbances, Flotation column, Process optimization.

1. Introduction

The global competition drives to improve the performance of processes in the industry. The RTO is a powerful tool to increase the efficiency of a process. However, there is an inherent difficulty to reach optimal operating points, due to the available models represent partially the process phenomenology. Modifier Adaptation is a RTO methodology capable to find a point that satisfies the necessary conditions of optimality of an uncertain process using models with structural mismatch. To do so, MA uses available measurements to correct the model-based optimization with experimental gradients of the objective function J_m and constraints C_m . This methodology was defined by Chachuat et al. (2009) and afterward by Marchetti et al. (2009) Eq. (1) shows the modified optimization problem, which includes the modifier of the objective function λ_k , and the modifiers of the constraints γ_k and ε_k .

$$\begin{aligned} \min_{u \in U} J_m(u, \alpha) + \lambda_k(u - u_k) \\ \text{s.t. :} \\ C_m(u, \alpha) + \gamma_k^T(u - u_k) + \varepsilon_k \leq 0 \end{aligned} \quad (1)$$

$$\begin{aligned}
\lambda_k^T &:= \nabla_u J_p(u_k) - \nabla_u J_m(u_k, \alpha) \\
\gamma_k^T &:= \nabla_u C_p(u_k) - \nabla_u C_m(u_k, \alpha) \\
\varepsilon_k^T &:= C_p(u_k) - C_m(u_k, \alpha)
\end{aligned} \tag{2}$$

Where $u_k \in \mathfrak{R}^{n_u}$ represents the actual operating point, which is calculated at the previous RTO iteration, and subscripts m and p indicates if the quantity either has been calculated using the available model or estimated from the process, respectively. The modifiers $\lambda_k \in \mathfrak{R}^{n_u}$, $\gamma_k \in \mathfrak{R}^{n_c \times n_u}$ and $\varepsilon_k \in \mathfrak{R}^{n_c}$ are estimated using Eq. (2).

In the last few years, research has advanced focusing the efforts on improving the estimation of the modifiers, whether searching for a more reliable and robust gradient estimation (Bunin et al., 2012; Marchetti et al., 2010; Gao et al., 2016) or avoiding the gradient estimation step (Navia et al., 2015), among others.

Regarding MA applications, it has been performed with low numbers of input variables and with known noise characteristics. Also, in MA application it has been assumed that the rate of change of the disturbances is lower than settling time of the process (Darby et al., 2011), which implies that the performance of the algorithms has been evaluated assuming either constant uncontrolled variables, or disturbances with low frequency changes, such as step or ramp functions (Wenzel et al., 2015). However, in practice, it is expectable that disturbances may change with higher frequencies, which can affect the gradient estimation step using previous measurements. This fact motivates the study of methods to take into account the available information of disturbances in the estimation of process gradients.

In this work, it is presented a proposal to take into account the information of both decision variables (u) and disturbances (ξ), in order to obtain an accurate estimation of the gradient of the process with respect to u . With this in mind, the aim is to have an optimization layer capable of tracking and maintaining the optimal condition of the plant, in spite of changes in measured or estimated disturbances.

The paper is organized as follows. Section 2 describes the proposed method that includes the information of disturbances. Section 3 presents the application of proposed methodology in a simulated flotation column for copper concentration. Section 4 shows the results, and section 5 presents the conclusions.

2. Extended method for systems with disturbances

In this work, we propose the extension of the dual methodology for experimental gradient estimation, to take into account explicitly the available information of ξ , assuming that these variables can be measured or estimated. To compute the experimental gradients it is necessary to use the differences of the actual measurements with respect to the $n = n_u + n_\xi$ previous operating points, as Eq. (3) shows.

$$\bar{\mu}_k^j \approx \bar{S}_k \nabla_{\bar{u}} y_{p,k}^j, \quad j = 1, \dots, n_c + 1 \tag{3}$$

Where $\bar{u} := [u, \xi]^T$, $\bar{S}_k := [\Delta \bar{u}_{k,1}, \dots, \Delta \bar{u}_{k,n}]$ and $\bar{\mu}_k^j = [\Delta y_{p,k,1}^j \dots \Delta y_{p,k,n_u}^j]^T$, with $\Delta \bar{u}_{k,i} = \bar{u}_k - \bar{u}_{k-i}$. Under the assumption that \bar{S}_k is nonsingular, the gradient of process variable y_p^j , with respect to the input variables can be obtained from Eq. (4).

$$\nabla_{\bar{u}} y_{p,k}^j \approx (\bar{S}_k)^{-1} \bar{\psi}_k^j \tag{4}$$

To ensure identifiability, an additional constraint must be added to the modified optimization problem, as Eq. (5) shows. This restriction is analogous to the dual constraint presented in Marchetti et al. (2010).

$$\begin{aligned} \min_{u \in U} & J_m(u, \alpha) + \lambda_k^T (u - u_k) \\ \text{s.t. :} & \\ & C_m(u, \alpha) + \gamma_k^T (u - u_k) + \varepsilon_k \leq 0 \\ & |\Delta \bar{u}_{k+1,1}^T \tau_k| \geq \delta \end{aligned} \tag{5}$$

Where τ_k is the vector orthonormal to the subspace formed by $W_k = \langle \{\Delta \bar{u}_{k,1}, \dots, \Delta \bar{u}_{k,n-1}\} \rangle$, and δ is a value greater than zero. As the value of ξ_{k+1} is unknown when the RTO is solved, this must be estimated from available models using previous values. Once the system reaches the steady state, the dual constraint must be reevaluated with the measured or estimated value of ξ_k . Since matrix \bar{S}_k has an independent part, it is necessary to evaluate the cases of ξ when identifiability problems may arise. However, lineal dependency in disturbances is an improbable case, considering the expected stochastic nature of uncontrolled process variables.

3. Application to flotation column

The process simulated in this work is the flotation of copper sulphides, which represent the species with more abundance in Chile. Industrial flotation has three main interconnected zones: rougher, scavenger and cleaner, plus a regrinding stage (Fig. 1b). In particular, we are interested in the cleaning zone of the flotation circuit, where columns are used because of their capability to increase the concentration of the product.

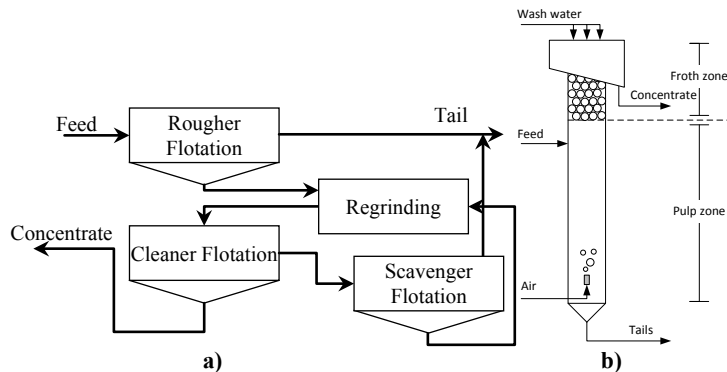


Figure 1. a) Diagram of flotation circuit. b) Diagram of flotation column.

Fig. 1b shows a diagram of a flotation column. This equipment has three inflows: feed pulp, air and wash water; and two outflows: concentrate and tail. Feed pulp with the valuable mineral comes from rougher cells and enters in the middle section of the column. Airflow is injected into the bottom to generate bubbles to collect the floatable particles. Wash water is introduced at the top of the column by countercurrent with

respect to air to decrease the concentration of gangue in the top outflow (concentrate). On the other hand, the tail flow leaves the column at the bottom. It is possible to distinguish two zones in the flotation column (Fig. 1b): collection and cleaning zone. In the collection zone, floatable particles from the feed pulp collide with air bubbles and they are transported to the top. In the cleaning zone, the froth is formed because of the addition of chemical reagents and wash water cleans the froth from gangue particles.

The decision variables of the process are the froth level (H_f), and air hold-up (ε_G). On the other hand, the input variables that are not controlled (ξ) correspond to the characteristics of the feed: concentration of copper, solid percentage and particle diameter.

The metallurgical model used in this work is a combination of phenomenological and empiric models of the flotation process, that represents a three-phase system with variable inputs conditions proposed by Finch & Dobby (1990), and the use of exponential functions to calculate the recovery in the zones of the column proposed by Yianatos et al. (1998, 2005).

Although flotation can be described as a pseudo-first-order reaction, the physical dependencies for recovery are still not fully understood (Savassi, 2005). Taking this into account, the uncertainty has been implemented as a modelling mismatch in the physicochemical description of the recovery of valuable mineral and gangue, as it was presented by Navia et al. (2016). This implies a structural uncertainty, since the influence of operational conditions in the kinetic constant has been neglected in the model, unlike the process, where they depend on internal flows.

The objective function J_m is the profit in the flotation column, where the effect of contiguous units are included, see Eq. (6).

$$J_m := C_E + C_L + C_R - I \quad (6)$$

In Eq. (6), C_E is the cost of the energy for pumping the slurry and compressing the air, C_L is the cost of the metallurgical losses in the scavenger stage (proportional to the copper that cannot be recuperated in the column stage), C_R is the cost associated to the regrinding process, and I represents the incomes of the process. The inequality constraints in the optimization problem are related to operational limitations and with the metallurgical result. Table 1 shows the values of upper and lower bounds for the constraints and for the decision variables.

Table 1. Upper and lower bounds of the optimization problem.

Bounds	J_G [cm/s]	J_w [cm/s]	J_B [cm/s]	R_{Cu} [%]	x_C [%]	H_f [cm]	ε_G [%]
Lower	1.0	0.04	0.0	55	22	40	8
Upper	2.0	0.4	0.28	100	34	120	15

Where J_i represents the superficial velocity inside the column, for $i = G, w, B$, where G means gas, w wash water and B is the Bias, defined as the difference between wash water and tails flow. Also, R_{Cu} is the copper recovery and x_C is the concentrate grade.

4. Results

In this section are shown the simulation results obtained in the flotation column system. In each graph, the optimum of the model (u_m^*) is the red dashed line, the optimum of the process (u_p^*) is the blue dash-dot line and the operating value of the variable (u_k) is the

solid black line. Additionally, the limits of the decision variables are the dashed grey lines (u^L, u^U), and the disturbances (ξ_k) are the solid black lines.

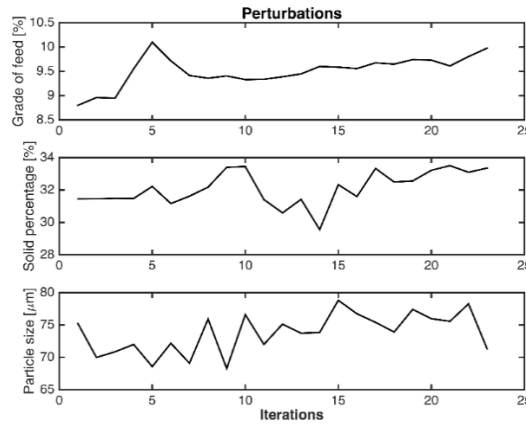


Figure 2. Inputs variables versus iterations number.

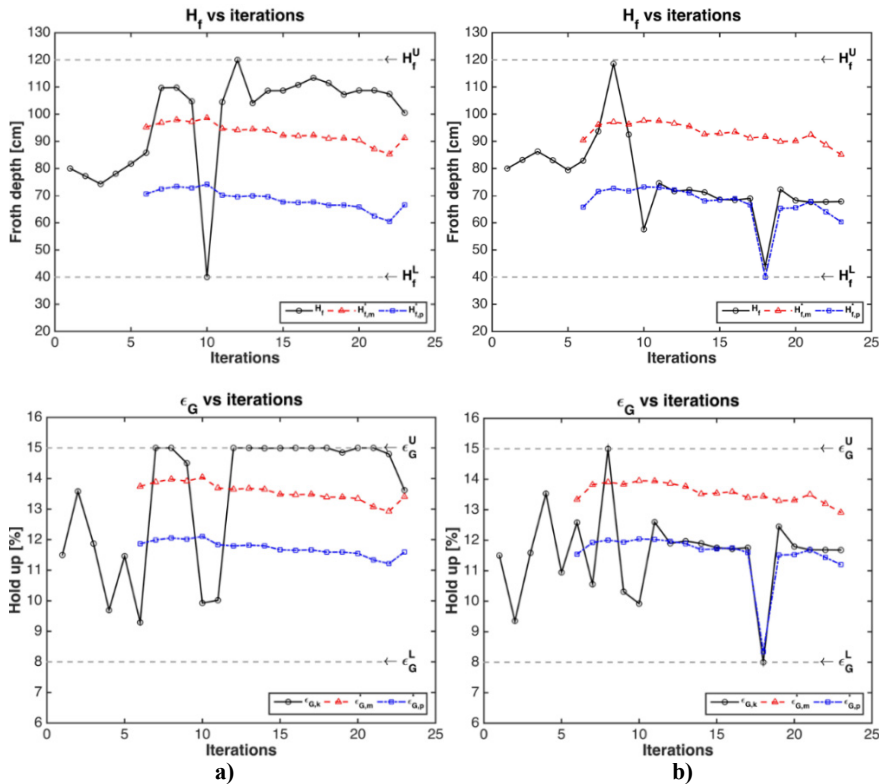


Figure 3. Decision variables in simulation a) without corrections and b) with correction in the estimation of process gradients.

For the simulation of the process, it is assumed that both decision variables and disturbances changes between each steady state. Fig.2 shows the changes of ξ during

the application of the optimization layer. These data were simulated using an ARIMA model, trained with real data.

The Fig. 3a shows the evolution of the decision variables without the correction in the estimation of the experimental gradient. It can be noted that even when the gradient was estimated using the traditional dual approach, and the value of the disturbances were updated in the model based optimization, the RTO couldn't detect the optimum of the process, which in fact changes because of the perturbations. On the other hand, Figure 3b shows the evolution of the decision variables correcting the gradient with the proposed extended dual approach. It can be seen that the adjustment of the gradient allows the RTO to converge and track the optimum of the process, in spite of changes in the disturbances. As the only difference between the results shown in Fig. 3a and Fig. 3b is the estimation of the gradient, it can be said that neglecting the effect of disturbances in the calculation of the process derivatives, can compromise the convergence properties of the MA methodology.

5. Conclusions

The results presented in this work show that the optimal operation of the system changes under time-varying input conditions. Therefore, if the gradient estimation step does not consider the disturbances, the system could not converge to the desired operational point. In other words, the use of the proposed extended gradient estimation method allows tracking the optimal operational conditions with continuously changing disturbances, assuming that they can be measured or estimated. In the studied process, this represents an increase in the profit of 3.5%.

6. Acknowledgements

Financial support of Chilean agency CONICYT (FONDECYT project No. 11160203).

References

- Bunin, G. A., François, G., and Bonvin, D. (2012). Exploiting local quasiconvexity for gradient estimation in modifier-adaptation schemes. Paper presented at the American Control Conference (ACC), 2012.
- Chachuat, B., Srinivasan, B., and Bonvin, D. (2009). Adaptation strategies for real-time optimization. *Computers & chemical engineering*, 33(10), 1557-1567.
- Darby, M. L., Nikolaou, M., Jones, J., and Nicholson, D. (2011). RTO: An overview and assessment of current practice. *Journal of process control*, 21(6), 874-884.
- Finch, J. A., and Dobby, G. S. (1990). *Column flotation*: Pergamon Press.
- Gao, W., Wenzel, S., and Engell, S. (2016). A reliable modifier-adaptation strategy for real-time optimization. *Computers & chemical engineering*.
- Marchetti, A., Chachuat, B., and Bonvin, D. (2009). Modifier-Adaptation Methodology for Real-Time Optimization. *Industrial & engineering chemistry research*, 48(13), 6022-6033.
- Marchetti, A., Chachuat, B., and Bonvin, D. (2010). A dual modifier-adaptation approach for real-time optimization. *Journal of process control*, 20(9), 1027-1037.
- Navia, D., Villegas, D., Cornejo, I., and de Prada, C. (2016). Real-time optimization for a laboratory-scale flotation column. *Computers & chemical engineering*, 86, 62-74.
- Savassi, O. (2005). A compartment model for the mass transfer inside a conventional flotation cell. *International journal of mineral processing*, 77(2), 65-79.
- Wenzel, S., Gao, W., & Engell, S. (2015). Handling Disturbances in Modifier Adaptation with Quadratic Approximation. *IFAC-PapersOnLine*, 48, 132-137.
- Yianatos, J., Bergh, L., and Cortés, G. (1998). Froth zone modelling of an industrial flotation column. *Minerals Engineering*, 11(5), 423-435.
- Yianatos, J., Bucarey, R., Larenas, J., Henríquez, F., and Torres, L. (2005). Collection zone kinetic model for industrial flotation columns. *Minerals Engineering*, 18(15), 1373-1377.

Towards the cooperative-based control of chemical plants

Bogdan Dorneanu^{a,*}, Evgenia Mechleri^a, Harvey Arellano-Garcia^a

^a*Department of Chemical and Process Engineering, Faculty of Engineering and Physical Sciences, University of Surrey, Guildford, Surrey, GU2 7XH, United Kingdom*

^{*}*b.dorneanu@surrey.ac.uk*

Abstract

This contribution presents the proof of concept for a consensus-based approach for the design and assessment of control structures in chemical plants. The applicability of the proposed approach is demonstrated on an existing mini-plant. For this purpose, a reduced dynamic model that considers a simplified structure of the plant, consisting of feed preparation, reaction, and downstream processing, is used to assess the control structure of the mini-plant using the consensus algorithm. The reduced model is used to assess the control structure of the mini-plant reactor, considering the relevant operational and safety variables.

Keywords: consensus problem, cooperative control, optimal control, multi-agent networks

1. Introduction

Modern large-scale industrial plants are complex dynamical systems which consist of highly interconnected and interdependent elements. The control of such systems is usually achieved via hierarchical multi-layered structures, benefitting from their inherent properties such as modularity, scalability, adaptability, flexibility, and robustness (Stanković et al, 2008). However, with the rapid development of Industry 4.0, there are continuously new requirements for controllers to meet. In the control layer, the controllers should automatically adapt to the changed systems structures, process parameters, and production planning with high efficiency and good quality. Thus, highly flexible dynamic optimal control with high performance is required. To this end, the consensus problem has received extensive attention in the distributed coordination and cooperative control of dynamic agents (Ren & Beard, 2005; Hui, 2010; Zhao et al, 2011; Tan et al, 2015; Lee et al, 2017), but less or no attention in chemical process engineering. Many consensus approaches focus on networks of homogeneous agents, where the states have exactly the same dimensions (Qin et al, 2017), hence they are considered states of the consensus protocol as well. In chemical engineering applications, the states of the agents have different dimensions, as the process units will often have non-identical dynamics, which will make impossible to achieve an internal state agreement at this level. An agent represents an element of a system's network composed of (many) interacting sub-systems, connected via flow of energy, materials, information, etc. Each element may consist of a series of sub-systems in itself, and might or might not be controlled. In the following sections an approach for applying the consensus problem to assess the control structure of a chemical mini-plant

is presented. To reduce the computational effort of the proposed algorithm, a structure-retaining model reduction (Dorneanu, 2017) is applied to the full dynamic model.

2. Cooperative control problems

The key idea of cooperative control is that a team of agents (or dynamic systems) must be able to respond to unanticipated changes in the environment by agreeing to what change took place, and by asymptotically approaching a common value of a shared variable of interest. In networks of agents, a consensus algorithm (or protocol) is an interaction rule that specifies the information exchange between an agent and all of its neighbours on a network (Olfati-Saber et al, 2007).

Considering the process system, S , that includes a number of N units, described by the following model:

$$\begin{aligned} \frac{dx_i(t)}{dt} &= f_i(x_i(t), u_i(t)) \\ y_i(t) &= g_i(x_i(t), u_i(t), p_i) \end{aligned} \quad (1)$$

With the initial conditions:

$$x_i(t_0) = x_{i,0} \quad (2)$$

Where t is the time variables, $x_i(t) \in \mathfrak{R}^{n_i}$ is the state variables vector of unit i , $u_i(t) \in \mathfrak{R}^{m_i}$ is the input variables vector of unit i , $y_i(t) \in \mathfrak{R}^{p_i}$ is the output variables vector of unit i , n_i is the state space dimension of unit i , m_i is the dimension of the input vector of unit i , p_i is the dimension of the output vector of unit i , f_i is the function describing the dynamics of the unit i , while g_i is the function describing the way in which the observations are deduced from the state and the input.

A simple consensus algorithm to reach an agreement regarding the state of n_z agents can be expressed as (Olfati-Saber et al, 2007):

$$\frac{dz_i(t)}{dt} = \sum_{j \in N_{z,i}} (z_j(t) - z_i(t)) \quad (3)$$

Where $z_i \in \mathfrak{R}^{n_z}$ is the protocol state.

The consensus protocol defined by equation (3) is said to solve the consensus problem for the system (1) if the following condition holds:

$$\lim_{t \rightarrow \infty} \|z_j(t) - z_i(t)\| = 0 \quad \forall i, j = 1, \dots, n_z \quad (4)$$

The cooperative protocol is defined as shown in Figure 1: the dynamic controller i receives information from the process unit i , in the form of the difference of the steady state value of the output variable y_i^P , as well as information from the dynamic controller

of the neighboring agents j , in the form of the consensus variable v_i , and corrects the input u_i^P . For an agent i , the variable v_i is calculated as:

$$v_i = \sum_{j \in N_{z,i}} (z_j(t) - z_i(t)) \quad (5)$$

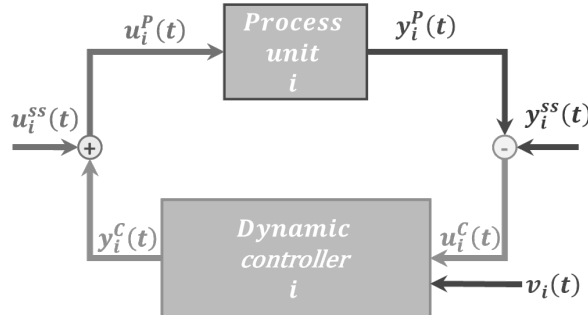


Figure 1. Block diagram of the cooperative control

The dynamics of the controller is defined as the linear model:

$$\begin{aligned} \frac{dz_i(t)}{dt} &= A_i^C z_i(t) + B_i^C u_i^C(t) + F_i^C v_i(t) \\ y_i^C(t) &= C_i^C z_i(t) + D_i^C u_i^C(t) + G_i^C v_i(t) \end{aligned} \quad (6)$$

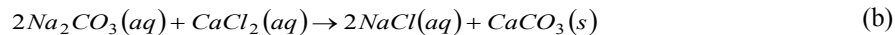
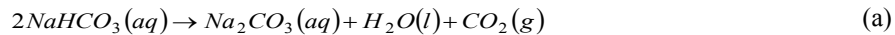
Where A_i^C , B_i^C , C_i^C , D_i^C , F_i^C , G_i^C are matrices to be determined.

3. The mini-plant

3.1. Process description

The plant (Figure 2) produces sodium ion solution as sodium chloride (saline) solution for sale to fine chemical, pharmaceutical and food industry. The raw material is sodium chloride (NaCl) contaminated with calcium chloride (CaCl_2), which is pre-mixed with a stoichiometrically calculated amount of sodium bicarbonate (NaHCO_3). This feedstock is fed into a reactor vessel charged with pre-heated water and the reaction temperature is maintained at 65°C .

The following two reactions take place inside the reactor:



The suspension is then pumped by a positive displacement pump through a plate filter, which removes a high proportion of the CaCO_3 . The output stream splits into a product and a recycle line. The recycle is fed back to the reactor, while the product is passed through a polishing filter, to remove any remaining solids, and then to the lot tank. The CO_2 resulted in the first reaction is then adsorbed in an alkaline solution.

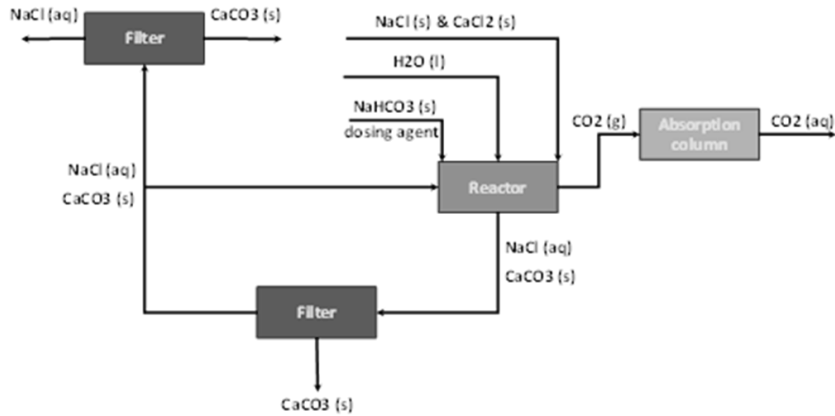


Figure 2. Simplified structure of the mini plant

3.2. Dynamic model

A dynamic model for the simplified process presented in Figure 2 is developed using Aspen Plus[®] Dynamics. The reactor is modelled using the RStoic model from the software library, assuming a conversion of 75% for each of the two reactions. The reactor dimensions are specified as follows: length, $L = 1$ m, and diameter, $D = 0.62$ m. A single stage flash separator is used for the CO_2 adsorption unit, with the dimensions specified as: $L = 0.8$ m, and $D = 0.1$ m. All the other units in the process flowsheet are assumed to be instantaneous. The dynamic model can be written in mathematical form as shown in equation (1).

3.3. Reduced model

To reduce the computational effort required by the proposed algorithm, the structure-retaining model reduction (Dorneanu, 2011) was applied to the full dynamic model: the model is decomposed into models of individual units by cutting streams of material, these models are linearized and a balanced model-order reduction is applied to obtain their reduced models.

Following the application of this approach, the dynamic model in equations (1) is approximated in state-space form as:

$$\frac{d\tilde{x}_i(t)}{dt} = \tilde{A}_i \tilde{x}_i(t) + \tilde{B}_i \tilde{u}_i(t) \quad (1')$$

$$\tilde{y}_i(t) = \tilde{C}_i \tilde{x}_i(t) + \tilde{D}_i \tilde{u}_i(t)$$

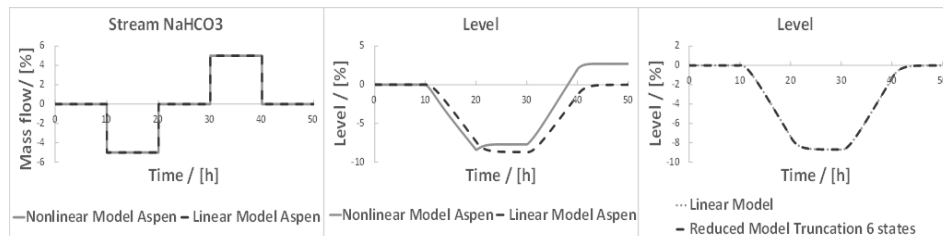


Figure 3. Response of the reactor level to disturbance on the flowrate of NaHCO_3

The linearization leads to a model with 9 states, which is reduced using Matlab[®] to a model with 6 states using model-order reduction via balanced realization. The reactor duty, the flowrates of the reactor's inlet feed streams (NaCl + CaCl₂, NaHCO₃ and the Recycle), and the mass fraction of their components are defined as input variables, while the reactor's pressure, temperature and level, as well as the reactor outlet stream and the mass fraction of its components are defined as the output variables for the linearization.

The agreement between the full dynamic model and the linear model, and between the linear model and the reduced model are presented in Figure 3. The graphs show the changes in the reactor level when a change is applied on the NaHCO₃ feed flowrate. The results are presented as variation from the steady state values.

3.4. Consensus-based control of the mini-plant

The condition defined by equation (4) implies the solution of an optimization problem defined as:

$$\text{Minimize} \quad \|v_i\| \quad (7)$$

$$\begin{aligned} \text{subject to} \quad & \frac{d \tilde{x}_i^P(t)}{dt} = \tilde{A}_i \tilde{x}_i^P(t) + \tilde{B}_i \tilde{u}_i^P(t) \\ & \tilde{y}_i^P(t) = \tilde{C}_i \tilde{x}_i^P(t) + \tilde{D}_i \tilde{u}_i^P(t) \\ & \tilde{y}_i^P(t) \geq 0 \\ & \frac{dz_i(t)}{dt} = A_i^C z_i(t) + B_i^C u_i^C(t) + F_i^C v_i(t) \\ & y_i^C(t) = C_i^C z_i(t) + D_i^C u_i^C(t) + G_i^C v_i(t) \end{aligned}$$

The optimization problem resulting from applying the consensus protocol for the reactor system defined in equation (1') is implemented in GAMS[®] (Tawarmalani & Sahinidis, 2005).

As the software cannot handle differential equations, the equations (1') and (6) are discretized for 100 time steps. The state-space models are discretized using the Matlab[®] c2d toolbox, using the zero-order hold method. Thus, equations (1') are rewritten as:

$$\tilde{x}_i^P[k+1] = \tilde{x}_i^P[k] + \tilde{A}_{i,d} \tilde{x}_i^P[k] + \tilde{B}_{i,d} \tilde{u}_i^P[k] \quad (1'')$$

$$\tilde{y}_i^P[k] = \tilde{C}_{i,d} \tilde{x}_i^P[k] + \tilde{D}_{i,d} \tilde{u}_i^P[k]$$

Where $\tilde{A}_{i,d}$, $\tilde{B}_{i,d}$, $\tilde{C}_{i,d}$, $\tilde{D}_{i,d}$ are the discretized forms of the state-space matrices.

Moreover, in order to make the optimization more computationally efficient, the $\|v_i\|$ is rewritten as:

$$\|v_i\| = \sqrt{(v_i)^2 + \varepsilon} \quad (8)$$

Where $\varepsilon \geq 0$

For applying the consensus approach, the inlet feed stream of NaHCO_3 is initially decreased by 5% (from its steady state value) between the times steps 20 and 40. All the other input variables are fixed at their steady state values. In the same time, between the time steps 30 and 50, it is assumed that the first filter unit in the process flowsheet is sending information in the form of the state variable of its controller, fixed at the value of $z_j(k) = 1e - 4$. The reactor level is bounded between 0.7 and 0.9 m. The reactor temperature and pressure are fixed at their steady state values, 65 °C and 1 bar, respectively.

4. Conclusions

An approach to apply the consensus algorithm for the design and control structures of chemical plants is presented. The approach is applied for the control of the reactor inside an existing mini-plant, while it receives information from the controller of only one other neighbouring unit in the form of a constant value of its state for a fixed amount of time. Moreover, a disturbance is applied on one of the reactor's inlet feed stream. The reactor level is kept between defined bounds.

Future work involves, in a first stage, the application of the algorithm when both units communicate in real time the state of their controller, followed by solving the consensus problem for all the units in the mini-plant flowsheet.

References

- Stanković, M.S., Stanković, S.S., & Stipanović, D.M., 2008, Consensus based multi-agent control structures, Proceedings of the 47th IEEE Conference on Decision and Control, 4364-4369
- Qin, J., Ma, Q., Shi, Y., Wang, L., 2017, Recent advances in consensus of multi-agent systems: A brief survey, IEEE Transactions of Industrial Electronics, Vol. 64, No. 6, 4972-4983
- Dorneanu, B., 2011, Model Reduction in Chemical Engineering: Case studies applied to process analysis, design and operation, PhD thesis
- Ren, W., Beard, R.W., 2005, Distributed consensus in multi-vehicle cooperative control, Springer-Verlag, London
- Hui, Q., 2010, Hybrid consensus protocols: an impulsive dynamical approach, International Journal of Control, Vol. 83, No. 6, 1107-1116
- Zhao, Y., Guanghui, W., Zhisheng, D., Xiang, X., 2011, A new observer-type consensus protocol for linear multi-agent dynamical systems, Proceedings of the 30th Chinese Control Conference, 5975-5980
- Tan, C., Liu, G.P., Shi, P., 2015, Consensus of networked multi-agent systems with diverse time-varying communication delays, Journal of the Franklin Institute, Vol. 352, Issue 7, 2934-2950
- Lee, S.J., Lee, J.M., Wu, J., Allgöwer, F., Suh, J.C., Lee, G., 2017, Consensus algorithm-based approach to fundamental modelling of water pipe networks, AIChE Journal, Vol. 63, No. 9, 3860-3870
- Olfati-Saber, R., Fax, J.A., Murray, R.M., 2007, Consensus and cooperation in networked multi-agents systems, Proceedings of the IEEE, Vol. 95, No. 1, 215-233
- Tawarmalani, M., Sahinidis, N.V., 2005, A polyhedral branch-and-cut approach to global optimization, Mathematical Programming, 103 (2), 225-249

A multiparametric analysis of molecular complexities vs. economic data towards the continuous pharmaceutical manufacturing (CPM) of antibiotics

Mabel E. Ellerker, Samir Diab, Dimitrios I. Gerogiorgis*

School of Engineering (IMP), University of Edinburgh, Edinburgh, EH9 3FB, UK

D.Gerogiorgis@ed.ac.uk

Abstract

Continuous pharmaceutical manufacturing (CPM) has a documented potential to reduce production costs, offering opportunities to simultaneously streamline product development and improve economics for the pharmaceutical industry. Selecting technically feasible and economically viable candidate active pharmaceutical ingredients (APIs) for CPM is imperative for this transition to succeed. The present paper outlines a statistical correlation analysis of structural complexity and trade statistics for antibiotics, towards establishing economically viable CPM candidates. Bertz molecular complexity indices (CIs) are compared with molecular weights and price, sales and revenue data to identify the strength of correlation among variables. Sales data show that penicillins and quinolones are the most economically promising antibiotic families, composing 60% of total antibiotic revenues in the period 2009-2011. Spearman's rank correlation coefficients confirm strong monotonic relationships between antibiotic Bertz CIs and trade parameters. To the best of our knowledge, this is the first study highlighting promising antibiotics towards systematising CPM pursuits.

Keywords: Continuous Pharmaceutical Manufacturing (CPM), statistics, antibiotics.

1. Introduction

The pharmaceutical industry faces increasing financial pressure due to globalised competition and rapidly increasing R&D expenditure: these pressing challenges can be alleviated by a judicious shift from the currently prevalent batch production to Continuous Pharmaceutical Manufacturing (CPM) (Anderson, 2012). Economic analyses are required for systematic evaluation to identify economically viable compounds for CPM. Antibacterial drugs, also known as antibiotics, have revolutionized modern medicine, and are an essential part of human life; however, their production is often expensive due to the elaborate processes required to obtain their complex molecular structures. Previous work has established that antibiotics have a particularly high economic potential for CPM, based on recent UK trade data for a vast dataset of currently marketed and regulated antibiotics (Nagy et al., 2016). While it is essential to ensure a robust continuous flow synthetic route is established for a candidate API prior to CPM implementation (Plutschack et al., 2017), identifying the economic viability of a new production paradigm for an API is equally important.

Statistical analysis of economic trade data for antibiotics can highlight promising candidates for CPM implementation, if a continuous route is established and scalable.

Molecular complexity indices (CIs) are important tools for predicting toxicological and physicochemical properties of chemical structures in drug design and pharmaceutical development (Li and Eastgate, 2015). This paper conducts statistical analyses between structural metrics and pharmaceutical trade data, to identify correlations between CIs and demand of various antibiotics, potentially highlighting promising API candidates for CPM implementation. We emphasise that such a statistical correlation analysis can be a very useful (not the sole) criterion for CPM opportunity identification, and must be used in tandem with pharmacokinetic, pharmacodynamic (PKPD) and clinical evidence.

2. Methodology and Analysis

2.1 Economic Data

Acquiring recent economic trade data is essential for conducting an accurate economic analysis of candidate antibiotics for CPM implementation. Sales and price data for the period 2009-2011 for 37 antibiotics from lists of the best performing antibiotics by sales (Vitaku, 2010; FDA, 2010; FDA, 2012) and those on the World Health Organisation (WHO) essential medicine lists (WHO, 2017) have been compiled. These antibiotics represent societally important products with high economic potential: the most recent economic data have been used, to ensure relevance to pharmaceutical industry trends.

2.2 Molecular Complexity

In this work, we quantify complexity via the Bertz CI, which is a weighted sum of numbers of different groups on organic molecules, including rings, non-aromatic unsaturated C-atoms, heteroatoms and chiral centres (Bertz, 1981). Bertz CI values for the full list of antibiotics considered are available in the literature (PubChem, 2017).

2.3 Statistical Correlations

A wide range of statistical correlation coefficients exist to determine the strength of different types of correlation between two sets of data. Spearman's rank correlation coefficients (r_s , Eq. 1) have been calculated to determine the strength of a monotonic relationship between two data sets. Here, d is the difference in rank of members of each dataset and n is the length of the dataset. The strength of correlation is quantified by the magnitude of the coefficient: $r_s = 0.6-0.8$ indicates a "strong" correlation and $r_s > 0.80$ shows a "very strong" indication of a monotonic relationship between two data sets.

$$r_s = 1 - \frac{6 \sum d^2}{n(n^2 - 1)} \quad (1)$$

3. Results and Discussion

3.1 Economic Data vs. Antibiotic Complexity Indices and Families

Fig. 1 shows Bertz CIs for the full set of antibiotics considered here; antibiotics are arranged in order of ascending MW. Bertz CI values generally increase with MW, reflecting the increasing number bond connections and variety of functional groups present in larger molecules. Economic data were compiled and compared for this set of antibiotics to establish promising antibiotics with high potential for CPM application.

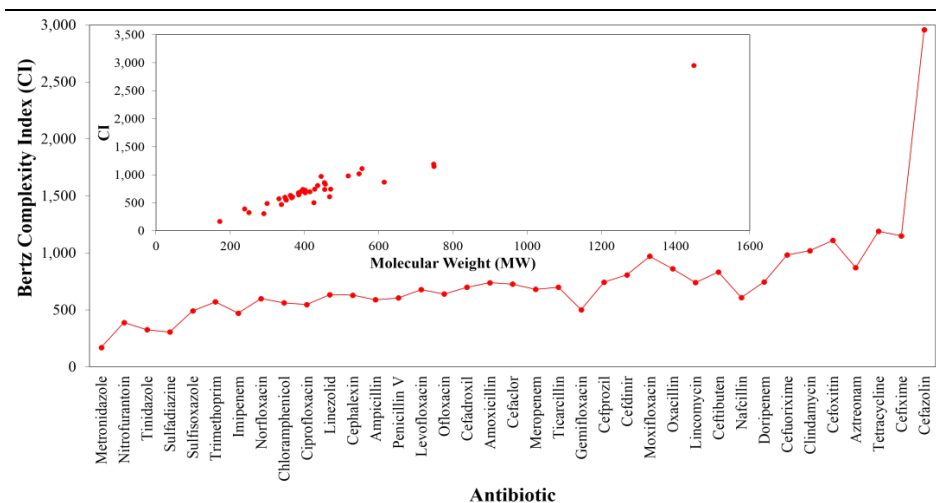


Figure 1: Bertz complexity index (CI) as a function of antibiotic molecular weight.

Fig. 2 shows compiled sales and price data for the total list of antibiotics. Antibiotics are arranged in order of ascending average sales (by mass) over the period of 2009-2011. From the set of antibiotics considered, amoxicillin has significantly higher sales over other antibiotics. Amoxicillin is a broad-spectrum antibiotic with various applications, and thus its wide utility makes it particularly important in modern society (Kaur et al., 2011). Cephalexin, ciprofloxacin, piperacillin and penicillin V are the subsequent best-performing antibiotics in terms of sales. Comparison of the economic performance of different antibiotic families can give an indication of antibiotics with CPM potential. Prices for different antibiotics vary significantly, thus annual revenues from different antibiotics allow an alternative economic comparison of promising antibiotic families.

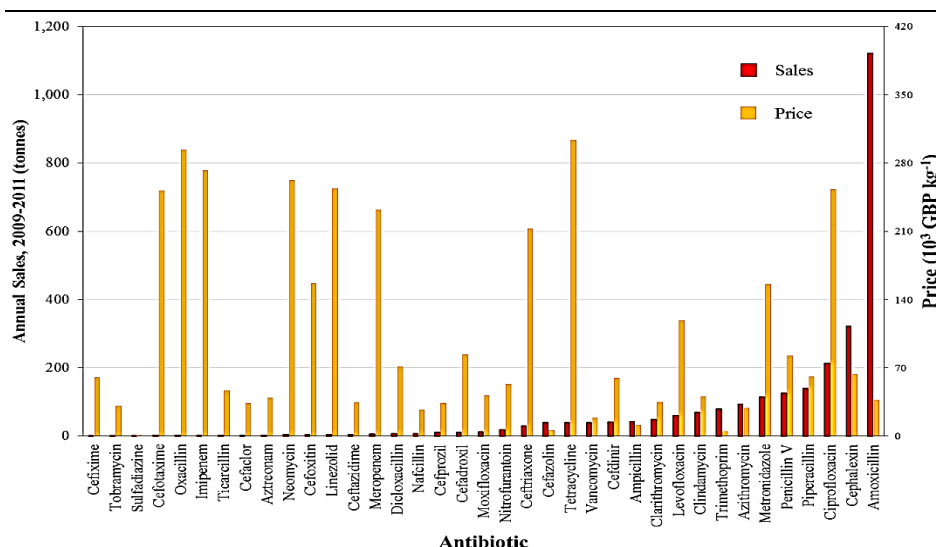


Figure 2: Average antibiotic annual sales (2009-2011) and unit prices (mass bases).

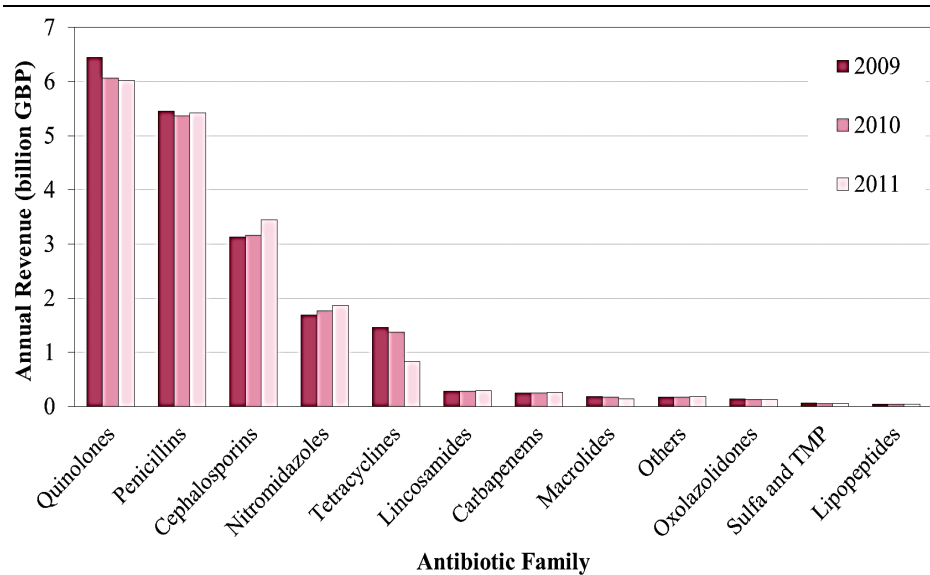


Figure 3: Annual revenues of different antibiotic families (2009-2011).

Fig. 3 compares annual revenues of the highest performing antibiotic families over the years for which sales and price data are available (2009-2011). Quinolones and penicillins dominate the pharmaceutical industry for antibiotics, contributing 60% of the total antibiotic revenue and are thus of high commercial importance. Fluctuation is recognised in all families of antibiotics present, but most notably for quinolones (a reduction of 0.38 billion GBP is clear in 2009-2010). Nevertheless, these families of antibiotics are consistently high performers, presenting strong economic incentives.

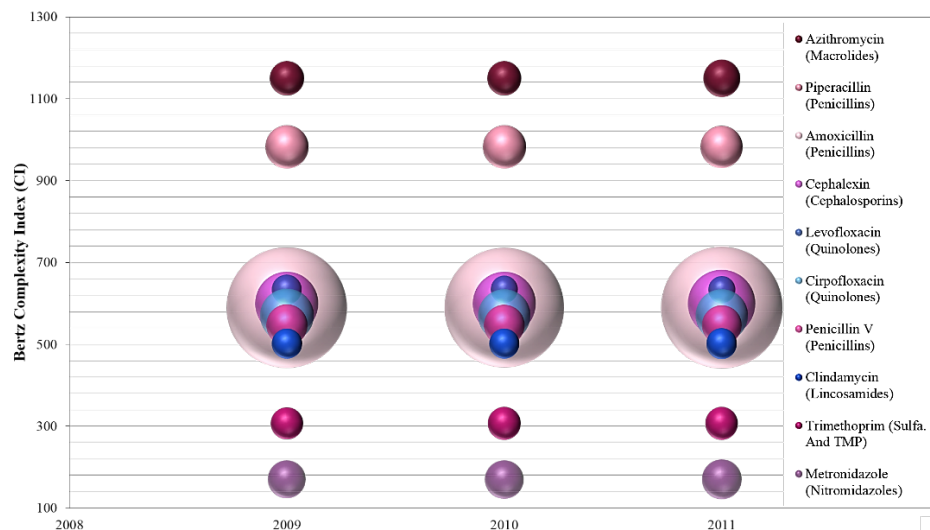


Figure 4: Bertz complexity index (CI) for the top 10 antibiotics by annual sales.

Over the period 2009-2011, revenues for quinolones, tetracyclines and macrolides decrease annually, while revenues for cephalosporins and nitromidazoles increase. Despite these changes, the overall market revenue remains relatively consistent between 2009-2011 (average = $\pm 3\%$), indicating a consistently high market for antibiotics. Economic stability of revenues is a key factor in new product R&D (Teoh et al., 2015), as is ensuring a technically feasible continuous flow synthesis (CPM) route for the API.

Fig. 4 shows sales volumes (bubble radius) of the top 10 antibiotics by sales and their Bertz CIs over the period 2009-2011. Amoxicillin and cephalexin contribute the highest sales volumes and thus strong market opportunities for UK production are evident. Amoxicillin, piperacillin and penicillin V belong to the penicillin family and ciprofloxacin and levofloxacin belong to the quinolone family, those that dominate the pharmaceutical industry (Fig. 3). Size variation for bubbles of each antibiotic is minimal over the period considered (2009-2011), indicating little variation in sales volumes; thus, each antibiotic listed is a consistently high marketing drug. All antibiotics shown in Fig. 4 are strong performers based on structure-trade correlation, thus potentially promising CPM implementation candidates, if continuous synthesis routes are available.

3.2 Statistical Correlation of Complexity Index with Economic Data

Spearman's rank correlation coefficients between different datasets are shown in Table 1. A "very strong" correlation ($r_s > 0.8$) exists between Bertz CI and MW due to the increasing size and complexity of molecules with increasing number and diversity of functional groups and bond types present as MW increases. as expected from the results presented in Fig. 1. "Strong" correlations ($0.6 < r_s < 0.8$) exist between sales and price data and molecular complexity. Fig. 5 shows average antibiotic sales (2009-2011) and prices versus Bertz CIs associated with the correlation Spearman's rank coefficients presented in Table 1. The strength of correlation between economic data and molecular complexity is directly related to the high performance of the antibiotics considered in the data set; correlations are made between the most recent economic data available.

Table 1: Spearman's rank correlation coefficient between paired data sets.

	$\log_{10}(\text{Bertz CI})$	$\log_{10}(\text{Average Sales, 2009-2011})$	$\log_{10}(\text{Price})$
MW	0.976	0.621	0.687
Bertz CI	n/a	0.634	0.718

3.3 Discussion

The present work has established penicillins and quinolones as economically promising candidates for CPM, based on previous work highlighting antibiotics as a promising class of APIs for CPM implementation (Nagy et al., 2016). Statistical analyses indicate strong monotonic relationships between Bertz CIs and economic data for the set of antibiotics considered here, which can be further validated with a wider data set where available. Addressing technical challenges in switching from batch to continuous manufacturing routes for candidate APIs is equally important to highlighting economic potential of antibiotics (Bana et al., 2017); these efforts must be conducted in tandem to establish the strongest candidate APIs for CPM implementation (Teoh et al., 2015) to facilitate the rapid transition of manufacturing paradigm in the pharmaceutical industry.

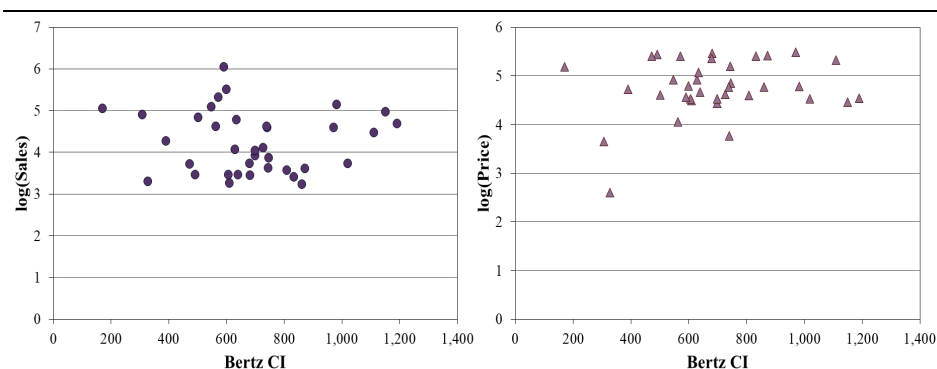


Figure 5: Antibiotic average sales (2009-2011) and prices vs. Bertz complexity index.

4. Conclusions

The statistical analysis of economic data indicates that penicillins and quinolones dominate the antibiotic market in terms of annual sales volumes and revenue, emerging as the most promising candidates for CPM. Amoxicillin contributes the most significant portion of total revenue (2009-2011) for the antibiotics considered here, followed by cephalexin and ciprofloxacin. Bertz CIs of a wide variety of antibiotics have been compiled and analysed vs. relevant economic data. Statistical analysis highlights a strong correlation between molecular complexity (MW, Bertz CI) with sales and price. The need for systematic evaluation of more trade data over a longer horizon is clear, as is the high incentive for selecting penicillins and quinolones as viable CPM candidates.

5. Acknowledgements

Ms. Mabel Ellerker acknowledges an EquateScotland CareerWISE (Women in Science & Engineering) Summer Research Placement Fellowship (University of Edinburgh). Mr. Samir Diab gratefully acknowledges the financial support of the Engineering and Physical Sciences Research Council (EPSRC) via a Doctoral Training Partnership (DTP) PhD fellowship awarded by the University of Edinburgh (EP/N509644/1).

References

- N. G. Anderson, 2012, *Org. Process Res. Dev.*, 16, 852–869.
- S. H. Bertz, 1981, *J. Am. Chem. Soc.*, 103, 3599–3601.
- FDA Food and Drug Administration, 2010, *Sales of Antibacterial Drugs in Kilograms*, 4–6.
- FDA Food and Drug Administration, 2012, *Sales of Antibacterial Drugs in Kilograms*, 5–8.
- S. Kaur, R. Rao and S. Nanda, 2011, *Int. J. Pharm. Pharmaceut. Sci.*, 3, 30–37.
- J. Li and M. D. Eastgate, 2015, *Org. Biomol. Chem.*, 13, 7164–76.
- B. Nagy, G. Marosi, D. I. Gerogiorgis, 2016, *Comput.-Aided Chemical Engineering*, 1045–1050.
- M. Plutschack, B. Pieber, K. Gilmore and P. H. Seeberger, 2017, *Chem. Rev.*, 117, 11796–11983.
- PUBCHEM Statistical Database, National Institutes of Health (NIH), Bethesda, MD, USA.
- S. K. Teoh, C. Rathi and P. Sharratt, 2015, *Org. Process Res. Dev.*, 20, 414–431.
- E. Vitaku, E. A. Ilardi and J. T. Njardarson, 2010, *J. Chem. Ed.*, 87, 1348.
- H. W. Whitlock, 1998, *J. Org. Chem.*, 63, 7982–7989.
- WHO World Health Organisation, 2017, *WHO Model List of Essential Medicines*, 20.

Combined Use of Bilevel Programming and Multi-objective Optimization for Rigorous Analysis of Pareto Fronts in Sustainability Studies: Application to the Redesign of the UK Electricity Mix

Phantisa Limleamthong,^a Gonzalo Guillén-Gosálbez,^{a,*}

^a*Centre for Process Systems Engineering, Imperial College of Science, Technology and Medicine, South Kensington Campus, London, SW7 2AZ, UK*

g.guillen05@ic.ac.uk

Abstract

Multi-objective optimization (MOO) has emerged as the preferable approach to tackle sustainability problems. The solution of MOO models is generally expressed as a set of Pareto optima, representing optimal trade-offs between given criteria. Identifying the final Pareto solution from this set for practical implementation is a challenging task, particularly when several criteria and decision-makers are involved in the analysis. In this work, we propose the rigorous method based on bilevel optimization and MOO to support decision-making in the post-optimal analysis of Pareto fronts. Our approach is capable of selecting non-dominated solutions which are particularly appealing for decision-makers, quantifying the distance between any suboptimal point of a MOO model and its Pareto front, and establishing improvement targets for suboptimal solutions that if attained would make them optimal. Overall, our method allows analyzing Pareto fronts and identifying a final Pareto point to be implemented in practice without the need to define explicit weights. We illustrate the capabilities of our approach through its application to the optimization of the UK electricity mix according to several sustainability indicators.

Keywords: Multi-objective optimization, Bilevel optimization, Sustainable development, Sustainability targets, Electricity generation

1. Introduction

Developing more sustainable systems requires the simultaneous consideration of a wide range of economic, environmental and social indicators. However, this task is quite challenging since inherent trade-offs between these criteria naturally arise.

Multi-objective optimization (MOO) has emerged as one of the most common techniques employed in sustainability problems. One major advantage of MOO is that it requires no articulation of decision makers' preferences via subjective weights. The typical outcome of MOO models, as applied to sustainability problems, is given by a Pareto front representing optimal trade-offs between economic, environmental and social criteria. The key characteristic of this frontier is non-inferiority, which means that by moving along its trajectory no objective can be improved without deteriorating at least another one. Unfortunately, these Pareto fronts are seldom analyzed in detail, leaving the task of selecting a final Pareto solution to be implemented in practice to decision-makers.

In this work, the task of exploring the Pareto frontier and selecting a final solution is posed as a bilevel programming problem. Hence, we combine multi-objective optimization and bilevel programming to facilitate the post-optimal analysis of Pareto fronts and avoid the need to define subjective weights in an explicit manner.

The paper starts by presenting mathematical background and proposed method in Section 2. A real-world case study of the UK electricity mix is illustrated in Section 3, followed by the results in Section 4. Finally, the conclusions are drawn at the end of the paper.

2. Methodology

In this section, we first introduce the mathematical background and address problem statement, followed by proposing mathematical approach to tackle this task.

2.1. Mathematical background and problem statement

Consider the following multi-objective problem (M.1):

$$\begin{aligned} \min_x \quad & \{f_1(x), \dots, f_k(x)\} \\ \text{s.t.} \quad & g(x) \leq 0 \\ & h(x) = 0 \end{aligned} \tag{M.1}$$

Where x denotes decision variables, $f_1(x)$ to $f_k(x)$ represent economic, environmental and social concerns, and $g(x)$ and $h(x)$ are the inequality and equality constraints given by the system under study. Consider the multi-dimensional function $f: R^n \rightarrow R^m$ and let X be the set of feasible solutions in the space R^n , and Y the feasible set of objectives values in R^m such that $Y = \{y \in R^m : y = f(x), x \in X\}$. Let $P(Y)$ defined as the Pareto frontier of the model, then the goal of the analysis sought is to find a point y^* in $P(Y)$ and its corresponding vector of decisions variables values x^* in X that optimizes a function $F(x, y)$ of x and y . That is, we aim to identify the values x^*, y^* such that $y^* = f(x^*)$, and at the same time $(x^*, y^*) = \arg \min F(x, y)$.

2.2. Proposed mathematical approach

2.2.1. Identifying specific points in the Pareto front using bilevel optimization:

Our approach to find Pareto points that minimize a given function $F(x, y)$ relies on formulating and solving a bilevel optimization problem. Bilevel programming problems consist of two nested optimization problems where the outer one is constrained by the optimal solution of the inner one. Here, the inner problem representing MOO guarantees the solution found is Pareto optimal, while the outer one minimizes a distance metric calculated considering a given suboptimal solution whose performance needs to be improved. Note that function $F(x, y)$ can accommodate any different distance metrics and alternative objective functions that reflect decision makers' preferences.

We next apply the ε -constraint method to the MOO problem, where $f_1(x)$ is kept as a main objective to be minimized subject to the others being less than or equal to the epsilon value. Hence, this task can be formulated as a bilevel optimization problem as follows:

$$\begin{aligned} \min_{\varepsilon_i} \quad & F(x, y_1(x), \dots, y_m(x)) \\ \text{s.t.} \quad & \min_x y_1(x) \\ & g(x) \leq 0 \\ & h(x) = 0 \\ & y_i(x) \leq \varepsilon_i \quad \forall i, i \neq 1 \end{aligned} \tag{M.2}$$

That is, the outer problem seeks the epsilon value ε_i^* that lead to an associated Pareto solution x^* calculated by the inner one. Note that it is possible to solve the bilevel problem by replacing the inner problem with its KKT conditions if the problem is LPs and convex NLPs. However, solving bilevel MILPs, MINLPs and nonconvex NLPs is more challenging, since this approach does not ensure convergence to the global

optimum. Some algorithms (Bard and Moore, 1990; Colson et al., 2007) have been put forward to solve the latter problems efficiently but the area is still under development.

2.2.2. Simplifying the post-optimal analysis and establishing improvement targets:

Furthermore, we can define improvement targets for any suboptimal solution based on the performance of point x^* . More precisely, let x^{sub} be a suboptimal solution of model M.2 and $\%imp_i$ denotes the percentage improvement in objective i that solution x^{sub} needs to accomplish to become optimal. We can define improvement targets for this solution as percentage difference between its performance and the performance of point x^* as follow: $\%imp_i = (y_i(x^*) - y_i(x^{sub})) / y_i(x^{sub}) \times 100\%$.

3. Case study: Application to the redesign of the UK electricity mix

We illustrate the capabilities of our approach through a case study addressing the improvements of the current UK electricity mix. Generally, the business as usual solutions are suboptimal and need to be improved to become efficient. Hence, the goal of the analysis is to identify a Pareto point representing an efficient electricity mix such that its distance with respect to the current mix is minimal.

3.1. Data sources and assumptions

The data used in this study was retrieved from the work by Stamford and Azapagic (2014). We selected six specific electricity generation technologies which are expected to play a vital role in the UK mix. For simplicity, we selected total levelized cost as economic indicator and global warming potential (gwp) as environmental indicator.

3.2. Mathematical formulation

Here, we aim to minimize all indicators subject to bounds on the electricity generation of each technology and a constraint for demand satisfaction. The ε -constraint method and KKT condition were applied to the MOO problem. The economic objective is kept as main objective while the environmental objective is treated as auxiliary ε -constraint. The general model which can be applied with multi-criteria case is given below.

$$\min_{\varepsilon_i} \sum_{j \in J} ((GEN_j^{p*} - GEN_j^{bau}) / GEN_j^{bau})^2 \quad (M.3a)$$

$$s.t. \quad \underline{\varepsilon}_i \leq \varepsilon_i \leq \overline{\varepsilon}_i \quad \forall i, i \neq cost \quad (M.3b)$$

$$x_{cost,j} - \mu_j^{\leq} + \mu_j^{\geq} + \lambda + \sum_{i, i \neq cost} (x_{i,j} \times \mu_i^{\leq}) = 0 \quad \forall j \quad (M.3c)$$

$$\sum_{j \in J} GEN_j = dem \quad (M.3d)$$

$$\underline{GEN}_j + s_j^{\leq} = GEN_j \quad \forall j \quad (M.3e)$$

$$\overline{GEN}_j + s_j^{\geq} = \overline{GEN}_j \quad \forall j \quad (M.3f)$$

$$\sum_{j \in J} (x_{i,j} \times GEN_j) + s_i^{\leq} = \varepsilon_i \quad \forall i, i \neq cost \quad (M.3g)$$

$$\mu_j^{\leq} - UY_j^{\leq} \leq 0 \quad \forall j \quad (M.3h)$$

$$s_j^{\leq} - U(1 - Y_j^{\leq}) \leq 0 \quad \forall j \quad (M.3i)$$

$$\mu_j^{\geq} - UY_j^{\geq} \leq 0 \quad \forall j \quad (M.3j)$$

$$s_j^{\geq} - U(1 - Y_j^{\geq}) \leq 0 \quad \forall j \quad (M.3k)$$

$$\mu_i^{\leq} - UY_i^{\leq} \leq 0 \quad \forall i, i \neq cost \quad (M.3l)$$

$$s_i^{\leq} - U(1 - Y_i^{\leq}) \leq 0 \quad \forall i, i \neq cost \quad (M.3m)$$

$$\mu_j^{\leq}, \mu_j^{\geq}, \mu_{i, i \neq cost}^{\leq}, s_j^{\leq}, s_j^{\geq}, s_{i, i \neq cost}^{\leq}, GEN_j \geq 0; Y_j^{\leq}, Y_j^{\geq}, Y_{i, i \neq cost}^{\leq} \in \{0, 1\}$$

Where the associated notation is given below:

Indexes/sets	J	Set of electricity generation technologies indexed by j
	I	Set of objectives indexed by i
Variables	GEN_j	Electricity generation of technology j , GWh/year
	ε_i	The value of objective i
Parameters	\overline{GEN}_j	Upper bound on the generation of technology j , GWh/year
	\underline{GEN}_j	Lower bound on the generation of technology j , GWh/year
	GEN_j^{bau}	The business as usual generation of technology j , GWh/year
	$x_{cost,j}$	Cost per GWh of technology j , £/GWh
	$x_{i,j}$	Attribute value of objective i where $i \neq cost$
	dem	Total UK electricity demand, GWh/year
	λ	Multiplier for the electricity demand equality constraint
	$\mu_j^{\leq}, \mu_j^{\geq}, \mu_{i,i \neq cost}^{\leq}$	Multiplier variable for the upper, lower bound, ε -constraint
	$s_j^{\leq}, s_j^{\geq}, s_{i,i \neq cost}^{\leq}$	Slack variable for the upper, lower bound, ε -constraint
	$Y_j^{\leq}, Y_j^{\geq}, Y_{i,i \neq cost}^{\leq}$	Binary variable for the epsilon inequality constraint
	U	Large parameter, assumed equal to 10^6

The outer problem of the model defines the distance with respect to the original mix. This objective function reflects the following decision-making strategy: to improve the sustainability performance of the UK electricity mix so as to achieve the Pareto optimality subject to minimum changes in the generation of each technology. Note that this model allows the decision-makers to focus on a specific suboptimal point, for example, the current electricity mix in this study. Hence, the solution to the model would represent the best Pareto optimal point to which the given suboptimal point could approach with least effort to change from its original state. The choices of a given suboptimal point could, therefore, possibly lead to different points in the Pareto set. Moreover, this model can also accommodate the different distance metrics by just simply modify the objective function of the outer problem in M.3a. For instance, we want to minimize the distance, however, this time in terms of objective space rather than the generation space. Where $x_{i,total}$ is defined as the total value of objective i , $\forall i \in I$, we can replace M.3a with the following equation: $\min_{\varepsilon_i} \sum_{i \in I} ((x_{i,total} - \sum_{j \in J} (x_{i,j} \times GEN_j)) / x_{i,total})^2$.

4. Results and discussion

4.1. Bi-criteria case

4.1.1. Pareto front analysis

In this case study, we consider two objectives to be minimized i.e. cost and gwp. The Pareto frontier shows three major different sections as shown in Figure1. In section A, at low level of cost, significant improvements of up to 35% reductions in gwp can be achieved at a marginal increase (1%) in cost. Figure2 shows the corresponding mix of technologies of the Pareto points presented in Figure1. For the entire section A, gas – as the cheapest alternative – is at its upper bound to ensure minimum cost. Moving away from the minimum cost point where the gwp objective gains more importance, the model decides to reduce coal (the greatest gwp contributor) until reach its lower bound in which 14% decrease in its generation could substantially trim down gwp. In section B, gas is

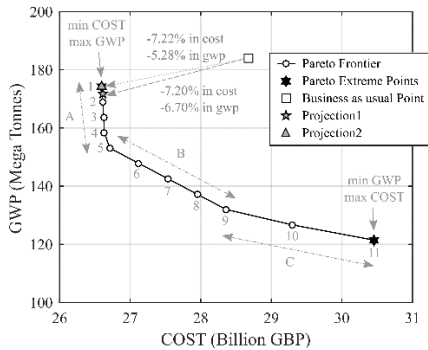


Figure1. Pareto frontier for bi-criteria case

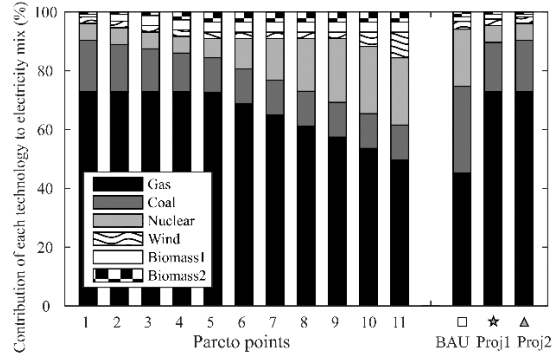


Figure2. Breakdown of technologies for bi-criteria case

replaced by nuclear to reduce further the gwp. Nuclear generation continuously increases until reaches its upper bound at the beginning of section C. From this point forward, coal stays at its lower bound and gas gradually decreases to its lower bound to minimize gwp. This is compensated by an increase in the generation of wind. Note that the results shown above may vary if the lower and upper bounds on the technologies are changed.

4.1.2. Analysis of projections and its improvement targets

We next solve model M.3 to identify the point in the Pareto set with respect to two projecting objective functions as mentioned in section 3.2. The bilevel model was solved by reformulating the inner problem using the KKT conditions, thereby leading to a convex MINLP. The mathematical model was implemented in GAMS 24.7.1 and solved with CPLEX 12.6.3.0 on an Intel® Core™ i7-3770 processor operating at 3.40 GHz. It took around 0.171 CPUs to achieve global optimality. The BAU solution has a total cost of £28.67bn and a gwp of 183.97 Mt. The first projection point with minimum changes in the generation has a cost of £26.60bn and a gwp of 171.65 Mt. To achieve this point, the current UK mix needs to reduce its cost and gwp by 7.20% and 6.70%, respectively. This could be done by increasing further the generation from gas and reducing the generation of nuclear, wind and biomass2 until they reach their lower bound as shown in Figure2. The second projection point with minimum changes in objective values corresponds to the minimum cost point, implying a 7.22% decrease in cost and 5.28% decrease in gwp. These targets are similar to the previous ones including their corresponding electricity portfolio as shown in Figure2. However, comparing between the two projected points, the first shows a lower reduction in cost (7.20% vs 7.22%), but leads to a significantly larger reduction in gwp (6.70% vs 5.28%).

4.2. Multi-criteria case

Incorporating more objectives could lead to a more realistic representation of the problem but add complexity to the bilevel model. In this case, we additionally incorporate working injuries (wi) into the problem as social indicator. We generated 1000 points of the Pareto set following a similar approach as before, but this time sampling the epsilon values from a uniform distribution with given lower and upper bounds. The Pareto solutions are depicted in Figure3. We next solved the model M.3 with another objective of wi to be minimized. It was implemented in GAMS and solved with CPLEX 12.6.3.0 which took around 0.094 CPUs to solve each instance of the problem. The Pareto solution that is closest in generation values to the BAU alternative has a cost of £28.27bn, emissions of 134.86 Mt, and injuries of 427.71 people/year. Taken the BAU solution as starting point, this solution entails reduction targets of 1.38% in cost, 26.69% in gwp, and 38.14% in wi. Compared to the bi-criteria case, the projected point shows larger cost but better value of

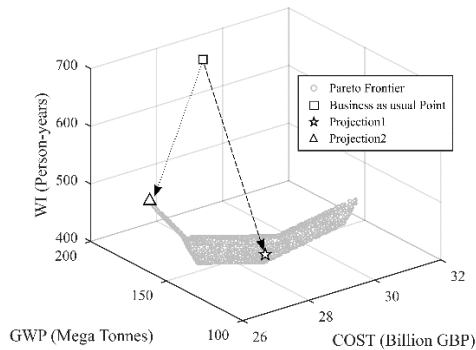


Figure3. Pareto frontier for 3Obj case

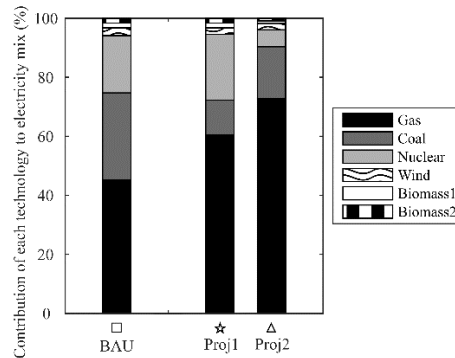


Figure4. Breakdown of technologies for 3Obj case

gwp. These targets could be achieved by reducing coal (the greatest gwp and wi contributor) to its lower bound and increasing gas and nuclear as shown in Figure4. The second projection point with minimum changes in objective values yields the same targets as bi-criteria case, which corresponds to £26.60bn in cost, 174.25 Mt of gwp and 495 people/year of wi, leading to reductions of 7.22%, 5.28% and 28.43% in these objectives, respectively. Comparing between the two projected solutions, the first shows a much lower reduction in cost, but brings about a significantly larger reduction in gwp and wi.

5. Conclusions

Multi-objective optimization (MOO) has been perceived as a common tool to address sustainability problems. The solution of MOO models is given by a Pareto front that requires decision-makers to identify the final solution to be implemented. In this study, we proposed a systematic approach based on bilevel programming and MOO to facilitate the analysis of Pareto front and establish optimal targets for suboptimal alternatives. We have implemented our approach to optimize the UK electricity mix according to some sustainability criteria, where a bi-criteria and multi-criteria cases were explored with two different projecting functions. The analysis of the Pareto frontier reveals that there are clear inherent trade-offs between the given criteria, which are strongly connected to the performance of each technology. The example of two projecting objective functions, i.e. minimum changes in generation and minimum changes in objective values, gives two different projected targets. This means that the model offers the flexibility to adopt any distance metric that particularly reflects decision makers' preferences. Overall, our bilevel-MOO-based approach allows analyzing Pareto fronts and selecting a final Pareto point to be implemented in practice without the need to define subjective weights. Our goal is to guide policy-makers and engineers in the transition towards a more sustainable society by supporting multi-criteria decision-making in sustainability problems.

References

- Bard, J.F., Moore, J.T., 1990. A Branch and Bound Algorithm for the Bilevel Programming Problem. *SIAM J. Sci. Stat. Comput.* 11, 281–292. doi:10.1137/0911017
- Calvete, H.I., Galé, C., 2011. On linear bilevel problems with multiple objectives at the lower level. *Omega* 39, 33–40. doi:10.1016/j.omega.2010.02.002
- Colson, B., Marcotte, P., Savard, G., 2007. An overview of bilevel optimization. *Ann. Oper. Res.* 153, 235–256. doi:10.1007/s10479-007-0176-2
- Stamford, L., Azapagic, A., 2014. Life cycle sustainability assessment of UK electricity scenarios to 2070. *Energy Sustain. Dev.* 23, 194–211. doi:10.1016/j.esd.2014.09.008

An effect of explosion venting panel using CFD in low pressure hydrogen facilities

Seungsik Cho,^a Jaewon Lee,^a Sunghyun Cho,^a Hyungjoon Yoon,^a and Il Moon^{a*}

^a*Department of Chemical and Biomolecular Engineering, Yonsei University, 50 Yonsei-ro, Seodamun-gu, Seoul 03722, Republic of Korea*

ilmoon@yonsei.ac.kr

Abstract

Hydrogen has been widely recognized as an energy source to replace fossil fuel due to its environmental friendly element and renewable properties. However, it also has disadvantages such as a wide range of flammability (4~75%), low minimum ignition energy (0.2mJ), etc. So, there have been studies to prevent explosions by creating ventilation systems which focus on effectively releasing leaked hydrogen gas. Despite hours of ventilation, several experimental results show the concentration still being maintained higher than 4%. Therefore, it is necessary to consider the countermeasures to minimize damage when explosion actually occurs due to the incomplete effect of ventilation. In this study, the FLACS Computational Fluid Dynamics(CFD) program was used to verify the reduced damage when the Explosion Venting Panel(EVP), which discharges overpressure and unburned gas, is applied in comparison to the enclosed hydrogen facilities that can give the biggest damage. The model was designed based on the test bed created with the same specifications as the low-pressure hydrogen facilities built in Ulsan, Korea. Until now, existing EVP studies attempted to prove how well their models fit with the actual experiments. However, those studies did not show the level of damage caused by overpressure. So, this study aims to provide a concrete numerical value of the damage caused by the explosion and to express damaging levels this value can cause. First, the size, number, and location of the EVP are selected to find the optimal placement. Second, scenarios are chosen according to the Korea Occupational Safety and Health Agency(KOSHA) guide. They are then, simulated based on the first criterion. Lastly, the installation distance of the blast wall is suggested in consideration of the damage to the surrounding facilities. As a result, with the frequently occurring accident case, the measured overpressure in the EVP applied case was 35% lower than that of the enclosed hydrogen facilities. In addition, the pressure measured less than 0.069 barg, a safely considered measure in all methods applied in the first criterion, proving the installation of the EVP as an effective solution. However, in the worst case, even with the installation of the EVP, the overpressure over the 0.069 barg was measured up to a 5m radius to the low-pressure hydrogen facilities. Therefore, it was confirmed that installation of blast wall was necessary as a mitigation plan. In conclusion, with the occurrence of hydrogen explosion, EVP applied resulted in lower overpressure than that of the enclosed hydrogen facilities. This study provides concrete numerical values for both the overpressure and the damage distance caused by the explosion. It also suggests an alternative to minimizing the damage, which is expected to be important reference when applying EVP and building a blast wall in various hydrogen related facilities.

Keywords: CFD, Explosion venting panel, Explosion, Blast wall

1. Introduction

Hydrogen is a clean energy and a new approach to answering the environmental pollution from the consumption of fossil fuel, but hydrogen working systems have potential safety problems (Yong Cao et al. 2017). Hydrogen has large laminar burning velocity (up to 3.50 m/s in NTP air) and wide flammability (4~75%). These properties may lead to hydrogen explosions which will give severe damages (D. Makarov et al. 2009). Therefore, it is important to take measures against the possibility of an explosion. Explosion venting panel(EVP) is the cheapest and most practical explosion mitigation method for the enclosure by discharging the overpressure of burned and unburned gas (Jingde Li et al. 2017). Many studies have been extensively conducted to figure out mechanism and phenomena of explosion. Qi bao et al. (2006) performed lots of experiments to investigate the generation mechanisms of the dominant overpressure transients. C. Regis Bauwens et al. (2009) suggested a simple model that agrees with experimental data based on the ignition location, obstacles, and vent size. E. Vyazmina (2016) approached numerically using CFD programs to validate experiments related to the explosion when EVP applied. Through those researches, EVP design standards like EN-14994 (2007), NFPA-68 (2013) were established and adopted (Jingde Li et al. 2017). However, studies have been focused on the validation process between their model and experiment data. Therefore, not many studies on the effect of EVP compared to the enclosed hydrogen facilities have been carried out.

In this work, explosion simulations are performed to find the optimal EVP systems according to the selected scenarios while changing the ignition position, EVP area, and size. In addition, based on the result of the scenario, the blast wall installation is additionally proposed as a mitigation plan to minimize damages to the internal facilities as well as the surrounding area.

2. CFD simulation and scenario decision

2.1. Modelling

A hydrogen town which uses low-pressure (below 0.1bar) hydrogen for its facilities was built at Ulsan, Korea in 2012. By making petrochemical products in a petrochemical industry park, the resulting by-product of hydrogen is produced and transported to the hydrogen town. Amongst several sectors, the fuel cell sector, which produces and supplies electricity to each apartment, is the most important sector that must be managed safely. The model was designed based on the test bed built in the Korea Gas Safety Research Centre to experiment several cases of hydrogen dispersion and explosion. The dimension of the fuel cell sector is 2.6m, 2.8m, and 2.1m in x, y, and z direction, respectively. Inside of the fuel cell sector, there are several components such as fuel cell, pipes, and fans. The schemes of the hydrogen town and the fuel cell sector are shown in Figure 1. In this work,



Figure 1. The hydrogen town and test bed (the fuel cell sector)

all the simulations are carried out by the CFD based software FLACS v10.4. The k-epsilon turbulence model is used, and the SIMPLE pressure correction algorithm is applied to calculate the compressible flows. All the components are illustrated through boxes and cylinders in pre-processor CASD of FLACS.

2.2. Scenarios decision

The scenarios are chosen based on the Korea Occupational Safety and Health Agency (KOSHA) guide. It is important to choose applicable scenarios since we are not able to conduct every accident case. KOSHA guide suggests the selection of the worst leakage scenario and the arbitrary leakage scenario. The worst leakage scenario is a virtual accident with the longest distance from the end point where the explosion occurred. The end point is the overpressure above 0.069 barg which can cause fatal damage to the human body. In this study, the worst leakage scenario of the 20mm pipe in the fuel cell sector being completely broken is selected because the amount of leakage is the greatest. In the case of the arbitrary leakage scenario, it is defined as a virtual accident that can occur frequently in exception to the worst leakage scenario. The arbitrary leakage scenario is assumed to have a leakage with the gap area of 20% of the 20mm pipe. Therefore, specific scenarios were determined by checking whether the concentration in the fuel cell sector was within the flammability when it leaked for 100 seconds to each corresponding area.

2.3. Case studies

To confirm the effectiveness of the EVP, the area of the EVP, the number of the EVP, and ignition positions were changed in each of the selected scenarios and compared to the enclosed hydrogen facilities using the FLACS v10.4. In terms of the selected scenarios, explosion simulations with different variables including three areas of the EVP ($0.64, 0.81, 1.00 \text{ m}^2$) and three cases of the number is carried out and recorded by 26 monitor points inside and outside of the fuel cell sector. The simulation conditions are shown in Figure 2 and Figure 3. The EVP was opened at 0.002 barg to allow quick opening even at small pressures, and the POPOUT relief panel model was applied in FLACS. Table 1 can be referred to configure the effect of the overpressure from each case on structure and the human body. The effect of the EVP is confirmed by checking the distance of the end point and whether there is a pressure above 0.069 barg in the internal facility or outside. The installation of the blast wall is considered based on the EVP simulation results.

3. Results

3.1. Scenario results

The concentration changes of the fuel cell sector due to leakage and dispersion according to each leakage scenario with time are shown in Table 2. In the worst leakage scenario,

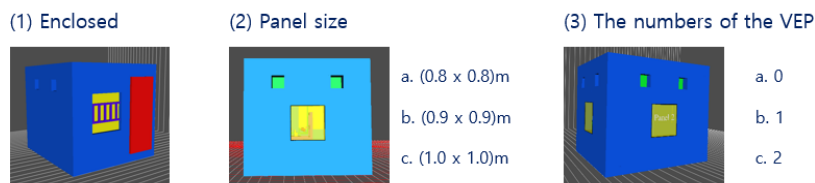


Figure 2. EVP conditions on the fuel cell sector

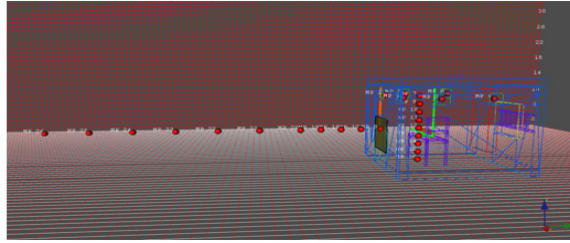


Figure 3. The geometry of the fuel cell sector

Table 1. Effect of the overpressure on structures and the human body

Overpressure (barg)	wind speed (m/s)	Effect on the human body	Effect on structures
0.069	16.987	Light injuries from fragments occur	Window glass shatters
0.138	31.292	People injured by flying glass and debris	Moderate damage to houses (windows and doors blown out and severe damage to roofs)
0.207	45.598	Serious injuries are common, fatalities may occur	Residential structures collapse
0.689	131.429	Most people are killed	Reinforced concrete buildings are severely damaged or demolished
1.379	224.414	Fatalities approach 100%	Heavily built concrete buildings are severely damaged or demolished

there is a total hydrogen flammability distribution change from 4% to 75% within 35 seconds of the leak. In this work, explosion simulation was validated with the experiments conducted by Korea Gas Safety by varying the hydrogen-air mixture(ER0) to determine which concentration has the greatest overpressure (Young-Do Jo et al. 2010). The maximum explosion pressure of hydrogen-air mixture is shown in Figure 4; the value at 31% was selected as the worst leakage scenario result. In the case of an arbitrary leakage scenario, the flammability is first observed at the leakage area with a high concentration as soon as leakage occurs. Then, the entire internal fuel cell sector gains concentration that can cause explosion 17 seconds after the leak. The arbitrary leakage scenarios are selected at both the leakage area and around the fan, as these serve as high chances of an ignition source within the fuel cell sector. Therefore, three scenarios in total were selected and EVP was applied to each scenario.

Table 2. The concentration changes of the fuel cell sector after the leakage

The worst leakage scenario (D=20mm, whole destruction)	Time(s)	0.0	1.0	2.0	5.0	10.0	15.0	20.0	35.0
	Concentration leakage start (%)		4.0	9.0	23.0	38.0	50.0	61.0	75.0
The arbitrary leakage scenario (D=20mm, partial destruction (20%))	Time(s)	0.0	0.1~15.0	17.0	32.0	40.0			
	Concentration leakage start (%)		28.0 (leakage area)	4.0 (Inside)	8.0 (Inside)	10.0 (Inside)			

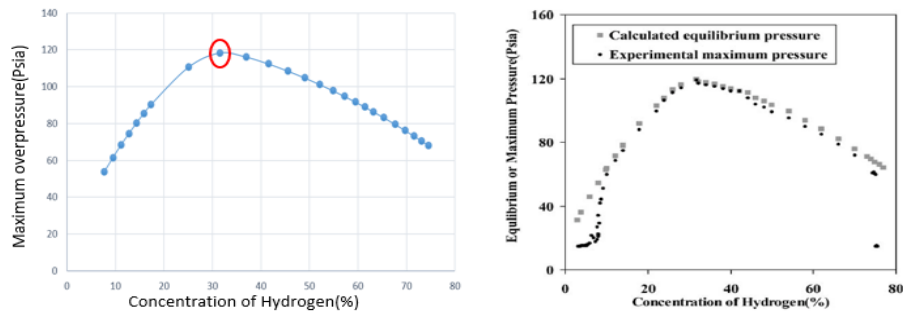


Figure 4. Maximum explosion pressure of hydrogen-air mixture

3.2. Simulation results

As seen from Table 3, EVP simulation conducted under the conditions mentioned in Section 2.3. In the worst leakage scenario, the overpressure is reduced when applied EVP in all cases. However, since the worst leakage scenario causes the greatest damage in all cases, the overpressure is higher than the largest value of the reference table. This can lead to not only the complete destruction of the internal facilities, but also the surrounding facilities as well. Therefore, a blast wall must be installed to minimize damage to surrounding facilities. The effect of the blast wall is shown in Figure 5. Unlike the worst leakage scenario, the overpressure result is significantly reduced to less than the end point pressure of 0.069 barg by installing the EVP in two arbitrary leakage scenarios. As the area of the EVP increases from 0.64 to 1.00, the overpressure gradually decreases. With case of increasing of the EVP number, the overpressure decreases sharply.

Table 3. The overpressure in the worst leakage scenario and the arbitrary leakage scenario

	EVP size (m ²)	The worst leakage scenario		The arbitrary leakage scenario			
				Leakage area		Around Fan	
		H ₂ (%)	Maximum pressure (barg)	H ₂ (%)	Maximum pressure (barg)	H ₂ (%)	Maximum pressure (barg)
(1) Confined	X		7.151		0.279		2.697
	0.64		4.691		0.046		0.042
(2) EVP size	0.81	31.55	4.307	28	0.034	7.73	0.020
	1.00		3.554		0.022		0.013
(3) The number of EVP	0.64 (#2)		2.697		0.013		0.008

4. Conclusion

This research suggests the effect of EVP to minimize damage caused by explosion in a hydrogen facility. Because many validation studies have resulted in the reliability of the simulation results, FLACS v10.4 is used to perform research. Based on the KOSHA guide, the worst leakage scenario and the arbitrary leakage scenario are determined by the actual leakage and dispersion simulation results. The arbitrary leakage scenario shows a significant reduction in overpressure when EVP is installed. However, in the worst leakage scenario, because of the large damage, installation of EVP is hard to reduce damage below the pressure of end point and can cause damage to surrounding facilities. Therefore, a blast wall must be installed. Further research is needed on the installation

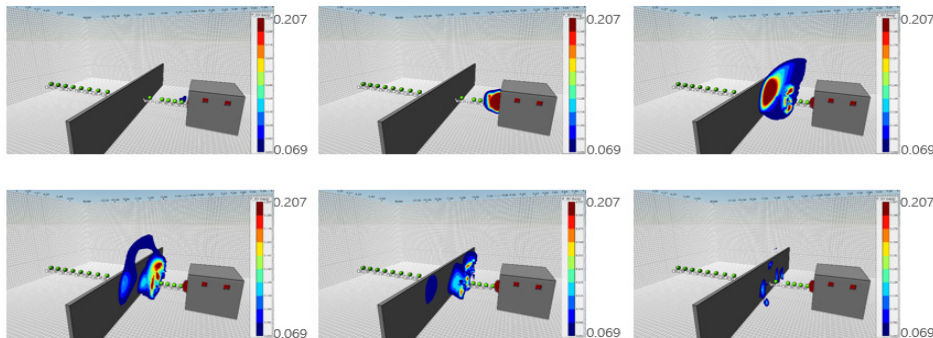


Figure 5. The overpressure changes in the blast wall installed

cost and installation distance of the blast walls. This EVP research provides specific numerical values for the damage distance and overpressure of internal facilities and the surroundings. This study aims to serve as reference to addressing the safety issues related to the overpressure caused by hydrogen explosion at facilities similar in size to the fuel cell sector.

References

- Yong Cao, Jin Guo, Kunlun Hu, Lifeng Xie, Bin Li, 2017, Effect of ignition location on external explosion in hydrogen-air explosion venting, *International journal of hydrogen energy*, 42, 10547-10554.
- D. Makarov, F. Verbecke, V. Molokov, O. Roe, M. Skotenne, A. Kotchourko, A. Lelyakin, J. Yanez, O. Hansen, P. Middha, S. Ledin, D. Baraldi, M. Heitsch, A. Efimenko, A. Gavrikov, 2009, An inter-comparison exercise on CFD model capabilities to predict a hydrogen explosion in a simulated vehicle refuelling environment, *International journal of hydrogen energy*, 34, 2800-2814.
- Jingde Li, Francisco Hernandez, Hong Hao, Qin Fang, Hengbo Xiang, Zhan Li, Xihong Zhang, Li Chen, 2017, Vented Methane-air Explosion Overpressure Calculation-A simplified approach based on CFD, *Process safety and environmental protection*, 109, 489-508
- Qi Bao, Qin Fang, Yadong Zhang, Li Chen, Shigang Yang, Zhan Li, 2016, Effects of gas concentration and venting pressure on overpressure transients during vented explosion of methane-air mixtures, *Fuel*, 175, 40-48
- C. Regis Bauwens, Jeff Chaffee, Sergey Dorofeev, 2010, Effect of Ignition Location, Vent Size, and Obstacles on Vented Explosion Overpressures in Propane-Air Mixtures, *Combustion Science and Technology*, 182, 1915-1932
- E. Vyazmina, S. Jallais, 2016, Validation and recommendations for FLACS CFD and engineering approaches to model hydrogen vented explosions: Effects of concentration, obstruction vent area and ignition position, *International journal of hydrogen energy*, 41, 15101-15109
- E. Papanikolaou, A.G. Venetsanos, G.M. Cerchiara, M. Carcassi, N. Markatos, 2011, CFD simulations on small hydrogen release inside ventilated facility and assessment of ventilation efficiency, *International journal of hydrogen energy*, 36, 2597-605.
- Zipf, R., Cashdollar, K. Effects of blast pressure on structures and the human body. Atlanta: The National Institute for Occupational Safety and Health, 2005.
- Young-Do Jo, Daniel A. Crawl, 2010, Explosion Characteristics of Hydrogen-Air Mixtures in a Spherical Vessel, *Process safety progress*, 29, 216-223

Control of the Steady-State Gradient of an Ammonia Reactor using Transient Measurements

Harro Bonnowitz^a, Julian Straus^b, Dinesh Krishnamoorthy^b, Esmail Jahanshahi^b
and Sigurd Skogestad^{b*}

^a*Department of Chemistry, Technische Universität Berlin, Berlin, Germany*

^b*Department of Chemical Engineering, Norwegian University of Science and Technology, Trondheim, Norway*
sigurd.skogestad@ntnu.no

Abstract

This paper presents the application of a steady-state real-time optimization strategy using transient measurements to an ammonia synthesis reactor case. We apply a new method for estimating the steady-state gradient of the cost function based on linearizing a dynamic model at the present operating point. The gradient is controlled to zero using a standard feedback controller, for example, a PI-controller. The applied method is able to adjust fast to the new optimal operation in case of disturbances. The advantage compared to standard steady-state real-time optimization is that it reaches the optimum much faster and without the need to wait for steady-state to update the model. It is significantly faster than classical extremum-seeking control and does not require the measurement of the cost function and additional process excitation. Compared to self-optimizing control, it allows the process to achieve the true optimum.

Keywords: Optimal Control, Extremum-Seeking Control, Reactor Control, Measurement Based Optimization

1. Introduction

The general aim of a process plant is to operate at the economic optimum. Different approaches are available in the literature for driving a process to its optimal operation point. The traditional approach is steady-state real-time optimization (RTO) in which a rigorous steady-state model is used for computing optimal setpoints. The necessary model reconciliation requires however that the plant is at steady-state before each reoptimization. This is a fundamental limitation of RTO as it may lead to suboptimal operation most of the time (Darby et al., 2011).

Self-optimizing control (SOC) (Skogestad, 2000) alleviates this problem through keeping the operation close to the optimum at all times by controlling selected controlled variable at a constant setpoint. Therefore, it can be used for close to optimal operation while waiting for the steady-state. The implementation is very fast and simple, but in case of unknown or large disturbances, the setpoints need to be updated using some other approach.

An alternative to RTO is a data-based approach, e.g. extremum-seeking control (ESC), which uses the plant measurements to drive the process to its optimal operation (Krstić and Wang, 2000). This is achieved by estimating the steady-state gradient from the input to the cost and using a small I-controller to drive the gradient to zero. Closely related approaches are the “hill-climbing” controller of Shinsky used recently by Kumar and Kaistha (2014) and the NCO-tracking approach

of Bonvin and coauthors (Franois et al., 2005). Their main advantage is that they are model free. The main challenge in these methods is the accurate estimation of the steady-state gradient from dynamic measurements. This normally requires constant excitations that are slow enough such that the dynamic system can be approximated as a static map (Krstić and Wang, 2000). As a result the convergence to the optimum is usually very slow. In the presence of abrupt disturbances, extremum-seeking control also causes unwanted deviations as discussed by Kumar and Kaistha (2014) and Krishnamoorthy et al. (2016).

A newer method for optimal operation is economic nonlinear model predictive control (E-NMPC), which handles the dynamic process behaviour, operational constraints, and leads to the optimal inputs for multivariable processes. Nevertheless, solving the optimization problem for a large-scale problem is computationally intensive and can potentially lead to computational delay.

In this paper, a new model-based dynamic gradient estimation (Krishnamoorthy et al., 2018, in preparation) is applied to drive the process to optimal operation. In contrast to standard ESC, the exact steady-state gradients is estimated based on the dynamic model of the process and hence no excitations are required. For the proposed method there is no need to measure the cost directly. Moreover, reoptimization is done by feedback control and solving the optimization problem is not necessary.

Heat-integrated processes, like the ammonia synthesis reactor (Morud and Skogestad, 1998) considered in this paper, are widespread in case of exothermic reactions to utilize the reaction heat. However, limit-cycle behaviour and reaction extinction may occur in the case of disturbances due to the positive feedback imposed through the heat integration (Morud and Skogestad, 1998). Straus and Skogestad (2017) proposed the application of E-NMPC for optimal control of the ammonia reactor to avoid this behaviour. In this paper, the application of the new feedback method is suggested to drive this process to optimal operation without the need of nonlinear dynamic optimization as is the case with E-NMPC or dynamic RTO.

2. Steady-state gradient control using transient measurements

We consider a process that can be modelled as a nonlinear dynamic system of the form

$$\dot{\mathbf{x}} = \mathbf{f}(\mathbf{x}, \mathbf{u}, \mathbf{d}) \quad (1)$$

$$\mathbf{y} = \mathbf{h}_y(\mathbf{x}, \mathbf{u}) \quad (2)$$

where $\mathbf{x} \in \mathbb{R}^{n_x}$, $\mathbf{u} \in \mathbb{R}^{n_u}$, $\mathbf{d} \in \mathbb{R}^{n_d}$, and $\mathbf{y} \in \mathbb{R}^{n_y}$ are the states, available control inputs, disturbances, and measurements. The cost does not need to be directly measured. In the proposed method, a state estimator such as an extended Kalman filter (EKF) (Simon, 2006) is applied to estimate the states \mathbf{x} of the system by using the measurements and the dynamic model, given in Eqs. (1) and (2).

Let the cost be modelled as $J = h_J(\mathbf{x}, \mathbf{u})$ with $h_J : \mathbb{R}^{n_x} \times \mathbb{R}^{n_u} \rightarrow \mathbb{R}$. A local linear state-space model, given by the Eqs. (3) and (4), can be obtained through linearization around the current operation point, as shown by Krishnamoorthy et al. (2018, in preparation).

$$\dot{\mathbf{x}} = \mathbf{A}\mathbf{x} + \mathbf{B}\mathbf{u} \quad (3)$$

$$J = \mathbf{C}\mathbf{x} + \mathbf{D}\mathbf{u} \quad (4)$$

where $\mathbf{A} = \partial\mathbf{f}/\partial\mathbf{x}$, $\mathbf{B} = \partial\mathbf{f}/\partial\mathbf{u}$, $\mathbf{C} = \partial h_J/\partial\mathbf{x}$, and $\mathbf{D} = \partial h_J/\partial\mathbf{u}$. In order to derive the steady state gradient, we set $\dot{\mathbf{x}} = 0$ and can derive in deviation variables

$$\Delta J = (-\mathbf{C}\mathbf{A}^{-1}\mathbf{B} + \mathbf{D})\Delta\mathbf{u} \quad (5)$$

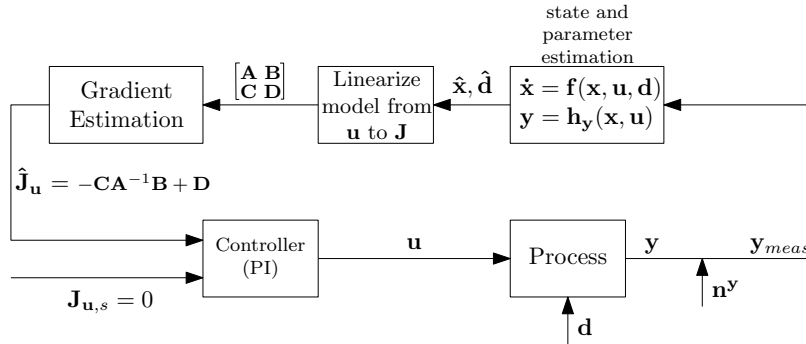


Figure 1: Block diagram of the proposed method.

which, since $\Delta J = \mathbf{J}_u \Delta \mathbf{u}$, gives the following estimate or prediction of the steady-state gradient:

$$\hat{\mathbf{J}}_u = -\mathbf{C}\mathbf{A}^{-1}\mathbf{B} + \mathbf{D} \quad (6)$$

We want to drive the system to an optimal steady-state where $\mathbf{J}_u = 0$, so even if the system is not at steady-state, we can use feedback control with $\mathbf{y} = \hat{\mathbf{J}}_u$ as “measurements” to drive the system to the optimal steady-state and by that satisfying the necessary conditions of optimality (Krishnamoorthy et al., 2018, in preparation). Any feedback controller, such as a PI controller, can be used to bring the gradient to zero. It is important to note that by using a nonlinear state estimator and a dynamic model for estimating the steady-state gradient \mathbf{J}_u , we can use transient measurements, without the need to wait for steady-state, as in traditional RTO. The scheme of the proposed method is shown in Figure 1. The disturbances can be estimated as well through the extension of Eq. (1) to an augmented system (Simon, 2006).

3. Model and problem formulation

The model of the ammonia reactor and all the model assumptions are based on Morud and Skogestad (1998)’s stability analysis. The process, shown in Figure 2, consists of 3 sequential reactor beds and the feed is split into 4 streams. The model is a differential algebraic system, where the differential equations describe the temperature evolution in the reactor beds and the algebraic equations represent the corresponding mass fraction of ammonia. There are 3 split-ratios or $\mathbf{u}_0 = [u_{0,1} \ u_{0,2} \ u_{0,3}]^T$ which are controlled by local temperature controllers. This is necessary for stabilizing the process. The temperature controllers are incorporated into the model in continuous time increasing the number of states by 3. This leads to $\mathbf{u} = [T_{m,1}^{sp} \ T_{m,2}^{sp} \ T_{m,3}^{sp}]^T$. The temperature controllers are modelled as single-input single-output integrator controllers, as the response can be approximated as a proportional process. The SIMC rules (Skogestad and Grimholt, 2012) were applied for the slave controllers tuning.

The state estimation is performed using an EKF (Simon, 2006). To this end, the model was reformulated as a system of ordinary differential equations. Each reactor bed in the model consists of n discrete volumes, which can be modelled as a CSTR cascade. This leads for each reactor bed to a total of $2n$ state variables per time step. For any CSTR reactor j in the CSTR cascade, the differential equations for the ammonia weight fractions $w_{\text{NH}_3,j}$ can be formulated as seen in Eq. (7), in which $\alpha = 0.33$ represents the bed void fraction, $\rho_g = 50 \text{ kg/m}^3$ the density of the gas,

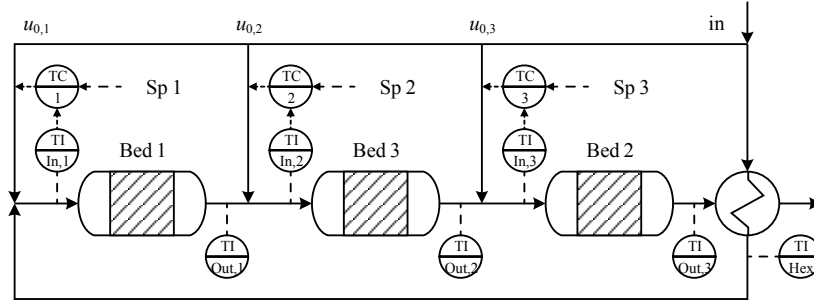


Figure 2: Heat-integrated 3 bed ammonia synthesis reactor with cascade control. The setpoint of the slave temperature loop is given by the proposed method.

and $V_j = V_{bed}/n$ the volume of each CSTR reactor j (Morud, 1995).

$$\frac{dw_{NH_3,j}}{dt} = \frac{\dot{m}_{j-1}w_{NH_3,j-1} - \dot{m}_jw_{NH_3,j} + m_{cat,j}r_{NH_3,j}}{V_j\rho_g\alpha} \quad (7)$$

To summarize, we can write, $\mathbf{x} \in \mathbb{R}^{6n+3}$, $\mathbf{u} \in \mathbb{R}^3$ in the system, given in Eqs. (1) and (2).

In contrast to Straus and Skogestad (2017), full state knowledge is not assumed in this paper. The measurement set for state estimation is given by the inlet and outlet temperature of each reactor as well as the outlet temperature of the heat exchanger (see Figure 2). In real plants the catalyst activity is changing over time, which is difficult or impossible to measure and leads to a plant-model mismatch. To take into account industrial applicability, we assume, that the catalyst activity is not measured, but included in the model as an uncertain parameter. Hence, the states and the uncertain parameter are combined to the augmented states with $d = [a_{cat}]$, what results in an augmented system. To optimize the operation, we want to maximize the (mass) extent of reaction.

$$\xi = \dot{m}_{in}(w_{NH_3,3n} - w_{NH_3,in}) \quad (8)$$

This results in a cost function $J = -\xi$. In this case, a cascade control is used, where the master controllers drive the three gradients to zero by giving new set points to three slave control loops. The EKF and the proposed method were implemented in discrete time. The controller of the proposed method are single-input single-output controllers. The continuous time process model, given in Eq. (1), was modelled using CasADi (Andersson, 2013) and integrated with CVODES, which is part of the SUNDIALS package (Hindmarsh et al., 2005)

4. Results

In the following section, we consider a disturbance in the feed flow and a plant-model mismatch, given by a mismatch in the catalyst activity. In all cases, we have three inner stabilizing temperature loops as indicated by the letter ‘‘T’’ on the plots. In addition, the results are compared to pure self-optimizing control (SOC) and extremum-seeking control (ESC) in the optimization layer. The integrated cost difference (loss) J_{int} is used for comparison of the different methods,

$$J_{int}(t) = \int_0^t [\xi_{opt,SS}(t') - \xi(t')] dt' \quad (9)$$

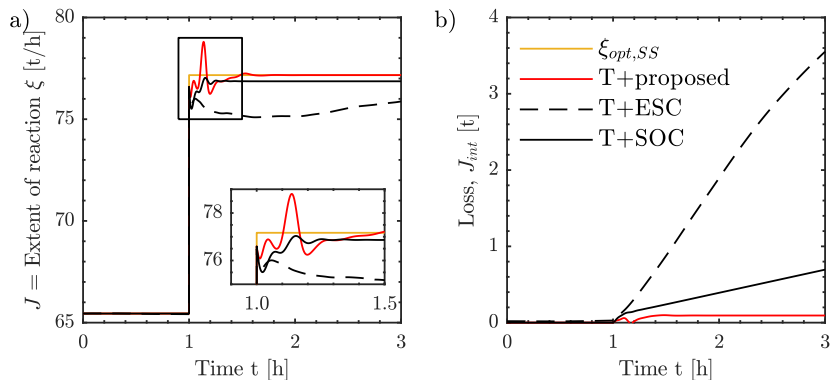


Figure 3: Responses of the alternative methods in a) the extent of reaction and b) the integrated loss to a disturbance in the feed flowrate of $\Delta \dot{m}_{in} = -15$ kg/s at time $t = 1$ h. $\xi_{opt,SS}$ represents the steady-state optimal extent of reaction.

First we simulate a disturbance change in the inlet flowrate \dot{m}_{in} to evaluate the performance of the control structure. The results for a decrease in the feed flowrate of $\Delta \dot{m}_{in} = -15$ kg/s at time $t = 1$ h are presented in Figure 3. The new proposed method gives fast disturbance rejection and settles down at the new optimal operation after about 30 min, as seen Figure 3 a). SOC is equally fast, but it does not quite reach the new optimum. This leads to a continuous increase in the integrated loss for SOC as seen in Figure 3 b). If we compare the proposed method to ESC as optimizing control, the proposed method is much faster and therefore causes a lower integrated cost difference of $J_{int}(t_{end}) = 0.1$ t. This is because the data-based gradient estimation takes longer time for accurate gradient estimation and the controller gain has to be small to satisfy stability. The application of extremum-seeking controllers does not converge to the steady-state optimum in the investigate time frame and requires 13 h.

In the second simulation, we consider plant-model mismatch. The results for a decreased catalyst activity Δa_{cat} by 20 % at time $t = 1$ h, which normally occurs slowly over a longer period of time, are presented in Figure 4. Therefore, the activity of the catalyst, or more specifically the

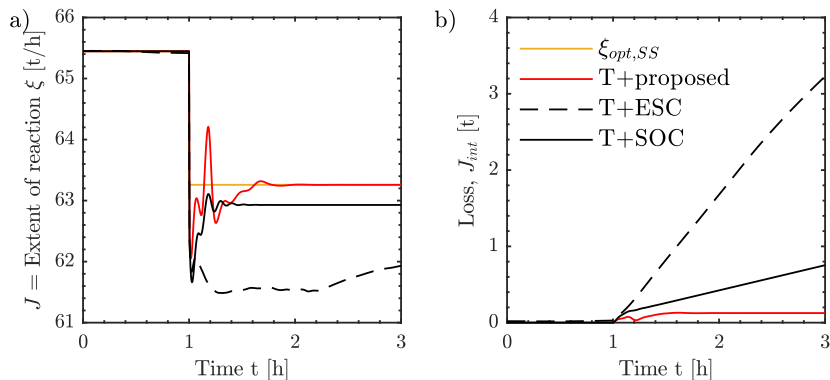


Figure 4: Responses of the alternative methods in a) the extent of reaction and b) the integrated loss to a plant-model mismatch of $\Delta a_{cat} = -20$ % at time $t = 1$ h. $\xi_{opt,SS}$ represents the steady-state optimal extent of reaction.

pre-exponential factor of the Arrhenius equation, spontaneously changes between the model used for the simulations and the model for the state estimation. The simulation shows that the proposed method is performing well even in the presence of a plant-model mismatch. This is because we are able to estimate the real value of the catalyst activity using the augmented EKF framework. About 1.5 minutes after the activity change, the mismatch as well as the states are estimated correctly. The proposed method is much faster than T+ESC, which in turn results in a lower total loss as seen in Figure 4 b). Again, SOC is equally fast, but the real optimum is not reached. The proposed method causes a total integrated cost difference of about $J_{int}(t_{end}) = 0.12$ t of ammonia for the considered case with plant-model mismatch.

5. Conclusion

We have applied a new method of utilizing transient measurements and a dynamic estimator to estimate the steady-state gradient and then using a simple PI controller for driving the process to its optimal operation. For an ammonia synthesis reactor with both disturbances and plant-model mismatch, the proposed method outperforms comparable control strategies. The industrial applicability is conceivable due to the usage of only seven measurements of the process besides the used dynamic model. An extended Kalman filter (EKF) allows the estimation of the steady-state gradients, even in case of plant-model mismatch by including unmeasured but modelled parameters in the estimator.

References

- J. Andersson, October 2013. A General-Purpose Software Framework for Dynamic Optimization. PhD thesis, Arenberg Doctoral School, KU Leuven, Department of Electrical Engineering (ESAT/SCD) and Optimization in Engineering Center, Kasteelpark Arenberg 10, 3001-Heverlee, Belgium.
- M. L. Darby, M. Nikolaou, J. Jones, D. Nicholson, 2011. RTO: An overview and assessment of current practice. *Journal of Process Control* 21 (6), 874 – 884.
- G. Franois, B. Srinivasan, D. Bonvin, 2005. Use of measurements for enforcing the necessary conditions of optimality in the presence of constraints and uncertainty. *Journal of Process Control* 15 (6), 701 – 712.
- A. C. Hindmarsh, P. N. Brown, K. E. Grant, S. L. Lee, R. Serban, D. E. Shumaker, C. S. Woodward, 2005. SUNDIALS: Suite of nonlinear and differential/algebraic equation solvers. *ACM Transactions on Mathematical Software (TOMS)* 31 (3), 363–396.
- D. Krishnamoorthy, E. Jahanshashi, S. Skogestad, 2018, in preparation. A feedback RTO strategy using transient measurements.
- D. Krishnamoorthy, A. Pavlov, Q. Li, 2016. Robust extremum seeking control with application to gas lifted oil wells. *IFAC-PapersOnLine* 49 (13), 205–210.
- M. Krstić, H.-H. Wang, 2000. Stability of extremum seeking feedback for general nonlinear dynamic systems. *Automatica* 36 (4), 595–601.
- V. Kumar, N. Kaistha, 2014. Hill-climbing for plantwide control to economic optimum. *Industrial & Engineering Chemistry Research* 53 (42), 16465–16475.
- J. Morud, Dec. 1995. Studies on the Dynamics and Operation of integrated Plants. PhD thesis, The Norwegian Institute of Technology, Department of Chemical Engineering, NTNU, Trondheim.
- J. C. Morud, S. Skogestad, 1998. Analysis of instability in an industrial ammonia reactor. *AIChE Journal* 44 (4), 888–895.
- D. Simon, 2006. Optimal state estimation: Kalman, H infinity, and nonlinear approaches. John Wiley & Sons.
- S. Skogestad, 2000. Plantwide control: the search for the self-optimizing control structure. *Journal of Process Control* 10 (5), 487 – 507.
- S. Skogestad, C. Grimholt, 2012. *The SIMC Method for Smooth PID Controller Tuning*. Springer London, London, pp. 147–175.
- J. Straus, S. Skogestad, June 2017. Economic NMPC for heat-integrated chemical reactors. In: 2017 21st International Conference on Process Control (PC), pp. 309–314.

A Simultaneous Parameter and State Estimator for Polymerization Process Based on Molecular Weight Distribution

Jiayuan Kang^a, Zhijiang Shao^a, Xi Chen^{a*}, Lorenz T. Biegler^b

^a*State Key Laboratory of Industrial Control Technology, College of Control Science and Engineering, Zhejiang University, Hangzhou, Zhejiang 310027 P.R. China*

^b*Department of Chemical Engineering, Carnegie Mellon University, Pittsburgh, Pennsylvania 15213, United States*
xi_chen@zju.edu.cn

Abstract

Key polymer properties are substantially related to the polymer molecular weight distribution (MWD). Kinetic-based MWD models involves mass balances for all chain types and for all possible chain lengths. These models are predictive and exhibit a large-scale nature. The numerical solution is expensive, especially for on-line optimization in a state/parameter estimator. Thus, MWD monitoring using first-principles models has rarely been studied. In this work, we developed a simultaneous parameter and state estimator for MWD in the framework of moving horizon estimation (MHE). A reduced order model is proposed based on null-space projection method. The reformulated model predicts a MWD profile without calculating all possible chains. The large-scale MWD model is reduced to a manageable number of equations. Then, the MHE framework is designed based on the reformulated model, where the parameters and states are estimated simultaneously. Numerical results show that by introducing MWD as state variables, the prediction accuracy is significantly improved. It is advantageous to introduce the slow measurement of MWD for polymer quality monitoring/control although the different measurement rates need to be coordinated.

Keywords: Reduced model, molecular weight distribution, moving horizon estimation.

1. Introduction

Key polymer properties are substantially related to the polymer molecular weight distribution (MWD) (Soares et al. 2012). On-line monitoring and prediction of dynamic MWD profiles are highly important for quality control of polymerization processes. High-dimensional MWD profiles and time-variant features are hard to describe with data-driven models. The use of first-principles models for on-line monitoring and control has received significant attention in recent years. Modelling MWD based on first principles involves writing the mass balances for all chain types and for all possible chain lengths. However, theoretically this requires simultaneously solving an infinite number of equations. Solving such a large system is challenging and computationally expensive, especially for on-line applications. Thus, MWD monitoring using first principles models has rarely been studied. In the previous work, we developed a fast sensor for dynamic MWD based on rigorous models (Kang et al. 2017). The prediction accuracy is maintained by correcting the model parameters through off-line

measurement. A common problem encounters in the model-based estimators due to the drifting and distortion of the model parameters (Baranwal et al. 2015). Thus, to improve prediction performance of the estimator, parameters need to be estimated simultaneously with the states by introducing on-line measurement.

In polymerization processes, measurements are not available at the same rate. The temperatures or pressures can be measured very quickly, but the polymer quality indices take longer. The common estimators usually use the fast measurements under the assumption that all states of interests are observable from them. However, this assumption does not always hold. López-Negrete and Biegler (2012) developed a moving horizon estimator by introducing slow measurement to improve the prediction quality of average molecular weight (AMW). Given that AMW is derived by MWD measurements, it is worth investigating the estimator based on MWD.

In this work, we developed a simultaneous parameter and state estimator in the framework of moving horizon estimation (MHE). The most challenging problem is that the MWD is a profile measurement and the state variables can be 10000 or more. Therefore, model order reduction is required to reduce the degrees of freedom (DOF) and improve the computational efficiency of the estimator. A reformulated MWD model is proposed based on null-space projection method (Nie et al. 2013). The estimator is designed based on the reduced order model. Numerical results show that by introducing MWD as state variables, prediction accuracy is significantly improved. The slowly measured MWD profile provides much more information, which benefits the performance of the estimator.

2. Dynamic Reduced Order Models for MWD

Population balances are widely accepted in modelling the polymerization process. Mass balances for all chain types and for all possible chain lengths are simultaneously solved and MWD and AMW can be derived based on the molecule fraction of each chain calculated. For most macro quality indices such as AMW, moment method (Mastan et al, 2015) is practical way to reduce the complexity of population balances. However, the information about individual chains is sacrificed and thus is not able to predict MWD. Though the Flory distribution is applied in many steady state situations, it does not apply for dynamic processes. Population balances are still necessary in most cases.

A simplified butadiene rubber (BR) polymerization process is investigated in this study. The catalyst system is hydrolyzed with complex reactions, and monomer-free sites are generated. The polymer chains grow at the active sites and transfer to the ethylene monomer. The mechanism can be very complex, but here only the fundamental polymerization kinetics are modelled. By assuming that the polymerization happens in a CSTR, the following population balances are derived:

$$\frac{dP_0(j)}{dt} = r_a(j) - k_p(j)MP_0(j) + k_{iM}(j)M \sum_{r=1}^{N_r} P_r(j) - k_d(j)P_0(j) \quad (1a)$$

$$\frac{dP_r(j)}{dt} = -k_p(j)M(P_r(j) - P_{r-1}(j)) - k_{iM}(j)MP_r(j) \quad (1b)$$

$$\frac{dD_r(j)}{dt} = k_{iM}(j)MP_r(j) \quad (1c)$$

$$\frac{dM}{dt} = - \sum_{j=1}^{N_s} \sum_{r=0}^{N_r} (k_p(j) + k_{iM}(j))MP_r(j) \quad (1d)$$

where $P_0(j)$, $P_r(j)$, $D_r(j)$ and M represent the concentration of active sites, living chains with length r , dead chains with length r and monomer, respectively; $j \in \{1, 2, \dots, N_s\}$ is the active sites type and N_s is supposed to 2; N_T is the maximum length of chains considered, which could be 100000 or more. The catalyst hydrolysis reaction is not included because the moisture content of water is unmeasurable in the plant. Consequently, the kinetic parameters of the hydrolysis reaction are hard to estimate. We simplify this reaction to a source term of $P_0(j)$, denoted as $r_a(j)$ in Eq. (1a).

The dynamic MWD is calculated by

$$w_r(t) = \sum_{j=1}^{N_s} (P_r(j) + D_r(j)) / \sum_{r=0}^{N_T} \sum_i^{N_s} (P_r(j) + D_r(j)) \quad (2)$$

Eq. (1)(2) contain $2N_T N_s + N_s + 1$ differential equations and N_T algebraic equations. This model exhibits a large-scale nature. Although the dynamic MWD can be calculated by accumulating the instantaneous distribution in short time intervals (see Soares et al. 2012). It is not applied for the estimators because of its nested calculation nature. To overcome these computational difficulties, a reduced order model is presented.

In polymerization processes, the propagation rates k_p are significantly higher than the other rates. Consequently, the living and dead polymer chains represent quite different behaviours. The living polymer chains are fast consuming, and the life time is in the order of seconds. The dead polymer chains are slowly cumulative, and the life time can be as long as the resistance time of the reactor. Eq. (1)(2) result in a two-time scale model and incur numerical calculation issues.

Null-space projection method (Nie et al. 2012) is a systematic reformulation procedure of reaction equation systems. The fast and slow reactions are separated after a sequence of matrix operations. By employing this method, mass balance of the monomer-free sites in Eq. (1a) can be reformulated as:

$$\frac{dP_0(j)}{dt} = r_a(j) - k_d(j)P_0(j) \quad (3a)$$

The fast reactions are sketched by two equilibrium equations:

$$k_p(j)MP_0(j) - k_{iM}(j)MY(j) = 0 \quad (3b)$$

$$-k_p(j)M(P_r(j) - P_{r-1}(j)) - k_{iM}(j)MP_r(j) = 0 \quad (3c)$$

where $Y(j) = \sum_{r=1}^{N_T} P_r(j)$ is introduced as a pseudo component.

By further substitution of Eq. (3b)(3c), the decomposition of coupling living chain lengths is accomplished:

$$P_r(j) = \left(\frac{k_p(j)}{k_p(j) + k_{iM}(j)} \right)^r P_0(j) \quad (3d)$$

The population balances of slow reactions remain, i.e., (1c)(1d).

The dynamic MWD is calculated by adding another differential equation:

$$\frac{dC}{dt} = \sum_{j=1}^{N_s} (k_p(j) + k_{iM}(j))MY(j) \quad (4a)$$

$$w_r(t) = \sum_{j=1}^{N_s} (P_r(j) + D_r(j)) / C \quad (4b)$$

By combining Eq. (1c)(1d), (3a)(3b)(3d) and (4), a chain decoupling model is obtained. This model provides the property of sampling in large chain intervals instead of all the chains. The reformulated model can figure out a MWD profile using $\delta N_T N_s + N_s + 2$

differential equations and $\delta N_T N_s + \delta N_T + N_s$ algebraic equations, where the sampling chains δN_T can be less than 100 but N_T can be 100000 or more.

3. Moving Horizon Estimation Based on MWD

Moving horizon estimation is an efficient strategy for constrained state estimation in nonlinear systems. The basic idea of MHE is to estimate the state trajectory using only the past N measurements, where N is referred to the length of horizon window. A nonlinear programming (NLP) problem is formulated at each sample time where a batch of past measurements is introduced and the states are estimated simultaneously. The horizon window allows incorporation of both frequent and infrequent measurements where the slow ones can be introduced as they are available.

The MHE formulation is shown as

$$\min_{z_{l-N}} \|z_{l-N} - \bar{z}_{l-N}\|^2 W_z + \sum_{l=0}^N \|y_l - \bar{y}_{l+k-N}\|^2 W_y \quad (5a)$$

$$\text{s.t. } z_{l+1} = f(z_l, u_l) + w_l \quad (5b)$$

$$y_l = h(z_l) + v_l \quad (5c)$$

where the process is assumed to be modelled by Eq. (5b)(5c), z_l is the vector of states, u_l is the vector of inputs, y_l is the vector of measurements, w_l is the vector of unknown disturbances, and v_l is the vector of measurement noise. The noise variables are assumed to be independent of states and $w_l \sim N(0, Q_l)$ and $v_l \sim N(0, R_l)$. W_z , W_y represent the inverse of the covariance matrices of the prior state estimates \bar{z}_{l-N} and measurement \bar{y}_{l+k-N} , respectively. The state vector in Eq. 5. is denoted as $z_l = [x_l, p_l]$, where x_l are the reactant concentrations, and p_l are kinetic parameters and $r_a(j)$. It is also assumed the bounds and constraints of states can be further added in the NLP formulation.

The determination of states that can be estimated depends on how much information is contained in the measurement. MWD is a profile measurement and has much more information than other scalar measurements such as AMW and monomer concentration. The reduced order model avoids calculating all the chains and allows estimating the MWD states $D_i(j)$ directly.

4. Results & Discussion

4.1. Model validation

The proposed dynamic MWD model is validated in a simulation of grade transition. The conventional method is compared for predictive consistence and computational efficiency. The reduced order model allows sampling in large chain intervals. In this case, the chain lengths are sampled evenly in logarithm scale with $\delta N_T = 40$. Fig. 1. shows the MWDs predicted by the reduced model and cumulative Flory method. The MWDs predicted by the two methods overlapped. The reduced order model predicted the same results using 40 chains rather than 50000 chains in cumulative Flory method.

The computational efficiency is also investigated. The cumulative Flory method cannot deal with the large-scale population balances, and a moment model is used instead. This approach spends most computational efforts in cumulate the instantaneous distributions. The total time cost is 78.3 s. However, the reduced order model uses manageable number of population balances to predict the dynamic MWD with time cost of 8.7 s. Over 90% time cost is saved. Moreover, the model scale is significantly smaller which can be implemented in a state estimator.

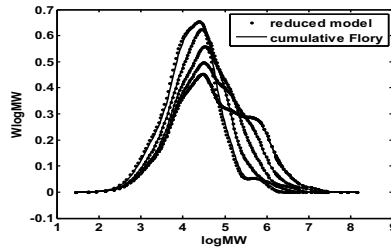


Fig. 1. Dynamic MWDs along time

4.2. Estimation case study

In this section, the reduced order model (i.e. Eq. (1c)(1d), (3a)(3b)(3d) and (4)) is used to estimate dynamic MWD of the BR process. We assume that the fast measurements are given by the monomer concentrations which can be measured by a refractometer. The MWDs are measured slowly through GPC. We also assume that the monomer concentrations are sampled every 10 min while the MWDs are sampled every 30 min. The horizon is set as 60 min. The unknown catalyst term $r_a(j)$ is chosen as model parameters p_l to be estimated. It is also assumed that $r_a(j)$ can be formulated as a random walk, i.e., $p_{l+1} = p_l + w_k^p$, where w_k^p is a Gaussian noise associated with p_l .

Three estimation schemes are designed for comparison as shown in Table 1. The difference lies in what kind of slow measurement is used. MHE-M only uses fast measurement but MMHE-MW and MMHE-MWD introduce slow measurement of AMW and MWD, respectively. The information contained in the measurements determines how many DOF of z_{l-N} in Eq. (5a) can be introduced.

Table 1. Three estimation schemes

Estimator scheme	Fast measurement	Slow measurement	DOF of z_{l-N}
MHE-M	Monomer concentration	-	$r_a(j)$
MMHE-MW	Monomer concentration	AMW	M, $r_a(j)$
MMHE-MWD	Monomer concentration	MWD	M, $D_r(j), r_a(j)$

Fig. 2. shows the comparison between some of the estimated states using the three estimation schemes, with respect to the real values. Fig. 2(a). shows the estimated AMW. MHE-M predicts AMW by correcting the catalyst hydrolysis parameters. The trend of the dynamics is captured but visible error exists between the estimated and real AMW. By introducing slow measurement of the polymer quality indices (AMW or MWD), the prediction error of AMW is significantly reduced. In other words, the observability is improved in MMHE-AMW and MMHE-MWD. The performance of MWD prediction is characterized by the sum square error (SSE) to the real MWD profile. Fig. 2(b). shows the benefit by introducing the full MWD profile as state

variables. The MMHE-MWD achieves the best prediction accuracy. The SSE of estimated MWD using MMHE-MWD is about 50% less than that of MHE-M and MMHE-MW. Besides, the estimation results of MMHE-MWD converges faster than the others. The slow measurement of MWD profile provides much more information which benefits the estimability of parameters and observability of states.

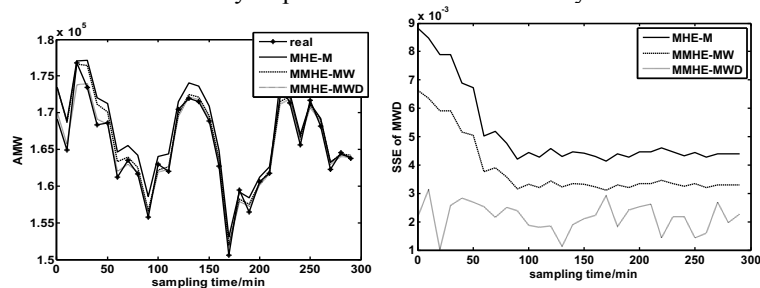


Fig. 2. (a) estimated AMW (b) SSE of estimated MWD

5. Conclusions

In this paper, we proposed a simultaneous parameter and state estimator for MWD in the MHE framework. It is challenging to estimate the MWDs directly due to the large-scale nature of the MWD model. To overcome this issue, a reformulated MWD model is proposed based on null-space projection method. The large-scale MWD model is reduced to a manageable one without essentially affects the predictive performance. The estimator is designed based on the reduced order model. The numerical results show that by introducing MWD as state variables, the prediction accuracy is significantly improved. The slow measurement of MWD profile provides much more information which benefits the performance of the estimator.

Acknowledgements

The authors gratefully acknowledge the financial support of the National Key Research and Development Program of China (No. 2017YFE0106700) and the NSFC-Zhejiang Joint Fund for the Integration of Industrialization and Informatization (No. U1509209).

References

- Y. Baranwal, P. Ballal, M. Bhushan, 2015, Modified minimum variance approach for state and unknown input estimation, *Computer-Aided Chemical Engineering*, 37, 1553-1558.
- J. Kang, Z. Shao, X. Chen, X. Gu, L. Feng, 2017, Fast and reliable computational strategy for developing a rigorous model-driven soft sensor of dynamic molecular weight distribution, *Journal of Process Control*, 56, 79-99.
- R. López-Negrete, L. T. Biegler, 2012, A moving horizon estimator for processes with multi-rate measurements: a nonlinear programming sensitivity approach, *Journal of Process Control*, 22, 677-688.
- E. Mastan, S. Zhu, 2015, Method of moments: a versatile tool for deterministic modeling of polymerization kinetics, *European Polymer Journal*, 68, 139-160.
- Y. Nie, L. T. Biegler, C. M. Villa, J. M. Wassick, 2013, Reactor modeling and recipe optimization of polyol processes: polypropylene glycol, *AIChE Journal*, 59, 2515-2529.
- J. B. P. Soares, T. F. L. McKenna, 2012, *Polyolefin reaction engineering*, Wiley-vch Verlag GmbH & Co. KGaA, Weinheim, Germany, 2012.

Unsupervised Automatic Updating of Classification Models of Fault Diagnosis for Novelty Detection

Mohammad Hamed Ardakani ^a, Ahmed Shokry ^{a,c}, Gerard Escudero ^b, Moisés Graells ^a, Antonio Espuña ^{a*}

a Department of Chemical Engineering, Universitat Politècnica de Catalunya. EEBE, Eduard Maristany, 10-14, 08019 Barcelona, Spain

b Department of Computer Science, Universitat Politècnica de Catalunya. EEBE, Eduard Maristany, 10-14, 08019 Barcelona, Spain

c Department of Mechanical Design and Production Engineering, Faculty of Engineering, Zagazig University, Zagazig, Egypt

Abstract

Novelty Detection (ND) methods are mainly developed to detect novel samples without a clear and general strategy for updating the Fault Detection and Diagnosis (FDD) system. The present study addresses this problem through developing an automatic unsupervised data driven framework for updating FDD systems for the ND purpose. The proposed method is based on the combination of One Class Classifiers (OCCs) that is used to detect samples following novel patterns (i.e. faults), and automatic clustering technique to diagnose them according to novel clusters (i.e. figure out the specific novel fault type). The FDD updating is performed by modifying the existing clusters and detecting new clusters for assembling models in an unsupervised automatic mode. An observer is also incorporated for data processing and enhancing the FDD robustness. The proposed framework is studied and validated via its application to a simulated benchmark case study consisting of three coupled tanks. The results show that the framework can efficiently manage classification models, learn novel clusters, and update FDD system.

Keywords: Updating, Novelty detection, One class classifier, Clustering, Observer

1. Introduction

Supervised FDD approaches are based on the assumption that the available process data could be labeled regarding normal and different faulty conditions (Qin, 2012). On the other hand, unsupervised approaches are usually applied in more realistic situations, when there is no prior information about the fault types in the process.

Clustering is an unsupervised learning method which partitions an unlabeled dataset into subgroups (i.e. clusters) of similar objects based on the knowledge extracted from these data (Das, et al., 2008). Clustering methods can be divided into automatic and non-automatic techniques. For the non-automatic type, the number of clusters must be priori specified for the clustering technique, while in automatic clustering, the optimal number of clusters is determined by the clustering technique without any prior knowledge.

Gama (2010) defines ND as recognizing novel concepts that could refer to the appearance of new concepts, changes in available concepts or presence of the noise in predefined concepts. OCC is a type of algorithm mainly developed for dealing with ND. The OCC algorithm determines the smallest hypersphere enclosing the training samples (Shawe et al., 2004) and next all samples lying outside the hypersphere are classified as

novel/ negative. A particular advantage of the OCC algorithm is that its training requires only positive examples, while other machine learning algorithms need positive and negative samples. One Class Support Vector Machines (OCS) is an applicable algorithm of OCC and there are different kernel types that could be applied with it. The kernel methods compromise between the module that maps the input data from original space to the feature space and a learning algorithm that understands linear patterns in the feature space.

Most of the researches in ND is only concentrated in detecting new classes, but not to the exploitation of these new knowledge. This study presents a data driven FDD framework based on the use of OCC and automatic clustering, allowing both novelty detection and FDD updating in an unsupervised manner. The framework automatically updates the FDD after diagnosing new class(es) by a set of OCCs and unsupervised automatic clustering.

2. Methodology

2.1. Problem definition and proposed framework

The problem consists in periodically updating the classification models to automatically learn changing conditions and new process faults. Consider an initial dataset, X , that is a collection of $s=1,2,\dots,S$ process vector states, which are in turn a set of $i=1,2,\dots,I$ scaler measurements, $X = \{\mathbf{x}_s\} = \{\mathbf{x}_{si}\}$. Assume no simultaneous faults so that this initial dataset X may be automatically clustered into F disjoint subsets by a clustering function, Eq.(1), $C(X, \beta)$:

$$C(X, \beta) \Rightarrow \begin{cases} A_f \subseteq X & \forall f : A_f \cap A_{f \neq f} = \emptyset \wedge |A_f| \geq \beta \\ B = X \setminus A & (A \equiv \cup A_f) \\ \bar{C}(\mathbf{x}_s) = f & \forall \mathbf{x}_s \in A_f \\ \bar{C}(\mathbf{x}_s) = 0 & \forall \mathbf{x}_s \in B \end{cases} \quad (1)$$

Which produces the set of labeled set A , a set of unlabeled samples B , and the function $\bar{C}(\mathbf{x}_s)$ providing the label for each sample \mathbf{x}_s . A cluster threshold parameter (β) needs to be tuned as a minimum size for each cluster, $\beta \leq |A_f|$, and consequently determines the complementary set B . If the true label of each sample $L(\mathbf{x}_s)$ was a priori known, then the Clustering Accuracy (CA) of each subset/cluster can be assessed as Eq. (2).

$$CA_f = \sum_{x_s \in A_f} \frac{\neg \{ \bar{C}(x_s), L(x_s) \}}{|A_f|}, \quad \forall f \quad (2)$$

Given the F clusters, supervised classifiers are developed accordingly. In order to set up the OCCs, each cluster is randomly divided into two disjoint subsets including training, A_f^t , and validation subset, A_f^v , Eq. (3):

$$A_f^t \cup A_f^v = A_f, \quad A_f^t \cap A_f^v = \emptyset \quad \text{being} \quad |A_f^t| = \alpha |A_f| \quad \text{and} \quad |A_f^v| = (1 - \alpha) |A_f| \quad (3)$$

In which α needs to be selected. The prediction of each OCC for each sample, $h_f(\mathbf{x}_s)$ is set to meet the conditions in Eq. (4):

$$h_f(\mathbf{x}_s) = \begin{cases} 1 & \text{if } \mathbf{x}_s \in A_f \\ 0 & \text{if } \mathbf{x}_s \notin A_f \end{cases}, \forall \mathbf{x}_s \quad (4)$$

The Individual Prediction Performance (IPP) of each OCC could be estimated for new dataset $X^* = \{\mathbf{x}_{s^*}\}$ using Eq. (5):

$$IPP_f = \sum_{\mathbf{x}_{s^*} \in X^*} \frac{\neg \vee \{h_f(\mathbf{x}_{s^*}), L(\mathbf{x}_{s^*})\}}{|X^*|} \quad \forall f \quad (5)$$

The assumption of no simultaneous faults allows defining a net prediction given by the whole set of OCCs for each new sample $H(\mathbf{x}_{s^*})$, which also allows assigning the new sample to the A or B subsets; this is given by Eq. (6)

$$H(\mathbf{x}_{s^*}) = \begin{cases} f & \text{if } \neg \vee \{h_f(\mathbf{x}_{s^*}), \forall f \in F\} \wedge h_f(\mathbf{x}_{s^*}) \\ 0 & \text{otherwise } \left(\neg \vee \{h_f(\mathbf{x}_{s^*}), \forall f \in F\} \right) \end{cases} \quad (6)$$

Finally, the Net Prediction Performance (NPP) for dataset X^* can be calculated based on Eq. (7):

$$NPP = \sum_{\mathbf{x}_{s^*} \in X^*} \frac{\neg \vee \{H(\mathbf{x}_{s^*}), L(\mathbf{x}_{s^*})\}}{|X^*|} \quad (7)$$

The implementation of this scheme is done with the framework proposed in this study, Figure (1) and Figure (2), that has two main modules:

- The Offline Model Updating (OMU) module, Figure (2) , and
- The Online Monitoring (OM) module, Figure (3).

The initial dataset, X , must be processed by the OMU module in order to determine the cluster dataset(A), the classification models (OCCs), the Updating Threshold (UT) value, and the unlabeled dataset, B . UT is minimum number of samples in B^* for calling OMU, based on Figure (2), and B^* is the unlabeled dataset for online samples. UT is successively updated by the summation of the Updating Threshold Parameter (UTP) and the number of samples in the current dataset B ($UT \leftarrow UTP + |B|$).

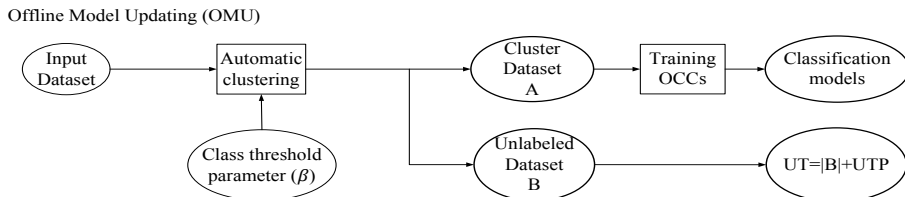


Figure 1. Proposed framework: OMU module.

UTP is a parameter that must be tuned, experimentally. In the OM module, Figure (2), the online samples are initially processed by observer and then are classified by set of OCCs, Eq. (6). The online samples that are diagnosed as elements of subsets A_f are discarded, while those that do not clearly belong to any of the subsets are kept and assigned to the unlabeled dataset for online samples B^* . After adding each sample to the unlabeled dataset, B^* , in online monitoring module, a condition must be checked: “Do number of samples in unlabeled dataset, B^* , meet the UT?”

Furthermore, for practical implementation another condition must be checked: “it is not updating?” that implies OMU is on progressing or not. If answers of both conditions are “Yes” then OMU will be triggered by online monitoring module. In this case, the inlet dataset of the OMU X^* is the total of B^* and clusters datasets A , Figure (2).

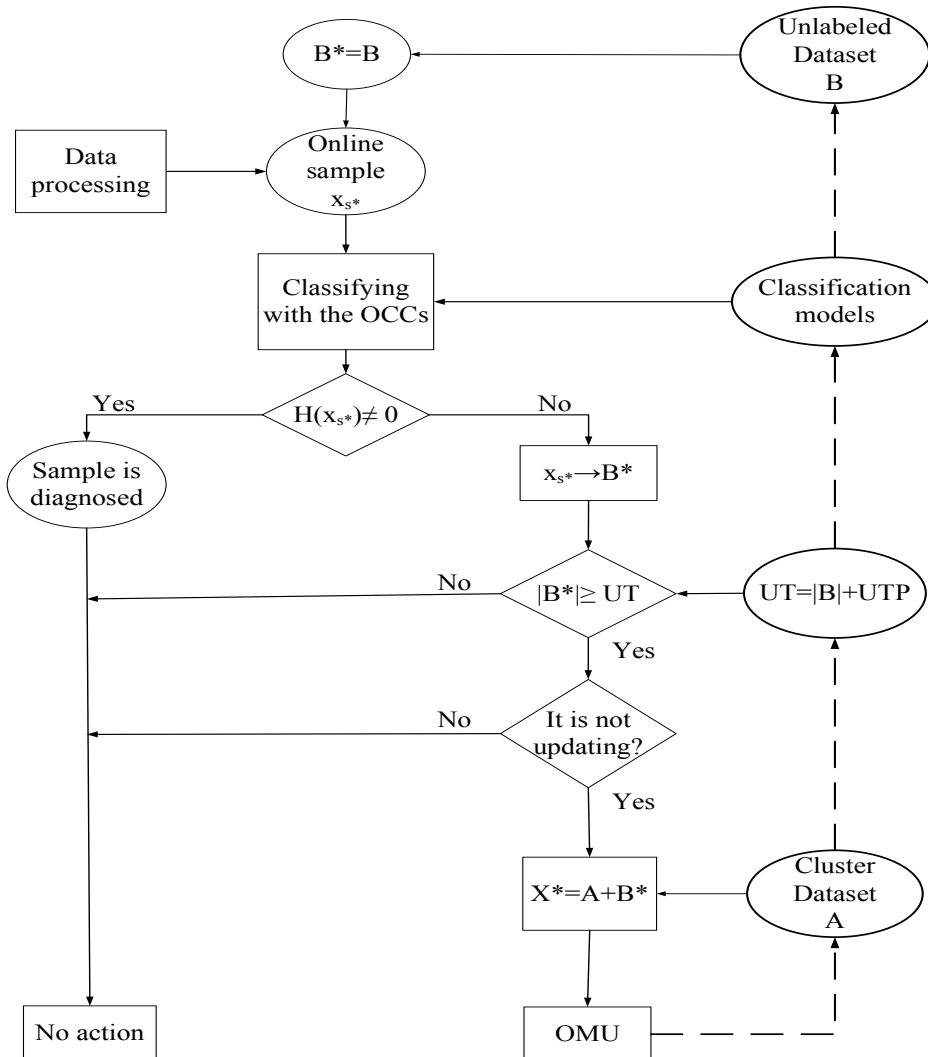


Figure 2. Proposed framework: OM module.

3. Case Study

A benchmark case study (Patton, et al., 1994) is used to validated the proposed framework. The system consists of three interconnected tanks, which are supplied with liquid by two pumps with flowrates $Q_1(t)$ and $Q_2(t)$. The tank levels $h_1(t)$, $h_2(t)$ and $h_3(t)$ are considered as the measured variables with sampling period each second. In addition to Normal (Nr) condition, the process is subjected to three faults: Fault 1 (F1) is the leaking in tank 1, Fault 2 (F2) is the plugging in tank 2 and Fault 3 (F3) is the leaking in tank 3. Both of the inlet flowrates are steady at magnitudes of $Q_1(t)=3 \times 10^{-3} (m^3/s)$ and $Q_2(t)=2.5 \times 10^{-3} (m^3/s)$. The Leaking and plugging flowrates are set to be between 10% and 25% of the inlet flow. Gaussian errors are introduced to the measured variables representing the sensors noise, for more details about the case setting see (Shokry, et al., 2016). Figure (3) presents the considered fault pattern influencing the process, where it is assumed that in the initial dataset X , there are two clusters including Nr and F1. During the 1000 seconds two new faults (F2 and F3) appear, while during the four time intervals (separated by dashed vertical lines) the fault pattern is switched. In Figure (3), during each time interval, the faults sequence are arranged from top to bottom: as an example, in the first interval, the normal condition occurs along the first 100 s. , F2 takes place along the subsequent 50 s. then F1 happens along the following 100 s.

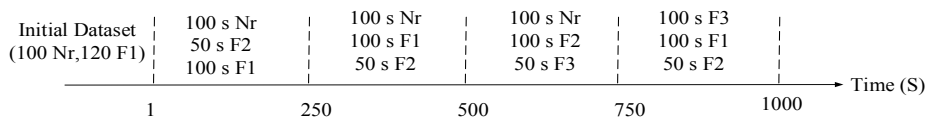


Figure 3. Fault pattern.

4. Application and Results

α , β and UTP are selected, experimentally, to be 0.8, 30 and 80, respectively. For the initial dataset the CA is 99%, while the CPU time is 3.2 second. During 1000 second based on fault pattern two times OMU is called. For the first call of OMU the CA is 95% and CPU time is 15.7 s., while for the second call these amounts are 95.2% and 15.7 s., respectively. In the first 250 seconds NPP is 95.2% and after detecting 80 new samples the first call of OMU starts at 475 s. and also from 491 s. the OCS_F2 is available. The second call of OMU starts at 760 s. and from 776 s. the OCS_F3 starts to monitor the system. Table (1) presents overall IPPs of the classifiers and also overall NPP.

Table 1. Overall IPP and NPP

$1 \leq t \leq 1000 \text{ s}$	Correct	Incorrect	IPP/NPP (%)
OCS Nr	964	36	96.4
OCS_F1	980	20	98.0
OCS_F2	478	31	93.9
OCS_F3	224	0	100.0
H (Net prediction)	931	69	93.1

F3 samples before 776 s. are labeled as B^* and then they are diagnosed as F3. Overall NPP is 93.1%, implying 931 correct predictions. Figure (4) presents overall

performance of the framework. In Figure (4), the thin striped rectangle in front of the F2 from 1 s. till 491 s. indicates during that time interval F2 samples are not diagnosed as defined class. For F3 samples the thin striped rectangle is drawn till 776 s. and after that they are diagnosed as defined class.

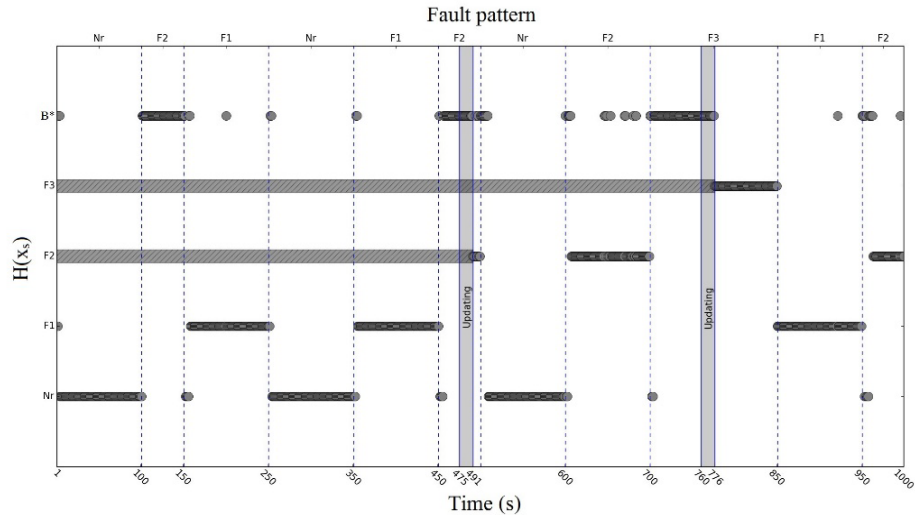


Figure 4. Performance of the framework.

5. Conclusions

In the present study a framework for unsupervised automatic updating of data driven FDD is addressed that is based on applying automatic clustering, OCCs and observer. While observer provides the error features for being replaced with the measured features, OCCs do ND and automatic clustering recognizes the new classes. Based on the framework, always the most relevant samples to the current conditions of the system are employed to train and update the FDD. The investigation is done by applying three tank benchmark while 1000 seconds are studied in which two new clusters appear in the system. Reasonable performance and accuracy of different tasks of the framework imply reliability of it.

6. References

- H. Das, S. Abraham, A. Konar, (2008), Automatic Clustering Using an Improved Differential Evolution Algorithm. *IEEE Transactions on Systems, Man and Cybernetics-Part A: Systems and Humans*, 38(1), 218–237.
- J.Gama, (2010), *Knowledge discovery from data streams*, CRC Press.
- R. J. Patton, J. Chen, , & Siew, T. M. (1994). Fault Diagnosis in Nonlinear Dynamic Systems via Neural Networks. *Proc. of IEE Int.Conf. on Control*, (389), 1–6.
- S. J. Qin, (2012), Survey on data-driven industrial process monitoring and diagnosis, *Annual Reviews in Control*, 36(2), 220–234.
- J. Shawe-Taylor, N.Cristianini, (2004), *Kernel methods for pattern analysis*, Cambridge university press.
- A.Shokry, M. Ardakani, G. Escudero, M. Graells, A. Espuña, (2016), Kriging based Fault Detection and Diagnosis Approach for Nonlinear Noisy Dynamic Processes. In *Computer Aided Chemical Engineering*, Vol. 38, pp. 55–60.

Development of a fuzzy system for dissolved oxygen control in a recombinant *Escherichia coli* cultivation for heterologous protein expression

Rafael A. Akisue,^a Antonio C. L. Horta,^{a,b} Ruy de Sousa Jr.^{a,b*}

^aGraduate Program in Chemical Engineering, Rod. Washington Luís km 235, São Carlos 13565-905, Brazil

^bFederal University of São Carlos, Rod Washington Luís km 235, São Carlos 13565-905, Brazil

ruy@ufscar.br

Abstract

One very important bioprocess is the cultivation of recombinant *E. coli* for expression of heterologous protein. For this, High Cell Density Cultures is one of the most widely used technique. Therefore, researchers from the Chemical Engineering Department of Federal University of São Carlos (UFSCar) developed a very useful computer program (SUPERSYS_HCDC) that, among other functions, presents a hybrid system with a PID for agitation and a decision tree for air and oxygen flow rates that controls the percentage of dissolved oxygen in the cultivation (nowadays some commercial controllers also offers this cascade control). However, in particular, delays may occur in the device responsible for air and oxygen injection into the bioreactor, since the decision tree provides no smooth responses. The original system presented operates by introducing steps in the air and oxygen flow rates. Under the light of the above-mentioned facts, fuzzy reasoning was used to develop a fuzzy controller, aiming to improve dissolved oxygen control in recombinant *E. coli* cultivation for heterologous protein production. At first, fuzzy logic toolbox was used to generate a control algorithm implemented in a MATLAB code. Secondly, the membership function parameters were optimized using ANFIS tool. Finally, in order to perform tests using the fuzzy controller, it was coupled to a neural network model of the process. This was created using artificial neural network toolbox and *E. coli* cultivation data. Results for oxygen and air flow rates indicated that the trends of aeration required by *E. coli* cultivation were fulfilled. Using the fuzzy controller, it was possible to maintain the percentage of dissolved oxygen around the set point value of 30%. In general, the fuzzy controller responses were smoother than those provided by the decision tree, in a way that the dissolved oxygen peaks were softened.

Keywords: Fuzzy Logic, Dissolved Oxygen, Artificial Neural Network, recombinant *Escherichia coli*, SUPERSYS_HCDC.

1. Introduction

The *Streptococcus pneumoniae* or pneumococcus is an important human pathogen, whose virulence factor is in its polysaccharide capsule. Thus, a capsular polysaccharide (PS) vaccine was created based on the idea that antibodies formed against the PS are effective in immunizing. However, the capsular polysaccharide does not have the capacity of activating T lymphocytes cells, responsible for the immunological memory.

One solution found was the conjugation of the polysaccharide with a protein that enhances the immune response (generating immunological memory).

Well characterized genetics and physiology and a established recombinant DNA technology were determinant factors that made *Escherichia coli* the pioneer organism for recombinant protein production. One of the wildest known technic for *E. coli* culture is the High-Cell-Density Cultivation (HCDC). Within this context, researchers from LaDABio Laboratory at the Chemical Engineering Department of Federal University of São Carlos (DEQ/UFSCar) developed the SUPERSYS_HCDC (Horta et al., 2014). The program in equipped with, among other functions, a hybrid system that aims to control the dissolved oxygen in the cultures. It is composed by a PID controller to manipulate agitation speed and a decision tree to manipulate air and oxygen flow rates. However, in particular, the decision tree does not provide smooth responses, revealing the need of improvements in the automatic control system of air and oxygen flow rates (Horta, 2011). Thus, this work aimed to develop a fuzzy system for dissolved oxygen control in a recombinant *E. coli* cultivation for heterologous protein expression.

2. Literature Review

The SUPERSYS_HCDC was developed in LabView platform and MATLAB code. It has, among its control modules, an automatic hierarchic hybrid module for dissolved oxygen concentration control. In order to meet the high oxygen consumption rates in a HCDC of *E coli*, the dissolved oxygen concentration control was designed using a hybrid system. It was composed by a PID controller (acting directly in the agitation speed) and a heuristic algorithm (modulating air and oxygen flow rates). The code for this heuristic control action consists of a decision tree as it is shown in Figure 1.

```

SCENARIO 1:
  If  $Agit < 0.7 * Agit_{SL}$  and  $QO2_{-1} > 0$ 
     $QAIR = QAIR_{-1} + \Delta$ 
     $QO2 = QO2_{-1} - \Delta$ 

SCENARIO 2:
  If  $Agit \geq 0.99 * Agit_{SL}$  and  $DO < DO_{IL}$ 
    SCENARIO 2a:
      If  $QAIR_{-1} + QO2_{-1} \geq Q_{MAX}$ 
         $QAIR = QAIR_{-1} - \Delta$ 
         $QO2 = QO2_{-1} + \Delta$ 
      SCENARIO 2b:
        If  $QAIR_{-1} + QO2_{-1} < Q_{MAX}$ 
           $QAIR = QAIR_{-1} + \Delta$ 
           $QO2 = QO2_{-1}$ 
  
```

Figure 1: Pseudocode for air and oxygen flow rate control

In Figure 1, $Agit$ and $Agit_{SL}$ are agitation speed and agitation superior limit, $QO2$ and $QAIR$ are oxygen and air flow rates, respectively, Δ is a constant value, DO and DO_{IL} are dissolved oxygen and dissolved oxygen inferior limit and Q_{MAX} is the maximum gas flow rate. The pseudocode is interpreted as it follows: if the agitation speed is low (lower than 70% of the agitation superior limit) in a scenario where oxygen is already being injected in the system, air flow rate should be increased and oxygen enrichment in the system should be decreased. However, if the agitation speed is near its maximum (equal to or higher than 99% of the agitation superior limit) and even so, the dissolved oxygen concentration in the system is low, two options are presented: it is observed if

air and oxygen flow rates sum exceeds the maximum gas flow rate. If yes, then air flow rate should be decreased and oxygen enrichment should be increased. If not, air flow rate should be increased and oxygen enrichment should be maintained. This original system operates by introducing steps in the oxygen and air flow rates (Horta, 2011). Thus, in this work, fuzzy reasoning (Zadeh, 1994) was used to improve it.

3. Methodology

The development of the fuzzy control system, which includes the establishment of the linguistic variables, the membership functions (and its optimum parameters) and the fuzzy rules, was carried out using two powerful computational tools: Fuzzy Inference System (FIS) and the Adaptive Neuro Fuzzy Inference System (ANFIS), both of them available on MATLAB Fuzzy Logic Toolbox.

Initially, three subroutines were created using MATLAB FIS editor. The first, called “Delta” (responsible for analysing the size of the variations in air and oxygen flow rates), and two subroutines called “Princ” (responsible for verifying if there will be an increment or a decrease of delta in air (“Princ1”) and oxygen (“Princ2”) flow rates). Figure 2 shows the input and output linguistic variables of each subroutine along with their respective linguistic values.

Subroutine	Input variable	Linguistic Value	Output variable
“Delta”	QO2ant: Previous Oxygen Flow Rate (L/min)	LP: Low and Positive MP: Medium and Positive HP: High and Positive	Delta
“Princ1”	CX: Microorganism Concentration (g/L)	LP: Low and Positive HP: High and Positive	QarEscolha
	AgitMed: Agitation Speed (rpm)	LP: Low and Positive HP: High and Positive VHP: Very High and Positive	
	DO: Dissolved Oxygen (%)	LP: Low and Positive MP: Medium and Positive HP: High and Positive	
	QarSe: Auxiliary Variable	NO YES	
	Mi: Specific Growth Rate (1/h)	LP: Low and Positive MP: Medium and Positive	
“Princ2”	CX: Microorganism Concentration (g/L)	LP: Low and Positive HP: High and Positive	QO2Escolha
	AgitMed: Agitation Speed (rpm)	LP: Low and Positive HP: High and Positive VHP: Very High and Positive	
	DO: Dissolved Oxygen (%)	LP: Low and Positive MP: Medium and Positive HP: High and Positive	
	QarSe: Auxiliary Variable	NO YES	
	Mi: Specific Growth Rate (1/h)	LP: Low and Positive MP: Medium and Positive	

Figure 2: Input (along with their linguistic values) and output variables of the subroutines

The input variable for “Delta” subroutine is QO2ant. Its output variable is Delta. For both “Princ1” and “Princ2” subroutines, the input variables are: CX, AgitMed, DO, QarSe (which is an auxiliary variable that allows the choice between the IF or IF NOT option in the decision tree, after air and oxygen flow rates sum) and Mi. Their output variables are QarEscolha e QO2Escolha, respectively, that determine whether there will be an increase or a decrease of delta in air or oxygen flow rates (respectively).

FIS editor allows users to define the membership function's shape and parameters. However, when discerning them heuristically by simple data analysis becomes impractical, the Adaptive Neuro Fuzzy Inference System is a valuable asset. It can perform membership function parameters optimization, using a set of functions, in order to build a fuzzy inference system from input and output data available.

For the "Delta" fuzzy inference system, the parameter optimization was performed using MATLAB Gaussian type 2 membership function (gauss2mf) for input variables, as it is shown by Equation 1:

$$f(x, \sigma, c) = e^{-\frac{(x-c)^2}{2\sigma^2}} \quad (1)$$

Gauss2mf is a combination of two sets of parameters. The first one, specified by σ_1 e c_1 , determines the left part of the curve. The second set, specified by σ_2 e c_2 , determines the right part of the curve.

Three fuzzy rules were adjusted for "Delta" by ANFIS tool, one of them exemplified by Equation 2:

$$\text{If } QO2_{ant} \text{ is LP then Delta is } F_1. \quad (2)$$

In which F_1 is a linear function, as it is shown in Equation 3:

$$F_1 = \alpha QO2_{ant} + \beta \quad (3)$$

In which α is the input variable (QO2ant) coefficient and β is the linear coefficient.

For the "Princ" fuzzy inference systems, the parameter optimization was performed using MATLAB Gaussian type 1 membership function (gauss1mf).

72 fuzzy rules were adjusted for both "Princ1" and "Princ2" using ANFIS tool, one of them exemplified by Equation 4:

$$\text{If } CX \text{ is LP and AgitMed is LP and DO is LP and QarSe is NO and Mi is LP then } QarEscolha \text{ is } F_1' \quad (4)$$

In which F_1' is a linear function, as it is shown by Equation 5:

$$F_1' = a \cdot Cx + b \cdot AgitMed + c \cdot DO + d \cdot QarSe + e \cdot Mi + f \quad (5)$$

In which a, b, c, d, and e are CX, AgitMed, DO, QarSe and Mi coefficients respectively, and f is the linear coefficient.

In order to test the fuzzy controller, it was coupled to a neural network model of the process. This was created using MATLAB Artificial Neural Network toolbox and *E. coli* cultivation data. The optimized (by ANFIS) fuzzy controller was coupled with the neural model of the process and with the PID controller for agitation speed. From

previous values of microorganism concentration (CX_{t-1}), dissolved oxygen (DO_{t-1}), Agitation speed ($Agit_{t-1}$), Air (Qar_{t-1}) and oxygen ($QO2_{t-1}$) flow rates and specific growth rate (μ_{t-1}), the fuzzy controller provides the subsequent air and oxygen flow rates. These data are passed on to a first neural network, which estimates the dissolved oxygen percentage. This result is used to update the agitation speed by the PID controller. This new set of data (DO_t , $Agit_t$, Qar_t and $QO2_t$) is passed on to a second neural network in order to assess microorganism concentration (CX_t). This result is used to estimate the specific growth rate (μ_t). For the next step, the simulator feeds back and updates all these values to the fuzzy controller. The flowchart of the simulator is described in Figure 3.

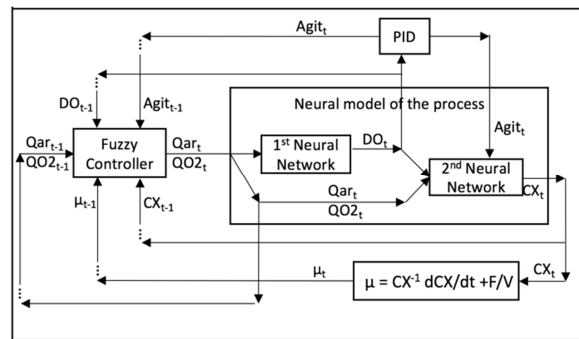


Figure 3: Flowchart of the simulator

For the purpose of this article dynamic neural networks were used, since they are more powerful than the static ones (due to the presence of memory). The neural networks were created using MATLAB Neural Network Time series application. To train the first neural network, a nonlinear input-output problem was selected. Data set was randomly divided by the application for training (70%), validation (15%) and testing (15%). The architecture chosen was one hidden layer (with 15 neurons, 4 delays and a sigmoidal activation function) and one output layer (with one neuron and a linear activation function). To train the second neural network an analogous procedure was adopted. However, in this case, a hidden layer with 4 neurons and 4 delays was employed.

E coli cultivation data sets for heterologous protein production employed in the development (through ANFIS) of the fuzzy controller and in the construction of the neural model of the process were provided by Horta (for details, see Horta, 2011).

4. Results

After parameters optimization by ANFIS and extensive training of several neural networks, the finest simulated results for air and oxygen flow rates are shown in Figures 4A and 4B, respectively. Using the fuzzy controller, it was possible to maintain the dissolved oxygen percentage near its optimum value of 30%, with almost no offset, as it is shown in Figure 4C. The dotted line represents the experimental data controlled using the original decision tree. The continuous line represents the simulated data controlled using the new fuzzy logic system (fuzzy controller).

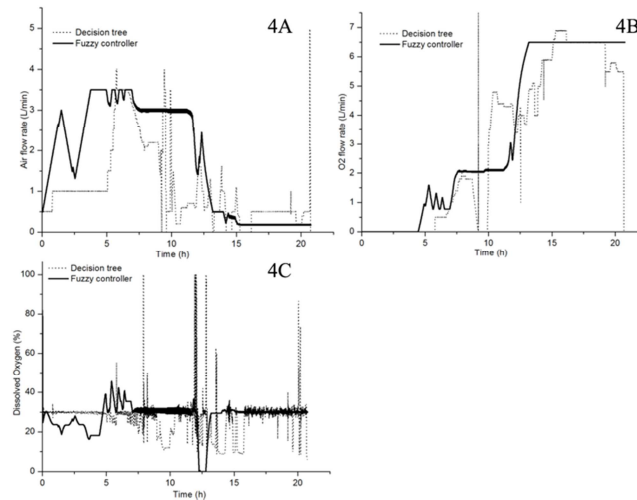


Figure 4: Results of the fuzzy controller using the simulator

The trends in air and oxygen flow rates required by the *E. coli* cultivation for heterologous protein production were followed successfully by the fuzzy controller. In general, the dissolved oxygen peaks were softened, that is, fuzzy controller responses were smoother than those provided by the decision tree. Very important to say that this smoother behaviour leads to an increase in the flow meter's lifetime, given its sensitivity to abrupt oscillations in air and oxygen flow rates.

5. Conclusions

It can be concluded that it was possible to fuzzyfy the existing decision tree/pseudocode for dissolved oxygen control. This new controller provided smoother responses than those provided by the previous one. In general, the dissolved oxygen peaks were softened, that is, the fuzzy controller responses were smoother than those provided by the decision tree. This could lead to a decrease in the metabolic stress suffered by the microorganism and consequently an increase in productivity, given its sensitivity to abrupt oscillations in dissolved oxygen percentage during the cultivation.

References

- A.C.L. Horta, 2011. Sistema automático de supervisão e controle de cultivos de alta densidade celular de *E. coli* recombinante. Doctoral dissertation. Federal University of São Carlos. Brazil.
- A.C.L. Horta, A.J. Silva, C.R. Sargo, A.M. Velez, M.C. Gonzaga, R.C. Giordano, V.M. Gonçalves, T.C. Zangirolami, 2014. A supervision and control tool based on artificial intelligence for high cell density cultivations. *Brazilian Journal of Chemical Engineering*, 31, 457-468.
- L.A. Zadeh, 1994. Fuzzy Logic, Neural Networks, and Soft Computing. *Communications of the ACM*, 37, 77-84.

Acknowledgements

To CNPq, CAPES and FAPESP for the financial support.

Logistics optimization for dispositions and depooling of distillates in oil-refineries: closing the production scheduling and distribution gap

Brenno C. Menezes,^{a,*} Jeffrey D. Kelly,^b Ignacio E. Grossmann^c

^a*Department of Chemical Engineering, University of São Paulo, Av. Prof. Luciano Gualberto trav.3 n.380, São Paulo, SP 05508-010, Brazil*

^b*Industrial Algorithms Ltd., 15 St. Andrew Road, Toronto, ON MIP4C3, Canada*

^c*Department of Chemical Engineering, Carnegie Mellon University, 5000 Forbes Av., Pittsburgh, PA 15213, United States*

brennocm@usp.br

Abstract

At the edge of the manufacturing of crude-oil distillates into refined final products, the production scheduling and distribution gap can be reduced by optimizing production rundown switches of dispositions of distillates in a mixed-integer linear model (MILP) considering discrete time-steps of days, shifts or hours for a delivery horizon of weeks or months. From the process network down to the product distribution side, there are definitions on the assignments and amounts of distillates to be dispatched downstream for further process- and blend-shops considering diverse tank farms and nodes for the distribution. However, such integration of the refining process and tank storage systems can become intractable for industrial-sized problems with complex scheduling configurations considering time-varying rundown supply rates, product demands and pricing. For this, we propose to model the dispositions of distillates using unit-operations as modes of transportation from the distillation sources to the tanks of process-shops and blend-shops for downstream processing and blending before the primary distribution. Additionally, by solving with pooling (groups of tanks) first then post-solve to depool by disaggregating the pooled solution, the determination of the distillate dispositions to tank assignments is facilitated given that scaling to industrial-sized cases without tank aggregation is complicated as highlighted in the examples. Better prediction of the operations scheduling by using small discrete time-steps within a planning horizon allows opportunities for exploring the contract and spot market plays of the finished products.

Keywords: crude-oil distillates, product scheduling, rundown switches, depooling.

1. Introduction

In the process industries with a wide variety of different quality feeds and products, especially in oil-refining and petro-chemicals manufacturing, the high-performance and complex refining of crude-oils into products can be achieved, for example, considering integrated approaches of the following subsystems: a) raw material or feed procurement, shipping, unloading, storage, dieting and charging, b) combined operations of process-

shops and blend-shops, c) management of intermediate and final product inventories, d) sales and distribution of refined products.

From the monthly and weekly procurement planning cycle up to the daily and hourly production scheduling from crude-oils to distilled products or distillates, an enterprise-wide optimization (EWO) strategy can feedback decisions from a lower to an upper level for a new search of a solution, updating lower level results as targets and reducing time-grids in upper level re-optimizations (Menezes et al., 2017). However, there are many challenges to develop such an EWO approach from the scheduling of product to the primary distribution management that typically evolves from time-steps of an hour, shift, day to those found in planning considering weeks, months and quarters.

First, to efficiently maintain the production for downstream process units, tanks or any modes of transport, a wide scheduling optimization shall determine production rundown switches in days, shifts or hours (small-buckets) for a delivery horizon of weeks or months (big-buckets), yielding models with hundreds or thousands of time-periods. Therefore, despite the quality and nonlinear aspects in the production network, which in turn can still be modified in downstream process-shops and blend-shops, a logistics optimization primarily must find the dispatching routes or dispositions of the distillates using a mixed-integer linear (MILP) model. This quantity and logic programming involves variables of networked amounts of flows and holdups, assignment of dispatching routes modeled as modes of operations, constraints for running-gauge and standing-gauge tanks of intermediate and final inventories, operations of blend-shops, multiproduct liftings via multiple mode of transport such as trucks, pipelines, ships, rails, etc.

Second, the complex scope of the MILP logistics optimization for disposition of distillates may count on simplifications to be solvable. We address the use of a depooling heuristic to facilitate the scaling to industrial-sized cases. Pooling and depooling is shown to help manage the temporal and structural degeneracy and symmetry of stocking and dispatching the intermediate tanks with distillates. Logistics pooling or group of tanks to depooling of individual ones is determined in a post-optimization step and sometimes referred to in industry as tank rotation, swinging or round-robin. The assignment of each disposition to the multiple tanks of the pooled group is performed before the processing and blending operations are executed. If an infeasibility occurs in the depooling sub-problem, then a modification to the filling (stocking) and/or drawing (dispatching) side of the tank flows can be made and the pooled problem re-run.

By solving such complicated logistics problem with a discrete time-step of around hours for a month as the time horizon, makes the production-distribution business more competitive since both fixed contracts and variable spot markets of feeds and products compete and complement each other. It maintains the balance between sustainability and profitability, the former via long-term contracts and the latter relying on short-term opportunities in the spot markets. Finally, we highlight examples varying the topology (unpooled vs. pooled) for some distillate inventories. They are solved for 1, 2 and 4 hours as time-step using the best MILP solvers in the market considering both feasibility and optimality as their focus since there is a balance between finding new feasible solutions and proving that the current solution is optimal. Although we expect a faster first solution in the feasibility focus, the optimality one maybe faster overall as seen in the examples.

2. Scheduling and primary distribution of products

In the logistics mixed-integer linear programming (MILP) problem (P), the objective function (1) maximizes the gross margin of product revenues considering the production scheduling and distribution network represented in Figure 1, which is constructed in the unit-operation-port-state superstructure (UOPSS) formulation (Kelly, 2005; Zyngier and Kelly, 2012). The UOPSS objects are: a) unit-operations m for sources and sinks of perimeters (\diamond), tanks (\triangle) and continuous-processes (\boxtimes) and b) the connectivity or routes involving arrows (\rightarrow), in-port-states i (\circ) and out-port-states j (\otimes). Unit-operations and arrows have binary and continuous variables (y and x , respectively).

The semi-continuous constraints in Eq. (2) control the networked quantity-flows for the connections $x_{j,i,t}$, the throughputs or charge-sizes of the unit-operations $x_{m,t}$ (except tanks) and tank holdups, inventory levels or lot-sizes $xh_{m,t}$, where x_t and y_t are generic continuous and binary variables. Eq (3) imposes that the sum of the connected arrows arriving in the inlet-ports i (or mixers) of unit-operation m ($m \notin M_{TK}$) are bounded by their throughputs (flows). Similarly, in Eq. (4) the sum of the arrows leaving from the outlet-ports j (or splitters) of m ($m \notin M_{TK}$) must be between bounds of their throughputs. The quantity balance of inventory or holdup for unit-operations of tanks ($m \in M_{TK}$) in Eq. (5) considers initial inventories $xh_{m,t-1}$ and inlet and outlet streams of the tanks. Eq. (6) is a material balance in blenders M_{BL} to assure that there is no accumulation of material in these types of units. In Eq. (7), for all physical units, at most one unit-operation m (as $y_{m,t}$ for procedures, modes, dispositions or tasks) is permitted in U at a time t . The remaining logistics calculations can be found in Kelly et al. (2017). Unit-operations m for tanks, blenders, and products belong, respectively, to the sets M_{TK} , M_{BL} , and M_P . The port-states j' and i'' represent upstream and downstream ports connected, respectively, to the in-port-states i and out-port-states j of unit-operations m . For $x \in \mathbb{R}^+$ and $y \in \{0,1\}$:

$$(P) \text{ Max } Z = \sum_t \sum_{m \in M_P} \text{price}_{m,t} x_{m,t} \quad (1)$$

$$\bar{x}_t^L y_t \leq x_t \leq \bar{x}_t^U y_t \quad \forall t \quad (2)$$

$$\frac{1}{\bar{x}_{m,t}^U} \sum_{j'} x_{j',i,t} \leq y_{m,t} \leq \frac{1}{\bar{x}_{m,t}^L} \sum_{j'} x_{j',i,t} \quad \forall i, m, t \quad (3)$$

$$\frac{1}{\bar{x}_{m,t}^U} \sum_{i''} x_{j,i'',t} \leq y_{m,t} \leq \frac{1}{\bar{x}_{m,t}^L} \sum_{i''} x_{j,i'',t} \quad \forall j, m, t \quad (4)$$

$$xh_{m,t} = xh_{m,t-1} + \sum_{j'} x_{j',i,t} - \sum_{i''} x_{j,i'',t} \quad \forall m \in M_{TK}, t \quad (5)$$

$$\sum_i \sum_{j'} x_{j',i,t} = \sum_{i''} x_{j,i'',t} \quad \forall m \in M_{BL}, t \quad (6)$$

$$\sum_{m \in U} y_{m,t} \leq 1 \quad \forall t \quad (7)$$

The flowsheet in Figure 1 shows an example of a typical crude-oil refinery network for the production and distribution of medium to heavy final fuels considering given amounts of distillates produced in two crude-oil distillation units CDU1 and CDU2. The distilled kerosene (KERO), light gasoil (LGO) and heavy gasoil (HGO) streams can be dispatched to feed tanks for processing in units such as hydrotreaters, dryers, blenders or directly to a finishing tank for commercialization. The transport of products considers pipelines, trucks, ships, rails and other local market deliveries to supply the multiple consumers under precise product demands.

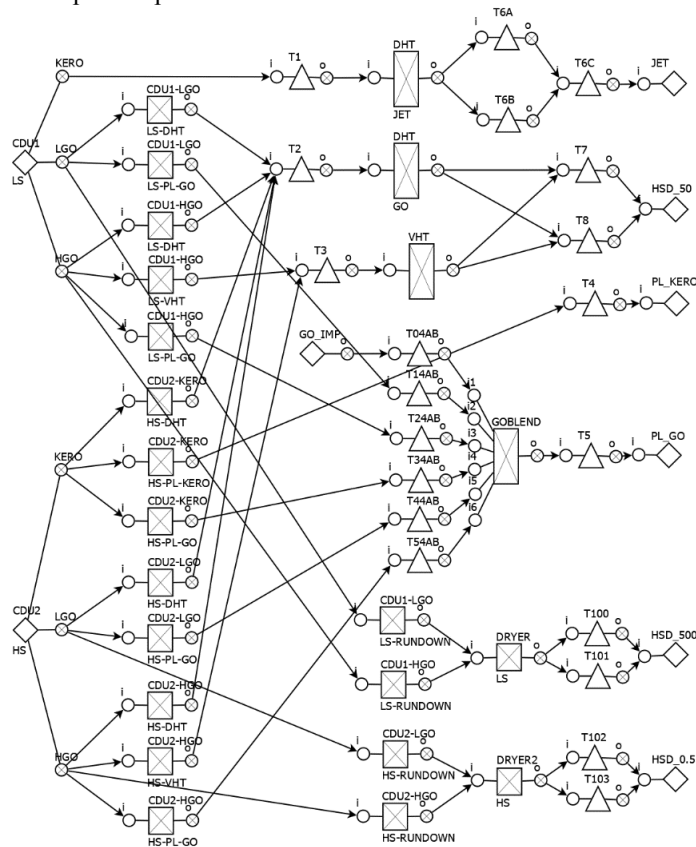


Figure 1. Medium to heavy distillates: production and distribution scheduling flowsheet.

In Figure 1, DHT-JET and DHT-GO represent the same physical hydrotreater DHT with JET (Jet Fuel) and GO (Gasoil) as modes of operation. VHT is a hydrotreating unit for HGO, the dryers of light and heavy HGO are the units DRYER and DRYER2 and the blender of HGO is the unit GOBLEND. The dispositions of the distillates in Figure 1 show: a single mode for KERO from CDU1, 3 modes of operations for CDU2-KERO and LGO from both CDU1 and CDU2 towers and HGO from both CDU1 and CDU2 with 4 modes. Transformations in DHT and VHT are disregarded, although a reduction on the yields of the medium distillates are expected by the secondary carbon chain cracking and the replacement of heteroatoms and metals by hydrogen. Both T2 and T3 in Figure 1 are pooled tanks with 5 and 2 aggregated tanks, respectively.

3. Dispositions and depooling of networked amounts or allocations

Figure 1 shows the dispositions of the distillates as modes of operations for KERO, LGO and HGO streams. However, to avoid degeneracy and symmetry among the assignments of the dispositions to their possible connected tanks, a *pooled* problem can be solved first and the disposed amounts of the distillates can be considered as sources (e.g., CDU1-LGO) in a *depooling* step of the downstream processing unit-operations (e.g., DHT-GO), as seen in Figure 2 for 5 physical tanks in the depooling of T2. Additional constraints to the depooling are related to multi-use of the source and sink ports, fill-draw delays and switching-when-full, switching-when-empty, etc. (Zyngier and Kelly, 2009).

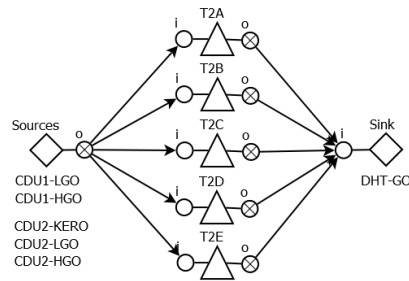


Figure 2. Depooling sub-network for tank T2 in Figure 1.

4. Examples

The example in Figure 1 is performed in the structural-based UOPSS framework found in the semantic-oriented modeling and solving platform *IMPL* (Industrial Modeling and Programming Language) from Industrial Algorithms Limited using Intel Core i7 machine at 3.70 GHz (in 8 threads) with 64GB of RAM. The logistics optimization for the proposed MILP in a time-horizon of 31 days with 1, 2 and 4 hours as time-step is solved using the latest version of CPLEX (v 12.71) and GUROBI (v 7.5.1). As seen in Table 1, the fastest solution for 1h time-step without pooling or aggregation of the tanks T2 and T3 (the unpooled problem) is optimized with GUROBI in about one half of an hour where its pooled problem is solved in around 2 minutes. For the pooled cases, the post-optimized sub-problems for depooling of T2 and T3 are solved within seconds with no infeasibilities. The depooling problem of T2 (Figure 2) has (in thousands) 13.6 equations and 8.2 continuous and 7.4 binary variables.

Table 1. Statistics of the problems for 1, 2 and 4 hours as time-step (at 1% MILP gap).

Topology	Focus	CPU (min)			GUROBI			Equations (in thousands)	Continuous/ Binary Variables for 1h
		CPLEX 1h	2h	4h	1h	2h	4h		
unpooled	feasibility	333.3	65.4	23.9	33.5	23.0	1.2	380.3	125.0 / 112.9
	optimality	785.3	190.0	32.2	29.1	18.5	1.0		
pooled	feasibility	60.7	18.6	4.1	4.3	2.8	0.7	304.7	107.6 / 85.8
	optimality	35.3	112.4	0.8	1.7	2.0	0.4		

Figure 3 shows the dispositions of the CDU1-HGO considering the possible destinations.

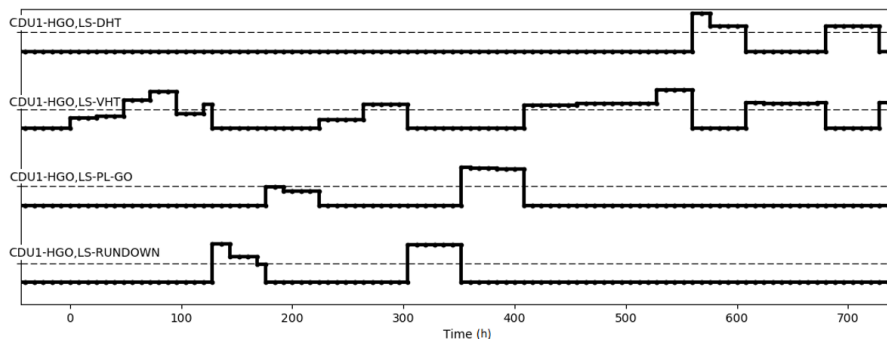


Figure 3. CDU1-HGO dispositions throughout the network.

5. Conclusions

A wide scope and scale for mapping of flows and holdups of intermediate and final products are determined in our proposed logistics optimization for the oil-refinery production- and demand-chains specific to distillates. This can potentially guide operational and marketing / sales teams to explore both contract and spot market opportunities on a day-by-day business basis taking advantage of a short-term hourly production-based scheduling solution within a planning perspective. At the edge of the modeling and solving capabilities, the aggregation, grouping or pooling of tanks and its disaggregation or depooling into individual and detailed tank assignments, has been shown to significantly reduce the computing time without any or limited loss in the accuracy of the scheduling results.

References

- J.D. Kelly, 2005. The Unit-Operation-Stock Superstructure (UOSS) and the Quantity-Logic-Quality Paradigm (QLQP) for Production Scheduling in The Process Industries. In Multidisciplinary International Scheduling Conference Proceedings: New York, United States, p. 327-333.
- J.D. Kelly, B.C. Menezes, F. Engineer, I.E. Grossmann, 2017, Crude-Oil Blend Scheduling Optimization of an Industrial-Sized Refinery: a Discrete-Time Benchmark. In Foundations of Computer Aided Process Operations, Tucson, United States.
- B.C. Menezes, I.E. Grossmann, J.D. Kelly, 2017, Enterprise-wide Optimization for Operations of Crude-Oil Refineries: Closing the Procurement and Scheduling Gap, *Comput Aided Chem Eng*, 40, 1249-1254.
- D. Zyngier, J.D. Kelly, 2012, UOPSS: A New Paradigm for Modeling Production Planning and Scheduling Systems. In European Symposium in Computer Aided Process Engineering: London, United Kingdom, p. 15146-56.
- D. Zyngier, J.D. Kelly, 2009, Multi-product Inventory Logistics Modeling in The Process Industries. In: Wanpracha Chaovalitwongse, Kevin C. Furman, Panos M. Pardalos (Eds.) Optimization and logistics challenges in the enterprise. Springer optimization and its applications, 30, Part 1, 61.

Multi-objective Optimization of the Energy System in an Iron and Steel Plant for Energy Saving and Low Emissions

Yujiao Zeng^a, Xin Xiao^{a*}, Jie Li^b, Fei Song^a

^a*Division of Environment Technology and Engineering, Institute of Process Engineering, Chinese Academy of Sciences, Beijing, 100190 P. R. China*

^b*School of Chemical Engineering and Analytical Science, The University of Manchester, Manchester, M13 9PL UK*

Email: xxiao@ipe.ac.cn

Abstract

The energy system in the iron and steel industry significantly contributes to the large energy consumption and emissions of CO₂ and some air pollutants such as SO₂ and NO_x. Therefore, optimization of the energy system is highly desired in order to reduce energy consumption and those emissions. In this paper, a multi-objective multi-period planning model is developed for optimization of the energy system in an iron and steel plant, incorporating some important practical features such as fuel selection, gasholder level control, minimum heating requirements for single and mixed consuming users and ramp rate limits. The objective is to minimize the economic cost and environmental impact simultaneously. To solve the multi-objective optimization model, a new improved multi-objective particle swarm optimization algorithm is proposed, incorporating self-adaptive mutation and effective constraint handling strategies. The results demonstrate the superiority of the proposed approach to solve the multi-objective optimization problem.

Keywords: multi-objective optimization, environmental impact, integrated energy system, improved multi-objective particle swarm, iron and steel

1. Introduction

The iron and steel industry is one of the largest energy consumers and emission sources of CO₂ and some air pollutants such as SO₂ and NO_x, accounting for about 18% of total industry final energy consumption and about 7% of the total CO₂ emissions in the world. The energy system in the iron and steel plant significantly contributes to the large energy consumption and those emissions. Therefore, optimization of the energy system is highly desired in order to reduce energy consumption and emissions of CO₂ and air pollutants.

The energy system in a typical iron and steel plant is illustrated in Figure 1, which is usually integrated with the production system. Optimization of such energy system involves simultaneous optimization of byproduct gases, steam and electricity distributions in production units, fuel boilers, steam turbines, combined heat and power units and waste heat and energy recovery units, which is not trivial. Generation rates of byproduct gases and demands of byproduct gases, steam and electricity from production units vary from time to time, increasing complexity. Decisions on burner switches in a

boiler and electricity purchase or sale make a combinatorial problem. With strict environmental regulations, environmental impact should be minimized simultaneously with economic indicators, resulting in a multi-objective optimization problem.

Many efforts have been made on planning and scheduling of production processes, such as steelmaking and continuous casting process (Li et al., 2012) and steelmaking continuous casting-hot rolling process (Tang et al., 2016) without considering energy optimization. Very few contributions related to optimization of the energy system in an iron and steel plant have been reported (Junior et al., 2016). They mainly focused on optimal supply of byproduct gases in gasholders and boilers. Zeng et al. (2018) developed a multi-period mixed-integer linear programming model for simultaneous optimization of byproduct gases, steam and electricity distributions. All of them mainly involve minimization of the economic impact of the energy system without considering the environmental impact.

In this paper, we develop a multi-objective multi-period planning model for the integrated energy system in an iron and steel plant. Some important practical features such as fuel selection, gasholder level control, minimum heating requirements for single and mixed consuming users and ramp rate limits are also incorporated into the model. The objective is to minimize the economic cost and environmental impact simultaneously. The environmental impact is assessed in terms of the release cost of the emissions including CO_2 , SO_2 , and NO_x . To solve the developed multi-objective optimization model, a new improved multi-objective particle swarm optimization (MOPSO) algorithm is proposed, incorporating self-adaptive mutation and effective constraint handling strategies. The results demonstrate that the proposed approach successfully solves the multi-objective optimization problem and obtains better solutions than actual operation. Compared with the single objective optimization, the proposed approach can generate nondominated solutions which span well over the entire Pareto optimal front surface.

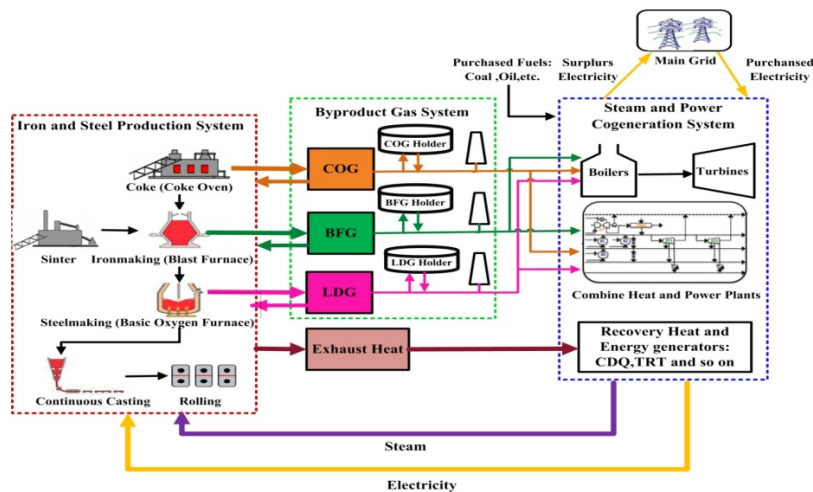


Figure 1 Integrated energy system in a typical iron and steel plant

2. Problem statement

Figure 1 illustrates the integrated energy system in a typical iron and steel plant. There are G ($g = 1, 2, \dots, G$) byproduct gas holders, I ($i = 1, 2, \dots, I$) fuel boilers, J ($j = 1, 2, \dots, J$) steam turbines, K ($k = 1, 2, \dots, K$) CHP units, M ($M = 1, 2, \dots, M$) waste heat and energy recovery units and U ($u = 1, 2, \dots, U$) production units. There are also D ($d = 1, 2, \dots, D$) pollutants including CO₂. **Given:** 1) Data of byproduct gas holders, fuel boilers, steam turbines, CHP units and waste heat and energy recovery units; 2) generation rate profiles of byproduct gases and demand profiles of byproduct gases, steam and electricity of production units; 3) economic and environmental data of the energy system; 4) planning horizon. **Determine:** 1) selection of byproduct gases, coal, and natural gas in boilers; 2) optimal byproduct gas distribution among production units, boilers, and CHP units; 3) inventory profiles of gasholders; 4) power generation plan; 5) operational plan for boiler burners. **Assumptions:** 1) all parameters are deterministic; 2) byproduct gas generation are piecewise constant; 3) demands of byproduct gases, steam, and electricity in production units are piecewise constant; 4) startups and shutdowns are not involved. More details can be referred to Zeng et al. (2018).

3. Mathematical formulation

The planning horizon is divided into T periods ($t = 1, 2, \dots, T$) based on the piecewise constant generation rate and demand profiles of byproduct gases, steam and electricity. The length of each period t is denoted as τ_t .

3.1. Objective functions

The economic objective is the minimization of total operating cost denoted as EOC , which is the same as that in Zeng et al. (2018).

$$EOC = C_{fuel} + C_{electricity} + C_{Penalty_1} + C_{Penalty_2} + C_{Penalty_3} + C_{Penalty_4} + C_{maintenance} \quad (1)$$

The environmental impact is assessed in terms of the release cost of emissions including CO₂ and some air pollutants such as SO₂ and NO_x, which is denoted as EVC .

$$EVC = \sum_{t=1}^T EV_d \cdot PE_{d,t} \cdot \tau_t \quad (2)$$

where, EV_d is environmental value for pollutant d , $PE_{d,t}$ is the emission amount of pollutant d in period t .

3.2. Pollutant emission calculation

The amount of CO₂, SO₂ and NO_x released can be calculated as:

$$PE_{CO_2,t} = 1.964 \times 10^{-6} \times \sum_g R_{g,t} \alpha_{CO_2}^g + 1.964 \times 10^{-6} \times \sum_g R_{g,t} (\alpha_{CO}^g + \alpha_{CO_2}^g + \alpha_{CH_4}^g) + 3.667 \times \sum_{i=1}^I F_{i,t}^{coal} \beta_C^{coal} \gamma_{CO_2}^{coal} + 3.667 \times \sum_{i=1}^I F_{i,t}^{oil} \beta_C^{oil} \gamma_{CO_2}^{oil} \quad (3)$$

$$PE_{SO_2,t} = 2 \times 0.8 \times \sum_{i=1}^I F_{i,t}^{coal} \beta_S^{coal} (1 - \eta_S^{coal}) + 2 \times \sum_{i=1}^I F_{i,t}^{oil} \beta_S^{oil} (1 - \eta_S^{oil}) \quad (4)$$

$$PE_{NO_x,t} = 1.63 \times \sum_{i=1}^I F_{i,t}^{oil} (\beta_N^{oil} \gamma_N^{oil} + 0.000938) \quad (5)$$

where, α_{CO} , α_{CO_2} , and α_{CH_4} are volume fraction of CO, CO₂ and CH₄ in the byproduct gas, respectively; β_C , β_S and β_N are mass fraction of carbon, sulfur and nitrogen in the fossil fuel, respectively; γ_{CO_2} is the conversion rate of carbon to CO₂; η_s is desulfurization efficiency; γ_N is the conversion rate of nitrogen to nitrogen oxides.

3.3. Pollutant emission limits

$$PE_{d,i} \leq LEM_d \quad (6)$$

where LEM_d is maximum emissions of pollutant d .

3.4. Other constraints

The other constraints include energy balance for byproduct gas, steam and power, operational constraint of gasholders and boiler burners, ramp rate limits of power generation units, and byproduct gas constraints for production units. These constraints can also be found in Zeng et al. (2018).

4. Improved multi-objective particle swarm optimization algorithm

An improved multi-objective particle swarm optimization (IMOPSO) is proposed for solving the proposed model by combining the classical MOPSO with time variant parameters, a self-adaptive mutation operator and effective constraint handling strategies.

(1) Time variant parameters

Time variant parameters are adopted to help the algorithm explore the search space more efficiently. The inertia weight w and acceleration coefficient c_1 are allowed to decrease linearly with iteration, while acceleration coefficient c_2 is allowed to increase linearly with iteration from $c_{2,min}$ to $c_{2,max}$.

(2) Self-adaptive mutation

To enhance the diversity of nondominated solutions, a self-adaptive mutation strategy is introduced to IMOPSO by incorporating two different mutation operators below,

$$x_{mutant,1}(k) = x_k(k) + Y \cdot [x_{r_1}(k) - x_{r_2}(k)] + (1 - Y) \cdot [x_{r_3}(k) - x_{r_4}(k)] \quad (10)$$

$$x_{mutant,2}(k) = x_k(k) \cdot [1 + gaussian(\sigma)] \quad (11)$$

where, r_1 , r_2 , r_3 and r_4 are random integers distributed uniformly between 1 and the population size. $r_1 \neq r_2 \neq r_3 \neq r_4$; Y is a uniform random number within [0, 1]; $gaussian(\sigma)$ is a Gaussian distributed random number with mean of 0 and a variance of σ .

After all velocities and positions of the particles have been updated, the above operators are used to generate two temporary positions for each particle based on the original positions. The better one between the original position and the temporary position is accepted as the next generation position of the particle.

(3) Constraints handling

The most popular way to handle constraints is to impose penalties for violated constraints. However, it requires a careful fine tuning of the penalty factors in order to approach the feasible region efficiently. In this work, we adopt multiple powerful

constraint handling strategies which can bias the optimization toward the feasible region without enforcing any restrictions. A heuristic strategy based on priority is used to handle energy balance constraints and a feasibility-based selection technique is employed to deal with inequality constraints. Details of these strategies can be referred to Zeng and Sum (2014).

5. Computational results

We use the proposed model and Improved MOPSO algorithm to solve three industrial examples from an iron and steel plant in China. All data can be found in Zeng et al. (2018). The planning horizon is 24 hours, which is divided into 12 intervals with sampling rate of 2 hours based on energy demand profiles. Examples 1-2 have single objectives. While Example 1 involves minimization of the operating cost, Example 2 is to minimize environmental cost only. Example 3 is to minimize economic cost and environmental impact simultaneously.

Figure 2 depicts a Pareto-optimal front for Example 3 from the proposed improved MOPSO approach. The Pareto optimal solution set including 20 nondominated solutions is generated in a single run. It can be observed that a high reduction in the economic cost is gained when passing from the left extreme C (minimum environmental cost) to point B than when passing from point B to the right extreme A (minimum operating cost). This means that passing from solution C to B provides a small increment in the environmental cost but produces a high decrease in the operating cost.

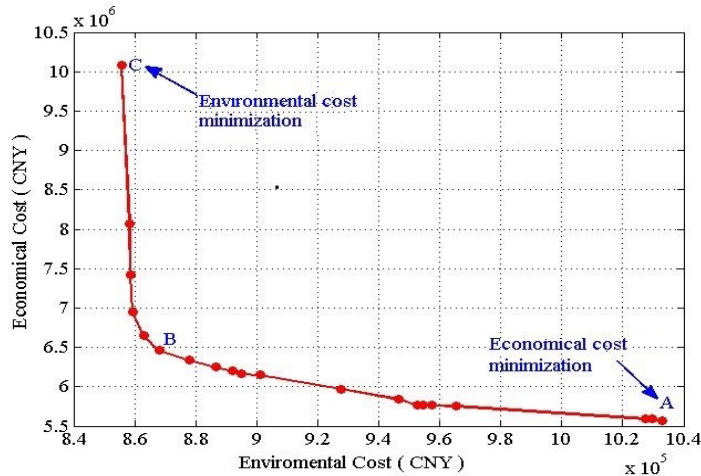


Figure 2 Pareto-optimal front for Example 3 from the proposed approach

Table 1 gives a detailed comparison for Examples 1-3 and actual operation. The results show that both the operating cost and environmental impact for Examples 1-3 are reduced compared to the actual operation. It is also can be observed that the results from the proposed approach are almost identical to those with single objective optimization. This demonstrates the effectiveness of the proposed improved MOPSO for solving the multi-objective problem as the best solution of each objective along with a set of nondominated solutions can be obtained in a single run.

6. Conclusions

In this paper, a multi-objective multi-period MILP model was developed for optimal distribution of byproduct gas, electricity and steam in an iron and steel plant. The objective is to minimize total operating cost and environmental impact simultaneously. A new improved MOPSO algorithm was proposed for solving the proposed model. The results demonstrated that the proposed approach successfully solved the multi-objective optimization problem and obtained better solutions than actual operation. Compared with the single objective optimization, the proposed approach can generate nondominated solutions which span well over the entire Pareto optimal front surface.

Table 1 Comparative results for Examples 1-3 and actual operation

	Actual operation	Proposed Approach		Single objective optimization	
		Minimize EOC	Minimize EVC	Minimize EOC	Minimize EVC
EOC (¥)	5,802,752	5,548,557	10,078,123	5,544,182	9,772,964
EVC (¥)	1,138,382	1,029,659	855,723	1,032,942	858,457
CO ₂ (t)	4,861	4,161	3,455	4,175	3,466
SO ₂ (t)	49.62	45.94	38.24	46.09	38.36
NO _x (t)	90.84	82.28	68.35	82.55	68.56

Acknowledgment

Yujiao Zeng would like to acknowledge financial support from the National Natural Science Foundation of China (61603370) and Major Science and Technology Program for Water Pollution Control and Treatment (2015ZX07202013-003).

References

- V. Junior, J. Pena, J. Salles, 2016, An improved plant-wide multiperiod optimization model of a byproduct gas supply system in the iron and steel-making process, *Applied Energy*, 164, 462-474.
- J. Li , X. Xiao, Q. Tang, C. Floudas, 2012, Production Scheduling of a Large-Scale Steelmaking Continuous Casting Process via Unit-Specific Event-Based Continuous-Time Models: Short-Term and Medium-Term Scheduling, *Industrial & Engineering Chemistry Research*, 51(21), 7300-7319.
- L. Tang, Y. Meng, Z. Chen, J. Liu, 2016, Coil Batching to Improve Productivity and Energy Utilization in Steel Production, *Manufacturing & Service Operations Management*, 18(2), 62-78.
- Y. Zeng, X. Xiao, J. Li, L. Sun, C. Floudas, 2018, A Novel Multi-Period Mixed-Integer Linear Optimization Model for Optimal Distribution of Byproduct Gases, Steam and Power in an Iron and Steel Plant, *Energy*, 143, 881-899.
- Y. Zeng, Y. Sun, 2014, An Improved Particle Swarm Optimization for the Combined Heat and Power Dynamic Economic Dispatch Problem, *Electric Power Components & Systems*, 42(15), 1700-1716.

Dynamic process simulation based process malfunction analysis

Alex Kummer, Tamás Varga

Department of process engineering, University of Pannonia, H-8200 Veszprém, Hungary

kummera@fmt.uni-pannon.hu

Abstract

With improving industrial chemical technologies the Hazard and Operability Analysis (HAZOP) or other safety analysis becomes more difficult to perform, because the technologies become more integrated and complex. Applying dynamic HAZOP can help the experts to explore all hazard situations in a technology based on dynamic process simulation. In this work a framework for exploring hazard events is suggested to support the safety analysis. The proposed framework works via OPC (Open Platform Communication) connection between MATLAB and Aspen HYSYS dynamic process simulator. Concentration of cumene-hydroperoxide (CHP) in vacuum column is chosen as a case study to show how the framework can be applied to analyze process safety related situations. The hazard events are generated through controller failures with significant changes in setpoints for a specific time. The events can be ranked based on the consequences, which can be significant in different perspectives. The most important is to analyze the temperature and pressure trajectories during the event, although the required time and energy to reach the normal conditions again can be evaluated too. All these parameters are considered in the qualification and ranking process of each investigated process malfunction.

Keywords: HYSYS-MATLAB connection, controller failure, consequence matrix, dynamic HAZOP, safety analysis

1. Introduction

A chemical process often uses operating conditions (temperature, pressure) that may represent a risk, and may lead to deviations that can generate hazardous events. Plant equipment, including pumps, compressors, and control equipment may fail too in spite of the correct maintenance policy. Possibility of human error is present in chemical industry, because operators can make mistakes which may lead to a hazard situation. Finally, chemicals by themselves may be toxic, flammable and/or explosive. All of these elements, and their interactions constitute process safety (Stoessel 2008).

Risk identification is essential for ensuring acceptable safe operation of a process (Berdouzi et al. 2017). In literature, there are several definition of risk, Aven and Renn proposed 9 general risk definitions, like expected value loss, probability of an undesirable event, uncertainty of outcome, or combination of probability and consequence (Villa et al. 2016). The most often used risk definition is the measure of the probability and severity of adverse effects. Risk can be calculated for different hazard scenarios, like cooling water loss, pump failure, etc. Hazard scenarios are

determined using Process Hazard Analysis (PHA) methods. The most commonly used PHA method is Hazard and Operability (HAZOP) study (Baybutt 2015). Basically, HAZOP study is a qualitative method, but without knowing the system behavior during malfunctions, a completely reliable safety study cannot be performed. Applying dynamic process simulators (DPS) can reveal the effects of different malfunctions, and the evolution of variables can be analyzed.

Many simulations of chemical processes can be found in literature related to process safety analysis. Eizenberg examined the possible deviations at the oxidation of 2-octanol and determined practical safety threshold values (Eizenberg, Shacham, and Brauner 2006). Wende Tian proposed DynSim-HAZOP using Aspen Dynamics, and based on the developed DPS, next to the well-defined deviations (high feed temperature, low feed flow, etc.), it is able to quantitatively analyze the out of control incidents too (clogged valve, pipeline leakage, scale formation, etc.) (Tian, Du, and Mu 2015).

In this work the analysis of vacuum distillation column is chosen to investigate different process malfunctions. The examined process unit is applied in an internal step in phenol production technology. The cumene-hydroperoxide (CHP) route to phenol was developed by Hercules and BP Chemicals. Almost all produced phenol is from synthetic processes. Nowadays worldwide phenol production is based on this technology. The simulator of vacuum distillation column is built in Aspen HYSYS.

An Open Platform Communication (OPC) is built between MATLAB and Aspen HYSYS. Therefore, data from dynamic simulator can be evaluated easily in MATLAB, and consequence matrix can be calculated. Quantifying the severity of consequences is important in hazard analysis, DPS based consequence matrix can give more precise and valuable information about the possible operation malfunctions. Values of consequence are determined for different process malfunctions based on a dynamic process simulator.

2. Methodology to assess consequence

Fatine Berdouzi suggested a methodology to quantify and decrease the risk of operation (Berdouzi et al. 2017). Their consequence identification method is extended with taking into account the energy consumption, and the time of malfunction. First of all, thermokinetic and thermal stability data are required in order to characterize the system. Besides that, a detailed description of the process is necessary to get information about the process units, control strategies, operating conditions and about the dynamic characteristics of the system. Reliable safety study cannot be done without knowing the process in detail. Second of all, based on a qualitative HAZOP analysis the crucial scenarios need to be simulated. Simulation results allow quantifying the effects of malfunctions according to temperature and pressure amplitude, malfunction duration, and energy consumption. Luyben suggests different levels of safety constraints and actions for reactor safety analysis (Luyben 2012). In our case, the suggested threshold values are presented in consequence matrix (Table 1), where *AH* means high alarm value, *op* means operating value, t_{PS} and t_{mf} mean plant start (or unit) and malfunction duration, *des* means design parameter, *set* stands for Pressure Safety Valve set pressure. C_{AEC} and C_{MD} constants are applied to define the threshold values of average energy (AEC) consumption and malfunction duration (MD).

Table 1 Consequence matrix

CI	Pressure	Temperature	Average energy consumption (AEC)	Malfunction duration (MD)
0	$P_{op} < P_{AH}$	$T_{op} < T_{AH}$	$Q_{op} < c_{AEC1} Q_{op}$	$t_{mf} < c_{MD1} t_{PS}$
1	$P_{AH} < P_{op} < P_{set}$	$T_{AH} < T_{op} < T_{des}$	$c_{AEC1} Q_{op} < Q_{op} < c_{AEC2} Q_{op}$	$c_{MD1} t_{PS} < t_{mf} < c_{MD2} t_{PS}$
2	$P_{set} < P_{op} < P_{des}$	-	$c_{AEC2} Q_{op} < Q_{op} < c_{AEC3} Q_{op}$	$c_{MD2} t_{PS} < t_{mf} < c_{MD3} t_{PS}$
3	$P_{des} < P_{op}$	$T_{des} < T_{op}$	$c_{AEC3} Q_{op} < Q_{op}$	$c_{MD3} t_{PS} < t_{mf}$

An override condition is applied in defining the consequence index of average energy consumption and malfunction duration. If the operating pressure or temperature exceed the design parameter, then the average energy consumption (AEC) and malfunction duration (MD) consequence index (CI) automatically becomes three.

$$IF P_{des} < P_{op} \text{ or } T_{des} < T_{op} \text{ THEN } CI_{AEC} = 3 \text{ and } CI_{MD} = 3$$

The “0” CI index value refers the lowest severity, and the “3” CI index refers the highest severity in risk calculation.

3. Case study

The first step in phenol production is oxidation of cumene to cumene-hydroperoxide (CHP) with 25-30% conversion. Phenol comes from cleavage of CHP, but in the previous step the diluted CHP has to be concentrated. The concentration of CHP (to ~60w%) is done in vacuum distillation column, where the bottom product is the concentrated CHP, and cumene comes as a distillate. The developed process simulator of vacuum distillation column is shown in Figure 1. DPS include hydrodynamics and hydrostatic calculations, therefore it helps to develop an adequate simulator of the process unit.

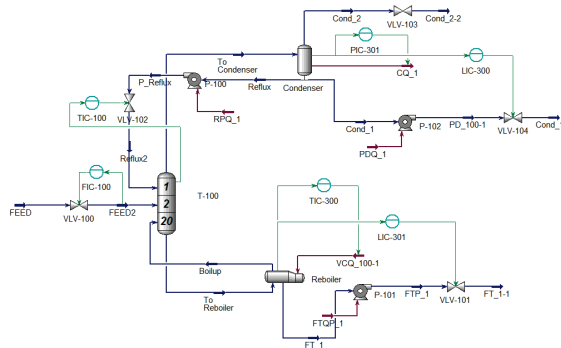


Figure 1 Process simulator of vacuum distillation column

The operation of T-100 vacuum column is controlled by tuned PI controllers. Tuning is done by Aspen HYSYS Autotuner module. FIC-100 controls the flow rate of feed cumene-CHP mixture. LIC-300 and LIC-301 controls the level in the reflux drum and reboiler by opening the outlet valve. The temperature of reboiler is controlled by TIC-300 controller. TIC-100 controls the tray temperature by reflux flow rate. The pressure of condensate tank is controlled via PIC-301 by cooling the condensate tank with cooling water.

4. Consequence assessment

Seven process malfunctions are chosen to test the suggested consequence quantification and corresponding consequences are analyzed. Five controller failure are simulated, where the setpoint of controllers are increased by twenty percent for two minutes. Beside controller failures, reflux pump failure and lack of cooling water are simulated too, both of them lasted two minutes. Every malfunction occurs at the start of the third minute. The trajectories of some important state variables as a result of malfunctions can be seen in Figure 2-3.

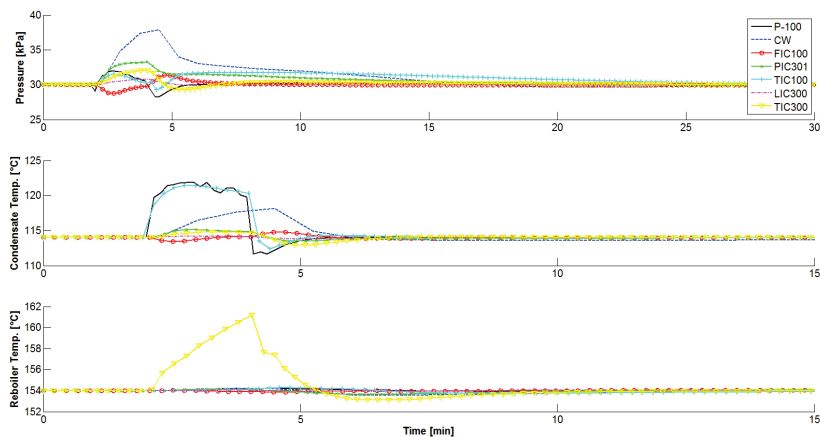


Figure 2 Pressure and temperature trajectories due to process malfunctions (FIC-100 failure: red, PIC-301 failure: green, TIC-100 failure: cyan, LIC-300 failure: magenta, TIC-300 failure: yellow, , lack of cooling water (CW): blue, P-100 reflux pump failure: black)

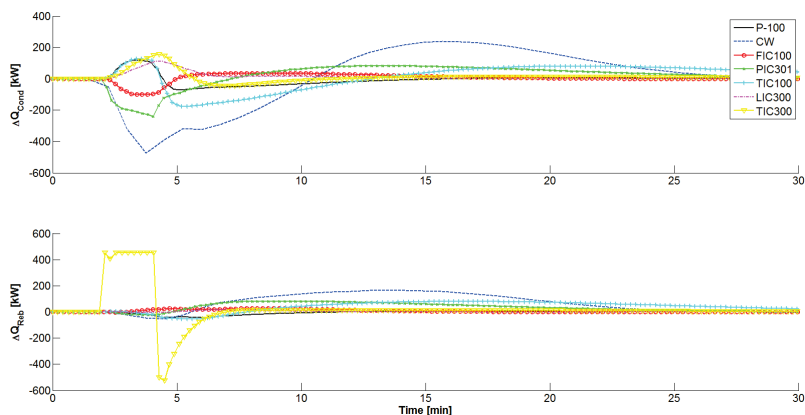


Figure 3 Energy consumption trajectories due to process malfunctions (FIC-100 failure: red, PIC-301 failure: green, TIC-100 failure: cyan, LIC-300 failure: magenta, TIC-300 failure: yellow, , lack of cooling water (CW): blue, P-100 reflux pump failure: black)

The trajectories are analyzed according to the described method (in methodology section), and the consequence indexes are calculated. The threshold values are listed in Table 2. Threshold values are defined for this case, and for every other case it should be

checked based on a DPS of the investigated system. Last two columns are the value of constant parameters from Table 1.

Table 2 Threshold values in consequence matrix calculation

	Pressure [kPa]	Temperature in reflux drum [°C]	Temperature in reboiler [°C]		AEC [-]	MD [-]
Alarm HIGH	32	116	158	$c_{AEC1-CMD1}$	0.005	0.05
Set pressure	110	-	-	$c_{AEC2-CMD2}$	0.01	0.1
Design parameter	120	140	200	$c_{AEC3-CMD3}$	0.05	0.5

Table 3 shows the critical values during process malfunctions. Maximum pressure in the reflux drum, maximum temperature in reflux drum and in reboiler, AEC for returning the system into normal operating conditions, and the required time to return into normal operating point can be seen.

Table 3 Critic values for calculation of consequence matrix

	P_{max} [kPa]	$T_{max\ reflux}$ [°C]	$T_{max\ reb}$ [°C]	AEC [kW]	MD [h]
FIC-100 failure	31.37	114.80	154.04	8.26	0.67
PIC-301 failure	33.30	115.13	154.12	27.57	0.95
TIC-100 failure	34.69	121.43	154.28	27.07	1.09
LIC-300 failure	30.76	114.17	154.02	10.32	0.59
TIC-300 failure	32.06	114.76	161.37	24.06	0.54
lack of CW	39.03	118.94	154.22	48.23	0.71
P-100 failure	31.99	121.89	154.24	-4.78	0.60

Table 4 Consequence matrix of T-100 malfunctions

	CI_p	CI_T	CI_o	CI_t	$\sum CI$
FIC-100 failure	0	0	0	2	2
PIC-301 failure	1	0	2	2	5
TIC-100 failure	1	1	2	2	6
LIC-300 failure	0	0	1	2	3
TIC-300 failure	1	1	2	2	6
lack of CW	1	1	2	2	6
P-100 failure	0	1	0	2	3

Table 4 shows the result of consequence analysis. Under CI_p and CI_T columns the value "1" means the analyzed process malfunctions does not cause any dangerous situation, although it indicates alarm sign. However, the analyzed process malfunctions cause higher energy consumption, and it takes relatively long time to get the operating unit back to normal operating condition. The sum of consequence indexes can be used in risk calculation as severity.

$$Risk = \sum CI \cdot Probability \quad (1)$$

5. Conclusions

In this work, a quantitative definition of process malfunction consequences is suggested. Dynamic process simulators are helpful in identifying hazard events, and relevant information can be collected about the evolution of variables during process malfunctions. Aspen HYSYS is used to analyze several process malfunction of vacuum distillation column. MATLAB and Aspen HYSYS are connected via OPC to evaluate the gained data. DPS allows the quantification of consequences. Consequence matrix includes the effect on pressure, temperature, average energy consumption and malfunction time duration. The operation malfunctions can be ranked based on the consequence matrix. In our case TIC-300, TIC-100 controller failure and the lack of cooling water has the highest severity, therefore these malfunctions need higher attention during unit operation. Severity is included in consequence matrix, therefore the risk can be defined using consequence matrix.

Acknowledgment

We would like to express our acknowledgement for the financial support of Széchenyi 2020 under the GINOP-2.2.1-15-2017-00059.

References

- Baybutt, Paul. 2015. "A Critique of the Hazard and Operability (HAZOP) Study." *Journal of Loss Prevention in the Process Industries* 33 (January):52–58. <https://doi.org/10.1016/j.jlp.2014.11.010>.
- Berdouzi, Fatine, Claire Villemur, Nelly Olivier-Maget, and Nadine Gabas. 2017. "Dynamic Simulation for Risk Analysis: Application to an Exothermic Reaction." *Process Safety and Environmental Protection*, October. <https://doi.org/10.1016/j.psep.2017.09.019>.
- Eizenberg, Shimon, Mordechai Shacham, and Neima Brauner. 2006. "Combining HAZOP with Dynamic Simulation—Applications for Safety Education." *Journal of Loss Prevention in the Process Industries* 19 (6):754–61. <https://doi.org/10.1016/j.jlp.2006.07.002>.
- Luyben, William L. 2012. "Use of Dynamic Simulation for Reactor Safety Analysis." *Computers & Chemical Engineering* 40 (May):97–109. <https://doi.org/10.1016/j.compchemeng.2012.02.013>.
- Stoessel, Francis. 2008. *Thermal Safety of Chemical Processes*. Weinheim, Germany: Wiley-VCH Verlag GmbH & Co. KGaA. <https://doi.org/10.1002/9783527621606>.
- Tian, Wende, Tingzhao Du, and Shanjun Mu. 2015. "HAZOP Analysis-Based Dynamic Simulation and Its Application in Chemical Processes: HAZOP Based Dynamic Simulation." *Asia-Pacific Journal of Chemical Engineering* 10 (6):923–35. <https://doi.org/10.1002/apj.1929>.
- Villa, Valeria, Nicola Paltrinieri, Faisal Khan, and Valerio Cozzani. 2016. "Towards Dynamic Risk Analysis: A Review of the Risk Assessment Approach and Its Limitations in the Chemical Process Industry." *Safety Science* 89 (November):77–93. <https://doi.org/10.1016/j.ssci.2016.06.002>.

Virtual inflow estimation with simplified tuning using cascaded and Kalman-like least squares observers

Christoph Josef Backi^{a,*} and Sigurd Skogestad^a

^a*Department of Chemical Engineering, Norwegian University of Science and Technology (NTNU), NO-7491 Trondheim, Norway*
christoph.backi@ntnu.no

Abstract

Multiphase metering is often unavailable, unreliable or expensive, which makes model-based, virtual monitoring a cheap and reliable alternative in order to obtain information about e.g. the inflows to a device. This paper presents an approach for inflow estimation to a gravity separator based on a standard Extended Kalman Filter. Potential improvements include a cascaded structure, a Kalman-like least squares observer with forgetting factor, and a combination of these.

Keywords: Virtual metering, estimation, observer design, gravity separator, oil and gas

1. Introduction

Gravity separators are used in the oil- and gas-industry for bulk separation of gas, water and hydrocarbons (oil and condensate). Further purification is achieved in downstream equipment such as hydrocyclones, gas scrubbers, gas flotation units or membranes. Backi and Skogestad (2017a) introduced a simple model for gravity separators based on first principles. A schematic of the model is presented on the left side in Figure 1, where the multiphase stream enters the inlet zone, flows through the active separation zone (length L) and leaves in the outlet zone.

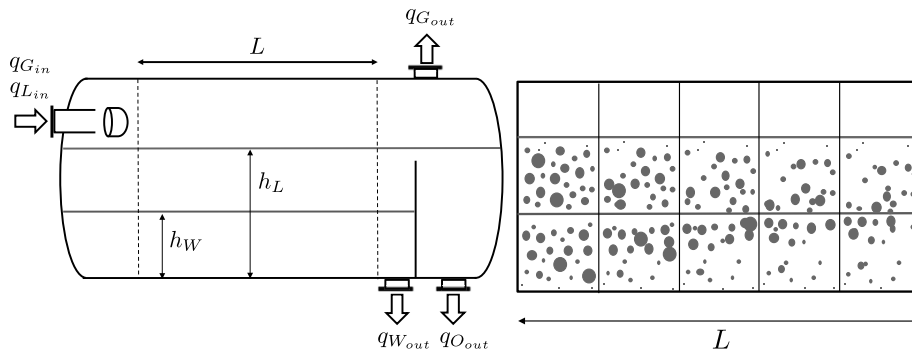


Figure 1: Schematics of the separator (left) and the droplet evolution in the active separation zone (right)

The model regards the in- and outflow dynamics of a multiphase stream consisting of oil, gas and water. Furthermore, the model incorporates static droplet calculations primarily based on *Stokes' law*, which gives vertical velocities for a droplet size class dispersed in a continuous phase. These

vertical velocities of droplets are compared to the droplets' horizontal velocity as they move along the separator and ultimately give the volume of separated droplets (the ones that reach the oil-water-interface). A schematic of the droplet evolution is presented on the right-hand side in Figure 1. For now, we do neither consider coalescence and breakage nor a dense-packed (emulsion) layer between the water- and oil-continuous phases.

It is desired to obtain as much information about the separator conditions as possible. For example, quantifying the inflows of gas and liquid to the separator and consequently also to the downstream equipment is advantageous regarding optimal operation and, in case of severe slugging events, to launch counter-measures. Multiphase metering, however, is often not applicable, too expensive or unreliable and thus the exact composition of the inlet stream to the gravity separator might be unknown. Therefore, dynamic model-based monitoring and estimation can be a reliable and cheap solution to determine these inflows (Backi and Skogestad, 2017b).

The remainder of the paper is structured as follows: Section 2 introduces the mathematical model, whereas Section 3 provides the methodology behind the observer designs. The results are presented in Section 4, while the paper is concluded in Section 5.

2. Mathematical Model

The three dynamic state variables in the original model (Backi and Skogestad, 2017a) are the total liquid level h_L , the water level h_W and the gas pressure p . This model serves as plant in the simulations. For the observer model, the state equations are augmented by quasi-stationary equations for the two inflows $q_{L,in}$ and $q_{G,in}$, which act as disturbances, as well as the effective split ratio γ , which defines the split of oil and water entering the water-continuous phase:

$$\frac{d\hat{h}_L}{dt} = \hat{f}_1 = \frac{\hat{q}_{L,in} - q_{W,out} - q_{O,out}}{2L\sqrt{\hat{h}_L}(2r - \hat{h}_L)}, \quad \frac{d\hat{q}_{L,in}}{dt} = \hat{f}_4 = 0, \quad (1)$$

$$\frac{d\hat{h}_W}{dt} = \hat{f}_2 = \frac{\hat{q}_{L,in}\hat{\gamma} - q_{W,out}}{2L\sqrt{\hat{h}_W}(2r - \hat{h}_W)}, \quad \frac{d\hat{q}_{G,in}}{dt} = \hat{f}_5 = 0, \quad (2)$$

$$\frac{d\hat{p}}{dt} = \hat{f}_3 = \frac{RT\frac{\rho_G}{M_G}(\hat{q}_{G,in} - q_{G,out}) + \hat{p}(\hat{q}_{L,in} - q_{L,out})}{V_{Sep} - \hat{V}_L}, \quad \frac{d\hat{\gamma}}{dt} = \hat{f}_6 = 0, \quad (3)$$

where r denotes the radius of the separator, L indicates the length of the active separation zone, $\mathbf{u} = [q_{W,out} \ q_{O,out} \ q_{G,out}]^T$ is the vector of manipulated variables (outflows of continuous water, oil and gas phases, respectively), universal gas constant R , gas temperature T , gas density ρ_G and molar gas mass M_G . Furthermore, V_{Sep} indicates the volume of the active separation zone and the estimated liquid volume is given as

$$\hat{V}_L = \frac{r^2L}{2} \left[2\cos^{-1}\left(\frac{r - \hat{h}_L}{r}\right) - \sin\left(2\cos^{-1}\left(\frac{r - \hat{h}_L}{r}\right)\right) \right].$$

The state vector of estimates can be written as $\hat{\mathbf{x}} = [\hat{h}_L \ \hat{h}_W \ \hat{p} \ \hat{q}_{L,in} \ \hat{q}_{G,in} \ \hat{\gamma}]^T$ whose first three states are assumed measurable. Hence, the output matrix is $\mathbf{y} = \mathbf{C}\hat{\mathbf{x}}$ with $\mathbf{C} = [\mathbf{I}_3 \ \mathbf{0}_{(3 \times 3)}]$, where \mathbf{I}_3 denotes an identity matrix of size 3 and $\mathbf{0}_{(3 \times 3)}$ indicates a matrix of zeros of size 3×3 . Note that in simulations the pressure differential equation is scaled to the unit bar.

3. Methods

We design an observer that estimates the inflows of liquid and gas to the separator as well as the effective split ratio in the water-continuous phase. The inflows constitute disturbances to the process

and hence an observer should be able to track these fluctuations. In Backi and Skogestad (2017b), an Extended Kalman Filter (EKF) in its standard continuous-time formulation was designed and implemented for the given estimation task providing full observability.

For the EKF design, the well-known differential Matrix-Riccati-Equation (DMRE) is solved in order to obtain the time-varying Kalman feedback gain $\mathbf{K}(t)$

$$\frac{d\mathbf{P}(t)}{dt} = \mathbf{A}(t)\mathbf{P}(t) + \mathbf{P}(t)\mathbf{A}^T(t) - \mathbf{K}(t)\mathbf{C}\mathbf{P}(t) + \mathbf{Q}, \quad \mathbf{K}(t) = \mathbf{P}(t)\mathbf{C}^T\mathbf{R}^{-1}, \quad (4)$$

where $\mathbf{P}(t)_{(6 \times 6)}$ is the state covariance matrix, $\mathbf{A}(t)_{(6 \times 6)} = \frac{\partial \hat{\mathbf{f}}(\hat{\mathbf{x}}, \mathbf{u})}{\partial \hat{\mathbf{x}}}$ denotes the time-varying Jacobian of (1)–(3), $\mathbf{Q}_{(6 \times 6)}$ and $\mathbf{R}_{(3 \times 3)}$ are the process and measurement noise covariance matrices.

3.1. Alternative observer design

An alternative, simple and practical observer design with potentially improved performance can be a Kalman-like least squares observer (KF-like LSO) with forgetting factor, as introduced in its discrete-time formulation in Johnstone et al. (1982) and further developments by Hammouri and De Leon Morales (1990) as well as Haring (2016), who introduced a continuous-time formulation.

In its deterministic sense, the Kalman Filter is a least-squares observer and hence the KF-like LSO is closely related to the EKF. In fact, the only difference between the two observer designs is found in the way the DRME is calculated, which looks as follows for the KF-like LSO

$$\frac{d\mathbf{P}(t)}{dt} = \mathbf{A}(t)\mathbf{P}(t) + \mathbf{P}(t)\mathbf{A}^T(t) - \mathbf{K}(t)\mathbf{C}\mathbf{P}(t) + \lambda\mathbf{P}(t), \quad \mathbf{K}(t) = \lambda\mathbf{P}(t)\mathbf{C}^T\mathbf{R}^{-1}, \quad (5)$$

where λ is the scalar forgetting factor.

The implementation of the observer design (5) can be advantageous compared to the EKF since the tuning procedure is simpler. Instead of tuning the process covariance matrix $\mathbf{Q}_{(6 \times 6)}$, which typically is a diagonal matrix with 6 tuning parameters, now only the scalar λ has to be defined, in addition to the measurement noise covariance matrix $\mathbf{R}_{(3 \times 3)}$.

3.2. Cascaded observer design

Investigating the structure of the model (1)–(3), it can be seen that the two equations (1) can be decoupled from the remaining equations, since estimation of $\hat{q}_{L,in}$ can be solely achieved by using (1) in 'Observer 1'. Consequently, the estimates of \hat{h}_L and $\hat{q}_{L,in}$ can be utilized in a cascaded structure as inputs to 'Observer 2', which includes the remaining four equations in (2) and (3).

A schematic of this cascaded structure is shown in Figure 2. By implementing the cascaded design,

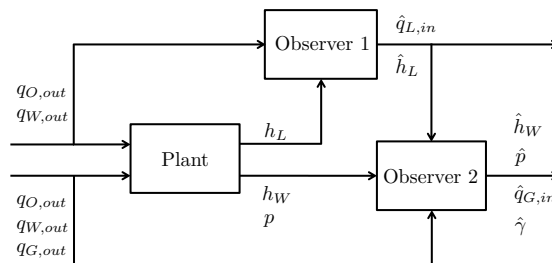


Figure 2: Schematic of the cascaded observer design in combination with the plant model

the tuning procedure for (5) gains one tuning variable, since now two observers instead of one are designed, each with a tuning variable λ .

The cascaded structure can not only be advantageous for the observer design (5), but the decoupling into two observers also has benefits when tuning the standard EKF (4). The original matrix $\mathbf{Q}_{(6 \times 6)}$ gets split up into two matrices $\mathbf{Q}_{1,(2 \times 2)}$ and $\mathbf{Q}_{2,(4 \times 4)}$, for which the tunings can be chosen more easily since there is less coupling between the single entries.

3.3. PI controller

The three state variables h_L , h_W and p are controlled by simple PI controllers, which rely solely on the estimated state variables. The controllers have the form $K(s) = K_p \left(1 + \frac{1}{\tau_I s}\right)$ and have been tuned by applying the SIMC tuning rules (Skogestad, 2003). The parameters K_p and τ_I as well as the tuning variable τ_c are shown in Table 1.

Table 1: Parameters for the three PI controllers

	τ_c	K_p	τ_I
water level	5 s	6.49	20 s
liquid level	5 s	5.063	20 s
pressure	5 s	0.0541	20 s

The rates of change for controller action are limited to $\pm 0.05 \text{ m}^3 \text{ s}^{-2}$ and the respective outputs are bounded between 0 and $1 \text{ m}^3 \text{ s}^{-1}$, respectively.

4. Results

In this Section, we present simulation results for the cascaded KF-like LSO and compare its performance to the EKF, both for cascaded and standard formulations. The simulation parameters can be found in Backi and Skogestad (2017a,b), but the tuning parameters for the observers will be presented. To render the simulations more realistic, we added white noise to all measurements, to the state derivatives in the plant model (process noise) and to the nominal inflows $q_{L,in}$ and $q_{G,in}$. These have been implemented in MATLAB Simulink as band-limited white noise processes with a noise power of 10^{-1} , sample time 0.1 s and a seed of [23341].

4.1. EKF

Here, we present results for the EKF both in standard and cascaded formulations. Figure 3 shows the results for the standard EKF design, whereas the simulations for the cascaded EKF design are presented in Figure 4 for direct comparison. The estimation of the measurable state variables do not differ for both cases, however, there is a clear improvement for the cascaded structure in terms of estimating the liquid inflow. A slight drawback is the noisier estimation of the split factor $\hat{\gamma}$. It must be noted that the split factor cannot reach its nominal value since the static droplet calculations are included in the plant model, but not in the observer model, hence a plant-model-mismatch is the consequence.

The observer parameters have been chosen as $\mathbf{Q} = \text{diag} [10^{-2} \ 10^{-1} \ 10^4 \ 10^1 \ 10^0 \ 10^0]$ and $\mathbf{R} = \text{diag} [10^0 \ 10^0 \ 10^4]$ for the standard EKF and $\mathbf{Q}_1 = \text{diag} [10^0 \ 10^1]$, $\mathbf{R}_1 = 10^1$ as well as $\mathbf{Q}_2 = \text{diag} [10^{-2} \ 10^4 \ 10^0 \ 10^0]$ and $\mathbf{R}_2 = \text{diag} [10^{-1} \ 10^4]$ for the cascaded design.

4.2. KF-like LSO

This Section presents results for the KF-like LSO for both the standard implementation and the cascaded structure in Figures 5 and 6, respectively. It can be seen that the overall estimation

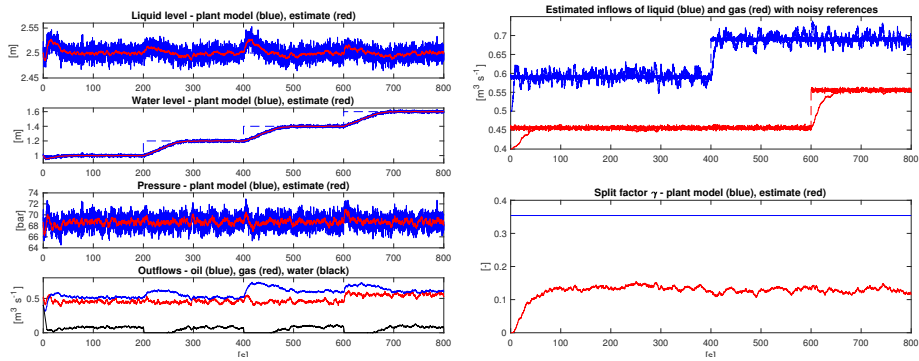


Figure 3: Results for the EKF in standard form: Measurable state variables, their estimates and manipulated variables on the left, disturbance variables and their estimates on the right

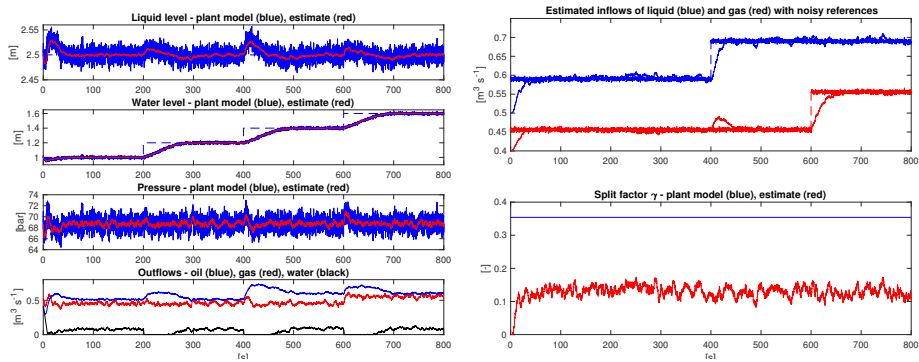


Figure 4: Results for the EKF in cascaded form: Same order of plots and signals as before

performance is much better compared to the EKF in the previous example. What is remarkable is that the cascaded structure in Figure 6 shows slightly worse performance compared to the standard structure in Figure 5, especially when comparing the estimate for the gas inflow after $t = 400$ s. This phenomenon, however, can also be seen in the EKF and might be caused by some delay introduced by the cascaded structure.

The observer parameters have been chosen to be $\lambda = 10^{-1}$ and $R = \text{diag} [10^0 \quad 10^0 \quad 10^4]$ for the standard formulation and $\lambda_1 = 10^{-1}$, $R_1 = 10^1$ as well as $\lambda_2 = 10^{-1}$ and $R_2 = \text{diag} [10^{-1} \quad 10^2]$ for the cascaded structure.

5. Discussion

In this paper, we presented observer designs for virtual inflow monitoring in gravity separation devices with simplified tuning procedures. We demonstrated in simulations that the KF-like LSO, compared to the EKF, performs generally better despite its simpler tuning. The cascaded structure clearly has a positive influence on the estimate of the liquid inflow for the EKF, but does not improve the overall performance of the KF-like LSO. The simpler tuning of the KF-like LSO makes it superior to the EKF, at least for the presented application, where a better noise suppression is the consequence.

Generalization of the results to virtual flow metering in other applications is not automatically

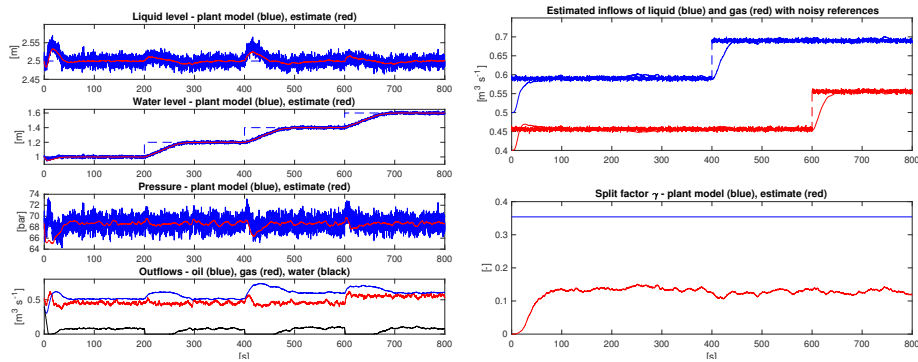


Figure 5: Results for the KF-like LSO in standard form: Same order of plots and signals as before

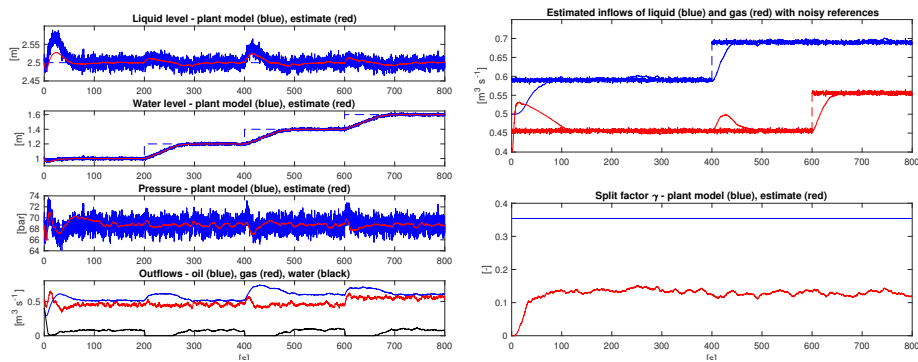


Figure 6: Results for the KF-like LSO in cascaded form: Same order of plots and signals as before

implied. The presented observer designs are based on a process model together with available measurements, which might be substantially different for other applications.

6. Acknowledgement

The authors gratefully acknowledge the financial support provided by the Norwegian Research Council in the project SUBPRO (Subsea production and processing).

References

- C. J. Backi, S. Skogestad, 2017a. A simple dynamic gravity separator model for separation efficiency evaluation incorporating level and pressure control. In: Proceedings of the 2017 American Control Conference. Seattle, USA, pp. 2823–2828.
- C. J. Backi, S. Skogestad, 2017b. Virtual inflow monitoring for a three phase gravity separator. In: Proceedings of the 1st IEEE Conference on Control Technology and Applications. Kohala Coast, USA, pp. 1499–1504.
- H. Hammouri, J. De Leon Morales, 1990. Observer synthesis for state-affine systems. In: Proceedings of the 29th IEEE Conference on Decision and Control. Honolulu, USA, pp. 784–785.
- M. A. M. Haring, 2016. Extremum-seeking control: convergence improvements and asymptotic stability. Ph.D. thesis, Norwegian University of Science and Technology.
- R. M. Johnstone, C. R. Johnson, R. R. Bitmead, B. D. Anderson, 1982. Exponential convergence of recursive least squares with exponential forgetting factor. In: Proceedings of the 21st IEEE Conference on Decision and Control. Orlando, USA, pp. 994–997.
- S. Skogestad, 2003. Simple analytic rules for model reduction and PID controller tuning. *Journal of Process Control* 13, 291–309.

Smarter process engineering across the plant life-cycle: CAPE 4.0 in industrial practice

David Elixmann*, Michael Imle, Markus Feist, Rolf-Dieter Becher

BASF SE, Carl-Bosch-Straße 38, 67056 Ludwigshafen/Rhein, Germany

david.elixmann@basf.com

Abstract

Digital trends in industry 4.0 are rapidly moving towards comprehensive connectivity and higher transparency in all manufacturing processes. It is expected that “process engineering 4.0” will turn data into value for chemical companies by increasing efficiency throughout the plant life-cycle. By improving efficiency in design and planning processes, by helping plant operators and engineers to better understand and operate their processes, and by reducing the effort required for “high end” CAPE techniques. These are dynamic simulation, operator training simulation, and real time optimization. First examples are soft sensors that enable operators to understand and optimize the process in real time based on simulations of dedicated equipment, as towers or heat exchangers.

Keywords: process operations, operator support system, process design & optimization, industry 4.0, Process industry

1. Introduction

“Data is the new oil” is the paradigm for an information industry that regards today’s data flows as a resource much like oil: Immensely useful for a plethora of new applications, and immensely valuable for those who control its sources and know how to process it into products and services. (cf. Simon and de Prato, 2015)

BASF’s own 4.0 initiatives in the field of computer-aided process engineering focus on the fields of predictive maintenance, supply chain optimization on the “Verbund” level, and engineering data management. They are expected to have a high impact on process simulation, plant design, process control and automation. It is expected that “process engineering 4.0” will turn data into value for BASF by increasing efficiency throughout the plant life-cycle:

Modern CAPE software with better mathematical solvers, improved user interfaces and better access to engineering databanks are expected to reduce the effort required for modelling and simulation activities in plant design. (cf. Marquardt 1996)

The integration of real-time plant data interfaces within process simulation tools is expected to significantly reduce the effort required to deploy process simulation models as online advisory tools. This will make it easier for process engineers to provide simulation consultancy and advice to plant operators, enabling them to better understand and operate their plants.

The simplification of process simulation work flows and the improved accessibility of equation-oriented modelling techniques is expected to make “high-level” CAPE techniques such as dynamic simulation and real-time optimization (RTO) sufficiently accessible to no longer require highly trained specialists, but young professionals with only a few years of process modelling experience. This would let young professionals quickly learn and apply these techniques on their own, greatly reducing the effort to create and maintain applications based on these techniques. (cf. Elixmann et al. 2014; Engl et al. 2010; Müller et al. 2017)

Key to these expectations is the concept of the “virtual plant” which embodies the idea of fully digitally supported engineering, operation and maintenance. The virtual plant is the digital representation of a real or planned chemical plant’s process behaviour, its control system configuration, the three-dimensional arrangement of its mechanical and electric equipment, its piping system, and its civil engineering structure.

BASF’s engineering & maintenance unit is investigating lighthouse projects to test whether these expectations are justified. There is a high willingness to invest into tools and training, should these lighthouse projects identify potential added value for the company’s process engineering discipline.

2. Results and discussion

An initial lighthouse project centres on soft sensors for heat exchanger fouling coefficients. Besides of this, foaming factors in absorption columns, supersaturation in absorption columns, and infrequently measured product concentrations in distillation units can be predicted and used as soft sensor (Burdorf et al. 2017; Imle et al. 2014). The modelling concepts behind these applications are not new, and have been taught to engineering students for decades (cf. Klatt and Marquardt 2007). However, the deployment and maintenance of such applications has in the past been regarded as too time consuming to allow these to become a routine activity. Experiences at BASF indicate that this is no longer the case, and that these applications can be justified on relatively small project budgets, or even as “side products” of conventional debottlenecking projects.

Other lighthouse projects involve the set-up of dynamic process simulation models in advance of plant modification projects and distributed control system (DCS) migration projects, and the conversion of process simulation models built for plant design projects into predictive process models for RTO projects. In the past, dynamic simulation models or predictive RTO models have only rarely been developed within BASF’s process engineering unit, since the effort to train engineers in the highly specialized tools for these complex modelling tasks could not be economically justified. There are indications that newer process simulation software and better deployment tools may change this situation, enabling a much higher degree of in-house development or preparation of such process models.

3. Outlook

It is possible that within a short time the assessment of software tool capabilities may change drastically from “It’s too complex for anyone but a specialist” to “Maybe we can actually train young professionals on these tools without putting them on a track to become expert specialists”.

If this were to change, demands on process engineers’ skills and methods could be expected to change substantially. To take advantage of more capable CAPE tools and plant data interfaces, process engineers must possess skills that at present are not considered to be critical in chemical engineering education.

Process engineers on “virtual plant” projects must develop a deeper understanding of their chemical plants. To develop practical CAPE 4.0 solutions, they must work with plant dynamics, process control, plant hydraulics, and measurement technology. They need to understand the chemistry and thermodynamics of their plants not just at the plants’ design conditions, but also under transient conditions, to build a predictive process model. This goes beyond the level of understanding required for a conventional steady-state process design task.

Their process models must robustly simulate plant behaviour not just at steady-state design conditions, but also across a wide range of plant operating conditions. Simulated equipment conditions must match actual observed operating conditions with higher accuracy than required for the original equipment design. Heat exchanger models must be able to accurately predict outlet temperatures and heat loads depending on inlet temperatures and process flow rates. Compressor models need to be extended to include performance curves across the expected operating range of the compressor unit.

Since these and other, similar requirements generally make the simulation models more complex and less robust, process engineers involved in “CAPE 4.0” projects must also become familiar with previously little used simulation techniques and rarely considered technical aspects of their simulation models. Troubleshooting a complex, equation-oriented steady-state simulation intended for a real-time online application requires that the engineer understands certain mathematical concepts such over/under-specification of equation systems, and diagnosing ill-posedness of process models (a frequent problem when on-line process models are automatically parameterized with plant data). Troubleshooting a dynamic process simulation requires some knowledge of the different ways in which a differential-algebraic equation system can become unsolvable.

Lastly, there is the challenge of interdisciplinary environments. “CAPE 4.0” projects will involve not just process engineers who develop sophisticated models, but also plant managers and operators who are the custodians of process know-how, and automation engineers who deploy those process simulation models as part of advanced process control systems. There exists at present only a fuzzily delineated division of work between process modelling experts and automation experts, because both roles are usually staffed with people from similar education backgrounds. The plant manager and operators, on the other hand, may often have no prior experience with simulation methods at all. It is very important that capabilities and limitations of the CAPE tools are clearly communicated at the beginning of these projects.

Some young process engineers who are now graduating from universities already possess deeper modelling and simulation know-how than past generations. Nevertheless, we see that there is still a skill gap between the requirements of the

“CAPE 4.0” working environment, and the skills that universities teach their chemical engineering students. Because CAPE teams are frequently the entry points and initial training environment for young graduates, a personnel turnover in CAPE teams of 50% within 5 years is not uncommon. Furthermore, internal demand for engineering skills within chemical corporations tends to place a higher emphasis on training young professionals well-rounded engineering skills rather than training them to a high degree of specialization in CAPE techniques. This implies that young professionals will only have a limited time available for learning the above mentioned “CAPE 4.0” skills on the job, if they were not acquired at university. We foresee a high demand from the chemical industry for engineers with strong foundations in systems engineering, process dynamics and control engineering.

We call on university educators who are now teaching the next generation of process engineers to place emphasis on these skills which are the key to interdisciplinary understanding and problem solving problem-solving skills in the field of CAPE 4.0.

4. Conclusions

Virtual plant based workflow and methods are only getting started now. There are great possibilities once their feasibility is proven, and the best ways to deploy state of the art software have been identified.

Soft sensor methods are already at the point where such applications can easily be developed by individual process engineers using state of the art process simulation software. Demand for dynamic simulations and RTO applications can be expected to take off rapidly once expectations for easier model development are realized.

Education of future process engineers is key to enable wider spread of high end “CAPE 4.0” methods.

References

- A. Burdorf, D. Elixmann, M. Imle, 2017, Accelerate conceptual process engineering using Column Analysis in Aspen Plus V9, OPTIMIZE 2017
- D. Elixmann, J. Puschke, H. Scheu, R. Schneider, I. Wolf, W. Marquardt, 2014, A software environment for economic NMPC and dynamic real-time optimization of chemical processes. at - Automatisierungstechnik. 62, 150-161
- G. Engl , A. Kröner , M. Pottmann , Computer Aided Chemical Engineering, Vol. 38 (Eds: S. Pierucci , G. Buzzi Ferraris), Elsevier, Amsterdam 2010, 451 – 456.
- M. Imle, E. von Harbou, L. Brachert, K. Schaber, H. Hasse, 2014, Predicting supersaturation by rate-based simulations of reactive absorption, Chemical Engineering Science, 118, 41-49.
- KU. Klatt, W. Marquardt, 2007, Perspectives for process systems engineering – a personal view from academia and industry, Computer Aided Chemical Engineering, 24, 19-32.
- W. Marquardt, 1996, Trends in computer-aided process modeling, Computers & Chemical Engineering, 20, 591-609.
- D. Müller, B. Dercks, E. Nabati, M. Blazek, T. Eifert, J. Schallenberg, U. Piechottka, K. Dadhe, 2017, Real-Time Optimization in the Chemical Processing Industry, Chemie Ingenieur Technik, 89, 1464-1470.

- J. Simon, G. de Prato, 2015, Is data really the new “oil” of the 21st century or just another snake oil? Looking at uses and users (private/public). 26th European Regional Conference of the International Telecommunications Society, San Lorenzo de El Escorial, Spain

Network formulations for the design and scheduling of multiproduct batch plants with parallel lines

Floor Verbiest^{a,*}, Tânia Pinto-Varela^b, Trijntje Cornelissens^a and Ana Barbosa-Póvoa^b

^a*ANT/OR - Operations research group, Dpt. of Engineering Management, University of Antwerp, Prinsstraat 13, Antwerp 2000, Belgium*

^b*CEG-IST, Instituto Superior Técnico, Universidade de Lisboa, Av Rovisco Pais 1, Lisbon 1049-001, Portugal*
floor.verbiest@uantwerpen.be

Abstract

Parallel production lines are a design option often used in chemical batch plants. In recent research, this option has been introduced into the strategic multiproduct batch plant design problem, assuming a single product campaign mode of operation. However, to accommodate for other modes of operation and different production strategies, more explicit scheduling should be considered. In this paper, the combined design and scheduling optimization of multiple lines multistage plants is addressed. More specifically, we explored the Resource-Task Network formulation, in which constraints were included to exploit the sequential characteristics of the problem under study. Furthermore, two solution approaches were studied: a general holistic one and, triggered by the rapid increase in problem size and computational expense, a decomposition approach. In this decomposition approach, the problem is divided into smaller subproblems, by fixing the number of lines, which are iteratively solved. The performance of both approaches are compared via several illustrative examples.

Keywords: design and scheduling, batch plants, parallel lines, Resource-Task Network

1. Introduction

The strategic design of chemical batch plants is a challenging research problem that has been studied extensively in the past decades. Over the years, the design models have been extended with strategic choices on e.g. different modes of operation and several design options (Barbosa-Póvoa, 2007). Recently, Verbiest et al. (2017) introduced parallel production lines, as a new design option, into the multiproduct multistage batch plant design problem. The aim of the corresponding MILP is to determine the optimal number of lines to install, the number and size of equipment units at every stage of every line and the assignment of products to every line, assuming a single product campaign mode of operation. However, despite the work already developed, other modes of operation and different production strategies need to be accounted for, which triggers the introduction of more explicit scheduling.

The optimization of plant design in combination with scheduling has already been explored via different methodologies, such as network formulations (Barbosa-Póvoa, 2007). These network formulations are proven to be powerful for this combined optimization, mainly for multipurpose plants (Pinto et al., 2008). However, in recent years, researchers have shown an increased interest

in applying these formulations to multiproduct multistage problems, i.e. sequential processes, as well (e.g. Castro and Grossmann (2005); Sundaramoorthy and Maravelias (2011)).

Motivated by these successful applications and the inherent flexibility of network representations (Méndez et al., 2006), this work explores the applicability of the Resource-Task Network (RTN) formulation, with discrete time representation, for the design and scheduling of multiproduct multistage batch plants with parallel lines. The RTN is a generic representation, originally formulated by Pantelides (1994), that is characterized by resources and tasks. The resources can be non-renewable resources, e.g. materials, or renewable resources, e.g. equipment units, that are produced and consumed by tasks (i.e. operations). Due to its generality, however, RTN models tend to increase fast in size, and accordingly in computational complexity (Méndez et al., 2006), so that adapted solution approaches are requested.

In the next section (Section 2), an overview of the problem considered is given together with the application of the RTN formulation. To tackle the computational complexity that is coupled with larger problems, an adapted (decomposed) solution approach is presented in Section 3. Some illustrative examples are studied in Section 4, where we compare the results of the adapted solution approach with the results obtained from solving the general (holistic) model. We end with a conclusion and some directions for future research.

2. Modeling framework

2.1. Problem characterization

The installation of parallel production lines in chemical batch plants is a design option frequently used in industry (Hill et al., 2016). These parallel lines are installed on the same production site and operate simultaneously, but independently, from one another. The lines have the same number of stages, so that production may be split over the optimal number of lines installed (see Figure 1). The presence of such parallel lines often allows for a reduction in total cost as not all products have to share all equipment any more, leading to smaller equipment and lower operating costs. Furthermore, products with similar characteristics are often grouped into product families and the dedication of these lines to particular products or product families may again reduce total operating costs by avoiding high contamination costs (Verbiest et al., 2017).

Within this setting, the aim of the problem is to determine:

- The optimal design of the plant. This encompasses the number of lines to install and, for every installed line, the number and size of units for every stage.
- The optimal schedule of the plant. This includes the product-to-line assignment, the number and size of batches of every product on every line and the corresponding timings and sequences of the batches on every line.

so as to minimize investment and operating costs.

2.2. Mathematical representation

The problem under study considers a multistage multiple lines batch plant producing P products i over ST stages st , where every stage performs a batch operation. There is the possibility to install at most L lines l with the same number of stages ST . The demand for every product and the total horizon are known upfront. A more detailed description is given in Verbiest et al. (2017).

In the RTN formulation of this plant, the sets considered are: (1) non-renewable resources r that represent the raw materials, intermediate states and finished products (the latter are equal to number of products P); (2) renewable resources j which are all the equipment units installed in every stage st of every line l and, finally, (3) tasks k that represent an operation in stage st of line l needed to produce product i . Every task k is characterized by a pair of variables: an integer variable N_{kt}

and a continuous one ξ_{kt} . These variables can be interpreted, respectively, as the number of units used by task k at time t and the total amount of material processed by these tasks (i.e. batch sizes). Moreover, every task has a fixed processing time (τ_k) and is linked to a unit j with a utilization factor (ϕ_{kj}), comparable to size factors defined in Verbiest et al. (2017).

Figure 1 illustrates an RTN representation of a batch process to produce one product (FP1). This process consists of 3 stages and at most 3 lines are allowed to be installed. The RTN requires 8 non-renewable resources r , 9 renewable resources j and 9 tasks k . Finally, the task-to-unit relation is shown as well

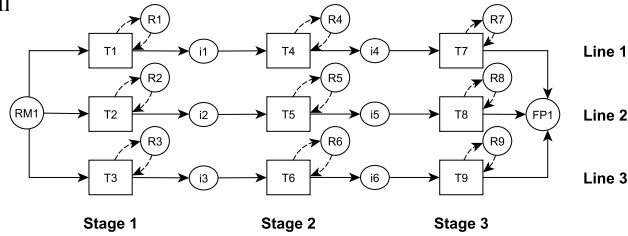


Figure 1: RTN representation of a batch multiple lines plant, producing 1 product

The main assumptions considered are: (1) Process/recipes are determined upfront; (2) Deterministic demand and process parameters, with the demand fulfilment for every product a hard constraint; (3) Only batch processing equipment is considered, with known unit-task compatibility; (4) Zero-wait policy between batch stages; (5) No batch splitting or mixing is allowed; (6) Identical parallel batch equipment per unit j , at most Δ^{max} , operating in-phase and used by one task at a time; (7) Discrete set of S equipment sizes V_s for all renewable resources j to choose from.

The objective of the developed MILP is to minimize the total cost, given by:

$$\sum_j \left(CCf_j \Delta_j + \sum_s V_s^{CCv_j} z_{js} \right) + \sum_k \sum_t N_{kt} CO_k \tag{1}$$

The first term are the capital costs that consist of a fixed component and a volume dependent component. The cost coefficients CCf_j, CCv_j are given, with $CCv_j < 1$ and equal costs for units j belonging to the same stage st . Δ_j is an integer variable indicating the number of identical units installed of resource j . The size choice of every unit is defined by V_s , the equipment size s chosen out of the given set, and the binary variable z_{js} that indicates if unit j has size s . The second term represents the operating cost, with CO_k being a known task-dependent cost coefficient and N_{kt} the integer variable that defines the number of units used by task k at time t .

As products in multistage multiple lines plants, once assigned to lines, go sequentially through all the stages of that line, batch preservation has to be guaranteed and constraints (2) and (3) are included in comparison to general (multipurpose) network models.

$$\xi_{kt} = \xi_{k'(t+\tau_k)} \quad \forall t, k, k' \text{ with } k' \text{ the task performed in the next stage after } k \tag{2}$$

This constraint enforces the batch integrity over the process, and states that if a task k at time t was executed, then exactly τ_k later, the task k' on the following stage of the same line will start and will have the same continuous extent.

An analogous constraint (Eq.(3)) is posed on the integer extent of the task (N_{kt}). However, it is an inequality since the units used by every task may differ from stage to stage because of possible differences in the units installed in every stage of a line.

$$N_{kt} \leq \Delta^{max} N_{k'(t+\tau_k)} \quad \forall t, k, k' \text{ with } k' \text{ the task performed in the next stage after } k \tag{3}$$

The remaining constraints are taken from the general RTN-model (see (Pantelides, 1994)), hence they will not be discussed. The two solution approaches studied use the mathematical representation presented above, with the holistic approach solving this model as it is using the Gurobi 7.0

solver. The adaptations made in the decomposition approach are discussed in the next section.

3. Decomposition solution approach

Since in the RTN formulation of the multistage multiple lines design problem the number of tasks and states increase very fast, the problem as such becomes difficult to solve in a reasonable computation time. In order to tackle the computational complexity, we propose a decomposition solution approach in which the holistic problem is divided into smaller problems, which are iteratively solved. The decomposition is done by fixing the number of lines, as this decision has a high impact on the model size (for every line l , for every product i , st numbers of tasks have to be specified). The procedure contains the following steps:

Step 1 Set the number of lines (NumbLin) equal to 1 and include a very large upper bound (UB) on the objective function

Step 2 Solve the subproblem (min. *TotalCost*, with a fixed NumbLin) using RTN with the extra constraint $UB > TotalCost$.

If the subproblem is infeasible - stop calculation and go directly to Step 4

Step 3 Update upper bound: $UB = TotalCost$

Step 4 If $NumbLin < L$, increase NumbLin with 1 and go back to Step 2.

The expected gains of this approach in comparison to solving the general holistic model are 3-fold: Firstly, at every iteration, the models considered are smaller in size, and thus, easier to solve. This can be illustrated on Figure 1: when solving a fixed 1 line model, we only have to consider 3 tasks, 4 non-renewable resources and 3 renewable resources, instead of respectively 9, 8 and 9. Secondly, after every iteration, the best solution found so far is updated and included as an upper bound in the next iteration. With this extra constraint, it might be unnecessary to solve all L models as worse solutions would make the calculations stop. Finally, as in every model the number of lines is fixed, the following constraint, existent in the original model, can be modified:

$$\sum_s z_{js} \leq 1 \quad \forall j \quad \rightarrow \quad \sum_s z_{js} = 1 \quad \forall j \quad (4)$$

and an additional constraint can be included:

$$\Delta_j \geq 1 \quad \forall j \quad (5)$$

With these constraints, the model is forced to install at least 1 unit of every renewable resource and to choose exactly 1 size out of the set of sizes. So, we limit the search possibilities given to the model.

4. Examples

To illustrate the performance of the proposed decomposition approach (Case a) and its comparison with the holistic formulation (Case b), three examples are used.

4.1. Process description

The processes can be described as chemical batch plants in which the demand for a certain number of products, belonging to certain product families, needs to be fulfilled within a predefined planning horizon. In order to produce these products, different operations (stages) are needed. For every stage a maximum number of identical units are operating in-phase and sizes are chosen out of a given set. Furthermore, the number of lines that can be installed on the production sites is limited. Table 1 gives a summary of the production data for every example, whereas the cost coefficients are given in Table 2. Note that capital costs are identical for units j belonging to the same stage st and operating costs are assumed the same for all tasks per product per line.

Table 1: Main production data - 3 illustrative examples

	Products	Prod Fam.	Stages	Parallel Equipm.	Sizes	Lines	Horizon	Demand (x10 ³)						
								P1	P2	P3	P4	P5	P6	P7
Ex1	3	3	4	3	5	4	15	1.83	1.57	0.99				
Ex2	7	3	3	3	4	3	12	2.55	1.95	2.2	1.0	1.9	1.45	2.5
Ex3	3	3	3	3	4	3	24	9.5	6.7	5.7				

Table 2: Main cost data - 3 illustrative examples

	Capital cost coefficients, per stage		Operating cost coefficients, per product per line			
	CC _f	CC _v				
Ex1	{300, 250, 230, 275}	{0.67, 0.65, 0.60, 0.62}	{50, 95, 85, 50}; {95, 50, 70, 95}; {85, 70, 50, 85}			
Ex2	{450, 400, 380}	{0.67, 0.65, 0.60}	{50, 90, 90}; {50, 90, 90}; {90, 50, 65}; {90, 50, 65}; {90, 65, 50}; {90, 65, 50}; {90, 65, 50}			
Ex3	{450, 400, 380}	{0.67, 0.65, 0.60}	{50, 90, 90}; {90, 50, 65}; {90, 65, 50}			

4.2. Results

The results of the 3 examples, and the computational statistics of the 2 approaches, are shown in Table 3. The optimality gap was set to 0% and the computational time was limited to 3 h.

Table 3: Results - Case (a) Decomposition (Decomp.) vs Case (b) Holistic (Hol.) approach

	Example 1 (3 Prod., 4 Stages, max.4 lines - H15)				Example 2 (7 Prod., 3 Stages, max.3 lines - H12)				Example 3 (3Prod, 3 Stages, max.3 lines - H24)				
	(a) Decomp.		(b) Hol.		(a) Decomp.		(b) Hol.		(a) Decomp.		(b) Hol.		
	1L	2L	3L	4L	1L	2L	3L	3L	1L	2L	3L	3L	
Sol.	5768	4711	Stop	Stop	4711	infeas.	8982	8360	8360	9691	7726	Stop	7726
Gap (%)	0	0	/	/	0	/	0	0	9.16	0	0	/	2.74
CPU (s)	14.88	107.19	/	/	4572.39	0.0	388.88	4748.09	3h	2.40	2568.28	/	3h
Var.	5173	18,896	/	/	72,262	4926	17,244	37,122	37,122	4266	14,868	/	31,950
Bin Var.	200	400	/	/	800	264	528	792	792	228	456	/	684
Const.	3321	6546	/	/	13,125	4115	8055	11,994	12,046	3718	7288	/	10,912

All numerical results were obtained using the Gurobi 7.0 optimizer on an Intel(R) Core(TM) i7-4790 CPU, 3.60GHz and 16 GB of RAM

As can be seen from Table 3, the proposed decomposition approach obtained the same solutions as the holistic approach. These solutions correspond to the installation of 2 parallel lines in examples 1 and 3, and of 3 lines in example 2. However, the decomposition approach reaches the optimal solutions with a significant lower computation time. For example 1, both solution methods found the optimal solution (gap: 0%), but the decomposition approach uses only 3% of the time when compared to the holistic approach. For example 2 and 3, the holistic approach was not able to reach an optimality gap of 0% after 3h, while the decomposition approach reached the optimal solutions in 1.5h and 45min, respectively. Finally, the problem characteristics are listed in the last 3 rows. It can be seen that in the decomposition approach smaller problems are solved, leading to reduced computing times.

Due to space limitations, we will only discuss example 3 more in detail. For this case, it is optimal to install a plant that consists of 2 lines (with a capital cost of 4351 and an operating cost of 3375). It is feasible to produce all products on 1 line, however, this is more expensive: the lower capital costs of 4021 (-7.5%) do not offset the high operating costs of 5670 (+68%) that are incurred when all product(families) are produced together. Furthermore, the solution of the 2-lines model considered as an upper bound in the 3-lines model leads to an early termination of the procedure, as this extra constraint could not be satisfied.

The selected equipment units (size and number) in every stage of the 2-lines plant as well as the proposed schedule are shown in Figure 2. Product 1 is produced entirely on line 1 and product 2 on line 2. Although it is less expensive to produce product 3 in combination with product 2 (lower operating costs per task as specified in Table 2), it is not feasible to make all the batches of 3 on line 2 (without having to increase the design). Hence, it is also produced on line 1.

As the present work is an extension of the work of Verbiest et al. (2017), it is important to compare the solution found in this work with the one obtained when solving the original MILP model with

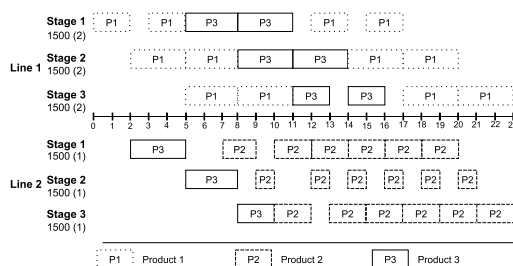


Figure 2: Optimal plant design and corresponding schedule of example 3

single product campaign mode of operation. The optimal solution found there is a 3-lines plant, instead of a 2-lines plant, that has a lower total cost. However, the proposed solution as it is, is infeasible since no detailed schedule was considered. Indeed, the total time spent on every product is based on the product cycle times, which is an underestimation. Hence, the combined design and scheduling problem results in more realistic solutions, supporting more thorough testing of the decomposition solution approach and further investigation of other adaptations in the future.

5. Conclusion

In this paper, the design and scheduling of multiproduct multistage chemical batch plants equipped with parallel production lines is investigated. More specifically, we applied the RTN formulation to solve this problem, in which some constraints that account for the sequential process were included. Besides solving the RTN model holistically, a decomposition solution approach is proposed to address the computational burden that is coupled with the rapid increase in problem sizes. In this approach, the problem is divided into smaller RTN-based subproblems, each with a fixed (incrementing) number of lines, which are solved iteratively. Three illustrative examples were solved with both approaches and it was found that the decomposition solution approach reached the optimal solutions with significantly lower computation times. Finally, the importance of simultaneously designing and scheduling batch plants is also demonstrated. As future work, further research should be carried out to explore other problem specific-adaptations and to thoroughly test the approach, so that ultimately the models can account for more responsive production strategies.

6. Acknowledgements

This work was supported by the Research Foundation - Flanders (FWO) and by Portugal 2020, POCI-01-0145-FEDER-016418 by UE/FEDER through the program COMPETE2020.

References

- A. P. Barbosa-Póvoa, 2007. A critical review on the design and retrofit of batch plants. *Comp. & Chem. Eng.* 31 (7), 833–55.
- P. M. Castro, I. E. Grossmann, 2005. New continuous-time milp model for the short-term scheduling of multistage batch plants. *Ind. Eng. Chem. Res.* 44 (24), 9175–9190.
- A. Hill, T. Cornelissens, K. Sørensen, 2016. Efficient multi-product multi-bom batch scheduling for a petrochemical blending plant with a shared pipeline network. *Comp. & Chem. Eng.* 84, 493–506.
- C. A. Méndez, J. Cerdá, I. E. Grossmann, I. Harjunkoski, M. Fahl, 2006. State-of-the-art review of optimization methods for short-term scheduling of batch processes. *Comp. & Chem. Eng.* 30 (6), 913–46.
- C. C. Pantelides, 1994. Unified frameworks for optimal process planning and scheduling. In: *Proceedings on the 2nd conference on foundations of computer aided operations*. Cache Publications New York, pp. 253–74.
- T. Pinto, A. P. F. D. Barbosa-Póvoa, A. Q. Novais, 2008. Design of multipurpose batch plants: A comparative analysis between the stn, m-stn, and rtn representations and formulations. *Ind. Eng. Chem. Res.* 47 (16), 6025–6044.
- A. Sundaramoorthy, C. T. Maravelias, 2011. A general framework for process scheduling. *AIChE J.* 57 (3), 695–710.
- F. Verbiest, T. Cornelissens, J. Springael, 2017. Design of a chemical batch plant with parallel production lines: Plant configuration and cost effectiveness. *Comp. & Chem. Eng.* 99, 21–30.

Fault detection of fermentation processes

Ernie Che Mid, Vivek Dua*

*Department of Chemical Engineering, Centre of Process System Engineering (CPSE),
University College London, Torrington Place, London WC1E 7JE, United Kingdom*

**Email: v.dua@ucl.ac.uk*

Abstract

Fault detection is becoming an important issue in fermentation processes. Any improper formulation or contamination in the fermentation may change the kinetic model parameters and lead to a process fault. In this work, a square system of parametric nonlinear algebraic equations is formulated and solved symbolically to obtain the kinetic model parameters as an explicit function of measurements, so as to estimate the parameters to detect and diagnose the faults in fermentation processes. A number of scenarios are considered to show the effectiveness of the presented approach. The proposed approach successfully estimates the model parameters and detects the faults in the system.

Keywords: Fault detection, fermentation, parameter estimation, multiparametric programming

1. Introduction

Fermentation is a process in which biomass gets converted into products such as alcohol or acid. Fermentation process is highly sensitive to small changes in operating limits that may affect the final product quality if changes happen during crucial stages of operation. Therefore the operation of fermentation must be maintained within specific limits. The process of detecting and diagnosing fault in industrial processes is thus required to be implemented in early operation to maintain the product quality and reduce production cost (Isermann, 1993; Mhaskar et al., 2006; Venkatasubramanian et al., 2003).

A number of studies have demonstrated the fault diagnosis in fermentation processes (Birol et al., 2002; Monroy et al., 2012). For glutamic acid fermentation, the diagnosis has been reported using wavelet analysis (Zhao et al., 1999; Ma et al., 2003), using extended Kalman filter and neural networks (Liu, 1999), and using support vector machines (Ma et al., 2007). However, the mentioned approaches are computationally demanding (Liu, 1999) and the diagnosis becomes difficult when more than one fault takes place simultaneously. In this work we propose a method to detect faults using multiparametric programming to address some of these issues for fermentation processes.

In our earlier work (Che Mid & Dua, 2017) a methodology based on multiparametric programming, to obtain the model parameters as an explicit function of the measurements, was presented. In that work a square system of parametric nonlinear algebraic equations was obtained by formulating optimality condition. These equations were then solved symbolically to obtain model parameters as an explicit function of measurements. In glutamic acid fermentation process (Ma et al., 2003), the state

variables are represented by the concentration of biomass, substrate and product. These state variables cannot be measured online and therefore this methodology cannot be directly applied. Therefore in this work, we present a methodology for the cases where the state variables cannot be measured but can be estimated from other measurable quantities such as pH, dissolved oxygen and temperature. By monitoring the estimated kinetic model parameters, process faults can be detected and diagnosed. The estimated kinetic model parameters should be close to observed parameters when no fault is present and any substantial discrepancy between the estimated and observed parameters indicates changes in the process and can be interpreted as a fault.

2. Fault detection using Multiparametric Programming

In fault detection, the objective is to estimate parameters, $\boldsymbol{\theta}$, such that the error, ε_{FD} , between the measurements, \hat{x}_j , and the model predicted value of state variables, x_j , is minimized as follows:

$$\varepsilon_{FD} = \min_{\boldsymbol{\theta}, \mathbf{x}(t)} \sum_{j \in J} \sum_{i \in I} \{\hat{x}_j(t_i) - x_j(t_i)\}^2 \quad (1)$$

Subject to:

$$\frac{dx_j(t)}{dt} = f_j(\mathbf{x}(t), \mathbf{u}(t), \boldsymbol{\theta}, t), j \in J \quad (2)$$

$$x_j(t=0) = x_j^0, j \in J \quad (3)$$

$$t \in [0, t_f] \quad (4)$$

where $\mathbf{x}(t)$ is the J-dimensional vector of state variable in the given ODE system, $\mathbf{u}(t)$ is the vector of control variables, and $\boldsymbol{\theta}$ is the vector of parameters. In our previous work (Che Mid & Dua, 2017), a solution technique for fault detection using multiparametric programming (MPP) to estimate the model parameters, $\boldsymbol{\theta}$, was presented. The model parameters, $\boldsymbol{\theta}$, are considered as optimization variables and the measurements, $\hat{x}_j(k+1)$, as the parameters in the context of multiparametric programming. The algorithm for model-based parameter estimation for fault detection using multiparametric programming is summarized as below (Che Mid & Dua, 2017):

(i) Discretize nonlinear ODE model in Equation (2) to algebraic equations using Euler's method and solve on the interval, $t \in [0, t_f]$ and step size, Δt , as given in Equation (5)

$$x_j(k+1) = x_j(k) + \Delta t f_j(\mathbf{x}(k), \mathbf{u}(k), \boldsymbol{\theta}) \quad (5)$$

(ii) Formulate fault detection optimization problem as a nonlinear programming (NLP) problem. For $I=1$, substituting Equation (5) in Equation (2), the fault detection problem is given as in Equations (6) to (8)

$$\varepsilon_{MPP} = \min_{\boldsymbol{\theta}, \mathbf{x}_j(k=1)} \sum_{j \in J} \{\hat{x}_j(k+1) - x_j(k+1)\}^2 \quad (6)$$

Subject to:

$$h_j = x_j(k+1) - x_j(k) - \Delta t f_j(\mathbf{x}(k), \mathbf{u}(k), \boldsymbol{\theta}) = 0, j \in J \quad (7)$$

$$x_j(k=0) = x_j^0, j \in J \quad (8)$$

where h_j represents the set of nonlinear algebraic equations obtained by discretizing the ODEs given by Equation (2) and shown in Equation (5).

(iii) Formulate Karush-Kuhn-Tucker (KKT) conditions for Equations (6) to (8) as given by Equations (9) to (12). The Lagrangian function is given by

$$L = g + \sum_{j \in J} \lambda_j h_j \quad (9)$$

$$\text{where } g = \{\hat{x}_j(k+1) - x_j(k+1)\}^2 \quad (10)$$

The KKT conditions are given by the Equality Constraints as follows

$$\nabla_{\theta} L = \nabla_{\theta} g + \nabla_{\theta_j} \sum \lambda_j h_j = 0 \quad (11)$$

$$h_j = 0 \quad (12)$$

(iv) Solve the Equality Constrains in Equations (11) and (12) of the KKT conditions parametrically to obtain Lagrange multiplies and model parameters, $\theta(\hat{x})$, as a function of measurements.

(v) Screen the solutions obtained in the previous step and ignore solutions with imaginary parts.

(vi) Calculate the estimated model parameters, θ , using the measurement, \hat{x} by simple evaluation of $\theta(\hat{x})$.

(vii) Diagnose fault by monitoring the changes of the model parameters. The estimated model parameters should be close to observed parameters when no fault is present. Any substantial discrepancy between the estimated and observed parameters indicates changes in the process and can be interpreted as a fault.

3. Fermentation Processes

The dynamic model of the glutamic acid fermentation process is as follow (Ma et al., 2003):

$$\frac{dX}{dt} = \mu X \quad (13)$$

$$\frac{dP}{dt} = bX \left(\frac{S}{K_s + S} \right) \quad (14)$$

$$\frac{dS}{dt} = -\frac{1}{Y_G} \frac{dX}{dt} - \frac{1}{Y_P} \frac{dP}{dt} - mX \quad (15)$$

where X , P and S are the concentrations of biomass, product and substrate with $X(0) = 0.03g/l$, $P(0) = 0g/l$ and $S(0) = 101.2g/l$. These state variables can not be measured on-line but can be estimated from other measurable quantities such as pH, dissolved oxygen and temperature. μ is the growth rate of the biomass and given as $\mu = \mu_m(1 - X/x_m)$. $b = 0.358h^{-1}$ is the maximum production rate, $K_s = 12.04g/l$ is the saturation constant of substrate, $Y_G = 0.436$ is the yield coefficient of biomass, $Y_P = 0.645$ is the yield coefficient of product, $m = 0.105h^{-1}$ is the maintenance coefficient of the biomass, $\mu_m = 0.767h^{-1}$ is the maximum growth rate of the biomass and $x_m = 6.43g/l$ is the maximum biomass concentration. Any improper formulation or contamination in the fermentation will change the kinetic model parameters, such as

μ_m and Y_p , and lead to a process fault (Ma et al., 2003). In this work, the kinetic model parameters, μ_m and Y_p , are obtained as explicit functions of measurements and estimated for fault detection using multiparametric programming algorithm as described in the previous section. The discrete-time fault detection problem is formulated as the nonlinear programming (NLP) problem using the discretization of ODE model as follows:

$$\varepsilon_{MPP} = \min_{\mu_m, Y_p} \sum_{k=0}^K \left\{ (\hat{X}(k+1) - X(k+1))^2 + (\hat{P}(k+1) - P(k+1))^2 + (\hat{S}(k+1) - S(k+1))^2 \right\} \quad (16)$$

Subject to:

$$h_1 = X(k+1) - X(k) - \Delta t \mu_m \left(1 - \frac{X(k)}{x_m} \right) X(k) = 0 \quad (17)$$

$$h_2 = P(k+1) - P(k) - \Delta t b X(k) \left(\frac{S(k)}{K_s + S(k)} \right) = 0 \quad (18)$$

$$h_3 = S(k+1) - S(k) - \Delta t \left(-\frac{1}{Y_G} \mu_m \left(1 - \frac{X(k)}{x_m} \right) X(k) - \frac{1}{Y_P} b X(k) \left(\frac{S(k)}{K_s + S(k)} \right) - m X(k) \right) = 0 \quad (19)$$

The Equations (17) to (19) are substituted into Equation (16) to obtain:

$$g = (\hat{X}(k+1) - (\Delta t \mu_m \left(1 - \frac{X(k)}{x_m} \right) X(k) + X(k)))^2 + (\hat{P}(k+1) - (\Delta t b X(k) \left(\frac{S(k)}{K_s + S(k)} \right) + P(k)))^2 + (\hat{S}(k+1) - (\Delta t \left(-\frac{1}{Y_G} \mu_m \left(1 - \frac{X(k)}{x_m} \right) X(k) - \frac{1}{Y_P} b X(k) \left(\frac{S(k)}{K_s + S(k)} \right) - m X(k) \right) + S(k)))^2 \quad (20)$$

The gradient of g with respect to μ_m and Y_p are given by

$$\frac{\partial g}{\partial \mu_m} = ((2X(k)(\Delta t X(k) - \Delta t x_m)(\hat{X}(k+1) + (X(k)(\Delta t \mu_m X(k) - x_m - \Delta t \mu_m x_m)) / x_m)) / \mu_m) + ((2\Delta t X(k)(1 - X(k)/x_m)(\hat{S}(k+1) - \Delta t (S(k)/\Delta t - mX(k) - (\mu_m X(k)(1 - X(k)/x_m)) / Y_G - (bS(k)X(k)) / ((K_s + S(k)) Y_P)))) / Y_G = 0 \quad (21)$$

$$\frac{\partial g}{\partial Y_p} = -(2b\Delta t S(k)X(k)(\hat{S}(k+1) - \Delta t (S(k)/\Delta t - mX(k) - (\mu_m X(k)(1 - X(k)/x_m)) / Y_G - (bS(k)X(k)) / ((K_s + S(k)) Y_P)))) / ((K_s + S) Y_P^2) = 0 \quad (22)$$

The equality constraints in Equations (21) and (22) are solved analytically in Mathematica, and the solution is given by

$$\mu_m = \frac{(X(k) - \hat{X}(k+1))x_m}{\Delta t X(k)(X(k) - x_m)} \quad (23)$$

$$Y_p = \frac{b\Delta t S(k)X(k)Y_G}{(K_s + S(k))(X(k) - \hat{X}(k+1) + S(k)Y_G - \hat{S}(k+1)Y_G - \Delta t m X(k)Y_G)} \quad (24)$$

The kinetic model parameters, μ_m and Y_p , are given by Equations (23) and (24) are obtained as explicit function of measurements and estimated by simple function evaluation.

4. Result

The whole fermentation period is of about 15 hours. In this work, the state variables X , P and S are estimated from other measurable quantities such as pH, dissolved oxygen and temperature. The kinetic model parameters values are estimated by Equations (23) and (24) for every minute sampling time for two scenarios, fault free and faulty scenarios. In fault free scenario, the measurement for X , P and S are shown in Figure 1 with noise included. The estimated kinetic model parameters, μ_m and Y_p , are shown in Figure 2. The figure shows that estimated kinetic model parameters are close to the true value and no fault was detected. In faulty scenario, the kinetic model parameters are changed as shown in Table 1 and the measurement for X , P and S for all the faults are shown in Figure 3. The estimated maximum growth rate of the biomass and yield coefficient of product are shown in Figures 4 and 5. From these figures, we can see that after 5 h, the estimated values of μ_m and Y_p change for each faulty scenario. It indicates that process fault has started occurring in the fermentation process. Fault is declared in the system after 5h.

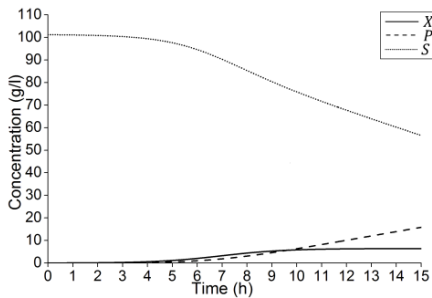


Figure 1: State variables profile for fault free scenario

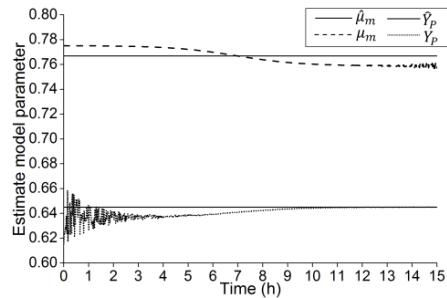


Figure 2: Estimated model parameters, μ_m and Y_p for fault free scenario

Table 1. Faulty scenario for glutamic acid fermentation

Faulty kinetic parameters	Fault 1	Fault 2	Fault 3	Fault 4
μ_m	Decrease 10 %	Increase 10 %	Decrease 15 %	Increase 15 %
Y_p	Decrease 10 %	Increase 10 %	Decrease 15 %	Increase 15 %

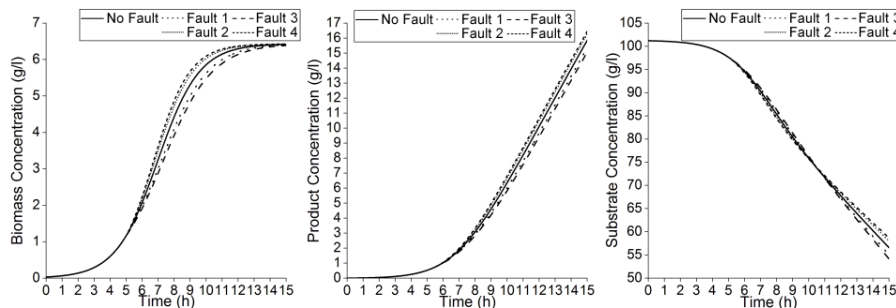
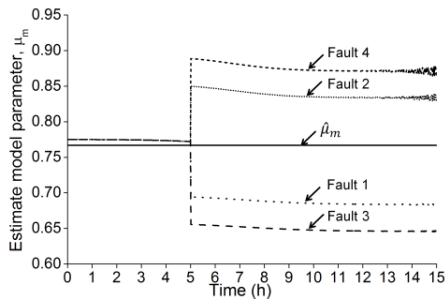
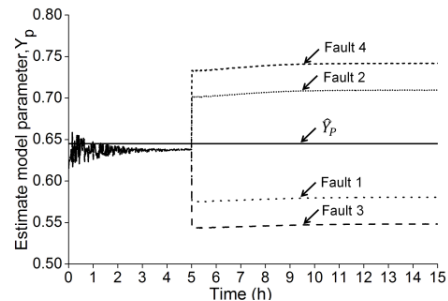


Figure 3: State variables profile for faulty scenarios

Figure 4: Estimated μ_m for faulty scenariosFigure 5: Estimated Y_p for faulty scenarios

5. Concluding Remarks

Parameter estimation based fault detection of fermentation processes is proposed using multiparametric programming. By monitoring the kinetic model parameters, process faults can be detected and diagnosed. In this work, a square system of parametric nonlinear algebraic equations was solved symbolically to obtain the model parameters as an explicit function of measurements. The model parameters are thus computed efficiently by performing simple function evaluations, without the need to solve an online optimization problem. This method is able to obtain model parameters as an explicit function of measurements and accurately estimate the kinetic model parameters value. The issues pertaining to fault tolerant control will be the subject of future work.

References

- E. Che Mid & V. Dua. 2017. Model-Based Parameter Estimation for Fault Detection Using Multiparametric Programming. *Industrial and Engineering Chemistry Research*,56(28),8000-8015.
- G. Birol, C. Ündey, & A. Çinar. 2002. A modular simulation package for fed-batch fermentation: Penicillin production. *Computers and Chemical Engineering*, 26(11),1553-1565.
- I. Monroy, K. Villez, M. Graells, & V. Venkatasubramanian. 2012. Fault diagnosis of a benchmark fermentation process: A comparative study of feature extraction and classification techniques. *Bioprocess and Biosystems Engineering*, 35(5), 689-704.
- L. Ma, F. Wang, Y. Jiang, & F. Gao. 2003. A Fault Diagnosis Method for Fermentation Process. *IFAC Proceedings*, 37(1), 661-665.
- L. Ma, J. Wang, & Z. Liu. 2007. A Fault Diagnosis Method Based on Composite Model and SVM for Fermentation Process, 2007 IEEE International Conference on Control and Automation, 3107-3110.
- P. Mhaskar, A. Gani, N. H. El-farra, C. Mcfall, P. D. Christofides, & J. F. Davis. 2006. Integrated Fault-Detection and Fault-Tolerant Control of Process Systems. *AIChE Journal*, 52(6), 2129-2148.
- R. Isermann. 1993. Fault diagnosis of machines via parameter estimation and knowledge processing-Tutorial paper. *Automatica*, 29(4), 815-835.
- V. Venkatasubramanian, R. Rengaswamy, K. Yin, & S. N. Kavuri. 2003. A review of process fault detection and diagnosis Part I: Quantitative model-based methods. *Computers & Chemical Engineering*, 27(3), 293-311.
- W. Liu. (1999). An extended Kalman filter and neural network cascade fault diagnosis strategy for the glutamic acid fermentation process. *Artificial Intelligence in Engineering*,13(2),131-140.
- Z. Zhao, X. Gu, & W. Jiang. 1999. Fault Detection Based on Wavearx Neural Network. *IFAC World congress*,1,7826-7831.

Nonlinear model predictive control application for gas-lift based oil production

Simone C. Miyoshi,^a Matheus Nunes,^{b,*} André Salles,^b Argimiro R. Secchi,^c
Maurício B. de Souza Jr.,^c Amanda L. Brandão^b

^a *Universidade Federal de São Carlos, Rod. Washington Luís (SP 310), km 235, São Carlos-SP 13565-905, Brazil*

^b *Pontifícia Universidade Católica do Rio de Janeiro, Rua Marquês de São Vicente, 225 - Gávea, Rio de Janeiro-RJ 22453-900, Brazil*

^c *Universidade Federal do Rio de Janeiro, Centro de Tecnologia - Cidade Universitária, Rio de Janeiro-RJ 21941-972, Brazil*

matnunes@aluno.puc-rio.br

Abstract

This work investigates the application of Nonlinear Model Predictive Control (NMPC) using Hammerstein Models in an offshore oil production well with gas-lift. The problem is especially challenging from the control point of view because it presents regions with gain sign inversion. This reversion of the gain direction makes this problem difficult to control with the usual Model Predictive Control (MPC) or even with the traditional Proportional-Integral-Derivative (PID) controllers. Thus, it is proposed to investigate the use of methodologies applying NMPC based on Hammerstein model combined with the Moving Horizon Estimator (MHE) approach. The oil flow rate is controlled by the gas-lift flow rate through the gas-lift choke valve. The plant was described by a mathematical model including the gas-lift well, the flowline and the production choke valve. Some control scenarios were tested and the nonlinear model predictive controller was capable to successfully stabilize the process.

Keywords: Nonlinear Model Predictive Control, Gas-lift, Process Control, Hammerstein Model, Moving Horizon Estimator.

1. Introduction

Artificial lifting techniques were developed due to the need of extracting oil from reservoirs which do not have enough energy to push the oil from its bottom to the platform, being the gas-lift one of the most widely applied methods. It consists in adding gas to the upcoming fluid, what increases the fraction of dissolved gas and lowers the mixture density. Despite the gas-lift's advantages such as low costs and simple operation, according to Eikrem et al. (2006), the technique can be affected by severe flow oscillations due to the casing-heading instability, a phenomenon that is originated by the interaction between the injected gas and the multiphase fluid inside the tubing. Once this effect happens, it decreases average production and the oscillations generated may also damage downstream equipment.

In the related literature, many papers focus on gas-lift optimization, for instance, the work of Alarcón et al. (2002). This work introduces a function in order to model the steady state oil production flow according to the gas-lift flow.

Plucenio et al. (2009) apply an extension of the predictive control to a simulated well that operates by continuous gas injection. The control algorithm does not consider constraints and the internal model was obtained from the linearization of the system by parts along the prediction horizon. The controlled variables of the system are the pressure drop in the production tube and the wellbore pressure. While the manipulated variables are based on the reference values of the gas-lift flow controller and the reference value of the wellhead pressure controller.

Cota and Reis (2012) investigate the application of linear multivariable predictive control applied in offshore systems. The approaches were tested using multi-layer MPC to increase oil productivity and to maintain BSW (basic sediments and water) and TOG (oil and grease content) indices within a range of acceptable values. As result, it was verified that the approach based on a linear model, despite stabilizing the process, presents limitations due to the presence of nonlinearities associated to the manipulated variables.

Eikrem et al. (2006) proposed a dynamic nonlinear model of a production well to implement a simulation that aims to stabilize the oscillations by applying a PI controller. However, when considering more complex implementations and more severe conditions, a more sophisticated control strategy may be required.

The work of Miyoshi et al. (2017) analyzed a class of problems that present static gain sign inversion, leading to unreachable setpoints, and proposed the use of Hammerstein block-oriented models in a nonlinear predictive control (NMPC) whose states are previously obtained by the application of a moving horizon estimator (MHE). As the oil production well studied in this current work belongs to this class of problems, the approach proposed by Miyoshi et al. (2017) was applied to control this process.

2. Methodology

The model of the gas-lift well was based on the work of Eikrem et al. (2006), considering the adaptations suggested by Ribeiro et al. (2016), to approximate the simulation of an actual well behavior, and was implemented in MATLAB and solved with ode15s. The well is composed by an annular, through which the gas is injected, and the production tube, through which the fluid flows from the reservoir to the production choke.

As the chosen NMPC approach was based on Hammerstein internal model, after selecting the variables of interest, it was necessary to make the identification of the steady state and the dynamic models of the process subject to gas-lift changes.

Once the nonlinear steady state profile of the variables was known, the MATLAB Curve Fitting Toolbox™ was applied to fit the functions proposed by Alarcón et al. (2002), corresponding to the nonlinear block of the Hammerstein model. The quality of the fit was based on the value of R^2 .

Based on the dynamic behavior of the oil production to the step changes in the input variables, the linear dynamic model was built as a combination of two first order transfer functions in parallel, corresponding to the dynamic block of the Hammerstein model. Then, the following parameters were estimated: k_1 , k_2 , τ_1 and τ_2 , solving a least-square problem with the Nelder–Mead optimization method.

The MHE was implemented based on Rao and Rawlings (2001) and Miyoshi et al. (2017) and the NMPC was implemented based on Miyoshi et al. (2017). Table 1

summarizes the applied control strategies and the respective controlled and manipulated variables.

Table 1 – Control Strategies Summary

Control Strategy	Controlled Variable	Manipulated Variable
PI	Wellbore pressure	Gas-lift choke valve opening
NMPC	Oil production flow	Gas-lift flow

3. Results

3.1. System Simulation

The results obtained for the system simulation obtained by applying the modified model developed by Eikrem et al. (2006) and Ribeiro et al. (2016) are shown in Figure 1.

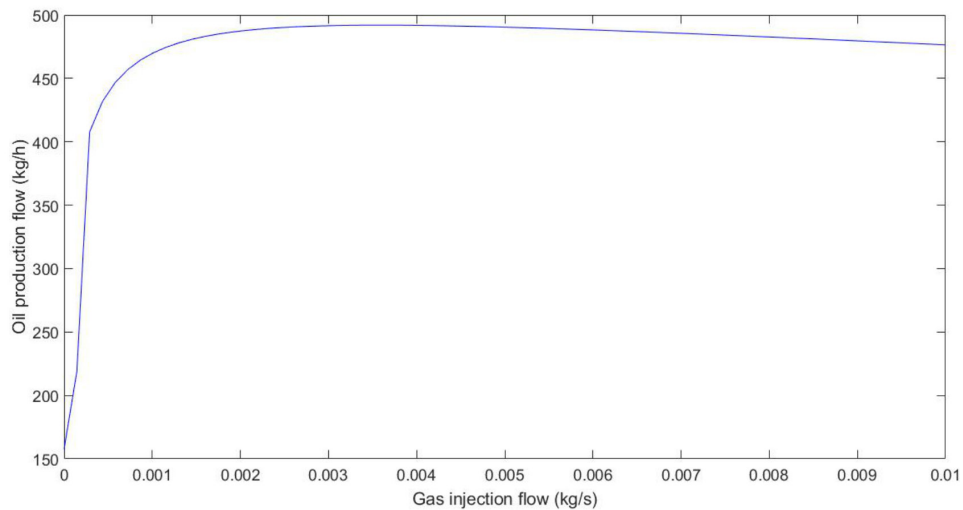


Figure 1 – Nonlinear static behavior obtained from steady state solutions for both gas-lift injection and oil production flow rates.

Figure 1 represents the static behavior that relates gas injection flow rate (kg/s) with oil production flow rate (kg/h). The graphical behavior indicates a convex profile, typical in this type of system. It can be observed that the oil rate increases until it reaches a maximum value, then it starts to decrease. This result shows that the increase of the gas-lift flow rate does not necessarily lead to an increase in the oil production.

The steady state function that represents the graphical behavior of the system was determined, with the use of MATLAB’s curve fitting tool, as presented in Equation (1). This function was obtained by empirically modifying the equation suggested by Alarcón et al. (2002), resulting in an R^2 value of 0.9812. The variable x represents the gas-lift flow rate (kg/s), while y is the oil production flow rate (kg/h).

$$y = -3.246x + 35.18x^2 - 237.3x^3 + 0.2603x^{-0.1361} - \frac{1.954 \times 10^{-5}}{x} + 0.08193 \ln(x) + 0.05311 \exp(x) \quad (1)$$

The obtained dynamic model was a second order transfer function that corresponds to the sum of two first order systems in parallel. Table 2 summarizes the estimated parameters. The parameters k_1 and k_2 represent the transfer function gains, while τ_1 and τ_2 are the time constants.

Table 2 – Transfer Function Parameters.

k_1	k_2	τ_1 (s)	τ_2 (s)
2.50	-1.88	3.50	5.53

The resulting Hammerstein model was tested with a step disturbance in gas-lift flow to verify if it could represent the oil production system as shown in Figure 2.

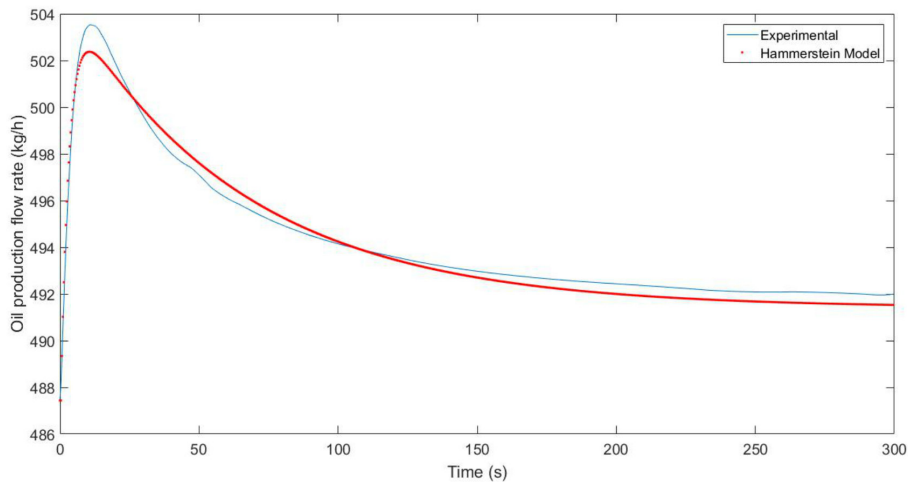


Figure 2 – Response of Hammerstein model compared to oil production system response to a step disturbance in gas-lift flow.

As result, the mean absolute percentage error between the Hammerstein model and the simulated well behavior was lower than 1%.

3.2. Moving Horizon Estimator

Another simulation was carried out to verify the performance of the moving horizon estimator, which is shown in Figure 3. This step is also important to provide the states required by the NMPC.

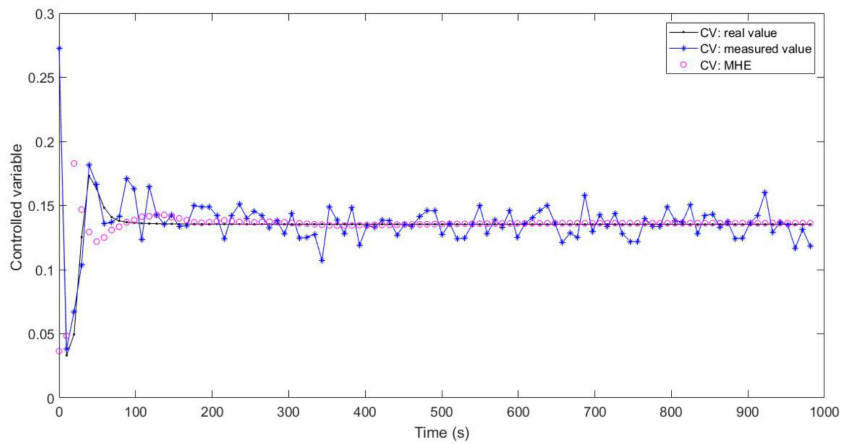


Figure 3 – MHE parameters estimation. CV represents the controlled variable (oil flow); the dots indicate the real values and the asterisks indicate the measured values, while the circles are the estimated values.

Figure 3 shows that after a short period the method can accurately estimate the real value, based on previously obtained measured values, successfully estimating the model states.

3.3. Nonlinear Predictive Control

The results of the application of the NMPC can be observed in Figure 4, showing how it can successfully stabilize the system oscillations. The setpoint is intentionally increased until it reaches an infeasible region. Then, it is finally decreased. This procedure is executed to observe the controller behavior when submitted to a gain sign inversion.

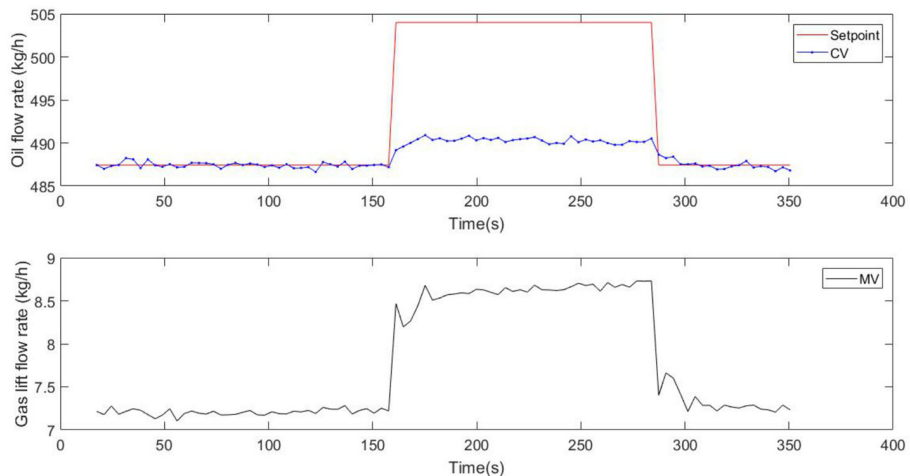


Figure 4 – NMPC results. MV in the bottom graph represents the manipulated variable (gas flow); the continuous line in the top graph indicates the setpoint and the dots are the predicted values of the controlled variable.

It is clear how the predictive control is able to overcome the gain sign inversion problem. These results were only possible due to the MHE accurate state predictions which were applied to the Hammerstein block-oriented model, also considering the Equation (1). Another significant result is the reduction of the computational costs.

Figure 4 shows that the NMPC can control this system in an infeasible setpoint region. The regular approaches of linear MPC controllers and the PID are not usually able to control the system after this region due to the occurrence of a gain sign inversion (Miyoshi et al., 2017).

4. Conclusions

In this paper, a NMPC based on Hammerstein models was applied to an offshore oil production well, in which gas-lift is used as lifting technique. The application aimed to control the oil production flow rate in an infeasible setpoint region by manipulating the gas-lift flow rate. A nonlinear function that represents the dynamic model was obtained with a relative error below 1%, and a moving horizon estimator could successfully estimate the states of the Hammerstein model to fulfill the predictive control structure.

The results showed that the proposed structure can control the system even in regions of gain sign inversion, which could not be achieved with linear control strategies. Therefore, the application of this methodology has potential to perform a significant increase in oil production at short processing time and low computational cost.

References

- G. Alarcón, C. Torres, L. Gómez, 2002, Global optimization of gas allocation to a group of wells in artificial lift using nonlinear constrained programming, *Journal of Energy Resources Technology - Transactions-American Society of Mechanical Engineers*, v. 124, p. 262-268.
- R. Cota, Y. Reis, 2012, *Controle Preditivo em Sistemas de Produção Offshore*, Federal University of Rio de Janeiro, p. 89. Rio de Janeiro, Brazil.
- G. Eikrem, O. Aamo, B. Foss, 2006, Stabilization of Gas-Distribution Instability in Single-Point Dual Gas-Lift Wells, *SPE Production & Operations*, p. 252-259.
- S. Miyoshi, A. Secchi, M. de Souza, 2017, Nonlinear Model Predictive Control based on Hammerstein Model, In: *10th World Congress of Chemical Engineering, 2017, Barcelona. Anais do 10th World Congress of Chemical Engineering*.
- A. Plucenio, D. Pagano, E. Camponogara, A. Truple, A. Teixeira, 2009, Gas-lift optimization and control with nonlinear MPC, *Proceedings of IFAC: International Symposium on Advanced Control of Chemical Processes*, v. 7, p. 904-909.
- C. Rao, J. Rawlings, 2001, Constrained process monitoring: moving-horizon approach, *AIChE J.*, v. 1, p. 97-109.
- C. Ribeiro, S. Miyoshi, A. Secchi, A. Bhaya, 2016, Model Predictive Control with Quality Requirements on Petroleum Production Platforms, *Journal of Petroleum Science and Engineering*, v. 137, p. 10-21.

System identification for a system subjected to persistent disturbances

Roberto Mei^a, Massimiliano Grosso^a, Federico Desotgiu^a, Stefania Tronci^{a*}

^a*Dipartimento di Ingegneria Meccanica, Chimica e dei Materiali, Università degli Studi di Cagliari, Via Marengo 2, 09123, Cagliari, Italy*

**stefania.tronci@dimcm.unica.it*

Abstract

This paper is aimed to analyse possible approaches for addressing multivariable system identification in presence of persistent disturbances. The main objective is to find a solution that is applicable to systems like wastewater treatment plants. Indeed, this type of processes can effectively improve their efficiency by means of advanced controllers, but their identification is quite difficult for the presence of continuous time varying characteristics of the feed flow rate. Optimal design of experiments is applied to the Benchmark Simulation Model no. 1 (Gernaey et al., 2014), and an adequate estimation of the process gains is obtained with multivariable identification if nonlinear models are used to describe the manipulated inputs – outputs relationships.

Keywords: system identification, disturbances, multivariable system, NARX

1. Introduction

Process control is an essential aspect for all industrial plants to guarantee safety, ambient protection and specifications. The development of control systems requires accurate mathematical models, which can be obtained either with a first principles approach or from experimental black-box model identification (Ghadipasha et al., 2015; Cogoni et al., 2014). In the latter case, experimental tests done on plant are needed. During these trials, the normal functioning of the plant is suspended. Based on the time needed, which is typically long, the economic efforts for this activity suspension can be significant. For example, the design of a Model Predictive Control needs about 50% of the time of the whole project (Darby and Nikolau, 2012). This need of time is due because, even though typical industrial system present a large amount of inputs and outputs, experimental tests for model identification are done singularly for each manipulated input. A multivariable system identification can contribute to reduce the amount of time needed for these activities and therefore costs. This is especially true when historical databases of the plant do not contain the required input-output information or they are not even available.

In this work, the possibility to perform a multivariable system identification for a wastewater treatment plant has been studied. For this purpose, the Benchmark Simulation Model no. 1 (hereafter referred as BSM1) has been used. This benchmark is a simulation environment which consents to simulate a wastewater plant composed of five reactors and one settler connected in series. The inlet flow (the wastewater) enters, together with the internal recycle and the external recycle, to the first reactor (which is an anoxic environment), passes through all the reactors and finally comes to the settler where clarified water and wastage are separated. In Figure 1 a simplified scheme of the plant is reported (for more technical details about the Benchmark please refer to Gernaey et al., 2014).

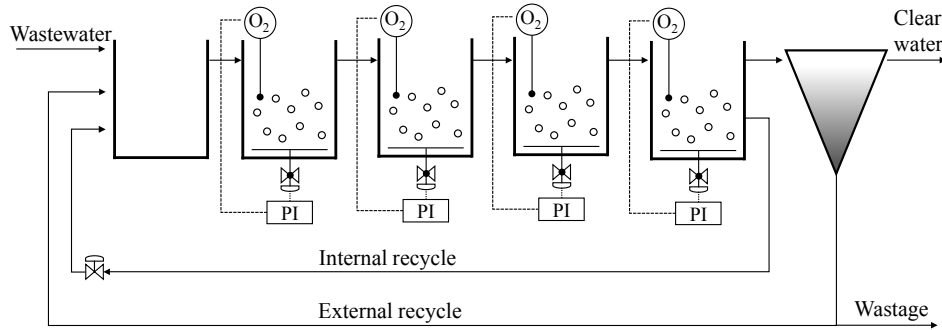


Figure 1: scheme of BSM1 plant.

The system identification methodology studied in this work focused only on the biological part of the plant, and it is an improvement of the methodology already applied in Foscoliano et al. (2016) and Mulas et al. (2015), where model predictive controllers were applied for controlling the concentration of nitrite and ammonia nitrogen on the reactors. Because of this the outputs chosen for the identification approach reported in the present paper are NO_2^- and NO_3^- nitrogen concentration in reactor 2 (SNO-R2) and NH_4^+ and NH_3 nitrogen concentration in reactor 5 (SNH-R5), according with Foscoliano et al (2016a,b). To control these two outputs, it was decided to use five manipulated inputs: the set-point of oxygen concentrations in reactor 2, 3, 4 and 5 (SP-SO_i , $i=2,\dots,5$) and the flow rate of internal recycle (Q_A). For the control of oxygen concentration four PI controllers have been designed to act on the transfer rate of oxygen in each aerated reactor. The crucial aspect is represented by the choice of variations to apply on manipulated inputs during the system identification phase, in order to maximize the amount of information about the system in the shortest possible time.

2. Inputs generation

For the choice of the best combination of uncorrelated inputs to use during the identification phase, the D-optimal design was used (Goodwin and Payne, 1977) with the objective to reduce the tests for system identification. In fact, the system should be excited in such a way that all interesting areas of the input space and the relevant frequencies are covered. Let us consider a multi-input and multi-output (MIMO) system composed of m outputs and n inputs. Such system can be describe as reported in Eq. (1), where $\mathbf{y}(t) \in \mathcal{R}^{m \times 1}$ is the outputs vector, $\mathbf{u}(t) \in \mathcal{R}^{n \times 1}$ is the manipulated inputs vector, $\mathbf{G}(t) \in \mathcal{R}^{m \times n}$ is the gains matrix and $\mathbf{e}(t) \in \mathcal{R}^{m \times 1}$ is the noise measurements vector.

$$\mathbf{y}(t) = \mathbf{G} \cdot \mathbf{u}(t) + \mathbf{e}(t) \quad (1)$$

Assuming the number of outputs and inputs equal to N , it is possible to write the matrices \mathbf{Y} and \mathbf{U} containing, respectively, the values of the m outputs and n inputs for each N -nth sampling time (Eq. (2) and (3)).

$$\mathbf{Y} = \begin{bmatrix} y_1(1) & \cdots & y_m(1) \\ \vdots & \ddots & \vdots \\ y_1(N) & \cdots & y_m(N) \end{bmatrix} \quad (2)$$

$$\mathbf{U} = \begin{bmatrix} u_1(1) & \cdots & u_n(1) \\ \vdots & \ddots & \vdots \\ u_1(N) & \cdots & u_n(N) \end{bmatrix} \quad (3)$$

Applying the least squares method, it is possible to define the estimator $\hat{\mathbf{G}}$ of \mathbf{G} (Eq. 4), where $\mathbf{X} = \mathbf{U}^T \mathbf{U}$ is called ‘information matrix’.

$$\hat{\mathbf{G}}^T = (\mathbf{U}^T \mathbf{U})^{-1} \mathbf{U}^T \mathbf{Y} = (\mathbf{X})^{-1} \mathbf{U}^T \mathbf{Y} \quad (4)$$

The D-optimal design is based on the maximization of the determinant of the \mathbf{X} matrix. If the number of samples N is relatively high and the estimator is impartial, the covariance matrix C_m can be found as reported in Eq. (5) (Goodwin and Payne, 1977; Darby and Nikolaou, 2014).

$$C_m \approx \frac{\mathbf{X}}{N-1} \quad (5)$$

If the determinant of C_m is near 1 the obtained inputs are uncorrelated and the determinant of the \mathbf{X} matrix is maximized, meaning that this combination of inputs can be used for the identification.

To study the possibility of multivariable identification in different cases, various configurations of uncorrelated inputs have been used. These designs have been generated in order to satisfy the conditions explained before. Each input variable can assume only its minimum or its maximum value, according to Table 1, varying according to step functions. For each design, three parameters, reported in Table 2, have been settled: the total time, representing the duration of the simulation (and, in real condition, of the identification performed on the plant); the step time, representing the minimal duration of a step; the switching frequency, representing the probability that a step has a value opposite to the previous step.

Table 1: minimum and maximum values for manipulated inputs

Manipulated input	Min	Max
Oxygen in reactor 2	0.25 g/m ³	0.75 g/m ³
Oxygen in reactor 3	1.50 g/m ³	2.50 g/m ³
Oxygen in reactor 4	1.75 g/m ³	2.25 g/m ³
Oxygen in reactor 5	1.25 g/m ³	1.75 g/m ³
Internal recycle	49804.2 m ³ /d	60871.8 m ³ /d

3. Multivariable system identification

To simulate the behaviour of the plant when a multivariable system identification is performed in real condition, the system was simulated using an inlet flow rate consisting of 17 variables describing typical dynamic variations for a wastewater flow. Details about this flow can be found at benchmark group website: <http://www.benchmarkwwtp.org/>.

The identification was carried out using the conditions reported in Tables 1 and 2, and before starting the step variations the system has been initialized simulating it for 15 days using a constant inlet flow and constant inputs. Then, for further 15 days, the variable inlet flow and constant manipulated inputs were used. Finally, for a period of time depending on the selected design, simulations were carried on using the variable

inlet flow and the manipulated variable inputs designed as described in the previous chapter.

Because the goal of this work is to assess if a multivariable system identification can be successfully applied to a system with time varying disturbances, some simulations were carried out to obtain reference values for the process. In particular, ideal conditions with constant pollutant loads were considered for calculating the gains of the process and comparing them with the ones obtained performing the identification as we were in a real plant (varying disturbances).

Table 2: parameters for the designed simulations

Design	Total time [d]	Step time [d]	Switching frequency
1	60	1	0.2
2	60	2	0.2
3	120	5	0.2
4	120	5	0.5
5	120	0.5	0.2
6	60	0.5	0.2
7	30	1	0.2
8	30	0.5	0.2
9	90	1	0.2
10	90	2	0.2

For every simulation, the obtained data of nitrate and nitrite nitrogen in reactor 2 (SNO-R2) and NH_4^+ and NH_3 nitrogen in reactor 5 (SNH-R5) were used separately for the identification process. The description of the data obtained for the multivariable identification process was first performed by means of a linear model. Such approach failed because the output signals were not correctly described. A nonlinear approach was therefore used and 10 nonlinear autoregressive models with exogenous inputs (1 for each couple output – input) were trained to describe the behaviour of the selected output in response to a step test (both positive and negative variations) of the selected input. Every single neural network was considered capable of describing the system if the following criterions were satisfied: 1) sign of the gain consistent with the process; 2) comparable order of magnitude both for positive and negative variations (bearing in mind the non-linearity of the process); 3) order of magnitude consistent with the process by considering the ideal situations of constant inlet conditions as described in the previous paragraph.

4. Results

Among all the designs studied, design number 3 is the one who returned the best results, therefore at least four months of experimental tests are needed. Figure 2 shows inlet ammonia flow rate, which is one example of the several process disturbances, the step applied to the manipulated inputs and the outputs (SNO-R2, SNH-R5) behaviour. The identification procedure should properly separate the effects of the disturbances to that of the manipulated inputs on the outputs and 10 NARX models formed by 2 past inputs and 2 past measured outputs (sampling time equal to 15 minutes) were able to give the

better description of input-output relationships. It is important to note the disturbances are not used as inputs of the NARX models, because in real plants they are not usually measured.

To evaluate the identification carried on, the gains of the 5x2 system have been predicted with the autoregressive models considering average process conditions and the obtained values are compared with the one calculated in the ideal case (single step and constant disturbances).

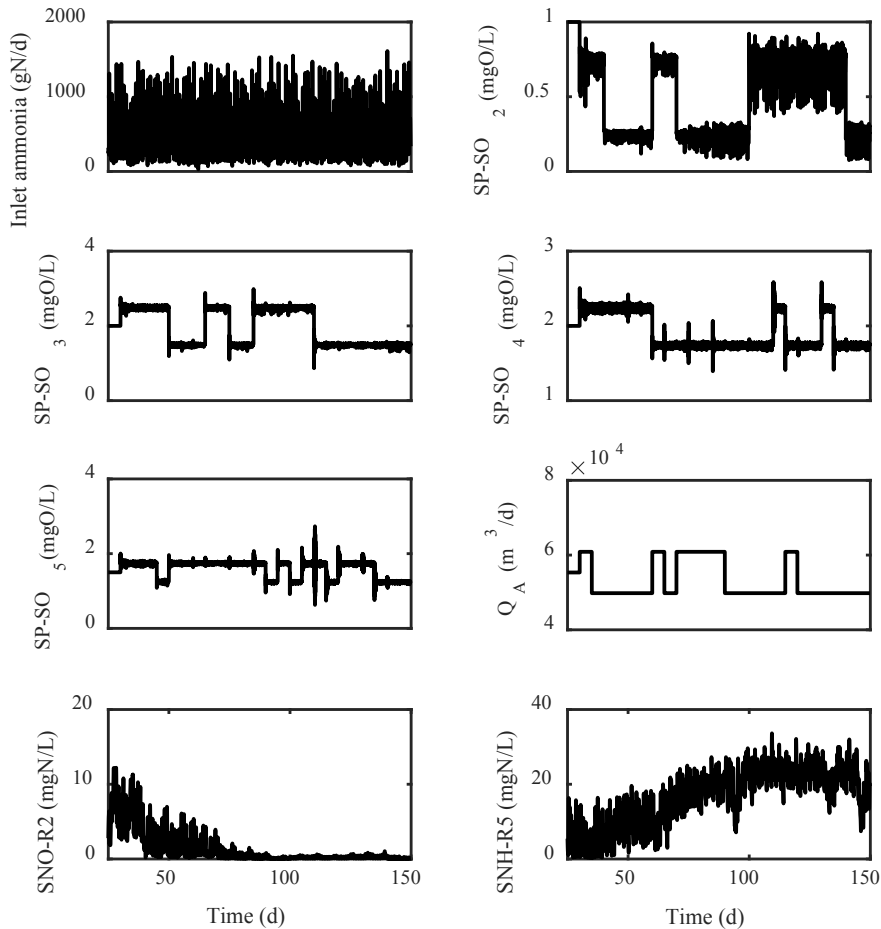


Figure 2: inputs and outputs behaviour during the multivariable step-tests.

The results are reported in Table 3, and it can be observed that the sign of the constant gain is correct for each multivariable identification, but the values are generally different of one order magnitude with respect to the single step. It is worth noting that the process shows highly nonlinear behaviour and that the multivariable identification with NARX has been conducted when the influent is subjected to large variations in terms of concentration, wastewater flow rate and temperature.

5. Conclusions

System identification for a multivariable system continuously excited by varying disturbances was accomplished using optimal design of experiment to establish the step changes program. The proposed system identification strategy could potentially reduce the amount of time needed for an input-output system identification done singularly in plant and therefore reduce costs. The obtained results are promising for evaluating information related to process gain, but the procedure did not allow the obtainment of reliable characteristic times of the process, and this aspect will be addressed in the future.

Table 3: results of the multivariable identifications compared to single step identifications

Manipulated input	SNO-R2		SNH-R5	
	Multivariable identification	Single step identification	Multivariable identification	Single step identification
Oxygen in reactor 2	0.126263	1.054	-0.875272	-0.106
Oxygen in reactor 3	0.044981	0.374	-0.245492	-0.116
Oxygen in reactor 4	0.379313	0.339	-1.740404	-0.113
Oxygen in reactor 5	0.021692	1.247	-0.125783	-0.201
Internal recycle	3.628257e-06	7.049E-05	0.000855	3.740E-06

References

- G. Cogoni, S. Tronci, R. Baratti, J.A. Romagnoli, 2014, Controllability of semibatch nonisothermal antisolvent crystallization processes. *Industrial & Engineering Chemistry Research*, 53(17), 7056-7065.
- M. L. Darby, M. Nikolaou, 2012, MPC: current practice and challenges. *Control Eng. Pract.* 20, 328-342.
- M. L. Darby, M. Nikolaou, 2014, Identification test design for multivariable model-based control: An industrial perspective, *Control Eng. Pract.* 22, 165-180.
- C. Foscoliano, S. Del Vigo, M. Mulas, S. Tronci, 2016a, Improving the wastewater treatment plant performance through model predictive control strategies, *Computer Aided Chemical Engineering*, 38, 1863-1868.
- C. Foscoliano, S. Del Vigo, M. Mulas, S. Tronci, 2016b, Predictive control of an activated sludge process for long term operation. *Chemical Engineering Journal*, 304, 1031-1044.
- K. Gernaey, U. Jeppsson, P. Vanrolleghem, J. Copp, 2014, *Benchmarking of Control Strategie for Wastewater Treatment Plants*. IWA Publishing, London.
- N. Ghadipasha, J.A. Romagnoli, S. Tronci, R. Baratti, 2015, On-line control of crystal properties in nonisothermal antisolvent crystallization. *AIChE Journal*, 61(7), 2188-2201.
- G. C. Goodwin, R. L. Payne, 1977, *Dynamic System Identification: Experiment Design and Data Analysis*, Academic Press, New York.
- M. Mulas, S. Tronci, F. Corona, H. Haimi, P. Lindell, M. Heinonen, R. Vahala, R. Baratti, 2015, Predictive control of an activated sludge process: An application to the Viikinmäki wastewater treatment plant. *J. Proc. Control* 35, 89-100.

Towards Obviating Human Errors in Real-time through Eye Tracking

Mohd Umair Iqbal,^a Babji Srinivasan,^a Rajagopalan Srinivasan^{b,*}

^a*Indian Institute of Technology Gandhinagar, Gujarat, 382355, India*

^b*Indian Institute of Technology Madras, Tamil Nadu, 600036, India*

babji.srinivasan@iitgn.ac.in, raj@iitm.ac.in

Abstract

To minimize human errors (principal reasons for accidents in process industries) it is imperative to understand their cognitive workload, the excess of which is often a preliminary state leading to human errors. In this work, we have devised a methodology based on an eye tracking parameter—gaze entropy—to gauge the variation of cognitive work load on a control room operator. The study highlights the potential of gaze entropy in observing the variation of cognitive workload with learning. The patterns observed have a potential to minimize human errors and improve safety in process industries.

Keywords: Human errors, eye tracking, cognitive workload, process safety, learning

1. Introduction

Industries have developed and adopted numerous technological advancements to enhance safety in the workplace. Despite these advancements, incidents continue to happen in process industries leading to financial and human losses (Mannan, 2004; Fernholz, 2014). A detailed analysis of various incidents reveal that human error is one of the principal causes for failure to control the plant in the process industries. Incorrect decisions made by the human operator could severely impact the process safety as exemplified by the incidents at Three Mile Island Nuclear plant (1979), BP's Texas City chemical plant (2005), Bayer CropScience pesticide production facility (2008) and Indonesian Air Asia QZ-8501 (2014) aviation accident. The traditional approach has been to look at human error as the initiating event of incidents, one that has a given likelihood of occurrence, similar to the way that a piece of hardware is expected to fail at some frequency. However, understanding of human errors is a challenging task—there is limited availability of human error data in public domain due to various sensitivity and propriety issues. Further, unlike machines, humans are more unpredictable as their thought process is influenced by various internal factors (like fatigue, sleep, ability, etc.) as well as external factors (like organisational culture, work environment, etc.). For machines the failure probability is predicted by using historical failure data related to the equipment. To minimize equipment failures, periodic checks and maintenance are required to maintain their health. The relatively high frequency of change in the thought process of humans demands a procedure to tackle human errors in a different way from that of machines. There is a need for continuous monitoring of the thought process in humans, and understand how learning impacts the thought process. Improvement in performance due to learning can be seen as analogous to equipment

improvement after periodic maintenances. Improvement in learning needs to be gauged in real time. This real time monitoring of humans has to be based on some measures which allow us to continuously trace the changing thought process so that real time interventions could be introduced to check for any aberrant behaviour or activity, and accordingly kick in preventive measures. Such interventions can reduce the human errors by inducing learning and reducing the amount of cognitive workload. Experts have already suggested the need to understand the cognitive aspects and of process operators (such as information processing, workload and decision making) under various conditions to understand and mitigate human errors (Bullemer and Nimmo, 1994; Manca et al., 2013). We believe that cognitive workload is an important component to understand human errors. There is a strong relation between the two—while human errors are defined as a mismatch between the demands of a process and the human capability (Embrey, 1994), mental workload, at the most general level, is defined as a relation between the mental resources demanded by a process and the resources that can be supplied by the operator (Parasuraman, 2008). Thus, addressing the issue of cognitive workload (overload). Further, we believe that the changes in cognitive workload are also strongly associated with learning—a significant parameter to minimize mistakes and errors. Its developments with learning will help address the broad issue of human errors and, hence, process safety.

2. Literature Survey

Cognitive Workload is defined as the total amount of mental effort and resources required by a human at any given time to handle a situation (Parasuraman, 2008). Cognitive workload is experienced when the working memory processing demands, for a task, exceed the learner's cognitive capacity (Mayer and Marenco, 2003). Cognitive workload is one of the important cognitive engineering constructs that influences the decision making process of the humans (Parasuraman, 2008; Zheng et al., 2015; Rodríguez et al., 2015). Researchers in safety critical domains such as aviation, driving and healthcare industries have attempted to understand cognitive workload by measuring various psychophysiological quantities such as Electroencephalography (EEG), galvanic skin resistance, heart rate, eye movements and pupil diameter. Due to its non-invasive nature and ease of use, eye tracking measures have been widely used to understand the cognitive workload of humans. For instance, during simulated surgical tasks, it was observed that higher pupil dilations correlated with increase in task complexity (Zheng et al., 2015). Experiments conducted to assess the workload of air traffic controller concluded that increase in subjective workload translated into an increase in the pupil diameter amplitude (Rodríguez et al., 2015). Another study revealed that changes in mental workload can be quantified by frequency domain analysis of pupil size measurements, with an increase in workload correlated with increase in power level at low frequencies (Peysakhovich et al., 2015).

More recently, we have conducted experimental studies on ethanol simulator plant to understand the cognitive behaviour of control room operators. In these studies, participants were attending various tasks that required them to take intervening actions upon alarm(s) to bring the plant back to normal conditions. Eye gaze studies revealed the existence of specific pattern in participants who have completed the task using single manipulated variable (Sharma et al., 2016). Pupillometry studies indicate that the size of the pupil correlates closely with their ability to successfully perform the necessary tasks to keep the process within safe limits (Bhavsar et al., 2015).

A lot of work has been done, as already discussed, to investigate various facets of cognition, there have been a few studies also to assess the impact of learning on cognitive workload. According to cognitive load theory when a person learns a task the effort needed to carry the task decreases because of the reduced need to process the information, a portion of which goes to long-term memory. Sibley et al. (2011) showed that the cognitive workload, as measured by pupil diameter, decreases with learning as the participants perform a heading task involving virtual unmanned aircraft vehicle. Burge et al. (2013) studied the mechanism underlying change in performance by analysing the pupil diameter variation. They concluded that the participants' performance increases because of the increase in efficiency due to improved allocation of cognitive resources by training. Literature related to the understanding of cognitive behaviour during tasks involving plant operators trying to tackle abnormal situations in real time is at best limited (Bhavsar et al., 2015). Further, the assessment of learning by measuring the entropy changes in real time during similar disturbance rejection tasks is hardly available, to the best of our knowledge. In this work we have attempted to find a relation between learning and cognitive workload (an overload of which increases the chances of error) using gaze entropy. By tracing the cognitive workload we can predict whether learning is occurring, and according take measures to make both these parameters favourable.

3. Experimental Methodology

The experiment consists of monitoring an ethanol production plant (See Figure 1), and taking appropriate action (s) (by an operator) to bring the plant back to normal state if any disturbance occurs. For detailed description of the experimental set-up and process the reader is referred to Iqbal and Srinivasan (2017).

The study involved 5 post graduate students of chemical engineering at Indian Institute of Technology Gandhinagar. They were given a reading manual that explained the ethanol production process, followed by a video training on how to operate the plant. To keep trace of the participants' gaze during the experiment we used a Tobii TX 300 remote eye tracker, and followed standard five point eye tracking calibration procedure to ensure validity of gaze data. The nature of the tasks performed by the participants and results obtained are discussed in next section.

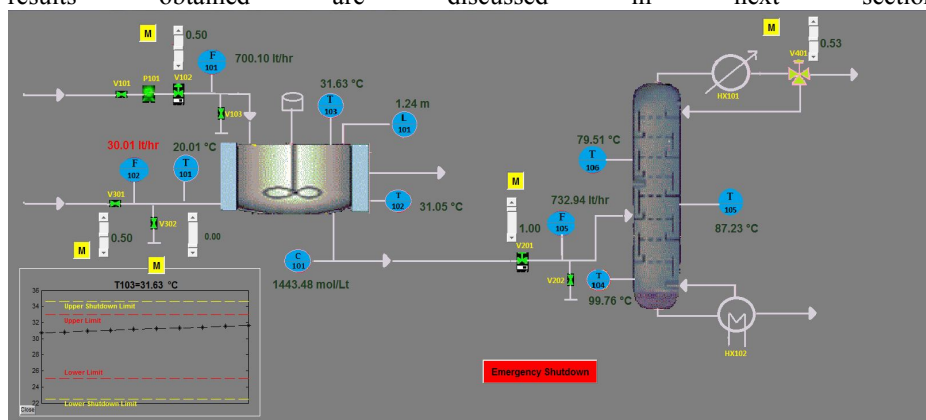


Figure 1 Human Machine Interface of an ethanol production plant

4. Results and Discussion

A typical task involves bringing a process variable(s) to within the acceptable limits as specified by the region between upper limit and lower limit in Figure 1. As soon as the alarm is triggered the participant gets to know about the disturbance in the plant, tries to comprehend the situation and accordingly takes some action(s). Now consider a typical scenario involving such a

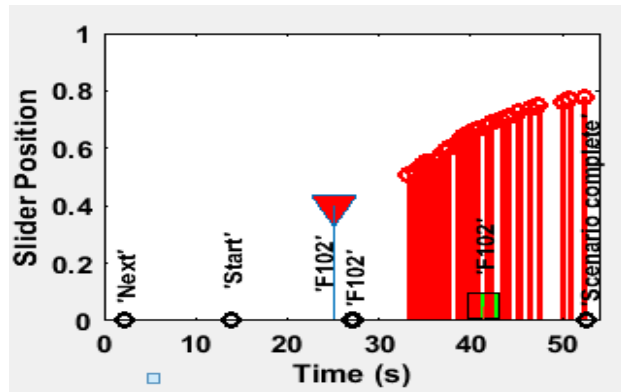


Figure 2 Slider position trend with time

task. The participant clicks on the start button to activate the Human Machine interface (Figure 1) at around 15 seconds (Figure 2). At around 25 seconds, the flow rate of the coolant goes outside the alarm-limits, turning the tag F102's value from blue to red, and simultaneously triggers an alarm (shown by inverted triangle). These developments alert the operator and possibly result in change in his cognitive workload. The operator tries to bring the disturbed process variable to within acceptable limits by changing the slider position to control the flow through coolant valve. The shift in slider position is shown in the figure by changing height of the stems in Figure 2. Thus, at around 33s the operator starts to move the slider controlling the coolant flow rate, and the alarm is cleared at around 42 s, as shown by the box 'F102' in Figure 2. Comparative analysis for gaze entropy during these tasks was done for five participants. The gaze entropy was determined for two time regions of the experiment: i) Region one: From first slider action to the last slider action (i.e. from around 33s to 53s) ii) From first alarm (shown by inverted triangle) to first slider action (i.e. the region from 25s to 33 s).

Task one involved handling a disturbance which involved change in coolant flow rate to outside the alarm limits. The correct action involved moving the coolant slider to appropriate position to bring the flowrate back to acceptable limits. It is not necessary that a participant always started with the correct slider action. Task two also involved the same disturbance but an additional problem of coolant valve getting stuck and hence not responding. The operators had to identify a bypass valve (V302) and use it to bring the disturbed coolant flow rate to within acceptable limits. Task two and one are similar in a way that both involve bringing the coolant flowrate to within acceptable limits by increasing the flow in the coolant line. Figure 3 shows the gaze entropy for different participants performing two similar tasks—Task 1 and Task 2—in region one (already defined). However, for the Task 2, the first slider action corresponds to a normally working slider which could be a bypass valve or any other slider which he or she perceives to be the correct one. Figure 4 shows gaze entropy in the region starting with time when the first alarm occurs to the time when he identifies the first perceived correct slider.

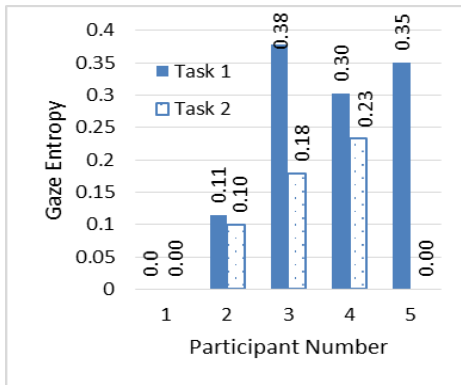


Figure 3 Comparative gaze entropy for different participants from first slider to last slider action

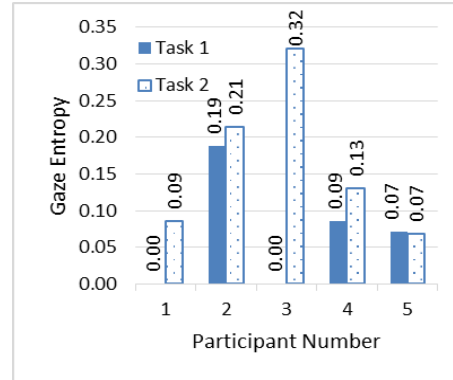


Figure 4 Comparative gaze entropy for different participants from first alarm to first slider action

The results shown in Figure 3 show that the gaze entropy for four participants decreases as they go to perform Task 2 after previously performing Task 1. The decrease in entropy demonstrates learning by a participant and the change in his mental state from having ‘more entropy’ to ‘less entropy’. The decrease in entropy and hence cognitive workload can be attributed to relative relief of the working memory load due to compensation from prior belief/learning (Joseph, 2013). We believe that if learning fails, gaze entropy may not decrease significantly as it decreases during learning. There are some zero values of entropy as well as can be seen in Figure 3. These signify that the participant might have been confident while performing the task. He might have been sure that a particular slider action is going to bring the process variable back to within acceptable limits, and as such is fixing his gaze in the same region on HMI. Thus, gauging this parameter will help us to keep track of the operator’s cognitive load and consequently learning.

The results from Figure 4 depict that the cognitive work load of a participant can increase if things go against the intuition developed by previous experience. The participants, after the same alarm is triggered and after their learning experience, would try to bring back the coolant flow rate to within acceptable limits by using the coolant valve but since the coolant valve had got stuck for Task 2, it takes them some time to realize that, and during that realization time their cognitive workload increases. Thus, as shown in Figure 4, the gaze entropy increases for four participants as the participant goes to perform Task 2, after having performed Task 1 previously.

5. Conclusions

In this work we have proposed a technique based on measurement of gaze entropy to gauge the cognitive workload of a human operators induced by the interaction between the nature of task and their abilities and/or perception about the task. Gaze entropy gives us a deep insight into the learning by an operator. Higher gaze entropy signifies a higher cognitive workload. Lower values of gaze entropy while performing a similar task previously reflects the potential of gaze entropy being a measure of learning. Knowing the real time trend of cognitive workload on operators and aberrations (if any) has a potential of minimizing human errors by providing necessary interventions in real time. These interventions may even include triggering of a warning to a more expert special-

operator asking for his intervention if the variables involved are critical safety variables, thereby enhancing learning. In this way human errors can be obviated in real time and will also allow for self-introspection by operators to improve their skills with the passage of time. This will ensure not just the existence of a safer workplace, but will also minimize the effects of various accidents on our environment by eliminating, or at least minimizing, their frequency of occurrence. Our future work will focus on developing a robust index based on many gaze parameters to measure cognitive workload on control room operators in real time.

References

- Bhavsar, P., Srinivasan, B. and Srinivasan, R., 2015. Pupillometry based Real-time Monitoring of Operator's Cognitive Workload to Prevent Human Error during Abnormal Situations. *Industrial & Engineering Chemistry Research*, 55(12), pp.3372-3382.
- Embrey, D.E., Kontogiannis, T., & Green, M. (1994). *Guidelines for preventing human error in process safety*. New York: Center for Chemical Process Safety, American
- Fernholz, G. (2014). *The Impact of the Operator on Plant Safety*. Retrieved from http://iom.invensys.com/EN/SoftwareGCC14Presentations/SimSci/SS_S_T-03B_The_Impact_of_the_Operator_on_Plant_Safety.pdf
- Joseph, S. (2013). Measuring cognitive load: A comparison of self-report and physiological methods (pp. 1-98). Tempe, AZ: Arizona State University.
- Manca, D., Brambilla, S., & Colombo, S. (2013). Bridging between virtual reality and accident simulation for training of process-industry operators. *Advances in Engineering Software*, 55, 1-9.
- Mannan, S., 2004. *Lees' Loss prevention in the process industries: Hazard identification, assessment and control*.
- Mayer, R. E., & Moreno, R. (2003). Nine ways to reduce cognitive load in multimedia learning. *Educational psychologist*, 38(1), 43-52.
- Parasuraman, R., Sheridan, T. B., & Wickens, C. D. (2008). Situation awareness, mental workload, and trust in automation: Viable, empirically supported cognitive engineering constructs. *Journal of Cognitive Engineering and Decision Making*, 2(2), 140-160.
- Peysakhovich, V., Causse, M., Scannella, S. and Dehais, F., 2015. Frequency analysis of a task-evoked pupillary response: Luminance-independent measure of mental effort. *International Journal of Psychophysiology*, 97(1), pp.30-37.
- Sharma, C., Bhavsar, P., Srinivasan, B. and Srinivasan, R., 2016. Eye gaze movement studies of control room operators: A novel approach to improve process safety. *Computers & Chemical Engineering*, 85, pp.43-57.
- Zheng, B., Jiang, X. and Atkins, M.S., 2015. Detection of Changes in Surgical Difficulty Evidence From Pupil Responses. *Surgical innovation*, 22(6), pp.629-635.
- Iqbal, M. U., & Srinivasan, R. (2017). Simulator based performance metrics to estimate reliability of control room operators. *Journal of Loss Prevention in the Process Industries*.
- Bullemer, P. T., & Nimmo, I. (1994, October). Understanding and supporting abnormal situation management in industrial process control environments: a new approach to training. In *Systems, Man, and Cybernetics. IEEE International Conference on Humans, Information and Technology*.1, 391-396.
- Sibley, C., Coyne, J., & Baldwin, C. (2011, September). Pupil dilation as an index of learning. In *Proceedings of the Human Factors and Ergonomics Society Annual Meeting (Vol. 55, No. 1, pp. 237-241)*. Sage CA: Los Angeles, CA: SAGE Publications.
- Rodríguez, S., Sánchez, L., López, P., & Cañas, J. J. (2015, September). Pupillometry to assess Air Traffic Controller workload through the Mental Workload Model. In *Proceedings of the 5th International Conference on Application and Theory of Automation in Command and Control Systems (pp. 95-104)*. ACM.

Online Monitoring of an Enzymatic Reactor based on Density Measurements

Emilio Granada-Vecino, Mauricio Sales-Cruz, Teresa Lopez-Arenas*

Departamento de Procesos y Tecnología, Universidad Autónoma Metropolitana - Cuajimalpa, Av. Vasco de Quiroga 4871, 05300 Mexico City, Mexico

mtlopez@correo.cua.uam.mx

Abstract

In this work, a monitoring strategy is presented to infer unmeasured concentrations and estimate the kinetic parameter of inhibition in an enzymatic reactor. The reaction corresponds to the hydrolysis of cellulose to produce glucose, in batch and isothermal conditions. The strategy is based on a softsensor that consists of a model-based state estimator and considering only density measurements. The reactor model and the softsensor performances are validated with experimental data, obtaining satisfactory estimates. The strategy could be extended to other bioreactors.

Keywords: Bioreactor, monitoring, state estimator, density.

1. Introduction

Online monitoring of bioreactors is increasingly important in industrial processes. First, bioreactors are relevant because more products (pharmaceuticals, food, fuel, etc.) are obtained sustainably through biotechnology. In particular, sugars (as glucose, sucrose, etc.) are essential compounds in bioreactors, as they participate in enzymatic or fermentation reactions as substrates or products. Undoubtedly, an important problem for the correct bioreactors monitoring and control is the sugar concentration inference, preferably through low-cost, reliable and fast-response sensors (Pohlscheidt et al., 2013). Through its monitoring, it is possible to control the substrate feed, to avoid the reaction inhibitions, to ensure the process operability, and to guarantee the product quality. Today, new sensors provide more possibilities for online monitoring, which are based on the measuring of physical, chemical or biological properties such as refractometers, viscometers, respirators, etc. Sugars are commonly measured using a biochemical analyser (as Life Sciences YSI), whose use is off line, with delay time and moderate operating cost. It is useful, accurate and reliable for research purposes, but not for industrial purposes.

In this work, an online monitoring system is proposed to infer the glucose (product) concentration in an enzymatic hydrolysis reactor, using cellulose as substrate and *Trichoderma reesei* as enzyme. The isothermal batch reaction is carried out in an experimental lab reactor, where density is measured by an online densitometer for monitoring purposes, and glucose concentration is measured by an off line biochemical analyser for validation purposes. First, a dynamic model is considered assuming a Michaelis-Menten reaction including product inhibition. Then, the online monitoring strategy is based on the development of a soft-sensor that is the association of: (a) a sensor (hardware), which allows online measurements; and (b) a state estimation algorithm (software), which can provide online estimates of unmeasurable states. For

the latter, a nonlinear geometric state estimator (Alvarez and Lopez, 1999) is used that relies on a dynamic process model and the observability property, presenting advantages in terms of mathematical solvability, convergence criteria, systematic construction and manageable tuning technique.

The results obtained are satisfactory for the states and parameter estimation. First, the reactor model is experimentally validated using the off line glucose concentration measurements. Next, it is determined that state estimation is feasible from an observability analysis. Finally, the dynamic softsensor is implemented, achieving an adequate estimation of the sugar concentration (with small deviation) and an inference of the non-measurable concentration of cellulose.

2. Process Description

2.1. Enzymatic hydrolysis reaction

The enzymatic hydrolysis reaction of α -cellulose (substrate, S) is considered to produce glucose (product, P), catalysed by *Trichoderma reesei* cellulase (enzyme, E). The initial concentrations were $S_0 = 15$ g/L of cellulose and $E_0 = 2$ ml/L of enzyme, pH was set at 4.5 with a buffer solution, and temperature was fixed at 50 °C. In particular, the enzymatic hydrolysis reaction of cellulose follows a Michaelis-Menten type kinetics with competitive product inhibition (Bisswanger, 2008), given by the following reaction rate (r_p):

$$r_p = \frac{V_{max} S}{K_m + S + (K_m / K_I) P} \quad (1)$$

Where the kinetic parameters defined by V_{max} , K_m and K_I are the fundamental pillars to understand the behaviour of enzymes. V_{max} represents the maximum rate at which the reaction rate can occur, K_m can be assumed as an inverse measure of the enzyme affinity for the substrate, and K_I is an inverse measure of the affinity of the enzyme for the inhibitor. In a previous work (Lopez-Arenas et al., 2017), the kinetic parameters were estimated for several initial substrate concentrations ($5 \text{ g/L} \leq S_0 \leq 15 \text{ g/L}$) through optimization, finding the optimum values of $V_{max} = 0.683 \text{ g/L/h}$ and $K_m = 13.634 \text{ g/L}$; while the value of K_I was S_0 -dependent ($0.3 \text{ g/L} < K_I < 1.5 \text{ g/L}$).

2.2. Experimental System

A stirred tank (stainless steel) reactor was used, operated in batch under isothermal conditions, with a nominal volume of 1 L (Figure 1a). The reactor has a mechanical agitation system, steam condenser, heating / cooling jacket, and automatic measurement sensors for pH and temperature. The experimental system is connected to a computer for heating control and data acquisition (Figure 1b).

Several samples were taken and filtered (since cellulose is not soluble) to measure the glucose concentration and the mixture density. The glucose concentration was measured off-line with a biochemical analyser (YSI 2900), to have measurements that allow the validation of the reactor model. While density measurements were taken with a density meter (Anton Paar, DMA 35), to be used in the online monitoring system.



Figure 1. Experimental system: (a) reactor and (b) data acquisition and control system.

3. Methodology

3.1. Reactor Model

The dynamic model of the reactor is given by the mass balances of substrate and product, additionally the inhibition parameter K_I is added as a system state with to its online estimation:

$$\frac{dS}{dt} = -r_p, \quad S(0) = S_0; \quad \frac{dP}{dt} = r_p, \quad P(0) = 0; \quad \frac{dK_I}{dt} = 0, \quad K_I(0) = K_{I0} \quad (2)$$

The mixture density (ρ) was calculated according to the additivity of specific volumes:

$$\underbrace{\frac{1}{\bar{V}_m}}_{\text{mixture}} = \underbrace{\frac{x_s}{\bar{V}_s}}_{\text{buffer solution}} + \underbrace{\frac{x_g}{\bar{V}_g}}_{\text{glucose}} \quad (3)$$

Leading to the following expression (were α , β , γ are constant values):

$$\rho = \frac{\alpha + P}{\beta + \gamma P} := h(P) \quad (4)$$

3.2. The observability analysis

First, the reactor model, Eq. (2), is written in vector form, together with the density as unique measure variable ($y = \rho$):

$$\dot{\mathbf{x}} = \mathbf{f}(\mathbf{x}), \quad \mathbf{x}(0) = \mathbf{x}_0; \quad y = h(x); \quad \text{where } \mathbf{x} = [S, P, K_I]^T \quad (5)$$

The reactor motion $\mathbf{x}(t)$ is RE (robustly exponentially) - detectable (i.e. partial observable) with the observability index $\kappa = 2$, and the state partition

$$\mathbf{x}_I = [P, K_I]^T \quad \text{observable states}; \quad \mathbf{x}_{II} = [S]^T \quad \text{unobservable state} \quad (6)$$

if the two following conditions are met along the reactor motion $\mathbf{x}(t)$: (a) an invertibility condition, which means the map $\phi(\mathbf{x})$ is invertible for \mathbf{x}_I , and (b) a stability condition, which means the unobservable dynamics $\mathbf{x}_{II}(t)$ is stable. Where the map ϕ (given by the measured outputs and some of their time-derivatives) and the observability matrix \mathbf{Q} are given by:

$$\phi(x) = [y, \dot{y}]^T = [h(x), g(x)]^T; \quad \mathbf{Q} = \frac{\partial \phi}{\partial \mathbf{x}_I} \quad (7)$$

The assessment of the invertibility condition can be verified if $\text{Rank}[\mathbf{Q}] = \kappa = 2$, or else, if $\det[\mathbf{Q}] \neq 0$ for all time. In fact this condition was evaluated numerically as can be seen in Figure 2a, showing that $\det[\mathbf{Q}] > 0$ for $P \neq 0$ and $P \neq S_0$. The stability condition is equivalent to verify that the dynamics $\dot{S} = -r_p$ is stable, considering $P(t)$ and $K_I(t)$ as nominal known motions. The dynamics is stable if the eigenvalue of its linear equation has strictly negative real part. This is verified also numerically along the reactor motion as shown in Figure 2b.

As the two conditions are met, therefore the reactor motion is RE-detectable for all time, except for $P = 0$ and $P = S_0$; which are the extremes of the reaction (the initial point at $t = 0$ and the end point when the conversion is 100%). The first one can be avoided for the implementation of the softsensor (it can be implemented a few seconds after the start of the reaction), and the last point is not reachable physically since there is product inhibition, thus a complete conversion cannot be reached.

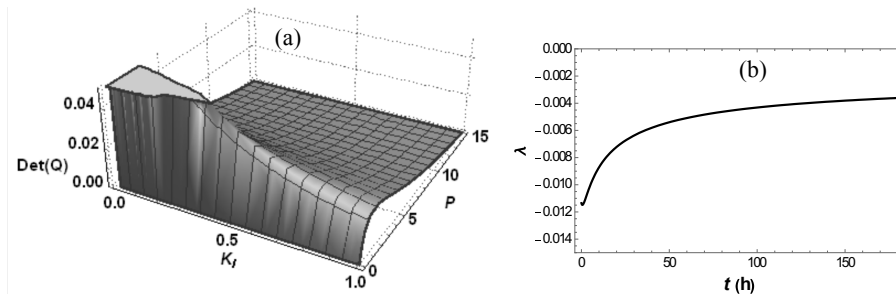


Figure 2. Observability analysis: (a) determinant of \mathbf{Q} , (b) eigenvalues of $\dot{\mathbf{x}}_{II}$.

3.3. State estimator design

The construction of the geometric estimator (Luenberger-like high-gain) follows from a straightforward consequence of the detectability property, according to the following expression (see Theorem 1 in Alvarez and Lopez, 1999). So that the estimator for the case study is given by

$$\dot{\hat{\mathbf{x}}}_I = \mathbf{f}_I + \mathbf{Q}^{-1} \mathbf{K}_o (y - \hat{y}) + \mathbf{Q}^{-1} \mathbf{\Pi} \mathbf{K}_{int} \int_0^\tau (y - \hat{y}) d\tau, \quad \hat{\mathbf{x}}_I(0) = \hat{\mathbf{x}}_{I0} \quad (8)$$

$$\dot{\hat{\mathbf{x}}}_II = \mathbf{f}_{II}, \quad \hat{\mathbf{x}}_{II}(0) = \hat{\mathbf{x}}_{II0}; \quad \hat{y} = h(\hat{\mathbf{x}}_I) \quad (9)$$

Here \mathbf{K}_o and \mathbf{K}_I are the gain matrices which should be chosen such that the estimation error dynamics is stable. It can be seen that the observable dynamics [Eq. (8)] has three terms: (i) a predictor term given by the model, (ii) a proportional corrector term driven by the estimation error, and (iii) an integral corrector. While the unobservable part [Eq. (9)] only has a predictor term given by the model. According to the tuning strategies for the geometric estimator given in Alvarez and Lopez (1999), the gains can be evaluated as follows:

$$\mathbf{K}_o = \begin{bmatrix} k_1 \\ k_2 \end{bmatrix}, \quad \mathbf{K}_{int} = \begin{bmatrix} 0 \\ k_{int} \end{bmatrix}; \quad k_1 = (2\zeta + 1)\omega_o s_o, \quad k_2 = (2\zeta + 1)\omega_o^2 s_o^2, \quad k_{int} = \omega_o^3 s_o^3 \quad (10)$$

Where ζ is the damping factor, which can be set as $\zeta = 0.71$ in order to have a response with moderate oscillations. While ω_o is the characteristic frequency, which can be selected for a reactor as $4/(\text{total reaction time})$. So that the only tuning parameter is s_o , which is the settlement factor of the estimator, which must be greater than 1.

4. Results and Discussion

Here is worth of mention that the experimental data for glucose concentration (shown in Figure 3) are off-line lab analysis plotted for comparison purposes, while density measurements are the only measured output used in the softsensor implementation. Several experiments were carried out with different initial concentration of substrate (S_0), but due to the lack of space only one case study is shown for $S_0 = 15$ g/L.

First the reactor model, Eq. (2), was validated using the known parameters (V_{max} , K_m) and assuming a value of $K_I = 0.8$ g/L. It can be seen in Figure 3a that the dynamic response for glucose concentration (thin lines) has the tendency behaviour but is does not match correctly. Similar response occurs for the density model, Eq. (4), as shown in Figure 3b, where the density is underestimated.

Then the softsensor was implemented, Eqs. (8)-(9), assuming same previous initial conditions and a parameter tuning fixed at $s_o = 13$. Figure 3a shows the concentration dynamic response, where it can be seen that the softsensor is able to infer quite close to the experimental trajectory, due to the correction done to the density estimation (as shown in Figure 3b). While the kinetic parameter K_I was online estimated according the changes of the reactor motion, reaching a quasi-constant end value of 0.34 g/L (see Figure 3c). Finally, Figure 3d shows how the measured output converges in an approximate time of 50 h, which means that from this point the estimated values are reliable.

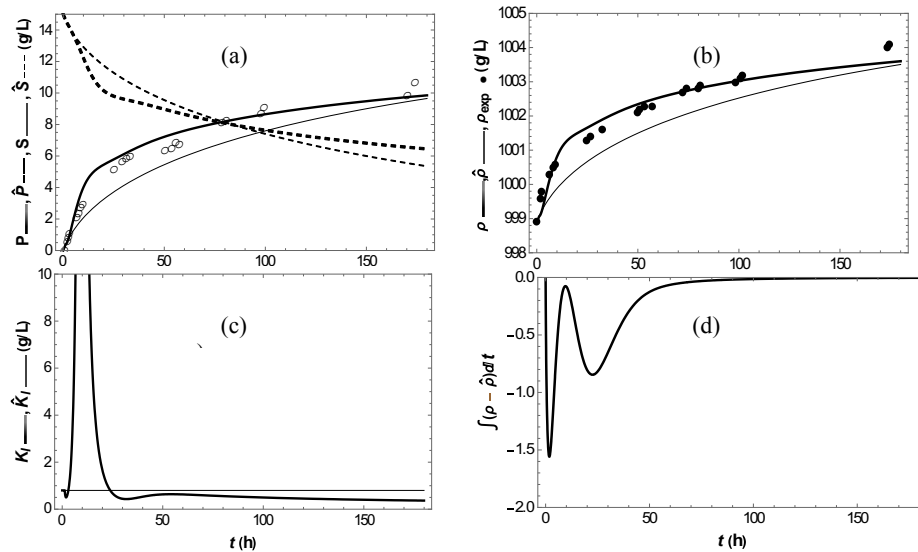


Figure 3. Dynamic response of the model and the softsensor: (a) estimated (unmeasured) concentrations, (b) measured density, (c) estimated inhibition parameter, (d) integral error.

5. Conclusions

An online monitoring strategy has been proposed to estimate unmeasured concentrations and a kinetic parameter in an enzymatic reactor, using only online measurements of density. The strategy minimizes time delays during monitoring, which raises an alternative of lower cost and greater accessibility, compared to the monitoring systems currently used based on discrete concentration measurements. The methodology proposed in this work can be extended to monitor other kind of reactors, such fermenters, but it could be also combined with other techniques for parameter estimation.

Acknowledgments

Financial support is acknowledged from the Energy Sustainability Fund 2014-05 (Conacyt-Sener), Mexican Bioenergy Innovation Centre, Bioalcohols Cluster (249564).

References

- J. Alvarez, T. Lopez, 1999, Robust dynamic state estimation of nonlinear plants, *AIChE J.* 45, 107-123.
- H. Bisswanger, 2008, *Methods*, in *Enzyme Kinetics: Principles and Methods*, Second Edition, Wiley-VCH Verlag GmbH & Co. KGaA, Weinheim, Germany.
- T. Lopez-Arenas, E. Granada-Vecino, M. Sales-Cruz, 2017, Parameter and state estimation techniques for an enzymatic reactor. 10th World Congress of Chemical Engineering, Spain.
- M. Pohlscheidt, S. Charaniya, C. Bork, 2013, *Bioprocess and fermentation monitoring*, Upstream Industrial Biotechnology, Vol. 2, John Wiley & Sons.

Optimal Strategic Planning of Integrated Petroleum and Petrochemical Supply Chain

Rahayu Ginanjar Siwi^a, Furqan Aljumah^a, Jie Li^{a*}, Xin Xiao^b

^a*School of Chemical Engineering and Analytical Science, The University of Manchester, Manchester M13 9PL, United Kingdom*

^b*Institute of Process Engineering, Chinese Academy of Sciences, Beijing 100190, China*
jie.li-2@manchester.ac.uk

Abstract

In this work we develop a novel multi-objective multi-period MINLP model for optimal strategic planning of entire petroleum and petrochemical supply chain (PPSC) to support decision making for petroleum and petrochemical industries. Nonlinear behaviour of the oil reservoir is considered for accurate prediction of crude production. More important, environmental impact based on Eco-indicator 99 is introduced as an objective function in addition to economic performance. The multi-objective model is converted to a single-objective by employing the weighting-sum method, which is solved to ε - global optimality using the proposed two-step procedure. An industrial-scale example is solved to show the capability of the proposed model and solution approach. The results clearly demonstrate the effect of considering environmental impact on the operation of PPSC.

Keywords: Petroleum supply chain, multi-objective, environmental impact, mixed-integer nonlinear programming (MINLP)

1. Introduction

The petroleum and petrochemical industry plays an important role in satisfying world energy demand and supporting our daily life. Petroleum-based fuel still owns the largest contribution of the global energy consumption by 30% in 2040 (U.S. Energy Information Administration, 2016). It is compulsory for these industries to develop optimal strategical plan for their supply chain to improve total profit and reduce environmental impact.

The entire petroleum and petrochemical supply chain (PPSC) can be divided into upstream, midstream, and downstream segments (Sahebi et al., 2014). While the upstream refers to crude exploration, production and transportation of crude oil to refineries, the midstream covers activities in refineries, petrochemical plants and chemical plants. The downstream focuses on storage and distribution to the customers.

A considerable amount of efforts encompassed the upstream of PPSC only (Gupta and Grossmann, 2012; Sahebi et al., 2015). For instance, Gupta and Grossmann (2012) developed an efficient multi-period MINLP model for optimal planning of offshore oil and gas field infrastructure. Nonlinear behaviour of the reservoir was considered for accurate prediction of crude production. Sahebi et al. (2015) designed the upstream crude supply chain by simultaneously considering economic performance and environmental impact. Some recent efforts addressed the integrated upstream and

midstream segments of PPSC (Azadeh et al., 2017). Azadeh et al., (2017) proposed a MILP model for design of upstream and midstream segments of PPSC to maximize economic performance only. It is clear that there is no strategic planning optimization model covering all segments of PPSC to optimize economic performance and environmental impact simultaneously.

In this work, we develop a novel multi-objective multi-period MINLP model for strategic planning of entire PPSC covering upstream, midstream and downstream segments to support decision making for petroleum and petrochemical industries. The entities in PPSC include oil wells, production platforms, refineries, petrochemical and chemical plants as well as an external market in each segment. The decisions include selection of potential facilities, technologies, locations, products and transportation modes, as well as establishment time of each facility. To predict the crude production accurately, nonlinear behaviour of the reservoir is considered. Environmental impact based on Eco-indicator 99 method (Goedkopp and Mark, 2015) is introduced as an objective function in addition to economic performance. The multi-objective model is converted to a single-objective by employing the weighting-sum method, which is solved to ϵ - global optimality using the proposed two-step procedure. An industrial-scale example is to illustrate the capability of the proposed model and solution approach. The results clearly demonstrate the effect of considering environmental impact on the operation of PPSC.

2. Problem Statement

A general PPSC is illustrated in Figure 1. There are W ($w = 1, 2, \dots, W$) oil wells, PP ($pp = 1, 2, \dots, PP$) platforms, F ($f = 1, 2, \dots, F$) refineries, PC ($pc = 1, 2, \dots, PC$) petrochemical plants, DC ($dc = 1, 2, \dots, DC$) chemical plants, and MD ($md = 1, 2, \dots, MD$) markets. Different technologies are used in some entities including WT ($wt = 1, 2, \dots, WT$) extraction technologies in oil wells, PT technologies ($pt = 1, 2, \dots, PT$) separating water from the crude oil and ST ($st = 1, 2, \dots, ST$) storage technologies in platforms, RT ($rt = 1, 2, \dots, RT$) refining technologies in refineries, CT ($ct = 1, 2, \dots, CT$) transforming technologies in petrochemical plants, and TT ($tt = 1, 2, \dots, TT$) technologies in chemical plants. Between two entities, there are TM ($tm = 1, 2, \dots, TM$) transportation modes.

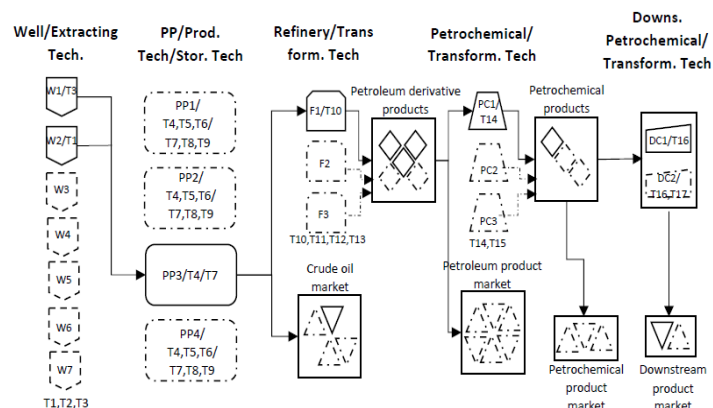


Figure 1 Petroleum and petrochemical supply chain where the dotted line represents the potential facilities and the steady line means readily operated facilities

Given: (1) economic data such as capital cost for establishment of each entity, unit operating cost of each potential technology, and capital and operating cost of every transportation mode; (2) potential location of each entity and capacity; (3) nonlinear behavior of oil reservoir; (4) demand and price of commodity; (5) environmental data for all entities and transportation modes; (6) the planning horizon. *Determine:* (1) allocation and establishment of each facility; (2) selection of technology for each built facility; (3) selection of transportation modes between two entities; (4) selection and allocation of external market; (5) selling amount of each product to external market and subsequent processing plant. *Assume:* oil wells produce the same type of crude oil. The objective is to maximize economic performance and minimize environmental impact, simultaneously.

3. Mathematical Formulation

The planning horizon is divided into T ($t = 1, 2, \dots, T$) periods with the length of each period as $\tau(t)$.

3.1. Economic objective

The economic objective is to maximize net present value (NPV), represented as follows,

$$NPV = \sum_t \frac{TCF(t)}{(1+i)^{(t-1)}} \quad (1)$$

where, TCF_t is total cash flow in period t and i is the interest rate. Details about the calculation of total cash flow can be referred to Azadeh et al. (2017).

3.2. Environmental impact

The environmental impact ($Eco99$) is counted based on Eco-indicator 99 method.

$$Eco99 = \sum_d f(d) \times Dam(d) \quad (2)$$

where, $Dam(d)$ is defined as the environmental damage d . $f(d)$ is the normalised weight of damage d . The environmental damage includes human health, ecosystem quality and resources depletion, which is contributed from contaminants released from utility consumption and direct emissions. More details can be referred to Sahebi et al. (2015).

3.3. Oil well constraints

We define binary variables $yw(w, wt, t)$ to represent if an oil well w uses extraction technology wt in period t . At most one technology is used for a well at a time. Then,

$$\sum_{wt} yw(w, wt, t) \leq 1 \quad \forall w, t \quad (3)$$

The total crudes extracted from the well is defined as $WTQ(w, t)$, the crude extracted from the oil reservoir using technology wt at a time is denoted as $WQ(w, wt, t)$.

$$WTQ(w, t) = \sum_{wt} WQ(w, wt, t) \quad \forall w, t \quad (4)$$

The capacity for each technology is represented as,

$$cl^L(w, wt) \cdot yw(w, wt, t) \leq WQ(w, wt, t) \leq cl^U(w, wt, t) \cdot yw(w, wt, t) \quad \forall w, wt, t \quad (5)$$

$$WTQ(w,t) \leq capw(w,t) \quad \forall w, t \quad (6)$$

0-1 continuous variables $xw(w,wt,t)$ are defined as the establishment of new well w using technology wt at period t .

$$\sum_{wt} \sum_t xw(w,wt,t) \leq 1 \quad \forall w \quad (7)$$

$$xw(w,wt,t) = yw(w,wt,t) - yw(w,wt,t-1) \quad \forall w, wt, t \quad (8)$$

We introduce binary variables $y1(w,pp,tm,t)$ as the existence of transportation mode between oil well w and production platform pp . The amount of crudes transported from well w and platform pp using transportation mode tm at t is denoted as $Q1(w,pp,tm,t)$.

$$WTQ(w,t) = \sum_{pp} \sum_{tm} Q1(w,pp,tm,t) \quad \forall w, t \quad (9)$$

$$c^L(tm) \cdot y1(w,pp,tm,t) \leq Q1(w,pp,tm,t) \leq c^U(tm) \cdot y1(w,pp,tm,t) \quad \forall w, t \quad (10)$$

We define 0-1 continuous variables $x1(w,pp,tm,t)$ to exhibit the establishment of new transportation mode between well w and platform pp .

$$\sum_t x1(w,pp,tm,t) \leq 1 \quad \forall w, pp, tm \quad (11)$$

$$x1(w,pp,tm,t) = y1(w,pp,tm,t) - y1(w,pp,tm,t-1) \quad \forall w, pp, tm, t \quad (12)$$

3.4. Crude production constraints for platforms

$$PTQ(pp,t) = \sum_w \sum_{tm} Q1(w,pp,tm,t) \cdot ofr(w,t) \quad \forall pp, t \quad (13)$$

where, $ofr(w,t)$ is the water-oil ratio from well w at period t and $PTQ(pp,t)$ denotes crude oil volume produced from a production platform.

3.5. Other constraints

We have many similar constraints for production platform, refineries, petrochemical plants, chemical plants and external markets for oil, petroleum products, petrochemicals, and chemicals as those for oil wells, which are not given in this paper.

3.6. Nonlinear behavior for oil reservoir

The maximum crude oil flowrate and the water-oil ratio changes nonlinearly with the fraction of oil recovered due to the decreasing reservoir pressure as the crude oil extraction progressing. More details can be referred to Gupta and Grossmann (2012).

$$capw(w,t+1) = a1(w) \cdot fc^3(w,t) + b1(w) \cdot fc^2(w,t) + c1(w) \cdot fc(w,t) + d1(w) \quad \forall w, t < T \quad (14)$$

$$fc(w,t) = \sum_{s < t} WTQ(w,s) / REC(w) \quad \forall w, t < T \quad (15)$$

The oil fraction in the 'raw' crude oil by the end of period t is represented by,

$$ofr(w,t) = a2(w) \cdot fc^3(w,t) + b2(w) \cdot fc^2(w,t) + c2(w) \cdot fc(w,t) + d2(w) \quad \forall w, t \quad (16)$$

We complete our novel optimization model for all segments of PPSC, which is a large-scale multi-objective multi-period MINLP model.

4. Solution approach

The multi-objective feature is handled using weighting sum method (Sahebi et al., 2015) by firstly normalizing each objective function using its maximum and minimum values.

$$\tilde{f}_1 = \frac{NPV - NPV^L}{NPV^U - NPV^L} \quad \tilde{f}_2 = \frac{Eco99^U - Eco99}{Eco99^U - Eco99^L} \quad (17-18)$$

Then, a new combined objective is expressed using respective weight factors w_1 and w_2 .

$$f_3 = w_1 \cdot \tilde{f}_1 + w_2 \cdot \tilde{f}_2 \quad (19)$$

To solve the model to ε - global optimality, two-step procedure is proposed as follows,

Two-step procedure: For each combination of w_1 and w_2 , the solution with $w_1 = 1$ and $w_2 = 0$ is used to initialize DICOPT for the generation of a good feasible solution. Then the obtained feasible solution from DICOPT is used as a start point for ANTIGONE for ε - global optimality.

5. Computational Studies

An industrial-scale example is solved to demonstrate the capability of the proposed model and solution approach. There are 7 oil wells with 2 operated and 5 potential wells, 4 production platforms with 1 operated and 3 potential platforms, 3 refineries with 1 operated and 2 potential, 3 petrochemical plants with 1 operated and 2 potential, and 2 chemical plants with 1 operated and 1 potential, as illustrated in Figure 1. Each entity involves different potential technologies for potential facilities such as 3 extraction technologies for oil wells, 3 production and 3 storage technologies for platforms, 4 for refineries, 2 for petrochemical plants and 2 for chemical plants. Five transportation modes are considered including offshore and onshore pipelines, oil tanker, railcar and truck. This example is solved using DICOPT and ANTIGONE in GAMS 24.7 on a workstation with Intel® Core™ i5-6200U CPU 2.30 GHz with 8 GB RAM under Windows 10 Home 64.

Table 1 Computational results for the example with different weight factors

No.	f_3	NPV		EQ		RD	HH	$Eco99$
		w_1	(1×10^6 USD)	w_2	(1×10^9 USD)	(1×10^9 USD)	(1×10^9 USD)	(1×10^9 USD)
1	1.003	0.000	183.666	1.000	282.212	1118.028	624.252	586.191
2	0.914	0.125	2778.713	0.875	311.549	1228.705	686.607	645.003
3	0.846	0.250	10232.296	0.750	525.614	2077.406	1160.084	1089.760
4	0.870	0.375	13248.627	0.625	662.597	2610.669	1460.100	1371.213
5	0.883	0.500	13401.480	0.500	687.322	2705.741	1513.595	1421.515
6	0.925	0.625	14163.211	0.375	739.031	2905.274	1628.133	1528.028
7	0.944	0.750	14031.286	0.250	742.639	2921.861	1636.209	1535.911
8	0.962	0.875	14183.189	0.125	768.178	3020.074	1692.074	1588.116
9	1.001	1.000	14136.932	0.000	766.423	3010.489	1687.122	1583.588

Note that HH is human health, EQ is ecosystem quality and RD is resources depletion

The MINLP model consists of 18,588 binary variables, 59,358 continuous variables and 81,633 constraints. The results are presented in Table 1. As seen in Table 1, the values of $Eco99$ increase with the increase of w_1 , whereas NPV values is increased gradually, indicating the environmental performance conflicts with the economic objective. Table 2 gives different technologies selected in each facility. From Table 2, when w_1 increases,

the technology with lower cost is selected such as oil extraction technology wt1 since the technology with lower cost usually produce worse environmental impact, which can be seen from wells #2, #3, #6, and #7. Since the well #1 uses the extraction technology wt3 in the beginning, it do not change technology throughout the entire period. This is also true for the well #4 and #5 with fixed technology of wt2. By taking higher consideration of environmental impact, the technology selection will switch from more economical technologies to more environmentally friendly technologies (e.g., wt1 to wt3).

Table 2 Selected technology in each facility for the example with different weight factors

Entities	#	Case No								
		1	2	3	4	5	6	7	8	9
Oil well (<i>w</i>)	1	wt3	wt3	wt3	wt3	wt3	wt3	wt3	wt3	wt3
	2	wt1	wt1	wt1	wt1	wt1	wt1	wt1	wt1	wt1
	3	wt3	wt3	wt2	wt2	wt1	wt1	wt1	wt1	wt1
	4	wt3	-	wt2	wt2	wt2	wt2	wt2	wt2	wt2
	5	wt3	-	wt2	wt2	wt2	wt2	wt2	wt2	wt2
	6	wt3	wt3	wt2	wt2	wt1	wt1	wt1	wt1	wt1
	7	wt3	wt3	wt2	wt2	wt2	wt2	wt2	wt1	wt1
Production platforms (<i>pp</i>)	1	-	-	pt3/st3	pt3/st3	pt3/st1	-	-	-	-
	2	-	pt3/st3	pt2/st2	pt3/st3	pt3/st3	pt2/st2	pt1/st3	pt1/st2	pt1/st2
	3	pt1/st1	pt1/st1	pt1/st1	pt1/st1	pt1/st1	pt1/st1	pt1/st1	pt1/st1	pt1/st1
	4	pt3/st3	-	pt3/st3	pt3/st3	pt3/st3	pt2/st2	pt2/st1	pt2/st1	pt1/st1
Refinery (<i>f</i>)	1	rt1	rt1	rt1	rt1	rt1	rt1	rt1	rt1	rt1
	2	-	-	rt2	rt2	rt2	rt2	rt2	rt2	rt2
	3	rt3	rt4	rt4	rt3	rt3	rt4	rt4	rt4	rt4
Petrochemical plant (<i>pc</i>)	1	ct1	ct1	ct1	ct1	ct1	ct1	ct1	ct1	ct1
	2	ct2	ct2	ct2	ct1	ct1	ct1	ct1	ct1	ct1
	3	-	-	-	-	-	-	-	-	-
Downstream chemical plant (<i>dc</i>)	1	-	-	-	-	-	-	-	-	-
	2	tt2	tt1	tt1	tt1	tt1	tt1	tt1	tt1	tt1

6. Conclusions

In this work, we developed a novel multi-objective multi-period MINLP model for strategic planning of entire PPSC covering upstream, midstream and downstream segments to support decision making for petroleum and petrochemical industries. Nonlinear behaviour of the reservoir was employed for accurate prediction of crude production. Environmental impact as well as economic performance was optimized simultaneously. The multi-objective model was converted to a single-objective by employing the weighting-sum method, which was solved to ϵ - global optimality using the proposed two-step procedure. The computational results clearly demonstrate the effect of considering environmental impact on the operation of PPSC.

References

- A. Azadeh, F. Shafiei, R. Yazdanparast, J. Heydari, A. Keshvarparast, 2017, Optimum integrated design of crude oil supply chain by a unique mixed integer nonlinear programming model, *Ind. Eng. Chem. Res.*, 56, 19, 5734-5746
- R. Goedkopp, S. Mark, "Eco-indicator 99 methodology report," Amersfoort, 2015.
- V. Gupta and I. E. Grossmann, 2012, An efficient multiperiod MINLP model for optimal planning of offshore oil and gas field infrastructure, *Ind. Eng. Chem. Res.*, 51, 6823-6840.
- H. Sahebi, S. Nickel, and J. Ashayeri, 2014, Strategic and tactical mathematical programming models within the crude oil supply chain context-A review, *Comput. Chem. Eng.*, 68, 56-77.
- H. Sahebi, S. Nickel, and J. Ashayeri, 2015, Environmentally conscious design of upstream crude oil supply chain, *Pet. Abstr.*, 55, 11501-11511.
- U.S. Energy Information Administration, *International Energy Outlook 2016*, 2016.

Real-Time Nonlinear State Estimation in Polymerization Reactors for Smart Manufacturing

Santiago D. Salas^a, Jorge Chebeir^a, Stefania Tronci^b, Roberto Baratti^b, José A. Romagnoli^{a*}

^a*Department of Chemical Engineering, Louisiana State University, Baton Rouge, LA 70809, United States of America*

^b*Dip. di Ingegneria Meccanica, Chimica e dei Materiali, Università degli Studi di Cagliari, Cagliari 09123 Italy*

**jose@lsu.edu*

Abstract

A high order Geometric Observer (GO) and a *hybrid* discrete-time extended Kalman filter (*h*-DEKF) are assessed in real-time towards data reconciliation and comprehensive polymer characterization. The nonlinear estimators are tested under a set of experiments using the data provided by the state-of-the-art smart sensor Automatic Continuous Online Monitoring of Polymerization reactions (ACOMP). To design the GO three different high-order structures are evaluated in terms of their robustness and performance. The gains of the GO are set following a systematic approach with a distinction between pure measurements and Lie derivatives. The *h*-DEKF design follows an auto-tuned error driven initialization of the free-parameters where different metaheuristic algorithms are employed for tuning. Both nonlinear estimators are contrasted for applications in the Smart Manufacturing of polymers. The aqueous polymerization of acrylamide using potassium persulfate as initiator demonstrates the effectiveness and flexibility of the estimator for real-time applications.

Keywords: Free-radical polymerization, nonlinear state estimation, geometric observer, extended Kalman filter.

1. Introduction

The chemical industry demands practical tools for the Smart Manufacturing of chemicals with target final properties. Polymers represent a significant portion of this industry, and its synthesis involves complex processes. Major concerns in polymerization include the intricacy of the mathematical model as well as inadequate or nonexistent real-time characterization techniques. A major goal in polymerization facilities is to achieve a target molecular weight distribution (MWD). After the chemical structure, MWD is the most important parameter controlling the physical, mechanical and processing properties of polymers. Nonetheless, the online monitoring of MWD by hardware sensors is currently not feasible at industrial scale. This scenario motivates the search for adequate state observers to generate a basis for model-based monitoring/control systems.

The utilization of state observers has a significant role on establishing the necessary model-based tools for the polymerization industry. The prevalent high cost of reliable sensors represents a major concern. Even if measurements are economically available

for the system, they are often inaccurate or contaminated by noise. In this context, state observers can suffice the lack of genuine measurements for control systems. State observers can infer significant unmeasured properties of the polymer during synthesis, providing model-centric monitoring and control capability that prevent shifting from desired final key properties.

In this work, a high-order GO and an h -DEKF are compared based on their ability in data reconciliation and state estimation. The comparison criteria includes robustness, estimation of unmeasured properties and stability. The ACOMP provides real-time measurements of monomer concentration, weight-average molecular weight and volume of contents inside the reactor (Reed, 2013). Using the available measurements and an upgraded version of the model developed by Ghadipasha et al. (2016), both nonlinear estimators are adapted to the underlying process. The GO (Alvarez & Fernandez, 2009) is principally characterized by its applicability to either observable or detectable systems. The design of the GO includes a robust local convergence and a systematic construction-tuning procedure. The h -DEKF is constructed in a similar fashion to the one in Salas et al. (2017). The difference resides in the determination of covariance error matrices, which are obtained following an auto-tuned error-driven approach. Then, both nonlinear state estimation methods are contrasted for applications in the Smart Manufacturing of polymers. The aqueous polymerization of acrylamide using potassium persulfate as initiator serves as an illustrative example to demonstrate the effectiveness of the real-time nonlinear state estimation and enhanced monitoring. The estimation strategies are tested under a range of conditions.

2. Background

2.1 Nonlinear Model

The adopted model of the polymerization reactor was based on Ghadipasha et al. (2016) and is here summarized

$$\frac{dN_m}{dt} = -(k_p + k_{fm})P_0N_m + F_mC_{mf} - F_{out}C_m \quad (1a)$$

$$\frac{dN_i}{dt} = -k_dN_i + F_iC_{if} - F_{out}C_i \quad (1b)$$

$$\frac{dN_s}{dt} = -k_{fs}N_sP_0 + F_iC_{sif} + F_mC_{smf} - F_{out}C_s \quad (1c)$$

$$\frac{d(\lambda_0V)}{dt} = (k_{fm}N_m + k_{td}P_0V + k_{fs}N_s)\alpha P_0 + \frac{1}{2}k_{tc}P_0^2V - F_{out}(\lambda_0) \quad (1d)$$

$$\frac{d(\lambda_1V)}{dt} = [(k_{fm}N_m + k_{td}P_0V + k_{fs}N_s)(2\alpha - \alpha^2) + k_{tc}P_0V] \frac{P_0}{(1-\alpha)} - F_{out}(\lambda_1) \quad (1e)$$

$$\frac{d(\lambda_2V)}{dt} = [(k_{fm}N_m + k_{td}P_0V + k_{fs}N_s)(\alpha^3 - 3\alpha^2 + 4\alpha) + k_{tc}P_0V(\alpha + 2)] \frac{P_0}{(1-\alpha)^2} - F_{out}(\lambda_2) \quad (1f)$$

The available measurements, along with their dependency on the state variables, are

$$C_m = \frac{N_m}{V}, \quad M_w = w_m \frac{\lambda_2}{\lambda_1}, \quad V = \frac{\lambda_1 V w_m}{\rho_p} + \frac{N_m w_m}{\rho_m} + \frac{N_s w_s}{\rho_s} + \frac{N_i w_i}{\rho_i} \quad (2)$$

The other not measured polymer properties to be estimated are

$$M_n = w_m \frac{\lambda_1}{\lambda_0} \quad (3a)$$

$$\frac{d g(m,n)}{dt} = \frac{k_p N_m P_0}{\lambda_1 V} \left[\left(\frac{m(1-\alpha)+\alpha}{\alpha} \right) \alpha^{m-1} - \left(\frac{(n+1)(1-\alpha)+\alpha}{\alpha} \right) \alpha^n \right] - \frac{1}{\lambda_1 V} g(m,n) \frac{d(\lambda_1 V)}{dt} \quad (3b)$$

For a detailed model description and definition of variables and constants, please see Ghadipasha et al. (2016). The above model could be recast, in compact notation, as

$$\dot{\mathbf{x}}(t) = f(\mathbf{x}, \mathbf{u}), \quad \mathbf{x}(t_0) = \mathbf{x}_0 \quad (4a)$$

$$\mathbf{y} = \mathbf{h}(\mathbf{x}) \quad (4b)$$

where, $\mathbf{x} = [N_m, N_i, N_s, \lambda_0 V, \lambda_1 V, \lambda_2 V]^T$ is the 6-dimensional state vector, $\mathbf{u} = [F_m, F_i, T]^T$ and $\mathbf{y} = [C_m, M_w, V]^T = [h_1(\mathbf{x}), h_2(\mathbf{x}), h_3(\mathbf{x})]^T$ are the 3-dimensional vectors of controlled variables and measurement ones.

2.2 Observability and Detectability

Even though the ACOMP represents a major advancement in providing online measurements of polymer properties, the complete state vector can seldom be measured. The number of online measurements is lower than the number of states required to fully describe the dynamics of the system. The implementation of a dynamic nonlinear state estimator is necessary for better comprehension of the evolution of state variables as well as to improve the available measurements. The effectiveness of the process monitoring depends on basic properties of the model: the observability and detectability. As reported by *Alvarez & Fernandez (2009)*, it is possible to assess the observability of a nonlinear system through the definition of the observability map $\boldsymbol{\phi}(\mathbf{x}, \mathbf{u}) = [\phi_1, \phi_2, \dots, \phi_m]^T$.

$$\boldsymbol{\phi}(\mathbf{x}, \mathbf{u}) = [\phi_1, \phi_2, \dots, \phi_m]^T, \quad \phi_i = (h_i, L_f^1 h_i, \dots, L_f^{k_i-1} h_i) \quad (5a)$$

where, $L_f^j h_i$ are the recursive j^{th} Lie derivatives of the time varying scalar field h_i along the vector f , k_i is the observability index of the i^{th} output and k is the estimator order given in Eq. (5b).

$$k = k_1 + k_2 + \dots + k_m \quad (5b)$$

For n states, the system is observable if the rank of the observability matrix is $k = n$. When $k < n$, there are unobservable states and the system is RE-exponentially estimable if the unobservable motion is stable. In this case, there is a differentiation between distinguishable and undistinguishable states.

2.3 Geometric Observer

The nonlinear estimation here reconstructs the polymerization dynamics (1-3) based on the GO proposed by *Alvarez & Fernandez (2009)*. The observer is reported in compact notation in Eq. (6a) for innovated and in Eq. (6b) for non-innovated states. Innovated states are those states which are corrected using the available measurements, while non-innovated states are obtained from the model (open-loop).

$$\hat{\mathbf{x}}_i(t) = f_i(\hat{\mathbf{x}}, \mathbf{u}) + (\partial_x \boldsymbol{\phi}(\hat{\mathbf{x}}, \mathbf{u}))^{-1} \mathbf{K}[\mathbf{y} - \mathbf{h}(\hat{\mathbf{x}})] \quad (6a)$$

$$\hat{\mathbf{x}}_v(t) = f_v(\hat{\mathbf{x}}, \mathbf{u}) \quad (6b)$$

In Eq. 6, $\hat{\mathbf{x}} = (\hat{\mathbf{x}}_i, \hat{\mathbf{x}}_v)$ is the estimated state vector; $\hat{\mathbf{x}}_i$ and $\hat{\mathbf{x}}_v$ are the vectors of the innovated and non-innovated states (*Tronci et al., 2005*), respectively; \mathbf{K} is a block diagonal matrix and its values are set in such a way that the error dynamics remain stable.

2.4 h-DEKF Implementation

The *h-DEKF* follows a similar structure as presented by *Salas et al. (2017)*. Here, it is enough to outline the basic concepts on which the DEKF relies. For details on the governing equations, please refer to *Simon (2006)*. The inferential procedure is,

$$\hat{\mathbf{x}}_{j+1/j+1} = \hat{\mathbf{x}}_{j+1/j} + \mathbf{K}_{j+1}[\mathbf{y}_{j+1} - \mathbf{h}_{j+1}(\hat{\mathbf{x}})]. \quad (7)$$

where $\hat{\mathbf{x}}_{j+1/j+1}$ represents the state estimate at time $(j + 1)$ on the basis of the model prediction $\hat{\mathbf{x}}_{j+1/j}$. \mathbf{K}_{j+1} is the filter gain matrix that weights the relative importance given to the model predictions and to the actual measurements. The filter gain matrix is constructed on the basis of the error covariance matrices of the measurements (\mathbf{R}) and the model (\mathbf{Q}) (Simon, 2006) that can be regarded as tuning parameters. The tuning problem of the filter is expressed as the minimization of the sum of the product between an absolute error vector, the inverse of the measurement error covariance matrix and the transposed absolute error vector, as given in Eq. (8).

$$\min \sum_{j=1}^n [\bar{y}_j - h(\hat{\mathbf{x}}_j)] \mathbf{R}^{-1} [\bar{y}_j - h(\hat{\mathbf{x}}_j)]^T \quad (8)$$

The *h-DEKF* tuning was performed using a genetic algorithm (GA) (Kapanoglu et al, 2007), differential evolution (DE) (Storn & Price, 1997) and particle swarm optimization (PSO) (Poli et al, 2007). Each algorithm has 30 independent runs of 1500 fitness function evaluations each, and, because the methods are population-based, 50 generations of a population size of 30 are chosen for all cases. For the GA, the selected crossover fraction is 0.6, extra-range for crossover is 0.4, mutation fraction set to 0.4, mutation rate to 0.1 and the selection method is fixed as random. Regarding the DE, the crossover rate is 0.7 and the scaling factor is randomly selected between the bounds [0.2, 0.8]. Finally, the PSO uses as parameters 1 for the initial inertia weight, 0.99 for the damping ratio, 1.5 for the cognitive coefficient and 2.0 for the social coefficient.

3. Results

The proposed nonlinear state estimation approaches were tested on a polymerization pilot plant consisting of a 1.5 L reactor monitored by the ACOMP system and auxiliary fittings and instruments (Salas et al. 2017). Recipes for three optimal semi-batch experiments corresponding to increasing, constant, and decreasing M_w time-evolution trajectories are generated by the minimization of a multi-objective dynamic optimization problem (Ghadipasha et al. 2016).

The analysis of the observability matrix shows that only 5 out of 6 states are observable, in which $\lambda_0 V$ is the not observable state. For the high-order estimator, the Lie derivative of two measurements are necessary. The combinations of possible integer k_i include: $(k_1, k_2, k_3) = (2, 2, 1)$, $(k_1, k_2, k_3) = (2, 1, 2)$ and $(k_1, k_2, k_3) = (1, 2, 2)$, where the first integer refers to C_m , the second to M_w and the third to V . The values of the coefficient of the gain matrix \mathbf{K} in (4) have been selected analyzing the natural frequencies of the system and they are set equal 0.4 for measurements and 10^{-8} for the Lie derivatives.

The different observer structures are compared in terms of the minimum singular value (σ_0), and condition number ($\eta = \sigma_{max}/\sigma_0$) of the observability matrix, in the understanding that the better estimation should be characterized by the highest σ_0 and the lowest η (Porru & Özkan, 2017). For this purpose, three different trajectories of M_w have been studied and the observability matrix was calculated along the trajectories. Results for the initial condition are reported in Table 1 and show that the innovation of 5 states with structures $(2, 2, 1)$ and $(1, 2, 2)$ depict a higher σ_0 with respect to $(2, 1, 2)$ in all cases. This behavior does not change along the trajectories. These phenomena can be explained by considering that h_2 is the only function depending on $\lambda_2 V$; therefore, by using its Lie derivative, it is possible to gain more information on $\lambda_2 V$. Configuration $(2, 2, 1)$ shows the lowest condition number for all cases, and appears to be the most promising structure. However, this structure fails to converge in some of the studied

trajectories (Increasing M_w trajectory) when tested in the set of available experiments. Thus, the structure that shows better performance is $(1,2,2)$, which can be explained by considering that C_m is more susceptible to introduce errors to the system with respect to V , which can have an impact on the robustness of the estimation.

The h -DEKF exhibits stable behaviour and ability in predicting unmeasured properties. In addition, the DE algorithm showed the best performance in achieving the best minimum value in average during tuning. The GO shows a slightly better ability in data reconciliation as it accomplishes better the task of reducing the noise of measurements, but the h -DEKF shows a better performance with respect to GO in predicting unmeasured properties for all cases. The comparison of the GO and h -DEKF is illustrated by Figure 1 and 2, for a representative increasing and decreasing M_w experiments.

Table 1: Minimum singular values and condition number for high order structures

Trajectory	Structure	$(2,2,1)$	$(2,1,2)$	$(1,2,2)$
Increasing M_w	σ_0	7.67E-05	1.13E-19	7.67E-05
	η	2.08E+10	4.83E+23	6.55E+14
Constant M_w	σ_0	7.82E-05	1.14E-21	6.13E-20
	η	2.68E+10	4.79E+25	8.9E+23
Decreasing M_w	σ_0	7.75E-05	3.76E-20	8.08E-20
	η	2.85E+10	1.45E+24	6.74E+23

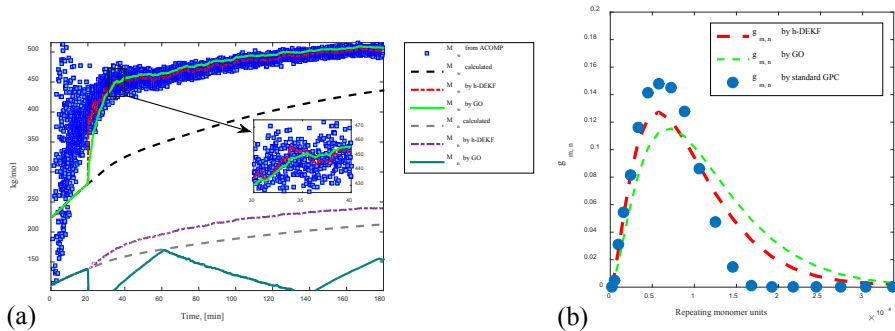


Figure 1: Increasing M_w trajectory. a) Weight average and number average molecular weight evolution, b) Experimental and estimated final chain length distribution.

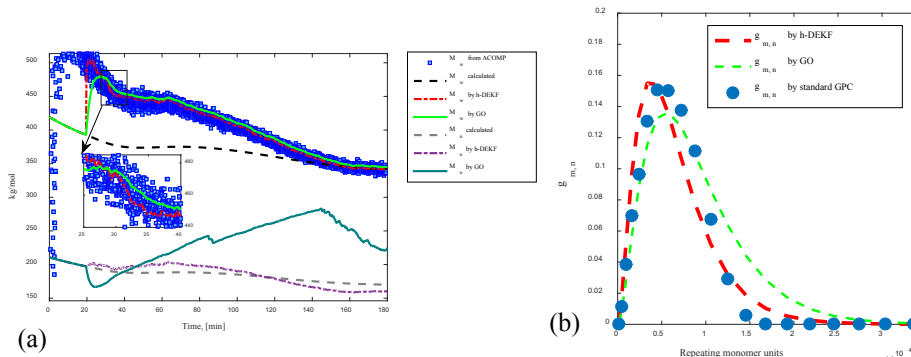


Figure 2: Decreasing M_w trajectory. a) Weight average and number average molecular weight evolution, b) Experimental and estimated final chain length distribution.

4. Conclusions

In this work, two different nonlinear state observers, GO and h -DEKF, are assessed and compared for reconstructing unmeasured properties i.e., number-average molecular weight and molecular weight distribution, while performing signal processing for the Smart Manufacturing of polymers. A response analysis determines the performance of each nonlinear observer. The h -DEKF leads to better results with respect to GO to infer MWD, but the GO offers better capability in data reconciliation. However, the h -DEKF presents for this case a better performance overall. The reasons of such finding could be related to the selected GO structure, which involves a high order structure that utilizes all possible Lie derivatives of the measured variables. This makes the estimation more sensitive to measurement and model errors/noise.

Therefore, a full order GO might not be the best choice for this application, which opens a venue to study in the future. The possibility of implementing lower order structures to increase the observer robustness without reducing the estimation performances represents a deeper study on the possible structures and combination of innovated states. The inclusion of robust and flexible state observers in model-centric tools permits a more efficient and effective operation during polymer synthesis.

References

- J. Alvarez, C. Fernandez, **2009**. Geometric estimation of nonlinear process systems, *J Process Contr.*, 19, 247-260.
- N. Ghadipasha, A. Geraili, J.A. Romagnoli, C.A. Castor, M. F. Drenski, W.F. Reed, **2016**. Combining On-Line Characterization Tools with Modern Software Environments for Optimal Operation of Polymerization Processes. *Processes*, 4, 5.
- M. Kapanoglu, İ. O. Koca, Ş. Erdogmus, **2007**. Genetic algorithms in parameter estimation for nonlinear regression models: an experimental approach. *J. Stat. Comput. Simul.*, 77, 851-867.
- R. Poli, J. Kennedy, T. Blackwell, **2007**. Particle swarm optimization. An overview. *Swarm Intell.*, 1, 33-57.
- M. Porru, L. Özkan, **2017**. Monitoring of Batch Industrial Crystallization with Growth, Nucleation, and Agglomeration. Part 2: Structure Design for State Estimation with Secondary Measurements. *Ind Eng Chem Res.*, 56, 9578–9592.
- W. F. Reed, A. M. Alb, **2013**. *Monitoring polymerization reactions: from fundamentals to applications*. John Wiley & Sons.
- S. D. Salas, N. Ghadipasha, W. Zhu, J. A. Romagnoli, T. McAfee, W. F. Reed, **2017**. Online DEKF for State Estimation in Semi-Batch Free-Radical Polymerization Reactors. *Computer Aided Chemical Engineering. Elsevier*, 40, 1465-1470.
- D. Simon, **2006**. Optimal state estimation: *Kalman, H infinity, and nonlinear approaches*. John Wiley & Sons.
- R. Storn, K. Price, **1997**. Differential evolution - A simple evolution strategy for fast optimization. *J. Glob. Optim.*, 11, 341-359.
- S. Tronci, F. Bezzo, M. Barolo, R. Baratti, **2005**. Geometric observer for a distillation column: development and experimental testing. *Ind Eng Chem Res.*, 30, 1870-1880.

Optimisation of water supply systems in the water – energy nexus: Model development and implementation to support decision making in investment planning

Christiana M. Papapostolou^{a*}, Emilia M. Kondili^a, Georgios Tzanes^b

^a*Optimisation of Production Systems Laboratory,
Mechanical Engineering Department, Piraeus University of Applied Sciences, 250 P.
Ralli and Thivon Av., 122 44 Athens Greece*

^b*Soft Energy Applications and Environmental Protection Laboratory
Mechanical Engineering Department, Piraeus University of Applied Sciences, 250 P.
Ralli and Thivon Av., 122 44 Athens Greece
ekondili@puas.gr*

Abstract

Water resources availability, in terms of quality and quantity, is a very crucial issue in many areas of the world; especially in areas with water shortage and varying and time dependent water demand. Lately, it has become obvious that water supply chain problems are also inherently linked to the energy availability and quality of an area, leading to the so called water – energy nexus problems. The present work is a continuation of our ongoing research in the optimisation of water and energy supply chain in terms of maximising the overall benefit of the integrated system, whilst satisfying the conflicting demands. The objective of the work is to expand the model for water supply optimisation to take into account all the potential water supply sources intending to support decision making in investments planning, with environmental considerations.

Keywords: water resources optimisation, water energy integration, economic and environmental criteria

1. Introduction. Scope and objectives of the work

Water resources availability, in terms of quality and quantity, is a very crucial issue in many areas of the world; especially in areas with water shortage and varying and time dependent water demand. Lately, it has become obvious that water supply chain problems are also inherently linked to the energy availability and quality of an area, leading to the so called water – energy nexus problems. In parallel, energy is a focal point in the water supply since in many cases it is in fact the limiting factor for the implementation of various water supply methods. For example, desalination methods being technologically mature and easily accessible, could provide easy and not particularly expensive water. However, the high energy demand of desalination methods sets constraints in the implementation of the method.

Furthermore, water recycle from waste water treatment plants may also provide a very important water supply method in various areas where there is no other method that

could be applied. However, the water transportation from the production point to the distribution network requires energy and again the two problems may be considered in an integrated manner. For the application of the developed framework, a case study in Cyclades island has been carried out in order to designate optimum water supply chain characteristics, along with the solution of the energy supply chain (ESC) problem, ultimately aiming to maximise the total benefit of the systems – as this is defined in the work. The results of the problem solution, the applicability of the model in various water – energy nexus as well as the importance and relevance of the issue in the CAPE community are also highlighted in the work.

Over the past decade, the integrated approach for the solution of water and energy problems, i.e. the so called ‘water – energy nexus’ has become a topic of increasing attention for the scientific communities and practitioners in the field. There is a continuous increase in the academic papers as well as in the professional studies demonstrating the improving capacity of the scientific community to assess in an integrated approach the water and energy problems.

Indicatively some of the most recent works related to the water – energy nexus may be cited. Saeed Kaddoura and SamehEl Khatib (2017) make a detailed review of the existing nexus modelling tools used for integrated policy making and identify the capabilities and limitations of each modelling tool in order to help readers select the appropriate tool for their objective.

Jiangyu Daia et al (2018) in their very recent research work make an extensive survey of recent scientific literature on the water-energy nexus, where 70 studies were identified and 35 were selected as comprehensive case studies for review. From this review it is clear that the research on water-energy nexus has seen a significant increase in both the number of studies and the capacity of the scientific community to productively assess water and energy interlinkages at a higher resolution. Fewer approaches are designed to support governance and implementation of technical solutions, and this is considered to be a priority challenge area for the scientific community if it aims to achieve greater impact on resource policy and management.

Daniel J. Garcia and Fengqi You (2016) relate the Water – Energy – Food nexus approach with Process Systems Engineering principles and identify process systems engineering research opportunities to appropriately model and optimize the nexus. It is clear from their work that there are further challenges with appropriate system boundary definitions and challenges in modeling the decision-making and conflicting objectives of multiple stakeholders in the nexus.

Focusing attention in the very crucial issue of water resources management and its sustainability considerations, Pires et al evaluate how indicators related to water use and management perform against a set of sustainability criteria assessing 170 indicators through an international panel of experts that evaluated whether they fulfil the four sustainability criteria: social, economic, environmental, and institutional.

Studying all these works it is obvious that very significant progress has been achieved but still there is a very wide scope for further work in the field since there are many features of the integrated problem that are not well understood yet and there is a very challenging area of problems that is focused either in specific geographical regions or in very specific characteristics of the problem itself.

The present work is a continuation of our ongoing research in the optimisation of water and energy supply chain in terms of maximising the overall benefit of the integrated system, whilst satisfying the conflicting demands. The objective of the work is to expand the model for water supply optimisation to take into account all the potential water supply sources along with their environmental and social impacts intending to support decision making in investments planning.

2. Case study

The optimisation model that has been developed in Papapostolou et al (2017) is implemented for a small island in Cyclades complex, called Iraklia. Iraklia - named after the Greek mythological god Hercules - is the westernmost island of the Small Cyclades complex with an area of 18 thousand square kilometres, located 18 nautical miles southern of Naxos, the largest island of Cyclades complex. The small island has 151 inhabitants settled in Panagia and Agios Georgios, the main settlement and the port, respectively.

At each aforementioned locations, there are two water tanks: the one in Panagia can store up to 1000m³, while the capacity of the Agios Georgios is 500m³. The latter presents significant water shortages, especially during the summer months which up till now have been met via ship-transfers (Figure 1), with a specific water transportation cost of ~15€/m³. For that purpose, the state has financially supported the installation of a desalination plant (300m³/day), which will be powered by a local diesel power station.

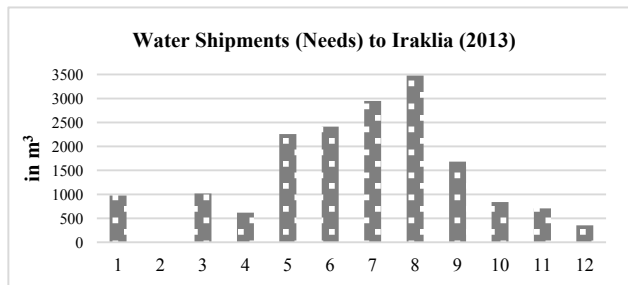


Figure 1: Annual water shipments to Iraklia throughout 2013 (YPEKA, 2016)

In Iraklia, as in most of the Aegean Sea islands, the electricity needs present a large fluctuation between winter and summer seasons, mainly attributed to tourism. More specifically, the load peak, which occurs during August, is nearly 4 times the average load during winter. The water demand has also a similar profile through time. Considering that the new desalination plant will produce as much water as is currently transported and the existing water supply strategy wherein the available water tanks' level should remain constantly at their maximum capacity, the electricity demand fluctuation will further be increased.

To deal with the load demand additions and to further reduce the total operational cost of the system, the option of installing RES is evaluated, accounting typical investment costs per kW installed for the diesel (850€/kW), wind (1400€/kW), PV (1200€/kW) and

for the energy-storage (Batteries 650€/kWh), desalination (1667 €/m³) for a project life-span of 25 years and granting typical annual fixed costs (See Tables 1, 2) whilst only for the diesel power station the specific fuel cost at (1.7€/lt) applies. Additionally, in an effort to predict more accurately the actual costs, the replacement of infrastructure parts has also been considered, as follows in Eq. (1):

$$\begin{aligned}
 & \text{ECONV} \\
 &= \frac{\sum_r \left[\frac{Pr_r * INVr_r}{*(1+n*FCr_r)} \right] + \sum_s \left[\frac{Ps_s * INVs_s}{*(1+n*FCs_s)} \right] + \sum_{wr} \left[\frac{Pwr_{wr} * INVwr_{wr}}{*(1+n*FCwr_{wr})} \right]}{(1+i)^n} \\
 &+ \frac{n * (\sum_t \sum_r EGrt_r * FCr_r + \sum_t \sum_s ESgt_s * FCs_s + \sum_t \sum_{wr} Fwrt_{wr} * FCwr_{wr})}{(1+i)^n} \quad (1)
 \end{aligned}$$

where the “r”, represents the different set of resources (wind, diesel and PV), “s” the storage station(s), “wr” the water resources (shipment and desalination) and “P” the nominal capacity of the resources, storage stations and water resources accordingly. Moreover, the installation cost “INV”, and the annual fixed cost “FC” are also considered for a time horizon “n” of 25 years, with an inflation rate “i” of 3%.

Table 1: Problem design parameters

Parameter	Assigned Values
Ship transfer water - cost (€/m ³)	10
Diesel fuel cost	1.7€/lt
Desalination capacity	300 m ³ /day
Water reservoir	500 m ³
Initial water level	100m ³
Batteries Depth of Discharge	90%
Desalination energy consumption	5kWh/m ³
Inflation rate	3%

Table 2: Problem cost parameters

Cost Parameter	Assigned Values
*Wind park installation cost (€/kW) ¹	1,350
*PV park installation cost (€/kW) ²	1,200
*Diesel station cost (€/kW) ³	850
*Battery specific cost (€/kWh) ⁴	650
*RO desalination plant cost (€/m ³) ⁵	1667
Annual fixed cost	3% x total initial cost ¹ 1.5% x total initial cost ² 5% x total initial cost ³ 0.5% x total initial cost ⁴ 2% x total initial cost ⁵

So, under the model setup introduced by Papapostolou et al. (2017), energy and water demand fulfillment will be investigated under a set of energy SCs (wind, PV, diesel and battery energy storage). The following equation describes the energy balance to be preserved, for each time step t (8760 hours per year), for s=1, one battery storage station Eq. (2):

$$\sum_r EGrt_r + ESgt_s - ESst_s - Edwrt_{wr} - \sum_u Edu_u = 0 \quad (2)$$

Where, $EGrt_r$ is the energy production of the specific resource (wind, PV, diesel), $ESgt_s$ is the energy retrieved from the battery bank, $ESst_s$ is the energy stored at the battery bank, Edu_u represents the electricity needs of the island users “u” and $Edwrt_{wr}$ stands for the electricity needs of the desalination plant. The hourly electricity requirements of the desalination plant are estimated by utilizing commercialized desalination infrastructure

technical specifications and by considering monthly sea water temperature factors. The water salinity is assumed equal to 39 psu. The water demand profile is estimated by considering the annual needs and typical monthly factors of water consumption, as arisen by historical data.

3. Results – Discussion

With the constraints of 100% energy and water demand fulfilment, and in search of the optimal sizing in terms of nominal power of the ESCs, the aforementioned model has been implemented. The most cost-efficient solution, in long term, with a great environmental performance is presented at Table 3: a small-scale PV, a wind turbine, a conventional power plant and an energy storage station have been selected in order to cover the electricity needs, including the desalination plant’s load demand.

Table 3: Results in terms of Nominal Power (NP)nominal power of the energy SCs

NP of the Diesel Power Plant (MW)	NP of the Wind Farm (MW)	NP of the PV Park (MW)		Capacity of the Energy Storage System (MWh)	NP of the Desalination (MW)
0.35	0.81	0.4		0.5	0.06

The proposed solution satisfies the electricity needs through RES, by approx. 92%, reducing the CO₂ emissions from 1110 tn/y, a value that corresponds to 100% coverage by a diesel-fired power plant, to 83 tn/y. The proposed solution requires a relative high capital expenditure due to the RES investment incorporation (approx. 1.87 MEUROS), however leads to the minimum possible present value of the total costs for a 25year operation of the system.

For the selected ESCs, representative operational profiles are depicted in Figure 2, for a set of typical days during the summer (August) period. As one may observe, under the resulted reasonable energy ESCs sizing, energy demand is met, allowing the minimum possible operation of the diesel power plant whilst also storing energy in days of RES surplus.

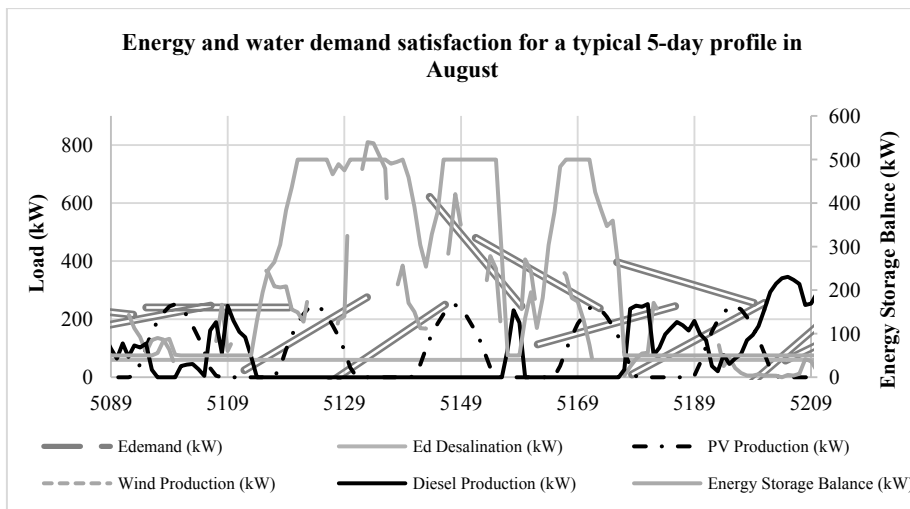


Figure 2: ESCs operation during August

4. Conclusions

In this work an integrated framework for the optimisation of water and energy supply systems is investigated through the model implementation in a small island in Cyclades. This small island faces electrical power and water outages, especially during the summer months, when the local population increases by approximately 500%. The implementation of the proposed framework results in the most cost-efficient solution, while it has a huge positive impact in the system's environmental performance. More specifically, model implementation results in the sizing of the RES- based desalination configuration (desalination plant and the associated wind, PV and battery energy supply system), of the diesel power station. In addition, it satisfies both the energy and water demand profile of the island, all accounting economic and environmental considerations.

This is an interesting case study on its own, as well as compared to the current proposed-by-the state water supply solution for the island which involves only a desalination plant powered by a diesel station, with no provision for load-demand increase and relevant shut downs that may occur during the touristic infusion of summer months. Especially when in operation the environmental criteria, the selection of RES-based desalination plant is grounded. The proposed framework may equally be applied to more complicated water and energy SCs with different not only resources on the demand side but also more end customers that need to be satisfied simultaneously.

Acknowledgements

The Post-doctoral Research was undertaken with a scholarship fund by IKY, Act "Supporting Post-Academic Researchers", with resources from the Operational Program "Human Education Development and Lifelong Learning", priority axes 6,8,9, co-funded by the European Social Fund - ESF and the Greek State.

References

- Jiangyu Dai, Shiqiang Wu, Guoyi Han, Josh Weinberg, Qianqian Yang, Water-energy nexus: A review of methods and tools for macro-assessment, *Applied Energy*, Volume 210, 15 January 2018, Pages 393-408
- Daniel J. Garcia, Fengqi You, The water-energy-food nexus and process systems engineering: A new focus, *Computers & Chemical Engineering*, Volume 91, 4 August 2016, Pages 49-67
- Saeed Kaddoura, Sameh El Khatib, Review of water-energy-food Nexus tools to improve the Nexus modelling approach for integrated policy making, *Environmental Science & Policy*, Volume 77, November 2017, Pages 114-121
- A.Pires, J.Morato, H.Peixoto, V.Botero, L.Zuluaga, A.Figueroa, Sustainability Assessment of indicators for integrated water resources management, *Science of The Total Environment*, Volume 578, 1 February 2017, Pages 139-147
- C. Papapostolou, E. Kondili, J.K. Kaldellis, 2017, Optimising the total benefit of water resources management in combination with the local energy systems in remote communities taking into account sustainability, *Computer Aided Chemical Engineering*, 40, 2689-2694
- [YPEKA] Misnistry of Enevrioment and Energy, 2015, River Basin Management Plan of the Aegean Islands (EL 14), Text only in Greek, URL: wfdver.ypeka.gr/el/management-plans-gr/

Planning the Drilling Rig Activities – Routing and Allocation

M. Sadegh Tavallali^{*}, Marzieh Zare

Department of Chemical Engineering, Shiraz Branch, Islamic Azad University, Shiraz, Iran 71987-74731

tavallali@iaushiraz.ac.ir

Abstract

Drilling well in petroleum fields is a highly complex task and managing a drilling rig fleet is even a more difficult issue, with various financial motivations and threads. Probably the most challenging issue is to efficiently allocate rigs to potential drilling sites and also to effectively determine the path of rig movements between the target drilling locations. The latter is rarely addressed in the open literature. Mathematical programming offers promising decision support models for such problems, hence in this study a time continuous optimization model is developed to minimize the overall drilling costs, and simultaneously plan the rig activities. The possibility of rig outsourcing is also embedded in the model and tested on an example. The results indicate 5.6% less total drilling costs.

Keywords: Drilling Rig, Routing, Planning, Mathematical Programming

1. Introduction

In contrast to the crude oil price, the energy demand is constantly increasing. This situation has created a sophisticated challenge for drilling companies, i.e. drilling activities should expand in spite of the current tight economic situation. Moreover, drilling is not a static activity, rather it is inherently a dynamic process (Tavallali et al. 2013), where not only the timing for well drilling, and rig movement should be rigorously planned, but also the rig routing, and possible rig outsourcing should be considered over the project horizon. Finally, the various alternatives for decisions such as rig-to-drilling site allocation, rig movement path selection, drilling timing make the drilling management problem an excessively combinatorial issue. Although there has been some attempts to study this complex problem (Van Den Heever and Grossmann 2000), still there exists important gaps (Tavallali et al. 2016). Firstly, this problem (and well placement as a tightly related task) is mostly modelled as a discrete time problem (Iyer et al. 1998, Tavallali 2015), thus there are many limitations in determining the practical drilling or movement durations. Secondly, to our knowledge, rig outsourcing is not addressed in the open literature, whereas this is a usual practice, especially for private drilling companies. Thirdly, although rig-to-well allocation is studied, however we are only aware of the study by (Iyer et al. 1998), who tackled rig movement planning in different regions of a field.

There exists a problem similar to the drilling rig planning in petroleum upstream industry and that is workover rig planning (WRP) (Aloise et al. 2006). Workover rigs are used to service wells which were already in operation. WRP is usually modelled as a time-discrete problem, with the objective of minimizing petroleum production loss.

That is an approximation for the volume of hydrocarbon that could be produced if the well was in service. In contrast to drilling operations, there are no standard drilling activities involved in WRP.

A practical approach for addressing the planning problem of drilling rig activities can be to use and modify the WRP concept to address the technical demands of drilling industry. This approach is utilized in this study. Moreover, we focus on the rig routing and movement problem, and tackle the three limitations of drilling planning studies mentioned above with a continuous time model.

2. Problem Definition

A drilling company should plan for drilling N wells using Y number of drilling rigs during a time window of T days. To be specific, the problem is as follows:

Given: Number and location of target wells, drilling rigs and rig terminals, geometry and the duration of each drilling, economic and financial data

Assumption: No idle duration between drilling activity of each rig

Policy: No drilling happens at the terminals and if required, new rigs can be outsourced from specific terminals.

Aim: Minimizing the overall costs of the project.

By determining: The drilling plan, rig-to-well allocation, and rig routing (movement from well-to-well)

3. Modeling

Sets and indices: Here we use $i = 1, 2, 3, \dots, I$ to refer to drilling rigs, $j = 1, 2, 3, \dots, J$ to show the target drilling wells/sites, and $k = 0, 1, 2, 3, \dots, K$ to represent the activity sequence. The sequence idea is defined to ensure the flexibility of tailoring a time continuous model. Finally, we define $OI \subseteq I$ to refer to the owned and outsourced rigs, and $JT \subset J$ to show the terminal sites were rigs can be stored.

Binary variables: y_{ij}^k is 1 if rig i starts drilling well j in the k -th sequence and 0 otherwise. Moreover $z_{ijj'}^k$ is 1 if rig i moves from site/well j to the site/well j' in the k -th sequence and 0 otherwise. Finally, it is assumed that the initial sequence shows the initial condition were no drilling was in operation, hence we set $y_{ij}^0 = 0$ and $z_{ijj'}^0 = 0$;

Constraints: Various logical, and techno-economic constraints are involved in this problem. In the interest of space, the most important ones are presented here.

Each well is drilled only once and obviously by at most one drilling rig. No drilling happens at terminals.

$$\sum_i \sum_k y_{ij}^k \alpha_{ij} = 1 \quad j \notin JT \quad (1)$$

Here α_{ij} is a binary parameter which is 1 if rig i can drill well j and 0 otherwise. This is fixed priori based on the technical requirements of well j and capabilities of rig i .

Moreover, each rig can drill only one well during each sequence.

$$\sum_j y_{ij}^k \alpha_{ij} \leq 1 \quad j \notin JT \quad (2)$$

The maximum allowable drilling length of each rig (q_i) is limited and hence that should not be more than the length of target well j .

$$l_j \sum_k y_{ij}^k \alpha_{ij} \leq q_i \quad j \notin JT \quad (3)$$

Based on the policies of the company, the operations are continuous and back-to-back.

$$y_{ij}^k \alpha_{ij} \leq \sum_{j'} y_{ij'}^{k-1} \alpha_{ij'} \quad j \neq j' \quad (4)$$

Rig routing is done by tracking the sequential activities of each rig at different sites.

$$z_{ijj'}^k \alpha_{ij} \alpha_{ij'} \leq (y_{ij}^k \alpha_{ij} + y_{ij'}^{k+1} \alpha_{ij'}) - 1 \quad j \neq j'; \quad k < K \quad (5)$$

Additionally, once rig i moves out of site j it should reach only one site. This is similar to a logical mass balance.

$$\sum_{j'} \sum_i z_{ijj'}^k \alpha_{ij} \alpha_{ij'} \leq 1 \quad j \neq j'; \quad k < K \quad (6)$$

Moreover, we assume that only one rig can move between two sites in a same sequence.

$$\sum_j \sum_{j'} z_{ijj'}^k \alpha_{ij} \alpha_{ij'} \leq 1 \quad j \neq j'; \quad k < K \quad (7)$$

The allocation decision is tightly related to the drilling time duration of each well. Considering the required rig travelling time from its initial position to the site j to be ft_{ij} , i.e. first traveling time. The very first drilling begins at least after this time duration is passed:

$$\sum_i ft_{ij} y_{ij}^1 \alpha_{ij} \leq dt_j \quad j \notin JT \quad (8)$$

where dt_j is the time of drilling initiation. Drillings should be finished before the end of contract deadline:

$$dt_j + \sum_i \sum_k \left(d_{ij} y_{ij}^k \alpha_{ij} + tt_{ij} z_{ij}^k \alpha_{ij} \right) \leq T \quad j \notin JT \quad (9)$$

Here d_{ij} is a parameter showing the drilling duration of well j by rig i , and tt_{ij} is a parameter showing the traveling time of rig i from initial site j to the final site j' .

Objective function: The total project cost (TC) should be minimized, by minimizing the costs of outsourcing rigs (C_{OS}), drilling (C_D), and rig movement:

$$\min TC = C_{OS} + C_D + C_{RM} \quad (10)$$

$$C_{OS} = \sum_{i \in OI} \sum_{j \notin JT} \sum_k C_{1ij} \left(d_{ij} y_{ij}^k \alpha_{ij} + \sum_{j'} tt_{ij} z_{ij}^k \alpha_{ij} \alpha_{ij'} \right) \quad (11)$$

$$C_D = \sum_i \sum_{j \notin JT} \sum_k \left(Cv_{ij} lv_j + Cd_{ij} ld_j \right) y_{ij}^k \alpha_{ij} \quad (12)$$

$$C_{RM} = \sum_i \sum_j \sum_{j'} \sum_k C_{2ij} t_{ij} z_{ij}^k \alpha_{ij} \alpha_{ij'} \quad (13)$$

where C_{1ij} , Cv_{ij} , Cd_{ij} and C_{2ij} are in order the unit costs of rig outsourcing, vertical and deviated drilling, and finally the rig movement. Additionally lv_j and ld_j are vertical and deviated lengths of well j .

4. Example

We evaluated the performance of the aforementioned model for a planning project with an operational time window of 365 days, 3 drilling rigs (with different technical specifications), three terminals and 5 potential (distributed) drilling sites. Total number of sequences was set as $K = 4$. This problem had 653 equations, 209 binaries and 18 continuous variables. DICOPT solver of GAMS 24.9.1 was used on a laptop with Intel CPU 3210M @ 2.50 GHz with 5.84 GB RAM to solve that.

Figure 1 shows the potential allocations (and hence routing) with dotted arrows and the depth of each site is shown in parenthesis. To evaluate the performance of the above model, we firstly chose a base case with 76, 107 and 122 days of operation for rig $i1$ to $i3$ respectively. That yielded total cost of 28.4 MM\$. Then solve the aforementioned model. Its final solution is shown with solid lines on Figure 1. The final costs was 26.8

MM\$ based on the assumed economic coefficients, i.e. almost 5.6% lower than the base case.

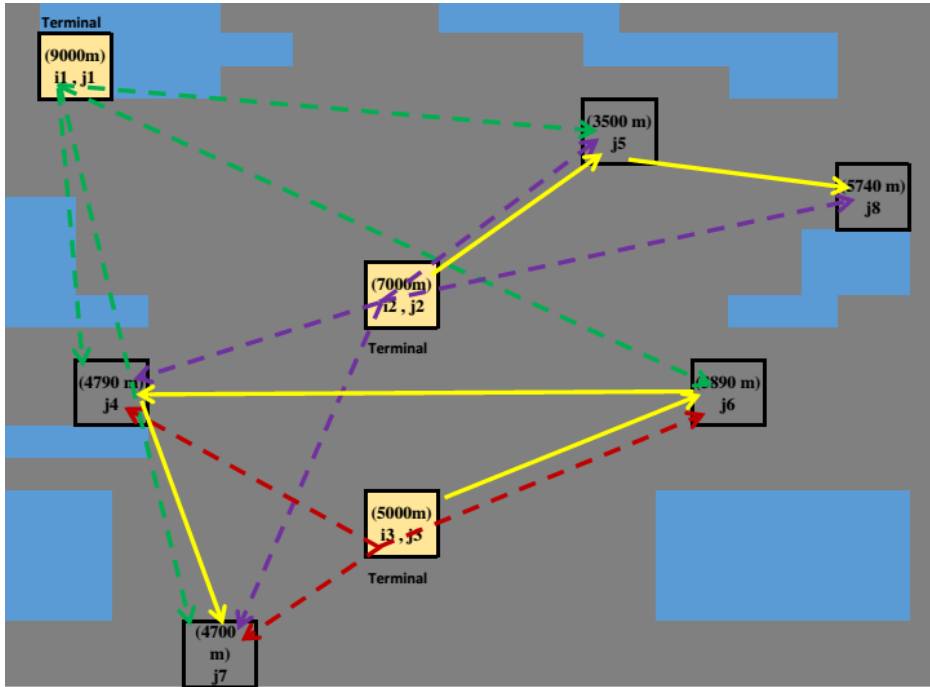


Figure 1: The bird view map of the field under study.

The selected allocations are shown in solid yellow lines.

As can be seen all drillings are done by $i2$ and $i3$ rigs and $i1$ is not utilized. Analysing the solution reveals that this is due to the fact that $i1$ is offered as an option for rig outsourcing and its selection could impose higher costs for the project. Hence that is prevented.

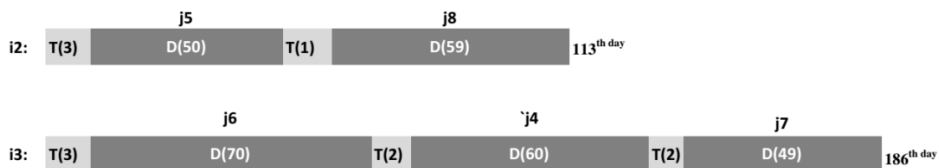


Figure 2: The drilling plan

T and D refer to the number of days spent for traveling and drilling.

Figure 2 represents the drilling plan. In this figure T and D refer to the number of days spent for traveling and drilling. According to Figure 1 and 2, rig $i2$ has taken 3 days to move from $j2$ to reach $j5$, where it was in operation for 50 days. Then another 4 days

was spent to move this rig to the new site at $j8$ to start 59 days of drilling. A similar path vs. time description can be easily extracted for rig $i3$. The drilling tasks of Rig $i2$ and $i3$ finished at 113th and 186th days of service respectively. It shows that the postulated 365 days of operation is not a tight constraint for this problem.

5. Conclusion

In this work we presented a decision support tool for minimizing the overall drilling costs, and simultaneously plan the rig activities with focus on rig routing. Significant number of logical constraints involved in this combinatorial problem was the main challenge for efficient planning. Modeling the problem as a time continuous model could hinder this thread. The results of an example showed how mathematical programming could effectively facilitate decision making about rig outsourcing, routing and movement. It was shown that our model could outperform a base case with 5.6% lower total drilling costs.

Acknowledgement

The authors are thankful to the technical experts from North Drilling Company (Iran) who helped with the initial discussions, and Professor IA Karimi (National University of Singapore), and D. Baxendale who led the previous projects on the related topics.

References

- Aloise, D. J., D. Aloise, C. T. Rocha, C. C. Ribeiro, J. C. Ribeiro Filho and L. S. Moura (2006). "Scheduling workover rigs for onshore oil production." Discrete Applied Mathematics **154**(5): 695-702.
- Iyer, R. R., I. E. Grossmann, S. Vasantharajan and A. S. Cullick (1998). "Optimal Planning and Scheduling of Offshore Oil Field Infrastructure Investment and Operations." Industrial and Engineering Chemistry Research **37**(4): 1380-1397.
- Tavallali, M., F. Bakhtazma, A. Meymandpour, F. Sadeghi, M. Hamed and I. Karimi (2015). A Drilling Scheduling Toolbox for Oil and Gas Reservoirs. Computer Aided Chemical Engineering, Elsevier. **37**: 2453-2458.
- Tavallali, M., I. Karimi, K. Teo, D. Baxendale and S. Ayatollahi (2013). "Optimal producer well placement and production planning in an oil reservoir." Computers & Chemical Engineering **55**: 109-125.
- Tavallali, M. S., I. Karimi and D. Baxendale (2016). "Process systems engineering perspective on the planning and development of oil fields." AIChE Journal **62**(8): 2586-2604.
- Van Den Heever, S. A. and I. E. Grossmann (2000). "An iterative aggregation/disaggregation approach for the solution of a mixed-integer nonlinear oilfield infrastructure planning model." Industrial and Engineering Chemistry Research **39**(6): 1955-1971.

Decision support platform based on intelligent mathematical modeling agents

Edrisi Muñoz^{a,*}, Elisabet Capón-García^b, Luis Puigjaner^c

^a *Centro de Investigación en Matemáticas A.C., Jalisco S/N, Mineral y Valenciana 36240, Guanajuato, México*

^b *Control and Optimization, ABB Switzerland Ltd, Segelhofstrasse 1K, 5405 Baden-Daettwil, Switzerland*

^c *Chemical Engineering Department, EEBE, Universitat Politècnica de Catalunya, Av. Eduard Maristany, 10-14, 08019 Barcelona, Spain*

emunoz@cimat.mx

Abstract

Decision support systems must provide the tools for effective problem management thus improving the whole decision process, from problem conception to solution implementation. However, model creation heavily depends on the modeler's expertise and the problem conception. This work focuses on automating the problem modeling and creating semantically enriched models. As a result, the modeler is supported in the modeling process. An automated modeling platform is developed, which encompasses mathematical models, their formal representation and the semantic model of the represented system. In addition, intelligent agents are designed in order to provide additional reasoning capabilities and create case rules for model creation, problem application storage and usage. A case study is performed using a scheduling modeling and solution example. Specifically, a systematic approach to scheduling model selection and solution implementation is achieved, thus enabling the bridge between theoretical developments and industrial practice.

Keywords: automated support system, decision support, reasoning agents, artificial intelligence.

1. Introduction

Decision support systems must provide the tools for effective problem management thus improving the whole decision process, from problem conception to solution implementation. In particular, a key piece of decision-making consists of the formal system representation, namely the system model, which captures those features that are necessary and sufficient to reach consistent decisions. However, model creation heavily depends on the modeler's expertise and the problem conception.

Likewise, the integration and management of data and information flows among different process operation levels is a common topic in the planning and scheduling areas, having a close relation with the area of supply chain. In order to improve the management of data and information flow among organizations, tools based on knowledge models seem to be a promising approach. Thus, organizations need knowledge management and organizational memory tools that encourage users and

foster collaboration while capturing, representing and interpreting corporate knowledge resources and their meaning.

Besides, during the last years the need for infrastructures continuously and coherently support for fast and reliable decision-making activities related to the production process, has revealed paramount importance (Varma et al., 2007). Moreover, efforts in this direction have result in works that presents ideas, theories, mathematical models, and practical systems in diversified domains integrated with semantics (Tanvir, 2012). Besides, Gonzales et al. 2014 uses semantic networks for improving the understanding the modeling of a physical phenomenon of engineering or other knowledge domain. This work is applied for teaching tasks, but make use of basic semantics.

The presented work develops a decision support platform based on knowledge management and intelligent agents for improving modeling. Specifically, this work focuses on the semantic and knowledge base exploitation of decision support systems. Specifically, the goal consists of automating the problem modeling and creating semantically enriched models. As a result, the modeler is supported in the modeling process and the dependence on own criteria and experience is reduced. An automated modeling platform is developed, which encompasses mathematical models, their formal representation and the semantic model of the represented system. In addition, intelligent agents are designed in order to provide additional reasoning capabilities and create case rules for model creation, problem application storage and usage. Indeed, agent routines are designed to automate the modeling and reach new decisions based on the problem description and previous experience.

2. Methodology

This work designs an agent-based structure for supporting decision-support, and applies the result to a planning and scheduling problem. Therefore, this section firstly introduces the planning and scheduling problems. Next, the operations research and mathematical modeling frameworks are established, together with the semantic approach to the problem description. Finally, the agent-based structure and rules are presented.

2.1. Planning and scheduling

Planning and scheduling problems at process industry have been tackled even before first computer appeared. The problem of what, where and how to produce has been defined as a complex problem that implies data and information of the whole production system. Information and data arrive from different layers involved in the production process, ranging from regulatory control, supervised control to single site production planning and enterprise supply chain planning.

At the production site level, the planning task aims to define how to meet the production targets in the site. Basically, this task makes decisions about resources allocation for each batch to be produced, as well as, how many batches of each product should be produced. Finally, as a result the best sequence in which resources should be used along the production is obtained.

The real-time production level, scheduling is concerned in how to predict the starting and finishing times of the required operations according to the on-going state of the plant. This level of detail is able to assure that the predicted schedule is feasible as it

involves a greater level of detail, using online information coming from the process plant. What is more, if any deviation of time occurs, this level is in charge of performing rescheduling actions resulting in changes to the predicted schedule.

2.2. Knowledge management framework (Domain knowledge)

The use of semantic models, so called ontologies or knowledge models, allow the formalization of the knowledge in different domain areas. The first ontology concern to describes the overall process system engineering environment. Such semantic model is based on ANSI/ISA-88 and 95 standards (Munoz, 2012, 2013, respectively). On the one hand, ANSI/ISA-88 standards compilation (International Society for Measurement and Control, 1995, 2003) allow the representation on the recipe model. Recipes manage the sufficient and necessary information in order to automate the data transaction task. On the other hand, ANSI/ISA-95 compilations (International Society for Measurement and Control, 2008) allow integrating information and data from recipes to the production schedule system. As a result Enterprise Ontological Project (EOP) describes semantically those specific functionalities in the process system-engineering domain reaching from operational to strategic functions.

2.3. Operations research and mathematical programming

Operations research (OR) is an interdisciplinary branch of mathematics, which uses mathematical models and tools to achieve optimal, or near optimal decisions in complex decision-making problems. OR techniques actually constitute the major part tools applied to solve problems. As one of the main tools for OR, mathematical programming is concerned with the study of problems in which one seeks to minimize or maximize a real valued function of a set of decision variables by systematically choosing the values of the decision variables from within an allowed set. The resulting mathematical model is a set of mathematical relations such as equations, inequalities, logical dependencies, etc., which correspond to physical or logical relationships in a real life problem. An OR ontology has been already developed to capture the elements involved in the creation of decision support systems (Muñoz et al. 2015).

The three initial steps to reach a problem analysis in OR and their adaptation to the problem of process planning and scheduling for this work are as follows: (i) observe the system: it includes the definition of the product(s) to be produced and the corresponding site recipe (procedure specific), the definition of the master recipe (process specific), and production order(s), including order request quantity & due date; (ii) problem definition: it consists of establishing the single or multiple objective, such as timing, financial, environmental, as well as the system constraints, represented as element – value source pairs; and, (iii) model construction: it consists of creating a basic structure for modeling, namely the objective function with inline labels, and the constraint elements which include labels and relations to the objective function.

The basic structure in an OR problem consists of a set of mathematical equations which model a problem with the aim to optimize it. Such equations are basically objective function and system constraints. An objective function is an equation with representative elements. In this work, both the objective function and the representative elements associated to the variables are assigned to representative labels, which allow further categorization and classification of the system. The objective function has to be optimized (minimization or maximization), and contains specific mathematical operations and impact values (values). As for the system constraints, their structure comprises equations, which represent the constraints based on elements within the

system. This work assigns to the constraints and the elements a representative label. Finally, additional constraints, such as those related to non-negativity and the element behavior (binary, integer, etc.) could be also considered from a given set elements or the problem structure.

2.4. Agent system structure

The proposed framework consists of a set of agents, which have different functions and communicate among them. In order to have a common vocabulary, all the agents rely on the ontologies described in sections 2.2 and 2.3.

The solution mechanisms consists of the following steps: (i) problem definition, (ii) modeling process for reaching a problem model, (iii) model analysis, (iv) model solutions, and (v) problem conclusions. Based on the solutions in (iv), we can make inferences and reach the decisions about the problem in (v). Finally, the assessment of decisions goodness is fed back to the agent system.

Each of the steps in the solution mechanism is represented as an agent of the system, which communicates with other existing agents. The multiple agents have different functions, which can be broadly classified as follows: (i) communication agents, (ii) search agents, (iii) classification agents, and (iv) solution agents.

For every problem instance, the problem features are recorded within the problem database by means of the communication agent. The problem features include the set of parameters, assumptions and decision variables required to solve the problem. In addition, the problem features must refer to any constraint (e.g. physical, design, operational) that the system has to consider. Therefore, the problem instantiation relies on the EOP ontology and the mathematical features described in the mathematical modeling ontology. Next, the optimization objective(s) are formalized within the communication agent. Overall, a specific problem statement is obtained.

Next, the communication agent prepares a problem summary for the classification agent, which analyses the problem according to a knowledge-driven classification procedure, and proposes a solution strategy based on similitude measure of the current problem instance with (i) existing problems already tackled in the past and stored in the database, (ii) existing problem approaches derived from the literature. As a result, a set of ranked solution approaches is proposed to the decision-maker.

The so-called search agent has two main functions. On the one hand, it looks for similar cases stored in the database with the current case, and compares them with the current problem instance in order to identify differences and similitudes. Therefore, it supports the classification agent and presents to the decision-maker the most similar cases. On the other hand, after the selection of the solution strategy the search agent creates the required information for the solution agent to tackle the problem.

Finally, the solution agent iterates with the solution algorithms in order to reach the optimal solution for the problem instance. The solution agent also sends the set of problem solutions to the decision maker and stores them in the database for future operation.

The different agents and the whole framework have been programmed in Jython, which combines the programming language in Python and the availability to use Java APIs, and communicate to the ontological models.

3. Case study

A case study for a multi-objective scheduling problem is solved. Specifically, a multi-product batch plant for acrylic fibers production is considered (Capon et al. 2011, 2012). The production plant consists of a 14 production stages with product dependent changeovers among three different final products. Three multi-objective optimization strategies are considered, namely a mathematical programming with a normalized constraint method (MP) (Capon et al. 2011), a genetic algorithm (GA) and a hybrid optimization approach (HA) (Capon et al. 2012). Several problem objectives are considered, such as productivity (P), total environmental impact (TEI), makespan (M) and total profit (TP). The problem instances solved in the original papers are the basis for the database of this problem, a total of 415 problem solutions are included with different problem description and objective function values.

Next, the framework including the different agents is tested with new problem parameters and results are shown in Table 1. The first column includes the problem size (number of batches for each problem), whereas the second column is related to the objective function. On the other hand, the third column presents the selection of the solution implementation, the fourth column shows the value of the objective function, and the fifth the distance to the best optimal solution found.

From Table 1, it can be seen that for small problem instances the rigorous mathematical programming approach is proposed, whereas large problem instances are better solved with genetic algorithm. In addition, the selection of the objective function also has an important role in the selection of the solution strategy. Indeed, for productivity maximization the hybrid approach is selected. In most cases, the distance of the solution proposed by the agent-based system to the optimal solution is lower than 5%. Therefore, this framework represents a systematic approach to scheduling model selection and solution implementation, thus enabling the bridge between theoretical developments and industrial practice, with high-level decision support to the engineers, who do not need to have a thorough understanding of the solution techniques.

Table 1. Results for different problem instances from agent-based framework, where (P,TEI,M,TP) stand for (productivity, total environmental impact, makespan and total profit) and (MP, GA, HA) stand for (mathematical programming, genetic algorithm and hybrid approach).

Number batches (A/B/C)	Obj. function	Solution approach	Solution value	Optimal solution value
2/2/2	P	MP	1.085	1.087
2/2/2	TEI	MP	24.1	24.1
2/2/2	M	MP	24	24
14/8/10	P	HA	1.071	1.072
14/8/10	TEI	MP	180.2	178.9
14/8/10	M	GA	164.3	162.8
16/14/12	P	HA	1.083	1.085
16/14/12	TP	MP	$2.1 \cdot 10^5$	$2.2 \cdot 10^5$

4. Conclusions

This work has developed an agent-based approach for automating the problem modeling and solution in any engineering domain, which requires model-based decision support. As a result, the decision-maker is supported in the modeling process and good solutions can be reached with limited knowledge on the solution techniques. An automated modeling platform is created, which encompasses mathematical models, their formal representation and the semantic model of the represented system. In addition, intelligent agents are designed in order to provide additional reasoning capabilities and create case rules for model creation, problem application storage and usage. For illustrating purposes, a case study is performed using a scheduling of a multiproduct batch plant. For that case, solutions within 5% optimality are obtained. As a result, a systematic approach to scheduling model selection and solution implementation is achieved, thus enabling the bridge between theoretical developments and industrial practice. Overall, this work presents a platform for enhanced problem solving and improved decision-making.

References

- E. Capon-Garcia et al. (2011). Multiobjective optimization of multiproduct batch plants scheduling under environmental and economic concerns. *AIChE J.*, 57, 2766-2782.
- E. Capon-Garcia et al. (2012). Multiobjective Evolutionary Optimization of Batch Process Scheduling Under Environmental and Economic Concerns. *AIChE J.*, 59, 429-444.
- Gonzales et al. (2014). Mathematical modeling using semantic networks for teaching. *European Journal of Education Sciences*, 1, 3, 81-96.
- International Society for Measurement and Control. (1995). Batch control. Part 1. Models and terminology. International Standard, ISA Society.
- International Society for Measurement and Control. (2003). Batch control. Part 3. General and Site Recipe Models and Representation. International Standard, ISA Society.
- International Society for Measurement and Control. (2008). Enterprise-Control System Integration. Part 1. Models and terminology. International Standard, ISA Society.
- E. Muñoz et al. (2012). Ontological framework for enterprise-wide integrated decision-making at operational level. *Comp. & Chem. Eng.*, 42, 217-234.
- E. Muñoz et al. (2013). Integration of enterprise levels based on an ontological framework, *Chem. Eng. Res.&Des.*, 91, 1542-1546.
- E. Muñoz et al. (2015). ,Operations Research Ontology for the Integration of Analytic Methods and Transactional Data. in *Trends and Applications in Software Engineering*, 139 - 145.
- Tanvir M., (2012). Semantics: Advances in Theories and Mathematical Models. InTech.
- V. Varma et al. (2007). Enterprise-wide modeling & optimization - An overview of emerging research challenges and opportunities. *Comp. & Chem. Eng.*, 31, 692-711.

Leak Detection Modeling Of a Pipeline Using Echo State Neural Networks

Alexandre M. Ribeiro^a, Caroline D. Grossi^b, Brunno F. Santos^b, Rejane B. Santos^{a*}, Ana M. F. Fileti^c

^a *Chemical engineering course, Federal Institute of Education, Science and Technology of South of Minas Gerais – (IFSULDEMINAS). Avenida Maria da Conceição Santos, 900, Parque Real, Pouso Alegre- MG, 37560-260, Brazil.*

^b *Departament of Chemical and Material Engineering (DEQM). Pontifical Catholic University of Rio de Janeiro(PUC-Rio) . Rua Marquês de São Vicente, 225 – Gávea, Rio de Janeiro- RJ, 22430-060, Brazil.*

^c *School of Chemical Engineering (FEQ), Department of Chemical Systems Engineering (DESQ), University of Campinas (UNICAMP). Rua Albert Einstein, 500 – Cidade Universitária, Campinas – SP, 13083-852, Brazil.*

*E-mail: rejane.santos@ifsuldeminas.edu.br

Abstract

Considering the importance of monitoring piping systems, the aim of this work is to develop a technique to detect gas leaks in pipes, based on acoustic method. A copper tubing $\frac{1}{2}$ in diameter and 53 m in length was assembled in laboratory, operating with continuous supply of compressed air, under various operating conditions with initial pressure of 1 kgf / cm². We analysed the signals of five microphones, installed inside the tubing, generated by the occurrence of gas leakage. The microphone signals in the time domain were converted to the frequency domain via the fast Fourier transform (FFT). The microphone signals in the frequency domain used as an input of the artificial neural network (ANN) of the type Echo State Network (ESN) to determine the occurrence or not of leakage (model output). From the results, it was observed that the leaks were adequately detected. The neural model presented a percentage of correctness of approximately 81% indicating the occurrence or not of leakage in the line.

Keywords: Pipeline, leak, Echo State Networks

1. Introduction

In addition to the use of piping networks as a means of transport for gases and liquids over long distances, these systems have been widely used in the distribution of gas directly in homes and at commercial points, usually called piped gas. The piped gas has become a comfort solution in civil construction. Because it is transported through pipelines in a continuous way, the gas, fuel, does not need storage, avoiding risks with deposit and releasing useful area in the buildings. On the other hand, there is a need for operational reliability of these piping systems, minimizing the risk of leakage, which can lead to disastrous consequences for families, pollution problems to the environment, and can also cause serious financial losses. There are several studies in the literature

about the detection of leaks in pipes, for example, ZHANG *et al.* (2004), TAGHVAEI *et al.* (2006), TOLSTOY *et al.* (2009), YANG *et al.* (2008), largely based on process variables measurements, as pressure and flow obtained from the pipe.

Therefore, it was intended in the present work to contribute to the development and testing of techniques to detect occurrences of leaks. The method chosen was the acoustic method, due to the great ease in detecting small leaks in ducts in a short time, as well as the low investment used in this method. The signals emitted by the acoustic sensors were used as input of a neural model (ESN) with the purpose of analysing the data in order to identify the occurrence of the leak.

Neural networks are a technique of Artificial Intelligence (AI) that has the ability to learn from experiences, improving their performances and adapting to changes in the environment. Among the main incentives for its use is the success of the works of BELSITO *et al.* (1998) and SANTOS *et al.* (2014), among others, developed studies using neural networks as a data analysis tool to detect leaks, showing promising results.

2. Methodology

In this study, the characteristics of the signals from microphones generated by gas leakage in a $\frac{1}{2}$ in diameter and 53 m long copper tubing were analysed in a laboratory under different operating conditions.

To perform the experiments, compressed air was used as the working fluid. The leaks were simulated through holes along the pipe, with different magnitudes and with a manometric pressure of 1 kgf/cm².

The experimental system was represented by a fixed gas pipe in a metal structure, as can be seen in Figure 1. The system consists of 8 pressure transducers to analyse the internal pressure along the pipe, 15 microphones, 12 points to cause rupture type leakage or to branch pipes, using ball valves, 7 holes along the pipe with different diameters for leak simulation.

In the experimental prototype, 15 microphones were installed along the tubing, but only 5 (M1, M2, M3, M4 and M14) were evaluated in the present study. The microphones M1, M2, M3, M4 and M14 are at 0.1 m; 3.3 m; 7.7 m; 11.4 and 49.3 m from the start of the pipe.

The holes were implemented in the pipe to simulate a leak as close as possible to a real situation, differing from a ruptured situation. The holes are at different locations along the pipe with different diameter sizes, varying between 0.5 and 4 mm.

In order to detect the leak more easily through the microphone signal, a digital filter was implemented in *Labview* (software used for monitoring and data acquisition). In the present work a sampling rate of 33 kHz was defined, respecting the Nyquist theorem.

The leaks were triggered manually. Before initializing the data acquisition program, a person would close the hole chosen for testing with his finger and at the right time was removed from the pipeline, causing the leak. This form was chosen in order to avoid noises inherent in valve openings if the leaks were also automated. When the data acquisition program was finalized, the data file was generated, producing acoustic sensors information in time domain and frequency domain with different leak sizes, non-leak situations, two leak cases occurring simultaneously and simulation having

branching in the line through valves connected to a 6 m long flexible pipe, according to Table 1.



Figure 1. Experimental leak detection system in gas piping.

Table 1 - Operating conditions.

Experiments	Operational situations
1	Leaks with diameters from 0.5 to 4 mm.
2	No leaks - only laboratory noise, air conditioning on and people walking.
3	No leaks - Constant beats on the pipe with a metallic instrument.
4	No leaks - constant beats in the pressure vessel with a metal instrument.
5	No leaks - line branching through the use of valves
6	Line branching and leak occurrence simultaneously
7	Occurrence of two leaks simultaneously

Branch situation in the line, means a simulation of gas consumption output in the residence, such as gas outlet to the stove, shower etc. Such situations do not represent a leak.

With the acquisition system in operation, connected to the instruments installed in the copper tubing, spectral analysis of the microphone signals (frequency domain analysis) was done through *Labview* software. Through the FFT it was possible to analyse the characteristic (predominant) frequencies in different operating situations, with and without leakage.

To determine the occurrence and size, training of a neural model with data from the fast Fourier transform (FFT) was performed, with some frequency signals chosen using as input to the neural model.

The neural modelling algorithm was implemented in MATLAB R2016a Software. The developed ANN was the echo state networks (ESN) based on JAEGER et al. (2001). This type of ANN has randomly connected hidden layer called reservoir (as a recurrent neural network). The use of ESN implies to tune some parameters in the algorithm: the number of input; the number of output; the number of neurons inside the reservoir, the weight matrix making the link between the input layer and the reservoir; the weight matrix representing the link between the reservoir and the ESN output; Spectral Radius, and Connection Percent. In the reservoir activation function was used hyperbolic tangent (tanh) and the output layer was used identity. The output weights (in ESN) were optimized by a multilinear regression (for instance by using the generalized matrix

inversion Moore-Penrose. Thus, the training process was simplified and this allowed finding the global optimum of the weight optimization problem. The performance of the model was analyzed according to error index.

An ESN is composed by input layer, the reservoir and the output layer. According to Jaeger et al. (2001), the activation of internal units is showed in Eq. (1).

$$x_{k+1} = f(W^{in}u_{(k+1)} + Wx_k + W^{back}y_k) \quad (1)$$

where $u_{(k+1)}$ is the exogenous input with dimensionality n , x_k is the internal states with dimensionality M , and y_k is the output. W^{in} and W is the input and internal (neurons in the reservoir) weights. The W^{back} is the output feedback weights and f is known as activation function which most of the time is hyperbolic tangent (tanh).

The output is calculated according to Eq. (2).

$$y_{k+1} = f^{out}(W^{out}(u_{(k+1)}, x_k, y_k)) \quad (2)$$

Where y_{k+1} is the output of the ESN, W^{out} denotes the output weights and f^{out} is the activation function of output neurons (mostly identity).

This output has recurrent connections in the reservoir. The backpropagation is given random weights (W^{back}), which are fixed and do not change during subsequent training. The connections between the reservoir and the output unit, W^{out} , are the only ones that change during training.

The signals of the five were used as inputs to the neural network to determine the occurrence or not of leaks (model output). However, the data file from each microphone subjected to fast Fourier transform consists of 9394 frequency signals (in the range between 500 and 16000 Hz), totalling 46970 frequency signals. Due to the difficulty in working with 46970 inputs in a neural model, a training was performed with 200 frequency spectrum signals (obtained from the FFT), with 40 signals from each microphone. These frequencies were determined by analysing all operational situations, verifying the frequencies that showed the greatest changes.

3. Results and analysis

With the experimental data coming from the microphones, signals of different frequencies were obtained using FFT. The Fast Fourier Transform (FFT) of the microphone signals (M1, M2, M3, M4 and M14) was performed in order to differentiate each case, that is, a frequency domain analysis for each situation mentioned in Table 1.

It can be seen from Figure 2 that for each tested situation a frequency spectrum with different profile was obtained. The first situation (letter a) refers to a normal noise from the laboratory (only air conditioning connected and possibly people walking near the system) without occurrence of leaks, the second situation (letter b) refers to an occurrence of leakage in the hole (diameter 3 mm) with 4.7 m distance from M1.

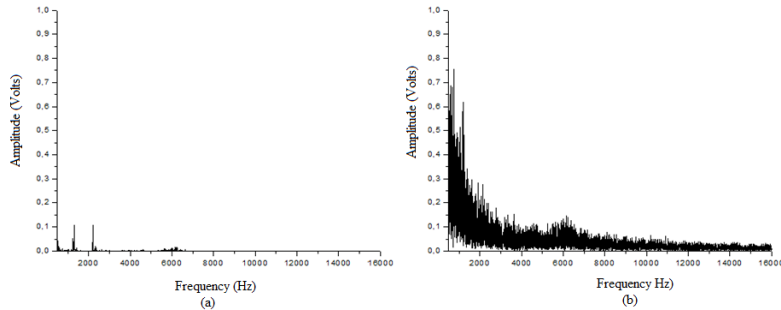


Figure 2. Frequency spectrum of microphone signals M1.

To perform the leakage detection of a low pressure gas piping system, the artificial neural networks technique was used as a tool to monitor the experimental system, receiving information from the microphones installed in the piping.

The experimental tests were performed in several operating situations (without and with leaks in different sizes), generating a database, which was divided into training data and data for the neural model offline test. In the test file was used data from an operational situation not used in training. For the training of the neural networks, the frequency signals of the microphones were used as input to the neural model to determine the occurrence or not of leaks (model output).

In order to perform the training of the neural model, the frequencies to enter the neural network were initially determined. We selected 40 frequencies of each microphone, totalling 200 entries in the neural model. These frequencies were determined by analysing all operational situations, verifying the frequencies that showed the greatest changes.

The best configuration of the parameters obtained from the various tests analysed was the number of neurons inside the reservoir 205, the weight matrix making the link between the input layer and the reservoir 1, the weight matrix representing the link between the reservoir and the ESN output 0.008, Spectral Radius 0.8 and Connection Percent 0.5, training correlation coefficient 0.9009 and training equation of the line $y = 0.8113x + 0.1315$.

The off-line test performed using 200 frequencies frequency spectrum signals obtained from the five microphones, presented a percentage of hit of approximately 80,0 %, indicating the occurrence or not of leaks in the line, according to Figure 3. All the 0.5 values, calculated by the ESN, were considered as no occurrence of leakage, while values greater than 0.5 were considered as presence of leakage. Figure 3 indicates the difference between data calculated by the ESN model and the experimental data, proving the satisfactory performance of the developed neural models.

Approximately 647 data vectors were used in test set of the developed model. Among these points, the maximum errors obtained were in situations with 0.5 mm leakage, indicating the non-occurrence of leaks and in situations with simulation of a branch on the line going at once with the leak, only indicating the branch line. But considering that there is a branch in the pipeline, the disturbance is probably something that is not permanent, so when the branch line is closed, the neural model will correctly indicate the occurrence of leaks.

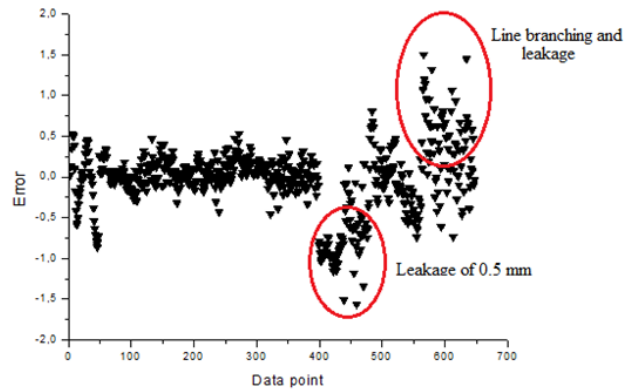


Figure 3. Difference between actual data and data computed by the Echo State Network.

4. Conclusions

Through the analysis of microphone signals in the frequency domain (through the FFT), it was possible to differentiate the several situations tested with and without occurrence of leaks, thus detecting when there was actually leakage.

It was possible to determine the occurrence of leaks through developed ESN model, with promising results, due to good agreement of the predicted with experimental data. The off-line test performed using 200 frequency spectrum signals from the five microphones showed percentage accuracy of approximately 80%, indicating the occurrence or not of leaks in the line.

5. References

- BELSITO, S., LOMBARDI, P., ANDREUSSI, P and BANERJEE, S. Leak Detection in Liquefied Gas Pipelines by Artificial Neural Networks. *AIChE Journal*, v.44, n.12; p. 2675, Dec 1998.
- JAEGER, H., The “echo state” Approach to Analysing and Training Recurrent Neural Networks – with an Erratum note. *Fraunhofer Institute for Autonomous Intelligent Systems* January 26, 2001.
- SANTOS, R. B.; SOUSA, E. O. DE; SILVA, F. V. DA; CRUZ, S. L. DA; FILETI, A. M. F. Detection and on-line prediction of leak magnitude in a gas pipeline using an acoustic method and neural network data processing. *Brazilian Journal of Chemical Engineering*, v. 31, p. 145-153, 2014.
- TAGHVAEI, M., BECK, S.B.M. and STASZEWSKI, W.J. Leak detection in pipeline networks using low-profile piezoceramic transducers. *Journals Wiley Inter Science*, p.1063-1082, 2006.
- TOLSTOY, A., HOROSHENKOV, K.V. and BIN ALI, M.T. Detection pipe changes via acoustic matched field processing. *Journal Applied Acoustics*, p.695-702, 2009.
- YANG, J., WEN, Y. e LI, P. Leak acoustic detection in water distribution pipelines. *World congress on intelligent control and automation*; Chongqing, China, p. 25-27, 2008.
- ZHANG, S., ASAKURA, T., HAYASHI, S. Gas Leakage Fault Detection of Pneumatic Pipe System Using. *JSME International Journal*, v. 47, n. 2, 2004.

Economic Model Predictive Control of a Wastewater Treatment Plant using Neural and Fuzzy models

Silvana Revollar^{a*}, Hernán Álvarez^b, Rosalba Lamanna^c, Pastora Vega^a,
Alejandro Goldar^c

^a*Dpto. Informática y automática. Universidad de Salamanca, Salamanca, 37008, España.*

^b*Escuela de Procesos y Energía. Universidad Nacional de Colombia, Medellín, Colombia*

^c*Dpto. Procesos y sistemas. Universidad Simón Bolívar, Caracas, 89000, Venezuela.*

Abstract

To improve efficiency in wastewater treatment plants, suitable optimization and control strategies for the activated sludge process are imperative. Therefore, adequate models for estimation of the critical variables are also vital. In this work, neural networks and fuzzy models are identified from data collected from a standard benchmark simulation platform (BSM1) used to represent the activated sludge process. These models are embedded in an economic predictive controller designed to regulate critical variables to ensure the desired effluent quality with the minimum energy consumption.

Keywords: Economic model predictive control, neural networks, fuzzy systems

1. Introduction

The awareness on reducing water pollution has been reflected on stricter effluent requirements and economic penalties for discharges out of specification. Hence, the wastewater industry has focused on achieving the desired effluent quality while increasing the efficiency of the Activated-Sludge Process (ASP) which is the biological treatment at the core of most Wastewater Treatment Plants (WWTPs). This research addresses the implementation of advanced model predictive control (MPC) strategies to optimize the operation of the ASP increasing the economic efficiency of WWTPs.

Many controllers tested in the ASP are designed for the tracking of a conservative set-point for the dissolved oxygen (DO) concentration (Amand et al., 2013). Nevertheless, the variations in the influent loading could be considered for improving the economic performance of the plant given that the effort required to treat the wastewater depends on the pollution load. Some works have proposed the use of hierarchical control strategies to optimize the operating point taking advantage of the variability of the load (Vega et al., 2014). More recently, Zeng and Liu, (2015) and Revollar et al. (2017) implemented economic model predictive controllers (EMPCs) to perform the dynamic optimization of the operation of WWTPs using single layer structures.

In the execution of such tasks, the estimation of the critical variables that affect the performance of the treatment and the prediction of the plant behaviour require the use of adequate models. Non-linear dynamic models of the ASP are precisely the type needed

when dealing with high interactions (Moscoso-Vasquez, et al., 2014) in optimization and control applications. Complex, high dimensional models as the ASMs of the International Water Association, are costly to use and with parameters hard to identify. Therefore, more efficient solutions, as models based on artificial intelligence, are desirable. In Goldar et al. (2014) an artificial neural network is successfully implemented for predictions in a multivariable non-linear model predictive control strategy used for the tracking of dissolved oxygen and nitrates concentration set-points. Very few applications of these kinds of models for the optimization of economics in advanced control schemes are found in the literature. In this work, neural networks and fuzzy models are identified to be implemented as prediction models in an economic model predictive control strategy.

The paper contains a description simulation platform used to represent the activated sludge process (BSM1) in section II and the formulation of the EMPC problem in section III. Section IV presents the attainment of the neural and fuzzy models, its structure, and validation results, as well as their implementation in the EMPC strategy. Conclusions and projections of this work are outlined in section V.

2. The Activated Sludge Process

A benchmark simulation protocol representing the activated sludge process (BSM1) has been developed by working group No. 1, within COST Actions 624 and 682 (Alex et al., 2008). The BSM1 plant layout is presented in Fig. 1, the simulation platform includes simulation models, influent loads, test procedures and evaluation criteria. The model considers 13 state variables in each reactor and describes 8 biological processes. Detailed information regarding the mathematical model, physical parameters and influent profile can be found in Alex et al. (2008).

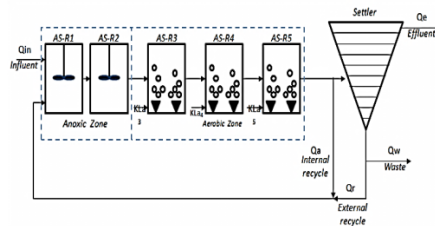


Figure 1. General scheme of the treatment plant of BSM1.

2.1. Control problem

The control strategy proposed in the BSM1 platform for the operation of the activated sludge process consist on the regulation of the dissolved oxygen (DO) concentration at the end of the aeration zone (S_{O_2}), and the nitrate concentration at the end of the anoxic zone (S_{NO_2}) using two PI control loops. The manipulated variables are the oxygen transfer coefficient (KLa) and the internal recycle flow (Q_a). The DO concentration in the aerobic zone is maintained close to the reference value that ensures an appropriated nitrification; however, an excessive amount of oxygen saturates the system and increases unnecessarily the aeration energy.

In this paper, a single layer multivariable economic model predictive control strategy is considered to achieve an efficient operation of the activated sludge process, minimizing

the energy consumption while attaining the desired effluent quality. The BSM1 dry-weather profile (Alex et al., 2008) is used to characterize the influent disturbances.

3. Economic model predictive controller (EMPC) formulation

Two approaches are distinguished in the EMPC formulation: economic optimizing controller and the economic-oriented tracking controller. In the economic optimizing control the optimal values of the control inputs (\mathbf{u}) are computed directly from the optimization of the economic performance. In the economic oriented tracking controller, an economic index is added to the classical model predictive control objective function. A generalized mathematical description including both alternatives is presented here.

3.1. General formulation of the EMPC

The standard non-linear model predictive control (MPC) cost function is a quadratic penalization of the deviation of the state (\mathbf{x}) from the desired operating point (\mathbf{x}_r) and the magnitudes of the inputs adjustment. W_x , W_u and W_n are the weights assigned to each objective.

$$J_{NMPC}(\hat{\mathbf{x}}(t), \mathbf{u}(t)) = |\hat{\mathbf{x}}(t) - \mathbf{x}_r|_{W_x}^2 + |\mathbf{u}(t) - \mathbf{u}(\tau_{k-1})|_{W_u}^2 + |\hat{\mathbf{x}}(\tau_N) - \mathbf{x}_r|_{W_n}^2 \quad (1)$$

In a general formulation including both EMPC approaches, the cost function measures the control performance (J_{NMPC}) and the economic performance (J_{ECO}).

$$\min_{\mathbf{u} \in \mathcal{S}(\tau)} \int_0^{\tau_N} (w_E \cdot J_{ECO}(\hat{\mathbf{x}}(t), \mathbf{u}(t)) + w_C \cdot J_{NMPC}(\hat{\mathbf{x}}(t), \mathbf{u}(t))) dt \quad (2)$$

The constraints and initial conditions are defined by equations (Eq. 3, 4, 5), being τ the sampling time and \mathbf{v} the measured disturbances:

$$\dot{\hat{\mathbf{x}}}(t) = f(\hat{\mathbf{x}}(t), \mathbf{u}(t), \mathbf{v}(t)) \quad (3)$$

$$\hat{\mathbf{x}}(0) = \mathbf{x}(\tau_k) \quad (4)$$

$$g(\hat{\mathbf{x}}(t), \mathbf{u}(t)) \leq 0, \quad \forall t \in [0, \tau_N) \quad (5)$$

3.2. Economic model predictive control of the activated sludge process

In the implementation of the EMPC to the activated sludge process, only the influent variables that have a major impact on the process are measured at each sampling time to perform the optimization. They are the influent flow rate (Q_{in}), the readily biodegradable substrate concentration ($S_{S,in}$) and the ammonium concentration ($S_{NH_4,in}$).

The performance indices adopted to assess dynamically the economic performance in the EMPC are the pumping energy and the aeration energy. The pumping energy (PE) represents the energy use for the pumping of internal recycle flow (Q_a).

$$PE = \frac{1}{T} \int_{t_0}^{t_f} (0.004 \cdot Q_a(t)) dt \quad [kWh/d] \quad (6)$$

The Aeration Energy (AE) is calculated from the oxygen transfer coefficient (KLa).

$$AE = \frac{S_{O,sat}}{T \cdot 1.8 \cdot 1000} \int_{t_0}^{t_f} V_2 \cdot KLa(t) dt \left[\frac{kWh}{d} \right] \quad (7)$$

The economic cost function (J_{ECO}) used in the EMPC implementation is an overall cost index (OCI) that includes PE, AE and the fines for off-specification ammonium concentration in the effluent (Ammonium concentration in the effluent is approximated by S_{NH5}). w_1 and w_2 are chosen here as $w_1 = w_2 = 1 \text{ EUR/kWh}$

$$OCI = \left(w_1 \cdot \frac{1}{T} \int_{t_0}^{t_f} (0.004 \cdot Q_a(t)) dt + w_2 \cdot \frac{S_{O,sat}}{T \cdot 1.8 \cdot 1000} \int_{t_0}^{t_f} V_2 \cdot KLa(t) dt + w_3 \cdot 8.2 \cdot \max(0, S_{NH5} - 4) \cdot Q_e \right) [EUR/d] \quad (8)$$

4. Identification of the models and implementation in the EMPC

The identification of the ASP is carried out considering the most important variables and all the biological mechanisms that govern the ASP, to provide an accurate representation of the whole non-linear process behaviour. A back-propagation feed-forward-neural-network model and a Takagi-Sugeno multidimensional fuzzy inference model are identified from data collected from the benchmark to predict the output variables: dissolved oxygen (DO) concentration at the end of the aeration zone (SO5) and the nitrate concentration at the end of the anoxic zone (SNO2).

Several test trainings are carried out, obtaining the best quality of information when perturbations are introduced as constant-frequency steps sequences of pseudo-random amplitude. This protocol is applied to the manipulated inputs KLa and Q_a or eventually superimposed to the dry weather profiles of the influent perturbations Q_{in} , SS_{in} and SNH_{in} .

For the neural model, the multi-layered, non-recurrent net structure known as Feed-forward Neural Network (FNN) is chosen because of its flexibility, and the simplicity of the training procedure when compared to recurrent networks. The structure of the neural networks is described in figure 2a. The typical training and cross validation practice is used to adjust the networks coefficients, by means of the well-known Levenberg-Marquardt algorithm, found in the Neural Networks Toolbox of Matlab [®].

For the fuzzy model, a Takagi-Sugeno fuzzy inference system (FIS) is selected, using as a consequent for each rule a linear affine function of the input variables. The FIS is based on multi-dimensional antecedent fuzzy sets (MDAFS) in such a way that a variable to variable partition is not required, instead, the partition is automatically done directly over all input variables producing a set of multi-dimensional clusters or rules. Three 3 clusters, equivalent to 3 fuzzy rules, are the best FIS configuration, which is the one used here (see figure 2b).

The FNN and FIS models are simulated under dry weather conditions and the step disturbances in oxygen mass transfer coefficient (KLa) and internal recycle flow rate (Q_a). The behaviour of the output variables estimated by the FNN and FIS models are shown in figure 3, along with the process outputs from the BSM1. The precision of the estimation is very good, for the oxygen content as well as for the nitrates-nitrites

concentration, which validates the use of the FNN or FIS as prediction model in the EMPC framework.

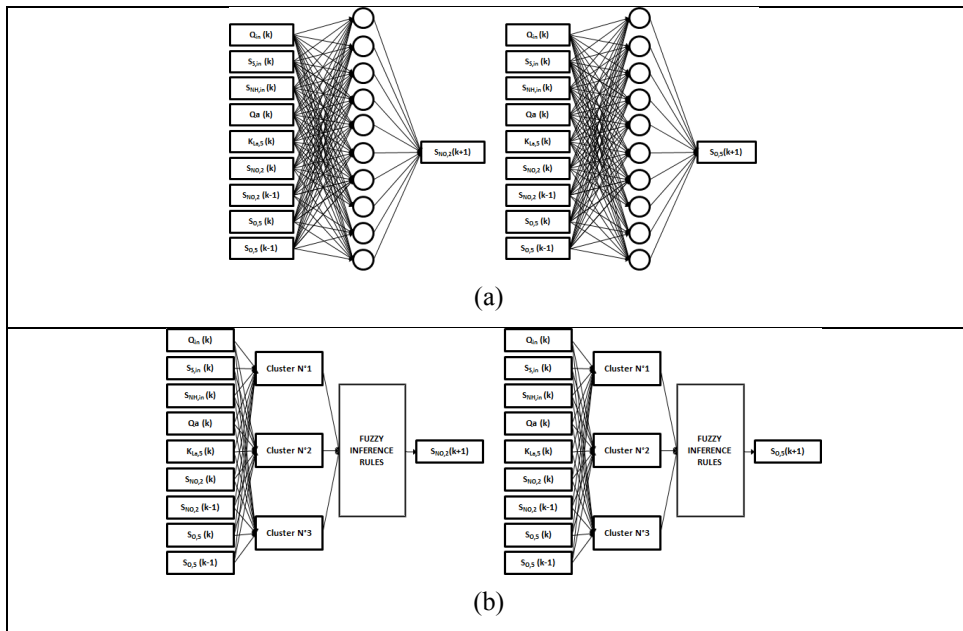


Figure 2. Structure of FNN (a) and FIS (b) models for estimation of S_{O_5} and S_{NO_2} .

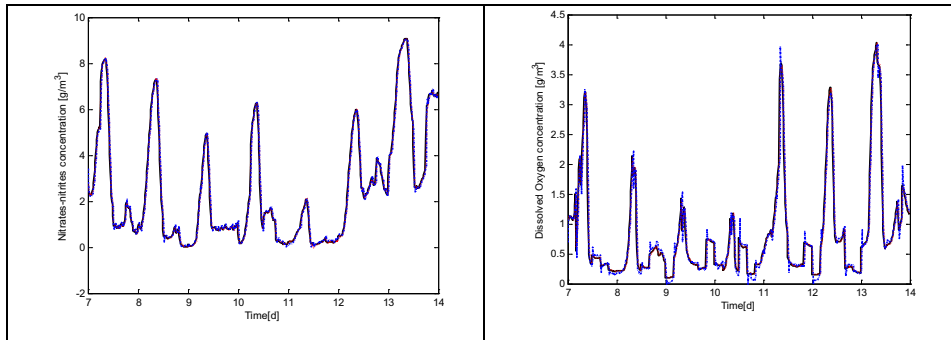


Figure 3. Validation of neural and fuzzy models for nitrates concentration S_{NO_2} and for dissolved oxygen concentration S_{O_5} . Solid line: Process; dotted line: FNN; dashed line: FIS.

The FNN and FIS models are implemented for predictions in the EMPC framework and the process performance using this controller is compared with the EMPC (named P-EMPC) and NMPC proposed in Revollar et al. (2017) that uses the reduced phenomenological model of the plant as prediction model (Figure 4). The weights of the EMPC cost function are $w_1=30$, $w_2=30$, $w_3=5$.

As seen on figure 4, the implementation of EMPCs for minimizing the energy consumption leads the S_{NO} and S_O concentration to the lower limits of the controlled variables. The behaviour of the EMPC using the FNN model is different from reduced

phenomenological model controller due to its ability to capture more precisely the process non-linear dynamics.

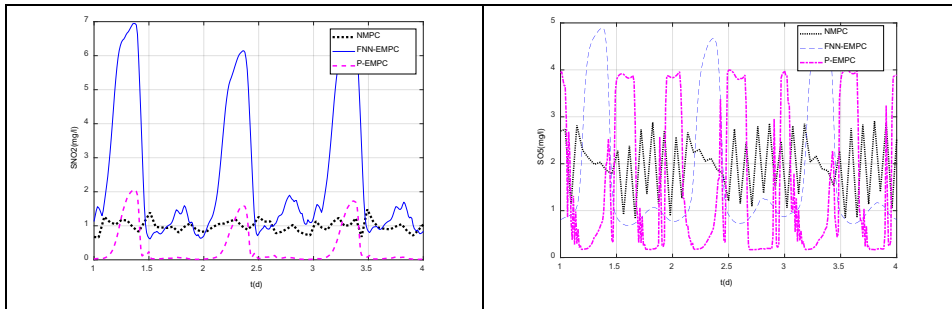


Figure 4. Comparison of the S_{NO_2} and S_{O_5} responses with the EMPC using the FNN model and the NMPC and EMPC using a reduced phenomenological model (Revollar et al. 2017)

5. Conclusions

In this work, the identification of the activated-sludge process with neural networks and fuzzy models is carried out using as the activated sludge process plant the challenging simulation benchmark BSM1. This simulator is an excellent tool to reproduce the complete, multifaceted nitrification-de-nitrification process. The capacity of the identified FNN and FIS for predictions is exploited in an EMPC strategy. The prediction estimates are acceptable for short horizons (twelve steps ahead), which makes them perfectly usable for economic predictive control applications.

References

- Amand, L. Olsson, G.; Carlsson, B. (2013) Aeration Control-A review. *Water Science & Technology*. 67(11): 2374-2397.
- Alex J.; Benedetti L.; Copp J.; Gernaey K.; Jeppsson U.; Nopens I.; Pons M.; Rieger L.; Rosen C.; Steyer J.; Vanrolleghem P.; Winkler S. Benchmark Simulation Model no. 1 (BSM1). IWA Taskgroup on benchmarking of control strategies for WWTPs.
- Goldar, A; S. Revollar, R. Lamanna, P. Vega. Neural NLMPC schemes for the control of the activated sludge process. 11th IFAC Symposium on Dynamics and Control of Process Systems, including Biosystems. June 6-8, 2016. NTNU, Trondheim, Norway
- Moscoso-Vasquez M.; Monsalve-Bravo G.; Alvarez, H. Model-based supervisory control structure for plantwide control of a reactor-separator-recycle plant. *Industrial & Engineering Chemistry Research*. Volume 53. Issue 52. pp 20177–20190. 2014
- Revollar, S.; Vega, P.; Vilanova, R.; Francisco, M. Optimal Control of Wastewater Treatment Plants Using Economic-Oriented Model Predictive Dynamic Strategies. *Applied Sciences* 7(8):813. August, 2017.
- Vega, P.; Revollar, S.; Francisco, M.; Martin, J. M. (2014) Integration of set point optimization techniques into nonlinear MPC for improving the operation of WWTPs. *Comput. Chem. Eng.* 68, 78–95.
- Zeng J.; Liu, J. (2015) Economic model predictive control of wastewater treatment processes. *Industrial & Engineering Chemistry Research*, 54, 5710-5721.

Bayesian estimation of product attributes from on-line measurements in a dropwise additive manufacturing system

Andrew J. Radcliffe*, Gintaras V. Reklaitis

Davidson School of Chemical Engineering, Purdue University, West Lafayette, IN, 47906, USA

aradcli@purdue.edu

Abstract

In the pharmaceutical industry, application of additive manufacturing technologies presents unique opportunities for monitoring and control of drug product quality through on-line image acquisition systems which estimate process output from images of emergent drops. For doses produced from pure fluids on-line imaging has demonstrated utility (Hirshfield, et al., 2015); however, processing of particulate suspensions requires consideration of uncertainty regarding gravity- and flow-mediated particle-liquid segregation. Even for well-mixed suspensions, random localization of particles during the necking of the liquid bridge results in variable drop trajectory (Furbank & Morris, 2004), which must be corrected for in the estimates of drop volume provided by an on-line imaging system. This work explores the use of Bayesian statistical models to resolve potential inaccuracy in drop volume estimates obtained by an on-line image sensor in a dropwise manufacturing process for suspension-based drug products. The framework in the case study presents a method by which uncertainty arising from on-line process measurements may be reconciled for through sufficient sampling and off-line analysis of process outputs.

Keywords: Bayesian inference, drug products, additive manufacturing

1. Introduction

Concurrent with the expansion of inkjet printing methods into precision materials (e.g. semiconductor, ceramics) industries, considerable research effort has been devoted to development/adaptation of inkjet technology for pharmaceuticals manufacturing. Applications of additive manufacturing technology have received substantial attention for production of oral solid doses (e.g. tablets, capsules, thin films). The mechanics of this fluid-based process facilitate monitoring and control of drug product properties, as the output of the system, individual drops, may be monitored in real time using an on-line imaging system (Hirshfield, et al., 2015). Recent work with homogenous fluids (solvents, melts) has demonstrated feasibility of an image capture system for process monitoring in dropwise additive manufacturing system (Hirshfield, et al., 2015, İçten, et al., 2015). However, quantification of process output with an image capture system becomes ambiguous for suspensions due the possibility of particle-liquid segregation during transit through the system. Additional uncertainty is presented by drop ejection, due to random localization of particles which may result in irregular drop trajectory; this manifests as uncertainty in the computation of drop volume from the on-line image

system. The optical sensor calibration is sensitive to the distance between drop and camera, for which variable drop trajectories would result in inaccurate drop volume estimates from the on-line image system. In this work, a Bayesian statistical model is applied to reconcile errors in computed/actual drop volumes from a set of suspension formulations and process conditions which yielded reproducible drops/products, as determined by gravimetric analysis. Multiple model structures are considered for estimation of actual drop volumes from computed drop volumes; prior information is obtained from separate experiments conducted at the same set of conditions. The estimated parameters from the statistical models are compared with predictions afforded by linear regression models, in both classical and Bayesian formulations.

2. Dropwise additive manufacturing platform, on-line image acquisition

The dropwise manufacturing system consists of a precision positive displacement pump, x-y staging, pump/staging controllers and on-line image acquisition system; the image acquisition system is comprised of a camera actuated by a motion sensor; the setup is a variant of the process described in (Hirshfield, et al., 2015). The mechanical action of the positive displacement pump forces fluid through the dispensing nozzle, which, dependent on process conditions and suspension properties, results in formation of one or more drops; the present work considered only the experimental conditions which produced a single drop per actuation event of the pump. A process diagram, including the image acquisition system, is presented in Figure 1.

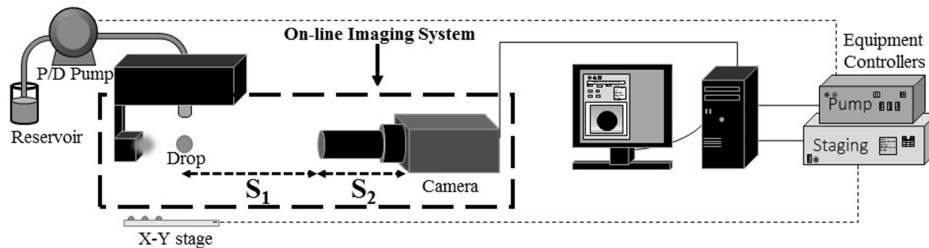


Figure 1. Process diagram for dropwise additive manufacturing system.

The on-line image acquisition system computes drop volume from the two-dimensional image by estimating the volume of the sphere from a stack of equivalent cylinders, for which diameters are defined using the drop edges; further detail is available in (Hirshfield, et al., 2015). A calibration procedure which defines a unit pixel in relation to physical dimensions is necessary to complete the volume estimate; this was performed in a configuration analogous to that depicted in Figure 2, with the drop replaced by an optical standard.

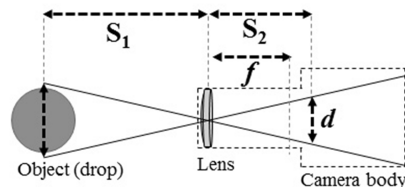


Figure 2. Ray tracing diagram for image acquisition system; drop not proportionate to scale.

The calibration procedure assumes constant values for system properties: S_1 (distance of object from lens), S_2 (distance from lens to image), f (focal length), and d (dimension of image sensor). As S_1 is determined by each the drop's trajectory, deviations result in errors for computed drop volume due to a changes in the effective magnification, which for a thin lens the linear magnification would change by a factor proportional to the ratio of ($S_{1,Calibration}/ S_{1,NEW}$). For pure fluids, the assumption of constant drop trajectory (fixed S_1) has demonstrated utility (Hirshfield, et al. 2015, İçten, et al, 2015); for particle suspensions, drop trajectory appears to be a distributed parameter (variable S_1).

3. Bayesian statistical modelling for actual drop volume in suspensions

Drops produced from suspensions exhibit larger variance in volume than drops from pure fluids due to the inherent heterogeneity imparted by particles. The presence of particles disrupt thinning of the fluid filament during drop break off at a length-scale proportional to particle size; for particle samples with a size distribution, this may cause drops to pinch off at different spatial locations, dependent on the presence of (relatively) large particles in the thinning filament (Furbank & Morris, 2004). Variability in the drop break off process may lead to altered drop trajectory, which may be one of several causes for discrepancies between computed drop volume and actual drop volumes as determined by gravimetric analysis. The severity of other process disturbances (flow-induced segregation; sedimentation) depends on suspension properties, process conditions and experimental timescale, thus, potential data sets for modelling were selected based on reproducible drop production which appeared to only exhibit error in computed drop volumes. This corresponded to drops produced from suspensions with particle volume fractions of 0.15-0.25 formulated from four pharmaceutical powders in a triglyceride oil carrier fluid; details related to particle characterization and properties may be found in (Radcliffe & Reklaitis, 2017).

The use of a statistical model for estimation of actual drop volume incorporates uncertainty into parameter estimates obtained using the computed drop volume as surrogate for actual drop volume. Several Bayesian model formulations with respective parameters sets and structures are developed for estimation of actual drop volume, based on future observation of computed drop volume. The Bayesian model results are compared with predictions from a linear regression model, for which unknown parameters are estimated by (1) ordinary least squares and (2) a Bayesian formulation of ordinary least squares. In the Bayesian models, informative prior distributions were estimated from the data (actual/computed drop volume) at given set of process conditions and suspension properties; the same data was used for the linear regression and Bayesian linear regression.

The first Bayesian model was structured with the likelihood based on the assumption that each computed drop volume (Y) was drawn from a normal distribution with parameters ($\theta_1 - \theta_2, \sigma^2$), in which ($\theta_1 - \theta_2$) and σ^2 are the mean and variance of computed drop volume. Actual drop volume (θ_1), and an offset parameter (θ_2), which represented a combined estimate of errors related to drop trajectory and other process disturbances; a multivariate normal distribution was assigned to (θ_1, θ_2) in order to preserve details of the relationship between the two parameters. The variance parameter (σ^2) of the likelihood was assigned a inverse gamma prior distribution, with parameters estimated from the data set; likewise, the mean vector and covariance matrix of the prior on (θ_1, θ_2) were estimated from the experimental data. Treatment of the future observations, y_i , individually or as a sample result in different interpretations of the

available information. Treated individually, the y_i 's are used to estimate $(\theta_1, \theta_2)_i$, and when treated together, the identity of y_i 's are subsumed under the sample average. Formulations produced by the dropwise platform contain 5-50 drops per dose, which motivates treatment of y_i 's using the sample average due to the large number of drops required by a dose regimen of 30 capsules. The joint posterior distribution for this model, conditioned on a future set of observations, Y , is given in Eq. (1).

$$p(\theta_1, \theta_2, \sigma^2 | \underline{Y}) = \frac{p(\underline{Y} | \theta_1, \theta_2, \sigma^2) p(\theta_2 | \theta_1) p(\theta_1) p(\sigma^2)}{p(\underline{Y})} \quad (1)$$

The second Bayesian model considers a case in which variable drop trajectory affects computed drop volumes through a magnification re-scaling factor proportional to $(S_{1,c}/S_{1,N})$, based on the image acquisition configuration and calibration. The likelihood distribution assumes that computed drop volume(s), Y , are drawn from a normal distribution with mean and variance parameters, θ_4/θ_5 , and σ^2 , respectively, which have known prior distributions. To preserve the relationship between them, the actual drop volume (θ_4) and scale parameter (θ_5) are assigned a multivariate normal distribution, with mean vector and covariance matrix estimates obtained from the experimental data. An inverse gamma distribution is assigned to the prior on σ^2 , with parameters estimated from the experiments. The joint posterior distribution for this model is given in Eq. (2), which treats the y_i 's using the sample average.

$$p(\theta_4, \theta_5, \sigma^2 | \underline{Y}) = \frac{p(\underline{Y} | \theta_4, \theta_5, \sigma^2) p(\theta_5 | \theta_4) p(\theta_4) p(\sigma^2)}{p(\underline{Y})} \quad (2)$$

The Bayesian models were compared with a normal linear model given two sets of parameters estimates obtained by: ¹ordinary least squares and ²Bayesian linear regression. The specifications of the linear model were as follows: actual drop volume, y , was the response variable; computed drop volume, X , was the explanatory variable; with parameter vector $\beta = [\beta_1, \beta_2]$; y , X were the same data as the prior distributions, which contained $n=39$ samples. In matrix form, the model consisted of the response column vector, y_i , design matrix X_{ij} with column $j=1$ specified as the control ($=1$), and column $j=2$ as the computed drop volumes and parameter vector, β ; the Bayesian procedure used the same model, but assigned a distribution to the variance of observations. As these were standard models in both cases, additional details are not included here, but may be found in reference texts (Gelman, et al., 2014).

4. Sampling from joint posterior distributions: Markov chain simulations

The joint posterior distributions presented in Eq. (1) and Eq. (2) are used to estimate actual drop volume for a given set of process conditions and suspension properties. For a given model, the joint posterior density was sampled using the Metropolis-Hastings algorithm in Markov chain simulations, with the density ratio defined using the proportionality of the joint posterior distribution of interest. The prior distribution was selected as the jumping distribution, which is used to generate of parameter proposals, θ_1^* ; proposals are evaluated using the ratio of the proposal joint posterior density (step θ^*) to that of the joint posterior density at the previous step (θ^{t-1}). The algorithm

proceeds by comparison of a random draw from the standard uniform distribution to the density ratio, r (Eq. (4)); θ^* is accepted as step t of the Markov chain when the density ratio is greater than the standard uniform draw, otherwise the algorithm proceeds from step θ^{t-1} (Chib & Greenberg, 1995). Markov chain simulations using the Metropolis-Hastings algorithm were executed and analysed in MATLAB; for a given joint posterior density, 10 chains with unique starting positions were simulated until the vectors of “accepted” posterior samples had lengths of 1,000,000; convergence monitoring and assessment of mixing followed the framework presented by (Gelman, et al. 2014).

5. Results and Discussion

Using the dropwise additive manufacturing platform, data sets consisting of n drops were generated; the on-line image acquisition system recorded a digital photograph of each drop, which landed in a pre-weighed container for gravimetric analysis. The actual volume of each drop was estimated from its mass, with a working assumption based on constant fluid density. The linked computed image volume and corresponding mass-based volume were used for estimation of prior distribution parameters in models 1, 2 and for the data used for linear regression.

The results of one case study, based on drops produced from micronized acetaminophen (20vol%) suspensions in triglyceride oil, are presented in Figures 3,4.

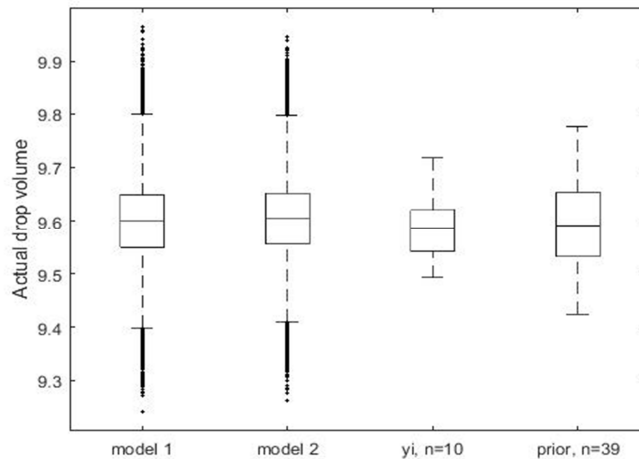


Figure 3. Posterior distributions of model 1,2 parameters (θ_1, θ_4), respectively, distribution of true values corresponding to y_i 's from the likelihood, and distribution of prior data.

The simulated posterior distributions are presented in Figure 3 as a box plot, in addition to the set of future observations of actual drop volume estimated from image (y_i in model 1,2 notation); the prior distribution of actual drop volume as the fourth entry. From Figure 3, it can be observed that model 1 and model 2 provide a reasonable estimate for mean value; however, the posterior distributions appear to have much longer tails as indicated by the whiskers – from a Bayesian perspective, this is not unexpected, as the posterior distribution includes uncertainty which has been specified in the model structure. In Figure 4, the Bayesian approach results in a larger confidence region than ordinary least squares, though the difference in mean predicted values is negligible.

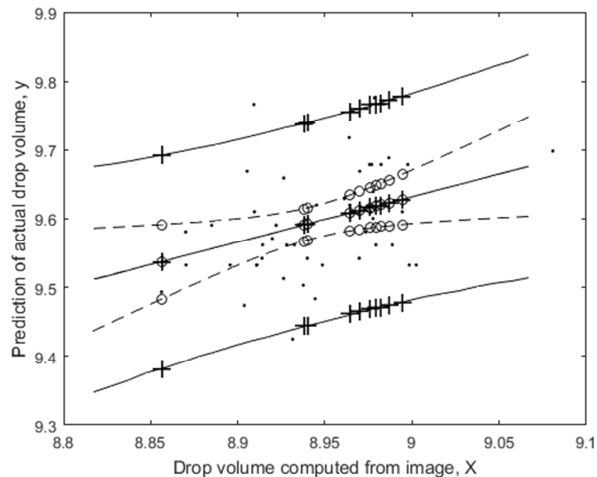


Figure 4. Predicted mean value, 95% confidence bounds of ordinary linear regression (dashed line, circle) and Bayesian linear regression (solid line, cross). Dots correspond to points to the associated actual/computed drop volume vectors.

6. Conclusions

In this study a Bayesian approach was developed for estimation of product parameters from observations made with offset; prior information from the pharmaceutical manufacturing system was used to update future estimates of drop volume output. The parameter estimates from the Bayesian posteriors provide reasonable estimates for items such as mean, variance, but with a more diffuse density than that observed in the data due incorporated uncertainty, which is also reflected in the respective confidence intervals of the ordinary/Bayesian linear regressions. For implementation in the dropwise manufacturing process, model complexity must at minimum reflect potential disturbances in the process, as demonstrated by peculiarities observed in using the on-line imaging system as the sole process monitor for suspension printing. An improved model necessitates additional explanatory variables such as concentration, which may assist in associating potential causes with experimental behaviour observed with suspensions.

References

- S. Chib & E. Greenberg, 1995, *The American Statistician*, 49, 327-335.
- R.J. Furbank & J.F. Morris, 2004, *Physics of Fluids*, 16, 1777-1790.
- A. Gelman, J.B. Carlin, H.S. Stern, D.B. Dunson, A. Vehtari, & D.B. Rubin, 2014, Boca Raton, FL: CRC press.
- L. Hirshfield, E. İçten, A. Giridhar, Z.K. Nagy, & G.V. Reklaitis, 2015, *Journal of Pharmaceutical Innovation*, 10, 140-155, 2015
- E. İçten, A. Giridhar, L.S. Taylor, Z.K. Nagy, and G.V. Reklaitis, 2015, *Journal of Pharmaceutical Sciences*, 104, 1641-1649
- Radcliffe, A. & G.V. Reklaitis, 27th European Symposium on Computer Aided Process Engineering, Oct. 1-5, 2017, Barcelona, Spain

Data Driven Reduced Order Nonlinear Multi-parametric MPC for Large Scale Systems

Panagiotis Petsagkourakis^a, Constantinos Theodoropoulos^{b*},

^a*School of Chemical Engineering and Analytical Science, The University of Manchester, M13 9PL, UK*

^{*}*k.theodoropoulos@manchester.ac.uk*

Abstract

Multiparametric model predictive control (mp-MPC) obtains an off-line feedback control law using parametric programming. Control of distributed parameter systems (DPS) remains a challenging task, as the system dynamics are infinite-dimensional. Model reduction techniques can produce a low-order system. In this work, a combined POD and recurrent artificial neural networks methodology is employed, in order to reduce the system, which can efficiently work for any simulator, including black-box ones. The reduced order model is then utilized by the mp-MPC. A novel strategy is introduced for computing the critical regions of the approximated mp nonlinear problem. The proposed algorithm produces an initial solution and accelerates the procedure, reducing the number of the required critical regions and the corresponding computational time. The effectiveness of the proposed algorithm is demonstrated for a tubular reactor where an exothermic reaction takes place.

Keywords: Model reduction, Distributed parameter systems, Artificial neural networks

1. Introduction

Model predictive control (MPC) is an online control methodology where a receding horizon is employed to compute the manipulated variables for an optimum trajectory (Theodoropoulos 2011). Online MPC may be computationally expensive, especially for the case of distributed parameter systems (DPSs) (Xie et al. 2015). The dissipative nature of such systems can be exploited for model order reduction (MOR). However, the application of online control action could be an obstacle even with the use of a reduced model. Fast MPC such as mp MPC is a powerful control methodology that computes offline the control actions as functions of the states (Pistikopoulos 2012) overcoming the online computational burden of the online MPC. Despite the fact that the majority of computations are performed off-line, the large size of the physical system may produce an intractable computational approach. Rivotti et al. 2012 combine nonlinear model order reduction, based on balancing of empirical gramians to reduce the size of the system with nonlinear multi-parametric MPC (Dominguez & Pistikopoulos, 2011). However, the latter methodology can still be prohibitive for complex large-scale systems, modelled by sets of PDEs and the complexity of equations can jeopardise the efficiency of the algorithm.

Data-driven methodology is employed in this work in order to create a considerably small approximation of the dynamical system. Proper orthogonal decomposition (POD) with recurrent artificial neural networks (rANN) is used to produce a data driven reduced order model that is then utilized in a novel mp algorithm suitable for such

systems. We propose a novel methodology that takes advantage of the collected trajectories in order to accelerate the computation of the mp MPC.

2. Artificial Neural Networks and Model Order Reduction

The focus of this work is on feedback control of spatially distributed processes described by a system of dissipative PDEs:

$$\frac{\partial x}{\partial t} = A(x, \frac{\partial x}{\partial z}, \dots, \frac{\partial^n x}{\partial z^n}) + B(z)u + F(x) \quad (1)$$

where A is a dissipative spatial differential operator, $F(x)$ is a nonlinear function and x , u , and y the states, manipulated, and output variables. Eq. 1 may be unavailable or complicated and Galerkin projection may be difficult to apply. This obstacle can be overcome employing data-driven methodology such as artificial neural networks with POD. Proper orthogonal decomposition (POD) is a widely used methodology for data compression that captures the most “energy” utilizing the method of snapshots (Sirovich 1987) in order to approximate the system eigen-functions. The ‘energy’ of a given mode is related to the magnitude of the eigenvalue corresponding to that mode. This methodology separates the spatial and temporal behaviour discretising the infinite dimensional states with a finite number of reduced states (dominant modes) that captures the most of the systems energy. The eigen-functions produced by this method are then used as global bases functions. The dominant modes can be computed using the \mathcal{L}_2 inner product as $a_i(t) = \int_V (x - \bar{x})\phi_i dz$, where $a_i(t)$ are the dominant modes, \bar{x} is the mean value of the snapshots, and ϕ_i are the computed eigen-functions.

After collecting the snapshots and computing the eigen-functions, a sub-set of snapshots can be used to train an ANN. Approximations using recurrent ANNs (rANN) is a popular methodology for nonlinear physical systems. The wide use of rANN is based on the universal approximation theorem stating that every non-linear dynamical system can be approximated to any accuracy providing enough (but always finite) hidden layers. The structure of the rANN can be relatively simple as the Nonlinear Autoregressive model process with exogenous input (NARX) or significantly complex as the so-called deep-ANN and convolutional ANN (cANN) (G et al. 2016) that have been widely used in image classification and face recognition. In this work, NARX models have been employed to keep the data set as small as possible due to their relatively simple structure. The NARX model is trained employing the back-propagation method and it is carried out in MATLAB R2017a with Neural Networks toolbox. Inputs for the rANN’s are the manipulated variables and the reduced states at the previous time instant.

At this point a special note is needed; POD and rANN are both data-driven methodologies; however a different treatment is required. The snapshots for the PODs can include steady-states; on the other hand rANN should not include steady-states (ss) as the rANN approximate the dynamical behaviour and a given ss will over-fit the network forcing it to duplicate satisfactory the ss but the transient behaviour will be jeopardised. That means that the corresponding data-sets employed for PODs and rANN should be in principle different.

3. Multiparametric Nonlinear MPC

The general optimal control problem can be seen as a continuous mp-nonlinear MPC, where the varying parameters are the current states and any other additional parameters such as set-points. This NLP problem can be formulated with $\theta = [a_0^T, u_{-1}^T, y_{ref}^T]^T$ as follows:

$$J(\theta) = \min_{a,u} h(a,u,\theta) = \min_{a,u} \sum_{i=1}^N \|y_i - y_{ref}\|_Q^2 + \sum_{i=1}^M \|\Delta u_i\|_R^2$$

$$u_i = u_{i-1} + \Delta u_i$$

$$G(a,u,\theta) = a_{i+1} - g(a_i, u_i) = 0$$

$$h_{in}(a,u,\theta) \leq 0$$

$$A\theta \leq b$$

(2)

where $\alpha_i = \alpha(t_i) = [a_1(t_i) \dots a_l(t_i)]^T$, N , M are the prediction and control horizon, respectively, u_{i-1} the manipulated variable at the previous time point, y_{ref} the set-point and g the reduced order rANN (section 2).

POD and rANN are employed, as described in section 2, to generate a reduced order model for Eq. 1 and the mp nonlinear MPC control problem uses the reduced order current states (dominant modes) a_0 reducing the size of θ . Nevertheless, the number of critical regions increases sharply, making the problem computationally intractable even for small sized problems (Grancharova and Johansen 2012). A novel algorithm is proposed in this section that produces a small number of critical regions using initially a multi-linear approximation for the system's dynamics and a step that refines the solution such that the error between the implicit NLP and the explicit approximation is within an a priori bound. The main idea behind the algorithm is to find multiple mp-QP such that the explicit solution can approximate Eq. 3 adequately enough. To do so the nonlinear components of the equation need to be linearized; however the main nonlinear function is the rANN. Therefore, an initial approximation using affine models is created by linearizing the system at multiple points. The first step of the algorithm takes advantage of the collected snapshots used in section 2. The data set is separated into a set of clusters using k-means (Hastie et al. 2009) and the corresponding centroids are computed. These points are then used as linearization points in order to construct a PWA model that is defined in polyhedral regions that are found employing Voronoi diagrams (this procedure can be enhanced using the algorithm of Breschi et al. 2016).

Subsequently, the refinement step follows, where the explicit solution is compared with the implicit NLP and more partitions are generated. The explicit solution is compared at the vertices of each critical region with the implicit solution. Every NLP problem is solved using a multiple shooting method which is suitable for stiff problems like the ones studied here, where the dynamics are given by a reduced order rANN. If the result of the comparison is not satisfactory then new approximate mp-QP is needed. In order to construct an mp-QP for each new partition the following approach is adopted; at the Chebyshev center of the partition a local mp-QP problem (one for each partition) is constructed in the form of Eq. 7:

$$\begin{aligned}
J(\theta) &= \min_U \frac{1}{2} \Delta U^T H \Delta U + (B + F(\theta - \theta_0))^T \Delta U + J^* \\
C \Delta U &\leq d \Delta \theta + E \\
A \theta &\leq b
\end{aligned} \tag{3}$$

with H, B, FC, d, E being the corresponding derivatives evaluated at the point of approximation for the computed for the optimum set of parameters. A scheme with numerical perturbations for the equality constraints is applied in order to compute the derivatives. If J^* is the optimal solution obtained with the multiple shooting method, for parameters θ_0 and optimal degrees of freedom U^* then, for example, the derivative of the objective function with respect to parameter θ_0 is computed as follows:

$$\frac{\partial h}{\partial \theta} = \frac{h(\alpha_{U^*, \theta_0 + \epsilon}, U^*, \theta_0 + \epsilon) - h(\alpha_{U^*, \theta_0 - \epsilon}, U^*, \theta_0 - \epsilon)}{2\epsilon} \tag{4}$$

where α_{U^*, θ_0} is the solution of $G(\alpha, U^*, \theta_0) = 0$ and $\alpha_{U^*, \theta_0 + \epsilon}$ the solution of $G(\alpha, U^*, \theta_0 + \epsilon) = 0$. This refinement procedure continues until an a priori tolerance is satisfied. If the new mp-approximation creates only one critical region that still does not provide an appropriate solution then the region should be divided according to a geometrical criterion (in this work a triangulation is employed). This approach may produce complex convex geometrical regions; however, overall the number of regions does not increase as steeply as in (Grancharova and Johansen 2012), and because of the good initial approximation the result doesn't produce many additional critical regions.

In the next section, this algorithm is employed to a system of PDEs after collecting a good set of snapshots in order to illustrate its computational capabilities.

4. Application

The effectiveness of the proposed algorithm is illustrated using a chemical engineering application; an exothermic tubular reactor. The physical system is described by two partial differential equations with Neumann boundary conditions:

$$\frac{\partial c}{\partial t} = \frac{1}{Pe_1} \frac{\partial^2 c}{\partial z^2} - \frac{\partial c}{\partial z} - Da c e^{\frac{\gamma T}{1+T}} \tag{5}$$

$$\frac{\partial T}{\partial t} = \frac{1}{Pe_2} \frac{\partial^2 T}{\partial z^2} - \frac{\partial T}{\partial z} - B Da c e^{\frac{\gamma T}{1+T}} + b (T_w - T) \tag{6}$$

Here c and T are the dimensionless concentration and temperature respectively, while T_w is the temperature of the cooling zone. The system's parameters are $Pe_1 = Pe_2 = 7$, $Da = 0.1$, $B = 2.5$, $b = 2$, and $\gamma = 6$. The eigenfunctions are computed employing the method described in section 2, where after the eigenanalysis 2 dominant modes capturing 99.8% of the system's energy are computed. A sub-set of the collected snapshots is utilized for the training of the rANN (rejecting the steady states). First, the

dominant modes are computed using Eq. 2 and then the rANN is trained with u_k, α_{k-1} being the inputs of the network and α_k the output. It is crucial that the validation error has to be adequately small as this model error propagates for predictions of larger time intervals during the actual simulation. The reduced model is then used to construct the NLP problem (with $Q=$ Identity matrix (I) and $R=0.01I$) at each Chebyshev center with $-1 \leq u_i \leq 1$ and $-1 \leq \alpha_i \leq 1$. Following the algorithm (section 3) the collected trajectories can then be used to identify the clusters and the mp problem is solved. Fig. 1a depicts two reduced variables at the final solution with the a priori tolerance=0.002. Overall 41 critical regions (~40 CPU-min) are constructed through the refinement process while the method proposed by Grancharova and Johansen 2012 produces 841 critical regions (over 4 CPU-hour). Then, the controllers are validated for different set-points and the results are depicted in Fig.2. The solution is adequately close to the actual implicit nonlinear MPC, and the controller approximates better the implicit NLP for the same a priori error bound. This shows the effectiveness of the proposed method. Furthermore, the error between the reduced order model and the actual system is higher than that produced by an equation-oriented methodology, thus it is important to use a method that will eliminate offsets. Here, in the on-line implementation the actual set-point is substituted by a new set-point which is actual one subtracted by the model error.

All the simulations are carried out using an i7 and 16 RAM single threaded machine. All the calculations are implemented in MATLAB, and each mp QP as well as each NLP problem, is solved using the toolbox POP (Pistikopoulos 2012) with NAG Mark 25.

5. Conclusions

We have developed a data-driven reduced order mp MPC suitable for large scale systems such as ones described by PDEs. A combined methodology of POD and rANN is employed to produce a reduced order system, without using the equations, which is then employed within a new nonlinear mp-MPC algorithm. The effectiveness of the proposed methodology is illustrated through the MPC of an exothermic tubular reactor described by complex nonlinear PDEs. The offline complexity is reduced and the approximated solution is obtained with computational efficiency using a multi-linear solution as an initial partition.

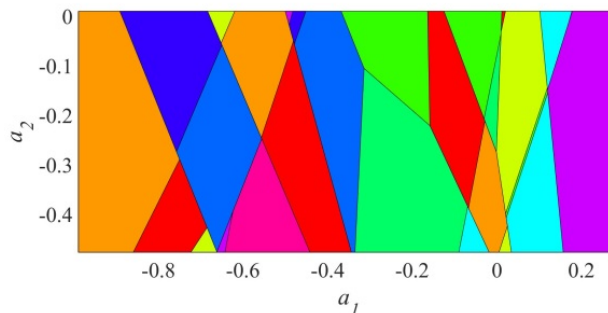


Figure 1: Critical regions for proposed method

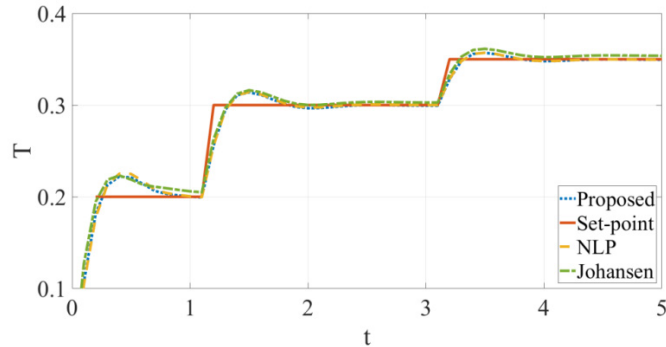


Figure 2: Solution for different set-points

References

- C. Theodoropoulos, 2011, *Optimisation and Linear Control of Large Scale Nonlinear Systems: A Review and a Suite of Model Reduction-Based Techniques*, Lecture Notes in Computational Science and Engineering, vol 75. Springer, Berlin
- W. Xie, I. Bonis, C. Theodoropoulos, 2015, Data-driven model reduction-based nonlinear MPC for large-scale distributed parameter systems, *Journal Process Control* 35:50–58.
- E. N. Pistikopoulos, 2012. From multi-parametric programming theory to MPC-on-a-chip multi-scale systems applications. *Computers and Chemical Engineering*
- P. Rivotti, R. S. C. Lambert, E. N. Pistikopoulos, 2012, Combined model approximation techniques and multiparametric programming for explicit nonlinear model predictive control. *Computers and Chemical Engineering*, 42, 277–287.
- L. F. Domínguez and E. N. Pistikopoulos, 2011, Recent Advances in Explicit Multiparametric Nonlinear Model Predictive Control, *Ind. Eng. Chem. Res.*, 50 (2), pp 609–619
- L. Sirovich, 1987, Turbulence and the dynamics of coherent structures, parts i–iii. *Quarterly of Applied Mathematics*, 45, 561–590
- I. Goodfellow, Y. Bengio, A. Courville, 2016, *Deep Learning (Adaptive Computation and Machine Learning series)*, MIT Press
- A. Grancharova, T.A. Johansen, 2012, *Explicit Nonlinear Model Predictive Control: Theory and Applications*
- I. Bonis, W. Xie, C. Theodoropoulos, 2014, Multiple model predictive control of dissipative PDE systems, *IEEE Transactions on Control Systems Technology*, 22(3), 1206–1214
- T. Hastie, R. Tibshirani, J. Friedman, 2009, *The Elements of Statistical learning: Data Mining Inference and Prediction*, Springer, 2
- V. Breschi, D. Piga, A. Bemporad, 2016, Piecewise affine regression via recursive multiple least squares and multicategory discrimination, *Automatica*, 73, 155–162

Model-based real-time prediction of corrosion in heat exchangers

Günther Holzer^a, Thomas Wallek^b

^a*Prozess Optimal CAP GmbH, Impulszentrum 1, 8250 Vorau, AT*

^b*Graz University of Technology, Institute of Chemical Engineering and Environmental Technology, Inffeldgasse 25/C, 8010 Graz, AT*

thomas.wallek@tugraz.at

Abstract

In the chemical and process industry a variety of thermal unit operations is applied in which gases or vapor mixtures must be cooled down to temperatures near the water dew point. Such mixtures often contain substances which tend to evolve corrosive characteristics in case the temperature unintentionally falls below the water dew point. In that particular case, depending on the gas composition, acids can be produced and may cause severe damage to heat exchangers. This kind of corrosion is called ‘pitting’ and may remain undetected for a long time, finally leading to a sudden failure of the equipment. One possible strategy to avoid ‘pitting’ is to use corrosion inhibitors, however, such inhibitors imply a significant increase of costs and are also difficult to dispense under varying process conditions. Consequently, most processes operate with a thermal safety distance to the water dew point in terms of pressure and temperature. A considerable drawback of this approach is that the capacity of the heat exchanging equipment is not fully utilized.

To overcome such limitations, this paper suggests a process prediction method for the real-time estimation of the lowest possible heat exchanger surface temperature in view of fully utilizing the optimization potential of the process. The key features of the new approach comprise (i) application of rigorous thermodynamics, considering all relevant facility components that are needed for a complete mass and energy balance, and (ii) a rigorous heat exchanger calculation providing surface temperatures and dead zone temperatures for the current thermodynamic state.

The thermodynamic calculation provides the theoretical water dew point as a function of the process parameters. Considering that sensitive variables such as the composition of the multicomponent process stream have a significant influence on the water dew point, the accurate thermodynamic description of the complete system poses one challenge of the method.

The customized CFD simulation which is integrated into the simulation model provides the complete spatial distribution of the heat exchanger surface temperatures and dead zone temperatures.

Both components are combined to a process prediction model, where an interface between the process prediction model and the process control system (PCS) is used for real-time transmission of the current process parameters to the model, and of

recommended process parameters generated by the model back to the PCS. These recommendations can either be used as guidelines for the operator or directly be implemented as PCS command variables in view of an automated optimal operation mode.

The proposed methodology couples rigorous thermodynamics with CFD simulation into a novel process prediction model which enhances the overall availability of the process significantly, ensures the definite prevention of ‘pitting’ and increases the efficiency of the process by at least one percentage point.

Keywords: corrosion, pitting, thermodynamics, CFD, process prediction

Control strategy for the Super Heat Integrated Distillation Column

Manuel Rodriguez^a, Ismael Diaz^a

^a *Universidad Politecnica de Madrid, Dpt. Of Chemical Engineering, C/ Jose Gutierrez Abascal 2, 28006 Madrid, ES*

manuel.rodriguez@upm.es

Abstract

Distillation is the most widely used in the separation section of a process. It consumes an important amount of energy (close to 40% of the energy of chemical process). Many different configurations to increase its thermodynamic efficiency have been proposed. The first modification was to add side heat exchangers and reboilers to reduce the duties of condenser and reboilers then a pressurized rectifying section was proposed so that the heat duty of the side condenser could be supplied to the side reboiler. This is basically the concept of what is called Heat Integrated Distillation Column (HIDiC). Recently Toyo Engineering Corporation has patented a new HIDiC called SuperHIDiC column concept, where it realizes the heat integration concept in a simplified manner. Using this column energy conservation is around 50% and greenhouse gas emissions are significantly reduced.

Objective is to develop a dynamic simulation of the column and to design the control structure. This will be based on a methyl ethyl ketone separation column.

First, we present the dynamic model, the designed column parameters and its performance in terms of energy consumption. After, we design and implement the control structure. This structure is evaluated under different production scenarios and disturbances and it is optimised for minimum total annual cost.

This work shows the potential of heat integrated columns and specifically of the recently developed by Toyo Eng. Corp. A control structure that minimises costs (capex and opex) is proposed and analysed showing possible operation problems and how interactions between the different control loops affect the column performance.

Keywords: energy integration, Distillation, Process control

Dynamic simulation and process control study for enhancing operability of small-scale BOG (Boil-off gas) re-liquefaction process in LNG-fueled ship

Hyunsoo Son^a, Jin-Kuk Kim^a, Dong-Hun Kwak^a

^a*Hanyang University, Dpt. of Chemical Engineering, 222 Wangsimni-ro, Seongdong-gu, Seoul 04763, KR*

jinkukkim@hanyang.ac.kr

Abstract

There has been an increasing demand for natural gas because it emits less greenhouse gases than conventional fossil fuels. Reinforcement of international regulation to reduce exhaust gas from ship also supports to fuel a ship with LNG (Liquefied natural gas). However, as LNG stored in a tank at low temperature keeps losing its heat into surroundings, generation of BOG (Boil-off gas) occurs. This necessitates the introduction of BOG re-liquefaction process because the accumulation of BOG not only leads to abnormal state in LNG tank but also decreases profitability.

While previous studies on BOG re-liquefaction processes are mostly limited to large-shipment capacity for LNG carriers using SS (steady state) simulation, this research aims at developing a novel framework for operational optimization of small-scale BOG re-liquefaction process equipped onto LNG-fueled ship by considering both SS and DS (dynamic state) simulation. For this purpose, the process is first designed with small-scale N₂-based reverse Brayton cycle which can be operated at offshore environments. Its feasibility is verified with SS simulation in a commercial simulator. Dynamic model developed in this study shows good agreement with SS simulation, indicating that the model is suitable for analyzing dynamic behaviors and control systems. Sensitivity analysis based on the SS simulation is also carried out for key design and operating parameters with which operation strategy for dealing with unexpected changes is obtained and guidance for achieving more economic operation, leading to the reduction of shaft power consumption for the cycle, is gained.

Process dynamics can be better predicted with DS model built in this study and robust control is effectively ensured with the proposed control logic. This improvement is essential to prevent unexpected operational failure (e.g. surging and thermal shock) or unwanted deterioration in system performance, due to disturbance in the feed and operating conditions.

There are various control mechanisms available for BOG re-liquefaction process. For example, LNG temperature can be controlled by either feed-backward or feed-forward way and faster dynamic response can be achieved with feed-forward way. The most robust control scheme which has stability and high energy efficiency is chosen such that manipulated and controlled variables are paired in a logical manner followed by investigating impacts of disturbances, like change in feed gas temperature. Furthermore, various operational scenarios are systematically investigated in the context of HAZOP

(Hazards and operability study), where DS simulation is utilized for optimizing system performance or minimizing energy consumption. In conclusion, practical and cost-effective operational guidelines are systematically obtained through the proposed operating strategy and control system.

Keywords: BOG re-liquefaction process, reverse Brayton cycle, dynamic modeling

Acknowledgement

This work was supported by the World Class 300 Project(R&D)(No. S2305678) of the SMBA (Korea).

Global Optimization Algorithm for Multi-period Design and Planning of Centralized and Distributed Manufacturing Networks

Cristiana Lara^a, Ignacio Grossmann^a

^aCarnegie Mellon University, Department of Chemical Engineering, Center for Advanced Process Decision-Making, 5000 Forbes Avenue, Pittsburgh, PA 15213, US

cristianallara@cmu.edu

Abstract

Distributed and modular manufacturing has arisen as a promising option for supply chain networks in which the transportation is the main bottleneck. However, economies of scale will always favor large scale centralized production. Therefore, there is a need for a general framework that can support this decision taken into account the potential tradeoffs (Lara et al., 2016). In this paper, we address the design and planning of manufacturing networks considering the option of centralized and/or distributed facilities. This multi-period problem involves the selection of which facilities to build in each time period, and their location in the continuous 2-dimensional space, in order to meet demand and maximize profits.

The problem is formulated as a version of the continuous facility location and allocation problem with limited capacity, also known as the Capacitated Multi-facility Weber Problem (CMWP) (Brimberg et al., 2008). The objective of this type of problem is to determine locations in continuous 2-dimensional space for opening new facilities based on their maximum capacity and the given coordinates of the suppliers or customers. We propose an extension of the original CMWP that considers fixed cost for opening new facilities, fixed transportation costs, and two sets of fixed-location points: suppliers i and customers j (Lara et al., 2017), and investment decisions in different time periods. The model is a multi-period nonlinear Generalized Disjunctive Programming (GDP), reformulated as a multi-period nonconvex Mixed-Integer Nonlinear Programming (MINLP).

We develop a bilevel decomposition algorithm that consists of decomposing the problem into a master problem and a subproblem. The master problem is based on a relaxation of the nonconvex MINLP, which yields an MILP that predicts the selection of facilities and their links to suppliers and customers, as well as a lower bound on the cost of problem. The subproblem corresponds to a nonconvex NLP of reduced dimensionality that results from fixing the binary variables in the MINLP problem, according to the binary variables predicted in the MILP master problem. Based on the bounding properties of their subproblems, ϵ -convergence is proved for this algorithm.

The applicability of the proposed model and solution framework are illustrated with case studies for different industries, including biomass and shale gas. The results show that the algorithm is more effective at finding global optimal solutions than general purpose global optimization solvers tested.

Keywords: supply chain optimisation, Planning, global MINLP

References

Lara, C.L., Grossmann, I.E., "Global Optimization for a Continuous Location-Allocation Model for Centralized and Distributed Manufacturing," in *Proceedings of 26th European Symposium on Computer Aided Process Engineering*, June 2016, Portorož, Slovenia.

Brimberg, J., Hansen, P., Mladonovic, N., Salhi, S., "A survey of solution methods for the continuous location allocation problem," *International Journal of Operational Research*, vol.5, pp. 1–12, Jan. 2008.

Lara, C.L., Trespalacios, F., Grossmann, I.E., "Global Optimization Algorithm for Capacitated Multi-facility Continuous Location Allocation Problems", *Submitted for publication*, 2017.

Optimal Integrated Facility for Waste Processing

Edgar Martín-Hernández^a, Apoorva M. Sampat^b, Victor M. Zavala^b, Mariano Martín^{a*}

^a *Department of Chemical Engineering. University of Salamanca. Pza. Caidos 1-5, 37008 Salamanca, Spain.*

^b *Department of Chemical and Biological Engineering. University of Wisconsin-Madison, 1415 Engineering Dr. Madison, WI 53706, USA.*

mariano.m3@usal.es

Abstract

An integrated facility for the processing of waste to recover power and high value-added products is conceptually designed. The process is based on the anaerobic digestion of different types of manure (cattle, pig, poultry, and sheep). The products obtained in the process are biogas composed of methane and carbon dioxide, and a nutrient-rich effluent. The biogas produced is cleaned and used in a gas turbine to produce electrical power while the hot flue gas obtained from combustion is fed to a steam turbine to produce additional power. The nutrient-rich effluent can be processed to recover the nutrients using technologies such as filtration, coagulation, centrifugation, and struvite precipitation. The design problem is formulated as a Mixed-Integer Nonlinear Program (MINLP), which incorporates detailed physical and economic evaluation models. We have found that struvite production in fluidized beds is the technology of choice to recover nutrients from all manure sources. It was found that the power produced strongly depends on the manure composition and exhibits high cost variability. In particular, it was found that the investment cost of the power produced ranges from 4,000 €/kW in case of poultry manure to 25,000 €/kW in the case of cattle or pig manure.

Keywords: anaerobic digestion, manure, power production, optimization

1. Introduction

Countries across the globe generate large amounts of waste. While many of these waste streams can be used as a source of power and chemical products, identifying suitable cost-effective technologies to achieve this is challenging. Anaerobic digestion (AD) is deemed as a promising technology to treat these residues to produce biogas, which can be used as a source of energy or chemicals (Hernández et al., 2017). However, AD technologies also generate a nutrient-rich residual stream called digestate that must be treated to prevent soil and water contamination (Sampat et al., 2017). Diverse processing technologies exist to achieve this.

In this work, a systematic design framework is proposed to optimize the simultaneous production of energy from biogas obtained by the AD of cattle, sheep, poultry, and pig manure, along with the recovery of nitrogen and phosphorous from the digestate. The proposed framework determines the optimal technology configuration, equipment

sizing, and operational conditions for various compositions of manure and digestate and revenues for biogas, electricity, and fertilizer.

2. Process superstructure

The proposed process consists of four sections: biogas production, biogas purification, electrical power generation, and nutrient recovery from the digestate. The biomass together with water and nutrients (manure slurry) are fed to a bioreactor (1), where the mixture is anaerobically digested to produce biogas and a decomposed substrate (digestate). The biogas is sent to the purification section (2) to remove H_2S in a fixed-bed reactor and to eliminate CO_2 and traces of NH_3 in a pressure swing adsorption (PSA) system. The biogas is then fed to a gas turbine (3) and the flue gas used to produce steam for a steam turbine (4). The digestate can be processed through a number of technologies to remove nitrogen and phosphorous. Several options are considered such as filtration (5), centrifugation (6), coagulation (7), and struvite production using either a fluidized bed reactor (FBR) (8) or a continuous stirred tank reactor (CSTR), (9). Figure 1 shows a scheme of the process. Four different types of manure (cattle, pig, sheep, and poultry) are processed through this to evaluate the power production and the best nutrient recovery technology.

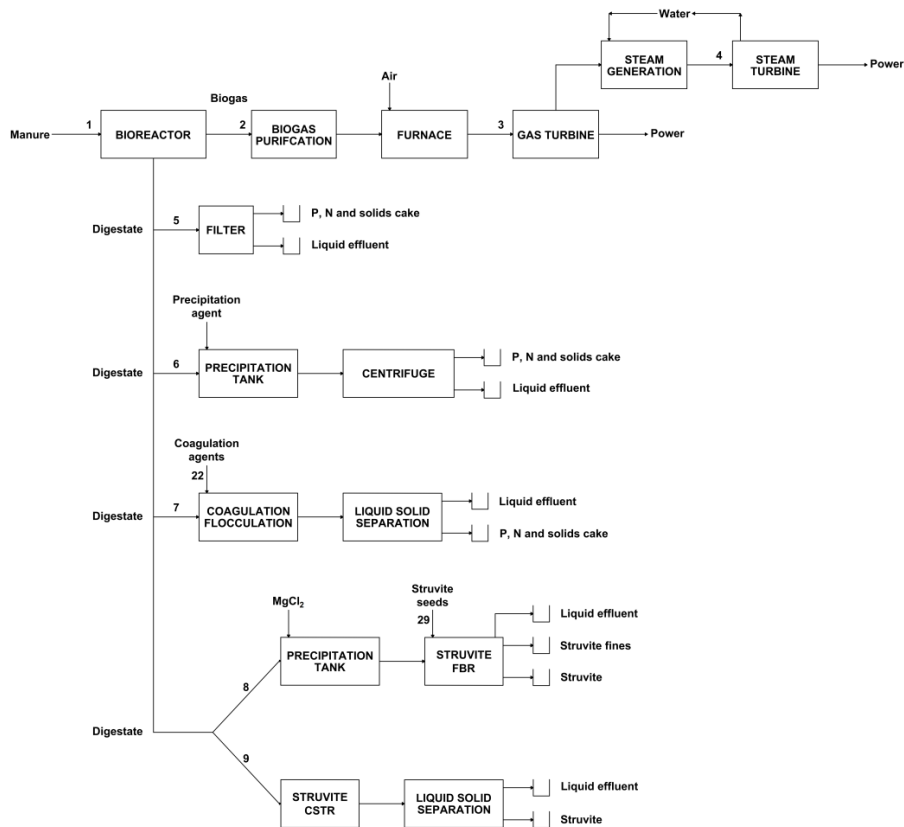


Figure 1.- Superstructure for manure processing to power and nutrients.

3. Modelling issues

The performance of the different unit operations is evaluated in the process by using detailed models that comprise mass and energy balances, thermodynamics, chemical and vapor-liquid equilibria, and product yield calculations based on experimental data.

- The anaerobic reactor: is modeled by using mass balances of the species involved in the production of biogas and digestate. Inorganic nitrogen, organic nitrogen, sulfur, carbon, and phosphorus balances are formulated by using the composition of volatile solids in manure (León and Martín, 2016)

- The gas purification section consists of a number of stages to remove H_2S , CO_2 , and NH_3 . The removal of H_2S is carried out in a bed of Fe_2O_3 that operates at 25-50 °C producing Fe_2S_3 . CO_2 is adsorbed using a packed bed of zeolite 5A. The typical operating conditions for PSA systems are low temperature (25 °C) and moderate pressure (4.5 bar). Together with CO_2 , ammonia and water are adsorbed.

- The gas turbine is modeled as a compression section for the biogas and another one for the air, a combustion chamber modeled as adiabatic and an expansion considered polytropic with a coefficient equal to 1.3, computed offline in CHEMCAD[®], and an efficiency of 85%.

- The steam turbine is modeled as a regenerative Rankine cycle. Surrogate models for the enthalpies and entropies as a function of the pressures and temperatures allow the optimization of the operating conditions (Martín and Martín, 2013).

- Four different technologies are considered for the recovery of nitrogen and phosphorous, namely, filtration, centrifugation, coagulation, and struvite production using either a stirred tank or fluidized bed reactors. These processes have been modeled using mass balances, removal yields, and equipment and operating cost correlations:

- Filtration: This technology consists of a filter that contains a reactive medium to help remove phosphorus. P removal using reactive filtration takes place through various mechanisms depending on the characteristics of the filter media. Five different types of filter media have been evaluated: wollastonite, Polonite[®], Filtra P[®], dolomite, and metallurgical slag. The removal yield of P and N for the different filter media is shown in Table 1.

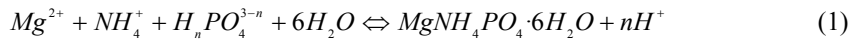
Table 1. Recovered P and N yield for different filter media.

Media/Nutrient	Polonite	Filtra P	Wollastonite	Dolomite	Metal slag
P (% recovered)	96.7 ^a	98.2 ^a	51.1 ^a	44.0 ^b	85.6 ^a
N (% recovered)	18.0 ^c	50.0 ^c	70.0 ^d	50.0 ^c	67.0 ^f
	<i>a: Gustafsson et al., 2008.</i>	<i>c: Kietlinska and Renman, 2005.</i>			<i>e: Aziz et al., 2004.</i>
	<i>b Pant et al., 2001.</i>	<i>d: Lind et al., 2000.</i>			<i>f: Yang et al., 2009</i>

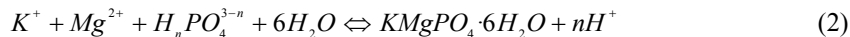
- Coagulation: Nutrients are recovered together with other sedimented solids by clarification. Phosphorus is removed mainly in the form of metal hydroxides, which is the dominant process at typical plant pH values. Nitrogen elimination is related to the removal of the colloidal matter (Aguilar et al., 2002). Different coagulation agents are considered: $FeCl_3$, $Fe_2(SO_4)_3$, $Al_2(SO_4)_3$, and $AlCl_3$. The removal efficiency achieved is similar for the different coagulant agents, with values up to 99% for phosphorus and 57% for nitrogen (Aguilar et al., 2002).
- Centrifugation: It separates solid and liquid phases to recover nutrients from the digestate. The advantage of this system is the simple equipment used. Precipitant agents can be added to improve the removal efficiency significantly. Previous studies show that an appropriate mixture of $CaCO_3$ and $FeCl_3$ promotes nutrients recovery. In particular, a ratio of 0.61 kg $CaCO_3$ and 0.44 kg of $FeCl_3$ per kilogram

of total solids in the raw material inlet stream, achieves a removal efficiency up to 95% and 47 % for P and N respectively (Meixner et al., 2015).

- Struvite production: P and N can be recovered from digestate through the formation of struvite, which is a phosphate mineral with a chemical formula of $MgNH_4PO_4 \cdot 6H_2O$. The advantage of this technology is that struvite is a solid with a high nutrients density, it is easy to transport, and it can be used as a slow-release fertilizer without any post-processing (Doyle and Parsons, 2002). The removal of nutrients via struvite precipitation follows the reaction shown below, which requires the addition of $MgCl_2$ and which results in the production of struvite crystals:



Due to the presence of potassium in the digestate, together with struvite, another product called potassium struvite or K-Struvite, is also produced that affects the amount of $MgCl_2$ used. In this case, the ammonia cation is substituted by the potassium cation.



Because the formation of struvite is favoured over the formation of K-Struvite, it is considered that only 15% of the potassium contained in the digestate will react to form K-Struvite (Zeng and Li, 2006). The mass balance for the reactors is given by the stoichiometry of the reactions above.

Two different types of reactors can be used to obtain struvite, either a stirred tank (CSTR) or a fluidized bed reactor (FBR). In case of the FBR, struvite is recovered from the bottoms and the liquid is processed through a hydrocyclone to avoid discharging fines. In the case of CSTR tanks, a centrifuge is used to recover the struvite. Seeding can be used to help grow the crystals (Doyle and Parsons, 2002). Due to the substantial increase in the struvite formation yield, the addition of struvite seeds in both cases is selected. The reaction takes place at about 27°C, with the addition of $MgCl_2$ at a concentration of 57.5 mg/dm³ (Zhang et al., 2014). A Mg:P molar ratio of 2 (Bhuiyan et al., 2008) is used.

The problem is formulated as an MINLP for the different filter media and coagulant agents. In the first stage, the detailed model is solved to determine the best filter and coagulant agent using economic cost functions. For that purpose the benefit obtained is maximized the benefit including the income obtained by selling the recovered nutrients minus the operational cost, which are function of recovered P and N yields, equipment cost and final cake moisture content, among other aspects.

Next, the superstructure is optimized to determine the optimal power and nutrient recovery technologies. Since the superstructure model is highly non-linear, to avoid integer variables and discontinuities when deciding on the selection digestate treatment technologies smooth approximations and continuous reformulations have been developed. The resulting problems are NLPs with 5,000 variables and 4,000 equations written in GAMS[®] that are solved using a multistart initialization procedure with CONOPT as preferred solver.

4. Results

4.1.-Operating conditions

In the case of cattle, pig, and poultry manure, the gas exhaust from the gas turbine reaches a temperature of 2,400 °C and a pressure of 8.2 bar before expansion. However, sheep manure shows different values. In particular, while the exhaust temperature is similar, the pressure is 15.6 bar, almost twice the value found for the rest of the raw materials. Furthermore, the flue gas exits the turbine at 300 °C below that when the rest of the manure types are used. This flue gas will later be used within the heat integration step. Moreover, while the high-pressure section of the steam turbine operates at 125 bar for cattle, pig, and poultry manure, in case of sheep manure it operates at 95 bar. This is related to the lower gas temperature from the gas turbine since the overheated steam needs to be produced using that stream. Intermediate and low pressures are the same in the steam turbine using any of the manure types, but the exhaust pressure of the steam is higher in case of sheep manure. Table 2 shows the products obtained from the various manure types, power, biogas, and digestate. Poultry waste is more efficient towards power production, due to its higher organic content. In all cases the FBR reactor for the production of struvite is the selected technology to recover N and P. In Table 2 it is possible to see the effect of the fact that cattle and pig manure are mostly liquids, since most of the product is digestate, almost 98%, while the use of poultry or sheep manure reduces the production of digestate to 75% and 88% respectively, increasing the production of biogas and power.

Table 2.- Process optimization results for considered manures

Manure	Power (kW)	Biogas comp. (CH ₄ /CO ₂ ratio)	Digestate treatment technology	Product recovered	Biogas / Manure ratio	Digestate / Manure ratio
Cattle	2,612	0.816	FBR struvite	Struvite	0.0208	0.9794
Pig	2,612	0.816	FBR struvite	Struvite	0.0208	0.9794
Poultry	31,349	0.818	FBR struvite	Struvite	0.2499	0.7526
Sheep	14,106	0.818	FBR struvite	Struvite	0.1217	0.8795

4.2.-Economic evaluation

Table 3- Electricity production cost and net present value (NPV) for the facility considering different raw materials

Raw material	Annual production costs (M€/y)	Electricity production cost (€/kWh)	Net Present Value
Cattle manure	12.04	0.45	-1.93x10 ⁷
Pig manure	12.07	0.45	-1.96x10 ⁷
Poultry manure	25.51	0.03	2.85x10 ⁸
Sheep manure	15.53	0.10	5.46x10 ⁷

To estimate the production cost, 20 years of plant life is considered, with a capacity factor of 98%. The equipment amortization represents at least 43% of the production costs. This share increases up to 60% in the case of poultry manure. As the investment is lower, the annual cost for other items is almost constant and their contribution to the electricity cost plays a more important role. The purchase of chemicals is the second most important contribution to the cost of electricity with a share of up to 23% for the use of cattle or pig manure and down to 16 % in the case of sheep manure. The electricity production costs obtained are presented in Table 3. The NPV has also been calculated as a measure of the project profitability. An electricity sale price of 0.06 €/kWh is assumed following current European values, to compare the profitability of this project at a discount rate of 3 %, typical in Spain.

5. Conclusions

In this work, integrated facilities for the production of biogas-based electrical power and fertilizers from manure have been designed. A two-step procedure has been used. First, the individual detailed models for each digestate treatment technology are used to formulate MINLP models aiming at selecting the best configuration for that technology: the best precipitation agent and filter media. In the second step, a superstructure is formulated including the best configuration of each technology. The results show that FBR technologies are preferred to recover nutrients. Furthermore, for poultry and sheep manure it is possible to produce electricity at a competitive price. The investment cost is highly dependent on the water and organic content of the manure type, ranging from 70 M€ to 208 M€. However, for these cases of high investment cost, the production cost of power is the most competitive due to the large production capacity. Competitive values of 4,000 €/kW for poultry manure are obtained, due to the highly concentrated manure, while large values of 25,000 €/kW installed are reported in case of cattle or pig manure.

6. References

- A. Kietlinska, G. Renman, 2005. An evaluation of reactive filter media for treating landfill leachate. *Chemosphere* 61, 933–940.
- A.M. Sapat, E. Martín, M. Martín, V.M. Zavala, 2017. Optimization Formulations for Multi-Product Supply Chain Networks. *Comp. Chem. Eng.* 104, 296–310.
- B. Hernández, E. León, M. Martín, 2017. Bio-waste selection and blending for the optimal production of power and fuels via anaerobic digestion. *Chem. Eng. Res. Des.*, 121, 163–172.
- B.B. Lind, Z. Ban, S. Bydén, 2005. Nutrient recovery from human urine by struvite crystallization with ammonia adsorption on zeolite and wollastonite. *Bioresour. Technol.* 73, 169–174.
- D. J. Doyle, S.A. Parsons, 2002. Struvite formation, control and recovery. *Water Res.* 36, 3925–3940.
- E. León, M. Martín, 2016. Optimal production of power in a combined cycle from manure based biogas. *Energy Conv. Manag.* 114, 89–99.
- H.A. Aziz, M.N. Adlan, M.S. Mohd Zahari, S. Alias, 2004. Removal of ammoniacal nitrogen (N-NH₃) from municipal solid waste leachate by using activated carbon and limestone. *Waste Manage. Res.* 22, 371–375.
- H.K. Pant, K.R. Reddy, E. Lemon, 2001. Phosphorus retention capacity of root bed media of sub-surface flow constructed wetlands. *Ecol. Eng.* 17, 345–355.
- J. Yang, S. Wang, Z. Lu, J. Yang, S. Lou, 2009. Converter slag–coal cinder columns for the removal of phosphorous and other pollutants. *J. Hazard. Mater.* 168, 331–337.
- J.P. Gustafsson, A. Renman, G. Renman, K. Poll, 2008. Phosphate removal by mineral-based sorbents used in filters for small-scale wastewater treatment. *Water Res.* 42, 189–197.
- K. Meixner, W. Fuchs, T. Valkova, K. Svardal, C. Loderer, M. Neureiter, G. Bochmann, G. B. Drog, 2015. Effect of precipitating agents on centrifugation and ultrafiltration performance of thin stillage digestate. *Sep. Pur. Technol.* 145, 154–160.
- L. Martín, M. Martín, 2013. Optimal year-round operation of a Concentrated Solar Energy Plant in the South of Europe App. *Thermal Eng.* 59, 627–633.
- L. Zeng, X. Li, 2006. Nutrient removal from anaerobically digested cattle manure by struvite precipitation. *J. Environ. Eng. Sci.* 5, 285–294.
- M.I. Aguilar, J. Sáez, M. Lloréns, A. Soler, J.F. Ortuño, 2002. Nutrient removal and sludge production in the coagulation-flocculation process. *Water Res.* 36, 2910–2919.
- M.I.H. Bhuiyan, D.S. Mavinic, F.A. Koch, 2008. Phosphorus recovery from wastewater through struvite formation in fluidized bed reactors: a sustainable approach. *Water Sci. & Technol.* 57, 175–181.
- T. Zhang, P. Li, C. Fang, R. Jiang, 2014. Phosphate recovery from animal manure wastewater by struvite crystallization and CO₂ degasification reactor. *Ecol. Chem. Eng. S.* 21, 89–99.

Assessing Energy and CO₂ Emission Reduction from Ammonia Production by Chemical Looping as Innovative Carbon Capture Technology

Dora-Andreea Chisalita, Letitia Petrescu, Ana-Maria Cormos,
Calin-Cristian Cormos *

*Babes-Bolyai University, Faculty of Chemistry and Chemical Engineering,
Arany Janos 11, Postal code: RO-400028, Cluj-Napoca, Romania*

cormos@chem.ubbcluj.ro

Abstract

The paper evaluates the technical performances of an ammonia production plant having an output of 2500 t/day. Mass and energy integration aspects of natural gas conversion (conventional steam reforming, autothermal reforming and chemical looping), carbon capture unit by gas-liquid and gas-solid systems, ammonia production and associated heat recovery and their influence on the overall ammonia production performances are discussed in detail. The ammonia production concepts were modelled and simulated using a process flow modelling software (ChemCAD). The obtained simulation results were used to assess the overall technical and environmental indicators of the ammonia production plant. Three case scenarios with CO₂ capture were considered for investigation. Industrial and experimental data were used to validate the models. The results show that the chemical looping system has significant advantages compared to the natural gas reforming technologies coupled with the gas-liquid absorption technology such as: lower specific fossil energy consumption (8.3 MWth/t NH₃ vs. 9.6 - 9.9 MWth/t NH₃), higher carbon capture rate (99.9 % vs. 60 – 90 %), lower specific CO₂ emissions (7 kg/t NH₃ vs. 230 - 900 kg/t NH₃ for plants with CO₂ capture based on gas-liquid absorption and about 2000 kg/t NH₃ for plant without CO₂ capture), lower plant complexity. The presented technical analysis of the different ammonia production cases shows very promising options to significantly reduce the fossil energy consumption as well as the carbon footprint of this important industrial sector.

Keywords: Ammonia production; Carbon Capture, Utilisation and Storage (CCUS) technologies; Chemical looping; Computer Aided Process Engineering (CAPE) tools.

1. Introduction

Reducing the energy consumption and CO₂ emissions from heat and power sector as well as from other energy-intensive industrial applications (e.g. metallurgy, cement, petro-chemistry) is of paramount importance today in order to satisfy the 2 °C pathway by 2050. Carbon capture and storage (CCS) is, at present, the most suitable option for capturing CO₂ from carbon-intensive industrial processes which can arise either from energy consumption, either from the process itself (raw materials undergo chemical or physical transformations in which CO₂ is formed as by-product) (IEA, 2016).

Ammonia is the second largest inorganic chemical produced worldwide (after sulphuric acid) being used predominantly within fertilizer industry, being an indispensable

chemical in meeting society's needs. On the other hand, ammonia production is highly carbon-intensive, relying on fossil fuels both for energy production and as feedstock for H₂ synthesis, accounting for about 1.5 % of total anthropogenic CO₂ emissions.

Today, ammonia is produced in more than 90 % of the cases following the Haber-Bosch synthesis process in which hydrogen and nitrogen are reacted over an iron promoted catalyst at high temperatures and pressure. Nitrogen is taken from air, while hydrogen is largely obtained from catalytic reforming of natural gas (48 %) and in smaller fractions from oil reforming (30 %), coal gasification (18 %) and water electrolysis (4 %) (Abbasi and Abbasi, 2011). The state of the art technology for hydrogen production used industrially in ammonia production facilities is steam-methane reforming (SMR). The SMR-based ammonia process releases into the atmosphere about 1.5 tonnes of CO₂ per tonne of ammonia (without considering urea production) according to Bicer et al. (2016). Although water electrolysis-based processes have the prospect of introducing a low-carbon hydrogen production pathway, they are more energy intensive as well as more resource and cost-demanding than the currently used fossil energy carriers.

Among the various carbon capture methods suitable to be implemented in an ammonia production plant, two reactive gas-liquid and gas-solid options are evaluated in this paper in pre-combustion CO₂ capture configurations. The first evaluated CO₂ capture option (considered as a reference case) is based on gas-liquid absorption using chemical solvents (methyl-diethanol-amine - MDEA). The second capture option is based on innovative chemical looping system (using iron oxides as oxygen carrier) for pre-combustion CO₂ capture. As key advantages of chemical looping cycle in comparison to gas-liquid absorption one can mention: better high temperature heat recovery potential and improved energy conversion efficiency with subsequent reduction of fossil fuel consumption and CO₂ emissions. The carbon capture rate for chemical looping system is almost total (99.9 %) in contrast with the reforming technologies (60 % for conventional steam reforming and 90 % for autothermal reforming).

2. Cases description and modeling assumptions

There are different carbon capture options suitable for industrial applications such as: absorption (chemical or physical), adsorption and more advanced capture technologies such as chemical looping combustion. In this paper, different ammonia production routes were considered leading to the development of three case studies:

Case 1: Ammonia production with SMR and MDEA-based CO₂ capture;

Case 2: Ammonia production with ATR and MDEA-based CO₂ capture;

Case 3: Ammonia production with chemical looping.

A schematic representation of the evaluated ammonia synthesis processes is depicted in Figure 1 and a description of each case is detailed below.

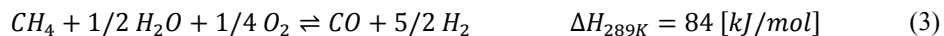
Case 1 describes a conventional ammonia production process with hydrogen being produced from steam methane reforming (SMR). SMR is based on an equilibrium limited and highly endothermic reaction (Reaction 1), for which the required energy is supplied by burning additional natural gas in a secondary reformer. The obtained process gas contains up to 30 % CO and is converted to CO₂ and H₂ through the water gas shift (WGS) reaction (Reaction 2). In a next step, CO₂ is removed by gas-liquid chemical absorption using MDEA as solvent.





Chemical absorption of CO₂ by MDEA is described by an absorption-desorption cycle that takes place in two interconnected columns: absorber and desorber. The sour gas to be treated is fed into the bottom section of the absorber where it is contacted counter-currently with lean chemical solvent which gradually absorbs CO₂. The CO₂ rich solvent is then pumped to the top of the desorber column where it is regenerated by increasing the temperature and releasing the captured CO₂. Although chemical absorption using alkanolamines is a mature technology being already implemented industrially in ammonia plants, the process is highly energy intensive, more specifically the thermal energy required for the amine's solution regeneration leads to increased operating cost and reduces the energy efficiency of the plant (Sreenivasulu, 2015).

Case 2 is to a large extent similar with Case 1, containing the same process steps: desulphurization, reforming, WGS and CO₂ removal by MDEA, with the exception of the reforming section which in this case is based on autothermal reforming (ATR) instead of SMR. ATR is another catalytic reforming technology, still under development, that combines the SMR with partial oxidation of methane in the same step according to Reaction (3). In this case, the heat required for the endothermic reaction reaction is generated in-situ by the partial oxidation of the fuel.



Compared to the SMR, ATR has an improved methane conversion as it operates at higher temperatures (600-1050 °C vs. 500-900 °C); the main difference between the two reforming technologies is that SMR uses oxygen as a heat source in a secondary reformer, while ATR directly combusts part of the methane with oxygen.

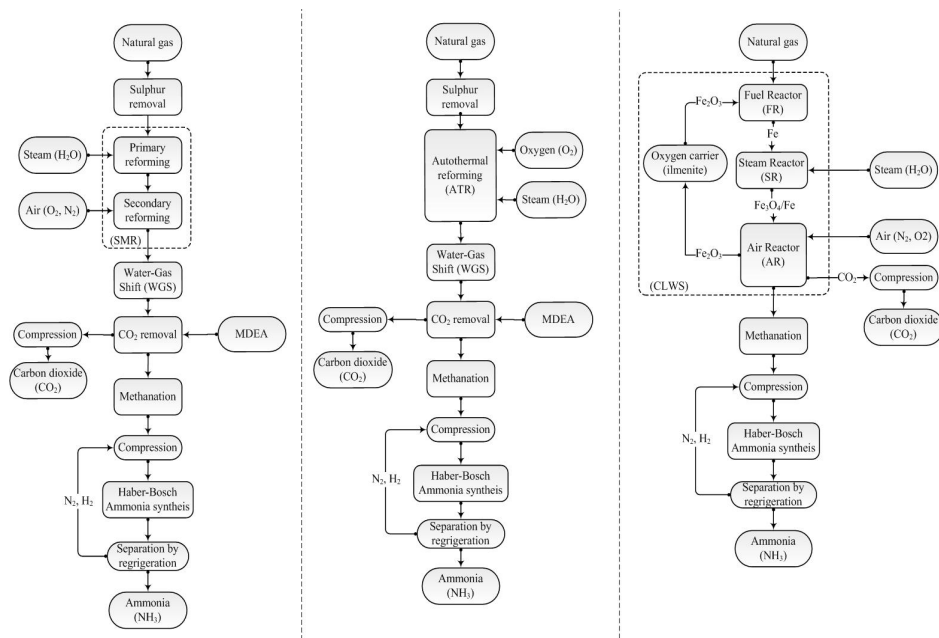


Figure 1. Ammonia production routes: Case 1 (left), Case 2 (middle), Case 3 (right)

Case 3 integrates hydrogen production and CO₂ capture in a single unit by incorporating chemical looping, a new emerging technology that received a lot of attention in the past years, into the ammonia production process. Fuel conversion takes place using the oxygen released by an oxygen carrier (OC) that circulated between two interconnected reactors: a fuel reactor (FR) where the fuel is converted to CO₂ and H₂O and an air reactor (AR) where the OC is regenerated by oxidation with air. As the air and fuel never get mixed, the combustion products are no longer diluted with nitrogen and thus an almost pure stream of CO₂ can be obtained by condensing the H₂O, eliminating a highly energy intensive separation unit. Chemical looping can also be used for hydrogen production, either by integration with the conventional reforming technologies (supplying oxygen for ATR or heat in SMR) either by taking advantage of the potential of some OC to be oxidized by steam to produce hydrogen.

The latter option is referred by Abad (2015) as chemical looping with water splitting (CLWS) and consists in replacing totally or partially the oxidation taking place in the AR with oxidation with steam in an additional steam reactor. Iron-based oxygen carriers are suitable for CLWS as they have high reactivity with the selected fuel and high conversion towards syngas production. Also they possess multiple oxidation states in order to be capable to oxidize the fuel in the fuel reactor and being partially oxidized by steam in the steam reactor, according to the following reactions (Fan, 2010):

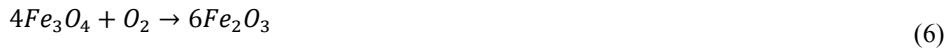


Table 1. Design and modeling assumption of evaluated ammonia plant concepts

Process Unit	Assumptions
Air separation unit (ASU)	100 % N ₂ purity, 98.5 % O ₂ purity @ 2 bar pressure ASU power consumption: 200 kWh/t oxygen
Sulphur removal unit	>98 % H ₂ S removed
Steam methane reforming (SMR)	500-900 °C; 27-29 bar; ~3.2 steam to NG ratio; ~55 % additional NG burned in the secondary reformer
Autothermal reforming (ATR)	600-1050 °C; 28-30 bar; ~0.15 steam to NG ratio; ~0.5 O ₂ to NG ratio
MDEA CO ₂ capture unit	50 wt% MDEA solution; Absorption/desorption columns: 30/10 stages
Chemical looping unit	oxygen carrier ilmenite; air reactor temperature 1000°C; fuel reactor temperature 700 °C; steam reactor temperature 700°C; generated steam pressure 28 bar;
CO ₂ compression	120 bar CO ₂ delivery pressure; 85 % compressor efficiency
Water gas shift reactors	High temperature shift (HTS): 400-450 °C; 27-29 bar Low temperature shift (LTS): 250-260 °C; 26-28 bar
Methanation reactor	50-300 °C; 25-16 bar; 99 % CO conversion

A summary of the modeling assumption considered for all case scenarios investigated is presented in Table 1. All case scenarios produce ammonia through the Haber-Bosch synthesis process having an output of 2500 t/day; nitrogen is obtained from the atmosphere by cryogenic air separation, this being the most efficient and cost-effective method to produce nitrogen at industrial scale. After the CO₂ capture unit, in all cases, a final removal of carbon oxides is completed by a methanation step after which the actual ammonia synthesis is carried out in the Haber-Bosch process.

3. Results and discussions

The investigated case scenarios were modeled and simulated using the process simulator ChemCAD. The developed models were validated by comparison to industrial data (Voldsund et al., 2016). Thermal integration by pinch methodology was performed for all considered designs for maximizing the overall energy efficiency (10 °C was considered as minimum temperature difference between the hot and cold streams). Figure 2 depicts the hot and cold composite curves for ammonia synthesis coupled with the chemical looping processes (Case 3).

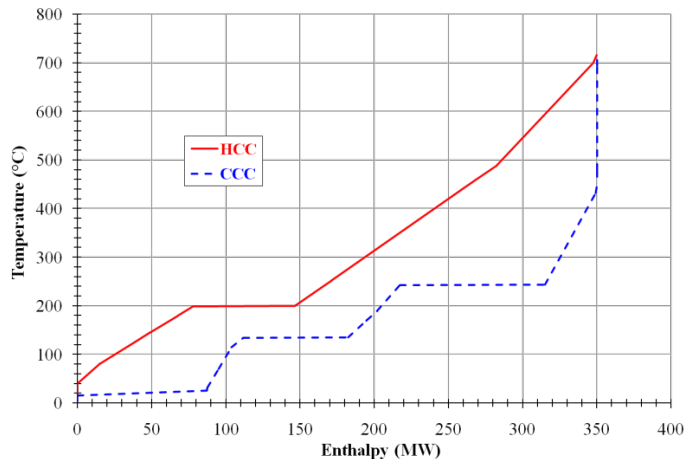


Figure 2. Hot and cold composite curves for the chemical looping unit coupled with ammonia synthesis (Case 3)

The main technical and environmental indicators of the evaluated scenarios are listed in Table 2. Looking at the results, one can notice that coupling ammonia production with chemical looping leads to a significant reduction in CO₂ emissions of about 99 % compared to the conventional ammonia production route and 64 % compared to MDEA-based capture coupled with ATR (6.43 kg/t NH₃ vs. 903.91-231.82 kg/t NH₃). Also, employing chemical looping into the ammonia production route brings a lower specific fossil energy consumption of about 14-16 % compared to Case 1 and Case 2. Although the ancillary power consumption for the chemical looping coupled ammonia production (Case 3) is about 1.6 % higher than the conventional ammonia production route (Case 1) and 1.2 % higher than in Case 2, it is covered by the additional energy production obtained from steam generation using recovered heat from the chemical looping process streams. Besides ammonia output, there is also an oxygen output for Cases 1 and 3, in comparison with Case 2 where oxygen is burned in the ATR reactor providing the heat required to drive the endothermic reforming reaction.

Table 2. Overall plant performance

Main Plant Data	Units	Case 1	Case 2	Case 3
Ammonia output	t/h	104.16	104.16	104.16
Fuel (NG) thermal energy	MW _{th}	1,025.62	1,004.46	865.65
Gross power output	MW _e	53.63	70.41	113.51
Ancillary power consumption	MW _e	53.63	70.41	84.16
Net power output	MW _e	0.00	0.00	29.35
Oxygen output	t/h	25.80	0.00	25.80
CO ₂ output (emissions)	t/h	94.15	24.14	0.67
Carbon capture rate	%	60.00	90.00	99.90
Specific CO ₂ emissions	kg/t NH ₃	903.91	231.82	6.43
Specific fossil energy consumption	MW _{th} /t NH ₃	9.84	9.64	8.31

4. Conclusions

This paper evaluates the energy and CO₂ emission reduction from an ammonia production plant considering three hydrogen production paths (conventional steam methane reforming, autothermal reforming and chemical looping) and two carbon capture technologies (gas-liquid absorption by MDEA and iron-based chemical looping). As the results show, the chemical looping system has key advantages compared to the natural gas reforming technologies coupled with CO₂ capture by gas-liquid absorption, such as lower specific fossil energy consumption, higher carbon capture rate, lower specific CO₂ emissions and lower plant complexity (the innovative chemical looping technology integrates in a single unit both hydrogen production and CO₂ capture). As overall conclusion, the chemical looping option is very promising for reducing significantly the carbon footprint and the fossil energy consumption of this important industrial sector with possible application in other industrial sectors too.

Acknowledgement

This work was supported by a grant of Ministry of Research and Innovation, CNCS – UEFISCDI, project ID PN-III-P4-ID-PCE-2016-0031, within PNCDI III.

References

- A. Abad, 2015, Chapter 15: Chemical looping for hydrogen production, Calcium and Chemical Looping Technology for Power Generation and Carbon Dioxide (CO₂) Capture, Woodhead Publishing Series in Energy, Cambridge, UK
- T. Abbasi, S.A. Abbasi, 2011, Renewable hydrogen: Prospects and challenges, Renewable and Sustainable Energy Reviews, 15, 3034-3040
- Y. Bicer, I. Dincer, C. Zamfirescu, G. Vezina, F. Raso, 2016, Comparative life cycle assessment of various ammonia production methods, Journal of Cleaner Production, 135, 1379-1395
- L.S. Fan, 2010, Chemical looping systems for fossil energy conversions, AIChE Wiley, Canada
- IEA, 2016, 20 Years of Carbon Capture and Storage - Accelerating future deployment, France
- B. Sreenivasulu, D.V. Gayatri, I. Sreedhar, K.V. Raghavan, 2015, A journey into the process and engineering aspects of capture technologies, Renewable and Sustainable Energy Reviews, 41, 1324-1350
- M. Voldsund, K. Jordal, R. Anantharaman, 2016, Hydrogen production with CO₂ capture, International Journal of Hydrogen Energy, 41, 4969-4992

Use of excess heat from ethylene recycling in a low-density polyethylene production plant

Rodolfo D.C. Matos^a, Isabel M. João^{a,b}, João M. Silva^{a,c,*}

^a*ISEL - Instituto Superior de Engenharia de Lisboa, R. Cons. Emídio Navarro, 1959-007 Lisboa, Portugal*

^b*CEG-IST, Instituto Superior Técnico, Av. Rovisco Pais, 1049-001 Lisboa, Portugal*

^c*CATHPRO-CQE, Instituto Superior Técnico, Av. Rovisco Pais, 1049-001 Lisboa, Portugal*

jmsilva@deq.isel.ipl.pt

Abstract

The recovery of the wasted heat is an effective way of improving the energy efficiency of industry sites and can contribute to the reduction of the operating costs and the CO₂ emissions. In the production of low density polyethylene, the polymerisation reaction is carried out with a large excess of ethylene at very high pressure. The excess ethylene is separated at an intermediate pressure (around 280 bar and 310 °C) and then it is recycled. In this recycle, the stream is cooled in several steps to temperatures close to 35 °C before being recompressed. In some units, the first cooling is carried out with air coolers up to temperatures around 130 °C. In a unit with a recycle of 33 t/h, this cooling corresponds to releasing to the atmosphere about 4.6 MW of thermal power. We present a study of different alternatives for the use of this excess heat. We studied the implementation of a refrigeration cycle by absorption with LiBr/H₂O, the production of steam and the electricity generation by Rankine and Kalina cycles. The Aspen HYSYS process simulator was used to study the different alternatives. The capital cost was estimated for each of the evaluated options as well as the benefits expected to be obtained. In the study conditions, the absorption refrigeration cycle is the best solution presenting a return period of 3 years.

Keywords: excess heat, energy efficiency, economic evaluation.

1. Introduction

The comfort brought by technological evolution is reflected on population growth. The more people there are the more needs and demands are to satisfy, consequently increasing energy expenditure. The smashing majority of energy is obtained from non-renewable feedstock like coal, natural gas, and oil (BP, 2017). However, their finite nature, the increasing CO₂ concentrations in atmosphere and the several conflicts between nations shouldn't be overlooked. The development of both renewable energy and efficiency technologies are fashionable and useful ways to reduce fossil fuel dependency and extend its life expectancy. Heat and power integration fits the latest category (Walsh and Thornley, 2012). Although there are several definitions to excess heat, here it is treated as suggested by Viklund and Johansson (2014): a sub-product of an industrial activity, which may or may not be able to recover internally through thermodynamic optimisation of a process.

In 2010, approximately 11.3 EJ out of 26.2 EJ were rejected by the EU as industrial waste heat, which represents 43% of the total energy produced. Motivated by the recovery of the economic crisis and sustainable growth, the recovery of excess heat has become an important goal in increasing energy efficiency (Viklund and Johansson, 2014).

2. Case study

A LDPE production plant consisting of two production lines has served as basis to the study. In each line, the excess ethylene recycles at a nominal flow of 33 t/h, at 310 °C and 280 bar. During the recycling process, it is intended to reduce the stream temperature to approximately 35 °C before recompression. The first step of the cooling is taken out with an air cooler, which cools the stream down to 130 °C, releasing 4.6 MW of heat per production line.

Globally, the needs of the LDPE plant are chilled water where 4.535 MW of energy are consumed, a minimum 2.2 t/h of high pressure steam (40 bar), a maximum 4 t/h of low pressure steam (7 bar) and 385 t/h of hot water.

The heat recovery hypothesis studied throughout this work consisted strictly in commercially available technologies to recover this heat. Two power production cycles, Rankine (Chen et al., 2010) and Kalina (Rodríguez et al., 2013), a LiBr/water absorption system (Srihirin et al., 2001) and the production of hot utility by heat exchanging were explored with the aid of the simulator Aspen HYSYS.

3. Results and discussion

3.1. Power cycles

A total of 23 fluids, most of which being on the review done by Chen et al. (2010), were tested on these simulations. Property packages were chosen based on the minimum squared error between the heat of vaporisation and the property package data for each fluid, on an adequate range of pressures. For ethylene, being in supercritical state, the property for comparison was the heat capacity.

3.1.1. Rankine cycle

In the first part of this study, condensation had bottom limits of 50 °C and 1 bar, and evaporation had the upper limit of 290 °C (assuming $\Delta T_{\min} = 20^\circ\text{C}$) and the critical pressure of the working fluid. Another restriction is that no fluid can condense inside the turbine. The results of the best fluids are shown in Table 1, with R-601 (pentane) being the most promising fluid.

After selecting the most promising fluid, ethylene stream cooling was bottom bounded at 130 °C, to respect the original process restrictions. Condensation was also allowed at 45 °C, using cooling water (CW) from 25 to 35 °C. After that, an integrated Rankine cycle was built to test its own integration advantages. The integration allows the stream sited before the evaporator to heat the stream before the condenser. This requires less CW to condensate more working fluid (Table 2).

Table 1 – Preliminary performance results for the best fluids tested in the simple Rankine cycle.

Fluid	T _{condenser} (°C)	P _{condenser} (bar)	T _{max} (°C)	P _{evaporator} (bar)	Fluid flow (t/h)	CW flow (t/h)	COP ¹	W _{out} (kW)
R-245ca	45	2.04	171	37	64.2	344	0.132	815
R-601	45	1.36	195	55	30.1	338	0.148	913
R-717	45	17.8	290	112	10.7	333	0.158	788
Hexane	70	1.05	234	30	28.6	28.6	0.144	809

¹Coefficient of performance, $COP = W_{out}/Q_{in} = (W_{turbine} - W_{pump})/Q_{evaporator}$

Table 2 – Comparison between simple and integrated Rankine cycle configurations for R-601, with ethylene cooling down to 130 °C.

Rankine configuration	T _{condenser} (°C)	P _{condenser} (bar)	T _{max} (°C)	P _{evaporator} (bar)	Fluid flow (t/h)	CW flow (t/h)	COP	W _{out} (kW)
Simple	45	1.36	195	33	30.1	338	0.154	713
Integrated	45	1.36	195	33	35.9	326	0.183	849

3.1.2. Kalina cycle

Previous restriction on ethylene cooling was set from the beginning and the vapour fraction in the generator was limited between 0.5 and 0.9. In this cycle, multistate turbines are also accepted (Bombarda et al., 2010). The main variable in this cycle is the mixture NH₃/H₂O, in the working fluid. Concentrations of 60, 70, 75 and 80 % (m/m) were simulated. Table 3 shows a maximum on W_{out} for 70 % NH₃, with the restrictions above. With this composition, low and high temperature heat exchangers were added, as schemed by Rodríguez (2013), to evaluate the efficiency changes in the system. Restrictions to the ΔT_{min} made it impossible to cool the ethylene down to 130 °C, but 172.2 °C instead. Still, it is interesting how the integration increases the cycle performance itself.

Table 3 – Simulation results for the Kalina cycle.

NH ₃ (%m/m)	T _{absorber} (°C)	P _{absorber} (bar)	Vapour fraction	T _{generator} (°C)	P _{generator} (bar)	Fluid flow (t/h)	CW flow (t/h)	COP	W _{out} (kW)
60	45	11.2	0.9	245	89	9.6	351	0.136	642
70	45	12.8	0.9	246	113	10.4	346	0.147	692
75	45	13.5	0.9	236	113	10.9	346	0.147	690
80	45	14.3	0.9	255	113	11.6	347	0.146	687
Kalina cycle with heat integration									
70	45	12.8	0.9	246	113	10.7	248	0.199	713

The analysis of the results obtained for the Rankine and Kalina cycles showed that the former had a better performance with a simpler configuration and at lower pressure.

3.2. Hot utility production by heat exchanging

Hot utility is produced directly by heating water with the ethylene stream. The study comprises the production of high and low pressures steam, and hot water needed in the process. Results are presented in Table 4. In the case of the production of steam at 7 bar it is possible to satisfy the needs of the process with only one of the production lines. Using both lines, ethylene temperature can be at 230 °C. The hot water process needs can be almost met by using the two production lines with ethylene at 130 °C.

Table 4 – Ethylene usage and hot utility production

Hot utility	Ethylene flow, required initial temperature	Production	Process needs
Steam, 40 bar	33 t/h, 310 °C	2.1 t/h	> 2.2 t/h
Steam, 7 bar	33 t/h, 310 °C	5.6 t/h	4 t/h
	66 t/h, 229.8 °C	4 t/h	
Hot Water, 95 °C	33 t/h, 130 °C	192 t/h	385 t/h
	66 t/h, 130 °C	384 t/h	
	33 t/h, 310 °C	1,180 t/h	

3.3. Refrigeration cycle – LiBr/H₂O absorption system

For the analysis of the refrigeration cycle, catalogues were consulted. Knowing the chilled water needed for both process lines, made possible to identify the amount of hot utility necessary to feed to the absorption system, which in turn led to the quantity of ethylene flow needed to produce that hot utility. Table 5 summarises the main results obtained for both single and double effect LiBr/H₂O absorption systems.

Table 5 – Ethylene flow to satisfy the needs in chilled water with LiBr/H₂O absorption system

Absorption cycle	Ethylene flow, required initial temperature	Production	Process needs
Single effect, hot water (90 °C)	41.7 t/h, 310 °C	4,554 kW	4,535 kW
	66 t/h, 243.4 °C		
Single effect, steam (1 bar)	46.4 t/h, 310 °C	4,676 kW	4,535 kW
	66 t/h, 256.1 °C		
Double effect, steam (8 bar)	32.3 t/h, 310 °C	4,652 kW	4,535 kW
	66 t/h, 248.6 °C		

4. Economic analysis

To carry out the economic evaluation of the different solutions studied, the following starting variables were used: annual operating time of 8,000 h, an energy price of 75 €/MWh, a low-pressure steam (7 bar) price of 18.9 €/t, an investment depreciation period of 10 years with constant rate of return, internal rate of return of 10% and project lifetime of 15 years. For this analysis, the income can be defined as the benefits in energy saving achieved with the implementation of each solution (Table 6).

Table 6 – Estimation of the annual benefits after investing on each technology.

	Power (Rankine)	Refrigeration (Double effect absorption chiller)	Hot utility (Steam 7 bar)
Net power (MW)	0.9	4.535	-
Steam (t/h)	-	-	4
Annual benefits (k€)	540	2,721	606

The equipment cost was estimated taking into account information provided by the suppliers of the solutions for Rankine and absorption cycles and with Aspen Economic Estimation for other equipment. The fixed capital cost was estimated using the Lang factors (Peters et al., 2003) and the results are present in the Table 7.

Table 7 – Fixed capital investment estimation via Lang factors.

	Rankine	Absorption chiller	Steam 7 bar
Main equipment cost (k€) ^v	1,200	528	-
2 water pumps for steam (k€) ^s	81	81	81
2 water pumps for chilled water (k€) ^s	-	Existent	-
2 cooling water pumps (k€) ^s	188	469	-
Ethylene/water heat exchanger (k€) ^s	1,000	1,000	1,000
Flash separator (k€) ^s	-	121	121
Total equipment cost, E (k€)	2,469	2,199	1,202
Equipment installation, instrumentation and control, piping and electrical installations, 142 % E (k€)	3,506	3,123	1,707
Direct plant cost (sum) (k€)	5,975	5,322	2,909
Engineering and supervision, and construction expenses, 74 % E (k€)	1,827	1,627	889
Direct and indirect costs (sum), C (k€)	7,802	6,949	3,798
Contractor's fee and contingency, 15 % C (k€)	1,170	1,042	570
Fixed capital investment (sum), FC (k€)	8,972	7,991	4,368
Annual depreciation, 10 % FC (k€)	897	799	437
Annual maintenance, 1.5 % FC (k€)	135	120	66

^v suppliers' information; ^s Aspen Economic Estimation

The cash flows for each year can be calculated taking into account the benefits, the depreciation, maintenance costs and the internal rate of return. The estimated cumulative cash flow after investing in one of the proposed solutions are present in Table 8. The refrigeration cycle by absorption with LiBr/H₂O is the solution with the best return of the investment with positive cumulative cash flow after the 3rd year.

Table 8 – Estimated cumulative cash flow after investing on each technology.

Year	Rankine	Abs. chiller	Steam 7 bar	Year	Rankine	Abs. chiller	Steam 7 bar
0	-8,973 k€	-7,995 k€	-4,370 k€	5	-4,038 k€	4,894 k€	-668 k€
1	-7,789 k€	-4,904 k€	-3,482 k€	6	-3,303 k€	6,813 k€	-117 k€
2	-6,713 k€	-2,094 k€	-2,675 k€	7	-2,635 k€	8,558 k€	384 k€
3	-5,735 k€	461 k€	-1,941 k€
4	-4,846 k€	2,783 k€	-1,274 k€	NPV=15	-382 k€	16,699 k€	2,419 k€

5. Conclusions

In this case study, lots of waste heat are available, so recovery is a right step to approach efficiency. Power cycles had efficiency limitations, with maximum performances around 20 %, reached at lower pressures in the Rankine cycle in relation to Kalina cycle. Heat driven LiBr/H₂O absorption refrigeration systems are available to substitute some power consuming traditional refrigeration cycles, due to cost benefit ratio and so the preferred solution for the use of excess heat from the ethylene recycle stream.

Acknowledgement

The authors would like to thank Fundação para a Ciência e Tecnologia for financial support through CQE (UID/QUI/00100/2013).

References

- P. Bombarda, C. Invernizzi, C. Pietra, 2010, Heat recovery from Diesel engines: a thermodynamic comparison between Kalina and ORC cycles, *Applied Thermal Engineering*, 30, 212-219.
- BP, 2017, BP Statistical Review of World Energy June 2017, <www.bp.com/content/dam/bp/en/corporate/pdf/energy-economics/statistical-review-2017/bp-statistical-review-of-world-energy-2017-primary-energy.pdf>, accessed on 17/07/2017.
- H. Chen, D.Y. Goswami, E.K. Stefanakos, 2010, A review of thermodynamic cycles and working fluids for the conversion of low-grade heat, *Renewable and Sustainable Energy Reviews*, 14, 3059-3067.
- M.S. Peter, K.D. Timmerhaus, R.E. West, 2003, *Plant Design and Economics for Chemical Engineers*, McGraw- Hill Chemical Engineering Series, New York.
- C.E.C. Rodríguez, J.C.E. Palacio, O.J. Venturini, E.E.S. Lora, V.M. Cobas, D.M. d. Santos, F.R.L. Dotto, V. Gialluca, 2013, Exergetic and economic comparison of ORC and Kalina cycle for low temperature enhanced geothermal system in Brazil, *Applied Thermal Engineering*, 52, 109-119.
- P. Srihirin, S. Aphornratana, S. Chungpaibulpatana, 2001, A review of absorption refrigeration technologies, *Renewable and Sustainable Energy Reviews*, 5, 343-372.
- S.B. Viklund, M.T. Johansson, 2014, Technologies for utilization of industrial excess heat: Potentials for energy recovery and CO₂ emission reduction, *Energy Conversion and Management*, 77, 369-379.
- C. Walsh, P. Thornley, 2012, Barriers to improving energy efficiency within the process industries with a focus on low grade heat utilization, *J. of Cleaner Production*, 23, 1, 138-146.

Flexible Hydrogen and Power Co - generation based on Dry Methane Reforming with Carbon Capture

Szabolcs Szima, Ana-Maria Cormos, Calin-Cristian Cormos *

*Babes-Bolyai University, Faculty of Chemistry and Chemical Engineering,
Arany Janos 11, Postal code: RO-400028, Cluj-Napoca, Romania*

cormos@chem.ubbcluj.ro

Abstract

This paper evaluates the dry reforming of methane (DRM) process with CO₂ capture using an alkanolamine gas - liquid absorption system for flexible hydrogen and power co-generation. The evaluated plant concepts consider a net power output of about 500 MW net with a flexible hydrogen thermal output in the range of 0 to 200 MW_{th}. The carbon capture rate of the CO₂ capture unit is higher than 90%. The evaluations used process flow modeling performed using ChemCAD process simulator, as well as, process integration techniques (e.g. thermal integration via pinch analysis) for quantification of mass & energy balances of the overall process. The analysis is geared toward assessment of key technical and environmental indicators of flexible hydrogen and power co-generation based on DRM with CO₂ capture such as: gross and net power output, hydrogen thermal output, cumulative energy efficiency, ancillary plant energy consumption, carbon capture rate, specific carbon dioxide emissions etc. As benchmark cases, conventional steam reforming and autothermal reforming, both equipped with CO₂ capture using gas-liquid absorption, are used for comparison reason of DRM technology. Potential production of other energy carriers (e.g. synthetic fuels like methanol) by dry methane reforming with CO₂ capture was also considered. As the key performance indicators show, the dry methane reforming process with CO₂ capture has some advantages in comparison to the conventional steam methane reforming and autothermal reforming such as: higher energy efficiency and carbon capture rate, lower specific CO₂ emissions, ability to process some of the captured CO₂ instead of energy-intensive steam used for conventional methane reforming etc.

Keywords: Flexible hydrogen and power co-generation; Dry methane reforming; Carbon Capture, Utilization and Storage (CCUS) technologies; CAPE tools.

1. Introduction

Carbon capture, utilization and storage (CCUS) technologies are expected to play a significant role in the near future for reducing the global greenhouse gas emissions and to ensure a sustainable development of energy - intensive industrial applications (e.g. heat and power sector, metallurgy, cement, petro - chemistry etc.). On the other hand, increasing the energy efficiency of fuel conversion processes as well as designing flexible energy conversion systems, able to timely respond to power grid variations are other significant ways to reduce both, fossil fuel consumptions and CO₂ emissions. Hydrogen is considered as one of the promising future energy carriers which is not involving fossil CO₂ emissions at the point of use. In addition, hydrogen (as well as

other chemicals used as energy carriers) has a distinct advantage in comparison to electricity that it can be easily stored to be used for power generation during the peak time or for other practical applications, like chemicals (Bailera et al., 2017).

Dry reforming of methane is a promising way to convert natural gas into syngas. According to Voldsund et al. (2016), nearly half of the global H₂ production is by natural gas steam reforming. In contrast with conventional steam reforming process, this procedure gives rise to a gas with a H₂/CO molar ratio of nearly 1:1 that is a feedstock for several processes. Garcia (2015) has reported that the main disadvantage of DRM is the catalyst deactivation due to carbon deposition. Although Ni-based catalysts are widely applied in the field, noble metal catalysts present less carbon deposits. From a kinetic perspective, the dry methane reforming process was described as methane decomposition on the catalyst followed by the gasification of these deposits.

In the present work the technology of CO₂ reforming was evaluated from a technical and environmental point of view. Comparisons between four operating scenarios were performed in order to better understand the behavior of the DMR plant. Thermal integration was applied to increase the energy efficiency. The obtained results for each scenario were compared to steam methane reforming and autothermal reforming, showing better performance in terms of natural gas consumption and efficiency.

2. Assessment methodology

While the heavy industry's energy demand is relatively constant during a 24 h cycle, private homes and small companies' power demand varies significantly. Similarly, with the constantly increase integration of the renewable energy sources (e.g. solar, wind) into the power grid, their production output depending significantly on the weather, induces fluctuations in the production / demand ratio. To counteract this issue, Gutiérrez-Martín and Rodríguez-Antón (2016) proposed the installation of a power to synthetic-natural-gas technology in the power grid to make use of the surplus energy as conventional power plants are designed to run at a constant production rate.

To catch up with today's market demand, in this paper a different approach is presented, one that uses flexible power plants to lower overproduction periods, reduce costs and lower carbon emissions. A DMR technology, offering the possibility of lowering its power output and produce H₂ during low energy demand periods, is investigated in the present paper. One of the main DMR outputs, H₂, can be later sold as a chemical or transformed into electrical energy when demand is high. For DMR simulation, the design assumptions presented in Table 1 were taken into consideration.

Table 1 Major design assumptions

Major design assumptions	
CH ₄ /CO ₂ ratio molar for reforming	1 / 1
CH ₄ purity	99.9 %wt
CO ₂ purity	99.9 %wt
Steam / carbon molar ratio for water gas shift	1.5
Oxygen source	Air

The process was build using the general structure of a reforming plant as presented in Figure 1. Methane and CO₂ are fed into the catalytic reactor that is designed as a shell and tube reactor. The catalyst is located in the tubes while in the shell the burning of methane maintains the desired temperature. Air is used as an oxygen source. The

product streams CO content is lowered using medium pressure steam in two, a high and low temperature shift reactor. The heat produced in the shift reactors is used to generate the necessary steam for it. H₂ purification is performed in the carbon capture unit where CO₂ is captured using a liquid phase absorber, 50 % wt. solution of methyl-diethanolamine (MDEA). A percentage of 98.75 % of the CO₂ is captured. The energy required for the regeneration of the solvent is obtained from the flue gases of the reactor. The leftover H₂ with CH₄ as a primary impurity is fed into the combined cycle gas turbine (CCGT) at the operating pressure of the gas turbine. High purity H₂ is obtained from the stream entering the GTCC. For power generation, a Mitsubishi Hitachi Power Systems M701G2 series gas turbine combined cycle was considered, with the following specifications: 334 MW net power output and 39.5 % net electrical efficiency for the gas turbine. The accompanying Rankin cycle was designed separately. The captured CO₂ and produced H₂ steams are compressed to 120 and to 60 bar, respectively.

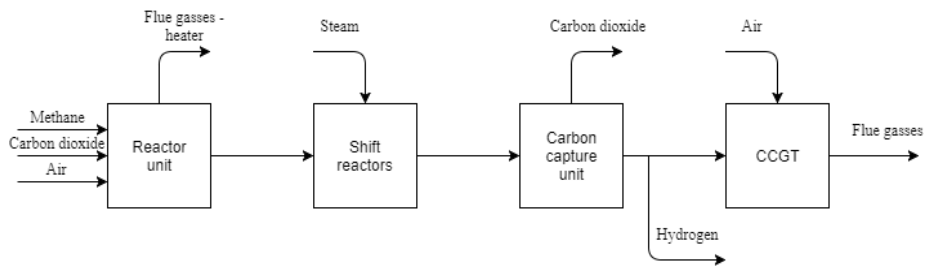


Figure 1. Process flow diagram of dry methane reforming with carbon capture

For the design of the dry methane reforming reactor, the use of kinetic data was selected. In order to verify the kinetic data available in the literature, this was compared to the results of the build-in thermodynamic functions in ChemCAD. The two showed very little difference. The reforming reactor was designed for a Ni/Al₂O₃ catalyst. This catalyst is frequently applied in the field and widely discussed in the literature (Abdullah et al., 2017). The kinetics selected is the one reported by Chein et al., (2017) applying to the two main reactions: dry reforming of methane and the reverse water-gas shift (RWGS). The side reactions describing the carbon formation were neglected. Both, previously mentioned reactions being highly endothermic, a significant amount of heat is used to maintain the desired high temperature of the reaction media. Following a thermodynamic study performed in ChemCAD, 920 °C was selected as an operating temperature. This value is in accordance with the data presented by Garcia (2015). To exemplify the impact of a carbon capture unit and of the lowered gas turbine feed rate over the system four scenarios were selected. The four scenarios are described more in detail in the following section. The base case (Case 1) was selected as having a dry reforming unit with two shift reactors connected to a CCGT to produce only power. No steps were taken to lower carbon emissions, only heat integration was performed. In Case 2, a CO₂ capture unit (based on gas-liquid absorption) is introduced to lower the greenhouse gas emissions. This scenario is important in order to quantify the energy penalty of using a CO₂ capture unit. The CO₂ stripped gasses are fed into the CCGT. In the third and fourth case studies (Cases 3 and 4) the hydrogen and power co-generation was assessed by gradually turned-down the gas turbine to produce hydrogen. The Case 3 is producing 100 MW_{th} and Case 4 200 MW_{th} of H₂. Two cases with lowered CCGT feed input were selected to easily describe linear variations in the behavior of the plant regarding lowered power production. The two lowered feed input case giving two data points and the case at full CCGT load being the third data point for each parameter.

3. Results and discussion

The previously mentioned cases, were modeled and simulated using ChemCAD 7.1 process simulator (Chemstations, 2017). The obtained models were used to calculate mass and energy balances in order to evaluate the key performance indicators and to perform thermal integration. As an example, Figure 2 presents the hot and cold composite curves of second case (dry methane reforming with carbon capture), the plant operating at full power load with carbon capture. A significant amount of energy is required for the regeneration of the CO₂ capture solvent (MDEA), which is also visible in the above - mentioned figure at about 125 °C. In the other three cases, similarly a considerable amount of energy is integrated to increase the efficiency of the plant.

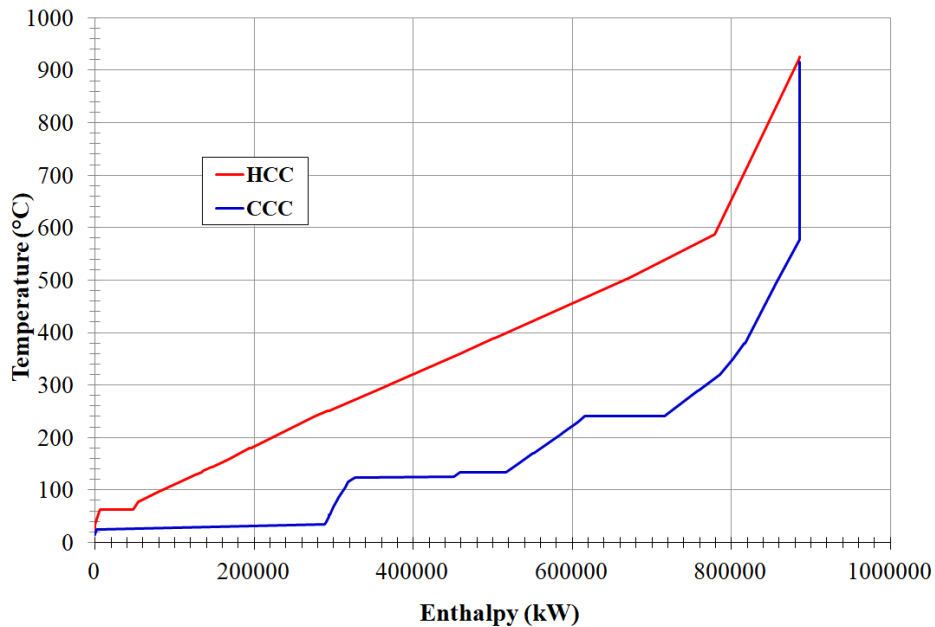


Figure 2. Hot and cold composite curves

In Table 2, the key performance indicators are presented for each investigated case. The energy input is the same in all four cases but depending on the downstream configuration, the efficiency and specific CO₂ emissions vary significantly. In Cases 1 and 2, the energy generated is almost the same, the difference in the expander output and the energy recovered in the Rankine cycle can be attributed to the solvent regeneration of the carbon capture unit. The sudden increase in the Rankine cycle output can be explained by the thermal integration of the plant. The same amount of heat is used in all three cases using carbon capture for heating the gas turbine inlet stream and powering the Rankine cycle. As the amount of gasses fed into the gas turbine dropped (CO₂ removed by the carbon capture unit), the amount of energy available for the Rankine cycle increased. The same trend can be noticed in the expander output section, as this is the unit setting up the desired pressure for the gas turbine. In the present plant configuration, the energy output of the CCGT is not affected by the introduction of the carbon capture unit, as this unit uses waste heat generated by the reactor.

Adding the carbon capture unit to the dry methane reforming plant lowers the global energy efficiency of the plant by 3 % as seen in the cumulative efficiency values. In Cases 3 and 4, the energy output of the gas turbine decrease significantly as expected with the decrease of fuel, however the efficiency penalty of the CCGT was only about 0.5 % in the verified two cases. The plant uses a significant amount of power to compress the CO₂ required for the plant, as it is considered that the gas is fed from a carbon capture unit at 1.5 bar. A similarly high quantity of energy is needed for the carbon capture unit to compress the gas. As the quantity of H₂ needed to compress is relatively small, compared to the amount of CO₂, the power needed for compression is also significantly lower. The cumulative efficiency of the plant shows a sudden decrease with the use of a carbon capture unit, however by the increase of H₂ production the overall (cumulative) energy efficiency of the plant increases significantly, overtaking the base case at maximum H₂ production capacity. The specific CO₂ emissions are calculated for power production thus explains the increase of the value as the H₂ ratio increases but when consider the overall energy production CO₂ emissions decrease.

Table 2. Comparison of simulated dry methane reforming scenarios

	Units	Case 1	Case 2	Case 3	Case 4
Natural gas input	t/h	79.89	79.89	79.89	79.89
Lower heating value LHV	MJ/kg		46.73		
Feedstock energy input	MW _{th}	1,037.00	1,037.00	1,037.00	1,037.00
Gas turbine output	MW _e	334.00	334.00	287.32	248.78
Steam turbine output	MW _e	173.22	174.73	152.91	132.60
Expander output	MW _e	4.60	1.56	3.14	2.58
Rankine cycle output	MW _e	40.22	12.72	16.28	15.79
Total power output	MW _e	551.75	522.59	459.65	399.75
H ₂ thermal output	MW _{th}	0.00	0.00	100.00	200.00
CO ₂ capture unit	MW _e	0.00	14.50	14.50	14.50
H ₂ compression unit	MW _e	0.00	0.00	1.12	2.25
Plant power unit	MW _e	12.93	12.54	12.54	12.27
Total power consumption	MW _e	12.93	27.04	28.17	29.02
Net power output	MW _e	538.83	495.55	431.49	370.73
Net power efficiency	%	51.95	47.78	41.60	35.74
Hydrogen efficiency	%	0.00	0.00	9.64	19.28
Cumulative plant efficiency	%	51.95	47.78	51.24	55.03
Carbon capture rate	%	0.00	64.40	64.40	64.40
CO ₂ emissions (power)	kg/MW _e	687.12	267.67	307.41	357.79
CO ₂ emissions (H ₂ +power)	kg/MW	687.12	267.67	249.57	232.41

Table 3 compares the obtained results for dry methane reforming to conventional steam methane reforming and autothermal reforming, as reported by Salkuyeh et al., (2017). The reference plants have a similar H₂ production rate as the one reported in this paper. The specific natural gas consumption of the dry methane reforming technology is lower than in the case of conventional steam reforming, however when compared to autothermal reforming the process has a significantly higher specific consumption. In terms of methane consumption, dry methane reforming technologies is located in between the technologies of steam methane reforming and autothermal reforming.

Table 3. Comparison of various methane reforming technologies

	Dry methane reforming	Steam methane reforming	Autothermal reforming
Natural gas consumption (t/t _{H2})	4.70	5.20	3.80
CO ₂ captured (t/t _{H2})	13.97	13.20	10.20
Hydrogen production rate (MW, LHV)	566.80	630	630

4. Conclusions

Lowering the electric grid energy surpluses can decrease the energy production prices as well as the carbon emissions. Power plants with flexible energy conversion capabilities can be actively applied to combat this issue. Dry reforming of methane is a promising alternative for steam methane reforming, the technology that is used today predominantly for obtaining H₂ from natural gas. In this work, four DRM scenarios were investigated to describe the behavior and the energetic aspect of this reforming technology, when coupled to a carbon capturing unit and when the GTCC is operated at lower capacities. DRM was also compared to conventional steam methane reforming, showing benefits in term of reducing the specific fuel (methane) consumption. The flexible hydrogen and power co-generation show its benefits in term of increasing the cumulative energy efficiency of the plant as well as decreasing the specific CO₂ emissions when the hydrogen output is increasing.

Acknowledgement

This work was supported by a grant of Ministry of Research and Innovation, CNCS – UEFISCDI, project ID PN-III-P4-ID-PCE-2016-0031: "*Developing innovative low carbon solutions for energy-intensive industrial applications by Carbon Capture, Utilization and Storage (CCUS) technologies*", within PNCDI III.

References

- B. Abdullah, N. A. A. Ghani, D. N. Vo, 2017, Recent advances in dry reforming of methane over Ni-based catalysts, *Journal of Cleaner Production*, 162, 170-185
- M. Bailera, N. Kezibri, L. M. Romeo, S. Espatolero, P. Lisbona, C. Bouallou, 2017, Future applications of hydrogen production and CO₂ utilization for energy storage: Hybride Power to Gas-Oxycombustion power plants, *International Journal of Hydrogen Energy*, 42, 19, 13625-13632
- R. Y. Chein, W. H. Hsu, C. T. Yu, 2017, Parametric study of catalytic dry reforming of methane for syngas production at elevated pressures, *International Journal of Hydrogen Energy*, 42, 21, 14485-14500
- Chemstations, 2017, ChemCAD 7, www.chemstations.com, Accessed 8 December 2017
- L. García, 2015, Hydrogen production by steam reforming of natural gas and other nonrenewable feedstocks, *Compendium of Hydrogen Energy*, 83-104,
- F. Gutiérrez-Martín, L. M. Rodríguez-Antón, 2016, Power-to-SNG technology for energy storage at large scales, *International Journal of Hydrogen Energy*, 41, 42, 19290-19303
- Z. K. Salkuyeh, B. A. Saville, H. L. MacLean, 2017, Techno-economic analysis and life cycle assessment of hydrogen production from natural gas using current and emerging technologies, *International Journal of Hydrogen Energy*, 42, 30, 18894-18909
- M. Voldsund, K. Jordal, R. Anantharaman, 2016, Hydrogen production with CO₂ capture, *International Journal of Hydrogen Energy*, 41, 9, 4969-4992

Parameter estimation for modelling of organophilic pervaporation

Andras Jozsef Toth,^{*,a} Eniko Haaz,^a Szabolcs Solti,^b Nora Valentinyi,^a Anita Andre,^a Daniel Fozer,^a Tibor Nagy,^a Peter Mizsey,^{a,c}

^a*Department of Chemical and Environmental Process Engineering, Műegyetem rkp. 3., Budapest, 1111, Hungary*

^b*Szelence Kamionmosó, Ipartelep, Szabadegyháza, 2431, Hungary*

^c*Department of Fine Chemicals and Environmental Technology, Egyetemváros C/1 108., Miskolc, 3515, Hungary*

andras86@kkft.bme.hu

Abstract

The work is motivated by an industrial environmental problem, which is ethanol removal from aqueous mixture. To complete this goal organophilic pervaporation of ethanol/water mixture through commercially available Sulzer PERVAP™ 4060 is investigated to obtain information about the removal of ethanol. The experimental results are obtained at different feed ethanol concentrations and temperatures. Our experimental data are evaluated with the semi-empirical pervaporation model (Valentinyi et al. 2013) of our improvement and it is found that the model can be applied also for this organophilic case. Linear and quadratic surfaces suiting (Model III) are also investigated in order to estimate partial permeate flux. The results of parameter estimation and modelling of the pervaporation show that the novel model that considers the concentration dependency of the transport coefficient (Model II) is also capable for the modelling of organophilic pervaporation and results in a better fit to the experimental data, than basic pervaporation model (Model I) and Model III.

Keywords: organophilic pervaporation, parameter estimation, model development, ethanol removal

1. Introduction

The pervaporation (PV) process can be used for dehydration of organics or for the removal of low concentration organics from aqueous mixtures (Ki Hong and Hi Hong 1999, Konieczny et al. 2008, Liang et al. 2004) and also for organic-organic separation. Depending on the permeating component two main areas of pervaporation can be identified: hydrophilic and organophilic pervaporation (Toth et al. 2015, Van der Bruggen and Luis 2014, Zhang et al. 1992).

Pervaporation is a separation method that is considered as green technology because of its low energy consumption. The mechanism of component separation in a liquid mixture by PV is complex but it can be explained with the solution-diffusion mechanism. It consists of the following steps: solution of the preferred component in the membrane; preferential diffusion of the component through the membrane material and desorption and evaporation on the permeate side into the vapour phase. One of the important features of describing PV is the transmembrane flux described in a general

form by Fick II equation. Apart from the simplicity of this equation the diffusion coefficient has complicated concentration dependency for non-ideal systems. Therefore scientists have been working on developing new models for pervaporation. Major models found in the literature, are the empirical model, pore-flow model; total solvent volume fraction model, and solution–diffusion model (Heintz and Stephan 1994a, b, Lipnizki and Trägårdh 2001, Luis and Van der Bruggen 2015, Marriott and Sørensen 2003, Schaetzel et al. 2004, Wijmans and Baker 1995). Crucial requirements of modelling, beside simplicity, are applicability of these models in flowsheeting environment (Valentínyi et al. 2013).

2. Material and methods

The novel model developed and tested by Valentínyi et al. (2013) on several hydrophilic PV case studies has proved to be a good one for the description of PV for engineering applications and design. The basic equation of this model is (J: partial permeate flux):

$$J_i = \frac{1}{1 + \{\bar{D}_i \cdot \exp(B \cdot x_{i1})\} / (Q_0 \cdot p_{i0} \cdot \bar{V}_i)} \cdot \frac{[\bar{D}_i \cdot \exp(B \cdot x_{i1})]}{\bar{V}_i} \cdot \left(\frac{p_{i1} - p_{i3}}{p_{i0}} \right) \quad i = (1, \dots, k) \quad (1)$$

The model is an improvement of Rautenbach's work (Rautenbach et al. 1990) and the improvements consider the concentration dependencies of the transport coefficient and the temperature dependencies of PV. First the parameters of the two models (Model I: Rautenbach, Model II: novel one) have to be estimated based on measured data. These parameters are the transport coefficients, permeability coefficients, activation energies (\bar{D}_i , Q_0 and E_i) and the B parameters that shows the concentration dependencies of the transport coefficients. The estimations are completed with the STATISTICA® program environment. Permeate flux can be also estimated directly with STATISTICA® from experiments results with surface suiting, it is called as Model III. Linear and quadratic surfaces are also applied.

The main aim of this paper is to extend Model II in the case of organophilic separation and to comparison of accuracy of these models. The verification can be obtained with objective function, that is minimized the deviation of the modelled and the measured values.

$$OF = \sum_{i=1}^n \left(\frac{J_{i,measured} - J_{i,modelled}}{J_{i,measured}} \right)^2 \quad (2)$$

PV of ethanol (EtOH) and water mixture using organophilic Sulzer PERVAP™ 4060 membrane is studied at different feed ethanol concentrations (x_{F-EtOH} : 5, 10, 15, 20 m/m%) and temperatures (T: 313K, 333K and 353K). The experimental set up is a P-28 membrane unit from CM-Celfa Membrantechnik AG. The flat sheet membrane with 28 cm² effective area is placed on a sintered disc separating the feed and the permeate sides. The volume of the feed tank is 500 ml. Cross-flow circulation velocity is kept at a permanent value of ~182 l/h. The vacuum on the permeate side is maintained with VACUUMBRAND PC2003 VARIO vacuum pump and kept at 2 torr (2.67 mbar). The isotherm conditions are assured with a thermostate. The permeate is collected in two traps connected in series and cooled with liquid nitrogen to prevent loss of the permeate (Toth and Mizsey 2015). The organic content of the feed, permeate and retentate are measured with Shimadzu GC2010Plus+AOC-20 autosampler gas chromatograph with a

CP-SIL-5CB column connected to a flame ionization detector, EGB HS 600 (Toth 2015, Toth et al. 2017).

3. Results and discussion

The minimized objective functions and estimated values for \bar{D}_i , E_i , and B parameters of the three models are shown in Table 1 (Model I: basic Rautenbach, Model II: improved model, Model III: quadratic surface model).

Table 1 Estimated parameters for ethanol-water mixture with Sulzer PERVAP™ 4060 membrane and objective functions resulted by the three models

	Model I		Model II		Model III	
	Water	EtOH	Water	EtOH	Water	EtOH
\bar{D}_i [kmol/m ² h]	0.014	0.074	0.027	0.074		
E_i [kJ/kmol]	31376	33071	31352	33077		
B [-]			-0.71	-0.04		
OF [-]	0.011	0.165	0.001	0.153	0.021	0.182

It can be seen that Model II has the lowest OF and the accuracy of PV models are better all case of water flux than ethanol flux. The comparison of the measured and calculated partial fluxes are presented in Figure 1 and Figure 2.

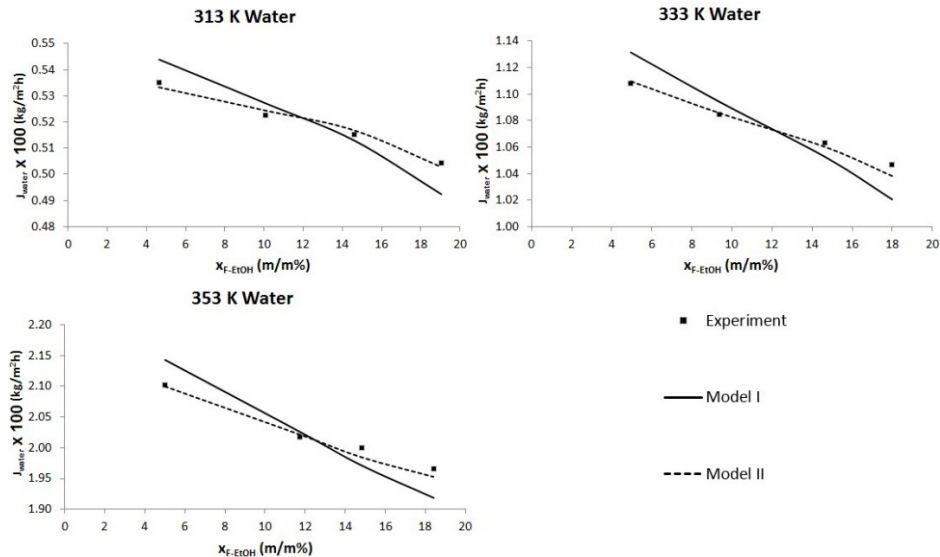


Figure 1. Measured partial fluxes of ethanol compared to fluxes calculated with Model I and Model II at 313K, 333K, 353K in a function of feed ethanol content in weight percent with Sulzer PERVAP™ 4060 membrane

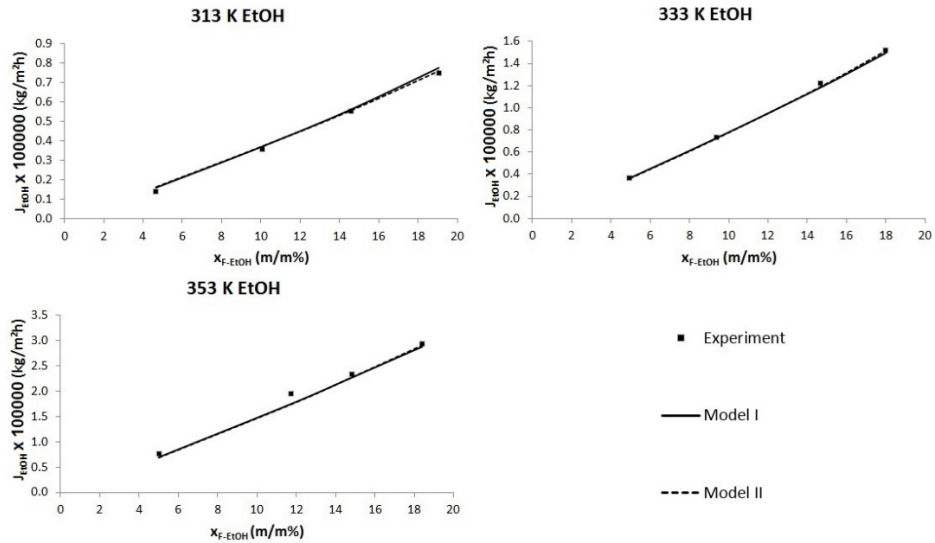


Figure 2. Measured partial fluxes of ethanol compared to fluxes calculated with Model I and Model II at 313K, 333K, 353K in a function of feed ethanol content in weight percent with Sulzer PERVAP™ 4060 membrane

Figure 3 shows the linear surface suiting with STATISTICA® software. The dependent variable is ethanol flux and independent variables are x_{F-EtOH} and $x_{F-EtOH} \cdot T$. The white discrete points mean the experimental data and below Figure 3 the equation of surface can be seen (Eq. (3)). Using Eq. (3) partial ethanol flux can be calculated.

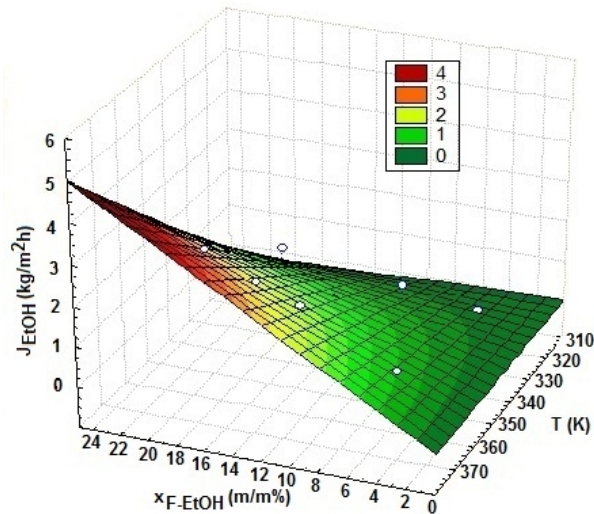


Figure 3. Linear surface in the function of ethanol flux, feed ethanol concentration and feed temperature (Virag 2007)

$$J_{EtOH} = -0.907485 \cdot x_{F-EtOH} + 0.002992 \cdot T \cdot x_{F-EtOH} \quad (3)$$

Figure 4 shows the quadratic surface suiting with STATISTICA®. In this case the dependent variable is J_{EtOH} and the independent variables are as follows: T , x_{F-EtOH} , $x_{F-EtOH} \cdot T$ and T^2 .

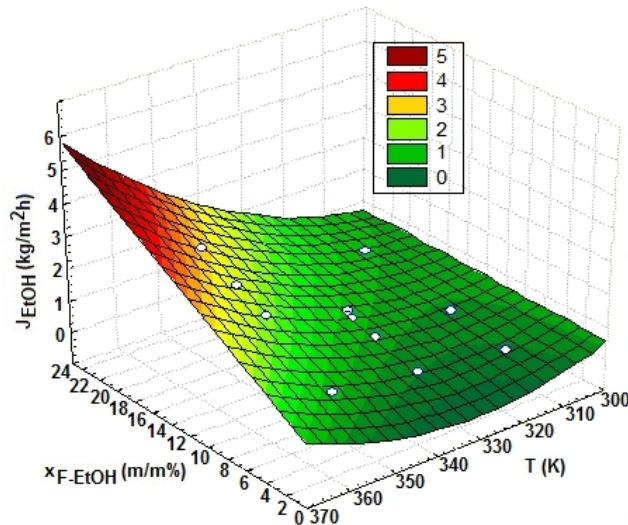


Figure 4. Quadratic surface in the function of ethanol flux, feed ethanol concentration and feed temperature (Virag 2007)

$$J_{EtOH} = 89.19 - 0.53 \cdot T - 0.80 \cdot x_{F-EtOH} + 0.0008 \cdot T^2 + 0.0027 \cdot x_{F-EtOH} \cdot T \quad (4)$$

It can be seen the quadratic surface model (Figure 4) estimates better the experimental data than linear surface model (Figure 3). The results suggest that linear correlation describe inaccurately the organophilic pervaporation. Many authors have suggested an exponential relationship between diffusion coefficient and feed concentration (Shelden and Thompson 1984, Valentínyi et al. 2013).

4. Conclusions

It can be concluded Model II results in a better fit to the experimental data, than Model I and III. The results of parameter estimation show that Model I estimates the measured fluxes higher than measured, especially in the case of ethanol content, because of that the transport coefficient depends on a greater extent of the feed composition. This dependency is found to be an exponential one also for our organophilic pervaporation. It can be stated the surface models, although simple and fast methods, cannot give fairly accurate estimate.

The authors would like to acknowledge the financial support of János Bolyai Research Scholarship of the Hungarian Academy of Sciences and OTKA 112699 project. This research was supported by the European Union and the Hungarian State, co-financed by the European Regional Development Fund in the framework of the GINOP-2.3.4-15-2016-00004 project, aimed to promote the cooperation between the higher education and the industry and the ÚNKP-17-3-I New National Excellence Program of the Ministry of Human Capacities.

References

- A. Heintz, W. Stephan, 1994a, A generalized solution-diffusion model of the pervaporation process through composite membranes Part I. Prediction of mixture solubilities in the dense active layer using the UNIQUAC model, *J Membrane Sci* 89, 1-2, 143-151.
- A. Heintz, W. Stephan, 1994b, A generalized solution-diffusion model of the pervaporation process through composite membranes Part II. Concentration polarization, coupled diffusion and the influence of the porous support layer, *J Membrane Sci* 89, 1-2, 153-169.
- Y. Ki Hong, W. Hi Hong, 1999, Influence of ceramic support on pervaporation characteristics of IPA/water mixtures using PDMS/ceramic composite membrane, *J Membrane Sci* 159, 1-2, 29-39.
- K. Konieczny, M. Bodzek, D. Panek, 2008, Removal of volatile compounds from the wastewaters by use of pervaporation, *Desalination* 223, 1-3, 344-348.
- L. Liang, J. M. Dickson, J. Jiang, M. A. Brook, 2004, Effect of low flow rate on pervaporation of 1,2-dichloroethane with novel polydimethylsiloxane composite membranes, *J Membrane Sci* 231, 1-2, 71-79.
- F. Lipnizki, G. Trägårdh, 2001, Modelling of pervaporation: Models to analyze and predict the mass transport in pervaporation, *Separ Purif Method* 30, 1, 49-125.
- P. Luis, B. Van der Bruggen, 2015, *Pervaporation, Vapour Permeation and Membrane Distillation*, pp. 87-106, Woodhead Publishing, Oxford.
- J. Marriott, E. Sørensen, 2003, A general approach to modelling membrane modules, *Chem Eng Sci* 58, 22, 4975-4990.
- R. Rautenbach, C. Herion, U. Meyer-Blumentoth, 1990, Pervaporation membrane separation processes, *Membrane Science and Technology Series* 1, 181-191.
- P. Schaetzel, C. Vaucclair, Q. T. Nguyen, R. Bouzerar, 2004, A simplified solution-diffusion theory in pervaporation: The total solvent volume fraction model, *J Membrane Sci* 244, 1-2, 117-127.
- R. A. Sheldon, E. V. Thompson, 1984, Dependence of diffusive permeation rates and selectivities on upstream and downstream pressures. IV. Computer simulation of nonideal systems, *J Membrane Sci* 19, 1, 39-49.
- A. J. Toth, 2015, *Liquid Waste Treatment with Physicochemical Tools for Environmental Protection*, PhD Thesis, Budapest University of Technology and Economics, Budapest.
- A. J. Toth, A. Andre, E. Haaz, P. Mizsey, 2015, New horizon for the membrane separation: Combination of organophilic and hydrophilic pervaporations, *Sep Purif Technol*, 156, 2, 432-443.
- A. J. Toth, E. Haaz, T. Nagy, R. Tari, A. J. Tarjani, D. Fozér, A. Szanyi, K.-A. Koczka, L. Racz, G. Ugro, P. Mizsey, 2017, Evaluation of the accuracy of modelling the separation of highly non-ideal mixtures: extractive heterogeneous-azeotropic distillation, *Comput-Aided Chem Eng. España, A., Graells, M. and Puigjaner, L. (eds)*, pp. 241-246, Elsevier.
- A. J. Toth, P. Mizsey, 2015, Methanol removal from aqueous mixture with organophilic pervaporation: Experiments and modelling, *Chem Eng Res Des* 98, 123-135.
- N. Valentinyi, E. Cséfalvay, P. Mizsey, 2013, Modelling of pervaporation: Parameter estimation and model development, *Chem Eng Res Des* 91, 1, 174-183.
- B. Van der Bruggen, P. Luis, 2014, Pervaporation as a tool in chemical engineering: a new era? *Curr Opin Chem Eng* 4, 47-53.
- B. Virag, 2007, *Investigation of ethanol-water mixture with organophilic pervaporation*, MSc Thesis, Budapest University of Technology and Economics, Budapest.
- J. G. Wijmans, R. W. Baker, 1995, The solution-diffusion model: a review, *J Membrane Sci* 107, 1-2, 1-21.
- S. Q. Zhang, A. E. Fouda, T. Matsuura, 1992, A study on pervaporation of aqueous benzyl alcohol solution by polydimethylsiloxane membrane, *J Membrane Sci* 70, 2-3, 249-255.

Simultaneous Optimization of Multistream Heat Exchangers and Processes

Yingzong Liang^a, Keat Ping Yeoh^a, Ergys Pahija^a, Pui Ying Lee^a, Chi Wai Hui^{a,*}

^a*Department of Chemical and Biological Engineering, The Hong Kong University of Science and Technology, Clear Water Bay, N.T., Hong Kong*

kehui@ust.hk

Abstract

Multistream heat exchangers (MHEXs) find application in a variety of energy intensive cryogenic processes. However, simultaneous optimization of process and MHEXs is often hindered by its nonlinear behavior and combinatory difficulties, which lead to low computational efficiency and poor solution qualities. In this paper, we present a mixed-integer nonlinear programming (MINLP) framework that comprises heat recovery of MHEXs, thermodynamics, vapor-liquid equilibrium, and other unit operations of the process. The MHEXs model combines the concept of Pinch analysis and multi-M formulation that improves solution efficiency by reducing the number of binary variables and nonconvexity of the model. The framework is applied to an industrial air separation unit (ASU) with multiple MHEXs to demonstrate its effectiveness.

Keywords: multistream heat exchangers, heat integration, process optimization

1. Introduction

Multistream heat exchanger (MHEX) is a type of processing units that simultaneously transfers heat among multiple process streams. Thanks to its compact structure and exceptional energy recovery efficiency, MHEXs find extensive applications in energy intensive processes including air separation (Pattison and Baldea, 2015), food and pharmaceutical production (Galeazzo et al., 2006), hydrocarbon processing (Shah et al., 2000), hydrogen purification and liquefaction (Christopher and Dimitrios, 2012), liquefied natural gas (LNG) production (Kamath et al., 2012), power generation (Memmott et al., 2017), and refrigeration processes (Thonon, 2008).

Much effort has been dedicated to model and optimize MHEXs to achieve higher economic-energy efficiency of process design. Hasan et al (2009) applied the concept of superstructure (Yeomans and Grossmann, 1999) to simulate MHEX, and formulated an mixed-integer nonlinear programming (MINLP) model to optimize heat recovery of MHEX. However, the complex superstructure is often computationally expensive, which brings greater difficulty to the simultaneous process and MHEX optimization. Kamath et al. (2012) presented a nonlinear programming (NLP) formulation of MHEX based on the concept of Pinch analysis (Kemp, 2011, Liang and Hui, 2016). The major challenge of the NLP formulation is the nonlinear approximation of *max* function, which can leads to error in energy balance and numerical difficulties.

Despite intensive research, MHEXs remain difficult to model due to the complexity of unknown stream data (e.g. temperatures and flow rates), resulting in bilinear function and discrete/nonlinear formulation for the heat integration model which is computationally expensive. To exacerbate the issue, simultaneous optimization of MHEXs and processes requires flash calculation of process streams and computation of other equipment that involve nonlinear thermodynamics constraints. Thus, it is significant to develop a rigorous and computationally efficient modeling framework to achieve simultaneous optimization of MHEXs and processes.

This paper aims to develop a mathematical model for simultaneous MHEXs and processes optimization. Discontinuous *max* function and nonlinear approximation of MHEX are circumvented by multi-M method (Hui, 2014) to reduce the nonconvexity and number of binary variables of the model. The resulting optimization problem is formulated as an MINLP model, which simultaneously maximizes heat recovery of the MHEXs and minimize operating cost of the process. The model subjects to the constraints of energy balance, constraints to enforce temperature difference of heat transfer in MHEXs, and constraints of the other unit operations and thermodynamics. We apply the proposed model to an industrial air separation process with multiple MHEXs to demonstrate its effectiveness.

2. Mathematical model

This section presents a framework for simultaneous MHEXs and process optimization. The framework includes heat recovery of MHEXs, thermodynamics, and other unit operations. The proposed model is formulated as an MINLP due to the bilinear function of process streams' enthalpy calculation and discrete nature of the multi-M formulation that handles the *max* functions.

Heat recovery in an MHEX can be considered as heat integration of multiple process streams without hot and cold utility. Therefore, the concept of Pinch analysis is applicable to the modeling of MHEXs. Moreover, the simultaneous MHEXs and process optimization requires modeling methods that are able to handle variable stream data. To achieve simultaneous optimization, we propose a method adapted from Hui's (2014) multi-M formulation to model the MHEXs. The model assumes counter-current of hot and cold streams at the MHEXs. Additionally, the heat capacity of a stream is assumed temperature independent in liquid phase, vapor phase, and phase change. The stream data (e.g. inlet/outlet temperatures and flow rates) can be varied or fixed. The model is formulated as follows.

$$\max \varphi(x) = \sum_{i \in H} CP_{i,e} \cdot f_{i,e}(t_{i,e}^{in} - t_{i,e}^{out}) \quad (1)$$

$$\min \psi(x) = \sum_{n \in N} cost_n \quad (2)$$

s.t.

$$\sum_{i \in H} CP_{i,e} \cdot f_{i,e}(t_{i,e}^{in} - t_{i,e}^{out}) = \sum_{i \in C} CP_{i,e} \cdot f_{i,e}(t_{i,e}^{out} - t_{i,e}^{in}) \quad e \in E \quad (3)$$

$$qsoa_{j,e} \geq qsia_{j,e} \quad j \in I, e \in E \quad (4)$$

$$qsoa_{j,e} = \sum_{i \in H} CP_{i,e} \cdot f_{i,e} (tp_{i,j,e}^{in} - tp_{i,j,e}^{out}) \quad j \in I, e \in E \quad (5)$$

$$qsia_{j,e} = \sum_{i \in C} CP_{i,e} \cdot f_{i,e} (tp_{i,j,e}^{out} - tp_{i,j,e}^{in}) \quad j \in I, e \in E \quad (6)$$

$$tp_{i,j,e}^{in} \leq t_{i,e}^{in} + M1_{i,j,e}^{in} (1 - y_{i,j,e}^{in}) \quad i \in I, j \in I, e \in E \quad (7)$$

$$t_{i,e}^{in} \leq tp_{i,j,e}^{in} \quad i \in I, j \in I, e \in IE \quad (8)$$

$$tp_{i,j,e}^{in} \leq t_{j,e}^p + M2_{i,j,e}^{in} \cdot y_{i,j,e}^{in} \quad i \in H, j \in I, e \in E \quad (9)$$

$$t_{j,e}^p \leq tp_{i,j,e}^{in} \quad i \in H, j \in I, e \in E \quad (10)$$

$$tp_{i,j,e}^{in} \leq t_{j,e}^p - \Delta T_e^{min} + M2_{i,j,e}^{in} \cdot y_{i,j,e}^{in} \quad i \in C, j \in I, e \in E \quad (11)$$

$$t_j^p - \Delta T_e^{min} \leq tp_{i,j,e}^{in} \quad i \in C, j \in I, e \in E \quad (12)$$

$$tp_{i,j,e}^{out} \geq t_{i,e}^{out} \quad i \in I, j \in I, e \in E \quad (13)$$

$$tp_{i,j,e}^{out} \geq t_{j,e}^p \quad i \in H, j \in I, e \in E \quad (14)$$

$$tp_{i,j,e}^{out} \geq t_{j,e}^p - \Delta T_e^{min} \quad i \in C, j \in I, e \in E \quad (15)$$

$$t_{j,e}^p = t_{i,e}^{in} \quad i \in H, j \in I, e \in E \quad (16)$$

$$t_{j,e}^p - \Delta T_e^{min} = t_{i,e}^{in} \quad i \in C, j \in I, e \in E \quad (17)$$

$$g(x, w) = 0 \quad (18)$$

$$h(x, w) \leq 0 \quad (19)$$

Here H and C respectively are the sets of hot and cold process streams. I is a set of process streams ($I = H \cup C$). E is a set of MHEXs. $f_{i,e}$, $CP_{i,e}$, $t_{i,e}^{in}$ and $t_{i,e}^{out}$ denote molar flow rate, heat capacity, inlet temperature, and outlet temperature of process streams, respectively. $tp_{i,j,e}^{in}$ and $tp_{i,j,e}^{out}$ respectively are pseudo inlet and outlet temperatures of stream i at MHEX e regarding pinch candidate j . $qsoa_{j,e}$ is enthalpy of hot streams above pinch candidate j , and $qsia_{j,e}$ is enthalpy of cold streams above pinch candidate j . $t_{j,e}^p$ is pinch candidate. $y_{i,j,e}^{in}$ is binary variables to determine the values of pseudo inlet temperatures. $M1_{i,j,e}^{in}$ and $M2_{i,j,e}^{in}$ are big-M parameters. ΔT_e^{min} is the minimum temperature difference for heat recovery.

Eq. (1) is the objective function to maximize overall heat recovery of MHEXs. Eq. (2) is the objective function to minimize operating cost of process. Eq. (2) represents energy balance of MHEXs, in which heat recovery obeys the conservation of energy. Eqs. (3)-(16) guarantee feasible heat transfer between hot and cold streams with temperature differences greater than or equal to ΔT_e^{min} . Eq. (3) ensures heat surplus above all pinch candidates. Eqs. (4) and (5) calculate the enthalpy of hot and cold streams above $t_{j,e}^p$ using the pseudo temperatures, which are determined by the multi-M constraints (Eqs. (6)-(14)). Eqs. (15) and (16) calculate pinch candidate $t_{j,e}^p$. Eqs. (17) and (18) represent the constraints of thermodynamics and unit operations (e.g. compressors and valves).

To illustrate the multi-M formulation, we take the calculation of pseudo temperatures of hot streams (Eqs. (6)-(9), (12) and (13)) for instance. Pseudo inlet temperature $tp_{i,j,e}^{in}$ is computed by Eqs. (6)-(9). If $t_{i,e}^{in} \geq t_{j,e}^p$, $y_{i,j,e}^{in}$ must be equal to 1, and hence Eq. (6) is reduced to $tp_{i,j,e}^{in} \leq t_{i,e}^{in}$, and Eq. (8) is relaxed into $tp_{i,j,e}^{in} \leq t_{i,e}^{in} + M1_{i,j,e}^{in}$. Together with Eq. (7), there is $tp_{i,j,e}^{in} = t_{i,e}^{in}$. Similarly, for $t_{i,e}^{in} \leq t_{j,e}^p$, we have $tp_{i,j,e}^{in} = t_{j,e}^p$. Pseudo outlet temperature $tp_{i,j,e}^{out}$ can be calculated via Eqs. (12) and (13) without using binary

variable. These constraints ensure the hot streams' enthalpy above $t_{j,e}^p$ is not overestimated. Different from previous methods, the multi-M formulation avoids nonlinear formulation and reduces the number of binary variables that improve solution efficiency of the model.

3. Case study

The proposed modeling framework is applied to an ASU process to demonstrate its performance. Figure 1 shows a simplified flowsheet of the MHEXs in an industrial ASU. The process involves 2 MHEXs, 3 hot streams, 4 cold streams, 2 water coolers, 2 air compressors, 1 expansion turbine, and 1 expansion valve. Cooling of the ASU is delivered by the compressors, and is recovered by the MHEXs. The thermodynamics of the process is modeled based on Soave-Redlich-Kwang (SRK) method (Soave, 1972). Streams' data of the ASU process are listed in Table 1. The composition of the process streams are presented in Table 2. The operating conditions of the equipment are specified in Table 3. The minimum temperature difference ΔT_e^{min} is equal to 3 K. In this example, the major variables are the flow rate and outlet temperatures of the process streams. The model is implemented on GAMS 27.4 and is solved by BARON.

Table 4 shows the optimal solutions of the example. 2 points of interest, namely the maximum heat recovery solution and minimum operating cost solution, are presented. The results suggest that increasing outlet temperature and flow rate of H2 can increase heat recovery. However, the increase flow rate of H2 results in greater energy consumption of the compressors, which leads to higher operating cost.

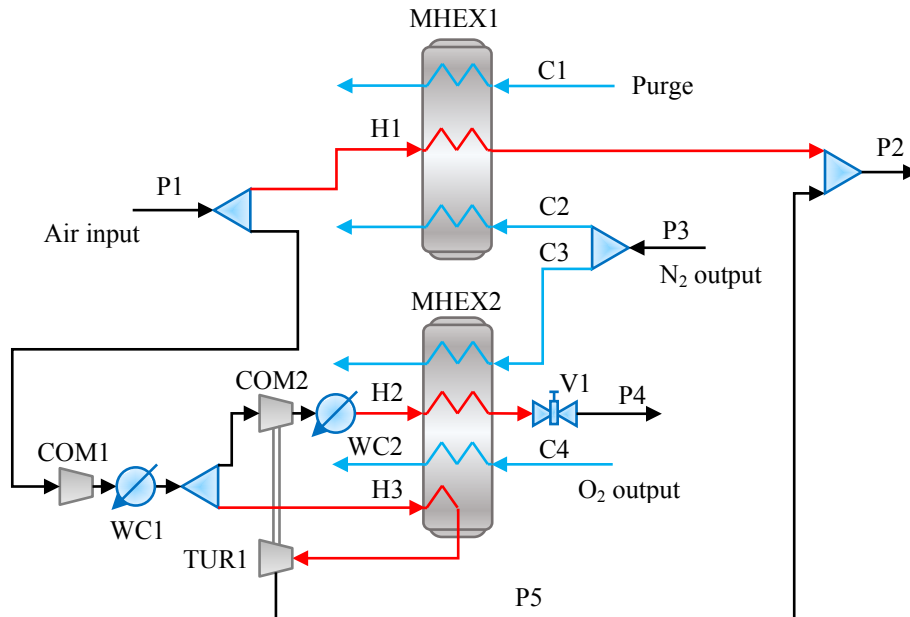


Figure 1 Simplified MHEXs of an industrial ASU.

Table 1 Data of process streams.

Stream	t_i^{in} (K)	t_i^{out} (K)	f_i (mol/s)	cp_i (J/mol·K)	p_i (kPa)
H1 (g-m)	284.2	98.15-102.2	≤ 800.0	-	610.0
H2 (g-l)	313.2	98.15-102.2	≤ 800.0	-	6,350
H3 (g-g)	313.2	-	≤ 800.0	30.94	4,000
C1 (g-g)	97.70	-	40.00	30.36	590.0
C2 (g-g)	89.15	-	≤ 620.0	29.38	130.0
C3 (g-g)	89.15	-	≤ 620.0	29.38	130.0
C4 (l-g)	99.99	-	140.0	-	8500
P1 (g)	-	284.2	800.0	-	610.0
P2 (m)	-	98.15-102.2	≤ 800.0	-	610.0
P3 (g)	-	89.15	620.0	-	130.0
P4 (m)	-	98.15-102.2	≤ 800.0	-	610.0
P5 (m)	-	98.15-102.2	≤ 800.0	-	610.0

Table 2 Process streams composition (mol %).

	P1	C1	P3	C4
N ₂	78.85	65.27	96.00	1.00
O ₂	21.15	34.73	4.000	99.000

Table 3 Operating condition of the units.

Unit	Outlet pressure (kPa)	Unit	Outlet temperature (K)
COM1	4,000	WC1	313.2
COM2	6,350	WC2	313.2
TUR1	610.0		
VI	610.0		

Table 4 Optimal solutions of the ASU example.

	Max heat recovery	Min operating cost
Heat recovery (kW)	5276	5170
Operating cost	6813	6372
H1 flow rate (mol/s)	331.3	325.1
H2 flow rate (mol/s)	191.7	185.3
H3 flow rate (mol/s)	277.1	289.6
H1 outlet temperature (K)	100.5	100.5
H2 outlet temperature (K)	97.20	96.70
H3 outlet temperature (K)	142.8	152.2
C2 flow rate (mol/s)	365.9	352.9
C3 flow rate (mol/s)	245.1	267.1
C1 outlet temperature (K)	251.2	253.5
C2 outlet temperature (K)	251.2	253.5
C3 outlet temperature (K)	310.1	298.5
C4 outlet temperature (K)	310.1	298.5

4. Conclusions

This paper proposed a modeling framework for simultaneous MHEXs and process optimization. The framework applied the multi-M formulation (Hui, 2014) to model MHEXs that allowed variable stream data, avoided nonlinear approximation, and reduced the number of binary variables to achieve higher solution efficiency. Rigorous thermodynamics method can be integrated into the framework so that it is applicable to various process design problems. A realistic ASU design problem with multiple MHEXs was investigated using the proposed framework. The computational results demonstrated that the framework is able to solve complex process optimization problem. Ultimately the model will be extended to the entire ASU flowsheet including the separation process, which enables the analysis of the trade-offs between energy consumption, product purity, heat recovery, and investment of ASU process.

Acknowledgement

The authors would like to thank the financial support from the Hong Kong Research Grants Council General Research Fund (16211117), Guangzhou Science and Technology Project (201704030136), and the Studentship from the Energy Concentration program of the School of Engineering at the Hong Kong University of Science and Technology.

References

- Christopher, K., Dimitrios, R., 2012. A review on exergy comparison of hydrogen production methods from renewable energy sources. *Energy & Environmental Science*. 5, 6640-6651
- Galeazzo, F.C., Miura, R.Y., Gut, J.A., Tadini, C.C., 2006. Experimental and numerical heat transfer in a plate heat exchanger. *Chemical Engineering Science*. 21, 7133-7138
- Hasan, M., Karimi, I., Alfadala, H., Grootjans, H., 2009. Operational modeling of multistream heat exchangers with phase changes. *AIChE J.* 1, 150-171
- Hui, C., 2014. Optimization of heat integration with variable stream data and non-linear process constraints. *Comput. Chem. Eng.* 0, 81-88
- Kamath, R.S., Biegler, L.T., Grossmann, I.E., 2012. Modeling multistream heat exchangers with and without phase changes for simultaneous optimization and heat integration. *AIChE J.* 1, 190-204
- Kemp, I.C., 2011. Pinch analysis and process integration: a user guide on process integration for the efficient use of energy. Butterworth-Heinemann
- Liang, Y., Hui, C., 2016. A shortcut model for energy efficient water network synthesis. *Appl. Therm. Eng.*, 88-91
- Memmott, M.J., Wilding, P.R., Petrovic, B., 2017. An optimized power conversion system concept of the integral, inherently-safe light water reactor. *Ann. Nucl. Energy*, 42-52
- Pattison, R.C., Baldea, M., 2015. Multistream heat exchangers: Equation-oriented modeling and flowsheet optimization. *AIChE J.* 6, 1856-1866
- Shah, R., Thonon, B., Benforado, D., 2000. Opportunities for heat exchanger applications in environmental systems. *Appl. Therm. Eng.* 7, 631-650
- Soave, G., 1972. Equilibrium constants from a modified Redlich-Kwong equation of state. *Chemical Engineering Science*. 6, 1197-1203
- Thonon, B., 2008. A review of hydrocarbon two-phase heat transfer in compact heat exchangers and enhanced geometries. *Int. J. Refrig.* 4, 633-642
- Yeomans, H., Grossmann, I.E., 1999. A systematic modeling framework of superstructure optimization in process synthesis. *Comput. Chem. Eng.* 6, 709-731

Population Balance Equation Applied to Microalgae Harvesting

Pui-Ying Lee^a, Ergys Pahija, Ying-Zong Liang, Keat-Ping Yeoh, Chi-Wai Hui^{*}

Department of Chemical and Biomolecular Engineering, The Hong Kong University of Science and Technology, Clear Water Bay, Hong Kong SAR

kehui@ust.hk

Abstract

Population Balance Equation is extended to model microalgae harvesting processes, such as centrifugation and sedimentation, to provide an accurate prediction of cell recovery rates. By analyzing changes in cell size distributions, the model can effectively examine how harvesting efficiencies would affect or be influenced by cell characteristics, such as size and density. Cell behaviors at different size ranges in the dewatering methods are studied to evaluate their variations with harvesting time as well as recovery rate for process optimization. Experiments of sedimentation and centrifugation on a microalgae species called *Chlorella* are carried out to validate the model. With measurements of optical densities and size distributions of the cell cultures, size specific densities of microalgae are derived to further improve the mathematical model.

Keywords: Microalgae harvesting, Cell characteristics, Population Balance Equation

1. Introduction

Microalgae, a fast-growing photosynthetic microorganism with high lipid content, is a promising bio-resource of biofuel. Production steps of microalgae for biofuel mainly include cultivation, harvesting and oil extraction, in which harvesting is regarded as a bottleneck accounting for around 20-30 % of the costs due to the dilute culture of microalgae, small cell size and similar density with water (Danquah et al., 2009). Therefore, optimizing the harvesting efficiency is essential to the development of the production process into an industrial scale. Extensive research efforts have been dedicated to evaluate efficiencies of various harvesting methods such as centrifugation and sedimentation from an experimental approach for maximizing the recovery. Nevertheless, not many modeling works of the processes have been performed and very few concerns have been raised towards the interrelationship between cell recovery rates and cell characteristics, such as size and density (Shelef et al., 1984). Stokes Law has been suggested to apply to govern settling behaviors of microalgae in both sedimentation and centrifugation by relating settling velocities of the processes to cell diameters and densities (Al hattab et al., 2015), but more individual cell characteristics should be taken into considerations for improving accuracies of the predicted results.

This study applies Population Balance Equation (PBE) to simulate the microalgae harvesting process. PBE has been commonly employed to characterize evolutions of particle populations in chemical processes, such as polymerization reaction, mixing and

crystallization. Some studies used PBE for modelling of bacteria (Ramkrishna, 2000) or microalgae growth (Pahija et al., 2017). A few applied PBE to modeling separation processes (Grimes, 2012) such as microalgae pre-concentration or harvesting (Sirin 2013). Sirin's work in PBE was limited for flocculation process to estimate the sedimentation rate and floc size distribution. In the following sections, PBE is applied to modeling sedimentation and centrifugation processes for microalgae harvesting.

2. Methodology

A Population Balance Equation (PBE) model is developed to characterize centrifugation and sedimentation of microalgae. The aim of the model is to find out size dependent recovery and selectivity of these two methods at different operating conditions such as operating time, rotation speed, etc. Experimental data is used to verify the model.

2.1. Population Balance Equation model

A simplified form of PBE (Randolph and Larson, 1988) for describing evolutions of particle growth commonly includes two terms as follow:

$$\frac{\partial n(t, d)}{\partial t} + \frac{\partial [G \cdot n(t, d)]}{\partial d} = 0 \quad (1)$$

The two terms on the left side of the equation represent the change in particle number densities with time and size respectively, in which n is number density, t is time and G is growth rate of particles. For the centrifugation and sedimentation of microalgae, the growth of cells is neglected. Instead, the variation of number density was caused by the size and density differences of the cells. The modified PBE equation becomes the follow:

$$\frac{\partial n(t, h, d)}{\partial t} = \frac{\partial [v(t, h, d) \cdot n(t, h, d)]}{\partial h} \quad (2)$$

where $v(t, h, d)$ is the cell travelling velocity and h is the distance travelled.

It is assumed that the cells reach their terminal velocities within a negligible time, so the $v(t, h, d)$ becomes $v(d)$ that depends only on cell size. Using discretization method to solve equation (2) would give the following equation, in which N denotes the number of cells.

$$N(t + 1, h, d) = N(t, h, d) + v(d) \frac{\Delta t}{\Delta h} [n(t, h - 1, d) - n(t, h, d)] \quad (3)$$

Centrifugation and sedimentation of particles in fluid has been modelled commonly by Stokes Law (Lamb, 1945). It is applicable to systems with dilute suspensions, homogeneous fluid, spherical particles and low Reynolds number (<1), which are fulfilled by the microalgae culture. Equation (4) and (5) are employed for centrifugation and sedimentation respectively to calculate the corresponding cell terminal velocities.

$$v_{t,c} = \frac{(\rho_p - \rho_f)r\omega^2d^2}{18\eta} \quad (4)$$

$$v_{t,s} = \frac{(\rho_p - \rho_f)gd^2}{18\eta} \quad (5)$$

which $v_{t,c}$ and $v_{t,s}$ are terminal velocities of the cells in centrifugation and sedimentation respectively, ρ_p and ρ_f are cell density and fluid density respectively, d is cell diameter, η is fluid viscosity, r is centrifuge radius, ω is centrifuge rotational speed and g is gravity.

In addition, Langevin Equation (Langevin, 1908) describing Brownian motion is employed to govern thermal vibrations of the cells in the fluid. The motion is particularly significant in small cells since the velocity is inversely proportional to cell diameter as illustrated in equation (6).

$$v_B = \sqrt{\frac{4kT}{3\pi\eta d}} \quad (6)$$

which v_B is the velocity of cells induced by Brownian motion and k is Boltzmann constant with the value of $1.38 \times 10^{-23} \text{ m}^2 \text{ kg s}^{-2} \text{ K}^{-1}$, while T (temperature) is assumed to be 298 K. The cell travelling velocity $v(d)$ in equation (3) is denoted by summing up equation (4) and (6) for centrifugation and summing up equation (5) and (6) for sedimentation.

The impacts of concentration effect and wall effect have been investigated and are found to be negligible due to the dilute cell culture and the small cell size to tube diameter ratio.

2.2. Experiments

Experiments of centrifugation and sedimentation are performed in 15ml centrifuge tubes with a diameter of 17 mm and a height 120 mm. For centrifugation, a centrifuge (Hettich EBA 20) with a radius of 0.044m and the rotational speed of 500 rpm is used. Forces added to the vertically tilted tubes are dominantly in horizontal directions and cells travelling beyond half of the tube diameter (8.5 mm) are considered captured. Cells mainly stick on one side of the wall which is farther away from the center after centrifugation and samples are taken in the middle of the other half of the tube at 1, 2, 3 and 4 minutes. For sedimentation, forces are mainly in vertical directions and cells travelling beyond half of the tube height (60 mm) are considered captured. Samples are taken in the middle of the upper part of the tube at 3, 10, 35, 55, 75, 120, 180 and 270 minutes. In every sampling, electronic pipettes are used to take 1.5 mL solution for optical density (OD) measurement by a photospectrometer and 10 μL solution for size distribution analysis using a microscope and computer software. A calibration curve relating OD and cell concentrations are experimentally obtained prior to the harvesting experiments. The gravity, fluid density and viscosity are assumed to be 9.81 ms^{-2} , 1000 kg m^{-3} and 0.00089 Pas respectively for calculations.

3. Result and Discussion

Numerical simulations of the developed PBE model are performed to predict number densities of the microalgae harvested after centrifugation and sedimentation. Figure 1a and 1b show the experimental data and simulation results of centrifugation and sedimentation respectively.

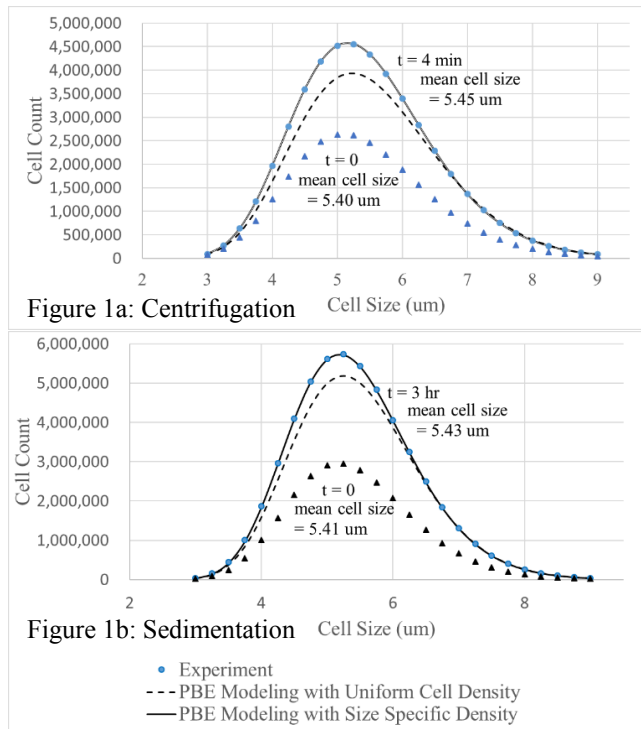


Figure 1. Experimental data and simulation results with uniform and size specific densities

The dash lines in the graph are the simulated results by assuming uniform cell densities ($1,070 \text{ kgm}^{-3}$) over different sizes, which the value is obtained from literature (Bonner, 1985). However, it is observed that the error with this assumption is significant as denoted in the figure. Therefore, the relationship between cell density and size is revised by analysing the data collected in the experiments. By evaluating the optical densities and size distributions of the centrifugation samples, the number of captured cells in each size is known. The sets of data are fitted into the PBE model and by allowing the travelling velocity $v(d)$ in equation (3) to vary, the velocity of each size of the cells is obtained. Finally, with equation (4) and (6), the size specific densities of cells can be calculated by plugging in the corresponding cell size and velocity.

The change in cell density with size is shown in Figure 2. The mean cell density is $1,110 \text{ kgm}^{-3}$ with a density range between $1,044$ to $1,137 \text{ kgm}^{-3}$, which is close to the literature value of $1,070 \text{ kgm}^{-3}$. The densities first increase with size and then decrease after the cells grow to a larger size of approximately 3.75 um . This observation perfectly aligns with the dark and light cycle of microalgae (Tamiya et al., 1953). First born cells,

also called nascent dark cells, consist of materials similar to those of their mother cells, which are composed of a higher portion of lipids with low densities. Along their growth to the next stage of active dark cells, fundamental cell materials are developed at the main priority so the cell densities rise. When the cells are mature and enter the stage of light cells, additional nutrients would be converted to lipids as an energy storage, resulting in the trend of varying cell densities throughout the life cycles.

Conventional methods to obtain algal densities mainly involve measurements of cell size and dry mass of the whole algal culture for calculating the average density value (Hu, 2014). However, it is too complicated to be possible to attain a full spectrum of cell densities varying with size accurately. This new approach to study the size specific behaviours of cells during harvesting can derive the relationship between cell density and size. Not only can it provide better understandings of cell characteristics as well as the growth kinetics, but also it can be performed without destroying the cells since drying is not required.

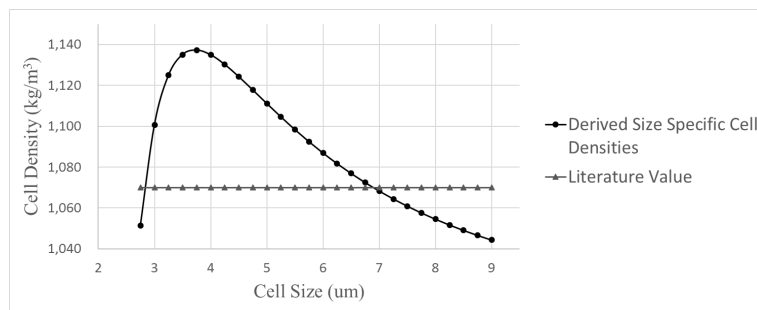


Figure 2. Size Specific Densities of Chlorella Cells

After substituting the derived size specific densities into the PBE model, as shown in Figure 1, the numerical solutions of both centrifugation and sedimentation converge on experimental results. This validates the accuracy and stability of the proposed model. After both harvesting methods, peaks of the cell size distributions shift to the right, representing that larger cells are generally more favorable as expected. This is because travelling velocities of cells in Stokes' Equation are proportional to the square of cell diameters, while in Langevin Equation, the velocities are inversely proportional to the square root of the diameters, which slightly hinders the shifts of the peaks to the right. On the other hand, the variations in size specific cell densities also affect the obtained size distributions since densities are directly proportional to terminal velocities of the cells.

4. Conclusion

Population Balance Equation is modified to model microalgae harvesting processes of centrifugation and sedimentation. Experimental data of the two methods is analysed by using a size specific approach and is combined with the mathematical model to predict harvesting efficiencies of the cells at different sizes. By studying optical densities and size distributions of the cells harvested after the experiments, a full spectrum of size specific densities is obtained with a range from 1,044 to 1,137 kgm^{-3} . It is found that the cell density first increase with cell size at the early stage until the size becomes around 3.75 μm and then decrease afterwards due to variations in cell compositions throughout

the life cycle. On the other hand, the numerical solutions obtained from the developed PBE model are validated by the experimental results, proving that it can efficiently generate stable and accurate solutions to characterise changes in number densities of microalgae at each size after harvesting. In this case, the harvesting efficiencies can be well predicted in relation to cell characteristics together with operation parameters of centrifugation and sedimentation.

References

1. M. Al hattab, A. Ghaly, A. Hammoud, 2015. Microalgae harvesting methods for industrial production of biodiesel: Critical review and comparative analysis. *Journal of Fundamentals of Renewable Energy and Applications* 5, 154.
2. JS. Bonner, 1985. The vertical transport and aggregation tendency of freshwater phytoplankton. PhD Dissertation, Clarkson University, Potsdam, New York.
3. MK. Danquah, L. Ang, N. Uduman, N. Moheimani, GM. Forde, 2009. Dewatering of microalgal culture for biodiesel production: exploring polymer flocculation and tangential flow filtration. *Journal of Chemical Technology and Biotechnology* 84, 7, 1078-1083.
4. BA. Grimes, 2012. Population balance model for batch gravity separation of crude oil and water emulsions. Part I: model formulation. *Journal of Dispersion Science and Technology* 33, 4.
5. MJ. Hounslow, RL. Ryall, VR. Marshall, 1988. A discretized population balance for nucleation, growth and aggregation. *AIChE Journal* 38, 1821-1832.
6. W. Hu, 2014. Dry weight and cell density of individual algal and cyanobacterial cells for algae. Master of Science Dissertation. University of Missouri-Columbia, Columbia, Missouri.
7. H. Lamb, 1945. *Hydrodynamics*. Dover Publications, Inc., 599.
8. P. Langevin, 1908. On the theory of Brownian motion. *Comptes Rendus Mathematique* 146, 530–533.
9. E. Pahija, Y. Liang, CW. Hui, 2017. Determination of microalgae growth in different temperature condition using a Population Balance Equation. *Chemical Engineering Transactions* 6, 721-726.
10. D. Ramkrishna, 2000. Population balances theory and applications to particulate systems in engineering. Academic Press. 355, 115.
11. G. Shelef, A. Sukenik, M. Green, 1984. Microalgae harvesting and processing: A literature review. Solar Energy Research Institute. Golden. DOI: 10.2172/6204677.
12. S. Sirin, 2013. Pre-concentration strategies for microalgae harvesting as biorefinery process chain. PhD Dissertation, Universitat Rovira I Virgil, Tarragona.
13. H. Tamiya, T. Iwanmura, K. Shibata, E. Hase, T. Nihei, 1953. Correlation between photosynthesis and light-independent metabolism in the growth of *Chlorella*. *Biochimica et Biophysica Acta* 12, 1-2, 23-40.

Total Site Utility Systems Structural Design Considering Environmental Impacts

Timothy G. Walmsley^{a,*}, Xuexiu Jia^a, Petar S. Varbanov^a, Jiří J. Klemeš^a, Yutao Wang^b

^a*Sustainable Process Integration Laboratory – SPIL, NETME Centre, Faculty of Mechanical Engineering, Brno University of Technology, Brno, Czech Republic*

^b*Department of Environmental Science and Engineering, Fudan University, Shanghai 200433, China*

walmsley@fme.vutbr.cz

Abstract

The aim of this study is to optimise the structural design of a central utility system for a Local Integrated Energy Sector, considering its environmental performance, such that Total Annual Cost is minimised. Environmental performance is captured by Greenhouse Gas emissions, Water, and Particulate Matter (PM) Footprints. To obtain the minimum cost solution, a Utility Systems Planner (USP) tool has been developed within the P-graph framework using a superstructure. The USP is applied to a case study with a chemical processing site and district energy demands. With the historically lower than average coal prices, the optimisation favours a utility system based on a coal boiler (68.4 MW) supplemented by geothermal clean energy plant (3 MW) to satisfy the 53 MW of process heat. Increasing the GHG emissions price from 5 €/t to 20 €/t shifts the optimisation in favour of natural gas as the primary fuel. Further increases in GHG prices to 95 €/t changes the optimal solution to biomass as the fuel with geothermal heat. Solitary focus on GHG emissions and its price, however, overlooks the immediate environmental impact of PM. Policy constraints on PM emissions to be at a safe level reverts the optimal solution to use natural gas as the fuel.

Keywords: Total Site; Process Integration; P-graph; Energy Planning.

1. Introduction

Growing global concern for pollution and irreversible environmental damage continues to drive governments and policymakers to implement incentives for clean and efficient energy supply. Reducing resource consumption through Locally Integrated Energy Sectors - LIES (Perry et al., 2008) and Total Site Heat Integration - TSHI (Klemeš et al., 1997) in addition to clean energy conversion technologies are meaningful ways to minimise harmful pollutants and conserve limited resources. Footprints metrics (Čuček et al., 2012) can help to capture the full environmental performance of an energy system. Quantifying the environmental footprints and intensities for a system represents a step forward (Ren et al., 2017), with the next step to influence industrial practice by identifying positive changes to typical technology selection, design, integration, and/or operation. For processing sites, the design and operation of the central utility system play a key role in achieving environmental performance goals.

There are three groups of studies that relate to the subject of the current paper. First, many recent studies have focused waste heat utilisation and utility systems optimisation without explicit consideration for environmental performance. For example, Oluleye et al. (2016) evaluated a range of waste heat utilisation technologies for industrial sites to increase overall energy efficiency. Second, studies have considered quantifying and comparing the environmental performance of a utility system to show the benefit of one technology over another. For example, Kelly et al. (2014) quantified the environmental performance of Combined Heat and Power (CHP) to demonstrate its important role in reducing electricity grid GHG emissions in the UK. Third, studies have focused on the design and optimisation of conventional central utility system, which consists of boilers and steam and gas turbine networks. For example, Luo et al. (2014) applied a multi-objective optimisation to determine a low-emissions utility system consisting of boilers, gas turbines, steam turbines, condensers, and let down valves, as well as emissions abatement technologies, with both coal and natural gas as the fuels. In general, these three areas of related research have lacked robust connections between the technology selection, optimisation, and integration of a site's central utility system and its environmental performance. The range of considered fuels and renewable energy sources, technologies, and environmental impacts have also been narrow. Addressing these gaps in literature is the focus of the study.

The aim of this study is to optimise the structural design of a Total Site (or LIES) central utility system, which cogenerates heating, cooling and power, considering its environmental performance such that Total Annual Cost is minimised. The study extends the work of Walmsley et al. (2018) that introduced a new Utility Systems Planner (USP) tool built as a P-graph superstructure (Friedler et al., 1996), to include estimations and pricing of three environmental footprints: Greenhouse Gas, Water, and Particulate Matter Footprints. The novelty of this work is derived from the comprehensive nature of the utility system superstructure in combination with accounting for environmental performance. Three scenarios are investigated using different environmental prices and constraints and, for each scenario, the USP superstructure is solved for minimum cost. A case study is presented to illustrate the new tool and its application.

2. Environmental Footprints

Utility systems are significant consumers of water and energy resources. In this study, environmental footprints related to these consumptions and emissions are incorporated into the optimisation of the utility system. Water Footprint (WF), initiated by Hoekstra and Huang (2002), has been well developed to quantify the amount of direct and indirect water use of a process, product or region. GHG Footprint (GHGF) is the total amount of GHG released from an operation (Čuček et al., 2012), expressed in the equivalent t of CO₂. A comprehensive estimation of WF and GHGF normally includes direct emissions from fuels and indirect emissions of fuel and material inputs. In studying a CHP system, Ren et al. (2018) found that >99.9 % of WF and GHGF was derived from emissions directly or indirectly relating to fuel consumption. As a result, this study approximates these footprints by only accounting for fuel-related emissions. Particulate Matter (PM) footprint measures the specific mass flow rate of particulates from direct and indirect fuel combustion (Yang et al., 2017). In this study, the PM Footprint (PMF) is defined by the PM10 criterion.

3. Utility System Planner

The USP superstructure, shown in Figure 1, contains a comprehensive range of fuels and resources as inputs to the central utility system, including Electricity, Biomass, Coal, Natural Gas (NG), Geothermal Heat, and Water. It also incorporates estimates for direct and indirect environmental footprints for GHG, PM10, and water. These are placed at the top of the superstructure. Below the fuels/resources are the energy conversion technologies, including Electric Boiler, Biomass Boiler, Coal Boiler, NG Boiler, NG Combined Cycle Gas Turbine (CCGT), NG Reciprocating Gas Engine (GE), Geothermal Clean Steam station, Thermal Vapour Recompression (TVR), Mechanical Vapour Recompression (MVR), Organic Rankine Cycle (ORC), Heat Pump (HP), Absorption Chiller (ACH), Electric Chiller (EC), Steam Turbine Stages (STS), and Let-down Valves (LV). These operations generate 9 intermediates utility levels. Varying shades of red through to orange for the lines and nodes indicate the hot utility levels from electricity through to hot water. Cold utility and water are indicated by lines with blue shades. These utilities then satisfy the energy demands of the industrial site and district heating and cooling.

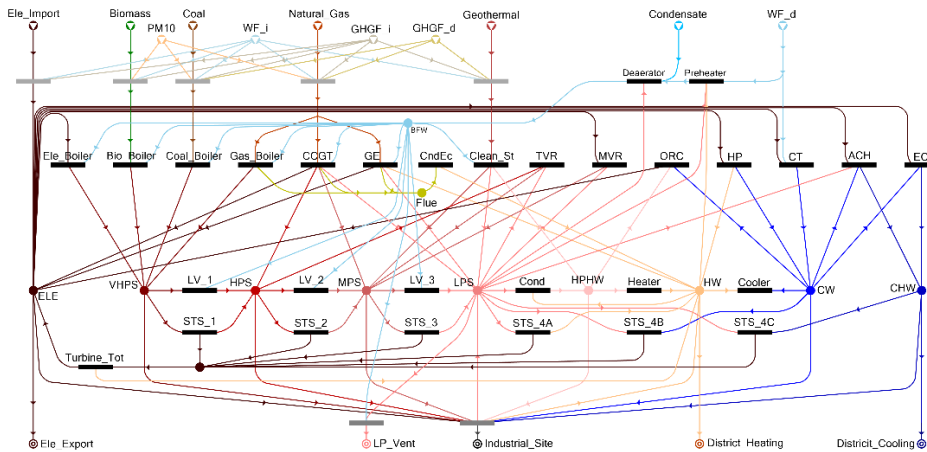


Figure 1: Utility Systems Planner tools – initial superstructure.

4. Method

The method to consider environmental performance in the USP involved three steps:

1) Estimate direct and indirect Emissions Factors (EF) for Greenhouse Gas, Water, and Particulate Matter (PM10). The estimation of each footprint is based on a coefficient approach, which can estimate the footprint of each fuel and resource input using Eq. (1).

$$F = F_d + F_i = \sum_{j=1}^n (\dot{m}_j \times EF_j)_d + \sum_{k=1}^n (\dot{m}_k \times EF_k)_i \quad (1)$$

Where F is the considered environmental footprint, EF is the emission factor for the considered impact, \dot{m} is the flow rate of the fuel, resource or material, subscripts d and i represent direct and indirect quantities.

2) Solve the USP superstructure to find the cost-optimal solution. The objective function of the USP is minimum Total Annual Cost (TAC), Eq. (2), i.e. the sum of utility cost (UC), annualized capital cost (CC), and operating and maintenance (OM).

$$TAC = UC + CC + OM \quad (2)$$

3) Project and input GHG emissions price increases to test various scenarios and constraints using the USP tool by finding the minimum cost solutions.

5. Locally Integrated Energy Sector case study

The considered LIES encompasses a representative industrial chemical processing site and the heating and cooling needs of the surrounding district. Figure 2 presents the Site Utility Grand Composite Curves for the industrial site and the entire LIES. The industrial site has a utility system Pinch between the MPS and LPS levels, which extends to between the MPS and CW levels once the district demands are included.

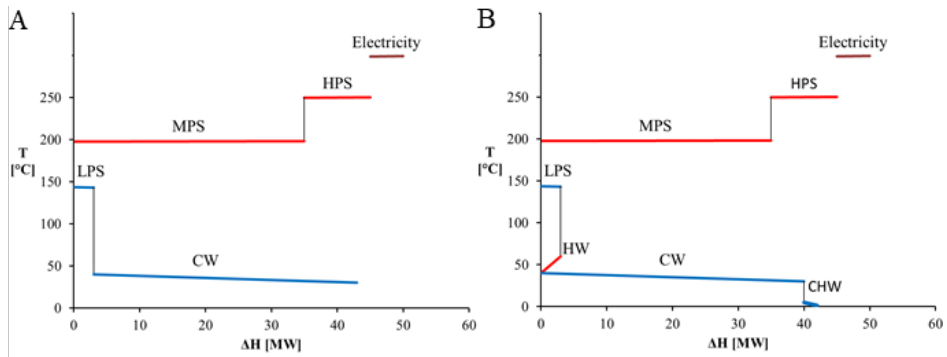


Figure 2: Site Utility Grand Composite Curves for the industrial site (A) and LIES (B).

Table 1 presents the energy prices and emissions factors for GHG and PM10 as well as water use rates (Gerbens-Leenes et al., 2008). For details on performance ratios of each energy conversion process, refer to the previous study by Walmsley et al. (2018).

Table 1: Initial industrial energy prices and GHG, PM10, and water emissions factors.

	Electricity	Biomass	Coal	NG	Geothermal
Price (€/GJ)	22.3	8.0	5.0	7.0	3.0
GHG Direct (kg/GJ)			91.4	55.2	1.3
GHG Indirect (kg/GJ)	77.6	0.8	0.4	5.5	0.2
Water Indirect (t/GJ)	6.8	70	0.2	0.1	0.5
PM10 Direct (g/GJ)		50	45	<0.1	

5.1. Scenario 1: Current energy and GHG emissions prices

The first scenario looked at the optimal solution based on present energy (Table 1) and GHG emissions prices (5 €/t). The energy prices are estimates based on Eurostat (2017). For these inputs, the USP consumes 68.4 MW_f of coal and 3 MW_f of geothermal heat. A two-stage steam turbine from VHPS to HPS and MPS (6.1 MW_{el}) means the self-sufficient in terms of electricity demand. This solution differs from Walmsley et al. (2018) due to the extension of the USP to include coal as a fuel option.

5.2. Scenario 2: Increasing GHG emissions price

The second scenario investigated the impact of varying the GHG emissions price from 5 €/t to 100 €/t (using 5 €/t increments) on the optimal USP solution with a focus on the fuel selection as shown in Figure 3. The GHG price increase was applied in the USP model to both direct (on-site) and indirect (off-site) GHG emissions. Conventionally, the emitter pays the cost of GHG emissions but then passes the cost on to the buyer, i.e. the utility operator. This means if the GHG price increases, the anticipated price of delivered fuels to a site will also increase to account for upstream GHG emissions cost.

Figure 3 shows that as the GHG emissions price increases from 5 €/t to 10 €/t, the amount of coal use slightly declined and replaced by geothermal. Once the price reached 15 €/t, the optimal solution comprised a coal boiler (60 MW_f), NG boiler (3 MW_f), and geothermal clean steam plant (10 MW_f) with the addition of an ORC unit (0.2 MW_{el}) to fully utilise the increased low-grade heat from geothermal. With the price between 20 €/t to 90 €/t, the solution changes to primarily use NG (56.9 MW_f) complemented by geothermal heat (10 MW_f) as well as electricity grid imports (0.3 MW_{el}). Once the price reaches 95 €/t the solutions changes to biomass (78.2 MW_f) with geothermal heat (10 MW_f) and grid electricity (0.3 MW_{el}).

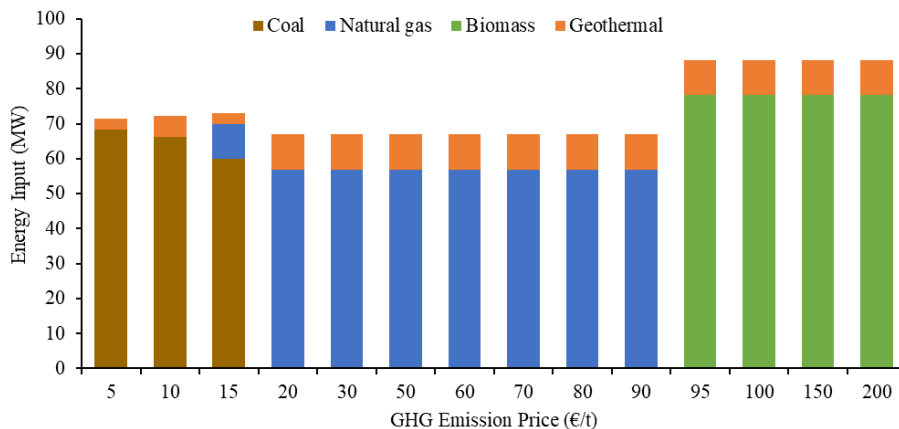


Figure 3: Impact of GHG emissions price on the optimal fuel selection.

5.3. Scenario 3: PM10 constraint

Sole focus on the present is likely to mean an industrial site will use coal as the primary energy source since it's the lowest cost option. The GHG price must quadruple before NG becomes the economically favoured option and may happen in the long-term future. Coal, however, has an immediate environmental impact – PM emissions (11.1 kg/h in the original solution). PM is a significant cause of haze as well as respiratory health issues. Using local regulations, a PM emissions constraint may be placed on the system design. If the PM10 rate was limited to <0.01 kg/h, NG is the lowest cost solution.

6. Conclusions

Environmental performance during the cost-optimisation of a central utility system has been quantified using Greenhouse Gas (GHG), Water, and Particulate Matter (PM) Footprints with the recently developed Utility Systems Planner (USP) tool. For the case study, current energy and emissions prices led to the cost-optimal solution of using coal

as the primary energy source. Significant price changes are needed to shift the cost-optimal solution away from coal. For example, the GHG price must quadruple before Natural Gas (NG) becomes the cost-optimal solution. However, excessive particulate emissions from coal and other solid fuels have proven to cause serious health issues. Placing a constraint on PM emissions shifts the cost-optimal solution to choose NG. Future work will look at the impact of water price on the USP optimisation.

Acknowledgement

This research has been supported by the EU project “Sustainable Process Integration Laboratory – SPIL”, project No. CZ.02.1.01/0.0/0.0/15_003/0000456 funded by EU “CZ Operational Programme Research, Development and Education”, Priority 1: Strengthening capacity for quality research, in a collaboration agreement with Fudan University, China.

References

- L. Čuček, J.J. Klemeš, Z. Kravanja, 2012, A Review of Footprint analysis tools for monitoring impacts on sustainability, *Journal of Cleaner Production*, 34, 9–20.
- Eurostat, 2017, Database - Eurostat, Eurostat <ec.europa.eu/eurostat/web/energy> accessed 24.04.2017.
- F. Friedler, J.B. Varga, E. Fehér, L.T. Fan, 1996, Combinatorically Accelerated Branch-and-Bound method for solving the MIP model of Process Network Synthesis, Chapter In: *State of the Art in Global Optimization*, Springer, Boston, USA, 609–626.
- W. Gerbens-Leenes, A.Y. Hoekstra, T.H. van der Meer, 2008, The water footprint of bioenergy and other primary energy carriers, *Value of water - No. 29*, Delft, The Netherlands.
- A.Y. Hoekstra, P.Q. Hung, 2002. Virtual water trade. A quantification of virtual water flows between nations in relation to international crop trade. *Value of water - No. 11*, Delft, The Netherlands.
- K.A. Kelly, M.C. McManus, G.P. Hammond, 2014, An energy and carbon life cycle assessment of industrial CHP in the context of a low carbon UK, *Energy*, 77, 812–821.
- J.J. Klemeš, V.R. Dhole, K. Raissi, S.J. Perry, L. Puigjaner, 1997, Targeting and design methodology for reduction of fuel, power and CO₂ on Total Sites, *Applied Thermal Engineering*, 17(8–10), 993–1003.
- X. Luo, J. Hu, J. Zhao, B. Zhang, Y. Chen, S. Mo, 2014, Multi-objective optimization for the design and synthesis of utility systems with emission abatement technology concerns, *Applied Energy*, 136(Supplement C), 1110–1131.
- G. Oluleye, M. Jobson, R. Smith, S.J. Perry, 2016, Evaluating the potential of process sites for waste heat recovery, *Applied Energy*, 161(Supplement C), 627–646.
- X.Y. Ren, X.X. Jia, P.S. Varbanov, J.J. Klemeš, Z.-Y. Liu, 2017, Targeting the cogeneration potential for Total Site utility systems, *Journal of Cleaner Production*, 170, 625–635.
- T.G. Walmsley, X. Jia, M. Philipp, A. Nemet, P.Y. Liew, J.J. Klemeš, P.S. Varbanov, 2018, Total Site utility system structural design using P-graph, *Chemical Engineering Transactions*, 63, 31–36.
- S. Yang, B. Chen, M. Wakeel, T. Hayat, A. Alsaedi, B. Ahmad, 2017, PM_{2.5} footprint of household energy consumption, *Applied Energy*, DOI: 10.1016/j.apenergy.2017.11.048.

Decarbonisation of the Industrial Sector by means of Fuel Switching, Electrification and CCS

Sandro Luh^{a,b,*}, Sara Budinis^a, Thomas J. Schmidt^{c,d} and Adam Hawkes^a

^a*Imperial College London, Dpt. of Chemical Engineering, South Kensington Campus, London SW7 2AZ, United Kingdom*

^b*ETH Zurich, Dpt. of Mechanical and Process Engineering, Raemistrasse 101, 8092 Zurich, Switzerland*

^c*ETH Zurich, Laboratory of Physical Chemistry, Dpt. of Chemistry and Applied Biosciences, Raemistrasse 101, 8092 Zurich, Switzerland*

^d*Paul Scherrer Institute, Electrochemistry Laboratory, 5232 Villigen PSI, Switzerland*
Sandro.Luh@web.de

Abstract

The industrial sector will have to undergo major changes in order to reduce its emissions with the goal of climate change mitigation. In this context, the iron and steel subsector accounts for the highest CO₂ emissions share. This work uses a simulation model of the global energy system and quantifies the impacts of different measures for CO₂ reduction (such as fuel switching, electrification and Carbon Capture and Storage - CCS) on investment and operation decisions. The reported scenarios consider the implementation of a CO₂ price as a policy instrument to decarbonise the industrial sector. The selected case study covers steel production in the USA up to the year 2050. The results show that single measures such as fuel switching, electrification and CCS adoption alone have a limited impact on the decarbonisation of the iron and steel sector and should be rather implemented all together in an integrated approach towards climate change mitigation.

Keywords: energy, emissions, steel, CCS, integrated assessment model

1. Introduction

The global industrial sector is characterised by high Total Final Energy Consumption (TFEC) (36 % of the global TFEC in 2014) and high CO₂ emissions (24 % of the total global CO₂ emissions) (IEA, 2017). Consequently, decarbonisation of this sector plays a crucial role in order to meet ambitious climate targets. A broad set of measures, including electrification (assuming an increasingly decarbonised power supply), fuel switching and CCS, is required to decarbonise this sector (IPCC, 2014).

This work is motivated by investigating the potential of increased electrification in the iron and steel subsector. The reasons for this are twofold. Firstly, among the five most energy-intensive industrial subsectors, the biggest increase of electricity-proportion from TFEC in ambitious climate scenarios is assumed for iron and steel (from 12 % in 2014 to 25 % in 2060 in the 2 °C scenario) (IEA, 2017). Secondly, steel making is the industrial subsector with the highest overall CO₂ emissions (28 % of the global industrial CO₂ emissions) (IEA, 2017). While electrification is even more likely to happen in non-energy-intensive subsectors, these subsectors do not account for large shares of CO₂

emissions (IEA, 2017). Therefore, iron and steel has the highest potential for overall CO₂ emission mitigation by increased electrification. This paper goes beyond the investigation of electrification's potential. Further, it aims to examine the potentials for fuel switching and CCS penetration as suitable options for decarbonisation pathways in the iron and steel subsector. In order to explore these potentials, the Industrial Sector Module (ISM) of the MUSE model (ModUlar energy system Simulation Environment) was used.

The World Steel Association (Worldsteel, 2016) has reported that 98 % of the globally mined iron ore is used as primary input for steel making and that global crude steel production has reached 1,670 Mt in 2014. Primary production technologies for crude steel are Blast Furnace-Basic Oxygen Furnace (BF-BOF), Direct Reduced Iron-Electric Arc Furnace (DRI-EAF) and Smelt Reduction-BOF (SR-BOF). Recycled steel (scrap) allows to produce secondary steel by means of the scrap-EAF technology (IEA-ETSAP, 2010).

2. Methodology

2.1. Integrated Assessment Models (IAMs)

IAMs are global models of the energy system, which quantify production of material commodities, consumption of energy commodities and their corresponding impacts on climate change over time (IPCC, 2014). They mainly consider representations of climate, human systems (e.g. energy and economic system) and natural systems in order to produce pathways of energy and greenhouse gas emissions in return (IPCC, 2014).

2.2. The MUSE model

MUSE is a global IAM where demand, conversion and supply of energy interact according to the market equilibrium principles. The model has a modular structure where each specific energy sector is modelled using a bottom-up approach based on a detailed techno-economic characterisation of the technologies as well as of the key indicators, which determine the stakeholders' investments in that sector (Giarola et al., 2017).

In this paper, the focus will be on the ISM of MUSE. The ISM first simulates how the demand of industrial commodities might grow as well as how the existing stock might retire. A linear decommissioning profile is in place in order to represent the remaining lifetimes of existing plants in the base years (2010 and 2014).

The total capacity $C_{new\ plants, t}$ that must be installed in a period t includes the retired capacity ($C_{retired, t}$) and the increase of the demand (D_t) from the previous period divided over a facility utilization factor (UF)

$$C_{new\ plants, t} = C_{retired, t} + \frac{(D_t - D_{t-1})}{UF} \quad (1)$$

Then the ISM uses a merit-order approach to rank the available technologies and decide which technologies to bring online until the demand is met. In particular, in order to make investment decisions for new plants, investors' key metric is the Net Present Value (NPV):

$$NPV = \sum_{t=1}^T \frac{CF_t}{(1+r)^t} - CF_0 \quad (2)$$

where CF_t represents the net cash flow during time period t , CF_0 is the total initial investment cost and r is the interest rate (assumed to be 10 % in the model).

When a technology is available, the Discounted Cash Flow (DCF) is taken into account in order to decide which plants among the existing plants are operated for production:

$$DCF = \sum_{t=1}^T \frac{CF_t}{(1+r)^t} \quad (3)$$

The metrics are based on CAPEX (specific CAPital EXpenditures) and OPEX (specific fixed OPERational Expenditures, including CO₂ price), which are defined in the model for each technology. The major constraints for new capacity addition of each technology include annual maximum growth rate, annual maximum capacity addition and total maximum capacity in a region.

2.3. Relevant assumptions and data sources

The MUSE model has been calibrated for 2010 and 2014 in order to match the overall fuel and electricity consumption from the IEA (2016). Regional demand projections of single commodities are based on regressions of historical data for the past 25 years (UNSD, 2017). Emissions from electricity generation and international trade of material commodities were not included in the case study.

Specific Energy Consumption (SEC) for the iron and steel sector has been selected according to the recent literature (IEA, 2017; Morfeldt et al., 2015; van Ruijven et al., 2016). Prices for fuel and electricity have been selected according to IEA's (2014) 450 ppm scenario. CAPEX were averaged from the investment cost given by Morfeldt et al. (2015) and van Ruijven et al. (2016). OPEX were selected from Morfeldt et al. (2015). For plants with CCS, CAPEX and OPEX are in 2010 48 % (2030: 32 %) higher than for plants without CCS (IEA-ETSAP, 2010). CCS energy penalty was assumed to be 12 % (IEA-ETSAP, 2010). An utilization factor of 90 % was assumed for all plants.

3. Case Study

3.1. Steel making

In this paper, the selected case study covers the production of iron and steel in the USA up to the year 2050. Steel is mainly produced by the technologies BF-BOF, DRI-EAF and scrap-EAF. In ambitious climate scenarios, the SR-BOF technology is expected to penetrate the market in the future (IEA, 2017). While the primary steel technologies mainly use iron ore as raw material, the scrap-EAF technology is reliant on the availability of scrap to produce secondary steel. The energy consumption of the latter technology requires 6.7 GJ per ton of produced crude steel, which is about one third of the average energy intensity of the primary technologies (IEA, 2017). A wider adoption of the scrap-EAF technology has the potential to decrease the specific energy consumption of the sector and therefore its greenhouse gas emissions. However, the scrap-EAF technology is limited by scrap availability, which is expected to increase globally by 80 % until 2050 as steel is highly recyclable (Worldsteel, 2016). The BOF and EAF technologies have accounted for 73.7 % and 25.8 % of global steel production in 2014, respectively (Worldsteel, 2016).

According to Worldsteel (2016), 80 Mt of crude steel were produced in the USA in 2010. In comparison to the global average (29 % in 2010), in the USA a large share of steel is produced by EAF technologies (61 %) (Worldsteel, 2016). The TFEC in this sector in the USA was 706 PJ in 2010 (IEA, 2016). In the same year, the iron and steel sector in the USA was accounting for CO₂ emissions from fuel combustion of 49.1 Mt_{CO₂} (IEA, 2016).

3.2. Scenarios

Two scenarios were simulated to analyse the decarbonisation of the iron and steel sector in the USA. The first scenario (S1) does not include a CO₂ price, while the second scenario (S2) includes a moderate price on CO₂ emissions (averaged by Budinis et al. (2016) from '450 ppm full technology'-scenarios of selected IAMs in IPCC (2014)).

The maximum annual growth rate for the scrap-EAF technology was set to 1 %, based on expected development of scrap availability in the USA (Worldsteel, 2016). Growth rate for primary steel production technologies was set to 3 % in order to meet the projected steel demand while showing investments in a wider range of technology options.

4. Results and Discussion

Figure 1 shows the overall supply of steel by technology for S1 (left hand side) and S2 (right hand side). Both scenarios show an increasing share of the scrap-EAF technology (from 52 % to 58 % for S1 and to 61 % for S2). The remaining demand is met by BF-BOF and DRI-EAF technologies. In both scenarios, technologies with relatively high share of electricity consumption (i.e. both EAF technologies) increase their overall market share from 61 % up to 82 % (S1) and 79 % (S2). However, as the availability of scrap is a limiting factor, EAF technologies cannot penetrate the market even further.

Figure 2 is reporting fuel shares for the two scenarios. While coal, the cheapest but also the most CO₂ producing fuel, covers in 2050 62 % of the market in S1, it only covers 16 % of the market in S2, due to the implemented CO₂ price. In contrast, natural gas and electricity gain increasing market shares in S2. It should be considered that the TFEC in S1 increases between 2010 and 2050 by 69 %, while it increases in S2 only by 28 %.

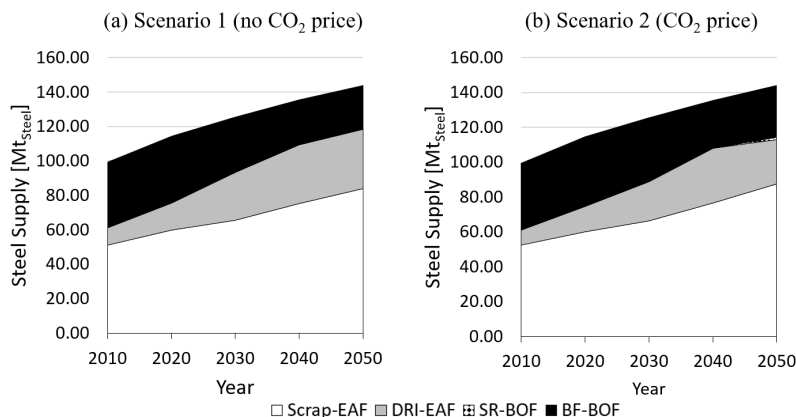


Figure 1. Projections of steel supply by different process technologies in the USA between 2010 and 2050. (a) shows S1, (b) shows S2.

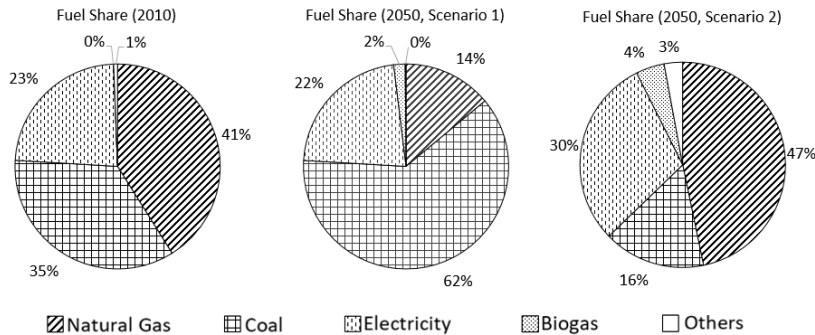


Figure 2. Fuel shares in USA's iron and steel sector in 2010 and in 2050 (S1 and S2). 'Others' include forest residues, heavy fuel oil, liquefied petroleum gas and naphtha.

Even though the share of EAF technologies increases in both scenarios, overall electrification is only found in S2. No overall electrification is found in S1, because more fuels (mainly coal) with a lower net calorific value than today will be used. This results in a higher demand of fuel per electricity and does therefore offset the increasing electrification from the growing share of EAF technologies.

Figure 3 reports the produced CO₂ emissions, disaggregated in CO₂ emitted to the atmosphere and CO₂ captured by CCS, for both scenarios. The results show that CO₂ emissions increase (+79% until 2050) when no CO₂ price is in place (S1). While total produced CO₂ emissions in S2 stay almost constant over time, an increasing share of these emissions will be captured and stored. The results show that the implementation of the CO₂ price results in 2050 in 30% of the steel produced by CCS technologies. As this happens to technologies with relatively high CO₂ emissions, up to 61% of the produced CO₂ is captured. This trend shows that the CO₂ price makes investors tend to invest into plants that provide CCS. However, the main barriers for CCS are political and societal issues, which were not taken into account within the model.

Emissions from electricity generation are not considered within this study (in 2010, specific CO₂ emissions were 0.52 kt_{CO2}/GWh, resulting in additional 23,500 kt_{CO2} for the iron and steel sector (EIA, 2012)). The electrification in S2 is consequently only an effective measure for decarbonisation when the power sector can generate sustainable and cost-effective electricity, by means of renewable sources and CCS. Overall, a CO₂ price is pushing the iron and steel sector towards less CO₂ producing technologies and fuels.

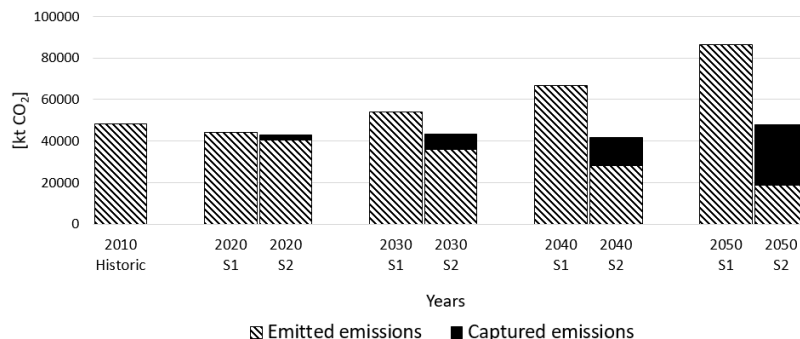


Figure 3. Produced CO₂ emissions (for S1 and S2) from the production of iron and steel in the USA, disaggregated in CO₂ emitted to the atmosphere and CO₂ captured by CCS.

5. Conclusion

This work has shown the penetration of different technologies into the market, with and without CO₂ price, in order to analyse potentials for fuel switching, electrification and CCS to decarbonise the industrial sector with focus on iron and steel in the USA.

The results have demonstrated that the assumed CO₂ price pushes investors towards less emitting fuels. Moreover, with and without CO₂ price, electrification takes place by means of EAF technologies' adoption. However, without CO₂ price this effect will be offset due to use of fuels with low net calorific value. Finally, the price for CO₂ emissions leads investors to invest in CCS plants, especially for CO₂ intensive technologies.

Each of the three measures has limited impact on the decarbonisation of the iron and steel sector, therefore they should be implemented all together in an integrated approach towards climate change mitigation. While CCS could be limited by political and societal factors that were not taken into account by the model, electrification by means of a shift to EAF technologies is limited by scrap availability. Therefore, the scrap recycling rate should be maximised. Other measures, such as energy and material efficiency, should also be implemented in order to reach ambitious climate goals.

Acknowledgement

The authors acknowledge the financial support of the Sustainable Gas Institute, Imperial College London, and of ETH Zurich.

References

- S. Budinis, S. Krevor, N. Mac Dowell, N. Brandon & A. Hawkes, 2016, Can technology unlock 'unburnable carbon'?, Sustainable Gas Institute, Imperial College London
- EIA (U.S. Energy Information Admin.), 2012, available at: <https://eia.gov/> [12/12/2017]
- S. Giarola, S. Budinis, J. A. Sachs, A. Hawkes, 2017, Long-term decarbonisation scenarios in the industrial sector, International Energy Workshop 2017
- IEA (International Energy Agency), 2014, World Energy Outlook 2014
- IEA, 2016, World Extended Energy Balances, UK Data Service, available at: <http://stats.ukdataservice.ac.uk/> [01/12/2017]
- IEA, 2017, Energy Technology Perspectives 2017, including database, available at: <http://iea.org/etp/etp2017/> [01/12/2017]
- IEA-ETSAP (Energy Technology Systems Analysis Programme), 2010, Technology Brief, available at: <https://iea-etsap.org/index.php/energy-technology-data/> [01/12/2017]
- IPCC, 2014, Climate Change 2014: Mitigation of Climate Change. Contribution of Working Group III to the Fifth Assessment Report of the Intergovernmental Panel on Climate Change
- J. Morfeldt, W. Nijs, S. Silveira, 2015, Journal of Cleaner Production, vol. 103, p. 469 – 482
- B. J. van Ruijven, D. P. van Vuuren, W. Boskaljon, M. L. Neelis, D. Saygin, M. K. Patel, 2016, Resources, Conservation and Recycling, vol. 112, p. 15 - 36
- UNSD (United Nations Statistics Division), 2017, available at: <http://data.un.org> [02/12/2017]
- Worldsteel (The World Steel Association), 2016, available at: <https://worldsteel.org/> [01/12/2017]

Solvent use optimization on polyphenols extraction from grape marc involving economical aspects

R. de Mattos,^{a*} B. Zecchi,^a P. Gerla,^a A. Ferrari^b

^a*Department of Unitary Operations in Chemical Engineering and Food Engineering- Chemical Engineering Institute - Engineering School – Universidad de la República, Julio Herrera y Reissig 565, CP 11300, Montevideo, Uruguay*

^b*Chemical & Process Systems Engineering Group – Chemical Engineering Institute - Engineering School – Universidad de la República, Julio Herrera y Reissig 565, CP 11300, Montevideo, Uruguay*

*rdmattos@fing.edu.uy

Abstract

Polyphenol's extraction from grape marc (GM) represents an interesting alternative for valorisation of an industrial waste, with an important economic and environmental impact. Solid-liquid extraction is improved by using higher quantities of solvent, but this generates a much more energy intensive process for solvent evaporation in later stages. The objective of this study was to find the optimal operational conditions in a polyphenol's extraction process from GM, aiming to reach the maximum economical profit for the system. It is considered a multistage batch solid-liquid extraction system using fresh solvent (ethanol-water mixture) in each stage. A MINLP structure is proposed for the optimization with the following decision variables: the number of stages, the solvent/GM mass ratios and temperatures for each stage. The difference between the income from product sales (powder extract rich in polyphenols) and the operational costs (basically related with energy consumption) was maximized. The MINLP was solved using DICOPT solver in GAMS, and also employing a genetic algorithm in Matlab. In both cases identical results were obtained, with low computational costs, indicating that non-convexities would be negligible. The obtained results show that for optimum solvent use three contact stages must be realized, and the solvent/GM mass ratio and temperature for all stages must be the same adding 4 liters of solvent at 80 °C per GM kilogram. In these conditions the objective function reaches a value of 3.12 dollars per GM kilogram.

Keywords: Grape marc, Polyphenols, Solid-liquid extraction, Optimization.

1. Introduction

Grape marc (GM) represents an industrial waste from wine fermentation having high polyphenol content with antioxidant properties which is beneficial on human health. Extracts obtained from GM have a wide range of applications such as cosmetics, food and pharmaceutical industry (Fontana et. al; 2013). Conventional solid-liquid systems are the most applied technologies for antioxidant extraction from vegetal sources (Zhu et. al; 2015).

Proper selection of operational conditions is essential to achieve maximum global performance of the process in conventional solvent extraction (CSE). Operation

variables having high incidence on the CSE include: the type of solvent used, the time and the form of contact between solid and solvent, the solvent/solid mass ratio and the solvent temperature (Chan et al., 2014). Ethanol-water mixtures are an attractive option for use in industrial processes because of its low cost and its safety quality for use in food. Previous studies have confirmed that a 50 % (v/v) concentration of ethanol in the hydroalcoholic solution is the most effective for recovery of phenolic compounds from grape residues (Bucic'-Kojic et al. 2009). Other unit operations are required after extraction, such as distillation, evaporation and spray drying to obtain powder as final product. Polyphenol's extraction is improved by using higher quantities of solvent, but this generates a much more energy intensive process for solvent evaporation in later stages. There are many works published in which operating variables such as temperature and the amount of solvent used for polyphenols extraction from GM have been optimized. Most of them are based on response surface methodology maximizing the extraction yield (Shi et al., 2003). However, none of these optimization works consider economic aspects involved in the unit operations such as distillation, evaporation and drying required after the extraction to obtain the final product.

The aim of this study was to apply first-principles models and modern optimization methods to find the optimal operational conditions in a polyphenol's extraction process from GM, aiming to reach the maximum economical profit for the global system.

2. Materials and Methods

2.1. Process Description

The process to obtain a powder extract rich in polyphenols from GM is represented in Figure 1 (GM drying and milling stages previous of extraction process are not presented in the figure).

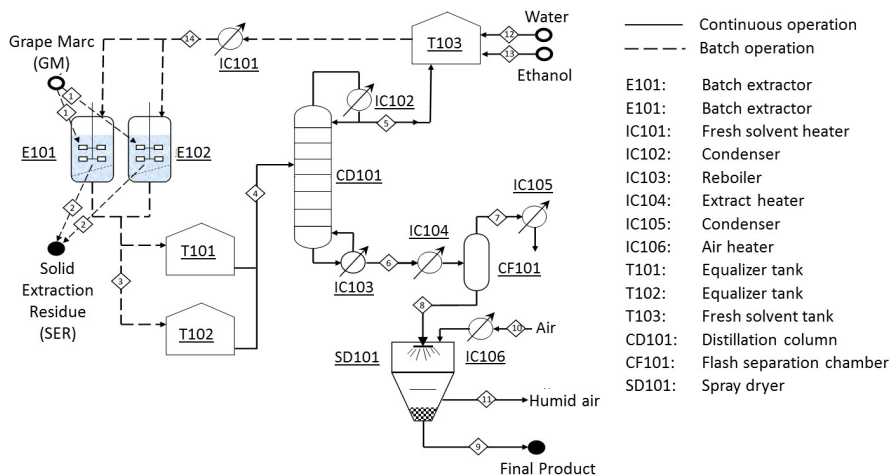


Figure 1: Proposed process for the obtention of a polyphenolic extract from GM.

A multistage sequential batch solid-liquid extraction system is considered (units E101 and E102). Cs_o is the total polyphenols compounds (TPC) in GM in grams of gallic acid equivalent (GAE) per kilogram [gGAE/kg]. The extraction solvent is a solution of 50 %

ethanol/water (v/v) and fresh solvent is used in each extraction stage. Extracts obtained are equalized (units T101 and T102) and then are fed to a distillation column (unit CD101). The residue from this column is fed into a one-stage flash evaporation system (units IC104, CF101 and IC105), without recovering the water stream going out of IC105. The concentrated extract is spray dried (unit SD101) obtaining a powder rich in polyphenols with a moisture content (X_p) of 11.1 % (dry basis) and a concentration of TPC ($C_{TPC,p}$) of 0.3 grams of GAE per gram of dry matter (Spigno et al.; 2007).

2.2. Polyphenols extraction modelling

Equilibrium at each extraction stage was assumed. This assumption is reasonable if the contact time in each stage is around 60 minutes, according to kinetic data from batch extraction published by Sant'Anna et al. (2012). Final TPC concentration in extracts after k stages is calculated from the TPC balance according to Eq. (1).

$$C_{f,k} = \frac{C_{S_{k-1}}}{L_k + \frac{K_k}{\rho_s}} \quad (1)$$

Where $C_{f,k}$ [gGAE/m³] is the final TPC concentration in the extract in k stage; $C_{S_{k-1}}$ [gGAE/kg], the final TPC concentration in the solid in $k-1$ stage; L_k [m³/kg], the solvent/GM mass ratio used in k stage; K_k [dimensionless], the TPC partition coefficient in k stage; and ρ_s [kg/m³], the solid density. The final TPC concentration in the solid at k stage is obtained by mass balance according to Eq. (2).

$$C_{S_k} = C_{S_{k-1}} - L_k C_{f,k} \quad (2)$$

The temperature incidence at k stage (T_k) is evaluated by the TPC partition coefficient function conforming to Eq. (3).

$$K_k = K_o \exp \left[\frac{\Delta H^\circ}{R} \left(\frac{1}{T_k + 273} - \frac{1}{T_o + 273} \right) \right] \quad (3)$$

Where K_o is the partition coefficient evaluated at T_o [°C] temperature; R , the ideal gas constant (1.987 cal/mol.K); and ΔH° [cal/mol], an enthalpy parameter of the model.

The following values were determined in a recent work (in progress by the authors): C_{S_o} =25.5 gGAE/kg, ρ_s =868.7 kg/m³, T_o =60 °C, K_o =5.20 and ΔH° =11.3 cal/mol. These values were determined with a more complete model (also including the dynamic behavior of the extraction processes) by fitting with experimental data published by Sant'Anna et al. (2012).

2.3. Product sale income and operation costs predictions

Product sale income (*PSI*) is calculated according to Eq. (4) in dollars per kilogram of dried and milled GM that is subjected to extraction. It is assumed that all TPC extracted with solvent is present in the final product obtained at the spray dryer.

$$PSI = PSP \left(\frac{1 + X_p}{1000 \cdot C_{TPC,p}} \right) \left[\left(\sum_{k=1}^m L_k C_{f,k} \right) - L_{ret} C_{f,m} \right] \quad (4)$$

Where PSP is the product sale price, assumed at 47 \$/kg (Casas et al; 2008); m the number of contact stages each of them with the addition of fresh solvent; and L_{ret} [m³/kg], the extract volume retained in solid extraction residue (SER) per kilogram of GM. Laboratory separation experiments allowed to estimate that SER obtained from one kilogram of GM, retains one liter of liquid extract ($L_{ret}=0.001$ m³/ kg).

The total operating cost in dollars per kilogram of dry and milled GM is calculated according to Eq. (5). Where $\alpha=66$ \$/m³ includes the costs due to: 1) solvent replacement not recovered from the extract, 2) energy dissipation in IC102 and IC105, and 3) energy consumption in IC103, IC104 and IC106; $\beta=0.08$ \$/m³°C represents the energy cost in IC101; T_{mean} [°C] is the arithmetic mean of all T_k values; T_{in} [°C], the solvent temperature in T103 (estimated to 32 °C); and $\gamma=0.24$ \$/kg represents the cost of solvent replacement not recovered from SER. α , β and γ values were calculated considering a price of 0.6 \$/kg for ethanol (Dimou et al., 2016) and 1.9 \$/t for process water required for solvent replacement. Energy dissipation cost was estimated for a price of 0.015 \$/t of cooling water (Dimou et al., 2016) and considering a range of 10 °C in the cooling tower. Energy consumption cost was estimated for a fuel oil price of 0.72 \$/L, and assuming a boiler that generate 13 kilograms of steam per liter of fuel oil. Solvent and energy dissipation/consumption requirements were calculated from the corresponding mass and energy balances. It is assumed that the ethanol retained in SER is not recovered. Mass and energy balances in distillation column were solved by a process simulation software (Aspen Plus, V8.4) resulting that 99.8 % of ethanol is recovered in distilled stream. Equilibrium conditions were assumed at 40 °C in CF101, and the outlet temperature in IC104 was set at 100 °C in order to prevent thermal degradation of phenolic compounds. Energy efficiency in SD101 was assumed to 57 %.

$$COST = \alpha \left[\left(\sum_{k=1}^m L_k \right) - L_{ret} \right] + \beta \left(\sum_{k=1}^m L_k \right) (T_{mean} - T_{in}) + \gamma \quad (5)$$

2.4. MINLP strategy for problem resolution

The structure of the optimization problem (MINLP) is given by Eq. (6). The difference between incomes from product sales and costs is assumed as the objective function to be maximized. Decision variables are: y_k , binary variables indicating whether stage k is performed ($y_k=1$) or not ($y_k=0$); and L_k and T_k , the solvent/GM mass ratio and temperature for each stage respectively. A maximum of seven contact stages with fresh extraction solvent is allowed (k : 1 to 7). The MINLP problem was solved in GAMS win664 24.8.5 software using DICOPT solver, and in Matlab R2015 using *ga* function for genetic algorithm implementation. It allows comparing performances between deterministic and non-deterministic tools and trying to deal with eventual non-convexities in the problem structure. The codes were executed in an Intel(R) Core(TM) i3-3240 CPU@3.4 GHz processor with 8 GB RAM memory.

$$\begin{aligned}
 & \max \quad z(x, y) = PSI(x, y) - COST(x, y) \\
 & x: L_k, T_k \\
 & y: y_k \\
 & \text{s.t:} \\
 & \text{Eq (2) to Eq.(5) and } C_{f,k} = (1 - y_k)C_{f,k-1} + y_k \left(\frac{Cs_{k-1}}{L_k + \frac{K_k}{\rho_s} + \varepsilon} \right) \\
 & y_{k+1} \leq y_k ; y_k L_{\min} \leq L_k \leq y_k L_{\max} ; T_{in} \leq T_k \leq T_{in} + y_k \Delta T_{\max} \\
 & L_k ; T_k \in \mathfrak{R}^n ; y_k \in \{0,1\}
 \end{aligned} \tag{6}$$

Where $\varepsilon=1\text{E-}7 \text{ m}^3/\text{kg}$ is a constant small value just introduced to avoid division by zero errors; $L_{\min}=0.004 \text{ m}^3/\text{kg}$ is the minimum solvent/GM mass ratio to ensure sufficient contact between solid-solvent and an adequate condition for mixing; $L_{\max}=0.05 \text{ m}^3/\text{kg}$ is a sufficiently large value; and $\Delta T_{\max}=48 \text{ }^\circ\text{C}$ is the maximum temperature increment allowed in IC104. This limits the maximum extraction temperature to $80 \text{ }^\circ\text{C}$ in order to prevent thermal degradation of phenolic compounds.

3. Results and Discussion

The solution found for the problem was the same with both methods and with low computational costs (resolution time of 4.22 s for ga function and 1.88 s for DICOPT). The optimal values for decision variables are shown in Table 1. The objective function reaches a value of 3.12 \$/kg and only three contact stages must be realized to maximize it. The cost associated to this optimal value is in the same order of magnitude respect to the one obtained in a similar process from Dimou et al. (2016). Respect to the optimal solvent/GM mass ratio, the results are the same for all stages and equal to the lower bound ($L_{\min}=0.004 \text{ m}^3/\text{kg}$). This result suggests that it is convenient to dose the extraction solvent in minimum quantities and in many contact stages. The optimal extraction temperature in all stages is $80 \text{ }^\circ\text{C}$, which is the maximum allowed in the problem to avoid possible polyphenols thermal degradation. This result is reasonable since as higher the temperature, higher the partition coefficient. As deterministic and non-deterministic approaches performed similar respect to the optimal solution, it could be stated that the current problem would present a convex nature. In this sense, the results can be interpreted as global optimization. Experimental data (Sant'Anna et al.; 2012) used for fitting the model, set a higher solvent/GM mass ratio ($0.05 \text{ m}^3/\text{kg}$) than the optimal, so new data should be obtained for further model validation in optimal conditions. In order to analyze the confidence of the results, a sensitivity analysis was carried out considering a variation of $\pm 30 \%$ for two relevant inputs (Cs_o and PSP), one at a time, resulting in the same values for the decision variables.

Table 1: Results for the optimization problem

k values	y_k	$L_k (\text{m}^3/\text{kg})$	$T_k (^\circ\text{C})$
For $k=1$ to 3	1	0.004	80
For $k=4$ to 7	0	0	32

4. Conclusions

A multistage sequential batch solid-liquid polyphenol's extraction process from GM was modeled and implemented in Matlab and GAMS. It assumed equilibrium conditions for each extraction stage in order to work with a simple but representative model. Optimal and confident operational conditions (number of stages, solvent/GM mass ratio, and temperatures) were found in order to achieve the maximum economical profit for the global system. Deterministic and non-deterministic optimization approaches were applied for solving the corresponding MINLP problem. Both methods revealed similar results, with a low computational burden, indicating that non-convexities would be negligible in this problem. A more completed work including model validation with new experiments, and the extraction process dynamics considering all solid-liquid contact times as additional decision variables, is in progress by the authors.

5. Acknowledgements

The research that brought the experimental results on this publication was economically supported by Agencia Nacional de Investigación e Innovación under the code POS_NAC_2016_1_130867.

References

- A. Bucic'-Kojic', M. Planinic', S. Tomas, L. Jakobek, M. Seruga, 2009, Influence of solvent and temperature on extraction of phenolic compounds from grape seed, antioxidant activity and colour of extract, *Int. J. Food Sci. & Technol.* 44, 2394-2401.
- E. Casas, M. Faraldi, M. Bildstein, 2008, Manual de Compuestos bioactivos a partir de residuos del procesamiento de la uva, BIOACTIVE-NET, https://www.ainia.es/html/portal_del_asociado/uva.pdf
- C. Chan, R. Yusoff, G. Ngoh, 2014, Modeling and kinetics study of conventional and assisted batch solvent extraction, *Chem. Eng. Research and design* 92, 1169-1186.
- C. Dimou, A. Vlysidis, N. Kopsahelis, S. Papanikolaou, 2016, Techno-economic evaluation of wine lees refining for the production of value-added products, *Biochem. Eng. J.* 116, 157-165.
- A.R. Fontana, A. Antonioli, R. Bottini, 2013, Grape Pomace as a Sustainable Source of Bioactive Compounds: Extraction, Characterization, and Biotechnological Applications of Phenolics. *J. Agric. Food Chem.* 61, 8987-9003.
- V. Sant'Anna, A. Brandelli, L.D. Ferreira Marczak, I.C. Tessaro, 2012, Kinetic modeling of total polyphenol extraction from grape marc and characterization of the extracts. *Separation and Purification Technology.* 100, 82-87
- J. Shi, J. Yu, J. Pohorly, J.C. Young, M. Bryan, Y. Wu, 2003, Optimization of the extraction of polyphenols from grape seed meal by aqueous ethanol solution, *Food, Agric. & Environment* 1(2), 42-47.
- G. Spigno, L. Tramelli, D.M. De Faveri, 2007, Effects of extraction time, temperature and solvent on concentrations and antioxidant activity of grape marc phenolics, *J. Food Eng.* 81, 200-208.
- F. Zhu, B. Du, L. Zheng, J. Li, 2015, Advance on the bioactivity and potential applications of dietary fibre from grape pomace. *Food Chemistry.* 186, 207-212.

Integrated Process Design and Optimization of a Nitrogen Recovery in Natural Gas Processing with Varying Feed Composition

Yongseok Lee,^a Youngsub Lim,^b Chonghun Han^{a,*}

^a*Seoul National University, School of Chemical and Biological Engineering, Building 302, 1 Gwanak-ro Gwanak-gu, Seoul, Korea, Republic of*

^b*Seoul National University, Department of Naval Architecture and Ocean Engineering, Building 34, 1 Gwanak-ro Gwanak-gu, Seoul, Korea, Republic of*

chhan@snu.ac.kr

Abstract

In this study, two cryogenic nitrogen recovery processes integrated with natural gas liquefaction and NGL (Natural Gas Liquid) recovery are optimized using a commercial chemical process design simulator, gProms Processbuilder v.1.1 which is powerful at complex optimization problem. The difference of each process is the way the nitrogen is removed from product LNG: Stand-alone and integrated one for nitrogen removal unit. These two processes are compared with each other in terms of plant specific energy (kWH/kg_{LNG}) with respect to varying nitrogen content in the feed gas. In order for clear comparison, each process would meet the same product specification of flowrate and composition for NGL, LNG, and vent N₂ stream and nitrogen contents in the feed gas vary from 0 to 20mol%. Consequently, as the nitrogen content in the feed increases, the specific energy also increases for both processes while the integrated configuration becomes more efficient than the other after around 13 mol%. It should be noted that all of the optimization results for each process configuration are improved compared with those from other researches which have the similar configuration. From this study, we could be ready for a recent trend occurring in natural gas processing. This trend would last for more than decades and the way this study aimed could be reasonable guidelines for other chemical process designs.

Keywords: Process Integration, Optimization, Industrial Application

1. Introduction

In recent small to mid-size onshore LNG plants and some shale gas export projects, nitrogen recovery in natural gas processing has been of great importance as nitrogen content in the pipeline feed gas varies over time and location. When it comes to nitrogen recovery, possible nitrogen sinks in natural gas process are product LNG (N₂ less than 1 mol%), fuel gas, and/or vent gas (N₂ more than 99 mol%). Among these three sinks, the demand of fuel gas which is generated conventionally from an end-flash drum decreases as compressor drivers are gradually switched from steam turbines to aero-derivative gas turbines or electric motors which require less or no fuel gas for energy source in a plant. Then the rest of nitrogen should be vented to atmosphere while meeting the environmental regulations which limit the hydrocarbon content less than 1mol% in vent gas. These two major trends in recent LNG projects of varying feed composition and decreasing plant fuel

demand makes it necessary to completely recover nitrogen from methane in the product LNG, as traditional LNG process would generate large fuel gas and lose too much methane with the same conditions. In this study, two major nitrogen removal options are optimized and compared in terms of plant energy efficiency: one for standalone NRU, and the other for Integrated NRU. From this results, design favourability could be evaluated for each process for varying nitrogen content in the feed.

2. Conceptual Process Design

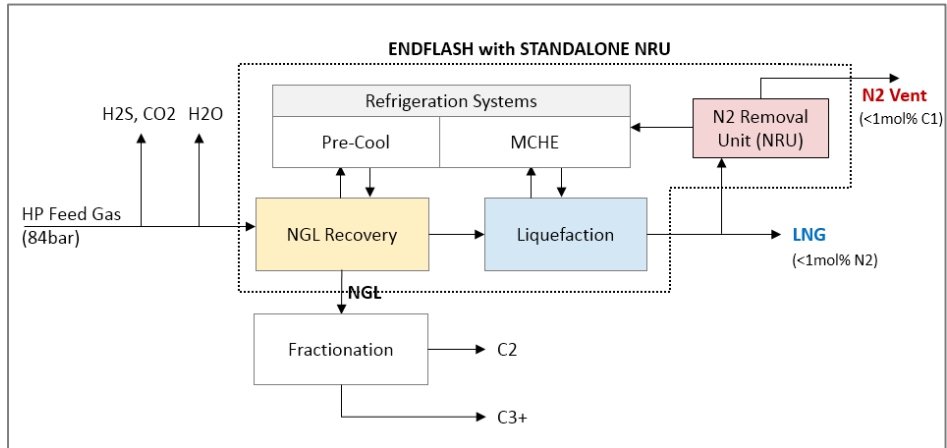


Figure 1. LNG Production Process with Standalone NRU

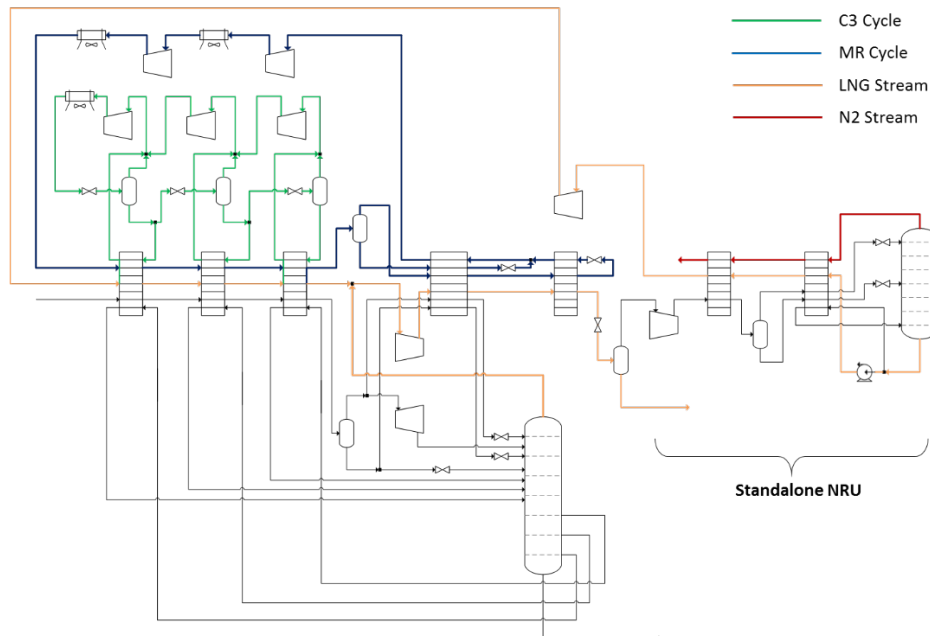


Figure 2. Process Flow Diagram for LNG Production Process with Standalone NRU

Integrated processes for LNG and NGL co-production with two nitrogen recovery schemes are illustrated in Figure 1 and 3, and each process flow diagrams are shown in Figure 2 and 4. For standalone NRU, NGL is firstly withdrawn from treated feed gas through GSP (Gas Subcooled Process) and C1 rich overhead stream is condensed and subcooled heading for end-flash drum to produce LNG. As nitrogen content in the feed increases, more flash gas from the drum is generated to meet the N₂ content specification in product LNG. In order to recover enough C1, N₂ is completely separated from C1 through standalone NRU and vented to atmosphere. For integrated one, N₂ separated between NGL recovery and liquefaction so that cryogenic heat source necessary in NRU is provided from refrigeration system in complete heat transfer network.

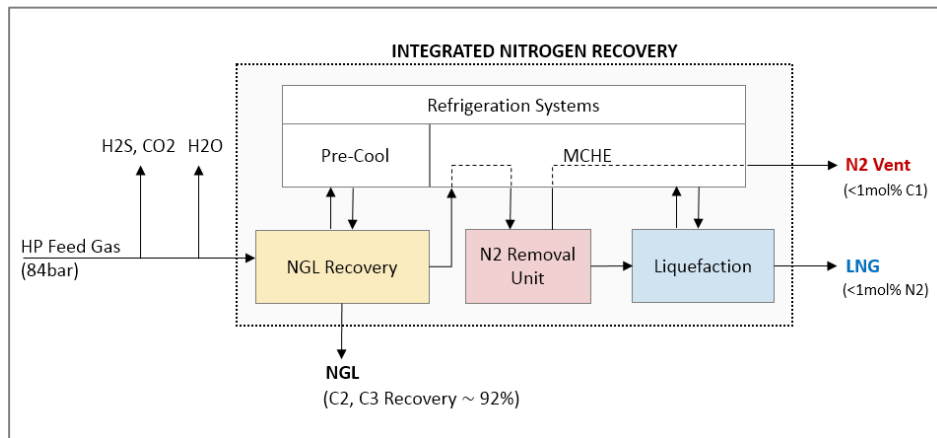


Figure 3. LNG Production Process with Integrated NRU

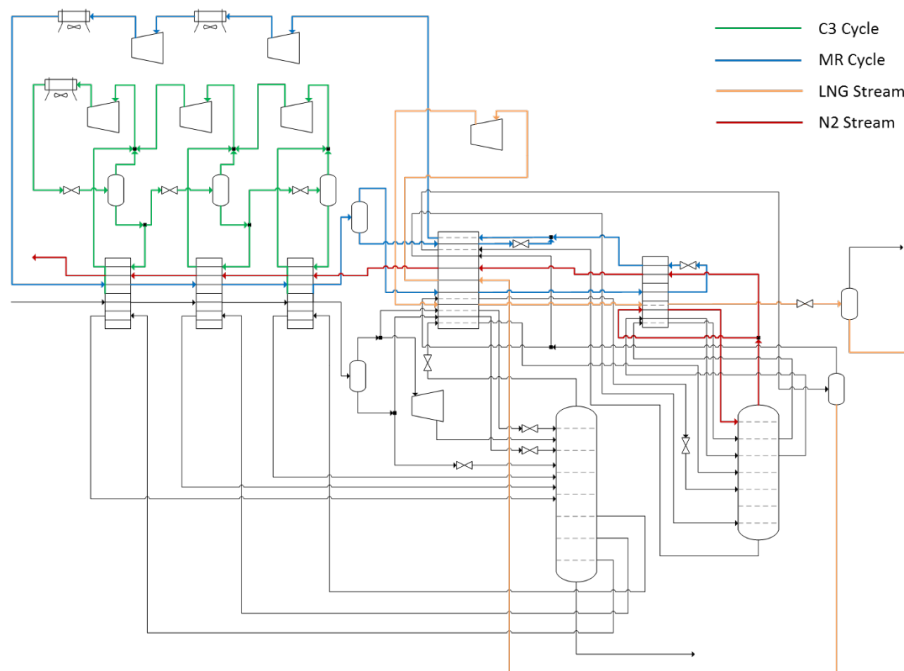


Figure 4. Process Flow Diagram for LNG Production Process with Integrated NRU

3. Optimization

Optimization structure is listed in Table 1. Objective function is specific power which is total power consumption for 1kg LNG production for 1 hour. In order to compare their energy efficiency clearly, product specification like C1, C2 recovery and impurity content and thermodynamic feasibility in heat transfer are constrained. As both standalone NRU and integrated one have same scheme for NGL recovery and refrigeration cycle (C3-MR) before nitrogen recovery section, they share similar control variables for optimization. Exceptionally for NRU, as standalone one should have additional compressor and two heat exchanger and integrated one draws two vapour side streams in rectifying section in the column for minimizing exergy loss in heat transfer, it makes few difference in the variable selection. In this chapter only 5 mol% N₂ Feed is evaluated for brevity.

Table 1. Optimization Structure for Standalone and Integrated NRU Process

	Standalone NRU	Integrated NRU
Objective Function	specific power [kWH/kg _{LNG}]	
Control Variables		
NGL Recovery	Cold reflux temperature Cold reflux flow ratio Side stream(1, 2, 3) flowrate	
MR Cycle	Pressure (High/Low) Heat exchanger outlet temperature (4th, 5th) Flowrate Composition(N ₂ , C1, C2, C3)	
C3 Cycle	Flowrate Split flow ratio	
NRU	NRU bottom pressure NRU reboling split ratio/ Flowrate NRU reflux split ratio/ Flowrate Compression ratio (Feed) Side stream Flowrate (1, 2)	
Inequality Constraints	C1 recovery > 0.99, C2 recovery > 0.92 N ₂ content in LNG < 0.01 C1 content in vent N ₂ < 0.01 MSHE MTA(Minimum Temperature Approach) > 3K	

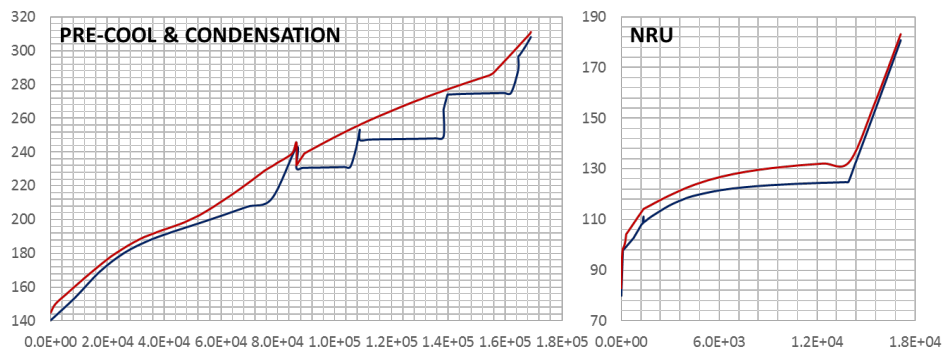


Figure 5. Composite Curve of Multi-stream Heat Exchangers in Standalone NRU process

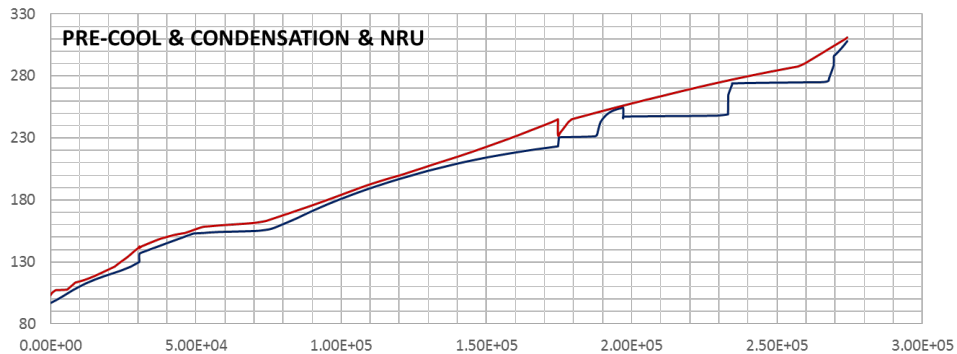


Figure 6. Composite Curve of Multi-stream Heat Exchangers in Integrated NRU process

After optimization, objective function value of each process is 0.39 for standalone and 0.48 kWh/kg_{LNG} for integrated one. Composite curves of heat transfer in all of the MSHE (Multi-Stream Heat Exchanger) are shown in Figure 5, 6. For standalone one, NRU plot is added as it has additional two heat exchangers independent on main heat transfer section for NRU feed precooling. It can be noticed from both plots that optimization of which the objective function is specific power minimize exergy loss in whole heat transfer section narrowing the space between hot and cold curves meeting 3K MTA constraints.

4. Varying Feed Composition

With respect to varying nitrogen content in the feed from 0 to 20 mol%, both processes can be optimized with similar optimization technique as shown in Table 2 and Figure 7. All three process also including base case (C3-MR LNG production process without NRU) lose their energy efficiency as nitrogen content in the feed increases, and it could be seen that any design with nitrogen content around 20 mol% is unfeasible for plant operation. Especially for base case, it should be noted that C1 recovery for LNG production drops significantly from 1.0 to 0.1 as nitrogen content increases because simple end-flash after liquefaction cannot afford to recover enough methane in order to meet the product specification of nitrogen content less than 1 mol% (C1 recovery for other cases is set to 1 for any nitrogen content). For two alternatives for nitrogen recovery, around 13mol% of nitrogen in the feed is the criteria for thermodynamically favourable design for LNG production. Integrated scheme also has less equipment like multi-stream heat exchanger and compressor so that it could have more favourability for highly leaner feed gas which contains larger nitrogen.

Table 2. Objective function values for varying nitrogen content in the feed

N ₂ Content		0	5	10	15	20
C1 Recovery for Base		1.00	0.79	0.56	0.28	0.08
Specific Power [kWh/kg _{LNG}]	Base	0.31	0.32	0.41	0.62	1.53
	Standalone	-	0.39	0.53	0.77	1.08
	Integrated	-	0.48	0.64	0.72	0.95

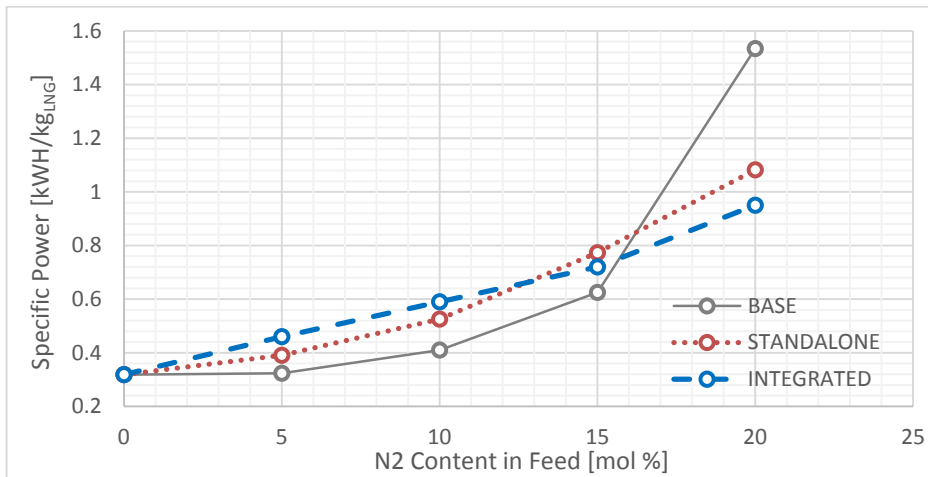


Figure 7. Comparison of Specific Power w.r.t. Varying N₂ Content in Feed

5. Conclusions

For varying feed composition in natural gas processing, two major nitrogen recovery scheme are optimized and evaluated for design favourability in terms of energy efficiency. In order to compare both processes clearly, product specification and thermodynamic feasibility like minimum temperature approach in heat transfer are fixed and optimization is performed for all discrete points (each process with nitrogen from 0 to 20 mol%) even for base case. Consequently two NRU options could completely recover nitrogen with reasonable energy efficiency for nitrogen content below 20 mol% in the feed. Especially integrated option becomes more favour after around 13mol% that standalone one, so that integrated design could be practically recommended for highly lean feed gas from unconventional natural gas sources like shale gas.

References

- B. Ghorbani, M. H. Hamed, and M. Amidpour, 2016, Development and optimization of an integrated process configuration for natural gas liquefaction (LNG) and natural gas liquids (NGL) recovery with a nitrogen rejection unit (NRU), *Journal of Natural Gas Science and Engineering*, 34, 590-603
- C. M. Ott, M. J. Roberts, S. R. Trautmann, and G. Krishnamurthy, 2015 Oct., State-of-the-art nitrogen removal methods from Air Products for liquefaction plants, *LNG journal*.
- F. Chen, M. J. Okasinski, and T. M. Sabram, 2016 April, Novel Nitrogen Removal Schemes For LNG Plants with Electric Motor Drive and Varying Feed Composition, *LNG 18 Perth Australia*.
- M. Mehrpooya, M. Hossieni, and A. Vatani, 2014, Novel LNG-based Integrated Process Configuration Alternatives for Coproduction of LNG and NGL, *Industrial & Engineering Chemistry Research*, 53, 17705-17721
- M. Wang and A. Abbas, 2016, Natural gas liquids (NGL) recovery in the liquefied natural gas production, *Computer Aided Chemical Engineering*, 38, 1207-1212

Sequential Flowsheet Optimization: Maximizing the Exergy Efficiency of a High-Pressure Water Scrubbing Process for Biogas Upgrade

Alberto T. Penteadó^{a,*}, Jan C. Schöneberger^b, Erik Esche^a, Hamid R. Godini^a, Günter Wozny^a and Jens-Uwe Repke^a

^a*Process Dynamics and Operations Group, Technische Universität Berlin, Sekretariat KWT 9 - Straße des 17. Juni 135, 10623 Berlin, Germany*

^b*Chemstations Europe GmbH, Lindencorso - Unter den Linden 21, 10117 Berlin, Germany*
alberto.penteado@tu-berlin.de

Abstract

Biogas is an important renewable energy source and potential raw material for the chemical industry. Its utilization frequently requires a treatment and/or upgrade step. The aim here is to maximize the exergy efficiency of a high-pressure water scrubbing process for upgrading biogas into biomethane by coupling a sequential modular simulation flowsheet with different optimization algorithms. By setting adequate operating pressures, and reducing cycle water and stripping air flowrates, an exergy efficiency of 92.4 % is reached.

Keywords: biogas, biomethane, high-pressure water scrubbing, sequential modular simulation, black-box optimization

1. Introduction and Motivation

Biogas is a mixture containing 50-75% CH₄, 30-50% CO₂, as well as H₂O, N₂, O₂, and minor amounts of contaminants such as H₂S, NH₃, aromatics, and siloxanes (Rasi et al., 2007). It is produced from the anaerobic digestion of different substrates by methanogenic bacteria. It plays an important role in a sustainable energy mix because, differently from other renewables, its production does not rely solely on climatic factors. The European Union has set a target of having 20% of its 2020 energy demand supplied by renewable systems, out of which at least 25% can originate from biogas (Holm-Nielsen et al., 2009). Biogas can be utilized for electricity and heat generation within a Combined Heat and Power (CHP) plant. The methane in biogas can alternatively be converted into syngas via reforming (Chen et al., 2017) or ethylene via oxidative coupling (Penteadó et al., 2017). A base treatment, consisting of cooling and drying followed by the removal or reduction of the H₂S content, is required prior to most biogas utilizations (Holm-Nielsen et al., 2009). The biogas upgrade consists in the removal of CO₂ to increase the gas' calorific value to that of pipeline-quality natural gas. The resulting gas is often called biomethane and can be employed as a vehicular fuel, in fuel cells, or injected into the natural gas grid.

Different processes are available to upgrade the biogas. Sun et al. (2015) published a major review on the available methods. The selection is done on a case-by-case basis, by considering the specific raw biogas composition, amount and nature of contaminants, production scale, application requirements, and available infrastructure and utilities. The most common ones are High Pressure Water Scrubbing (HPWS), Amine Scrubbing (AMS), Pressure Swing Adsorption (PSA), Gas Permeation (GP), and Cryogenic Distillation (CD) (Sun et al., 2015). Hybrid concepts can also be

employed to explore the main advantages of each technology (Scholz et al., 2013). The HPWS is one of the most used biogas upgrade technologies in Europe (Scheffelowitz et al., 2015). A quantitative comparison of the upgrade cost is presented in Figure 1. The calculation is done with the Biomethane Calculator (Miltner et al., 2013). Given inputs such as feed gas flow and composition; desired upgrading technology; and the required biomethane purity, the software yields methane recovery, production, investment and operating costs, and the specific biomethane production cost, thus enabling a preliminary assessment of upgrading plants. It can be seen from Figure 1, that for the gas composition and flow rate used in this study and specified in Table 1, the HPWS is very competitive. It tends to get even more competitive for larger scale plants.

A number of authors have assessed the HPWS process from an energy and economic standpoint. Rottunno et al. (2017) modeled this process in Aspen Plus using rigorous rate-based simulations to design the absorption and stripping columns. Budzianowski et al. (2017) also developed non-equilibrium Matlab models for a number of different configurations of HPWS and Near Atmospheric Pressure Water Scrubbing (NAPWS), using plant data for model validation, and finally estimating the energy requirement for the upgrade process in each configuration. The study concludes that using high pressure absorption, intermediary flash for methane recovery, and stripping for water regeneration provides an efficient solution. Wylock and Budzianowski (2017) later extend the previous contribution considering only the scrubber-flash-stripper configuration and focusing on the sizing of the column packing height, and further performance estimation for the system. While all of these studies perform the sizing and rating of the absorption and stripping columns using rigorous rate-based models, the operating conditions are determined by heuristics, experience, or by carrying out extensive simulations and sensitivity studies with one parameter being varied at the time, potentially leading to sub-optimal results. In contrast, the present study aims at determining the operating conditions for a HPWS process by means of mathematical optimization. The objective is to maximize the process' exergy efficiency given 8 continuous and bounded decision variables subject to product specification constraints. To this purpose, a framework for the optimization of sequential modular simulations is developed.

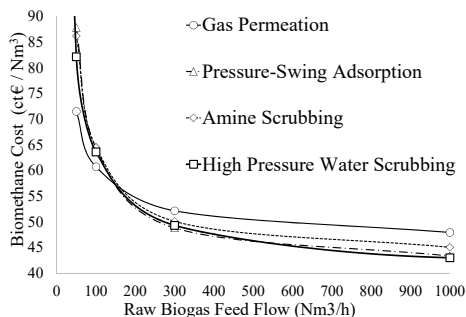


Figure 1: Comparison between different biogas upgrading technologies

2. Methods

A HPWS process using a scrubber-flash-stripper configuration is modeled in the software Chemcad7. The simulation flowsheet is presented in Figure 2. The raw biogas (stream 1) is pressurized in a three stage compression section (equipment 1, 20 and 4) with intermediate cooling (equipment 2, 21, 5) in the upstream of the absorption column or scrubber (equipment 6). In the scrubber, the biogas is contacted with pressurized water fed to the top of the column. The gases dissolve in water, allowing the removal of the CO_2 and H_2S , but also causing some CH_4 losses. The biomethane (stream 8), leaves the column at the top. The bottoms (stream 9) is then flashed (equipment 8) to an intermediate pressure in order to recover some CH_4 , which is recycled back to an intermediate compression stage. The flash's liquid (stream 12) enters the second column, where CO_2 and H_2S are stripped out with air (stream 13), which is fed via a blower (equipment 10). The stripper (equipment 9) is operated at a pressure of 1.1 bar. The regenerated water is partially purged

(stream 18), mixed with fresh water (stream 20), pumped to the absorption pressure (equipment 17), and passes through a heat exchanger (equipment 18) before being recirculated back to the absorption column. The gas stream leaving the stripper column passes a bio-filter (equipment 19) that removes the H_2S before leaving the process e.g. through a stack. The 8 continuous decision variables to be determined are the two intermediary pressures in the compression, the absorption pressure, the temperature of the gas and the liquid fed to the absorber, the cycle water and stripping air flowrates, and the cycle water purge ratio. Their initial values and bounds are listed in Table 2.

2.1. Modeling

The Volume-Translated Peng-Robinson Equation of State is used to model the system, allowing for consistent physical and chemical exergy calculations in both liquid and gas phases in all streams. The table of binary parameters is completed by using data from Schmid et al. (2014) and with Twu parameters from Dortmund Data Bank (2015). More modeling details and validations are described by Schöneberger and Fricke (2017).

A typical biogas composition, as given by Rasi et al. (2007), is assumed according to Table 1. The biomethane must contain at least 96 mol% of CH_4 and maximum 20 ppmv of H_2S . Compressors have an adiabatic efficiency of 50 % and inter-stage cooling to 5 K above dew point. Cooling water is available at 298 K.

Cycle water make-up is provided as saturated steam at 1.1 bar. This is done to reflect the exergy consumption for the water treatment and penalize fresh-water consumption, which would otherwise have zero physical exergy. The water pump (equipment 17) has an adiabatic efficiency of 70 %. Stripping air is fed at 298 K, 1.013 bar, and dry. Pressure drop in exchangers is neglected. The absorber and stripper are packed columns using Mellapak 250Y with 20 and 10 stages respectively. The use of non-equilibrium models largely increases computational effort and column flooding can cause non-convergence of the flowsheet, which are drawbacks for the application of such models within optimization. A rate-based model is, therefore used to estimate Murphree efficiencies that are then set constant in the equilibrium stage model used in the optimization.

Table 1: Raw biogas feed stream

Flow	300	Nm ³ /h
Temperature	348	K
Pressure	1.0	bar
Composition		
N ₂	0.97	mol%
O ₂	0	mol%
CH ₄	60	mol%
CO ₂	36	mol%
H ₂ S	0.03	mol%
H ₂ O	3.0	mol%

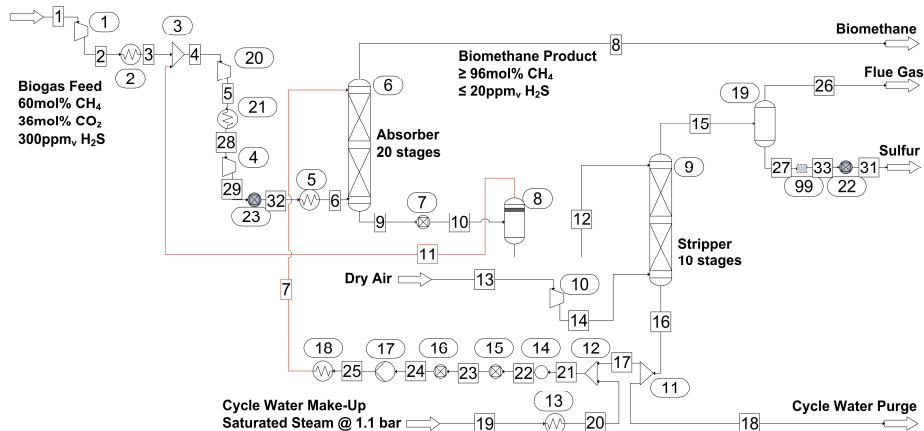


Figure 2: Simulation flowsheet of the HPWS process implemented in Chemcad7

2.2. Exergy Calculation

The exergy efficiency is taken as the main objective for the optimization, as it reflects thermodynamic inefficiencies that translate into operating cost (energy consumption) and environmental impact (methane slip). The exergy rate of a stream is given as the sum of its physical and chemical exergy rates, calculated as in Equations 1 and 2 respectively. The thermodynamic environment is defined at 298 K and 1.0 bar. Diederichsen reference environment and ideal mixing is assumed for chemical exergies. For the work streams in the compressors and pump, the exergy rate is equal to the calculated power. The exergy efficiency, given by Equation 3, is defined as the ratio between the recovered exergy rate in the form of the biomethane product stream and all exergy fed to the process in the form of electricity to run compressors and the pump, the biogas feed stream, the stripping air, and the steam make-up for the water cycle.

$$\dot{E}_s^{PH} = \dot{H}_s(T_s, p_s, z_s) - \dot{H}_s(T^{ref}, p^{ref}, z_s) - T^{ref} \cdot [\dot{S}_s(T_s, p_s, z_s) - \dot{S}_s(T^{ref}, p^{ref}, z_s)] \quad (1)$$

$$\dot{E}_s^{CH} = \dot{n}_s \cdot \sum_{c=1}^{NC} [z_{s,c} \cdot e_c^{CH} + R \cdot T^{ref} \cdot z_{s,c} \cdot \ln(z_{s,c})] \quad (2)$$

$$\eta_{exergy} = \frac{\dot{E}_8}{\dot{W}_1^{el} + \dot{W}_{20}^{el} + \dot{W}_4^{el} + \dot{W}_{10}^{el} + \dot{W}_{17}^{el} + \dot{E}_1 + \dot{E}_{19} + \dot{E}_{13}} \quad (3)$$

3. Optimization Framework

The aim is to maximize the value of the exergy efficiency. Constraints are set for a minimum CH₄ content of 96.0 mol% and a maximum H₂S content of 20 ppm_v in the biomethane product gas. To solve this NLP, a framework is developed in Matlab by using the OPC Toolbox to communicate with the Chemcad7 flowsheet as a black-box simulation server, as well as different optimizers. The implementation allows for an easy and flexible objective formulation in Matlab, by reading the enthalpy and entropy rates from the Chemcad7 flowsheet, and calculating the exergy rates and then returning the negative value of the exergy efficiency to the optimizer. In a similar fashion, the constraints are evaluated inside Matlab by reading the composition of the product stream. To avoid additional unnecessary time-consuming simulations, values are saved in variables accessible by both functions. With a single black-box simulation, it is possible to evaluate the objective and the constraints. The same is true for numerical evaluation of gradients and jacobians, if required by the optimizer.

Black-box optimization with sequential modular flowsheets is difficult because the problem structure typically causes the objective function to be discontinuous, non-differentiable, not defined in many points, noisy, and subject to relaxable and unrelaxable nonlinear constraints from the simulation environment (Martelli and Amaldi, 2014). The use of gradient-based algorithms, which are the preferred choice, can therefore become very challenging. The numerical gradients might be undefined, expensive to evaluate, or simply of no use because of poor quality. Hence, direct search methods became very popular among engineers and researchers to deal with this type of optimization (Martelli and Amaldi, 2014).

To allow for enough flexibility, both gradient-based and direct-search algorithms are implemented in the framework: Matlab's Genetic Algorithm (GA) and Particle-Swarm Optimization (PSO) solvers, and the Mesh Adaptive Direct Search (MADS) algorithm NOMAD (Le Digabel, 2011) provided in the OPTI-Toolbox (Currie and Wilson, 2012). In order to use the available Sequential Quadratic Programming (SQP) algorithm provided with Chemcad7, an additional VBA unit operation is added to the flowsheet and programmed to calculate the objective value. It is not the aim of this study to provide a rigorous solver benchmark, but rather demonstrate the flexibility and try to achieve better results by exploiting the advantages of each search method.

Table 2: Decision variables and results

Variables	Units	Lower Bound	Upper Bound	Initial Value	Results			
					GA	PSO	MADS	SQP
Exergy Efficiency	%	0	100	55.48	90.16	92.34	92.39	92.40
Function Evaluations	-	0	-	-	6,480	2,053	530	461
Intermediate Pressure	bar	1.1	15.0	2.6	6.91	6.48	8.30	7.72
Intermediate Pressure 2	bar	1.1	20.0	7.5	13.07	12.53	11.50	14.48
Absorber Pressure	bar	1.1	25.0	17.5	21.42	21.15	24.87	25.00
Liquid Feed Temperature	K	303	353	305	332	303	303	303
Gas Feed Temperature	K	303	353	323	328	351	353	303
Cycle Water Flowrate	Nm ³ /h	5	500	236	29.19	30.61	25.21	25.92
Stripping Air Flowrate	Nm ³ /h	10	1000	850	690.92	35.54	39.14	42.21
Purge Ratio	-	0.01	0.1	0.03	0.017	0.01	0.01	0.01

4. Results

The optimal value for the purge ratio is found to be at its lower bound. Even though a smaller purge requires a higher water recirculation rate and more pump duty, the effect of the reduced fresh water requirement and its associated exergy is much more pronounced. As expected, the liquid feed temperature is also at its lower bound. The gas feed temperature has little influence to the efficiency. The intermediate pressure 2 can be almost independently optimized. However, the intermediary/flash pressure, absorption pressure, cycle water flow rate, and stripping air flow rates are highly coupled and many points with high exergy efficiencies, i.e. $\geq 90\%$, have been found at fairly different conditions as intermediary results. A higher absorption pressure increases the compression duty, but reduces the required cycle water and stripping air flow rates to keep the product purity constraints fulfilled.

In this study, a rational exergy efficiency of 92.40 % has been reached. A large reduction in cycle water and stripping air flow rates could be achieved, while keeping the product within specification. Although not exactly an exergy efficiency, Rotunno et al. (2017) applied a conversion factor of 0.41 to transform primary energy into electricity and then calculated an efficiency of 87.3 % for a HPWS process using the same configuration. The results of this study are, thus in the same order of magnitude from previously published results. The optimal absorption pressure is found to be in its upper bound and above the initial point of 17.5 bar and above the range of 7-12 bar found as typical values in other literature cases such as (Budzianowski et al., 2017), (Wylock and Budzianowski, 2017), and (Rotunno et al., 2017). The reason is probably that considering the water make-up stream to be saturated steam over-penalizes the water usage and leads to an operating point at a higher pressure and with lower water recirculation and fresh water consumption. Nevertheless, if the water make-up stream would be liquid at ambient conditions, it would have zero physical exergy and lead to excessive use of water. To avoid this, a different objective function, e.g. operating cost, can be used in future studies.

The SQP algorithm is the most efficient and effective of the tested solvers, reaching a stationary point within 47 iterations and 461 function evaluations. The gradients are built by central finite differences with the default step size of 0.005. It is essential to keep the step size long enough compared to the simulation tolerance. Most numeric gradient methods used in optimization have a way lower step size by default, e.g. 10^{-6} , while tear-stream tolerances in sequential simulations is often 10^{-3} or 10^{-4} . The solver NOMAD with orthogonal polling directions provided great usability with significant objective improvement with its parameters left to default. For GA and PSO, a way larger number of function evaluations is required to reach similar objective values.

5. Conclusion

In this contribution, the operating conditions of a high-pressure water scrubbing process using a scrubber-flash-stripper configuration is determined by mathematical optimization. An operating point with 92.40 % exergy efficiency is achieved using a SQP algorithm. A flexible framework for the optimization of sequential modular simulations is developed and presented. Future works include extending its usability to handle larger and more complex flowsheets with integer and binary decisions. Parallelization must also be addressed given the speed-up potential.

6. Acknowledgement

Alberto T. Penteado acknowledges the funding from CAPES / Brazil (11946/13-0). Financial support from the Cluster of Excellence Unifying Concepts in Catalysis by the German Research Foundation (DFG EXC 314) and from the German Federal Ministry of Education and Research (BMBF 10044119) are also gratefully acknowledged.

References

- W. M. Budzianowski, C. E. Wylock, P. A. Marciniak, 2017. Power requirements of biogas upgrading by water scrubbing and biomethane compression: Comparative analysis of various plant configurations. *Energy Conversion and Management* 141, 2–19.
- X. Chen, J. Jiang, K. Li, S. Tian, F. Yan, 2017. Energy-efficient biogas reforming process to produce syngas: The enhanced methane conversion by O_2 . *Applied Energy* 185, 687–697.
- J. Currie, D. I. Wilson, 2012. Opti: Lowering the barrier between open source optimizers and the industrial matlab user. In: N. Sahinidis, J. Pinto (Eds.), *Foundations of Computer-Aided Process Operations*. Savannah, Georgia, USA. Dortmund Data Bank, 2015. Ddb explorer version 2015. URL www.ddbst.com/free-software.html
- J. B. Holm-Nielsen, T. Al Seadi, P. Oleskowicz-Popiel, 2009. The future of anaerobic digestion and biogas utilization. *Bioresour. Technol.* 100 (22), 5478–5484.
- S. Le Digabel, 2011. Algorithm 909. *ACM Transactions on Mathematical Software* 37 (4), 1–15.
- E. Martelli, E. Amaldi, 2014. Pgs-com: A hybrid method for constrained non-smooth black-box optimization problems. brief review, novel algorithm and comparative evaluation. *Computers and Chemical Engineering* 63, 108–139.
- M. Miltner, A. Makaruk, M. Harasek, Oct. 2013. Biomethane calculator version 2.1.1. Software. URL bio.methan.at
- A. T. Penteado, M. Kim, H. R. Godini, E. Esche, J.-U. Repke, 2017. Biogas as a renewable feedstock for green ethylene production via oxidative coupling of methane: Preliminary feasibility study. In: *Chemical Engineering Transactions*. Vol. 61. The Italian Association of Chemical Engineering, pp. 589–594.
- S. Rasi, A. Veijanen, J. Rintala, 2007. Trace compounds of biogas from different biogas production plants. *Energy* 32 (8), 1375–1380.
- P. Rotunno, A. Lanzini, P. Leone, 2017. Energy and economic analysis of a water scrubbing based biogas upgrading process for biomethane injection into the gas grid or use as transportation fuel. *Renewable Energy* 102, 417–432.
- M. Scheftelowitz, N. Rendsberg, V. Denysenko, J. Daniel-Gromke, W. Stinner, K. Hillebrand, K. Naumann, D. Peetz, C. Hennig, Thran D., M. Beil, J. Kasten, L. Vogel, 2015. *Stromerzeugung aus biomasse (vorhaben iia biomasse): Zwischenbericht mai 2015*.
- B. Schmid, A. Schedemann, J. Gmehling, 2014. Extension of the vtp group contribution equation of state: Group interaction parameters for additional 192 group combinations and typical results. *Industrial & Engineering Chemistry Research* 53 (8), 3393–3405.
- M. Scholz, B. Frank, F. Stockmeier, S. Falß, M. Wessling, 2013. Techno-economic analysis of hybrid processes for biogas upgrading. *Industrial & Engineering Chemistry Research* 52 (47), 16929–16938.
- J. Schöneberger, A. Fricke, 2017. Optimizing the exergetic efficiency of a pressurized water process for bio gas cleaning. *Chemical Engineering Transactions* 57, 457–462.
- Q. Sun, H. Li, J. Yan, L. Liu, Z. Yu, X. Yu, 2015. Selection of appropriate biogas upgrading technology—a review of biogas cleaning, upgrading and utilisation. *Renewable and Sustainable Energy Reviews* 51, 521–532.
- C. E. Wylock, W. M. Budzianowski, 2017. Performance evaluation of biogas upgrading by pressurized water scrubbing via modelling and simulation. *Chemical Engineering Science*.

Extensions for Multi-Period MINLP Superstructure Formulation for Integration of Thermal Energy Storages in Industrial Processes

Anton Beck^a and René Hofmann^{a,b,*}

^a*AIT Austrian Institute of Technology GmbH, Center for Energy, Sustainable Thermal Energy Systems, Giefinggasse 2, 1210 Wien, Austria*

^b*Technische Universität Wien, Institute for Energy Systems and Thermodynamics, Getreidemarkt 9/BA, 1060 Wien, Austria*
René.Hofmann@tuwien.ac.at

Abstract

In this paper, extensions to the MINLP superstructure formulation for multi-period heat exchanger network synthesis (HENS) proposed by Zhang (2006) which is based on the work by Yee and Grossmann (1990) are introduced. These modifications allow for simultaneous HENS including storage-subsystems with different characteristics. Besides stratified tanks and two-tank systems models for latent heat thermal storages (LHTS) and sensible storages are presented. Also, a sequential targeting procedure for the integration of storages is presented which combines insights from pinch analysis methods and a MINLP-formulation to calculate an approximation for optimal storage size and melting temperature. The results of the proposed integration procedure for thermal energy storages is demonstrated using a case study adapted from literature.

Keywords: Mathematical Programming, Heat Integration, Thermal Energy Storage, Latent Heat Thermal Storage, Pinch Analysis

1. Introduction

The synthesis of cost-efficient heat exchanger networks (HENs) has been a topic of scientific interest for several decades now. However, only little research has been done towards the combination with cost-efficient storage integration for multi-period plant operation. Anastasovski (2017) used Pinch Technology for the introduction of two-tank systems in HENS. Storage costs are obtained by variation of storage parameters and temperature differences. Chen and Ciou (2008) proposed a MINLP superstructure formulation for cost-efficient indirect heat recovery using thermal energy storage. A sequential design procedure for HENS with selection of an optimal utility system and storage integration was proposed by Mian et al. (2016). They tried to overcome the drawbacks of the sequential approach by applying the derivative-free hybrid algorithm PGS-COM by Martelli and Amaldi (2014). To our best knowledge, no work has been published on cost-optimal HENS combined with the integration of LHTS or sensible storages with fixed mass. A rigorous optimization procedure for the integration of thermal energy storages such as multi-tank systems but also LHTS might be a door opener for industrial application of these heat recovery systems. In this paper an extension to the simultaneous MINLP superstructure formulation for multi-period HENS proposed by Zhang (2006) is presented that allows for storage integration with different characteristics. For the integration of LHTS and sensible storages with fixed mass such as fluidized bed regenerators (FBR) a targeting stage is proposed to identify (sub)-optimal storage mass.

2. Storage Integration Algorithm

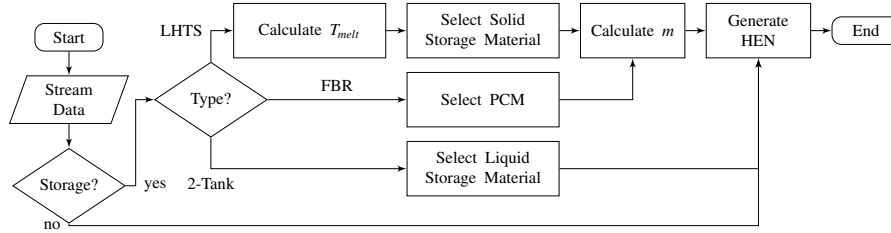


Figure 1: Flow chart for the storage integration algorithm

The combination of simultaneous HENS for multi-period problems and the integration of thermal energy storages leads to a highly complex optimization problem. To reduce problem complexity a storage integration algorithm is proposed which splits the selection of the storage type, storage material and storage mass and thus storage capacity into individual problems. These are treated sequentially according to Fig. 1. A MILP targeting formulation described in section 2.1 is used to calculate the phase change temperature T_{melt} for LHTS which is then used to manually select a suitable phase change material. Also, storage materials for the FBR and two-tank system are selected by the user. For storages with fixed storage mass and variable storage temperature (LHTS, FBR) the target formulation is then used to find the optimal storage size. Finally, the extended MINLP superstructure formulation for multi-period HENS and storage integration (section 2.3) is set up with the predefined storage parameters to find the cost-optimal mixed heat recovery system.

2.1. Storage Target

The targeting procedure for the integration of sensible and latent thermal energy storage with fixed storage mass is formulated as a MILP model which is based on modified Grand Composite Curves (mGCC) which are similar to the shifted Grand Composite Curves (GCC) proposed by Bandyopadhyay et al. (2010) for total site integration. These curves are obtained by removing the "pockets" from the GCC, splitting it at the pinch point and shifting the two new curves back by $\Delta T_{min}/2$. The mGCCs, just like the GCC, provide information at which temperature heating or cooling can be supplied to the process. Within the MILP model the mGCCs for every operation period are then formulated as piecewise linear functions using binary variables. The optimal trade-off between storage size and external utility is then found by variation of the storage size and solving the MILP formulation until no improvement of the objective value can be obtained. No individual process streams and no individual heat exchangers are considered which makes the problem relatively easy to solve.

2.2. Storage Models

In this work generic models for LHTS, FBR and two-tank or stratified tank systems are presented which can be used in both the targeting formulation and the extended superstructure. All storages are modelled as a mass points (uniform temperature in the storage), process streams are connected to the storages by an intermediate storage cycle (ISC) via heat exchangers (HEXs), the storage state is equal at the beginning and the end of the process duration and the storage temperature during each time interval is considered to be equal to the storage temperature at the end of each individual time interval. The model equations for the cumulated storage energy and the ISC are equal for all storage types. The cumulated energy for each operation period $Q_{cum,p}$ in the storages is calculated as

$$Q_{cum,P} = Q_{shift} + \sum_{p=1,\dots,P} \dot{Q}_{charge,p} \Delta t_p - \sum_{p=1,\dots,P} \dot{Q}_{discharge,p} \Delta t_p, \quad Q_{shift} \geq 0, \quad P = 1, \dots, NOP \quad (1)$$

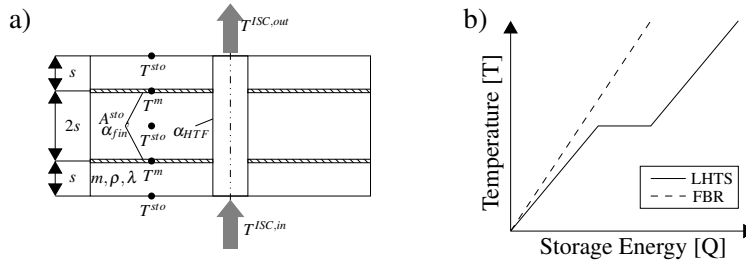


Figure 2: Schematic storage model and QT-characteristics for LHTS and FBR

where Q_{shift} is the storage load at the beginning of the storage cycle. $\dot{Q}_{charge,p}$ and $\dot{Q}_{discharge,p}$ are the charging and discharging loads of operation period p with the duration Δt_p . NOP is the number of operation periods. Simultaneous charging and discharging is not allowed and is prohibited by the constraints $z_{ikp}^{ISC} \leq 1 - y_p$ and $z_{jkp}^{ISC} \leq y_p$ where y_p are binaries that decide whether the storage is charged or discharged. The binary variables z_{ikp}^{ISC} and z_{jkp}^{ISC} determine whether the HEXs between the process streams (hot process stream i , cold process stream j) and the ISC are active in temperature stage k . For the two-tank model no HEX between the ISC and the storage vessels is needed as the heat transfer fluid (HTF) is stored directly. The lower and upper temperatures in the ISC correspond to the temperatures of the hot and cold storage tanks ($T_p^{ISC,hot} = T^{sto,hot}$, and $T_p^{ISC,cold} = T^{sto,cold}$). The minimum storage mass m is calculated by the nonlinear equation

$$Q_{cum}^{ub} - Q_{cum}^{lb} = (T^{sto,hot} - T^{sto,cold})cpm \quad (2)$$

where Q_{cum}^{ub} and Q_{cum}^{lb} are the maximum and minimum values of $Q_{cum,p}$. Opposed to two-tank systems in LHTS and FBR a HEX between the ISC and the storage is needed which is used for both charging and discharging. The necessary heat transfer area A^{sto} for this HEX is calculated by

$$A^{sto} \geq \frac{\sum_i \sum_k \dot{Q}_{ikp}^{ISC} + \sum_j \sum_k \dot{Q}_{jkp}^{ISC}}{U \Delta T_p^{sto}} \quad (3)$$

where \dot{Q}_{ikp}^{ISC} and \dot{Q}_{jkp}^{ISC} are the heat loads from the process streams to the ISC, ΔT_p^{sto} is the temperature difference between the storage fins T^m and the storage material T^{sto} . and U is the overall heat transfer coefficient in the storage HEX. ΔT_p^{sto} is calculated by

$$\Delta T_p^{sto} \leq T_p^{sto} - T_p^m + \Gamma y_p, \quad \Delta T_p^{sto} \leq T_p^m - T_p^{sto} + \Gamma (1 - y_p) \quad (4)$$

where Γ is a sufficiently large number used to activate and deactivate Eq. (4). The overall heat transfer coefficient U is derived from a simple model according to Fig. 2. The LHTS and FBR are modelled as shell and tube storages with radial fins that stretch out to the shell. It is assumed that the tube area is negligible compared to the fin area and thus all heat transfer is performed by the fins which are assumed to operate at the arithmetic mean of the HTF in- and outlet temperatures ($T^m = (T^{ISC,in} + T^{ISC,out})/2$). The characteristic length s for heat conduction is then calculated by $s = \frac{m}{A^{sto}\rho}$. The heat transfer coefficients from HTF to the fins α_{HTF} and from the fins to the storage medium α_{sto} are assumed to be infinite for the LHTS. This way the overall heat transfer coefficient is a function of the HEX area A^{sto} , the storage mass m , the thermal conductivity of the storage material λ and its density ρ . For the FBR model heat conduction is assumed to be negligible and a constant heat transfer coefficient between the fins and the storage material α_{sto} is assumed.

Table 1: Stream data and cost coefficients

	T _{in} (°C)	T _{out} (°C)	CP (kW/K)	Start (h)	End (h)
H1	170	50	3	0.3	0.8
H2	190	80	4	0.25	1
C1	100	160	8	0	0.5
C2	40	155	10	0.5	0.7
UT h	250	250	-	-	-
UT c	10	15	-	-	-

Exchanger cost = $1000+175[A(m^2)]^\beta \text{€y}^{-1}$, Storage cost (LHTS/FBR/2-tank) = $10,000/20,000/6,000[m(kg)/\rho(kg/m^3)]+50.7[A(m^2)]^\beta \text{€y}^{-1}$, $\beta = 0.6$, hot utility cost = $252 \text{€y}^{-1} \text{ kW}^{-1}$, cold utility cost = $22.68 \text{€y}^{-1} \text{ kW}^{-1}$, $dT_{min} = 5^\circ \text{C}$, years $y = 3$

Table 2: Storage material properties

	LHTS	FBR	2-tank
Material	Erythritol ^a	Quartz sand	Therm. oil
cp_s (kJ/kgK)	1.38	0.83	-
cp_l (kJ/kgK)	2.76	-	2
Δh (kJ/kg)	339.8	-	-
λ_s (W/mK)	0.733	-	-
λ_l (W/mK)	0.326	-	-
ρ (kg/m ³)	1390*	1300	1000
	(1480, 1300)		
T_{melt} (°C)	117.7	-	-

*average value, ^aF. Agyenim and I. Knight (2007)

$$U_{LHTS} = \frac{1}{\underbrace{\frac{1}{\alpha_{sto}} + \frac{s}{\lambda}}_0 + \underbrace{\frac{1}{\alpha_{HTF}}}_0} = \frac{\lambda}{s} = \frac{\lambda A^{sto} \rho}{m}, \quad U_{FBR} = \frac{1}{\underbrace{\frac{1}{\alpha_{sto}} + \frac{s}{\lambda}}_0 + \underbrace{\frac{1}{\alpha_{HTF}}}_0} = \alpha_{sto} = const. \quad (5)$$

For the LHTS different values for λ and thus U_{LHTS} are used for solid, liquid and transition phase, where for the transition the average of the solid and liquid values is used. Eq. (3) is adapted using the binary variables which are also used to model the piecewise linear QT-characteristics. This characteristic shown in Fig. 2 provides a relation between the storage temperature and the stored energy and depends on storage mass, specific heat cp , phase change enthalpy Δh and melting temperature T_{melt} . For FBR this characteristic is linear for fixed storage mass.

2.3. Extended Superstructure

In this paper a multi-period formulation based on the MINLP superstructure proposed by Zhang (2006) is used and extended for storage integration. The objective function in the extended version considers HEX between process streams and ISC, storage HEX in the case of LHTS or FBR and the mass of the storage material. The costs for storage construction and storage equipment are assumed to be proportional to the mass of the storage material and are considered in the cost coefficient for storage mass.

3. Example

To demonstrate the integration procedure a slightly adapted version of an example from Kemp (2007) was investigated. The example consists of two hot and two cold process streams with different start and end times leading to 6 operation periods. The process is assumed to be cyclic with a cycle duration of one hour. For higher accuracy for storage heat flows of LHTS and FBR all operation periods were split into two periods with equal durations. The stream data and cost coefficients, which are rough estimates based on material costs, are presented in Table 1.

In the targeting phase for the integration of a LHTS system an ideal phase change temperature for the PCM of 120°C was found. The sugar alcohol Erythritol with a phase change temperature of 117.7°C was then selected as storage material. For the FBR quartz sand and for the two-tank system thermal oil were selected as storage materials. The properties of the selected storage materials are shown in Table 2. The heat transfer coefficient between the fins and the storage material in the FBR was assumed to be $0.3 \text{ kW/m}^2 \text{K}$ based on the work by Molerus et al. (1995). The obtained targets for ideal storage masses for LHTS and FBR were 710.3 kg and 1725.5 kg respectively. After material selection and targeting for storage mass the extended multi-period MINLP superstructure was solved using the local MINLP solver DICOPT (Discrete and Continuous Optimizer)

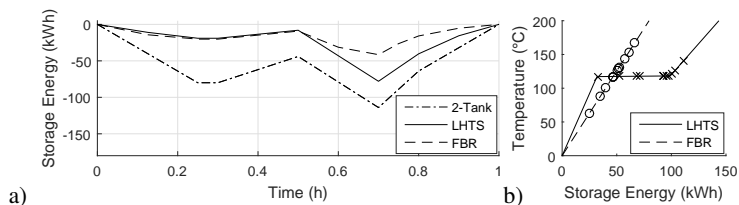


Figure 3: a) Cumulated storage energy over process duration for two-tank system, LHTS and FBR, b) QT-diagram with storage states

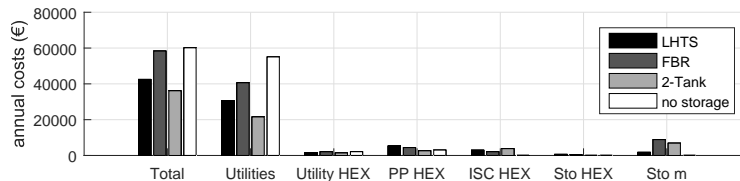


Figure 4: Annual cost analysis for the obtained HEN with LHTS, FBR, two-tank system and without storage integration (PP= direct heat integration)

which is based on the outer approximation method with equality relaxation strategies presented by Viswanathan and Grossmann (1990). DICOPT was initialized using an approximate solution obtained by solving a linearized version of the formulation.

Fig. 3 a) shows the cumulated storage energy over time. Using the two-tank system the highest heat recovery was obtained followed by the LHTS system. The integration of the FBR yielded the lowest heat recovery which can also be seen from the utility costs in Fig. 4. In Fig. 3 b) a QT-diagram is presented which shows that the LHTS system operates in phase transition and in the liquid phase of the storage medium. The temperature range within the storage is small compared to the FBR where the storage temperature ranges from 62.5 to 166.8 °C. The two-tank system operates at 165 and 105 °C and the optimal storage mass is 3420 kg.

Comparison of the annual costs of the optimized heat recovery systems and the HEN without storage integration (Fig. 4) shows that the two-tank system is the most cost-efficient solution with total annual costs of 36,122 € compared to 60,116 € for the case without storage. Although, the costs for the storage vessels of the two-tank system exceed the cost for the LHTS, higher heat recovery can be obtained which makes the storage more cost-efficient. The least cost-efficient storage is the FBR with high costs for the storage vessel and low heat recovery. The HENs for all cases are presented in Fig. 5. The HENs with LHTS and two-tank system have one less utility exchanger than the HEN without storage integration. All four process streams are connected to the ISC. Using the FBR no reduction in the the number of utility HEXs was obtained.

4. Conclusion

The proposed procedure for storage integration allows for simultaneous optimization of HENs and storage subsystems. Storage models for two-tank systems, LHTS and FBR that will be validated in future work were presented that can be included in superstructure formulations for HENS. This allows for scenario analysis of different types of storages. The proposed targeting procedure helps to select a PCM with a suitable melting temperature for LHTS and to reduce problem complexity by providing estimates for optimal storage size. In the presented example a conventional two-tank storage system resulted in the lowest annual costs. Although, other storage systems might

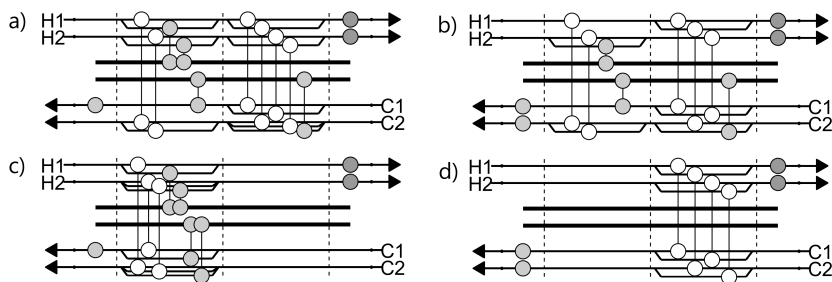


Figure 5: Optimal HENs: a) LHTS, b) FBR, c) two-tank system d) no storage

be the better alternative if condensing and evaporating process streams are considered or for high temperature application. Whether storage integration is worthwhile highly depends on the costs for storage equipment and additional utilities. Also, low period durations for cyclic processes favour the integration of storage systems as higher heat recovery per storage volume can be obtained.

5. Acknowledgement

This integration method of thermal energy storages and the corresponding project were initiated and could be realized by means of the endowed professorship through the cooperation between AIT (Austrian Institute of Technology) and TU Wien (Vienna University of Technology) in the research-field of Industrial Energy Systems.

References

- A. Anastasovski, 2017. Design of heat storage units for use in repeatable time slices. *Applied Thermal Engineering* 112, 1590–1600.
- S. Bandyopadhyay, J. Varghese, V. Bansal, 2010. Targeting for cogeneration potential through total site integration. *Applied Thermal Engineering* 30 (1), 6–14.
- C.-L. Chen, Y.-J. Ciou, 2008. Design and optimization of indirect energy storage systems for batch process plants. *Industrial & Engineering Chemistry Research* 47 (14), 4817–4829.
- M. F. Agyenim, I. Knight, 2007. The use of phase change material (pcm) to improve the coefficient of performance of a chiller for meeting domestic cooling in wales. 2nd PALENC Conference and 28th AIVC Conference on Building Low Energy Cooling and Advanced Ventilation Technologies in the 21st Century, September 2007, Crete island, Greece 1.
- I. C. Kemp, 2007. *Pinch Analysis and Process Integration*. Elsevier.
- E. Martelli, E. Amaldi, 2014. Pgs-com: A hybrid method for constrained non-smooth black-box optimization problems. *Computers & Chemical Engineering* 63, 108–139.
- A. Mian, E. Martelli, F. Maréchal, 2016. Multi-period sequential synthesis of heat exchanger networks and utility systems including storages. In: 26th European Symposium on Computer Aided Process Engineering. Vol. 38 of *Computer Aided Chemical Engineering*. Elsevier, pp. 967–972.
- O. Molerus, A. Burschka, S. Dietz, 1995. Particle migration at solid surfaces and heat transfer in bubbling fluidized beds—ii. prediction of heat transfer in bubbling fluidized beds. *Chemical Engineering Science* 50 (5), 879–885.
- J. Viswanathan, I. Grossmann, 1990. A combined penalty function and outer-approximation method for minlp optimization. *Computers & Chemical Engineering* 14 (7), 769 – 782.
URL <http://www.sciencedirect.com/science/article/pii/0098135490870854>
- T. F. Yee, I. E. Grossmann, 1990. Simultaneous optimization models for heat integration-ii. heat exchanger network synthesis. *Computers & Chemical Engineering* 14 (10), 1165–1184.
- W. V. N. Zhang, 2006. Design of flexible heat exchanger network for multi-period operation. *Chemical Engineering Science* 61 (23), 7730–7753.

Dynamic simulation of a post-combustion CO₂ capture pilot with assessment of solvent degradation

Hana Benkoussas^a, Grégoire Léonard^a, Madalina Ioana Burca^b, Ana-Maria Cormos^{b,*}

^a *Université de Liège, Department of Chemical Engineering, Allée de la Chimie B6a, Liège Sart Tilman, 4000, Belgium*

^b *Universitatea Babeș-Bolyai, Faculty of Chemistry and Chemical Engineering 11 Arany Janos, RO-400028, Cluj-Napoca, Romania.*

Cani@chem.ubbcluj.ro

Abstract

To predict solvent degradation in an industrial CO₂ capture process and for a better understanding of the interactions between solvent degradation and performance of the capture process, an existing dynamic model of an amine based pilot plant for carbon capture has been improved and adapted at the University of Babeș-Bolyai on the basis of the kinetic model of solvent oxidative degradation proposed at the University of Liège. The developed dynamic model has been used to simulate the transient behavior of the CO₂ capture process with assessment of solvent degradation.

Keywords: CO₂ capture, dynamic model, solvent degradation

1. Introduction

Amine solvent based post-combustion capture is an efficient technique and it is based on an absorption-regeneration loop. However, there are many operational drawbacks for usage of amine solvents in industrial application. Among others, corrosion limits the amine concentration in the solution, thermal degradation may happen in the regeneration step and oxidative degradation is occurring in the presence of oxygen in the flue gas typical of absorber conditions. Moreover, the presence of impurities (SO_x, NO_x and fly ash) also leads to amine solvent degradation. These drawbacks lead to an increase in the process cost and environmental concerns, as the properties of the solution may be affected by the presence of degradation products that can also be emitted to the atmosphere. Previous results studying degradation in CO₂ capture pilot plants showed that oxidative degradation due to the presence of oxygen in the flue gas is the main degradation pathway (Lepaumier et al. 2011, Léonard et al. 2015a). In a first attempt to extrapolate these results, a steady-state model with assessment of solvent degradation has been developed (Léonard et al. 2014a; Léonard et al. 2015a) with assumptions allowing to consider degradation as a pseudo steady-state phenomenon. In a recent work, a dynamic prediction of solvent degradation has been proposed by Dhingra et al. (2017) as a function of the concentration of dissolved iron ions in the amine solution based on experimental results from 3 different pilot plants. However, this dynamic model does not consider the whole absorption-regeneration process, nor does it consider the influence of varying the operating parameters of the process.

On the other side, power plants are required to be operated in dynamic scenarios, due to the timely variation of the grid demand. The importance of dynamic models resides in the ability to study and to predict the dynamic behavior of a plant as function of time, which cannot be done with steady-state models. Therefore, these models allow the development of complex control strategies and the study of flexible operation of the plant. There are various dynamic models published in the literature, describing the absorption based CO₂ capture process. These models are used for process design improvement, dynamic behavior analysis, flexible operation studies etc. (Gaspar and Cormos, 2010). But these dynamic models neglect the degradation of the solvent, considering only the reaction between amine and CO₂. The aim of the present work was thus to update a dynamic model of amine-based CO₂ capture absorber validated with pilot plant data and to make it suitable for simulating the oxidative degradation of the solvent based on previous experimental results.

2. Mathematical model

The dynamic model of CO₂ absorption process in alkanolamine solution consists of partial differential equations that describe the total mass, component and energy balances of liquid and gas phases and constitutive relations (used to assess the physical and thermodynamic properties of the system). The developed model is based on the two-film theory and is using the following assumptions (Gaspar and Cormos, 2010): counter current plug flow regime of the two phases inside the column; the concentration of CO₂ and O₂ at gas-liquid interface are approximated using Henry's law; liquid and gas phases are assumed to be an ideal mixture; chemical reactions take place only in the liquid phase and the vapors condense at the gas-liquid interface; heat transfer by radiation as well as by conduction in the axial direction are neglected ; and finally, the fresh solvent is assumed to have been 100% regenerated. The partial differential equations of the model were discretized by spatial derivatives using first order approximations, and all mathematical equations have been implemented in MATLAB/Simulink.

2.1 CO₂ reaction kinetic model

The absorption chemical reaction is presented below:



The reaction mechanism implemented in the present model is based on data revised by Versteeg et al. (1996). The reaction between CO₂ and primary/secondary amines can be described with zwitterion mechanism. According to this mechanism the overall reaction order for MEA has a value of two. The reaction rate follows 2nd order kinetics and can be written as:

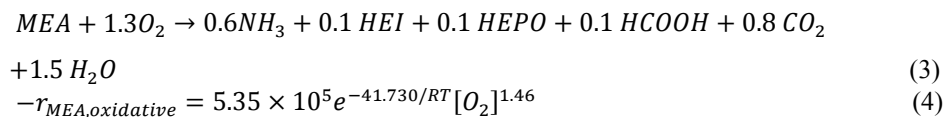
$$r = k_d \cdot C_{CO_2} \cdot C_{MEA} - k_r \cdot C_{MEACOO^-} \cdot C_{MEAH^+} \quad (2)$$

Where: $k_d = 4.4 \times 10^8 \cdot e^{-5400/T}$ [m³/mol.s] and k_r is computed from the reaction equilibrium constant (Versteeg et al. 1996).

2.2 Oxidative kinetic model

Amine solvent oxidative degradation is a very slow process. A pilot plant sample showed a degradation rate of 4% of MEA 30 wt.% after 45 days, when treating a flue gas containing about 5% O₂ in an absorption-regeneration loop (Lepaumier, 2008). In order to build a kinetic model of oxidative degradation of MEA, various accelerated experiments have been performed under conditions of pressure and temperature more severe than those of the pilot plant, using a Degradation Test Rig (DTR) developed at the University of Liège. The relevance of accelerated conditions is evidenced by reproducing in seven days lab experiments with similar degradation pathways as observed in CO₂ capture pilot plants (Léonard et al. 2015a).

Oxygen absorption into MEA aqueous solution can be described by two elementary processes: diffusion of gaseous O₂ through gas-liquid interface and chemical reaction with MEA taking place in the bulk of liquid phase. The oxygen mass transfer is described by the two-film theory considering a low reaction rate of oxidative degradation process. The exact reaction chemistry of oxidative degradation is not determined because of the complexity of the free-radical degradation kinetics. Based on the experimental results, Leonard et al. (2014b) proposed an apparent reaction mechanism consisting in an irreversible reaction implying the main identified degradation products. This apparent mechanism is reported in equation (3) and its kinetics is given in equation (4):



Where: R is the universal gas constant (8.314J/molK), T the temperature (K) and [O₂] the concentration of dissolved oxygen(mol/L). The value for the activation energy is given in J/mol and the pre-exponential unit is(mol/Ls)/(mol/L)^{1.46}.

3. Results

The developed dynamic model has been used to simulate the transient behavior of the CO₂ absorption process into an aqueous solution of MEA with assessment of solvent degradation. The capture rate equals about 97%. The solvent is recycled, in order to observe the solvent loss through degradation, while the gas flow is continuously fed to the absorber column. The experimental results published in literature by Aroonwilas et al. (2004) (pilot plant parameters: 30 wt.% MEA; Sultzer DX packing; absorber diameter 0.02 m, packed height 2 m) are used to validate the developed absorption model. A good correlation between experimental and simulation results with regards to CO₂ molar fraction was observed (R=0.98).

The simulation results showed 0.034 wt.% MEA degradation per day in case of 0.54 Nm³/h gas flow rate with 6 % of O₂ and 9.2 % of CO₂. The flue gas was considered to be under atmospheric pressure and at 298K. In the column, the concentration of O₂ in the gas flow and the O₂ dissolved into the liquid phase show slight variations around the values of 2.5 10⁻³ mol/L and 7.8 10⁻⁵ mol/L respectively. In Table 1, the oxidative degradation of the solvent is presented in weight % / day, for various operation conditions. As one can observe, the degradation effect is directly influenced by the increase of the oxygen concentration in the flue gas, but also by the flue gas flow rate.

Table 1. Solvent concentration variation for different operation conditions

Operation parameter	Degradation rate (wt.% /day)
Nominal values: $F_G = 1.64 \cdot 10^{-4} \text{ m}^3/\text{s}$; $C_{O_2} = 6 \text{ \%v}$; $C_{CO_2} = 9.2\text{ \%v}$.	0.034
+ 10% F_G	0.041
- 10% F_G	0.030
$C_{O_2 \text{ in}} = 8 \text{ \%v}$.	0.047
$C_{O_2 \text{ in}} = 4 \text{ \%v}$.	0.024

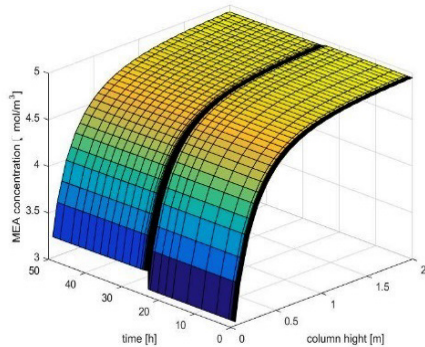


Figure 1. Absorber MEA concentration profile for 10% gas flow rate decrease

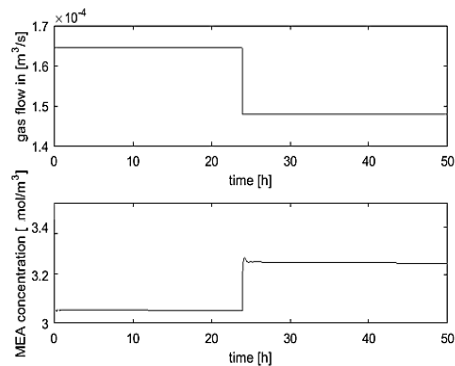


Figure 2. Absorber MEA output for 10% gas flow rate decrease

The increase by 10% of the gas flow rate causes a small increase in the oxygen concentration profile in the liquid, leading to an increase of MEA degradation to 0.041 wt.% per day. The O_2 concentration in the liquid and the system temperature were stabilized in 5000 s at the new steady-state, in case of 10% step change. The effect of the variation of the flue gas flow on the MEA concentration and temperature profiles in the column is showed in Figure 1 and Figure 3. For a more detailed view, the MEA output concentration is also presented in Figure 2. It is noticed that the decrease of the gas flow leads to an increase of the MEA concentration. This is not directly related to solvent degradation, but rather to the fact that when we decrease the flue gas flow, a lower absolute amount of CO_2 is absorbed in the column, leading to a larger relative concentration of MEA in the rich solvent. However, as the concentration of MEA is not considered in the kinetic model for solvent degradation, this variation of the amine concentration is not the reason for the change in the degradation rate. Instead, as can be seen in Figure 3, the modification of the gas flow leads to temperature variations in the column due to the exothermicity of the CO_2 absorption. In case of flue gas flow increase, the resulting temperature increase has two consequences. First, the oxygen equilibrium concentration in the liquid is decreased following Henry's law, and second the reaction rate of the oxidative degradation is increased. In total, following the two-film assumption with slow reaction rate in the liquid, this leads to an increase in the MEA degradation rate when the gas flow rate is increased.

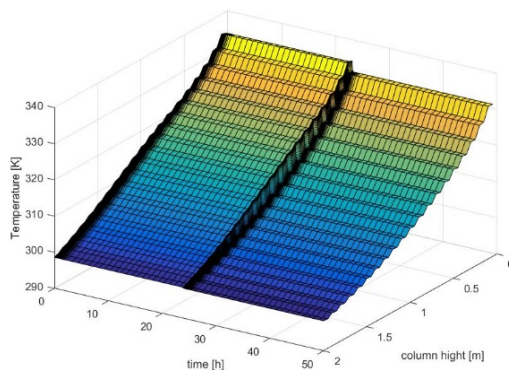


Figure 3. Temperature profile in the absorber for 10% gas flow rate decrease

We also observed the effect of a change in the oxygen concentration in the flue gas, varying from 6 % to 4 and 8% respectively. A new steady-state has been achieved in 500 s after the disturbance. It appeared logically that the increase of oxygen concentration leads to more MEA degradation. The change with 2 % vol of O₂ input concentration causes a modification of ~0.010 wt% MEA degradation per day.

The predicted amount of MEA loss, in the presence of 6% of oxygen and 9.2 v% of CO₂ equals to 8.17 g MEA/t CO₂. Moser et al. (2011) report a degradation rate of 284 g MEA/t CO₂ in the pilot plant and in the absence of degradation inhibitors. Leonard et al. (2015b) report a degradation rate of 82 g MEA/t CO₂ when including the kinetic model for solvent oxidative degradation described by equation 4 in Aspen Plus steady-state model. This latter represents another pilot plant and other flue gas conditions (pilot plant described by Knudsen et al. (2011)). As a consequence, there is still a non-negligible difference between these simulation results, and also when compared with pilot plant results. The discrepancies observed between the present model and the steady-state model could be explained by the fact that in the case of our dynamic model, the inlet gas temperature of the absorber is lower than the typical gas temperature in the absorber (298 K instead of 313-323 K), limiting the degradation rate. Also some variables have been neglected in both degradation models that could explain the differences with the pilot plant results, such as the presence of impurities like SO_x, NO_x, dissolved metals and fly ash.

4. Conclusion

In this work, an existing dynamic model of amine based carbon capture has been improved and adapted by integration of the kinetic models for solvent degradation. In the model, the mass and energy balance equations of liquid and gas phases are used to describe the components concentrations and temperature profiles inside the packed column.

The developed dynamic model has been used to simulate the transient behavior of the CO₂ capture process with assessment of solvent degradation, in conjunction with integrated power plant. Typical disturbances have been investigated, such as the step increment in the flue gas flow rate with respect to its nominal operating point and the variation of oxygen concentration. The results show that the increases of flue gas flow

and oxygen concentration both lead to the increase of MEA degradation. However, discrepancies are observed between the present dynamic modeling approach and a previous steady-state model, probably due to the operating conditions of the modeled set-up so further work is required to confirm this assumption. Nevertheless, the present modeling approach may be successfully used to study the influence of varying operating conditions on the degradation of amine solvent. Further developments may include the influence of the amine concentration on the degradation kinetics. The entire absorption-regeneration loop may also be considered to study with more accuracy the process dynamics. Finally, further variations of the input conditions should be evaluated.

Acknowledgement

This work was supported by Wallonie-Bruxelles International and by a grant of the Romanian National Authority for Scientific Research UEFISCDI: PN-III-P3-3.1-PM-RO-BE-2016-0008 “Dynamic simulation of a post-combustion CO₂ capture pilot with assessment of solvent degradation”.

References

- A. Aroonwilas, A. Veawab, 2004. Characterization and Comparison of the CO₂ Absorption Performance into Single and Blended Alkanolamines in a Packed, *Industrial Engineering Chemical Research*, 43, 2228-2237
- G. Léonard, D. Toye, G. Heyen, 2015a, Relevance of accelerated conditions for the study of monoethanolamine degradation in post-combustion CO₂ capture. *Canadian Journal of Chemical Engineering*, 93 (2), 348.
- G. Leonard, C. Crosset, D. Toye, G. Heyen, 2015b, Influence of process operating conditions on solvent thermal and oxidative degradation in post-combustion CO₂ capture. *Computers and Chemical Engineering*, 121-130.
- G. Léonard, D. Toye, G. Heyen, 2014a, Experimental study and kinetic model of monoethanolamine oxidative and thermal degradation for post-combustion CO₂. *International Journal of Greenhouse Gas Control* 30, 171–178.
- G. Léonard, D. Toye, G. Heyen, 2014b, Assessment of Solvent Degradation within a Global Process Model of Post-Combustion CO₂ Capture. *Proceedings of the 24th European Symposium on Computer Aided Process Engineering – ESCAPE 24*.
- G.F. Versteeg, L.A.J. Van Dijk, W.P.M. Van Swaaij, 1996. On the kinetics between CO₂ and alkanolamines both in aqueous and non-aqueous solutions. *Chemical Engineering Journal* 144, 113-158.
- H. Lepaumier, 2008, Etude des mécanismes de dégradation des amines utilisées pour le captage du CO₂ dans les fumées. Phd thesis. University of Savoie.
- H. Lepaumier, E. da Silva, A. Einbu, A. Grimstvedt, J. Knudsen, K. Zahlsen, H. Svendsen, 2011, Comparison of MEA degradation in pilot-scale with lab-scale experiments. *Energy Procedia* 4, 1652-1659.
- J. Gaspar, A. M. Cormos, 2010, Dynamic modeling and validation of absorber and desorber columns for post-combustion CO₂ capture. *Computers and Chemical Engineering* 35, 2044-2052.
- J. Knudsen, J. Andersen, J. Jensen, O. Biede, 2011, Evaluation of process upgrades and novel
- P. Moser, S. Schmidt, K. Stahl, 2011, Investigation of trace elements in the inlet and outlet streams of a MEA-based post-combustion capture process – results from the test programme at the Niederaussem pilot plant. *Energy Proc*, 4: 473–9.
- S. Dhingra, P. Khakharia, A. Rieder, A. Cousins, A. Reynolds, J. Knudsen, J. Andersen, R. Irons, J. Mertens, M. Abu Zahra, P. Van Os and E. Goetheer, 2017, Understanding and Modelling the Effect of Dissolved Metals on Solvent Degradation in Post Combustion CO₂ Capture Based on Pilot Plant Experience. *Energies*, 10, 629.

A computer-aided analysis on regional power and heat energy systems considering socio-economic aspects: A case study on an isolated island in Japan

Yasunori Kikuchi,^{a,b,*} Yuko Oshita,^c Miwa Nakai,^a Aya Heiho,^a
Yasuhiro Fukushima,^d

^a *Presidential Endowed Chair for “Platinum Society”, The University of Tokyo, 7-3-1 Hongo, Bunkyo-ku, Tokyo 113-8656, Japan*

^b *Department of Chemical System Engineering, The University of Tokyo, 7-3-1, Hongo, Bunkyo-ku, Tokyo 113-8656, Japan*

^c *Faculty of Maritime Sciences, Kobe University, 5-1-1 Fukaeminami-machi, Higashinada-ku, Kobe, 658-0022, Japan*

^d *Department of Chemical Engineering, Tohoku University, 6-6-07 Aramaki-aza-aoba, Aoba-ku, Sendai-shi, Miyagi 980-8579, Japan*

kikuchi@platinum.u-tokyo.ac.jp

Abstract

Socio-economic aspects of technology implementation should be carefully examined in the design of regional energy systems. In this paper, we conducted a computer-aided socio-economic analysis on regional energy systems in isolated islands. Existing developed models were simultaneously utilized for characterizing the applicable technology options. At the same time, we analysed economic circulations induced by the utilization of locally available resources such as the residues of agriculture and forestry, which may twist the faucet of the cash effluent from the regions. A case study was conducted in an isolated island in Japan, Tanegashima, to demonstrate proposed computer-aided socio-economic analysis. The results clarified that the region-specific conditions on industrial structures can be revealed and visualized by preparing customized input-output table for the region. For the analysis of socio-economic aspects of newly installed technologies, computer-aided tools should be able to estimate the elements of input-output table based on the technological modelling with the locally customized input-output table.

Keywords: sugarcane bagasse, life cycle assessment, input-output table.

1. Introduction

The design of energy systems has become an issue all over the world. A single optimal system cannot be suggested, because the availability of infrastructure and resources should be considered locally with their social acceptability (Kikuchi et al., 2017). A computer-aided approach is necessitated for specifying possible solutions considering multiple requirements on energy such as low carbon resources, high stability, and high economic performance.

In this paper, we conducted a computer-aided socio-economic analysis on regional energy systems in isolated islands. Existing developed models on sugar mill (Ouchida et al., 2017) and wood-chip derived power generation (Kanematsu et al., 2017) were simultaneously utilized for characterizing the applicable technology options. At the same time, we analysed economic circulations induced by the utilization of locally available resources such as the residues of agriculture and forestry, which may twist the faucet of the cash effluent from the regions. A case study was conducted in an isolated island in Japan, Tanegashima, to demonstrate proposed computer-aided socio-economic analysis.

2. Materials and method

2.1. Requirements of socio-economic analysis in regional energy system design

As the elements in technology assessment, the relationships among sociosphere, econosphere, and technosphere are taken into account. Figure 1 schematically shows the elements of technology assessment represented as spheres related with technology implementation. Sociosphere includes the social systems and their thinking ways such as security, lifestyles, and health motivated or incentivized by general values and norms. Econosphere is composed of multiple-scale economy, e.g., industrial, regional, national, and global economy, which can be represented as their cash flows based on profitability of industrial activities. Technosphere means more technology-based systems which can be represented as mass or energy balance based on their conversion and efficiency originating from the mechanisms on natural sciences. Politisphere can be related with all other spheres by regulating the activities in technosphere based on the public benefits. These spheres have been recognized as the interfaces of interdisciplinary research to frame the actual situation for implementing novel factors such as marketing-natural environment (Neace, 1995), entrepreneurship ecosystems (Frederick, 2011), and interpretation of quantified environmental impact by life cycle assessment (LCA) (Hofstetter, 1998).

In micro-communities, the social aspects are important for renewable energy systems (Neves et al., 2014), the quantification of which can be conducted partly by contingent valuation methods, such as willingness to pay (Stigka et al., 2014). Sociotechnical research can provide wider feasibility checks on the outcome of technologies (Geels et al., 2017). The “feasibility” of technologies and systems has various aspects from technological, economic, and social viewpoints. The phases of technology development represented by technology readiness level (e.g., Australian Renewable Energy Agency, 2014) or technology implementation (Kaya and Okuwada, 2015) point out such feasibility. For example, the technological feasibility should be checked in multiple scales of production: laboratory, bench, and demonstration scales. The economic feasibility, including micro and macro level, should also be confirmed after demonstration experiments before commercialization. The social feasibility, generally represented as social acceptability and preference, is necessitated for letting the technologies and systems embedded in society, which is needed for radical innovation such as deep decarbonization (Geels et al., 2017). At that time, the general input-output tables (IO-tables) adopted in existing models for energy systems analysis such as the MARKAL (ESTAP, 2017) is not appropriate for the detail analysis in regional systems because the industrial structures are individually different from region to region.

Especially, the central industries in regions should be carefully considered in socio-economic analysis to visualize the effects of technology implementation. However, the construction of IO-table specified for a region requires a plenty of efforts to survey the sufficient quantity of data with adequate quality.

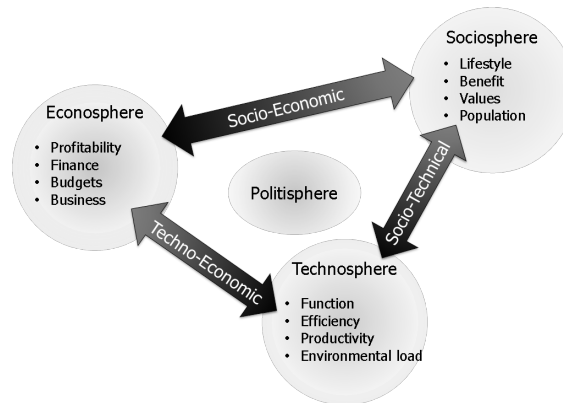


Figure 1 Spheres to be considered for energy system design

2.2. Case study in Tanegashima, Japan

Tanegashima is one of remote islands in Kyushu area of Japan that have independent electricity grids from four main islands of Japan. The power mix is mainly composed of diesel engines, the power generation costs of which are relatively higher than the other areas in four main islands in Japan due to the transport of fuels from oil refinery in main islands and technical staffs for maintenance, and so on. In such region, the social issues on energy security and depopulation have become critical rather than the most of other areas in Japan. A revitalization of the region has been strongly necessitated.

Several projects on energy systems in Tanegashima have been launched. The cane sugar mill at Tanegashima has a possibility to produce power and heat for the regional energy systems utilizing the excess bagasse (Ouchida et al., 2017) and unused woody biomass (Kikuchi et al., 2016). Woody biomass can also be utilized for the small- and medium-sized combined heating and power production (CHP) considering the available timber supply inside of Tanegashima (Kanematsu et al., 2017). The waste cooking oils had been converted into biodiesel by conventional wet-processing methods in Tanegashima and are applied into the demonstration experiments of solid catalyst method, a novel biodiesel production method (Chen et al., 2017). Regarding cane sugar mill, especially, the preferences of residents to the utilization of their unused sugarcane-derived resources are relatively high (Kikuchi et al., 2017). In addition to the previous studies on the techno-economic (Ouchida et al., 2017) and sociotechnical (Kikuchi et al., 2017) analyses on the advanced use of biomass-derived CHP installed at cane sugar mill at Tanegashima, a socio-economic analysis based on the Tanegashima-customized IO-table is conducted in this paper.

The customized IO-table for Tanegashima was constructed by the modification of IO-tables of Okinawa prefecture, Kagoshima prefecture, and whole Japan with the investigation of actual financial statements of industries. The changes of internal production and added values induced by the power generation based on the mixed bagasse and woody biomass, and biodiesel production were calculated by existing

developed models for material and energy flows in cane sugar mills (Ouchida et al., 2017) and their applicability as industrial symbiosis (Kikuchi et al., 2016), the temporal profile of locally available foresee resources considering sustainable foresee management toward leveled age class distribution in Tanegashima (Kanematsu et al., 2017), and biodiesel production with ion-exchange resin catalyst process (Chen et al., 2017). Note that the IO-table of Tanegashima has some uncertainties in the values due to the limitation of data availability. The calculation includes the effects of the cultivar shifting, ethanol production from molasses fermentation, biomass-derived power production, and biodiesel production from waste cooking oils.

3. Results

Figure 2 schematically show the results of analysis on the technologies in cane sugar mill. The power capacity at cane sugar mill can be higher than the half of maximum capacity by utilizing excess bagasse and currently available woody biomass (Kikuchi et al., 2016). This can be increased over 1,500 kW considering the shift of sugarcane cultivars (Ouchida et al., 2017) and the possible timber supply in sustainable forest management (Kanematsu et al., 2017). The shift of sugarcane cultivars can decrease the life cycle greenhouse gas (GHG) emissions by replacing the electricity from power grid (Ouchida et al., 2017) and enhance the profitability of sugarcane industries (Ouchida et al., 2017). The consumer preferences on renewable resources indicate the higher preferences to bagasse in Tanegashima (Kikuchi et al., 2017).

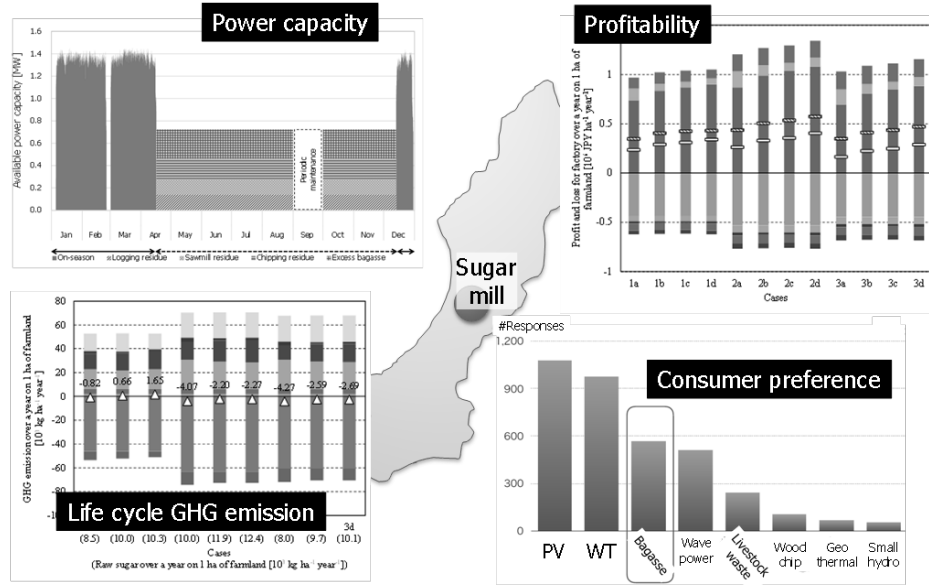


Figure 2 Previous analyses on the energy systems surroundings of cane sugar mill at Tanegashima; The combined heating and power production from cane sugar mill utilizing excess bagasse (Ouchida et al., 2017) and wood chip (Kikuchi et al., 2016).

Figure 3 shows the preliminary calculation results of the changes of the internal production and added values induced by the technology implementation in Tanegashima.

The biomass-derived power utilized excess bagasse and woody biomass. The cultivar of sugarcane was also shifted from NiF8 to NiF18 (Ouchida et al., 2017). The results indicate the increase in internal production and added values of sugarcane sector by this cultivar shift. Although it leads to the increase of internal production of raw sugar, the added value of raw sugar was decreased. This is because the current subsidies for raw sugar production in Japan was increased by the increase of sugarcane harvesting. The net of such positive and negative effects reached positive. This is nation-specific condition on production. Additionally, the power grid decreases the internal production, but increase the added value. This is a region-specific condition in Tanegashima and other remote islands. The electric power companies operate their power plants as deficit production, which needs the deficit covering from their other branches in other regions, i.e., the main island of Kyushu, Japan. The decrease of production lead to the increase of added value at Tanegashima.

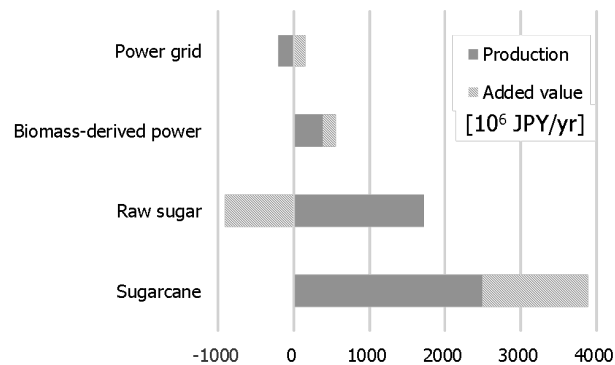


Figure 3 Input-output analysis of the changes in internal production and added values induced by the technology implementation in cane sugar mill at Tanegashima.

4. Conclusion

The socio-economic analysis should be based on the region-specific conditions. General methods of socio-economic analysis cannot deal with such detail facts of energy systems. Our results clarified that the region-specific conditions on industrial structures can be revealed and visualized by preparing customized input-output table for the region. For the analysis of socio-economic aspects of newly installed technologies, computer-aided tools are needed to estimate the elements of IO-table based on the technological modelling, which can take into account the novel technology implementation. At the same time, the locally customized IO-table is also prepared for the detail analysis of socio-economic aspects of technology implementation by dividing or modifying generally available IO-tables normally including multiple local government and regions.

Acknowledgement

The authors acknowledge the support given by Shinko Sugar Mill Company, Nishinoomote-shi, Nakatane-cho, Minamitane-cho, and the Tanegashima Forestry Cooperative. Part of this study was financially supported by the Ministry of Agriculture, Forestry and Fisheries of Japan (Rural Biomass Research Project, BUM-Cm6500), the Japan Society for the Promotion of Science (JSPS) KAKENHI Grant Number 16H06685 (Research Activity start-up), 17K12857 (Young Scientists B), 16H06126

(Young Scientists A), 15H01750 (Scientific Research A), and 26285080 (Scientific Research B), and the Environment Research and Technology Development Fund (IRF-1503). Activities of the Presidential Endowed Chair for “Platinum Society” in the University of Tokyo are supported by the KAITEKI Institute Incorporated, Mitsui Fudosan Corporation, Shin-Etsu Chemical Co., ORIX Corporation, Sekisui House, Ltd., and East Japan Railway Company.

References

- Australian Renewable Energy Agency, 2014. Technology Readiness Levels for Renewable Energy Sectors. <https://arena.gov.au/assets/2014/02/Technology-Readiness-Levels.pdf>
- I.C. Chen, N. Shibasaki-Kitakawa, H. Ohno, Y. Fukushima, 2017. Implementation of a novel biodiesel production system in local community, *Proceeding of EcoDesign 2017*.
- The Energy Technology Systems Analysis Program (ETSAP), 2017. MARKAL, <https://iea-etsap.org/index.php/etsap-tools/model-generators/markal>
- H.H. Frederick, 2011. The role of universities as entrepreneurship ecosystems in the era of climate change: A new theory of entrepreneurial ecology, the Second Entrepreneurship and Management International Conference, Perlis, Malaysia.
- F.W. Geels, B.K. Sovacool, T. Schwanen, S. Sorrell, 2017, Sociotechnical transitions for deep decarbonization. *Science*, 357(6357), 1242-1244.
- P. Hofstetter, 1998. Perspectives in life cycle impact assessment: a structured approach to combine models of the technosphere, ecosphere and valuesphere, Dissertation ETH No. 12806, <http://e-collection.library.ethz.ch/view/eth:41276>, ETH Zurich, Zurich, Switzerland
- Y. Kanematsu, K. Oosawa, T. Okubo, Y. Kikuchi, 2017, Designing the scale of a woody biomass CHP considering local forestry reformation: A case study of Tanegashima, Japan, *Applied Energy*, 198, 160-172.
- A. Kaya, K. Okuwada, 2015. Investigating the courses of implementation by describing research performance, *Sociotechnica*, 12, 12-22.
- Y. Kikuchi, Y. Kanematsu, M. Ugo, Y. Hamada, T. Okubo, 2016, Industrial Symbiosis Centered on a Regional Cogeneration Power Plant Utilizing Available Local Resources: A Case Study of Tanegashima, *Journal of Industrial Ecology*, 20(2) 276-288.
- Y. Kikuchi, M. Nakai, K. Oosawa, Y. Kanematsu, K. Ouchida, T. Okubo, 2017, A computer-aided socio-technical analysis on national and regional energy systems considering local availability of renewable resources, *Computer-Aided Chemical Engineering*, 40, 2485-2490
- M.B. Neace, 1995. The marketing-natural environment interface in the classroom: model for discussion, *Journal of Marketing Theory and Practice*, 3(4), 33-37.
- D. Neves, C.A. Silva, S. Connors, 2014. Design and implementation of hybrid renewable energy systems on micro-communities: a review on case studies. *Renewable & Sustainable Energy Reviews*, 31, 935–946.
- K. Ouchida, Y. Fukushima, S. Ohara, A. Sugimoto, M. Hirao, and Y. Kikuchi, 2017, Integrated design of agricultural and industrial processes: A case study of combined sugar and ethanol production. *AIChE Journal*, 63(2), 560-581.
- E.K. Stigka, J.A. Paravantis, G.K. Mihalakakou, 2014. Social acceptance of renewable energy sources: a review of contingent valuation applications. *Renewable & Sustainable Energy Reviews*, 32, 100–106.

Simulation-based Analysis of Sewage Sludge Treatment Considering Regional, Social, and Technological Characteristics

Akinori Shimizu,^{a+} Tatsuya Okubo,^a Yasunori Kikuchi^{a,b*}

^a *The University of Tokyo Department of Chemical System Engineering 7-3-1, Hongo, Bunkyo-ku, Tokyo Japan*

^b *The University of Tokyo Organization for Interdisciplinary Research Project 7-3-1 Hongo, Bunkyo-ku, Tokyo Japan*

kikuchi@platinum.u-tokyo.ac.jp

Abstract

The effective utilization of sewage sludge has attracted increasing attention, so various technologies are under vigorous research and developments. However, the discussion of general applicability and effectiveness of those technologies throughout diverse regions are not sufficient due to the limitation of regional data of existent sewage sludge treatment plants (STPs). A technological simulator was constructed which can characterize 149 technology scenarios and regional parameters of a thousand STPs located in Japan were prepared by utilizing statistics and the geological information system application. The analysis of sewage sludge treatment considering regional, social, and technological characteristics was performed with the index of life-cycle greenhouse gas emission by inputting prepared parameters of each STP into the constructed simulator. It was revealed that each technology has different performance according to the regional characteristics. The importance of considering actual regional characteristics was suggested.

Keywords: Sewage sludge utilization, Resource recovery Regional analysis, LCA, GIS

1. Introduction

The effective utilization of sewage sludge has attracted increasing attention as it is ubiquitous biomass and contains many useful ingredients like carbon and phosphorus, each of which can substitute exhaustible fossil fuels and phosphorus rocks, respectively. Other than simple incineration or landfill, there exists many emerging technologies and system options for utilizing the sludge. Between the alternative options, various kinds of trade-offs are often observed; some other options reduce the amount of greenhouse gas (GHG) emission at the sludge treatment plant (STP) but increase GHG at the landfill site. To discuss such trade-off quantitatively, life-cycle-based analyses have been often conducted (Pasqualino et al., 2009). Such analyses need inventory data for each scenario. In preparing many sets of inventory data for the analyses, simulation-based approaches are helpful because they can complement data of hypothetical scenarios and even save much time and money which are necessary for actual surveys.

As for utilization of biomass, analysis and discussion should be conducted according to the regional characteristics as the optimum option is dependent on each plant. (Kikuchi et al., 2015). However, most conventional researches assessing technologies for sewage sludge utilization were conducted by only considering specific regional conditions

(Mills et al., 2014), so quantitative discussion about the effect and importance of regional conditions was hardly performed. It seems that one of the biggest barriers is difficulty of collecting regional characteristics. Instead of collecting regional data manually or assuming regional parameters, accessing statistics and calculating by the geological information system (GIS) application leads to more granular information with less workload. Although the applicability and effectiveness of the GIS application in assessing alternatives options were mentioned (Goulart et al., 2017), few researches adopted GIS for data collection so far (Tampio et al., 2017).

In this study, 149 kinds of technology scenarios were generated by combining conventional, emerging technologies whose technological parameters were extracted from dozens of patents, papers, reports etc. Technological characteristics were synthesized into the technology simulator for assessing life-cycle GHG emission (LC-GHG) of each technology scenario. Parameters sets of each STPs which reflect regional and social characteristics in Japan were obtained from statistics, GIS calculations. Those parameters sets were input to the technology simulator to analyse the performance of technology scenarios at each STP.

2. Materials and method

2.1. Definition of requirements for the technological simulator and regional parameters

First principle of sludge treatment is detoxifying by treatments such as landfilling. Besides, incineration, anaerobic digestion and composting have been conducted to reduce the volume and odor of sludge conventionally. For further efficient utilization, various technologies are under research and development such as pyrolysis gasification, incineration power generation, etc. (Rulkens 2008) and phosphorus recovery from sludge, returning water, ash etc. (Cieslik and Konieczka, 2017). Simulation-based approach is effective to conduct iterative analyses in considering many kinds of scenarios and many sets of parameters of STPs.

It is well known that processes such as anaerobic digestion or dewatering change the condition of sludge and those changes affect the efficiency of subsequent processes. Therefore, each process should not be regarded as independent, but rather, subordinate to previous processes. Hence, the simulator for analyses should incorporate each technology option as unit process which calculate the conditions of processed materials based on the parameters of input materials to the process.

One of the most important parameters which affect the performance is the scale of STP as there are huge scale merits in power generation efficiency or construction. Besides scale, transportation distance to facilities which utilize sludge-derived products is regarded as an important parameter. In addition, temperature at each region affects the amount of heat needed for anaerobic digestion or other thermal processes and concentration of phosphorus and nitrogen in sludge also affect the collection rate of phosphorus recovery, the burden of returning water. These are regarded as distinctive parameters to each STP, so considered in the analyses below.

As for assessing GHG emission, LC-GHG emission from construction of equipment, consumption of chemicals, electricity, heavy oil, transportation, landfilling and deduction of sludge-derived products are considered in addition to actual emission of CH₄ and N₂O through each process. It is reported that dismantling comprises less than 2 percent of whole LC-GHG, so dismantling was excluded from consideration in this study.

2.2. Construction of the technological simulator and requirements for regional parameters

The adopted technologies are following: anaerobic fermentation, thermal hydrolysis of excess sludge, 2 dewatering methods (using organic with and without inorganic coagulants), 5 sludge stabilization methods (incineration, pyrolysis gasification with power generation, fuelization, composting, slagging), 4 phosphorus recovery methods (magnesium ammonium phosphate (MAP) recovery from digested sludge or returning water, hydroxyapatite (HAP) recovery from returning water or ash). Descriptions of some technologies are as follows. Dewatering by organic and inorganic coagulant leads to lower moisture content, but more phosphorous precipitates. Thermal hydrolysis improves the digestion rate of excess sludge but consumes much energy to increase the temperature of excess sludge to 170 °C. Dewatered sludge is dried by consuming heavy oil in fuelization, which produce coal-substituting fuel used in coal or biomass power plants. To analyse the result of each combination of technologies quantitatively, every technology was modelled to calculate the condition of sludge after treatment at the technology.

Process flow and the analysis boundary of sewage sludge treatment in the simulator is shown in Figure 1. 149 technology scenarios were generated by combining each technology. All utility input, output, transportation load and emission are counted from treating thickened sludges to the utilizing products or landfilling in each scenario. Technological characteristics were collected from various papers (Nakakubo et al., 2012), patents, literatures and reports (MLIT, 2015). To convert inventory data into LC-GHG, a variety of databases were referred (Nansai and Moriguchi, 2012, AIST and JEMAI, 2016, Swiss Centre for Life Cycle Inventories, 2010). Integrating the models of technologies, the simulator was constructed on the application soft of “Microsoft® Excel®”.

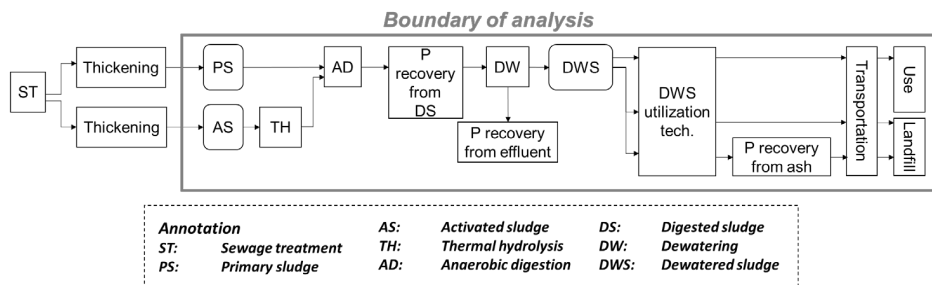


Figure 1: Process flow and the analysis boundary of sewage sludge treatment

Table 1: Parameter sets of two STPs.

STP	Distance to nearest facility		Annual average temperature of sewage	Primary sludge		Activated sludge		Total nitrogen amount
	Landfill site	Biomass/coal power plant		Total amount	Phosphorus amount	Total amount	Phosphorus amount	
[–]	[km]	[km]	[°C]	[t-DS/year]	[kg/year]	[t-DS/year]	[kg/year]	[kg/year]
A	27.92	5.24	14	2842	1407	745	5630	80225
B	4.76	4.68	15	183	1385	22	4399	32020

2.3. Preparation of parameters of each STP and synthesis into data sets

Data of the amount of and concentration of phosphorus, nitrogen in primary and activated sludge, water temperature was obtained from statistics (JSWA, 2016), some of which were calculated by considering the mass balance between input sewage and discharge water. Distances between each STP and facilities of using sludge-derived products were calculated by using “Esri® Arc GIS®” as follows. Firstly, positional information of STP, coal power plants and landfill sites was collected using the constructed database (MLIT, 2012). These parameters are thought to reflect regional and social characteristics around each STP. Prepared parameter sets of two STPs are shown in Table 1.

3. Results and discussions

3.1. Results of simulation

LC-GHG of 149 technology scenarios at a thousand STPs are calculated. Here, two STPs whose parameter sets are described in Table 1 are chosen as examples for brief explanation of the results (Figure 2). As shown in Figure 2, the GHG of each scenario and at each STP has different value. Generally, GHG values of scenarios are smaller in STP A than in STP B which is thought to be because of the scale merit. This is consistent with conventional knowledge about sludge treatment facilities. However, at the same time, some scenarios like scenario 75 and 128 have almost the same GHG values, which imply that scale merit of those scenarios are not significant as those two scenarios comprise technologies which need lower capital investment. Such differences of tendency can be observed throughout the simulations.

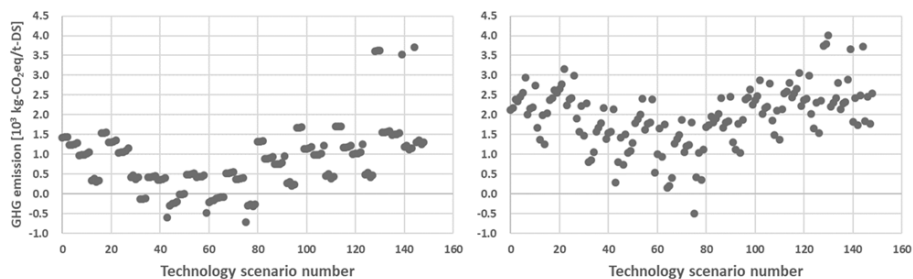


Figure 2: GHG emission of each technology scenario. (left: STP of A, right: STP of B)

Table 2: GHG emission of 4 technology scenarios at STP A and B.

Scenario	0	3	7	11
STP	[10 ³ kg-CO ₂ /t-DS]			
A	1.43	1.24	0.98	1.05
B	2.13	2.34	2.01	1.67

For further discussion, GHG values of some scenarios are listed in Table 2. Scenarios referred here are as follows; scenario 0 is the one of simple incineration after dewatering by only organic coagulant. In scenario 3, the process of anaerobic digestion and power generation by using methane is added to scenario 0. In scenario 7, the process of hydrothermal treatment before digestion to promote anaerobic digestion is still more

added to scenario 3. Scenario 11 replaces the dewatering process of scenario 0 with dewatering using organic and inorganic coagulants together.

Comparing the values of GHG emission at STP A and B, all scenarios give lower values to STP A with bigger sludge scale which is alike the tendency in Figure 2. Introducing anaerobic digestion can reduce GHG emission at STP A, but rather increase at STP B. At STP A, combining hydrothermal treatment with anaerobic digestion further decreases GHG emission. Even though only anaerobic digestion increases GHG emission at STP B, anaerobic digestion with hydrothermal treatment can reduce GHG emission. Dewatering using organic and inorganic coagulants together lead to less moisture content in dewatered sludge, which can reduce electricity and heavy oil consumption at incineration process. Thanks to these merits, both STPs can receive benefit from substituting the method of dewatering. Interestingly, the scenario which gives the lowest GHG emission among the 4 scenarios is different to each STP; scenario 7 is the lowest at STP A and scenario 11 is at STP B.

3.2. Discussions

From the results of simulations, it seems that regional and social characteristics affect the effectiveness of the technology, and optimum technology scenario varies at each STP. These results based on detailed regional characteristics are informative not only for actual decision-making of each STP to opt out technologies, but also for the companies, researchers to acknowledge what kind of technologies are appropriate, needed nation-widely. Extensive discussions of other technology scenarios, other indicators, and at other STPs are currently coped with and to be reported soon.

The approach adopted in this study makes it easy to extend the subjects of assessment by using simulation-based and statistical data, once the simulation structure is constructed. However, there needed many assumptions to perform analysis because of lack of statistical data of each STP and research time limitation; composition of sludge was calculated partly using the uniform value taken at the specific STP, the assumption that facilities around STP can accept whole sludge in each technology scenario was adopted etc. To improve the accuracy of simulations, these assumptions should be reviewed, discussed, and agreement should be built among the researchers. At the same time, maintaining databases for regional assessments should be promoted, especially in developing countries to induce development and installation of appropriate technologies in each place.

4. Conclusions

We analysed the LC-GHG of various technology scenarios at a thousand STPs in Japan by combining the technological simulator and prepared parameter sets of each STP. It was revealed that parameters which reflect social and regional characteristics certainly affected the LC-GHG of each technology scenario. Different optimum scenarios at each STP are different are partly discussed quantitatively in this report. These knowledges would be informative not only for actual decision-makers at each STP, but also for researchers and ministries who conduct research and subsidize various technologies. For refined research using regional data, it is implied that maintaining precise databases is needed.

Acknowledgement

Part of this study was financially supported by the Japan Society for the Promotion of Science (JSPS) KAKENHI Grant Number 16H06126 (Young Scientists A), 15H01750

(Scientific Research A), and 26285080 (Scientific Research B). Activities of the Presidential Endowed Chair for “Platinum Society” in the University of Tokyo are supported by the KAITEKI Institute Incorporated, Mitsui Fudosan Corporation, Shin-Etsu Chemical Co., ORIX Corporation, Sekisui House, Ltd., and East Japan Railway Company.

References

- B. Cieslik and P. Konieczka, 2017, A review of phosphorus recovery methods at various steps of wastewater treatment and sewage sludge management. The concept of “no solid waste generation” and analytical methods, *Journal of Cleaner Production*, 4. 1728–1740.
- L. M. Goulart Coelho, L. C. Lange, and H. M. Coelho, 2017, Multi-criteria decision making to support waste management: A critical review of current practices and methods, *Waste Management & Research*, 1, 3–28.
- Japan Sewage Works Association (JSWA), 2016 Sewage statistics, Japan.
- Y. Kikuchi, Y. Kanematsu, M. Ugo, Y. Hamada, and T. Okubo, 2015, Industrial Symbiosis Centered on a Regional Cogeneration Power Plant Utilizing Available Local Resources: A Case Study of Tanegashima, *Journal of Industrial Ecology*, 2. 276–288.
- N. Mills, P. Pearce, J. Farrow, R. B. Thorpe, and N. F. Kirkby, 2014, Environmental & economic life cycle assessment of current & future sewage sludge to energy technologies, *Waste Management*, 1, 185–195.
- Ministry of Land, Infrastructure, Transport and Tourism (MLIT), 2012 data of country value information of waste treatment facilities, <http://nlftp.mlit.go.jp/ksj/gml/datalist/KsjTmplt-P15.html>. Japan.
- Ministry of Land, Infrastructure, Transport and Tourism (MLIT), 2015, Revised Guideline of Technologies of Energy Utilization of Sewage Sludge, Japan.
- T. Nakakubo, A. Tokai, and K. Ohno, 2012, Comparative assessment of technological systems for recycling sludge and food waste aimed at greenhouse gas emissions reduction and phosphorus recovery, *Journal of Cleaner Production*, 157–172.
- K. Nansai and Y. Moriguchi, 2012, Embodied energy and emission intensity data for Japan using input–output tables (3EID): For 2005 IO table, CGER, National Institute for Environmental Studies, Japan, <http://www.cger.nies.go.jp/publications/report/d031/index.html>
- National Institute of Advanced Industrial Science and Technology (AIST) & Japan Environmental Management Association for industry (JEMAI), 2016, LCI database IDEA version 2.1.2., Japan.
- J. C. Pasqualino, M. Meneses, M. Abella, and F. Castells, 2009, LCA as a decision support tool for the environmental improvement of the operation of a municipal wastewater treatment plant, *Environmental Science and Technology*, 9, 3300–3307.
- W. Rulkens, 2008, Sewage Sludge as a Biomass Resource for the Production of Energy: Overview and Assessment of the Various Options, *Energy Fuels*, 1, 9–15.
- Swiss Centre for Life Cycle Inventories, 2010, ecoinvent version 2.2.
- E. Tampio, E. Lehtonen, V. Kinnunen, T. Mönkäre, S. Ervasti, R. Kettunen, S. Rasi, and J. Rintala, 2017, A demand-based nutrient utilization approach to urban biogas plant investment based on regional crop fertilization, *Journal of Cleaner Production*, 19–29.

Increasing Energy Efficiency in Pulp and Paper Production by Employing a New Type of Latent Heat Storage

Christoph Zauner^{a,*}, Rene Hofmann^{a,b}, Bernd Windholz^a

^a*AIT Austrian Institute of Technology, Center for Energy, Giefinggasse 2, 1210 Vienna*

^b*TU Wien, Institute of Energy Systems and Thermodynamics, Getreidemarkt 9/302*

christoph.zauner@ait.ac.at

Abstract

In pulp and paper production black liquor is burnt to recover base chemicals and to generate electricity and steam which is e.g. used in papermaking machines. In the event of paper tearing excess steam has to be condensed usually. We propose a latent thermal energy system to recover that energy and re-use it in the papermaking machines. A storage model was developed and experimentally verified by a lab-scale prototype. For the specific process, we designed a tube-bundle storage using thermally conductive HDPE as PCM and show that up to 30 MWh can be recovered per day. Finally, we describe the potential of storages to improve energy generation and efficiency in plants.

Keywords: pulp and paper, steam, latent heat storage, process integration, simulation

1. Introduction and Motivation

In pulp and paper production black liquor is a waste product resulting from the kraft process. To recover the base chemicals (NaOH, NaS) and the energy contained within the dissolved carbon compounds, the substance is burnt. The resulting steam is employed to produce electricity and in different processes (see section 4). Roughly half of the steam extracted from the turbine at 3 bars and 150 °C is used at the papermaking machines. Thus, in the event of paper tearing a large amount of excess steam cannot be utilized and has to be cooled in an auxiliary condenser.

In total 319 events per year with a maximum of 200 tons occurred at Smurfit Kappa Nettingsdorfer (SKN) (Figure 1). In 77 % the amount of excess steam was below 55 tons, which will be used as sizing input for the thermal storage system. The insert shows that excess steam events occur roughly once a day and last for up to a few hours with a maximum mass flow rate around 55 tons/hour and an average of 22 tons/hours.

The main idea to improve the efficiency of the plant is to store the energy contained in the excess steam instead of condensing it. We propose a latent heat storage system capable of storing that energy to generate steam at a later time. When the papermaking machines resume production after a paper tearing event, our systems adds additional steam to reduce the shutdown period, increase production capacity and save energy.

2. Latent Heat Storage

Making use of the high phase change enthalpy between melting and solidification, one can design energy storages with high thermal capacity. Since 2013 AIT investigates new phase change materials (PCMs), heat exchangers (HEX) and PCM storages based

on polymers. Especially high density polyethylene is a promising candidate because of several advantages (C. Zauner (2016), C. Zauner (2017), Marx (2017)). Recent work within the project StoreITup-IF shows promising results for the development of thermally conductive polymers suitable for PCM storages (H. Weingrill (2016)). For such materials, one can use a tube bundle heat exchanger and still achieve excellent storage power, which will be shown in more detail below.

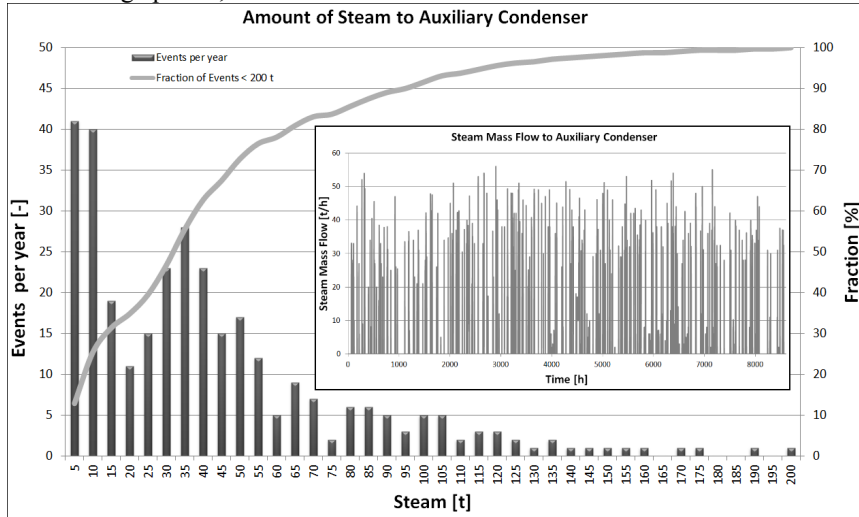


Figure 1: Histogram of excess steam at SKN that had to be actively cooled in the auxiliary condenser. Insert: Annual distribution of events and steam mass flow rate to the aux. condenser.

To be able to design the storage, we developed a 3-dimensional node model consisting of the following physical relationships (Figure 2):

- A lumped capacitance model using a Gaussian distribution describes the HDPE phase change material at each node with appropriate constants c_i :

$$\frac{dQ_{pcm}}{dt} = m_{pcm} c_p \frac{dT_{pcm}}{dt}, \quad c_p(T) = c_0 + c_1 + c_2 \exp\left(-\frac{1}{2} \left(\frac{T - T_{phch}}{\sigma}\right)^2\right) \quad (1)$$

- Heat transfer between two adjacent radial PCM-nodes i and $i+1$ is modelled by conduction (convection can be neglected due to the high viscosity):

$$\frac{dQ_{i+1-i}}{dt} = 2\pi l \lambda_{PCM} \ln\left(\frac{r_{i+1}}{r_i}\right) (T_{i+1} - T_i) \quad (2)$$

- The heat transfer between the tube and the heat transfer fluid is modelled using well-known correlations from literature (VDI 2010).
- In addition, the tubes are longitudinally discretized and connected in series.

A lab-scale prototype filled with roughly 100 kg of HDPE was designed, built by a subcontractor and characterized at the thermal storage test lab at AIT (Figure 2). Thermal oil was used as heat transfer medium. The energy and power characteristics were calculated from measured inlet and outlet temperatures as well as mass flow. Figure 3 shows the characterization results for a step response as well as a comparison between measurements and simulation. Excellent agreement was achieved and proves that the model can be used for storage design as was intended.

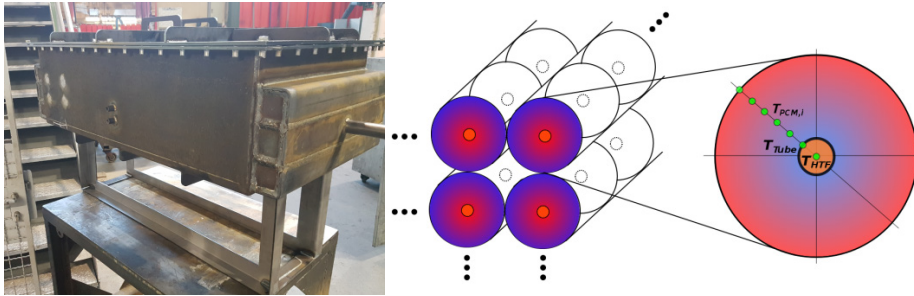


Figure 2: Lab-scale prototype (left) and schematics of the storage model (right).

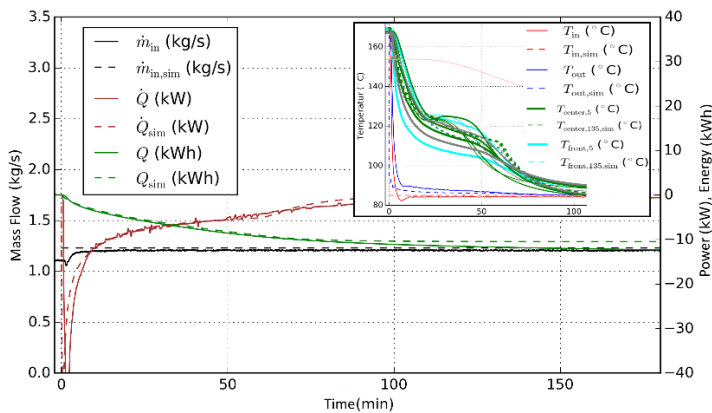


Figure 3: Power characteristics, stored energy of the lab-scale storage prototype for a discharging step response. Solid lines represent measurements and dashed lines simulation results.

3. Waste-to-Energy System using Latent Heat Storage

Based on the plant data presented above, we designed a latent heat storage system that is capable of storing the energy contained in 55 tons of steam (150 °C, 3 bar) which would otherwise have to be cooled by the auxiliary condenser (Figure 4, left).

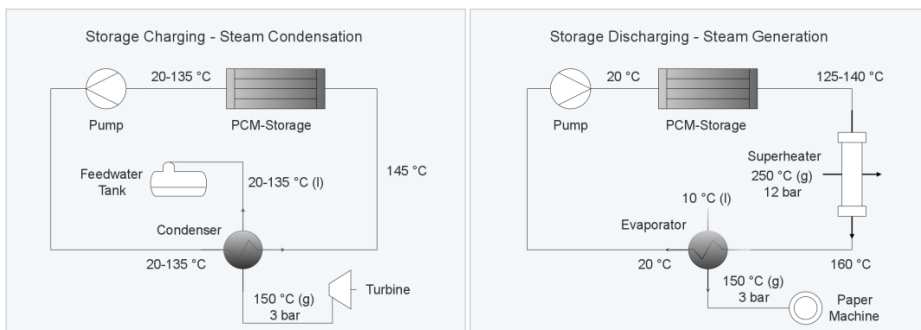


Figure 4: Left: Schematics of the system for charging the PCM storage with excess steam in the event of paper tearing. Right: Schematics of generating steam by discharging the storage.

The system was modelled and simulated in Modelica/Dymola. We use pressurized water in the storage loop to transfer a constant power of 15 MW from a condenser into the storage (charging: Figure 5). As PCM we use a thermally conductive HDPE (10

W/mK). The mass flow within the storage loop has to be controlled as shown to condense a constant excess steam flow of 22 tons/hour. The condensed water is transferred back into the feedwater tank to retrieve the remaining energy. Within this process of charging, the different layers of PCM are subsequently molten (observe the plateau around 130 °C) and heated from 20 °C to about 140 °C.

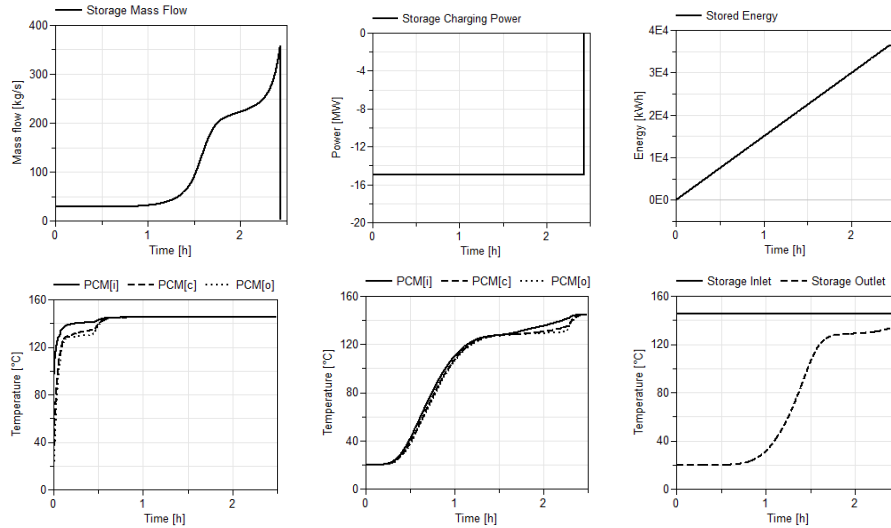


Figure 5: Bottom left: PCM temperatures close to the inlet of the storage (i...innermost node close to the tube, c...center node, o...outermost node). Bottom center: PCM temperature at the center of the storage.

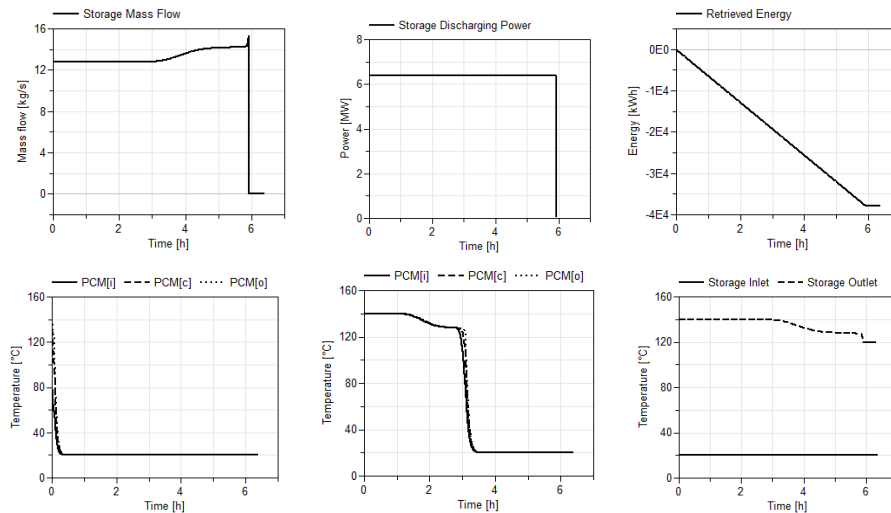


Figure 6: Bottom left: PCM temperatures close to the inlet of the storage (i...innermost node close to the tube, c...center node, o...outermost node). Bottom center: PCM temperature at the center of the storage.

In order to generate steam, the system on the right-hand-side of Figure 4 is used. The storage is discharged (Figure 6) using a constant inlet temperature of 20 °C which is heated up to 125 – 140 °C by crystallizing the PCM. A superheater fed by high pressure steam from the turbine is employed to heat the pressurized water further up to 160 °C. Adjusting the mass flow, a constant storage discharging power of 6.4 MW can be achieved, which is supplemented by 1.1 MW from the superheater. Thus, in this particular scenario, one can generate 10 tons/hour of steam (150 °C, 3 bars) over a period of roughly 6 hours, which can be used elsewhere (e.g. paper machines).

Table 1: Summary of PCM storage characteristics

	Energy [MWh]	Power [MW]	Amount of Steam [t]
Charging	36.4	15	55
Discharging	37.8	6.4	60 ¹
¹ The difference between charging and discharging is due to the energy supplied by the superheater.			

4. Steam Utilization

A typical integrated paper production process including waste-to-energy utilization starts with pulp production (screening, chip piles, digesters), proceeds to the pulp washing and storage (evaporation), the recovery paper treatment (pulper, screening) over the refining to the paper machine (wire-press-dryer section, pop roller, winder) different energy systems namely lime kiln, black liquor steam generator, and a 3-pass shell steam boiler are installed as energy supply system to fulfil the overall thermal and electricity energy demand. The black liquor steam generator is the base energy supply for the thermal and the electricity demand whereas the 3-pass shell steam boiler acts as peak load boiler.

According to Austropapier (2017) the end energy use in the industrial sector pulp and paper is 15700GWh per year with an electric portion of 33% and a sector share in industrial energy use of rd. 18%. The mechanical digestion (groundwood) 1100-1200 [kWhel/t] and thermo-mechanical digestion (mechanical pulp) 1800-3600 [kWhel/t] are one of the electrical major process-specific key figures in the papermaking process, ECJR (2015). One of the thermal major process-specific key figures are the paper machine (thermal energy input for drying processes in the paper machine and for the after-treatment steps) with 1200 [kWhth/t] and chemical digestion and black liquor recycling with total 1400-2100 [kWhth/t] (ECJR (2015)). Within the chemical digestion any flexibility measures by implementation of thermal energy storages (TES) is possible as a result of high thermal energy demand and batch process mode (ECJR (2015)). Some process integration options in the pulp and paper industry for energy system enhancing are discussed in Pettersson (2003) and Söderman (2003); any synthesis could be performed using pinch-analyses or optimization methods. On one hand side during paper production the required heating demand varies significantly and often abruptly. On the other hand side the overall paper process design specifies and restricts the flexibility and load change behaviour. As one major part the boiler construction design plays an important role. Any flexibility causes the change of pressure and therefore ideally the saturated steam temperature resulting in stresses to comply all permissible gradients in thick-walled components and limit values on the system (Hofmann (2014)).

TES can therefore contribute ideally to ride-through (bridging power failures), power quality (compensation of voltage fluctuations), energy management (decoupling of production fluctuations), and peak shaving. Thus the start-up process of the overall system (paper mill and steam boiler) may be speeded-up to decrease any production outages. Based on the examinations in Hofmann (2014), it is possible to provide parameters to optimally design the load change and start-up process of a peak load boiler. There are many parameters during a start-up/load change process to be fulfilled and it is often helpful to carry out a comprehensive FEM calculation (stress range, safety etc.) alongside an EN12952-15 calculation in combination with a temperature difference measurement device built-in into the e.g. drum shell to assign the permissible temperature differences to the current pressure to ensure compliance (Hofmann (2013)). To smoothening the steam extraction and reduce fatigue loads of components caused by cyclic loads (permissible stress ranges) TES can be ideally integrated into the process by additionally reducing the heat input of the peak load boiler significantly.

5. Conclusions

We developed a latent heat storage system that can be used to retrieve energy in the event of paper tearing in a pulp and paper plant. A storage model was experimentally validated and employed to recover up to 30 MWh per day. Finally, we showed how storages can be used to improve energy efficiency and generation.

6. Acknowledgement and Author Contributions

The Austrian Research Promotion Agency (FFG) is gratefully acknowledged for funding this work under Grant No. 838669 (StoreITup!) and No. 848914 (StoreITup-IF) conceived, submitted and lead by C.Z. The PhD supervisor of C.Z., R.H., initiated the paper and developed the storage use case together with C.Z. and M. Strach (Smurfit Kappa Nettingsdorfer). C.Z. designed, modelled, simulated and characterized the storages with the great help of B.W. and F. Hengstberger and content-wise discussions with R.H. Chapters 1-3 were written by C.Z., chapter 4 by R.H. and commented by all authors, F.H. and M. Strach.

7. References in the text

- K. Marx, A. Sommer, W. Hohenauer, T. Barz, *Computer Aided Chem. Eng.* 40 (2017), 211-216
- VDI Gesellschaft Verfahrenstechnik und Chemieingenieurwesen, *VDI Heat Atlas* (2010)
- H. Weingrill, W. Hohenauer, K. Resch-Fauster, L. Gnegeler, C. Zauner, *Thermam* (2016)
- C. Zauner, F. Hengstberger, M. Etzel, D. Lager, R. Hofmann, H. Walter, *Appl. Energy* 179 (2016)
- C. Zauner, F. Hengstberger, B. Mörzinger, R. Hofmann, H. Walter, *Appl. Energy* 189 (2017)
- R. Hofmann, T. Walch, A. Kolbitsch, *Kraftwerkstechnisches Kolloquium* (2013), 35 – 46
- R. Hofmann, A. Kolbitsch, *Power-Gen Europe*, Paper No. T6S5O30, Cologne, Germany, (2014)
- Austropapier, *Branchenbericht 2016/17*. Hg. v. Vereinigung der Österr. Papierindustrie (2017).
- ECJR, *BAT reference doc. for the production of pulp, paper and board* (directive 2010/75/EU)
- F. Pettersson, J. Söderman, *Computer Aided Chem. Eng.* 13, (2003), 1043-1048
- J. Söderman, F. Pettersson, *Computer Aided Chem. Eng.* 14, (2003), 1061-1066

The role of CCS and biomass-based processes in the refinery sector for different carbon scenarios

Julia Sachs^{a*}, Sukma Hidayat^a, Sara Giarola^b and Adam Hawkes^a

^a*Chemical Engineering Department, Imperial College London, Kensington, London SW7 2AZ, United Kingdom*

^b*Earth Science, Imperial College London, Kensington, London SW7 2AZ, United Kingdom*

j.sachs@imperial.ac.uk

Abstract

This paper studies technological pathways in the refinery sector, such as fuel switching, carbon capture and storage (CCS), energy efficiency as well as retrofit decisions (i.e. upgrading, scaling-up, and equipment modernisation) with the aim of decarbonisation. A global refinery outlook is presented for a 2.5 °C and 2 °C climate target scenario from 2010 through to 2050. The results highlight that a full portfolio of technologies (non-conventional processes, gas-/coal- based, with/without CCS, and biomass- based process) is necessary. Among the conventional refineries, only the most efficient ones or those investing in CCS to increase competitiveness and reducing emissions, can stay in the market.

Keywords: refinery, energy, emissions, carbon capture and storage.

1. Introduction

Refinery is responsible for 6 % of the total global CO₂ emissions (Brown, 2010) and represents one of the largest energy consumers. Although the carbon emission reduction targets in transport fuels (EC, 2009, EPA, 2007), have affected the operating strategies of many facilities as well as stimulated new investments in biorefineries (IEA Bioenergy Task 42, 2009, Mathews, 2008), the sector needs to undergo huge changes to address the challenges of decarbonisation. CCS is also deemed to play a fundamental role in this transition (IEA, 2016 (a)). In this regard, the investors's risk-aversion makes the diffusion of novel and expensive technologies more difficult.

Refineries have aimed at increasing their competitiveness in many ways, from the economies of scale to the equipment modernisation (Oil & Gas Journal, 2017). To capture the variety of industrial strategies for competitiveness in a carbon-constrained world, this paper examines the potential pathways for decarbonisation in terms of fuel switching, CCS, efficiency improvements, and typical retrofit decisions such as upgrading, scaling-up, and equipment modernisation. The analysis is carried out using a simulation approach where investors decide according to the profitability of the assets.

2. Methodology

Among the considered technologies, conventional refineries dominate the existing assets and are available in many configurations. They are classified according to the

number of processing units: distillation (atmospheric or vacuum), catalytic cracking, thermal cracking (delayed cooking or visbreaking), and hydrocracking leading to eight different refinery types (Table 1). For example, A only consists of a distillation unit; E adds a thermal cracking unit which enables the processing of different fuel types; C has the most complex configuration as it includes all the possible process units.

Table 1. The conventional refinery types

Type	Distillation	Thermal	Catalytic	Hydro	Refinery, Location	Crude Oil	Upgrade options
A	X	-	-	-	Fina Petroleos de Angola, Luanda	Light	-
B	X	X	X	-	OMV AG, Schwechat	Medium	C
C	X	X	X	X	Petroleum Co. of Trinidad and Tobago Ltd., Pointe-a-Pierre	Heavy	-
D	X	-	-	X	Coraf, Pointe-Noire	Medium	H,G,C
E	X	X	-	-	Ceylon Petroleum Corp., Sapugaskanda	Medium	H,B,C
F	X	-	X	-	Tema Oil Refinery Co. Ltd., Tema	Light	G,B,C
G	X	-	X	X	Jordan Petroleum Refinery, Zarqa	Medium	C
H	X	X	-	X	Bahrain Petroleum Co., Sitra	Medium	C

X: available; -: not available

As shown in Table 1, a prototype was selected to characterize the techno-economic parameters (i.e. product yield, carbon emission, capital costs, variable costs, fixed costs, and efficiency) of all refinery types (IEA 2016 (b), Gary, 2007, Maples, 2000). Every refinery type differs in terms of cost, output share, as well as fuel used (light, medium, and heavy oil) and can make specific investment decisions. While all the refineries can decide to modernize the equipment, scaling-up or investing in CCS, the upgrade to a more complex configuration is applicable to all refineries but type A and C. While scaling-up and modernization can increase the capacity or replace the aging processing units to extend lifetime, upgrading improves the performance of the refining process or reduces its emissions by adding CCS. The capital cost for retrofitting was derived by excluding some construction costs such as cost of establishing a company, the land and layout costs (for modernizing), the recruitment, training and start-up costs (for modernizing and scaling-up) (Favennec, 2001). The cost for upgrading was calculated by the difference between the cost of the more complex refinery and the cost of the current refinery.

3. Biorefinery and Refinery Sector Model within MUSE

MUSE, the ModULAR energy systems Simulation Environment, is an energy systems modelling framework designed to enable long-term analyses of the energy system transitions (S. Giarola, 2017). MUSE is a partial equilibrium model based on microeconomic foundations. It applies a modular approach to the modelling of the energy systems where the specific drivers of investments and operation are tailored to represent that observed in each specific energy sector. In its global version, MUSE models the global energy systems (i.e. including demand, transformation/conversion

and supply sectors) with a geographical disaggregation into 28 regions. Within the MUSE framework, the biorefinery and refinery sector model (BRMS) belongs to the conversion sectors which link supply and demand by transforming primary fuels to secondary fuels. The main focus lies on the production planning and capacity investments of the sector. Each technology is modelled using a bottom-up approach based upon the definition of the specific techno-economic and environmental characteristics for each of the 28 regions of MUSE. The initial stock in the base year and its decommissioning profiles are defined exogenously; forward demand of fuels, prices of primary energy commodities and carbon are dynamically exchanged with the core algorithm of MUSE. For an accurate determination of the production planning on long-term investment decisions, the BRMS uses a two-step simulation approach (Figure 1) to model investment decisions and operating strategies in the market. To capture the wide technology range in the refinery sector 39 plant types are considered and given in Table 2. This list is limited to existing fuel production routes where future productions paths, e.g. using solar energy, are not considered

Table 2 Refining technologies considered in BRSM MUSE

Conventional Refinery		Non-conventional Refinery	Bio-based Refinery		
1.	Refinery A	17.	GTL: Fischer-Tropsch	26.	BTL Direct
2.	Refinery B	18.	GTL: Fischer-Tropsch + CCS	27.	BTL Indirect: FT
3.	Refinery C	19.	CTL Direct: hydrogenation	28.	BTL Indirect: FT + CCS
4.	Refinery D	20.	CTL Indirect: Fischer-Tropsch	29.	Biomass to ethanol: 1 st Gen.
5.	Refinery E	21.	CTL Indirect: Fischer-Tropsch + CCS	30.	Biomass to ethanol: 2 nd Gen.
6.	Refinery F	22.	Electricity to hydrogen (electrolysis)	31.	Biomass to ethanol: 3 rd Gen
7.	Refinery G	23.	Gas to hydrogen	32.	Biomass to hydrogen
8.	Refinery H	24.	Gas to hydrogen + CCS	33.	Biomass to hydrogen + CCS
9.	Refinery A + CCS	25.	Coal to hydrogen	34.	Biomass to biodiesel
10.	Refinery B + CCS		Coal to hydrogen + CCS	35.	Biomass to biogas
11.	Refinery C + CCS			36.	Landfill to biogas
12.	Refinery D + CCS			37.	Biomass to biogas + upgrade
13.	Refinery E + CCS			38.	Biomass to biosyngas
14.	Refinery F + CCS			39.	Biomass to biosyngas + upgrade
15.	Refinery G + CCS				
16.	Refinery H + CCS				

In the first step, the BRSM is designed to model the production of secondary energy commodities, including petroleum and non-petroleum products as well as biofuels.

A merit-order approach based on plant Gross Margin, representing the portion of each dollar of revenue that the company retains as gross profit, is used. The decision metric is calculated by

$$Gross\ Margin = \frac{\sum_i^N X_i P_i - \sum_j^M X_{con,j} P_j - X_c CP}{\sum_j^M X_{con,j} P_j} \quad Eq. 1$$

where $P_{i/j}$ is Price of product i/j ; X_i is amount of product i ; $X_{con,j}$ is the amount of input productions consumed; X_c is the CO2 emission; CP is the CO2 price. Based on the mix of technologies used, the required amount of primary energy commodities, the emissions and the market price of secondary fuels are determined.

In the second step, the BRMS estimates the capacity expansion required to meet the commodity demand and the potential profitability of a refinery upgrade, considering the decommissioning profile of the existing stock and simulates the operation of an asset as well as the consumption of primary energy. The investment decision is determined by looking at the future demand and available stock of refineries for a pre-defined number

of years ahead (typically 10). All potential new technologies and upgrading decisions are considered one by one in comparison to the existing technologies. An algorithm that determines the production of all refineries based on the current demand is carried out to determine the net present value (NPV), representing the profitability over the refinery lifetime, given for the possible set of new technologies. The NPV of each plants is calculated as

$$NPV = \sum_{t=1}^T \frac{C_t}{(1+r)^t} - C_0 \quad \text{Eq. 2}$$

where C_t is cash flow, C_0 is the capital cost, and r is the interest rate. All potential new technologies and upgrading decision are further ranked according to their NPV and one by one considered for commissioning. New plants are directly added to the system where retrofitting will be commissioned if it can increase the profitability of the corresponding existing assets.

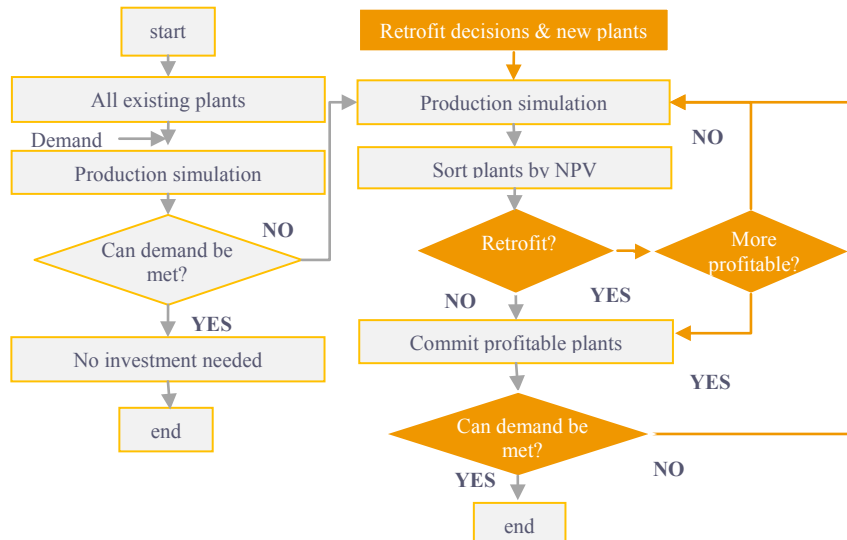


Figure 1 Flow chart of the functionality of the investment algorithm integrated in the BRMS

4. Case Study and Analysis

The transition of the refinery sector is analysed for three different carbon cost scenarios; zero carbon price scenario, 2.5 °C scenario and 2 °C scenario. The carbon prices for the refinery sector are determined using the carbon budget provided in (Rogelj, 2015). The analysis focuses on the uptake of bio-based refineries, non-conventional refineries (Table 2), and refineries with CCS with 90% capture rate as well as the difference in investments in retrofits and new plants. The results for the different scenarios are illustrated in Figure 2. In case of zero carbon price, the trend in the refinery sector is to shift towards more flexible large scale refineries, while the smallest ones are forced out of the market. This results from the upgrade of several unprofitable plants to more economic refinery types and the up-scaling and modernization of large scale plants with

a high NPV. The highest share of 72 % of refinery C tends to indicate that more complex and flexible technologies are favoured. In the 2.5 °C and 2 °C scenario, refineries in combination with CCS appear in the market.

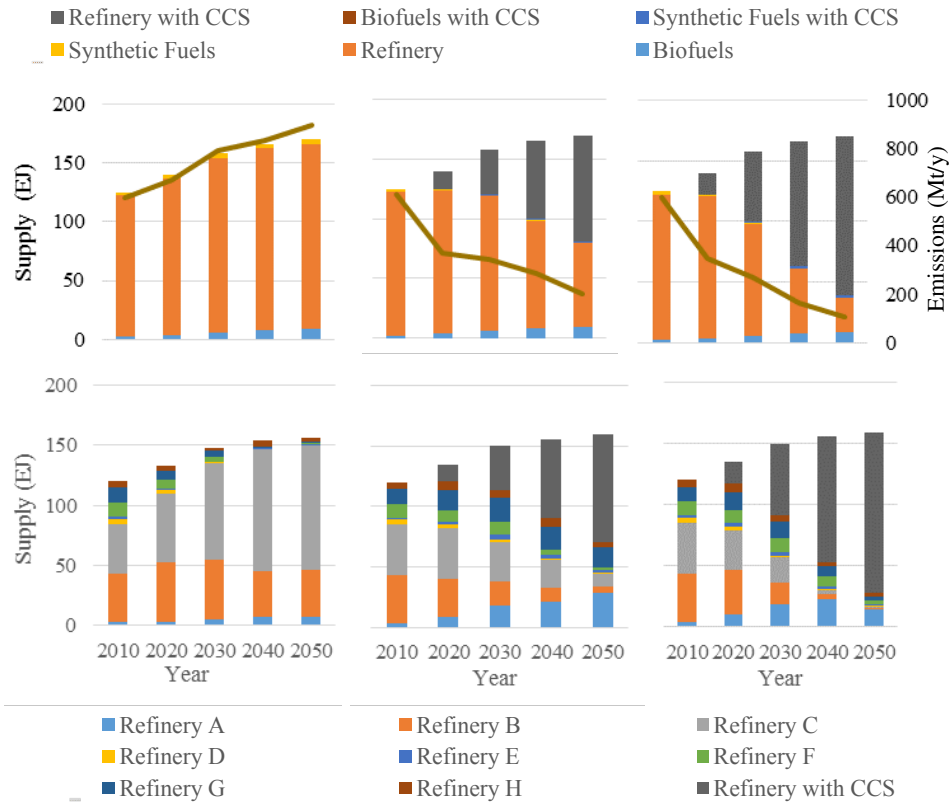


Figure 2 Production by refinery type and year for zero carbon scenario (left), 2.5 °C scenario (middle) and 2 °C (right). The top graph shows the mix of different technologies, the bottom one illustrates the conventional refineries.

It is interesting to see that for carbon scenarios of 2.5 °C, there is a mix of all refinery types, with a predominance of type A (17 %) and G (10 %) without CCS, as they have the lowest emissions of the conventional refineries, where B and C have the highest share 34 % and 26 % respectively, among refineries with CCS; on the other side, there is uptake shift towards the integration of CCS to refinery type A (15 %), for a 2 °C scenario. The increase of bio-based refineries, in particular with CCS, increases with an escalating carbon price since these refinery types show zero net emissions and can yield negative emissions coupled with CCS. These present the most valuable technology options for a further limitation of the emissions in the refinery sector beyond the 2 °C scenario.

The most popular retrofit decision for the zero carbon price scenario presents the upgrading followed by scaling-up and modernization. This changes for the different carbon scenarios where the most popular retrofit option is given by the upgrade of CCS or the modernization and only a few refineries are upgraded to different refinery types

or scaled up. An interesting observation can be made in the investment in modernization measures for all scenarios. Modernizations of refineries are only conducted for larger scale refineries, since it is not economic to maintain small scale refineries due to their unprofitability.

5. Conclusion

This paper shows the impact of changes in the refinery sector due to retrofit and fuel switching on carbon emission profiles. The results of the different decarbonisation scenarios emphasize that a large portfolio of technologies is needed to achieve a decarbonisation of the global refinery sector. In particular, conventional refineries with CCS will still play an important role since the current refinery sector is dominated by conventional refineries and the integration of CCS units presents the most economical approach to face climate change. Biorefineries, with and without CCS, are essential on the other hand for a climate target beyond 2 °C.

References

- J. Brown, 2010, Global Technology Roadmap for CCS in Industry Sectoral Assessment: Refineries, Det Norske Veritas
- Environmental Protection Agency (EPA), 2007, The United States Environmental Protection Agency (EPA): Renewable Fuel Standard Program, <https://www.epa.gov/renewable-fuel-standard-program> [29/01/ 2017]
- European Community (EC), 2009, Directive 2009/28/EC of the European Parliament and of the Council of 23 April on the Promotion of the Use of Energy from Renewable Sources and Amending and Subsequently Repealing Directives 2001/77/EC and 2003/30/EC
- J. Favennec, 2001, Refinery operation and management. Paris, Technip.
- S. Giarola, S. Budinis, J. Sachs and A. Hawkes , 2017, Long-term decarbonisation scenarios in the industrial sector. International Energy Workshop, Maryland, USA
- J. H . Gary, G. E. Handwerk, and M. J. Kaiser, 2007, Petroleum refining : technology and economics. 5th edition. Boca Raton, CRC Press.
- IEA, 2016 (a), Speeding up Carbon Capture and Storage needed to meet climate goals, <https://www.iea.org/newsroom/news/2016/november> [13/09/ 2017].
- IEA, 2016 (b), Summary energy balances: World energy balances, 1960-2014, Tech. rep., UK Data Service
- IEA Bioenergy Task 42, 2009, Biorefineries: adding value to the sustainable utilisation of biomass.
- W. Maas, 2016, CCS Demonstration at Shell, <https://d2oc0ihd6a5bt.cloudfront.net/> [13/09/ 2017].
- R. E. Maples, 2000, Petroleum refinery process economics. 2nd edition. Tulsa, Okla., PennWell.
- J.A. Methews, 2008, Biofuels, climate change and industrial development: can the tropical South build 2000 biorefineries in the next decade? *Biofuels, Bioproducts and Biorefining*. 2 (2)
- Oil & Gas Journal, 2017, Refining and Processing. <http://www.ogj.com/oil-processing/refining.html> [13/09/ 2017].
- J. Rogelj, G. Luderer, R. C. Pietzcker, E. Kriegler, M. Schaeffer, V. Krey, K. Riahi , 2015, Energy system transformations for limiting end-of-century warming to below 1.5 °C, *Nature Climate Change*, 5, 519

Modelling and optimization of a geotextile dewatering tubes process

Franco Mangone*, Jimena Ferreira, Adrián Ferrari, Soledad Gutiérrez

Chemical and Process Systems Engineering Group – Chemical Engineering Institute - Engineering School – Universidad de la República, Julio Herrera y Reissig 565, PC 11300, Montevideo, Uruguay

Abstract

Sludge dewatering represents the general process of removing moisture from a sludge in order to reduce its total volume, and this is desirable in most cases for minimizing downstream sludge management and transportation costs. Many different technologies exist to accomplish this goal, such as decanter centrifuge and diverse press-like units. A simple alternative to these mechanical equipment are the geotextile dewatering tubes, which are disposable bags to which sludge is continually fed until a critical volume is reached, and then are allowed to drain naturally. Apart from having a simple operation, these bags allow for sludge accumulation over extended periods of time, until it is transported to the disposal site.

Although the process is apparently simpler than other alternatives, it involves a set of decisions such as feeding patterns, number of required bags and sequencing, etc., which could lead to sub-optimal utilization of the technology. The aim of this study is to detect these critical decisions, and then analyze strategies to optimize the process. The model used to represent the process will be the one proposed by Yee and Lawson (2012) will be used.

Optimization of the processing capacity of an individual tube is carried out, by finding a minimal operation time which in turn ensures that the optimization objective is achieved, as is described throughout this study.

Keywords: Dewatering tubes, Sludge, Optimization

1. Introduction

Among the several sludge dewatering systems available, geotextile tubes represent one of the simplest alternatives due to the lack of mechanical components in the equipment, and the simplicity of operation. They consist on tubes to which sludge is continually fed until a critical volume is reached, and then they are allowed to drain naturally. This pattern is repeated until enough solids are contained inside of the tube, and at that point they are cut open and their content is disposed of.

An optimal operation of this system involves decision making, such as when to stop dewatering for every cycle, the number of units needed for a tube network, etc. Also, the process might be affected by upstream conditions such as sludge purge frequency and flow, which could also be decision variables for a more plant-wide problem. The present work will focus on the optimization of a single tube operation, in terms of the

selection of the corresponding cycle times. No previous information regarding this matter was found in literature.

2. Modelling

A correct operative representation of a dewatering tube can be quite challenging because of how intricately the involved phenomena are related: a detailed model should incorporate a correct calculation of the tube's volume, which is related to tensile forces of its material and also to the forces applied by the contents of the bag, which vary during the operation. In this sense, Yee and Lawson (2012) described a simple model which gives a good approximation to the full operation discussed above. They tested it using gypsum slurry and contaminated sediments in order to conduct validation, yielding very good agreement with experimental data. A diagram summarizing the stages that are discussed next is available in Yee and Lawson (2012), see Figure 3 in their publication. Essentially, these stages are characterized by (i) a different size (i.e., volume and height; the length is fixed) of the tube, as well as (ii) different zones (i.e., a suspension, settling, and settled zone) that develop in the tube.

2.1. Filling

The operation is divided into filling and drawdown stages. Yee and Lawson (2012) propose that the modelling for both stages can be clearly differentiated. They assume that during filling, the output flow (the clarified liquid that drains through the tube wall) can be directly related to the feed flow, via a simple relationship given by Eq. (1):

$$\frac{Q_{out}}{Q_{in}} = A_P \cdot n_{in} = A_P \cdot (1 - \phi_{in}) \quad (1)$$

Where Q_{in} and Q_{out} represent the total feed and output flow rates (m^3/h) respectively; n_{in} is the porosity of the feed (dimensionless); ϕ_{in} is the volumetric solids fraction in the feed (dimensionless); and A_P is a parameter called "floc quality factor", dimensionless. This equation assumes that the turbulence inside the bag during filling is enough to resuspend any previously sedimented solids, and thus offering no additional resistance to permeate flow. It is possible to calculate the filling time using a simplified mass balance, given by Eq. (2):

$$\frac{\Delta V_T}{\Delta t} = Q_{in} - Q_{out} \quad (2)$$

Where V_T and t represent the bag volume (m^3) and time (h). The filling time can be calculated by knowing the set final volume (V_{max}), given by the manufacturer, as well as the initial volume for each cycle. Then, performing a mass balance in the tube, ϕ can be calculated for the final time, being the initial condition for the next drawdown phase.

2.2. Drawdown

During this stage, sedimentation occurs and the clarified liquid flow is hindered because of the additional resistance created by the sediment. To account for this phenomenon, Yee and Lawson (2012) utilize a variation of the equation proposed by Richardson and Zaki (1954) for hindered settling, represented by Eq. (3):

$$\frac{dh_T}{dt} = -(1 - \phi)^q \quad (3)$$

Where h_T is the total height of the tube (m); ϕ is the mean volumetric solids fraction of the contained sludge (dimensionless); and q is an empirical power factor, which relates to the resistance offered by the sediment. The height of the tube is related to the total volume through an empirical relationship proposed by Yee et al. (2012) and correlated with the more rigorous analysis of Leshchinsky et al. (1996) and Palmerton (2002), presented in Eq. (4):

$$V_T = L_T D_T^2 \left[\left(\frac{h_T}{D_T} \right)^{0.815} - \left(\frac{h_T}{D_T} \right)^{8.6} \right] \quad (4)$$

Where L_T is the total length of the tube (m) and D_T is the theoretical diameter (m), which corresponds to the diameter if the tube was completely filled, adopting a cylindrical shape. This equation gives good estimates for the volume in a range of h_T/D_T lower than 0.7. Additionally, it is possible to effectuate a solids mass balance between any two given times during drawdown. Assuming that no solids escape the tube, and taking the initial conditions for this phase ($\phi_0, V_{T,0}$), it is possible to state the following:

$$\phi = \frac{\phi_0 \cdot V_{T,0}}{V_T} \quad (5)$$

Then, by substituting Eq. (5) and Eq. (4) into Eq. (3), an ordinary differential equation is obtained, but because exponents are not integers, it cannot be solved by separating variables. Although an analytical solution is difficult to obtain, a numerical solution to the problem can be obtained. The original resolution proposed by Yee and Lawson (2012) involved a very simple discretization, but in this case, more accurate ODE solvers will be used.

3. Optimization

In the context of utilization of a single dewatering tube, the optimization in this work focuses on maximizing the capacity of the system, which translates into maximizing the amount of sludge that it admits over the full operating period. Depending on the particularities of the plant where the tube is installed, feed conditions might change and more degrees of freedom could be added to the problem. For simplicity, a first approach will be considered in which a constant feed flow is assumed during filling, and no flow is admitted into the system during drawdown.

The final moisture content and final tube volume for the entire operation (N cycles) are set as terminal constraints for the problem. In this sense, the objective will be to achieve these final conditions in the minimum time possible. This problem is analogous to studying the ratio between total drawdown time and total filling time, because the latter is fixed if a starting volume is given, due to the fact that the final volume is also fixed because of the maximum height condition. Therefore, the involved decision variables are the drawdown time spans, and also the number of cycles.

The problem to analyse represents a mixed integer non-linear programming (MINLP) problem. In order to reduce the complexity of the problem, a fixed number of cycles N will be assumed, and optimization will be carried out.

The resulting optimization problem is described by the following equations:

$$\min_{t_{cycle,n}} \sum_n t_{cycle,n} \quad n = 1, 2, \dots, N$$

$$\text{s.t.} \begin{cases} \text{Modelling: ODE system} \\ \phi(t = t_f) \geq 0.3 \\ V_T(t = t_f) \geq 0.85 \cdot V_{max} \\ t_{cycle,n} = t_{fill,n} + t_{draw,n} \end{cases}$$

Where t_{cycle} is the cycle time (h); t_{fill} and t_{draw} , represent the duration of filling and drawdown stages (h); t_f , is the final time for the whole process (h); and n , represent the cycle number.

Table 1 - Parameter values used for simulation

Parameter	Value	Dimensions
ϕ_{in}	0.05	-
Q_{in}	10	m ³ /h
L_T	20	m
D_T	2.9	m
$h_{T,max}$	2	m
A_P	0.7	-
q	18	-

Where $h_{T,max}$ is the maximum height of the bag, which is related to the V_{max} given by the manufacturer.

Optimization was carried out in Matlab R2015a using *fmincon* function and choosing solver *SQP*. The process parameters utilized during all calculations are shown in Table 1. Terminal conditions (final volume and moisture) would depend on local legislation and manufacturer recommendations, and the values utilized are taken just for the purpose of simulation. Additionally, the number of cycles N was set at 6 for the purposes of this simulation.

4. Results and discussion

The optimization results are shown in Figure 1.

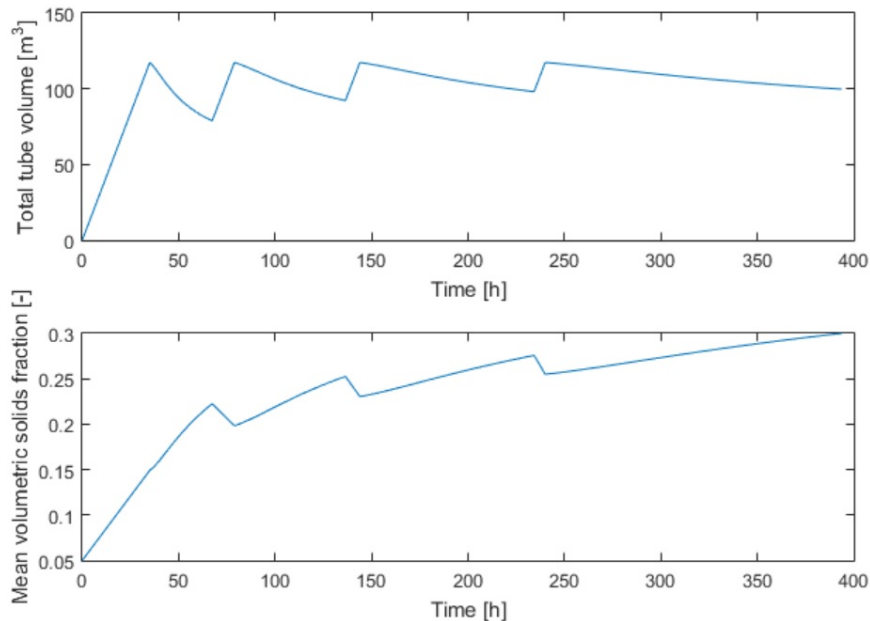


Figure 1 - Simulation result at optimal operation.

The life time of the tube in optimal conditions is 393.6 hours. For comparison, a valid operative strategy would be to fix the drawdown cycle times at a value, for example 100 hours, and calculate the number of cycles needed. In this case, 5 cycles are needed to satisfy the final conditions, with a total operation time of around 670 hours, more than 50% above the optimal time calculated. The ratio of drawdown times to filling times was reduced to a minimum, thus ensuring maximum tube capacity.

Table 2 - Results for optimal cycle times

Cycle	Filling time (h)	Drawdown time (h)
1	35.0	0
2	0	0
3	0	32.2
4	11.5	57.5
5	7.51	90.5
6	5.76	154

A closer inspection of the solution to the problem reveals that the solver assigns a value of zero to some cycle times, which can be seen in Table 2. By doing this, the number of “effective” cycles in the solution (4) is lower than the one originally assumed (6), as is clear in Figure 1. Forcing any value of N lower than four will yield suboptimal solutions to the overall optimization problem as can be observed in Table 3.

Table 3 - Optimal total time for different values of N

Value of N	Total dewatering time (h)
2	1.29E4
3	419
4	394
5	394
6	394

This means that the simulation will yield the same result for any N equal or greater than four. For a more generic problem, carrying out optimization with increasing values of N until the solution presents times with a value of zero, will lead to the determination of the value of N that produces an optimal result. A simple iterative strategy is used in place of a MINLP solver.

5. Conclusion

Modelling of a geotextile dewatering tubes process was implemented in Matlab. Optimal operation for a single bag was studied under the assumption of a constant feed flow from the upstream wastewater treatment plant. The use of an MINLP structure was avoided by proposing an equivalent NLP problem, which is easier to solve. The results showed that the bag throughput was improved, and with a reduction in the required number of cycles respect to traditional strategies. An increase in drawdown times is observed as further cycles are started. Bag network analysis and optimization under feeding scheduling, including upstream conditions and constraints, represent an interesting challenge for the future.

References

- T. W. Yee and C. R. Lawson, 2012, "Modelling the geotextile dewatering tube process", *Geosynthetics international*, **19**, No. 5, 339-353
- T. W. Yee, C. R. Lawson, Z. Y. Wang, L. Ding, Y. Liu, 2012, "Geotextile tube dewatering of contaminated sediments, Tianjin Eco-City, China", *Geotextiles and Geomembranes*, **31**, 39-50
- J. F. Richardson and W. N. Zaki, 1954, "Sedimentation and Fluidisation. Part 1.", *Trans. Inst. Chem. Eng.* **32**, 35-53
- D. Leshchinsky, O. Leshchinsky, H. I. Ling, P. A. Gilbert, 1996, "Geosynthetic tubes for confining pressurized slurry: some design aspects", *Journal of Geotechnica Engineering*, **122**, No. 8, 682-690
- J. B. Palmerton, 2002, "Distinct element modelling of geosynthetic fabric containers", *Proceedings of the 7th International Conference of Geosynthetics, Nice, France*, **3**, 1021-1024

Innovative Temperature Swing Adsorption Simulation Model for Biogas Upgrading

Hannes Vogtenhuber^{a,*}, Elisabeth Sonnleitner^b, Franz Helminger^c, René Hofmann^a, Gerhard Schöny^b, Veronika Wilk^c, Michael Lauerma^c, Andreas Werner^a and Hermann Hofbauer^b

^a*TU Wien, Institute for Energy Systems and Thermodynamics, Getreidemarkt 9/302 1060 Vienna, Austria*

^b*TU Wien, Institute for Chemical Engineering, Getreidemarkt 9/166 1060 Vienna, Austria*

^c*AIT, Center for Energy, Giefingasse 2, 1210 Vienna, Austria*
hannes.vogtenhuber@tuwien.ac.at

Abstract

A multi-stage fluidized bed system for temperature swing adsorption (TSA), which uses solid amine sorbents for CO₂ capture and a heat pump for further optimization of the energy consumption, is studied in detail. The present work introduces detailed models for the most important aspects of the process, in order to study interactions in a simulation model. The overall efficiency depends on three different aspects: adsorption efficiency, heat transfer and heat recovery with a heat displacement system. These three modeling aspects have been combined to gain information about different limiting factors of the proposed TSA process for biogas upgrading. With the new TSA process model, a tool has been created which enables the design and dimensioning of a biogas upgrading plant, as well as the comparison to other biogas upgrading processes.

Keywords: modeling and simulation, fluidized bed, TSA, CO₂ capture, biogas upgrading

1. Introduction

Nowadays, it becomes more important to find alternatives to fossil fuels in order to reduce CO₂ emissions to the atmosphere. For example bio-methane from biogas upgrading can be used as a replacement for natural gas. Biogas contains about 15-40% CO₂ and 60-85% CH₄, depending on its feedstock (Ryckebosch et al., 2011). To supply bio-methane to the natural gas grid, a CO₂ capture process is required to fulfill the quality requirements. Several adsorption processes, such as pressure swing adsorption (PSA), membrane separation, amine scrubbing and physical adsorption, have been reported during the last few decades (Ryckebosch et al., 2011). None of them delivers an optimal solution when it comes to the costs of the upgrading step. More recently, an adsorption technology with solid amine sorbents in a temperature swing adsorption process (TSA) within a multi-stage fluidized bed system has been proposed for post-combustion CO₂ capture applications and may represent a cost efficient alternative to existing biogas upgrading processes. (Pröll et al., 2016; Schöny et al., 2017). The regeneration of the solid sorbent material is performed in the TSA system by lifting the temperature in contrast to the temperature for adsorption, which is performed at lower temperatures (temperature swing adsorption). Many adsorption separation processes, such as pressure swing adsorption (PSA), are based on fixed bed systems, which are operated in batch mode and have limited heat transfer rates (Nikolaidis et al., 2015). The introduced TSA fluidized bed system has an advantage over fixed bed systems, because of a continuous process

operation. In the proposed TSA process, the stages are operated in a counter current flow of the solid sorbents and the gas stream. In contrast to the application of TSA in post-combustion CO₂ capture, biogas upgrading with the proposed TSA process allows for the integration of a high temperature heat pump, due to smaller plants and therefore lower total heat requirement than in post-combustion CO₂ capture. Due to this advantage, the integration of a high temperature heat pump is proposed, in order to enable heat recovery from the exothermic adsorption and use this heat for the endothermic desorption. To enable an optimal heat displacement, every stage is equipped with immersed heat exchangers in the fluidized bed, which are designed in order to allow for preferably high heat transfer rates. As the efficiency of the heat pump is dependent on the necessary temperature swing between adsorber and desorber, the efficiency of heat transfer via the heat exchangers is essential. A simplified IPSEproTM model for the proposed TSA process for biogas upgrading, has been recently proposed by authors of this work (Vogtenhuber et al., 2017). Based on this work, in the following an introduction of the three main process aspects of the extended TSA simulation model will be presented.

2. Process Modeling Aspects

The process model is based on the IPSEproTM model that was previously introduced by (Vogtenhuber et al., 2017). The core of the simulation tool is represented by individual fluidized bed stage unit models that are connected to reassemble a 5x5-stage TSA process set up (see Figure 1).

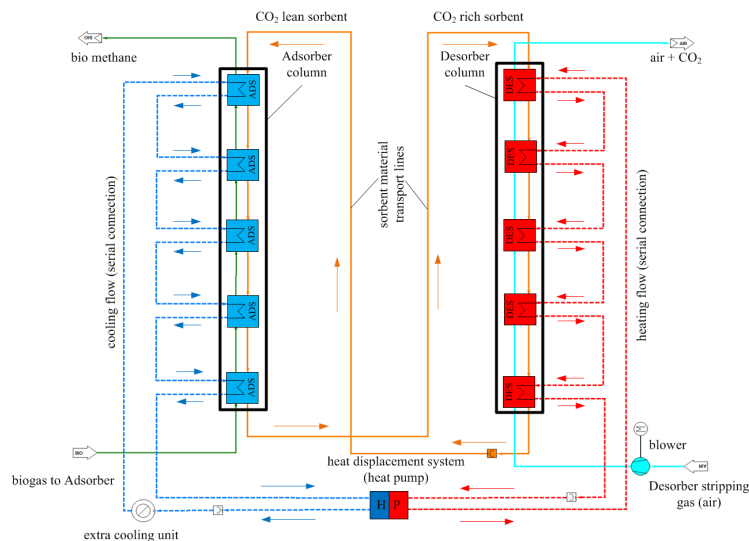


Figure 1: IPSEproTM simulation model

Each stage is based on mass and energy balances for all involved species in the gas and solid streams, according to Figure 1. Isothermal operating conditions as well as ideal gas-solids contact and ideal mixing of the fluidized sorbent material are assumed for each stage unit.

2.1. Adsorption Efficiency Modeling

The first aspect is based on the adsorption behavior of the gas species on the solid sorbent and deals with the deviation from equilibrium conditions. The assumption of having ideally mixed solids requires the CO₂ partial pressure in the outgoing gas stream to be determined by the equilibrium loading of the sorbent material within the stage. In order to determine the CO₂ equilibrium

loading, the adsorption model by Toth (Do, 1998) was used in this work. With the fitting of the Toth model parameters to experimentally determined CO₂ adsorption equilibria data, a suitable mathematical description of the CO₂ equilibrium adsorption capacities can be gained. The experimentally determined CO₂ equilibrium adsorption data on a solid amine sorbent (Lewatit® VP OC 1065), as well as the respective Toth parameter fitting was recently presented by authors of this work (Sonnleitner et al., 2017). With the fitted parameters, adsorption capacities at temperatures and CO₂ concentrations, which were not obtained experimentally, can be calculated. The calculated adsorption capacities reflect the capacity at equilibrium conditions, and presume ideal conditions, where the sorbent is exposed long enough to the adsorptive to reach equilibrium loading. The Toth model was embedded in the process simulation model, and allows for calculation of the CO₂ adsorption on any sorbent material, where a respective Toth parameter set is available.

Based on the findings in a previous study by authors of this work (Sonnleitner et al., 2017), the examined adsorbent material is considered to interact with CO₂, but not with CH₄ and therefore, no transport of CH₄ from the adsorber to the desorber needs to be considered. However, differences in the gas compositions are considered in the energy balances by accounting for the corresponding heat capacities of the individual gas streams. Furthermore, it is expected that H₂O, which is present in the biogas stream, plays an essential role for the overall heat management system. Veneman et al. (2015) determined a significant H₂O adsorption, which suggests a transport of H₂O from the adsorber to the desorber. Therefore, it was decided to incorporate a suitable model for H₂O adsorption in the simulation model.

The influence of other trace gases contained in the biogas, such as H₂S and NH₃, on adsorption properties, are currently not considered in the model, due to a lack of experimental data. Nevertheless, a potential co-adsorption of these species, on the solid amine sorbent material, as suggested by Belmabkhout et al. (2011), may be incorporated in the existing model, after further experimental evaluation. In case of a potential co-adsorption, the costs, for additional gas treatment to reach the specification for biomethane, may be reduced.

During experiments in an existing bench scale unit (Schöny et al., 2017), findings regarding the real behaviour of a 5x5-stage process have been gained. These experiments revealed that, operating conditions such as the gas-solid contact time and adsorption kinetics need to be considered. Therefore, an additional parameter, the stage efficiency, has been added. The stage efficiency reflects, based on experimental findings the proportionally reduced capacity of the sorbent under certain limiting operation conditions. The potentially limiting factors can be either a too high solids circulation rate, which may not ensure a long enough residence time to reach equilibrium loading, or low CO₂ concentrations, which potentially need more solids residence time in each stage. Another limiting factor could be the adsorber temperature, which may slow down the adsorption speed and equilibrium loading may not be reached at low temperatures, as reported for other solid amine sorbents. In order to assess and quantify the respective limitation on the stage efficiency, further experiments will be performed in the bench scale unit. Based on these results, process parameter dependent stage efficiencies will be incorporated in the simulation model, to indicate real operating performance.

As adsorption of CO₂ by the sorbent material is an exothermic process and desorption is an endothermic process, heat exchangers are included for the supply of the required cooling and heating demand in each stage. The total energy demand in the individual stages is the sum of the latent heat demand for adsorption/desorption of the CO₂ and the sensible heat demand for lowering/lifting the temperature of the incoming sorbent and gas stream. Whilst in the simplified adsorption IPSEpro™ model, no limitation on heat exchanging capacity is specified; in reality, the heat exchanger design is essential for the overall process in order to ensure a proper heat management. Therefore, the second modeling aspect deals with the proper design and construction for the heat exchangers to supply the required energy within the stages.

2.2. Heat Transfer Modeling

First of all, fluidized bed regimes are significantly better regarding the heat transfer, compared to other contacting regimes (i.e. fixed- and moving bed). As mentioned before, isothermal operation of each stage is considered, thermal fly-wheel and the mixing behaviour of the fluidized solids. To control and maintain the process temperature within the unit model, heat exchange with a heating or cooling medium is considered. The exchanged heat \dot{Q}_{cond} can be derived from the energy- and mass balance of the unit (see Figure 1) and is according to Eq. (1).

$$\pm \dot{Q}_{\text{thermal}} + \dot{Q}_{\text{cond}} = \dot{m}_{\text{sorb}} \cdot c_{p,\text{sorb}} \cdot (T_{\text{des}} - T_{\text{ads}}) + \dot{m}_{\text{gas}} \cdot c_{p,\text{gas}} \cdot (T_{\text{des}} - T_{\text{ads}}) \quad (1)$$

Depending on either adsorption or desorption, the term \dot{Q}_{thermal} has a positive or negative sign, due to the respective exothermal or endothermal reaction. The conducted heat \dot{Q}_{cond} between fluidized bed and stage heat exchanger is based on Fourier's law and can be defined as:

$$\dot{Q}_{\text{cond}} = \dot{m}_{\text{fl}} \cdot c_{p,\text{fl}} \cdot (T_{\text{fl},\text{in}} - T_{\text{fl},\text{out}}) \quad (2)$$

$$\dot{Q}_{\text{cond}} = k \cdot A_{\text{hex}} \cdot LMTD \quad (3)$$

where Eq. (2) comprises the fluid mass flow \dot{m}_{fl} through the heat exchanger tube and the temperature difference ΔT_{fl} between inflow and outflow of the cooling/heating medium. Another expression of the term \dot{Q}_{cond} is provided in the Eq. (3), where A_{hex} is the needed heat exchanger surface, $LMTD$ the logarithmic mean temperature difference and k the overall heat transfer coefficient between heating or cooling medium and the fluidized bed, through the tube-wall. The overall heat transfer coefficient equation is presented in the following general form:

$$k = \left(\frac{1}{\alpha_{\text{FB}}} + \frac{d_{\text{out}}}{2 \cdot \lambda} \cdot \ln \frac{d_{\text{out}}}{d_{\text{in}}} + \frac{d_{\text{out}}}{d_{\text{in}} \cdot \alpha_{\text{in}}} \right)^{-1} \quad (4)$$

where d_{in} and d_{out} are the tube diameters of the immersed heat exchanger. The heat transfer coefficient between tube and fluidized bed α_{FB} is the sum of the particle convective term $\alpha_{\text{par,conv}}$, the gas convective term $\alpha_{\text{gas,conv}}$ and the radiation term α_{rad} .

$$\alpha_{\text{FB}} = \alpha_{\text{par,conv}} + \alpha_{\text{gas,conv}} + \alpha_{\text{rad}} \quad (5)$$

The radiation term in Eq. (5) becomes more important at temperatures above 400°C and is therefore insignificant for this application (i.e. regeneration temperature $\approx 100^\circ\text{C}$). Literature offers a great spectrum of correlations of wall-to-bed heat transfer in fix or fluidized bed regimes. Many of them calculate the maximum heat transfer coefficients in a certain optimum fluidization range. Only few mathematical models, like Molerus et al. (1995) and Martin (2010), are able to describe the overall fluidized bed heat transfer coefficient as a function of superficial gas velocity and the tube diameter of the immersed heat exchanger. Another important influence factor on the mathematical model is the particle diameter of the used solid sorbent. Therefore, these two models will be incorporated into the simulation model, for calculation of the heat transfer coefficient α_{FB} . Further, the heat exchanger design within the adsorption/desorption stages plays an important role with regard to good heat transfer rates and performance of the heat pump. Different heat exchanger tube diameters and of course different layouts, especially tube bundles, in-line and staggered configuration particularly, influence the wall-to-bed heat transfer coefficient (Hofer et al., 2017). Currently, the implemented mathematical model in the simulation tool, is not able to represent suitable heat exchanger designs. Ongoing experiments investigate the aftermath of different heat exchanger arrangements with finned tubes in terms of heat transfer coefficient, compared to bare tube arrangements within a fluidized bed. Hence, bare tube and finned tube heat exchanger layouts will be implemented into a special circulating fluidized bed test rig with amine sorbent (i.e. to represent real process conditions) as bed material. Results from the empirical experiments will be used to evaluate possible new correlations or improve existing models to predict heat transfer coefficients regarding to parameters mentioned before. The potentially improved and adapted mathematical model will be incorporated to the IPSEproTM simulation model.

2.3. Modeling of the closed loop heat pump cycle

In order to ensure a proper heat recovery in the proposed TSA process, the third aspect deals with the integration of a heat pump model with standard components, such as heat exchangers, compressors, expansion valves, control systems, sensors, etc. The numerical models of the vapour compression heat pump for the heat displacement in the TSA process are written in the modeling language Modelica™. The models in Modelica™ are mathematically described by differential, algebraic and discrete equations. For the heat pump model, to be integrated in the TSA process, two configurations are considered, a single-stage heat pump cycle with optional internal suction gas heat exchanger, see Figure 2 (left) and a cascade configuration, see Figure 2 (right). The main components of the single-stage heat pump cycle are the compressor, the heat exchangers and the refrigerant. In principle, the cascade configuration consists of two single-stage heat pump cycles interconnected with an evaporator-condenser. For both configurations mass and energy balances equilibrium models have been used and following main model components are implemented to fulfill the requested temperature range.

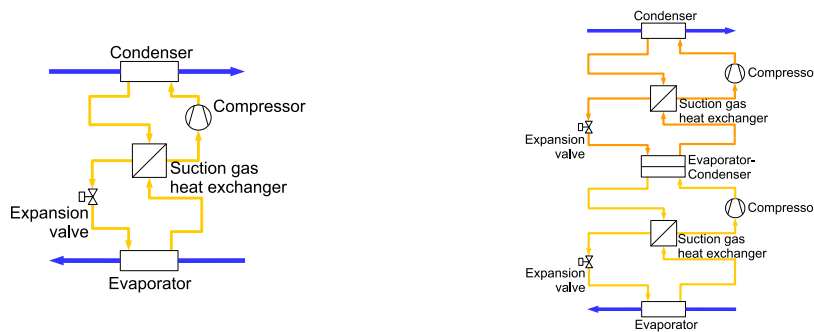


Figure 2: Single-stage heat pump cycle with optional internal suction gas heat exchanger (left) and Cascade configuration (right)

For the single-stage heat pump cycle, the fluid properties of R600 and R1234ZE(Z) are implemented. For the cascade configuration the combinations of R717/ R1234ZE(Z), R1234ZE(E)/ R1234ZE(Z), R717/ R600, R600a/ R600, R600a/ R1234ZE(Z) and R717/ R1336mzz-Z are implemented on the low temperature stage/high temperature stage. All the necessary fluid data is provided by existing Refprop (NIST, 2017) representations.

In order to describe the compression cycle, the isentropic and the volumetric efficiency are prescribed. They are usually given as a function of pressure ratio and condensing or evaporating temperature. An ideal isentropic compression is complemented by different physical effects, such as pressure drop on the suction and the discharge side, internal leakage, re-expansion of the compressed fluid and mechanical friction. The volumetric efficiency gives the relation between the geometrical mass flow and the actual mass flow in the compressor. The geometrical mass flow can be calculated with the known refrigerant properties on the suction side and the prescribed swept volume. The volumetric efficiency gives the relation between the geometrical mass flow and the actual mass flow over the compressor. The geometrical mass flow can be calculated with the known refrigerant properties on the suction side and the swept volume. In order to enable a quick comparison of different heat pump configurations, heat exchanger models based on the Number of Transfer Units method (NTU) are used. This method provides correlations between the heat flow rate and the required thermal conductance, depending on the heat exchanger geometry, which can be found in the literature (VDI, 2013). For the numerical comparison of the different heat pump configurations, the temperature input parameters of the heat exchangers (evaporator, condenser

and internal suction gas heat exchanger) are set equally.

3. Results and Conclusion

The introduced three aspects are implemented in an existing TSA system model in the IPSEpro™ environment. The process model for adsorption behavior (section 2.1) can be used to determine problematic operation conditions that are related to performance losses. High heat transfer rates between heat exchanger equipment and the fluidized bed can be ensured by optimal superficial gas velocity and optimized heat exchanger design and layout. A quick comparison of different heat pump configurations for the process heat supply, can be conducted by applying the introduced numerical models in the new simulation tool. Due to the interactions, of the three presented model aspects, several different operation modes of the TSA process are possible. For example, the optimum temperature for adsorption, which influences the performance of the heat pump, can be calculated with the TSA system model. Resulting from the empirical evaluation of the influence of different process parameters on the ideal model assumptions, a simulation tool has been created, which allows for more accurate process investigations for the future design of a TSA plant. The simulation model, will allow planning and dimensioning of a biogas upgrading plant, as well as for comparison to other biogas upgrading processes.

4. Acknowledgment

This project is funded by the Climate and Energy Fund and is carried out within the framework of the Energy Research Program 2015 (FFG project no. 853612).

References

- Y. Belmabkhout, N. Heymans, G. de Weireld, A. Sayari, 2011. Simultaneous adsorption of H₂S and CO₂ on triamine-grafted pore-expanded mesoporous MCM-41 silica. *Energy & Fuels* 25 (3), 1310–1315.
- D. D. Do, 1998. *Adsorption Analysis: Equilibria and Kinetics*. Imperial College Press, London.
- G. Hofer, G. Schöny, J. Fuchs, T. Pröll, 2017. Investigating wall-to-bed heat transfer in view of a continuous temperature swing adsorption process. *Fuel Processing Technology* 169, 157–169.
- H. Martin, 2010. *Wärmeübergang in Wirbelschichten: VDI-Wärmeatlas, 2nd Edition*. VDI-Buch. Springer-Verlag Berlin Heidelberg, Berlin.
- O. Molerus, A. Burschka, S. Dietz, 1995. Particle migration at solid surfaces and heat transfer in bubbling fluidized beds—ii. prediction of heat transfer in bubbling fluidized beds. *Chemical Engineering Science* 50 (5), 879–885.
- G. N. Nikolaidis, E. S. Kikkinides, M. C. Georgiadis, 2015. Modelling and simulation of pressure swing adsorption (PSA) processes for post-combustion carbon dioxide (CO₂) capture from flue gas. In: *12th International Symposium on Process Systems Engineering and 25th European Symposium on Computer Aided Process Engineering*. Vol. 37 of *Computer Aided Chemical Engineering*. Elsevier, pp. 287–292.
- NIST, 2017. Nist reference fluid thermodynamic and transport properties database (refprop): Version 9.1. URL <https://www.nist.gov/srd/refprop>
- T. Pröll, G. Schöny, G. Sprachmann, H. Hofbauer, 2016. Introduction and evaluation of a double loop staged fluidized bed system for post-combustion CO₂ capture using solid sorbents in a continuous temperature swing adsorption process. *Chemical Engineering Science* 141, 166–174.
- E. Rytkebosch, M. Drouillon, H. Vervaeren, 2011. Techniques for transformation of biogas to biomethane. *Biomass and Bioenergy* 35 (5), 1633–1645.
- G. Schöny, F. Dietrich, J. Fuchs, T. Pröll, H. Hofbauer, 2017. A multi-stage fluidized bed system for continuous CO₂ capture by means of temperature swing adsorption – first results from bench scale experiments. *Powder Technology* 316, 519–527.
- E. Sonnleitner, G. Schöny, H. Hofbauer, 2017. Assessment of zeolite 13X and Lewatit® VP OC 1065 for application in a continuous temperature swing adsorption process for biogas upgrading. *Biomass Conversion and Biorefinery*. VDI (Ed.), 2013. *VDI-Wärmeatlas, 11th Edition*. Springer Vieweg, Berlin and Heidelberg and London and New York.
- R. Veneman, N. Frigka, W. Zhao, Z. Li, S. Kersten, W. Brilman, 2015. Adsorption of H₂O and CO₂ on supported amine sorbents. *International Journal of Greenhouse Gas Control* 41, 268–275.
- H. Vogtenhuber, R. Hofmann, G. Schöny, J. Pirkelbauer, M. Fraubaum, F. Helming, A. Werner, H. Hofbauer, 2017. Development of an Efficient Heat Balance Concept for a TSA-Process Considering Heat-Pump Integration. In: *10TH International Conference on Sustainable Energy and Environmental Protection*. University of Maribor, pp. 1–6.

Reduced Model Describing Efficient Extraction of Hydrogen Transported as Co-Stream in the Natural Gas Grid

Werner Liemberger^{a,*}, Martin Miltner^a and Michael Harasek^a

^aTU Wien, Institute of Chemical, Environmental & Bioscience Engineering, A-1060 Vienna, Getreidemarkt 9/166, Austria
werner.liemberger@tuwien.ac.at

Abstract

The world's energy demand is increasing since years. Together with environmental issues (e.g. global warming) and energy security concerns, renewable energies are on the rise. As these are less predictable the importance of a cost effective and environmentally friendly energy storage and transportation system increases.

A solution might be hydrogen (H₂), as the gas has a high energy density and might be a future energy carrier. In a power-to-gas context electrical energy is used to produce H₂ via water electrolysis. The gas can be stored and transported, most cost- and energy-efficient via pipelines.

However, pipelines are capital intensive so the current natural gas-grid could be used to co-transport H₂. According to national pipeline regulations low H₂ concentrations are already possible (e.g. 4% (v/v) in Austria). While the injection is straightforward, the extraction is challenging. In previous work a process has been identified, experimentally validated and optimised via process simulation, that is able to extract H₂ at fuel cell quality (99.97% (v/v) according to ISO 14687-2:2012).

The previously gained knowledge is used in the current work to create a reduced model (combination of principal component analysis and trained artificial neural network). The model has a significantly increased performance compared to the whole process simulation. Therefore, it is computationally less expensive and can be easily implemented in further investigations like GIS based analysis and economic evaluations as done in ongoing work.

Keywords: hydrogen infrastructure, process simulation, future technology, fuel cell hydrogen, artificial neural network

1. Introduction

In the last decades, the awareness of climate change increased much. It is assumed that global warming can be reduced by reducing global greenhouse gas emissions. Therefore, renewable energies gain in importance. As these energy resources are less predictable than conventional, controlling electrical excess energy is more difficult.

The electrical excess energy is mostly stored and used when needed. Currently, the only large scale available storing technologies are pumped hydro-electric energy storage (PHES) and compressed air storage (CAS). For the future it is estimated, that 600 TWh have to be stored (Blanco and Faaij, 2018) which is higher than the potential of PHES. CAS could fulfil this, but the potential of chemical energy storage (like power-to-gas) is greater.

In a power-to-gas concept, hydrogen (H_2) is produced via water electrolysis from electrical excess energy. The gas can be stored, transported (most energy- and cost-efficient via pipeline) and re-electrified. As currently only 16×10^3 km of H_2 pipeline networks exist, the natural gas grid (already 2.2×10^6 km in Europe (Eurogas, 2015)) might be an option, especially when using it to co-transport H_2 , which is already allowed up to a certain limit (e.g. 4%(v/v) in Austria). In previous work (e.g. see Liemberger et al. (2017a)) a process has been presented, that is able to extract this H_2 , transported with the natural gas grid, at fuel cell quality (e.g. use for mobility).

The process, based on membrane technology and pressure swing adsorption, has been investigated experimentally and optimised with process simulation. Due to non-linear coupled equations its convergence is difficult and time-consuming. Further, when investigating internal recycles (required for a higher total H_2 recovery at lower energy demand), numerous recycle stream ratios are possible ($> 5 \times 10^5$ cases), increasing the simulative effort significantly. This makes it difficult to implement the full process simulation in detailed geographic information system (GIS) based and economic analyses. Therefore, a reduced model is required.

1.1. Process Simulation

In previous work (Liemberger et al., 2017b), several process designs have been studied via process simulation and optimisation to identify an energy efficient process design. Two designs are shown in Fig. 1, a simple (PR1; see Fig. 1(a)) one and a more complex (PR9; see Fig. 1(b)).

The simulations were done in MATLAB[®] (R2016b) with an in-house developed solution-diffusion based membrane model, a splitter model for the PSA and an isentropic compression model (adjusted by an efficiency coefficient of 72 %).

The membrane separation uses a solution-diffusion approach to determine the transmembrane flux for each component (function of difference in partial pressure and permeance). For multicomponent gases this leads to a system of coupled non-linear differential equations. The used in-house developed code uses a finite difference approach to solve this equation system in the modelled module. For more detailed information on the modelling approach see Liemberger et al., 2017b.

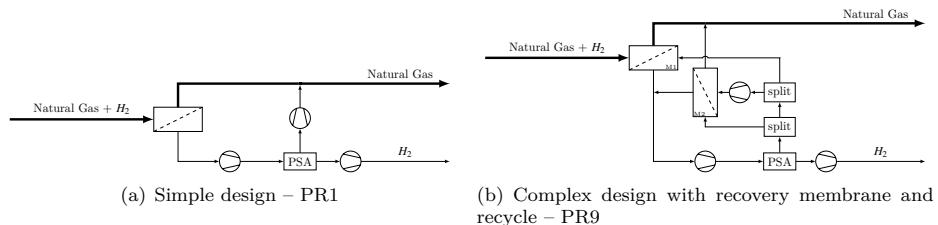


Figure 1: Investigated schemes with membrane pre-enrichment and a purification via PSA

The work has shown, that the process design with recovery membrane and sweep gas streams (PR9) requires the lowest specific amount of energy for the extraction of H_2 from mixtures with natural gas. Further, PR9 is able to achieve higher total H_2 recovery rates than PR1.

While the simulation of PR1 is straight forward (no recycle stream), the one of PR9 is more complex (higher degree of freedom). The configuration of both splitters as well as the

recovery membrane leads to two recycle streams. In case more gas is recycled, the total H_2 recovery can be increased. However, as the gas has to be re-compressed internally, more energy is required. This trade-off is an optimisation problem, computationally intense to solve. Therefore, the current work uses data from extensive simulation with rigorous model for a reduced model, easy to apply in further investigations like economic evaluations.

1.2. Model Reduction – Artificial Neural Network

Several modelling techniques are known in literature like partial least squares regression (PLS), principal component analysis (PCA) and artificial neural networks (ANNs) (Balabin et al., 2011).

In a PCA possible correlated variables are converted to a set of linearly uncorrelated values, called principal components.

ANNs are used to solve several problems, e.g., in process identification, classification, data analysis, control and fault detection (e.g. see Azlan Hussain, 1999). While they are used in several chemical engineering sectors like (i) oil and gas industry, (ii) environment, (iii) biotechnology, (iv) polymer industry, (v) nanotechnology (vi) mineral industry and others (Pirdashti et al., 2013) their public awareness has increased in the last decades due to big data and image recognition issue.

In an ANN simple mathematical operations (so called neurons) are combined with weighted connections (values adjusted during training). The final model is able to represent the data and might be suitable to predict new cases correctly (in this case the correct energy demand).

Depending on the way the neurons are connected different types can be encountered, mainly (i) feed-forward (single-layer perceptron, multilayer perceptron and radial based) and (ii) recurrent (Hopfield, Elman, Jordan and recurrent multilayer) neural networks are used (Pirdashti et al., 2013).

2. Methods

In the current work, a PCA is used in combination with an artificial neural network, trained with previously gained data from Liemberger et al. (2017b). The data was randomly split into a training (70% of data), test (15%) and validation (15%) set. Beside feed concentration (H_2 , CH_4 and CO_2), feed pressure, PSA recovery and membrane selectivity the total H_2 recovery is used as input parameter to the ANN.

A feed-forward network with 15 hidden layers was taken (see Fig. 2), as it had the best performance. The network contains seven layers with a hyperbolic tangent sigmoid transfer function, followed by three layers with a positive linear transfer function and five additional layers with hyperbolic tangent sigmoid transfer function. Finally, the output is scaled via a linear regression layer.

Before applied to the ANN the input data is pre-processed. The values are first cleaned (removal of constant rows) and normalised (scaled to a range from -1 to 1). Then principal components are gained via PCA and used as input variables to the ANN. The ANN is trained to produce values between -1 and 1 which are rescaled to the original output unit in a post-processing step. Finally, the specific energy demand is computed.

The network was trained supervised (model results are known from process simulation) where the model performance was evaluated by the mean square error (MSE). During the training the weight and bias values are updated in order to reduce the MSE. This was

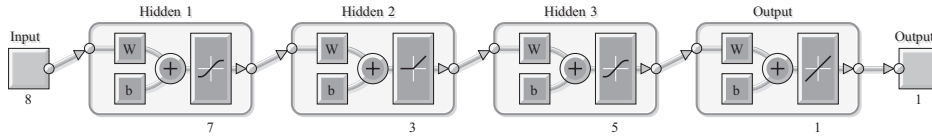


Figure 2: Feed-forward ANN with 8 input variables, multiple hidden layers and one output variable, representing the specific energy demand

efficiently done with a Levenberg-Marquardt backpropagation algorithm implemented in the Neural Network Toolbox of MATLAB® R2016b.

To minimise overfitting a validation data set was used during the training. This dataset is taken to test if the model accuracy increases within the training, or if only the accuracy of model increases for the applied training data. In case the accuracy of the validation data set stays the same, the network has been overfitted and the training process is stopped.

After training the gained ANN is tested with unused data (test set).

Beside this standard procedure to create a neural network some example cases are investigated to check the plausibility of the gained results, especially for cases not included in the training, validation and test data.

3. Results and Discussion

3.1. Training, Validation and Testing

Fig. 3 shows the model quality for training, validation and test data. As it can be seen, all results are positive with determination coefficients (R^2) of 0.99879 (training data), 0.99863 (validation data) and 0.99872 (test data).

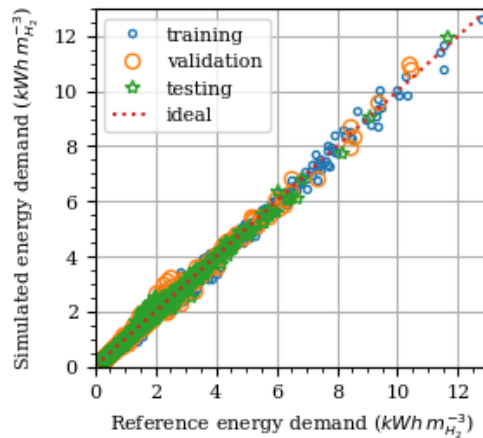


Figure 3: Regression plot of training, validation and test data of the ANN

3.2. Plausibility Checks

The plausibility checks are performed for various input parameters. If not changed during the variation the following variables have been chosen: (i) feed concentration H_2 4%(v/v), CO_2 1%(v/v), (ii) 51 bar feed pressure, (iii) selectivity of 75.68 for H_2/CH_4 , 3.37 for H_2/CO_2 and (iv) 80% PSA recovery. The current work uses a compression efficiency of 72% as this can be scaled directly and does not require a complex model.

3.2.1. Variation of H_2 Feed Concentration

In Fig. 4(a) the influence of the H_2 feed concentration is presented. A higher H_2 feed concentration requires less energy (at the same total H_2 recovery) for the extraction. The ANN slightly overestimates the compression energy at low concentrations, while the others are in good agreement. For the cases with 5%(v/v) H_2 (not part of the data set) it can be seen that the predicted energy demand looks reasonable.

3.2.2. Variation of Feed Pressure

Several feed pressures have been analysed and the results are presented in Fig. 4(b). Higher feed pressures reduce the required amount of energy. Anyhow, the off-gas has to be re-compressed to the feed pressure level. Subsequently, it is a trade-off between better membrane separation efficiency (greater pressure difference) and an increased re-compression effort. The ANN is in good agreement with the process simulation. However, the ANN curves are slightly wavy. Therefore, it is assumed that the model quality could be improved with more training data, varying the pressure.

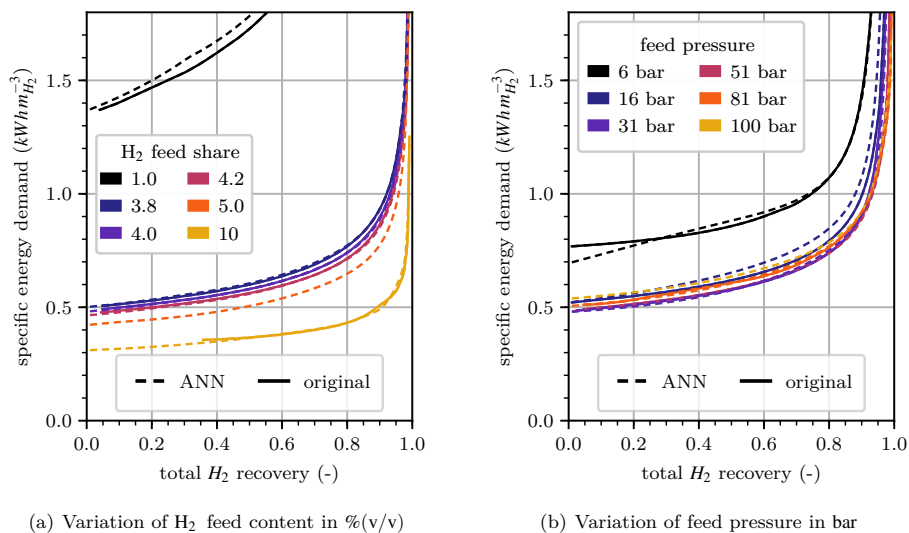


Figure 4: Variation of feed conditions (H₂ content and pressure)

3.2.3. Variation of Membrane Selectivity of H₂/CH₄

For the efficient separation a selective membrane is required. The influence of this material dependent parameter has been investigated and is shown in Fig. 5(a). The predicted values are in good agreement with the provided process simulation data. A higher selectivity reduces the energy demand, as the membrane separation is more efficient. The modelled energy demand for selectivity values that were not included in the data sets (see 150 and 250) look reasonable.

3.2.4. Variation of PSA Recovery

A higher PSA recovery reduces the required amount of energy as already presented in Liemberger et al. (2017b). The reduced model is able to properly predict the effect of changing the PSA recovery as shown in Fig. 5(b) of the dataset (70 %, 80 % and 90 %). Further, the prediction of an in-between value, 85 %, looks promising.

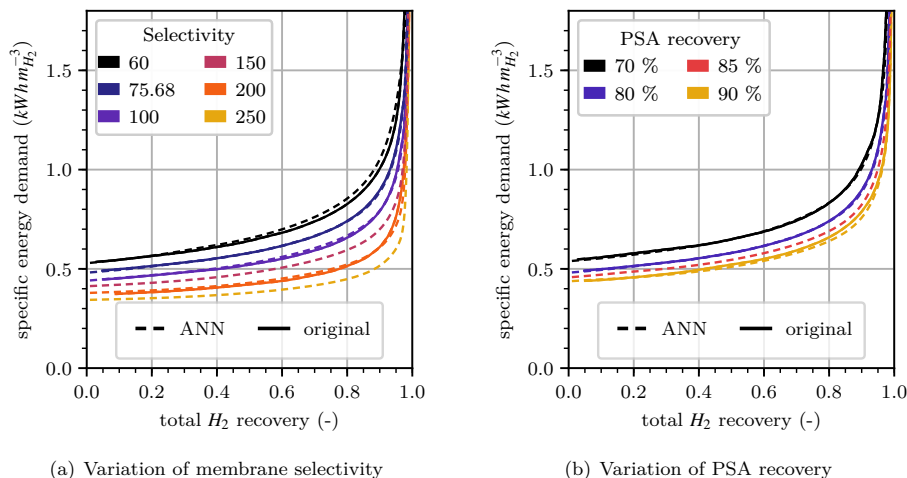


Figure 5: Variation of membrane H_2/CH_4 selectivity and PSA recovery

4. Conclusion and Outlook

This work presents a trained artificial neural network to predict the specific amount of energy required for the extraction of H_2 transported as co-stream with natural gas based on various input parameters like feed concentration, pressure, PSA recovery and more.

Beside results of the network creation step (network quality) further plausibility checks are shown. In conclusion the work presents a suitable method and model to identify the required energy demand used in ongoing work for detailed economic and siting evaluations.

References

- Azlan Hussain, M., 1999. Review of the applications of neural networks in chemical process control — simulation and online implementation. *Artificial Intelligence in Engineering* 13 (1), 55–68. doi: 10.1016/S0954-1810(98)00011-9.
- Balabin, R. M., Lomakina, E. I., Safieva, R. Z., 2011. Neural network (ANN) approach to biodiesel analysis: Analysis of biodiesel density, kinematic viscosity, methanol and water contents using near infrared (NIR) spectroscopy. *Fuel* 90 (5), 2007–2015. doi: 10.1016/j.fuel.2010.11.038.
- Blanco, H., Faaij, A., 2018. A review at the role of storage in energy systems with a focus on Power to Gas and long-term storage. *Renewable and Sustainable Energy Reviews* 81, 1049–1086. doi: 10.1016/j.rser.2017.07.062.
- Eurogas, 2015. Statistical Report. Last accessed on 15.12.2017. URL <http://www.eurogas.org/uploads/2016/flipbook/statistical-report-2015/>
- Liemberger, W., Groß, M., Miltner, M., Harasek, M., 2017a. Experimental analysis of membrane and pressure swing adsorption (PSA) for the hydrogen separation from natural gas. *Journal of Cleaner Production*, 896–907 doi: 10.1016/j.jclepro.2017.08.012.
- Liemberger, W., Halmschlager, D., Miltner, M., Harasek, M., 2017b. Efficient Extraction of Hydrogen Transported as Co-Stream in the Natural Gas Grid: The Importance of Process Design: submitted. *Applied Energy*.
- Pirdashti, M., Curteanu, S., Kamangar, M. H., Hassim, M. H., Khatami, M. A., 2013. Artificial neural networks: Applications in chemical engineering. *Reviews in Chemical Engineering* 29 (4), 205–239. doi: 10.1515/revce-2013-0013.

Packed bed sorption enhanced methane reforming on CaO/CuO/Al₂O₃(NiO) catalyst

Giuseppe Diglio^a, Piero Bareschino^a, Erasmo Mancusi^{a,*}, Francesco Pepe^a,
Dawid Hanak^b, Vasilije Manovic^b

^a*Dipartimento di Ingegneria, Università degli Studi del Sannio, Piazza Roma 21, Benevento 82100, Italy*

^b*Combustion and CCS Centre, Cranfield University, Cranfield MK43 0AL, United Kingdom*

erasmo.mancusi@unisannio.it

Abstract

An autothermal sorption-enhanced steam methane reforming in a packed-bed reactor for production of high-purity hydrogen was studied by means of 1D numerical model. The reactor utilises a CaO/CuO/Al₂O₃(NiO) catalyst. This process is characterised by a number of challenges, such as the choice of the operating conditions to ensure both a production of high-purity H₂ stream and an autothermal sorbent regeneration stage. This paper addresses these challenges through numerical simulation. The results for the system cyclically operated in a packed-bed showed a methane conversion of 95%, and a hydrogen yield and selectivity around 3 mol_{H₂}·mol_{CH₄}⁻¹ and 90%, respectively.

Keywords: hydrogen, calcium oxide, copper oxygen carrier, nickel catalyst, fixed bed.

1. Introduction

Hydrogen is a secondary form of energy mainly produced by Steam Methane Reforming (SMR). However, SMR has two main drawbacks: the reforming reactions are strongly endothermic, hence an external heater is needed, and the effluent is a mixture of H₂ and CO, therefore a post-processing unit is required to obtain an enriched-H₂ gas stream (Marabàn and Valdés-Solis, 2007). Sorption-Enhanced Steam Methane Reforming (SE-SMR) is currently investigated as a feasible solution to address such drawbacks (Broda *et al.*, 2013). Reforming catalyst (Ni) and CO₂ solid sorbent, usually CaO, are mixed in order to carry out CH₄ reforming and CO₂ adsorption simultaneously, thus producing a high-purity H₂ stream. While the H₂ production and CO₂ adsorption stage is globally autothermal (Broda *et al.*, 2013), the heat required by endothermic sorbent regeneration reaction is the main drawback of SE-SMR. To overcome this engineering challenge, a novel CaO-based sorbent mechanically mixed with Cu-based oxygen carrier and Ni-based catalyst was recently developed. Such material enables providing the heat for calcination reaction by means of exothermic Cu reduction reaction (Manovic and Anthony, 2001). This study aims to prove the technical feasibility, and contribute to the scale-up and commercialisation, of this near-zero CO₂ hydrogen production technology.

2. Kinetic scheme and mathematical model

The adopted kinetic scheme is reported in Table 1. Three main stages can be distinguished in SE-SMR, namely reforming/CARBonation (CAR), OXidation (OX) and reduction/CALcination (CAL) stage. In CAR stage, methane and steam are fed to the reactor. Reforming reactions (R1-R3), methane decomposition (R4), carbon gasification by steam (R5) and by CO₂ (R6), as well as carbonation reaction (R7) occur simultaneously. As a result, a stream of high-purity H₂ leaves the reactor. In OX stage, a lean oxygen-nitrogen mixture is fed to the reactor and oxidation of Ni (R8), of Cu (R9), and of the carbon deposited onto the catalyst surface (R10) takes place. In CAL stage, CuO (R11-R13) and NiO (R14-R17) reduction reactions occur at the expenses of CH₄ oxidation, simultaneously with sorbent regeneration (calcination reaction, R18).

Table 1 – Kinetic scheme adopted.

Reaction	$\Delta H^0, \text{J}\cdot\text{mol}^{-1}$	
<i>Reforming/Carbonation stage</i>		
$\text{CH}_4 + \text{H}_2\text{O} \xrightarrow{\text{Ni}} \text{CO} + 3\text{H}_2$	206	R1
$\text{CO} + \text{H}_2\text{O} \xrightarrow{\text{Ni}} \text{CO}_2 + \text{H}_2$	-41	R2
$\text{CH}_4 + 2\text{H}_2\text{O} \xrightarrow{\text{Ni}} \text{CO}_2 + 4\text{H}_2$	165	R3
$\text{CH}_4 + \text{Ni} \xrightarrow{\text{Ni}} \text{Ni-C} + 2\text{H}_2$	74	R4
$\text{C} + \text{H}_2\text{O} \xrightarrow{\text{Ni}} \text{CO} + \text{H}_2$	131	R5
$\text{C} + \text{CO}_2 \xrightarrow{\text{Ni}} 2\text{CO}$	172	R6
$\text{CaO} + \text{CO}_2 \rightarrow \text{CaCO}_3$	-179	R7
<i>Oxidation Stage</i>		
$2\text{Ni} + \text{O}_2 \rightarrow 2\text{NiO}$	-479	R8
$2\text{Cu} + \text{O}_2 \rightarrow 2\text{CuO}$	-312	R9
$\text{C} + \left(\frac{I+\psi}{2}\right)\text{O}_2 \rightarrow \psi\text{CO}_2 + (I-\psi)\text{CO}$	[-787, -110]	R10
<i>Reduction/Calcination stage</i>		
$4\text{CuO} + \text{CH}_4 \rightarrow 4\text{Cu} + \text{CO}_2 + 2\text{H}_2\text{O}$	-178	R11
$\text{CuO} + \text{CO} \rightarrow \text{Cu} + \text{CO}_2$	-127	R12
$2\text{CuO} + 2\text{H}_2 \rightarrow 2\text{Cu} + 2\text{H}_2\text{O}$	-86	R13
$2\text{NiO} + \text{CH}_4 \rightarrow 2\text{Ni} + 2\text{H}_2 + \text{CO}_2$	161	R14
$\text{NiO} + \text{CO} \rightarrow \text{Ni} + \text{CO}_2$	-43	R15
$\text{NiO} + \text{H}_2 \rightarrow \text{Ni} + \text{H}_2\text{O}$	-2	R16
$\text{NiO} + \text{CH}_4 \rightarrow 2\text{Ni} + 2\text{H}_2 + \text{CO}$	203	R17
$\text{CaCO}_3 \rightarrow \text{CaO} + \text{CO}_2$	179	R18

The kinetic expressions of reaction rates are reported in Diglio *et al.* (2017a, 2017b, 2018). To describe axial concentration and temperature profiles in the reactor, a 1D pseudo-homogenous packed-bed model was used, as reported by Eqs. (1-4):

$$\varepsilon_g \frac{\partial C_i}{\partial t} + u_{sg} \frac{\partial C_i}{\partial z} = \varepsilon_g \frac{\partial}{\partial z} \left(D_{ax} \frac{\partial C_i}{\partial z} \right) - r_i \rho_{oc} \quad (1)$$

$$\frac{dX_k}{dt} = \sigma \frac{r_k}{C_k^0}, \quad \frac{dC_C}{dt} = r_C \quad (3)$$

$$\left[\varepsilon_g c p_g \rho_g + (1 - \varepsilon_g) c p_s \rho_{oc} \right] \frac{\partial T}{\partial t} + u_{sg} c p_g \rho_g \frac{\partial T}{\partial z} = \varepsilon_g \frac{\partial}{\partial z} \left(\lambda_{eff} \frac{\partial T}{\partial z} \right) + \rho_{oc} \sum_j (r_{R_j} \Delta H_{R_j}) \quad (2)$$

$$\frac{dP}{dz} = \frac{150 \mu_g (1 - \varepsilon_g)^2}{d_p^2 \varepsilon_g^3} u_{sg} + \frac{1.75 (1 - \varepsilon_g) \rho_g}{d_p \varepsilon_g^3} u_{sg}^2 \quad (4)$$

where C is the gas concentration in $\text{mol}\cdot\text{m}^{-3}$, C_C is the carbon concentration in $\text{kg}_C\cdot\text{kg}_{oc}^{-1}$, C_k^0 is the initial concentration of solid species in the carrier in $\text{mol}\cdot\text{kg}_{oc}^{-1}$, T is the temperature in K, X is the solid conversion, P is the pressure in Pa, ε_g is the bed void fraction, u_{sg} is the gas superficial velocity in $\text{m}\cdot\text{s}^{-1}$, z is the axial variable in m, D_{ax} is the axial dispersion, ρ_{oc} and ρ_g are the density of oxygen carrier and gas, respectively, in $\text{kg}\cdot\text{m}^{-3}$, $c p_g$ is the gas heat capacity in $\text{J}\cdot\text{kg}^{-1}\cdot\text{K}^{-1}$, μ_g is the gas viscosity in $\text{Pa}\cdot\text{s}$, λ_{eff} is the effective thermal conductivity in $\text{W}\cdot\text{m}^{-1}\cdot\text{K}^{-1}$, t is the time in s, d_p is the particle diameter in m, r is the reaction rate in $\text{mol}\cdot\text{kg}_{oc}^{-1}\cdot\text{s}^{-1}$, ΔH is the reaction enthalpy in $\text{J}\cdot\text{mol}^{-1}$, i is the gas species (CH_4 , H_2 , CO_2 , H_2 , CO , CO_2 , O_2 , N_2), k is the solid species (Ni, Cu, CaO).

The rates of consumption or formation of gas, r_i , and solid, r_k and r_C , species are determined by summing up the reaction rates of that species in all the reactions R_j ($j=1, \dots, 18$). To account for catalyst deactivation due to carbon deposition on its surface, with the exception of (R7), (R18), and (R10), all reaction rates were scaled by a deactivation function, ranging from 0 (fully poisoned catalyst) to 1 (carbon free catalyst), according to Diglio *et al.* (2016). The CO_2 adsorption capacity of the sorbent decreases in few carbonation/calcination cycles, after that assumes an almost constant value over around 50 cycles. To take into account the decay in CO_2 capture capacity, the approach suggested by Fernandez *et al.* (2012) was adopted, by assuming a maximum absorption capacity of 40% of its nominal value. The cyclic nature of SE-SMR was mathematically expressed by assuming that the initial conditions for each step (CAR, OX and CAL) are equal to the ones from the previous step. In addition, Danckwerts and Neumann boundary conditions were used. For evaluation of temperature, pressure and composition dependencies of reaction enthalpies, transport coefficients, and gas properties, the state-of-art correlations and assumptions were adopted. Further details can be found in Diglio *et al.* (2017a). The numerical model was solved using the commercial software Comsol Multiphysics®. Reactor length, L , was discretised with 1000 nodes and it was carefully checked whether further refinements of the spatial discretisation did not produce any significant variations in the computed concentration and temperature profiles. The validation of the model is reported in Diglio *et al.* (2017a, 2017b, 2018).

3. Results and discussion

Operating conditions, reactor and catalyst data used in the simulations are reported in Table 2. The period, and the consequent feed switch strategy, of each stage is not fixed *a priori*. Instead, a control that checks the conditions for switching between each stage based on the outlet gas stream composition was set up. Figure 1 reports gas molar fractions on dry basis at the reactor outlet as a function of time during the first CAR (A), OX (B) and CAL (C). During CAR, a high-purity H₂ gas stream is obtained (~95%). H₂ content of the outlet gas stream decreases as CaO sorbent approaches its saturation capacity, while CH₄ content increases. In order to ensure a high-purity H₂ production, the control orders the system to stop the CAR when outlet H₂ molar fraction decreases below 0.85 (Fig. 1A). With the aim to ensure thermal-neutral conditions during OX and to avoid high temperatures, which could lead to solid material deactivation, an inlet O₂ molar fraction around 0.03 is guaranteed by recirculating the nitrogen obtained at the outlet of the reactor. This stage should ensure that both Ni and Cu in the solid material are completely oxidized, thus the control ceases OX only when inlet O₂ molar fraction is detected at the reactor outlet (Fig. 1B). During the CAL, the heat released by exothermic Cu reduction should drive endothermic Ni reduction and sorbent regeneration. With this aim, a mixture of CH₄ and CO₂ is fed to the reactor with a CO₂-to-CH₄ feed ratio able to ensure autothermal conditions (Qin *et al.*, 2015; also see Table 2). Consequently, only steam and CO₂ are detected at the exit of the reactor. The control orders the system to stop the CAL when both CH₄ and CO₂ outlet molar fractions reach their feeding value. The former condition ensures that both Ni and Cu are fully reduced, while the latter ensures that the sorbent is fully regenerated (Fig. 1C). Starting from these results, cyclic operation consisting of a sequence of carbonation/reforming-purge-oxidation-purge-calcination-purge stages was considered. The purge stage between calcination and carbonation aims to pressurize the bed until $P_{CAR/OX}$ since the calcination stage is carried out at atmospheric pressure. The period of each purge stage was fixed to 100 s.

Table 2 – Parameters used in the simulations.

Parameter	Value
Feed temperature, T_f	1073 K
Initial temperature of the bed, T_0	1073 K
Carbonation and oxidation Pressure, $P_{CAR/OX}$	3.5 MPa
Calcination Pressure, P_{CAL}	101325 Pa
Reactor length, L	1 m
Reactor diameter, d_r	0.05 m
Particle diameter, d_p	0.01 m
Bed void fraction, ε_g	0.5
Mass of the solid in the reactor, m_s	1.6 kg
Mass fraction of sorbent, ω_{CaO}	0.45
Mass fraction of nickel, ω_{Ni}	0.10
Mass fraction of copper, ω_{Cu}	0.45
H ₂ O-to-CH ₄ feed ratio during CAR	5
CO ₂ -to-CH ₄ feed ratio during CAL	2.3
Mass flux of the gas phase in the CAR and CAL, $G_{CAR/CAL}$	1 kg·m ⁻² ·s ⁻¹
Mass flux of the gas phase in the OX, G_{OX}	10 kg·m ⁻² ·s ⁻¹

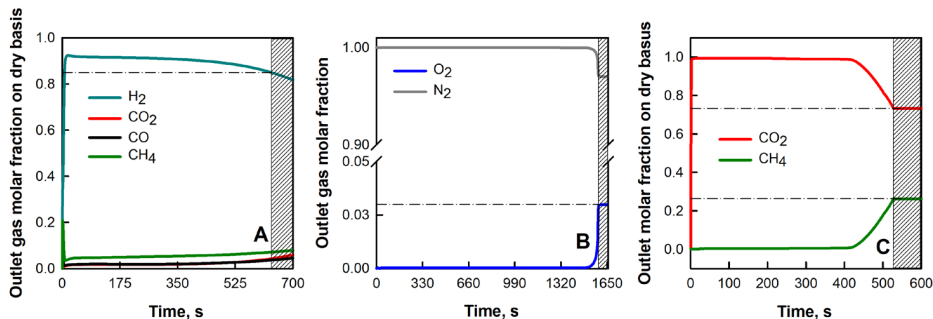


Figure 1 – Outlet gas molar fractions during the first CAR (A), OX (B) and CAL (C).

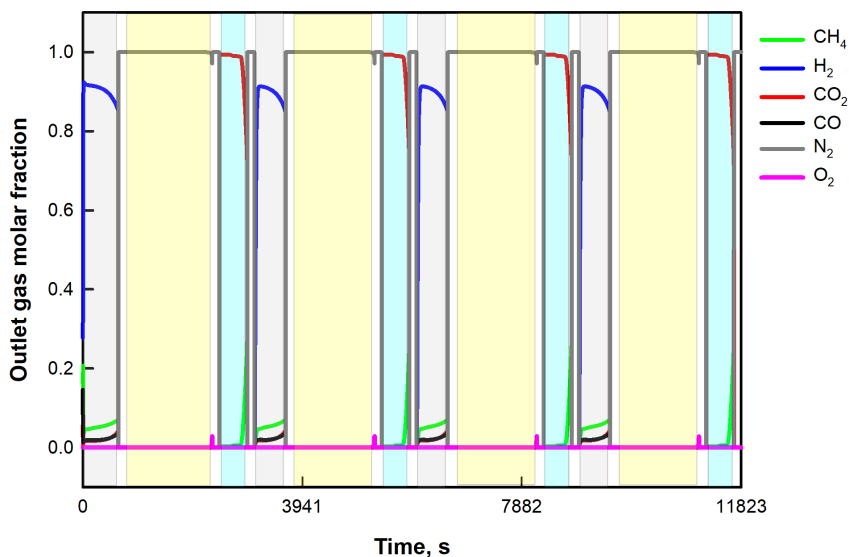


Figure 2 – Outlet gas molar fractions during multiple carbonation/reforming (in grey), purge (in white), oxidation (in yellow) and reduction/calcination (in blue) cycles as function of the time.

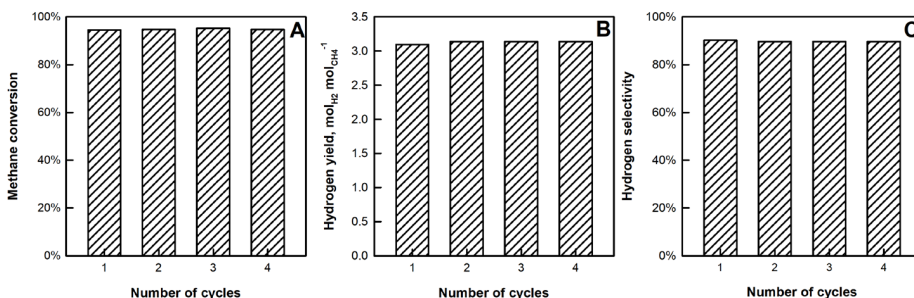


Figure 3 – Average CH₄ conversion in per cent (A), H₂ yield (B) and selectivity in per cent (C) during reforming/carbonation stage for all 4 SE-SMR cycles.

The results of cyclic operation of SE-SMR are reported in Fig. 2 in terms of outlet molar fractions as function of the time. It has been shown that 4 steps of cyclic operation are enough to attain regime conditions. Indeed, the period of each stage (*i.e.* the width of colourful strings in Fig. 3) reaches a constant value after just the first cycle. In Fig. 3, CH₄ conversion (A), H₂ yield (B) and selectivity (C) are reported as average values of reforming/carbonation stages for the 4 steps of cyclic operations: CH₄ conversion is around 95%, while H₂ yield and selectivity are about 3 mol_{H₂}·mol_{CH₄}⁻¹ and 90%, respectively. These last two parameters are higher than corresponding ones found in literature for alternative H₂ production process (Diglio et al., 2016).

4. Conclusions

A numerical investigation of autothermal SE-SMR process in packed-bed based on a CaO/CuO/Al₂O₃(NiO) catalyst is presented. The SE-SMR is intrinsically periodic, as reforming/carbonation, oxidation and reduction/calcination stages cyclically follow each other. A 1D pseudo-homogeneous model was used to find the operating conditions ensuring high-purity H₂ production over carbonation stage, thermal-neutrality over oxidation stage, and an autothermal reduction/calcination stage. The switch between each stage was dictated by monitoring outlet gas composition. At regime conditions, hydrogen yield and selectivity of 3 mol_{H₂}·mol_{CH₄}⁻¹ and 90% were reached, respectively.

References

- M. Broda, V. Manovic, Q. Imtiaz, A.M. Kierzkowska, E.J. Anthony, C.R. Muller, 2013, High-purity hydrogen via the sorption-enhanced steam methane reforming reaction over a synthetic CaO-based sorbent and a Ni catalyst, *Environ. Sci. Technol.*, 47, 6007-6014.
- G. Diglio, P. Bareschino, E. Mancusi, F. Pepe, 2016, Chemical Looping Reforming: Impact on the Performances Due to Carbon Fouling on Catalyst, *Comput.-Aided Chem. En.*, 38, 229-234.
- G. Diglio, P. Bareschino, E. Mancusi, F. Pepe, 2017a, Numerical assessment of the effects of carbon deposition and oxidation on chemical looping combustion in a packed-bed reactor, *Chem. Eng. Sci.*, 160, 85-95.
- G. Diglio, P. Bareschino, E. Mancusi, F. Pepe, 2017b, Techno-economic analysis of sorption-enhanced steam methane reforming in a fixed bed reactor network integrated with fuel cell, *J. Power Sources*, 364, 41-51.
- G. Diglio, D.P. Hanak, P. Bareschino, F. Pepe, V. Manovic, 2018, Modelling of sorption-enhanced steam methane reforming in a fixed bed reactor network integrated with fuel cell, *Appl. Energ.*, 210, 1-15.
- J.R. Fernandez, J.C. Abadanes, G. Grasa, 2012, Modelling of sorption enhanced steam methane reforming in adiabatic fixed bed reactor, *Chem. Eng. Sci.*, 137, 254-267.
- V. Manovic, E.J. Anthony, 2001, CaO-based pellets with oxygen carriers and catalysts, *Energ. Fuel*, 25, 4846-4853.
- G. Maraban, T. Valdés-Solis, 2007, Towards the hydrogen economy?, *Int. J. Hydrogen Energ.*, 32, 1625-1637.
- C. Qin, B. Feng, J. Yin, J. Ran, L. Zhang, V. Manovic, 2015, Matching of kinetics of CaCO₃ decomposition and CuO reduction with CH₄ in Ca-Cu chemical looping, *Chem. Eng. J.*, 262, 665-675.

A Heat Load Distribution Method for Retrofitting Heat Exchanger Networks

Hür Bütün^{a*}, Ivan Kantor^a, Alberto Mian^a and François Maréchal^a

^a*École Polytechnique Fédérale de Lausanne, IPESE, Sion, Switzerland*
hur.butun@epfl.ch

Abstract

Fluctuating energy prices, increasing environmental concerns, and regulations push industries toward more energy efficient plants. Process integration (PI) techniques, proven to be effective in providing solutions with improved energy and material efficiencies often neglect modifications to the heat exchanger network (HEN). HEN design methods have been studied extensively to overcome this drawback of process integration but often still focus on grassroots design to suggest retrofits. This work proposes a method to solve heat load distribution (HLD), a sub problem of HEN design, in the context of retrofit problems. The problem is solved using a mixed integer linear programming (MILP) model with integer cuts (IC) to obtain many retrofit options with high computational speed. The model is built on previously developed methods for PI (Maréchal and Kalitventzeff, 2003) and HEN design (Ciric and Floudas, 1989; Mian et al., 2016), such as mathematical programming (MP) and pinch analysis (PA). The objective function of the proposed method is minimisation of the estimated cost of the modifications required in an existing HEN, by considering the costs of repiping, additional heat exchanger area and additional heat exchangers. The estimated area of the potential stream matches is calculated using graphical techniques on the process integration results and taking into account correction factor. The additional heat exchanger area is constrained to practical limits available in the literature. The cost of heat exchanger area is calculated using piece-wise linearization of nonlinear cost functions. Solving the model yields information on stream matches and their heat loads as well as identifying which streams should be repiped and which heat exchangers should be modified or replaced. An industrial case study is solved to show the effectiveness of the proposed method resulting in annualized cost reductions of 9% considering the HEN design alone and 29% with modifications to the utility system to include heat pumping.

Keywords: process integration, heat exchanger network, retrofit, heat load distribution

1. Introduction

Industrial energy consumption represents 26% of the European total; industry is therefore incentivized by regulatory bodies to improve energy efficiency. Improving energy efficiency in industry has thus been a primary concern in research studies. PI techniques emerged after the oil crisis in 1970s and are still relevant and effective energy targeting methods to solve industrial energy efficiency problems (Klemeš and Kravanja, 2013). PI results typically propose solutions that require modifications to existing plants. Although investment in new technologies and equipment is considered with PI techniques, heat exchanger modifications are typically neglected. Several methods are available to include the cost of the modifications in the heat exchangers within PI (Bütün et al., 2017) or as post-processing (Ahmad et al., 1990). However, without knowing the

HEN superstructure or even the stream matches, estimation from these methods might deviate significantly from the real cost. HEN design has been deeply studied to improve calculation of the total cost of energy saving measures.

Yee and Grossmann (1990) proposed the SYNHEAT model using mixed integer non-linear programming (MINLP) to solve energy targeting, the matches between hot and cold streams and the optimal superstructure of the HEN simultaneously. One of the nonlinear constraints in HEN is calculation of logarithmic mean temperature difference (LMTD). Barbaro and Bagajewicz (2005) eliminated the nonlinear LMTD constraints by using fixed temperature intervals and formulated the HEN problem in the form of MILP by using linear cost functions.

Since heat exchanger network design is a difficult problem to solve, decomposition methods for dividing and solving it as several subproblems have been developed. The most common three subproblems of HEN are energy targeting (i.e. energy integration), minimum number of hot-cold stream matches (i.e. HLD) and minimum heat exchanger area cost (i.e. HEN superstructure). François and Irsia (1989) proposed the SYNEP model which solves the heat exchanger network subproblems by including heuristics. Mian et al. (2016) improved the heat exchanger network superstructure by allowing both parallel and series configurations and coupled MP methods with particle swarm optimization.

Retrofitting problems are currently the focus of many European industries since energy efficiency improvements are implemented on existing sites. Ciric and Floudas (1989) proposed a method to solve the HLD subproblem by including retrofit constraints. Afterward, a MINLP model formulation (Ciric and Floudas, 1990) was used to find the optimal retrofit superstructure applying an iterative procedure. Nguyen et al. (2010) proposed a MILP formulation using the fixed temperature interval model of Barbaro and Bagajewicz (2005).

A gap is identified for solving the HLD in retrofit situations since existing methods either do not clearly state how LMTD is calculated (Ciric and Floudas, 1989) or use predefined temperature intervals and linear cost functions (Barbaro and Bagajewicz, 2005) to fit within the MILP domain. This paper proposes a method to solve HLD retrofit problems based on the work of Ciric and Floudas (1989). The results of HLD can be used for heat exchanger network design in case of unsplit acyclic HENs or can be followed by superstructure synthesis.

2. Methodology

2.1. Energy integration

The energy integration (i.e. targeting) subproblem must be solved prior to considering HLD. The problem is defined with a set of units (**U**) consisting of the set of process units (**PU**) with fixed sizes and utility units (**UU**) which are scheduled using binary variables (y) and sized using continuous variables (f). The energy and material flows are modelled as thermal and mass streams with set of streams (**S**). Streams are assigned to units such that sizing and scheduling agree with their containing units. The details of the MILP formulation of energy integration can be found in Marechal and Kalitventzeff (2003).

2.2. LMTD calculation from graphical methods

LMTD evaluation is nonlinear and hence cannot be calculated within an MILP. One novelty this paper brings is the LMTD estimation at the level of HLD. The method to obtain vertical segments from the composite curves (Ahmad et al., 1990) is adapted. This way the LMTD for each vertical zone in the composite curve can be obtained. However, HLD is formulated with temperature intervals. The $LMTD_{ijk}$ of the hot ($i \in \mathbf{H}$) and cold ($j \in \mathbf{C}$) streams in each temperature interval ($k \in \mathbf{K}$) is calculated by taking the weighted average of the LMTD of the vertical segments in the

temperature interval. Afterwards, this parameter is used to calculate the area required for the heat transfer of the match i - j using Eqns. (1) and (2).

$$A_{ijk} = \frac{\dot{Q}_{ijk}}{U_{ijk} \cdot \text{LMTD}_{ijk} \cdot F_{corr}} \quad \forall i \in \mathbf{H}, j \in \mathbf{C}, k \in \mathbf{K} \quad (1)$$

$$A_{ij} = \sum_{z=1}^{\mathbf{K}} A_{ijk} \quad \forall i \in \mathbf{H}, j \in \mathbf{C} \quad (2)$$

2.3. Heat load distribution for retrofitting

The HLD problem is defined from the results of energy integration (EI). The units that are not used in EI are removed from the set of units for HLD. Since HLD focuses on heat, it only considers thermal streams from the overall set of streams. The unit sizes and hence the heat load of the streams are fixed as parameters. The existing heat exchangers in the system are defined as a set (\mathbf{X}). To model the stream segments, the set of stream groups (\mathbf{SG}) is used. As such, when a stream with phase change or varying heat capacity is defined, a stream for each segment is created but all are assigned to the same stream group. Stream groups are then separated into the set of hot stream groups (\mathbf{HG}) and the set of cold stream groups (\mathbf{CG}). The matches are created between $i \in \mathbf{HG}$ and $j \in \mathbf{CG}$ using binary variables (y_{ij}). The problem size is therefore greatly reduced in problems with segmented streams compared to existing methods available in literature. The heat load of the stream matches is determined using the heat flow model presented by (Floudas et al., 1986). Modifications in the existing heat exchanger network are classified into six categories as proposed by (Circic and Floudas, 1989). Each stream pair in the solution can be defined according to the required modifications, or lack thereof.

- **Category 1: No modification, no cost.** The existing stream match is housed in the current heat exchanger. Hence, no modification is required. The matches are assigned to this category using set **C1**
- **Category 2: Moving the heat exchanger.** The existing stream match is housed in an existing exchanger, though not the one currently employed for this purpose. Hence, this category requires moving the heat exchanger. The matches are assigned to this category using set **C2**
- **Category 3: Repiping one stream.** A new match is housed in a heat exchanger from the existing network which was housing either the cold or the hot stream of the match. The matches are assigned to this category using set **C3**
- **Category 4: Repiping two streams.** A new match is housed in a heat exchanger from the existing network which had no connection with either the cold or hot stream of current network. The matches are assigned to this category using set **C4**
- **Category 5: Purchasing a new heat exchanger.** An existing stream match is housed in a new heat exchanger. The matches are assigned to this category using set **C5**
- **Category 6: Purchasing a new heat exchanger and repiping.** A new stream match is housed in a new heat exchanger. The stream matches are assigned to this category using set **C6**

In contrast to the methods available in literature, only the matches that include at least one stream group from a process unit are considered for the listed retrofitting categories. This approach omits the cost of heat exchangers between utility units (e.g. boiler and steam network), thus only optimising interactions which affect the process units.

The cost of modifications according to the retrofitting categories can be summarised as moving a heat exchanger, repiping stream(s) and purchasing a new heat exchanger. In addition, when one of the heat exchangers from the existing networks is reused, its area can be increased (i.e. additional heat exchanger area). The cost of moving heat exchangers, repiping and additional heat exchanger area are calculated using linear formulas found in Rezaei and Shafiei (2009). Cost calculation for new heat exchangers is completed by applying piece-wise linearization to nonlinear

cost estimation formulae. The objective Eqn. (3) is minimization of the total modification cost required in the network.

$$\begin{aligned} \min_{y,n,A} & \sum_{y_{ijx}}^{C2} y_{ijx} \cdot c^{move} + \sum_{y_{ijx}}^{C3} y_{ijx} \cdot c^{rep1} + \sum_{y_{ijx}}^{C4} y_{ijx} \cdot c^{rep2} \\ & + \sum_{n_{ij}}^{C5} (n_{ij} \cdot c^{inst} + A_{ij}^{purc}) + \sum_{n_{ij}}^{C6} (n_{ij} \cdot c^{inst+rep2} + A_{ij}^{purc}) + \sum_{A_{ijx}}^X A_{ijx}^{add} \end{aligned} \quad (3)$$

The retrofit constraints are given in Eqns. (4) to (8). An existing heat exchanger is assigned to maximum one stream match by Eqn. (4). Each match is assigned to either an existing heat exchanger or a new one by Eqn. (5). Heat exchanger area required for each match must be equal to the heat exchanger area used from the existing exchangers and the new heat exchanger area using Eqn. (6). The new heat exchanger area assigned to a stream match is equal to either heat exchanger area added to an existing exchanger or the area of a purchased heat exchanger (i.e. a new heat exchanger) by Eqn. (7). The additional area to the existing heat exchangers is constrained to the practical limits by Eqn. (8). The heat flow model and the equations concerning stream matches can be found in Mian et al. (2016). Tbl. 1 depicts the description of the symbols used in the formulation.

$$\sum_{i=1}^{HG} \sum_{j=1}^{CG} y_{ijx} \leq 1 \quad \forall x \in \mathbf{X} \quad (4)$$

$$y_{ijx} + n_{ij} - y_{ij} = 0 \quad \forall i \in \mathbf{HG}, j \in \mathbf{CG}, x \in \mathbf{X} \quad (5)$$

$$A_{ij}^{new} + A_{ijx}^{exist} - A_{ij} = 0 \quad \forall i \in \mathbf{HG}, j \in \mathbf{CG}, x \in \mathbf{X} \quad (6)$$

$$A_{ij}^{new} = A_{ijx}^{add} + A_{ij}^{purc} \quad \forall i \in \mathbf{HG}, j \in \mathbf{CG}, x \in \mathbf{X} \quad (7)$$

$$A_{ijx}^{add} \leq A_{ijx}^{exist} \cdot add^{max} \quad \forall i \in \mathbf{HG}, j \in \mathbf{CG}, x \in \mathbf{X} \quad (8)$$

Table 1: Description of the symbols in the formulation

Symbol	Description	Symbol	Description
y	Binary to decide a stream match	$exist$	Existing
n	Binary to decide a new stream match	add	Additional
A	Area of the stream match	$purc$	Purchase
\dot{Q}	Heat load	$move$	Moving
\bar{U}	Overall heat transfer coefficient	$rep1$	Repiping 1 stream
F_{corr}	LMTD correction factor	$rep2$	Repiping 2 streams
c	Specific cost	$inst$	Installation

3. Case Study

An industrial production plant is studied to apply the proposed method. In the current state of the site, heat recovery between hot and cold processes is not applied. Therefore, all process heating requirements are supplied by the heating utilities and hot processes are cooled by cooling utilities. The existing plant uses a boiler to provide heating which is distributed to processes through the steam network. Air and water heat exchangers are both used to supply the process cooling requirements. The list of process streams, their current stream matches and heat exchanger area are given in Tbl. 2.

In addition to the existing utilities, integration of two heat pumps is considered. The evaporation and condensation temperature levels of the heat pumps are decided based on the grand composite curve (GCC) of the plant.

Table 2: Streams and initial heat exchanger areas of the case study

Stream	T _{in} [°C]	T _{out} [°C]	T _{sat} [°C]	ΔQ [kW]	Area [m ²]	Stream	T _{in} [°C]	T _{out} [°C]	T _{sat} [°C]	ΔQ [kW]	Area [m ²]
C1	51	56	56	404	5.5	H4	55	33	-	1150	121.2
C2	79	84	84	2172	35.5	H5	44	31	-	246	34.9
C3	61	66	66	284	4.1	H6	47	40	-	144	19.5
C4	58	63	63	1894	26.9	H7	67	35	67	1340	475
C5	60	65	65	1960	41.6	H8	86	35	86	1172	304.7
C6	43	100	100	1974	61.3	H9	57	35	57	2488	1095.5
C7	43	100	100	824	25.6	H10	67	35	67	1286	451.9
C8	63	68	68	1442	31.5	H11	67	31	67	780	283.1
C9	53	58	58	420	8.4	H12	69	35	69	2256	776.9
H1	53	31	-	610	70.4	H13	177	40	61	2574	806.9
H2	50	38	-	46	4.7	H14	81	39	81	730	195.6
H3	41	32	-	2218	332.8	H15	58	35	-	680	431

4. Results and discussion

The current energy bill of the plant is calculated to represent the base case scenario (BCS) and hence provide a basis of comparison for benefits of the energy saving solutions. EI is carried out in several scenarios. energy saving scenario 1 (ES1) presents a scenario where investment in new energy conversion technologies is not desired. Improvements in energy efficiency must therefore be through better use of the resources and systems available on the plant. In energy saving scenario 2 (ES2), integration of heat pumps is also considered.

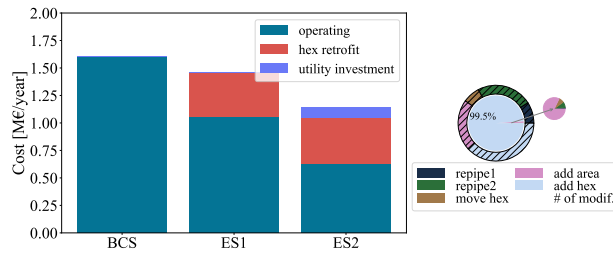


Figure 1: Cost comparison of scenarios (left), distribution modifications in ES2 (right)

EI is followed by HLD retrofit optimization for each scenario (excluding the base case) which yields annualized cost estimation of the heat exchanger network modifications to achieve the improvements in energy efficiency assuming 20 years of life time and 8% interest rate. In Fig. 1 the comparison of the base case and energy saving scenarios can be seen. Operating cost is reduced by 33% with more efficient use of the steam network and another 28% with the integration of heat pumps. When the cost of the modifications estimated by HLD and the cost of the heat pumps are considered, the reduction in the total cost becomes 9% and 29% in ES1 and ES2, respectively. The details of heat exchanger network modifications for ES2 are given in Fig. 1. The distribution of the number of modifications of each type can be seen in the outer pie chart while the distribution of the cost of the modifications is plotted in the inner chart. The cost of the modifications is dominated by the cost of new heat exchangers added to the network. Since the remaining contributions are marginal, the distribution of cost amongst them is plotted separately. The cost of adding area to the existing heat exchangers has the largest cost contribution. One reason for this distribution is that repiping and moving heat exchangers have unit cost per modification while additional heat exchanger area also depends on the size of the modification.

In HLD, because of the nature of the problem, it is possible to obtain the same or similar objective function evaluations with different configurations. In industrial applications, these alternatives are important to provide several options for improvement since not all constraints are accounted for in the formulation of the optimization. IC is applied to the HLD retrofit of ES2. The comparison of IC scenarios is depicted in Fig. 2. With the integer cut solutions, ten different modification combinations are proposed, with objective values within 1% of the optimal.

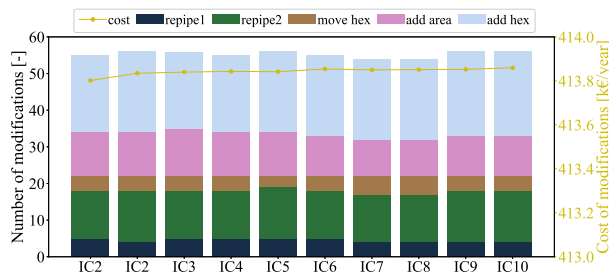


Figure 2: Integer cuts results

5. Conclusion

In this work, a mathematical programming method is proposed to solve HLD in the context of retrofit problems. The categories of modifications are defined as moving heat exchangers, repiping stream(s) of an existing heat exchanger, adding heat exchanger area to the existing heat exchangers and adding new heat exchangers. The method is applied to a real industrial problem where the total cost of the system was reduced by 29% considering integration of new utilities, more efficient use of the existing ones and the estimated cost of the modifications in the heat exchanger network. Multiple options for retrofitting were obtained by applying integer cuts in HLD. The method can be used to make preliminary retrofit decisions as well as to determine the stream matches prior to HEN superstructure synthesis.

6. Acknowledgements

This project has received funding from the European Union's Horizon 2020 research and innovation programme under grant agreement No 679386.

References

- Ahmad, S., Linnhoff, B., Smith, R., Jul. 1990. Cost optimum heat exchanger networks—2. targets and design for detailed capital cost models. *Computers & Chemical Engineering* 14 (7), 751–767.
- Barbaro, A., Bagajewicz, M. J., Aug. 2005. New rigorous one-step MILP formulation for heat exchanger network synthesis. *Computers & Chemical Engineering* 29 (9), 1945–1976.
- Büttin, H. E., Kantor, I. D., Maréchal, F., 2017. A process integration method with multiple heat exchange interfaces. *Proceedings of ECOS 2017*, 1447–1460.
- Ciric, A., Floudas, C., Jun. 1989. A retrofit approach for heat exchanger networks. *Computers & Chemical Engineering* 13 (6), 703–715.
- Ciric, A. R., Floudas, C. A., Feb. 1990. A mixed integer nonlinear programming model for retrofitting heat-exchanger networks. *Industrial & Engineering Chemistry Research* 29 (2), 239–251.
- Floudas, C. A., Ciric, A. R., Grossmann, I. E., Feb. 1986. Automatic synthesis of optimum heat exchanger network configurations. *AIChE Journal* 32 (2), 276–290.
- François, M., Irsia, B., Apr. 1989. Synep1 : A methodology for energy integration and optimal heat exchanger network synthesis. *Computers & Chemical Engineering* 13 (4-5), 603–610.
- Klemeš, J. J., Kravanja, Z., Nov. 2013. Forty years of Heat Integration: Pinch Analysis (PA) and Mathematical Programming (MP). *Current Opinion in Chemical Engineering* 2 (4), 461–474.
- Marechal, F., Kalitventzeff, B., Oct. 2003. Targeting the integration of multi-period utility systems for site scale process integration. *Applied Thermal Engineering* 23 (14), 1763–1784.
- Mian, A., Martelli, E., Maréchal, F., Jan. 2016. Framework for the Multiperiod Sequential Synthesis of Heat Exchanger Networks with Selection, Design, and Scheduling of Multiple Utilities. *Industrial & Engineering Chemistry Research* 55 (1), 168–186.
- Nguyen, D. Q., Barbaro, A., Vipanurat, N., Bagajewicz, M. J., Jul. 2010. All-At-Once and Step-Wise Detailed Retrofit of Heat Exchanger Networks Using an MILP Model. *Industrial & Engineering Chemistry Research* 49 (13), 6080–6103.
- Rezaei, E., Shafiei, S., Sep. 2009. Heat exchanger networks retrofit by coupling genetic algorithm with NLP and ILP methods. *Computers & Chemical Engineering* 33 (9), 1451–1459.
- Yee, T., Grossmann, I., Oct. 1990. Simultaneous optimization models for heat integration—II. Heat exchanger network synthesis. *Computers & Chemical Engineering* 14 (10), 1165–1184.

Combining Biomass, Natural Gas, and Carbonless Heat to Produce Liquid Fuels and Electricity

Leila Hoseinzade, Thomas A. Adams II*

*Department of Chemical Engineering, McMaster University, 1280 Main St W,
Hamilton, Ontario, L8S 4L8, Canada
tadams@mcmaster.ca*

Abstract

In this study, a new Biomass-Gas-Nuclear heat-To-Liquid fuel (BGNTL) process is presented which uses high-temperature nuclear heat as the heat source for steam methane reforming (SMR). This process co-produces liquid fuels (Fischer-Tropsch liquids, methanol and DME) and power. The BGNTL process was simulated using a combination of different software packages including gPROMS, MATLAB, ProMax, and Aspen Plus. This included the use of a rigorous multi-scale model for the nuclear-heat-powered SMR reactor which was developed in a prior work in gPROMS. Energy efficiency and cradle-to-grave life cycle inventory and life-cycle impact analyses of greenhouse gas (GHG) emissions were accomplished to analyze the environmental impacts of the BGNTL system. Plant performance was compared with a base case Biomass-Gas-To-Liquid (BGTL) process at the same size. In both processes, a carbon capture and storage (CCS) option is considered. It has been found that both processes result in negative total life cycle GHG emissions due to the use of biomass as one of the feedstocks and CCS. Furthermore, the results of this study demonstrate that BGNTL process has 5% lower direct GHG emissions and 13% lower life cycle GHG emissions compared to the BGTL process due to the nuclear heat integration. Also, by using nuclear heat, fossil fuel consumption decreased by up to 10%.

Keywords: Biomass, Natural gas, Carbonless Heat, Polygeneration.

1. Introduction

When oil prices are high, there is significant incentive to use alternative methods of producing gasoline and diesel such as the gas-to-liquids process (GTL). Previous studies have shown that instead of using gas only, processes which integrate natural gas with other fuels can exploit certain synergies that yield both higher energy and carbon efficiencies (Khojasteh and Adams, 2013, Adams and Barton, 2011). In this process, natural gas and coal are used as the source of carbon, while heat and electricity are provided by an advanced type of nuclear energy source called a Modular Helium Reactor (MHR) (Adams and Barton, 2011). This forms the coal-gas-and-nuclear-to-liquids (CGNTL) process, which can be better both environmentally and economically than coal-to-liquids (CTL), coal-and-gas-to-liquids (CGTL), and other processes. However, even though the CO₂ can be eliminated during processing, one cannot prevent the CO₂ emissions from using the gasoline. Furthermore, coal is not of much interest to the Province of Ontario, Canada due to lack of local coal mines and the lack of political support. A recent study (Scott and Adams, 2016) presented a biomass-gas-and-nuclear-to-liquids (BGNTL) process to co-produce fuels and power which is meant to specifically take advantage of Ontario's interests and resources. In this process, nuclear

energy was used to power a copper-chloride cycle that produced hydrogen for syngas upgrading. However, it was found that it was not economical to use nuclear energy in this way (Scott and Adams, 2016). Instead, other approaches which take better advantage of the high-temperature ($>800^{\circ}\text{C}$) heat produced by some nuclear reactors may be preferable. This study presents the BGNTL process which uses high temperature nuclear heat as the heat source of steam methane reforming process and compares the efficiency and environmental impacts of this process with the BGTL process.

2. Methodology

Figure 1 shows the schematic of the BGTL and BGNTL processes. The process starts with biomass gasification using the high purity oxygen from the air separation unit (ASU), steam, and CO_2 . The produced hot syngas transfers its heat via a radiant syngas cooler (RSC) to either the integrated steam reforming process in the BGTL case or the steam generator in heat recovery steam generator (HRSG) section for BGNTL case. Then, the raw syngas is desulfurized in both cases and clean syngas is sent to the syngas mixing section. In the BGTL case, this CO-rich syngas is mixed with the hydrogen-rich syngas from the integrated RSC/SMR, syngas from the auto-thermal reforming (ATR) sections, and shifted syngas from the water gas shift (WGS) section to achieve a certain H_2/CO ratio for downstream processes. In the BGNTL case, CO-rich syngas is mixed with H_2 rich syngas from the integrated SMR/high temperature gas-cooled reactor (HTGR) to adjust the H_2/CO ratio. In this case, a WGS section is not necessary since nuclear-driven syngas has very high hydrogen content and all of the CO-rich syngas is required to obtain the desired H_2/CO ratio for Fischer-Tropsch (FT) synthesis and MeOH & DME processes.

The mixed syngas then is split into three streams and sent to either FT synthesis to produce gasoline and diesel, to the MeOH & DME section to produce DME and MeOH, or to the power generation section which includes gas turbine (GT) and solid oxide fuel cell (SOFC) sub-systems. The SOFC exhaust gas is mostly water and CO_2 which can be easily separated by CO_2 compression. The waste heat from the sections is recovered in the HRSG unit to produce steam for the plant needs and electricity via steam turbines if extra heat is available. Finally, 90% of the CO_2 in the FT feed syngas is removed using MDEA solvent, then this purified CO_2 and CO_2 from SOFC is compressed up to 150 bar for sequestration.

To simulate the BGTL and BGNTL processes, a combination of Aspen Plus V10, ProMax, gPROMS, and MATLAB software packages were used. Aspen Plus was used to model most of the process sections except CO_2 removal and integrated steam reforming sections. The PR-BM physical property package was used for most of the Aspen Plus simulations except the water-only streams in which NBS/NRC tables were applied, CO_2 /water mixture at high pressures for which PSRK was used, and MeOH/DME separation for which NRTL-RK was used. ProMax software was employed to model the CO_2 removal section due to more accurate physical property models (TSWEET) for this system. This model was developed by Adams et al. (2014). A reduced order model (ROM) of this process was developed based on the ProMax results and implemented in Aspen Plus. Also, gPROMS was used to model the integrated RSC/SMR system and integrated HTGR/SMR processes. The RSC/SMR process used in the BGTL case was modeled and validated using experimental data by Ghouse et al. (2015). Scott et al. (2016) developed a ROM of this process based on the

results of this model and implemented that in Aspen Plus. In addition, the integrated HTGR/SMR section of BGNTL process was modeled in gPROMS by Hoseinzade et al. (2017) and validated using two pilot scale facility design data.

Both BGTL and BGNTL cases were sized to have 1270 MW_{HHV} thermal input including woody biomass, natural gas, and nuclear energy (in the BGNTL case only). The amount of biomass fed is 100 tonne/hr in both cases; however, the amount of natural gas and nuclear heat are varied accordingly, noting that the ratio between natural gas and nuclear heat in the integrated HTGR/SMR is fixed based on design limits. Table 1 shows the raw material and energy input to the base case BGTL and BGNTL plants. Note that the nuclear heat input is nearly identical to the thermal output (115 MW_{th}) of the Peach Bottom I helium-cooled reactor constructed in 1967 (LaBar et al., 2010). Utility requirements in the plant such as steam and electricity are generated in the plant. As a result of using nuclear energy in the BGNTL process, fossil fuels consumption approximately decreased by 10%.

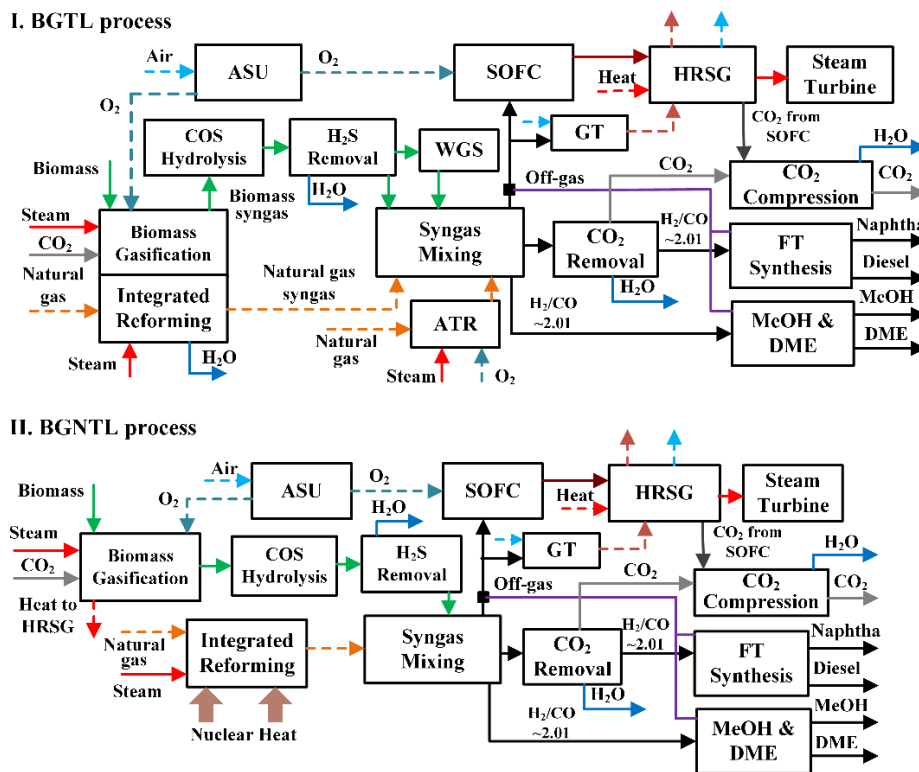


Figure 1. Schematic of BGTL and BGNTL processes.

Table 1. Thermal inputs to the plant (HHV basis where applicable).

Plant	Biomass (MW _{th})	NG feed to SMR (MW _{th})	NG feed to ATR (MW _{th})	Nuclear heat (MW)	Extra heat/power (MW)
BGTL	550.0	169.3	550.7	-	-
BGNTL	550.0	600.5	-	119.5	-

3. Results and discussions

To evaluate the performance of the BGNTL process, its energy efficiency, carbon efficiency, and environmental impacts are compared to the BGTL process. To have a consistent basis for the comparison, the total thermal input, operating conditions, and CO₂ capture percentages are set to be the same. In addition, the syngas molar split fraction to each of the FT, MeOH & DME, SOFC, and GT routes, and the molar percentage of MeOH product used for DME production is fixed and the same for both cases.

To develop the reduced order model of the integrated HTGR/SMR system, the rigorous model developed in gPROMS by Hoseinzade et al. (2017) was applied. The studied HTGR/SMR plant is a shell and tube heat exchanger which high temperature helium gas is flowing in the shell side, and methane is reformed to syngas in the tube side. This system contains 199 SMR tubes placed in a shell with 14 (m) length and 2.7 (m) inner diameter. To collect the data from the model, the natural gas flow rate and steam to carbon ratio in the feed were selected as the independent variables. 55 data points were randomly generated using Latin Hypercube (LH) sampling, and the key output variables including the methane and steam conversions, heat duty, reformer exit temperature and pressure drop were recorded for each data point. 40 data points were used to train the model for each of the outputs, and 15 data points were applied to test the accuracy of the model. The MVR method was employed to develop the ROM for each of the outputs. For many of the variables, a second-order polynomial was the best fit. In addition, for all of the cases, R² of both training and testing was over 0.99.

In addition, the CO₂ removal process used a MDEA / piperazine blend as the solvent with a 90% CO₂ capture rate. This model then was used to build a ROM to implement in Aspen Plus. 100 data points were generated using LH sampling to train and test the developed ROM. 75% of the data were applied to the training, and the rest was used for the testing. Independent variables of this model include the CO₂ flow rate in the feed and solvent to feed molar ratio. Key output variables were the CO₂, H₂S, and water flow rate in the outlet streams, makeup solvent amount, reboiler and condenser duties in the stripper, different cooler duties, pump power, and outlet stream pressure. The ROM was developed based on the MVR as the previous case, and the model accuracy for the train and test were demonstrated by an R² over 0.98 for all the cases.

For the given feed conditions in Table 1, simulation results for the BGTL and BGNTL cases are shown in Table 2. The results show that electricity percentage of the BGNTL process is higher than the BGTL plant; however, liquid fuels and chemicals rate is slightly lower than the BGTL process due to lower natural gas feed rate.

Table 2. Simulation results.

Plant	Naphtha (tonne/hr)	Diesel (tonne/hr)	MeOH (tonne/hr)	DME (tonne/hr)	Electricity (MW)
BGTL	2.7	5.8	4.1	47.9	45.9
BGNTL	2.4	5.2	3.7	42.7	67.1

To evaluate the performance of the plants, energy efficiency is used as one of the indicators. Energy efficiency for a plant is defined as the ratio of the sum of produced power and HHV of produced fuels to the sum of total HHV of the feedstocks and

nuclear heat thermal input (Khojashteh and Adams, 2013). The energy efficiencies of plants with the given conditions in Table 1 and results in Table 2 are calculated as 47.27% for the BGTL case and 44.21% for the BGNTL process. The lower efficiency of the BGNTL plant is due to the lower fuel production rate comparing to the BGTL. The carbon efficiency is defined as the percentage of the carbon atoms in the feed converted into the liquid fuels (Khojasteh and Adams, 2013). The carbon efficiency is 40.06% for the BGNTL process and 41.57% for BGTL. The carbon efficiencies of the plants are close, however, the BGTL carbon efficiency is slightly higher.

To evaluate the environmental impacts of both processes, a cradle to grave GHG emission analysis was conducted. In both cases, all of the CO₂ produced in the SOFC section and 90% of the CO₂ in the FT feed syngas is captured. The only direct GHG emissions from the plant are the GT emissions. To estimate the cradle-to-plant-gate GHG emissions, woody biomass cradle-to-plant-gate emission was considered as 0.133 tonne CO₂e/tonne (Zhang et al., 2010) and natural gas well-to-plant-gate emission was counted as 7.2 g CO₂e/MJ_{th,HHV} (Scott and Adams, 2016). Furthermore, a credit was considered for using biomass by estimating the equivalent CO₂ in biomass based on the carbon atom balance. The plant gate-exit-to-grave emissions include the GHG emissions from the produced fuels' dispensing, distribution and consumption stages. It is assumed that fuel dispensing and distribution GHG emissions are 138 g CO₂e/GJ and 575 g CO₂e/GJ, respectively; plant-to-grave emissions of gasoline and diesel are assumed to be 19.64 lbs CO₂e/gallon and 22.38 lbs CO₂e/gallon, respectively (Scott and Adams, 2016). The plant-to-grave emissions of methanol and DME were also estimated based on fully combusting those and calculated as 1.37 and 1.91 kg CO₂e/kg, respectively. Net sequestered CO₂ also represents the total CO₂ captured subtracted from any CO₂ input to the plant.

Table 3 shows the GHG emission results for the BGTL and BGNTL plants with and without CCS. The negative value for net CO₂e emissions represents the reduction in GHG emissions. Based on the results, both processes end up with a net reduction in GHG emissions, however, BGNTL process achieves 13.4% more life cycle GHG emission reduction and 5% less direct CO₂ emissions in the plant due to using nuclear energy. Based on the GREET (2017) model the cradle-to-plant gate-exit GHG emissions of coal-based DME is 92,700 gCO₂e/GJ_{DME} and its gate-exit-to-grave emissions are 60,280 gCO₂e/GJ_{DME} (Scott and Adams, 2016), so the cradle to grave GHG emissions of coal based DME is 152,990 gCO₂e/GJ_{DME}.

Table 3. Cradle to grave GHG emissions of the plants for 85% capacity.

GHG emission (tCO ₂ e/yr)	BGTL/CCS	BGNTL/CCS	BGTL/ woCCS	BGNTL/ woCCS
Direct GHG emissions	216,780	204,400	1,231,500	1,172,300
Cradle-to-plant-gate- entrance GHG emissions	-896,410	-916,940	-896,040	-916,940
Net sequestered	-941,210	-893,112	0	0
Plant-gate-exit-to-grave GHG emissions	914,990	814,310	911,450	813,390
Net Cradle-to-grave GHG emissions	-705,120	-791,340	1,327,700	1,149,500
Net Cradle-to-grave GHG emissions (gCO ₂ e/GJ _{HHV})	-48,372	-58,128	88,307	84,536

4. Conclusions

A base case design for the BGNTL process was presented and its performance was demonstrated by comparing the plant thermal and carbon efficiencies and life cycle GHG emissions to the base case BGTL process of the same size. It was found that both processes have significant negative net lifecycle GHG emissions owing to the sequestration of biogenic carbon. Even without sequestration, the lifecycle GHG emissions of the products are much lower than fossil fuels. However, BGNTL/CCS has 13% lower life cycle GHG emissions and 5% lower direct GHG emissions than BGTL/CCS owing to the use of nuclear energy. The BNGTL and BGTL have similar carbon efficiencies, but the BNGTL thermal efficiency is lower for this product mix.

In this work, the presented model used a mixture of products and technologies (such as both SOFCs and GT), but in practice, only a subset of these would be chosen. This was done because in future work, the model will be used in a superstructure optimization framework which will choose key process design parameters, outputs, and technologies based on a combination of economic and environmental objective functions. Based on the present results, the BGNTL process is expected to be more expensive but have less environmental impact than BGTL, and the optimization-based analysis will be used to better understand this trade-off. This will also determine if the integrated HTGR/SMR approach to integrating nuclear energy is preferable to the copper-chlorine cycle.

5. Acknowledgments

Financial support from the Ontario Ministry of Innovation via Early Researcher Award ER13-09-213 with matching support from the McMaster Advanced Control Consortium is gratefully acknowledged.

References

- T. A. Adams II, P. I. Barton, 2011, Combining coal gasification, natural gas reforming, and solid oxide fuel cells for efficient polygeneration with CO₂ capture and sequestration, *Fuel processing Technology*, 92, 10, 2105-2115.
- T. A. Adams II, Y. Khojasteh Salkuyeh, J. Nease, 2014, Processes and Simulations for Solvent-based CO₂ Capture and Syngas Cleanup. In: *Reactor and Process Design in Sustainable Energy Technology*, ed: Fan Shi. Elsevier: Amsterdam. ISBN 978-0-444-59566-9.
- GREET 2017, U-Chicago Argonne LLC, Argonne, USA.
- J. H. Ghouse, D. Seepersad, T. A. Adams II, 2015, Modelling, simulation and design of an integrated radiant syngas cooler and steam methane reformer for use with coal gasification, *Fuel Processing Technology*, 138, 378-389.
- L. Hoseinzade, T. A. Adams II, 2017, Modeling and simulation of an integrated steam reforming and nuclear heat system, *International Journal of Hydrogen Energy*, 42, 39, 25048-25062.
- Y. Khojasteh Salkuyeh, T.A. Adams II, 2013, Combining coal gasification, natural gas reforming, and external carbonless heat for efficient production of gasoline and diesel with CO₂ capture and sequestration, *Energy Conversion and Management*, 74, 492-504.
- M. P. LaBar, A. S. Shenoy, W. A. Simon, E. M. Campbell, Y. A. Hassan, 2010, The Gas-Turbine Modular Helium Reactor in: *Nuclear Energy Materials and Reactors – Vol. II*, Y.A. Hassan and R.A. Chaplin, eds., EOLSS Publications.
- J. A. Scott, T. A. Adams II, 2016, Design, Simulation and Optimization of a Biomass-Natural-gas-and-Nuclear to Liquid Fuels and Power Process, Master's Thesis, McMaster University.
- Y. Zhang, J. McKechnie, D. Cormier, R. Lyng, W. Mabee, A. Ogino and H. L. Maclean, 2010, Life Cycle Emissions and Cost of Producing Electricity from Coal, Natural Gas, and Wood Pellets in Ontario, Canada. *Environmental Science & Technology*, 44, 1, 538-544.

Optimisation of Wastewater Treatment and Recovery Solutions in Industrial Parks

Edward O'Dwyer^{a,*}, Hongcheng Wang^b, Ai-jie Wang^b, Nilay Shah^a and Miao Guo^{a,*}

^a*Centre for Process Systems Engineering, Department of Chemical Engineering, Imperial College London, South Kensington Campus, London SW7 2AZ, United Kingdom*

^b*Chinese Academy of Sciences, Key Laboratory of Environmental Biotechnology, Research Center for Eco-Environmental Sciences, Chinese Academy of Sciences, Beijing 10085, China*

**e.odwyer@imperial.ac.uk, *miao.guo@imperial.ac.uk*

Abstract

A considerable amount of carbon-containing and nutrient-rich waste resources are generated globally each year, which could be converted via various routes to bioenergy and other value-added bio-products. In an industrial park setting in which multiple waste-streams of different compositions along with various treatment/recovery technologies may be present, significant opportunities for symbiotic interaction exist through appropriate coordination. To enable such a shift, this work introduces an optimisation framework suitable for handling such a problem, thus providing the potential for significant reductions in the environmental and financial costs associated with the wastewater treatment process. A superstructure is proposed whereby different waste streams of varying flow rates and compositions are input and acted on by a combination of different treatment/recovery technologies to produce a set of treated output streams. The process is captured within a Mixed-Integer Linear optimisation formulation (MILP), in which a combined set of (typically competing) objectives capturing the financial, energy and environmental considerations associated with the problem, is minimised. Variables representing design and operational decisions as well as time-varying flow rates and compositions are included, while the physical limitations of the system and the design requirements of the outputs are also captured.

Keywords: wastewater, optimisation, industrial process design

1. Introduction

Globally, expanding populations and rapid urbanisation, particularly in the Global South, are leading to grand challenges at the nexus of resources, water and waste. The projected 50% increase in global population in the 21st century (United Nations, Department of Economic and Social Affairs, Population Division (2017)), combined with non-OECD economic growth is expected to bring a increase in energy demand of over 30%, while intensifying the resource scarcity challenge e.g. for non-renewable phosphorus. Moreover, rising waste generation brings additional stress. Globally, out of a total of 0.12–4.3 kg per day per capita solid waste, 59%–68% is organic fraction and significant amount of (330km³, per year) municipal wastewater is generated (Hoorweg and Bhada (2012)). The global trajectory of solid waste growth is projected to rise to 6 million tonnes per year with a similar organic fraction level by 2025 and to exceed 11 million tonnes per day by 2100 under a *business as usual* scenario (Hoorweg et al. (2013)); such an increasing waste trend is particularly intense in less developed countries.

To achieve the responsive management of the environment and natural resources, a paradigm shift to resource-circular systems with waste recovery is underway. Industrial parks or complexes launched in many countries (Zhang et al. (2016)) offer potential solutions to integrate functional industry networks with eco-efficient design and value-added ecosystem services. For effective strategic planning (e.g. location selection) in such an industrial park context, water remediation strategies can play a critical role in the overall park sustainability. Despite the modelling advances in process design and rigorous life cycle sustainability evaluation, an integrated system modelling framework that can bridge process synthesis and resource recovery network planning in an industry park context remains a gap.

Defined in (Chertow (2000)) as *industrial symbiosis*, traditionally separate industries engaging in collective approaches to physical exchanges of materials, by-products, energy and water can lead to globally advantageous operation (Afshari et al. (2017)). Development methodologies for eco-industrial parks that can exploit these industrial symbioses are studied in (Farel et al. (2016)), with the particular relevance to developing countries of such methodologies emphasised in (Shi et al. (2010)). As is highlighted in (Rubio-Castro et al. (2010)), the integration of wastewater streams from different streams generated from industries of close proximity can lead to reductions in the quantity of wastewater discharged as well as the fresh water requirement.

Effective design of an eco-industrial park-wide treatment scheme requires an optimal mix of technologies to be chosen at an optimal set of locations in terms of the financial and economic performance indicators. In (Puchongkawarin et al. (2015)), a strategy for optimisation of the wastewater treatment process is defined, while in (Rubio-Castro et al. (2010)), a formulation is defined for determining an optimal wastestream network configuration in a park-wide context. In this paper, an MILP optimisation methodology is developed to bridge the gap between process and network optimisations. Given a known set of industrial wastewater producers, the formulation determines an optimal set of locations and types of waste treatment and resource recovery units to provide economically and environmentally desirable performance, while adhering to physical and regulation-based constraints. The formulation can incorporate transport considerations, circular bio-economy factors and policy-driven incentives such as taxes and subsidies.

2. Optimisation Framework and Objective Formulation

The wastewater treatment process can be comprised of many stages in which various technological pathways can be implemented to remove pollutants, recover resources and extract valuable by-products (e.g. energy) from wastewater streams. In an industrial park context, different classes of industry producing a wide range of waste streams of varying compositions can be present at a single location. If each waste producer is considered only in isolation, a decentralised set of treatment plants is required, which may not operate to maximise the economic and environmental targets of the park as a whole. Alternatively, a centralised treatment plant to which all waste streams are fed could be employed, benefiting from economies of scale; however, transportation of the waste streams is required and the treatment process must be designed to handle a wider range of waste flows and compositions.

Appropriate design of the treatment and resource recovery process for the complete industrial park, exploiting symbioses present between the different industries while combining decentralised and centralised strategies, requires an optimisation framework that can handle both spatial and temporal aspects with the flexibility needed to cater to a wide spectrum of stakeholders and technological pathways. By integrating local constraints and global objectives, the developed framework seeks to achieve this holistic design aim. The constraints and objectives associated with the proposed MILP formulation are given here.

2.1. Mapping waste production

To enable the wide range of waste producers that may exist in a given industrial park to be captured within the optimisation framework, each individual waste producer is characterised only by its location and by the flow-rate and composition of the waste produced. To efficiently define location, the specific industrial park is divided into a grid of arbitrarily sized cells. This allows distances between waste producers and treatment facilities to be approximated. Wastewater stream compositions are characterised in the model as a set of P parameters and constituent component concentrations. This set can include the chemical oxygen demand (COD), nitrogen concentration, phosphorus concentration and protein content. Depending on the context, these can be considered pollutants or useful resources. In a network of X cells with J waste streams, the parameters p of stream j generated in cell x at time t are then given as $gen_{j,x,p,t}$, while the flow rate of the stream is $fl_{j,t}m^3/h$.

2.2. Resource Removal and Recovery

As the global bio-economy becomes more advanced, the ability to recover resources to prevent depletion (e.g. Phosphorus) or for use as an energy source (e.g. as biogas) is likely to act as an ever-greater influence on the wastewater treatment facility design process (Venkata Mohan et al. (2016)). Here, the technologies used in the overall treatment process are categorised as treatment technologies and recovery technologies. The former category includes options such as aerobic membrane bioreactors, de-watering, de-nitrification and clarification units which reduce the pollutant concentration, while technologies classified here as recovery technologies include anaerobic digestion and ion exchange strategies in which useful resources are extracted from the stream.

The treatment technologies generically form the set Tr , with the presence of a particular treatment unit tr for waste stream j in cell x indicated by the binary term $\alpha_{j,x,tr}$. Each class of treatment technology introduces a change in each waste stream parameter p of $\Delta P_{tr,p}^t$. Similarly, Rec denotes the set of potential recovery units. The presence of a particular recovery unit re is indicated by the binary term $\beta_{j,x,re}$ and each class of recovery technology introduces a change in each waste stream parameter p of $\Delta P_{re,p}^r$. Additionally, a recovery unit can extract a certain proportion of the components of a wastestream on which it acts. The recovery efficiency is denoted for technology type re as $R_{re,p}$.

The composition of discharged waste from stream j is given as:

$$dis_{j,p,t} = \sum_{x \in X} \left(gen_{j,x,p,t} - \sum_{tr \in Tr} \alpha_{j,x,tr} \Delta P_{tr,p}^t - \sum_{re \in Rec} \beta_{j,x,re} \Delta P_{re,p}^r \right) \quad \forall p \in P; t \in T \quad (1)$$

The quantity of recovered resources from stream j is then given by:

$$rs_{j,p,t} = fl_{j,t} \sum_{x \in X} \sum_{re \in Rec} \beta_{j,x,re} R_{re,p} \Delta P_{re,p}^r \quad \forall p \in P; t \in T \quad (2)$$

To limit the discharge of excessive levels of pollutants, constraints can be enforced on the concentration of particular components in each wastestream. Where P_p^{max} and P_p^{min} are the upper and lower bounds associated with stream parameter p , the constraints can be defined for stream j as:

$$dis_{j,p,t} - P_p^{max} \leq 0 \quad \forall p \in P; t \in T \quad (3)$$

$$P_p^{min} - dis_{j,p,t} \leq 0 \quad \forall p \in P; t \in T \quad (4)$$

Maximum and minimum flow restrictions are included for each technology, with the assumption that each treatment and recovery plant can take in multiple wastestreams. For the treatment technologies these are defined as:

$$Fl_{tr}^{min} - \sum_{j \in J} fl_{j,t} \alpha_{j,x,tr} \leq 0 \quad \forall x \in X; tr \in Tr; t \in T \quad (5)$$

$$\sum_{j \in J} fl_{j,t} \alpha_{j,x,tr} - Fl_{tr}^{max} \leq 0 \quad \forall x \in X; tr \in Tr; t \in T \quad (6)$$

Where $u \ll 1$ is an arbitrarily small constant, the presence of at least one treatment or recovery unit in cell x visited by stream j can be represented by the binary term $v_{j,x}$.

$$v_{j,x} \geq u \left(\sum_{tr \in Tr} \alpha_{j,x,tr} + \sum_{re \in Rec} \beta_{j,x,re} \right) \quad \forall j \in J; x \in X \quad (7)$$

Similarly, the presence of a specific treatment unit in cell x applied to any stream is given by $\omega_{x,tr} \geq u \sum_{j \in J} \alpha_{j,x,tr}$ with the presence of a recovery technology given as $\phi_{x,re} \geq u \sum_{j \in J} \beta_{j,x,re}$.

2.3. Spatial aspects and transportation networks

To enable the costs associated with the transportation of the waste streams to be taken into account, the distance travelled by each stream must be included as an optimisation variable. The presence of a transport pathway between the waste generation at x and the waste treatment and recovery location at x' is given for stream j by the binary variable $\gamma_{j,x,x'}$ formed as:

$$\gamma_{j,x,x'} \geq G_{j,x} v_{j,x'} \quad \forall x \in X; x' \in X \quad (8)$$

where $G_{j,x} = 1$ if the waste stream j originates at x and is 0 otherwise.

Using $\ell_{x,x'}$ to represent the distance between cell x and x' (this distance matrix can be pre-defined to enable spatial and geographical restrictions associated with pipework installation to be considered), the transport distance for the j^{th} stream is then:

$$len_j^{ot} = \sum_{x \in X} \sum_{x' \in X} \gamma_{j,x,x'} \ell_{x,x'} \quad (9)$$

2.4. Defining the Objective

Effective wastewater treatment in an industrial park context is a subjective matter, with local and global priorities varying across different stakeholders. These priorities can conflict. While local government may have environmental targets, individual waste producers may have a more economically focussed preference. Furthermore, the specific environmental and economic indicators will be contextual, as different regions and countries seek to satisfy different demands and considerations. Once again, to maintain the flexibility of the optimisation framework, both environmental and economic objectives are incorporated in a manner that allows for the optimisation to be aligned with specific scenarios by choosing suitable weights.

To determine the associated capital costs, an approximate cost per unit distance of pipework is defined as Cap^l . The operational and maintenance costs of transporting waste per unit distance is then given as Op^l . The transport costs for the full network $Cost^l$ are defined for the time period T as:

$$Cost^l = \sum_{j \in J} \left(Cap^l len_j^{ot} + \sum_{t \in T} Op^l fl_{j,t} len_j^{ot} \right) \quad (10)$$

In addition to the transport costs highlighted in Eq.(10), capital costs exist for the construction of each treatment and recovery unit. These are denoted respectively as Cap^t and Cap^r . Similarly, operational costs for treating $1m^3$ of waste for one hour are defined for each treatment and recovery unit as Op^t and Op^r . The total costs for the treatment processes are then defined as:

$$Cost^t = \sum_{x \in X} \sum_{tr \in Tr} \left(Cap_{tr}^t \omega_{x,tr} + \sum_{t \in T} Op_{tr}^t \sum_{j \in J} fl_{j,t} \alpha_{j,x,tr} \right) \quad (11)$$

The costs for the recovery processes $Cost^r$ are similarly defined.

In a well functioning bio-economy, the ability to sell any valuable resources extracted from the waste streams can act as an incentive. Furthermore, costs associated with the disposal of undesired waste can be included (Op^{dis}). Subsidy and taxation policies can play a large role in the economic viability of the park's wastewater treatment strategy. In the proposed framework, a taxation cost can be applied to each specific disposed waste constituent, while subsidies for the recovery of bio-products can be included to incentivise environmentally beneficial operation. Aside from economic incentives and taxes, the recovery or disposal of specific resources can be targeted directly in the objective. The weights associated with this cost (w_p^a and w_p^b) can be arbitrarily chosen, depending on the needs of the user. These costs are given here as:

$$Cost^{fin} = \sum_{j \in J} \sum_{p \in P} \sum_{t \in T} \left((Op_p^{dis} + Tax_p + w_p^a) dis_{j,p,t} - (Price_p + Sub_p + w_p^b) rs_{j,p,t} \right) \quad (12)$$

The full objective J to be minimised is then given as:

$$J = Cost^t + Cost^r + Cost^r + Cost^{fin} \quad (13)$$

3. Framework Implementation

To demonstrate the operation of the optimisation framework, a simple case-study is presented here in which a hypothetical eco-industrial park consisting of 4 waste producing industries seeks to achieve the most cost effective approach for the treatment and recovery of the produced wastewater. The different wastestreams are characterised by the respective concentrations of each of three different components: COD, total nitrogen (TN), total phosphorus (TP). These compositions are taken from Henze and Comeau (2008). Two types of treatment unit and two types of recovery unit can be implemented at any location in a 4x4 grid, which represents the spatial layout of the park (as it is assumed that no physical barriers are present, euclidean distances are used to determine transport lengths). Capital and operational costs are estimated for the treatment and recovery plants as well as the transportation of waste to the plants. Policy-based costs and subsidies are neglected here. The optimisation is carried out using the CPLEX solver in GAMS v.24.9.1.

As notional cost values are used here, the exact cost impact of the optimisation-based approach is unlikely to be instructive; however, the importance of taking a holistic perspective when designing such facilities in an industrial park context can be illustrated. To do so, three different scenarios are shown here. In the first scenario, a high transport cost is assumed, while the sale of resources is assumed to not be possible. In the second scenario, the transport costs are reduced, while in the final scenario, the ability to profit from the recovery from the wastestreams of one of the components is introduced. As is shown in Fig. 1, the locations and technology types chosen for optimal performance are significantly different, with both decentralised and centralised approaches favoured, depending on the scenario. Beyond this simple illustrative case used here to emphasise the purpose of the methodology, the model has been applied to hypothetical design studies in which GPS-X and CapdetWorks were applied in simulation and techno-economic analyses; the modelling framework is also currently being expanded to incorporate the experimental work being carried out at the Chinese Academy of Sciences, where the reactor design and technology development are being developed for the case-specific industrial park in China.

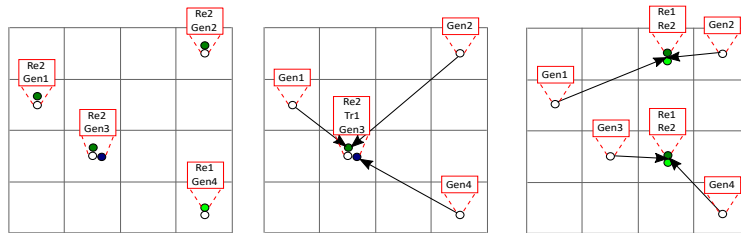


Figure 1: Three design scenarios for wastewater treatment in eco-industrial park

4. Conclusion

The concept of Industrial Symbiosis, through which advantageous operation of the various actors in an eco-industrial park context is achieved by process integration has long been established. In this paper, the concept is applied to the design of park-wide wastewater treatment and resource recovery strategies. An MILP-based optimisation framework is formulated which enables the locations and types of treatment and recovery technologies to be optimised. The formulation takes into account financial aspects such as the capital and operational costs for the technologies themselves, the costs associated with the transport of waste around the park and other policy-based taxes and subsidies. Aside from the environmental constraints on pollutants in the waste streams, benefits associated with the recovery of valuable resources and by-products can be included. The framework is flexible enough to allow for an arbitrarily large range of technologies to be considered while also enabling individual user preferences to be incorporated. This flexibility is shown in a hypothetical case study in which changing contextual parameters are captured in the framework to produce the most suitable treatment design approach.

References

- H. Afshari, R. Farel, Q. Peng, 2017. Improving the Resilience of Energy Flow Exchanges in Eco-Industrial Parks: Optimization Under Uncertainty. *ASCE-ASME J. Risk and Uncert. in Engrg. Sys., Part B: Mech. Engrg.* 3 (2), 021002.
- M. R. Chertow, nov 2000. Industrial Symbiosis: Literature and Taxonomy. *Annual Review of Energy and the Environment* 25 (1), 313–337.
- R. Farel, B. Charrière, C. Thevenet, J. H. Yune, 2016. Sustainable Manufacturing Through Creation and Governance of Eco-Industrial Parks. *Journal of Manufacturing Science and Engineering* 138 (10), 101003.
- M. Henze, Y. Comeau, 2008. Wastewater Characterization. In: M. Henze, M. van Loosdrecht, G. Ekama, D. Brdjanovic (Eds.), *Biological Wastewater Treatment: Principles Modelling and Design*. IWA Publishing, London, Ch. 3, pp. 33–52.
- D. Hoornweg, P. Bhada, 2012. What a Waste. *A Global Review of Solid Waste Management*. Urban development series knowledge papers 281 (19), 44 p.
- D. Hoornweg, P. Bhada-Tata, C. Kennedy, 2013. Waste production must peak this century. *Nature* 502 (7473), 615–617.
- C. Puchongkawarin, C. Gomez-Mont, D. C. Stuckey, B. Chachuat, 2015. Optimization-based methodology for the development of wastewater facilities for energy and nutrient recovery. *Chemosphere* 140, 150–158.
- E. Rubio-Castro, P.-O. J. MMara, Mahmoud M. El-Halwagi, M. Serna-González, A. Jiménez-Gutiérrez, 2010. Water Integration of Eco-Industrial Parks Using a Global Optimization Approach. *Industrial & Engineering Chemistry Research* 49 (20), 9945–9960.
- H. Shi, M. Chertow, Y. Song, 2010. Developing country experience with eco-industrial parks: a case study of the Tianjin Economic-Technological Development Area in China. *Journal of Cleaner Production* 18 (3), 191–199.
- United Nations, Department of Economic and Social Affairs, Population Division, 2017. *World Population Prospects The 2017 Revision Key Findings and Advance Tables*. Tech. rep.
- S. Venkata Mohan, G. N. Nikhil, P. Chiranjeevi, C. Nagendranatha Reddy, M. V. Rohit, A. N. Kumar, O. Sarkar, 2016. Waste biorefinery models towards sustainable circular bioeconomy: Critical review and future perspectives. *Biore-source Technology* 215, 2–12.
- C. Zhang, L. Zhou, P. Chhabra, S. S. Garud, K. Aditya, A. Romagnoli, G. Comodi, F. Dal Magro, A. Meneghetti, M. Krafi, 2016. A novel methodology for the design of waste heat recovery network in eco-industrial park using techno-economic analysis and multi-objective optimization. *Applied Energy* 184, 88–102.

Integration of carbon dioxide and hydrogen supply chains

Anton Ochoa Bique,^a Tuan B.H. Nguyen,^a Grazia Leonzio,^b Christos Galanopoulos,^a Edwin Zondervan,^{a,*}

^a*Bremen University, Dep. Production Engineering, Germany*

^b*University of L'Aquila, Dep. Chemical Engineering, Italy*

edwin.zondervan@uni-bremen.de

Abstract

In this work, the impact of Carbon Capture, Utilization, and Storage (CCUS) as a potential technology to reduce Germany's carbon dioxide (CO₂) emissions is studied. Carbon dioxide is used as a raw material for methanol production in the global market. Carbon dioxide is captured from power plants and can be reacted to methanol with renewable hydrogen. The study shows that the integration of hydrogen- and carbon dioxide supply chains is only feasible if the electricity needed for renewable hydrogen can be delivered for free.

Keywords: carbon dioxide capture and storage, MILP modeling, Hydrogen supply chain, methanol synthesis, carbon dioxide reduction.

1. Introduction

Oxfam (2017) reported for 2017 five major environmental and humanitarian disasters that can be attributed to climate change. Many scientists have linked global temperature rise (and climate change) to increasing levels of greenhouse gases in our atmosphere. One of the main greenhouse gases is carbon dioxide. In 2016 the global carbon dioxide emissions were approximately 36 Gtons and trends show that emissions will keep growing if nothing is done.

The main sources of carbon dioxide emissions stem from the energy production via fossil sources such as coal and oil. Future scenarios for energy production we will remain dependent on fossil fuel resources (the NPS, New Policies Scenario and the 450S scenario stay below an average temperature increase of 2 °C, see the report by the International Energy Agency. 2015).

This all indicates that there is an urgent need to reduce carbon dioxide emissions to our atmosphere. This might be viewed as an environmental alarm bell. However, as chemical engineers, we can view this as an opportunity to serve and supply many different sectors: carbon dioxide can be used to produce fuels, construction materials, food, polymers, etc. Germany can take a leading role here.

In the Climate Action Programme 2020 (Nature Conservation Federal Ministry for the Environment, 2014) Germany aims at dramatically reducing its carbon dioxide emissions. As a result of the energie-wende (energy transition), Germany has massively invested in renewable energy production. However, conventional coal and gas-fired

power plants still largely supply the German energy landscape. This is due to the discontinuous availability of renewable energy and its problematic storage.

The aim of this work is to setup and study an economically and technologically functioning supply chain for the utilization of carbon dioxide that is captured from major stationary point emission sources throughout northern Germany. A potential application of carbon dioxide is the reforming of it into methanol for which Germany has an annual demand of 940 ktons per year. The hydrogen that is needed for producing methanol can be generated via water electrolysis with renewable energy.

2. Model description

We will geographically restrict the area of interest to the federal states of Northwest Germany (Lower-Saxony, Bremen, Hamburg, and Schleswig-Holstein) and explore different scenarios of a potential future supply chain network. We will evaluate two cases: one in which we focus on meeting demand for methanol and in the other to maximize carbon dioxide reductions. For each case a spatially explicit mixed integer linear program (MILP) optimization model is developed in the Advanced Interactive Multidimensional Modeling (AIMMS) software, targeting the economically optimized supply chain structure.

The generated network (see Figure 1) consists of one carbon dioxide dominated- (upper part of Figure 1), one hydrogen dominated- (lower part of Figure 1), and one storage/utilization dominated section (shown on the right side of Figure 1). The power plants are the sources of carbon dioxide dominated section. With pressure swing adsorption, amine absorption or membranes the capture of carbon dioxide from these sources is possible. Afterwards, carbon dioxide is transported to a storage or methanol production site. The sources of the hydrogen section are at locations near excess renewable energy production. With this energy, hydrogen can be produced via electrolysis. To transport the hydrogen to the methanol sites pipelines are used. Currently, the model considers only one storage site. The potential locations where methanol can be produced are at all the locations of the power plants and excess energy production sites. In this network, the sources represent the suppliers (of carbon dioxide and hydrogen) and the carbon dioxide storage and methanol production locations can be seen as the demand sites.

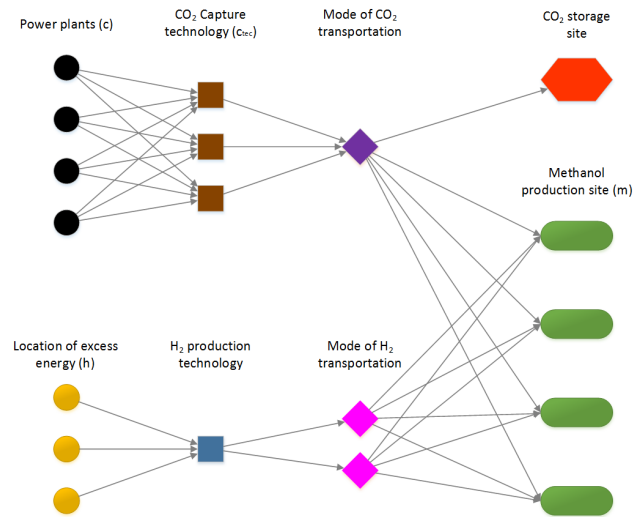


Figure 1: Network scheme of the CCS/CCUS Supply Chain

Form modeling the following assumptions are made:

- A capture plant is located at a carbon dioxide source to avoid the transportation of flue gas;
- a capture node can be connected by only one carbon dioxide source;
- the mode for transporting carbon dioxide is always pipeline;
- the H₂ production plants are located on the coast of the North Sea, near excess energy production;
- each location of excess energy can only provide one node of hydrogen production, and each hydrogen production node can only be provided by one location;
- hydrogen is produced through electrolysis;
- methanol is produced by direct, single step hydrogenation;
- all products can be sold at a stable price;
- there is only one carbon dioxide storage site, which has an infinite storage capacity;
- the network structure is fixed; time-dependent values are calculated to a yearly average through the specific lifetime of the component;

The type, location and yearly carbon dioxide emissions and flue gas compositions at the point sources are known. In addition, the cost and efficiencies of the capture and compression technologies that can be selected are given. Further, the carbon dioxide transportation via pipeline with its distances and costs are known. The location, price and amount of excess energy of the hydrogen sources are known and also the electrolysis as hydrogen production technology with its cost parameters are known. For the hydrogen transport technologies also distances and costs are given. For the methanol production plants, the hydrogenation of carbon dioxide is selected. For the methanol production plant also the locations and costs are given. Ultimately, the carbon dioxide storage site is going to be at Altmark while the storage costs, the methanol demand, and the carbon dioxide reduction target are fixed (the interested reader may contact the authors for the detailed dataset).

The objective is to minimize the costs of the supply chain which are composed of costs for carbon capture and compression, carbon dioxide transport, hydrogen production and transport, methanol production and carbon dioxide storage.

The following decisions must be made to minimize the costs: selection of the capture plant and the quantity that each plant captures, selection of the capture technology for each plant, used hydrogen production location and the quantity of produced hydrogen, transport mode for hydrogen, transport pathway for carbon dioxide and hydrogen, storage and methanol production site (inclusive the amount of stored CO_2 / produced methanol).

3. Data collection

For the hydrogen production facilities, a study from the Jülich Research Institute (D. Krieg, 2012) was used to identify the major offshore wind parks that can produce renewable electricity. These locations and capacities of these power sources provide power for the hydrogen production plants (HPP). We assume that the HPP should be located near the power sources.

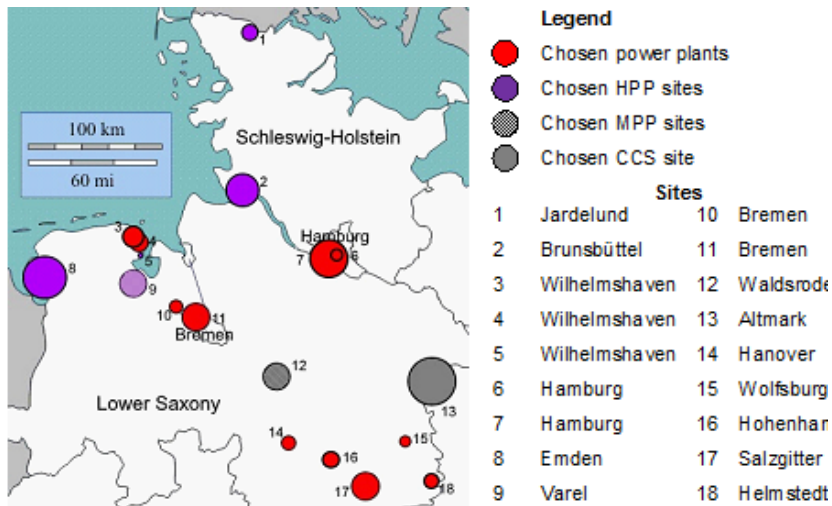


Figure 2 – Overview of all considered sinks and sources of the supply chain

A DEHSt report (Deutsche Emissionshandelsstelle, 2016) on power plant emissions was used to identify the major point sources of carbon dioxide. When considering only sources that emit 1 Mton or more, already more than half of the total carbon dioxide can be accounted for. All hydrogen production sites and carbon dioxide emission sites can be used as a methanol production plant (MPP). From the BMWi report (Federal Ministry for Economic Affairs and Energy, 2016) we identified one major carbon storage site (CCS). (See Figure 2).

4. Results and discussion

The model is formulated as a mixed integer linear programming model and has 4.950 constraints, 7.510 continuous variables, and 663 integer variables. AIMMS is used as optimization platform, and CPLEX 12.7 is selected as the preferred solver.

Two scenarios were evaluated. A methanol-driven scenario (to satisfy and/or to maximize methanol production) and a carbon dioxide-driven scenario (focusing on the reduction of carbon dioxide emissions to achieve the German emission targets for 2020). For both scenarios, the effect of electricity costs for hydrogen production and the possibility to store carbon dioxide were investigated; this leads per scenario to three alternative cases. The main outcomes are found in Figures 3 and 4.

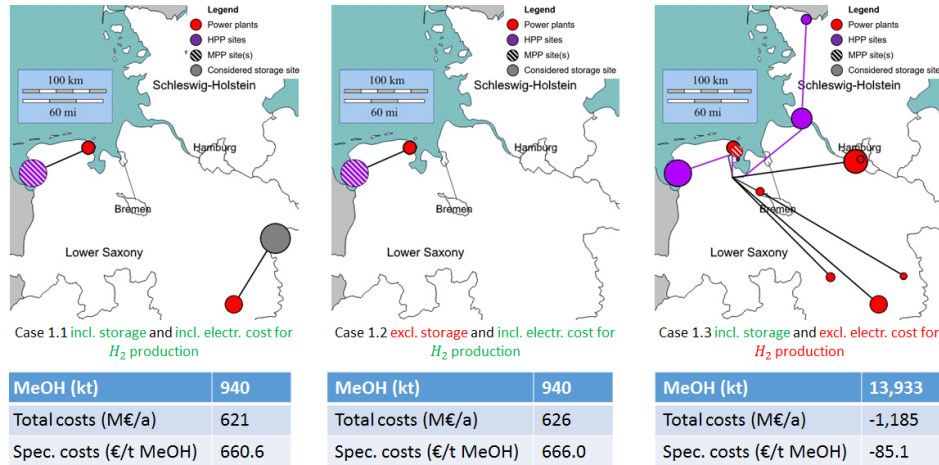


Figure 3 – Proposed structures for a methanol-driven supply chain

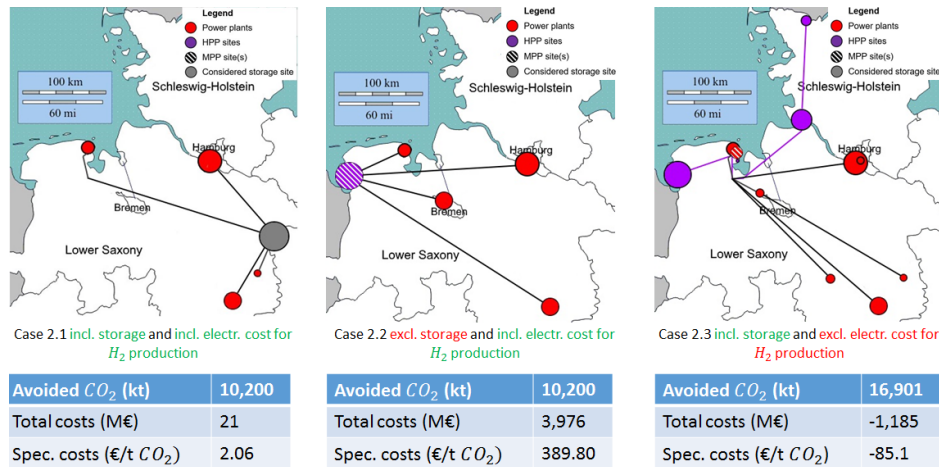


Figure 4 – Proposed structures carbon-dioxide-driven supply chain

The first scenario is the methanol-driven one. In this case including the option to store CO₂ and electricity costs for H₂ production (0.06 €/kWh; case 1.1), the specific MeOH production costs are 660.6 €/ton. Approximately the same costs were found in the case excluding the storage option and including electricity costs (case 1.2) with specific MeOH production costs of about 666.0 €/ton. The second scenario is carbon dioxide-driven one. Case 2.1 including storage option and electricity costs for H₂ production, leading to specific CO₂ avoidance costs of 2.06 €/ton. These marginal expenses are achieved by full storage of the captured amount of CO₂. Excluding storage option and

including electricity costs for H_2 production (case 2.2), leading to an economically intractive solution with nearly 390 €/ton avoided CO_2 . Based on public perception against storage option, the comparison of cases leads to the selection of case 1.2 as the most realistic scenario for a future supply chain.

5. Conclusions

A MILP model for the integration of carbon dioxide and hydrogen supply chain networks has been developed. This model has been used to investigate the techno-economic feasibility of such supply chain in northern Germany. Two scenarios were proposed, the first considered scenario is the methanol-driven one. The specific MeOH production costs are calculated to 660.6 €/ton. These costs are almost double the costs of the current methanol prices. The second scenario is based on carbon dioxide reduction. This scenario results in a price of nearly 390 €/ton avoided CO_2 . Moreover, when an including storage option, with free power for H_2 production the total costs reduce drastically for both scenarios and the network becomes economically feasible. However, it is noted that at this time the model does not limit the scale up of the MPP.

6. Acknowledgements

The authors gratefully thank Mr. Kevin Schmidtke, Mr. Sebastian Schulze and Mr. Sven Charmeteau who are students in the Process Systems Engineering Laboratory of Bremen University for their contributions to this project.

References

- Deutsche Emissionshandelsstelle (DEHSt), 2016, Kohlendioxidemissionen der emissionshandelspflichtigen stationären Anlagen und im Luftverkehr in Deutschland im Jahr 2015. VET-Bericht.
- Federal Ministry for Economic Affairs and Energy (BMWi), 2016, Fifth Monitoring Report "The Energy of the Future".
- International Energy Agency, 2015, Key world energy statistics.
- D. Krieg, 2012, Konzept und Kosten eines Pipelinesystems zur Versorgung des deutschen Straßenverkehrs mit Wasserstoff. Vol. 144.
- Nature Conservation Federal Ministry for the Environment, 2014, Building and Nuclear Safety (BMUB), The German Government's Climate Action Programme 2020.
- Oxfam, 2017, Unrooted by climate change – responding to the growing risk of displacement, Briefing paper.

Multi-objective Optimization of a Carbon Dioxide Utilization Superstructure for the Synthesis of Formic and Acetic Acid

Juan D. Medrano-García^{*}, Rubén Ruiz-Femenia, José A. Caballero

^a*University of Alicante, Institute of Chemical Process Engineering, P.O.99, E-03080, Alicante, Spain*

jd.medrano@ua.es

Abstract

Worldwide carbon dioxide emissions are constantly increasing. Carbon Capture and Storage emerged as a temporary solution to this problem, but even if these emissions were to be drastically decreased, the stored gas has to be given a purpose. The aim of this work is the study of the synthesis of carbon monoxide from CO₂ and its utilization as a raw material in acetic and formic acid synthesis. We propose a superstructure in which we include several consuming and non CO₂ consuming syngas synthesis technologies, an H₂/CO separation step and the CO utilization section. We solve the multi-objective optimization problem minimizing the Total Annualized Cost (TAC) and Global Warming Potential (GWP) as our economic and environmental indicators. Results show that the Tri-reforming process can be used to reduce emissions in the synthesis of CO and both acids, while Partial Oxidation results in a lower economic investment and a higher GWP.

Keywords: multi-objective optimization, CO₂ emission reduction, synthesis

1. Introduction

Synthesis gas (syngas) production is the cornerstone of many industries. This H₂/CO mixture is mainly produced from gasification (coal, heavy hydrocarbons) or reforming (light hydrocarbons). Steam, oxygen, carbon dioxide or mixtures of them act as reforming agents and react with the carbon source at high temperatures. Depending on the agent employed, the reaction conditions and composition of the synthesized syngas can greatly differ among technologies. The required composition of the mixture varies between applications, being the most common H₂/CO ratios of two (methanol and Fischer-Tropsch synthesis) or higher (hydrogen production). The synthesis of ethanol and higher alcohols, dimethyl ether and oxo-alcohols use lower H₂/CO ratios of about 1. However, if the ratio is reduced even further, the resulting gas is pure carbon monoxide. This gas is used without any hydrogen in the synthesis of small organic compounds, such as formic and acetic acid.

The synthesis of syngas is usually the most impactful step in both cost and emission in the synthesis of a syngas derived product. When the carbon source is natural gas (methane), the conversion to syngas is called reforming. Several technologies have been developed for the reforming of methane (Figure 1). The classic technologies offer syngas with high hydrogen content (Steam Methane Reforming, SMR) or with reduced operating investment (Partial Oxidation, POX; Auto-thermal Reforming, ATR;

Combined Reforming, CR). However, newer technologies, which are able to consume CO₂ (Dry Methane Reforming, DMR; Bi-reforming, BR; Tri-reforming, TR), even if they are more cost intensive or produce syngas with lower H₂/CO ratios, are still interesting options due to a reduced environmental impact under specific situations.

In a previous work, we studied the cost and emission associated with the synthesis of syngas for several compositions and pressures of the product (Medrano-García et al., 2017). The results showed that, when synthesizing syngas with an H₂/CO ratio of one at low pressure, an actual net consumption of CO₂ can be achieved with the proper syngas synthesis technology selection and separation unit configuration. This result led us to wonder the outcome of the synthesis at an even lower ratio, which is essentially carbon monoxide synthesis.

In this work, we propose a process superstructure in which several syngas synthesis technologies, a specific separation scheme to purify CO from syngas and two CO utilization processes (formic and acetic acid) are included. We apply the ϵ constraint method (Ehrgott & Wiecek, 2005) to solve the multi-objective optimization problem minimizing the Specific Total Annualized Cost (STAC) and Global Warming Potential (GWP), which result in clear trade-offs between both objectives.

2. Methodology

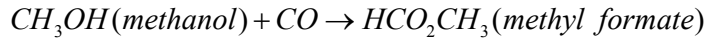
2.1. Superstructure overview

We propose a process superstructure (Figure 1) to tackle this optimization problem. The superstructure consists of a syngas synthesis, a CO separation, and a CO utilization section. The syngas synthesis section takes into account seven different alternatives (Figure 1) to produce the mixture. All of these alternatives use the methane reforming reaction for the synthesis but differ in the reforming agent employed, as well as the reaction conditions. The CO separation section consists of an initial flash unit, used to condense water, and two Pressure Swing Adsorption (PSA) units. The first one (PSA1) preferentially adsorbs H₂ (adsorption at 30 bar, desorption at 1 bar, 90 % H₂ recovery and 99.5 % purity (Chiang & Chang, 2014)), while the second one (PSA2) does the homologue for CO (3 bar adsorption, 90% recovery and 99 % purity (Kasuya & Tsuji, 1991)). The rejected flow of PSA2 passes through a diglycolamine (DGA) absorber which removes CO₂ (Nuchitprasittichai & Cremaschi, 2011), and the rest of the gases are burnt to fuel the reformer reactor. The H₂ flow separated in PSA1 can also be used to fuel the reformer reactor or in the production of electrical energy throughout a fuel cell. The use of a fuel cell is restricted by a maximum flow of H₂ that can enter this unit, but several fuel cells can be installed simultaneously to overcome the limit at the cost of a higher capital investment ((Chiang & Chang, 2014)). The maximum production of electricity allowed corresponds to the maximum electricity demand of the system. Finally, the CO utilization section consists of two different full processes: formic acid and acetic acid synthesis.

2.1.1. Formic acid synthesis

Formic acid (FAc) can be synthesized through methyl formate hydrolysis, oxidation of hydrocarbons or hydrolysis of formamide. In this work, we use the first method since not only uses CO as a raw material but it is also the most extended technology for formic acid synthesis worldwide (Hietala et al., 2000). The process flow diagram

proposed can be seen in Figure 2. First, CO and methanol in a proportion of 3.2:1 (MeOH/CO) are compressed to 45 bar and mixed. The mixture is heated up to 80 °C and enters the methyl formate (MeF) reactor R1 in which the following reaction takes place with a 95 % conversion of CO:



After the reaction, the mixture pressure is reduced to 9 bar and enters distillation column C1 where most of the methanol is recovered and sent back to the pressurization section along with the uncondensable CO. The distillate, which contains mainly methyl formate, is then mixed with water with a proportion of 5:1 (W/MeF). The mixture is heated up to 120 °C and enters the formic acid reactor R2:



The mixture enters distillation column C2 which separates the pairs MeF/MeOH and Water/Fac. The pair MeF/MeOH enters distillation column C4 where MeF exits as distillate and is recycled to the entrance of reactor R2, while MeOH exits as the bottom product and is recycled back to the MeOH and CO compression section. The pair Water/Fac enters distillation column C3 where the product formic acid is retrieved at an 85 wt% purity, and water is obtained as distillate which is recycled back at the entrance of reactor R2. Production of formic acid is set to close to 80 kt/y.

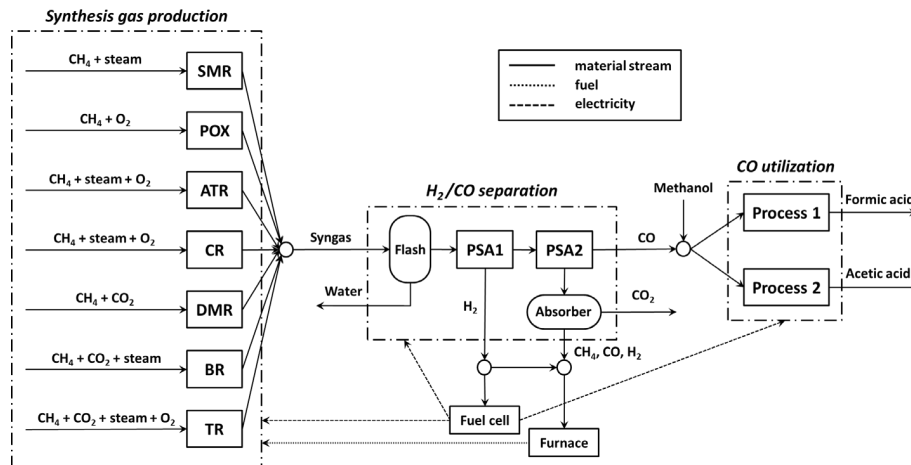


Figure 1. Process superstructure for the synthesis, purification and utilization of carbon monoxide.

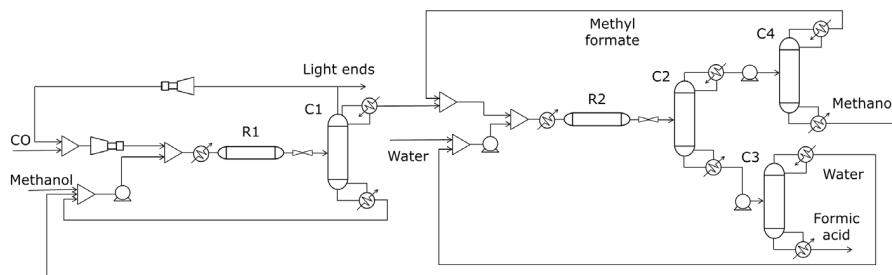


Figure 2. Proposed formic acid production flowsheet (Process 1).

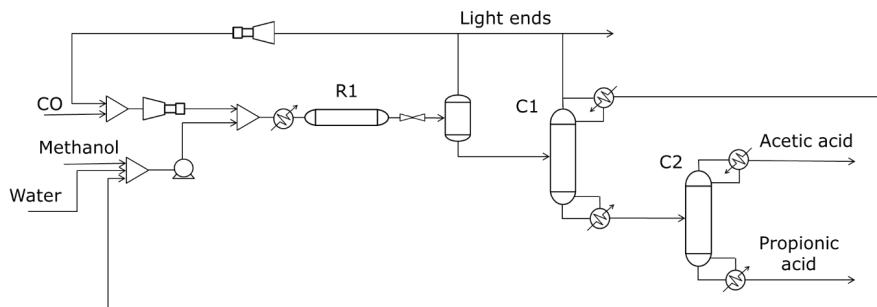
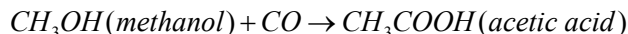


Figure 3. Proposed acetic acid production flowsheet (Process 2).

2.1.2. Acetic acid synthesis

The synthesis of acetic acid also has several procedures (fermentation, carbonylation of methanol, direct oxidation of saturated hydrocarbons, oxidation of acetaldehyde, synthesis from ethylene or ethane). We choose carbonylation of methanol for acetic acid synthesis due to it being the most important (Monsanto process, now improved by the Cativa process) (Le Berre et al., 2000). The proposed process diagram can be seen in Figure 3. A mixture of methanol and water (4.5 wt %) is compressed to 30 bar and mixed with CO. This water does not participate directly in the main reaction but it is necessary to activate the catalyst. The reactants are heated up to 175 °C and enter the acetic acid reactor R1, which main reaction is:



Methanol selectivity in the reactor reaches 99 %. The remaining methanol is transformed into propionic acid, which is the main byproduct of this process. Carbon monoxide selectivity only achieves 90 % due to the unavoidable reaction with water in the so called Water Gas Shift (WGS) reaction, which produces H_2 and CO_2 . After the reaction, the pressure is reduced to 1 bar and the mixture enters a flash unit in which most of the uncondensable gases (CO , CO_2 , and H_2) are separated. The liquid phase then enters distillation column C1. The rest of the gases are separated, mixed with the vapor phase of the flash unit and recycled after a 50 % purge. The purged gases are used as fuel. The distillate, formed mainly by methanol and water is recycled to the beginning of the process. Acetic and propionic acid exit the column as the bottom product, and enter distillation column C2. Here, propionic acid 99 wt% is obtained as a byproduct, and acetic acid 98 wt% is purified in the distillate. Production of acetic acid is set to approximately 100 kt/y.

2.2. Multi-objective optimization problem

The calculation of the composition of the synthesized syngas, utility consumption and capital cost is carried out using linear models obtained from simulations in Aspen HYSYS according to the optimal operating conditions specified in the literature. In addition, heat integration was applied before building the models (Medrano-García et al., 2017). Similarly, for the formic and acetic acid synthesis, we also built linear models which parameters depend on the total acid production.

We address the existence or inexistence of a unit or syngas technology using the Generalized Disjunctive Programming (Raman & Grossmann, 1994). The proposed disjunctions are then translated into algebraic equations using the Hull reformulation

(Lee & Grossmann, 2000). We apply the ϵ constraint method to solve the resulting MILP using an economic (Specific Total Annualized Cost, STAC) and environmental (Global Warming Potential, GWP) indicator to study the different scenarios (minimum cost and minimum emission) in the synthesis and utilization of CO proposed.

3. Results and discussion

We solved the MILP problem with GAMS and using the solver CPLEX. This problem consists of 336 equations and 345 variables, 18 of which are binary variables. Formic and acetic acid process flowsheets were simulated using Aspen HYSYS.

The trade-off between cost and emission of the synthesis of CO as well as the consumption of CO₂ can be seen in Figure 4. The lowest cost synthesis (0.149 \$/kg CO) is achieved using POX as the only reforming technology. However, this technology also provides the highest emission (0.904 kg CO₂-eq/kg CO). On the other hand, the use of TR achieves the lowest emission possible (0.602 kg CO₂-eq/kg CO) at the cost of increasing the STAC (0.258 \$/kg CO). The intermediate Pareto points consist of linear combinations of these extreme solutions. A direct CO₂ generation (up to 0.640 kg CO₂/kg CO) occurs at lower values of STAC (use of POX), however, at the maximum value of STAC (use of TR) a consumption of 4.162 kg CO₂/kg CO can be achieved.

The results of the synthesis of formic and acetic acid can be seen in Figure 5, and are obtained by varying the CO source (cost and emission) and maintaining constant the rest of process variables. It can be seen that the effect in STAC of the formic acid synthesis reaches almost a 20 % while the reduction in GWP barely surpasses a 5 %. However, when synthesizing acetic acid, an increase above 11 % of the cost results in a significant reduction of more than 15 % of the emissions, which sets carbonylation of methanol for the synthesis of acetic acid as an interesting process for further studies related to CO₂ reutilization.

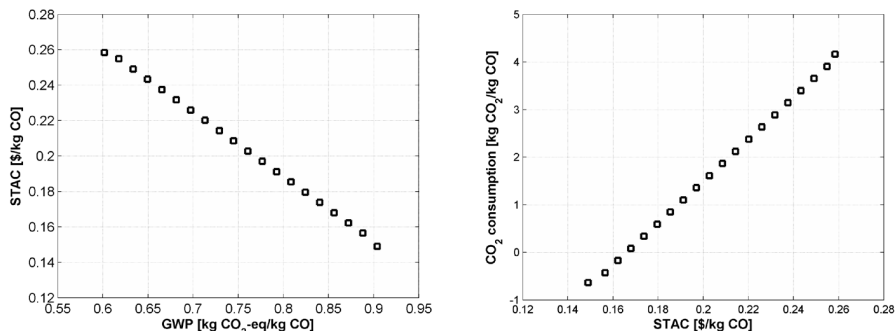


Figure 4. STAC vs GWP (left) and net CO₂ consumption vs STAC (right) of the synthesis of CO.

4. Conclusions

We performed multi-objective optimizations to study the effect in the Specific Total Annualized Cost and Global Warming Potential of the synthesis of CO using CO₂. The use of CO₂ as a raw material through the Tri-reforming process decreases the emission a 33.4 % but increases the cost of the process up to a 73.1 % from its synthesis by Partial Oxidation. In the synthesis of formic acid, increasing the STAC a 19.9 % can result in a decrease of the GWP of a 5.2 %. On the other hand, when synthesizing acetic acid, a

reduction of a 15.5 % in GWP can be achieved by increasing an 11.3 % the cost of the synthesis.

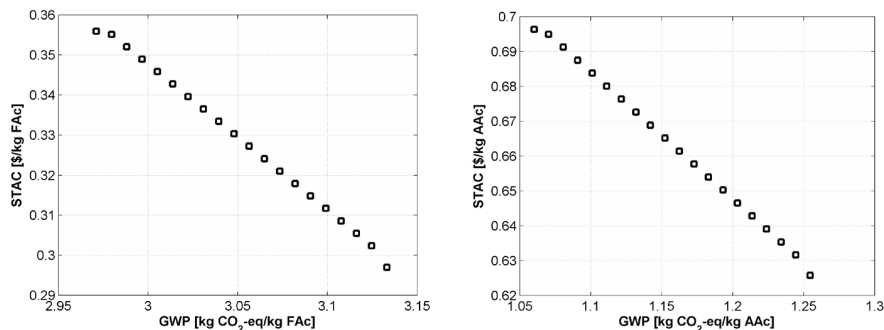


Figure 5. STAC vs GWP for the synthesis of formic acid (left) and acetic acid (right).

Acknowledgements

The authors gratefully acknowledge financial support to the Spanish «Ministerio de Economía, Industria y Competitividad» under project CTQ2016-77968-C3-2-P (AEI/FEDER, UE) and «Generalitat Valenciana: Conselleria de Educació, Investigació, Cultura y Deporte» for the Ph.D. grant (ACIF/2016/062).

References

- Chiang, Y. C., & Chang, C. T. (2014). Single-objective and multiobjective designs for hydrogen networks with fuel cells. *Industrial and Engineering Chemistry Research*, 53, 6006-6020.
- Ehrgott, M., & Wiecek, M. M. (2005). Multiobjective programming. In *International Series in Operations Research and Management Science* (Vol. 78, pp. 667-722).
- Hietala, J., Vuori, A., Johnsson, P., Pollari, I., Reutemann, W., & Kieczka, H. (2000). Formic Acid. In *Ullmann's Encyclopedia of Industrial Chemistry: Wiley-VCH Verlag GmbH & Co. KGaA*.
- Kasuya, F., & Tsuji, T. (1991). High purity CO gas separation by pressure swing adsorption. *Gas Separation & Purification*, 5, 242-246.
- Le Berre, C., Serp, P., Kalck, P., & Torrence, G. P. (2000). Acetic Acid. In *Ullmann's Encyclopedia of Industrial Chemistry: Wiley-VCH Verlag GmbH & Co. KGaA*.
- Lee, S., & Grossmann, I. E. (2000). New algorithms for nonlinear generalized disjunctive programming. *Computers & Chemical Engineering*, 24, 2125-2141.
- Medrano-García, J. D., Ruiz-Femenia, R., & Caballero, J. A. (2017). Multi-objective optimization of combined synthesis gas reforming technologies. *Journal of CO₂ Utilization*, 22, 355-373.
- Nuchitprasittichai, A., & Cremaschi, S. (2011). Optimization of CO₂ capture process with aqueous amines using response surface methodology. *Computers & Chemical Engineering*, 35, 1521-1531.
- Raman, R., & Grossmann, I. E. (1994). Modelling and computational techniques for logic based integer programming. *Computers & Chemical Engineering*, 18, 563-578.

Concentrating High Purity CO₂ from Syngas after Oxy-fuel Combustion by Pressure Swing Adsorption Process

Cheng-Tung Chou,^{a*} Bi-Ching Wu,^a Tien-Lin Wu,^a Hong-Sung Yang,^b Chia-Hsuan Shen,^c

^a*Department of Chemical and Materials Engineering, National Central University, No. 300, Zhongda Rd., Zhongli District, Taoyuan City 32001, Taiwan*

^b*Department of Applied Cosmetology, Hwa Hsia University of Technology, Gongzhuang Rd., Zhonghe District, New Taipei City 23568, Taiwan*

^c*Department of Mechanical Engineering, Chang Gung University, Wenhua 1st Rd., Guishan District, Taoyuan City 33302, Taiwan*

t310030@ncu.edu.tw

Abstract

This research experimentally studied the concentration of high purity CO₂ from syngas after oxy-fuel combustion by pressure swing adsorption (PSA) process, so that the purified CO₂ can be captured and utilized/stored to reduce greenhouse gas emission. First, UOP 13X was used as adsorbent in this study due to its high adsorption amount and the selectivity of CO₂ to N₂ usually increasing with temperature. Then breakthrough curves and desorption curves were discussed by changing the feed flow rate and feed composition and were verified with a simulation program. Finally, carbon dioxide was purified by a single-bed four-step pressure swing adsorption process. The feed gas of PSA process was 95% CO₂ / 5% N₂, simulating syngas after oxy-fuel combustion. Variables such as vacuum pressure, adsorption time, cocurrent depressurization time and countercurrent depressurization time were discussed to find their effects on CO₂ recovery and purity in order to study the optimal operating conditions for obtaining high purity CO₂.

Keywords: Pressure swing adsorption, Carbon dioxide purification, UOP 13X zeolite

1. Introduction

Since Industrial Revolution in 19th century, the requirement of fossil fuels increases dramatically because of the rapid growth of economy. The large amount of greenhouse gases, especially CO₂, influences the climate change seriously. The United Nations signed the Paris Agreement in April 2016 in order to control the rate of temperature raising. The agreement includes restricting the increase of temperature within 1.5~2 °C and balancing CO₂ emission/nature consumption before 2050. Due to the legal validity of this agreement, the signatories show their determination to solve global warming.

There are several major technologies to capture carbon dioxide: absorption, cryogenic separation, membrane separation, high temperature solid looping systems and

adsorption (Abanades et al., 2015). Among these technologies, pressure swing adsorption (PSA) has advantages of low cost and being easy to operate. PSA can separate different gas mixtures by various adsorbents, which makes it very competitive.

In this study, carbon dioxide from the feed of syngas after oxy-fuel combustion was purified by PSA process. H_2 , CO , CO_2 , CH_4 , H_2O , and a small amount of N_2 and Ar are the typical syngas composition (Todd, 2000). After the syngas passes through the oxy-fuel combustion and water removal, the output gas concentration of CO_2 is about 95 % - 97.4 %. The feed of syngas composition is simplified as a mixture of 95 % CO_2 and 5 % N_2 , and UOP 13X zeolite is used as the adsorbent. Based on the breakthrough curve and desorption curve experiments, we carried out the single-column four-step pressure swing adsorption procedure to purify carbon dioxide and explored various variables to find the optimum operating conditions to obtain more valuable, high purity carbon dioxide.

2. Experimental Description

Adsorption amount and adsorption isotherm were obtained by using Micro-Balance Thermo Cahn D-200. Breakthrough curves, desorption curves and PSA process experiments were performed by adsorption bed. The concentration of outlet gas was detected by Thermo Fisher Scientific Trace-1300 GC. The single-bed four-step PSA process is shown as Figure 1 and the steps are pressurization, adsorption, cocurrent depressurization, and countercurrent depressurization respectively. The experiments started with a set of basic experiment, the operating conditions are shown in Table 1.

Table 1. Basic operating conditions of single-bed four-step PSA process.

Feed composition	95% CO_2 , 5% N_2
Pressurization time (s)	150
Adsorption time (s)	70
Cocurrent depressurization time (s)	170
Countercurrent depressurization time (s)	140
Feed pressure (atm)	3.47
Bed temperature (K)	358

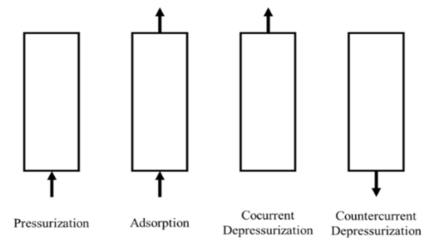


Figure 1. Schematic diagram of single bed four-step PSA process.

3. Model Description

3.1. Mathematical modelling

The PSA dynamic model is made up of several partial differential equations, and the following assumptions are made:

1. Mass transfer resistance between gas phase and solid phase is considered; linear driving force model is used.
2. Extended Langmuir-Freundlich equation is used to calculate the adsorption amount.
3. Only axial concentration and temperature gradient are considered.
4. The ideal gas law is applied.
5. Non-isothermal system is assumed.
6. The pressure drop along the bed can be neglected due to large particle size.

The above assumptions are used in following equations (Huang et al., 2006):

Overall mass balance:

$$-\frac{\partial q}{\partial z} = \frac{\varepsilon A}{R} \frac{\partial (P/T)}{\partial t} + (1 - \varepsilon) A \sum_{i=1}^n \frac{\partial n_i}{\partial t} \quad (1)$$

Mass balance for component i:

$$\frac{\partial}{\partial z} \left(\frac{\varepsilon AD_{m,j} P}{RT} \frac{\partial y_i}{\partial z} \right) - \frac{\partial (y_i q)}{\partial z} = \frac{\varepsilon A}{R} \frac{\partial}{\partial t} \left(\frac{y_i P}{T} \right) + (1-\varepsilon) A \frac{\partial n_i}{\partial t} \quad (2)$$

Energy balance:

$$\begin{aligned} (A\bar{k}) \frac{\partial^2 T}{\partial z^2} - \frac{\partial}{\partial z} (\bar{C}_p q T) - \pi D h (T - T_w) \\ = \frac{\varepsilon A}{R} \frac{\partial}{\partial t} (\bar{C}_p P) + (1-\varepsilon) A \sum_{i=1}^n \frac{\partial}{\partial t} [n_i (\bar{C}_{p,i} T - H_i)] + (1-\varepsilon) \rho_s \hat{C}_p A \frac{\partial T}{\partial t} \end{aligned} \quad (3)$$

Linear driving force model:

$$\frac{\partial n_i}{\partial t} = k_{LDF,i} (n_i^* - n_i) \quad (4)$$

3.2. Adsorption isotherm on UOP 13X zeolite

The isotherm parameters of CO₂ and N₂ are regressed from measured adsorption data at different temperature. The model parameters of different gas adsorption on UOP 13X zeolite for Eq. (5) are listed in Table 2.

Langmuir-Freundlich isotherm for multiple components:

$$q_i^* = \frac{n_i^*}{\rho_s} = \frac{q_{m,i} b_i y_i^{m_i} P_j^{m_j}}{1 + \sum_{j=1}^n b_j y_j^{m_j} P_j^{m_j}} \quad (5)$$

Table 2. Values of model parameters in Eq. (5) for UOP 13X zeolite.

	Carbon dioxide	Nitrogen
a _{1,1} (mol/kg)	6.05	1.17×10 ²
a _{1,2} (mol/kgK)	-4.20×10 ⁻³	-1.28×10 ⁻¹
b _{1,0} (1/atm)	6.80×10 ³	1.65×10 ⁴
b _{1,1} (K)	1.90×10 ³	9.79×10 ²
m _{1,1} (-)	9.67×10 ⁻¹	1.12
m _{1,2} (K)	-2.33×10 ¹	-1.40×10 ²

$$\begin{aligned} q_{m,i} &= a_{i,1} + a_{i,2} T \\ b_i &= b_{i,0} \exp(b_{i,1}/T) \\ m_i &= m_{i,1} + m_{i,2}/T \end{aligned}$$

4. Results and Discussion

4.1. Adsorbent selection

The adsorbents from different companies such as COSMO 5A, UOP 5A, COSMO 13X, and UOP 13X were discussed respectively, and then the selectivities were calculated by Eq. (6) with feed concentration 95 % CO₂ and 5 % N₂ at different feed pressure: 1, 1.5, and 2 atm at various temperature.

$$\alpha_p = \left[\left(\frac{q_{\text{CO}_2, \text{pure}}^*}{q_{\text{N}_2, \text{pure}}^*} \right) \frac{y_{\text{N}_2}}{y_{\text{CO}_2}} \right]_{\text{feed}} \quad (6)$$

Table 3 shows that COSMO 13X and UOP 13X have higher adsorption amounts of CO₂ than 5A. Figure 2 is the comparison of selectivity of different adsorbents at different temperature. We can see that except the selectivity of COSMO 13X is higher than that of UOP 13X at 298 K, the selectivities of COSMO 13X are lower than those of UOP 13X at other temperatures. Most of all, the selectivity of UOP 13X usually increases with temperature. The range of operating temperature can be wider when the CO₂ is purified with 13X zeolite, so we choose UOP 13X zeolite as the adsorbent in this experiment.

Table 3. Adsorption amount of different adsorbents at different temperature with 1 atm. (unit: mol/kg)

Temperature (K)	COSMO 5A		UOP 5A		COSMO 13X		UOP 13X	
	CO ₂	N ₂	CO ₂	N ₂	CO ₂	N ₂	CO ₂	N ₂
298	3.427	0.445	3.407	0.555	3.926	0.338	3.808	0.347
328	2.965	0.237	3.035	0.306	3.277	0.224	3.318	0.237
338	2.834	0.225	2.975	0.266	3.015	0.215	3.047	0.228
348	2.779	0.199	2.747	0.231	2.586	0.184	2.824	0.207
358							2.761	0.148
368							2.621	0.144
378							2.336	0.122
398							1.857	0.112
418							1.681	0.098
458							1.047	0.094

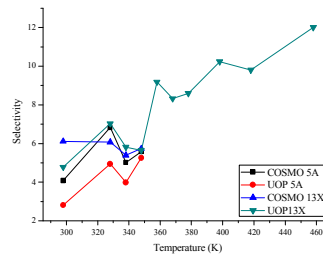


Figure 2. Selectivity of different adsorbents at 1 atm.

4.2. Comparison of experiment and simulation for breakthrough curve and desorption curve

This comparison is used to verify the mass transfer coefficient ($k_{LDF,i}$) of linear driving force model predicted by theory (Ruthven and Farooq, 1990). The results are shown in Figure 3 and Figure 4. It shows that our simulation results are close to the experimental data. Therefore, the accuracy of simulation program can be trusted.

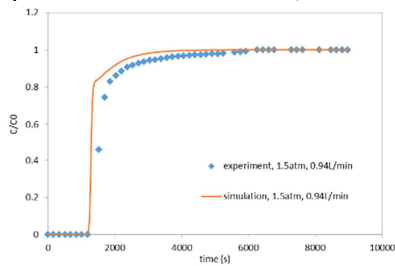


Figure 3. Breakthrough curve of CO₂ for gas mixture. (50 % CO₂, 50 % N₂)

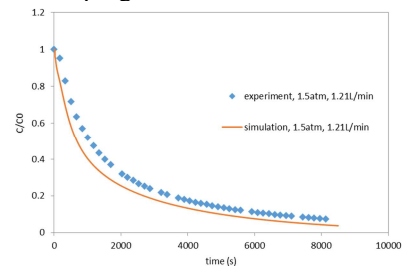


Figure 4. Desorption curve of CO₂ by pure helium.

4.3. Comparison of different operating conditions for breakthrough curve and desorption curve

Effect of feed flow rate on breakthrough curve

Figure 5 is breakthrough curve of CO₂ at 1.72 atm and 298 K with different feed flow rate. The flow rates are 1.137 L/min, 0.788 L/min, and 0.511 L/min respectively. As observed from the figure, when the flow rate increases, the feed amount of CO₂ increases, resulting in a faster breakthrough in the adsorption bed.

Effect of feed composition on breakthrough curve

With the increasing concentration of CO₂, the feed amount of CO₂ increases. Therefore, the time for adsorption bed to achieve breakthrough reduces, resulting in a faster breakthrough in the adsorption bed.

Effect of feed flow rate on desorption curve

Figure 6 is breakthrough curve of CO₂ at 1.72 atm and 298 K with different feed flow rate. The flow rate are 1.737 L/min, 1.660 L/min, and 1.156 L/min respectively. When the H₂ flow rate increases, the feed amount of H₂ increases, resulting in decreasing the concentration of CO₂ in gas phase and increasing desorption rate of CO₂.

Effect of feed composition on desorption curve

Due to the different feed concentration of CO₂, which would change denominator C₀ of the dimensionless concentration during CO₂ desorption process, with higher feed

concentration of CO₂, its dimensionless concentration would decline more until the dimensionless concentration of CO₂ reaches 0.

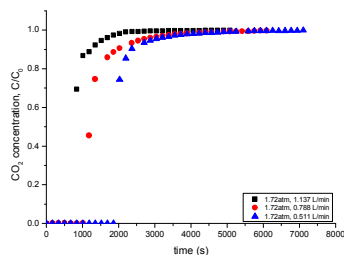


Figure 5. CO₂ breakthrough curves at 298 K with different feed flow rate.

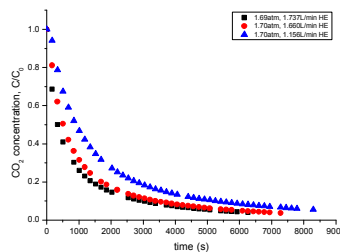


Figure 6. CO₂ desorption curves at 298 K with different He feed flow rate.

4.4. One-bed four-step PSA process

To separate high purity CO₂ from syngas after oxy-fuel combustion, one-bed four-step PSA process is used. There are many operating variables discussed, and the main experimental results are as following:

Effect of cocurrent depressurization time

As shown in Figure 7, with the increase of cocurrent depressurization time, the purity of CO₂ at the bottom product increases and the recovery decreases. N₂, as the weakly adsorbate in adsorbent, would be discharged as the cocurrent depressurization time increasing. When the bottom concentration of CO₂ increases, there will be more CO₂ discharged from the top of the bed at the same time. Therefore, the longer the cocurrent depressurization time, the more CO₂ that flows from the top stream, resulting in a decrease in the recovery of CO₂ at the bottom stream.

Effect of adsorption time

As shown in Figure 8, with the increase of adsorption time, the purity of CO₂ at the bottom is similar and the recovery decreases. As the adsorption time increases, the total amount of gas entering the bed increases, so that more CO₂ exits from the top of the bed. Therefore, the recovery at the bottom is relatively lower, but the concentration of CO₂ at the bottom is similar.

Effect of countercurrent depressurization pressure

As shown in Figure 9, with the increase of countercurrent depressurization pressure, the purity of CO₂ at the bottom increases and the recovery decreases. As the countercurrent depressurization pressure increases, the adsorption bed of bottom product discharge less, so that the bottom of the recovery decreases. The lower countercurrent depressurization pressure it is, the more amount of N₂ at the bottom it emits. Therefore, the bottom CO₂ purity decreases.

Effect of countercurrent depressurization time

As shown in Figure 10, increasing the vacuum time will cause the concentration of CO₂ at the bottom of the bed to go up first and then down, and the recovery will rise slightly. When the vacuum time increases from 140 s to 300 s, the adsorbent has a better desorption efficiency. This increases the amount of CO₂ released from the bottom of the bed, so it can improve the bottom concentration of CO₂. When the vacuum time increases from 300 s to 450 s, not only we can have more CO₂ from the bottom of the bed, but also get the N₂ amount relatively high. Hence, the bottom concentration of CO₂ decreases. If the bottom of the product flow slightly increases, the concentration keeps almost the same, so the recovery increases slightly.

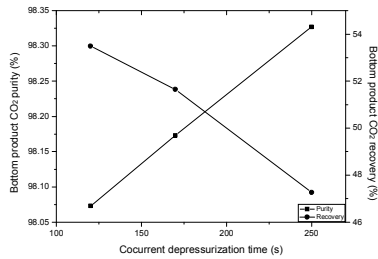


Figure 7. Effect of cocurrent depressurization time on bottom product CO₂ purity and recovery.

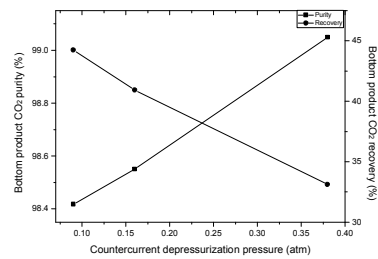


Figure 9. Effect of countercurrent depressurization pressure on bottom product CO₂ purity and recovery.

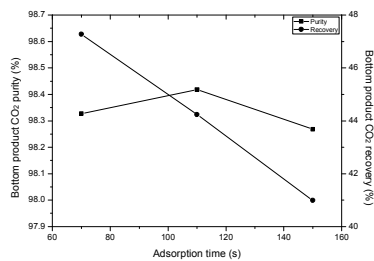


Figure 8. Effect of adsorption time on bottom product CO₂ purity and recovery.

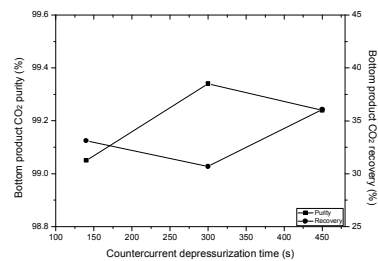


Figure 10. Effect of countercurrent depressurization time on bottom product CO₂ purity and recovery.

5. Conclusion

This research experimentally studied the concentration of high purity CO₂ from syngas after oxy-fuel combustion by PSA and also developed a simulation program. By the analysis of the adsorption amount and the selectivity of CO₂ to N₂ over different adsorbents, we chose UOP 13X zeolite as the adsorbent due to its high adsorption amount and the selectivity of CO₂ to N₂ usually increasing with temperature.

Breakthrough curves and desorption curves were discussed by changing the feed flow rate and feed composition. Increasing feed flow rate and enhancing the carbon dioxide portion in feed of CO₂/N₂ could help the adsorption bed to reach breakthrough faster in the breakthrough experiments. The adsorption isotherm parameters were regressed from experimental adsorption data, which were used in simulation. The simulation results of breakthrough curves and desorption curves agreed quite well with the experimental data, which shows the simulation program can be trusted.

Finally, CO₂ was purified by a single-bed four-step PSA process. The feed gas of PSA process was 95 % CO₂/5 % N₂. After a series of experiments, we found that the optimal operating conditions are feed pressure 3.47 atm, bed temperature 358 K, cocurrent depressurization pressure 1.33 atm, countercurrent depressurization pressure 0.38 atm, pressurization time 150 s, adsorption time 110 s, cocurrent depressurization time 250 s and countercurrent depressurization time 300 s. The experimental results of final conditions are 99.34 % purity and 30.69 % recovery of CO₂ at bottom product.

Acknowledgement

The authors gratefully acknowledge the financial support of the NEP-II program of Ministry of Science and Technology, Taiwan under project number MOST 106-3113-E-008-004.

References

- J. C. Abanades, B. Arias, A. Lyngfelt, T. Mattisson, D. E. Wiley, H. Lic, M. T. Ho, E. Mangano and S. Brandani, 2015, "Emerging CO₂ capture systems," *International Journal of Greenhouse Gas Control*, vol. 40, pp. 126-166.
- D. M. Todd, 2000, "Gas Turbine Improvements Enhance IGCC Viability," 2000 Gasification Technologies Conference, San Francisco, CA.
- W. J. Huang, C. Y. Chen, and C. T. Chou, 2006, "Concentration and recovery of SO₂ from flue gas by pressure swing adsorption," *J. Chin. Inst. Chem. Eng.*, vol. 37, pp. 149-157.
- S. Ruthven and D. M. Farooq, 1990, Heat effects in adsorption column dynamics. 2. Experimental validation of the one-dimensional model, *Ind. Eng. Chem. Res.*, vol.29, pp. 1084-1090.

Flow diagram of waste double base propellant treatment including fluidized bed reactor

Raymoon Hwang^a, Jiheon Lee^a, Inkyu Lee^a, Hyunsoo Kim^b, Jungsoo Park^b, Oh Min^c, Il Moon^{a,*}

^a*Department of Chemical and Biomolecular Engineering, Yonsei University, 50 Yonsei-ro, Seodaemun-gu, Seoul 03722, Republic of Korea.*

^b*Department of Chemical Engineering, Hanbat National University, 125 Dongseo-daero, Ou-seong-koo, Daejeon, Republic of Korea*

^c*Agency of Defense Development, NE32, Republic of Korea*

ilmoon@yonsei.ac.kr

Abstract

Dealing with explosive wastes appropriately is a difficult problem recently. Many of them are just being buried and some of them are being treated. The main method to treat explosive wastes is to burn it with Rotary-kiln reactor. However this has a risk of explosion during the process because it is based on explosion mechanism. In addition, Rotary-kiln method can not deal with enough amount of explosive waste because Rotary-kiln method use batch reactor. Lastly, because of the limit of non-successive process, the efficiency of the purification process is low which results in an incomplete combustion. This incomplete combustion makes the exhaust gas more dirty which contains more harmful substances. To overcome the limits of Rotary-kiln method which are introduced above, development of combustion-based process is necessary. Therefore, a flow diagram which includes fluidized bed reactor was developed with Aspen Plus. A mixture of explosive waste slurry and water with the same ratio was fed in the fluidized bed reactor. Also, additional units were chosen and designed which clean exhaust gas to make the reactor more adaptable. The proposed process was thermodynamically analyzed and the efficiency evaluation was held. Also, the improvement possibility of the process was derived. The final exhaust gas from this process satisfied the environment regulation of Korea. This process can deal with 3000 ton/yr which is the total amount of waste propellant in Korea, while the exhaust gas fits the regulation of CO 25ppm/hr, NO₂ 0.10ppm/hr. This study is expected to contribute to the improvement of the efficiency of the explosive waste treatment process and the possession of domestic technology in Korea.

Keywords: fluidized bed reactor, flow diagram, double base propellant.

1. Introduction

The explosive waste treatment has been a major issue in chemical engineering field. The most common method to treat the explosive waste is burring in land. In this point of view explosive wastes in land occurs environment contamination in various aspects including groundwater contamination. Because of its toxicity, pancytopenia or cancer may occur(treatment methods for the remediation of nitroaromatic explosives). In this

point of view, an adequate method to make these wastes unarmful is required. Harmless wastes can be achieved by burning process. However, burning explosive materials have to be dealt carefully because it has explosive possibility. Rotary-kiln method is generally used in explosive waste treatment process. It was introduced at 1989 in Germany according to Poulin(2010). But Rotary-kiln method can not deal with massive amount of wastes. Moreover, it has a possibility of explosion during the process. To overcome this disadvantage of the Rotary-Kiln, this study proposed a new explosive waste treatment process with fluidized bed. With the benefit of fluidized bed reactor, the amount of allowance of propellant is larger comparing with Rotary-Kiln reactor. In this research, a treatment process of exhaust gas is introduced. The exhaust gas properties are calculated by the computer flow dynamic(CFD) by J.lee(2016) technology and the overall process flow scheme was configured and simulated.

2. Process descriptions

NO, NO₂, CO, CO₂ is target gases ingredients in this process. Table 1 shows the composition of exhaust gas from the fluidized bed reactor. Components which affect the environment are in Table 1 are NO, NO₂, CO, CO₂ according to the environment regulations at Republic of Korea. To satisfy the regulations, each components have to be handled appropriately before discharging it to the air. The schematic process flow diagram of the suggested process is illustrated in Figure 1.

Table 1. Composition of the exhaust gas from the incinerator

	Mole fraction	Mole flow (kmol/hr)
Water	0.023	6.69
NO ₂	0.005	1.49
NO	0.001	0.17
N ₂	0.767	220.37
O ₂	0.199	58.58
CO ₂	0.015	4.48
CO	0.008	2.30
total	1	294.09

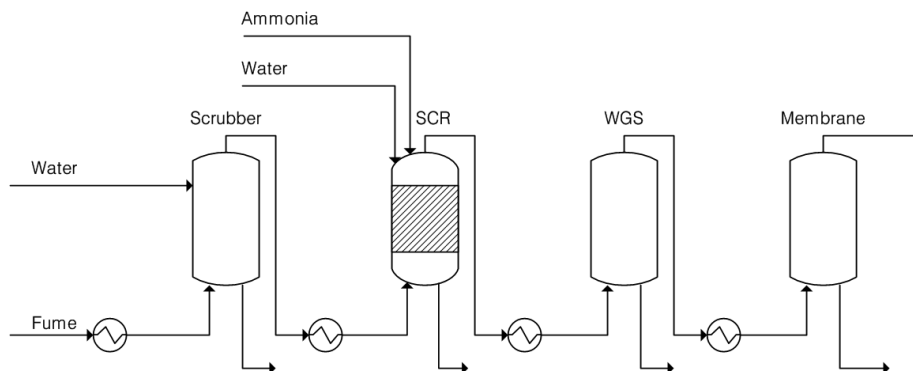


Figure 1. Overall flow diagram of the treatment process

2.1. NOx abatement process

Generally, there are two types of methods reducing NOx. One is wet method which uses the absorption principle and the other is dry process which use chemical interaction between NOx and other components. To define an appropriate unit to decrease NOx, both of the wet method and dry method were used to supplement the drawbacks of each other. At wet method, water was simulated as an absorbent. On the other hand, V₂O₅-TiO₂ catalyst was applied when simulating dry method. Equation (1) is the main reaction of wet method.



The main purpose of this reactor is to separate NO₂ from the exhausted gas. Because this is an equilibrium based unit, the conversion ratio was assumed as 0.9 according to the reference, Sweedney et al.(1999). On the other hand, a selective catalyst reduction reactor was used to simulate the process of abatement of NO. The inputted kinetics are equation (2) ~ (11).



$$-\frac{4dNO}{dt} = 1.5 \times 10^7 e^{-\left(\frac{E_1}{RT}\right)} (P_{NH_3})^{0.0005} (P_{NO})^1 (P_{O_2})^{0.5} \quad (3)$$

$$E_1=15\text{kcal/gmol} \quad (4)$$



$$-\frac{2dNO_2}{dt} = 1.5 \times 10^7 e^{-\left(\frac{E_2}{RT}\right)} (P_{NO_2})^1 (P_{NH_3})^{0.0005} (P_{O_2})^{0.5} \quad (6)$$

$$E_2=14.5\text{kcal/gmol} \quad (7)$$



$$+\frac{4dNO}{dt} = 1.5 \times 10^7 e^{-\left(\frac{E_3}{RT}\right)} (P_{H_2O})^{0.3} (P_{N_2})^0 \quad (10)$$

$$E_3=10\text{kcal/gmol} \quad (11)$$

The selective catalyst reduction(SCR) was simulated as a plug flow reactor. In the simulation which was handled in this research, scrubber mainly abated NO₂. To separate NO and NO₂ efficiently, scrubber and SCR was placed.

2.2. CO abatement process

To capture CO, water-gas shift reaction was used. According to the reference, the conversion ratio of CO was higher than 90% at 400°C. And when the H₂O/CO ratio was 7.5:1. To get reduce CO, water-gas shift reaction like equation (12) ~ (13) was used.



$$\Delta H = -41.2 \text{ kJ/mol}, \Delta G = -28.6 \text{ kJ/mol} \quad (13)$$

In according water-gas shift reactor in upon gas treatment system, Ni-Al₂O₃ catalyst was used. The conversion ratio at WGS reactor was 0.99.

2.3. CO₂ abatement process

To capture CO₂, a membrane reactor was used. The membrane is of asymmetric cellulose acetate hollow-fiber membrane. The separate ratio of CO₂ was 0.99. As a result, combined treatment process is shown at Figure 3. NO_x is captured at scrubber and catalyst reactor, CO is captured at water-gas shift (WGS) and CO is treated at membrane reactor.

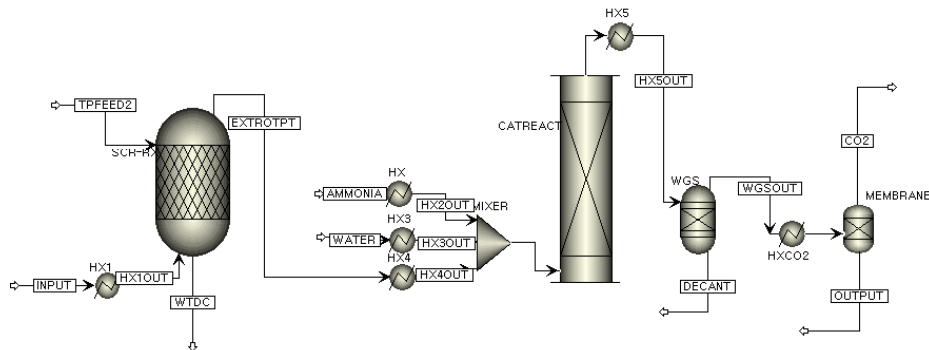


Figure 3. Overall treatment process with simulation conditions

The overall process diagram is the exhaust gas treatment system. First, NO and NO₂ are separated with the scrubber and selective catalyst reduction (SCR). Six heat exchangers are placed to use the energy more efficiently. Because ammonia and water is the feed of NO abatement process, the SCR has three inputs. After separating NO_x, CO and CO₂ is treated gradually. The temperature and pressure conditions are shown in Table 2.

Table 2. Specifications of each units

	Temperature(°c)	Pressure (bar)
Scrubber	32.22	1
SCR	284.53 ~ 319.22	1
WGS	25	1
Membrane	25	1

3. Results

The final exhaust gas have reached the environmental regulation at Republic of Korea. Little amount of NO₂ was released and output of NO was 5ppm.

Table 3. Mole flow of inlet and outlet of each units

	Inlet (kmol/hr)	Outlet of NO _x abatement system (kmol/hr)	Outlet of WGS reactor (kmol/hr)	Outlet (kmol/hr)
Water	6.85	11.47	0.01	0.01
NO ₂	1.49	0	0	0
NO	0.17	5.19e-6	5.19e-6	5.13e-6
CO ₂	4.48	4.48	6.76	0.34
CO	2.30	2.30	0.02	0.02
N ₂	220.37	221.22	221.22	219.00
O ₂	58.58	58.35	58.35	57.77

After a proper amount of environmental harmful exhaust gas was achieved, building heat exchanger network was proceeded. During design, I.Lee(2017) was referred. With the heat curve of the process shown in Figure 4 and the temperature profile is summarized in Table 4, heat exchanger network was achieved as shown on Figure 6.

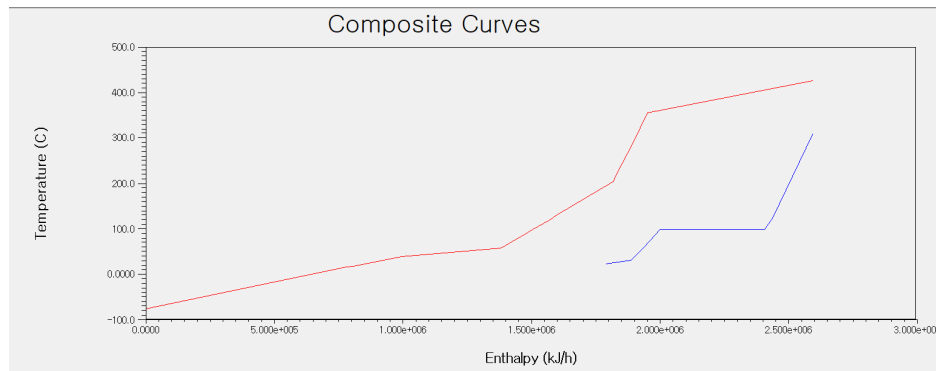


Table 4. Heat integration table

	Inlet T (°C)	Outlet T (°C)	MC _p (kJ/hr)	HTC (kJ/hr)	Flow rate (kg/hr)
WATER to HX3OUT	25.0	125.0	-	473,000	180.0
AMMONIA to HX2OUT	100.0	90.0	801.2	8012	360.0
EXTROTPT to HX4OUT	32.2	310.0	855.5	237,600	832.3
RECOU to HXOUT	206.3	-75.0	-	1,645,000	1372
SO ₂ to HX1OUT	356.9	17.8	-	302,800	843.7
INPUT To HXOUTSOX	426.9	356.9	9178	642,400	8437
SCR-RX heat	25.0	32.2	13210	95,420	-

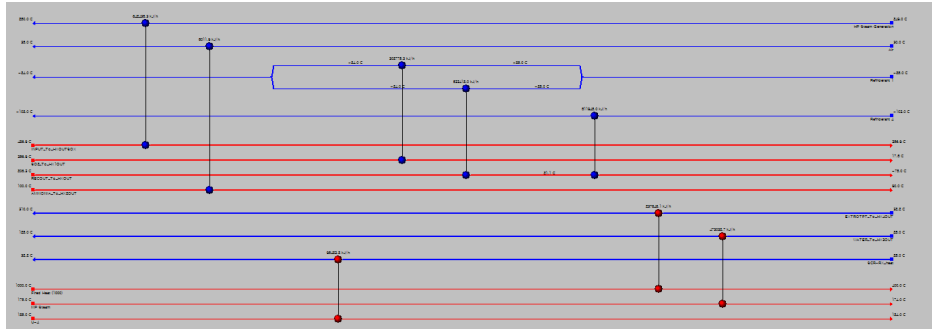


Figure 6. Heat exchanger network result

The most energy effective heat exchanger network point was heat exchange between HXOUT and RECOU. As a result, the proposed heat exchanger network (HEN) process can save energy by 833,412 kJ/hr. Including upon point, eight points are being exchanged to save energy.

4. Conclusions

To separate NO and NO₂ successfully and efficiently, both of SCR and scrubber have to be used. With upon four units, the final exhaust gas from the treatment process has satisfied the environmental regulation of Republic of Korea. Also, with the benefit of the heat exchanger network, almost 4 million kJ/hr of energy can be saved. With this simulated facility, large scale of waste ammunition can be treated. Because a lot of waste water occurs during the process, additional treatment system has to be handled to make a more comprehensive treatment system.

References

- C.Y.Pan,1986 ,Gas separation by High-Flux, Asymmetric Hollow-Fiber Membrane, AIChE Journal, Vol.32, No. 12, 2020-2027
- J.Lee,C.Park,2017,Simulation of waste propellant combustion process in fluidized bed incinerator, Theories and applications of chemical engineering, Vol.23, 205
- I.Lee, J.Park,2017, Conceptual design and exergy analysis of combined cryogenic energy storage and LNG regasification processes: Cold and power integration, Energy, Vol.140, Part 1, 106-115
- I.Poulin,2010, Literature review on demilitarization of munitions, DRDC Valcartier Tm, November, 2010-213
- Yue Li, Qi Fu, Maria Flytzani-Stephanopoulos, 1999, Low-temperature water-gas shift reaction over Cu- and Ni-loaded cerium oxide catalysts, Applied catalysis B: Environmental 27 (2000), 179-191
- Sweedney, Andrew Jeffery,1999,Computer Simulation and Optimization of the NO_x Abatement System at the Radford Facility and Army Ammunition Plant, etds, 03042000-11000048

Integration of Renewable Resources into Petroleum Refining

Mohamed Al Jamri, Robin Smith*, Jie Li

Centre for Process Integration, School of Chemical Engineering and Analytical Science, The University of Manchester, Manchester M13 9PL, UK

robin.smith@manchester.ac.uk

Abstract

Integration of renewable resources into transportation fuel system requires investigation of resource compatibility with existing infrastructure and exploitation of potential integration points within transportation fuel system. This work focuses on co-processing fast pyrolysis oil (FPO) in refinery FCC units. In this work, a novel methodology is proposed for the modelling of catalytic cracking of a blend of vacuum gas oil (VGO) and fast pyrolysis oil in an advanced cracking evaluation (ACE-R) FCC unit. A new molecular-level characterisation method, based on MTHS matrix approach, is developed for the characterisation of blended feedstock. Molecular-level reaction models are then constructed based on large scale and complex reaction networks synthesised using MTHS matrix framework. The total number of reactions used to synthesise the reaction network in this work is 328. Kinetic parameters tuning problem is formulated as an optimisation problem in which the objective function is to minimise the difference between measured and predicted products yields at various conversion levels. An overall good agreement between measured and predicted yields is obtained using the developed kinetic model for VGO: FPO blending ratio, C/O ratio and reaction temperature of 95:5, 5 and 530°C, respectively. PONA composition in each layer of product stream (e.g. gasoline, diesel, gasoil, etc.), as well as oxygen compounds compositions and oxygen content is predicted. This creates potentials for rigorous optimisation of process parameters for refinery profit maximisation or better products' quality control. The methodology developed in this work can easily be extended to model other refinery processes.

Keywords: Catalytic cracking, Fast pyrolysis oil, biomass, refinery, MTHS matrix.

1. Introduction

Integration of renewable energy sources into transportation fuel system is increasingly becoming a priority for several developed countries, especially in Europe and North America. For example, EU members' aim to increase the share of renewable energy sources in their transportation fuel system from the current value of 6.5% to 10% by 2020 (The European Commission, 2015). In order to achieve this goal, infrastructure-compatible refinery bio-intermediates or completely fungible finished biofuels are considered to be the most, and perhaps, the only viable option which can help fulfilling this regulation requirement.

Second generation biofuels are produced from lignocellulosic biomass (mainly agriculture residues) and considered to be promising and sustainable option, especially since it does not create competition with food industry. Production of biofuels from second generation biomass can be achieved via two distinctive routes. The first route

starts with the gasification of solid biomass, which destroys the biomass building blocks to form carbon monoxide and hydrogen. Gasification products are then used as a feed for Fischer-Tropsch (FT) synthesis process or other liquid synthesis processes (MeOH or olefins synthesis), where synthetic liquid fuels are manufactured according to fuels' standards and refinery requirements. The second route involves the conversion of biomass polymers (cellulose, hemicellulose and lignin) into smaller molecules in the form of dense and viscous oil (bio oil) via pyrolysis processes. Obtained liquid asset is then upgraded via catalytic means in order to produce refinery intermediates and/or finished fuels. While the first option gives the refiner more control over yields and specifications of the various fuels cuts, the opportunities of integrating bio-intermediates using this route into existing refineries' infrastructure is limited. The second option, on the other hand, gives refiners more opportunities to exploit spare capacity available in their upgrading units, and allow them to use economy of scale to decrease the extra cost induced from introducing biomass into existing plants.

Co-processing biomass pyrolysis oil in refinery FCC process emerges as a promising option for the integration of renewable resources into transportation fuels system. This is mainly due to the ability of FCC units in handling different feedstocks and the tolerance of FCC catalyst to oxygenates, water, carbon monoxide and carbon dioxide. However, the effects of introducing bio oil to such a large and important refinery process must be carefully examined. In this work, the effects of co-processing bio oil with VGO in catalytic cracking unit (MAT) is investigated via process modelling techniques. The proposed method includes detailed, molecular-level characterisation of feed and product streams, as well as detailed reaction network and kinetic models which consider the complex interactions between the various molecules on the surface of cracking catalyst.

2. Integrated Modelling Methodology

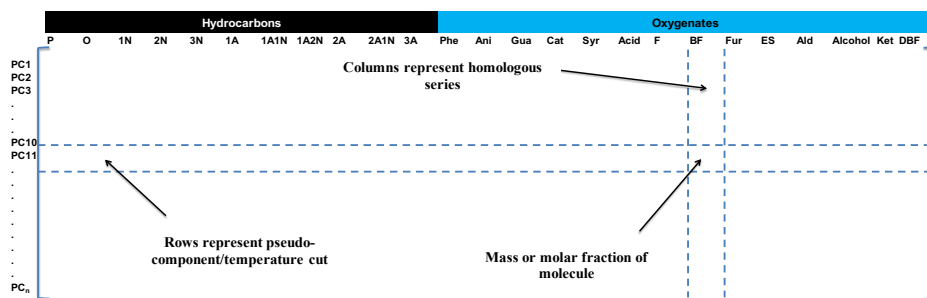


Figure 1. Proposed MTHS Matrix Framework for Representation of Mixed Stream

Characterisation of process stream is a fundamental step in the development of process models. For complex reactive processes, such as upgrading processes found in petroleum refineries (e.g. FCC), characterisation of process stream has significant effects on model's quality and suitability for process integration and optimisation. For complex chemical streams, characterisation step involves measurements of bulk properties, as well as quantities of the various chemical families found in the stream.

2.1. Feed Characterisation Methodology

Stream characterisation for model development of refinery process is not trivial. Experimental approaches, although provide detailed molecular-level information, are time consuming and expensive. Non-experimental methods, such as pseudo-components and structural parameters approaches are fast and simple in application, however, does not provide molecular information, therefore, not compatible with reaction models.

Stream characterisation approach adopted in this work attempts to provide detailed molecular-level information compatible with reaction models, efficiently and at low cost. Molecular Type and Homologous Series (MTHS) matrix approach uses 2-D matrix to represent the size and type of a given molecule or lump in the characterised stream (Figure 1). The compositional matrix is obtained by solving an optimisation problem in which the objective function is to minimise the difference between measured and predicted bulk properties and structural information (Figure 2). The resultant matrix comprises petroleum-based hydrocarbon molecules, as well as bio-based oxygenated homologous series representing bio oil fraction in the blended stream.

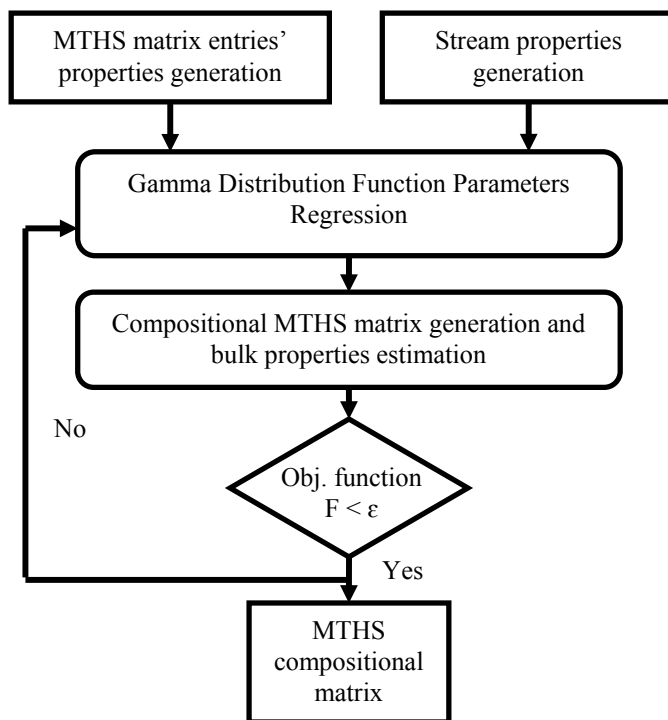


Figure 2. MTHS matrix Solution Algorithm

The proposed methodology has been tested against a blend of vacuum gas oil (VGO) and fast pyrolysis oil (FPO) at blending ratio of 95:5. The results exhibit maximum error of 8% in the prediction of stream density.

2.2. Reaction Network Modelling Methodology

Reaction network synthesis procedure starts by determining reaction pathways, kinetic expressions and kinetic parameters values. The literature is rich in hydrocarbons

reactions pathways and kinetic information (Jacob *et al.*, 1976; Araujo-Monroy and López-Isunza, 2006), however, the information available on bio molecules reaction pathways and kinetic data is scarce. In this work, hydrocarbons reaction network proposed by Gómez-Prado (2009) is adopted to represent catalytic cracking reactions of hydrocarbon molecules in feed stream. Reaction pathways for bio molecules are deduced from model compounds studies for catalytic conversion of bio oil (Adjaye and Bakhshi, 1995a), while kinetic expressions and initial values for kinetic parameters are taken from previous works in literature (Adjaye and Bakhshi, 1995b).

The developed reaction model includes 328 reactions used to describe the behaviour of 58 lumps and chemical species inside the reactor. The model exhibits ability in handling different feedstocks as well as different blending ratios (VGO and FPO) without the necessity of kinetic parameters re-fitting. In addition, industrial requirements for products quality control are fulfilled in this model. This is mainly due to the ability of this model in tracking structural groups (PONA) as well as oxygenated compounds at each boiling level of product stream.

The values of kinetic parameters are regressed using hybrid optimisation technique. In order to reduce the number of variables in the optimisation model, it was assumed that same types of reactions have similar activation energies. This resulted in a total of 14 optimisation variables, which are activation energies for 14 different types of reaction families included into the model. Because of non-linearity found in the optimisation/regression model, stochastic search method (Genetic Algorithm) has been used to increase the chance of obtaining a solution in the vicinity of global optimum. A deterministic search technique (SQP) has been used to improve the quality of the solution obtained by GA. The results obtained using this hybrid optimisation scheme show good agreement between predicted and measured products' yields.

3. Results and Discussion

Table 1. Predicted Composition of Blended Stream (VGO:FPO = 95:5)

	Light gas	L. gasoline	H. Gasoline	Diesel	Gasoil	Residues
P	7.67E-01	2.59E-02	7.01E-01	6.09E+00	2.99E+01	1.83E+01
O	0.00E+00	0.00E+00	1.85E-05	4.48E-03	1.74E-01	1.80E-01
N	0.00E+00	0.00E+00	0.00E+00	0.00E+00	8.66E+00	1.20E+01
A	0.00E+00	0.00E+00	0.00E+00	0.00E+00	1.96E+01	1.49E-02
Phenolic	0.00E+00	3.19E-01	3.76E-01	1.02E-01	3.33E-02	6.49E-02
Acid & ES	0.00E+00	1.18E+00	8.38E-01	5.37E-02	8.91E-04	1.24E-06
Ald & Ket	0.00E+00	5.26E-01	1.75E-02	2.66E-04	6.64E-07	0.00E+00
Alcohols	0.00E+00	1.77E-02	3.13E-04	4.07E-06	0.00E+00	0.00E+00

The developed characterisation methodology has been used for the characterisation of a blend of 95 wt. % VGO and 5 wt. % FPO stream which is used as a feed for catalytic cracking unit. The compositional matrix obtained is condensed to show the total composition of each structural group in each fraction in the feed stream (Table 1). The

results obtained are compared with measured experimental data for the characterised stream. The results showed a maximum error of 8% in density predictions.

Compositional matrix obtained from characterisation step is fed to the reaction model and tested against a set of experimental data. Table 2 shows a comparison between measured and predicted yield values obtained from the model. Figure 3 is a parity plot used to measure the accuracy of the developed model. The figure exhibits R^2 (index of correlation) value of 0.985, indicating good accuracy of fitting parameters obtained.

Table 2. Comparison between Predicted and Measured Yields

WHSV	6		8		12		24	
	Pred.	Exp.	Pred.	Exp.	Pred.	Exp.	Pred.	Exp.
Dry Gas	1.47	2.54	1.46	2.21	1.43	2.06	1.40	1.87
LPG	38.40	39.91	37.60	39.47	35.34	34.50	33.27	30.05
Gasoline	29.26	30.73	29.22	29.48	29.03	28.22	28.75	27.48
LCO	15.59	12.59	16.09	15.11	17.52	18.80	18.84	22.77
HCO	9.26	8.14	9.71	8.17	11.04	11.13	12.35	12.84
Coke	6.02	6.08	5.92	5.56	5.65	5.29	5.39	4.99

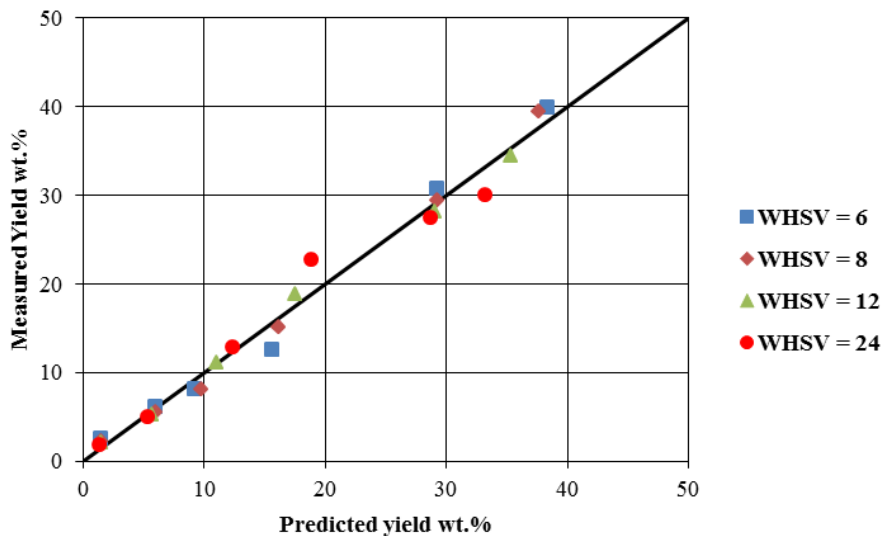


Figure 3. Parity Plot of Model Predicted Yields and Experimentally Determined Yields

The novelty in this work is the ability of the proposed method in predicting the composition of the various oxygenated groups in each fraction of product stream. For example, Figure 4 shows the composition of phenolics and alcohols in diesel product fraction as a function of conversion. Validation of the values obtained is a matter of data availability.

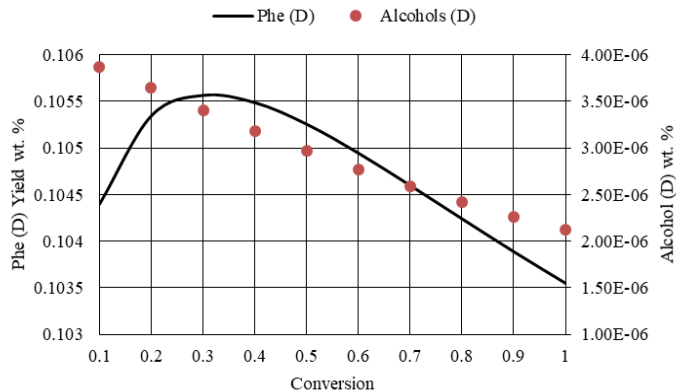


Figure 4. Composition of Phenolics and Alcohols in Diesel Fraction

4. Conclusions

A methodology for molecular-level characterisation of mixed petroleum and bio oil streams is proposed. The methodology eliminates the need for detailed laboratory based characterisation by converting bulk properties of mixed streams, which are readily available and easily measured, into detailed molecular-level information via optimisation-based model. The proposed characterisation model is integrated into a novel catalytic cracking reaction model in which 328 reactions are used to describe the behaviour of 58 lumps inside a pilot plant scale MAT unit. The results obtained exhibits good accuracy when compared with experimental results and previous models with similar complexity.

References

- Adjaye, J. D. and Bakhshi, N. N. (1995a) 'Catalytic conversion of a biomass-derived oil to fuels and chemicals II: Chemical kinetics, parameter estimation and model predictions', *Biomass and Bioenergy*, 8(4), pp. 265–277. doi: [https://doi.org/10.1016/0961-9534\(95\)00019-4](https://doi.org/10.1016/0961-9534(95)00019-4).
- Adjaye, J. D. and Bakhshi, N. N. (1995b) 'Production of hydrocarbons by catalytic upgrading of a fast pyrolysis bio-oil. Part II: Comparative catalyst performance and reaction pathways', *Fuel Processing Technology*, 45(3), pp. 185–202. doi: [https://doi.org/10.1016/0378-3820\(95\)00040-E](https://doi.org/10.1016/0378-3820(95)00040-E).
- Araujo-Monroy, C. and López-Isunza, F. (2006) 'Modeling and Simulation of an Industrial Fluid Catalytic Cracking Riser Reactor Using a Lump-Kinetic Model for a Distinct Feedstock', *Industrial & Engineering Chemistry Research*. American Chemical Society, 45(1), pp. 120–128. doi: 10.1021/ie050503j.
- Jacob, S. M. et al. (1976) 'A lumping and reaction scheme for catalytic cracking', *AIChE Journal*. American Institute of Chemical Engineers, 22(4), pp. 701–713. doi: 10.1002/aic.690220412.
- Juan Luis Gómez Prado (2009) *Integrated Methodology for the Modelling of Refinery Fluid Catalytic Cracking Units*. University of Manchester. doi: 10.1016/S0306-4522(99)00245-6.
- The European Commission (2015) *Renewable energy statistics*. Available at: http://ec.europa.eu/eurostat/statistics-explained/index.php/Renewable_energy_statistics (Accessed: 1 June 2017).

Simulation of CO₂ Geological Storage Together with a Water Alternating Gas Process for Oil Production in Fang Oilfield (Thailand)

Kreangkrai Maneeintr,^{a,*} Hutthapong Yoosook^a

^a*Carbon Capture, Storage and Utilization Research Group, Department of Mining and Petroleum Engineering, Faculty of Engineering, Chulalongkorn University, Bangkok 10330 Thailand.*

Kreangkrai.M@chula.ac.th

Abstract

Due to the environmental concern, carbon dioxide (CO₂) emission into the atmosphere has been the main issue in petroleum industries. The sources of CO₂ come from natural gas processing and other processes. The current technology to mitigate CO₂ is carbon capture, storage and utilization (CCSU). However, oil is expected to produce more because of the higher consumption. Therefore, CO₂ geological storage in depleting oilfield together with an enhanced oil recovery can be a better technology to meet both targets. The excellent example of this technology is the Weyburn Project in Canada that can store CO₂ and produce more oil as well as prolong the reservoir life simultaneously. For this project, the technology is applied with the depleting oilfield for both oil production and CO₂ storage in Northern Thailand by using simulation model with the real data of the oilfield. Water alternating gas (WAG) process for enhanced oil recovery (EOR) is used to improve the mobility of the flooding system resulting in better sweep efficiency and an improvement in the oil recovery. Consequently, the objective of this research is to evaluate CO₂ injection together with WAG process as well as to investigate the effects the parameters such as chasing water rate and total HCPV injection on oil production, CO₂ consumption and sequestration. The total HCPV used in this study is ranged from 0.5 to 1.5 and the results are compared with that of CO₂ flooding. From the simulation, the results report that oil can be produced up to 57% recovery, CO₂ consumption is approximately 3 scf/bbl. Furthermore, CO₂ consumption increases with total HCPV injection. The results of this study can be applied as a fundamental data to develop the CO₂-EOR project in the depleting oilfield in the North of Thailand for both oil production and CO₂ storage in the future.

Keywords: Enhanced oil recovery, carbon dioxide, water alternating gas, CO₂ injection.

1. Introduction

The injection of CO₂ into oil reservoir is one method of enhanced oil recovery (EOR). The main recovery mechanisms are to reduce oil viscosity and to trap gas (Mohammed-Singh et al., 2006). In addition, CO₂-EOR can reduce Greenhouse Gas (GHG) emission to atmosphere (Le Gallo et al., 2002). Currently, there are three main operating strategies for CO₂ injection, including CO₂ Huff-n-Puff, CO₂ flooding, and water alternating gas (WAG). The operations of CO₂ Huff-n-Puff are injecting of CO₂ into oil reservoir until reaching of desired slug volume. Then, the well is shut-in for 2 to 4

weeks as a soaking period (Wang et al., 2013). Subsequently, the well is opened to produce back both oil and injected CO₂. These processes are repeated between 2 to 5 cycles or operated until insufficient oil production (Whittaker and Perkins, 2013). The cycle of CO₂ injection proved to be the most suitable for reservoirs with relatively small pool size (Song and Yang, 2013). Therefore, CO₂ Huff-n-Puff usually perform as pilot test in many field to confirm reservoir fluid response with injected CO₂ before beginning of full field implementation of CO₂ flooding or WAG (Simpson, 1988).

CO₂ flooding is a method by injected CO₂ into reservoir (Holm, 1982). However, the application of CO₂ flooding may potentially have problems of viscous fingering that caused of early breakthrough and poor sweep efficiency (Donaldson et al., 1989). To reduce the problem, the alternating slugs of injected water and CO₂ is applied to the field that known as water alternating gas (WAG) process. Moreover, the huge amount of CO₂ consumption in the conventional CO₂ flooding usually limits its widespread application and allows WAG to be taking place due to economic decision (Zekri et al., 2011). Finally, the integrated CO₂ Huff-n-Puff and WAG technique seem to be the effective process.

2. Reservoir model

The compositional reservoir simulator provided by CMG was used as a tools to construct the 3D reservoir model and to compare the results. The heterogeneous reservoir model was created based on a reservoir data in Fang oilfield, Thailand as shown in Figure 1. The pattern of producer and injector was quarter five-spot pattern that included one injector and producer at the opposite corner of this model. The reservoir properties of this models are summarized in Table 1. The API gravity of the reservoir fluid is about 31°API.

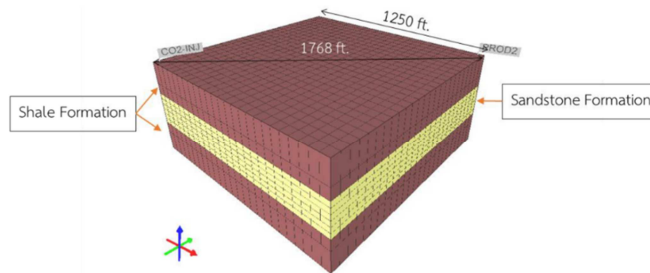


Figure 1. Reservoir model with location of injection and production wells

Table 1 Reservoir properties using for created reservoir model

Parameter	Values	Unit
Grid Dimension	25 x 25 x 6	Block
Reservoir Size	1250 x 1250 x 30	Ft.
Average Porosity	0.25	Fraction
Average Horizontal Permeability	150	mD
Average Vertical Permeability	15	mD
Rock Compressibility	0.000003	1/PSI
Initial Reservoir Pressure	680	PSI
Reservoir Temperature	144	°F
Reservoir Type	Sandstone	

3. Results and discussion

3.1. Sensitivity Analysis of CO₂ Huff-n-Puff

The sensitivity of these parameters on oil recovery factor is presented in Figure 2. In addition the most important parameter is production time, followed by production rate, HCPV injection, and injection time. And, the range for the incremental oil recovery factor at three cycle of CO₂ Huff-n-Puff process is 2.61% to 4.98% of original oil in place (OOIP).

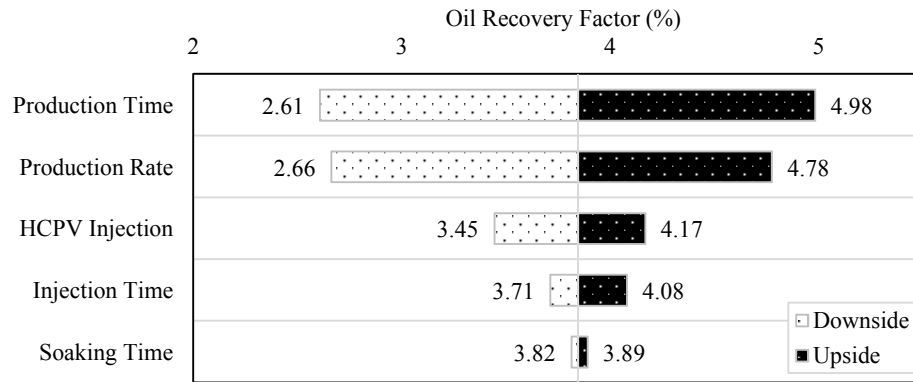


Figure 2. Sensitivity analysis of oil recovery factor using CO₂ Huff-n-Puff process

3.2. Effect of Chasing Water Rate

The effect of chasing water rate of 300, 450, and 600 BWPD on oil recovery factor and CO₂ utilization was investigated as presented in Figure 3. The results showed that higher oil recovery can be obtained by additional injection rate. Moreover, the increasing of chasing water rate can reduce CO₂ utilization at all CO₂ HCPV injection. The lowest CO₂ utilization is achieved when injection of 600 BWPD at 0.5 HCPV that is about 13 scf/stb.

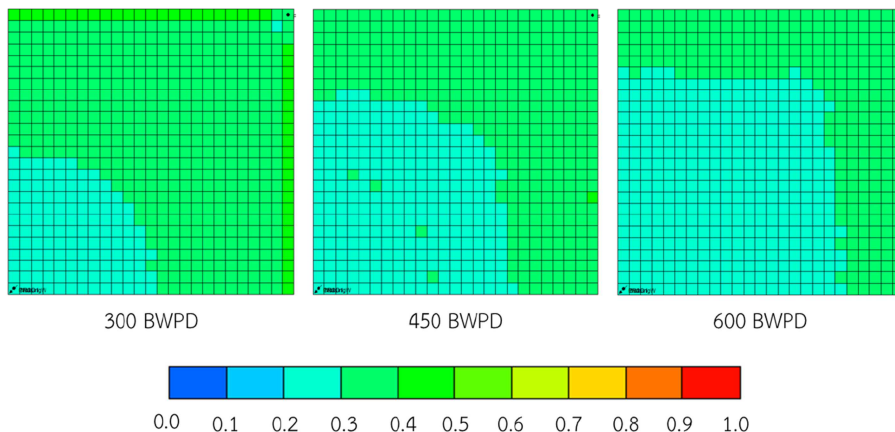


Figure 3. Effect of chasing water injection rate on oil recovery

3.3. Effect of CO₂ HCPV Injection

The HCPV injection has an effect on the performance of integrated CO₂ Huff-n-Puff and WAG technique as presented in Figure 4. The results showed that the highest oil recovery factor of each chasing water injection rate is obtained by injecting 2.0 HCPV of CO₂. When chasing water is injected at 300, 450, and 600 bwpd, oil recovery factor is achieved at the maximum values of 62.2, 64.3, and 65.7% of OOIP, respectively. The main reasons that can explain these circumstances are CO₂ solubility into crude oil and oil swelling factor. Sasaki et al., (2013) stated that the swelling factor increased by added reservoir pressure and CO₂ solubility also increased rapidly by increasing pressure below bubble point. Also, the results indicated that increasing of HCPV injection provides higher CO₂ utilization for every chasing water rate. The lowest CO₂ utilization is 13.2 scf/stb.

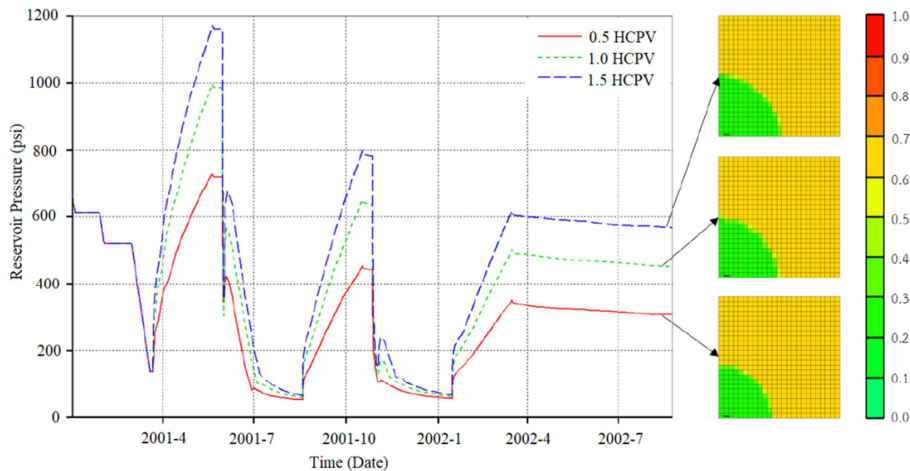


Figure 4. Effect of CO₂ HCPV injection on reservoir pressure and drainage area

3.4. Comparative study

From the simulation results, the highest oil recovery was achieved by using integrated CO₂ Huff-n-Puff and WAG method, followed by conventional CO₂ flooding method, as shown in Figure 5. With the natural flow, only 2% of OOIP can be recovered because the reservoir contained insufficient pressure. Once, the conventional CO₂ flooding process is applied into the field, it can improve oil recovery about 23% of OOIP beyond primary recovery. Moreover, the integrated CO₂ Huff-n-Puff and WAG process presents the highest oil recovery compared to others mentioned processes that it can recover oil up to 63% of OOIP. Comparing to other methods, the integrated CO₂ Huff-n-Puff and WAG method could produce oil 61% of OOIP more than primary recovery production. 38% of OOIP is recovered higher than the use of conventional CO₂ flooding. And, CO₂ utilization of the integrated CO₂ Huff-n-Puff and WAG method is 27.43 scf/stb that much lower than the use of conventional CO₂ flooding method which required up to 69.02 scf/stb. Finally, the main recovery mechanisms of the integrated CO₂ Huff-n-Puff and WAG method are reservoir pressure maintenance, oil displacement by CO₂ and water, sweep efficiency improvement, oil viscosity reduction due to oil swelling, and trapped gas effect.

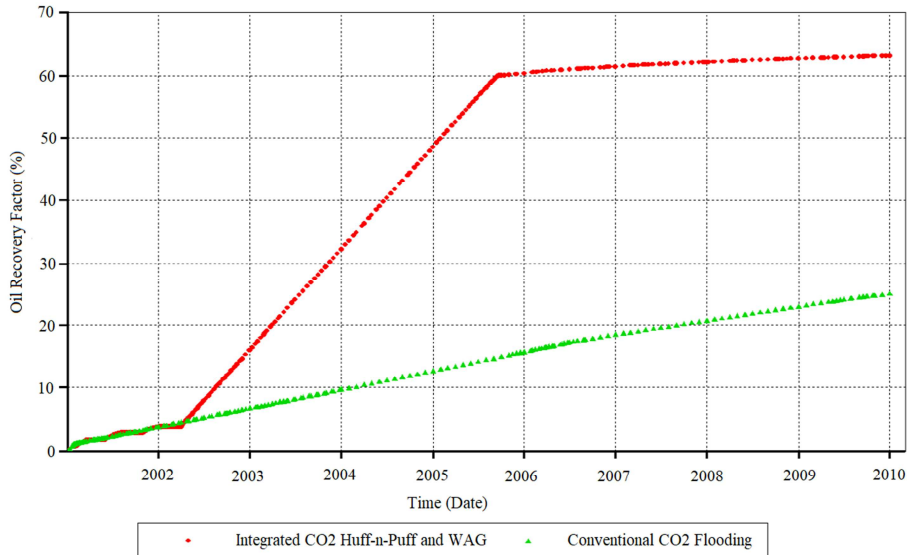


Figure 5. Comparison of oil recovery factor for different recovery techniques

4. Conclusions

Based on the results of this study, it can be concluded that the key operational parameters of CO₂ Huff-n-Puff process in depleting reservoir are oil production rate and production time. Thus, these two parameters should be sufficient to produce the injected CO₂ and crude oil from reservoir until reservoir pressure nearly reaches inadequate pressure to recover oil. An integrated CO₂ Huff-n-Puff and WAG technique provides higher oil recovery than conventional CO₂ flooding technique due to the CO₂ EOR mechanisms and sweep efficiency improvement.

The main EOR mechanisms are reservoir pressure maintenance, oil viscosity reduction due to oil swelling, crude oil displacement by CO₂ and water, sweep efficiency improvement, trapped gas effect, and injected fluid's mobility reduction. Conventional CO₂ flooding provides the poor performance because very high mobility of CO₂ can cause the early breakthrough that allows low volumetric sweep efficiency. The chasing water rate has significant effect on the performance of integrated CO₂ Huff-n-Puff and WAG technique to enhanced oil recovery. Also, increasing CO₂ HCPV injection in integrated CO₂ Huff-n-Puff and WAG technique slightly offers additional oil recovery factor due to increased swelling factor and CO₂ solubility. However, the exceeding CO₂ HCPV injection requires considerable more amount of CO₂ that will extremely increase CO₂ utilization. Compared to other methods, the integrated CO₂ Huff-n-Puff and WAG method can provide higher oil recovery than other techniques.

5. Acknowledgements

The authors would like to thank Chevron Thailand Exploration and Production, Ltd. and the Ratchadapisek Sompoch Endowment Fund (2016), Chulalongkorn University (CU-59-003-IC) for financial support of this study.

References

- E.C. Donaldson, G.V. Chilingarian, T.F. Yen, 1989, Gas Injection, Enhanced Oil Recovery II Processes and Operations, Volume 2, ELSEVIER, Amsterdam, P. 99.
- Y. Le Gallo, P. Couillens, T. Manai, 2002, CO₂ Sequestration in Depleted Oil or Gas Reservoirs, SPE International Conference on Health, Safety and Environment in Oil and Gas Exploration and Production, 20-22 March, Kuala Lumpur, Malaysia.
- L.W. Holm, 1982, CO₂ Flooding: Its Time Has Come, Journal of Petroleum Technology, 34 (12) pp. 2739-2745.
- L.J. Mohammed-Singh, A.K. Singhal, S. Sim, 2006, Screening Criteria for CO₂ Huff 'n' Puff Operations, the SPE symposium on improved oil recovery, 22-26 April Tulsa, Oklahoma, USA.
- K. Sasaki, Y. Sugai, C. Or, H. Kono, 2013, CO₂ Solubility Characteristics of Crude Oils related to Carbon Capture and Utilization (CCU), G-COE Program Kyushu University Novel Carbon Resource Sciences newsletter, 8, pp. 5-8.
- M.R. Simpson, 1988, The CO₂ Huff 'n' Puff Process in Bottomwater-Drive Reservoir, Journal of Petroleum Technology, 40 (07).
- C. Song, D. Yang, 2013, Performance Evaluation of CO₂ Huff-n-Puff Processes in Tight Oil Formations, SPE Unconventional Resources Conference Canada, 5-7 November, Calgary, Alberta, Canada.
- Z. Wang, J. Ma, R. Gao, F. Zeng, C. Huang, P. Tontiwachwuthikul, Z. Liang, 2013, Optimizing Cyclic CO₂ Injection for Low- permeability Oil Reservoirs through Experimental Study, SPE Unconventional Resources Conference Canada, 5-7 November, Calgary, Alberta, Canada.
- S. Whittaker, E. Perkins, 2013, Technical Aspects of CO₂ Enhanced Oil Recovery and Associated Carbon Storage, Global CCS Institute.
- A.Y. Zekri, M.S. Nasr, A. AlShobakyh, 2011, Evaluation of Oil Recovery by Water Alternating Gas (WAG) Injection - Oil-Wet & Water-Wet Systems, SPE Enhanced Oil Recovery Conference, 19-21 July, Kuala Lumpur, Malaysia.

A Multi-period Mixed Integer Linear Program for Assessing the Benefits of Power to Heat Storage in a Dwelling Energy System

Gbemi Oluleye,^{a,*} John Allison,^b Nick Kelly,^b Adam Hawkes,^a

^a*Centre for Process Systems Engineering, Imperial College London, South Kensington Campus, London SW7 2AZ, United Kingdom*

^b*Department of Mechanical and Aerospace Engineering, University of Strathclyde, Glasgow G1 1XQ, United Kingdom*

o.oluleye@imperial.ac.uk

Abstract

In this paper a novel multi-period MILP model is developed, and applied to show how: (1) integrating thermal energy storage with ASHP (i.e. power to heat storage) reduces the ASHP peak and total electricity demand by 78.2 % and 8.4 % respectively, and (2) proper sizing of the ASHP reduced its total electricity demand by 35%. The accuracy of the model is improved by using fewer time slices to capture technology and energy demand characteristics. Storage size and operation are determined based on the energy demand and economic price signals.

Keywords: heat electrification, ASHP, TES, MILP, domestic heating.

1. Introduction

Decarbonisation of domestic heating through electrification of heat, could go a long way in achieving the global energy-related CO₂ target of 50 % below current levels in 2050 (IEA, 2011). Air Source Heat Pumps (ASHP) are the preferred early option for heat decarbonisation especially where heat networks are not cost effective (Love et al., 2017). However, increased electricity demand is a challenge with heat electrification. In GB, for a 20 % heat pump uptake, the national grid evening peak demand increases by 14 % (Love et al., 2017), thus requiring new investments in both transmission and generation capacity to maintain security of supply. Integration of TES with ASHP, and proper sizing of the ASHP could reduce both the peak and total electricity demand. Therefore, tackling this challenge would go a long way in increasing deployment of ASHP. The system configuration and operating strategy of a dwelling energy supply system has been determined based on MILP models (Iturriaga et al., 2017). To simplify the representation of energy demand and technology characteristics, a 1 h time slice for reference days is applied in Iturriaga et al. (2017). Hourly time slices neglect the peak energy demand and are below the trading period of the national grid. Therefore making the existing model inadequate to design a system with ASHP and TES, and illustrate how both the peak and total electricity demand of the ASHP can be reduced. Even though 5 min time slice is applied in Zhang et al. (2012), the impact of TES was not investigated, and design was for reference days. Renaldi et al. (2017) designed for 365 days but an hourly time slice was applied. Therefore two challenges of integrating power to heat storage in dwelling identified from the literature survey are: (1) increased electricity demand, and (2) lack of

accurate systems integration method. The novel framework developed in this work addresses both challenges and proves the hypothesis that integrating TES with ASHP, and proper sizing of the ASHP could reduce both its peak and total electricity demand.

2. Methodology

The core of the developed methodology is the mathematical optimization model. The model presents a systematic framework for integrating power to heat storage in a dwelling energy system. The dwelling energy system refers to a generic plant with the layout in Figure 1. A graphical overview of the methodology is presented in Figure 2.

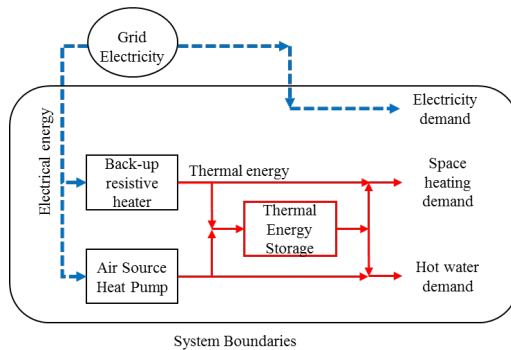


Figure 1. Dwelling energy system with air source heat pump and back-up resistive heater layout. The ASHP converts electricity imported from the grid to heat.

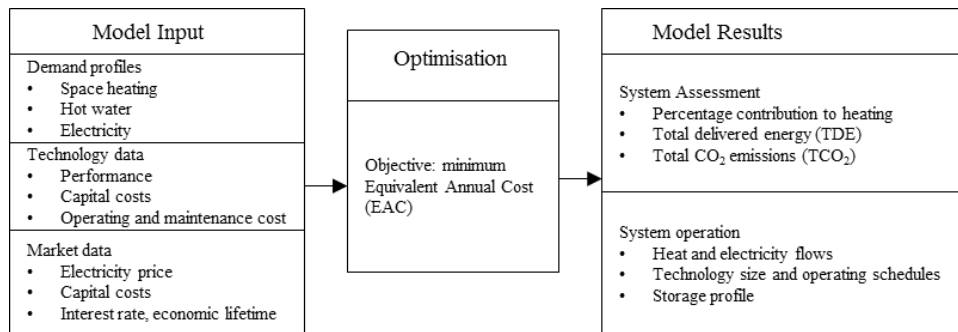


Figure 2. Methodology overview

The design objective in Eq. (1) is the sum of the annualised capital cost (ACC), the fuel cost (FC), maintenance cost (MC) and grid electricity import ($W_{GRID,IMP}$). Heat (Q) and electricity (W) balances were defined as part of the system constraint. The heat balance is the sum of the heat from the ASHP i , and heat delivered from storage, less the sum of heat fed into storage and the heat demand for every time slice r . The electricity balance is the sum of electricity imported to satisfy demand, electricity imported for the ASHP i less electricity demand for all time slice r . Another constraint was introduced such that the size of the ASHP is not exceeded in all time slice r . Other constraints for the existence and operation of the ASHP and TES are presented in Eq. (2) to Eq. (8). The TDE and TCO₂ were used to assess the system. The TDE is the fuel value of the total electricity imported, and the TCO₂ is CO₂ from total electricity import.

$$\text{Min} : [\text{ACC} + \text{FC} + \text{MC} + \text{W}_{\text{GRID,IMP}}] \quad (1)$$

$$Q_{i,r} - L \times Z_{i,r} \geq 0; \quad \forall i \in I, r \in R \quad (2)$$

$$Q_{i,r} - U \times Z_{i,r} \leq 0; \quad \forall i \in I, r \in R \quad (3)$$

$$Z_{i,r} - Y_i \leq 0; \quad \forall i \in I, r \in R \quad (4)$$

$$Q_{\text{out},r} - U_{\text{TES}} \times Y_{\text{TES},r} \leq 0 \quad \forall r \in R \quad (5)$$

$$Q_{\text{in},r} - U_{\text{TES}} \times (1 - Y_{\text{TES},r}) \leq 0 \quad \forall r \in R \quad (6)$$

$$0 \leq \left[\sum_{r=1}^r \left(\left(\frac{Q_{\text{TES,in},r} \times \eta_{\text{charge}}}{\eta_{\text{discharge}}} - \frac{Q_{\text{TES,out},r}}{\eta_{\text{discharge}}} \right) \times \text{ts}_r \right) + (Q_{\text{TES}} \times \text{ISH}) \right] \leq Q_{\text{TES}} \quad (7)$$

$$(Q_{\text{TES}} \times \text{ISH}) - 0.1 \leq \sum_{r=1}^r \left(\left(\frac{Q_{\text{TES,in},r} \times \eta_{\text{charge}}}{\eta_{\text{discharge}}} - \frac{Q_{\text{TES,out},r}}{\eta_{\text{discharge}}} - \frac{Q_{\text{TES}} \times \theta}{24} \right) \times \text{ts}_r \right) + (Q_{\text{TES}} \times \text{ISH}) \leq Q_{\text{TES}} \times \text{ISH} + 0.1 \quad (8)$$

Where Z and Y are binary variables for technology operation and existence, U and L define the upper and lower operational limits, θ is the daily TES loss, ISH is the initial store heat and η represents the efficiency. The above model was formulated in GAMS 24.7.3, and solved using Lindo Global solver on a 64 bit 3.40 GHz Intel ® Core™ i7-6700 CPU with 32 GB RAM.

3. Case study

In this case study, ASHP and TES are integrated into a detached house in the UK (121 m² floor area). The total electricity and heat (both space heating and hot water) demand are 8,387 kW_e and 11,620 kW_{th} respectively. The peak electricity and heat demand are 9.1 kW_e and 27.2 kW_{th}. The sizes of ASHP considered are 14, 8, 5 and 2 kW_{th}. The ASHP have electric resistance heaters as back-up and the size of the store is determined optimally. Further details of the house and assumed market data are in Oluleye et al. (2017). The electricity demand for the house and the ASHP electricity requirements (without TES) are presented in Figure 3 for all ASHP sizes. The ASHP peak electricity demand is more than twice that of the house demand. The peak electricity demand increases as the size of the ASHP decreases (Figure 3). As the ASHP size reduces, the contribution from the back-up resistive heater increases (Figure 4a). For a 2 kW_{th} ASHP, the back-up resistive heater contributes 45 % to the heat demand; therefore increasing the peak. When TES is integrated, the ASHP diverts heat to the store during off-peak hours and the contribution of heat from the resistive heater reduces (Figure 4b). The

combination of the two reduces the peak and total electricity demand (Figure 5). The 14 kW_{th} ASHP electricity demand is 50.6 % more than the building electricity demand, 8 kW is 51.4 % more, 5 kW is 56 % more and 2 kW is 87 % more (Table 1). For all sizes design with TES is more economic, the total delivered energy and CO₂ emissions are lower (Table 1). Reducing the peak electricity demand using power to heat storage reduces the investment in new transmission and generation capacity for the national grid.

When the model is run to consider discrete equipment sizing, the 5 kW_{th} ASHP was selected because it has the lowest EAC (Table 1). Compared to the worst case ASHP size (2 kW_{th}), the optimum size (5 kW_{th}) reduces the additional electricity demand by 35.38 %.

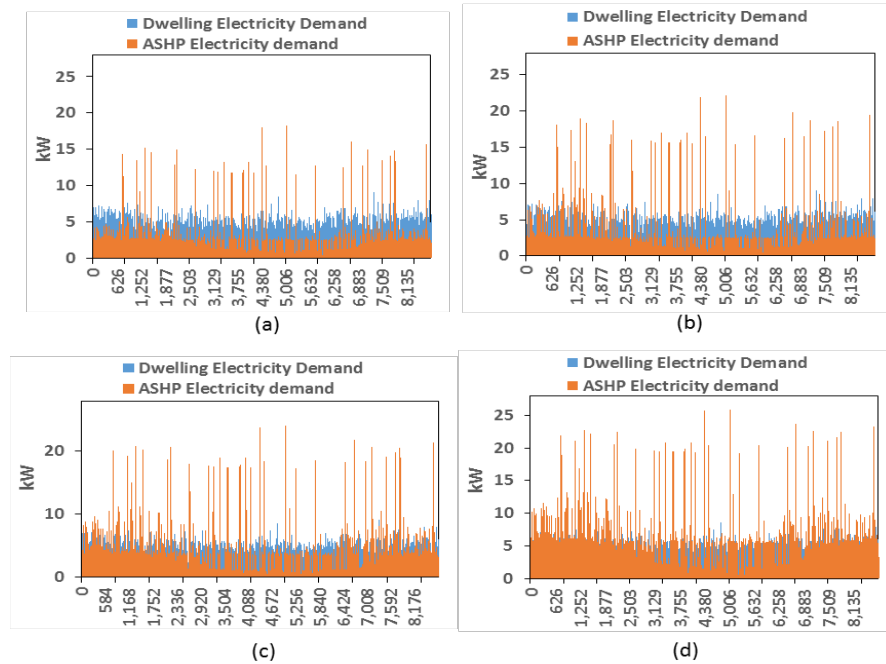


Figure 3. Electricity demand profile for (a) 14 kW_{th}, (b) 8 kW_{th}, (c) 5 kW_{th} and (d) 2 kW_{th}

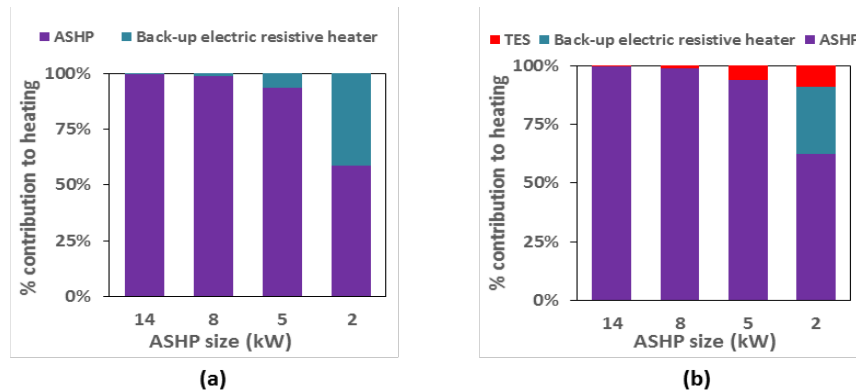


Figure 4. Contribution to heating for (a) design without TES, and (b) design with TES

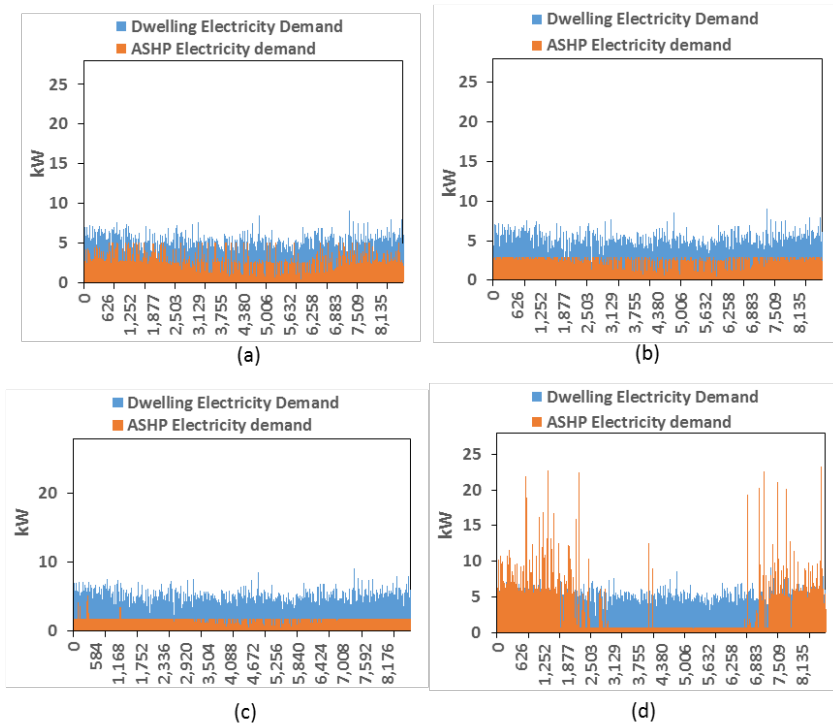


Figure 5. Electricity demand profile (design with TES) for (a) 14 kW_{th}, (b) 8 kW_{th}, (c) 5 kW_{th} and (d) 2 kW_{th}

Table 1. Model results summary

		EAC (£/y)	TDE (kWh/y)	TCO₂ (kg/y)	W_{ASHP,total} (kW)	W_{ASHP,Peak} (kW)
14 kW	No TES	2,183.5	31,580	5,642	4,245	18
	TES	2,183.8	31,535	5,634	4,227	5
8 kW	No TES	2,099	31,756	5,673	4,315	22
	TES	2,094	31,558	5,638	4,236	3
5 kW	No TES	2,075	32,710	5,844	4,697	24
	TES	2,029	31,709	5,665	4,297	5
2 kW	No TES	2,362	39,139	6,992	7,269	26
	TES	2,296	37,713	6,737	6,698	23

4. Conclusions

A novel multi-period MILP model is developed for integrating ASHP and TES (i.e. power to heat storage) in a dwelling. The model is used to determine whether power to

heat storage can reduce both the total and peak electricity demand required by the ASHP. The framework considers optimal sizing (in this case the ASHP and storage size are determined based on the energy demand and economic price signals) and operational planning. A case study was carried to demonstrate the validity and soundness of the approach. Results show that whilst proper sizing of ASHP reduces its total electricity demand, integrating TES reduces both the peak and total electricity demand. The results obtained and the framework are useful in determining the role of power to heat storage in decarbonising domestic energy systems. Even though we can achieve reduction in the ASHP total and peak electricity demand, connecting large number of heat pumps results in excessive voltage drop beyond allowed limits. Future work will to determine the maximum number of heat pumps to prevent excessive voltage drop.

Acknowledgement

The authors would like to thank EPSRC for funding the research reported in this paper under grant EP/N021479/1 as part of its Thermal Energy Challenge programme.

References

- International Energy Agency, Technology Roadmap Energy-efficient Buildings: Heating and Cooling Equipment. Available at https://www.iea.org/publications/freepublications/publication/buildings_roadmap.pdf, sessed 05/10/2017.
- E. Iturriaga, U. Aldasoro, A. Campos-Celador, J. M. Sala, 2017 A general model for the optimization of energy supply systems of buildings, *Energy*, 138, 954 – 966
- J. Love, A. Z. Smith, S. Watson, E. Oikonomou, A. Summerfield, C. Gleeson, R. Lowe, 2017, The addition of heat pump electricity load profiles to GB electricity demand: Evidence from a heat pump field trial, *Applied Energy*, 204, 332-342
- G. Oluleye, A. D. Hawkes, J. Allison, N. Kelly, J. Clarke, 2017, An optimisation study on integrating and incentivising Thermal Energy Storage (TES) in a dwelling energy system, In: Sustainable Development of Energy, Water and Environment Systems Conference
- R. Renaldi, A. Kiprakis, D. Friedrich, 2017, An optimisation framework for thermal energy storage integration in a residential heat pump heating system, *Applied Energy*, 186, 520 – 529
- D. Zhang, L. G. Papageorgiou, E. S. Fraga, 2012, Optimisation based analysis of a dwelling with an air source heat pump, *Computer Aided Chemical Engineering 22nd European Symposium on Computer Aided Process Engineering*, 312-316

Numerical Representation for Heat Exchanger Networks Binding Topology and Thermodynamics

Petar S. Varbanov^a, Timothy G. Walmsley^a, Michael Walmsley^b,
Jiří J. Klemeš^a, Zdravko Kravanja^c

^a*Sustainable Process Integration Laboratory – SPIL, NETME Centre, Faculty of Mechanical Engineering, Brno University of Technology, Brno, Czech Republic*

^b*Energy Research Centre, School of Engineering, University of Waikato, Private Bag 3105, Hamilton, New Zealand*

^c*University of Maribor, Faculty of Chemistry and Chemical Engineering, Smetanova ulica 17, 2000 Maribor, Slovenia*

varbanov@fme.vutbr.cz

Abstract

This paper introduces a new tool for HEN analysis and optimisation, tailored to retrofit for improving heat recovery. The HEN Matrix provides a scalable HEN representation, suitable for both mathematical treatment and interactive use by engineers, thus having the potential to further facilitate the work of energy managers and site engineers for improving the energy and emission performance of industrial sites. The types of industry expected to benefit from this decision-making tool include Oil and Gas, Chemicals, Food, Textiles, Pulp and Paper. The provided case study illustrates the usefulness and engineering potential of the new concept.

Keywords: Heat Exchanger Network, Retrofit, Matrix, Scalability

1. Introduction

Heat recovery in industry and residential applications plays an important part in reducing simultaneously costs, fuel consumption and environmental footprints. Process Integration (PI) and its core discipline – Heat Integration (Klemeš et al., 2014), have been assisting the improvement the process performance. Focusing on existing plants, there has been recently a resurgence in retrofit methods for heat recovery in industry – especially in the field of Heat Exchanger Networks (HENs) introducing the Energy Transfer Diagram (ETD, Bonhivers et al., 2014). That work has provided the thermodynamic reasoning and initial ETD, clearly showing the heat flows through energy systems, connecting the hot and cold utilities via the served processes. That has been followed by other developments – the “Network Table” (Bonhivers et al., 2017b) and Heat-Exchanger Load diagram (HELD) (Bonhivers et al., 2017a), giving rise to Bridge Analysis, which is itself a step-forward from a previous work on paths construction for HEN retrofit (Varbanov and Klemeš, 2000). Walmsley et al. (2017) have improved the concept, defining a Modified ETD (M-ETD), to show regions of net heat surplus/deficit within HENs, providing clearer insights to identify possible retrofit bridges for improving heat recovery.

These developments have marked a clear trend in binding together the topology and thermodynamic representations of a HEN using graphical means and matrix-style

representation. The current work takes this trend further by providing a combined HEN representation – a HEN Retrofit Dashboard (HENRD). This includes linking several modules: (a) the HEN topology, (b) the ETD Net Cascade Table (Walmsley et al., 2017), which is the numerical representation of the ETD and shows the net cascade of each individual heat exchanger within the HEN, and (c) the ETD plot.

The ETD plot allows to identify promising options visually, which is suitable for smaller HENs. Devising a numerical representation of the ETD, while respecting the HEN topology, provides the opportunity to automate the decision-making process and scale up its application to large retrofit problems (e.g. >40 streams). These tools are complemented by the Grid Diagram (Klemeš et al., 2014), including optionally its variations – the Shifted Retrofit Thermodynamic Diagram (Yong et al., 2015) and the Retrofit Tracing Grid Diagram (Nemet et al., 2015). The aim of this contribution is to develop a robust and scalable HEN retrofit tool, suitable for large retrofit problems (e.g. >40 streams), for improving the performance of industrial, commercial, administrative and residential facilities. The new tool is illustrated on a case study.

The next section overviews the evolution of the retrofit-related HEN representations, showing how the HENRD offers the means for devising improved methods for HEN retrofit with the right balance of automation and user interaction.

2. Analysis of HEN representations for retrofit

There have been several HEN representations, used for evaluation and improvement of the networks. The Grid Diagram (GD, Linnhoff and Flower, 1978) is a well-established, compact and intuitive HEN representation, clearly showing the network topology, stream temperatures and HE loads. In this capacity, it is an excellent tool for simulating, designing or retrofitting visually small-size HENs. The GD can also be used for displaying even larger-scale HENs within software tools (i-Heat, 2017).

The GD has been widely applied for HEN retrofit. One of the fundamental works on HEN retrofit (Tjoe and Linnhoff, 1986) introduced the of area efficiency as an indication the degree of the current network area utilisation. In that work, the GD was used for identifying heat exchangers (HEs) transferring heat across the Pinch (Linnhoff and Flower, 1978), performing the so called Cross-Pinch Analysis.

The Retrofit Thermodynamic Diagram (RTD, Lakshmanan and Bañares-Alcántara, 1996) was presented and extended later (Lakshmanan and Bañares-Alcántara, 1998). It is a variation of the GD, which represents HENs by showing both the temperature span and process stream CPs. This allows showing explicitly the heat exchanged between streams. A further development has been the Shifted Retrofit Thermodynamic Diagram (SRTD, Yong et al., 2015) which incorporates the minimum allowed temperature difference (ΔT_{\min}). Nemet et al., (2015) proposed the Retrofit Tracing Grid Diagram (RTGD), emphasising temperature feasibility and path tracing.

An interesting HEN visualisation by Gadalla (2015) plots the heat exchangers of a network as arrows of the temperatures of hot process streams versus those of the cold process streams. The indication of the Pinch point locations is performed by a pair of lines – a horizontal and a vertical one. This tool (T_H - T_C Plot) allows to easily spot the Cross-Pinch heat transfer, the Network Pinch (NP), and which are the Pinching Matches.

These HEN representations, as well as the Problem Table (PT, Linnhoff and Hindmarsh, 1983) and the M-ETD (Walmsley et al., 2017) form a pool of available tools for HEN analysis and improvement by parameter adjustment and retrofit.

However, when dealing with HEN retrofit, it is important to account for most system properties simultaneously. Moreover, the HEN size in terms of number of streams and/or HEs poses a challenge for visually inspecting the heat paths and system connections. With increasing the network size, the clutter on any of these visualisations grows exponentially and hinders the purely visual comprehension of the network interactions and the possible improvement options. This observation reveals also the need for scalability of the employed tools. Following the above reasoning, Table 1 compares the tools against the important criteria.

Table 1. Comparison of the HEN representations

	GD	(S)RTD	RTGD	T_H-T_C Plot	PT	(M-)ETD
Topology	Yes	Yes	Yes			
HE identification	Yes	Yes	Yes	Yes		Yes
Stream temperatures	Yes	Yes	Yes	Yes		
Stream CPs		Yes				
HE loads	Yes	Yes	Yes			Partly
Cross-Pinch heat transfer	Yes	Yes	Yes	Yes Explicit		Yes Implicit
NP identification	Yes	Yes	Yes	Yes Explicit		
Pinching Matches identification	Yes	Yes Explicit	Yes Explicit	Yes Explicit		
ΔT_{\min} embedded		Yes - SRTD			Yes	Yes – one of the variations
Heat Recovery Targets					Yes	Yes
Scalability	Limited				Yes	Limited

It can be seen from Table 1, that the considered HEN representations are suitable for different aspects of HEN analysis. All of them, except the PT, feature limited scalability, stemming from the goal of the diagrams to visualise each heat exchanger and each process stream in the HEN in specific ways. From these tools, only the PT features sufficient scalability, as it provides a collective numerical representation of the HEN streams and has a matrix form, suitable for mathematical treatment.

3. The HEN Matrix and the HEN Retrofit Dashboard

The M-ETD features a direct connection to the PT for a HEN problem. It is constructed using calculations of the HEs, sliced by temperature intervals, defined by the shifted start/end process stream temperatures - supplemented by temperature boundaries

stemming from the HEN topology. In this way, it bears the potential to be converted into a scalable tool. What is missing from the M-ETD, is the link to the HEN topology and to the process streams. The HEN Matrix, has to combine several key features:

- (i) Superimpose the HEs on the temperature intervals, so that each HE is sliced within the intervals it intersects with.
- (ii) Show visually and numerically the connections HEN topology.
- (iii) Minimise the clutter by providing a seamless representation.

While the GD variations can satisfy part of these requirements, they tend to clutter very quickly with the increase of the HEN complexity. The HEN Matrix represents all process streams and all heat exchangers within the columns of a table, while the rows are taken by temperature boundaries and temperature intervals. Combining the HEN Matrix with the M-ETD forms the HENRD (Figure 1). The tool is demonstrated in the next section.

4. Retrofit case study

A four-stream problem from Klemeš et al. (2014) is used to demonstrate the application of the new tools. The problem consists of two hot streams and two cold streams with two recovery exchangers, one heater and two coolers. The maximum energy recovery target for the retrofit problem is 1,950 kW. More details on this problem can be found in Walmsley et al. (2017). Figure 1 presents the proposed HENRD. Walmsley et al. (2017) demonstrated the M-ETD contains sufficient information to identify retrofit bridges between coolers and heaters as well as its maximum duty. A key limitation of the M-ETD is the lack of information regarding topology of the HEN. This study tackles the topology limitation through the HENRD where a vertical grid diagram is overlaid with the M-ETD Net Cascade Table and placed beside the M-ETD.

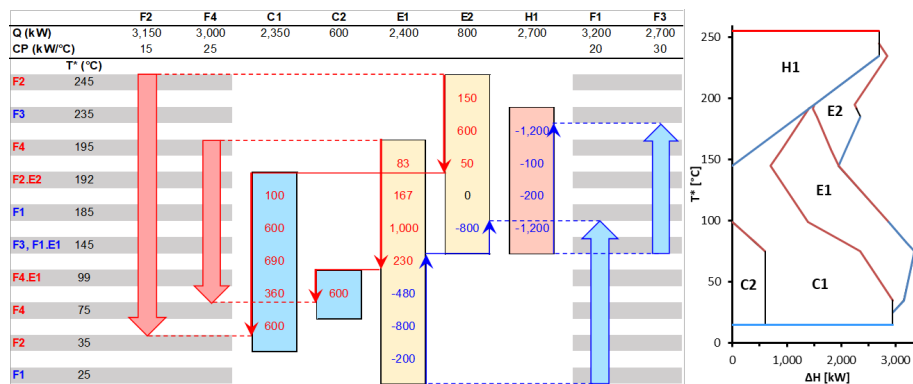


Figure 1. HEN Retrofit Dashboard for four-stream case study

Using the M-ETD, a retrofit bridge above the Pinch between C1 to E2 to H1 can be identified with a maximum duty of 700 kW (Figure 2). This bridge can then be translated to the rest of the HENRD. The topological details inform the designer that hot stream F2 is the same for both E2 and C1. If an additional exchanger between F2 and F3 (700 kW; T^* range = 195 – 245 °C), it will shift E2 to lower T^* intervals resulting in F2 leaving E2 at a lower temperature, which will reduce the C1 duty by 700 kW. So,

although the bridge displays as two steps, the only major physical change is one extra exchanger.

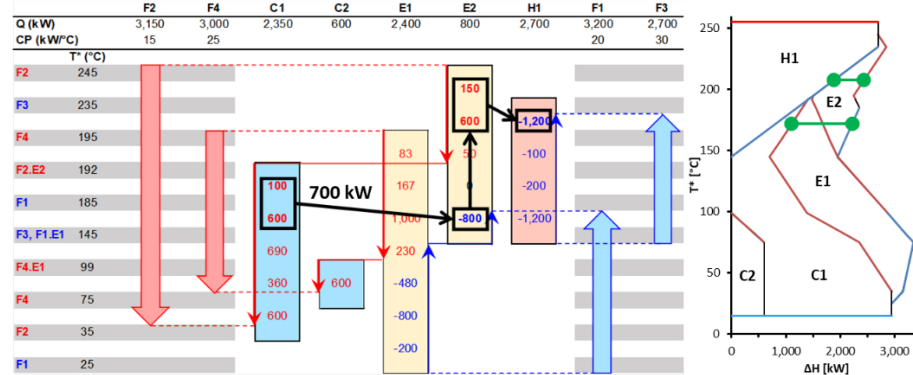


Figure 2. HEN Retrofit Dashboard for simple retrofit option

A second retrofit bridge can be identified on the HENRD (Figure 3). This bridge extends the total energy savings to reach its targeted maximum. A similar analysis of the topology leads to identifying the need for two new recovery exchangers for the second bridge.

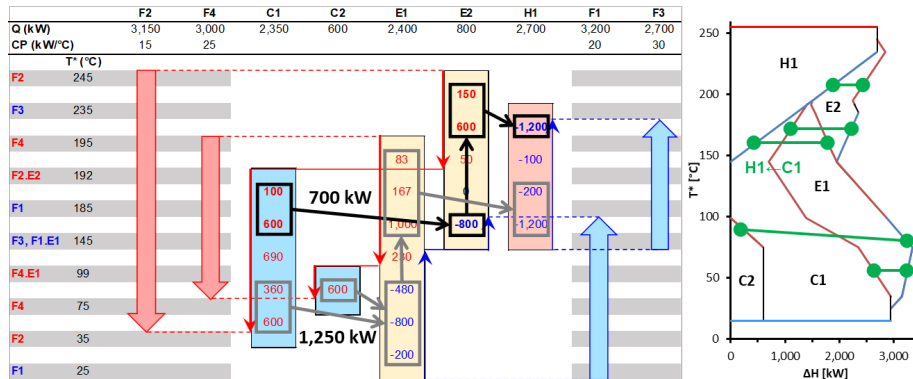


Figure 3. The HEN Retrofit Dashboard for maximum energy recovery retrofit option

5. Conclusions

The current paper proposes a new scalable tool for representing HENs for simulation, optimisation and retrofits, named the HEN Matrix. When combined with the well-known Grid Diagram and the Modified ETD, they have the potential to become the kernel of a powerful HEN Retrofit Dashboard - a tool for interactive HEN optimisation and evolution, which should be able to exploit both active engineer involvement and mathematical optimisation, in order to achieve heat recovery improvement at minimum cost, in a transparent manner. The provided case study clearly shows the usefulness of the proposed tools in representing a HEN, its analysis and targeting the retrofit steps. The future work will be directed towards tackling larger-scale HENs, binding the tools to underlying mathematical optimisation models and the full development of the HENRD.

Acknowledgement

This research has been supported by the EU project “Sustainable Process Integration Laboratory – SPIL”, project No. CZ.02.1.01/0.0/0.0/15_003/0000456 funded by EU “CZ Operational Programme Research, Development and Education”, Priority 1: Strengthening capacity for quality research, in a collaboration with the University of Waikato – New Zealand and the University of Maribor – Slovenia.

References

- J.-C. Bonhivers, A. Alva-Argaez, B. Srinivasan, P.R. Stuart, 2017a, New analysis method to reduce the industrial energy requirements by heat-exchanger network retrofit: Part 2 – Stepwise and graphical approach, *Applied Thermal Engineering*, 119, 670-686.
- J.-C. Bonhivers, M. Korbel, M. Sorin, L. Savulescu, P.R. Stuart, 2014, Energy transfer diagram for improving integration of industrial systems, *Applied Thermal Engineering*, 63(1), 468–479.
- J.-C. Bonhivers, B. Srinivasan, P.R. Stuart, 2017b, New analysis method to reduce the industrial energy requirements by heat-exchanger network retrofit: Part 1 – Concepts, *Applied Thermal Engineering*, 119, 659-669.
- M.A. Gadalla, 2015. A new graphical method for pinch analysis applications: Heat exchanger network retrofit and energy integration. *Energy*, 81, 159–174.
- i-Heat, 2017. Process Integration provide the latest technology in state-of-the-art software. <www.processint.com/chemical-industrial-software/>, Accessed 20/12/2017.
- J.J. Klemeš, P.S. Varbanov, S.R. Wan Alwi, Z.A. Manan, 2014. *Process Integration and Intensification: Saving Energy, Water and Resources*, De Gruyter, Berlin, Germany.
- R. Lakshmanan, R. Bañares-Alcántara, 1996, A Novel Visualisation Tool for Heat Exchanger Network Retrofit, *Industrial & Engineering Chemistry Research*, 35, 4507-4522.
- R. Lakshmanan, R. Bañares-Alcántara, 1998, Retrofit by inspection using thermodynamic process visualisation, *Computer & Chemical Engineering*, 22(1), S809-S812.
- B. Linnhoff, J.R. Flower, 1978. Synthesis of heat exchanger network: I. Systematic generation of energy optimal networks, *AIChE Journal*, 24, 633 – 642.
- T.N. Tjoe, B. Linnhoff, 1986. Using pinch technology for process retrofits. *Chemical Engineering*, 93: 47–60.
- B. Linnhoff, E. Hindmarsh, 1983. The Pinch Design Method for Heat Exchanger Networks. *Chemical Engineering Science*, 38(5), 745-763.
- P. Varbanov, J. Klemeš, 2000. Rules for Paths Construction for HENs Debottlenecking. *Applied Thermal Engineering*, 20(15-16), 1409–1420.
- M.R.W. Walmsley, N.S. Lal, T.G. Walmsley, M.J. Atkins, 2017. A Modified Energy Transfer Diagram for Heat Exchanger Network Retrofit Bridge Analysis. *Chemical Engineering Transactions*, 61, 907-912, DOI:10.3303/CET1761149.
- J.Y. Yong, P.S. Varbanov, J.J. Klemeš, 2015. Heat Exchanger Network Retrofit supported by Extended Grid Diagram and Heat Path Development, *Applied Thermal Engineering*, 89, 1033–1045, doi: 10.1016/j.applthermaleng.2015.04.025.

Optimisation of Integrated Bioenergy and Concentrated Solar Power Supply Chains in South Africa

Massimo Liu^a, Koen H. van Dam^b, Antonio M. Pantaleo^{b,c}, Miao Guo^{b*}

^a*Imperial College London, Energy Futures Lab, Department of Mechanical Engineering, South Kensington Campus, London SW7 2AZ, United Kingdom*

^b*Imperial College London, Department of Chemical Engineering, South Kensington Campus, London SW7 2AZ, United Kingdom*

^c*University of Bari Aldo Moro, Department of agro-environmental sciences, Via Amendola 165/A 70125 Bari, Italy*

**miao.guo@imperial.ac.uk*

Abstract

Climate change and energy security are complex challenges whose solutions depend on multi-faceted interactions between different actors and socio-economic contexts. Energy innovation through integration of renewable energies in existing systems offers a partial solution, with high potential identified for bioenergy and solar energy. In South Africa there is potential to further integrate renewable energies to meet local demands and conditions. Various concentrated solar power (CSP) projects are in place, but there is still land available to generate electricity from the sun. In combination with sustainable biomass resources these can offer synergetic benefits in improving the power generation's flexibility. While thermodynamic and thermo-economic modelling for hybrid CSP-Biomass technology have been proposed, energy modelling in the realm of supply chains and demand/supply dynamics has not been studied sufficiently.

We present a spatially and temporally Mixed Integer Linear Programming (MILP) model, to optimize the choice and location of technologies in terms of economic cost while being characterised by realistic supply/demand constraints as well as spatially-explicit environmental constraints. The model is driven by electricity demand, resource availability and technology costs as it aspires to emulate key energy and sustainability issues. A case study in the South African province of Gauteng was implemented over 2015-2050 to highlight the potential and challenges for hybrid CSP-Biomass and integrated systems assessment and the applicability of the modelling approach.

From the range of hybrid CSP-Biomass technologies considered, based on detailed techno-economic characteristics from the literature, the Biomass only EFGT plant is identified as the cost optimal. When distributed generation (DG) technologies, small-scale Solar PV and Wind Turbines were introduced to the model as a competing alternative, they were demonstrated to be more economically optimal (€65 mil against €85 mil with CSP-Biomass Industrial scale), driven by technology learning cost reductions, evidencing the case for DG technologies to gain momentum. Together these scenarios highlight the possible carbon savings from integrating multiple renewable energy technologies.

Keywords: Solar, Bioenergy, Renewables, South Africa.

1. Introduction

Driven by the growing global population and economic development, energy consumption is expected to increase by 48% by 2040 (EIA, 2016), which will exert unprecedented stress on environmental degradation and resource depletion. To combat climate change, the renewed commitments under the 2015 Paris agreement to maintain global average temperature are a testament to the decarbonisation acceleration (UNFCCC, 2015). Global and national policies have been addressing energy demand stress in conjunction with greenhouse gas (GHG) reduction, by actively promoting the low-carbon renewable energy sources (RES) technologies, which are projected to represent 50% the global energy generation by 2030 (Goldman Sachs, 2017). The integration of renewable energy in existing energy infrastructure offers one of the solutions to low-carbon economy transition, with high potential identified in the use of bioenergy and solar energy (IEA, 2015). Dispatchable renewable energy plants such as reservoir hydro, biomass and CSP with storage have been installed with more frequency, contributing to energy flexibility in the respective systems (REN21, 2016). Biomass and CSP in particular offer strong potential as they have the capability to store solar energy in addition to being well distributed globally and thus being a relatively accessible source of energy (Rosillo-Calle, et al., 2015). These technologies have contributed to grid flexibility and grown distributed generation, which has gained significant momentum in developing countries (REN21, 2016). Together they offer a technology solution with the potential of achieving environmental sustainability and economic viability. This paper focuses on the Hybrid CSP-Biomass integration in the context of South Africa.

South Africa has been swiftly implementing policies towards a low carbon economy that diversifies its energy mix by moving away from the current coal-dominant electricity generation (over 90%) (IEA, 2017). Despite the significantly increased electricity access (35% to 86% of population) in South Africa in the last two decades, over 60% of population in African continent still has no access to modern energy and infrastructure (projected to decrease to 35% by 2040) (AFDB, 2013), which constrains the regional economy and livelihood improvement; whereas two third of the Africa's electricity is supplied by South Africa (AFDB, 2013). The renewable energy is expected to play significant roles within the overall African energy portfolio to tackle the energy poverty and insecurity (IEA, 2017) as well as achieve the South African national targets on universal electricity access by 2025 (GNESD, 2017). Despite the modelling advances in thermodynamic and thermo-economic aspects, a gap emerged on the renewable energy system integration considering demand/supply dynamics in Africa. By applying MILP optimization approach, this study aims to advance the understanding of the hybrid CSP-Biomass system design at the spatial and temporal scales under the supply-demand as well as environmental constraints in South Africa.

2. Technology Description

CSP-Biomass Hybrid technology is still at early-development stage with significant data gaps emerged. In this study, the proposed technologies and the respective techno-economic characteristics were based on a combination of case studies (based on ENEA Archimede project, Griffith, Thermosolar Borges), and performances of operating plants (Thermosolar Borges). The range of technologies possesses different levels of biomass-

solar hybridisation and as such different techno-economic characteristics with varying outputs and resource requirements.

Specific CSP cost studies and analysis by IEA (for technology learning), NREL and IRENA were also used to gather more detailed costing data on the different components and resources required (i.e. water, land). These enabled to introduce variations to the representative technologies. An example of such variation is using dry cooling technology instead of the conventional wet cooling, which in turn has an impact on the capital input and operational cost, energy generation and efficiency.

In addition to these technologies, data for distributed renewable energy generation technologies in the form of small scale Solar PV and Wind turbines were collected to compare the industrial scale CSP-Biomass plants with DG technologies on a ‘per year’ basis. Table 1 shows the technologies included in the model.

Table 1 – Technologies modelled (NREL, 2013; Peterseim *et al.*, 2014; Pantaleo *et al.*, 2017)

Technology	DNI	Water (m ³ /yr)	Rated Output (MW)	MWh/Tonne Biomass
100% Biomass	NA	15,000	1.4	0.612
Pantaleo D (Wet Cooling) TES (1.3h)	2,256	32,283	1.4	0.769
Pantaleo E (Wet Cooling) (TES 5h)	2,256	41,997	1.4	1
B50 (Griffith) (Wet)	2,100	480,900	30	1.866
Borges Thermosolar (Wet) – peak	1,800	294,000	22.5	1.96
Borges Thermosolar (Wet) – night (no solar, biomass only)	2,130	159,000	12	1
Pantaleo D (Dry Cooling) TES (1.3h)	2,256	2,001	1.4	0.715
Pantaleo E (Dry Cooling) (TES 5h)	2,256	2,603	1.4	0.93
B50 (Griffith) (Dry)	2,100	29,815	30	1.735
Borges Thermosolar (Dry) – peak	1,800	18,228	22.5	1.823
Borges Thermosolar (Dry) – night (no solar, biomass only)	2,130	9,858	12	0.93

3. Methodology

The fundamental concept is to investigate the potential of the novel Hybrid CSP-Biomass renewable power generation in South Africa under a context with strong policy support for RES and abundance in biomass and solar resources. In addition to the insights into the economic feasibility of the technologies, the model aims to reflect the

underpinning sustainability challenges which are characterised by the supply chain, supply/demand constraints capturing the variability in electricity demands and resources. A spatial-temporal MILP model was formulated and solved in AIMMS using the CPLEX solver.

Table 2 Nomenclature for optimisation model

Sets	Description
g, k	Set of Cell locations $g \in G$
n	Set of biomass residue (source) locations
c	Set of candidate location cells for plant installation (demand location)
t	Time $\in \{Year\}$
b	Set of biomass residues= {maize residue, wheat residue, etc.}
m	Transport mode = {truck, rail}
kpi	Set of KPI = {cost, emissions}
p	Set of plant technology candidates
Binary Variables	
$A_{c,p}$	Existence of technology location cell.
$Flow_{n,c}$	presence of a link between a technology with a biomass field
Continuous Variables	
$EPro_{c,t,p}$	Energy production of a technology in a period (non-linear) (MWh)
$Tflow_{n,c,b,m}$	Transport flow of biomass between a biomass field and a technology location in a given period. (Tonne)
$TotalCost$	Total economics costs (Euro)

As presented in Eq.(1), the objective function is to minimise the total costs which account for the costs incurred by -1) the infrastructure ($CInf_{kpi,t}$, Eq. (2)) dependent on the annuity factor (Af_p) and related CAPEX cost ($Icon_{kpi,t,p}$); 2) cost of operation ($COp_{kpi,t}$, Eq. (3)) of plant technology determined by the energy production ($EPro_{c,t,p}$), the variable ($IOpVar_{kpi,t,p}$) and fixed ($IOpFix_{kpi,t,p}$) cost of operation; 3) and the supply chain costs of the biomass ($CBPro_{kpi,t}$, Eq. (4)) which are depend on direct (machinery, labour, fuel costs) and indirect costs (compensation in soil for loss of nutrients from removal of biomass residues) in the harvesting, collection, and treatment ($ICult_{kpi,b,t}$); 4) the cost related to the transport of the biomass ($CTn_{kpi,t}$, Eq. (5)), which depends on unit transport cost ($ITn_{kpi,m,t}$) and distance ($Dn_{n,c}$) is also included but is expected to represent a small share of the total costs.

$$TotalCost = \sum_{kpi,t}^{KPI,T} (CInf_{kpi,t} + COp_{kpi,t} + CBPro_{kpi,t} + CTn_{kpi,t}) \quad (1)$$

$$CInf_{kpi,t} = \sum_{c,p}^{C,P} Icon_{kpi,t,p} \times Af_p * A_{c,p} \quad (2)$$

$$COp_{kpi,t} = \sum_{c,p}^{C,P} IOpVar_{kpi,t,p} \times EPro_{c,t,p} + \sum_{c,p}^{C,P} IOpFix_{kpi,t,p} \times A_{c,p} \quad (3)$$

$$CBPro_{kpi,t} = \sum_{n,c,p,m}^{N,C,P,M} ICult_{kpi,b,t} \times Tflow_{n,c,b,m,t} \quad (4)$$

$$CTn_{kpi,t} = \sum_{n,c,p,m}^{N,C,P,M} ITn_{kpi,m,t} \times Dn_{n,c} \times Tflow_{n,c,b,m,t} \quad (5)$$

The model takes into account a range of constraints that ensure the method feasibility and applicability, which can be summarised as follows (formulation not included here):

- Total number of technology plants in operation per location is upper bounded by user-defined parameters;
- Logic constraints on the existence and number of links between biomass source n and technology plant location c ;
- Transport distance is constrained by user-defined upper bound;
- Equality and inequality constraints on the biomass supply-demand balances and flows;
- Inequality constraints on water and land resource availability and direct normal irradiance (DNI);
- Constraints on plant capacity and operational time.

4. Case Study: Gauteng Province (South Africa)

Table 3 - Data Inputs

Solar DNI	2,266 kWh/m ²
Biomass Availability	24,500Tonne
Unmet Electricity Demand to Satisfy	11.07 TWh/annum

Table 4 --Scenarios' key cost results in 2015

Scenario 1 (1 Technology Only)	223,428.00 kEuro
Scenario 2 (Multiple Technologies)	85,191.00 kEuro
Scenario 3 (Multiple Techs with DG)	65,162.00 kEuro

The modelled results indicated that among the technologies considered, the biomass externally-fired gas turbine remained the most cost optimal option, which can be explained by the CSP’s high CAPEX intensity and comparatively lower load factors. The cost optimisation scenario runs showed that DG technologies provide more economically competitive solutions. Throughout the time periods (2010s-2050s) modelled, the scenarios executed with DG technologies presented lower cost solutions in comparison with the scenarios without DG technologies (Figure 1). Technology learning effects represented as pivotal for DG technologies selected by the model.

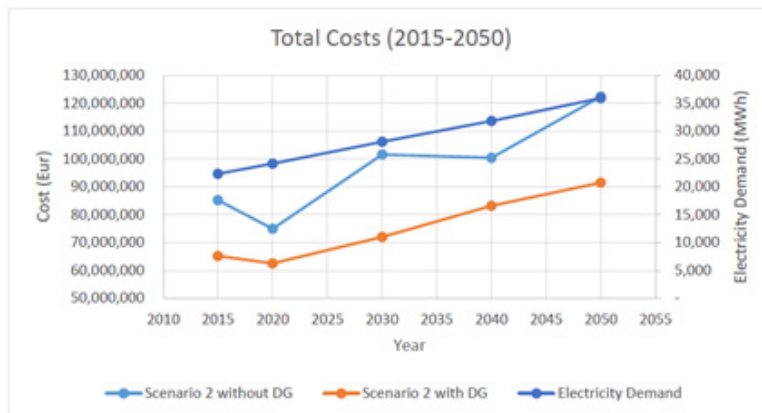


Figure 1. Cost profiling for scenarios with/without DG technologies

While centralised generation of energy has demonstrated better economic performances due to the scaling-up effects, densification of generation and higher efficiencies, the advent of small scale generation technologies has been able to satisfy energy needs due to better geographical and operational flexibility compared with centralised generation. The input data used to characterise these DG technologies reflected their advantages, which were confirmed by the projected technology learning, in particular in attracting investments which in turn is expected to drive the economic profiles of the technology.

5. Conclusion

The optimisation model presented in this study generated insights into the economically feasible technology solutions under a given context. Such modelling approach could be widely applicable to inform decision-makers in terms of renewable energy integration system design. The model is capable of executing scenarios with a range of technologies considering their economic profiles incurred by capital inputs, technology operation, and transportation and sourcing of biomass feedstock. This model can be further expanded and adapted to a wider range of renewable energy systems. This study revealed that the small scale solar PV and wind turbines are more cost effective to satisfy the specified electricity demands than the large scale hybrid CSP-Biomass plants modelled. Such research findings are driven by a range of modelling factors including the low operation of technologies caused by the difference between demand and rated output of the technologies, the uneven use of resources (biomass residues), negligible resource footprint (water, land) assumed for the DG technologies. Thus it is worth implementing more small scale systems in the region to exploit the abundant solar and biomass residue resource potential. The South African region modelled in the case study showed great potential with abundant solar and biomass resources, and the urgent needs in African continent to increase the electricity access suggest the opportunity for RES generation systems in South Africa which is in line with the national/regional strategy.

References

- AFDB, 2013. African Development Report 2012
- EIA, 2016. *World Energy demand and economic outlook 2016 with projections to 2040*, Washington, DC: U.S. Energy Information Administration.
- Goldman Sachs, 2017. *The Low Carbon Economy*.
- UNFCCC, 2015. *UN Climate Change Newsroom*.
- GNESD & UNEP, 2015. *Biomass Residues as Energy Source to improve energy access and local economic activity in low HDI regions of brazil and colombia (BREA)*, s.l.: Global Network on energy for sustainable development (GNESD).
- IEA, 2017. *Global Renewable Energy*.
- IEA, World Energy Outlook 2015. 2015
- NREL. (2016, February). *Distributed Generation Renewable Energy Estimate of Costs*. Retrieved August 1, 2017, from NREL: https://www.nrel.gov/analysis/tech_lcoe_re_cost_est.html
- Pantaleo, A., et al. (2017). Novel Hybrid CSP-Biomass CHP for flexible generation: thermo-economic analysis and profitability assessment. *Applied Energy* 204, Oct 2017
- Rosillo-Calle, F., de Groot, P., Hemstock, S. L., & Woods, J. (2015). *The Biomass Assessment Handbook* (second edition ed.). New York: Routledge, Taylor & Francis
- Peterseim, J., White, S., Tadros, A., & al., e. (2014). Concentrating solar power hybrid plants - enabling cost effective synergies. *Renewable Energy*, 67, 178-185.

Use of Artificial Intelligence to Experimental Conditions Identification in the Process of Delignification of Sugarcane Bagasse from Supercritical Carbon Dioxide

Isabelle C. Valim,^a Artur S. C. Rego,^a Alex Queiroz,^b Vinnicius Brant,^b Antônio A. F. Neto,^b Cecília Vilani,^a Brunno F. Santos^{a*}

^a*Department of Chemical and Material Engineering (DEQM). Pontifical Catholic University of Rio de Janeiro (PUC-Rio). Rua Marquês de São Vicente, 225 – Gávea, Rio de Janeiro – RJ, 22430-060, Brazil.*

^b*SENAI Innovation Institute for Green Chemistry. Rua Morais e Silva, 53, Bloco 9, 2^o andar – Maracanã, Rio de Janeiro – RJ, 20271-030, Brazil.*

bsantos@puc-rio.br

Abstract

This study evaluated the use of artificial neural networks (ANN) as tools to predict and identify the experimental conditions used in the process of delignification of sugarcane bagasse using supercritical carbon dioxide (ScCO₂). The experimental conditions varied from 35 – 100°C to temperature, 75 – 300 bar to pressure and 0 – 100% to ethanol content, used as co-solvent in the extraction. HPLC and determination of insoluble lignin (Klason lignin) analysis were performed to evaluate the efficiency of the process. A database was constructed with the information of the experiments, dividing them into groups of training (70%) and test (30%). The models were obtained using toolbox of the MATLAB R2016b. In the developed neural network, the data obtained by the different techniques of analysis were used as neurons in the input layer and the percentage of insoluble lignin was used as neuron in the output layer. The performance of the neural network was evaluated by the correlation coefficient (R²) and the error indexes (MSE and SSE). The process of sugarcane bagasse delignification using ScCO₂ showed good yields. The model developed from the neural network was satisfactory, since the R² value was 99.58% and the error index values were 0.176 to SSE and 0.0147 to MSE.

Keywords: Sugarcane Bagasse, Lignin, Supercritical Carbon Dioxide, Artificial Neural Networks, Failure Prediction.

1. Introduction

Sugarcane bagasse is a vegetal biomass that has much potential for use because of its structural elements: cellulose, hemicellulose and lignin. In order to use it as a raw material to produce new compounds, sugarcane bagasse needs to undergo a pre-treatment process, leading to the removal of lignin from the vegetable fibers. Thus, cellulose and hemicellulose become more available for subsequent processes like chemical or enzymatic hydrolysis leading to improved fermentation procedure, for example, in the production of 2^o generation ethanol. The methodology of delignification

of biomass using ScCO₂ is a clean process that aims at the non-formation of intermediate residues.

The use of ANN modelling in chemical processes has increased because of its simplicity in solving complex problems. Alberton et al., 2016 uses ANN modelling to correlate compositions and properties as viscosity index of the extracted and raffinate phases in the liquid-liquid extraction process of API I group lubricants.

With the creation of recent technologies and the increase in the volume of instrumental data obtained every day, the use of ANN model in the identification of process conditions to avoid operational errors becomes relevant, since it is a technique that simulates the human reasoning, bringing greater security to the accomplishment of tasks. In the context of pretreatment of sugarcane bagasse, Valim et al., 2017 uses ANN for prediction and failures detection in the process.

2. Materials and Methods

2.1. Process of sugarcane bagasse delignification using supercritical carbon dioxide

Based on Rabelo et al., 2014 the sugarcane bagasse used in this work was washed under a stream of tapwater, dried in an oven at 45 °C for 48 h to reduce bagasse moisture content. The lignocellulosic biomass was homogenized in an electric crusher to reduce particle size, fragmented into small fine particles and stored in a dessicator with no moisture for later use in the delignification experiments with supercritical carbon dioxide pretreatment.

The use of co-solvents in supercritical fluid extraction has been used to improve efficiency, increasing productivity and modifying process selectivity (Dalmolin et al., 2010). In this work, the co-solvent used was commercial ethanol 92.8 °INPM.

According to Pasquini et al., 2005, temperature, pressure and co-solvent content are variables that influence the process of delignification of the biomass with ScCO₂. The experiments were carried out in a temperature range of 35 °C to 100 °C, in a pressure range of 75 bar to 300 bar and in a co-solvent content range of 0 % to 100 %. The reactions were processed in a Maqnagua supercritical extraction set. 46 g of the biomass was placed in the extractor, where 500 mL of the co-solvent solution was added. The reaction occurred for 1 h. After this time, the extract is collected and the sugarcane bagasse after pretreatment is washed with 550 mL of NaOH 1% (w/v) to remove the adsorbed lignin in the biomass fibers. The obtained pulp was filtered, washed with water and dried in an oven for further analysis. All tests were performed in duplicate.

2.2. Klason lignin determination

To determine the content of lignin insoluble was used the standard methodology NREL (60) (Sluiter et al., 2008). An aliquot of 300 mg was removed from the pulp obtained after delignification. This sample was hydrolysed with H₂SO₄ 72 % (v/v) for approximately 2 h. The acid was diluted to 4 % (v/v) and the sample was placed in an autoclave at 121 °C for 1 h. A vacuum filtration was performed in the autoclave solution using pre-weighed crucibles. The crucible with the filtered solid was placed in an oven at 105 °C for 12 h.

Eq. (1) shows the calculation of the lignin insoluble percentage in biomass, where m_1 corresponds to the mass of the empty crucible and m_2 corresponds to the mass of the crucible with the filtrate, after the autoclave stage.

$$\%Lignin = \left(\frac{m_2 - m_1}{0.3} \right) \cdot 100 \quad (1)$$

2.3. Glucose and Xylose determination

Aliquots of each hydrolysate, obtained after filtration of the acid hydrolysis, were neutralized with sodium bicarbonate to neutral pH. The neutralized hydrolysates were filtered directly into vials using 0.22 μm Milipore filters.

These samples were subjected to High Performance Liquid Chromatography (HPLC) analyses using a SUPELCOSIL LC NH₂ (250 x 4.6 mm) on a Shimadzu chromatograph. As a mobile phase, a aqueous solution of 75% acetonitrile with a flow rate of 1 mL/min at 25 °C was used. The compounds were monitored with a Shimadzu RID-10A refractive index detector.

The standard curve for the quantification of sugars in the samples consisted of seven points ranging from 0.1 g/L to 4 g/L. The solutions were prepared from standard solutions of 50 g/L glucose and xylose.

2.4. Artificial neural network architecture

An ANN topology was selected to predict the Klason lignin content in each sample of the experiment. In this study, MATLAB R2016b was used. The activation functions for the hidden layer neurons tested were *tansig* and *logsig* and the training algorithms were *trainbr* and *trainlm*.

To evaluate the performance of the ANN, the error indexes SSE (Sum of Squared Errors) and MSE (Mean Squared Error) were observed. In addition, other aspects such as value of Coefficient of Determination (R^2) and number of network parameters were evaluated.

3. Results and Discussion

3.1. Quantitative analysis of the sample fractions after pretreatment

Table 1 shows the insoluble lignin content in sugarcane bagasse, as well the glucose and xylose concentrations present in the biomass in each experiment. The BT sample refers to sugarcane bagasse before pretreatment using ScCO_2 and is used only as a reference.

The study presents preliminary quantitative results where it is possible to observe that in the biomass samples after pretreatment with ScCO_2 there was a reduction in the insoluble lignin content, suggesting that the difference, based on BT sample, was lignin removed in the extraction process.

It was expected that the samples with lower Klason lignin content presented higher concentrations of available sugars, since lignin acts as a protection for the cellulosic structure.

Regarding glucose concentration, the results were consistent, since the sugarcane bagasse samples after pretreatment, except sample 4, showed an increase when

compared to the BT sample. However, the sample 5, which presented a lower content of insoluble lignin, did not present the highest glucose concentration.

Table 1. Results of HPLC and Klason lignin analyzes on sugarcane bagasse samples before and after pretreatment using ScCO_2 .

Sample		Temperature (°C)	Pressure (bar)	Co-solvent (%)	Klason lignin (%)	Glucose (g/L)	Xylose (g/L)
BT	A	-	-	-	20.57%	0.73	0.64
	B				20.33%	0.70	0.65
1	A	74	190	50	19.03%	0.89	0.64
	B				18.23%	0.89	0.64
2	A	35	300	100	18.23%	0.89	0.61
	B				17.40%	0.88	0.60
3	A	91	75	100	16.20%	0.72	0.44
	B				14.93%	0.72	0.43
4	A	84	180	50	14.80%	0.62	0.47
	B				15.13%	0.60	0.47
5	A	47	75	0	15.40%	0.81	0.81
	B				14.53%	0.84	0.91

Regarding xylose concentration, the values obtained for the sugarcane bagasse samples after pretreatment remained similar when compared to the BT sample, except 3 and 4 that presented lower values. Sample 5, however, showed a significant increase in xylose concentration relative to the others.

3.2. ANN training and testing

The results of HPLC analysis and determination of insoluble lignin were used for ANN training (70% of the data set) and testing (30% of the data set). The mean results of each experiment were calculated to obtain more data for the neural modelling.

The variables used as neurons in the input layer were the Klason lignin content in biomass, glucose concentration and xylose concentration. The variable used as neuron in the output layer was the experimental condition identifier.

Table 2 shows some ANN topologies developed in this work. The selected ANN model presented 3 neurons in the hidden layer, being the simplest topology. The activation function used was logsig and the training algorithm was trainbr. This ANN, in addition to presenting a better correlation coefficient, presents SSE and MSE error indexes satisfactory.

Table 2. Some ANN topologies used in the model proposed in the delignification process of sugarcane bagasse with ScCO_2 , besides the activation function, training algorithm and the adjustment values obtained for each case.

Experimental condition identification in sugarcane bagasse after pretreatment						
Number of neurons in input layer	Number of neurons in hidden layer	Activation function	Training algorithm	R ²	SSE	MSE
3	4	tansig	trainlm	97.95%	0.080	0.0066
3	4	logsig	trainlm	96.82%	1.96E-04	1.63E-05
3	4	tansig	trainbr	99.38%	0.159	0.0133
3	4	logsig	trainbr	99.50%	0.133	0.0111
3	3	tansig	trainlm	97.21%	0.033	0.0027
3	3	logsig	trainlm	53.72%	7.52E-04	6.27E-05
3	3	tansig	trainbr	99.51%	0.133	0.0111
3	3	logsig	trainbr	99.58%	0.176	0.0147

Figure 1(a) shows the topology used, as well as the training algorithm and the SSE error index obtained. It is important to note that approximately 5 effective parameters were used in the ANN during the training, discarding the possibility of overfitting in the ANN model. Thus, it can be stated that the small number of experimental data obtained did not affect the model quality, since it was not necessary to use more than 5 arrays for ANN training. Figure 1(b) shows the R² values of 99.58% for the training stage obtained for the applied ANN topology. This ANN presented an SSE performance value of 0.176 and MSE of 0.0147.

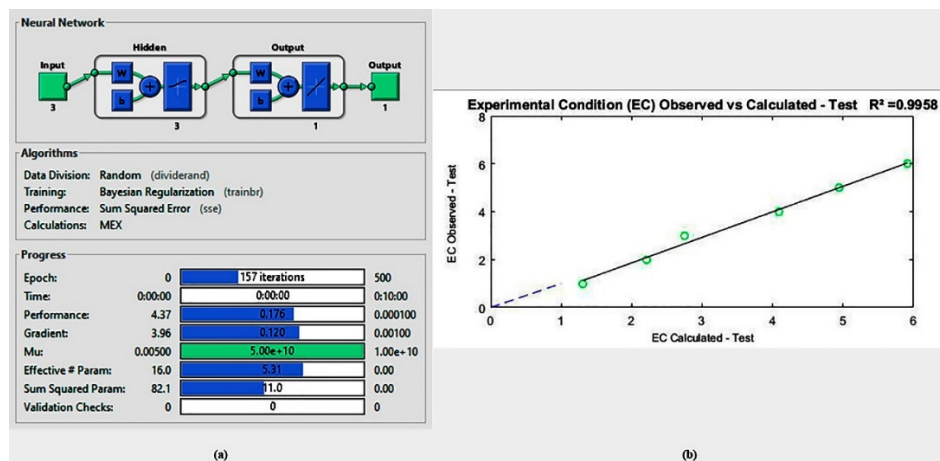


Figure 1. (a) Image obtained from MATLAB R2016b software that shows the ANN topology, as well as the training algorithm and the SSE error index obtained during the training stage. (b) Regression diagram for the ANN test stages used to predict the experimental condition used in the delignification process of sugarcane bagasse with ScCO_2 .

It is important to emphasize the importance of the construction of a model for the experimental conditions identification used during the delignification process of sugarcane bagasse with ScCO₂, due that the experimental results obtained have values very close to each other. This factor can cause confusion and insecurity in the operator who, when supported by an ANN model for identification, can prevent operational errors occurring.

4. Conclusions

The applied lignin extraction methodology was proven efficient, confirmed by the quantitative HPLC and determination of Klason lignin analyses. The most suitable condition for the process was the use of 0% ethanol as co-solvent at 47 °C and 75 bar resulting in lower insoluble lignin content and higher available sugars concentration. Data extracted from the analyses were essential for the ANN training, due to the low standard deviation of the analyses, increasing the quality of the selected ANN model. Regarding the predictions of the proposed model, the proposed ANN topology is considered adequate, since it presented satisfactory performance, confirmed by the observed SSE, MSE and R² values. Further experiments are needed to obtain more data and improve ANN training. However, the obtained ANN shows potential to be used, identifying with 99.58% safety the experimental conditions used during the process.

References

- Alberton, K. P. F., Lima, A. D., Nogueira, W. S., Gomes, L. C., Melo, P. A., Secchi, A. R., Jr, M. B. S., 2016, Neural networks modeling of dearomatization of distillate cuts with furfural to produce lubricants, *Computer Aided Chemical Engineering*, 38, 247-252.
- Dalmolin, I., Mazutti, M. A., Batista, E. A. C., Meireles, M. A. A., Oliveira, J. V., 2010, Chemical characterization and phase behaviour of grape seed oil in compressed carbon dioxide and ethanol as co-solvent, *The Journal of Chemical Thermodynamics*, 42, 797-801.
- Pasquini, D., Pimenta, M. T. B., Ferreira, L. H., Curvelo, A. A. S., 2005, Sugarcane bagasse pulping using supercritical CO₂ associated with co-solvent 1-butanol/water, *The Journal of Supercritical Fluids*, 34, 125-131.
- Rabelo, S.C., Andrade, R.R., Filho, R.M., Costa, A.C., 2014, Alkaline hydrogen peroxide pretreatment, enzymatic hydrolysis and fermentation of sugarcane bagasse to ethanol, *Fuel*, 136, 349–357.
- Sluiter, A., Hames, B., Ruiz, R., Scarlata, C., Sluiter, J., Templeton, D., Crocker, D., 2008, Determination of structural carbohydrates and lignin in biomass, *Laboratory analytical procedure*, 1617, 1-16.
- Valim, I. C., Fidalgo, J. L. G., Rego, A. S. C., Vilani, C., Martins, A. R. F. A., Santos, B. F., 2017, Neural network modeling to support an experimental study of the delignification process of sugarcane bagasse after alkaline hydrogen peroxide pretreatment, *Bioresource Technology*, 243, 760-770.

Including Agricultural and Organic Waste in Food-Water-Energy-Waste Nexus Modelling and Decision-Making

Daniel J. Garcia^a and Fengqi You^{b*}

^a*Northwestern University, 2145 Sheridan Road, Evanston, IL, 60626, USA*

^b*Cornell University, 318 Olin Hall, Ithaca, NY, 14853, USA*

fengqi.you@cornell.edu

Abstract

The Food-Energy-Water-Waste Nexus (FEWWN) represents the interconnections between food, energy, water, and waste production systems and has become a key research area in recent years. Enormous quantities of agricultural and organic wastes are produced throughout the FEWWN, representing a hurdle to sustainability. Often, these wastes are not treated appropriately because their true costs are not only rarely quantified, but they are also usually externalised to the surrounding communities and environments. In this work, we address this shortcoming from a systems perspective fused with approaches from ecological economics and ecosystem service valuation. We construct a bioenergy production framework where the bioenergy may be produced from ethanol and/or agricultural and organic wastes. If waste is converted, we consider the regenerated ecosystem services as an economic benefit. We apply the framework to a multiobjective case study on the US state of Illinois where 160 PJ of bioenergy is to be produced considering objectives of net cost and Green GDP. Green GDP ranges from -\$125M/y to \$132M/y with corresponding net costs ranging from \$107M/y to \$260M/y.

Keywords: Biofuels, sustainability, Food-Energy-Water-Waste Nexus, ecosystem services

1. Introduction

Systems researchers have recently increased focus on the Food-Energy-Water (FEWN) Nexus (Garcia and You, 2016) and the broader Food-Energy-Water-Waste Nexus (FEWWN) (Garcia and You, 2017a). Sustainability of the Nexus is critical as global population increases, resource availability decreases, and the effects of climate change increase. A key hurdle towards sustainability of the FEWWN is waste production and management. Enormous quantities of agricultural and organic wastes are produced at nearly all scales and links along FEWN supply chains. Food supply chains are particularly wasteful; in the US, only about 70% (Garcia and You, 2017a) of the produced food is eaten – the rest is wasted along the way. Other unavoidable wastes are produced. For example, livestock produce copious amounts of manure. Waste throughout the FEWWN often occurs because the true cost of producing the waste is either not considered or is externalised to surrounding communities and the environment. However, these costs must be quantified and utilised in decision-making if the FEWWN is to become sustainable.

Ecosystems provide essential services – called Ecosystem Services (ES) – to humanity that make our lives possible, such as nutrient cycling within a forest or flood management from mangroves (World Resources Institute, 2005). Agricultural and organic wastes produced throughout the FEWWN can degrade local ecosystems in many ways, diminishing the level of ES they can provide. Swine manure often spills into nearby creeks, rivers, and streams, killing fish, impacting the local water supply, and dramatically reducing recreation in the area. It is not enough to focus on ecosystem impacts of only waste systems, however, as other FEWWN systems also impact ecosystems. Clearing forests for cropland to grow feedstocks for bioethanol destroys the services originally provided by the forest. Ecological economists aim to quantify the value of the services local ecosystems provide. There are many ways ES are valued. However, despite the importance of considering ecosystem health in sustainable decision-making, quantitative valuation of the negative or positive impact on ES by a proposed process or supply chain is rarely considered. In this work, we integrate ES valuation methods including the hedonic pricing method and an aggregated biome-services approach into a FEWWN decision-making modelling framework for bioenergy production. We consider “Green GDP” as an optimisation objective, which accounts for the value of ecosystems destroyed/regenerated. Total cost of the bioenergy production strategy is another objective in the multi-objective framework. We propose a framework that considers the value of ES destroyed by bioethanol production via conversion of land to managed cropland for feedstock production and the value of ES regenerated by conversion of agricultural and organic waste to renewable energy. We apply the framework to a case study on the US state of Illinois.

2. Problem Statement

The proposed framework can account for bioenergy production costs in tandem with changes in ES from conversion of livestock manure to bioenergy, restoring local ES, and conversion of forests/pastures to cropland to grow bioenergy feedstocks, destroying local ES. Thus, the framework is best applied at the local or regional scales. Taking the perspective of some local/regional government, the framework considers two objectives of minimum net production cost and maximum Green GDP. Bioenergy may be produced as either bioethanol or electricity from biogas produced from swine manure. Bioethanol may be produced from corn grain, corn stover, or switchgrass from any mix of 9 bioethanol production pathways, with different feedstock pretreatment options. Base operating and capital costs are known for a given capacity of each pathway. Instead of allowing each pathway to scale, we fix costs and capacities and allow multiple plants to be constructed. An example pathway is dilute acid pretreatment of switchgrass to fermentation and distillation (Humbird et al., 2011). We work with the US EPA’s level 4 ecoregions (Woods et al., 2006) to represent the different ecosystems and Monfreda’s Agro-Ecological Zones to estimate corn yields Monfreda et al. (2009). We utilise data from Kang et al. (2014) to estimate switchgrass yields. Population statistics, median household values, statistics on swine farms (number of farms and number of hogs on each farm), electricity prices, and existing cropland area are taken from the US DOE, USDA, and the US Census Bureau. Process data on biogas production systems from anaerobic digestion of swine manure is taken from Cowley et al. (2014) for two systems – complete mix/plug flow reactors and covered lagoons. Gains/losses in ES value are calculated in a few ways. For biomass feedstock production for ethanol, we assume the original ecosystem is cleared for managed

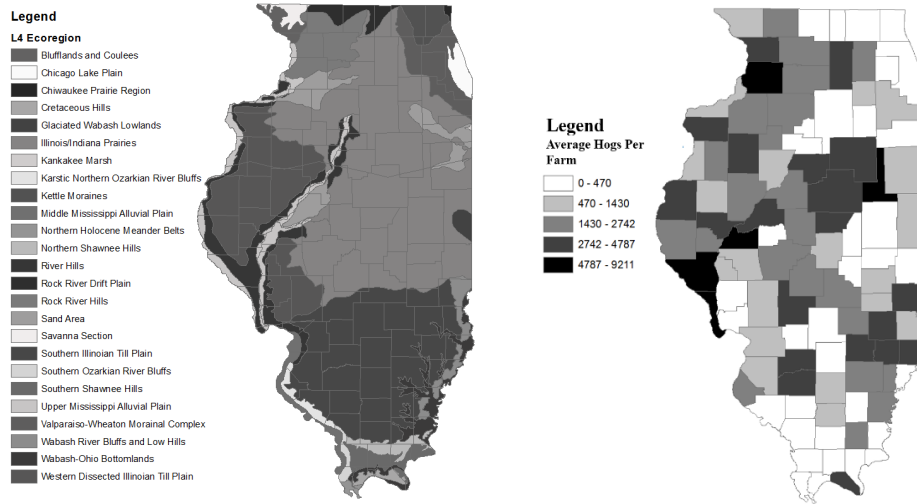


Figure 1. Selected data. Illinois ecoregions (left), and average hogs per farm (right).

feedstock cropland. Spatially explicit ES values are taken from The Economics of Ecosystems and Biodiversity (van der Ploeg and de Groot, 2010), database and applied in this framework via the benefit transfer approach. Values for each ecosystem (temperate grassland, temperate forest, floodplains) were aggregated with data from this database as per the method outlined in Garcia and You (2017b). We assume conversion of swine manure to biogas regenerates ES that were diminished before the manure was handled properly. Following an avoided cost/remediation approach, we assume creeks, rivers, and streams no longer become polluted by manure spills if a digester is constructed on nearby swine farms. These costs are estimated with historical records of relevant government fees and fines. Finally, we integrate the hedonic valuation approach for swine manure on nearby property values. If a farmer decides to convert the swine manure to bioenergy, we assume nearby property values no longer decrease due to odors, threats of spills, human health issues, etc. as quantified statistically by Herriges et al., (2005). We model an expected increase in nearby property values when manure is converted. The magnitude of the increase depends on distance from the hog farm and size of the hog farm. Next, the framework is applied to a case study on bioenergy demand in the US state of Illinois (Figure 1). Illinois produced approximately 160 PJ of corn ethanol in 2016, so we aim to identify from where the next 160 PJ of bioenergy should come to help Illinois reach its 20-25% renewable energy target by 2025.

3. Methodology

We processed, integrated, and analysed spatial data in ArcGIS 10.5 (ESRI, 2017). The data was imported into the mathematical programming model. Parameters are in lowercase with variables in uppercase (Table 1).

$$\min \sum_x \sum_c CC_{xc} \cdot \left(ic/1 - (1+ic)^t \right) + OC_{cx} - H_{cx} \cdot hfs_c \cdot ec_c \cdot ber - E_c \cdot epr \quad (1)$$

$$\min \sum_c E_c \cdot epr + EV + SP - \sum_b \sum_c EL_{bc} \cdot esval_b \quad (2)$$

$$\text{s.t. } ed \leq \sum_c \sum_x E_c + H_{cx} \cdot hfs_c \cdot ber \quad (3)$$

$$E_c = \sum_r \sum_c \sum_{x=eth} \sum_b CR_{rcxb} \cdot py_{rx}, \forall c \quad (4)$$

$$NT_{cx} \cdot bcap_x = \sum_r \sum_b CR_{rcxb}, \forall c, x \quad (5)$$

$$\sum_x \sum_{r=stover} \sum_b CR_{rcxb} \leq ssf \cdot \left(sa_c + \sum_x \sum_{r=corn} \sum_b CR_{rcxb} \right), \forall c \quad (6)$$

$$CC_{xc} = (NT_{cx} + H_{cx}) \cdot bcc_x, \forall c, x \quad (7)$$

$$OC_{cx} = (NT_{cx} + H_{cx}) \cdot boc_{cx}, \forall c, x \quad (8)$$

$$\sum_b EL_{b,c} \leq flm_c, \forall c \quad (9)$$

$$EV = \sum_c \sum_x H_{cx} \cdot mhv_c \cdot hi \cdot (sm_c \cdot hq_c (pcsqd + pcsqu) + sm_c \cdot hh_c \cdot pcsh + lg_c \cdot hoh_c \cdot pcloth) \quad (10)$$

$$SP = \sum_c \sum_x H_{cx} \cdot sab \quad (11)$$

$$EL_{bc} = \sum_b \sum_x CR_{rcxb} \cdot cy_{rb}, \forall b, c \quad (12)$$

$$\sum_x H_{cx} \leq hf_c, \forall c \quad (13)$$

where sets x, c, r, b represent bioenergy production options, c is counties, r is ethanol feedstocks, and b is BAMAs. The objective (1) accounts for annualised capital costs, annual operating costs, and revenue from electricity and ethanol. Objective (2) calculates the change in Green GDP, considering ethanol produced, changes in property values via the hedonic pricing method, avoided costs of cleanup/litigation for manure spills, and the value of lost ecosystems by clearing for ethanol feedstock production. Constraint (3) ensures bioenergy targets are met. Constraints (4)-(5) calculate ethanol produced. Constraint (6) controls stover utilisation. Constraints (7) and (8) calculate costs. Constraint (9) controls how much land may be converted to cropland. Constraints (10)-(12) calculates regenerated/lost ES values via the hedonic pricing method, avoided cost method, and aggregated valuation method, respectively. Constraint (13) ensures that no more hog farms install biogas-electricity generators than exist in each county.

4. Results and Discussion

All experiments were performed on a DELL OPTIPLEX 790 desktop PC with an Intel (R) Core (TM) i5-2,400 CPU @ 3.10 GHz and 8 GB RAM. We handle the multiobjective component of the problem with the ϵ -constraint method (Hwang and Masud, 2012). The mixed integer problems consisted of 4,596 equations, 32,338 continuous variables, and 1,326 discrete variables. All models and solution procedures were coded in GAMS 24.8.5 (Brooke et al., 1988). with the CPLEX 12 solver.

The Pareto-optimal frontier is shown in Figure 2. Green GDP ranges from -\$138M/y to \$144M/y, and the net cost ranges from \$107M/y to \$260M/y. Green GDP increases sharply from -\$125M/y to \$132M/y around a net cost of approximately \$200M/y. This sharp increase is likely primarily due to a shift from largely corn-based ethanol production in the lower cost solutions to utilising corn stover instead at the higher cost solutions. However, hog farms begin choosing to convert manure to biogas and electricity around this point as well. Small gains in Green GDP are made on either side of this sharp increase, reflecting hog farms who decide to convert manure to electricity. At the lowest cost solution, no farmers convert manure to electricity, while at Point A

Table 1. Parameters (lower case) and variables (upper case) in the model.

CC_{cx}	Capital costs	t	Annualisation timeframe (20 years)
H_{cx}	Number of hog farms in county c that integrate biogas technology x	epr	Ethanol selling price (avg 2012 spot price)
OC_{cx}	Operating costs	flm_b	Convertible land in county c
SV	Spill ES value loss avoided	cy_{rb}	Yield of crop r in BAMA b
E_c	Ethanol produced in county c	$esval_b$	Value of ES in BAMA b
EL_{bc}	Area of BAMA b lost in county c	hfs_c	Average hog farm size in county c
CR_{rcxb}	Mass of feedstock r grown in county c and BAMA b for conversion in x	hi	Annualised mortgage factor
NT_{cx}	Number of plants x in county c	ed	Bioenergy target
EV	Hedonic ES value recaptured	ec_c	Electricity cost in county c
sa_b	Original stover availability	ber	Biogas-electricity conversion rate
ic	Interest rate of capital	ssf	Sustainable stover harvest factor
bcc_x	Reference capital cost of x	$bcap_x$	Reference capacity of x
bop_{cx}	Reference operating cost of x in c	$bfop_x$	Reference fixed operating cost of x
mhv_c	Median property value in county c	py_{cx}	Conversion of r to ethanol in x
sm_c	1 if average hog farm in c is small	lg_c	1 if average hog farm in c is large
hq_c	Households within 0-0.4 km	hh_c	Households within 0.4-1.2 km in c
sab	ES value loss from manure spill avoided	$pcsqd$	Home value decrease 0.4 km downwind small hog farm
$pcsqu$	Home value decrease 0.4 km upwind small hog farm	$pcsh$	Home value decrease 1.2 km from small hog operation
$pcloh$	Home value decrease 2.4 km from large hog farm	hf_c	Number of hog farms in county c
hoh_c	Households within 2-2.8 km in c		

most do. Interestingly, fewer farmers convert manure to electricity at Point B than Point A. This may be due to the nature of the ϵ -constraint method combined with the increased cost of using corn stover over corn grain to produce ethanol. We chose the net cost as the constrained objective using the ϵ -constraint method. Thus, if corn stover is more costly to convert to ethanol, there is less “budget” in the net cost to convert manure to electricity. Using corn stover results in larger ES savings due to no longer clearing land; stover may be harvested from corn already produced. Thus, stover production is prioritised over manure conversion at Point B. Most of the Green GDP gain comes from growing corn in counties with lower BAMA values and by converting manure in counties with high median housing values. More farmers convert manure to

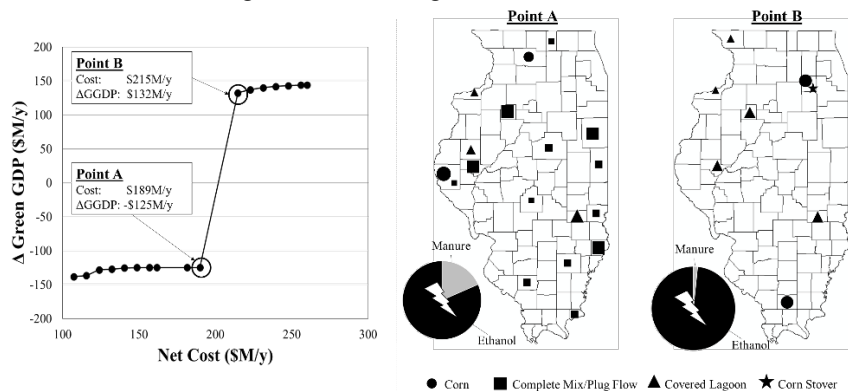


Figure 2. Pareto-optimal curve (left). Detailed results on Points A and B (right). Pie charts represent portion of bioenergy from ethanol and conversion of manure to biogas and electricity.

electricity from Point B to the highest Green GDP solution, where, as in Point A, all farmers convert manure to electricity. More farmers build covered lagoons over complete mix/plug flow reactors to convert manure to biogas and electricity in Point B.

5. Conclusion

A modelling framework for a bioenergy production strategy considering ethanol production and conversion of agricultural and organic wastes to biogas and electricity was presented. This work represents the first time several such impacts are valued and quantified via a range of ES valuation techniques. We applied the framework to a case study on bioenergy production in the US state of Illinois with two objectives of minimum net cost and maximum Green GDP. Considering ES values was shown to influence decision-making. Green GDP ranged from -\$125M/y to \$132M/y with associated net costs of \$107M/y to \$260M/y.

References

- A. Brooke, D. Kendrick, A. Meeraus, 1988, GAMS, a user's guide, ACM Signum Newsletter, 23(3-4).
- Cowley, C., B. W. Brorsen, D. Hamilton, 2014, Economic Feasibility of Anaerobic Digesters with Swine Operations, Agricultural & Applied Economics Association's 2014 Annual Meeting, Minneapolis, MN, July 27-29, 2014.
- Environmental Systems Research Institute (ESRI), 2016, ArcGIS Desktop: Release 10. Redlands, CA.
- D. J. Garcia, F. You, 2016, The water-energy-food nexus and process systems engineering: A new focus, *Computers & Chemical Engineering*, 91, 49-67.
- D. J. Garcia, F. You, 2017a, Systems engineering opportunities for agricultural and organic waste management in the food-water-energy nexus, *Current Opinion in Chemical Engineering*, 18, 23-32.
- D. J. Garcia, F. You, 2017b, Introducing Green GDP as an Objective to Account for Changes in Global Ecosystem Services Due to Biofuel Production, ESCAPE27 paper 3336.
- J. A. Herring, S. Secchi, B. A. Babcock, 2005, Living with hogs in Iowa: the impact of livestock facilities on rural residential property values, *Land Economics*, 81 (4), 530-545.
- C. L. Hwang, A. S. Masud, 2012, Multiple objective decision making-methods and applications: a state-of-the-art survey, 164, Springer Science & Business Media.
- D. Humbird, R. Davis, L. Tao, C. Kinchin, D. Hsu, A. Aden, 2011, Process Design and Economics for Biochemical Conversion of Lignocellulosic Biomass to Ethanol: Dilute-Acid Pretreatment and Enzymatic Hydrolysis of Corn Stover, National Renewable Energy Laboratory, Golden, CO, United States.
- S. Kang, S. S. Nair, K. L. Kline, J. A. Nichols, D. Wang, W. M. Post, C. C. Brandt, S. D. Wullschlegel, N. Sing, X. Wei, 2014, Global simulation of bioenergy crop productivity: analytical framework and case study for switchgrass, *GCB Bioenergy*, 6, 14-25.
- C. Monfreda, N. Ramankutty, T. W. Hertel, 2009, Global agricultural land use data for climate change analysis, GTAP Working Paper 40.
- S. van der Ploeg, R. S. de Groot, 2010, The TEEM Valuation Database – a searchable database of 1310 estimates of monetary values of ecosystem services, Foundation for Sustainable Development, Wageningen, The Netherlands.
- A. J. Woods, J. M. Omernik, C. L. Pederson, B. C. Moran, 2006, Level III and IV ecoregions of Illinois, EPA/600/R-06/104, USEPA National Health and Environmental Effects Lab, Corvallis, OR.
- World Resources Institute, 2005, Millenium Ecosystem Assessment: Ecosystems and Human Well-Being: Biodiversity Synthesis, World Resources Institute, Washington, DC, United States.

Optimum Utilization of Biomass for the Production of Power and Fuels using Gasification

Ahmed AlNouss,^{a,b} Gordon Mckay,^b Tareq Al-Ansari^{b,*}

^a*Department of Chemical Engineering, College of Engineering, Qatar University, Doha, Qatar*

^b*Division of Sustainable Development, College of Science and Engineering, Hamad Bin Khalifa University, Qatar Foundation, Doha, Qatar*

talansari@hbku.edu.qa

Abstract

The state of Qatar strives to diversify its energy portfolio whilst minimizing potential impacts on the environment from released wastes of multiple sectors. The current energy portfolio utilizes fossil fuels to drive the power sector which releases GHG's into the atmosphere. There has been significant progress in diversifying the global energy mix in order to limit GHG emissions. Biomass, which is a CO₂ neutral organic fuel, serves as a potential energy source for the generation of sustainable heat and power. The objective of this paper is to model a system that utilizes waste biomass from Qatar built environment to generate a high-energy product gas that contains hydrogen, carbon monoxide, and methane. There is a strong sustainable development component where there is a reduction in biomass waste and consumption of raw material as natural gas consumption is reduced. As such, the biomass can be utilized to generate a valuable product, whilst reducing GHG's and Qatar's dependency on reserves of natural gas. Gasification is considered as the preferred option for the processing of biomass where the product gas mixture (syngas) can be used to power generators/gas-turbines and produce clean energy since the process is carbon neutral. The syngas can be also used in the petrochemical industry to produce ammonia and methanol and reduce local dependency on natural gas. In this study, a computer simulation model of the biomass gasifier was developed using Aspen Plus considering Qatar's biomass characteristics. The results demonstrated the possibility to utilize domestic feedstock in Qatar such as date palm residues amongst others to generate syngas. Furthermore, the study determines the optimum blends of biomass feedstocks which are to be utilized in the existing gasification processes.

Keywords: biomass, gasification, date pits, optimization, nexus

1. Introduction

Like most countries, one of the main challenges facing the State of Qatar is the need to develop holistic waste management strategies which reduce environmental impacts from generated waste, estimated at 1.8 kg per capita per day (Ahmad, 2016). Coupled to this is the need to prolong the life time of natural resources, i.e. natural gas. Currently Qatar utilizes this commodity to meet its domestic needs for power, converted to LNG and other chemicals for export. Incidentally, Qatar strives to diversify its energy portfolio with the forthcoming integration of solar energy into the domestic electricity

grid. The management of biomass through a holistic utilization strategy can contribute towards national objectives of enhanced resource productivity, environmental protection and economic diversity. Biomass, which is a CO₂ neutral organic fuel, serves as potential energy source and renewable feedstock for the generation of sustainable heat and power (Gordillo et al., 2009). Gasification is considered as the preferred option for the processing of biomass where the product gas mixture (syngas) can be used to power generators/gas turbines and produce clean energy since the process is carbon neutral. The syngas can also be used to produce high value petrochemicals such as ammonia and methanol.

The objective of this paper is to model a gasification system that utilizes the waste biomass from Qatar built environment to generate a high-energy product gas that contains hydrogen, carbon monoxide, and methane. As such, the biomass can be utilized to generate a valuable product, whilst reducing GHG's and Qatar's dependency on the nation's reserves of natural gas. Furthermore, considering the various types of solid waste available in Qatar such as sewage sludge, date palm waste, and other organic waste, this study will determine the optimum blend of biomass feedstock which can be utilized in existing gasification processes to produce optimum product output. This study differs from other literature studies in terms of its optimization nature by including various biomass feedstocks that includes date pits. The potential of biomass gasification for the State of Qatar has been demonstrated through an energy, water and food (EWF) nexus case study for a hypothetical food security scenario for the State of Qatar (Al-Ansari et al., 2016). In this study, manure is gasified to produce syngas which is utilized for power generation purposes within the overall EWF nexus.

Since 2001, biomass gasification (BG) has received widespread importance in both academia and industry. This is primarily due to the need to mobilize effective strategies to combat climate change and the volatile oil prices. BG technology can reduce the generated carbon to hydrogen (C/H) ratio leading to a higher calorific value content and a favourable H₂ fraction. Furthermore, outputs from BG also yields many useful products, which include bio-fuels, bio-char, syngas, power, heat, and fertilizer. Syngas is a key product of BG and it mainly consists of Carbon monoxide (CO), Hydrogen (H₂), Methane (CH₄) and Carbon dioxide (CO₂). It is an important element in the production of environment-friendly fuels and chemicals and in the generation of power. However, various types of contaminants are associated with syngas production such as tars, sulphur inorganic compounds, particulates and nitrogenous compounds. The properties and quality of the gasification product and its associated contaminates depends on the gasifying agent, feedstock material and dimensions, reactor conditions and design, presence of sorbent and catalyst (Sikarwar et al., 2016).

Aspen plus, a process modelling software, has successfully been utilized to simulate gasification process systems. Incidentally, those related to biomass are less extensive than other sources of fuel used in gasification such as coal (Puig-Arnavat et al., 2010). Doherty et al. developed an Aspen plus model to simulate biomass gasification in a steam blown dual fluidized bed (DFB). The model is developed based on Gibb's free energy minimization and restricted equilibrium methods. The results demonstrated agreement with published data for syngas composition, heating value and cold gas efficiency (CGE) (Doherty et al., 2013). Trop et al. studied co-gasification of torrefied wood biomass and municipal sewage sludge for the production of methanol using Aspen Plus. A techno-economic study was performed in comparison with coal

gasification, where the results showed that the biomass combination can serve as a potential alternative (Trop et al., 2016). Han et al. developed a similar model for downdraft biomass gasification. The model was first validated with experimental data and then a sensitivity analysis was utilized to perform an investigation on the effect of gasification temperature, biomass moisture content and equivalence ration on the quality of synthesis gas (Han et al., 2017).

2. Model Development

The base model developed in this project is based on air-steam gasification of different feedstocks available in the State of Qatar to generate H₂-rich syngas. The Aspen Plus flowsheet of the biomass gasifier is modelled based on the assumptions of steady state, zero-dimensional, isothermal operation, atmospheric gasification pressure (P_g) (~1 bar) operation, neglected pressure drops, ideal gases, char is 100% carbon (C), tar formation is neglected, fuel bounds N₂, S, and Cl₂ are converted to NH₃, H₂S and HCl, respectively, instantaneous drying and pyrolysis, and heat loss from the gasifier is neglected.

Table 1: Proximate and ultimate analyses of biomass feedstocks

Mass Flow (tons/y)	Manure	Sludge	Date Pits
	5.27x10 ⁵	3.65 x10 ⁴	7.60x10 ³
Proximate analyses (wt %)			
Volatile matter	64.97	8.1	77.7
Fixed carbon	13.46	17.8	16.311
Ash	21.57	65.8	0.98
Moisture	27.4	8.3	5.01
Ultimate analyses (wt %)			
C	37.05	50.38	50.84
H	5.06	6.12	6.83
O	31.44	14.9	37.88
N	3.66	2.89	4.45
S	0.45	0.25	0
Cl	0.97	0	0
Ash	21.37	65.8	0.98
LHV (dry basis) (MJ/kg)	19.09	16.40	25.30

The equation of state selected for this model is Peng-Robinson with Boston-Mathias modifications. Biomass streams representing manure, dried sewage sludge and date pits feedstocks are specified as non-conventional streams with, ultimate and proximate analyses and assumed flow rates illustrated in Table 1. Stream thermodynamic conditions of 1 bar and 25 °C are assumed in accordance with the assumption of atmospheric conditions (Doherty et al., 2013). The mass yields of the non-conventional biomass streams into conventional components, have been determined and set using a calculator block according to the following formulation:

Table 2: Calculator block formulations of conventional components yield

WATER = PROXANAL(1)	[1]	CARBON = ULTANAL (2) / 100 * FACT	[6]
H2O = WATER / 100	[2]	H2 = ULTANAL (3) / 100 * FACT	[7]
FACT = (100 - WATER) / 100	[3]	N2 = ULTANAL (4) / 100 * FACT	[8]
ASH = ULTANAL(1) / 100 * FACT	[4]	CL2 = ULTANAL (5) / 100 * FACT	[9]
SULF = ULTANAL (6) / 100 * FACT	[5]	O2 = ULTANAL (7) / 100 * FACT	[10]

The outlet stream from the reactors is fed to a separator block to separate out the ash content. The rest of the components are directed to a stoichiometric reactor where 100%

of the fuel bound N_2 , S and Cl_2 are converted to NH_3 , H_2S and HCl , respectively through the following reactions:



The resulted components are removed from the main fuel stream via a separator. The main fuel stream is then fed to the gasifier simulated using a Gibbs reactor. The other two feed streams are the air and steam needed to gasify the biomass. The air stream is fed with specified mole fractions of 0.95 O_2 , 0.016 N_2 , and 0.034 Ar, which is the typical quality of air from an air separation unit. The temperature and pressure of the air and steam streams are set to 450 °C and 1 bar. The assumed gasification air-biomass ratio (GATBR) is 0.6. Whereas, the injected steam mass flowrate is calculated based on the mass flowrate of the biomass and its moisture content along with a 0.75 steam to biomass ratio (STBR). The gasification reactor is modelled utilizing the minimization of Gibb's free energy while restricting the chemical reaction equilibrium. The following reactions were specified with zero temperature approach:



Another Gibbs reactor block is utilized to perform the water shift and methanation reactions; Eq. (17) and (18), by means of restricting the reaction's equilibrium through specifying temperature approach values of (-265 °C and -90 °C respectively). This temperature approach values ensure that the model outputs a realistic syngas composition. The exit stream represents the final output syngas stream from the model.

3. Results

After the development of the air-steam gasification model, the biomass feedstock is optimized in order to find optimum blended feedstock. The optimization involves maximizing the syngas production whilst constraining the $H_2:CO$ ratio in accordance with the different syngas utilization processes, in particular the generation of power and liquid fuels (Iaquaniello et al., 2012). The results are summarized in Table 3.

The different $H_2:CO$ ratios have led to different blends of the biomass feedstocks. A Sensitivity analysis is then applied to understand the effect of changing the key gasification process parameters on the operating conditions and produced results as illustrated on Figures 1-4. The parameters considered include the: gasification temperature (T_g) and pressure (P_g), gasification air-biomass ratio (GATBR) and steam to biomass ratio (SATBR). The main observation results are, syngas composition in dry Vol%, lower heating value (LHV) in dry mass basis, cold gas efficiency (CGE) which is a measure of produced syngas heating value to biomass heating value. It can be seen that the LHV, CGE and syngas compositions demonstrate unrealistic results when the operating conditions.

Table 3: Results of biomass feedstock blends optimization

H ₂ :CO ratio	2:1	3:1	4:1
Syngas Composition, dry basis (mol%)			
N ₂	0.45	0.67	1.12
CO	20.20	12.57	6.02
CO ₂	35.90	48.65	68.79
H ₂	40.40	37.71	24.06
CH ₄	3.06	0.40	0.01
Feed Blend (wt%)			
Manure	0.16	39.15	46.69
Date Pits	99.68	39.15	6.62
Sludge	0.16	21.69	46.69
Syngas Yield (kg product/kg Feed)			
	2.27	2.13	1.96
LHV at 0 °C, dry basis (MJ/m ³)			
	8.20	6.21	4.07

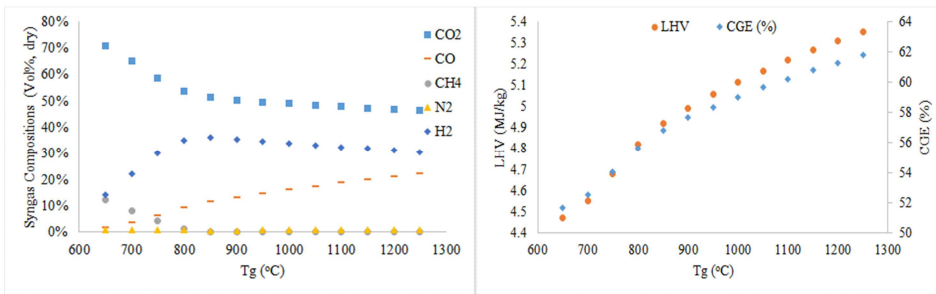


Figure 1: Effect of changing gasification temperature (T_g) (STBR = 0.75, GATBR = 0.6, P_g = 1 bar)

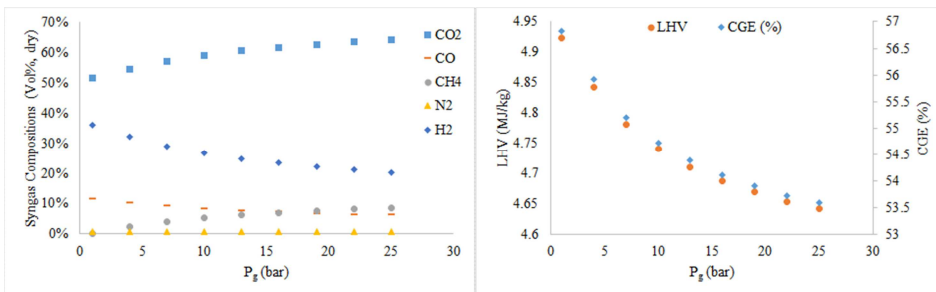


Figure 2: Effect of changing gasification pressure (P_g) (STBR = 0.75, GATBR = 0.6, T_g = 850 °C)

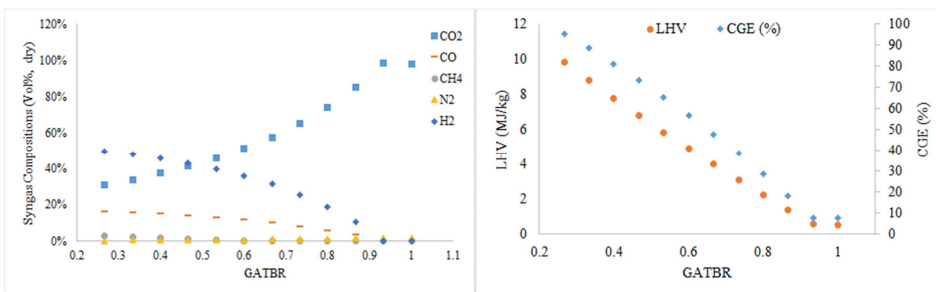


Figure 3: Effect of changing gasification air-biomass ratio (GATBR) (STBR = 0.75, P_g = 1 bar, T_g = 850 °C)

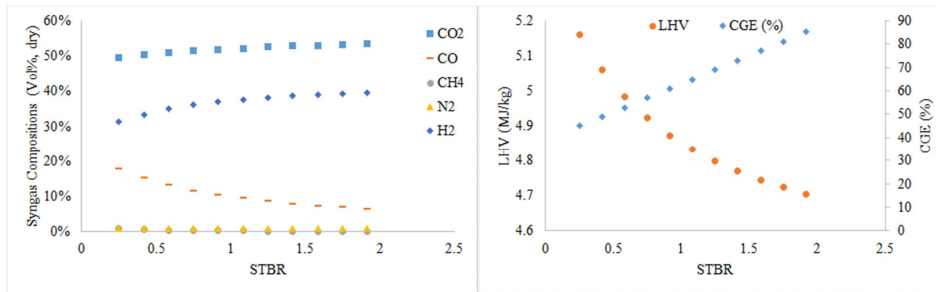


Figure 4: Effect of changing steam to biomass ratio (STBR) (GATBR = 0.6, $P_g = 1$ bar, $T_g = 850$ °C)

4. Conclusions

This study demonstrated a methodology to maximise product output for a biomass gasification process through optimising a feedstock blend for a case study in the State of Qatar. From the results, it can be deduced that the LHV and CGE and syngas composition demonstrate unrealistic results when the biomass gasification process is operating under non-optimum conditions. Alternatively, optimal conditions in terms of gasification temperature (T_g) and pressure (P_g), gasification air-biomass ratio (GATBR), and steam to biomass ratio (STBR) demonstrate improvement in simulation output because of the higher presence of H₂ and CO in the produced syngas. This presence has been reflected in the increase of lower heating value and cold gas efficiency.

References

- F. Ahmad, 2016, Sustainable solutions for domestic solid waste management in Qatar, Qatar University.
- T. Al-Ansari, A. Korre, Z. Nie, and N. Shah, 2016, Integration of Biomass Gasification and CO₂ Capture in the LCA Model for the Energy, Water and Food Nexus, *Computer Aided Chemical Engineering*, 38, 2085-90.
- W. Doherty, A. Reynolds, and D. Kennedy, 2013, Aspen plus simulation of biomass gasification in a steam blown dual fluidised bed.
- G. Gordillo, K. Annamalai, and N. Carlin, 2009, Adiabatic fixed-bed gasification of coal, dairy biomass, and feedlot biomass using an air–steam mixture as an oxidizing agent, *Renewable Energy*, 34, 12, 2789-97.
- J. Han, Y. Liang, J. Hu, L. Qin, J. Street, Y. Lu, and F. Yu, 2017, Modeling downdraft biomass gasification process by restricting chemical reaction equilibrium with Aspen Plus, *Energy Conversion and Management*, 153, Supplement C, 641-48.
- G. Iaquaniello, E. Antonetti, B. Cucchiella, E. Palo, A. Salladini, A. Guarinoni, A. Lainati, and L. Basini, 2012, Natural Gas Catalytic Partial Oxidation: A Way to Syngas and Bulk Chemicals Production, *Natural Gas - Extraction to End Use*, Ch. 12.
- M. Puig-Arnavat, J.C. Bruno, and A. Coronas, 2010, Review and analysis of biomass gasification models, *Renewable and Sustainable Energy Reviews*, 14, 9, 2841-51.
- V.S. Sikarwar, M. Zhao, P. Clough, J. Yao, X. Zhong, M.Z. Memon, N. Shah, E.J. Anthony, and P.S. Fennell, 2016, An overview of advances in biomass gasification, *Energy & Environmental Science*, 9, 10, 2939-77.
- P. Trop, M. Agrez, D. Urbancl, and D. Goricanec, 2016, Co-gasification of torrefied wood biomass and sewage sludge, *Computer Aided Chemical Engineering*, 38, 2229-34.

An energy, water and food nexus approach aiming to enhance food production systems through CO₂ fertilization

Tareq Al-Ansari^{a*}, Rajesh Govindan^a, Anna Korre^b, Zhenggang Nie^b, Nilay Shah^c

^a*Division of Sustainable Development, College of Science and Engineering, Hamad Bin Khalifa University, Qatar Foundation, Doha, Qatar*

^b*Department of Earth Science and Engineering, Royal School of Mines, Imperial College, London SW7 2BP, U.K.*

^c*Department of Chemical Engineering, Imperial College, London SW7 2AZ, U.K.*

*talansari@hbku.edu.qa

Abstract

As part of the drive for global food security, all nations will need to intensify food production, including those situated in hyper arid climates. The State of Qatar is one such example of a national system that whilst it is presented with environmental challenges, seeks to enhance food security. The energy, water and food (EWF) nexus approach is an effective means to accurately ascertain resource consumption, identify synergies and trade-offs, and quantify environmental burdens in the delivery of products and services. The EWF nexus theory has been uniquely applied to a hypothetical food system in Qatar where sub-system model's representative of EWF systems are developed. It has been suggested that the fertilization of agricultural systems with CO₂ can enhance their productivity. The study described in this paper considers the life cycle yield improvements which can be made possible at the farm level by utilizing the captured CO₂. This requires a modification of the EWF nexus model to consider the spatial characteristics of the modelled elements. The newly built model is used to investigate the CO₂ transport methods (pipeline and truck), and distance that CO₂ captured from combined cycle gas turbine (CCGT) and biomass integrated gasification combined cycle (BIGCC) sub-systems which may then be transported for CO₂ fertilization, and yield improvements to be justified from an energy utilization perspective. In this regard, an integrated analysis using GIS-based optimization is applied where the sub-systems are represented as geospatial elements together with their design constraints, such as the capacity-related parameters of the fertilization systems, and the energy requirements of the transport network connecting the CO₂ sources with the fertilization systems at multiple greenhouse locations in Qatar. These form part of the problem formulation for the determination of optimal locations of food production systems using Non-Linear Programming (NLP) to ensure the feasibility of CO₂ fertilization and realize environmental improvements within the overall EWF nexus framework. The results indicate the optimal locations and extents for new greenhouse developments that are constrained by the available farming infrastructures and CO₂ transportation options to balance for the net energy and water requirements for food production.

Keywords: EWF nexus, Food security, Meta-Heuristics, Life cycle, Agriculture

1. Introduction

Holistic approaches such as the energy, water and food (EWF) nexus are critical for addressing integrated challenges in uncertain environments. The State of Qatar is situated in a region characterised by a complex environment. Its climate is hyper arid, with high average temperatures and humidity, posing multiple challenges with respect to food production. Historically, Qatar has imported a vast majority of its food requirements from overseas markets. However, this is likely to change with the inception of food security projects, which are designed to increase Qatar's domestic food production capacity. Doing so will require a mobilisation of multiple resource sectors in order to transform the domestic food production operating within a challenging environment.

Agricultural intensification, as witnessed in the past, involved unsustainable practices, which has led to widespread environmental degradation. Going forward, the importance of understanding the relationship between the environment and food security outcomes will be critical, as agricultural productivity essentially depends on the condition of the environment. This introduces the notion of 'sustainable intensification', which is related to the need to meet the demands of nutritional demands of a growing environment without furthering degradation to the natural environment (Godfray and Garnett, 2014). There is much discussion on the effect of the elevated levels of CO₂ in the atmosphere on crops. The general consensus is that higher crop yields will be produced as a result. This is because CO₂ is an essential compound in the photosynthesis process where its carbon content is utilised to form carbohydrates. Furthermore, increasing concentrations of CO₂ inhibits the loss of water also known as transpiration due to increased resistance from the stomata. It has also been suggested that increased temperature and decreased soil moisture would have a negative impact on crop yields. This, however, would be offset by the natural fertilization of crops from the increasing concentration of CO₂ in the atmosphere (Lawlor and Mitchell, 1991). Moreover, the fertilization of plants using CO₂ not only results in increases in dry matter production, but is accompanied by improvements of water utilization efficiency (WUE) (Kimball and Idso, 1983).

The objective of this study is to utilize the EWF nexus model previously developed by the authors to explore the potential of enhancing agricultural productivity through CO₂ fertilization. The study utilizes a hypothetical food security scenario for the State of Qatar previously evaluated using a EWF Nexus approach (Al-Ansari et al., 2016; 2017). The case studied involves raising domestic production by 40 %. The configurations utilized in this research are adopted from Al-Ansari et al. (2016; 2017) as detailed in Table 1 utilising combined cycle gas turbine (CCGT), post carbon capture (PCC), biomass integrated gasification combined cycle (BIGCC) and bioenergy carbon capture and storage (BECCS) for power generation. The purpose of this work is, however, not to attempt to predict potential crop improvements from CO₂ fertilization, but to quantify the minimum yield improvement using an indirect, but related, measure of reduction in transpiration from crops that would be required in order to balance the amount of energy (or equivalent water requirement) used for CO₂ capture, compression and transportation to the agriculture zone, i.e. greenhouse. The objective in this case is to improve system wide WUE. It should be noted that calculations of expected crop productivity increase from CO₂ fertilization are not within the scope of this study. This research identifies the increase in energy required to enable CO₂ fertilization, which would need to be balanced out by increases in crop productivity, which in turn result in an overall reduction in the water requirement and, therefore, energy consumption.

Table 1. Scenario development

Scenario	a	b	c
Integration of PCC	CCGT is used to power all water and food sub-systems.	PCC is integrated with the CCGT powering the water sub-system.	PCC is integrated with the CCGT powering the water and food sub-systems.
Integration of PV and BECCS (BIGCC + PCC)	<i>BIGCC power is distributed amongst the water and food sub-systems.</i>		
	CCGT is used to power all water and food sub-systems.	PV is integrated to power the water sub-system. The food sub-system is powered with the CCGT integrated with PCC.	PV is integrated to power the water and food sub-systems

2. Available data and assumptions

The problem formulation developed in this study is based on multimodal datasets for the State of Qatar, each of which provides spatial information for: (a) distribution of land use for farming activities; (b) distribution of solar irradiance; (c) the locations of the major sources of CO₂ emissions; and (d) possible modes of CO₂ transport that are of interest in the current study, namely pipelines and road transport. Fig 1 illustrates the country wide distribution of resources, indicating the relevant spatial parameter inputs used in the formulation.

The extent of the feasible region for the determination of optimal greenhouse locations was based on the percentage of land use under the category of green areas, as shown in Fig 1(a), available from the public databases of the Ministry of Development Planning and Statistics (MDPS) in Qatar. The locations were assumed to be constrained to ensure the availability of infrastructure to provide resources, such as water for irrigation, fertilizer, and transportation, where necessary. Thus, a cut-off percentage of 20 % was assumed in this study to ensure that the proposed locations for greenhouses are within a radial distance of 5 km from existing farming areas.

An important part of the input data considered in this study is the spatial distribution of solar radiation component reported as Direct Normal Irradiance (DNI) and indicated as contours in Fig 1(b), modified after Martín-Pomares *et al.* (2017). The DNI was used to determine the depth of evapotranspiration, characterizing the loss of water (in mm/day) from agricultural lands, in general. It was assumed that the water loss is owing to transpiration in crops only, which constitutes up to 10 % of evapotranspiration (Doorenbos, 1977), and that it also applies to greenhouses with minimal control on the direct sunlight radiation, air temperature, air humidity and wind (Fazlil-Ilahil, 2009).

Additionally, the locations of CCGT and BIGCC power plants are indicated in Fig 1(c). A BIGCC plant, however, does not currently exist and was assumed to be located closer to the city of Doha, as it is expected that most of the biomass waste would be generated from this region which has the highest population density. With regards to the options for transportation of CO₂ captured from the power plants, underground pipelines and road transport were assumed (Fig 1(d)). The service pipeline corridors are already available in the State of Qatar, and thus any proposal for laying new pipelines for CO₂ transportation are expected to follow these routes as per the local regulations. It is also assumed that the

road network would be utilized only for the last mile delivery of CO₂ to the greenhouses to minimize any service delays or potential hazards caused by CO₂ transportation. In view of this, the distance of road transport was assumed to not exceed 10 km.

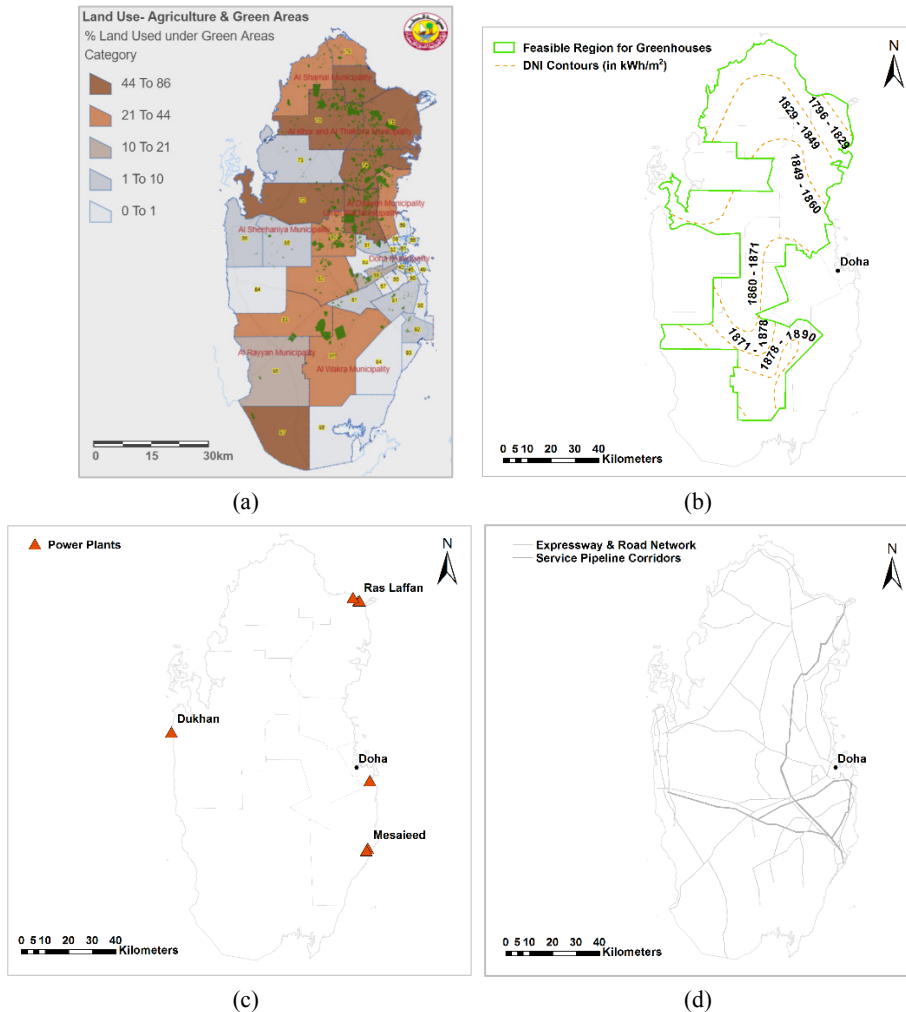


Fig 1. Maps of (a) agricultural land use and % coverage by the agricultural sector for municipalities, according to the 2015 census by MDPS, Qatar; (b) DNI contours (modified after Martín-Pomares *et al.* (2017)) for regions with the potential for new greenhouse development; (c) locations of CCGT and BIGCC power plants; and (d) transport network infrastructure available for the alignment with possible transportation of CO₂ from power plants to greenhouses.

3. Methodology

A non-linear programming (NLP) formulation was developed to determine the optimal location and minimum required area of greenhouses, based on the available data and assumptions posed as constraints in the problem. The nomenclature of variables used in the formulation is as follows:

Decision variables

- X_G, Y_G : easting and northing of the greenhouse (in metres).
- A_G : area of the greenhouse (in m^2).

Estimated variables

- X_F, Y_F : easting and northing of existing agricultural fields (in metres).
- X_D, Y_D : easting and northing of proposed CO_2 distribution centres (in metres).
- E_{CCT} : total energy consumption for CO_2 capture, compression and transport from the power plant to the greenhouse (in MWh/year), after Nie *et al.* (2011) and Al-Ansari *et al.* (2017).
- W_G : DNI equivalent for water loss (in MWh/ m^2), after Martín-Pomares *et al.* (2017).
- k_1 : conversion factor for equivalent water consumption (in m^3), after Al-Ansari *et al.* (2017).
- k_2 : conversion factor for equivalent depth of evapotranspiration (in m^3 /year), after Doorenbos (1977).

The optimization problem was posed with the objective of minimizing the net water consumption in the network subject to non-linear constraints, as follows:

$$\begin{aligned} & \text{Minimize } \{k_1 \times E_{CCT}(X_G, Y_G) - k_2 \times A_G \times W_G(X_G, Y_G)\} \\ & \text{subject to,} \\ & (X_G - X_D)^2 + (Y_G - Y_D)^2 \leq 10,000^2, \\ & (X_G - X_F)^2 + (Y_G - Y_F)^2 \leq 5,000^2, \text{ and} \\ & X_G, Y_G \in \text{DNI contour set.} \end{aligned} \tag{1}$$

4. Results

The NLP formulation in Eq. (1) was subsequently solved using a meta-heuristic algorithm called simulated annealing to determine the optimal solutions. Fig 2 illustrates the results obtained after solving the NLP problem described in the earlier section. It should be noted that multiple locations of CO_2 distribution centres were assumed at the intersections of pipelines and roadways for simplification purposes.

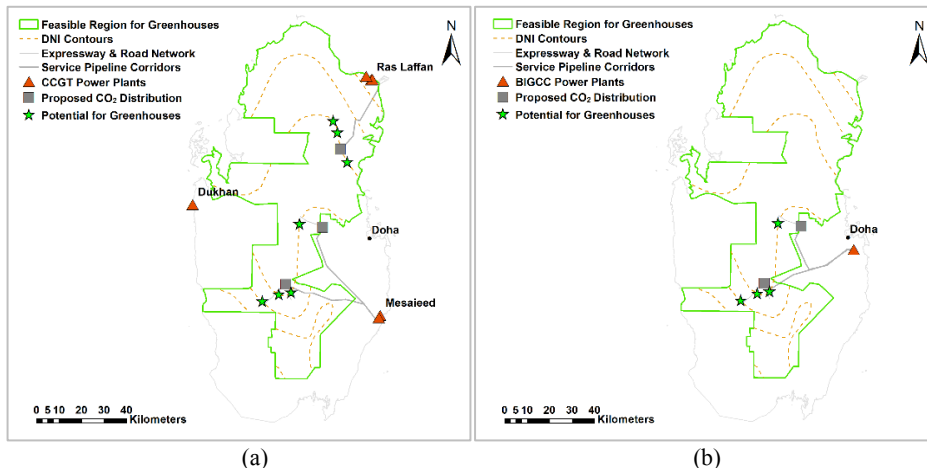


Fig 2. Optimized locations of greenhouses in the case of CO_2 captured from: (a) CCGT plants; and (b) BIGCC plants.

The optimal locations of the greenhouses are constrained on the DNI contour lines, which are used to estimate the water losses owing to crop transpiration. In addition, the ranges of the minimum area required for greenhouses were estimated under different scenarios of CO₂ captured from: (a) CCGT plants: 32,000 to 35,000 m²; and (b) BIGCC plants: 13,000 to 14,000 m², to minimize the net water consumption, or result in net water savings.

5. Conclusions

The authors present a decision framework based on the EWF nexus approach for the development of new greenhouses with the aim to enhance domestic food production in the State of Qatar. The results obtained thus far are promising from an environmental perspective, as the emission reduction that can be potentially achieved by the CO₂ fertilization network is around 0.5Mt/year considering the integration of capture technology for both CCGT and BIGCC, with the potential benefit of saving precious water resource. However, for such a solution to be viable, the question of economic feasibility needs to be addressed. This is a limitation of the analysis presented here, and is currently being studied under this framework.

References

- Al-Ansari, T., Korre, A., Nie, Z., Shah, N., 2016, Integration of Biomass Gasification and CO₂ Capture in the LCA model for the Energy, Water and Food Nexus, proceedings of the 26th European Symposium on Computer Aided Process Engineering: Escape 26, June 12 – 14, Slovenia.
- Al-Ansari, T., Korre, A., Nie, Z. and Shah, N., 2017. Integration of Greenhouse Gas Control technologies within the Energy, Water and Food Nexus to enhance the environmental performance of food production systems. *Journal of Cleaner Production*, 162, pp. 1592-1606.
- Doorenbos, J., 1977. Guidelines for predicting crop water requirements (No. C 25366). FAO, Roma (Italia).
- Fazlil-Ilahil, W.F., 2009. Evapotranspiration models in greenhouse (Doctoral dissertation, M. Sc. Thesis. Wageningen Agricultural University, The Netherlands).
- Godfray, H. C., Beddington, J. R., Crute, I. R., Haddad, L., Lawrence, D., Muir, J. F., Pretty, J., Robinson, S., Thomas, S. M., and Toulmin, C., 2010, Food security: the challenge of feeding 9 billion people, *Science*, 327, 812-8.
- Kimball, B., and Idso, S., 1983, Increasing atmospheric CO₂ effects on crop yield, water use and climate, *Agricultural Water Management*, 7, 55-72.
- Lawlor, D. W. and Mitchell, R. A. C., 1991, The effects of increasing CO₂ on crop photosynthesis and productivity: a review of field studies, *Plant, Cell and Environment*, 14, 807-818.
- Martín-Pomares, L., Martínez, D., Polo, J., Perez-Astudillo, D., Bachour, D. and Sanfilippo, A., 2017. Analysis of the long-term solar potential for electricity generation in Qatar. *Renewable and Sustainable Energy Reviews*, 73, pp.1231-1246.
- Nie, Z., Korre, A. and Durucan, S., 2011. Life cycle modelling and comparative assessment of the environmental impacts of oxy-fuel and post-combustion CO₂ capture, transport and injection processes. *Energy Procedia*, 4, pp.2510-2517.

Energy and water integration for the design of sustainable total textile waste refinery

Athanassios Nikolakopoulos,^{a*} Antonis Kokossis^a

^a*National Technical University of Athens, Department of Chemical Engineering,
9 Heroon Polytechniou Street, Athens 15780, Greece.*

nikolako@mail.ntua.gr

Abstract

This paper presents a process design method using combined energy and water integration for a complete textile waste refinery process. The proposed method consists of a superstructure model taking into account balanced energy and water minimization targets and produces energy and water networks of maximum efficiency. It produces significant results both for independent and combined water and energy integration; Savings up to 71% for heating and 86% for cooling can be achieved by standalone energy integration and savings up to 38% for water consumption by applying independent water integration. On the other hand, combined energy and water integration can lead to 74.5% energy and 36% water savings, thus an increase of 3.5% in energy savings at the expense of just 2% reduction in water savings.

Keywords: water integration, energy integration, mathematical programming, superstructure model.

1. Introduction

The present work coordinates established and original Process Integration technologies to the solution of a new problem; the design of the sustainable Total Textile Waste Refinery (TTWR); a new waste recycling and refining process, that it is being currently developed in the course of the European Horizon2020 research project RESYNTEX. It uses the complete spectrum of waste textiles as feedstock, aiming to provide a holistic response to the largely overlooked waste textile management problem. TTWR is now just before the phase of pilot construction and process integration technologies are currently implemented to accelerate the design solution.

TTWR consists of gate links between textile materials with commodity and specialty products and chemicals. Feedstock includes the entire range of textile fibres and final products including bio-ethanol, adhesives used in the wood-based panel production, PET bottles and PA-derived value-added chemicals. Without any water integration attempts the water consumption is as high as 52 tonnes per tonne of feedstock, and it is shared among reaction and separation stages (mostly washing and filtration steps) at a 2:1 ratio. Contrary to the textile fabrication processes which uses an average of 30 MJ/kg of fabric (Kalliala and Nousianinen, 1999), TTWR is more energy intensive, requiring more than 53 MJ/kg of feedstock. The majority of the energy requirements (~40%) is used in reactions, which are mainly neutral thermochemical hydrolyses at high temperatures for PAs and PET, and biochemical hydrolyses at mild temperatures. Considering that water is

used at high ratios compared to the feedstock material in all reactions, it is also the main energy carrier in the reactors. This evidence indicates clear scope for a combined energy and water integration study, since water is used both as a cleaning agent for removing dyes and impurities as well as the main heating medium. Novel process integration tools have been developed for assessing alternative process integration scenarios and achieving maximum efficiencies in energy and water use in modern biorefineries (Koufolioulis et al., 2014; Nikolakopoulos and Kokossis, 2017a). Also, total waste management and recycle design technology has been produced to enable the development of designs for processes with minimum environmental impact (Nikolakopoulos and Kokossis, 2017b).

A new tool is proposed in this paper for targeting maximum energy and water efficiencies in the TTWR. It is developed by using a mathematical programming superstructure model which balances the preference towards energy and water saving goals. The application of the proposed tool in the design of the TTWR is able to produce significant energy and water saving targets, that may reach up to 71% for energy and 36% for water.

2. Methodology

The concept of combined heat and water integration is based on the idea of combining and reusing at water-using operations outlet water streams coming from other operations and also splitting and reusing outlet streams at other operations for reducing heating and cooling requirements and at the same time reduce fresh water requirements.

In order to calculate the reuse flowrates between operations that minimize the total fresh water use and the same time minimized energy requirements for heating water streams a superstructure of the processes is constructed to account for all possible connections between water using operations. The superstructure is represented by the superstructure model described next.

The objective function maximizes the weighted sum of normalized water and energy savings; W^S and E^S given by equations 32 and 33 respectively, where FW^{init} and TQ^{init} is the total fresh water and energy consumption prior to integration and FW , TQ^S are the consumptions after integration respectively. Depending on the value of the weighting factor a ; $0 \leq a \leq 1$, different balances between fresh water and energy use minimization are introduced, i.e. when $a = 1$, minimization of energy is neglected, while the opposite stands for $a = 0$, when water use minimization is not considered. In all cases though, the mass and energy balances are satisfied, resulting in feasible networks.

$$\max Z = a \cdot W^S + (1 - a) \cdot E^S \quad (1)$$

s.t.:

The total flow of fresh water required is:

$$FW = \sum_{i=1}^{No} Fwin_i \quad (2)$$

The wastewater flow is:

$$FWW = \sum_{j=1}^{S_j} FTPdis_j \quad (3)$$

The total flow of contaminants in the wastewater flow is:

$$FWW \cdot Cout, env = \sum_{j=1}^{S_j} FTPdis_j \cdot CoutTP_j \quad (4)$$

Equation (5) is the mass balance of water around operation i considering diluted streams, i.e. $Fin_i + Mc_i = Fout_i$, where Mc_i is the mass of contaminants removed by water in operation i .

$$Fin_i = Fout_i \quad (5)$$

Mass of contaminants removed by water in operation i , where Cin_i and $Cout_i$ are the inlet and outlet concentrations for operation i .

$$Mc_i = Fin_i (Cout_i - Cin_i) \quad (6)$$

Inlet flow for process i , summing up fresh water, reused water and treated water. The recycled flowrates are set to 0 for this study.

$$Fin_i = Fwin_i + \sum_{ii=1}^{No} Freuse_{ii,i} + \sum_{j=1}^{S_j} FTPtoP_{j,i}, \quad \forall i \quad (7)$$

Mass of contaminant entering operation i

$$Fin_i \cdot Cin_i = \sum_{ii=1}^{No} Freuse_{ii,i} \cdot Cout_{ii} + \sum_{j=1}^{S_j} FTPtoP_{j,i} \cdot CoutTP_j, \quad \forall i \quad (8)$$

Outlet from process i , including the waste water and water reused to other processes

$$Fout_i = Fwwout_i + Frest_i, \quad \forall i \quad (9)$$

The water reused from process i to the rest of the water using operations is:

$$Frest_i = \sum_{ii=1}^{S_j} Freuse_{i,ii}, \quad \forall i \quad (10)$$

The wastewater from operation i driven to the treatment process is:

$$Fwwout_i = \sum_{j=1}^{S_j} FPtoTP_{i,j}, \quad \forall i \quad (11)$$

The inlet flowrate for treatment process j is:

$$Ft_j = \sum_{i=1}^{No} FPtoTP_{i,j} + \sum_{jj=1}^{S_j} FTPtoTP_{jj,j}, \quad \forall j \quad (12)$$

The inlet mass flowrate of contaminant for treatment process j :

$$Ft_j \cdot CinTP_j = \sum_{i=1}^{No} FPtoTP_{i,j} \cdot Cout_i + \sum_{jj=1}^{S_j} FTPtoTP_{jj,j} \cdot CoutTP_{jj}, \quad (13)$$

The flowrate of treated water going to water using operations (= 0), other treatment processes (= 0) and to discharge is:

$$Ft_j = \sum_i^{No} FTPtoP_{j,i} + \sum_{jj}^{S_j} FTPtoTP_{jj,j} + FTPdis_j, \quad \forall j \quad (14)$$

$$FTPtoTP_{j,jj} = 0, \quad \forall j = jj \quad (15)$$

$$Freuse_{i,ii} = 0, \quad \forall i = ii \quad (16)$$

The mass of contaminant treated by wastewater treatment processes, is equal to the total mass of contaminant removed by water in water-using operations minus the

mass of contaminant discharged to the environment:

$$\sum_j^{S_j} Ft_j (CinTP_j - CoutTP_j) = \sum_i^{No} Mc_i - F_{ww} * Cout_{env}, \quad \forall i \quad (17)$$

Equation (18) is the inlet flowrate binary constraint for process j

$$Ft_j \leq z_j \cdot M \quad (18)$$

Equation (19) is the inlet concentration constraint for treatment process j

$$CinTP_j \leq Cin \max TP_j, \quad \forall j \quad (19)$$

The environmental limit concentration constraint is:

$$Cout_{env} \leq Ce \quad (20)$$

The maximum inlet concentration constraint for operation I is:

$$Cin_i \leq C_i^{in,max} \quad (21)$$

The maximum outlet concentration constraint for operation I is:

$$Cout_i \leq C_i^{out,max} \quad (22)$$

Equations (23-25) are the binary water using operation constraints

$$Freuse_{i,ii} \leq zp_{i,ii} \cdot M, \quad \forall i \neq ii \quad (23)$$

$$Freuse_{ii,i} \leq zp_{ii,i} \cdot M, \quad \forall i \neq ii \quad (24)$$

$$zp_{ii,i} + zp_{i,ii} \leq 1, \quad \forall i \neq ii \quad (25)$$

The heat coming in the heat exchanger before process I is:

$$Qin_i = \sum_{ii} (1000 * Freuse_{ii,i} \cdot Cp \cdot Tp_{ii}^{out} / 3600) \quad (26)$$

Equation (27) is the constraint for inlet energy in operation i .

$$Qin_i \leq Q_i^r \quad (27)$$

The additional heat required before entering operation i after integration is:

$$Q_i^{add} = Q_i^r - Qin_i \quad (28)$$

The total additional heat required for heating of streams before entering the unit operations is:

$$TQ^{add} = \sum Q_i^{add} \quad (29)$$

Inequality (30) represents the calculation of the overall energy savings.

$$Q_{ik}^s \geq Q_{ik}^{init} - (Q_{ik}^r - Qin_{ik}) \quad (30)$$

The total energy savings are:

$$TQ^s = \sum_{ik} Q_{ik}^s \quad (31)$$

The total water savings {0, 1} are:

$$W^s = \frac{FW^{init} - FW}{FW^{init}} \quad (32)$$

The total energy savings {0, 1} are:

$$E^s = \frac{TQ^{init} - TQ^s}{TQ^{init}} \quad (33)$$

3. Results

Water and energy consumption before any integration is 3.218 t/h and 192 kW respectively. By applying independent water and energy integration the respective consumptions are reduced to 1.998 t/h and 56 kW resulting in 38 % and 71 % savings for water and energy respectively. Using the model (1-33), and a range of different values for the parameter a , the superstructure is optimized, resulting in different water management networks for the of RESYNTEX process with increasing complexity as a increases. Table 1 reports the savings in fresh water and energy by first applying the superstructure optimization approach and then the conventional energy integration technology, accounting for the new, reduced energy requirements for the water streams entering the water-using operations. By varying the values of a , the region of attainable combined water and energy savings can be constructed. On the curve that fits the points lay all feasible combinations. Above and below the curve, no combinations are feasible in terms of network design.

Table 1 Water and energy savings vs values of a

a	Water consumption (t/h)	Water savings	Energy consumption (kW)	Energy savings (%)
0.2	2030	36 %	48.96	74.5
0.5	2025	37 %	50.16	73.95
0.8	2008	38 %	53.41	72.18

For values of $a = 0.8$ and 0.9 the Table 2 and Table 3 demonstrate - by presenting the resulting flows between water using operations - that by increasing water savings the resulting network becomes more complex and therefore difficult and costly to construct and operate. For $a = 0.8$ 14 operations connections are resulting, while for $a = 0.9$, 19 connections between water using operations are required at the benefit of insignificant increase in savings >38%. Small reduction in water savings results in significant reduction in energy requirements and network complexity.

Table 2 Water network flowrates for $a = 0.8$; water savings 38%

Process	1	2	5	6	7	9	10
2	0.179		0.004	0.004		0.003	
3	0.031	0.476			0.052		
7		0.003	0.1	0.073		0.011	0.044
8			0.101	0.13			

Thus, it is preferable to take advantage of larger energy requirements reduction versus trivially increased water savings, which at the same time are followed by increased and undesired network complexity. A realistic network (Figure 1) is produced by setting $a = 0.2$, which results into 9 connections with flowrates reasonable in terms of justifying a connection (piping and pumping) between operations.

Table 3 Water network flowrates for $a = 0.9$; water savings > 38%

Processes	1	2	3	4	5	6	7	9	10
2	0.153			0.008	0.039				
3	0.32	0.238							
7		0.024	0.002		0.064	0.087		0.015	0.04
8	0.013	0.013	0.019	0.025	0.016	0.02	0.094		0.031

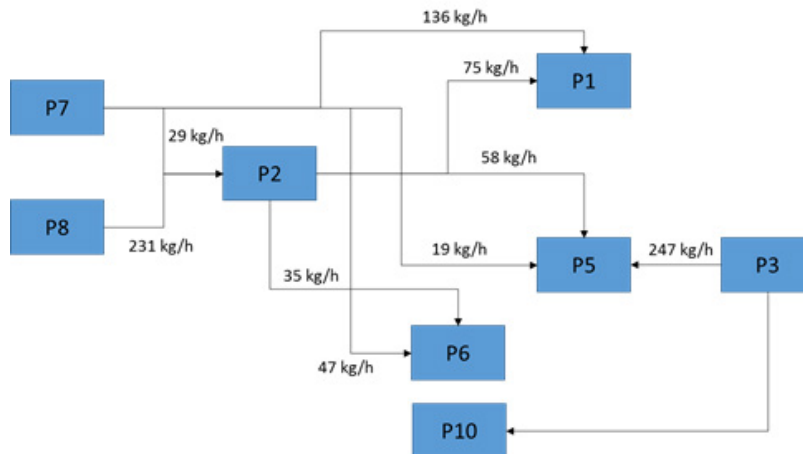


Figure 1 Proposed water network for $a = 0.2$

4. Conclusions

Energy and water integration produce significant results; up to 71% and 86% heating and cooling energy savings respectively, for independent energy integration, 38% savings for independent water integration, while combined energy and water integration can lead to 74.5% energy and 36% water savings, thus an increase of 3.5% in energy savings at the expense of 2% water savings reduction. For water integration, assumptions on concentration limits will have to be validated experimentally. In any case, the computational tools are developed in parametric form and can easily be applied to different process scenarios as well underline assumptions. The integrated process designs will be used for the techno-economic evaluation and for producing the final designs. Future work will also target the reduction of chemicals consumption and the optimization of sustainability metrics, as for example the minimization of CO₂ emissions.

Acknowledgement

This project has received funding from the *European Union's Horizon 2020 research and innovation program* under grant agreement No 641942.



References

- Kalliala, E.M., Nousianinen, P., 1999. Life Cycle Assessment Environmental Profile of Cotton and Polyestercotton Fabrics. *AUTREX Res. J.* 1, 8–20.
- Koufoulioulos, D., Nikolakopoulos, A., Pyrgakis, K., Kokossis, A., 2014. A mathematical decomposition for the synthesis and the application of total site analysis on multi-product biorefineries. *Comput. Aided Chem. Eng.* 34, 549–554. doi:10.1016/B978-0-444-63433-7.50076-6
- Nikolakopoulos, A., Kokossis, A., 2017a. A problem decomposition approach for developing total water networks in lignocellulosic biorefineries. *Process Saf. Environ. Prot.* 109, 732–752. doi:10.1016/j.psep.2016.12.007
- Nikolakopoulos, A., Kokossis, A., 2017b. Targeting and synthesis of single-impurity total water systems using coordinated transshipment models. *Clean Technol. Environ. Policy* 1–19. doi:10.1007/s10098-017-1462-6

The potential for carbon dioxide capture and utilization within the State of Qatar.

Ali Attiq Al-Yaeeshi, Tareq Al-Ansari*, Rajesh Govindan

Divison of Sustainable Development, College of Science and Engineering, Hamad Bin Khalifa University, Qatar Foundation, Doha, Qatar

*talansari@hbku.edu.qa

Abstract

Global warming is directly related to the increasing GHG emissions from both natural and anthropogenic sources. The contribution of CO₂ emissions towards this phenomenon has propelled the international community to initiate research programs that aim to mitigate the emissions through process efficiency improvements, in addition to capturing CO₂ from flue gases at the power plant stacks. Such options have become especially attractive for implementation when they are economically viable. In this regard, one of the most promising technological approach is Carbon Capture and Utilization (CCU). It aims to reduce CO₂ emissions from electricity production and other chemical process industries by capturing CO₂ and subsequently utilizing it in several applications, such as for Enhanced Oil Recovery within the oil and gas industry. The optimum utilization of CO₂ as feedstock potentially enhances the efficiency of chemical conversion processes resulting in useful products of economic value. The objective of this study is to assess the integration of CO₂ utilization within existing processes and technologies to create economic opportunities within the State of Qatar. The methodology includes the development of a geospatial database - comprising information on the CO₂ sources and sinks, and the transport network linking them using GIS - followed by the techno-economic assessment and single-objective linear programming of the proposed CO₂ utilization network which includes the fertilizer and chemical additives industries in Qatar. It was shown that by linking the market prices of value-added products, namely urea and methanol, the optimal solution of the distribution and utilization of CO₂ within the industrial network changes, whilst considering the revenue and profit functions as the network objectives in separate case studies.

Key words: CO₂ Utilization, Linear Programming, Methanol, Urea

1. Introduction

The State of Qatar has recorded rapid economic growth as a result of the continuous development of its vast hydrocarbon resources. Industrial development of this kind will have corresponding environmental challenges in the form of GHG emissions. Qatar is a signatory to the Paris climate agreement which commits all participating nations to reduce their emissions. The development of alternative energy technologies, energy efficiency initiatives, and Carbon Capture and Storage (CCS) programs are critical to both satisfying energy demand and ensuring sustainable development (Ebinger *et al.*, 2011). Significant research and development has focused on CCS, as it is considered a possible strategy to maintain hydrocarbon-driven power generation whilst mitigating CO₂ emissions. In fact,

CCS has the potential to contribute to one-sixth of the emission reduction required by 2050 IEA (2013). The utilization of CO₂ in what is known as carbon capture and utilization (CCU) programs avoids the need to store CO₂ in underground storage sites. CCU enables the creation of an eco-system which encourages the recycling of CO₂ and conversion into value-added products, such as urea, methanol and cement, in addition to its possible utilization for enhanced oil recovery (EOR). An example of the latter is the world's largest EOR project called the 'Weyburn-Midale project' in Canada which has been injecting over 2 Mt CO₂/year for the past 15 years from a coal gasification plant into the Weyburn oil field (Brown, 2017). In the case of Qatar, however, utilization of CO₂ for EOR is yet to be practised commercially. This is primarily due to the lack of fully characterized CO₂ storage options and remains under study (Al-Menhali, 2016).

Multiple studies have considered CCU approaches for industrial zones within the State of Qatar. Using a systems approach, Al-Mohannadi *et al.* (2016) developed cost optimal allocations of natural gas with and without restriction of CO₂ emissions across multiple sources and multiple sinks. It was concluded that the use of renewable energy in power generation could save natural gas allocation and achieve CO₂ emission reduction and additional revenue. Alternatively, reducing the CO₂ emissions can be achieved by the integration of renewable energy systems, where it may compensate the energy lost due to carbon management strategies (Al-Mohannadi, *et al.* 2017). Furthermore, the integration of waste heat and carbon management system to achieve low cost net reductions in CO₂ emissions was also proposed to meet a specified emissions target for an industrial park (Hassiba, 2016). Hassiba and Linke (2017) aims to overcome the limitation of the sequential approach with an integrated optimization model to minimize the overall cost of the CO₂ emissions reduction, while simultaneously exploring the synergy amongst heat and carbon management integration in an industrial park for a pre-specified CO₂ reduction target. In addition, the model also considers renewable thermal energy options to be explored as additional possibilities to reduce CO₂ emissions. Multi-period carbon integration was proposed by Al-Mohannadi, *et al.* (2016) to optimize the transition planning over a time horizon which enables certain emission cuts in future dates.

The objective of this study is to develop an integrated methodology by considering the economic drivers of CO₂ utilization options. It considers a single CO₂ capture system located at the source with the highest CO₂ emissions, thereby reducing the cost of the required compression system and pipeline network. Based on this, a single-objective optimization framework using linear programming (LP) is proposed in order to find solution points that maximizes revenues/profits through increased production rate at the sinks, depending on the market prices of value-added products, whilst achieving CO₂ emissions reduction. This approach was applied for the fertilizer and methanol plants located in the Messaid industrial zone in Qatar as a special case study.

2. Available Data

The following subsections describe the data related to a specific CO₂ source, namely Qatar Aluminium (Qatalum), and two potential sinks that have been identified for the economic utilization of CO₂, namely Qatar Fertilizer Company (QAFCO) and Qatar Fuel Additives Company (QAFAC) in the Messaid industrial zone. The related costs for these include the capital cost of capture system, the cost of CO₂ compression and transportation, and other operating costs associated with the sinks.

2.1. CO₂ Source Data

The CO₂ emissions from Qatalum is around 4.7 Mt/year (DCLG, 2015), making it the highest emitter in the Messaid industrial zone. The capture of CO₂ is assumed to be achieved by chemical absorption using amine solvents, and thus the maximum achievable capture removal efficiency of 90% was assumed. Based on this the estimated cost of the capture system is around \$40/t of CO₂ (Hildebrand, 2009). This corresponds to an estimated capital cost of the capture system of approximately \$169 million.

2.2. CO₂ Compression and Transport Data

Compression is needed to overcome the pressure drop in pipelines and to meet sinks pressure requirements. The unit cost of compression and transportation per 100 km of the pipeline is approximately \$1.5/tCO₂ (Herzog et al., 2004). In this case study, the total cost of compression and transport to both QAFAC and QAFCO is approximately \$0.5 million.

2.3. CO₂ Sinks Data

2.3.1 Urea production

In this study, it is proposed that a reliable external source of CO₂ supply would be provided via CO₂ capture and utilization in order to produce additional urea with the excess ammonia available. Five ammonia plants are currently operating in the State of Qatar. In the event of an ammonia plant shutdown, there still exists an opportunity to sustain the production of urea by sourcing the excess ammonia and CO₂ from other operating plants. Qatar Fertilizer Company (QAFCO) exports around 15% of its ammonia produced which amounts to approximately which equals approximately 0.55 Mt/year in 2014. However, in this study it is suggested that it would be useful to monitor the price of ammonia in the Middle East spot market because in 2016 it had faced competition with the price of urea, thus leading to the essential question of whether it is more valuable to produce greater quantities of urea for export rather than exporting the surplus ammonia. On average, the 2016 prices of ammonia and urea were \$220/tonne and \$300/tonne respectively (Argus Media, 2017). Moreover, according to the relation between these products, one tonne of urea can be produced from 0.57 tonne of ammonia and 0.74 tonne of CO₂ (Park, 2001). Thus, if the exported amount of ammonia (0.55 Mt/year) is reacted with CO₂ (0.74 Mt/year), it would result in the production of 1.3 Mt of urea/year. When this quantity is exported, it would generate a revenue of \$390 million, which is greater than that generated by exporting the excess ammonia (approximately \$121 million), based on 2016 prices. In addition, the capital cost for the urea plant corresponding to this production capacity is approximately \$610 million (Kable, 2017).

2.3.2 Methanol production

Qatar Fuel Additives Company (QAFAC) operates a methanol plant based on natural gas feed (mainly methane C1) with a capacity around 3,000 tonne/day. The average market price was around \$220/t of methanol in 2016 (Argus Media, 2016). In this study, it is proposed that an external CO₂ source can be utilised to meet methanol production targets by integrating CO₂ source to the methanol synthesis unit with 500 t/day (Al-Hitmi, 2012). Additionally, an opportunity exists for QAFAC to increase the production of methanol by using hydrogen, which is available in Messaid, together with the captured CO₂ as raw materials with ratio H₂/CO₂ 3:1 (Pérez-Fortes, et al., 2016). This option can potentially contribute to a relatively higher net reduction in CO₂ emissions

for the same methanol production target. The capital cost of methanol plant corresponding to this target was estimated to be approximately \$1,200 million, with the average price of \$4,000/t of hydrogen (Pérez-Fortes, et al., 2016).

3. Methodology

The LP formulation for the proposed CO₂ utilization network, as illustrated in Fig 1, considers CO₂ resource allocation from Qatalum to QAFAC and QAFCO, constrained by their utilization capacities.

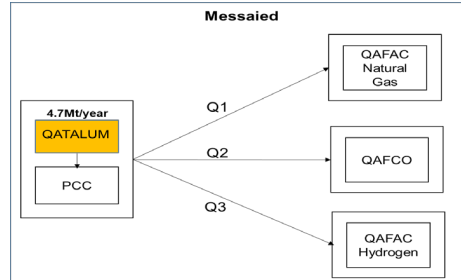


Fig.1 Proposed CO₂ utilization network in the Messaid industrial zone.

The nomenclature of variables used in the LP formulation is as follows:

Decision variables

- Q₁: fraction of CO₂ transported from Qatalum to QAFAC (using NG).
- Q₂: fraction of CO₂ transported from Qatalum to QAFACCO.
- Q₃: fraction of CO₂ transported from Qatalum to QAFAC (using hydrogen).

Parameters related to Qatalum

- η : efficiency of CO₂ capture system = 0.9.
- e : CO₂ emissions rate = 4.7 Mt/year.
- C_1 : cost factor incurred through CO₂ capture = $\eta \times e \times \$40/\text{t CO}_2$.

Parameters related to QAFAC (using natural gas)

- d_2 : pipeline distance from Qatalum = 3km.
- ρ : density of natural gas = 0.9 kg/m³
- C_{21} : CAPEX of methanol plant = \$1,200 million.
- C_{22} : cost factor incurred through CO₂ transportation = $\eta \times e \times (d_2/100) \times \$1.5/\text{t CO}_2$
- C_{23} : cost factor incurred from natural gas purchase = $\eta \times e \times 0.82 \times \$2.5/\text{ft}^3 \text{ NG} \times \rho$
- R_2 : revenue factor from methanol = $\eta \times e \times 1.82 \times \$220/\text{t methanol}$.

Parameters related to QAFACCO

- d_3 : pipeline distance from Qatalum = 5km.
- C_{31} : CAPEX of urea plant = \$610 million.
- C_{32} : cost factor incurred through CO₂ transportation = $\eta \times e \times (d_3/100) \times \$1.5/\text{t CO}_2$
- R_3 : revenue factor from urea = $\eta \times e \times 1.82 \times \$300/\text{t urea}$.

Parameters related to QAFAC (using hydrogen)

- d_4 : pipeline distance from Qatalum = 3km.
- C_{41} : cost factor incurred through CO₂ transportation = $\eta \times e \times (d_4/100) \times \$1.5/\text{t CO}_2$
- C_{42} : cost factor incurred from hydrogen purchase = $\eta \times e \times \$4000/\text{t H}_2$
- R_4 : revenue factor from methanol = $\eta \times e \times 1.82 \times \$220/\text{t methanol}$.

The goal is to find optimal solutions for allocation with the potential to maximize profit from the products manufactured at the sinks within the network. In effect, this also leads to the reduction in CO₂ emissions in an economical manner. Hence:

$$\begin{aligned} & \text{Maximize } \{Q_1 \times (R_2 - C_{11} - C_{21} - C_{22} - C_{23}) + Q_2 \times (R_3 - C_{11} - C_{31} - C_{32}) + Q_3 \times \\ & (R_2 - C_{11} - C_{41} - C_{42})\} \\ & \text{subject to,} \\ & Q_1 + Q_2 + Q_3 \leq 1, \\ & Q_1 \times \eta \times e \leq 0.60 \times 10^6, \\ & Q_2 \times \eta \times e \leq 1.01 \times 10^6, \\ & Q_3 \times \eta \times e \leq 1.83 \times 10^6, \\ & Q_1 \times (R_2 - C_{11} - C_{21} - C_{22} - C_{23}) \geq 0 \text{ (profit constraint for QAFAC using natural} \\ & \text{gas).} \\ & Q_2 \times (R_3 - C_{11} - C_{31} - C_{32}) \geq 0 \text{ (profit constraints for QAFAC), and} \\ & Q_3 \times (R_2 - C_{11} - C_{41} - C_{42}) \geq 0 \text{ (profit constraint for QAFAC using hydrogen).} \end{aligned} \quad (1)$$

3. Results

Tables 1 and 2 indicate the optimized CO₂ allocations when: (a) the profit constraint is non-negative as indicated in Eq. 1; and (b) the profit constraint is relaxed, i.e. the utilization network is only optimized for revenue, and thus can potentially make a loss.

Table 1. The profit constraints are non-negative.

Decision Variables (fractional amount of CO ₂ from QATALUM)	
Q ₁	0.0322
Q ₂	0.0453
Q ₃	0
Objective (Profit) \$	9.89x10⁷

Table 2. The profit constraints are relaxed.

Decision Variables (fractional amount of CO ₂ from QATALUM)	
Q ₁	0.142
Q ₂	0.241
Q ₃	0.431
Objective (Profit) \$	-6.06 x10⁹

The results illustrate that when the CCU network optimization is applied for the specified case study, a clear benefit is achieved in terms of generating revenues/profits at the sinks, whilst simultaneously reducing carbon emissions. The CCU network model is considered economically attractive when the price of methanol and urea increases, driven by the high demand, particularly in the Asian and European markets. The results of this study indicate the total CO₂ flow rate from the source to the sinks once the model optimized for profit and revenue are 0.3Mt/y and 3.4Mt/y respectively. In Table 1, the results correspond to the case where the model is optimized for profit such that the CO₂ will be consumed at a lower rate. On the other hand, the results in Table 2 correspond to the case where the model is optimized for revenue such that CO₂ is consumed more efficiently, whilst making a loss. These results suggest that the environmental and economic objectives are competing, as expected. Moreover, this is also a consequence of the high price of hydrogen as a raw material for the methanol plant. However, it is envisaged that the recovery of any network losses could be carried out within a time horizon of 5 to 10 years, subject to the demand, and consequently the selling price, of the value-added products.

4. Conclusion

The analysis presented considers CCU to increase methanol and urea production, whilst reducing CO₂. The approach demonstrates the potential economic benefit of a proposed CCU network in Qatar which is dependent on the market prices of value-added products. Considering that price fluctuations exist, future work will capture this effect by considering the economic life cycle of the network at the plant-level and modelling the economic objective in terms of the net present value (NPV) and internal rate of return (IRR), which will be implemented within a multi-period optimization formulation.

References

- Al-Mohannadi, D.M., Abdulaziz, K., Alnouri, S.Y. and Linke, P., 2017. On the synthesis of carbon constrained natural gas monetization networks. *Journal of Cleaner Production*, 168, pp.735-745.
- Al-Mohannadi, D.M., Alnouri, S.Y., Bishnu, S.K. and Linke, P., 2016. Multi-period carbon integration. *Journal of Cleaner Production*, 136, pp.150-158.
- Al-Mohannadi, D.M. and Linke, P., 2016. On the systematic carbon integration of industrial parks for climate footprint reduction. *Journal of Cleaner Production*, 112, pp.4053-4064.
- Argus Media, 2016, Argus Methanol Annual 2016, Available from: <http://www.argusmedia.com/petrochemicals/2016-methanol-annual/> [Accessed 7 December 2017].
- Argus Media, 2017, Argus Ammonia Market Summary, Available from: <http://view.argusmedia.com/rs/584-BUW-606/images/Argus%20Ammonia%20%282017-08-03%29.pdf> [Accessed 7 December 2017].
- Al-Menhali, A., 2016. Multiphase flow for CO₂ injection in saline aquifers and oil reservoirs: multi-scale observations (Doctoral dissertation, Imperial College London).
- DCLG., 2015, Environmental Impact Assessment, Department for Communities and Local Government, 1-98. Available from: <https://www.gov.uk/guidance/environmental-impact-assessment#mitigation-measures> [Accessed 7 December 2017].
- Ebinger, C., Hultman, N., Massy, K., Avasarala, G. and Rebois, D., 2011. Options for Low-carbon Development in Countries of the Gulf Cooperation Council. Policy.
- Hassiba, R.J., Al-Mohannadi, D.M. and Linke, P., 2017. Carbon dioxide and heat integration of industrial parks. *Journal of Cleaner Production*, 155, pp.47-56.
- Hassiba, R.J. and Linke, P., 2017. On the simultaneous integration of heat and carbon dioxide in industrial parks. *Applied Thermal Engineering*, 127, pp.81-94.
- Herzog, H. and Golomb, D., 2004. Carbon capture and storage from fossil fuel use. *Encyclopedia of energy*, 1(6562), pp.277-287.
- Hildebrand, A. N., 2009, Strategies for Demonstration and Early Deployment of Carbon Capture and Storage: A Technical and Economic Assessment of Capture Percentage. Available from: http://sequestration.mit.edu/pdf/AshleighHildebrand_Thesis_May09.pdf [Accessed 7 December 2017].
- IEA, 2013, Technology Roadmap: Carbon Capture and Storage, France [Online], Available from: <http://www.iea.org/publications/freepublications/publication/technologyroadmapcarbonsaptureandstorage.pdf> [Accessed 7 December 2017].
- Kable Intelligence Limited, 2017, QAFCO V and VI Projects, Qatar, Available from: <http://www.chemicals-technology.com/projects/qafco-v-vi/> [Accessed 7 December 2017].
- Park, M., 2001. Fertilizer Industry, Woodhead Publishing [Accessed 7 December 2017]
- Al-HitmiKMR.QAFAC:Carbondioxiderecoveryplant,Sustainable Technologies, Systemsand Policies2012 Carbon Captureand Storage Workshop:22 <http://dx.doi.org/10.5339/stsp.2012.ccs.22> [accessed 18 February 2018]
- Pérez-Fortes, M., Schöneberger, J.C., Boulamanti, A. and Tzimas, E., 2016. Methanol synthesis using captured CO₂ as raw material: techno-economic and environmental assessment. *Applied Energy*, 161, pp.718-732.

Optimization of Batch Heteroazeotropic Distillation Operational Strategies with Entrainer Recycle

Laszlo Hegely*, Peter Lang

Budapest University of Technology and Economics, Department of Building Service and Process Engineering, Muegyetem rkp. 3-9, H-1111 Budapest, Hungary

hegely@mail.bme.hu

Abstract

The batch heteroazeotropic distillation (BHAD) separation of a minimum boiling azeotropic mixture (isopropyl alcohol(A) – water(B)) with toluene as entrainer(E) is simulated and optimized with GA. The production cycle consists of processing three consecutive batches. Both BHAD operational modes (sequential (Mode I) and simultaneous (Mode II) distillation + decantation) are studied. The E-rich phase and (eventually) the off-cut can be recycled to the next batch to reduce the loss of both isopropyl alcohol and the entrainer. The optimization variables are the amount of E added to the charge and the reflux ratios of the steps. The effect of the recycling is discussed and the optimization results are compared with those of the non-optimized processes.

Keywords: batch heteroazeotropic distillation, optimization, entrainer recycle.

1. Introduction

For the separation of azeotropic mixtures a special distillation method, such as batch heteroazeotropic distillation (BHAD) must be applied. By BHAD an entrainer (E) is added to the binary mixture (A-B) before the start of the distillation which forms at least one heteroazeotrope with the original components. The liquid-liquid split (decantation) makes the separation feasible. BHAD can be performed by two operational modes. The whole amount of the E-lean phase is usually withdrawn; it is partially refluxed only if the E-rich phase does not provide sufficient reflux.

By Mode I, the distillation and decantation are performed sequentially (the whole amount of the E-rich phase is withdrawn with the E-lean one) while in Mode II simultaneously. By Strategy A of Mode II the whole amount of the E-rich phase is refluxed, by Strategy B, one part of it is also withdrawn.

The majority of E is present in the E-rich phase and a much smaller part of it in the E-lean one. For both economic and environmental reasons, E must be recycled and reused in the next batch. Luyben and Chien (2010) studied the dehydration of acetic acid with isobutyl acetate (E) by Mode II (Strategy A) without optimization where E was recycled.

In our previous work (Hegely and Lang, 2017), the dehydration of isopropanol(A)-water(B) mixture of azeotropic composition with toluene (E) was studied. Calculations were performed for Mode I and both strategies of Mode II. The values of the operational parameters were chosen to obtain a high specific product flow rate (SPF: amount of product/duration of the process). Strategy A of Mode II gave the highest recovery, but it was much slower than Mode I. Strategy B gave unsatisfactory results. In a cycle of 3

batches recycling made Mode I infeasible for Batch III because of the accumulation of B, while it had favourable effects (increased recovery, faster production) for Mode II. The goals of this work is to optimize the three-batch processes with a genetic algorithm (GA). The objective function to be maximized is the profit of the individual batches, which are optimized separately. The dynamic simulation is performed by ChemCAD. The description of the phase equilibria is made more accurate than it was in our previous work.

2. The separation process

The components form a ternary and three binary minimum boiling azeotropes (Table 1). The UNIQUAC binary interaction parameters were taken from Stankova et al. (1970) for the VLE and from Washburn and Beguin (1940) for the LLE at 25 °C (temperature of the decanter) which can be produced with inexpensive cooling water.

Table 1. Calculated boiling point (T_{bp}) and composition of the azeotropes (1.013 bar).

	T_{bp} (°C)	A (mol%)	B (mol%)	E (mol%)
ABE	76.6	36.4	37.7	25.9
ABE – E-rich phase (25 °C)		39.3	31.6	29.1
ABE – E-lean phase (25 °C)		14.3	84.5	1.2
AB	80.0	67.6	32.4	-
AE	81.3	81.3	-	18.7
A	82.3	100	-	-
BE	84.8	-	56.4	43.6
B	100.0	-	100	-
E	110.6	-	-	100

The composition of the ABE azeotrope is in acceptable agreement with the experimental one (33.6 % A, 38.5 % B and 27.9 % E). The azeotrope is close to the binodal solubility curve, thus it is important to calculate it accurately. (By repeating the calculations for Mode II, the production time was only the fifth of that of Hegely and Lang (2017)).

The aim is to produce A as the still residue in 98 mol% purity. For Mode I, processing of Batch I has the following steps:

- Step 0: Warming up of the charge (fresh feed+E) onto its boiling point and heating-up of the column under total reflux ($R = \infty$). This step is finished when the composition of the top vapour is close to that of the ternary heteroazeotrope.
- Step 1: Production of distillate with overall composition close to that of the ternary heteroazeotrope. The distillate has two liquid phases, and decantation is performed later in the distillate accumulator. A finite reflux ratio ($R_1 < \infty$, optimization variable) is applied. This step is finished when the aqueous phase disappears in the decanter. The E-rich phase of the accumulated distillate is recycled to the next batch.
- Step 2: Off-cut collection under $R_2 < \infty$ (optimization variable) to remove B and E from the still. This step is finished when the concentration of A in the still (product) reaches its specified value. The off-cut cannot be recycled (high B content).

For Mode II, only the differences are highlighted:

- Step 0: E is filled into the decanter instead of the still, as this was found to be more favorable (Hegely and Lang, 2017). This step includes the filling up of the decanter, and is finished when the prescribed levels of both liquid phases are reached.
- Step 1: Removal of B in the form of E-lean phase. Both liquid phases have a constant level in the decanter. The excess of E-lean phase is withdrawn as distillate, while that

of the E-rich phase is refluxed entirely to the column (Strategy A). R_1 is determined by the phase ratio (ca. 7.7 mol/mol) of the condensate. This step is finished when the E-lean phase disappears or the concentration of A in the still reaches the prescribed purity. The E-rich can be recycled to the next batch by mixing it to the fresh feed.

- Step 2: The off-cut can be recycled, as its B content is low.

For Batches II and III, Step 0 is slightly different from those of Batch I. The E-rich phase and the off-cut of the previous batch are mixed to the fresh feed before distillation. Fresh E can also be added to the charge (Mode I) or to the decanter (Mode II).

3. Optimization method

The three batches are optimised consecutively, that is, each batch is optimised separately for the charge composition (x_{Ch}) obtained by mixing fresh feed and the material recycled from the previous batch. The mass of fresh feed is calculated so as to always obtain the same charge volume (1.16 m³) before the addition of E.

The objective function (OF) to be maximized is the profit of the individual batches:

$$OF = p_A m_{pA} - p_E m_E - c_{inc} m_{inc} - c_{st} Q_{st} t \quad (1)$$

where m_{pA} is the mass of the product A, m_E is that of the fresh E, and m_{inc} is that of liquid to be incinerated (E-lean phase and for Mode I, the off-cut). p_A is the price of the product A (1 \$/kg), p_E is the price of E (0.672 \$/kg). c_{inc} is the cost of incineration (0.21 \$/kg), c_{st} is cost of heating steam (low pressure (4 bar) 8.308 \$/GJ), Q_{st} is the heat duty (0.4 GJ/h), and t is the duration of the whole process including warming-up of the charge.

For Mode I, the optimization variables are the amount of E added to the fresh feed (F_E) and the reflux ratios of the steps: R_1 , R_2 . The upper bound of F_E is 6.32 kmol, above which x_{Ch} is located in the distillation region, where E is the stable node instead of A. The lower bound for the reflux ratios is 0.2, the upper one is 10 and 15, respectively. The optimization of Mode I is performed by a real-coded elitist GA written in VBA under Excel. The parameters of the GA: mutation probability: 5 %, crossover probability: 70 %, population size: 30, number of generations: 100. OF is evaluated by dynamic simulation using different modules of the flow-sheet simulator ChemCAD. The failure to reach the specified purity of the product is penalized by changing the value of OF to -10,000 \$.

For Mode II, the possible optimization variables are F_E and R_2 , if taking off-cut is necessary. We found (Hegely and Lang, 2017) that an off-cut is only necessary above a certain F_E value. As we will show later, at the optimal F_E value, the prescribed purity is reached during Step 1, and no off-cut is taken. This reduces the optimization problem to a one-dimensional one, therefore the use of GA is not necessary.

The column has $N=28$ theoretical stages (excluding the reboiler and the condenser), with a liquid hold-up of 2 dm³/stage. Q_{st} is 400 MJ/h. The hold-up of the total condenser is 40 dm³. The hold-up of the decanter (83.1 dm³) is chosen to ensure a residence time of 5 min. The hold-up of the heavy (E-lean) phase is 6.4 dm³. For Mode I, Step 0 lasts 1 h. The column design is fix, but N could be included in the optimization when a new column is designed. This would change the optimal values of R , but not the main conclusions.

4. Optimization results

4.1. Mode I

For Batch I, the optimal F_E and reflux ratios are higher than in the non-optimized process (Table 2). The optimization made the process economical, mostly by increasing the amount of the product (income) and considerably decreasing the incineration cost (C_{inc}) by practically eliminating the off-cut (decreased from 7.05 to 0.01 kmol) due to the increased R_1 . The amount of the two-phase distillate increased, but only its E-lean phase has to be incinerated (1.83 instead of 1.05 kmol).

Table 2. Charge compositions, optimal values of the parameters, costs and profit of the optimized and non-optimized processes (Mode I).

Batch	$x_{Ch,A}$ mol%			F_E , kmol	R_1	R_2	Income, \$	Cost, \$			Profit, \$
	A	B	E					E	Incin.	Steam	
Optimized I	67.4	32.6	0.0	4.39	2.98	13.13	393	272	26	33	79
II	46.9	30.8	22.3	-	1.93	11.51	110	0	16	24	70
III	49.0	29.8	21.2	0.02	1.94	11.21	162	1	10	23	128
Non-optimized I	67.4	32.6	0.0	4.00	2.00	9.00	350	248	82	36	-16
II	55.8	31.0	13.2	1.56	2.00	9.00	237	96	10	20	110
III	47.5	30.4	22.2	0.09	2.00	9.00	78	6	28	20	25

The total amount of the E-rich phase from Batch I cannot be recycled to the next batch. The amount of recycled material is so high (15.96 kmol) that only 1.52 kmol fresh feed can be treated. The composition of the recycled material (Figure 1, point R) lies outside the distillation region where A is stable node, and by mixing this low amount fresh feed to it, the x_{Ch} of Batch II (point Ch) lies also outside the desired region. This means that E would be obtained as still residue instead of A, so the amount of recycled material must be reduced. The hold-up is recycled entirely, as its composition is favourable, but the amount of E-rich phase recycled is reduced so that x_{Ch} lie just inside the feasible region. However, this means that fresh E cannot be added to the charge, as it would move the composition outside of the region, thus F_E is not an optimization variable for Batch II.

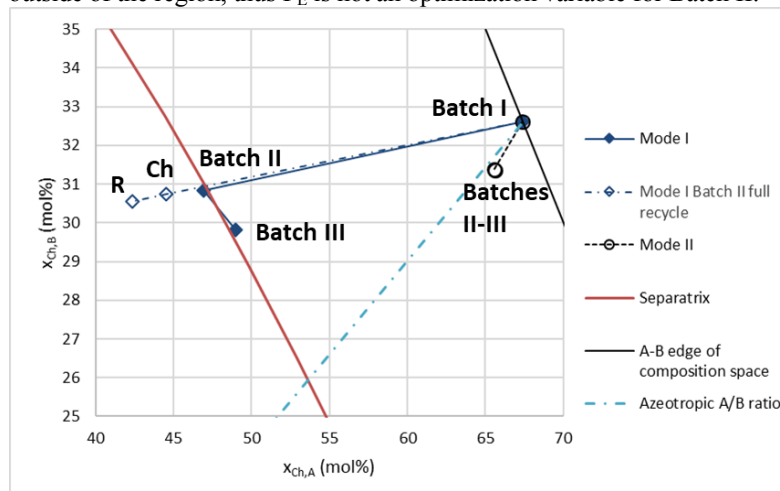


Figure 1. The effect of recycling on charge composition by the different operational policies

The charge of Batch II has a low A/B ratio and high E content. This is the result of taking very low amount of off-cut, which is advantageous for Batch I, but significantly reduces the income of Batch II. The profit is lower than that of the non-optimized process. The reflux ratios of Batch II are lower than those of Batch I; R_1 is similar to that of the non-optimized process, while R_2 is higher. Unlike for Batch I, the total amount of the E-rich phase can be recycled to Batch III, so F_E is again an optimization variable.

By Batch III, x_{Ch} is more favourable than that of Batch II (Figure 1) with a higher A/B ratio. The small change in x_{Ch} results in a significant increase of the income and profit. Practically no fresh E is needed, and the reflux ratios are similar to those of Batch II.

The optimization more than doubled the profit of the cycle. The total income is identical, but the cost of E (C_E) and C_{inc} are greatly reduced. The recycling greatly affects the results (Table 3). The amount of fresh E is greatly reduced, but so is that of the fresh feed and the product, although the recovery of A (η_A) increases. The duration is shorter with recycling, but SPF decreases. However, without recycling the amount of material to be incinerated is ten times more, making the process uneconomical (total profit: -299 \$).

Table 3. Results of the optimized three batch processes (with and without recycle) for Mode I.

	F_E , kmol	Fresh feed, kmol	Product, kmol	Total non- recycled, kmol	Duration, h	SPF, kmol/h	η_A , %
Batch I	4.39	20.0	6.58	1.85	10.0	0.657	47.8
Batch II	0.00	3.07	1.80	2.26	7.1	0.254	21.3
Batch III	0.02	4.01	2.68	1.71	6.8	0.394	30.4
Total	4.41	27.1	11.1	5.81	23.9	0.463	59.4
No recycle	13.2	60.0	19.7	48.6	30.1	0.657	47.8

4.2. Mode II

For the optimal amount of E, no off-cut is necessary, thus F_E is the only optimization parameter (results in Tables 4 and 5). For Batch I, its effect was studied in the range 0.65-0.9 kmol. On the increase of F_E , m_{PA} increases. The increase of C_E is obvious. Both the cost of heating steam and C_{inc} have a minimum as a function of F_E . The minimum of C_{inc} is a result of two effects. By increasing F_E , it takes more time to remove E from the still. By decreasing it, however, the level of the aqueous phase in the decanter reaches its prescribed value slower. Nevertheless, the variation of C_{inc} is very slight. The profit has a minimum at $F_E=0.7$ kmol. Its total variation in the range studied is less than 9 \$.

Table 4. Charge compositions, optimal values of F_E , costs and profit of the optimized and non-optimized processes (Mode II).

	Batch	x_{Ch} , mol%			F_E , kmol	Income, \$	Cost, \$			Profit, \$
		A	B	E			E	Incin.	Steam	
Optimized	I	67.4	32.6	0.0	0.7	656	43	36	42	535
	II	65.6	31.4	3.1	0.09	617	6	33	41	536
	III	65.6	31.3	3.1	0.09	617	6	33	41	536
Non-optimized	I	67.4	32.6	0.0	0.843	670	52	37	45	533
	II	65.5	31.4	3.1	0.242	629	15	34	44	535
	III	65.6	31.3	3.1	0.240	629	15	34	44	536

As 0.60 kmol E is recycled to Batch II, only a small E make-up is necessary. Instead of the value necessary to reach 0.7 kmol ($F_E=0.104$ kmol), the optimal F_E value was lower

(0.09 kmol). The main differences between Batches I and II are that in Batch II, the A/B ratio of the charge is higher (Figure 1), and the greater part of E is initially in the still. The income of Batch II is lower, but so is C_E , thus the same profit is reached. By Batch III, x_{Ch} is almost identical to that of Batch II, thus optimization was deemed unnecessary.

Recycling reduces the amount of fresh E needed to less than half, but also the amount fresh feed processed by 12 % (Table 5). However, due to the increase in η_A , the amount of product is lower only by 4 %. The duration of the production is also lower with recycle. If no recycling is applied, C_{inc} is 50 \$ instead of 36 \$, thus recycling is preferable not only environmentally, but economically, as well.

Table 5. Results of the optimized three batch processes (with and without recycle) for Mode II.

	F_E , kmol	Fresh feed, kmol	Product, kmol	Total non- recycled, kmol	Duration, SPF, h	η_A , %
Batch I	0.7	20.0	11.1	6.7	12.7	0.872 80.4
Batch II	0.09	16.6	10.4	6.2	12.4	0.840 79.7
Batch III	0.09	16.5	10.4	7.5	12.4	0.838 79.6
Total	0.88	53.1	31.8	20.5	37.5	0.850 87.1
No recycle	2.1	60.0	33.2	24.0	38.1	0.872 80.4

In the non-optimized process, the decanter was completely filled with E in Batch I, and for Batches II-III, only the E lost in the previous batch was added to the decanter. The higher F_E increased both C_E and m_{pA} , however the profit was only very slightly lower for every batch. The charge compositions (without the E added) were almost identical to those of the optimized process. These results indicated, as well, that the profit is not very sensitive to the value of F_E , which could enable a robust technology in practice.

5. Conclusions

Dehydration of the isopropanol(A)-water(B) azeotrope with toluene as entrainer (E) by batch heteroazeotropic distillation was optimised by a GA. One production cycle consists of three batches. The E-rich phase is recycled to the next batch to reduce the loss of A and E. The profit of each batch was maximised separately. Optimization variables were the amount of E added (F_E) and the reflux ratio of the steps (R_1 , R_2). By Mode I, optimization greatly increased the profit by reducing the cost of E and incineration. The amount of recycled material was high, which significantly decreased the capacity, and changed the charge composition, but without E recycling, the process was uneconomical. By Batch II, the E-rich phase was only partially recycled to ensure the feasibility of A production and no fresh E was added. By Mode II, taking off-cut was not necessary at the optimal F_E . Since the profit was not very sensitive to F_E , the optimization only increased it slightly. Recycling reduced the E consumption to less than half, increased the recovery of A, but also reduced the amount of fresh feed treated. Mode II was superior to Mode I in every respect except the amount of non-recycled material. With E recycling, fresh E had to be added to Batch I by both modes, and Batches II-III required only a small E make-up. Future work could include simultaneous optimization of the batches that is computationally more intensive as the number of variables is three times higher.

Acknowledgement

This work was supported by OTKA (Project No.: K-120083).

References

- L. Hegely, P. Lang, 2017, Entrainer Recycle for Batch Heteroazeotropic Distillation, *Chemical Engineering Transactions*, 61, 949-954.
- W.L. Luyben, I.L. Chien, 2010, *Design and Control of Distillation Systems for Separating Azeotropes*, John Wiley & Sons, Inc., Hoboken, New Jersey, USA, 421-422.
- L. Stankova, F. Vesely, J. Pick, 1970, *Collect. Czech. Chem. Commun.* 35, 1.
- E.R. Washburn, A.E. Beguin, 1940, *J. Am. Chem. Soc.*, 62,579.

Energy Efficient Design of Ionic Liquid based Gas Separation Processes

Xinyan Liu^{a,b}, Xiaodong Liang^a, Xiangping Zhang^b, Suojiang Zhang^b, Georgios M. Kontogeorgis^{a*}, Rafiqul Gani^a

^a *Department of Chemical & Biochemical Engineering, Technical University of Denmark, DK 2800 Kgs. Lyngby, Denmark*

^b *Beijing Key Laboratory of Ionic Liquids Clean Process, State Key Laboratory of Green Process and Engineering, Institute of Process Engineering, Chinese Academy of Sciences, Beijing 100190, China*
gk@kt.dtu.dk

Abstract

Gas separation processes are among the most important operations in the oil and gas related industries. The most common separation technology applied is distillation, which consumes large amounts of energy. Because of the good stability, non-volatility, tunable viscosity and designable properties, ionic liquids (ILs) are regarded as novel potential solvents and alternative media for gas absorption. Therefore, a strategy for hybrid gas separation process synthesis where distillation and IL-based absorption are employed for energy efficient gas processing has been developed. In this work, a three-stage methodology proposed for hybrid gas separation process design and evaluation is proposed: IL screening, where a systematic screening method together with a database tool is established to identify suitable ILs; process design, where the important design issues (amounts of solvent needed, operating temperatures and pressures, evaporation conditions, etc.) are determined; process simulation and evaluation, where the final separation process results are concluded.

Keywords: gas separation; ionic liquids; property model; process design

Introduction

Currently, traditional gas separation technologies are energy intensive distillation and solvent based absorption operations or flux limited adsorption and membrane-based operations. For most gas mixtures, the most common separation technology applied is distillation, which consumes large amounts of energy to give the high purity products. These distillation columns operate at low temperatures and high pressures and therefore require high energy consumption, leading to negative environmental impacts. Therefore, an alternative scheme, taking advantage of each individual technology, a hybrid gas separation scheme of combining distillation with absorption separation processes is proposed.

Due to designable properties as well as good stability and non-volatility, ionic liquids (ILs) are regarded as potential mass separating agents for gas absorption. In this work, a strategy for hybrid gas separation process synthesis where distillation and IL-based absorption are employed for energy efficient gas processing is presented. Most of the developments related to the use of ILs for gas absorption have concentrated on the CO₂ capture capacities of different ILs, which points to the potential of an IL-based gas decarbonization technology (Liu et al., 2016). Encouraged by good absorption of CO₂ with ILs, new studies have focused on the solubility of other gases in ILs. However, the

thousands of ILs that may be potentially applicable, makes it a challenging task to search for the best one for specific gas absorptions from different raw gas. In addition to the solubility of the selected gas in the solvent (ILs or other organic chemicals), the selectivity of the IL solubility for the gases to be separated is also very important, together with other pure component properties of ILs. Therefore, before a selection-screening method for ILs for use in absorption based gas separation tasks can be developed, the needed properties must be available in the form of data or property models from which they can be obtained. Several options, such as, group contribution (GC) based UNIFAC (Lei, Dai, Wang, & Chen, 2014) or the COSMO-RS method (Klamt & Eckert, 2000) can be applied for solubility and selectivity predictions, while a database or GC-based models for pure component properties may be used. In this paper, in order to lay a foundation for ILs screening and design, a database, containing experimental data for different gas solubility and Henry's law constants for gases in ILs, is established. Both the COSMO-RS method and the UNIFAC model are applied for the needed predictions of gas solubility in ILs. Further, a hybrid gas separation scheme to separate gases from a model shale gas mixture is developed and evaluated.

Methodology

In this work, a three-stage methodology for hybrid gas separation process design and evaluation is proposed. The first stage involves IL screening, where a systematic screening method together with a database tool is established to identify suitable ILs based on a collection of gas solubility data, Henry's law constant data as well as data estimated through reliable predictive models, for example, COSMO-RS (Klamt & Eckert, 2000), UNIFAC (Lei et al., 2014). Further, design of problem specific ILs for different gas-IL systems is developed. It should be noted that models and data operate at multi-scale. The second stage is process design, where the important design issues such as the amount of solvent needed, operating conditions (temperature and pressure), and solvent recovery are determined. This stage operates at macro scale. A hybrid gas separation scheme is designed to replace the conventional distillation process, where the only energy requiring step in the hybrid process is the flash-evaporation step (and the low energy consuming pre-distillation step, if employed). Potentially a large reduction of energy consumption is therefore possible by switching from distillation to the hybrid-absorption scheme for selective gas separation tasks. For example, replace distillation by absorption to remove only the gases present in smaller amounts in the gas mixture, thereby letting the larger amounts to go free as the exhaust gas product. This small amount of absorbed gas is easily separated from the IL solvent through evaporation or distillation, which only consumes a small fraction of the total energy of the conventional distillation based process. The third stage involves verification, sustainability and economic analysis based on rigorous process simulation of the generated hybrid gas separation process. Application of the methodology is highlighted for a gas separation problem involving a model shale gas mixture.

Database and model library

Database library

The database includes collected measured solubility data and Henry's law constant of gases in ILs at different temperatures. It covers 16 gases 260 ILs for the gas solubility data and 11 gases 110 ILs for the Henry's law constants. It also includes predicted data from COSMO-RS, covering 16 gases for 13585 ILs.

Property library

The solubility data generated through COSMO-RS have been reported (ref) to be useful for qualitative screening, where the activity coefficient calculated from the interaction of charge screening on molecular surface can be employed. However, a comparison between experimental activity coefficients of different gases in ILs and the COSMO-RS predicted values revealed that while for some light hydrocarbon gases, such as C_2H_4 and C_2H_6 , a fairly accurate model could be obtained (see Fig 1), for the CO_2 and CH_4 solubility, the errors were too large (see Fig 2). Equations 1-2 give the correlations obtained from the COSMO-RS and experimental data for gas solubility of C_2H_4 and C_2H_6 (see Table 1). For CO_2 solubility in IL, a new UNIFAC model is developed using the available experimental data only. Table 2 lists the 14 pairs of parameters (a_{ij}) that are fitted for 22 IL- CO_2 systems, containing 2 main cations with different alkyl chain as substituent and 11 anions. For CH_4 solubility in IL, only experimental data is used, until the extended UNIFAC-IL model parameters are available.

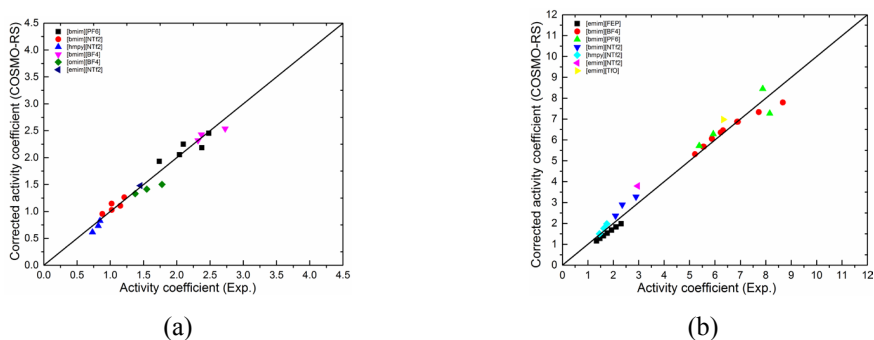


Figure 1 Activity coefficient comparison between experiment and COSMO-RS: (a) C_2H_4 in ILs (b) C_2H_6 in ILs

Table 1 COSMO-RS corrected model

Gas	Corrected model	Equation
C_2H_4	$\gamma_{cor}^{\infty} = 1.582\gamma_{cosmo}^{\infty} + 1.268 - 0.00466T$	Eq.(1)
C_2H_6	$\gamma_{cor}^{\infty} = 1.1488\gamma_{cosmo}^{\infty} + 2.41 - 0.006699T$	Eq.(2)

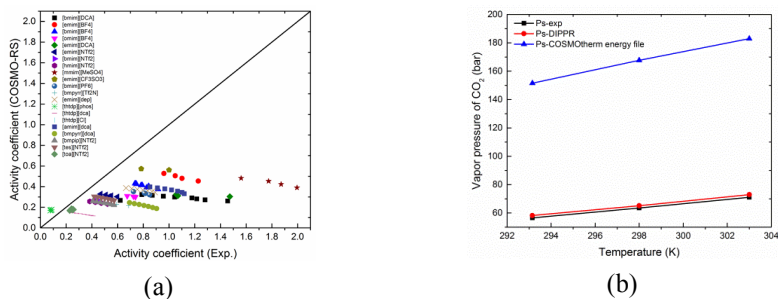


Figure 2 Comparison for activity coefficient of CO_2 in ILs between experiment and COSMO-RS a); Vapor pressures of CO_2 as a function of temperature from 3 sources b)

Main Group	0	1	2	3	4	5	6	7	8	9	10	11	12	13	14	
	CO ₂	CH ₄	[m]	[Py]	[DMP]	[BF ₄]	[PF ₆]	[Tf ₂ N]	[SCN]	[CH ₃ SO ₄]	[DCA]	[NO ₃]	[Cl]	[TfO]	[eFAP]	
0	0															
1	0	0														
2			0													
3				0												
4					0											
5						0										
6							0									
7								0								
8									0							
9										0						
10											0					
11												0				
12													0			
13														0		
14															0	

Figure 3 Fitted parameters for the UNIFAC-IL model

Case study

As a case study, the separation of gases from model shale gas with 5 gases (H₂, CO₂, CH₄, C₂H₄, C₂H₆) is considered as a conceptual example. The undesired absorbed gas is the one in the largest amount (CH₄, whose concentration is 80%) and H₂, which is lower boiling point than CH₄. Using the available data (measured and predicted), the Henry's law constants for CO₂ is plotted against selectivity of CO₂/CH₄ for different ILs and temperatures (see Fig 4).

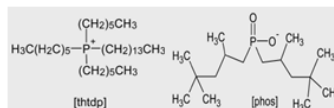
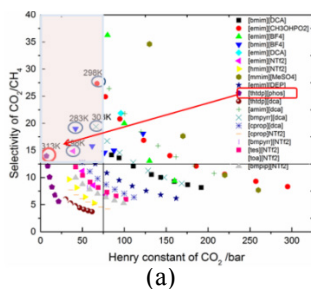


Figure 4 Henry's law constant of CO₂ versus selectivity of CO₂/CH₄ (a); best IL structure (b)

The optimal IL should have low Henry's law constant of CO₂ and high selectivity of CO₂/CH₄, that is, lie in the area with colored background. With the temperature increase, the solubility of CO₂ and selectivity of CO₂/CH₄ all decrease. As IL= [thtdp][phos] shows the lowest Henry's law constant at relatively high temperature, it means that it may have a lower Henry's law constant and higher selectivity when the temperature is decreased. Therefore, it is selected as the potential solvent. The correlated models are used (Eqs. 1-2) for the other two gases (C₂H₄, C₂H₆). The selected IL turned out to have higher solubility for C₂H₄ than C₂H₆, and acceptable selectivity with respect to CH₄.

Based on the screening result, a preliminary scheme is generated, as shown in Figure 5. As a replacement for the distillation column, an absorber with the selected IL is considered. The objective of this design is to obtain 99% CO₂ removal and a 90% CH₄ recovery rate, and high utilization efficiency for the other two light hydrocarbon gases. The selected IL is first used to absorb CO₂, C₂H₄ and C₂H₆, which are then further separated by distillation or membrane (Tula et al., 2017). To obtain a high recovery rate of CH₄, it has one stream recycle to the absorber. Only 17% of the total gas needs to be absorbed, based on preliminary mass and energy balance, the amount of IL needed for 100 kmol/hr model shale gas separation is estimated to be 171 kmol/hr and the energy required for the evaporation of the gases is 13.5 kJ/mol gas. Although the price of the IL

is higher than the organic amine-based solvent for CO₂ capture (Huang et al., 2014), its advantage of no solvent loss and the low energy regeneration consumption indicates a long-term benefit. As one part of this case study, our group has evaluated an IL-based CO₂ capture process previously. Based on the economic analysis, it is turned out that the percentage of solvent cost in the total capture cost is very low (almost 1%) as solvent used is significantly lower. Up on request, the detailed simulation results from AspenPlus can be obtained from the authors.

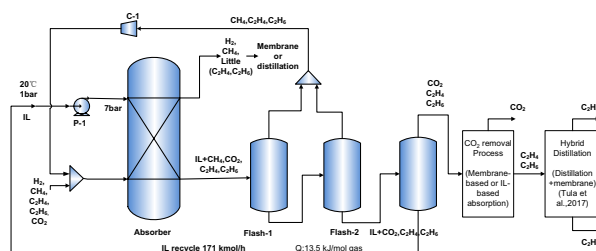


Figure 5 Preliminary schemes for shale gas separation

Note, however, that for the purposes of simulation in AspenPlus, the NRTL model needed to be used. This means that the gas solubility data are used to regress the needed NRTL parameters. So, the screening and IL selection is made with data plus predictive GC based models, while the verification is made with the NRTL model for a fixed IL. A sensitivity analysis for the IL amount and pressure of absorber is performed to find the operation condition (amount of solvent and pressure). As shown in Figure 6, with the increase of IL flowing into the absorber, the capture rate of CO₂ increases suddenly and C₂H₄ and C₂H₆ increase slightly, the recovery of CH₄ firstly increases suddenly but slightly decreases because of being absorbed by IL. With the increase of pressure in absorber, the capture rate of C₂H₄, C₂H₆ and recovery of CH₄ all increase slightly, and the capture rate of CO₂ stays at the highest rate (99.9%) because of the highest solubility.

Conclusion and future work

This work laid a good foundation for novel IL-based hybrid gas separation process synthesis. The database contains sufficient experimental data on solubility and Henry's law constant of several gases in ILs. Hence, thermodynamic models, including correlated model regressed with data from the COSMO-RS model and a new UNIFAC model for gas-IL systems have been developed and validated. On the basis of the database and model library, a three-stage framework for the ILs screening, gas separation process design and evaluation has been implemented and validated with a case study involving the design of a hybrid gas separation scheme for model shale gas mixture. IL- based CO₂ capture, as the main part of this case, has been rigorously simulated and analyzed. The result indicates that because of the low solvent investment occupied percentage, the total separation cost of the IL-based processes is still reduced compared with traditional solvent absorption. Future work is continuing to make the economic analysis of the whole process and develop the UNIFAC model for more gas-ILs systems together with hybrid schemes for energy, cost efficient and environmentally benign gas separation systems.

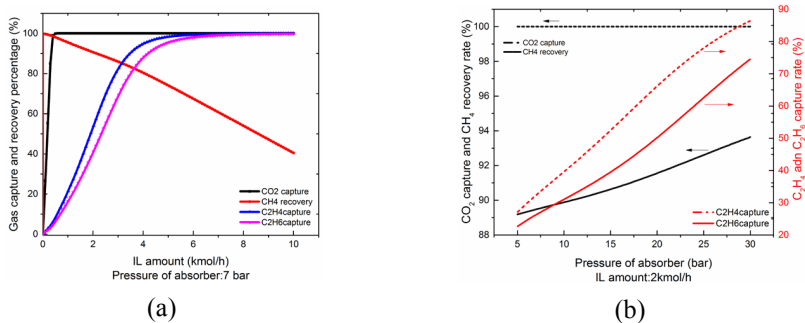


Figure 6 Sensitivity analysis for IL amount (a) and pressure of absorber (b)

References

- Huang, Y., Zhang, X., Zhang, X., Dong, H., & Zhang, S. (2014). Thermodynamic Modeling and Assessment of Ionic Liquid-Based CO₂ Capture Processes. *Ind. Eng. Chem. Res.*, 53(29), 11805-11817.
- Klamt, A., & Eckert, F. (2000). COSMO-RS: a novel and efficient method for the a priori prediction of thermophysical data of liquids. *Fluid Phase Equilibria*, 172, 43-72.
- Lei, Z., Dai, C., Wang, W., & Chen, B. (2014). UNIFAC model for ionic liquid-CO₂ systems. *AIChE Journal*, 60(2), 716-729.
- Liu, X., Huang, Y., Zhao, Y., Gani, R., Zhang, X., & Zhang, S. (2016). Ionic Liquid Design and Process Simulation for Decarbonization of Shale Gas. *Industrial & Engineering Chemistry Research*, 55(20), 5931-5944.
- Tula, A. K., Befort, B., Garg, N., Camarda, K. V., & Gani, R. (2017). Sustainable process design & analysis of hybrid separations. *Computers & Chemical Engineering*, 105, 96-104.

Techno-Economic Analysis of CO₂ Capture Processes from Coal-fired Power Plants

Seokwon Yun^a, Sunghoon Lee^a, Jin-Kuk Kim^a

^a*Hanyang University, Dpt. of Chemical Engineering, 222 Wangsimni-ro, Seongdong-gu, Seoul 04763, KR*

jinkukkim@hanyang.ac.kr

Abstract

Environmental regulations for flue gas emitted from coal-fired power plants in past mainly focused on sulfur oxides (SO_x), nitrogen oxides (NO_x) and particulate matter (PM) generated during combustion. Actions and regulations for preventing global climate change have been actively addressed in these days and considerable attentions are being paid to the implementation of CO₂ capture and sequestration technologies. A wide range of CO₂ separation techniques based on amine solvents, CO₂ adsorbents, membranes and so on, are available and each technology has own technical advantages and disadvantages. Therefore, Techno-Economic Analysis (TEA) is required to compare CO₂ separation processes in a systematic and fair manner and, hence, to gain full understanding of techno-economic impacts associated with the introduction of CO₂ capture processes in process industries.

This presentation discusses costing basis and assumptions required for TEA, as well as explains costing methodology based on multi-parameters scaling concept. Major equipment cost, indirect cost (e.g. EPC cost, owner's cost, contingency, etc.) and operating & maintenance cost are considered for economic costing. In order to improve the accuracy of TEA results, reliable costing data and scale parameters are applied, based on industrial practices. Widely-practiced values for finance-related parameters, like interest rate and project life time for economic analysis, are adopted. The economics of several post-combustion CO₂ capture processes applied for coal-fired power plant is analyzed with the proposed TEA tool. A case study is carried out to demonstrate the applicability of TEA tool for evaluating CO₂ removal technologies and to provide economic impacts associated with capture processes. Process optimization is conducted for each CO₂ removal technology and TEA is made for the optimized process configurations with optimal operating conditions, as unrealistic results may be obtained with non-optimal process design. The process optimization is carried out with integrated framework in which process simulator and in-house models are linked with an optimization solver.

Techno-economics of CO₂ capture processes was evaluated on the basis of the Cost of Electricity (COE), the cost of CO₂ captured and the cost of CO₂ avoided. Breakdown of TEA results for each technology are made and compared to obtain comparative guidance for areas of further process development. Because the introduction of CO₂ capture process results in process changes/modifications of the power plant, increase in cost for power plant and CO₂ capture process is separately analyzed. Sensitivity analysis

is also done to understand impacts on costing when key design or costing parameters are varied.

Keywords: CO₂ capture, techno-economic analysis, post combustion

Acknowledgement

This research was supported by the Korea Carbon Capture & Sequestration R&D Center (KCRC) through the National Research Foundation of Korea (NRF) funded by the Ministry of Science, ICT (NRF-2014M1A8A1049338).

Process design of absorption-membrane hybrid CO₂ capture systems for coal-fired power plant

Mun-Gi Jang^a, Sunghoon Lee^a, Seokwon Yun^a, Jin-Kuk Kim^a

^a*Hanyang University, Dpt. of Chemical Engineering, 222, Wangsimni-ro, Seongdong-gu, Seoul, KR*

jinkukkim@hanyang.ac.kr

Abstract

Global warming is now a global issue and about 42% of CO₂ emissions are associated with power plants in 2013 (IEA, 2015). Significant efforts have been made to the development of CO₂ capture technologies for power plants.

Technical progress being made in the area of CO₂ capture has mainly focused on single separation technology, namely, absorption, adsorption, cryogenic systems, membrane, etc (Freeman et al., 2012). In order to complement shortcomings of each technology and to maximize synergetic benefits, the attention of hybrid process using more than one CO₂ capture technology simultaneously has been recently drawn.

This study focuses on process design of CO₂ capture systems in coal-fired power plant by combining absorption and membrane separation methods together. Two absorption-membrane hybrid options for separating CO₂ from flue gas are investigated. Process modeling was carried out with Unisim® and Matlab® in an integrated manner. The hybrid process considered in this study is categorized to series and parallel schemes, according to the linking structure between absorption and membrane process.

For the hybrid series process, the flue gas emitted from the boiler is subjected to the absorption process to remove CO₂, while non-treated flue gas is fed into the membrane process in which a portion of the combustion air for the boiler is used as sweep gas to generate pressure gradient. CO₂ is then passed from the flue gas into the sweep air stream which is fed to the boiler. Accordingly, CO₂ concentration of the flue gas is increased, with which energy required for desorbing CO₂ in the stripper can be reduced.

In the hybrid parallel process, the flue gas discharged from the boiler is divided into two streams. One is fed to the absorption process, and the other is used as air sweep gas in membrane process. As CO₂ concentration of the flue gas increases and the feed flowrate to the absorption process decreases, there is a possibility to reduce capital cost of absorption process.

Case study was performed such that key design variables, including absorption CO₂ removal rate (only to parallel process), MEA solvent flowrate, the ratio of air entering the membrane, and membrane area were varied and their techno-economic impacts were evaluated in a holistic manner.

With the case study, it was found that hybrid process based on series arrangement can reduce reboiler duty for a stripper column, while hybridized parallel process can reduce the absorption column cost. In order to fully appreciate hybrid process between absorption and membrane, further detailed verification for potential negative impacts on power generation would be required if air sweeping were utilized in hybrid arrangement.

Keywords: simulation, CO₂ capture, hybrid process

References

IEA, 2015. "CO₂ Emissions From Fuel Combustion IEA Statistics." International Energy Agency: highlights. France: International Energy Agency (2015).

Freeman, Brice, et al. "Hybrid membrane-absorption CO₂ capture process." *Energy Procedia* 63 (2014): 605-613.

Feasibility of energy integration for high-pressure biofuels production processes

Luis Alberto Villegas-Herrera^a, Fernando Israel Gómez-Castro^{a,*}, Araceli Guadalupe Romero-Izquierdo^a, Claudia Gutiérrez-Antonio^b, Salvador Hernández^a

^a*Departamento de Ingeniería Química, División de Ciencias Naturales y Exactas, Campus Guanajuato, Universidad de Guanajuato, Noria Alta S/N, Guanajuato, Gto., 36050, México*

^b*Facultad de Química, Universidad Autónoma de Querétaro, Centro Universitario, Av. Cerro de las Campanas S/N, Santiago de Querétaro, Qro., 76010, México.*

fgomez@ugto.mx

Abstract

The production of renewable fuels has been proposed as a feasible alternative, in the short- and medium-term, to mitigate the environmental impact due to the use of fossil fuels for the transport sector. Biodiesel and biojet fuel are promising fuels to partially replace their corresponding fossil fuels. To produce biodiesel, processes with supercritical alcohols shows some advantages over the traditional base-catalyzed processes, e.g., no undesired reactions occur when the raw material has high concentration of free fatty acids. It is worth to mention that this process operates at high pressure and temperature, so the energy demand is elevated. On the other hand, the biojet fuel production through the hydrotreatment process has been developed as a feasible alternative, due to its similarity with the conventional refining processes. Like the supercritical process for biodiesel production, bio-jet fuel production requires high pressure and temperature, thus having high energy requirement. In both processes, distillation, an energy-intensive separation process, is used to generate the desired hydrocarbons fractions. Thus, to determine potential reduction in the total energy requirements for both processes, the feasibility of energy integration between the supercritical biodiesel process and the hydrotreating process to produce bio-jet fuel is studied in this work. By this approach, reductions on the utilities costs are expected if compared with the individual processes. Also, due to energy integration, which reduces the external energy requirements, global environmental impact is expected to be reduced as well.

Keywords: process integration, hydrotreating, supercritical transesterification

1. Introduction

The current high energy demand, the instability on the fossil fuels price, and the increment of the concentration of greenhouse gases emissions make necessary the development of alternative energy sources; these sources allow to address those drawbacks, such as the production of renewable fuels. In the transport sector, among the main fuels used to satisfying the society requirements, diesel and jet fuel have high demand. Among the pathways to produce biodiesel, the use of supercritical alcohols has been proposed to perform the transesterification and esterification reactions, avoiding

the side reactions that occur in the traditional based-catalyzed process. Moreover, supercritical process can use low-quality or waste vegetable oils without a previous treatment, reducing the processing cost by 60-80% (Lee et al., 2011). It is important to mention that most of the supercritical processes require only few equipment compared to conventional processes (Gómez-Castro et al., 2017). Nevertheless, due to the high pressure and temperature conditions, under which the supercritical process operates, the energy demand is considerably high. On the other hand, bio-jet fuel is an emergent biofuel which has taken importance on the last years (Gutiérrez-Antonio et al., 2015a), due to the growth in the aviation sector. Bio-jet fuel can be produced using vegetable oils as raw material, converting it into a renewable fuel through two reaction steps. The first one is the hydrotreating step; the second one is formed by hydrocracking and hydroisomerization reactions (Gutiérrez-Antonio et al., 2015b). Like the supercritical process for biodiesel production, bio-jet fuel production requires high pressure and temperature, thus having high energy requirement. Moreover, the desired hydrocarbon fractions are obtained through distillation, which is known as an energy-intensive separation process. In 2017, Gómez-Castro et al. studied the energy and mass integration of a supercritical biodiesel process and a bioethanol production process from lignocellulosic biomass. The energy and mass integration were feasible, nevertheless, savings of 4.4% and 7.7% were obtained for heating and cooling, respectively; these energy savings are low, and they do not compensate the additional investment required. This tendency is due to high differences between temperature levels of both processes (Gómez-Castro et al., 2017). In this work, energy integration is proposed between the supercritical and the hydrotreating processes to produce biodiesel and bio-jet fuel, respectively; the aim is to reduce the use of external energy and improve the energetic savings. The design and simulation of both processes are performed, realizing a sensitivity analysis in the process equipment, aiming to reduce energy requirement for the individual processes as much as possible. Then, a pinch analysis takes place to identify the potential of process integration to reduce the total energy requirement for both processes. By this approach, reductions on the utilities costs are expected, if compared with the individual processes. In addition, global environmental impact are expected to be reduced, since the energetic requirements are almost fully satisfied by the energy delivered in the processes.

2. Process simulation

The design and simulation of both processes has been performed in Aspen Plus V. 8.0. For biodiesel production, according with Gómez-Castro et al. (2017), 1,284 kg/h of vegetable oil, represented as a mixture of triolein (70 mol %) and oleic acid (30 mol %) enter to the process; along with 3,358 kg/h of supercritical ethanol. The biodiesel production is roughly 12,000 t/y, being considered as a small-scale one (Skarlis et al, 2012). The reactants streams are conditioned at 330°C and 200 bar, before entering to the transesterification and esterification reactor. Kinetic parameters for a first-order model have been used to represent the reactions; which were obtained by adjusting the data reported by Varma et al. (2010). Due to high operational conditions, after reaction zone the pressure is reduced to 1 bar for entering the separation zone; where ethanol is recovered. The biodiesel and glycerol are separated by decanting. It is worth to mention that glycerol's purity is 99.5 mol %, which make it available as solvent. UNIFAC has been used to describe phase equilibrium. The flowsheet for the supercritical biodiesel process is shown in Figure 1.

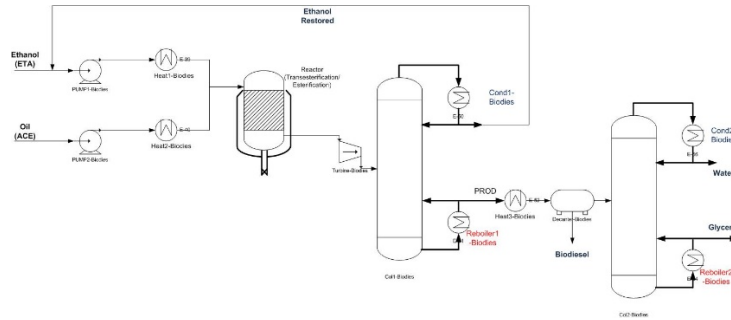


Figure 1. Supercritical biodiesel production flowsheet (Gómez-Castro et al., 2017).

On the other hand, the hydrotreating process to produce biojet fuel is integrated by two consecutive reactors and a separation zone, which is a direct distillation scheme. The vegetable oil used is *Jatropha Curcas* from Mexico; represented as a mixture of triolein (42 % wt), trilinolein (44% wt), tripalmitin (11 %wt) and tristearin (3 % wt), as major weight components. 1,710 kg/h of *Jatropha Curcas* oil enter to the process. Moreover, the hydrogen feeding enters in a ratio of 1500 mL of H₂/mL of oil to avoid coke formation (Gutiérrez-Antonio et al., 2017a). In the first reactor, hydrotreating reactions are carried out at 320°C and 80 bar; where the reactants must be conditioned before entering the reactor. A first-order lumped kinetic model, proposed by Sharma et al. (2012) has been used to represent this reaction zone. Carbon dioxide and carbon monoxide, water and lineal hydrocarbons are obtained as products. The first three compounds are separated before entering the hydrocracking – hydroisomerization reactor. The hydrocracking reaction is represented by the model of Shayegh et al. (2012); while hydroisomerization reaction is represented through the kinetic model proposed by Calemma et al. (2000). It is worth to mention that there is no additional feed of hydrogen, due to the excess introduced in the first reactor is enough for the whole reactive section (Gutiérrez-Antonio et al., 2016b). The operational conditions are 480°C and 80 bar. The stream leaving the second reactor is conditioned to 1 bar before entering the distillation train. Four products are obtained in this stage: light gases (C1-C4), naphthas (C5-C7), biojet fuel (C8-C16) and green diesel (C17-C21). The biojet fuel obtained by this process is roughly 3,671,000 L/y; quantity required by the Bajío International Airport to satisfy its renewable fuel demand, according with ASTM D7566 (Vásquez et al., 2017). Figure 2 shows the flowsheet for this process.

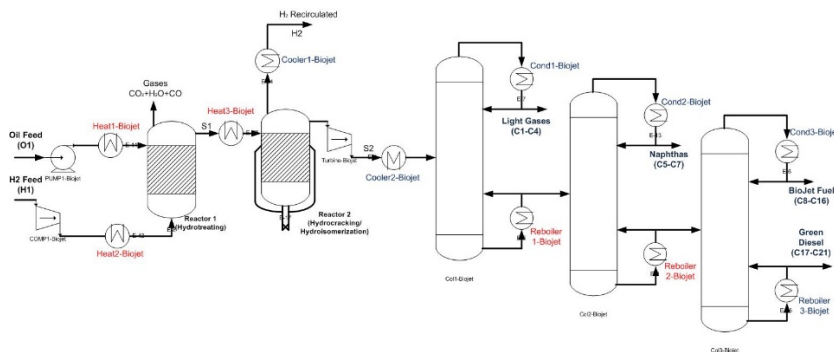


Figure 2. Bio-jet fuel production flowsheet (Gutiérrez-Antonio et al. 2016a).

In both processes, a sensitivity analysis has been performed for all process equipment with degrees of freedom, to minimize the energy requirements and keeping the quality required for the process streams.

3. Feasibility of energy integration

For both processes, the energetic analysis of all streams has been performed to obtain its enthalpy and temperature levels. Moreover, the equipment with energy inputs or outputs inside the process have been identified. At once, the heat cascade to predict the minimal heating and cooling services has been calculated, according with the pinch point analysis (Linnhoff et al., 1983). The minimal external services for both processes are then compared with the energy requirements of the individual processes; as well as the energetic savings obtained by the previous energetic integration for supercritical biodiesel and bioethanol processes (Gómez-Castro et al, 2017).

4. Results

The results of this work are presented and analysed in this section. The energetic characteristics of the streams entering and leaving the process equipment, the exothermal energy of reaction zone and the energy requirements for the distillation columns inside the supercritical biodiesel process are presented in Table 1. The same information for biojet fuel process is shown in Table 2. The total heating requirements for the streams in both processes is 2,143.40 kW, while total cooling requirements are 1,185.73 kW. It can be seen that, heating of ethanol previous to the transesterification/esterification reactor requires the highest quantity of steam for both processes. It can also be noticed that the condenser of the first distillation column for the biojet fuel process requires the use of a refrigerant. R-717 can be used for the temperature levels shown.

Table 1. Data for the equipment and streams, biodiesel process.

EQUIPMENT/STREAM	T _{IN} (°C)	T _{OUT} (°C)	HEAT DUTY (KW)
ACE	67.41	330	203.24
PROD	175.69	25	-108.79
ETA	98.59	330	1,012.27
COND1	80.10	78.02	-328.21
COND2	167.91	86.31	-6.23
REBOILER 1	161.82	175.69	12.12
REBOILER 2	267.59	314.23	31.46
REACTOR	--	--	-31.41

Table 2. Data for the equipment and streams, bio-jet fuel process.

EQUIPMENT/STREAM	T _{IN} (°C)	T _{OUT} (°C)	HEAT DUTY (KW)
H1	-192.86	320	80.00
S2	409	27.22	-492.11
O1	64.05	320	252.36
H2	480	320	-124.28
S1	342.02	425.56	221.69
COND1	-9.89	-21.31	-28.02
COND2	61.51	41.068	-47.68
COND3	245.96	233.61	-50.41
REBOILER 1	65.69	86.95	67.15
REBOILER 2	262.01	297.87	188.06
REBOILER 3	369.04	375.24	75.05
REACTOR 1	--	--	-787.45
REACTOR 2	--	--	-3.59 x 10 ⁻⁴

According with the pinch point analysis, the pinch point temperature for hot streams has been detected at 109.7°C, while for the cold streams 98.59°C, using a $\Delta T = 10^\circ\text{C}$. The minimal requirements of heating and cooling calculated by heat cascade are 1,129.07 kW and 63.078 kW, respectively. Savings around 47% may be achieving for heating utilities through energetic exchange between process streams, while, the savings in cooling requirements can be roughly 95%.

Feasibility of energy integration has been established for the streams in both processes. Moreover, the energy released by the reaction zone in the supercritical process and in the first reaction zone from hydrotreating process (around 819 kW) can be recovered, generating saturated steam with enough energy to satisfy the heating requirement in two distillations columns in the supercritical process. Likewise, the heating requirements for two distillation columns in the conventional train for bio-jet fuel process can be provided. Through this strategy, the whole savings for heating utilities are around 60%. On the other hand, in both process a turbine was installed to reduce the pressure before a distillation column. The electrical energy released for this equipment in both processes is 110.65 kW, covering roughly 67% the total electrical demand for the whole process. It is worth to mention that a flow of 3,131.7 kg/h is recovered and recirculated in the supercritical process to reduce the fresh ethanol stream. Likewise, the hydrogen stream recovered with a flow rate of 191.62 kg/h in the bio-jet fuel process is conditioned for return to the feed process.

5. Conclusions

Feasibility of energetic integration between supercritical biodiesel process and bio-jet fuel processes has been analysed. Savings of roughly 60% in heating requirements and 95% for cooling utilities have been obtained through the pinch point analysis; and by removing the released exothermal energy by transesterification – esterification reactions and by the hydrotreatment reactor. Obtained savings indicate that energy integration between the supercritical biodiesel process and the hydrotreating process for the production of bio-jet fuel has high potential for energy saving.

References

- V. Calemma, S. Peratello, C. Perego, 2000, Hydroisomerization and hydrocracking of long chain n-alkanes on Pt/amorphous SiO₂-Al₂O₃ catalyst, *Appl. Catal. A.*, 190, 1, 207.
- F.I. Gómez-Castro, M.G. Aldana-González, C. Conde-Mejía, C. Gutiérrez-Antonio, A.G. Romero-Izquierdo, R. Morales-Gutiérrez, 2017, Process integration for the supercritical production of biodiesel and the production of lignocellulosic bioethanol, *Computer Aided Chemical Engineering*, 40, 931-936.
- C. Gutiérrez-Antonio, A.G. Romero-Izquierdo, F.I. Gómez-Castro, S. Hernández, 2016a, Energy integration of a hydrotreatment process for sustainable biojet fuel production, *Ind. Eng. Chem, Res.*, 55, 8165-8175.
- C. Gutiérrez-Antonio, A.G. Romero-Izquierdo, F.I. Gómez-Castro, S. Hernández, A. Briones-Ramírez, 2016b, Simultaneous energy integration and intensification of the hydrotreating process to produce biojet fuel from *Jatropha curcas*, *Chemical Engineering and Processing*, 110, 134-145.
- S. Lee, D. Posarac, N. Ellis, 2011, Process simulation and economic analysis of biodiesel production process using fresh and waste vegetable oil and supercritical methanol, *Chemical Engineering Research and Design*, 89, 12, 2626-2642.
- B. Linhoff, E. Hindmarsh, 1983, The pinch design method for heat exchanger networks, *Chemical engineering science*, 38, 5, 745-763.
- R.K. Sharma, M. Anand, B.S. Rana, R. Kumar, S. Farooqui, M.G. Sibi, A.K. Sinha, 2012, *Jatropha*-oil conversion to liquid hydrocarbon fuels using mesoporous titanosilicate supported sulfide catalysts, *Catal. Today*, 198, 1, 314.
- F. Shayegh, A. Farshi, A. Dehghan, 2012, A kinetics lumped model for VGO catalytic cracking in a fluidized bed reactor, *Pet. Sci. Technol.*, 30, 9, 945.
- S. Starliks, E. Kondili, J.K. Kaldellis, 2012, Small-scale biodiesel production economics: a case study focus on Crete Island, *Journal of Cleaner Production*, 20, 1, 20-26.
- M.C. Vásquez, E.E. Silva, E.F. Castillo, 2017, Hydrotreatment of vegetable oils: a review of the technologies and its developments for jet biofuel production, *Biomass and Bioenergy*, 105, 197-206.

Design of a low-cost process for the production of biodiesel using waste oil as raw material

Roberto Gasca-González,^a Fernando Israel Gómez-Castro,^{a,*} Araceli Guadalupe Romero-Izquierdo,^a Eric Zenón- Olvera,^b Claudia Gutiérrez-Antonio^c

^a*Departamento de Ingeniería Química, División de Ciencias Naturales y Exactas, Campus Guanajuato, Universidad de Guanajuato, Noria Alta S/N, Guanajuato, Gto. 36050, México.*

^b*Centro del Cambio Global y la Sustentabilidad del Sureste, Calle Centenario del Instituto Juárez S/N, Villahermosa, Tab., 86080, México.*

^c*Facultad de Química, Universidad Autónoma de Querétaro, Centro Universitario, Av. Cerro de las Campanas S/N, Santiago de Querétaro, Qro. 76010, México.*

fgomez@ugto.mx

Abstract

Biodiesel is a promissory candidate to partially replace the use of fossil diesel in engines and other devices for energy production; it is composed by a combination of alkyl esters. It can be produced mainly from vegetable oils; which cost represents around 60-80% of the total production cost of biodiesel, affecting the selling price of the biofuel. Thus, the use of waste oils as raw material has been studied in the last years, because they are a cheaper alternative. However, they usually have a high content of free fatty acids, thus its conversion into alkyl esters require additional steps; since alkaline transesterification of oils with a high composition of free fatty acids is accompanied by saponification reactions. Usual pre-treatments involve the use of acid, homogeneous catalysts to transform the fatty acids into alkyl esters. On the other hand, the conversion of the oil into biodiesel is performed by reactions with alcohols, usually methanol which is produced commonly from petrochemical routes; this fact makes the production of biodiesel less sustainable. An alternative alcohol to produce biodiesel is ethanol, which can be obtained from other bioprocesses. In this work, the design of a low-cost biodiesel production process is reported, using waste cooking oil as raw material. Simulations of the process are performed in the process simulator Aspen Plus. Sensitivity analysis are performed to the equipment with degrees of freedom, to determine the design with the lowest energy requirement. Total annual costs and environmental impact are evaluated for the process.

Keywords: Waste oil, biodiesel production, process design, sustainable processes.

1. Introduction

The use of biofuels has been established as a strategy to reduce the mankind dependence on fossil fuels. Moreover, the partial substitution of fossil fuels with renewable fuels is expected to reduce the environmental impact due to the use of fuels in human activities. Biodiesel is one of the most known liquid biofuels, widely used in diesel engines, mixed with fossil diesel. This renewable fuel is obtained from raw materials rich in

triglycerides, as vegetable oils or animal fats. Nevertheless, one of the main contributions to the total annual cost in the biodiesel production is given by the raw material; thus, the use of waste oils has been proposed as an alternative raw material to reduce these costs (Lee et al., 2011). One of the main drawbacks of such approach is the high content of free fatty acids in the waste oils, which can cause saponification if basic catalysts are used (Gómez-Castro et al., 2015). To avoid such side reaction, an acid pre-treatment is commonly used, allowing the reduction of the concentration of free fatty acids in the stream entering to the basic transesterification reactor (Zanuttini et al., 2014).

One of the most important parameters to consider in the biodiesel production, together with the raw material, is the alcohol to be used as reactant. The alcohol most commonly used to perform the esterification and transesterification reactions is methanol, because the reaction with the triglycerides is fast, and it can easily dissolve sodium hydroxide. Nevertheless, methanol is toxic and relatively expensive. An alternative reactant is ethanol, which is less toxic; also, it can be produced from renewable raw materials, which may reduce the environmental impact due to the biodiesel production. One of its main disadvantages is its lower reaction rate, compared with methanol, and the azeotrope formed with water. These two issues cause the need of modified processing routes to transform the oils into biodiesel. According to the literature, the use of ethanol as reactant for the transesterification of waste oils has been performed through sonication (Martinez-Guerra and Gude, 2014), lipases (Ferrero et al., 2016), hydrotalcite catalysts (Ma et al., 2016), among others; in particular, the recovery of ethanol in these works is not addressed. Nevertheless, there have been several attempts to recover unreacted alcohol from the output mixture of the transesterification process through stripping or vacuum distillation or to remove it by flash evaporation or heating the mixture to 120 °C (Yaakob et al., 2013). To the authors' knowledge the use of glycerol, byproduct in biodiesel production, as solvent for the ethanol recuperation has not been reported. Therefore, in this work a proposal for a biodiesel production process from waste oil using ethanol as reactant is presented. The design of the process is constrained in terms of the raw material available in the municipality of Emiliano Zapata, Tabasco, México, where the plant is expected to be constructed. The flowsheet required to produce the biofuel is presented, and separation steps are proposed to reach the desired quality of biodiesel. Also, the recovery of ethanol is performed with glycerol, a byproduct in biodiesel production. The process is then assessed in terms of total annual costs, environmental impact and energetic efficiency, to determinate the economic potential of the proposed flowsheet to produce a competitive biofuel.

2. Case study

5,000 L per month of oil are treated, since it is the estimated availability of waste oil in the municipality of Emiliano Zapata, Tabasco, México. This amount of waste oil is equivalent to a daily feed of 163 kg. The waste oil is composed by fatty acids (6 wt%) and triglycerides (94 wt%). The distribution of components in the oil is shown in Table 1.

The oil composition shown in Table 1 is modelled for the production of biodiesel. Due to the high composition of free fatty acids, an acid pre-treatment is required. Moreover, since ethanol will be used as reactant, a purification step must be proposed to obtain a

high-purity biofuel. Finally, the design of the reactors is constrained because it must be adjusted to existent equipment.

Table 1. Composition for the raw material (Bulla Pereira, 2014).

Component	Mass composition
Palmitic	12.3 wt%
Oleic	24.0 wt%
Linoleic	56.6 wt%
Linolenic	7.1 wt%

3. Methodology

As aforementioned, 163 kg/h of waste oil are treated to obtain biodiesel. The process is simulated in the software Aspen Plus V8.4. In the simulator, thermodynamic data is not available for all the components, mainly for the ethyl esters; so, they are estimated using the group contribution methods available on the simulator, and the Constantinou-Gani method to determine the formation enthalpy and Gibbs energy. The phase equilibrium has been modelled using the UNIQUAC method, according to the diagram reported by Carlson (1996), considering the characteristics of the components involved.

Once the components are loaded and the thermodynamic model has been selected, the flowsheet is developed. The first step is the acid pre-treatment, where the RBatch module has been used, with a molar ratio ethanol/oil of 6:1 and 1 wt% of sulfuric acid as catalyst. The kinetic model used to represent the reaction is that reported by Neumann et al. (2016). Here, the main design variables are the reaction time and the temperature, which are modified in order to maximize the conversion of fatty acids. The size of the reactors cannot be modified, since they already exist. The stream leaving the first reactor enters to a neutralization equipment, which has been simulated using a RStoic module. The produced salt is removed by a filter. The stream leaving the neutralization step enters to a second reactor, where transesterification occurs with sodium hydroxide. Ethanol is fed in a 6:1 ratio with oil. The reaction takes place in a batch reactor (RBatch module). Once more, the effect of the reaction time and the temperature is analyzed. The kinetic model of da Silva et al. (2008) is used to represent the reaction. Finally, the purification train is established. In a first stage, a decanter is used to separate the glycerol phase from the biodiesel phase. The glycerol phase is neutralized using phosphoric acid. The solid by-product is removed by a filter. The resulting stream contains mainly glycerol and some water. On the other hand, the biodiesel is washed, representing the washing equipment as a liquid-liquid extraction column. The excess of water is removed from the biodiesel stream in a flash drum, to reach the biodiesel composition indicated by the international standards. The other stream leaving the washing tower contains ethanol and water, where the ethanol must be recovered. Nevertheless, the presence of water causes the formation of an azeotrope, which makes the separation difficult. An extractive distillation column is used to obtain ethanol with purity of 99.5 mol%. Glycerol is used as extraction agent, as recommended by Navarrete-Contreras et al. (2014). Such agent is obtained as by-product in the

reaction steps, so it can be used in the extractive distillation system. A sensitivity analysis is performed on this column, to obtain the design with the lowest heat duty. Then, the glycerol is purified in a conventional column. A simplified representation of the whole process is shown in Figure 1. Once the process has been simulated and the required yields and purities obtained, the capital costs of the process are computed using the Guthrie method (Turton et al., 2012), while the operation costs are estimated in terms of the utilities requirement. Environmental impact is computed in terms of the carbon dioxide emissions of the process, which are directly related with the total heat duty and the temperature levels required. The CO₂ emissions are estimated using the method proposed by Gadalla et al. (2005).

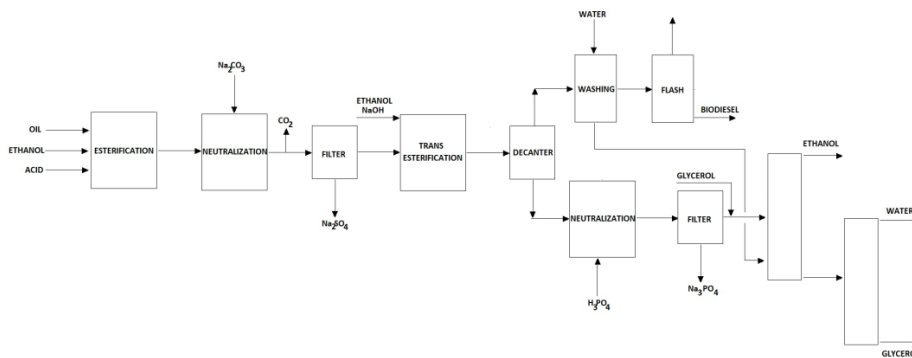


Figure 1. Block diagram of the biodiesel production process

4. Results

In this section, some of the major results of the analysis are presented. In the case of the esterification reactor, it has been determined that operating at 70°C with $t = 30$ min is enough to obtain conversion of fatty acids around 99 mol%. In the case of the transesterification reactor, the best temperature was determined as 70°C, with $t = 15$ min, obtaining conversion around 96 mol% of triglycerides to biodiesel. Other of the main equipment in the process is the extractive distillation column, which was designed with 12 stages, feeding the ethanol/water stream in stage 10, while the glycerol/water stream is fed in the stage 3. The whole process has energy requirement of 108 kW, where the flash drum contributes with around 62% of the total heating requirement of the process. The ethanol recovery train contributes with 36%.

Table 2 shows the equipment costs estimated with the Guthrie method, together with the operational costs and the total annual cost. It is important to notice that the total capital cost must be annualized to obtain the total annual cost (TAC). To do this, recovery time has been assumed to be 10 years. In the utilities cost, only the costs for steam and water are included. Here, the utilities cost represents around 46% of the total annual cost.

Table 3 shows the computed CO₂ emissions for the whole process. The use of two possible fuels to produce the steam is considered: gasoil and natural gas. As expected,

using natural gas reduces around 33% the carbon dioxide emissions in comparison with gasoil.

Table 2. Costs for the proposed biodiesel process.

Capital cost (USD)	Variable cost (USD/y)	TAC (USD/y)
221,009	18,693	40,794

Table 3. Emissions of carbon dioxide for the biodiesel process.

Carbon dioxide emissions (kg/h)	
Gasoil	Natural gas
38.12	25.61

The selling cost for biodiesel has been estimated, following the approach of Santana et al. (2010); where the annual equivalent cost, the annual operation cost and the annual production of biodiesel are involved. Also, the quantity of glycerol produced inside the process is considered. For the proposed process, the annual production of biodiesel is 57,115 kg/y, which is derived from the mean generation of residual oil in the municipality of Emiliano Zapata, Tabasco, México. Moreover, the process produces 2,621 kg/y of glycerol, which could be sold or used to partially fulfill the solvent requirements in the extractive distillation column. With this information, it has been determined that the unitary cost for the biodiesel obtained in the proposed process is 0.865 USD/l. The obtained cost is lower than the mean cost of fossil diesel in Mexico (around 0.965 USD/l), making the process competitive.

5. Conclusions

The design and simulation of a biodiesel production process from waste oil using ethanol as reactant has been proposed. The design of the process has been performed using CAPE tools, as the process simulator Aspen Plus. For this process, some of the equipment has been already acquired, particularly the reactors, which constrains the design step. The effect of the design variables in the main equipment of the process has been studied through sensitivity analysis, to generate a process with low energy requirement. One of the main differences with the traditional processes using methanol is the necessity of using special separation processes to recover the ethanol. In terms of the cost of the product, it has been estimated that the process has potential to produce a biofuel with lower selling cost than fossil diesel.

References

A.E. Bulla Pereira, 2014, Diseño del proceso de producción del biodiésel a partir de aceites de fritura (Spanish), Universidad Nacional de Colombia, Bogotá, Colombia, 1-135.

- E.C. Carlson, 1996, Don't gamble with physical properties, *Chemical Engineering Progress*, October, 35-46.
- N.L. da Silva, E.C. Rivera, C.B. Batistella, D.R. de Lima, R. Maciel Filho, M.R. Wolf Maciel, 2008, Biodiesel production from vegetable oils: operational strategies for large scale systems, *Computer Aided Chemical Engineering*, 25, 1101-1106
- G.O. Ferrero, H.J. Rojas, C.E. Argaraña, G.A. Eimer, 2016, Towards sustainable biofuel production: Design of new biocatalyst to biodiesel synthesis from waste oil and commercial ethanol, *Journal of Cleaner Production*, 139, 495-503.
- M.A. Gadalla, Z. Olujic, P.J. Jansens, M. Jobson, R. Smith, 2005, Reducing CO₂ emissions and energy consumption of heat-integrated distillation systems, *Environmental Science & Technology*, 39, 17, 6860-6870.
- F.I. Gómez-Castro, J.G. Segovia-Hernández, S. Hernández, V. Rico-Ramírez, C. Gutiérrez-Antonio, A. Briones-Ramírez, I. Cano-Rodríguez, Z. Gamiño-Arroyo, 2015, Analysis of alternative non-catalytic processes for the production of biodiesel fuel, *Clean Technologies and Environmental Policy*, 17, 7, 2041-2054.
- S. Lee, D. Posarac, N. Ellis, 2011, Process simulation and economic analysis of biodiesel production processes using fresh and waste vegetable oil and supercritical methanol, *Chemical Engineering Research and Design*, 89, 12, 2626-2642.
- Y. Ma, Q. Wang, L. Zheng, Z. Gao, Q. Wang, Y. Ma, 2016, Mixed methanol/ethanol on transesterification of waste cooking oil using Mg/Al hydrotalcite catalyst, *Energy*, 107, 523-531.
- E. Martínez-Guerra, V.G. Gude, 2014, Transesterification of waste vegetable oil under pulse sonication using ethanol, methanol and ethanol-methanol mixtures, *Waste Management*, 34(12), 2611-2620.
- S. Navarrete-Contreras, M. Sánchez-Ibarra, S. Hernández, A.J. Castro-Montoya, F.O. Barroso-Muñoz, 2014, Use of glycerol as entrainer in the dehydration of bioethanol using extractive batch distillation: simulation and experimental studies, *Chemical Engineering and Processing: Process Intensification*, 77, March, 38-41.
- K. Neumann, K. Werth, A. Martín, A. Górak, 2016, Biodiesel production from waste cooking oils through esterification: catalyst screening, chemical equilibrium and reaction kinetics, *Chemical Engineering Research and Design*, 107, March, 52-62.
- G. Santana, P. Martins, N. de Lima da Silva, N. Batistella, C. Maciel Filho, M. Wolf Maciel, 2010, Simulation and cost estimate for biodiesel production using castor oil, *Chemical Engineering Research and Design*, 88, 5, 626-632
- R. Turton, R.C. Bailie, W.B. Whiting, J.A. Shaeiwitz, D. Bhattachayya, 2012, Analysis, synthesis, and design of chemical processes, 4th edition, Prentice Hall, New Jersey, 951-982.
- Z. Yaakob, M. Mohammad, M. Alherbawi, Z. Alam, K. Sopian, 2013, Overview of the production of biodiesel from waste cooking oil, *Renewable and Sustainable Energy Reviews*, 18, 184-193.
- M.S. Zanuttini, M.L. Pisarello, C.A. Querini, 2014, Butia Yatay coconut oil: process development for biodiesel production and kinetics of esterification with ethanol, *Energy Conversion and Management*, 85, 407-416

Energetic assessment of lignin extraction processes by simulation

Javier Fernández-Rodríguez, María González Alriols*, Fabio Hernández Ramos, Jalel Labidi

Biorefinery Processes Research Group, Chemical & Environmental Engineering Department, University of the Basque Country UPV/EHU, Plaza Europa 1, 20018. Donostia, Spain.

maria.gonzalez@ehu.eus

Abstract

The energetic requirements of several processes for high-purity lignin production from lignocellulosic waste streams has been studied in this work, based on simulation analysis performed with experimental data. The introduced variables were: two different raw materials (almond shell and olive tree pruning), the use of a pre-treatment stage and the application of two different sulphur-free delignification methods (organosolv and soda processes) with their subsequently lignin precipitation steps. In total, four scenarios were approached and assessed in terms of desirable product yields, water and chemical consumptions and energetic duties. Results showed a more efficient process when almond shell was used as raw material. In terms of the delignification process, organosolv method required a much lower quantity of chemicals due to the recycle and recirculation of the solvent (ethanol). The energy consumption associated to this recycle implied an increase of 18-12 % in the total energy consumption. On the other hand, lignin product yield was higher with soda process although its chemical consumption was found to be much higher, in terms of soda and sulfuric acid requirements.

Keywords: lignocellulosic biomass, biorefinery, lignin, energetic efficiency, simulation

1. Introduction

Technological routes and projects in which lignocellulosic biomass is used to produce energy and bio-based chemicals and materials have been increasing nonstop in the last years. Research and commercial efforts have been focused on improving the biorefinery processes making them susceptible of competing with the petrochemistry market (Montazeri and Eckelman, 2016). A variety of biomass pre-treatment strategies have been applied to separate the lignocellulosic biomass structure into cellulose, hemicelluloses and lignin, including the use of bases, such as sodium hydroxide, organic alcohols and acids (organosolv treatments) or ionic liquids. The lignin fraction has frequently been considered a by-product from the polysaccharides isolation process for biofuels production via hydrolysis and fermentation. Nevertheless, lignin has proved to have a big potential for the production of added-value chemicals and materials, due to the variety of functional groups in its chemical structure (Thakur et al., 2014). These lignin-based products must be competitive with their petroleum-derived counterparts. At this point, it is very important to design energy efficient process for the lignin

extraction and purification. Otherwise, it would be difficult to offer an actual alternative to consolidated products based on fossil resources (Mabrouk et al., 2016).

In this work, the lignin extraction and purification processes from two different lignocellulosic biomass sources (almond shell and olive pruning) by two different pre-treatments (organosolv and soda) are presented. The target has been the designing of an energy efficient process by simulating with using Aspen Plus[®] software the different sequences in order to minimize its energy consumptions.

2. Simulation procedure

2.1. Processes description

Experimental data was reported in a previous work (Fernández-Rodríguez et al., 2017), where almond shell and olive tree pruning were used as feedstock for lignin extraction. Compositions of these raw materials are described in Table 1.

Table 1. Chemical characterization of raw materials (Fernández-Rodríguez et al., 2017).

Macro-components	Composition (%)	
	Almond Shell	Olive Tree Pruning
Cellulose	39.93	50.01
Hemicellulose	8.29	12.74
Lignin	50.86	22.33
Extractives	0.07	11.46
Ashes	0.86	3.46

These materials were subjected to an autohydrolysis pre-treatment to increase lignin concentration prior the delignification stage. Reaction was carried out at 180 °C, using only water as reagent in a 1:8 solid/liquid ratio. After that stage, solid material was cleaned and driven to a pulping stage where lignin was extracted. Organosolv pulping was conducted using a mixture of ethanol/water (70/30 V/V) at 200 °C in a 1:6 solid/liquid ratio, whereas soda process was carried out at 121 °C using a NaOH 7.5 wt.% solution as reagent in the same solid/liquid ration of organosolv method. Regardless the used process, after the delignification stage, the undissolved solid was cleaned in two steps, first with the same solvent utilized in the reaction; and then with water to obtain a pulp enriched in cellulose. On the other hand, the black liquor obtained after the reaction was led to a precipitation stage. In the organosolv process, lignin was precipitated with the addition of acidified water (pH= 2) and then filtered to obtain lignin as the solid fraction. On the other hand, the soda black liquor was precipitated by lowering the pH down to 4 by sulfuric acid addition (96 wt.%). The filtered cake was then washed with water to remove the excess of salts that were generated by this precipitation method.

2.2. Simulation

Based on the experimental results of the above described processes, a simulation by Aspen Plus V8.8 was build up to stablish mass and energy balances that could allow to determine the influence of raw materials and delignification methods used in the energy requirements of the processes. The processes flowsheets are presented in Figures 1 and 2. The organosolv process includes a solvent recovering stage. Hence, a recirculation of

ethanol by distillation was proposed to reutilize this compound in the reactor and as washing stream.

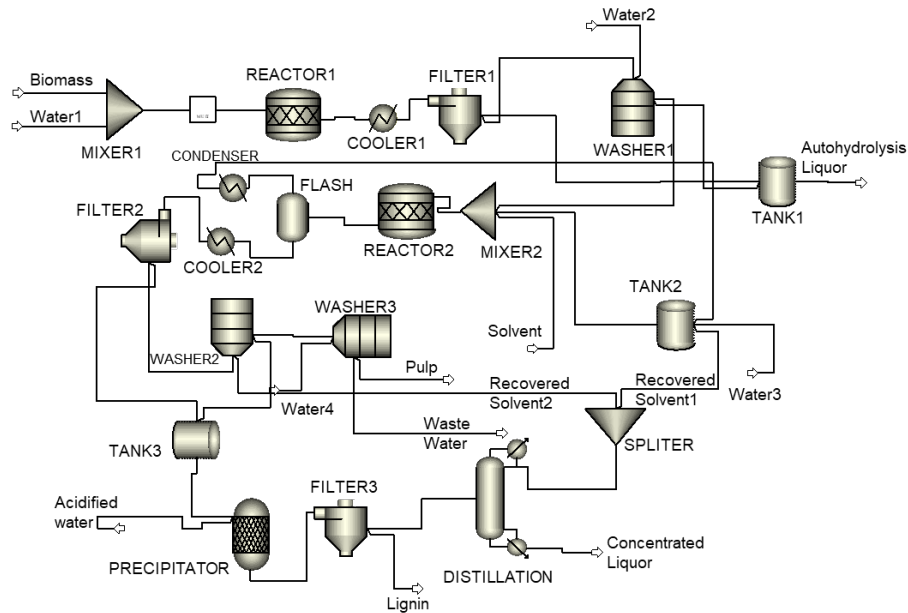


Figure 1. Flowsheet of the organosolv process.

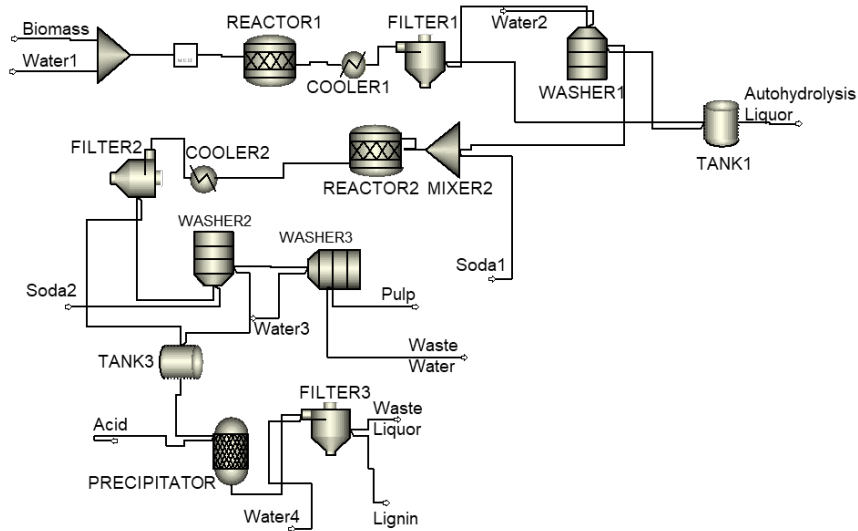


Figure 2. Flowsheet of the soda process.

NRTL-RK model was selected to simulate the thermodynamic properties of the streams involved in the process. The simulation basis was 100 kg/h of dry raw materials and 800 kg/h of water to the autohydrolysis reaction. A description of the equipment used in these processes is detailed in Table 2. The distillation column for ethanol recovery in the organosolv process was designed to obtain a recovered stream with the same ethanol

mass fraction as it was introduced to the system (74.7 wt.%). Reactions happening in autohydrolysis, delignification and precipitation stages were adjusted stoichiometrically following the experimental yields obtained (Fernández-Rodríguez et al., 2017). Lignin stream was obtained completely dry and with the same purity as it was experimentally reported (Fernández-Rodríguez et al., 2017).

Table 2. Blocks design for the simulation process.

Equipment	Aspen Module	Specification	
		Organosolv	Soda
MIXER1	Mixer	1 bar	
REACTOR1	RStoic	180 °C, 0 vapor fraction	
COOLER1	Heater	25 °C, 1 bar	
FILTER1	SSplit	Solid stream: 80 wt.% consistency	
WASHER1	SSplit	Water:solid cleaning ratio of 2.5:1, Solid stream outlet at 90 wt. consistency	
TANK1	Mixer	1 bar	
TANK2	Mixer	1 bar	
MIXER2	Mixer	1 bar	
REACTOR2	RStoic	200 °C, 0 vapor fraction	
FLASH	Flash2	1 bar, adiabatic	
CONDENSER	Heater	1 bar, 0 vapor fraction	
COOLER2	Heater	1 bar, 25 °C	
FILTER2	SSplit	Solid stream: 80 wt.% consistency	
WASHER2	SSplit	Solvent:solid cleaning ratio of 2:1, Solid stream outlet at 90 wt. consistency	
WASHER3	SSplit	Water:solid cleaning ratio of 2:1, Solid stream outlet at 90 wt. consistency	
TANK3	Mixer	1 bar	
PRECIPITATOR	RStoic	1 bar, adiabatic	
FILTER3	SSplit	Solid stream dry	
DISTILLATION	RadFrac	1 bar, 4 stages, reflux ratio 1.5	-
SPLITER	SSplit	Stream to Washer2 2:1 to solid	-

3. Results

The comparison of the analysed scenarios is represented in Table 3. Process efficiency was evaluated in terms of water and chemicals (ethanol or soda) consumptions and total energy duties.

Table 3. Main results for the different processes approached. AO: almond shell, organosolv; OO: Olive tree pruning, organosolv; AS: Almond shell, soda; OS: Olive tree pruning, soda.

	Units	AO	OO	AS	OS
Lignin yield	%	4.63	2.81	10.1	6.91
Pulp yield	%	49.7	47.3	37.4	28.2
Solvent consumption	kg/h	20.11	18.40	427.8	387.6
Water consumption	kg/h	1626	1553	1072	1029
Acid	kg/h	-	-	39.01	35.40
Waste streams	kg/h	1693	1622	1594	1520
Energy requirement	kW	432.3	495.4	353.1	435.6

The generated waste streams were also considered as they should be treated before their disposal. The influence of the raw material used in the process can be noticed in all the

measured parameters. Almond shell presented in all cases, the highest lignin and pulp production yields for the same biomass feed to the system. When using this raw material, lignin yield was found to be 63.7 % higher than the obtained with olive pruning, for the organosolv process and 47 % higher in the case of soda process. The obtained pulp yields were found to be similar for both materials in the organosolv process but 33 % higher for almond than in the soda process. A higher chemicals consumption was needed when almond shell was used, particularly, a 10 % more of the reagents for the pulping stage (either ethanol or soda) was required and a 4% more of water. As a consequence, higher waste streams flow was produced (between 4-10 % of increase with regard to olive pruning scenarios). Regarding energy duties, lower energy consumption was experimented for almond processes. On the other hand, the influence of the used pulping process was particularly remarkable when comparing the lignin production yield, as the one obtained by the soda process was more than a 50% higher than the obtained by the organosolv method. However, lower pulp yields (24% in case of almond and 40 % for olive tree pruning) were obtained by the soda process. The comparison of both processes in terms of solvents consumption was favourable to the organosolv, since the ethanol recovery led to a very low consumption rate of this compound (0.25 times the quantity of used biomass), whereas in soda process the required soda solution quantity was around 4 times the quantity of the used biomass. Furthermore, soda process water requirement was 30 % higher than the quantity used in the organosolv scheme, due to the great quantity needed in the precipitation stage. In addition, the waste stream quantities were similar, (5-6 % lower for organosolv process). In terms of energy duties, the inclusion of the distillation stage for organosolv process led to an increase of 18-12 % in the total energy consumption. The evaluation of the energetic duties of both processes was carried out by the quantification of each stage with energy requirements. In Figure 3, the energy duties of the involved are presented.

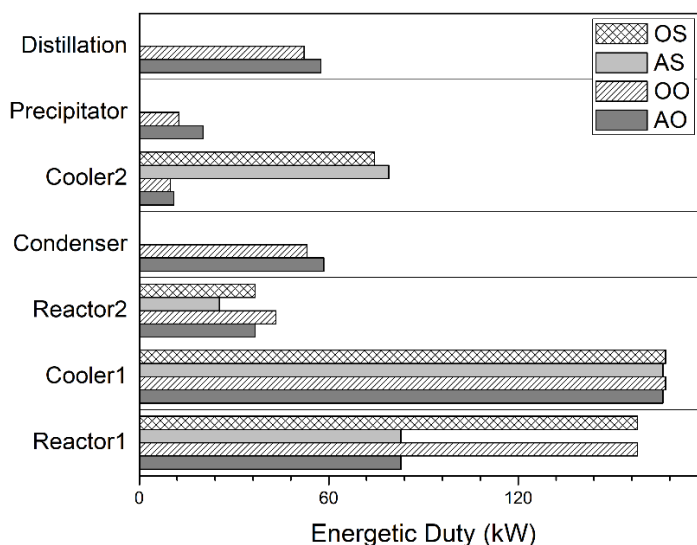


Figure 3. Energy duties of the process stages. AO: almond shell, organosolv; OO: Olive tree pruning, organosolv; AS: Almond shell, soda; OS: Olive tree pruning, soda.

The stage with the highest energy duty was the heat exchanger “Cooler1”, after the autohydrolysis reaction. Concretely, this stage implied between 33 and 47 % of the total energy duties depending on the case of study. Autohydrolysis reaction was the operation with the second highest heat duty of the process. A considerable difference was found in this stage depending on the used raw material. Olive tree pruning required a higher heat contribution than almond shell in this operation. Distillation heat duty supposed only 13-10 % of the total energy duty for organosolv processes, indicating that, the inclusion of the distillation stage, did not led to a huge increase in total energy consumption. Furthermore, the organosolv process presented an advantage in the cooling of the stream produced in delignification stage by the inclusion of the flash unit and condenser to recirculate the ethanol. In the case of the soda process, the whole stream exiting the delignification reactor needed to be cooled. As summary, organosolv process presented higher energy duty considering the global process. However, its reduction in solvent consumption was found to be higher than the increase of energy duty. Therefore, a compromise should be set to determine what scenario would the most interesting.

4. Conclusions

Simulation by Aspen Plus V8.8 has been successfully applied to different scenarios based on experimental data. Almond shell was more suitable for lignin generation than olive tree pruning with lower energetic duty regardless the delignification method used. In terms of the delignification method used, soda process presented better values for lignin obtaining, whereas the pulp stream flow was lower. Much higher consumptions of solvent and acid were required in the soda scheme, while its was energetic duties were lower than the ones associated to the organosolv process. Regarding the energetic duties for each stage, the main energy consumption was located in the autohydrolysis stage. The identifying of the most critical points for energetic duties will lead to an energetic integration process in a further work.

Acknowledgements

This work was funded by the Spanish Ministry of Economy and Competitiveness (CTQ2016-78689-R) and the Basque Government (IT1008-16).

5. References

- J. Fernández-Rodríguez, X. Erdocia, C. Sánchez, M. González Alriols, J. Labidi, 2017, Lignin depolymerization for phenolic monomers production by sustainable processes, *Journal of Energy Chemistry* 26 (4), 622-631.
- A. Mabrouk, X. Erdocia, M. González Alriols, M. Razak Jeday, J. Labidi, 2016, Exergy analysis: An optimization tool for the performance evaluation of an organosolv process, *Applied Thermal Engineering* 106, 1062-1066.
- M. Montazeri, M.J. Eckelman, 2016, Life cycle assessment of catechols from lignin depolymerization, *ACS Sustainable Chemistry Engineering*, 4(3), 708-718.
- V.K. Thakur, M.K. Thakur, P. Raghavan, M.R. Kessler, 2014, Progress in green polymer composites from lignin for multifunctional applications: A review, *ACS Sustainable Chemistry and Engineering*, 2(5), 1072-1092.

Retro-Techno-Economic-Environmental Analysis (RTEEA) from the cradle: a new approach for process development

Andrew M. Elias^a, Felipe F. Furlan^{b*}, Marcelo P. A. Ribeiro^{a,b}, Roberto C. Giordano^{a,b}

^a *Chemical Engineering Graduate Program, Federal University of São Carlos, PPGEQ/UFSCar, Via Washington Luiz, km 235, São Carlos, SP, 13565-905, Brazil.*

^b *Department of Chemical Engineering, Federal University of São Carlos, UFSCar, Via Washington Luiz, km 235, São Carlos, SP, 13565-905, Brazil*

furlan@ufscar.br +55 16 33066877

Abstract

The chance of a successful industrial implementation of innovative or unconventional processes can be greatly enhanced if the analysis of economic feasibility and environmental impacts is performed from the beginning. In this study, Retro-Techno-Economic Analysis was expanded into Retro-Techno-Economic-Environmental Analysis (RTEEA), combining Life Cycle Analysis (LCA) metrics with economic ones, in order to define regions of feasible operation for the process. In addition, the selection of key process variables was done through global sensitivity analysis (GSA). RTEEA was applied to the case study, the production of succinic acid (SAc) from sugarcane sucrose. Greenhouse gases emissions (GHG, in kg CO₂ eq./kg SAc) and the process Net Present Value (NPV) were chosen as performance metrics. For mapping the GSA response surface, Latin hypercube sampling was used. Sensitivity analysis pointed out that GHG is only influenced by yeast selectivity while NPV was more sensitive to concentration, productivity and yeast selectivity (99.6% of explained variance). The feasible region is bounded by the limits in yeast selectivity and by the infinite productivity curve (obtained assuming instantaneous reaction). The methodology was able to identify the main process variables that influence the process economic and environmental performance, derive their threshold values, and make explicit their relations.

Keywords: global sensitivity analysis, life cycle assessment, feasible space, process simulation.

1. Introduction

To avoid potential losses of research and development (R&D) investments, it is necessary to screen possible economic bottlenecks, providing targets for the experimental teams ever since the beginning of the experiments (Furlan et al., 2016).

Indeed, Process Systems Engineering (PSE) tools, allied to techno-economic analysis (TEA) and life cycle assessment (LCA) can be useful for verifying and understanding the techno-economic feasibility and environmental impact of new processes. Usually, when the economic and environmental performance are considered, the best operational condition for an individual piece of equipment is not optimal for the whole process. Therefore, it is essential to include plantwide simulations, based on reliable experimental data, in order to verify the feasibility of the proposed solution according to techno-economic and environmental criteria.

TEA and LCA are usually used to assess the economic and environmental performance of predefined process conditions. RTEA (Furlan et al., 2016) is a novel approach that turns this problem upside down, providing targets of key process variables for R&D teams, in order to seek for feasible operational conditions, taking into account the overall process. In this work, RTEA was expanded to RTEEA (Retro-Techno-Economic-Environmental Analysis), incorporating life cycle assessment. This methodology is presented here, using NPV and GHG as metrics to define feasible regions. Rather than reporting an extensive techno-economic-environmental analysis of a process, a case study is reported, exemplifying a real application of the methodology. Therefore, techno-economic analysis and life cycle assessment were applied to the production of succinic acid from sucrose. Global sensitivity analysis (GSA) was carried out to search, with statistical criteria, the process variables that have the greatest influence on the process performance. This methodology can be used only in equation-oriented simulators (where no order is imposed to solve the system of equations), without relying on an external convergence loop.

2. Methodology

The production of succinic acid (SAC) from sugarcane sucrose by fermentation is described by Efe et al. (2013). RTEEA methodology is constituted by four parts: construction of a base case, incorporation of TEA and LCA analysis in the simulation, selection of key variables through global sensitivity analysis and delimitation of the feasible space. The Net Present Value (NPV) was chosen as economic metric while greenhouse gas (GHG) emissions was chosen as environmental metric. The techno-economic analysis was performed by Furlan et al. (2016) in a previous work. The cradle-to-gate GHG emissions of the production of succinic acid from sucrose was calculated using LCA methodology. The functional unit was defined as 1 kg of SAC. The system boundaries include the cultivation of sugarcane, conversion of sugarcane to sucrose and the microbial synthesis of succinic acid from sucrose. The 2007 Intergovernmental Panel on Climate Change (IPCC) Global Warming Potentials (GWPs) method was employed to convert GHG emissions to CO₂-equivalent emissions. The emission of CO₂ eq associated with the sugarcane cultivation and the process of sugarcane conversion to sucrose were obtained from Figueiredo et al. (2010) as 241 kg CO₂ eq (t sugarcane)⁻¹. GHG emissions for the process simulation were estimated by inserting equations and data from Weidema et al. (2013) into EMSO. Electricity and steam requirements obtained from the case study simulations were used to determine GHG emissions associated with energy consumption.

GSA indicated the process variables that have more influence on economic and environmental feasibility. Mapping of the response surface was carried out by Latin Hypercube Sampling (LHS), ensuring that the ensemble of random numbers generated was representative of the real variability of the parameters in the simulated process (Saltelli et al. 2008). Six process variables were initially selected: succinic acid concentration in the bioreactor, yeast specific productivity (SAC produced/yeast mass/reaction time), yeast selectivity (SAC produced/ethanol produced), selectivity of the adsorption column used to recover SAC, sucrose conversion, and crystals' drying temperature. To avoid a type II error when classifying an important factor as non-influential, the Latin hypercube was constructed with 10^4 points (Saltelli et al. 2008). Selection of the key variables was based on a cumulative explained variance. In order to provide a graphical representation of the responses, only the three most influential variables were selected.

For the RTEEA methodology it is essential that the variables chosen for analysis are inputs (i.e., process constraints). If not, other specified variable, correlated with the desired one, must be freed in order to keep the degrees of freedom null. The equation that equals the economic/environmental metrics with a threshold value was solved together with the model equations of the process (mass and energy balances, thermodynamics relations, etc). RTEEA swaps the specification of the chosen variables (which become output variables of RTEEA) for this equation. Zero net present value (NPV=0) and GHG emission by petrochemical route for SAC production were chosen as these threshold values. Detailed information can be found in Furlan et al. (2016).

The platform for the simulations was the software EMSO (Environment for Modelling, Simulation and Optimization, Soares and Secchi, 2003), an equation-oriented simulator.

3. Results and Discussion

To demonstrate the potential of this methodology, the production of SAC from sucrose was chosen as case study, based on a process described by Efe et al. (2013). The TEA was performed by Furlan et al. (2016) and compared to the original work.

The cradle-to-gate LCA was incorporated in the simulations, in order to determinate the GHG emissions of the whole production process. The major GHG contribution comes from agricultural management, which impacts directly on sucrose production.

The global sensitivity analysis was performed based on the previously described variables. Among more than 800 process variables, the selected ones were chosen in order to avoid type I errors, which indicates that a non-influential factor was defined as important (Saltelli et al., 2008). The analysis was performed in order to evaluate the total explained variance, based on the determination coefficient (R^2). Table 1 shows the R^2 calculated based on the data regression generated by LHS. The regression equations were composed by the mean of the all NPV and GHG values calculated in a simulation plus the linear and quadratic effects of the variable and the combinations of them, providing an equation with 28 terms.

Table 1: Coefficient of the determination (R^2) of the regressions: selected results with greater R^2 . When #1 is assigned to a variable, its linear and quadratic terms are taken into account. Variables i and j cross-terms are only considered when #1 is assigned for both variables i and j . The six elected variables were: succinic acid concentration (Csa), yeast productivity (Pr), sucrose conversion (Conv), succinic acid to ethanol selectivity (Select), selectivity of the adsorption column (Sel_ad) and the crystals' drying temperature (Temp). The number of variables analyzed at same time change, in order to determine the metric's most influential factor. Grey cells are the ones with the highest R^2 for each number of analyzed variables.

Simultaneously analyzed variables	Occurrence of the variable						R^2	
	Csa	Pr	Conv	Select	Sel_ad	Temp	NPV	GHG
5	1	1	1	1	1	0	0.9962	0.9944
4	1	1	1	1	0	0	0.9962	0.9943
3	1	1	0	1	0	0	0.9960	0.9941
2	1	1	0	0	0	0	0.9234	0.0864
	0	1	0	1	0	0	0.1089	0.9941
1	0	0	0	1	0	0	0.0014	0.9937
	1	0	0	0	0	0	0.6719	0.0395

GSA clearly shows the effect of the process variable on the performance metric. Succinic acid concentration has the greatest effect on process NPV, but its determination coefficient is low (0.6719). When two variables are considered simultaneously, the total explained variance increases. A maximum R^2 value of 0.9234 for the NPV occurs when Csa is combined with productivity. Adding yeast selectivity increases total variance explained to 0.9960. Using more than 3 process variables does not provide any relevant increment on correlation. GHG, on the other hand, is most influenced by yeast selectivity (0.9937 explained variability), while other variables have minor effects. Thus, as can be seen in Figure 1, the GHG performance is only limited by the yeast metabolism (Efe et al., 2013) and by the selectivity calculated based on GHG emissions for a petrochemical route for succinic acid production (Cok et al, 2013).

Based on Figure 1, that bounds the GHG feasible region, RTEEA was performed in order to determine economic feasibility. Figure 2 shows the isoeconomic surfaces (for $NPV = 0$) in terms of the process variables selected using GSA.

Productivity's effect on minimum feasible succinic acid concentration is greater at low selectivity. Nevertheless, this effect quickly decreases as selectivity increases. Selectivities above 12 have almost no effect on Csa, for productivities above 100

g/kg/h. Therefore, if selectivities above 12 are already achieved, there is no reason to invest on

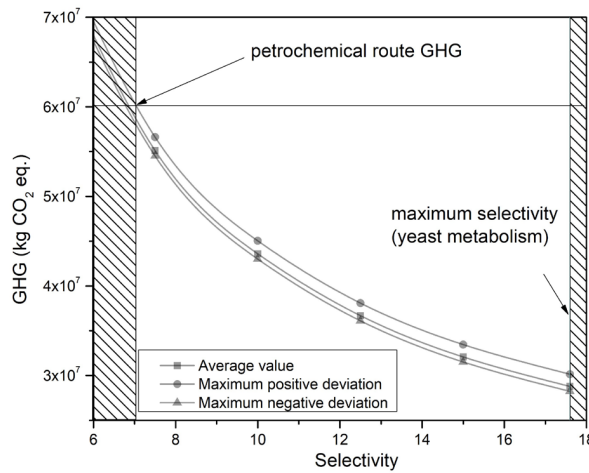


Figure 1: GHG performance based on yeast selectivity. The petrochemical route emissions (1.94 kg CO₂ eq /kg SAc) provide the minimum value for selectivity, 7.02 (Cok et al, 2013) and the yeast metabolism the maximum value, 17.6 (Efe et al., 2013).

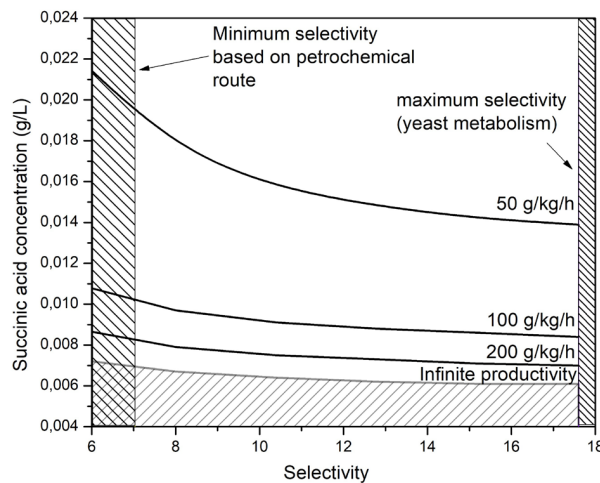


Figure 2: Succinic acid concentration (g/L) as function of the yeast selectivity (SAc produced/ethanol produced). The continuous lines are contour plots of isoeconomic surfaces (NPV=0) for various specific yeast productivities (SAc produced/yeast mass/reaction time). Feasible area (NPV>0) is above each line. Hatched areas are unfeasible regions.

increasing it. A better strategy is to increase succinic acid concentration, by increasing yeast resistance or by different process intensification techniques. Additionally, selectivities above 7 already lead to lower GHG emissions than petrochemical based succinic acid's. These comments exemplify how lab experiments can be quickly evaluated, and a new search direction for designing experiments can be derived, using RTEEA diagrams.

4. Conclusions

In this work, environmental analysis was coupled with techno-economic one to derive goals to R&D teams. The RTEEA methodology, an extension of RTEA, was able to identify the main process variables that influence the process economic and environmental performance, obtain their threshold values, and make explicit their relations. A case study was used to demonstrate the methodology capabilities. A set of six process variables were initially analyzed and their number reduced using global sensitivity analysis. With this methodology, a diagram was built which can be used to quickly derive new goals and directions for process development.

5. Acknowledgements

The authors would like to thank to the FAPESP-BIOEN (process n° 2016/10636-8) and A. M. Elias scholarship from CAPES.

References

- Cok, B., Tsiropoulos, I., Roes, A. L., Patel, M. K., 2013, Succinic acid production derived from carbohydrates: An energy and greenhouse gas assessment of a platform chemical toward a bio-based economy. *Biofuels, Bioprod. Bioref.* 8, 16-29.
- Efe, Ç., van der Wielen, L. A. M., Straathof, A. J. J., 2013, Techno-economic analysis of succinic acid production using adsorption from fermentation medium. *Biomass Bioenergy* 56, 479-492.
- Figueiredo, E. B., Panosso, R. A., Romão, R., Scala Jr, N. L., 2010, Greenhouse gas emission associated with sugar production in southern Brazil, *Carbon Balance and Management* 5:3.
- Furlan, F. F., Costa, C. B. B., Secchi, A. R., Woodley, J. M., Giordano, R. C., 2016, Retro-Techno-Economic Analysis: Using (Bio)Process Systems Engineering Tools to Attain Process Target Values, *Industrial and Engineering Chemistry Research* 55 (37), 9865-9872.
- Saltelli, A., Ratto, M., Andres, T., Campolongo, F., Cariboni, J., Gatelli, D., Saisana, M., Tarantola, S., 2008, *Global Sensitivity Analysis: The Primer*; John Wiley & Sons: Chichester, U.K.
- Soares, R. P., Secchi, A. R., 2003, Emso: A new environment for modelling, simulation and optimisation. *Computer Aided Chemical Engineering* 14, 947-952.
- Weidema, B.P., Bauer, C., Hischier, R., Mutel, C., Nemecek, T., Reinhard, J., Vadenbo, C.O., Wernet, G., 2013, *Overview and Methodology: Data Quality Guideline for the Ecoinvent Database Version 3, Ecoinvent Report, St. Gallen, Switzerland.*

Dynamic Modeling of Butanol Production from Lignocellulosic Sugars

Cansu Birgen^{a,*} and Heinz A. Preisig^a

^a*Department of Chemical Engineering; NTNU; Trondheim, Norway*
cansu.birgen@ntnu.no

Abstract

We proposed a dynamic model for butanol production from glucose and xylose as representative lignocellulosic sugars. The model consists of the extended Monod model for growth on mixed sugars with the effect of noncompetitive inhibition between them. The Luedeking-Piret model was used for butanol production. Sugar uptake equations were derived through a semi-empirical approach by employing yield coefficients. The proposed model has 10 parameters. We estimated the parameters by using data from a feed interval of a fed-batch fermentation experiment, which we performed with glucose and xylose by *Clostridium beijerinckii* NCIMB 8052. Parameter estimation imposed a constrained optimization problem where the objective was to minimize the sum of squared error (SSE) between the predicted and observed values of components. The constrained nonlinear optimization problem was solved using `fmincon` in MATLAB 2017b Optimization Toolbox based on the interior point algorithm. The problem was solved after 90 iterations and 1141 function evaluations resulting an SSE value of $8.9417e-14$. We validated the model with data sets of four other feed intervals, and the index of model accuracy, which was sum of squared relative error (SSRE) was 2.2245. We conducted the sensitivity analysis with end point deviations to identify the critical parameters. Substrate affinity constant for xylose, K_{sX} had the highest impact on cell mass, xylose and butanol concentrations, and had the second greatest effect on glucose concentration. This is the first study which addresses the dynamic modeling of simultaneous utilization of lignocellulosic sugars for butanol production. The proposed model is the first attempt to incorporate the interaction between sugars. The methodology we proposed provides an understanding in the dynamics of the butanol production from glucose and xylose, and it can further be used for guiding optimal process design and operation.

Keywords: dynamic modeling, butanol, lignocellulosic sugars, glucose, xylose

1. Introduction

Butanol has become a popular renewable energy carrier due to the depletion of fossil fuel resources and raising environmental concerns. However, its production has feedstock availability and low yield challenges. Ezeji et al. (2014) suggested that the exploitation of all the sugars bound in lignocellulosic biomass can contribute to solving these problems. Current studies mainly focus on single sugar systems, especially glucose, which does not reflect the true nature of the butanol production process from lignocellulosic sugars. Therefore, understanding the multiple sugar utilization in mixed form, the interactions between the sugars and resulting effect on cell mass growth and product formation is crucial. Our main objective is to develop a dynamic model for production of butanol from a mixture of glucose and xylose as representative lignocellulosic sugars. The developed systematic approach for dynamic modeling can also be applied for other types of microorganisms and sugars.

2. Theory

2.1. Kinetic model for butanol production from glucose and xylose

In this study, we established the kinetic model based on unstructured mathematical models which have typically been used to estimate the state of butanol production Srivastava and Volesky (1990). We developed a dynamic model for the process which describes cell mass growth, X , butanol production, B , and uptake of glucose, S_G and xylose, S_X .

In our previous study, we showed that the interaction between sugars was significant and in non-competitive inhibitory form Birgen et al. (2018b). Cell mass growth on glucose is shown in Equation 1 and, growth on xylose is shown in Equation 2.

$$\mu_G = \frac{\mu_{max_G} * S_G}{K_{S_G} * S_G * (1 + \frac{S_X}{K_{S_X}})} \quad (1)$$

$$\mu_X = \frac{\mu_{max_X} * S_X}{K_{S_X} * S_X * (1 + \frac{S_G}{K_{S_G}})} \quad (2)$$

where μ_{max_G} and μ_{max_X} are maximum specific growth rates on glucose and xylose, respectively. K_{S_G} and K_{S_X} are substrate affinity constants for glucose and xylose. Cell mass concentration change over time is shown in Equation 3.

$$\frac{dX}{dt} = (\mu_G + \mu_X) * X \quad (3)$$

Glucose uptake and xylose uptake are given in terms of the amounts utilized for cell mass growth and product formation, which can be seen in Equation 4 and Equation 5, respectively.

$$\frac{dS_G}{dt} = -\frac{1}{Y_{X/S_G}} * \mu_G * X - \frac{1}{Y_{B/S_G}} * \mu_G * X \quad (4)$$

where Y_{X/S_G} is the cell yield on glucose and Y_{B/S_G} is the butanol yield on glucose.

$$\frac{dS_X}{dt} = -\frac{1}{Y_{X/S_X}} * \mu_X * X - \frac{1}{Y_{B/S_X}} * \mu_X * X \quad (5)$$

where Y_{X/S_X} is the cell yield on xylose and Y_{B/S_X} is the butanol yield on xylose. The kinetic model for butanol formation is developed using the Luedeking-Piret model which only has a growth associated part as shown in Equation 6.

$$\frac{dB}{dt} = Y_{B/X_G} * \mu_G * X + Y_{B/X_X} * \mu_X * X \quad (6)$$

where Y_{B/X_G} is the butanol yield on cell mass utilizing glucose and Y_{B/X_X} is the yield on cell mass utilizing xylose.

2.2. Parameter estimation for kinetic model

Parameters of fermentation model that are listed in Section 2.1 are unknown a priori, therefore, we must estimate them from experimental data. In this work, the measured concentrations of cell mass, glucose, xylose, and butanol are used:

$$y = [[X] [S_G] [S_X] [B]]^T$$

for estimation of parameters

$$\Theta = [\mu_{max_G} \ K_{S_G} \ \mu_{max_X} \ K_{S_X} \ Y_{X/S_G} \ Y_{B/S_G} \ Y_{X/S_X} \ Y_{B/S_X} \ Y_{B/X_G} \ Y_{B/X_X}]^T$$

The parameter estimation poses a nonlinear least-squares optimization problem

$$\hat{\Theta} = \underset{\Theta}{\operatorname{argmin}} \sum_{i=1}^{N_m} \sum_{j=1}^{N_v} |\bar{y}_{ij} - y_{ij}|^2 \quad (7)$$

where $\hat{\Theta}$ denotes the estimated value of the kinetic parameters Θ ; and \bar{y} and y denote the measured and predicted concentration of the components; N_m is the number of measured components which is 4; N_v is the number of measurement points which is 14; and the subscript ij denotes the j^{th} value of the i^{th} measured component.

The objective of the parameter estimation problem in Equation 7 is to determine the parameters, Θ by minimizing the squared difference between the predicted and measured concentration of the components in y . The constrained nonlinear optimization problem is solved in using `fmincon` in MATLAB 2017b Optimization Toolbox based on the interior point algorithm together with `ode45` solver for the mass balance equations.

The parameter bounds considered in the optimization problem are given in Table 1. The parameter bounds for yield coefficients were determined using stoichiometric relations between the components Mayank et al. (2013). Rest of the parameter bounds were taken from literature Buehler and Mesbah (2016) and Eom et al. (2015).

2.3. Sensitivity analysis of kinetic model parameters

We conducted the sensitivity analysis 10% variations in each of 10 parameters presented in Section 2.1. The sensitivity can be measured by comparing the final concentrations with perturbed and unperturbed parameters. End point deviations (ED) of cell mass, glucose, xylose and butanol as a result of each parameter perturbation are assessed. ED is calculated as in Equation 8.

$$ED_i^P (\%) = \frac{y_i(\Theta + \Delta\Theta, t_{end}) - y_i^{ref}(\Theta, t_{end})}{y_i^{ref}(\Theta, t_{end})} \quad (8)$$

where $y_i(\Theta, t_{end})$ and $y_i(\Theta + \Delta\Theta, t_{end})$ represent the simulated concentration of i^{th} component in the fermenter at time t_{end} associated with unperturbed parameter Θ and perturbed parameter $\Theta + \Delta\Theta$, respectively. $y_i^{ref}(\Theta, t_{end})$ is the end concentration of the i^{th} component in the reference.

2.4. Model validation

We obtain the model after parameter estimation, and perform model simulations to check its validity for other feed intervals in the fed-batch fermentation experiment. We calculated sum of squared relative error (SSRE) between the predicted and observed values of the components as a quantitative measure of model accuracy, shown in Equation 9.

$$SSRE = \sum_{t=0}^{t_{end}} \left(\frac{\bar{y}_i(t) - y_i(t)}{\bar{y}_i(t)} \right)^2 \quad (9)$$

where $\bar{y}_i(t)$ and $y_i(t)$ denote the measured and predicted concentration of the components at time t , the subscript i denotes value of the i^{th} measured component.

3. Results and discussion

The optimization problem was solved after 90 iterations and 1141 function evaluations resulting an objective function, SSE value of $8.9417e-14$. First order optimality was $1.683e-07$. The optimization problem was solved when the size of the current step was less than the selected value of the step size tolerance, $1.0e-18$ and constraints were satisfied to within the selected value of the constraint tolerance which was set to $1.0e-12$. The estimated parameters are shown in Table 1.

Table 1: Estimates and bounds of model parameters.

Parameter	Lower bound	Upper bound	Initial point	Estimate
μ_{maxG}	0	1	0.5	0.3550
K_{SG}	0	2.5	1.25	0.8698
μ_{maxX}	0	1	0.5	0.3110
K_{SX}	0	2.5	1.25	0.8466
$Y_{X/SG}$	0	0.689	0.345	0.3982
$Y_{B/SG}$	0	0.412	0.206	0.2527
$Y_{X/SX}$	0	0.689	0.345	0.4294
$Y_{B/SX}$	0	0.494	0.247	0.3311
$Y_{B/XG}$	0	5	2.5	2.0367
$Y_{B/XX}$	0	5	2.5	1.5364

After the parameter estimation, we performed model simulations. Predicted and observed data are shown in Figure 1.

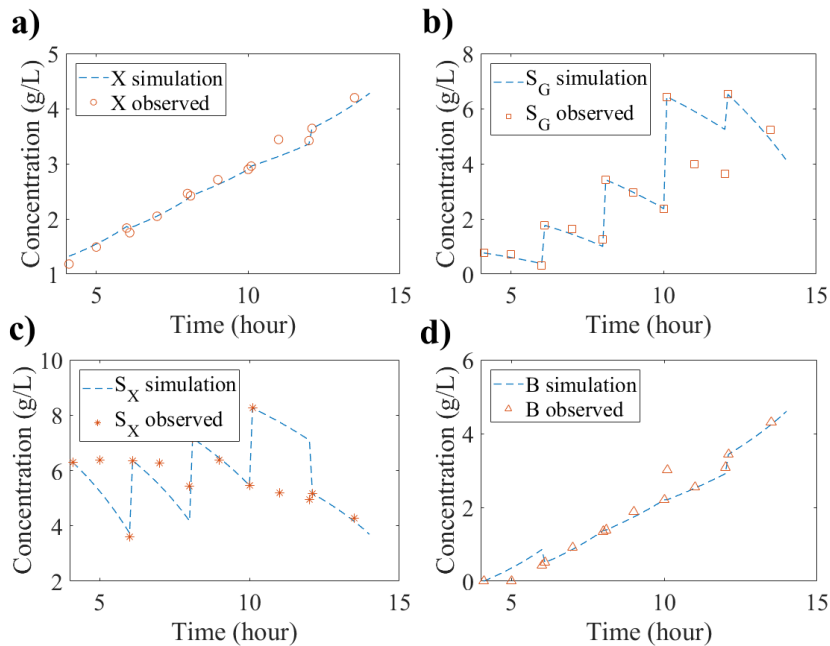


Figure 1: Predicted and observed values of a) cell mass concentration, b) glucose concentration, c) xylose concentration, d) butanol concentration.

The maximum specific growth rate on glucose was higher than on xylose, because its utilization yields more ATP and results in a higher cell mass growth rate. Furthermore, substrate affinity constant for glucose is larger indicating a lower affinity for glucose than xylose. This can be explained by our fermentation start up strategy that enables simultaneous utilization of sugars Birgen et al. (2018a), where the cells are first grown on a medium containing only xylose. Both the cell mass yield, Y_{X/S_X} and butanol yield, Y_{B/S_X} on xylose was higher than on glucose, which supports our motivation to investigate further on fermentation of xylose and other sugar mixtures.

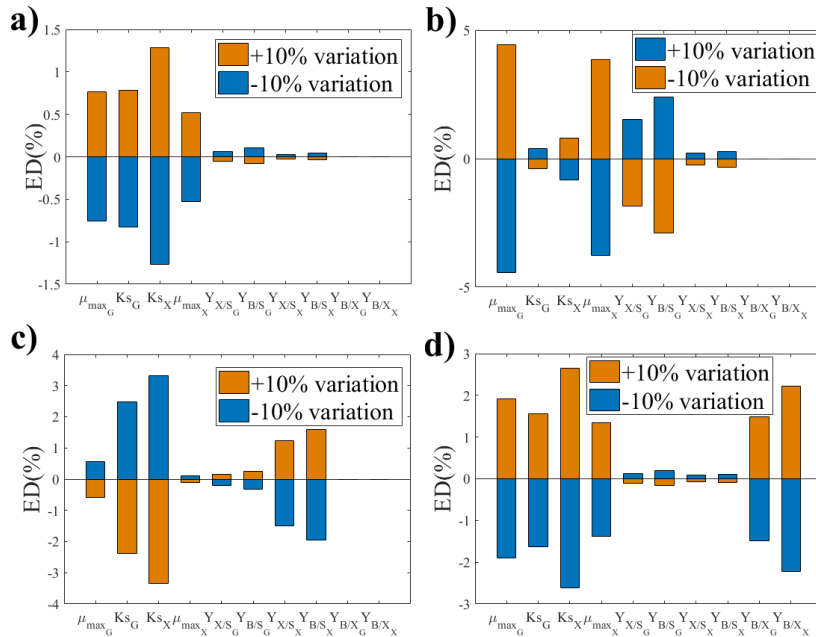


Figure 2: Sensitivity analysis results for a) cell mass concentration, b) glucose concentration, c) xylose concentration, d) butanol concentration.

We performed model validation with other feed intervals in the fed-batch fermentation data. We calculated SSRE between the observed and predicted values of the concentrations for quantitative measurement of the model accuracy. SSRE was 2.2245, which is in the range of previous findings for similar modeling approaches Eom et al. (2015).

In the sensitivity analysis of the model parameters, the reference trajectory was the concentration at the end of the feed interval in the fed-batch fermentation resulting from successive simulation under given design and operation variables. Figure 2 shows the results of the sensitivity analysis for the concentrations of cell mass, glucose, xylose and butanol. Substrate affinity constant for xylose, K_{S_X} showed substantial effects on all components.

Since our target product is butanol, we focus on the parameters which has the greatest influence on its final concentration. The second greatest influence was from the butanol yield on xylose utilizing cells, Y_{B/X_X} . Next critical parameter was the μ_{max_G} . Yield coefficients related to glucose and cell yield coefficient on xylose, Y_{X/S_X} and butanol yield coefficient on xylose, Y_{B/S_X} had a minor influence on the final butanol concentration.

4. Conclusions

We proposed a dynamic model for butanol production from glucose and xylose as representative lignocellulosic sugars. The model consists of the extended Monod model for growth on mixed sugars with noncompetitive interaction between the sugars. The Luedeking-Piret model was used for butanol production. Sugar uptake equations derived through a semi-empirical approach by employing yield coefficients. The proposed model has 10 parameters. We estimated the parameters by using data from fed-batch fermentation experiments, which we performed with glucose and xylose by *Clostridium beijerinckii* NCIMB 8052. Parameter estimation imposed a constrained optimization problem where the objective was to minimize the sum of squared errors (SSE) between the predicted and observed values of components. The constrained nonlinear optimization problem was solved using `fmincon` in MATLAB 2017b Optimization Toolbox based on the interior point algorithm. Sensitivity analysis showed that Substrate affinity constant for xylose has the greatest impact on cell mass, butanol, glucose and xylose concentrations. In addition, yield coefficients were critical parameters for butanol concentration. The main contributions of this paper can be stated as below:

1. This is the first study which addresses the dynamic modeling of utilization of lignocellulosic sugars in mixed form for butanol production.
2. This paper provides insight into contributions of each sugar to cell mass growth and butanol formation by parameter estimation of yield coefficients.
3. The proposed model is the first attempt to incorporate the interaction between sugars.

The methodology we proposed provides an understanding in the dynamics of the butanol production from glucose and xylose, and it can further be used for guiding optimal process design and operation.

5. Acknowledgment

EcoLodge - Efficient production of Butyl-Butyrate from Lignocellulose derived Sugars (NFR246821) has received funding from Norwegian Research Council under ENERGIX programme and Ministry of Science and Technology, Government of India (INT/NOR/RCN/P-06/2015).

References

- C. Birgen, S. Markussen, A. Wentzel, H. A. Preisig, B. Wittgens, 2018a. The effect of feeding strategy on butanol production by *clostridium beijerinckii* ncimb 8052 using glucose and xylose. *Chemical Engineering Transactions* 65.
- C. Birgen, S. Markussen, A. Wentzel, H. A. Preisig, B. Wittgens, 2018b. Modeling the growth of *clostridium beijerinckii* ncimb 8052 on lignocellulosic sugars. *Chemical Engineering Transactions* 65.
- E. A. Buehler, A. Mesbah, 2016. Kinetic study of acetone-butanol-ethanol fermentation in continuous culture. *PLoS one* 11 (8), e0158243.
- M.-H. Eom, B. Kim, H. Jang, S.-H. Lee, W. Kim, Y.-A. Shin, J. H. Lee, 2015. Dynamic modeling of a fermentation process with ex situ butanol recovery (esbr) for continuous biobutanol production. *Energy & Fuels* 29 (11), 7254–7265.
- T. C. Ezeji, S. Liu, N. Qureshi, 2014. Mixed sugar fermentation by clostridia and metabolic engineering for butanol production. *Biorefineries: Integrated biochemical processes for liquid biofuels*. Elsevier BV, 191–204.
- R. Mayank, A. Ranjan, V. S. Moholkar, 2013. Mathematical models of abe fermentation: review and analysis. *Critical reviews in biotechnology* 33 (4), 419–447.
- A. Srivastava, B. Volesky, 1990. Updated model of the batch acetone-butanol fermentation. *Biotechnology letters* 12 (9), 693–698.

Enzymatic keratin hydrolysis: Dynamic modelling, parameter estimation and validation

Alistair Rodman^a, Francesco Falco^b, Dimitrios I. Gerogiorgis^{a*}, Krist V. Gernaey^b

^a *School of Engineering (IMP), University of Edinburgh, Edinburgh, EH9 3FB, UK*

^b *DTU Chemical Engineering, Technical University of Denmark, 2800 Kgs. Lyngby, DK*

D.Gerogiorgis@ed.ac.uk

Abstract

Keratin rich waste material is an abundant by-product from the agroindustry, particularly the meat and poultry industries: skin remains, bristle, animal hair, horns and hooves, feathers, etc. This waste may not be incinerated due to environmental concerns, so producers seek waste valorization by upcycling this non-biodegradable by-product by depolymerization to extract soluble proteins, which can be used as animal feed supplements. This can be performed thermally, however high temperature processing destroys amino acids which are necessary in the product and are costly to later supplement. A novel two-stage enzymatic de-polymerization process for keratin is being investigated. The first stage involves growing the microbial keratinases on a substrate sample, and is optimized for maximal enzyme production. The second stage uses the keratinases in a bioreactor optimized for substrate hydrolysis. The enzymatic hydrolysis mechanism for keratin is not well documented rendering current the current industrial application limited. This paper presents lab scale experimental results from the second (hydrolysis) stage using a keratinolytic enzymatic cocktail with the filamentous bacterium *Amycolatopsis keratiniphila D2* (DSM 44409). Dynamic state data for the product (protein) and substrate (keratin) concentrations following varying substrate loading has been used to construct the first reduced order model for the enzymatic hydrolysis of waste keratin. Potential model applications include to dynamically optimize this second process stage by computing optimal dosage strategies (keratin deposit intervals and volume) to minimize processing time and cost to dispose or repurpose the biochemical waste.

Keywords: keratin, enzymatic hydrolysis, dynamic modelling, parameter estimation.

1. Introduction

1.1. Background

Keratin rich waste material is an abundant by-product from agroindustrial activities, particularly the meat and poultry industries (Daroit and Brandelli, 2014): skin remains, bristle, animal hair, horns and hooves, feathers, etc. It is estimated that five million tonnes per year of keratin waste is produced in these industries (Brebu and Spiridon, 2011), which is classified as a low-risk animal by-product. This constitutes the third most abundant renewable polymeric material present in nature after cellulose and chitin. This solid residue is not suitable for human consumption and must be treated for safe disposal, providing financial and environmental incentives for process development.

Recently, producers seek waste valorization by upcycling this non-biodegradable by-product by depolymerization to extract soluble proteins from the residual biomass to produce a saleable by-product, for example as an animal feed supplement. The aquaculture industry is one of the fastest growing sectors in food production, accounting for approximately half of the seafood consumed in the world. The availability of risk-free, easily accessible and economical feed ingredients for sustainable aquaculture production plays a key role in global food security; proteins obtained from the biodegradation of keratin could replace a significant fraction of the fish meal used in aquaculture feed formulation. Fish meal constitutes one of the main ingredients of fish feed and represents about 40% of its total weight (Fang et al., 2013), suggesting vast potential demand for such a product, under given purity and food safety specifications.

1.2. Enzymatic keratin bioprocessing

Traditionally keratin hydrolysis has been performed thermally (Jeske et al., 1976; Orzeszko and Sutarzewicz, 1979), however high temperature processing destroys amino acids necessary for the product to be used as animal feed and are costly to later supplement. Keratins are fibrous structural proteins containing many disulfide bonds in their primary structure. Based on their secondary structure, keratins, are divided into α - and β -keratin. The α -type (hard keratin) has a higher cysteine content which allows the formation of a larger number of disulfide bridges between cross-linking protein chains, rendering them water-insoluble and resistant to lysis by conventional proteolytic enzymes. Select bacteria, actinomycetes and keratinophilic fungi, have been found capable of synthesizing microbial keratinases (enzymes which hydrolyse keratins) when in an environment that the only source of carbon, nitrogen, sulphur and energy is from keratin biomass. Therefore, biodegradation using keratinolytic bacteria is an attractive way of converting keratinic waste into products of practical industrial value (Al-Musallam et al., 2003). This can include acting as a fish meal replacement in feeds for the aquaculture industry, where the product has an improved amino acid profile compared to thermal keratin processing (Korniłowicz-Kowalska and Bohacz, 2011).

Therein a novel two stage process can be performed for the conversion of keratin rich waste material into a useful protein rich product. Firstly, a keratin sample is used as a bacteria feed to promote the synthesis of microbial keratinases. Here, keratin consumption is not of interest and the process stage should be optimized solely for enzyme production and growth. Subsequently keratin hydrolysis may be performed using the enzyme produced in the previous stage. The two processes (enzyme synthesis and hydrolysis) are favoured in drastically different conditions, so staging is essential. The two stages can be physically separated via a cross-flow ultrafiltration membrane step, with each stage cyclically repeated in order to achieve semi-continuous operation.

It is desirable to perform the keratin degradation process stage at high solids loadings to maximize product titer and reduce process water, energy usage, and reactor size (Gong et al., 2015). As this is an industrial process in its infancy, the enzymatic hydrolysis mechanism is not well documented, rendering current industrial application limited. Therein lies a strong incentive for dynamic modelling of keratin hydrolysis, to facilitate high-fidelity process simulation and optimisation (Rodman and Gerogiorgis, 2017).

2. Materials and Methods

2.1. Enzyme preparation

Lab scale hydrolysis experiments have been performed using a keratinolytic enzymatic cocktail with the filamentous bacterium *Amycolatopsis keratiniphila* D2 (DSM 44409), first reported by Al-Musallam et al. (2003). The bacterium was cultivated on mineral keratin medium with the following composition: 0.75 g L⁻¹ NaCl, 1.75 g L⁻¹ K₂HPO₄, 0.25 g L⁻¹ MgSO₄·7H₂O, 0.055 g L⁻¹ CaCl₂, 0.010 g L⁻¹ FeSO₄·7H₂O, 0.005 g L⁻¹ ZnSO₄·7H₂O and 1% w/w poultry by-product meal (PBM) keratin powder. The medium is sterilized at 121 °C (20 min), and free keratinase extract is obtained for hydrolysis.

2.2. Keratinase activity screening

To screen for suitable reaction temperatures, enzymatic activity was monitored over time following isothermal incubation by assaying with azokeratin as a substrate. A range of temperatures were screened between 30 and 50°C, where an inherent trade off exists between increased initial activity and increasing activity decay rate. It was found that at 40 °C the activity was suitably high and did not decay prohibitively quickly, and has thus been implemented as the experimental and model reaction temperature.

2.3. Dynamic state data

Vials containing 2 mL keratinase preparation and varying solids loading (PBM meal) were placed in a thermoshaker at 40 °C and 600 rpm. At fixed time intervals, triplicate vials were removed for each solid loading considered. A sample from each vial was taken and the protein content determined by bicinchoninic acid (BCA) assay, and the remaining vial contents vacuum filtered, dried and weighed to determine residual substrate mass. Two campaigns were performed: firstly, initial reaction kinetics for four substrate concentrations (1.5, 3, 5 and 7% w/w) were considered with samples taken over time in the first hour, a period in which the consumption rate is approximately constant at the maximum (initial) value. Secondly, three substrate concentrations were considered (3, 5 and 7% w/w) with the hydrolysis performed for 72 h to construct state profiles for both substrate, $[K]$, and product, $[P]$, throughout the entire reaction duration.

3. Experimental Results and Dynamic Model Parameter Estimation

The keratinase activity profile at 40 °C can be seen in Fig. 1a, with Fig. 1b representing the initial substrate consumption rates at differing solid loadings. The gradients from Fig. 1b are used in the Lineweaver-Burk plot (Fig. 1c) to elucidate initial reaction kinetics. Fig. 2 presents the experimental state data over a 72-hr experimental campaign.

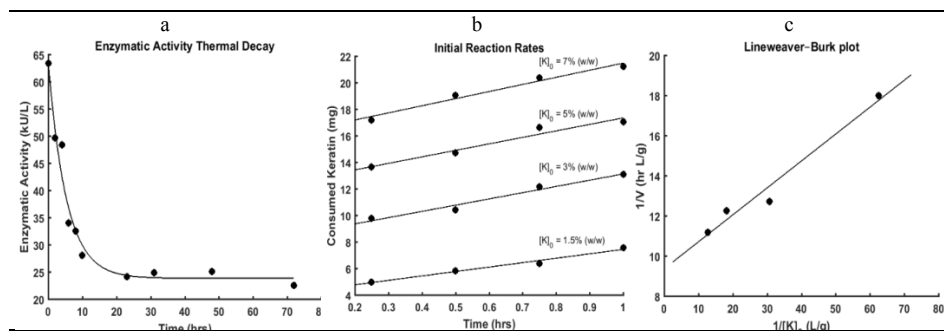


Figure 1. Enzyme activity, initial reaction rates and Lineweaver-Burk plot ($T = 40\text{ }^{\circ}\text{C}$).

Based on the experimental results, the following model is proposed for the enzymatic hydrolysis of keratin. The substrate is considered to consist both hydrolysable, $[K]_H$, and non-readily hydrolysable, $[K]_{NH}$, components (Eq. 1), where the later refers to keratins which *A. keratiniphila D2* is unable to digest. The hydrolysable fraction, H , is defined by Eq. (2). The consumption rate of the readily hydrolysable substrate is considered as the product of three factors (Eq. 4). Firstly, the Michaelis–Menten expression, φ_1 , describes the reaction kinetics (Eq. 5). Secondly, φ_2 relates to the keratinase activity: this term differs from a conventional two parameter first order activity decay expression by the addition of residual activity (R_A). This is a result of an enzyme cocktail being present in place of a single cell type, where components of the cocktail have drastically differing decay timescales at this reaction temperature. The residual activity represents the activity of the cells that do not notably decay within the hydrolysis timescale, which is visible from the activity in Fig. 1a plateauing well above 0. Lastly, an inhibition term, φ_3 , is considered as a function of the product concentration (Eq. 7), representing the proteins being produced impeding the keratin-enzyme interaction. A product ratio, f , relates protein production to substrate consumption, with the remainder of the consumed substrate mass consisting of released fats, lipids, peptides etc.

$$[K] = [K]_{NH} + [K]_H \quad (1)$$

$$[K]_H = H \cdot [K] \quad (2)$$

$$\frac{d[K]_H}{dt} = -r \quad (3)$$

$$r = \varphi_1 \cdot \varphi_2 \cdot \varphi_3 \quad (4)$$

$$\varphi_1 = \frac{V_{max} \cdot [K]_H}{K_M + [K]_H} \quad (5)$$

$$\varphi_2 = [E] = e_i \cdot \exp(-k_D \cdot t) + R_A \quad (6)$$

$$\varphi_3 = \frac{K_I}{K_I + [P]} \quad (7)$$

$$\frac{d[P]}{dt} = f \cdot r \quad (8)$$

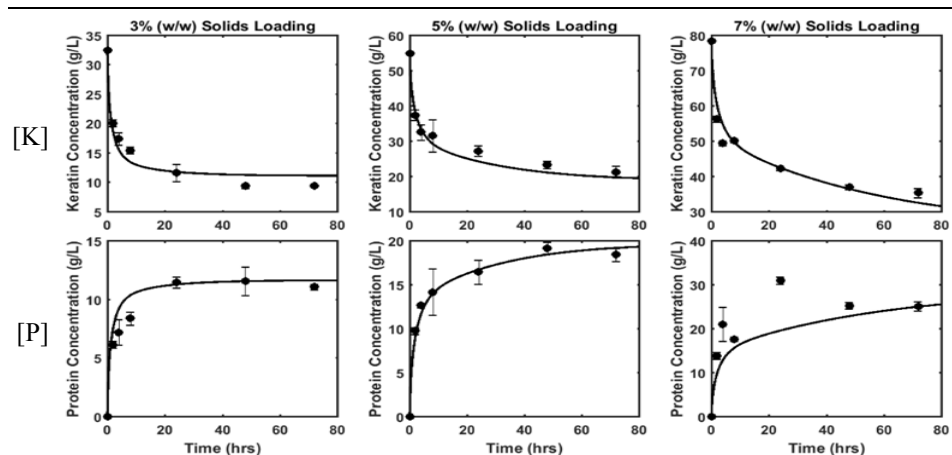


Figure 2. Dynamic model trajectories vs. experimental data for substrate and product.

Table 1. Dynamic model parameter values computed for enzymatic keratin hydrolysis.

Parameter	Symbol	Value	Units	Data Source
Hydrolysable substrate fraction	H	0.63	(-)	Fig. 2
Maximum reaction velocity	V_{max}	3.20	$\text{g L}^{-1} \text{hr}^{-1}$	Fig. 1c
Michaelis–Menten constant	K_m	14.29	g L^{-1}	Fig. 1c
Initial enzymatic activity	e_i	39.96	kU L^{-1}	Fig. 1a
Enzyme decay constant	k_D	0.188	hr^{-1}	Fig. 1a
Residual enzyme cocktail activity	R_A	23.91	kU L^{-1}	Fig. 1a
Product inhibition constant	K_I	0.328	g L^{-1}	Fig. 2
Product ratio	f	0.548	(-)	Fig. 2

Of the eight model parameters, three (e_i , k_D and R_A) can be fit from the activity assay profile (Fig. 1a), whose solid line shows the fit using parameter values from Table 1. Two parameters (V_{max} and K_m) are determined directly using the initial kinetics via the Lineweaver-Burk plot method (Fig. 1c). Additionally, f can be directly inferred as the ratio between the protein and keratin state derivatives in Fig. 2, while H can be considered as the average of the total substrate fraction digested after the reaction is completed. Subsequently, the remaining model parameter, K_I , is estimated by minimizing the sum squared error between model and experimental data points, defined by Eq. 9 and solved using MATLAB (fminsearch); ode45 is used for model integration.

$$\min \sum (f(\mathbf{x}_j, \theta) - y_j)^2 \quad (9)$$

Here, $f(\mathbf{x}_j, \theta)$ is the model predicted keratin and protein state trajectory for experiment j , θ is the parameter vector and y_j is the experimental state trajectory. The data sets for 3% and 7% w/w initial substrate concentration were used in the fitting, leaving the 5% w/w profile as a supplementary dataset which is used for comparisons for model validation.

4. Discussion

It can be seen from Fig. 2 that the proposed model is able to effectively describe the key behaviour observed in the experimental data, both for keratin consumption and protein production. The dataset not used in the model parameter determination (5% w/w loading) shows good agreement between experimental data and the model prediction, suggesting the model can accurately describe keratin hydrolysis at 40 °C with *A. keratiniphila* D2. The model can be used to compute optimal substrate dosage strategies towards processing time and cost minimization in biochemical waste keratin hydrolysis.

The model assumption of a fixed fraction of the substrate being hydrolysable, H , is not able to fully capture the observed phenomena where yield decreases with solids loading. As a result, the model under-predicts keratin consumption at 3% w/w solids, and over predicts for 5% and 7% w/w (Fig. 2). If the value of H is defined individually for each solid loading campaign according to the observed experimental yield in that campaign and the model parameters re-determined, the fit is exceptional. This indicates that if the mechanism behind diminishing yield with increasing substrate concentration can be incorporated into an updated model it would be even more accurate in representing the dynamic system. It is known that as solids loading increases, factors that were insignificant in low-solid systems become more prominent (Modenbach and Nokes, 2013), which can restrict substrate conversion yield at higher loading and is found to be the case here. It is possible that mass transfer between the keratin and enzyme is becoming impeded at high substrate concentrations due to reduced free water content as the liquid absorbs into the biomass, as has been observed in high-solids enzymatic

cellulose hydrolysis (Hodge et al., 2009), a reactive system known to have many parallels to keratin hydrolysis; however further experimental work is necessary to confirm whether this is the precise mechanism responsible for the observed phenomena. Moreover, further experimental work to investigate parameter temperature dependence will have great value towards process development, facilitating model implementations towards simultaneous optimization of reactor temperature profile and keratin dosing.

5. Conclusions

The hydrolysis of keratin rich material with keratinolytic bacteria is an attractive way of transforming undesirable waste from agroindustrial activities into products of practical industrial value. A lab-scale experimental campaign has been performed, enabling the successful parameterization of a dynamic model for enzymatic hydrolysis of keratin. Michaelis–Menten kinetics with product inhibition allows the observed behaviour of the reactive system to be captured, with the model fit showing good agreement with experimental data. The development of such a model is an important contribution towards improving the competitiveness of this novel means of waste valorization via computational simulation, optimization and development of hydrolysis reactors. The model assumption of a fixed fraction of the substrate being hydrolysable cannot fully capture the observed phenomena, inasmuch as yield decreases with solids loading. Further experimental work is necessary to explore this advance, with the aim of better describing the apparent inhibition effect at higher substrate content, thus increasing model fidelity and enabling dynamic optimization of the keratin hydrolysis reactor.

6. Acknowledgements

The authors gratefully acknowledge the financial support of the Eric Birse Charitable Trust for a Birse PhD Fellowship, and to the Royal Society of Edinburgh (RSE) for the John Moyes Lessells Travel Scholarship (to DTU), both awarded to Mr A. D. Rodman.

References

- A. Al-Musallam, S. Al-Zarban, Y. Fasasi, R. Kroppenstedt & E. Stackebrandt, 2003. *Amycolatopsis keratiniphila* sp. nov., a novel keratinolytic soil actinomycete from Kuwait. *International Journal of Systematic and Evolutionary Microbiology*, **53**(3): 871-874.
- A. Modenbach & S. Nokes, 2013. Enzymatic hydrolysis of biomass at high-solids loadings—a review. *Biomass and Bioenergy*, **56**: 526-544.
- A. Rodman & D. Gerogiorgis, 2017. Dynamic optimization of beer fermentation: Sensitivity analysis of attainable performance vs. product flavour constraints. *Computers and Chemical Engineering*, **106**: 582-595.
- D. Hodge, N. Karim, D. Schell & J. McMillan, 2009. Model-based fed-batch for high-solids enzymatic cellulose hydrolysis. *Applied Biochemistry and Biotechnology*, **152**(1): 88-107.
- G. Orzeszko & D. Sutarzewicz, 1979. Bristle utilization. *Meat Management*, 48-51.
- J. Gong, Y. Wang, D. Zhang, R. Zhang, C. Su, H. Li, ... & J. Shi, 2015. Biochemical characterization of an extreme alkaline and surfactant-stable keratinase derived from a newly isolated actinomycete *Streptomyces aureofaciens* K13. *RSC Advances*, **5**(31): 24691-24699.
- J. Jeske, W. Doruchowski & H. Weislo, 1976. The assessment of by-product management in the poultry industry. *Food Industry*, **30**: 255-257.
- T. Kornilowicz-Kowalska & J. Bohacz, 2011. Biodegradation of keratin waste: theory and practical aspects. *Waste Management*, **31**(8): 1689-1701.
- Z. Fang, J. Zhang, B. Liu, G. Du & J. Chen, 2013. Biodegradation of wool waste and keratinase production in scale-up fermenter with different strategies by *Steno-trophomonas maltophilia* BBE11-1. *Bioresource Technology*. **140**: 286-291.

Adaptation of a Monte Carlo method to the hydrotreating of bio-oil model compounds

Ana R. Costa da Cruz^a, Jan Verstraete^{a,*}, Nadège Charon^a, Jean-François Joly^a

^aIFP Energies nouvelles, Rond-point de l'échangeur de Solaize, 69360 Solaize, France

*jan.verstraete@ifpen.fr

Abstract

Lignocellulosic biomass, like oil fractions, is a source of hydrocarbons. The transformation from biomass to liquid hydrocarbons passes by several processes: pretreatment, conversion, followed by post-treatment. In one of the possible transformation schemes, the biomass undergoes fast pyrolysis, and the produced bio-oils are upgraded through hydroconversion and hydrotreating. Similar to the heavy oil fractions, bio-oils are complex mixtures and, consequently, they have a complex reaction behaviour. For this reason, in the present work, the reaction pathways of model molecules representative of bio-oil are studied under hydrotreating conditions over a NiMo/Al₂O₃ catalyst. To simulate the various transformations, a kinetic Monte Carlo method, called Stochastic Simulation Algorithm, is applied to guaiacol, furfural and D-glucose and compared to the experimental results.

Keywords: Bio-oil Model Compounds, Hydrotreating, Kinetics, Monte Carlo.

1. Introduction

To face the actual energetic dilemma, eco-friendly technologies are being studied. From the array of renewable energies, biomass takes a prime role, as it presents a higher energetic potential. This source, like the petroleum fractions, is a carbon-based reserve. It can therefore be transformed into chemical building blocks and fuels. In order to achieve this goal, biomass must undergo several transformations: biomass pretreatment, conversion, and upgrading. In one of the possible transformation schemes, the biomass undergoes fast pyrolysis to transform it into intermediate compounds such as bio-char, gases and bio-oil. These substances are subsequently upgraded and valorised. Through a dedicated upgrading process scheme that includes a series of hydrotreating and hydroconversion steps, the fast pyrolysis bio-oil is converted into valuable products.

Both the hydrotreating and hydroconversion steps have been studied by the scientific community (Elliot, 2007; Wang et al., 2013; Zacher et al., 2014). However, driven by the difficulty in understanding the bio-oil complexity, several authors turned to representative single model compounds and mixtures of these (Furimsky, 1999; Wang et al., 2013). Through these models, the reaction mechanisms, both of single molecules and mixtures, began to be documented. However, such type of experimental studies is not sufficient to uncover the global reaction network of actual bio-oils.

The present work proposes a new approach to investigate the reaction networks and the reactivity of bio-oils. A “on-the-fly” method, termed Stochastic Simulation Algorithm, allows the construction of a modelling and simulation tool for the conversion of bio-oil. This technique generates the reaction network while the simulation is unrolling thereby

avoiding the pre-definition of the bio-oil reaction pathways. Already applied to complex oil fractions (Oliveira, 2013; Oliveira et al., 2016; Lopez-Abelairas et al., 2016), this tool promises a potential solution for unravelling the global reaction network of bio-oils. Limited by the feed complexity, the present work will focus on the transformation of model compounds.

2. Model Development

The Stochastic Simulation Algorithm (SSA) (Gillespie, 1976; Gillespie, 1992) is based on the randomness of events, which can be represented by their occurrence probability. This algorithm is a kinetic Monte Carlo (kMC) method, which describes the evolution of a molecular system, molecule by molecule, and event by event. Unlike classic procedures, this method can describe the evolution of a molecular mixture over time without a pre-defined reaction network.

The stochastic approach is based on the identification of all possible reaction events at a given moment in time and on the calculation of the reactivities for each event, through the stochastic rate parameter (c_v) and the several combinations in which the reactants may collide and react (h_v). As described by Gillespie (1976; 1992), for monomolecular reactions, as in the case of hydrotreating reactions with hydrogen in excess, the combinatorial parameter equal 1, as there is only one possibility of collision. Furthermore, for the same type of reactions, Gillespie (1976; 1992) showed that the stochastic rate parameter can be determined by the deterministic rate parameter (k_v). Combining this information with the Arrhenius law, the stochastic rate parameter is given by Equation (1).

$$c_v = c_v(T_{ref}) \exp\left(-\frac{E_a}{R} \left(\frac{1}{T} - \frac{1}{T_{ref}}\right)\right) \quad (1)$$

where c_v is the stochastic rate constant of the reaction type v at the reaction temperature, $c_v(T_{ref})$ is the stochastic rate constant of the reaction type v at the reference temperature T_{ref} , E_a is the activation energy, R is the ideal gas constant, T is the temperature of the system, and T_{ref} is the reference temperature.

After calculating the apparent first order rate coefficients for the reactions, the reaction probability can be generated for each reaction event, as shown in Equation (2).

$$P_v = \frac{h_v c_v}{\sum_i^M (h_i c_i)} \quad (2)$$

By assembling all the probabilities of all molecules, the overall reactivity allows to determine, via Monte Carlo sampling, the time interval until the next reaction. A first random number (RN_1) is drawn to determine the reaction time step (Δt) between the current time t and the time at which the next, yet undefined, reaction will occur. This reaction time step is calculated by Equation (3), as proposed by Gillespie (1976; 1992).

$$\Delta t = -\frac{\ln(RN_1)}{\sum_i^M (h_i c_i)} \quad (3)$$

A second random number (RN_2) is drawn to select, from the normalized discrete probability density function (D_R), the next reaction (μ). More precisely, the reaction selection step is performed by drawing a number between zero and one. The value of this random number selects the next reaction from the cumulative probability distribution (D_R), as shown in Equation (4).

$$D_R(\mu-1) < RN_2 < D_R(\mu) \quad (4)$$

After calculating the time step and selecting the reaction, the reaction system is updated by executing the selected reaction, i.e. replacing the reactant(s) by the product(s), and incrementing the simulation time according to reaction time step (Δt). The simulation proceeds reaction by reaction, through the sampling of the mentioned variables. The procedure is repeated until the final simulation time is reached, leading to the set of product molecules.

The SSA requires as inputs a list of reactant molecules, the different types of reactions that can occur and the kinetic parameters associated to these transformations. Due to its stochastic nature, this method generates a different outcome for each simulation. Therefore, as with any stochastic approach, the method has to be based on several simulations, each of which calculates discrete time trajectories of molecular populations. Their average profile will converge to the same results as deterministic methods.

3. Results and Discussion

For the simulation of the hydrotreating of guaiacol, furfural and D-glucose (fructose), the reactions for demethylation, demethoxylation, transalkylation, dehydrogenation, hydrodeoxygenation, decarbonylation and hydrogenation of unsaturated bonds and rings were implemented. For the various model molecules, the SSA method is able to predict the expected trends, not only for the conversion of the reactants, but also for the generation of the various products and for the hydrogen consumption. Additionally, this approach also predicts the transformation of the intermediates into smaller molecules.

Due to the high reactivity of the model compounds, the heating and cooling periods contribute significantly to the overall conversion. Hence, the reactor simulations need to account for these dynamic periods.

3.1 Guaiacol simulation and kinetic model

The first application of our kinetic model has simulated the hydrotreating of guaiacol. The model results were compared to the experimental data obtained by Ozagac (2016) for the hydrotreating of guaiacol over a NiMo/Al₂O₃ catalyst in a batch reactor at 13 MPa and 300 °C and for reaction times of 3 h and of 5 h. For the experiments, a blank run was performed and showed an initial conversion of 10 % after the heating up the batch reactor to 300 °C and cooling it down to ambient temperature.

For the conversion of guaiacol into hydrocarbons, only the hydrogenation of rings, demethylation, demethoxylation, transalkylation, and hydrodeoxygenation reactions

were considered. The kinetic parameters of the reactions were estimated based on the guaiacol conversion for the three batches. For all these reactions, the same energy of activation was considered in order to reduce the number of kinetic parameters to be estimated. The reactions during the thermal history of the experiments (heating, reaction and cooling) were also taken into account.

A good agreement is observed with the experimental results, as shown in Figure 1 and Figure 2. The model predicts, within the error of the experimental data, the correct order of magnitude for the conversion of guaiacol and the selectivities towards methanol, phenol and dialcohols.

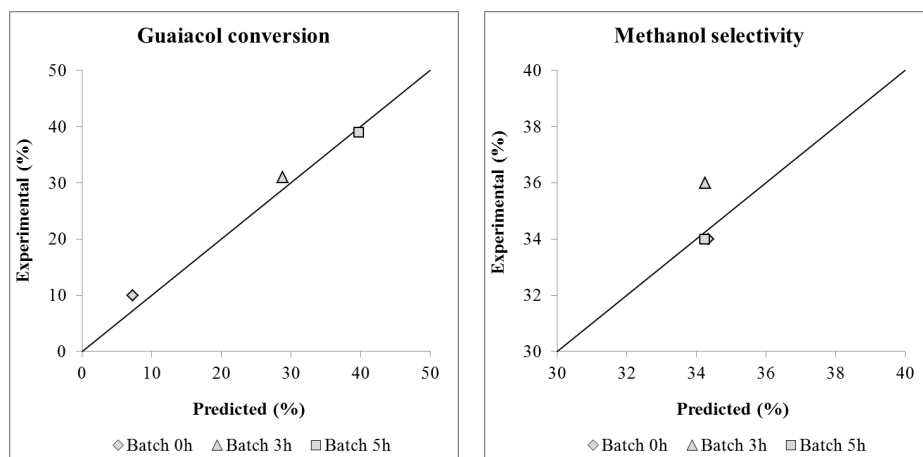


Figure 1 - Stochastic simulation of guaiacol hydrotreating based on the average of 50 simulations with 10000 molecules: a) Guaiacol conversion (%), b) Methanol selectivity (%).

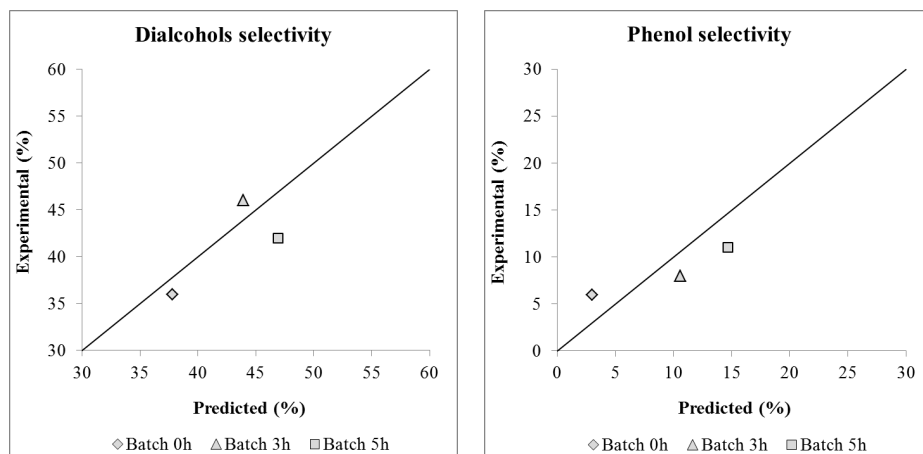


Figure 2 - Stochastic simulation of guaiacol hydrotreating based on the average of 50 simulations with 10000 molecules: a) Dialcohols selectivity (%), b) Phenol selectivity (%).

3.2 Furfural and D-Glucose simulation

By extrapolating the kinetic parameters obtained for guaiacol according with Elliot (2007) reactivity scale, it is possible to simulate the hydrotreating for both furfural and D-glucose.

Similar to the guaiacol simulation, the reactions considered represent only the conversion of furfural and D-glucose into hydrocarbons. For the dehydrogenation, hydrodeoxygenation, decarbonylation and hydrogenation of unsaturated bonds and rings, the same energy of activation was once again considered. The thermal behaviour of the reactor during heating, reaction and cooling was again taken into account.

The simulations for both compounds were performed at 13 MPa and 300 °C during 1 h. As shown in Figure 3, the disappearance of furfural (monoaldehyde) is leads to the generation of monoalcohols, by hydrodeoxygenation, and hydrocarbons, by decarbonylation, as seen in the experimental results of Ozagac (2016).

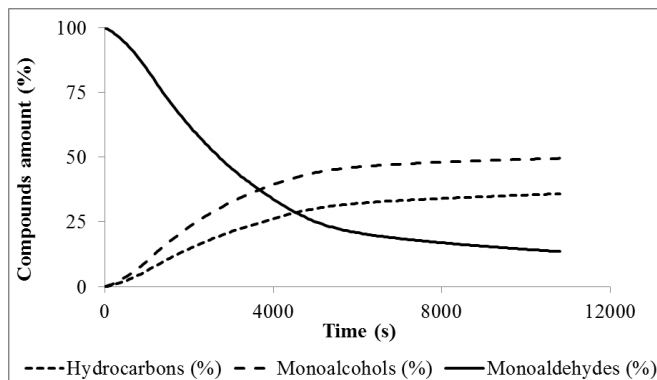


Figure 3 - Stochastic simulation of furfural hydrotreating based on the average of 50 simulations with 10000 molecules: Major compounds fraction (%).

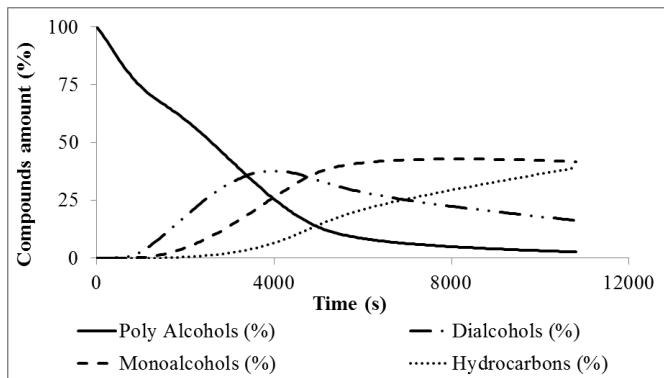


Figure 4 - Stochastic simulation of D-glucose hydrotreating based on the average of 50 simulations with 10000 molecules: Major compounds fraction (%).

The gradual loss of the hydroxyl group, as shown in Figure 4, reflects a transformation of D-glucose via dehydration and hydrodeoxygenation. As seen in the experimental results of Ozagac (2016), both pathways are the main conversion routes of D-glucose into hydrocarbons, thus illustrating the consistency between the simulations and the experimental results.

4. Conclusions

The SSA methodology was applied to bio-oil model molecules. The kinetic model generated is able to simulate the reactions of guaiacol under hydrotreating conditions. The simulations showed the correct trends when compared to available experimental data. The model was also used to simulate the hydrotreating for both furfural and D-glucose. Access to further experimental data will allow to compare these simulations to experimental data, and to improve and extend the proposed kinetic model.

The results presented here also show that the SSA method is an excellent simulation tool for complex reaction networks without the need for a pre-defined reaction network. Additionally, these simulations enable a better understanding of these systems, making the SSA method suitable to be applied to a full range bio-oil.

References

- Elliott DC (2007) Historical Developments in Hydroprocessing Bio-oils. *Energy Fuels* 21(3):1792–1815.
- Furimsky E (2000) Catalytic hydrodeoxygenation. *Applied Catalysis A: General* 199(2):147–190
- Gillespie DT (1976) A general method for numerically simulating the stochastic time evolution of coupled chemical reactions. *Journal of Computational Physics* 22(4):403–434.
- Gillespie DT (1992) A rigorous derivation of the chemical master Equation. *Physica A: Statistical Mechanics and its Applications* 188(1-3):404–425.
- Lopez-Abelairas M, Oliveira LP, Charon N, Verstraete JJ (2016) Application of Monte Carlo Techniques to LCO Gas Oil Hydrotreating: Molecular Reconstruction and Kinetic Modelling. *Catal. Today* 271, 188-198.
- Oliveira LP (2013) Développement d'une méthodologie de modélisation cinétique de procédés de raffinage traitant des charges lourdes, École Normale Supérieure de Lyon
- Oliveira LP, Hudebine D, Guillaume D, Verstraete JJ, Joly JF (2016) A Review of Kinetic Modeling Methodologies for Complex Processes. *Oil Gas Sci. Technol. – Rev. IFP Energies nouvelles* 71(3):45.
- Ozagac M (2016) Etude mécanistique de l'hydroconversion catalytique de bio-huiles de pyrolyse. PhD, Université Claude Bernard - Lyon 1.
- Wang H, Male J, Wang Y (2013) Recent Advances in Hydrotreating of Pyrolysis Bio-Oil and Its Oxygen-Containing Model Compounds. *ACS Catalysis* 3 (5), 1047-1070.
- Zacher AH, Olarte MV, Santosa DM, Elliott DC, Jones SB (2014) A review and perspective of recent bio-oil hydrotreating research. *Green Chem* 16:491-515.

Ontology Modelling for Lignocellulosic Biomass: Composition and Conversion

Madeleine Bussemaker*, Nikolaos Trokanas, Linsey Koo, Franjo Cecelja

Univeristy of Surrey, Guildford GU2 7XH, UK

m.bussemaker@surrey.ac.uk

Abstract

This paper presents an expansion of an already developed ontology BiOnto (Trokanas, Bussemaker, Velliou, Tokos, & Cecelja, 2015) and processing technology eSymbiosis ontology (Raafat, Trokanas, Cecelja, & Bimi, 2013) towards valorisation of lignocellulosic biomass. The ontology provides a reference model interpretable by humans and computers by further classifying and characterizing lignocellulosic biomass (LCB) in several ways, such as: lignin, hemicellulose and cellulose content, C5 and C6 composition, elemental composition, and heat value. Similarly, LCB processing technologies are classified and characterised based on the input of LCB components, with related conversion rates of specific components. The combination of these classifications can elucidate additional information to assist in decision making for the ontology user. For example, the theoretical conversion rates of C5 and C6 polymeric sugars to ethanol are 0.5987 and 0.5679, then by employing the inference capabilities of the knowledge model, the user can gain insights into theoretical ethanol yields for various biomass types based on their C5 and C6 polymeric composition. This can also be applied to theoretical and actual yields of technologies modelled within the ontology, providing a useful reference tool for biorefinery development.

Keywords: lignocellulose, ontology, biomass, biorefining.

1. Introduction

In the process engineering ontologies are commonly used for knowledge representation. Historically, their potential has been recognised in many different domains such as the biomedical (Musen et al., 2012), legal (Casellas et al. 2011), financial (Montes et al. 2005), agricultural (Soergel et al. 2006), as well as chemical and process engineering.

Lignocellulosic biomass (LCB) is an attractive feedstock for numerous biorefining processing technologies due to its low cost, abundance and widespread availability. The technology configuration for LCB biorefining varies according to the desired end products and LCB composition. In addition, the characteristics of the conversion of the LCB depends on the characteristics and composition of the feedstock LCB. For example, pyrolysis to bio-oil, hydrolysis and fermentation to ethanol, anaerobic digestion for bio-gas and pelletisation for heat fuel are all processes that convert LCB based on alternate characteristics of the feedstock such as heating value, carbohydrate content, sugar composition, and lignin components. Therefore and as proposed in this paper, it is of interest to model the knowledge available around lignocellulosic biomass, to capture its development to enable facile analysis of biomass conversion potential for various applications. To the best of the authors' knowledge this is the first presentation

of the knowledge modelling of LCB to this level of detail for conversion using a range of technologies. This in turn can assist in decision making for the development and operation of LCB biorefineries.

2. Biomass Classification and Characterisation

The BioOnto ontology structure has been described previously (Trokanas, Bussemaker et al. 2015). In brief, this includes the classification of biomass as a material and using the following material properties: *PlatformMaterial*, *MaterialbyPhysicalForm*, *FeedstockMaterial*, *WasteBiomass* and *Other*. Here the names of the properties are self-explanatory.

The volatile nature of biomass makes it essential to characterise different types of biomass in detail. Characterisation addresses many aspects of the biomass, mainly focusing on the characteristics that affect its processing. In BiOnto, all types of biomass are characterised to primarily reflect composition of interest, which are further enhanced by introducing the restrictions on properties with user defined ranges (Figure 1).

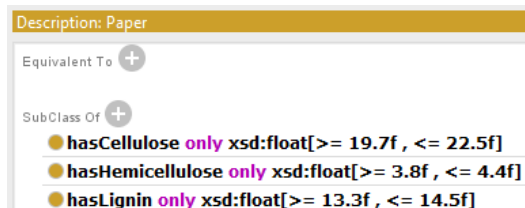


Figure 1 Restrictions for Paper

In cases where more complex information is required, characterisation is extended to include other composite elements of biomass. Looking for example at certain types of lignocellulosic biomass, information vital to decision making goes beyond the content of cellulose, hemicellulose and lignin to the specific composition of these three building blocks. The example of Aspen, a type of hardwood, is presented in Figure 2. Again here the names of ontology classes and properties are self-explanatory.

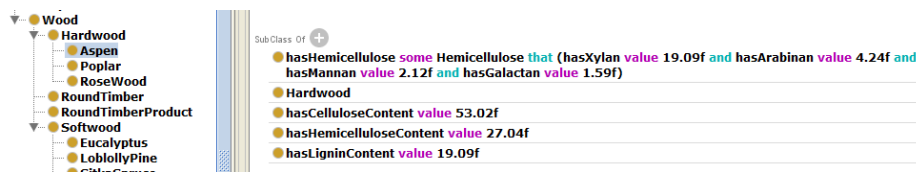


Figure 2 Characterising Aspen

To achieve this level of detail it is also important to take advantage of the advanced expressivity of ontology language OWL2 (Welly et al. 2004) and more specifically the keyword 'that', which enables one level of reification statements.

An excerpt of a detailed characterisation of the composition for lignocellulosic biomass types is presented in Table 1.

Table 1 LCB Characterisation

	Cellulose (C6)	Hemicellulose (C5 and C6)	Lignin
Aspen	53.02	27.04	19.09
Poplar	43.67	19.55	27.23
Switchgrass	33.75	26.02	16.82
CornStover	37.4	27.3	18
Mixed hardwood	42.6	18.7	28.3
Loblolly Pine	43.6	21.2	26.8
Eucalyptus	46.7	13.8	29.4

Then, additional detail such as the sugar components of the hemicellulose within the biomass are also modelled (Table 2).

Table 2. Composition of Hemicellulosic components of LCB

	Xylan (C5)	Arabinan (C5)	Mannan (C6)	Galactan (C6)
Aspen	19.09	4.24	2.12	1.59
Poplar	15.63	0.71	2.27	0.94
Switchgrass	22.13	2.81	0.19	0.89
CornStover	21.1	2.6	1.6	2
Mixed hardwood	15.1	0.5	2.1	1
Loblolly Pine	6.6	1.6	10.8	2.2
Eucalyptus	12.3	0.2	0.6	0.7

One of the complexities of biomass is the reporting of composition and the non-uniformity of compositions of various feedstocks. For instance, hemicellulosic sugars are often reported as their polymeric form (xylan, mannan, galactan, arabinan), of the corresponding monomers (xylose, mannose, galactose, arabinose). However, within the plant the hemicellulose actually occur as combinations of these components, such as arabinoxylans, glucomannans, xyloglucan and glucuronoxylans which are composed of the monomeric sugars, including glucose. Current technologies are mostly aimed at conversion of the sugars in biomass which relies on knowledge of the C6 and C5 sugar composition which can be inferred from the hemicellulosic and cellulosic composition. As biorefining technologies are developed, alternative targeted approaches to other biomass components are likely such as recent interest in arabinoxylans. Hence the ontology provides a method/framework to catalogue biomass types for varieties of uses.

3. Biorefining Processing Technologies Classification and Characterisation

The ontology part representing biorefining technologies consist of 3 sub-ontologies: i) ByProcessType, ii) ByProcessStage and iii) ByProductHeatingValue, as described previously (Trokanas, Bussemaker et al. 2015).

Biorefining technologies have been modelled in detail to widen the scope of potential applications. Each biorefining technology in BiOnto, has been modelled in terms of

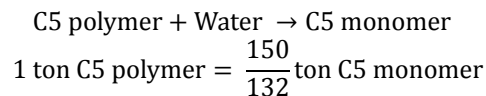
feedstock materials, output products and by-products. Operational characteristics have also been modelled for each technology. These include conversion rate, required/permissible moisture content, operating temperature and product heating value. This information has been modelled using restrictions on properties. The example of a fixed bed gasifier is presented in Figure 3. The restrictions in Figure 3, describe FixedBedGasifier technologies, which is defined having a conversion rate between 60-80%. The same technology has a defined range of product heating value (≤ 5) that leads to the reclassification of this technology as a low heating value technology.

Superclasses	
●	Gasification
●	hasConversionRate only int [60 , <= 80]
●	hasEndUse only GaseousFuel
●	hasInput only (LignocellulosicBiomass or SewageSludge)
●	hasMoistureContent only int [<= 20]
●	hasOutput only Biogas
●	hasPhase value "Main-processing"
●	hasProductHeatingValue only int [4 , <= 5]
●	hasSideProduct only FlyAsh
●	hasTemperature only int [780 , <= 1400]
Inherited anonymous classes	
●	hasPlatform some Syngas
●	hasTemperature some int
●	hasProductHeatingValue some int
●	hasEndUse only EndUse
●	hasOutput only Material

Figure 3 Fixed-bed Gasifier Restrictions

In addition to the cataloguing of technologies, theoretical yields have been modelled based on known stoichiometry, assisting the user in decision making at a more granular level. Often technologies give an overall conversion rate, however in reality, if considering an alternate biomass, the conversion rate will be more dependent on the composition of the biomass. For example, the reactions and theoretical conversion rates of hydrolysis and fermentation, which are dependent on the C5 and C6 sugar composition within the biomass type. Here we show the example of the C5 hydrolysis and fermentation below:

Hydrolysis:



Every process is explicitly defined in the ontology, as demonstrated in Figure 4 and Figure 5.

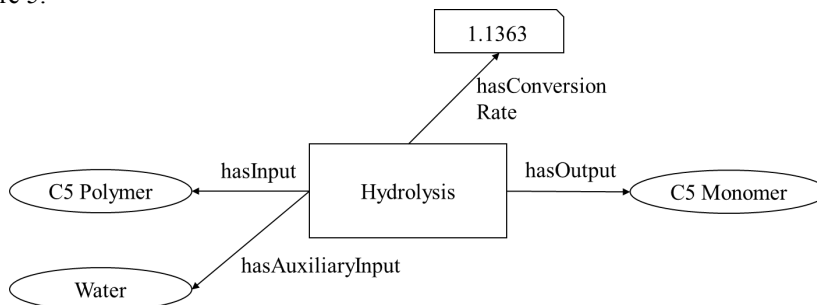


Figure 4 Hydrolysis model

Fermentation

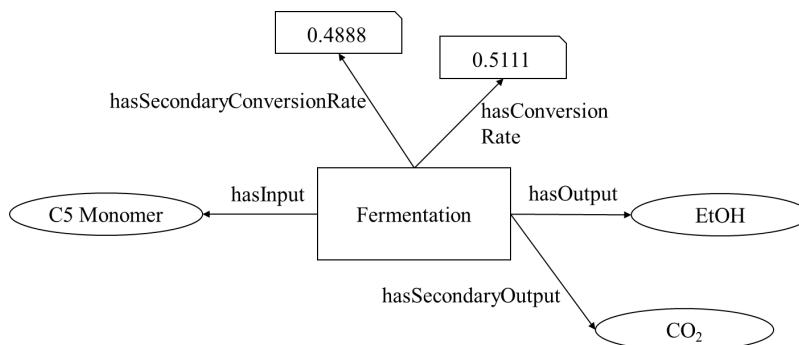
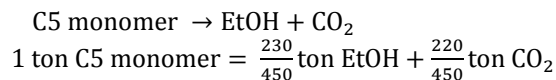


Figure 5 Fermentation model

The explicit modelling of each process, in combination with the graph nature of the ontology, allow the extraction of new knowledge, in the form of valorisation paths for inputs as well as processing paths for targeted outputs. This is achieved with the use of semantic rules. The following rule, modelled in SPARQL, identifies potential paths for a specific input (?targetInput) and constructs a new process in the ontology model. The new process is characterised by a new theoretical conversion rate, derived from the individual conversion rates from the processes involved. The new process is also linked to each step, to provide a level of provenance for the user.

```

CONSTRUCT {
    ?newProcess a Process .
    ?newProcess hasOutput ?output2 .
    ?newProcess hasInput ?targetInput .
    ?newProcess hasConversionRate ?overallConversion .
    ?newProcess hasStep1 ?process1 .
    ?newProcess hasStep2 ?process2 .
}
WHERE {
    ?process1 hasInput ?targetInput .
    ?process1 hasOutput ?output1 .
    ?process1 hasConversionRate ?rate1 .
    ?process2 hasInput/^hasOutput ?process1 .
    ?process2 hasConversionRate ?rate2 .
    ?process2 hasOutput ?output2 .
    BIND(?rate1 * ?rate2 AS ?overallConversion)
    BIND(UUID() AS ?newProcess)
}
    
```

In the case of the processes presented in Figures 4 and 5, the new conversion rates are calculated as:

$$1 \text{ ton C5 polymer} = \frac{69}{117} \text{ ton EtOH}$$

$$1 \text{ ton C6 polymer} = \frac{46}{81} \text{ ton EtOH}$$

4. Using BiOnto

BiOnto has been developed in order to expand the previously developed ontology for industrial symbiosis, called eSymbiosis ontology (Cecelja, Raafat et al. 2015). However, it has the potential to support other applications, serving as a common vocabulary and classification of biomass and bio-processing technologies. Current implementation supports selection of Biomass Type, Output and Platform material. The characterization allows for investigations into biomass types and theoretical yields using the information provided by the ontology. For example, if the user is interested in theoretical ethanol yields from various biomass types. It also has a potential to support various aspects of biorefining decision making, the aspects which is currently being tested in practice.

5. Conclusions

The presented ontology models biomass and biorefining technologies in detail, allowing the ontology to be used in a range of applications. Validation was performed through case study in Industrial Symbiosis domain where the ontology was used to collect information from the users and identify symbiotic matches between available feedstocks and technologies. Further testing was performed with data and model integration approach in the domain of biorefining. However, BiOnto is open to other applications as well. Future plans include the use of BiOnto to enable model and data integration in biorefining domain and incorporation of the ontology in the decision making process of value chain modelling for biorefineries.

References

- Montes, M. M., Bas, J. L., Bellido, S., Corcho, O., Losada, S., Benjamins, R., Contreras, J., "WP10: Case Study eBanking D10. 7 Financial Ontology." Data, information and process integration with semantic web services, FP6-507483 (2005).
- Casellas, Núria. Legal ontology engineering: Methodologies, modelling trends, and the ontology of professional judicial knowledge. Vol. 3. Springer Science & Business Media, 2011.
- Cecelja, F., T. Raafat, Trokanas, N., Innes, S., Smith, M., Yang, A., Zorogios, Y., Korkofygas, A., Kokossis, A., (2015). "e-Symbiosis: technology-enabled support for industrial symbiosis targeting SMEs and innovation." *Journal of Cleaner Production* 98: 336-352.
- Musen, M.A., Noy, N.F., Shah, N.H., Whetzel, P.L., Chute, C.G., Story, M.A., Smith, B. and NCBO team, "The national center for biomedical ontology." *Journal of the American Medical Informatics Association* 19.2 (2011): 190-195.
- Raafat T, Trokanas N, Cecelja F, Bimi X., "An ontological approach towards enabling processing technologies participation in industrial symbiosis." *Computers & Chemical Engineering* 59 (2013): 33-46.
- Soergel D, Lauser B, Liang A, Fisseha F, Keizer J, Katz S., "Reengineering thesauri for new applications: the AGROVOC example." *Journal of digital information* 4.4 (2006).
- Trokanas, N., Bussemaker, M., Velliou, E., Tokos, H. and Cecelja, F., (2015). "BiOnto: An Ontology for Biomass and Biorefining Technologies." *Computer Aided Chemical Engineering* 37: 959-964.
- Welty C, McGuinness DL, Smith MK., (2004). "OWL Web Ontology Language Guide - www.w3.org." Retrieved 17/07/2016, from www.w3.org.

Optimization of Cellulose Hydrolysis in a Non-ideally Mixed Batch reactor

F. Fenila^a, Yogendra Shastri^{a*}

^aDepartment of Chemical Engineering, Indian Institute of Technology Bombay, Mumbai, India - 400076

*fenila@iitb.ac.in, *yshastri@che.iitb.ac.in*

Abstract

Non-ideal mixing is an important challenge in industrial scale enzymatic hydrolysis reactors. This work, therefore, optimizes a hydrolysis reactor after considering non-ideal mixing. The flow rate of heating fluid was used as the decision variable for maximization of glucose problem, and flow rate of the heating fluid and enzyme loading was used as decision variables for maximization of profit problem. The non-ideal mixing was represented by dividing the reactor into three levels and each level comprising 12 compartments connected to each other by circulation and exchange flows. Multiple cases with the substrate either uniformly or non-uniformly distributed in the reactor were studied. It was observed that the optimal decision variables for maximization of glucose problem were dependent on the substrate distribution for the initial hours of hydrolysis and the optimal decisions do not differ much in the later stages of hydrolysis. For maximization of profit problem, the enzyme requirement changed significantly, but the flow rate of heating fluid did not change much for the ideally mixed reactor. However, for the non-ideally mixed reactor, both the flow rate of the heating fluid as well as the enzyme requirement changed significantly. The use of optimal decisions from a non-ideally mixed reactor instead of an ideally mixed one lead to 3.19 % and 6.63 % reduction in deviation of glucose and profit from ideally mixed reactor.

Keywords: Mixing, Optimization, Cellulose, Hydrolysis

1. Introduction

Optimization of enzymatic hydrolysis of cellulose is important to improve economic efficiency by increasing yields, reducing enzyme requirements or both. However, most of the optimization studies in the literature are carried out assuming a well-mixed reaction system. This assumption is not suitable for large-scale industrial reactors and insoluble substrates like cellulose, especially at high solid loadings. Under these conditions, the problems related to heat and mass transfer are more prominent. Moreover, local hot spots for temperature and enzyme concentration may be created. This reduces the overall conversion of cellulose to glucose. Therefore, considering the non-ideality in mixing is essential. Selecting the appropriate reactor design, and impeller type are design decisions to address this problem. Impeller speed can also be manipulated to achieve better mixing. Additionally, conversion in non-ideally mixed reactors can be increased by regulating operating variables such as the rate of heating, amount and feeding rate of substrate and enzyme. Optimizing the operating variables is also desirable as it gives an additional degree of freedom to address issues of uncertainties in feedstock composition and reaction kinetics. This work, therefore, explores this option to optimize an industrial scale non-ideally mixed reactor. The

benefit of this approach is quantified by simultaneously studying the well-mixed reactor system.

The article is arranged as follows. The non-ideal mixing and cellulose hydrolysis models are explained in Section 2. Sections 3 and 4 discuss the glucose maximization and profit maximization problems, respectively, and the important conclusions are summarized in Section 5.

2. Model Description

Computational fluid dynamics (CFD) is a good method to understand the mixing behaviour. However, using a CFD model for optimization studies will lead to computational complexity. Compartment modelling approach, on the other hand, is less complicated than CFD and represents non-ideal mixing reasonably well. Cui et al. (1996) represented a reactor mixed with multiple impellers using compartment modelling approach. In this approach, the reactor is divided into smaller compartments of equal volume connected by circulation flow and exchange flow due to mixing. The flow rate generated by the circulation flow and exchange flow are functions of impeller type and dimensions (Cui et al., 1996). This model has been widely adapted in literature to study non-ideal mixing (Vrábel et al., 1999; Caccavale et al., 2011).

In this work, the approach proposed by Cui et al. (1996) was adapted for a reactor with a single impeller. The reactor was divided into three levels along the vertical direction, and each of these levels was further divided into 12 compartments of equal volume which are assumed to be well mixed. These compartments are connected to each other by circulation flow (F_C) along the radial direction and exchange flow along the axial direction (F_E). The circulation and exchange flow rates are functions of impeller geometry and mixing speed. Level 1 (top level) and Level 3 (bottom level) are mixed by circulation flow $F_C/2$ whereas level 2 (middle level) is mixed by circulation flow F_C due to proximity to the impeller. The previous studies using this approach had considered the non-ideal mixing of single phase reaction mixture. However, the enzymatic hydrolysis involves a multi-phase solid-liquid mixture. Therefore, an additional parameter representing the efficiency of multi-phase mixing was added, based on a similar approach used in literature for liquid-gas systems.

The reaction kinetics for conversion of cellulose to cellobiose and glucose in each of the reactor compartments were modelled based on Kadam et al. (2004). The thermal deactivation kinetics of cellulase (E_1) and β -glucosidase (E_2) were based on Caminal et al. (1985), where the model parameters were re-estimated using experimental data from the literature. The changes in the concentration of cellulose, cellobiose, cellulase, and β -glucosidase in every compartment due to reaction and mixing were tracked using Eq. 1. The reactor was assumed to be at an initial temperature of 298 K, and a heating fluid of 328 K was passed through the jacket enclosing the reactor. The temperature changes in the jacket and reactor compartments were modelled based on energy balance equations (Eq. 2, 3). The following equations are written for component 'i' in compartment 'h'

$$\frac{dC_{i,h}}{dt} = R_{exn_i} + \frac{F_C}{V} (C_{i,s} - C_{i,h}) + \frac{F_E}{V} (C_{i,l} + C_{i,u} - 2C_{i,h}) \quad (1)$$

$$\frac{dT_j}{dt} = \sum_{h=1}^{n_c} \beta_h \frac{US(T_{Rh} - T_j)}{V_j \rho_j C_{pj}} + \frac{(T_{in} - T_j)}{V_j} \quad (2)$$

$$\frac{dT_{Rh}}{dt} = -\beta_h \frac{US(T_{Rh} - T_j)}{V_c \rho C_{pr}} + \frac{F_c(T_{Rs} - T_{Rh})}{V_c} + \frac{F_E(T_{Rl} - T_{Ru} - 2T_{Rh})}{V_c} \quad (3)$$

$i=1,2,\dots,5$ and $h=1,2,\dots,36$.

In Eq. 1, $C_{i,h}$ is concentration of i^{th} component in h^{th} compartment. $R_{\text{ex}n_i}$ refers to the formation or conversion of i^{th} component. F_C is the circulation flow rate (m^3/s), F_E is the exchange flow rate (m^3/s), and V is the volume (m^3). $C_{i,s}$, $C_{i,l}$, and $C_{i,u}$ (g/L) are the concentration of i^{th} component in side, lower and upper compartments, respectively. In Eq. 2, T_j , β , U , S , T_{Rh} , V_j , T_{in} are the jacket temperature (K), fraction of heat transfer area available, heat transfer coefficient ($\text{kJ/h.m}^2.\text{K}$), temperature in compartment 'h' (K), jacket volume (m^3), and temperature of heating fluid at jacket inlet, respectively. β_h , T_{Rs} , T_{Rl} , T_{Ru} , and V_C are the fraction of heat transfer area available for compartment 'h', temperature of side compartment (K), temperature of lower compartment (K), temperature of upper compartment (K), and compartment volume (m^3).

This model was used to study a 3 m^3 enzymatic hydrolysis reactor. The reactor and impeller dimensions from Corre a et al. (2016) were adapted, and solid loading was 10 %. The initial cellulose and background glucose and xylose loadings were chosen based on the typical composition of acid pretreated lignocellulosic substrate. The composition used was 49 g/L of cellulose, 14.85 g/L of glucose, and 11.35 g/L of xylose. The enzyme concentration and background glucose and xylose were considered same in all reactor compartments. The mixing efficiency parameter was estimated based on mixing speed of 470 rpm and assuming that a completely mixed system is obtained in 35 h. Two different problems, namely maximization of glucose at the final time and maximization of batch profit, were solved. The economic parameters were taken from literature. The flow rate of jacket fluid was used as decision variable for glucose maximization, while flow rate of jacket fluid and enzyme loading were used as decision variables for profit maximization problem. Optimization studies were solved with the initial substrate along the the top (level 1) or bottom (level 2) or side compartments.

3. Maximization of glucose

Maximization of glucose problem was solved for batch times 12 hr to 72 hr (Fig. 1). The results showed that the optimal flow rate for non-ideal mixing was higher than that of ideal mixing for all batch times. This was because the heat supplied by the heating fluid in the reactor jacket does not reach the inner compartments effectively with non-ideal mixing and hence more heat has to be supplied to the reactor. The optimal flow rate for non-ideal mixing was 86.8 times higher than that for ideal mixing for 12 hr batch time. Non-ideal mixing in addition to small batch time was the reason for this observation. However, the difference in non-ideal and ideal mixing case reduced drastically for batch times of 24 hr and higher (Fig. 1). Availability of larger mixing time, in addition to degradation of enzyme upon exposure to higher temperature for a longer time, was the reason. It was also observed that the optimal flow rate was dependent on the initial substrate distribution in the reactor. However, this difference again diminished as the batch time increased beyond 24 hr.

The final glucose concentration was highest when ideal mixing was assumed, and the corresponding optimal heating fluid flow was used. The benefit of the proposed approach was quantified by applying the solution for an ideal reactor to a non-ideally mixed reactor ("Ideal optima" in Fig. 2), which is the conventional approach. The deviation in glucose concentration from the ideal case for this option was then compared with the deviation for optimal solution considering non-ideal mixing (proposed approach, "Non-ideal optima" in Fig. 2). The results showed that the proposed approach provided noticeable benefit as compared to the conventional approach, especially for smaller batch times. When the substrate was present in level 1,

the reduction in deviation from ideal was very less because, except the side compartment, the compartments in level 1 were not in direct contact with the walls of the reactor. However, when the substrate was present in level 3 or sides or uniformly distributed, there was a noticeable reduction in the deviation in glucose concentration from ideal.

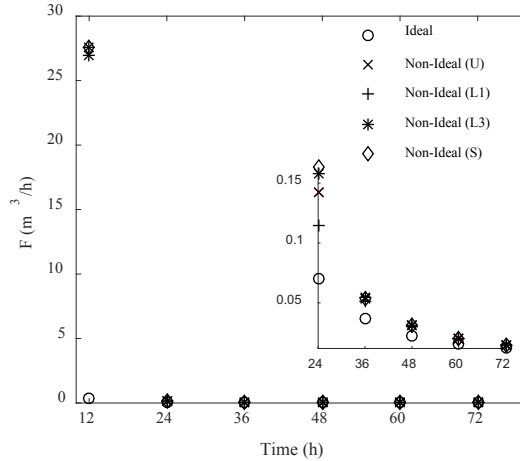


Figure 1: Flow rate of heating fluid required for maximization of glucose for the ideally mixed reactor and non-ideally mixed reactor with the different initial distribution of substrate. (U-uniformly mixed substrate, L1 - substrate in top compartments only, L3 - substrate in bottom compartments only, S- substrate along sides only)

4. Maximization of profit

The significant increase in the optimal flow rate of jacket fluid for the non-ideal case has not resulted in substantial increase in the glucose concentration. This makes the economic feasibility of the optimal solutions questionable. Therefore, the maximization of profit problem was solved with flow rate of heating fluid, enzyme loading as decision variables. The cost of enzymes E_1 and E_2 were assumed to be 368 Rs./kg and the cost of heating was assumed as 7.12 Rs./kW. The revenue from glucose was 52 Rs./kg. For ideal mixing, even though the optimal enzyme loading of both cellulase (E_{1T}) and β -glucosidase (E_{2T}) reduced, the heating fluid flow rate was similar to that for glucose maximization problem. However, for non-ideal mixing, a significant reduction in the flow rate of heating fluid as well as E_1 was observed (Fig. 3). The reduction in E_1 could be due to the high cost associated. However, E_2 , which costs the same as E_1 , was found to increase which could be because E_2 used was already low. Subjecting the reduced amount of enzymes to higher temperature will lead to loss of enzyme due to deactivation and hence reduced profit. In case of different initial distribution of substrate, all the non-ideal scenarios were less profitable than ideal one. Similar to maximization of glucose problem, significant reduction in the deviation of profit from ideally mixed reactor was observed when optimal decisions corresponding to non-ideal mixing pattern and substrate distribution was used instead of optimal decisions from ideally mixed reactor (Fig. 4).

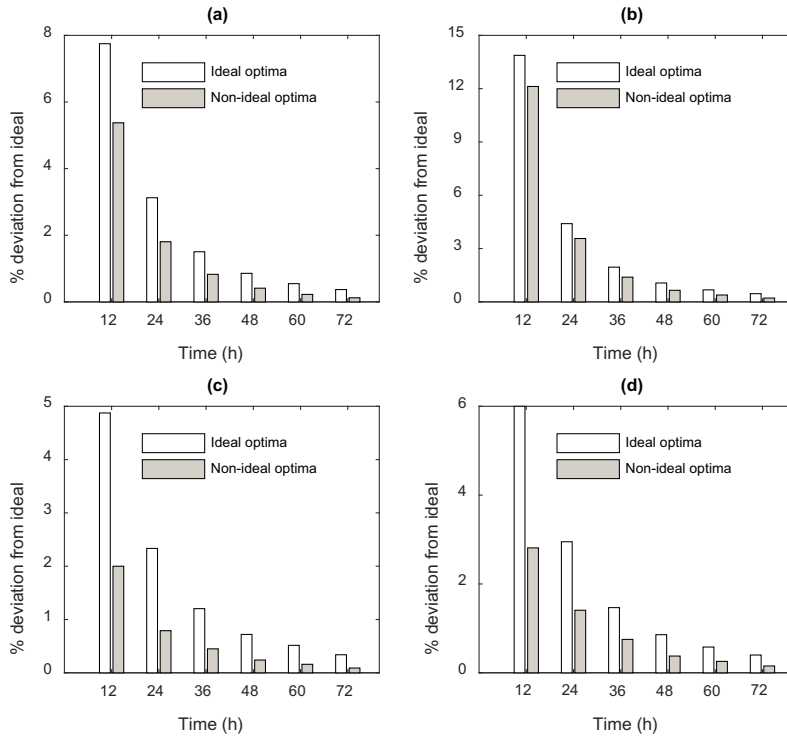


Figure 2: Glucose concentration for different initial substrate distributions with optimal flow rate of jacket fluid from ideally and non-ideally mixed reactors. (a) Uniform substrate (b) Substrate in level 1 only (c) Substrate in level 3 only (d) Substrate along sides only.

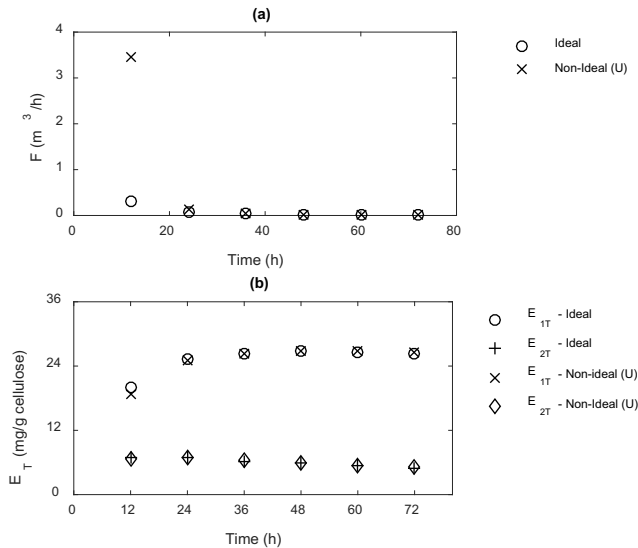


Figure 3: Flow rate and enzyme loading comparisons for ideally mixed and non-ideally (uniform substrate) mixed reactors for maximization of profit

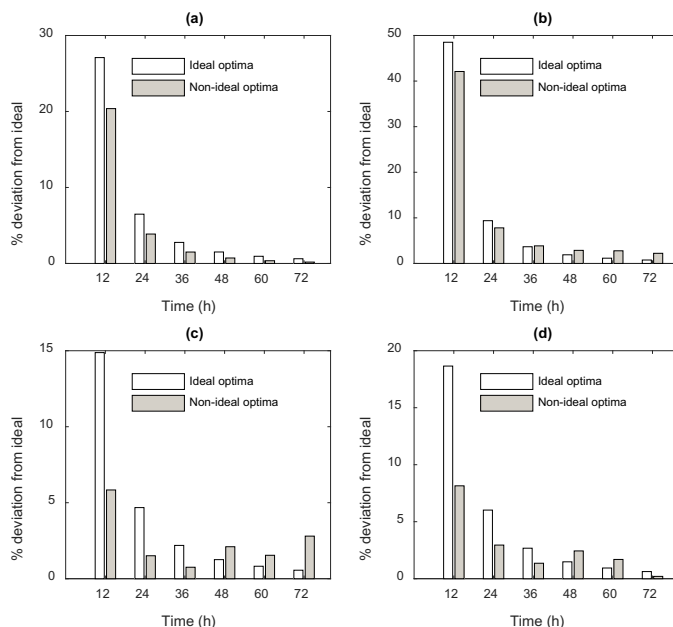


Figure 4: Profit for different initial substrate distributions with optimal flow rate of jacket fluid from ideally and non-ideally mixed reactors. (a) Uniform substrate (b) Substrate in level 1 only (c) Substrate in level 3 only (d) Substrate along sides only

5. Conclusions

This work optimized the enzymatic hydrolysis batch reactor considering non-ideal mixing. The results showed that the use of optimal decisions from non-ideally mixed reactor over an ideally mixed reactor was beneficial in terms of glucose concentration as well as profit for shorter batch times. Significant change in enzyme loading between maximization of glucose and maximization of profit problems for ideally mixed reactor was observed. For non-ideally mixed reactor, in addition to significant changes in the enzyme loading, the optimal flow rate also changed significantly between maximization of glucose and maximization of profit problems. The use of optimal decisions from a non-ideally mixed reactor instead of an ideally mixed one lead to 3.19 % and 6.63 % reduction in deviation of glucose and profit from ideally mixed reactor. These results provide guidelines for optimally operating industrial reactors.

References

- F. Caccavale, M. Lamarion, F. Pierri, F.,V. Tufano, 2011, Springer-Verlag London.
- G. Caminal, J. Lopez-Santin, and C. Sola, 1985, *Biotechnol. Bioeng.* XXVII, 1282–1290.
- K.L. Kadam, E.C. Rydholm, J.D. McMillan, 2004, *Biotechnol. Prog.*20(3), 698–705.
- L.J. Correã, A.C. Badino, A.J.G. Cruz, 2016, *Biopro.*39, 825–833.
- P. Vrabel, R.G.J.M. Van Der Lans, Y.Q. Cui, K. Ch, A.M. Luyben 1999, *Trans IChemE*, 77, 291-302.
- Y.Q. Cui, R.G.J.M. Van der Lans, H.J. Noorman, K. Ch, K.C.A.M. Luyben, 1996, *Chem. Eng. Res. Des.*74(2), 261–271.

Combined basic and fine chemical biorefinery concepts with integration of processes at different technology readiness levels

Sara Badr,^a Jane Yee Yap,^b July Tan,^b Matty Janssen,^c Elin Svensson,^d Stavros Papadokonstantakis^{a,*}

^a*Chalmers University of Technology, Department of Space, Earth and Environment, Hörsalsvägen 7B, Gothenburg 412 96, Sweden*

^b*UCSI University, Department of Chemical and Petroleum Engineering, No.1, Jalan Menara Gading, 56000 Cheras, Kuala Lumpur, Malaysia*

^c*Chalmers University of Technology, Department of Management and Economics, Rännvägen 6B, Gothenburg 412 96, Sweden*

^d*CIT Industriell Energi AB, Sven Hultins gata 9, Gothenburg 412 88, Sweden*
stavros.papadokonstantakis@chalmers.se

Abstract

Biorefineries offer promising alternatives to the use of fossil fuels to produce energy and chemicals. This work describes the development of a biorefinery concept to produce adipic acid from Swedish forest residues and lutein from micro-algae. A description is provided for each process line available, its technology readiness level (TRL) and the tools available to model it. Scenarios of the integrated concept are built with associated material flow analysis. Key results of the material inventory of the base case scenario are presented as well as insights into the development of further scenarios. Material flow inventories can then be further used for economic and environmental assessment. Major challenges of integration are discussed in terms of uncertainties and data gaps for processes with low TRL such as scaling up lab experiments, understanding the restrictions of material recycling and its impact on process performance. The feedback given through these scenarios can help guide further experimental efforts.

Keywords: Process design, Process modelling, Biomass, Integrated system

1. Introduction

Problems such as climate change and resource depletion pose significant challenges in the 21st century. There is increasing pressure to find more sustainable solutions to produce energy and materials. While the use of renewable sources of energy, such as wind and solar power, can reduce the world's dependence on fossil fuels, 85 % of the chemicals used today are produced via non-renewable sources (Morales et al., 2017). Second and third generation biorefineries provide promising alternatives to the use of fossil fuels to produce energy and chemicals. In a biorefinery concept, where an array of value added chemicals are produced, mass and energy integration of the different chemical production lines is crucial to maintain the feasibility of the design concept in terms of reduced costs and environmental impacts.

The biorefinery concept described in this work combines the production of a bulk product, adipic acid (AA), from forest residues (GROT abbreviation in Swedish) in Sweden and a fine chemical, lutein, from micro-algae. AA is an important high-volume chemical that is produced from petroleum derivatives such as benzene, cyclohexane and phenol. It is mainly used in the production of nylon which has wide ranging and fast-growing applications such as in the automotive industry and footwear sectors. Lutein is a carotenoid that has several uses in the food and pharmaceutical industries. It is a high-value chemical with growing market demand. It is currently produced from marigold flowers.

The continuous development of new processes is a key factor in increasing the efficiency of biorefineries and their competitiveness. The incorporation of new concepts and process alternatives in the design phases of biorefineries can help identify more optimum process operation alternatives, as well as better integration and symbiosis potential. Technology readiness level (TRL) is a measure of the maturity of a process alternative. TRL 1 is the lowest and denotes a technology where only basic principles are reported, while TRL 9 is the highest where the technology is proven in an actual operational environment. Despite the advantages of incorporating promising new technologies in early design stages, the integration of several process lines at different TRLs is a major design challenge. The variation in the quality and sources of data could pose an obstacle to integration efforts.

This work describes the development of scenarios for the integrated biorefinery concept, the different production lines with their uncertainties at their respective TRL and the consequent challenges and restrictions of formulating and analysing integrated scenarios.

2. Biorefinery processes

Figure 1 shows the schematic of the proposed biorefinery concept and proposed production lines and their current TRLs. The different process lines can be connected through the recycling of water, CO₂, nutrients, and heat streams across the process. Optimizing key connection points is the basis for process integration efforts. In this section a description of the biorefinery, its products and investigated technologies is given as well as the data sources and modelling tools available. An accounting of integration restrictions as well as process uncertainties is also provided.

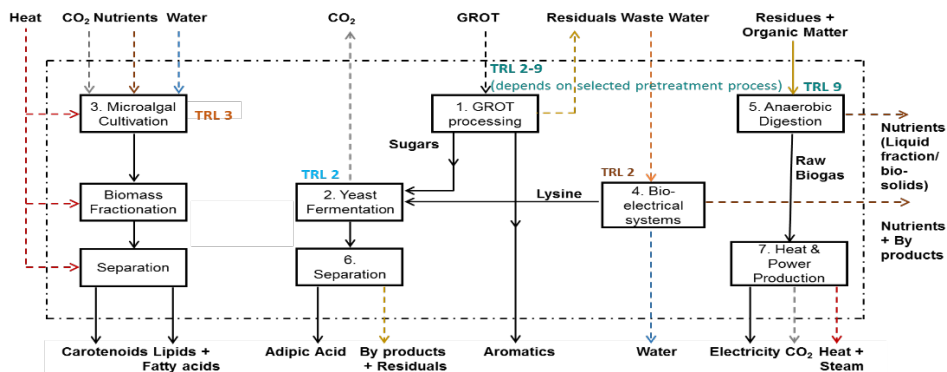


Figure 1. Biorefinery concept starting from GROT and micro-algae

Forest residues are processed to produce sugars, which are fermented to produce AA as the main bulk product. The choice of the GROT pre-treatment method can influence the range of by-products available as well as define the TRL of this process section. An effective pre-treatment method would allow for the efficient separation of lignin, cellulose and hemicellulose fractions. Steam explosion at 7 bar and 140 °C is used as a first step in the pre-treatment process to open up the biomass fibers followed by a refining step and an acidic or alkaline pre-treatment step. Pre-treatment using acids (e.g. sulfuric acid) is the conventional industrially established method. However, it suffers from several disadvantages including lower quality lignin fractions and increased impurities that may inhibit the subsequent fermentation, and thus require further processing steps (Kumar and Sharma, 2017). The use of alkaline pre-treatment maximizes the potential use of lignin as a starting material for chemical production rather than its use only as an energy source. The Kraft cooking method using sodium sulphide, hydroxide and carbonate has been extensively used in the pulp and paper industry. Another method under investigation is the soda cooking method as a sulphur free alternative to the Kraft method (Bose et al., 2009). Lignin produced from the Kraft method can be separated from the cooking liquor using the LignoBoost process, and then converted into aromatics and bio-oil by mixing the lignin with K_2CO_3 and phenol and brought to the reaction conditions at 350 °C and 25 MPa (Nguyen et al., 2014). Lignin through this process yields 27 % aromatics mainly anisoles and alkyphenols among others and 55 % bio-oil product of a higher heating value than lignin and the rest is char. Experimental data are used to carry out a material flow analysis of the steam explosion, Kraft and soda cooking methods, while literature data is used for the LignoBoost and lignin depolymerization processes. Figure 2 shows a schematic of the alkaline pre-treatment with Kraft cooking with subsequent lignin valorization processes.

Cellulose and hemicelluloses produced then go through hydrolysis which yields a mixture of pentoses and hexoses. These sugars are then fermented to produce AA via lysine in a two-step process (Burgard et al., 2013). Data regarding the conversion of glucose to lysine are obtained from experimental procedures reported in literature (Kiefer et al., 2004). There is still an ongoing exploration to find a suitable microorganism to increase yields of AA, with the major obstacle to achieving high enough rates for commercialization being the tolerance to the AA product (Karlsson et al., 2017). As such, this section of the process has one of the lowest TRLs in the biorefinery concept with many uncertainties that can severely affect the overall process. Examples of such uncertainties include the possibility of carrying out the process to produce lysine at more concentrated sugar levels than 40 mM glucose as reported in literature, which would be too dilute for commercial applications, and whether similar conversion rates and products can be expected for sugars other than glucose. Theoretically a 90 % conversion of lysine to AA is possible; however, without large scale experiments, this value remains uncertain. The effect of possible impurities from the pre-treatment section is also uncertain. The recovery of AA from the fermentation broth is rigorously modelled using the process simulation software Aspen Plus V8.8. The process features the concentration of AA through a multiple effect evaporator, followed by crystallization and filtration as shown in Figure 2.

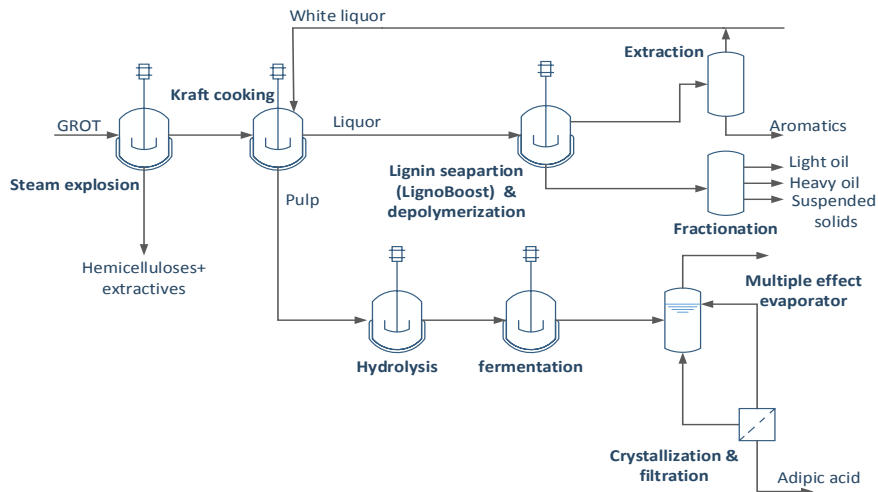


Figure 2. Major units of the alkaline pre-treatment of GROT with lignin valorization and the AA production line

The lutein production line starts with the cultivation of the micro-algae followed by flocculation, sedimentation and centrifugation. The supernatant fraction is recycled while the solid fraction is dried and methanol is used to extract lutein. The solvent is then recycled while the remaining biomass can be utilized as protein rich animal feed. Data are obtained from experimental procedures and the process is described by Mayers et al. (2016). The solvent recovery process is modelled in Aspen Plus V8.8.

Waste water streams from the process are sent to an anaerobic digestion unit to produce biogas, which is an industrially established process. Two reactor configurations are investigated for anaerobic digestion, one using a continuous stirred tank reactor (CSTR) and the other using an internal circulation (IC) reactor.

Another investigated technology with a low TRL where data are also only available at lab scale is the use of bioelectrical fermentation systems to produce chemicals such as lactic acid and lysine (Xafenias et al., 2017). This presents an opportunity for waste streams and nutrients to be utilized, while increasing the biorefinery product portfolio and enhancing the yield of AA by recycling lysine. However, a major challenge to integration efforts is the lack of data considering scale-up as well as the application to sugars other than glucose that might be present in waste streams, in addition to the inhibiting effects that impurities from waste streams or the upstream pre-treatment of GROT may incur.

3. Results and discussion

To tackle the difficulties posed by uncertainties described in the previous section, scenarios are created where all processes are simplified and represented through material and energy flow inventories. These inventories are then used to carry out capital and operating cost evaluations and life cycle assessment. All scenarios must have a pre-treatment option, an AA production line and an anaerobic digestion unit. The microalgae and the bioelectrical fermentation units are optional. Figure 3 shows the range of possible scenarios. Table 1 shows an excerpt from the material flow inventory

of the base case scenario, denoted by the dotted lines in Figure 3, where key process units are combined to produce 10,000 t/y AA: 1) the alkaline pre-treatment unit with the Kraft cooking, 2) AA production assuming conversion of only glucose at 40 mM to lysine and 90 % conversion of lysine to AA, 3) Anaerobic digestion unit and 4) the micro-algae unit with a maximum productivity 19 t biomass/ha/y and a maximum available area of 10 ha with CO₂ recycled from the AA fermentation unit.

AA currently has a market size of about 3,800,000 t/y. Extrapolating from the base case scenario presented in Table 1 shows that the production of 100,000 t/y of AA would require 1.9 Mt/y of GROT which is comparable to the entire Swedish yearly production. Physical availability of GROT is then the limit for production, where the only way to increase AA yield beyond these values is by converting other sugars that were considered inert in this scenario, given that already a 90 % conversion of lysine to AA was assumed.

Table 1 also shows that the microalgae production line and its requirements are very small compared to the size of the AA line. Lutein has a price that is 3 orders of magnitude higher than AA, but material requirements for this line can be very small in comparison to the main bulk line. For example, the microalgae line represents less than 0.07 % of the NaOH requirements in the combined process, despite being a major cost and environmental factor for the non-integrated micro-algae line. Moreover, water, nutrients, CO₂ and energy for drying can all be recycled from the main line. However, caution should be taken regarding impurities, while NH₃ present in the water streams as a by-product of AA production could be beneficial for the microalgae, other impurities such as traces of sugars could be detrimental. The CO₂ recycled should be from the fermentation unit rather than from the combustion of lignin for example, to avoid affecting the ability to market the micro-algae line products as of food grade quality.

Different scenarios would yield varying product portfolios. It is important to note that the scenarios discussed here are only those which would highly impact the process yield, but not those that would affect the performance. For example, in the microalgae line the use of chemicals for sedimentation and flocculation (e.g. NaOH) can be replaced by more intensive energy use for centrifugation, but the yield of lutein is unaffected. Another example would be the number and configuration of the evaporators in the AA line.

An understanding of the impact of impurities is crucial to continue building scenarios, e.g. the use of IC reactors in anaerobic digestion units may reduce the equipment size drastically, but such reactors are more sensitive to solid particles.

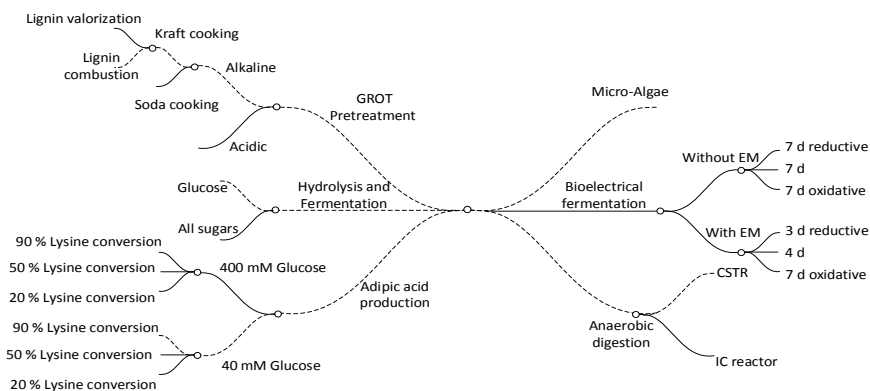


Figure 3. Depiction of the range of process scenarios. Dotted lines show chosen base case scenario.

Table 1. Excerpt from inventory analysis of base case scenario

Input	t/y	Output	t/y
GROT	190,000	Adipic acid	10,000
Methanol	750	Lignin	34,000
NaOH	2,300	Biomethane	3,000
		Lutein	0.95

4. Conclusions

This work describes the development of a biorefinery concept to produce bulk and fine chemicals. It has been shown that evaluating technologies at different TRLs can be difficult due to the uncertainties incurred at the preliminary stages of process development and varying levels of available data sources and quality. However, the questions generated at this stage may be valuable to guide further experimental efforts, e.g. by repeating experiments at expected impurity levels. Scenarios can be created to determine the cut-off levels for the feasibility of a process, e.g. minimum conversion of lysine to AA for the process to be commercially valid, or the required size of bioelectrical fermentation unit to be economically feasible within this concept. Results generated from the material and energy flow inventories of these scenarios would be used for further economic and environmental assessments. With material integration, recycling of process material including impurities is inevitable. Developing an understanding of the impacts and restrictions of material integration is crucial for further design development. It is important in the case of integrated scenarios, to identify and fully characterize the bottleneck technologies and thus determine the size of a biorefinery concept like this one.

References

- S.K. Bose, S. Otori, D. Kanungo, R.C. Francis, N.H. Shin, 2009, Mechanistic Differences Between Kraft and Soda/AQ Pulp. Part 1: Results from Wood Chips and Pulps, *Journal of Wood Chemistry and Technology*, 29, 214-226.
- A.P. Burgard, P. Pharkya, R.E. Osterhout, 2013, Microorganisms for the production of adipic acid and other compounds. Genomatica Inc., US 8592189 B2.
- E. Karlsson, V. Mapelli, L. Olsson, 2017, Adipic acid tolerance screening for potential adipic acid production hosts, *Microbial cell factories*, 16, 20.
- P. Kiefer, E. Heinzle, O. Zelder, C. Wittmann, 2004, Comparative metabolic flux analysis of lysine-producing *Corynebacterium glutamicum* cultured on glucose or fructose, *Applied and Environmental Microbiology*, 70, 229-239.
- A.K. Kumar, S. Sharma, 2017, Recent updates on different methods of pretreatment of lignocellulosic feedstocks: a review, *Bioresources and Bioprocessing*, 4, 7.
- J.J. Mayers, A. Ekman Nilsson, E. Svensson, E. Albers, 2016, Integrating Microalgal Production with Industrial Outputs—Reducing Process Inputs and Quantifying the Benefits, *Industrial Biotechnology*, 12, 219-234.
- M. Morales, T. Pielhop, P. Saliba, K. Hungerbühler, P. Rudolf von Rohr, S. Papadokonstantakis, 2017, Sustainability assessment of glucose production technologies from highly recalcitrant softwood including scavengers, *Biofuels, Bioproducts and Biorefining*, 11, 441-453.
- T.D.H. Nguyen, M. Maschietti, T. Belkheiri, L.-E. Åmand, H. Theliander, L. Vamling, L. Olausson, S.-I. Andersson, 2014, Catalytic depolymerisation and conversion of Kraft lignin into liquid products using near-critical water, *The Journal of Supercritical Fluids*, 86, 67-75.
- N. Xafenias, C. Kmezik, V. Mapelli, 2017, Enhancement of anaerobic lysine production in *Corynebacterium glutamicum* electrofermentations, *Bioelectrochemistry*, 117, 40-47.

CFD modelling of organosolv lignin extraction in packed beds

Michael Harasek*, Bahram Haddadi, Christian Jordan, Anton Friedl

^a Technische Universität Wien, Institute of Chemical, Environmental and Biological Engineering, Getreidemarkt 9/166, 1060 Vienna, Austria

michael.harasek@tuwien.ac.at

Abstract

Integrated biorefinery concepts have become important sustainable alternatives for the production of fuels and chemicals to replace fossil feedstocks. The utilization of lignocellulosic biomass frequently requires the extractive separation of lignin from cellulose and hemi-cellulose. Minimizing solvent usage and maximizing lignin extraction help to make this process more efficient. The extraction process is often carried out in packed beds, where a uniform distribution of the solvent in the packed bed helps to maximize the contact time between solvent and particles and increase the efficiency. Computational fluid dynamics simulations can give a very detailed view about the flow behaviour and distribution in these packed bed systems.

In this study, a packed bed of particles was created using an in house discrete element method code. A packing geometry was extracted and meshed, and the flow field was solved using the open-source package OpenFOAM[®]. Radial and axial distribution of the porosity and also the velocity distribution and high velocity points along the bed were extracted and analyzed. Pressure drop and residence time distribution at different flow rates were extracted and compared.

It was observed that the pressure drop along the bed height increases non-linearly with the flow rate and the RTD narrows representing a more uniform flow through the packed bed but shorter contact time between solvent and particles.

Keywords: Computational Fluid Dynamics (CFD), Lignin, Organosolv, Extraction, Discrete Element Method (DEM).

1. Introduction

Integrated bio-refinery concepts have become important sustainable alternatives for the production of fuels and chemicals to replace fossil feed stocks (Cherubini, 2010). The utilization of lignocellulosic biomass frequently requires the separation of lignin from cellulose and hemi-cellulose. Solvent extraction of lignin using alcohol/water mixtures at elevated temperatures and pressures - the organosolv process - has recently gained more attention due to high quality sulfur-free lignin which can be produced from a variety of different biomass feedstock. A key parameter for the success of the technology is to minimize the use of solvent and maximize the lignin extraction efficiency (Sluiter et al., 2008).

Usually, the extraction process is performed in fixed bed extractors where the solvent mixture is passed over the biomass packed bed. A uniform distribution of the solvent

through the packed bed helps to maximize the extraction by increasing the contact time and surface area of the solvent. In addition, multiple solvents may be used, in the case of exchange of solvent "A" by solvent "B" minimizing the mixing of the solvents is of interest, too. Thus, the extractor design with a proper solvent distribution is essential (Delgado, 2006).

In this study, the flow pattern, wall effects, pressure drop and residence time distribution of the water/ethanol mixture through a biomass lignin extraction process using computational fluid dynamics (CFD) were investigated and the effect of flow rate on these parameters was studied.

2. Methodology

The analysis of random packings of particles poses a great challenge on CFD as the creation of the complex, unstructured geometry cannot be created with usual CAD tools. A code based on discrete element modelling (DEM) from TU Wien using particle clumps to consider non-spherical or fibrous biomass particles was used in combination with the open-source CFD tool OpenFOAM® (version 4.1, 2016) for the simulation of the flow (Haddadi et al., 2016). An automated procedure was generated to prepare the filling of the extractor geometry with arbitrary non-spherical finite geometries representing the biomass pieces, including the STL file creation and meshing through SnappyHexMesh. The developed workflow also contains the computational extraction of general packing properties, e. g. the void fraction distribution over radius or bed length. This information reveals non-ideal structures in vicinity of the walls or macrovoids inside the packing which may cause short-cuts or channelling.

3. Packing creation

Packing was created using an in-house discrete element method (DEM) code. DEM is a numerical approach for modelling large number of particles interacting with each other. There are various methods for simulating non-spherical particles. A very well established model is the multi-sphere approach. In this approach the non-spherical particles are represented by overlapping sub-spherical particles which interact just with sub-spheres from other particle clumps. However, these sub-sphere particles are smaller and have higher overlaps compared to the main particle characteristic length, resulting in a more accurate representation of the non-spherical particle. An optimum sub-sphere size is important for reasonable particle representation and computational time. The contact between sub-spheres with each other and the walls were modelled using the soft-sphere approach (Norouzi et al., 2016).

In this study, a packed bed of cylindrical rods with two different sizes was created. The particle size and DEM clumps properties are listed in Table 1.

Table 1: Particles size and DEM clump properties

	Length [mm]	Diameter [mm]	Sub-sphere diameter [mm]	Sub-sphere overlap [%]
Particle 1	30	5	5	70
Particle 2	40	4	4	70

Around 1400 particles (50 % particle 1 + 50 % particle 2) were randomly packed into a cylindrical bed with a radius of 75 mm. the particles were released from a flat plane

300 mm above the bottom of the bed. Particles had an initial velocity of 0.15 m/s along the gravitational direction. The gravity was 9.8 m/s^2 along the bed axis, the created packing consisting of the clumps can be seen in Figure 1 – a. After packing the particles into the bed the representing particles' surface stereolithography (stl) was extracted to be meshed in the next step (Figure 1 - b).

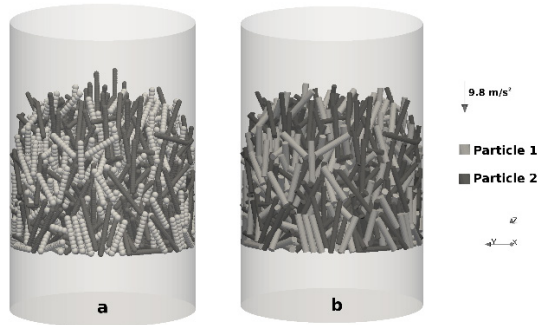


Figure 1: Created packing, a – clumps, b – stl

4. Meshing and solution

The created stl geometry was meshed using the open-source meshing tool snappyHexMesh. The packing stl file was inserted into a cubic background mesh with mesh size of 5 mm (Figure 2 – a). The base mesh was refined up to three levels on the particles edges and two levels on the particles body. In each refinement level the background mesh is divided into two cells in each direction (overall eight new cells per each refinement level). In the next step the mesh points are moved to be placed on the stl surface (snapping). The final mesh had around 2.4 million cells (Figure 2 – b, c, d).

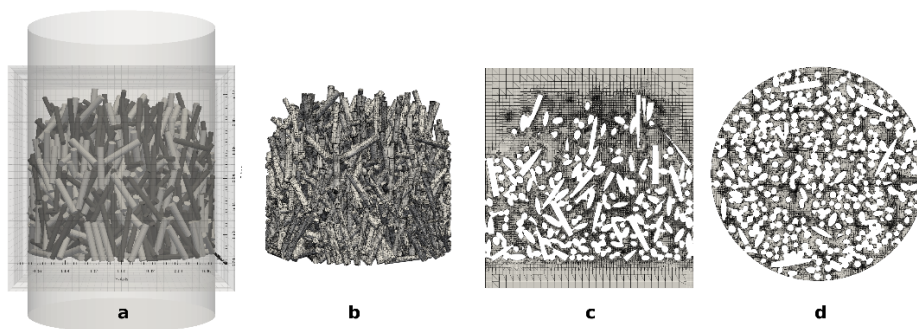


Figure 2: Mesh, a – Inserted background mesh, b – Particles mesh, c – Vertical symmetry mesh cross section, d – Horizontal symmetry mesh cross section

Fluid flow through the meshed packed bed was simulated using the open-source CFD package OpenFOAM[®]. A steady state incompressible solver was selected (simpleFoam) which was based on the semi-implicit method for pressure linked equations (SIMPLE) pressure-velocity coupling algorithm and the residence time distributions were calculated using scalarTransportFoam which solves a scalar transport equation based on

the velocity field derived from simpleFoam. The liquid used in the simulations was a 60 % volume mixture of ethanol/water entering the bed from bottom (z direction) at 0.01 m/s and exiting from top at ambient conditions (298 K and 10^5 Pa). The initial and boundary conditions are listed in Table 2.

Table 2: Boundary conditions and initial conditions

	Velocity [m/s]	Pressure [Pa]	RTD scalar [-]
Inlet	0.01	Zero gradient	1.0
Outlet	Zero gradient	10^5	Zero gradient
Walls	No slip	Zero gradient	Zero gradient
Particle 1	No slip	Zero gradient	Zero gradient
Particle 2	No slip	Zero gradient	Zero gradient
Internal field	0.0	10^5	0.0

Gravity was 9.8 m/s^2 along the bed axis. The density of the mixture was 891 kg/m^3 and the dynamic viscosity was $0.0023 \text{ Pa}\cdot\text{s}$. The Reynolds number was below 600 based on the maximum local velocity and Sauter mean particle diameter; therefore all the simulations were performed laminar.

5. Results and discussion

5.1. Radial and axial porosity

The overall porosity of the bed was around 0.61. As shown in Figure 3 axial and radial porosities are also extracted and plotted. The axial porosity shows the bed porosity along the main bed axis from bottom of the packing to the top of the packing. At the bottom of the packing because of the wall effect between particles and walls the porosity is higher, then it sharply decreases and - toward the top of the bed - it increases again representing a looser packing at the top of the packing.

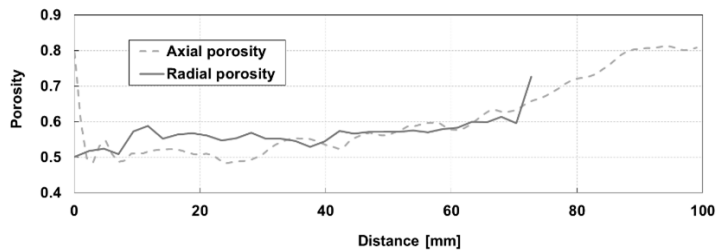


Figure 3: Bed porosity along the bed height and radius (wall at a radial distance of 75 mm, top of the bed at axial distance of 100 mm)

On the other hand the radial porosity is the lowest in the centre of the bed which shows a denser packing of the particles in that region. By moving along the radius from centre of the bed toward the wall the porosity remains almost constant and then it rises close to the walls because of the particle wall effect.

5.2. Pressure drop

Pressure drops along bed height at 10 equally distanced positions were extracted and plotted. Figure 4 shows the relative pressure to the outlet (10^5 Pa) excluding the hydrostatic pressure, by moving from bottom of the bed to the top of the bed the pressure decreases, and this decrease is not linear because of the non-linearity in the bed porosity. The overall pressure drop along the bed is around 12 Pa.

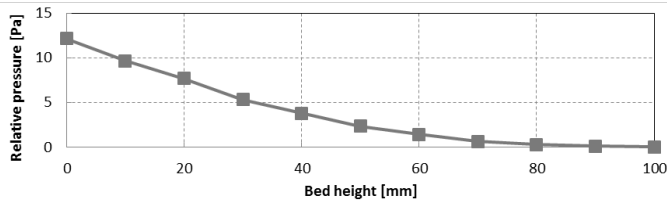


Figure 4: Relative pressure along bed height

Also the inlet flow rate was varied to study the effect of the flow rate on the pressure drop along the bed height (excluding hydrostatic pressure). For this purpose the inlet velocity of the packed bed was increased from 0.01 m/s up to 0.05 m/s. As expected, by increasing the inlet velocity the pressure drop along the bed also increases (Figure 5).

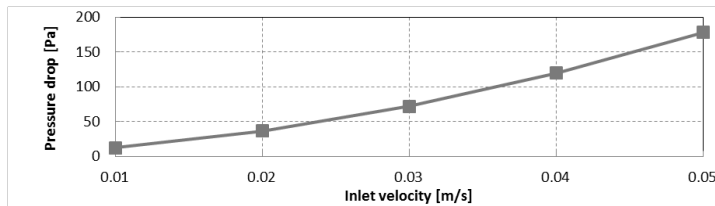


Figure 5: Pressure drop along bed height versus inlet velocity

5.3. Velocity

In detailed CFD studies also the velocity distribution in the bed can be extracted and analyzed. Based on the performed simulations the highest velocity in the bed is around 0.12 m/s and occurs close to the walls. In Figure 6 velocity contour plots at different heights from bottom of the packed bed are extracted. Some high velocity spots can be observed close to the walls which show the channeling in the bed and smaller contact time between particles and liquid and consequently lower extraction performance. Also high velocity points are shown in Figure 6, all the regions with velocity higher than $8 \times$ inlet velocity are extracted and plotted. Most of these regions are close to the walls which also confirm the non-ideal distribution of the flow in the packed bed.

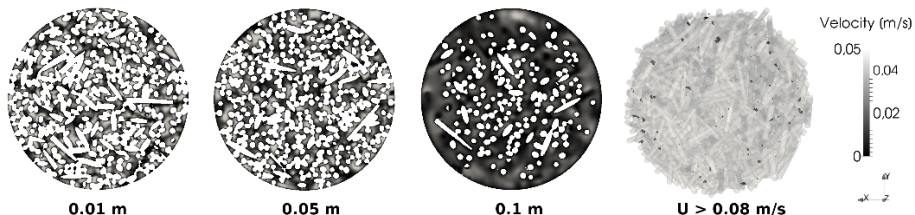


Figure 6: Velocity magnitude contour plots at different heights from bottom of the packed bed and high velocity points with velocity $8 \times$ bigger than the inlet velocity

5.4. Residence time distribution

Figure 7 shows the residence time distribution for the investigated packed bed at different Re numbers (particle based). By increasing Re (inlet velocity) the relative breakthrough time is slightly reduced, but the slope of the sigmoidal breakthrough curve is higher. The RTDs clearly show strong non-ideality in the flow structure in the packing.

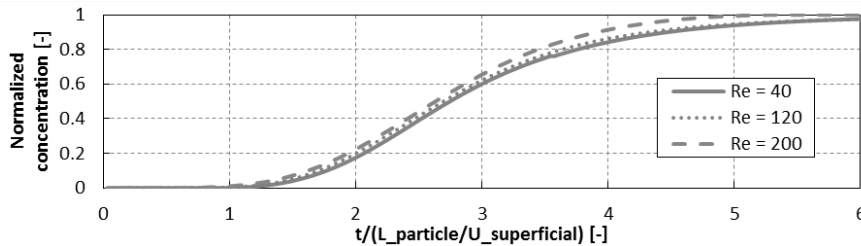


Figure 7: RTD curve at different Reynolds numbers

6. Conclusion and outlook

In this study organosolv solvent flow over a packed bed was investigated. A packed bed geometry of two different types of cylindrical particles representing straw-like biomass was created using an in-house DEM code. The required stl file of the packing geometry was also generated by the in-house DEM code, and a mesh was prepared in OpenFOAM[®]. A generic workflow is now available to generate packings from multiple arbitrary non-spherical particle geometries.

Porosity distribution along the bed height and bed radius were extracted and analyzed. In addition, pressure profiles and pressure drops in the bed were investigated at different flow rates, and high velocity points in the bed were extracted. Most of the high velocity points were close to the walls due to higher porosities in the near-wall regions. Significant non-idealities in the fluid flow occur in these type of beds. As a consequence, liquid redistribution plates or other design measures may be required to improve the extraction process. As a next step, the lignin extraction process – dissolving lignin from the biomass particles resulting in a species source term in the extraction fluid – will be implemented based on previous CFD studies of adsorption processes (Haddadi et al., 2016).

References

- F. Cherubini, 2010, The biorefinery concept: Using biomass instead of oil for producing energy and chemicals, *Energy Conversion and Management*, 51(7), 1412-1421.
- J.M.P.Q. Delgado, 2006, A critical review of dispersion in packed beds, *Heat and Mass Transfer*, 42(4), 279-310.
- B. Haddadi, C. Jordan, H.R. Norouzi & M. Harasek, 2016, Investigation of the pressure drop of random packed bed adsorbers, *Chemical Engineering Transactions*, 52, 439-444.
- A. Sluiter, B. Hames, R. Ruiz, C. Scarlata, J. Sluiter, D. Templeton & D. Crocker, , 2008, Determination of structural carbohydrates and lignin in biomass, *Laboratory analytical procedure*, 1617, 1-16.
- H.R. Norouzi, R. Zarghami, R. Sotoudeh-Gharebagh, & N. Mostoufi, 2016, *Coupled CFD-DEM Modeling: Formulation, Implementation and Application to Multiphase Flows*, John Wiley & Sons.

Pyrolysis Kinetics of Genetically Engineered Hybrid Poplars for Bio-Oil Production

Vo The Ky,^a Jinsoo Kim^{a,*}

^a*Department of Chemical Engineering, Kyung Hee University, 1732 Deogyong-daero, Giheung-gu, Yongin-si, Gyeonggi-do 17104, Republic of Korea*

jkim21@khu.ac.kr

Abstract

In this study, hybrid poplars were genetically engineered to increase their biomass volume and change their biochemical composition to improve the pyrolytic production of bio-oil. Wild-type hybrid poplars (WT) and genetically engineered hybrid poplars (TP) were comparatively investigated with regard to their pyrolysis characteristics and kinetics via thermogravimetric analysis (TGA) and isothermal pyrolysis within a micro-tubing reactor. Model-free methods were used to determine the activation energy for the thermal decomposition of the WT and TP samples. The results showed that the activation energy of the WT sample was always greater than that of the TP sample at the same level of conversion. Isothermal pyrolysis experiments of the two biomass samples were performed at various temperatures (360–400°C) and durations (1–5 min) using a micro-tubing reactor. A reaction network and quantitative kinetic model were proposed for pyrolysis of the WT and TP samples. Kinetic parameters were obtained through an optimization function and used to explore the parameter space in order to predict product yields as a function of reaction time and temperature for both WT and TP feedstocks.

Keywords: pyrolysis, hybrid poplar, model-free method, reaction network, kinetic model.

1. Introduction

Pyrolysis of hybrid poplar trees has attracted considerable attention in recent years. Özyurtkan et al. (2008) investigated the effects of carbonization conditions of hybrid poplars such as the heating rate, particle size, and sweep gas flow using TGA method. The experimental results indicated that biochar yields decreased with an increased heating rate and sweep gas flow rate, but increased with an increase in particle size. Additionally, the kinetic parameters were also determined separately for the carbonization of cellulosic and lignin components of hybrid poplars. Xiang et al. (2016) studied the kinetic mechanism with regard to the thermal decomposition of hybrid poplar sawdust through thermogravimetric experiments at different heating rates and a model-free method was used to determine the kinetic parameters. In general, these studies focused on the pyrolysis characteristics and compositions of pyrolytic vapor products for hybrid poplar trees utilizing TGA and Py-GC/MS methods. However, there have been few studies regarding pyrolysis kinetics and quantitative kinetic models of

genetically engineered hybrid poplars, which is necessary for the design and operation of biomass pyrolysis systems.

In this study, WT were genetically engineered to TP to increase their biomass content and change their biochemical composition to improve the pyrolytic production of bio-oil for the first time. Afterwards, the pyrolysis characteristics and kinetics of both WT and TP samples were investigated via TGA and isothermal pyrolysis reactions in a micro-tubing reactor, respectively. For an improved understanding of the pyrolysis mechanism, a quantitative kinetic model was applied based on a reaction network for the pyrolysis of the WT and TP samples. Finally, kinetic parameters calculated from the kinetic model were used to predict the pyrolysis product distributions (biochar, bio-oil and gas products) as a function of reaction temperature and duration.

2. Pyrolysis kinetics of hybrid poplars

The kinetic parameters for pyrolysis of the WT and TP samples were determined through analyses of differential thermogravimetry (DTG) data obtained at different heating rates. For the global reaction scheme of solid biomass \rightarrow char + volatiles, the kinetic equation for the pyrolysis of biomass can be described as follows (Vo et al., 2017; Ma et al., 2015):

$$\frac{dX}{dt} = A \exp\left(-\frac{E}{RT}\right) f(X) \quad (1)$$

where A is the pre-exponential factor, E is the activation energy of the reaction, R is the universal gas constant, T is the absolute temperature, and X is the conversion value..

Integrating both sides of Eq. (1) after introducing the heating rate $\beta = dT/dt$ yields Eq. (2) (Vo et al., 2017):

$$g(X) = \frac{AE}{\beta R} \int_0^x \frac{dX}{f(X)} = \int_{T_0}^T \frac{A}{\beta} \exp\left(-\frac{E}{RT}\right) dt \quad (2)$$

In this study, the Kissinger-Akahira-Sunose (KAS) method and Flynn-Wall-Ozawa (FWO) method were used (Ceylan et al., 2014). These model-free methods have been widely used for the estimation of activation energy since they can be used without knowledge of the reaction model (Ceylan et al., 2014).

Based on Eq. (2), the KAS method can be derived as follows (Vo et al., 2017):

$$\ln\left(\frac{\beta}{T^2}\right) = \ln\left[\frac{AR}{Eg(X)}\right] - \frac{E}{RT} \quad (3)$$

and the FWO method can be expressed as follows (Takeo, 1965):

$$\ln(\beta) = \ln\left(\frac{AE}{Rg(X)}\right) - 5.331 - 1.052 \frac{E}{RT} \quad (4)$$

Using Eqs. (3) and (4), the apparent activation energy could be obtained from the plot of $\ln(\beta)$ versus $1000/T$ for the FWO method and $\ln(\beta/T^2)$ versus $1000/T$ for the KAS method at a given conversion X .

Fig. 1 (a-b) and Fig. 1(c-d) show the plots used for the KAS and FWO methods, respectively. Between the conversion range of 10–80%, the apparent activation energy values for the WT sample were 231.24–282.89 kJ/mol for KAS and 233.67–284.48 kJ/mol for FWO, respectively, while those for the TP sample were 169.16–234.58 kJ/mol for KAS and 167.66–231.26 kJ/mol for the FWO method.

Although the activation energy values calculated from the KAS and FWO methods showed very similar results, it was obvious that both the WT and TP samples exhibited different activation energy values due to different biochemical compositions (Slopiecka, et al., 2012). Between the conversion range of 10 to 35% for the WT sample and 10 to 40% for the TP sample, the activation energy increased with conversion, which could be attributed to the degradation of hemicellulose. Afterwards, the activation energy decreased with an increase in conversion up to 60% for both biomass samples, which could be due to the decomposition of cellulose crystals, of which the activation energy decreased with an increase in conversion (Hu et al., 2016). For conversion values above 60% for the WT and TP samples, the activation energy slowly increased due to the slow decomposition of lignin. The fluctuation in activation energy with conversion indicated that different pyrolysis mechanisms existed depending on the decomposition of different biochemical compositions (Hu et al., 2016). Also, the apparent activation energy of the WT sample was always higher than that of the TP sample at the same conversion value, which could be due to a higher lignin content in the WT sample (Burhenne, et al., 2013).

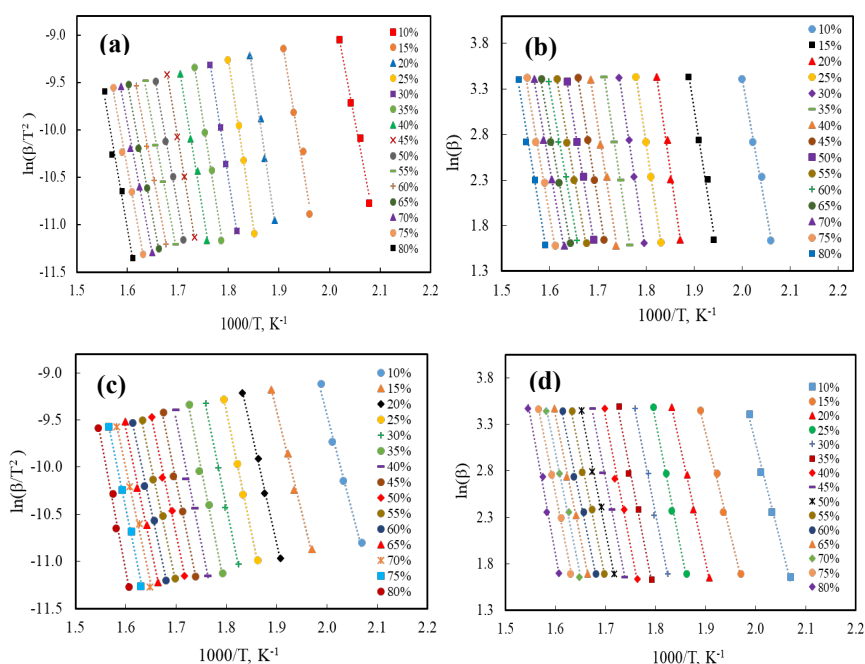


Fig. 1. KAS (a, c) and FWO (b, d) plots of the WT sample (a, b) and TP sample (c, d) at different conversion values. (Vo et al. (2017))

3. Kinetic model for pyrolysis of hybrid poplar trees

A previous study on pyrolysis of individual biomass component (hemicellulose, cellulose, and lignin) showed that the pyrolytic product included liquid oil and gas products. Among the products, the gas product could be produced directly from the degradation of biomass component or from the secondary cracking of volatiles (Yang et al., 2007). In this study, pyrolysis mechanisms were described as the independent primary thermal decomposition of hemicellulose, cellulose and lignin into a liquid phase (bio-oil) with gas products, followed by secondary cracking of the bio-oil to yield gas products. Based on this reaction network, a quantitative kinetic model was proposed for the isothermal decomposition of WT and TP samples in a micro-tubing reactor. For simplicity, it was assumed that all reactions were first-order and irreversible. By applying the apparent rate equation, the reaction rate for each pathway can be written as follows:

$$\text{Hemicellulose: } \frac{dx_{1,h}}{dt} = -(k_{1,h} + k_{2,h})x_{1,h} \quad (5)$$

$$\text{Cellulose: } \frac{dx_{1,c}}{dt} = -(k_{1,c} + k_{2,c})x_{1,c} \quad (6)$$

$$\text{Lignin: } \frac{dx_{1,l}}{dt} = -(k_{1,l} + k_{2,l})x_{1,l} \quad (7)$$

$$\text{Bio-oil product: } \frac{dx_2}{dt} = -k_3x_2 + k_{1,h}x_{1,h} + k_{1,c}x_{2,c} + k_{1,l}x_{1,l} \quad (8)$$

$$\text{Gaseous product: } \frac{dx_3}{dt} = k_{2,h}x_{1,h} + k_{2,c}x_{1,c} + k_{2,l}x_{1,l} + k_3x_2 \quad (9)$$

Here, $x_{1,h}$, $x_{1,c}$, $x_{1,l}$, x_2 , and x_3 correspond to the mass fractions of hemicellulose, cellulose, lignin, bio-oil, and gaseous products, respectively. The mass fractions of hemicellulose ($x_{1,h}$), cellulose ($x_{1,c}$), and lignin ($x_{1,l}$) in the original biomass are the product of the total solid fraction (x_1) and their fraction in dry ash-free biomass. This relationship can be illustrated by Eq. (10):

$$x_1 = x_{1,h} + x_{1,c} + x_{1,l} \quad (10)$$

The system of ordinary differential equations (5)-(9) was solved, and the rate constants (k_j) were estimated using a least-squares objective function (Q), which was defined as the summation of the squared differences between the experimental yield for each product fraction (x_i^{exp}) and the model value (x_i^{model}) at a given reaction temperature.

$$Q = \sum_i \sum_t [x_i^{\text{exp}}(t) - x_i^{\text{model}}(t)]^2 \quad (11)$$

A MATLAB optimization function was used to minimize the value of the objective function (Q) at each reaction temperature (Valdez and Savage, 2013). Initially, the boundary conditions of the rate constants were fixed within $0.00\text{--}0.48\text{ min}^{-1}$, and the fixed-step size for the solver was 0.05 seconds. These constrained conditions were short enough to avoid very long computational times but long enough to supply the fastest paths observed experimentally.

Fig. 2 shows correlations of the model (solid line) to the experimental product yield data (discrete points) obtained from pyrolysis of the WT and TP samples at various temperatures. In general, pyrolysis of the WT and TP samples revealed similar trends with regard to the evolution of solid, bio-oil and gas product yields according to the pyrolysis temperature and duration. Herein, it should be noted that the initial solid yields of 100% excluded the ash content of the woody biomass because most of the ash content was not involved in the conversion to pyrolytic products. As can be seen in Fig. 2, the bio-oil yield for both the WT and TP samples increased with an increase in reaction time at pyrolysis temperatures of 360 and 380 °C. However, at a pyrolysis temperature of 400 °C, the bio-oil yield increased dramatically only during the initial 3 minutes, afterwards the bio-oil yield began to decrease slightly with further reaction time. At a high pyrolysis temperature of 400 °C, the conversion of biomass into bio-oil was complete within a short reaction time; further reaction time facilitated the conversion of bio-oil to gas. The gas yield always increased with increases in reaction time and temperature for both the WT and TP samples.

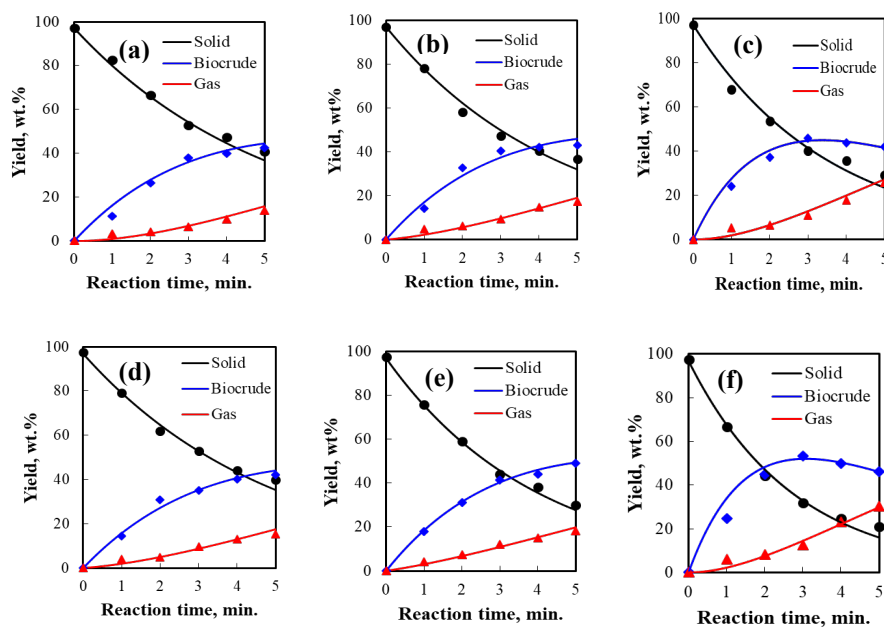


Fig. 2. Experimental (discrete points) and calculated (solid lines) yields of solid, bio-oil, and gas products as a function of reaction duration at various reaction temperatures for the WT (a, b, c) and TP (d, e, f) samples at 360 °C (a, d), 380 °C (b, e), and 400 °C (c, f). (Vo et al. (2017))

4. Conclusion

A comparative study on the pyrolysis characteristics and kinetics of WT and TP samples was performed via TGA and isothermal pyrolysis experiments. Between the conversion range of 10–80%, the apparent activation energy values for the WT samples were 231.24–284.48 kJ/mol while those for the TP samples were 167.66–234.58 kJ/mol. A quantitative kinetic model was applied to the isothermal experiment data. The results showed that the model accurately represented the experimental data for both the WT and TP samples. An estimation of the rate constants suggested that the dominant reaction pathway was the formation of bio-oil from cellulose and hemicellulose. Additionally, the TP samples always exhibited a higher rate constant for every reaction compared to the WT samples. This suggested the potential for genetic engineering to improve biomass feedstocks for the pyrolytic production of bio-oil.

References

- L. Burhenne, J. Messmer, T. Aicher, M.-P. Laborie. The effect of the biomass components lignin, cellulose and hemicellulose on TGA and fixed bed pyrolysis *J Anal Appl Pyrolysis*, 101 (2013), pp. 177-84
- S. Ceylan, Y. Topcu, Z. Ceylan. Thermal behaviour and kinetics of alga *Polysiphonia elongata* biomass during pyrolysis *Bioresour Technol*, 171 (2014), pp. 193-8
- M. Hu, Z. Chen, S. Wang, D. Guo, C. Ma, Y. Zhou, et al. Thermogravimetric kinetics of lignocellulosic biomass slow pyrolysis using distributed activation energy model, Fraser–Suzuki deconvolution, and iso-conversional method *Energy Convers Manage*, 118 (2016), pp. 1-11
- Z. Ma, D. Chen, J. Gu, B. Bao, Q. Zhang. Determination of pyrolysis characteristics and kinetics of palm kernel shell using TGA–FTIR and model-free integral methods *Energy Convers Manage*, 89 (2015), pp. 251-9
- M.H. Özyurtkan, D. Özçimen, A.E. Meriçboyu. Investigation of the carbonization behavior of hybrid poplar *Fuel Process Technol*, 89 (2008), pp. 858-63
- K. Slopiecka, P. Bartocci, F. Fantozzi. Thermogravimetric analysis and kinetic study of poplar wood pyrolysis *Applied Energy*, 97 (2012), pp. 491-7
- O. Takeo. A New Method of Analyzing Thermogravimetric Data *Bulletin of the Chemical Society of Japan*, 38 (1965), pp. 1881-6
- P.J. Valdez, P.E. Savage. A reaction network for the hydrothermal liquefaction of *Nannochloropsis* sp *Algal Res*, 2 (2013), pp. 416-25
- T.K. Vo, H.V. Ly, O.K. Lee, E.Y. Lee, C.H. Kim, J.-W. Seo, et al. Pyrolysis characteristics and kinetics of microalgal *Aurantiochytrium* sp. KRS101 *Energy*, 118 (2017), pp. 369-76
- T.K. Vo, J.-S. Cho, S.-S. Kim, J.-H. Ko, J. Kim, Genetically engineered hybrid poplars for the pyrolytic production of bio-oil: Pyrolysis characteristics and kinetics *Energy Convers Manage*, 153 (2017), pp. 48-59
- Y. Xiang, Y. Xiang, L. Wang. Thermal decomposition kinetic of hybrid poplar sawdust as biomass to biofuel *J Environ Chem Eng*, 4 (2016), pp. 3303-8
- H. Yang, R. Yan, H. Chen, D.H. Lee, C. Zheng. Characteristics of hemicellulose, cellulose and lignin pyrolysis *Fuel*, 86 (2007), pp. 1781-8

Model-based Fed-batch Algal Cultivation Strategy for Enhanced Starch Production

Gonzalo M. Figueroa-Torres,^a Jon K. Pittman,^b Constantinos Theodoropoulos^{a,*}

^a*Biochemical and Bioprocess Engineering Group, School of Chemical Engineering and Analytical Science, University of Manchester, M13 9PL, UK*

^b*School of Earth and Environmental Sciences, University of Manchester, M13 9PL, UK*
k.theodoropoulos@manchester.ac.uk

Abstract

Promoting and ensuring widespread usage of biofuels throughout the European Union are two crucial targets of the existing strategic measures tackling global warming (Eurostat, 2017). Selection of adequate biofuel feedstocks, however, remains a major challenge obstructing large-scale production of biofuels. Microalgal biomass has been recently recognized as a promising biofuel feedstock due to its ability to accumulate significant amounts of starch (a raw precursor of sugar-based fuels) and lipids, when grown under nutrient-limited conditions (Markou et al., 2012; Suganya et al., 2016). However, such strategies need to be carefully implemented since they are typically characterised by a trade-off between biomass growth and starch/lipid accumulation. We previously identified and validated a starch-enhanced batch-mode cultivation scenario by means of a kinetic model capable of predicting the nitrogen limited dynamics of mixotrophic algal growth and simultaneous starch and lipid formation (Figueroa-Torres et al., 2017). This work focuses on starch accumulation, and the validated model is exploited by establishing an optimal fed-batch cultivation strategy capable of enhancing starch formation whilst sustaining algal growth. Optimal fed-batch operating conditions were identified by means of a model-based optimisation study maximising starch concentration. The computed fed-batch starch-enhanced scenario was subsequently verified against experimental data obtained from lab-scale cultures of *Chlamydomonas reinhardtii* CCAP 11/32, which yielded a 37 % increase in starch concentration with respect to that obtained by standard batch operation. Results highlight the potential use of predictive kinetic model as optimisation tools for the establishment of large-scale algae-to-fuel cultivation strategies.

Keywords: microalgae, *Chlamydomonas reinhardtii*, modelling, fed-batch, biofuels.

1. Introduction

Transportation industries are responsible for more than two thirds of the total crude oil and petroleum products consumed throughout the European Union. In an effort to mitigate overconsumption of fossil-based fuels and their associated contribution to climate change, the European Council established a strategic framework mandating all Member States to use by 2020 a minimum 10 % of renewables sources, such as biofuels, to satisfy their transport fuel consumption (Eurostat, 2017). The race towards meeting such a renewable energy target requires the successful implementation of large-scale biofuel technologies. However, widespread production of biofuels from biomass has thus far been severely restricted by the use of traditional, but highly controversial,

food-based feedstocks and/or complex lignocellulosic materials (Chundawat et al., 2011; Suganya et al., 2016).

A promising alternative to traditional biofuel feedstocks is microalgal biomass because it naturally accumulates starch, a carbon-based compound from which sugar-based fuels (e.g. bioethanol, biobutanol) could be obtained. Nevertheless, optimal large-scale cultivation systems need to be developed before microalgal starch becomes a low-cost and renewable feedstock suitable for biofuel production. A popular algal cultivation strategy which significantly increases typical starch contents involves nitrogen limitation (Markou et al., 2012). However, such cultivation strategies should be carefully implemented to: i) prevent a decrease in overall biomass growth, and ii) additionally portray the dual distribution of the intracellular carbon pool towards not only starch, but also lipid formation (Bekirogullari et al., 2017). In our previous work, we identified optimal starch-enhancing batch-mode cultivation strategies by means of a robust modelling framework predicting nitrogen-limited mixotrophic algal cultivation dynamics (Figueroa-Torres et al., 2017). Thus, the focus of this study was to develop a model-based strategy for enhanced starch formation during fed-batch algal cultivation.

2. Modelling and optimisation of algal fed-batch cultivation

2.1 Kinetic modelling

The predictive kinetic model developed in Figueroa-Torres et al. (2017) is capable of portraying the nitrogen-limited mixotrophic growth dynamics of the following 8 cultivation variables: total biomass, X (gC L^{-1}); nitrogen N (gN L^{-1}); nitrogen quota q_N (gN gC^{-1}); acetic acid A (gC L^{-1}); starch S (gC L^{-1}); lipids L (gC L^{-1}); active biomass x^* (gC L^{-1}); and pH, H . The corresponding accumulation rate of each variable is described by the following set of ordinary differential equations:

$$\frac{dX}{dt} = \mu \cdot X \quad (1)$$

$$\frac{dN}{dt} = -\rho_N \cdot X \quad (2)$$

$$\frac{dq_N}{dt} = \rho_N - q_N \cdot X \quad (3)$$

$$\frac{dA}{dt} = -\frac{1}{Y_{X/A}} \cdot \frac{\mu_H(A)}{\mu_H(A) + \mu_P(I)} \cdot X \quad (4)$$

$$\frac{dS}{dt} = r_1 \cdot \frac{N_{\text{int}}^{n_S}}{N_{\text{int}}^{n_S} + (N_{\text{int}}^2/k_{i,S})^{n_S}} \cdot \left(1 + \frac{e^{\phi_S \cdot A_{\text{int}}}}{\mu}\right) \cdot \frac{k_1}{k_1 + N/N_0} \cdot \mu \cdot x^* - \frac{r_2}{q_N} \cdot X \quad (5)$$

$$\frac{dL}{dt} = r_3 \cdot \frac{N_{int}^{n_L}}{N_{int}^{n_L} + k_{s,L}^{n_L} + \left(N_{int}^2/k_{i,L}\right)^{n_L}} \cdot (\mu + 1) \cdot \frac{k_2}{k_2 + N/N_0} \cdot \mu \cdot x^* - \frac{r_4}{q_N} \cdot X \quad (6)$$

$$\frac{dx^*}{dt} = \frac{dX}{dt} - \left(\frac{dS}{dt} + \frac{dL}{dt} \right) \quad (7)$$

$$\frac{dH}{dt} = \left(\frac{x^* - x_0^*}{x^*} \right) \cdot K_H \cdot \frac{dx^*}{dt} \quad (8)$$

The specific growth rate, μ , is a function of: the heterotrophic growth (driven by the acetic acid concentration); the phototrophic growth (driven by the light distribution across the culture vessel); and the nitrogen-dependent growth (driven by the nitrogen quota):

$$\mu = \mu_{max} \cdot [w_H \cdot \mu_H(A) + w_P \cdot \mu_P(I)] \cdot \mu_N(q_N) \quad (9)$$

$$\mu = \mu_{max} \cdot \left(w_H \cdot \frac{A}{A + K_{s,A} + A^2/k_{i,A}} + w_I \cdot \frac{I}{I + K_{s,I} + I^2/k_{i,I}} \right) \cdot \left(1 - \frac{q_{N,0}}{q_N} \right) \quad (10)$$

As shown in Eq. (5) and Eq. (6), the formation of starch and lipid molecules is primarily regulated by the intracellular nitrogen ($N_{int} = q_N X$), and acetate ($A_{int} = A - A_o$) concentrations. On the other hand, the nitrogen uptake rate (ρ_N) shown in Eq. (2) and Eq. (3) is expressed as:

$$\rho = \bar{\rho}_{N,max}(X, N_0) \cdot \frac{N}{N + K_{s,N} + N^2/k_{i,N}} \cdot \frac{A}{A + K_{s,A,N} + A^2/k_{i,A,N}} \quad (11)$$

$$\bar{\rho}_{N,max}(X, N_0) = \rho_{N,max} \cdot \frac{N_o^n}{N_o^n + K_{N_o}^n} \cdot e^{-\phi_N \cdot X} \quad (12)$$

Kinetic parameter values throughout Eq's. (1) – (12), along with their corresponding definition and respective units, are summarised in Table 1.

2.2 Optimisation of fed-batch cultivation

The above modelling framework was shown to be a robust optimisation tool for the establishment of batch-mode cultivation strategies enhancing starch formation (Figueroa-Torres et al., 2017). However, a common setback of batch-mode systems is nutrient exhaustion, which causes cellular death towards the end of the cultivation and consequently halts starch production. Therefore, a model-based fed-batch strategy was envisaged whereby growing cultures undergoing nitrogen limitation were supplied with a pulse of acetic acid (major carbon source in standard TAP medium). Preliminary experiments, however, indicated that the above model was unable to capture the ability of growing cells to regain their nitrogen uptake capacity when supplied with a pulse of acetic acid. Therefore, the model was adjusted by: i) expressing the pulse-associated

nitrogen uptake rate as a function of the increase in biomass concentration from any starting cell density (i.e. $X-X_0$), rather than by just the residual biomass, and ii) by expressing the saturation constant, K_* , as a function of both the initial cell density and nitrogen concentration, as shown in Eq. (13).

$$\bar{\rho}_{N,\max}(X, N_0, X_0) = \rho_{N,\max} \cdot \frac{N_0^n}{N_0^n + [K_*/(1 + X_0/N_0)]^n} \cdot e^{-\phi_N \cdot (X - X_0)} \quad (13)$$

In order to establish an optimal starch-enhancing fed-batch cultivation strategy, the adjusted model was then employed to identify two operating parameters: i) the optimal injection time of the acetic acid pulse, t_{pulse} , and ii) the required concentration of acetic acid in the pulse, A_{pulse} . These operating parameters were identified by maximising the following objective function:

$$\text{Objective} = \max S(t_{pulse}, A_{pulse}) \quad (14)$$

where S is the predicted starch medium concentration, subject to the governing model equations (i.e. Eq.(1)-Eq.(13)), and t_{pulse} and A_{pulse} are the degrees of freedom. The maximisation problem was solved by means of a stochastic optimisation algorithm (simulated annealing), coupled with a deterministic method (SQP) as in Vlysidis et al. (2011). Both routines were implemented in Matlab R2015a.

3. Materials and methods

3.1 Strain and cultivation.

Experimentation was carried out with the strain *Chlamydomonas reinhardtii* CCAP 11/32c, maintained mixotrophically in standard TAP medium at 25 °C, 150 rpm, and a light/dark cycle of 16/8 h (Figueroa-Torres et al., 2017). Cultivation experiments were performed in multiple identical vessels containing 500 mL of TAP medium which allowed duplicate samples to be fully harvested throughout cultivation (before/after pulse injection). Growth was initiated by inoculating culture vessels simultaneously with a 1 mL aliquot of an active algal inoculum. Vessels were kept at the same environmental conditions described before. During the course of cultivation, a sterile nutrient pulse was aseptically injected into growing cultures as per the optimal fed-batch operating conditions (i.e. A_{pulse} and t_{pulse}) identified by the optimization study.

3.2 Analytical methods.

Biomass concentration (cell dry weight) was measured gravimetrically by drying harvested cultures overnight at 70 °C. Starch was quantified as per a Total Starch kit supplied by *Megazyme International, Ireland*. Lipids were quantified in a SOXTEC Unit 1043 using hexane as extracting agent as in Bekirogullari et al. (2017). Extracted lipids were then determined gravimetrically. Residual nitrogen concentration was measured in a TOC-VCSH/TNM-1, Shimadzu (Total Organic Carbon/ Total Nitrogen). Acetic acid was measured by HPLC (High Pressure Liquid Chromatography) using an Aminex HPX-87H column (8 m, 300x7.7mm) with sulfuric acid 5mM as mobile phase (50 °C and 0.6 mL min⁻¹) and a UV detector set at a wavelength of $\lambda=210$ nm.

4. Results and discussion

As described in the preceding section, the original maximum nitrogen uptake rate expression was modified to accurately portray algal growth dynamics subject to a single acetic acid pulse. Consequently, the values of the kinetic parameters in Eq. (13) (i.e. $\rho_{N,max}$, K^* , n , and ϕ_N) were re-identified as per the methodology of Vlysidis et al. (2011) to ensure that predicted dynamics were still consistent with those original datasets presented in Figueroa-Torres et al. (2017). Final parameter values are shown in Table 1.

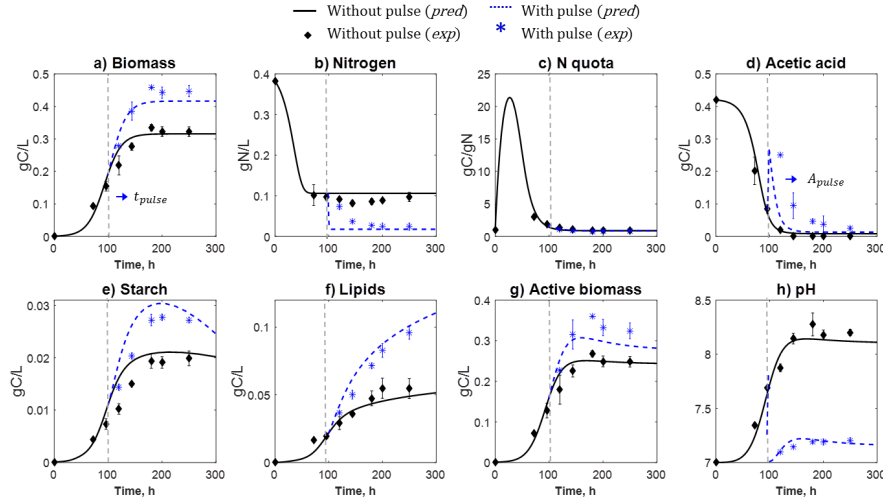


Figure 1. Predicted and experimental dynamics obtained by *Chlamydomonas reinhardtii* cultures grown under batch and fed-batch (pulse injection) cultivation.

The optimisation study was subsequently carried out with the adjusted model, which indicated that the optimal fed-batch operating conditions maximising starch concentration (i.e. Eq. (14)) required a nutrient pulse with concentration equivalent to $A_{pulse} = 0.21 \text{ gC L}^{-1}$, to be supplied at a time equivalent to $t_{pulse} = 97.5 \text{ h} \sim 100 \text{ h}$ (4th day). The pulse injection (10 mL) accounted for a 2% volume increase in the overall culture medium, and was considered negligible in calculations.

Table 1. List of parameter employed in the kinetic model (Figueroa-Torres et al., 2017).

Symbol	Definition	Value	Units	Symbol	Definition	Value	Units
μ_{max}	Maximum specific growth rate	0.106	h^{-1}	$K_{i,A,N}$	Uptake saturation constant, A	1.004	gC L^{-1}
$q_{N,0}$	Minimum nitrogen quota	0.876	gN gC^{-1}	$k_{i,A,N}$	Uptake inhibition constant, A	1.098	gC L^{-1}
$K_{i,A}$	Acetate saturation constant	1.789	gC L^{-1}	r_1	Rate of reaction	0.049	gC gC^{-1}
$k_{i,A}$	Acetate inhibition constant	0.109	gC L^{-1}	r_2	Rate of reaction	0.003	$\text{gN gC}^{-1}\text{h}^{-1}$
$K_{i,L}$	Light saturation constant	1.4	$\mu\text{mol m}^{-2}\text{s}^{-1}$	r_3	Rate of reaction	0.162	gC gC^{-1}
$k_{i,L}$	Light inhibition constant	186.52	$\mu\text{mol m}^{-2}\text{s}^{-1}$	r_4	Rate of reaction	0.005	$\text{gN gC}^{-1}\text{h}^{-1}$
$Y_{X/A}$	Yield coefficient	0.059	gC gC^{-1}	$k_{i,S}$	Inhibition constant	0.214	gN L^{-1}
σ	Light attenuation coefficient	1	$\text{L gC}^{-1} \text{m}^{-1}$	n_S	Shape parameter	4.145	-
$\rho_{N,max}$	Maximum nitrogen uptake rate	34.56	$\text{gN gC}^{-1}\text{h}^{-1}$	k_I	Regulation constant	0.110	-
K^*	* Saturation constant, N_0	0.310	gN L^{-1}	Φ_S	Regulation coefficient	0.675	L gC^{-1}
n	* Shape-controlling parameter	19.10	-	$K_{s,L}$	Saturation constant	0.023	gN L^{-1}
Φ_N	* Uptake regulation coefficient	138.74	L gC^{-1}	$k_{i,L}$	Inhibition constant	0.086	gN L^{-1}
$K_{s,N}$	Uptake saturation constant, N	0.163	gN L^{-1}	n_L	Shape parameter	1.812	-
$k_{i,N}$	Uptake inhibition constant, N	0.113	gN L^{-1}	k_2	Regulation constant	0.213	-

* Parameters re-identified in this work accounting for pulse-associated nitrogen uptake.

The computed optimal fed-batch strategy was validated experimentally and further compared against a simple batch control case. Both predicted and experimental dynamics are shown in Figure 1, where it is observed that the adjusted kinetic model was capable of accurately describing the dynamics of biomass growth, nutrient uptake, and starch and lipid formation both before and after the pulse addition. Compared to standard batch-mode, fed-batch conditions yielded 37% increase in starch concentration with a corresponding 76% increase in lipids. The effect of acetic acid, an organic carbon source, has been shown to enhance microalgal growth in *C. reinhardtii* when compared to standard phototrophic conditions which rely solely on inorganic CO₂ (Bekirogullari et al., 2017). Results from this work further show the advantage of fed-batch cultivation, where the exhaustion of carbon (e.g. acetate) leading to cell death is avoided.

5. Conclusions

A model-based optimisation study was carried out to identify optimal operating parameters suitable for the enhancement of starch formation by fed-batch algal cultivation. The optimisation problem (i.e. maximising starch formation) was solved by means of a global optimisation algorithm, subject to a validated predictive kinetic model for nitrogen-limited mixotrophic algal growth. The computed fed-batch optimal cultivation strategy yielded a 37% increase in starch against standard batch cultivation and was validated against experimentally generated data.

Acknowledgements

G. Figueroa-Torres kindly acknowledges CONACyT-México for its financial support.

References

- M. Bekirogullari, I.S. Fragkopoulos, J.K. Pittman, C. Theodoropoulos, 2017, Production of lipid-based fuels and chemicals from microalgae: An integrated experimental and model-based optimization study, *Algal Res.*, 23, 78–87.
- S.P.S. Chundawat, G.T. Beckham, M.E. Himmel, B.E. Dale, 2011, Deconstruction of Lignocellulosic Biomass to Fuels and Chemicals, *Annu. Rev. Chem. Biomol. Eng.*, 2, 121–145.
- Eurostat, Energy data, 2017, retrieved from: <http://ec.europa.eu/eurostat/web/energy/overview> [last accessed on: 08/12/17].
- G.M. Figueroa-Torres, J.K. Pittman, C. Theodoropoulos, 2017, Kinetic modelling of starch and lipid formation during mixotrophic, nutrient-limited microalgal growth, *Bioresour. Technol.*, 241, 868–878.
- G. Markou, I. Angelidaki, D. Georgakakis, 2012, Microalgal carbohydrates: an overview of the factors influencing carbohydrates production, and of main bioconversion technologies for production of biofuels, *Appl. Microbiol. Biotechnol.*, 96, 631–645.
- T. Suganya, M. Varman, H.H. Masjuki, S. Renganathan, 2016, Macroalgae and microalgae as a potential source for commercial applications along with biofuels production: A biorefinery approach, *Renew. Sustain. Energy Rev.*, 55, 909–941.
- A. Vlysidis, M. Binns, C. Webb, C. Theodoropoulos, 2011, Glycerol utilisation for the production of chemicals: Conversion to succinic acid, a combined experimental and computational study, *Biochem. Eng. J.*, 58–59, 1–11.

Model-based process development for a continuous lactic acid bacteria fermentation

Robert Spann^a, Anna Eliasson Lantz^b, Christophe Roca^c, Krist V. Gernaey^a and Gürkan Sin^{a*}

^a*Process and Systems Engineering Center (PROSYS), Department of Chemical and Biochemical Engineering, Technical University of Denmark, Søtofts Plads Building 229, 2800 Kgs. Lyngby, Denmark*

^b*PILOT PLANT, Department of Chemical and Biochemical Engineering, Technical University of Denmark, Søtofts Plads Building 229, 2800 Kgs. Lyngby, Denmark*

^c*Chr. Hansen A/S, Bøge Allé 10-12, 2970 Hørsholm, Denmark*
gsi@kt.dtu.dk

Abstract

A mechanistic process model describing a lactic acid bacteria (LAB) fermentation was applied to develop a continuous fermentation process. Producing LAB for the dairy industry in a continuous cultivation, which would allow harvesting the cells during the cultivation, would reduce production costs compared to traditional batch processes. To this end, a validated mechanistic model of a *Streptococcus thermophilus* fermentation was used for a model-based continuous process evaluation. The fermentation model consists of biological and chemical mechanisms including a description of the growth rate as a function of pH and inhibition effects of metabolites. The optimal dilution rate and substrate concentration in the feed were estimated in order to maximize the cell yield (biomass concentration) and to minimize the waste of substrate during the continuous fermentation in a 50 m³ bioreactor for two scenarios: downstream capabilities are i) flexible, and ii) fixed. The biomass concentration is restricted by the growth-inhibiting lactic acid concentration, which is produced by the growing bacteria. Furthermore, the substrate, which is supplied by the feed, should be consumed completely in the fermentation and not wasted in the bioreactor effluent owing to raw material costs. The resulting non-linear optimization problem was formulated and solved in MATLAB[®]. A Monte Carlo simulation showed the robustness of the results, where a biomass concentration of 5 g L⁻¹ could be achieved in the continuous fermentation with a substrate wastage of less than 3 % in the bioreactor effluent. The productivity of the continuous process was similar to a traditional batch process, but frequent cleaning and sterilization are no longer necessary in a continuous process resulting in a shorter unproductive downtime of the bioreactors. This promising potential of a continuous process for LAB cultivations encourages pilot-scale studies for a comprehensive techno-economic evaluation.

Keywords: continuous lactic acid bacteria fermentation, modelling, process development, Monte Carlo simulation

1. Introduction

Mechanistic models are increasingly applied in the biotechnological industry in order to develop, understand, optimize, monitor, and control fermentation processes. They can support the development of fermentation processes and give insight into the process during operation. There are several applications for mechanistic models: E.g. they may be applied offline to determine appro-

appropriate process operation conditions and control strategies, or online as soft sensor for model-based monitoring and control (Mears et al., 2017).

In this study, a mechanistic model describing a *Streptococcus thermophilus* fermentation was applied to design a continuous fermentation process. The food industry strives for continuous fermentations to reduce production costs compared to traditional batch fermentations, which are still the standard operation. The model predicted biological state variables, such as the biomass, substrate (lactose), and lactic acid concentrations. In addition, the model predicted the pH of the fermentation broth by solving the dissociation reactions of the charged components, as lactate, ammonia, carbonate and phosphate. The aim of this study was to propose the optimal process conditions for a continuous lactic acid fermentation to design a beneficial process compared to a batch process. To this end, the model was utilized to optimize the dilution rate and substrate concentration in the feed stream by maximizing the biomass concentration and reducing the substrate waste in the bioreactor effluent.

2. Nomenclature

Symbol	Description		
C_i	concentration (g L ⁻¹)	μ_{max}	max. specific growth rate (h ⁻¹)
F	medium flow rate (L h ⁻¹)	α	growth related production coefficient of lactic acid (g g ⁻¹)
K_I	substrate inhibition constant (g L ⁻¹)	σ_{pH}	std. deviation in the pH function
K_S	limiting substrate constant (g L ⁻¹)		
K_{La}	lactate inhibition parameter (L g ⁻¹)		
$K_{P,La}$	2. lactate inhibition param. (L g ⁻¹)		
$K_{P,pH1}$	lactate inhibition pH parameter	Subscripts i	
$K_{P,pH2}$	2. lactate inhibition pH parameter	La	dissociated lactic acid
pH_{opt}	optimal pH in the pH function	P	by-product: lactic acid
t_{lag}	lag-time coefficient (h)	S	substrate: lactose
V	volume of the bioreactor (L)	S_i	lactose in the feed inlet
Y_{gal}	galactose yield (g g ⁻¹)	X	biomass

3. Materials and Methods

3.1. Fermentation Model

A first principles model describing the homolactic *S. thermophilus* fermentation was applied for a continuous fermentation. The model was validated previously with 2 L batch fermentations at different pH set points (pH 5.5 - 7.0) and initial lactose (substrate) concentrations (20 and 70 g L⁻¹). Furthermore, the model was validated with a continuous accelerostat fermentation at lab-scale to ensure that the model predicts limiting substrate conditions as they occur in continuous cultivations, as well (manuscript in preparation). The studied strain consumes lactose, yielding biomass, lactic acid, and galactose because galactose is not metabolized but secreted. In the present study, the bacterial cells (biomass) are the product of interest. The growth rate expression (Eq. (1)) depends on the lag time, lactose inhibition and limitation (Åkerberg et al., 1998), pH dependent lactate inhibition, and the pH of the cultivation broth (Schepers et al., 2002).

$$\frac{dC_X}{dt} = \mu_{max} \cdot (1 - e^{-t/t_{lag}}) \cdot \frac{C_S}{C_S + K_S + \frac{C_S^2}{K_I}} \cdot \frac{1}{1 + e^{\frac{K_{P,La} \cdot (C_{La} - K_{La})}{1 + e^{\frac{1}{K_{P,pH1} \cdot (pH - K_{P,pH2})}}}}} \cdot e^{-\frac{(pH_{opt} - pH)^2}{\sigma_{pH}^2}} \cdot C_X - \frac{F}{V} \cdot C_X \quad (1)$$

Table 1: Kinetic parameters for the dynamic model of the *S. thermophilus* fermentation.

Parameter	Unit	Value	95 % confidence interval (CI)		Reference
K_I	g L^{-1}	164			(Åkerberg et al., 1998)
K_{La}	g L^{-1}	19.80	19.71	19.89	parameter estimation
$K_{P,La}$	L g^{-1}	0.24	0.17	0.30	parameter estimation
$K_{P,pH1}$		20			expert knowledge*
$K_{P,pH2}$		7			expert knowledge*
K_S	g L^{-1}	0.79			(Åkerberg et al., 1998)
pH_{opt}		6.38	6.28	6.50	parameter estimation
t_{lag}	h	1			expert knowledge*
Y_{gal}	g g^{-1}	0.69	0.61	0.76	parameter estimation
α	g g^{-1}	5.19	5.18	5.20	parameter estimation
μ_{max}	h^{-1}	2.06	2.03	2.08	parameter estimation
σ_{pH}	h^{-1}	1.42	1.35	2.50	parameter estimation

*) consultation of process experts.

The expression for the lactic acid secretion rate as by-product (Eq. (2)) is considered to be growth dependent (Peng et al., 1997).

$$\frac{dC_P}{dt} = \alpha \cdot \frac{dC_X}{dt} - \frac{F}{V} \cdot C_P \quad (2)$$

The lactose uptake rate expression (Eq. (3)) is the sum of the growth and lactic acid secretion rate expressions taking the secretion of galactose (Y_{gal}) into account.

$$\frac{dC_S}{dt} = \frac{F}{V} \cdot (C_{Si} - C_S) - (1 + Y_{\text{gal}}) \cdot \left(\frac{dC_X}{dt} + \frac{dC_P}{dt} \right) \quad (3)$$

The chemical model (for the pH calculation) comprises the dissociation reactions of the charged components in the fermentation broth, such as lactate, ammonia, carbonate, phosphate, and water (Musvoto et al., 2000). The kinetic model has been implemented in MATLAB® (The MathWorks®, Natick, MA) and the ODEs were solved with the ode15s solver. The kinetic parameters (Table 1) were derived from a consistent parameter estimation as described in Spann et al. (2017).

3.2. Design of the continuous fermentation conditions

The continuous process was a single stage chemostat cultivation without recirculation, hence the process is continuously fed with the growth medium and the culture broth is withdrawn at the same rate in order to maintain the bioreactor volume constant. The target product of the fermentation

Table 2: Description of the design problem (LB: lower bound, UB: upper bound).

Scenario	Description	Flow rate [$\text{m}^3 \text{h}^{-1}$]		C_{Si} [g L^{-1}]	
		LB	UB	LB	UB
Scenario 1	50 m^3 bioreactor downstream flexible	1	20	50	150
Scenario 2	50 m^3 bioreactor downstream restricted		fixed to 10	50	150

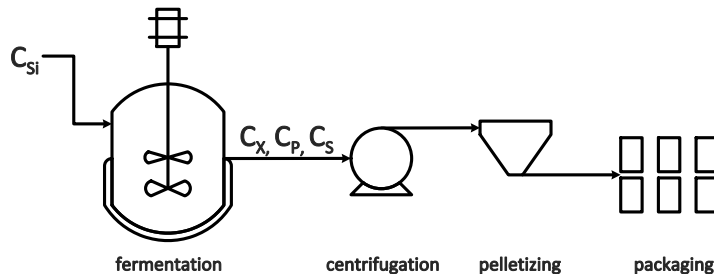


Figure 1: Scheme of the continuous lactic acid bacteria fermentation and downstream units.

process are the cells, as they are used in the dairy industry for yoghurt and cheese production, subsequently. Optimal process conditions for a continuous *S. thermophilus* fermentation process were predicted for two scenarios (Table 2): Scenario 1) A 50 m³ bioreactor is available and the downstream units will be built based on the calculated bioreactor effluent flow rate (Fig. 1). Scenario 2) A 50 m³ bioreactor and the downstream units for centrifugation and pelletizing are already available with given capacities. The flow rate is fixed to 10 m³ h⁻¹ here. For scenario 1, the feed flow rate and lactose concentration in the feed solution were optimized. For scenario 2, only the lactose concentration in the feed solution was optimized. The carbon source lactose will be growth limiting. The challenge of the design problem for an optimal feed flow rate and inlet substrate concentration was that the lactic acid concentration in the broth is determined by the biomass concentration but lactic acid inhibits biomass growth at the same time. The objective was: i) to maximize the biomass concentration in the bioreactor effluent; and, ii) to minimize the waste of substrate in the bioreactor effluent for both scenarios. The objective function was solved in MATLAB using the built in solver, fmincon. The mean values of the biological model parameters were used in the optimization step.

3.3. Monte Carlo simulation

100 independent input samples were created in the probability range [0 1] with the Latin Hypercube Sampling (LHS) technique (McKay et al., 1979; Sin et al., 2009). Then, the Iman Conover method (Iman and Conover, 1982) was applied to induce the correlation between the model parameters, which was derived from a parameter estimation. The samples were finally converted into the real parameter space using the Matlab function icdf, in which all uncertainties were assumed to be normally distributed. A Monte Carlo simulation of the continuous fermentation process was performed considering both the biological model parameter uncertainties (Table 1) and variations of the lactose concentration in the feed (which was obtained in the previous optimization step) with $3\sigma = 10\%$.

4. Results and Discussion

Two scenarios were investigated considering both the new construction of the production facilities (scenario 1), and the limitations of an already available plant (scenario 2). For scenario 1, the capacities of the downstream units were considered to be flexible. A flow rate of 5 m³ h⁻¹ was estimated with a lactose concentration of 54 g L⁻¹ in the feed solution (Fig 2). For scenario 2, an already existing production plant was assumed given limitations in the flow rates. Here, the estimated lactose concentration in the feed solution was 50 g L⁻¹. More lactose would be wasted in the bioreactor effluent in scenario 2 since the dilution rate is almost twice as high as in scenario 1, and the lactic acid bacteria cannot consume all the supplied lactose at this high rate.

The continuous fermentation starts with a batch phase with 65 g L^{-1} lactose initially (Fig. 3). During the exponential growth in the batch phase, the biomass concentration increased before the continuous fermentation started. The optimal time to switch from the batch to continuous mode will not be easily detectable since there is no dissolved oxygen (DO) tension signal in this non-aerated cultivation, where DO is usually used in aerated cultivations to monitor biomass activity. However, the base addition rate will in this case indicate when growth slows down as lactic acid secretion is diminished at the same time (data not shown). The Monto Carlo simulations considering model parameter uncertainties and variations of the lactose concentration in the feed inlet show that the considered uncertainties had a minor effect on the target biomass concentration with acceptable $3\sigma < 0.5 \text{ g L}^{-1}$.

A continuous cultivation could be a profitable alternative to a batch process for the industrial production of lactic acid bacteria as the cells are the desired product that can be produced in a continuous manner, similar to primary metabolites. In addition, naturally derived lactic acid bacteria might be less prone to genetic instability, which might for example be an issue in a continuous cultivation with genetically modified organisms that are often used in the pharmaceutical industry. However, the application of a continuous cultivation is quite limited in the biotechnological industry so far. This might be mostly because of the risk for process contaminations, which could cause more harm in a continuously operated reactor than a batch culture. Nevertheless, especially in the presented lactic acid bacteria cultivation, the lactic acid concentration is already inhibiting the growth of many contaminants as the lactic acid concentration will be higher than 25 g L^{-1} . In a traditional batch process with an initial lactose concentration of 65 g L^{-1} a biomass concentration of 6 g L^{-1} was reached (see the initial batch phase in Fig. 3). The batch process will be, however, more expensive than the continuous culture due to more frequent cleaning, sterilization, pre-culture preparation tasks, etc., provided that the continuous process could be maintained stable with a low risk of failure.

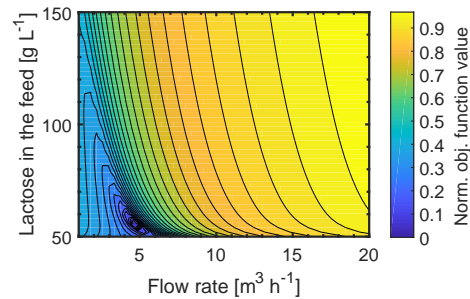


Figure 2: Contour plot of the normalized objective function value with respect to the lactose concentration in the feed and the feed flow rate. The minimum for scenario 1 is at $F = 5 \text{ m}^3 \text{ h}^{-1}$ and $C_{Si} = 54 \text{ g L}^{-1}$. The minimum for scenario 2 is at the lower limit $C_{Si} = 50 \text{ g L}^{-1}$ with the given $F = 10 \text{ m}^3 \text{ h}^{-1}$.

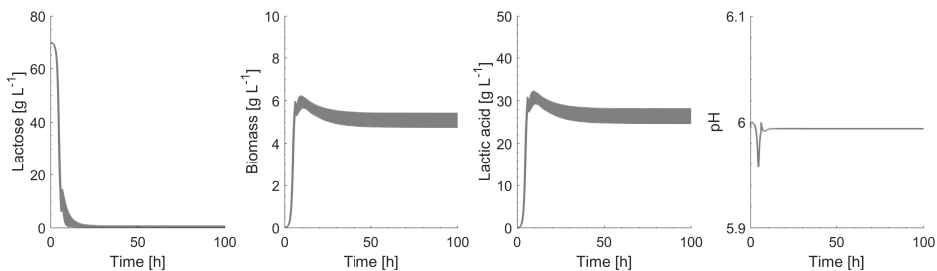


Figure 3: A continuous *S. thermophilus* fermentation with a batch phase in the beginning. 95 % confidence bounds for the limiting substrate lactose, dry cell weight, lactic acid concentration, and the pH (from left to right). A Monte Carlo simulation of 100 input samples was performed considering model parameter uncertainties, and variations of the lactose concentration in the feed solution.

Mechanistic models, as applied in the present study, are preferably used for off-line cultivation process development because of their many advantages (Mears et al., 2017): Mechanistic models are often able to extrapolate to process conditions outside the conditions that were used to develop the model. In addition, mechanistic models provide a flexible model structure that could be adjusted to several processes by adjusting the model parameters. Furthermore, some companies prefer to apply mechanistic models, e.g. for control purposes, because they want to understand where the predictions derive from, instead of following a black-box prediction. Due to these advantages, one should accept a longer model development and validation time of a mechanistic model compared to black-box models.

Further research is necessary to validate the presented model predictions in lab- or pilot-scale experiments. Biotechnological companies and further studies could use the presented case study by also including an economical objective function, e.g. considering sales revenue and expenses, such as operation and raw material costs, in order to design the most profitable continuous cultivation.

5. Conclusion

This study used a mechanistic model describing the production of *S. thermophilus* in a fermentation process to propose the optimal conditions for a continuous cultivation. The fermentation conditions were estimated for two scenarios: downstream capabilities are i) flexible, and ii) fixed. A continuous process is regarded as more cost effective than a traditional batch process, and especially mechanistic models are valuable for process design purposes because they might be capable to predict also conditions which were not experimentally investigated beforehand. In conjunction with uncertainty considerations, a probability distribution of the model prediction was obtained and the uncertainty in the biomass prediction was low, which shows the robustness of the model for analysis. Further studies are needed to validate the model predictions experimentally at pilot-scale and economic issues could be included in the optimization problem.

6. Acknowledgement

This project has received funding from the European Union's Horizon 2020 research and innovation program under the Marie Skłodowska-Curie grant agreement No 643056 (Biorapid project).

References

- Åkerberg, C., Hofvendahl, K., Hahn-Hägerdal, B., Zacchi, G., 1998. Modelling the influence of pH, temperature, glucose and lactic acid concentrations on the kinetics of lactic acid production by *Lactococcus lactis* ssp. *lactis* ATCC 19435 in whole-wheat flour. *Applied Microbiology and Biotechnology* 49, 682–690.
- Iman, R. L., Conover, W. J., 1982. A distribution-free approach to inducing rank correlation among input variables. *Communications in Statistics - Simulation and Computation* 11 (3), 311–334.
- McKay, M. D., Beckman, R. J., Conover, W. J., 1979. Comparison of Three Methods for Selecting Values of Input Variables in the Analysis of Output from a Computer Code. *Technometrics* 21 (2), 239–245.
- Mears, L., Stocks, S. M., Albaek, M. O., Sin, G., Gernaey, K. V., 2017. Mechanistic Fermentation Models for Process Design, Monitoring, and Control. *Trends in Biotechnology* 35 (10), 914–924.
- Musvoto, E., Wentzel, M., Loewenthal, R., Ekama, G., 2000. Integrated Chemical-Physical Processes Modelling - I. Development of a Kinetic-Based Model for Mixed Weak Acid/Base Systems. *Water Research* 34 (6), 1857–1867.
- Peng, R. Y., Yang, T. C. K., Wang, H.-e., Lin, Y.-c., Cheng, C., 1997. Modelling of Lactic Acid Fermentation - An Improvement of Leudeking's Model. *Journal of the Chinese Agricultural Chemical Society* 35 (5), 485–494.
- Schepers, W. A., Thibault, J., Lacroix, C., 2002. *Lactobacillus helveticus* growth and lactic acid production during pH-controlled batch cultures in whey permeate/yeast extract medium. Part II: kinetic modeling and model validation. *Enzyme and Microbial Technology* 30, 187–194.
- Sin, G., Gernaey, K. V., Neumann, M. B., van Loosdrecht, M. C. M., Gujer, W., 2009. Uncertainty analysis in WWTP model applications: A critical discussion using an example from design. *Water Research* 43 (11), 2894–2906.
- Spann, R., Roca, C., Kold, D., Eliasson Lantz, A., Gernaey, K. V., Sin, G., 2017. A Consistent Methodology Based Parameter Estimation for a Lactic Acid Bacteria Fermentation Model. In: España, A., Graells, M., Puigjaner, L. (Eds.), *Proceedings of the 27th European Symposium on Computer Aided Process Engineering - ESCAPE 27*. Elsevier, p. 3042.

A Global State Feedback Linearization and Decoupling MPC of a MIMO Continuous MSMMPR Cooling Crystallization Process

Ravi Parekh,^a Brahim Benyahia,^{a*} Chris D. Rielly^a,

^a*Loughborough University, Loughborough, Leicestershire, LE11 3TU, UK*

b.benyahia@lboro.ac.uk

Abstract

Continuous manufacturing of pharmaceuticals requires effective control strategies to meet the tightly regulated critical product quality attributes, which has triggered a wide interest in model predictive control (MPC) techniques. This study applies a linear form of MPC to a nonlinear seeded continuous MSMMPR crystallization process of acetaminophen in water, by using a global linearization technique; input-output state-feedback linearization (SFL). The two novelties are the application of MPC with SFL to continuous crystallization for SISO and MIMO systems; and the handling of the constraints as part of the SFL framework. For a single-input single-output system (SISO), MPC with SFL is applied to achieve a supersaturation reference trajectory by manipulating the coolant temperature subject to bounds and constraints. Additionally a multiple-input multiple-output (MIMO) case is presented using MPC with SFL and decoupling (SFLD). The supersaturation control from SISO was implemented in conjunction with crystal mean size control by manipulating the seed loading rate within bounds. The SISO configuration managed to control the crystallization process to within 1% of a prescribed set-point value within 2 residence times. In contrast, the MIMO controller was only able to stay within 4% of the set-point after 10 residence times, likely due to the highly coupled effects of the inputs on the outputs, which are lost in part due to the SFLD.

1. Introduction

The pharmaceutical industry is currently facing the challenges of transforming traditional batch production methods to robust continuous manufacturing processes, which can reduce manufacturing costs and time, whilst producing more consistent product (Mascia et al., 2013, Benyahia, 2018). Alongside this paradigm shift, the pharmaceutical industry is increasingly seeking advanced optimization and control strategies to meet tight regulatory requirements (Lakerveld et al., 2015). One tool that can effectively achieve these objectives is model predictive control (MPC): a powerful model-based optimization and control technique that has been used across many industrial sectors. Many pharmaceutical processes are complex with nonlinear dynamics and exhibit a highly coupled multiple-input multiple-output (MIMO) structure, one notable example being crystallization, making it a good candidate to demonstrate MPC capabilities (Lakerveld et al., 2013, Benyahia et al., 2012).

Nonlinear control techniques, such as nonlinear MPC (NMPC), have emerged to control nonlinear processes, such as polymerisation. Examples of the implementation of the NMPC on crystallization were also reported more recently. Nagy (2009) implemented

NMPC onto a batch crystallizer to control the crystal size distribution and Damour et al (2010) presented the implementation of NMPC on an industrial crystallizer using an artificial neural network model. Despite this relative success, NMPC is not as computationally efficient as linear MPC. The developed of robust control of nonlinear systems with MPC is one area still in need of further exploration and one particular technique of interest is input-output state-feedback linearization (SFL), a subset of global linearization.

The pairing of MPC with SFL can be used for single-input single-output (SISO) systems and has been applied to batch crystallization for supersaturation control (Jansen, 2011), but without implementation of realistic bounds or constraints on the manipulated input (coolant temperature). One potential constraints application for SFL is introduced by Schnelle and Eberhard (2015) for trajectory tracking of a multibody system, and should be suitable for crystallization control. Additionally, MIMO MPC is a desirable control configuration and can be achieved using SFL with decoupling (SFLD). Few applications of MPC with SFLD have been reported in the open literature; Chang and Chen (2015) applied the approach to a proton exchange membrane fuel cells. In crystallization control, Hernandez et al (2012) implemented nonlinear MIMO control onto continuous cooling crystallization using SFLD but with a proportional-integral-derivative (PID) controller. The most notable contribution on constraint handling for SFLD is by Deng et al (2009) using a dynamic neural network to handle constraints, but this would be too computationally expensive for controlling a crystallization process in real-time. Therefore a combination of approaches is needed to demonstrate the effectiveness of constrained MPC with SFL/SFLD for crystallization.

This paper discusses the application of bounded and constrained MPC with SFL to a continuous MSMPR crystallization simulation for SISO control of: supersaturation by manipulating the cooling jacket temperature; and number averaged mean crystal size by manipulating the seed loading. Moreover, the MIMO control of the above system is also demonstrated with bounds and constraints using MPC with SFLD, to establish if this control technique is adequate for MIMO control of a continuous crystallization process.

2. Model and Control Method

2.1. Crystallization Model

Cooling crystallization processes operate by cooling a solution with a dissolved solute into an unstable region where there is a driving force for the solute to crystallize out of solution by nucleation, or growth on existing crystals suspended in the mixture. Crystals may also be fed into the crystallizer as a seed to promote growth and suppress nucleation. To capture these kinetics and associated properties, the crystallizer model equations include the population (Eqs. 1 & 2), mass (Eq. 3) and energy balances (Eq. 4), the system-specific crystallization kinetics (Eqs. 5 & 6) and thermodynamic solubility. The population balance equation is simplified to only include nucleation and size independent growth kinetics, and subsequently can be solved using the method of moments. The mass balance is in terms of the concentration of solute dissolved in solvent, the kinetic equations for nucleation and growth are power laws, and solubility is a second order polynomial with respect to solution temperature.

$$\frac{d\mu_0}{dt} = B + \frac{F_{in}}{V} \mu_{0,in} M - \frac{F_{out}}{V} \mu_0 \quad (1)$$

$$\frac{d\mu_i}{dt} = iG\mu_{(i-1)} + \frac{F_{in}}{V} \mu_{i,in} M - \frac{F_{out}}{V} \mu_i \quad i = 1, \dots, 3 \quad (2)$$

$$\frac{dC}{dt} = -k_v \rho_c 3G\mu_2 + \frac{F_{in}}{V} C_{in} - \frac{F_{out}}{V} C \quad (3)$$

$$\frac{dT}{dt} = -\frac{UA_c(T - T_c)}{\rho V c_p} + \frac{F_{in}}{V} T_{in} - \frac{F_{out}}{V} T \quad (4)$$

$$B = k_b (C - C^*)^b \mu_2 \quad (5)$$

$$G = k_g (C - C^*)^g \quad (6)$$

Here, k_b and b are empirically derived nucleation kinetic parameters, and similarly k_g and g are growth parameters. F_{in} and F_{out} are the volumetric flow in and out respectively, V is the volume, μ_i is the i^{th} moment and $\mu_{i,in}$ are the i^{th} moments of the seed distribution. The shape factor of crystals and crystal density are k_v and ρ_c respectively, the overall heat transfer coefficient is U , the area of heat transfer is A_c and the density and specific heat capacity of the coolant fluid are ρ and c_p respectively. The two inputs (i.e. manipulated variables) are the temperature of the coolant T_c and the seed loading multiplier M .

2.2. Model Predictive Control with State Feedback Linearization

The model predictive control framework for a SISO MPC with SFL is shown in figure 1. There is an input u into the crystallizer and a measured output y . The output is passed to a predictor model in the MPC; this also receives a set of transformed inputs from the optimizer in the MPC \hat{v} to determine the future output trajectory \hat{y} . The trajectory is compared to a set-point or reference trajectory y_{ref} and the vector of errors e is passed into a constrained optimization problem for minimization. Once the optimal transformed inputs are found, the input and output horizons are calculated and the first transformed input v from the vector \hat{v} is passed into the control law, with the current process states from the crystallizer, to find the next input u to the process. The MIMO case is an extension of the SISO framework where there are 2 inputs and 2 outputs for the simulated crystallizer and 2 reference trajectories whose tracking problems are described by a single optimizer, and the control law replaced with a decoupling matrix.

The control law for the SISO system is shown in equation 7 (Jansen, 2011). The decoupling matrix for the MIMO case is shown in equation 8 and the SFLD control law in equation 9 (Deng et al, 2009). The decoupling matrix must be square and non-singular (invertible) to determine feasible control laws (equation 9).

The SISO supersaturation control case has a set-point of 0.006 g/g where a bounded coolant temperature (between 273 K and 340 K) and constrained to change no more than 2 K min^{-1} , is used a manipulated variable. The seed moments are calculated for a seed loading of 0.5 g L^{-1} and $10 \text{ }\mu\text{m}$ seed size along with a seed loading multiplier of $M = 1$. With a residence time of 15 minutes, the ideal case for SISO is to start-up the MSMPR and reach steady state, at which point the supersaturation will be within 1% of the set-point, in a short time. The MIMO case is an extension of SISO where there is

also a targeted set-point that consists in achieving a crystal size of 20 μm at steady state using the seed loading multiplier as a manipulated variable, bounded between 0.25 and 2. Similar performance criteria to the SISO case were used in the MIMO case.

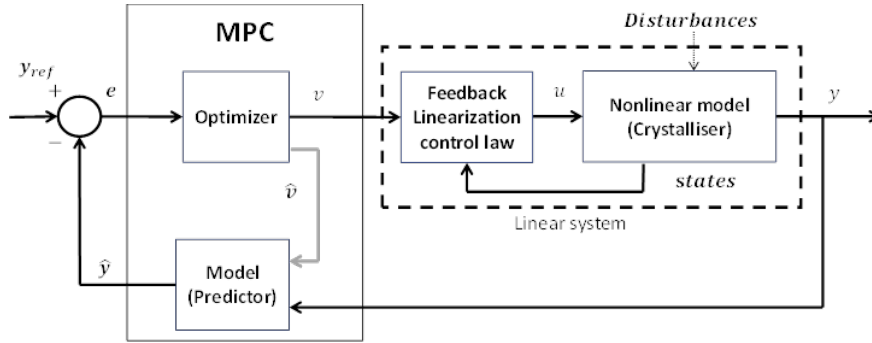


Figure 1 – Model Predictive Control with State Feedback Linearization

$$u = \frac{v - \sum_{k=0}^{r-1} \beta_k L_f^k y}{\beta_r L_g L_f^{r-1} y} \quad \begin{cases} L_g L_f^k y = 0 & k = 0, \dots, r-2 \\ L_g L_f^{r-1} y \neq 0 \end{cases} \quad (7)$$

$$E = \begin{bmatrix} \beta_{1,r_1} L_{g_1} L_f^{r_1-1} y_1 & \dots & \beta_{1,r_1} L_{g_n} L_f^{r_1-1} y_1 \\ \vdots & \ddots & \vdots \\ \beta_{n,r_n} L_{g_1} L_f^{r_n-1} y_n & \dots & \beta_{n,r_n} L_{g_n} L_f^{r_n-1} y_n \end{bmatrix} \quad \text{where } L_g \text{ and } L_f \text{ are Lie derivatives} \quad (8)$$

$$u = -E^{-1} \begin{pmatrix} \sum_{k=0}^{r_1} \beta_{1,k} L_f^k x_1 \\ \vdots \\ \sum_{k=0}^{r_n} \beta_{n,k} L_f^k x_n \end{pmatrix} + E^{-1} v \quad (9)$$

3. Results and Discussion

3.1. SISO MPC with SFL

The SISO MPC with SFL results for supersaturation control by manipulating the coolant temperature of the crystallizer is shown in figure 2. The top graph is the output and at the bottom is the input. The supersaturation was within 1% of the target of 0.006 g/g within 2 residence times during start-up and maintained throughout, meanwhile all the input changes are feasible. The coolant and solution temperatures are changing over 10 residence times though, indicating a slow progress to steady state. Despite that, it is clear from these results that the input is capable of controlling this crystallizer to steady state without violating the bounds or constraints. This demonstrates a working MPC controller with SFL for this SISO configuration; another set of results has also been obtained for a second SISO configuration to control the crystal mean size to a target

size, by allowing the seed loading multiplier to change within bounds, with a fixed coolant temperature, and the results will be published in detail in an extended version of this article.

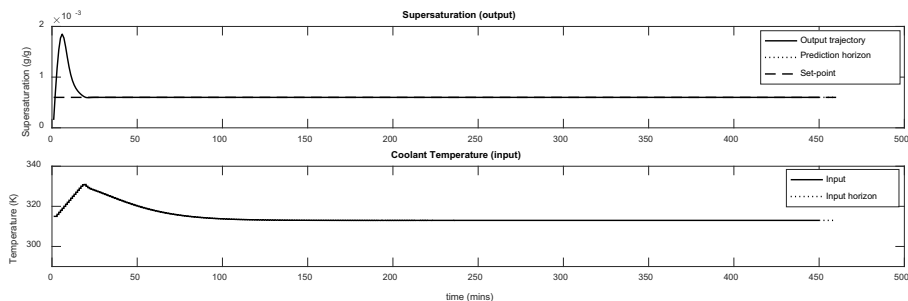


Figure 2 – SISO MPC with SFL for supersaturation control

3.2. MIMO MPC with SFLD

The two SISO results are used independently to validate that this method of constraint handling does indeed work for MPC with SFL and further to inform some set points or trajectories for the MIMO case. The latter is important because of the coupled dynamics; the seed loading will be used to control the crystal mean size but will also affect the supersaturation consumption; similarly, the temperature of the coolant is used to control the supersaturation, but also affects the mean crystal size.

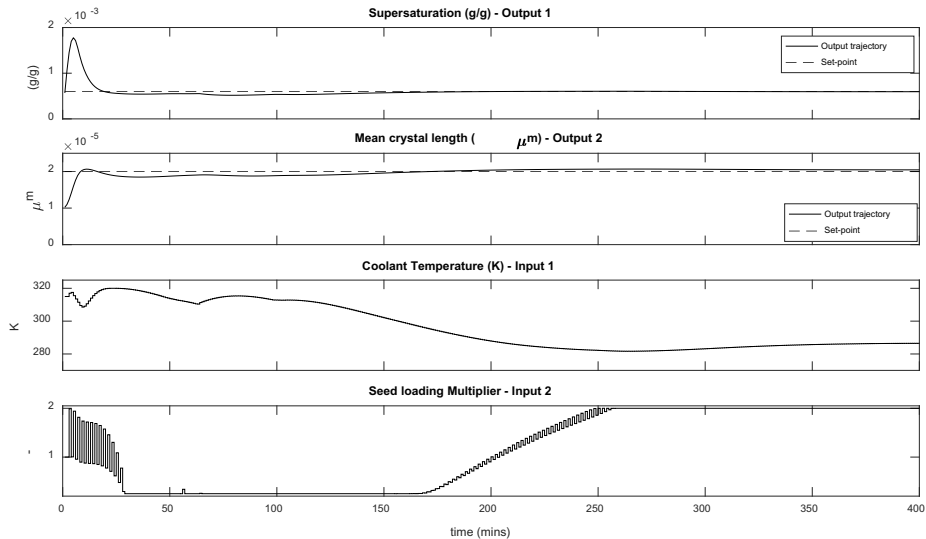


Figure 3 – MIMO MPC with SFLD for supersaturation and mean-size control

The results of the MIMO MPC with SFLD are shown in figure 3 where the top two graphs are the outputs (supersaturation and crystal mean size), with their respective inputs being the bottom two graphs. Both output set-points are met while the inputs are feasible. However, the outputs are only within 15% of the set-points at 5 residence times, and within 4% after 10. The settling time is larger than the one observed with the SISO approach too, which is likely due to the simultaneous coupled effects of seed

loading and coolant temperature. Although these are drawbacks, the results sufficiently demonstrate that the crystallization process can be controlled using this constrained MIMO MPC with SFLD, but not as effectively as SISO.

4. Conclusions

A SISO MPC with SFL and constraints has been applied to supersaturation control of a continuous crystallizer and the coolant temperature input changes did not violated their bounds and constraints. A MIMO MPC with SFLD was also developed and applied to the crystallizer but was not as effective as SISO, with longer time to steady state and 3% further away from the set-point, likely due to the decoupling procedure. However, the MIMO system did not violate constraints and did demonstrate a steady convergence towards the set-points, so is suitable as a controller for crystallization.

References

- B. Benyahia, 2018, Applications of a plant-wide dynamic model of an integrated continuous pharmaceutical plant: Design of the recycle in the case of multiple impurities. In Process Systems Engineering for Pharmaceutical Manufacturing: From Product Design to Enterprise-Wide Decisions. In Singh, R and Yuan, Z (ed) Process Systems Engineering for Pharmaceutical Manufacturing: From Product Design to Enterprise-Wide Decisions, Elsevier, (In press)
- B. Benyahia, R. Lakerveld, P. I. Barton, 2012, A Plant-wide Dynamic Model of a Continuous Pharmaceutical Process, *Industrial and Engineering Chemical Research*, 51, 15393-15412
- L. Y. Chang, H. C. Chen, 2014, Linearization and Input-Output Decoupling for Nonlinear Control of Proton Exchange Membrane Fuel Cells, *Energies*, 7, 591-606
- C. Damour, M. Benne, B. Grondin-Perez, J. P. Chabriat, 2010, Nonlinear predictive control based on artificial neural network model for industrial crystallization, *Journal of Food Engineering*, 99, 225-231
- J. Deng, V. M. Becerra, R. Stobart, 2009, Input Constraints Handling in an MPC/Feedback Linearization Scheme, *Int. J. Appl. Math. Comput. Sci.*, 19, 219-232
- P. A. Q. Hernandez, R. O. Perez, S. T. Avila, S. H. Castro, 2012, Nonlinear MIMO Control of a Continuous Cooling Crystallizer, *Modelling and Simulation in Engineering*, 2012.
- P. N. J. M. Jansen, 2011, State Feedback Linearization of a seeded batch cooling crystallizer for supersaturation control, *IEEE*
- R. Lakerveld, B. Benyahia, P. L. Heider, H. Zhang, A. Wolfe, C. Testa, S. Ogden, D. R. Hersey, S. Mascia, J. M. B. Evans, R. D. Braatz, P. I. Barton, 2015, The Application of an Automated Control Strategy for an Integrated Continuous Pharmaceutical Pilot Plant, *Organic Process Research & Development*, 19, 1088-1100
- S. Mascia, P. L. Heider, H. Zhang, R. Lakerveld, B. Benyahia, P. I. Barton, R. D. Braatz, C. L. Clooney, J. M. Evans, T. F. Jamison, K. F. Jensen, A. S. Myserson, B. L. Trout, 2013, End-to-end continuous manufacturing of pharmaceuticals: integrated synthesis, purification, and final dosage formation, *Angewandte Chemie International Edition*, 52, 12359-12363
- Z. K. Nagy, 2009, Model based robust control approach for batch crystallization product design, *Computers and Chemical Engineering*, 33, 1685-1691
- F. Schnelle, P. Eberhard, 2015, Constraints mapping in a feedback linearization/MPC scheme for trajectory tracking of underactuated multibody systems, *IFAC*, 48, 446-451

Models for Designing Hydrogen Peroxide Decontamination Processes in Sterile Drug Product Manufacturing

Keisho Yabuta,^a Haruka Futamura,^b Koji Kawasaki,^c Masahiko Hirao,^a
Hirokazu Sugiyama^{a,*}

^a*Department of Chemical System Engineering, The University of Tokyo, 7-3-1, Hongo, Bunkyo-ku, 113-8656, Tokyo, Japan*

^b*Technical Research Center, Airex Co., Ltd., 3-139, Asayama, Tokai-shi, 476-0006, Aichi, Japan*

^c*President, Airex Co., Ltd., Airex Co., Ltd., 14-13, Tsubaki-cho, Nakamura-ku, Nagoya-shi, 453-0015, Aichi, Japan*

sugiyama@chemsys.t.u-tokyo.ac.jp

Abstract

We developed models for designing rapid and effective H₂O₂ decontamination processes in the manufacturing of sterile drug products such as injectables. Decontamination is a critical change over process to establish proper environment, e.g., isolator, for sterile filling, with a trade-off between the level of sterility assurance and the hours of time required. Our model defines these performances as the objective functions, and H₂O₂ injection profile and initial humidity in the isolator as the design variables. Using statistical methods, a set of models was developed and validated, where experiments with an industrial-scale isolator provided necessary data. The models were applied in a case study where Pareto-optimal conditions could be indicated given the target concentration of H₂O₂ in the isolator. The study revealed that around 10% of the process time could be reduced at most, without compromising the sterility assurance, which is significantly relevant to the productivity of drug manufacturing.

Keywords: multiobjective design, statistical modeling, drug product manufacturing, biopharmaceuticals, change-over

1. Introduction

Sterile drug products such as injectables of biopharmaceuticals are filled into vials in isolators or in clean rooms, where the environment must be sterile. Decontamination is a critical change over process to irreversibly deactivate, namely kill, microorganisms in the isolator, before a batch operation of filling can start. As a disinfection agent, hydrogen peroxide (H₂O₂) is used typically in the industry. The process consists of two steps: (a) sterilization by injecting H₂O₂ into the air of the isolator, and (b) aeration by ventilating the inside air for decreasing H₂O₂ concentration to a target, e.g., 0.5 ppm. One of the key issues is the time intensity; for example the entire process takes up to ten hours while the filling of injectables takes a couple of hours. This time-intensive process is, and will be more critical for the productivity due to the trend of small scale production along with the introduction of personalized medicine. However, realization

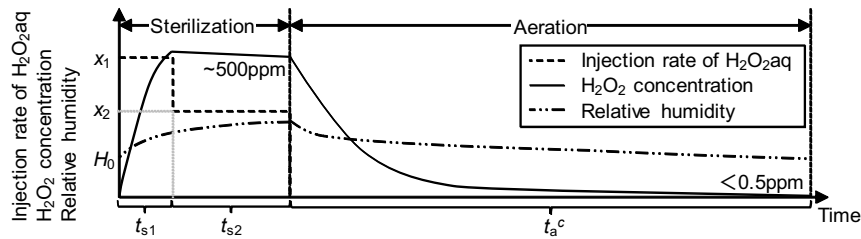


Figure 1. Injection profile and measured profile of decontamination process

of rapid decontamination processes is not simple because sterility assurance and speedy completion of the process are competing objectives.

In the literature, some authors tackled this relevant but complex process. Unger-Bimczok et al. (2008) identified H₂O₂ concentration and humidity as important parameters; Radl et al. (2009, 2011) developed models for analyzing physical behavior of H₂O₂. Wang et al. (2014) showed that the residual H₂O₂ after aeration may oxidize products during storage; Hubbard and Eppler (2015) investigated the uptake of H₂O₂ into a product for understanding the oxidation effect. Our group proposed the decision-support model for shortening the time required by the decontamination process (Sugiyama et al., 2017). However, design of decontamination processes requires incorporation of various aspects such as quality, productivity, or safety, which need to be incorporated into decision-making. In this study, we present a set of process models which can be applied to the multiobjective design of decontamination processes considering rapidity and sterility.

2. Model development

2.1. Overview

The design variables were defined as injection rate x [g/min] and injection time t [min] of H₂O₂(aq), and initial relative humidity H_0 [%] in the isolator. Figure 1 shows typical profiles of H₂O₂(aq) injection, and measured H₂O₂ concentration and humidity. In sterilization, H₂O₂(aq) is injected into the isolator at rates of x_1 and x_2 during the time t_{s1} and t_{s2} , respectively. In aeration, H₂O₂ concentration, which is around 500 ppm at the beginning, is decreased until the target concentration such as 0.5 ppm by ventilating the air inside the isolator.

As the objective functions, sterility assurance level (SAL; PIC/S, 2011) and process time were considered. SAL is an industrially known indicator that represents the probability of a microorganism to be present in the product, and thus the degree of sterility assurance of an operation. SAL is defined as Eq.(1):

$$SAL = 10^{-n} \quad (1)$$

where n is an index number. A larger value of n means that the operation ensures a higher level of sterility. Process time t_{total}^c is defined as Eq.(2):

$$t_{total}^c = t_{s1} + t_{s2} + t_a^c \quad (2)$$

where t_a^c is aeration time for decreasing H₂O₂ concentration to target value c .

For mathematically connecting the design variables to the objective functions, intermediate indicators D-value [min] (ISO, 2006) and the amount of H₂O₂aq loaded per unit volume of an isolator, Q [g/m³], were considered. D-value is the time duration required for killing 90 % of the surviving microorganisms, i.e., small D-value means high disinfection efficacy. Generally, D-value is calculated according to an industrially established procedure using biological indicator (BI), a microbiological sampler that contains a predetermined number of microorganisms. Using D-value Eq. (1) can be transcribed as Eq.(3):

$$SAL = 10^{6 - \frac{t_{s1} + t_{s2}}{D}} \tag{3}$$

where the constant six is the standard value in the evaluation of SAL. The parameter Q can be calculated using Eq.(4):

$$Q = \frac{x_1 t_{s1} + x_2 t_{s2}}{V_{iso}} \tag{4}$$

where V_{iso} [m³] is volume of the isolator, and Q was reported as the important parameter for the process (Sigwarth and Moirandat, 2000). Among these parameters, there are two relationships that need to be quantified: (i) between design variables and D-value, and (ii) between design variables and aeration time. In order to describe these relationships as model equations, experiments were conducted using a typical industrial-scale isolator.

2.2. Experiment

Figure 2 shows the isolator used in experiments (Airex Co., Ltd.) which has the volume of 2.4 m³ as V_{iso} , and four gloves for intervention and tank and evaporator of H₂O₂aq (omitted in the figure). Inside of this isolator was almost empty: only a metallic mesh and measurement instruments were present, and the isolator did not have any manufacturing equipment such as filling machine. For the sake of simplicity, H₂O₂ concentration, relative humidity, and temperature were considered homogeneous inside the isolator. The injection technology of H₂O₂ is an Airex system, which generates

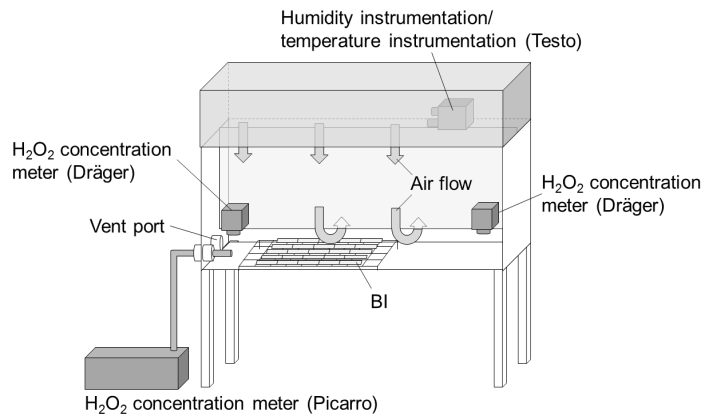


Figure 2. Isolator used in experiments

condensate of H₂O₂ and H₂O during sterilization. The measurement instruments used in the experiments were three H₂O₂ concentration meters (Dräger and Picarro), and instrumentation for humidity and temperature (Testo). The air inside the isolator was circulated from the start of the process until the middle of aeration, and was ventilated afterwards for aeration. Several sets of BIs (Mesa Labs), which were placed on the metallic mesh, were periodically taken out from the isolator through a vent port set-by-set. Each set of the BIs was then separately cultivated to determine the D-value. In the experiments, H₂O₂aq of 35 wt% (Wako Pure Chemical Industries), and liquid cultivation media (Atect) were used.

Among the design variables, x_1 , x_2 , t_{s2} , and H_0 were varied in the experiment. The parameter t_{s1} was kept constant in order to describe the dependence of D-value on x_1 , which was considered the most critical for disinfection. The entire decontamination process was performed 31 times. D-value was calculated from the seven-day-cultivation result of the BIs according to the minimized Limited Spearman Karber Method (LSKM) (Sigwarth and Moirandat, 2000). The parameter t_a^c was determined as the time point when the H₂O₂ concentration went below the fixed target concentration c .

2.3. Model development and validation

The models for evaluating SAL and process time were developed based on the regression analysis from the experiment result. Among 31 data points, 26 data points were used for developing the models, and residual five data points were used for validating the models. If all of five data points were included inside the 95% prediction interval of the model equation, the model was judged as validated.

The D-value estimation model was developed as follows:

$$D = 3.7 - 0.72x_1 \quad (5)$$

which was then validated according to the criteria, and this equation can be used in the same range as the experimental condition. The units of the first and second coefficients on the right side are min and min²/g, respectively. R-squared was 0.885. As for the result of t_a^c , where c was set as 0.5 ppm, the developed model was as follows:

$$t_a^{0.5 \text{ ppm}} = 0.90 + 1.6Q + 0.37H_0 \quad (6)$$

This model equation was validated as well, and the valid range of this equation is same as Eq.(5). The units of the first, second, and third coefficients on the right side are min, m³min/g, and min, respectively. Figure 3 presents the result and model validation where all of the five data points for validation were included in the 95 % of prediction interval. R-squared was 0.742. Based on these models, the process time and SAL can be evaluated using Eq.(2) and Eq.(3), respectively.

3. Application of the model

As an application of the developed models, this paper presents the design of decontamination process for the isolator shown in Figure 2, with specifying c as 0.5

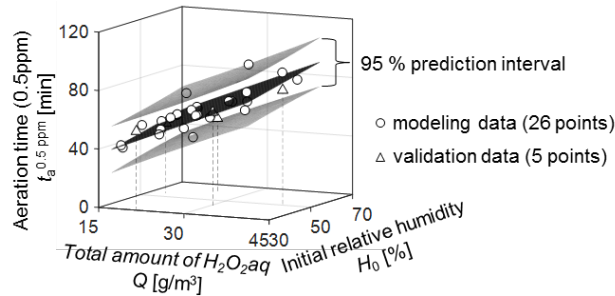


Figure 3. Result and model validation of aeration time

ppm. All parameters in the evaluation were same as the values and the ranges used in the experiments except for t_{s2} , which was considered modifiable in this investigation.

Figure 4 shows the evaluation result, and this contour plot is valid for the fixed t_{s1} and t_{s2} , which are constant values in this case. SAL was independent on the initial relative humidity H_0 because only injection rate x_1 was statistically relevant in estimating D-value. The condition which gave better SAL was larger x_1 , while the condition which gave shorter process time was smaller x_1 and smaller H_0 ; Pareto optimal conditions were described as the chain line. Figure 5 shows the multiobjective evaluation of the entire alternative conditions for decontamination covered in Figure 4. Evidently, the trade-off relationship between sterility assurance and process time was observed. From Figure 5, the alternatives on the left side line are Pareto optimal, the selection of which depends on the priority in the drug manufacturer. One extreme option was SAL of 10^{-7} and process time of 77 min (point A), and the other extreme option was 10^{-18} and 101 min (point B). At one SAL, process time has a range around 10 %, i.e., there is a possibility that maximum 10 % of process time can be shortened without sacrificing SAL.

For the actual development of the isolator, the results in Figure 5 can be used to determine initial but promising conditions before introducing various equipment inside. Further experiments are needed to decide the final conditions after installing equipment such as filling machine, however, the availability of good initial conditions would reduce try-and-errors, and thus accelerate the development. The results in Figure 5 can also be used for similar isolators like the one shown in Figure 2, which is industrially typical regarding volume and H_2O_2 evaporation system.

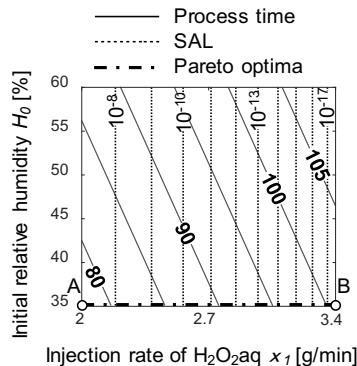


Figure 4. Evaluation result of Process time and SAL

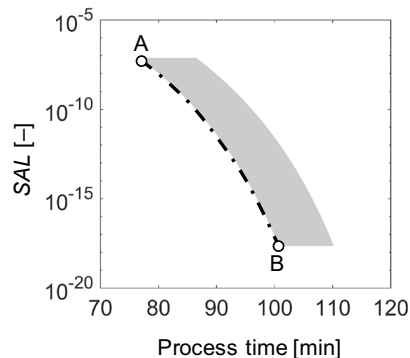


Figure 5. Multiobjective evaluation result

4. Conclusions and outlook

We presented a set of validated statistical models for designing rapid and effective H₂O₂ decontamination processes in sterile drug product manufacturing. The models can estimate SAL and process time, with the input information on injection rate and time of H₂O₂, and initial relative humidity inside the isolator. Experiments were performed using an industrial-scale isolator to obtain necessary data for model development as well as validation. The multiobjective evaluation result also indicated that around 10 % of process time can be reduced at most without sacrificing the SAL. For the actual isolator development, the obtained results can be used to determine initial but promising conditions, which can accelerate the development by reducing try-and-errors.

The future plan is to develop physical models for elucidating the relationship between physical phenomena such as condensation of H₂O₂ and the experiment results obtained in this study. The integration of physical and statistical models will enhance the application capability for various types of isolators and also clean rooms.

Acknowledgements

The authors would like to thank the experts from Airex Co., Ltd. for the contribution to the experiments and fruitful discussion. Financial supports by Grant-in-Aid for Young Scientists (A) No. 17H04964 from Japan Society for the Promotion of Science are also acknowledged.

References

- A. Hubbard, K. Eppler, 2015, Measuring hydrogen peroxide residuals and product exposure on isolator and rabs filling lines, *BioPharma Asia*, 4, 5, 26–33
- International Organization for Standardization (ISO), 2006, ISO 11138-1 Sterilization of health care products -- Biological indicators -- Part 1: General requirements
- Pharmaceutical Inspection Convention Pharmaceutical Inspection Co-Operation Scheme (PIC/S), 2011, Validation of aseptic processes, Available at: <https://www.picscheme.org/layout/document.php?id=153> (Accessed December. 7, 2017)
- S. Radl, S. Ortner, R. Sungkorn, J. G. Khinast, 2009, The engineering of hydrogen peroxide decontamination systems, *J. Pharm. Innov.*, 4, 2, 51–62
- S. Radl, S. Larisegger, D. Suzzi, J. G. Khinast, 2011, Quantifying absorption effects during hydrogen peroxide decontamination, *J. Pharm. Innov.*, 6, 4, 202–216
- V. Sigwarth, C. Moirandat, 2000, Development and quantification of H₂O₂ decontamination cycles, *PDA J. Pharm. Sci. Technol.*, 54, 4, 286–304
- H. Sugiyama, K. Matsunami, K. Yabuta, 2017, Process systems engineering approaches for drug product manufacturing: from tablets to injectables, *Comput. Aided Chem. Eng.*, 40, 2785–2790
- B. Unger-Bimczok, V. Kottke, C. Hertel, J. Rauschnabel, 2008, The influence of humidity, hydrogen peroxide concentration, and condensation on the inactivation of *geobacillus stearothermophilus* spores with hydrogen peroxide vapor, *J. Pharm. Innov.*, 3, 2, 123–133
- W. Wang, A. A. Ignatius, S. V. Thakkar, 2014, Impact of residual impurities and contaminants on protein stability, *J. Pharm. Sci.*, 103, 5, 1315–1330

Multi-flowrate Optimization of the Loading Phase of a Preparative Chromatographic Separation

Anton Sellberg, Mikael Nolin, Anton Löfgren, Niklas Andersson and Bernt Nilsson*

*Department of Chemical Engineering, Lund University, P.O. Box 124, SE-221 00 Lund, Sweden
bernt.nilsson@chemeng.lth.se*

Abstract

This contribution consists of a multi-flow rate optimization method to maximize the key performance indicators, yield, degree of resin utilization and productivity for a chromatographic loading step. The protein adsorption to the resin is modeled using a mechanistic column model with a steric mass action adsorption isotherm. The model was used to optimize the flow rate trajectories and the loading duration by using a simultaneous method where the controls and state variables were discretized using a direct and local collocation method on finite elements in the temporal dimension and a finite volume weighted essentially non-oscillatory scheme in the spatial dimension. The discretized nonlinear program was solved using an interior point method. The two and three dimensional pareto fronts for the multi-objective optimization are presented and the multi-flow rate strategy showed considerable improvement in all objectives at different points on the pareto front.

Keywords: Modelling, Optimization, Collocation, Protein, Chromatography

1. Introduction

Purification of proteins typically consists of a clarification step, a chromatographic capture step and one or several additional orthogonal chromatography steps. This contribution is concerned with the loading of the chromatography columns and mainly the loading of the capture step. Since the capacity of chromatographic resins are low, resin utilization is of great importance. Resin utilization is especially important in the capture step since the capture step receives the highest amount of product protein and makes use of expensive resin, e.g. protein A or mixed-mode resins. In addition to resin utilization, product yield and production rate needs to be taken into account when optimizing the loading phase. To increase the resin utilization and product yield several design and control approaches have been suggested. Capture-SMB (Angarita et al., 2015) and periodic counter current chromatography, which uses two and three columns in sequence to fully load one of the columns while collecting the product breakthrough on the following column. Both of these approaches have the drawback of needing extra columns and equipment as well as a flow rate limitations due to the increased pressure drop over the interconnected columns. Another approach has been to use dual-flowrate loading strategies on a single column to maximize the dynamic binding capacity and productivity. This approach does not need any extra equipment or columns and still outperforms single loading strategies (Ghose et al., 2004).

The aim of this study is to expand the dual-flowrate strategy to include any number of flowrates during the loading. This is achieved by mechanistic modeling of the process and discretization of the temporal domain while keeping a constant flowrate in each time horizon, i.e. piecewise constant controls. Yield, production rate and degree of resin utilization are identified as key process indicators (KPIs) which are weighed together to form a scalar objective. This approach results in

a large-scale dynamic optimization problem constrained by partial differential algebraic equations which is solved for both single and multiple flowrates and variable loading time. A case study where a 4 g/L lysozyme solution is loaded on a 1 ml prepacked Sepharose SP Fast Flow column is presented to show the advantages of the multi-flow rate strategy compared to the single flow rate strategy.

2. Chromatography Model

The Transport-Dispersive Model (Schmidt-Traub et al., 2006) was used to model the breakthrough curves of protein during column loading. The model equations, Eq. 1 and 2, are defined over the spatial, $z \in [z_0, z_f]$ and temporal, $t \in [t_0, t_f]$ domain. The mass-balance over the mobile and stationary phase is governed by:

$$\frac{\partial c_\alpha}{\partial t} = \frac{\partial}{\partial z} \left(D_{\text{ax}} \frac{\partial c_\alpha}{\partial z} - \frac{\dot{Q}}{\varepsilon_t A_c} c_\alpha \right) - \frac{1 - \varepsilon_c}{\varepsilon_t} \frac{\partial q_\alpha}{\partial t}, \quad \alpha \in \{\text{lys}, s\} \quad (1)$$

$$\frac{\partial q_\alpha}{\partial t} = \begin{cases} -k_{\text{film}}(q_\alpha - q_\alpha^*) & \text{for } \alpha = \text{lys} \\ -\nu \frac{\partial q_{\text{lys}}}{\partial t} & \text{for } \alpha = s \end{cases} \quad (2)$$

where c_α is the concentration of component α in the mobile phase, t is time, z is the spatial coordinate, D_{ax} is the axial dispersion, \dot{Q} is the volumetric flow rate, ε_t is the total void, ε_c is the column void, A_c is the column cross section area, k_{film} is the film mass transfer parameter, q_α is the concentration of component α in the stationary phase, ν is the characteristic charge of lysozyme and q_α^* is the adsorbed concentration of component α at equilibrium with the mobile phase, which is governed by the steric mass action isotherm (Brooks and Cramer, 1992):

$$0 = c_\alpha - \frac{1}{K_M} \frac{q_\alpha^* c_s^\nu}{\left(\Lambda - (\sigma + \nu) q_\alpha^* \right)^\nu} \quad (3)$$

where K_M is the equilibrium constant, Λ is the total ion exchange capacity and σ is the steric shielding parameter. The SMA isotherm was then reparametrized according to:

$$K_{\text{eq}} = K_M \Lambda^\nu, \quad q_{\text{max}} = \Lambda (\sigma + \nu)^{-1} \quad (4)$$

where K_{eq} is the new equilibrium constant for adsorption and desorption of lysozyme and q_{max} is the maximum concentration for adsorbed lysozyme. The total film mass transfer resistance is the sum of the inner and outer film resistance. The total film mass transfer parameter, the inner film transfer parameter (k_s) and the outer film transfer parameter (k_o) depends on the stationary phase saturation and flow rate according to (Steinebach et al., 2016):

$$k_{\text{film}} = \left(\frac{1}{k_s} + \frac{1}{k_o} \right)^{-1}, \quad k_s = k'_s \frac{(1 - \Gamma)^{1/3}}{1 - (1 - \Gamma)^{1/3}}, \quad k_o = k'_o \left(\frac{\dot{Q}}{A_c \varepsilon_c} \right)^{1/3} \quad (5)$$

where k'_s is the inner film mass transfer resistance parameter, Γ is the saturation level of the stationary phase, i.e. $\Gamma = q_\alpha / q_{\text{max}}$ for rectangular isotherms and k'_o is the outer film mass transfer resistance parameter. Danckwert boundary conditions are used for the column inlet and homoge-

neous von Neumann conditions are used at the column outlet:

$$D_{\text{ax}} \frac{\partial c_{\alpha}(t, z_0)}{\partial z} - \frac{\dot{Q}}{A_c \varepsilon_t} c_{\alpha}(t, z_0) = \frac{\dot{Q}}{A_c \varepsilon_t} c_{\text{load}, \alpha} \Pi(t, t_0, \Delta t_{\text{load}}) \quad (6)$$

$$D_{\text{ax}} \frac{\partial c_s(t, z_0)}{\partial z} - \frac{\dot{Q}}{A_c \varepsilon_t} c_s(t, z_0) = \frac{\dot{Q}}{A_c \varepsilon_t} c_{A, s} \quad (7)$$

$$\frac{\partial c_{\alpha}(t, z_f)}{\partial z} = 0 \quad (8)$$

$$\frac{\partial c_s(t, z_f)}{\partial z} = 0 \quad (9)$$

where $c_{\text{load}, \alpha}$ is the load concentration of component α , $\Pi(t, t_0, \Delta t_{\text{load}}) \in [0, 1]$ is a smooth rectangular function in the temporal horizon $[t_0, t_0 + \Delta t_{\text{load}}]$, Δt_{load} is the load time and $c_{A, s}$ is the salt concentration in the low salt buffer. At the start of each run the column only contains low salt buffer. The column void, ε_c , was 0.3 and the total void, ε_t , was 0.9. The isotherm and mass transfer coefficients are summarized in Table 1.

Table 1: Model parameters used to model the adsorption of lysozyme to the resin.

q_{max} [mol m ⁻³]	ν [-]	K_{eq} [(mol m ⁻³) ^{ν}]	k'_s [s ⁻¹]	k'_0 [m ^{-1/3} s ^{-2/3}]	Pe [-]
17.6	5.97	$3.40 \cdot 10^{14}$	$1.11 \cdot 10^{-13}$	$2.42 \cdot 10^{-2}$	0.50

3. Multi-Objective Dynamic Optimization Problem

To formulate the optimization problem, a well-defined objective function is needed. The basis of the objective functions is the three different key performance indicators (KPIs) for the process. The KPIs are weighed together to form the objective function. In this case yield, $Y(t)$, productivity, $P(t)$ and degree of stationary phase utilization, $U(t)$ are the KPIs of the process. The KPIs are defined as:

$$Y(t) = m_c(t) m_{\text{in}}(t)^{-1}, \quad (10)$$

$$P(t) = m_c(t) \left[\Delta t_{\text{load}} + \Delta t_w \right]^{-1}, \quad (11)$$

$$U(t) = m_c(t) \left((1 - \varepsilon_t) V_c q_{\text{max}} \right)^{-1} \quad (12)$$

where m_c is the amount of lysozyme adsorbed to the stationary phase, m_{in} is the amount of lysozyme loaded to the column, Δt_w is the time it takes to wash, clean and regenerate the column and V_c is the column volume. The amount of lysozyme adsorbed to the stationary phase and loaded is defined as:

$$\frac{dm_{\text{in}}(t)}{dt} = \Pi(t, t_0, \Delta t_{\text{load}}) \dot{Q}(t) c_{\text{feed}}, \quad (13)$$

$$\frac{dm_c(t)}{dt} = \Pi(t, t_0, \Delta t_{\text{load}}) \frac{1 - \varepsilon_c}{\varepsilon_t} A_c \int_{z_0}^{z_f} \frac{dq_{\text{lys}}}{dt} dz \quad (14)$$

The cost function for the optimization can then be expressed as:

$$- \left[\omega_Y \bar{Y}(t_f) + \omega_P \bar{P}(t_f) + \omega_U \bar{U}(t_f) \right] + R_Q \sum_{i=1}^{N_Q-1} \Delta \hat{Q}_i^2, \quad (15)$$

$$\sum_{i \in \{Y, P, U\}} \omega_i = 1 \quad (16)$$

where the bracketed term is the weighted normalized KPIs, the second term is penalizing the squared difference between two flow rates and R_Q is the penalizing weight. The penalizing term is added to make the resulting flow rate trajectory smoother and to avoid pressure spikes caused by a large step-wise change in flow rate. The complete multi-objective dynamic optimization problem can finally be formulated as:

$$\min. \quad - \left[\omega_Y \bar{Y}(t_f) + \omega_P \bar{P}(t_f) + \omega_U \bar{U}(t_f) \right] + R_Q \sum_{i=1}^{N_Q-1} \Delta \dot{Q}_i^2, \quad (17a)$$

$$\text{w.r.t. } \mathbf{x} : [t_0, t_f] \rightarrow \mathbb{R}^{N_x}, \quad \mathbf{y} : [t_0, t_f] \rightarrow \mathbb{R}^{N_y},$$

$$\mathbf{Q} \in \mathbb{R}^{N_Q}, \quad \Delta t_{\text{load}} \in \mathbb{R},$$

$$\text{s.t. } \mathbf{0} = \mathbf{F}(t, \dot{\mathbf{x}}(t), \mathbf{x}(t), \mathbf{y}(t), \dot{\mathbf{Q}}(t), \Delta t_{\text{load}}), \quad \mathbf{x}(t_0) = \mathbf{x}_0, \quad (17b)$$

$$\mathbf{g}_e(t, \dot{\mathbf{Q}}(t)) = 0, \quad (17c)$$

$$Q_L \leq \dot{Q}(t) \leq Q_U, \quad \Delta t_L \leq \Delta t_{\text{load}} \leq \Delta t_U, \quad (17d)$$

$$\forall t \in [t_0, t_f]$$

The optimization variables consist of the piecewise constant flow rates, \mathbf{Q} , the free manipulated variable, Δt_{load} , the state variables, $\mathbf{x} = (c_{\text{lys}}, q_{\text{lys}}, c_s, m_c, m_{\text{in}})$ and the algebraic variable $\mathbf{y} = q_{\text{lys}}^*$. The trajectories \mathbf{x} are determined by the PDAE in Eq. (17b), the equality constraint on \mathbf{Q} in each time horizon in Eq. (17c) and the bounds on \mathbf{Q} and Δt_{load} in Eq. (17d).

4. Modeling and Optimization Environment

The model presented in section 2 and the dynamic optimization problem presented in section 3 were implemented in the Modelica and Optimica languages. The open-source platform JModelica.org (Åkesson et al., 2010) was used for both simulation and optimization purposes. The spatial domain was discretized using 25 finite volumes and a weighted essentially non-oscillating (Shu, 1998) scheme with 3 sub-stencil was used to approximate the convective and diffusive flux.

For simulation purposes the model was compiled to a functional mock-up unit before being interfaced with CVode from the SUNDIALS solver suite (Hindmarsh et al., 2005). The backward differentiation formula and a relative and absolute tolerance of 10^{-10} was used to simulate the model. The multi-objective dynamic optimization problem presented in section 3 was solved using a direct and local collocation method with 150 finite elements. Each element contained two Radau points and the solution was estimated using Lagrange polynomials (Magnusson and Åkesson, 2015). The nonlinear program resulting from the collocation was solved using the the primal-dual interior point method IPOPT (Wächter and Biegler, 2006) and the linear solver MA57 from HSL (HSL, 2013). The automatic differentiation package, CasADi (Andersson, 2013), was used to compute the first- and second-order derivatives. The starting point of the optimization was obtained by simulating the flow rate trajectory with a constant control signal of 2 ml min^{-1} . The optimization was solved with a tolerance of 10^{-8} .

5. Results and Discussion

Two different cases were optimized to assess the performance of the suggested multflow rate loading strategy. The conventional single flow rate i.e. $N_Q = 1$ was used as a base case and a multflow rate strategy with $N_Q = 50$ was used to demonstrate the advantages with multflow rate loading. The resulting breakthrough curves and optimal flow rates for two different objective weight combinations can be seen in Figure 1. Subplot a) and c) has the objective weights, $\omega_P = 0.440$,

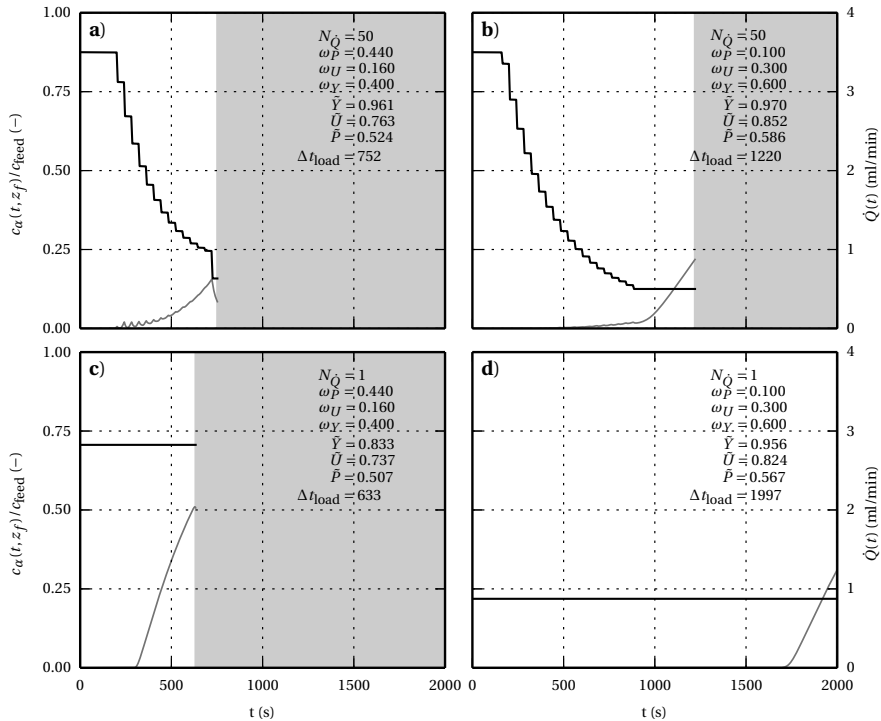


Figure 1: Optimal breakthrough trajectories for the column. The solid black step-function is the flow rates used to load the column, the solid gray line is the protein breakthrough at the column outlet and the gray area indicates the reduction in cycle time, i.e. $t_f - \Delta t_{load}$. The solution to the optimization problem using $N_Q = 50$ is shown in subplot a) and b). The solution to the optimization problem using $N_Q = 1$ is shown in subplot c) and d).

$\omega_U = 0.160$ and $\omega_Y = 0.400$, which results in comparable results with respect to utilization and productivity but the multi-flow rate strategy has a 15% increase in yield. Comparing the results in subplot b) and d), 1.5 – 3.4% lower results in all objectives can be observed for the single flow rate strategy while loading 777s (63.7%) longer than the multi-flow rate strategy. Thus if only a shorter loading time can be allowed, the results of the single flow rate strategy will decrease more than the results of the multi-flow rate strategy. Furthermore any time-saving improvements to the elution, cleaning and regeneration strategy i.e. lowering of Δt_w in Equation 11, will result in a higher relative improvement in production rate for the multi-flow rate strategy.

For each of the cases, a three-dimensional and three two-dimensional pareto fronts were sampled, presented in Figure 2. The complex trade-off between the three objective functions can be seen in the three-dimensional pareto plot. For combinations containing a high weight in yield the multi-flow rate strategy shows better performance in all objectives compared to the single flow rate strategy. This is due to the fact that for single flow rate loading having a large weight on yield means running the process at a low flow rate to avoid protein breakthrough. A constant low flow rate also means that only a small amount of protein will be loaded onto the column i.e. resin utilization and production rate will be low. For the multi-flow rate strategy the process can be run at high flow rates until breakthrough occurs and then gradually decrease the flow rate to maximize the amount of protein loaded while minimizing the breakthrough.

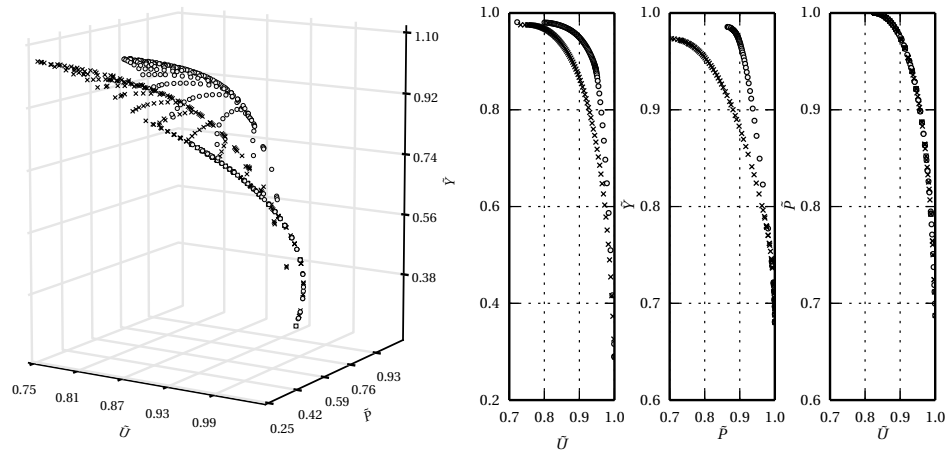


Figure 2: The multi-flow rate strategy is the o markers while the single flow rate strategy is x in all subplots. The result from the tri-objective optimization is presented in the leftmost sub-plot. The three two dimensional sub-plot show the pareto front with one objective fixed to zero.

6. Conclusions

The presented multi-flow rate approach outperforms the single flow-rate for most points on the three dimensional pareto front. The advantage is most pronounced for pareto solutions where no objective function has a weight of zero. However the multi-flow strategy still outperforms the single flow strategy for most weight combinations if $\omega_P = 0$ or $\omega_U = 0$. For $\omega_Y = 0$, the single and multi-flow rate strategies collapse to the same Pareto front because breakthrough of protein has no impact on the production rate and resin utilization, instead all the solutions uses the highest flow rate and only Δt_{load} varies between solutions.

References

- J. Åkesson, K.-E. Årzén, M. Gäfvert, T. Bergdahl, H. Tummescheit, 2010. Modeling and optimization with optimica and JModelica.org-Languages and tools for solving large-scale dynamic optimization problems. *Computers and Chemical Engineering* 34 (11), 1737–1749.
- J. Andersson, October 2013. A General-Purpose Software Framework for Dynamic Optimization. PhD thesis, Arenberg Doctoral School, KU Leuven, Department of Electrical Engineering (ESAT/SCD) and Optimization in Engineering Center, Kasteelpark Arenberg 10, 3001-Heverlee, Belgium.
- M. Angarita, T. Müller-Späh, D. Baur, R. Lievrouw, G. Lissens, M. Morbidelli, 2015. Twin-column CaptureSMB: a novel cyclic process for protein affinity chromatography. *Journal of Chromatography A* 1389, 85–95.
- C. A. Brooks, S. M. Cramer, 1992. Steric mass-action ion exchange: displacement profiles and induced salt gradients. *AIChE Journal* 38 (12), 1969–1978.
- S. Ghose, D. Nagrath, B. Hubbard, C. Brooks, S. M. Cramer, 2004. Use and optimization of a dual-flowrate loading strategy to maximize throughput in protein-affinity chromatography. *Biotechnology progress* 20 (3), 830–840.
- A. C. Hindmarsh, P. N. Brown, K. E. Grant, S. L. Lee, R. Serban, D. E. Shumaker, C. S. Woodward, 2005. SUNDIALS: suite of nonlinear and differential/algebraic equation solvers. *ACM Transactions on Mathematical Software* 31 (3), 363–396.
- HSL, 2013. A collection of fortran codes for large scale scientific computation. <http://www.hsl.rl.ac.uk/>.
- F. Magnusson, J. Åkesson, 2015. Dynamic optimization in JModelica.org. *Processes* 3 (2), 471–496.
- H. Schmidt-Traub, M. Schulte, A. Seidel-Morgenstern, 2006. Preparative chromatography: of fine chemicals and pharmaceutical agents. John Wiley & Sons.
- C.-W. Shu, 1998. Essentially non-oscillatory and weighted essentially non-oscillatory schemes for hyperbolic conservation laws. In: *Advanced numerical approximation of nonlinear hyperbolic equations*. Springer, pp. 325–432.
- F. Steinebach, M. Angarita, D. J. Karst, T. Müller-Späh, M. Morbidelli, 2016. Model based adaptive control of a continuous capture process for monoclonal antibodies production. *Journal of Chromatography A* 1444, 50–56.
- A. Wächter, L. T. Biegler, 2006. On the implementation of an interior-point filter line-search algorithm for large-scale nonlinear programming. *Mathematical Programming* 106 (1), 25–57.

Mathematical modelling of moisture migration in confectionery multicomponent food systems

Paschalia Mavrou,^a Rex Thorpe,^b William Frith,^c Guoping Lian,^{b,c} Tao Chen^{b*}

^a*Centre for Environment and Sustainability, University of Surrey, Guildford, GU2 7XH, United Kingdom*

^b*Department of Chemical and Process Engineering, University of Surrey, Guildford, GU2 7XH, United Kingdom*

^c*Unilever Research Colworth, Sharnbrook, MK44 1LQ, United Kingdom*

t.chen@surrey.ac.uk

Abstract

Moisture migration occurring during storage in multicomponent food systems is one of the most common problems facing the food manufacturing industry. An example for such a food system is a mass of ice cream in contact with a wafer. In this work, a dynamic moisture migration model for a confectionery food system consisting of a wafer separated by a moisture barrier from a high water activity component (e.g. ice cream) is developed. The 1D diffusion equation was solved for the barrier and wafer each having different transport properties. The developed model predicts the moisture content of the wafer in different locations throughout the product's shelf life.

Keywords: mathematical modelling, moisture migration, multicomponent food.

1. Introduction

Moisture migration in manufactured foods can significantly affect their quality, nutrition, sensory attributes and shelf life. It can occur between foods and the surrounding atmosphere or between different compartments of manufactured foods when they have different water activities. Changes in food attributed to moisture migration include softening, toughening, breakdown, swelling or shrinkage of the material (Roudaut and Debeaufort, 2011). Such changes can have a detrimental effect on the organoleptic properties of the food leading to consumer rejection.

Several studies can be found in published literature on moisture migration in food materials. However, in most moisture migration is usually coupled with a heat transfer process (e.g. baking, freezing). A smaller number of studies is focused on moisture migration in multicomponent food systems during storage at constant temperature. Hao et al. (2016) investigated moisture migration in a biscuit – hawthorn and a biscuit – agar gel system at 25°C. Guillard et al., (2003a) studied a two component food system of a sponge cake in contact with a fresh wet filling at 20°C. Gulati et al. (2015) studied moisture migration in a bread with a chicken filling sandwich during storage at 25°C.

In several food systems, an edible moisture barrier can be employed between two different water activity materials to minimise moisture transfer. An example for such a material is chocolate flavoured films which have been extensively used in the confectionery industry. Biquet and Labuza, (1988) conducted a study to experimentally

evaluate a semisweet dark chocolate film as a moisture barrier at 20°C. Guillard et al. (2003b) evaluated the barrier properties of various edible films at 20°C while Bourlieu et al., (2006) characterised nine lipid-based edible barrier films at the same temperature.

In this work a phenomenological model to predict dynamic moisture migration for a multicomponent food system has been developed using food material transport properties as inputs. Experimental data obtained at room temperature conditions are used to predict the moisture content in the different components in contact. Room temperature conditions are significantly higher than the temperature of interest for this application. However, this study aims to present the predictive capabilities of the model and serves as a starting point for further investigation.

2. Models and methods

The system used as a case study consists of a wafer cone internally coated with moisture barrier and it is filled with ice cream as seen in Figure 1. The product is usually packaged in a material considered mostly impermeable to moisture.

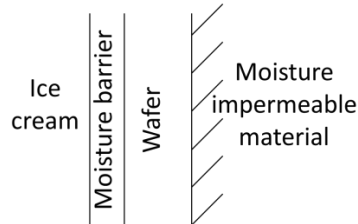


Figure 1: Different components of the investigated system

2.1. Moisture transfer

To simulate the moisture migration a 1D mass transfer equation is used (Guillard et al., 2003a). As the driving force for moisture migration is the water activity (α_w) gradient between the materials in contact, the mass transfer equation needs to be expressed in terms of α_w :

$$\frac{\partial X}{\partial t} + D_{eff} \frac{\partial^2 X}{\partial x^2} = \frac{\partial X}{\partial \alpha_w} \frac{\partial \alpha_w}{\partial t} + D_{eff} \frac{\partial}{\partial x} \left(\frac{\partial X}{\partial \alpha_w} \frac{\partial \alpha_w}{\partial x} \right) = 0 \quad (1)$$

where X (wt/wt) is the moisture content calculated on a wet base, D_{eff} (m^2/s) is the effective diffusivity, x (m) is the location and t (s) the time. Solving the above equation requires information specific to each material at the temperature of interest. These are the materials' D_{eff} and moisture sorption isotherms both usually obtained experimentally.

Equation (1) is a 2nd order partial differential equation and it is usually solved numerically. Different methods can be used as the finite element method (Hao et al. 2016) or finite differences (Guillard et al., 2003a).

2.2. Moisture sorption isotherms

Moisture sorption isotherms relate α_w to the corresponding material X . They are unique for each material and temperature and they are usually obtained gravimetrically. To obtain moisture absorption isotherms an initially dry sample is placed in environments of increasing α_w . For each α_w level, the weight of the sample is measured continuously until equilibrium is observed. In theory equilibrium is established when the weight of the sample remains constant over time. However, in practice the sample is considered at equilibrium when the change of weight over a predefined period of time is sufficiently small (Bourlieu et al., 2006).

2.3. Effective diffusivity

The sorption kinetics data obtained from the sorption experiments can be used to obtain the D_{eff} values assuming they are constant for each α_w step. The data can be fitted to an analytical solution of the mass transfer equation to obtain the D_{eff} . Fick's 2nd law can be solved analytically for a variety of common geometries such as infinite plane, cylinder and sphere. For a flat sample whose geometry can be simulated as an infinite plane, the analytical solution is (Guillard et al., 2003a):

$$m(t) = m_0 + (m_\infty - m_0) \left[1 - \frac{8}{\pi^2} \sum_{n=0}^{\infty} \frac{1}{(1+2n)^2} \exp \left[-(1+2n)^2 \pi^2 \frac{D_{eff} t}{h^2} \right] \right] \quad (2)$$

where m (kg) is the mass of the sample, m_0 (kg) is the mass at $t=0$, m_∞ (kg) the mass at equilibrium and h (m) the thickness of the sample.

3. Implementation

3.1. Material moisture sorption isotherms

The wafer's moisture sorption isotherm was experimentally obtained at 25°C. This temperature was selected to allow for comparisons against published data. The Direct Vapour Sorption (DVS) equipment manufactured by Surface Measurement Systems was used. The sample is initially desiccated and then humidity is increased in a stepwise manner. The thickness of the wafer is ca. 2.4mm.

Water activity was increased from 0 to 0.9 with a 0.1 increment and the maximum investigated α_w was 0.95. Equilibrium was assumed to have been achieved when the change of sample mass over 5 minutes became smaller than 0.002%/min. The obtained wafer moisture sorption isotherm is shown in Figure 2a.

For the mathematical representation of the isotherms a variety of models can be found in published literature but not all of them give a good fit for all food materials throughout the entire α_w range. The best fit for the wafer isotherm was found to be given using the Freundlich model (Chen and Chen, 2014) described by equation (3):

$$X = 0.5176(a_w)^{4.050} \quad (3)$$

Currently, no isotherm has been obtained for the moisture barrier. However, to be able to use the developed model the use of an isotherm is imperative. The isotherm presented in Guillard et al., 2003b was used where authors used the Ferro – Fontan model to fit

the data which is described by equation (4). The isotherm was obtained at 20°C and is shown in Figure 2b.

$$X = \left[\ln \left(\frac{1.895}{a_w} \right) \left(\frac{1}{0.634} \right) \right]^{-9.312} \quad (4)$$

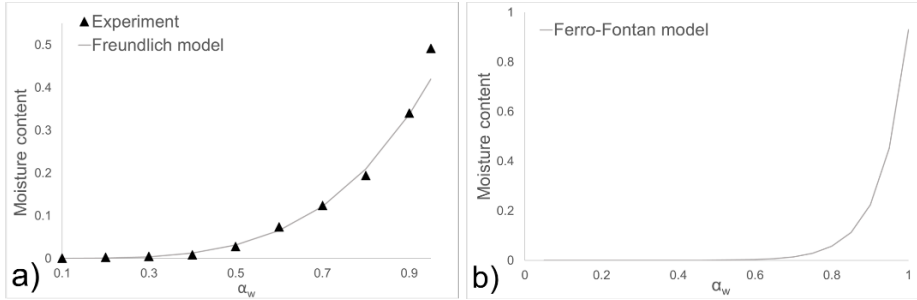


Figure 2: a) Wafer moisture sorption isotherm, b) Dark chocolate flavoured coating moisture sorption isotherm in Guillard et al., (2003b).

From Figure 2 it can be observed that for the same value of α_w the wafer absorbs more moisture compared to the moisture barrier suggesting it's more hygroscopic.

3.2. Material effective diffusivities

For the wafer the data obtained from the moisture sorption isotherm experiments were used. As the geometry of the wafer can be simulated as an infinite plane equation (2) was used to fit the D_{eff} value for each α_w step. An average value for the entire investigated α_w range was used equal to $5.41 \cdot 10^{-11} \text{ m}^2/\text{s}$.

No sorption kinetics data were available for the moisture barrier. However, permeability data obtained at 4°C using the water method ("ASTM Standard test methods for water vapor transmission of materials," 1995) were available. Combining the definition of the flux with and Fick's first law an average D_{eff} value of $5.94 \cdot 10^{-13} \text{ m}^2/\text{s}$ was calculated.

3.3. Phenomenological model for moisture migration in an ice cream cone

Equation (1) was solved numerically using the method of lines (Cutlip and Shacham, 1998). To use this method the materials are separated in grids and their X is calculated at each location using equation (1) for different time intervals.

The boundary conditions are obtained from the description of the system as shown in Figure 1. On the left hand side, the moisture barrier is in direct contact with a mass of ice cream calculated to be at $\alpha_w=0.84$. On the right hand side, the wafer is assumed to be in contact with a moisture impermeable barrier. The number of grids required to discretise the moisture barrier was selected to be 200. As the thickness of the moisture barrier is ca. 0.6mm and the wafer's 2.4mm, to maintain constant grid thickness in both materials, the number of grids required to discretise the wafer was found to be 800.

The initial condition for the system is that $\alpha_w=0.45$ in both materials. This value is calculated using the wafer's isotherm as at the start of the manufacturing process for the wafer $X=2\%$. Uniform initial conditions are used to ensure the only α_w gradient is between the ice cream and the first grid of the moisture barrier.

4. Results and discussion

The time allowed for the simulation is 48 hours as the moisture barrier appears to equilibrate with the ice cream fast. This can be attributed to the isotherm which was obtained at 20°C, a temperature significantly higher than the temperatures of interest for this application. Therefore, this study serves to showcase the predictive capabilities of the model and serve as an initial starting point for future investigation at lower temperatures.

4.1. Space domain

Figure 3 depicts the a_w and corresponding X of the materials in contact as a function of space after 6, 24 and 48 hours.

Water activity in all test locations increases over time. Closer to the ice cream the increase is more prominent as the flux is higher due to the higher a_w gradient. The same effect can be observed in Figure 3b. The discontinuity in this Figure occurs at the interface between the two materials and is a result of the materials having different isotherms leading to different X for the same a_w .

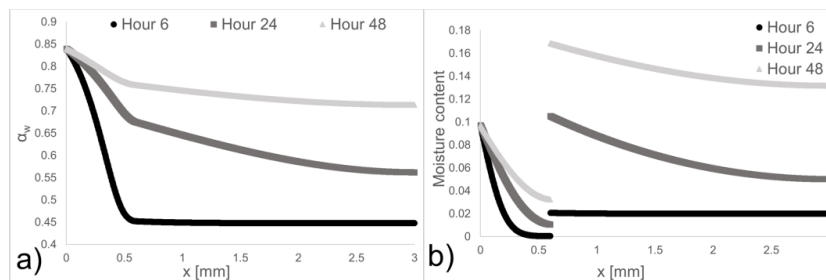


Figure 3: a) Water activity as a function of space after 6, 24 and 48 hours, b) Moisture content as a function of space after 6, 24 and 48 hours.

4.2. Time domain

Figure 4 depicts the a_w and corresponding X of the employed materials as a function of time at specific locations. Two locations in each material were selected to represent the areas closest to the boundaries and areas close to the interface. It is observed that for the location closest to the ice cream, a_w increases rapidly and reaches approximately equilibrium with the ice cream in about 48 hours. For the other investigated locations, a plateau is initially observed before a_w starts to increase. This is because moisture must progress through all previous locations and the D_{eff} of both the chocolate layer and the wafer present significant resistance.

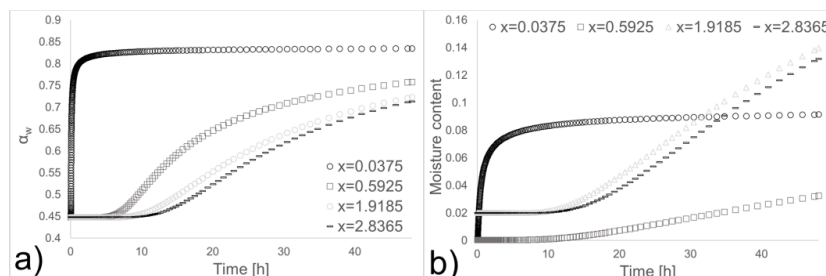


Figure 4: a) Water activity as a function of time at specific locations, b) Moisture content as a function of time at specific locations.

In Figure 4b the significance of the moisture sorption isotherms is showcased. Location $x=0.5925\text{mm}$ in the moisture barrier has a significantly higher α_w , compared to the wafer location at $x=1.9185\text{mm}$. However, the corresponding X of the moisture barrier's location is lower than the wafer's. This is due to the wafer being more hygroscopic and thus absorbing more moisture for the same α_w value.

5. Conclusions

A mathematical model for the prediction of moisture migration in a multicomponent system was presented. Experimental and published data at room temperature conditions were used as inputs to calculate the X of the different materials in contact in different locations over time. The moisture barrier at room temperature conditions cannot protect the wrapping wafer effectively as it appears to be reaching equilibrium with the high α_w material in 48 h.

Further work is required to obtain input data for different temperatures including below zero conditions. As the model considers a uniform moisture barrier layer using data at different temperatures will allow the designers to understand whether moisture migration occurs through the materials (diffusion limited). Otherwise this suggests the presence of imperfections in the moisture barrier whose influence should be investigated.

Acknowledgements

Unilever and EPSRC funding is gratefully acknowledged.

References

- ASTM Standard test methods for water vapor transmission of materials, 1995. , in: Annual Book of ASTM Standards. ASTM, Philadelphia, PA.
- B. Biquet, T.P. Labuza, 1988. Evaluation of the Moisture Permeability Characteristics of Chocolate Films as an Edible Moisture Barrier. *J. Food Sci.* 53, 989–998.
- C. Bourlieu, V. Guillard, H. Powell, B. Vallès-Pàmies, S. Guilbert, N. Gontard, 2006. Performance of lipid-based moisture barriers in food products with intermediate water activity. *Eur. J. Lipid Sci. Technol.* 108, 1007–1020.
- H.-Y. Chen, C. Chen, 2014. Equilibrium relative humidity method used to determine the sorption isotherm of autoclaved aerated concrete. *Build. Environ.* 81, 427–435.
- M. B. Cutlip, M. Shacham, 1998. The numerical method of lines for partial differential equations.
- V. Guillard, B. Broyart, C. Bonazzi, S. Guilbert, N. Gontard, 2003a. Evolution of moisture distribution during storage in a composite food modelling and simulation. *J. Food Sci.* 68, 958–966.
- V. Guillard, B. Broyart, C. Bonazzi, S. Guilbert, N. Gontard, 2003b. Preventing Moisture Transfer in a Composite Food Using Edible Films: Experimental and Mathematical Study. *J. Food Sci.* 68, 2267–2277.
- T. Gulati, A. K. Datta, C.J. Doona, R.R. Ruan, F.E. Feeherry, 2015. Modeling moisture migration in a multi-domain food system: Application to storage of a sandwich system. *Food Res. Int.* 76, 427–438.
- F. Hao, L. Lu, J. Wang, 2016. Finite Element Analysis of Moisture Migration of Multicomponent Foods During Storage. *J. Food Process Eng.* n/a-n/a.
- G. Roudaut, F. Debeaufort, 2011. Moisture loss, gain and migration in foods, in: Kilcast, D., Subramaniam, P., *Food and Beverage Stability and Shelf Life.* p. 63.

Model predictive control for automated anesthesia

Adriana Savoca, Jessica Barazzetta, Giuseppe Pesenti, Davide Manca*

*PSE-Lab, Dipartimento di Chimica, Materiali e Ingegneria Chimica “Giulio Natta”
Politecnico di Milano, Piazza Leonardo da Vinci 32, Milano 20133, Italy
davide.manca@polimi.it*

Abstract

The main challenge of anesthesia is the maintenance of the desired sedation level before, during, and after the induction. We developed an in-silico model-based control loop for the administration of an analgesic opioid, remifentanyl, and of an anesthetic, propofol. The patients' response (i.e. the real process) is predicted in-silico by a physiologically-based pharmacokinetic model, conjugated with suitable pharmacodynamic models that simulate the dynamic response of heart rate, arterial pressure, and bispectral index. We simulated the induction phase of anesthesia and obtained a fast and safe patient's response by setting the arterial pressure and bispectral index as controlled variables, and implementing proper bounds on both the plasma concentration and the controlled variables.

Keywords: model-based control, anesthesia, analgesia, pharmacokinetics, pharmacodynamics.

1. Introduction

Different drugs are responsible for the anesthesia cocktail, i.e. (i) a hypnotic for unconsciousness, (ii) an analgesic for pain relief, (iii) a neuro-muscular blocker to avoid undesired reflex activity. Most of these drugs feature a narrow therapeutic range that makes their titration critical. The anesthesiologist usually selects an initial dose according to standard protocols. This dose is then subject to variations based on measurable (e.g., hemodynamics, muscle and cerebral activity) and subjective (e.g., eyes movement, response to calling) physiological indicators of the patient's status. Indeed, the induction allows reaching a certain “depth of anesthesia” (DOA) that has to be kept throughout the operation (i.e. maintenance) until the end of the surgery. In engineering terms, the anesthesiologist acts as a “human” feedback controller and implements actions based on the patient's response. The actuator of this control-loop is usually a target control infusion (TCI) pump, which implements a three-compartment pharmacokinetic (PK) model to determine the infusion rate that allows achieving the desired target concentration. However, these models do not have any correspondence with the real physiology of human body, and the adaptive parameters are often identified by fitting the measured drug concentration in healthy volunteers (Minto et al., 1997; Schnider et al., 1998). Therefore, these models may not be suitable to determine the adequate anesthesia dose for special population (e.g., ill, elderly). Recent years have seen a rising interest in the application of medical devices for Physiological Closed-Loop Control (PCLC) (FDA, 2015). Anesthesia practice may benefit from the introduction of automated controllers. In fact, the anesthesiologist's control action is intrinsically subjective and intermittent, and often irregular, with possible adverse effects on the patient's health and longer times for recovery. Researchers are

investigating different control strategies, e.g., PID, fuzzy controllers, neural networks, model-based control (FDA, 2015). Anesthesia challenges call for (i) robustness towards disturbances (i.e. nociceptive stimuli) and measured variables noise, (ii) control effort minimization to avoid overdosing, (iii) management of drugs dynamics and interactions that may alter pharmacokinetics and pharmacodynamics. Model predictive control (MPC) can tackle these tasks. We developed an in-silico loop for anesthesia induction and maintenance with co-administration of the hypnotic propofol and the analgesic remifentanyl.

2. Methods

Figure 1 shows the structure of an in-silico loop for induction and maintenance of anesthesia. For the sake of correctness, we introduced a “mismatch” between (i) the model that represents the real patient and (ii) the model implemented in the controller. We chose to use a physiologically-based (PB) PK model (Abbiati et al. (2016)) to represent in-silico the PK response of the real human body. This model is more complex than classical PK models, as it features compartments that correspond to real tissues and organs and includes realistic metabolism/elimination paths. Indeed, PBPK models are nearer to the anatomy and physiology of patients and this makes the individualization of both prediction and treatment easier.

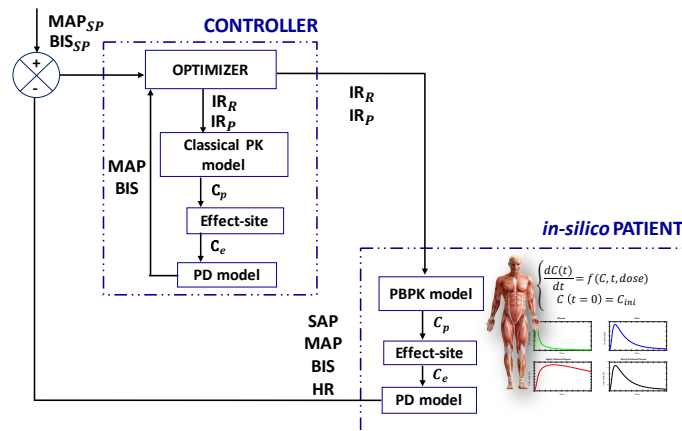


Figure 1 - In-silico loop scheme for control of anesthesia with propofol and remifentanyl. The main elements are: (i) the controller PK three-compartment model combined with Hill equation (PD), (ii) the real patient model, i.e. PBPK model combined with Hill equation (PD), (iii) the optimizer, (iv) the control specifications on MAP and BIS, (v) the manipulated variables IR_R and IR_P (remifentanyl and propofol infusion rates, respectively).

Our PBPK model is conjugated to suitable pharmacodynamic (PD) models (i.e. modified Hill equation) as discussed in Savoca et al. (2017), to predict mean arterial pressure (MAP), systolic arterial pressure (SAP), heart rate (HR), and bispectral index (BIS). In particular, AP and HR depend on remifentanyl concentration while BIS depends on propofol concentration, as it is an unconsciousness measure that depends on the hypnotic. The MPC controller implements a classical three-compartment PK model, which is simpler and faster than the PBPK counterpart. Once again, the adopted PD models remain the same. We use PK model parameters for remifentanyl from Minto et

al. (1997) and for propofol from Schnider et al. (1998). The manipulated variables are remifentanyl and propofol infusion rates. The corresponding controlled variables are MAP and BIS. We chose MAP as the analgesia controlled variable over HR and SAP, because (i) it is more reliable than SAP and DAP, and (ii) the PD model provided better results in the validation phase with experimental data from the scientific literature. However, the objective function includes a penalty when the plasma concentration overflows the therapeutic range. We chose BIS as the hypnosis controlled variable because several authors consider it a reliable measure of the sedation level. We remain aware of some controversies arising in case of neuromuscular-blocking agents use (Schuller et al., 2015). Eq. (1) is the objective function that is minimized at each discrete control time k of the prediction horizon. The result of the optimization is a set of optimal control actions evaluated over a specific control horizon. The first control action is assessed in-silico using the PBPK/PD model whose output is passed at the following time instant to the controller as an input value.

$$\min_{\mathbf{u}(k), \mathbf{u}(k+1), \dots, \mathbf{u}(k+h_c-1)} \left\{ \sum_{j=k+1}^{k+h_p} \left[w_y e_y^2(j) + PF_x(j) \right] + \sum_{i=k}^{k+h_p-1} \left[w_u \Delta \mathbf{u}^2(i) \right] \right\} \quad (1)$$

The first term in Eq. (1) accounts for the minimization of the distance of the model prediction from the assigned set-point trajectory. The second term minimizes the control effort to avoid steep changes of the manipulated variables (i.e. the infusion rates). In addition, we implemented suitable penalty functions for the plasma concentration and the controlled variables MAP and BIS (summarized in PF_x). The MPC code is written in Fortran 90.

3. Results

3.1. Induction and maintenance simulation

The goal of induction is to rapidly reach a desired DOA level (i.e. setpoint in control terminology). It is worth underlining that the scientific literature does not provide any unique definition of DOA. We define DOA as BIS=45 [-] and MAP=70 [mm Hg], since the sedation range is BIS=40-60 [-], and MAP is around 70 [mmHg] in conditions of adequate analgesia. These are the setpoints assumed for induction and maintenance in our simulations. The control action starts 5 min after the simulation begins (to simulate the pre-induction phase when a null drug concentration corresponds to baseline values of awake patients, i.e. MAP=100 [mmHg] and BIS=90 [-]). The desired DOA level is achieved with a balanced control action (Figure 2, medium panel) that is steep at $t=5$ min (i.e. bolus) to ensure fast reaching of the set point (see top panel) but decreases gradually once it is reached. The rise-time of MAP is 2.69 min. The time required for unconsciousness (i.e. the time for BIS to reach 70 [-]) is 1.593 min, while the time to start incision (i.e. BIS=50 [-]) is 2.814 min. It is worth observing that in both cases (i.e. remifentanyl and propofol) the concentration remains within the therapeutic range (remifentanyl 3-8 ng/mL ensures adequate analgesia while 1.3-6.8 $\mu\text{g/mL}$ is the therapeutic blood range for propofol). Particularly, the controller prioritizes the error of set point term rather than the plasma concentration PF, as the MAP set point is maintained even though the controller model analgesic concentration is below the adequate range. The physiological time delay between the drug concentration in plasma and the corresponding clinical effect is represented by the lag between plasma and effect-site compartments (bottom panel).

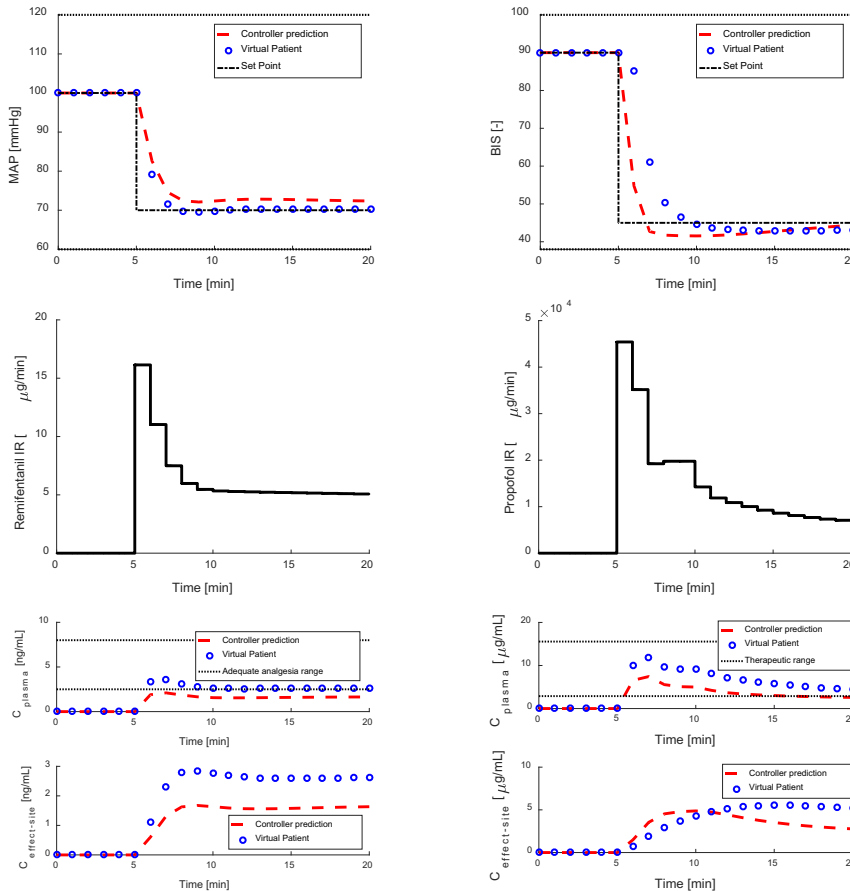


Figure 2 - Simulation of the induction phase. Left diagrams refer to analgesia while right diagrams refer to hypnosis. (Top) Dynamics of controlled variables. (Medium) Manipulated variables. (Bottom) Time profiles of monitored plasma (top) and effect-site (bottom) pharmacokinetics predicted by the controller model (red dashed line) and the virtual patient model (blue circles).

This delay depends on distribution/diffusion processes, age, presence of impairments, and PK input. Therefore, different PK models for the same drug display different lags.

The CPU time for the simulation of 20 control actions (discrete control time=1 min), as shown in Figure 2, is 10.05 s (Intel® Core™ i7-3770 CPU @ 3.40 GHz, 8 GB RAM), proving that the in-vivo and online application of MPC to surgical anesthesia is today feasible. Figure 3 shows that in absence of disturbances, after the induction, the controller can maintain both MAP and BIS target values for a prolonged time (i.e. the duration of the surgical procedure, hereby assumed 50 min) without showing any stability problems.

3.2. End of surgery simulation

Unlike the simulation of Section 3.1 based on a 50 min surgical maintenance, we now want to reproduce the end of surgery at $t=30$ min (by modifying the MAP and BIS

setpoints to 100 and 90, respectively), which corresponds to the completion of drugs infusion.

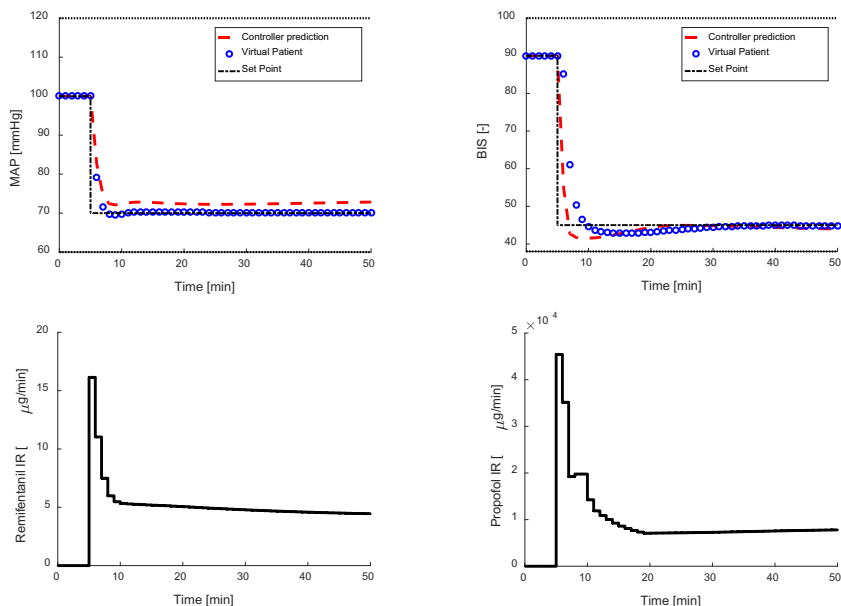


Figure 3 - Controlled (top panel) and manipulated (bottom panel) variables during maintenance phase (on the left, MAP dynamics; on the right, BIS dynamics). The duration of the surgical procedure is 50 min. The controller can maintain the targeted set points with no instabilities.

As expected, the manipulated variables go to zero and, since the drugs are progressively cleared from the virtual patient body, the pharmacological effects (i.e. MAP and BIS) increase towards the baseline values, i.e. awake patient (Figure 4). The estimated time for recovery from anesthesia is around 46.22 min, which is consistent with real surgeries. In fact, although the recovery time from opioids and hypnotics is subject to inter-individual differences, Misal et al. (2016) report that “complete physiologic recovery takes place by 40 min in 40% of the patients”. For the sake of clarity, it is important to underline that the controller is not responsible in influencing the velocity of the curve after the infusion ends, as there are not any antidotes to remifentanyl and propofol. Consequently, the profile depends on the metabolic and elimination characteristics of the patient, i.e. the PBPk/PD model. The recovery from anesthesia is very critical and we are aware that in the practice BIS and MAP observations are not sufficient. Other measurable and non-measurable (i.e. movement, response to calling) variables must be considered to assess the level of awareness. For this reason, the expertise of the anesthesiologist remains essential.

4. Conclusions

According to our findings, the designed MPC controller allows achieving a safe induction with plausible results concerning the end of surgery. The use of a PBPk/PD model leaves space for treatment personalization and analysis via in-silico simulation. In fact, “special” individuals can be simulated, such as ill patients. Future work will investigate the controller response to intraoperative disturbances, e.g., nociceptive

stimuli. The final goal of our research line is clinical validation. In this case, the controller would feature the PBPK/PD model and the patient would be in-vivo rather than in-silico. This is a key point as, in the literature, to our knowledge, no one has combined anesthesia control with the physiological approach to PK/PD modeling.

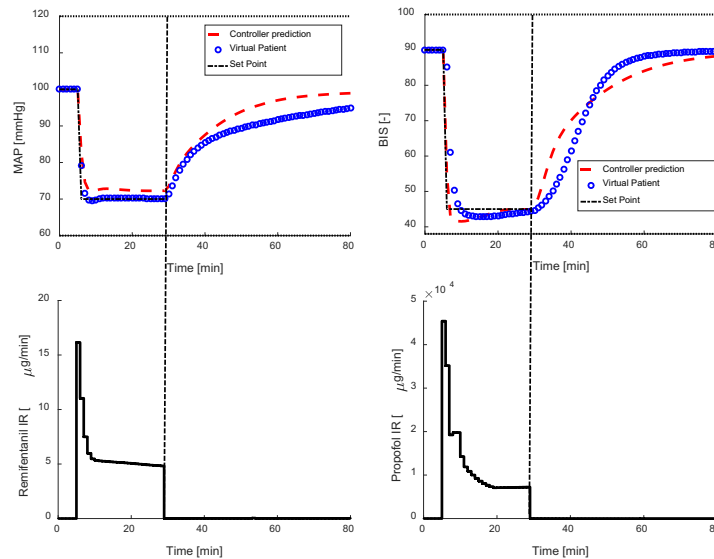


Figure 4 - Controlled (top panel) and manipulated (bottom panel) variables after the end of anesthesia. Control action stops at $t=30$ min, as shown by the vertical dotted line.

References

- Abbiati, R.A., Lamberti, G., Grassi, M., Trotta, F., Manca, D. (2016). Definition and validation of a patient-individualized physiologically-based pharmacokinetic model. *Computers & Chemical Engineering*, 84, 394-408.
- FDA, the Food and Drug Administration (2015). Physiological Closed-Loop Controlled (PCLC) Medical Devices – Discussion Paper for Workshop 1-20.
- Minto, C.F., Schnider, T.W., Egan, T.D., Youngs, E., Lemmens, H.J., Gambus, P.L., Billard, V., Hoke, J.F., Moore, K.H., Hermann, D.J., Muir, K.T., Mandema, J.W., Shafer, S.L. (1997). Influence of age and gender on the pharmacokinetics and pharmacodynamics of remifentanyl. I. Model development. *Anesthesiology*, 86, 10-23.
- Misal, U.S., Joshi, S.A., Shaikh, M.M. (2016). Delayed recovery from anesthesia: A postgraduate educational review. *Anesthesia, Essays and Researches*, 10, 164-172.
- Savoca, A., Abbiati, R.A., Manca, D. (2017). Performance of classical and physiologically-based PK-PD modelling for prediction of remifentanyl hemodynamic effects, *Computer Aided Chemical Engineering* (Vol. 40, pp. 2755-2760): Elsevier.
- Schnider, D.M., Thomas W., Minto, M.B.C., Charles F., Gambus, M.D., Pedro L., Andresen, M.D.C., Goodale, D.D.S.P., David B., Shafer, M.D., Steven L., Youngs, M.D., Elizabeth J. (1998). The Influence of Method of Administration and Covariates on the Pharmacokinetics of Propofol in Adult Volunteers. *Anesthesiology*, 88, 1170-1182.
- Schuller, P.J., Newell, S., Strickland, P.A., Barry, J.J. (2015). Response of bispectral index to neuromuscular block in awake volunteers. *Br J Anaesth*, 115 Suppl 1, i95-i103.

Process modelling, design and technoeconomic evaluation for continuous paracetamol crystallisation

Hikaru G. Jolliffe, Dimitrios I. Gerogiorgis*

School of Engineering (IMP), University of Edinburgh, Edinburgh, EH9 3FB, UK

D.Gerogiorgis@ed.ac.uk

Abstract

Continuous Pharmaceutical Manufacturing (CPM) has received significant research interest as a way to achieve a step-change in the performance of pharmaceutical production, where innovations are incremental at best due to the current paradigm – batch production – being a relatively mature technology. In this work, a Continuous Oscillatory Baffled Crystalliser (COBC) for paracetamol crystallisation has been modelled and optimal design and operation has been determined via nonlinear optimization (NLP). Clear trends emerge, with rate of antisolvent use having a marked impact of COBC volumes; crystal seed mass loading also has a strong effect. However, there are tradeoffs between mass efficiency, cost and volume, and product crystal size. The trends and optima illustrate how process modelling, simulation and optimisation provide clear insights into process performance and decisions on acceptable tradeoffs.

Keywords: Continuous Oscillatory Baffled Crystalliser (OBC), paracetamol.

1. Introduction

Pharmaceutical production has long relied solely on batch processing, and while it has many benefits including equipment flexibility and the know-how of a mature technology, in an environment of growing R&D expenditure and a greater awareness of and a drive to be more sustainable, research interest has turned towards Continuous Pharmaceutical Manufacturing (CPM); continuous production can achieve higher yields purities, better heat and mass transfer, decreased processing times, and better efficiency and reliability. The need for cost-effective R&D methodologies brings process modelling and simulation to the forefront of initial stages of process option evaluation. Furthermore, they are also of great utility in evaluating alternative design parameters for existing or newly developed processes (Benyahia et al., 2012). Continuous crystallisation has received significant research attention toward developing separation technologies for CPM, with both stirred tanks and tubular crystallisers types studied in great detail (Ferguson et al., 2014; McGlone et al., 2015; Diab and Gerogiorgis, 2017).

In previous work, we have used modelling and simulation to economically evaluate two CPM processes, and we have also used nonlinear optimisation of these process models to determine optimal design and operating parameters for key product separation operations (Jolliffe and Gerogiorgis, 2017a, 2017b). In the present work, we systematically incorporate models for continuous crystallisation, published crystallisation kinetic data, and economic analysis into a nonlinear optimisation model

to determine optimal crystallisation operation and design for the recovery of an analgaesic Active Pharmaceutical Ingredient (API), paracetamol. This key API has been widely used as a model API for CPM studies, with published data on crystallisation kinetics available (Brown et al., 2015; Cruz et al., 2016). The impact of temperature, crystalliser size and configuration, antisolvent type and quantity, and flowrate are considered. The optimisation cases are formulated into a nonlinear optimisation model to determine optimal Continuous Oscillatory Baffled Crystalliser design variables and process conditions. Technical (API recovery), environmental (E-factor) and economic metrics (Capital Expenditure, CapEx) are used for comprehensive process evaluation.

2. Continuous Oscillatory Baffled Crystallisers (COBC)

Continuous Oscillatory Baffled Crystallisers (COBC) are a development of Oscillatory Baffled Reactors, and in essence are a series of baffles in long (i.e. high length-to-diameter ratio) tubes, and in appearance are similar to Plug Flow crystallisers with baffles. COBC units tend to offer improved performance over the latter, as well as over batch crystallisers. They offer improved scaling, heat and mass transfer and decreased processing times (Lawton et al., 2009). COBC units operate by inducing an oscillatory flow in the fluid contents, and there is also a net flow through the unit (as this is a continuous process) which is independent of the oscillatory flow. The use of a reciprocating pump is a common way to generate the oscillatory flow: as the fluid moves back and forth across the baffles, the eddies generated enhance mixing and thus improve local crystallisation performance considerably. Baffle design primarily varies in terms of the orifice-to-internal diameter ratio, the gap between the baffles and the number of orifices in the baffles; in some cases constrictions are used instead of baffles.

3. Nonlinear optimisation and process model

The objective function to be minimized is a Capital Expenditure (*CapEx*) function (Eq. 1), from a capacity-power law using crystalliser volume. The coefficient a and exponent n were generated by fitting publicly available data for cost and capacity of commercial COBC units. Crystalliser volume is computed in a relatively straightforward manner (Eq. 2), from total volumetric throughput and the residence time required to achieve the desired objectives (such as yield). The population balance (Eq. 3) and mass balance (Eq. 4) are solved via a moment transformation (Eq. 5) (Brown et al., 2014). Key variables in (Eq. 5) include characteristic crystal length L (m), growth rate G (m s^{-1}). The volume shape factor k_v is taken to be 0.866, typical for the monoclinic Form I of paracetamol which is often encountered (Brown and Ni, 2011), and the crystal density ρ_{API} is 1.3 g.cm^{-3} . Nucleation is considered to be negligible, so the Br_o^j terms are ignored. Growth rate G is computed via the an empirical correlation (Eq. 6) (Brown and Ni, 2011), where ΔC_{API} is the degree of supersaturation (Eq. 7), \dot{Q}_{AS} is the rate of antisolvent addition in mL min^{-1} , and the oscillatory flow Reynold Number Re_o (Eq. 9). In the latter term angular velocity $\omega = 2\pi f_{osc} a_{osc}$ (ms^{-1}) replaces the superficial fluid velocity found in the normal (Net Flow) Reynolds Number (Re_n , Eq. 9). Here, f_{osc} and a_{osc} are the frequency and amplitude of the fluid oscillation, respectively (normally taken to be 2 Hz and 10 mm in this model). In the literature, values for both Re_o and Re_n are suggested to achieve the best mixing, often above 300 for the former and above 50 for the latter. In this model we have imposed similar requirements, although with a higher Re_o ; values over 4,000 are reported (Brown and Ni, 2011). The Re_o to Re_n ratio (ψ) has an optimal mixing interval; operation may vary outside reported ranges (Eq. 9) by as much as 10%.

The solubility of paracetamol in different solvent systems has been commonly studied in the literature. Here, the use acetone as process solvent is modelled, with either water or toluene as antisolvent. Empirical values for paracetamol were taken fitted high order polynomial surrogate equations to calculate solubilities (Eq. 8) (Fig. 1). With water use there is a solubility peak, and within a certain range adding water will in fact increase API solubility. To avoid this, the rate of antisolvent use was limited to a range of 50:50 to 20:80 by weight (process solvent acetone : antisolvent). It transpires that the use of toluene results in highly impractical residence times and volumes (very long/large), and so the results presented in this work refer to the use of water as an antisolvent.

Seed crystal loading can vary from 0.5% to 2.0% by weight (seed w.r.t. solvent and antisolvent). The following assumptions are made: a) seed crystals are monodisperse (i.e. of same size) and of monoclinic Form I; b) no nucleation, agglomeration or

$$\min CapEx = aV_{COBC}^m \quad (1)$$

s.t.

$$V_{COBC} = \dot{Q}_{Tot} \tau_{req} \quad (2)$$

$$\frac{\delta n}{\delta t} + G \frac{\delta n}{\delta L} = 0 \quad (3)$$

$$\frac{dC_{API}}{dt} = -3\rho_{API}k_v G \int_0^\infty L^2 n dL \quad (4)$$

$$\mu_j = \int_0^\infty L^j f_n(L, t) dL, \quad \begin{bmatrix} \dot{\mu}_0 \\ \dot{\mu}_1 \\ \dot{\mu}_2 \\ \dot{\mu}_3 \\ \dot{\mu}_{C_{API}} \end{bmatrix} = \begin{bmatrix} B \\ G\mu_0 + Br_0 \\ 2G\mu_1 + Br_0^2 \\ 3G\mu_2 + Br_0^3 \\ -\rho_{API}k_v(3G\mu_1 + Br_0^3) \end{bmatrix} \quad (5)$$

$$G \cdot 10^8 = 3.78 \cdot 10^{-12} \Delta C_{API}^{1.570} \dot{Q}_{AS}^{1.158} Re_o^{2.155} + 21.50 \quad (6)$$

$$\Delta C_{API} = C_{API} - C_{API}^{sat}, \quad S = \frac{C_{API}}{C_{API}^{sat}} \quad (7)$$

$$C_{API}^{sat} = \sum_{i=0}^n \sum_{j=0}^k a_{ij} m_{AS, \%}^i T^j \quad (8)$$

$$Re_o = \frac{2\pi f_{osc} a_{osc} \rho_{mix} d}{\mu_{mix}} > 1000, \quad Re_n = \frac{\rho_{mix} u_{net} d}{\mu_{mix}} > 40, \quad 10 > \psi = \frac{Re_o}{Re_n} > 4 \quad (9)$$

$$0.5 \leq ASR \leq 0.8 \quad (10)$$

$$0.5 \frac{kg_{seed}}{kg_{solvent}} \leq 100SMR \leq 2.0 \frac{kg_{seed}}{kg_{solvent}} \quad (11)$$

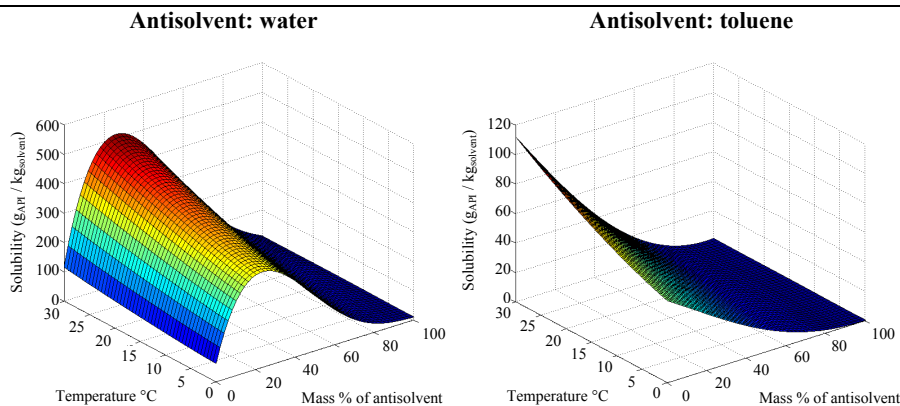


Figure 1. Paracetamol solubility in acetone-antisolvent mixtures (Granberg and Rasmuson, 2000).

breakage of crystals; c) crystal growth rates are size-independent; d) no impurities; e) sufficient heat transfer available to maintain a linear cooling profile. In terms of temperature, the inlet temperature can vary between 30 to 70 °C, and cooled to 5 °C; an inlet temperature of 50 °C is the default studied, and the other values investigated to see how optimality varies. Likewise, seed crystal size has been set at 40 microns by default, and larger sizes are investigated to study the optimal solution variation. Separate optimisation cases are formulated for varying inlet temperature and seed crystal size.

The MATLAB solver employed here is a constrained minimization routine (trust region reflective algorithm) with tolerances (stopping criteria) set to 10^{-6} . Gradients have been computed by the solver itself, and the solution time is reasonably fast, ranging between 30–100 seconds (the latter is the time required to generate capital expenditure response surfaces, while the time to run a single optimisation case is between 5–10 seconds). As stated, separate cases were formulated for initial temperatures. Separate cases were also performed for seed crystal sizes. A quick global search has been performed by checking convergence from multiple initial starting points; the runs always converged to the same point, and the absence of other local minima can be concluded with high confidence.

4. Results and discussion

Given a desired yield of 50%, the total cost response surface for an inlet temperature of 50 °C and a seed crystal size of 40 microns is given in Fig. 2A. The optimal solution (cost = 101,370 GBP) is pushed to bounds. It is evident that the rate of antisolvent use affects the total cost more significantly than the seed mass loading. Greater rates of antisolvent use result in lower costs via lower required residence times, due to faster growth rates. The tabulated values (Table 1) illustrate how the optimum changes with varying inlet temperatures, with a constant seed crystal size of 40 microns. Increasing the inlet temperature can drastically lower the cost via small required volumes and residence times. We can also see how the product crystal size varies, increasing with inlet temperature (and lowering with lower inlet temperature). This makes sense, as we assume the same initial supersaturation ratio ($S = 1.5$, Eq.7) in all cases: the higher the inlet temperature the higher the inlet solubility, thus higher supersaturation, thus greater API content, thus greater API precipitation for the same yield, thus larger product crystal sizes (as seed count is the same). Table 1 presents how capital cost, volume, residence time and product crystal size vary as a function of the seed crystal size used.

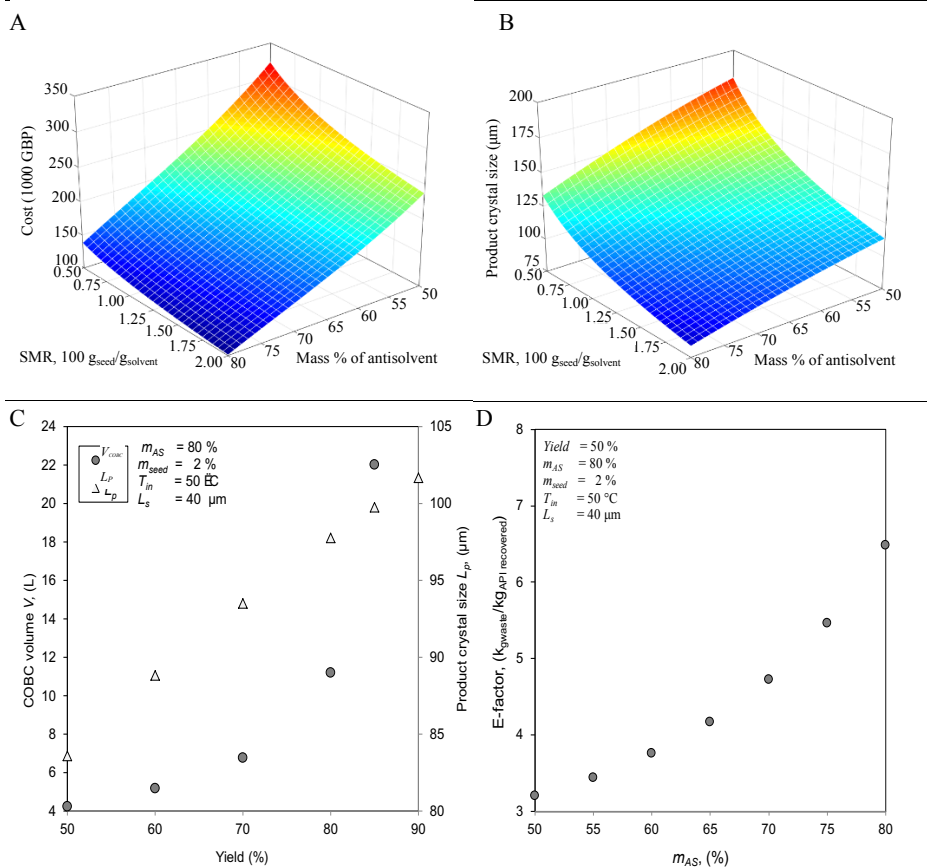


Figure 2. Total cost (A) and product crystal (B) response surfaces, volume and product size variation with required yield (C), and E-factor variation with antisolvent use (D).

For the same inlet temperature of $50^\circ C$; optima variation is less pronounced as with different inlet temperatures. Of course, for a given seed mass loading, larger seed crystal sizes mean lower seed counts. The response surface for product crystal size is given in Fig. 2B. Lower antisolvent amount results in larger product crystals; again, this is an effect of seed count. With lower antisolvent amount, the mass of seed crystals added in absolute terms is less. Therefore, the seed count will lower, meaning crystals must grow more in order to achieve the same yield. The reason lower seed mass loading increases product size is similar. The change in required COBC volumes as a result of oscillation in the COBC unit is straightforward (values not shown): Higher angular velocities (ω , a combination of the oscillation frequency and amplitude) produce a clear trend of lower volumes; this is to be expected, as higher ω increases Re_o , which increases growth rates. Fig. 2C illustrates the variation of volumes and product crystal sizes for different required target yields (other results here are for a 50% yield). The inlet temperature is $50^\circ C$, with a seed crystal size of 40 microns. Product crystal size increases linearly, while crystalliser volumes increase exponentially; achieving 90% yield is impractical.

Table 1. Optima variation for differing inlet temperatures (left) and seed crystal size (right).

T_{in} (°C)	Seed crystal size $L_s = 40\mu\text{m}$				Inlet temperature $T_{in} = 50^\circ\text{C}$				
	CapEx (10^3 £)	V_{COBC} (L)	τ_{req} (s)	L_p (μm)	L_s (μm)	CapEx (10^3 £)	V_{COBC} (L)	τ_{req} (s)	L_p (μm)
70	37.032	0.941	91	118.0	80	161.060	8.499	822	167.2
60	60.337	1.954	189	99.2	70	147.280	7.435	719	146.3
50	101.370	4.250	411	83.6	60	132.970	6.380	617	125.4
40	170.600	9.265	896	71.5	50	117.700	5.315	514	104.5
30	283.530	19.822	1917	62.4	40	101.370	4.250	411	83.6

Finally, evaluating E-factors (mass of waste per unit mass of product; a measure of mass efficiency – lower is better) in Fig. 2D, we can see that for a given yield they worsen with increasing antisolvent quantity; E-factor is invariant with seed mass loading. However, with worsening E-factor, costs improve, highlighting the conflicting requirements in process design and evaluation, and the need for tradeoff decisions.

5. Conclusions

The solved optimisation cases illustrate the benefits and drawbacks of different combinations of solvent and antisolvent, in both technical and sustainability terms, and the varying impacts of inlet temperature, seed mass loading, seed crystal size, mechanical operation of the crystalliser, and rate of antisolvent use. For a desired yield of 50 %, the latter has the most significant effect on crystalliser cost (Capital Expenditure), while seed mass loading also has a strong effect. Higher required yields require exponentially larger and more costly crystallisers. The tradeoff between material efficiency (which has been calculated by means of the E-factor metric), and volumes and cost, underscores competing objectives that frequently arise during process design.

6. Acknowledgements

Mr. Hikaru G. Jolliffe gratefully acknowledges the financial support of the Engineering and Physical Sciences Research Council (EPSRC) via a Doctoral Training Partnership (DTP) PhD fellowship awarded by the University of Edinburgh (EP/M506515/1).

References

- Benyahia, B. et al., 2012. *Ind. Eng. Chem. Res.* 51, 15393–15412.
- Brown, C.J. et al., 2015. *Chem. Eng. Process. Process Intensif.* 97, 180–186.
- Brown, C.J. et al., 2014. *CrystEngComm* 16, 8008–8014.
- Brown, C.J., Ni, X., 2011. *Cryst. Growth Des.* 11, 719–725.
- Cruz, P. et al., 2016. *CrystEngComm* 18, 9113–9121.
- Diab, S., Gerogiorgis, D.I., 2017. *Org. Process Res. Dev.* 21, 924–926.
- Ferguson, S. et al., 2014. *Cryst. Growth Des.* 14, 617–627.
- Granberg, R.A. and Rasmuson, A.C., 2000. *J. Chem. Eng. Data*, 45, 478–483.
- Hodges, P., 2015. <http://www.nitechsolutions.co.uk>, accessed 9/11/2017.
- Jolliffe, H.G., Gerogiorgis, D.I., 2017a. *Ind. Eng. Chem. Res.* 56, 4357–4376.
- Jolliffe, H.G., Gerogiorgis, D.I., 2017b. *Comput. Chem. Eng.* 103, 218–232.
- Lawton, S. et al., 2009. *Org. Process Res. Dev.* 13, 1357–1363.
- McGlone, T. et al., 2015. *Org. Process Res. Dev.* 19, 1186–1202.

Process modelling, simulation and technoeconomic optimisation for continuous pharmaceutical manufacturing of (*S*)-warfarin

Samir Diab, Dimitrios I. Gerogiorgis*

School of Engineering (IMP), University of Edinburgh, Edinburgh, EH9 3FB, UK

D.Gerogiorgis@ed.ac.uk

Abstract

Continuous pharmaceutical manufacturing (CPM) has the potential to attain several technical and operational economic benefits compared to the currently prevalent batch production paradigm. Despite the variety of demonstrated continuous flow syntheses of active pharmaceutical ingredients (APIs), the limited number of cost-effective continuous separations is a bottleneck to end-to-end CPM. Establishing promising APIs for integrated CPM is paramount. (*S*)-Warfarin is an anticoagulant API whose continuous flow synthesis features a single reaction with high enantiomeric selectivity followed by liquid-liquid extraction (LLE). This work describes the steady-state process modelling and technoeconomic optimisation for the upstream CPM of (*S*)-warfarin, implementing reactor design and LLE solvent comparison for purification. Ethyl acetate, isopropyl acetate, isobutyl acetate, 1-heptanol, 1-octanol and heptane are candidate LLE solvents. Reported reaction conversions and computed LLE efficiencies allow mass balance calculation and total cost estimation to establish promising LLE solvents. The nonlinear optimisation problem is formulated for total cost minimisation. Liquid-liquid phase equilibria, API phase compositions and solubilities for LLE design are implemented via surrogate polynomials based on extensive UNIFAC modelling; API recovery rates are calculated via detailed mass transfer correlations. The methodology used here screens optimum process configurations to achieve a technoeconomically optimal design for a continuous (*S*)-warfarin manufacturing plant.

Keywords: Continuous Pharmaceutical Manufacturing (CPM), (*S*)-warfarin.

1. Introduction

Continuous pharmaceutical manufacturing (CPM) is a key area of green chemistry research with the potential for significant technical, operational and economic benefits over currently prevalent batch manufacturing methods (Koenig and Dillon, 2017). Despite the numerous demonstrations of continuous flow syntheses (Britton and Raston, 2017) towards active pharmaceutical ingredients (APIs), including end-to-end production campaigns (Adamo et al., 2016), only certain synthetic routes benefit from continuous operation (Hartman et al., 2011) and the lack of demonstrated continuous purification and separation methods integrated in CPM plants is an important obstacle (Bana et al., 2017). Establishing promising APIs for CPM application and screening for those with the highest likelihood of success is imperative for the elucidation of potential process configurations and successful implementation of continuous manufacturing routes (Teoh et al., 2015), and process modelling is critical in performance evaluation.

(*S*)-Warfarin is an anticoagulant API, commonly known as Coumadin[®], commonly used for the treatment of deep vein thrombosis and pulmonary embolism (Porter, 2015). The continuous flow synthesis of (*S*)-warfarin features a single reaction and subsequent liquid-liquid extraction (LLE) process (Porta et al., 2015). Comparison of different conceptual separation process alternatives is essential for establishing cost-effective, materially efficient designs for upstream CPM configurations. Screening of candidate continuous LLE configurations for CPM of this API has yet to be conducted; process modelling, simulation and optimisation of continuous separation processes are valid alternatives to laborious experimental efforts for rapid design space investigation to elucidate technically feasible and economically viable processes (Jolliffe et al., 2018).

Here, we implement steady-state process modelling and nonlinear optimisation for the upstream CPM of (*S*)-warfarin, including continuous flow synthesis and LLE. Flowsheet development based upon the published continuous synthetic route and a conceptual continuous LLE process are presented, comparing various separation solvents. Thermodynamic models for liquid-liquid phase composition and API solubility prediction in non-ideal, multicomponent mixtures for LLE design are described. Nonlinear optimisation problem formulation for total cost minimisation are presented. Minimum total costs, optimal API recoveries and material efficiencies for different process configurations are compared to establish promising LLE solvents.

2. Process Modelling and Nonlinear Optimisation

2.1 Continuous Flow Synthesis and Process Flowsheet

The flowsheet for the CPM of (*S*)-warfarin (API) is shown in Fig. 1 (Porta et al., 2015). The continuous flow synthesis of the API features the nucleophilic addition of 4-hydroxy-coumarin with benzalacetone in the presence of trifluoroacetic acid (TFA) and a chiral amine catalyst at 75 °C in 1,4-dioxane, with a reported conversion of 61%. Aqueous HCl (10% w/w) is added to the reactor effluent before entering the LLE unit. Upon addition of the candidate LLE solvent, the process forms an organic (product) phase containing recovered API and an aqueous (waste) phase, between which API partitions. Several candidate separation solvents are compared for continuous LLE: ethyl acetate (EtOAc), isopropyl acetate (iPrOAc), isobutyl acetate (iBuOAc), 1-heptanol (HepOH), 1-octanol (OcOH) and *n*-heptane (nHep), as per (Alder et al. (2016).

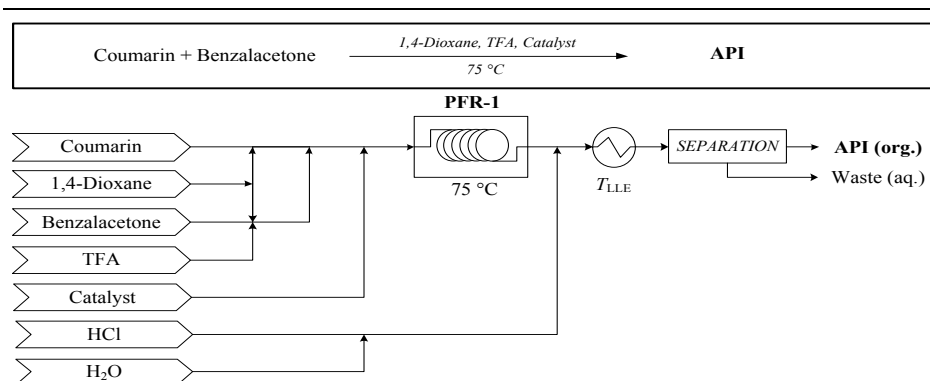


Figure 1: Process flowsheet for continuous (*S*)-warfarin production (Porta et al., 2015).

2.2 Separation Design and Thermodynamic Modelling

Continuous separation (LLE) processes are modelled as single-stage mixer-settlers at $T_{LLE} = 20, 40, 60$ °C and solvent feed rates $r = 1-4$ (mass basis). The rate of API recovery, \dot{f} , is described by Eq. 1. K is the overall mass transfer coefficient, a is the volume-specific interfacial area, V_{LLE} is the tank volume, and C^* and C are the theoretical and equilibrium API concentrations in the product phase, respectively. k_i and Sh_i are phase mass transfer coefficients and Sherwood numbers, respectively, D_{API} is the API diffusivity, d_{32} is the dispersed phase Sauter mean droplet diameter, Sc is the Schmidt number, Fr is the Froude number, EO is the Eotvos number, ϕ is the dispersed phase volume fraction, Re_i is the impeller Reynolds' number, d_i and d_t are the impeller and tank diameters, respectively, We is the Weber number, N_i is the impeller rotation speed, ρ_c is the continuous phase density and σ is the interfacial surface tension (Skelland and Moetti, 1990).

$$\dot{f} = KaV_{LLE}(C^* - C) \quad (1)$$

$$K = (k_c^{-1} + k_d^{-1})^{-1} \quad (2)$$

$$Sh_d = \frac{k_d d_{32}}{D_{API,d}} = 6.6 \quad (3)$$

$$Sh_c = \frac{k_c d_{32}}{D_{API,c}} = 1.25 \cdot 10^{-5} Sc_c^{1/3} Fr_c^{5/12} EO^{5/4} \phi^{-1/2} Re^{2/3} \left(\frac{d_i}{d_{32}}\right)^2 \left(\frac{d_{32}}{d_t}\right)^{1/2} \quad (4)$$

$$d_{32} = \begin{cases} 0.052 d_i We^{-0.6} \exp 4\phi & , We < 10^3 \\ 0.390 d_i We^{-0.6} & , We > 10^3 \end{cases} \quad (5)$$

$$We = \frac{d_i^3 N_i^2 \rho_c}{\sigma} \quad (6)$$

$$a = \frac{6\phi}{d_{32}} \quad (7)$$

Phase compositions and mixture API solubilities are predicted via the UNIFAC model. LLE stage efficiencies (E_{LLE}) allow calculation of actual product API concentrations from theoretical API concentrations in the product phase.

$$E_{LLE} = ((Ka\tau_{LLE})^{-1} + 1)^{-1} \quad (8)$$

2.3 Nonlinear Optimisation Formulation

The aim of the optimisation is to minimise the total cost objective function (*Cost*).

$$\min Cost = CapEx + \sum_{t=1}^{\tau} \frac{OpEx}{(1+y)^t} \quad (9)$$

$$\tau_{LLE} > 0 \quad (10)$$

$$1 < r < 4 \quad (11)$$

The discount rate ($y = 5\%$) accounts for inflation and τ is the plant lifetime (20 years). Annual operation of 8,040 hours is considered. Optimisation decision variables are the LLE residence time (τ_{LLE}) and relative solvent feed rate (r). Capital (*CapEx*) expenditure includes battery limits installed costs, construction and working capital; operating expenditure (*OpEx*) is the sum of material costs, utilities and waste handling requirements (Schaber et al., 2011). Solvent recovery after LLE is assumed to be 70%; all material requirements are scaled to account for reaction and separation inefficiencies.

3. Results and Discussion

Minimum total costs for each LLE solvent and operating temperature are shown in Fig. 2. The LLE solvent with the lowest minimum total costs is iBuOAc ($293.87 \cdot 10^6$ GBP, 60°C), followed by EtOAc ($299.91 \cdot 10^6$ GBP, 20°C) and iPrOAc ($299.93 \cdot 10^6$ GBP, 60°C). These solvents perform comparably due to their similar molecular structures and polarities, inducing similar phase compositions and thus comparable API recoveries. This effect is also observed for HepOH and OcOH, which attain the next lowest total costs ($339.43 \cdot 10^6$ GBP and $324.54 \cdot 10^6$ GBP, respectively) both operating at $T_{\text{LLE}} = 60^\circ\text{C}$. The poorest performance is attained via nHep (min cost = $350.52 \cdot 10^6$ GBP, 60°C).

For most cases, increasing operating temperature leads to lower total costs due to the enhanced mass transfer (recovery) rates of API into the product phase, which requires shorter LLE tank residence times (lower *CapEx*) and material requirements (lower *OpEx*) to meet the plant capacity of 100 kg per annum. When nHep is implemented as a separation solvent, *OpEx* is significantly higher for all LLE operating temperatures (20 , 40 , 60°C) considered, due to the low API recoveries attainable in comparison to other separation solvents considered in this work (Fig. 3). In all process configurations, the solvent feed rate (r) is pushed to its lower bound ($= 1$). The solvent feed rate and its assumed recovery following LLE directly affects materials and waste treatment costs (key *OpEx* components). The sensitivity of total cost minima to varying solvent recovery can be readily compared using the methodological framework described here.

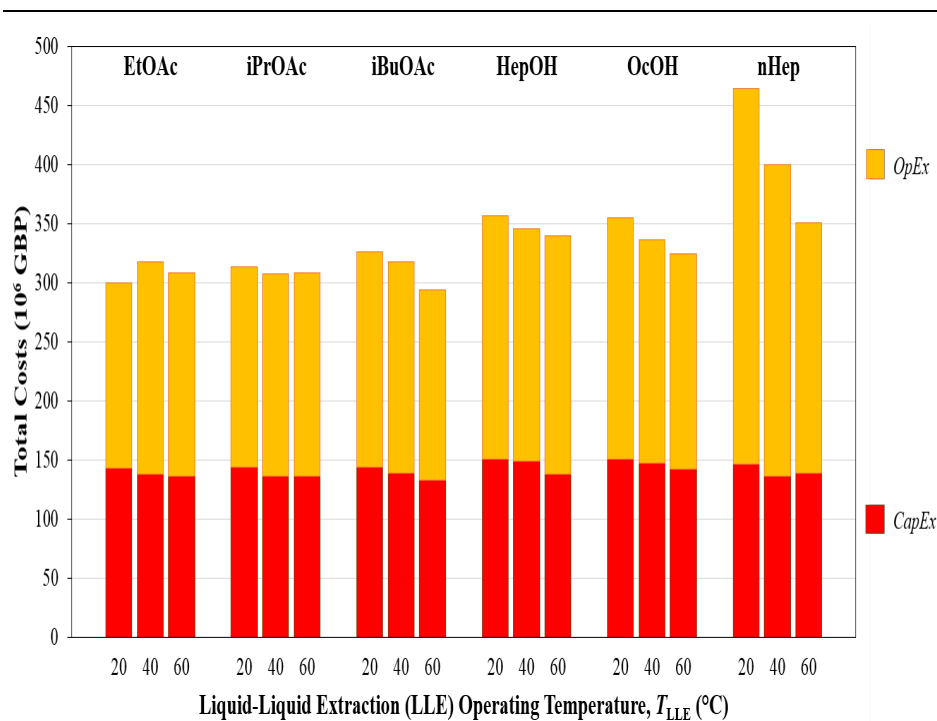


Figure 2: Minimum total costs attainable for different continuous LLE configurations.

Attainable E -factors for all processes vary between 57–127; whilst these values are high in comparison to other manufacturing sectors ($E < 0.1$ for oil and gas processing), they are reasonable for pharmaceutical manufacturing processes (Roschangar et al., 2015). The E -factor variations are directly related to corresponding API recoveries; as API recovery increases, material requirements and waste (and thus the E -factor) decrease. Implementing the process configuration with the lowest total costs (iBuOAc, 60 °C) attains $E = 58.4$, which is very low in comparison to other configurations in this work.

The described framework can be used to perform sensitivity analyses with respect to economic data (e.g. varying material prices, rates of interest for inflation) and other operational assumptions (e.g. achieved solvent recovery). It also allows the investigation of the effect of scaling plant capacity on total cost components and E -factors, an essential consideration during process development. Candidate separation solvents investigated for application here have been selected based upon their suitability for LLE (i.e. exhibit rapid phase splitting with the process mixture and are considered suitable with respect to detailed EHS criteria). (*S*)-Warfarin is available in both liquid (dispersion) and solid (tablet) formulations, and thus consideration of crystallisation and downstream processing following the upstream CPM considered in this work. Consideration of the effects of LLE solvent choices and resulting API recoveries and purities in the organic product phase on the requirement for additional purification prior to further processing will aid LLE solvent selection. The methodology described in this work can be implemented for other APIs requiring continuous LLE, provided that kinetic and thermodynamic data are available for modelling and total cost minimisation.

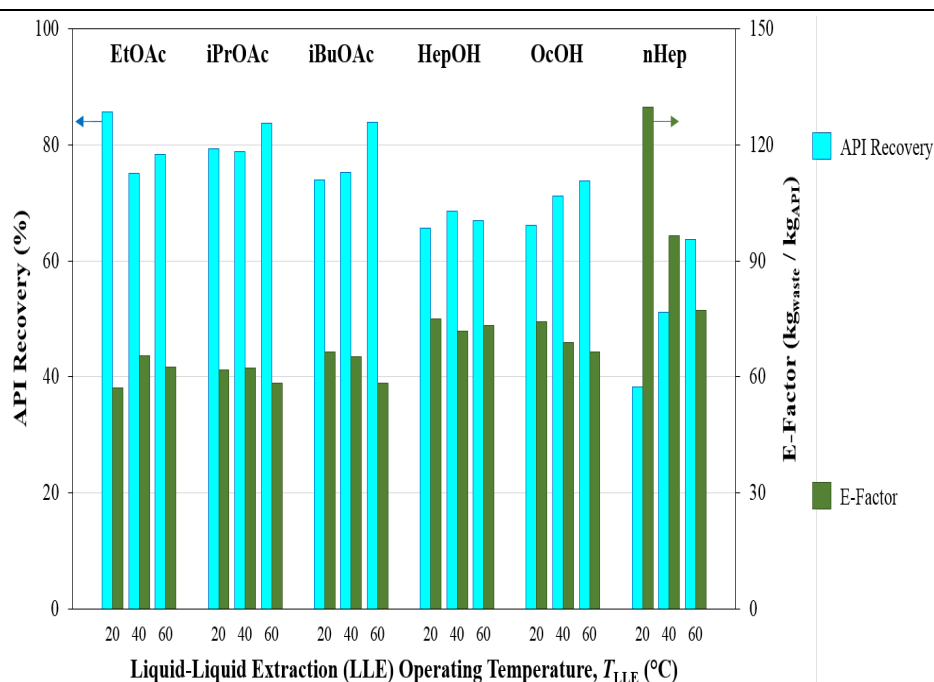


Figure 3: API recoveries and E-factors corresponding to total cost minima.

4. Conclusions

This paper presents the systematic evaluation of six candidate separation solvents for the continuous liquid-liquid extraction (LLE) of (*S*)-warfarin following the experimentally demonstrated continuous flow synthesis (Porta et al., 2015). Comparison of minimum total costs via nonlinear optimisation with LLE solvent feed rate and tank residence time as decision variables establish promising candidate LLE solvents for the CPM of (*S*)-warfarin. Isobutyl acetate (iBuOAc) emerges as a promising candidate LLE solvent, attaining the lowest minimum total costs of $293.87 \cdot 10^6$ GBP and a reasonable E-factor of 58.4, followed by ethyl acetate and isobutyl acetate. The considered alcohols (1-heptanol and 1-octanol) and *n*-heptane attain inferior performance (higher total costs) due to lower maximum (theoretical) API recoveries estimated by the UNIFAC method.

The technoeconomic and environmental impact analyses presented in this work can inform the future design of CPM processes for this societally important API. Consideration of wider operating parameter sets and additional LLE solvents can be performed by adapting the existing framework, given the availability of required thermodynamic data and physical properties. Sensitivity analyses with respect to varying performance assumptions (e.g. varied attainable reaction and separation efficiencies upon scale up) and economic considerations (available solvent recovery, interest rates etc.) can be implemented within the framework and will add robustness to the presented results. Consideration of carrier and separation solvent combinations on subsequent upstream (e.g. crystallisation) and downstream (product formulation) unit operations is essential for successful implementation of a fully continuous process.

5. Acknowledgements

Mr. Samir Diab gratefully acknowledges the financial support of the Engineering and Physical Sciences Research Council (EPSRC) via a Doctoral Training Partnership (DTP) PhD fellowship awarded by the University of Edinburgh (EP/N509644/1).

References

- A. Adamo, R. L. Beingessner, M. Benham, J. Chen, T. F. Jamison, K. F. Jensen, J. C. M. Monbaliu, A. S. Myerson, E. M. Revalor, D. R. Sneed, T. Stelzer, N. Weeranoppanant, S. Y. Wong and P. Zhang, 2016, *Science*, 352, 61–67.
- C. M. Alder, J. D. Hayler, R. K. Henderson, A. M. Redman, L. Shukla, L. E. Shuster and H. F. Sneddon, 2016, *Green Chem.*, 18, 3879–3890.
- P. Bana, R. Örkényi, A. Lakó, K. Lövei, G. I. Túrós, J. Éles, F. Faigl and I. Greiner, 2017, *Bioorg. Med. Chem.*, 25, 6180–6189.
- J. Britton and C. L. Raston, 2017, *Chem. Soc. Rev.*, 52, 10159–10162.
- R. Hartman, J. McMullen and K. Jensen, 2011, *Angew. Chem. Int. Edit.*, 50, 7502–7519.
- H. G. Jolliffe, S. Diab and D. I. Gerogiorgis, 2018, *Org. Process Res. Dev.*, 22, 40–53.
- S. Koenig and B. Dillon, 2017, *Curr. Opin. Green Sust. Chem.*, 7, 56–59.
- R. Porta, M. Benaglia, F. Coccia, S. Rossi and A. Puglisi, 2015, *Symmetry*, 7, 1395–1409.
- W. R. Porter, 2010, *J. Comput. Aid. Mol. Des.*, 24, 553–573.
- F. Roschangar, R. Sheldon and C. Senanayake, 2015, *Green Chem.*, 17, 752–768.
- S. D. Schaber, D. I. Gerogiorgis, R. Ramachandran, J. M. B. Evans, P. I. Barton and B. L. Trout, 2011, *Ind. Eng. Chem. Res.*, 50, 10083–10092.
- R. Sheldon, 2012, *Chem. Soc. Rev.*, 41, 1437–1451.
- A. H. P. Skelland and L. T. Moetti, 1990, *Ind. Eng. Chem. Res.*, 29, 2258–2267.
- S. K. Teoh, C. Rathi and P. Sharratt, 2015, *Org. Process Res. Dev.*, 20, 414–431.

Dynamic modelling and simulation of reactive transport phenomena in an amperometric blood glucose biosensor

Fergus McIlwaine, Dimitrios I. Gerogiorgis

School of Engineering (IMP), University of Edinburgh, Edinburgh, EH9 3FB, UK

Abstract

The treatment of diabetes as well as several other diseases which affect millions of patients worldwide strongly depend on deploying affordable technologies for frequent and accurate monitoring of blood glucose concentrations. Both theoretical and experimental investigations of novel blood glucose biosensor concepts pave the way for fast efficiency analysis of candidate biosensor designs. Recent studies have addressed the operation of amperometric biosensors, within which a combination of an enzymatic reaction and an enzyme deposited on an electrode allows for conclusive blood glucose detection. This paper models a single droplet of blood on an amperometric glucose biosensor to investigate the sensitivity of sensor performance to varying transport phenomena parameter values. The work presents a comprehensive sensitivity analysis, based on a new two-dimensional spatiotemporal model (constructed in MATLAB) which studies the combined reactive transport phenomena within a blood droplet deposited on an enzyme-coated surface. The sensitivity analysis explores the variation of electrode response (current density) and concentration profiles throughout the droplet and the enzyme layer subject to varying initial conditions and component diffusivities. Results clearly indicate a strong dependence of output profiles on the said sensitivity parameters: ensuring high current density (especially for small droplet volumes) is a prerequisite for developing reliable glucose biosensors of high accuracy and precision.

Keywords: Modelling; simulation; diabetes; glucose; biosensors; reaction-diffusion.

1. Introduction

Approximately 5% of the UK population have some form of diabetes: many patients require home glucose biosensors (Peng et al., 2016). Diabetes treatment is dependent upon the availability of reliable and affordable technologies to monitor blood glucose levels. The development of low-cost but high-fidelity biosensors for blood monitoring is pivotal, especially for underprivileged communities and countries with growing populations but modest healthcare expenditure. Both theoretical and experimental investigations of novel blood glucose biosensor concepts are essential, particularly because the latter is essential to determine prior to industrial-scale production ventures (Cambiaso et al., 1996). Recent studies consider amperometric biosensors, in which an enzymatic reaction on an enzyme-coated electrode allows the measurement of blood glucose concentrations (Baronas and Kulys, 2008). Modelling and simulation allows the effects of many parameters to be studied with relative ease and speed compared to experimental methods. This paper models a single droplet of blood on an enzyme coated electrode, modelling a glucose biosensor. Sensitivity analyses of blood glucose concentration variation for different transport properties allows insight into essential design considerations for the development of high-fidelity glucose biosensors.

2. Sensor Model

The blood droplet contacts an enzyme coated electrode. It is assumed that blood droplet geometry remains fixed. The 2D model domain is split into two subdomains: the droplet and the enzyme, which are created in MATLAB using finite difference analysis.

2.1 System Geometry

The system is modelled as a half ellipse (the blood droplet) on a rectangle (the enzyme coating). Dimensions of the droplet and enzyme considered are shown in Fig. 1.

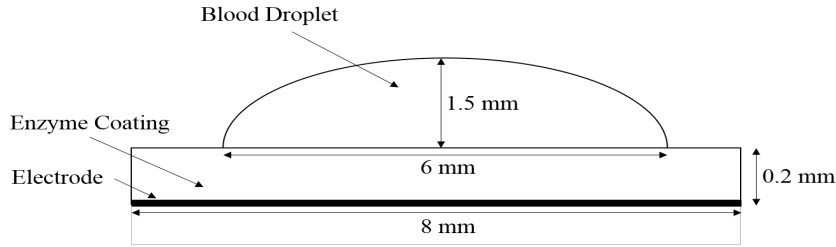
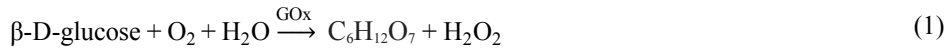


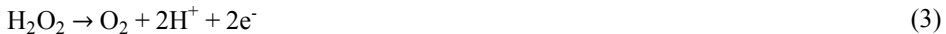
Figure 1: Geometry of a blood droplet on the enzyme-coated electrode of a glucose biosensor.

2.2 Enzymatic Reaction

The enzyme (Glucose Oxidase, GOx) is immobilised in the coating and catalyses the reaction of glucose to gluconic acid ($C_6H_{12}O_7$) and hydrogen peroxide (H_2O_2).



where E is the enzyme, C is the substrate-enzyme complex, S is the substrate (glucose) and P is product. Rate constants of the forward and backward reactions (Eq. 2) are k_{1+} and k_{2+} , respectively. Current is produced by the oxidation of H_2O_2 (Eq. 3).



2.3 Transport Phenomena: Partial Differential Equations (PDEs)

Reactant and product diffusion occurs in the blood droplet; chemical reaction only occurs at the enzyme layer. Mass transfer is modelled via Fick's second law of diffusion

$$\frac{\partial C_S}{\partial t} = D_{S,1} \nabla^2 C_S \quad (4)$$

$$\frac{\partial C_P}{\partial t} = D_{P,1} \nabla^2 C_P \quad (5)$$

where $D_{S,1}$ and $D_{P,1}$ are the diffusivities of S and P in the droplet, respectively, and C_S and C_P are the concentrations of S and P in the droplet respectively. Reaction occurs in the immobilized enzyme layer; concentrations obey the reaction-diffusion PDEs (eqs. 6-7).

$$\frac{\partial C_S}{\partial t} = D_{S,2} (\nabla^2 C_S) - \frac{V_{\max} C_S}{K_M + C_S} \quad (6)$$

$$\frac{\partial C_P}{\partial t} = D_{P,2} (\nabla^2 C_P) + \frac{V_{\max} C_S}{K_M + C_S} \quad (7)$$

where V_{\max} is the maximum enzymatic rate ($= k_{2+} C_S$), K_M is the Michaelis-Menten constant, $D_{S,2}$ and $D_{P,2}$ are the diffusivities of S and P in the enzyme, respectively.

2.4 Dimensionless model

We introduce the dimensionless parameters X , Y , T , \bar{S} and \bar{P} as the dimensionless 2D spatial coordinates (x and y), time coordinate (t), C_S and C_P , respectively. Dimensionless parameters are calculated as the ratio of the dimensional coordinate to a characteristic value. The reaction-diffusion PDE for glucose become dimensionless when substituted (eqs. 8-9). $L^* = 1$ mm, $T^* = 10$ s and $U^* = 4$ mmol L⁻¹ are the characteristic values for spatial coordinates, the time coordinate and concentrations, respectively.

$$\frac{\partial \bar{S}}{\partial T} = \frac{D_s}{L^{*2}} (\nabla^2 \bar{S}) - \frac{V_{\max} \bar{S}}{K_M + S^* \bar{S}} \quad (8)$$

$$\frac{\partial \bar{P}}{\partial T} = \frac{D_s}{L^{*2}} (\nabla^2 \bar{P}) + \frac{V_{\max} \bar{S}}{K_M + S^* \bar{S}} \quad (9)$$

2.5 Boundary Conditions

No flux conditions exist on the curved surface of the droplet, i.e. $\nabla \bar{S} = 0$, $\nabla \bar{P} = 0$. On the electrode, it is assumed that P is readily consumed (i.e. $\bar{P} = 0$) and there is a no flux condition for S. On the edges of the electrode, we assume $\bar{S} = 0$, $\bar{P} = 0$. Furthermore, we assume no flux conditions in the area of enzyme which is not contacting the droplet.

Table 1: Base-case kinetic and transport parameters and initial conditions for the model.

Parameter	Units	Value
k_{+1}	m ³ mol ⁻¹ s ⁻¹	1.20·10 ⁻²
k_{-1}	s ⁻¹	0.68·10 ⁻³
k_2	s ⁻¹	5.00·10 ⁻²
k_M	mol m ⁻³	4.22
E_0	mol m ⁻³	1.25·10 ⁻¹
V_{\max}	mol m ⁻³ s ⁻¹	6.30·10 ⁻³
$D_{S,\text{droplet}}$	m ² s ⁻¹	6.00·10 ⁻¹⁰
$D_{S,\text{enzyme}}$	m ² s ⁻¹	3.00·10 ⁻¹⁰
$D_{P,\text{droplet}}$	m ² s ⁻¹	6.00·10 ⁻¹⁰
$D_{P,\text{enzyme}}$	m ² s ⁻¹	3.00·10 ⁻¹⁰
C_{S0}	mmol L ⁻¹	4.00

3. Results and Discussion

Reaction kinetic and transport phenomena parameters and initial conditions (including the initial enzyme concentration, E_0) used as a base case in the model are shown in Table 1. The choice of initial glucose (substrate) concentration, C_S , is based on the minimum fasting blood glucose concentration for a healthy individual (Sarwar et al., 2010). Sensitivity analyses investigate the effect of varying reactant and product diffusivities in the droplet and enzyme layer and initial blood glucose concentration on the glucose biosensor electrode current density, as well as output reactant and product concentration profiles. Other parameters are kept constant for all sensitivity analyses.

Fig. 2 shows sensitivity analyses for the transient current density of the biosensor electrode. At low substrate diffusivities in the droplet ($D_{S,\text{droplet}}$), longer timescales are required for substrate to reach the enzyme layer and produce current (Eq. 3); consequently, a plateau in current density is gradually attained. For high $D_{S,\text{droplet}}$, substrate reaches the enzyme layer faster than it is reacted, leading to an initial peak in

current density followed by a gradual decrease. For low substrate diffusivities in the enzyme layer ($D_{S,enzyme}$), lesser enzyme layer surface areas are available for substrate reaction, and hence current density peaks are observed followed by gradual decline. As $D_{S,enzyme}$ increases, a greater surface area is available for reaction, and thus plateaus are gradually attained. As product diffusivities in the droplet ($D_{P,droplet}$) increase, less product produced in the enzyme layer occupies enzyme surface area for reaction, hence induced current densities increase. When product diffusivity in the enzyme layer ($D_{P,enzyme}$) is lower, less area is available for reaction, due to the lower propensity for product transport from enzyme, and longer times are required for maximum currents.

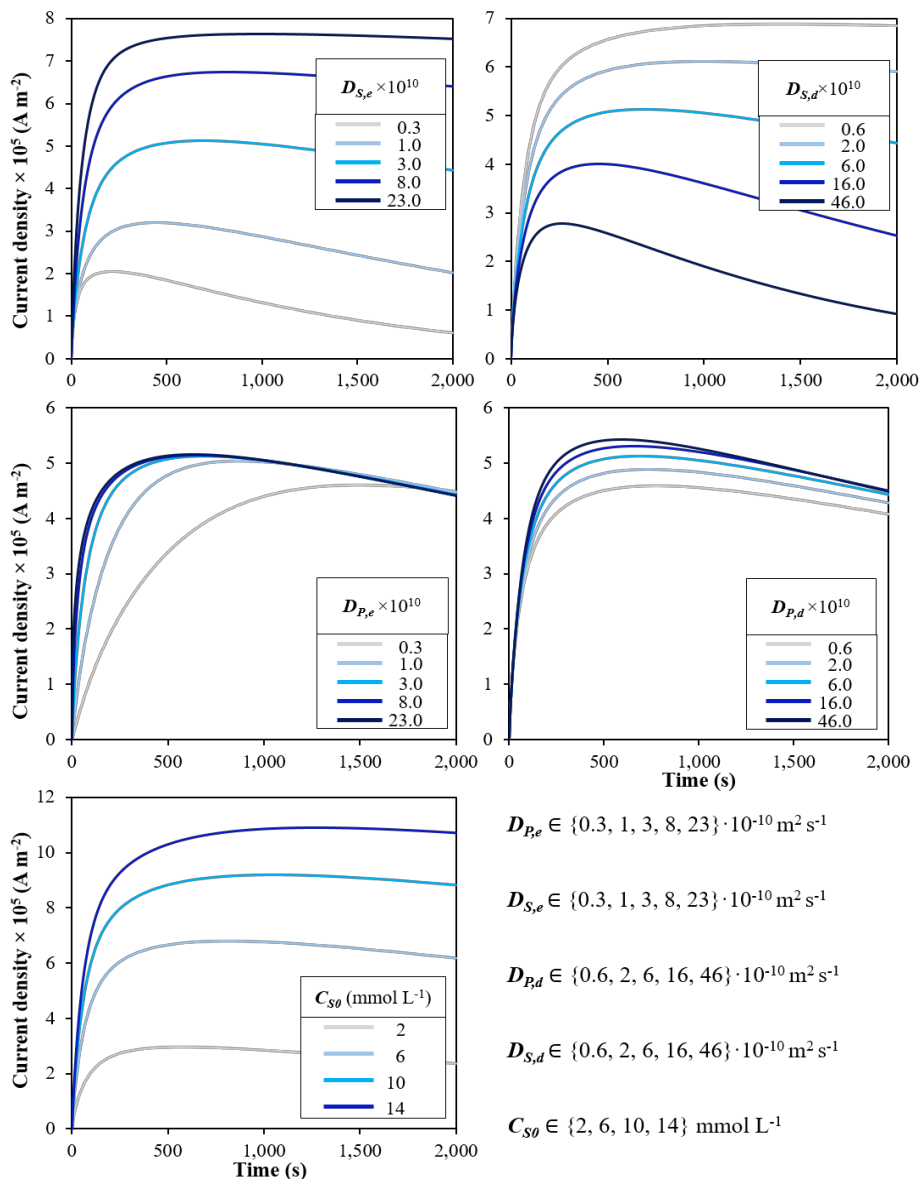


Figure 2: Effect of model parameters on transient biosensor electrode current densities.

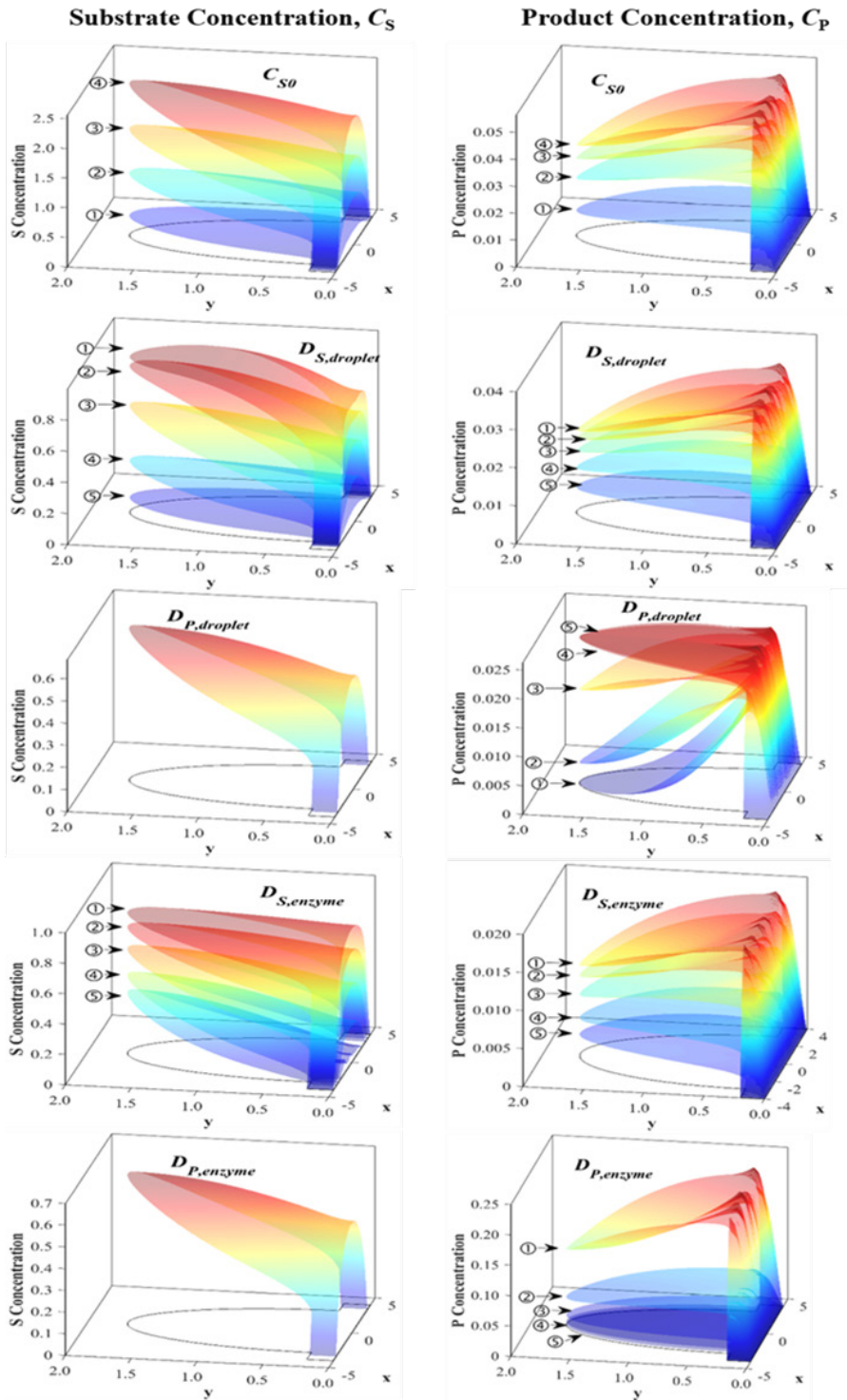


Figure 3: Sensitivity of output concentration profiles vs. model parameters (Table 2).

Table 2: Parameter variation for the model-based sensitivity analysis shown in Fig. 3.

Fig. 3 notation	C_{S0} (mmol L ⁻¹)	$D_{enzyme} \cdot 10^{10}$ (m ² s ⁻¹)	$D_{droplet} \cdot 10^{10}$ (m ² s ⁻¹)
①	2.0	0.3	0.6
②	6.0	1.0	2.0
③	10.0	3.0	6.0
④	14.0	8.0	16.0
⑤	–	23.0	46.0

Transient current densities illustrated in Fig. 3 clearly increase with initial blood glucose concentrations; greater initial substrate (glucose) concentrations incur greater amounts of H₂O₂, which thus induces greater current (eqs. 1-3). Current densities plateau beyond 500 s for all initial concentrations considered. Biosensor performance is strongly dependent on patient-to-patient physiological variability, as well as on the temperature dependence and sensitivity of hence varying enzymatic reaction kinetic parameters.

Fig. 3 shows the variation of substrate and product concentration profiles in the droplet with varying transport properties; parameter values associated with individual analyses are provided in Table 2. Increasing initial blood glucose concentrations lead to higher concentration profiles throughout the droplet. As substrate diffusivity in the droplet ($D_{S,droplet}$) increases, concentrations decrease throughout the droplet; expectedly, product concentrations decrease with increasing distance (y) from the enzyme layer. Increasing product diffusivity in the droplet ($D_{P,droplet}$) significantly affects profiles due to the effect of product diffusion on enzyme layer surface availability discussed previously. Increasing substrate diffusivities in the enzyme layer ($D_{S,enzyme}$) result in decreasing concentrations in the analysed blood droplet. Increasing product diffusivities in the enzyme layer ($D_{P,enzyme}$) incur rapidly decreasing product concentrations in the droplet due to the preferential diffusion of product in the enzyme layer to the blood droplet.

4. Conclusion

Numerical modelling of a blood droplet on a glucose biosensor with parametric sensitivity analysis has been conducted to investigate the sensitivity of glucose biosensor performance to essential operating parameters. Transient electrode responses (current densities) vary significantly with initial blood glucose concentration. Sensitivity analyses show larger electrode responses are gained for higher enzyme layer diffusivities. This work illustrates the importance of ensuring high current densities for effective biosensor performance and the potential for tuning enzyme layer properties for the design of high-fidelity glucose biosensors for their application in modern medicine.

5. Acknowledgements

The authors gratefully acknowledge the support of Prof. Hugh McCann (Head of the School of Engineering, University of Edinburgh) via a HoS Undergraduate Summer Research Placement Fellowship awarded to Mr. F. McIlwaine. Helpful discussions with Mr. Samir Diab, Drs N. Radacsi (UoE) and H.L. Tan (UiTM) are also acknowledged.

References

- R. Baronas and J. Kulys, 2008, *Sensors*, 8, 4800-820.
- A. Cambiaso, L. Delfino, M. Grattarola et al., 1996, *Sensors and Actuators*, 33, 203-207.
- X. Peng, X. He, D. Liu et al., 2016, *Value Health*, 19, A683-A684.
- N. Sarwar, P. Gao, S. R. K. Seshasai et al., 2010, *Lancet*, 375, 2215-2222.

Industrial Scale Experiments towards the Development of Process Evaluation Models for Continuous Pharmaceutical Tablet Manufacturing

Kensaku Matsunami,^a Takuya Nagato,^b Koji Hasegawa,^b Masahiko Hirao,^a
Hirokazu Sugiyama^{a,*}

^a*Department of Chemical System Engineering, The University of Tokyo, 7-3-1 Hongo, Bunkyo-ku, Tokyo, 113-8656, Japan*

^b*Research & Development Department, Powrex Corporation, 8-121-1 Kitaitami, Itami-shi, Hyogo, 664-0831, Japan*

sugiyama@chemsys.t.u-tokyo.ac.jp

Abstract

Large-scale experimental results are presented, which compared batch and continuous pharmaceutical tablet manufacturing towards the development of process evaluation models. In the experiment, fluidized bed, high shear, and continuous granulators were used with the same raw materials, and the similarities and differences in the process and the products were analyzed. The maximum scale was 100 kg/lot. The experimental results were compared regarding quality of granules as well as tablets, and also regarding economic performance of the process. The analysis revealed significant differences in the product such as size/shape of granules; yield of the process was found to be an improvement opportunity for the continuous technology. Based on these findings, a strategy was created to develop models that can support process design of tablet manufacturing with considering product quality and process performance.

Keywords: Continuous manufacturing, granulation, product quality, economy, process design

1. Introduction

Continuous manufacturing is attracting attention in the pharmaceutical industry as an alternative to conventional batch manufacturing (Lee et al., 2015). Different authors contributed to the computer-aided design/operation of continuous manufacturing processes, such as Jolliffe and Gerogiorgis (2016) for active pharmaceutical ingredients (APIs), or Singh et al (2015) and Kruisz et al (2017) for tablets. Currently, the industry is highly interested in the capability of this novel manufacturing technology, especially regarding product quality and process economy. With a focus on tablet manufacturing, Järvinen et al (2015) compared product quality, and Sugiyama et al (2017) compared the economic performance of batch and continuous technologies.

For process designers, models would be of high relevance that could estimate the resulting performance depending on the technology choice given the product components. Meng et al (2017) presented the effects of the process- and design-parameters on granule size distribution in the continuous technology, with comparing physical properties of granules. However, the previous experiments remained on a small

scale, which leaves the opportunity for a larger scale investigation to develop realistic models. In this work, we

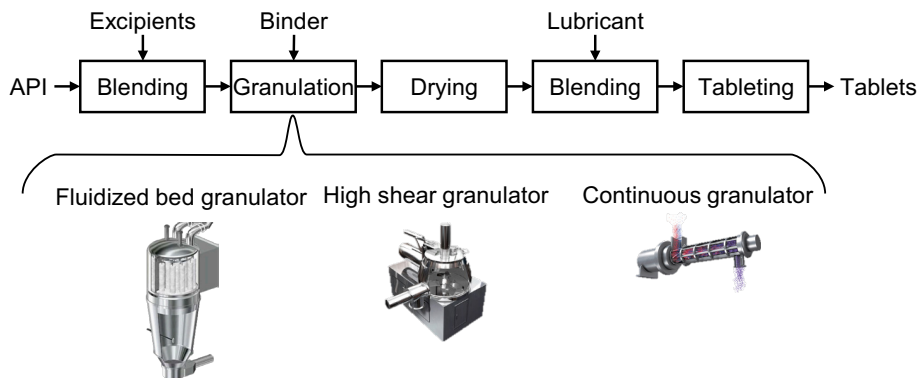


Figure 1 Manufacturing processes and granulators used in the experiments

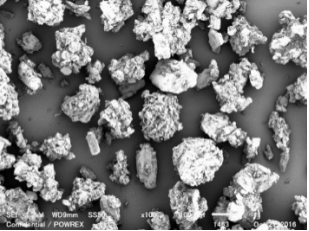
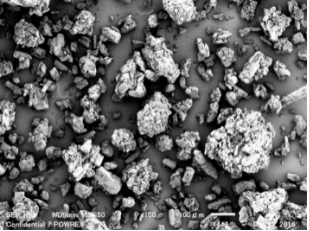
performed large-scale experiments at maximum 100 kg/lot, for comparing batch and continuous tablet manufacturing technologies, towards the development of design-support models for the industry.

2. Materials and methods

Tablets were produced in the experiment, which contained 30 % ethenzamide and 70 % consisting of mannitol and crystalline cellulose as excipients, hydroxypropyl cellulose as a binder, and magnesium stearate as a lubricant. Figure 1 shows the manufacturing process consisting of the units of mixing, granulation, drying, blending, and compression. Wet granulation method was applied in the experiments; Figure 1 also shows the granulators used. The initial experiment was conducted at the scales from 5 to 10 kg/lot, and the full-scale experiment was done at the scale of 100 kg/lot. As shown in Figure 1, two types of batch technology and one type of continuous technology were adopted in the experiment. The speed of the continuous granulation was set as 25 kg/h. Although the mechanics of granulator were different between batch and continuous technologies, same materials were used with the same condition through the experiments.

During and after the experiments, quality of granules and tablets, and the characteristics of the process were assessed for analyzing the differences between batch and continuous technologies. Particle shape, particle size, and bulk density were measured for the granules, and hardness, API content, and dissolution were measured for the tablets. For assessing the tablets, the following was set as the target: (i) tablet hardness is higher than 40 N, (ii) API content is between 95 % and 105 % of an absolute target, and (iii) dissolution rate is higher than 80 % within 30 minutes. The processes were characterized by the yield of the entire process, the causes of losses, and the amount of each loss cause. Here, yield was defined as the mass ratio of the total amount of the final tablet to that of the input raw materials. For the sake of space, this paper reports the results of the full-scale experiment mainly, with focusing on fluidized bed granulation and continuous granulation.

Table 1 Characterization results of granules and tablets

	Batch technology (fluidized bed)	Continuous technology
Granules		
SEM pictures		
Mean diameter	1.627×10^{-4} m	2.031×10^{-4} m
Loose bulk density	348 kg/m^3	510 kg/m^3
Tablets		
Tablet hardness	65 N	65 N
API content	97.5 %	99.3 %

3. Results

3.1. Characterization results of granules

The upper three rows of Table 1 shows the characterization results of granules: scanning electron microscopy (SEM) pictures, mean diameter, and loose bulk density. The SEM pictures suggest that the granules produced by fluidized bed granulation were porous, and those by continuous granulation were spherical. From the results of mean diameter and loose bulk density, the granules produced by the fluidized bed were smaller and had a lower density than those by continuous granulation.

3.2. Characterization results of tablets

The lower two rows of Table 1 shows the characterization results of tablets: tablet hardness and API content, which satisfied the target values specified.

Figure 2 (a) shows the comparative results of dissolution test between batch and continuous technologies, where all tablets achieved the target value, i.e., higher than 80 % within 30 minutes. In the pharmaceutical industry, so-called similarity factor f_2 is widely used to evaluate the similarity of one dissolution profile with the other. The

$$f_2 = 50 \cdot \log \left\{ \left[1 + \frac{1}{n} \sum_{t=1}^n (R_t - T_t)^2 \right]^{-0.5} \times 100 \right\} \quad (1)$$

factor f_2 is defined as Eq. (1):

where the parameters n and R_t/T_t represent the number of time points, and the dissolution values at time t . If value of f_2 is higher than 50, dissolution of produced tablets is regarded as equivalent to the reference in the industry. The calculated value of f_2 between

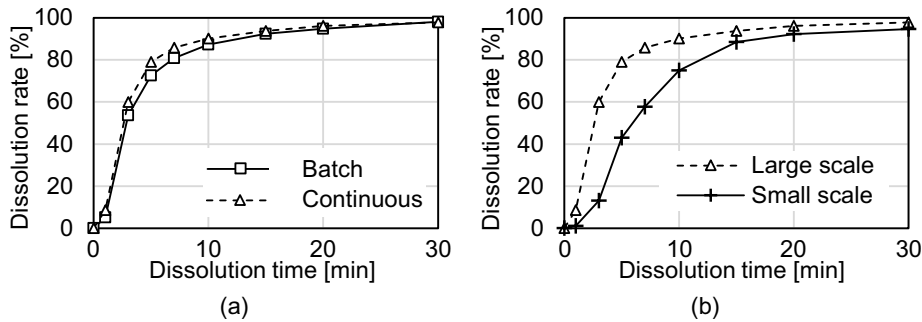


Figure 2 Results of dissolution test: (a) comparison between batch and continuous and (b) comparison between large and small scale in continuous technology

batch (fluidized bed) and continuous was 76.0, which conformed the capability of the continuous technology at an industrial scale. Further new findings were obtained by comparing the results of dissolution tests between small- and large-scale experiments.

Figure 2 (b) shows the comparative results of dissolution test between the initial (5 kg/lot) and the full-scale (100 kg/lot) experiments in continuous technology. Although same equipment was used in both two experiments, the value of f_2 was calculated as 38.2, i.e.,

the profiles were judged as different. When the full-scale experiment was conducted for the first time, all the conditions were specified the same as in the initial experiment, except for the running time (changed from 12 minutes to 4 hours). However, the completion of the four-hour-operation needed adjustment of machine equipment and also the inlet water content, which caused the difference of the dissolution profile. This experiment was an actual case where the scale-up, which is believed to be easy in continuous technology, was not straightforward.

3.3. Characterization results of process

Regarding the performance of the process, yield was analyzed by measuring and calculating the amount of the final products and losses, which is summarized in Figure 3. In batch technology, yield was more than 93 % where the major causes of losses were sticking to the granulator and condition setting of compression. However in continuous technology, yield was 89 %, and a major cause of losses was stabilization at the beginning of the process.

Regarding this improvement opportunity of the continuous technology, a further investigation was performed on the dynamic variation of mean granule diameter monitored by a process analytical technology (PAT) tool. This PAT tool was only for monitoring, and not for controlling the process. In the experiment, nine minutes were needed until the mean diameter of granules became stable, until which the products were discarded. The total rejected amount was 3.75 kg, i.e., 3.53 % lowering of yield, indicated as “stabilization of the process” Figure 3 (b). However, after this nine minutes, mean granule diameter and also dissolution profiles of the sampled tablets were not changing significantly, i.e., the process was stable for the remaining running time. These findings indicate that stabilizing the start-up operation is a great improvement opportunity for continuous technology to be economically competitive against batch technology.

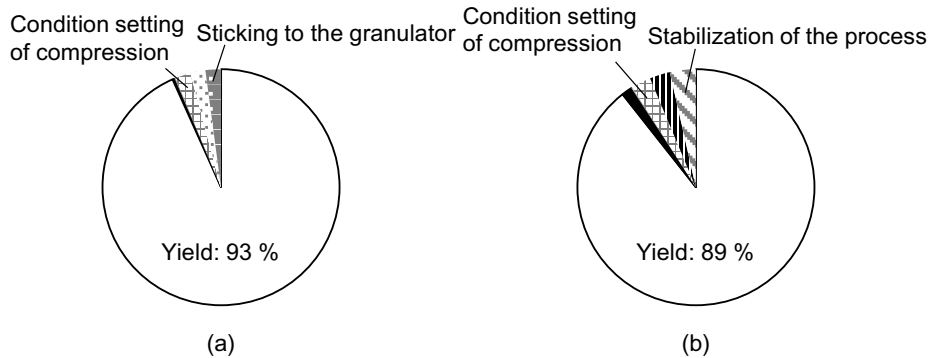


Figure 3 Results of yield and losses: (a) batch technology (high shear granulation), and (b) continuous technology

4. Strategy for model development

This chapter presents the way to utilize the results of large-scale experiments towards the development of process evaluation models. Figure 4 shows an overview of the models to be developed. The input parameters are defined, which could affect the quality of granules and tablets, such as physical properties of raw materials, machine types, and process conditions. The final objectives are the set of information that the process designer would require for decision making, such as dissolution profile of tablets. Also, the intermediate objectives are defined that are affected by the input parameters and affect the final objectives, such as bulk density of granules. The strategy is to describe each relationship in the entire system (indicated by arrows in Figure 4) as a mathematical model (indicated by the equation in Figure 4).

The experimental results shown in the previous chapter serve as the initial step of such model development. For example, a relationship was observed between the machine types, i.e., fluidized bed or continuous granulator, and the physical properties of granules/tablets, e.g., size/shape, or tablet hardness. Process conditions such as the water content amount during granulation process were also found to influence on the dissolution profile of the tablets in the continuous manufacturing. Quantifying such tendency on continuous technology is already novel by itself, because the knowledge of the process/technology is still to mature, as compared to long-established batch technology.

Our strategy for the model development is to conduct further experiments with varying the values of the input parameters and to investigate the impact on the outcome. Design of Experiments (DoE) based approach is currently undertaken to find the critical input parameters, considering both physical properties of raw materials and process conditions.

5. Conclusions and outlook

We presented 100 kg-scale experimental results on batch and continuous manufacturing technologies towards the development of design-oriented process evaluation models. To our knowledge, this is the first time report of the industrial scale experiments of continuous technology, being compared with the conventional batch technology. In the experiment, differences were observed in the granule properties between two technologies, however, looking into the obtained tablets, the dissolution profile was

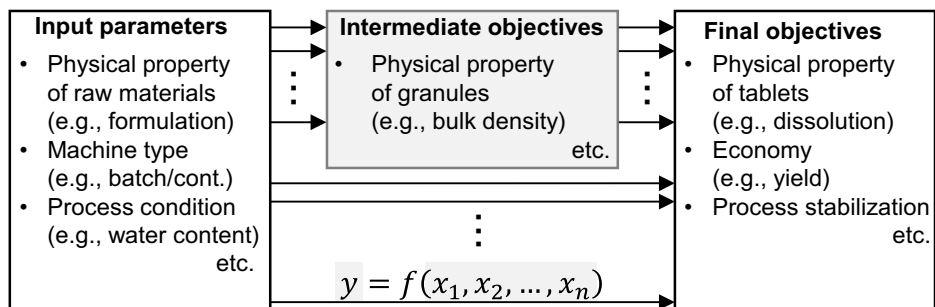


Figure 4 Overview of process evaluation models

similar, and the quality was all above the target values. Regarding continuous technology, stabilization of the start-up operation was identified as the opportunity to reduce the product loss and to improve economic performance. As to the future work, further DoE-based experiments will provide the information for developing process evaluation models that can be comprehensively used for process design of pharmaceutical tablet manufacturing.

Acknowledgement

Financial supports by Grant-in-Aid for Young Scientists (A) No. 17H04964 from Japan Society for the Promotion of Science are acknowledged.

References

- M. A. Järvinen, M. Paavola, S. Poutiainen, P. Itonen, V. Pasanen, K. Uljas, K. Leiviskä, M. Juuti, J. Ketolainen, K. Järvinen, 2015. Comparison of a continuous ring layer wet granulation process with batch high shear and fluidized bed granulation process, *Powder Technol.*, 275, 113–120
- H. G. Jolliffe, D. I. Gerogiorgis, 2016. Plantwide design and economic evaluation of two Continuous Pharmaceutical Manufacturing (CPM) cases: Ibuprofen and artemisinin, *Comput. Chem. Eng.*, 91, 269–288
- J. Kruisz, J. Rehrl, S. Sacher, I. Aigner, M. Horn, J. G. Khinast, 2017. RTD modeling of a continuous dry granulation process for process control and materials diversion, *Int. J. Pharm.*, 528, 334–344
- S. L. Lee, T. F. O'Connor, X. Yang, C. N. Cruz, S. Chatterjee, R. D. Madurawe, C. M. V. Moore, L. X. Yu, J. Woodcock, 2015. Modernizing pharmaceutical manufacturing: from batch to continuous production, *J. Pharm. Innov.*, 10, 191–199
- W. Meng, S. Oka, X. Liu, T. Omer, R. Ramachandran, F. J. Muzzio, 2017. Effects of process and design parameters on granule size distribution in a continuous high shear granulation process, *J. Pharm. Innov.*, 12, 283–295
- R. Singh, A. D. Román-Ospino, R. J. Romañach, M. Ierapetritou, R. Ramachandran, 2015. Real time monitoring of powder blend bulk density for coupled feed-forward/feed-back control of a continuous direct compaction tablet manufacturing process, *Int. J. Pharm.*, 495, 612–625
- H. Sugiyama, K. Matsunami, K. Yabuta, 2017. Process systems engineering approaches for drug product manufacturing from tablets to injectables, *Comput. Aided Chem. Eng.*, 40, 2785–2790

A Process System Approach to Nose-to-Brain Delivery of Biopharmaceutics

Costas Kiparissides,^{a,b*} Aleck H. Alexopoulos,^b Philippos Karageorgos,^b
Athina Vasileiadou^b and Vassilis Bourganis^b

^a *Department of Chemical Engineering, Aristotle University of Thessaloniki, 54124, Thessaloniki, Greece.*

^b *Chemical Process & Energy Resources Institute, 6th km Harilaou-Thermi rd., P.O. Box 60361, 57001, Thessaloniki, Greece*

costas.kiparissides@cperi.certh.gr

Abstract

A process systems approach towards the development and integration of computational models to describe the application, adhesion, spreading, and stability of a reacting hyaluronic acid gel onto the Olfactory mucous layer as well as the release of drug from particles dispersed in the hydrogel matrix, diffusion, and transfer through the mucous layer is described. The initial results from this systems approach reveal the connection between the physico-chemical processes which can lead to design limitations, e.g., gel extrusion time influences the extent of spreading on the mucous layer.

Keywords: adhesion, spreading, gelation, hydrogel, olfactory.

1. Introduction

Central nervous system (CNS) disorders (e.g., multiple sclerosis, Alzheimer's, Parkinson's, etc.) represent a growing public health issue, primarily due to the increased life expectancy and the aging population. The treatment of such disorders requires the delivery of therapeutic compounds to the brain in sufficient amounts to elicit a pharmacological response. The role of the nose as an entry point for the brain-targeted delivery of various medications has long been identified, revealing an unprecedented opportunity to deliver drugs to the brain, thus posing a promising alternative to intravenous delivery. Although highly advantageous due to its non-invasive nature, rapid onset of action, highly localized delivery, and low systemic exposure, the delivery of medications to the brain via the nasal cavity exhibits particular challenges associated with poor permeability across biological barriers (e.g., nasal and olfactory mucosae) and poor stability attributed to enzymatic activity observed in the nasal cavity.

The development of an innovative nanotechnology-based formulation is described that can be applied to the nasal olfactory region for the chronic treatment of CNS disorders. The novel formulation consists of biodegradable polymer nanoparticles loaded with drugs (e.g., long-acting cognition enhancing insulin analogues). The drug loaded particles are embedded into a biodegradable hydrogel that is deposited, via a nasal endoscopic applicator as a thin liquid-gelling film, onto the olfactory region (Figure 1). By controlling the molecular and morphological properties of the biodegradable hydrogel and the embedded polymeric nanocarriers, a controlled and sustained release of the therapeutics can be achieved thus resulting in improved drug delivery.

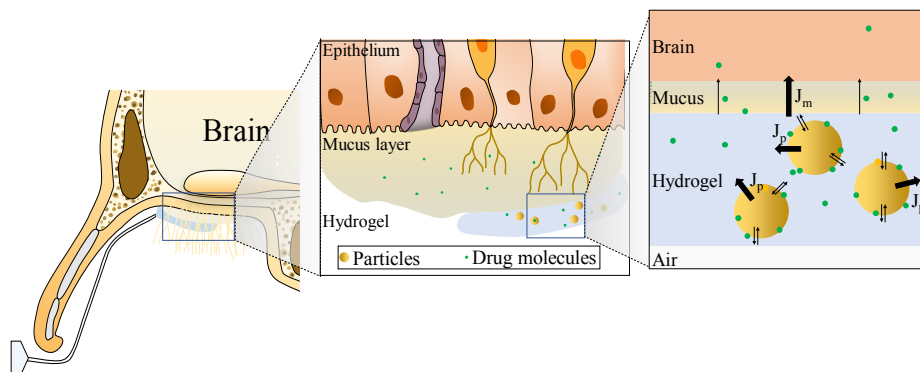


Figure 1. Hydrogel application, spreading, adhesion and drug release

In this work, a process systems computational approach, comprising models at different time and length scales, is applied to elucidate the fundamental physical, transport and biological processes related with nose-to-brain delivery of biopharmaceutics. In particular, it includes a CFD-based computational model to describe the flow of a reactive polymer solution through an applicator in terms of flow rate and tube characteristics (e.g., tip geometry, diameter). The extrusion of the reactive polymer solution and its conversion to a solid hydrogel film is examined for different tip placements, tip shapes, and total extruded matrix volume. The muco-adhesive forces, which control the hydrogel film spreading, are considered via the development of a hydrogel/mucus model. The long-term stability of the deposited hydrogel matrix is examined in terms of the hydrogel swelling and degradation kinetics. A dynamic drug release model is developed to describe the drug release rate from the drug-loaded microcarriers embedded in the hydrogel matrix in terms of molecular and morphological properties of polymeric carriers-hydrogel system. From the numerical solution of the above computational models, the dynamic drug mass transfer rate from the hydrogel matrix to the mucosa interface will be calculated. Finally, the drug flux from the hydrogel-mucosa interface to the olfactory bulb (i.e., drug transfer through the mucous layer in series with the epithelium) will be calculated.

The various mathematical models will be integrated following a PSE approach to obtain a general computational framework that will identify the key characteristic system's design parameters that will optimize the complex formulation-deposition process to achieve a desired therapeutic effect.

2. Computational Model

The overall model integration is shown in Figure 2. There are two groups of sub-models which differ mostly in their time scale. Group A describes the extrusion of the gelling hyaluronic acid solution as well as the hydrogel adhesion, spreading, and stability on the olfactory mucous layer. Group B describes the long terms changes in hydrogel (i.e., due to gelation, swelling, and degradation), the drug diffusion, and the transfer rate through the olfactory mucous layer. The underlying models are tightly interconnected in each group. Group A and B are connected only by the hydrogel shape after the end of the application process (gel shape, $G(x,y,z,t_{ext})$).

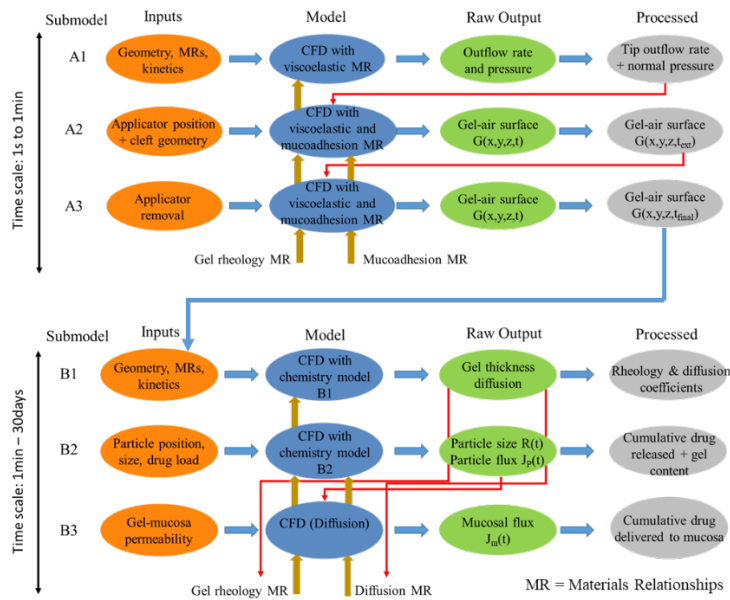


Figure 2. Modelling approach in N2B-patch programme. (de Baas, 2017).

In order to design an optimal in-situ gelling system the relationship between gelation, delivery (i.e., extrusion from the applicator tube), attachment (i.e., mucoadhesion), spreading, and stability must be described (i.e., Group A models in Figure 2). These factors are shown in Figure 3. The hydrogel is formed in situ according to a characteristic gelation time, t_{gel} . The hydrogel is delivered to the olfactory mucosa via extrusion from an applicator tube with an application time of t_{ext} . The hydrogel adheres to the mucous layer and spreads, with a characteristic time of t_{spr} , under the influence of surface forces and viscoelasticity which vary with continuing gelation.

It is clear that if the application time is larger than the gel time $t_{ext} \gg t_{gel}$ then the extrusion process becomes problematic. Moreover, if $t_{gel} \ll t_{spr}$ there is insufficient spreading over the mucous layer, while if $t_{gel} \gg t_{spr}$ the gel will deform under the influence of gravity and detach due to capillary instability.

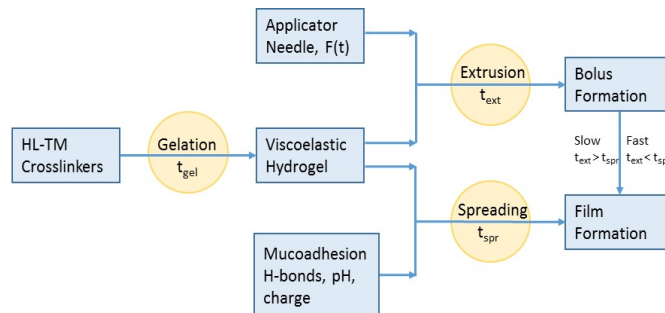


Figure 3. Key mechanisms involved in hydrogel extrusion, gelation, and spreading.

2.1. Applicator Flow.

In the applicator device hyaluronic acid (HA) and cross-linking fluids are mixed in situ and then directed to the applicator tip in the Olfactory cleft while undergoing gelation. For this system it can be shown that both the Reynolds and the Dean numbers are small, i.e., $\ll 1$. Consequently there are no inertial or secondary-flow effects and the problem can be treated as steady-state creeping flow through a straight tube.

The pressure drop through the applicator tube is determined by (Bird et al., 1987):

$$\Delta P = \frac{8Q}{\pi R^4} \int_0^L \eta(z) dz \quad (1)$$

where Q is the flow rate and $\eta(z)$ is the shear viscosity which varies with position due to the gelling reaction. For HA solutions the shear-viscosity over a range of shear rates from 10^{-3} to 10^3 s^{-1} were reported by Malecki et al. (2007) and have been found to follow a power law model, e.g., with coefficients: $m=14$ and $n = 0.2951 \text{ wt. \%}$.

Assuming a simple first order scheme for the gelling kinetics and extending the shear-rate behavior of the HA solution to the early phase of gelation by increasing the low shear-rate power-law viscosity value Eq.1 can be solved. The computed pressure drop, increases with the Damköhler-I number, $Da = t_{\text{ext}}/t_{\text{gel}}$, which is equal to the ratio of the extrusion to the gelation times. The key design criteria is to maintain $Da < 1$ because for larger values, i.e., $Da > 1$ the pressure drop in the applicator tube increases significantly. A similar approach can be employed with more detailed kinetic schemes for gelation. CFD simulations can also be performed to include the static mixer and examine the extent of mixing and also possible dispersion effects within the applicator tube.

2.2. Droplet Spreading.

To examine the spreading of large hydrogel droplets on solid surfaces the approach described by Härth and Schubert (2012) is employed where the droplet shapes are approximated with spherical caps. This is a good approximation if the droplet radius is significantly larger than the capillary length.

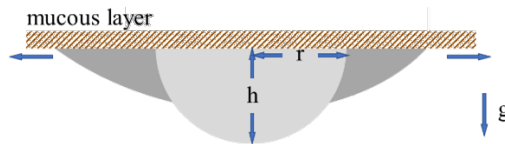


Figure 4. HA droplet spreading over the olfactory mucous surface

The net driving force, F_{tot} , for deformation and spreading of the hydrogel droplet is a sum of capillary, gravitational, viscous, and elastic terms.

$$F_{\text{tot}} = F_C + F_G + F_V + F_E \quad (2)$$

If it is further assumed that the net acceleration is zero, then the rate of change in the radius, dr/dt , can be obtained according to:

$$0 \approx 2\pi r \left(S + \gamma_L \frac{2r^2}{r^2 + h^2} \right) + \frac{4\rho g V^2}{3\pi r^3} + \frac{r^6 \eta \frac{dr}{dt}}{\xi V^2} + 2\pi r h \frac{\eta}{\lambda} f\left(r, \frac{t}{\lambda}\right) \quad (3)$$

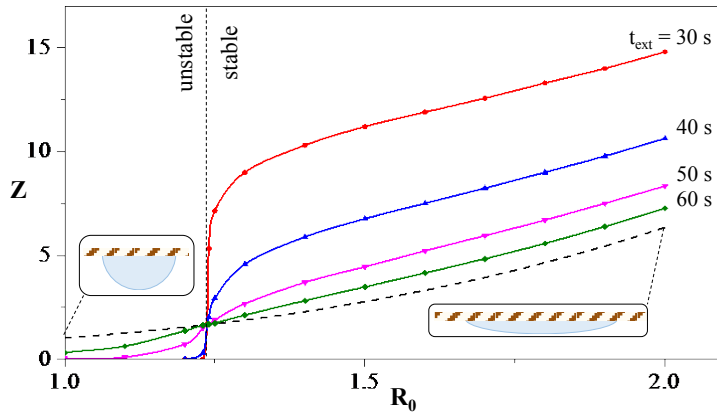


Figure 5. Initial (dashed line) and final (full line) droplet aspect ratios, i.e., $Z = r/h$, for different extrusion times and initial droplet radii, R_0 . ($V = 2 \text{ cm}^3$, $\gamma = 45 \text{ mN/m}$, rheology data from Lee et al., 2008).

where γ_L is the surface tension, S is the spreading coefficient, V is the droplet volume, ρ is the hydrogel density, $\xi = 37.1 \text{ m}^{-1}$, and f is an elastic spreading function.

In Figure 5 the spreading of hydrogel droplets on the olfactory mucous layer is shown. It is clear that the final aspect ratio depends strongly the initial contact radius of the droplet as well as the applicator extrusion time due to the gelling reaction and changing rheological properties. Capillary instability occurs below values of $R_0 = 1.237$, which corresponds to a critical Bond number of:

$$Bo = \rho g R_0^2 / \gamma = 12 \tag{4}$$

It should be noted that small unstable droplets (i.e., $z < 1.665$ and $R_0 < 1.237$) can be kinetically stable due to the increasing elasticity and viscosity of the hydrogel.

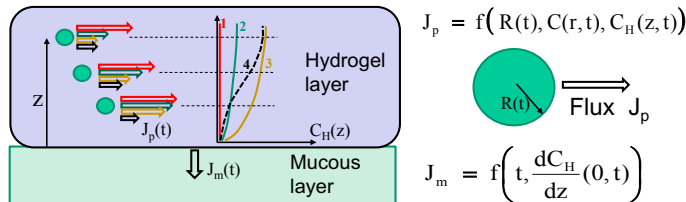


Figure 6. HA droplet spreading over the olfactory mucous surface

2.3. Drug Release and Diffusion.

The drug release and diffusion is also a highly complicated process operating over longer times (days and weeks instead of seconds) Figure 6. The drug is released from the dispersed particles and then transfers through the hydrogel to the olfactory mucous layer. At the same time there is continuing gelation combined with swelling and degradation of the hydrogel. Consequently the particles experience continuously changing local environments and therefore drug release rates. The flux from the hydrogel to the mucous layer controls the net flux to the brain and is connected to the particle release flux according to Eq. (5).

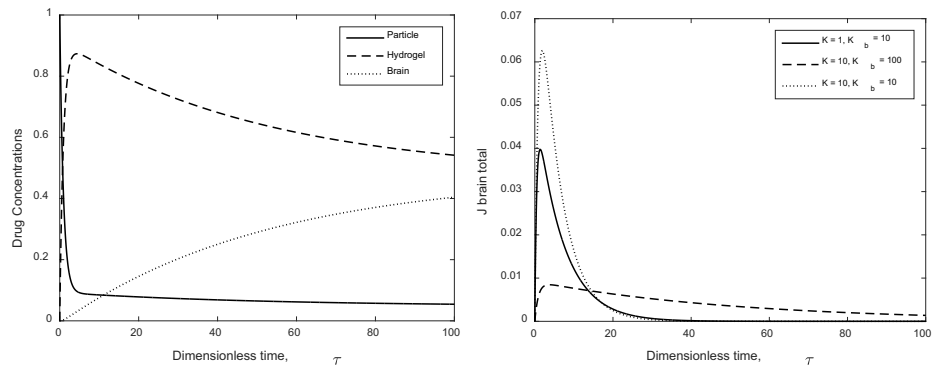


Figure 7. Hydrogel drug transfer. (a) Dimensionless drug concentration in the particle, hydrogel, and brain, (b) Total flux to the brain. K is a dimensionless drug release rate and K_b is a dimensionless ratio of release to mucous layer transfer rates.

$$J_m(t) = NJ_p(t) + \frac{d}{dt} \int_0^H C_H(z, t) dz \quad (5)$$

where N is the particle and C_H the drug concentrations in the hydrogel.

In the case of surface loaded drug release by adsorption/desorption dynamics the drug concentration and hydrogel to mucous layer flux are shown in Figure 7.

3. Conclusions

A process systems approach taking into account the key processes and their relevant time and length scales is necessary to describe nose to brain drug delivery using hydrogel films. The applicator function depends critically on the extrusion and gelation times while the hydrogel gel spreading depends on the applied volume and the extrusion time. Different flux behaviour can be found depending on the state of the hydrogel, the drug diffusion coefficient, and the particle loading profile.

Acknowledgement

This work is part of the N2B-patch EU Horizon 2020 No. 721098 programme.

References

- R.B. Bird, R.C. Armstrong, and O. Hassager, 1987, Dynamics of polymeric liquids. Volume 1. Fluid mechanics. 2nd Edition, John Wiley & Sons, New York.
- A.F. de Baas (Ed.), 2017, Modelling in H2020 LEIT-NMBP Programme Materials and Nanotechnology projects, 6th version, ISBN 978-92-79-63185-6, 278-286.
- M. Härth and D.W. Schubert, 2012, Simple Approach for Spreading Dynamics of Polymeric Fluids, *Macromol. Chem. Phys.*, 213, 654–665.
- F. Lee, J.-E. Chung, M. Kurisawa, 2008. An injectable enzymatically crosslinked hyaluronic acid-tyramine hydrogel system with independent tuning of mechanical strength and gelation rate, *Soft Matter*, 4, 880–887.
- A. Malecki, A.-L. Kjøniksen, B. Nyström, 2007, Anomalous Viscosity Behavior in Aqueous Solutions of Hyaluronic Acid, *Polymer Bulletin*, 59, 217–226.

Artificial vision system for the online characterization of the particle size distribution of bulk materials on conveyor belts

Mario Soprana,^a Andrea C. Santomaso,^b Pierantonio Facco^{a,*}

^a*CAPE-Lab, Computer-Aided Process Engineering Laboratory, Department of Industrial Engineering, via Marzolo 9, 35131 Padova, Italy*

^b*APT-Lab, Advanced Particle Technology laboratory, Department of Industrial Engineering, via Marzolo 9, 35131 Padova, Italy*

pierantonio.facco@unipd.it

Abstract

In this work, a methodology is presented to develop an artificial vision system to characterize the particle size distribution of granular products in motion on a conveyor belt. This methodology exploits the wealth of information stored in videos of the bulk material and, in particular, the information on the particle size distribution is extracted by multivariate and multiresolution image texture analysis.

The method is applied to the case of a granulated microcrystalline cellulose directly discharged from a hopper on a conveyor belt. The effectiveness of the presented methodology to estimate the particle size distributions is demonstrated in terms of estimation accuracy, velocity, reliability, and non-invasiveness of the system.

Keywords: granular materials, conveyor belt, particle size distribution, multivariate image analysis, multiresolution texture analysis.

1. Introduction

The characterization of the particle size distribution (PSD) of a granular material is of paramount importance in a wide series of industrial sectors (e.g.: pharmaceutical industry, food manufacturing, mineral or metals treatment). Typically, the PSD of a granular product can be characterized by means of hand-made measurements, which require trained and dedicated personnel who sieve and weigh samples of the granular materials. Unfortunately, this off-line procedure entails the loss of time, money and part of the material.

Among the innovative analytical technologies, artificial vision systems (AVS) gained great interest (Gosselin et al., 2008), because of their versatility, rapidity and the relatively low cost. However, the available AVS are limited to at-line systems that carry out the measurement of single particles, but do not measure the PSD from the bulk granular material.

Few examples of AVS were developed to characterize a granulate material from the granulate bulk. These methods exploit multivariate image texture analysis to describe the texture of the product surface that is included in an image scene. The textural information on the spatial variability of the light intensity are extracted, in such a way as

to relate image texture to the granulate PSD. These methodologies were proposed in different sectors, such as batch crystallization monitoring (Calderon De Anda et al., 2005), pharmaceutical powders classification (Garcia-Muñoz and Carmody, 2010) and particle growth monitoring in granulation (Nalesso et al., 2015). However, these applications are limited to the description of unimodal PSDs in terms of average particle diameter and particle diameter standard deviation.

Recently, Facco et al. (2017) proposed a systematic methodology for the development of an AVS for the estimation of multi-modal granulate materials PSDs from multivariate and multiresolution texture analysis of images of the product bulk. This comprehensive methodology was developed in the case of a static application within a laboratory environment, when the granulate material is settled in a static sample holder.

In this work, the methodology proposed by Facco et al. (2017) is extended to a dynamic case study in which the granular materials are moved by means of a conveyor belt and the collected images are the frames of a video. The proposed methodology is tested in the case of a granulated microcrystalline cellulose (MCC), which is a common excipient frequently utilized in the pharmaceutical manufacturing.

2. Experimental apparatus and video collection system

The experimental campaign was carried out in the apparatus that is represented in the scheme of Figure 1. The experimental system was composed by:

- a wedge shaped hopper with an outlet size of $0.075 \text{ m} \times 0.045 \text{ m}$ located at a distance of 0.005 m from the conveyor belt. The granulate material layer left on the conveyor belt was about 0.005 m thick and 0.110 m wide;
- a conveyor belt 0.750 m long and 0.250 m wide. The conveyor belt was moved by means of a three-phase electric motor (C.A.T.I. S.p.A., Padova, Italy) with a frequency of 50 Hz and a power of 0.37 kW , whose velocity was controlled by a Micromaster 420 inverter (SIEMENS, GmbH, Manchester, U.K.);
- an artificial vision system for the collection of the granulate mixtures videos (approximately of the duration of 20 s , each).

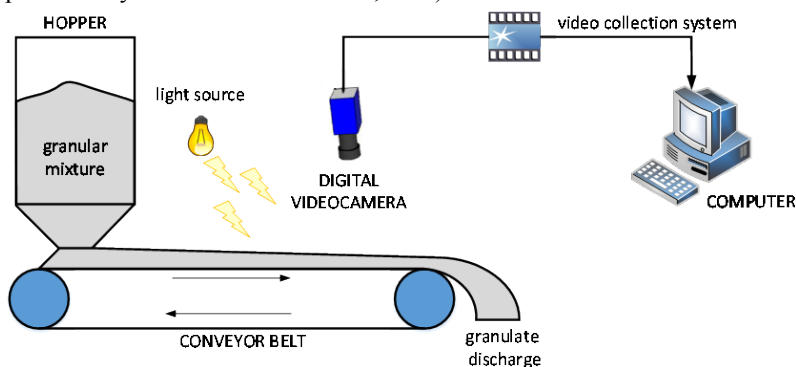


Figure 1. Scheme of the experimental apparatus for the collection of videos of granulate materials moved by means of a conveyor belt.

The image acquisition system was made of a digital mvBlueFox videocamera (Matrix Vision GmbH, Oppenweiler, Germany) with USB interface with proprietary

wxPropView software, which collected the videos at a rate of 10 frames per second. The camera was equipped with a F 3.5 diaphragm (utilized at its maximum aperture) and a Fujinon lens whose focal length is 25 mm. A lighting system was adopted to light up the mixtures. This was composed of a 180 LEDs ring with a power of 4.8 W for each LED. This was also used to shade the inspected granular material from the external environmental light.

3. Data collection and artificial vision system

In this work, the methodology adopted to build the AVS is the one proposed by Facco et al. (2017) and represented in Figure 2. This methodology is divided in two parts:

- design of experiments for mixture preparation and data collection;
- artificial vision system development and validation.

The data collection was organized preparing several batches of granulate MCC according to the procedure described in Nalesso et al. (2015). The granular material was sieved (Retsch AS 200, Germany) in 4 different classes (namely, 4 different ranges of particle size): range A of 600-800 μm particles, range B of 800-1000 μm particles, range C of 1000-1400 μm particles, and range D of 1400-2000 μm particles. These granular classes were then mixed in different proportions to prepare the granulate mixtures to be analyzed by the AVS.

Design-of-experiments (DoE; Montgomery, 2008) was then utilized to design the granulate mixtures. In particular, a space filling design was used, based on the algorithm of Kennard and Stone (1969) to suggest the mixtures to be prepared. A total of $N=100$ mixtures were prepared varying the factors of the DoE. The cumulative weight fractions of the granulate classes were varied on 11 levels: $y_i = 0.00, 0.10, 0.20, \dots, 0.90, 1.00$. Videos were collected for each mixture (appropriately charged and mixed in the hopper) that was moved by the conveyor belt. Three typical images [768 pixel \times 1024 pixel] collected in a video are shown in Figure 3. Only the images where granular material was present without including any portion of the conveyor (Figure 3b) were considered. A number of $R = 5$ frames of each mixture were extracted from the respective video (the image scene of each frame did not overlap with that of the following).

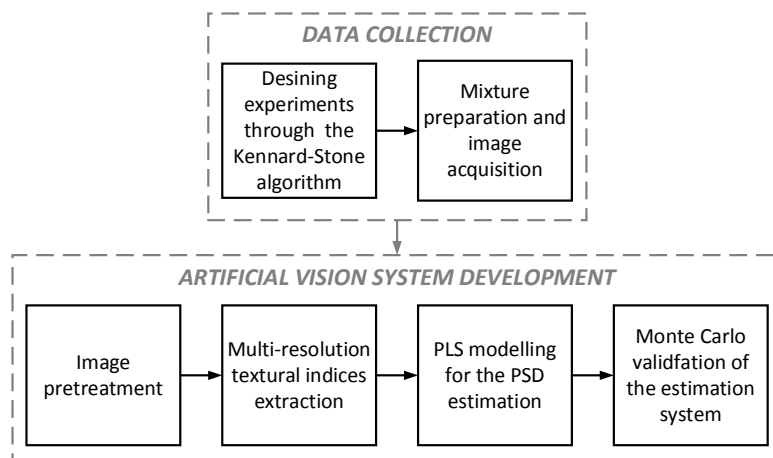


Figure 2. Scheme of the methodology proposed by Facco et al. (2017) to develop artificial vision systems for the PSD estimation in granulate mixtures.

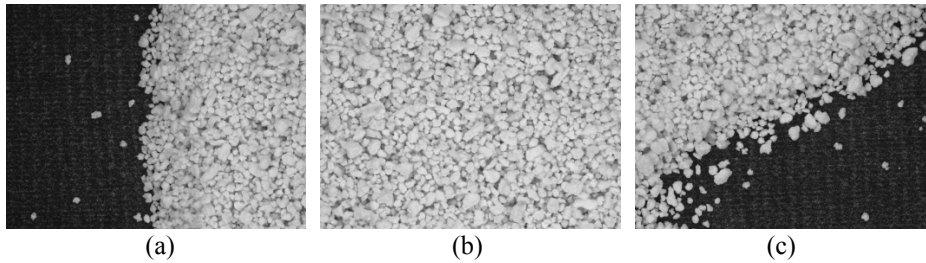


Figure 3. Typical images of a collected video for a granulate mixture: (a) initial image; (b) image scene during the video; (c) final image. Images containing portions of conveyor belt such as (a) and (c) were discarded before the analysis.

The artificial vision system was calibrated according to the methodology proposed by Facco et al. (2017):

- images were pretreated through image adjustment and wavelet detrending (Addison, 2002) to remove the effect of both the light shades and granulate surface curvature;
- multiresolution textural indices were extracted from the pretreated images following the procedure suggested by Facco et al. (2010). Wavelet decomposition was adopted to extract multiple resolution scales ($M=6$) of the pretreated images and $S=6$ statistical indices (e.g.: mean, standard deviation, skewness, kurtosis, entropy, energy) were then calculated from the histogram of pixel light intensities for every scale;
- multiway Partial Least Squares (PLS; Geladi and Kowalski, 1986; Nomikos and MacGregor, 1995) was used to estimate the cumulative weight fractions of the granulate classes in a mixture from the multiresolution textural indices, used as predictors. In particular, a global PLS model was used to identify the 30 calibration mixtures that were more similar to the validation one; than a local PLS model (Shank et al., 1998) was built on the selected mixtures for the estimation of the granulate mixture PSD in validation. Local models are tailored on each specific validation sample and guarantees a higher specificity of the model, accordingly ensuring better estimation performance than a global estimation model. Note that, the predictors, originally organized in a three dimensional matrix $\underline{\mathbf{X}} [N \text{ mixture} \times (M \cdot S) \text{ textural indices} \times R \text{ video frames}]$ were treated with a hybrid unfolding of the data, as suggested by Facco et al. (2017). This allows dealing with both the correlation among multiresolution textural indices within single frames of a video and, at the same time, correlation between the textural indices of different frames of the video. As a consequence, the hybrid unfolding helps to consider all the effects of the local differences among the frames, the local inhomogeneity of the mixture in the image scene, and also the effect of partial segregation;
- the estimation model was finally validated through a Monte Carlo procedure in $N_{IT} = 100$ iterations. In each iteration $N_C = 80$ (over the total 100) randomly selected mixtures were used for local PLS model calibration, and other $N_V = 10$ were randomly selected for validation.

4. Results

Two typical examples of estimated PSD are presented in Figure 4. Figure 4a shows the estimated PSD for the validation mixture #1, in which the PSD is uni-modal. The estimation performance is satisfactory, because the estimated value (i.e., the grey dashed

line) is very close to the real measured PSD (i.e., black line). The maximum error in this case is ~4.1% in correspondence of the cumulative weight fraction of the classes A+B.

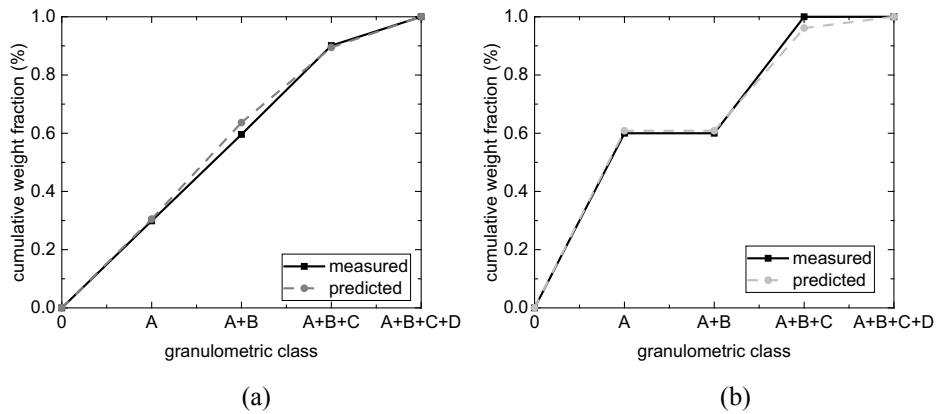


Figure 4. Examples of estimated PSD compared to real measured ones: a) validation sample #1; b) validation sample #2.

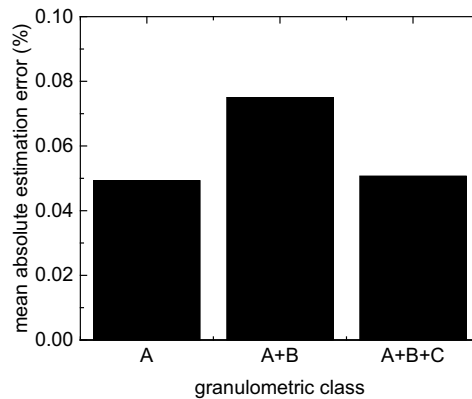


Figure 5. Mean absolute PSD estimation error for the cumulative weight fractions of the granulometric classes A, B and C.

Figure 4b shows the case of validation mixture #2, which clearly displays a bi-modal PSD. In this case, the estimation performance is absolutely accurate, as well. In fact, the estimation errors are below 4%, and the multi-modal trend is fully identified.

Finally, the mean absolute estimation error for the estimation of the PSD is considered to evaluate the estimation performance of the model with the Monte Carlo validation procedure which include $N_{IT} = 100$ iterations of the random partition of the available mixtures in $N_C = 80$ randomly selected mixtures considered for calibration and $N_V = 10$ randomly selected mixtures for validation. The mean absolute error of estimation MAE is used as an estimation performance index:

$$MAE = \frac{1}{N_{IT}N_V} \sum_{h=1}^{N_{IT}} \sum_{v=1}^{N_V} |y_{h,v} - \hat{y}_{h,v}| \quad (1)$$

where the error is the difference between the measured value of the cumulative weight fraction $y_{h,v}$ at iteration h and for validation mixture v , and its estimated value $\hat{y}_{h,v}$. The error is averaged on all the N_{IT} iterations and on all the N_V validation samples.

It can be observed that the estimation performance of the AVS are very good, because the *MAE* is well below 10% for all the granulometric classes, where 10% is the width among the different levels of the factors utilized in the DoE.

5. Conclusions

This work extended the use of a methodology to develop an artificial vision system to estimate the particle size distribution of granular materials in bulk mixtures to the case in which the material is moved in conveyor belts. The proposed methodology utilized digital videos of a granular bulk. The outcomes demonstrated that the particle size distribution of a granulated product can be estimated very satisfactorily from videos of a bulk mixture in movement on conveyor belts, also in case of multi-modal particle size distributions.

Future works will be oriented to two main aspects: the development of a method to identify the most appropriate number of videos to calibrate an accurate and reliable system and the test of robustness of the proposed system to disturbances that are related to the different conveyor belt velocity and to particle segregation.

References

- P. S. Addison, 2002. The illustrated wavelet transform handbook: introductory theory and applications in science, engineering, medicine and finance, CRC Press, Boca Raton.
- J. Calderon De Anda, X. Z. Wang, K. J. Roberts, 2005. Multi-scale segmentation image analysis for the in-process monitoring of particle shape with batch crystallisers, *Chem. Eng. Sci.*, 60, 4, 1053–1065.
- P. Facco, A. C. Santomaso, M. Barolo, 2017, Artificial vision system for particle size characterization from bulk materials, *Chem. Eng. Sci.*, 164, , 246-257.
- P. Facco, E. Tomba, M. Roso, M. Modesti, F. Bezzo, M. Barolo, 2010, Automatic characterization of nanofiber assemblies by image texture analysis, *Chemom. Intell. Lab. Syst.*, 103, 1, 66–75.
- S. García-Muñoz, A. Carmody, 2010, Multivariate wavelet texture analysis for pharmaceutical solid product characterization, *Int. J. Pharm.*, 398, 1-2, 97–106.
- P. Geladi, B. R. Kowalski, 1986, Partial least-squares regression: a tutorial, *Anal. Chim. Acta*, 185, 1–17.
- R. Gosselin, C. Duchesne, D. Rodrigue, 2008, On the characterization of polymer powders mixing dynamics by texture analysis, *Powder Technol.*, 183, 2, 177–188.
- R.W. Kennard, L. A. Stone, 1969, Computer aided design of experiments, *Technometrics*, 11, 137–148.
- D. C. Montgomery, 2008, Design and Analysis of Experiments, John Wiley & Sons, New York.
- S. Nalesso, C. Codemo, E. Franceschinis, N. Realdon, R. Artoni, A. C. Santomaso, 2015, Texture analysis as a tool to study the kinetics of wet agglomeration processes, *Int. J. Pharm.*, 485, 1-2, 61–69.
- P. Nomikos, J. F. MacGregor, 1995, Multi-way partial least squares in monitoring batch processes, *Chemom. Intell. Lab. Syst.*, 30, 1, 97–108.
- J. S. Shenk, M. O. Westerhaus, P. Berzaghi, 1998, Investigation of a LOCAL calibration procedure for near infrared instruments, *J. Infrared Spectrosc.*, 5, 4, 223–232.

Automatic controller failure detection with application in model based control of an *E. coli* fed-batch

Sophia Ulonska^{a,+}, Julian Kager^{a,+} and Christoph Herwig^{a,b,*}

^aICEBE, TU Wien, Gumpendorfer Straße 1a 166/4, 1060 Wien, Austria

^bCD Laboratory on Mechanistic and Physiological Methods for Improved Bioprocesses, TU Wien, Gumpendorfer Straße 1a 166/4, 1060 Wien, Austria

* Corresponding author.

⁺ Contributed equally to the paper.

christoph.herwig@tuwien.ac.at

Abstract

Advanced model based control strategies are necessary for efficient bioprocess control. In order to ensure continued control it is essential to detect controller failures in time. Redundant controllers allow for detailed diagnostics and maintenance during the process. Within this contribution a hierarchical combination of three different controllers was developed for setpoint control of biomass specific uptake rates of glucose and lactose of a green fluorescent protein producing *E. coli* strain. To achieve this, a model predictive controller (MPC) based on a dynamic mechanistic model for biomass growth and substrate uptake, a controller based on biomass estimates derived from elemental balancing of inflows and outflows (EBC) as well as an open-loop controller with predefined feed profiles were combined. A strategy was developed to trigger reversible switches between the different controllers in case of failures. To achieve this, measures for failure detection were identified. This permanent controller diagnostic and automatic controller switches are essential tools allowing continued control even in case of malfunctions.

Keywords: bioprocess control, controller diagnostics, failure detection, model based control, model predictive control, state observer

1. Introduction

E. coli processes are frequently used for the production of biopharmaceuticals (Sanchez-Garcia et al. (2016)). In order to guarantee the quality of their products, producers have to control and continuously improve their production processes which is further motivated by PAT (FDA (2004)) and QbD (FDA (2008)) guidelines. Model based methods are powerful tools to achieve efficient processes with constant quality. They allow the control of only indirectly measurable physiological entities such as growth, uptake and production rates (Schaepe et al. (2014)). Various model types can be applied, e.g. purely data-driven models (Kadlec et al. (2009)), models based on first principles (Wechselberger et al. (2013)) or mechanistic models (Jenzsch et al. (2006)).

Open loop control systems following a predefined feed trajectory are widespread due to their simplicity (Stanke and Hitzmann (2012)). Simple models can be used to define the feed trajectory: exponential feeding based on a constant substrate to biomass conversion rate was successfully used to maintain high growth in non-recombinant *E. coli* strains (Lee (1996)). However, without feedback for biomass growth this strategy might fail in case of deviations (e.g. because of a changed yield coefficient due to increased by-product formation). More elaborate controllers are

based on elemental balances (Wechselberger et al. (2013)). Biomass formation rates are estimated by consumed oxygen and emitted carbon. Feed addition is based on the current biomass estimation. However, the underlying model is only valid in case of strict sugar limitation and predictions are not possible. Dynamic models allow the usage of nonlinear MPC's, where optimized inputs (e.g. feed rates) are applied. Additionally, technical and physiological constraints can be defined. Typically, the real-time optimization is performed based on the most probable state of the system. This is determined by state observers based on measurements and model predictions. Examples are Kalman or particle filters (Goffaux and Wouwer (2005); Simon (2006)). Successful MPC implementations can be found in oil refineries and chemical plants (Qin and Badgwell (2003)), whereas applications in biopharmaceuticals industry are still rare (Sommeregger et al. (2017)). Uncertainty about the model, severe non-linearities or limited measurements are the main reasons why those powerful controllers can fail in practice. Typical measures to repair a failed controller include laborious and time-consuming steps like parameter re-estimation or elaborate analysis of offline samples. Therefore it is important to have a back-up controller running in parallel in case of failures. Within this contribution, a methodology is suggested, which bases on the combination of different controllers to achieve efficient and continued control. For this, we combine a MPC based on a mechanistic process model, a controller based on elemental balances (EBC) and an open-loop controller based on a predefined feed trajectory. The control goal was simultaneous control of two interdependent substrates (glucose and lactose) in a green fluorescent protein (GFP) producing *E. coli* fed-batch process (Wurm et al. (2017)). Controller reliability was automatically evaluated by statistical and biological measures. By diagnosis of failures, automatic switches between super-ordinate and subordinate controllers are triggered to ensure reliable and continued control. The outline of this contribution is a description of the process and the three different controllers. Failure diagnostics for the different controllers were then presented, followed by a description of our combined control strategy.

2. Materials and Methods

2.1. Cultivations

Fermentations were conducted in a parallel bioreactor system (DASGIP, Eppendorf AG, Germany). GFP producing *E. Coli* cells were cultivated in chemically defined media with a limited amount of glucose (5 g/L). After C-source depletion, a fed-batch on glucose was conducted for around 12 hours with feed (450 g/L glucose) addition via peristaltic pumps (DASGIP MP8, Eppendorf AG, Germany). Afterwards the induction phase started by additionally feeding lactose (180 g/L). The pH, measured by potentiometric pH sensors (Hamilton, Switzerland), was maintained at pH 7 by adding NH_4OH (12.5 %), which was used additionally as N-source. Oxygen saturation measured by optical DO probes (Hamilton, Switzerland) was kept over 30 % by increasing the oxygen content in the inflow air, which was supplied with 2 vvm via a L-sparger. Four dip tubes were used for feed, base addition and offline sampling. The exhausted gas composition was analysed by a ZrO_2 sensor for O_2 and an infrared sensor for CO_2 analysis (DASGIP GA4, Eppendorf AG, Germany). Dry cell weight (DCW) was determined by centrifugation (4500g, 4 °C, 10 min) of 1 mL cultivation broth and subsequent drying of the cell pellet at 105 °C for 48 h. Cell-free samples of the cultivation broth were analysed for concentrations of substrates and metabolites by HPLC (Agilent Technologies, USA) with a Supelco gel C-610 H ion exchange column (Sigma-Aldrich, USA) and a refractive index detector (Agilent Technologies, USA). The mobile phase was 0.1 % H_2PO_4 with a constant flow rate of 0.5 mL/min.

2.2. Controllers

In order to maintain the predefined biomass specific uptake rates of glucose and lactose three different controllers were implemented.

MPC: The controller was based on a mechanistic model for cell growth on two substrates. Specific uptake rates of glucose and lactose were modelled Monod-like. Maximal specific lactose uptake rate was assumed to depend on specific glucose uptake rate as described in Wurm et al. (2017). The model described biomass with an error below 5 %. An extended Kalman filter (EKF), as described in Simon (2006), was taken for filtering, which was based on oxygen uptake rate (OUR) and carbon emission rate (CER) measurements. They were predicted with an error below 5-10 %. The objective function for the optimization was to minimize the deviation between the defined setpoints for specific glucose and lactose uptake rates and the model predictions, constrained by maximal feed-rates and reactor volume. Additionally, highly varying feed rates were penalized. The optimization algorithm, an adaptation of the Nelder-Mead method, was implemented in Python. Data transfer from and to the DASGIP process control software was performed via Open Platform Communications (OPC).

EBC: A controller relying on elemental balances was used. It is assumed that substrate, ammonia and oxygen are converted to biomass and carbon dioxide. The unknown biomass formation rate can be determined by applying elemental balances such as the C-balance or the degree of reduction balance. Based on measured reactor inflows (feeds and air supply) and outflows (offgas composition and sample volume) the formed biomass was estimated as described in Wechselberger et al. (2013). Based on this estimation the feed rates needed to maintain the predefined set points were directly calculated. The algorithm was implemented in the process control software (DASGIP Control v4.5, Eppendorf AG, Germany) and works only in sugar limited fed-batch processes with negligible product and by-product formation. Update frequency was a time interval of 60 s.

Open-loop: As the simplest feed controller constant or exponentially increasing feeds as described in Lee (1996) were included and implemented directly in the process control software.

3. Results and Discussion

The MPC and the EBC were tested in simulations on historical datasets and were also applied in the described microbial process. Generally, all three controllers showed the ability to maintain the desired specific uptake rates of glucose and lactose. Results can be found in Kager et al. (2017) and Wurm et al. (2018). Nevertheless, several controller malfunctions occurred and could be described.

3.1. MPC failure detection

Besides system breakdowns, failures of the MPC were observed mainly because of wrong estimations due to the model (inappropriate parameters or structure) or the Kalman filtering process. The most promising indicators to recognize these failures automatically were identified as follows: (1) Time-out errors were used to detect system breakdowns. (2) The covariance matrix P computed during the EKF procedure is a classical criterion to assess the reliability of the estimates of the EKF. However, the EKF is known to (possibly) fail due to inappropriate configuration (Dochain (2003); Agarwal and Bonvin (1989)). In a few cases numerical instabilities were observed leading to overestimated or underestimated covariances (Huang et al. (2008)). Therefore, additionally (3) directly the distance between the model and the measurements was considered. In Figure 1 an example for measurements and filtered estimates of CER (A), OUR (B) and biomass (C) in the induction phase is shown. The offline samples for biomass show an overestimation after 23 hours. The entries of P indicating variances of biomass did not behave conspicuously. However, the percentual deviation of OUR was bigger than 5 % after 23.6 hours; for CER this was observed after 25.4 hours. The reason for the deviation was an underestimation of glucose consumption and an overestimation of the biomass yield. Parameter recalibration of the related parameters would lead to better predictions. This example shows, that deviations higher than 5% for one of the measurements are indicators for deviations between model and process.

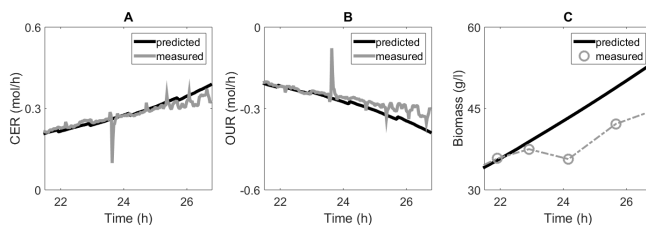


Figure 1: Real-time diagnostic of MPC: A) measured and estimated CER, B) measured and estimated OUR, C) offline reference measurements and estimation of biomass.

3.2. EBC failure detection

The carbon and the degree of reduction balance can be used to determine the unknown biomass formation rate. This over-determined equation system allows to improve estimation accuracy by data reconciliation and to check data consistency (Wechselberger et al. (2013); Jobe et al. (2003)). For the latter the h -value can be used: the hypothesis is tested whether deviations are only due to expected measurement errors or additionally due to gross errors, such as neglected metabolites, changing metabolism or others (Van der Heijden et al. (1994)). In our application values above 3.68 (95 % confidence level) indicate the existence of such gross errors. The threshold for the h -value depends on the degree of redundancy as well as on the desired confidence level (Jobe et al. (2003)).

In addition to the statistical h -value, the biomass to substrate yield can be used for estimator diagnostics. Although not stringently constant over the whole process (Wechselberger et al. (2013)) substrate to biomass yields are by nature within certain ranges. A yield around 0.5 g biomass/g glucose is often reported for *E. coli* (Shiloach and Fass (2005)). Ranges between 0.3 and 0.6 were selected to be physiologically meaningful.

In Figure 2 the h -value (A), the yield (B) as well as offline data for glucose and lactose concentrations (C) are shown for a real fermentation process. From 20 hours onwards, the h -value is several times above the threshold of 3.68. Additionally, from 24 hours onwards the online calculated yield drifted. Both measures indicate potential malfunction of the controller. This is confirmed by offline analysis of sugar concentrations, which revealed accumulation of glucose and lactose. In this case the assumptions of the EBC are no longer valid. Violations at the beginning of the fed-batch phase after 5 hours were due to inaccurate measurements in the offgas composition.

3.3. Overall control scheme

As described above, the MPC as well as the EBC might fail. Diagnostics to recognize them were defined. Typically elaborate and time-consuming measures to overcome the controller failure like parameter re-estimation or analysis of the sugar concentrations have to be performed. However, due to the swift growth of the bacteria, rapid responses will be needed. This can be ensured by automatic switches to another, in this situation possibly more reliable controller.

In Figure 2 D a possible switch is shown. To prevent glucose accumulation, caused by the faulty EBC, alternative outputs from MPC or open loop could be used. Applying a constant feed could effectively prevent further accumulation of substrates, but desired uptake rates are no longer maintained and will decrease over time. The MPC is favourable as it optimizes the current and future process inputs to reach the desired objectives. In our case, the feed pumps would be turned off until the accumulated substrate is consumed, followed by an optimized feeding profile in order to maintain a constant uptake rate. The underlying model is extendable and works also in case of substrate accumulation. However, the MPC might fail due to too simplified model assumptions,

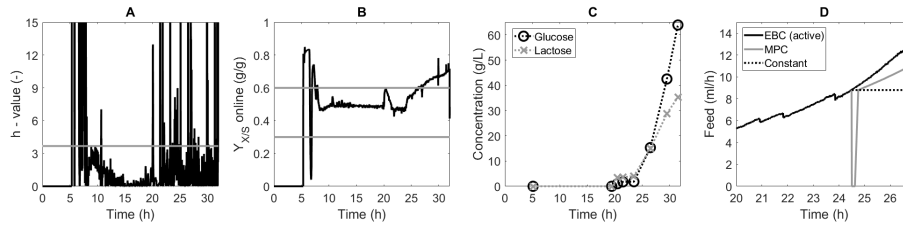


Figure 2: Real-time diagnostic of EBC: A) h-value trajectory, B) online biomass to substrate yield estimation, C) offline reference measurements of sugars, D) glucose feeds of implemented controllers.

wrong parameters or errors during the filtering process. In those cases a switch back to EBC can give more reliable results and lead to more stable behaviour. However, as noted above, the EBC is not operational in case of substrate accumulation or noisy or imprecise measurements. The overall control scheme is shown in Figure 3. If the MPC is expected to fail (indicated by timeout errors, the covariance matrix or deviations from the measurements), a switch to the EBC is performed. In case the EBC possibly fails, which is analysed by the h-value and the yield ($Y_{X,S}$), a constant feed is performed to avoid substrate accumulation. However, as soon as the superordinate controller is expected to work again, a switch back to it is performed. Thresholds as well as update rates should be defined by evaluating historical datasets.

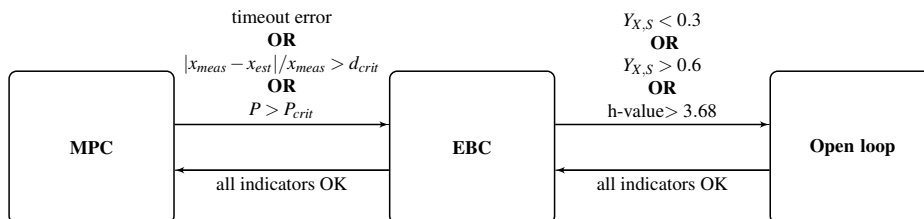


Figure 3: Implemented controller scheme ensuring the safe usage of advanced controllers in highly dynamic microbial processes. Automatic switches are performed according to online diagnostics.

4. Conclusions

Summing up, for the model predictive controller (MPC) as well as the elemental balance controller (EBC) measures were defined to identify controller failures. For the MPC these were timeout errors, the covariance matrix P of the EKF and deviations between estimates and measurements. For the EBC, the h-value as well as the biomass to substrate yield were taken to detect gross errors. To ensure continued process control even in case of failures, a strategy was developed that triggered automatic switches between the different controllers. Especially in processes with relatively fast dynamics, like *E. coli* fed-batches the implemented control scheme enabled the usage of MPC while ensuring continued control in case of malfunctions. Within this system MPC's can be further developed and tested in biopharmaceutical processes, triggering the usage of these promising controllers. In the current application an extended model as well as additional measurement devices could further improve the quality of the MPC and allow complex control of unmeasurable variables considering physiological and technical constraints.

5. Acknowledgements

Financial support was provided by the Austrian research funding association (FFG) under the scope of the COMET programme within the research project Industrial Methods for Process Analytical Chemistry - From Measurement Technologies to Information Systems (impACTs) (contract # 843546). We thank Philip Waite for proofreading and linguistic revision.

References

- M. Agarwal, D. Bonvin, 1989. Limitations of the extended Kalman filter for batch reactors. *IFAC Proceedings Volumes* 22 (8), 299–306.
- D. Dochain, 2003. State and parameter estimation in chemical and biochemical processes: a tutorial. *Journal of process control* 13 (8), 801–818.
- FDA, 2004. Guidance for industry: PAT A framework for innovative pharmaceutical development, manufacturing, and quality assurance. DHHS, Rockville, MD.
- FDA, 2008. Guidance for industry. Q8 (R2) pharmaceutical development.
- G. Goffaux, A. V. Wouwer, 2005. Bioprocess state estimation: some classical and less classical approaches. In: *Control and Observer Design for Nonlinear Finite and Infinite Dimensional Systems*. Springer, pp. 111–128.
- G. P. Huang, A. I. Mourikis, S. I. Roumeliotis, 2008. Analysis and improvement of the consistency of extended Kalman filter based SLAM. In: *Robotics and Automation, 2008. ICRA 2008. IEEE International Conference on*. IEEE, pp. 473–479.
- M. Jenzsch, R. Simutis, A. Luebbert, 2006. Generic model control of the specific growth rate in recombinant *Escherichia coli* cultivations. *Journal of biotechnology* 122 (4), 483–493.
- A. M. Jobe, C. Herwig, M. Surzyn, B. Walker, I. Marison, U. von Stockar, 2003. Generally applicable fed-batch culture concept based on the detection of metabolic state by on-line balancing. *Biotechnology and bioengineering* 82 (6), 627–639.
- P. Kadlec, B. Gabrys, S. Strandt, 2009. Data-driven soft sensors in the process industry. *Computers & Chemical Engineering* 33 (4), 795–814.
- J. Kager, J. Fricke, U. Becken, C. Herwig, 2017. A Generic Biomass Soft Sensor and Its Application in Bioprocess Development. Application Note 357, Eppendorf GmbH, Juelich, Germany.
- S. Y. Lee, 1996. High cell-density culture of *Escherichia coli*. *Trends in biotechnology* 14 (3), 98–105.
- S. J. Qin, T. A. Badgwell, 2003. A survey of industrial model predictive control technology. *Control engineering practice* 11 (7), 733–764.
- L. Sanchez-Garcia, L. Martín, R. Mangués, N. Ferrer-Miralles, E. Vázquez, A. Villaverde, 2016. Recombinant pharmaceuticals from microbial cells: a 2015 update. *Microbial cell factories* 15 (1), 33.
- S. Schaepe, A. Kuprijanov, C. Sieblist, M. Jenzsch, R. Simutis, A. Lubbert, 2014. Current advances in tools improving bioreactor performance. *Current Biotechnology* 3 (2), 133–144.
- J. Shiloach, R. Fass, 2005. Growing *E. coli* to high cell density: a historical perspective on method development. *Biotechnology advances* 23 (5), 345–357.
- D. Simon, 2006. *Optimal state estimation: Kalman, H infinity, and nonlinear approaches*. John Wiley & Sons.
- W. Sommeregger, B. Sissolak, K. Kandra, M. von Stosch, M. Mayer, G. Striedner, 2017. Quality by control: Towards model predictive control of mammalian cell culture bioprocesses. *Biotechnology Journal* 12 (7), 1600546–1600552.
- M. Stanke, B. Hitzmann, 2012. Automatic control of bioprocesses. In: *Measurement, Monitoring, Modelling and Control of Bioprocesses*. Springer, pp. 35–63.
- R. Van der Heijden, B. Romein, J. Heijnen, C. Hellinga, K. Luyben, 1994. Linear constraint relations in biochemical reaction systems: II. Diagnosis and estimation of gross errors. *Biotechnology and bioengineering* 43 (1), 11–20.
- P. Wechselberger, P. Sagmeister, C. Herwig, 2013. Real-time estimation of biomass and specific growth rate in physiologically variable recombinant fed-batch processes. *Bioprocess and biosystems engineering* 36 (9), 1205–1218.
- D. J. Wurm, J. Hausjell, S. Ulonska, C. Herwig, O. Spadiut, 2017. Mechanistic platform knowledge of concomitant sugar uptake in *Escherichia coli* BL21 (DE3) strains. *Scientific Reports* 7, 45072.
- D. J. Wurm, J. Quehenberger, J. Mildner, B. Eggenreich, C. Slouka, A. Schwaighofer, K. Wieland, B. Lendl, V. Rajamanickam, C. Herwig, et al., 2018. Teaching an old pet new tricks: tuning of inclusion body formation and properties by a mixed feed system in *e. coli*. *Applied microbiology and biotechnology* 102 (2), 667–676.

A Novel Dynamic Model of Plate Heat Exchangers Subject to Fouling

Shunfeng Guan^a, Sandro Macchietto^{a*}

^a*Department of Chemical Engineering, Imperial College London, South Kensington Campus, London SW7 2AZ, UK*

s.macchietto@imperial.ac.uk

Abstract

The modelling of plate heat exchangers (PHEs) for dairy applications is revisited utilising recent concepts that have proved very effective in different but related areas, in particular dealing with fouling in tubular exchangers and crude oil refinery applications.

The approach initially proposed by Georgiadis and Macchietto (2000) is followed, but coupled with a more detailed 2D distributed model capable of describing and characterising deposit layer growth. The proposed model, illustrated for a single channel in a PHE, includes an improved milk and protein aggregation/deposition model, independent deposition on the plates at each side of the channel, the interaction of local operating conditions and deposit formation (via a moving boundary at the fluid-deposit interface), and the asymmetric deposition due to different boundary conditions at the two sides of a plate. It is shown that the model adequately predicts the distribution of deposit along the plates and provides useful insights into problematic plate regions.

Keywords: dairy processes, energy recovery, plate heat exchanger, fouling, dynamic model.

1. Introduction and background

Plate heat exchangers (PHEs) are widely used, particularly in the food industries, as they are compact, configurable in different arrangements (Figure 1) and easily cleaned. The deposition of materials on hot surfaces (fouling) reduces thermal and hydrodynamic performance, requires periodic cleaning (often after just few hours of operation) with heavy economic and productivity losses. Simulation models help predict these effects and enable smarter operation and design decisions. In spite of a rich literature there is still significant interest in improving models accuracy and useability in practical applications. Current mechanistic models of PHEs dynamic behaviour with fouling typically rely on simplifying assumptions, limiting their predictive ability. Deposit changes inside the PHE plates are either ignored or captured indirectly as an overall thermal fouling resistance. Computational Fluid Dynamics (CFD) models (e.g. Choi et al., 2013) start to include relevant detailed hydrodynamics, e.g. plates corrugations, with good results. However the CFD environment and solution times (often days) prevent incorporating other aspects (e.g. control) and their use for optimising PHEs design and operation within overall heat exchanger networks, for example, to optimise cleaning schedules. Here, the modelling of PHEs fouling for dairy applications is revisited utilising recent concepts that proved very effective in related areas, in particular for fouling in tubular exchangers and crude oil refinery applications. The basic mechanistic,

1D distributed, dynamic model approach initially proposed by Georgiadis and Macchietto (2000) is followed, however coupled with a more detailed 2D distributed model capable of describing and characterising deposit layer growth, of the type used by Coletti and Macchietto (2011) and refined by Diaz Bejarano et al. (2016). The goal is to develop a more predictive, yet far simpler model than CFD ones, enabling its use in optimisation of single PHEs and whole heat exchanger networks that include PHEs. In the following, the proposed model is illustrated for a single channel in a PHE subject to milk fouling, with validation against experimental results. Results for full PHEs will be presented elsewhere.

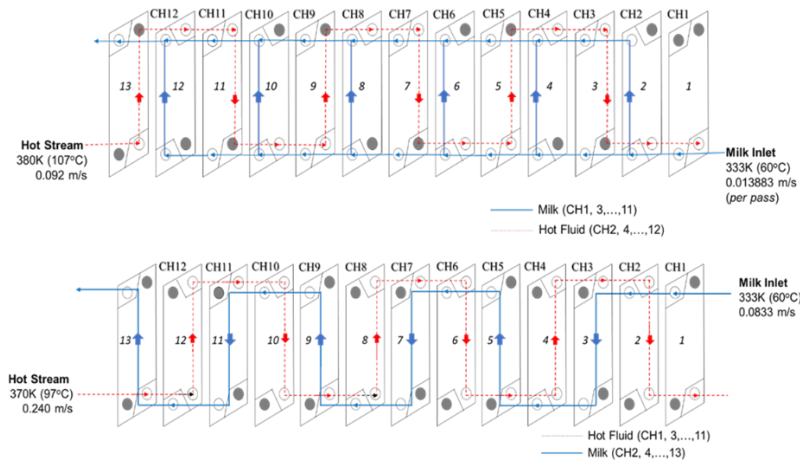


Figure 1. Two different Plate Heat Exchanger arrangements: 1 (top) and 2 (bottom).

2. Model of PHE plate with fouling deposition

The well-established β -lactoglobulin reaction scheme (Georgiadis & Macchietto, 2000) was used to model milk deposition, with some parameter changes to better characterise the protein polymerisation process above 90 °C. The PHE channel model considers the independent growth of a fouling layer on each of the two hot walls j and $j+1$ of a channel j where a fouling fluid flows, being heated. The model (Figure 2) is distributed in 2D, longitudinally (coordinate x) and across (coordinate y) the plate. Uniform distribution is assumed along the plate width, W . Five domains (left to right) are defined along the plate length, $x = [0, L]$:

- 1) Ω_W^L : Left plate wall domain, between outer and inner plate walls, $y = [-P_o, -P_i]$;
- 2) Ω_L^L : Left plate deposit layer domain, $y = [-P_i, -P_{flow,L}]$;
- 3) Ω_F : Channel fluid flow domain, $y = [-P_{flow,L}, P_{flow,R}]$;
- 4) Ω_L^R : Right plate deposit layer domain, $y = [P_{flow,R}, P_i]$;
- 5) Ω_W^R : Right plate wall domain, $y = [P_i, P_o]$;

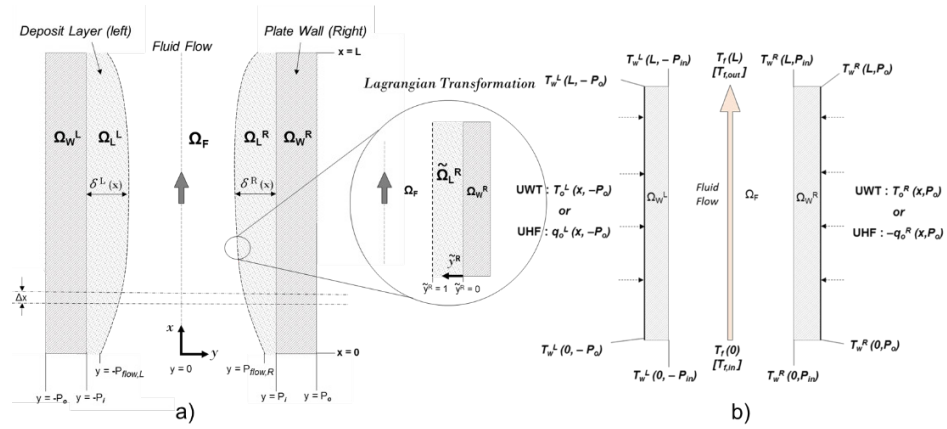


Figure 2. Channel j delimited by plates j (on left) and $j+1$ (on right), 5 domains modelled, reference coordinates and Lagrangian transformation a). Boundary conditions applied b).

The temperature profiles in each domain are given by a thermal balance over a differential element Δx (Figure 2). Assuming uniform plate geometry and constant material properties (wall thermal conductivity, λ_w , density, ρ_w , specific heat capacity, Cp_w), the standard heat conduction equation and Fourier's law give the local temperature T_w^i (K) in the plate wall vs time and location (x, y) and the heat flux q_w^i (W/m²) across the wall:

$$\frac{\rho_w Cp_w}{\lambda_w} \frac{\partial T_w^i(x, y)}{\partial t} = \frac{\partial^2 T_w^i(x, y)}{\partial y^2}; \quad \forall i = L, R \quad (1)$$

$$q_w^i(x, y) = -\lambda_w \frac{\partial T_w^i(x, y)}{\partial y}; \quad \forall i = L, R \quad (2)$$

The two deposit domains, Ω_L^L on the left and Ω_L^R on the right plates of the channel are modelled as a conductive fouling layer, assuming constant deposit density, ρ_L , specific heat capacity, Cp_L and thermal conductivity, λ_L , no deposit ageing, and no heat source and variations in the x -direction:

$$\frac{\rho_L Cp_L}{\lambda_L} \frac{\partial T_L^i(x, y)}{\partial t} = \frac{\partial^2 T_L^i(x, y)}{\partial y^2}; \quad \forall i = L, R \quad (3)$$

T_L^i is the local temperature of the deposit layer (K), and λ_L is the thermal conductivity (W/m.K), both of which are functions of spatial coordinates (x, y) as well as time. The heat flux at any point along the thickness of the deposit is:

$$q_L(x, y) = -\lambda_L(x, y) \frac{\partial T_L^i(x, y)}{\partial y}; \quad \forall i = L, R \quad (4)$$

To more easily solve the system of PDEs, the moving boundary between each deposit layer and the fluid is dealt with using a Lagrangian transformation, as in Diaz-Bejarano et al. (2016). The transformed dimensionless deposit domain, $\tilde{\Omega}_L^R$, now with a constant boundary, is shown in Fig. 2a. For the new right domain, $\tilde{\Omega}_L^R$, \tilde{y}^R , Eq. 3 and 4 become:

$$\frac{\rho_L Cp_L}{\lambda_L} \left(\frac{\partial T_L^R(x, \tilde{y}^R)}{\partial t} - \frac{\tilde{y}^R}{\delta^R(x)} \delta^R(x) \frac{\partial T_L^R(x, \tilde{y}^R)}{\partial \tilde{y}^R} \right) = \frac{1}{\delta^R(x)^2} \frac{\partial}{\partial \tilde{y}^R} \left(\frac{\partial T_L^R(x, \tilde{y}^R)}{\partial \tilde{y}^R} \right) \quad (5)$$

$$q_L(x, \tilde{y}^R) = \frac{\lambda_L}{\delta^R(x)} \frac{\partial T_L^R(x, \tilde{y}^R)}{\partial \tilde{y}^R} \quad (6)$$

For the new left domain, $\tilde{\Omega}_L^L$, \tilde{y}^L , Eq. 3 and 4 become:

$$\frac{\rho_L C p_L}{\lambda_L} \left(\frac{\partial T_L^L(x, \tilde{y}^L)}{\partial t} - \frac{\tilde{y}^L}{\delta^L(x)} \dot{\delta}^L(x) \frac{\partial T_L^L(x, \tilde{y}^L)}{\partial \tilde{y}^L} \right) = \frac{1}{\delta^L(x)^2} \frac{\partial}{\partial \tilde{y}^L} \left(\frac{\partial T_L^L(x, \tilde{y}^L)}{\partial \tilde{y}^L} \right) \quad (7)$$

$$q_L(x, \tilde{y}^L) = -\frac{\lambda_L}{\delta^L(x)} \frac{\partial T_L^L(x, \tilde{y}^L)}{\partial \tilde{y}^L} \quad (8)$$

where $\dot{\delta}^i$ (m/s), the rate of change in fouling layer thickness, δ^i , over time represents the volumetric flux of deposit material, in $\text{m}^3/\text{m}^2 \cdot \text{s}$.

$$\dot{\delta}^i = \frac{d}{dt} (\delta^i); \quad \forall i = L, R \quad (9)$$

A standard enthalpy balance applies to the fluid domain:

$$\begin{aligned} \frac{\partial}{\partial t} (\rho_f C p_f T_f A_{flow}) &= -\frac{\partial}{\partial x} (\rho_f C p_f T_f u_f A_{flow}) + \frac{\partial}{\partial x} \left(\lambda_f A_{flow} \frac{\partial T_f}{\partial x} \right) \\ &+ Wh(T_L^R|_{\tilde{y}=1} - T_f) + Wh(T_L^L|_{\tilde{y}=1} - T_f) \end{aligned} \quad (10)$$

where $T_f(x)$ is the fluid bulk temperature (K), $u_f(x)$ (m/s) is the mean fluid velocity derived from the flow area, A_{flow} , h is the local film heat transfer coefficient and W is the plate width (wetted perimeter). The fluid physical properties, $\rho_f(x)$, $C p_f(x)$, and $\lambda_f(x)$ are functions of the mean fluid temperature at each local point. The variation in $A_{flow}(x)$ is due to the moving deposit boundaries on both sides of the plate.

$$A_{flow}(x) = W(P_{flow,L} + P_{flow,R}) \quad (11)$$

The Biot number is broken down into a local thermal resistance variable, providing insights into the fouling thickness along the plate length. This neglects possible fouling removal (due to shear forces), but nonetheless provides useful distributed information on the deposit. Using the Biot number definition of Fryer and Slater (1985):

$$Bi = \frac{h_f^o \delta_d}{\lambda_d} \quad (12)$$

into the rate of deposition yields the following expression:

$$\frac{d \delta_d(x)}{dt} = \lambda_d \left(\frac{\beta k_w C_{AP}^*}{h_f^o} \right) \quad (13)$$

where h_f^o (W/m²·K) is the local heat transfer coefficient for the fluid in clean conditions and other variables as in Fryer and Slater (1985). The layer thickness, δ_d , is determined by integrating eq. 13, given the thermal conductivity, λ_d , of the newly deposited layer.

Uniform Wall Temperature (UWT) boundary conditions were used here, i.e. a constant wall temperature was fixed on the outside of each plate. Various single channels of a PHE undergoing heating were simulated, starting from clean conditions. A first-order backwards discretisation method was used with 50 points in the axial flow direction and 10 points along the y axis for the plate domains. Similar temperature profiles were generated with 10 to 500 discretisation points across the layer thickness (y axis) without impacting accuracy, so 10 points were used. Temperature dependent milk physical

properties were used (De Jong, 1997). The single channel model contains 1445 variables and simulation of 6 h of heating takes about 11.45 s of CPU time using gPROMS.

3. Results, discussion and conclusions

The model described was used to simulate the dynamic fouling behaviour of 5 individual channels (no. 3, 5, 7, 9 and 11 in Arrangement 1, Figure 1). Channel 1 was omitted as negligible fouling was recorded (Delplace et al., 1997). Average plate temperatures calculated from a previous model were taken as the UWT boundary values for the *right* and *left* plates of each channel (Table 1). Except for channel 3, these outside temperatures on the two walls are asymmetric. Table 1 also details for each channel the results obtained after 6 h of simulation: outlet milk temperatures, mass of deposit (overall and on each of the two side walls) and max deposit thickness on each side. The total deposit mass on channels 3, 5 and 7 match exceptionally well the available experimental data for similar conditions (Delplace et al., 1997). For channels 9 and 11 the deposited masses are substantially over-predicted. A plausible cause is that the heating loads in the latter channels are higher, involving temperatures beyond 363 K (90°C) where the kinetic parameters used in the fouling reaction schemes are known to diverge from those at a lower temperature range (Jun & Puri, 2006). An identical deposit mass profile was generated on the plates on either side of channel 3, as its boundary conditions were symmetrical. For all other plates, deposition is different on the left and right plates, which have different UWT boundary temperatures. The deposit thickness distribution along channels 3, 5, 7 (Figure 3), shows that (for the imposed conditions), except for channel 3, fouling is not uniform along the flow axis, with most deposit near the end of the plates and asymmetrical on the two side plates.

Table 1. Boundary conditions and summary of results after 6h of operation for each channel, using the 2D distributed model

Channel No.		3	5	7	9	11
UWT (K) <i>Boundary Condition</i>	<i>R</i>	355.00	359.30	362.10	366.89	369.97
	<i>L</i>	355.00	356.66	360.50	363.49	368.30
Milk Outlet Temp. (K)		354.89	357.84	361.15	365.01	368.95
Total Deposit Mass (g)		1.59	4.21	8.09	12.62	16.19
Experimental Total Deposit Mass ^a (g)		1.50	4.00	7.00	8.50	12.00
Deposit Mass on each plate (g)	<i>R</i>	0.79	2.84	4.74	7.78	8.69
	<i>L</i>	0.79	1.36	3.35	4.84	7.50
Maximum Deposit Thickness (mm)	<i>R</i>	0.0101	0.0275	0.0379	0.0485	0.0518
	<i>L</i>	0.0101	0.0147	0.0281	0.0334	0.0450

R: Right plate of channel, *L*: Left Plate of channel; ^aDelplace et al. (1997)

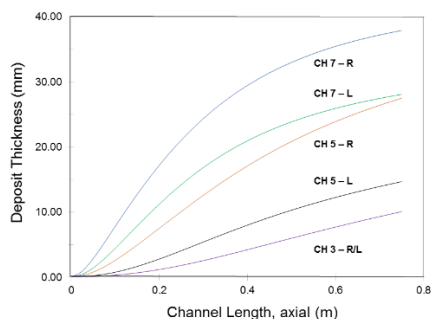


Figure 3. Deposit thickness distribution along channel length after 6 h of operation.

The new model accounts for interaction of local operating conditions and deposit and asymmetric deposition due to different boundary conditions at the two sides of a channel. It predicts the distribution of deposit along the plates and gives useful insights into problematic plate regions. It is a suitable component for industrial PHEs configurations, for simulation, to determine optimal operation and cleaning policies, and to study optimal sensor locations as required for online monitoring.

4. Acknowledgements

The financial support by the Ministry of Environment and Water Resources, Singapore, and the Dept of Chem Eng, Imperial College London (SG), and useful discussions with M Georgiadis, E. Diaz-Bejarano and F. Coletti are gratefully acknowledged.

References

- Choi, W., Jun, S., Nguyen, L. T., Rungraeng, N., Yi, H., Balasubramanian, S., Puri, V. M. & Lee, J., 2013, 3- D Milk Fouling Modeling of Plate Heat Exchangers with Different Surface Finishes Using Computational Fluid Dynamics Codes. *J Food Process Eng.* 36 (4), 439-449
- Coletti, F. & Macchietto, S., 2011, A Dynamic, Distributed Model of Shell-and- Tube Heat Exchangers Undergoing Crude Oil Fouling. *Ind. Eng. Chem. Res.* 50 (8), 4515-4533.
- De Jong, P. (1997). Impact and control of fouling in milk processing. *Trends in Food Science & Technology.* 8 (12), 4011-405.
- Delplace, F., Leuliet, J. C. & Tissier, J. P. (1994) Fouling Experiments of a Plate Heat Exchanger by Whey Protein Solutions. *Food and Bioproducts Processing: Transactions of the Institution of Chemical Engineers, Part C.* 72 163-169.
- Diaz-Bejarano, E., Coletti, F. & Macchietto, S., 2016, A new dynamic model of crude oil fouling deposits and its application to the simulation of fouling- cleaning cycles. *AIChE J.* 62 (1), 90-107.
- Fryer, P. J. & Slater, N. K. H., 1985, A direct simulation procedure for chemical reaction fouling in heat exchangers. *The Chemical Engineering Journal*, 31 (2) 97-107.
- Georgiadis, M. C. & Macchietto, S., 2000, Dynamic modelling and simulation of plate heat exchangers under milk fouling. *Chemical Engineering Science.* 55 (9), 1605-1619.
- Jun, S. & Puri, V. M., 2006, A 2D dynamic model for fouling performance of plate heat exchangers. *Journal of Food Engineering.* 75 (3), 364-374.

Risk based approach for batch release

Linus Mockus^a, Gintaras Reklaitis^a, Kenneth Morris^b, David LeBlond^c

^a*Purdue University, West Lafayette IN 47907-2100, US*

^b*Long Island University, Arnold & Marie Schwartz College of Pharmacy and Health Sciences, 75 Dekalb Avenue, Brooklyn, New York 11201-8423, US*

^c*Cmc Statistics, 3091 Midlane Drive, Wadsworth, IL 60083, US*

lmockus@purdue.edu

Abstract

Release of manufactured lots is a major decision point in reaching the goal of a customer – the product quality is reasonably good – and of manufacture – no rework/scrap/lost revenue. In this study we will focus on pharmaceutical industry (solid dosage form).

Adaptive Bayesian sample size determination. In this study we used adaptive Bayesian approach to determine the number of lots needed to estimate inter/intra lot variability. This was dictated by limited number of lots available in the study. Specifically, a linear random effects model was built and fitted to tablet data from multiple lots. The estimate was considered accurate enough when change in signal (or variability estimates) disappeared within noise. In our case we considered 1% of label claim as noise level. However, if signal to noise ratio was high, additional lot was sampled. Sampling included traditional content uniformity and dissolution testing. In order to be consistent with pharmacopeia 10 tablets from a lot were used for content uniformity testing while 12 tablets from the same lot were used for dissolution testing. Manufacturer, however, may not need this step since historical production information may be used to estimate the inter/intra lot variability by employing Bayesian methodology. It is important to note that analytical variability component was factored out which is not easily done with traditional frequentist methodology.

Estimation of probability that product is within specifications at given confidence level. The next step was to estimate the probability of product being within specifications at a given confidence level which is metrics used for lot release by ASTM E2709–12 standard. However, the approach delineated in the standard was extended by Bayesian treatment. Specifically, inter/intra lot variability estimates were used to determine the probability while confidence level was replaced by the Bayesian credible interval concept. As delineated in ASTM E2709–12 standard this non-trivial task using frequentist methodology was very straightforward when using Bayesian methodology.

We propose that lot can be released (consistently with ASTM E2709–12 standard) when the probability of product being within specifications at a given confidence level is high enough not to cause any harm to the patient. In order to determine the probability threshold, we propose to perform virtual clinical study with Simcyp or PK-Sim to determine if there is no harm to the patient and drug product is efficacious, i.e. drug plasma levels are within therapeutic window for prescribed dosing regimen.

We verified the proposed methodology on seven immediate release products from different manufactures. We found that there are large differences in inter/intra lot variability between different manufacturers. Based on our experience more than six lots are typically required to establish accurate variability estimate.

The current pharmacopeia doesn't incorporate inter lot variability and therefore our proposed approach is more restrictive in the sense that it allows releasing lots that contain safer and more efficacious product than using existing lot release criteria. It is based on FDA's risk based approach. From manufacturers perspective it supports the FDA's quality metrics initiative to assure that only safe and quality medicine is being produced. While this study considered solid dosage form the proposed methodology could be easily generalized for different dosage forms and any batch processing industries.

Keywords: Risk analysis; batch release

Computational Improvements for the Eddy Dissipation Concept by Operator Splitting and Tabulation

Eva-Maria Wartha^{a*}, Markus Bösenhofer^{a,b} and Michael Harasek^a

^aTechnische Universität Wien, Getreidemarkt 9/166, 1060 Vienna, Austria

^bK1-MET GmbH, Stahlstraße 14, Betriebsgebäude (BG) 88, 4020 Linz, Austria
eva-maria.wartha@tuwien.ac.at

Abstract

The Eddy Dissipation Concept (EDC) is a well working concept for turbulent reacting flows, which depicts the influence of chemical reactions as well as turbulence. The problem when using detailed chemical mechanisms - necessary for more information about radical species and pollutants - is the vastly increased computational demand. Operator splitting and in situ adaptive tabulation (ISAT) can be a way to reduce the computational effort and improve the application of detailed chemical mechanisms with the EDC. Two operator splitting mechanisms are presented and used for the simulation of Sandia Flame D. The computational time can be decreased and the results fit well to the experimental results.

Keywords: turbulent combustion, OpenFOAM, Eddy Dissipation Concept (EDC), operator splitting, in situ adaptive tabulation (ISAT)

1. Introduction

Simulation can be a great tool to improve the understanding of complex processes and consequently enhance efficiency and reduce emissions. In many systems, such as biomass combustion, pulverized coal combustion or blast furnaces, gas phase combustion occurs and needs to be modeled.

The Eddy Dissipation Concept (EDC) (Magnussen, 1981) is a widely used combustion model, which couples the effect of chemical reactions and the effect of turbulence. It has been widely used for many applications, e.g. by Zahirović et al. (2010), Stefanidis et al. (2006) and Rehm (2010). When using detailed chemical mechanisms the computational demand increases significantly compared to global or skeletal mechanisms. Therefore, computational improvements for the EDC are necessary to make use of detailed chemical mechanisms possible to enable additional insight on radical species or NO_x formation.

In situ adaptive tabulation (ISAT) has been proposed by Pope (1997) to decrease the computational time for reactive flow calculations. Originally, it has been used in combination with PDF methods, but it can also be used in conjunction with the EDC. In the EDC the species concentration in the reacting structures can be described by an ordinary differential equation (ODE)-system. Mixing and chemical reactions are taken into account there. ISAT can only be used for the chemical part of the equations, since taking both into account would distort the table and make a look-up inefficient, (Pope, 1997) and (Rehm, 2010). Therefore, operator splitting has to be used to split the ODE and enable ISAT.

Rehm (2010) presented two operator splitting methods for the EDC. The computational

time could not be reduced there, but also no results with regard to the accuracy were presented.

In the following the EDC and operator splitting methods are explained. These methods are then used to simulate Sandia Flame D in OpenFOAM, a turbulent methane-air jet flame. Experimental flame data from Barlow and Frank (1998) and Schneider et al. (2003) is used to validate the simulation results. Moreover, operator splitting and direct integration results are compared.

2. Model Description

2.1. Eddy Dissipation Concept

The EDC models the interaction between turbulence and chemical reactions. It assumes that the fluid consists of surroundings and fine structures, whose size is in the order of the Kolmogorov length scale (Magnussen, 1981). Since educts need to be mixed on a molecular scale to react, reactions only occur in the fine structures.

Magnussen (1981) derived the description of the fine structures based on an energy cascade model. The fine structure fraction γ^* is expressed by the turbulent kinetic energy k , the dissipation rate ε , the kinematic viscosity ν and a constant $C_\gamma = 2.13$, Eq.(1). The mass transfer between the fine structures and the surroundings per unit of mass of the fine structures and time can also be expressed by ν , ε and $C_\tau = 0.41$, Eq.(2). The residence time in the fine structures τ^* is the reciprocal of \dot{m}^* . The mass transfer per unit of fluid \dot{m} can be calculated by the mass transfer per unit of mass of the fine structures and the fine structure fraction, Eq.(2).

$$\gamma^* = C_\gamma^3 \left(\frac{\nu \varepsilon}{k^2} \right)^{\frac{3}{4}} \quad (1)$$

$$\dot{m}^* = \frac{1}{C_\tau} \left(\frac{\varepsilon}{\nu} \right)^{\frac{1}{2}} = \frac{1}{\tau^*} = \gamma^* \frac{1}{\dot{m}} \quad (2)$$

To obtain the mass transfer rate for one species R_i^* per unit volume of the reacting fine structure fraction χ , the species concentration in the fine structures and the surroundings is required, Eq. (3). The concentration and the density in the fine structures and the surroundings are also taken into account. When using the detailed chemistry approach, the fraction of the reacting fine structures χ is usually set to one, as suggested by Gran and Magnussen (1996). The relation between some property Ψ in the surroundings (\circ), the fine structures ($*$) and the fluid average ($\bar{}$) is given in Eq.(4).

$$R_i^* = \frac{\dot{m}^* \rho^*}{1 - \gamma^* \chi} \left(\frac{\bar{c}_i}{\bar{\rho}} - \frac{c_i^*}{\rho^*} \right) \quad (3)$$

$$\bar{\Psi} = \gamma^* \chi \Psi^* + (1 - \gamma^* \chi) \Psi^\circ \quad (4)$$

Different concepts exist to model the chemical reactions in the fine structures: the fast chemistry approach (Magnussen, 1981), the local extinction approach (Byggstoyl and Magnussen, 1983) or the detailed chemistry approach (Gran and Magnussen, 1996). To use a detailed chemical mechanism, the latter has to be used. There, the fine structures are treated as adiabatic and isobaric perfectly stirred reactors (PSRs). This leads to the following set of ODEs, Eq.(5). Where h^* is the enthalpy, p^* the pressure and Y_i^* the

mass fraction of species i in the fine structures. $\dot{\omega}_i$ denotes the reaction rate and Y° the concentration of species i in the surroundings.

$$\frac{dh^*}{dt} = 0 \quad \frac{dp^*}{dt} = 0 \quad \frac{dY_i^*}{dt} = \dot{\omega}_i + \frac{1}{\tau^*} (Y_i^\circ - Y_i^*) \quad (5)$$

2.2. Operator Splitting

Operator splitting splits the species conservation equation in Eq.(5) into a chemical and a mixing part, solves them separately and combines the solutions to get a solution of the original ODE. Two second order operator splitting methods, Strang splitting and Staggered splitting, which are used for the simulation in OpenFOAM are presented here.

2.2.1. Strang Splitting

The chemical subproblem is denoted by A and the mixing one by B. Strang splitting (Strang, 1963), shown in Figure 1, provides a solution of the original ODE by first solving subproblem A on a time interval $\Delta t/2$, Eq.(6). Then subproblem B is solved on a time interval Δt with the solution from A as its initial condition, Eq.(7). The final solution, marked by a circle, Eq.(9) is obtained by solving subproblem A again on the remaining time interval $\Delta t/2$, Eq.(8).

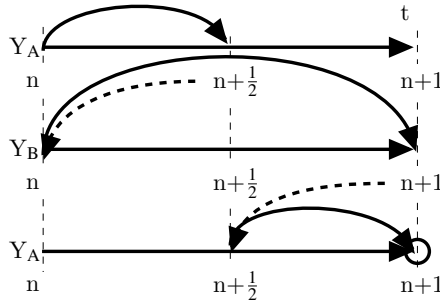


Figure 1: Strang splitting scheme

$$\frac{d(Y_i^*)_A}{dt} = \dot{\omega}_i \quad \text{with } (Y_i^*)_A(t=0) = Y_i^*(t=0) \quad (6)$$

$$\frac{d(Y_i^*)_B}{dt} = \frac{1}{\tau^*} (Y_i^\circ - Y_i^*) \quad \text{with } (Y_i^*)_B(t=0) = (Y_i^*)_A(t = \Delta t/2) \quad (7)$$

$$\frac{d(Y_i^*)_A}{dt} = \dot{\omega}_i \quad \text{with } (Y_i^*)_A(t = \Delta t/2) = (Y_i^*)_B(t = \Delta t) \quad (8)$$

$$Y_i^*(t = \Delta t) = (Y_i^*)_A(\Delta t) \quad (9)$$

2.2.2. Staggered Splitting

Figure 2 shows the solution procedure of the Staggered splitting scheme. Subproblem A is solved for a time step Δt from n to $n+1$ and subproblem B is solved from $n+\frac{1}{2}$ to $n+\frac{3}{2}$, taking the solution from subproblem A as initial condition. The solution is approximated by the mean of the solutions of subproblem A and B marked by circles in Figure 2, Eq.(10). The initial time step, needs special treatment: the mixing subproblem is solved on a time interval $\Delta t/2$ to obtain the initial conditions for subproblem A.

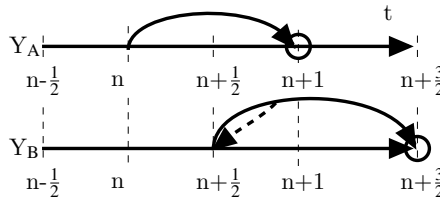


Figure 2: Staggered splitting, adapted from Ren and Pope (2008)

$$Y_i^*(t=n) = \frac{1}{2} \left((Y_i^*)_A(t=n+1) + (Y_i^*)_B \left(t = n + \frac{3}{2} \right) \right) \quad (10)$$

3. Simulation Details

Sandia Flame D was simulated in OpenFOAM using the in-house solver rhoEdcFoam. A 2D-wedge was simulated with a grid of 4329 cells (4218 hexahedras and 111 prisms). A transient simulation was conducted for 0.5 seconds to achieve a description of the steady-state of the flame. Radiation was neglected due to studies showing, that radiation has a minor impact on the results (Li et al., 2017).

For the chemical reactions the detailed chemical mechanism GRI-3.0 from Smith et al. (2017), including 53 species and 325 reactions, was used. The simulations have been conducted with direct integration and the presented operator splitting methods in conjunction with ISAT. The retrieval tolerance for ISAT was set to 10^{-4} . The results from a simulation using a global mechanism are also added for comparison.

The presented operator splitting methods are second order methods, i.e. the error is proportional to $\mathcal{O}(\Delta t^2)$. To improve the predictions and limit the error done by operator splitting, a maximum operator splitting time step size of $\Delta t = 10^{-3}$ s and $\Delta t = 10^{-4}$ s was tested.

4. Results and Discussion

Figure 3(a) to Figure 3(c) show the centerline profiles of temperature, CO₂ and NO mass concentration for the different simulations (x/d represents the axial position normalized by the jet diameter $d=7.2$ mm). The results from direct integration fit best to the experimental results for temperature and CO₂ mass concentration. The profiles show, that operator splitting approximates the solution well, but is a bit less accurate. For the NO mass concentration the solution from Staggered splitting fits even better to the experimental results than the direct integration.

To quantify the accuracy of the predictions, the sum of squared errors (SSE) was calculated for all available data points and for different quantities (temperature T, velocity u, and different species concentrations). The SSE was normalized to the SSE of direct integration to compare the different simulation settings (Figure 3(d)). Staggered splitting seems to be even more accurate than direct integration. The improved predictions could result from increased stability or be due to error compensation resulting from taking the mean in Eq. (10). Strang splitting gives in general better predictions than the global mechanism but gives less accurate predictions than the other simulations.

Figure 3(e) to Figure 3(h) show results from Staggered splitting and Strang splitting with and without limited time step size. The time step size was limited to 10^{-3} s and 10^{-4} s for Staggered splitting. The profiles of the temperature at the centerline (Figure 3(e) and Figure 3(g)), show that the limited splitting schemes give a bit improved, especially smoother, predictions. The SSE was calculated and normalized to the simulations without time step limitation. For Staggered splitting, the limited case gives improved predictions for all quantities, except methane. The smaller limit for the time step, i.e. 10^{-4} s, did not lead to a significant improvement. Therefore, the time step limit was only set to 10^{-3} s for Strang splitting.

For Strang splitting the improvement is not as big and also for methane no improvement is achieved through the limited time step size. In general the limited time step size gives a bit more accurate predictions, with only minimally increased computational demand.

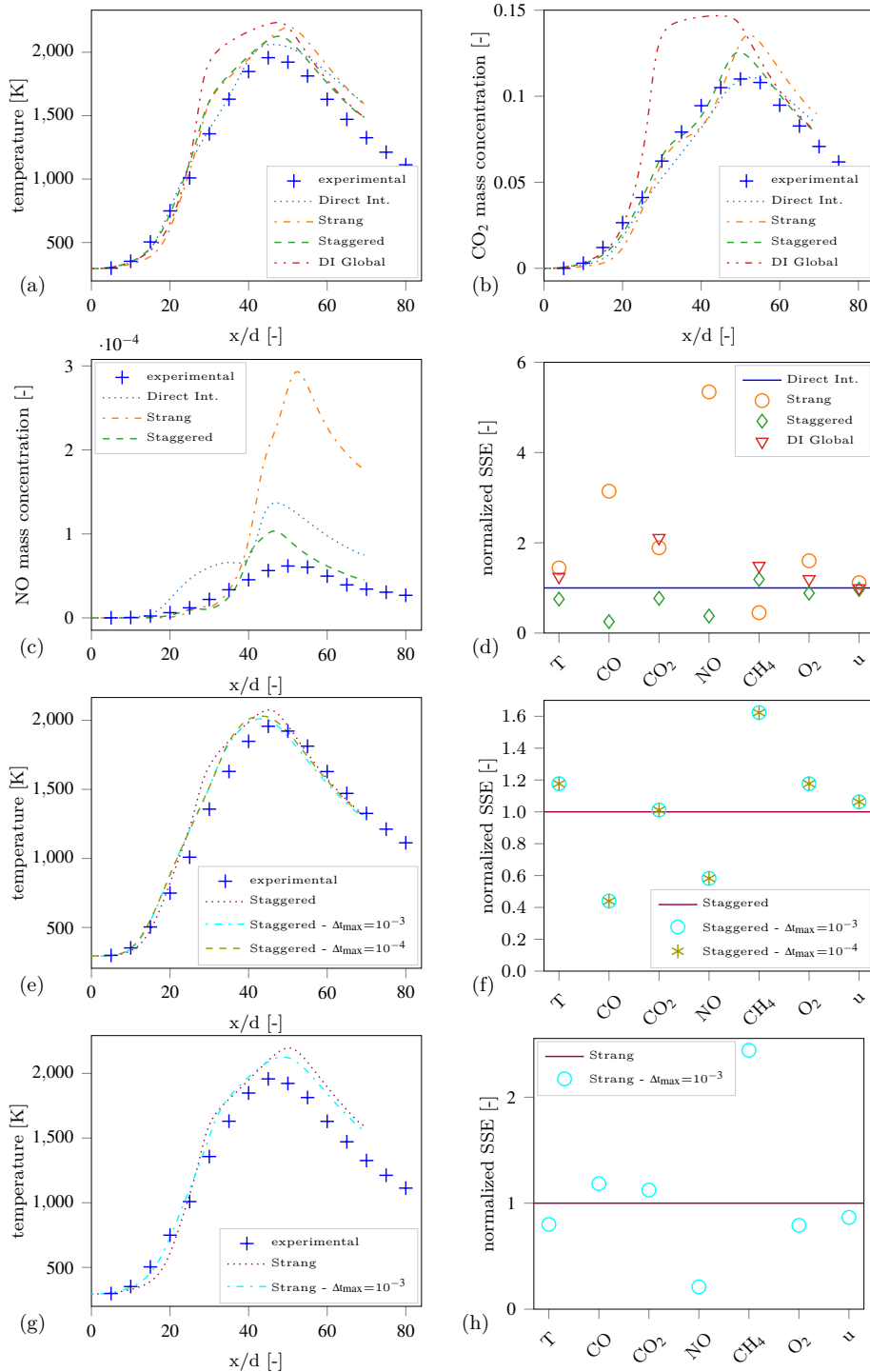


Figure 3: Comparison of simulation results and experimental data for (a) temperature (b) CO_2 and (c) NO mass concentration and (d) comparison of the normalized SSE for all data points; Results using limited time steps in (e) to (h)

Since the simulations were not carried out on the same computers, the computational time can only be roughly compared. Using Strang splitting with an ISAT-tolerance of 10^{-4} , the computational time could be reduced by approximately 23 % compared to direct integration. Further comparisons on the computational time with different ISAT settings and without ISAT are presented by Wartha (2017).

Staggered splitting is even faster than Strang splitting, since it needs less function calls for one operator splitting step. The reduction of computational time for Staggered splitting compared to Strang splitting is around 20 %.

5. Conclusion and Outlook

The use of a detailed chemical mechanism is important to predict species like radicals or pollutants, which are not present in global mechanisms. The presented operator splitting methods, Strang and Staggered splitting, work and can reduce the computational demand when detailed chemical mechanisms are used in conjunction with the EDC. Good predictions for temperature and concentrations have been achieved for Sandia Flame D. For some cases Staggered splitting gives even better results than direct integration. Furthermore, the computational demand is smallest for Staggered splitting. Therefore, Staggered splitting seems to be the best choice.

To substantiate those findings, further test cases with other flames should be conducted to ensure, that the presented findings are also valid for other combustion regimes.

References

- R. S. Barlow, J. H. Frank, 1998. Effects of turbulence on specific mass fractions in methane/air jet flames. Twenty-Seventh Symposium (International) on Combustion 27, 1087–1095.
- S. Byggstoyl, B. Magnussen, 1983. A model for flame extinction in turbulent flow. Fourth Symposium on Turbulent Shear Flows 4, 32–38.
- I. R. Gran, B. F. Magnussen, 1996. A Numerical Study of a Bluff-Body Stabilized Diffusion Flame. Part 2. Influence of Combustion Modeling And Finite-Rate Chemistry. Combustion Science and Technology 119, 191–217.
- Z. Li, A. Cuoci, A. Sadiki, A. Parente, 2017. Comprehensive numerical study of the Adelaide Jet in Hot-Coflow burner by means of RANS and detailed chemistry. Energy 139, 555–570.
- B. Magnussen, 1981. On the structure of turbulence and a generalized eddy dissipation concept for chemical reaction in turbulent flow. 19th American Institute of Aeronautics and Astronautics Aerospace Science Meeting, 1–6.
- S. B. Pope, 1997. Computationally efficient implementation of combustion chemistry using in situ adaptive tabulation. Combustion Theory and Modelling 7830 (1), 41–63.
- M. Rehm, 2010. Numerische Strömungssimulation der Hochdruckvergasung unter Berücksichtigung detaillierter Reaktionsmechanismen. Ph.D. thesis, Technische Universität Bergakademie Freiberg.
- Z. Ren, S. B. Pope, 2008. Second-order splitting schemes for a class of reactive systems. Journal of Computational Physics 227 (17), 8165–8176.
- C. Schneider, A. Dreizler, J. Janicka, E. P. Hassel, 2003. Flow field measurements of stable and locally extinguishing hydrocarbon-fuelled jet flames. Combustion and Flame 135 (1-2), 185–190.
- G. P. Smith, D. M. Golden, M. Frenklach, N. W. Moriarty, B. Eiteneer, M. Goldenberg, C. T. Bowman, R. K. Hanson, S. Song, W. C. J. Gardiner, V. V. Lissianski, Z. Qin, 2017. GRI-MECH 3.0. URL <http://www.me.berkeley.edu/gri-mech/>
- G. D. Stefanidis, B. Merci, G. J. Heynderickx, G. B. Marin, 2006. CFD simulations of steam cracking furnaces using detailed combustion mechanisms. Computers and Chemical Engineering 30 (4), 635–649.
- G. Strang, 1963. Accurate partial difference methods I: Linear cauchy problems. Archive for Rational Mechanics and Analysis 12 (1), 392–402.
- E.-M. Wartha, 2017. A Study on New Developments and Chemical Time Scale Definitions for the Eddy Dissipation Concept. Master's thesis, Technische Universität Wien.
- S. Zahirović, R. Scharler, P. Kilpinen, I. Obernberger, 2010. Validation of flow simulation and gas combustion sub-models for the CFD-based prediction of NOx formation in biomass grate furnaces. Combustion Theory and Modelling 15, 61–87.

Active Learning of Process Control

Manuel Rodríguez^{a*}, Alberto Prada^a, Ismael Díaz^a, Emilio Gonzalez^a, María González-Miquel^a

^a*Universidad Politecnica de Madrid, José Gutierrez Abascal 2, Madrid 28006, Spain*
manuel.rodriguez@upm.es

Abstract

Process Control is a course that needs a thorough understanding of how the different unit operations work and what are the implications of changing operation variables in a process. This paper presents how education innovation can help students to improve their learning and understanding of the different concepts and thus to get better results in the subject and to achieve the desired outcomes. The Process Control Course is taught in the Bachelor Degree in Chemical Engineering at the Technical University of Madrid. Different methodologies have been integrated and used in the course as: flipped classroom, peer instruction, and gamification. In order to implement the mentioned methods, the following material has been developed: screencasts, concept tests, trivia contest and simulations besides the traditional material (slides and text). First year results show high student motivation, higher participation in class and better results (marks) in the subject.

Keywords: Active learning, adaptive learning, flipped classroom, gamification, just in time teaching.

1. Introduction

Lecturing has been the usual way of instruction since universities were founded more than 900 years ago. There are theories emphasizing the need of changing this approach to allow the students develop their understanding. Active learning, understood as an instructional method that engages students in the learning process, seems fundamental in the new teaching/learning paradigm which is student-centered. Freeman et al (2014), did a meta-analysis study where they demonstrate that active learning increases performance in STEM (Science, Technology, Engineering and Mathematics) disciplines. New education methodologies exist to tackle this new way of teaching.

One of the most used learning approaches related with active learning, Lucke and Dunn (2017), is flipped (or inverted) classroom, which can be defined, as stated by Lage et al. (2000): “Inverting the classroom means that events that have traditionally taken place inside the classroom now take place outside the classroom and vice versa”. This definition is somehow limited and we prefer the definition given by Bishop and Verleger (2013): “[...] is a new pedagogical method, which employs asynchronous video lectures and practice problems as homework, and active, group-based problem solving activities in the classroom. It represents a unique combination of learning theories [...]”. Another important learning methodology is game-based learning or gamification. In Bodnar (2014), they explore the impact of gamification in students in an engineering discipline getting very positive results. This paper is focused on active learning of the subject Process Control. Some previous experiences can be found in

literature related to applying the flipped classroom to this subject, like in Marlin (2016) but it is basically based on the flipped classroom methodology. Our approach, although relying in flipping the classroom, extends this method with the use of other learning experiences as gamification, peer instruction, group problem solving or simulations.

1.1. The motivation

How to select the best control structure for a unit operation or a reactor? How many degrees of freedom does a process have for control? How to develop a P&I starting with a process flowsheet from scratch? These questions are addressed and explained in the course Process Control. This course needs a thorough understanding of the operations to be controlled and the implications of all the units in a process. These concepts are difficult to grasp for many students and they stay in a quite passive attitude, so a different innovative approach has been implemented in order to increase students understanding and participation.

1.2. The objective

The main objective is to foster a student-centred learning methodology. A motivating active learning that allows a personalized evolution of the student. This objective is decomposed in the following sub-objectives:

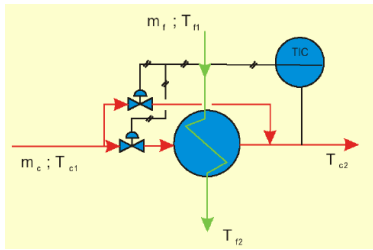
- Implement a new student centred learning methodology
- Increase student motivation and participation in class
- Increase the understanding of the more complex concepts by the students
- Improve student results and the outcomes acquired
- Make the students aware of the importance of self-learning

2. The active learning approach

In this approach, different education innovation experiences have been integrated. Although the core methodology is flipped classroom, it is complemented with gamification activities, adaptive learning and peer instruction. In order to implement the methodology, the following elements have been developed: screencasts, concept tests, dynamic simulations and gamification (trivia like).

2.1. Educational material

•Concept tests: These correspond to the contents of the course and are focused on checking the students comprehension. They are multiple choice questions, like the one shown in Fig. 1.



Next figure shows a control scheme where the valves:

- Must have the same pressure drop
- One must have greater pressure drop than the other
- Both must be fail open or fail close
- One must be fail open and the other fail close
- a) and c) are correct
- b) and d) are correct

Figure 1. Concept test example

- Gamification: Trivia like competition, single elimination tournaments or spotting errors (in given P&Is) competition have been developed.
- Screencasts: Educational videos have been recorded for every topic. These are the main material for flipping the classroom. The videos have a teacher narrative to explain the main concepts of the lessons and they have a lecture-like format. This is a very valuable material as it allows the student to assimilate the concepts prior to the classroom and they are available for reviewing as needed depending on the learning evolution of the student. Videos solving problems (basically developing the control structure of a process) have also been recorded. Fig. 2. shows a snapshot of the explanation of Valve Position Control.

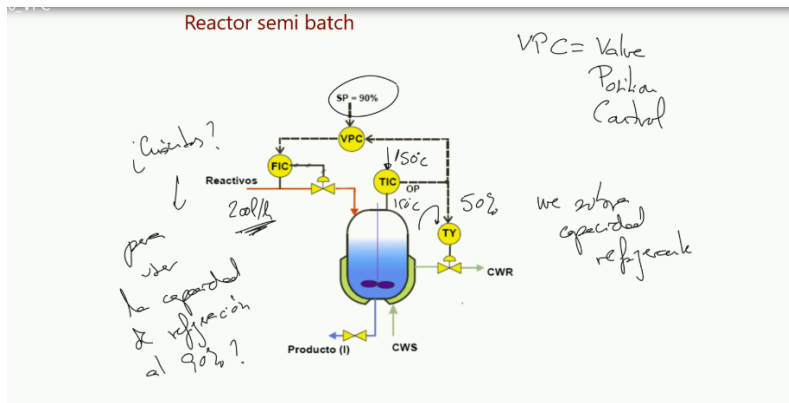


Figure 2. Snapshot of a screencast explaining Valve Position Control in a semi batch reactor

- Simulations

An operator training simulator has also been developed. It has a HMI (Human Machine Interface) as shown in Fig 3. It allows to act as an operator and perform tasks such as: change operation modes (manual, automated), tune controllers, see variables evolution, etc.

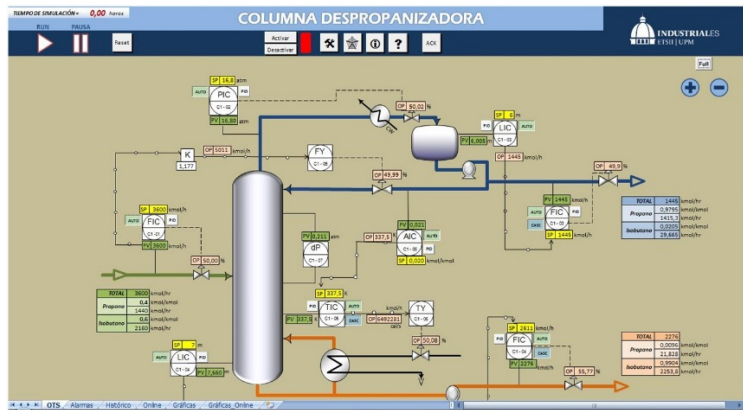


Figure 3. Snapshot of the OTS showing a distillation column with its control

2.2. Methodology

The methodology applied is not based on a single one but on the application and integration of several ones, like the ones that are described below.

- Flipped classroom

This methodology has been applied using educational videos/screencasts and complemented with traditional material as slides or texts. The student learns by himself in advance the contents of the topic to be discussed in the following class.

- Peer instruction: This is achieved using concept tests. Individual student understanding is evaluated through the use of concept tests. Then small groups of students get together and think about the more difficult topics (tests with more wrong questions) and the test is run again. Finally, the instructor explains the topic in detail.

- Gamification: The main purpose of gamification is to improve the classroom experience and to have more active and participative classes. Gamification is a powerful methodology since it can motivate the students and help to fix concepts however it has to be used with caution and keeping in mind its final objective: learn and understand (in a funnier way).

The above methodologies (along with some others) are used in an integrated and varied way allowing to have motivated students and helping to fix concepts.

3. Implementation

Screencasts along with slides are provided beforehand to flip the classroom. Concept tests (implemented using the *Gopollock* platform – gopollock.com–) are made at the beginning of the class to check the understanding of the students and to work on the more difficult concepts. The students comment on the question and it is answered again (peer instruction), finally, the instructor gives the explanation. Dynamic simulations are provided so they can check how different control loops work. Besides from time to time a gamification activity is done covering several lessons.

All these activities are complemented with the use of a virtual environment (Operator Training System - OTS) of a process plant previously developed. The OTS allows the student to operate a plant, changing its conditions, operating parameters, activate alarms, see the evolution of variables, change the tuning of controllers, etc.

It is important to change what is done from class to class. If the same procedure is regularly done then the students will, finally, lose the motivation and the effort that has been put into the development of these educational methodologies will be partially lost. In the subject of Process Control, the use of concept tests are not used in every class (they are used in about 30-40% of the classes). Not all the course topics are explained flipping the classroom, some of them are explained in a traditional way but always keeping in mind to have an active and participative audience. Interaction while presenting the lesson has been achieved in this case using *Mentimeter* (mentimeter.com), a platform that allows to create different type of questions that the students answer and see the results in real time as they are answering. Fig 4. shows a summary of the implementation done. Students get the screencasts and additional educational material before class. Then concept tests are done in class along with peer instruction. Team work for case based problems and for theory topic discussion are created. Some gamification activities (in the figure a tournament recreating Game of Thrones is shown, where the teams were families and the winner got the Iron Throne – besides some extra points).

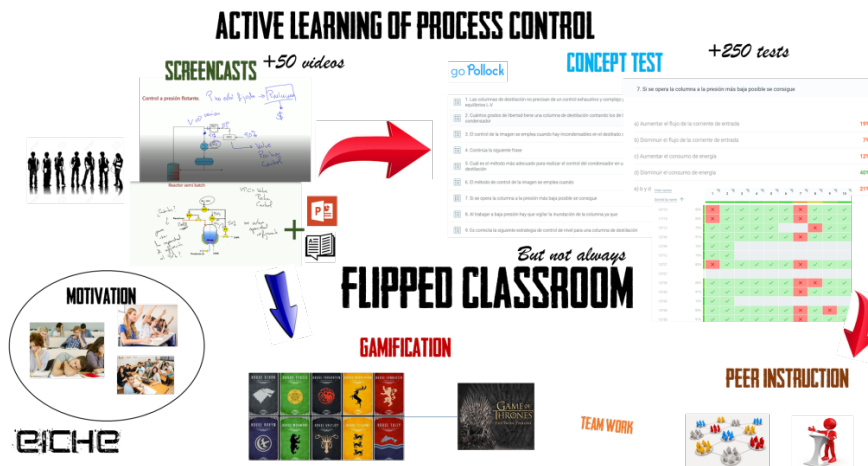


Fig 4. Implementation of active learning for process control

3.1. Results

The results obtained come from a one year experience. Most of the students prefer this approach to the classic one of traditional teaching with slides. Some motivation has to be included in order to get most of the class having the previous work, needed to have the flipped classroom, done. The incentive used is getting marks after completing the activity (it is not necessary that all the activities provide marks). As a result the class is more dynamic and active and the student participation is much higher. The core of the contents are more progressively learned along the course and the use of the tests shows

that the concepts are better understood. At this moment partial results are available. A process control theory exam has been done. Results compared with the two preceding years are presented in Table 1:

Table 1. Results obtained in the last four years

Year	Average grade (out of 10)	% Passed	% Failed	Students
2017	7.4	91	9	54
2016	6.8	67	34	39
2015	5.6	72	23	43
2014	6.7	75	25	32

Although these results have to be taken with caution it seems that a significant improvement has been achieved. Not only in the students that have passed the theory exam but in the average grade obtained.

4. Conclusions

New innovative education methodologies are not just a hype but a true improvement over traditional ones. Implementing a flipped classroom allows to focus on the difficult parts of the lessons, instead of giving time to all the concepts as in the traditional approach. Students are more active, motivated and get a better understanding. Flipped learning is a useful methodology but it is not the only one and abusing of it or of any other will make it quite less efficient. An important conclusion of this project is that what best fits for a new way of teaching or better a new way of learning is using several approaches (flipped classroom, gamification, peer instruction, team work, case based learning, etc). This will make the students alert, motivated and highly participative.

References

- J.L. Bishop, M. Verleger. The Flipped Classroom: A Survey of the Research. 120th ASEE Annual Conference, American Society for Engineering Education, Atlanta, 2013
- C. A. Bodnar, R.M. Clark. Exploring the impact game-based learning has on classroom environment and student engagement within an engineering product design class. Proceedings of the Second International Conference on Technological Ecosystems for Enhancing Multiculturality, 191-196, 2014
- S. Freeman, S. L. Eddy, M. Mc Donough, M.K. Smith, N. Okoroafor, H. Jordt, M. P. Wenderoth. Active learning increases student performance in science, engineering, and mathematics. PNAS, 111: 8410:8415
- M.J. Lage, G.J. Platt, and M. Treglia. Inverting the classroom: A gateway to creating an inclusive learning environment. The Journal of Economic Education, 31(1):30-43, 2000.
- T. Lucke, P.K. Dunn. Activating learning in engineering education using ICT and the concept of 'Flipping the classroom'. European Journal of Engineering Education, 42: 45-57, 2017
- T. Marlin. The Flipped Classroom: A Survey of the Research. 120th ASEE Annual Conference, American Society for Engineering Education, Columbus, Ohio, 2017

Combining Open Source and Easy Access in the field of DEM and coupled CFD-DEM: LIGGGHTS®, CFDEM®coupling and CFDEM®workbench

Dr. Alice Hager^{a*}, Dr. Christoph Kloss^a and Dr. Christoph Goniva^a

^a*DCS Computing GmbH, Industriezeile 35, 4020 Linz, Austria*

alice.hager@dcs-computing.com

Abstract

Discrete Element Method (DEM) and DEM coupled to Computational Fluid Dynamics (CFD-DEM) are powerful techniques for optimization and design of particle processes. Macroscopic granular particles or flow involving fluids and granular particles are everywhere - in industry, environment and everyday lives: sugar, sand, ores, tablets, chemicals, biomass, detergents, plastics, crops, fruits need to be harvested, produced, processed, transported and stored.

We highlight our vision of providing cutting edge simulation technology to an open public via the open source CFD-DEM software CFDEM®coupling (cf., Goniva et al. (2012)) and the open source DEM software LIGGGHTS® (cf., Kloss et al. (2012)).

While open source guarantees transparency and security of investment it does not automatically enable everyone to easily apply the software. Often the installation of the required operating system or third-party software are hindering potential users from using open source software. By developing the commercial GUI CFDEM®workbench we provide an easy access route to the complex field of DEM and CFD-DEM modelling, which is fully compatible to its open source advantages. It combines the strength of the open source simulation software with the comfort of a guidance through the installation and setup process. We give an introduction to the software tool and highlight possible applications in fields such as steel industry, chemical industry, pharmaceutical industry, consumer goods industry, agricultural machinery production, food production, powder metallurgy and plastics production.

Keywords: CFD-DEM, DEM, Open Source, GUI

1. Introduction

The multidisciplinary of modern computer aided process engineering leads to a variety of challenges, some of which are listed here:

- process / operating conditions
- determination of main influence factors
- development of models for depicting the different physical effects
- transferring the models to efficient computational tools
- choosing appropriate material parameters
- model setup and simulations with interpretation of results

Each of the mentioned points comes with very specific requirements that differ strongly: In some areas detailed knowledge about the process itself is necessary while in others programming skills or a fundamental theoretical background is required. There are many experts that work on one or a couple of the mentioned points, but it rarely happens that a single person covers the complete list of tasks. Besides developments in the dedicated areas it is particularly important to create strong links between them to guarantee a possibly complete information transfer and optimal usage of the different tools. Thus, either a strong team of experts or an efficient and easy-to-use workflow is needed to tackle modern CAD engineering tasks.

With the combination of LIGGGHTS®, CFDEM®coupling and CFDEM®workbench we provide a combination of versatile tools that on the one hand allow for the implementation of new models by scientists, developers and students and on the other hand support a straight forward application by engineering experts. The modular structure of the open source DEM code LIGGGHTS® and the open source CFD-DEM code CFDEM®coupling makes it possible to apply newly developed models universally. This paves the way to de-couple scientific model development and its industrial application. Fig. 1 for example shows a selection of particle types, which can be used in combination with different physical models.

In this paper we first introduce the theoretical background of DEM and coupled CFD-DEM. Then we propose two entirely different approaches for applying LIGGGHTS® and CFDEM®workbench: the objective of the first example is the application of a complex, already implemented model and the specialisation on the variation of material parameters. The second example shows the implementation of a new model and its application in a simulation. Both examples demonstrate ways for teaching simulation tools for computer aided process engineering.

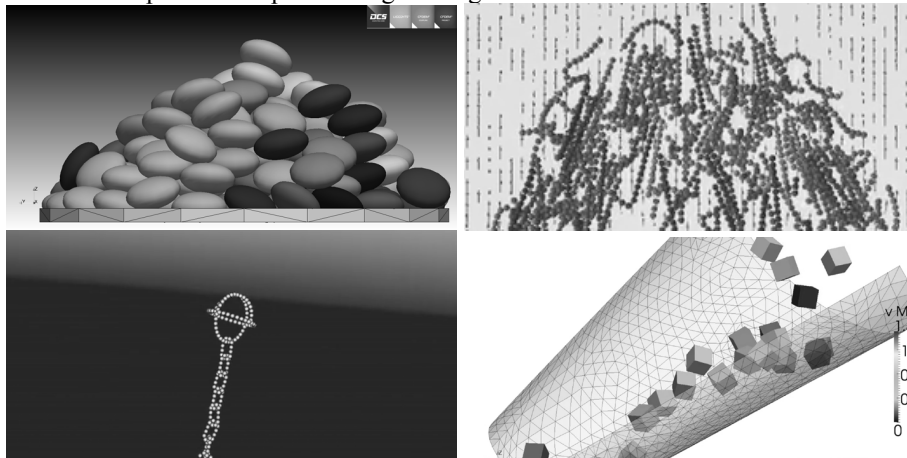


Figure 1. Different particle types in LIGGGHTS®: superquadrics (top left), flexible fibers (top right), a buoy on a chain modeled by complex multispheres (bottom left) and convex particles (bottom right).

2. Theoretical background – The governing equations

The discrete element method (cf., Cundall and Strack (1979)) is a Lagrangian method, in which the trajectory of each particle is calculated explicitly under simultaneous consideration of the different forces in the system. In pure DEM calculations these are

particle-particle as well as particle-wall interaction forces, in coupled calculations also the impact of the surrounding fluid is considered. The governing equations for the translational and rotational motion are based on Newton's second law (cf., Kloss et al. (2012)):

$$m_p \frac{du_p}{dt} = F_{p,p} + F_{p,w} + m_p g + F_{p,f} \quad (1)$$

$$I_p \frac{d\omega_p}{dt} = T_p \quad (2)$$

Here m_p is the mass of particle p , v_p is its velocity, $F_{p,p}$ stands for the particle-particle and $F_{p,w}$ for the particle-wall forces. The term $F_{p,f}$ stands for the forces that are exerted by the surrounding fluid. For calculating the contacts between the particles and particles and walls, the so-called soft-sphere approach (cf., Cundall and Hart (1992)) is used. In this method the particles in contact have a slight overlap and elastic, plastic and frictional forces are calculated with the aid of the spatial overlap. LIGGGHTS® provides a large number of different models for handling normal and tangential contacts as well as the effect of friction, rolling resistance, cohesion, liquid films etc. Models for computing the contribution of $F_{p,f}$ are available in CFDEM®coupling.

Coupled CFD-DEM comes in two flavours, namely as resolved and unresolved CFD-DEM. The first method is a direct numerical simulation method where each particle is resolved within the fluid mesh, in the second method the particles are smaller than the cells of the fluid mesh. The latter method was first introduced by Tsuji et al. (1993) and is suitable for running simulations with large numbers of particles. The governing equations are the volume averaged Navier Stokes equations:

$$\frac{\partial \alpha \rho}{\partial t} + \nabla \cdot (\alpha \rho U) = 0 \quad (3)$$

$$\frac{\partial \alpha \rho U}{\partial t} + \nabla \cdot (\alpha \rho U U) - \nabla \cdot (\alpha \tau) = -\alpha \nabla p + R_{s,l} + \alpha \rho g, \quad (4)$$

where α denotes the voidfraction of the fluid, ρ its density, U the fluid velocity, p the pressure, τ the stress tensor and $R_{s,l}$ the solid-liquid interaction force, which is computed as following:

$$R_{s,l} = K_{s,l} (U - U_s), \quad (5)$$

where $K_{s,l}$ is the interaction force coefficient and U_s the average particle velocity calculated on the cells of the fluid mesh (cf., Goniva et al. (2012)).

3. Example A: Studying the behavior of a load responsive wall in the presence of cohesive granular matter

The use scenario in this case is a process engineer without deep knowledge on the DEM and the underlying equations can set up a case study that relies on highly complex models.

The basic setup of the case consists of a cylinder which is closed by a plate. The plate is defined in a load responsive manner, i.e. it starts to tilt in y-direction as soon as a load is applied. Particles are inserted into the cylinder and under the influence of gravity they start to settle. As soon as they hit the plate, the latter tilts enough for displaying a gap, though which particles could fall out of the cylinder. The load reduces, since the kinetic energy of the particles is absorbed by the plate and the gap is closed again. Fig. 2 gives an overview of the case setup.

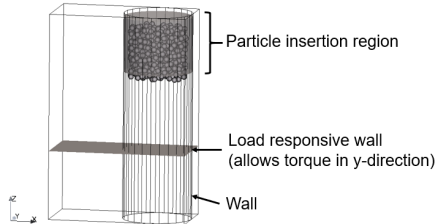


Figure 2. A pack of particles is inserted in a cylinder. As soon as they exert force on the plate, it starts to tilt.

It is assumed that the granular material is cohesive, and that the user wants to determine the cohesiveness for which a certain fraction of the material exits the cylinder. One of the provided cohesion models for particle-particle and particle-wall contacts (e.g. sjkr, c.f., DCS Computing GmbH. (2016)) is chosen and the parameter for the cohesion energy density is varied. Fig. 3 shows results and the comparison of the particle number for two different cases. While for the lower cohesion there is still a significant number of particles that falls out, the higher cohesion leads to the formation of a clump and only few particles exit.

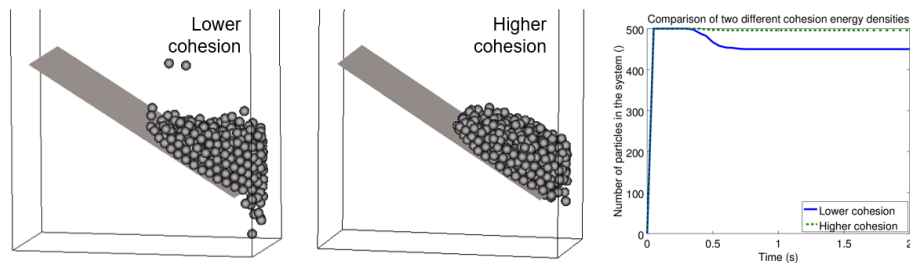


Figure 3. Comparison of the results of calculations for low and high cohesive energy density. For the lower value more particles leave the domain while for the higher value most of the mass remains.

The workbench automatically saves all particle data such as position, radius, velocity, angular velocity, force, etc., all global data such as number of particles, kinetic energy of the system, etc. and all forces and torques on the plate. For visualization one can either use paraview (for the particle data, see the two images in Fig. 3), the live-graph-view that comes with the workbench (esp. suitable for monitoring the results during the simulation) or other tools as for example octave for comparing the global data of several simulations (see plot in Fig. 3).

4. Example B: Implementation of a lubrication force model and its application

In this example we show how one can use the advantages of the open source framework of LIGGGHTS® to implement a new model in combination with the flexibility of CFDEM®workbench for using it in simulations. The use scenario here is a scientist developing a new model which is then applied by an engineer.

The motivation for the new model is the following: when colliding particles are surrounded with a fluid or even a gas, the displacement of the fluid in the gap between two particles causes a force – the lubrication force. In many cases this force is relatively small and thus neglected, but when considering highly viscous fluids or light and small particles it might be worth considering. The formulation of the lubrication force F_{lub} (cf., e.g., Davis et al. (1986)) is given as

$$F_{\text{lub}} = -6\pi\mu r_{ij}^2 \left(\frac{1}{h} \right) v_n, \quad (6)$$

where r_{ij} is the effective radius defined as

$$\frac{1}{r_{ij}} = \frac{1}{r_i} + \frac{1}{r_j}, \quad (7)$$

with i and j denoting two arbitrary particles. h is the minimal distance between the surfaces, μ the dynamic fluid viscosity and v_n the relative velocity of the two particles.

4.1. Implementation

The lubrication force acts when two particles approach each other or move away from each other after a collision, i.e. when two particles are close but not in contact. This makes the lubrication force similar to a cohesion. For implementing the model one can now use an arbitrary cohesion model as template and start to replace the equations. When implementing the model one has to limit the radius of action of the lubrication force – for very small values of h the force would become too big and if h becomes too large, the contact search would become too expensive. This approach was also used by Sun and Xiao (2016) in their implementation. Fig. 4 shows two small parts of the implementation.

```

if(h<minDist || h>deltaC)
{
    if(scddata.contact_flags)
        *scddata.contact_flags &= ~CONTACT_COHESION_MODEL;
    return;
}

// force component
const double mult = 6.*M_PI*mu*r_ij*r_ij/h;
const double fx = mult*vn2;
const double fy = mult*vn2;
const double fz = mult*vn3;

```

Figure 4. Two small code snippets of the implementation: radius of action of the lubrication force model is limited (left), computation of the force components (right).

4.2. Application

While the implementation of the new model requires deeper knowledge of the code and the equations, its application is relatively simple within CFDEM®workbench. The user has to select the option “custom” for all cohesion models (for the particles this setting is made in the pair_style tab, for the walls the cohesion model has to be selected in the wall/gran tabs), and define the custom cohesion model “lubrication” in the Custom Settings tab. As the lubrication force requires information about the fluid viscosity, an additional custom global property must be added (cf., Fig. 5). The remaining settings are identical to the ones of the original case.

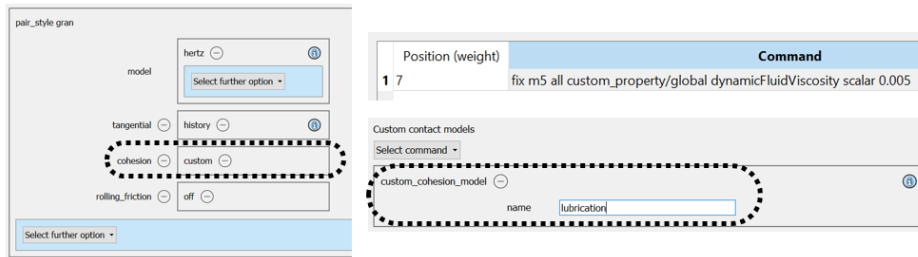


Figure 5. Necessary settings for using the lubrication force model in CFDEM®workbench.

Conclusion

With the presented software tools we bridge the gap between research, development, application and education. With CFDEM®workbench we lower the entry barrier for users to access the capabilities to the complex simulation engine LIGGGHTS® while the advantages of open source are fully maintained. This approach is not only advantageous to industry, where development and application often happen in different divisions, but also for education, where time limitations often make it difficult to teach complex methods that can easily be applied and modified at the same time. Currently it is already possible to run one-way coupled fluid-particle simulations, which consider the impact of a fluid field on the particles or the prepare the DEM side for a fully coupled simulation. The future goal is to bring CFDEM®coupling to the workbench as well.

References

- P.A. Cundall and R.D. Hart, 1992, Numerical modelling of discontinua, *Eng. Computation*, 9, 2, 101-113
- P.A. Cundall and O.D.L. Strack, 1979, A distinct element model for granular assemblies, *Géotechnique*, 29, 47-65
- R.H. Davis, J. Serasyssol and E.J. Hinch, 1986, The elastohydrodynamic collision of two spheres, *J. Fluid Mech.*, 163, 479
- C. Goniva, C. Kloss, N.G. Deen, J.A.M. Kuipers and S. Pirker, 2012, Influence of rolling friction modelling on single spout fluidized bed simulations, *Particuology*, DOI 10.1016/j.partic.2012.05.002
- C. Kloss, C. Goniva, A. Hager, S. Amberger and S. Pirker, 2012, Models, algorithms and validation for opensource DEM and CFD-DEM, *An Int. J.* 2012 - Vol. 12, No.2/3 pp. 140 – 152
- DCS Computing GmbH, 2016, LIGGGHTS® v3.x Documentation / gran cohesion sjkr model, https://www.cfdem.com/media/DEM/docu/gran_cohesion_sjkr.html
- Y. Tsuji, T. Kawaguchi and T. Tanaka, 1993, Discrete particle simulation of two-dimensional fluidized bed, *Powder Technol.*, 77, 1, 79-87
- R. Sun and H. Xiao, 2016, SediFOAM: A general-purpose, open-source CFD-DEM solver for particle-laden flow with emphasis on sediment transport, *Comput. Geosci.*, 89, 207-219
- Z.Y. Zhou, S.B. Kuang, K.W. Chu and A.B. Yu, 2010, Discrete particle simulation of particle-fluid flow: model formulations and their applicability, *J. Fluid Mech.*, 661, 482-510

Open-use and community-based tools for education in process system engineering: industrial applications from decision automation to data analytics

Brenno C. Menezes,^{a,*} Jeffrey D. Kelly^b

^a*Department of Chemical Engineering, University of São Paulo, Av. Prof. Luciano Gualberto trav.3 n.380, São Paulo, SP 05508-010, Brazil*

^b*Industrial Algorithms Ltd., 15 St. Andrew Road, Toronto, ON MIP4C3, Canada*

brennocm@usp.br

Abstract

As part of the freeware, open-use and community-based movement on education in the process system engineering discipline, we present the *OpenIMPL* initiative that is a forum to exchange ideas, learnings, know-how, experiences and data using the free training license of IMPL (Industrial Modeling and Programming Language) for open-use. IMPL is both a structural and semantic language with its concepts, constructs and configurations of the Unit-Operation-Port-State Superstructure (UOPSS) and the terms and details of its Quantity-Logic-Quality Phenomena (QLQP). This forum is primarily intended to discuss problems found in the Batch and Continuous Process Industries when solving design, planning, scheduling, optimization, control, parameter estimation, data reconciliation and simulation examples although interesting and suitable instances found in other industries are also welcome and encouraged. By extensively performing industrial applications around research and development types of initiative, we provide industrial modeling frameworks (IMF) as a jump-start to an industrial project implementation since it can be easily enhanced, extended, customized, modified, etc. to meet the diverse needs of your project and as it evolves over time and use. IMF's also provide graphical user interface prototypes for drawing the flowsheet and typical Gantt charts and trend plots to view the solution of quantity, logic and quality time-profiles. Current developments use Python integrated with open-source Gnome Dia and Matplotlib modules respectively, but other prototypes embedded within Microsoft Excel/VBA for example can be created in a straightforward manner. The primary purpose of the IMF's is to provide a timely, cost-effective, manageable and maintainable deployment of applications to formulate and optimize complex industrial manufacturing systems in either off-line or on-line environments. Using IMPL alone would be somewhat similar (but not as bad) to learning the syntax and semantics of an AML (Algebraic Modeling Language), although in IMPL there is no needs of coding all of the necessary mathematical representations of the problem including the details of digitizing your data into time-points and periods, demarcating past, present and future time-horizons, defining sets, index-sets, compound-sets to traverse the network or topology, calculating independent and dependent parameters to be used as coefficients and bounds and finally creating all of the necessary variables and constraints to model the complex details of logistics (discrete) and quality (nonlinear) industrial optimization

problems. Therefore, IMF's and IMPL give to the end-user, in our opinion, a more elegant and structured approach to industrial modeling and solving so that you can capture the benefits of advanced decision-making faster, better and cheaper. Upon agreement to join in the community of the industrial optimization and estimation applications, all model and/or problem data used with the free training license of IMPL must be made available to the *OpenIMPL* initiative. As such, it is the sole responsibility of the academic, non-commercial and/or home user to ensure that the model and/or problem data can be released and shared publicly.

Keywords: Education, open-use, enterprise-wide optimization, industrial modeling and programming language

An interactive virtual laboratory for process engineering education

Diana Ibet Roman-Sanchez^a, Teresa Lopez-Arenas^a, Mauricio Sales-Cruz^a

^a*Universidad Autónoma Metropolitana - Cuajimalpa, Avenida Vasco de Quiroga 4871, Col. Santa Fe Cuajimalpa, Delegación Cuajimalpa de Morelos, C.P. 05348, Ciudad de México, MX*

asales@correo.cua.uam.mx

Abstract

At present, technological innovation can be used as a tool in the teaching-learning process through the implementation and use of an interactive virtual laboratory. Large-scale resources could be simulated, overcoming the drawbacks associated with the physical space, infrastructure and instrumentation required to carry out process engineering practices at different levels (laboratory, pilot and industrial). In this type of laboratory, students can enter a virtual environment where they must apply the acquired knowledge to select solution options and make decisions in situations similar to a real environment, allowing them to experience the resulting consequences.

The LaVIP (for its acronym in Spanish for Virtual Laboratory of Process Engineering) is being developed at the Universidad Autónoma Metropolitana (Cuajimalpa Campus), where practices are being implemented that support undergraduate degrees such as chemical engineering, biological engineering and related. In particular, this work shows the methodology used for the development and implementation of the LaVIP, as well as the results of an interactive virtual practice for an isothermal batch reactor where an enzymatic hydrolysis reaction occurs.

The LaVIP is accessed through a website, which includes the information architecture of an educational platform that guides the user, providing tools to: (i) motivate and involve the student in the development of a practice in a quasi-real environment, and (ii) improve teaching and evaluate learning. The educational platform is developed using usability techniques, maintaining indispensable characteristics such as access security, an intuitive environment, access to information (offering resources such as glossary, help, descriptions, etc.), student progress monitoring, and a simple administration portal.

The functions and executable programs of process engineering practices are developed using the Matlab Production Server application. This tool provides web clients, which through a process and administration server allow users to run programs developed in Matlab without having an own license. The main server is able to generate scripts, which are used in the website developed in the standard HTML5 language.

As case study, the calculations and analysis of an isothermal batch reactor where the enzymatic hydrolysis of cellulose to produce glucose is carried out. The kinetics is Michaelis-Menten type and the main objective is to determine the values of the kinet

- (1) trial and error, where the kinetic parameters are estimated from a plot of experimental data;
- (2) linear regression, where the parameters are calculated from the linearization of the Michaelis-Menten equation; and
- (3) optimization, where an objective function is minimized to determine the optimal parameter values.

So far, LaVIP has its own systematic development process for lab practice implementation. Currently its use is internal and being in evaluation. In the future, more practices will be added and LaVIP use will open for other institutions.

Keywords: modelling, simulation, education, virtual lab, reactor engineering

Author Index

A

Abildskov, J., 287
Abonyi, J., 1003
Adams II, T.A., 845, 1401
Akisue, R.A., 1129
Akkerman, R., 651, 1063
Al-Ansari, T., 537, 1481, 1487, 1499
Alexopoulos, A.H., 1661
Al Jamri, M., 1439
Aljumah, F., 1201
Alkatheri, M., 91
Allison, J., 1451
Almansoori, A., 91
Almeida-Trasvina, F., 621
AlNouss, A., 145, 1481
Al-Obaidi, M.A., 19
Alriols, M.G., 1535
Al-Sobhi, S.A., 145
Álvarez, H., 1237
Alves, R.M.B., 597
Alvim, R., 25
Al-Yaeeshi, A.A., 1499
Alzyod, S., 451
Amini, S., 247
Anantpinijwatna, A., 49, 73
Anda, M., 313
Andersson, N., 1619
Andersson, S., 247
Andre, A., 1287
Anne, S.B., 893
Appel, S., 737
Ardakani, M.H., 1069, 1123
Arellano-Garcia, H., 211, 821, 1087
Arruda, L.V.R., 931
Arsenyeva, O., 181, 289
Arsenyev, P., 289
Asiagbe, K.S., 79
Asprion, N., 43
Assawasaengrat, P., 409
Attarakih, M., 427, 451
Audino, F., 223
Avraamidou, S., 391

B

Bachmann, G., 985
Backi, C.J., 1153
Badino, A.C., 175
Badr, S., 1577
Bahri, P.A., 55, 313
Bakošová, M., 961

Baratti, R., 1207
Barazzetta, J., 1631
Barbosa-Póvoa, A.P., 773, 809, 815, 931,
949, 991, 1165
Bardow, A., 307, 325
Bareschino, P., 1389
Bari, I.D., 585
Barla, F., 903
Barletta, D., 193, 585
Barthe-Delanoë, A.M., 785
Bart, H.-J., 427, 451
Becher, R.-D., 1159
Bechtsis, D., 439
Beck, A., 1335
Benjelloun, S., 229
Benkoussas, H., 1341
Benyahia, B., 1607
Bergh, L., 1081
Berinde, D.A., 711
Betancourt-Torcat, A., 91
Beykal, B., 421
Biegler, L.T., 1117
Bildea, C.S., 711, 791
Bique, A.O., 603, 1413
Birgen, C., 1547
Boer, D., 457
Bogataj, M., 549
Boix, M., 67, 803
Bonamy, C., 31
Bonnowitz, H., 1111
Bortz, M., 43
Bösenhofer, M., 1687
Böttcher, R., 43
Bouaswaig, A.E.F., 139
Bourganis, V., 1661
Brandão, A.L., 1177
Brandenbusch, C., 103
Brant, V., 1469
Braz, C.G., 25
Briceño, L., 1081
Bublitz, S., 403
Budinis, S., 1311
Burca, M.I., 1341
Bussemaker, M., 1565
Bütün, H., 1395

C

Caballero, J.A., 463, 657, 731, 1419
Cabo, D., 1075
Cakir, R., 67

- Calvo-Serrano, R., 133
 Camarda, K., 543
 Campos, A.L., 483
 Capón-García, E., 1225
 Cárdenas-Guerra, J.C., 513
 Carmeliet, J., 525
 Carrero-Parreño, A., 657
 Carvalho, A., 253, 773, 809
 Castiglioni, A., 651
 Castro, P.M., 973
 Cecelja, F., 471, 495, 563, 1565
 Chachuat, B., 597
 Champa, V., 409
 Charon, N., 1559
 Chebeir, J., 1207
 Chen, T., 937, 1625
 Chen, X., 1117
 Chen, Y., 851
 Chhabra, P., 157
 Chisalita, D.-A., 1269
 Chkifa, A., 229
 Choi, Y., 693
 Chomette, G.A., 669
 Cho, S., 1105
 Chou, C.-T., 1425
 Chován, T., 349
 Chuang, Y.C., 937
 Chu, H.-Y., 761
 Ciahotný, K., 253
 Cloete, H., 247
 Cloete, S., 247
 Coelho, F.A., 483
 Colombo, M., 79, 1027
 Consuegra, F.E., 259
 Contreras-Zarazúa, G., 579
 Cormos, A.-M., 1269, 1281, 1341
 Cormos, C.-C., 1269, 1281
 Cornelissens, T., 979, 1165
 Costa da Cruz, A.R., 1559
 Cremaschi, S., 519
 Cruz, A.J.G., 175
 Csukás, B., 223
 Čuček, L., 863
- D**
- da Silva, C., 773
 Dalle Ave, G., 907
 Dam, K.H.V., 1463
 Damartzis, T., 669
 Darvehei, P., 55
 Das, T., 1015
 de Dios, L.G., 67
 de Mattos, R., 1317
 Demirskyy, O., 289
 de Moraes, M.G.F., 997
- Demouling, M., 169
 de Oliveira Filho, P.B., 361
 De Prada, C., 1081
 Desotgiu, F., 1183
 de Souza, M.B., 997, 1177
 de Sousa, R., 1129
 de Souza, L.M., 31
 Dhar, S., 205
 Diab, S., 1093, 1643
 Díaz, I., 121, 285, 1257, 1693
 Diaz, M.S., 271
 Diglio, G., 1389
 Domenech, S., 803
 Dorgo, G., 1003
 Dorneanu, B., 1087
 Dua, V., 1171
- E**
- Èerveðanský, I., 687, 779
 Ejeh, J.O., 633
 Elekidis, A.P., 1051
 Elias, A.M., 1541
 Elixmann, D., 1159
 Ellerker, M.E., 1093
 Elsidó, C., 373
 Elve, A.T., 235, 241
 Engell, S., 301, 907, 1009
 Epelle, E.I., 127
 Erdmann, E., 433
 Esche, E., 403, 955, 1329
 Escudero, G., 1069, 1123
 Espuña, A., 163, 223, 265, 501, 531, 749,
 1069, 1123
 Estrada, V., 271
 Ewertowska, A., 457
- F**
- Fabricatore, N., 743
 Facco, P., 1667
 Fairweather, M., 61, 79, 555, 1027
 Falco, F., 1553
 Fechtner, M., 295
 Feist, M., 1159
 Fenila, F., 1571
 Fernández-Rodríguez, J., 1535
 Fernengel, J., 97
 Ferrari, A., 1317, 1371
 Ferreira, J., 1371
 Figueroa-Torres, G.M., 1595
 Fikar, M., 1045
 Fileti, A.M., 1231
 Filipe, R., 291
 Fozer, D., 1287
 Frauzem, R., 13
 Friedl, A., 1583

Friedler, F., 869
 Frith, W., 1625
 Fritz, L., 271
 Fukushima, Y., 1347
 Fürer, F., 525
 Furlan, F.F., 1541
 Futamura, H., 1613

G

Gabrielli, P., 525
 Galanopoulos, C., 1413
 Galvanin, F., 355
 Gandiglio, M., 415
 Gani, R., 13, 737, 851, 857, 875, 887, 893,
 905, 1513
 Gao, J., 591
 Garcia, D.J., 1475
 García-García, J.C., 513
 Garcia, M., 1075
 García-Sánchez, M., 839
 Garg, N., 875
 Gasca-González, R., 1529
 Gazzani, M., 525
 Genty, L., 803
 Georgiadis, G.P., 1075
 Georgiadis, M.C., 1051, 1075
 Gerla, P., 1317
 Gernaey, K.V., 1553, 1601
 Gerogiorgis, D.I., 127, 1093, 1553, 1637,
 1643, 1649
 Giarola, S., 415, 1365
 Gioiella, F., 193
 Giordano, R.C., 1541
 Girardin, L., 1057
 Giuliano, A., 193, 585
 Gjøby, J.M., 1021
 Glaser, T., 115
 Godini, H.R., 1329
 Goebel, R., 115
 Goen Ho, 313
 Goes, P., 507
 Goldar, A., 1237
 Gómez-Castro, F.I., 331, 639, 755, 1523,
 1529
 Gong, J., 1
 Goniva, C., 247, 1699
 González, E.J., 121, 1693
 González-Miquel, M., 121, 1693
 Govindan, R., 537, 1487, 1499
 Graciano, J.E.A., 597
 Graells, M., 223, 501, 749, 1069, 1123
 Granada-Vecino, E., 1195
 Grimm, F.A., 421
 Grossi, C.D., 1231
 Grossmann, I.E., 373, 657, 1135, 1261

Grosso, M., 1183
 Guan, S., 1679
 Guillén-Gosálbez, G., 133, 445, 1099
 Guittard, P., 767
 Gundersen, T., 489
 Guo, M., 833, 1407, 1463
 Gurker, T., 247
 Gutiérrez-Antonio, C., 639, 1523, 1529
 Gutierrez, J.P., 433
 Gutiérrez, S., 1371

H

Haaz, E., 1287
 Haddadi, B., 1583
 Hager, A., 1699
 Hajizeinalibioki, S., 211
 Hanak, D., 1389
 Han, C., 1323
 Han, J., 723
 Hanulová, L., 961
 Haragovics, M., 1003
 Harasek, M., 1383, 1583, 1687
 Harbottle, D., 61
 Harjunkoski, I., 907
 Hasegawa, K., 1655
 Hawkes, A., 415, 1311, 1365, 1451
 Hayashi, S., 663
 Hegely, L., 1505
 Heiho, A., 1347
 Helminger, F., 1377
 Hennen, M., 307
 Hernández, S., 331, 639, 1523
 Herwig, C., 1673
 Hidayat, S., 1365
 Hinrichsen, O., 97
 Hirao, M., 1613, 1655
 Hjaila, K., 501
 Hofbauer, H., 1377
 Hoffmeyer, M., 271
 Hoffrogge, D.F., 307
 Hofmann, R., 925, 1335, 1359, 1377
 Hohl, L., 31
 Hollermann, D.E., 307
 Holzer, G., 1255
 Horta, A.C.L., 1129
 Hoseinzade, L., 1401
 Hsu, S.-H., 937
 Hui, C.-W., 1293, 1299
 Hwangbo, S., 343
 Hwang, R., 1433

I

Iakovou, E., 439
 Illner, M., 31
 Imle, M., 1159

Imsland, L., 139
 Iqbal, M.U., 1189
 Isafiade, A.J., 675

J

Jahanshahi, E., 1111
 Jang, M.-G., 1521
 Janssen, F.A.L., 109
 Janssen, M., 1577
 Jaramillo, I., 151
 Jäschke, J., 1021
 Jaubert, J.-N., 767
 Javaloyes-Antón, J., 463, 731
 Jeenchay, J., 385
 Jelihi, P., 609
 Jeng, J.-C., 761
 Jhamb, S., 887
 Jia, X., 1305
 Jiménez-Esteller, L., 457
 Jiménez-González, C., 7
 Jiménez, L., 445
 João, I.M., 1275
 Jolliffe, H.G., 1637
 Joly, J.-F., 1559
 Jonkman, J., 651
 Jordan, C., 1583
 Jörke, A., 85

K

Kager, J., 1673
 Kalemi, E., 495, 563
 Kang, J., 1117
 Kantor, I., 1395
 Kapnisi, M., 645
 Kapustenko, P., 289
 Karageorgos, P., 1661
 Kara-Zaïtri, C., 19
 Karimi, I.A., 157
 Kaspereit, M., 295
 Kather, M., 109
 Kawasaki, K., 1613
 Kelly, J.D., 1135, 1705
 Kelly, N., 1451
 Kenig, E.Y., 181, 397
 Khusanov, A., 289
 Kienle, A., 85, 295
 Kikuchi, Y., 1347, 1353
 Kim, G.-H., 279
 Kim, H., 1433
 Kim, J., 693, 723, 1589
 Kim, J.-K., 901, 1259, 1519, 1521
 Kinaci, M.E., 217
 Kiparissides, C., 1661
 Kiss, A.A., 791, 827
 Kitchaiya, P., 49, 409

Kittisupakorn, P., 615, 967
 Klamt, A., 9
 Kläs, T., 169
 Klemeš, J.J., 1305, 1457
 Kloss, C., 247, 1699
 Klymenko, O.V., 211
 Koèi, V., 253
 Kokossis, A.C., 573, 645, 903, 1493
 Koller, M., 925
 Koltsaklis, N.E., 1051
 Konaem, W., 967
 Kondili, E.M., 1213
 Kontogeorgis, G.M., 737, 851, 857, 875,
 887, 1513
 Koo, J., 279
 Koo, L., 471, 495, 563, 1565
 Kopanos, G.M., 163, 1075
 Korre, A., 537, 1487
 Koumaditi, E., 851
 Kouyialis, G., 565
 Kovacs, Z., 869
 Kraft, M., 157
 Kraume, M., 31
 Kravanja, Z., 549, 705, 863, 1457
 Krishnamoorthy, D., 1015, 1111
 Kröger, L.C., 109
 Kronqvist, J., 463
 Kruber, K.F., 325
 Ksiazkiewicz, A., 109
 Kummer, A., 1147
 Kwak, D.-H., 1259
Ky, Vo., 1589

L

Labidi, J., 1535
 Lamanna, R., 1237
 Lang, P., 1505
 Lantz, A.E., 1601
 Lanzini, A., 415
 Lara, C., 1261
 Lara, R.J., 271
 Latifi, A., 229
 Lauer mann, M., 1377
 Leal, A.L., 187
 LeBlond, D., 1685
 Lee, C.-J., 627
 Lee, I., 1433
 Lee, J., 1105, 1433
 Lee, P.Y., 1293, 1299
 Lee, S., 901, 1519, 1521
 Lee, Y., 1323
 Lee, Y.-W., 279
 Leira, F.M., 139
 Le Lann, J.M., 785
 Leo, E., 1009

Léonard, G., 1341
 Leonhard, K., 109, 325
 Leonzio, G., 1413
 Letsios, D., 565
 Lian, G., 1625
 Liang, X., 887, 1513
 Liang, Y.-Z., 1293, 1299
 Lichtenegger, T., 217
 Liemberger, W., 1383
 Liesche, G., 881
 Li, J., 477, 1033, 1141, 1201, 1439
 Lima, C., 949
 Limleamthong, P., 1099
 Lim, Y., 1323
 Liu, C., 857
 Liu, M., 1463
 Liu, S., 633
 Liu, X., 1513
 Lobo-Oemichen, R., 839
 Löfgren, A., 1619
 Lopez-Arenas, T., 839, 1195, 1707
 Lopez, M., 1075
 Luh, S., 1311
 Luna, M.F., 943
 Lupera, G., 163, 531
 Lu, X., 857

M

Macchietto, S., 1679
 Madabhushi, P.B., 845
 Magatão, L., 931
 Mahmoud, B.H., 61
 Maia, L.K.K., 603
 Malakul, P., 13
 Manca, D., 433, 603, 743, 1631
 Mancusi, E., 1389
 Mandade, P., 717
 Mandani, F., 543
 Maneeintr, K., 1445
 Mangone, F., 1371
 Mannan, M.S., 705
 Manovic, V., 1389
 Mantia, F.L., 603
 Manzi, J., 507
 Maréchal, F., 669, 1057, 1395
 Markoš, J., 687, 779
 Marmolejo-Correa, D., 513
 Martelli, E., 373
 Martínez, E.C., 943
 Martín-Hernández, E., 1263
 Martín, M., 567, 1263
 Martins, F.G., 187
 Mateo-Sanz, J.M., 445
 Matos, H.A., 25, 291
 Matos, R.D.C., 1275

Matsegora, O., 289
 Matsunami, K., 1655
 Mavrou, P., 1625
 Maxeiner, L.S., 301
 Mazzotti, M., 525
 McIlwaine, F., 1649
 Mckay, G., 1481
 Mecheri, M., 767
 Mechleri, E., 1087
 Medina-González, S., 531
 Medrano-García, J.D., 731, 1419
 Mei, R., 1183
 Meira, W.H.T., 931
 Mele, F.D., 501
 Mendes, A., 25
 Menezes, B.C., 1135, 1705
 Mészáros, A., 961
 Mhamdi, A., 109
 Mian, A., 1395
 Mid, E.C., 1171
 Mihal', M., 687, 779
 Milhorn, A., 391
 Miltner, M., 1383
Min, Oh., 1433
 Misener, R., 565
 Miskolczi, N., 349
 Misra, A., 31
 Mitsos, A., 109
 Miyoshi, S.C., 1177
 Mizsey, P., 1287
 Mockus, L., 1685
 Moheimani, N.R., 55
 Mohseni, M., 169
 Molla, G.S., 287
 Montastruc, L., 67, 803
Moon, Il., 1105, 1433
 Morakabatchiankar, S., 501
 Morales, J.M., 949
 Morales-Rodriguez, R., 513, 755
 Moraru, M.D., 711
 Morgado, J.F., 247
 Morris, K., 1685
 Mortimer, L.F., 61
 Mostafaei, H., 973
 Mousqué, F., 803
 Mujtaba, I.M., 19
 Municchi, F., 247
 Muñoz, E., 1225
 Murathathunyaluk, S., 49
 Murray, P., 525
 Muthia, R., 827

N

Nagato, T., 1655
 Nagy, T., 1287

Nagy, Z.K., 681
 Nakai, M., 1347
 Nascimento, M.L.F., 361
 Natarajan, A.P.A., 699
 Navia, D., 1081
 Négny, S., 785, 803
 Neto, A.A.F., 1469
 Neves, F., 931
 Neveux, T., 767
 Nguyen, T.B.H., 1413
 Niederkleine, I., 115
 Nie, Z., 1487
 Nikolakopoulos, A., 1493
 Nilsson, B., 1619
 Ning, C., 319, 913
 Njobuenwu, D.O., 79, 555
 Nogueira, J., 483
 Nolin, M., 1619
 Nopens, I., 293
 Nunes, M., 1177

O

Obermeier, A., 955
 Ochoa-Tapia, A., 839
 O'Dwyer, E., 1407
 Ogholaja, T., 555
 Okubo, T., 1353
 Oluleye, G., 415, 1451
 Onel, M., 421
 Oravec, J., 961
 Orehounig, K., 525
 Orosz, A., 869
 Oshita, Y., 1347
 Osorio, M., 259
 Otero, M.V., 567

P

Padungwatanaroj, O., 337
 Pahija, E., 1293, 1299
 Pankajakshan, A., 355
 Pantaleo, A.M., 1463
 Papadokonstantakis, S., 1577
 Papageorgiou, L., 633
 Papapostolou, C.M., 1213
 Parekh, R., 1607
 Park, D., 279
 Park, J., 1433
 Patrascu, I., 791
 Paulen, R., 1045
 Paulo, H., 991
 Peakall, J., 61
 Penteado, A., 1329
 Pepe, F., 1389
 Perederic, O.A., 737
 Pereira, R.D., 175

Pérez-Cisneros, E.S., 839, 905
 Pérez-Moya, M., 223
 Pesenti, G., 1631
 Peters, B., 169
 Petrescu, L., 1269
 Petsagkourakis, P., 1249
 Phillips, T.D., 421
 Pich, A., 109
 Pigler, P., 1003
 Pinheiro, C.I.C., 291
 Pintariè, Z.N., 863
 Pinto-Varela, T., 991, 1165
 Piper, M., 397
 Pistikopoulos, E.N., 11, 391, 421, 705
 Pittman, J.K., 1595
 Poletto, M., 193, 585
 Pöllabauer, F., 985
 Ponce Ortega, J.M., 331
 Ponce-Rocha, J.D., 755
 Pontes, K.V., 361
 Poulimenos, D., 439
 Pozo, C., 445, 457
 Prada, A., 1693
 Preisig, H.A., 235, 241, 1547
 Prieto, C.G., 271
 Privat, R., 767
 Psycha, M., 645
 Puen, A., 1081
 Puigjaner, L., 1225
 Pulluru, S.J., 1063
 Pyrgakis, K.A., 573

Q

Qian, H., 857
 Quaglio, M., 355
 Queiroz, A., 1469
 Quinta-Ferreira, R., 247
 Quintanilla, P., 1081

R

Rabhi, A., 229
 Radcliffe, A.J., 1243
 Radl, S., 247
 Rakovitis, N., 1033
 Ramírez-Márquez, C., 567, 579
 Ramos, F.H., 1535
 Rattanatum, T., 13
 Rätze, K.H.G., 881
 Rego, A.S.C., 1469
 Reklaitis, G.V., 1243, 1685
 Relvas, S., 931, 949
 Repke, J.-U., 31, 403, 955, 1329
 Revollar, S., 1237
 Reyes-Labarta, J.A., 657
 Reyes-Lúa, A., 1015

- Ribeiro, A.M., 1231
Ribeiro, J.C., 187
Ribeiro, J.P., 815
Ribeiro, M.P.A., 1541
Rice, H.P., 61
Rielly, C.D., 1607
Ritter, J., 43
Roca, C., 1601
Rocha, J., 25
Rodman, A., 1553
Rodríguez, F., 199
Rodríguez, M., 121, 285, 1257, 1693
Romagnoli, J.A., 1207
Roman-Sanchez, D.I., 1707
Romero-Izquierdo, A.G., 1523, 1529
Rosa, D., 507
Roth, M., 139
Ruiz-Femenia, R., 657, 731, 1419
Rusyn, I., 421
Ruszczynski, L., 287
- S**
- Sachs, J., 1365
Saez, D.S., 211
Salas, S.D., 1207
Sales-Cruz, M., 839, 905, 1195, 1707
Salles, A., 1177
Sampat, A.M., 1263
Sánchez, A., 151, 199
Sánchez Medina, E.I., 845
Sanchez Perez, J.M., 67
Sánchez-Ramírez, E., 579, 755
Sangwon Ryu, 279
Santarelli, M., 415
Santomaso, A.C., 1667
Santos, A., 809
Santos, B.F., 483, 1231, 1469
Santos, R.B., 1231
Sarup, B., 737
Sarwar, O., 391
Sauvage, S., 67
Savoca, A., 1631
Schack, D., 881
Scharzec, B., 561
Scheffczyk, J., 325
Schmidt, T.J., 1311
Schneiderbauer, S., 217
Schneider, S.M., 139
Schöneberger, J.C., 1329
Schöny, G., 1377
Scotti, F., 743
Seabra dos Reis, M.P., 1039
Sebastia-Saez, D., 821
Secchi, A.R., 997, 1177
Sechi, S., 415
Seckendorff, J.V., 97
Segovia-Hernández, J.G., 331, 567, 579, 755
Seidel, C., 85
Seidel-Morgenstern, A., 85
Sellberg, A., 1619
Shah, N., 537, 1407, 1487
Shang, C., 919
Shao, Z., 1117
Sharma, A., 1045
Shastri, Y., 717, 797, 1571
Shen, C.-H., 1425
Shimizu, A., 1353
Shokry, A., 163, 265, 531, 1069, 1123
Siemanond, K., 337, 367, 379, 385, 663
Silva, A.M.S., 187
Silva, J.M., 291, 1275
Sin, G., 287, 1601
Siniscalchi, A.G., 271
Sioungkrou, E., 903
Sithanandam, S., 699
Siwi, R.G., 1201
Skiborowski, M., 103, 115, 325, 561
Skogestad, S., 1015, 1111, 1153
Smith, R., 477, 621, 1439
Smutná, J., 253
Sofia, D., 193
Sója, J., 349
Solti, S., 1287
Somoza-Tornos, A., 749
Song, F., 477, 1141
Son, H., 1259
Sonnleitner, E., 1377
Soprana, M., 1667
Soren, A., 797
Soria-Ornelas, M.L., 639
Spann, R., 1601
Springael, J., 979
Srichanvichit, K., 49
Srinivasan, B., 205, 1189
Srinivasan, R., 205, 1189
Sriprom, P., 409
Stadler, P., 1057
Štefanica, J., 253
Straus, J., 1111
Suciu, R., 1057
Sugiyama, H., 1613, 1655
Sundaramoorthy, A.S., 699
Sundmacher, K., 881
Sunghyun Cho, 1105
Suwatthikul, A., 615, 967
Svensson, E., 1577
Szilagyi, B., 681
Szima, S., 1281

T

Tan, J., 1577
 Tavallali, M.S., 1219
 Tawai, P., 367
 Temmann, P., 103
 Theodoropoulos, C., 1249, 1595
 Thévenin, D., 31
 Thorpe, R., 1625
 Threerachannarong, N., 379
 Tian, X., 37
 Tian, Y., 705
 Till, Z., 349
 Torres, M.A., 291
 Torres-Rivas, A., 457
 Toth, A.J., 1287
 Touche, I., 67
 Tovazhnianskyi, V., 289
 Tran, J., 181
 Trokanas, N., 471, 563, 1565
 Tronci, S., 1183, 1207
 Tzanes, G., 1213

U

Ulonska, S., 1673
 Uribe-Ramirez, A.R., 331

V

Vakilifard, N., 313
 Valencia, G.E., 259
 Valentinyi, N., 1287
 Valim, I.C., 1469
 Van Dam, K.H., 1463
 van der Ham, A.G.J., 827
 van der Padt, A., 651
 Varbanov, P.S., 1305, 1457
 Vargai, P., 779
 Varga, M., 223
 Varga, T., 349, 1147
 Varshney, D., 717
 Vasileiadou, A., 1661
 Vazquez-Castillo, J.A., 567, 579
 Vázquez, D., 731
 Vega, P., 1237
 Velázquez-Guevara, M.A., 331
 Verbiest, F., 979, 1165
 Verheyleweghen, A., 1021
 Verstraete, J., 1559
 Vieira, M., 991
 Vikse, M., 489
 Vilani, C., 1469
 Vilard, C., 991
 Villegas-Herrera, L.A., 1523
 Viveros-García, T., 839
 Vlachos, D., 439
 Vocciante, M., 397

Vogtenhuber, H., 1377
 Vollbrecht, B., 85
 Vooradi, R., 893
 Vyhmeister, E., 531

W

Wallek, T., 985, 1255
 Walmsley, M., 1457
 Walmsley, T.G., 1305, 1457
 Wang, A.-J., 1407
 Wang, H., 1407
 Wang, M., 421
 Wang, X., 907
 Wang, Y., 1305
 Wartha, E.-M., 1687
 Wassermann, T., 609
 Wenzel, S., 301
 Werner, A., 1377
 Wilk, V., 1377
 Windholz, B., 1359
 Windmeier, C., 955
 Woodley, J.M., 737, 851, 875
 Wozny, G., 1329
 Wright, F.A., 421
 Wu, B.-C., 1425
 Wu, O., 139
 Wu, T.-L., 1425

X

Xao, X., 1201
 Xiao, X., 477, 1141

Y

Yabuta, K., 1613
 Yang, H.-S., 1425
 Yang, J.-H., 627
 Yang, M., 37
 Yap, J.Y., 1577
 Yeoh, K.-P., 1293, 1299
 Yoo, C.K., 343
 Yoon, H., 1105
 Yoosook, H., 1445
 You, F., 1, 37, 319, 591, 913, 919, 1475
 Yuan Yao, 937
 Yu, H., 489
 Yun, S., 1519, 1521

Z

Zakuciová, K., 253
 Zare, M., 1219
 Zauner, C., 1359
 Zavala, V.M., 1263
 Zecchi, B., 1317
 Zeng, Y., 477, 1141
 Zeng, Z., 519

Zenón-Olvera, E., 1529
Zhang, N., 477, 1033
Zhang, S., 1513
Zhang, X., 1513
Zhao, Q., 767
Zhou, L., 157, 421
Zhu, W., 857

Zibart, A., 397
Ziogou, C., 1075
Zirngast, K., 863
Zondervan, E., 603, 609, 1413
Zore, Ž., 863
Zotică, C., 1015
Zurano-Cervelló, P., 445

